Geofluids

Disaster Mechanisms Linked to the Role of Fluids in Geotechnical Engineering

Lead Guest Editor: Yi Xue
Guest Editors: Guanglei Zhang, Chuangzhou Wu, Kai Yao, and Jia Liu

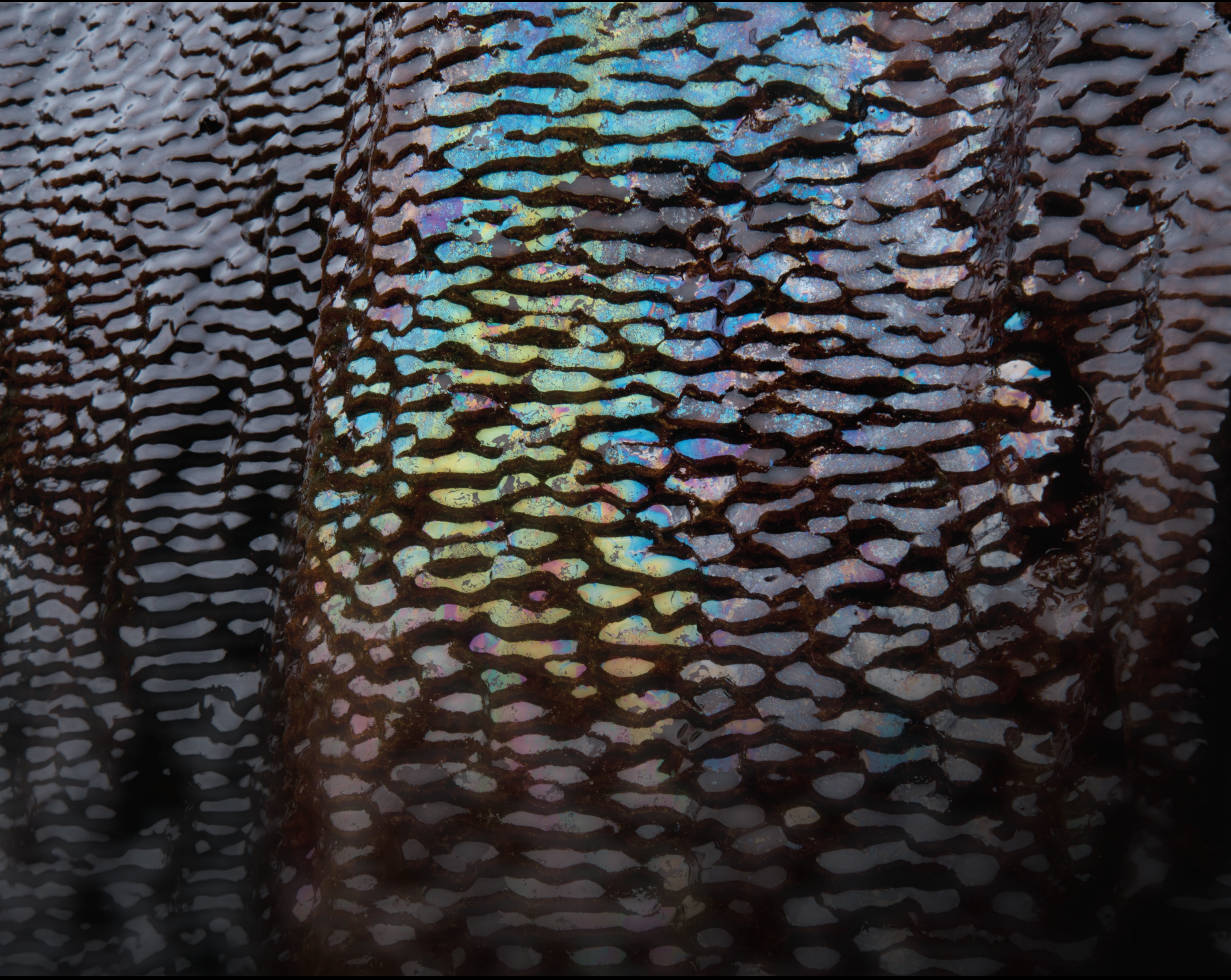

Disaster Mechanisms Linked to the Role of Fluids in Geotechnical Engineering

Geofluids

Disaster Mechanisms Linked to the Role of Fluids in Geotechnical Engineering

Lead Guest Editor: Yi Xue
Guest Editors: Guanglei Zhang, Chuangzhou Wu, Kai Yao, and Jia Liu

Bisheng Wu, China
Da-yang Xuan, China
Yi Xue, China
HE YONGLIANG, China
Fan Yang, China
Zhenyuan Yin, China
Sohrab Zendehboudi, Canada
Zhixiong Zeng, Hong Kong
Yuanyuan Zha, China
Keni Zhang, China
Mingjie Zhang, China
Rongqing Zhang, China
Xianwei Zhang, China
Ye Zhang, USA
Zetian Zhang, China
Ling-Li Zhou, Ireland
Yingfang Zhou, United Kingdom
Daoyi Zhu, China
Quanle Zou, China
Martina Zucchi, Italy

Contents

Contents

Contents

Contents

Hindawi
Geofluids
Volume 2022, Article ID 7332182, 9 pages
https://doi.org/10.1155/2022/7332182

Research Article

Disastrous Mechanism of Water Burst by Karst Roof Channel in Rocky Desertification Mining Area in Southwest China

Jie Suo,[1] Qirong Qin,[1] Wenqiang Wang,[2,3] Zhenhua Li ,[2,3] Cunhan Huang,[2,3] Youlin Xu,[4] and Zuguo Chen[5]

[1]*School of Geoscience and Technology, Southwest Petroleum University, Chengdu, 610500 Sichuan, China*
[2]*School of Energy Science and Engineering, Henan Polytechnic University, Jiaozuo, 454000 Henan, China*
[3]*Collaborative Innovation Center of Coal Work Safety and Clean High Efficiency Utilization, Jiaozuo, 454000 Henan, China*
[4]*Institute of Mining Engineering, Guizhou Institute of Technology, Guiyang, 550003 Guizhou, China*
[5]*Xintian Coal Mine, Yonggui Energy Development Co., Ltd., Qianxi, 551500 Guizhou, China*

Correspondence should be addressed to Zhenhua Li; jzlizhenh@163.com

Received 22 April 2021; Revised 7 February 2022; Accepted 5 March 2022; Published 18 March 2022

Academic Editor: Jia Liu

With the development of coal mining in rocky desertification mining area in Southwest China, water burst is becoming an important disaster in coal mine. In order to grasp the evolution characteristics of water gushing channels in coal mining in rocky desertification mining area, the 1402 working face in Xintian Coal Mine is taken as the research object, and the occurrence of aquifers on the roof of the working face is analyzed, and the water filling path of the aquifers is explored. Besides, the evolution characteristics of water passage in coal seam mining are comprehensively analyzed, by the methods of physical similarity simulation, numerical simulation, and microseismic monitoring. The results show that the key water resource is the atmospheric precipitation, which enters the mine through the original karst fissure and mining-induced fissure. With the continuous advance of working face, the fracture height of overburden increases gradually. Specifically, when the advancement distance of working face exceeds 135 m, the water-conducting cracks in the overlying strata develop to the bottom boundary of the Yulongshan limestone aquifer, and then, the mining-induced fracture and aquifer are conducted; when the working face advances 190 m, the overall overburden mining fissure is divided into fissure opening zone and fissure closed zone. Meanwhile, most of the microseismic events occur in the middle part of the karst roof, and the maximum height of microseismic event is 40 m away from the bottom boundary of the Yulongshan limestone, during the advancing process of the working face. When the mining fissure is connected with the original karst fissure, atmospheric precipitation enters the aquifer through the original karst fissure and enters the gob of working face through the mining fissure. The research results provide the references for prediction and prevention for the water burst disaster in rocky desertification mining area in Southwest China.

1. Introduction

As one of the most important coal bases in Southwest China, Guizhou is known as the "Southwest Coal Sea" [1, 2]. At the same time, it is also the largest and most concentrated area of karst distribution in China. The exposed area of limestone reaches 73% of the total area of the province [3, 4]. The underground karst fissures are highly developed in this area. Most of the atmospheric rainfall are not stored on the surface, which flows into the underground karst aquifer [5]. When mining coal seams in karst mining areas, roof karst water seriously threatens the safe and efficient mining of coal in mines [6, 7]. Therefore, it is of great significance to study the evolution characteristics of water gushing channels in karst roof of mining areas, which is beneficial for guiding coal mining in rocky desertification mining area in Southwest China.

Many scholars at home and abroad have done lots of research work on the development height and characteristics of the water-conducting fracture zone in the karst coal roof.

In terms of the development characteristics and laws of the water-conducting fractured zone, researchers represented by Liu Tianquan [8] have summarized and obtained the empirical formula for the development height of the water-conducting fractured zone through years of field research and analysis; Qiao et al. [9] systematically summarized the research progress of aerosol water from four aspects, namely, the formation mechanism of roof aerosol water, disaster-causing mechanism, water disaster prediction and early warning, and key prevention and control technologies; Yang and Xu [10] comprehensively employed the methods of theoretical analysis, similar material tests, and numerical simulation to obtain the evolution law of the water-conducting fracture zone in a large mining height face; Lai et al. [11] used physical similar material simulation experiments, combined with the total station and borehole peep monitoring, 3DEC, and SPSS statistical analysis software, and obtained the migration law of overlying strata in coal seam mining, the development and evolution of fractures, and the distribution characteristics of water-conducting fracture zones; Zou et al. [12] used FLAC3D software to calculate and analyze the plastic failure zone, displacement field, and stress field distribution characteristics of the surrounding rock above the stope before and after the fully mechanized caving work passes the fault and obtained the formation mechanism of the water channel; Wang et al. [13] used theoretical analysis and field detection to obtain the characteristics of the development height of roof water-conducting fractures under the influence of the key layer structure with the mining thickness, and the development height is affected by both the mining thickness and the key layer structure; Zhang et al. [14–16] used the theory of elastic foundation beams to establish a mechanical analysis model for the height of the overburden water-conducting fissure zone of the block-filled stope; Zhu et al. [17] built a coal seam mining model in the karst cave area and obtained the development characteristics of roof mining cracks during coal seam mining; Wang et al. [18] used similarity simulation and theoretical analysis to propose a composite mechanism model of “elastic thin plate” and “parallel pressure arch” for the migration of overlying strata in high-strength mining under three-dimensional spatial conditions; Liu et al. [19] used the borehole television system and borehole simple hydrological observation method, combined with similarity simulation and numerical simulation, and obtained the development characteristics of the overlying water-conducting fissure zone in fully mechanized caving mining in deep and extra-thick coal seams. In terms of the height of the water-conducting fissure zone, Y. P. Zhang et al. [20] used a combination of field measurement, numerical simulation, and similarity simulation to obtain the overburden failure height of the deep thick coal seam in the west of Mongolia with the large mining height; Guo et al. [21] used the method of on-site ground drilling flushing fluid leakage and theoretical analysis methods to obtain the height of the water-transmitting fracture zone in top coal mining under soft and hard alternate overburden conditions; Yang et al. [22] comprehensively used downhole borehole water injection loss observation, borehole television, and numerical simulation technology to obtain the development height of water-conducting fracture zone in fully mechanized caving mining under thick loose layer and weak overburden. In terms of water flow height prediction, Shi et al. [23, 24] combined principal component analysis (PCA), genetic algorithm (GA), and optimized Elman neural network to establish PCA-GA-Elman for the height prediction of water flow fracture zone development. Based on neural network algorithms, Z. H. Li et al. [25] selected mining thickness, mining depth, working face inclination length, coal seam inclination, and overlying rock structure characteristics as the main influencing factors for the height of the water-conducting fissure zone. Based on the particle swarm (POS)-support vector regression (SVR) research method, Xue et al. [26] constructed the Ordos Basin Jurassic coal field water-transmitting fractured zone height prediction model.

The above research results have an important guiding significance for coal mining under water bodies, but there are few studies on the development height and development rules of water-conducting fissures in karst mining areas [27, 28]. This paper employs a combination of theoretical analysis, similarity simulation, numerical simulation, and field microseismic monitoring to analyze the source and volume of water inrush from coal seam mining in karst areas. Through similarity simulation and numerical simulation, the process of connection between the water conduction fissures and the original karst fissures is proved, and the water inrush model for coal seam mining in karst areas is proposed, and the coal seam mining in karst mining areas is mastered. Therefore, the evolution characteristics of roof water gushing channels provide an important reference for safe and efficient coal mining in rocky desertification mining area in Southwest China.

2. Mining and Hydrogeological Conditions

2.1. Water Source of Mine Water Filling. Xintian Mine is located in Qianxi County, Bijie City, Guizhou Province. This area is a typical karst mining area. Mine water is mainly filled with two major water sources, namely, atmospheric precipitation and underground karst water. Atmospheric precipitation is the main source of replenishment for surface water and underground karst water, which restricts the dynamic changes in the flow of surface rivers and mines. According to the meteorological data provided by the Qianxi County Meteorological Bureau, the annual rainfall in the mining area is about 940~1090 mm, and the rainy season is from May to September, accounting for about 80% of the annual rainfall. Under normal circumstances, atmospheric precipitation mainly replenishes the Yulongshan limestone aquifer through shallow weathering fissures, structural fissures, and sinkholes. Continuous rainfall increases the water supply to the underground Yulongshan limestone aquifer, so atmospheric precipitation is the direct water source for filling water in the shallow limestone aquifer of the mine. When the mining fissure is connected to the aquifer, the aquifer becomes a direct source of water for the mine.

The water richness of the aquifer in the Yulongshan section of the Yelang Formation in the mining area is generally not strong and extremely uneven. However, affected by the structure of the fault and lateral fracture zone, the karst is strongly developed, and the underground karst space is connected with the surface karst, especially during rainfall. Atmospheric precipitation and surface water leak along surface creeks and sinkholes to replenish the ground, resulting in a large amount of groundwater enrichment in the limestone aquifer in the Yulongshan section, which becomes an enrichment zone for groundwater. The lower part contains the limestone of the Changxing Formation with an average thickness of 35 m. Because there is a water barrier in the middle, and the stratum is not exposed, deep buried, and poor replenishment conditions, the limestone of the Changxing Formation is a weak aquifer.

2.2. Mine Water Filling Channel. The water-filled channel in the karst mining area is composed of the original karst fissures and mining fissures, which is different from the water-filled channels in ordinary mining areas only by the mining fissures. The original fissures include weathered zones, faults, collapse pits, sinkholes, and underground karst fissures. Mining fissures are the fractures formed by the collapse of the roof of underground coal mining, forming the water-filling channel of the karst mining area. When the mining fissures and karst fissures are connected, karst water continuously flows into the well, seriously affecting the safe and efficient mining of the working face.

2.3. Overview of Test Working Face. The 1402 working face of Xintian Coal Mine is selected as the test working face, which has a strike length of 147 m and a slope length of 1148 m. The average mining thickness of the coal seam is 3 m, and the average inclination angle is 3°. The working face elevation is +912~+948 m. The working face is located to the north of the three main lanes in the south wing, 1401 mined area on the east, 1404 unmined working face on the west, 1402 bottom extraction lane under 1402 belt transport lane, and original 1# bottom extraction under 1402 track transport lane. The surface is barren hills, and the buried depth is more than 340 m, and the mining has little impact on the ground. The layout of 1402 working face is shown in Figure 1.

3. Similarity Simulation of Evolution Characteristics of Water Gushing Channel

3.1. Model Design and Establishment. According to the mining geological conditions of the 1402 working face, the buried depth of working face is about 340 m, and the mining thickness of the coal seam is only 3 m. In consideration, if the similarity ratio is small, the geometric similarity ratio is selected as 1 : 100; and the length, width, and height of the selected similarity simulation test bench are2500 mm × 200 mm × 1300 mm, and the simulated rock layer height is 120 m. According to similarity simulation principles, the top loading of the model fails to simulate the weight of the rock formation. According to the original model, the loading value is

$$q_p = \frac{P}{F} = \gamma_p (H - H_l). \tag{1}$$

The load value q_m on the model is

$$q_m = \frac{q_p}{C_L \cdot C_\gamma} = \frac{\gamma_P (H - H_1)}{C_L \cdot C_\gamma}, \tag{2}$$

where q_p is the prototype unsimulated rock formation pressure, KPa; H is the mining depth, m; H_1 is the height of the simulated roof rock formation, m; the thickness of the unsimulated overburden is 280 m, where the average bulk density of the overburden is 2800 KN/m^3; and the load q_m applied to the model is 3484 KPa. This load is compensated by the pressure of the hydraulic column on the test bench. Two displacement measuring lines are arranged on the model, a total of 48 displacement measuring points, and each measuring point is 10 cm apart. The 1# measuring line is located at the interface of the limestone top plate of the Changxing Formation, and the 2# measuring line is located at the interface of the limestone floor of the Changxing Formation. In order to eliminate the influence of the boundary, 30 m coal pillars are left on the left and right sides of the model, and the excavation is carried out gradually from right to left, shown in Figure 2.

This experiment uses sand as aggregate, calcium carbonate and gypsum as cementing materials, and borax as retarder. According to the calculation method of the simulated strength value of similarity materials, a reasonable ratio of similarity materials in each layer is obtained. According to the cross-sectional area of the model frame, the thickness of the rock (coal), and the geometric similarity ratio, the weight of the similarity material of each rock (coal) layer is calculated (considering the richness factor of 1.2), and the proportion number and parameters are shown in Table 1.

3.2. Development Characteristics of Water Gushing Channels

3.2.1. Fracture Characteristics of Overlying Strata. The mining method of oblique mining is adopted in the 1402 working face. During the mining process, collapse, subsidence, and layer separation occur in sequence above the gob. When the working face advances to 85 m, the overburden fracture occurs for the fifth cycle. The overburden collapse height is 24 m, and the fracture angle on the side of the working face is 55°, which is smaller than the fracture angle at the open cut. The lower part contains the limestone of the Changxing Formation. There are a large number of separation zones, and the mining cracks do not penetrate the limestone of the Changxing Formation; when the working face advances to 150 m, the overburden fracture occurs in the ninth cycle. The overburden fracture height is 85 m, and the fracture angle on the side of the working face is 56°, and the fracture angle at the open cut is 60°, and the fracture angle between the two fracture lines is 60°. The strata span is 80.6 m, and the mining fissures have fully developed to the top of the

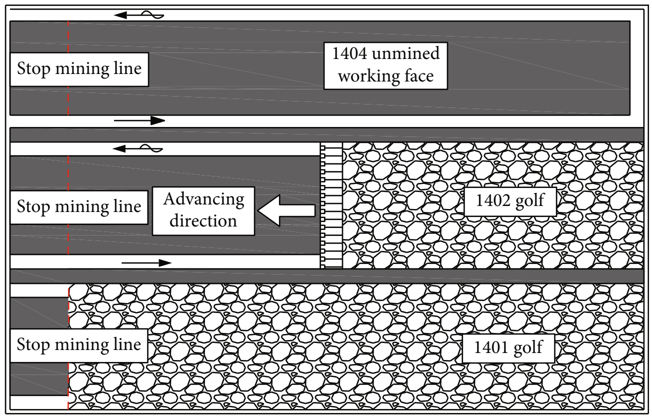

Figure 1: Schematic layout diagram of 1402 working face.

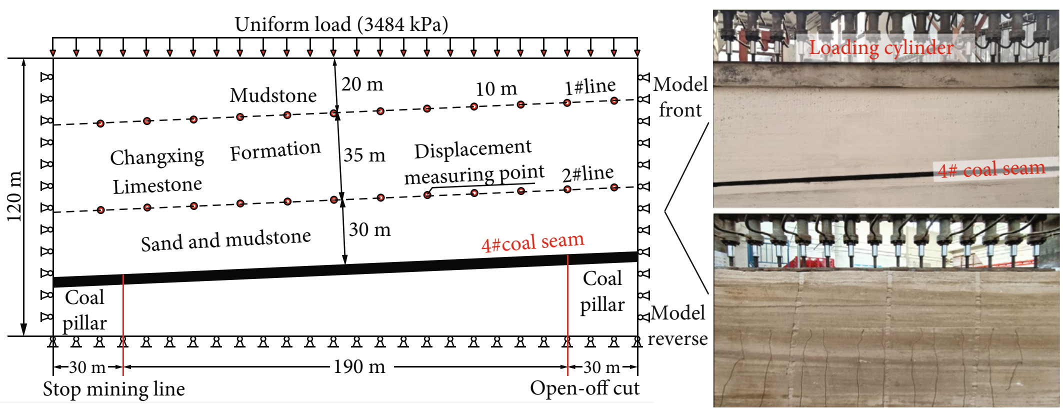

Figure 2: Displacement measuring point arrangement and excavation position.

Table 1: Similarity simulation test ratio and parameters.

No.	Lithology	Thickness (cm)	Matching number	Compressive strength (MPa)	Tensile strength (MPa)	Cohesion (MPa)	Density (g/cm^3)
1	Sand and mudstone	20	655	29.9	2.31	9.91	2.770
2	Limestone	35	437	51.4	5.70	17.12	2.800
3	Sand and mudstone	30	655	29.9	2.31	9.91	2.770
4	4# Coal	3	773	3.9	0.28	1.23	1.461
5	Sand and mudstone	32	655	29.9	2.31	9.91	2.770

model, indicating that the fracture height of the fissures has reached the Yulongshan limestone floor at this time; when the working face advances to 190 m, the overburden fracture occurs for the thirteenth cycle. The fracture angle on the side of the working face is 52°, and the fracture angle at the open cut is 60°, and the strata span between the two fracture lines is 132.6 m. The fractured height of the fissure has reached the inside of Yulongshan limestone. When the 4# coal seam is excavated, there are 13 periodic roof breaks in the overburden. The first break step is 35 m, and the average periodic break step is 11.9 m. The mining fissures are connected to the Yulongshan limestone aquifer, shown in Figure 3.

During the excavation of the working face, the overburden fracture height is recorded. When the working face advances to 95 m, the overburden fracture height is 45 m, and the limestone of the Changxing Formation has been fractured; when the working face advances to 110 m, the Changxing Formation is completely broken; when the working face advances to 135 m, the overburden fracture height is 85 m, indicating that the cracks have developed to the top of the model. Due to the size of the model, with the further excavation of the coal seam, the height of the overburden cracks no longer changes on the model. However, the limestone of the Yulongshan section gradually

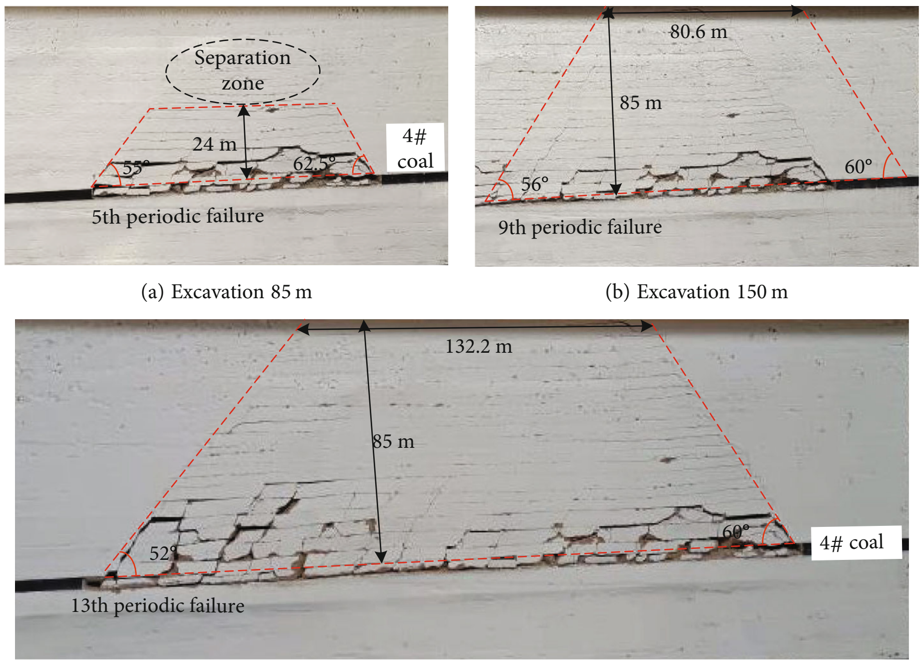

(a) Excavation 85 m

(b) Excavation 150 m

(c) Excavation of 190 m

Figure 3: Periodic weighting of coal seam.

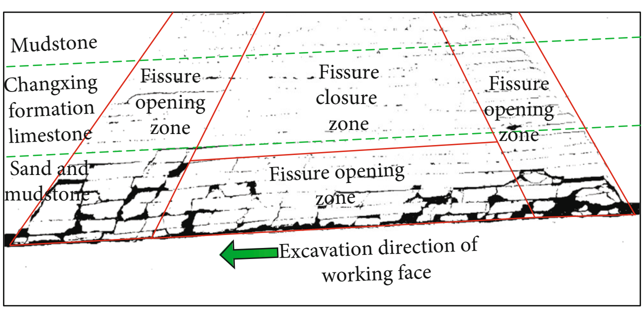

Figure 4: Fissure field in mining 4# coal seam.

breaks in actual conditions, and the mining fissures continue to expand into the limestone of the Yulongshan section.

3.2.2. Displacement of Overlying Rock. The displacement change of the limestone roof in the Changxing Formation during the mining process of the 4# coal seam is obtained. When the working face advances to 110 m, the survey line begins to bend and deform, indicating that the upper part of the Changxing Formation limestone begins to bend and sink; when the working face advances to 120 m, the maximum subsidence value of 1# survey line is -507.3 mm, and the limestone of Changxing Formation breaks and sinks at this time; with the continuous advancement of working face, the displacement curve sinks periodically. After the working face is mined, the maximum sinking value of the 1# survey line is -1006 mm.

The displacement change of the limestone floor in the Changxing Formation during the mining process of the 4# coal seam is obtained. When the working face advances to 85 m, the 2# survey line is bent and deformed. At this time, the limestone floor of the Changxing Formation breaks and sinks. With the continuous advancement of the working face, the floor sand and mudstone layers are periodically broken. When the coal seam is excavated, the maximum subsidence of the 2# survey line is -1332.1 mm.

3.2.3. Fissure Field. The sketch map of the distribution of overburden cracks in the 4# coal seam after mining is shown in Figure 4. The overburden fissure field is divided into fissure opening area and fissure closure area. The opening angle of the overburden rock near the working face and the open cut is relatively large, and the fissures are more developed. The water conductivity is strong, and the upper fissures in the middle of the gob are closed due to compaction, and the water conductivity is poor. After the coal seam is fully mined, the mining fissures have developed to the top of the model and are connected to the Yulongshan limestone aquifer. The roof water enters the gob through mining fissures. Because it is inclined mining, the karst water in the gob flows to the working face, which is consistent with the water gushing phenomenon that occurs in the actual coal seam mining process.

4. Field Measurement of Breaking Height in Overlying Rock

4.1. Layout of Microseismic Monitoring Points. According to the general principle that all measuring points form a spatial body, candidate points for the station layout of the microseismic monitoring system of Xintian Mine have been

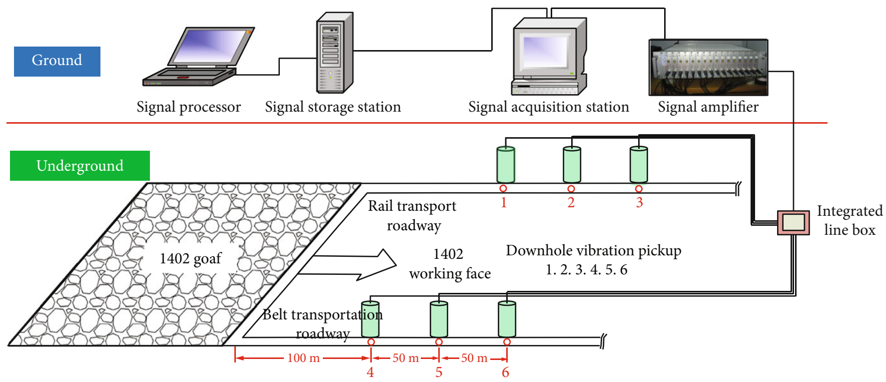

Figure 5: Working principle and schematic diagram of measuring point layout.

Table 2: Optimal plan for measuring point layout.

N0.	Location	Coordinate *X*	*Y*	*Z*
1	1402 Track roadway	3001528.013	35608039.428	930.590
2	1402 Track roadway	3001547.067	35608007.589	921.339
3	1402 Track roadway	3001569.681	35607977.316	913.300
4	1402 Belt roadway	3001407.313	35607944.994	937.110
5	1402 Belt roadway	3001428.630	35607914.794	931.960
6	1402 Belt roadway	3001452.382	35607880.289	925.357

selected. The schematic diagram of the designed layout of measuring points is shown in Figure 5.

The optimal plan for the location of the measuring point determined by analysis and measurement calculation is shown in Table 2.

4.2. Analysis of Microseismic Monitoring Results. The distribution of microseismic events was monitored from November 11, 2019, to January 5, 2020. The microseismic events mostly occurred in front of the work and were mostly biased towards the 1402 belt lane, and the energy range was in the range of 0~1000 J. There were only four microseismic events in the mined-out area behind the working face, with energy three times greater than 1000 J.

The cross-sectional view of the microseismic event in the track lane at 1402 working face is obtained. The microseismic event gradually decreases in the front of the working face, but the energy of the event increases as it goes up. There are three locations in front of the work where the energy of the microseismic event exceeds 100 J. One of them is the bottom of the Changxing Formation limestone, and the remaining two are located inside the Yulongshan limestone. The two locations are 5 m and 45 m away from the bottom boundary of the Yulongshan rock formation, and the highest point is 125 m from the roof of 4# coal seam.

The section view of the microseismic event at the 1402 working face is obtained. During the monitoring period, the upper rock formations at the 1402 working face have four relatively large vibrations, all with energy greater than 100 J. Moreover, the locations of the incidents are basically near the vertical line of the working face. The positions from bottom to top are as follows: 3 m below the Changxing Formation limestone floor, 1 m below the Yulongshan limestone floor, and 45 m above the Yulongshan limestone floor.

During the monitoring period, microseismic events mostly occur on the leading working face. Large energy events exceeding 100 J are mainly concentrated in the middle of the working face and lagging behind the working face and occur in the upper part of the gob behind the working face. According to the microseismic event profile, the maximum height of the microseismic event is located at the Yulongshan limestone 125 m away from the 4# coal seam. Therefore, the height of the water gushing channel develops to the Yulongshan limestone, and the water gushing channel is connected to the Yulongshan limestone cave.

5. Analysis of Mine Water Inflow Process

After the working face is fully recovered, there is continuous water gushing to the working face behind the working face. Temporary water pumps are installed on the working face to pump the water to the storage tank of the stop line. After the precipitation, it is discharged into the underground silo through the water pump, shown in Figure 6.

5.1. Analysis of Mine Water Inflow. By analyzing the average monthly water inflow from April 2015 to October 2019 and the atmospheric rainfall data in the area, the relationship between atmospheric rainfall and mine water inflow is obtained, shown in Figure 7. The change in mine water inflow is closely related to atmospheric rainfall, indicating that there is a water inflow channel between the mine and the ground, resulting in an increase in mine water inflow after atmospheric rainfall.

5.2. Mine Water Gushing Process. Based on the hydrogeological conditions of the mining area, a conceptual model of karst roof gushing water is proposed, shown in Figure 8. There are many bead-shaped sinkholes on the surface. The limestone karst fissures in the upper part of the Yulongshan section are relatively developed, and the karst fissures in the lower part are poorly developed. Gas and rain tend to enter underground karst caves and karst fissures through sinkholes and surface karst cracks, becoming a potential threat to coal mining. Xintian Coal Mine mainly mines the 4# and 9# coal seams. With the increase of the mining space

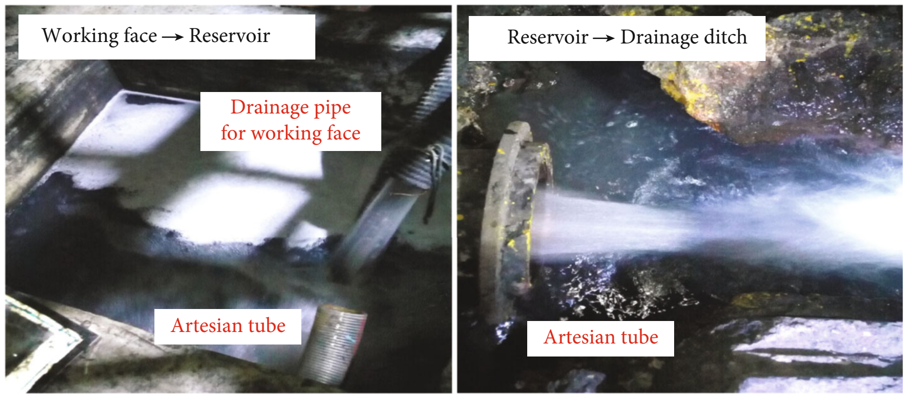

FIGURE 6: Underground gushing and drainage situation.

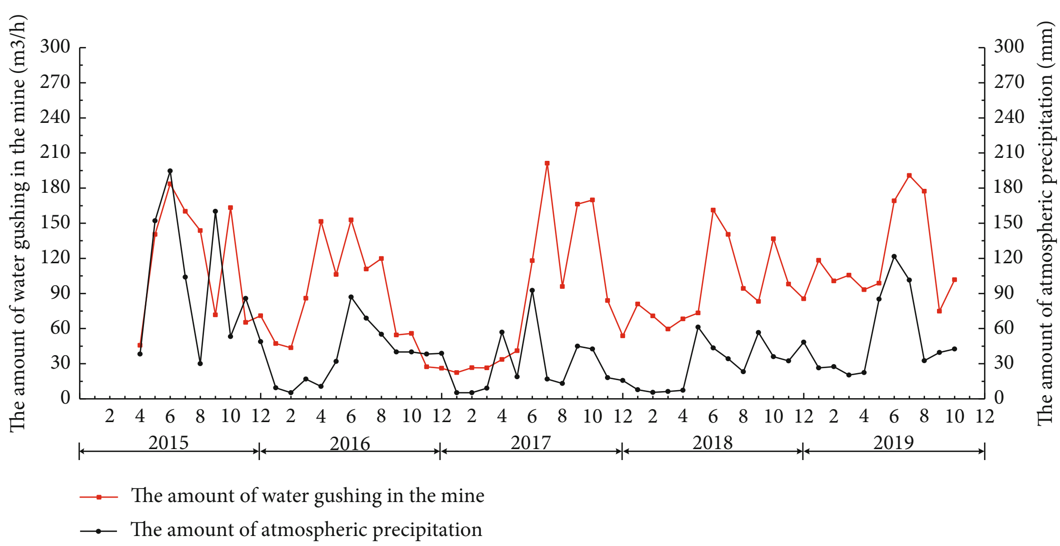

FIGURE 7: The relationship between mine water inflow and atmospheric rainfall in Xintian Mine.

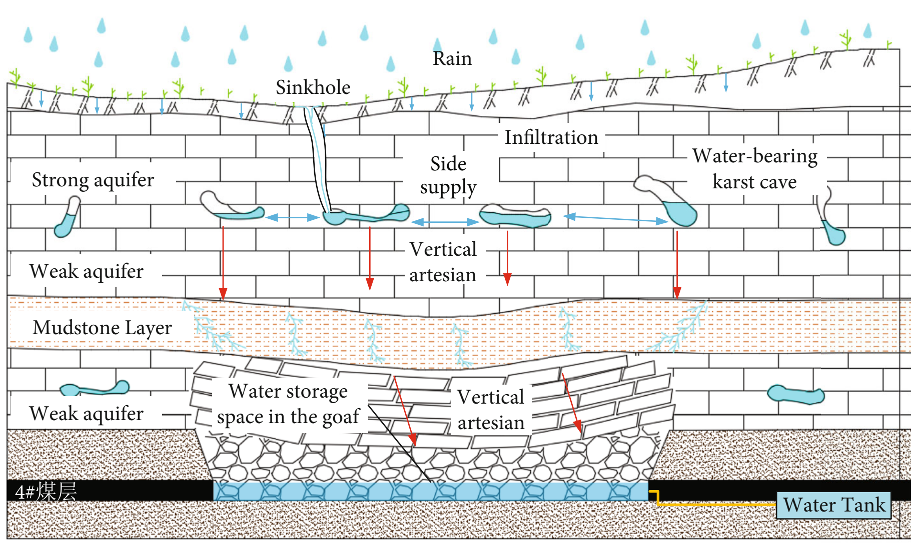

FIGURE 8: Conceptual model of water inrush from karst roof in coal mining.

of the 4# coal seam, the mining fissures gradually develop upwards, and the original fissures further develop and expand under the influence of mining.

When the distance between the coal seam and the aquifer reaches the critical value of water gushing, the original karst fissures and mining fissures are connected to form a water gushing channel between the surface-karst cave-working face or gob. When 4# coal seam is mined in Xintian Mine, the working face is threatened by roof karst water, and the mining work of 9# coal seam is also threatened by roof karst water.

6. Conclusion

(1) Atmospheric precipitation in karst areas is the key supply water source for the Yulongshan limestone aquifer, which enters the mine through the original karst fissure and mining-induced fissure. Besides, the Yulongshan limestone aquifer is the direct source of water gushing in the mine

(2) There are ultrahigh-conductivity fracture zones in coal seam mining in karst mining areas. When the working face advances 135 m, the fissure develops to the Yulongshan limestone floor. With the continuous advancement of the working face, the height of the water-conducting fissure zone continues to develop upwards. The final monitoring results show that the development height of water-conducting fissure zone is 125 m

(3) When the 4# coal seam is fully mined, the mining fissure is connected to the karst fissure, and a water gushing channel is formed between the surface, the karst cave, and the working face (or gob). On this basis, a conceptual model of karst roof gushing in coal mining in rocky desertification mining area is proposed

Data Availability

The data used to support the findings of this study are included within the article.

Conflicts of Interest

The authors declare that they have no conflicts of interest.

Acknowledgments

This work was supported by the National Natural Science Foundation of China (52174073, 41972175, and 51774110) and the Natural Science Foundation of Henan Province (222300420007).

References

[1] S. J. Wang, “Discussion on the concept deduction of karst rocky desertification and its scientific connotation,” *China Karst*, vol. 2002, no. 2, pp. 31–35, 2002.

[2] Z. W. Liu, M. Q. Zhang, and S. R. Wang, “Catastrophe prediction and treatment technology of karst tunnel,” *Second edition, Beijing: Science Press, vol.*, vol. 2007, 2007.

[3] Z. Z. Cao, Y. L. Ren, Q. T. Wang, B. H. Yao, and X. C. Zhang, “Evolution mechanism of water-conducting channel of collapse column in karst mining area of Southwest China,” *Geofluids*, vol. 2021, 2021.

[4] Y. Xue, J. Liu, P. G. Ranjith, Z. Zhang, F. Gao, and S. Wang, “Experimental investigation on the nonlinear characteristics of energy evolution and failure characteristics of coal under different gas pressures,” *Bulletin of Engineering Geology and the Environment*, vol. 81, no. 1, article ???, 2022.

[5] J. Liu, Y. Xue, Q. Zhang, H. Wang, and S. Wang, “Coupled thermo-hydro-mechanical modelling for geothermal doublet system with 3D fractal fracture,” *Applied Thermal Engineering*, vol. 200, article 117716, 2022.

[6] P. Hou, Y. Xue, F. Gao et al., “Effect of liquid nitrogen cooling on mechanical characteristics and fracture morphology of layer coal under Brazilian splitting test,” *International Journal of Rock Mechanics and Mining Sciences*, vol. 151, p. 105026, 2022.

[7] Y. Xue, J. Liu, P. G. Ranjith, X. Liang, and S. Wang, “Investigation of the influence of gas fracturing on fracturing characteristics of coal mass and gas extraction efficiency based on a multi-physical field model,” *Journal of Petroleum Science and Engineering*, vol. 206, article 109018, p. 109018, 2021.

[8] State Coal Industry Bureau, “Coal pillars and coal mining regulations for buildings, water bodies, railways and main shafts,” *Beijing: Coal Industry Press*, vol. 2000, no. 1, pp. 225–233, 2000.

[9] W. Qiao, Z. W. Wang, W. P. Li et al., “The formation mechanism, hazard mechanism and prevention technology of coal mine roof separation water damage,” *Journal of China Coal Society*, vol. 46, no. 2, pp. 507–522, 2021.

[10] Y. L. Yang and G. G. Xu, “Evolution of water-transmitting fault zone in large mining height working face under Luohe sandstone aquifer,” *Coal Mine Safety*, vol. 52, no. 3, pp. 30–35, 2021.

[11] X. P. Lai, X. D. Zhang, P. F. Shan, F. Cui, B. W. Liu, and R. Bai, “Development law of water-conducting cracks in overlying strata in mining of three-soft coal seams under thick loose layers,” *Chinese Journal of Rock Mechanics and Engineering*, vol. 40, no. 9, pp. 1739–1750, 2021.

[12] G. H. Zou, C. Zhang, D. Tian et al., “Research on the formation mechanism of the water channel through the overlying strata of the fault group in fully mechanized caving face,” *Metals and Minerals*, vol. 539, no. 5, pp. 65–70, 2021.

[13] X. Z. Wang, J. L. Xu, H. K. Han, J. F. Ju, and Y. T. Xing, “Stepped development characteristics of roof water-conducting fissure height with mining thickness,” *Journal of China Coal Society*, vol. 44, no. 12, pp. 3740–3749, 2019.

[14] Y. Zhang, S. Cao, T. Wan, and J. Wang, “Field measurement and mechanical analysis of height of the water flowing fracture zone in short-wall block backfill mining beneath the aquifer: a case study in China,” *Journal of Mining & Safety Engineering*, vol. 2018, no. 1, pp. 1–12, 2018.

[15] Y. Zhang, S. G. Cao, X. P. Lai et al., “Analysis of the mechanical characteristics of the development of water-transmitting fractures in the overlying rock in short-wall block mining,” *Journal of China Coal Society*, vol. 45, no. S2, pp. 551–560, 2020.

[16] Y. Zhang, S. G. Cao, X. P. Lai, C. Z. Zhao, and S. Y. Du, "Research on development mechanism and control of water-conducting fissures in overlying rock in short-wall block-filling mining," *Journal of Mining & Safety Engineering*, vol. 36, no. 6, pp. 1086–1092, 2019.

[17] C. Q. Zhu, D. G. Cui, Z. Zhou, Q. F. Li, and Y. J. Huang, "Similarity simulation of mining fissure development and cave failure characteristics in karst mining area," *Chinese Journal of Underground Space and Engineering*, vol. 15, no. 1, pp. 93–100, 2019.

[18] Y. G. Wang, W. B. Guo, E. H. Bai et al., "Study on the characteristics and mechanism of overlying strata migration in high-strength mining," *Journal of China Coal Society*, vol. 43, no. s1, pp. 28–35, 2018.

[19] Y. F. Liu, S. D. Wang, and X. L. Wang, "Development characteristics of water conducting fracture zone in overlying strata in fully mechanized caving mining in deep and extra-thick coal seam," *Journal of China Coal Society*, vol. 39, no. 10, pp. 1970–1976, 2014.

[20] Y. P. Zhang, Y. G. Zhang, Y. T. Liu, Y. J. Song, and Q. Y. Zhao, "Research on overburden failure height of large-cutting height fully mechanized face in deep thick coal seam in western Mengxi," *China Safety Science Journal*, vol. 30, no. 8, pp. 37–43, 2020.

[21] W. B. Guo, G. Z. Lou, and B. C. Zhao, "Research on the height of water-conducting fracture zone in top coal caving mining with soft and hard overlying strata in Lugou coal mine," *Journal of Mining & Safety Engineering*, vol. 36, no. 3, pp. 519–526, 2019.

[22] D. M. Yang, W. B. Guo, G. B. Zhao, Y. Tan, and W. Q. Yang, "Development height of water-conducting fracture zone in fully mechanized caving mining under thick loose layer and weak overburden," *Journal of China Coal Society*, vol. 44, no. 11, pp. 3308–3316, 2021.

[23] L. Q. Shi, H. B. Wu, Y. L. Li, and W. K. Li, "PCA-GA-Elman optimization model for predicting the development height of water-conducting fracture zone," *Journal of Henan Polytechnic University (Natural Science Edition)*, vol. 40, no. 4, pp. 10–18, 2021.

[24] L. Q. Shi, H. Q. Xin, P. H. Zhai et al., "Study on the calculation of the height of the water conducting fracture zone under the condition of large mining depth," *Journal of China University of Mining and Technology*, vol. 41, no. 1, pp. 37–41, 2012.

[25] Z. H. Li, Y. C. Xu, L. F. Li, and C. Z. Zhai, "Prediction of the height of water conducting fracture zone based on BP neural network," *Journal of Mining & Safety Engineering*, vol. 32, no. 6, pp. 905–910, 2015.

[26] J. K. Xue, H. Wang, C. H. Zhao, J. Yang, Z. F. Zhou, and D. B. Fang, "Prediction of the height of water-transmitting fissure zone and roof water filling mode of Jurassic coalfield in Ordos Basin," *Journal of Mining & Safety Engineering*, vol. 37, no. 6, pp. 1222–1230, 2020.

[27] Y. Xue, J. Liu, X. Liang, S. Wang, and Z. Ma, "Ecological risk assessment of soil and water loss by thermal enhanced methane recovery: numerical study using two-phase flow simulation," *Journal of Cleaner Production*, vol. 334, article 130183, p. 130183, 2022.

[28] Z. Z. Cao, Y. F. Xue, H. Wang, J. R. Chen, and Y. L. Ren, "The non-Darcy characteristics of fault water inrush in karst tunnel based on flow state conversion theory," *Thermal Science*, vol. 25, no. 6, pp. 4415–4421, 2021.

Hindawi
Geofluids
Volume 2021, Article ID 5552016, 13 pages
https://doi.org/10.1155/2021/5552016

Research Article

Stress Distribution and Failure Characteristics of Stope Overburden of an Inclined Coal Seam

Xin Liu, Jian Sun, and Yong Yang

State Key Laboratory of Mining Response and Disaster Prevention and Control in Deep Coal Mines, Anhui University of Science and Technology, Huainan 232001, China

Correspondence should be addressed to Jian Sun; sj323@cumt.edu.cn

Received 25 February 2021; Accepted 9 November 2021; Published 8 December 2021

Academic Editor: Yi Xue

The stress distribution, failure depth, and shape and range of overlying strata of the stope are important bases for the prevention of roof water hazards and determination of reasonable locations of roof roadways. Based on the hydrogeological data of the E9103 workface, FLAC numerical simulation software was used to establish a numerical calculation model of the overlying strata of the E9103 inclined coal seam, and the stress distribution and failure characteristics of the overlying strata were analyzed. The development height of the caving and water-flowing fractured zones in the overlying strata of the workface was determined. Results showed that the stress reduction area appeared above the goaf in the form of an "arched" distribution, and tensile stress occurred in the local area of the overburden. The overburden relief arch of the workface was symmetrically distributed along the advanced direction and asymmetrically distributed along the inclined direction, with the arch crown deflecting above the workface. The horizontal and vertical displacements of the overlying strata of the stope increased with the advancing distance of the workface. The horizontal displacement in the x-direction presented two obvious regions, and the critical points of the two regions moved forward with the advancement of the workface and showed a certain degree of symmetry. The horizontal displacement in the y-direction presented an "inverted bowl" distribution and increased with the advancement of the workface. The main failure forms of the overlying strata of the workface were a tensile and shear failure, and shear failure was dominant in the upper direction. The height of the overburden caving zone in the workface had little relationship with the advancing distance of the workface and increased slowly as the advancing distance of the workface increased. The development height of the caving zone is 7.2–18.13 m. The development height of the water conduction fissure zone increased rapidly with the increase in the advancing distance of the workface. When the advancing distance was equal to the length of the workface, the development height of the water conduction fissure zone was flat and basically maintained at a stable value. The development height of the water conduction fissure zone is 30.8–62.2 m. These research findings have important engineering importance for ensuring safe and efficient mining of E9103 workface.

1. Introduction

Coal seam mining destroys the original stress balance state of overburden strata; causes stress redistribution in the surrounding rocks of the stope; forms stress concentration and stress reduction areas; leads to the deformation, movement, separation, fracture, and collapse of overburden strata in the stope; and results in caving zone, water conduction fissure zone, and bending zone [1–5]. Determining the development height of the caving and water conduction fissure zones of a mining workface is conducive to predicting and preventing roof water disasters when the confined aquifer and water accumulate in the goaf in the overlying strata of a coal seam [6–8]. Therefore, research on the stress distribution, failure characteristics, and influence range of overlying strata is the premise and basis for realizing safe mining under confined water, determining the reasonable position of roof roads, and judging the influence of lower coal mining on upper coal mining [9–13].

At present, research on the stress distribution and failure characteristics of overlying strata of stope mainly involves numerical simulation, similar simulation, and field

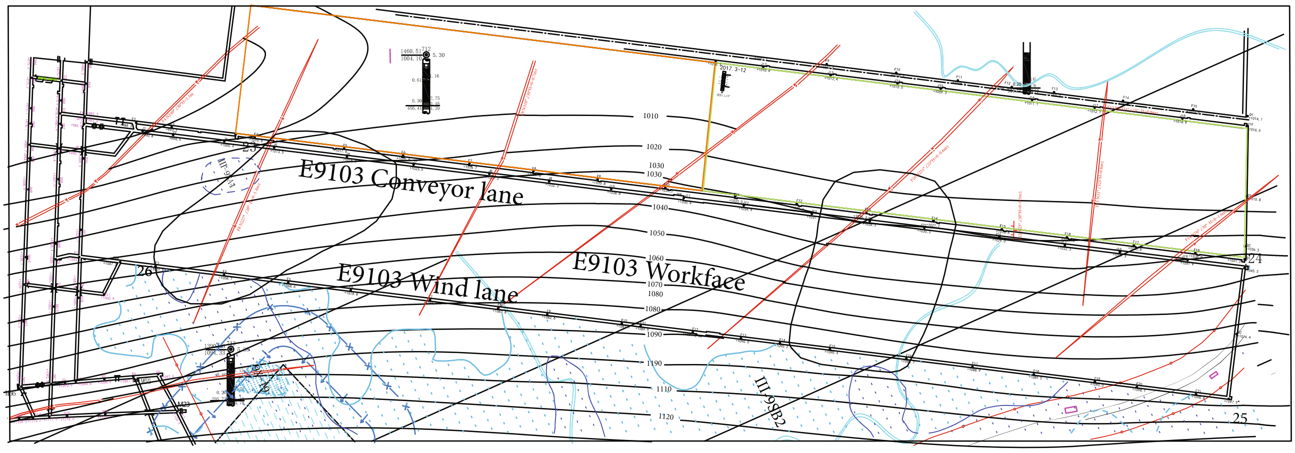

Figure 1: Plan of E9103 workface.

monitoring. These methods provide technical support and safety guarantee in realizing safe mining under confined water, determining the reasonable position of roof roads, and judging the influence of lower coal mining on upper coal mining. Wang et al. [14] studied the dynamic evolutionary characteristics and spatiotemporal coupling effect of mining pressure, strata movement, and fracture distribution in a deep stope by using comprehensive methods composed of numerical simulation, similar simulation, and field monitoring. The dynamic response mechanism of mining stress, overlying strata displacement, and roof fracture fields has also been investigated. To obtain the reasonable position of roadways in the upper coal seam, Huang et al. [15] studied the morphology characteristics of the fractured zone and the concentrated stress distribution in surrounding rock induced by the mining of the lower coal seam by using theoretical analysis, field testing, and numerical simulation. They proposed two schemes for roadway positions, namely, inner and outward stagger modes, and avoided the influence of the fractured zone and concentrated stress field effectively. Based on the engineering background of Dananhu No. 1 Coal Mine in Xinjiang, Lai et al. [16] studied the overburden fracture and water conduction characteristics of fully mechanized top coal caving mining in a soft roof-coal-floor coal seam under an extremely arid climate. Their research provided a scientific basis for the safe mining of fully mechanized top-coal caving workface in soft roof-coal-floor coal seams and the determination of proper water-retaining mining schemes. Yang et al. [17] used the 11915 workface of a mine as an example and applied three methods, namely, borehole water leakage, borehole TV, and numerical simulation, to observe the height of the water conduction zone.

The abovementioned research results play an effective guiding role in ensuring the safety of coal mine production. Based on the engineering background of E9103 workface mining in Linfen Tianyu Hengjin Coal Mine and the hydrogeological data of the workface, a numerical calculation model of mining overburden in the E9103 inclined coal seam workface was established through FLAC numerical simulation software in this study. The stress distribution, failure characteristics, and development height of the overburden caving and water conduction fissure zones were simulated and analyzed. The research results have important engineering guiding significance for ensuring safe and efficient mining of the E9103 workface.

2. Numerical Calculation Model of the Mining Overburden of an Inclined Coal Seam

2.1. Engineering Background. Linfen Tianyu Hengjin Coal Mine of Anhui Wanbei Coal Electricity Group mainly mines nos. 9 and 10 coal seam. The E9103 workface is the second fully-mechanized top-coal caving workface in the first east mining area of the mine. The workface is located in the east wing of the Nanshan inclined shaft, and the cut hole is constructed close to the protective coal pillar line of the mining boundary. The outer horizontal distance of the machine lane is 8 m from the E9101 workface goaf, and the outer side of the wind lane is the solid coal that has not yet been mined. The line is estimated to be 197 m away from Dongyi transportation uphill. The length of the transportation roadway is 1718 m. The ventilation roadway is 1739 m long and 190 m wide on the average in the E9103 workface. The coal seam floor elevation of the workface is +1015 m to +1117 m, the average thickness of the coal seam is 4.50 m, the inclination angle of the coal seam is 14° to 18°, and the average inclination is 16°, as shown in Figure 1. The immediate roof and the main roof of the E9103 workface are shallow marine limestone with high compressive strength (the average compressive strength is 29.6 MPa), which makes it difficult for the roof to fall. The immediate floor of the E9103 workface is made up of mudstone, no. 11 coal seam, mudstone, and limestone.

The no. 2 coal seam above the E9103 workface has been mined. Water accumulation in the goaf and the roof sandstone aquifer (K5, K7, and no. 2 coal roof sandstone aquifer) are the main sources of water inrush to the workface. If the water conduction fissure zone communicates with the water accumulated in the goaf and aquifer of roof sandstone after the E9103 workface is mined, the safe production of the mine will be threatened. To ensure normal and safe mining, the stress distribution and failure characteristics of the

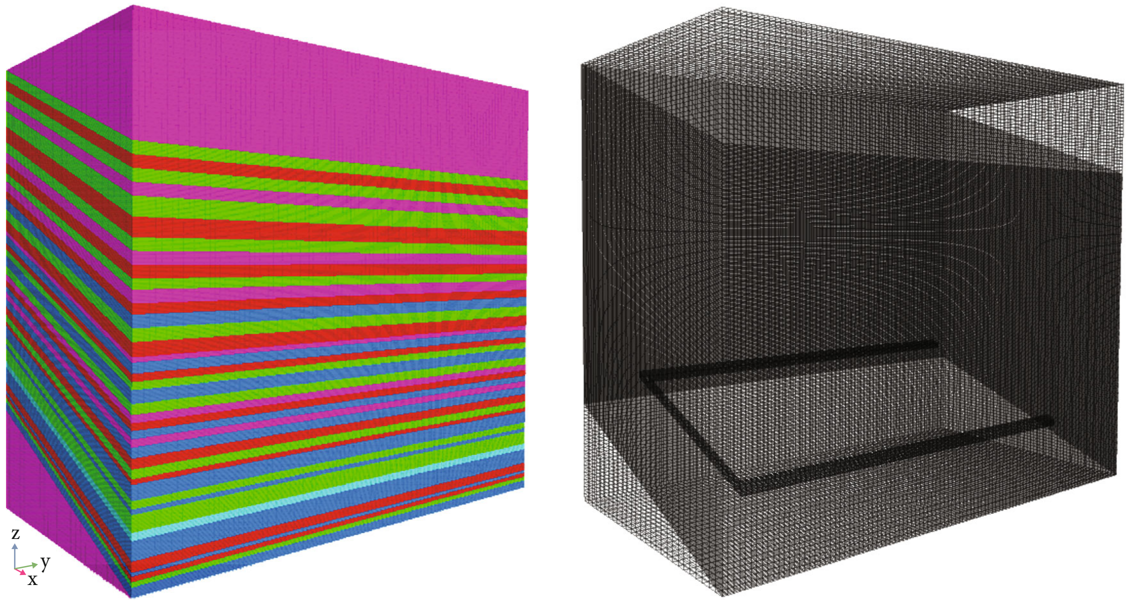

Figure 2: Numerical calculation model of E9103 workface.

overlying strata in the E9103 workface must be studied, the development height of the water conduction fissure zone must be determined, and corresponding technical measures should be formulated for water hazard prevention and control in accordance with the existing geological and hydrological data of the mine. Doing so will guarantee safe and efficient production of the mine.

2.2. Computational Models and Simulation Parameters. Based on the comprehensive geological histogram of the E9103 workface of Hengjin Coal Mine, a numerical calculation model of the overlying strata of an inclined coal seam was established, as shown in Figure 2. In the model, the x-direction is the inclined direction of the workface, the y-direction is the strike direction, the inclined length (x-direction) is 300 m, and the strike length (y-direction) is 500 m. The inclination angle of the rock and coal seam is 16°, and 50 m coal pillars are set around the workface. Excavation is carried out from $y = 50$ m and stopped at $y = 450$ m, with a total of 400 m forward excavation. The bottom surface of the model constrains the displacement in the vertical direction, and the front and rear sides restrain the displacement in the horizontal direction. The upper surface of the model is a free surface, and the overlying strata (except the coal seam roof) are loaded to the upper surface of the model in the form of uniform load (applied load of 8.2 MPa). The physical and mechanical parameters of the roof and floor of the inclined coal seam workface in the model are shown in Table 1.

During model calculation, the calculation grid is divided according to the geometric size of the model, and the corresponding physical and mechanical parameters are provided to the rock layer. Then, the stress equilibrium state of the original rock of the model is calculated. The model is excavated step by step with 20 m excavation per step and 20 excavations in total at one time. The movement, deformation, and failure laws of the overlying strata of the E9103 workface are simulated under different driving distances. At the end of each excavation calculation, the information of the simulation unit and the joint is extracted to analyze the change rule of the stress distribution and failure characteristics of the overlying strata of E9103 workface with the advancing distance of the workface and to reveal the evolution rule of the overburden movement and development height of the water conduction fissure zone in E9103 workface.

2.3. Constitutive Model and Coal-Rock Parameters. The approximate ideal elastic-plastic model is used for the numerical calculation model, and Mohr-Coulomb yield criterion is adopted for the failure criterion. The Mohr-Coulomb yield criterion can be expressed as follows:

$$\begin{cases} f^s = \sigma_1 - \sigma_3 N_\varphi + 2C\sqrt{N_\varphi}, \\ f^t = \sigma_3 - \sigma^t, \end{cases} \tag{1}$$

where σ_1 and σ_3 are the maximum and minimum principal stresses, respectively; C and φ are the cohesive force and internal friction angle, respectively; σ^t is the tensile strength of the material; $\sigma^t_{\max} = c/\tan\varphi$; and $N_\varphi = 1 + \sin\varphi/1 - \sin\varphi$. When $f^s = 0$, the material undergoes shear failure, and when $f^t = 0$, the material undergoes tensile failure.

The physical and mechanical parameters of coal and rock mass involved in the elastic-plastic model of the Mohr-Coulomb yield criterion include bulk modulus B, shear modulus S, cohesion C, internal friction angle φ, and mass density D. B and S are determined according to elastic

Table 1: Physical and mechanical parameters of roof and floor of E9103 workface.

No.	Lithology	Thickness (m)	Density ($kg.m^{-3}$)	Bulk modulus (GPa)	Shear modulus (GPa)	Tensile strength (MPa)	Cohesion (MPa)	Internal friction angle (°)
1	Medium sandstone	44.0	2650	2.21	1.15	2.4	2.50	32
2	Fine sandstone	9.5	2620	1.93	1.00	2.20	2.78	36
3	Siltstone	4.0	2650	2.08	1.33	1.84	2.55	37
4	Fine sandstone	8.0	2650	1.93	1.00	2.20	2.78	36
5	Mudstone	5.0	2650	1.78	0.92	0.88	1.84	29
6	Siltstone	4.0	2650	2.08	1.33	1.84	2.55	37
7	Mudstone	6.0	2650	1.78	0.92	0.88	1.84	29
8	Siltstone	9.0	2650	2.08	1.33	1.84	2.55	37
9	Coal seam	4.5	1400	1.51	0.77	0.65	1.90	25
10	Mudstone	4.0	2650	1.78	0.92	0.88	1.84	29
11	Fine sandstone	7.0	2650	1.93	1.00	2.20	2.78	36
12	Mudstone	3.0	2650	1.78	0.92	0.88	1.84	29
13	Fine sandstone	6.0	2650	1.93	1.00	2.20	2.78	36
14	Siltstone	6.0	2650	2.08	1.33	1.84	2.55	37
15	Mudstone	3.0	2650	1.78	0.92	0.88	1.84	29
16	Medium sandstone	20.0	2650	2.21	1.15	2.4	2.50	32

modulus E and Poisson ratio μ of coal and rock mass, and the relationships between them are as follows:

$$\begin{cases} B = \dfrac{E}{3(1-2\mu)}, \\ S = \dfrac{E}{2(1+\mu)}. \end{cases} \quad (2)$$

3. Stress Distribution of Overlying Strata under Mining in an Inclined Coal Seam

After coal seam mining, the overlying strata moved and deformed, resulting in stress redistribution and the emergence of pressure phenomena in the workface. Figure 3 shows a cloud diagram of the vertical stress distribution of the overlying strata of E9103 workface at different advancing distances. Correspondingly, Figure 4 shows the variation rule of the vertical stress concentration coefficient with the change of advancing distance. The excavation of the workface destroys the stress balance state of the original rock, resulting in the stress redistribution of the stope surrounding rock and the formation of mining disturbance. The change in advancing distance reflects different disturbance and destruction ranges of the overburden coal and rock mass caused by coal seam mining.

When the workface is pushed forward for 40 m, stress concentration occurs in the coal and rock mass in the front and rear of the workface. The peak vertical stress in front of the workface reaches 14.38 MPa, and the stress concentration coefficient is 1.78 (Figure 4). Meanwhile, a stress reduction area appears above the goaf of the workface in the form of an "arch" distribution, and tension stress occurs in the local area of the overburden layer. The occurrence of tensile stress, which causes macrotensile damage to the roof of the goaf, is the dominant factor for the collapse and destruction of overlying strata and the main reason for the development of fracture and fissure in the lower part of the fissure zone. With the increase in the advancing distance in the workface, the mining disturbance range is enlarged continuously, and the low-stress area above the goaf develops upward in the form of an "arch." When the workface is pushed to 200 m, the peak bearing pressure at the rear of the workface reaches the maximum value of 21.01 MPa, and the stress concentration factor is 2.6 (Figure 4). As the workface continues to advance, the increasing trend of peak bearing pressure gradually slows down, as shown in Figures 3(f)–3(j). This result indicates that the mine pressure is relatively obvious during the first meeting period of the workface. It also suggests that safe production, such as roof management during the first meeting period and its following period, should be strengthened when the workface is recovered.

Figure 5 shows a cloud diagram of the vertical stress distribution of the overlying strata in the workface along the inclined direction of the coal seam during the advancing process of the E9103 workface (200 and 400 m). The distribution characteristics of the vertical stress field of the overlying strata in the workface at different positions along the inclined direction of the coal seam are similar to those along the strike direction of the workface. Stress concentration areas occur in the coal and rock mass in front of and behind the workface, and stress reduction areas occur in the goaf area of the workface and gradually develop upward in the form of an "arch." Figure 5 shows that with the advancing of the workface, the mining space gradually forms, the overlying strata of the workface move and are destroyed under the action of gravity, the immediate roof directly falls down, and the main roof breaks, resulting in mining failure crack and the redistribution of the overlying strata of the workface. The relief arch of the overlying strata basically shows a

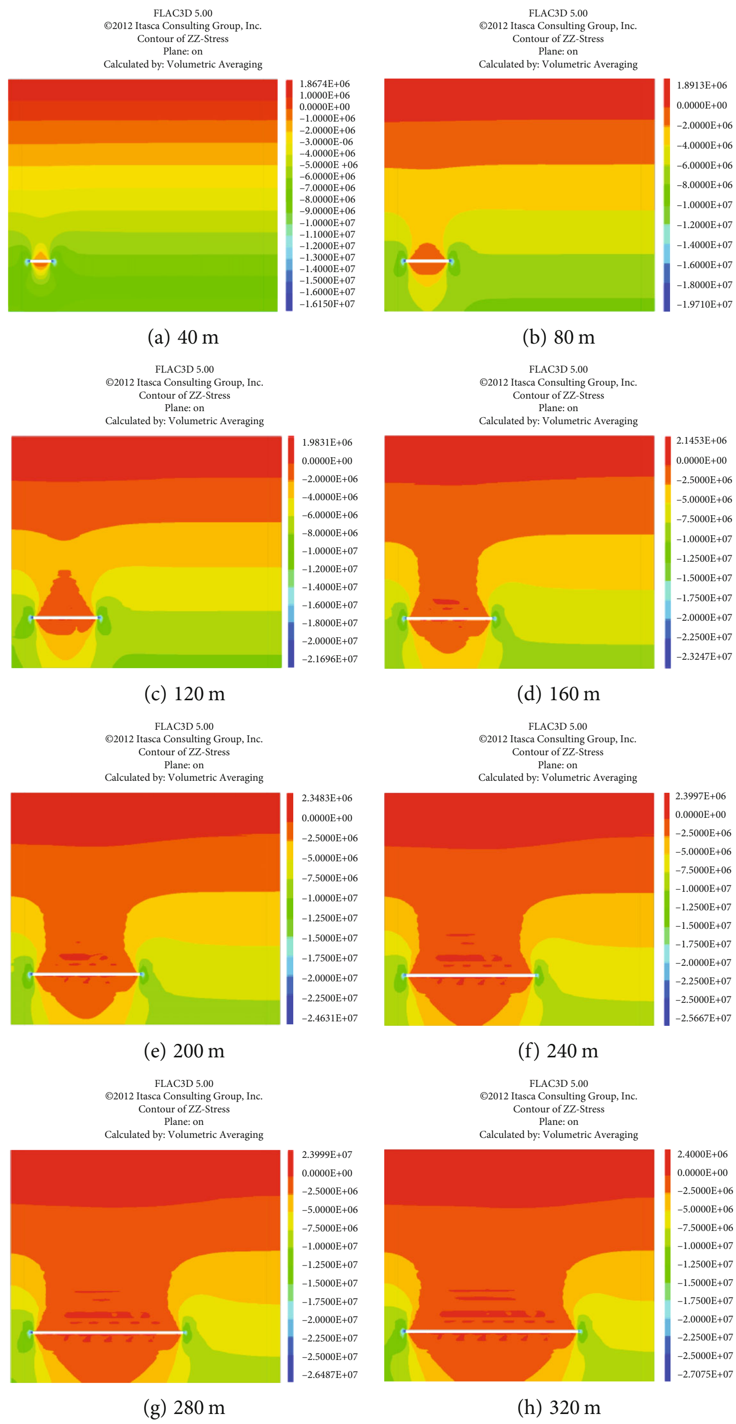

Figure 3: Continued.

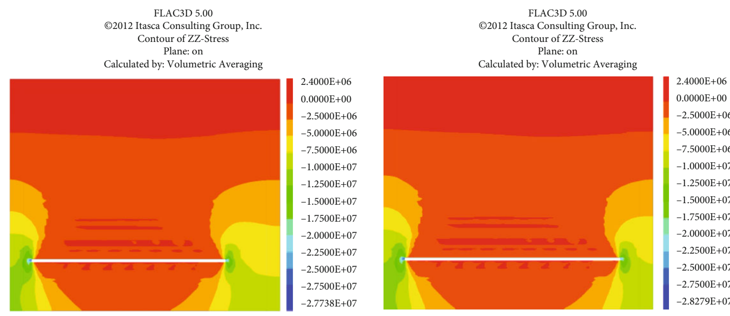

(i) 360 m (j) 400 m

FIGURE 3: Cloud diagram of vertical stress distribution of overlying strata of E9103 workface at different advancement distances.

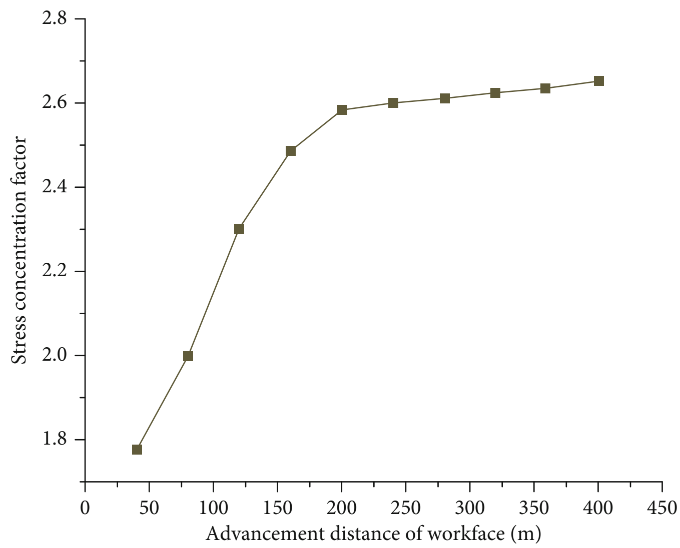

FIGURE 4: Variation regularity of vertical stress concentration coefficient of overlying strata of E9103 workface at different advancement distances.

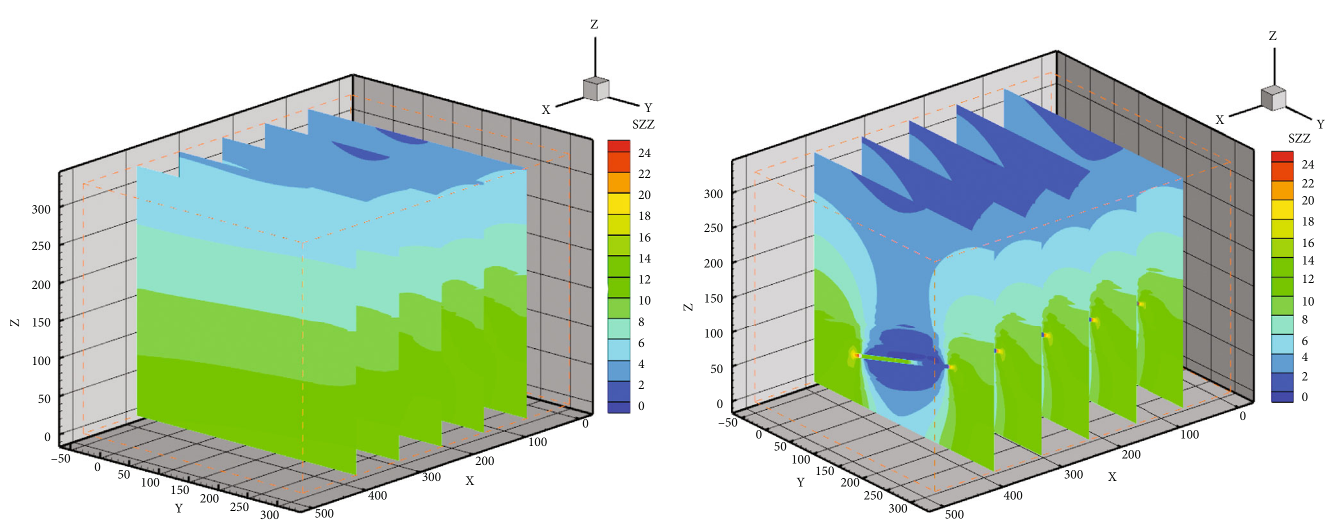

(a) 200 m (b) 400 m

FIGURE 5: Cloud diagram of vertical stress distribution of overlying strata of workface along the inclined direction of coal seam during advancing process (200 m and 400 m).

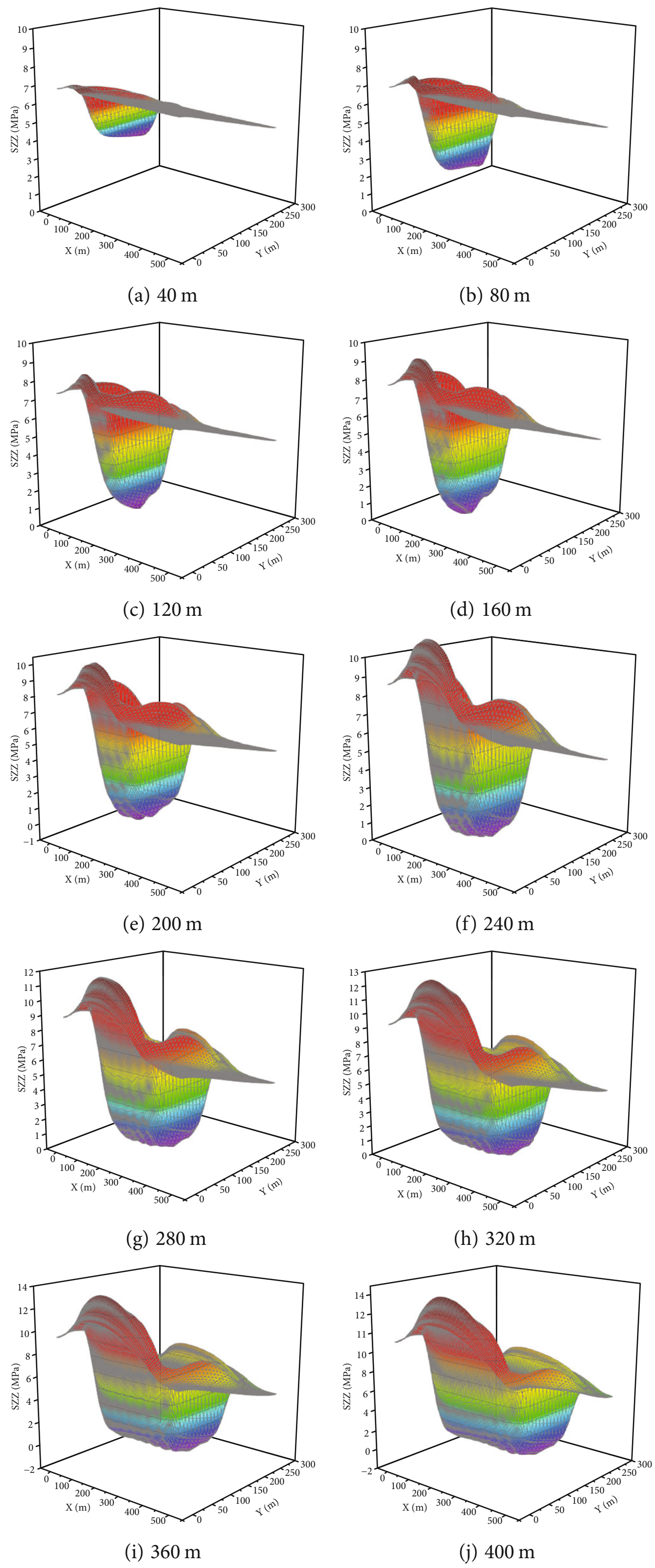

FIGURE 6: Three-dimensional surface diagram of vertical stress of surrounding rock of E9103 workface at different advancement distances.

symmetrical distribution along the advancing direction of the workface, whereas the relief arch of the overlying strata presents an asymmetrical distribution along the inclined direction of the workface, and its vault is inclined above the workface. The stress distribution of the overlying strata of the stope along the inclined direction of the coal seam is completely different from that of the overlying strata of the workface of the horizontal coal seam.

Figure 6 shows a 3D surface diagram of the vertical stress of the surrounding rock of E9103 workface at different advancing distances. Correspondingly, Figure 7 shows a curve of the vertical stress of the surrounding rock of the E9103 workface with advancing distance of the workface. The stress of the surrounding rock changes with the increase in the advancing distance after the E9103 workface is mined, and areas of stress increase and decrease emerge to some extent. Local tensile stress occurs in the goaf area, leading to tensile failure of coal and rock mass and fracture.

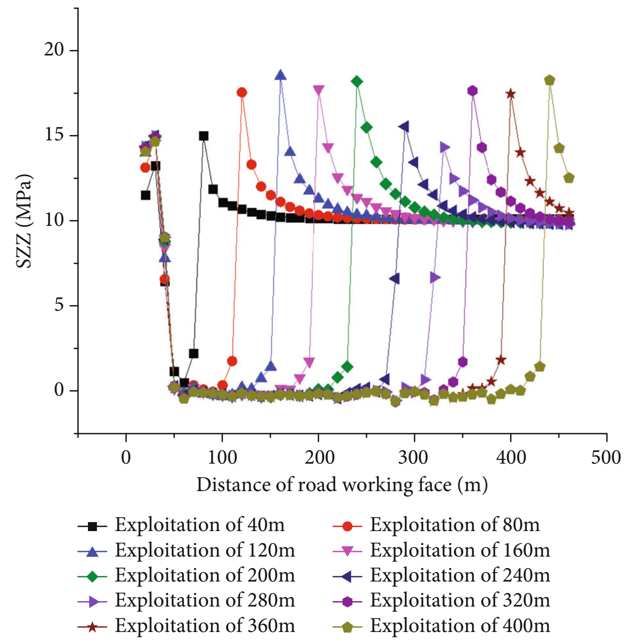

Figure 7: Variation curve of vertical stress of surrounding rock of E9103 workface at different advancement distances.

4. Displacement Characteristics of the Mining Overburden of an Inclined Coal Seam

Figure 8 shows the vector distribution of the displacement of the overlying strata when the E9103 workface is pushed to 400 m. The overlying strata of the stope move and deform with the advancement of the workface. The roof strata in the goaf move toward the goaf continuously, forming the subsidence area of the overlying strata, and the movement direction of the underlying floor strata in the goaf is opposite to that of the roof strata, forming a bottom drum area. The displacement vector value of the overlying roof and underlying floor strata in the goaf decreases with the increase in the distance from the goaf.

Figure 9 shows the variation curves of the horizontal displacement (x and y directions) and vertical displacement (z direction) of the overburden of E9103 workface with different advancing distances. The horizontal and vertical displacements of the overlying strata of the stope increase with the advancing distance of the workface. Figure 9(a) indicates that the horizontal displacement in the x-direction presents two obvious areas. The horizontal movement direction of the overlying strata in a certain distance ahead of the open-off cut is consistent with the advancing direction of the workface (the x-direction displacement is greater than zero), whereas the horizontal movement direction of the overlying strata in a certain distance behind the stopping line is opposite to the advancing direction of the workface (the x-direction displacement is less than zero). With the increase in the advancing distance of the workface, the critical point of the domain (x-direction displacement equals zero) moves forward constantly, presenting certain symmetry. Figure 9(b) shows that the horizontal displacement in the y-direction presents a distribution pattern of an "inverted bowl." The distribution is symmetrical in the central position of the goaf. With the continuous advancement of the workface, the horizontal displacement in the y-direction increases continuously, which may conducive to the formation of the failure fissures of the overlying strata. Figure 9(c) indicates that the vertical displacement of the overlying strata of the stope increases continuously with the advancement of the workface, and the influence range increases continuously.

5. Failure Characteristics of Overburden Rock during Mining in an Inclined Coal Seam

After workface mined, the damage on the overlying strata of the stope presents obvious zonation. In accordance with the theory of mine pressure and strata control, the overlying strata of the workface after mining generally form caving, fissure, and bending subsidence zones from the bottom to the top, in which the height of the development of the falling and fissure zones (called "two-zones" parameter) is an important technical parameter for safe production of the workface. The distribution form and development height of overlying strata of the stope are closely related to the geological conditions of the workface and essential in guiding the prevention and control of water hazards. In the following part, the development characteristics of the "two-zones" of overlying strata in E9103 inclined coal seam workface are analyzed from two perspectives, namely, plastic failure characteristics of overlying strata and stress discrimination method.

5.1. Distribution Characteristics of the Plastic Zone of Stope Overburden. After yielding, the overlying strata of the stope enter a plastic state, and their integrity is destroyed. On the one hand, the inherent cracks in the rock mass further expand and extend; on the other hand, new cracks are generated. These cracks connect with each other and form a water conduction crack passage. The failure characteristics of the plastic zone of the overlying strata can intuitively reflect the failure form, which is one of the main bases for analyzing the development height of the "two-zones" of the overlying strata and for determining the height of the maximum water conduction fissure zone. A distribution

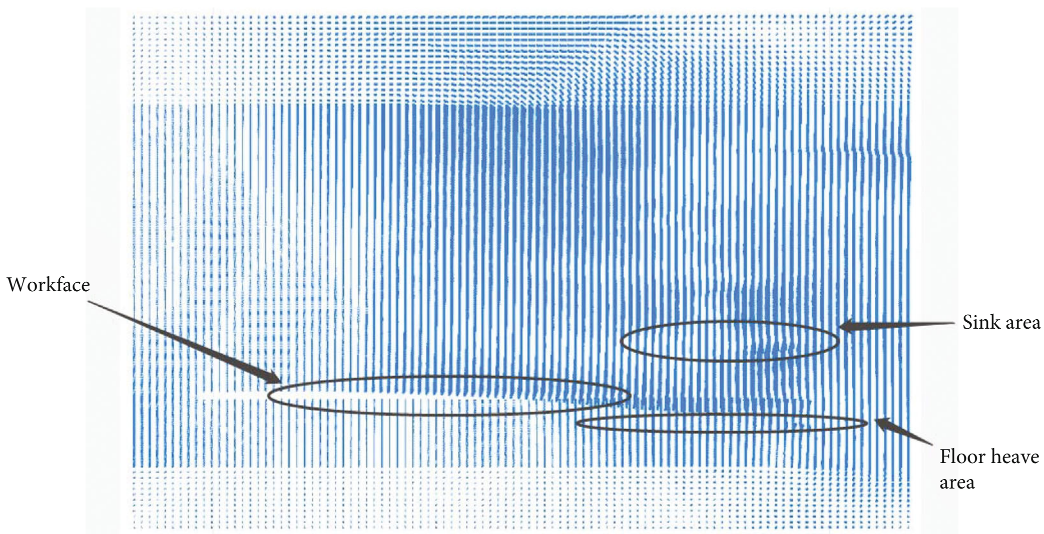

Figure 8: Vector distribution of overburden displacement of overlying strata when E9103 workface advances to 400 m.

cloud diagram of the plastic zone of overlying strata in the direction of the strike and inclination of the workface when the E9103 workface is advanced to 400 m is shown in Figure 10.

The distribution cloud diagram of the plastic area of the overlying strata shows that the rock in the goaf is mainly caused by tensile and shear failure then by shear failure upward. The overlying strata after mining can be roughly divided into five deformation and destruction areas from top to bottom; the five are nondestroyed area, plastic deformation area, tension crack area, tension damage area, and local tension area. The failure form of the overlying strata is a symmetrical "arched" distribution along the advancing direction of the workface; it is also an asymmetrical "arched" distribution along the inclined direction of the coal seam, and the broken vault deviates from the middle to the upper part of the workface. The failure form of the overlying strata along the inclined direction of the coal seam is completely different from that along the workface of the horizontal coal seam. After coal seam mining, the height of the fissure zone of the overlying strata of the stope is mainly affected by the range of plastic zones above the coal and rock mass and above the goaf before and after the workface. Rocks in the caving zone are generally in the localized tension zone, and the plastic zone is mainly characterized by tension failure. Figure 10 shows that the height of the caving and water conduction fissure zones of the workface is 18.13 and 62.2 m, respectively (the maximum height of the plastic zone).

5.2. Failure Characteristics of the "Two-Zones" of Overlying Strata. The stress discrimination method is adopted to calculate the stress of each joint by using different strength and yield criteria and to judge whether the point has yielded failure by using the stress state of the joint. Tensile stress and small compressive stress zones are areas where cracks develop. The upper bounds of tension failure and tension fracture zones are important criteria for determining the height of the caving and water conduction fracture zones. Figure 11 shows a sketch of the maximum principal stress, minimum principal stress, and horizontal stress of the overlying strata of the stope when the E9103 workface is advanced to 400 m.

The principal stress nephograms in Figures 11(a) and 11(b) show that the maximum principal stress distribution is similar to that of the saddle and basically consistent with that of the plastic zone. The minimum principal stress develops upward in the form of an arch. The horizontal stress nephograms in Figures 11(c) and 11(d) show that the vertical zone of horizontal stress of the overlying strata of the stope is obvious. Tensile stress occurs in a certain range over the goaf. The tensile stress gradually transforms into compressive stress, and the horizontal stress isoline becomes sparse after exceeding the range. According to the magnitude and nature of horizontal and principal stresses, it can be divided into three zones, namely, bidirectional tension stress zone, tension-compression stress zone, and compression stress zone. The bidirectional tensile stress area shows that the maximum and minimum principal stresses are greater than 0, which is mainly distributed in the strata of the caving zone in the goaf. When the tensile stress exceeds the ultimate tensile strength of the rock mass, the rock mass breaks and collapses, and the stress is released and transferred. The tensile and compressive stress areas show that the maximum principal stress is greater than 0, and the minimum principal stress is less than 0, which is mainly distributed outside the rock mass of the caving zone, and the rock mass is subject to a certain direction of tensile stress. When the compressive stress is higher than the tensile strength, shear and tensile fractures are produced. The compressive stress zone shows that the maximum and minimum principal stresses are less than 0. The caving zone is generally located in the bidirectional tensile stress zone and tension-compression stress zone of the overlying strata. The main failure forms are tension and shear failures. The

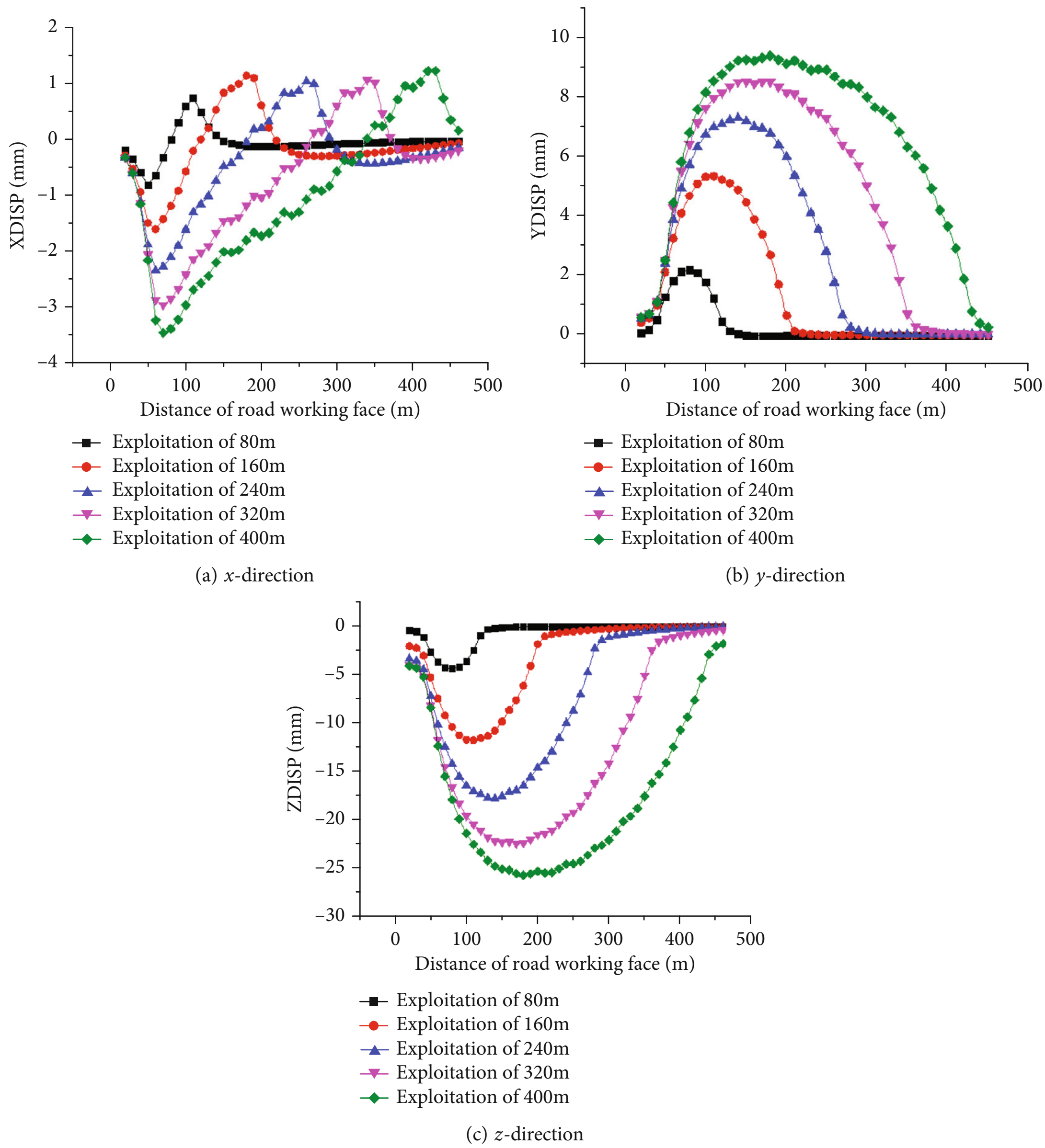

Figure 9: Variation curves of horizontal displacement (x-direction and y-direction) and vertical displacement (z-direction) of overburden of E9103 workface at different advancement distances.

magnitude of principal stress and rock mass properties controls the development height of the caving zone and the openness, density, and penetration of mining cracks.

Rock is a compressive and non-tensile material. Generally, if the maximum and minimum principal stresses of the overlying strata in the goaf are tensile stresses, the rock will experience comprehensive tensile failure, and the roof will fall to form a caving zone. If only one of the principal stresses is tensile stress, visible cracks will occur perpendicular to the tensile stress, forming a fractured zone. The positive tensile stress is set, the main stress of the overlying strata is taken as the range of tensile stress of the caving zone, and the range of the main stress in one direction is adopted as the height of the obvious fissure zone. Figure 12 shows the variation in the development height of the caving and fracture zones of the overlying strata of E9103 workface at different advancing distances. Figure 12 indicates that when the workface is advanced for 40 m, the heights of the caving and fracture zones are 7.2 and 30.8 m, respectively. When the workface is advanced for 80 m, the height of the caving zone is 8.5 m, and the height of the fracture zone is 40.5 m. When the workface is advanced for 120 m, the heights of the caving and fracture zones are 10.82 and 47.3 m, respectively. When the workface is advanced for 160 m, the height of the caving zone is 12.5 m, and the height of the fracture zone is 52.1 m. When the workface is advanced for 200 m, the heights of the caving and fracture zones are 14.18 and 56.11 m, respectively. When the workface is advanced for 240 m, the heights of the caving and fracture zones are 15.62 and 57.34 m, respectively. When the workface is advanced for 280 m, the height of the caving zone is 16.91 m, and the height of the fracture zone is 58.2 m.

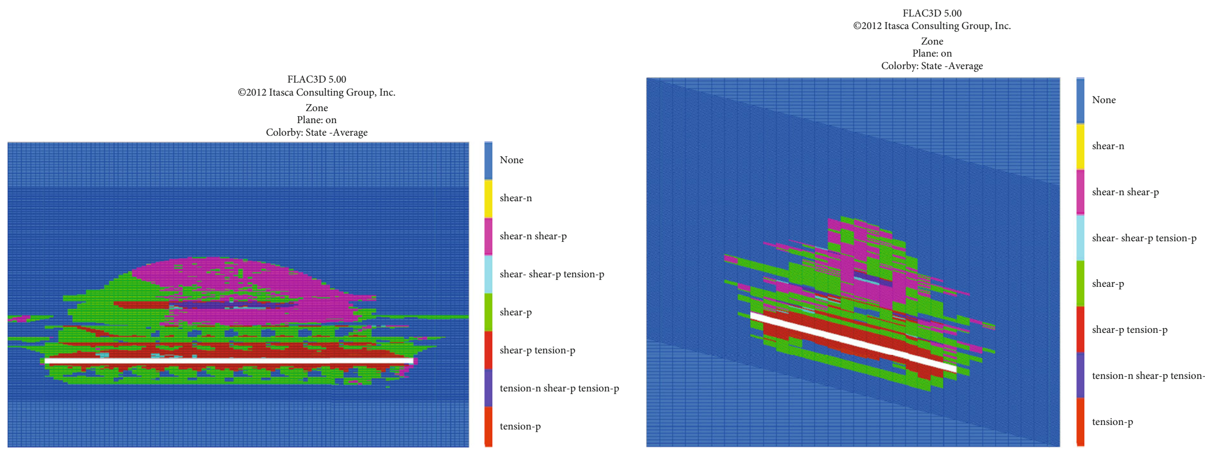

(a) Advanced direction of workface

(b) Inclined direction of workface

Figure 10: Cloud diagram of workface orientation and inclination plasticity zone distribution as E9103 workface advances to 400 m.

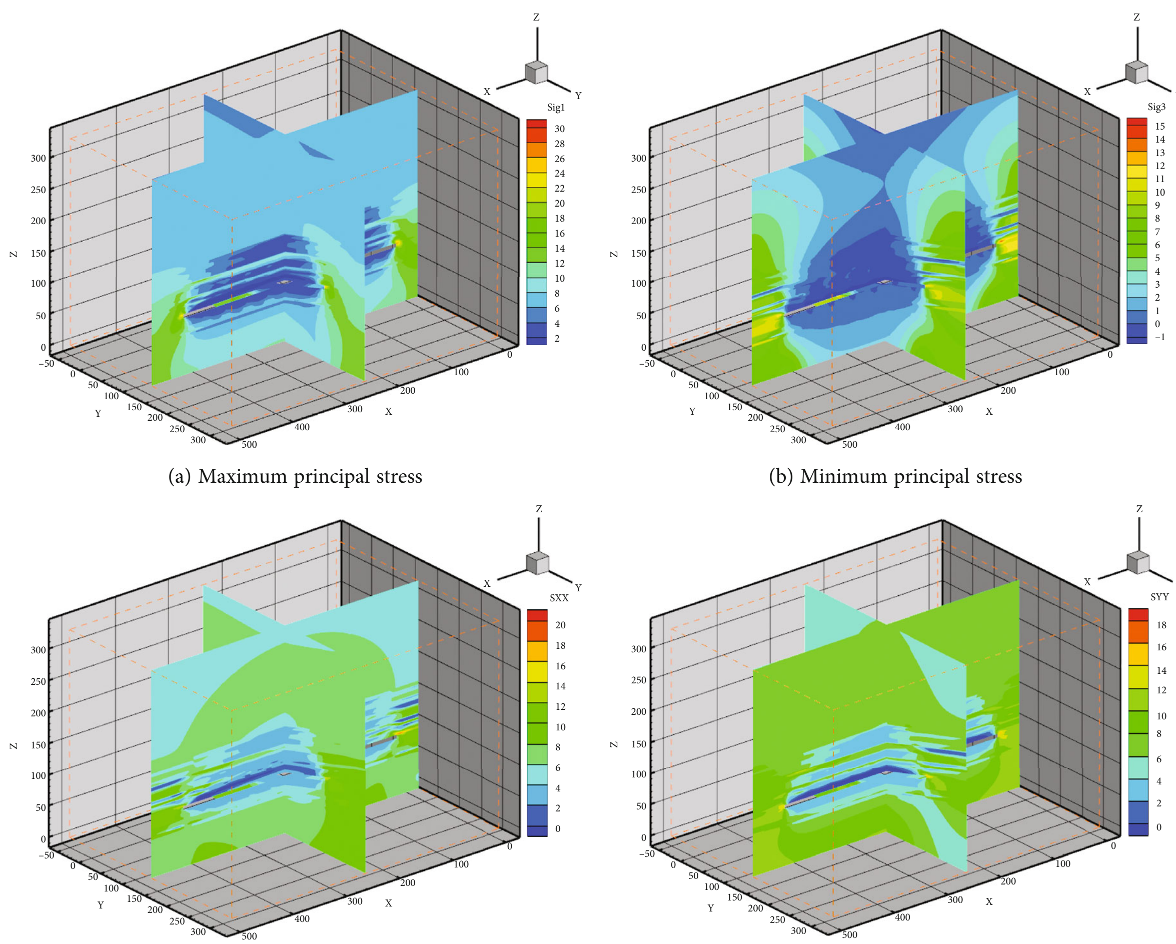

(a) Maximum principal stress

(b) Minimum principal stress

(c) Horizontal stress SXX

(d) Horizontal stress SYY

Figure 11: Cloud diagrams of maximum principal stress, minimum principal stress, and horizontal stress of overlying strata when E9103 workface advanced to 400 m.

When the workface is advanced for 320 m, the height of the caving zone is 15.88 m, and the height of the fracture zone is 59.1 m. When the workface is advanced for 360 m, the heights of the caving and fracture zones are 17.61 and 59.8 m, respectively. When the workface is advanced for 400 m, the heights of the caving and fracture zones are

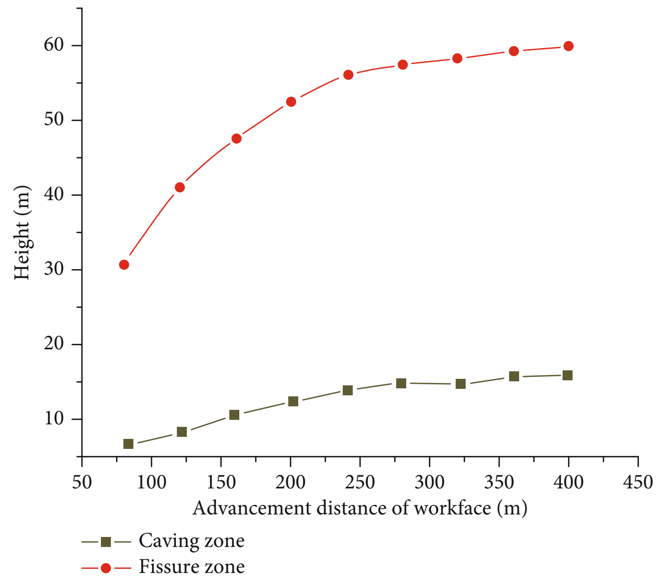

FIGURE 12: Development height of the overlying strata of caving zone and fissure zone at different advancement distances of E9103 workface.

18.13 and 62.2 m, respectively. In conclusion, the height of the overburden caving zone has little to do with the advancing distance of the E9103 workface; it increases slowly with the advancing distance of the workface, and the height of the caving zone is 7.2–18.13 m. The height of the fracture zone increases rapidly with the advancing distance of the workface. It tends to be flat when the advancing distance is equal to the length of the workface and remains at a stable level; the development height of the fracture zone is 30.8–62.2 m.

6. Conclusions

On the basis of the hydrogeological data of the E9103 workface in Hengjin Coal Mine, a numerical calculation model of the overlying strata of the E9103 inclined coal seam workface was established by applying FLAC numerical simulation software. The stress distribution and failure characteristics were simulated and analyzed, and the development heights of the caving and water conduction fissure zones of the E9103 workface were confirmed. The following main conclusions were obtained:

(1) After the E9103 workface is mined, stress reduction zones emerge above the goaf, and these are in the form of "arches." Tension stresses occur in the local area of the overlying strata. The relief arch of the overlying strata is symmetrically distributed along the advancing direction of the E9103 workface, asymmetrically distributed along the inclined direction, and its arch is inclined above the workface

(2) The horizontal and vertical displacements of the overlying strata of the E9103 workface increase with advancing distance. The horizontal displacement in the x-direction presents two obvious areas, and the critical point of both areas moves forward with the workface, showing a certain symmetry. The horizontal displacement in the y-direction presents an "inverted bowl" distribution and increases with the advancement of the workface

(3) The overlying strata in the E9103 workface are mainly tensile and tensile–shear failure and then upward shear failure. The overlying strata in the caving zone are generally in the local tension area, and the plastic zone is mainly tension failure. The height of the caving zone in the E9103 workface has little relationship with advancing distance, and it increases slowly with advancing distance. The development height of the caving zone is 7.2–18.13 m. The development height of the water conduction fissure zone increases rapidly with advancing distance. When the advancing distance is equal to the length of the working face, the development height of the fissure zone is flat and basically maintains a stable value. The development height of the water conduction fissure zone is 30.8–62.2 m

Data Availability

Without any supplementary materials for this study, all the data, tables, and pictures have been presented in the paper.

Conflicts of Interest

The authors declare that they have no conflicts of interest regarding the publication of this paper.

Acknowledgments

This study was supported by the National Natural Science Foundation of China (no. 51974010).

References

[1] M. Qian and P. Shi, *Ground Pressure and Strata Control*, China University of Mining & Technology Press, Xuzhou, China, 2003.

[2] X. Zhang Pingsong, G. L. Shiang, and W. Rongxin, "Prospect and progress of deformation and failure monitoring technology of surrounding rock in stope," *Coal Science and Technology*, vol. 48, no. 3, pp. 14–35, 2020.

[3] Z. Dan, Z. Pingsong, S. Bin, W. Hongxian, and L. Changsheng, "Monitoring and analysis of overburden deformation and failure using distributed fiber optic sensing," *Chinese Journal of Geotechnical Engineering*, vol. 37, no. 5, pp. 952–957, 2015.

[4] L. Jia, X. Yi, C. Wei, H. Peng, W. Songhe, and L. Xin, "Variational phase-field model based on lower-dimensional interfacial element in FEM framework for investigating fracture behavior in layered rocks," *Engineering Fracture Mechanics*, vol. 255, article 107962, 2021.

[5] Y. Xue, T. Teng, F. Dang, Z. Ma, S. Wang, and H. Xue, "Productivity analysis of fractured wells in reservoir of hydrogen and carbon based on dual-porosity medium model," *International Journal of Hydrogen Energy*, vol. 45, no. 39, pp. 20240–20249, 2020.

[6] State Bureau of Coal Industry, *Regulations of Buildings, Water, Rail Way and Main Well Lane Leaving Coal Pillar and Press Coal Mining*, China Coal Industry Publishing House, Beijing, 2000.

[7] H. Bingxiang, X. Liu Changyou, and Jialin, "Research on through degree of overlying strata fracture fissure induced by mining," *Journal of China University of Mining & Technology*, vol. 39, no. 1, pp. 45–49, 2010.

[8] L. Yu, L. Qimeng, L. Wenping, and H. Youbiao, "Height of mining-induced fractured zones in overlying strata and permeability of rock with nonpenetrative fractures," *Geofluids*, vol. 2020, 13 pages, 2020.

[9] C. Xianggang, Q. Wei, L. Li, J. Chuanwen, and N. Lei, "Model of mining-induced fracture stress-seepage coupling in coal seam over-burden and prediction of mine inflow," *Journal of China Coal Society*, vol. 45, no. 8, pp. 2890–2900, 2020.

[10] S. Jian, W. Lianguo, and Z. Guangming, "Stress distribution and failure characteristics for workface floor of a tilted coal seam," *KSCE Journal of Civil Engineering*, vol. 23, no. 9, pp. 3793–3806, 2019.

[11] W. Cheng, Z. Nong, X. Li Guichen, Q. D. Xingliang, and Z. Nianchao, "Control principles for roadway roof stabilization in different zones during ascending mining," *Journal of China University of Mining & Technology*, vol. 41, no. 4, pp. 543–550, 2012.

[12] Z. Wei, Z. Dongsheng, C. Jianben, X. Wang Xufeng, and Mengtang, "Determining the optimum gateway location for extremely close coal seams," *Journal of China University of Mining & Technology*, vol. 2, pp. 182–188, 2012.

[13] Z. Shizhong, F. Gangwei, C. Ling et al., "Disaster control of roof falling in deep coal mine roadway subjected to high abutment pressure," *Geofluids*, A. Brogi, Ed., vol. 2021, Article ID 8875249, 17 pages, 2021.

[14] W. Xinfeng, G. Mingzhong, and L. Longqin, "Spatiotemporal coupling law of mining pressure, strata movement and fracture field distribution in deep stope," *Journal of Mining & Safety Engineering*, vol. 33, no. 4, pp. 604–610, 2016.

[15] H. Wanpeng, X. Wenbin, Z. Yongsheng, and L. Chao, "Reasonable layout of roadways for upward mining technology of close coal seams," *Chinese Journal of Rock Mechanics and Engineering*, vol. 36, no. 12, pp. 3028–3039, 2017.

[16] L. Xingping, C. Feng, C. Jiantao, L. Zhaohai, and Y. Lei, "Analysis on characteristics of overlying rock caving and fissure conductive water in top-coal caving working face at three soft coal seam," *Journal of China Coal Society*, vol. 42, no. 1, pp. 148–154, 2017.

[17] Y. Daming, G. Wenbing, Z. Gaobo, T. Yi, and Y. Weiqiang, "Height of water-conducting zone in longwall top-coal caving mining under thick alluvium and soft overburden," *Journal of China Coal Society*, vol. 44, no. 11, pp. 3308–3316, 2019.

Hindawi
Geofluids
Volume 2021, Article ID 5549223, 11 pages
https://doi.org/10.1155/2021/5549223

Research Article

A Study of Instantaneous Shear Mechanical Properties on the Discontinuity of Rock Mass Based on 3D Morphological Properties

Qingzhao Zhang,[1,2] Zejun Luo ,[1,2] Bo-An Jang,[3] Qiuyi Wang,[4] Zhen Zhong ,[5] and He Jiang[6]

[1]*Department of Geotechnical Engineering, Tongji University, Shanghai, China*
[2]*Key Laboratory of Geotechnical and Underground Engineering of Ministry of Education, Tongji University, Shanghai, China*
[3]*Department of Geophysics, Kangwon National University, 1Kangwondaehak-gil, Chuncheon-si, Gangwon-do 24341, Republic of Korea*
[4]*Yunnan Gongdong Expressway Construction Headquarters, Kunming, China*
[5]*Key Laboratory of Rock Mechanics and Geological Hazards of Zhejiang Province, Shaoxing University, Zhejiang Province, China*
[6]*YCIC Highway Construction Co., Ltd, Kunming, China*

Correspondence should be addressed to Zhen Zhong; zhongzhen@zju.edu.cn

Received 13 February 2021; Revised 2 November 2021; Accepted 11 November 2021; Published 28 November 2021

Academic Editor: Kai Yao

In order to study the instantaneous mechanical properties of rock mass discontinuities with different 3D morphologies during the shear process, the Brazilian splitting method is used to prepare natural rock mass discontinuities, and the high-precision 3D scanning test of discontinuities is carried out. The Z_2 is selected as the evaluation parameter of the discontinuities. Based on the graded cyclic shear test results of discontinuities, the influence of the morphology characteristics on the strength and deformation characteristics is analyzed. With the increase of shear times, the 3D morphology characteristic parameters of the structural plane decrease steadily after the graded cyclic shear. Based on the test curve, the graded cyclic shear characteristics of rock mass discontinuities are analyzed from the shear deformation, and the shear process of the discontinuities is finely divided by combining with the variation characteristics of shear stiffness. Combined with the 3D morphology parameters, an empirical formula for the shear strength of discontinuities is proposed. Through verification, the effect of the new model is better than that of the classical JRC-JCS model.

1. Introduction

The discontinuities in jointed rock mass play a dominant role in the deformation and damage of rock mass. Due to the existence of discontinuities, the rock mass has complex engineering properties, which leads to anisotropy and heterogeneity [1]. Meanwhile, it also destroys the integrity of the rock mass and greatly reduces the material properties of the rock mass, which is the primary factor that affects the stability of engineering rock mass [2]. Therefore, scholars have always been focusing on the study on the mechanical properties and parameter selection of the discontinuities of rock mass.

The morphological properties of the discontinuities of rock mass have a significant impact on their mechanical properties [3, 4]. Speaking of two-dimensional morphological properties of discontinuities, the most famous of which is the joint morphology characterized by joint roughness coefficient (JRC) of the discontinuities proposed by Barton and Choubey [5]. The method has now been recommended by the International Society for Rock Mechanics and Engineering. In fact, many scholars have modified and improved the

JRC evaluation method and also established a quantitative empirical relationship between different statistical parameters and JRC values by measurement and statistical methods [6–9]. Since Prof. Mandelbrot proposed the theory of fractal geometry [10], some scholars have applied it to the study of jointed morphology. Kulatilake et al. and Zhu et al. [11, 12] separately established an empirical relationship between fractal dimensions and JRC indicators, so that JRC indicators can be obtained by a fractal method. In recent years, the characterization method for the 3D morphology of discontinuities has become a hot topic in the research of morphological characteristics. Belem et al. [13] discussed the 3D roughness coefficient characterizing the morphology of several discontinuities and studied the variation law of the roughness coefficient in the shear process of discontinuities. Grasselli et al. [14] studied the morphological properties of discontinuities with 3D morphology scanning technology, proposing to describe the 3D morphological properties of discontinuities with new 3D morphological parameters. Xia et al. [15] studied the description of the 3D morphology of discontinuities in different contact states and proposed the method of calculating morphological parameters. Rabczuk et al. [16, 17] described a new approach for modelling discrete cracks in mesh-free methods. At present, the study on the morphological properties of discontinuities and their characterization methods has been mature, but it still needs to be further improved. The characterization methods of 3D morphology of discontinuities have higher requirements for measurement accuracy, and the characterization parameters are complex, which are not conducive to popularization and promotion.

Shear strength is one of the basic mechanical properties of discontinuities, and rich research results have now been achieved. Among the studies on the strength properties of discontinuities, the most representative of which is three strength formulas of discontinuities, i.e., Patton's formula, Ladanyi's formula, and Barton's formula, and most of the follow-up studies are carried out based on these three formulas. Patton introduced undulating angle into Mohr-Coulomb criterion in the 1960s and established the bilinear shear strength criterion of discontinuities. Barton [18] established the famous empirical formula of JRC-JCS peak shear strength based on JRC indicators. Chen et al. [19] constructed the model of peak shear strength based on the function relationship between normal stress and peak-dilation angle of discontinuities. Park et al. [20] constructed a shear constitutive model of discontinuities based on 3D morphological parameters. Based on the study of the 3D morphology of discontinuities. Xia et al. [21] carried out a comprehensive study on the 3D peak shear strength of discontinuities and constructed a 3D model of peak shear strength. Ge [22] established the empirical formula for the peak shear strength of discontinuities based on the 3D morphological parameter BAP. Compared with the strength properties of the discontinuities of rock mass, the study on its deformation properties is inferior in both depth and breadth, but the scholars at home and abroad have never stopped studying the deformation properties of discontinuities [23, 24]. Yin et al. [25] constructed a new discontinuities constitutive model based on cyclic shear test and numerical simulation and reflected the impact of the wear of discontinuities on its frictional characteristics and dilation characteristics in the model. Li and Du [26] explored the shear deformation characteristics of discontinuities based on the shear test on artificial discontinuities. Huang et al. [27] simulated the shear test on the regularly dentate discontinuities with different normal stresses and angles based on PFC2D program and analyzed the law of shear deformation and strength. Gui [28] established the jointed peak shear displacement model based on the direct shear test on artificial discontinuities and proposed the constitutive model of joint shear and the shear dilatancy mode. The research results of the mechanical properties of discontinuities are mainly in the artificially prefabricated regular discontinuities, while there are relatively less studies on the natural rock mass discontinuities. In particular, there are few studies considering the 3D morphological properties of rock mass discontinuities.

The morphological properties of discontinuities are fundamental for studying the strength theory, but it is difficult to apply the current strength model due to the complex characterization method of 3D morphological properties of discontinuities. In this paper, several samples of discontinuities of natural rock mass are prepared through artificial fracturing with the help of 3D morphology scanning technology, and the 3D morphological properties are evaluated. The graded cyclic shear test of discontinuities is carried out based on different 3D morphological properties, and the impact of which on the strength of discontinuities is analyzed based on the test results. From the angle of changes in shear strength, the deformation properties of discontinuities in the shear process are studied, and the empirical formula of shear strength of discontinuities considering 3D morphological properties is established.

2. Materials and Methods

2.1. Sample Preparation. Ten natural gneiss blocks are selected to prepare $100 \times 100 \times 100$ mm $(L \times W \times H)$ cube samples, and the 100×100 mm $(L \times W)$ discontinuities of rock mass are obtained by the Brazil split test in the direction parallel to that of the gneiss schistosity, and the samples of discontinuities are numbered from p-i, as shown in Figure 1.

2.2. Scanning Test on 3D Morphology of Discontinuities. In order to quantitatively characterize the impact of 3D morphology of the discontinuities on the shear strength, as shown in Figure 2, TJXW-3D rock surface morphometry is used to determine the surface morphology of the discontinuities of rock mass. Ten samples of discontinuities in total are selected for graded cyclic shear test. After each direct shear test, the samples shall be provided with 3D morphological scanning for 10 s, with a scanning accuracy of $\pm 20\,\mu$m, so as to accurately obtain 3D morphological data of the discontinuities, as shown in Figure 3.

2.3. Graded Cyclic Direct Shear Test. The CSS-1950 biaxial rheological rock tester in the Key Laboratory of Geotechnical and Underground Engineering, as shown in Figure 4, is used

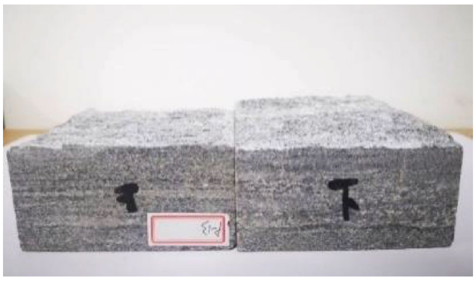

Figure 1: Gneiss discontinuities.

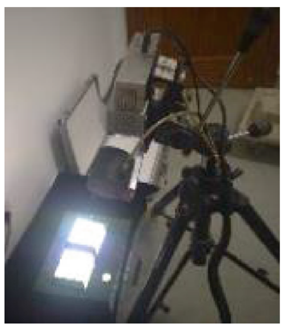

Figure 2: Surface morphometer.

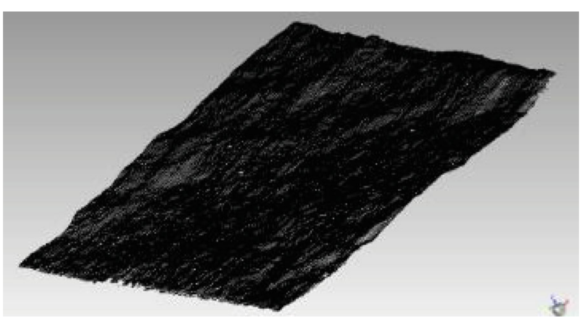

Figure 3: 3D morphological data of discontinuities.

Figure 4: CSS-1950 biaxial rheological rock tester.

to carry out the graded cyclic shear test on the discontinuities of rock mass. The maximum pressure of the tester is 500 kN in the direction of vertical axis and 300 kN in the horizontal direction, and the control accuracy of the loading system is 1%.

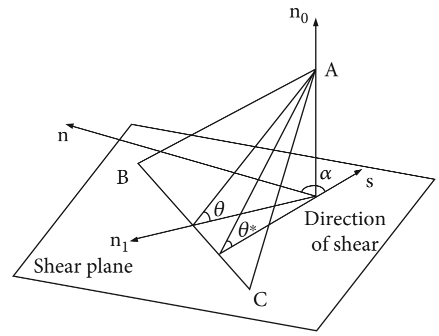

Figure 5: Geometrical relationship diagram of jointed elementary apparent dip algorithm.

The normal load of rock mass shear test shall be determined by the uniaxial compressive strength of rock mass samples. The average uniaxial compressive strength obtained by the uniaxial ultimate compressive strength test on 5 cylindrical samples is 50.5 MPa.

As the anisotropy of discontinuities is complex, the sample blocks are tested by loading the graded cyclic shear under different normal stresses. 5 sample blocks of the discontinuities of natural rock mass are selected. Each sample block of discontinuities is subject to five direct shear tests, respectively (under the normal stresses of 2.5 MPa, 3.75 MPa, 5 MPa, 6.25 MPa, and 7.5 MPa), and the shear rate is 0.5 MPa/min, so that the c and φ values and the morphological changes of each discontinuities are obtained in combination with the test results.

3. 3D Morphological Evaluation of the Discontinuities of Rock Mass

3.1. 3D Morphological Indicators of Discontinuities. Based on a number of shear tests on the discontinuities of rock mass, it is found that there is only partial contact between the top and bottom of rock discontinuities in the shear process, and such contact only appears on the slope facing the shear direction. When determining the 3D morphological properties of discontinuities, parameters facing the shear direction shall be used to reflect the effective shear resistance of the discontinuities. Grasselli et al. studied the morphological properties of discontinuities by means of 3D morphological scanning and pointed out the geometrical relationship between the triangular elementary apparent dip of discontinuities (θ^*) and the shear direction with reference to the concept of effective shear angle (i.e., apparent dip θ^*) [14], as shown in Figure 5.

As shown in Figure 6, the formula of calculating the apparent dip (θ^*) is as follows:

$$\theta^* = \tan^{-1}(-\tan\theta \times \cos\alpha), \tag{1}$$

$$\cos\theta = \frac{\boldsymbol{n} \times \boldsymbol{n_0}}{|\boldsymbol{n}| \times |\boldsymbol{n_0}|}, \tag{2}$$

$$\cos\alpha = \frac{\boldsymbol{s} \times \boldsymbol{n_1}}{|\boldsymbol{s}| \times |\boldsymbol{n_1}|}, \tag{3}$$

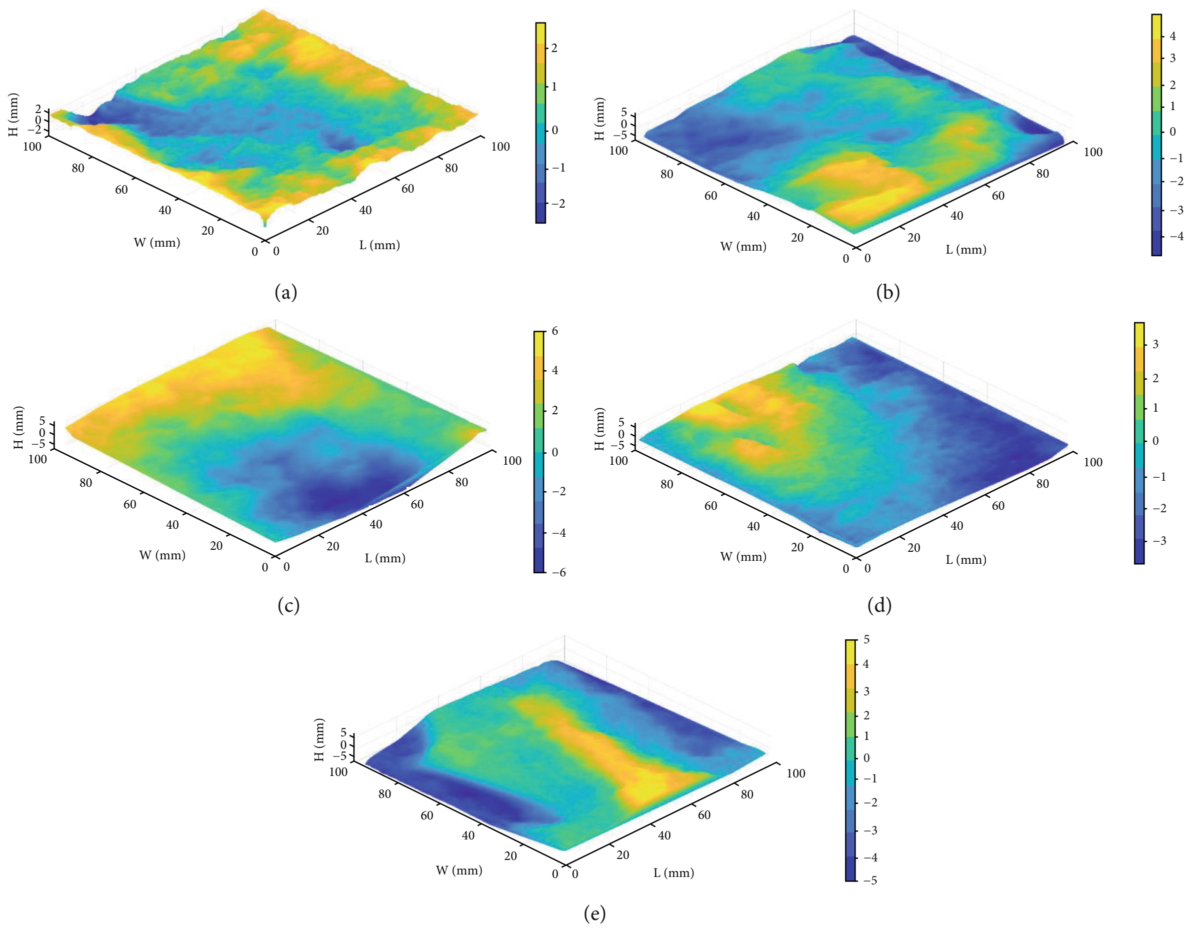

Figure 6: Initial 3D Morphology of Discontinuities. (a) p-1. (b) p-2. (c) p-3. (d) p-4. (e) p-5.

where θ refers to the true dip of triangular element of the discontinuities, α refers to the included angle of triangular element of the discontinuities in dip direction and shear direction, n refers to the outer normal vector of joint element, n_0 refers to the outer normal vector of shear plane, n_1 refers to the projected vector of n in shear direction, and s refers to the vector of joint in shear direction.

Tse and Cruden [29] obtained a logarithmic regression relationship between JRC and Z_2 of joint curve from 10 Barton standard contour curves, which was the most widely used. Yu and Vayssade [30] used a linear relationship to describe the relationship between JRC and Z_2. In 2010, Tatone and Grasselli [31] also proposed to use the exponential relation to represent the relationship between JRC and Z_2. The above research results show that Z_2 can better describe the undulation characteristics of joint.

The relief data after Delaunay in the previous section is calculated according to formula (1), so as to obtain the effective shear dip (θ^*) of each triangular elementary plane.

In this study, according to the effective shear dip (θ^*) calculated of each triangular elementary plane, the formula of calculating the root-mean-square (Z_2) of slope is put forward as follows:

$$Z_2 = \sqrt{\frac{\sum_{i=1}^{n}\left(\tan^2\theta_i^*\right)}{n}}, \tag{4}$$

where θ_i^* refers to the effective shear dip of any triangular element and n refers to the number of effective shear dips on the whole joint surface.

Formula (4) is related to the effective shear dip of discontinuities only. The root-mean-square (Z_2) of relief slope finally determined can be used to accurately describe the morphological properties of the whole discontinuities, and the calculation is fast, so that it can be used as a valid parameter for describing the morphological properties of discontinuities.

3.2. Calculation of 3D Morphological Property Indicators of Discontinuities. The point cloud data obtained by scanning the morphology of discontinuities is a coordinate system based on the morphometry projection center, and the samples are placed at will during scanning, so the coordinates shall be transformed before calculating the morphological parameters in order to get the triangular metadata under the standardized coordinate system. Later, the MATLAB program is used to transform the coordinates for the triangular point cloud data, so as to get the triangular elementary data of discontinuities under the global coordinate system, as shown in Figure 6. Also, formula (4) is used to calculate the root-mean-square (Z_2) of slope, a 3D morphological parameter of discontinuities. In this paper, the Z_2 of discontinuities is used to characterize the 3D morphological properties of discontinuities, and the results are shown in Table 1.

Table 1: Root-mean-square values of discontinuities.

Sample No.	Initial	First shear	Second shear	Third shear	Fourth shear	Fifth shear
p-1	0.252	0.262	0.225	0.220	0.215	0.211
p-2	0.280	0.290	0.278	0.275	0.262	0.260
p-3	0.273	0.257	0.234	0.238	0.201	0.198
p-4	0.238	0.234	0.224	0.214	0.208	0.205
p-5	0.279	0.266	0.240	0.233	0.223	0.213

According to the changes in 3D morphological property parameters obtained, as shown in Figure 7, the morphological properties and variation trend of discontinuities can be evaluated, so as to better analyze the variation characteristics of discontinuities in the shear test. The curve in Figure 7 shows a steady decreasing trend, indicating that graded cyclic direct shear conditions, slight cutting, and slip occur to the discontinuities, which slowly reduces the roughness of the discontinuities. However, some data in the curve fluctuate, indicating that obvious shear phenomenon may have occurred during the shear process, which significantly changed the shape of the discontinuities, leading to sudden increase or decrease of Z_2. Finally, the three-dimensional morphology parameters of the discontinuities show a decreasing trend, which reflects that the morphology of the discontinuities tends to be smooth and stable in the multistage shear process.

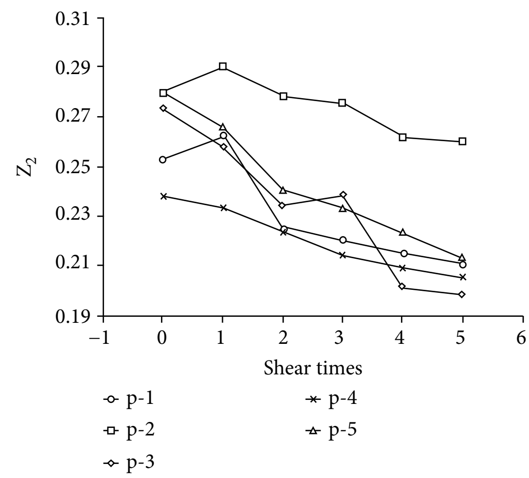

Figure 7: Root-mean-square values of discontinuities.

4. Study of Shear Deformation Properties of Different 3D Morphological Discontinuities

4.1. Shear Deformation Properties of Different 3D Morphological Discontinuities. As discontinuities are complex, the deformation properties are determined by the characteristics of the surface morphology and materials, and Ladanyi and Archambault [32] divided the shear deformation of discontinuities into two parts, i.e., cut deformation and frictional deformation. In the discontinuities with same 3D morphological properties, the greater the normal stress is, the higher the peak strength is, and the more obvious the peak is.

As shown in Figure 8 (p-i-zj-l), due to the effect of stress concentration, when the shear stress exceeds the maximum stress that "convex" can bear, it will cause wear and damage to the surface of discontinuities. When the "convex" is cut off largely, the shear stress will be released largely with an obvious stress drop. Later, the discontinuities will start to have yield failure and generate a large relative displacement to enter the stage of macroslip, and the shear stress is largely provided by frictional force.

As shown in Figure 8 (p-i-zj-2~5), the morphological properties of stress-displacement curve (MPa mm) have significantly changed as compared with first shear. The curve shows a period of significant linear increase in early loading but is missing in the original peak stage and goes directly into the yield stage, so that the shear stress has no obvious change with the increase of shear displacement. It is because the obvious "convex" on the surface of discontinuities has been cut off during first shear, the discontinuities tend to show "smooth" relief. As the number of shears increases, the whole discontinuities become smoother, the cut phenomenon gradually disappears, and the shear force of the discontinuities is mainly provided by frictional force. Therefore, after the first shear, it is difficult to observe any stress drop in the stress-strain curve as the number of shears increases, and the curve tends to be smoother, which also proves that only the existence of "convex" on the surface of discontinuities makes the discontinuities have a peak during first shear.

4.2. Shear Stiffness Properties of Discontinuities in the Shear Process. From the changes in the shear stiffness of discontinuities in the shear process, the shear process of discontinuities can be described in detail. According to formula (5), the shear stiffness of the discontinuities in the shear process can be calculated. The sample p-1 is used to draw the stress-stiffness-deformation curve, as shown in Figure 9.

$$ks = \frac{\Delta\tau}{\Delta D}. \tag{5}$$

In Figure 9, the shear stiffness shows certain fluctuations. Shear stiffness increases as shear deformation increases at the very beginning, and this stage corresponds to the compaction section (OA section) in the shear curve. Afterwards, shear stiffness sharply increases with deformation, and this stage corresponds to AB section in the shear curve; when shear stress reaches the stress τ_B, the shear stiffness hits the peak, and it later starts to drop, and this stage corresponds to BC section in the shear curve, that is, the sample starts to soften after hardening to the greatest extent; AC section tends to be approximately linear, and this stage is what we called the phase of linear elasticity.

When shear stiffness drops to a certain extent, the shear deformation curve tends to have obvious yield characteristics. At this time, the shear stiffness of discontinuities drops rapidly, and this stage corresponds to CD section in the shear curve, which is the yield stage, as shown in the shear stiffness curve after point N given in Figure 9. When the shear deformation hits the peak, the deformation value

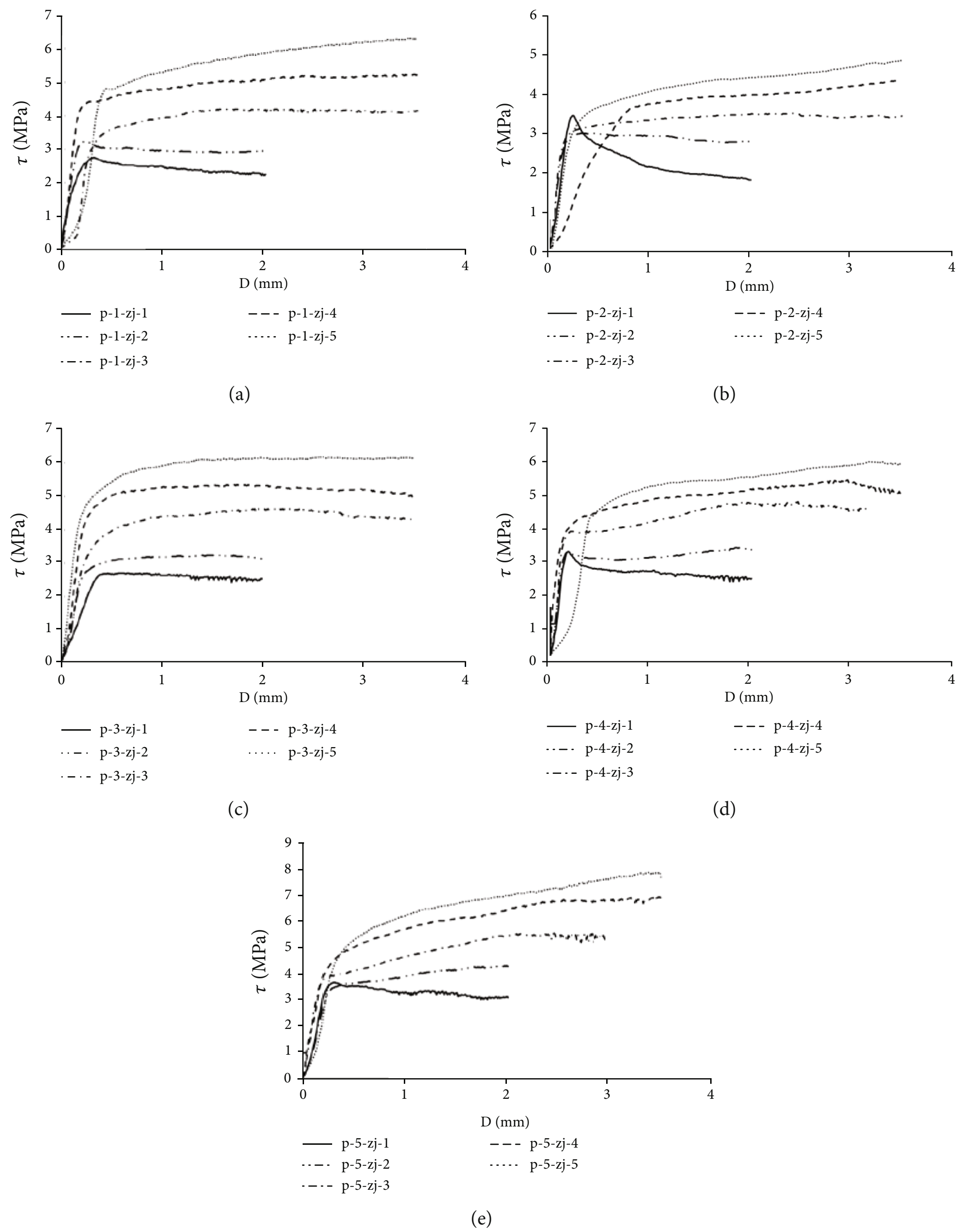

Figure 8: Direct shear stress-displacement curve (MPa mm) of discontinuities with 3D morphological properties under different normal forces. (a) p-1. (b) p-2. (c) p-3. (d) p-4. (e) p-5.

corresponding to point D, the shear stress is maximum, while the shear stiffness is close to zero. When the stress exceeds point D, the shear deformation curve starts to drop, the shear stiffness is negative, and this stage corresponds to the postpeaking phase (DE section), during which the shear stiffness also becomes close to zero from negative.

5. Study of Shear Strength Properties of Different 3D Morphological Discontinuities

5.1. Characteristics of Shear Strength Changes in Discontinuities. As this group of tests is cyclic shear tests on the same sample of discontinuities under different normal pressures, the data processing method may be different. Based on a number of direct shear tests on samples of artificial JRC discontinuities, Wang et al. [33, 34] proposed that the shear strength of discontinuities can be divided into two parts, i.e., the strength component related to the cut and friction.

$$\tau = S_{JRC} + S_f. \tag{6}$$

As it can be seen from formula (6), in the shear process, the shear strength of discontinuities can be divided

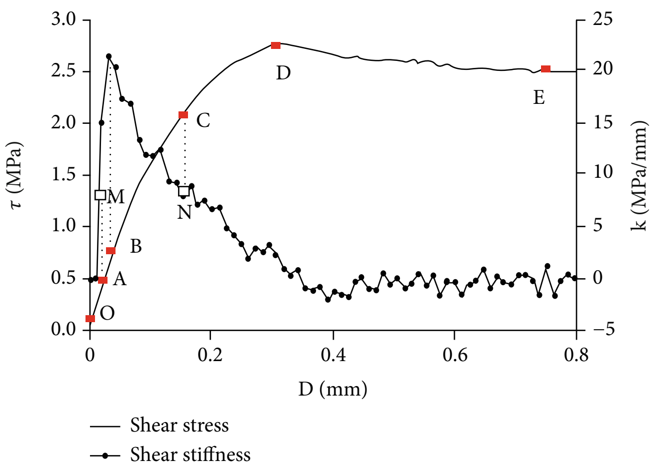

Figure 9: Shear stress-shear stiffness-shear deformation curve.

into two parts, i.e., cut related to JRC and friction between discontinuities. Therefore, it is considered in this paper that this is also the case with the discontinuities of natural rock mass, so that the peak shear strength of discontinuities of natural rock mass can be deemed as being composed of cut and friction approximately.

Figure 10 gives the diagram of strength components of discontinuities of natural rock mass in the shear process. In order to restore the impact of the cut of discontinuities, the peak strength of first shear is subtracted by the residual strength to get the shear stress generated by the cut of discontinuities, which shall later be added to the corresponding friction stress again after the follow-up shears, so as to approximately restore the corresponding peak shear strength of each shear of discontinuities.

$$\tau_i = \tau_c + \tau_{fi}, \tag{7}$$

where $i = 2, 3, 4, 5$, which refers to the ith test.

Therefore, according to the above theory and combined with test results, the peak strength of each shear of discontinuities is restored approximately, as shown in Table 2.

After certain correction, each block of the discontinuities has a good linear correlation with the peak shear strength under different normal forces, so as to finally determine the basic mechanical parameters of the discontinuities, as shown in Table 3 and Figure 11.

5.2. Empirical Formula of Shear Strength Considering 3D Morphology. The peak shear strength of discontinuities has always been a hotspot and difficult subject in the field of rock mass mechanics in the past few decades. Most of the peak shear strength formulas proposed so far follow the form of the Mohr-Coulomb formula. Barton first proposed that the shear strength of discontinuities is mainly composed of three parts: peak dilation angle, i.e., the dip of shear path tangent in the peak state; convex shear part, which represents the contribution of convex shear damage to jointed strength; and basic friction angle, which is mainly determined by material properties [5]. Based on the direct shear test on

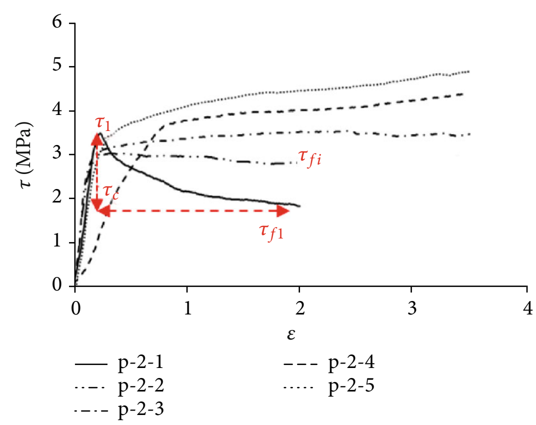

Figure 10: Diagram of strength components.

irregular discontinuities in the state of normal stress, Patton considered that the irregular jointed surface morphology has a significant impact on the peak shear strength of the joint [35]. Therefore, Patton established a relational expression between dilation angle and normal stress with different morphological parameters, deeming that the shear strength of the joint is jointly determined by normal stress (σ_n) and internal friction angle (φ_b).

$$\tau_p = \sigma_n \tan\left(\varphi_b + i_p\right), \tag{8}$$

where τ_p refers to the peak shear strength, σ_n refers to the normal stress, φ_b refers to the internal friction angle, and i_p refers to the dilation angle.

Based on the Patton model and in combination with the model of Qian [36], the empirical formula for shear strength of discontinuities was proposed by considering the influence of 3D morphology:

$$\tau_p = \sigma_n \tan\left[\varphi_b + \arctan\left(Z_2\right)\right], \tag{9}$$

where τ_p refers to peak shear strength, σ_n refers to normal

Table 2: Peak shear strength of discontinuities (unit: MPa).

Sample No.	τ_1	τ_{f1}	τ_c	τ_2	τ_{f2}	τ_3	τ_{f3}	τ_4	τ_{f4}	τ_5	τ_{f5}
p-1	2.75	1.94	0.81	3.74	2.93	4.99	4.18	5.89	5.08	6.69	5.88
p-2	3.47	1.84	1.63	4.45	2.82	5.14	3.51	5.62	3.99	6.06	4.43
p-3	2.7	2.5	0.2	3.34	3.14	4.81	4.61	5.53	5.33	6.35	6.15
p-4	3.13	2.33	0.8	3.99	3.19	5.32	4.52	5.73	4.93	6.1	5.3
p-5	3.7	3.13	0.57	4.89	4.32	6.06	5.49	7.37	6.8	8.17	7.6

Table 3: Basic mechanical parameters of discontinuities.

Sample No.	2.5	3.25	5	6.25	7	Fitted curve	R^2	Frictional angle φ (°)	Cohesive force (c)
p-1	2.75	3.74	4.99	5.89	6.69	$y = 0.8269x + 0.843$	0.9913	39.61	0.843
p-2	3.47	4.45	5.14	5.62	6.06	$y = 0.52x + 2.4522$	0.9543	27.49	2.4522
p-3	2.7	3.34	4.81	5.53	6.35	$y = 0.788x + 0.7637$	0.9953	38.26	0.7637
p-4	3.13	3.99	5.32	5.73	6.1	$y = 0.6412x + 1.7764$	0.9643	32.68	1.7764
p-5	3.7	4.89	6.06	7.37	8.17	$y = 0.9392x + 1.5298$	0.9879	43.23	1.5298

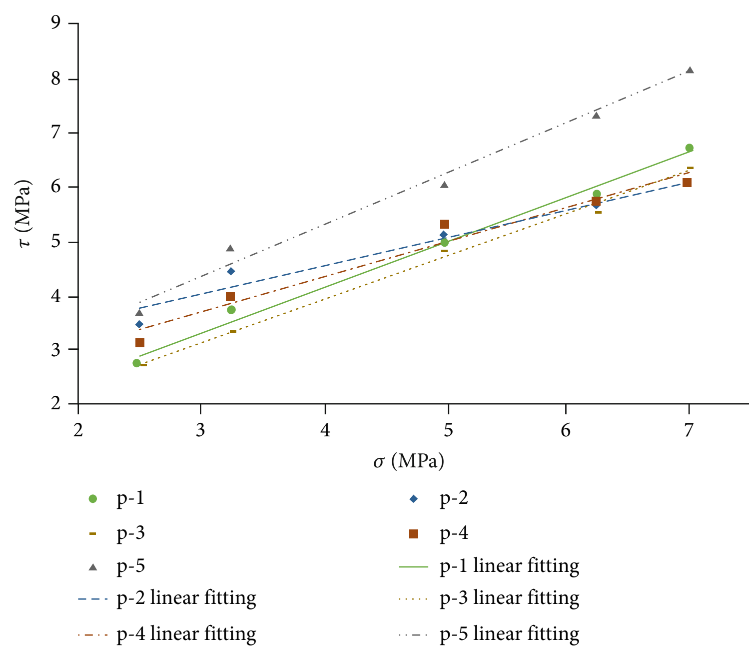

Figure 11: Relationship between different normal stresses and shear forces on discontinuities.

stress, and φ_b refers to internal friction angle. When the normal stress is 0, arctan (Z_2) can be used to characterize the initial dilation angle that is related to 3D morphological properties of the joint. As for smooth flat discontinuities, the 3D morphological parameter is 0, and the formula is simplified into $\tau_p = \sigma_n \tan(\varphi_b)$, which is consistent with the classical Mohr-Coulumb criterion.

The comparison between the test result of peak shear strength of discontinuities and the calculated result of the formula (9) is shown in Figure 12, from which it can be seen that the theoretical value of formula (9) and test result maintain good consistency at the beginning of the cycle. As the number of cycles increases, the deviation between test value and theoretical value grows, which is because the test value of peak shear strength has been restored by certain means, but as the normal pressure increases, the peak shear strength restored is still low, so that the deviation grows under high normal stress.

The empirical formula of shear strength considering 3D morphological parameters of discontinuities obtained is simple and clear in expression, each of whose parameters can be obtained quickly, and it can be used to rapidly evaluate the morphological properties and estimate the shear strength of discontinuities, so that it is suitable for the discontinuities of hard rock mass.

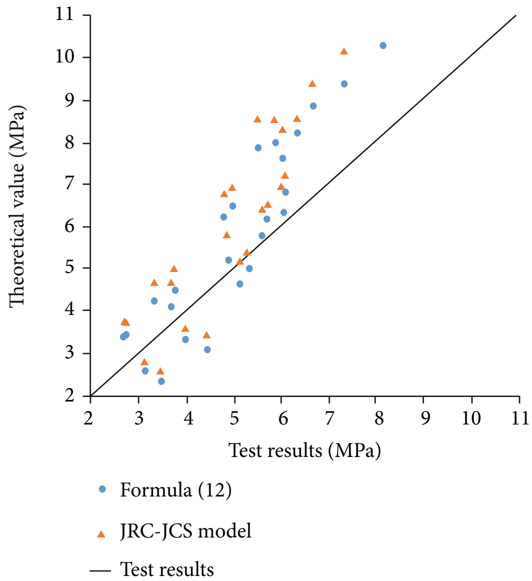

Figure 12: Comparison diagram of test results and theoretical value of the model.

5.3. Model Validation of Shear Strength considering 3D Morphology. Barton and Choubey [5] proposed the most commonly used JRC-JCS formula based on a large number of direct shear tests on the discontinuities of rock mass:

$$\tau = \sigma_n \times \tan\left[JRC \lg\left(\frac{JCS}{\sigma_n}\right) + \varphi_b\right], \qquad (10)$$

where φ_b refers to the basic internal friction angle, σ_n refers to the normal stress, and JCS refers to the compressive strength of the wall of discontinuities.

Based on Barton's standard profile line, Tse and Cruden [29] found by studying surface geometrical parameters that the correlation between the root-mean-square (Z_2) of slope and roughness coefficient JRC of discontinuities is the best, and the correlation coefficient is 0.986, as shown in formula (12). In this paper, the root-mean-square (Z_2) is substituted into formula (11) in order to deduce the roughness coefficient JRC of discontinuities, which is later substituted into formula (10) in order to calculate the corresponding peak shear strength. The calculation results are shown in Figure 12.

$$JRC = 32.20 + 32.47 \lg (Z_2) \, [29]. \qquad (11)$$

In order to quantitatively evaluate the effect of two models on the predicted peak shear strength, the mean deviation formula is used to characterize the accuracy of the calculation model, and the smaller the mean deviation is, the closer the calculated value of the model is to the measured value. The mean deviation is defined below [37–39]:

$$\bar{\sigma}_{avg} = \frac{1}{n}\sum_{i=1}^{n}\left|\frac{\tau_{mea} - \tau_{est}}{\tau_{mea}}\right| \times 100\%, \qquad (12)$$

Table 4: Mean deviation between calculated value and test value of two models.

	After first shear	After first two shears	After three shears	After four shears	After five shears
Formula (11)	22.12%	21.23%	20.81%	21.48%	21.40%
JRC-JCS	27.40%	26.24%	25.39%	27.35%	27.63%

where $\bar{\sigma}_{avg}$ refers to mean deviation, τ_{mea} refers to the test value of jointed peak shear strength, τ_{est} refers to the calculated value of jointed peak shear strength, and n refers to the number of joint test groups.

Based on 25 shear tests, the mean deviations of formula (9) and JRC-JCS formula in different stages are shown in Table 4. If analyzed from mean deviation, it can be seen that as the number of cycles increases, the mean deviation of formula (9) remains stable and is smaller than that of the classical JRC-JCS formula, which indicates that the model has stable prediction ability, the calculated value can be well fitted with the test value, and the model effect is superior to the classical Barton's formula.

6. Conclusion

In this paper, an integrated study is carried out on the morphological properties and shear properties of the discontinuities of natural rock mass, and a high-accuracy 3D morphology scanning test on the discontinuities is conducted to evaluate the 3D morphological properties of the discontinuities of rock mass. In addition, based on the graded cyclic shear test of discontinuities, the impact of the morphological properties of discontinuities of natural rock mass on the strength properties and deformation properties of discontinuities are analyzed and concluded, and the main conclusions are as follows:

(1) Based on the results of the 3D morphology scanning test on the discontinuities of natural rock mass, the root-mean-square (Z_2) of slope is selected as the parameter for evaluating morphological properties, and it is found that the morphological parameter shows a trend of steady decline as the number of shears increases

(2) Based on the graded cyclic shear test curve, the graded cyclic shear properties of the discontinuities of rock mass are analyzed from shear deformation, and the shear process of discontinuities is refined in combination with the characteristics of the change in shear stiffness

(3) Based on the graded cyclic shear test on the discontinuities of natural rock mass, the strength properties and deformation properties of discontinuities in the process of graded cyclic shear process are analyzed, and a method that is suitable for determining the strength parameter of discontinuities in the graded

cyclic shear process is proposed. Also, combined with the 3D morphological parameter, the empirical formula of shear strength of discontinuities considering 3D morphological properties is proposed, which is compared with the classical JRC-JCS formula in order to validate the proposed shear strength model.

Data Availability

All data and models generated or used during the study appear in the submitted article.

Conflicts of Interest

The authors declare that they have no conflicts of interest.

Acknowledgments

This work was supported by the National Natural Science Foundation of China (No. 41977227), the Key Laboratory of Rock Mechanics and Geohazards of Zhejiang Province, Key Technology of Highway Tunnel Safety Construction Under Complex Condition in Eastern Yunnan Mountainous Area, Research on Key Technology of Corrugated Steel Assembly Rapid Initial Support Structure for Highway Tunnel, the Shanghai Rising-Star Program (No. 17QC1400600), and the Shanghai Municipal Science and Technology Major Project (No. 2017SHZDZX02).

References

[1] Q. Z. Zhang, *Study on the shear creep characteristics of rock mass discontinuity*, Tongji University, 2011.

[2] D. L. Qi, *Fuzzy measure method of the analysis for jointed rock slope stability*, Hebei University, 2015.

[3] Z. Y. Luo, S. G. Du, and M. Huang, "Experimental study of stress effect on peak friction angle of rock structural plane," *Chinese Journal of Rock Mechanics and Engineering*, vol. 33, no. 6, pp. 1142–1148, 2014.

[4] C. C. Xia and Z. Q. Sun, *Joint mechanics of engineering rock mass*, Tongji University Press, 2002.

[5] N. Barton and V. Choubey, "The shear strength of rock joints in theory and practice," *Rock Mechanics*, vol. 10, no. 1-2, pp. 1–54, 1977.

[6] Y. Li and Y. Zhang, "Quantitative estimation of joint roughness coefficient using statistical parameters," *International Journal of Rock Mechanics and Mining Sciences*, vol. 77, pp. 27–35, 2015.

[7] G. Zhang, M. Karakus, and H. Tang, "A new method estimating the 2D joint roughness coefficient for discontinuity surfaces in rock masses," *International Journal of Rock Mechanics and Mining Sciences*, vol. 72, pp. 191–198, 2014.

[8] X. G. Liu, W. C. Zhu, and Q. L. Yu, "Estimation of the joint roughness coefficient of rock joints by consideration of two-order asperity and its application in double-joint shear tests," *Engineering Geology*, vol. 220, pp. 243–255, 2017.

[9] S. G. Du, S. F. Yang, and Z. Jiang, "A new technique for fast measurement of," *Journal of Engineering Geology*, vol. 10, no. 1, pp. 98–102, 2002.

[10] B. B. Mandelbrot, "The fractal geometry of nature," *American Journal of Physics*, vol. 51, no. 3, pp. 286-287, 1983.

[11] P. H. S. W. Kulatilake, P. Balasingam, J. Park, and R. Morgan, "Natural rock joint roughness quantification through fractal techniques," *Geotechnical and Geological Engineering*, vol. 24, no. 5, pp. 1181–1202, 2006.

[12] Z. D. Zhu, F. D. Xing, and W. P. Qu, "Fractal description of two-phase medium cementation plane roughness coefficient between rock and concrete," *Journal of China Coal Society*, vol. 31, no. 1, pp. 20–25, 2006.

[13] T. Belem, F. Homand-Etienne, and M. Souley, "Quantitative parameters for rock joint surface roughness," *Rock Mechanics and Rock Engineering*, vol. 33, no. 4, pp. 217–242, 2000.

[14] G. Grasselli, J. Wirth, and P. Egger, "Quantitative three-dimensional description of a rough surface and parameter evolution with shearing," *International Journal of Rock Mechanics and Mining Sciences*, vol. 39, no. 6, pp. 789–800, 2002.

[15] C. C. Xia, W. M. Xiao, and W. Wi, "Calculation method for three-dimensional composite topography of joint under different contact conditions," *Chinese Journal of Rock Mechanics and Engineering*, vol. 29, no. 11, pp. 2203–2210, 2010.

[16] T. Rabczuk, G. Zi, S. Bordas, and H. Nguyen-Xuan, "A simple and robust three-dimensional cracking-particle method without enrichment," *Computer Methods in Applied Mechanics & Engineering*, vol. 199, no. 37-40, pp. 2437–2455, 2010.

[17] T. Rabczuk and T. Belytschko, "Cracking particles: a simplified meshfree method for arbitrary evolving cracks," *International Journal for Numerical Methods in Engineering*, vol. 61, no. 13, pp. 2316–2343, 2004.

[18] N. Barton, "Review of a new shear-strength criterion for rock joints," *Engineering Geol*, vol. 7, no. 4, pp. 287–332, 1973.

[19] S. G. Chen, J. G. Cai, and J. Zhao, "Discrete element modelling of an underground explosion in a jointed rock mass," *Geotechnical and Geological Engineering*, vol. 18, no. 2, pp. 59–78, 2000.

[20] J. W. Park, Y. K. Lee, and J. J. Song, "A constitutive model for shear behavior of rock joints based on three-dimensional quantification of joint roughness," *Rock Mechanics and Rock Engineering*, vol. 46, no. 6, pp. 1513–1537, 2013.

[21] C. C. Xia, Z. C. Tang, and Y. L. Song, "A new peak shear strength formula for matching irregular joints based on 3D morphology parameters," *Chinese Journal of Rock Mechanics and Engineering*, vol. 32, no. S1, pp. 2833–2839, 2013.

[22] Y. F. Ge, *Research on roughness and peak shear strength for rock discontinuities based on BAP*, China University of Geosciences, 2014.

[23] B. Laganyi and G. Archambault, "Simulation of shear behaviour of a jointed rock mass," *Proceedings of the 11th Symp. on Rock Mechanics. [S. l.]*, W. H. Somerton, Ed., , pp. 105–125, AIME, 1970.

[24] N. Barton, *Modeling rock joint behavior from in-situ block tests: implications for nuclear waste repository design*, Office of Nuclear Waste Isolation, Columbus, 1982.

[25] X. J. Yin, G. L. Wang, and C. H. Zhang, "Study of constitutive model for rock interfaces and joints under cyclic shear loading," *Engineering Mechanics*, vol. 22, no. 6, pp. 97–103, 2005.

[26] Q. S. Li and S. J. Du, "Surface roughness analysis of rock joints under different shear deformation histories," *Rock and Soil Mechanics*, vol. 6, pp. 850–855, 2004.

[27] D. Huang, R. Q. Huang, and L. Pe, "Shear deformation and strength of through-going saw-tooth rock discontinuity," *Journal of China Coal Society*, vol. 7, 2014.

[28] Y. Gui, *Study on the surface degradation under shearing and the coupled shear-flow properties of rock joints*, Tongji University, 2018.

[29] R. Tse and D. M. Cruden, "Estimating joint roughness coefficients," *International Journal of Rock Mechanics & Mining Sciences & Geomechanics Abstracts*, vol. 16, no. 5, pp. 303–307, 1979.

[30] X. B. Yu and B. Vayssade, "Joint profiles and their roughness parameters," *International. Journal of Rock Mechanics and Mining Sciences*, vol. 28, no. 4, pp. 333–336, 1991.

[31] B. S. A. Tatone and G. Grasselli, "A new 2D discontinuity roughness parameter and its correlation with JRC," *International Journal of Rock Mechanics and Mining Sciences*, vol. 47, no. 8, pp. 1391–1400, 2010.

[32] B. Ladanyi and G. Archambault, "Simulation of shear behavior of a jointed rock mass," in *The 11th US Symposium on Rock Mechanics. American Rock Mechanics Association*, OnePetro, 1969.

[33] Z. Wang, M. R. Shen, G. H. Tian, and Q. Z. Zhang, "Time-dependent strength of rock mass discontinuity with different values of JRC," *Chinese Journal of Rock Mechanics and Engineering*, vol. 36, Supplement 1, pp. 3287–3296, 2017.

[34] Z. Wang, L. L. Gu, M. R. Shen, F. Zhang, G. K. Zhang, and S. X. Deng, "Influence of shear rate on the shear strength of discontinuities with different joint roughness coefficients," *Geotechnical Testing Journal*, vol. 43, no. 3, p. 20180291, 2020.

[35] F. D. Patton, "Multiple modes of shear failure in rock," in *In Proc First Congress of International Society of Rock Mechanics*, pp. 509–513, Lisbon, Portugal, 1966.

[36] X. Qian, *Study of shear-flow coupled behaviors of rock joints under high seepage pressure*, Tongji University, Changsha, 2018.

[37] P. H. S. W. Kulatilak, G. Shou, and T. H. Huang, "New peak shear strength criteria for anisotropic rock joints," *International Journal of Rock Mechanics & Mining Sciences & Geomechanics Abstracts*, vol. 32, no. 7, pp. 673–697, 1995.

[38] J. Yang, G. Rong, and D. Hou, "Experimental study on peak shear strength criterion for rock joints," *Rock Mechanics and Rock Engineering*, vol. 49, no. 3, pp. 821–835, 2016.

[39] N. Vu-Bac, T. Lahmer, X. Zhuang, T. Nguyen-Thoi, and T. Rabczuk, "A software framework for probabilistic sensitivity analysis for computationally expensive models," *Advances in Engineering Software*, vol. 100, pp. 19–31, 2016.

Hindawi
Geofluids
Volume 2021, Article ID 3143024, 14 pages
https://doi.org/10.1155/2021/3143024

Research Article

Quantitative Identification of the Water Resistance Capacity of Composite Strata in Mining Coal Seam Floors

Xinyi Wang,[1,2,3] Fang Li,[1] Qi Wang,[4] Bo Chen,[1] Yu Zou,[5] and Bo Zhang[6]

[1]*Institute of Resources & Environment, Henan Polytechnic University, Jiaozuo 454000, China*
[2]*Collaborative Innovation Center of Coalbed Methane and Shale Gas for Central Plains Economic Region, Jiaozuo 454100, China*
[3]*Collaborative Innovation Center of Coal Work Safety and Clean High Efficiency Utilization, Jiaozuo 454100, China*
[4]*College of Geosciences and Engineering, North China University of Water Resources and Electric Power, Zhengzhou 450045, China*
[5]*Jiangmen Branch Bureau of Hydrology, Guangdong Provincial Bureau of Hydrology, Jiangmen 529000, China*
[6]*Institute of Energy and Chemical Industry, China Pingmei Shenma Group, Pingdingshan 467000, China*

Correspondence should be addressed to Qi Wang; wangqi@ncwu.edu.cn

Received 14 April 2021; Revised 23 August 2021; Accepted 24 September 2021; Published 20 October 2021

Academic Editor: Chuangzhou Wu

In coal seam mining, the water resistance of the floor composite strata is the key to determining whether water disaster occurs or not and to formulating water control countermeasures. Taking the Pingdingshan Coalfield No. 8 mine and Shoushan mine as the research objects, the thickness ratio of plastic brittle rock, core recovery rate, thickness of effective aquiclude, fault complexity, composite compressive strength, and equivalent water resistance coefficient were selected as the index factors. The comprehensive weight of each index factor was determined by using the entropy weight theory. The water resistance of the J_{16-17} coal seam floor composite rock in the study area was quantitatively evaluated using the fuzzy variable set mathematical model and was divided into five grades: extremely weak, weak, medium, strong, and very strong. The results show that the J_{16-17} coal floor composite rock layers with strong and very strong water resistance areas account for 23.64% of the total area, the medium areas account for 58.26%, and the weak and extremely weak areas account for 18.1%. These results provide support for the accurate assessment of water inrush hazards of a coal floor.

1. Introduction

In the process of mining Permian Carboniferous coal seams in North China coalfields, water inrush from an Ordovician or Cambrian thick limestone aquifer is always a threat. These bottom plates usually experience high water pressure and are rich in water [1, 2]. The composite rock layer is composed of sandstone, mudstone, thin limestone, and a thin coal seam. Between the coal seam and thick limestone is the barrier for resisting high water pressure and preventing groundwater from rising. Therefore, it is of great theoretical and practical significance to quantitatively evaluate the water resistance capacity of the composite rock strata, which can scientifically formulate water prevention and control countermeasures to reduce the degree of harm from water inrush in an area.

At present, many experts and scholars have carried out research work on the water resistance of rock formations. Yang [3] believed that the essence of mining under pressure is the existence of combined water, which makes the rock strata have the ability of water resistance and decompression, and proposed the concept of water resistance coefficient. Qian et al. [4] and Miao and Qian [5] put forward the "key layer" theory for judging water inrush from coal floors. Xu et al. [6] based on the investigation of the floor lithology, strata combination relationship, and karst development conditions of a certain wellfield proposed that at least 25 m upper Cambrian limestone could be used as an aquiclude, which significantly improved the mining conditions of the coal seam. Zhang et al. [7] studied the relationship between water resistance capacity of rock strata and its structural composition and combination form through laboratory tests and proposed that the combination with better water resistance ability should start with soft rock strata and alternate soft and hard rock strata. Yin and Hu [8] took structure, in situ stress, and rock permeability as the influencing factors of the water resistance capacity of rock strata and concluded that the water resistance capacity of mudstone, siltstone, medium sandstone, and limestone ranges from large to small. Feng et al. [9] used experiments and numerical simulations to study the effects of different lithological characteristics of the aquiclude on its water resistance capacity. Li et al. [10] faced the problem of the stability of the water resistance rock mass of the karst tunnel, only considered the safe thickness of the water resistance rock mass, and did not consider the joints and permeability of the rock mass, which has certain limitations. Sun et al. [11] studied the influence of thickness, layer, length, cohesion, and internal friction angle on the water resistance capacity of the key composite aquiclude and concluded that the water pressure that can withstand is in a quadratic parabola relationship with its thickness. The greater the thickness, the better the water resistance capacity. Xu et al. [12] analyzed the lithology, void structure, and permeability characteristics of Fengfeng Formation from a micro-macro scale and made a quantitative study on its water resistance capacity. Lyu and Xie [13] and Zhang et al. [14] used statistical analysis and laboratory experiments to study the lithologic combination characteristics, rock mechanical strength, water properties, and permeability of coal seam overburden rock and evaluated the comprehensive water resistance capacity. Wang [15] studied the water resistance capacity of overlying rock from the strength, anisotropy, rheology, and expansibility of rock.

As shown above, the research on the water resistance capacity of rock layers has developed from the initial consideration of a single factor such as rock thickness or lithologic difference [16–20] to a comprehensive analysis of multiple factors such as lithology combination, rock mass strength, and permeability, making the evaluation system more and more perfect. However, due to insufficient field data and difficulty in quantifying index factors, the existing evaluation index system often ignores the influence of geological structure, mining failure, and equivalent water resistance of different lithology and rock formations. In addition, in the existing research results, the analytic hierarchy process or grey correlation method is commonly used to calculate the weight of index factors, so that the calculation results are greatly influenced by the subjective shortcomings. In this paper, the thickness ratio of plastic brittle rock, core recovery rate, thickness of effective aquiclude, fault complexity, composite compressive strength, and equivalent water resistance coefficient were selected as index factors, covering many factors affecting the water resistance capacity of composite strata on coal floor. The comprehensive weight determined by entropy weight theory overcomes the subjective and objective randomness of the traditional method. The fuzzy variable set theory can describe the characteristics of things under the combined action of multiple index factors and has realized the quantitative identification of water resistance capacity of composite rock strata. The research results are expected to provide technical support for an accurate evaluation of water inrush risk from coal floors.

2. Determination of Index Factors

2.1. Strata Structure of Coal Seam Floors. The area of the No. 8 mine and Shoushan mine, located in the eastern Pingdingshan Coalfield, is 68.35 km^2. At present, mainly the $J_{16\text{-}17}$ coal is mined. The thickness of the coal seam has a range of 2-3.8 m, with an average thickness of 2.44 m. The main threatening aquifer of the baseplate is a Cambrian limestone aquifer with a thickness greater than 200 m. The coal seam and Cambrian limestone are composed of sandy mudstone, medium-fine sandstone, thin coal seam, thin limestone, and bauxite mudstone. The floor rock structure of the $J_{16\text{-}17}$ coal is shown in Figure 1. The thickness is 68-77 m, and the mean value is 71.3 m.

2.2. Index Factor Selection. During coal mining, the main factors controlling the water resistance of the floor composite rock layer are the lithological structure, integrity, thickness of effective aquiclude, fault development, compressive strength, and permeability.

The floor of the Ji Formation coal seam is an interbed of brittle sand (limestone) and plastic mudstone. The more sand (limestone) layers and the thicker the single layer, the more easily the floor is damaged by excavation; while the mudstone layers depend on elastic deformation to decompose stress under load, the more numerous and thicker the mudstone layers, the better the water resistance of the rock layers. Lithological structure is usually characterized by the ratio of brittle rock thickness to plastic rock thickness revealed by drilling holes (thickness ratio of plastic brittle rock).

The integrity of the rock mass represents the degree of development of cracks in the rock mass. It reflects the permeability and water-bearing capacity of the rock mass. Therefore, it is an important index for evaluating the water resistance of the rock formation. Integrity is often indicated by the ratio of the core length to the thickness of the formation (core recovery rate) during drilling. The lower the recovery is, the more fractured the rock is, the better the permeability is, and the stronger the water-bearing capacity is.

The thickness of the aquiclude is the distance between the mining coal seam and the main threatening aquifer, and the disturbance destroy depth of the floor is the disturbance destroy depth under the mining condition of the coal seam. The thickness of effective aquiclude is the difference between the two. Based on the lithological structure and rock mass integrity, the greater the effective aquiclude is, the stronger the ability to resist water pressure damage, and the lower the possibility of water inrush from the floor.

Faults and associated fissures not only destroy the integrity of the rock layers but also are important water diversion channels. The more developed the interruption layers in the coal seam floor, the denser the tensional faults are, the more serious the rock layers are damaged, and the higher the frequency of water inrush occurs. Once water inrush occurs,

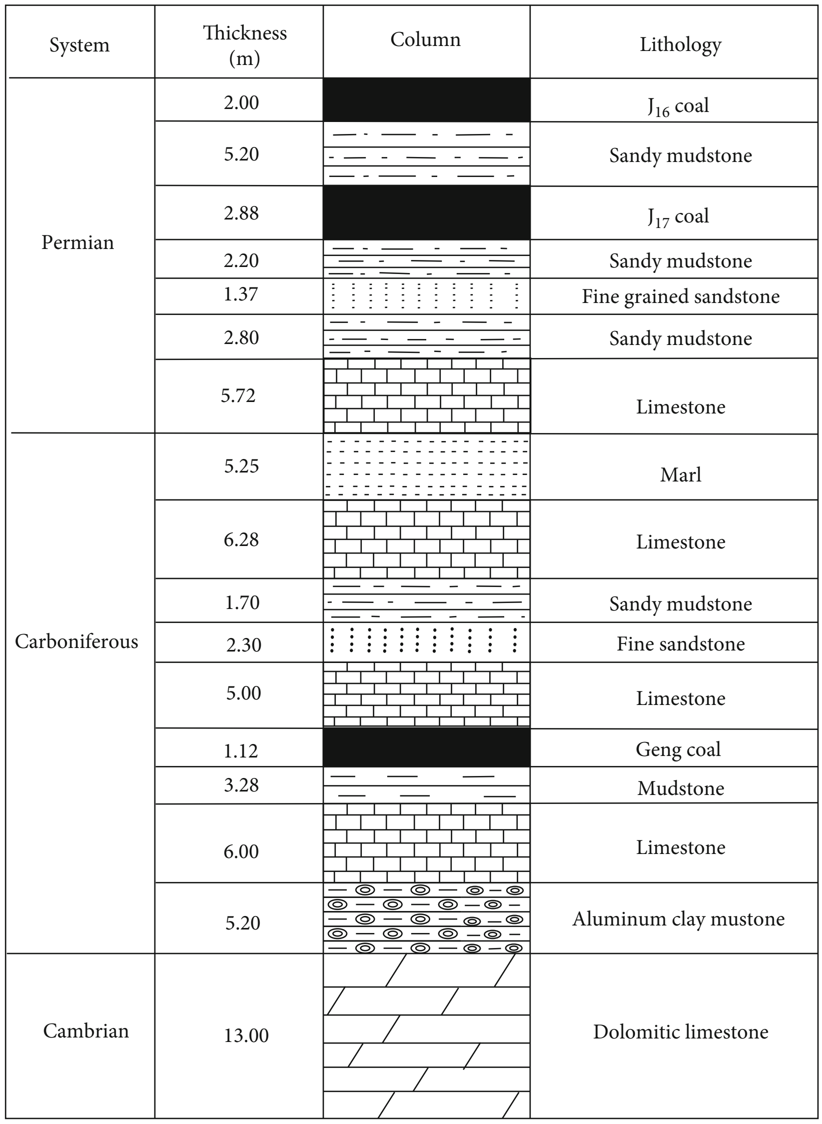

FIGURE 1: Column diagram of coal floor of the $J_{16\text{-}17}$ Formation.

the greater the water volume is. Fault development is often indicated by fault complexity.

The ability of the rock formation to resist water pressure is closely related to its own compressive strength. Hard limestone and sandstone have high compressive strength, but poor plasticity and weak water-retaining ability, while soft mudstone has the opposite characteristics: low compressive strength, good plasticity, and good water-retaining ability. The compressive strength of the multirock combination of the coal floor is characterized by the composite compressive strength.

The more permeable the composite rock layer in the coal seam floor is, the higher the rise height of groundwater under the same water pressure and the greater the possibility of water inrush. In order to facilitate the uniform comparison and analysis of permeability for the different lithological rocks, the equivalent water resistance coefficient is often used to indicate the permeability of rocks. When the lithological thickness and equivalent water-proofing coefficient of each rock layer are known, the equivalent water resistance coefficient of the composite rock layer can be obtained as the basis for determining the water-resistance capacity of the floor.

Therefore, we selected six factors, including the thickness ratio of plastic brittle rock, the core recovery rate, the thickness of effective aquiclude, fault complexity, composite compressive strength, and equivalent water resistance as the index factors to evaluate the water resistance of the coal seam floor rock.

3. Index Factor Quantization

3.1. Thickness of Effective Aquiclude. The thickness of effective aquiclude in the coal seam floor can play the role of water blockage [21]. The calculation formula is [22]

$$t = M - C_P, \tag{1}$$

$$C_P = 0.0085H + 0.1665\alpha + 0.1079L - 4.3579, \quad (2)$$

where t is the effective thickness of the aquiclude, m; M is the total thickness of the aquiclude, m; C_p is the disturbance destroy depth of the floor, m; L is the inclined length of the working face, m; H is the mining depth of the coal layer, m; and α is the inclination angle of the coal layer.

The average destruction depth of the Ji Group coal floor disturbance for the No. 8 mine and Shoushan mine calculated by formula (2) is shown in Table 1.

We take drilling hole No. 1 as an example, located in the No. 8 coal mine. The total thickness of the floor rock of the $J_{16\text{-}17}$ coal exposed by drilling is 68.14 m. First, the disturbance damage depth of the floor rock is 20.41 m (Table 1). Then, according to Equation (1), the effective thickness of the aquiclude is calculated to be 47.73 m. Analogously, the effective water-resistant thickness of 48 boreholes is calculated, and their contours are drawn (as shown in Figure 2).

3.2. The Complexity of the Fault. Fault complexity is often expressed by fractal dimension and calculated by fractal theory [23]. The smaller the fractal dimension is, the lower the complexity of the fault layer.

$$\lg N(r) = -D_S \lg r + A, \quad (3)$$

where A is constant and D_S is the fractal dimension value.

Firstly, the region containing fractal is divided into several square blocks according to certain rules. The blocks containing fractal are numbered one by one, and the similarity ratio $r = 1$, 1/2, 1/4, and 1/8 are taken, respectively. The blocks are subdivided into 1, 4, 16, and 64 square grids. Count the number of grids $N(r)$ occupied by the fractal body at different scales in a certain segment and establish the lg (r)-$lgN(r)$ double logarithmic coordinate system with formula (3). Then, the slope of the fitted line and the correlation coefficient are obtained by the least square method, and the absolute value of the slope is the value of the fractal dimension.

According to the actual situation, this paper divided the mining area into 600×600 mm square blocks. The number of mesh $N(r)$ covering faults when $r = 600$, 300, 150, and 75 mm is calculated successively, and the obtained results are shown in Table 2. The contour of fault fractal dimension is shown in Figure 3.

3.3. Composite Compressive Strength. In this study, a total of 60 cores were collected from seven boreholes in the $J_{16\text{-}17}$ coal floor, including 25 mudstone, 25 sandstone, and 10 limestone samples. The test results of the compressive strength are shown in Table 3.

The order of compressive strength is plastic mudstone < brittle limestone < brittle sandstone. Although brittle rock has a high compressive strength, it easily fractures under load, and its water resistance performance is poor, while plastic mudstone exhibits contrary behaviors. The research results show that when the compressive strength of brittle rock is twice that of plastic rock, the water resistance capacity of the latter is 2.5-3 times that of the former [24]. According to the manual of mine geology [25], the conversion coefficient of the compressive strength for different rocks is shown in Table 4.

Table 1: List of disturbance damage depths of the Ji Group coal floor (m).

Mine	α (°)	L (m)	H (m)	C_p (m)
No. 8 mine	17	140	804.76	20.41
Shoushan mine	10.17	160	713	20.65

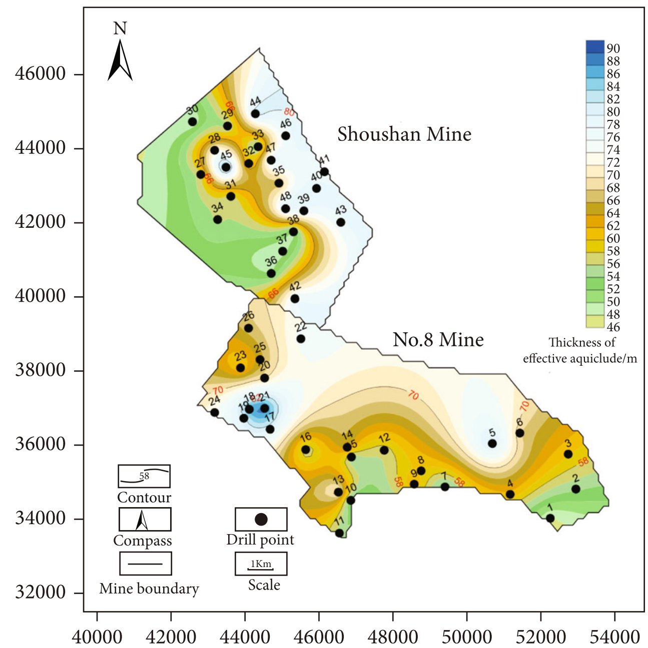

Figure 2: Contour map of the thickness of the effective aquiclude.

The compressive strength of the composite rock formation is calculated as follows:

$$\bar{p} = \sum_{i=1}^{n} p_i \times \tau_i \times \gamma_i, \quad (4)$$

where $\bar{p}$ is the composite compressive strength of the rock strata, MPa; P_i is the average compressive strength of each rock layer, MPa; τ_i is the ratio of thickness of each rock layer; and γ_i is the conversion coefficient of the compressive strength of each rock layer, MPa/m.

Taking the No. 1 drilling hole of the No. 8 mine as an example, the thickness ratios of the mudstone, limestone, and sandstone are 58.61%, 31.57%, and 9.83%, respectively. The composite compressive strength calculated by using Equation (4) combined with Tables 3 and 4 is 4.87 MPa. Following the same procedure, the composite compressive strength of the 48 boreholes can be obtained, and the contour lines are drawn (as shown in Figure 4).

The figure shows that the compressive strength of the $J_{16\text{-}17}$ coal floor composite rock layer is 4.00-7.43 MPa, and the mean value is 5.71 MPa. At present, the water pressure

Table 2: Quantitative values of the index factors.

Drilling hole	Thickness ratio of plastic brittle rock	Core recovery rate	Thickness of effective aquiclude	Fault factor values	Composite compressive strength	Equivalent water resistance coefficient
1	1.4158	0.7840	47.73	0.8432	4.87	0.9410
2	1.0978	0.8795	54.39	1.2114	5.38	0.9685
3	1.1437	0.7255	60.16	1.4051	5.24	0.9251
4	0.9832	0.7500	61.49	0.8772	5.52	0.9196
5	0.4547	0.7626	82.06	1.1708	6.75	0.8285
6	0.8891	0.6579	68.03	1.1863	5.74	0.9492
7	1.2344	0.6879	51.77	1.3911	5.14	0.9528
8	0.9676	0.8300	59.51	1.3214	5.54	0.9143
9	0.9948	0.8100	62.23	1.2141	5.51	0.9310
10	0.8373	0.7243	50.35	0.8021	5.70	0.9042
11	1.2413	0.5881	55.18	0.7392	5.03	0.8816
12	0.9411	0.5223	56.52	1.1883	5.52	0.8659
13	0.8551	0.7988	72.24	0.8609	5.74	0.8913
14	0.6670	0.7131	66.02	1.2704	6.13	0.8490
15	0.7282	0.7300	54.06	1.1801	5.99	0.8629
16	0.7286	0.6500	55.42	1.1174	5.73	0.8533
17	0.8972	0.5178	80.13	0.6891	5.66	0.9018
18	0.4423	0.5650	87.61	1.0870	6.81	0.8354
19	0.8691	0.5500	81.05	0.8817	5.69	0.8818
20	0.7293	0.6975	69.32	0.9017	6.05	0.9053
21	0.9372	0.4363	89.77	0.8195	5.53	0.8659
22	0.6177	0.9226	75.05	0.8745	6.27	0.8508
23	0.6608	0.7508	59.65	0.7917	6.18	0.8750
24	0.7382	0.5876	74.00	0.6451	5.93	0.8342
25	0.6804	0.9000	65.17	0.8504	6.14	0.8847
26	0.7033	0.8996	66.95	0.7936	6.06	0.8705
27	0.8139	0.9060	61.15	0.8942	5.36	0.9137
28	0.7064	0.8471	74.35	0.9661	5.78	0.8677
29	0.3347	0.7330	58.90	1.1468	6.93	0.8736
30	0.7952	0.7953	54.25	1.3911	5.63	0.8872
31	0.2857	0.8829	60.65	0.8917	7.06	0.8500
32	0.6667	0.9149	62.90	0.8060	5.96	0.9001
33	0.5720	0.9098	56.93	0.8794	6.26	0.9179
34	0.4793	0.8400	60.37	0.8929	6.37	0.8885
35	0.8096	0.8694	68.65	0.8635	5.78	0.9527
36	0.4583	0.8462	55.81	1.1781	6.46	0.8629
37	0.5239	0.8464	55.18	1.2118	6.22	0.8500
38	1.3847	0.8479	55.25	1.1817	4.77	0.9226
39	0.6517	0.8700	77.83	0.9677	5.84	0.8673
40	0.1599	0.7889	79.58	0.8598	7.43	0.7724
41	0.2780	0.6980	75.73	0.8697	6.84	0.7943
42	0.5179	0.8500	78.00	0.8837	6.28	0.8772
43	0.6748	0.8540	77.80	1.0656	5.61	0.8444
44	0.4013	0.9300	81.41	1.1236	6.71	0.8844
45	0.7415	0.9150	86.90	0.7696	5.80	0.9075
46	0.4563	0.8520	77.09	0.9230	6.46	0.8845
47	0.6197	0.9490	79.80	0.8511	6.02	0.9158
48	0.7681	0.8090	80.72	0.9761	5.70	0.9040

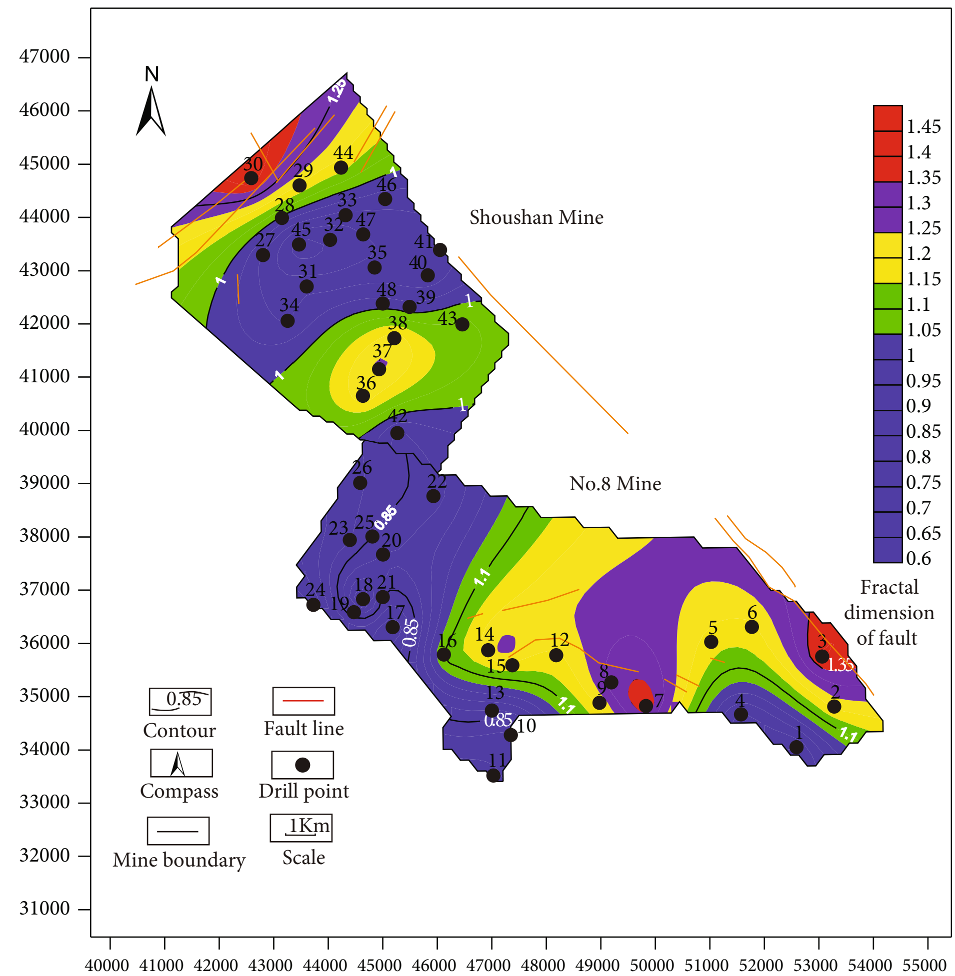

FIGURE 3: Contour map of the fault fractal dimension.

TABLE 3: Compressive strength of each lithology test in the study area (MPa).

Mine	Mudstone	Sandstone	Limestone
Shoushan mine	41.43	73.72	90.10
No. 8 mine	37.60	84.83	93.12

TABLE 4: Conversion coefficient of test compressive strength for each lithology.

Lithology	Conversion factor (MPa/m)
Mudstone, marl, clay, shale	0.05
Sand shale	0.07
Sandstone, no karst limestone, marl	0.10

of the Cambrian limestone in the study area is 0.38-4.94 MPa, and the mean value is 2.63 MPa. The composite rock layer in its natural state can fully resist water pressure. However, under the influence of faults and mining, the water-resistant performance of the coal seam floor rock will be significantly reduced, which shows the necessity of a multifactor evaluation of the water-resistance capability.

3.4. Equivalent Water Resistance Coefficient. Referring to the existing literature [26–28], the equivalent water resistance coefficients of different rock layers are listed in Table 5.

The equivalent water resistance coefficient of the composite rock formation is calculated as follows [28]:

$$\bar{q} = \sum_{i=1}^{n} \tau_i \times \lambda_i, \tag{5}$$

where $\bar{q}$ is the equivalent water resistance coefficient; τ_i is the ratio of thickness of each rock layer; and λ_i is the conversion value of equivalent water resistance coefficient.

Based on the rock layer thickness revealed by drilling and the equivalent water resistance coefficient values listed in Table 5, the equivalent water resistance coefficient of the composite rock layers for the $J_{16\text{-}17}$ coal floor in 48 drilling holes was obtained. The contours are shown in Figure 5.

3.5. Index Factor Set. The thickness ratio of the plastic brittle rock and core recovery rate can be counted according to the drilling disclosure information. Quantitative values of the six index factors corresponding to the 48 boreholes are shown in Table 2. In order to correspond to the evaluation of the

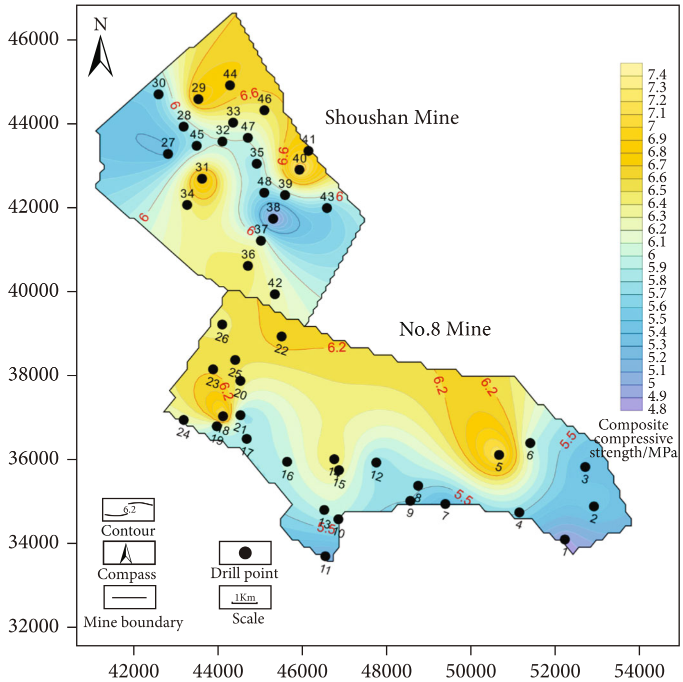

Figure 4: Contour map of composite compressive strength.

Table 5: Conversion value of the lithology equivalent water resistance coefficient.

Lithology	Conversion value of equivalent water resistance coefficient
Mudstone, marl, clay, shale	1.0
Sandstone	0.4
Sand shale	0.8
Mine	0.7
Gravel, gravel, etc.	0

water-resistance of the rock formation, the value of the fault complexity factor is taken as the reciprocal of the fractal dimension.

4. Index Factor Weight

It is very important to choose a scientific mathematical method to determine the weight of the index factors. Referring to the existing research results [29], this paper chooses nine-scale AHP and gray correlation analysis to calculate the subjective and objective weights and then couples them to determine the comprehensive weights.

4.1. Subjective Weight. The AHP establishes a hierarchical structure model, constructs a judgment matrix, and calculates the weight of each factor's influence on the overall goal [30, 31]. As shown in Table 6, the target layer is the evaluation of the water resistance of the coal seam floors. The criterion layer divides the index factors into 3 categories, and the scheme layer includes 6 index factors.

Starting from the criterion level, referring to expert opinions to construct secondary indicators, the judgment matrix

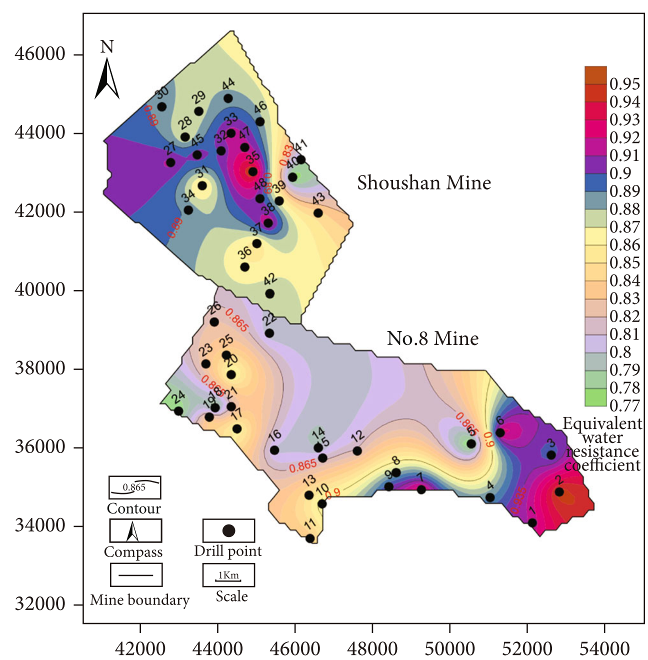

Figure 5: Contour map of the equivalent water resistance coefficient.

of geological structure and disturbance damage, compression resistance and permeability, lithology combination and water blocking performance is

$$R_B = \begin{bmatrix} 1 & 5/2 & 2 \\ 2/5 & 1 & 2/3 \\ 1/2 & 3/2 & 1 \end{bmatrix}. \tag{6}$$

Table 6: Hierarchical structure performance index of aquiclude.

Target layer	Criteria layer	Scheme layer
Evaluation of water resistance of the coal seam floors (A)	Geological structure and disturbance damage (B1)	The thickness of effective aquiclude (C1)
		Fault factor values (C2)
	Compression resistance and permeability (B2)	Composite compressive strength (C3)
		Core recovery rate (C4)
	Lithology combination and water blocking performance (B3)	Equivalent water resistance coefficient (C5)
		Thickness ratio of plastic brittle rock (C6)

Table 7: Subjective weight determined by AHP.

Indicators	Thickness ratio of plastic brittle rock	Core recovery rate	Thickness of effective aquiclude	Fault factor values	Composite compressive strength	Equivalent water resistance coefficient
Subjective weight	0.2321	0.1578	0.1311	0.3932	0.0395	0.0464

Table 8: Objective weight from the grey correlation analysis method.

Indicators	Thickness ratio of plastic brittle rock	Core recovery rate	Thickness of effective aquiclude	Fault factor values	Composite compressive strength	Equivalent water resistance coefficient
Objective weight	0.1366	0.1616	0.1617	0.1529	0.1601	0.2271

The calculated feature vector $\omega_B = (0.5242, 0.1973, 0.2785)$. $CR_B = 0.0036 < 0.1$; it satisfies the consistency condition.

Similarly, the judgment matrices of the six indicator factors are

$$R_{C1} = \begin{bmatrix} 1 & 1/3 \\ 3 & 1 \end{bmatrix}, R_{C2} = \begin{bmatrix} 1 & 1/4 \\ 4 & 1 \end{bmatrix}, R_{C3} = \begin{bmatrix} 1 & 1/5 \\ 5 & 1 \end{bmatrix}. \tag{7}$$

The calculated feature vector $\omega_{C1} = (0.25, 0.75)$, $\omega_{C2} = (0.2, 0.8)$, $\omega_{C3} = (0.1667, 0.8333)$. $CR_{C1} = CR_{C2} = CR_{C3} = 0 < 0.1$; it satisfies the consistency condition.

The weights of the 6 index factors are

$$\begin{aligned} \Theta_1 &= 0.5242 \times (0.25,0.75) = (0.1311,0.3932), \\ \Theta_2 &= 0.1973 \times (0.2,0.8) = (0.0395,0.1578), \\ \Theta_3 &= 0.2785 \times (0.1667,0.8333) = (0.0464,0.2321). \end{aligned} \tag{8}$$

By calculating $CR = 0.0000 < 0.1$, it satisfies the consistency condition, indicating that the constructed judgment matrix is reasonable. The subjective weight of the six index factors is shown in Table 7.

4.2. Objective Weight. The objective weight can be calculated by using the grey correlation analysis method. According to the index factor values corresponding to the 48 boreholes (Table 2), the overall reference sequence [32] is obtained as follows:

$$X_0 = \{89.77, 0.6451, 7.43, 0.975, 0.949, 1.4158\}. \tag{9}$$

After initial value processing of X_0 [33], the correlation degree can be further calculated:

$$\begin{aligned} \gamma_0 &= (\gamma_{01}, \gamma_{02}, \gamma_{03}, \gamma_{04}, \gamma_{05}, \gamma_{06}) \\ &= (0.3891, 0.3679, 0.3853, 0.3888, 0.5467, 0.3288). \end{aligned} \tag{10}$$

Then, the weights of the six index factors [34] can be obtained, and their values are shown in Table 8.

4.3. Comprehensive Weights. According to the subjective and objective weights, the following formula can be used to calculate the comprehensive weight [35]:

$$\omega_i = \frac{(\omega_{1i} * \omega_{2i})^{0.5}}{\sum_{i=1}^{n} (\omega_{1i} * \omega_{2i})^{0.5}}, \tag{11}$$

where ω_{1i} and ω_{2i} are the subjective and objective weights, respectively. Further application of entropy weight theory can calculate the relative entropy value:

$$H(U, V) = \sum_{i=1}^{n} U_i \ln \frac{U_i}{V_i}, \tag{12}$$

where $H(U, V)$ is the relative entropy of U and V, and n is the number of indicators.

Table 9: Comprehensive weight of index factors.

Indicators	Thickness ratio of plastic brittle rock	Core recovery rate	Thickness of effective aquiclude	Fault factor values	Composite compressive strength	Equivalent water resistance coefficient
Comprehensive weight	0.1955	0.1753	0.1599	0.2692	0.0873	0.1127

The comprehensive weights of the six index factors determined by formula (11) are shown in Table 9. The relative entropies of the comprehensive weights with the subjective and objective weights can be calculated by formula (12) (as shown in Table 10).

Table 10: Relative entropy of weight.

Weight	Comprehensive weight and subjective weight	Comprehensive weight and objective weight
Relative entropy	0.073	0.089

Obviously, the relative entropies are less than 0.1 and tend to 0, which indicates that the consistency between the comprehensive weight and the subjective and objective weight is high [36]. That is, the comprehensive weight can effectively combine the subjective and objective weights, and its weight distribution is more scientific and reasonable.

5. Identification of Water Barrier Ability

5.1. Model Building

5.1.1. Level Matrix Establishment. According to the existing index factor data with reference to the existing research results [37], the water-insulation capacity of the composite strata in the coal seam floor can be divided into five grades, namely, extremely weak (I), weak (II), medium (III), strong (IV), and very strong (V).

Assuming that the mean value of an indicator factor is x and the mean square deviation is s, according to the mean-variance method, a recognition interval composed of five levels can be established. The calculation formulas are as follows:

$$I_{ab} = [[0, \bar{x} - s][\bar{x} - s, \bar{x} - 0.5s][\bar{x} - 0.5s, \bar{x}][\overline{x,}\bar{x} + 0.5][\bar{x} + 0.5s, \bar{x} + s]],$$
$$I_{cd} = [[0, \bar{x} - 0.5][0, \bar{x}][\bar{x} - s, \bar{x} + 0.5s][\bar{x} - 0.5s, \bar{x} + s][\bar{x} + s, \bar{x} + 2s]],$$
$$I_M = \left[\frac{(a+b)}{2}\right]. \tag{13}$$

The standard interval matrix of the six index factors corresponding to the five levels can be determined:

$$I_{ab} = \begin{bmatrix} [0, 0.4625] & [0.4625, 0.6016] & [0.6016, 0.7407] & [0.7407, 0.8798] & [0.8798, 1.019] \\ [0, 0.6491] & [0.6491, 0.712] & [0.712, 0.7749] & [0.7749, 0.8378] & [0.8378, 0.9007] \\ [0, 55.83] & [55.83, 61.51] & [61.51, 67.19] & [67.19, 72.87] & [72.87, 78.55] \\ [0, 0.7956] & [0.7956, 0.8948] & [0.8948, 0.9939] & [0.9939, 1.093] & [1.093, 1.192] \\ [0, 5.371] & [5.371, 5.655] & [5.655, 5.94] & [5.94, 6.225] & [6.225, 6.509] \\ [0, 0.845] & [0.845, 0.865] & [0.865, 0.885] & [0.885, 0.9051] & [0.9051, 0.9251] \end{bmatrix}. \tag{14}$$

The index factor range matrix constructed as

$$I_{cd} = \begin{bmatrix} [0, 0.6016] & [0, 0.7407] & [0.4625, 0.8798] & [0.6016, 1.019] & [1.019, 1.297] \\ [0, 0.712] & [0, 0.7749] & [0.6491, 0.8378] & [0.712, 0.9007] & [0.9007, 1.027] \\ [0, 61.51] & [0, 67.19] & [55.83, 72.87] & [61.51, 78.55] & [78.55, 89.9] \\ [0, 0.8948] & [0, 0.9939] & [0.7956, 1.093] & [0.8948, 1.192] & [1.192, 1.39] \\ [0, 5.655] & [0, 5.94] & [5.371, 6.225] & [5.655, 6.509] & [6.509, 7.078] \\ [0, 0.865] & [0, 0.885] & [0.845, 0.9051] & [0.865, 0.9251] & [0.9251, 0.9651] \end{bmatrix}. \tag{15}$$

The index factor matrix is

$$I_M = \begin{bmatrix} 0.2313 & 0.5321 & 0.6712 & 0.8103 & 0.9494 \\ 0.3246 & 0.6806 & 0.7435 & 0.8064 & 0.8693 \\ 27.92 & 58.67 & 64.35 & 70.03 & 75.71 \\ 0.3978 & 0.8452 & 0.9443 & 1.043 & 1.143 \\ 2.685 & 5.513 & 5.798 & 6.082 & 6.367 \\ 0.4225 & 0.855 & 0.875 & 0.895 & 0.9151 \end{bmatrix}. \tag{16}$$

5.1.2. Level Eigenvalue Determination. For a borehole, the relative difference matrix and relative subordination matrix can be obtained by comparing the quantified values of the six index factors with the corresponding data of the matrices I_{ab}, I_{cd}, and I_M [38, 39]. For borehole 1, the relative difference matrix is

$$D_A(u) = \begin{bmatrix} -1 & -1 & -0.9475 & 0.0111 & -1 \\ -1 & -1 & -0.9475 & 0.0107 & 0.3775 \\ 0.0324 & 0.0010 & 0.0003 & 0.0003 & -1 \\ -1 & -1 & 0.9414 & 0.1196 & -1 \\ 0.3366 & 0.0126 & 0.0079 & 0.0036 & -1 \\ -1 & -1 & -0.9475 & 0.1051 & -1 \end{bmatrix}. \tag{17}$$

Table 11: Evaluation results of each borehole in the mining area.

Drilling hole	Level eigenvalue $\alpha = 1, \beta = 1$	$\alpha = 1, \beta = 2$	$\alpha = 2, \beta = 1$	$\alpha = 2, \beta = 2$	Mean	Waterproof ability grade
1	3.6544	3.5047	4.1654	3.9117	3.8091	IV
2	3.502	3.4306	4.0213	3.9278	3.7204	IV
3	3.6759	3.5109	4.239	3.9485	3.8436	IV
4	3.7136	3.5287	4.2675	3.9754	3.8713	IV
5	2.2395	2.3538	1.9527	2.1855	2.1829	II
6	3.7877	3.6014	4.5335	4.2561	4.0447	IV
7	3.588	3.4534	4.2084	3.9854	3.8088	IV
8	3.7403	3.5429	4.2758	3.9915	3.8876	IV
9	3.6678	3.5091	4.2116	3.9349	3.8308	IV
10	3.2876	3.2574	3.6278	3.5052	3.4195	III
11	3.1764	3.2221	3.2825	3.3479	3.2572	III
12	2.3663	2.2988	2.5043	2.4577	2.4068	II
13	3.3073	3.2887	3.5358	3.5015	3.4083	III
14	2.1647	2.2678	1.9389	2.1243	2.1239	II
15	2.5617	2.606	2.5215	2.6208	2.5775	III
16	2.279	2.3811	2.0797	2.2682	2.252	II
17	3.296	3.2668	3.6164	3.5123	3.4229	III
18	2.2245	2.3447	1.9259	2.1655	2.1652	II
19	3.182	3.2255	3.2919	3.354	3.2634	III
20	3.7163	3.5353	4.1929	3.9606	3.8513	IV
21	2.3663	2.2988	2.5043	2.4577	2.4068	II
22	2.2127	2.3157	1.9924	2.1817	2.1756	II
23	2.9916	3.0838	2.9515	3.1097	3.0342	III
24	2.2272	2.3463	1.9305	2.1691	2.1683	II
25	3.2634	3.2673	3.4148	3.4315	3.3442	III
26	2.8611	2.9716	2.7547	2.9459	2.8833	III
27	3.7387	3.5425	4.2704	3.9899	3.8854	IV
28	2.4441	2.3738	2.5554	2.5058	2.4698	II
29	2.9519	3.0502	2.886	3.0575	2.9864	III
30	3.2971	3.288	3.4872	3.4804	3.3882	III
31	2.1914	2.2944	1.9676	2.1556	2.1522	II
32	3.3017	3.2728	3.608	3.5157	3.4246	III
33	3.7246	3.5343	4.2739	3.9827	3.8789	IV
34	3.3003	3.2884	3.5022	3.4872	3.3945	III
35	3.5887	3.4537	4.2099	3.9861	3.8096	IV
36	2.5617	2.606	2.5215	2.6208	2.5775	III
37	2.1914	2.2944	1.9676	2.1556	2.1522	II
38	4.6934	4.5189	5.2535	4.9613	4.8568	V
39	2.4271	2.3573	2.5431	2.4942	2.4554	II
40	1.8025	1.8694	1.6102	1.7337	1.754	I
41	1.7928	1.8653	1.6009	1.7255	1.7461	I
42	3.0531	3.1345	3.0596	3.1939	3.1103	III
43	2.2044	2.3317	1.8922	2.1376	2.1415	II
44	3.255	3.2636	3.4034	3.4245	3.3366	III
45	4.7221	4.5373	5.2134	4.9691	4.8605	V
46	3.2578	3.2649	3.4072	3.4269	3.3392	III
47	4.7378	4.541	5.2804	4.9908	4.8875	V
48	3.2883	3.2582	3.6268	3.5059	3.4198	III

Table 12: Classification standards for water resistance.

Waterproof ability grade	Extremely weak (I)	Weak (II)	Medium (III)	Strong (IV)	Very strong (V)
Level eigenvalue	$W < 2.0$	$2.0 \leq W < 2.5$	$2.5 \leq W < 3.5$	$3.5 \leq W < 4.5$	$W \geq 4.5$

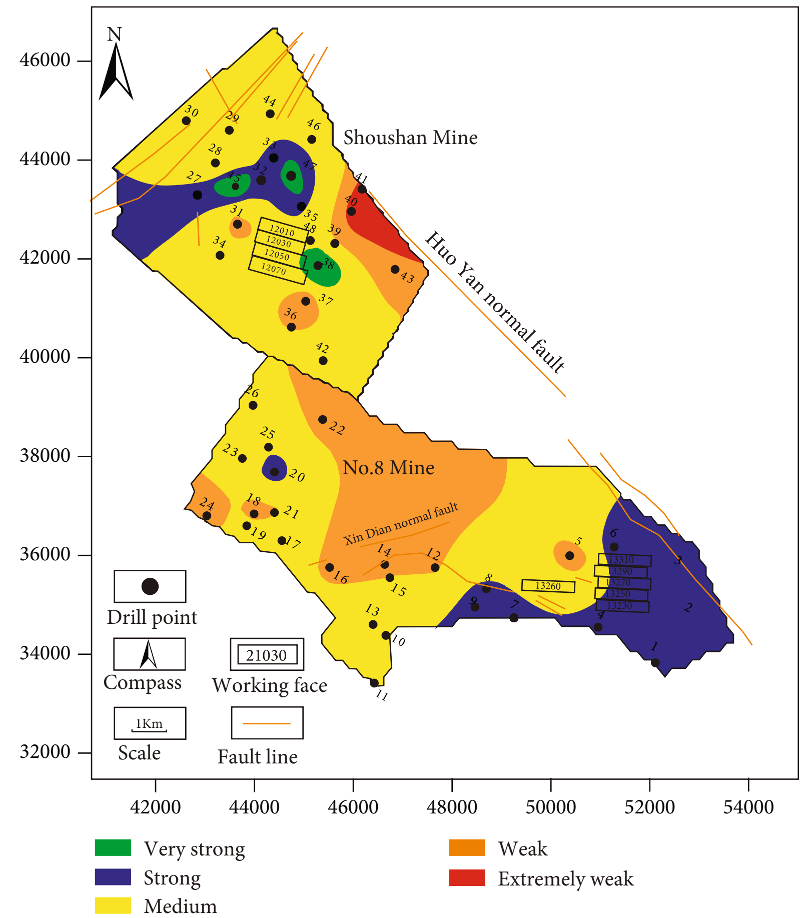

Figure 6: Zoning map of the water insulation capability for the $J_{16\text{-}17}$ coal floor composite stratum.

The relative membership matrix is

$$\mu_A(u) = \begin{bmatrix} 0 & 0 & 0.0263 & 0.5055 & 0 \\ 0 & 0 & 0.0263 & 0.5053 & 0.6887 \\ 0.5162 & 0.5005 & 0.5003 & 0.5001 & 0 \\ 0 & 0 & 0.7457 & 0.5598 & 0 \\ 0.6683 & 0.5063 & 0.5039 & 0.5018 & 0 \\ 0 & 0 & 0.0263 & 0.5525 & 0 \end{bmatrix}. \quad (18)$$

According to the principle of the fuzzy variable set, the relative membership matrix and the corresponding comprehensive weight are combined based on the requirements, and the hierarchical characteristic values under different parameters can be obtained.

$$H = \sum_{1}^{m} \frac{\mu_h}{\sum_1^m \mu_h} * h, \quad (19)$$

$$\mu_h = \frac{1}{1 + \left\{ \left(\sum_{i=1}^{n} [w_i (1 - u_A(ih))]^{\beta} \right) / \left(\sum_{i=1}^{n} [w_i u_A(ih)]^{\beta} \right) \right\}^{\alpha/\beta}}, \quad (20)$$

where $i = 1, 2, 3, \cdots, n$; n is the number of indicators; $h = 1, 2, 3, \cdots, m$; m is the number of evaluation index grades; w_i is the weight of the evaluation index (as shown in Table 9); $\mu_A(\mu_{ih})$ is the relative membership degree of the ith index under grade h; and α and β are optimization criteria and distance parameters, respectively, usually taking values 1 and 2.

According to formulas (19) and (20), the level eigenvalue of borehole 1 is

$$H = (3.6544, 3.5047, 4.1654, 3.9117). \quad (21)$$

The mean of the level eigenvalue is 3.8091. Similarly, the mean value of the grade characteristics of other boreholes can be calculated as shown in Table 11 (Note: α and β are the parameters of the compound operation of the fuzzy variable sets).

5.2. Water-Resistant Capacity Zoning. According to the hydrogeological conditions of the study area and the research results of others [38], the eigenvalue thresholds corresponding to the five levels of water insulation capacity are shown in Table 12.

According to the characteristic values of 48 drilling levels of the No. 8 mine and the Shoushan mine listed in Table 11, the water resistance capacity grade can be determined by the classification standard in Table 12. The values are also listed in Table 11. The corresponding partition of the water resistance capacity of the composite strata in the coal floor of the $J_{16\text{-}17}$ is shown in Figure 6.

The statistical analyses showed that the strong and very strong water resistance areas occupy 23.64% of the total area. The medium area accounts for 58.26%, and the weak and extremely weak areas account for 18.1%. The medium water insulation capacity is relatively high, and the weak and very weak areas are relatively small.

6. Discussion

It can be seen from the calculation process of AHP that the determination of the weight of indicator factors depends on the expert opinions or scores, and the results are easily affected by the subjective will of experts. Grey correlation method is based on the actual drilling data to determine the weight; it can avoid the impact of evaluator's subjective will, but the grey correlation analysis method uses the same weight set when calculating the optimal solution, it is difficult to reflect the optimization of the evaluation. Combined with the previous two methods, the comprehensive weight determined by the entropy weight method can not only reduce the interference of human factors but also fully reflect the actual field, and its results are more scientific and reliable.

In the present mine excavation project, the water resistance capacity is usually judged according to the thickness of the aquiclude. It can be seen from Table 2 that the effective water resistance thickness of Nos. 38, 40, and 41 are 55.25 m, 79.58 m, and 75.73 m, respectively. Based on this, it is judged that the water resistance of the rock formation near No. 38 borehole is weaker than 40 and 41 drilling. In fact, the existence of the Huoyan fault near boreholes 40 and 41 not only reduces the distance between the coal seam and the aquifer [39] but also destroys the integrity of the coal seam floor [40–42]. At the same time, it also changed the migration characteristics of groundwater [43], which greatly reduced the water resistance of the rock formation. In this paper, it is determined that the water resistance capacity of the rock strata at borehole No. 38 is class V, and that of the rock strata at boreholes Nos. 40 and 41 is class I (Table 11), that is, the water resistance capacity of borehole No. 38 is greater than that of boreholes Nos. 40 and 41. The results are credible.

It can be seen from Figure 6 that the water resistance level characteristic value of the composite rock layer of the coal seam floor in the west of the Shoushan mine and the southeast of the No. 8 mine is above 2.5, and the water resistance is relatively strong. Therefore, the possibility of water inrush from the floor during coal mining is relatively small. The mining activities of the No. 8 mine and the Shoushan mine are mainly carried out in areas with strong and medium water resistance. The 13230, 13250, 13260, 13270, 13290, and 13310 working faces of No. 8 mine have stopped mining. The 12010, 12030, 12050, and 12070 working faces of Shoushan mine have stopped mining.

There is no floor water inrush accident in these working faces, which shows that the evaluation results are in good agreement with the actual situation.

7. Conclusions

(1) Based on the comprehensive analysis of multiple influencing factors on the water resistance of the $J_{16\text{-}17}$ coal seam floor composite rock in the Pingdingshan Coalfield No. 8 mine and the Shoushan mine, we select the thickness ratio of plastic brittle rock, core recovery rate, thickness of effective aquiclude, fault complexity, composite compressive strength, and equivalent water resistance coefficient as the evaluation index factors. It provides a guarantee for identifying the water resistance of the composite rock layer of the coal seam floor

(2) Based on the analytic hierarchy process and grey relational analysis, the subjective and objective weights of the index factors are defined. The entropy weight theory is used to determine the comprehensive weights. Based on the fuzzy variable set theory, the mathematical model of water resistance evaluation is constructed, and the $J_{16\text{-}17}$ coal floor is quantitatively identified. The water resistance of the coal seam floor composite rock layer is divided into five grades: extremely weak, weak, medium, strong, and very strong, laying the foundation for the accurate assessment of the water inrush risk from the coal seam floor

(3) The areas with strong and very strong water resistance capacity of the $J_{16\text{-}17}$ coal floor composite rock in the No. 8 mine and the Shoushan mine account for 23.64% of the total area, the medium area accounts for 58.26%, and the weak and extremely weak areas account for 18.1%. Areas with medium water-resisting capacity accounting for relatively high, weak, and very weak areas are relatively small. The accurate evaluation and zoning of water-resistance capacity indicate the direction for the mine to take targeted measures to prevent and control floor water hazards

(4) The comprehensive weight of the index factors determined by the entropy weight theory reduces

the interference level of human factors. The fuzzy variable set theory realizes the quantitative evaluation of the water resistance of the composite rock under the action of multiple index factors. The actual excavation results on site have proved the reliability of the evaluation results. It provides a reference method for accurately distinguishing the water resistance of rock formations

Data Availability

The data used to support the findings of this study are included within the article.

Conflicts of Interest

The authors declare that they have no conflicts of interest.

Acknowledgments

This work was supported by the National Natural Science Foundation of China (41802186 and 41972254), Innovative Science and Technology Talents Team Construction Project of Henan Province (CXTD2016053), and Special Funds for Higher Education Basic Scientific Research Funds of Henan Province (NSFRF200103).

References

[1] S. N. Dong, X. M. Guo, Q. S. Liu, H. Wang, and S. Nan, "Model and selection criterion of zonal preact grouting to prevent mine water disasters of coal floor limestone aquifer in North China type coalfield," *Coal Geology & Exploration*, vol. 48, no. 4, pp. 1–10, 2020.

[2] Q. Wu, "Progress, problems and prospects of prevention and control technology of mine water and reutilization in China," *Journal of China Coal Society*, vol. 39, no. 5, pp. 795–805, 2014.

[3] S. A. Yang, "Water resistance coefficient and its application," *Coal Geology & Exploration*, vol. 3, pp. 41–46, 1986.

[4] M. G. Qian, X. X. Miao, and J. L. Xu, "Study on key strata theory in strata control," *Journal of China Coal Society*, vol. 3, pp. 2–7, 1996.

[5] X. X. Miao and M. G. Qian, "Advance in the key strata theory of mining rock mass," *Journal of China University of Mining & Technology*, vol. 1, pp. 25–29, 2000.

[6] Z. M. Xu, Y. J. Sun, W. H. Sui, G. W. Zhang, S. Li, and X. L. Huang, "The water isolating and hydrogeological structure characteristics for upper member of Cambrian limestone in coal floor," *Journal of Mining & Safety Engineering*, vol. 27, no. 3, pp. 399–403, 2010.

[7] W. Q. Zhang, B. Y. Li, and J. X. Li, "Water resistance and its relationship with structure components and configuration of rocks," *Coal Geology & Exploration*, vol. 4, pp. 41–44, 1992.

[8] S. X. Yin and W. Y. Hu, "Study of water resist property and its natural intrusion," *Coal Geology and Exploration*, vol. 36, no. 1, pp. 34–40, 2008.

[9] M. M. Feng, X. B. Mao, and Q. H. Zhu, "Effect of lithologic association of the water-resisting strata in coal seam floor on water insulating," *Journal of Mining & Safety Engineering*, vol. 27, no. 3, pp. 404–409, 2010.

[10] T. Li, L. Zhang, Q. Jiang, C. Feng, and R. Zhao, "Safe thickness and fracture evolution law determined for hydraulic fracturing of water-resistant rock mass with hidden karst based on GDEM," *Tunnel Construction*, vol. 41, no. 1, pp. 67–76, 2021.

[11] J. Sun, L. G. Wang, and H. Q. Hou, "Research on water-isolating capacity of the compound water-resisting key strata in coal seam," *Journal of China University of Mining & Technology*, vol. 42, no. 4, pp. 560–566, 2013.

[12] F. Xu, D. W. Jin, J. Z. Yang et al., "Multi-scale quantitative evaluation of water resistance capacity of Fengfeng formation in Baode Coal Mine," *Journal of China Coal Society*, vol. 46, no. 7, pp. 2379–2386, 2021.

[13] D. Lyu and Y. X. Xie, "Study on Paleogene rock structure characteristics and integrated water-resistance performance in Yilan mining area," *Safety in Coal Mines*, vol. 41, no. 3, pp. 44–47, 2020.

[14] Y. J. Zhang, Y. J. Song, P. P. Chen, and Z. L. Fan, "Study on comprehensive water insulated performances of deep Jurassic system rock strata," *Coal Science and Technology*, vol. 42, no. 8, pp. 98–98, 2014.

[15] W. B. Wang, "Research on lithology characteristic and water-resisting property of overlying strata under sea area," *Coal Mining Technology*, vol. 15, no. 3, pp. 10–13, 2010.

[16] W. Y. Hu and S. X. Yin, "Dynamic mechanism of water inrush from floor of mining face," *Chinese Journal of Rock Mechanics and Engineering*, vol. 29, no. S1, pp. 3344–3349, 2010.

[17] K. Cybulski, B. Malich, and A. Wieczorek, "Evaluation of the effectiveness of coal and mine dust wetting," *Journal of Sustainable Mining*, vol. 14, no. 2, pp. 83–92, 2015.

[18] Q. Yi, K. Xie, P. Sun, and Y. Kim, "Characterization of phosphorus in the sedimentary environments of inundated agricultural soils around the Huainan Coal Mines, Anhui, China," *Science of the Total Environment*, vol. 472, pp. 538–549, 2014.

[19] Z. B. Yang, "Application analysis of Slesarev formula in mine water prevention and control," *Safety in Coal Mines*, vol. 47, no. 9, pp. 190–193, 2016.

[20] W. Zhang, R. Y. Zhang, M. H. Yan et al., "Application of GIS technology in the calculation of water inrush coefficient of coal seam floor," *Coal and Chemical Industry*, vol. 39, no. 2, pp. 48–51, 2016.

[21] B. Zhang and X. F. Chang, "Prediction method and application of mining failure depth of coal seam floor," *Coal Technology*, vol. 37, no. 12, pp. 26–29, 2018.

[22] Y. C. Xu and Y. Yang, "Applicability analysis on statistical formula for failure depth of coal seam floor in deep mine," *Coal Science and Technology*, vol. 41, no. 9, pp. 129–132, 2013.

[23] D. K. Wang, F. C. Zeng, J. G. Wang et al., "Dynamic evolution characteristics and fractal law of loaded coal fractures by micro industrial CT," *Chinese Journal of Rock Mechanics and Engineering*, vol. 39, no. 6, pp. 1165–1174, 2020.

[24] Q. Ping, H. Zhang, and H. P. Su, "Study on dynamic compression mechanical properties of limestone with different lengths," *Chinese Journal of Rock Mechanics and Engineering*, vol. 37, no. S2, pp. 3891–3897, 2018.

[25] D. B. Chai, *Mine Geological Work Manual*, China Coal Industry Press, 1986.

[26] K. Zhou and B. Q. Wang, "The evaluation of equivalent thickness of water-resisting layer," *Coal and Chemical Industry*, vol. 39, no. 2, pp. 45–47, 2016.

[27] C. H. Han, J. C. Wei, D. L. Xie, J. G. Xu, W. J. Zhang, and Z. C. Zhao, "Evaluation of water abundance of

sandstone aquifer based on set pair analysis and variable fuzzy set coupling method: a case study of Jurassic Zhiluo Formation aquifer in Jinjiaqu well field, Ningdong mining area," *Journal of China Coal Society*, vol. 45, no. 7, pp. 199–201, 2020.

[28] Q. R. Liu, *Hydrogeological Characteristics and Exploration Evaluation Methods of Solid Deposits in China*, Petroleum Industry Press, 1995.

[29] X. Y. Wang, T. T. Wang, Q. Wang, X. Liu, R. Li, and B. J. Liu, "Evaluation of floor water inrush based on fractal theory and an improved analytic hierarchy process," *Mine Water and the Environment*, vol. 36, no. 1, pp. 87–95, 2017.

[30] G. X. Li, N. N. Liu, X. M. Wu, W. L. Liu, and R. M. Wang, "Application of optimal combination weighting model in water inrush evaluation of floor collapse column," *Safety in Coal Mines*, vol. 49, no. 11, pp. 194–198, 2018.

[31] L. Q. Shi, R. G. Zhang, J. Han, P. Z. Cong, D. X. Qin, and Y. C. Guo, "Water inrush risk assessment with multi-source information type fusion based on EWM-AHP comprehensive weighting," *Journal of Henan Polytechnic University*, vol. 39, no. 3, pp. 17–25, 2020.

[32] G. Xu, L. Wang, H. T. Wang, K. Wang, and Y. Z. Feng, "Prediction method of coal seam gas content based on grey theory and BP neural network," *Coal Technology*, vol. 38, no. 11, pp. 82–85, 2019.

[33] C. Cheng, *Research on Evaluation of Comprehensive Benefits of Isolated Buildings Based on Combined Weight and Grey Relation*, Northeast Forestry University, 2018.

[34] H. Tang, "The application of improved grey correlation analysis method in groundwater evaluation," *Northeast Water Resources and Hydropower*, vol. 38, no. 8, 2020.

[35] K. G. Li, M. L. Li, and Q. C. Qin, "Research on evaluation method of rockburst tendency based on improved comprehensive weighting," *Chinese Journal of Rock Mechanics and Engineering*, vol. 39, no. S1, pp. 2751–2762, 2020.

[36] G. J. Sun, X. Y. Huo, and X. J. Sun, "Evaluation method of four-parameter interval number based on combinator-weighted fuzzy matter-element," *Mathematics in Practice and Theory*, vol. 50, no. 19, pp. 288–295, 2020.

[37] Y. Chen, X. Wang, Y. Zhao, H. Shi, X. Liu, and Z. Niu, "Quantitative evaluation for the threat degree of a thermal reservoir to deep coal mining," *Geofluids*, vol. 2020, Article ID 8885633, 15 pages, 2020.

[38] X. Y. Wang, M. G. Yao, J. G. Zhang et al., "Risk assessment of coal seam floor water inrush based on improved AHP method and fuzzy variable set theory," *Journal of Mining and Safety Engineering*, vol. 36, no. 3, pp. 558–565, 2019.

[39] Z. Q. Song, J. Hao, J. Q. Tang, and Y. K. Shi, "Study on water inrush from fault's prevention and control theory," *Journal of China Coal Society*, vol. 38, pp. 1511–1515, 2013.

[40] Q. Z. Zhang, H. S. Jang, D. S. Bae, G. Y. Kim, and B. A. Jang, "Empirical rock mechanical site-descriptive modeling (RMSDM) for the Korea Atomic Energy Research Institute Underground Research Tunnel (KURT)," *Environmental Earth Sciences*, vol. 75, no. 10, 2016.

[41] C. Z. Wu, J. Chu, S. F. Wu, and Y. Hong, "3D characterization of microbially induced carbonate precipitation in rock fracture and the resulted permeability reduction," *Engineering Geology*, vol. 249, pp. 23–30, 2019.

[42] Q. Z. Zhang, C. Z. Wu, X. C. Fei, B. A. Jang, and D. Liu, "Time-dependent behavior of rock joints considering asperity degradation," *Journal of Structural Geology*, vol. 121, pp. 1–9, 2019.

[43] Y. H. Zhang, Z. Q. Xiong, X. F. Li, R. D. Peng, and Y. C. Li, "Study on technology of mine water disaster prevention and control in underground mine under complex hydrogeological conditions," *Coal Science and Technology*, vol. 49, no. 3, pp. 167–174, 2021.

Hindawi
Geofluids
Volume 2021, Article ID 8169926, 9 pages
https://doi.org/10.1155/2021/8169926

Research Article

Numerical Simulation of Dynamic Characteristics of Dam Concrete Based on Fuzzy Set

Fang Jianyin, Liu Ke, Dang Faning, and Li Shutian

Institute of Geotechnical Engineering, Xi'an University of Technology, Xi'an 710048, China

Correspondence should be addressed to Fang Jianyin; fjylxr@163.com

Received 11 April 2021; Accepted 16 September 2021; Published 4 October 2021

Academic Editor: Jinze Xu

The dynamic characteristics of concrete are the key point of the dam seismic safety design. In order to study the dynamic characteristics of concrete, a CT scan test of concrete under dynamic load was carried out; CT scan images of the concrete loading process were obtained. Based on the definition of integrity, integrity area, and intercepted sections in the quantitative zoning theory, the concrete CT images were divided into the hole or crack area ($P_{0-\lambda_1}$), hardened cement stone area ($P_{\lambda_1-\lambda_2}$), and aggregate area (P_{λ_2-1}). And the determination method of partition threshold is studied. Then, based on the CT resolution unit, a concrete numerical calculation model of structural random is established, and the numerical simulation experiment of concrete under uniaxial dynamic load is carried out. The results show that the concrete numerical calculation model of structural random is very close to the actual mesostructure of concrete, and the interface thickness between aggregate and hardened cement is very close to the actual interface thickness (which is 40~50 μm). Under the action of dynamic load, the damage of the sample is mainly concentrated in the upper part of the sample, and the damage is easy to occur at the initial defect place, and the damage occurs at multiple points at the same time. The damage crack is relatively straight, the phenomenon of the crack passing through the aggregate is obvious, and the crack expands along the fastest path of energy release.

1. Instruction

The mechanical properties of concrete are related to the safety evaluation of the dam concrete structure under dynamic load, which is the focus of current research. Since the concept of numerical concrete appeared, the mesoscale numerical model based on the finite element has been widely used in the study of dynamic characteristics of concrete.

Yong et al. [1] established a three-dimensional random aggregate model and carried out numerical simulation research on concrete target penetration tests by using LS-DYNA software. Chen et al. [2] developed a mesomechanical pretreatment algorithm to construct the random ellipsoidal aggregate model for the mesoscopic structure of fully graded concrete. Yuan et al. [3] studied the dynamic strength characteristics of dam concrete using the random aggregate model. Yue et al. [4] simulated the dynamic tensile properties of coral aggregate seawater concrete by using the 3D mesoscopic concrete model. In these models and methods, concrete is considered to be composed of aggregate, mortar, and interface [5–6]. The mortar matrix, aggregate, pore, and interface have significant influence on the mechanical properties of concrete [7–8]. Therefore, in the process of simulating the mechanical behavior and damage characteristics of concrete, it is very important to represent the mesostructure of concrete as realistically as possible in the numerical model. A large number of researchers [9–16] have reconstructed two-dimensional or three-dimensional concrete numerical calculation models based on X-ray CT scanning technology, and the mechanical properties of concrete are studied by using the model. Ju et al. [17] propose using a l CT technique to acquire the real structural information of SRM samples and constructing a 3D SRM model in PFC3D to represent SRM's real heterogeneity and irregular structure. Zheng et al. [18, 19] present a computer procedure for reconstructing the 3D porous structure of low-permeability sandstone based on the information of a reference model which is established from computed tomography (CT) images. To examine the development law of a coal fracture structure under uniaxial compression, tension, and shearing, Hao et al. [20] have scanned the coal after loading using computed tomography (CT) and segmented the coal matrix, minerals, and fractures in the CT scanning image of the coal by using a threshold segmentation method. Wang et al. [21, 22] have established the three-dimensional numerical model of a coal sample based on a CT scanning image and studied the seepage and deformation characteristics of different pore-fracture structures of coal at different temperatures.

However, the elements of these models have great singularity, and the thickness of the interface in the model is large, which still has a certain gap with the real concrete.

To this end, the CT test of concrete under dynamic uniaxial compression was carried out, and the concrete scanning images were quantitatively divided based on the damage zoning theory, and a structural random type numerical concrete model was established; the mechanical properties of concrete under uniaxial dynamic compression stress were studied by using the model.

1.1. Uniaxial Dynamic Compression CT Test. This test adopts the newly developed portable power loading equipment of Xi'an University of Technology, which is the first power loading test equipment with CT scanners in China [23]. The CT scanner uses a Marconi M8000 spiral CT scanner with an image size of 1024×1024. The maximum imaging speed is 0.5 seconds for four-layer scanning. The loading scanning device is shown in Figure 1.

This test uses a first-grade C15 concrete cylinder test piece, the diameter of the samples is 60 mm, and the length is120mm; the water-cement ratio is 0.4, and the aggregate particle size is 5–20 mm. Samples are cured for 28 days under standard conditions, and the test is then conducted.

In the test, the frequency of sinusoidal wave load was 2 Hz, and each amplitude had more than 3 vibration times, gradually increasing the amplitude. In the initial stage of uniaxial compression, stress control loading is adopted. After the second scan, the loading was changed to displacement control, and the load increment is 0.002 mm. During the scanning, the loading was stopped, but the unloading was not carried out, and the pressure peak was maintained. A total of 7 scans were carried out until the test was stopped when the sample was damaged. The scanning position is shown in Figure 2, and the CT images of sample damage are shown in Figure 3.

Figure 1: Portable dynamic loading equipment and CT scanner (reproduced from Fang et al. [24]).

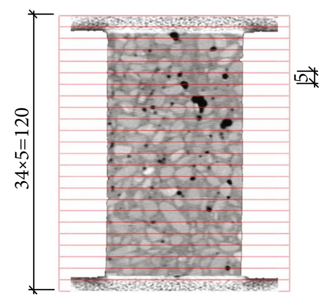

Figure 2: CT scan localization of the sample (reproduced from Fang et al. [24]).

2. The Establishment of "Structural Random Type Numerical Concrete Model"

2.1. Quantitative Partitioning Theory

2.1.1. Integrity Degree. On the basis of fuzzy mathematics theory, the entire CT scan image is called the whole field, which is represented by a set as $\Omega = \{(x, y, z) \mid (x, y, z)$ is an arbitrary point on the study object space area$\}$. Any point in the whole field is complete, but the integrity is different. On this basis, the integrity can be defined as follows:

$$P(x, y, z) = \frac{H(x, y, z) + 1000}{\max H(x, y, z) + 1000}, \tag{1}$$

where $H(x, y, z)$ is the CT number of the space point (x, y, z), which can be defined as follows:

$$H(x, y, z) = \frac{\mu t - \mu_w}{\mu_w} \times 1000, \tag{2}$$

where μ_t and μ_w are the X-ray linear attenuation coefficients of minerals and water in the scanned image, respectively.

According to this definition, the integrity degree is in the interval of $[0, 1]$.

With the increase of the load, the scanning images of each section are unique, and the CT number distribution of each section is different. The normalized CT number, integrity, and breakage have universal applicability, which greatly simplifies the research of concrete CT tests.

2.1.2. Horizontal Integrity Domain of λ. The integrity of the study area and the phenomenon of fracture were blurred by the concept of integrity degree. In order to study the crack evolution law of concrete with a clear physical concept and connect the macrofracture with the microdamage, the concept of integrity level is introduced here.

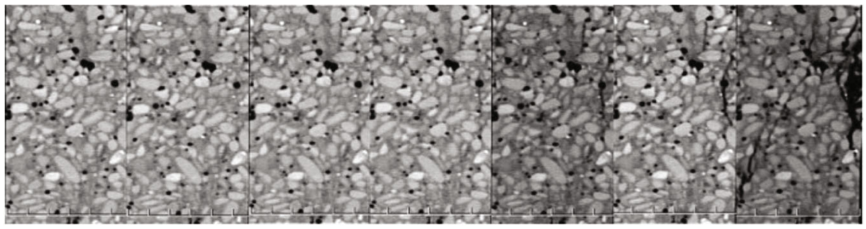

Figure 3: CT images of samples.

Assuming that $0 \le \lambda \le 1$, set

$$\{(x, y, z) \mid 1 \le P(x, y, x) \le \lambda, (x, y, z) \in \Omega\} \quad (3)$$

is defined as the λ level complete domain of the sample, expressed by P_λ.

The integrity domain P_λ is essentially the set of all CT resolution units whose CT number is greater than a certain threshold value. It can be seen that, as long as the value of λ is properly selected, P_λ represents the collection of all CT points whose density is less than a certain threshold, which is the crack area or the damage area.

Therefore, the λ horizontal integrity domain of the sample can be regarded as the damage region of classical damage mechanics or the crack of fracture mechanics, thus realizing the transition from microscopic to macroscopic and linking the damage and fracture of concrete.

2.1.3. (λ_1-λ_2) Intercepted Section. The study of λ horizontal integrity domain is only a resolution unit from 1 to λ. However, concrete is a multiphase material composed of aggregate, hardened cement, and cavity cracks. In order to distinguish them, the definition of $(\lambda_1$-$\lambda_2)$ intercepted section can be introduced to describe it.

Assuming that $0 \le \lambda_1 \le \lambda_2 \le 1$, set

$$\left\{(x, y, z) \mid \lambda_1 \le P(x, y, x) \le \lambda_2, (x, y, z) \in \Omega, ? 0 \le \lambda 1 \le \lambda 2 \le 1\right\} \quad (4)$$

is defined as $(\lambda_1 - \lambda_2)$ complete domain intercepted sections, expressed by $P_{\lambda_1-\lambda_2}$. In fact, the intercepted section is a statistical resolution unit in which the density of the sample is close within the interval $\lambda_1 - \lambda_2$. The connotation of the intercepted section is very simple, but its extension is very rich. In practice, the intercepted section can be applied to delamination of foundation, definition of joint interlayer, division of fracture zone, division of rock or concrete, definition of material integrity, damage and fracture zone, etc.

Figure 4 shows the partition intercepted sections of a scan section of a concrete sample. The intercepted sections can distinguish well the materials of different densities in the concrete, such as aggregates, cement mortar, and cracks.

2.2. Quantitative Partitioning. The specific definition is as follows:

When $0 \le P(x, y, x) < \lambda_1$, the material is believed to contain pores or is fractured. It is called the hole crack area and is denoted as $P_{0-\lambda_1}$.

When $\lambda_1 \le P(x, y, x) < \lambda_2$, the material integrity is considered general, and the material is in the hardened cement zone t and is denoted as $P_{\lambda_1-\lambda_2}$.

When $\lambda_2 \le P(x, y, x) \le 1$, the material integrity is high in the aggregate area (coarse and fine aggregates) and is denoted as P_{λ_2-1}.

λ_1 is the threshold of the crack zone and the hardened cement zone, and λ_2 is the threshold of the hardened cement and aggregate areas. λ_1 and λ_2 are the material parameters, which are constant.

The focus of the partition is how to determine reasonable partition thresholds λ_1 and λ_2. For homogeneous rocks, λ_1 and λ_2 can be obtained using the maximum–minimum method. However, for concrete, this method cannot be used. This method is proposed based on homogeneous materials. Hence, its applicability to heterogeneous materials, such as concrete, is limited. Therefore, the method of probability statistics is used to determine the threshold.

Concrete is a composite material composed of aggregates, mortar, and ITZ. The idea of partition indicates that a component of its resolution unit should be continuous and gradually distributed to avoid large jump changes. The distribution of the resolution units among different components is bound to a certain jump. This idea indicates that to select a CT scan as a universe Ω, a total of 137027 resolution units are required. The statistical relationship between the threshold and the resolution unit is shown in Figure 5, where the abscissa is the threshold, and the ordinate is the corresponding number of statistical units.

As shown in Figure 5, when the thresholds are approximately 0.7 and 0.84, the number of statistical resolution units has a large jump; therefore, λ_1 and λ_2 are 0.7 and 0.84, respectively.

2.3. Modeling Ideas. First of all, CT scan images need to be processed, which includes image positioning and image CT number extraction. The source program is written in FORTRAN language to read the CT scan data files, and the detailed location is carried out according to the image. The positioning accuracy is one CT resolution point (about 0.009 mm), based on which the reconstruction range of the model was determined, and then, the

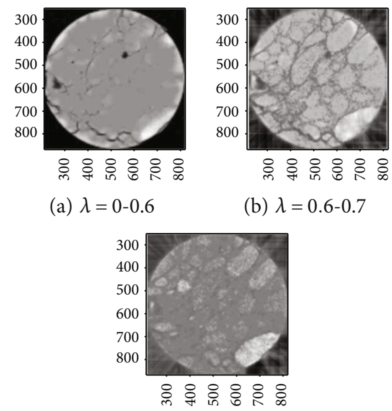

(a) $\lambda = 0$-0.6 (b) $\lambda = 0.6$-0.7 (c) $\lambda = 0.7$-1

Figure 4: Intercepted sections of complete domain.

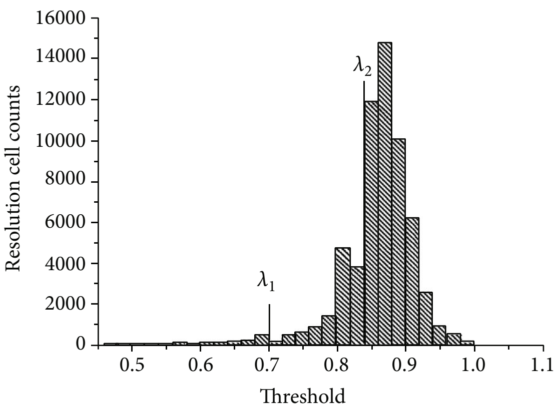

Figure 5: Relationship of threshold and resolution cell (reproduced from Fang et al. [24]).

CT number within the reconstruction range was extracted.

In the CT image, the larger the CT number, the higher the brightness, which represents the greater the density of the material. In the image, the brighter place is aggregate (coarse aggregate and fine aggregate), the gray area is mortar (the product of cement hydration and hardening), and the black area is the hole and crack.

Using the quantitative zoning theory, the FORTRAN source program was compiled to process the extracted CT numbers, and then, the "concrete numerical model of structure random" was reconstructed on the finite element software. The specific modeling ideas are shown in Figure 6.

The "concrete numerical model of structure random" established according to the above modeling ideas is shown in Figure 7.

3. Numerical Experimental Study Based on Structural Randomness

3.1. Numerical Test Conditions. In accordance with the physical tests, the material parameters as shown in Table 1 can be obtained.

In the numerical simulation, the constraint conditions are the full constraint of the sample bottom surface and the horizontal constraint of the sample top surface. The failure of concrete under load is caused by material damage. The elastoplastic damage model can be used as a theoretical tool to deal with the stress damage of concrete materials. Therefore, this paper uses the plastic damage model, which is based on plasticity and assumes that concrete material has two kinds of damage, one is the tensile damage d_t caused by the principal tensile stress, and the other is the pressure damage d_c caused by crushing under pressure. For damage variables d_t and d_c, their value range is $[0, 1]$. When 0, it means that the material is complete without damage, and when 1, it means that the material is completely damaged.

The model is described by effective stress and hardening variables:

$$\begin{gathered}
\bar{\sigma} = D_0^{\mathrm{el}} : \left(\varepsilon - \varepsilon^{\mathrm{pl}}\right) \in \left\{\bar{\sigma} | F\left(\bar{\sigma}, \tilde{\varepsilon}^{\mathrm{pl}}\right) \leq 0\right\}, \\
\dot{\bar{\sigma}}^{\mathrm{pl}} = h\left(\bar{\sigma}, \tilde{\varepsilon}^{\mathrm{pi}}\right) * \dot{\varepsilon}^{\mathrm{pl}}, \\
\dot{\varepsilon}^{\mathrm{pl}} = \dot{\lambda} \frac{\partial G(\bar{\sigma})}{\partial \bar{\sigma}}.
\end{gathered} \tag{5}$$

$\dot{\lambda}$ and F should satisfy the Kuhn-Tucker condition, namely, $\dot{\lambda} F \leq 0$, $\dot{\lambda} \geq 0$, $F \leq 0$.

Cauchy stress can be obtained by using damage factor $d(\bar{\sigma}, \tilde{\varepsilon}^{\mathrm{pl}})$ and effective stress:

$$\sigma = (1 - d)\bar{\sigma}. \tag{6}$$

The damage deformation of the material under uniaxial tensile load is shown in Figure 8. σ_{c0} is the stress at failure. When the stress is before the initial yield stress σ_{c0}, the relationship between tensile stress and strain is linear (linear elastic relationship), and then, the material enters the softening deformation stage. In this process, the stiffness of the material degenerates. When the material cracks, the strain

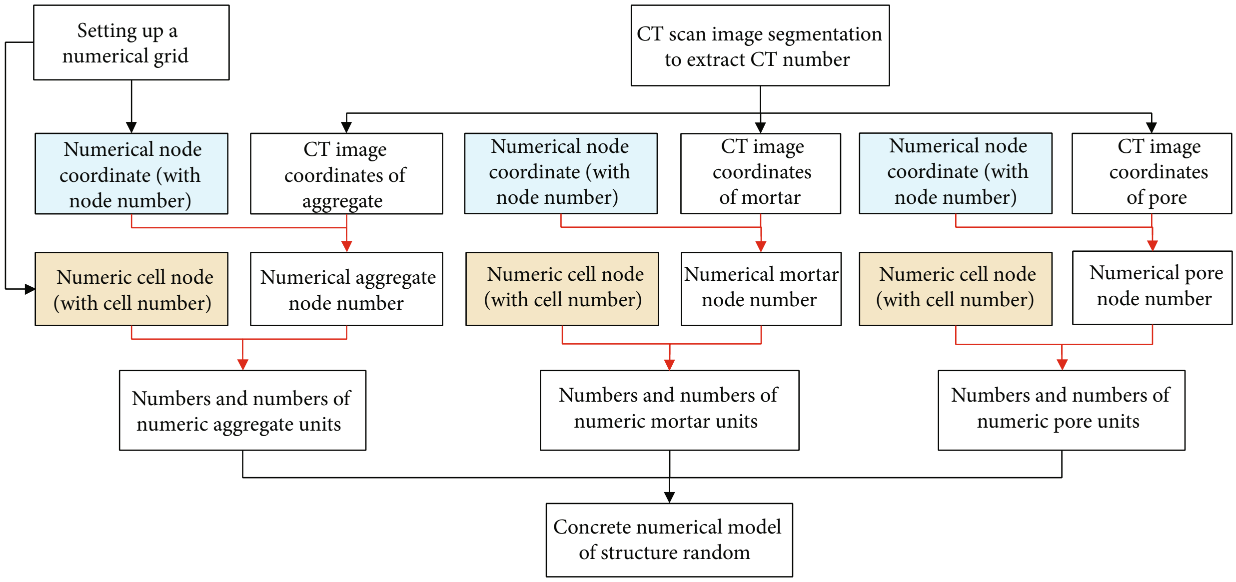

FIGURE 6: Model ideas of concrete numerical model of structure random.

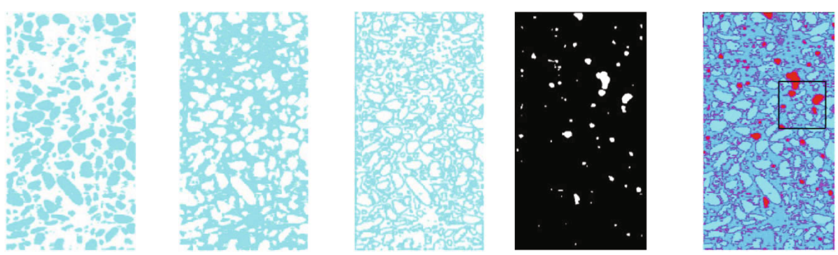

(a) Aggregate (b) Cement mortar (c) ITZ (d) Hole (e) The overall model

FIGURE 7: Concrete numerical model of structure random.

TABLE 1: Material parameter of concrete components (reproduced from Fang et al. [24]).

Material	Elastic modulus (GPa)	Poisson's ratio	Tensile strength (MPa)	Density (kg/m^3)
Aggregate	58.731	0.2407	9.25	2800
Motor	17.458	0.1960	2.78	2200
ITZ	13.967	0.2000	1.56	2000

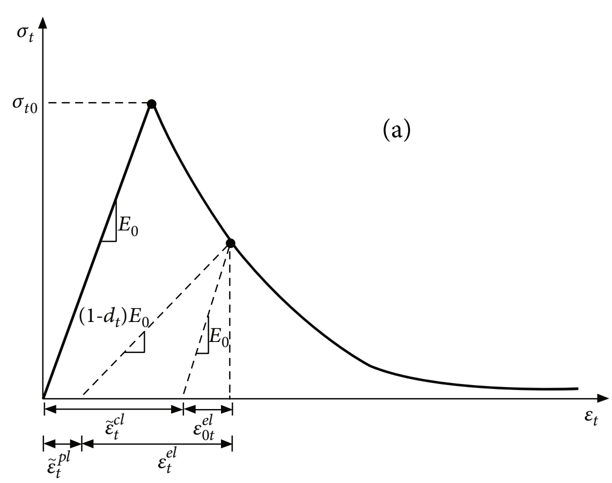

FIGURE 8: Tensile stress and strain.

can be expressed as

$$\tilde{\varepsilon}_t^{\mathrm{ck}} = \varepsilon_t - \varepsilon_{0t}^{\mathrm{el}},$$
$$\varepsilon_{0t}^{\mathrm{el}} = \frac{\sigma_t}{E_0}. \quad (7)$$

It can be obtained from Figure 8:

$$\tilde{\varepsilon}_t^{\mathrm{pl}} = \tilde{\varepsilon}_t^{\mathrm{ck}} - \frac{d_t}{(1-d_t)}\frac{\sigma_t}{E_0}. \quad (8)$$

Under the action of uniaxial compression load, when the stress is before the initial yield stress (σ_{c0}), the stress-strain relationship of the material is linear elastic, and this stage is the elastic deformation stage. When the stress is between σ_{c0} and the ultimate stress (σ_{cu}), the material is in the strengthening stage, and then, the strain continues to increase and the material enters the softening stage.

According to $\tilde{\varepsilon}_c^{\mathrm{in}}$ (inelastic strain), the corresponding hardening data can be obtained.

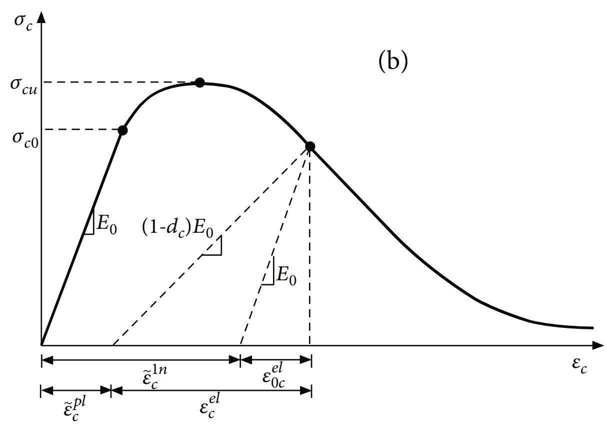

Figure 9: Compression stress and strain.

As can be seen from Figure 9, $\tilde{\varepsilon}_c^{\mathrm{in}}$ has the following relationship with $\varepsilon_{0c}^{\mathrm{el}}$:

$$\begin{aligned} \tilde{\varepsilon}_c^{\mathrm{in}} &= \varepsilon_c - \varepsilon_{0c}^{\mathrm{el}}, \\ \varepsilon_{0c}^{\mathrm{el}} &= \frac{\sigma_c}{E_0}. \end{aligned} \tag{9}$$

Therefore, it can be obtained from Figure 9.

$$\tilde{\varepsilon}_c^{\mathrm{pl}} = \tilde{\varepsilon}_c^{\mathrm{in}} - \frac{d_c}{(1-d_c)}\frac{\sigma_c}{E_0}. \tag{10}$$

Then, the stress-strain relationship under tension and compression can be obtained:

$$\sigma_t = (1-d_t)E_0\left(\varepsilon_t - \tilde{\varepsilon}_t^{\mathrm{pl}}\right), \tag{11}$$

$$\sigma_c = (1-d_c)E_0\left(\varepsilon_c - \tilde{\varepsilon}_c^{\mathrm{pl}}\right). \tag{12}$$

The model assumes that the stiffness degradation is isotropic and can be described by a scalar parameter D:

$$\begin{aligned} E &= (1-d)E_0(0 \le d \le 1), \\ (1-d) &= (1-s_t d_c) - (0 \le s_t, s_c \le 1). \end{aligned} \tag{13}$$

s_t and s_c are related to the stress state of the material and can be expressed as

$$\begin{aligned} s_t &= 1 - w_t r^*(\bar{\sigma}_{11}) - 0 \le w_t \le 1, \\ s_c &= 1 - w_c[1 - r^*(\bar{\sigma}_{11})] - 0 \le w_c \le 1, \\ r^*(\bar{\sigma}_{11}) &= H(\bar{\sigma}_{11}) = \begin{cases} 1\ (\bar{\sigma}_{11} > 0), \\ 0\ (\bar{\sigma}_{11} < 0), \end{cases} \end{aligned} \tag{14}$$

where w_t and w_c are weight factors. According to Figure 10, when $\tilde{\varepsilon}_c^{\mathrm{pl}} = 0$, $d_c = 0$, then

$$(1-d) = (1-s_c d_t) = 1 - (1 - w_c(1-r^*)d_t). \tag{15}$$

In equation (15), when the material is in the state of tensile stress, $r * (\bar{\sigma}) = H(\bar{\sigma}) = 1$ and $d = d_t$. When the material is in the state of compressive stress, $d = (1-w_c)d_t$. If $w_c = 1$, then $d = 0$, the compression stiffness has been restored at this time. If $w_c = 0$ and $d = d_t$, the stiffness is not restored. If $0 \le w_c \le 1$, the stiffness is partially restored.

Due to the great difference between the tensile and compressive properties of concrete, the damage factor D can be calculated according to the tensile and compressive conditions, respectively. The compressive damage factor can be obtained from equation (12):

$$d_c = \frac{1 - \sigma_c E_0^{-1}}{\varepsilon_c - \tilde{\varepsilon}_c^{\mathrm{pl}}}. \tag{16}$$

By substituting $\varepsilon_c = \varepsilon_c^{\mathrm{in}} + \varepsilon_{0c}^{\mathrm{el}}$ and $\varepsilon_{0c}^{\mathrm{el}} = \sigma_c E_0^{-1}$ into equation (12), we can get

$$d_c = 1 - \frac{\sigma_c E_0^{-1}}{\tilde{\varepsilon}_c^{\mathrm{pl}}(1/b_c - 1) + \sigma_c E_0^{-1}}, \tag{17}$$

where $b_c = \tilde{\varepsilon}_c^{\mathrm{pl}}/\varepsilon_c^{\mathrm{in}}$.

Similarly, the cordera damage factor:

$$d_t = 1 - \frac{\sigma_t E_0^{-1}}{\tilde{\varepsilon}_t^{\mathrm{pl}}(1/b_t - 1) + \sigma_t E_0^{-1}}, \tag{18}$$

where $b_t = \tilde{\varepsilon}_t^{\mathrm{pl}}/\varepsilon_t^{\mathrm{ck}}$.

3.2. Analysis of Test Results. According to the above calculation conditions, the concrete numerical simulation test is carried out, and the nephogram of displacement and damage of the specimen under dynamic load with the change of load can be obtained, as shown in Figures 11 and 12.

It can be seen from Figure 11 that the longitudinal displacement of the concrete sample changes more evenly at the initial stage of loading. The displacement at the top of the sample is larger than that at the bottom, and there is a sudden change in the displacement near the initial defects (holes and cracks). This is due to the stress concentration near the initial defect, which leads to the strain localization of the specimen, which is consistent with the understanding of the compression densification of the specimen. With the further increase of displacement loading, new damage cracks appear in the specimen, and the displacement of the initial defect in the specimen mutates further, resulting in more uneven displacement in the whole section of the specimen. It can be found from Figure 11 that the more concentrated the initial defects are, the easier the specimen will be damaged, the more obvious the stress concentration is, and the more obvious the displacement mutation is. This explains the origin of strain localization from one side.

It can be seen from Figure 12 that under the dynamic load, the damage in the sample is mainly concentrated in the upper part of the sample, and it is easy to cause damage in the initial defects of the sample, and multipoint damage occurs at the same time. The damage crack is relatively

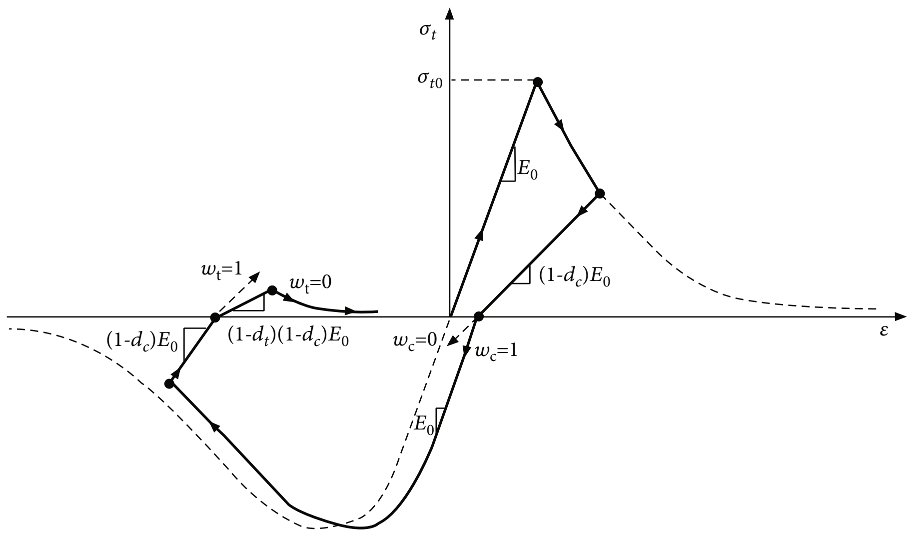

Figure 10: Stress cycling curve of concrete under uniaxial loading.

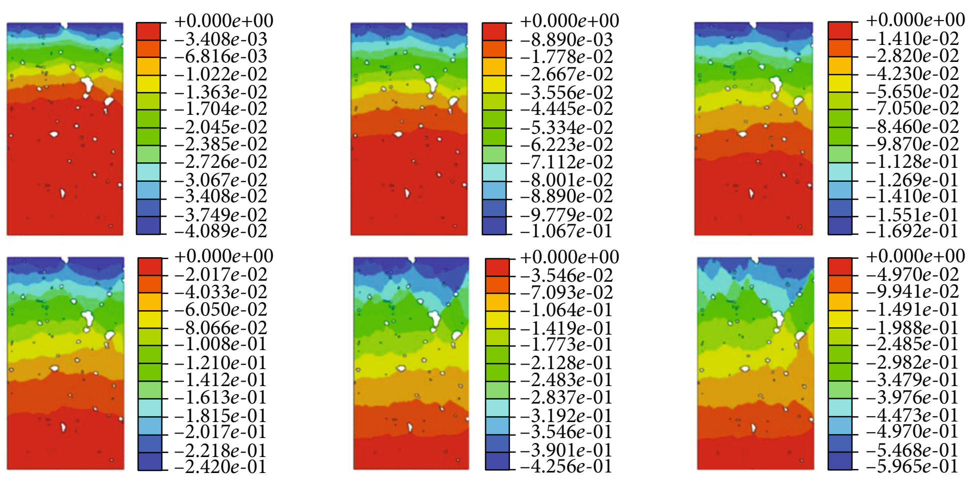

Figure 11: Longitudinal displacement of concrete under dynamic loading.

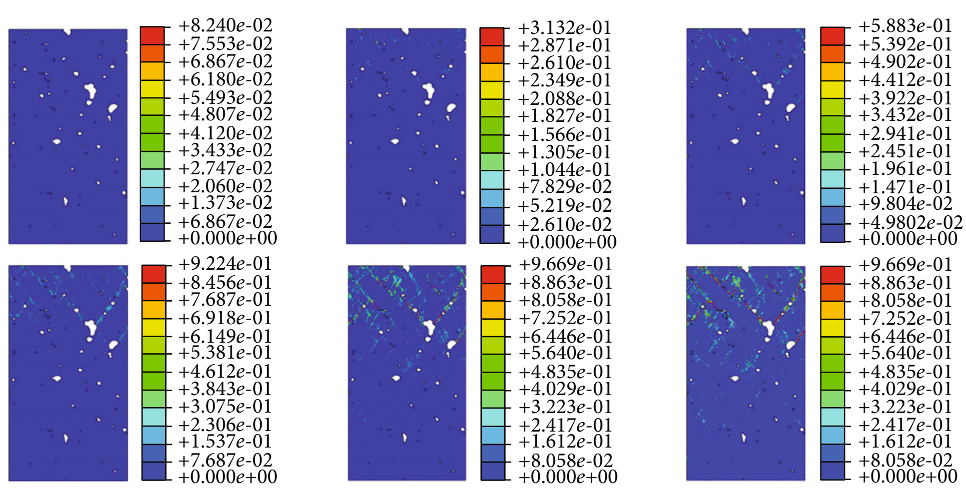

Figure 12: Damage evolution of concrete.

straight, and the phenomenon around the aggregate is not obvious. In some places, there is a phenomenon that the crack passes through the aggregate. This is different from the development of cracks around the interface with weak aggregate strength under static load.

The main reason is that under the action of dynamic load, due to the fast loading rate, the crack develops rapidly, so the crack has no time to follow the weak surface around the aggregate but follows the path of rapid energy release. This is consistent with the results of the physical CT test of coagulation under dynamic action.

Through the above analysis, it is found that the dynamic numerical simulation test by using the "structural random concrete numerical model" shows that the displacement and damage change law of concrete is very similar to the conclusion of the current physical test institute, which indicates that the model established in this paper is more practical in simulating the dynamic test of concrete.

4. Conclusions

In this paper, the CT test of concrete under dynamic uniaxial compression was carried out, the "structure random concrete numerical model" was constructed based on the CT images, and the mechanical properties of concrete under uniaxial dynamic compression stress were studied by using the model. The conclusions of this study are as follows.

(1) Based on the concrete CT test of dynamic loading and quantitative partition theory, the probabilistic statistical method to determine the subdivision threshold is proposed, and the "structure random concrete numerical model" was established based on CT resolution units. The "concrete numerical model of structure random" is very close to the real mesostructure of concrete; it can describe the mesostructure of concrete and can reflect the aggregate and the hardening cement interface. Moreover, the thickness of the interface is about 0.04 mm, which is very close to the real interface thickness (about 10-50 μm)

(2) Under the action of dynamic load, the damage in the sample is mainly concentrated in the upper part of the sample, and it is easy to cause damage in the initial defects of the sample, and multipoint damage occurs at the same time. The damage crack of concrete develops rapidly; the crack does not have enough time to follow the weak side around the aggregates but follows the path of energy release fast

Data Availability

The basic data supporting my research results can be found in the article.

Conflicts of Interest

The authors declare that they have no conflicts of interest.

Acknowledgments

The research is funded by the Natural Science Foundation of China (No. 51979225), Natural Science Foundation of Shaanxi Provincial Department of Education of China (No. 18JK0547), Science and technology innovation project of Xi'an University of Technology (No. 2016CX026), and Xi'an University of Technology School Doctor Gold (No. 107-451116012).

References

[1] Y. Yong, Y. Deng, and C. Daiguo, "Numerical modeling study on the penetration impact of concrete mesoscopic composition," *Chinese Journal of Applied Mechanics*, vol. 1, pp. 69–75, 2015.

[2] C. Chen, S. Bai, Y. Huang, L. Lam, Y. Yao, and L. M. Keer, "3D random packing algorithm of ellipsoidal particles based on the Monte Carlo method," *Magazine of Concrete Research*, vol. 73, no. 7, pp. 343–355, 2021.

[3] Q. I. N. Yuan, C. H. A. I. Jun-rui, and D. A. N. G. Fa-ning, "Numerical analysis on static and dynamic strength of dam concrete," *Journal of Water Resources and Architectural Engineering*, vol. 11, no. 1, pp. 1–6, 2013.

[4] C. J. Yue, H. Y. Ma, H. F. Yu et al., "Experimental and three-dimensional mesoscopic simulation study on coral aggregate seawater concrete with dynamic direct tensile technology," *International Journal of Impact Engineering*, vol. 150, p. 103776, 2021.

[5] W. Ren, Z. Yang, R. Sharma, C. Zhang, and P. J. Withers, "Two-dimensional X-ray CT image based meso-scale fracture modelling of concrete," *Engineering Fracture Mechanics*, vol. 133, pp. 24–39, 2015.

[6] H. S. Wong, M. Zobel, N. R. Buenfeld, and R. W. Zimmerman, "Influence of the interfacial transition zone and microcracking on the diffusivity, permeability and sorptivity of cement-based materials after drying," *Magazine of Concrete Research*, vol. 61, no. 8, pp. 571–589, 2009.

[7] Q. Yu, H. Liu, T. Yang, and H. Liu, "3D numerical study on fracture process of concrete with different ITZ properties using X-ray computerized tomography," *International Journal of Solids and Structures*, vol. 147, pp. 204–222, 2018.

[8] H. Wang, Z. Huang, L. Li, Z. You, and C. Yu, "Three-dimensional modeling and simulation of asphalt concrete mixtures based on X-ray CT microstructure images," *Journal of Traffic and Transportation Engineering (English Edition).*, vol. 1, no. 1, pp. 55–61, 2014.

[9] T. I. A. N. Wei, D. A. N. G. Fa-ning, and C. H. E. N. Hou-qun, "CT experimental study on failure characteristics of concrete under dynamic loading," *Journal Of Earthquake Engineering And Engineering Vibration*, vol. 31, no. 1, pp. 30–34, 2011.

[10] J. Kollmann, G. Lu, P. Liu et al., "Parameter optimisation of a 2D finite element model to investigate the microstructural fracture behaviour of asphalt mixtures," *Theoretical and Applied Fracture Mechanics*, vol. 103, p. 102319, 2019.

[11] Z. Wang, H. Li, and X. Lan, "Formation damage mechanism of a sandstone reservoir based on micro-computed tomography," *Advances in Geo-Energy Research*, vol. 5, no. 1, pp. 25–38, 2021.

[12] Y. Zhao, J. Jiang, Y. Dai, L. Zhou, and F. Ni, "Thermal property evaluation of porous asphalt concrete based on heterogeneous

meso-structure finite element simulation," *Applied Sciences*, vol. 10, no. 5, p. 1671, 2020.

[13] Y. Xue, T. Teng, F. Dang, Z. Ma, S. Wang, and H. Xue, "Productivity analysis of fractured wells in reservoir of hydrogen and carbon based on dual-porosity medium model," *International Journal of Hydrogen Energy*, vol. 45, no. 39, pp. 20240–20249, 2020.

[14] X. Wang, H. Yin, X. Zhao, B. Li, and Y. Yang, "Microscopic remaining oil distribution and quantitative analysis of polymer flooding based on CT scanning," *Advances in Geo-Energy Research*, vol. 3, no. 4, pp. 448–456, 2019.

[15] H. Elaqra, N. Godin, G. Peix, M. R'Mili, and G. Fantozzi, "Damage evolution analysis in mortar, during compressive loading using acoustic emission and X-ray tomography: effects of the sand/cement ratio," *Cement and Concrete Research*, vol. 37, no. 5, pp. 703–713, 2007.

[16] L. Zhu, D. Faning, and D. Weihua, "Coupled X-ray computed tomography and grey level co-occurrence matrices theoryas a method for detecting microscopic damage of concrete under different loads," *China Civil Engineering Journal*, vol. 53, no. 8, pp. 97–107, 2020.

[17] Y. Ju, H. Sun, M. Xing, X. Wang, and J. Zheng, "Numerical analysis of the failure process of soil–rock mixtures through computed tomography and PFC3D models," *International Journal of Coal Science & Technology*, vol. 5, no. 2, pp. 126–141, 2018.

[18] J. Zheng, Y. Ju, and X. Zhao, "Influence of pore structures on the mechanical behavior of low-permeability sandstones: numerical reconstruction and analysis," *Int J Coal Sci Technol*, vol. 1, no. 3, pp. 329–337, 2014.

[19] Y. Xue, J. Liu, P. G. Ranjith, X. Liang, and S. Wang, "Investigation of the influence of gas fracturing on fracturing characteristics of coal mass and gas extraction efficiency based on a multi-physical field model," *Journal of Petroleum Science and Engineering*, vol. 206, p. 109018, 2021.

[20] D. Hao, S. Tu, C. Zhang, and H. Tu, "Quantitative characterization and three-dimensional reconstruction of bituminous coal fracture development under rock mechanics testing," *Fuel*, vol. 267, p. 117280, 2020.

[21] G. Wang, X. Qin, D. Han, and Z. Liu, "Study on seepage and deformation characteristics of coal microstructure by 3D reconstruction of CT images at high temperatures," *International Journal of Mining Science and Technology*, vol. 31, no. 2, pp. 175–185, 2021.

[22] L. Zhu, F. Dang, Y. Xue, K. Jiao, and W. Ding, "Multivariate analysis of effects of microencapsulated phase change materials on mechanical behaviors in light-weight aggregate concrete," *Journal of Building Engineering*, vol. 42, p. 102783, 2021.

[23] T. I. A. N. Wei, D. A. N. G. Fa-ning, D. I. N. G. Wei-hua, L. I. A. N. G. Xin-yu, and C. H. E. N. Hou-qun, "Development of a dynamic loading apparatus for CT experiment and its application," *Rock and Soil Mechanics*, vol. 31, no. 1, 2010.

[24] J. Fang, Y. Pan, F. Dang, X. Zhang, J. Ren, and N. Li, "Numerical reconstruction model and simulation study of concrete based on damaged partition theory and CT number," *materials*, vol. 12, no. 24, p. 4070, 2019.

Hindawi
Geofluids
Volume 2021, Article ID 6423048, 15 pages
https://doi.org/10.1155/2021/6423048

Research Article

An Estimation Model for Hydraulic Conductivity of Low-Permeability and Unfilled Fractured Granite in Underground Water-Sealed Storage Caverns

Yangbing Cao, Weiguo Gong, Xiangxiang Zhang, Junxi Chen, and Zhenping Huang

Zijin School of Geology and Mining, Fuzhou University, Fuzhou 350116, China

Correspondence should be addressed to Yangbing Cao; cybing1140504@163.com

Received 21 April 2021; Accepted 24 August 2021; Published 27 September 2021

Academic Editor: Yi Xue

The permeability of rock mass is closely related to the stability and safety of underground structure, especially in underground water-sealed storage caverns. With regard to the estimation approaches in predicting the hydraulic conductivity of fractured granite in water-sealed storage caverns, there are some limitations of parameter selection leading to poor applicability. Focusing on the contribution of the water conduction fractures (WCF) to the hydraulic conductivity, we attempted to propose a novel model, the CA model, for estimating its hydraulic conductivity based on the fracture orientation index and the normal stress index by analyzing the borehole wall imaging results and borehole water-pressure test results in the site of underground water-sealed storage caverns. The results indicated that the proposed model is suitable for low-permeability and unfilled fractured granite, exhibiting good effectiveness by clarifying the relation between geomechanical parameters and hydraulic behavior. Further, the parameters upon which the proposed model is based are representative and easy to obtain, which has certain guiding significance and reference value for analyzing the permeability characteristics of similar rock masses.

1. Introduction

At present, many underground water-sealed storage caverns are located in the low-permeability and unfilled fractured granite area. A large number of random joints result in distinct heterogeneity and anisotropy in the permeability of fractured granite. With the abovementioned features of granite, most underground water-sealed storage caverns for oil or liquefied petroleum gas make the groundwater flow in complex fracture networks, forming a stable seepage field by constructing a water curtain system, so as to achieve the long-term storage of oil or liquefied petroleum gas. However, groundwater seepage may not only weaken the granite strength but form local high-pressure seepage resulted from water-sealed conditions, resulting in some geological disasters such as block falling or block sliding.

Therefore, the groundwater seepage characteristics of fractured granite in these water-sealed storage cavern areas become a critical issue to study the stability of surrounding granite and the evolution of seepage field. Specifically, the construction of the seepage medium model, as well as the determination of hydraulic conductivity, is the most essential question. Currently, the seepage medium model of the rock mass can be divided into three categories: the equivalent continuum medium model [1–3], double-medium model [4, 5], and discrete fracture network (DFN) model [6–8]. However, the equivalent continuum model is only applicable to large-scale loose or broken rock with a representative elementary volume (REV). In addition to a small-scale REV, the input parameters of the dual medium model are complex and possess a wide range of assumptions. Meanwhile, the two types of continuous medium models do not involve the specific spatial distribution of the water conduction fractures (WCF), and they are difficult to characterize the heterogeneity and discontinuity of seepage in the rock mass, making them unsuitable for the underground water-sealed storage caverns. Note that the WCF is a class of rock mass fracture belonging to the primary seepage zone. Generally, primary seepage zones are some fractures with high permeability or distinct systematic distributions as well as a combination of the two in rock mass. The DFN model assumes that flow and solute transport occur primarily within fractures [9]. Therefore, by accurately describing the geometric parameters (orientation, spacing and aperture, etc.) and hydraulic parameters (hydraulic aperture, etc.) of each fracture in the fracture network, the geometric and hydraulic characteristics of the WCF can be described. Thus, the heterogeneity and seepage anisotropy of the fractured rock mass can be determined. This model has been widely used in the stability and seepage analysis of high and steep rock slopes and underground caverns with small research areas and requires high research degree and calculation accuracy [10, 11]. In summary, the fractured granite of the underground water-sealed storage cavern can be examined as a fractured seepage network comprising WCF, enabling seepage calculations to be conducted using the DFN model with a calibrated hydraulic conductivity.

Methods for determining the hydraulic conductivity of fractured rock mass mainly include the field hydraulic test method, inverse analysis method, and empirical estimation method. The field hydraulic test method [12, 13] obtains the hydraulic conductivity of rock mass via an analytical calculation of water-pressure test and pumping test data in situ. However, because of its high cost as well as technology and time requirements, its precision and scope are limited, and it is difficult to reflect the hydraulic conductivity characteristics of the rock mass of the entire study area. Meanwhile, the inverse analysis method [14, 15] is based on the monitoring data of groundwater flow rate or velocity. The hydraulic conductivity of a rock mass is calculated via analytical or numerical methods, but it often provides a no-unique solution, which affects the accuracy. Finally, the empirical estimation methods mainly include the fracture network measurement method, fracture network numerical test method, and geological index estimation method. Among these, in the fracture network measurement method [16–18], the geometric parameters of fractures in the measurement and statistic area are substituted into the permeability tensor formula to obtain the initial value of the equivalent permeability tensor, which must then be corrected using the hydraulic test method or inverse analysis method. The fracture network numerical test method [19–21] was proposed by Long et al. [19] to determine the REV and equivalent permeability tensor of rock mass. However, the understanding of the existence and size effect of the REV is not uniform, which makes it difficult to establish the numerical model.

The geological index estimation method can be divided into single index and comprehensive index estimation methods. Currently, many scholars use a single index, such as depth [22, 23], P-wave velocity (V_p) [24], geoelectrical parameters [25], or rock quality designation (RQD) [26, 27], to establish an empirical formula to predict the hydraulic conductivity of rock mass. Moreover, existing estimation models based on the comprehensive index have also made great progress. Hsu et al. [28, 29] defined a comprehensive index HC that considers the RQD, depth index (DI), lithology permeability index (LPI), and gouge content designation (GCD) index and estimated the hydraulic conductivity of fractured sedimentary rock by establishing a power function relationship between the hydraulic conductivity (K) and HC index. Song et al. [30] proposed the RMP index, which considers the RQD, rock integrity designation (RID), fracture aperture designation (AD), and LPI and established a power function relationship to estimate the hydraulic conductivity of the underground water-sealed caverns for liquefied petroleum gas (LPG) engineering site. Chen et al. [31] developed the ZRF model, which considers the buried depth (Z), RQD, and GCD, in order to estimate the hydraulic conductivity of the granite in a hydropower station. Thus, geological index estimation models are simple and practical and have a certain application value in stability and permeability research of rock mass engineering. However, as geological indices of rock mass are adopted mainly to characterize rock mass mechanics, the indices may not be entirely applicable to hydraulic behavior [32]. Therefore, the proposed models lack key parameters, such as the fracture orientation and hydraulic aperture, which control the hydraulic conductivity of rock mass and cannot form a connection between the seepage model of the fractured media and permeability of the fractured rock mass.

Based on the field test results of borehole water-pressure tests and borehole wall imaging tests of rock mass in a underground water-sealed storage cavern, this paper discusses the existing estimation indices and models and innovatively introduces geometric characteristic parameters such as the fracture orientation, number, and aperture of the WCF. Finally, we proposed a new model for estimating hydraulic conductivity that uses normal stress on the WCF and fracture orientation as its basic parameters. In addition, this model examines the influence of RQD, fracture spacing, and density on the permeability of the rock mass by considering the number of fractures. Based on the estimation results, it is proven that the proposed model can accurately reflect the permeability characteristics of fractured granite in the study area, thereby providing a reference for estimating the hydraulic conductivity and engineering application of other rock masses.

2. Hydraulic Conductivity Distribution Characteristics of Rock Mass in the Underground Water-Sealed Storage Caverns

2.1. Geological and Hydrogeological Setting. In this study, the underground water-sealed storage cavern area is situated in the eastern coastal area of Shandong Province, China. The research object of this study is a water-sealed storage cavern for propane on the east side of the project area. As shown in Figure 1, the study area is located in a transition zone between hills and alluvial plains. The altitude of the ground surface ranges from 15 m to 40 m, the topographic slope gradient is less than 5°, and the overall dip direction of the slope is westward. Because of the construction of ancillary facilities on the ground, the surface morphology is required to create a flat with the final elevation of approximately 30 m. In the study area, fine-grained monzonitic granite and marble occurred in the northeast of it, and the surface is covered with thin Quaternary overburden. The grained monzonitic granite was formed in the early stages of the Yanshan period

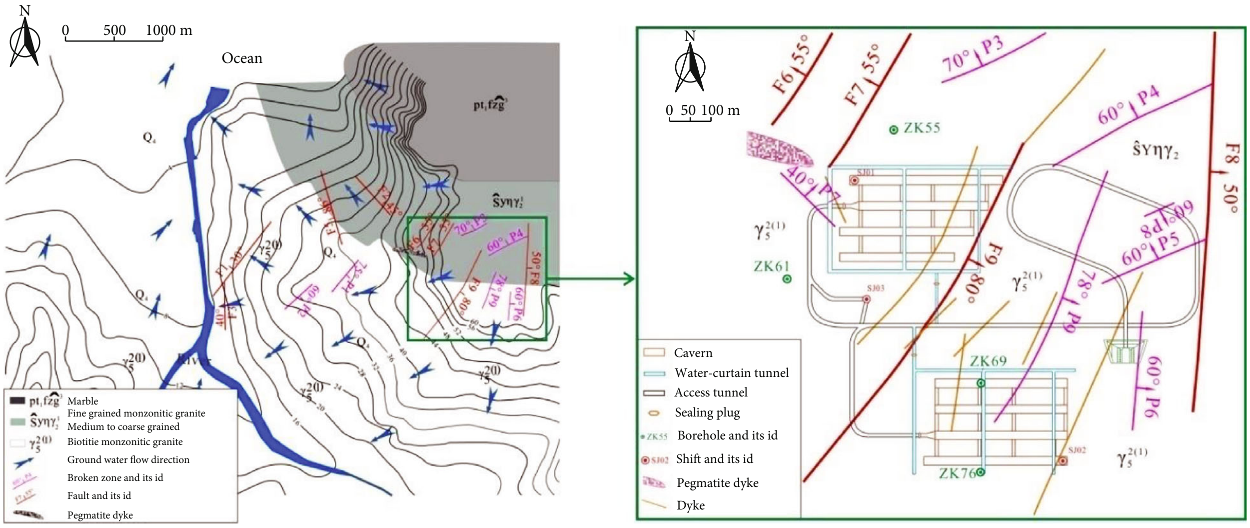

Figure 1: Geological and hydrogeological setting: (a) the regional area and (b) the study area.

which has a blocky structure and is generally medium to coarse grained. It is relatively hard rock accounting for more than 80% of the cavern rock mass. The rock mass of the slightly weathering layer has high strength, and the fractures range from extremely low developed to low developed. This is the main rock constructing the cavern, and the basic quality grade of the rock mass is II-III. The cavern construction is greatly influenced by secondary faults and joints distributed in the engineering area. According to the survey results of faults and discontinuities, the faults within the cavern site mainly include fault F9 and fracture zone P9. The remaining faults or fracture zones are far from the caverns and are small scale, barely influencing the cavern construction.

The hydrogeological survey revealed that the groundwater is mainly recharged by the vertical infiltration of atmospheric precipitation and lateral groundwater in mountainous areas, whereas it is mostly discharged by surface runoff with small infiltration. As illustrated in Figure 1, groundwater flows from higher altitudes areas of the eastern mountains to the western and northern regions and finally into the adjacent river and ocean. According to the laboratory and in situ test results, the granite matrix has very low permeability and porosity. Because of the development of joints, the low-permeability value of the rock matrix, and the large hydraulic gradient in the slightly weathered granite, groundwater mainly flows through the complex fracture network. Moreover, it appears to be the primary pathway in some broken areas and fracture concentrated belts. Therefore, the hydrogeological conditions of the study area highly obey the assumption of the fracture network model.

In the fresh or slightly weathered granite, the geostress was measured in two vertical boreholes using the hydraulic fracturing method. The classical theory of hydraulic fracturing was proposed by Hubbert and Willis [33]. To date, it has been deeply developed in theory and widely used in the geostress measurement and the stimulation technique of oil and gas reservoirs in the petroleum industry [34–36]. The conditions of this study area obey the assumptions of the hydraulic fracturing classical theory, including the test section of the rock which is homogeneous, isotropic, linear elastic, intact, and impermeable, and there is one principal stress direction parallel to the borehole axis. Because the final altitude of the ground surface will be flat, it is assumed to be a plane with a 30 m altitude in the following regression analysis. Therefore, the calculation of the geostress can be transformed to a planar stress issue with a circular hole in an infinite plate [34]. In addition, it was predetermined that the tensile stress is positive, and the compressive stress is negative. The maximum and minimum horizontal principal stresses are, respectively, 13.71 MPa and 8.05 MPa in the corresponding design altitude range of the cavern floor. Thus, it can be judged that the site is an area of medium and low in situ stress in accordance with the Chinese standard for engineering classifications of rock mass [37]. After tensor transformation, tensor averaging, and a linear regression analysis, the direction of the maximum principal stress was determined to be NE78° along the horizontal plane. Assuming that the weight density of the rock mass was 27 kN/m^3, the fitting relationships between the principal stresses and altitude are as follows:

$$\begin{cases} \sigma_H = 0.0361h - 6.0651, \\ \sigma_h = 0.0206h - 3.9489, \\ \sigma_v = 0.027h - 0.81, \end{cases} \tag{1}$$

where σ_H, σ_h, and σ_v are the maximum principal stress (MPa), intermediate principal stress (MPa), and minimum principal stress (MPa), respectively, and h is the altitude (m).

Borehole wall imaging tests were conducted in 28 boreholes using borehole televiewer technology and the latest digital panoramic borehole camera system (DPBCS) [38]. The DPBCS were employed as follows: a digital high-definition camera device in front of the probe can record a continuous, magnetically orientated, digital, 360° color image of the borehole wall. The depth and plane orientation are measured by the wheel and magnetic electronic compass

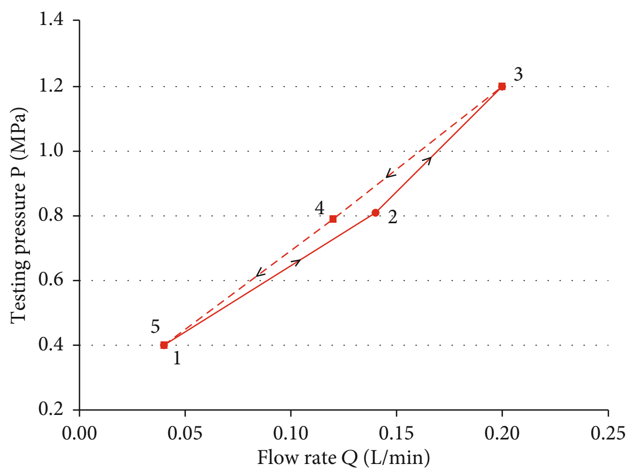

FIGURE 2: Diagram of stable flow rate and testing pressure variation at the five test stages.

of the DPBCS, respectively, and the annular borehole wall image is obtained. Then, in the flattened pattern, the annular borehole wall image is converted into a two-dimensional panoramic image in the order of N-E-S-W-N. Using the established coordinate system, it is reduced to a real borehole wall image. Finally, image interpretation software can be used to process the image to obtain the orientation, location, geometrical aperture, spacing, and filling content. After completing abovementioned steps, it was found that the fractures of the slightly weathered rock mass were basically closed, and there was no filled medium inside. However, not all the data from DPBCS and interpretation software are available, and geometrical aperture is also difficult to accurately process as the use of rigorous mathematical formulas and interpretation algorithms produce errors. Therefore, this study mainly conducted permeability analyses and hydraulic conductivity estimations based on the fracture orientation, number, spacing, and other geometric parameters.

2.2. Analysis of Borehole Water-Pressure Test Data. In accordance with the Chinese code of water-pressure tests in boreholes for water resources and hydropower engineering (CCWPT) [39], a total of 609 test sections were then subjected to double-packer water-pressure tests adopted intelligent water-pressure testers. Each test section is divided into three levels of pressure and three or five stages owing to the depth of the test section. Figure 2 shows the basic curve between the test pressure (P) and input flow (Q) of the test section when five stages existed. According to the CCWPT, if the absolute differences in the flow rate between stages 4 and 2 (or between stages 3 and 1 if there are only three stages) and between stages 5 and 1 are less than 1 L/min, or the relative errors are less than 5%, the boost and the buck phases in the P-Q curve can be considered to be basically coincident. In this study, the flow rate of every stage was invariably less than 1 L/min; so, the absolute difference was less than 1 L/min. Thus, the P-Q curves conform to the type of laminar flow, meaning that the fracture water flowing in the low-permeability and unfilled fractured granite was considered to be laminar flow.

Owing to the fact that the groundwater flow through the fracture was laminar, the Lugeon value of the rock mass in the test sections can be calculated using formula (2), except for the test sections with high permeability around the fracture zone or a joint dense development zone.

$$q = \frac{Q_{\max}}{L \bullet P_{\max}}, \tag{2}$$

where q (Lu) is the Lugeon value, L (m) is the length of the test section, $Q_{\max}$ (L/min) is the maximum flow rate for each test stage (the third stage if five stages exist and the second stage if three stages exist), and $P_{\max}$ (MPa) is the maximum testing pressure for each test stage (the third stage if five stages exist and the second stage if three stages exist).

The distribution of the Lugeon values in the fresh or slightly weathered granite is illustrated in Figure 3. A three-parameter Weibull distribution was used to fit the results, revealing a shape parameter of 0.80, a scale parameter of 0.061, and a location parameter of 0.001. In addition, the results show that the permeability of the cavern site is mainly distributed in 0.001–0.20 Lu, with an average of 0.082 Lu and a maximum of 1.098 Lu. Therefore, according to the CCWPT, the rock mass in the study area is mainly low permeability or extremely low permeability.

According to the method suggested in the CCWPT, when the test section is below the groundwater level, q < 10 Lu and the fracture flow are laminar. Thus, the equivalent hydraulic conductivity of the rock mass in the test section can be calculated using formula (3), which was proposed by Hvorslev [40]. Figure 4 illustrates the distribution characteristics of the hydraulic conductivity of 599 test sections in the fresh or slightly weathered granite area (without considering the test sections with larger K values around the fracture zone or joint dense development zone). A three-parameter Weibull distribution was used to fit the data. Based on the fit, the shape parameter was found to be 0.851, the scale parameter was 7.2×10^{-4}, and the location parameter was 3.6×10^{-6}. After obtaining the distribution model and statistical characteristics of the random variables, the Monte Carlo method can be used for generation in computer software [34].

$$K = \frac{Q}{2\pi LH} \ln \left[\frac{L}{2r} + \sqrt{1 + \left(\frac{L}{2r} \right)^2} \right], \tag{3}$$

where K is the hydraulic conductivity, Q is the flow rate, r is the radius of the borehole, H is the testing pressure head, and L is the same as above.

2.3. Applicability of the Single Index Estimation Method of Hydraulic Conductivity. At present, many empirical models use a single index, such as depth (Z or DI), P-wave velocity of rock mass (V_p), or rock quality designation (RQD), to estimate the hydraulic conductivity of rock mass. These

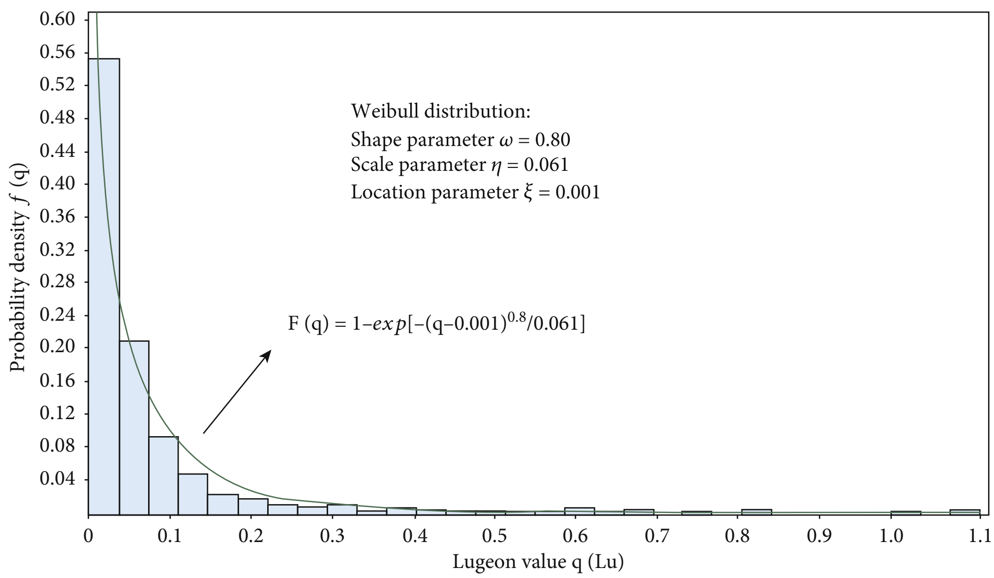

Figure 3: Distribution characteristics of Lugeon values in fresh or slightly weathered granite.

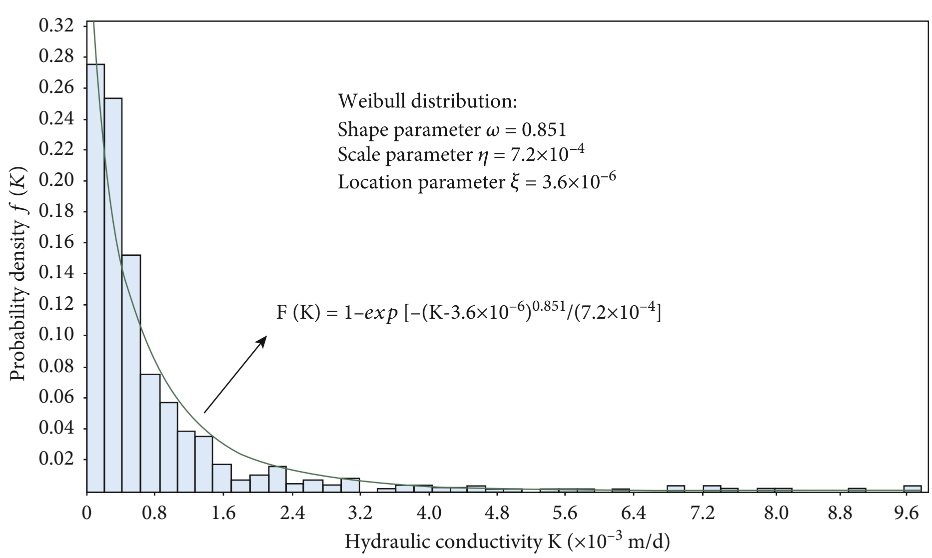

Figure 4: Distribution characteristics of hydraulic conductivity in fresh or slightly weathered granite.

indices are mostly based on the relationship between the degree of fracture development and the corresponding index. Then, we explored whether the above indices are suitable for estimating the hydraulic conductivity of fractured granite in the study area.

According to the results of the water-pressure tests, Figure 5 demonstrated the distribution of hydraulic conductivity of rock mass with depth. It can be seen that the hydraulic conductivity is mainly concentrated in the range of 10^{-5} – 10^{-2} m/d, and it is irregular at each depth, reaching even three orders of magnitude differences at the same depths. Further, it was found that with increasing depth, the hydraulic conductivity of each borehole exhibited the following changes:

(1) In a small portion of the boreholes, with increasing depth, the hydraulic conductivity of the rock mass remained basically unchanged, only experiencing a very slight fluctuation

(2) In a small portion of the boreholes, with increasing depth, the hydraulic conductivity of the rock mass remained basically unchanged, and only in dense local fractures or large fractures did the hydraulic conductivity increase sharply

(3) In most boreholes, the hydraulic conductivity of the rock mass changes irregularly with increasing depth, and the relationship between the hydraulic conductivity and depth is disordered

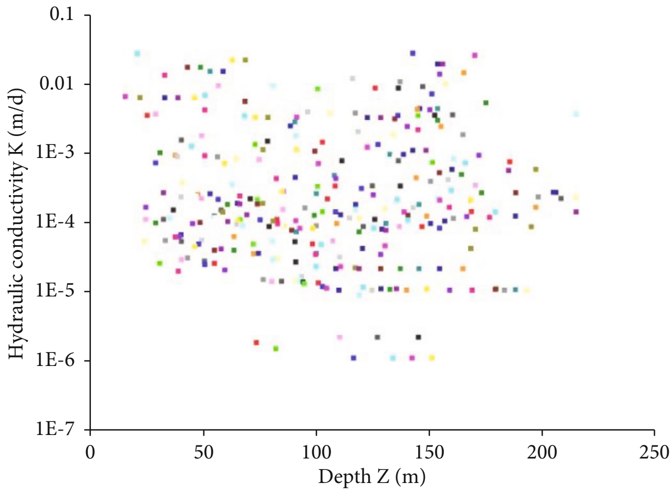

Figure 5: Scatter diagram of hydraulic conductivity distribution in study area.

The permeability of the granite at the site is closely related to the distribution characteristics of the fractures and the integrity of the rock mass, which can be characterized by the RQD and RID, in which the RQD refers to the cumulative length of core pieces longer than 100 mm in a run (R_S) divided by the total length of the core run (R_T) under standard drilling processes, and *RID* is obtained using the following:

$$\mathrm{RID} = \left(\frac{V_p}{V_r}\right)^2, \tag{4}$$

where V_p is the elastic P-wave velocity of the rock mass, and V_r is the elastic P-wave velocity of the rock block. As RQD and RID are both, to a certain extent, influenced by development density, size, and aperture of fractures, the relationship between rock permeability and the fracture distribution and rock integrity can be described using RQD and V_p.

Based on the core logging results of the boreholes and the test results of the P-wave velocity, the average P-wave velocity of the rock mass in each borehole was found to be between 4.8 km/s and 5.2 km/s. Further, it was found that most boreholes are similar to the K-RQD and K-V_p curves of ZK55 shown in Figures 6 and 7, respectively, which both exhibit no obvious regularity and large dispersion.

In summary, the single index method of estimating hydraulic conductivity, including the index of depth, *RQD*, and P-wave velocity, is not suitable to directly estimate the hydraulic conductivity of the rock mass in the study area. Therefore, based on the paradigm of the comprehensive index estimation method, a new estimation model to estimate the hydraulic conductivity of low-permeability and unfilled fractured granite in underground water-sealed storage caverns must be proposed considering the comprehensive effect of multiple indices.

3. Hydraulic Conductivity Estimation Model of Low-Permeability and Unfilled Fractured Granite

3.1. Model Construction and Parameter Selection. The permeability of fracture media in the DFN depends almost entirely on the spatial structure of the fracture system; meaning, the relationship between the fracture properties and permeability can be clarified by establishing a simple medium model of fractured rock mass. Snow [16] assumed that there was a water-conducting fracture network composed of n groups of directional fractures in a medium of pure fractured rock mass, and that the fracture water took a laminar flow. Therefore, the permeability tensor of each group of the WCF was superimposed based on the cubic law of the parallel plate model, and considering geometric factors, such as the fracture orientation, spacing, and hydraulic aperture, the following permeability tensor calculation formula was proposed, which is referred to as the snow model:

$$K_{\mathrm{SNOW}} = \frac{g}{12\nu}\sum_{i=1}^{n}\frac{b_i^3}{S_i}\begin{bmatrix} 1-n_{xi}^2 & -n_{xi}n_{yi} & -n_{xi}n_{zi} \\ -n_{yi}n_{xi} & 1-n_{yi}^2 & -n_{yi}n_{zi} \\ -n_{zi}n_{xi} & -n_{zi}n_{yi} & 1-n_{zi}^2 \end{bmatrix}, \tag{5}$$

where K_{SNOW} (m/s) is the hydraulic conductivity tensor of the rock mass, g (m/s^2) is the gravitational acceleration, ν (m^2/s) is the kinematic viscosity, b_i (m) is the average hydraulic aperture of group i, S_i (m) is the space of group i, n_{xi}, n_{yi}, and n_{zi} are components in the x, y, and z directions, respectively, of the unit normal vector of group i fracture, and n is the number of fractures.

Snow [16] considered the number of fractures to reflect the spacing and density of the fractures by superposing the hydraulic conductivity tensor of all the WCF, which is actually the contribution of rock integrity parameters to the

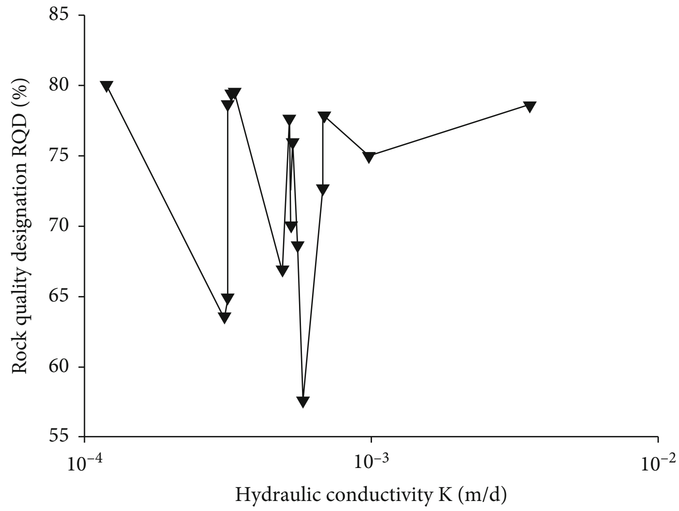

Figure 6: Relationship curve between hydraulic conductivity (K) and rock quality designation (RQD).

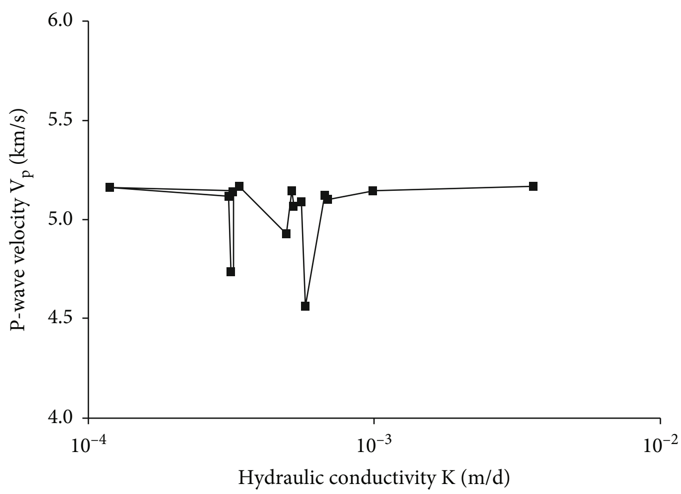

Figure 7: Relationship curve between hydraulic conductivity (K) and P-wave velocity (V_p).

hydraulic conductivity. Further, the snow model is suitable for laminar flow and clean fractures, which are consistent with the characteristics of the granite in the study area. Therefore, the snow model can be simplified into two parts: the orientation of all fractures and the hydraulic aperture. According to the superposition principle of the hydraulic conductivity tensor and considering the number of fractures, the fracture orientation index and hydraulic aperture index were tentatively selected to establish a new model for predicting the hydraulic conductivity of the low-permeability and unfilled fractured granite in underground water-sealed storage caverns. The hydraulic aperture is mainly controlled by normal stress, contact area, geometrical aperture, and roughness of the fracture, and it is difficult to determine the hydraulic aperture directly. Previous relevant studies [34, 41, 42] show that the quantitative relationship exists distinctly between normal stress and fracture hydraulic aperture. Fortunately, the normal stress of fractures is relatively easy to obtain in engineering; so, it was selected to replace the index of hydraulic aperture for the construction of the estimation model. Therefore, the normal stress, as a comprehensive index, combined with the orientation index of the discontinuity can comprehensively characterize the hydraulic behavior of the fracture.

The hydraulic conductivity tensor of the rock mass is based on the permeability characteristics of the WCF. However, according to the results of the borehole water-pressure tests and borehole wall imaging tests in the study area, it was found that not all fractures are the WCF, and most have no seepage significance. As the orientation of the WCF determines the primary seepage direction of the rock mass, the fracture network model needs to be characterized emphatically. Therefore, in the case of existing fracture orientation index, the proposed model introduces orientation index of the WCF to characterize the contribution of the hydraulic characteristics of the WCF to the permeability of the rock mass.

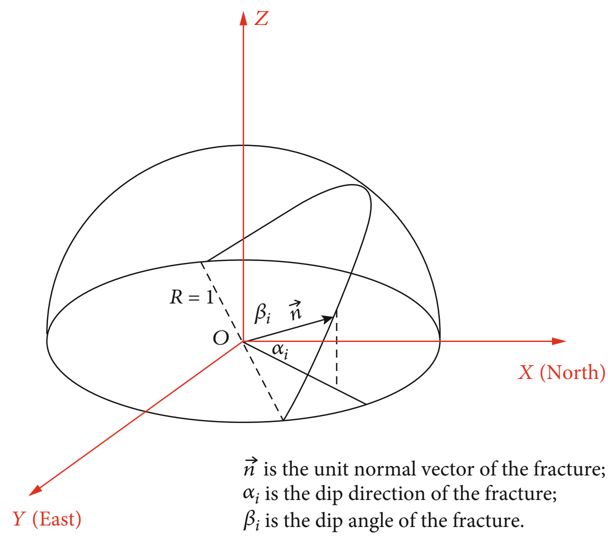

FIGURE 8: Schematic diagram of unit normal vector of fracture orientation in geographic coordinate system.

3.2. Novel Model for Estimating Hydraulic Conductivity of Fractured Granite in Water-Sealed Storage Caverns. Based on the snow model and fracture network model elements, this study used the fracture orientation (denoted as A or A_j) and the normal stress (σ_n) of the WCF as the basic index to characterize the geometric characteristics of the fracture and the hydraulic properties of the WCF, respectively, and proposed an estimation model for hydraulic conductivity of the low-permeability and unfilled fractured granite in underground water-sealed storage caverns, called the CA model:

$$K = \alpha \bullet A + \beta \bullet C_{\text{wcf}} + \gamma, \tag{6}$$

where α, β, and γ are empirical constants, and K (cm/s) is the hydraulic conductivity of each test section. The index A represents the contribution of the orientation of all fractures to the hydraulic conductivity, and C_{wcf} is an integrated hydraulic index representing the contribution of all the WCF to hydraulic conductivity of rock mass. Therefore, the name of the CA model is taken from the main indices C_{wcf} and A. In terms of the unit of two parameters, the index A proposed in this study is dimensionless, and the unit of the index C_{wcf} is MPa^{-3}. Although the unit is different, the model only uses its numerical value.

(1) The method for obtaining the index A. It is assumed that the contribution of the orientation of n fractures to the hydraulic conductivity of the rock mass at a certain depth range is A_n. Based on the principle of permeability tensor superposition, the following formula can be obtained:

$$A_n = \sum_{i=1}^{n} A_i = \sum_{i=1}^{n} \begin{bmatrix} 1 - n_{xi}^2 & -n_{xi}n_{yi} & -n_{xi}n_{zi} \\ -n_{yi}n_{xi} & 1 - n_{yi}^2 & -n_{yi}n_{zi} \\ -n_{zi}n_{xi} & -n_{zi}n_{yi} & 1 - n_{zi}^2 \end{bmatrix}. \tag{7}$$

If the dip direction of fracture i is α_i, the dip angle is β_i, the x -axis points to the east, the y-axis points to the north, the z -axis points upwards, and a space rectangular coordinate system ENZ(xyz) is constructed. As shown in Figure 8, the x, y, and z components of the normal vector of the ID i of the fracture are expressed as follows:

$$\left.\begin{aligned} n_{xi} &= \sin \alpha_i \bullet \sin \beta_i \\ n_{yi} &= \cos \alpha_i \bullet \sin \beta_i \\ n_{zi} &= \cos \beta_i \end{aligned}\right\}. \tag{8}$$

The eigenvalues of A_n was calculated and denoted as A_1, A_2, and A_3, of which the three eigenvectors are the principal directions of the eigenvalues. The fracture orientation index A is defined as the geometric mean value of the eigenvalue A_n, as follows:

$$A = \sqrt[3]{A_1 \bullet A_2 \bullet A_3}, \tag{9}$$

where the physical meaning of A is the contribution of the orientation of all fractures to the hydraulic conductivity in the depth range of the test section. Therefore, the orientation index of fractures can be obtained by simultaneous formulas (7), (8), and (9).

(2) The method for obtaining the index C_{wcf}. To obtain C_{wcf}, the identification and selection of WCF should be conducted first to determine the mathematical relationship between the hydraulic parameters of the WCF and the hydraulic conductivity of the rock mass. Firstly, based on borehole wall image tests and water-pressure tests data, the hydraulic conductivity of each test section and internal fractures orientation was obtained. Secondly, the orientation ranges of fractures with a small hydraulic conductivity in the test section need to be screened out, and it was considered that it does not belong to the primary

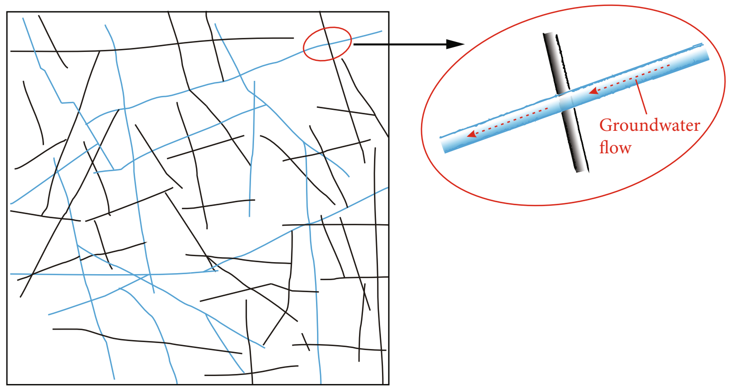

Figure 9: The WCF and the direction of groundwater flow in fracture system (the blue line represents the WCF, and the black line represents ordinary discontinuities).

seepage zone. Finally, it was removed from the orientation range of the test sections with large hydraulic conductivity, and what were retained were the WCF and its orientation in each test section. Based on the DFN model of a real discrete fracture network generated using a Monte Carlo simulation by Min et al. [6], Figure 9 represents the WCF selected from fracture network and internal groundwater seepage

Although we have selected the normal stress index (σ_n) instead of the hydraulic aperture (e_h) of the WCF to build the new model, it still plays a role as a bond between the hydraulic conductivity of rock mass and normal stress on the fracture. Based on the research results of Cao et al. [34] on the fracture hydraulic aperture of slightly weathered granite which located nearby the study area, it was assumed that a rock mass test section with upper and lower surfaces parallel to its contained fracture and with a distance of L between the two interfaces. Other parameters were kept the same as previously mentioned. The hydraulic conductivity K_r of the fractured rock mass is the superposition of the hydraulic conductivity of each fracture in the test section as follows:

$$K_r = \sum_{i=1}^{n} \frac{g(e_h)^3}{12\nu L} \cdot A_i. \tag{10}$$

Thus, the basic relationship between hydraulic aperture and normal stress was obtained, in which the quantitative relationship is given by fitting the average variation characteristics [34].

$$e_h = \frac{292.1}{\sigma_n + 1.78}. \tag{11}$$

According to formulas (10) and (11), the relationship between hydraulic conductivity and normal stress on the WCF of the fractured granite in the study area can be summarized as follows:

$$K_r \approx \sum_{i=1}^{n} \frac{g}{12\nu L} \cdot \frac{aA_i}{\sigma_{ni}^3}, \tag{12}$$

where a is constant. Therefore, the contribution index of the WCF to the hydraulic conductivity is

$$C_{wcf} = \sum_{j=1}^{N} \frac{A_j}{\sigma_{nj}^3}. \tag{13}$$

To facilitate the calculation in formula (13) and relate the physical meaning of A_j to A, A_j represents the contribution value of the orientation of all the WCF in the test section to the hydraulic conductivity of the rock mass, and the calculation method is the same as that used for the index A. When there is no WCF in the test section, that is, the number N of the WCF in the test section is 0, $C_{\mathrm{wcf}} = 0$. As the index A includes the contribution of some WCF orientation to the hydraulic conductivity of the rock mass, and because the relationship between the normal stress of the fracture and the hydraulic conductivity of the rock mass obtained by formula (12), it is appropriate to divide A_j into ${\sigma_{nj}}^3$, which not only avoids the issue that the geometric parameter of the WCF repeatedly lead to excessive weights in the estimation of the hydraulic conductivity but also possesses some theoretical and logical basis. The introduction of correction parameters α, β, and γ does not make the three terms of formula (6) have a large difference, especially when $C_{\mathrm{wcf}} = 0$.

The normal stress σ_{nj} of the WCF is calculated using the following steps. First, the fracture depth can be obtained from the location from the borehole wall image. Combined with the altitude of the borehole orifice, the fracture altitude can be calculated. Then, the principal stresses σ_H, σ_h, and σ_v at the fracture location can be obtained by substituting the fracture altitude into formula (1). Next, a unified spatial coordinate system of the principal stresses is constructed, as shown in Figure 10, wherein the H -axis positively points to the direction of the maximum principal stress, the h-axis positively points to the direction of the intermediate principal stress, and the v-axis points positively upward. According to second law of Cauchy stress, using the geometric relationship, the dip angle β and the adjusted dip direction α of the fracture are transformed into the rectangular

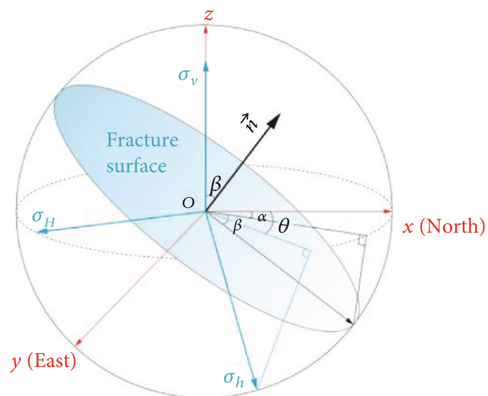

Figure 10: Schematic diagram of the orientation of discontinuity orientation in principle stress space.

coordinate system of the principal stress space to obtain the normal stress of the WCF:

$$\sigma_n = n_H^2\sigma_H + n_h^2\sigma_h + n_v^2\sigma_v, \tag{14}$$

where n_H, n_h, and n_v are the unit normal vectors of the fracture in the principal stress space coordinate system.

In summary, the hydraulic parameters A_j of the WCF are calculated by formulas (7), (8), and (9), just like index A. Substituting σ_{nj} calculated by formula (14) and A_j into formula (13), C_{wcf} can be easily acquired. According to the CA model, the empirical constants α, β, and γ can be gained from linear regression. Thereby, the estimated hydraulic conductivity K of the CA model is finally obtained.

4. Engineering Application and Reliability Analysis of CA Model

4.1. Parameter Fitting of the CA Model in the Study Area. Based on the interpretation results of borehole wall imaging and water-pressure test data of low-permeability and unfilled fractured granite in situ, we calculated the values of A, C_{wcf}, and $K_{\text{in-situ}}$ (the in situ test values of hydraulic conductivity from double-packer borehole water-pressure test) of each test section in ZK61 and ZK69, as listed in Table 1. The fracture strike range with low hydraulic conductivity ($K < 5 \times 10^{-5}$ m/d) was removed from the strike range with high hydraulic conductivity ($K > 5 \times 10^{-3}$ m/d), and that of the WCF was obtained as 0°–20°, 30°–50°, 330°–340°, and 350°–360°. In addition, according to the results of the borehole wall image, it was found that the dip direction of the dominant fractures in the rock mass is mainly distributed in the intervals 80°–90°, 110°–140°, and 270°–300°.

The CA model was used to fit the test data of ZK61 and ZK69, and the model parameters are listed in Table 2. The spatial variation characteristics of the regional geological conditions and permeability may be the reason for the different fitting parameters of the CA model in two boreholes. Given that ZK61 and ZK69 are located in the same engineering site, they have similar geological and hydrogeological

Table 1: Test results of boreholes in the study area.

Borehole	Depth [m]	Index A	Index C_{wcf}	$K_{\text{in-situ}}$ [m/d]
ZK61	31-41	6.899	0	7.91×10^{-5}
	41-51	12.024	0	9.75×10^{-3}
	51-61	7.584	0	3.60×10^{-4}
	61-71	8.087	2.53×10^{-3}	4.29×10^{-4}
	71-81	6.563	1.34×10^{-2}	5.67×10^{-4}
	81-91	3.773	5.85×10^{-3}	4.01×10^{-5}
	91-101	6.543	5.44×10^{-3}	3.91×10^{-4}
	101-111	2.386	7.30×10^{-3}	1.74×10^{-4}
	111-121	2.972	7.41×10^{-3}	4.25×10^{-4}
	121-131	1.791	0	1.46×10^{-4}
	131-141	5.685	3.55×10^{-2}	6.85×10^{-4}
	151-161	3.394	7.01×10^{-3}	4.12×10^{-4}
	161-171	3.187	1.16×10^{-3}	1.55×10^{-4}
	171-181	6.429	4.24×10^{-3}	1.90×10^{-4}
	181-191	3.696	4.12×10^{-3}	3.99×10^{-4}
	191-201	2.851	3.48×10^{-3}	2.97×10^{-4}
	201-211	8.035	5.02×10^{-3}	2.09×10^{-4}
ZK69	33-43	5.592	2.90×10^{-2}	1.23×10^{-4}
	42-52	6.761	1.30×10^{-2}	1.22×10^{-4}
	51-61	5.254	1.86×10^{-2}	9.54×10^{-5}
	60-70	5.367	4.30×10^{-3}	2.36×10^{-4}
	69-79	2.826	8.72×10^{-3}	2.01×10^{-4}
	78-88	6.147	1.80×10^{-3}	4.48×10^{-4}
	87-97	8.933	3.27×10^{-3}	1.94×10^{-4}
	96-106	5.094	6.54×10^{-3}	6.34×10^{-4}
	105-115	7.738	3.07×10^{-3}	8.57×10^{-4}
	114-124	10.473	1.96×10^{-2}	3.63×10^{-4}
	123-133	5.895	3.42×10^{-3}	4.13×10^{-4}
	132-142	3.958	0	4.37×10^{-4}
	141-151	0.633	0	1.11×10^{-4}
	150-160	4.931	0	1.04×10^{-4}
	159-169	1.185	1.24×10^{-2}	1.48×10^{-4}
	168-178	2.713	8.79×10^{-4}	1.30×10^{-4}
	177-187	4.574	4.13×10^{-3}	2.19×10^{-4}
	186-196	8.045	1.34×10^{-1}	2.65×10^{-3}
	195-205	8.279	1.33×10^{-1}	2.08×10^{-3}
	204-214	1.404	9.13×10^{-2}	1.15×10^{-3}
	213-223	4.096	6.33×10^{-3}	8.40×10^{-4}

Table 2: Fitting results of CA model parameters.

Boreholes	α	β	γ	R^2
ZK61	2.89×10^{-6}	1.30×10^{-2}	1.95×10^{-4}	0.78
ZK69	1.84×10^{-5}	1.40×10^{-2}	9.88×10^{-5}	0.74
All	2.04×10^{-5}	1.38×10^{-2}	7.40×10^{-5}	0.85

conditions, and the hydraulic conductivity is mainly concentrated in the magnitude of 10^{-4}–10^{-3} m/d. Moreover, the CA model was used to fit the two boreholes tests data simultaneously, and the estimation results are in accordance with the test results in situ ($R^2 = 0.85$). Therefore, the model proposed in this study is suitable for projects that have similar engineering geological conditions to that of the water-sealed storage caverns. According to the aforementioned research, the CA model may be more appropriate to estimate the hydraulic conductivity of rock mass with low permeability and internal unfilled fractures.

4.2. Verification and Reliability Analysis of the CA Model. Since this study has proposed a new model, it is necessary to test it, which is an inevitable process of scientific research. Moreover, the superiority of the new model needs to be demonstrated from the comparison with other models. Therefore, existing indices or models should be summarized and used to predict the hydraulic conductivity of low-permeability and unfilled fractured granite. The prediction results of CA model and previous models are compared with the $K_{\text{in-situ}}$ to explicate its superiority.

(1) The HC model and the RMP model. Existing comprehensive indices or estimation models mainly consider rock integrity (characterized by the RID or RQD), depth index (DI or Z), lithology permeability index (LPI), gouge content designation (GCD), and fracture aperture designation (AD) as basic parameters. To be specific, the HC index and the RMP index are the most representative, as follows:

$$\text{HC} = (1 - \text{RQD})(1 - \text{GCD})(\text{DI})(\text{LPI}), \tag{15}$$

$$\text{RMP} = (1 - \text{RQD})(1 - \text{RID})(\text{AD})(\text{LPI}), \tag{16}$$

where $\text{LPI} = 0.15$ is for granite through the classification of rock permeability [28]. Among these, the GCD is calculated using the following equation:

$$\text{GCD} = \frac{R_G}{R_T - R_s}, \tag{17}$$

where R_G is the total length of filling content and $\text{GCD} = 0$ for the unfilled granite in the study area. In addition, the HC index defined DI as the buried depth index:

$$\text{DI} = 1 - \frac{L_C}{L_T}, \tag{18}$$

where L_C is a depth that is located at the middle of a double-packer test interval in the borehole, and L_T is total borehole length. However, as the hydraulic conductivity of the rock mass is independent of the length of the borehole, the selected index DI may be unreasonable. The fracture aperture parameter (AD) in the RMP index is defined as the ratio of the sum of fracture aperture d_A and the length L of the test section. Since the two models are based on the HC index and RMP index, respectively, they can be called the HC model and RMP model. Based on two comprehensive indices, the two estimation models were used in estimating the hydraulic conductivity of sedimentary rocks with gouge filled and water-sealed storage caverns with unfilled granite, respectively.

$$K = b(\text{HC})^c, \tag{19}$$

$$K = m(\text{RMP})^n, \tag{20}$$

where b, c, m, and n are all fitting parameters. Using the HC model, the hydraulic conductivity of ZK76 at different depths in the study area was estimated, and the results are listed in Table 3.

Based on the empirical RMP model, the hydraulic conductivity of the ZK76 at different depths was estimated, and the estimation results are listed in Table 4.

(2) The ZRF model. In addition to considering RQD, the ZRF model introduced Z and GCD to predict the hydraulic conductivity of fractured rock mass at the site of Yagen-II Hydropower Station in China. The expression of the ZRF model is

$$\lg K = \kappa + \lambda \cdot PD + \omega \cdot \lg Z, \tag{21}$$

$$\text{PD} = (1 - \text{RQD})(1 - \text{GCD}), \tag{22}$$

where κ, λ, and ω are empirical constants. The hydraulic conductivity of the ZK76 at different depths was estimated by the ZRF model, and the results are listed in Table 5.

(3) Analysis of the CA model and applicability comparison with other models. Based on the water-pressure test of ZK76, the hydraulic conductivity of rock mass in each depth section was calculated according to formula (3). According to the interpretation results of wall imaging of ZK76, the location and orientation of all fractures in each depth section were obtained. Based on the data of orientation and hydraulic conductivity, the location and orientation of WCF were then picked out. Equations (7)–(9) were used to calculate A and A_j; the normal stress σ_{nj} of the WCF was calculated by combining formulas (1) and (14). According to Table 2, the fitting parameters of the CA model are as follows: $\alpha = 2.04 \times 10^{-5}$, $\beta = 1.38 \times 10^{-2}$, and $\gamma = 7.40 \times 10^{-5}$. Substituting the above parameters and basic indices into the CA model

Table 3: HC model estimation results of ZK76.

Z [m]	1-RQD	DI	1-GCD	LPI	$K_{\mathrm{HC\,model}}$ [m/d]
35	0.36	0.840	1.0	0.150	3.55×10^{-5}
45	0.33	0.795	1.0	0.150	2.91×10^{-5}
55	0.3	0.749	1.0	0.150	2.35×10^{-5}
65	0.18	0.703	1.0	0.150	1.07×10^{-5}
75	0.23	0.658	1.0	0.150	1.36×10^{-5}
85	0.31	0.612	1.0	0.150	1.86×10^{-5}
95	0.19	0.566	1.0	0.150	8.51×10^{-6}
105	0.18	0.521	1.0	0.150	7.04×10^{-6}
125	0.2	0.429	1.0	0.150	6.24×10^{-6}
135	0.14	0.388	1.0	0.150	3.32×10^{-6}
155	0.13	0.292	1.0	0.150	2.02×10^{-6}
165	0.11	0.247	1.0	0.150	1.27×10^{-6}
175	0.15	0.201	1.0	0.150	1.47×10^{-6}
185	0.24	0.155	1.0	0.150	1.97×10^{-6}
195	0.14	0.110	1.0	0.150	5.79×10^{-7}
205	0.23	0.064	1.0	0.150	5.46×10^{-7}

Table 4: RMP model estimation results of ZK76.

Z [m]	1-RQD	1-RID	AD	LPI	$K_{\mathrm{RMP\,model}}$ [m/d]
35	0.36	0.25	6.72×10^{-4}	0.15	4.63×10^{-4}
45	0.33	0.18	1.04×10^{-3}	0.15	4.72×10^{-4}
55	0.30	0.14	1.23×10^{-3}	0.15	4.04×10^{-4}
65	0.18	0.11	9.75×10^{-4}	0.15	1.72×10^{-4}
75	0.23	0.11	7.91×10^{-4}	0.15	1.78×10^{-4}
85	0.31	0.11	1.12×10^{-3}	0.15	3.11×10^{-4}
95	0.19	0.08	1.31×10^{-4}	0.15	2.41×10^{-5}
105	0.18	0.08	8.97×10^{-4}	0.15	1.22×10^{-4}
125	0.20	0.08	5.92×10^{-4}	0.15	9.29×10^{-5}
135	0.14	0.08	3.35×10^{-4}	0.15	4.17×10^{-5}
155	0.13	0.08	6.73×10^{-4}	0.15	7.15×10^{-5}
165	0.11	0.08	2.48×10^{-4}	0.15	2.60×10^{-5}
175	0.15	0.08	3.07×10^{-4}	0.15	4.10×10^{-5}
185	0.24	0.08	6.92×10^{-4}	0.15	1.25×10^{-4}
195	0.14	0.10	8.38×10^{-4}	0.15	1.12×10^{-4}
205	0.23	0.10	1.25×10^{-3}	0.15	2.43×10^{-4}

$$K = \alpha \bullet A + \beta \bullet \left(\sum_{j=1}^{N} \frac{A_j}{\sigma_{nj}^3} \right) + \gamma. \tag{23}$$

The prediction result of hydraulic conductivity of ZK76 has been listed in Figure 11, which also involved the estima-

Table 5: ZRF model estimation results of ZK76.

Z [m]	1-RQD	1-GCD	PD	$K_{\mathrm{ZRF\,model}}$ [m/d]
35	0.36	1.0	0.36	3.01×10^{-4}
45	0.33	1.0	0.33	2.06×10^{-4}
55	0.3	1.0	0.30	1.47×10^{-4}
65	0.18	1.0	0.18	6.53×10^{-5}
75	0.23	1.0	0.23	7.63×10^{-5}
85	0.31	1.0	0.31	1.07×10^{-4}
95	0.19	1.0	0.19	5.00×10^{-5}
105	0.18	1.0	0.18	4.34×10^{-5}
125	0.2	1.0	0.20	4.18×10^{-5}
135	0.14	1.0	0.14	2.81×10^{-5}
155	0.13	1.0	0.13	2.36×10^{-5}
165	0.11	1.0	0.11	2.00×10^{-5}
175	0.15	1.0	0.15	2.38×10^{-5}
185	0.24	1.0	0.24	3.75×10^{-5}
195	0.14	1.0	0.14	2.05×10^{-5}
205	0.23	1.0	0.23	3.25×10^{-5}

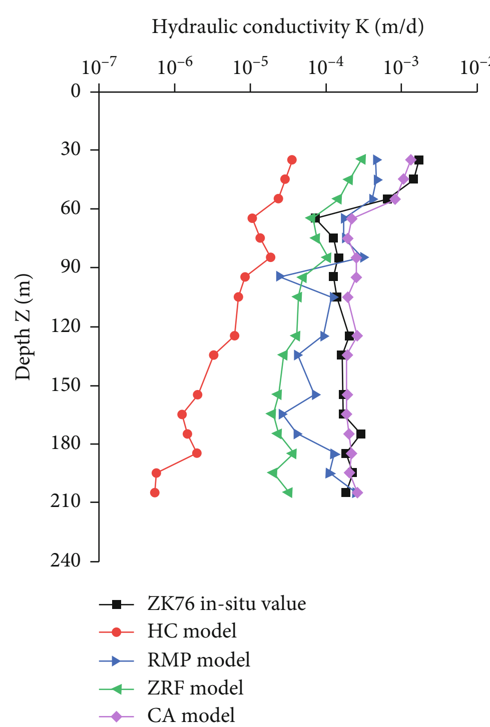

Figure 11: Comparison between the estimated values of hydraulic conductivity.

tion results of the HC model, RMP model, ZRF model, and in situ measured values of ZK76. It can be seen that the new CA model provides significantly better results than the existing models. Specifically, the root mean square error of the CA model is 3.76×10^{-5} m/d, which is far less than that of the HC, RMP, and ZRF models (respectively, 1.46×10^{-4} m/d, 1.02×10^{-4} m/d, and 1.24×10^{-4} m/d), and the relative errors are 45.0%, 95.8%, 64.1%, and 70.6%, respectively. Thus, the CA model is more suitable and accurate in estimating the hydraulic conductivity of low-permeability and unfilled fractured granite in underground water-sealed storage caverns.

5. Discussion

Existing comprehensive indices or models are not suitable for the low-permeability and unfilled fractured granite in underground water-sealed storage caverns as the aforementioned LPI and GCD lead to a weak representation and poor correlations between the geological parameters and the hydraulic conductivity, resulting in large estimation errors. Although the RMP model has been proposed for fractured granite of LPG caverns in adjacent areas, it commonly overestimated the contribution of rock integrity to the hydraulic conductivity by simultaneously adding the RQD and RID parameters. Therefore, the randomness of discontinuities causes large fluctuations in the hydraulic conductivity of the rock mass at different depths by affecting the integrity of rock mass. In addition, the fracture aperture designation is difficult to measure, which may be another cause of errors.

Compared with existing models, the CA model considers the characteristics of the seepage fracture network model of the rock mass. Based on the snow model, the number of fractures is introduced to reflect the integrity of the rock mass, and the orientation of fractures is considered to reflect the permeability of the rock mass. Moreover, the proposed model considers the characterization of mechanical and hydraulic properties of the rock mass and has a certain theoretical basis. Simply put, the CA model has only two basic parameters: fracture orientation index (A) and normal stress index (σ_n), which can be easily obtained using test data in situ. Thus, it is reliable to estimate the hydraulic conductivity of the cavern granite. However, this model is dependent on the number and accuracy of the in situ data, and it may be difficult to identify the WCF. Therefore, an accurate screening method for the WCF must be explored.

A sensitivity analysis of the fracture orientation index and normal stress index of the model indicated that the change in the hydraulic conductivity caused by σ_n is much larger than that caused by A when the two parameters change by the same multiple. This shows that the influence of the normal stress of the fracture on the rock mass permeability is greater than that on the fracture orientation. This is because the normal stress controls the magnitude of the permeability of the rock mass, whereas the fracture orientation determines the seepage direction. Further, it shows that the normal stress index selected in this study is reasonable to construct the new model.

6. Conclusions

(1) Existing models have difficulty accurately reflecting the hydraulic conductivity characteristics of low-permeability and unfilled fractured granite in underground water-sealed storage caverns. The rock mass was regarded as a fractured network comprising WCF; using the test data of borehole wall imaging and water-pressure tests of fractured granite of an underground water-sealed storage caverns, the fracture orientation index and normal stress index were selected as basic parameters, and the CA model for estimating hydraulic conductivity was established by introducing the WCF contribution index C_{wcf}

(2) The hydraulic conductivity of ZK76 in the study area was estimated using the CA model to determine its reliability. Compared with the existing models, the estimation results of the CA model were closest to the in situ measured values which have a high accuracy. Further, it is extremely suitable for estimating the hydraulic conductivity of low-permeability and unfilled fractured granite in underground water-sealed storage caverns which can also be applied for similar rock mass

(3) The paper proposed a screening method of the water conduction fractures (WCF) that mainly consists of the following steps. Firstly, the appropriate method should be used to determine the hydraulic conductivity of each test sections. Secondly, the strike and orientation of internal fractures were obtained based on survey results of borehole wall image tests and water-pressure tests. Thirdly, the fracture strike range in the test section with low hydraulic conductivity was removed from the strike range with high hydraulic conductivity, and the WCF in rock mass was then identified. In addition, the study indicated that the WCF orientation can be determined only by the dominant fractures orientation in the study area of the underground water-sealed storage caverns

(4) A sensitivity analysis of the parameters of the CA model revealed that the influence of the normal stress of the fracture on the permeability of rock mass is greater than the fracture orientation

Data Availability

The data used to support the findings of this study are available from the corresponding author upon request.

Conflicts of Interest

The authors declare that there is no conflict of interest regarding the publication of this paper.

Acknowledgments

This study was funded by the Natural Science Foundation of Fujian Province of China (Grant No. 2019J05036 and No. 2020J05133), the Geological Research Project of Bureau of Geology and Mineral Exploration and Development Guizhou Geological of China (Qiandikuang Kehe [2020]

No. 1), and the Fuzhou University Testing Fund of Precious Apparatus (Grant No. 2020T007).

References

[1] M. Oda, "An equivalent continuum model for coupled stress and fluid flow analysis in jointed rock masses," *Water Resources Research*, vol. 22, no. 13, pp. 1845–1856, 1986.

[2] J. He, S. H. Chen, and I. Shahrour, "Numerical estimation and prediction of stress-dependent permeability tensor for fractured rock masses," *International Journal of Rock Mechanics and Mining Sciences*, vol. 59, pp. 70–79, 2013.

[3] G. Rong, J. Peng, X. J. Wang, G. Liu, and D. Hou, "Permeability tensor and representative elementary volume of fractured rock masses," *Hydrogeology Journal*, vol. 21, no. 7, pp. 1655–1671, 2013.

[4] Y. Xue, T. Teng, F. Dang, Z. Ma, S. Wang, and H. Xue, "Productivity analysis of fractured wells in reservoir of hydrogen and carbon based on dual-porosity medium model," *International Journal of Hydrogen Energy*, vol. 45, no. 39, pp. 20240–20249, 2020.

[5] B. Li, R. Liu, and Y. Jiang, "A multiple fractal model for estimating permeability of dual-porosity media," *Journal of Hydrology*, vol. 540, pp. 659–669, 2016.

[6] K. B. Min, J. Rutqvist, C. F. Tsang, and L. R. Jing, "A block-scale stress-permeability relationship of a fractured rock determined by numerical experiments," *Geo-Engineering Book Series*, vol. 2, pp. 269–274, 2004.

[7] A. Yaghoubi, "Hydraulic fracturing modeling using a discrete fracture network in the Barnett shale," *International Journal of Rock Mechanics and Mining Sciences*, vol. 119, pp. 98–108, 2019.

[8] N. Huang, R. C. Liu, Y. J. Jiang, and Y. F. Cheng, "Development and application of three-dimensional discrete fracture network modeling approach for fluid flow in fractured rock masses," *Journal of Natural Gas Science and Engineering*, vol. 91, article 103957, 12 pages, 2021.

[9] B. Figueiredo, C. F. Tsang, A. Niemi, and G. Lindgren, "Review: the state-of-art of sparse channel models and their applicability to performance assessment of radioactive waste repositories in fractured crystalline formations," *Hydrogeology Journal*, vol. 24, no. 7, pp. 1607–1622, 2016.

[10] P. Gattinoni and L. Scesi, "An empirical equation for tunnel inflow assessment: application to sedimentary rock masses," *Hydrogeology Journal*, vol. 18, no. 8, pp. 1797–1810, 2010.

[11] C. Yu, S. C. Deng, H. B. Li, J. C. Li, and X. Xia, "The anisotropic seepage analysis of water-sealed underground oil storage caverns," *Tunnelling and Underground Space Technology*, vol. 38, pp. 26–37, 2013.

[12] F. W. Tesema and M. Ekmekci, "Use of packer test results in hydrogeological characterization: a comparison of calculation methods for a representative value," *Momona Ethiopian Journal of Science (MEJS)*, vol. 11, no. 1, pp. 52–69, 2019.

[13] Y. F. Chen, S. H. Hu, R. Hu, and C. B. Zhou, "Estimating hydraulic conductivity of fractured rocks from high-pressure packer tests with an Izbash's law-based empirical model," *Water Resources Research*, vol. 51, no. 4, pp. 2096–2118, 2019.

[14] J. M. Hong, Y. F. Chen, M. M. Liu, and C. B. Zhou, "Inverse modelling of groundwater flow around a large-scale underground cavern system considering the excavation-induced hydraulic conductivity variation," *Computers and Geotechnics*, vol. 81, pp. 346–359, 2017.

[15] L. Gan, G. Chen, and Z. Z. Shen, "A new approach to permeability inversion of fractured rock masses and its engineering application," *Water*, vol. 12, no. 3, p. 734, 2020.

[16] D. T. Snow, "Anisotropie permeability of fractured media," *Water Resources Research*, vol. 5, no. 6, pp. 1273–1289, 1969.

[17] G. M. Cheng, F. S. Ma, S. J. Wang, X. J. Chen, and R. M. Yuan, "Permeability study of fractured rock mass based on geometry measuring method," *Chinese Journal of Rock Mechanics and Engineering*, vol. 21, pp. 3595–3599, 2004.

[18] X. Y. Song, Y. T. Liu, X. E. Jiang, Z. P. Ding, and L. Xue, "A novel approach to assessing the anisotropic permeability parameters of fractured media," *IOP Conference Series: Materials Science and Engineering*, vol. 474, no. 1, article 012043, 2019.

[19] J. C. S. Long, J. S. Remer, C. R. Wilson, and P. A. Witherspoon, "Porous media equivalents for networks of discontinuous fractures," *Water Resources Research*, vol. 18, no. 3, pp. 645–658, 1982.

[20] P. Blum, R. Mackay, M. S. Riley, and J. L. Knight, "Performance assessment of a nuclear waste repository: upscaling coupled hydro- mechanical properties for far-field transport analysis," *International Journal of Rock Mechanics and Mining Sciences*, vol. 42, no. 5-6, pp. 781–792, 2005.

[21] J. Zhang, L. Y. Yu, H. W. Jing, and R. C. Liu, "Estimating the effect of fractal dimension on representative elementary volume of randomly distributed rock fracture networks," *Geofluids*, vol. 2018, Article ID 7206074, 13 pages, 2018.

[22] Z. Q. Wei, P. Egger, and F. Descoeudres, "Permeability predictions for jointed rock masses," *International Journal of Rock Mechanics and Mining Sciences and Geotechnics Abstracts*, vol. 32, no. 3, pp. 251–261, 1995.

[23] V. Piscopo, A. Baiocchi, F. Lotti et al., "Estimation of rock mass permeability using variation in hydraulic conductivity with depth: experiences in hard rocks of western Turkey," *Bulletin of Engineering Geology and the Environment*, vol. 77, no. 4, pp. 1663–1671, 2018.

[24] J. Huang, P. F. Zhou, X. W. Jiang, and D. L. Zhang, "Estimation of depth-decaying hydraulic conductivity using sonic velocity," *Journal of Beijing Jiaotong University*, vol. 36, no. 4, pp. 101–104, 2012.

[25] S. Chandra, S. Ahmed, A. Ram, and B. Dewandel, "Estimation of hard rock aquifers hydraulic conductivity from geoelectrical measurements: a theoretical development with field application," *Journal of Hydrology*, vol. 357, no. 3-4, pp. 218–227, 2008.

[26] İ. Öge, "Assessing rock mass permeability using discontinuity properties," *Procedia Engineering*, vol. 191, pp. 638–645, 2017.

[27] X. W. Jiang, L. Wan, and X. S. Wang, "Estimation of rock mass deformation modulus using variations in transmissivity and RQD with depth," *International Journal of Rock Mechanics and Mining Sciences*, vol. 46, no. 8, pp. 1370–1377, 2009.

[28] S. M. HSU, M. C. CHUNG, C. Y. KU, C. H. Tan, and S. Y. Chi, "A rock mass classification scheme for estimating hydraulic conductivity of fractured rocks," in *Geocongress 2008*, pp. 452–459, Reston, VA, 2008.

[29] C. Y. Ku, S. M. HSU, L. B. Chiou, and G. F. Lin, "An empirical model for estimating hydraulic conductivity of highly disturbed clastic sedimentary rocks in Taiwan," *Engineering Geology*, vol. 109, no. 3-4, pp. 213–223, 2009.

[30] K. Song, E. C. Yan, and G. Chen, "Hydraulic conductivity estimation of rock mass in water sealed underground storage caverns," *Chinese Journal of Rock Mechanics and Engineering*, vol. 33, no. 3, pp. 575–580, 2014.

[31] J. Chen, M. M. Liu, X. Li, Y. F. Chen, and C. B. Zhou, "A geological indexes-based empirical model for estimation of permeability coefficient in fractured rock mass," *Rock and Soil Mechanics*, vol. 37, no. 6, pp. 1706–1714, 2016.

[32] A. Shahbazi, A. Saeidi, and R. Chesnaux, "A review of existing methods used to evaluate the hydraulic conductivity of a fractured rock mass," *Engineering Geology*, vol. 265, article 105438, 2020.

[33] K. M. Hubbert and D. G. Willis, "Mechanics of hydraulic fracturing," *Transactions of the AIME*, vol. 4597, no. 210, pp. 153–166, 1957.

[34] Y. B. Cao, X. T. Feng, E. C. Yan et al., "Calculation method and distribution characteristics of fracture hydraulic aperture from field experiments in fractured granite area," *Rock Mechanics and Rock Engineering*, vol. 49, no. 5, pp. 1629–1647, 2016.

[35] X. X. Zhang, J. G. Wang, X. L. Wang, and F. Gao, "Numerical performances of invariable and moving boundary methods during fluid penetration into anisotropic porous media," *Computers and Geotechnics*, vol. 121, article 103458, 2020.

[36] Y. Xue, J. Liu, P. G. Ranjith, X. Liang, and S. Wang, "Investigation of the influence of gas fracturing on fracturing characteristics of coal mass and gas extraction efficiency based on a multi-physical field model," *Journal of Petroleum Science and Engineering*, vol. 206, article 109018, 2021.

[37] GB/T50218-2014, *Standard for Engineering Classifications of Rock Mass, Standard*, China Planning Press, Beijing, China, 2014.

[38] S. J. Li, X. T. Feng, C. Y. Wang, and J. A. Hudson, "ISRM suggested method for rock fractures observations using a borehole digital optical televiewer," *Rock Mechanics and Rock Engineering*, vol. 46, no. 3, pp. 635–644, 2013.

[39] SL31-2003, *Water-pressure Tests in Boreholes for Water Resources and Hydropower Engineering, Standard*, China Water Power Press, Beijing, China, 2003.

[40] M. J. Hvorslev, "Time lag and soil permeability in groundwater observations," *U.S. Army Bulletin*, vol. 36, p. 50, 1951.

[41] H. S. Lee and T. F. Cho, "Hydraulic characteristics of rough fractures in linear flow under normal and shear load," *Rock Mechanics and Rock Engineering*, vol. 35, no. 4, pp. 299–318, 2002.

[42] X. X. Zhang, J. G. Wang, F. Gao, and X. L. Wang, "Numerical study of fracture network evolution during nitrogen fracturing processes in shale reservoirs," *Energies*, vol. 11, no. 10, p. 2503, 2018.

Hindawi
Geofluids
Volume 2021, Article ID 9994477, 15 pages
https://doi.org/10.1155/2021/9994477

Research Article

Investigation on Dewatering of a Deep Shaft in Strong Permeable Sandy Pebble Strata on the Bank of the Yellow River

Yuchao Zheng[1] **Jianyong Lei**[1] **Fei Wang**[2] **Liang Xiang**[2] **Jianfeng Yang**[1] **and Qingshuai Xue**[3]

[1] *Key Laboratory of Transportation Tunnel Engineering, Ministry of Education, School of Civil Engineering, Southwest Jiaotong University, Chengdu 610031, China*
[2] *China Railway First Survey and Design Institute Group Co., Ltd., Xian 710043, China*
[3] *Shenyang Qipeng Group Co., Ltd., Shenyang 110027, China*

Correspondence should be addressed to Yuchao Zheng; zhengyc218@126.com

Received 6 March 2021; Revised 17 August 2021; Accepted 29 August 2021; Published 24 September 2021

Academic Editor: Yi Xue

This paper reports the dewatering scheme of a deep excavation in sandy pebble strata. The excavation is in high permeability strata and is close to the Yellow River, making the dewatering difficult during construction. At present, few researchers have specially studied the dewatering scheme of deep excavations in strong permeable strata near the water resource. Field pumping test was conducted before the excavation activity, and the permeability coefficient of the strata was obtained by reverse analysis. According to the characteristics of the project, the dewatering scheme of "waterproof curtain + base grouting + pumping" was proposed. The influence of vertical waterproof curtain and base grouting on dewatering was analyzed by numerical simulation. In the construction process, the field water table and ground settlement were measured. The results show that (1) the groundwater table versus permeability coefficient curve shows three different stages and (2) the dewatering scheme of "waterproof curtain + base grouting + pumping" is effective for deep excavation in strong permeable strata.

1. Introduction

Many deep excavations or ventilation shafts have been designed and constructed in the rail transit projects, power tunnels, and water conveyance tunnels [1–3]. The construction of excavation pits below the groundwater table needs to lower the water table below the excavation face, so the dewatering scheme is vital. Effective dewatering measures are aimed at preventing uplift and fail of the base, avoiding quicksand and piping, and improving the stability and keeping the excavation face dry [4]. However, the dewatering work will lead to ground settlement inevitably. An ideal situation is to obtain the required drawdown with the least volume of pumped water to reduce the adverse impact on the surrounding environment [5, 6].

There are two common dewatering methods for excavation pits, one only uses pumping well and the other method is the cowork of pumping well and waterproof curtain. The pumping well method pumps out a large amount of groundwater, which forms a large cone of depression. The surrounding ground settlement will also be serious, which will damage the safety of adjacent buildings if any. Therefore, the combination of pumping well and waterproof curtain is widely used because of its less impact on the environment. For the excavation pit, because the diaphragm wall can be used as both a supporting structure and a good waterproof curtain, the cowork of waterproof curtain and pumping well is used for dewatering frequently [7–9].

Many researchers have studied on dewatering of deep excavations. Liu et al. [10] proposed inflow prediction formulas for excavation pits with partial penetrating curtains in high-permeability aquifers. Other researchers [11–13] focused on the deformation mechanism of diaphragm wall and ground settlement induced by dewatering. Zeng et al.

[14] and Zeng et al. [15] investigated ground settlement caused by preexcavation dewatering.

In excavation pit dewatering, in addition to pumping well and diaphragm wall, horizontal barriers have also been used. The base grouting was carried out for the excavation pit dewatering of Fuzhou Metro Line 2 [16], China, but there was no further analysis on base grouting. Granata and Leoni [17] reported a case that designed a grout blanket in order to decrease the water inflow from the bottom of the excavation, and the work focused mainly on the grouting activity quality control. It can be seen from the above practices that placing horizontal barriers is conducive to dewatering work when excavation under complex geological conditions.

In the past, it was rare to encounter an excavation pit with all the flowing three characteristics including a large excavation depth, a short distance from river, and high permeability sandy pebble strata. However, during the dewatering of the ventilation shaft between Lanzhou City University Station and South Shen'an Bridge Station of Lanzhou Metro Line 1, Gansu Provence, China, it encountered all these three characteristics. The depth of the shaft reaches 45.1 m, and the horizontal distance between the Yellow River embankment and the shaft center is only 105 m.

Both numerical simulation method and field observation were adopted in this paper. The influence of base grouting and waterproof curtain on dewatering was analyzed by numerical simulation. Then, the proposed dewatering scheme of "waterproof curtain + base grouting + pumping" was simulated. Field groundwater table and ground settlement were measured, and assembled data verified the results of the numerical simulation.

2. Project Background

2.1. Location of the Shaft. Lanzhou City is located on the floodplain of the upper reaches of the Yellow River. The shield tunnel of Lanzhou Metro Line 1 was bored underneath the bed of the Yellow River for about 317 m between Lanzhou City University Station and South Shen'an Bridge Station. A ventilation shaft was necessary in the north bank of the Yellow River for shield machine receiving and ventilation. Considering the depth of the tunnel and site conditions, the depth of the shaft reaches 45.1 m, and the horizontal distance between the Yellow River embankment and the shaft center is only 105 m. The location of the shaft is shown in Figure 1.

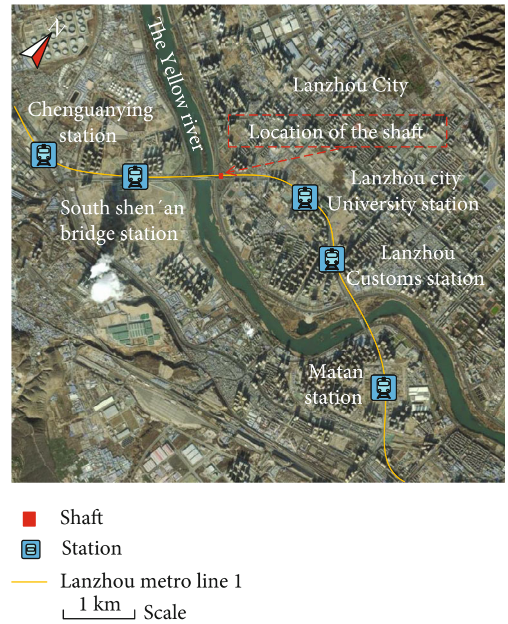

Figure 1: Location of the shaft.

2.2. Geology and Hydrogeology

2.2.1. Geology Conditions. Geological and hydrological conditions play a decisive role in the design of dewatering scheme. The geotechnical engineering investigation showed that the local strata were Quaternary, including 1-1 miscellaneous fill, 2-1 loess soil, 2-6 medium sand, 2-10 pebble, and 3-11 pebble, as shown in Figure 2. Medium sand was only sporadically distributed. The thickness of pebble 2-10 ranged from 5.7 m to 15.5 m, and that of pebble 3-10 was 200 m to 300 m. Consequently, 2-10 pebble and 3-11 pebble were mainly considered in this project for their large thicknesses.

A series of field tests (e.g., pumping test, field shear test, see Figure 3, and dynamic penetration test) and laboratory tests (e.g., grain size analysis and shear test) were carried out. The uniformity coefficient (C_u) of 2-10 pebble and 3-11 pebble is 159.04 and 19.34, respectively, and the coefficient of curvature (C_c) is 131.67 and 14.64, respectively. The grain size larger than 20 mm accounted for 63.5% of 2-10 pebble, and that value of 3-11 pebble is 64.53%. Figure 4 shows the 3-11 pebble layer. The suggested property parameters of the strata are shown in Table 1.

2.2.2. Hydrogeology. Groundwater mainly occurred in 2-10 pebble stratum and 3-11 pebble stratum, belonging to phreatic water with a water table of about -9.6 m, which was slightly higher than the water table of the Yellow River. The hydraulic connection between aquifer 2-10 and aquifer 3-11 was good. No confined water was found.

Two groups of single-well field pumping test were carried out to obtain the hydrogeology parameters. In each group, pumping tests of large drawdown, medium drawdown, and small drawdown were carried out. Four wells with the same diameter and depth were arranged in each group, one well served as pumping well, and the other three served as observation wells. According to field pumping tests, composition analysis of the aquifers, and regional engineering experience, the average permeability coefficient of each stratum was determined roughly, as shown in Table 1.

The permeability coefficient of anisotropic geotechnical medium is difficult to obtain directly, especially in complex geological conditions. The field pumping tests combined with inverse analysis can overcome the problem [5, 8, 18, 19]. Group-well pumping tests were carried out in the shaft, and an inverse analysis for hydrological parameters was carried out by Visual Modflow, a three-dimensional finite difference groundwater flow model software.

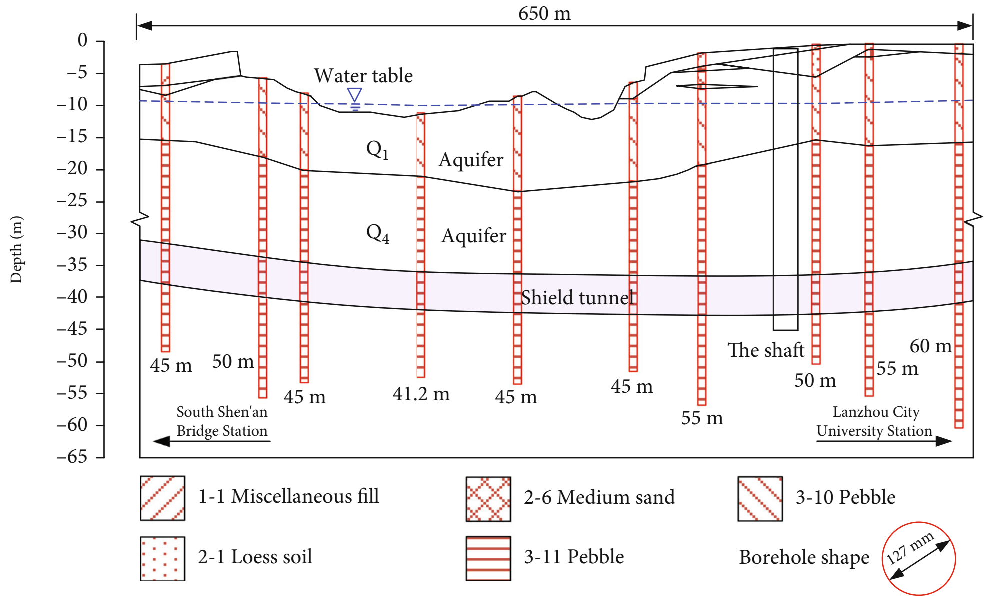

Figure 2: Longitudinal stratigraphic section.

Figure 3: Field shear test.

Figure 4: 3-11 pebble.

The permeability coefficients of 2-10 pebble and 3-11 pebble are shown in Table 2. It indicates that the horizontal permeability coefficient (K_H) is larger than the vertical permeability coefficient (K_V).

2.3. The Challenges. To summarize, the construction of the shaft presented several characteristics, including high permeability of aquifers, a large depth, and a short distance from the Yellow River. It brought several challenges:

(1) Dewatering was difficult. Due to the high permeability coefficient and strong seepage, it is uncertain that the water level can be reduced to the safe level only by the pumping well and vertical waterproof curtain

(2) In the thick and sandy pebble strata, the diaphragm wall is prone to defects which lead to leakage

(3) Construction safety risk is high. Due to the high water table and strong permeable aquifers, water table inside the pit will rise rapidly once the dewatering system fails, resulting in serious consequences

2.4. Preliminary Dewatering Scheme

2.4.1. Barrier Effect of Waterproof Curtain. The diaphragm wall is widely used for dewatering. In thick aquifer, diaphragm wall cannot penetrate to the aquitard [8]. Therefore, groundwater flows into the excavation pit through the bottom of the diaphragm wall [8, 11, 20]. The principle of diaphragm wall that can be used for dewatering is its barrier effect on seepage. It changes the seepage direction and seepage path of groundwater [21, 22].

(1) Seepage direction: the underground water flows into the pumping well horizontally without a barrier such as diaphragm wall. When pumping is conducted in cases with a barrier, the groundwater flow is three dimensional, both horizontal seepage and vertical seepage exist simultaneously [21, 22]. The vertical seepage consumes more energy and produces larger drawdown than the horizontal one for the vertical hydraulic conductivity is smaller than the horizontal conductivity [8]

Table 1: Strata property parameters.

Strata	Cohesion c (kPa)	Friction angle φ (°)	Density ρ (g/cm^3)	Void ratio e	Deformation modulus E_0 (MPa)	Permeability coefficient k (×10^{-4}m/s)
1-1 miscellaneous fill	0	12	1.71	—	5	0.58~0.93
2-1 loess soil	19	24.7	1.66	0.84	—	0.35~0.58
2-6 medium sand	0	30.0	1.90	—	12	2.3~2.90
2-10 pebble	0	35.0	2.17	0.282	45	6.60~7.41
3-11 pebble	15	43.0	2.28	0.288	50	5.79~6.37

Table 2: Inverse analysis results of permeability coefficient (×10^{-4} m/s).

Aquifers	Permeability coefficient	
	K_V	K_H
2-10 pebble layer	5.83	7.52
3-11 pebble layer	5.41	6.60

(2) Seepage path: the water outside the pit needs to bypass the bottom of the barrier to flow into the well in case of the existence of a barrier. It means that the barrier lengthens the seepage path so that the seepage time is also increased. In the initial stage of pumping, groundwater discharge mainly comes from inside the excavation pit. Groundwater head outside the pit begins to decline after a certain time because of the extension of the seepage path [21, 22]

2.4.2. Overview of the Shaft. The geometry of the shaft is rectangular in the plane with a size of 33.4 m × 20.4 m (see Figure 5), and the depth of the shaft was 45.1 m. The horizontal distance between the Yellow River embankment and the shaft center is only 105 m.

Given the wide use of diaphragm wall and pumping well, as well as some successful cases of base grouting, the dewatering scheme of "waterproof curtain + base grouting + pumping " was proposed.

Considering both dewatering design and excavation pit supporting design, the shaft was divided into 5 floors, named F1 to F5 from top to bottom, as shown in Figure 6. The shaft was composed of main structures (including side wall, floor slab, beam and column), the inner diaphragm wall (inner waterproof curtain) and the outer diaphragm wall (outer waterproof curtain) (see Figure 6). The main structures were made of reinforced concrete. The inner diaphragm wall was made of C40 (its Young's modulus $E = 34$ GPa) reinforced concrete with a thickness of 1.2 m and a depth of 60.1 m. The outer plain concrete diaphragm wall was 0.8 m thick and 51.1 m deep. Sleeve-valve-pipe grouting (base grouting) was implemented in a range of 10 m below the bottom to improve the strata properties.

In order to ensure safety of shield boring, side grouting reinforcement range was in the shield passing area between the outer waterproof curtain and the inner waterproof curtain at the depth of 32.15 m to 50.15 m, as shown in Figure 6.

The space was divided into three parts by the two waterproof curtains, as shown in Figure 5. The space inside the inner waterproof curtain was area I, the space between the inner waterproof curtain and outer waterproof curtain was area II, and the space outside the outer waterproof curtain was area III.

2.4.3. Drawdown Required. Limit equilibrium method assumes that water inrush does not occur when the gravity of the overlying soil is larger than the water pressure under a coefficient, expressed as [9, 23]

$$F = \frac{\gamma_s(H - h_s)}{\gamma_w(H - D)}, \tag{1}$$

where F is the safety factor, h_s is the excavation depth (m), D is the water head of confined aquifer (m), H is the depth of the confined aquifer roof (m), γ_s is the unit weight of soil between the excavation pit bottom and the confined aquifer roof, with a value of 21 kN/m^3 here, and γ_w is the unit weight of base grouting area, with a value of 25 kN/m^3 in this paper.

Formula (1) was used to obtain the safety water table required by 7 different excavation depths (excavation depth: 10 m, 20 m, 30 m, 31.2 m, 35 m, 40 m, and 45.1 m). The comparison of excavation depth and safe water table is as Table 3 at safety factor $F = 1.2$. The limit excavation depth of the shaft was 31.2 m. Therefore, when the excavation depth was less than 31.2 m, pumping inside the shaft prevailed to make the excavation face dry. When the excavation face was lower than -31.2 m, pumping wells inside and outside the shaft should work together.

2.4.4. Layout of Pumping Wells. It was preliminarily designed to arrange 9 pumping wells (W1 to W9, among which W5 was for observation, also represented by O1) in area I, 6 pumping wells (W10 to W15) in area II, and 52 pumping wells (W16 to W67, among which W47, W53, W59, and W65 were observation wells, also represented by O2 to O5, respectively) in area III. Figure 7 shows the layout of the pumping wells. Details of pumping wells are shown in Table 4. The depth of the wells in area I was 55 m with a diameter of 650 mm and a filter length of 15 m. The 6 wells in area II were 60 m deep and were steel pipe wells. Cement well with a depth of 60 m, a diameter of 800 mm, and a filter length of 30 m was adopted in area III.

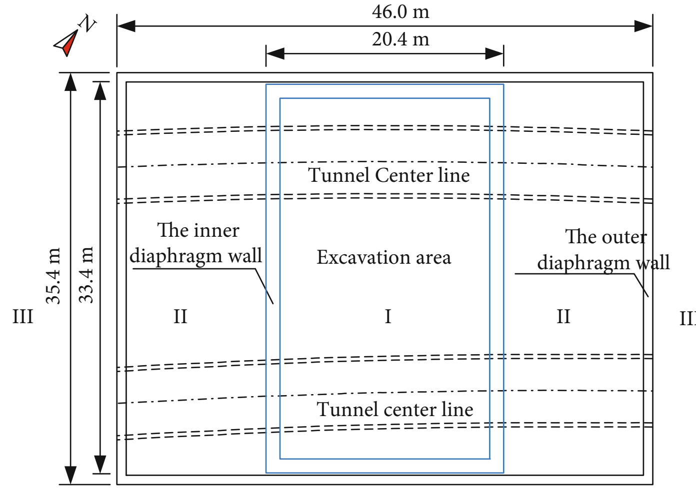

Figure 5: Top view of the shaft.

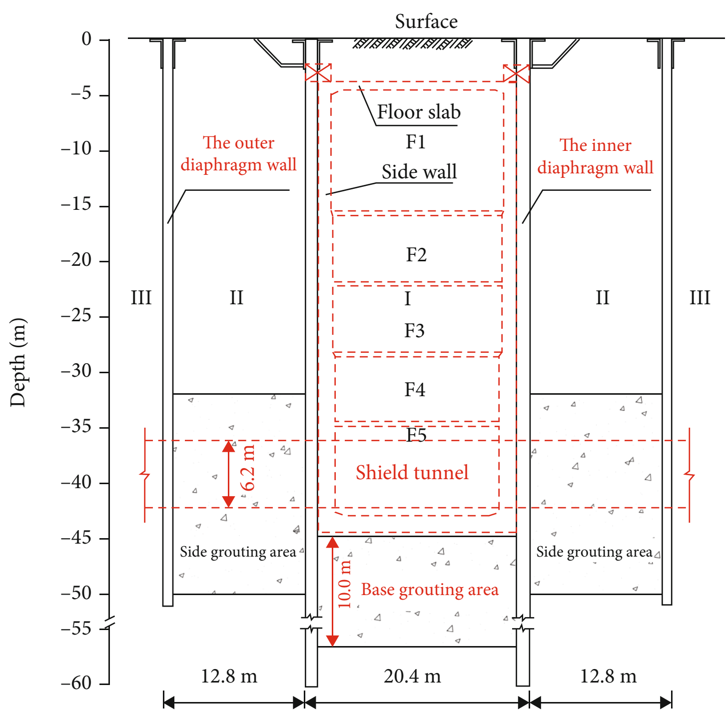

Figure 6: Section view of the shaft.

Table 3: Comparison of excavation depth and safe water table (m).

Excavation depth	Safe water table outside the shaft	Drawdown required
10	-10	0
20	-10	0
30	-10	0
31.20 (critical excavation depth)	-10	0
35	-16.7	6.7
40	-25.4	15.4
45.1	-34.2	24.2

3. Numerical Simulation

The feasibility of the planned dewatering scheme needs to be examined. This section mainly focuses on three issues: (i) the influence of vertical waterproof curtain on dewatering, (ii) the influence of base grouting on dewatering, and (iii) the numerical simulation of the proposed dewatering scheme of "waterproof curtain + base grouting + pumping."

3.1. Mechanism of Seepage Analysis. Formula (2) [4, 9] is the governing equation of three-dimensional transient flow in anisotropic porous media. It is also the constitutive model used in this paper. In Visual Modflow, the numerical

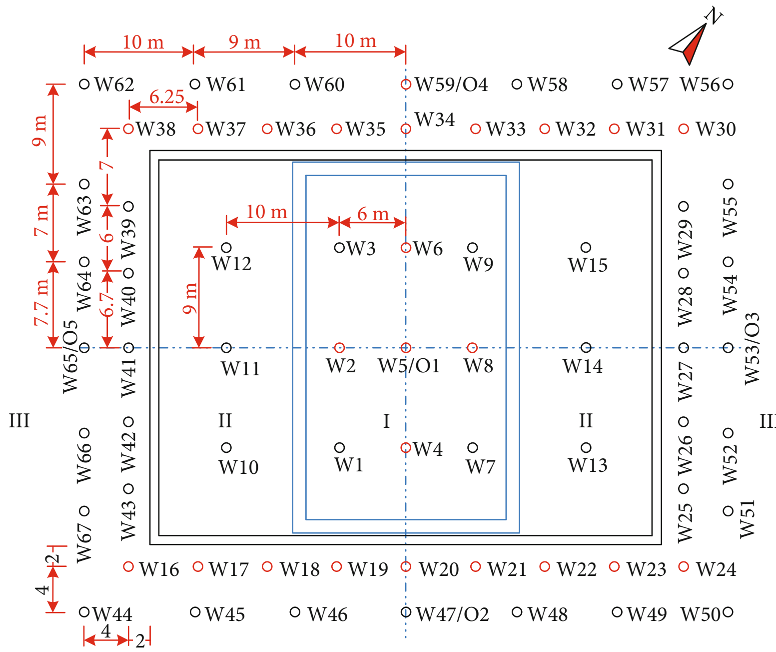

Figure 7: Layout of pumping wells (m).

Table 4: Details of pumping wells.

Well location	Quantity	Diameter (mm)	Filter length (m)	Depth of well (m)	Type of well
In area I	9	650	15	55	Steel pipe well
In area II	6	650	30	60	Steel pipe well
In area III	52	800	30	60	Cement well

simulation model can be obtained by discretizing the mathematical model with the finite difference method.

$$\begin{cases} \dfrac{\partial}{\partial x}\left(k_{xx}\dfrac{\partial h}{\partial x}\right)+\dfrac{\partial}{\partial y}\left(k_{yy}\dfrac{\partial h}{\partial y}\right)+\dfrac{\partial}{\partial z}\left(k_{zz}\dfrac{\partial h}{\partial z}\right)-W=S_s\dfrac{\partial h}{\partial t}, & (x,y,z)\in\Omega, \\ h(x,y,z,t)\big|_{\Gamma_1}=h_1(x,y,z), & (x,y,z)\in\Gamma_1, \\ k_{xx}\dfrac{\partial h}{\partial n_x}+k_{yy}\dfrac{\partial h}{\partial n_y}+k_{zz}\dfrac{\partial h}{\partial n_z}\big|_{\Gamma_2}=q(x,y,z,t), & (x,y,z)\in\Gamma_2, \\ h(x,y,z,t)\big|_{t=t_0}=h_0(x,y,z), & (x,y,z)\in\Omega, \end{cases} \tag{2}$$

where k_{xx}, k_{yy}, and k_{zz} are the hydraulic conductivity in the x, y, and z directions (cm/s); h is the water table in position (x, y, z) (m); S_s is the specific storage rate in position (x, y, z) (m^{-1}); n_x, n_y, and n_z are the unit normal vectors on boundary Γ_2 along the x, y, and z directions, respectively; W is the recharge and discharge of the groundwater (d^{-1}); t is time (h); Γ_1, Γ_2 are the first and second types of boundary condition, respectively; q is the lateral recharge per unit area on boundary Γ_2 (m^3/d); h_0 (x, y, z) is the initial water table in position (x, y, z) (m); and Ω is the calculation domain.

3.2. *Influence of Vertical Waterproof Curtain*

3.2.1. Analysis Cases. Four analysis cases were set to analyze the influence of waterproof curtain on excavation pit dewatering, as shown in Table 5. There was no waterproof curtain

Table 5: Four analysis cases.

Case	Inner waterproof curtain	Outer waterproof curtain	Base grouting
1	×	×	×
2	√	×	×
3	√	√	×
4	√	√	√

Table 6: Parameters of aquifers in the model.

Aquifer	Specific storage S_s (1/m)	Specific yield S_y	Permeability coefficient (m/s)
2-10 pebble	5.0×10^{-4}	0.2	K_V 5.83×10^{-4}
			K_H 7.54×10^{-4}
3-11 pebble	5.0×10^{-4}	0.2	K_V 5.41×10^{-4}
			K_H 6.60×10^{-4}

in case 1, the inner waterproof curtain was set in case 2, and the inner and outer waterproof curtains were set in case 3. From case 1 to case 3, all 67 pumping wells were on working. In case 4, both base grouting and the two waterproof curtains were set, the permeability coefficient of base grouting area was 1.0×10^{-7} m/s, and 52 pumping wells outside the pit and 3 in area I were turned on. Simulation time of each case was 10 days.

3.2.2. Three-Dimensional Seepage Model. Considering the influence range of dewatering, the size of the model was determined to be 1200 m × 1200 m, and the height was 150 m. In Visual Modflow, the analysis type was transient flow for this simulation.

The boundary condition was simulated by Constant Head package with the water table of -10.0 m. Using the River package to simulate the Yellow River, its water table was set at -10.0 m. The coordinate origin was situated at the center of the shaft surface. Waterproof curtain was simulated by Wall package with the permeability coefficient of 1.84×10^{-12} m/s (considering the antiseepage grade of P8). Pumping wells were simulated by the Well package. According to the results of the field pumping tests, the pumping rate of each well in area I and area II was set to 100 m^3/h while the pumping rate of each well in area III was 150 m^3/h. Aquifers of 2-10 pebble and 3-11 pebble were mainly considered in the model. Hydrological parameters of the aquifers were determined according to the results of the field pumping tests and inverse analysis, and the values used in the simulation are as shown in Table 6.

The model for case 4 is as shown in Figure 8, and Figure 9 presents the model of diaphragm wall and pumping wells. It was divided into 8 layers vertically. The horizontal mesh became sparse from the shaft center to outside, a total of 214 rows and 214 columns. The finite difference mesh had a total of 416025 nodes and 366368 elements.

3.2.3. Results. Figure 10 shows the cone curve of depression in each case. The cone curve of depression became steep near the Yellow River and relatively flat away from the Yellow River.

In case 1, the cone curve of depression was smooth, and water table in area I was reduced to -35.0 m. In case 2 to case 4, the water table in area I was -46.9 m, -51.0 m, and -53.3 m, respectively.

For the water table in area I: in case 1, the water table cannot be lowered to the bottom of the pit, and the water table in case 2 to case 4 was lower than the bottom of the pit. The drawdown in case 3 was 11.1% more than that in case 2. The drawdown in case 4 was 17.3% more than that in case 2. The drawdown in case 4 was 5.6% greater than that in case 3, although the number of pumping wells in case 4 was only 82.1% of that in case 3.

For the water table in area II: on the Yellow River side, the water table of case 1 to case 4 was -33.9 m, -29.2 m, -34.2 m, and -43.6 m, respectively. Obviously, neither case 1 nor case 2 can meet the safety requirement. Case 3 can just meet the requirement, and case 4 can meet the requirement. The drawdown of case 4 was 1.39 times than that of case 3.

The above analysis account for the cowork of base grouting and two vertical waterproof curtains forms a relatively impervious space and isolates the hydraulic connection of inside and outside the shaft.

3.3. Influence of Base Grouting

3.3.1. Analysis Cases. Grouting is an effective method to block water in underground engineering [24]. Grouting reinforcement of weak strata improves the mechanical properties (compression modulus, cohesion, friction angle, and permeability coefficient) of the reinforced area. Some mesotable studies such as literatures [25, 26] involved the diffusion mechanism of slurry and tried to simulate it by numerical method. However, the determination of parameters is complicated, and its applicability needs to be improved in practice.

In this paper, the grouting effect is considered from a macro perspective. Permeability coefficient is set in the base grouting area to reflect the reinforcement effect in simulation. In each analysis cases, the two waterproof curtains were set; the differences were the permeability coefficient of the base grouting area and the number of pumping wells in operation. For the permeability coefficient of the base grouting area, there were 10 different values (6×10^{-4} m/s, 4.5×10^{-4} m/s, 3.2×10^{-4} m/s, 2.2×10^{-4} m/s, 1.4×10^{-4} m/s, 8.5×10^{-5} m/s, 4.4×10^{-5} m/s, 1.9×10^{-5} m/s, 5.8×10^{-6} m/s, and 7.5×10^{-7} m/s). For pumping wells, all 52 wells in area III and all 6 wells in area II were in operation in each case, and the number of pumping wells in area I varied from 1 to 9. A total of 53 analysis cases were simulated. The simulation time was 30 days.

The constitutive model used was transient flow. The size of the model was 1200 m × 1200 m × 150 m. It was divided into 8 layers, 214 rows and 214 columns with a total of 416025 nodes and 366368 elements. The boundary condition of constant water head was simulated by Constant Head package with the water table of -10.0 m. The Yellow River

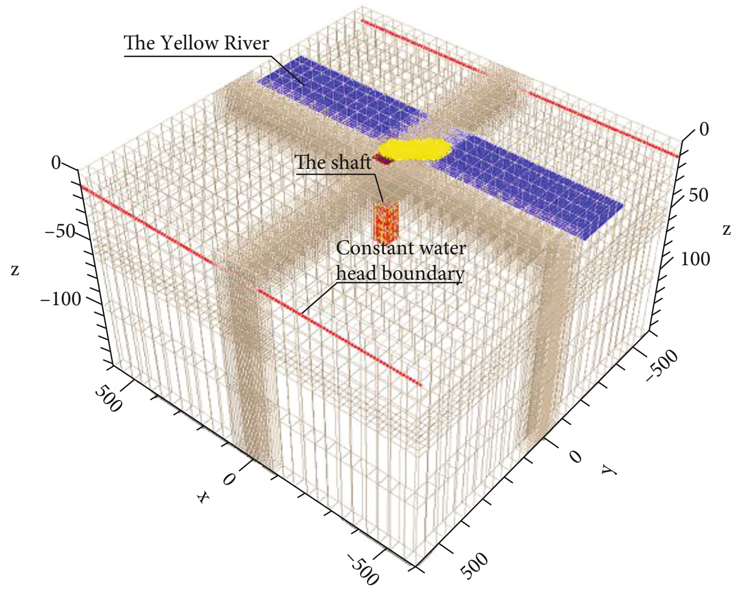

Figure 8: Mesh of three-dimensional model.

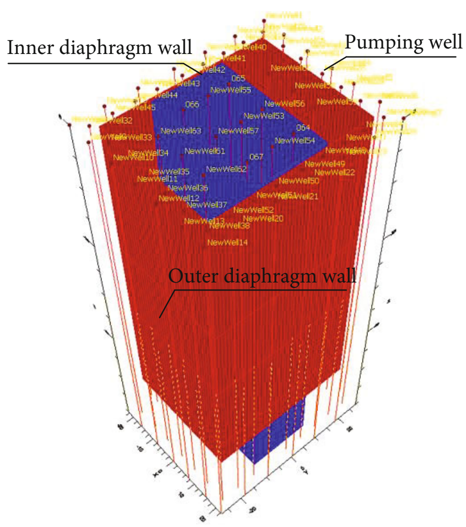

Figure 9: Model of diaphragm wall and pumping well.

was simulated by River package with the water table of -10.0 m. Waterproof curtain was simulated by Wall package with the permeability coefficient of 1.84×10^{-12} m/s. Pumping wells were simulated by the Well package. The pumping rate of each operative well in area I and area II was set to 100 m^3/h while in area III the pumping rate was 150 m^3/h. The pumping rate of the inoperative well was set to 0 m^3/h. Hydrological parameters of the aquifers are as shown in Table 6.

3.3.2. Result. The water table in area I is shown in Figure 11. From the perspective of slope, the groundwater table versus permeability coefficient curve shows three different stages.

Stage 1: when the permeability coefficient is greater than 1.4×10^{-4} m/s, the curve is almost a flat line. In this stage, with the decrease of permeability coefficient, the water table is slowly decreasing. According to different curves, the decline of water table in area I is mainly affected by the number of pumping wells in area I.

Stage 2: the curvature of curve changes rapidly. The permeability coefficient is between 1.9×10^{-5} m/s and 1.4×10^{-4} m/s in this stage. With the decrease of permeability coefficient, the decline rate of groundwater table accelerates.

Stage 3: the water table shows a linear downward trend with a large slop. When the permeability coefficient is less than 1.9×10^{-5} m/s, the water table decreases linearly with the decrease of permeability coefficient.

The dewatering results are closely related to the permeability coefficient of the grouting area. A large permeability coefficient does no obvious effect on dewatering. A small permeability coefficient significantly benefits the dewatering work while it is difficult to achieve. Therefore, the permeability coefficient of grouting area should be controlled in stage 3. For this project, the coefficient is recommended to be 1×10^{-7} m/s.

3.4. Simulation of Dewatering Scheme. In Sections 3.2 and 3.3, the effect of vertical waterproof curtain and base grouting on dewatering is analyzed, but the process of dewatering is not considered. According to the analysis in Section 2.4.3, the required drawdown is different under different excavation depths. Therefore, in the actual excavation process, the dewatering well should be turned on in several stages according to the excavation depth. In this part, the proposed dewatering scheme of "waterproof curtain + base grouting + pumping" is simulated.

3.4.1. Simulation Process. The simulation was carried out in 9 stages, shown in Table 7. The simulation process is as follows: in stage 1, pumping is not carried out because the groundwater table is about -10 m. In stage 2, turn on 2 wells in area I. In stage 3, turn on 4 wells in area I. Stage 4 is to

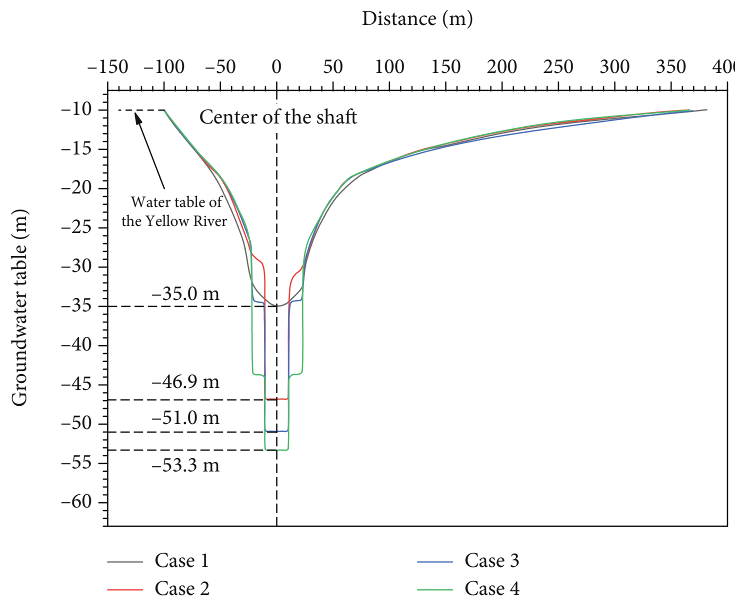

FIGURE 10: Cone curves of groundwater depression of the 4 analysis cases.

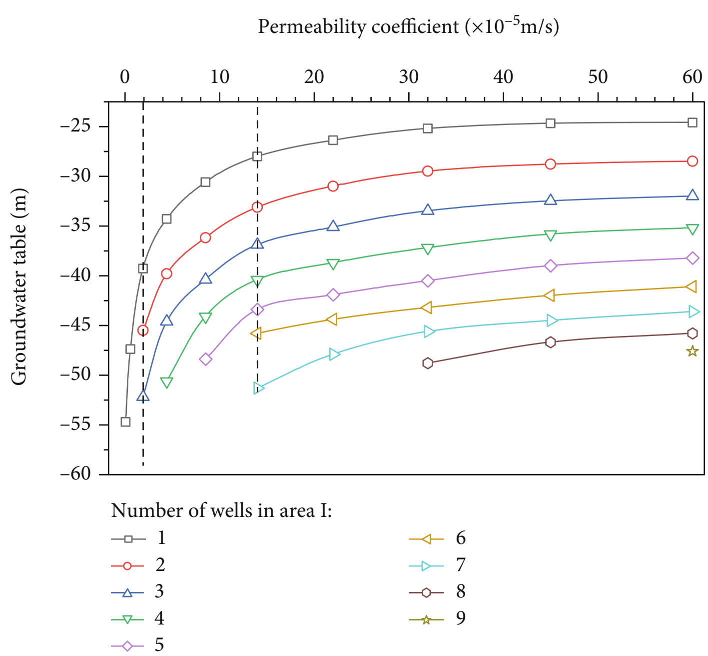

FIGURE 11: Water table of different analysis cases.

turn on 6 wells in area I. Thereafter, the permeability coefficient of the base grouting area is set to 1×10^{-7} m/s. Then, turn on 1 well in area I, 6 wells in area II, and 4 wells in area III to conduct the stage 5 analysis. In stage 6, the number of wells in area III is 12. In stage 7, the number of wells in area III is 20. In stage 8, 40 wells are in operation in area III. In stage 9, 52 wells are working in area III.

The constitutive model used was transient flow. The size of the model was 1200 m × 1200 m × 150 m which was divided into 8 layers, 214 rows and 214 columns with a total of 416025 nodes and 366368 elements. The boundary condition was simulated by Constant Head package with the water table of -10.0 m. The Yellow River was simulated by River package with the water table of -10.0 m. Waterproof curtains were simulated by Wall package with the permeability coefficient of 1.84×10^{-12} m/s. The pumping rate of each operative well in area I and area II was set to 100 m^3/h while in area III the pumping rate was 150 m^3/h. The pumping rate of the inoperative well was 0 m^3/h. Hydrological parameters of the aquifers are as shown in Table 6. The permeability coefficient of the base grouting area was 1×10^{-7} m/s.

Table 7: Operation scheme of pumping wells.

Stage	Number of pumping wells			Water table (m)		Excavation depth (m)	Description
	Area I	Area II	Area III	Area I	Area II		
1	—	—	—	-10.0	-10.0	0.00~10.00	Excavation of F1
2	2	—	—	-18.4	-10.0	10.00~17.68	
3	4	—	—	-25.6	-10.0	17.68~24.08	Excavation of F2
4	6	—	—	-32.5	-10.0	24.08~30.48	Excavation of F3
Grouting the base during the excavation of F3 with the target permeability coefficient of 1×10^{-7} m/s							
5	1	6	4	-54.2	-17.4	30.48~35.50	Excavation of F4
6	1	6	12	-54.2	-20.1	35.50~36.78	
7	1	6	24	-54.4	-24.1	36.78~39.00	
8	1	6	40	-54.8	-28.8	39.00~42.00	Excavation of F5
9	1	6	52	-54.8	-34.2	42.00~45.10	

3.4.2. Result. The water table of different stages is shown in Table 7. From stage 1 to stage 4, there was no grouting at the base, and the pumping wells in the area I varied from 0 to 6. The water table in area I dropped from -10.0 m to -32.5 m while the water table in area II changed little. It shows that the pumping well in area I cannot effectively lower the water table in area II when there is no grouting at the base. Since the critical excavation depth is 31.2 m, the purpose of pumping is to reduce the water table in area I to ensure the dryness of the excavation face. According to the water table of simulation results, the excavation depth of each stage can be obtained. And F1 to F3 can be excavated during stage 1 to stage 4, shown in Table 7.

After the base grouting, the water table in area I maintained between -54.2 m and -54.8 m from stage 5 to stage 9. As the number of pumping wells in area III increased from 4 to 52, the water table in area I changed little, while the water table in area II decreased from -17.4 m to -34.2 m. After the base grouting was completed, a horizontal waterproof curtain was formed. Only one pumping well was needed inside the pit to keep the water table below -54.2 m. The decrease of water table in area II was mainly due to the increase of the number of wells in area III. According to the water table inside the pit and outside the pit, F4 and F5 can be excavated during stage 5 to stage 9, as shown in Table 7.

4. Field Observation

The dewatering scheme of “diaphragm wall + base grouting + pumping” was used, and the ventilation shaft was accomplished. Field observation data were validated against the simulation results to verify the reliability of the three-dimensional model.

4.1. Field Dewatering

4.1.1. Excavation Strategies. The results of numerical simulation indicated that the preliminary designed dewatering scheme of “diaphragm wall + base grouting + pumping” was effective. And it was used in the construction of the shaft. The overview of the shaft is provided in Section 2.4.2. Figure 7 shows the layout of the pumping wells.

The shaft was constructed by reversed construction method. It was excavated in layers using mechanics. Firstly, the inner diaphragm wall and the outer waterproof curtain were constructed, and the sleeve-valve-pipe grouting method was used for side grouting. Secondly, preexcavation pumping test was conducted to check the reliability of the dewatering scheme and the quality of the diaphragm wall. Thirdly, it constructed the capping beam of the inner diaphragm wall and the horizontal reinforced concrete strut beam at the top of the main structure. Then, the shaft was excavated from F1 to F5 one after another; the construction sequence of each floor was excavating to bottom of each floor, applying horizontal strut beam, and concreting the side wall of the same floor. During the excavation of F3 layer, base grouting was carried out, and the target permeability coefficient was 1.0×10^{-7} m/s. After receiving of the shield machine, the construction of the floor slab was conducted from F5 to F1. Finally, the ground was restored.

In excavation engineering, it is generally necessary to lower the water table to 0.5 m below the excavation face. Therefore, this paper took the water table 0.5 m below the excavation face as the water table control criterion.

In order to reduce the impact of dewatering on the environment, the staged dewatering strategy was implemented according to different excavation depths referring to the excavation stages in Table 7. During the excavation of the initial 10 m, no pumping well was required. During the excavation of the remaining part of F1, turn on 2 wells in area I. With the deepening of excavation, the number of pumping wells was gradually increased according to the actual situation of the site.

4.1.2. Preexcavation Pumping Test. The preexcavation pumping test is an effective method to check the reliability of the dewatering scheme and the quality of the diaphragm wall [27]. Therefore, the preexcavation pumping test was conducted after the construction of diaphragm wall.

Only 5 pumping wells were constructed in area I and 19 in area III for the preexcavation pumping test (each well was marked in red in Figure 7, and among which W5, W24,

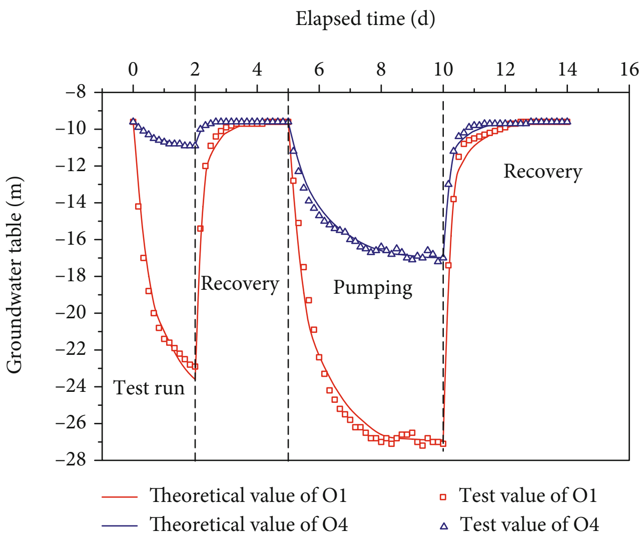

FIGURE 12: Water table of preexcavation pumping test and inverse analysis.

W38, and W59 were used as observation wells). During the pumping test, 4 pumping wells in area I were in operation for trial operation for 2 days, and then, all 20 pumping wells were turned on. The pumping was stopped after the water table of the observation wells was stable. The measured groundwater table of wells O1 and O4 is as shown in Figure 12.

Inverse analysis was carried out by Visual Modflow based on preexcavation pumping test results, and the inverse analysis results of well O1 and well O4 are as shown in Figure 12. The permeability coefficients of aquifer 2-10 and aquifer 3-11 were obtained accurately. Vertical permeability coefficient (K_V) and horizontal permeability coefficient (K_H) of aquifer 2-11 were 5.65×10^{-4} m/s and 7.15×10^{-4} m/s, respectively. For aquifer 3-11, K_V was 5.34×10^{-4} m/s and K_H was 6.34×10^{-4} m/s. Given the diaphragm wall had been completed before the preexcavation test, the effect of diaphragm wall was also taken into consideration in the inverse analysis. The existence of the diaphragm wall made the results of the two inverse analysis (the other inverse analysis is in Section 2.2) different with the maximum difference of 4.92%. It can be explained that the parameters used in the modeling were precise enough. The pumping tests verified the quality of the diaphragm wall was good.

4.1.3. Grouting Parameters. The grouting will directly affect the dewatering results. Splitting grouting method was adopted for the base grouting. PVC sleeve-valve-pipe with a diameter of 65 mm was used. The grouting boreholes were arranged with equilateral triangles with a spacing of 1.2 m. The target diffusion radius of each grouting hole was 0.8 m, as shown in Figure 13. The grouting material of the upper 3 m of the base grouting area was ordinary Portland cement, and the water-cement ratio was controlled between 0.8 : 1 and 1 : 1. The grouting material of the lower 7 m was mixed slurry made of ordinary Portland cement and sodium silicate with a volume ratio of 1 : 0.8. The grouting pressure was 2 to 3 MPa.

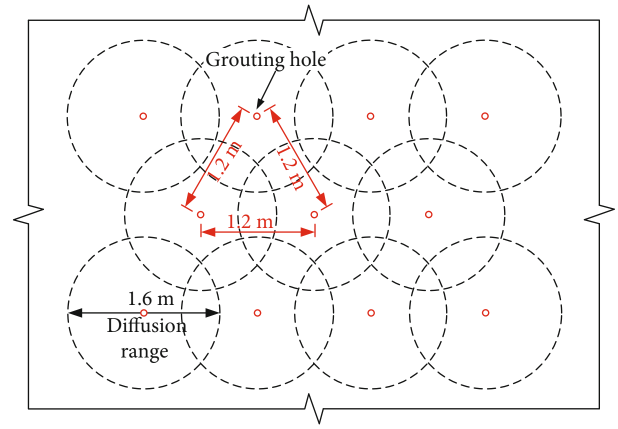

FIGURE 13: Layout of grouting hole and slurry diffusion.

4.2. Water Table Observation. The observation of the groundwater table (observation points WT1 to WT7 are shown in Figure 14) began from June 26, 2015, to April 24, 2016, lasting for 304 days [2]. Groundwater table versus time curve is plotted, such as shown in Figure 15.

Starting from June 26, 2015, all pumping wells were put into trial operation for 13 days. From the 13th day to the 97th day, F1 and F2 were excavated. At this stage, according to the excavation progress, the pumping wells in area I were turned on step by step to ensure the water table in the pit was below the excavation face beyond 0.5 m. The drawdown in area II and area III was very weak, and the water table difference of each observation well (WT1 to WT6) was very small. It can be interpreted that the groundwater discharge mainly comes from inside the excavation pit in this stage.

During the excavation of F3, in order to prevent inrush, some wells outside the pit were turned on, and the water table of observation wells WT1 to WT4 dropped to -15 m. Water table in area II changed about 2.7 m. Water table in area I dropped to about -36.2 m.

From the 138th day to the 230th day, F4 and F5 were excavated. During this time, all 6 wells in area II were in operation and the number of pumping wells in area III was gradually increased in several stages. As a result, the water table in area III gradually reduced to -36 m while the water table in area II rapidly dropped to about -35 m. The water table in area I was -46.1 m. After the bottom of the shaft was constructed, the number of pumping wells reduced in two stages until the water table returned to normal table. Moreover, during the construction, no obvious leakage was found in the waterproof curtain.

4.3. Ground Settlement Observation. The measurement of ground settlement began from June 26, 2015, lasting for 340 days. The observation points are shown in Figure 14. The settlement versus time curve is shown in Figure 16.

It can be seen from Figure 16 that ground settlement is closely related to dewatering process. In the construction run, the maximum settlement was -6.56 cm, which was acceptable.

Most of the settlement occurred in the 1st day to the 138th day, that was, during the excavation of F1 to F3. According to GS09-5, the settlement occurred during the

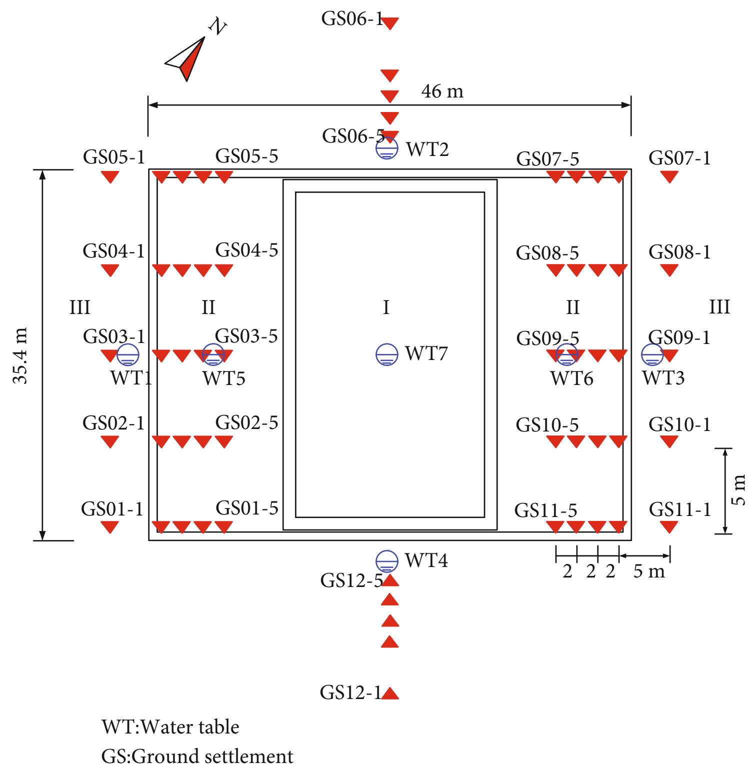

Figure 14: Layout of observation points for underground water table (WT) and ground settlement (GS). (The numbers of the 2nd to the 4th observation points on each observation section are not marked.)

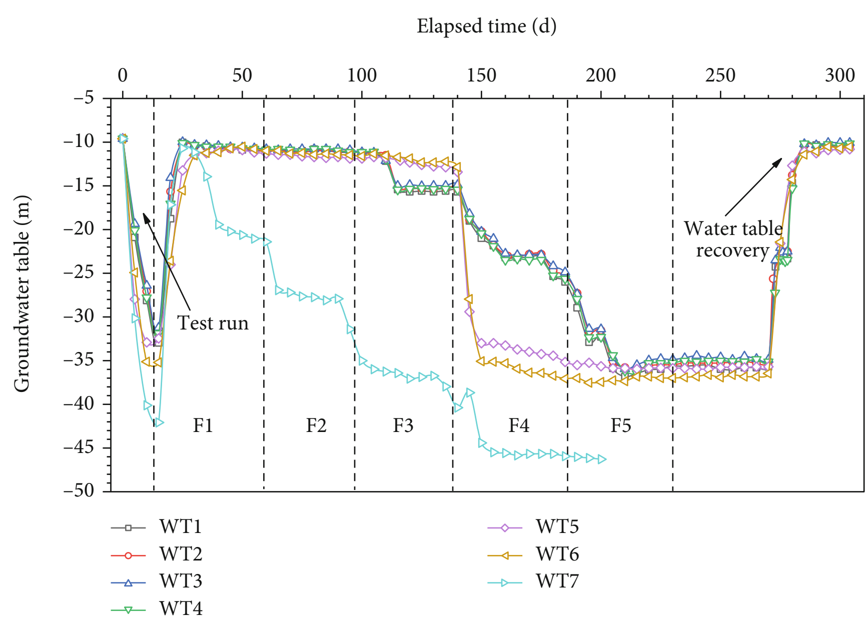

Figure 15: Observation results of underground water table.

excavation of F1 to F3 which accounts for 88.4% of the maximum settlement. There may be two reasons for this. First, the upper structures were not stable during this time; the effect of dewatering and excavation unloading together leads to large ground settlement. Second, the base was grouted during the excavation of F3, and the upper structure was gradually stable. The base grouting area, the diaphragm wall, and the horizontal strut beam formed a combined support system, and the structural stiffness increased, which led to the following excavation cause small settlement.

During the excavation of F4 to F5, the ground settlement gradually stabilized. After concreting the bottom of the shaft,

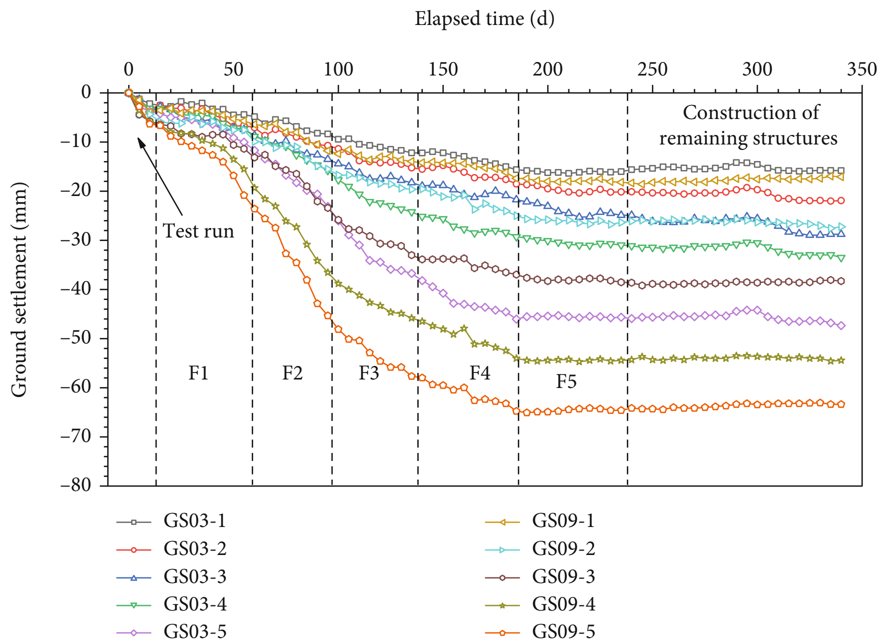

FIGURE 16: Ground settlement curve.

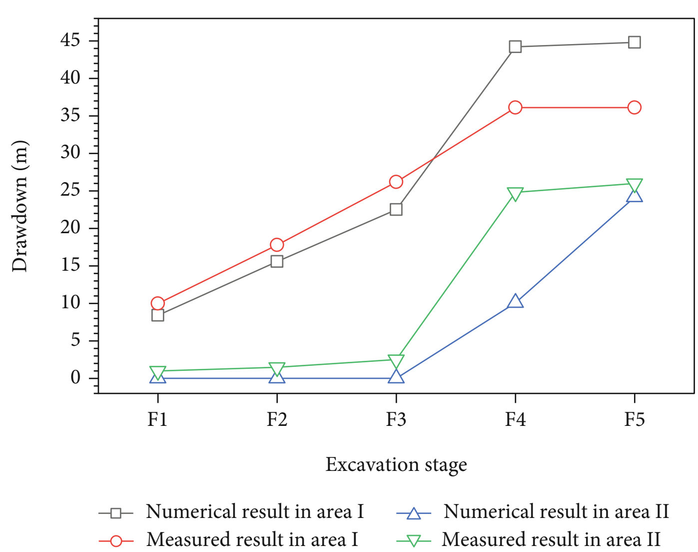

FIGURE 17: Comparison of drawdown.

the ground settlement raised slightly due to the recovery of groundwater table.

5. Validation

Since the ground settlement is not considered in the numerical simulation, the main parameter for validation is the groundwater table. The measured water table is compared with the numerical results of Section 3.4.2, as shown in Figure 17.

During the excavation of F1, the drawdown obtained by numerical simulation was 8.4 m and the measured drawdown was about 10 m in area I, which indicated that the simulation result is 16% smaller than the measured result. The simulated result of drawdown in area I was 12.3% lower than the measured one during the excavation of F2.

During the excavation of F3, the water table in area II decreased to -12.5 m, which was 2.5 m deeper than the simulation result. The simulated result of drawdown in area I was 14.1% smaller than the measured result.

During the excavation of F4, the water table in area I was -46.1 m, while the numerical result was -54.2 m. The water table in area II was -35 m, while the simulated result was -20.1 m.

During the excavation of F5, the drawdown in area I was 36.1 m, while the numerical result was 44.8 m. The measured drawdown in area II was about 26 m, while the simulated result was 24.2 m, and the difference was only 6.9%.

To summarize, the measured results are in good agreement with the numerical results during the excavation of F1 to F3 and F5. The difference is mainly reflected in the excavation of F4. This is because in order to ensure the safety of the project, the pumping wells in area III was increased during the excavation of F4. Therefore, the numerical simulation is reliable.

6. Conclusions

In this paper, the method of numerical simulation was adopted to analyze the dewatering scheme. The project was successfully implemented, which verified the reliability of the dewatering analysis. The following conclusions are obtained:

(1) The groundwater table versus permeability coefficient curve shows three different stages. The permeability coefficient of grouting area is recommended to be controlled in stage 3. For this project, the recommended value is 1×10^{-7} m/s

(2) The design of the inner waterproof curtain and outer waterproof curtain leads to a large drawdown. When two waterproof curtains are used, the drawdown is 11.1% larger than that in case with one waterproof curtain

(3) The dewatering scheme of "waterproof curtain + base grouting + pumping" is effective for deep excavation in strong permeable strata

Data Availability

The data used to support the findings of this study are available from the corresponding author upon request.

Conflicts of Interest

The authors declare that there is no conflict of interest regarding the publication of this paper.

Acknowledgments

The authors would like to thank the financial support from China Railway First Survey and Design Institute Group Co., Ltd. and Lanzhou Rail Transit Co., Ltd. (Grant No. 13-17). Thanks are due to the China Railway First Survey and Design Institute Group Co., Ltd. and the China Railway No.14 Engineering Group Co., Ltd. for providing great assistance in field water table observation and land subsidence observation.

References

[1] T. Schwamb, K. Soga, R. J. Mair et al., "Fibre optic monitoring of a deep circular excavation," *Proceedings of the Institution of Civil Engineers-Geotechnical Engineering*, vol. 167, no. 2, pp. 144–154, 2014.

[2] Y. C. Zheng, J. Xiong, T. Liu, X. B. Yue, and J. L. Qiu, "Performance of a deep excavation in Lanzhou strong permeable sandy gravel strata," *Arabian Journal of Geosciences*, vol. 13, no. 4, 2020.

[3] N. E. Faustin, M. Z. E. B. Elshafie, and R. J. Mair, "Case studies of circular shaft construction in London," *Proceedings of the Institution of Civil Engineers-Geotechnical Engineering*, vol. 171, no. 5, pp. 391–404, 2018.

[4] J. X. Wang, X. T. Liu, J. X. Liu, L. B. Wu, Q. F. Guo, and Q. Yang, "Dewatering of a 32.55 m deep foundation pit in MAMA under leakage risk conditions," *KSCE Journal of Civil Engineering*, vol. 22, pp. 2784–2801, 2018.

[5] J. X. Wang, X. T. Liu, Y. B. Wu et al., "Field experiment and numerical simulation of coupling non-Darcy flow caused by curtain and pumping well in foundation pit dewatering," *Journal of Hydrology*, vol. 549, pp. 277–293, 2017.

[6] Y. Tan, Y. Lu, and D. L. Wang, "Deep excavation of the Gate of the Orient in Suzhou stiff clay: composite earth-retaining systems and dewatering plans," *Journal of Geotechnical and Geoenvironmental Engineering*, vol. 144, no. 3, p. 05017009, 2018.

[7] E. Pujades and A. Jurado, "Groundwater-related aspects during the development of deep excavations below the water table: a short review," *Underground Space*, vol. 6, no. 1, pp. 35–45, 2021.

[8] J. X. Wang, B. Feng, T. P. Guo, L. G. Wu, R. X. Lou, and Z. Zhou, "Using partial penetrating wells and curtains to lower the water level of confined aquifer of gravel," *Engineering Geology*, vol. 161, pp. 16–25, 2013.

[9] Y. You, C. H. Yan, B. T. Xu, S. Liu, and C. H. Che, "Optimization of dewatering schemes for a deep foundation pit near the Yangtze River, China," *China, Journal of Rock Mechanics and Geotechnical Engineering*, vol. 10, no. 3, pp. 555–566, 2018.

[10] L. H. Liu, M. F. Lei, C. Y. Cao, and C. H. Shi, "Dewatering characteristics and inflow prediction of deep foundation pits with partial penetrating curtains in sand and gravel strata," *Water*, vol. 11, no. 10, p. 2182, 2019.

[11] L. Zhang, X. J. Zhou, Y. D. Pan, B. W. Zeng, D. F. Zhu, and H. Z. Jiang, "Design of groundwater extraction in open cut foundation pit and simplified calculation of ground subsidence due to dewatering in sandy pebble soil strata," *Advances in Civil Engineering*, vol. 2020, 25 pages, 2020.

[12] Y. Chen, W. Zhao, P. J. Jia, and J. Y. Han, "Proportion analysis of ground settlement caused by excavation and dewatering of a deep excavation in sand area," *Indian Geotechnical Journal*, vol. 48, no. 1, pp. 103–113, 2018.

[13] Y. Mei, D. Zhou, X. Wang et al., "Deformation law of the diaphragm wall during deep foundation pit construction on lake and sea soft soil in the Yangtze River Delta," *Advances in Civil Engineering*, vol. 2021, 11 pages, 2021.

[14] C. F. Zeng, X. L. Xue, G. Zheng, T. Y. Xue, and G. X. Mei, "Responses of retaining wall and surrounding ground to pre-excavation dewatering in an alternated multi-aquifer-aquitard system," *Journal of Hydrology*, vol. 559, pp. 609–626, 2018.

[15] C. F. Zeng, X. L. Xue, and M. K. Li, "Use of cross wall to restrict enclosure movement during dewatering inside a metro pit before soil excavation," *Tunnelling and Underground Space Technology*, vol. 112, p. 103909, 2021.

[16] C. Cao, C. Shi, L. Liu, and J. Liu, "Evaluation of the effectiveness of an alternative to control groundwater inflow during a deep excavation into confined aquifers," *Environmental Earth Sciences*, vol. 79, no. 22, 2020.

[17] R. Granata and F. Leoni, *In: 5th International Conference on Grouting, Deep Mixing, and Diaphragm Walls, Grouting 2017, July 9, 2017 - July 12, 2017*, American Society of Civil Engineers (ASCE), Honolulu, HI, United states, 2017.

[18] M. Calvello and R. J. Finno, "Selecting parameters to optimize in model calibration by inverse analysis," *Computers and Geotechnics*, vol. 31, no. 5, pp. 410–424, 2004.

[19] X. H. Deng, D. Y. Yuan, D. S. Yang, and C. S. Zhang, "Back analysis of geomechanical parameters of rock masses based on seepage- stress coupled analysis," *Mathematical Problems in Engineering*, vol. 2017, 13 pages, 2017.

[20] E. Pujades, A. Lopez, J. Carrera, E. Vazquez-Sune, and A. Jurado, "Barrier effect of underground structures on aquifers," *Engineering Geology*, vol. 145-146, pp. 41–49, 2012.

[21] S. L. Shen, Y. X. Wu, and A. Misra, "Calculation of head difference at two sides of a cut-off barrier during excavation dewatering," *Computers and Geotechnics*, vol. 91, pp. 192–202, 2017.

[22] H. M. Lyu, S. L. Shen, Y. X. Wu, and A. N. Zhou, "Calculation of groundwater head distribution with a close barrier during excavation dewatering in confined aquifer," *Geoscience Frontiers*, vol. 12, no. 2, pp. 791–803, 2021.

[23] J. X. Wang, X. T. Liu, J. D. Xiang, Y. H. Jiang, and B. Feng, "Laboratory model tests on water inrush in foundation pit bottom," *Environmental Earth Sciences*, vol. 75, no. 14, 2016.

[24] C. Y. Jia, H. L. Wang, H. Q. Liu, G. B. Zhang, and K. H. Sheng, "Research on the technology of plugging gushing water in the vertical shaft under complicated conditions," *Geofluids*, vol. 2020, 17 pages, 2020.

[25] X. L. Liu, F. Wang, J. Huang, S. J. Wang, Z. Z. Zhang, and K. Nawnit, "Grout diffusion in silty fine sand stratum with high groundwater level for tunnel construction," *Tunnelling and Underground Space Technology*, vol. 93, p. 103051, 2019.

[26] G. X. Zhu, Q. S. Zhang, R. T. Liu, J. W. Bai, W. Li, and X. Feng, "Experimental and numerical study on the permeation grouting diffusion mechanism considering filtration effects," *Geofluids*, vol. 2021, 11 pages, 2021.

[27] G. Zheng, C. F. Zeng, Y. Diao, and X. L. Xue, "Test and numerical research on wall deflections induced by pre-excavation dewatering," *Computers and Geotechnics*, vol. 62, pp. 244–256, 2014.

Hindawi
Geofluids
Volume 2021, Article ID 7126013, 9 pages
https://doi.org/10.1155/2021/7126013

Research Article

Influence of Water-Cement Ratio on Viscosity Variation of Cement Grout in Permeation Grouting

Gaohang Lv,[1] Jian Liu,[2] Bo Han,[1] Tiantao Zhang,[2] Quanyi Xie,[2] and Xueshen Zhang[2]

[1] *School of Civil Engineering, Shandong University, Jinan 250061, China*
[2] *School of Qilu Transportation, Shandong University, Jinan 250002, China*

Correspondence should be addressed to Quanyi Xie; quanyixiesdu@163.com

Received 22 April 2021; Revised 15 July 2021; Accepted 1 September 2021; Published 24 September 2021

Academic Editor: Chuangzhou Wu

Diffusion radius is an important construction parameter, because it can significantly influence the grouting effectiveness. Theoretical models in predicting diffusion radius have been practiced, but there are still significant discrepancies between theoretical calculations and realistic results in the practical construction. One of the critical reasons for the misprediction is the time-dependent behavior of the cement grout, which is significantly affected by the water-cement ratio (W/C). Therefore, this paper experimentally and numerically studies the influence of W/C on the viscosity variation of the grout and grouting process. Firstly, the apparent viscosity of the cement grout under different W/C is tested by a rotational viscometer in a laboratory experiment. Subsequently, based on the laboratory tests, numerical models are established to investigate the influence of W/C on the diffusion process of cement grout in sand layers. According to the laboratory results, the apparent viscosity of cement grouts decreases with the increase of W/C. Besides, the apparent viscosity increases with time, while the increasing range of apparent viscosity firstly increases and then decreases as W/C increases. Based on the simulated results, when W/C changes from 0.8 to 1.1, the diffusion radius at 60 min experiences a less and less obvious increase under the given grouting pressure for permeation grouting in the sand layer. When W/C is 0.9, the relative error reaches to 37.65% at 60 min, which is slightly lower than that of 0.8. However, when W/C changes from 0.9 to 1.0, the relative error becomes very narrow (21.36%), and this figure is much lower than that of 0.8 or 0.9. The simulation results are verified by field test, and the relative error is 6%, which proves the effectiveness of the analysis. Therefore, the cement permeation model considering viscosity variation of the grout is a reasonable alternative in the real project. At the same time, the time-dependent behavior of cement grouts should be considered, especially when using cement grouts with a low water-cement ratio in the practical engineering.

1. Introduction

Unfavorable foundation is a common problem in civil engineering and transport engineering. The cost for foundation treatment sometimes can make up more than half of the total cost in engineering construction, so that the foundation improvement becomes critically important. Permeation grouting with cement grouts has been widely utilized for foundation improvement because of its simple construction and high efficiency [1–3]. However, grouting effectiveness in practical engineering is significantly affected by the properties of grouting materials and geological conditions [4]. In addition, a reasonable estimation of grouting parameters before practical engineering will help grouting construction meet requirements at a relatively low price. In order to improve the accuracy of calculation, scholars have investigated permeation grouting from different points of view. For example, some put forward theoretical calculations based on a few assumptions and simplifications. Yang et al. [5] and Ye et al. [6] established theoretical models based on different constitutive models of flow pattern and deduced the calculation formulas for diffusion range or grouting pressure for permeation grouting. Besides, some researchers studied permeation grouting using experimental and numerical methods. For example, Celik [7] investigated the features of cement-based permeation grout based on some important grout parameters, such as the rheological properties, coefficient of permeability to grout, and injectability of cement grout. Similarly, based on the immiscible multiphase flow theory, Coskun and Tokdemir [8] established the mathematical model of permeable grouting in fully saturated soil. Furthermore, Fu et al. [9] proposed a mathematical model of seepage grouting according to the self-weight effect of slurry and established a prediction model of Bingham cement slurry setting size. Apart from that, Fu et al. developed a set of grouting test devices, which consist of a power device, pressure-bearing slurry tank, and several test frames [9]. The compressive strength, deformation modulus, and permeability coefficient were selected as the evaluation indexes of the grouting reinforcement effect.

On the other hand, researchers attach importance to the influence of grouts on grouting effectiveness. Among others, some scholars have tried to improve the theoretical formulas by using new methods in order to obtain more accurate rheological parameters. Dai and Bird [10] provided another approach to the establishment of a Reynolds-type equation in lubrication theory by variational theory. Beyond that, Rahman et al. [11, 12] measured the static and dynamic yield stresses with different measurement techniques. In addition, other scholars explored the influence of grouting materials on the diffusion process. Indeed, the power expended by the injection mechanism is the energy dissipated by viscous effects. Based on this fact, El Tani [13] obtained the radial flow rate of cement grout in a rock fracture from Bingham's relation. Zhang et al. [14] regarded the quick setting slurry as a Bingham liquid of time-dependent behavior and employed an even capillary group model to describe the porous flow process. They suggested that the spatial uneven distribution of viscosity should be considered carefully in the grouting design. At present, researches focus on either viscosity measurement or viscosity variation under single W/C. Investigation on the influence of W/C on viscosity variation and the diffusion process is relatively rare. Besides, the discrepancy between the diffusion radius considering time-dependent behavior and that not considering different W/C has not been quantitatively studied.

Therefore, in this work, laboratory experiments and numerical simulations are carried out to investigate the influence of W/C on the diffusion radius of cement grouts in the sand layer as well as the discrepancies between the diffusion radius considering time-dependent behavior and that not considering. In particular, firstly, a laboratory test was performed to measure the apparent viscosity of cement grouts under different W/C, after which the viscosity variation characteristics were investigated by fitting the measured apparent viscosity with ORIGIN. Subsequently, based on the obtained time-dependent behavior of cement grouts, calculation models were established by COMSOL to simulate the diffusion process of the cement grout in the sand layer. Apart from that, the simulated results considering and not considering time-dependent behavior under different W/C were compared, and the influence of W/C on cement permeation grouting was analyzed.

2. Laboratory Experiment on Viscosity of Cement Grout

2.1. Experiment Instruments and Testing Material. The laboratory experiments focus on investigating the rheological properties of pure cement grouts, and the concerned W/C range is 0.5-1.1, widely used in practical engineering. According to Ruan [15], cement grouts under W/C 0.5-0.7 can be classified as power-law fluid, while grouts under W/C 0.8-1.0 are generally classified as Bingham fluid.

Figure 1: YDNJ-160A-type mixer.

In the experiment, the YDNJ-160A-type mixer (Figure 1) was employed in preparing the fresh cement grouts. In order to accurately measure the apparent viscosity, the NXS-11B-type rotational viscometer (Figure 2) was adopted, and the main technique indexes of the viscometer are shown in Table 1.

The cement used in the experiment is Portland cement (PC) graded 42.5 produced by Sunnsy Group in Jinan. The main chemical composition is shown in Table 2.

2.2. Test Procedure. Fresh cement grouts under W/C 0.5~1.1 were firstly produced and kept in the thermostat with temperature of 20°. Subsequently, the apparent viscosity of grouts was measured from the very beginning to 40 min every 10 minutes. Then, the viscosity variation characteristics of cement grouts under different W/C were analyzed by fitting the measured apparent viscosity with ORIGIN software. Finally, mathematical equations describing the time-dependent behavior of cement grouts under different W/C were formed (specification for geotechnical tests).

2.3. Discussion of Experimental Result. The apparent viscosity of cement grouts under different W/C is shown in Table 3. Based on previous researches [16], the relationship between apparent viscosity of cement grouting materials and time could be fitted as a natural logarithm function.

The fitting curves are shown in Figures 3 and 4. According to Figures 3 and 4, at the same moment, the apparent viscosity of grouts decreases when W/C increases from 0.5 to 1.1, and the apparent viscosity under W/C 0.5-0.7 is an order of magnitude higher than that of 0.8~1.1. Besides, the increasing range of apparent viscosity firstly increases and then decreases as W/C increases. When W/C is 0.5 and 0.6, the increasing range is less than 2 times of the initial viscosity. As W/C increases from 0.7 to 0.9, the increasing

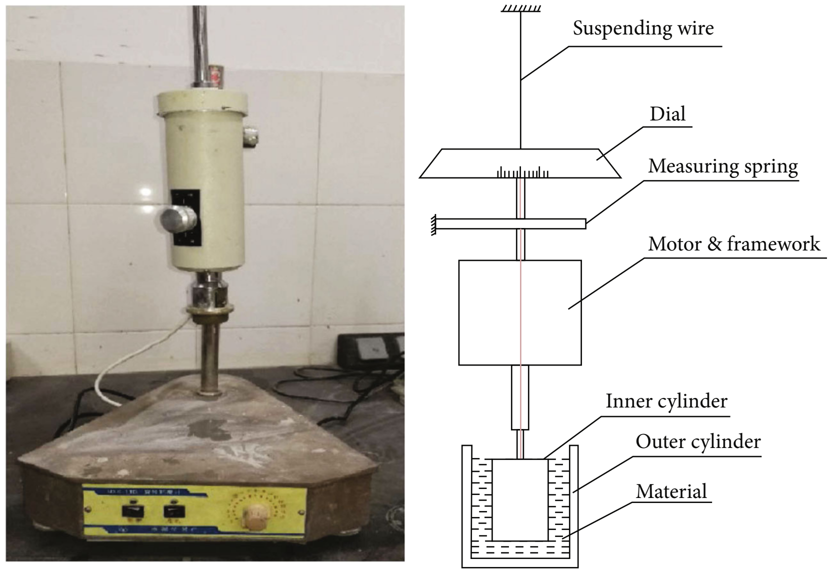

Figure 2: NXS-11B-type rotational viscometer.

Table 1: Main technique indexes of rotational viscometer.

Technique indexes	Parameters
Measurement range (η)	$2.8 \sim 1.78 \times 10^7$ mPa · s
Shear stress range (τ)	$27.67 \sim 21970$ Pa
Shear rate range (D_S)	$1.23 \sim 996\ s^{-1}$
Rotational speed	$5.6 \sim 360$ r/min
Reproducibility	±1% (FS)
Environmental temperature	$+5 \sim 35^{\circ}$

Table 2: Main chemical composition of PC.

Material	CaO (%)	SiO_2 (%)	Al_2O_3 (%)	Fe_2O_3 (%)	Fineness (m^2/kg)	Specific gravity (kg/m^3)
PC	62.60	22.61	4.35	2.46	342	2980

range increases from 3.74 times to 4.39 times. However, the increasing range drops from 4.08 times to 3.32 times when W/C increases from 1.0 to 1.1. In conclusion, the influence of W/C on time-dependent behavior firstly increases and then decreases as W/C increases.

Consequently, the time-dependent behavior of the cement grout must be considered to ensure the grouting effectiveness during the design and construction period.

According to the test results, the variation rules of shear strength and density of slurry under different water-cement ratios are analyzed, as shown in Figures 5 and 6. Obviously, with the increase of the water-cement ratio, the density decreases linearly, and the shear strength also decreases. When the W/C is greater than 0.9, the change trend decreases.

Table 3: Measured apparent viscosity of cement grouts under different W/C.

W/C	Apparent viscosity (mPa·s)				
	0 min	10 min	20 min	30 min	40 min
0.5	932.54	992.06	1021.83	1349.21	1507.94
0.6	344.41	422.18	516.62	538.84	599.94
0.7	77.23	80.01	83.34	10.00	288.86
0.8	27.78	28.89	46.12	55.56	94.57
0.9	14.29	24.61	28.89	37.23	62.79
1.0	12.24	23.89	24.61	33.89	49.99
1.1	12.22	15.00	27.23	33.34	40.56

3. Numerical Simulation Analysis

Based on the obtained time-dependent behavior of cement grouts, COMSOL is employed to simulate the diffusion process of cement grouts and calculate the diffusion radius under different W/C. Given that permeation grouting under constant grouting pressure is widely used in practical engineering, this research focuses on the influence of W/C on the grouting process under the given grouting pressure. The concerned subjects are the cement grout under W/C 0.8~1.1 because there are many related theoretical analyses about Bingham fluid [17], and it is convenient to compare with the simulated results. In fact, cement grout with W/C in the vicinity of 1.0 has been widely used in practical engineering.

Viscosity is deemed as a constant, and it is equal to the initial viscosity when the time-dependent behavior is not considered. While viscosity variation is taken into account, the changing viscosity is equivalent to a mean viscosity by integration. The equation could be expressed as follows:

$$\bar{\mu} = \int_0^t \frac{\mu(t)dt}{t}, \tag{1}$$

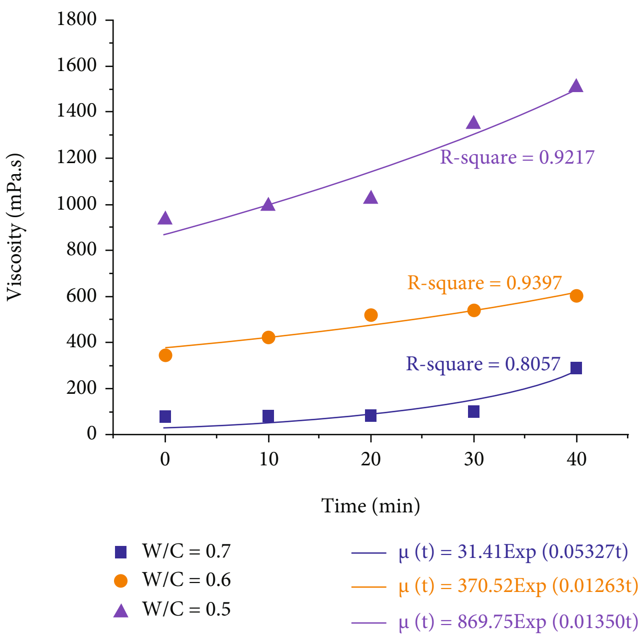

Figure 3: Fitting curves of viscosity of cement grouts (W/C = 0.5 ~ 0.7).

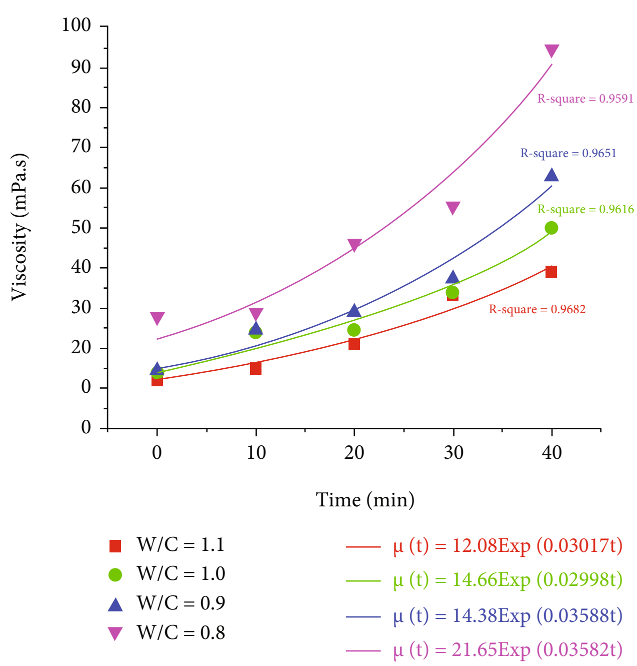

Figure 4: Fitting curves of viscosity of cement grouts (W/C = 0.8 ~ 1.1).

$$\beta = \frac{\int_0^t \mu(t)dt/t}{\mu_w}, \tag{2}$$

where $\bar{\mu}$ and μ_w are the mean viscosity of the cement grout and the viscosity of water, respectively; β is the viscosity ratio between the cement grout and water, and t is the whole grouting time.

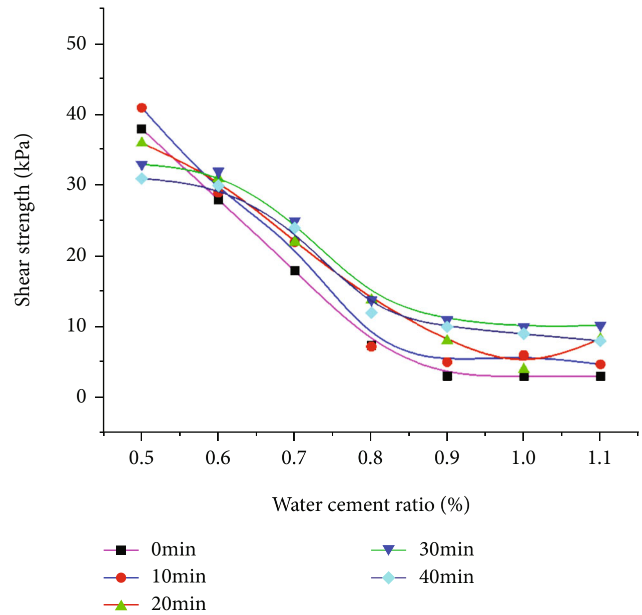

Figure 5: Fitting curves of viscosity of cement grouts (W/C = 0.8 ~ 1.1).

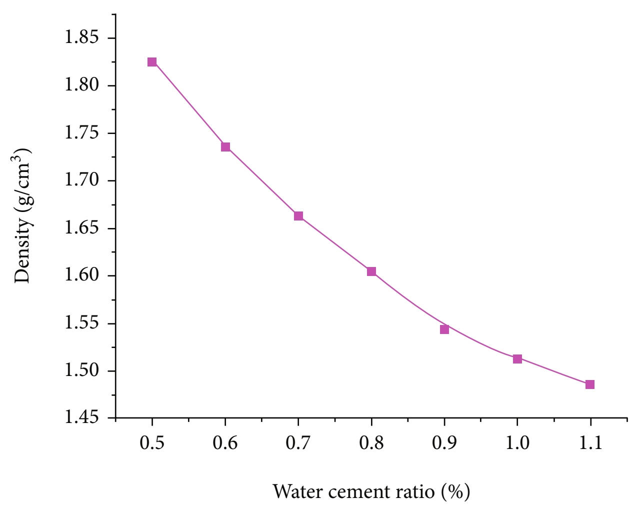

Figure 6: Fitting curves of viscosity of cement grouts (W/C = 0.8 ~ 1.1).

3.1. Parameter Setting. Before establishing the calculation model, some assumptions are made as follows:

(1) Gravity is negligible during the grouting process

(2) The yield strength is regarded as a constant with a value of 3 Pa

(3) The permeation grouting starts from the grouting pipe bottom, and the grout penetrates into the sand layer spherically under a grouting pressure of 300 kPa

In the solid mechanics module, the surface is set as a free deformation boundary. The left and right boundaries of the

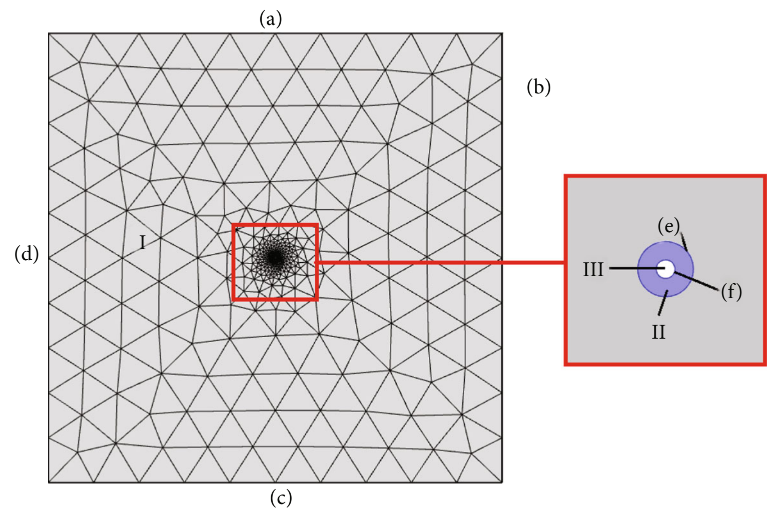

Figure 7: Calculation model of numerical simulation.

Table 4: Numerical model parameters.

Parameters	Value
Density of cement grout	1520 kg/m^3
Viscosity of cement grout	Calculated by Equation (1)
Density of water	1000 kg/m^3
Permeability of soil (K_1)	6.31e-11 m^2
Porosity of soil	0.35
Water-cement ratio	0.97

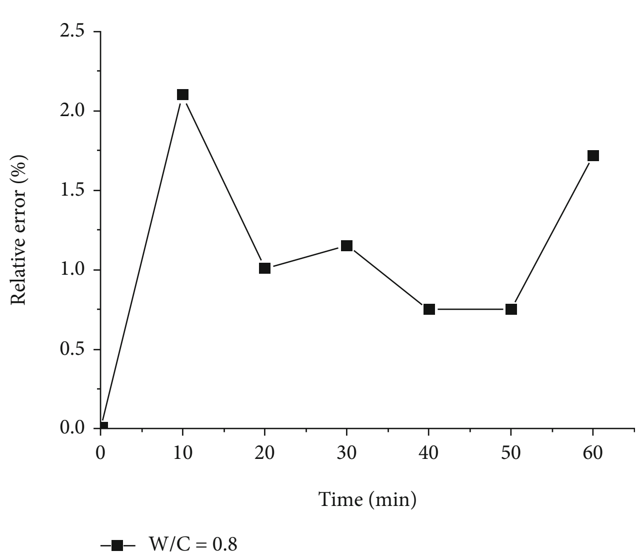

Figure 8: Relative error between theoretical diffusion radius and simulated radius (W/C = 0.8).

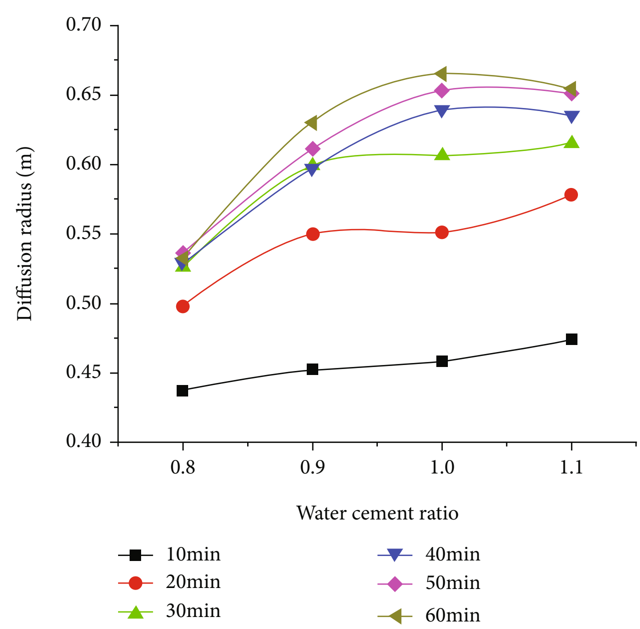

Figure 9: Diffusion radius of cement grouts under different W/C.

model are set as the roller support boundaries, which only allow vertical displacement, rather than lateral displacement. The lower boundary of the calculation model is set as a fixed boundary. In the seepage mechanics module, the height of the groundwater level is set to be consistent with the surface height, and the left and right boundaries and the lower boundary of the calculation model are set as a no-flow boundary, that is, the seepage velocity ≠ 0.

The model of the numerical simulation is displayed in Figure 7, and the main parameters of the numerical model are presented in Table 4. The right part in Figure 7 is the local enlarged drawing of the grouting hole. In the initial condition, Part I and Part II are full of water and cement slurry, respectively, and Part III is the grouting hole with a radius of 30 mm. The entrance of the grout is Boundary (F), and the exit is Boundaries (A), (B), (C), and (D).

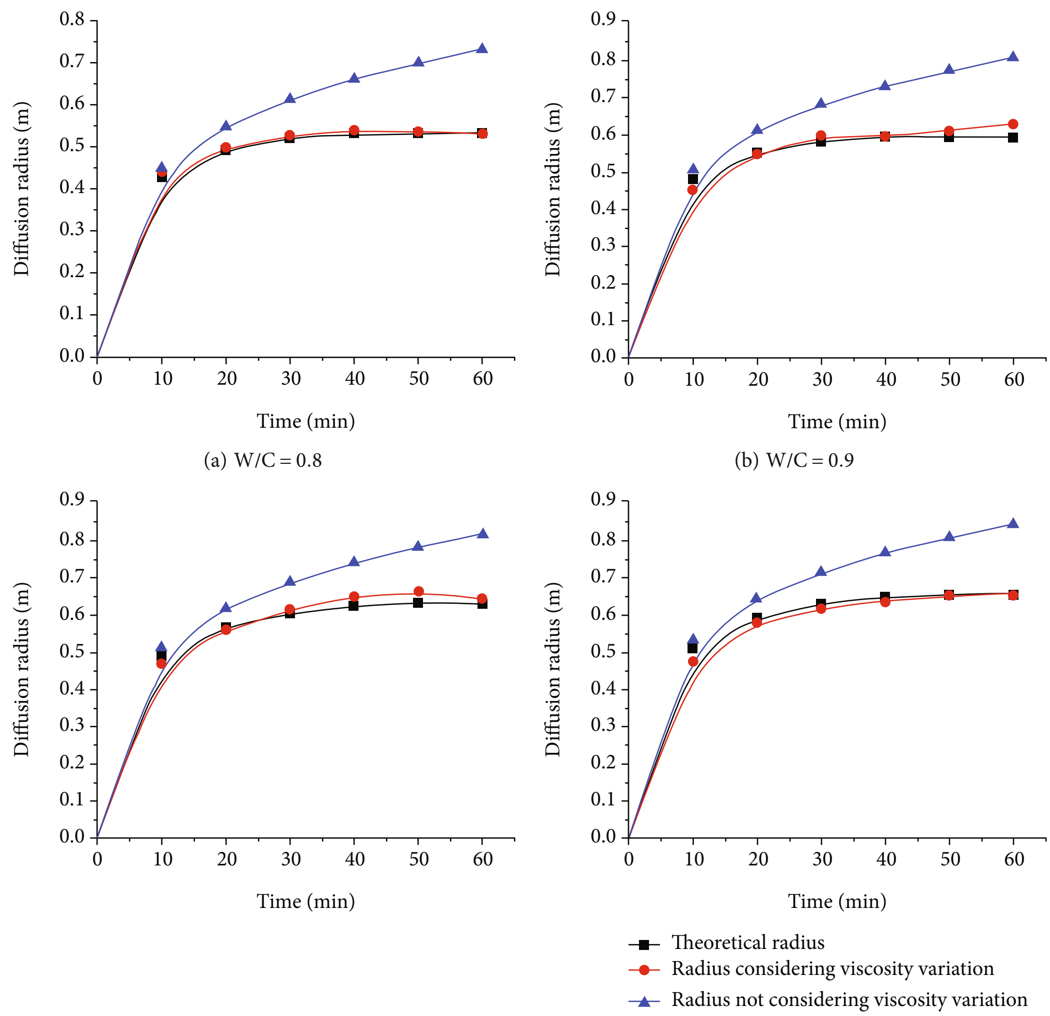

(a) W/C = 0.8

(b) W/C = 0.9

(c) W/C = 1.0

(d) W/C = 1.1

Figure 10: Diffusion radius comparison (W/C = 0.9).

3.2. Validity of Numerical Model. Prior to grouting simulation considering different W/C, the validity of the calculation model is firstly proven by comparing the simulated results with the results calculated via a widely accepted theoretical calculation [18]. The diffusion radius considering a time-dependent behavior can be theoretically calculated according to

$$p_1 - p_0 = \frac{\beta \varphi r_1^3 \gamma_w}{3Ktl_0} + \frac{4}{3}\lambda(r_1 - r_0), \tag{3}$$

$$K = \frac{K_1 \gamma_w}{\mu_w} = \frac{\varphi b^2 \gamma_w}{8\mu_w}, \tag{4}$$

$$\lambda = \frac{2\tau_0}{b}, \tag{5}$$

where $p_1 - p_0$ is the pressure difference; K, β, φ, and γ are the permeation coefficient, the ratio between the cement grout and water viscosity, the porosity of the sand layer, and the unit weight of water, respectively; r_1 and r_0 are the diffusion radius and the radius of the grouting pipe, respectively; and

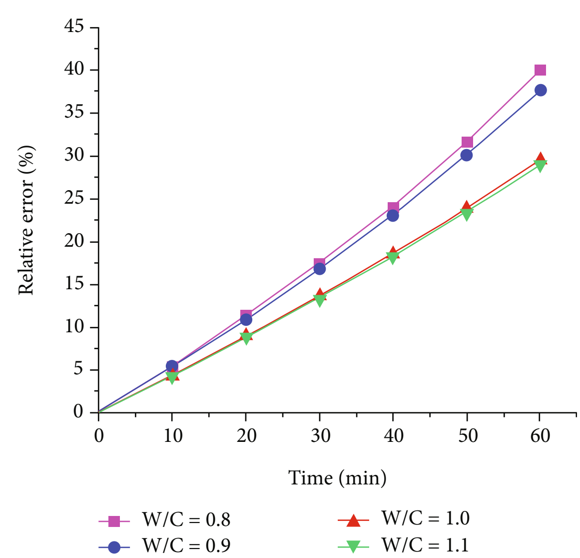

Figure 11: Relative error between theoretical diffusion radius obtained and simulated results not considering time-dependent behavior.

(a) Setting out and drilling

(b) Excavation exploration process

FIGURE 12: Field test of grouting diffusion radius.

λ, τ_0, and b are the starting pressure, yield stress, and capillary radius, respectively.

Based on the obtained results, the relative error between the diffusion radius obtained by theoretical calculation and the numerical simulation when W/C is 0.8 is shown in Figure 8. It is noteworthy that the relative errors are within 3%, manifesting that numerical simulation can well reflect the diffusion process. Thus, it is a reasonable alternative to use COMSOL to further analyze the influence of W/C on the grouting process.

After proving the validity of the calculation model, comprehensive investigations are carried out to explore the influence of W/C on the diffusion radius of permeation grouting in the sand layer. Besides, the relative error with regard to considering the time-dependent behavior of viscosity under different W/C is quantitatively analyzed.

3.3. Discussion of Simulated Result

3.3.1. Influence of W/C on Diffusion Radius. The diffusion radius of cement grouts under different W/C is shown in Figure 7. According to Figure 9, the diffusion radius increases as W/C increases from 0.8 to 1.1, indicating that larger W/C will lead to a larger diffusion radius. In particular, when W/C changes from 0.8 to 0.9, the diffusion radius at 60 min experiences a dramatic increase with the increasing range of 18%. The increasing trend becomes less obvious when W/C rises from 0.9 to 1.1. In addition, the diffusion radius under the same W/C increases with time and the growth rate becomes small. The attenuation rate decreases as W/C increases from 0.8 to 1.1. One possible reason lies in that the grouting pressure attenuates faster for cement grouts with higher W/C, because high-concentration cement grouts need more energy when diffusing in the sand layer.

3.3.2. Influence of W/C on the Relative Error of Diffusion Radius with Regard to Considering Time-Dependent Behavior. The simulated results considering time-dependent behavior and not considering time-dependent behavior and the theoretical diffusion radius under different W/C are compared. Based on the obtained results, the diffusion radius under the water-cement ratios of 0.8-1.1 is shown in Figure 10. Notably, theoretical radiuses and simulated results considering time-dependent behavior under all W/C show good agreements and keep steady after 40 min, which tallies with the actual conditions. With the attenuation of the grouting pressure, the diffusion radius marginally increases and eventually approaches a constant value. By contrast, the diffusion radius not considering a time-dependent behavior dramatically rises with time, resulting in an increasing gap with the theoretical radius or simulated result considering the viscosity variation of cement grouts.

TABLE 5: Comparison of diffusion radius.

Water-cement ratio	0.8	0.9	1	1.1
Simulation results (m)	0.74	0.81	0.82	0.84
Test result (m)	0.77	0.84	0.89	0.92

In order to quantitatively investigate the influence of W/C, the relative errors between simulated results not considering viscosity variation and the theoretical radius under different W/C are obtained (see the result in Figure 11). The influence of W/C on the relative error of the diffusion radius with regard to considering the viscosity variation decreases as W/C increases from 0.8 to 1.1. When W/C is 0.8, the relative error sharply enlarges with time, reaching to nearly 40% at 60 min. Similarly, when W/C is 0.9, the relative error reaches to 37.65% at 60 min, which is slightly lower than that of 0.8. However, when W/C varies from 0.9 to 1.0, the relative error becomes more narrow (21.36%), and this figure is much lower than that of 0.8 or 0.9. The relative error experiences a slight drop when W/C increases to 1.1, possibly because the time-dependent behavior weakens when W/C increases.

3.3.3. Field Test of Grouting Diffusion Radius. In order to verify the analysis and numerical simulation results, this paper conducted field grouting tests in the Yellow River impact area. According to the above simulation parameters, the slurry of different water-cement ratio is set, and the grouting time is 60 minutes (technical specification for earth dam grouting). In the wake of grouting, after 72 hours, the grouting part is excavated (see Figure 12).

After excavation, the grouting radius under different water-cement ratios is calculated in detail (see the specific parameters in Table 5).

The field test results reveal that with the increase of the water-cement ratio, the grouting diffusion radius increases

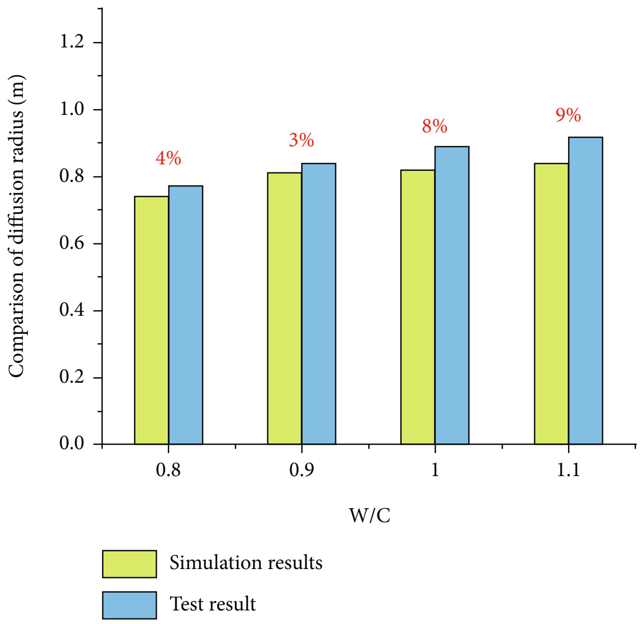

FIGURE 13: Data comparison.

gradually. Moreover, the test and simulation results are compared. It is found that the average error of the slurry diffusion radius between the simulation results and the field test results is 6% (see Figure 13), and the simulation results are in good agreement with the test results, which verifies the analysis conclusions in this paper.

4. Conclusion

In order to investigate the viscosity variation of cement grouts under different W/C and the influence of W/C on the permeation grouting process in the sand layer, this paper carried out laboratory experiments and numerical simulations. In particular, laboratory tests focus on studying the influence of W/C on the apparent viscosity of pure cement grouts. Subsequently, numerical simulation is conducted to reproduce the grouting process of cement grouts and study the diffusion radius when considering the time-dependent behavior under different W/C. Based on the obtained results, the following conclusions are drawn:

(1) The apparent viscosity of cement grouts decreases with the increase of W/C. The apparent viscosity increases with time. Besides, the increasing range of apparent viscosity firstly increases and then decreased as W/C increases

(2) When W/C changes from 0.8 to 1.1, the diffusion radius of cement grouts at 60 min experiences a less and less obvious increase under a given grouting pressure for permeation grouting in the sand layer

(3) For the investigated cases, the relative error of the diffusion radius obtained by theoretical analysis and numerical simulation not considering viscosity variation drops when W/C increases

(4) According to the test results, the grouting diffusion radius increases gradually, and the test and simulation results are compared. It is found that the average error of the slurry diffusion radius between the simulation results and the field test results is 6%, and the simulation results are in good agreement with the test results

Data Availability

Some or all data, models, or code generated or used during the study are available from the corresponding author upon request.

Conflicts of Interest

We declare that we do not have any commercial or associative interest that represents a conflict of interest in connection with the work submitted.

Acknowledgments

This work was supported by the Shandong Key Research and Development Plan (2019JZZY010429) and the Science and Technology Plan of the Shandong Transportation Department (2019B48).

References

[1] S. C. Li, R. T. Liu, Q. S. Zhang, and X. Zhang, "Protection against water or mud inrush in tunnels by grouting: a review," *Journal of Rock Mechanics and Geotechnical Engineering*, vol. 8, no. 5, pp. 753–766, 2016.

[2] H. J. Seo, H. Choi, and I. M. Lee, "Numerical and experimental investigation of pillar reinforcement with pressurized grouting and pre-stress," *Tunnelling and Underground Space Technology*, vol. 54, pp. 135–144, 2016.

[3] Q. Zhang, H. B. Wang, R. T. Liu et al., "Infiltration grouting mechanism of porous media considering diffusion paths of grout," *Yantu Gongcheng Xuebao/Chinese Journal of Geotechnical Engineering*, vol. 40, pp. 918–924, 2018.

[4] Z. Li, L. Zhang, Q. Zhang, R. Liu, W. Yang, and Y. Chu, "Simulation test for permeation grouting reinforcement effect of sand layer," *Meitan Xuebao/Journal of the China Coal Society*, vol. 43, pp. 3488–3497, 2018.

[5] Z. Yang, X. Niu, K. Hou et al., "Study on diffusion parameters of Bingham fluid based on column-hemispherical penetration grouting," *Journal of Sichuan University (Chinese Journal of Geotechnical Engineering)*, vol. 28, no. 12, pp. 47–53, 2015.

[6] F. Ye, C. F. Gou, Z. Chen, Y. P. Liu, and J. L. Zhang, "Back-filled grouts diffusion model of shield tunnel considering its viscosity degeneration," *Zhongguo Gonglu Xuebao(China Journal of Highway and Transport)*, vol. 26, no. 1, pp. 127–134, 2013.

[7] F. Celik, "The observation of permeation grouting method as soil improvement technique with different grout flow models," *Geomechanics and Engineering*, vol. 17, no. 4, pp. 367–374, 2019.

[8] S. B. Coskun and T. Tokdemir, "Modelling of permeation grouting through soils," *Journal of Applied Engineering Sciences*, vol. 10, no. 1, pp. 11–16, 2020.

[9] Y. Fu, X. Wang, S. Zhang, and Y. Yang, "Modelling of permeation grouting considering grout self-gravity effect: theoretical and experimental study," *Advances in Materials Science and Engineering*, vol. 2019, Article ID 7968240, 16 pages, 2019.

[10] G. Dai and R. B. Bird, "Radial flow of a Bingham fluid between two fixed circular disks," *Journal of non-Newtonian fluid mechanics*, vol. 8, no. 3-4, pp. 349–355, 1981.

[11] M. Rahman, U. Håkansson, and J. Wiklund, "In-line rheological measurements of cement grouts: effects of water/cement ratio and hydration," *Tunnelling and Underground Space Technology*, vol. 45, pp. 34–42, 2015.

[12] M. Rahman, J. Wiklund, R. Kotzé, and U. Håkansson, "Yield stress of cement grouts," *Tunnelling and Underground Space Technology*, vol. 61, pp. 50–60, 2017.

[13] M. El Tani, "Grouting rock fractures with cement grout," *Rock Mechanics and Rock Engineering*, vol. 45, no. 4, pp. 547–561, 2012.

[14] Q. N. Zhang, L. W. Zhang, X. Z. Zhang, R. Liu, M. Zhu, and D. Zheng, "Grouting diffusion in a horizontal crack considering temporal and spatial variation of viscosity," *Yanshilixue Yu Gongcheng Xuebao/Chinese Journal of Rock Mechanics and Engineering*, vol. 34, pp. 1198–1210, 2015.

[15] W. J. Ruan, "Spreading model of grouting in rock mass fissures based on time-dependent behavior of viscosity of cement-based grouts," *Chinese Journal of Rock Mechanics and Engineering*, vol. 24, no. 15, pp. 2709–2714, 2005.

[16] W. J. Ruan, "Research on diffusion of grouting and basic properties of grouts," *Chinese Journal of Geotechnical Engineering*, vol. 27, no. 1, pp. 69–73, 2005.

[17] A. Franci and X. Zhang, "3D numerical simulation of free-surface Bingham fluids interacting with structures using the PFEM," *Journal of Non-Newtonian Fluid Mechanics*, vol. 259, pp. 1–15, 2018.

[18] X. Y. Kong, *Advanced Mechanics of Fluids in Porous Media*, University Of Science And Technology of China Press, 2010.

Hindawi
Geofluids
Volume 2021, Article ID 6745900, 9 pages
https://doi.org/10.1155/2021/6745900

Research Article

Evaluation Method of Granite Multiscale Mechanical Properties Based on Nanoindentation Technology

Man Lei,[1,2] **Fa-ning Dang**,[1,2] **Haibin Xue**,[1,2,3] **and Mingming He**[1]

[1]*Institute of Rock and Soil Mechanics, Xi'an University of Technology, Xi'an 710048, China*
[2]*State Key Laboratory of Ecohydraulics in Northwest Arid Region, Xi'an University of Technology, Xi'an 710048, China*
[3]*National Engineering Laboratory for Surface Transportation Weather Impacts Prevention, Kunming 650200, China*

Correspondence should be addressed to Haibin Xue; xhbyts2013@163.com

Received 15 April 2021; Revised 2 August 2021; Accepted 12 August 2021; Published 15 September 2021

Academic Editor: Constantinos Loupasakis

In order to study the mechanical properties of granite at the micro- and nanoscale, the load-displacement curve, residual indentation information, and component information of the quartz, feldspar, and mica in granite were obtained using a nanoindentation test, a scanning electron microscope (SEM), and X-ray diffraction (XRD). The elastic modulus and the hardness of each component of the granite were obtained through statistical analysis. Treating rock as a composite material, the relation between the macro- and microscopic mechanical properties of rock was established through the theory of micromechanical homogenization. The transition from micromechanical parameters to macromechanical parameters was realized. The equivalent elastic modulus and Poisson's ratio of the granite were obtained by the Self-consistent method, the Dilute method, and the Mori-Tanaka method. Compared with the elastic modulus and the Poisson ratio of granites measured by a uniaxial compression test and the available data, the applicability of the three methods were analyzed. The results show that the elastic modulus and hardness of the quartz in the granite is the largest, the feldspar is the second, the mica is the smallest. The main mineral contents in granite were analyzed using the semiquantitative method by XRD and the rock slice identification test. The elastic modulus and the Poisson ratio of granite calculated by three linear homogenization methods are consistent with those of the uniaxial compression test. After comparing the calculation results of the three methods, it is found that the Mori-Tanaka method is more suitable for studying the mechanical properties of rock materials. This method has an important theoretical significance and practical value for studying the quantitative relationship between macro- and micromechanical indexes of brittle materials. The research results provide a new method and an important reference for studying the macro-, micro-, and nanomechanical properties of rock.

1. Introduction

Granite is widely used in the construction of hydropower stations, underground nuclear waste storage, and tunnel engineering because of its good mechanical properties, such as dense structure, high strength, and resistance to weathering. Many scholars have done a lot of research on the macro-, micro-, and nanomechanical properties of rocks [1–4]. However, there are relatively few studies on the transition from the micro- and nanoscale mechanical properties to the macromechanical properties of rocks. The microstructure of granite and its mechanical properties are studied by the nanoindentation technology in this paper. Here, an attempt to study the macromechanical properties of the granite from the micro- and the nanoscale of minerals is made.

Nanoindentation is a very effective method to study the micro- and nanomechanical properties of materials [1, 2, 5–7]. In recent years, researchers have begun to use this method to study the mechanical properties of rocks. Viktorov et al. [8] studied the strength and deformation properties of minerals in rocks by using nanoindentation. Zhu et al. [9] reported a study to assess nanoindentation mapping of mechanical properties of natural rocks. Zhang et al. [10] studied the micromechanical properties of granite by the nanoindentation test, which provided a reference for determining the macromechanical properties of rock from a microscopic perspective. Liu et al. [11] obtained the quantitative relationship between fracture toughness and elastic modulus of shale based on the energy analysis method, which provided a good perspective for understanding the nanomechanical behavior of rocks. All in all, regarding rocks as homogeneous materials, many scholars studied the micro- and nanomechanical properties of rocks by the nanoindentation technique. However, there are relatively few studies that consider the heterogeneous characteristic of rock and reveal the macromechanical properties of granite from the micromechanical properties of minerals.

Due to the difficulty of taking standard core samples in deeply buried engineering and the destruction of the original structure by sampling in important parts of existing engineering, a large number of macromechanical tests cannot be carried out. In this case, the macromechanical parameters of rocks can be calculated by the micro- and nanomechanical parameters, and nanoindentation technology is an effective way to measure the micro- and nanomechanical parameters of materials. In other words, the micromechanical properties of rocks can be obtained by nanoindentation tests and related algorithm; however, the macromechanical behavior of rocks are usually more focused in practical engineering. Therefore, it is a key scientific problem to establish the relationship between the macro- and micromechanical indexes of rocks at different scales. Bobko et al. [12], Chen et al. [13], and Abou et al. [14] proposed some homogenization methods and micromechanical models to estimate the macromechanical properties of materials. The advantages and disadvantages of each method were analyzed.

Granite is regarded in this paper as a material mainly composed of quartz, feldspar, and mica. The linear homogenization theory of composite materials is introduced into the cross-scale study of the macro-, micro-, and nanomechanical properties of granite. The quantitative relationship between the micromechanical indexes and the macromechanical indexes is established by using the Self-consistent method, the Dilute method, and the Mori-Tanaka method. Comparing the results calculated by these three methods with the mechanical parameters measured by the experiment and combining with the advantages and disadvantages of the three methods, an appropriate method is recommended to analyze the relationship between macro- and micromechanical properties of granite. The research results will be helpful in studying the micro- and nanomechanical properties of rocks and in realizing the transition from micro- and nanomechanical parameters to macromechanical parameters.

2. Test Techniques and Procedures

2.1. Testing Device. Nanoindentation is a kind of testing technology where an indenter is pressed vertically into the sample surface and the indentation depth and the corresponding load are recorded. The micro- and nanomechanical parameters of the material are calculated according to the load-displacement curve of the material. The nanoindentation tests are carried out on the Agilent Nanoindenter G200, which is shown in Figure 1. Load control mode is adopted in the test. The maximum load of the test is 500 mN, and the load resolution is 50 nN. The Berkovich indenter is selected for this test. The maximum indenter displacement is 1.5 mm. The maximum press-in depth is 500 μm, and the displacement resolution is 0.01 nm.

2.2. Determination Method of Elastic Modulus and Hardness. Figure 2 shows the three-stage process curves of a typical sample under single loading, holding, and unloading [15]. In the loading stage, the indentation depth increases with the load, and elastoplastic deformation occurs. In the unloading stage, only elastic deformation can be recovered, so this stage can be used to determine the mechanical indexes such as elastic modulus and hardness of materials [11, 16].

Nanoindentation tests can obtain elastic modulus E, hardness H, contact stiffness S, creep stress index, fracture toughness, and so on. Elastic modulus and hardness are very important and commonly used. Contact stiffness is defined as the slope of the tangent line at the maximum load on the unloading curve, which can be expressed as follows:

$$S = \frac{dP}{dh}\Big|_{h=h_m}. \quad (1)$$

The reduced modulus is calculated as follows [17]:

$$E_r = \frac{\sqrt{\pi}}{2\beta} \cdot \frac{S}{\sqrt{A}}. \quad (2)$$

The contact area A is related to the contact depth h_c, which can be expressed as follows:

$$A = f(h_c). \quad (3)$$

For the Berkovich indenter, the contact depth can be calculated as follows:

$$h_c = h - \varepsilon \frac{P}{S}. \quad (4)$$

The hardness is expressed as follows:

$$H = \frac{P}{A}. \quad (5)$$

The yield strength can be obtained as follows:

$$\sigma_y \approx \frac{H}{3}. \quad (6)$$

Elastic modulus can be calculated as follows:

$$\frac{1}{E_r} = \frac{\left(1 - \nu^2\right)}{E} + \frac{\left(1 - \nu_i^{\,2}\right)}{E_i}, \quad (7)$$

Figure 1: Agilent Nanoindenter G200.

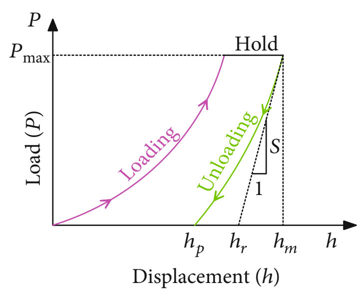

Figure 2: A typical load-displacement curve in nanoindentation tests (h_p: residual indentation depth after unloading; h_r: indentation depth at the intersection of the tangent line at the maximum load on the unloading curve and the displacement axis; h_m: maximum indentation depth before unloading).

or

$$E = \left(1 - \nu^2\right)\left[\frac{1}{E_r} - \frac{1 - \nu_i^2}{E_i}\right]^{-1}, \tag{8}$$

where β is an indenter correction coefficient and ε is a constant related to the indenter shape. With regard to a regular pyramid Berkovich indenter, $\beta = 1.034$, $\varepsilon = 0.75$ [18]. h_c (nm) is the contact depth. A (nm^2) is the contact area, which can be calculated as $A = 24.56h_c^2$ [18]. E_r is the reduced elastic modulus, which stands for the interaction effect between the indenter and indented material. E_i and ν_i represent the elastic modulus and the Poisson ratio of the indenter, respectively. For the diamond indenter used in the present study, $E_i = 1141$ GPa, $\nu_i = 0.07$. ν is the Poisson ratio of the indented material. In this paper, the mechanical properties of the three minerals were measured by a noncrack pressing test.

2.3. Test Procedures. The nanoindentation tests require that the surface of the indented material should be smooth as possible. During the test, the diamond indenter is pressed vertically into the sample surface. The elastic deformation begins to occur on the sample surface. The plastic deformation and even crack occurs with the increase of load. The indentation is left after the completion of each point test. Finally, the load-displacement curve can be obtained, which is shown in Figure 2. The elastic modulus and hardness of the sample can be calculated by the characteristic parameters on the curve. Elastic modulus is an essential parameter for evaluating the brittleness of rock while hardness can be utilized to describe the difficulty of a rock surface being indented [1]. Both of which are important indexes to evaluate the mechanical properties of the materials [16, 18].

The granite in this paper is taken from the Qinling Mountains. The samples are relatively fresh and retain the structural characteristics of magma crystallization. It is a semi-idiomorphic granular granite and mainly composed of quartz, plagioclase, alkaline feldspar, and mica. The test procedures are detailed as follows:

(1) Firstly, the granite sample is processed into a cuboid with a length of 15 mm, a width of 15 mm, and a height of 5 mm. The sample surface is polished with 100#, 600#, 800#, 1000#, 2000#, 5000#, and 7000# gold matte paper in turn. The grinding time on each kind of gold matte paper is not less than 40 minutes. At the same time, a surface roughness meter is used to randomly scan the sample surface, thus ensuring that the *Ra* is not greater than 5 μm. Then, the sample is cleaned with ultrasonic waves to make sure that there is no debris on the sample surface. Finally, the prepared sample is placed in an oven at 50°C for 24 to 48 hours until it is completely dried up

(2) After the polishing and drying phases, the sample is put on the support platform within the work space of the indentation instrument at a temperature of 20 ± 1°C and a relative humidity of 42%. The sample surface is observed using an optical microscope to identify the minerals, and the indentation test on the mineral is carried out. Figure 3 shows microscopic images of quartz, feldspar, and mica. In this test, a single load-unload mode is used

(3) After the indentation tests, the sample is observed by SEM to obtain the morphology and distribution characteristics of various minerals and the residual indentation on different minerals. The semiquantitative phase analysis is carried out by XRD and a rock slice identification test to obtain the volume percentage of each mineral in granite

3. Results and Discussion

3.1. Mineral Microstructure and Content. Figure 3 shows microscopic images of quartz, feldspar, and mica. It can be seen that the surface of quartz is very smooth, feldspar is second, and the surface of biotite is black and biotite has a lamellar structure.

Figure 4 shows typical residual indentation images of quartz, feldspar, and mica. These images are obtained by SEM. The residual indentation of quartz is complete and clear, the residual indentation morphology is consistent with the indenter shape, and no obvious cracks occur in Figure 4(a), which indicates that the elastic properties of quartz is good. The residual indentation of feldspar is slightly deeper than that of quartz, and the indentation edge has a bulge deformation in Figure 4(b), which indicates that

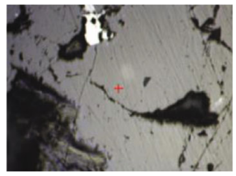

(a) Quartz

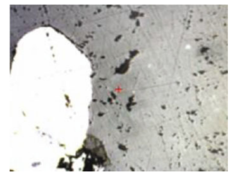

(b) Feldspar

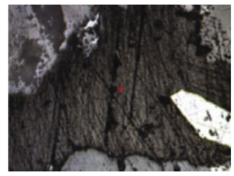

(c) Mica

Figure 3: Microscopic images of three minerals (magnification 250x).

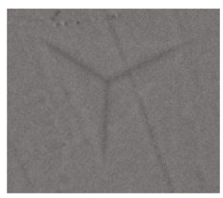

(a) Quartz

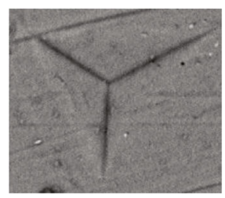

(b) Feldspar

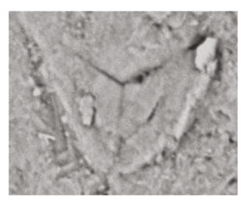

(c) Mica

Figure 4: Typical residual indentation images of three minerals.

the mechanical properties of feldspar is slightly worse than quartz. Slight flaking occurs around the residual indentation of mica, and the residual indentation morphology is incomplete and unclear in Figure 4(c), which indicates that the mechanical properties of mica is worst.

The composition and content of minerals can be obtained by X-ray diffraction (XRD) and rock slice identification test. Figure 5 shows the XRD energy spectrum of granite and the pie chart of the volume percentage of the main minerals. The results show that the granite contains 25.2% quartz, 61.6% feldspar (26.5% potassium feldspar and 35.1% plagioclase), 10.9% mica, and 2.3% other minerals. Due to the small proportion of other minerals, their effects on the mechanical properties of granite are ignored.

3.2. Analysis of Elastic Modulus and Hardness of Minerals. According to the results of nanoindentation tests, the elastic modulus and hardness of the main minerals in granite can be obtained. In the calculation process, the Poisson ratio of quartz, feldspar, and mica are 0.20, 0.25, and 0.30, respectively [19]. Material cracking under loading will affect the accuracy of elastic modulus and hardness, so the elastic modulus and hardness of the material are calculated by nanoindentation tests without cracking. The critical load for cracking of quartz and feldspar is between 20 mN and 50 mN and that of mica is between 5 mN and 10 mN. Therefore, the maximum load of quartz and feldspar is 20 mN, and the loading time is 20 seconds. The maximum load of mica is 5 mN, and the loading time is 5 seconds. The loading rate is 1 mN/s, and the holding time is 10 seconds for three minerals.

Figure 6 shows the load-displacement curves of nanoindentation for quartz, feldspar, and mica under loading and unloading. It can be seen that the loading and unloading process of minerals in granite can be divided into the compaction stage (OA), the elastoplasticity stage (AB), the holding stage (BC), and the unloading stage (CD). The deformation of mica is the largest, feldspar is the second, and quartz is the smallest. The above law is consistent with the law of residual indentation deformation. The compaction stage of quartz is much shorter than mica. Under the same holding time, the creep deformation of mica is the largest, followed by feldspar and quartz. These indicate that quartz has a dense structure, high stiffness, and good mechanical properties, while mica has a relatively loose structure, small stiffness, and poor mechanical properties.

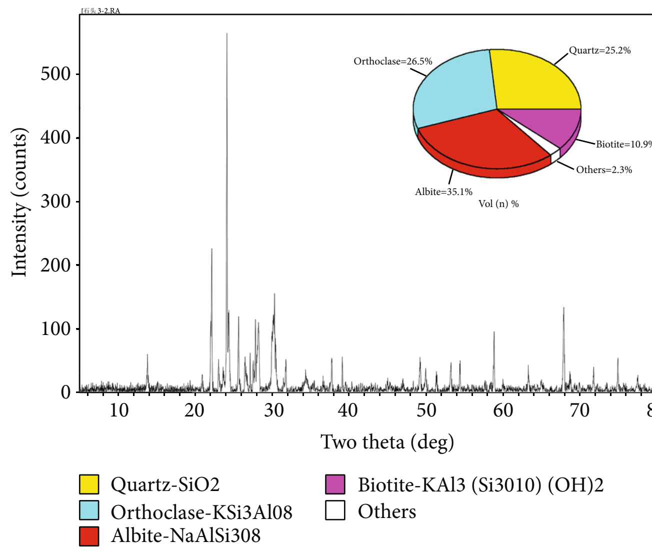

Figure 5: XRD energy spectrum of granite and pie chart of the volume percentage of the main minerals.

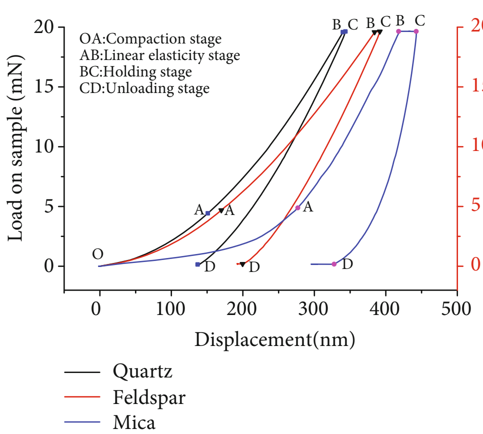

Figure 6: Load-displacement curves of quartz, feldspar, and mica.

Figure 7 is the distribution histogram of the elastic modulus and hardness of quartz. It can be seen that the distribution of the elastic modulus and hardness of quartz is in accord with the normal distribution and is concentrated. By statistical analysis and calculation, the elastic modulus of quartz is 101.34 ± 9.53 GPa and the hardness is 12.72 ± 2.17 GPa.

Figure 8 is the distribution histogram of the elastic modulus and hardness of feldspar. It can be seen that the distribution of the elastic modulus and hardness of feldspar conforms to the normal distribution and is relatively concentrated. By statistical analysis and calculation, the elastic modulus of feldspar is 82.47 ± 10.29 GPa and the hardness is 9.20 ± 1.68 GPa.

Figure 9 is the distribution histogram of the elastic modulus and hardness of mica. It can be seen that the amplitude of the elastic modulus and hardness of mica changes greatly. By statistical analysis and calculation, the elastic modulus of mica is 25.88 ± 8.33 GPa and the hardness is 1.78 ± 0.75 GPa.

4. Homogenization Methods and Techniques

Granite is a three-phase composite material, which is composed of quartz, feldspar, and mica. These three minerals are randomly distributed. The elastic properties of these different minerals are obtained by nanoindentation tests. The relative content of each mineral is obtained by XRD and the rock slice identification test. On this basis, the macroscopic elastic properties of granite are estimated by the Self-consistent method, the Dilute method, and the Mori-Tanaka method.

4.1. Self-Consistent Method. The Self-consistent method was first used by Hershey for the study of polycrystals [20]. The method is further developed and used by Hill to study the elastic modulus of composites [21]. The Self-consistent method replaces the anisotropic composite with an idealized homogeneous continuum. This substitution is based on the equalization of strain energy stored or dissipated by the material at a certain volume range. When the scale range is much larger than the local characteristic size of the anisotropic material, the mechanical behavior of the two media is the same. The effective modulus of the composite material can be expressed as follows [22]:

$$\bar{C} = C_0 + \sum_{r=1}^{N=1} c_r (C_r - C_0) \left[I + \bar{P}_r \left(C_r - \bar{C} \right) \right]^{-1}, \qquad (9)$$

where C_0 and C_r are the modulus of the mineral with the largest content and the modulus of phase r, respectively. c_r is the volume fraction of phase r. I is the tensor related to the shape of the inclusion. $\bar{P}_r$ is the P tensor when phase r is placed in the unknown composite material as the matrix. It is related to the shape of the inclusion and the unknown modulus $\bar{C}$ of the composite. This is an implicit equation of the effective modulus of the composite. The self-

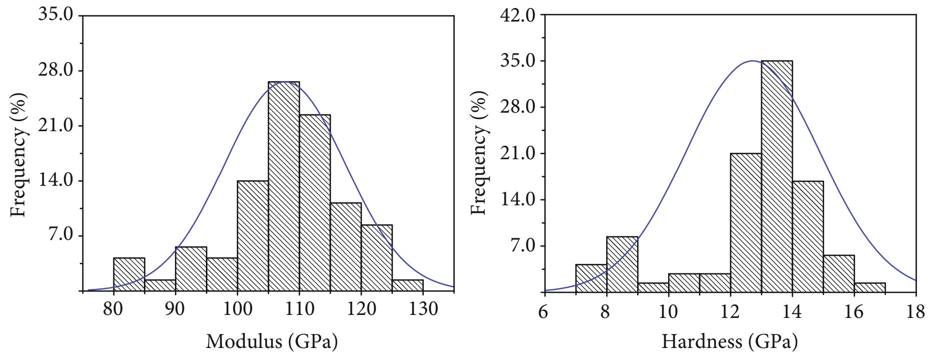

FIGURE 7: Distribution histogram of the elastic modulus and hardness of quartz.

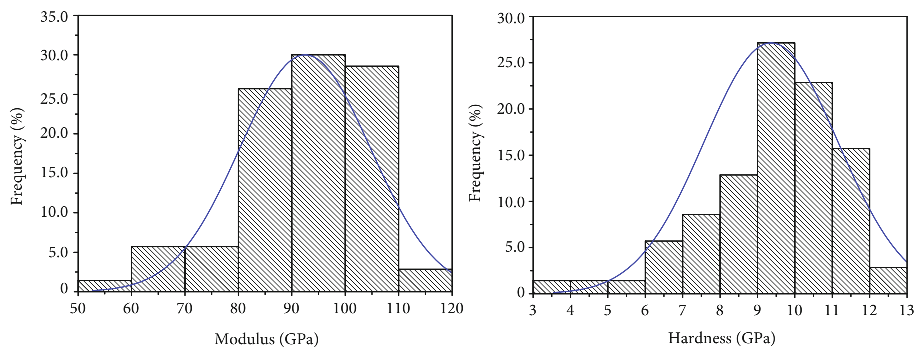

FIGURE 8: Distribution histogram of the elastic modulus and hardness of feldspar.

consistent method can be used to estimate the effective modulus of the composite by solving this equation.

The implicit equations of effective shear modulus and bulk modulus of granite are obtained by using the simplified algorithm for an isotropic tensor and are shown as follows:

$$G^{\mathrm{hom}} = \sum_{r=0} c_r \frac{5G_r \cdot G^{\mathrm{hom}}\left(3K^{\mathrm{hom}} + 4G^{\mathrm{hom}}\right)}{G^{\mathrm{hom}}\left(9K^{\mathrm{hom}} + 8G^{\mathrm{hom}}\right) + 6G_r\left(K^{\mathrm{hom}} + 2G^{\mathrm{hom}}\right)}, \tag{10}$$

$$K^{\mathrm{hom}} = \sum_{r=0} c_r \frac{k_r\left(3K^{\mathrm{hom}} + 4G^{\mathrm{hom}}\right)}{3K_r + 4G^{\mathrm{hom}}}, \tag{11}$$

where G^{hom} and K^{hom} represent the effective shear modulus and bulk modulus of granite after homogenization, respectively. G_r and K_r are the shear modulus and bulk modulus of phase r, respectively. The calculation formulas are as follows:

$$G_r = \frac{E}{2(1+\nu)}, \tag{12}$$

$$K_r = \frac{E}{3(1-2\nu)}, \tag{13}$$

where E and ν are the elastic modulus and the Poisson ratio of the minerals, respectively.

4.2. Dilute Method. It is assumed that the concentration of inclusions in the composite are small, and the interactions between them are negligible. The multiple inclusion problem can be turned into a single inclusion problem, and the inclusions can be separated from each other [23]. The effective modulus of the composite is predicted as follows [22]:

$$\bar{C} = C_0 + \sum_{r=1}^{N-1} c_r\left[\left(C_r - C_0\right)^{-1} + P_r\right]^{-1}. \tag{14}$$

Considering that there is no interaction between inclusions and assuming that inclusions are spherical particles, the macroscopic elastic properties of granite are obtained by the Dilute method and are shown as follows [14]:

$$K^{\mathrm{hom}} = K_0 + \sum_{r=1}^{N} c_r \frac{(K_r - K_0)(3K_0 + 4G_0)}{3K_r + 4G_0}, \tag{15}$$

$$G^{\mathrm{hom}} = \sum_{r=1}^{N} c_r \frac{5G_0(G_r - G_0)(3K_0 + 4G_0)}{G_0(9K_0 + 8G_0) + 6G_r(K_0 + 2G_0)}, \tag{16}$$

where K_0 and G_0 are the bulk modulus and shear modulus of the minerals with the largest content. Other symbols have the same meanings as above.

4.3. Mori-Tanaka Method. The Mori-Tanaka method was proposed by Mori and Tanaka in 1973 when they were studying the work hardening of dispersion-hardened

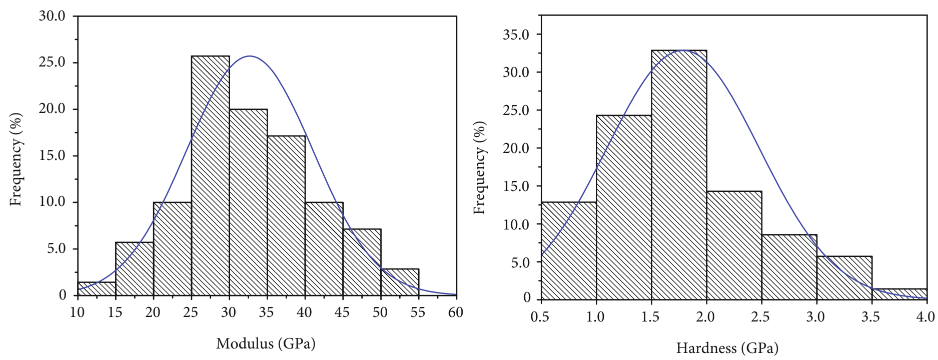

Figure 9: Distribution histogram of the elastic modulus and hardness of mica.

materials [24, 25]. This is a method for calculating the equivalent elastic modulus of heterogeneous materials based on Eshelby's equivalent inclusion principle. The Mori-Tanaka method takes interactions between inclusions into account and assumes that each inclusion is embedded in an infinite matrix. The effective modulus of a composite can be expressed as follows [22]:

$$\bar{C} = C_0 + \sum_{r=1}^{N-1} c_r \left[(C_r - C_0)^{-1} + c_0 P_r \right]^{-1}. \tag{17}$$

The bulk modulus and shear modulus of granite are expressed as follows:

$$K^{\mathrm{hom}} = \frac{\sum_{r=0} c_r (K_r / 3K_r + 4G_0)}{\sum_{s=0} c_s / 3K_r + 4G_0}, \tag{18}$$

$$G^{\mathrm{hom}} = \frac{\sum_{r=0} c_r G_r / G_0 (9K_0 + 8G_0) + 6G_r (K_0 + 2G_0)}{\sum_{s=0} c_s / G_0 (9K_0 + 8G_0) + 6G_s (K_0 + 2G_0)}, \tag{19}$$

where K_0 and G_0 are the bulk modulus and shear modulus of mica, respectively. Considering that the pore structure of mica is obvious, the bulk modulus and shear modulus of mica are expressed as follows:

$$K_0 = \frac{4(1-\varphi) K_s G_s}{4G_s + 3\varphi K_s}, \tag{20}$$

$$G_0 = \frac{(1-\varphi) G_s}{1 + 6\varphi (K_s + 2G_s / 9K_s + 8G_s)}, \tag{21}$$

where K_s and G_s are the bulk modulus and shear modulus of mica regardless of pore structure, respectively. φ is the porosity of mica, which is estimated to be 5% in this paper.

4.4. Comparative Analysis of Calculation Results. The equivalent bulk modulus and shear modulus of granite are obtained by the above methods and procedures. The elastic modulus and the Poisson ratio can be calculated as follows:

$$E^{\mathrm{hom}} = \frac{9K^{\mathrm{hom}} \cdot G^{\mathrm{hom}}}{3K^{\mathrm{hom}} + G^{\mathrm{hom}}}, \tag{22}$$

$$\nu^{\mathrm{hom}} = \frac{3K^{\mathrm{hom}} - 2G^{\mathrm{hom}}}{6K^{\mathrm{hom}} + 2G^{\mathrm{hom}}}. \tag{23}$$

The mechanical parameters of granite obtained by three homogenization methods are shown in Table 1. It can be seen that the elastic modulus and the Poisson ratio calculated by three homogenization methods are in accordance with them obtained by uniaxial compression tests. The elastic modulus of granite obtained by the Self-consistent method, the Dilute method, and the Mori-Tanaka method are 74.13 GPa, 76.59 GPa, and 73.91 GPa, respectively. The Poisson ratio of granite obtained by the three methods are 0.241, 0.244, and 0.246, respectively. Compared with the measured values, the deviation rates of the elastic modulus are 26.5%, 30.7%, and 26.1% and those of the Poisson ratio are 3.6%, 2.4%, and 1.6%, respectively.

Through comparative analysis of the advantages and disadvantages of three homogenization methods, the Self-consistent method is more suitable for isotropic and homogeneous materials without a matrix and does not consider the material porosity, the Dilute method is suitable for materials with a small inclusion content and does not consider the interaction between inclusions, but the Mori-Tanaka method can consider the pores and the interaction between inclusions. The Mori-Tanaka method is suitable for the transition of granite mechanical parameters from microscale to macroscale.

Through comparative analysis of the calculation results with the measured values, the elastic modulus obtained by the three homogenization methods are higher than the measured value. The possible reasons are as follows: (1) Samples of a macromechanical property test are large in size and contain many defects such as microcracks and micropores. When the samples are under loading, the microcracks are more likely to propagate. (2) It is assumed that mineral particles are arbitrary spherical particles for three homogenization methods, while the actual shapes of mineral particles are quite different. (3) The actual distribution, arrangement, and bonding action of minerals in granite are different from the calculation assumptions of various methods.

Although the granite mechanical parameters obtained by the three homogenization methods are different from the measured values in a certain range, the homogenization method plays an important role in the evaluation of the

Table 1: Compared analysis of the calculation results with the measured values.

	Bulk modulus: K^{hom} (GPa)	Shear modulus: G^{hom} (GPa)	Elastic modulus: E^{hom} (GPa)	Poisson's ratio: ν^{hom}
Self-consistent method	47.64	29.88	74.13	0.241
Dilute method	49.77	30.80	76.59	0.244
Mori-Tanaka method	48.53	29.65	73.91	0.246
Test measurement	—	—	58.6	0.250

mechanical properties of rock-soil materials and has an engineering practical value. It will be the focus and hotspot of future research on the analysis of factors causing deviation and the application of optimization homogenization method in rock-soil materials.

5. Conclusion

The elastic modulus and hardness of quartz, feldspar, and mica in granite were statistically analyzed by a nanoindentation test. The residual indentation information of three minerals in granite were analyzed by SEM. The relative content of three minerals in granite were obtained by XRD and a rock slice identification test. The Self-consistent method, the Dilute method, and the Mori-Tanaka method were used to realize the transition of granite mechanical parameters from microscale to macroscale. The main conclusions are as follows:

(1) The distribution of the elastic modulus and the hardness of the three minerals in granite is basically in accord with the normal distribution. The mechanical parameters of mica are more discrete, because the mechanical properties of mica are poor and the nanoindentation test is easily affected by other impurities

(2) The morphology and residual indentation of the three minerals in granite were obtained by SEM, which provides an effective method and reference for the study of rock mechanical properties. XRD and rock slice identification test shows that the content of quartz, feldspar, and mica in granite are 25.2%, 61.6%, and 10.9%, respectively

(3) Three homogenization methods were used to realize the transition of granite mechanical parameters from microscale to macroscale. The calculation results are in accordance with uniaxial compression test results. Among the three methods, the Mori-Tanaka method is more suitable for the transition of granite mechanical parameters from microscale to macroscale. The homogenization method of a composite plays an important role in studying the mechanical properties of rock-soil materials and has an engineering practical value. The research results provide a new method and an important reference for studying the macro-, micro-, and nanomechanical properties of rock

Data Availability

The data used to support the findings of this study are available from the corresponding author upon request.

Conflicts of Interest

The authors declare no conflict of interest.

Acknowledgments

The authors acknowledge the support from the National Natural Science Foundation of China (Nos. 51979225 and 52009107), the Natural Science Basic Research Plan in Shaanxi Province of China (No. 2020JQ-627), the Opening Research Fund of National Engineering Laboratory for Surface Transportation Weather Impacts Prevention (No. NEL-2020-02), and the Ministry of Water Resources Public Welfare Industry Scientific Research Project (No. 201501034-04).

References

[1] Z. Ma, R. Pathegama Gamage, and C. Zhang, "Effects of temperature and grain size on the mechanical properties of polycrystalline quartz," *Computational Materials Science*, vol. 188, article 110138, 10 pages, 2021.

[2] Z. Ma, R. Pathegama Gamage, and C. Zhang, "Application of nanoindentation technology in rocks: a review," *Geomechanics and Geophysics for Geo-Energy and Geo-Resources*, vol. 6, no. 4, pp. 1–27, 2020.

[3] Y. Xue, J. Liu, P. G. Ranjith, X. Liang, and S. Wang, "Investigation of the influence of gas fracturing on fracturing characteristics of coal mass and gas extraction efficiency based on a multi-physical field model," *Journal of Petroleum Science and Engineering*, vol. 206, article 109018, 2021.

[4] Y. Xue, T. Teng, F. Dang, Z. Ma, S. Wang, and H. Xue, "Productivity analysis of fractured wells in reservoir of hydrogen and carbon based on dual-porosity medium model," *International Journal of Hydrogen Energy*, vol. 45, no. 39, pp. 20240–20249, 2020.

[5] C. Wang, *Study of deformation behavior of nanocrystalline nickel using nanoindentation techniques*, vol. 8, University of Tennessee, Knoxville, 2010.

[6] S. Naderi, M. A. Dabbagh, M. A. Hassan, B. A. Razak, H. Abdullah, and N. H. Abu Kasim, "Modeling of porosity in hydroxyapatite for finite element simulation of nanoindentation test," *Ceramics International*, vol. 42, no. 6, pp. 7543–7550, 2016.

[7] M. Tanguy, A. Bourmaud, and C. Baley, "Plant cell walls to reinforce composite materials: relationship between

nanoindentation and tensile modulus," *Materials Letters*, vol. 167, pp. 161–164, 2016.

[8] S. D. Viktorov, Y. I. Golovin, A. N. Kochanov et al., "Micro- and nano-indentation approach to strength and deformation characteristics of minerals," *Journal of Mining Science*, vol. 50, no. 4, pp. 652–659, 2014.

[9] W. Z. Zhu, J. J. Hughes, N. Bicanic, and C. J. Pearce, "Nanoindentation mapping of mechanical properties of cement paste and natural rocks," *Materials Characterization*, vol. 58, no. 11-12, pp. 1189–1198, 2007.

[10] F. Zhang, H. Guo, J. Zhao, and D. Hu, "Experimental study of micromechanical properties of granite," *Chinese Journal of Rock Mechanics and Engineering*, vol. 36, no. s2, pp. 3864–3872, 2017.

[11] K. Liu, M. Ostadhassan, and B. Bubach, "Applications of nanoindentation methods to estimate nanoscale mechanical properties of shale reservoir rocks," *Journal of Natural Gas Science and Engineering*, vol. 35, pp. 1310–1319, 2016.

[12] C. P. Bobko, B. Gathier, J. A. Ortega, F. J. Ulm, L. Borges, and Y. N. Abousleiman, "The nanogranular origin of friction and cohesion in shale—a strength homogenization approach to interpretation of nanoindentation results," *International Journal for Numerical and Analytical Methods in Geomechanics*, vol. 35, no. 17, pp. 1854–1876, 2011.

[13] Q. Chen, M. M. Nezhad, Q. Fisher, and H. Zhu, "Multi-scale approach for modeling the transversely isotropic elastic properties of shale considering multi-inclusions and interfacial transition zone," *International Journal of Rock Mechanics and Mining Sciences*, vol. 84, pp. 95–104, 2016.

[14] A. Abou-Chakra Guéry, F. Cormery, J. F. Shao, and D. Kondo, "A comparative micromechanical analysis of the effective properties of a geomaterial: effect of mineralogical compositions," *Computers and Geotechnics*, vol. 37, no. 5, pp. 585–593, 2010.

[15] J. Hay, "Introduction to instrumented indentation testing," *Experimental Techniques.*, vol. 33, no. 6, pp. 66–72, 2009.

[16] Y. T. Cheng, Z. Li, and C. M. Cheng, "Scaling relationships for indentation measurements," *Philosophical Magazine A*, vol. 82, no. 10, pp. 1821–1829, 2002.

[17] R. B. King, "Elastic analysis of some punch problems for a layered medium," *International Journal of Solids and Structures*, vol. 23, no. 12, pp. 1657–1664, 1987.

[18] W. C. Oliver and G. M. Pharr, "An improved technique for determining hardness and elastic modulus using load and displacement sensing indentation experiments," *Journal of Materials Research*, vol. 7, no. 6, pp. 1564–1583, 1992.

[19] M. F. Cai, *Rock Mechanics and Engineering*, Science Publishing House, Beijing, 2002.

[20] A. V. Hershey, "The elasticity of an isotropic aggregate of anisotropic cubic crystals," *Journal of Applied Mechanics*, vol. 21, pp. 236–241, 1964.

[21] R. Hill, "Continuum micro-mechanics of elastoplastic polycrystals," *Journal of the Mechanics and Physics of Solids*, vol. 13, no. 2, pp. 89–101, 1965.

[22] G. Shen, G. Hu, and B. Liu, *Mechanics of Composite Materials*, Tsinghua University Press, Beijing, (Second Edition) edition, 2013.

[23] A. Zaoui, "Continuum micromechanics: survey," *Journal of Engineering Mechanics*, vol. 128, no. 8, pp. 808–816, 2002.

[24] T. Mori and K. Tanaka, "Average stress in a matrix and average elastic energy of materials with misfitting inclusions," *Acta Metallurgica et Materialia*, vol. 42, no. 7, pp. 597–629, 1973.

[25] Y. Benveniste, "On the Mori-Tanaka's method in cracked bodies," *Mechanics Research Communications*, vol. 13, no. 4, pp. 193–201, 1986.

Hindawi
Geofluids
Volume 2021, Article ID 6622380, 13 pages
https://doi.org/10.1155/2021/6622380

Research Article

Creep Characteristics of Different Saturated States of Red Sandstone after Freeze-Thaw Cycles

Yongxin Che, Yongjun Song, Jianxi Ren, Jiaxing Chen, Xixi Guo, Hao Tan, and Mengling Hu

College of Architecture and Civil Engineering, Xi'an University of Science and Technology, Xi'an 710054, China

Correspondence should be addressed to Yongjun Song; songyj79@163.com

Received 3 January 2021; Revised 8 June 2021; Accepted 21 August 2021; Published 10 September 2021

Academic Editor: Kai Yao

To investigate the creep mechanical characteristics of rocks in different saturated states after freeze-thaw cycles, samples with different saturations (30%, 50%, 70%, 90%, and 100%) were selected for nuclear magnetic resonance (NMR), scanning electron microscopy (SEM), and uniaxial compression creep tests. The internal microscopic damage of the rock sample and mechanical characteristics under long-term loading are analyzed after the action of freeze-thaw cycles. The test results show that, as the saturation increases, the T2 spectrum distribution shifts to the right. The spectrum area gradually increases as the porosity increases. The critical saturation of freeze-thaw damage occurs when the saturation increases from 70% to 90%. It can be seen from the SEM image that the number of pores inside the rock samples gradually increases with increases in saturation, leading to the appearance of cracks. Under long-term loading, the saturation has a significant influence on the time-efficiency characteristics of sandstone freeze-thaw. As the saturation increases, the creep deformation gradually increases. After reaching 70%, the axial creep strain increases significantly. The rate of creep is accelerated, the creep failure stress is reduced, and the creep time under the last level of stress is significantly increased. A modified viscous-plastic body is connected in series to the basic Burgers model, the freeze-thaw-damage viscous element is introduced, and the creep parameters are fitted using test data. The results will provide a reference for long-term antifreeze design for rock engineering in cold areas.

1. Introduction

Rock masses in cold regions are subjected to the thermal action of seasonal changes and day-night cycles for long periods of time, leading to severe damage and deterioration. Geotechnical engineering in mines and tunnels in the cold regions of western China operate in freeze-thaw environments, with significant loads and surrounding rock pressure for extended periods of time. Rock creep under long-term loading significantly affects the long-term stability of rock masses. If the long-term effects of freeze-thaw and load are not considered at the same time, it will bring safety hazards to engineering construction in cold areas. Therefore, studying the creep characteristics of rock-mass engineering under the action of freeze-thaw cycles and investigating the time-efficiency characteristics play an important role in ensuring the long-term stability of rock-mass engineering in cold regions.

In recent years, Li et al. [1] investigated the influence of the number of freeze-thaw cycles and graded loads on creep and established a nonlinear creep constitutive model of freeze-thaw sandstone. Zhou et al. [2] conducted a triaxial unloading creep test on sandstone; the results showed that both the unloading process and the freeze-thaw cycle can improve the creep deformation of the rock sample, where radial deformation is more sensitive. Chen et al. [3] conducted triaxial creep tests on quartz sandstone after different freeze-thaw cycles. The research showed that the microdamage caused by freezing and thawing can lead to strong creep characteristics; the creep mechanical parameters are obviously changed with the increase in freeze-thaw cycles. Yang et al. [4] carried out triaxial creep tests and microscopic tests under the freeze-thaw cycle and systematically analyzed the operating mechanism of the effects of freezing and thawing on the creep characteristics of gneiss. Liu et al. [5] carried out a triaxial creep test on carbon shale under freeze-thaw action and determined the nonlinear characteristics of creep damage. It was concluded that, under the combined action of freeze-thaw and creep, the freeze-thaw action would accumulate rock damage and accelerate creep failure. Zhang et al. [6] proposed the freeze-thaw rock damage viscous element and constructed a constitutive model for granite freeze-thaw shear creep. Zhou et al. [7, 8] carried out mechanical and micro-microscopic tests on prefabricated fractured sandstone after freezing and thawing; the interaction mechanism of moisture inside the defective rock mass and the evolution of the fatigue damage zone of the rock mass have been fully studied under the action of freezing and thawing cycles.

It can be seen from the above research that the freeze-thaw cycle has a significant influence on the long-term mechanical properties of rocks; however, most current creep research is only carried out in the fully saturated state. Owing to the several changes in geology, geography, climate, and hydrology over the years, the water content of rock masses differs significantly.

McGreevy and Whalley [9] believed that the initial water content of a rock mass determines the degree of frost-heave damage, and the water content will fluctuate with the number of freeze-thaw cycles, freezing duration, and seasonal changes. Liu et al. [10] found that the freeze-thaw damage of rock masses is dependent on the initial saturation, which has an important influence on the frost-heave force. Only the rock masses that exceed the critical value of saturation will lead to effective freeze-thaw damage [11, 12]. Chen et al. [13] carried out uniaxial compression, longitudinal wave velocity, and porosity-measurement tests on tuffs with different initial saturations after the freeze-thaw process, and the results showed that a saturation of 70% is the critical value for effective freeze-thaw damage. The level of saturation has a significant influence on the long-term mechanical properties of the rock mass. Al-Omari et al. [14] found that the critical saturation is the main factor that dictates the freeze-thaw failure of limestone in the Chambord Castle in France. With the goal of understanding the time-efficiency deterioration of rocks at different saturations, Zhang et al. [15] proposed an elastic-viscous-plastic model based on a stress function of the influence of freeze-thaw cycles on the characteristics of saturated rocks and the rheological theory. Yang et al. [16] conducted a triaxial creep test for soft rock under water-bearing conditions, where the change law of creep deformation was analyzed. Liu et al. [17] tested slabs under different water-bearing conditions using the rock creep test and established the FLAC3D creep constitutive secondary development model, which considers the effect of water-bearing degradation. Zhang et al. [18] took the auxiliary tunnel of Jinping II Hydropower Station as an example to study the time-dependent deformation of rock tunnels and established a novel four-element fractional viscoplastic (FVP) model based on the test results. Wang et al. [19, 20] carried out uniaxial long-period cyclic load creep tests on rock salt specimens under different maximum cyclic stresses and cyclic periods and analyzed the law of creep stage, creep rate, and elastic modulus with stress and number of cycles.

Table 1: Composition of rock samples.

Quartz	Plagioclase	Calcite	Potash feldspar	Clay minerals and other constituents
53.0%	17.9%	8.9%	9.9%	10.3%

The above studies have laid the foundation for understanding rock creep characteristics and the influence of saturation on rock instantaneous mechanical properties under the effect of freeze-thaw cycles. However, there are few reports on the long-term mechanical properties of rocks with different saturation levels under freeze-thaw cycles. This paper conducts NMR, scanning electron microscopy, and uniaxial compression creep tests on red sandstone in different states of saturation after freeze-thaw cycles and analyzes the microscopic and creep damage mechanisms. Based on the Burgers model, a freeze-thaw damage creep model—considering the effect of saturation—is established. Further, the experimental value and fitted theoretical values are compared, finally obtaining the creep parameters. The results of this research will provide a reference and basis for long-term antifreeze design for rock engineering in cold areas.

2. Materials and Methods

2.1. Rock Samples. The rock samples were taken from a tunnel slope in a cold region in western China. Owing to the differences in water content of slopes at different heights, the stability of the slope will gradually weaken under the action of freeze-thaw cycles and long-term loads [21]. The D8Venture X-ray single crystal diffractometer was used to analyze the mineral composition of the rock samples. The mineral composition is shown in Table 1. The internal particles of the rock sample were pore-type cemented, which is a moderately swollen weakly cemented soft rock.

In accordance with the test regulations of the International Society of Rock Mechanics, the rock sample was processed into a standard cylinder with a diameter of 50 mm and a height of 100 mm. A rock sample with good integrity was selected and baked in an oven at 105°C for 24 hours; the primary wave velocity and dry density of rock samples were measured after cooling. The variation range of primary wave velocity and dry density states that ($1832 < v < 1865$ m/s) and ($2.30 < \rho < 2.32$ g/cm^3), respectively. Three groups were subjected to nuclear magnetic resonance (NMR), conventional uniaxial compression tests, and uniaxial compression creep tests, totaling 15 rock samples, as shown in Figure 1(c). The average values of the initial basic physical parameters for the rock samples are shown in Table 2.

2.2. Test Plans

2.2.1. Preparation of Rock Samples with Different Saturated States. All rock samples were subjected to forced saturation for 24 hours using a vacuum saturating machine to obtain completely saturated rock samples. The rock sample was subsequently naturally air-dried, and its quality was monitored at regular intervals until the corresponding mass of the rock sample with different saturations (30%, 50%, 70%, 90%, and 100%) was obtained according to

$$m_t = m_{\mathrm{d}}(1-\omega) + \omega m_{\mathrm{s}}, \quad (1)$$

where m_t is the corresponding weight of the rock sample in different saturated states, m_{d} is the weight of the dry rock sample, ω represents the saturation of the rock samples, and m_{s} is the weight of the saturated rock sample. After obtaining the required saturation, the rock sample is sealed using plastic wrap and then packed in a plastic bag and sealed in water to keep the rock-sample saturation constant. Figure 1(e) shows the water sealing device for the rock samples.

2.2.2. Freeze-Thaw Cycle Test. Before the freeze-thaw cycle, the rock samples with different saturated states were placed in the water sealing device for a week to achieve a uniform distribution of water in the rock samples. The freeze-thaw cycle is carried out using a water-sealed device to keep the saturation stable. The rock sample is frozen for 12 hours at –20°C and thawed for 12 hours at 20°C. A freeze-thaw cycle takes place every 24 hours. The number of freeze-thaw cycles is set to 30, the approximate number of days in a month. The equipment for the freeze-thaw test is shown in Figure 1(d).

2.2.3. Nuclear Magnetic Resonance Test. After the freeze-thaw cycles, the first set of rock samples were vacuum saturated for 24 hours, and then, the nuclear magnetic resonance test was conducted. The nuclear magnetic resonance test equipment is shown in Figure 1(g). We used an NMR instrument (MacroMR12-150H-I, Suzhou Niumag Analytical Instrument Corporation, Suzhou, China) with a magnetic field strength of 0.3 ± 0.05 T, H proton resonance frequency of 12.77 MHz, and coil radio frequency pulse frequency of 1.499 MHz.

2.2.4. Creep Test. The conventional uniaxial compression test was performed on the second set of rock samples with different saturated states to obtain the stress level of creep. The loading is controlled by the deformation, with a loading rate of 0.002 mm/s, and the peak strength of rock samples with different saturation was obtained. The third group of rock samples determined the graded loading stress levels according to 30%, 40%, 50%, 60%, 70%, 80%, and 90% of the second group's peak strength. Each level was loaded for 24 h, and the loading rate was 0.02 MPa/s. The surrounding area of the rock samples was smeared with petroleum jelly and wrapped in a thin plastic rubber sleeve before loading to ensure the stability of the internal saturation during the loading process.

The test loading device uses the TAW-1000 rock mechanics testing machine, which can perform conventional uniaxial and triaxial compression and creep tests. The testing machine consisted of four main units: conventional triaxial, servo loading, deformation monitoring, and data acquisition units. The maximum axial stress can reach 1000 KN. The maximum confining stress can reach 100 MPa. The loading device is shown in Figure 1(f).

3. Results

3.1. Nuclear Magnetic Resonance Test after Freeze-Thaw Cycle

3.1.1. T_2 Spectrum Distribution Analysis. The rock sample mainly comprises a mineral skeleton and pores. In a fully saturated state, NMR can be used to detect the signal strength of water in each pore and the total porosity, which in turn can determine the nuclear magnetic resonance characteristics. The particle and surface characteristics of the rock samples are reflected by the specific surface area. The lateral relaxation time T_2 of the rock samples is determined by the fluid volume and the specific surface area in the rock pores [12]. Therefore, the T_2 spectrum can clearly and intuitively quantify the internal pore structure of the rock sample.

Figure 2 shows the distribution of the T_2 spectrum for rock samples with different saturated states after freeze-thaw cycles. The figure declares that, after the freeze-thaw cycles, the pore distribution of the rock samples presents a three-peak distribution and two peaks are the main representative forms. The variation trends of the T_2 spectrum distribution curves are very similar. They all gradually move to the upper-right corner as the saturation increases. Based on the principle that the relaxation time T_2 is positively correlated with the pore size, combined with the position where the T_2 spectrum distribution peak appears, different relaxation time intervals can be attributed to different pore types, namely, ($r < 0.1\,\mu$m, $T_2 < 7$ ms) micropores, ($0.1 < r < 1\,\mu$m, $7 < T_2 < 700$ ms) mesopores, and ($r > 1\,\mu$m, $T_2 > 700$ ms) macropores [22]. From the lateral relaxation time T_2, we can see that the pore-distribution characteristics change significantly as the saturation reaches 90%. After freezing and thawing, mesopores replace the small pores to a significant extent and become the main pore form, indicating that after the saturation reaches 70%, the rock sample freeze-thaw damage is mainly reflected in the development of micropores, which causes an increase in mesopores.

3.1.2. T_2 Spectrum Area and Porosity Analysis. The T_2 spectrum area of NMR can reflect the changes in the size and number of pores in the rock, and the peak area is positively correlated with the corresponding pore size and number [23]. The T_2 spectrum area is used to quantify the law governing the changes in the internal structure of rock samples with different saturations under freezing and thawing conditions, facilitating the evaluation of the degree of rock damage. Table 3 shows the total area of the T_2 spectrum and the areas of micropores, mesopores, and macropores under different saturation conditions after the freeze-thaw cycle. It is clearly observed that the total area of the T_2 spectrum gradually increases with increases in saturation.

During the freeze-thaw cycle of the rock samples, there is mutual conversion among the three types of pores. The degree of increase in the volume of each type of pore is not the same. The percentage of differing pore volumes in the total pore volume of the rock samples changes at different saturation levels. The proportion of the total area of the T_2

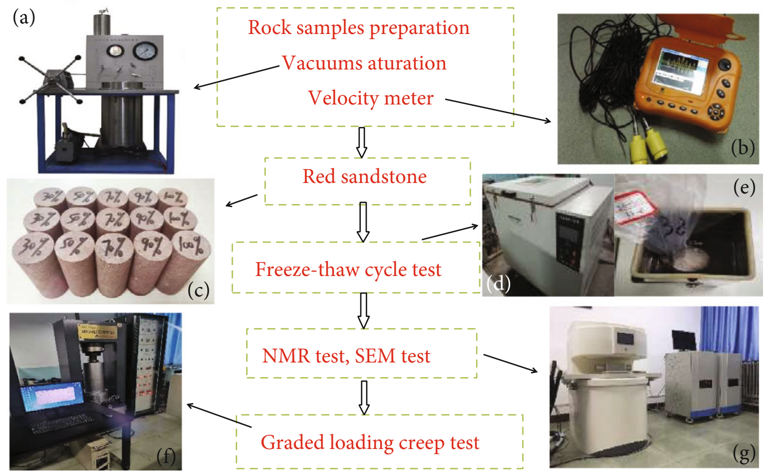

Figure 1: Flow chart of the experimental procedure.

Table 2: Average values of physical parameters for rock samples.

P-wave velocity (m/s)	Dry density (g/cm^3)	Porosity (%)	Saturated water content (%)	Saturated density (g/cm^3)
1863	2.31	9.56	5.29	2.45

spectrum is shown in Figure 3. It can be seen from the figure that the inside of the rock sample is mainly composed of micropores and mesopores after freeze-thaw cycles, which account for about 50% of the total pore volume—the ratio of macropores to the total volume of pores is below 2%. The damage of the rock samples caused by the freeze-thaw cycles is mainly in the form of micropores and mesopores. With increases in saturation, the percentage of mesopore area gradually increases, and when the saturation reaches 90%, the peak area of mesopores gradually becomes the main peak. It shows that, when the saturation increases from 70% to 90%, the internal frost-heave force of the rock sample increases continuously, and the critical value of freeze-thaw damage is reached [11].

3.1.3. Porosity Changes with Saturation. Porosity is the most commonly used and most important index for evaluating the characteristics of pores in porous materials. In this study, the change in the porosity of the rock sample after the freeze-thaw cycles was calculated using Equation (2) via the saturation method [24]:

$$\Phi = \frac{m_s - m_d}{\rho_w V_b}, \tag{2}$$

where Φ is the porosity of the rock sample, m_s is the weight of the saturated sample, m_d is the weight of the dry rock sample, ρ_w is the density of saturating water, and V_b is the bulk volume of the rock sample.

Figure 4 shows the change curve for porosity and the T_2 spectrum area of rock samples with respect to saturation after freeze-thaw cycles. The porosity of the rock sample exhibits a nonlinear growth trend with increases in saturation, indicating that the internal volume of the rock sample increases with an increase in the number of freeze-thaw cycles. When the saturation increases from 30% to 70%, the porosity only increases by 13.66%, the total area of the T_2 spectrum increases by 17.92%, and the rock sample damage is low. When the saturation changes from 70% to 100%, the porosity increased by 23.60%, the total area of the T_2 spectrum increased by 28.79%, and critical freeze-thaw damage occurred. Therefore, it is obvious that the pores grow slowly in the first stage and rapidly in the second. The damage inside the rock sample is smallest in the first stage; therefore, the porosity and total area of the T_2 spectrum increase slowly. The increase in porosity is mainly due to the soluble minerals and cement in the rock sample gradually dissolving with the increase in saturation, weakening the connections between particles. This makes the pore volume increase continuously, and the damage caused by frost heave is small. However, the effective freeze-thaw damage occurs in the second stage. As the saturation increases, the frost-heave force increases and the internal fissures of the rock sample expand. The continuous dissolution of soluble minerals and cement by water molecules aggravates the destruction of the rock structure. The pore size inside the rock sample changes significantly, resulting in an increase in the porosity and the total area of the T_2 spectrum [10]. From the above analysis, it can be concluded that the change in the internal microstructure of the rock sample by freeze-thaw cycles is greatly affected by the saturation level.

3.2. Scanning Electron Microscope Analysis. To further analyze the microstructural characteristics of the rock sample affected by saturation, slices were taken from the same position inside the rock sample after the freeze-thaw cycle, and the scanning electron microscopy test under 100x magnification was performed. The scanning result is shown in Figure 5. The PCAS software binarizes the information of the scanning electron microscope [25], and the black portion of the binarized image represents the pores and cracks of the

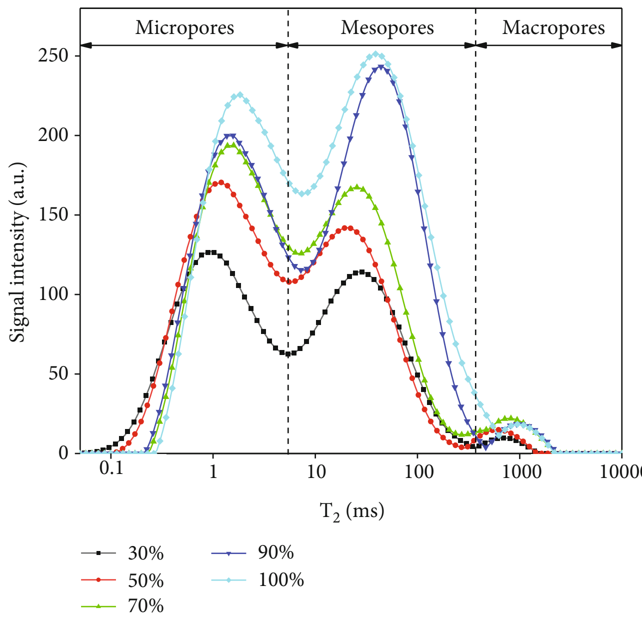

Figure 2: T_2 spectrum distribution of rock samples with different saturated states.

Table 3: NMR results of rock samples under different saturated states.

Saturation ω	Total area	Micropore area	Mesopore area	Macropore area
30%	11659	6021	5457	181
50%	12640	6831	5543	229
70%	13748	7100	6435	213
90%	15528	6868	8370	290
100%	15706	6550	8847	309

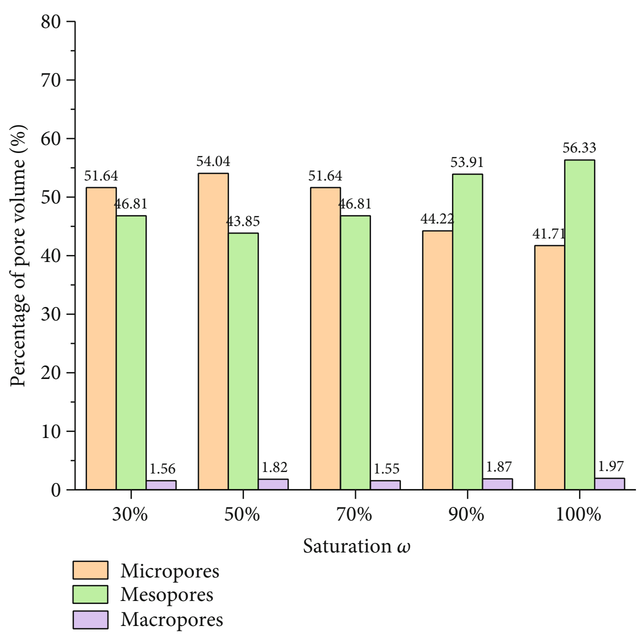

Figure 3: Proportional of three pore types in the total area of T_2 spectrum.

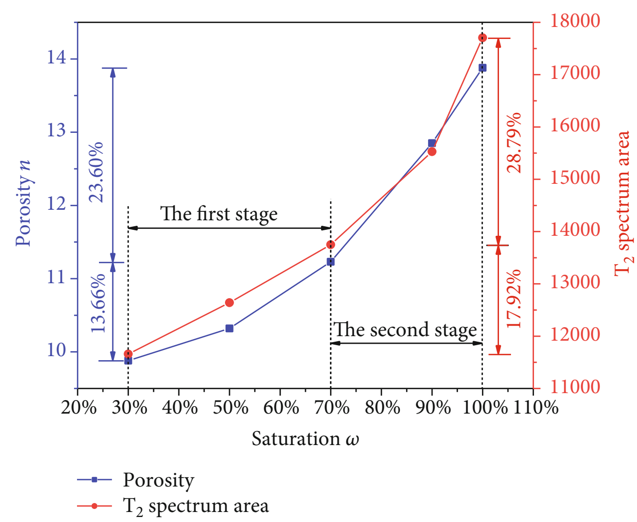

Figure 4: Porosity and T_2 spectrum area change curve with saturation.

scanned slice. From the binarization image, it is clearly observed that as the saturation gradually increases, the number of pores inside the rock sample increases and significant cracks develop. Under low-saturation conditions, owing to the small frost-heave force on the rock sample, even after 30 freeze-thaw cycles, the mineral particles of the rock sample are still tightly bonded, the grain boundary is not obvious, and the pores are fewer. As the saturation increases, particularly when it reaches 90%, the frost-heave force gradually increases, the bonding state of the cement and mineral particles in the rock sample gradually change, and the dissolution of the cement gradually accelerates. As a result, there is a significant loss of cement between particles, weakening their connection. Further, the dissolution holes increase in

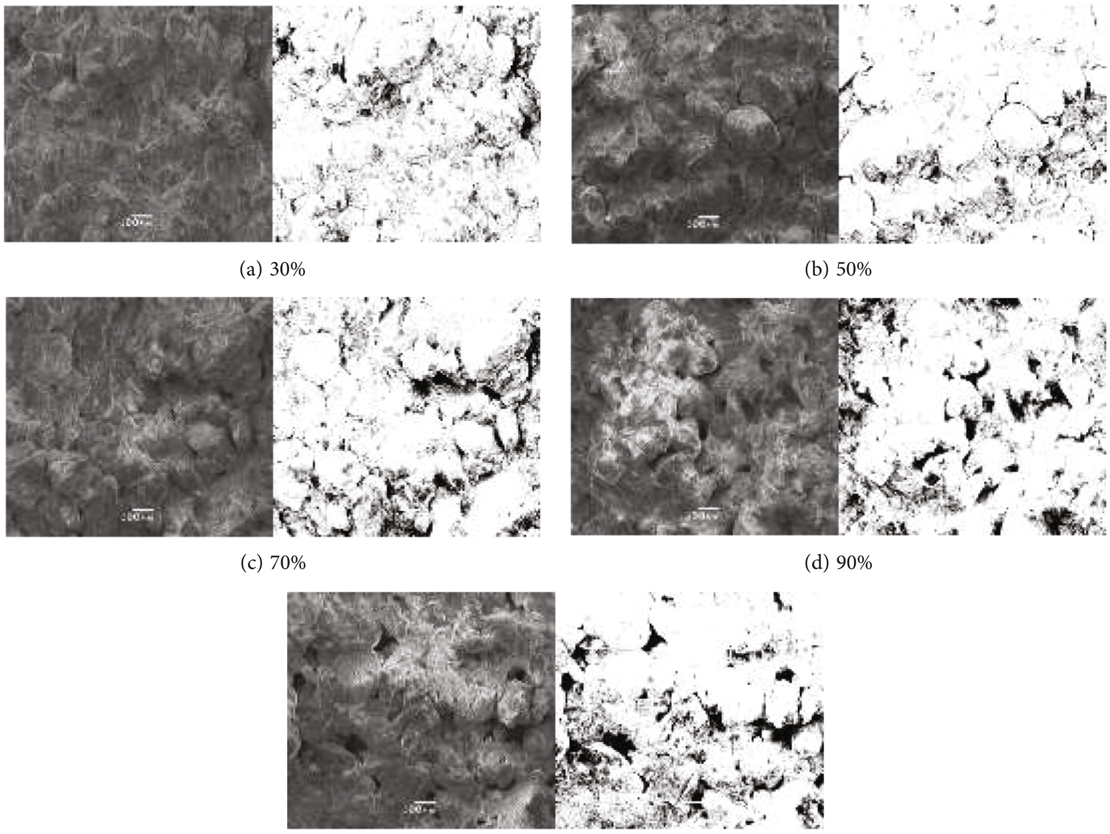

(a) 30%

(b) 50%

(c) 70%

(d) 90%

(e) 100%

Figure 5: Scanning electron microscopy and binarization images of rock samples with different saturations.

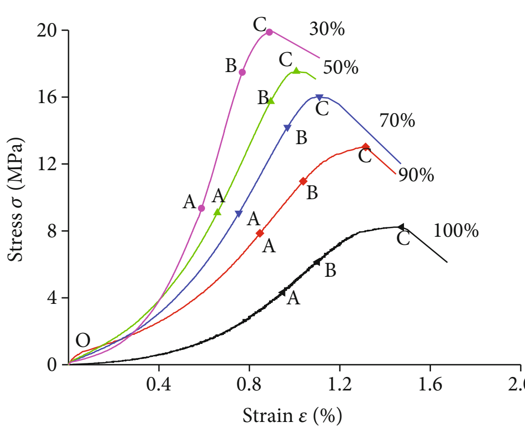

Figure 6: Stress-strain curves of differently saturated rock samples.

number and penetration cracks through particles appear. The above analysis demonstrates that, when the saturation reaches 70%, freeze-thaw cycle damage gradually appears, a value that can be used as the critical saturation for freeze-thaw damage.

3.3. Uniaxial Strength Test Analysis. To determine the loading classification, uniaxial compression tests on rock samples with different saturation states were carried out. The stress-strain curve is shown in Figure 6, and the test results are shown in Table 4. In the curve, OA is the compaction stage,

Table 4: Mechanical parameters of rock samples with different saturations.

Parameter	Saturation ω				
	30%	50%	70%	90%	100%
Uniaxial strength σ_f (MPa)	17.19	14.50	10.51	7.87	5.12
Elastic modulus E (GPa)	2.13	1.94	1.52	1.09	0.57

AB is the linear-elastic stage of pore and crack development, and BC is the plastic development stage [26]. The table shows that the strength and elastic modulus both decrease with increases in saturation. When the saturation increases from 30% to 70%, the decrease in strength and elastic modulus is smaller, decreasing by 38.86% and 28.64%, respectively; when the saturation is increased from 70% to 100%, it decreases by 51.29% and 62.5%, respectively, which represents a much larger decline than the former case. This shows that, under the action of freeze-thaw cycles, the instantaneous mechanical properties of rock samples are greatly affected by saturation, and the critical value of instantaneous mechanical damage occurs when the saturation increases from 70% to 90%.

3.4. Analysis of Creep Test Results

3.4.1. Influence of Saturation on Creep Deformation in Rock Samples. Figure 7 shows the uniaxial creep curves of rock

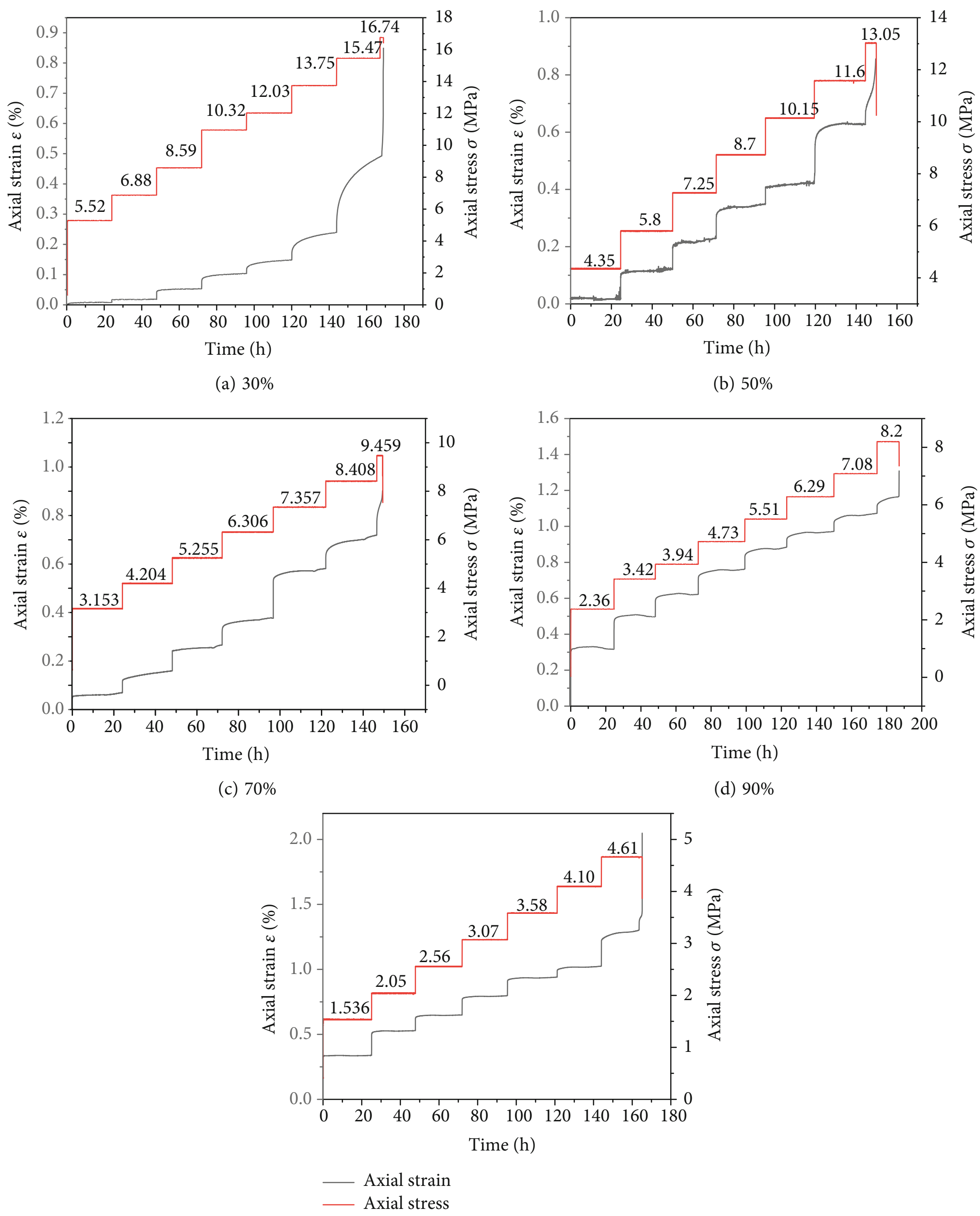

Figure 7: Creep curves of rock samples with different states of saturation.

Table 5: Axial creep strain of rock sample under graded loading.

Saturation ω	Axial creep strain of different graded loading stress levels $\varepsilon/10^{-2}$						
	30%	40%	50%	60%	70%	80%	90%
30%	0.0083	0.0175	0.0531	0.1035	0.1486	0.2394	0.4951
50%	0.0185	0.1225	0.2294	0.3485	0.4251	0.6264	0.8572
70%	0.0693	0.1594	0.2631	0.3745	0.5853	0.7165	0.9022
90%	0.3138	0.4926	0.6217	0.7624	0.8843	0.9717	1.1676
100%	0.3375	0.5216	0.6465	0.7975	0.9441	1.0171	1.4396

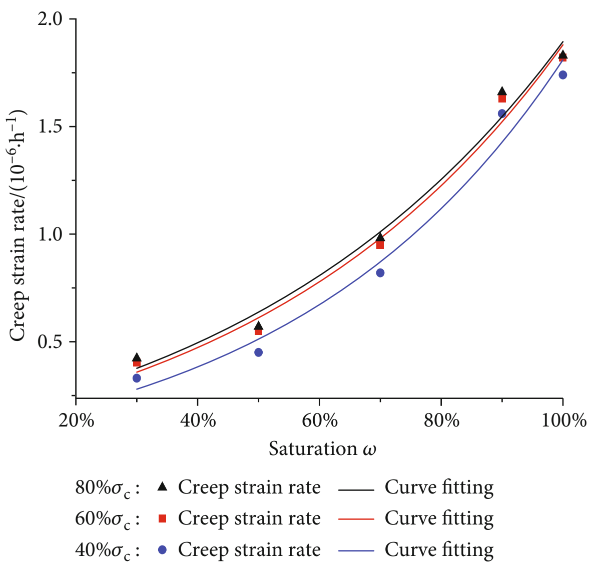

FIGURE 8: Steady-state creep rate under different loading stress levels.

samples with different saturated states after freeze-thaw cycles. The figure is visible that the rock sample immediately produces instantaneous strain under the action of axial stress, which gradually increases with increases in saturation. Under the action of long-term stress, the creep characteristics of rock samples are relatively obvious. As the stress increases, the creep deformation increases significantly, and the characteristics of decelerated creep and stable creep appear [27]. Under the action of the final load, the characteristics of accelerated creep appear, and the creep rate and creep deformation gradually increase with increases in creep time, until failure. As the saturation increases, the creep deformation gradually increases under the load of the same level, and the creep curve gradually becomes steeper. Looking at Table 5, under the first level of horizontal load, relative to the previous saturation level, the axial creep strain increment of the rock samples with 50%, 70%, 90%, and 100% saturation are 0.0102, 0.0508, 0.2445, and 0.0237, respectively; under the second level of horizontal load, the additional values are 0.105, 0.0369, 0.3332, and 0.029, respectively. From the above analysis, it can be concluded that, under the load of the same level, the axial creep strain of the rock sample gradually increases with the increase of saturation. This is because the internal damage of the rock sample is greatly affected by saturation under the action of a freeze-thaw cycle. According to the analysis in sections, when the saturation reaches 70%, the internal particle cementation of the rock sample weakens, and the number of pores increases, leading to a reduction in creep mechanical properties.

3.5. Influence of Saturation on the Creep Rate of Rock Samples. Figure 8 shows the steady-state creep rates of rock samples with different saturated states at 40%, 60%, and 80% loading stress levels. This is evident from the fitting curve that, under the same stress level, the steady-state creep rate of the rock sample increases nonlinearly with increases in saturation. Taking the 60% stress loading level as an example, when the saturation is low, the steady-state creep rate of the rock sample increases only slightly. When the saturation is 30%, the steady-state creep rate of the rock sample is 4.204×10^{-7}, and when the saturation is 50%, it is 5.562×10^{-7}, exhibiting an increase of 32.31%. As the saturation continues to increase, the increase in the steady-state creep rate of the rock sample gradually increases. When the saturation is 70%, the steady-state creep rate is 9.571×10^{-7}; when it reaches 90%, the steady-state creep rate is 1.634×10^{-6}, which is an increase of 70.73%. The same change pattern is also shown at the 40% and 80% loading stress level. It can be concluded that saturation has a great influence on the steady-state creep rate of the rock samples. As the saturation increases, the steady-state creep rate of the rock sample increases gradually. This could be because of the difference in the degree of damage caused by the freeze-thaw cycle to the rock samples in different saturated states. When the saturation reaches 70%, owing to the increase in internal water molecules, the frost-heaving force increases, causing internal pores and microcracks in the rock-sample structure to develop and expand, resulting in increased damage and the gradual deterioration of mechanical properties.

Under the final stage of loading, the rock samples with different saturated states underwent creep failure. The change of the curves of axial strain and creep strain rate under the final stress level with time is shown in Figure 9. To visually analyze the curve characteristics of the accelerated creep stage of a 100% saturation rock sample, only the portion of the curve after the axial-strain change is shown in the figure.

Under the action of freezing and thawing, the rock samples with different saturated states experienced the decelerated-creep stage, the stable-creep stage, and the accelerated-creep stage, and rapid destruction occurs in the accelerated creep stage; the creep-failure law is different under the action of the final level of stress. Further, 90% and 100% rock samples have a shorter accelerated creep stage, because when they reach a higher saturation, freezing and thawing cause their plasticity to decrease; as shown in the figure, the creep rate curve is approximately barrel-shaped—it first gradually decreases, then remains stable, and finally increases suddenly. The results of a comparison among the creep failure stress level, creep duration, and creep rate of rock samples in different saturated states under the action of freezing and thawing are shown in Table 6. The rock samples with a saturation of 30%, 50%, 70%, 90%, and 100% fail at stresses of 15.47 MPa, 13.05 MPa, 9.46 MPa, 8.2 MPa, and 4.61 MPa, respectively; at low levels of saturation, the creep time gradually decreases with increases in saturation. When the saturation is greater than 70%, the creep time gradually increases; the creep rate of the rock sample increases with increases in saturation.

3.6. Creep Failure Morphology. Table 7 shows the creep failure morphology and sketch map of rock samples with different saturated states after freeze-thaw cycles. It is clear that the failure mode of the rock sample is shear failure. When

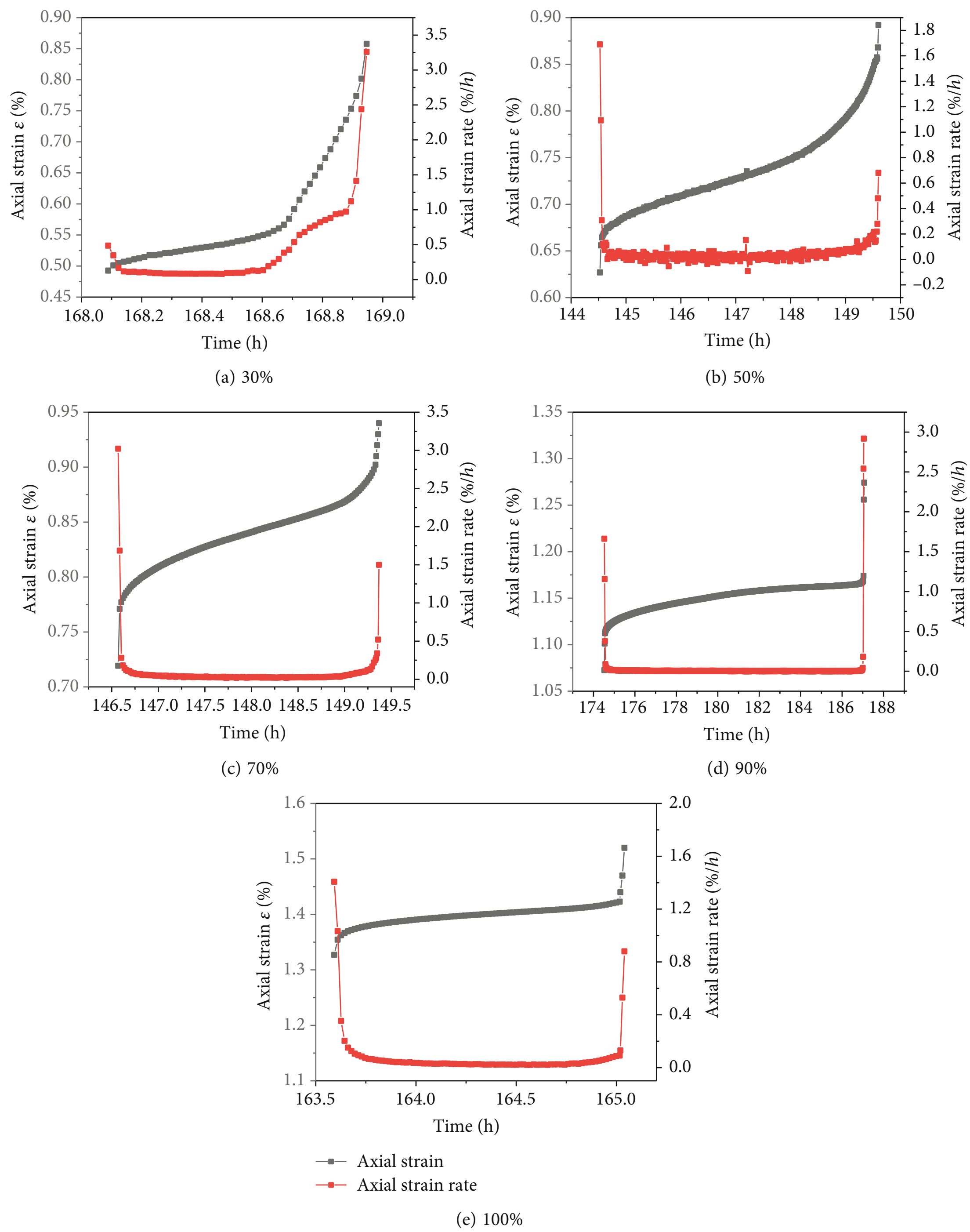

Figure 9: Change of creep rate of rock sample under failure stress.

the saturation is 30%, only one primary crack appears. As the saturation increases, the failure cracks of the rock sample gradually increase, and microcracks appear. The crack spacing of the rock sample gradually forms, and tension characteristics manifest. This is because, as the saturation increases, the freeze-thaw cycle causes the cementation between the particles of the rock sample to weaken, increasing cracks. The internal cracks in the rock sample structure gradually develop and expand under long-term loading, eventually evolving into multicrack shear failure [28].

4. Creep Model with Different Saturated States under Freeze-Thaw Cycles

4.1. Establishing the Creep Model. From the above experimental analysis, it can be concluded that rock samples with different saturated states, under the action of freezing and thawing, sequentially experience the decelerated-creep stage, the stable-creep stage, and the accelerated-creep stage. Further, the creep properties of the rock sample are related to the saturation, stress state, and loading time. The classic

Table 6: Creep parameters of specimens under failure stress.

Saturation ω	Failure stress σ (MPa)	Creep time (h)	Decelerated creep stage Initial creep rate	Stable creep stage Steady-state creep rate	Accelerated creep stage Accelerated creep rate
30%	16.74	0.96	2.829×10^{-6}	6.328×10^{-7}	1.726×10^{-6}
50%	13.05	5.33	3.357×10^{-6}	7.389×10^{-7}	2.185×10^{-6}
70%	9.46	2.73	1.583×10^{-6}	7.842×10^{-7}	2.603×10^{-6}
90%	8.20	12.74	3.824×10^{-6}	8.617×10^{-7}	3.015×10^{-6}
100%	4.61	25.59	0.426×10^{-5}	0.103×10^{-6}	0.413×10^{-5}

Table 7: Creep failure morphology of rock samples.

Test pattern	Saturation ω				
	30%	50%	70%	90%	100%
Destruction pattern					
Sketch	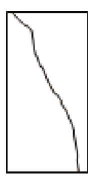	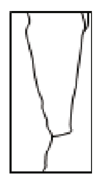	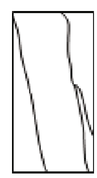	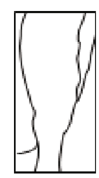	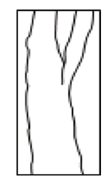

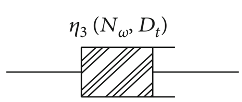

Figure 10: Freeze-thaw damage to viscous components.

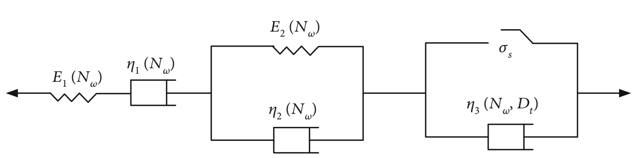

Figure 11: Creep model.

Burgers model can fully reflect the decelerated-creep and stable-creep stage during the creep test, but it cannot describe the accelerated-creep stage. Therefore, in this paper, a modified viscous-plastic body is connected in series on the basis of the Burgers model. By introducing the damage variable to consider the accumulation of damage in the creep process, describing the variation of the viscosity coefficient with the creep process and accounting for the effect of saturation on the viscosity coefficient, a freeze-thaw-damage viscous element was constructed. The viscous components are shown in Figure 10.

The freeze-thaw-damage viscous element is a Newtonian body, and its constitutive relationship is shown in

$$\sigma = \eta_3(N_\omega, D_t)\dot{\varepsilon}, \tag{3}$$

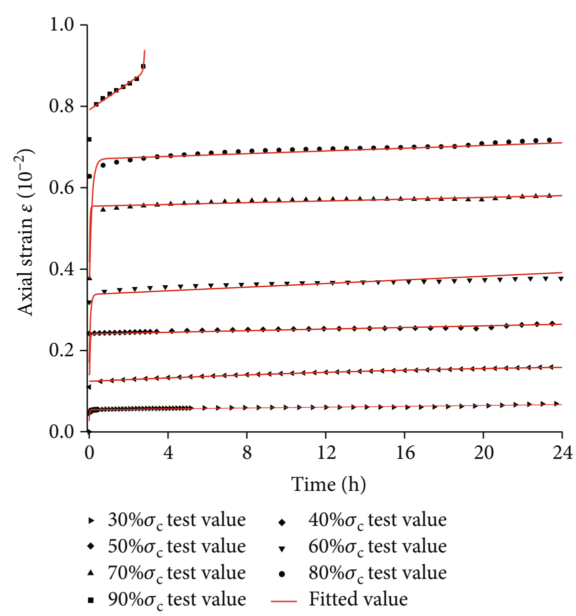

Figure 12: Creep verification curve of 70% saturation rock samples.

where σ is the stress of the viscous element, $\dot{\varepsilon}$ is the strain rate, and $\eta_3(N_\omega, D_t)$ is the viscosity coefficient of the freeze-thaw-damage viscous element.

Table 8: Creep model parameters of 70% saturation rock samples.

Saturation ω	Stress (MPa)	E_1	E_2	η_1	η_2	α	η_3	R^2
70%	3.153	0.384	0.624	46.326	13.68	_	_	0.95
	4.204	0.396	0.673	46.175	16.33	_	_	0.99
	5.255	0.382	0.531	46.158	15.37	_	_	0.94
	6.306	0.631	0.522	46.033	12.35	_	_	0.93
	7.357	0.543	0.501	44.384	17.95	_	_	0.94
	8.408	0.412	0.413	40.569	19.32	_	_	0.96
	9.459	0.596	0.338	33.218	26.31	0.037	8.236	0.99

Considering the influence of saturation and long-term loading on the viscosity coefficient, the coefficient of the viscous element is shown in

$$\eta_3(N_\omega, D_t) = \eta_3(N_\omega)(1 - D_t), \tag{4}$$

where $\eta_3(N_\omega)$ is the viscosity coefficient after a certain number of freeze-thaw cycles and D_t is the damage variable $(0 \le D_t < 1)$.

A significant amount of research has shown that the damage caused by long-term loading in the process of rock creep has a negative exponential function relationship with time [29], as shown in

$$D_t = 1 - e^{-\alpha t}, \tag{5}$$

where α is the coefficient related to the material properties and saturation of the rock sample and t is time.

Therefore, considering the joint influence of saturation and long-term load, the viscosity coefficient is

$$\eta_3(N_\omega, D_t) = \eta_3(N_\omega) e^{-\alpha(N_\omega)t}, \tag{6}$$

where $\alpha(N_\omega)$ is the material coefficient of the rock sample at a certain number of freeze-thaw cycles at a degree of saturation.

Therefore, the constitutive relationship of the viscous element is

$$\varepsilon = \frac{\sigma}{\alpha(N_\omega)\eta_3(N_\omega)} \left[e^{\alpha(N_\omega)t} - 1 \right]. \tag{7}$$

The model is composed of four parts connected in series: a water-containing elastic element, a water-containing viscous element, a water-containing viscoelastic element, and a water-containing viscous-plastic body. The creep model is shown in Figure 11, where E_1, E_2, η_1, and η_2 are parameters related to saturation; η_3 is the parameter related to loading time and saturation. The creep equation is obtained as shown in Equations (8) and (9):

when $\sigma \le \sigma_s$,

$$\varepsilon = \frac{\sigma}{E_1(N_\omega)} + \frac{\sigma}{\eta_1(N_\omega)} t + \frac{\sigma}{E_2(N_\omega)} \left(1 - e^{(E_2(N_\omega)/\eta_2(N_\omega))t} \right), \tag{8}$$

when $\sigma \ge \sigma_s$,

$$\begin{aligned} \varepsilon = {} & \frac{\sigma}{E_1(N_\omega)} + \frac{\sigma}{\eta_1(N_\omega)} t + \frac{\sigma}{E_2(N_\omega)} \left(1 - e^{(E_2(N_\omega)/\eta_2(N_\omega))t} \right) \\ & + \frac{\sigma - \sigma_s}{\alpha(N_\omega)\eta_3(N_\omega)} \left[e^{\alpha(N_\omega)t} - 1 \right]. \end{aligned} \tag{9}$$

4.1.1. Model Validation. The Boltzmann superposition principle is used to transform the creep curve under the staged-loading condition into the creep curve under the separate-loading condition. The 1stOpt mathematical optimization analysis software is used to identify the model parameters. The calculated results of the established freeze-thaw-damage creep model are in good agreement with the test results and can simultaneously describe instantaneous deformation, decelerated creep, stable creep, and accelerated creep processes. Owing to space limitations, only the creep verification curve and creep-parameter evolution results of the 70% saturation rock sample is listed, as shown in Figure 12 and Table 8.

5. Conclusions

The freeze-thaw cycle has a significant influence on the long-term mechanical properties of rocks. However, most current creep research is only carried out in the fully saturated state. This paper conducts NMR, scanning electron microscopy, and uniaxial compression creep tests on red sandstone in different states of saturation after freeze-thaw cycles. The main results of this research are summarized as follows.

Under the action of freeze-thaw cycles, as the saturation of rock samples increases, the T_2 spectrum distribution shifts to the right, the total area of the T_2 spectrum gradually increases, and the porosity increases. Further, when the saturation increased from 70% to 90%, the distribution characteristics of pores changed significantly. After freeze-thaw cycles, mesopores replaced micropores, becoming the main pore form.

By SEM image, it can be seen that the number of pores in the rock samples gradually increases with increasing saturation levels. When the saturation reaches 70%, freeze-thaw cycle damage gradually appears, the number of dissolution holes increases, and penetration fracture occurs in the particle.

Under uniaxial compression, rock samples in different saturated states experience the compaction stage, linear-elastic stage, and plastic stage. The instantaneous mechanical properties of rock samples are greatly affected by saturation. The critical value appears when the saturation increases from 70% to 90%.

Under long-term loading, saturation has a significant influence on the time-efficiency characteristics of the rock sample during the freeze-thaw cycle. With increases in saturation, the creep deformation gradually increases. When it reaches 70%, the axial creep strain increases greatly, the creep rate increases, the creep failure stress decreases, and the creep time under the final level of stress increases significantly. This shows that the saturation level of 70% is the critical saturation for the deterioration of the mechanical properties of the rock sample.

A modified viscous-plastic body is connected in series on the basis of the Burgers model. The damage accumulation and saturation change in the creep process are fully considered. The freeze-thaw-damage viscous element—with the viscosity coefficient $\eta_3(N_\omega, D_t)$—is introduced, and creep parameters were fitted using the experimental data. The numerical-calculation values of the model are in good agreement with the experimental values. The creep model established can accurately reflect the staged-loading creep state of rock samples in different saturated states under the action of freezing and thawing. The model can provide a theoretical basis for investigating the time-efficiency characteristics of rocks in different water-saturation states.

Data Availability

The data used to support the findings of this study are included within the article, displayed by figures and tables.

Conflicts of Interest

The authors declare no conflict of interest.

Acknowledgments

This research was supported by the National Natural Science Foundation of China (Nos. 11972283, 11872299, and 41702346) and the Natural Science Foundation of Shaanxi Province, China (No. 2017JM1039), which are greatly appreciated.

References

[1] J. L. Li, L. Y. Zhu, K. P. Zhou, S. P. Cao, and H. W. Liu, "Experimental investigation on the effects of ambient freeze-thaw cycling on creep mechanical properties of sandstone under step loading," *IEEE Access*, vol. 7, pp. 108513–108520, 2019.

[2] Z. J. Zhou, H. C. Zhan, J. Y. Hu, and C. N. Ren, "Characteristics of unloading creep of tuffaceous sandstone in East Tianshan Tunnel under freeze-thaw cycles," *Advances in Materials Science and Engineering*, vol. 2019, Article ID 7547564, 16 pages, 2019.

[3] G. Q. Chen, F. Guo, J. C. Wang, and Y. X. Zhou, "Experimental study on triaxial creep characteristics of quartz sandstone after freezing and thawing," *Rock and Soil Mechanics*, vol. 38, no. s1, pp. 203–210, 2017.

[4] X. R. Yang, J. N. Jiang, S. Y. Wang, and F. R. Zhang, "Experimental study on the creep characteristics of gneiss under freeze-thaw cycles," *Rock and Soil Mechanics*, vol. 40, no. 11, pp. 4331–4340, 2019.

[5] X. X. Liu, S. N. Li, Z. P. Xu, Y. Li, and Y. M. Zhou, "Research on the creep model of carbonaceous shale under freeze-thaw cycles," *China Journal of Highway and Transport*, vol. 32, no. 11, pp. 137–145, 2019.

[6] F. R. Zhang, J. N. Jiang, X. R. Yang, and F. Y. Shen, "Test and model study of granite shear creep under freeze-thaw cycles," *Rock and Soil Mechanics*, vol. 41, no. 2, pp. 509–519, 2020.

[7] Y. Niu, X. P. Zhou, J. Z. Zhang, and Q. H. Qian, "Experimental study on crack coalescence behavior of double unparallel fissure- contained sandstone specimens subjected to freeze-thaw cycles under uniaxial compression," *Cold Regions Science and Technology*, vol. 158, pp. 166–181, 2019.

[8] X. P. Zhou, Y. Niu, J. Z. Zhang, X. C. Shen, Y. Zheng, and F. Berto, "Experimental study on effects of freeze-thaw fatigue damage on the cracking behaviors of sandstone containing two unparallel fissures," *Fatigue & Fracture of Engineering Materials & Structures*, vol. 42, no. 6, pp. 1322–1340, 2019.

[9] J. P. McGreevy and W. B. Whalley, "Rock moisture content and frost weathering under natural and experimental conditions: a comparative discussion," *Arctic Antarctic and Alpine Research*, vol. 17, no. 3, pp. 337–346, 1985.

[10] Q. S. Liu, S. B. Huang, Y. S. Kang, and X. Z. Cui, "Research progress and thinking on freeze-thaw damage of fractured rock masses," *Chinese Journal of Rock Mechanics and Engineering*, vol. 34, no. 3, pp. 452–471, 2015.

[11] A. Prick, "Critical degree of saturation as a threshold moisture level in frost weathering of limestones," *Permafrost and Periglacial Processes*, vol. 8, no. 1, pp. 91–99, 1997.

[12] A. Prick, "Dilatometrical behaviour of porous calcareous rock samples subjected to freeze-thaw cycles," *Catena*, vol. 25, no. 1-4, pp. 7–20, 1995.

[13] T. C. Chen, M. R. Yeung, and N. Mori, "Effect of water saturation on deterioration of welded tuff due to freeze-thaw action," *Cold Regions Science and Technology*, vol. 38, no. 2-3, pp. 127–136, 2004.

[14] A. Al-Omari, K. Beck, X. Brunetaud, Á. Török, and M. Al-Mukhtar, "Critical degree of saturation: a control factor of freeze-thaw damage of porous limestones at Castle of Chambord, France," *Engineering Geology*, vol. 185, pp. 71–80, 2015.

[15] P. Zhang, Y. Zou, X. Wang, T. Jiang, H. Lin, and P. Cao, "An elasto-visco-plastic model based on stress functions for deformation and damage of water-saturated rocks during the freeze-thaw process," *Construction and Building Materials*, vol. 250, article 118862, 2020.

[16] X. R. Yang, J. N. Jiang, and Z. B. Jiang, "Study on creep test and damage model of soft rock under water content," *Rock and Soil Mechanics*, vol. 39, pp. 167–174, 2018.

[17] X. J. Liu, X. R. Liu, T. X. Wang, and J. B. Wang, "Study on creep constitutive model of shallow metamorphic slate considering water-bearing degradation effect," *Chinese Journal of Rock Mechanics and Engineering*, vol. 33, no. 12, pp. 2384–2389, 2014.

[18] J. Z. Zhang, X. P. Zhou, and P. Yin, "Visco-plastic deformation analysis of rock tunnels based on fractional derivatives,"

Tunnelling and Underground Space Technology, vol. 85, pp. 209–219, 2019.

[19] J. B. Wang, Q. Zhang, Z. P. Song, and Y. W. Zhang, "Experimental study on creep properties of salt rock under long-period cyclic loading," *International Journal of Fatigue*, vol. 143, p. 106009, 2021.

[20] J. B. Wang, Q. Zhang, Z. P. Song, and Y. W. Zhang, "Creep properties and damage constitutive model of salt rock under uniaxial compression," *International Journal of Damage Mechanics*, vol. 29, no. 6, pp. 902–922, 2020.

[21] X. D. Luo, N. Jiang, X. Y. Fan, N. F. Mei, and H. Luo, "Effects of freeze-thaw on the determination and application of parameters of slope rock mass in cold regions," *Cold Regions Science and Technology*, vol. 110, pp. 32–37, 2015.

[22] J. L. Li, R. B. Kaunda, and K. P. Zhou, "Experimental investigations on the effects of ambient freeze-thaw cycling on dynamic properties and rock pore structure deterioration of sandstone," *Cold Regions Science and Technology*, vol. 154, pp. 133–141, 2018.

[23] Y. J. Shen, Y. Z. Wang, X. Wei, H. L. Jia, and R. X. Yan, "Investigation on meso-debonding process of the sandstone-concrete interface induced by freeze-thaw cycles using NMR technology," *Construction and Building Materlals*, vol. 252, p. 118962, 2020.

[24] L. M. Anovitz and D. R. Cole, "Characterization and analysis of porosity and pore structures," *Reviews in Mineralogy and Geochemistry*, vol. 80, no. 1, pp. 61–164, 2015.

[25] B. Liu, J. Z. Shi, J. Zhou, and C. Tang, "Quantification and characterization of microporosity by image processing, geometric measurement and statistical methods: application on SEM images of clay materials," *Applied Clay Science*, vol. 54, no. 1, pp. 97–106, 2011.

[26] H. M. Zhang and G. S. Yang, "Experimental study on damage and mechanical properties of freeze-thawed rock," *Journal of China Coal Society*, vol. 38, no. 10, pp. 1756–1762, 2013.

[27] X. R. Yang, A. N. Jiang, and M. X. Li, "Experimental investigation of the time-dependent behavior of quartz sandstone and quartzite under the combined effects of chemical erosion and freeze-thaw cycles," *Cold Regions Science and Technology*, vol. 161, pp. 51–62, 2019.

[28] Y. S. Kang, C. C. Hou, B. Liu, Q. S. Liu, H. M. Sang, and Y. C. Tian, "Frost deformation and a quasi-elastic-plastic-creep constitutive model for isotropic freezing rock," *International Journal of Geomechanics*, vol. 20, no. 8, article 04020119, 2020.

[29] F. B. Chen, Q. J. Zuo, Y. Y. Wu, Z. J. Zhang, and X. Q. Zhao, "Study on the macro-fine-micro mechanism of slate expansion process in rich water environment," *Chinese Journal of Rock Mechanics and Engineering*, vol. 39, no. 1, pp. 126–137, 2020.

Hindawi
Geofluids
Volume 2021, Article ID 7194988, 18 pages
https://doi.org/10.1155/2021/7194988

Research Article

Experimental Study of Site-Specific Soil Water Content and Rainfall Inducing Shallow Landslides: Case of Gakenke District, Rwanda

Martin Kuradusenge,[1] Santhi Kumaran,[2] Marco Zennaro,[3] and Albert Niyonzima[4]

[1]*African Centre of Excellence in Internet of Things, University of Rwanda, KN 67, Kigali 3900, Rwanda*
[2]*School of ICT, The Copperbelt University, Kitwe 21692, Zambia*
[3]*International Centre of Theoretical Physics, Strada Costiera, 11, I-34151 Trieste, Italy*
[4]*School of Engineering, University of Rwanda, KN 67, Kigali 3900, Rwanda*

Correspondence should be addressed to Martin Kuradusenge; m.kuradusenge@ur.ac.rw

Received 24 April 2021; Revised 3 August 2021; Accepted 14 August 2021; Published 9 September 2021

Academic Editor: Guanglei Zhang

Shallow landslides are among the natural threats causing death and damage. They are mostly triggered by rainfall in mountainous areas where precipitation used to be abundant. The amount of rainfall inducing this natural threat differs from one site to another based on the geographical characteristics of that area. In addition to the rainfall depth, the determination of soil water content in a specific zone has a major contribution to the landslide prediction and early warning systems. Rwanda being a country with hilly terrains, some areas are susceptible to both rainfall and soil water content inducing landslides. But an analytical study of the physical threshold determination of both rainfall and soil water content inducing landslides is lacking. Therefore, this experimental study is conducted to determine the rainfall and soil water content threshold that can be fed in to the landslide early warning system (LEWS) for alert messages using the Internet of Things (IoT) technology. Various experiments have been conducted for the real-time monitoring of slope failure using the toolset composed of a rain gauge, soil moisture sensors, and a rainfall simulating tool. The results obtained show that the threshold for landslide occurrence does not solely correlate with the total rainfall amount (or intensity) or soil moisture, but also influenced by internal (geological, morphological) and environmental factors. Among the sampled sites, the sites covered by forest indicated no sign of slope failure, whereas sites with crops could slip. The experiments revealed that for a specific site, the minimum duration to induce slope failure was 8 hours, 41 minutes with the rainfall intensity of 8 mm/hour, and the soil moisture was above 90% for deeper sensors. These values are used as thresholds for LEWS for that specific site to improve predictions.

1. Introduction

Rainfall-induced shallow landslides are among the most natural disasters that causes deaths and substantial economic losses damaging infrastructure or plants in different mountainous regions around the world [1–3]. In Rwanda, about 1,000 landslide cases have been identified during the past decade [4], affecting a significant number of citizens, agriculture land, livelihoods, and infrastructure that are valued in billions of dollars. For instance, almost 200 people died by landslide incidences during 2016-2018 [5, 6]. The most susceptible areas in Rwanda are the northern and western provinces, which are characterized by mountains and steep slopes [7, 8].

Rainfall-induced landslides are mainly caused by intrinsic factors like geological and geomorphological parameters and extrinsic factors such as hydrological conditions, climatic conditions, earthquakes, and volcanic eruptions [9–11]. Hydrological factors such as rainfall and ground water table location influence the slope stability. The process of this type of natural disaster is intricate. The water content in the shallow soil is almost absent during the dry season. When it rains, the rainwater starts penetrating into the earth characterized by different permeability properties, and then, the ground becomes moist. It keeps on penetrating until it reaches the layer of low hydraulic conductivity where it accumulates up to the complete saturation level [12] and forces the grains of the soil to separate. The matric suction on the topsoil decreases, and once the ground is fully water-logged, the soil matric suction finally vanishes completely [13], making the ground unstable, and that is a critical condition for landslide risk [14]. Thus, depending on the other geophysical characteristics of the area, a landslide incidence may follow [14]. Chiorean in [15] describes the process of a rainfall-induced landslide as follows: (i) rainfall permeation results in a reduction of the matric suction of the slope soil, (ii) the diminution in soil matric suction decreases the soil shear strength, and (iii) the decrease in soil shear strength afterwards causes the slope to become unbalanced and finally fail. The matric suction (ψ_m) plays a crucial role in landslide occurrence and is defined as the difference between pore air pressure (u_a) and pore water pressure (u_w) [15–18].

$$\psi_m = u_a - u_w, \tag{1}$$

ψ_m is influenced by the movement of water (most of the time rainwater) within soil pores [19]. At the initial state, when the soil is free from water (dry), the soil has the peak value of matric suction, and this attains its lowest value (zero) when the soil is fully saturated [20].

Various mitigation methods have been utilized extensively to reduce the risk of landslide incidence. They include structured measures and nonstructured warning systems. Structural methods require high construction costs and may take many years [21]. Therefore, high precision LEWS is more efficient and should be emphasized.

Numerous studies have been undertaken broadly to reduce the impact of landslides on human lives and economic loss. They include various prediction models, susceptibility models, and landslide early warning systems (LEWS) [3, 10]. Some of the models establish the relationship between landslide occurrence and rainfall intensity through the laboratory field test as well as numerical analysis [22, 23]; others estimated the rainfall intensity and duration that could cause landslide incidences [10, 24–28]. Parameters used in each study are different and depend on the author selection and the availability of data. The most common parameters used in different studies are rainfall (external triggering factor) and internal factors such as slope (inclination, aspect), soil type, lithology, and land cover [29–35].

Past studies have used the laboratory flume test to identify the correlation between soil water content and landslide occurrence where rainfall, soil type (particle size), and slope inclination have been taken into consideration [16, 20, 36–39]. Others used empirical field tests [39, 40] or numerical modelling [3, 41], and various studies conducted on LEWS have generally used historical rainfall data together with landslide occurrence records to determine the rainfall threshold inducing landslides [34, 42–48]. The studies conducted in [22, 49–56] have shown that they have used antecedent rainfall as a key parameter that has a great impact on landslides' occurrence. In this research paper, the parameters considered are rainfall intensity together with soil moisture content (SMC) that can help to achieve a better landslide prediction modelling tool that might be used for LEWS. Though the preceding studies demonstrated the role that rainfall plays in triggering slope failure and came up with good results, the optimization is needed because of the complexity of conditions causing landslide incidence. Therefore, there is a need to derive the correlation between the present rainfall, antecedent rainfall, and the content of water in the soil at the time of slope failure to determine the site-specific threshold values of these parameters.

In relation to the above, the gaps found in the past studies is the exploration of how rainfall has different effects on slope stability according to the geophysical and environmental characteristics. For example, some experiments used the embankment soil in the slope flume [23, 57, 58] that has no original strength (cohesion) and could not provide a reliable threshold as the one conducted on the terrain. Therefore, the field experiment to determine the SMC and rainfall depth is of great importance for the LEWS. The present study was carried out on site and aimed at (1) analyzing how gradually the rainwater penetrates in to the soil during or after rainfall events until the landslide occurrence and (2) identifying the rainfall amount and threshold values for the SMC as a step prior to feed in to the LEWS using IoT technologies. Both quantitative statistical analysis and qualitative techniques were used through environmental covariates, namely, slope, soil type, vegetation (or land coverage), and rainfall intensity as an external parameter. The soil water content inducing landslides will be determined for each selected site. The geographical scope of the study is Gakenke district while the period of study is October 2019-June 2021 (21 months).

2. Materials and Methods

2.1. Study Area. This study was conducted in five sectors (Figure 1(c)) of Gakenke district (Figure 1(b)) located in the northern province of Rwanda (Figure 1(a)). The district shares borders with Rulindo, Burera, Musanze, Nyabihu, Kamonyi, and Muhanga Districts. The district comprises 19 administrative sectors divided into 97 cells, 617 villages. The district has an area of 704.06 km^2 [59]. The population density is 473 residents/km^2. The climate in this district is commonly the type of humid climate with the average annual temperature ranging between 16°C and 29°C. The rainfall is quite plentiful with a scale between 1,100 and 1,500 mm/yr. This district has four main seasons: the small dry season from January to February, a high rain season spans from March to May, marked by plentiful rainfall and landslide incidences, the long dry season extending from June to August, and finally, the short rain season from September to December. The high hills separated by rivers and swamplands characterize this district. The highest altitude

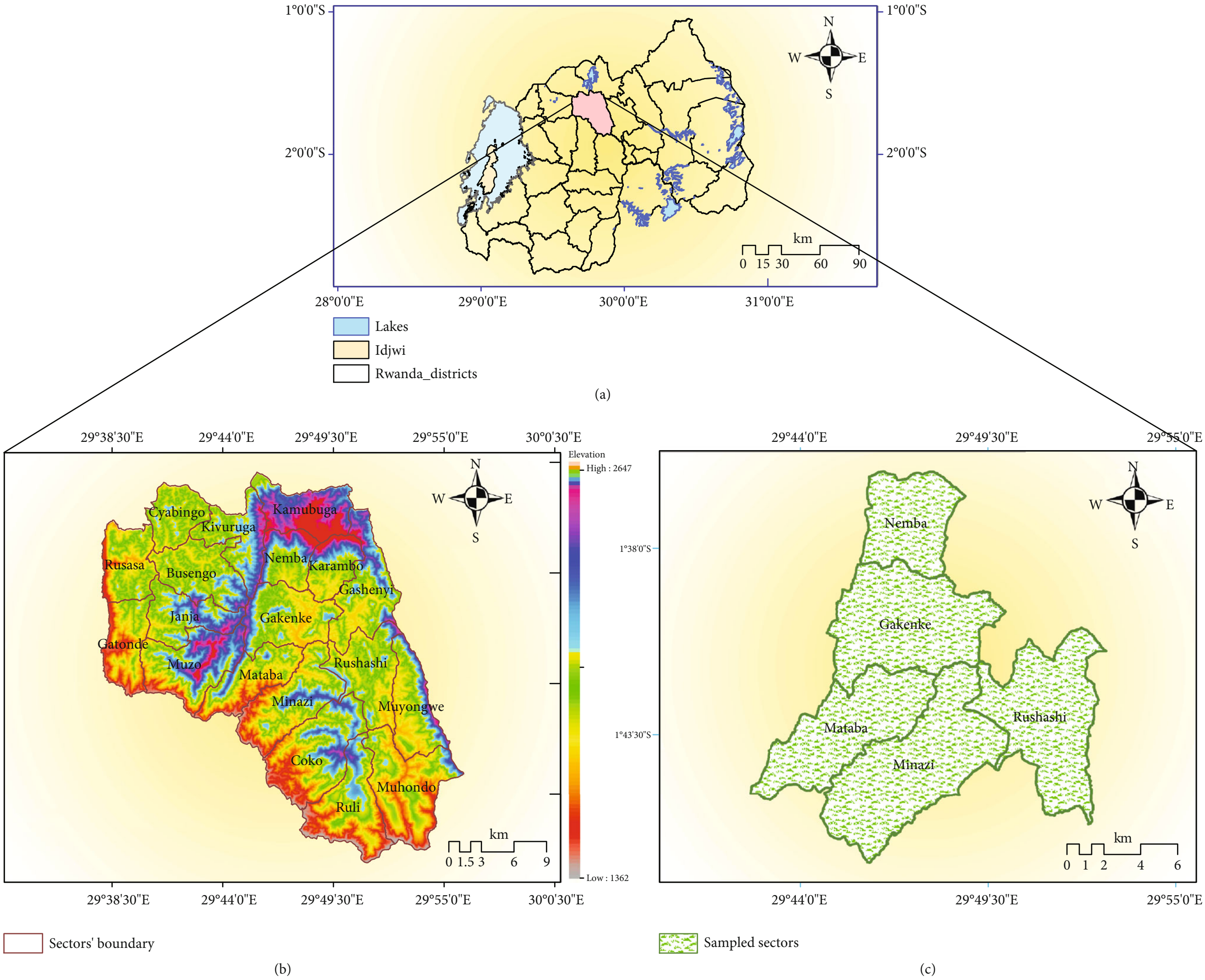

FIGURE 1: Study area: (a) Rwanda, (b) district elevation map and sectors' boundaries, and (c) district's sectors of experiments.

attains 2,647 meters (Mount Kabuye), whereas the lower altitude is 1,362 meters [59].

Due to its climatology and geographical characteristics such as topography and geology, the district is characterized by numerous landslides that cause few to many deaths and property damage in different heavy rainfall events [60–62]. In addition to the frequent and abundant rainfall, high slopes, land cover, and soil texture contribute to the slope failure in this region [63, 64]. The landslides in this region can be classified into two categories: (i) landslides related to natural slopes that initiate from anywhere on a hill slope (Figure 2(a)) and (ii) human-made slopes which are cut slopes related to house plots (Figure 2(b)), roads, or excavation activities.

2.2. Methods. The early warning system is one of the methods that can be used to reduce the risks related to landslides by providing incident information to the citizens prior to the occurrence. Two main methodological approaches can be used for landslide mitigation techniques. The first method uses physically based models considering the infinite soil mechanism; the second counts on experimental studies to determine the rainfall intensity and duration threshold [10, 12]. The challenge associated with the first approach is that the landslide can be detected but not predicted. The second approach can be appropriate, but the threshold for each influencing factor (such as hydrological, land use, lithological, and soil characteristics) should be determined [65]. In the current study, the rainfall intensity inducing shallow landslides is estimated considering the soil-forming factors and environmental covariates. Various experiments and numerical analysis were carried out for estimating the rainfall amount and the soil water content level that may lead to the slope failure.

2.2.1. Daily Rainfall Data. The slope failure in the study area and in the entire country is solely dependent on rainwater. Therefore, the rainfall data were necessary for this study.

(a) (b)

Figure 2: Pictures of landslides in the study area during 2016 (a) and 2020 (b) events.

Primary and secondary data have been used for both quantitative studies and qualitative assessment. Firstly, historical rainfall and soil moisture data were collected from the Rwanda Meteorology Agency for analysis of their correlation. Data from three rain gauge stations (Figure 3(d)) were used for primary analysis (Figure 4). This analysis was envisaged to identify rainfall amount-induced slope failures and landslide locations in the neighborhood of rain gauge stations.

Secondary, field work was conducted in the surrounding areas that have been characterized by at least two landslide incidences in the past 5 years. In this study, rain gauge and soil moisture sensors were used for real-time data collection.

2.2.2. Soil Moisture. In addition to the rainfall data, historical soil water content data were collected from the office in charge of meteorology and were analyzed (Figure 4(d)) on the basis that the SMC has a correlation with precipitation [66–69]. Moreover, studies revealed that the actual soil wetness can be achieved through in situ measurement [9, 70]. The soil moisture sensors were used to collect the soil water content on different sites (Figure 3(d)).

2.2.3. Slope. Various studies showed that the slope has a high impact on landslide occurrence. Steep slopes in several regions characterize Gakenke district where the slope angle can be more than 45 degrees. Other studies such as [51, 63] used 5 slope classes, whereas in this study, we grouped the first two classes because landslide cases are very few in areas with slopes less than 15%. According to the data source [71, 72], the slopes are categorized in four classes as indicated by Figure 3(c).

2.2.4. Soil Types. Geotechnical properties have an important impact on the slope stability [73]. In each test site, soil samples were collected and taken to the soil mechanics lab at the University of Rwanda to be tested for soil classification and other analysis. The soil classes found on the sampled sites are silty sand, sandy silt, sandy lean clay with gravel, lean clay, and elastic silt.

2.2.5. Land Cover. Land use is another factor contributing to the landslide occurrence. There are five different types of land cover in the study area: forest, cropland, grassland, built area, and water, but only the first three could be used in this study.

2.2.6. Experimenting Tools and Setup. To identify the rainfall influence on slope instability and its correlation with soil moisture, we used the rainfall simulator (Figure 5) for the direct in situ measurement of the soil humidity in various time durations until the slope starts indicating the sign of sliding such as a horizontal crack on the ground above the slope or sliding of cut slopes. The rainfall amount was recorded along with soil moisture at the interval of 49 seconds. The sensor-based monitoring tool was made of (i) the sensor node comprising three analog capacitive soil moisture sensors manufactured by Paialu, the operating voltage is 3.3~3.5 V to capture soil water content in various ground depths, and Arduino Uno Microcontroller ATmega328P; (ii) weather station consisting the transmitter (MISOL Model: WH40) and the receiver (model: WN5360); the communication between the transmitter and receiver was via wireless with a transmission frequency of 433 mhz and a maximum distance of 100 meters; (iii) a laptop with the Python code data logger to record readings from 3 sensors and convert into CSV file (Figure 6).

The soil moisture sensor used is a resistive sensor that outputs the voltage variation as water penetrates into the ground, i.e., the increase of the water in soil lowers the ground resistance that will then drop the voltage. By default, the sensor readings change from high to low when moisture is detected, and their values may differ from one sensor to another. Therefore, the output values from the sensors were calibrated in the Arduino IDE (Integrated Development Environment) by putting the sensors into an oven-dried soil and recording the readings and then putting the sensors in the fully wetted container of the soil (fully saturated) and again record readings. In the Arduino IDE, the maximum value (reading in dried soil) was mapped to zero (0) and the minimum (reading in wetted soil) to 100. Three sensors

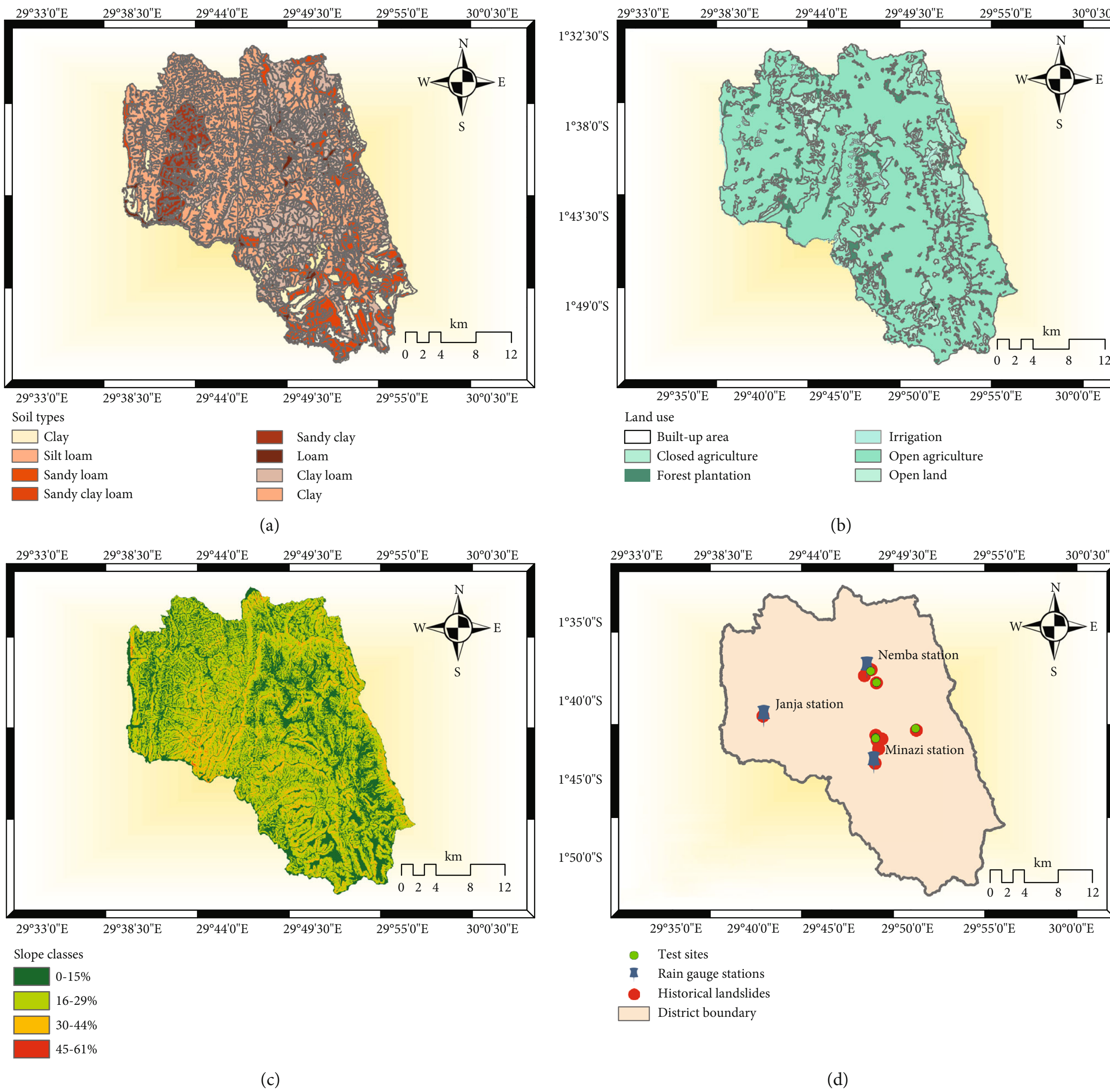

Figure 3: Maps: (a) soil types, (b) land use classification, (c) slope classification, and (d) rain gauge and test site locations.

were placed in different ground depths as indicated in Table 1.

2.2.7. Experimental Sites. All field experiments were conducted in the surrounding zones that have the historical background of landslides (Figure 3(d)). Different representative sites were chosen according to the geotopographical and environmental features including slope, soil types, and land use as indicated in Table 2.

At least two experimental tests were done at each site plot to test the reoccurrence of the slope failure. After the first two tests, one more test was conducted for that indicated at least one landslide to prove the reliability of the results.

3. Results and Discussion

3.1. Soil Classification Test Results. Five main sites were chosen as sample sites (SA, SB, SC, SD, and SE). Samples of soil were taken for the laboratory test of soil particle size distribution analysis because this plays an important role on different hydrologic features such as water retention characteristics and slope failure as well. The table below (Table 3) summarizes the relative composition of the soil in the sampled sites.

As shown in Table 2, from each site, two or three plots were sampled (except site SB) to identify the soil-related effects on the infiltration process. Some of the plot samples were found to have different soil textures. For

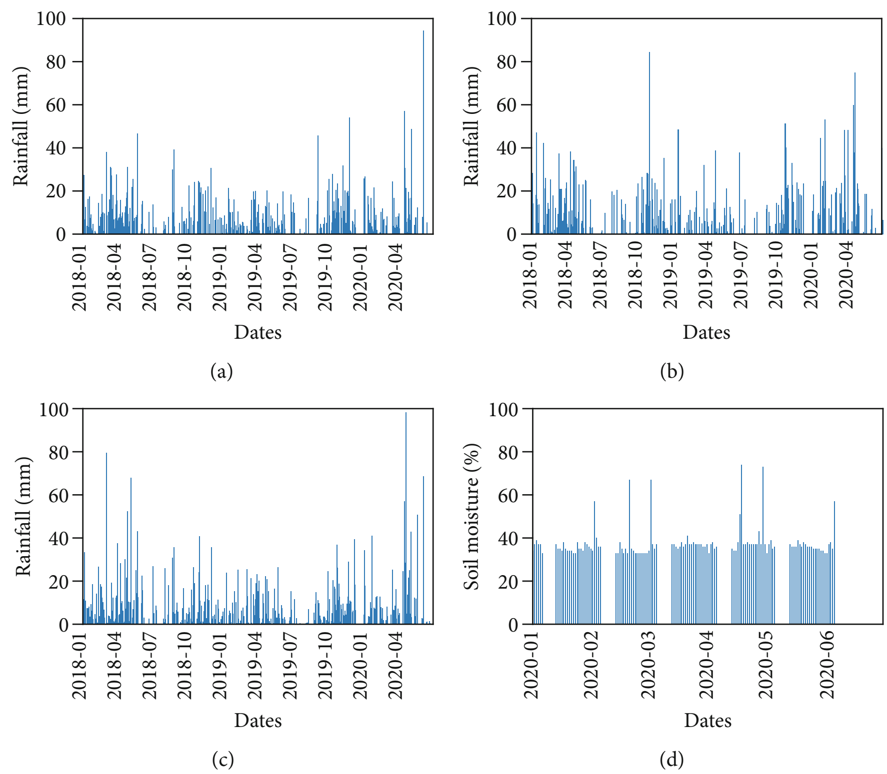

FIGURE 4: Past daily rainfall in the district of Gakenke from three rain gauge stations and one soil moisture station: (a) Janja, (b) Minazi, (c) Nemba, and (d) Rushashi soil moisture station.

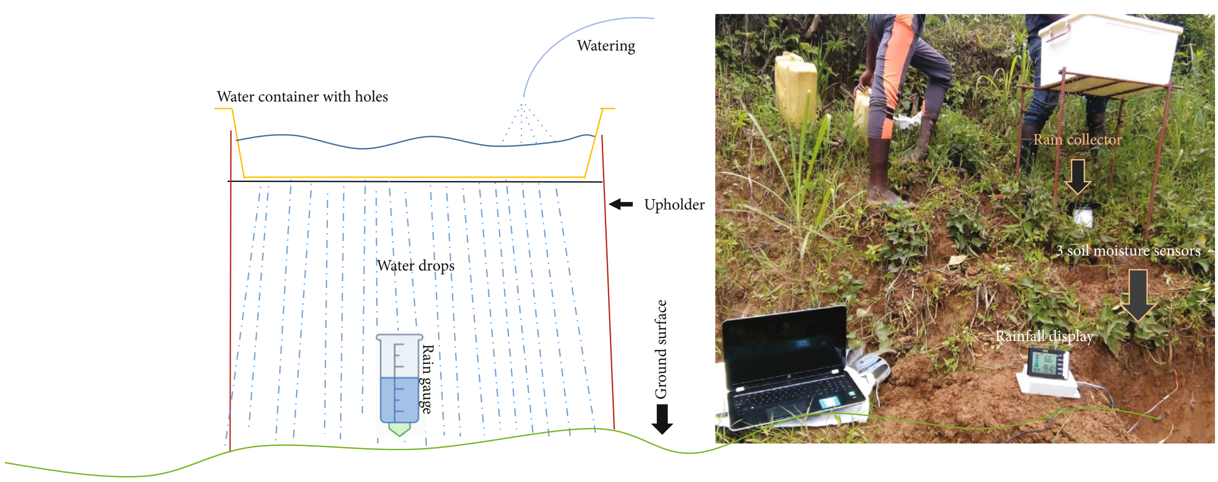

FIGURE 5: Rainfall simulator.

instance, the soil types on site SA were silty sand and sandy silt for SA1 and SA2, respectively. Likewise, site SE plots had elastic silt and lean clay for SE1 and SE2, respectively.

3.2. Simulation Results. The rainfall simulation was applied to the selected sites while recording the rainfall amount and soil moisture content (using a wireless rain gauge and three sensors, respectively) until the slope sliding (or crack) is observed or not. The activity took different durations depending on the site. The limit of rainfall simulation and duration was based on the rainfall events that induced landslides recently (Figure 4) or in the past [51]. Out of twenty-nine (29) experimental tests carried out on 11 plots, sixteen of them (55.5%) resulted in slope failure (or crack) as shown in Table 4.

As shown in Table 2, most sites are characterized by steep and very steep slopes, while the laboratory results indicate that lean clay and elastic silt are the most dominant soil classes in the sampled sites. The results in Table 4 show that landslides are possible in all categories of soil except in sandy lean clay with gravel, which is less represented among the

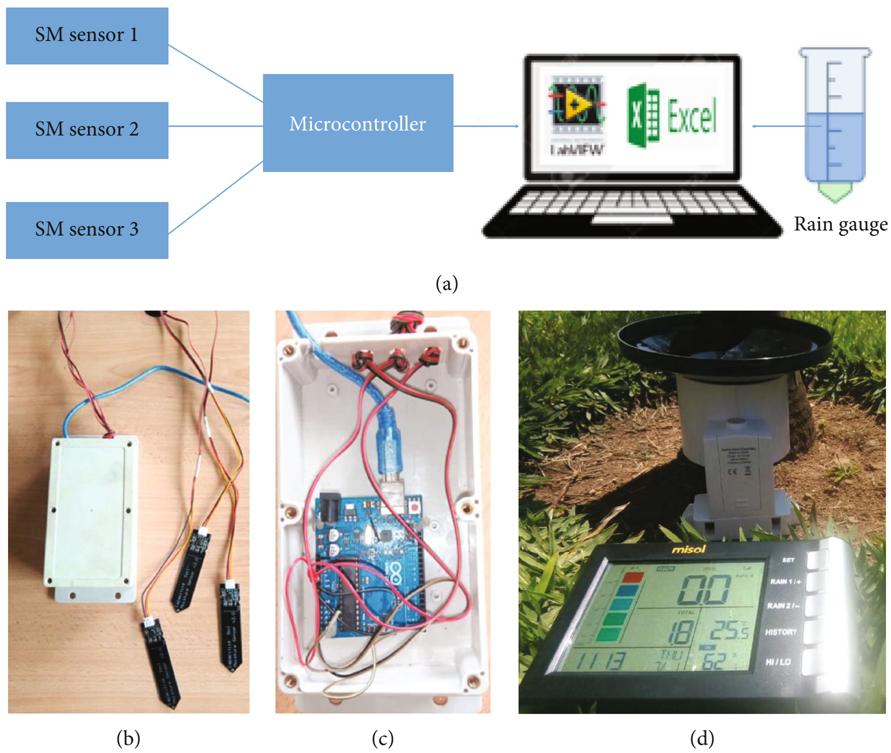

Figure 6: The block diagram and tool set of monitoring equipment: (a) block diagram, (b) sensor node box, (c) inside box, and (d) rain gauge with a digital display.

Table 1: In-ground depth placement of sensors.

Sensor	Site plot Depth placement (m)										
	SA1	SA2	SB	SC1	SC2	SC3	SD1	SD2	SD3	SE1	SE2
Sensor1	0.2	0.2	0.2	0.2	0.2	0.2	0.2	0.2	0.2	0.2	0.2
Sensor2	0.6	0.6	0.5	0.6	0.7	0.6	0.6	0.6	0.6	0.5	0.6
Sensor3	1.2	1.1	0.9	1.2	1.3	1.2	1.1	1.2	1.2	1	1.2

Table 2: Geotopographical characteristics of representative sites in the study area.

#	Site	Location (sector, cell, village)	Plot	Slope (°)	Land cover	Number of experiments
1	SA	Minazi, Raba, Ndegamire	SA1	26.4	Crops	3
2			SA2	35.3	Grass	2
3	SB	Mataba, Buyange, Gabiro	SB	41.8	Forest	2
4			SC1	47.2	Crops	3
5	SC	Rushashi, Mbogo, Gisanze	SC2	28.9	Crops	3
6			SC3	39.7	Grass	3
7			SD1	49.5	Forest	3
8	SD	Gekenke, Rusagara, Museke	SD2	31.3	Crops	3
9			SD3	29.8	Grass	3
10	SE	Nemba, Gisozi, Karukara	SE1	28.6	Forest	2
11			SE2	24.4	Crops	3

Table 3: Soil particle size and classification.

Sample	Gravel (%)	Sand (%)	Fines (%)	LL (%)	PL (%)	PI (%)	Group symbol	Group name
SA	1	52	48	37	25	12	SM	Silty sand and sandy silt
SB	24	24	53	41	23	18	CL	Sandy lean clay with gravel (SLC/G)
SC	0	10	90	42	25	17	CL	Lean clay
SD	0	3	97	66	37	29	MH	Elastic silt
SE	0	10	90	42	23	16	CL	Elastic silt and lean clay

Table 4: Observed simulation results.

Site	Soil type	Intensity (mm/h)/duration (hours, minutes)			Slope failure observed
		Test 1	Test 2	Test 3	(tests 1, 2, and 3)?
SA1	Silty sand	8.7/10 h15	8.7/12 h31	8.7/11 h45	Y, N, N
SA2	Sandy silt	8.7/11 h03	8.7/11 h26	NA	N, N, -
SB	SLC/G*	8.4/11 h33	8.4/12 h24	NA	N, N, -
SC1	Lean clay	9.4/10 h59	7.8/10 h27	7.8/10 h23	N, Y, Y
SC2	Lean clay	7.8/9 h04	7.8/8 h48	7.8/9 h40	Y, Y, Y
SC3	Lean clay	9.4/9 h54	7.8/9 h32	7.8/10 h37	Y, Y, N
SD1	Elastic silt	11.1/10 h37	7.2/11 h04	NA	N, N, -
SD2	Elastic silt	8.0/8 h41	7.2/11 h10	7.2/11 h21	Y, Y, N
SD3	Elastic silt	7.2/9 h36	7.2/11 h58	7.2/9 h37	Y, Y,Y
SE1	Elastic silt	10.8/11 h14	7.7/10 h14	NA	N, N, -
SE2	Lean clay	7.7/9 h11	7.7/8 h53	7.7/9 h28	Y, Y, Y

selected sites because the sampled sites are those that had landslides in the past.

3.3. Correlation between Rainfall and Soil Moisture Content. The shortest time used to simulate rainfall and provoke slope failure was 8 h41 at a rainfall rate (intensity) of 8 mm/h. This occurred on site SD2 where the land is covered by crops at the slope of 31.3°. The soil moisture at the point of failure was 82%, 92%, and 95% Figure 7(a). In addition to other factors, the short duration to simulate slope failure is linked to the antecedent rainfall indicated by high initial soil moisture.

The nearby site SD3 was selected with a different land cover (grass) and the slope inclination of 29.8°. The slope failure was observed for all three tests on this site after 9 h36, 11 h58, and 9 h37 with the rainfall intensity of 7.2 mm/h. This took different duration of rainfall simulation to induce landslide, but the soil moisture content recorded by the three sensors was above 80% for the top sensor, while the deeper sensors recorded more than 90% as shown in Figures 8(a)–8(c). Furthermore, three tests conducted on site SC2 resulted in slope failure. This site has a slope inclination of 28.9° and the land used for agriculture (covered by crops). The maximum soil moisture content attained by the three sensors was 98%, while the least value was 86% recorded by the top sensor (sensor1) during the first test (Figure 8). As shown in Table 4, the duration for each test was different due to factors like the initial soil moisture content (prior to the experiment) or other internal geological factors.

It was also observed that the two sites were characterized by lean clay. It indicates that this soil type is more susceptible to landslides because even on sites SC1 and SC3, two tests out of three resulted in slope failure. On site SC1, the rainfall simulation of 10 h59 and intensity of 9.4 mm/h did not result in slope failure, while the last two tests at the intensity of 7.8 mm/h resulted in slope failure after 10 h27 and 10 h23, respectively. On the other hand, the first two tests on site SC3 resulted in slope failure; however, the last did not even show up any sign of sliding. Figure 9 shows the correlation between rainfall and soil moisture content for the two sites.

The land covered by *Eragrostis spectabilis* type of grass has shown to be resistive to rainwater infiltration in the soil. This is the only one site among the grass-covered plots (Figures 10(a) and 10(b)) that did not show up any sign of slope failure for the first two tests. However, out of the three tests carried out on site SA1, only one slope failure was observed as shown in Table 4. Generally, the simulation took a long duration on sites that did not show up any sign of slope failure compared to those manifested landslides. The reason was to test the effect of daily total cumulative rainfall and duration on landslide occurrence. Figures 10(a)–10(f) show that the simulated cumulative rainfall was about 100 mm while the duration was more than 11 hours (Table 4).

The common feature for the sites that did not show up any sign of slope failure is the land cover, as they are covered by forest (Figures 10(c)–10(f)), whereas the other one is covered by grass (Figures 10(a) and 10(b)). Figures 10(a)–10(f) also indicate that, even though it required a long duration of

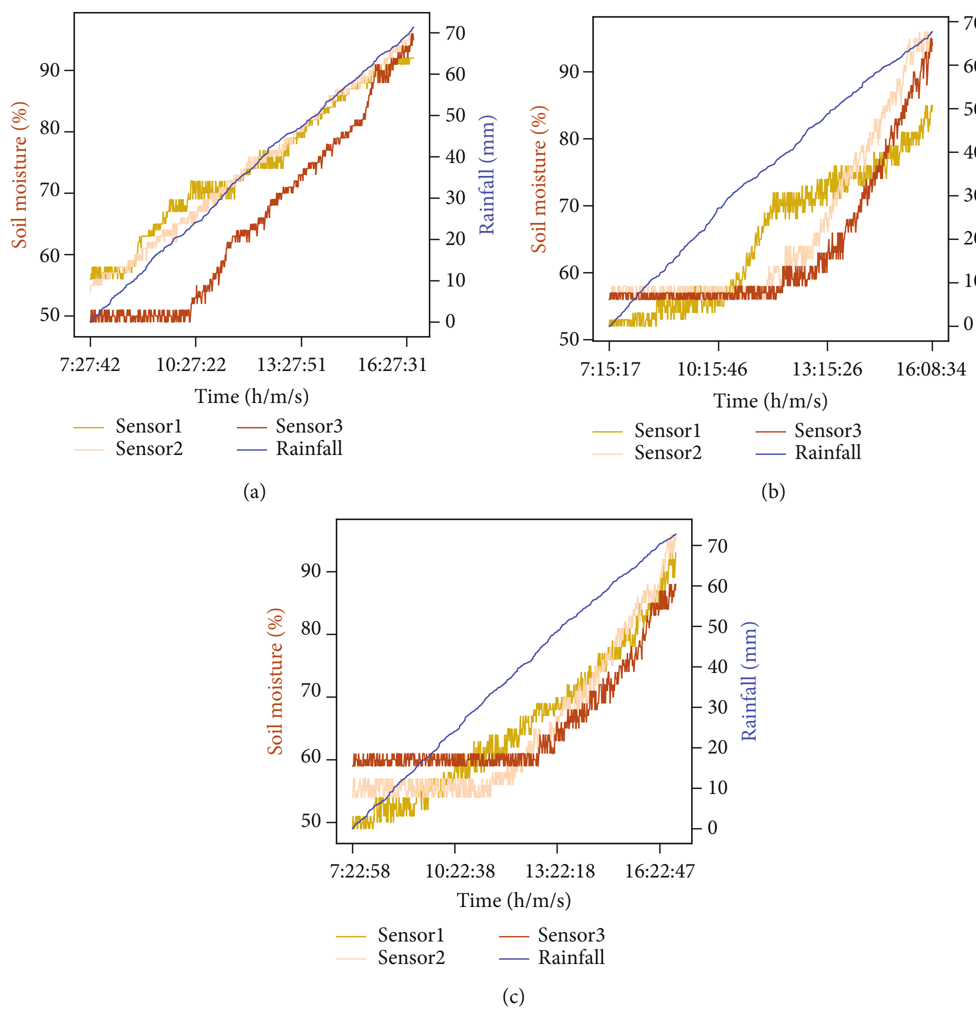

Figure 7: Variation of soil moisture content versus cumulative rainfall for three experimental tests on site SD2. The slope failure was observed for the first two tests (a, b) and did not occur during the last test (c).

simulation and the high amount of total rainfall, in some cases, the saturation level was less than 90% for the three sensors (Figures 10(a) and 10(c)–10(f)). This means that it requires a long time to make the soil fully saturated with the slopes covered by forest or protected by *Eragrostis spectabilis*.

From the figures above, the linear regression of both rainfall and soil moisture (Figure 11) is observed due to the continuous simulation of rainfall. In practice, this is not the case because rainfall is characterized by discontinuous events (with interevent periods) of different durations. Even though one-day rainfall can reach the values simulated in this study, the duration expands to many hours or else can be related to the previous rainfall events (antecedents). Hence, the use of soil moisture sensors for LEWS has a crucial importance because their data are informative to the antecedent rainfall.

The first two figures (Figures 11(a) and 11(b)) compare cropland and forestland, respectively. As shown by the slope lines of the best fit, the slope of 0.4 indicates that the infiltration rate was faster for crop land than that of forest land and got saturated before forest land (slope = 0.2). Likewise, in Figures 11(c) and 11(d), slope = 0.7 for cropland and 0.4 for forestland.

3.4. Slope Failure, Total Rainfall, and Intensity. The numerical analysis of rainfall intensity and duration (Table 4) shows that each site required different duration and rainfall intensity to initiate the slope failure. This shows that the thresholds for the two parameters are not identical and in case to be identical, all other factors should be identical which is almost impossible for different sites. As shown in Figure 12, there are many landslide cases that occurred when the rainfall intensity was lower than that of the highest intensity.

3.5. Slope Failure and Geoenvironmental Factors. It is not forthright to explain the correlation between hydrological and mechanical processes occurred before and during the slope failure. Although the triggering factors may be clearly known, the process itself is complex. Rainfall has been

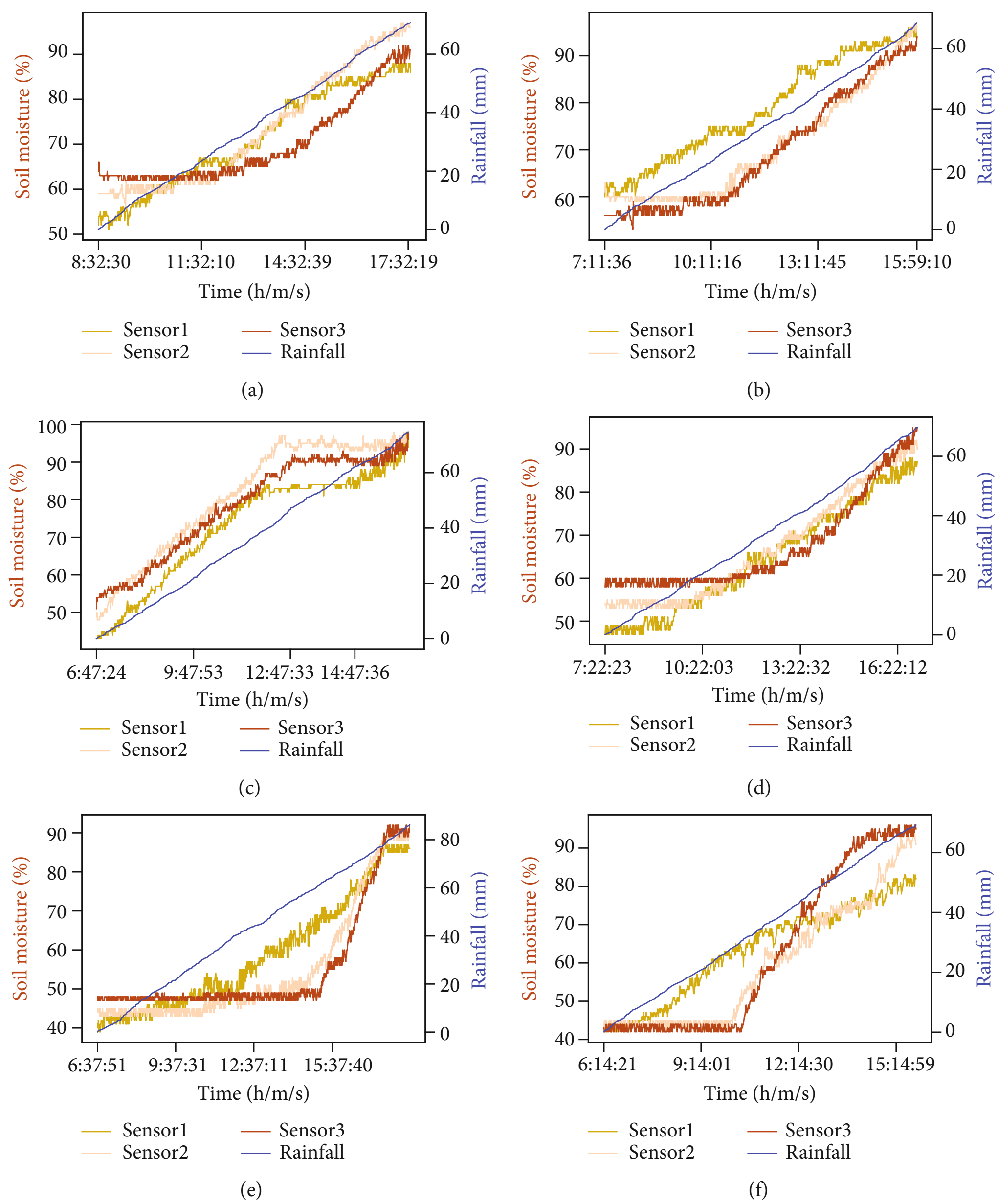

Figure 8: Variation of soil moisture content versus rainfall for three tests on site SC2 (a–c) and site SD3 (d–f).

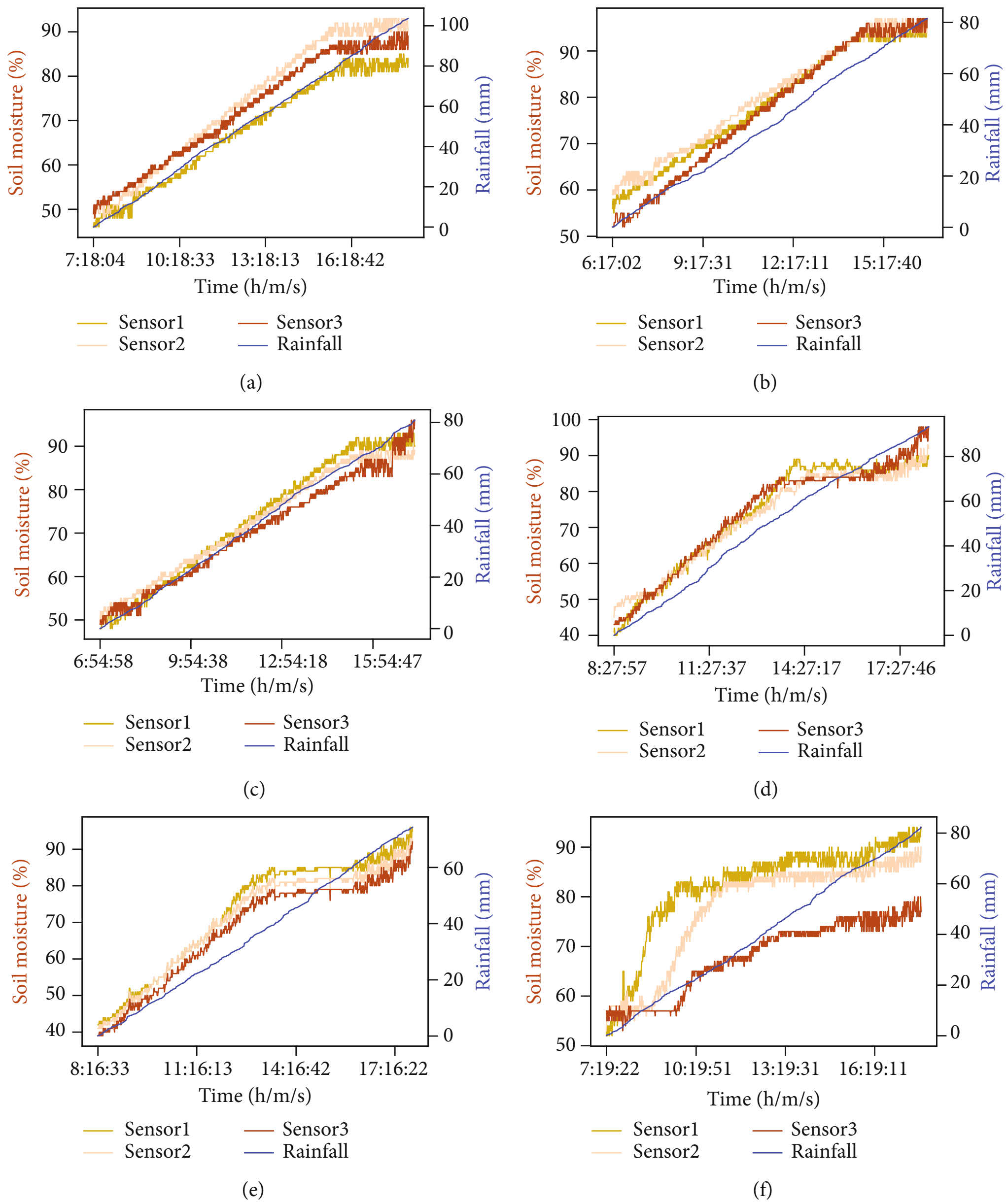

Figure 9: Variation of soil moisture content versus rainfall for three tests on site SC1 (a–c) and site SC3 (d–f).

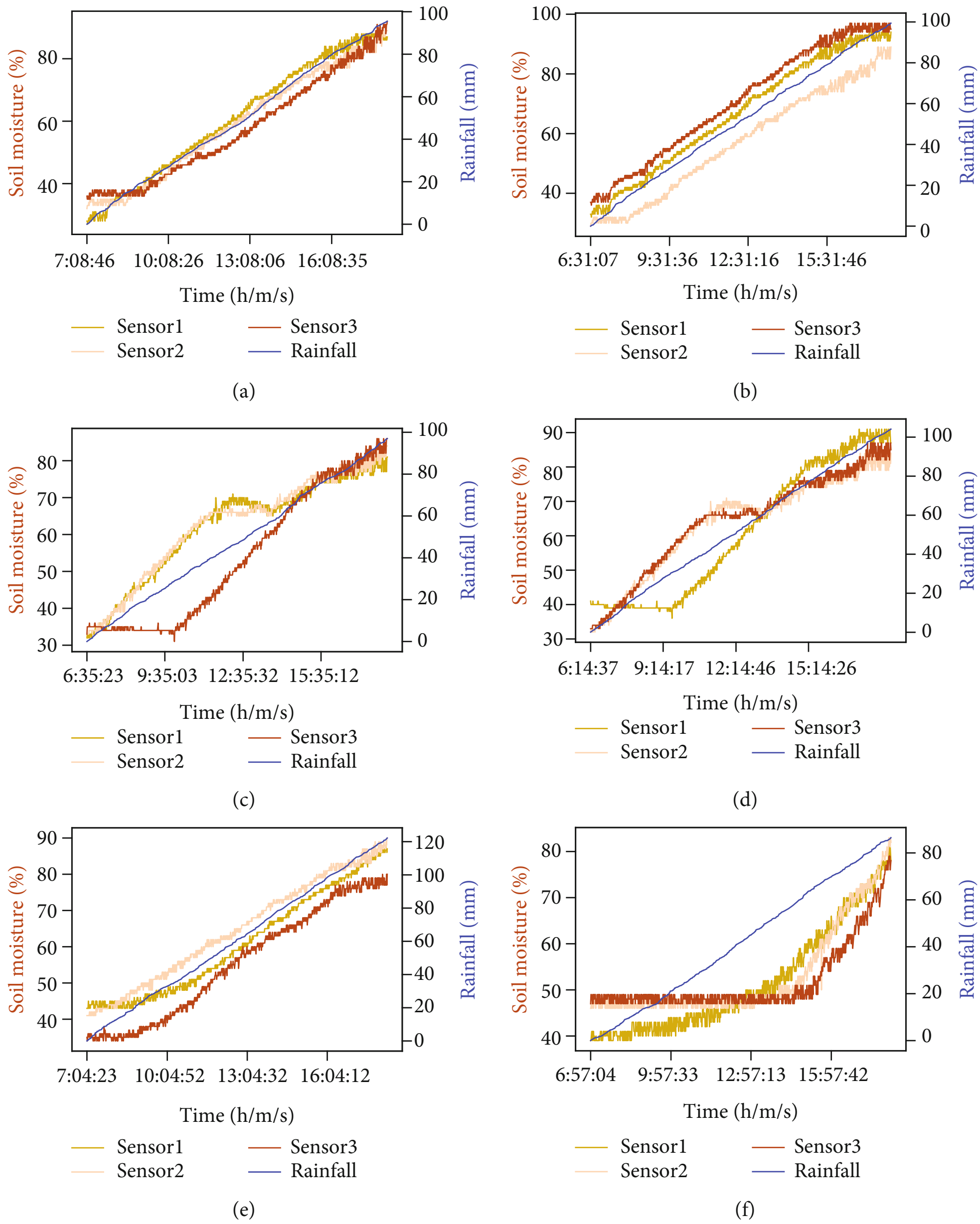

Figure 10: Variation of soil moisture content versus rainfall for sites SA2 (a, b), SB (c, d), and SE1 (e, f).

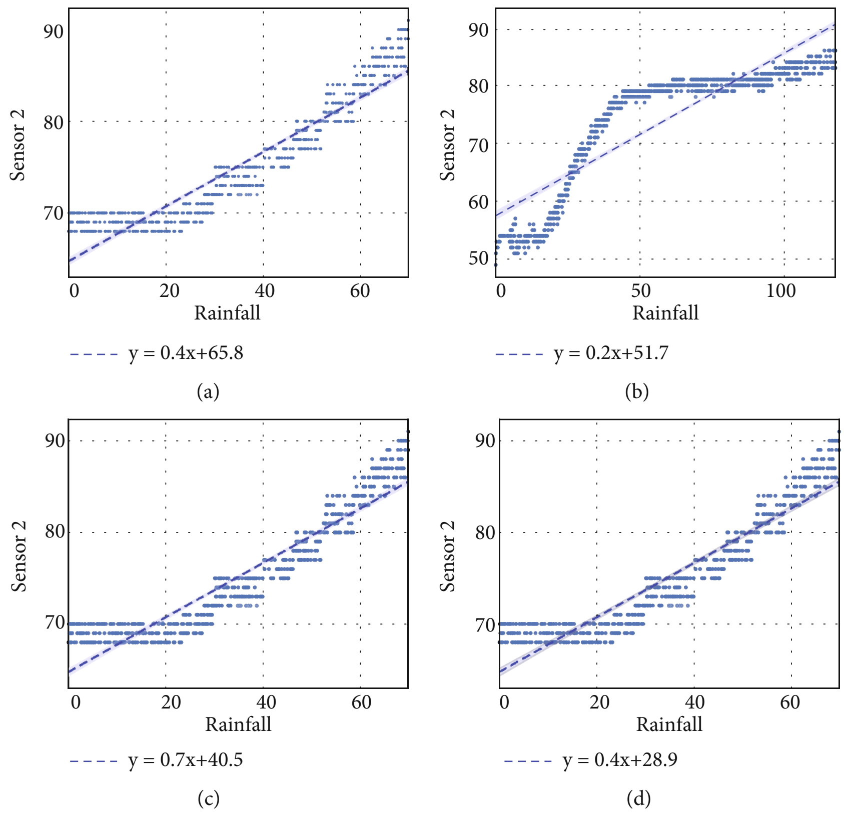

Figure 11: Rainfall vs. soil moisture: (a) SD2, (b) SD1, (c) SE2, and (d) SE1.

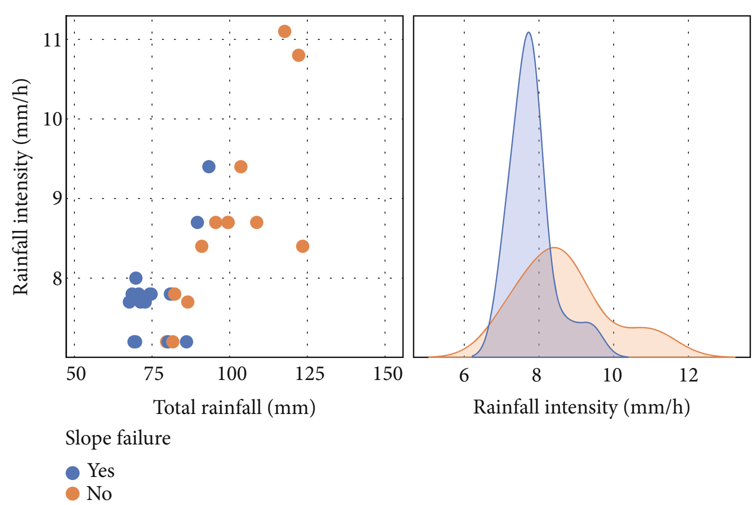

Figure 12: Slope failure vs. total rainfall and intensity.

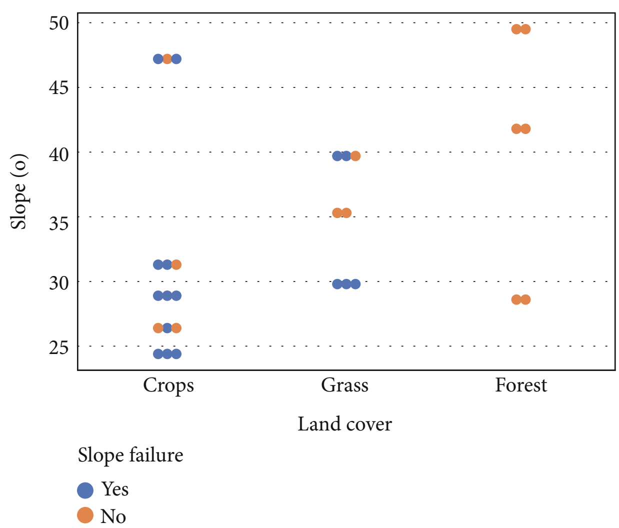

FIGURE 13: Slope failure vs. slope angle and land cover.

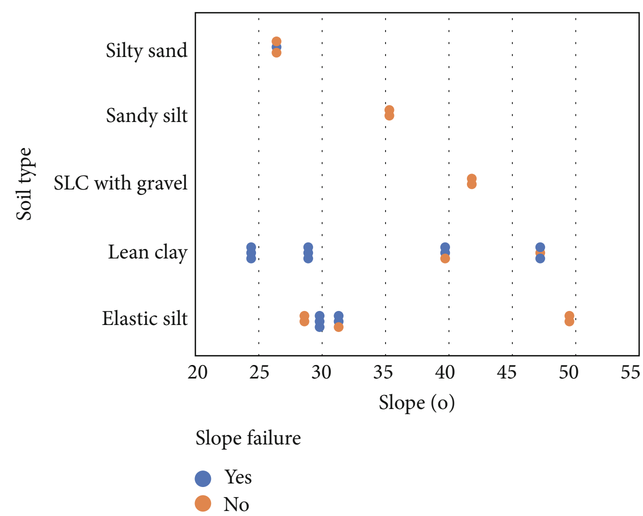

FIGURE 14: Slope failure vs. soil type.

discussed in the literature as external landslides' causing factor, but cannot be considered alone without the physical characteristic changes of the soil at the near stage of sliding. The rainfall intensity and duration that are the basis of the hazard prediction cannot be determined because their values cannot be the same in all susceptible areas characterized by different environment factors. Therefore, the field experimental analysis was crucial in this study to identify the threshold of both rainfall and soil water content leading to water-induced shallow landslides in different susceptible locations.

3.5.1. Landslides, Slope, and Land Cover. Although steep slopes are associated with landslide occurrence, in this study, it has been realized that very steep slopes (45° and higher) are not more prone to soil failure compared to the slopes < 45° and >25° (Figure 13). Two reasons that may justify this statement are as follows: (i) the most very steep slopes are characterized by sturdy rocks that make the slopes to be more stable; (ii) due to the high inclination, much rainfall water runs off instead of seeping into the soil compared to the moderate slopes. Apart from the slope inclination, the rainwater runoff also depends on the land cover and soil texture.

There was no landslide indication observed on all sites covered by forest, although long duration has been used for simulating rainfall (more than 11 hours). This is an indication of the role of forest cover to slope stability. In the study area, most of the forest areas are at the same time covered by *Eragrostis spectabilis*, which is a natural grass type found in the high mountains in the study area. Site SA2 was covered by this type of grass and did not show up any sign of slope failure.

3.5.2. Landslides, Slope, and Soil Types. Table 4 shows that the soil types in most of the sampled sites are lean clay and elastic silt. The results do not really indicate which soil type is more susceptible to landslides. But the sites were selected based on the historical background of landslide events, and the laboratory tests reveal the two types of soil that are most dominant among the sampled sites. It was noted that the sites (lean clay or elastic silt) that did not indicate any sign of slope failure are those that were protected by forest or have the high slope angle. Therefore, lean clay and elastic silt are the most affected by landslides compared to the other types of soil in the sampled sites (Figure 14).

3.6. Rainfall and Soil Moisture Thresholds. The maximum records of rainfall and soil moisture content from the experiments conducted in this study help us establish thresholds for both parameters in the specific sites (area of study). As stated earlier, three sensors were placed in various depths underground for knowing which one can better predict landslide incidence. Red dots in Figure 15 are more clustered in the right lower corner of the figures, indicating that the slope failure was observed when sensor 1 recorded greater than 80% and 90% for sensors placed deeper (sensor 2 and sensor 3). The minimum rainfall inducing slope failure as indicated by the same figure is around 70 mm. Therefore, we can conclude that these values can be used for local LEWS. On the other hand, rainfall can be used for regional LEWS as it is not possible identifying the soil moisture content at each and every site. Even though a rainfall of more than 100 mm did not cause slope failure according to this study, such daily rainfall depth is also dangerous as the increased rainwater runoff may cause floods, which can also depend on different factors (which is out of the scope of this study). It was also noted that the sites that did not experience any slope failure are those lands covered by forest or types of grass that reinforce the shear strength of the topsoil. But under normal circumstances, a one-day rainfall of more than 70 mm should be taken into consideration for early warning systems by considering the antecedent rainfall and other geofactors.

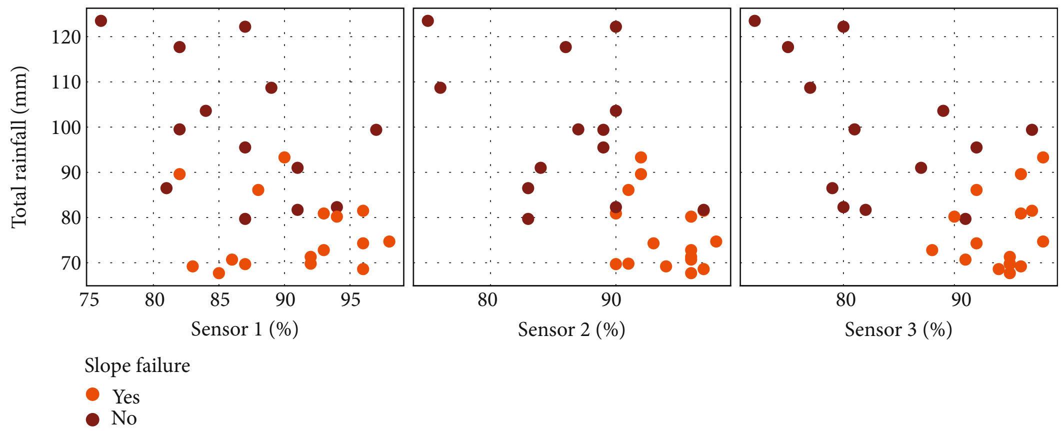

Figure 15: Rainfall and soil moisture thresholds.

As mentioned before, most of the nonlandslide cases in this study are related to the forestland cover that persists to rainwater penetration and requires more rainfall duration. This explains the reason of having less incidences with high total rainfall as shown in Figure 15. It was also explained that rainwater runoff was much more in very steep slopes than steep or medium slopes. Hence, the probability of slope failure increases with soil permeability which is dependent on the soil texture, rainfall intensity, and duration.

4. Conclusions

In this study, field experiments were conducted at various sites selected surrounding the areas that had landslide events in the past. The study consisted of the measurement of rainfall and soil water content using a rain gauge and soil moisture sensors. The site sample profile considered different parameters such as slopes, angles, soil texture, soil depths, and land coverage.

The experimental results show that rainfall triggers slope failure, and the total rainfall amount inducing this hazard depends on various other parameters. Rainfall alone cannot be considered as a parameter to predict slope failure, and it has an implication on the hydrological properties of the soil. In addition, the level of soil water content at the near stage of slope failure differs from one site to another depending on the internal and external features. In general, steep slopes are more susceptible to shallow landslide incidence compared to the very steep slopes. Furthermore, we noticed that land coverage plays an important role in the slope stability due to more time required for saturation of land covered by natural grass or forest than that covered by plants. This is because the vegetation adjusts the hydrological equilibrium of the involved location through the evapotranspiration process, whereas roots add some reinforcement by increasing soil shear strength [81–82] and the degree of slope stabilization varies according to the vegetation [83–86].

According to the experimental results in this study, the following major insights are taken: (i) a common threshold for rainfall intensity or soil water content could not be derived for LEWS. Instead, location-specific thresholds have to be determined using empirical models. Then, the identified threshold can specifically be used to predict the slope failure in areas with identical (or almost) geomorphological features. (ii) The daily rainfall of more than 70 mm and soil water content of more than 90% may lead to the landslide hazard depending on other geofactors in specific sites. (iii) The thresholds found in this study can be used in designing local LEWS for areas having almost similar environmental covariates or soil forming factors, especially for cut slopes (manmade slopes) such as in-house plots or roads. (iv) This study proposes similar experiments to be conducted at various sites to derive site-specific thresholds to feed in to local IoT-based LEWS as the parameters differ from one zone to another.

4.1. Future Work. In the next stage of our research, we expect to perform the environmental and soil analysis during the development of the prototype for LEWS.

Data Availability

All data used to achieve the objectives of this study are available online (ACEIoT portal at University of Rwanda). The uniform resource locator (URL) is found under reference [74].

Conflicts of Interest

The authors declare no conflict of interest.

Acknowledgments

The authors recognize and appreciate the inputs and contributions of government organs, specifically Rwanda Meteorology Agency, Ministry in Charge of Emergency Management, and the administration of Gakenke District. The support of the Soil Mechanics Laboratory in the Department of Civil, Environmental and Geomatic Engineering, and the Centre for Geographic Information System (CGIS), under the University of Rwanda is highly recognized and appreciated. This research was under the support of the African Centre of Excellence in the Internet of Things

(ACEIoT) running under the University of Rwanda, College of Science and Technology (UR-CST), and the APC was funded by the same centre.

References

[1] H. An, T. T. Viet, G. Lee et al., "Development of time-variant landslide-prediction software considering three-dimensional subsurface unsaturated flow," *Environmental Modelling & Software*, vol. 85, pp. 172–183, 2016.

[2] S. Jeong, K. Lee, J. Kim, and Y. Kim, "Analysis of rainfall-induced landslide on unsaturated soil slopes," *Sustainability.*, vol. 9, no. 7, pp. 1220–1280, 2017.

[3] A. Hidalgo, M. P. Obando, and M. P. Obando, "Effect of the rainfall infiltration processes on the landslide hazard assessment of unsaturated soils in tropical mountainous regions," in *Engineering and Mathematical Topics in Rainfall*, IntechOpen, 2018.

[4] J. B. Nsengiyumva, G. Luo, L. Nahayo, X. Huang, and P. Cai, "Landslide susceptibility assessment using spatial multi-criteria evaluation model in Rwanda," *International Journal of Environmental Research and Public Health*, vol. 15, no. 2, p. 243, 2018.

[5] MINEMA, *Minstry of Disaster Management and Refugee Affairs, Annual Report 2016 Desaster Response and Recovery Unity*, Kigali, 2016http://minema.gov.rw/fileadmin/user_upload/ANNUAL_DISASTER_EFFECTS_REPORT_2016.pdf.

[6] MINEMA, *Republic of Rwanda Ministry in Charge of Emergency Management*, Kigali, 2018http://minema.gov.rw/fileadmin/user_upload/Annual_Disaster_effects_Report_2018.pdf.

[7] *Republic of Rwanda Ministry of Emergence Management*, 2018, https://www.minema.gov.rw/fileadmin/user_upload/Minema/Publications/Contingency_Plans/Contingency_Plan_for_Floods_nd_Landslides.pdf.

[8] *Republic of Rwanda Ministry in Charge of Emergence Management*http://minema.gov.rw/uploads/tx_download/National_Risk_Atlas_of_Rwanda_electronic_version.pdf.

[9] A. J. Posner and K. P. Georgakakos, "Soil moisture and precipitation thresholds for real-time landslide prediction in El Salvador," *Landslides*, vol. 12, no. 6, pp. 1179–1196, 2015.

[10] M. B. Kenanoğlu, "Effect of unsaturated soil properties on the intensity- duration threshold for rainfall triggered landslides," *Teknik Dergi*, vol. 30, no. 2, pp. 9009–9028, 2019.

[11] H. F. Yeh and Y. J. Tsai, "Analyzing the effect of soil hydraulic conductivity anisotropy on slope stability using a coupled hydromechanical framework," *Water*, vol. 10, no. 7, p. 905, 2018.

[12] M. G. Persichillo, M. Bordoni, M. Cavalli, S. Crema, and C. Meisina, "The role of human activities on sediment connectivity of shallow landslides," *CATENA*, vol. 160, pp. 261–274, 2018.

[13] A. G. Li, Z. Q. Yue, L. G. Tham, C. F. Lee, and K. T. Law, "Field-monitored variations of soil moisture and matric suction in a saprolite slope," *Canadian Geotechnical Journal*, vol. 42, no. 1, pp. 13–26, 2005.

[14] S. Alsubal, N. b. Sapari, S. H. Indra, and M. A. M. A.-B. Harahap, "A review on mechanism of rainwater in triggering landslide," *IOP Conference Series: Materials Science and Engineering*, vol. 513, p. 12009, 2019.

[15] V.-F. Chiorean, "Determination of matric suction and saturation degree for unsaturated soils, comparative study - numerical method versus analytical method," *IOP Conference Series: Materials Science and Engineering*, vol. 245, p. 032074, 2017.

[16] M. Y. Fattah, A. H. Al-lami, and M. Ahmed, "Effect of initial water content on the properties of compacted expansive unsaturated soil," *Journal of Engineering*, vol. 21, no. 3, 2015.

[17] N. Lu, M. Asce, W. J. Likos, and M. Asce, "Suction stress characteristic curve for unsaturated soil," *Journal of Geotechnical and Geoenvironmental Engineering*, vol. 132, no. 2, pp. 131–142, 2006.

[18] C. W. W. Ng and B. Menzies, *Advanced Unsaturated Soil Mechanics and Engineering*, Taylor & Francis, New York, USA, 2007.

[19] R. Paul, *Field Measurement of Soil Suction Using Thermal Conductivity Matric Potential Sensors*, University of Saskatchewan, 1988.

[20] L. Ontrasio and L. Schilirò, "Inferences on modeling rainfall-induced shallow landslides from experimental observations on stratified soils," *Italian Journal of Engineering Geology and Environment*, vol. 18, no. 2, 2019.

[21] M. Jakob and I. T. O. I. T. Simpson, "A regional real-time debris-flow warning system for the District of North Vancouver, Canada," *Landslides*, vol. 9, no. 2, pp. 165–178, 2012.

[22] M. Hong, J. Kim, and S. Jeong, "Rainfall intensity-duration thresholds for landslide prediction in South Korea by considering the effects of antecedent rainfall," *Landslides*, vol. 15, no. 3, pp. 523–534, 2018.

[23] L. Montrasio and R. Valentino, "Experimental analysis and modelling of shallow landslides," *Landslides*, vol. 4, no. 3, pp. 291–296, 2007.

[24] P. Lumb, "Effect of rainstorms on slope stability," in *Symposium on Hong Kong Soils*, pp. 73–87, Local Property & Printing Company, Limited, 1962.

[25] P. Lumb, "Slope failures in Hong Kong," *The Quarterly Journal of Engineering Geology*, vol. 8, no. 1, pp. 31–65, 1975.

[26] P. Brand and E. W. Premchitt, "Relationship between rainfall and landslides in Hong Kong," in *4th International Symposium on Landslides*, pp. 377–384, Toronto, Canada, Canadian Geotechnical Society, 1984.

[27] P. J. Finlay, R. Fell, and P. K. Maguire, "The relationship between the probability of landslide occurrence and rainfall," *Canadian Geotechnical Journal*, vol. 34, no. 6, pp. 811–824, 1997.

[28] F. C. Dai and C. F. Lee, "Frequency-volume relation and prediction of rainfall-induced landslides," *Engineering Geology*, vol. 59, no. 3–4, pp. 253–266, 2001.

[29] B. T. Pham, B. Pradhan, D. Tien Bui, I. Prakash, and M. B. Dholakia, "A comparative study of different machine learning methods for landslide susceptibility assessment: a case study of Uttarakhand area (India)," *Environmental Modelling & Software*, vol. 84, pp. 240–250, 2016.

[30] M. Marjanović, M. Krautblatter, B. Abolmasov, U. Đurić, C. Sandić, and V. Nikolić, "The rainfall-induced landsliding in Western Serbia: a temporal prediction approach using Decision Tree technique," *Engineering Geology*, vol. 232, pp. 147–159, 2018.

[31] H. Hong, H. Shahabi, A. Shirzadi et al., "Landslide susceptibility assessment at the Wuning area, China: a comparison between multi-criteria decision making, bivariate statistical

and machine learning methods," *Natural Hazards*, vol. 96, no. 1, pp. 173–212, 2019.

[32] X. Sun, J. Chen, Y. Bao, X. Han, J. Zhan, and W. Peng, "Landslide susceptibility mapping using logistic regression analysis along the Jinsha river and its tributaries close to Derong and Deqin County, southwestern China," *ISPRS International Journal of Geo-Information*, vol. 7, no. 11, pp. 429–438, 2018.

[33] K. Martinović, K. Gavin, C. Reale, and C. Mangan, "Rainfall thresholds as a landslide indicator for engineered slopes on the Irish Rail network," *Geomorphology*, vol. 306, pp. 40–50, 2018.

[34] S. Peruccacci, M. T. Brunetti, S. L. Gariano, M. Melillo, M. Rossi, and F. Guzzetti, "Rainfall thresholds for possible landslide occurrence in Italy," *Geomorphology*, vol. 290, pp. 39–57, 2017.

[35] D. P. Kanungo and S. Sharma, "Rainfall thresholds for prediction of shallow landslides around Chamoli-Joshimath region, Garhwal Himalayas, India," *Landslides*, vol. 11, no. 4, pp. 629–638, 2014.

[36] L. Montrasio, L. Schilirò, and A. Terrone, "Physical and numerical modelling of shallow landslides," *Landslides*, vol. 13, no. 5, pp. 873–883, 2015.

[37] M. Ahmadi-adli, N. K. Toker, and N. Huvaj, "Prediction of seepage and slope stability in a flume test and an experimental field case," *Procedia Earth and Planetary Science*, vol. 9, pp. 189–194, 2014.

[38] Y. Chen, "Soil–water retention curves derived as a function of soil dry density," *GeoHazards*, vol. 1, no. 1, pp. 3–19, 2018.

[39] A. Saha, S. Sekharan, and U. Manna, "Evaluation of capacitance sensor for suction measurement in silty clay loam," *Geotechnical and Geological Engineering*, vol. 3, 2020.

[40] S. Chersich, "A simplified approach to assess the soil saturation degree and stability of a representative slope affected by shallow landslides in Oltrepò Pavese (Italy)," *Geosciences*, vol. 8, no. 12, p. 472, 2018.

[41] A. Farouk, L. Lamboj, and J. Kos, "A numerical model to predict matric suction inside unsaturated soils," *Acta Polytechnica*, vol. 44, no. 4, 2004.

[42] J. Ho and K. T. Lee, "Performance evaluation of a physically based model for shallow landslide prediction," *Landslides*, vol. 14, no. 3, pp. 961–980, 2016.

[43] M. T. Abraham, D. Pothuraju, and N. Satyam, "Rainfall thresholds for prediction of landslides in Idukki, India: an empirical approach," *Water*, vol. 11, no. 10, p. 2113, 2019.

[44] A. Rosi, T. Peternel, M. Jemec-Auflič, M. Komac, S. Segoni, and N. Casagli, "Rainfall thresholds for rainfall-induced landslides in Slovenia," *Landslides*, vol. 13, no. 6, pp. 1571–1577, 2016.

[45] G. Martelloni, S. Segoni, R. Fanti, and F. Catani, "Rainfall thresholds for the forecasting of landslide occurrence at regional scale," *Landslides*, vol. 9, no. 4, pp. 485–495, 2012.

[46] M. T. Abraham, N. Satyam, S. Kushal, A. Rosi, B. Pradhan, and S. Segoni, "Rainfall threshold estimation and landslide forecasting for Kalimpong, India using SIGMA model," *Water*, vol. 12, no. 4, 2020.

[47] G. Jordanova, S. L. Gariano, M. Melillo, S. Peruccacci, M. T. Brunetti, and M. J. Auflič, "Determination of empirical rainfall thresholds for shallow landslides in Slovenia using an automatic tool," *Water*, vol. 12, no. 5, p. 1449, 2020.

[48] L. Piciullo, S. L. Gariano, M. Melillo et al., "Definition and performance of a threshold-based regional early warning model for rainfall-induced landslides," *Landslides*, vol. 14, no. 3, pp. 995–1008, 2017.

[49] M. Melillo, M. T. Brunetti, S. Peruccacci, S. L. Gariano, A. Roccati, and F. Guzzetti, "A tool for the automatic calculation of rainfall thresholds for landslide occurrence," *Environmental Modelling & Software*, vol. 105, pp. 230–243, 2018.

[50] Y. Zhao, Y. Li, L. Zhang, and Q. Wang, "Groundwater level prediction of landslide based on classification and regression tree," *Geodesy and Geodynamics*, vol. 7, no. 5, pp. 348–355, 2016.

[51] M. Kuradusenge, S. Kumaran, and M. Zennaro, "Rainfall-induced landslide prediction using machine learning models: the case of Ngororero District, Rwanda," *International Journal of Environmental Research and Public Health*, vol. 17, no. 11, p. 4147, 2020.

[52] J. Uwihirwe, M. Hrachowitz, and T. A. Bogaard, "Landslide precipitation thresholds in Rwanda," *Landslides*, vol. 17, no. 10, pp. 2469–2481, 2020.

[53] A. Dikshit, R. Sarkar, B. Pradhan, S. Acharya, and K. Dorji, "Estimating rainfall thresholds for landslide occurrence in the Bhutan Himalayas," *Water*, vol. 11, no. 8, p. 1616, 2019.

[54] E. Monsieurs, O. Dewitte, and A. Demoulin, "A susceptibility-based rainfall threshold approach for landslide occurrence," *Natural Hazards and Earth System Sciences*, vol. 19, pp. 775–789, 2019.

[55] A. Terzis, A. Anandarajah, K. Moore, and I.-J. Wang, "Slip surface localization in wireless sensor networks for landslide prediction," in *Proceedings of the fifth international conference on Information processing in sensor networks - IPSN '06*, ACM: New York, 2006.

[56] A. Dikshit, N. Satyam, B. Pradhan, and S. Kushal, "Estimating rainfall threshold and temporal probability for landslide occurrences in Darjeeling Himalayas," *Geosciences Journal*, vol. 24, no. 2, pp. 225–233, 2020.

[57] L. Schilirò, G. P. Djueyep, C. Esposito, and G. S. Mugnozza, "The role of initial soil conditions in shallow landslide triggering: insights from physically based approaches," *Geofluids*, vol. 2019, Article ID 2453786, 14 pages, 2019.

[58] T. W. J. Van Asch, B. Yu, and W. Hu, "The development of a 1-D integrated hydro-mechanical model based on flume tests to unravel different hydrological triggering processes of debris flows," *Water*, vol. 10, no. 7, p. 950, 2018.

[59] G. District, *Republic of Rwanda Gakenke District Environmental and Social Management Plan (ESMP) Quality Basic Education for Human Capital Development QBE*, 2019.

[60] D. Karemera, *Landslide Victims Laid to Rest | The New Times | Rwanda*https://www.newtimes.co.rw/section/read/199730.

[61] R. Umurengezi, *Gakenke: Family of Eight That Perished in Landslide Buried*https://www.newtimes.co.rw/news/gakenke-family-eight-perished-landslide-buried.

[62] *Republic of Rwanda Gakenke District*, 2019, https://www.mineduc.gov.rw/fileadmin/user_upload/Mineduc/SPIU_Documents/ESMP/Gakenke/GAKENKE_DISTRICT-_ESMP_FOR_CONSTRUCTION_OF_CLASSROOMS_AND_LATRINES_SUB-PROJECTS_UNDER_RWANDA_QBE-HCD_PROJECT.pdf.

[63] G. G. Benineza, I. Rwabudandi, and M. J. Nyiransabimana, "Landslides hazards assessment using geographic information system and remote sensing: Gakenke District," *IOP Conference Series: Earth and Environmental Science*, vol. 389, no. 1, p. 012015, 2019.

[64] M. J. Claude, N. V. Martin, M. Abias et al., "Mapping landslide susceptibility and analyzing its impact on community livelihoods in Gakenke District, Northern Rwanda," *Journal of Geoscience and Environment Protection*, vol. 8, no. 5, pp. 41–55, 2020.

[65] G. T. Harilal, D. Madhu, M. V. Ramesh, and D. Pullarkatt, "Towards establishing rainfall thresholds for a real-time landslide early warning system in Sikkim, India," *Landslides*, vol. 16, no. 12, pp. 2395–2408, 2019.

[66] R. Sehler, J. Li, and H. Ye, "Investigating relationship between soil moisture and precipitation globally using remote sensing observations," *Journal of Contemporary Water Research & Education*, vol. 168, no. 1, pp. 106–118, 2019.

[67] Y. Zhang, J. Liu, X. Xu, Y. Tian, Y. Li, and Q. Gao, "The response of soil moisture content to rainfall events in semi-arid area of Inner Mongolia," *Procedia Environmental Sciences*, vol. 2, pp. 1970–1978, 2010.

[68] M. Fereidoon, M. Koch, and L. Brocca, "Predicting rainfall and runoff through satellite soil moisture data and SWAT modelling for a poorly gauged basin in Iran," *Water*, vol. 11, no. 3, 2019.

[69] B. Zhao, Q. Dai, D. Han et al., "Estimation of soil moisture using modified antecedent precipitation index with application in landslide predictions," *Landslides*, vol. 16, no. 12, pp. 2381–2393, 2019.

[70] A. Wicki, P. Lehmann, C. Hauck, S. I. Seneviratne, P. Waldner, and M. Stähli, "Assessing the potential of soil moisture measurements for regional landslide early warning," *Landslides*, vol. 17, no. 8, pp. 1881–1896, 2020.

[71] *Centre for GIS and Remote Sensing (CGIS) - College of Sciences and Technology*https://cst.ur.ac.rw/Centre-for-GIS-and-Remote-Sensing-CGIS.

[72] *Explore Maps - Rwanda Geoportal*http://geoportal.rlma.rw/maps/?limit=100&offset=0.

[73] G. Crosta, "Regionalization of rainfall thresholds: an aid to landslide hazard evaluation," *Environmental Geology*, vol. 35, no. 2–3, pp. 131–145, 1998.

[74] *Rainfall and Soil Moisture Data*, 2021, https://aceiot.ur.ac.rw/IMG/xlsx/sm-rf-data_allsites_martink.xlsx.

Hindawi
Geofluids
Volume 2021, Article ID 5510566, 9 pages
https://doi.org/10.1155/2021/5510566

Research Article

A Case Study on the Gas Drainage Optimization Based on the Effective Borehole Spacing in Sima Coal Mine

Ming Ji[1] **Zhong-guang Sun**[2,3,4] **and Wei Sun**[3]

[1]*Key Laboratory of Deep Coal Resource Mining, Ministry of Education of China and China University of Mining & Technology, Xuzhou 221116, China*
[2]*State Key Laboratory of The Gas Disaster Detecting, Preventing and Emergency Controlling, Chongqing 400037, China*
[3]*China Coal Technology and Engineering Group Chongqing Research Institute, Chongqing 400039, China*
[4]*State Key Laboratory for the Coal Mine Disaster Dynamics and Controls, Chongqing University, Chongqing 400044, China*

Correspondence should be addressed to Ming Ji; jiming@cumt.edu.cn

Received 26 February 2021; Revised 15 June 2021; Accepted 14 August 2021; Published 8 September 2021

Academic Editor: Yi Xue

Based on the dynamic expressions of permeability and porosity of the coal seam derived in the paper, a multiphysical field coupling numerical model of gas migration under the interaction of stress field and seepage field was established. The gas drainage project #3 Coal Seam operated by Sima Coal Industry Co., Ltd., was selected as the study object. Taking different drainage time periods in various positions of drainage holes into consideration, combined with the advance situation of the 1207 working face in the Sima Coal Mine, a mixed layout gas drainage scheme featured with the effective borehole spacing was obtained through the COMSOL multiphysics simulation. In addition, a series of field industrial tests were performed to validate the research result, revealing that comprehensively considering the extraction time of coal and optimizing the layout of extraction boreholes can effectively improve the engineering economic benefits.

1. Introduction

Coal seam gas drainage is one of the important measures to control mine gas [1, 2] However, a majority of researches take the effective drainage radius as the basis of drainage hole layout, overlooking the influences of the superimposed drainage and fracture expansion without taking the influence of different drainage times of drainage holes in different positions of the coal seam into account. Additionally, most researches adopt a single borehole layout, which often causes some common issues such as a waste of resource, uneven gas drainage, and failure of meeting relevant standards. Many existing studies fail to consider the establishment of a multiphysical field coupling model of gas migration under the interaction of the stress field and seepage field and overlook the dynamic nature of the permeability and porosity of the coal seam. All the aforementioned which are lacking in previous studies have made it necessary to conduct an in-depth optimization research on coal seam gas drainage.

In this paper, the gas drainage optimization of #3 Coal Seam in Sima Coal Industry Co., Ltd., of Lu'an Group was studied. Based on the changes of coal seam stress, gas pressure, and gas adsorption and desorption which tend to exert an important impact on the coal seam permeability and porosity, the dynamic expressions of coal seam permeability and porosity were deduced which was used to build the numerical model of a multiphysical field coupling for migration under the interaction of stress field and seepage field. Additionally, taking different drainage time periods in various positions of drainage holes into consideration, combined with the advance situation of the 1207 working face in the Sima Coal Mine, a mixed layout gas drainage scheme featured with the effective borehole spacing was obtained by the COMSOL multiphysics simulation. In addition, a series of field industrial tests were performed for the purpose of validating the research.

2. Gas Solid Coupling Analysis of Coal Seam Gas Migration

2.1. The Migration Law of Coal Seam Gas. Two types of gas flow in coal seams have been identified including the diffusion flow and the laminar flow targeting different types of coal seams [3–5]. Generally speaking, in the coal seam with a microporous structure or low permeability, the diffusion flow plays a critical role while in the coal seam with microporous structure or high permeability, the laminar flow dominates [6–8]. In this study, the gas flow in the process of drainage is treated as laminar flow, following Darcy's law.

A number of factors can affect the migration of coal seam gas, such as geological conditions of storage, occurrence of coal seam, mechanical properties of coal and rock, permeability and porosity of coal seam, gas adsorption capacity of coal seam, and gas pressure. Among those factors, gas pressure, gas adsorption capacity of coal seam, porosity, and permeability of coal seam are considered as the primary ones. Gas pressure is the driving force of gas migration while the gas adsorption capacity of coal seam decides the capacity of the coal seam to store gas. Meanwhile, the porosity and permeability are the indicators of smooth gas migration in the coal seam [9–11].

The gas pressure of the #3 Coal Seam in Sima mine was measured at 0.31 MPa which was used as the basic gas pressure of this study, despite that the gas pressure measured stayed below the critical value of 0.74 MPa. The gas adsorption constants a and b of the #3 Coal Seam were identified at about 17.52 $m^{3/}t$ and 0.75 MPa^{-1}, separately, which were considered low, indicating that the gas adsorption capacity of the #3 Coal Seam was weak. During the field drainage, several measures can be adopted to facilitate the drainage and extraction including the selection of the appropriate negative pressure of the drainage hole, the optimization of the layout of the hole, the promotion of the desorption of gas, and the increase of the gas diffusion and migration speed.

2.2. The Derivation of Dynamic Expressions of Porosity and Permeability of Coal Seam. During the gas extraction, the gas tends to be desorbed and migrated, exposing the coal skeleton to stress changes, resulting in small deformation, and the porosity and permeability change accordingly. According to the existing research and the field conditions of Sima mine and the 2D model in the numerical simulation calculation, the plane strain ε_s is introduced, leading to a modified dynamic expression of coal seam porosity [12–14].

$$\varphi = 1 - \frac{1-\varphi_0}{1+\varepsilon_s}\left(1 - \frac{\Delta p}{k_s}\right), \tag{1}$$

where φ_0 is the initial porosity of coal, ε_v is the volume strain, ΔP is the variation of gas pressure, $\Delta p = P - P_0$, P is the real time gas pressure, P_0 is the initial gas pressure, and k_s is the skeleton modulus of the coal and rock mass.

According to the Kozeny-Carman formula, combined with the previous dynamic expression of porosity, the modified dynamic expression of permeability can be obtained as follows:

$$k_e = \frac{k_0}{1+\varepsilon_s}\left[1 + \frac{\varepsilon_s + (\Delta p/k_s)(1-\varphi_0)}{\varphi_0}\right]^3, \tag{2}$$

where k_0 is the initial permeability of coal and ε_s is the plane strain.

2.3. The Multiphysical Field Coupling Model of Coal Seam Gas Migration. This study focuses on the deformation of the coal seam due to the forces imposed and the gas flow [15–18]. Therefore, the following assumptions have been made:

(1) The flow field formed by the gas drainage hole under a certain negative pressure is the radial flow field

(2) The adsorption content of the gas is described by the Langmuir equation

(3) Gas flow is described by Darcy's law

(4) The seepage process of the gas is regarded as an ideal isothermal process

(5) The coal seam is isotropic with only a small linear elastic deformation

(6) The influence of water in the coal seam on gas drainage is overlooked

Taking the assumptions listed above into consideration, the seepage movement of coal seam gas as the ideal gas should follow the control equations of gas flow listed as follows [13, 14, 19–25].

2.3.1. Law of Conservation of Mass. Gas in the coal seam often takes two forms including the free state and the adsorption state. Despite the statuses, the source and total amount of gas in the coal seam remain unchanged. In other words, the gas migration should first follow the law of conservation of mass:

$$\frac{\partial m}{\partial t} + \nabla \bullet \left(\rho_g q_g\right) = Q_p, \tag{3}$$

where m is the gas content (kg/m^3), ρ_g is the gas density (kg/m^3), q_g is the Darcy seepage velocity of gas (m/s), Q_p is the source or sink items (kg/(m^3·s)), and t is the time variable (s).

2.3.2. The State Equation of Gas. The gas in seepage movement is regarded as an ideal gas, which satisfies the equation of state of ideal gas:

$$\rho_g = \frac{M_g P}{RT}, \tag{4}$$

where M_g is the molecular weight of gas (kg/kmol), P is the gas pressure (Pa), R is the ideal gas constant (kJ/(kmol·K)), and T is the absolute temperature (K_o).

2.3.3. Langmuir Equation. The coal seam is a porous medium with many pores and fissures, in which gas coexists in the adsorption state and the free state. The Langmuir equation describing the gas content defines the relationship between gas adsorption and desorption with gas pressure:

$$m = \frac{M_g}{RT}\left(\frac{\varphi}{P_0} + \frac{ab\rho_s}{1+bP}\right)P^2, \tag{5}$$

where φ is the porosity, P_0 is the atmospheric pressure (Pa), a is the Langmuir constant (m^3/kg), b is the Langmuir constant (Pa^{-1}), and ρ_s is the coal seam density (kg/m^3).

2.3.4. Darcy's Law. When a pressure gradient is identified in the distribution of gas pressure in the coal seam, the gas migration will occur, which is often a linear seepage flow and follows Darcy's law:

$$q_g = -\frac{k_e}{\mu_g}\left(\nabla p + \rho_g g \nabla z\right)^2, \tag{6}$$

where q_g is the Darcy flow velocity (m/s), k_e is the permeability of the coal seam (m^2), μ_g is the gas dynamic viscosity (Pa·s), and g is the acceleration of gravity ($m \cdot s^{-2}$).

The process of gas extraction is featured with two physical phenomena including the seepage movement of gas as fluid and the microdeformation of coal. The stress and deformation of the coal body cause changes to the pore characteristics and then affect the gas seepage movement. Consequently, the gas seepage tends to change the gas pressure within the coal body, resulting in different effective stresses. The interaction of two phenomena acts like a chain reaction featured with mutual constraint and influence.

The dynamic expression of coal seam porosity is substituted into equation (5), then

$$m = \frac{M_g}{RT}\left[\frac{1}{P_0} - \frac{1-\varphi_0}{P_0(1+\varepsilon_s)}\left(1-\frac{\Delta P}{k_s}\right) + \frac{ab\rho_s}{1+bP}\right]P^2. \tag{7}$$

The dynamic expression of coal seam permeability is substituted into equation (6), then

$$q_g = -\frac{k_0\left(\nabla p + \rho_g g \nabla z\right)^2}{\mu_g(1+\varepsilon_s)}\left[1 + \frac{\varepsilon_s + (\Delta p/k_s)(1-\varphi_0)}{\varphi_0}\right]^3. \tag{8}$$

By substituting formula (4) and derived formulas (7) and (8) into formula (3), the following results are obtained:

$$\frac{\partial\left\{\left(M_g/RT\right)\left[1/P_0 - ((1-\varphi_0)/P_0(1+\varepsilon_s))(1-\Delta P/k_s) + ab\rho_s/(1+bP)\right]P^2\right\}}{\partial t} - \nabla \cdot \left\{\frac{M_g P k_0\left(\nabla p + \rho_g g \nabla z\right)^2}{RT\mu_g(1+\varepsilon_s)}\left[1 + \frac{\varepsilon_s + (\Delta p/k_s)(1-\varphi_0)}{\varphi_0}\right]^3\right\} = Q_p. \tag{9}$$

Formula (9) is the gas-solid coupling model finally derived in this paper. The model is embedded into the COMSOL multiphysics software for gas drainage optimization.

3. The Introduction of the Calculation Model

3.1. The Calculation Model Parameter Setting. Before establishing the numerical model, the determination of the relevant parameters involved is vital. Based on relevant literature and geomechanics tests, after testing and adjusting the coefficient of the COMSOL multiphysics 5.0 built-in module, the main parameters used in the model were obtained, as shown in Table 1.

Table 1: Model parameter.

Items	Symbol	Value
Gas density (kg/m^3)	rhog	0.716
Gas dynamic viscosity (Pa·s)	vl	1.08e-5
Equivalent compressibility of matrix (1/Pa)	χ_p	2.18e-3
Fluid compressibility (1/Pa)	chif	1.3942e-5
Coal density (kg/m^3)	rhoc	1470
Initial porosity of coal	φ_0	0.0318
Poisson's ratio of coal	mu	0.33
Initial permeability of coal (m^2)	k_0	0.907e-15
Young's modulus of coal (MPa)	E	3000
Initial pressure of coal gas (MPa)	P_0	0.31
Standard atmospheric pressure (Pa)	P_a	1.01e5
Biot-Willis coefficient	α_B	0.801

3.2. The Model Establishment. The original gas pressure of the #3 Coal Seam in the Sima mine was 0.31 MPa. Due to the large error of gas concentration measurement, the original gas pressure reduced by 30% was selected as the standard for the simulation, leading to setting the gas drainage standard pressure at 0.22 MPa.

In order to provide direct guidance to the field construction, the effective borehole spacing was introduced in the simulation. The gas pressure of the whole seam can be reduced to the maximum borehole spacing value within the standard pressure value after drainage for a certain period of time. In other words, through the numerical simulation, the most reasonable drilling spacing value can be determined, which not only meets the need of reducing gas pressure but also reduces the difficulty and cost of on-site construction.

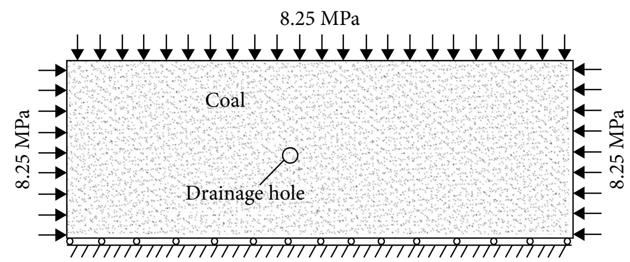

Figure 1: The calculation model.

The method similar to the "bucket theory" was used to calculate the effective drilling spacing, aiming to find out the area with the least superimposed effect of borehole pumping in the simulation calculation model and ensure that the pressure within the area drops right below the standard value.

The porous elastic module and Darcy's law module [13, 14, 26] in COMSOL were used in this simulation, and the required variables and parameters were inputted to the software. According to the actual drilling gas drainage process, an idealized two-dimensional calculation model with length × height of 16 m × 6.6 m was established as shown in Figure 1. The drainage boreholes were arranged in the middle of the model with the bottom as a fixed constraint. Meanwhile, the upper, left, and right boundaries have a boundary load of 8.25 MPa as the actual confining pressure condition. All sides of the model were airtight with an initial gas pressure of 0.31 MPa in the model.

As demonstrated in Figure 1, a drill hole was arranged in the 2D calculation module. Following the single variable method, the effective extraction radius corresponds to various diameters of extraction drill holes (95 mm, 113 mm, and 133 mm), extraction pressures (20 kPa, 25 kPa, 30 kPa, 35 kPa, 40 kPa, and 45 kPa), and extraction durations (90 d, 180 d, and 360 d). The detailed calculations are presented in Table 2.

According to Table 2, as the extraction duration, pressure, and diameter of the extraction drill hole increased, the effective radius of the single drainage hole increased, demonstrating a positive correlation.

Currently, the commonly adopted extraction drill holes are sized at113 mm in diameter and 133 mm in diameter, with the extraction pressure between 25 kPa and 40 kPa. The extraction often consumes substantial time, more than 1 year and even 2 to 3 years. Due to the relatively thicker coal seal in the Sima mine, multiple extraction holes in multiple layers were adopted. The extraction holes are often arranged in three ways including the three-flower style, four-flower style, and five-flower style, as demonstrated in Figure 2.

A few simulations with various conditions were performed including the extraction drill holes of 113 mm and 133 mm in diameter under the extraction pressure of 25 kPa, 30 kPa, 35 kPa, and 40 kPa. The extraction duration was set at 360 d. The calculation of the effective extraction radius is demonstrated in Figure 3 below.

Table 2: The simulation results of single-bore model.

Single bore		Effective radius of drainage (m)		
Hole diameter	Negative pressure	90 d	180 d	360 d
95 mm	20 kPa	0.45	0.57	0.72
95 mm	25 kPa	0.46	0.57	0.73
95 mm	30 kPa	0.46	0.58	0.74
95 mm	35 kPa	0.47	0.59	0.75
95 mm	40 kPa	0.47	0.60	0.76
95 mm	45 kPa	0.48	0.61	0.77
113 mm	20 kPa	0.48	0.60	0.76
113 mm	25 kPa	0.48	0.61	0.77
113 mm	30 kPa	0.49	0.62	0.78
113 mm	35 kPa	0.49	0.62	0.79
113 mm	40 kPa	0.50	0.63	0.80
113 mm	45 kPa	0.51	0.64	0.81
133 mm	20 kPa	0.50	0.63	0.80
133 mm	25 kPa	0.51	0.64	0.81
133 mm	30 kPa	0.51	0.65	0.82
133 mm	35 kPa	0.52	0.66	0.83
133 mm	40 kPa	0.53	0.67	0.84
133 mm	45 kPa	0.53	0.67	0.85

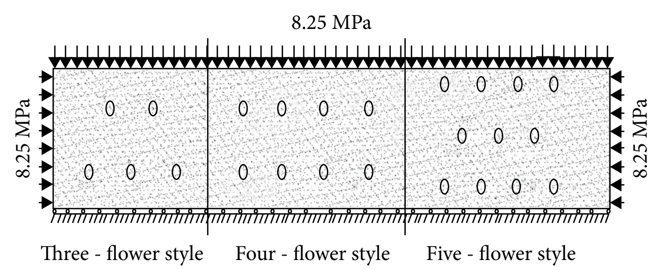

Figure 2: Three arrangements of drainage holes.

According to Figure 3, the drainage hole of 133 m in diameter demonstrated better extraction. The negative pressure of the extraction hole was 35kpa in the coal mining practice. The five-flower layout of the extraction holes was superior than the three-flower layout while the three-flower layout is superior the four-flower layout.

4. The Simulation and Analysis of the 1207 Working Face of Sima Coal

4.1. The Simulation Process Analysis. The strike length of the 1207 working face in the #3 Coal Seam of the Sima mine is 220 m with an inclined length of 1092 m. During the production, in order to ensure the safety of production, gas extraction was carried out. However, this kind of pumping scheme is single without considering the specific circumstances.

As mentioned previously, the drainage time greatly affects the gas drainage. Different drainage time periods should adopt different drainage hole layout schemes, such

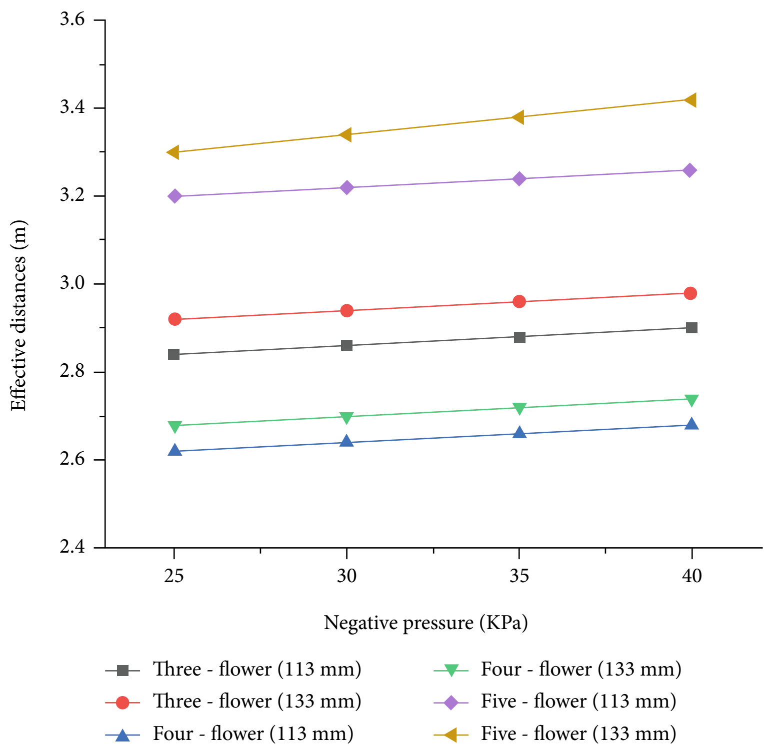

FIGURE 3: The effective distances between bores under different suction pressures.

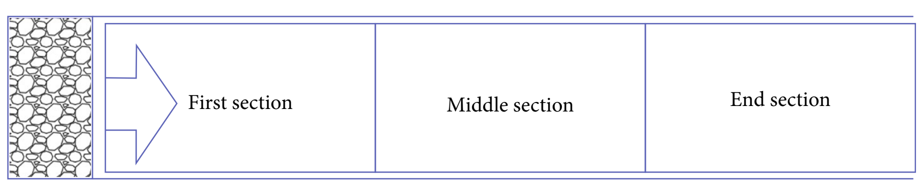

FIGURE 4: The sections divided in the roadway for extraction.

as different borehole spacings or patterns. As the no. 1207 working face advanced, different extraction durations were identified in different positions of extraction boreholes in the mining roadway. Under such circumstance, different sections should be divided based on the different extraction durations, allowing individual extraction design corresponding to different field conditions.

According to the comprehensive analysis of the driving speed, working face layout time, and mining speed of the mining roadway in the no. 1207 working face, and taking the drainage effectiveness into consideration, the coal seam gas drainage in the no. 1207 working face can be divided into three sections in simulation, as shown in Figure 4. The average extraction time of the three sections is 110D, 210D, and 310D, respectively.

The average extraction time, negative pressure, and hole diameter of the three sections were identified, and the gas extraction optimization of the three sections was also studied in detail. The calculation model of the optimization of the extraction changes from the single-row hole layout to the five-row pattern hole layout until the optimal result was obtained. Under the extraction of the experimental scheme, the goal of the whole layer of the #3 coal extraction up to 0.22 MPa was achieved.

4.2. The Analysis of Simulation Results

4.2.1. The Analysis of the First and Middle Sections. The extraction time of the first section and the middle section was set at 110 days and 210 days, respectively. According to the simulation calculation, the coal seam gas pressure can be reduced to the standard value within a fixed time only when the five-flower layout was adopted. Due to the different extraction durations, the effective drilling spaces of the two sections varied. The gas pressure cloud diagram in the simulation process is shown in Figures 5(a) and 5(b).

According to Figure 5, with more gas extraction, the pressure of the gas in the coal seam experienced constant changes. The gas pressure closer to the drainage hole dropped most. A further distance from the drainage hole leads to less decrease in the gas pressure until the threshold distance was reached where the gas pressure stayed at the initial value, indicating that the coal outside the impact boundary was not subject to the impacts of the extraction.

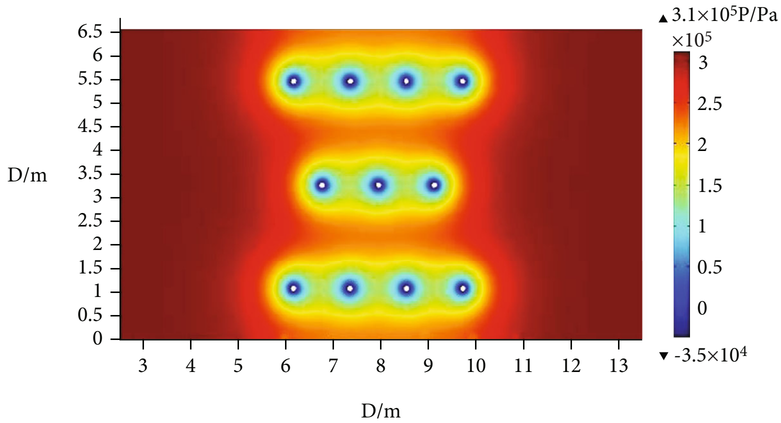

(a) The first section

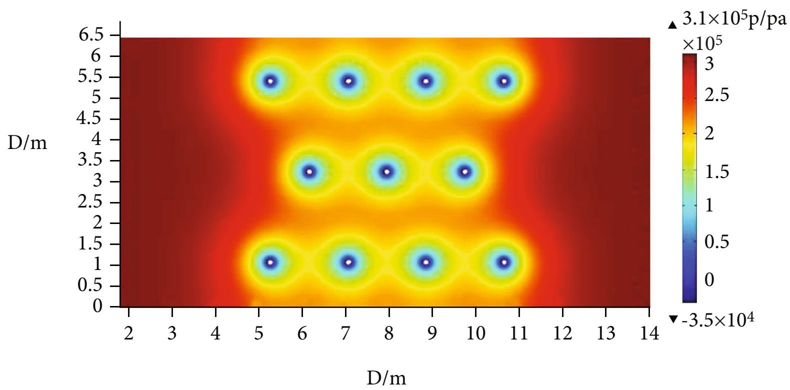

(b) The middle section

Figure 5: The gas pressure cloud diagram from simulation.

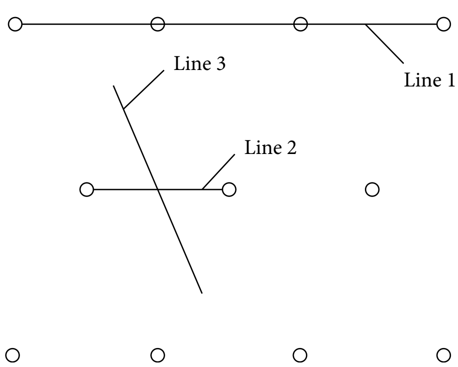

Figure 6: The structure line of the value line graph.

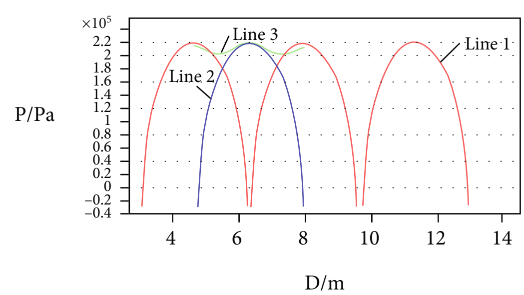

Figure 7: The value line graph.

In order to describe the gas pressure distribution in the five-flower arrangement, the structure line of the value line graph shown in Figure 6 was inserted into the simulated gas pressure cloud graph, which can vividly illustrate the distribution of the gas pressure value in the area wrapped by the five-flower hole. The value line graph is shown in Figure 7.

According to Figure 5, the maximum gas pressure in the wrapping area of the five-flower hole is 0.22 MPa, and the gas pressure in other places is lower than the set value. At this time, the distance between two adjacent drainage holes at the same level is concluded as the effective drilling spacing.

Table 3: Effective borehole spacing values in different sections.

Roadway segmentation	Extraction time	Horizontal effective drilling spacing value	Longitudinal row spacing
First segmentation	110 d	1.15 m	2.20 m
Middle segmentation	210 d	2.45 m	2.25 m

According to the simulation results, the effective drilling spacing values of the two sections in the five-flower arrangement are obtained, as shown in Table 3.

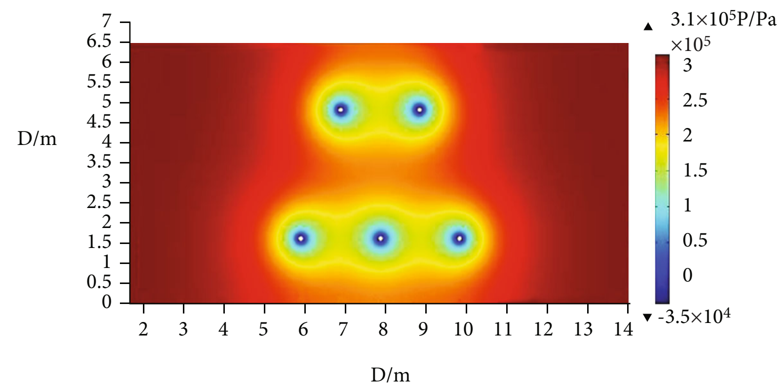

Figure 8: The gas pressure cloud diagram.

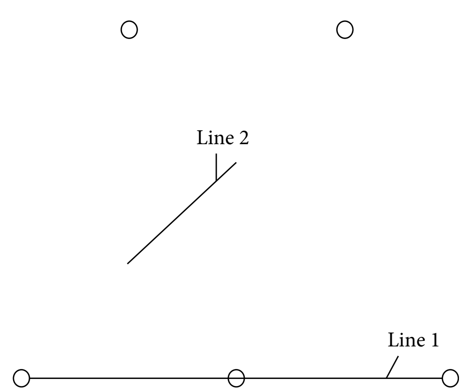

Figure 9: The structure line of the value line graph.

4.2.2. The Analysis of the Results of the End Sections. The extraction time of the end section was set at 310 days. The simulation suggests that the coal seam gas pressure can be reduced to the standard value within a fixed time when the three-flower arrangement was adopted. The gas pressure cloud diagram in the simulation process is shown in Figure 8.

Similarly, from Figure 8, being closer to the drainage hole leads to higher pressure drops. The gas pressure reaches the peak value of 0.22 MPa at the triangle center of gravity. In order to better describe the distribution of gas pressure in the three-flower hole, the construction line of the value-taking line diagram shown in Figure 9 was inserted into the simulated gas pressure cloud diagram, which can vividly illustrate the distribution of the gas pressure value in the area wrapped by the three-flower hole, and the value-taking line diagram is shown in Figure 10.

According to Figure 10, the maximum gas pressure in the wrapping area of the three-flower hole is 0.22 MPa, and the gas pressure in other places is lower than the set value. At this time, the distance between two adjacent extraction holes at the same level is the effective drilling spacing.

The simulation has suggested that the horizontal effective spacing between boreholes is 2.00 m with the vertical row spacing of 2.00 m when the three-flower pattern layout is adopted in the end section.

4.3. A Proposal of a Mixed Layout Scheme. According to the previous calculation results, a mixed layout scheme was developed specifically for the gas drainage in the no. 1207 working face of the Sima mine. The details are presented as follows.

The first section: a five-flower pattern layout was adopted with the horizontal drilling spacing of 1.15 m. The upper row of drilling is 5.50 m away from the floor longitudinally with the middle row of drilling 3.30 m away from the floor, and the bottom row of drilling1.10 m away from the floor.

The middle section: a five-flower pattern layout is adopted with the horizontal drilling spacing as 2.45 m. The upper row of drilling was 5.55 m away from the floor longitudinally with the middle row of drilling 3.30 m away from the floor, and the bottom row of drilling1.05 m away from the floor.

The end section: a three-flower pattern arrangement was adopted with the horizontal drilling spacing as 2.00 m. The upper row of drilling was 4.92 m away from the floor longitudinally with the bottom row of drilling 1.68 m away from the floor.

5. The Industrial Test

5.1. The Detailed Test Plan. In this industrial practice, the air-return roadway of the no. 1207 working face was selected. Without affecting the original production and extraction, the extraction practice test was carried out at 450 m~485 m in the middle section and 750 m~785 m in the end section of the air-return roadway. According to the previous calculation results, the specific scheme is proposed as follows:

(1) At 450 m~485 m in the middle section of the air-return roadway

The five-flower hole layout was adopted along with a negative pressure of 35 kPa, a diameter of 133 mm, an average length of 161 m, and a horizontal drilling spacing of 2.45 m. Longitudinally, the upper row of holes was 5.55 m away from the floor, with the middle row of holes 3.30 m away from the floor, and the bottom row of holes 1.05 m away from the floor.

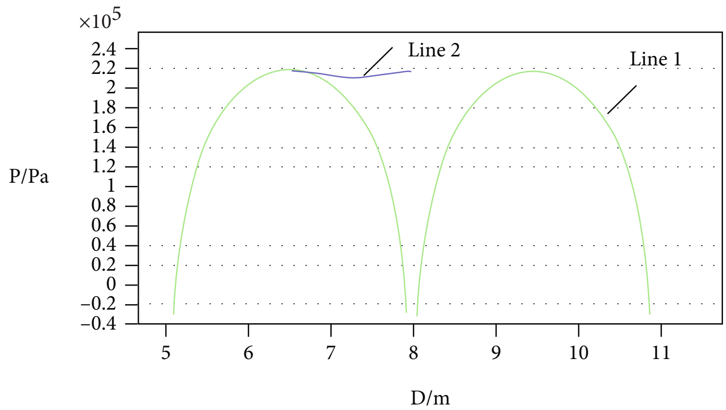

FIGURE 10: The value line graph.

(2) At 750 m~785 m in the end section of the air-return roadway

The three-flower hole layout was adopted with a negative pressure of 35 kPa, a diameter of 133 mm, an average length of 161 m, and a horizontal drilling spacing of 2.00 m. Longitudinally, the distance between the upper row and the floor was 4.92 m, with the distance between the bottom row and the floor at 1.68 m.

5.2. The Analysis of the Field Test. The industrial test scheme for gas drainage revealed that the drainage boreholes cover the coal seam effectively and evenly. The residual gas content in the middle and end sections of the air roadway was reduced by 31.24% and 32.16%, respectively, with the analytic gas content reduced by 46.86% and 49.81%, respectively, and the coal seam gas pressure reduced by 45.03% and 48.33%, respectively.

6. Conclusion

As the extraction duration, the negative pressure of the extraction, and the extraction drill hole diameter increase, the effective extraction radius of the single drainage hole increases, demonstrating a positive correlation.

Based on the simulation, a proposal including an effective spacing among extraction holes was developed. In the proposal, the extraction holes are arranged based on the effective drainage hole distances, taking various extraction durations corresponding to different locations in the roadway into consideration.

According to the gas pressure cloud diagram, a greater pressure drop is identified closer to the extraction hole. The gas pressure stays stable after reaching the threshold distance.

The gas pressure decreases with the increase of extraction time and finally grows stable. Some superposition effects have been identified between two drainage holes with a more intensive gas pressure drop in the superposition area.

Data Availability

The data used to support the findings of this study are available from the corresponding author upon request.

Conflicts of Interest

The authors declare that there are no conflicts of interest regarding the publication of this paper.

Acknowledgments

This paper was supported by the Priority Academic Program Development of Jiangsu Higher Education Institutions and the Natural Science Foundation of Chongqing, China (Grant No. cstc2019jcyj-msxmX0633 and No. cstc2020jcyj-msxmX0972), and the Science and Technology Planning Project of Jiulongpo District, China (Grant No. 2020-02-005-Y).

References

[1] Z. Yan, Y. Wang, J. Fan, Y. Huang, and Y. He, "Study on key parameters of directional long borehole layout in high-gas working face," *Shock and Vibration*, vol. 2021, Article ID 5579967, 14 pages, 2021.

[2] X. Guo, S. Xue, Y. Li, C. Zheng, and L. Xie, "Research on optimization of key areas of drainage borehole sealing in ultrathick coal seam," *Shock and Vibration*, vol. 2021, Article ID 5536196, 8 pages, 2021.

[3] J. Fan, *Research and Application of Gas Drainage Technology in Working Face of High Gas Coal Seam*, China Coal Research Institute, 2016.

[4] R. Pan, *Permeability evolution characteristics of loaded coal and its application in pressure relief gas drainage*, China University of mining and technology, 2014.

[5] J. Z. Zhou, C. F. Wei, W. T. Li, and H. L. Chen, "Analysis of saolid elastoplastic mechanics based on mathematical module of COMSOL Multiphysics," *Engineering Journal of Wuhan University*, vol. 48, no. 2, pp. 195–201, 2015.

[6] L. Si, H. Zhang, J. Wei, B. Li, and H. Han, "Modeling and experiment for effective diffusion coefficient of gas in water-saturated coal," *Fuel*, vol. 284, no. 15, article 118887, 2021.

[7] L. Si, J. Wei, Y. Xi et al., "The influence of long-time water intrusion on the mineral and pore structure of coal," *Fuel*, vol. 290, article 119848, 2021.

[8] F. Wang, J. He, Y. Liang, Y. Luo, Z. Liao, and L. Li, "Study on the permeability characteristics of coal containing coalbed

methane under different loading paths," *Energy Science and Engineering*, vol. 6, no. 5, pp. 475–483, 2018.

[9] B. Li, S. Xue, and C. Zheng, "Enhancing gas pre-drainage system performance based on fault tree failure analysis for environmental safety," *Fresenius Environmental Bulletin*, vol. 30, no. 2A, pp. 2137–2146, 2021.

[10] Z. Cheng, H. Pan, and Q. Zou, "Gas flow characteristics and optimization of gas drainage borehole layout in protective coal seam mining: a case study from the Shaqu coal mine, Shanxi province, China," *Natural Resources Research*, vol. 30, no. 2, pp. 1481–1493, 2021.

[11] C. Zhang, J. Xu, E. Wang, and S. Peng, "Experimental study on the gas flow characteristics and pressure relief gas drainage effect under different unloading stress paths," *Geofluids*, vol. 2020, Article ID 8837962, 10 pages, 2020.

[12] T. Li, B. Wu, and B. Lei, "Study on the optimization of a gas drainage borehole drainage horizon based on the evolution characteristics of mining fracture," *Energies*, vol. 12, no. 23, article 4499, 2019.

[13] B. LI, J. Wei, and L. Peng, "Numerical simulation on gas drainage of boreholes in coal seam based on gas-solid coupling model," *Computer Modelling & New Technologies*, vol. 18, no. 12A, pp. 418–424, 2014.

[14] J. Wei, B. Li, K. Wang, and D. Sun, "3D numerical simulation of boreholes for gas drainage based on the pore-fracture dual media," *International Journal of Mining Science and Technology*, vol. 26, no. 4, pp. 739–744, 2016.

[15] S. Li, "Solid-gas coupling model and numerical simulation of coal containing gas based on COMSOL multiphysic," *Advanced materials research*, vol. 616-618, pp. 515–520, 2013.

[16] X. Yang and X. Zhao, "Study on influence of complex stress on fracture damage of coal and rock mass in pressure relief borehole," *Science and technology in China*, vol. 9, no. 2, pp. 138-139, 2015.

[17] L. Han, "Numerical simulation of gas drainage based on fluid-solid-heat coupling model," *Journal of Liaoning Technical University (Natural Science Edition)*, vol. 32, no. 12, pp. 1605–1608, 2013.

[18] C. Li, *Study on the Relationship between Drilling Parameters and Gas Drainage Effect in the Coal Seam*, Henan Polytechnic University, 2014.

[19] C. Liu, G. Yin, M. Li et al., "Shale permeability model considering bedding effect under true triaxial stress conditions," *Journal of Natural Gas Science and Engineering*, vol. 68, article 102908, 2019.

[20] C. Liu, G. Yin, M. Li, D. Shang, B. Deng, and Z. Song, "Deformation and permeability evolution of coals considering the effect of beddings," *International Journal of Rock Mechanics and Mining Sciences*, vol. 117, pp. 49–62, 2019.

[21] Z. Sun, L. Li, F. Wang, and G. Zhou, "Desorption characterization of soft and hard coal and its influence on outburst prediction index," *Energy Sources, Part A: Recovery, Utilization, and Environmental Effects*, vol. 42, no. 22, pp. 2807–2821, 2020.

[22] Y. Xue, J. Liu, P. G. Ranjith, X. Liang, and S. Wang, "Investigation of the influence of gas fracturing on fracturing characteristics of coal mass and gas extraction efficiency based on a multi-physical field model," *Journal of Petroleum Science and Engineering*, vol. 206, article 109018, 2021.

[23] S. Hu, G. Tao, and L. Xiaohong, "Analysis and numerical simulation of fluid-structure coupling of gas drainage from boreholes," *Journal of Chongqing University*, vol. 34, no. 11, pp. 105–110, 2011.

[24] S. Wei, K. Ma, and B. Li, "Research on coal and gas outburst based on COMSOL multiphysics," *Coal*, vol. 19, no. 5, pp. 14–16, 2010.

[25] G.-Z. YIN, L. I. Ming-Hui, L. I. Sheng-Zhou, L. I. Wen-Pu, J.-W. YAO, and Q.-G. ZHANG, "3d numerical simulation of gas drainage from boreholes based on solid gas coupling model of coal containing gas," *Journal of China Coal Society*, vol. 38, no. 4, pp. 535–541, 2003.

[26] H. P. Xie, H. W. Zhou, D. J. Xue, and F. Gao, "Theory, technology and engineering of simultaneous exploitation of coal and gas in China," *Journal of China Coal Society*, vol. 39, no. 8, pp. 1391–1397, 2014.

Hindawi
Geofluids
Volume 2021, Article ID 4237061, 14 pages
https://doi.org/10.1155/2021/4237061

Research Article

Study on the Prediction of the Height of Two Zones in the Overlying Strata under a Strong Shock

Xingping Lai ,[1,2] Bowei Liu ,[1] Pengfei Shan ,[1,2] Feng Cui,[1,2] Yun Zhang,[1,2] Xudong Zhang,[1] Rui Bai,[1] and Xuan Wu[3]

[1]*School of Energy Engineering, Xi'an University of Science and Technology, Xi'an 710054, China*
[2]*Key Laboratory of Western Mines and Hazard Prevention, Ministry of Education, Xi'an 710054, China*
[3]*China-ASEAN Geosciences Cooperation Center (Nanning), Nanning, Guangxi 530023, China*

Correspondence should be addressed to Pengfei Shan; shanpengfei@xust.edu.cn

Received 22 April 2021; Accepted 14 August 2021; Published 7 September 2021

Academic Editor: Yi Xue

A development of overlying strata fractures and an unknown distribution of the two zones, which results from a strong shock tendency roof short-distance coal seam group mining, are the main problems faced by Xiashijie Coal Mine. Consequently, an experiment has been conducted; here are the steps: designing an underlying strata development law and the two-zone distribution physical similarity simulation test under the short-distance coal seam group combined mining, using the BT-AE to comonitor the fracture development law and the distribution characteristics of the caving zone and the water-conducting fractured zone, and combining with 3DEC comparative analysis. The results show that after the coal seam mining is over, the number of overlying fractures increases with depth, controlled by the mining stress field in the direction of 115° west from north to west. The direction of overlying fracture is mainly concentrated in the area of 300°~30°; the overlying fracture angles eventually develop to 81° and 74°, increasing by 15.7% and 8.8%, and the caving ratio and cracking ratio are 4.87 and 17.75. After comparing with the numerical calculation results, the reliability of the two zones obtained by the physical similarity simulation test is verified. The AE analysis results show that the "release-accumulate-release" energy evolution process of overlying rock fracture under mining conditions has a phased relationship with fracture expansion. The energy positioning results are consistent with the distribution of BT observation cracks, and the large energy events are mostly concentrated in the collapse zone, indicating that AE has the practicality of disaster warning. The results of this study provide scientific guidance for water-preserving mining under the combined mining of coal seams with a strong impact tendency roof in Xiashijie Coal Mine.

1. Introduction

As an important industrial raw material in China, coal resources will not change their dominant position for a long time. Xie et al. [1] proposed that China's total energy consumption demand in 2025 will be 5.5 to 5.6 billion tons of standard coal, accounting for 50% to 52% of full energy consumption. However, the mining of coal will inevitably cause the movement and fracture of the overlying strata and the formation of cracks at the same time. The existence of fissures will cause the overlying aquifer to seep to the working face and cause underground water inrush accidents. While water resources are wasted, it also brings major hidden dangers to underground safety production. Therefore, it is very necessary to study the development law of overlying fractures and the distribution patterns of the two zones after mining in a fully mechanized caving face.

Many scholars at home and abroad have made relatively mature researches in theory and practical applications for the evolution of overlying fractures and water conservation mining. Fan [2] puts forward some suggestions on water-preserving coal mining based on the perspective of scientific development. Wang et al. [3] proposed the characteristics of overburden failure and deformation caused by high-intensity mining and its impact on the environment and at the same time gave a formula for calculating the height of the "two zones" under high-intensity mining. Zhao et al. [4] suppressed the contact between the height of the water-conducting fissure zone and the strong aquifer of the overburdened rock to control the problem of water gushing in the overlying rock. Lai et al. [5] obtained the overlying rock migration damage height of fully mechanized caving face through physical similarity simulation research and determined the relationship between the measured resistance of the on-site support and the water conduction position and the amount of water conduction in the overlying rock fracture. Wang et al. [6] used the entropy method-cloud model to evaluate the ecological environment of certain mining areas that are mainly based on water conservation mining. Wang et al. [7] analyzed the positional relationship between coal seams and aquifers through the combination of indoor experiment and field and proposed to partition the stability of the mining water barrier and standardize the coal-mining method, in order to carry out scientific mining in mining areas with fragile ecological environment. Guo et al. [8] obtained the formation mechanism of the "two-zone" failure mode of overlying strata in high-strength mining by studying the failure transmission process of overlying strata. Cheng et al. and Xue et al. [9, 10] studied the evolution characteristics of the overburden fissure zone caused by the mining disturbance in the soft rock protection layer. Research by Yang et al. [11] showed that the water-conducting fracture zone under thick loose layer and weak overburden will go through four stages, and it will develop upward in the form of separation layer, mostly in the form of articulation. Wang et al. [12] found that through theoretical analysis and on-site detection and analysis that the height of the water-conducting fracture zone is affected by the thickness of the coal seam and the structure of key layers, and the height changes stepwise with the thickness of the coal seam. Zhao et al. [13] found that the height of the water-conducting fracture zone is affected by the thickness of the mining, the thickness of the bedrock, and the thickness of the load layer. Liu and Zhao [14] analyzed and verified the protective mechanism and effect of coal filling mining on the roof aquifer by constructing a mechanical model and similar simulation tests. Huang et al. [15] combined numerical calculation model with physical simulation and theoretical analysis and concluded that the evolution of overlying strata cracks is affected by the distance between coal pillars in different sections. Yang et al. [16] obtained the smallest safe waterproof coal pillar size through RFPA2D analysis. Fan and Liu [17] observed and analyzed the leakage vector of flushing fluid in downhole boreholes and the development of cracks in the hole wall and found that mining cracks showed a dynamic evolution characteristic of "generation-development-bridging." Wu et al. [18] quantitatively evaluated the mining disturbance area through observation of borehole images. Dong et al. [19] proposed a new technology for the protection of burnt rock water and its impact on coal mining. Guo and Dong [20] established a numerical model of groundwater seepage and studied the seepage laws of different aquifers affected by the fracture zone. Du et al. [21] proposed the principle of direct roof control for coal mining with strip structure filling "water retention-storage." Lai et al. [22–25] observed, analyzed, and determined the height and spatial distribution of the water-conducting fissure zone in the internal subsidence zone, and the fracture zone after the coal seam was excavated.

The abovementioned researches have made useful explorations on the evolution of fractures and the distribution of the two zones in my country's coal mine water conservation mining and laid a solid foundation for subsequent researches. In this paper, aiming at the joint mining of close-range coal seams with a strong impact tendency in Xiashijie Coal Mine, the method of physical similarity simulation test is used, the law of crack development and the distribution of the two zones are obtained through the drilling TV and acoustic emission monitoring system and establish a 3DEC numerical calculation model to verify it and provide a scientific basis for the safe production of Xiashijie Coal Mine and the protection of water resources.

2. Engineering Background

2.1. Geological Structure Characteristics and Coal Seam Occurrence in Xiashijie Coal Mine. Xiashijie Coal Mine is located in the northwest of Tongchuan City, Shaanxi Province. The mine field is 4 km long, with a slope of about 3.3 km wide and a coal-bearing area of 13.2 km^2. The mine has 127 million tons of recoverable reserves, and the original design service life is 101 years. The buried depth of the coal seam is 640 m, and the roof of the coal seam tends to impact. The bedding and fissures of the 3-2# coal seam are relatively developed, and the hardness of the 3-2# coal seam is medium. The first mining face is 2301 working face, the slope length is 210 m, and the mining thickness is 4.5 m. The 4-2# coal seam is relatively stable, with developed endogenous fissures, flakes, and collapses. The first mining face is 222 with an oblique length of 210 m and a mining thickness of 10.0 m.

2.2. Coal Roof and Floor Characteristics. The 3-2# coal seam is directly topped by dark-gray silty mudstone and siltstone, the rock layer is relatively broken, and the average thickness is 2.0 m. The 3-2# coal seam floor is gray to dark-gray siltstone, commonly known as black sandstone, with an average of 7.35 m.

The direct roof of 4-2# coal seam is dark gray-gray black siltstone, thin-layered, partially sandy mudstone and mudstone, and argillaceous cement. 4-2# coal seam floor is carbonaceous mudstone, black, thin-layered, and with an average thickness of 6.16 m. The mean distance between 3-2# coal seam and 4-2# coal seam is 21.76 m.

2.3. Mine Hydrological Characteristics. The surface of the mine is mostly covered by vegetation, with dense forests and vertical and horizontal valleys. There are no rivers and other water bodies. Due to the high terrain, there will be no water accumulation in the rainy season. Since the distance between 3-2# coal seam and 4-2# coal seam is 21.76 m, the water inflow of 3-2# coal seam is the same as that of 4-2# coal seam. In the mining of 3-2# coal seam, the normal water inflow of the mine is 100~120 m^3/h, and the maximum water inflow is 170 m^3/h.

According to the analysis of mine hydrogeological data, during the mining process of 222 working face, some sections of the water-conducting fracture zone will directly affect the Luohe Formation, and some sections of the Luohe Formation aquifer water indirectly enter the underground through the Yijun Formation. After the upper 2301 working face was mined, the structure of the overlying water-bearing (impermeable) layer was destroyed, and water in the goaf poured into the 222 working face. According to the "Mine Geological Report" (revised), it is estimated that the normal water inflow of 222 working face is 42.6 m^3/h, and the maximum water inflow is 223.7 m^3/h.

3. Experimental Study on the Development of Mining Overlying Strata and the Distribution of Two Zones

3.1. Physical Model Design. The Xiashijie Coal Mine was used as the experimental research object, and three-dimensional models with length, width, and height of 3.0 m, 0.2 m, and 1.7 m were selected. According to the similarity theory, the geometric similarity ratio is selected as 1 : 400, the stress similarity ratio is 1 : 600, and the pressure similarity ratio is $1:1.2\times10^7$. The similar materials required for the test are mainly sand, white powder, plaster of paris, mica, and water, among which fly ash is added when the coal seam is proportioned, and the mica powder is used for layering. According to the corresponding ratio, mix and stir evenly and then pave it on the model frame to simulate the process of deformation and collapse of different rock layers during the mining process. The physical and mechanical parameters and material loading ratio of coal-measure formation are shown in Table 1.

3.2. Test and Equipment Monitoring Program. There are 20 cm boundary coal pillars on both sides of the model. The working face advances from left to right, and a total of 260 cm is excavated. The experiment first simulates mining 3-2# coal seam, with a 1.5 cm stop for a total of 187 times. After the 3-2# coal seam is mined, 4-2# coal seam is mined with a 1.0 cm stop for a total of 260 times.

Two peepholes with the same diameter of 60 mm and depth of 150 cm are evenly arranged along with the model frame. The number from left to right is 1# drilling and 2# drilling, and the distance between the two drillings is 96 cm. When the overburden is destroyed by pressure, the GD3Q-GA drilling TV is used to observe the full-hole 360° through the peephole, and the collected images are processed to obtain a plane expansion map to observe the changes of the overburden. At the same time, the cracks in the stage can be fitted, the azimuth angle can be measured, and the number of cracks and the change law of azimuth can be obtained by analysis. The model test system is shown in Figure 1.

At the beginning of the test, the Express-8 acoustic emission system developed by the American company Mistral was used to monitor the amount of energy released during the overburden failure, the change in the severity of the damage, and the location of the event in real-time. By monitoring and analyzing the acoustic emission signal during the mining process of the working face, it can reflect the overburden failure, fracture, and the distribution law of the two zones during the mining process of the model working face.

4. Analysis of the Development of Cracks in the Overlying Rock and the Characteristics of the Two Zones

4.1. The Development Number and Direction Characteristics of Overlying Rock Fractures. The number of fractures in the overlying rock can objectively reflect the damage degree of the rock mass affected by mining disturbance. In this test, based on the structural plane joints measured by the borehole TV, a set of data for every 10 cm of the borehole depth is used to draw a figure of the number of cracks in the overburden rock in boreholes 1# and 2# after the mining of the two working faces and compare the two, as shown in Figure 2. After the end of mining in the 2301 working face and the 222 working face, due to the support of the main key layer, the number of cracks in the range of 1# drilling depth 60 cm~70 cm and 2# drilling 70 cm~80 cm is significantly less than the number of cracks in the upper and lower sections.

It can be seen from Figure 2 that after the rock formation is affected by mining disturbance, the number of fractures below the main key layer is more than the number of cracks above, and the number of overburdened fractures increases with the increase of drilling depth. That is to say, the roof overlying rock above the working face is damaged by mining disturbance, and there are many cracks.

The azimuth rose diagram of the model overlying cracks monitored by the borehole TV is shown in Figure 3. In the range of 0°~360°, the fissures in different orientations of the 1# and 2# boreholes in the two working faces are drawn for each 10° as a group. In Figure 3(a), after the end of the mining in the 2301 working face, the 1# borehole has 1 crack at 160°, 2 cracks in the range of 292.5°~315°, 1 crack at 335°, and 3 cracks in the range of 337.5°~360°; the remaining fissures are between 22.5° and 90°, of which there are 8 fissures in the range of 40° to 45°. In Figure 3(b), after the end of mining in the 2301 working face, the cracks in the 2# borehole are all distributed in the range of 0°~50°. In Figure 3(c), after the end of the mining in the 222 working face, there is 1 fissure at 358° and 4 fissures at 94° in No. 1 borehole. The remaining fissures are distributed in the range of 20°~90°; there are 12 cracks in the range of 54°~58°. Due to the interaction between the rock layers during the mining disturbance, the azimuth of the 1# borehole fissure after the end of mining in the 222 working face shifts clockwise from that of the 1# borehole fissure after the end of the 2301 working face, and the number of deep borehole cracks increased significantly. In Figure 3(d), after the end of the mining in the 222 working face, most of the fractures in borehole 2# are in the range of 0°~90°, and only 7 of the fractures are in the range of 337.5°~360°.

It can be seen from Figure 3 that the fissures in boreholes 1# and 2# are mainly concentrated in the area of 0°~90°,

Table 1: Physical and mechanical parameters of the model and material filling ratio.

Serial number	Lithology	Single layer thickness/m	1 cm ingredients River sand/kg	Plaster/kg	White powder/kg
1	Fine-grained sandstone	26.00	8.40	0.36	0.84
2	Siltstone	12.30	8.40	0.24	0.96
3	Conglomerate	52.10	8.40	0.50	0.72
4	Medium-grained sandstone	52.80	8.40	0.48	0.72
5	Sandstone	22.02	8.40	0.50	0.72
6	Medium-grained sandstone	28.73	8.40	0.48	0.72
7	Sandy mudstone	33.48	8.53	0.21	0.85
8	Coarse-grained sandstone	14.70	8.53	0.32	0.75
9	Sandstone	23.76	8.4	0.5	0.72
10	Medium-grained sandstone	69.11	8.4	0.48	0.72
11	Sandy mudstone	16.20	8.53	0.21	0.85
12	Medium-grained sandstone	5.00	8.4	0.48	0.72
13	Sandstone	17.80	8.4	0.5	0.72
14	Coarse-grained sandstone	14.60	8.53	0.32	0.75
15	Sandy mudstone	3.90	8.53	0.21	0.85
16	Coarse-grained sandstone	33.00	8.53	0.32	0.74
17	Sandstone	13.50	8.4	0.5	0.72
18	Coarse-grained sandstone	12.88	8.53	0.32	0.74
19	Sandy mudstone	27.18	8.53	0.21	0.85
20	Coarse-grained sandstone	12.90	8.53	0.32	0.75
21	Sandy mudstone	4.62	8.53	0.21	0.85
22	Siltstone	21.47	8.4	0.24	0.96
23	Sandy mudstone	23.03	8.53	0.21	0.85
24	Siltstone	7.36	8.4	0.24	0.96
25	Mudstone	8.74	8.53	0.21	0.85
26	Siltstone	11.02	8.4	0.24	0.96
27	Sandstone	9.07	8.4	0.5	0.72
28	Mudstone	7.07	8.53	0.21	0.85
29	Sandstone	12.16	8.4	0.5	0.72
30	Siltstone	7.24	8.4	0.24	0.96
31	3-2# coal	4.50	4.15	0.21	0.42
32	Siltstone	7.21	8.4	0.24	0.96
33	Sandstone	14.55	8.4	0.5	0.72
34	4-2# coal	10.00	4.15	0.21	0.42

while the true north direction of the borehole in the model is 60° west of the actual azimuth. Therefore, the overburden fractures in the mine are mainly distributed in the area of 300°~30°, indicating that the development and formation of the fractures in the borehole are mainly controlled by the mining stress field in the direction of 115° west of the true azimuth.

4.2. Internal Characteristics of Overlying Fractures. Figure 4 shows the imaging and statistical characteristics of the cracks of the overburden in the 1# borehole at the end of mining the 2301 working face. It can be seen from Figure 4 that within the range of 0 ~ 35.7 cm of the borehole, mining disturbance has fewer effects on the rock formation in this range, and the rock formation does not appear to sink or cracks. Within the range of 35.7 cm~73.4 cm in the borehole, the rock formation has moved with a little loosening and slagging phenomenon, and the fracture width is about 1.5 mm. Within the range of 73.4 cm~114.6 cm in the borehole, the rock formation forms fissures due to subsidence, but the fissure width is 2 mm. In the range of 114.6 cm~150.0 cm in the borehole, the roof collapsed, the rock formation is more severely damaged, the fracture width was 3 mm, and the crack length showed an overall upward trend with the increase of depth. It can be seen from the borehole TV monitoring that after the end of the mining in the 2301 working face, the height of the collapse zone is 4.9 cm, and the height of the water-conducting fractured zone is 37.4 cm through the 1# borehole monitoring. Corresponding to the 2301

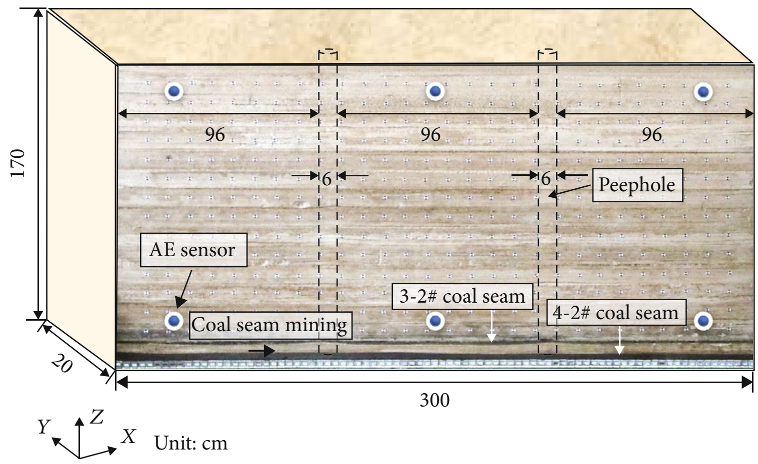

Figure 1: Similar material model and equipment layout.

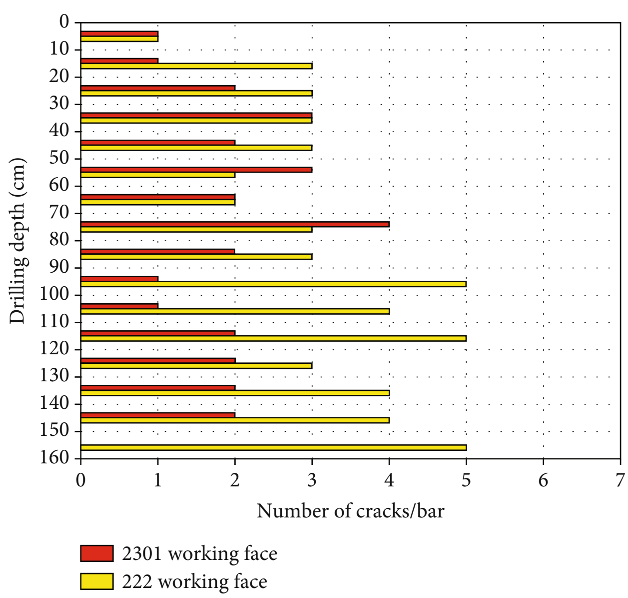

(a) Working face stoping ends 1# borehole overlying rock fissure diagram

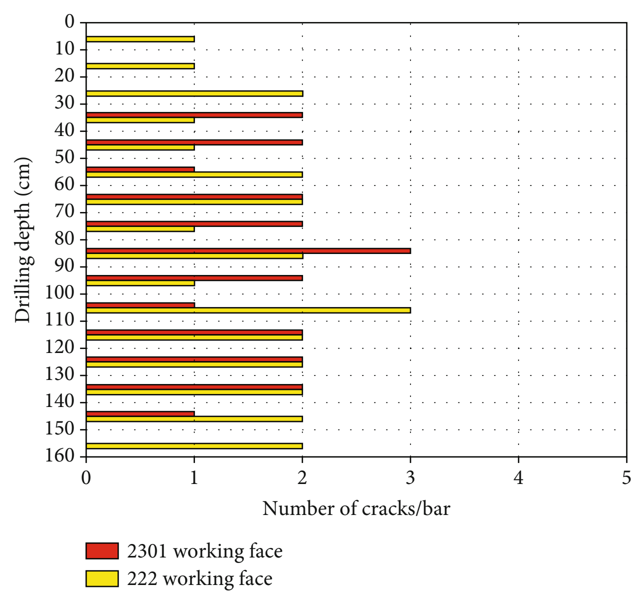

(b) Working face stoping ends 2# borehole overlying rock fissure diagram

Figure 2: Number of cracks in the overlying rock.

working face of Xiashijie Coal Mine after mining, the rock collapse zone is 19.6 m, and the water-conducting fractured zone is 149.6 m.

Figure 5 shows the imaging and statistical characteristics of the cracks of the overburden in the 2# borehole at the end of mining the 2301 working face. It can be seen from Figure 5 that within the range of 0 ~ 36.2 cm of the borehole, mining disturbance has fewer effects on the rock formation in this range, and the rock formation does not sink or crack. Within the range of 36.2 cm~74.7 cm of the borehole, the rock strata have moved, and some loosening and slagging phenomenon occurs. At this time, some cracks with a width of 1 mm are generated. In the range of 74.7 cm~116.8 cm in the borehole, the rock formations form a narrower and denser circumferential fissure due to subsidence. At the same time, the rock formations in this range are accompanied by shear failure, and longitudinal fissures are generated, and in some areas, the two kinds of fissures are staggered, forming interlaced fissures, and the width of the fissures is 2 mm. In the range of 116.8 cm~150.0 cm of the borehole, the roof collapsed obviously, and the rock strata suffered a tensile failure, and the damage is more serious. Within this range, the average crack width is 2.1 mm. Due to mining disturbances, the rock strata above the working face are seriously damaged, so the width and length of the cracks are larger than the upper strata, and the overall trend is increasing. It can be seen from the borehole TV monitoring that after the end of the mining in the 2301 working face, the height of the collapse zone is 5.2 cm, and the height of the water-conducting fractured zone is 37.6 cm through the monitoring of the 1# borehole; corresponding to the 2301 working face of Xiashijie Coal Mine after mining, the rock collapse zone is 20.8 m, and the water-conducting fractured zone is 150.4 m.

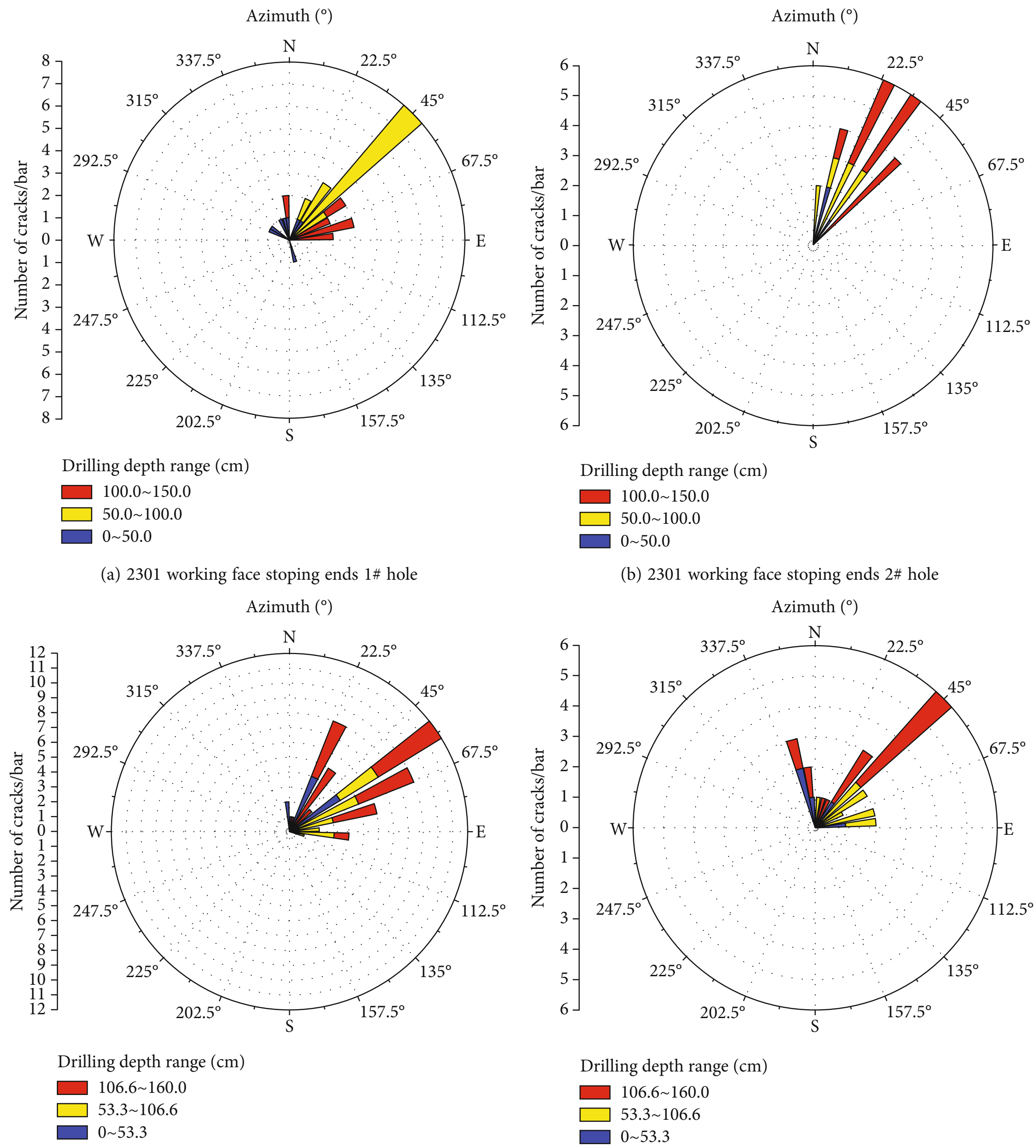

(a) 2301 working face stoping ends 1# hole

(b) 2301 working face stoping ends 2# hole

(c) 222 working face stoping ends 1# hole

(d) 222 working face stoping ends 2# hole

Figure 3: Azimuth rose diagram of overlying rock fractures.

Figure 6 shows the imaging and statistical characteristics of the cracks of the overburden in the 1# borehole at the end of mining the 222 working face. It can be seen from Figure 6 that within the range of 0 ~ 31.6 cm in the borehole, the rock strata bend and sink, and the separation layer has developed to the surface, producing small fissures with a width of 1 mm. In the range of 31.6 cm~62.7 cm in the borehole, there are a large number of cracks, and the width of the cracks develops to 2 mm; there is no connection between the rock layers, and this range is at the edge of the bending zone. Within the range of 62.7 cm~94.5 cm in the borehole, the rock formation closed the local fissures due to settlement and its own weight, and the width was reduced to 1 mm. Within the range of 94.5 cm~127.5 cm in the borehole, the lower rock strata are not compacted due to the collapse of the key layer to form a structure, and the crack width is 5 mm. Within the range of 127.5 cm~160.0 cm in the borehole, the roof collapsed obviously, and cracks with a width of 7 mm and a length of 55 mm were generated, and the rock formation was seriously damaged. It can be seen from the borehole TV monitoring that after the end of the mining in the 222 working face, the height of the collapse zone is

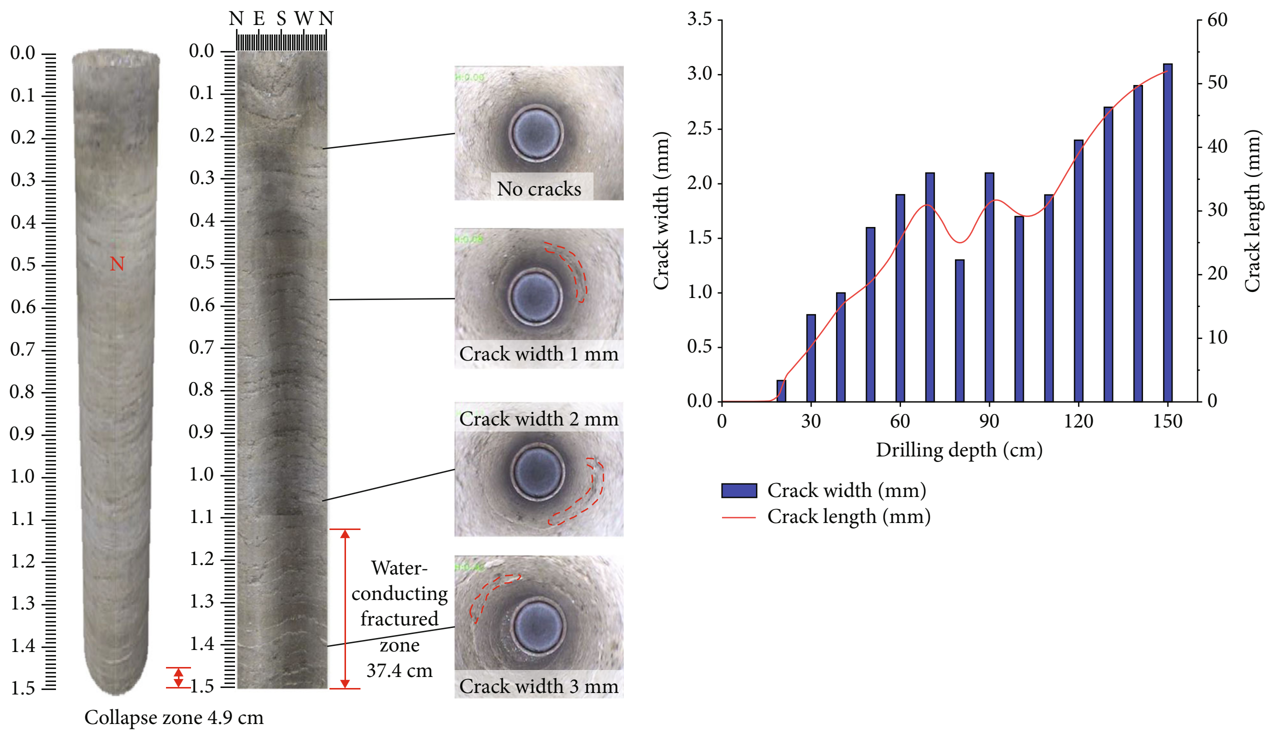

(a) Drilling panoramic fissure peep imaging

(b) Statistical characteristics of different depth cracks

FIGURE 4: The imaging and statistical characteristics of the overburden cracks in the 1# borehole after the end of mining the 2301 working face.

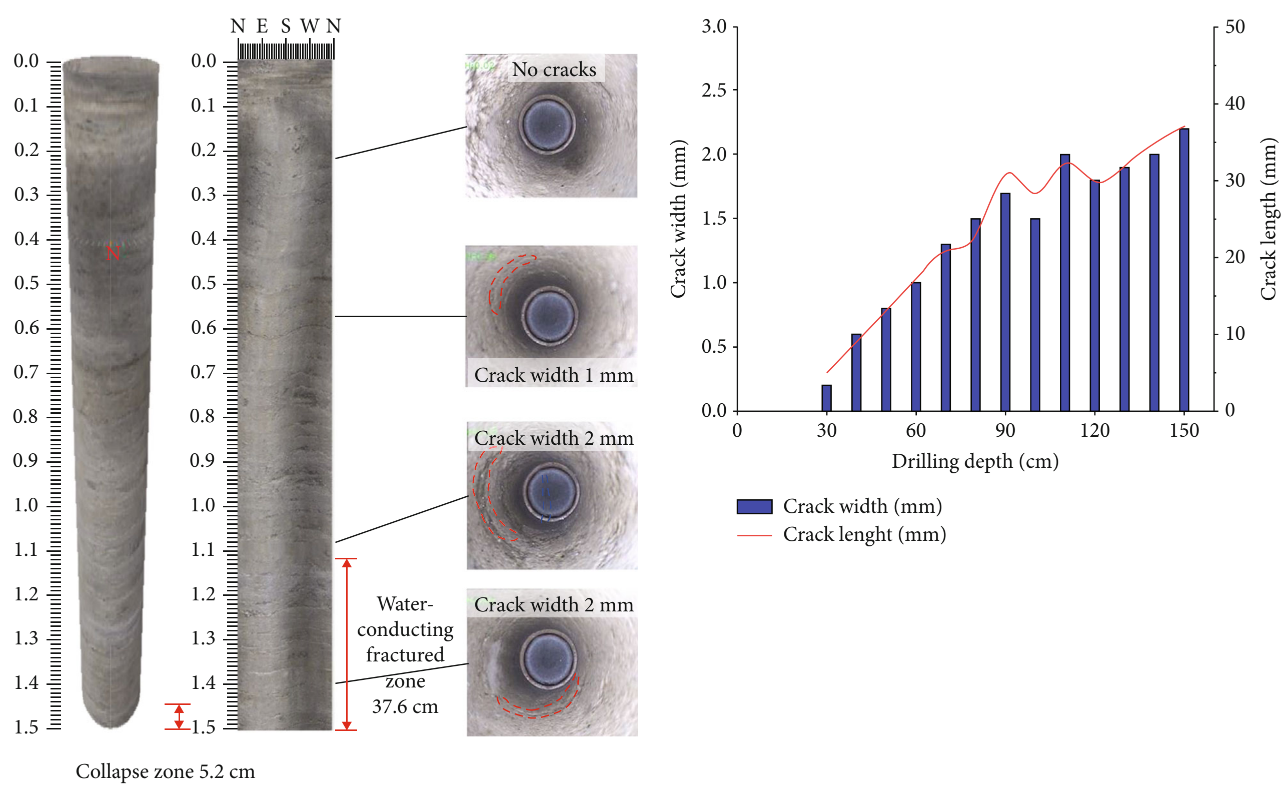

(a) Drilling panoramic fissure peep imaging

(b) Statistical characteristics of different depth cracks

FIGURE 5: The imaging and statistical characteristics of the overburden cracks in the 2# borehole after the end of mining the 2301 working face.

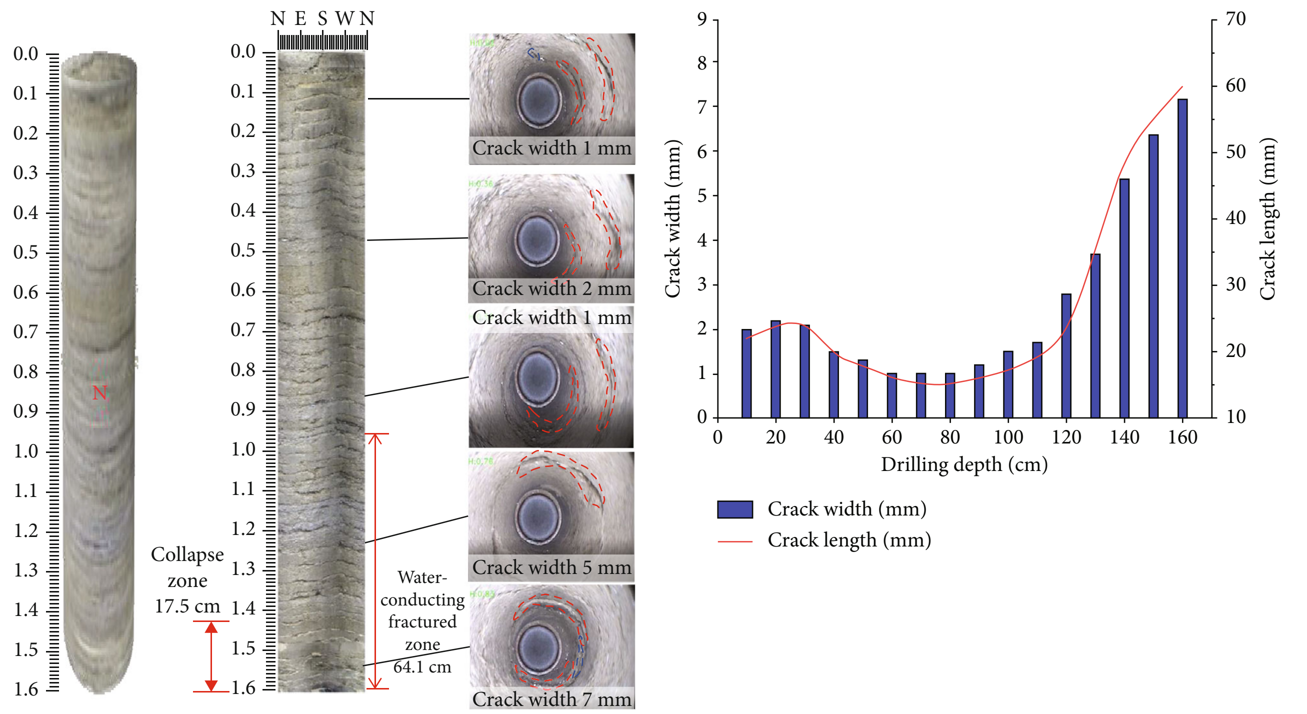

(a) Drilling panoramic fissure peep imaging

(b) Statistical characteristics of different depth cracks

Figure 6: The imaging and statistical characteristics of the overburden cracks in the 1# borehole after the end of mining the 222 working face.

17.5 cm, and the height of the water-conducting fractured zone is 64.1 cm through the 1# borehole monitoring; corresponding to the 222 working face of Xiashijie Coal Mine, the rock collapse zone is 70 m, and the water-conducting fractured zone is 256.4 m.

Figure 7 shows the imaging and statistical characteristics of the cracks of the overburden in the 2# borehole at the end of mining the 222 working face. It can be seen from Figure 7 that within the range of 0 ~ 40.6 cm in the borehole, the separation layer has developed to the surface, and the rock formation bends and sinks, resulting in cracks with an average width of 2.2 mm. Within the range of 40.6 cm~121.6 cm in the borehole, local fissures are closed due to rock settlement and self-weight, and the width of the fissures is reduced, with an average value of 1.8 mm. Within the range of 121.6 cm~160.0 cm of the borehole, the roof separation occurred obvious collapse phenomenon, local cracks with a width of 7 mm and a length of 60 mm were generated, and within this range, the average crack width was 5.3 mm, and the rock formation was seriously damaged. It can be seen from the drilling monitoring that after the end of the mining at the 222 working face, through the 2# drilling monitoring, the height of the collapse zone is 17.8 cm, and the height of the water-conducting fractured zone is 64.6 cm; corresponding to the 222 working face of Xiashijie Coal Mine, the rock collapse zone is 71.2 m, and the water-conducting fractured zone is 258.4 m.

Through the direct observation of the physical similar simulation test results and the indirect observation of the internal damage of the overlying rock through the borehole television, in the process of mining in the 3-2# coal seam 2301 working face, the range and height of the overburden damage continue to increase with the mining of the model. However, affected by the fragmentation and expansion effect of the coal and rock below, the increase in the damage height of the overburden gradually decreases with the increase in the number of pressures. After the end of the mining in the 2301 working face of the 3-2# coal seam, the rock activity stabilizes. When mining 4-2# coal seam 222 working face, with the continuous advancement of the working face, the roof of the coal seam sinks so that the upper collapsed rock layer continues to sink and damage to the bottom rock layer. The upper rock layer collapses sequentially due to periodic pressure. After the end of the stoping, a relatively stable squeeze equilibrium structure forms between the broken rock blocks and finally tended to a stable state. Observation from borehole 2# shows that the cracks have developed to the surface, and the number of cracks has increased significantly. The TV analysis results of the model borehole show that the evolution process of the overburden rupture is “Fracture expansion-Fracture-Collapse.”

4.3. Two-Zone Distribution Characteristics. Through the physical similarity simulation test, the heights of the two zones were measured in sequence after the end of the mining at the 2301 working face and the 222 working face, and the distribution maps of the two zones were drawn, as shown in Figures 8 and 9. To facilitate the observation of the failure mode of the rock formation, the fracture line of the rock formation has been added, and the angle measured. It can be seen from Figure 8 that after the end of mining in the 3-2# coal seam 2301 working face, the caving zone above the

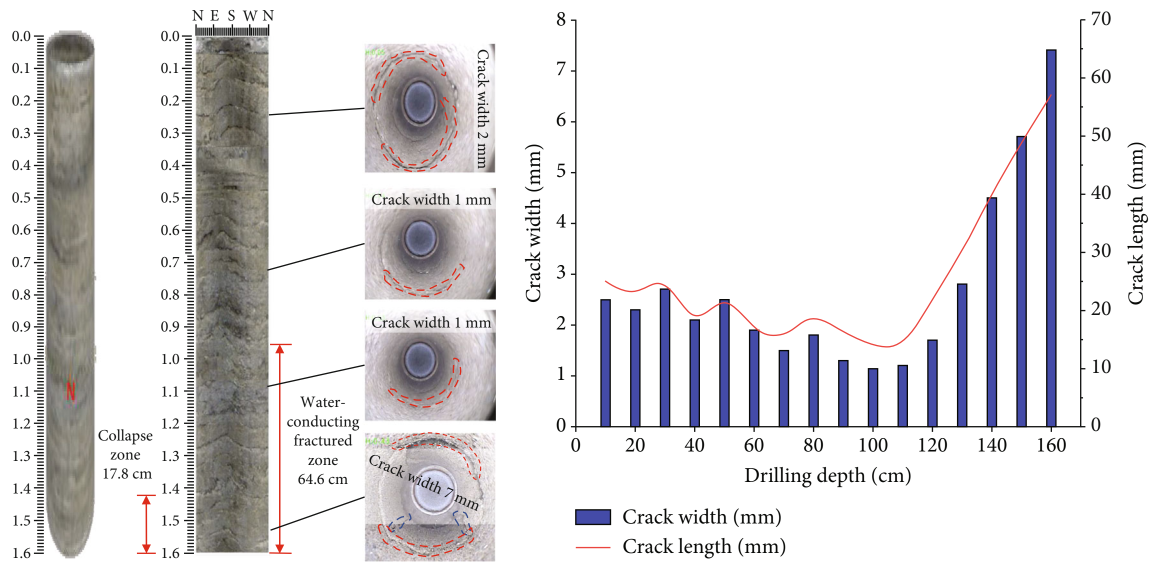

(a) Drilling panoramic fissure peep imaging

(b) Statistical characteristics of different depth cracks

Figure 7: The imaging and statistical characteristics of the overburden cracks in the 2# borehole after the end of mining the 222 working face.

working face is approximately trapezoidal in distribution. The breaking angle on the left side of the goaf is 70°, and the breaking angle on the right side is 68°. Because the coal pillars at the two ends of the working face have a supporting effect on the overlying strata, the displacement and deformation of the middle strata are larger than those on both sides; therefore, the height of the water-conducting fractured zone is slightly higher at both ends of the working face and lower in the middle, showing a "saddle-shaped" distribution.

After the stoping in the 4-2# coal seam 222 face, the distribution of the two zones is shown in Figure 9. It can be seen from Figure 9 that the mining of 222 working face caused a large-scale collapse of the rock layer between the two coals, and the damaged rock layer of the 3-2# coal seam continued to be bent and subsided after mining. The breaking angle on the left side of the goaf developed to 81°, and the breaking angle on the right side developed to 74°, increasing by 15.7% and 8.8%. The development height of the two zones continued to expand upward, and the development of the two zones was like a "saddle shape" until the end of the stoping.

Through borehole television monitoring, the heights of the overlying caving zone and water-conducting fractured zone after the end of mining in the 2301 and 222 working faces are shown in the table of the height of the two zones after the end of the mining in Table 2.

The results show that after the 3-2# coal seam is mined, the average height of the collapsed zone and the water-conducting fractured zone are 20.2 m and 150.0 m, and the caving ratio and the cracking ratio are 4.5 and 33.3. After the coal seam group stoping, the collapsed zone and water-conducting fractured zone eventually developed to 70.6 m and 257.4 m, and the caving ratio and the cracking ratio are 4.87 and 17.75, increasing by 15.7% and 8.8%.

According to Yu and Zhang [26], it is known that when the coal seam inclination angle is 0°~54° in the range of 0°~54°, the caving zone height formula (1) and the water-conducting fractured zone height formula (2) are as follows:

$$Hc = \frac{100\sum M}{2.1\sum M + 16} \pm 2.5, \quad (1)$$

$$Hf = \frac{100\sum M}{1.2\sum M + 2.0} \pm 8.9. \quad (2)$$

In which, $\sum M$ is the total thickness of the coal seam, and its cumulative thickness does not exceed 15 m; ± is the allowable range of error; Hc is the height of the collapse zone; Hf is the height of the fracture zone.

The average thickness of the 3-2# coal seam in the 2301 working face is 4.5 m, which can be calculated in the above formula (1) and formula (2), and the height of the collapse zone is in the range of 15.2 m~20.2 m. The height of the water-conducting fractured zone is in the range of 51.9 m~69.7 m. The average thickness of the 4-2# coal seam in the 222 working face is 10.0 m. After the 4-2# coal seam is stopped, the cumulative thickness of the coal seam is 14.5 m. Take it into the above formula (1) and formula (2) to calculate that the height of the collapse zone is in the range of 28.7 m~33.7 m. The height of the water-conducting fractured zone is in the range of 65.8 m~83.6 m. Table 3 shows the formula to calculate the height range of the two zones.

The development height of the two zones calculated by the formula has a large deviation from the development height of the two zones obtained by the physical similarity simulation experiment, which is not enough to support it. Because the coal seam of Xiashijie Coal Mine is buried at 640 m and belongs to a mine with a strong impact tendency, the development height of the two zones calculated by the conventional theoretical formula is quite different from the value of the physical similarity simulation test. Therefore, in order to verify the accuracy of the borehole TV

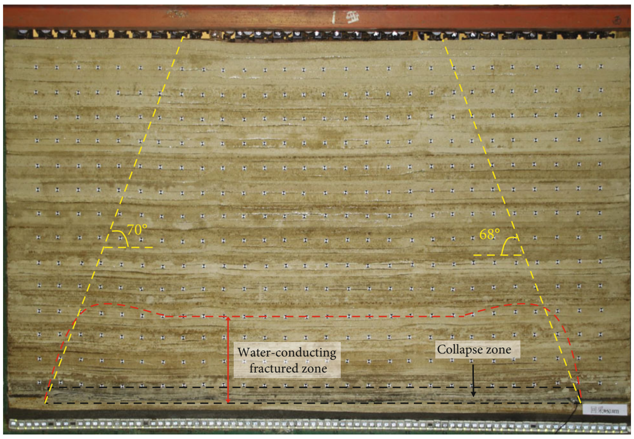

Figure 8: 3-2# coal seam's two-zone distribution map.

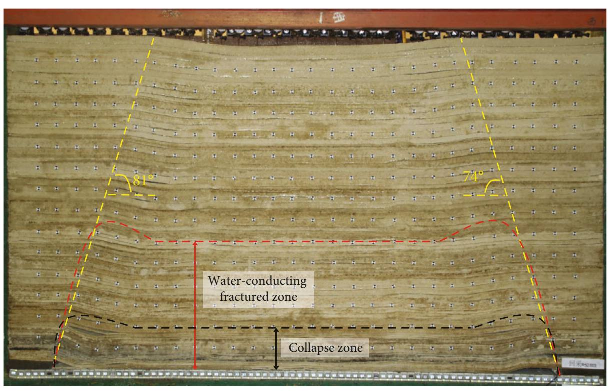

Figure 9: 4-2# coal seam's two-zone distribution map.

monitoring results, acoustic emission energy evolution positioning will be used to further analyze the development height of the two zones.

4.4. Positioning Analysis of Overburden Energy Evolution. With the aid of the location of acoustic emission events, the fissure development and the height of the two zones after joint mining of the coal seam group are inverted to verify the accuracy of the height of the two zones monitored by the borehole TV system. According to the size of the event energy, the acoustic emission events are divided into 4 different levels of less than 10,000, 10,000~50,000, and 50,000~100,000 and greater than 100,000 mV·μs. According to the frequency of the occurrence of acoustic emission events in the overburden and the location of the concentrated energy distribution, the distribution range of the collapse zone and water-conducting fractured zone is drawn.

From Figure 10, the three-dimensional location of the acoustic emission event at the end of mining at 2301 working face shows that after the end of mining in the 3-2# coal seam 2301 working face, the heights of the collapse zone and the water-conducting fractured zone are 20.8 m and 150.8 m, respectively, which are 0.6 m and 0.8 m apart from the average height of the two zones monitored by the borehole TV system. Due to coal mining, the overlying rock formations with a strong impact tendency are severely broken and damaged, so high-energy events are mostly concentrated in the collapse zone. The 3-2# coal seam is relatively thin. After the end of the mining, the rock in the middle of the model moved, and there were slag drop, loosening, and small cracks between the rock layers, so small energy events were scattered in the middle of the rock. The upper rock layer is less affected by mining disturbance, and the rock layer has no subsidence and cracks, so the acoustic emission monitoring system did not capture the energy event.

From Figure 11, the acoustic emission three-dimensional space positioning map of the 222 working face shows that, after the end of coal mining in the 4-2# coal seam 222 face, the heights of the collapse zone and the water-conducting fractured zone shown in the upper seismic source envelope of the face are 71.0 m and 258.0 m; the average height of the two zones differs from the height monitored by the borehole TV by 0.4 m and 0.6 m. When the 4-2# coal seam is completed mining, the rock layers among the coal seam groups have collapsed more severely, and the damage forms are obvious. Therefore, within the collapse zone, the large-energy events are significantly increased and become denser. Due to the collapse of the key layer to form a structure, the central rock layer sinks, and the local fractures are compacted. Therefore, the energy of small events is denser near the water-conducting fractured zone. After the coal seam group was mined, the surface subsided, and small cracks formed, so small energy events were scattered in the upper part of the model.

Acoustic emission monitoring results corroborate the results of borehole TV monitoring. The comprehensive analysis of borehole TV monitoring and acoustic emission monitoring shows that after the combined mining of deep roof coal seams with a strong impact tendency, the average height of the final collapse zone obtained from the physical similarity simulation test is 70.8 m, and the average height of the water-conducting fractured zone is 257.7 m. Through the energy location of the acoustic emission monitoring system, it can be known that large-energy events are mostly concentrated in the collapse zone, and there are more energy events near the contour of the water-conducting fractured zone than in the upper and lower parts. From this, it is known that the energy dissipation of the overburden rupture of the upper strata is "Release-Accumulate-Release," and the AE monitoring system can provide early warning for coal mine safety production.

5. Numerical Simulation Verification Analysis

5.1. Selection of Numerical Simulation Software and Determination of Calculation Parameters. The 3DEC software is currently an ideal numerical simulation software for simulating the movement process of a rock formation after it is broken. It can ideally analyze and study the potential failure modes of rock mass directly related to the discontinuous features. At the same time, it can also simulate the process of roof falling, collapse, and separation after coal seam excavation. A discrete element numerical model is constructed according to the characteristics of the coal and rock layers in the Xiashijie Coal Mine, and the height of

Table 2: The development height table of the two zones after the end of the working face.

Working face	1# drilling Height of collapse zone/m	1# drilling Height of fissure zone/m	2# drilling Height of collapse zone/m	2# drilling Height of fissure zone/m	Average Height of collapse zone/m	Average Height of fissure zone/m
2301 working face	19.6	149.6	20.8	150.4	20.2	70.6
222 working face	70.0	256.4	71.2	258.4	150.0	257.4

Table 3: Formula calculates the development height range of the two zones.

Working face stoping situation	Strike model overlying two zones Height range of collapse zone/m	Strike model overlying two zones Height range of fissure zone/m
2301 working face stoping end	15.2 ~20.2	51.9 ~69.7
222 working face stoping end	28.7 ~33.7	65.8 ~83.6

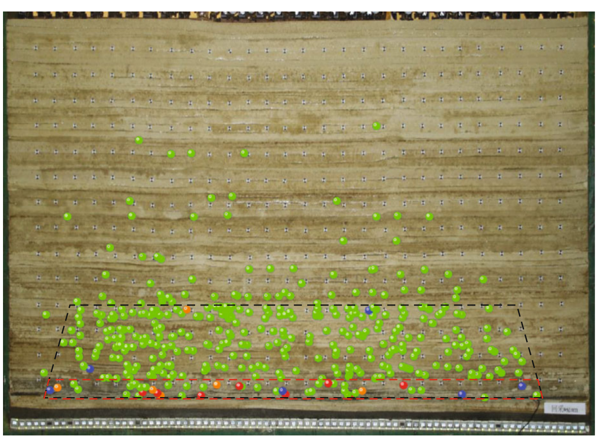

Figure 10: Three-dimensional location map of acoustic emission event at the end of mining at 2301 working face.

the two zones is comprehensively determined through numerical calculation.

According to the field geological data and rock mechanics test results, the final coal rock mechanics parameters are determined (Table 4) and provide a reliable basis for the numerical simulation calculation.

5.2. Establishment of the Numerical Calculation Model. The geological characteristics of the numerical model of the overburden failure characteristics and the mining sequence of the working face are consistent with the physical similarity simulation experiment, as shown in Figure 12. The model has a length of 1,200 m, a width of 80 m, and a height of 650 m.

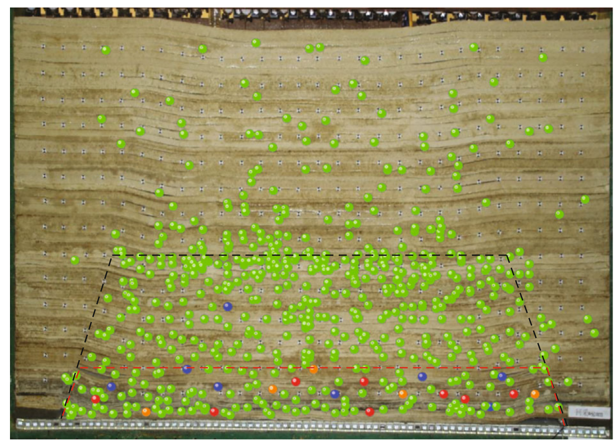

Figure 11: Three-dimensional location map of acoustic emission event at the end of mining at 222 working face.

5.3. Numerical Calculation Analysis Results. Figure 13 shows the distribution of overburden cracks in the 3-2# coal seam at the end of mining. During the advancing process of the 2301 working face, the continuous increase and expansion of cracks cause the rock formation to collapse continuously. Due to the influence of the boundary coal pillars, the overlying strata at both ends of the working face remained in a suspended state after the advancement of the 2301 working face is completed. The caving zone is mainly concentrated in the lower black dotted trapezoidal area with a height of about 18.4 m, the difference between the average height of the collapse zone measured by the similar simulation test BT-AE joint monitoring system of 20.5 m is 2.1 m, and the deviation is small. The water-conducting fractured zone is mainly concentrated in the red dotted trapezoidal area. The yellow rectangles on both sides are accompanied by the existence of fractures. The height of the water-conducting fractured zone is 147.6 m. Compared with the similar simulation test BT-AE joint monitoring system, the average height of the water-conducting fractured zone measured by 150.4 m differs by 2.8 m, and the error is small.

Table 4: Main coal and rock mechanical parameters.

Number	Lithology	Bulk density (kN/m^3)	Tensile strength (MPa)	Elastic modulus (GPa)	Internal friction angle (°)	Cohesion (MPa)	Poisson's ratio
1	Fine-grained sandstone	2.21	1.56	1.415	25.48	2.40	0.17
2	Siltstone	2.45	0.78	0.885	15.3	4.90	0.23
3	Conglomerate	2.64	3.02	0.345	34.72	2.91	0.19
4	Sandstone	2.35	0.88	0.925	11.8	3.47	0.25
5	Medium-grained sandstone	2.31	1.12	1.214	27.77	1.32	0.22
6	Sandy mudstone	2.54	0.23	0.346	26.28	0.48	0.27
7	Coarse-grained sandstone	2.41	0.48	0.817	30.84	1.65	0.25
8	Mudstone	2.62	0.95	1.321	27.21	1.88	0.25
9	3-2# coal seam	1.35	1.33	1.67	29.74	2.68	0.31
10	4-2# coal seam	1.45	1.86	1.84	30.87	3.61	0.21

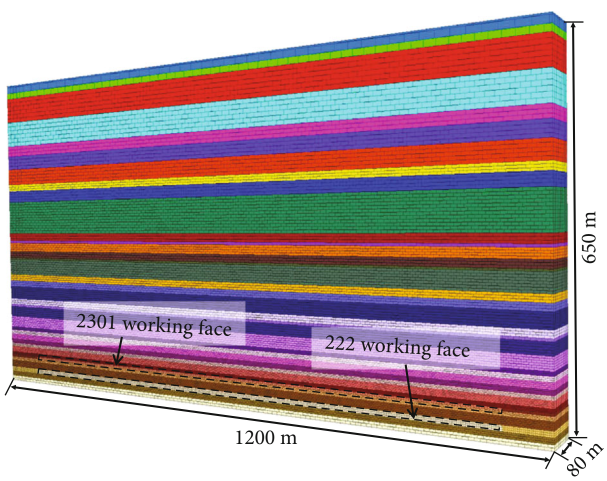

Figure 12: 3DEC numerical calculation model.

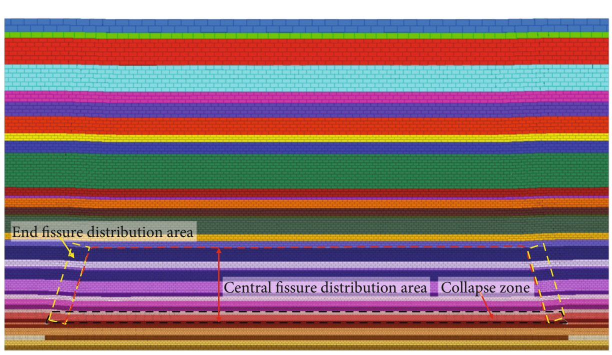

Figure 13: 3-2# coal seam overburden collapse characteristics at the end of mining.

Figure 14 shows the distribution of overburden cracks in the 4-2# coal seam after mining. During the advancing process of working face 222, the overlying rock strata are affected by mining disturbances and cause a large number of cracks and separations, causing collapse and subsidence.

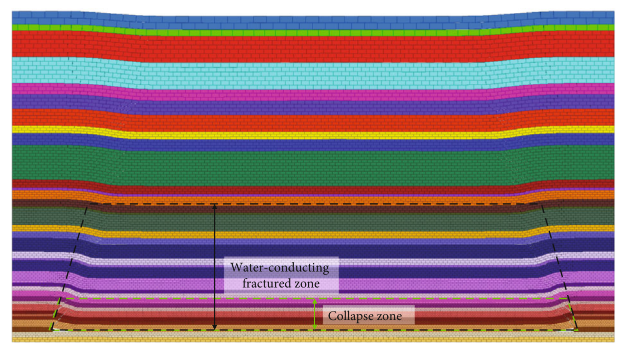

Figure 14: 4-2# coal seam overburden collapse characteristics at the end of mining.

The collapse zone is mainly concentrated in the green trapezoidal range, with a height of about 68.4 m. The difference between the average height of the collapse zone measured by the similar simulation test BT-AE joint monitoring system is 70.8 m by 2.4 m, and the deviation is small. Serious fracture damage occurs in the rock above the goaf at both ends of the working face, and the fracture cracks are more obvious. The rock layer near the coal roof was damaged to a greater extent, and the cracks are the most concentrated. However, the middle and upper rock layers squeeze and rub against each other after the collapse, and the number of cracks is significantly less than that of the lower rock layers. The crack zone is mainly concentrated in the black trapezoidal area with a height of 252.0 m. Compared with the similar simulation test BT-AE joint monitoring system, the average height of the fissure zone measured by the BT-AE joint monitoring system is different by 5.7 m, and the error is small.

Under the combined mining of coal seams with a strong impact tendency, there is a large error in the height of the two zones of overlying strata through numerical calculation and the height of the caving zone and the water-conducting fractured zone calculated by the empirical formula. The height of the two zones measured by the 3DEC numerical analysis is slightly smaller than the height of the two zones obtained by the physical similarity simulation experiment within a reasonable range, which well proves the accuracy of the two zones' height measured by the physical similarity simulation experiment.

6. Conclusions

(1) Under the condition of combined mining of the strong flushing coal seam group in the lower stone section, the number of overburden cracks increases with the depth, mostly near the roof. Controlled by the mining stress field in the direction of 115° west from north to west, the direction of the overburden cracks is mainly concentrated in the area of 300°-30°

(2) After the 3-2# coal seam is mined, the overburden fracture angles are 70° and 68°, respectively, and the caving ratio and cracking ratio are 4.5 and 33.3. After the coal seam group stoping, the overburden fracture angles eventually developed to 81° and 74°, increasing by 15.7% and 8.8%, and the caving ratio and cracking ratio are 4.87 and 17.75. After the 4-2# coal seam is mined, due to the fracture of the upper subkey layer, the cracks expand in a wide range, and the height of the cracked zone increases, which increases the proportion of the two zones. TV analysis of boreholes shows that the evolution characteristic course of overburden rupture is "fracture expansion-fracture-collapse"

(3) The AE analysis results show that the "release-accumulate-release" energy evolution process of overburden rupture under mining conditions has a phased relationship with fracture expansion, and the energy positioning results are consistent with the BT observation fracture distribution. Moreover, high-energy events are mostly concentrated in the collapse zone, indicating that AE has the practicality of disaster warning. When the coal seam is buried deep and has a tendency to impact, the height values of the two zones calculated by the empirical formula differ greatly from the actual height. To ensure the smooth progress of water-preserving mining, physical similarity simulation tests should be conducted reasonably through the BT-AE system joint monitoring and verified through discrete element numerical calculations to comprehensively determine the height of the water-conducting fractured zone. Formulate appropriate water prevention and control plans and programs to solve the problems of the development height of the two zones of the strong impact tendency roof and the prevention and control of water in the close coal seam group of Xiashijie Coal Mine

Data Availability

The test data used to support the findings of this study are included in the article. Readers can obtain data supporting the research results from the test data table in the paper.

Conflicts of Interest

No conflict of interest exists in the submission of this manuscript.

Authors' Contributions

The manuscript is approved by all authors for publication. All the authors listed have approved the manuscript that is enclosed.

Acknowledgments

This work is sponsored by the National Nature Science Foundation of China (Nos. 51904227 and 52004201) and the Shaanxi Natural Science Fundamental Research Program Enterprise United Fund (2019JLZ-04).

References

[1] H. P. Xie, L. X. Wu, and D. Z. Zheng, "Prediction on the energy consumption and coal demand of China in 2025," *Journal of China Coal Society*, vol. 44, no. 7, pp. 1949–1960, 2019.

[2] L. M. Fan, "Discussing on coal mining under water-containing condition," *Coal Geology & Exploration*, vol. 33, no. 5, pp. 53–56, 2005.

[3] Y. G. Wang, W. B. Guo, and E. H. Bai, "Characteristics and mechanism of overlying strata movement due to high-intensity mining," *Journal of China Coal Society*, vol. 43, no. S1, pp. 28–35, 2018.

[4] C. H. Zhao, D. W. Jin, and Z. X. Li, "Analysis of overlying aquifer water inrush under mining the Topmineable seam in Yushen Mining Area," *Journal of China Coal Society*, vol. 46, no. 2, pp. 523–533, 2021.

[5] X. P. Lai, F. Cui, and J. T. Cao, "Analysis on characteristics of overlying rock caving and fissure conductive water in top-coal caving working face at three soft coal seam," *Journal of China Coal Society*, vol. 42, no. 1, pp. 148–154, 2017.

[6] J. Q. Wang, M. Y. Lu, and Q. X. Wang, "Study on ecological environment assessment of water conservation mining based on entropy weight method and cloud model," *Coal Science and Technology*, pp. 1–8, 2020.

[7] S. M. Wang, Q. X. Huang, and L. M. Fan, "Study on overburden aquclude and water protection mining regionazation in the ecological fragile mining area," *Journal of China Coal Society*, vol. 35, no. 1, pp. 7–14, 2010.

[8] W. B. Guo, E. H. Bai, and G. B. Zhao, "Current status and progress on overburden and surface damage and prevention technology of high-intensity mining," *Journal of China Coal Society*, vol. 45, no. 2, pp. 509–523, 2020.

[9] X. Cheng, G. M. Zhao, and Y. M. Li, "Evolution of overburden mining-induced fractured zone and pressure-relief gas drainage in soft rock protective seam," *Journal of Mining & Safety Engineering*, vol. 37, no. 3, pp. 533–542, 2020.

[10] Y. Xue, J. Liu, P. G. Ranjith, X. Liang, and S. H. Wang, "Investigation of the influence of gas fracturing on fracturing characteristics of coal mass and gas extraction efficiency based on a multi-physical field model," *Journal of Petroleum Science and Engineering*, vol. 206, article 109018, 2021.

[11] D. M. Yang, W. B. Guo, and G. B. Zhao, "Height of water-conducting zone in longwall top-coal caving mining under

thick alluvium and soft overburden," *Journal of China Coal Society*, vol. 44, no. 11, pp. 3308–3316, 2019.

[12] X. Z. Wang, J. L. Xu, and H. K. Han, "Stepped development characteristic of water flowing fracture height with variation of mining thickness," *Journal of China Coal Society*, vol. 44, no. 12, pp. 3740–3749, 2019.

[13] B. C. Zhao, Z. R. Liu, and C. Tong, "Relation between height of water flowing fractured zone and mining parameters," *Journal of Mining & Safety Engineering*, vol. 32, no. 4, pp. 634–638, 2015.

[14] J. G. Liu and L. T. Zhao, "Theory of water protection and practice application in mining based on the backfilling mining technology," *Journal of China Coal Society*, vol. 39, no. 8, pp. 1545–1551, 2014.

[15] Q. X. H. J. Cao and J. W. Du, "Research on three-field evolution and rational coal pillar staggered distance in shallow buried closely spaced multi-seam mining," *Journal of China Coal Society*, vol. 44, no. 3, pp. 681–689, 2019.

[16] X. K. Yang, X. M. Zhang, and Z. J. Hou, "Numerical simulation of safety mining under a river in Yushuwan coal mine," *Journal of Mining & Safety Engineering*, vol. 25, no. 3, pp. 305–308, 2008.

[17] Z. L. Fan and Z. G. Liu, "Mud cover effect of mining-induced failure of soft overburden in thick clay strata," *Journal of Mining & Safety Engineering*, vol. 37, no. 6, pp. 1196–1204, 2020.

[18] F. Q. Wu, J. Y. Liu, T. Liu, H. Zhuang, and C. Yan, "A method for assessment of excavation damaged zone (EDZ) of a rock mass and its application to a dam foundation case," *Engineering Geology*, vol. 104, no. 3-4, pp. 254–262, 2009.

[19] S. N. Dong, Z. B. Yang, and Z. K. Ji, "Study on water-preserved mining technology of burnt rock aquifer beside the large reservoir in Shenfu mining area," *Journal of China Coal Society*, vol. 44, no. 3, pp. 709–717, 2019.

[20] X. M. Guo and S. N. Dong, "Seepage law of bedrock aquifer and water-preserved mining technology in deep coal seam mining," *Journal of China Coal Society*, vol. 44, no. 3, pp. 805–812, 2019.

[21] X. J. Du, G. R. Feng, and T. Y. Qi, "Roof stability analyses of "water-preserved and water-stored" coal mining with constructional backfill mining," *Journal of China Coal Society*, vol. 44, no. 3, pp. 821–830, 2019.

[22] X. P. Lai, M. F. Cai, F. H. Ren, M. Xie, and T. Esaki, "Assessment of rock mass characteristics and the excavation disturbed zone in the Lingxin Coal Mine beneath the Xitian river, China," *International Journal of Rock Mechanics & Mining Sciences*, vol. 43, no. 4, pp. 572–581, 2006.

[23] X. P. Lai, H. C. Xu, J. D. Fan et al., "Study on the mechanism and control of rock burst of coal pillar under complex conditions," *Geofluids*, vol. 2020, Article ID 8847003, 19 pages, 2020.

[24] X. P. Lai, J. J. Dai, and C. Li, "Analysis on hazard characteristics of overburden structure in steeply inclined coal seam," *Journal of China Coal Society*, vol. 45, no. 1, pp. 122–130, 2020.

[25] X. P. Lai, J. J. Dai, H. D. Xu, and X. Z. Chen, "Multifield environmental analysis and hazards prevention of steeply inclined deep coal mining," *Advances in Civil Engineering*, vol. 2021, Article ID 6651088, 12 pages, 2021.

[26] X. Y. Yu and E. Q. Zhang, *Mining Damage Science*, Coal Industry Press, Beijing, China, 2nd ed edition, 2010.

Hindawi
Geofluids
Volume 2021, Article ID 5536786, 12 pages
https://doi.org/10.1155/2021/5536786

Research Article

Experimental Study on Formation Slip under Injection-Production Interregional Pressure Difference Based on the Abnormal Similarity Theory

Chaoyang Hu[1], **Fengjiao Wang**[1], **Tingting Wang**[2], **Chi Ai**[1], and **Chenyu Wu**[3,4]

[1]*Laboratory of Enhanced Oil Recovery of Education Ministry, Northeast Petroleum University, Daqing, 163318 Heilongjiang, China*
[2]*School of Electrical Engineering and Information, Northeast Petroleum University, Daqing, 163318 Heilongjiang, China*
[3]*Daqing Oilfield Production Engineering Research Institute, Daqing, 163453 Heilongjiang, China*
[4]*Heilongjiang Provincial Key Laboratory of Oil and Gas Reservoir Stimulation, Daqing, 163453 Heilongjiang, China*

Correspondence should be addressed to Fengjiao Wang; wangfengjiao8699@126.com
and Tingting Wang; wangtingting@nepu.edu.cn

Received 18 February 2021; Accepted 11 August 2021; Published 7 September 2021

Academic Editor: Jia Liu

In oilfield development, the pore pressure difference between adjacent areas leads to cracks and slipping in the weak structural surface layer, which triggers the shear failure of the casing. The formation slip involves a large range of formation, and its amount is not proportional to the size of the slipping rock mass, which conventional physical models cannot simulate. In this study, based on the abnormal similarity theory, we derived the similarity coefficients of mechanical parameters with different horizontal and vertical proportions. Furthermore, an experimental device for simulating the formation crack and slip under interregional formation pressure difference was developed. Through the experiments, we obtained slip conditions under different pressure differences between adjacent areas and different oil layers and fault surface depths. The study shows that the pore pressure difference between adjacent areas is the driving force of the formation slips. The slip zone is located in the middle of two abnormal pressure zones, and the distance between the adjacent areas can affect the slip range. The deep burial of the oil layer and shallow depth of the weak structural surface can trigger a more significant formation slip. The experimental method proposed in this paper provides an experimental device and method for understanding the formation of cracks and slips on weak structural surfaces. The experimental results provide a theoretical basis for the prevention of shear-type casing damage caused by formation slip.

1. Introduction

When an oil field is developed, the average formation pressure difference between adjacent blocks gradually occurs, which leads to a formation pressure difference between adjacent areas. The pressure difference between adjacent areas can make the formation produce nonuniform longitudinal deformation and exert a force on the upper formation. For formations with weak upper horizontal structural surfaces, the pressure difference between the adjacent areas can lead to the formation of cracks and slips at the weak horizontal structural surfaces, leading to shear-type casing damage. Taking the Daqing Oilfield in China as an example, at the bottom of the Nen'er member in the upper oil layers, there is a mud-shale standard layer, which can be used as a standard for identifying other layers because of its obvious logging characteristics. This mud-shale standard layer has a small dip angle and a stable distribution throughout the entire region. There are a large number of low-strength fossils in the standard layer, which constitute the horizontal weak structural surface, and have been damaged in a large area, forming a horizontal crack surface. For example, after long-term high-pressure water injection and polymer injection development in the Daqing Oilfield, the Sazhong Development Zone has formed nine casing-damage concentration areas with a total area of 38.34 km^2. The casing damage rate in the concentration area is as high as 80%, and most are shear-type casing damage [1–4]. The casing damage in these areas has the characteristics of layer concentration, region concentration, and time concentration.

Domestic and foreign scholars have studied the mechanism of casing damage for many years, and both have confirmed that the change in reservoir injection and production pressure can cause the crack and slip of the horizontal weak structural surface [5–8]. At present, the typical research method is to use a finite element model and simulations to determine the influence of reservoir deformation on the degree of cracks, slips, and casing damage [9–11]. However, with the long-term overpressure development of oil fields, casing damage is increasingly frequent, and even regional casing damage is formed in the standard mud-shale formations of the Daqing Oilfield [12–14]. Because the mechanism of slip casing damage on the mud-shale crack surface is still not clear, and the mechanical model of formation slip and experimental methods have not been formulated, only field experience or conservative methods can be generally used for prevention measures at present. Additionally, a large area of injection reduction and closure of more than 100 injection wells in the casing damage area seriously affects the production of oil fields. The means of prevention and control are not informed, and the pertinence of the problem is poor, resulting in a lack of active monitoring of casing damage. Understanding the mechanism of casing damage is the key point to preventing, controlling, and managing casing damage on weak horizontal structure surfaces. Therefore, establishing a laboratory experimental device that simulates the sliding casing damage on a horizontal crack surface and reveals the mechanism of regional casing damage is critical.

It is important to verify the mechanism of standard layer shear-type casing damage through laboratory experiments [15, 16]. However, owing to the limitations of experimental conditions and measurement methods, there are only direct dynamic shear-type casing damage experiments and underground mining ground deformation experiments. Sun [17] used a high-strength expansion agent to simulate formation stress; they inserted the simulation casing into the middle of the device, then inserted the expansion agent into one side of the experimental device, and, through the expansion agent, simulated the formation near the wellbore to shear the casing directly. Yin [18] conducted a direct shear test on a J55 casing with a TS-1 casing damage testing machine independently developed for in situ stress by the Laboratory of China Petroleum Exploration and Development Research Institute. The above two experiments simulated the formation of shear-type casing damage, but the actual casing damage process was greatly simplified in the experiments. In the experiments, the source of shear force was a direct thrust from two sides, but it could not explain the source of shear stress in the actual formation. In addition, there are no other reports on laboratory experimental devices for shear-type casing damage in the petroleum development field.

In an indoor physical simulation experiment of formation deformation in the mining field, Gong et al. [19] established a simulation experiment device for mining subsidence under complex geological conditions by using a similar material model with a scale of 1 : 200, model frame length of 2.1 m, and height of 1 m. The model was divided into 10 layers. It was laid in layers, and the layers were separated using an appropriate amount of mica powder. Zou and Chai [20] established a similar two-dimensional model test-bed using similar materials for simulated formation and measured the displacement state of the simulated formation after mining using laser reflection. However, the above experimental equipment was mainly aimed at underground air excavation to surface deformation and cannot determine the role of regional formation pore pressure difference [21]. The slip of the horizontal weak structural surface was caused by the relative slip between layers inside the formation, which was quite different from the measurement purpose of this experiment. In addition, there are no reports on laboratory test equipment and methods for shear-type casing damage caused by formation slip.

In this study, we propose a set of experimental devices that can simulate and measure formation slip. Based on the abnormal similarity theory with different horizontal and vertical scale similarity ratios, we carried out a formation slip simulation experiment under injection-production interregional pressure difference. The corresponding measurement method and experimental steps of formation slip were designed according to the slip characteristics of the mud-shale crack surface. Based on the abnormal similarity theory, the corresponding relationship between the experimental model and the prototype formation slip was established, and the formation slip at different positions under different conditions was measured and compared with the theoretical calculation results, and the factors influencing the formation slip were analyzed.

2. Materials and Methods

2.1. Experiment Method Based on the Similarity Model. The formation swelling and deformation caused by pore pressure changes are from the underground target layer to several hundred meters above the ground and several thousand meters in the horizontal direction, which reflects two prominent problems: a big volume is involved [22–25] and the great difference between horizontal and vertical proportions. The sliding layer is not a water flooding reservoir, but the nonproduction horizontal layer is approximately 70 m above it. The geological conditions are shown in Figure 1.

To solve the above problems, the simulated formation material was used instead of the actual formation, and a similar method was adopted to conduct the simulation experiment. Model experiments with different aspect ratios were designed according to the characteristics of the formation. The dimensional analysis method (π theorem) is applied to derive the similarity relationship between each physical quantity and determine the similarity constant of each physical quantity. In this experiment, the horizontal and vertical dimensions of the geometric parameters were analyzed with different scaling coefficients, and the length dimensions representing the horizontal and vertical directions were taken as different dimensions, $[L_r]$ and $[L_z]$, respectively.

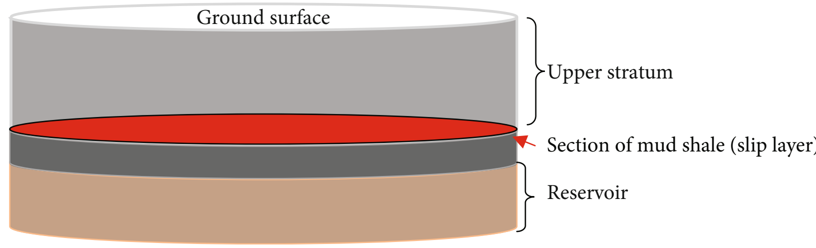

Figure 1: The geological conditions of slip layer.

According to the definition of each physical quantity, the dimensions of each physical quantity based on the above assumptions were obtained, as shown in Table 1.

D is the radial size (m) H is the vertical dimension (m), u is the radial displacement (m), w is the vertical displacement (m), σ_r is the radial stress (MPa), σ_z is the vertical stress (MPa), ε_r is the radial strain (nondimensional), ε_z is the vertical strain (nondimensional), E_r is the radial Young's modulus (MPa), E_z is the vertical Young's modulus (MPa), μ_{zr} is the radial Poisson's ratio (nondimensional), and μ_{rz} is the nondimensional vertical Poisson's ratio.

In this physical simulation experiment, the dimensions $[T]$ and $[M]$ corresponding to the basic dimension are determined in proportion, so only the change in dimension $[M]$ needs to be considered. Therefore, D, H, and E_r are taken as the basic dimensions to obtain the dimensionless π terms of other physical quantities, as shown in Table 2.

The horizontal and vertical similarity ratios of the physical model and formation prototype were different. According to the distortion compensation model, the respective π terms are assumed to form a product relation. Then, the relation between the independent π terms is as follows:

$$\pi = \left(A_1 \pi_{a_1}^{e_1}\right) \cdots \left(A_i \pi_{a_i}^{e_i}\right) f\left(\pi_{u_1}, \pi_{u_2}, \cdots\right), \tag{1}$$

where π_{ai} is the π term with dimensional parameters. When the parameters of some similar materials fail to meet the similarity ratio requirements in model design and material selection, they distort the model system. $\pi_{u1}$and π_{u2} are dimensionless parameter π terms, e_i is distorted idempotent, and A_i is an infinite constant.

The prediction coefficient δ_i generated by model distortion is expressed as follows:

$$\delta_i = \left(\beta_1^{-e_1}\right) \cdots \left(\beta_i^{-e_i}\right) \left[\frac{f(\pi_{u1}, \pi_{u2}, \cdots)_p}{f(\pi_{u1}, \pi_{u2}, \cdots)_m}\right], \tag{2}$$

where δ_i is the coefficient of prediction, β_i is the distortion coefficient of each parameter π term, $\beta_i = \pi_{im}/\pi_{ip}$, and π_{im} and π_{ip} are dimensionless π terms for each parameter. The subscript "p" represents the parameters of the formation prototype, and the subscript "m" represents the parameters of the experimental model.

Thus, the similarity ratio relation can be obtained as follows:

$$\begin{cases} C_u = \delta_1 C_D, \\ C_w = \delta_2 C_H, \\ C_{\sigma_r} = \delta_3 C_{E_r}, \\ C_{\sigma_z} = \delta_4 C_D{}^{-2} C_H{}^2 C_{E_r}, \\ C_{E_z} = \delta_5 C_D{}^{-2} C_H{}^2 C_{E_r}, \\ C_{\mu_{zr}} = \delta_6 C_D{}^{-2} C_H{}^2, \\ C_{\mu_{rz}} = \delta_7 C_D{}^2 C_H{}^{-2}, \end{cases} \tag{3}$$

where C_f is the similarity ratio of the parameter $f = (D, H, u, \cdots, \mu_{rz})$ and δ_i is the prediction coefficient generated by the model distortion.

Both experimental models and stratigraphic prototypes, simulated stratigraphic materials, and stratigraphic rocks can be considered as isotropic materials. Therefore, the following relations are obtained:

$$\delta_3 = \frac{C_D{}^2}{C_H{}^2}, \quad \delta_4 = \delta_5 \frac{C_D{}^2}{C_H{}^2}, \quad \delta_6 = \delta_7 \frac{C_D{}^4}{C_H{}^4}. \tag{4}$$

Then, the similarity ratio of the dimensionless parameters is obtained as follows:

$$C_{\varepsilon_r} = \frac{\varepsilon_{rp}}{\varepsilon_{rm}} = \frac{C_{E_r}}{C_{\sigma_r}} \frac{1 + 2\mu_{rzp}}{1 + 2\mu_{rzm}} = \frac{C_H{}^2}{C_D{}^2} \frac{1 + 2\mu_{rzp}}{1 + 2\mu_{rzm}}, \quad C_{\varepsilon_z} = \frac{\varepsilon_{zp}}{\varepsilon_{zm}} \frac{C_{E_z}}{C_{\sigma_z}} \frac{1 + 2\mu_{rzp}}{1 + 2\mu_{rzm}} = \frac{C_H{}^2}{C_D{}^2} \frac{1 + 2\mu_{rzp}}{1 + 2\mu_{rzm}}. \tag{5}$$

Table 1: Dimensions of physical quantities based on different horizontal and vertical length ratios.

Basic dimensions	D	H	u	w	σ_r	σ_z	ε_r	ε_z	E_r	E_z	μ_{zr}	μ_{rz}
$[M]$	0	0	0	0	1	1	0	0	1	1	0	0
$[L_r]$	1	0	1	0	0	-2	0	0	0	-2	2	-2
$[L_z]$	0	1	0	1	-1	1	0	0	-1	1	-2	2
$[T]$	0	0	0	0	-2	-2	0	0	-2	-2	0	0

In the design of a structure dissimilar model, factors such as type, material, manufacturing conditions, loading capacity, arrangement of measuring points, and equipment conditions should be considered comprehensively in the geometric size of the model. An experimental model that is too small will lead to high requirements for experimental processing and instrument measurement accuracy, and an excessively large experimental model will inconvenience the experiment. Therefore, it is necessary to consider these factors in selecting the experimental size and materials. For this experiment, given the lateral and vertical dimensional similarity ratio and mechanical parameters of the simulated stratum, the similarity ratio of the other parameters and the corresponding prediction coefficients can be obtained.

Considering the elastic modulus, strength, and actual processing capacity of each material comprehensively, soft polyvinyl chloride was selected as the simulated formation material of the similar model. Considering that the actual water injection pressure of the experimental model was generally less than 1.5 MPa, the simulated stress of the formation material is in the linear elastic deformation range. At the same time, under the action of interregional pore pressure, the formation prototype was in the linear elastic deformation range regardless of the oil layer, overburden, or even the surface position and did not involve nonlinear yield deformation and failure. Therefore, for the experiments, this polymer material could be used as a simulated stratum instead of rocks.

Thus, the experimental model and formation prototype parameters were obtained, as shown in Table 3.

According to the similarity theory, the similarity ratio and prediction coefficient of each parameter between the actual stratigraphic prototype and the experimental model of the upper and lower layers are shown in Tables 4 and 5, respectively.

The values of the corresponding parameters of the actual formation can be obtained by multiplying the parameters of the simulated formation in the experimental model with the corresponding parameter similarity ratio.

2.2. Equipment. The crack and slip of the horizontal weak structural surface at the bottom of the Nen'er member is caused by the vertical deformation of the bottom oil layer, which is characterized by no stress at the top and deformation at the bottom under the action of formation pressure. However, deformation through the formation pore pressure requires the accumulation of a large thickness, which cannot be achieved by laboratory experiments to produce the bottom deformation of the formation slip. In a previous finite element study, bottom water injection pressurization pressure was similar to that of interregional formation pore pressure. For this reason, we used bottom water injection pressurization to simulate the interregional formation pressure difference. However, this type of experimental equipment is unprecedented and requires additional design and manufacturing. To experimentally achieve formation slip deformation with different radial sizes, a flange adapter was used, which could correspond to the experimental materials with diameters of 250 mm, 300 mm, and 400 mm. In this experiment, a two-dimensional axisymmetric model was used. To ensure that the deformation of the equipment is very small when simulating formation deformation, steel equipment with a height of 1000 mm and a wall thickness of 40 mm that can withstand a pressure of 5 MPa without leakage was used. The maximum bearing capacity of the designed physical simulation device of a weak structure surface slip under the action of the interlayer pressure difference was 5 MPa, and the diagram of its structure is shown in Figure 2.

In the experiment, a combination of a manual pump and a constant-flux pump was used to inject liquid into the device to achieve pressurization. The maximum allowable pressure of the constant-flux pump was 42 MPa, the minimum flow rate was 0.001 mL/s, and the maximum flow rate was 1.000 mL/s. First, the manual pump was used for rapid pressurization. Then, when all the liquid in the pump was pumped into the equipment to reach the experimental pressure, the constant-flux pump was used for slow and accurate pressurization until the pressure required by the experiment was reached. The manual liquid booster pump, advection pump, and formation deformation test device were connected through six channels, and a pressure gauge was installed on the six channels to measure the internal liquid pressure (Figure 2).

2.3. Method for Measuring Formation Slip. By connecting the water injection pressurization system with the main experimental equipment, simulated formation expansion can be achieved. The vertical displacement of the formation was accurately measured with a displacement measurement device with an accuracy of 0.001 mm and a range of 15.000 mm. For continuous and stable measurements of the formation with the displacement measurement device, a custom steel plate was made to fix it. The middle and both ends of the customized steel plate were equipped with a drill hole. The drill hole in the middle was used to install the

Table 2: The dimensionless π term of each physical parameter.

Number	Parameter	Dimensionless π term	Number	Parameter	Dimensionless π term
1	Radial displacement	$\pi_1 = u/D$	2	Vertical displacement	$\pi_2 = w/H$
3	Radial Young's modulus	$\pi_3 = \sigma_r/E_r$	4	Vertical stress	$\pi_4 = \sigma_z/u^{-2}w^2E_r$
5	Vertical Young's modulus	$\pi_5 = E_z/u^{-2}w^2E_r$	6	Vertical Poisson's ratio	$\pi_6 = \mu_{zr}/u^{-2}w^2$
7	Vertical Poisson's ratio	$\pi_7 = \mu_{rz}/u^2w^{-2}$			

Table 3: Parameter comparison between the similar model and formation prototype.

Formation parameters	Similar model	Actual formation model
Elastic modulus	2.04 GPa	25 GPa
Poisson's ratio	0.31	0.25
Formation diameter	250 mm, 300 mm, 400 mm	1500 m, 1800 m, 2400 m
The total thickness of the formation	The upper formation 15.0 mm The lower formation 5.0 mm	The upper formation 600 m The lower formation 200 m

Table 4: Each prediction coefficient of the similar model.

Prediction coefficient generated by model distortion		Prediction coefficient generated by model distortion	
Transverse modulus of elasticity	$\delta_3 = 0.0900$	Longitudinal stress	$\delta_4 = 0.0081$
Longitudinal modulus of elasticity	$\delta_5 = 0.0900$	Transverse Poisson's ratio	$\delta_6 = 0.0726$
Longitudinal Poisson's ratio	$\delta_7 = 8.9606$		

Table 5: Similarity ratio of parameters between the actual formation prototype and similar model.

	D	H	σ_r	σ_z	ε_r	ε_z	E_r	E_z	μ_{zr}	μ_{rz}
Similarity ratio	12000	40000	62.12	62.12	0.662	0.662	10.288	10.288	7.353	7.353

displacement measurement device. The two ends could be fitted to the flange of the formation-deformation measuring device.

The soft adhesive of epoxy resin selected in the formation slip experiment, with an operation time of 4 h and solidification time of 12 h, was used to simulate the casing deformation and slip under the formation-deformation condition. The epoxy resin adhesive was formed by gradual thickening and condensation after mixing liquids A and B. The hardness and softness of the epoxy resin could also be adjusted according to the different formulations and solidification times. In this experiment, a soft adhesive with a solidification time of 12 h was selected. Both liquids A and B were of this type of epoxy resin adhesive and were low-viscosity solutions. After mixing, the viscosity gradually increases; good fluidity was maintained in the first 30 min, and the initial setting time was 4 h. From 4 h to 10 h, it became a solid, and the mobility almost disappeared, but the plasticity was strong; that is, after the deformation under the action of an external force, the shape could not be recovered. After 10 h, the plastic characteristics gradually transformed into elastic characteristics. After 12 h, the epoxy resin adhesive was set with strong elasticity and a certain memory effect; that is, after the external force was applied to deform it, the deformation could be recovered by removing the external force. The AB epoxy resin adhesive maintained a long fluidity time. In the slip experiment of a weak horizontal structural surface, the amount of expansion of the simulated material should be kept constant; thus, a material with moderate solidification time was needed to simulate the deformation condition of the casing in maintaining formation uplift. However, the preparation process took a long time, so the epoxy resin needed to maintain a certain period of fluidity before solidification. The solidified epoxy resin adhesive maintained its deformed state during solidification and returned to its original state when the force was removed. The epoxy resin adhesive is a fluid before curing and can deform with the internal deformation of the casing. Soft epoxy adhesives have good scalability after curing and are not easily damaged by large deformations. This type of epoxy resin deforms during disassembly, but the deformation is within the elastic range. After the epoxy resin adhesive was

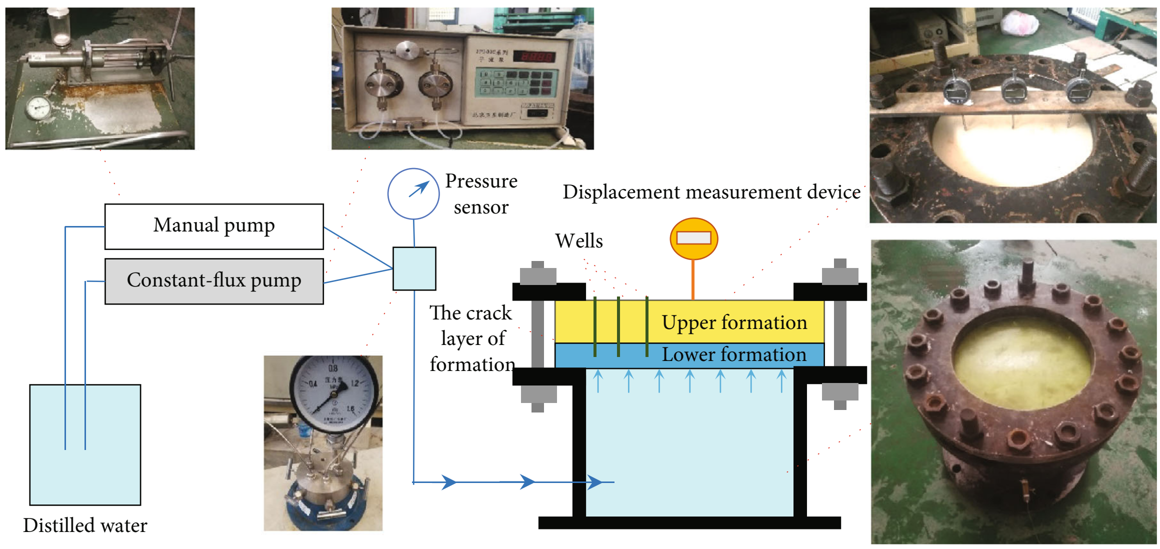

Figure 2: The connection diagram of the formation deformation experiment and stress measuring devices.

removed, it returned to the shape of the formation slip and did not affect the slip measurement results.

The epoxy resin was solidified in the hole, and after removing all external forces, the epoxy resin deformed to the solidified shape, that is, the hole position slippage state due to the formation expansion. This method can be used to easily observe the variation characteristics of slip at different planes for formation expansion induced by hydraulic fracturing. To avoid the mutual interference of the stress concentration near the hole, the spiral layout mode was selected after observing the hole layout. The holes of the simulated material were all distributed on the helix. This ensured that the spacing between the holes was the same and the straight distance between the holes was not too short. In the experiment, the distance between the actual holes was extended to an average of 34.6 mm by spiral distribution drilling. The shortest distance between two holes was 25.4 mm. The stress between holes with a diameter of 2 mm was very small.

If the method of injecting epoxy resin directly into the simulated formation was adopted, the epoxy resin glue would be completely cemented in the inner wall of the observed hole, and the epoxy resin glue would not be removable or would be seriously damaged after removal. Therefore, a method of inserting a polytetrafluoroethylene (PTFE) pipe into the hole to simulate the casing was designed. PTFE has a strong resistance to organic solvents and is not easy to glue. The epoxy resin adhesive did not stick to the PTFE after solidification and could be easily removed. In addition, in order to prevent the leakage of epoxy resin glue during injection and the experiment, a length of 1–2 mm at the bottom of the simulated casing of the PTFE pipe was sealed in advance. Because the epoxy resin adhesive was transparent, dye was added to the epoxy resin adhesive to change its color in order to facilitate observation in the experiment; the dye was very low in content, with only 0.1% concentration dying the epoxy resin. After the formation slip experiment was completed, the

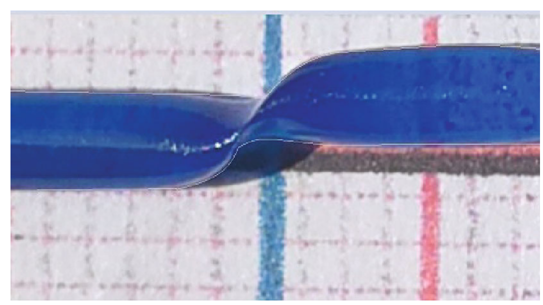

Figure 3: Enlarged image of simulated wellbore deformation.

morphology of the epoxy resin glue was the internal morphology of the observation hole. Owing to the small amount of deformation in the observation of the inner shape of the hole, there would be a large error in the direct measurement using the measuring tool; thus, the deformation could not be measured directly. In the actual measurement process, the deformation was obtained by enlarging a picture of the epoxy resin for accurate measurement and then reducing the corresponding multiple, as shown in Figure 3.

Through the magnification measurement method, the transverse shear deformation at the position of the crack-slip surface in the observation hole was obtained. Combined with the relationship between the formation slip and transverse shear deformation of the observation hole, the interlayer slip at the observation hole position was calculated, as shown in the following equation:

$$s_i = s_{i(w)} + d_w \alpha_w - D_c, \tag{6}$$

where s_i is the slip amount of the hole at the position numbered point i (mm), $s_{i(w)}$ is the transverse shear deformation of the bedding crack surface inside the hole at the point numbered point i (mm), d_w is the bit diameter (mm), α_w

Figure 4: Drilling and gluing.

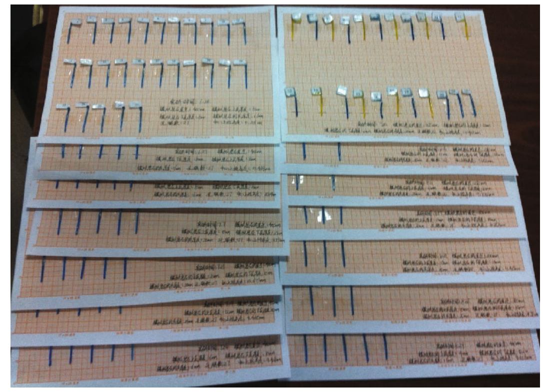

Figure 5: The borehole interior morphology after the formation slip experiment.

is the reaming rate of the bit (for PVC, an easy-to-drill material, the reaming rate is generally 5%), and D_c is the simulated casing outer diameter (mm).

2.4. Experimental Procedure

(1) The flange conversion joint corresponding to the experimental size of the experimental material was installed on the experimental equipment, and the water tank was filled with water in advance

(2) The simulated material was fixed to an experimental device. The simulated stratum was placed in the experimental device according to the designed sequence, and the bottom of the simulated stratum was sealed to prevent liquid leakage. The top bolt was tightened to fix the simulated formation boundary. Subsequently, the sealing and connectivity of the experimental device were examined

(3) The boreholes were marked on the simulated formation device according to the designed position, and the simulated boreholes were drilled with an electric drill, with the drilling depth guaranteed to meet the experimental requirements. This is shown in Figure 4

(4) Timing immediately started at the configuration of the epoxy resin adhesive. The prepared simulated casing was inserted into the simulated well, and the configured epoxy resin adhesive was injected into the simulated casing with a syringe installed with a long glue injection needle. The casing ensures that the epoxy resin adhesive will not flow into the micro-tensioned layer when the formation slips. The thickness of the casing was 0.1 mm, which hardly changed when the formation was deformed, and it did not affect the experimental results. The viscosity of the epoxy resin adhesive increased sharply. After 15 min, although the epoxy resin adhesive is still a fluid, it cannot be injected into the casing through a syringe, resulting in the failure of the experiment. Therefore, all epoxy resins should be injected into the simulated casing within 15 min

(5) The displacement measuring device was installed on the formation simulation device to detect the swelling displacement of the simulated material

(6) A manual pump was used to inject water into the pressurizing device and to apply pressure to the simulated material for recording the longitudinal deformation and water injection pressure data of the formation. The changes in value of the pressure gauge and displacement measuring device were observed. The water injection pressure in the experiment is different from the pore pressure in the actual formation; therefore, it cannot be directly used as the pore pressure of the formation. It must be equivalent to the pore pressure of the reservoir required by the simulation of the uplift of the formation center in the experiment and the corresponding uplift of the actual formation. During this period, it is necessary to find the corresponding relationship between the pore pressure variation and the experimental water injection pressure by numerical simulation. When the displacement measurement device reached the experimental design of longitudinal deformation, the pressure was stopped to keep the pressure unchanged. The above steps were carried out within 1 h after the epoxy resin adhesive was mixed, that is, before the initial setting of the epoxy resin adhesive

(7) A constant-flux pump was used to keep the pressure value of the bottom booster unchanged. Then, the epoxy resin adhesive took 12 h to set

(8) After 12 h, the drainage valve was opened to relieve pressure. Then, the pressure of the experimental equipment was removed, and the simulated casing in the simulated formation was removed. After the simulated casing was cut open, the epoxy resin adhesive reflecting the formation slip shape of each simulated well was removed and pasted on the coordinate paper with formation information to complete the slip measurement

Table 6: Experimental parameters of each group.

Serial number	The interregion formation pressure difference (MPa)	Abnormal formation pressure area (m)	The depth of formation (m)	The depth of horizontal weak structure surface (m)
1	1.59	1500	800	600
2	1.98	1500	800	600
3	2.38	1500	800	600
4	1.59	1800	800	600
5	1.59	2400	800	600
6	1.59	2400	640	600
7	1.59	2400	960	600
8	1.59	2400	800	560
9	1.59	2400	800	680

3. Experimental Result

The experimental device we developed was used to carry out several groups of formation slip experiments, and the formation slip distribution was measured under different pressures, simulated formation diameters, reservoir-buried thicknesses, and crack surface depths, and the internal morphology of the simulated well after deformation was obtained, as shown in Figure 5.

The mechanical parameters of the experimental model and the formation prototype were based on the data in Table 3. We conducted a total of 14 groups of experiments, nine of which were effective. Nine valid sets of experimental data are listed in Table 6.

The slip distributions on the crack surface between the top and bottom formations under different water injection pressures (serial numbers 1, 2, and 3) were compared for a simulated formation diameter of 250 mm, as shown in Figure 6.

The slip of the crack surface is a relative displacement, that is, the difference between the radial displacements of the upper and lower layers of the horizontal crack surface. In the simulation experiment, the displacement of the upper and lower parts of the crack surface could not be measured, and the slip could only be determined by observing the solidification shape of the epoxy resin adhesive in the borehole. The experimental results showed that after the deformation of the simulated formation bottom, the simulated formation above was deformed by pressure from the bottom. Although the layer in the middle of the simulated formation could maintain the longitudinal continuity of the stratum, it had a relative displacement in the horizontal direction. Although the surrounding area of the simulated formation was completely fixed and the center of the formation did not slip under symmetric action, there was also a slip in the middle. It can be seen from Figure 6 that under different vertical displacements of the formation center, the variation trend of the interlayer slip was the same, which first increased and then decreased with an increase in distance from the center. By comparing the slippage of different vertical displacements at the center of the formation, it was found that the slippage on the horizontal crack surface of the formation had a linear relationship with the longitudinal displacements at the center.

The actual slip of the formation can be obtained by multiplying the slip value by the transverse proportionality coefficient. The interregional formation pressure difference did not correspond to the water injection pressure at the bottom of the test equipment. The pressure difference between the adjacent regions of the actual formation can be calculated according to its effect on the formation. First, the corresponding relationship between the formation pressure difference and the vertical deformation of the surface center was calculated based on the finite element simulation. Then, according to the simulated uplift height multiplied by the longitudinal length ratio, the actual maximum vertical deformation height of the formation can be obtained to determine the regional formation pressure difference of the actual formation. Through calculations, it was determined that in the actual formation corresponding to the experimental conditions, the slip amounts at different positions corresponding to the interregional pressure difference (serial numbers 1, 2, and 3) were as in Figure 7.

Through scale conversion, the size of the experimental model was converted to the actual size of the formation, as shown in Figure 7. The origin of the r coordinate was the center of the abnormally high-pressure area, and the position $r = 1500$ m was the center of the low-pressure area. The slip of the crack surface occurred between the high-pressure and low-pressure zones, and the slip first increased and then decreased. In actual oil field production, formation slip will shear the wellbore on the slip surface, resulting in shear-casing damage. In the Daqing Oilfield, the crack surface was uncemented to prevent shear-casing damage, leaving room for formation slip. When the formation slip exceeded 60 mm, the formation would cause the shear deformation of the casing and affect the production of the oil and water wells. Based on this amount of slip, the maximum interregional formation pressure difference was 0.69 MPa for no casing damage occurred on this field.

The range of the interregional formation pressure difference also affects the slip on the horizontal crack surface of the horizontal weak structure layer. Therefore, experiments with different diameters were performed to simulate

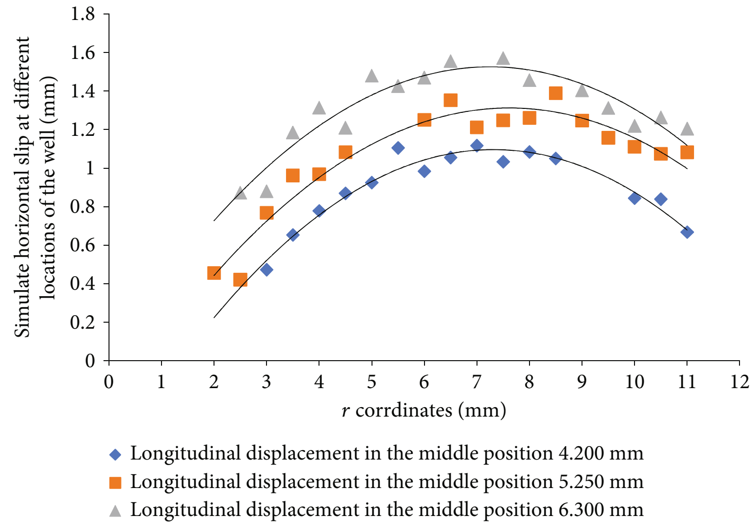

Figure 6: Trend diagram of the slippage experimental results in the mud-shale section under different pressures.

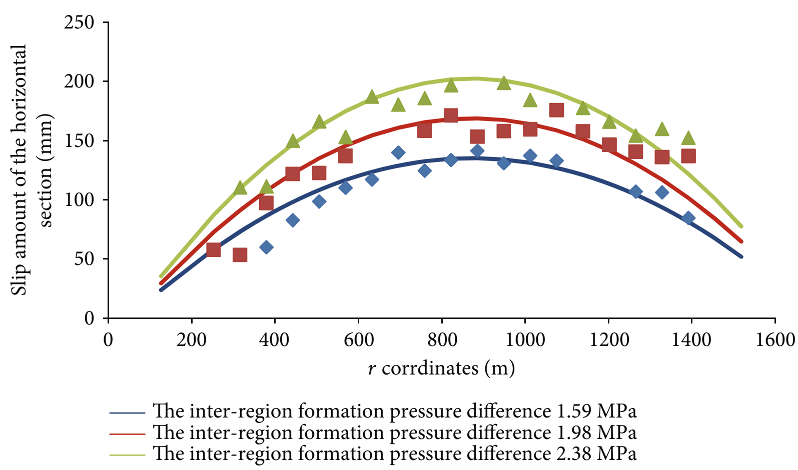

Figure 7: The section slippage in the actual formation of mud shale under different formation pore pressure difference between regions.

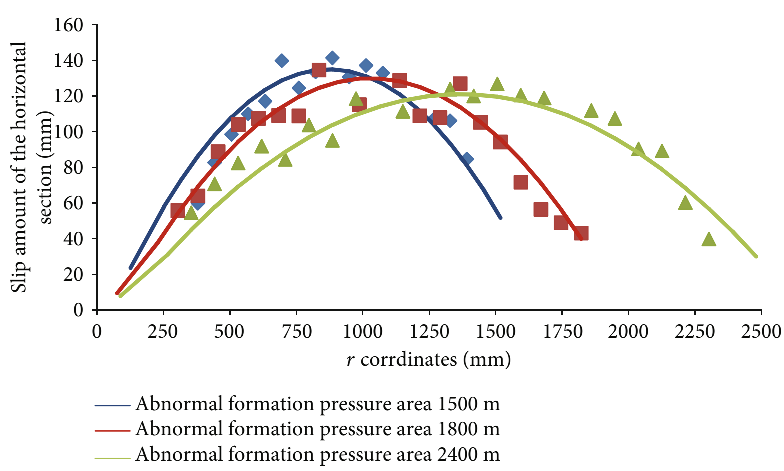

Figure 8: The section slippage in the actual formation of mud shale for a range of different formation pore pressure differences.

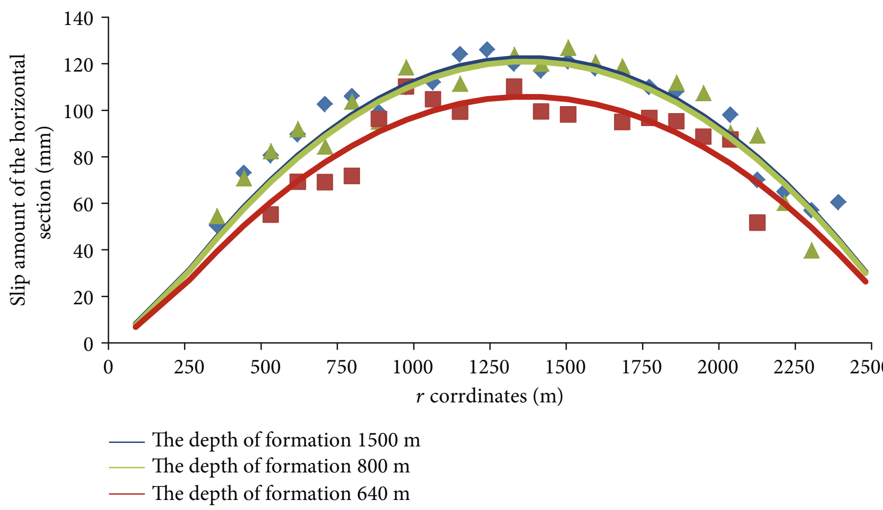

Figure 9: The section slippage in the actual formation of the mud-shale standard layer at different depths.

formation slip. The diameters of the experiment were 250 mm, 300 mm, and 400 mm (serial numbers 1, 4, and 5). The interlayer slip was measured and analyzed where all the longitudinal displacements of the formation center were 4.20 mm, and it was converted into the actual formation conditions under the formation pressure difference in the same area. The results are presented in Figure 8.

After transformation, the formation pressure difference between regions was 1.59 MPa. With an increase in the range of interregional formation pressure, the maximum value of slippage on the mud-shale crack surface decreased slightly and was extrapolated, and the influence range of the interzonal slippage increased. The top depth of the oil layer was different in different blocks, so the variation degree of slippage on the mud-shale crack surface would also change accordingly.

To study the effect of the reservoir depth on the interlayer slip, different simulated formation thickness experiments were carried out to analyze the formation slip under different standard depth conditions. The simulated material in this group was 400 mm in diameter, and the total thicknesses of the simulated formations were 24, 20, and 16 mm. The corresponding total thicknesses of the actual formations were 960 m, 800 m, and 640 m (serial numbers 7, 5, and 6). The relative position of the mud-shale standard layer remained unchanged, and the thickness ratio of the top and bottom layers was 3 : 1. Through the transformation of the measurement results to the actual formation, the slip distribution on the horizontal crack surface of the standard layer was calculated and obtained for an interregional formation pressure difference of 1.59 MPa and different top depths of the oil layers, as shown in Figure 9.

In terms of numerical value and trend, with the increase in reservoir depth, the maximum slip on the mud-shale crack surface increased; however, the increase was small. Within the range of the reservoir top depth in the Daqing Oilfield, the slip varied by 25% at most. The maximum value of slip and the distribution law of slip showed no obvious changes in the three groups of experiments.

To determine the influence of depth on the slippage of the mud-shale crack surface, 400 mm was selected to simulate the formation and ensure that the total thickness of the simulated formation was uniformly 20 mm. Three combined conditions of 13 mm: 7 mm, 15 mm: 5 mm, and 17 mm : 3 mm thickness of the upper and lower layers were studied, and the corresponding horizontal crack surface depths were 520 m, 600 m, and 680 m, respectively (serial numbers 8, 5, and 9). Through the transformation of the measured results to the actual formation, the slip distribution on the horizontal crack surface of the standard layer with different top depths of oil layers was calculated and obtained when the interregional formation pressure difference was 1.59 MPa, as shown in Figure 10.

The calculation results showed that the interlayer slip increased with the upward movement of the relative position of the standard layer. When the mud-shale standard layer was located in the middle of the oil layer and the surface, the maximum slip was caused by the interregional formation pressure difference. This law was very similar to the distribution law of shear stress; that is, under the action of interregional pressure difference, the formation shear stress accumulated from the bottom, reached a maximum in the middle of the formation, and became zero on the surface. In addition, from the calculation results, for different interregional formation pressure differences, action ranges, formation thicknesses, and crack surface depths, the comparison between the experimentally measured data and the theoretically calculated results was in good agreement. In the simulation experiment, a mud-shale standard interlayer slip was observed, the amount of interlayer slip under different conditions was measured, and the accuracy of the theoretical model of formation slip under the effect of interregional formation pressure difference was verified.

The experimental analysis showed that the interregional formation pressure difference between the bottom oil layers was the driving force for the slip of the mud-shale standard layer in the formation, and the formation pore pressure did not need to act directly on the

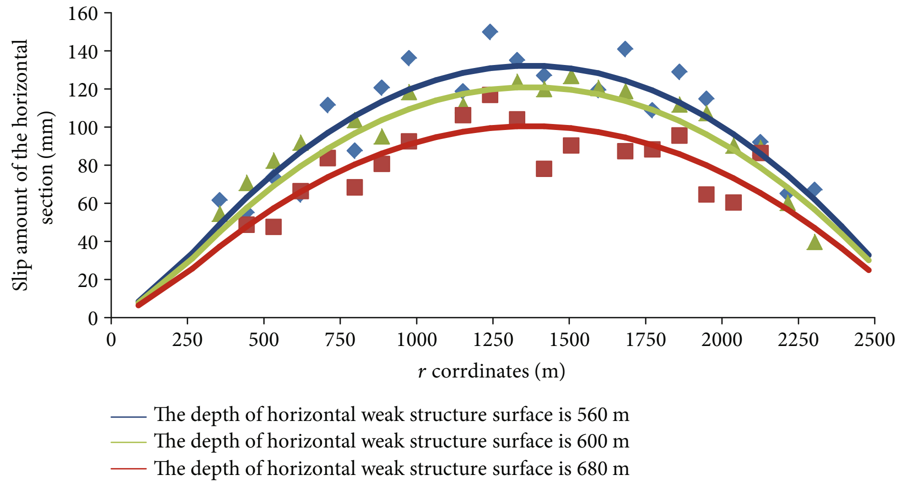

Figure 10: The section slippage of the actual formation of mud shale for different section depths.

formation where the crack surface was located. The interregional formation pressure difference acted on the formation below the crack surface at a certain distance; it could transfer the formation deformation to the crack surface and form the horizontal relative displacement through the uneven longitudinal deformation through the formation rock. When the distance of the interregion was greater than 1500 m, with an increase in the distance between regions, the maximum slip amount generated by the pressure difference between regions on the crack surface decreased slightly. However, the influence range of the slip amount increased. Under the actual stratigraphic conditions, the formation with a deep oil layer but relatively shallow horizontal weak structure surface had a relatively large slip amount caused by cracks. In oilfield development, in order to prevent casing damage caused by formation slip, the interregional formation pressure difference should be reduced to less than 0.69 MPa (taking Daqing Oilfield as an example). However, for formations with deep burial locations and relatively shallow horizontal weak structural surfaces, it should be emphasized to prevent and control the change in interregional formation pressure difference.

4. Conclusions

(i) In this study, the influence of formation slip due to interregional formation pressure difference was studied using the similarity model. This study solves the problem that indoor simulation experiments cannot be carried out because of the large gap between the horizontal and vertical ratios between the formation prototype and the experimental model. By reserving observation holes and placing soft epoxy resin in the holes and gradually solidifying it under loading conditions, the slip amount of the formation can be measured

(ii) The interregional formation pressure difference can cause relative slip at the weak horizontal structural surface. Shear-casing damage occurs when the local slip exceeds the limit that the wellbore can bear. The pressure difference between the safe zones to prevent casing damage can be obtained from the limit values of the maximum formation slip and shear-casing slip. Through this method, the safe interregion formation pressure difference in the Daqing Oilfield is 0.69 MPa

(iii) The maximum slip amount is located on the weak structural surface between the high- and low-pressure zones. An increase in the interregion spacing can affect the slip range. The formation with a deep burial location and a relatively shallow crack surface will result in a more serious formation slip

Data Availability

The data used to support the findings of this study are included within the article.

Conflicts of Interest

The authors declare that they have no conflicts of interest regarding the publication of this paper.

Acknowledgments

This research was supported by the National Natural Science Foundation of China (Youth Project) (Grant No. 51804076), Joint Guidance Project of Natural Science Foundation of Heilongjiang (Grant No. LH2021E016), China Postdoctoral Science Foundation (Grant No.2021M690528), Postdoctoral Projects in Heilongjiang Province (Grant No. LBH-Z20035), Youth Science Foundation of Northeast Petroleum University (Grant no. 2018QNL-19), and Research Initiation Foundation of Northeast Petroleum University (Grant No. 2019KQ14).

References

[1] L. He, Y. Ye, W. Qunyi, Y. Jianwen, and D. Huilan, "Challenges and countermeasures facing casing damage in Daqing oilfield," in *European Association of Geoscientists & Engineers, 67th EAGE Conference & Exhibition*, pp. 1–00557, Madrid, Spain, Jun 2005.

[2] J. Li, X. Lu, J. Li, Y. Cai, and G. Zeng, "Prediction method and field experiment of casing damage in fault block X of Daqing oilfield," *Acta Petrol Sinica*, vol. 29, no. 4, pp. 625–628, 2008.

[3] C. Hu, J. Gao, and Y. Liu, "The impact of casing damage critical condition on marker bed with differential internal and external pressure in Daqing oilfield," *Advances in Petroleum Exploration and Development*, vol. 11, no. 1, pp. 42–44, 2016.

[4] Y. H. Zhao, H. Q. Jiang, H. Q. Li et al., "Research on predictions of casing damage based on machine learning," *Journal of China University of Petroleum*, vol. 44, no. 4, pp. 57–67, 2020.

[5] S. Na, "Slip mechanism of fault due to pressure difference and analysis of casing damage," *Oil and Gas Field Surface Engineering*, vol. 29, no. 5, pp. 23–25, 2010.

[6] J. Chen, Q. Hu, and W. Wu, "Identification method for high-risk position of casing damage in the surface wellbore of a mining subsidence area based on laminate theory," *Disaster Advances*, vol. 6, pp. 139–148, 2013.

[7] L. Gao, L. Qiao, Z. Liu, Z. Zhuang, and H. Yang, "Numerical modeling and cementing countermeasure analysis of casing shear damage in shale reservoir," *China Petroleum Machinery*, vol. 44, no. 10, pp. 6–16, 2016.

[8] S. Q. Yang, P. F. Yin, and Y. H. Huang, "Experiment and discrete element modelling on strength, deformation and failure behaviour of shale under Brazilian compression," *Rock Mechanics and Rock Engineering*, vol. 52, no. 11, pp. 4339–4359, 2019.

[9] Z. Lian, G. Liu, B. Tang, F. Dong, and Y. Li, "Finite element analysis of casing damage in plastic flow formation," *Natural Gas Industry*, vol. 22, no. 6, pp. 55–62, 2002.

[10] H. Chen, N. Ge, and Q. Zhu, "Finite element modeling and mechanism analysis of casing damage in oil wells under liquid–solid interaction," *Journal of Computational and Theoretical Nanoscience*, vol. 19, no. 6, pp. 1701–1704, 2013.

[11] C. Hu, C. Ai, F. Tao, F. Wang, and M. Yan, "Optimization of well completion method and casing design parameters to delay casing impairment caused by formation slippage," in *SPE/IADC Middle East Drilling Technology Conference & Exhibition*, Abu Dhabi, UAE, 2016.

[12] W. Tao, Y. Shenglai, Z. Weihong et al., "Law and countermeasures for the casing damage of oil production wells and water injection wells in Tarim oilfield," *Petroleum Exploration and Development*, vol. 38, no. 3, pp. 352–361, 2011.

[13] E. Engin and O. Cam, "Mechanism analysis of casing damage induced by high pressure water injection in Daqing oilfield," *Journal of Psychiatric and Mental Health Nursing*, vol. 16, no. 5, pp. 462–472, 2010.

[14] Z. Kui, "Research and application of casing damage prevention and early warning system," *Journal of Yangtze University (Nat Sci Edit)*, vol. 9, no. 5, pp. 119–122, 2012.

[15] Z. Liwei, F. Lihua, and C. Yulian, "Research and application on the casing damage repairing technology of the block in tertiary oil recovery," *Science Technology and Engineering*, vol. 14, no. 23, pp. 46–50, 2014.

[16] C. C. Liu, "Casing damage mechanism analysis and preventive measures for oilfield water injection wells," *Petrochemical Technology*, vol. 26, no. 5, pp. 59–66, 2019.

[17] S. Guisheng, *Casing failure forecast and disposal countermeasure research*, Daqing Petroleum Institute, 2008.

[18] F. L. Yin, *The on-line monitoring technology for the casing outside pressure and the casing strain based on the fiber-optic sensing technology*, Harbin Institute of Technology, 2010.

[19] Y. Gong, F. Q. Tang, and J. Zhang, "Research of model test of surface movement and deformation by mining coal in loess mountain area," *Mine Surveying*, vol. 3, pp. 9–11, 2013.

[20] Y. F. Zou and H. B. Chai, *Similarity theory of mining subsidence and its application*, Science Press, 2013.

[21] X. Hui, H. T. Fei, T. Sun, J. Lin, L. Ma, and J. Yang, "Research and application of intelligent casing damage prevention and control system in Daqing oilfield," in *Proceedings of the International Field Exploration and Development Conference*, pp. 3853–3858, Xi'an, China, 2020.

[22] Y. Li, D. Jia, Z. Rui, J. Peng, F. Chunkai, and J. Zhang, "Evaluation method of rock brittleness based on statistical constitutive relations for rock damage," *Journal of Petroleum Science and Engineering*, vol. 153, pp. 123–132, 2017.

[23] T. Wang, T. Zhang, P. G. Ranjith et al., "A new approach to the evaluation of rock mass rupture and brittleness under triaxial stress condition," *Journal of Petroleum Science and Engineering*, vol. 184, article 106482, 2020.

[24] M. Sheng, S. Tian, B. Zhang, and H. Ge, "Frequency analysis of multi-sources acoustic emission from high-velocity waterjet rock drilling and its indicator to drilling efficiency," *International Journal of Rock Mechanics and Mining Sciences*, vol. 115, pp. 137–144, 2019.

[25] Y. Xue, J. Liu, P. G. Ranjith, X. Liang, and S. Wang, "Investigation of the influence of gas fracturing on fracturing characteristics of coal mass and gas extraction efficiency based on a multi-physical field model," *Journal of Petroleum Science and Engineering*, vol. 206, article 109018, 2021.

Hindawi
Geofluids
Volume 2021, Article ID 9965228, 11 pages
https://doi.org/10.1155/2021/9965228

Research Article

Experimental Investigations on Creep Behavior of Coal under Combined Compression and Shear Loading

Rongbin Hou [1,2], Leige Xu [1], Duoxin Zhang [1], Yanke Shi [1,2] and Luyang Shi [1]

[1] *School of Civil Engineering and Communication, North China University of Water Resources and Electric Power, Zhengzhou, 450045 Henan, China*
[2] *MWR Center for Levee Safety and Disease Prevention Research, Yellow River Institute of Hydraulic Research, Zhengzhou 450003, China*

Correspondence should be addressed to Rongbin Hou; hourongbin@ncwu.edu.cn and Yanke Shi; shiyanke@ncwu.edu.cn

Received 15 March 2021; Accepted 16 August 2021; Published 30 August 2021

Academic Editor: Yi Xue

The creep behavior of rock has received much attention for analyzing the long-term response and stability of underground rock engineering structures. Numerous studies have been carried out on the creep properties of various rocks under pure compression conditions. However, little attention has been paid to the creep behavior of rocks in a combined compression-shear loading state. In this work, a novel combined compression and shear test (C-CAST) system was used to carry out inclined uniaxial compression tests and creep tests for various inclination angles (0°, 5°, 10°, and 15°). The results revealed that the peak strength of the coal decreased with the inclination angle of the specimen, which could provide the basis for setting up a creep test scheme. Multistage compression-shear creep tests were carried out on specimens with different inclination angles. Based on the analysis of the creep test data, the creep behavior of the coal in a combined compression-shear state was studied. It was found that the specimen inclination affected the time-dependent deformation, long-term strength (LTS), and time to failure. Compared with the specimen under pure compression, the inclination specimens tend to produce large shear strain with time, while they were more prone to shear failure. The reduction of the long-term strength was closely associated with the increase of the specimen inclination angle when the angle was more than 5°. Moreover, the ratio of the peak strength to the LTS was not affected by the specimen inclination, which is considered an inherent characteristic. We anticipate that the results obtained will assist in pillar design and long-term stability analysis.

1. Introduction

Pillars are common rock structures in underground coal mining that are used to control ground subsidence [1, 2], protect a roadway [3–5], and isolate the underground water in a goaf [6–8]. The reasonable design of a coal pillar to ensure its long-term stability is the prerequisite for underground disaster prevention and ground-surface environment protection. Previous studies on the long-term stability of coal pillars have mostly assumed that the rock structures are in a pure compression loading condition [9–11]. Then, the uniaxial compressive strength (UCS) of coal is incorporated into the formula of the coal pillar strength estimation. However, the axes of the pillars are usually not parallel to the direction of maximum in situ principal stress in mining practices, such as the loading condition of coal pillars in an inclination coal seam. In this case, if the UCS of the rock is substituted into the strength formula of the inclination pillars, the strength of the coal pillar will be overestimated [12, 13]. Pariseau [14] and Foroughi and Vutukuri [15] have noted in their studies that the estimation of the pillar stability in an inclination coal seam becomes complicated based on whether or not the rock structures are in a compression-shear loading condition. Furthermore, some researchers have pointed out that the instability of pillars is also related to the creep behavior of rock [16–18]. For example, Yang et al. [17] pointed out that the creep behavior of rock cannot be ignored in the design of a coal pillar, as evidenced by a creep test and numerical analysis. Hence, a detailed understanding of the creep behavior of coal in a combined compression-shear loading condition is very important in mining, since it helps in the long-term stability analysis of coal pillars.

Creep is a phenomenon in which the deformation of solid materials increases with time under constant stresses below their peak strength. In order to better understand the long-term creep stability of coal pillars in mining projects, numerous creep experiments for coal have been performed in laboratories, and creep models have been put forward. Chen et al. [16] carried out a uniaxial creep test on coal from the Daizhuang Coal Mine in Shangdong, China, to acquire the initial creep stress and long-term strength of the coal for the long-term stability analysis of a coal pillar. Zhao et al. [19] conducted a triaxial creep test to analyze the effect of the creep load level on a time-dependent deformation. The results showed that the transient creep and the steady-state creep were obviously affected by the creep load, and the steady-state creep rate depended on the properties of the coal, the creep load, and the confining pressure. Cai et al. [20] analyzed the hardening damage mechanism of lean coal creep based on the phenomenon for which the instantaneous elastic modulus increased and the viscosity coefficient decreased in the uniaxial compression creep tests. Yang et al. [21] proposed a nonlinear viscoelastic and acceleration creep model of coal based on triaxial creep experiment results at various deviatoric stress levels, which could describe the complete creep stage of coal.

From the abovementioned studies, it is clear that a large number of research conclusions about creep can be well applied on the loading mode of uniaxial compression or triaxial compression. However, few researchers have investigated the time-dependent deformation and long-term strength of coal with a combined compression and shear loading condition. In recent years, the short-term strength, deformation, and microcrack fracturing behaviors of various rocks have been experimentally investigated for dynamic or quasistatic compression-shear loading conditions [12, 22, 23]. For example, Xu and Dai [23] analyzed the mechanical responses of brittle rocks with dynamic compression-shear loading by using a modified split Hopkinson pressure bar (SHPB) system. The results showed that the elastic modulus and the shear modulus were affected by the specimen inclination, and they exhibited loading-path insensitivity for high loading rates. He et al. [12] developed a C-CAST system to study the quasi-static mechanical properties and failure patterns of various rocks with a compression-shear loading condition. The experimental results indicated that both the elastic modulus and the peak strength of the rocks declined as the inclination angle of the specimens increased, and the rocks were prone to shear failure.

Previous studies have shed some light on the influence of specimen inclination perturbation on the short-term mechanical properties of rocks, and many efforts have been devoted to investigating the creep behavior of rocks via the uniaxial or triaxial compressive creep tests as well. Therefore, these findings can provide a good foundation for researching the creep behavior of coal with compression-shear loading. In this research, a series of combined compression-shear loading tests were performed first using the novel C-CAST system. The influence of the coal specimen inclination on the peak strength for compression-shear loading was studied. The results will provide guidance for the design of a compress-shear loading creep test scheme. Then, creep experiments were conducted under combined compression and shear loading conditions to investigate the effects of the specimen inclination on the time-dependent behavior. Additionally, the relationship between the long-term strength and peak strength under combined compression-shear loading conditions was obtained. Finally, the experimental results were discussed in terms of reducing the risk of coal pillar instability in mining engineering.

2. Experiments

2.1. Specimen Preparation. The experimental material used throughout this study was coal, which was collected from the Yuandian Coal Mine in Anhui Province, China. In order to maintain the consistency of the specimens, the coal specimens were cored parallel to the bedding of coal seam at the same construction site and wrapped in plastic sheets to prevent moisture loss. Then, according to the recommendation of the International Society for Rock Mechanics (ISRM), all of the specimens were prepared as cylinders with a diameter of 50 mm and precision ground to 100 ± 0.02 mm in length [24], as shown in Figure 1.

All of the prepared specimens for the experiments in this study needed to undergo strict screening. The specimen screening process was as follows. First, the specimens that had obvious flaws (cracks, pores, and inclusions) on the surface (Figure 1) were excluded. Then, the degree of uniformity among the remaining rock specimens was determined based on the measured P-wave velocity and density of the specimens. As a result of the obvious bedding effect of the wave velocity on the coal specimens [25], the P-wave velocity was measured along with two different diametrical directions and axial directions. The arrangement of ultrasonic transducers on a coal specimen for measuring the P-wave velocity is shown in Figure 2. The average values of the P-wave velocities in the axial direction and the diametrical direction for the specimens were 1537.52 m/s and 1354.78 m/s, respectively. The average density of the specimens was 1453 kg/m^3. In view of the P-wave velocity and density being closely related to the strength of the material [26], the specimens with densities from 1453 to 1453 kg/m^3 and with deviation of wave velocities less than 5% were selected for the subsequent tests.

2.2. Experimental Apparatus and Procedure. The tests were performed at room temperature (25°C) using the servohydraulic mechanic testing system and the novel C-CAST system at the China University of Mining and Technology. The servohydraulic rock mechanic testing system allowed a maximum axial loading of 1000 kN. The axial displacement was automatically recorded by the system. The C-CAST system was originally designed by Fidelis T. Suorineni in cooperation with the University of New South Wales, Australia [12]. Then, He et al. [10] modified the C-CAST system and obtained some valuable research results. In this study, the modified C-CAST system was installed in the

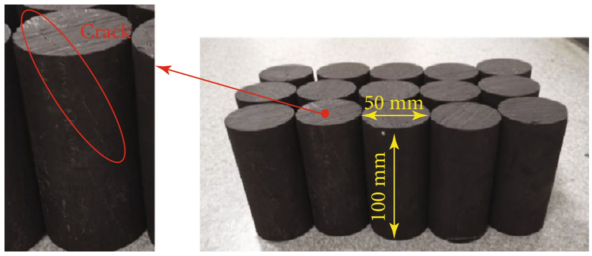

Figure 1: A selection of the coal specimens.

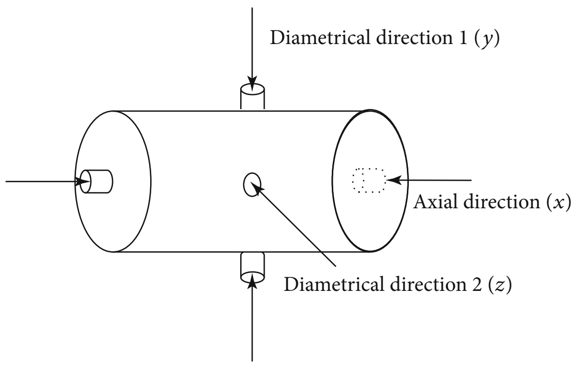

Figure 2: Arrangement of ultrasonic transducers on the coal specimen.

servohydraulic Rock Mechanics Testing System, which could conduct cylindrical specimen inclination loading experiments. The external loading force was applied by the servohydraulic rock mechanic testing system to the adaptors of the C-CAST system. The specimen and the loading diagram of the C-CAST device are shown in Figure 3. The vertical displacement and the loading force of the specimen could be monitored during the tests. Based on the monitoring data and the mechanical analysis, the axial stress, shear stress, axial strain, and shear strain of the specimen under combined compression-shear loading condition were obtained (see Section 2.3).

Understanding the compressive strength and deformation characteristic of rocks is the basis of designing rock creep tests. Therefore, obtaining the peak strength of specimens under compression-shear loading condition is the premise of subsequent creep tests. In this study, the uniaxial compression tests of specimens with four inclined angles were carried out. The inclination angle in this study was set to 0°, 5°, 10°, and 15°. The modified C-CAST system was loaded at a velocity of 0.3 mm/min for all the tests in this study. Five specimens were taken for testing in each test scenario. After the tests, the results that had the highest and lowest vertical peak load values in each test scenario were excluded, and then the peak values of the vertical load were obtained from the remaining three test results. The average values of the peak load for different test scenarios were 34, 31, 21, and 16 kN, which could be used to determine the loading level in the subsequent creep tests.

After the compression-shear tests, creep tests were conducted on the specimens with inclination angles of 0°, 5°,

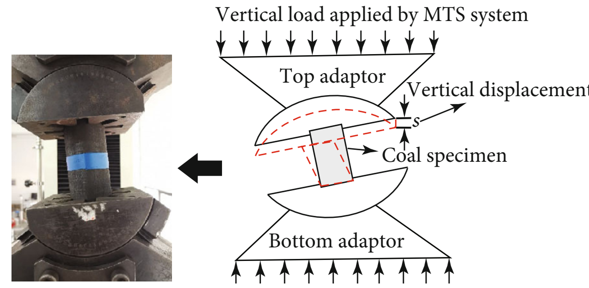

Figure 3: Specimen and loading diagram of C-CAST.

10°, and 15° with multilevel loading. In the creep tests, six creep loading stages were set up, and the vertical loading increment (Figure 3) from one level to the next was 4 kN. The vertical loading levels in the compression-shear creep tests are shown in Figure 4. Each loading level was maintained for 21600 s, except for the last step (at which point the specimens failed).

2.3. Data Processing. For the case of the conventional uniaxial compressive test and the uniaxial creep test, the specimen was in a pure compression state. The deformation state of the specimen before and after loading is shown in Figure 5. Then, the axial stress and strain of the specimen could be obtained from the following equations:

$$\sigma_0 = \frac{F_v}{A_0}, \varepsilon_0 = \frac{S}{L}, \tag{1}$$

where σ_0 and ε_0 are the axial stress and axial strain of the specimen, respectively, F_v and S are the load and displacement signals output directly from the rock mechanic testing system, respectively, and A_0 and L are the initial cross-sectional area and the axial length of the cylindrical specimen, respectively. Based on the laboratory tests and the above theoretical formulas, the mechanical properties of rock under uniaxial loading condition could be evaluated.

In this study, the specimen was obliquely installed on the C-CAST system with a certain inclination, and it was not in pure compression state after loading (i.e., a compression-shear state). Hence, the above equation (1) was no longer applicable for calculating the stress and deformation of the specimen for the compression-shear loading condition. In order to gain insight into the stress and deformation characteristics of the inclined specimen with the vertical loading condition (i.e., the specimen in the compression-shear state), it was necessary to propose a new data processing algorithm based on the experimental monitoring data.

Figure 6 shows the deformation shape of the specimen with the inclination angles of 0°, 10°, and 15° after the quasi-static compression-shear loading tests. From the figure, it can be noted that the deformation behavior of the specimen in the compression-shear loading test was obviously different from that in the pure compression tests. The cylindrical specimen showed axial compression and lateral expansion in the pure compressive state. However, there was a shear slip surface in the specimen in the compression-shear loading

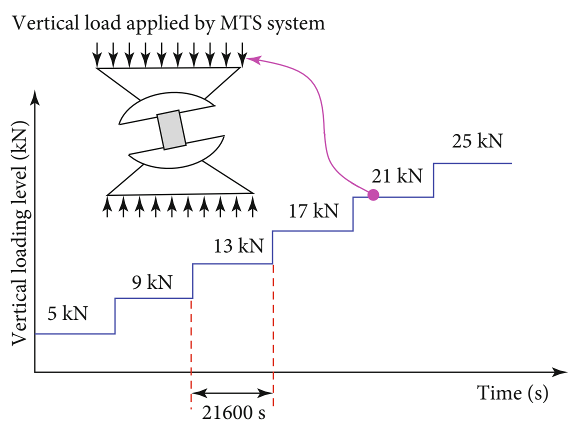

FIGURE 4: Creep loading levels conducted on the C-CAST system.

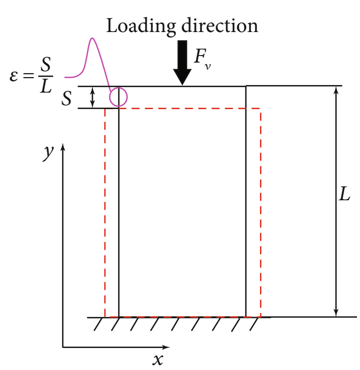

FIGURE 5: Deformation state of the cylindrical specimen in pure compression loading.

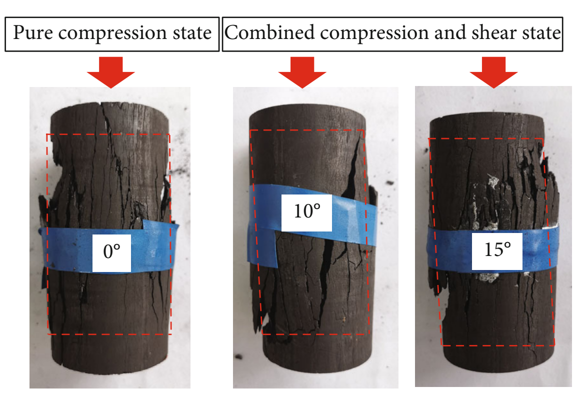

FIGURE 6: Deformation shape of the specimen at different inclination angles after the quasistatic compression-shear loading tests.

state. Thus, it could be concluded that the mechanical properties and the deformation behavior of the inclination specimen might be closely related to the shear stress component. According to the compression-shear loading test approach, the force analysis was sketched as shown in Figure 7 based on the small deformation hypothesis. The vertical loading force was decomposed to obtain the axial force (F_n) and the shear force (F_s) applied on the contact surface of the specimen. Additionally, after a certain vertical displacement

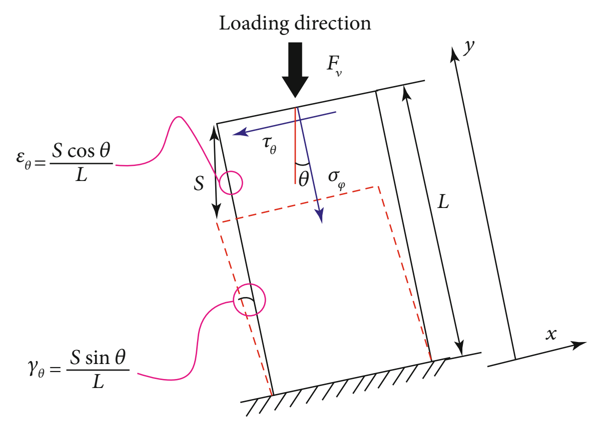

FIGURE 7: Sketch of force analysis of the specimen for the compression-shear loading condition.

(S) on the adaptor of the C-CAST system, there was some compressive and shear deformation. Hence, based on the above analysis, the axial stress and strain as well as the shear stress and strain could be calculated with the following equations:

$$\sigma_\theta = \frac{F_n}{A_0} = \frac{F_v \cos \theta}{A_0}, \tau_\theta = \frac{F_s}{A_0} = \frac{F_v \sin \theta}{A_0}, \quad (2)$$

$$\varepsilon_\theta = \frac{S \cos \theta}{L}, \gamma_\theta \approx \tan \gamma_\theta = \frac{S \sin \theta}{L}, \quad (3)$$

where θ denotes the inclination angle of the specimen on the C-CAST system, σ_θ and τ_θ are the axial stress component and the shear stress component of the specimen, respectively, and ε_θ and γ_θ are the axial strain and shear strain, respectively.

3. Experimental Results

3.1. Influence of Specimen Inclination on Peak Stress. As pointed out in Section 2.2, the peak stresses of the coal specimens at the inclination angles of 0°, 5°, 10°, and 15° were analyzed before the creep tests. According to equations (2) and (3), the axial stress, axial strain, shear stress, and shear strain of the inclination specimens were calculated. Then, the stress-strain curves of the specimens at various inclination angles were obtained, as shown in Figure 8. From the figure, it can be seen that the deformation characteristics of the coal samples at different inclination angles were basically the same. These deformation characteristics could be successively divided into the crack compaction, elasticity, yielding, and post peak failure stages. However, the peak strength and strain of the specimens with different inclination angles showed great diversity. As a whole, the peak strength and strain decreased with the increase of the inclination angle, but this law was not obvious when the inclination angle was in the range of 0°–5°.

Based on the vertical force data at the peak point of loading curves, the corresponding compression stress and shear stress (i.e., the peak stress) of each specimen were calculated,

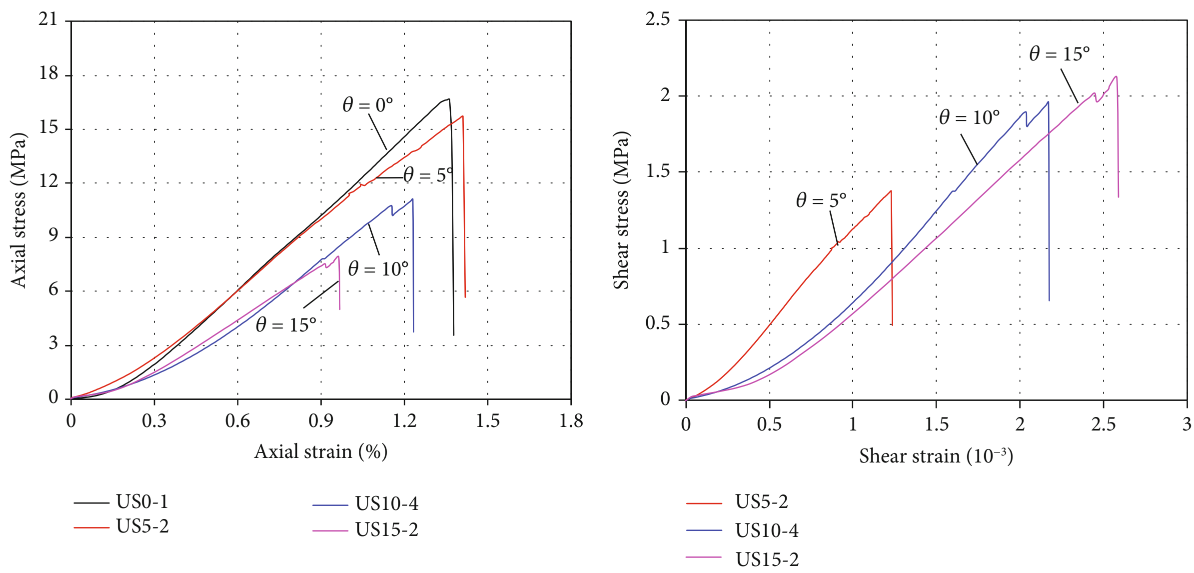

Figure 8: Stress-strain curves of the coal specimen at various inclination angles for the compression-shear loading condition.

Table 1: Compression stress and shear stress of specimens corresponding to the peak points.

Test scenario	Specimen number	Axial stress (MPa)	Shear stress (MPa)	Mean value of axial stress (MPa)	Mean value of shear stress (MPa)
	US0-1	16.21	0		
$\theta = 0^{\circ}$	US0-2	17.15	0	16.65	0
	US0-4	16.59	0		
	US5-2	15.57	1.36		
$\theta = 5^{\circ}$	US5-3	16.69	1.46	15.72	1.36
	US5-5	14.45	1.26		
	US10-1	11.46	2.02		
$\theta = 10^{\circ}$	US10-4	11.12	1.96	10.81	1.90
	US10-5	9.86	1.73		
	US15-1	8.45	2.26		
$\theta = 15^{\circ}$	US15-2	7.91	2.12	8.14	2.18
	US15-4	8.05	2.16		

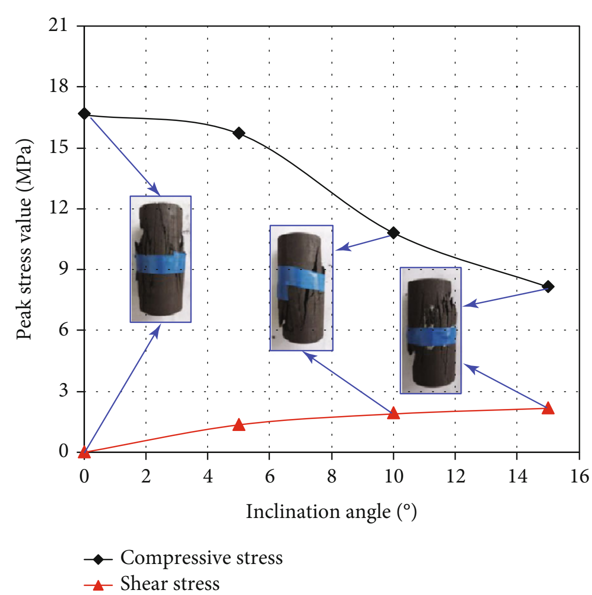

Figure 9: Relationship between specimen inclination and peak stress.

as listed in Table 1. The relationships between the average peak stresses and inclination angles of the specimens are shown in Figure 9. We concluded that the inclination angle had some effect on the peak stresses of the coal specimens. According to the comparison of the compression strength for uniaxial compressive condition, the peak compression stress of the specimen at the inclination angles of 5°, 10°, and 15° decreased by approximately 5.59%, 35.08%, and 51.11%, respectively. When the inclination angle was greater than 5°, the peak compression stress decreased linearly with the increase of the inclination angles. Moreover, it can be seen from Figure 9 that with the increase of the inclination angle of the specimen, the peak shear stress in the specimen increased gradually, and the failure pattern of the rock changed from splitting failure to shear failure.

3.2. Influence of Specimen Inclination on Time-Dependent Deformation. According to the creep test procedure described in Section 2.2, the variation of the axial and shear strains with time for the coal specimens with various inclination angles was plotted, as shown in Figure 10. It can be seen from the figure that the strain-time curves were smooth without fluctuation, which indicated that the deformation had good continuity with time. The deformation of the specimens included the instantaneous deformation in a sudden manner after the application of the load and the time-

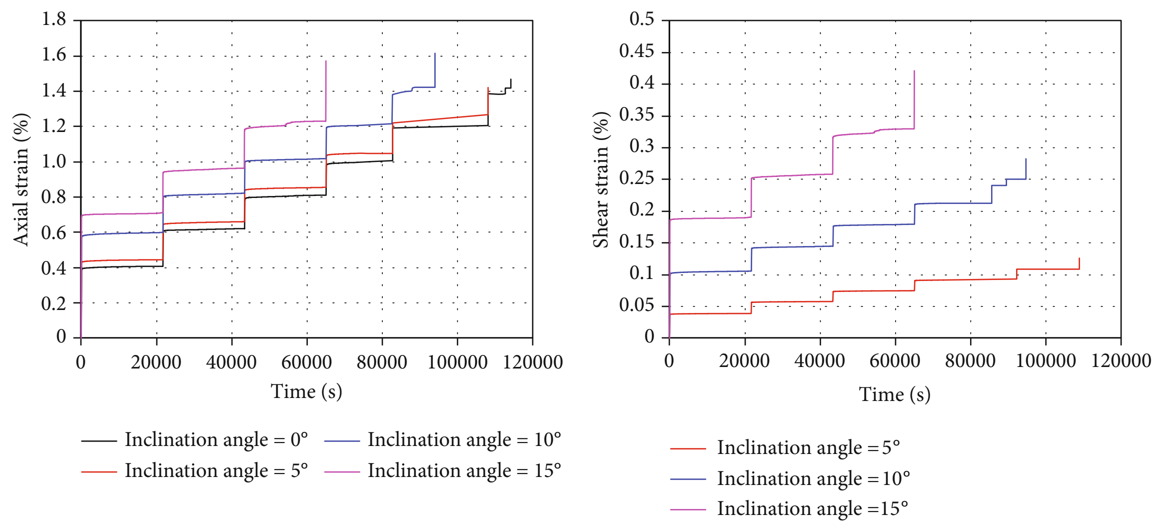

(a) Axial strain-time curve

(b) Shear strain-time curve

Figure 10: Strain-time curves of specimens with different inclination angles.

dependent deformation with the constant loading condition. Further, compared with the conventional uniaxial creep test (when the inclination angle was 0°), the specimens with a combined compression-shear condition seemed to be more prone to creep failure. The test results indicated that the duration of the creep for the coal specimens was significantly affected by the inclination angle for the same test scenario. For example, the durations of creep for the specimens with inclination angles of 0°, 5°, 10°, and 15° before specimen failure were 113764, 108634, 93496, and 65034 s, respectively. It could be deduced that the failure of the coal pillars was affected by the inclination angle of the coal seam. In deep coal pillar design and long-term stability analysis, the influence of the coal pillar inclination angle on the overall structural safety cannot be ignored.

According to the results of the multistage loading creep tests, the axial creep curves of the coal specimens with different inclination angles at each creep loading levels were obtained by using the Boltzmann superposition principle [27–29]. These curves are shown in Figure 11. It can be found from the figure that the axial creep strain increased over time under constant loading. The creep curves of the coal specimens clearly showed that the time-dependent behavior was related to the levels of the external load. At low creep stress levels (i.e., the first creep stress level in this study), there were only primary creep stages in which the strain rates gradually decreased to zero with time. With the increase of the creep load, the time-dependent deformation could be divided into two stages, a primary creep and a steady creep with a constant strain rate. At the final creep stress levels, three creep stages were exhibited, and the coal specimens failed after the tertiary creep stage of the accelerating strain rate. Additionally, it should be pointed out that the tertiary creep did not appear in the creep tests for specimens with inclination angles of 5° and 15°, which might have been due to the short duration of each creep level.

3.3. Influence of Specimen Inclination on Long-Term Strength. Many studies have shown that the strength of a rock mass with a long-term load is lower than its peak strength, and the instability of a rock structure shows obvious time correlation [30–32]. The long-term strength (LTS) of rock is a mechanical parameter reflecting the time-dependent characteristics, which plays a key role in the long-term stability analysis and life prediction of a rock structure [33–35]. At present, the methods used to determine the long-term strength of rock are mature, including the isochronous stress-strain curves method, the transition creep method, and the steady creep rate inflection point method. Among these methods, the isochronous stress-strain curves method is the most widely used method for determining the LTS of rock. Therefore, this method was used to identify the LTS of coal for different combined compression-shear states in this study.

The isochronous stress-strain curves reflected the variation of the creep stress and strain at the same duration. It should be pointed out that the inflection points of the isochronous stress-strain curves indicated the transformation of the deformation characteristics from viscoelasticity to viscoplasticity. Moreover, the accumulation of viscoplastic deformation with time would eventually lead to rock failure. Therefore, the stress corresponding to the inflection point of an isochronous stress-strain curve is generally defined as the LTS of rock [34–36]. In this study, for the sake of acquiring the LTS of coal specimens with different combined compression-shear conditions, the isochronous stress-strain curves (Figure 12) were drawn based on the process introduced by Tan [37].

As shown in Figure 12, the inflection point of the isochronal stress-strain curve was not evident with the limited test data and short test duration. However, the stress range of the inflection point of the isochronal curve could be obtained according to the creep stress levels. It can be seen from Figure 12 that the stress range of the LTS identified

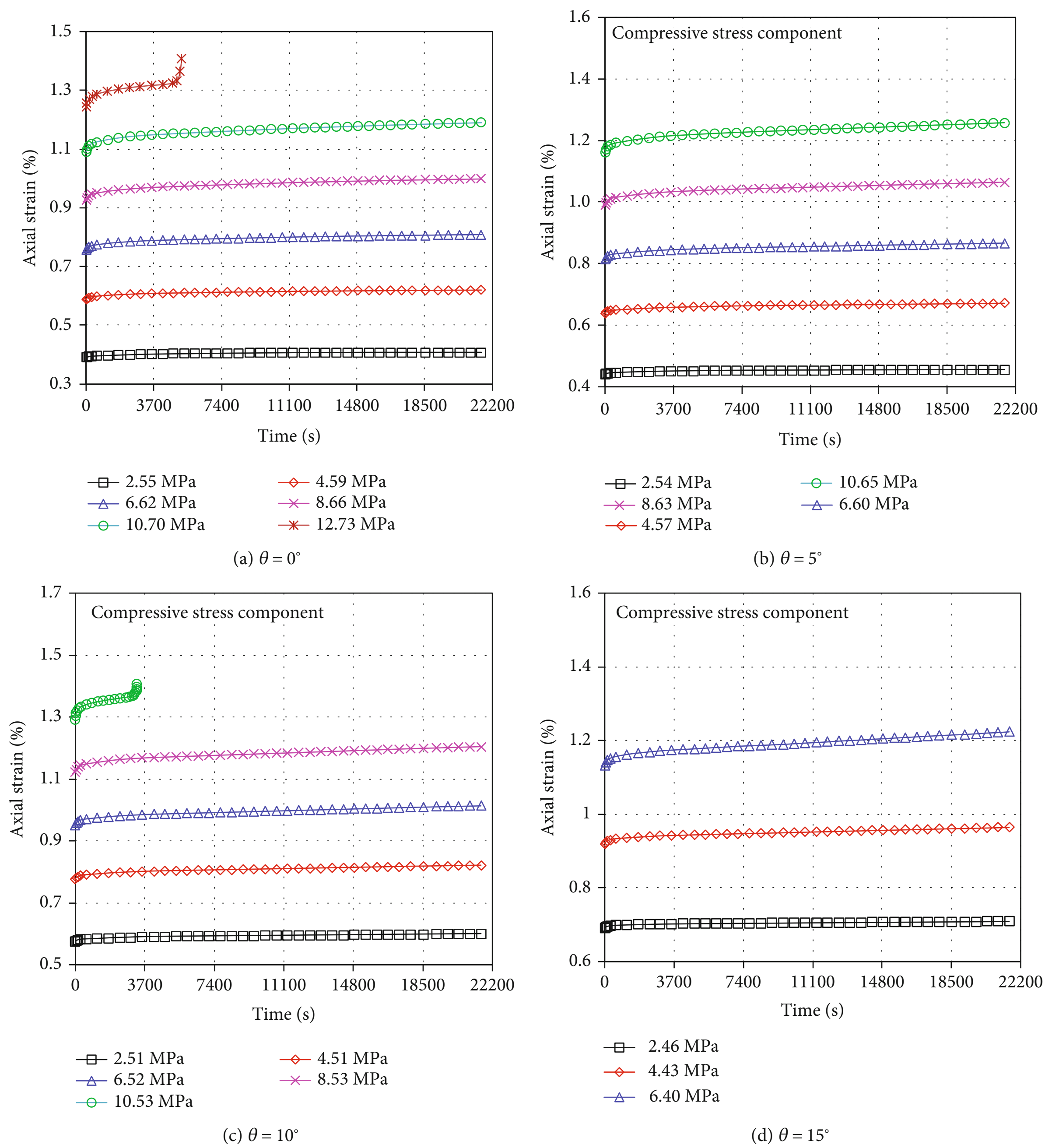

Figure 11: Axial creep curves of specimens with different inclination angles (θ) under compression-shear condition.

from the isochronous stress-strain curves was small. Thus, in order to quantitatively obtain the LTS of the coal for different combined compression-shear conditions, the average values of the stress range could be used as the LTS, and these values were 9.68, 9.64, 7.525, and 5.415 MPa, respectively. Figure 13 shows the relationship between the inclination angle of the specimens and the LTS of the coal. It can be seen that the LTS of coal decreased with the increase of the inclination angle. However, when the inclination angle of the specimen was less than 5°, the attenuation of the LTS was not obvious. When the inclination angle increased from 0° to 5°, 10°, and 15°, the LTS of the coal decreased by 0.41%, 22.26%, and 44.06%, respectively. It should be noted that the LTS of the coal specimen decreased noticeably if the specimen inclination was more than 5°.

The peak strength and the LTS of coal specimens with different inclination angles for the combined compression-shear loading condition are listed in Table 2. Moreover, the ratio of the peak strength to the LTS of the specimen under pure compression state was 55.41%, and the ratios of the inclined specimens in a combined compression-shear state were 61.32%, 66.53%, and 66.52%, respectively. The relationship between the peak strength and the LTS of the specimens in a combined compression-shear state seemed not to be affected by the specimen inclination angle. Therefore, this meant that if the ratio of the peak strength to the LTS of the

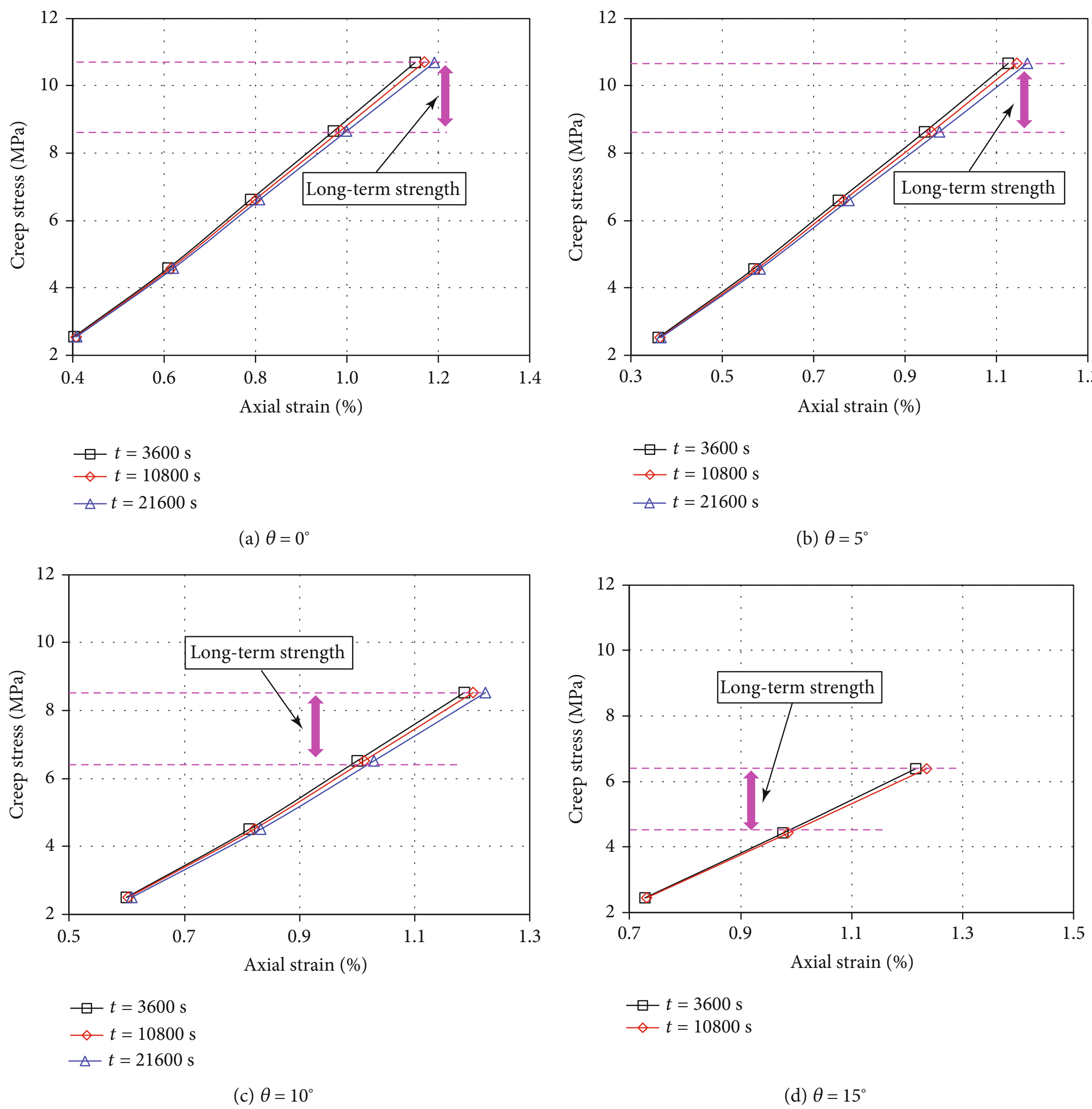

FIGURE 12: Isochronous stress-strain curves of coal specimens with different inclinations.

rock in a combined compression-shear state had been determined, the LTS of the rock specimens at any inclination angle could be estimated using the corresponding peak strength.

4. Implications for Mining Engineering

During the design and construction of underground engineering, understanding the creep behavior of rock is very important when evaluating the stability of rock construction, such as for deep rock pillars, underground oil or gas storage projects, and nuclear waste repositories. It is worth noting that these rock structures are commonly not in a pure compression state, such as the coal pillar in an inclined coal seam. However, it is very common to analyze the strength of a coal pillar based on the mechanical parameters obtained from a uniaxial compression test or creep test. Obviously, the inclination angle of a coal pillar is ignored when estimating the strength of the coal pillar based on this method. In fact, the coal pillar is in a combined compression-shear loading condition. Therefore, it can be inferred that if only the mechanical properties of rock under pure compression are analyzed to guide the underground rock engineering, then the design is not comprehensive.

In this research, we studied the influence of a combined compression-shear load on the creep behavior of coal via the uniaxial loading creep test of coal specimens with different inclination angles. The results obtained from these tests are useful for better understanding the deformation and creep failure of the coal pillar in an inclined coal seam under constant stress. It could be concluded from these test data that the angles between the axes of the coal pillars and the

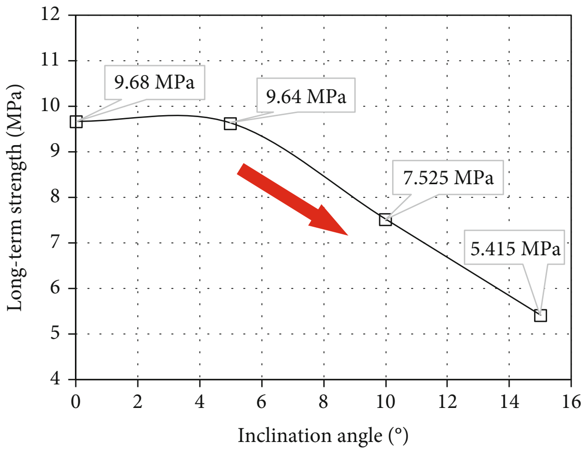

Figure 13: Relationship between inclination angle of specimens and long-term strength of coal in combined compression-shear condition.

Table 2: Peak strength (PS) and LTS of coal for different compression-shear states.

Inclination angle (°)	Peak strength (MPa)	LTS (MPa)	Ratio of PS to LTS
0	16.65	9.68	55.41%
5	15.72	9.64	61.32%
10	10.81	7.525	66.53%
15	8.14	5.415	66.52%

direction of the maximum principal stress would have a significant impact on the stability of the coal pillar. Since the shear deformation increased with time due to the shear stress component that was induced by the inclination angle, the incremental accumulation of the shear strain could drastically shorten the time-to-failure, as seen in the test illustrated in Figure 10. Moreover, the tests results showed that the long-term strength would decrease with the increase of the inclination angle. When analyzing the stability of a coal pillar in an inclined coal seam, if the existence of the shear strain was ignored, it might therefore lead to mine disaster. Therefore, we suggested that the influence of the seam inclination on the pillar strength should be considered while designing the pillar dimensions during mining activities.

In addition, the experimental results also showed that the time-dependent deformation and the long-term strength of the specimens with an inclination angle of 5° were not significantly different from those specimens under pure compression (i.e., inclination angle is 0°). It could be concluded that it was safe and feasible to design a coal pillar according to the conventional method when the inclination angle of the coal seam was less than 5°. The above results not only deepened the understanding of the time-dependent behavior of coal in a complex stress state but also provided a theoretical basis for a specific engineering application. However, it should be recommended that other rock types be similarly tested to gain a better understanding of the influence of a combined compression-shear load on creep behavior.

5. Conclusions

In this study, in order to investigate the time-dependent mechanical behavior of coal under a combined compression-shear load, a novel C-CAST system was used to carry out the creep tests. Then, a mechanical model was established, and a data processing method was proposed. The influence of the inclination angle on the peak strength, time-dependent deformation, and long-term strength of the coal specimens was analyzed. Some noteworthy conclusions are summarized as follows.

(i) The deformation and failure characteristics of coal for a quasistatic combined compression-shear loading condition were obviously different from those under pure compression. In the combined compression-shear tests, the shear deformation component increased with the inclination angle before failure. Moreover, the peak strength of the coal specimens decreased with the increase of the inclination angle as a result of the shear stress component

(ii) The pattern of the time-dependent deformation of coal in the combined compression-shear creep test was basically consistent with that of the uniaxial or triaxial compressive creep test, which included primary creep, steady creep, and tertiary creep. However, the duration of the creep before rock failure was obviously different for various compression-shear states (i.e., various inclination angles of the specimens). For the same vertical load, the larger inclined specimen was more prone to creep failure

(iii) The LTS of the coal under different compression-shear states was determined with the isochronous stress-strain method. When the inclination angle of the specimen was more than 5°, the LTS of the coal gradually decreased with the increase of the inclination angle. The ratio of the long-term strength to the corresponding peak strength of the coal was in the range of 61%–66%, which indicated that the relationship between the long-term strength and the peak strength was not significantly affected by the inclination angle of the specimen

Data Availability

All the data used to support the findings of this study are included within the article.

Conflicts of Interest

There are no conflicts of interest regarding the publication of this paper.

Acknowledgments

This research was funded by the Natural Science Foundation of China (grant number 52004098) and the Science and Technology Project of Henan Province (Nos. 192102310210 and 212102310951).

References

[1] W. J. Guo, H. L. Wang, and S. J. Chen, "Coal pillar safety and surface deformation characteristics of wide strip pillar mining in deep mine," *Arabian Journal of Geosciences*, vol. 9, no. 2, pp. 1–9, 2016.

[2] W. B. Zhu, J. M. Xu, J. L. Xu, D. Y. Chen, and J. X. Shi, "Pier-column backfill mining technology for controlling surface subsidence," *International Journal of Rock Mechanics and Mining Sciences*, vol. 96, pp. 58–65, 2017.

[3] Z. Zheng, Z. Q. Yang, H. Z. Zhu, F. L. He, C. Y. Du, and B. Q. Liu, "Study on reasonable coal-pillar width and surrounding-rock control of gob-side irregular roadway in inclined seam," *Journal of Mining and Safety Engineering*, vol. 36, no. 2, pp. 231–233, 2019, in Chinese.

[4] F. L. He and G. C. Zhang, "Pillar width determination and surrounding rocks control of gob-side entry with large cross-section and fully-mechanized mining," *Rock and Soil Mechanics*, vol. 37, no. 6, pp. 1721–1728, 2016, in Chinese.

[5] Y. Xue, Z. Z. Cao, and Z. H. Li, "Destabilization mechanism and energy evolution of coal pillar in rockburst disaster," *Arabian Journal of Geosciences*, vol. 13, no. 13, pp. 1–13, 2020.

[6] Q. Y. He, Y. C. Li, B. J. Zhou, B. Y. Wu, X. W. Zhang, and S. Zhang, "Mechanical properties of granite under quasi-static compression combined shear loading," *Journal of Mining and Safety Engineering*, vol. 37, no. 3, pp. 162–169, 2020, in Chinese.

[7] Y. Xue, J. Liu, P. G. Ranjith, X. Liang, and S. Wang, "Investigation of the influence of gas fracturing on fracturing characteristics of coal mass and gas extraction efficiency based on a multi-physical field model," *Journal of Petroleum Science and Engineering*, vol. 206, article 109018, 2021.

[8] Q. L. Yao, Q. Hao, X. Y. Chen, B. J. Zhou, and J. Fang, "Design on the width of coal pillar dam in coal mine groundwater reservoir," *Journal of China Coal Society*, vol. 44, no. 3, pp. 890–898, 2019.

[9] Y. Zhang, F. Ren, and X. Zhao, "Characterization of joint set effect on rock pillars using synthetic rock mass numerical method," *International journal of geomechanics*, vol. 17, no. 3, article 06016026, 2017.

[10] Q. Y. He, Y. C. Li, J. H. Xu, and C. G. Zhang, "Prediction of mechanical properties of igneous rocks under combined compression and shear loading through statistical analysis," *Rock Mechanics and Rock Engineering*, vol. 53, no. 2, pp. 841–859, 2020.

[11] L. Chen, X. B. Mao, and P. Wu, "Effect of high temperature and inclination angle on mechanical properties and fracture behavior of granite at low strain rate," *Sustainability*, vol. 12, no. 3, article 1255, p. 25, 2020.

[12] Q. Y. He, Y. C. Li, and S. She, "Mechanical properties of basalt specimens under combined compression and shear loading at low strain rates," *Rock Mechanics and Rock Engineering*, vol. 52, no. 10, pp. 4101–4112, 2019.

[13] F. Suorineni, P. Kaiser, J. J. Mgumbwa, and D. Thibodeau, "mining of orebodies under shear loading part 1–case histories," *Mining Technology*, vol. 120, no. 3, pp. 137–147, 2011.

[14] W. G. Pariseau, "Shear stability of mine pillars in dipping seams," in *The 23rd U.S. Symposium on Rock Mechanics (USRMS)*, American Rock Mechanics Association, 1982.

[15] M. Foroughi and V. Vutukuri, *Estimating elastic pillar stresses in inclined coal seams*, vol. 302, Transactions of Society for Mining, Metallurgy, and Exploration, Inc, 1997.

[16] S. J. Chen, W. J. Guo, G. Q. Cheng, and T. P. Zhao, "Research on creep supporting effect of deep strip pillar," *Journal of Mining and Safety Engineering*, vol. 29, no. 1, pp. 52–57, 2012, in Chinese.

[17] Y. J. Yang, H. Q. Duan, C. X. Liu, and Y. R. Hao, "Reasonable design of coal barrier pillar of roadway in deep mining considering long-term stability," *Journal of Mining and Safety Engineering*, vol. 34, no. 5, pp. 921–927, 2017, in Chinese.

[18] A. Sainoki and H. S. Mitri, "Numerical investigation into pillar failure induced by time-dependent skin degradation," *International Journal of Mining Science and Technology*, vol. 27, no. 4, pp. 591–597, 2017.

[19] H. B. Zhao, G. Z. Yin, and W. Z. Zhang, "Study of creep characteristics and constitutive relation of briquette under confining pressure," *Rock and Soil Mechanics*, vol. 30, no. 8, pp. 2305–2308, 2009, in Chinese.

[20] T. T. Cai, Z. T. Feng, D. Zhao, and Y. L. Jiang, "A creep model for lean coal based on hardening-damage mechanism," *Rock and Soil Mechanics*, vol. 39, no. s1, pp. 61–68, 2018, in Chinese.

[21] S. Q. Yang, P. Xu, and P. G. Ranjith, "Damage model of coal under creep and triaxial compression," *International Journal of Rock Mechanics and Mining Sciences*, vol. 80, pp. 337–345, 2015.

[22] H. B. du, F. Dai, Y. Xu, Z. L. Yan, and M. D. Wei, "Mechanical responses and failure mechanism of hydrostatically pressurized rocks under combined compression-shear impacting," *International Journal of Mechanical Sciences*, vol. 165, article 105219, 2020.

[23] Y. Xu and F. Dai, "Dynamic response and failure mechanism of brittle rocks under combined compression-shear loading experiments," *Rock Mechanics Rock Engineering*, vol. 51, no. 3, pp. 747–764, 2018.

[24] Ö. Aydan, T. Ito, U. Özbay et al., "ISRM suggested methods for determining the creep characteristics of rock," *Rock Mechanics and Rock Engineering*, vol. 47, no. 1, pp. 275–290, 2014.

[25] X. L. Xu, R. Zhang, F. Dai, B. Yu, M. Z. Gao, and Y. F. Zhang, "Effect of coal and rock characteristics on ultrasonic velocity," *Journal of China Coal Society*, vol. 40, no. 4, pp. 793–800, 2015.

[26] X. H. Liu, Q. J. Hao, S. Y. Wu, R. Zhang, and J. Yu, "Nonlinear mechanical properties of coal rock under quasi-static strain rate," *Journal of China Coal Society*, vol. 44, no. 5, pp. 1445–1473, 2019.

[27] R. B. Hou, K. Zhang, J. Tao, X. R. Xue, and Y. L. Chen, "A nonlinear creep damage coupled model for rock considering the effect of initial damage," *Rock Mechanics and Rock Engineering*, vol. 52, no. 5, pp. 1275–1285, 2019.

[28] Y. J. Song, Y. X. Che, L. T. Zhang, J. X. Ren, S. J. Chen, and M. L. Hu, "Triaxial creep behavior of red sandstone in freeze-thaw environments," *Geofluids*, vol. 2020, Article ID 6641377, 20 pages, 2020.

[29] Z. W. Zhou, W. Ma, S. J. Zhang, C. Cai, Y. H. Mu, and G. Y. Li, "Damage evolution and recrystallization enhancement of frozen loess," *International Journal of Damage Mechanics*, vol. 27, no. 8, pp. 1131–1155, 2018.

[30] N. A. Chandler, "Quantifying long-term strength and rock damage properties from plots of shear strain versus volume strain," *International Journal of Rock Mechanics and Mining Sciences*, vol. 59, pp. 105–110, 2013.

[31] L. Jian-feng, W. Lu, P. Jian-liang, Z. Lu, and B. Yu, "Experimental study on creep deformation and long-term strength of unloading-fractured marble," *European Journal of*

Environmental and Civil Engineering, vol. 19, supplement 1, pp. s97–s107, 2015.

[32] Y. Zhang, P. J. Jin, W. Y. Xu, H. B. Zhao, and S. H. Mei, "Experimental study of triaxial creep behavior and long-term strength of clastic rock in dam foundation," *Rock and Soil Mechanics*, vol. 37, no. 5, pp. 1291–1300, 2016, in Chinese.

[33] M. R. Shen and H. J. Chen, "Testing study of long-term strength characteristics of red sandstone," *Rock and Soil Mechanics*, vol. 32, pp. 3301–3305, 2011.

[34] L. Cong and X. L. Hu, "Triaxial rheological property of sandstone under low confining pressure," *Engineering Geology*, vol. 231, pp. 45–55, 2017.

[35] Z. W. Zhou, W. Ma, S. J. Zhang, H. M. Du, Y. H. Mu, and G. Y. Li, "Multiaxial creep of frozen loess," *Mechanics of Materials*, vol. 95, pp. 172–191, 2016.

[36] R. B. Hou, K. Zhang, and J. Tao, "Effects of initial damage on time-dependent behavior of sandstone in uniaxial compressive creep test," *Archives of Mining Sciences*, vol. 64, no. 4, pp. 687–707, 2019.

[37] T. Tan, "The mechanical problems for the long-term stability of underground galleries," *Chinese Journal of Rock Mechanics and Engineering*, vol. 1, pp. 1–20, 1982.

Hindawi
Geofluids
Volume 2021, Article ID 5527967, 12 pages
https://doi.org/10.1155/2021/5527967

Research Article

Study on Fracture Distribution and Local Brittleness Characteristics Based on Stepwise Regression Method

Wanchun Zhao,[1] **Xiaohan Feng**,[2] **and Tingting Wang**[3]

[1]*Institute of Unconventional Oil & Gas, Northeast Petroleum University, Daqing, Heilongjiang 163318, China*
[2]*School of Petroleum Engineering, Northeast Petroleum University, Daqing, Heilongjiang 163318, China*
[3]*School of Electrical Engineering & Information, Northeast Petroleum University, Daqing, Heilongjiang 163318, China*

Correspondence should be addressed to Tingting Wang; wangtingting@nepu.edu.cn

Received 24 February 2021; Revised 10 May 2021; Accepted 17 August 2021; Published 29 August 2021

Academic Editor: Jia Liu

The brittleness of rock is an important parameter that influences and controls the evolution mechanism of the fracture and formation of a fracture net. The existing methods of brittle characterization are describing the brittleness of rock mass as a whole. They lack reliability descriptions to guide the fracture strike and improve the volume of the reservoir. It is considered that the macroscopic brittle fracture of a rock is the process of continuous initiation and propagation of local fractures in the rock mass under the action of external loads. The macroscopic fracture is the appearance caused by a local rupture to a certain extent, and the local rupture is the root cause of macroscopic fracture. The study of the local brittleness of a rock can reveal the intrinsic nature of its fracture behavior and can reflect the evolution mechanism of fracture more directly and accurately. In this paper, coring sampling in field outcrop is first carried out, and the break evolution law of core is described by a CT scanner. The mineral compositions in the core are determined by a mineral analysis diffractometer. The regulation of the rock local brittleness with different mineral contents is analyzed. And a new method for local brittle region division and characterization of rock has been developed. This method gives the connotation relation of the rock brittle fracture as a whole induced by a local brittle fracture. And it provides a new approach to study the law of a rock fracture.

1. Introduction

With the shortening of the proven oil and gas reserves, unconventional oil and gas exploitation is the inevitable development trend in the future to ensure the sustained and stable oil and gas production. As a new type of clean energy, unconventional oil and gas has the advantages of wide resource distribution, abundant reserves, and long exploitation life. It has become a hot spot in global oil and gas exploration and development.

For unconventional oil and gas reservoir development, the large-scale volume fracturing method is often used to reform. This method is efficient and economical, and the effect of improving reservoir permeability is outstanding. The study shows that the brittleness of a rock can significantly affect the reservoir fracturing effect and wellbore stability [1]. Therefore, the evaluation of brittleness characteristics has become the primary factor to be considered in fracturing well selection and scheme design [2]. Statistical analysis shows that there are more than 30 methods to characterize brittleness [3–23]. Most of these methods are put forward to specific problems, applicable to different disciplines, each with its own advantages and limitations. During this period, Zhaoping and Suping [24] applied the methods of X-ray diffraction, fluorescence spectrum analysis, and mechanical test to study the mineral composition and chemical composition characteristics of coal-bearing mudstone. They established a qualitative and quantitative relationship between the mechanical properties (including uniaxial compressive strength and elastic modulus) of mudstone and its chemical composition (including SiO_2 and FeO) and found that the uniaxial compressive strength and modulus of elasticity of mudstone increased with the increase of SiO_2 content. Burnaman and other scholars [25, 26] consider that mineral composition is the internal reason for controlling rock brittleness and causing a difference in the fracture net fracturing effect and makes a three-terminal element diagram of a rock brittle to evaluate the brittleness qualitatively according to the relative content of minerals in shale. Wen-Long's [27] analysis shows that the rock with high contents of quartz, feldspar, and carbonate is brittle. This kind of rock is easy to form natural fractures and induced fractures under the action of external forces, and its development degree is generally positively correlated with the content of brittle minerals. Liu et al. [28] found that the mineral content, composition distribution, and fracture development characteristics are important internal controlling factors affecting the brittleness of rock mass. In the same year, Gale et al. [29] found a negative correlation between the clay mineral content and natural fracture development characteristics, as shown in Figure 1. Lin et al. [30] established a nonlinear viscoplastic element on the basis of time-dependent shear strength by connecting the plastic element representing shear strength with the viscous element in parallel and studied effectively the mechanical properties of rock from the point of difference of shear strength. Zhang et al. [31] are using the discrete element numerical method to establish five different numerical models of regular sawtooth joints, study the shear mechanical characteristics of joints under creep condition, and analyze the influence of creep on the mechanical characteristics of joints. Xiangyuan et al. [32] obtained that reservoir brittleness controlled the development characteristics and degree of natural fractures based on the analysis of Chang 7 tight reservoir in Longdong Area. The larger the reservoir brittleness is, the more likely the fracture will occur under the action of tectonic stress, which will lead to the increase of fracture development. That is, the higher the content of brittle minerals (quartz, calcite, dolomite, and feldspar) in shale, the more developed the natural fractures in the area and the larger the brittleness. And the higher the content of clay minerals, the less developed the natural fractures in the area and the larger the toughness, as shown in Figure 2.

At present, the following two methods are widely used to calculate the rock brittleness in the industry. One is the rock mineral analysis method proposed by Jravie et al. [33] in 2009. In this method, quartz is regarded as a brittle mineral. And the contents of quartz, carbonate rock, and clay are measured, so as to calculate the rock brittleness, as shown in formula (1).

$$\mathrm{BRIT} = \frac{V_{\mathrm{quartz}}}{V_{\mathrm{quartz}} + V_{\mathrm{carbonaterock}} + V_{\mathrm{clay}}} \times 100, \qquad (1)$$

where BRIT is the rock brittleness index and V is the mineral volume.

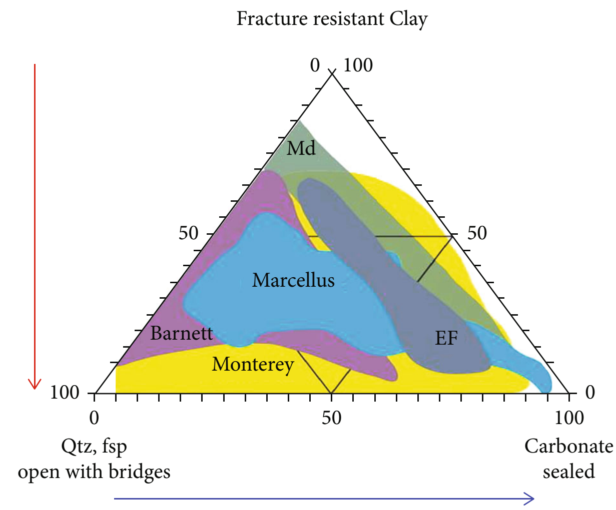

Figure 1: Mineral composition and fracture development diagram.

Another commonly used method for calculating rock brittleness is the elastic parameter method proposed by Xue et al. [34] in 2007, as shown in formula (2). According to this method, the higher the elastic modulus of rock is, the lower Poisson's ratio is, and the larger the rock brittleness is, as shown in Figure 3. The brittleness index of the rock is defined by the method of mechanics parameters, which is generally accepted and adopted in the field.

$$\mathrm{BRIT} = \frac{1}{2}\left(\frac{E - E_{\min}}{E_{\max} - E_{\min}} + \frac{\nu - \nu_{\max}}{\nu_{\min} - \nu_{\max}}\right) \times 100, \qquad (2)$$

where $E_{\max}$ is the maximum elastic modulus of the rock, $E_{\min}$ is the minimum elastic modulus of te rock, $\nu_{\max}$ is maximum Poisson's ratio of the rock, and $\nu_{\min}$ is minimum Poisson's ratio of the rock.

Both of these methods can accurately characterize the brittleness of reservoir rocks to a certain extent. However, the brittleness description is based on the analysis of the overall brittleness of the research object, and the influence of natural fracture development on rock brittleness in reservoir cannot be described. In 2015, Bing et al. [36] analyzed the acoustic emission signal of the fracturing test and found that the peak of AE accumulation events occurred before the pump pressure reached the peak rupture pressure. This phenomenon shows that before the macrofracture of the rock mass, many microfractures have appeared in it, and the accumulation of microfracture finally leads to the fracture of the core as a whole. Wang et al. [37] proposed a new index for the brittleness evaluation of rock mass based on catastrophe theory and found that the softening modulus and brittleness index changed in polynomial with the increase of confining pressure.

Therefore, it is considered in this paper that the macrobrittle fracture of the rock is a process of local fracture initiation, propagation, microfracture, and gradual deterioration of rock matrix under external loads. The study of the local brittleness characteristics of the rock mass can reveal the

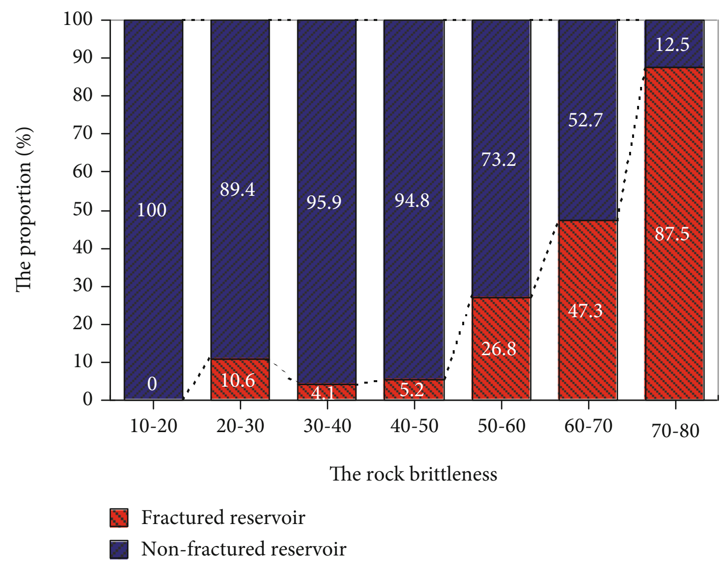

Figure 2: Brittleness and nature fracture relation chart.

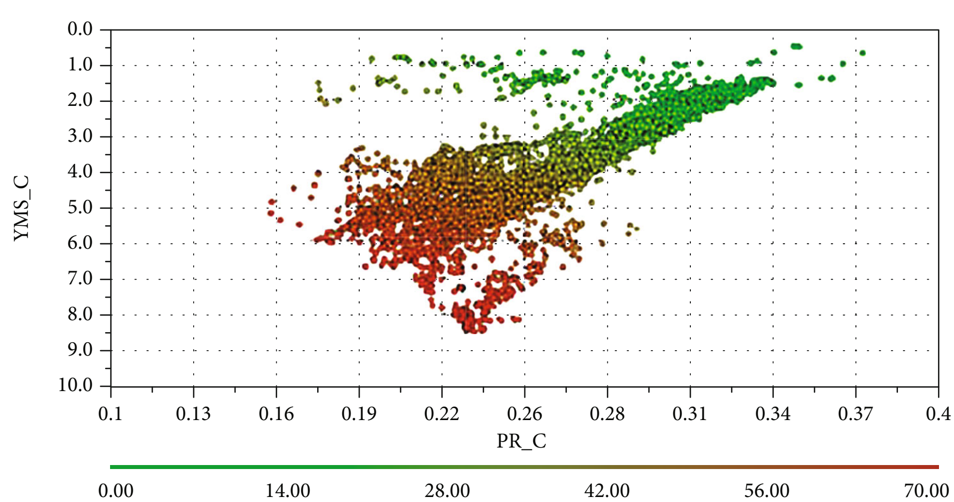

Figure 3: The influence chart of brittleness between the elastic modulus and Poisson ratio [35].

intrinsic essence of the rock microfracture behavior and can more directly and accurately reflect the fracturing capacity and fracture evolution mechanism. Firstly, the law of local fracture propagation and fracture in shale during compression test is analyzed by CT scanning. And a method for characterizing local brittleness of shale is established by means of diffraction analysis of the core mineral composition and stepwise regression method. Finally, the local brittle fracture law of an artificial fracture is analyzed by a hydraulic fracturing test.

2. Analysis of Shale Core Compressive Fracture Law by CT Scanning

In this paper, the SkyScan 1172 high-resolution CT machine is used for the CT scanning test, as shown in Figure 4. This machine is a product of SkyScan company in Belgium. It uses the principle of microfocus X-ray imaging to perform ultrahigh-resolution three-dimensional imaging, which can obtain high-precision three-dimensional images without damaging the core. It is small in size, high in resolution, and can observe very fine structure without sample preparation, dyeing, and slicing. The test cores are taken from layer B in block A in Liaohe Oilfield, as shown in Figure 5. The core is scanned by CT, and the fracture distribution of the sample after CT scanning is obtained in 30 s, 90 s, 120 s, and 180 s, as shown in Figure 6 [38].

The CT scan results show that the process of shale rupture begins with the formation of local short microfractures in the core between 0 and 30 s. With time between 30 s and 90 s, local microfractures grow longer and new ones form elsewhere. When the time reaches 120 s, the microfractures intersect and connect with others to form larger microfractures, which cause core instability and fracture at 180 s.

Figure 4: SkyScan 1172 high-resolution CT scanner.

Figure 5: The core sample for CT scan.

Therefore, the macrofracture of shale is the phenomenon caused by local fracture to a certain extent, and the local fracture is the fundamental cause of macrofracture.

3. Establishment of Rock Local Brittleness Characterization Method

Because the macrofracture of a rock is caused by the local brittle fracture and expansion, how to characterize the rock local brittleness has become an important research content in this paper. It is impossible to analyze the rock brittle distribution from the microscopic field by means of rock mechanical parameters or stress-strain tests. The mineral component analysis method is used to describe the rock brittle distribution in this paper. The mineral analysis method proposed by Rickman only considers the rock mineral composition itself, without considering the influence of rock heterogeneity, reservoir environmental factors, and the development of natural fractures. Therefore, this method is improved and perfected.

In this paper, the rock local brittleness distribution is analyzed based on reservoir heterogeneity. And the stepwise regression analysis is used to screen the main controlling factors to study the influence of different mineral components on the elastic modulus and Poisson's ratio of rock. This method means that when a phenomenon is affected by multiple factors at the same time, the inversion compact transformation method and bidirectional test method are used to gradually analyze the contribution of influencing factors to the explained variables. If the factor is discriminated, it will be introduced into the stepwise regression model. According to the F test, the significance analysis of the introduced parameters is conducted to determine whether the relevant parameters in the regression model need to be eliminated because of the change of contribution. After repeated screening and elimination, the optimal regression equation is established. The stepwise regression analysis can include many explanatory variables. The explanatory variables of this method are the rock elastic modulus and Poisson's ratio, and the explained variables are the content determination values of quartz, potassium feldspar, plagioclase, calcite, dolomite, analcite, siderite, pyrite, and clay minerals. The general form of the established regression model is

$$\widehat{Y} = \beta_0 + \beta_1 Z_{\text{quartz}} + \beta_2 Z_{\text{potassium-feldspar}} + \cdots + \beta_j Z_j, \tag{3}$$

where $\beta_j (j = 0, 1, 2, \cdots, 9)$ are regression coefficients, $\widehat{Y}$ are explained variables including the rock elastic modulus and Poisson's ratio, and Z_j (j = quartz, potassium, $\cdots$, clay minerals) are the experimental values of 9 explanatory variables that have significant influence on $\widehat{Y}$.

Because of the experimental data with n periods, the correlation coefficients between explanatory variables and explained variables are calculated based on these data, as shown in formula (4). The initial correlation coefficient matrix of regression analysis is established according to the correlation coefficient between different parameters, as shown in formula (5).

$$r_{XY} = \frac{\sum_{i=1}^{n} (X_i - \bar{X})(Y_i - \bar{Y})}{\sqrt{\sum_{i=1}^{n} (X_i - \bar{X})^2} \sqrt{\sum_{i=1}^{n} (Y_i - \bar{Y})^2}}, \tag{4}$$

$$R = \begin{bmatrix} r_{\text{quartzquartz}} & \cdots & r_{\text{quartz}Y} \\ \cdots & \cdots & \cdots \\ r_{Y\text{quartz}} & \cdots & r_{YY} \end{bmatrix}, \tag{5}$$

where X_i and Y_i are the experimental values of parameters, $\bar{X}$ and $\bar{Y}$ are the average values of parameters' experimental data, r_{XY} are the correlation coefficients between parameters X and Y, and R is to obtain the initial correlation coefficient matrix by one-to-one correspondence calculation of the research parameters.

According to the initial correlation coefficient matrix, the partial regression square sum u_i between explanatory variables and explained variables which represents the

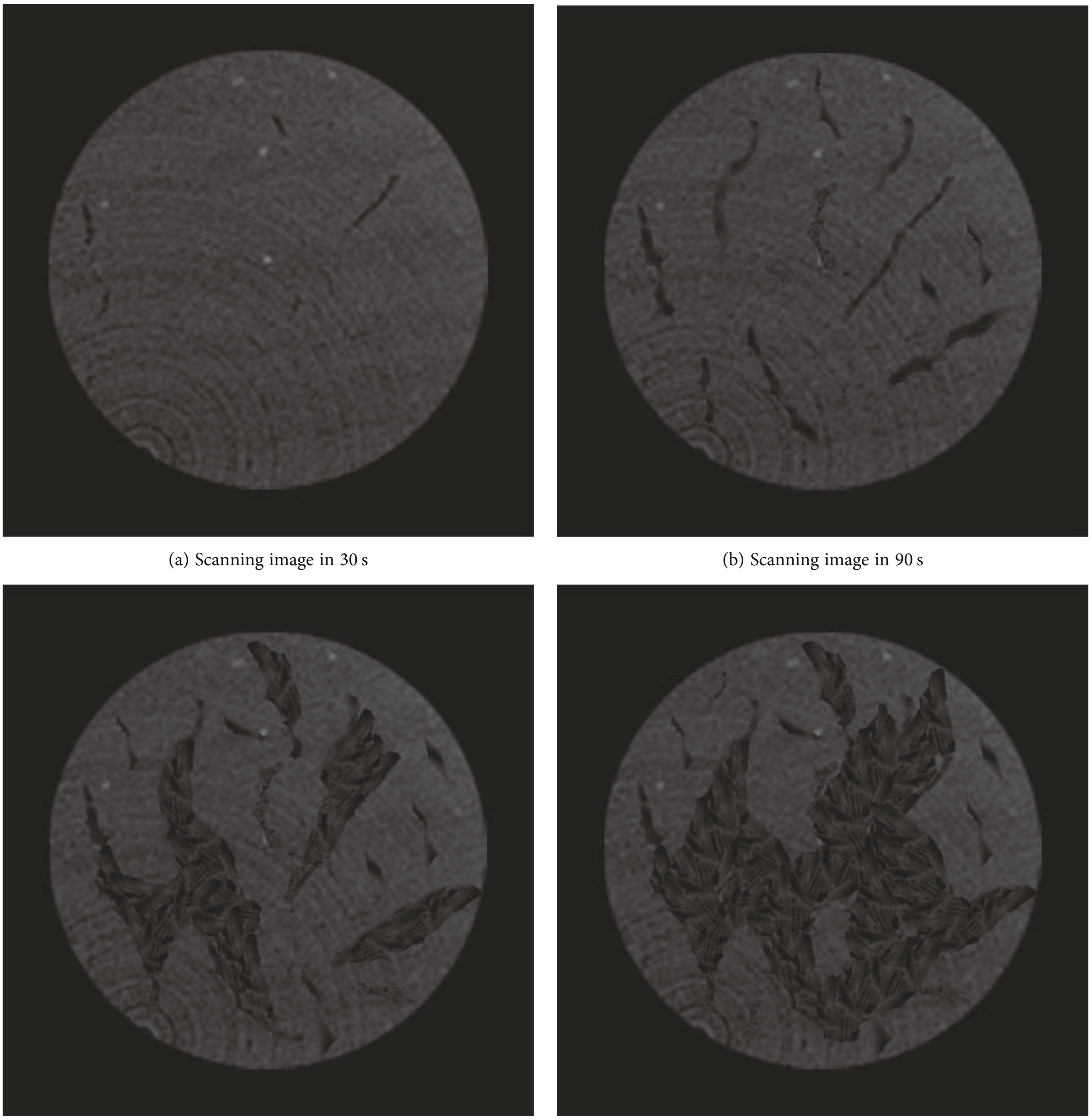

(a) Scanning image in 30 s

(b) Scanning image in 90 s

(c) Scanning image in 120 s

(d) Scanning image in 180 s

Figure 6: The fracture distribution images of CT scan core.

contribution of different parameters in regression equation, as shown in formula (6).

$$u_i = \frac{r_{iY}^2}{r_{ii}}. \tag{6}$$

The parameter which has a maximum partial regression square sum is selected as the introduction parameter and tested by the F test method. When the test result is larger than the empirical threshold, this parameter can be introduced into the regression equation as a regression parameter. Conversely, the parameter cannot be introduced into the regression equation and need to be eliminated. Its F test method is shown in formula (7). The critical threshold is determined by referring to the F distribution table.

$$F_{\text{in}} = \frac{u_i/f_1}{(r_{YY} - u_i)/f_2}, \tag{7}$$

where F_{in} is the F test value when the parameter is quoted; f_1 is the number of independent variables introduced this time, usually 1 is appropriate; $f_2 = n - m - 1$, in which n is the number of experimental groups and m

is the number of independent variables introduced into the regression equation.

When the parameter is quoted successfully, it is required to use it as the primary element. The contribution of this parameter should be eliminated by the inversion compact transformation method, and the new correlation coefficient matrix should be calculated. Through the new correlation coefficient matrix, the contribution degree of residual parameters can be calculated by partial regression square sum of research parameters, and then, the parameters of the newly introduced regression equation can be determined by F test. At the same time, due to the introduction of new parameters, the contribution of parameters in the regression equation needs to be redistributed, and the selected parameters need to be tested by F test in reverse to eliminate the parameters that cannot pass, as shown in formula (8).

$$F_{\text{out}} = \frac{u_i/f_1}{r_{YY}^{(l)}/f_2}, \tag{8}$$

where F_{out} is the F test value when the parameter is eliminated.

Repeatedly quoting and eliminating parameters until the regression equation cannot quote and eliminate any variables. In this case, all the selected parameters are independent variables for the regression equation.

After choosing the influencing parameters of the regression equation, the regression coefficients of each parameter can be calculated by formula (9). The regression coefficients of the unselected variables are all 0. After the calculation, the average value of the experimental data is substituted into the regression equation to calculate the regression coefficient β_0, as shown in formula (10).

$$\beta_i = \frac{\sigma_Y}{\sigma_i} r_{iY}^{(l)}, \tag{9}$$

$$\beta_0 = \bar{Y} - \sum_{i=1}^{9} \beta_i \bar{Z}_i, \tag{10}$$

where σ_i is the variance of the experimental data of parameter i, σ_Y is the variance of the experimental data of explained variable Y, $\bar{Z}_i$ is the average value of the experimental data of parameter i, and $\bar{Y}$ is the average value of the experimental data of explained variable Y.

After establishing a complete regression equation, the accuracy of the regression equation can be verified by significance analysis, and the calculation process is shown in formula (11). When the calculation result is larger than the critical threshold value, it shows that the regression equation is significant and the linear relationship is accurate, which can be used as an effective result.

$$F_{\text{significant}} = \frac{\left(1 - r_{YY}^{(l)}\right)/k}{r_{YY}^{(l)}/(n-k-1)}, \tag{11}$$

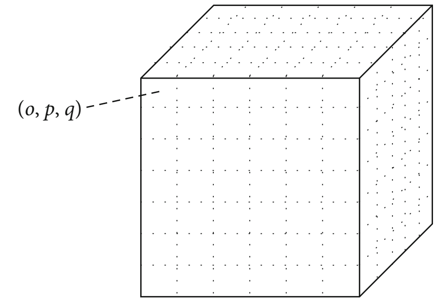

Figure 7: Sketch map of core discretization.

where $F_{\text{significant}}$ is the significant analysis result of regression equation and k is the principal element of the correlation coefficient matrix.

The regression equations of the rock elastic modulus and Poisson's ratio calculated by the stepwise regression analysis method are $\bar{E}$ and $\bar{\nu}$, respectively. So for a new core sample, it can be discretized into infinitesimal units, as shown in Figure 7.

At this time, each core unit can be represented by (o, p, q) in azimuth. The corresponding modulus of elasticity $\bar{E}_{(o,p,q)}$ and Poisson's ratio $\bar{\nu}_{(o,p,q)}$ are calculated according to the regression equation after the mineral composition content of each unit is determined. By substituting the results into the elastic parameter method in formula (2), the rock local brittleness expression formula can be obtained as follows:

$$\text{BRIT}_{(o,p,q)} = \frac{1}{2}\left(\frac{\bar{E}_{(o,p,q)} - E_{\min}}{E_{\max} - E_{\min}} + \frac{\bar{\nu}_{(o,p,q)} - \nu_{\max}}{\nu_{\min} - \nu_{\max}}\right) \times 100. \tag{12}$$

Formula (12) is the expression of rock local brittleness. This formula combines the study of reservoir environment to analyze and quantify the influence of mineral composition on the rock brittleness. The results are scientific and representative. And the local brittleness change low can be accurately characterized according to the heterogeneity of reservoir.

4. Case Verification

In this paper, the microarea mineral composition diffraction test is carried out by D8-ADVANCE X-ray diffractometer, as shown in Figure 8. This machine is produced by BRUKED-AXS Co. Ltd. of Germany, which is one of the most advanced X-ray diffractometer systems in the world. Its high-precision goniometer can satisfy the error of measuring peak position of any diffraction peaks in the whole spectrum range with the standard peak position not exceeding 0.01 degrees. The test cores are taken from layer B in block A in Liaohe Oilfield, with a total of 22 cores, as shown in Figure 9.

Firstly, mechanical parameters such as the elastic modulus and Poisson's ratio of test cores are measured by

Figure 8: D8-ADVANCE X-ray diffractometer.

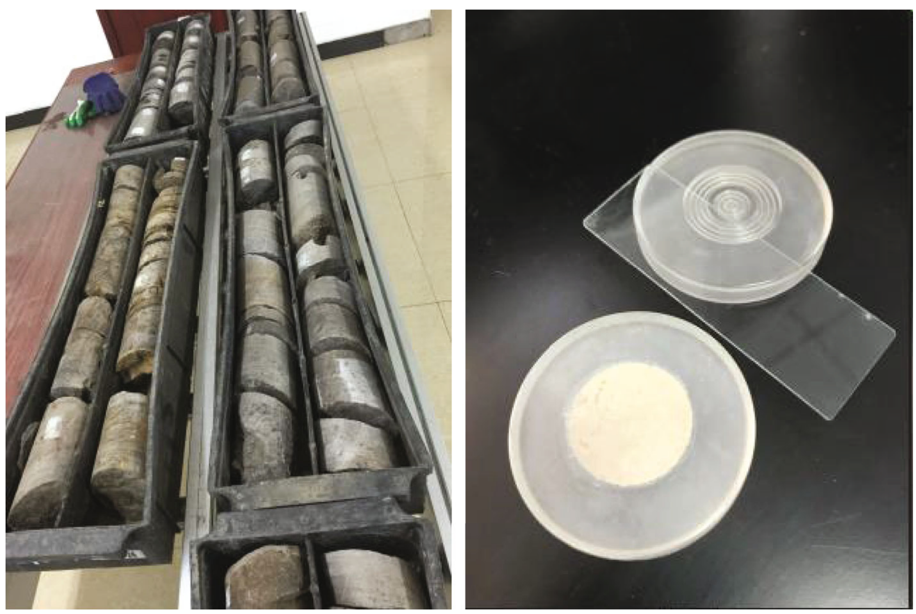

Figure 9: The core samples.

simulating the actual stress of the formation through the triaxial compressive test, and the mineral compositions of test cores are analyzed by an X-ray diffractometer. The specific data obtained are shown in Table 1.

According to the data analysis, the core samples taken in block A of Liaohe Oilfield are mainly composed of quartz, potassium feldspar, plagioclase, dolomite, and clay minerals. Some cores contain calcite, analcite, siderite and pyrite, and others are too low to be considered in this paper. The core elastic modulus is in the range of $[21.42, 31.79]$ and the Poisson's ratio is in the range of $[0.268, 0.312]$.

Through stepwise regression analysis, the initial correlation coefficient matrix R among elastic modulus, Poisson's ratio, and mineral contents are calculated as shown in Table 2.

The critical threshold of the model is mainly related to reliability and free degree, so the screening limit should not be too large; otherwise, the introduction of fewer variables will make the model impractical. In this paper, four parameters are introduced to establish the regression model, and the critical threshold is $F_{0.05}^{(4,17)}$. From the F distribution table, we can see that $F_{0.05}^{(4,17)} = 2.96$.

According to the stepwise regression analysis, the process of quoted and eliminating parameters of core elasticity modulus and Poisson's ratio by inversion compact transformation method and bidirectional test method is shown in Table 3.

After the influence parameters of the core elastic modulus and Poisson's ratio are quoted and eliminated for many times, the regression coefficients of the elastic modulus and

Table 1: The determination result of core mineral compositions and mechanical parameters.

Serial number	Quartz	Potassium feldspar	Plagioclase	Calcite	Dolomite	Analcite	Siderite	Pyrite	Clay minerals	Elastic modulus (GPa)	Poisson's ratio
	The type and content of minerals										
1	0.203	0.031	0.168	0.033	0.202	0.132	0.021	0.025	0.185	29.23	0.285
2	0.197	0.036	0.073	0.089	0.095	0.291	0.018	0.019	0.182	31.79	0.278
3	0.148	0.038	0.166	0.044	0.217	0.121	0.014	0.028	0.224	24.65	0.307
4	0.289	0.032	0.138	0	0.248	0.089	0	0	0.204	26.98	0.271
5	0.211	0.04	0.159	0.052	0.151	0.136	0.015	0.02	0.216	26.74	0.283
6	0.195	0.037	0.165	0.011	0.214	0.14	0	0	0.238	24.88	0.288
7	0.177	0.054	0.273	0	0.153	0.033	0	0.015	0.295	21.56	0.281
8	0.096	0.043	0.125	0	0.116	0.341	0.075	0.032	0.172	22.56	0.274
9	0.106	0.07	0.117	0.02	0.267	0.16	0.03	0.018	0.212	26.27	0.274
10	0.12	0.073	0.242	0.11	0.18	0.05	0.013	0.024	0.188	21.93	0.297
11	0.203	0.071	0.169	0.024	0.073	0.182	0.056	0	0.222	22.1	0.28
12	0.218	0.027	0.114	0.011	0.313	0.109	0.101	0	0.107	29.53	0.271
13	0.251	0.103	0.164	0	0.189	0.04	0.087	0.03	0.136	31.63	0.268
14	0.196	0.065	0.096	0.02	0.139	0.309	0	0	0.175	30	0.271
15	0.124	0.058	0.063	0.017	0.054	0.429	0.019	0	0.236	28.84	0.279
16	0.131	0.148	0.21	0.039	0.256	0.028	0.017	0.042	0.129	29.53	0.281
17	0.068	0.144	0.316	0.037	0.245	0	0.022	0.015	0.153	26.28	0.289
18	0.122	0.067	0.375	0.019	0.177	0.048	0.031	0	0.161	28.6	0.273
19	0.095	0.101	0.113	0.036	0.359	0.045	0.016	0.027	0.208	23.49	0.312
20	0.125	0.12	0.192	0.144	0.141	0.095	0.013	0.046	0.124	25.21	0.272
21	0.198	0.059	0.103	0.15	0.108	0.168	0.048	0	0.166	21.42	0.274
22	0.061	0.084	0.458	0.034	0.137	0.017	0.049	0	0.16	22.53	0.284

Table 2: The initial correlation coefficient matrix *R*.

	1	-0.50037	-0.45817	-0.13212	-0.05214	0.09481	0.05809	-0.24719	0.08393	0.35372	-0.39678
	-0.50037	1	0.36313	0.19435	0.19137	-0.45001	-0.03055	0.44192	-0.41878	0.00199	0.090176
	-0.45817	0.36313	1	-0.05867	0.01911	-0.65828	-0.02337	-0.07040	-0.12159	-0.27625	0.110721
	-0.13212	0.19435	-0.05867	1	-0.24949	-0.04570	-0.15995	0.27187	-0.27396	-0.23883	0.098718
	-0.05214	0.19137	0.01911	-0.24949	1	-0.57396	-0.00198	0.19780	-0.19621	0.11737	0.3602
$R =$	0.09481	-0.45001	-0.65828	-0.04570	-0.57396	1	0.02244	-0.20717	0.20291	0.19098	-0.27216
	0.05809	-0.03055	-0.02337	-0.15995	-0.00198	0.02244	1	-0.05565	-0.52406	0.06922	-0.36284
	-0.24719	0.44192	-0.07040	0.27187	0.19780	-0.20717	-0.05565	1	-0.24243	0.05379	0.230505
	0.08393	-0.41878	-0.12159	-0.27396	-0.19621	0.20291	-0.52406	-0.24243	1	-0.39416	0.357259
	0.35372	0.00199	-0.27625	-0.23883	0.11737	0.19098	0.06922	0.05379	-0.39416	1	/
	-0.39678	0.090176	0.110721	0.098718	0.3602	-0.27216	-0.36284	0.230505	0.357259	/	1

Poisson's ratio are calculated by formulas (10) and (11), as shown in Table 4.

By substituting the results of the stepwise regression analysis into formula (3), the regression model between the core elastic modulus, Poisson's ratio, and mineral compositions can be obtained as follows:

$$E = 37.6374 + 20.1992x_{\text{quartz}} - 38.5568x_{\text{calcite}} + 9.5781x_{\text{analcite}} - 60.0874x_{\text{siderite}} - 68.1563x_{\text{clay}}, \quad (13)$$

$$\nu = 0.2472 - 0.0714x_{\text{quartz}} + 0.0911x_{\text{clacite}} + 0.0813x_{\text{dolomite}} + 0.154x_{\text{clay}}. \quad (14)$$

According to the stepwise regression analysis, the main factors affecting the rock elastic modulus under simulated confining pressure include the contents of quartz, calcite, analcite, siderite, and clay minerals. And the main factors affecting rock Poisson's ratio include the contents of quartz, calcite, dolomite, and clay minerals. Among them, the content of quartz and analcite is positively correlated

Table 3: Flow table for introducing the elastic modulus and Poisson's ratio parameters.

Introduced variables	Elastic modulus E					Poisson's ratio ν				
	u_{max}	F_{in}	u_{min}	F_{out}	Results	u_{max}	F_{in}	u_{min}	F_{out}	Results
First variable	0.155	3.679			Clay minerals in	0.157	3.737			Quartz in
Second variable	0.151	4.126			Quartz in	0.154	4.237			Clay minerals in
Third variable	0.101	3.081	0.181	4.954	Calcite in	0.179	6..334	0.183	5.059	Dolomite in
Fourth variable	0.121	4.377	0.122	3.708	Siderite in	0.098	4.043	0.170	6.011	Calcite in
Fifth variable	0.099	4.253	0.143	5.144	Analcite in	0..008	0.314	0.135	5.572	End of regression
Sixth variable	0.013	0.530	0.126	4.467	End of regression					

Table 4: Stepwise regression analysis results.

Regression coefficient	Elastic modulus E	Poisson's ratio ν
Initial coefficient	37.6374	0.2472
Quartz	20.1992	-0.0714
Potassium feldspar	0	0
Plagioclase	0	0
Calcite	-38.5568	0.0911
Dolomite	0	0.0813
Analcite	9.5781	0
Siderite	-60.0874	0
Pyrite	0	0
Clay minerals	-68.1563	0.154

with the rock elastic modulus and the content of calcite, siderite, and clay minerals is negatively correlated with the rock elastic modulus. The content of calcite, dolomite, and clay minerals is positively correlated with rock Poisson's ratio, and the content of quartz is negatively correlated with rock Poisson's ratio.

The regression equations are tested and analyzed by significance test and R^2. The calculation by formula (12) shows that $F_{\text{elastic mod ulus}} = 5.396 > F_{0.05}^{(4,17)} = 2.96$ and $F_{\text{Poisson}}{}'{}^{\text{sratio}} = 6.073 > F_{0.05}^{(4,17)} = 2.96$. And the R^2 of the elastic modulus and Poisson's ratio are 0.913 and 0.936. This shows that the regression equations of the rock elastic modulus and Poisson's ratio are significant, and the linear relationships between rock mechanical parameters and mineral compositions are highly accurate, which can be used as an effective result.

According to the relationship between the elastic modulus, Poisson's ratio, and rock mineral composition, the elastic parameter method is introduced to analyze rock brittleness, and the following formula is obtained after substitution:

$$\mathrm{BRIT} = \frac{1}{2}\left[\frac{\begin{pmatrix} 37.6374 + 20.1992x_{\text{quartz}} - 38.5568x_{\text{calcite}} + \\ 9.5781x_{\text{analcite}} - 60.0874x_{\text{siderite}} - 68.1563x_{\text{clay}} \end{pmatrix} - E_{\min}}{E_{\max} - E_{\min}} + \frac{\begin{pmatrix} 0.2472 - 0.0714x_{\text{quartz}} + 0.0911x_{\text{clacite}} \\ +0.0813x_{\text{dolomite}} + 0.154x_{\text{clay}} \end{pmatrix} - \nu_{\max}}{\nu_{\min} - \nu_{\max}}\right] \times 100. \quad (15)$$

Formula (15) is the rock local brittleness evaluation model in Block A of Liaohe Oilfield. This model quantitatively establishes the relationship between the mineral composition in rock and the local brittleness, taking into account the actual reservoir environment and the influence of different mineral components on the development of natural fractures.

As shown in Figure 10, it can be found that the brittleness trend of different calculation methods is basically the same, which compared the rock brittleness calculated by mineral composition analysis method, elastic parameter method, and the new method. However, the rock mineral analysis method lacks quantitative characterization of mineral composition, and its calculated brittleness index is seriously low, which is quite different from the actual situation in the field. The difference of brittleness variation calculated by the elastic parameter method is large, which leads to great calculation errors. In this paper, the trend of the brittleness index of the new calculation method is the same as that of the elastic parameter method. However, considering the effect of different mineral compositions on reservoir brittleness, the calculation results are more precise and the calculation error of elastic parameter method is reduced. The calculation results are more in line with the actual situation of the study block.

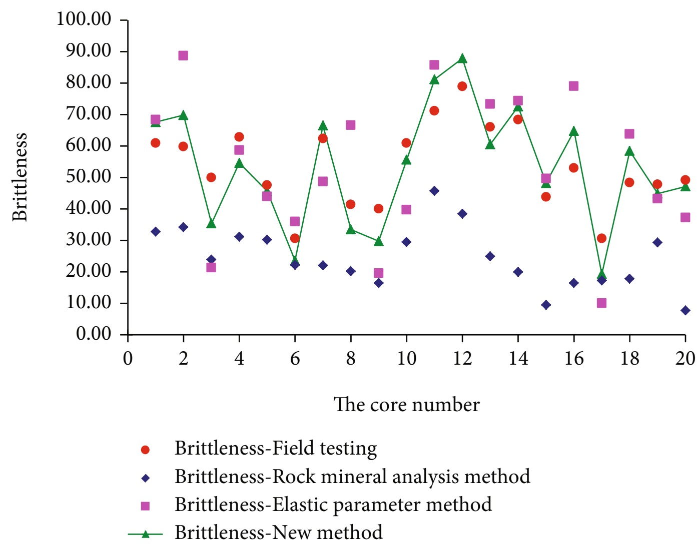

FIGURE 10: Brittleness results under different calculation methods.

5. Conclusion

(1) In this paper, the fracture states of the shale core at different times are observed by CT scanning tests. The results show that with the increase of time, local microfractures are first formed in the core. While the microfractures grow longer, new microfractures are formed elsewhere. Until a large number of microfractures intersect and communicate with each other, eventually leading to core instability and fracture. Therefore, it can be seen that the rock macrofractures are the appearance of local fractures after reaching a certain degree, and the local fractures are the fundamental cause of macrofractures

(2) The stepwise regression analysis method is used to quantitatively analyze the relationships between the rock elastic modulus, Poisson's ratio, and rock mineral compositions combined with the environment of the Liaohe Oilfield actual reservoir, which is the basis of establishing the characterization method of local shale brittleness. A new method for characterizing shale brittleness by rock mineral compositions is established in combination with the elastic parameter method, thus realizing the characterization of local brittleness of the discrete core. This method is scientific and representative and can describe the change rule of rock local brittleness accurately

(3) The results show that quartz, calcite, siderite, analcite, and clay minerals are the main influencing factors of the rock elastic modulus. Dolomite, calcite, quartz, and clay minerals are the main influencing factors of Poisson's ratio. Among them, quartz and analcite have a positive correlation with the elastic modulus, and calcite, dolomite, and clay minerals have a positive correlation with Poisson's ratio. Other minerals have negative correlations

(4) It can be seen from the comparative analysis that the new method of the local brittleness index characterizes the change rule of rock brittleness from the microcosmic point of view, and the results are the same as those of the elastic parameter method. It can precisely quantify the influence of different mineral components on the reservoir brittleness, reduce the calculation errors of elastic parameter method, and avoid the low calculation results of the rock mineral analysis method. The results are more in line with the actual situation of the study block

Data Availability

The data used to support the findings of this study are available from the corresponding author upon request.

Conflicts of Interest

The authors declare that they have no conflicts of interest.

Acknowledgments

This research was supported by the Talented Reserves of Heilongjiang Province Science Foundation for Distinguished Young Scholars of Northeast Petroleum University (SJQHB201802), National Natural Science Foundation of China (Grant Nos. 51404073 and 51574088), Natural Science Foundation of Heilongjiang Province of China (Young Scientists) (Grant No. QC2017043), 9th special China Postdoctoral Science Foundation projects (Grant No. 2016T90268), Heilongjiang Postdoctoral Foundation (LBH-TZ-0503), China Postdoctoral Science Foundation (Grant No. 2018M630335), Heilongjiang General Undergraduate Colleges and Universities Young Innovative Talents Training Plan (Grant No. UNPYSCT-2016084), and Key Young Project of Northeast Petroleum University "National Foundation" Cultivating foundation (Science) 2017.

References

[1] L. Qinghui, C. Mian, P. W. Fred, J. Yan, and L. Zhimeng, "Influences of engineering factors on shale gas production-take the Haynesville shale gas reservoir in North America for example," *Journal of Natural Gas Industry*, vol. 32, no. 4, pp. 54–59, 2012.

[2] F. Meng, H. Zhou, C. Zhang, R. Xu, and J. Lu, "Evaluation methodology of brittleness of rock based on post-peak stress-strain curves," *Rock Mechanics and Rock Engineering*, vol. 48, no. 5, pp. 1787–1805, 2015.

[3] H. Honda and Y. Sanada, "Hardness of coal," *Fuel*, vol. 35, p. 451, 1956.

[4] M. M. Protodyakonov, "Mechanical properties and drillability of rocks," in *Proceedings of the 5th Symposium on Rock Mechanics*, pp. 103–118, Twin Cities, USA, 1963.

[5] A. W. Bishop, "Progressive failure with special reference to the mechanism causing it," in *Proceedings of the Geotechnical Conference*, pp. 142–150, Oslo, 1967.

[6] V. Hucka and B. Das, "Brittleness determination of rocks by different methods," *International Journal of Rock Mechanics and Mining Sciences and Geomechanics Abstracts*, vol. 11, no. 10, pp. 389–392, 1974.

[7] B. R. Lawn and D. B. Marshall, "Hardness, Toughness, and brittleness: an indentation analysis," *Journal of American Ceramic Society*, vol. 62, no. 7-8, pp. 347–350, 1979.

[8] G. E. Andreev, *Brittle Failure of Rock Materials: Test Results and Constitutive Models*, A. A. Balkema Press, Netherlands, 1995.

[9] J. B. Quinn and G. D. Quinn, "Indentation brittleness of ceramics: a fresh approach," *Journal of Materials Science*, vol. 32, no. 16, pp. 4331–4346, 1997.

[10] V. Hajiabdolmajid and P. Kaiser, "Brittleness of rock and stability assessment in hard rock tunneling," *Tunneling and Underground Space Technology*, vol. 18, no. 1, pp. 35–48, 2003.

[11] R. Altindag, "The correlation of specific energy with rock brittleness concept on rock cutting," *Journal of the South African Institute of Mining and Metallurgy*, vol. 103, no. 3, pp. 163–171, 2003.

[12] H. Copur, N. Bilgin, H. Tuncdemir, and C. Balci, "A set of indices based on indentation test for assessment of rock cutting performance and rock properties," *Journal of the South African Institute of Mining and Metallurgy*, vol. 103, no. 9, pp. 589–600, 2003.

[13] S. Yagiz, "An investigation on the relationship between rock strength and brittleness," in *Proceedings of the 59th Geological Congress of Turkey*, p. 352, Ankara, Turkey, 2006.

[14] R. Rickman, M. J. Mullen, J. E. Petre, W. V. Grieser, and D. Kundert, "A practical use of shale petro- physics for stimulation design optimization: all shale plays are not clones of the Barnett Shale," in *SPE annual technical conference and exhibition*, pp. 1–22, Denver, Colorado, USA, 2008.

[15] T. Feng, X. B. Xie, W. X. Wang, and C. L. Pan, "Brittleness of rocks and brittleness indexes for describing rockburst proneness," *Mining and Metallurgical Engineering*, vol. 20, no. 4, pp. 18-19, 2000.

[16] C. Hu, F. Wang, and C. Ai, "An Improved New Convolutional Neural Network Method for Inverting the Pore Pressure in Oil Reservoir by Surface Vertical Deformation," *Lithosphere*, vol. 2021, no. 1, p. 5597238, 2021.

[17] L. Enlong and Z. Shen, "Study on brittleness of geomaterials," *Chinese Journal of Rock Mechanics and Engineering*, vol. 24, no. 19, pp. 3449–3453, 2005.

[18] C. H. Sondergeld, K. E. Newsham, J. T. Comisky, M. C. Rice, and C. S. Rai, "Petrophysical considerations in evaluating and producing shale gas resources," in *SPE unconventional gas conference*, pp. 1–17, Pittsburgh, Pennsylvania, USA, 2010.

[19] Q. H. Li, M. Chen, Y. Jin, F. P. Wang, B. Hou, and B. W. Zhang, "Indoor evaluation method for shale brittleness and improvement," *Chinese Journal of Rock Mechanics and Engineering*, vol. 31, no. 8, pp. 1680–1685, 2012.

[20] H. Y. Diao, "Rock mechanical properties and brittleness evaluation of shale reservoir," *Acta Petrologica Sinica*, vol. 29, no. 9, pp. 3300–3306, 2013.

[21] H. Zhou, F. Z. Meng, C. Q. Zhang, R. C. Xu, and J. J. Lu, "Quantitative evaluation of rock brittleness based on stress-strain curve," *Chinese Journal of Rock Mechanics and Engineering*, vol. 6, pp. 1114–1122, 2014.

[22] C. Yun, J. Yan, and C. Mian, "A rock brittleness evaluation method based on energy dissipation," *Chinese Journal of Theoretical and Applied Mechanics*, vol. 47, no. 6, pp. 984–993, 2015.

[23] T. Wu, *The Study on the Influencing Factors and Evaluation Method of Rock Brittleness in Shale Gas Reservoir*, The Southwest Petroleum University, 2015.

[24] M. Zhaoping and P. Suping, "Mudstone composition of coal measures and its influence on the mechanical properties," *Coal Geology & Exploration*, vol. 32, no. 2, pp. 14–16, 2004.

[25] M. D. Burnaman, W. Xia, and J. Shelton, "Shale gas play screening and evaluation criteria," *China Petroleum Exploration*, vol. 14, no. 3, pp. 51–64, 2009.

[26] A. Hofmann, C. Rigollet, E. Portier, and S. Burns, "Gas shale characterization - results of the mineralogical, lithological and geochemical analysis of cuttings samples from radioactive Silurian shales of a Paleozoic Basin," in *North Africa Technical Conference and Exhibition*, pp. 1–12, Cairo, Egypt, 2013.

[27] D. I. Wen-Long, L. Chao, L. I. Chun-Yan, H. U. Chang-Chun, J. Kai, and C. E. Wei-Te, "Dominant factor of fracture development in shale and its relationship to gas accu-mulation," *Earth Science Fronties*, vol. 19, no. 2, pp. 212–220, 2012.

[28] B. Liu, Y. F. Lü, Q. Ran, C. L. Dai, M. Li, and M. Wang, "Geological conditions and exploration potential of shale oil in Qingshankou Formation, Northern Songliao Basin," *Oil & Gas Geology*, vol. 35, no. 2, pp. 280–285, 2014.

[29] J. F. Gale, S. E. Laubach, J. E. Olson, P. Eichhuble, and A. Fall, "Natural fractures in shale: a review and new observations," *AAPG Bulletin*, vol. 98, no. 11, pp. 2165–2216, 2014.

[30] H. Lin, X. Zhang, R. Cao, and Z. Wen, "Improved nonlinear burgers shear creep model based on the time-dependent shear strength for rock," *Environmental Earth Sciences*, vol. 79, no. 6, pp. 1–9, 2020.

[31] X. Zhang, H. Lin, Y. Wang, R. Yong, Y. Zhao, and S. Du, "Damage evolution characteristics of saw-tooth joint under shear creep condition," *International Journal of Damage Mechanics*, vol. 30, no. 3, pp. 453–480, 2021.

[32] X. Zhao, L. Zeng, K. Zu, X. Hu, and J. Shi, "Brittleness characteristics and its control on natural fractures in tight reservoirs: a case study from Chang 7 tight reservoir in Longdong area of the Ordos Basin," *Oil & Gas Geology*, vol. 37, no. 1, pp. 62–71, 2016.

[33] D. M. Jarvie, R. J. Hill, T. E. Ruble, and R. M. Pollastro, "Unconventional shale-gas systems: the Mississippian Barnett Shale of north-central Texas as one model for thermogenic shale-gas assessment," *AAPG Bulletin*, vol. 91, no. 4, pp. 475–479, 2009.

[34] Y. Xue, J. Liu, P. G. Ranjith, X. Liang, and S. Wang, "Investigation of the influence of gas fracturing on fracturing characteristics of coal mass and gas extraction efficiency based on a multi-physical field model," *Journal of Petroleum Science and Engineering*, vol. 206, article 109018, 2021.

[35] R. Rickman, M. J. Mullen, J. E. Petre, W. V. Grieser, and D. Kundert, "A practical use of shale petrophysics for stimulation design optimization all shale plays are not clones of the Barnett shale," in *SPE annual technical conference and exhibition*, pp. 1–13, Denver, Colorado, USA, 2008.

[36] H. Bing, C. Mian, P. Tan, and D. Li, "Monitoring of hydraulic fracture network by acoustic emission method in simulated tri-axial fracturing system of shale gas reservoirs," *Journal of China University of Petroleum*, vol. 39, no. 1, pp. 66–71, 2015.

[37] T. Wang, T. Zhang, P. G. Ranjith et al., "A new approach to the evaluation of rock mass rupture and brittleness under triaxial stress condition," *Journal of Petroleum Science and Engineering*, vol. 184, article 106482, 2020.

[38] T. Wang, *Evolution Mode on Shale Fracture with Acoustic Emission Behavior*, The Northeast Petroleum University, 2017.

Hindawi
Geofluids
Volume 2021, Article ID 3963291, 14 pages
https://doi.org/10.1155/2021/3963291

WILEY | Hindawi

Research Article

Numerical Simulation of Nanosilica Sol Grouting for Deep Tunnels Based on the Multifield Coupling Mechanism

Dongjiang Pan,[1,2,3] **Kairong Hong**,[1,3] **Helin Fu**,[2] **Zhiguo Li**,[1,3] **Limeng Zhang**,[1,3] **Gaoming Lu**,[1,3] **Feixiang Sun**,[1,3] **and Shiyu Wen**[4]

[1]*China Railway Tunnel Group Co., Ltd., Guangzhou, Guangdong, China*
[2]*School of Civil Engineering, Central South University, Changsha, Hunan, China*
[3]*State Key Laboratory of Shield Machine and Boring Technology, Zhengzhou, Henan, China*
[4]*China Railway Development Investment Group Co., Ltd., Kunming, Yunnan, China*

Correspondence should be addressed to Dongjiang Pan; cumtpdj@163.com

Received 21 April 2021; Revised 18 July 2021; Accepted 12 August 2021; Published 26 August 2021

Academic Editor: Kai Yao

Grouting is an effective technical way for the construction of deep tunnels in unfavorable geological conditions. The fluid-solid-chemical coupling mechanism of grouting process is analyzed from the following three aspects: influence of physical properties of silica sol on permeability coefficient, dynamic changes of porosity and permeability of geotechnical media with seepage pressure, and governing equations for flow and mass transfer characteristics. A dynamically changing model for nanosilica sol grouting in deep tunnels is established, considering the changing physical properties of grout and surrounding rock. Based on the Xianglushan Tunnel of Yunnan Water Diversion Project, the temporal and spatial evolution of silica sol grout is studied. The effect characteristics of grouting pressure and initial permeability are clarified. The rationality of this model is verified by classical Newtonian fluid grouting theory. The main conclusions: with the molar concentration as the index, the grout range can be divided into the raw grout region and the transition region; with the decrease of the grouting pressure, the growth rate of the normal grouting radius and the axial grouting radius will gradually decrease; due to the mechanical dispersion and molecular diffusion, the range of the transition region will gradually increase with time. The ratio of the transition region to grouting radius fluctuates slightly with time under the initial permeability of 5 D. The fluctuation increases with the decrease of initial permeability, and the average ratio increases with the decrease of grouting pressure. This study can provide theoretical guidance for grouting design of deep tunnel engineering.

1. Introduction

Due to the influence of crustal movement, human excavation engineering, and weathering erosion, the rock mass contains not only macroscopic defects such as joints and cracks but also microscopic defects such as microcracks and micropores [1–4]. Grouting is an effective technical way for the construction of deep tunnels in unfavorable geological conditions [5–7]. Due to nanoparticle size, low viscosity, high injectability, and friendly to ecological environment, silica sol grouting has been widely used in petroleum engineering, groundwater protection engineering, tunnel construction, nuclear waste storage, liquefiable soil improvement, and other geotechnical fields [8–11].

Wang et al. [10, 12] investigated the rheological properties of nanosilica sol grout and derived an equation of real-time viscosity and permeability length. Fujita and Kobayashi [13] studied the transport mechanism of colloidal silica in unsaturated sand and the effect of charging properties of sand and silica particles by sand column experiment. In order to study the penetration law of silica sol in microcracks with a width of 40-50 microns, fluorescent whitening agent-ultraviolet observation method, microscopic observation method, and hydraulic experiment method were used to jointly predict and verify the penetration length and sealing effect of silica sol [14]. The influence of gel effect on the migration ability of silica sol in liquefied soil was studied by using soil column experiments and a pilot-scale facility [15–17]. The migration process of silica sol along the whole length of soil column, the gel capacity of silica sol when it reached the target area, the injection amount of silica sol, and the migration amount of silica sol with the concentration of chloride ion as the indexes were monitored during the soil column experiment. The flow laws of silica sol, epoxy resin, polyurethane, and cement-based grout in one-dimensional and two-dimensional fractured rock mass with different grouting modes (constant flow grouting, constant pressure grouting, and constant energy grouting) were studied by theoretical analysis [18]. An analytical model of colloidal silica gelling in groundwaters with varying pH and background electrolyte concentrations was developed and validated [19]; the model was then applied to a hypothetical case study to demonstrate its use in grout design, based on published in situ groundwater data from the Olkiluoto area of Finland. The pulsating grouting technology of silica sol was tested in a 500-meter-deep tunnel at Mizunami Underground Research Laboratory in Japan [20]. Pan et al. [21, 22] studied the influence characteristics and mechanism of fragmental size of broken coal mass on the injection regularity of silica sol grouting. Injection regularity of silica sol grouting in broken coal mass generally presented a three-stage regularity. The fragmental size had a great impact on the 2nd and 3rd stages.

In summary, previous experts have achieved fruitful research results about the injection law of silica sol grouting through numerical simulations, column tests, and field experiments. However, there are still some deficiencies in the study of the synergy effect of grouting material-surrounding rock physical properties on silica sol grouting in deep tunnels, and the study of multifield mechanism for silica sol grouting in deep tunnels is still insufficient.

In this paper, in order to explore the theoretical mechanism of nanosilica sol grouting technology for deep tunnels in unfavorable geological conditions, a dynamically changing model for silica sol grouting in deep tunnels is established, taking into account the changing physical properties of grout and surrounding rock. Based on the project background of Xianglushan Tunnel of Central Yunnan Water Diversion Project, the temporal and spatial evolution of Darcy velocity, viscosity, molar concentration, and fluid pressure of silica sol grouting are analyzed. The effects of grouting pressure and initial permeability of surrounding rock on permeability grouting characteristics of silica sol are explored. The rationality of this model is verified by combining the column theory and sphere theory.

2. Engineering Background and Grouting Material

Xianglushan Tunnel was located on the head of the Dali I Section, which was the first section of the main channel of the Central Yunnan Water Diversion Project (Figure 1). At the feasibility study stage, the total length of the section was 63.426 km [23]. For Xianglushan Tunnel, the burial depth in the area to the north of the trough valley of the Runan River was 600~1000 m. According to the stress assessment results of tunnel surrounding rock in the geological survey stage, the average weight of rock mass can be calculated as $26.5\,\mathrm{kN/m^3}$. The vertical stress of the surrounding rock at a buried depth of 1000 m was 26.50 MPa, which was a high level of ground stress. The statistics of conventional water pressure tests results showed that the overall permeability of the rock formations in the study area was weak water permeability ($1 \leq q$ (permeability rate) < 10 Lu, $10^{-5} \leq K$ (permeability coefficient) $< 10^{-4}$ cm/s), and some were medium permeable. The permeability of karst strata was stronger than that of nonkarst strata. Part of the medium permeability is mainly concentrated limestone, dolomitic limestone, argillaceous limestone, and sandstone of Songgui formation.

The drilling and blasting method and TBM method were used to construct the Xianglushan Tunnel, in which the TBM section was 35.37 km long. According to the information of exploration and design, the tunnel diameter of downstream TBM section was 9.8 m, in which Class IV and V surrounding rocks accounted for 53.14% (Table 1), and large deformation surrounding rocks accounted for 16.62%. Under the condition of naked tunnel, the length of the main tunnel section of Xianglushan Tunnel was 33.085 km with a specific yield greater than $3\,\mathrm{m^3/m\cdot d}$ in dry season.

Considering environmental protection, ecology, and flow control in the tunnel, in order to avoid more leakages in the tunnel, reduce the impact of pumping and drainage on groundwater environment and tunnel construction, groundwater should be plugged and drained in a way that followed the principle of "first plugging, and limited drainage." When the local hydraulic head of groundwater was less than 60 m, it was better to adopt the full plugging method; when the hydraulic head of groundwater was more than 60 m, drainage and guide mode should be adopted.

Silica sol was selected as sealing grouting material. It was a one-component nanogrouting material, which belonged to colloidal solution, odorless and nontoxic. Silica sol had a typical double-electron layer structure. The dominant size of the silica particles in silica sol was 8–12 nm. When strong electrolyte solution (i.e., catalyst) was added, the double-electron layer of colloidal particles was compressed and thinned, and the gel reaction began to take place. The viscosity of colloidal particles increased gradually [25, 26]. The catalyst chosen in the experiment was NaCl solution (Table 2). The gel time of silica sol can be adjusted according to the amount of catalyst. The gel reaction products had a good transmittance and compact microstructure (Figure 2).

3. A Dynamically Changing Model for Silica Sol Grouting in Deep Tunnels Based on the Multifield Coupling Mechanism

The injection process in a tunnel is a complex and changeable system problem: (a) geotechnical medium is multiscale, and different stress states of surrounding rocks at different positions in a tunnel lead to uneven development of fracture and pore; (b) geotechnical environment is multi-interface, such as grout-rock, grout-gas, and grout-water interfaces;

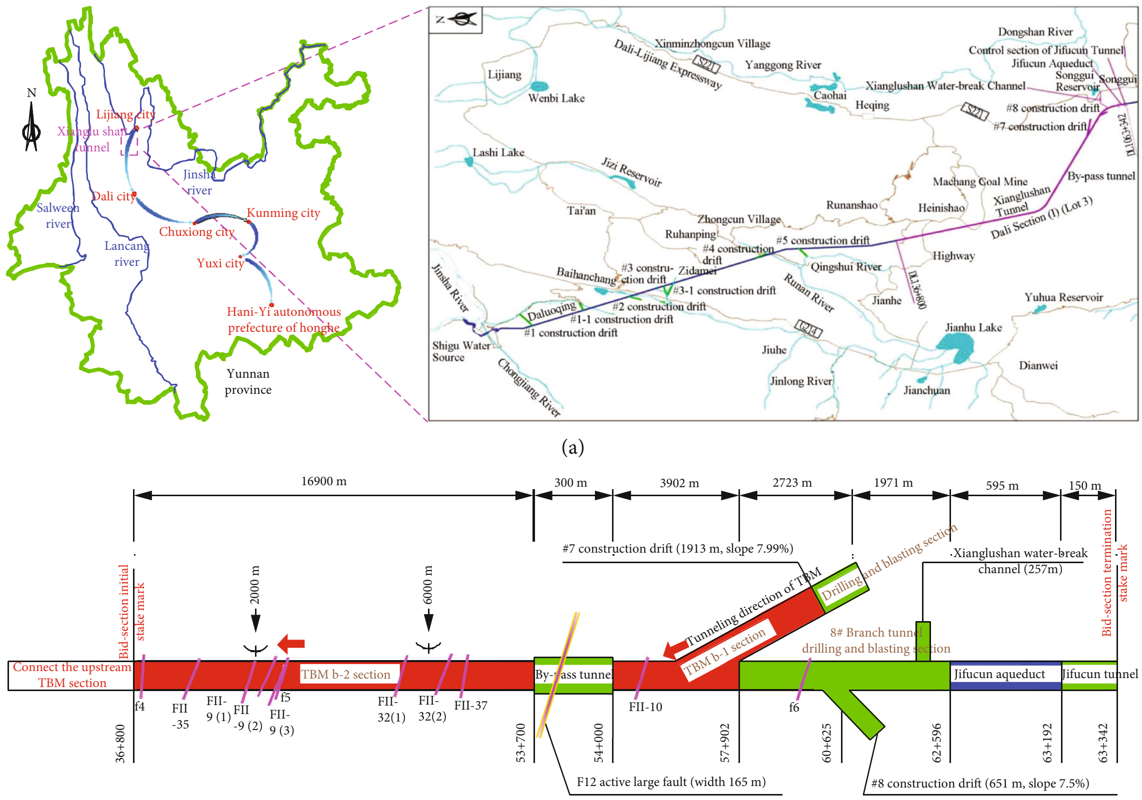

Figure 1: Overview of the downstream TBM (Tunnel Boring Machine) section of Xianglushan Tunnel. (a) Planning curve of the Central Yunnan Water Diversion Project and location of Xianglushan Tunnel; (b) working condition of the downstream TBM section of Xianglushan Tunnel.

Table 1: Mechanical parameters of Class IV and V rock mass in Xianglushan Tunnel.

Rock mass quality [24] Major classification	Minor classification	Uniaxial compression strength (MPa)	Intactness index of rock mass	Unit weight (kN/m^3)	Shear strength (MPa)	Deformation modulus (GPa)	Poisson's ratio
	IVa	30-40	0.45	23.5	0.6-0.7	3-5	0.27-0.28
IV	IVb	15-25	0.6	23.5	0.4-0.6	2-3	0.28-0.29
	IVc	5-10	0.55	22	0.3-0.4	1.5-2	0.29-0.30
	Va	10-20	0.4	22	0.2-0.3	0.7-1.5	0.30-0.31
V	Vb	5-10	0.3	22	0.1-0.2	0.2-0.7	0.31-0.32
	Vc	1-3	0.24	22	0.05-0.1	0.1-0.2	0.32-0.34

Table 2: Basic physical properties of silica sol and catalyst.

Properties	Silica sol	Catalyst
Viscosity	~10 mPa·s	~1 mPa·s
Density	1.1 kg/L	1.07 kg/L
pH	10	7
Concentration (% by weight)	SiO_2 15%	NaCl 10%

the permeability grouting presents nonlinear characteristics because of the different states, structures, and physical and chemical properties of the interfaces; (c) in the grouting process, there are many reactions, such as convection, molecular diffusion, mechanical dispersion, adsorption and retention, and gel reaction between silica sol and catalyst. These reactions will change the migration characteristics of fluids [27]. In this paper, the injection process of silica sol in deep tunnels is regarded as a multireaction coupled flow in porous media. The fluid-solid-chemical coupling mechanism of grouting process is analyzed from the following three aspects.

3.1. Influence of Physical Properties of Silica Sol on Permeability Coefficient. Assuming that the rock mass does not undergo hydration or expansion, the permeability

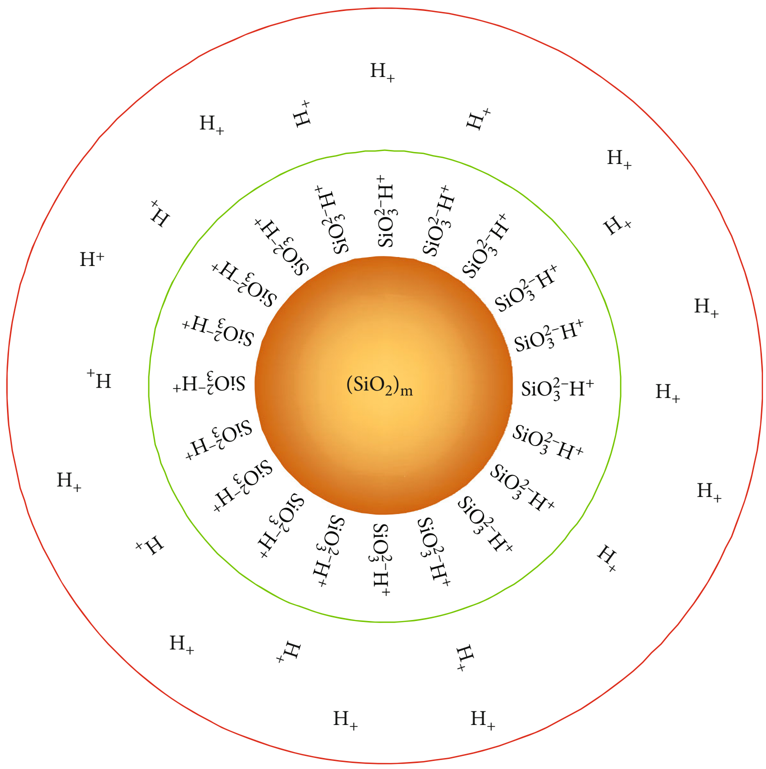

(a)

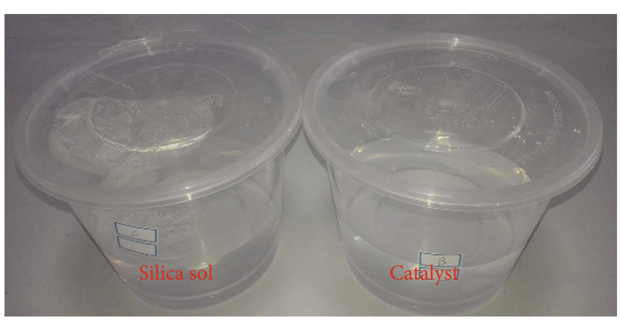

(b)

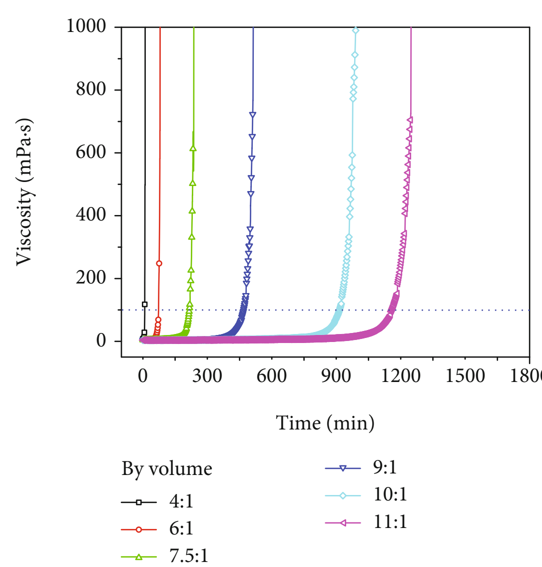

(c)

Figure 2: Continued.

(d)

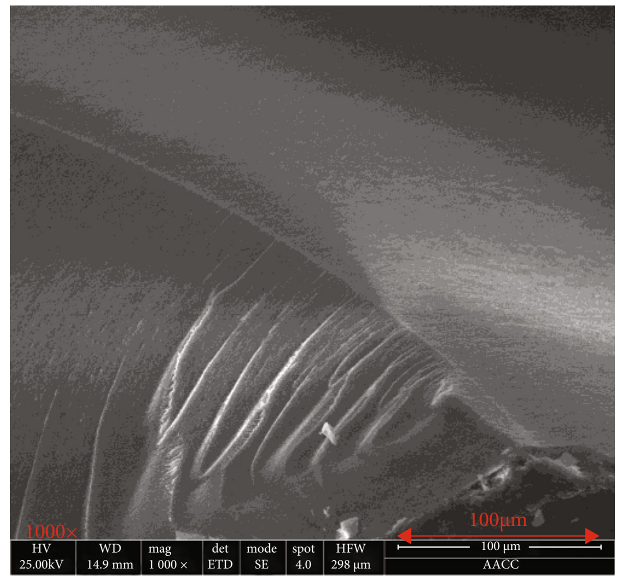

(e)

Figure 2: Double-electron layer structure and gel process of silica sol. (a) Double-electron layer structure of silica sol; (b) photo of silica sol and NaCl solution; (c) viscosity versus time curves for grout with different proportions; (d) gel reaction products; (e) scanning electron microscope photo of gel reaction products.

coefficient of grout is mainly restricted by two aspects: (a) the redistribution of surrounding rock stress field caused by engineering disturbances such as excavation and grouting; (b) the change of viscosity and density of grout caused by self-gel and dilution in groundwater. Self-gel is embodied in the dependence of viscosity on time; adsorption retention and dilution in groundwater are embodied in the dependence of viscosity on concentration and density on concentration.

3.1.1. Three-Dimensional Surface Equation for Viscosity-Time-Concentration of Grout. For silica sol with mass fraction of 15%, the molar concentration of silica is 2750 mol/m^3. The grout is prepared with silica sol : catalyst volume ratio of 9 : 1, and the viscosity is measured with an NDJ-5S rotary viscometer [28]. The function expression of fitting viscous time curve is as follows:

$$\mu = 7.32 \times 10^{-13} e^{t/1309.55} + 7.71 \times 10^{-3}, \tag{1}$$

where t is in seconds and μ is in Pa·s.

By using the linear interpolation algorithm [29], the three-dimensional surface equation of grout with respect to time and concentration can be obtained:

$$\mu(c, t) = \frac{7.32 \times 10^{-13} e^{t/1309.55} + 7.71 \times 10^{-3} - 0.001}{2750} c + 0.001, \tag{2}$$

where the preferable range of t is 0-36000 s and the preferable range of c is 0-2750 mol/m^3. As shown in Figure 3, a three-dimensional surface diagram is drawn.

3.1.2. Relationship between Density and Molar Concentration of Grout. The molar concentration of grout (9 : 1) is 2750 mol/m^3, and the density is 1097 kg/m^3; however, the molar concentration of water is 0 mol/m^3 and the density is 1000 kg/m^3. The molar concentration of silica sol grouting is basically proportional to its density, and the density of grout can be expressed as follows:

$$\rho = 1000 + \frac{97}{2750} c, \tag{3}$$

where ρ is the density of grout, kg/m^3.

(a)

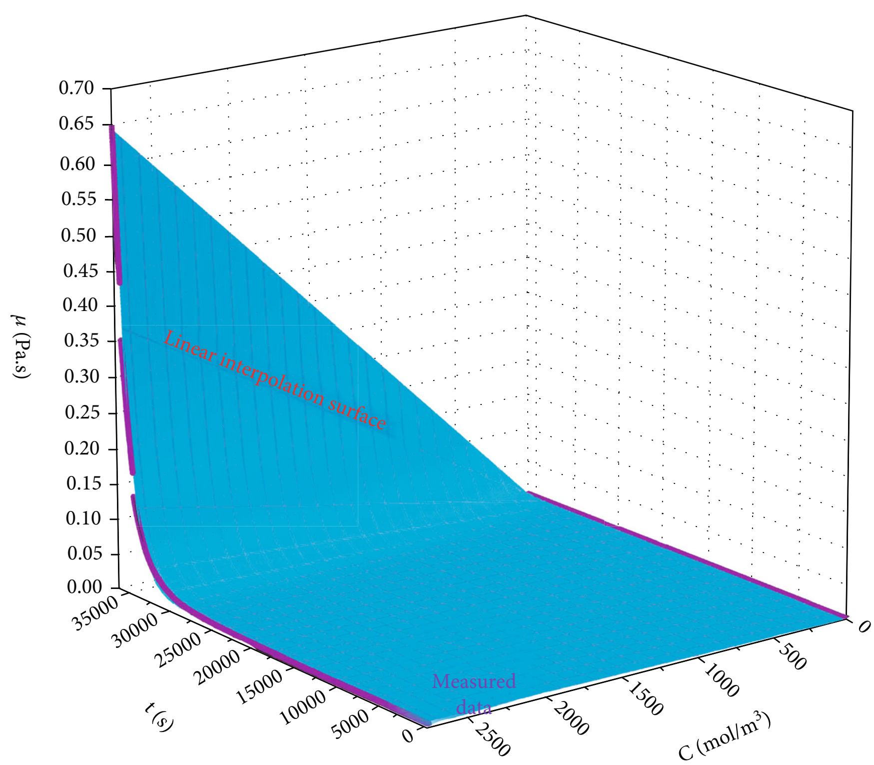

(b)

Figure 3: Rotation viscosity experiment: (a) NDJ-5S rotary viscometer; (b) linear interpolation three-dimensional surface of viscosity with time and concentration for grout.

3.2. Dynamic Changes of Porosity and Permeability of Geotechnical Media with Seepage Pressure. In the process of geotechnical grouting, the seepage pressure of grouting fluid will change the spacing or pattern of geotechnical particles, so that the actual porosity, permeability, and other physical parameters will dynamically change with the change of the seepage pressure, thereby affecting the seepage process. When neglecting the temperature effect, the relationship between the dynamic changes of porosity and permeability in geotechnical media under seepage pressure can be given as follows [30]:

$$\varphi = 1 - \frac{1-\varphi_0}{1+\varepsilon v}\left(1 - \frac{\Delta p}{E_s}\right), \tag{4}$$

$$k = \frac{k_0}{1+\varepsilon_v}\left(1 + \frac{\varepsilon_v}{\varphi_0} - \frac{\Delta p(1-\varphi)}{\varphi_0 \cdot E_s}\right)^3, \tag{5}$$

where φ is the dynamic porosity; k is the dynamic permeability; φ_0 is the initial porosity; k_0 is the initial permeability; ε_v is the volumetric strain; $\Delta p = p - p_0$ (p_0 is the initial pressure; p is current pressure); E_s is the bulk modulus of geotechnical media.

Combined with Equations (2), (3), and (5), a variable permeability coefficient model of silica sol grouting in the tunnel can be constructed:

$$K = \frac{k\rho g}{\mu}, \tag{6}$$

where K is the permeability coefficient.

3.3. Governing Equations for Flow and Mass Transfer Characteristics

3.3.1. Governing Equations for Grout Flow. The governing equations of grout flow can be expressed by Darcy's law [2].

$$\begin{aligned} &\frac{\partial(\varphi \cdot \rho)}{\partial t} + \nabla \cdot (\rho \mathbf{u}) = Q_m, \\ &\mathbf{u} = -\frac{k}{\mu}(\nabla p + \rho g \nabla D), \end{aligned} \tag{7}$$

where $\mathbf{u}$ is the Darcy velocity, m/s; ∇D is the unit vector in gravity direction; D is the vertical coordinates.

3.3.2. Governing Equation for Mass Transfer. Silica sol grouting approximately satisfies transport of diluted species in porous media [11]. Assuming that only convection, molecular diffusion, and mechanical dispersion are considered and that adsorption is not considered, the basic equation of solute transport is shown in the following:

$$\frac{\partial c_i}{\partial t} + \nabla \cdot (-D_i \nabla c_i) + \mathbf{u} \cdot \nabla c_i = R_i, \tag{8}$$

where c_i is the concentration of component i, mol/m^3; D_i is the molecular diffusion, m^2/s; R_i is the reaction rate of component i, mol/(m^3·s).

Because the gel reaction of silica sol is the gradual connection of colloidal particles into a network structure, the gel reaction can be regarded as not affecting the molar concentration of silica.

4. Numerical Model and Boundary Conditions

4.1. Parameter Values. COMSOL software is used for numerical calculation. As shown in Figure 4, the model size is 100 × 100 m, the diameter of tunnel is 9.8 m, the diameter of grouting borehole is 5 cm, and the length of borehole is 3 m. The numerical simulation process can be divided into three steps: in situ stress initialization, tunnel excavation, and borehole grouting. The values of parameters in the numerical model are shown in Table 1.

4.2. Boundary Conditions

4.2.1. Boundary Conditions for Solid Mechanics. The upper boundary condition is given stress of 25 MPa, the lower boundary condition is fixed constraint, the left boundary condition is symmetrical boundary condition, and the right boundary condition is roller support. The boundary condition of the tunnel is simplified to free. After boring, the grouting pipe is put in, and the boundary condition is simplified to zero radial displacement.

4.2.2. Boundary Conditions for Darcy's Law. The upper, lower, and right boundary conditions of the model are given hydraulic head of 50 m, and the left boundary condition is symmetrical. After tunnel excavation, timely grouting behind shield closes the cracks in surrounding rock, and the boundary condition for surrounding rock of tunnel is nonflowing. The boundary condition of borehole is given pressure of 2 MPa to simulate grouting pressure.

4.2.3. Boundary Conditions for Transport of Diluted Species in Porous Media. The upper, lower, and right boundary conditions of the model are given pressure of 0 mol/m^3, and the left boundary condition is symmetrical. The boundary condition of borehole is 2750 mol/m^3, which simulates the grout concentration at the injection end.

5. Results and Discussion

5.1. Injection Characteristics of Model with a Grouting Pressure of 2 MPa and an Initial Permeability of 5 D. Taking a calculation model with a grouting pressure of 2 MPa and an initial permeability of 5 D as an example, a monitoring line of 80 m in length is laid vertically in the grouting hole, and the permeability law of silica sol grouting in tunnel is analyzed. As shown in Figures 5(a)–5(e), there is a certain transition zone between groundwater and grout. Because Darcy velocity, viscosity, and permeability coefficient are dependent variables of molar concentration, 10% of initial molar concentration of grout (27.50 mol/m^3) is used as the index of grout penetration radius. Define the 10%~95% (27.50~2612.50 mol/m^3) of initial molar concentration for the transition region and 95%~100% of initial concentration for the raw grout region. The grouting radius and transition

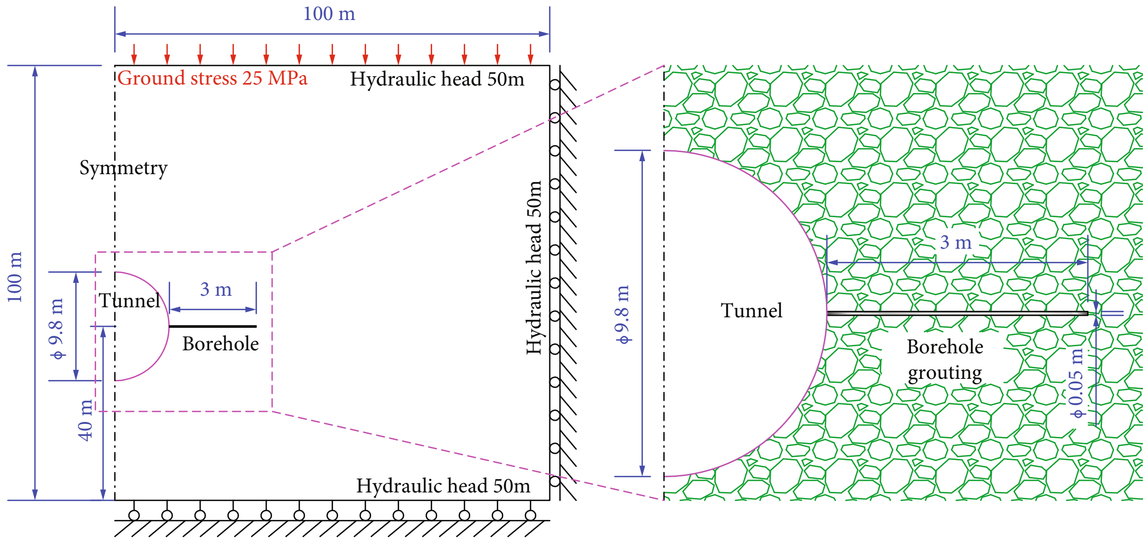

Figure 4: Schematic diagram of the numerical model.

region in different directions at different times are calculated, as shown in Figure 5(f).

The viscosity, molar concentration, and permeability coefficient in the raw grout region remain basically unchanged at the same time. The viscosity and molar concentration in the transition region decrease with the distance from the grouting hole, while the permeability coefficient increases with the distance from the grouting hole. Moreover, when the gel time is not exceeded, the viscosity increases slowly and remains at a low level for a long time, which basically coincides with the indoor test.

The Darcy velocity at the same location decreases with the increase of time. The maximum Darcy velocity at the 15th minute is 3.21×10^{-4} m/s, the maximum Darcy velocity at the 480th minute is 1.37×10^{-4} m/s, and the maximum Darcy velocity at the 560th minute drops sharply to 1.32×10^{-5} m/s. This is closely related to the late sharp increase in viscosity.

The normal grouting radius is higher than the axial grouting radius; the normal grouting radius, the axial grouting radius, and the transition region all increase with time, but the ratio of the transition region to the grouting radius remains at 36.22%.

5.2. Effect of Grouting Pressure on the Injection Characteristics. Silica sol grout can be regarded as Newtonian fluid. Column theory and sphere theory for uniform permeability of Newtonian fluid in stratum are shown in Equations (9) and (10) [32]. According to the values of parameters in Tables 2 and 3, the theoretical grouting radius is calculated:

$$h_1 = \frac{r_1^{\,2}\varphi\beta}{2Kt} \ln \frac{r_1}{r_0}, \tag{9}$$

$$r_1 = \sqrt[3]{\frac{3Kpr_0 t}{n\beta}}, \tag{10}$$

where h_1 is the difference between grouting pressure head and groundwater head, cm; r_1 is the grouting radius, cm; β is the viscosity ratio of grout to water; and r_0 is the radius of grouting pipe, cm.

Under the same initial permeability of 5 D, the numerical models with a grouting pressure of 2 MPa, 1.5 MPa, and 1 MPa are calculated, respectively. As shown in Figure 6, the numerical simulation and theoretical calculation of grout frontier under different grouting pressures are presented. The normal grouting radius is slightly higher than the axial grouting radius, the axial grouting radius is significantly higher than the column theoretical value, and the column theoretical value is higher than the sphere theoretical value. With the decrease of grouting pressure, the growth rates of normal grouting radius and axial grouting radius gradually decrease. When the grouting pressure is 2 MPa and 1.5 MPa, respectively, the numerical simulation value is larger than the calculation value of column theory, and the excess value is equal to the range of the transition region. The coincidence between the axial raw grout region and the column theoretical value is high, which indicates that column theory can explain the injection characteristics of raw grout region. The range of the transition region increases with time, which is attributed to the increasing effect of mechanical dispersion and molecular diffusion. The ratio of transition region to grouting radius fluctuates slightly with time under the same grouting pressure, and the average ratio increases slightly with the decrease of grouting pressure. The grouting design of the tunnel engineering should take into account not only the scope of the raw grout region but also the affluence factor of the transition region.

5.3. Effect of Initial Permeability on the Injection Characteristics. Under the same grouting pressure of 2 MPa, the numerical models with an initial permeability of 5 D, 0.5 D, and 0.05 D are calculated, respectively. As shown in Figure 7, the numerical simulation and theoretical

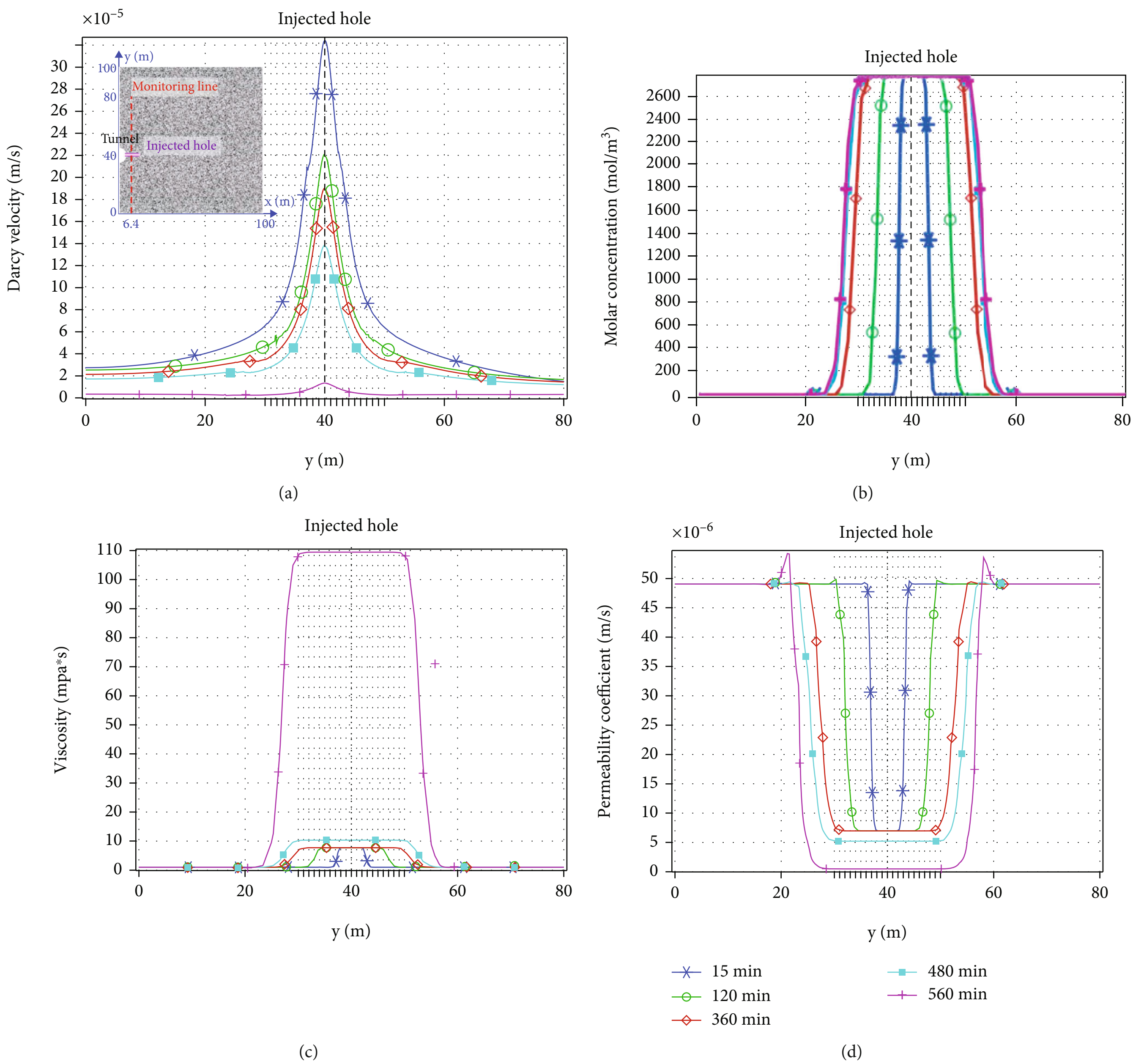

Figure 5: Continued.

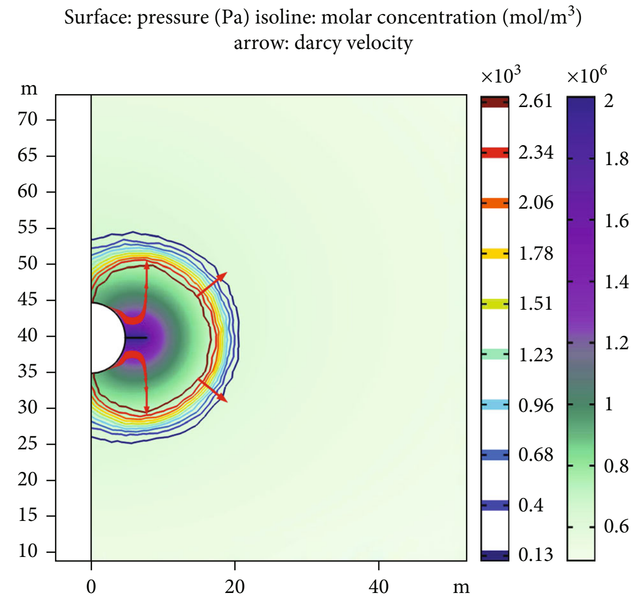

(e)

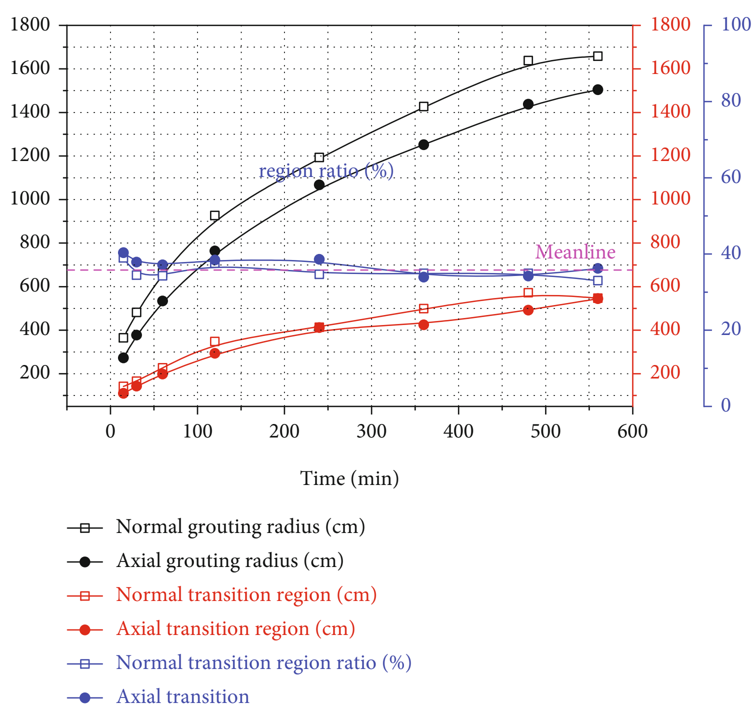

(f)

Figure 5: Permeability characteristics of the model with a grouting pressure of 2 MPa and an initial permeability of 5 D. (a) Distribution characteristics of Darcy velocity at different times; (b) distribution characteristics of viscosity at different times; (c) distribution characteristics of molar concentration at different times; (d) distribution characteristics of permeability coefficient at different times; (e) distribution characteristics of pressure, molar concentration, and Darcy velocity at 420th minute; (f) grouting radius and transition region in different directions at different times.

calculation of grout frontier under different grouting pressures are presented.

The normal grouting radius is slightly higher than the axial grouting radius, and the axial grouting radius is significantly higher than the value of column theory. With the decrease of initial permeability, the growth rates of normal and axial grouting radius decrease gradually. Under all initial permeability conditions, the axial raw grout region has a high degree of coincidence with the column theory, which indicates that the column theory can explain the injection characteristics of the axial raw grout region. And under the initial permeability of 0.05 D, the range of the

Table 3: Value of parameters in the numerical model.

Number	Medium	Parameters	Unit	Value or expression
1	Geotechnical medium	Deformation modulus	[Pa]	1.1×10^9
2		Poisson's ration	[1]	0.3
3		Density	[kg/m^3]	2200
4		Cohesion	[Pa]	0.25×10^6
5		Angle of internal friction	[degree]	30
6		Initial porosity	[1]	14%
7		Initial permeability	[m^2]	5×10^{-12}
8		Dynamic porosity	[1]	Equation (4)
9		Dynamic permeability	[m^2]	Equation (5)
10	Grout	Viscosity	[Pa·s]	Equation (2)
11		Density	[kg/m^3]	Equation (3)
12		Molecular diffusion*	[m^2/s]	1.2×10^{-11}
13		Mechanical dispersion	[m^2/h]	8.4×10^{-4} [17]

Note: *Stocks-Einstein equation can be used to calculate molecular diffusion [31].

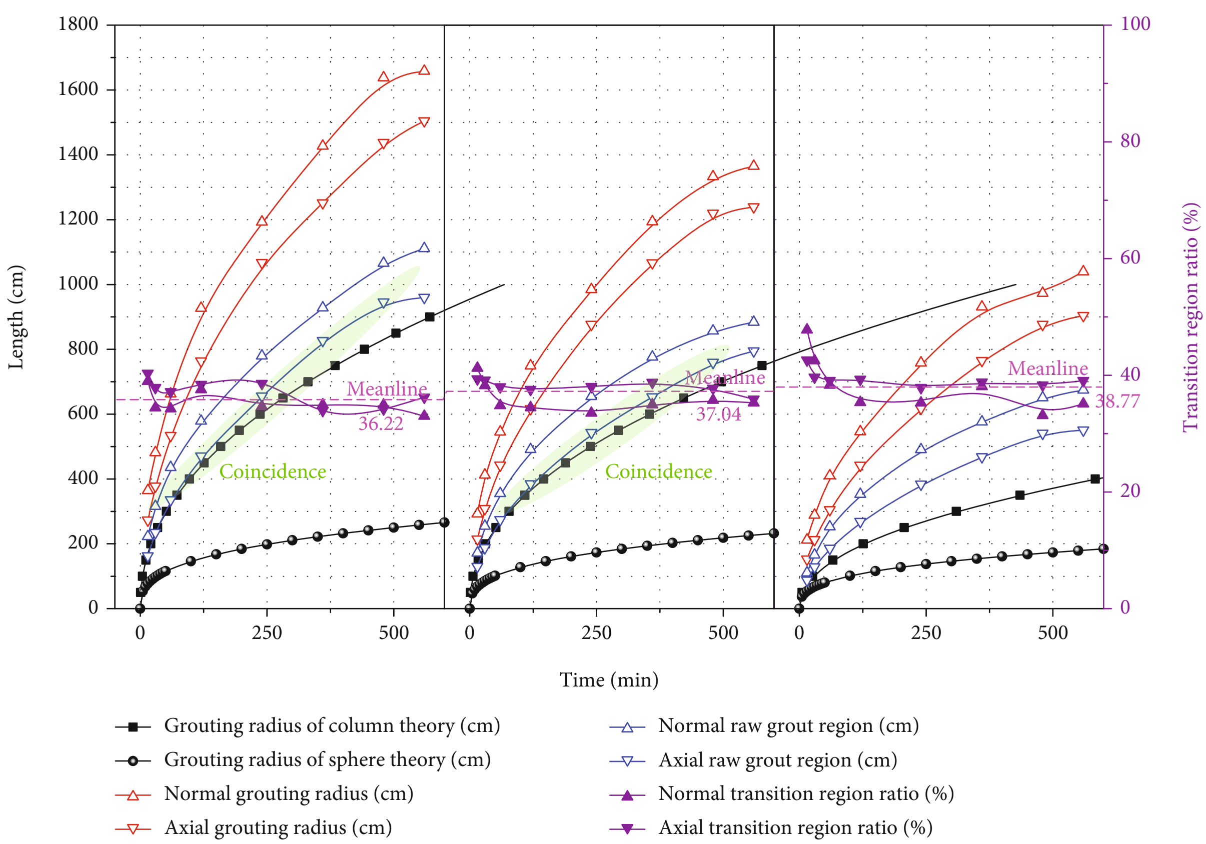

Figure 6: Comparisons between numerical simulation and theoretical calculation of grouting radius under different grouting pressures: (a) 2 MPa; (b) 1.5 MPa; (c) 1 MPa.

raw grout region is basically equal to the calculated values of column theory and sphere theory, which indicates that in the geotechnical medium media with low permeability, the multifield coupling mechanism of permeability grouting can explain the column theory and sphere theory well. The range of the transition region increases with time. Under the initial permeability of 5 D, the fluctuation of the ratio of the transition region to grouting radius is small, and the fluctuation increases with the decrease of the initial permeability, and the average ratio increases gradually with the decrease of

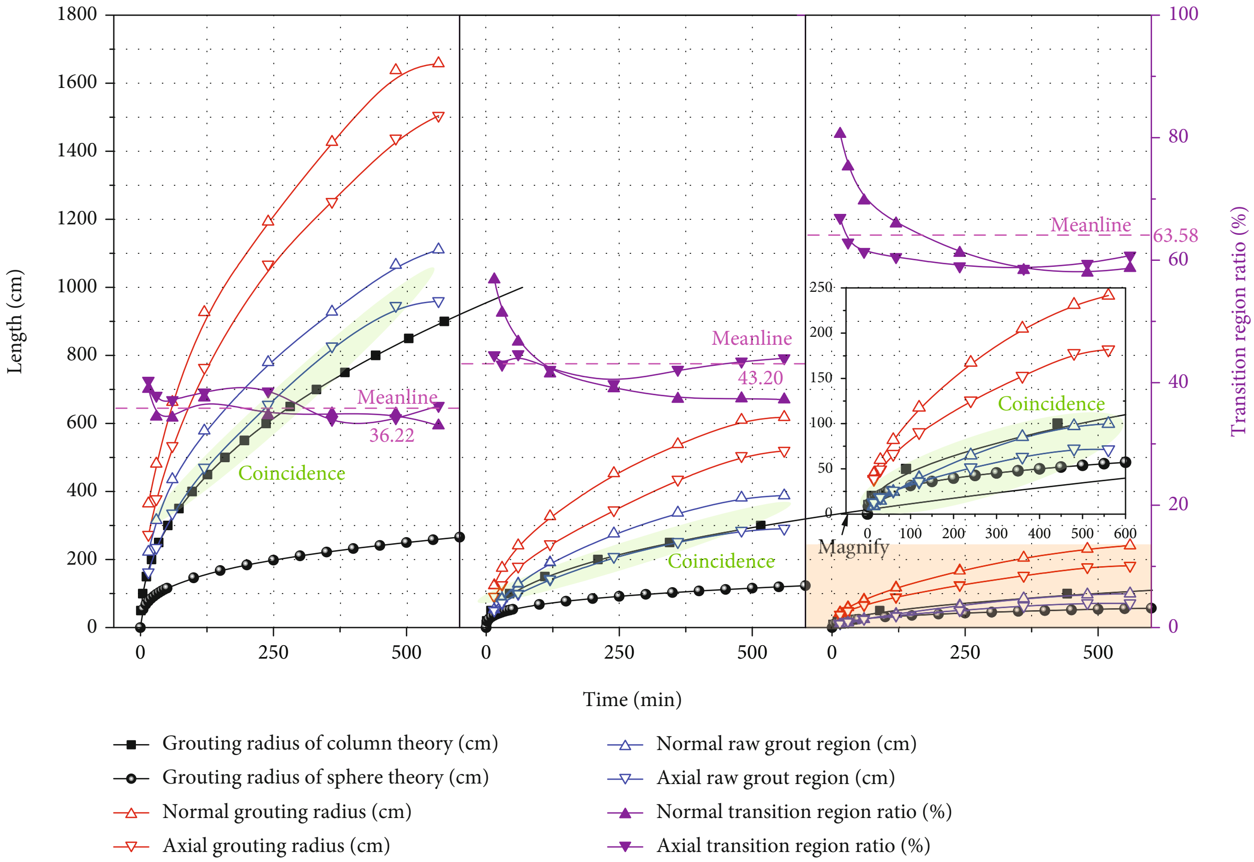

Figure 7: Comparisons between numerical simulation and theoretical calculation of grouting radius under different initial permeabilities: (a) 5 D; (b) 0.5 D; (c) 0.05 D.

the grouting pressure. The results show that for the grouting of low-permeability rock and soil medium, although the grouting radius is small, the range of the concentration gradient increases. Therefore, it is necessary to make full use of this phenomenon to develop a grouting material which is easy to diffuse and disperse. In addition, the maximum grouting radius is more than 16 m, so the "super grouting" technology can be developed without affecting the construction period. The fully enclosed grouting in full section of tunnel can be completed by using only two symmetrical grouting boreholes.

6. Conclusions

In order to explore the theoretical mechanism of nanosilica sol grouting technology for deep tunnels in unfavorable geological conditions, a dynamically changing model for nanosilica sol grouting in deep tunnels is established, taking into account the changing physical properties of grout and surrounding rock. Injection characteristics of nanosilica sol grouting in deep tunnels affected by grouting pressure and initial permeability are analyzed based on the project background of Xianglushan Tunnel of Central Yunnan Water Diversion Project. The rationality of this model can be verified by combining the column theory and sphere theory for Newtonian fluid. The main conclusions are as follows:

(1) The grout range can be divided into the raw grout region and the transition region with the molar concentration of silica as the index. Viscosity, molar concentration, and permeability coefficient in the raw grout region remain basically unchanged at the same time; in the transition region, viscosity and molar concentration decrease with the distance from the grouting hole, while the permeability coefficient increases with the distance from the grouting hole

(2) With the decrease of grouting pressure, the growth rates of normal grouting radius and axial grouting radius will gradually decrease; due to mechanical dispersion and molecular diffusion, the range of the transition region will gradually increase with time

(3) The ratio of the transition region to grouting radius fluctuates slightly with time under the initial permeability of 5 D, and the fluctuation increases with the decrease of initial permeability, and the average ratio increases with the decrease of grouting pressure

Data Availability

The data used to support the findings of this study are available from the corresponding author upon request.

Conflicts of Interest

The authors declare that they have no conflicts of interest.

Acknowledgments

This work was supported by the National Natural Science Foundation of China (Nos. 51978668, 42002281, and 51674244), the China Postdoctoral Science Foundation (No. 2020M683155), the Natural Science Foundation of Henan Province of China (Nos. 202300410001 and 202300410002), the Research and Development Program of China Railway Group Limited (No. 2020-zhongdazhuanxiang-04), and the Science and Technology Innovation Program of China Railway Tunnel Group Co., Ltd. (No. Suiyanhe 2020-12).

References

[1] F. Wang, T. Fruehwirt, and H. Konietzky, “Influence of repeated heating on physical-mechanical properties and damage evolution of granite,” *International Journal of Rock Mechanics and Mining Sciences*, vol. 136, p. 104514, 2020.

[2] W. Wu, F. Gong, and W. Yang, “Experimental simulation study of spalling in deep rectangular tunnel with plastic fine grain marble,” *Tunnelling and Underground Space Technology*, vol. 98, p. 103319, 2020.

[3] Q. He, Z. Liu, Y. Li, and D. Li, “Laboratory investigation on microcrack fracturing behaviour of granite under quasi-static combined compression and shear,” *Geomechanics and Geophysics for Geo-Energy and Geo-Resources*, vol. 7, no. 3, p. 52, 2021.

[4] M. Zaid, “Three-dimensional finite element analysis of urban rock tunnel under static loading condition: effect of the rock weathering,” *Geomechanics and Engineering*, vol. 25, pp. 99–109, 2021.

[5] D. Pan, *Permeation Law and Long-Term Solidification Stability Evaluation in Loose Coal with Silica Sol Grout, in: Shool of Mines*, China University of Mining and Technology, Xuzhou, 2018.

[6] S. He, J. Lai, L. Wang, and K. Wang, “A literature review on properties and applications of grouts for shield tunnel,” *Construction and Building Materials*, vol. 239, p. 117782, 2020.

[7] Q. Liu, X. Xu, and X. Tang, “A numerical study of the influence of cyclic grouting and consolidation using TOUGH2,” *Bulletin of Engineering Geology and the Environment*, vol. 80, no. 1, pp. 145–155, 2021.

[8] C. Hao, Y. Cheng, J. Dong, H. Liu, Z. Jiang, and Q. Tu, “Effect of silica sol on the sealing mechanism of a coalbed methane reservoir: new insights into enhancing the methane concentration and utilization rate,” *Journal of Natural Gas Science and Engineering*, vol. 56, pp. 51–61, 2018.

[9] C. Sogaard, J. Funehag, and Z. Abbas, “Silica sol as grouting material: a physio-chemical analysis,” *Nano Converg.*, vol. 5, no. 1, p. 6, 2018.

[10] P. Wang, S. Li, Y. Li et al., “Experimental research on rheological and mechanical properties of nano silica sol grout,” *Journal of Sol-Gel Science and Technology*, vol. 91, no. 1, pp. 178–188, 2019.

[11] C. Sogaard, K. Kolman, M. Christensson, A. B. Otyakmaz, and Z. Abbas, “Hofmeister effects in the gelling of silica nanoparticles in mixed salt solutions,” *Colloids and Surfaces a-Physicochemical and Engineering Aspects*, vol. 611, p. 125872, 2021.

[12] P. Wang, S. Li, S. Zhao, J. Li, and Y. Li, “Temperature effect on gelation time for nano-sized silica sol grout,” *Kuei Suan Jen Hsueh Pao/Journal of the Chinese Ceramic Society*, vol. 48, pp. 231–236, 2020.

[13] Y. Fujita and M. Kobayashi, “Transport of colloidal silica in unsaturated sand: effect of charging properties of sand and silica particles,” *Chemosphere*, vol. 154, pp. 179–186, 2016.

[14] J. Funehag and Å. Fransson, “Sealing narrow fractures with a Newtonian fluid: model prediction for grouting verified by field study,” *Tunnelling and Underground Space Technology*, vol. 21, no. 5, pp. 492–498, 2006.

[15] P. M. Gallagher and Y. Lin, “Colloidal silica transport through liquefiable porous media,” *Journal of Geotechnical and Geoenvironmental Engineering*, vol. 135, no. 11, pp. 1702–1712, 2009.

[16] M. Hamderi and P. M. Gallagher, “Pilot-scale modeling of colloidal silica delivery to liquefiable sands,” *Soils and Foundations*, vol. 55, no. 1, pp. 143–153, 2015.

[17] W. J. Richard, P. M. Gallagher, and Y. Lin, “Analytical model for transport of dilute colloidal silica dispersions through porous media,” *Journal of Geotechnical and Geoenvironmental Engineering*, vol. 144, 2018.

[18] M. E. Tani and H. Stille, “Grout spread and injection period of silica solution and cement mix in rock fractures,” *Rock Mechanics and Rock Engineering*, vol. 50, no. 9, pp. 2365–2380, 2017.

[19] M. Pedrotti, C. Wong, G. El Mountassir, and R. J. Lunn, “An analytical model for the control of silica grout penetration in natural groundwater systems,” *Tunnelling and Underground Space Technology*, vol. 70, pp. 105–113, 2017.

[20] M. Tsuji, S. Kobayashi, S. Mikake, T. Sato, and H. Matsui, “Post-grouting experiences for reducing groundwater inflow at 500 m depth of the Mizunami Underground Research Laboratory, Japan,” in *in: ISRM European Rock Mechanics Symposium - EUROCK 2017, International Society for Rock Mechanics and Rock Engineering*, p. 8, Ostrava, Czech Republic, 2017.

[21] D. Pan, K. Hong, H. Fu, J. Zhou, N. Zhang, and G. Lu, “Influence characteristics and mechanism of fragmental size of broken coal mass on the injection regularity of silica sol grouting,” *Construction and Building Materials*, vol. 269, 2020.

[22] D. Pan, K. Hong, H. Fu, J. Zhou, and N. Zhang, “Experimental study of the mechanism of grouting colloidal nano-silica in over-broken coal mass,” *Quarterly Journal of Engineering Geology and Hydrogeology*, pp. qjegh2020–qjegh2161, 2021.

[23] Y. Zhao, “The most representative national key water conservancy project under construction: central Yunnan water diversion project,” *Tunnel Construction*, vol. 39, pp. 511–522, 2019.

[24] D. Chen, F. Si, Y. Cai et al., “Code for engineering geological investigation of water resources and hydropower,” in *in, Ministry of Housing and Urban-Rural Development and General Administration of Quality Supervision*, p. 261, Inspection and Quarantine of the People’s Republic of China, 2008.

[25] G. I. Agapoulaki and A. G. Papadimitriou, “Rheological properties of colloidal silica grout for passive stabilization against liquefaction,” *Journal of Materials in Civil Engineering*, vol. 30, no. 10, p. 04018251, 2018.

[26] D. Pan, Z. Sun, J. Zhou, N. Zhang, Z. Yang, and Y. Qin, “Incorporating silica sol as a binder to improve long-term stability of

blocky coal," *Geotechnical and Geological Engineering*, vol. 38, no. 4, pp. 3597–3610, 2020.

[27] C. Zheng and G. D. Bennett, *Applied Contaminant Transport Modeling*, Wiley-Interscience, New York, 2nd edition, 2002.

[28] ASTM, *Standard Test Method for Viscosity and Gel Time of Chemical Grouts by Rotational Viscometer (Laboratory Method)*, West Conshohocken, PA, 2014.

[29] T. Koyama, T. Katayama, T. Tanaka, Y. Kuzuha, and Y. Ohnishi, "Development of a numerical model for grout injection and its application to thein situgrouting test at the Grimsel test site, Switzerland," *Geosystem Engineering*, vol. 16, no. 1, pp. 26–36, 2013.

[30] C. Pengda, L. Lu, T. Ju, and W. Daozeng, "Application of time-varying viscous grout in gravel-foundation anti-seepage treatment," *Journal of Hydrodynamics*, vol. 23, pp. 391–397, 2011.

[31] V. Potapov, K. Povarov, V. Podverbny, and O. Guseva, "Study of colloidal silica formation and precipitation in solution of Mutnovskoe hydrothermal field (Kamchatka, Russia)," *Proceedings World Geothermal Congress 2005*, R. N. Horne, Ed., , pp. 1–9, International Geothermal Association, Antalya, Turkey, 2005.

[32] J. Kuang, Y. Zan, J. Wang, and J. Du, *Grouting Theory and Engineering Example of Rock and Soil*, Science Press, Beijing, 2001.

Hindawi
Geofluids
Volume 2021, Article ID 2023782, 16 pages
https://doi.org/10.1155/2021/2023782

Research Article

Evolution Mechanism, Monitoring, and Early Warning Method of Water Inrush in Deep-Buried Long Tunnel

Wenfeng Tu, Liping Li, Shuai Cheng, Diyang Chen, Yongcai Yuan, and Yanhao Chen

Geotechnical and Structural Engineering Research Center, Shandong University, Jinan, Shandong 250061, China

Correspondence should be addressed to Liping Li; yuliyangfan@163.com

Received 22 April 2021; Accepted 11 August 2021; Published 25 August 2021

Academic Editor: Yi Xue

Water inrush is a serious disaster in tunnel construction. Because the process of water inrush is complicated and there is no effective monitoring and early warning method, the control of water inrush disaster is passive. Firstly, the failure mode and determination method of safety thickness of the antioutburst structure are summarized. The key breakthrough directions and development trends of water inrush mechanism was analyzed. Secondly, the sensitivity ranking and the adjunct characteristics of different types of precursor information are determined by the model test. An improved scheme of microseismic monitoring technology is proposed to locate the spatial position of the water inrush channel, and a multi-information time-space integrated monitoring method for an antioutburst structure is established. By analyzing the evolution law of multi-information in the process of water inrush, the evolution model and its identification method are put forward. Finally, the level of water inrush was determined through the analysis of the dynamic and static reserves of disaster source, and a multilevel and comprehensive warning system of tunnel water inrush is established. Through the remote real-time monitoring and early warning platform and its engineering application, the early warning of water inrush time trend and the early warning of water inrush rupture space position are realized.

1. Introduction

In recent years, with the development of infrastructure construction in China, a large number of tunnels were built in western mountainous areas. There are some difficulties in the construction of the tunnel, such as large buried depth, long tunnel line, high stress, strong karst, high water pressure, and frequent disasters [1]. Some serious geological disasters often occur during the construction of deep-buried tunnels [2, 3], which have the characteristics of high concealment, strong suddenness, and strong destructiveness. There have been many cases of casualties, equipment damage, and delays in construction due to water inrush of tunnels, as shown in Table 1 [4, 5].

With the large-scale construction of karst tunnels, many researchers carry on the study about the prevention and control techniques of water inrush [6, 7]. The occurrence and evolution of water inrush is a process of coupling force field and seepage field. For the progressive failure of water-resisting rock mass or the infiltration and instability of filling medium, researchers put forward the failure mode of the antioutburst structure using fracture mechanics and hydraulics, and proposed the mechanical model and criteria of water inrush [8, 9]. Some researchers analyzed the mechanism and evolution process of the seepage instability of filling [10–13]. The calculation method of the safe thickness of the antioutburst structure was established [14–17]. Numerical simulation is an important method to study water inrush [18, 19]. At present, the commonly used analysis software mainly includes FLAC-3D, RFPA, COMSOL PFC-3D, and PD, etc., and the research content includes seepage-stress coupling of rock mass, pore water pressure characteristics of mining rock mass, and stability of water-bearing faults and surrounding rocks [20–25]. However, due to limitations in software development, it is difficult to consider the complex construction geological environment of tunnel engineering. To verify the theory and make up for the inability of a mechanical model, researchers carried out some water inrush model tests, because of the unfavorable geological environment, the high osmotic pressure,

Table 1: Statistics on water inrush and mud disasters in tunnels.

Tunnel type	Tunnel name	Time/year	Disaster description
Railway tunnel	Yuanliangshan tunnel	2002	Large-scale water and mud inrush occurred 71 times. The highest water pressure reached 4.6 MPa. The maximum water inflow was 72,000 m^3/h, causing 9 deaths
	Maluqing tunnel	2005	A large-scale water and mud inrush occurred 19 times, causing 11 deaths
	Yesanguan tunnel	2007	In a half-hour, water irruption quantity is 151,000 m^3, and mudstone eruption quantity is 53,500 m^3, causing 10 deaths
	Guzishan tunnel	2011	A major water inrush occurred and the surface collapsed, causing 2 deaths
	Taoshuping tunnel	2014	Water inrush, causing 9 deaths
	Wulong tunnel	2002	There have been more than 10 large-scale water and mud inrush, with a maximum water inflow of 7.18 million m^3/d
	Yunwushan tunnel	2008	The water inflow is 46,000 m^3/d, and the maximum water inflow is 172,000 m^3/d
	Qiyueshan tunnel	2005	Exposing 187 large-scale karst pipes and caves, and causing large-scale water inrush for more than 20 times
	Dazhiping tunnel	2006	The water and mud inrush reaches more than 60,000 m^3 and then stabilizes at 8000 m^3
	Xiangshan tunnel	2009	The maximum water inflow reaches 7300 m^3/h, and multiple water inrush occurs within two years.
	Bahuashan tunnel	2006	The total water inflow is 15,000 m^3, and the protruding angle crushed stone is about 1800 m^3. There are 13 sudden water and mud inrush accidents before and after, and the 200 m long tunnel is inundated.
	Chaoyang tunnel	2018	The maximum water inflow was 1100 m^3/h, and the water output was estimated to be about 100,000 m^3 causing 3 deaths
Road tunnel	Zhongjiashan tunnel	2012	The water and mud inrush occurred 14 times in 3 months, the total mud volume exceeded 27,900 m^3, and the total water inrush exceeded 20,000 m^3
	Longtan tunnel	2006	Large-scale burst mud 2 times; the mud volume exceeded 9000 m^3, causing large-scale landslide 3 times
	Baiyunshan tunnel	2010	Large-scale instant burst mud 2000 m^3, maximum water inflow 300 m^3/h, surface subsidence 300 m^2, depth 20 m, 6 deaths
	Foling tunnel	2012	The inflow of water is 30,000 m^3, and the pumping water is 1.3 million cubic meters.
	Shangjiawan tunnel	2013	Three large-scale water inrush occurred in the same section, and the maximum amount of inrush of clay and water suddenly reached 7700 m^3.
	Anshi tunnel	2019	About 15,000 m^3 of mud and 800 m^3 of water gushed into the disaster site causing 12 deaths. Ten people were injured.

complex stress, and construction disturbance encountered during the construction process [26]. The test system of a similar physical model was used to study the seepage and deformation laws of surrounding rock under the combination of multiple factors, which provided a theoretical basis for the antiseepage reinforcement technology during the construction process [27–32].

Damage and destruction of the antioutburst structure will lead to the occurrence of water inrush. The damage process will be accompanied by various physical information (stress, strain, acoustic emission, etc.). Rock failure test is the basis to obtain the evolution law of multiple information. It is also an important basis for the monitoring design of the precursory information of the antioutburst structure [33–41]. Nevertheless, most of the basic mechanical tests use single information to explain the damage process of rock mass, and the influence of multiphysics coupling is not considered. Many researchers have developed similar material for the fluid-solid coupling model test [42]. Based on the different formation and experimental conditions, researchers found out the developmental characteristics of fissures under different stress and seepage pressures. In the real-time monitoring of geological disasters, the network application system was developed based on the internet of things, which was successfully applied in the instability monitoring of slope stability, mine impact pressure, and water inrush [43–48]. However, the monitoring method of water inrush mainly relies on geological precursor information and hydrogeological report. In the early warning of water inrush, D-S evidence theory, extension theory, and fuzzy evaluation [49–53] are applied to the fusion analysis of multi-information. The severity of the disasters induced by the disaster-causing structure was graded. This method determines the monitoring items such as water pressure, water quantity and quality, initial support, and surrounding rock stability [54]. Nevertheless, the correlation between precursor information and the water inrush model is not clear, and it is difficult to carry out the research work of early warning for a specific water inrush model.

Due to the complexity, suddenness, and diversity of the water inrush disasters in deep tunnels, it is necessary to summarize the different cases of water inrush disasters, analyze the types of different water inrush disasters, and study the mechanism of water inrush under different failure modes and the evolution law of precursor multiple information. Data mining is used to establish an information fusion recognition model to provide a basis for water inrush pattern recognition and fusion warning. Based on the analysis of multi-information fusion of water inrush, a monitoring and early warning system for water inrush disasters is established to realize early warning of water inflow, water inrush time, and location, which are effective measures to prevent and control sudden water disasters. Based on systematically summarizing the mechanism of sudden flooding, the research of this paper focuses on the multi-information fusion analysis and prediction and early warning of water inrush, and divides the water inrush hazard level by dynamic and static water quantity assessment. Through multi-information monitoring combined with microseismic monitoring technology positioning to carry out time-space warning, and achieve effective active prevention and control of major water inrush disasters, it can provide some reference and support for monitoring and warning of tunnel water inrush disaster.

2. Catastrophic Evolutionary Mechanism of Water Inrush

The formation of water inrush disasters of a tunnel is affected by many factors. According to different division principles, water inrush disasters are divided into various types. From the perspective of disaster sources, water inrush disasters are divided into crevice-type water inrush, fault-type water inrush, dissolution-cavity-type water inrush, and pipeline and underground dark river water inrush. Considering the different forms of disasters, water inrush disasters are divided into instantaneous water inrush, stable water inrush, and seasonal water inrush. According to the formation form of the water inrush channel, water inrush disasters are divided into geological defect type and nongeological defect type [10]. The evolution process of the water inrush channel is not only related to the properties of the channel but also closely related to external disturbance factors such as water pressure, ground stress, and blasting disturbance.

2.1. The Failure Mode of Antioutburst Structure. Based on the failure mode of the antioutburst structure, the water inrush type is divided into the progressive failure of the resistance structure and filling medium infiltration and instability. The progressive failure of the resistance structure is mainly caused by dynamic disturbance and hydraulic cleavage under high osmotic pressure. The instability of the filling structure can be divided into local osmotic instability and overall slip instability.

2.1.1. The Progressive Failure of Resistance Structure. Based on the division of the failure mode of the antioutburst structure, combined with the theory of fracture mechanics, structural mechanics, and rock mass dynamics, some mechanical models and water inrush criteria were established, such as tensile shear failure and compression shear failure models [55]. The discriminating conditions of the water inrush were obtained. The karst fissure water is prominently defined as the accumulative stage and the unstable stage, and the mechanical mechanism of the long-term interaction of water and rock before water inrush is studied. It is suitable for analyzing the control effect of karst water and water pressure on the stability of surrounding rock [56].

2.1.2. Filling Medium Infiltration and Instability. For filling faulty geological structures such as large cracks, faults, and karst pipes, the formation of water inrush channels is caused by seepage and catastrophic changes of internal filling media, such as fault activation and karst pipeline filling infiltration. From the permeability characteristics of the filling, the filling medium infiltration and instability can be divided into the permeation instability of the filling medium and slip instability of a filling belt [10].

(1) Permeability Instability of Filling Medium. When the filling geological structure is under strong osmotic pressure and excavation, the internal filling medium is continuously eroded which may lead to piping and soil flow. When the filling material is quickly flushed out, it leads to the formation of water inrush channels and causing the seepage instability of the filling medium [57].

(2) Slip Instability of Filling Belt. When there is a large-scale disaster source nearby and the filling geological structure is relatively weak or impervious, the filling structure has the dual characteristics of water blocking and water filling. This type of filling structure is relatively stable and has high water-blocking properties. When the filler is dense, heterogeneous structure with poor water permeability, or impermeable, the entire structure of the filling does not have the conditions for the formation of a potential water inrush channel. Sliding instability of filling belt is easy to occur under the action of strong seepage.

2.2. Minimum Antiburst Safety Thickness. By analyzing the failure mode of the anti-outburst structure and the evolution process of the catastrophe, the calculation method of the minimum antioutburst safety thickness of the tunnel is summarized. The water inrush from the karst tunnel face is caused by the dual action. On the one hand, the tunnel blasting excavation causes the intrinsic crack activation and expansion of the rock mass. On the other hand, under the continuous action of high karst water pressure, the rock mass is softened. Corrosion changes the effective stress between the cracks in the rock mass, causing the crack to expand and penetrate.

Different scholars have proposed some calculation models of antioutburst safety thickness for different engineering geological conditions. The tunnel floor is simplified as a cantilever beam for mechanical analysis using elastic theory. According to its structural integrity, it is divided into "complete rock formation" and "incomplete rock formation," and the calculation formula of the safe thickness of the tunnel floor is obtained [58]. Using fracture mechanics and hydraulics theory to analyze the hysteresis effect and multipath effect of tunnel water inrush, a safe thickness calculation model of rock wall based on critical water pressure is established [9]. Based on the analysis of system potential energy control parameters and catastrophic evolution path, a folding catastrophe model is proposed and the minimum safe thickness calculation formula for water inrush is established [59]. The existence of a safe thickness zone increases the difficulty of fracture propagation in hydraulic fracturing. As the excavation progresses, the relaxation zone gradually extends to the safe thickness zone, and the energy threshold of the hydraulic fracturing of the rock mass under the action of the high head is getting lower and lower. When the tunnel face is located within the minimum safe thickness range, the rock mass undergoes splitting and water inrush. The "three districts" theory holds that the area between the tunnel face and water-bearing body can be divided into three parts: the excavation disturbance zone in front of the face, the fracture zone around the water-bearing body, and the intact rock mass protection zone [55]. The water inrush is a dynamic process in which the excavation disturbs the fissure zone and the permeable fissure zone gradually increase, which is the progressive failure process of the antioutburst structure, and is shown as follows:

$$h_s \geq h_1 + \frac{1}{\pi}\left(\frac{k_{Ic}}{1.12p_w}\right)^2 + h_3, \tag{1}$$

where h_s is the area of rock protection thickness; h_1 is the slack thickness zone caused by construction; h_3 is a fractured zone, which is determined by geophysical exploration and drilling methods; k_{Ic} is the fracture toughness of rock; p_w is fissure water pressure.

In view of the water inrush caused by dynamic disturbance such as blasting excavation, the antioutburst structure of the karst tunnel is divided into blasting excavation disturbance zone L_c and hydraulic fracturing zone L_w [56]. In engineering practice, the blasting excavation disturbance zone L_c can be obtained by a field test, empirical estimation, and theoretical calculation. Hydraulic fracturing zone L_w under the action of the explosive stress wave is derived by analyzing the critical water pressure of the expansion and failure of water-bearing cracks in the tunnel face, as shown in equation (2) and equation (3). The formula for calculating the minimum safe thickness of the fractured rock mass is $L = L_c + L_w$.

$$L_w = \frac{11R}{17} \cdot \left\{ \ln \lambda - \ln \left[\lambda - \frac{2fP_w\sqrt{\pi a} - \sqrt{3}K_{\prod C} - 2c\sqrt{\pi a} + 2\tau_1 \left| K_{\prod}^{(2)} \right| \sqrt{\pi a}}{\gamma H \sqrt{\pi a}(f - f\cos 2\beta - \sin 2\beta)} \right] - \frac{f + f\cos 2\beta + \sin 2\beta}{f - f\cos 2\beta - \sin 2\beta} \right\}, \tag{2}$$

$$L_w = \frac{11R}{17} \cdot \left\{ \ln \lambda - \ln \left[\lambda - \frac{2fP_w\sqrt{\pi a} - \sqrt{3}K_{\prod C} - 2c\sqrt{\pi a} + 2\tau_1 \left| K_{\prod}^{(2)} \right| \sqrt{\pi a}}{\gamma H \sqrt{\pi a}(f - f\cos 2\beta + \sin 2\beta)} \right] - \frac{f + f\cos 2\beta - \sin 2\beta}{f - f\cos 2\beta + \sin 2\beta} \right\}. \tag{3}$$

2.3. Key Issues of Water Inrush Mechanism Research. The existing theoretical model has certain applicable conditions. For example, in view of the existence of karst caves at the tunnel floor, the beam-slab model simplifies the blast disturbance to the additional force on the rock mass, and hydrostatic pressure is treated as water pressure. The natural rock mass may not only break water in the intact rock mass but also break in the structural plane of the rock mass. Therefore, the criterion of water inrush for the progressive failure of resistance structure established by the theory of fracture mechanics is generally applicable to the brittle failure of rock mass which immediately changes from elastic deformation to sudden fracture. The applicability of this method is poor for large plastic deformation and failure of rock mass after elastic deformation. The calculation model of the safe thickness of the antioutburst structure only calculates the thickness of the protection zone, but the value of the fracture zone depends on the accuracy of the geophysical results, leading to a large error in the results. In summary, there are still many typical and difficult problems in the study of the evolution mechanism of water inrush in deep tunnels.

Firstly, detonation pressure and excavation unloading are the important factors affecting the water inrush of deep-buried rock mass. It is important to research the failure mechanism and seepage characteristics of rock mass under dynamic disturbance, strong unloading, and high osmotic pressure. It can reveal the mathematical relationship between stress, strain, seepage parameters, and groundwater flow variables. The establishment of a mathematical model of the evolution process of water inrush under the unloading disturbance and osmotic pressure is one of the difficulties in the study of the evolution mechanism of the inrush hydrodynamics.

Secondly, the deep burial depth and long tunnel line of tunnels bring high ground stress, strong osmotic pressure, and more complex regional seepage field evolution, making the catastrophe process of water inrush more complicated. Some research still needs improvement. Examples of these include the iterative method of seepage-stress-damage coupling of the calculation unit for transferring fluid pressure during rock mass rupture, the assignment method of transition conditions, and the boundary conditions between the fracture flow and the pipe flow model. There is no mature numerical method to simulate the water inrush.

Finally, the key control factors and corresponding control methods in the evolution process of water inrush and burst mud disasters under different disaster modes are still uncertain, making it difficult to establish corresponding decision-making models. Few scholars carry out research on the "control theory" of water inrush and burst mud disasters. It is an urgent need to carry out evolution mechanism of water inrush and disaster controlling method for collaborative research. A breakthrough is needed on the basic theoretical problem of the evolution mechanism with high pressure and large flow. It can effectively determine the key control factors and optimal control opportunities in different evolution stages of water inrush and provide theoretical support and method guidance for the active prevention and control of deep tunnel water inrush.

3. Real-Time Monitoring Method of Catastrophe Precursor Information

The evolution process of the water inrush disaster is a kind of dynamic damage process. The hydrothermal medium system, the hydrodynamic system, and the equilibrium state of surrounding rock mechanics changes sharply due to tunnel excavation, and the energy stored in the underground water is instantaneously released, carrying sediment and debris to the high speed of the excavation face [10]. It is a multifield coupling process integrating solid, liquid, and gas, which is accompanied by changes in information of multiple physical quantities. In view of the real-time monitoring of the evolution process of water inrush, the targets and contents of the water inrush disaster monitoring are clarified, and the fusion analysis is carried out under the coordination of multiple information monitoring to achieve effective disaster early warning.

3.1. Real-Time Monitoring Object for Water Inrush. During the construction of the tunnel, the static reserves of disaster sources can be detected through the geological forecast. The dynamic reserves of groundwater recharge can be estimated by the regional estimation of the supply channel [59], and the damage level can be quantified by the total quantity of water inrush. Through multi-information monitoring, the security situation of the antioutburst structure and the location of microseismic monitoring are analyzed. Finally, a comprehensive monitoring and early warning method based on the geological prediction of the disaster source, multi-information fusion monitoring of the antioutburst structure, and microseismic location of the water inrush channel is established.

3.1.1. Anti-outburst Structure Monitoring. The antioutburst structure is the last barrier to the occurrence of water inrush disaster. In the process of water inrush evolution, a large amount of mechanical physics information will change on the antioutburst structure. A monitoring method for the fusion analysis of displacement (on the surface), force field (inside), and microseismic (in the far field) is proposed. Through the long-term stable monitoring of the water inrush channel and the evolution state, combined with the water inflow estimation, the time and space warning of water inrush are finally realized, as shown in Figure 1 [60].

Based on the multi-information characteristics of the seepage instability of water-blocking rock mass and the filling structure, the monitoring principle and design method of "microseismic-seepage dominant, multi-information fusion" are proposed. Combined with previous numerical simulation results, water inrush simulation test was carried out to obtain the fusion evolution law of precursor information of rock mass instability and water inrush. Aiming at the types of different typical water inrush disasters, the sensitivity ranking of multi-information is proposed, as shown in Table 2, and the multi-information evolution model of different water inrush types can be obtained.

For the water inrush of the type of water-blocking rock mass destruction, the multi-information monitoring sensitivity of the microseismic information is stronger than other information because its antioutburst structure is fractured rock mass. During the process of rock mass rupture and stress redistribution, the microrupture develops inside the rock mass. The energy is released in the form of elastic waves, and the microseismic information is highlighted. In the water inrush caused by filling infiltration instability type, the antioutburst structure is mostly fault filling and pipeline filling. The brittle fracture of the medium is not obvious, resulting in the microseismic reaction that is not obvious, but the displacement information is sensitive during the evolution process.

3.1.2. Monitoring of Disaster Sources. The geological exploration technology is adopted to realize the spatial location and scale determination of the disaster source. The groundwater migration information is monitored, and the recharge water flow near the tunnel is estimated. The total amount of water inrush is the decisive factor in the classification of hazard levels, and it depends on the static and dynamic reserves of the disaster source. At present, the static reserves of disaster sources can be determined by advanced prediction methods such as induced polarization [61]. Determining the total amount of water inrush disasters and predicting the level of disaster damage can provide a theoretical basis for disaster control.

3.2. Monitoring of the Rupture Channel of the Anti-outburst Structure. As a kind of dynamic disaster, making full use of the information of a large number of mechanical and physical fields during the catastrophic process is the key to solving the problem of forecasting and warning of water inrush disasters. Therefore, a dynamic and static combined monitoring method is established by combining wireless sensing and cloud platform technology to realize

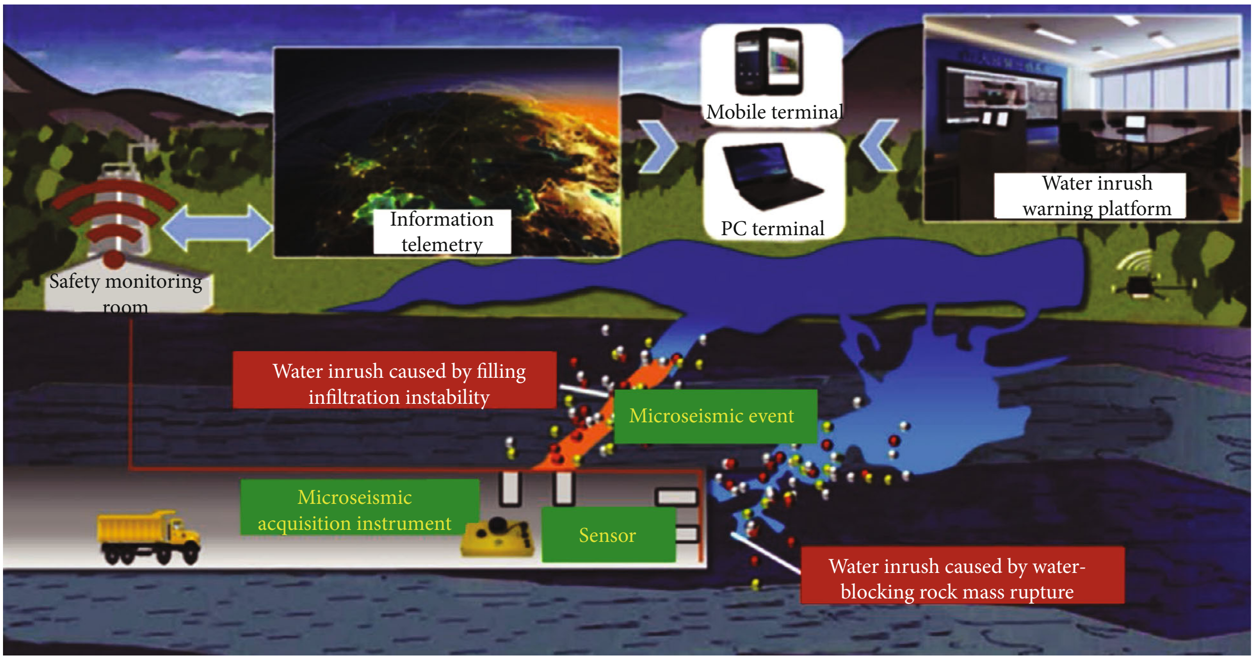

Figure 1: Microseismic monitoring design of antioutburst structure.

Table 2: Multi-information sensitivity ranking of water inrush [30].

Type of disaster	Monitoring object	Information sensitivity ranking	Nature
Water inrush caused by water-blocking rock mass destruction	Structure of fractured rock mass	Microseismic>stress field>displacement field>seepage field	Influence of seepage on microseismic information during rupture
Water inrush caused by filling infiltration instability	Fault filling, pipe filling	Displacement field>osmotic pressure>stress field>microseismic information	Influence of disturbance on the evolution process of multi-information

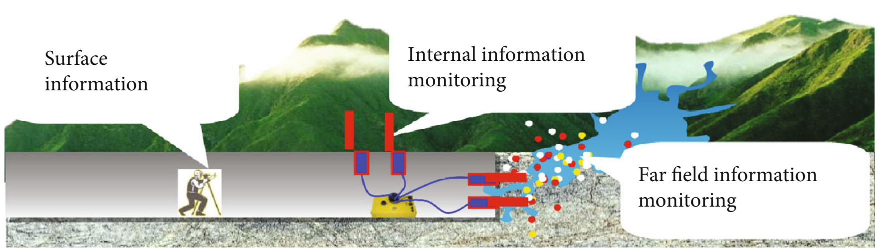

Figure 2: Dynamic monitoring of multifield information of water inrush.

surface information monitoring, internal information monitoring, and far field information monitoring in the disaster area, as shown in Figure 2. The surface information is mainly the displacement information of the surrounding rock surface, which can be obtained by monitoring and measuring means. The force field information such as stress and osmotic pressure inside the rock mass is monitored by sensor network in real time. At the same time, the remote field microseismic information monitoring in the disaster area is introduced, and a new multi-information monitoring method based on microseismic is proposed.

Through the research on multi-information monitoring and early warning methods of water inrush precursors in complex environment, the method of effective information identification and interference information elimination for water inrush precursors is proposed. Through the establishment of the basic theory of multi-information monitoring and early warning of the antioutburst structure and the comprehensive analysis of the evolution correlation and matching characteristics of each field of information to identify the evolution state of the disaster, the situation of the water inrush disaster is assessed. The time-oriented warning of the occurrence of the disaster is realized.

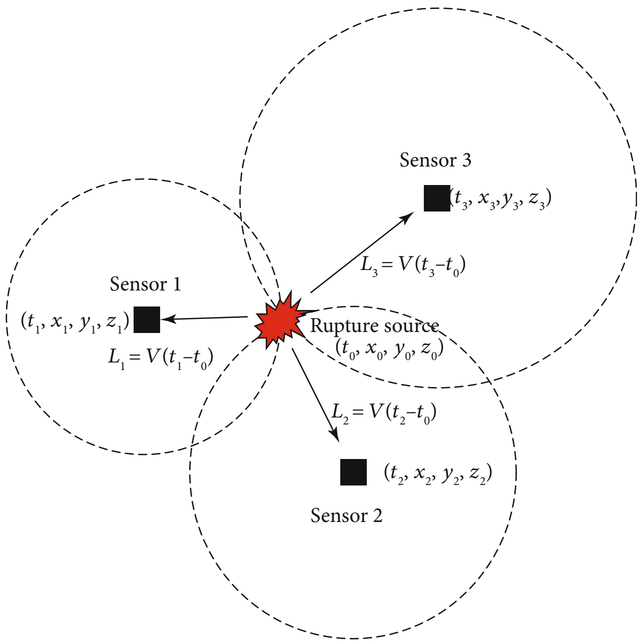

FIGURE 3: Microseismic event and positioning principle.

3.2.1. Positioning Method of Rupture Channel Based on Microseismic Monitoring. The research on monitoring and early warning of tunnel water inrush disaster shows that the water-blocking rock mass is anisotropic heterogeneous material. After the tunnel excavation disturbance, the stress redistribution occurs in the rock, so that the accumulated energy is released in the form of elastic waves. After the fluctuation is received by the sensor network, a shock response occurs, which is called a microseismic event. A large amount of microfracture leads to the penetration of cracks, which causes abnormal loosening of the original stable water-blocking surrounding rock. Therefore, the microseismic signal becomes an important precursor feature of dynamic disasters.

Figure 3 shows the positioning principle of the microseismic event. The sensor's point positions x_k, y_k, z_k and the signal acquisition time t_k by the sensor are known both in the initial construction and in the operation of the system. After measuring the original rock wave velocity $V_{P\text{-}S}$ by a blasting experiment, the path length of the microseismic signal collected by each sensor is shown as follows:

$$\Delta L_k = V_{P\text{-}S} \times \Delta t_k = V_{P\text{-}S} \times (t_{k+1} - \Delta t_k). \tag{4}$$

The distance from each sensor to the source point can be expressed as follows:

$$\Delta L_k = \sqrt{(x_k - x)^2 + (y_k - y)^2 + (z_k - z)^2}. \tag{5}$$

By arranging the sensor array in the tunnel, the automatic acquisition, transmission, and processing of the microseismic data can be realized. The location of the internal damage of the rock is determined by the microseismic positioning principle and is displayed on the three-dimensional map.

FIGURE 4: Model test of microseismic positioning.

FIGURE 5: Field verification of upgrades for microseismic equipment.

The microseismic monitoring technology has the characteristics of long-distance overall monitoring and 3D real-time monitoring, which achieves the purpose of monitoring the stability of the water-blocking rock mass.

3.2.2. Improved Microseismic Technology for Monitoring Water Inrush Disasters. The traditional microseismic monitoring technology is mostly used for monitoring and early warning of rockburst disasters in underground engineering. There are few applications for monitoring antioutburst structure in the water inrush disaster. As shown in Figure 4, the model test method is used to compare and

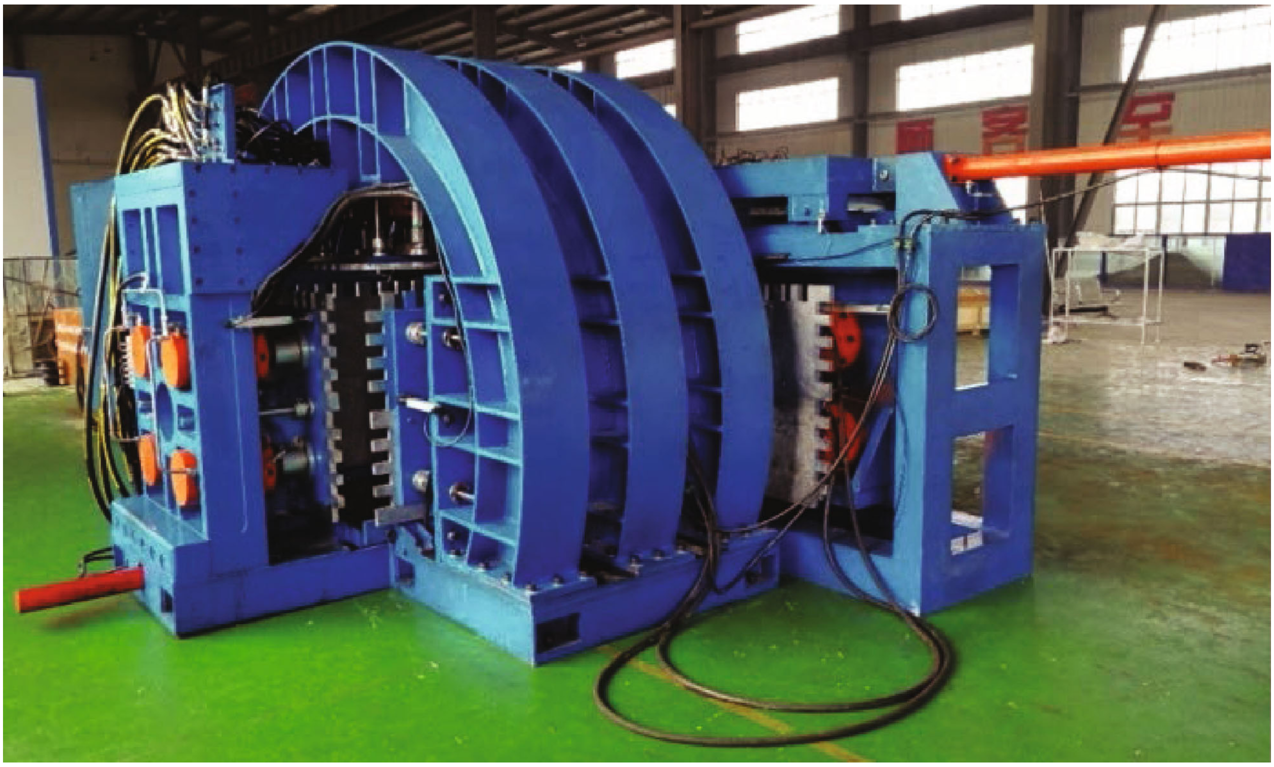

Figure 6: Model test and precursor information collection of water-blocking rock mass [30].

analyze the microseismic response law during the process of rupture of dry rock mass and water-rich rock mass, and provide a basis for exploring the difference between rock burst disaster and water inrush disaster [62]. Through the field application of microseismic technology in the water inrush disaster of tunnel engineering, the difference of the monitoring signal between the water inrush disaster and the rock burst disaster is found, as shown in Figure 5. The traditional microseismic monitoring system could not be directly applied to the monitoring of the water inrush disaster.

The parameters of the monitoring hardware are improved by upgrading the microseismic monitoring system from the software layer and the hardware layer, which is different from the conventional rockburst monitoring. The software is embedded in the filter program for rock cracking signal of water-rich mass. At the same time, in the aspect of data processing, the self-developed multi-information fusion analysis software TMIWS is embedded in the microseismic information processing system. It realizes the dual function of the identification of precursor information and the location of the water inrush channel.

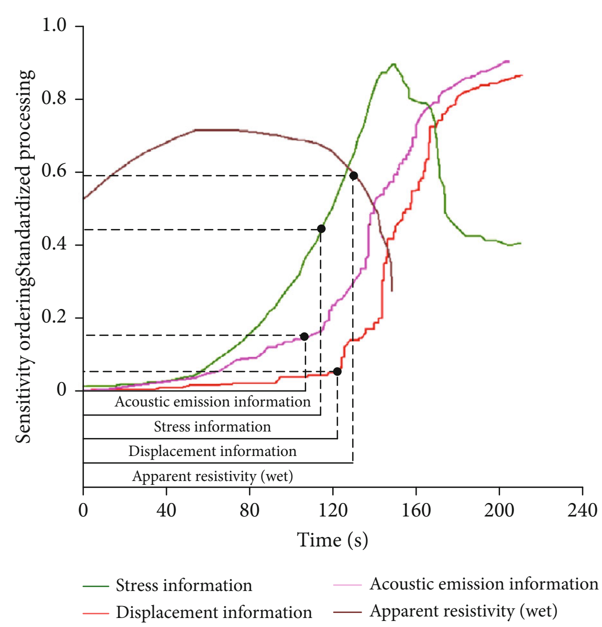

Figure 7: Rock mass fracture multiphysical parameter sensitivity ranking [30].

4. Multi-Information Fusion Analysis and Early Warning Technology

4.1. Matching Model of Multitype Water Inrush

4.1.1. Multifield Information Evolution Law of Rupture in Water-Bearing Rock Mass. The physical basis of monitoring and early warning of water inrush information is a large amount of precursor information generated during the instability of rock mass. These precursor information includes acoustic emission, apparent resistivity, stress, and displacement, as shown in Figure 6. It is more difficult to obtain all of this information accurately during the actual tunnel construction process, but the occurrence of this information is actually present.

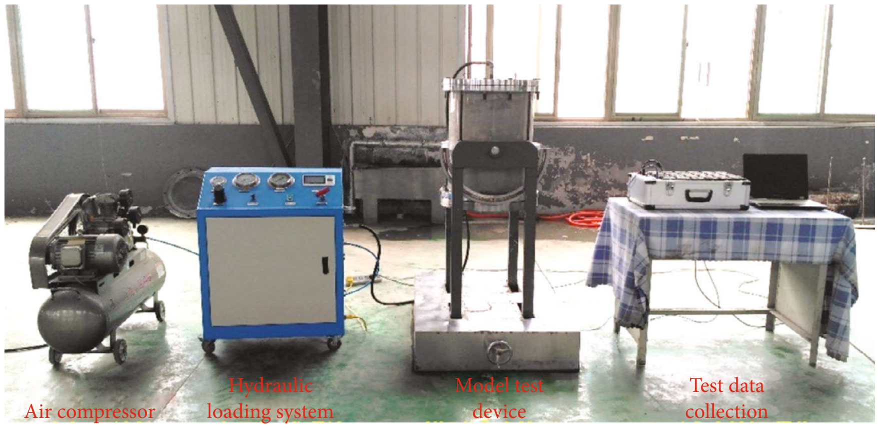

Figure 8: Physical simulation test system for seepage instability of water in the filling medium [30].

Through the model test of the rupture state of the tunnel surrounding rock, and combined with the numerical simulation results of the predecessors, the evolution law of the precursory information of the rock mass instability and water inrush is obtained and the multiphysical parameter sensitivity ranking of the rock mass rupture is performed, as shown in Figure 7. The sensitivity ranking of the critical points of the precursory information of the water inrush rock damage is acoustic emission information > stress information > displacement information > osmotic pressure information.

4.1.2. Evolution Law of Multifield Information of Water Inrush of Infiltration Instability. During the tunnel construction process, with the influence of the water-induced disaster-causing structure, as the tunnel surface is gradually approaching the water-induced disaster-causing structure, the water inrush channel gradually penetrates. When the excavation disturbance continues to occur, a large amount of water infiltrates into the tunnel. When the exposed structure is a filling medium, the filling medium is unstable and water inrush occurs. Figure 8 is a physical simulation test system for seepage instability and water inrush in tunnel filling medium.

The filling medium has less stress redistribution effect than the rock mass. Under the action of excavation disturbance, the filling structure is easy to deform. The internal stress redistribution is mainly concentrated in the weak boundary position, and the large-scale stress change occurs at the boundary, causing the slippage of the entire filling body or deformation near the dominant seepage channel. The sensitivity rankings of the precursor information are seepage information, displacement information, stress information, and acoustic emission information, as shown in Figure 9. In the construction process of the tunnel, combined with the results of the simulation test, the time node of the water quality changing from turbid to clear can be used as a discontinuity of precursor information for the seepage instability.

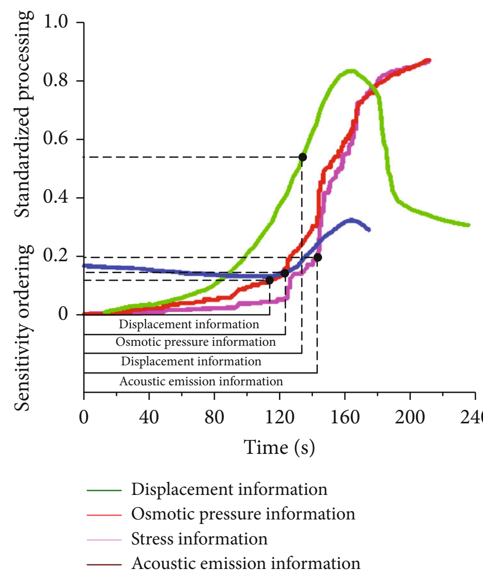

Figure 9: Classification of filling osmotic instability multiphysical parameters sensitivity [30].

4.2. Time-Oriented Warning Based on Multi-Information Fusion Analysis. The "five factors" that affect the occurrence of water inrush are physical properties, structure, stress, energy, and time. Based on these factors and the real-time monitoring data such as microseismic, displacement, stress, osmotic pressure, temperature, and resistivity, the situation assessment theory [63, 64] is introduced into the disaster prediction of water inrush. Using the method of log auditing [65, 66], real-time monitoring and correction of multiheterogeneous information is used to establish the water inrush potential prediction model. In view of the disadvantages of the Yager formula, based on the previous D-S fusion theory, an average weighted fusion algorithm of the probability of conflict of evidence is proposed. The distribution function of the probability of conflict of evidence is weighted according to the average support degree of each proposition and then distributed. Finally, a new D-S fusion theory is proposed. This method overcomes the shortcomings of the previous methods and forms a multivariate information fusion analysis method for the precursor of water surge. Based on the improved D-S fusion theory, a situational

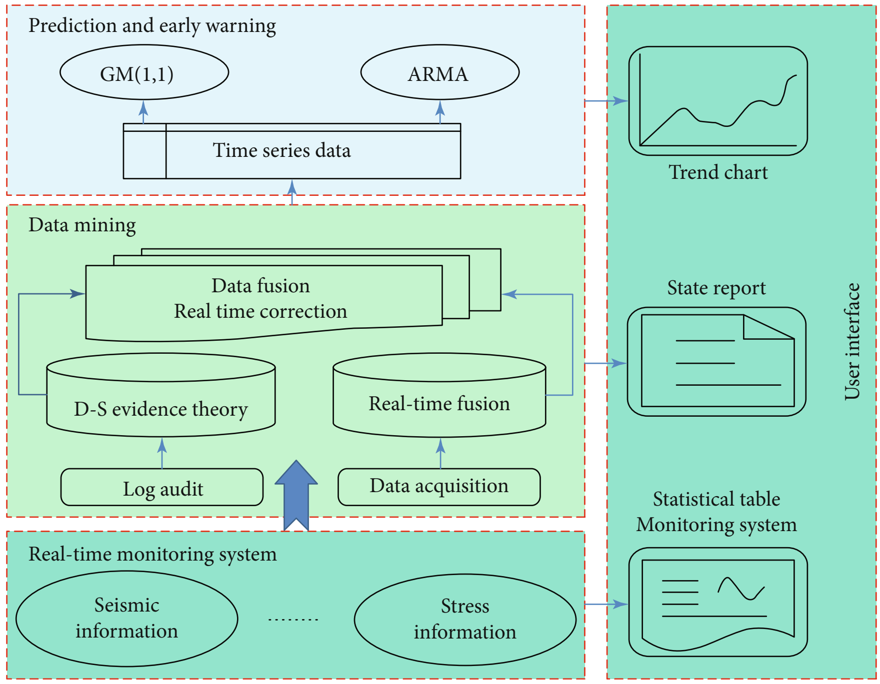

Figure 10: Fusion prediction method of water inrush situation.

fusion prediction method for water inrush predicting is proposed. Using this fusion prediction method, the water inrush condition is obtained in continuous time. The time tendency of the occurrence of a water inrush disaster is finally determined.

The implementation process of fusion prediction method of water inrush situation is as follows. First, the monitoring data and construction log obtained in the monitoring system such as microseismic, displacement, stress, osmotic pressure, temperature, and resistivity are converted into time series information. Secondly, during the entire information change process, a sliding window of ΔT (time) is set (the trailing edge of the sliding window is the real-time display time, the size of ΔT is freely set according to actual needs). Using the log audit method, the probability of occurrence of water inrush in the ΔT is quantified. Finally, multiphysical data is fusion analyzed by introducing the D-S fusion theory. The real-time data of the monitoring system corrects the fusion analysis results to meet the prediction of the change of the water inrush state. Based on the accurate prediction, the real-time status is obtained which fully reflects the actual situation of water inrush. Because the result of the water inrush prediction is a time series, the linear visual display is realized by using the GM$(1, 1)$, ARMA, and Holt-Winters model to predict the probability of the water inrush, as shown in Figure 10.

All the water inrush expectations are fused analysis by using improved D-S evidence fusion methods [30] to obtain the occurrence probability of water inrush. The precursory multi-information accompanying the occurrence of tunnel water inrush disaster includes microseismic, displacement, stress, osmotic pressure, temperature, and apparent resistivity. The information data that can be obtained in the actual construction process is limited. The formula for synthesizing the probability of occurrence of water inrush in three types of physical quantity monitoring systems is deduced.

$$\begin{cases} m(\phi) = 0, \\ m(A) = \prod_{id=1}^{5} m_{id}(A) + \lambda \cdot f(A), \\ m(\bar{A}) = 1 - m(A), \\ m(H) = 0, \end{cases} \tag{6}$$

where

$$\begin{aligned} \lambda &= 1 - \prod_{id=1}^{5} m_{id}(A) - \prod_{id=1}^{5} m_{id}(\bar{A}), \\ f(A) &= \frac{1}{5}\sum_{id=1}^{5} m_{id}(A). \end{aligned} \tag{7}$$

According to equation (6), the alarm log information data of the multiphysical monitoring system is analyzed by fusion to obtain the occurrence probability of water inrush, $\delta_{hp} = m(A)$.

Through the data mining of the precursor multi-information of water inrush in the ΔT, the real-time monitoring data of the around ΔT time are corrected to obtain the time series-based water inrush situation. Therefore, the water inrush situation can be predicted by GM$(1, 1)$. The GM$(1, 1)$ is the content of the grey system theory. It can find the regular and make predictions in a limited number of

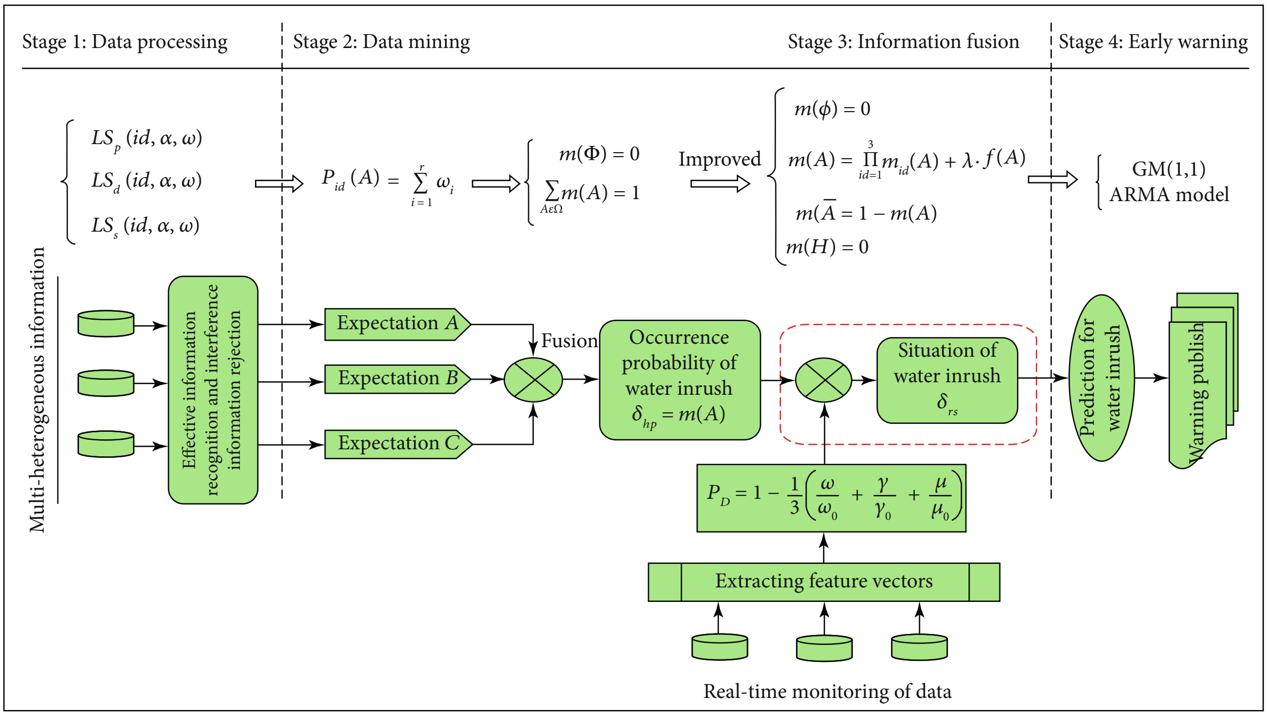

FIGURE 11: Fusion prediction model of water inrush.

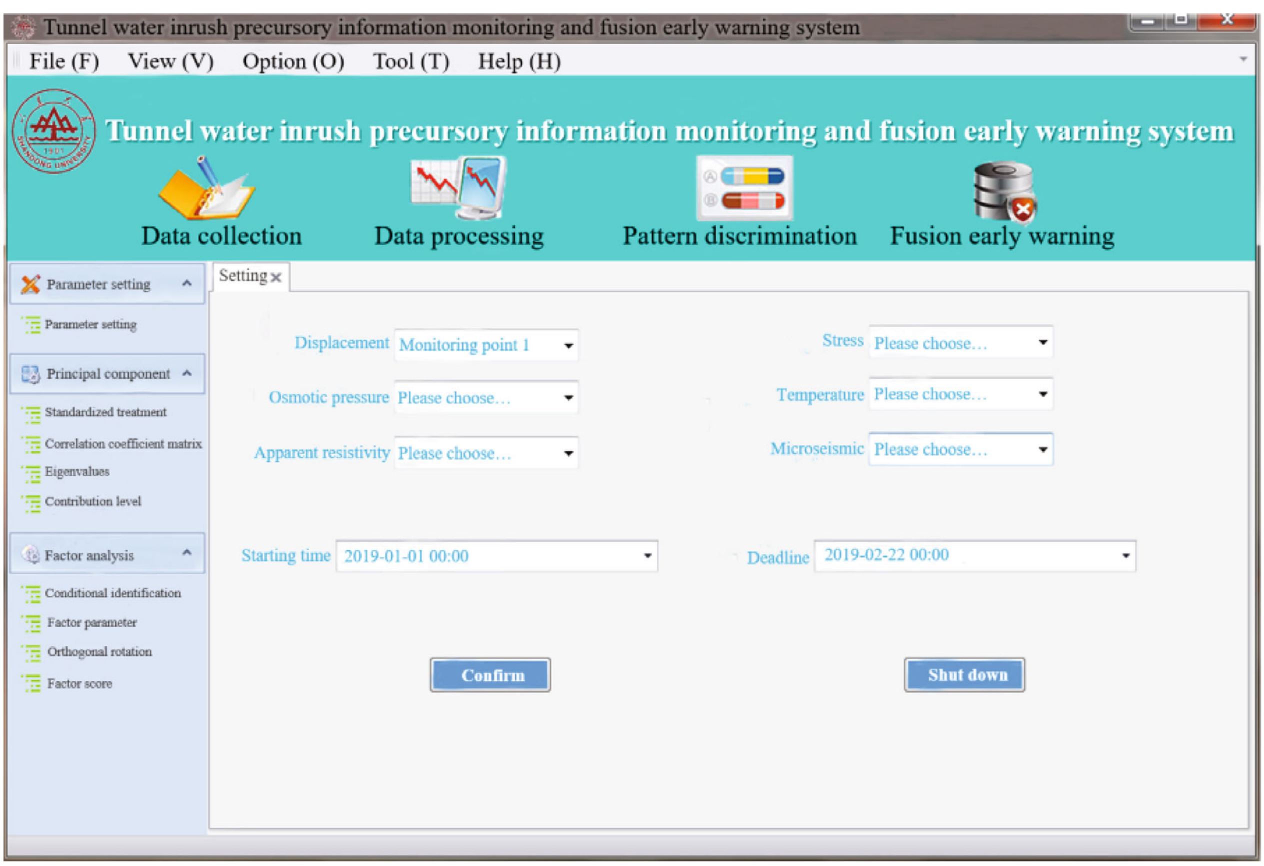

FIGURE 12: Monitoring and integration warning system for precursor information of water inrush [30].

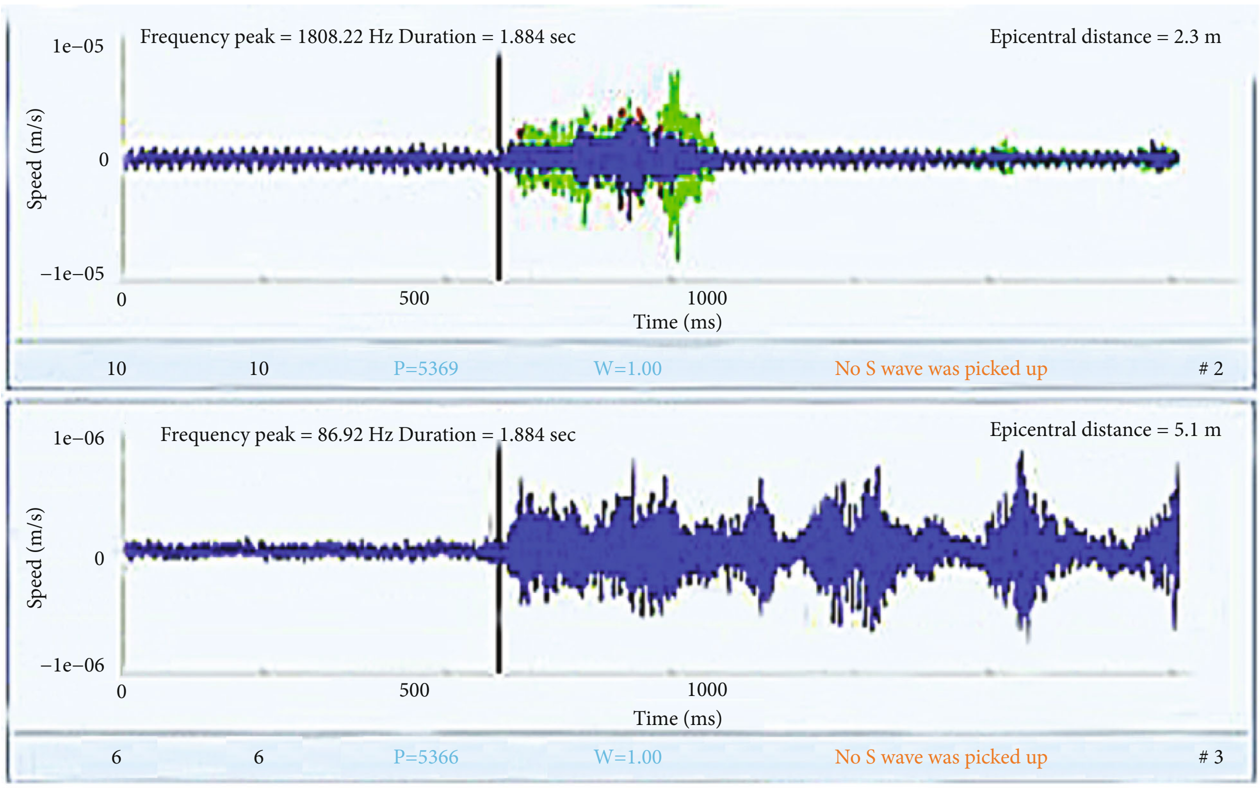

Figure 13: The microseismic monitoring signal of water inrush.

Figure 14: On-site water discharge.

Figure 15: Monitoring component installation.

data or discrete data, and draw the situational curve for visual expression. It also can assist the engineer to fully understand and grasp the development trend of the tunnel water inrush situation. A propensity warning for the occurrence of water inrush is achieved, as shown in Figure 11.

4.3. The Early Warning of Water Inrush Based on Microseismic Monitoring. If there are many recharge channels near the disaster source of the water inrush, when a water inrush disaster occurs, the water inrush channel will have a large amount of water supply. The turbulence signal generated by the water flow impinging on the channel wall can propagate in the anisotropic rock soil medium. Through the simulation test, the feasibility of capturing signals and inverting the positioning supply channel in the tunnel surface was verified. Therefore, a hydroacoustic detector and a microseismometer suitable for the monitoring of water inrush disasters of tunnel have been developed.

The microseismic monitoring equipment is combined with the wireless sensor network to form a real-time monitoring method for the water inrush multi-information carried by microseismic. Through the quantitative analysis of the multi-information situation, based on the established multi-information depth fusion algorithm, the situation of water inrush and the location of rupture channel are predicted to realize the continuous real-time monitoring and

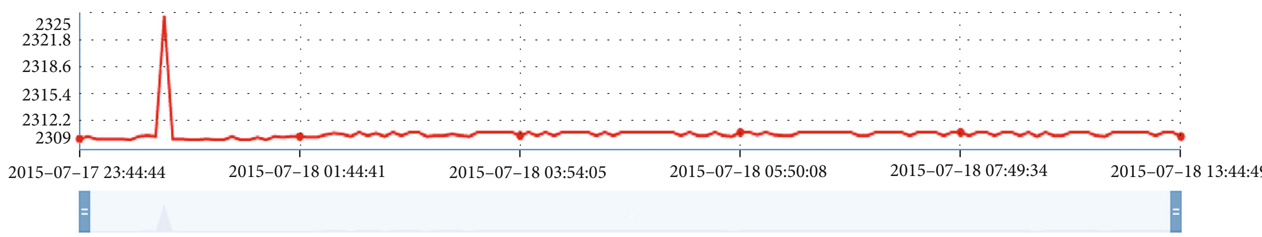

(a) Pore water pressure

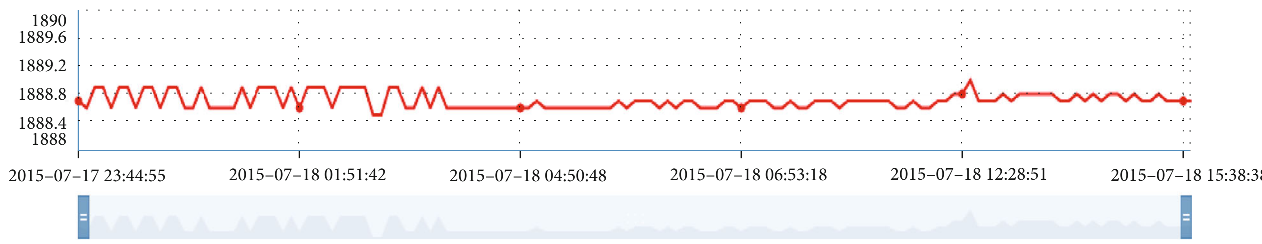

(b) The stress curve

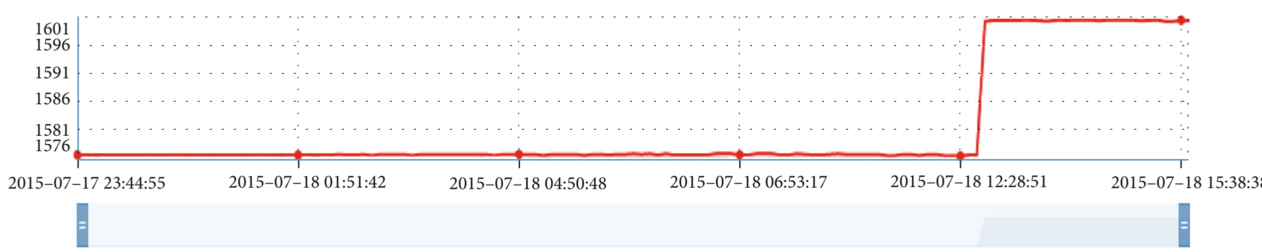

(c) The displacement curve

Figure 16: Monitoring data of physical quantity.

early warning of water inrush disaster, as shown in Figures 12 and 13.

During the tunnel construction process, disaster source static reserves are detected through the whole process of geological prediction. The dynamic reserve of groundwater recharge is estimated by the regional estimate of the recharge channel. The hazard level is quantified by the amount of water in the water inrush. Through the multi-information monitoring of the antioutburst structure, the analysis of the security situation of the antioutburst structure to determine the time tendency, and the microseismic monitoring to determine the location of the water inrush channel, a comprehensive monitoring and early warning method was established, based on the geological prediction of the disaster source, the multi-information fusion monitoring of the antioutburst structure, and the microseismic positioning of water channels.

5. Engineering Applications

The Yuelongmen tunnel of Sichuan Chenglan Railway is one of the most difficult railway projects in China. It is located in the alpine valley area on the eastern edge of the Qinghai-Tibet Plateau. Mountains and steep valleys surround it. It passes through Jiuzhaigou and the Giant Panda Protection Base. Accompanied by the collision between the Indian plate and the Eurasian plate, the topographical and geological conditions show typical "four poles and three highs" characteristics. The Yuelongmen tunnel is a double-hole tunnel with a total length of 19981 m for the left line and 20042 m for the right line. The tunnel passes through the Longmenshan active fault zone and fault fracture zone. The maximum depth of the tunnel is 1445 m. In the process of construction, disasters such as large deformation and water inrush frequently occur under high ground stress. In the D2K94 +645 ~ D2K94+675 mileage, through the deployment of monitoring sensors, video monitoring devices, and remote wireless transmission systems, a multi-information monitoring platform based on microseismic is built to monitor real-time multivariate precursor information, as shown in Figures 14 and 15. During the construction period, 27 small and medium-sized water inrush were accurately warned, and the water inrush situation was effectively controlled. The estimation method of the hydrostatic volume and dynamic reserves of the disaster source was proposed, and the hazard level warning was realized, ensuring safe construction in water. It guarantees the safe construction of the extremely high-risk section of the Yuelongmen tunnel and promotes its application throughout the entire railway.

The remote monitoring and early warning analysis system for major water inrush includes data acquisition, data processing, pattern discrimination, and fusion warning. Based on the remote real-time acquisition of physical quantity information to find the evolution law of precursor information of two kinds of water inrush, the water inrush pattern recognition and discrimination model was established to carry out accurate type identification of water inrush, as shown in Figure 16. A fusion analysis model of tunnel water inrush was established. Through the analysis of multi-information fusion, the evolution state of the water inrush was predicted in time. In space, the early warning technology of microseismic positioning channel and integrated multi-information prediction situation was used as an auxiliary to monitor and warn. Multiterminals, such as total monitoring center, on-site subcenter, base station, and internet, have realized real-time monitoring and early warning of tunnel water inrush in different places.

6. Conclusions

This paper systematically summarizes the failure mode, the occurrence criterion, and the safe thickness determination method of the antioutburst structure and expounds the catastrophic evolution process of the formation of the water inrush channel. The disaster source and antioutburst structure of water inrush were monitored in real-time to obtain the evolution law of precursory multi-information. Finally, the identification method of the precursor information of water inrush was established, and the propensity prediction of water inrush time was realized. The remote monitoring and early warning analysis system of major water inrush was established, which can provide the basis for prevention and control of disasters.

(1) The catastrophic evolution mechanism of the progressive failure of the resistance structure and the infiltration and instability of filling medium was explained. By systematically summarizing the existing theoretical model of water inrush, calculation method, and applicable conditions, this paper focuses on the hot and difficult problems, key breakthrough directions, and development trends of the mechanism research of water inrush. The research on the dynamic evolution mechanism of water inrush in deep tunnels provides theoretical support and method guidance for the active prevention and control of water inrush

(2) By comparing the application of microseismic monitoring in rockburst and water inrush, the improvement schemes of software and hardware for traditional microseismic technology of antioutburst structure were proposed to locate the rupture of the antioutburst structure. The scheme was embedded in the fusion early warning software. Then, the cluster analysis theory was used to realize the effective acquisition of precursory information of water inrush. The identification problem of the evolution of state and precursor information of water inrush was solved

(3) An improved D-S fusion method was introduced for the fusion analysis of multidimensional heterogeneous information. Combined with real-time monitoring data to correct the fusion analysis results, the tendency to predict the water inrush time was realized. Besides, the true state of the water inrush situation was comprehensively reflected. Considering the estimation of the static reserve and the dynamic reserves under the water supply replenishment of disaster sources, it can achieve the magnitude prediction of the water inrush. Finally, a monitoring and early warning analysis system for major water inrush was established

(4) Yuelongmen tunnel relies on the multi-information collection wireless transmission platform to establish a multilevel and comprehensive early warning system. It realized data cloud storage analysis and real-time monitoring and early warning of multiterminals. It realizes the time and space warning of major water inrush and promotes the development of active prevention and control of disasters

Data Availability

The data used to support the findings of this study are included within the article.

Conflicts of Interest

The authors declare that they have no conflicts of interest.

Acknowledgments

The research for this paper was supported by a project of the National Science Foundation for Distinguished Young Scholars of China (Grant No. 52025091), the National Natural Science Foundation of China (Grant Nos. 51909143, 52009076, and 52009070), a project of the Joint Funds of the National Natural Science Foundation of China (Grant No. U1934218), the Shandong Provincial Key Research and Development Program (Major Scientific and Technological Innovation Project) (Grant Nos. 2019JZZY010601 and 2019JZZY010428), and the China Postdoctoral Science Foundation (Grant Nos. 2020M682182 and 2021T140414).

References

[1] R. Q. Huang and X. N. Wang, “Analysis of major disaster geological problems in deep tunnel engineering,” *Hydrogeological Engineering Geology*, vol. 4, pp. 21–24, 1998.

[2] X. W. Luo and F. L. He, “A study of geological structures inclined to disaster and models of water burst in deep-buried long tunnels,” *Modern Tunnelling Technology*, vol. 51, no. 1, pp. 21–25, 2014.

[3] M. S. Wang and Z. S. Tan, “China tunnel and underground construction technology,” *Strategic Study of CAE*, vol. 12, no. 12, pp. 4–10, 2010.

[4] D. Y. Chen, *Study on water inrush mechanism and real-time monitoring method of karst cave in tunnels [Ph.D. thesis]*, Shandong University, Jinan, 2016.

[5] Y. G. Wang, *Study on scourge and prevention of karst tunnel water inrush [Ph.D. thesis]*, China Academy of Railway Sciences, Beijing, 2010.

[6] Z. W. Liu, *Karst waterburst mechanism and prevention countermeasures in Yuanliangshan tunnel [Ph.D. thesis]*, China University of Geosciences, Beijing, 2004.

[7] Z. W. Liu, M. C. He, and S. R. Wang, "Study on karst waterburst mechanism and prevention countermeasures in Yuanliangshan tunnel," *Rock and Soil Mechanics*, vol. 27, no. 2, pp. 228–232, 2006.

[8] J. X. Wang, B. Feng, and X. S. Zhang, "Hydraulic failure mechanism of karst tunnel surrounding rock," *Chinese Journal of Rock Mechanics and Engineering*, vol. 29, no. 7, pp. 1363–1370, 2010.

[9] J. Q. Guo and C. S. Qiao, "Study on water inrush mechanism and thickness of rock wall of karst tunnel face," *Journal of The China Railway Society*, vol. 34, no. 3, pp. 105–111, 2012.

[10] L. P. Li, *Study on evolution mechanism and application of water inrush disaster in high risk karst tunnel [Ph.D. thesis]*, Shandong University, Jinan, 2009.

[11] L. P. Li, D. Y. Chen, and S. C. Li, "Numerical analysis and fluid-solid coupling model test of filling-type fracture water inrush and mud gush," *Geomechanics and Engineering*, vol. 13, no. 6, pp. 1011–1025, 2017.

[12] Z. L. Nie, *Analysis for water burst mechanism and study on mechanical features of tunnel lining in water filled karst area [Ph.D. thesis]*, Southwest Jiaotong University, Chengdu, 2009.

[13] Z. Q. Zhou, L. P. Li, S. S. Shi et al., "Study on tunnel water inrush mechanism and simulation of seepage failure process," *Rock and Soil Mechanics*, vol. 41, no. 11, pp. 3621–3631, 2020.

[14] R. Q. Huang and X. N. Wang, "Analysis of hydraulic splitting in deep water tunnel gushing process," *Chinese Journal of Rock Mechanics and Engineering*, vol. 19, no. 5, pp. 573–573, 2000.

[15] X. J. Weng, *Study on inrush of water and mud mechanism and grouting control technology in water-rich fault fracture zone of tunnel [Ph.D. thesis]*, Shandong University, Jinan, 2014.

[16] J. W. Zhang, Y. Tan, and T. Chen, "Study on mechanism of batholite water inrush in lateral karst tunnel," *Journal of Highway and Transportation Research and Development*, vol. 34, no. 5, pp. 109–115, 2017.

[17] S. Q. Sun, P. He, G. Wang et al., "Shape characterization methods of irregular cavity using Fourier analysis in tunnel," *Mathematics and Computers in Simulation*, vol. 187, pp. 191–214, 2021.

[18] X. Zhang, D. J. Sanderson, and A. J. Barker, "Numerical study of fluid flow of deforming fractured rocks using dual permeability model," *Geophysical Journal International*, vol. 151, no. 2, pp. 452–468, 2002.

[19] L. Jing, Y. Ma, and Z. Fang, "Modeling of fluid flow and solid deformation for fractured rocks with discontinuous deformation analysis (DDA) method," *International Journal of Rock Mechanics and Mining Sciences*, vol. 38, no. 3, pp. 343–355, 2001.

[20] L. Q. Ma, D. S. Zhang, and X. X. Miao, "FLAC3D simulation of seepage law of mining rock mass," *Journal of Hunan University of Science and Technology (Natural Science Edition)*, vol. 21, no. 3, pp. 1–5, 2006.

[21] L. C. Li, C. A. Tang, and Z. Z. Liang, "Numerical analysis of pathway of groundwater inrush from faults in coal seam floor," *Chinese Journal of Rock Mechanics and Engineering*, vol. 28, no. 2, pp. 290–297, 2009.

[22] C. A. Tang, T. H. Yang, L. C. Li et al., "Numerical simulation of influence of pore water pressure on rock crack propagation," *Rock and Soil Mechanics*, vol. 24, no. S2, pp. 17–20, 2003.

[23] Z. Q. Zhou, P. G. Ranjith, W. M. Yang, S. S. Shi, C. C. Wei, and Z. H. Li, "A new set of scaling relationships for DEM-CFD simulations of fluid–solid coupling problems in saturated and cohesiveless granular soils," *Computational Particle Mechanics*, vol. 6, no. 4, pp. 657–669, 2019.

[24] Z. Q. Zhou, Z. H. Li, C. L. Gao et al., "Peridynamic microelastoplastic constitutive model and its application in the failure analysis of rock masses," *Computers and Geotechnics*, vol. 132, article 104037, 2021.

[25] C. L. Gao, Z. Q. Zhou, Z. H. Li, L. P. Li, and S. Cheng, "Peridynamics simulation of surrounding rock damage characteristics during tunnel excavation," *Tunnelling and Underground Space Technology*, vol. 97, article 103289, 2020.

[26] S. C. Li, C. L. Gao, Z. Q. Zhou et al., "Analysis on the precursor information of water inrush in karst tunnels: a true triaxial model test study," *Rock Mechanics and Rock Engineering*, vol. 52, no. 2, pp. 373–384, 2019.

[27] Y. C. Mo, *Stability research on high water pressure filled karst caves tunnel [Ph.D. thesis]*, Southwest Jiaotong University, Chengdu, 2009.

[28] Y. Q. Hu, Y. S. Zhao, and D. Yang, "Simulation theory & method of 3D solid-liquid coupling," *Journal of Liaoning Technical University*, vol. 2, pp. 204–206, 2007.

[29] S. C. Li, Y. Zhou, and L. P. Li, "Development and application of a new similar material for underground engineering fluid-solid coupling model test," *Chinese Journal of Rock Mechanics and Engineering*, vol. 31, no. 6, pp. 1128–1137, 2012.

[30] Y. C. Yuan, *Study on precursor information evolution law of water inrush and early warming method in tunnels and its engineering applications [Ph.D. thesis]*, Shandong University, Jinan, 2017.

[31] S. G. Song, S. C. Li, L. P. Li et al., "Model test study on vibration blasting of large cross-section tunnel with small clearance in horizontal stratified surrounding rock," *Tunnelling and Underground Space Technology*, vol. 92, p. 103013, 2019.

[32] L. P. Li, C. S. Shang, K. W. Chu et al., "Large-scale geomechanical model tests for stability assessment of super-large cross-section tunnel," *Tunnelling and Underground Space Technology*, vol. 109, article 103756, 2021.

[33] Z. P. Meng, M. S. Li, and P. Q. Lu, "Temperature and pressure under deep conditions and their influences on mechanical properties of sandstone," *Chinese Journal of Rock Mechanics and Engineering*, vol. 25, no. 6, pp. 1177–1181, 2006.

[34] H. R. Li, C. H. Yang, and Y. G. Liu, "Experimental research on ultrasonic velocity and acoustic emission properties of granite under failure process," *Chinese Journal of Geotechnical Engineering*, vol. 36, no. 10, pp. 1915–1923, 2014.

[35] J. Li, J. H. Yue, Y. Yang, X. Zhan, and L. Zhao, "Multi-resolution feature fusion model for coal rock burst hazard recognition based on acoustic emission data," *Measurement*, vol. 100, pp. 329–336, 2017.

[36] X. P. Zhang, Q. Zhang, and S. C. Wu, "Acoustic emission characteristics of the rock-like material containing a single flaw under different compressive loading rates," *Computers and Geotechnics*, vol. 83, pp. 83–97, 2017.

[37] S. C. Li, X. J. Xu, and Z. Y. Liu, "Electrical resistivity and acoustic emission response characteristics and damage evolution of sandstone during whole process of uniaxal compression," *Chinese Journal of Rock Mechanics and Engineering*, vol. 1, no. 33, pp. 14–23, 2014.

[38] S. C. Li, L. P. Li, S. C. Li et al., "Development and Application of Similar Physical Model Test System for Water Inrush of Underground Engineering," *Journal of Mining & Safety Engineering*, vol. 27, no. 3, pp. 299–304, 2010.

[39] S. C. Li, C. Hu, L. P. Li, S. G. Song, Y. Zhou, and S. S. Shi, "Bidirectional construction process mechanics for tunnels in dipping layered formation," *Tunnelling and Underground Space Technology*, vol. 36, pp. 57–65, 2013.

[40] S. X. Ling, Y. Ren, and X. Y. Wu, "Study on reservoir and water inrush characteristic in Nibashan tunnel, Sichuan Province, China," *Engineering Geology for Society and Territory*, vol. 6, pp. 577–582, 2015.

[41] Z. H. Wang, T. Su, H. Konietzky, Y. L. Tan, and G. L. Zhou, "Hydraulic properties of Beishan granite after different high temperature treatments," *Bulletin of Engineering Geology and the Environment*, vol. 80, no. 4, pp. 2911–2923, 2021.

[42] G. M. Zhang, K. Zhang, L. J. Wang, and Y. Wu, "Mechanism of water inrush and quicksand movement induced by a borehole and measures for prevention and remediation," *Bulletin of Engineering Geology and the Environment*, vol. 74, no. 4, pp. 1395–1405, 2015.

[43] H. Yuan, H. M. Zhong, and D. J. Lai, "Geological disaster online realtime monitoring and early-warning system research based on the Flex Viewer framework," *Journal of Natural Disasters*, vol. 22, no. 2, pp. 177–184, 2013.

[44] S. E. Ma, Z. R. Mei, and J. W. Zhang, "Geological structure quantitative evaluation and monitoring and early warning of water inrush and mud disaster in long tunnel," *Modern Tunnel Technology*, vol. 46, no. 2, pp. 99–104, 2009.

[45] Y. Q. Xu and J. Ma, "Dynamic monitoring and early warning system for geological disasters based on internet of things technology and its architecture," *Chinese Journal of Geological Hazard and Control*, vol. 24, no. 3, pp. 90–93, 2013.

[46] G. L. Sun, Z. G. Tao, and W. L. Gong, "Slope disaster monitoring and early warning network system and its engineering application," *Journal of China University of Mining and Technology*, vol. 46, no. 2, pp. 285–291, 2017.

[47] J. P. Sun, "Technologies of monitoring and communication in the coal mine," *Journal of China Coal Societ*, vol. 35, no. 11, pp. 1925–1929, 2010.

[48] S. Wang, L. P. Li, S. Cheng et al., "Study on an improved realtime monitoring and fusion prewarning method for water inrush in tunnels," *Tunnelling and Underground Space Technology*, vol. 112, article 103884, 2021.

[49] X. Kuang, M. Z. Bai, and C. L. Wang, "Research of comprehensive warning of water inrush hazards in karst tunnel based on fuzzy evolution method," *Journal of Highway and Transportation and Development*, vol. 27, no. 11, pp. 100–103, 2010.

[50] P. Zhao, X. L. Pei, and J. Xue, "Research on safety pre-warning management of building construction based on information fusion technique," *China Safety Science Journal*, vol. 19, no. 10, pp. 106–110, 2009.

[51] Y. N. Yang, H. P. Cao, and M. Xu, "Index system of risk assessment on karst tunnel water inrush disasters and value of quantitative method," *Geosience*, vol. 2, pp. 414–420, 2015.

[52] J. Liu and W. M. Wu, "Research on safety risk early warning model of large coal water disaster," *Chinese Coal*, vol. 5, pp. 122–124, 2017.

[53] P. Liu, J. F. Wang, and L. Y. Zhang, "Reliability study on coal mine water disaster early warning system based on extension evaluation," *Coal Technology*, vol. 34, no. 6, pp. 136–138, 2015.

[54] S. C. Li, Z. Q. Zhou, L. P. Li, Z. H. Xu, Q. Q. Zhang, and S. S. Shi, "Risk assessment of water inrush in karst tunnels based on attribute synthetic evaluation system," *Tunnelling and Underground Space Technology*, vol. 38, pp. 50–58, 2013.

[55] L. P. Li, S. C. Li, and Q. S. Zhang, "Study of mechanism of water inrush induced by hydraulic fracturing in karst tunnels," *Rock and Soil Mechanics*, vol. 31, no. 2, pp. 523–528, 2010.

[56] S. C. Li, Y. C. Yuan, and L. P. Li, "Water inrush mechanism and minimum safe thickness of rock wall of karst tunnel face under blast excavation," *Chinese Journal of Geotechnical Engineering*, vol. 37, no. 2, pp. 313–320, 2015.

[57] Z. Q. Zhou, *Evolutionary mechanism of water inrush through filling structures in tunnels and engineering applications [Ph.D. thesis]*, Shandong University, Jinan, 2016.

[58] S. J. Zang, "Theoretical on study minimum safe thickness of floors of tunnels in heavy karst areas during construction," *Tunnel Construction*, vol. 27, no. 5, pp. 17–19, 2007.

[59] M. Sun and W. N. Liu, "Research on water inrush mechanism induced by karst tunnel face with high risk," *Rock and Soil Mechanics*, vol. 32, no. 4, pp. 1175–1180, 2011.

[60] S. Cheng, *Microseismic mechanism and monitoring analysis method for water inrush in tunnels [Ph.D. thesis]*, Jinan, Shandong University, 2019.

[61] B. Liu, *Research on real-time monitoring of tunnel water-bearing geological structure based on resistivity method and IP method for advanced detection and water inrush disaster [Ph.D. thesis]*, Shandong University, Jinan, 2010.

[62] R. S. Jian, X. H. Ya, and H. M. Sun, "Situation assessment method of rock burst based on multi-source information fusion," *Journal of Mining & Safety Engineering*, vol. 31, no. 2, pp. 187–195, 2014.

[63] S. Bjørn and S. W. Hystad, "Situation awareness as a determinant for unsafe actions and subjective risk assessment on offshore attendant vessels," *Safety Science*, vol. 93, pp. 214–221, 2017.

[64] Y. Wei, Y. F. Lian, and D. G. Feng, "A network security situational awareness model based on information fusion," *Journal of Computer Research and Development*, vol. 46, no. 3, pp. 353–362, 2009.

[65] Y. Wei and Y. F. Lian, "A network security situational awareness model based on log audit and performance correction," *Chinese Journal of Computers*, vol. 32, no. 4, pp. 763–772, 2009.

[66] S. Wang, *Regional dynamic risk assessment and early warning of tunnel water inrush and application [M.S. thesis]*, Shandong University, Jinan, 2016.

Hindawi
Geofluids
Volume 2021, Article ID 5593448, 8 pages
https://doi.org/10.1155/2021/5593448

Research Article

Experimental Study on Water-Sand Seepage Characteristics in Fractured Rock Mass under Rheological Effect

Jiarui Chen,[1] **Hai Pu**,[2,3] **Jianxiong Liu**,[1] **Jihua Zhang**,[1] **Peitao Qiu**,[4] **Wenhu Gu**,[1] **Qirong Li**,[1] and **Zhendong Chen**[1]

[1]*Faculty of Architecture and Civil Engineering, Huaiyin Institute of Technology, Huai'an, Jiangsu 223001, China*
[2]*State Key Laboratory for Geomechanics & Deep Underground Engineering, China University of Mining & Technology, Xuzhou, Jiangsu 221116, China*
[3]*College of Mining Engineering and Geology, Xinjiang Institute of Engineering, Urumqi, Xinjiang 830091, China*
[4]*School of Civil Engineering, Xuzhou University of Technology, Xuzhou, Jiangsu 221018, China*

Correspondence should be addressed to Jianxiong Liu; 1011103615@qq.com

Received 24 February 2021; Accepted 13 August 2021; Published 21 August 2021

Academic Editor: Yi Xue

This study investigates water-sand bursting disasters associated with fractured rock that affect safe mining in the mining areas of Western China. A broken rock water-sand seepage rheological test device was developed, and rheological tests were conducted on multiple groups of broken rock samples with single-stage axial loading and different load levels. When the rheology of each group of broken rock samples was stable, water-sand mixed fluid was injected into the samples at a certain pressure gradient to conduct water-sand seepage tests on broken rock masses. It was found that when the porosity of a fractured rock mass is within a certain range, the water-sand mixed fluid does not completely pass through the fractured rock mass and some sand particles are filtered by the fractured rock sample. There is an exponential relationship between the sand breaking ability and the sand filtration ability of fractured rock and its initial porosity, and the permeability of fractured rock decreases by a certain extent after sand filtration. However, for different load levels, when the flow through a fractured rock mass tends to be stable, the final porosity of the fractured rock mass decreases exponentially with axial compression. Based on the classical Kelvin rheological model and the basic theory of fractional calculus, a new fractional rheological model has been proposed and the rheological parameters under different load levels were fitted to the model. The new fractional rheological model is better able to describe the rheological characteristics of broken mudstone.

1. Introduction

The removal of underground coal in China's western coal mining regions results in the formation of a goaf. Unsupported overburdened rocks undergo fractures that lead to interconnected cracks [1]. The seepage of mixed fluids formed by water and sand through the connected cracks within overburdened rocks can cause serious disasters from water and sand inrush [2], which seriously threaten production safety in western coal mines. The disasters caused by penetrating cracks are a threat to many projects [3, 4] and therefore a topic of intense research [5–11].

Backfilling of a goaf is currently considered to be the most effective manner to solve the problem of sedimentation. Rheological effects are encountered due to loading compaction of broken rock that occurs during backfilling. The creep mechanical properties of saturated bulky gangue materials have been studied by other researchers [12]. However, several problems involving the long-term stability of backfill projects are related to the passage of time [13], which include the creep properties of the filling material under the long-term effect of loading. The water-bearing state of broken rock is an important factor that affects its creep mechanical properties, and major project accidents may occur due to the instability of loose rock that increases with time [14–17].

Significant progress has been made in the research on the rheological characteristics of various types of rocks [18, 19]. However, most research has been conducted on whole-rock blocks [20] and research on the deformation characteristics of broken rock samples is lacking. Experimental research on creep has been conducted [21] on limestone rockfill material with a three-parameter model of rockfill material. When crushed rock is saturated with water, particle transfer and rearrangement occur due to external forces and the lubrication from water. Also, there are some differences between the rheological characteristics of saturated rock and dry rock. When rock particles are pushed against each other, they slide and deform to achieve a balance in the rheological process of the fractured rock. Rock particles are crushed directly due to external loads [22, 23], or smaller particles exit due to internal breakage or unstable crushing, which results in changes to the mechanical properties of broken rock. The changes in deformed seepage characteristics with time have been studied for broken sandstone [24], and unlike that of the entire rock blocks, the deformation scale of broken rocks under external forces is usually large. Also, changes in volume are much larger [25], resulting in changes in the porosity of broken rock and the surrounding rock space. These are crucial factors to consider [26] when addressing problems related to water and sand inrush in western coal mines. Physical quantities like elastic modulus and coefficient of viscosity of fractured rock change constantly during creep and compaction, and traditional rheological models are unable to fully describe such phenomena; the rheological equation of fractional calculus introduced in this study is well suited for the purpose.

The fractional-order system is a fundamental theory [27] that studies arbitrary order differentials and integrals. Integer-order differentials and integrals for arbitrary order extensions [28] in fractional calculus of mechanics are primarily applied in research on constitutive models of viscoelastic materials [29–31] and are currently one of the most active fields of research [32]. Kabwe et al. [33] proposed a fractional derivative viscoelastic (FDVP) constitutive model, which can estimate delayed deformation due to compression. Lokoshchenko et al. [34] considered the piecewise-constant time dependence of bending moment magnitude and direction and used a linear fractional creep model to determine the fracture time of a plate. A new rheological parameter for fractional derivative models has been proposed [35] by combining drawing-fitting and numerical methods in terms of the viscoelastic properties of materials.

This paper considers that the seepage characteristics of water-sand mixtures in a fractured rock mass are affected by the compaction characteristics of fractured rock mass and the water pressure gradient. The elastic modulus and coefficient of viscosity change continuously during the process of compaction and rheology of fractured rock. However, the elastic modulus and viscosity coefficient are constants in traditional rheological models. Hence, using traditional models to describe the rheological properties of fractured rock masses results in large errors. This paper adopts the fractional parameter α to represent equivalent changes in the relationship between elastic modulus and coefficient of viscosity. It replaces a Newton dashpot with an Abel dashpot based on a saturated broken mudstone compaction rheological experiment, and a new rheological model is obtained via a fractional Kelvin model connected in series to a three-parameter model using a combination theory. Also, the water-sand seepage characteristics of broken rock due to rheological effects are studied based on the new model. This study provides a reference for safe mining in China's western coal mines.

2. Test System and Solution

2.1. Test System and Material. Lateral flow occurs readily in loosely confined, pressure-free crushed rocks under axial pressure that are therefore unable to bear large loads. However, in certain situations, such as in coal mines and tunnels, broken rocks bear both large and small confined pressures. Therefore, a broken rock rheology-water and sand seepage test device (Figure 1(a)) was designed for testing, using an MTS816 electrohydraulic servo-controlled test system (Figure 1(b)).

The broken rock samples were mudstone particles with particle diameters of 5~8, 8~10, 10~12, 12~15, and 15~20 mm evenly mixed with a ratio of 1 : 1 : 1 : 1 : 1, and the density was $\rho = 2420\,\mathrm{kg/m^3}$ in the natural state. Sand in western mining areas is natural aeolian sand, with a particle size distribution of 20~220 mesh. Each test used a total of 1200 g of broken rock, and 500 g of sand. The inner diameter of the cylinder was 100 mm with a height of 250 mm.

2.2. Test Solution. A broken rock mass of mass m, fully moistened with water, was packed in the penetrator sleeve. Aeolian sand was then placed in the pressure-bearing ring and the sleeve was tapped lightly to compact the broken rock sample. The MTS816 was then started for loading, with the load being held at 0.05 kN for 10 minutes to stabilize the system and set the initial state. A preset load σ_i was then applied for the rheological test and the strain-stress curve of the broken rock was obtained. After a certain time t_i, the deformation of the broken rock sample stabilized and the distance h_i between the piston and the lower permeable plate was measured, which represented the height of the broken mudstone sample and was used to calculate the porosity of the broken mudstone, as shown in equation (1) as follows:

$$\phi_i = 1 - \frac{m}{\rho_{\mathrm{mudstone}} r^2 \pi h_i} \, (i = 1, 2, 3, 4), \tag{1}$$

where ϕ_i is the porosity of broken mudstone at time t_i of the test; m is the mass of the broken mudstone sample; ρ_{mudstone} represents mudstone density; r is the radius of the permeameter sleeve; h_i is the height of the mudstone test sample.

The pump was then switched on and water was pressurized to a certain pressure in the permeameter at which the deformation of the broken rock stabilized. The water-sand mixture formed when the water flow stirred up the sand particles inside the pressure-bearing ring via the broken rock, and seepage occurred. The sand particles were divided into three parts when the seepage was stable: one part (m_1) infiltrated with the water flow; a second part (m_2) resided within the broken rock due to the filtering of the broken rock framework; a third part (m_3) remained within the

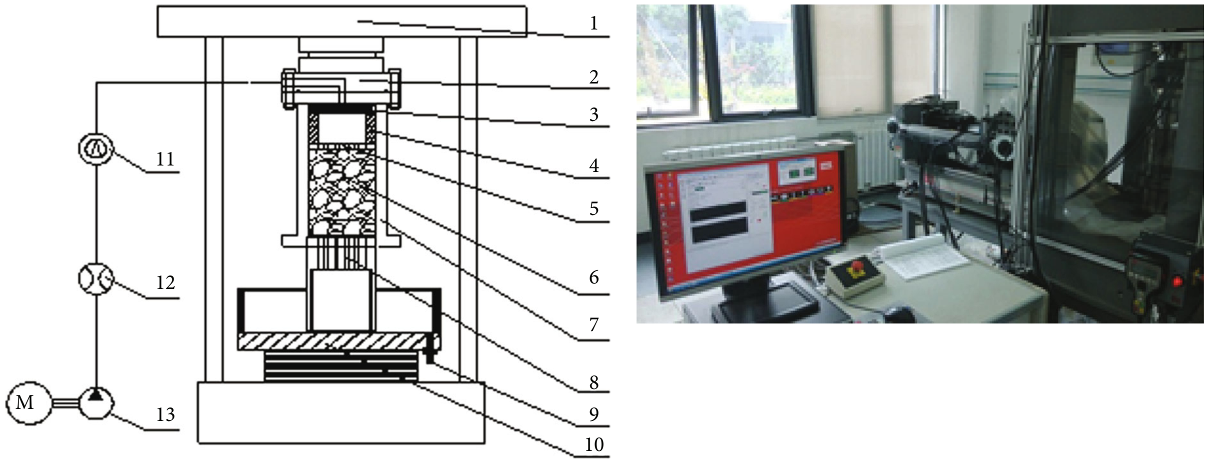

(a) Test system for rheology and seepage of broken rock

(b) MTS816 electrohydraulic servo-controlled test system

Figure 1: Test equipment. 1: MTS816; 2: permeameter base; 3: upper permeable plate; 4: pressure-bearing ring; 5: lower permeable plate; 6: broken rock; 7: permeameter sleeve; 8: piston; 9: tray outlet; 10: water-sand collection tray; 11: pressure gauge; 12: flowmeter; 13: speed regulation pump.

pressure-bearing ring. Among these, m_2 was the sand filtered by the broken rock and changed the porosity of the broken rock framework with the variation $\nabla\phi_i$:

$$\nabla\phi_i = \frac{m_2}{\rho_{\text{aeolian sand}} r^2 \pi h_i}, \tag{2}$$

where $\rho_{\text{aeolian sand}}$ represents the aeolian sand density.

Here, the porosity of the broken rock framework is represented by φ_i:

$$\varphi_i = \phi_i - \nabla\phi_i (i = 1, 2, 3, 4). \tag{3}$$

In the test, the pressure differential of the seepage decreased linearly along the axial permeameter when the seepage stabilized. The outlet and inlet pressures p were measured by the pressure gauge directly, and the outlet of the permeameter was connected to the atmosphere at pressure p_0. Hence, the formula for the pressure gradient Δp is as follows:

$$\Delta p = -\frac{\partial p}{\partial z} = \frac{p - p_0}{h_i}, \tag{4}$$

where z is the direction of the pressure gradient.

The volume flow (Q) through the permeameter per unit time was measured by the flowmeter and was used to calculate the speed of seepage v:

$$v = \frac{Q}{\pi r^2}. \tag{5}$$

In the test, when the water-sand seepage occurred, some of the particles resided inside the broken rock framework due to the effect of filtering and changed the porosity of the broken rock framework. It was very difficult to dynamically observe the internal framework since the entire test sample was in a confined environment. The change in the porosity and framework structure of the broken rock sample led to changes in its seepage characteristics. This paper reports an investigation of the characteristics of permeability, porosity, water infiltration, water-sand seepage, and sand filtration of broken rock through an analysis of the various deformation processes of broken rock. The seepage process can be assumed to conform to the law of Darcy:

$$-\frac{\partial p}{\partial z} = \frac{v\mu}{k}, \tag{6}$$

where k is permeability and μ is the kinetic viscosity of the fluid.

3. Analysis of the Rheological Characteristics of Broken Rock Based on the Fractional Calculus

3.1. Curve of the Rheological Test of Broken Mudstone. Axial loads of 12, 30, 60, and 120 kN were successively applied on the samples during the tests, with the corresponding stresses being 1.53, 3.82, 7.64, and 15.29 MPa. The corresponding heights at which the broken rock test samples for the above four loads stabilized rheologically were 119, 109, 101, and 94 mm, respectively. Figure 2 shows the strain-stress curves of the broken mudstone test samples.

It was observed that rock particles pushed against each other, slid to deform, and achieved a balance during the rheological processes of fractured rock samples. Rock particles were crushed directly under the effect of external load, smaller particles exited due to internal breakage or unstable crushing, and particle transfer and rearrangement were enhanced under the joint effect of water lubrication and external force. Unlike entire-rock compression tests, the rheological parameters of broken rocks vary due to the above reasons. The rheological parameters of rocks under varying loads, however, can be presumed to be constant and equal

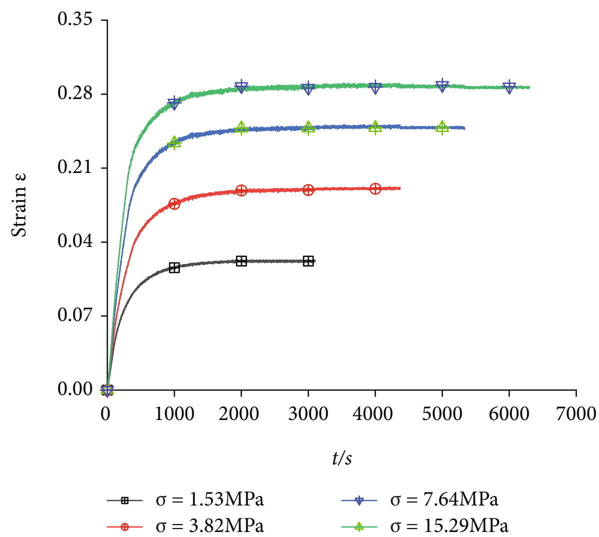

Figure 2: Test strain-time curves.

to the values obtained before crushing, for the entire-rock compression creeping test.

3.2. Basic Knowledge of Fractional Calculus. Among the many ways to define fractional calculus, the Riemann-Liouville definition is the most common. For any complex $\alpha > 0$, the integral fractional Riemann-Liouville definition is

$$I_{a+}^{\alpha} f(t) = \frac{1}{\Gamma(\alpha)} \int_a^t \frac{f(\tau)d\tau}{(t-\tau)^{1-\alpha}} (t > a, \alpha > 0), \quad (7)$$

where $\Gamma(\alpha) = \int_0^{\infty} t^{\alpha-1} e^{-t} dt$ is the Gamma function. When α is an integer, the definition of fractional calculus and integer calculus is

$$I_{a+}^{\alpha} f(t) = \frac{1}{(n-1)!} \int_a^t \frac{f(\tau)d\tau}{(t-\tau)^{1-n}} (n \in N). \quad (8)$$

The fractional Riemann-Liouville definition has super-singularity which is inconvenient for engineering and physical modeling. An Italian geophysicist, Caputo, proposed a definition of weakly singular fractional differentials, for $0 < \alpha < 1$, which is expressed as

$$D_t^{\alpha} f(t) = \frac{1}{\Gamma(1-\alpha)} \int_a^t \frac{f'(\tau)d\tau}{(t-\tau)^{\alpha}} (t > a). \quad (9)$$

The fractional derivative adopts the form $(d^{\alpha}/dt^{\alpha})f(t)$ for practical applications.

3.3. Fractional Form of the Viscous Element. The Newton dashpot, when extended from the integer to fraction form, is known as the Abel dashpot (Figure 3). Its constitutive equation is stated as

$$\sigma(t) = \eta^{\alpha} \frac{d^{\alpha} \varepsilon_b}{d^{\alpha} t} \; 0 \le \alpha. \quad (10)$$

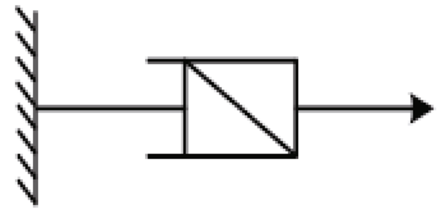

Figure 3: Abel dashpot.

Equation (10) may be rearranged as

$$\frac{d^{\alpha} \varepsilon}{d^{\alpha} t} = \frac{\sigma(t)}{\eta^{\alpha}}, \quad (11)$$

where ε is the strain on the viscous element and η is the viscous coefficient.

When $\sigma(t)$ is constant, i.e., the stress is unchanged, the two sides of equation (11) for the fractional integral can be written per the operator theory of fractional calculus of Riemann-Liouville as

$$J(t) = \frac{\varepsilon(t)}{\sigma} = \frac{1}{\eta^{\alpha}} \frac{t^{\alpha}}{\Gamma(1+\alpha)}. \quad (12)$$

Equation (12) may be converted to a dimensionless form, from which the strain curve of the fractional Abel dashpot can be obtained (Figure 4).

When $\alpha = 1$, the element represents an ideal fluid; when $\alpha = 0$, it represents ideal elasticity. The Abel dashpot can represent the properties of both solids and fluids and can hence be used to study the mechanical properties of rheological rock.

3.4. A Constitutive Model of Fractional Rheology. Figure 5 shows a fractional rheological model based on the Kelvin model:

This model is based on a three-parameter model in series, i.e., a fractional Kelvin model with Abel dashpots (Figure 5). The Kelvin model with an integer solution alone does not agree well with experimental data at the initial stage of creep, resulting in errors. After the introduction of fractional orders, the model was able to solve this problem well.

The total strain of the model can be expressed as follows:

$$\varepsilon = \varepsilon_0 + \varepsilon_1 + \varepsilon_2. \quad (13)$$

(1) Hooke's law for solids

$$\varepsilon_0(t) = \frac{\sigma}{k_0} \quad (14)$$

(2) Integer Kelvin model

$$\sigma = k_1 \varepsilon_1 + \eta \dot{\varepsilon}_1, \quad (15)$$

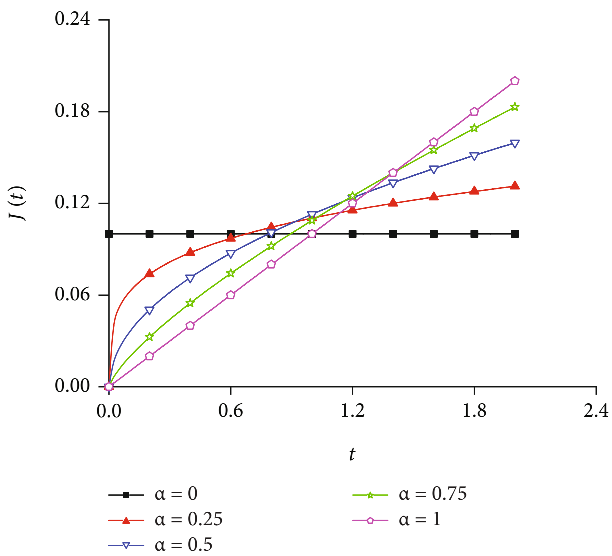

FIGURE 4: Strain characteristics of the Abel dashpot.

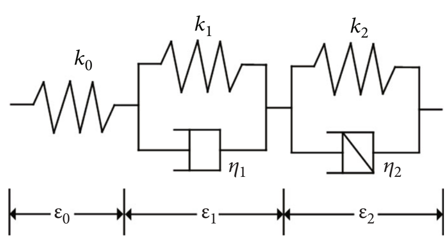

FIGURE 5: A fractional rheological model based on the Kelvin model.

$$\varepsilon_1(t) = \frac{\sigma}{k_1}\left(1 - e^{-tk_1/\eta_1}\right) \tag{16}$$

(3) Fractional Kelvin model

$$\sigma = k_2\varepsilon_2(t) + \eta\frac{d\varepsilon_2(t)}{dt} \tag{17}$$

According to the basic theory of fractional calculus, assume that $a = k_2/\eta_2$, $b = \sigma/\eta_2$. At $t = 0$, $\varepsilon_2 = 0$.

Equation (17) may then be written as follows:

$$\frac{d^\alpha\varepsilon_2(t)}{d^\alpha t} + a\varepsilon_2(t) = b. \tag{18}$$

Applying a Laplace transform to equation (18) yields

$$s^\alpha\varepsilon(s) + a\varepsilon(s) = \frac{b}{s}. \tag{19}$$

The following equation is then obtained:

$$\varepsilon(s) = \frac{b}{[s(s^\alpha + a)]}. \tag{20}$$

An inverse Laplace transform on equation (20) yields

$$\varepsilon_2(t) = b\int_0^t (t-s)^{\alpha-1}E_{\alpha,\alpha}[-a(t-s)^\alpha]\mathrm{d}s, \tag{21}$$

where $E_{\alpha,\beta}(z) = \sum_{n=0}^{\infty} z^n/\Gamma(n\alpha + \beta)$. Replacing a, b in equation (21), the following equation is then obtained:

$$\varepsilon_2(t) = \eta^{-1}\sum_{n=0}^{\infty}\frac{(-1)^n}{\Gamma(\alpha n + \alpha + 1)}\left[\eta\frac{t^\alpha}{k}\right]^{n+1}. \tag{22}$$

Considering the three-part strain, the constitutive equation of the fractional rheological model can be expressed as

$$\varepsilon(t) = \frac{\sigma}{k_0} + \frac{\sigma}{k_1}\left(1 - e^{-tk_1/\eta_1}\right) + \eta^{-1}\sum_{n=0}^{\infty}\frac{(-1)^n}{\Gamma(\alpha n + \alpha + 1)}\left[\eta\frac{t^\alpha}{k}\right]^{n+1}. \tag{23}$$

3.5. Analysis of the Experimental Results of Broken Mudstone Based on the New Fractional Rheological Model. To study the rheological characteristics of saturated broken mudstone and validate the accuracy of the new fractional rheological model, the 1stOpt mathematical software is applied to fit the parameters according to the data obtained from the experiment. The fitting effect is shown in Figure 6, based on the fractional rheological model (equation (23)).

It can be seen in Figure 6 that the fitting accuracy between the theoretical and experimental values is high. The fitting parameters are shown in Table 1.

Broken mudstone has remarkable creep characteristics, which can cause substantial changes in porosity and permeability. It is an important parameter that affects the safety of coal mining.

Porosity refers to the ratio of the pore volume and the total volume of the particles in the broken state:

$$n = \frac{V_s - V}{V_s}, \tag{24}$$

where n is the porosity; V is the particle volume of the broken rock sample; V_s is the total volume of the broken rock sample in the test. In this paper, the variation of the porosity of broken mudstone in a stable state of deformation for different levels of pressure is shown in Figure 7.

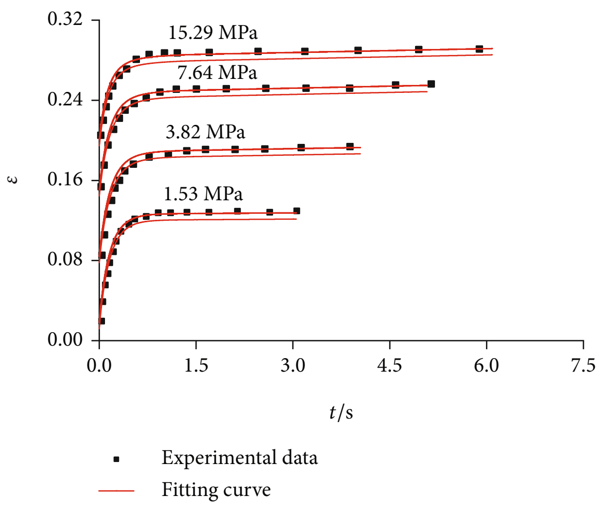

Figure 6: Rheological model fitting curve obtained from test results.

Table 1: Parameters of new fractional model.

Axial compression (MPa)	1.53	3.82	7.64	15.29
k_0 (MPa)	58.60	12.10	6.67	5.21
k_1 (MPa)	10.70	12.30	13.8	18.40
k_2 (MPa)	58.55	36.89	33.22	29.34
η_1 $(10^3\,\mathrm{s}\cdot\mathrm{MPa})$	1.80	2.08	2.20	2.40
η_2 $(10^3\,\mathrm{s}\cdot\mathrm{MPa})$	1.90	2.00	2.22	2.82
α	0.78	0.81	0.82	0.79

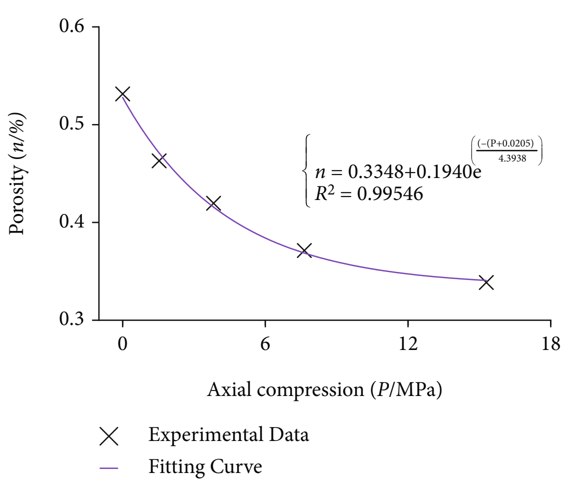

Figure 7: Porosity curve.

By fitting the data of steady-state porosity changes for different levels of pressure, the equation of the porosity curve is obtained as follows:

$$n = a \cdot e^{b \cdot P} + c, \tag{25}$$

Table 2: Water and sediment seepage test data of broken rock samples under different loads.

Stress level (MPa)	Initial porosity	v (mm/s)	m_1 (g)	m_2 (g)
1.53	0.263	4.69	42	112
3.82	0.296	4.71	65	111
7.64	0.331	4.78	106	109
15.29	0.374	4.96	161	103

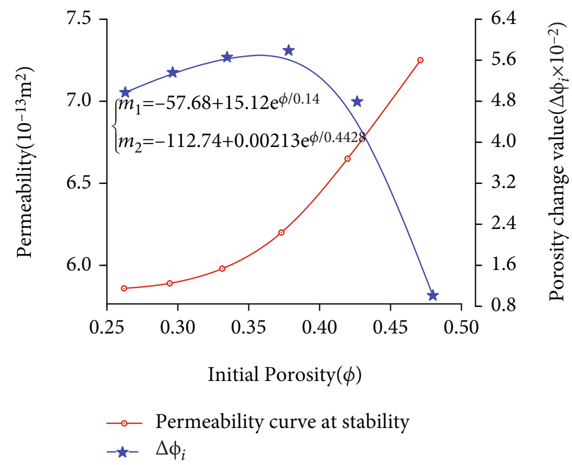

Figure 8: Relationship between initial porosity and seepage characteristics under axial loading.

where n is porosity; P is the axial pressure; parameters a, b, and c are constants, where $a = 0.193$, $b = -0.228$, and $c = 0.335$.

4. Water-Sand Seepage Characteristics of Fractured Rock due to Rheological Effects

The porous characteristics of a fractured rock skeleton are the basic factors that determine its permeability. According to the different heights, h_i, of the broken rock samples, the pump speed was adjusted and the water pressure P was changed to maintain the water pressure gradient Δp at 8×10^{-3} MPa/mm. The test data is shown in Table 2.

During the water and sediment seepage test, the porosity of broken rock changed due to filtration and the barrier effect of the broken rock skeleton. When the water and sediment seepage was stable, the masses of permeable sand particles (m_1) and filtered sand particles (m_2) were different for broken rock skeletons with different initial porosities. Figure 8 shows the relationship between the final porosity and permeability when the water-sand seepage was stable.

It can be seen in Figure 8 that water and sand seepage reduced the permeability of the fractured rock samples. When the initial porosity of the fractured rock was small, the change in porosity was large. In other words, sand particles may play a role in filling voids, thus reducing the possibility of a large-scale water inrush. When the initial porosity increased to a certain value, the porosity variation $\nabla\phi_i$ tended to be 0, the broken rock lost the ability to filter sand, and almost all sand particles exited the broken rock. Under these conditions, there was a great risk of water inrush and sand break.

When a steady seepage state was reached, the framework of the broken rock was filled with sand particles. It can be seen in Figure 8 that with an increase in initial porosity, the filtration quality of a broken rock sample decreased and the permeability increased. The relationship between the initial porosity and the quality of sand burst and filtration can be expressed by an exponential function (equation (26)):

$$\begin{aligned} m_1 &= -57.68 + 15.12 e^{\phi/0.14}, \\ m_2 &= -112.74 - 0.00213 e^{\phi/0.04428}. \end{aligned} \tag{26}$$

5. Conclusion

In this paper, an experimental study on the water-sand seepage characteristics of fractured rock under rheological action was conducted:

(1) Creep-time characteristic plots were obtained by conducting axial compression experiments on several groups of broken mudstone samples. During compaction of saturated broken rock samples, particle crushing and sliding deformations were encountered. During the compaction rheological process, the elastic modulus and viscosity coefficient of the samples changed continuously and the deformation characteristics were quite different from those of whole-rock compression. In this paper, a fractional-order parameter α was used to equivalently represent the continuous changes in the elastic modulus and viscosity coefficient. Based on fractional calculus and a three-parameter model, a fractional Kelvin model was connected in series with an Abel dashpot to form a new rheological model

(2) Creep data of broken mudstone under different pressures were obtained from axial compression tests of several groups of broken rock samples. The parameters of the new fractional rheological model were fitted using 1stOpt software, by inputting the creep parameters of broken mudstone samples under different pressures. Compared with the three-parameter model, the fitting accuracy of the fractional rheological model was higher. From the rheological data of broken mudstone samples, the values of the stable porosities of broken mudstone under various pressures were determined and the relationship between pressure and porosity was obtained by fitting the test data

(3) When the rheological tests of each group of broken rock were stable, a water pressure gradient of 8×10^{-3} MPa/mm was applied to the permeameter using a pump for each sample. The water-sand mixed fluid percolated through the broken rock samples, and the value of permeability obtained was $10^{-13}\,\mathrm{m}^2$. However, sand particles could not completely pass through the broken rock samples. Some sand particles were filtered and intercepted by broken rock and became part of the broken rock sample, thus changing its porosity and permeability. An exponential relationship between the initial porosity and the quality of sand burst and filtration was thereby obtained. This study guides the risk prediction and assessment of water and sand inrush in broken rock

Data Availability

The data used to support the findings of this study are included within the article.

Conflicts of Interest

The authors declare that they have no conflicts of interest.

Acknowledgments

This work was supported by the National Natural Science Foundation of China (nos. 51904113, U1803118, 51974296, and 51904112) and the 2019 Huaishang Talent Plan Program.

References

[1] H. Zhang, M. Tu, H. Cheng, and Y. Tang, “Breaking mechanism and control technology of sandstone straight roof in thin bedrock stope,” *International Journal of Mining Science and Technology*, vol. 30, no. 2, pp. 259–263, 2020.

[2] Y. Wang, F. Geng, S. Yang, H. Jing, and B. Meng, “Numerical simulation of particle migration from crushed sandstones during groundwater inrush,” *Journal of Hazardous Materials*, vol. 362, pp. 327–335, 2019.

[3] G. Zhang, Y. Jiao, H. Wang, Y. Cheng, and L. B. Chen, “On the mechanism of inrush hazards when Denghuozhai Tunnel passing through granite contact zone,” *Tunnelling and Underground Space Technology*, vol. 68, pp. 174–186, 2017.

[4] L. Huang, J. Ma, M. Lei, L. Liu, Y. Lin, and Z. Zhang, “Soil-water inrush induced shield tunnel lining damage and its stabilization: a case study,” *Tunnelling and Underground Space Technology*, vol. 97, p. 103290, 2020.

[5] G. Zhang, Y. Jiao, C. Ma, H. Wang, L. B. Chen, and Z. C. Tang, “Alteration characteristics of granite contact zone and treatment measures for inrush hazards during tunnel construction - a case study,” *Engineering Geology*, vol. 235, pp. 64–80, 2018.

[6] D. Zhang, X. Xie, M. Zhou, Z. K. Huang, and D. M. Zhang, “An incident of water and soil gushing in a metro tunnel due to high water pressure in sandy silt,” *Engineering Failure Analysis*, vol. 121, p. 105196, 2021.

[7] K. Xia, C. Chen, Y. Zheng et al., “Engineering geology and ground collapse mechanism in the Chengchao Iron-ore Mine in China,” *Engineering Geology*, vol. 249, pp. 129–147, 2019.

[8] G. Zhang, C. Wang, Y. Jiao, H. Wang, and L. B. Chen, “Deposits sources of inrush hazards for the Liangshan Tunnel passing through deeply buried granite,” *Tunnelling and Underground Space Technology*, vol. 92, p. 103058, 2019.

[9] L. Yu, C. Zhanqing, L. Shuncai, D. Feng, and Z. Lianying, “Experimental study on influence of the creeping of saturated

rock to mechanical properties [J]," *Mining Research & Development*, vol. 31, no. 6, pp. 51-52, 2011.

[10] M. Li, J. X. Zhang, X. X. Miao, and Y. L. Huang, "Strata movement under compaction of solid backfill body [J]," *Journal of China University of Mining & Technology*, vol. 43, no. 6, pp. 969–973, 2014.

[11] Y. Y. Wang, J. Qi, C. H. Yang, and J. Wei, "A study of nonlinear creep law in deep rocks [J]," *Rock and Soil Mechanics*, vol. 26, no. 1, pp. 117–121, 2005.

[12] Y. Xue, T. Teng, F. Dang, Z. Ma, S. Wang, and H. Xue, "Productivity analysis of fractured wells in reservoir of hydrogen and carbon based on dual-porosity medium model," *International Journal of Hydrogen Energy*, vol. 45, no. 39, pp. 20240–20249, 2020.

[13] Y. Xue, P. G. Ranjith, F. Dang et al., "Analysis of deformation, permeability and energy evolution characteristics of coal mass around borehole after excavation," *Natural Resources Research*, vol. 29, no. 5, pp. 3159–3177, 2020.

[14] G. He, E. Wang, and X. Liu, "Modified governing equation and numerical simulation of seepage flow in a single fracture with three-dimensional roughness," *Arabian Journal of Geosciences*, vol. 9, no. 1, 2016.

[15] X. Liu, S. Wang, S. Wang, and E. Wang, "Fluid-driven fractures in granular materials [J]," *Bulletin of Engineering Geology and the Environment*, vol. 77, pp. 621–636, 2015.

[16] X. L. Liu and S. Y. Wang, "Mine water inrush forecasting during the mining under waters [J]," *Disaster Advances*, vol. 5, no. 4, pp. 877–882, 2012.

[17] Y. L. Chen and R. Azzam, "Creep fracture of sandstones [J]," *Theoretical and Applied Fracture Mechanics*, vol. 47, no. 1, pp. 57–67, 2007.

[18] Y. Xin, M. Li, D. An, H. Ji, and J. Kang, "Experimental study on the instability mechanism of the major-defect fractured rock [J]," *Arabian Journal of Geosciences*, vol. 10, no. 14, pp. 1–12, 2017.

[19] O. Hamza and R. Stace, "Creep properties of intact and fractured muddy siltstone," *International Journal of Rock Mechanics and Mining Sciences*, vol. 106, pp. 109–116, 2018.

[20] F. Wu, H. Zhang, Q. Zou, C. Li, J. Chen, and R. Gao, "Visco-elastic-plastic damage creep model for salt rock based on fractional derivative theory," *Mechanics of Materials*, vol. 150, p. 103600, 2020.

[21] Z. Shen and Z. Kuizhi, "Back analysis of creep deformation of rockfill dams [J]," *Journal of Hydraulic Engineering*, vol. 6, pp. 1–6, 1998.

[22] Y. Xue, J. Liu, P. G. Ranjith, X. Liang, and S. Wang, "Investigation of the influence of gas fracturing on fracturing characteristics of coal mass and gas extraction efficiency based on a multi-physical field model," *Journal of Petroleum Science and Engineering*, vol. 206, p. 109018, 2021.

[23] L. Zhu, F. Dang, Y. Xue, K. Jiao, and W. Ding, "Multivariate analysis of effects of microencapsulated phase change materials on mechanical behaviors in light-weight aggregate concrete," *Journal of Building Engineering*, vol. 42, p. 102783, 2021.

[24] S. C. Li, Z. Q. Chen, X. X. Miao, and Y. Liu, "Experimental study on the properties of time-dependent deformation-seepage in water-saturated broken sandstone [J]," *Journal of Mining & Safety Engineering*, vol. 28, no. 4, pp. 542–547, 2011.

[25] L. Shuncai, C. Zhanqing, and Y. Liu, "Study on penetration features of coal rejects during constant load deformation test process [J]," *Coal Science and Technology*, vol. 41, no. 3, pp. 59–62, 2013.

[26] S. Wanghua, C. Guangtao, and Q. Dong, "Experimental research on critical percolation gradient of quicksand across overburden fissures due to coal mining near unconsolidated soil layers [J]," *Chinese Journal of Rock Mechanics and Engineering*, vol. 26, no. 10, pp. 2084–2091, 2007.

[27] R. Garra, F. Mainardi, and G. Spada, "A generalization of the Lomnitz logarithmic creep law via Hadamard fractional calculus [J]," *Chaos, Solitons & Fractals*, vol. 102, pp. 333–338, 2017.

[28] L. Zhuo and B. Xu, "Finite element method for viscoelastic fractional derivative model [J]," *Engineering Mechanics*, vol. 18, no. 3, pp. 40–44, 2001.

[29] Y. Feng, X. Yang, J. Liu, and Z. Q. Chen, "A new fractional Nishihara-type model with creep damage considering thermal effect," *Engineering Fracture Mechanics*, vol. 242, p. 107451, 2021.

[30] M. di Paola, L. Galuppi, and G. Royer Carfagni, "Fractional viscoelastic characterization of laminated glass beams under time- varying loading," *International Journal of Mechanical Sciences*, vol. 196, p. 106274, 2021.

[31] F. Wu, R. Gao, J. Liu, and C. Li, "New fractional variable-order creep model with short memory," *Applied Mathematics and Computation*, vol. 380, p. 125278, 2020.

[32] X. Xu and Z. Cui, "Investigation of a fractional derivative creep model of clay and its numerical implementation," *Computers and Geotechnics*, vol. 119, p. 103387, 2020.

[33] E. Kabwe, M. Karakus, and E. K. Chanda, "Creep constitutive model considering the overstress theory with an associative viscoplastic flow rule," *Computers and Geotechnics*, vol. 124, p. 103629, 2020.

[34] A. M. Lokoshchenko and L. V. Fomin, "Delayed fracture of plates under creep condition in unsteady complex stress state in the presence of aggressive medium," *Applied Mathematical Modelling*, vol. 60, pp. 478–489, 2018.

[35] T. Beda and Y. Chevalier, "New methods for identifying rheological parameter for fractional derivative modeling of viscoelastic behavior [J]," *Mechanics of Time-Dependent Materials*, vol. 8, no. 2, pp. 105–118, 2004.

Hindawi
Geofluids
Volume 2021, Article ID 1974451, 9 pages
https://doi.org/10.1155/2021/1974451

Research Article

Study of Tunnel-Face to Borehole ERI (TBERI) Measurement Configurations and Its Optimization

Wei Zhou,[1,2] Lichao Nie ,[1] Yongheng Zhang ,[1] Yonghao Pang,[1] Zhao Dong,[1] Zhimin An,[2] Zhengyu Liu ,[1] and Chuanyi Ma[3]

[1]*Geotechnical and Structural Engineering Research Center, Shandong University, Jinan 250061, China*
[2]*Shandong Transportation Planning and Design Institute Co., Ltd., Jinan 250031, China*
[3]*Shandong Hi-Speed Group Co., Ltd., Jinan 250104, China*

Correspondence should be addressed to Zhengyu Liu; liuzhengyu@sdu.edu.cn

Received 22 April 2021; Revised 12 July 2021; Accepted 10 August 2021; Published 19 August 2021

Academic Editor: Chuangzhou Wu

Most of the existing electrical-resistivity-based ahead prospecting methods in tunnel use only the tunnel cavity and tunnel face space to locate the water-bearing structures in front of the tunnel. However, due to the limitation of the narrow available space for arranging electrodes in tunnel, this kind of method is difficult to achieve more accurate image for water-bearing structures. The cross-hole electrical resistivity tomography (CHERT) and borehole-to-surface electrical resistivity tomography (BSERT) methods using borehole space have been proved effective means to achieve better images of deep anomalies on the surface. In this paper, the tunnel-face and borehole ERI (TBERI) method in tunnels was studied. To less affect the construction progress, the pole-pole configuration using a single borehole was studied in this paper. Moreover, the configuration is optimized based on the block weighted CR optimization strategy. After considering the data combination, an effective measurement configuration suitable for TBERI detection was formed. To accelerate calculation, some redundant data are removed from the obtained data after proposed block weighted optimization is conducted. By adopting the proposed configuration, the abnormal objects in the target area in the inversion are more accurate. The effectiveness of proposed configuration is verified by numerical simulation.

1. Introduction

In the past two decades, tunnel engineering has developed rapidly in the worldwide. Especially in Southwest China, a large number of roads, railways, and water diversion projects need to rely on tunnels to cross the complex terrains. However, disasters such as water inrush, collapse, and other geological disasters occurred during construction period would threat the construction progress even safety of the constructors. Geophysical prospecting method plays an important role in detecting anomalous bodies [1, 2]. In the field of water-conducting structure detection, the electrical resistivity (ER) method is widely applied because of its high sensitivity to water bodies [3–8]. However, conventional configuration which arrange electrodes on the surface is not close enough to the abnormal body located deep underground. Therefore, electrodes are then arranged in boreholes to obtain data containing more information of the abnormal body located deep underground, which is cross-hole or borehole-to-surface detection. This is an effective way to achieve fine detection of underground low-resistivity bodies [9, 10]. Similarly, for ahead prospecting methods conducting in tunnel environments, the space of ahead drilling borehole can also be used for borehole electrical resistivity (BER) detection.

At present, the cross-hole electrical resistivity tomography (CHERT) is a hot spot in engineering geophysical prospecting especially in the surface electrical detection. However, due to the narrow space in the tunnel, only one single borehole is often used. Therefore, the single-hole ER detection in the tunnel is the focus of our research. Recently, some scholars have conducted systematic research on the single borehole-to-surface ERT (BSERT) method in the surface detection situation. For example, Tsourlos et al. analyse the different types of BSERT configurations through the sensitivity distribution and the inversion result and conclude that the "in-hole data" is the main cause of symmetric artifacts [11]. They proposed solutions based on data deletion and weighted inversion and to a certain extent solved the problem of symmetric artifacts of the BSERT. Wang and Lin believe that the highly symmetrical distribution of sensitivity is the cause of symmetric artifacts [12]. The balance between detection resolution and the intensity of symmetric artifacts is a key issue in the selection of configurations. They optimized the data of the two configurations for joint inversion and used the weighted MOST method to improve the inversion results, effectively solving the problem of symmetric artifacts. Li et al. proposed the tunnel-face and borehole ERI (TBERI) configuration and applied in a subway tunnel engineering [13]. They proved the effectiveness of this method for detecting water bodies in front of the tunnel.

By adopting the TBERI configuration, more observed data can be obtained by increasing electrodes. However, due to the complex electromagnetic interference of the machine in the tunnel, the quality of the obtained data is uncertain. In order to solve similar problems in surface ERT, Wilkinson et al. proposed the Compare-R (CR) configuration optimization method based on the model resolution matrix of the data set in the surface ERT detection [14]. This optimization strategy can optimize the observation device based on the sensitivity matrix, which can reduce the number of electrodes and basically ensuring the overall quality of the data set, finally greatly reduce the amount of data. This method has been subsequently applied to a variety of electrical detection situations and has been further developed in the past decade [15, 16]. Wilkinson et al. improved the goodness function (GF) of CR method and realized adaptive optimized survey design by introducing block weighting [16]. Uhlemann et al. had made further improvements on this basis [17]. They introduced a weighting factor for electrode placement to achieve combined optimization of both measurement configuration and electrode placement.

In this paper, the optimization of measurement configuration of TBERI was studied. First, a measurement configuration of TBERI is proposed based on the application research of Li et al. [13]. Then, the TBERI measurement configuration is optimized based on the block weighted optimization method, and the optimized configuration is verified by one numerical simulation. Next, the optimization algorithm is introduced in the second chapter. Then, the results of block weighted optimization is shown in chapter 3 through the distribution image of the model resolution matrix. Finally, the effectiveness of the proposed method is verified by the inversion simulation results of the two anomalies.

2. Methodology

2.1. TBERI Measurement Configurations. TBERI is proposed to make full use of the tunnel face and forward drilling space. As shown in Figure 1(a), the size of the tunnel is assumed to be 9 m × 7 m with shape of horseshoe, and a 30 m long advance borehole was drilled in front of the tunnel face. Figure 1(b) shows the specific arrangement of electrodes on the tunnel face. The electrodes are divided into 7 rows; the spacing between each row is 1 m, and the distance between electrodes in the row is also 1 m. There is a 0.5 m gap between the electrode array and the upper and lower boundaries of the tunnel, and a total of 45 electrodes are arranged on the tunnel face. The electrodes in the borehole are arranged at equal intervals of 1 m, with a total of 30 electrodes.

It has to be noted that the pole-pole configuration was mainly discussed in this paper. Based on the configuration of A-M (A is located on the tunnel face, and M is located in the borehole) introduced by Wang and Lin [12], the AM configuration was additionally discussed (all electrodes are located in the borehole); these two kind of configurations are as shown in Figure 2. The A-M configuration can obtain 1,350 data, and the AM configuration can obtain a maximum of 435 data without considering the reciprocity of the electrodes. Combining the two pieces of data forms the basis for the next configuration optimization, the comprehensive data set $\mathbf{S_c}$. Although Tsourlos et al. have clearly pointed out that the in-hole data like AM configuration is not recommended [11], Wang and Lin believe that a balance should be struck between symmetric artifacts and resolution (however, they also exclude in-hole data) [12]. In the following content, the reason why we consider AM configuration will be explained.

Apparently, the AM configuration data is a kind of "in-hole data." This type of data has the typical characteristics of symmetrical distribution of sensitivity, which makes it difficult to perceive the orientation information of anomalies. This is also the cause of symmetrical artifacts. However, due to the full use of the drilling space, this type of data is sensitive to the depth information of the anomaly and is necessary for ensuring the deep detection capabilities of BSERT. Therefore, Wang and Lin recommended to combine different configuration data in order to improve the inversion result [12]. To verify the conclusion in tunnel environment, a numerical test is conducted. A $4 \times 4 \times 4\,\mathrm{m}^3$ block with resistivity of 10 Ω·m is assigned at a distance of 2 m from the borehole and 4.5 m from the tunnel face. Figure 3 shows the least-squares inversion results of different configurations (A-M or A-M + AM). It can be seen that although the addition of AM results in symmetry artifacts, the resistivity of the anomalies located deep in front of the tunnel face can be easily seen. Therefore, the AM configuration was considered to obtain a better inversion result.

2.2. Block Weighted CR Optimization Strategy. The optimization strategy will be briefly introduced in this part; detail content could refer to Tsourlos et al., Uhlemann et al., and Wilkinson et al. [11, 17, 18]. In the generalized inversion theory, the model resolution matrix $\mathbf{R}$ can be defined by the following formula [19]:

$$\mathbf{m}^{\mathrm{fit}} = \mathbf{R}\mathbf{m}^{\mathrm{true}}, \tag{1}$$

where the $\mathbf{m}^{\mathrm{fit}}$ and $\mathbf{m}^{\mathrm{true}}$ are simulated model and real model, respectively. The model resolution matrix quantifies the resolved degree of each grid. If each grid is perfectly resolved then $\mathbf{R} = \mathbf{I}$ [14]. For ease of calculation, after

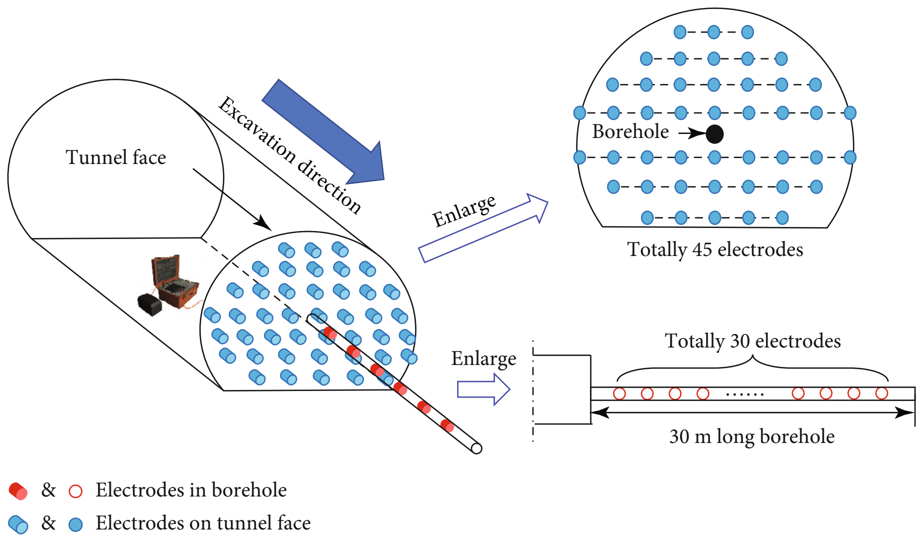

Figure 1: Sketch of TBERI electrode arrangement. (a) The three-dimensional overall diagram. (b) Electrode arrangement on the tunnel face. The electrodes arranged in rows as much as possible to cover the tunnel face. Totally 45 electrodes are placed in this case. (c) Electrode arrangement in the borehole. Generally, the electrodes in the borehole are arranged at equal intervals. Totally 30 electrodes are placed in this case.

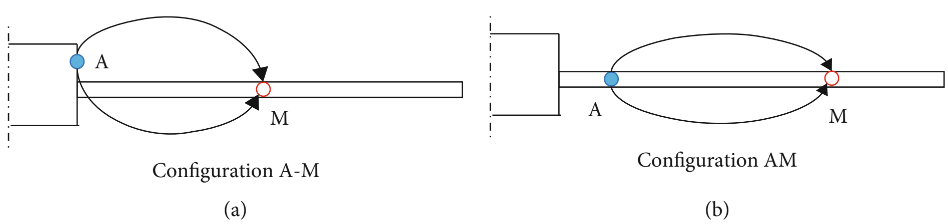

Figure 2: Sketch of two types of configurations. (a) A-M configuration. Electrode A is placed on the tunnel face while electrode M is placed in the borehole. (b) AM configuration. Both electrodes A and M are placed in the borehole.

linearization, **R** can be calculated by the following formula [20]:

$$\mathbf{R} = \left(\mathbf{J}^T\mathbf{J} + \mathbf{C}\right)^{-1}\mathbf{J}^T\mathbf{J}, \tag{2}$$

where J is Jacobian matrix and C is the regularization matrix [21]. The CR strategy is based on the calculation of **R**, selecting a subset $\mathbf{S_b}$ (the base set) from $\mathbf{S_c}$. Although $\mathbf{S_b}$ contains less data, its model resolution value is similar to $\mathbf{S_c}$. The complete flow chart of optimization progress is shown in Figure 3. In this progress, the goodness function (GF) is the key point to controlling the optimization process. It determines which data will eventually be selected into $\mathbf{S_b}$. The calculation formula of GF is as follows [14]:

$$\mathrm{GF} = \frac{1}{m}\sum_{j=1}^{m}\frac{R_{t,j}}{R_{b,j}}, \tag{3}$$

where $\mathbf{R_t}$ is the resolution of the base set plus the test configuration and $\mathbf{R_b}$ is the resolution of the base set. In each iteration of optimization, the single or multiple configurations with the highest GF value will be selected to be added to the base set. In order to add artificially controllable factors in the optimization process, Uhlemann et al. and Wilkinson et al. improved the calculation formula of GF [17, 18]:

$$\mathrm{GF} = \frac{1}{m{w_e}^{\beta}}\sum_{j=1}^{m}\frac{w_{t,j}\Delta R_{b,j}}{R_{c,j}}, \tag{4}$$

where w_t is the so called block weighting factor while ${w_e}^{\beta}$ is the weighting factor for electrode selection. In this paper, w_t was mainly considered because there is no need in this study to produce an "extremely focused" measurement configuration in TBERI. Therefore, β is set to 0, and ${w_e}^{\beta}$ will not work in the formula. In the subsequent numerical simulations, the depth range of the anomaly is assumed to be known based on the borehole information (for example, a low-resistivity body exists between 10 and 15 m). Based on this, the weighting factor w_t of the grid within the range of 10-15 m will be set to 1, while other grids will be set to 10^{-12}.

3. Numerical Simulations

3.1. Optimization Simulation. Firstly, an array optimization experiment was conducted, using the block weighted CR optimization strategy. A $15 \times 15 \times 30\,\mathrm{m}^3$ cube zone is

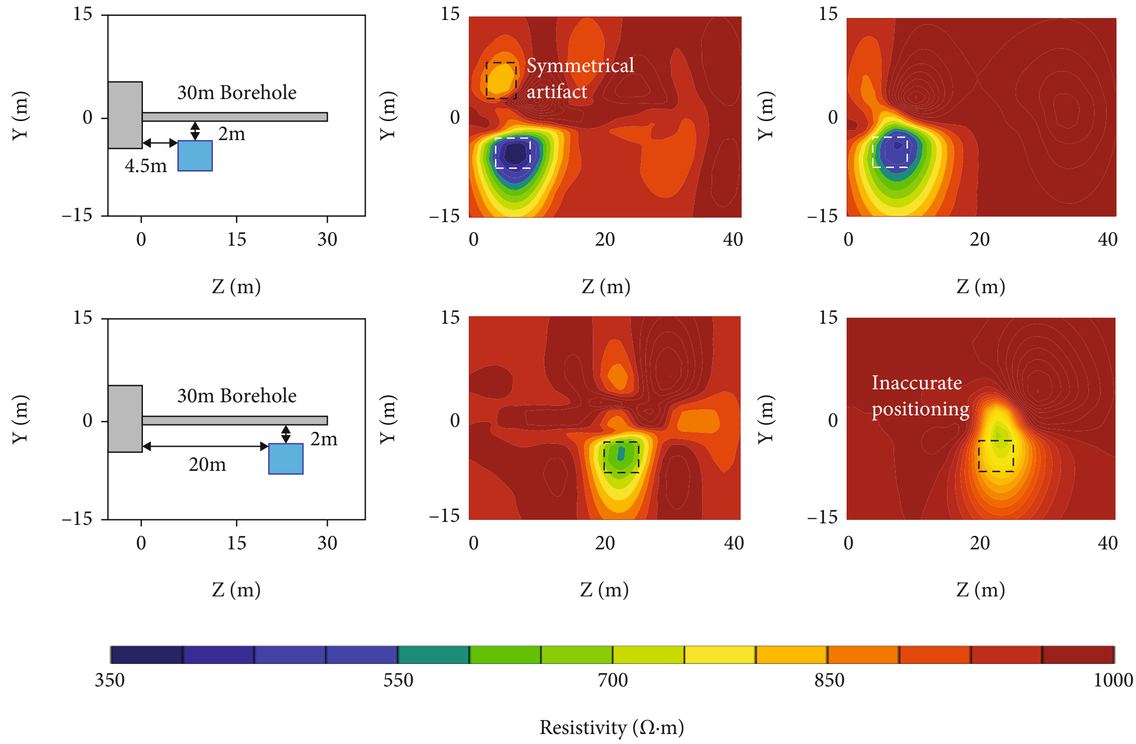

Figure 3: Inversion results of different configurations. (a, d) Schematic diagrams of low-resistivity anomaly models located at different depths; the background resistivity is 1000 Ω·m, and the anomaly resistivity is 10 Ω·m. (b, c) Inversion result of combined A-M + AM and single A-M for model in (a), respectively; the results are similar. However, there is a symmetrical artifact shown in (c). (e, f) Inversion result of combined A-M + AM and single A-M for model in (d), respectively. Obviously, for deep anomalies, the AM data can effectively improve the inversion result.

arranged in front of the tunnel face as the target as shown in Figure 4. The target zone is close to the borehole and the tunnel face. In the target zone, the weight factor w_t is set to 1, while the other zone is 10^{-12}. In this optimization, the comprehensive data set is the collection of all AM and A-M data. The electrode arrangement has been described in detail in Section 2.1. Under this electrode arrangement, the comprehensive data set could contain up to 1090 data. The initial data set is a set of data obtained by single data selected arbitrarily. After each optimization iteration is completed, 30 optimal data with the largest GF value will be added to the base set. The number of iterations is selected according to detecting requirement of the optimized configuration. In this paper, the optimization iteration process continues until there are more than 390 data in the base set.

Figures 5(a)–5(d) show the change process of the relative model resolution during the optimization iteration. Under the influence of the weighting factor in the GF formula, the optimization strategy tends to give priority to increasing the model resolution in the 0-15 m area in front of the tunnel face. It can be seen from the figure that the optimization strategy is to increase the model resolution of all grids in the range of 0-15 m overall, although half of the grids in this area have a weighting factor of 10^{-12}. For the area in 15 m to 30 m on the Z axis, the model resolution is obviously lower, which shows that the weighting factor plays a role in the optimization process. Figures 5(e) and 5(f) show the com-

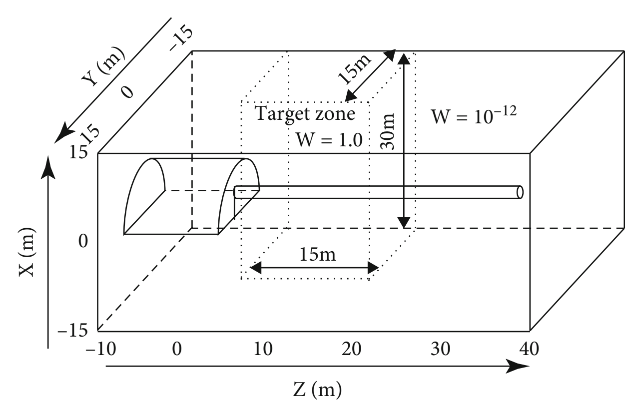

Figure 4: The three-dimensional schematic diagram of the TBERI model used in the optimization simulation. The cube marked with dotted line is the target zone, and the weighting factor inside is 1, while the factor of the other zone is 10^{-12}.

paration of the model resolution of the base set and comprehensive set. The model resolution of the base set is symmetrically distributed, and there is almost no asymmetric distribution although it has the difference in weight factors.

Figure 6 shows the value of the average relative model resolution during iteration. The solid purple line represents the change in the average relative model resolution in the

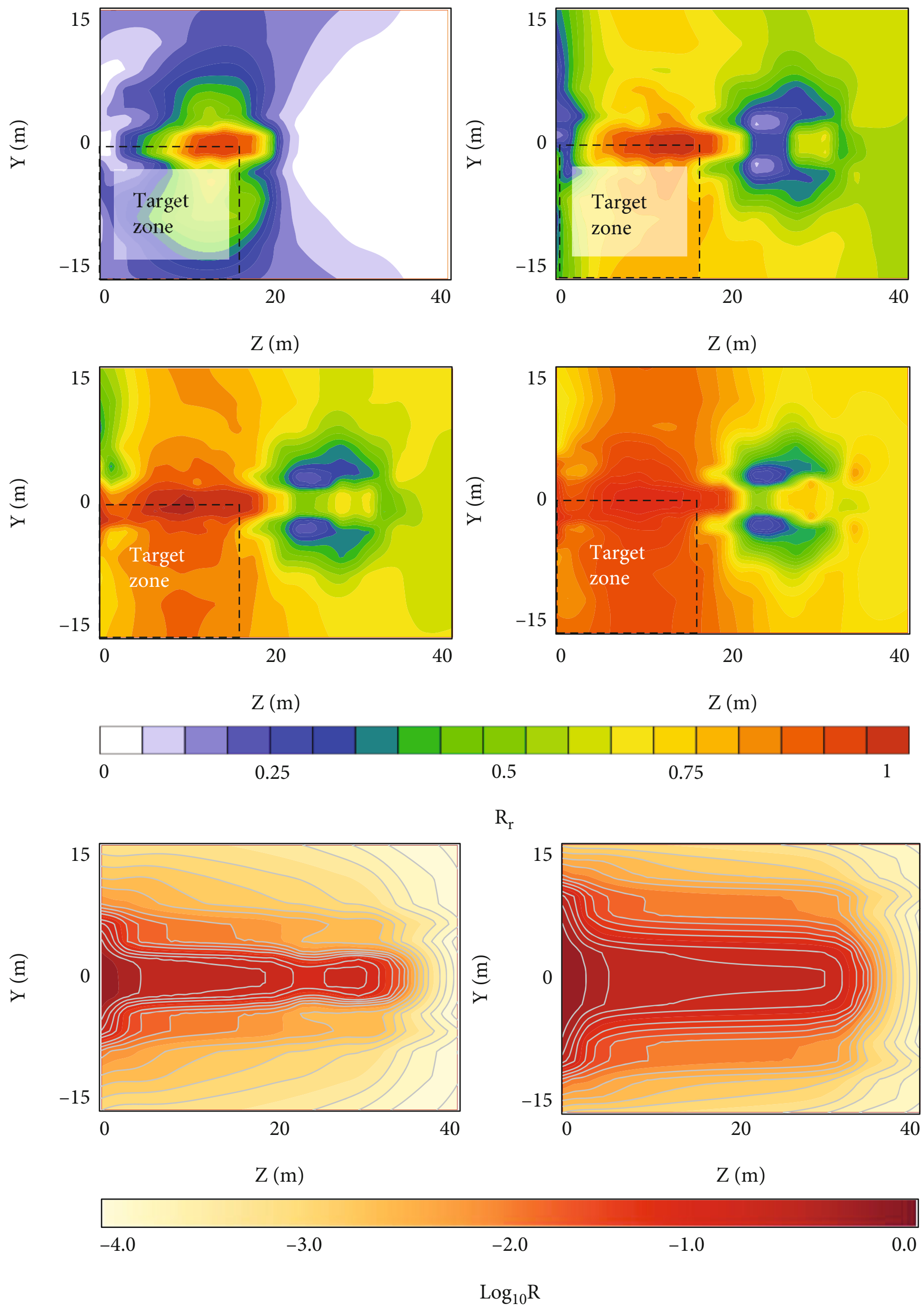

Figure 5: The relative model resolution distribution (a–d) of each stage of the optimization process and the model resolution comparison of the final result (e, f). (a–d) The relative model resolution distribution of the base set after 2, 6, 10, and 13 times optimization iteration. (e) The model resolution distribution of the base set after 13 times iteration. (f) The model resolution distribution of the comprehensive set.

target zone, and the red dotted line represents the change in the average relative model resolution in the whole zone. The average relative model resolution of the target zone is always greater than that of the whole zone. After 13 iterations, the average relative model resolution of the target zone reached about 0.85, while the whole area only reached about 0.7. This shows that the weighted optimization strategy can give priority to improving the model resolution of the target zone.

3.2. Inversion Simulation. In this section, three inversion simulations are calculated to compare the performance of the data set before and after optimization in the inversion. The first column of Figure 7 shows the model schematic diagrams of the three simulations. In the first simulation, a $4 \times 4 \times 4\,m^3$ block with resistivity of 10 Ω·m is assigned at a distance of 2 m from the borehole and 5 m from the tunnel face, and the low-resistance block is located in the target zone. In the second simulation, the low-resistance block of

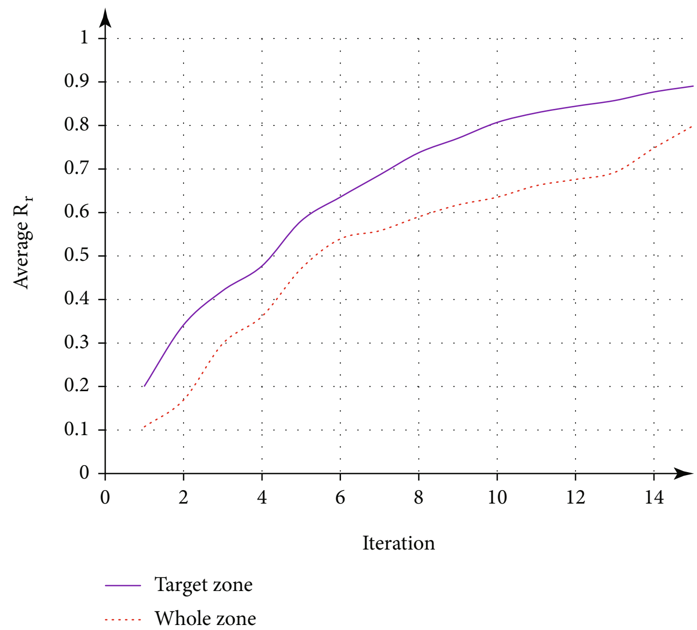

FIGURE 6: The curve of the average relative model resolution as the number of iterations increases. The solid purple line represents the change in the average relative model resolution in the target zone, and the red dotted line represents the change in the average relative model resolution in the whole zone.

the same size is set at a distance of 2 m from the borehole and 20 m from the tunnel face and is no longer in the target zone. In the third model, two low-resistance blocks were arranged inside and outside the target zone, and the size of the blocks is the same as the last two models. The resistivity of mentioned blocks above is 10 Ω·m, and the background resistivity is 1000 Ω·m. Three-dimensional least-squares inversion method with smooth constraints was used for inversion imaging. The forward simulation data used for inversion has been added with a certain degree of noise, and the noise application method can be referred to Bellmunt et al. [9]. The selection of noise-related parameters is related to Wang and Lin [12]. The iteration is terminated when the RMS value is less than 5%, and the number of iterations for each simulation is between 5 and 6 times. The second column is the inversion results using the comprehensive set, and the third column is the inversion results using the optimized measurement configuration. The centers of the low-resistance blocks are all located on the $X = 0$ m section, so the inversion results with the two-dimensional slice image of the $X = 0$ m section are also shown.

As shown in Figures 7(b) and 7(c), for the anomalous body located near to the tunnel face, the value of resistivity in the inversion result is more approach to the forward model. It is probably because the model resolution of the grid near to the tunnel face is higher than that of far grid. Because the optimized configuration uses less data than the original comprehensive configuration, some artifacts appear in the inversion results. Nevertheless, the resistivity value of the artifacts is much less than the anomalous bodies. Therefore, the optimized configuration is able to image the anomalous bodies. As shown in Figures 7(e) and 7(f), the location of the anomalous body is accurately imaged. As shown in Figures 7(h) and 7(i), both the anomalous bodies are imaged accurately. Similarly, the resistivity value of anomalous body near to the tunnel face is closer to the forward model than the farer one.

In the first simulation, the inversion results of the comprehensive set and the optimized data set are similar to each other, and both produce a certain degree of symmetrical artifact. In the second simulation, for the block located outside the target zone, the optimized data set showed a "blurred" imaging effect. In the third calculation example, when two blocks exist at the same time, the optimized data set can image the blocks in the target zone well but can only roughly image the block outside the target zone.

4. Discussions

Model resolution is one of the standard to evaluate the detecting ability of a configuration. Therefore, an optimization strategy could help select configuration pertinently. In the optimization simulation, selected one side of the borehole within the range of 0-15 m is selected as the target zone to get better inversion result within this area. In our thought, the distribution of resolution should be symmetrical because the model resolution on the side where the target zone is located is higher than the other side. However, the result obtained is an almost symmetrical model resolution distribution. We believe that this phenomenon is caused by the "in-hole data." As discussed by Tsourlos et al. and Wang and Lin [11, 12], the sensitivity of "in-hole data" is symmetrically distributed, and it has the same sensitivity to the grid at any angle around the borehole. Therefore, it is reasonable to speculate that the influence of "in-hole data" on the model resolution is also symmetric. Since we have considered

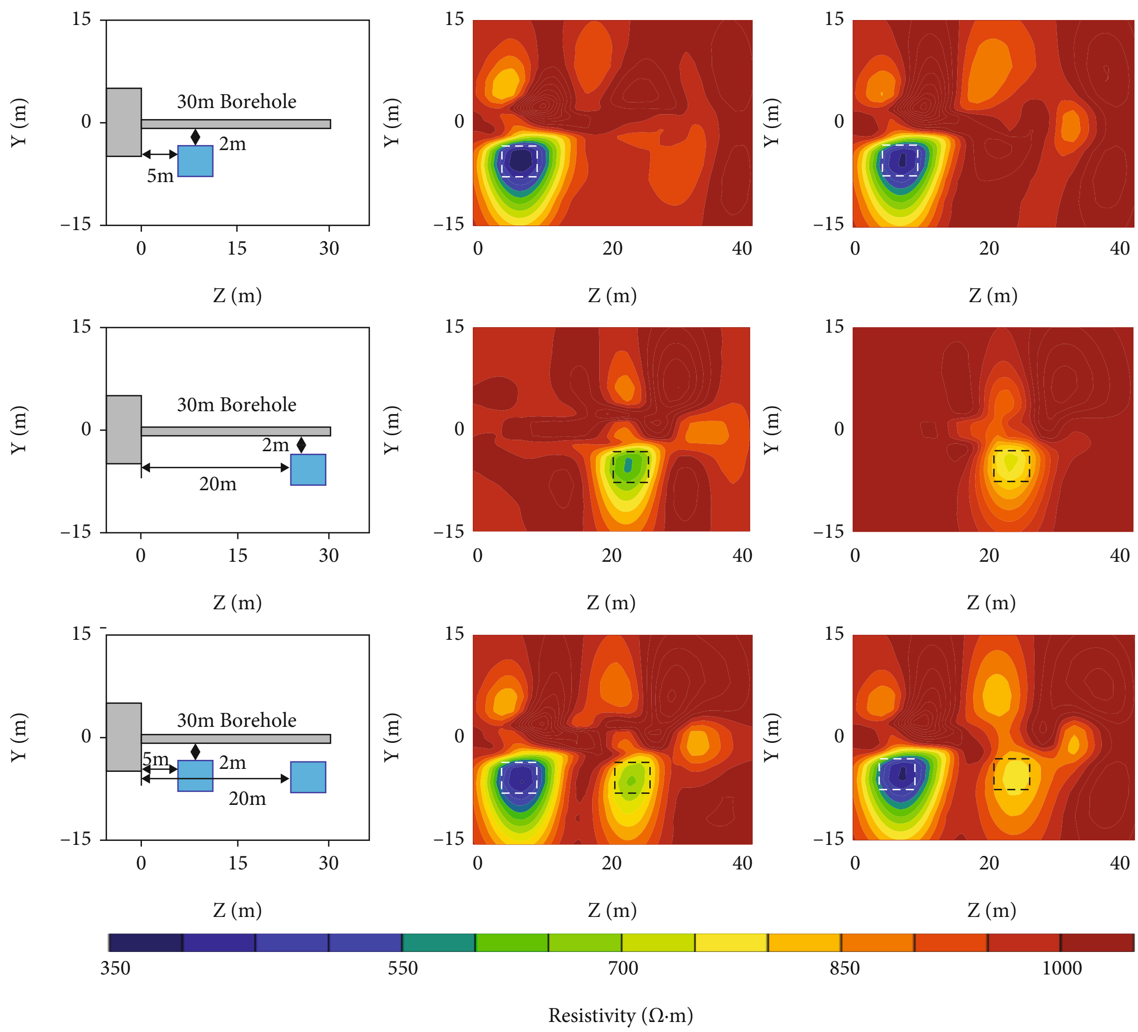

Figure 7: Two-dimensional slice map of inversion model and result. The first column is schematic diagrams of three inversion models, which are the model of low-resistance block inside the target area, the model of low-resistance block outside the target area, and the model of double low-resistance block. The second column is the inversion results using the comprehensive set, and the third column is the inversion results using the optimized measurement configuration.

"in-hole data" in the comprehensive set, these data will inevitably be selected into the base set during the optimization process. This results in a symmetrical distribution of the resolution of the optimized model. Although it is impossible to achieve accurate block weighting optimization in the range of 0-15 m, this algorithm still effectively distinguishes two regions in the depth direction. This is reflected in that the model resolution in the 0-15 m area is significantly higher than the 15-40 m area. At the same time, for specific engineering condition, the area of the target zone could be selected according to the demand.

The inversion result verifies the optimization effect. For anomalies in the target zone, the optimized data set basically retains the sensitivity to this zone, and the inversion results before and after optimization are basically the same. For anomalies after 15 m, due to the lower optimized model resolution of this zone, the inversion result of the optimized data set is obviously inferior to the inversion result of the comprehensive set. Through this optimization method of measurement configuration, we can greatly reduce the amount of data while preserving the model resolution of the target zone.

It has to be noted that the number of iterations is selected according to subjective demand. A method based on data set and resolution matrix should be proposed to the balance between calculation effectiveness and accuracy of the inversion result to evaluate the optimization progress objectively. The effectiveness of proposed strategy should be verified in field test.

5. Conclusions and Outlook

In this paper, a single-hole electrical resistivity detection method TBERI and two pole-pole configurations suitable for tunnels are proposed to obtain accurate inversion result. However, symmetrical artifacts appear in the inversion result of AM configuration. This confirms that the azimuthal information can only be retrieved by the potential electrodes arranged on tunnel face. Therefore, a comprehensive configuration including a single-hole electrical resistivity detection method TBERI and two pole-pole configurations is proposed. Then, block weighted CR optimization strategy is proposed to optimize the configuration for accurate and effective inversion. Based on the comprehensive set composed of A-M + AM configurations, about 60% of the data and achieved an average relative model resolution of 80% in the target zone are streamlined. Through three sets of inversion simulations, the effectiveness of this optimization method is verified: the imaging effect in the target zone is basically retained, while the imaging effect outside the target zone is weakened.

It has to be noted that only initially considered pole-pole configurations are considered in this paper. However, in the research of Wang and Lin [12], they have fully considered the tripole or quadrupole configurations. This will be what we will further study and discuss in TBERI in the future. In addition, this paper carried out a preliminary attempt on the pole-pole configuration of the measurement configuration optimization strategy and verified its effectiveness. In the follow-up study of the tripole or quadrupole configurations, as the amount of data will increase exponentially, it will be necessary to study its data reduction and optimization methods.

Data Availability

The data used to support the findings of this study are available from the corresponding author upon request.

Conflicts of Interest

The authors have no conflicts of interest to declare.

Authors' Contributions

Dr. Zhengyu Liu did the instruction and revision work of this paper. Mr. Wei Zhou and Mr. Lichao Nie completed the design of electrode arrangement and measurement configuration of the TBERI method in this paper. Mr. Yongheng Zhang carried out the work of writing this paper. Mr. Yonghao Pang and Mr. Zhao Dong carried out the block weighted optimization of the TBERI measurement configuration. Mr. Zhimin An and Mr. Chuanyi Ma carried out the calculation work of the numerical examples in this paper.

Acknowledgments

The research was supported by the Science & Technology Program of Department of Transport of Shandong Province (2019B47_2).

References

[1] S. Li, B. Liu, X. Xu et al., "An overview of ahead geological prospecting in tunneling," *Tunnelling and Underground Space Technology*, vol. 63, pp. 69–94, 2017.

[2] S. Li, R. Liu, Q. Zhang, and X. Zhang, "Protection against water or mud inrush in tunnels by grouting: a review," *Journal of Rock Mechanics and Geotechnical Engineering*, vol. 8, no. 5, pp. 753–766, 2016.

[3] S. Li, B. Liu, L. Nie et al., "Detecting and monitoring of water inrush in tunnels and coal mines using direct current resistivity method: a review," *Geotechnical Engineering*, vol. 7, no. 4, pp. 469–478, 2015.

[4] B. Liu, Q. Guo, S. Li et al., "Deep learning inversion of electrical resistivity data," *IEEE Transactions on Geoscience and Remote Sensing*, vol. 58, no. 8, pp. 5715–5728, 2020.

[5] Y. Pang, L. Nie, B. Liu, Z. Liu, and N. Wang, "Multiscale resistivity inversion based on convolutional wavelet transform," *Geophysical Journal International*, vol. 223, no. 1, pp. 132–143, 2020.

[6] M. H. Loke, J. E. Chambers, D. F. Rucker, O. Kuras, and P. B. Wilkinson, "Recent developments in the direct-current geoelectrical imaging method," *Journal of applied geophysics*, vol. 95, pp. 135–156, 2013.

[7] A. Revil, M. Karaoulis, T. Johnson, and A. Kemna, "Some low-frequency electrical methods for subsurface characterization and monitoring in hydrogeology," *Hydrogeology Journal*, vol. 20, no. 4, pp. 617–658, 2012.

[8] Y. Rubin and S. S. Hubbard, *Hydrogeophysics Vol 50*, Springer Science & Business Media, 2006.

[9] F. Bellmunt, A. Marcuello, J. Ledo, and P. Queralt, "Capability of cross-hole electrical configurations for monitoring rapid plume migration experiments," *Capability of cross-hole electrical configurations for monitoring rapid plume migration experiments*, vol. 124, pp. 73–82, 2016.

[10] K. Leontarakis and G. V. Apostolopoulos, "Laboratory study of the cross-hole resistivity tomography: the model stacking (MOST) technique," *Journal of Applied Geophysics*, vol. 80, pp. 67–82, 2012.

[11] P. Tsourlos, R. Ogilvy, C. Papazachos, and P. Meldrum, "Measurement and inversion schemes for single borehole-to-surface electrical resistivity tomography surveys," *Journal of Geophysics and Engineering*, vol. 8, no. 4, pp. 487–497, 2011.

[12] H. Wang and C.-P. Lin, "Cause and countermeasures for the symmetric effect in borehole-to-surface electrical resistivity tomography," *Journal of Applied Geophysics*, vol. 159, pp. 248–259, 2018.

[13] S. Li, S. Xu, L. Nie et al., "Assessment of electrical resistivity imaging for pre-tunneling geological characterization - a case study of the Qingdao R3 metro line tunnel," *Journal of Applied Geophysics*, vol. 153, pp. 38–46, 2018.

[14] P. B. Wilkinson, P. I. Meldrum, J. E. Chambers, O. Kuras, and R. D. Ogilvy, "Improved strategies for the automatic selection of optimized sets of electrical resistivity tomography measurement configurations," *Geophysical Journal International*, vol. 167, no. 3, pp. 1119–1126, 2006.

[15] F. M. Abdullah, M. H. Loke, M. Nawawi, and K. Abdullah, "Improving the resolution of 3-D resistivity surveys along the perimeter of a confined area using optimized arrays," *Pure and Applied Geophysics*, vol. 176, no. 4, pp. 1701–1715, 2019.

[16] P. B. Wilkinson, M. H. Loke, P. I. Meldrum et al., "Practical aspects of applied optimized survey design for electrical resistivity tomography," *Geophysical Journal International*, vol. 189, no. 1, pp. 428–440, 2012.

[17] S. Uhlemann, P. B. Wilkinson, H. Maurer, F. M. Wagner, T. C. Johnson, and J. E. Chambers, "Optimized survey design for electrical resistivity tomography: combined optimization of measurement configuration and electrode placement," *Geophysical Journal International*, vol. 214, no. 1, pp. 108–121, 2018.

[18] P. B. Wilkinson, S. Uhlemann, P. I. Meldrum et al., "Adaptive time-lapse optimized survey design for electrical resistivity tomography monitoring," *Geophysical Journal International*, vol. 203, no. 1, pp. 755–766, 2015.

[19] W. Menke, *Geophysical Data Analysis: Discrete Inverse Theory*, Academic press, 2018.

[20] M. H. Loke and R. D. Barker, "Least-squares deconvolution of apparent resistivity pseudosections," *GEOPHYSICS*, vol. 60, no. 6, pp. 1682–1690, 1995.

[21] M. H. Loke, I. Acworth, and T. Dahlin, "A comparison of smooth and blocky inversion methods in 2D electrical imaging surveys," *Exploration Geophysics*, vol. 34, no. 3, pp. 182–187, 2003.

Hindawi
Geofluids
Volume 2021, Article ID 5515052, 12 pages
https://doi.org/10.1155/2021/5515052

Research Article

Deformation Mechanism and Control of the Surrounding Rock during Gob-Side Entry Driving along Deeply Fully Mechanized Caving Island Working Face

Fei Liu [1] **and Yongsheng Han** [2]

[1] *School of Resources and Civil Engineering, Suzhou University, Suzhou, Anhui 234000, China*
[2] *Department of Water Resources Engineering, Shandong Water Conservancy Vocational College, Rizhao, Shandong 276826, China*

Correspondence should be addressed to Yongsheng Han; yongshenghan998@126.com

Received 24 February 2021; Accepted 30 July 2021; Published 19 August 2021

Academic Editor: Jia Liu

The deformation control of the surrounding rock during gob-side entry driving along deeply fully mechanized caving island working face is one of the main bottlenecks affecting the successful and efficient production in modern mining. The prior ordinary fully mechanized caving theories have been difficult in ensuring the safe and efficient mining along island working face during gob-side entry driving under the complex conditions in the west. Therefore, it is of great theoretical and practical significance to carry out the research on the deformation mechanism and control of the surrounding rock during gob-side entry driving along deeply fully mechanized caving island working face. This paper, by means of experimental research, theoretical analysis, numerical calculation, and field industrial test, systemically researched the deformation characteristics of the surrounding rock and the law of strata behaviors during gob-side entry driving along deeply fully mechanized caving island working face.

1. Introduction

Fully mechanized caving mining is an advanced coal mining method. Since it came out in the late 1950s, after decades of testing and application, it has been rapidly developed in nearly ten coal-producing countries [1] in the world. From the late 1970s to the early 1980s, fully mechanized caving mining became one of the main methods of mining high seams in France, Hungary, and the former Yugoslavia [2]. Fully mechanized caving mining technology [3–5], with its characteristics of low cost, low input, high yield, high efficiency, high benefit, safety and reliability, and simple system as well as its technical storage advantages has gradually replaced the slice longwall method and has become the main technical method to achieve high yield and high efficiency in mining high seams in China.

During fully mechanized caving mining, the backstopping roadway of the working face generally is developed along the coal seam floor. The roadway is a full coal road [6] whose roof and two sides are all coal. Setting coal pillars [7–10] has always been the traditional roadway protection method in coal mines. The traditional method of setting coal pillars is to set a coal pillar with a certain width between the transportation roadway in the upper section and the ventilation roadway in the lower section, so that the roadway in the lower section can avoid the fixed peak area of abutment pressure. The drifting and application of double transportation roadways in sections is simple in technical management, which is beneficial to ventilation, transportation, drainage, and safety [11]. However, the coal pillar loss is as high as 10%~30%; in addition, influenced by secondary mining [12, 13] of the ventilation roadway, it is difficult to maintain the roadway and the supporting cost is high. The propagation of abutment pressure from the coal pillar to the floor not only affects the mining of the adjacent coal seam and the stability of the floor roadway but also becomes a hidden trouble that causes strong strata behaviors. In order to improve the recovery rate of coals during fully mechanized caving mining, domestic scholars put forward a method, namely, setting narrow coal pillars in the backstopping roadway at the gob side during gob-side entry driving [14–19], and the coal pillar width is generally between 4and 7 m. Due to the increase of mining depth year by year, it is more and more difficult to maintain the roadway at the gob side during fully mechanized caving mining, which restricts the developing speed of a fully mechanized caving face and seriously affects the construction of a high-yield and efficient working face.

The coal pillar width is closely related to the strata behaviors [20] of the coal pillar, backstopping roadway support, maintenance cost, safe mining at the working face, and coal resource recovery rate. At present, some coal mines in China still rely on experience to determine the coal pillar width [21, 22], which lacks scientificity and pertinence. How to give consideration to resource recovery rate and the prevention of large deformation of the coal pillar and how to reasonably determine the coal pillar width has become a research topic for many scholars. Influenced by geological conditions, mining successions, and other factors [23], some mines adopt island working face mining in the mining process. However, compared with the nonisland working face, the law of overlying strata activity of the stope is very intense, the stress concentration degree is high [24, 25], and the strata behavior pressure is high. Therefore, it is of great theoretical significance and practical application value to carry out the research on the deformation mechanism and control of the surrounding rock during gob-side entry driving along the deeply fully mechanized caving island working face. Statistics of the roof fall accidents from year 2001 to 2013 is shown in Table 1.

Table 1: Statistics of the roof fall accidents from year 2001 to 2013.

Year	Number of roof fall events	Deaths
2001	267	380
2002	771	913
2003	1036	1239
2004	787	988
2005	749	913
2006	103	218
2007	36	144
2008	19	85
2009	14	43
2010	16	57
2011	15	64
2012	13	58
2013	9	21
Total	3835	5123

2. Engineering Geological Conditions

The experimental mine is located in Shaanxi province (Figure 1). The coal seam in the working face of the test area is stable, and the thickness of the coal seam is 7.2~8.46 m, with an average thickness of 7.83 m. The coal seam is nearly horizontal, and the dip angle is between 2° and 4°, with an average of about 3° coal seam with gangue 1~5 layers, thickness 0.20 m~2.10 m, average 1.15 m, and coal seam structure of 0.80 (0.20), 0.50 (0.30), 0.80 (0.70), 1.90 (0.30), and 5.60. Through the actual exposure of three main roadways and two roadways in the working face of 42 panels, the geological structure of the working face is simple, and no large structure is found. It is expected that there is no large geological structure in the process of mining. The roof lithology of the coal seam is mainly gray medium-grained feldspar quartz sandstone, followed by gray-black, dark gray siltstone, and fine sandstone interbeds. The floor is mainly gray miscellaneous carbonaceous mudstone, with a small amount of gray-white argillaceous sandstone. Detailed lithological descriptions of the rock strata are illustrated in Figure 2.

It can be seen from the experimental results (Figure 3 and Table 2) that the local surrounding rock components of roadway mainly include illite/montmorillonite mixed layer, quartz, calcite, kaolinite, siderite, and dolomite. Kaolin, illite, and montmorillonite are clay argillaceous expansive rocks with strong hydrophilicity and swelling in water. The fracture joints in the local surrounding rock of the roadway in the northern wing strata are developed, and the roadway is seriously flooded. Water is easy to enter the surrounding rock. The kaolinite and illite are softened, broken, and disintegrated when encountering water, while the montmorillonite expands when encountering water and then softens and loosens.

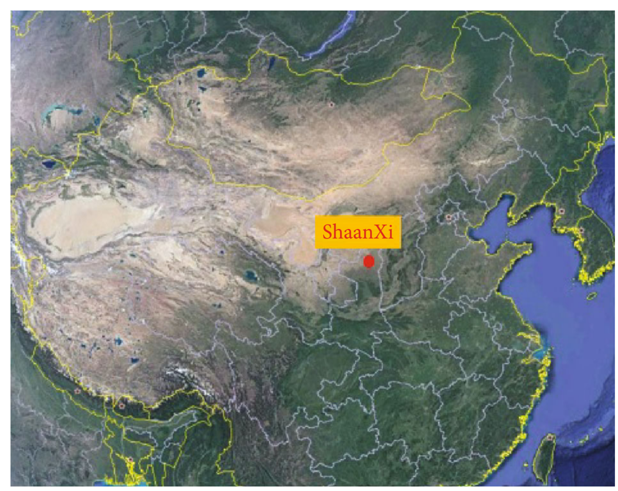

Figure 1: Location of the experimental mine, Shaanxi, China.

3. Theoretical Calculation of Narrow Coal Pillar Width along Goaf Roadway

Reasonable selection of the narrow coal pillar width in the roadway along the goaf is one of the key links in roadway excavation and support technology. A large or small coal pillar size is not conducive to roadway surrounding rock support and maintenance. According to the roadway protection mechanism of the narrow coal pillar along the goaf, the coal pillar is as small as possible under the premise of considering the improvement of the anchor force and support effect.

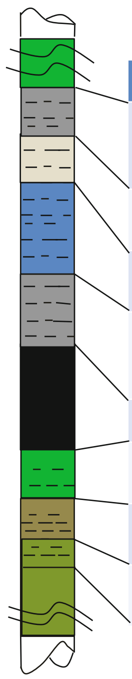

Thickness (m)	Lithology	Lithology description
4.33	Interbedding of siltstone and fine sandstone	Greyish black, dark grey oblique bedding and oblique wavy bedding
3.96	Siltstone and fine sandstone	Grayish white, grayish black, oblique wavy bedding
6.29	Medium sandstone	Gray white, composed of mica and quartz, argillaceous cementation
4.00	Siltstone	Dark gray, black gray, banded, microwave bedding
7.83	Coal	Black block
1.93	Fine sandstone	Dark gray, grayish brown, horizontal bedding
1.40	Carbonaceous mudstone	Black massive, intercalated with thin coal and sandy mudstone
1.00	Siltstone	Black, brownish black, horizontal bedding

Figure 2: Stratigraphic column and geological description.

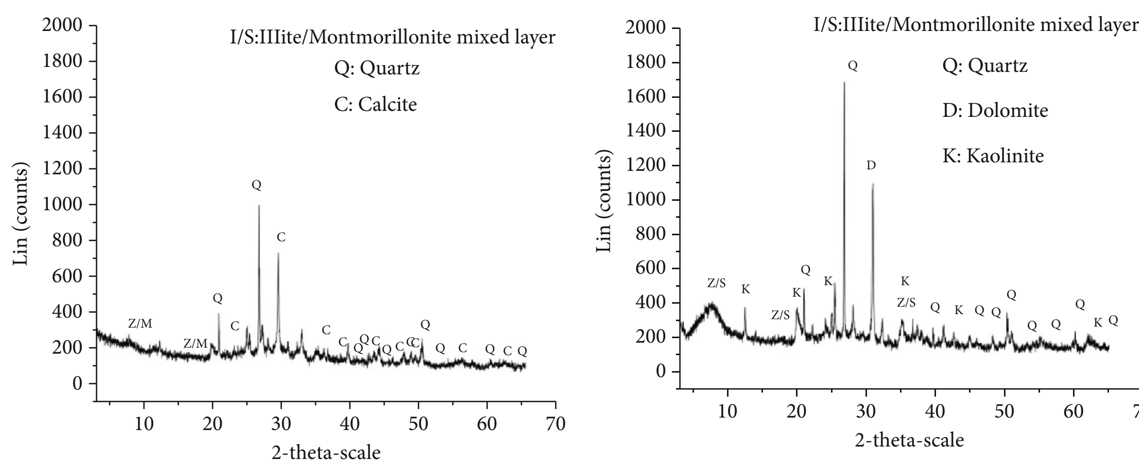

(a) #1 sample

(b) #4 sample

Figure 3: X-ray diffraction pattern.

According to the limit equilibrium theory [26] of coal pillar stability,

$$B = X_1 + X_2 + X_3, \tag{1}$$

where X_1 is the width of plastic zone generated in the coal body at the goaf side after the mining of the upper working face, and its value is calculated according to the following formula:

$$X_1 = \frac{mA}{2tg\varphi_0} \ln \left| \frac{k\gamma H + C_0/tg\varphi_0}{C_0/tg\varphi_0 + P_z/A} \right|, \tag{2}$$

where B is the coal pillar width; m is the height of roadway, 4.6 m; A is the coefficient of the horizontal pressure, 0.85; φ_0 is the internal friction angle of the coal seam interface, 30°; C_0 is the cohesive force of the coal seam interface, 5 MPa; k is the stress concentration factor, 3; γ is the average bulk density of overlying strata, 25 kN/m^3; H is the depth of the roadway, average 491 m, 500 m in the calculation; P_z is the support resistance of the anchor bolt to the coal side, 0.08 MPa; X_2 is the effective length of the anchor, 2.5 m; X_3 is the enrichment of the coal pillar width considering the large thickness of the coal seam and is generally calculated by 15~35% of the $X_1 + X_2$ value.

Substituting the mechanical parameters of the roadway surrounding rock and the assumed supporting parameters into the above formula, the theoretical value of the width of the narrow coal pillar along the goaf can be obtained, and the final calculated coal pillar width is 13.9-15.7 m. The

Table 2: Experimental results of X-ray diffraction.

Sample number	#1	#2	#3	#4	#5
Main components	I/S, Q, C	I/S, Q, K, S	Q, K, D, S	I/S, Q, D, K	Q, S, K

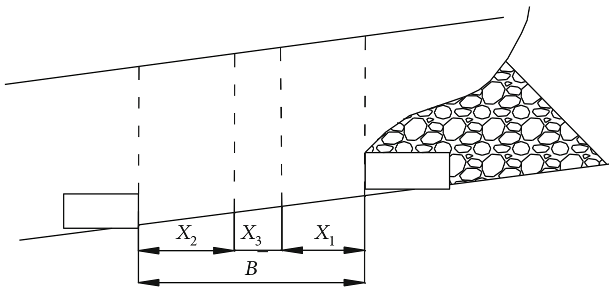

Figure 4: Calculation model of theoretical coal pillar width.

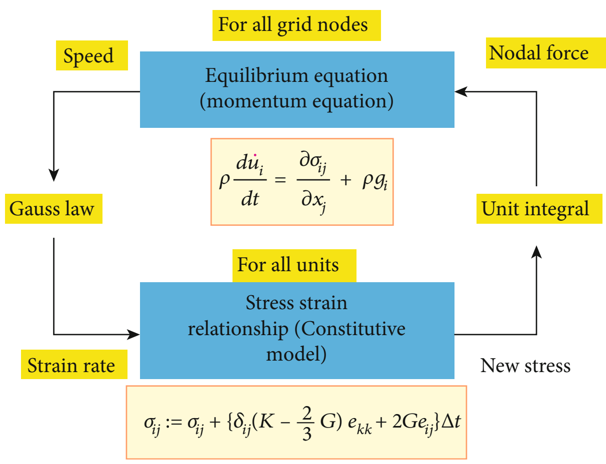

Figure 5: Solving process of FLAC^{3D}.

calculation model of theoretical coal pillar width is shown in Figure 4.

4. Finite Element Method Simulation

4.1. 3-D Fast Lagrangian Method. The 3-D fast Lagrangian method is a numerical analysis method based on the 3-D explicit finite difference method, which can simulate the 3-D mechanical behavior of rock and soil or other materials. 3-D fast Lagrangian analysis adopted the explicit finite difference scheme to solve the governing differential equation of the field and applied a mixed-unit discrete model to accurately simulate the yield, plastic flow, softening, and large deformation of materials. It had its unique advantages especially in the elastic-plastic analysis and large deformation analysis of materials, construction process stimulation, and other fields. The solving process of FLAC^{3D} is shown in Figure 5.

4.2. Establishment of Mechanical Calculation Model. The coal pillar width between the 4204 working face and the 4208 working face was 246~248 m. After roadway driving, the stress of the roof and the floor was redistributed, and the surrounding rock was deformed, moved, and even damaged.

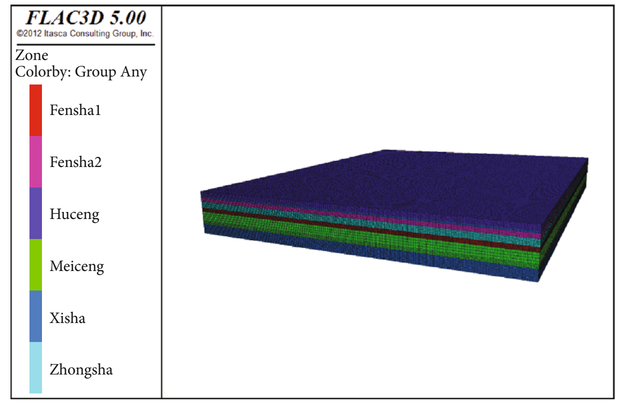

Figure 6: Initial model.

However, the range of the influence on the surrounding rock after roadway driving was definite, and the stress change could be ignored at a distance away from the roadway. Therefore, the sizes of the model of the 4206 island working face, the transportation roadway, and the ventilation roadway were designed as follows: length × width × height = 800 × 300 × 40 m, as shown in Figure 6.

Displacement boundary conditions of the model: rolling support was adopted in the X direction to limit the displacement in the X direction; rolling support was adopted in the Y direction to limit the displacement in the Y direction; displacement boundary was adopted at the bottom boundary of the model to limit the displacement in the Z direction; and the free boundary was adopted at the upper boundary of the model to apply vertical stress. The specific boundary conditions of the numerical model are shown in Figure 7.

4.3. Numerical Simulation Scheme Calculation. The displacement of the roof and floor of the transportation roadway and the stress state of the surrounding rock mass in the 4206 island working face in different support parameters were studied. According to the theoretical calculation results, the following three supporting schemes were selected for optimization. The simulation scheme is shown in Table 3.

5. Numerical Result Analysis

5.1. Stress Distribution Characteristics of the Surrounding Rock along the Island Working Face. From the perspective of safety, the narrow coal pillar was set in the stress-relaxed area or the original rock stress area as much as possible during gob-side entry driving. Therefore, the coal pillar width left in the two roadways along the 4206 working face should be larger than the range of the stress-relaxed area.

When backstopping the 4204 working face and the 4208 working face, with the development of the working face, the first weighting of the main roof formed an "O-X" fracture; the periodic weighting formed an arc triangle block at the

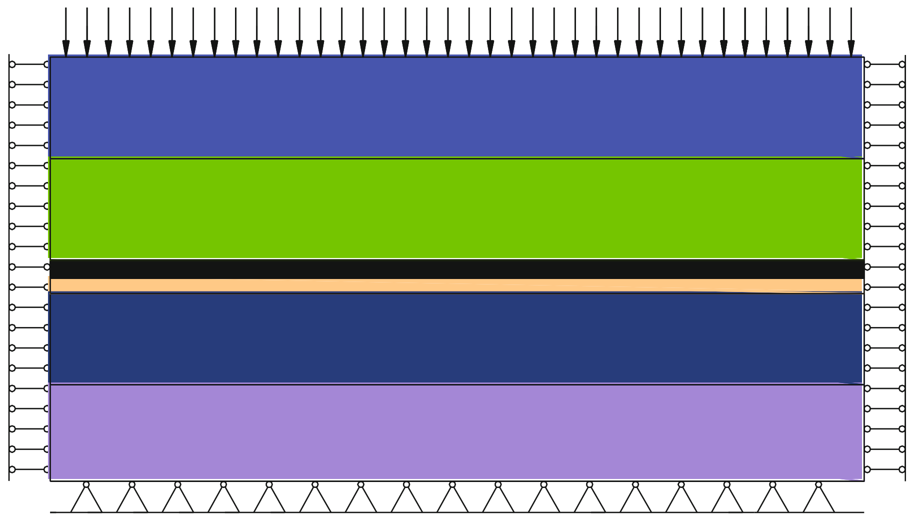

Figure 7: Boundary setting of numerical calculation model for gob-side entry driving in fully mechanized top coal caving face.

Table 3: Supporting scheme.

	Bolt	Anchor cable	Spacing between bolts	Spacing between anchor cables	Preload (moment)	Material
Scheme I	Roof: $\Phi 20 \times 2500$ Side: $\Phi 20 \times 2500$	Roof: $\Phi 21.8 \times 9600$ Side: $\Phi 21.8 \times 6500$	Roof: 800×800 Side: 800×800	Roof: 1600×800 Side : row spacing 800	Bolt: 300 N·m Anchor cable: 210 kN	Bolt: screw thread steel anchor cable: steel strand
Scheme II	Roof: $\Phi 20 \times 2500$ Side: $\Phi 20 \times 2500$	Roof: $\Phi 21.8 \times 9600$ Side: $\Phi 21.8 \times 6500$	Roof: 800×700 Side: 800×700	Roof: 1600×700 Side : row spacing 700	Bolt: 300 N·m Anchor cable: 210 kN	Bolt: screw thread steel anchor cable: steel strand
Scheme III	Roof: $\Phi 20 \times 2500$ Side: $\Phi 20 \times 2500$	Roof: $\Phi 21.8 \times 9600$ Side: $\Phi 21.8 \times 6500$	Roof: 700×700 Side: 700×700	Roof: 1600×700 Side : row spacing 700	Bolt: 300 N·m Anchor cable: 210 kN	Bolt: screw thread steel anchor cable: steel strand

end of the working face, which formed lateral abutment pressure along the 4206 island working face and directly influenced the stability of the set coal pillars during gob-side entry driving. The distribution of the lateral abutment pressure is shown in Figure 8.

A monitoring point was set up every 1 m from the edge of the gob, to monitor the vertical stress in the coal seam and determine the range of the stress-relaxed area and the stress-increased area. The monitoring data are shown in Table 4.

As can be seen from Figure 9, near the edge of the gob, due to the gob near the working face, the coal changed from the 3-D stress state to the 2-D stress state, and the stress inside the coal could be released to the gob. The closer it was to the gob, the more obviously the stress was released, so that the stress-relaxed area was formed at the edge of the gob; at the same time, the roof was broken at the edge of the gob, forming an arc triangular block. This structure caused pressure on the coal and formed stress concentration in front of the stress-relaxed area. That was the stress-increased area. For safety's sake and to reduce the deformation of the coal pillar, the stress-increased area was avoided when setting the coal pillar. As the position advanced forward into the coal, the influence of the stress release at the edge of gob and the bearing pressure of the arc triangle block on the original rock stress inside the coal became less. When the distance advanced forward enough, the surrounding rock stress returned to be the original rock stress. That was original rock stress area.

It can be seen from the curve that the stress-relaxed area was located 0 to 3 m from the edge of the gob and that the stress-increased area was located 3 to 25 m from the edge of the gob. The minimum vertical stress appeared at 1 m away from the gob, and the vertical stress concentration coefficient was 0.47. The maximum vertical stress appeared at 7 m away from the gob, and the vertical stress coefficient was 2.49; between 3 and 7 m, the vertical stress gradually rose at a faster rate, so it was not suitable to set the coal pillar. When it was 15 m, the vertical stress was 16.9 MPa and the vertical stress coefficient was 1.24, which was 124% of the original rock stress. The minimum vertical stress appeared at 25 m, and the vertical stress concentration coefficient was 1.

5.2. Optimization of Coal Pillar Size at the Island Working Face. In the theoretical calculation, the reasonable range of the width between two coal pillars in the roadway was 13.9~15.7 m, and the width of 12 to 16 m between two coal pillars was considered in the numerical calculation model. Theoretically, after the overlying strata of the gob at 4204 and 4208 working faces became stabilized, the distribution

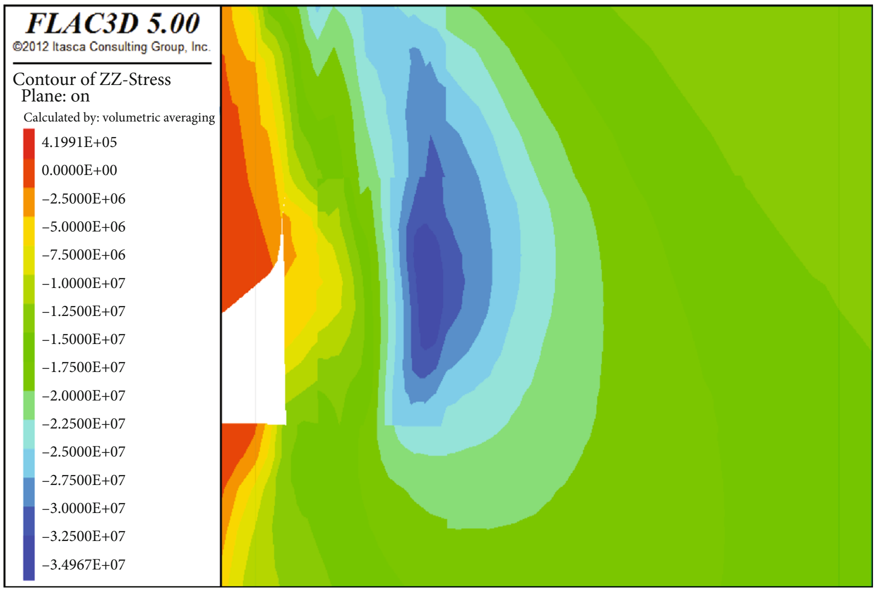

Figure 8: Lateral abutment pressure distribution of 4206 island working face.

Table 4: Monitoring table of vertical stress.

Monitoring point	Vertical stress (MPa)	Vertical stress concentration factor	Monitoring point	Vertical stress (MPa)	Vertical stress concentration factor
1	6.4	0.47	14	18.2	1.34
2	9.0	0.66	15	16.9	1.24
3	12.6	0.93	16	16.3	1.20
4	19.8	1.46	17	15.9	1.17
5	28.5	2.10	18	15.5	1.14
6	33.3	2.45	19	15.5	1.14
7	33.9	2.49	20	14.7	1.08
8	29.8	2.19	21	14.6	1.07
9	26.1	1.92	22	14.3	1.05
10	23.5	1.73	23	14.3	1.05
11	21.4	1.57	24	14.0	1.03
12	19.9	1.46	25	13.6	1.00
13	18.7	1.38			

of the surrounding rock stress and the coal pillar stress in the two roadways at the 4206 working face was the same. However, considering that the cross-section size of the transportation roadway was larger than that of the ventilation roadway (the curved cross-section of the transportation roadway was 5800 (width) × 4600 mm (medium height); the arc cross-section of the ventilation roadway was 5200 (width) × 3700 mm (medium height)), the surrounding rock stability of the transportation roadway and its influence on the coal pillar were greater than that of the ventilation roadway. Therefore, taking the coal pillar width in the transportation roadway as an example, the simulation research was carried out to select a reasonable coal pillar width. According to the simulation results, the vertical stress inside the coal pillar at 40 m behind the working face was largest, and the plastic zone was most completely developed. Considering that there was no air leakage among the 4206, 4204, and 4208 gob, the coal pillar in the gob shall not be permeated by cracks and still had a certain bearing capacity. When the coal pillar in the gob could ensure no air leakage and had a certain bearing capacity, the coal pillar during the driving period and the coal pillar in front of the working face during the backstopping period could also ensure no air leakage and have a bearing capacity. Therefore, taking the state of the coal pillar at the working face during the driving and backstopping period and that of the coal pillar 40 m from the back of the gob as the basis for comparison, we, respectively, compared the distribution of stress, deformation, and plastic zone of the coal pillars when the width was 12, 13, 14, 15, and 16 m, to determine the reasonable range of the coal pillar width.

5.2.1. During the Driving Period of the Roadway. The coal pillar stress and roadway deformation state during the driving period of the roadway are shown in Figure 10.

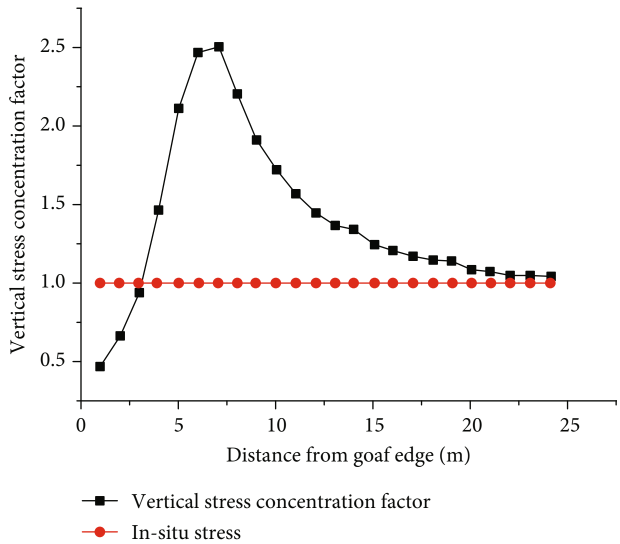

Figure 9: Lateral abutment pressure distribution curve of 4206 island working face.

It can be seen from the curve trend that as the coal pillar width increased between 12 and 15 m, the maximum vertical stress inside the coal pillar decreased. When the coal pillar width was small, the coal pillar was influenced by the abutment pressure of the roof, the bearing area was small, and the stress value was relatively large. As the coal pillar width increased continuously between 15 and 16 m, the maximum vertical stress inside the coal pillar continued to decrease, but the decreasing speed was slow. Therefore, it is not recommended to set the coal pillar at 16 m.

Although the maximum vertical stress inside the 15 m coal pillar was not the minimum, it differed from the 16 m coal pillar by less than 1%, which could be regarded as the same. At the same time, compared with the 16 m coal pillar, the width of the 15 m coal pillar was more reasonable and could save coal resources. Therefore, the 15 m coal pillar is preferred.

5.2.2. The Working Face during the Backstopping Period. The coal pillar stress and roadway deformation state at the working face during the backstopping period are shown in Figure 11.

When the coal pillar width was 12 m, the roadway deformation was largest. When the coal pillar width was 16 m, the deformation of the roadway was least, the surface displacement of the coal pillar side was 821 mm, the displacement of entity coal side was 441 mm, and the subsidence of the roof was 750 mm, so the deformation of the roadway was small. When the coal pillar width was 15 m, the curve tended to be stable. With the increase of the coal pillar width, the deformation of the surrounding rock continued to decrease but the change was not obvious.

When the coal pillar width was 12 m to 15 m, the deformation of the coal pillar in the roadway was reduced from 1513 to 845 mm, which was reduced by 44%; when the coal pillar width was 15 m to 16 m, the deformation of the coal pillar in the roadway decreased from 1513 to 821 mm, which was reduced by 46%. Compared with the 15 m wide coal pillar, the change was not obvious. Therefore, the 15 m coal pillar is preferred.

5.2.3. 40 m behind the Gob. The vertical stress, vertical stress concentration coefficient, and roadway deformation of the 40 m coal pillar behind the working face are shown in Figure 12.

When the coal pillar width was 12 to 15 m, the vertical stress inside the coal pillar in the roadway was reduced by 16% from 58.9 to 49.4 MPa; when the coal pillar width was 12 to 16 m, the vertical stress in the coal pillar in the roadway was reduced by 17% from 58.9 to 48.8 MPa. Compared with the 15 m coal pillar, the change was not obvious. Therefore, the 15 m coal pillar is preferred.

When the coal pillar width was 12 to 15 m, the deformation of the coal pillar was reduced by 27% from 3208 to 2327 mm; when the coal pillar width was 12 to 16 m, the deformation of the coal pillar was reduced by 30% from 3208 to 2258 mm. Compared with the 15 m coal pillar, the change was not obvious. Therefore, the 15 m coal pillar is preferred.

The distribution status of the stress, deformation, and plastic zone inside the coal pillar when the coal pillar width was 12, 13, 14, 15, and 16 m was analyzed, respectively, by numerical simulation calculation based on the state of the coal pillar during the roadway driving, of that at 40 m behind the gob, and of that at the working face. The results showed that when the coal pillar width was 15 m, the stress value inside the coal pillar was basically reduced to the lowest, and there was a 4 m elastic zone inside the coal pillar, which had better fire prevention and gas prevention ability; when the coal pillar width was between 12 m and 15 m, the maximum vertical stress inside the coal pillar was reduced with the increase of the coal pillar width; when the coal pillar width was 15 m, the roadway deformation tends to be stable, and the deformation of the surrounding rock continued to decrease with the increase of the coal pillar width, but the change was not obvious. Through the above analysis, it is determined that the recommended width of the coal pillar set in the two roadways of the 4206 island working face is 15 m.

5.3. Research on the Supporting Effect of the Island Working Face

5.3.1. Simulation Analysis of the Transportation Roadway during the Driving Period. As can be seen from Table 5, there was a big difference in the stress and deformation of the surrounding rock by different supporting schemes. In Scheme 1, the stress of the roadway side was relatively concentrated, the subsidence of the roof was large, the floor heave was obvious, and the deformation of the two sides was serious, indicating that the roadway support is insufficient in Scheme 1. Compared with Scheme 1, the stress of the surrounding rock was significantly reduced, and the deformation of the surrounding rock could be reduced by up to 81.7% in Scheme 2 and Scheme 3, indicating that Scheme 2 and Scheme 3

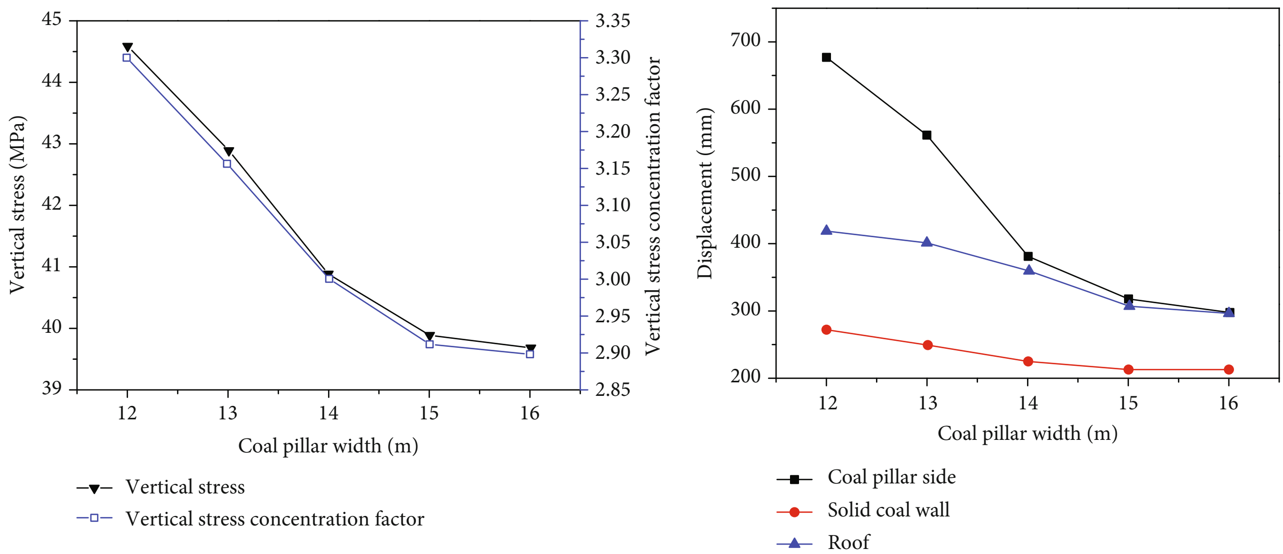

(a) Vertical stress and stress concentration factor in coal pillar

(b) Deformation of roadway

FIGURE 10: Variation trend of surrounding rock stability with coal pillar width during roadway excavation.

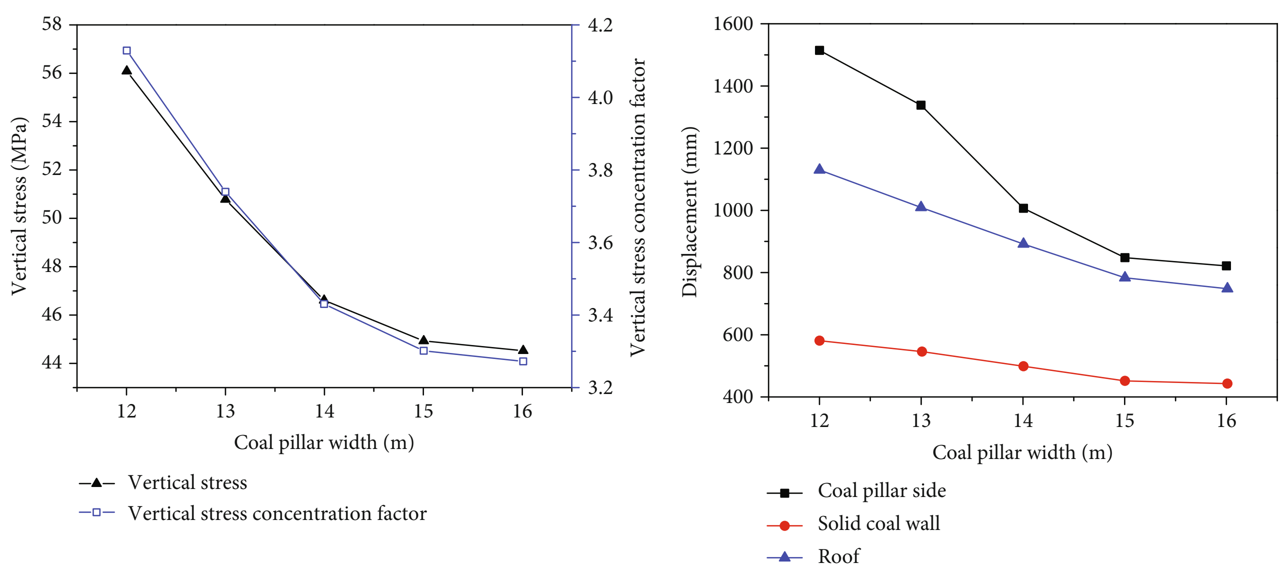

(a) Vertical stress and stress concentration factor in coal pillar

(b) Deformation of roadway

FIGURE 11: Variation trend of surrounding rock stability with coal pillar width during working face mining.

can maintain the stable state of the surrounding rock of the roadway, improve the stress distribution, and reduce deformation. Therefore, Scheme 2 or Scheme 3 should be selected as a reasonable supporting scheme.

It can be found from the table that both Scheme 2 and Scheme 3 had achieved a good effect on roadway support and significantly improved the deformation of the surrounding rock, while the supporting effects in Scheme 2 and Scheme 3 were not much different. Considering the economic benefits, Scheme 2 is preferred.

5.3.2. Simulation Analysis of the Transportation Roadway during the Backstopping Period at the 4206 Working Face. As can be seen from Table 6, there was a big difference in the stress and deformation of the surrounding rock in different supporting schemes. In Scheme 1, the stress of the roadway side was relatively concentrated, the subsidence of the roof was large, the floor heave was obvious, and the deformation of the two sides was serious, indicating that the roadway support is insufficient in Scheme 1. Compared with Scheme 1, the stress of the surrounding rock was significantly reduced, and the deformation of the surrounding rock could be reduced by up to 41.1% in Scheme 2 and Scheme 3, indicating that Scheme 2 and Scheme 3 can maintain the stable state of the surrounding rock of the roadway, improve the stress distribution, and reduce deformation. Therefore, Scheme 2 or Scheme 3 should be selected as a reasonable supporting scheme.

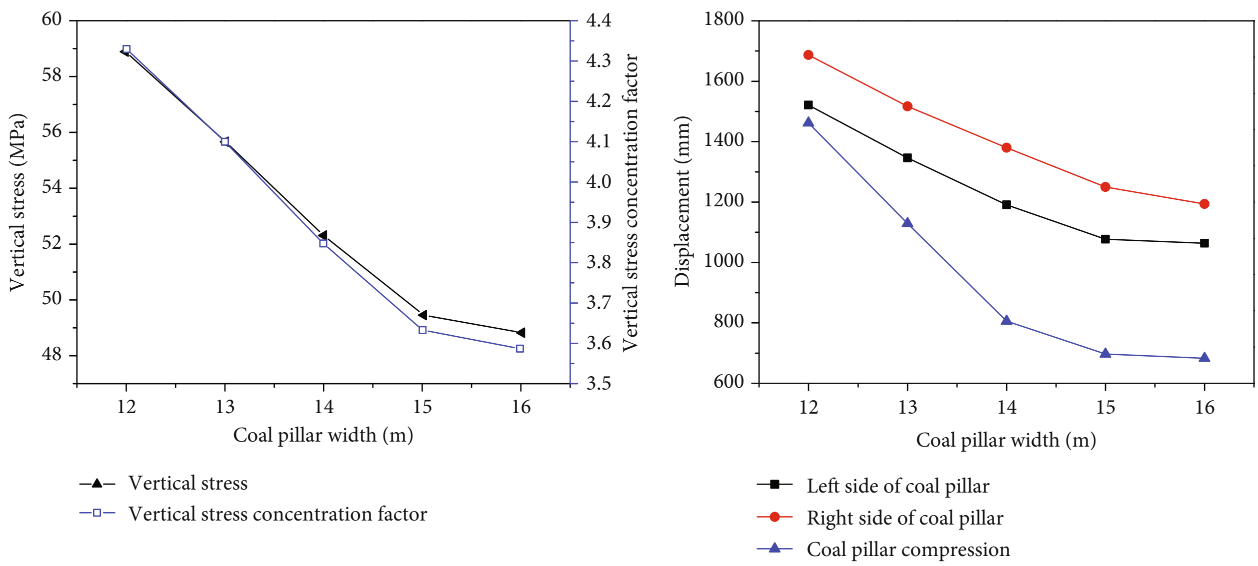

(a) Vertical stress and stress concentration factor in coal pillar

(b) Deformation of coal pillar

Figure 12: The stability of coal pillar 40 m behind goaf changes with the width of coal pillar.

Table 5: Comparison of simulation schemes for 4206 transport CIS trough.

Scheme name	Scheme I	Scheme II		Scheme III	
		Increment of decrease	Decrease percentage	Increment of decrease	Decrease percentage
Vertical stress (MPa)	25.8	4.4	17.1%	5.4	20.9%
Roof subsidence (mm)	310.8	244.2	78.6%	247.7	76.7%
Floor heave (mm)	88.1	39.5	44.8%	38.5	43.7%
Deformation of two sides (mm)	330	257.7	78.1%	269.7	81.7%

Table 6: Comparison of simulation schemes for 4206 transport CIS trough.

Scheme name	Scheme I	Scheme II		Scheme III	
		Increment of decrease	Decrease percentage	Increment of decrease	Decrease percentage
Vertical stress (MPa)	35.1	3	9%	3.1	9%
Roof subsidence (mm)	714	211	29.5%	238	33.3%
Floor heave (mm)	163	55	33.7%	67	41.1%
Deformation of coal pillar side (mm)	934	221	23.7%	267	28.6%
Deformation of stope side (mm)	430	141	32.8%	149	34.7%

It can be found from the table that both Scheme 2 and Scheme 3 had achieved a good effect on roadway support and significantly improved the deformation of the surrounding rock, while the supporting effects in Scheme 2 and Scheme 3 were not much different. Considering the economic benefits, Scheme 2 is preferred.

6. Practice of 4206 Transportation Roadway Support

6.1. Support Parameters of 4206 Transportation Roadway. Roof and side anchors are, respectively, $\Phi 20 \times 2500$ mm left-handed and right-handed nonlongitudinal reinforcement screw steel anchors, with spacing of 800×700 mm, and preload of 300 N·m. The roof anchor cable adopts Φ 21.8×9600 mm steel strand, spacing of 1600×700 mm, and preload of 210 kN. The side anchor cable adopts $\Phi 21.8 \times 6500$ mm steel strand, the row spacing is 700 mm, and the preload is 210 kN. The anchor mesh is laid flat, and the steel mesh and the mesh are pressed against each other for 100 mm, and each 100 mm is connected with iron wire. The specific support parameters are shown in Figure 13.

6.2. Observation Data Processing and Analysis. The 4206 island working face adopts gob-side entry driving with a coal pillar of 15 m and adopts the above strengthening support scheme. In the mining process of the 4206 isolated island working face, the cross point method is used to monitor the

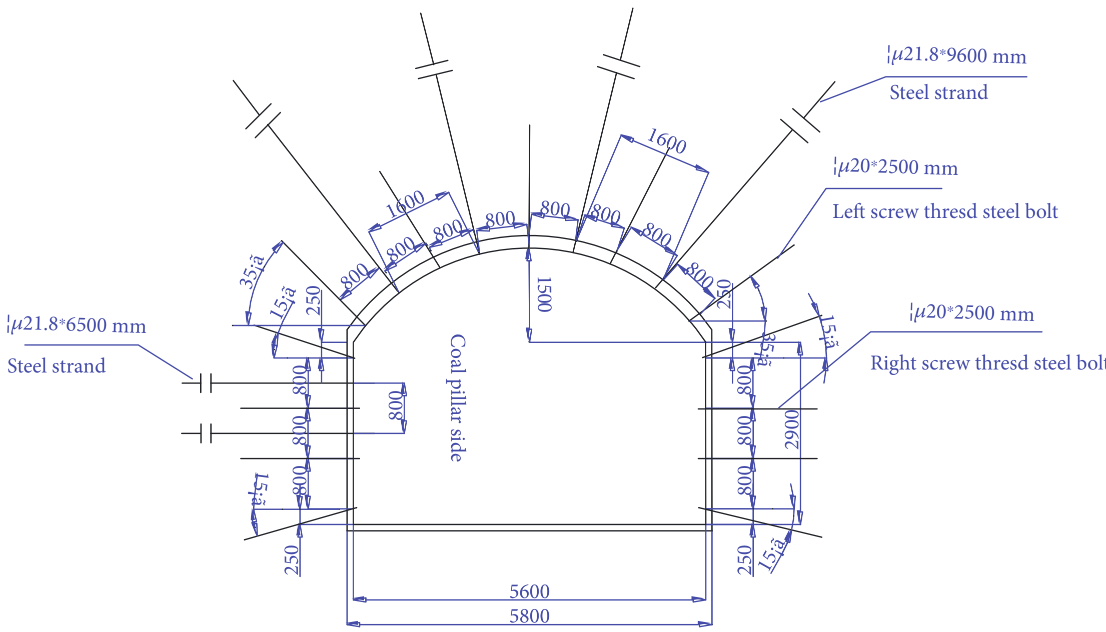

(a) Bolt support parameters of transport roadway

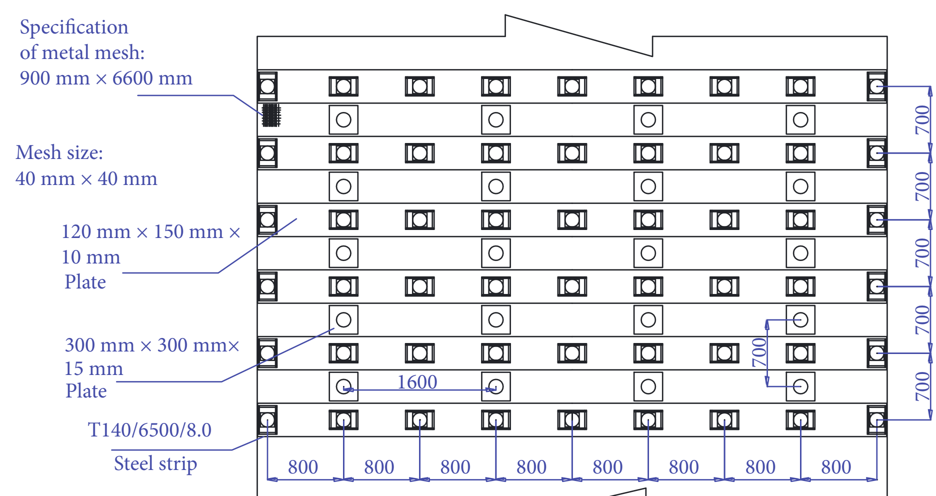

(b) Bolt-mesh support parameters of roof in transport roadway

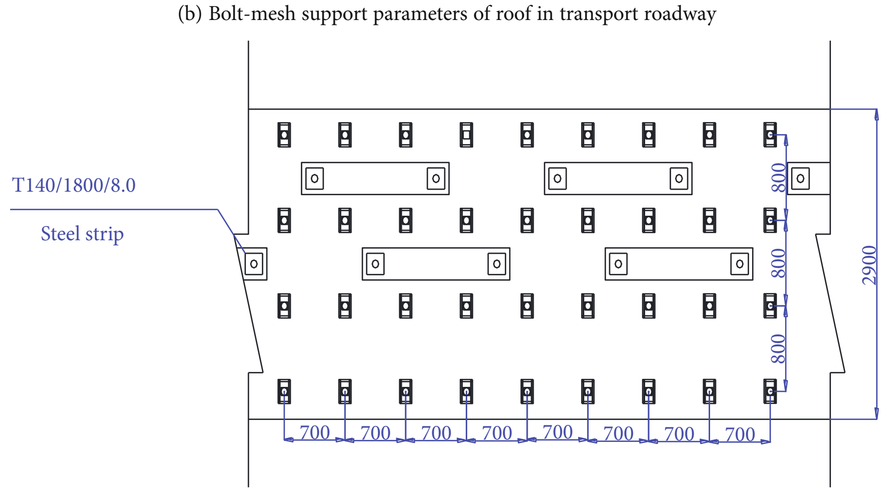

(c) Bolting distance between bolts at the side of transport roadway

Figure 13: Schematic diagram of support scheme for 4206 transport roadway.

deformation of the surrounding rock of the roadway. Under the mining influence of the 4206 isolated working face, the roof and floor convergence and the two-side convergence of the roadway are stable within 100 mm, and the coal pillar of roadway protection has not been significantly damaged. The deformation of the roadway is effectively controlled, which ensures the safety and stability of gob-side entry driving.

7. Conclusion

(i) The X-ray diffraction of the complete coal and rock samples in the test mine was studied. It was found that there were more illite and montmorillonite mixed layers in the #1, #2, and #4 samples, and kaolinite components were found in the #2, #3, #4, and #5 samples. The kaolinite and illite soften, break, and collapse when encountering water, while the montmorillonite expands when encountering water and then softens and loosen, resulting in serious deformation and failure of the roadway

(ii) According to the limit equilibrium theory of coal pillar stability, it is theoretically determined that the narrow coal pillar width of gob-side entry driving is between 13.9 and 15.7 m

(iii) The surrounding rock deformation mechanism of gob-side entry driving in the isolated island working face is analyzed, and the stress, deformation, and plastic zone distribution in the coal pillar are simulated and analyzed when the width of the coal pillar is 12, 13, 14, 15, and 16 m. Between 12 m and 15 m, with the increase of the coal pillar width, the maximum vertical stress in the coal pillar decreases. When the coal pillar width is 15 m, the deformation of the roadway tends to be stable. With the increase of the coal pillar width, the deformation of the surrounding rock continues to decrease, but the change is not obvious. Based on comprehensive consideration, it is determined that the recommended width of the coal pillar in two gateways of the 4206 island working face is 15 m

(iv) The support parameters of three different schemes are verified by numerical simulation, and the final support design scheme is determined. The field practice effect is good

Data Availability

The data used to support the findings of this study are available from the corresponding author upon request.

Conflicts of Interest

The authors declare no conflicts of interest.

Acknowledgments

This work is supported by the Jiangsu Youth Fund Project (No. BK20200634), the Excellent Young Talents Support Program in Colleges and Universities (No. gxyq2021221), and the Research Platform Open Project of Anhui Coal Mine Exploration Engineering Technology Research Center of Suzhou University (Nos. 2019ykf01 and 2016ykf02). We sincerely acknowledge the former researchers for their excellent works, which greatly assisted our academic study.

References

[1] Y.-H. Li, *Comparison study on the ground pressure characteristics of large height and top-caving mining face*, Henan Polytechnic University, 2012.

[2] J.-W. Li, *Study on surrounding rock control technology for gob-side entry retaining in top-coal caving mining face of Wuyang coal mine*, Liaoning Technical University, 2015.

[3] L. Yu, S.-H. Yan, H.-Y. Yu, and Z. Zhang, “Studying of dynamic bear characteristics and adaptability of support in top coal caving with great mining height,” *Procedia Engineering*, vol. 26, pp. 640–646, 2011.

[4] W. T. Liu, “Key mining technology for super-long fully mechanized top-coal caving face in soft thick seam,” *Coal Engineering*, vol. 15, no. 12, pp. 34–43, 2019.

[5] C.-H. Fang, *Study of the equipments matching es technology of the top-coal caving fully-mechanized face*, Shandong University of science and technology, 2009.

[6] L.-S. Zhou, *Study in failure and deformation character of entry along goaf and the technology of strata control about the fully mechanized sublevel caving in deep mine*, Shandong University of science and technology, 2006.

[7] W. Shi and X.-Z. Xu, “Research on reasonable size of protective coal pillars in coal section,” *Meitan Jishu/ Coal Technology*, vol. 29, no. 12, pp. 67–69, 2010.

[8] Y. Yang and R.-D. Tian, “Numerical simulation research on deformation of coal pillars under gangue filling condition,” *Journal of Liaoning Technical University (Natural Science Edition)*, vol. 35, no. 12, pp. 1390–1396, 2016.

[9] Q. Li, X.-B. Mao, W.-K. Bu, and Z.-G. Ma, “Mechanism of using waste-filling in roadway to control the deformation of covered rock strata,” *Journal of China University of Mining & Technology*, vol. 6, no. 37, pp. 745–750, 2008.

[10] J.-T. Zhang, D.-F. Zhang, W.-Y. Wang, X.-Q. Zhang, and X. Wang, “Reasonable width study of coal pillar preserving gateway in deep mining,” *Coal Technology*, vol. 33, no. 8, pp. 76–78, 2014.

[11] J.-L. Xi, *Study on large section roadway gob-side entry retaining technology in Tunlan*, China University of Mining & Technology (Beijing), 2013.

[12] R.-J. Si, F.-P. Li, L.-L. Zhao, L.-J. Xu, and H.-X. Feng, “Research on hydraulic fracturing roof cutting and roadway protection technology with wide sublevel coal pillar,” *Coal Science and Technology*, vol. 48, no. 7, pp. 282–287, 2020.

[13] Z.-X. Li and C. Wang, “Section design of mining roadway in "three soft" coal seam based on complex function method,” *Safety in Coal Mines*, vol. 46, no. 4, pp. 203–205, 2015.

[14] Q.-H. Ma and Y.-T. Wang, “Mechanism of narrow pillar protecting roadway and support technology of gob-side entry in deep mine,” *Journal of Mining and Safety Engineering*, vol. 26, no. 4, pp. 520–523, 2009.

[15] P. Gong, Z. Ma, R. R. Zhang, X. Ni, F. Liu, and Z. Huang, “Surrounding rock deformation mechanism and control technology for gob-side entry retaining with fully mechanized

gangue backfilling mining: a case study," *Shock and Vibration*, vol. 2017, Article ID 6085941, 15 pages, 2017.

[16] X.-H. Li, N. Zhang, and C.-J. Hou, "Rational position determination of roadway driving along next goaf for fully-mechanized top-coal caving mining," *Journal of China University of Mining & Technology*, vol. 29, no. 2, pp. 186–189, 2000.

[17] X.-Z. Hua, S. Liu, and Z.-H. Liu, "Research on strata pressure characteristic of gob-side entry driving in island mining face and its engineering application," *Chinese Journal of Rock Mechanics and Engineering*, vol. 30, no. 8, pp. 1646–1651, 2011.

[18] J.-B. Bai, *Surrounding Rock Control of Gob Side Entry Driving*, China University of Mining and Technology press, Jiangsu Xuzhou, 2006.

[19] K.-X. Zhang, Y.-J. Zhang, and Z.-Q. Ma, "Determination of the narrow pillar width of gob-side entry driving," *Journal of Mining&Safety Engineering*, vol. 32, no. 3, pp. 446–452, 2015.

[20] E.-B. Yi, D.-L. Xu, J. Sun, M.-L. Xie, and W.-X. Li, "Analysis on prevention and treatment of rock burst with different width coal pillars in isolated island working face," *Safety in Coal Mines*, vol. 42, no. 11, pp. 126–128, 2011.

[21] J.-M. Xi, J.-H. Mao, G.-S. Yang, and J.-F. Wang, "Numerical simulation study on rational coal pillar width in the roadway along goaf," *Coal Geology & Exploration*, vol. 36, no. 4, pp. 42–45, 2008.

[22] J.-D. Liu, *Study on reasonable width of sections coal pillar in mining the ultra-close multiple seam*, Xi'an University of Science and Technology, 2014.

[23] Z. Zhou, *Research on surrounding rock control technologies of narrow pillar of mining roadways in island coal face in thick coal seam*, Taiyuan University of Technology, 2014.

[24] B.-X. Huang, C.-Y. Liu, B.-S. Zheng, and Q.-Y. Chen, "Research on strata pressure characteristic of gob-side entry driving in island mining face and its engineering application," *Chinese Journal of Geotechnical Engineering*, vol. 29, no. 6, pp. 932–937, 2007.

[25] Y.-M. Cao, X.-Z. Hua, K. Yang, and L.-G. Qi, "Research on the laws of strata behavior in the gob-side entry of the island mining face," *Safety in Coal Mines*, vol. 44, no. 1, pp. 43–46, 2013.

[26] B. Yao, T.-H. Kang, and B. Yin, "Width optimization of narrow coal pillar of gob-side entry driving in isolated fully mechanized caving face," *Safety in Coal Mines*, vol. 49, no. 6, pp. 130–134, 2018.

Hindawi
Geofluids
Volume 2021, Article ID 6026229, 9 pages
https://doi.org/10.1155/2021/6026229

Research Article

Evolution Law of Gas Discharge of Carbon Monoxide in Mining Extra-Thick Coal Seam of Datong Mining Area

Zhanyuan Ma [1] and Feng Du [2,3]

[1] *Jinneng Holding Group, Datong 037000 Shanxi, China*
[2] *School of Energy Science and Engineering, Henan Polytechnic University, Jiaozuo, 454000 Henan, China*
[3] *Collaborative Innovation Center of Coal Work Safety and Clean High Efficiency Utilization, Jiaozuo, 454000 Henan, China*

Correspondence should be addressed to Feng Du; fdu_cumt@126.com

Received 14 April 2021; Revised 7 June 2021; Accepted 7 August 2021; Published 16 August 2021

Academic Editor: Jia Liu

In order to reveal the evolution law of gas discharge of carbon monoxide in mining an extra-thick coal seam of the Datong mining area by the numerical simulation and field monitoring test, the 8202 working face and 8309 working face in the Tongxin coal mine are chosen as the test sites. The results show that the seepage flow of carbon monoxide gas reaches $1.854 \times 10^{-8}\ \mathrm{m^3/s}$ in the #1 fracture after the #3 key stratum in the far field breaks in the 8202 working face, the seepage flow of carbon monoxide gas reaches $1.307 \times 10^{-7}\ \mathrm{m^3/s}$ in the #2 fracture, the seepage flow of carbon monoxide gas reaches $4.276 \times 10^{-7}\ \mathrm{m^3/s}$ in the #3 fracture, the seepage flow of carbon monoxide gas reaches $4.192 \times 10^{-7}\ \mathrm{m^3/s}$ in the #4 fracture, and the seepage flow of carbon monoxide gas reaches $1.623 \times 10^{-7}\ \mathrm{m^3/s}$ in the #5 fracture. The initial caving of the #3 key stratum in the far field occurs and collapses to the gob, when the working face in the #3-5 coal seam advances to 180 m, and the voussoir beam forms in the #3 key stratum. Besides, a shower shape was formed by the seepage flow of carbon monoxide gas, and the maximum flow in the working face reaches $4.562 \times 10^{-4}\ \mathrm{m^3/s}$. When the 8309 working face advances from 521.2 m to 556.4 m, the air pressure at the working face gradually rises and reaches the maximum magnitude and then begins to decrease; when the working face advances to 556.4 m, the air pressure at the working face reaches the maximum magnitude of 91.35 kPa. The gas discharge disaster of carbon monoxide in mining the extra-thick coal seam of the Datong mining area is effectively controlled by the dynamic balance multipoint control technology. The research results can be treated as an important theoretical basis for the prevention and treatment for carbon monoxide discharge disaster in mining the extra-thick coal seam of the Datong mining area.

1. Introduction

Coal resource is the one of the kinds of basic energy for economy and social development, and the sustainable development of the coal industry is closely related to economic and social development and energy security in China [1]. Besides, CO (carbon monoxide) is widely recognized as the most important symbol gas for detecting coal spontaneous combustion at the early stage [2]. However, CO overrunning occurs in a large number of field practices in coal mines, especially in mining the thick coal seam [3, 4]. Meanwhile, CO is a toxic and harmful gas, which poses a serious threat to the safety and health of miners [5]. The concentration of CO in the working face cannot exceed 0.0024%, which is the requirement of "the safety regulation for coal mining" in China [6, 7]. For example, the carbon monoxide gas discharge disaster occurred in the Tongxin coal mine in Shanxi province, which greatly affected the safety mining production [8, 9]. Therefore, it is of great significance to research the evolution law of gas discharge of carbon monoxide in mining an extra-thick coal seam, in order to guarantee the safe mining in the Datong mining area.

The scholars at home and aboard have carried out lots of research on the evolution law of gas discharge of carbon monoxide in mining a coal seam. Zhai et al. [10] analyzed the CO gas sources and influence factors in the working face and established a quantitative calculation model of the CO gas content, based on the CO gas produced mechanism from the coal oxidization process. Jia et al. [11] put forward the viewpoint that the source of carbon monoxide was comprised of the primal and secondary carbon monoxide by means of theoretical analysis combining with coal mine fire prevention theory, coal geology theory, gas geology theory, and coal chemistry theory. Yu et al. [12] analyzed the roof collapse of a crack zone in a carboniferous coal seam and the stress influence law of a coal pillar in a mined-out area of the Jurassic coal seam and obtained the mechanism of strong pressure revealed under the influence of a mining dual system of the coal pillar. Chen et al. [13] analyzed the overburden movement and failure law caused by double period coal seam mining by using the key strata theory, physical detection, and numeric simulation technology. Tang et al. [14] investigated the microseismic events of space-time evolution characteristics under the influence of a complex mined-out area at the upper Jurassic coal seam group and obtained the relationship of strata movement and rock pressure under the influence of double series coal seams. Meng [15] determined the cracking connection in the overburden strata above the double system seam mining in the Datong mining area, according to the discharging disaster of accumulated water and harmful gas in the gob, caused by the developed and connected cracks in the overburden strata above each seam after the mining of the multiseams. Zhang et al. [16] established a dynamic load calculation method for the unextracted area, coal pillar area, and mining collapse area of the upper coal seams and studied the dynamic deformation of overlying strata and pressure behavior, according to the mining condition of multiple coal seams with deep overburden strata and a large panel in the Datong mining area. Yu et al. [17] analyzed the impact process of a hard roof breaking to the gob and got the relationship between the axial force of the broken block and the broken expansion coefficient of caving coal-rock in the gob, in order to deal with the issue of the abnormal gas emission during periodic weighting, based on the "O-X"-type breaking of the hard roof.

At present, many scholars at home and abroad have studied the evolution law of gas discharge of carbon monoxide in mining a coal seam, whose thickness is less than 8 m [18–20]. The average mining thickness of the #3-5 coal seam in the Datong mining area is 15 m; therefore, the working face is easily connected with the above abandoned gob, where CO gas is accumulated by the mining-induced fractures in the overburden, leading to the gas discharge disaster of carbon monoxide. However, the evolution law of gas discharge of carbon monoxide in mining the extra-thick coal seam of the Datong mining area is not researched systematically and deeply [21–23]. Based on the mining and geological conditions of the 8202 working face and the 8309 working face in the Tongxin coal mine in Shanxi province, the evolution law of the gas discharge of carbon monoxide in mining the extra-thick coal seam of the Datong mining area is studied, by the numerical simulation and field monitoring test. The research results can be treated as an important basis for the prevention and treatment of carbon monoxide discharge disaster in mining extra-thick coal seams.

2. Numerical Calculation Simulation of Gas Discharge of Carbon Monoxide

2.1. Numerical Calculation Model. The numerical calculation model of the CO gas discharge is established in UDEC software, which is shown in Figure 1. The extra-thick coal seam is the coal seam whose thickness is larger than 8 m. There are three key strata in the overburden of the 8202 working face, namely, the #1 key stratum (lower part in the near field), #2 key stratum (upper part in the near field), and #3 key stratum (whole part in the near field). The key stratum refers to the stratum which controls the whole or partial overburden movement from the overburden to the surface. Besides, the thickness of the #14 coal seam is 4 m, the thickness of the #3-5 coal seam is 15 m, and the distance between the #14 coal seam and the #3-5 coal seam is 160 m.

In the numerical calculation simulation, the #14 coal seam is mined, followed by the #3-5 coal seam, and the mining step is 15 m. The gas pressure in the gob in the #14 coal seam is set to 0.1 MPa, and the gas pressure in the gob in the #3-5 coal seam is set as negative. The physical parameters of the rock mass are obtained by the rock mechanics experiments, as shown in Table 1.

2.2. Numerical Calculation Results. The initial caving of the direct roof occurs, when the 8202 working face in the #3-5 coal seam advances to 45 m, and the transverse fractures on the top rapidly develop to the bottom of the #1 key stratum in the near field. The pore pressure at the top of the #3 key stratum in the far field reaches the maximum of 0.1 MPa, and the pressure is not transferred to the bottom of the #3 key stratum in the far field, as shown in Figure 2.

The harmful gas in the gob comes from the left coal spontaneous combustion [24, 25]. And the discharge of harmful gas is controlled by negative pressure ventilation. From the perspective of flow distribution, the CO gas flow rate at both ends of the floor of the coal seam reaches the maximum magnitude 0.0293 m^3/s, since both ends of the gob of the #14 coal seam have the largest fracture development depth and fracture opening degree, located within 1 m below the floor at both ends. Besides, the flow rate outside 1 m below the floor of the coal seam rapidly drops to 1.362×10^{-7} m^3/s, which varies greatly in magnitude. Meanwhile, it is obvious that the seepage phenomenon occurs in some primary joints prefabricated in the #3 key stratum in the far field, and the seepage flow is 1.634×10^{-7} m/s, with the extremely low seepage flow. In addition, the maximum seepage flow of the roof of the #3-5 coal seam is 3.285×10^{-8} m/s, located at 7 m in the direct roof, which is mainly derived from the extremely low seepage flow generated by partial primary fractures, as shown in Figure 3.

The initial caving of the #1 key stratum in the near field occurs and collapses to the gob, when the working face in the #3-5 coal seam advances to 105 m. The distance between the #1 key stratum and the #2 key stratum in the near field is only 6 m. The overburden deformation and movement caused by the break of the #1 key stratum have a significant impact on the #2 key stratum, resulting in obvious longitudinal and transverse fractures in the #2 key stratum. The

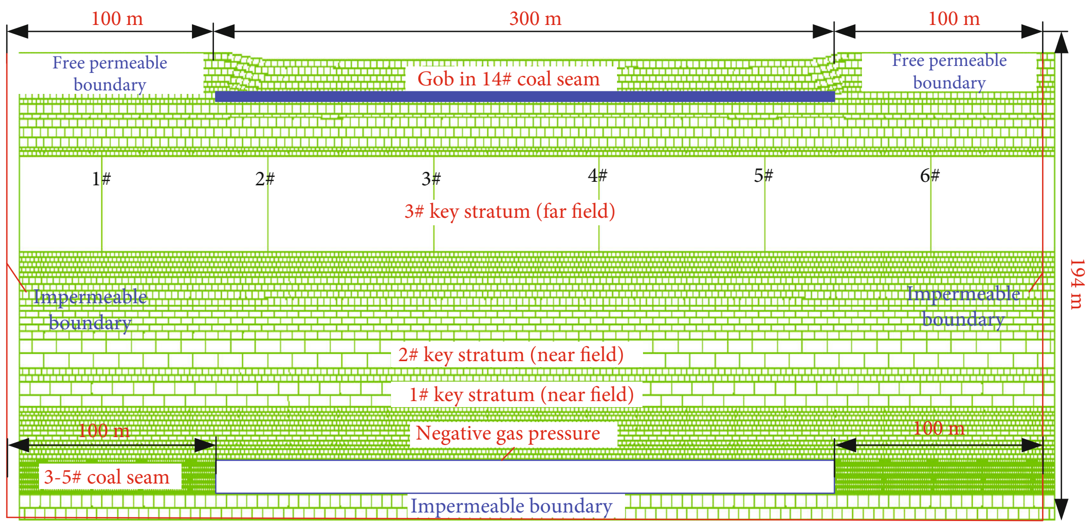

Figure 1: The numerical calculation model of gas discharge of carbon monoxide.

Table 1: The physical parameters of rock mass.

Rock strata	K (GPa)	G (GPa)	d (N·m^{-3})	f (°)	C (MPa)	t (MPa)
Coarse sandstone	10.85	7.5	2540	35	12.5	2.56
Sandy mudstone	30.35	14.74	2693	35	12.5	4.4
Medium sandstone	23.24	15.93	2654	35	12.5	5.72
Fine sandstone	19.79	19.86	2700	34	4.8	6.4
Siltstone	18.50	16.02	2604	34	4.8	4.89
Coal seam	3.89	1.59	1426	42	2.01	1.6

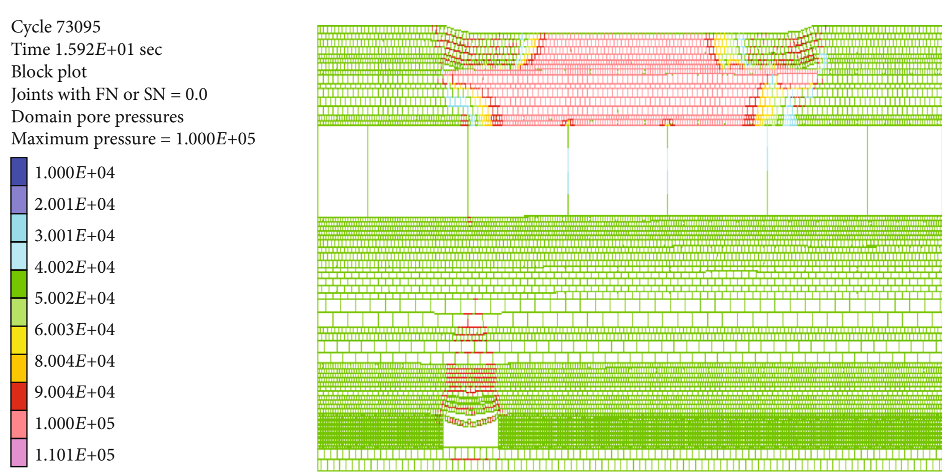

Figure 2: The pore pressure distribution in initial caving of direct roof.

maximum pore pressure above the key stratum in the far field is 0.1 MPa, as shown in Figure 4.

From the perspective of flow distribution, the fractures in overburden above the #1 key stratum in the near field further develop, especially the primary fractures of the key stratum in the far field; therefore, the CO gas penetrates down through primary fractures in the #3 key stratum with a small flow rate and enters the key seepage passage in the working face. The seepage flow of the #3 key stratum in the far field increases to 2.250×10^{-7} m^3/s, and the maximum flow in the working face reaches 1.655×10^{-4} m^3/s, which increases by nearly ten thousand times, as shown in Figure 5.

The initial caving of the #2 key stratum in the near field occurs and collapses to the gob, when the working face in the #3-5 coal seam advances to 120 m. Tensile fractures occur in the lower part of the #3 key stratum in the far field and the

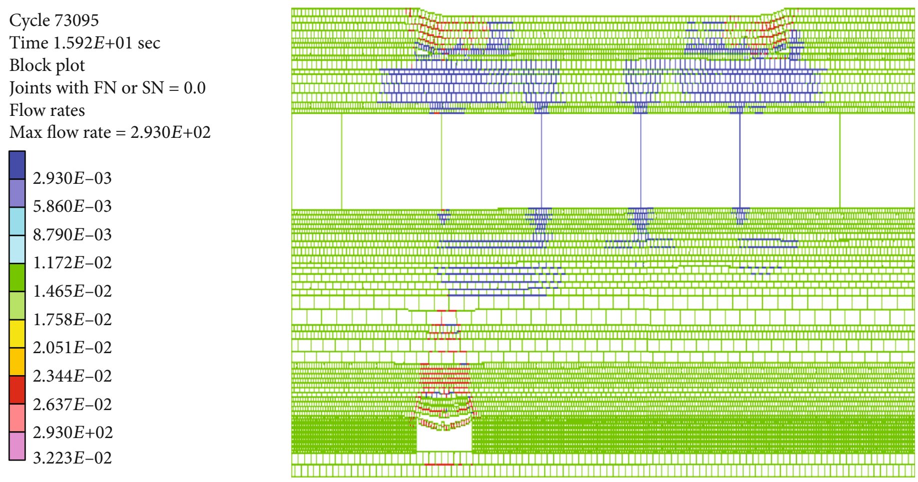

Figure 3: The flow distribution in initial caving of direct roof.

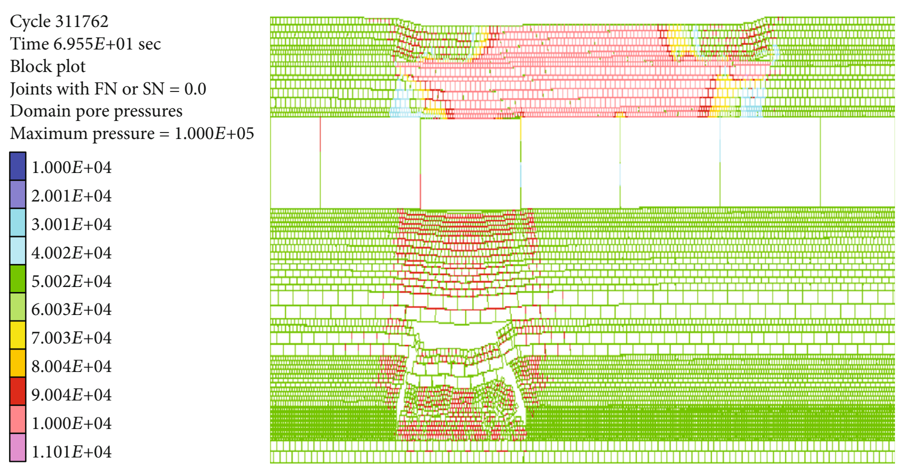

Figure 4: The pore pressure distribution in initial caving of #1 key stratum.

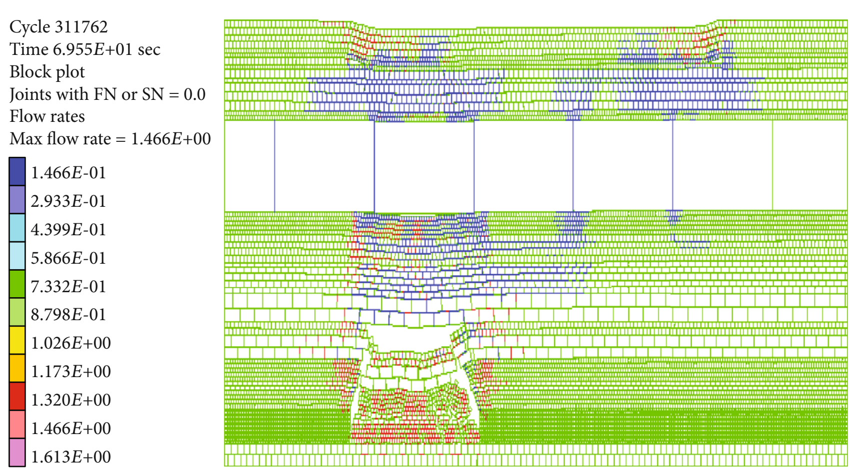

Figure 5: The flow distribution in initial caving of #1 key stratum.

upper part of the #3 key stratum above the central position of the gob. However, the development of fractures above the #3 key stratum is low, because the #3 key stratum is unbroken, whose deformation and movement is small. Meanwhile, the maximum pore pressure at the top of the #3 key stratum is almost constant, as shown in Figure 6.

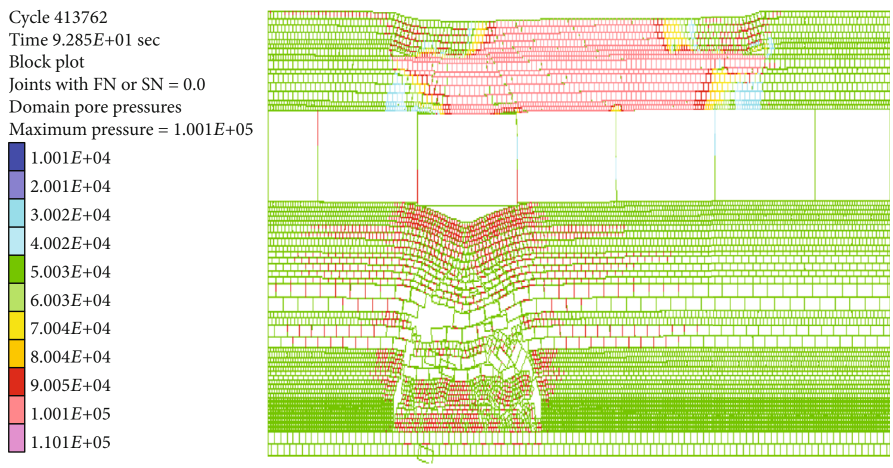

Figure 6: The pore pressure distribution in initial caving of #2 key stratum.

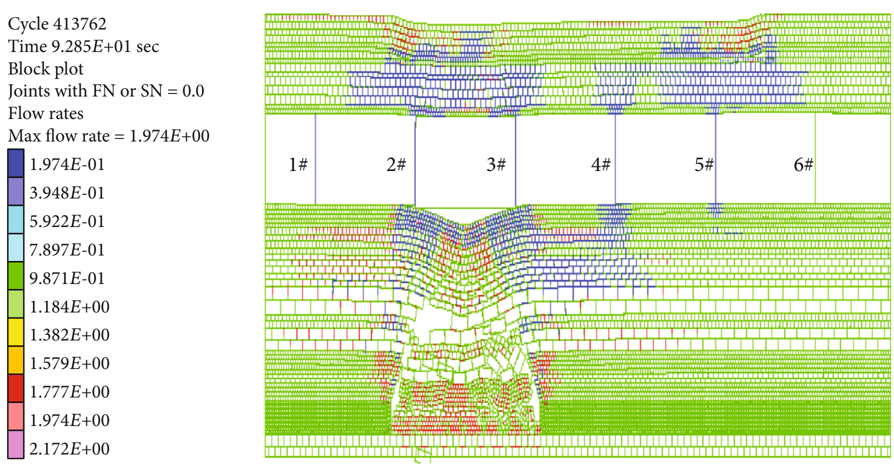

Figure 7: The flow distribution in initial caving of #2 key stratum.

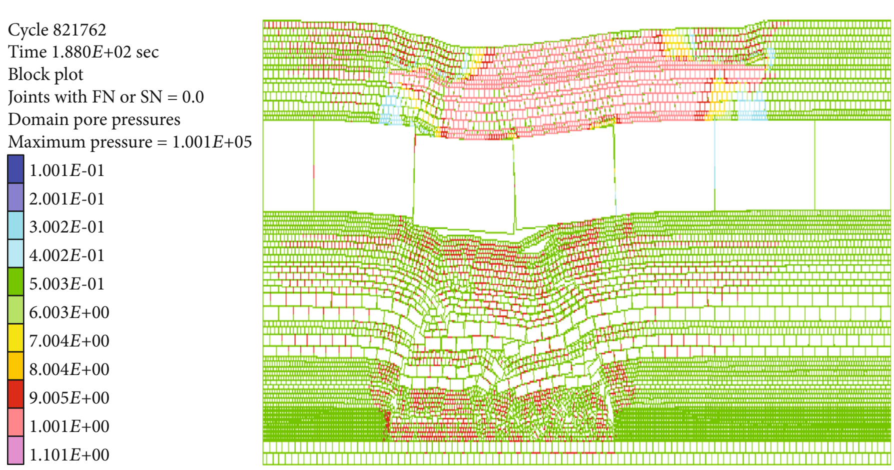

Figure 8: The pore pressure distribution in initial caving of #3 key stratum.

From the perspective of the flow distribution, the fracture opening of the #3 key stratum in the far field continues to increase, after the break of the #2 key stratum in the near field. Specifically, the seepage flow of the CO gas reaches 1.393×10^{-8} m^3/s in the #1 fracture, the seepage flow of the CO gas reaches 6.143×10^{-8} m^3/s in the #2 fracture, the seepage flow of the CO gas reaches 3.736×10^{-7} m^3/s in the #3 fracture, the seepage flow of the CO gas reaches $2.329 \times$

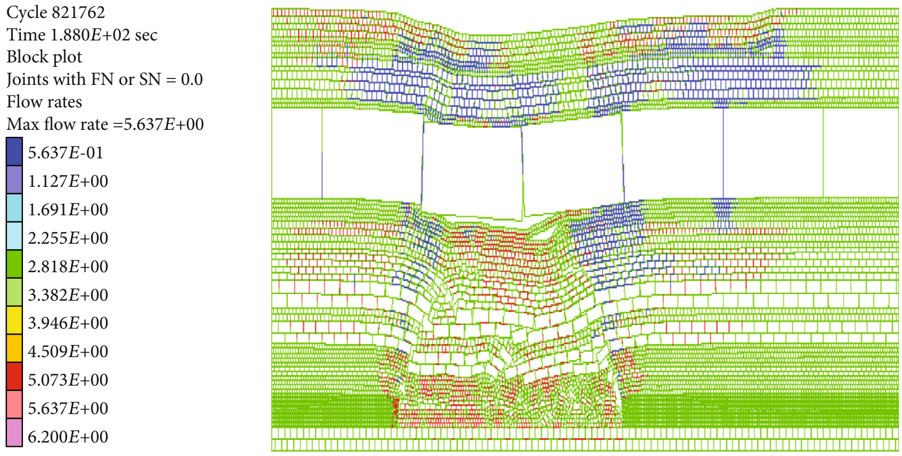

Figure 9: The flow distribution in initial caving of #3 key stratum.

(a) Empty box barometer

(b) Medium speed air gauge

(c) Dry and wet thermometer

(d) Ventilation multiparameter tester

Figure 10: Air pressure observation instruments.

Table 2: Comprehensive table of air pressure observations at the working face.

Number of times	Measurement points	1	2	3	4	5	6	7	8
1	Barometric pressure reading (mmHg)	679.8	679.6	679.5	679.1	678.5	678.0	678.5	678.5
	Pressure (kPa)	90.34	90.32	90.30	90.25	90.17	90.10	90.17	90.17
2	Barometric pressure reading (mmHg)	680.6	680.1	680.5	680.0	680.3	679.8	680.0	679.9
	Pressure (kPa)	90.45	90.38	90.43	90.37	90.40	90.34	90.37	90.36
3	Barometric pressure reading (mmHg)	683.4	683.3	683.2	682.9	682.6	683.1	682.6	682.2
	Pressure (kPa)	90.82	90.81	90.79	90.75	90.71	90.78	90.71	90.66
4	Barometric pressure reading (mmHg)	683.0	683.2	683.0	682.6	682.9	683.0	683.1	683.5
	Pressure (kPa)	90.77	90.79	90.77	90.71	90.75	90.77	90.78	90.83
5	Barometric pressure reading (mmHg)	683.7	683.4	683.1	682.9	682.9	682.9	683.0	683.5
	Pressure (kPa)	90.86	90.82	90.78	90.75	90.75	90.75	90.77	90.83
6	Barometric pressure reading (mmHg)	687.5	687.3	687.0	687.2	687.2	687.5	687.4	687.4
	Pressure (kPa)	91.37	91.34	91.30	91.33	91.33	91.37	91.35	91.35
7	Barometric pressure reading (mmHg)	687.8	687.8	687.6	687.8	687.0	686.2	686.5	687.2
	Pressure (kPa)	91.41	91.41	91.38	91.41	91.30	91.19	91.23	91.33
8	Barometric pressure reading (mmHg)	683.8	683.6	683.0	683.0	683.3	683.8	683.5	683.2
	Pressure (kPa)	90.87	90.85	90.77	90.77	90.81	90.87	90.83	90.79
9	Barometric pressure reading (mmHg)	684.5	684.6	684.6	684.5	684.6	684.7	684.9	684.6
	Pressure (kPa)	90.97	90.98	90.98	90.97	90.98	90.99	91.02	90.98
10	Barometric pressure reading (mmHg)	683.2	683	683.4	683.1	683.4	683.2	683.6	683.5
	Pressure (kPa)	90.79	90.77	90.82	90.78	90.82	90.79	90.85	90.83

10^{-7} m^3/s in the #4 fracture, and the seepage flow of the CO gas reaches 1.128×10^{-7} m^3/s in the #5 fracture. Besides, a shower shape is formed by the seepage flow of the CO gas, and the maximum flow in the working face reaches 8.285×10^{-4} m^3/s, as shown in Figure 7.

The initial caving of the #3 key stratum in the far field occurs and collapses to the gob, when the working face in the #3-5 coal seam advances to 180 m, and the voussoir beam forms in the #3 key stratum. The upper strata of the #3 key stratum in the far field are in the state of compression, and the strata dislocation appear in the tensile fractures, located in the two solid ends of the strata. With the continuous advance of the panel, the overburden strata fracture periodically, and a fracture surface with a certain angle is formed in the coal seam, which is called the fracture surface. Besides, the formed tensile fractures are the key seepage passage for the CO gas, which flows into the fractures in the #3 key stratum in the far field and enters the working face, through the fracture surface in the underlying overburden. The maximum pore pressure at the top of the #3 key stratum in the far field is almost constant, as shown in Figure 8.

From the perspective of the flow distribution, when the break of the #3 key stratum in the far field occurs, the seepage flow of the CO gas reaches 1.854×10^{-8} m^3/s in the #1 fracture, the seepage flow of the CO gas reaches 1.307×10^{-7} m^3/s in the #2 fracture, the seepage flow of the CO gas reaches 4.276×10^{-7} m^3/s in the #3 fracture, the seepage flow of the CO gas reaches 4.192×10^{-7} m^3/s in the #4 fracture, and the seepage flow of the CO gas reaches 1.623×10^{-7} m^3/s in the #5 fracture. Besides, a shower shape is formed by the seepage flow of the CO gas, and the maximum flow in the working face reaches 4.562×10^{-4} m^3/s, as shown in Figure 9.

3. Field Monitoring Test of Gas Discharge of Carbon Monoxide

3.1. Field Monitoring for Air Pressure. The Carboniferous #3-5 coal seam is mined at the working face in the Tongxin coal mine, and the fully mechanized caving mining technology is adopted. In order to verify whether the gas in the mined-out area has leaked, field monitoring for air pressure is carried out in the 8309 working face. Eight air pressure observation points are designed and arranged in the working face. The instruments used for barometric observation include empty box barometers, medium-speed wind meters, dry and wet thermometers, and ventilation multiparameter detectors, as shown in Figure 10.

The observation time of each measuring point is 15 minutes, and the field observation is made at the same time every day, ensuring that the observation interval is 24 hours, and the total observation period is 10 days. The observation results are shown in Table 2.

During the observation period, the air pressure of observation points is basically similar; therefore, the data of the #4 measuring point and the #5 measuring point are selected. When the working face advances from 521.2 m to 556.4 m, the air pressure in the working face gradually rises and reaches the maximum value and then begins to decrease; when the working face advances to 556.4 m, the air pressure at the working face reaches the maximum value of 91.35 kPa.

When the working face advances from 521.2 m to 546.8 m, the difference of the air pressure between the working face and the ground surface gradually decreases, the difference of the air pressure gradually increases from 546.8 m to 556.4 m, and the difference of the air pressure decreases from 556.4 m to 570.8 m.

3.2. Dynamic Balance Multipoint Control Technology. The negative pressure ventilation is adopted in the working face, which induces the CO gas from the overlying gob to leak to the working face, resulting in the CO gas concentration and harmful gas being overrun in the working face. Therefore, the dynamic balance multipoint control technology is put forward to deal with the practice problem. Three pressure-equalizing regulating valves are constructed in the intake airway. The first regulating valve is about 30 m away from the roadway entrance, and three local fans are installed in the intake airway in turn. Each fan has two stages, and the suction air volume is about 1000 m^3/min, the three fans are started at the same time, and the supply air volume reaches 2300 m^3/min. By gradually adjusting the intake airway and return airway to adjust the pressure difference and air volume inside and outside the damper, the purpose of CO emission control is effectively achieved.

4. Conclusions

(1) The initial caving of the #2 key stratum in the near field occurs when the 8202 working face in the #3-5 coal seam advances to 120 m. The seepage flow of the CO gas reaches 1.393×10^{-8} m^3/s in the #1 fracture in overburden, the seepage flow of the CO gas reaches 6.143×10^{-8} m^3/s in the #2 fracture, the seepage flow of the CO gas reaches 3.736×10^{-7} m^3/s in the #3 fracture, the seepage flow of the CO gas reaches 2.329×10^{-7} m^3/s in the #4 fracture, and the seepage flow of the CO gas reaches 1.128×10^{-7} m^3/s in the #5 fracture. Besides, the maximum flow in the 8202 working face reaches 8.285×10^{-4} m^3/s

(2) The initial caving of the #3 key stratum in the far field occurs when the working face advances to 180 m. The seepage flow of the CO gas reaches 1.854×10^{-8} m^3/s in the #1 fracture, the seepage flow of the CO gas reaches 1.307×10^{-7} m^3/s in the #2 fracture, the seepage flow of the CO gas reaches 4.276×10^{-7} m^3/s in the #3 fracture, the seepage flow of the CO gas reaches 4.192×10^{-7} m^3/s in the #4 fracture, and the seepage flow of the CO gas reaches 1.623×10^{-7} m^3/s in the #5 fracture. Besides, a shower shape is formed by the seepage flow of the CO gas, and the maximum flow in the working face reaches 4.562×10^{-4} m^3/s

(3) When the working face advances from 521.2 m to 556.4 m, the air pressure at the working face gradually rises and reaches the maximum value and then begins to decrease; when the working face advances to 556.4 m, the air pressure at the working face reaches the maximum value of 91.35 kPa. The difference of the air pressure gradually increases from 546.8 m to 556.4 m and decreases from 556.4 m to 570.8 m. Besides, the gas discharge disaster of carbon monoxide in mining an extra-thick coal seam is effectively controlled by the dynamic balance multipoint control technology

Data Availability

The data used to support the findings of this study are included within the article.

Conflicts of Interest

The authors declare that they have no conflicts of interest.

Acknowledgments

This work was supported by the National Natural Science Foundation of China (U1904128) and the Young Teacher Foundation of Henan Polytechnic University (2019XQG-08).

References

[1] H. X. Lin, F. Yang, Z. Z. Cao, Y. Wang, and X. J. Jiao, "Disastrous mechanism of water discharge in abandoned gob above the stope in mining extra-thick coal seam," *Geofluids*, vol. 2021, Article ID 6633517, 10 pages, 2021.

[2] J. Li, "Validation methods of upper long distance goaf harmful gas discharge based on drilling camera and tracer technology," *Safety in Coal Mines*, vol. 50, no. 8, pp. 80–83, 2019.

[3] B. Yu, W. B. Zhu, R. Gao, and J. R. Liu, "Strata structure and its effect mechanism of large space stope for fully-mechanized sublevel caving mining of extremely thick coal seam," *Journal of China Coal Society*, vol. 41, no. 3, pp. 571–580, 2016.

[4] Z. Z. Cao, Y. L. Ren, Q. T. Wang, B. H. Yao, and X. C. Zhang, "Evolution mechanism of water-conducting channel of collapse column in karst mining area of Southwest China," *Geofluids*, vol. 2021, Article ID 6630462, 8 pages, 2021.

[5] D. P. Zhang, Z. G. Wang, Y. Sun, and M. L. Zhou, "Research status and trend of CO overrunning in coal mines of China," *Safety in Coal Mines*, vol. 44, no. 4, pp. 183–185, 2013.

[6] Y. Xue, T. Teng, F. Dang, Z. Ma, S. Wang, and H. Xue, "Productivity analysis of fractured wells in reservoir of hydrogen and carbon based on dual-porosity medium model," *International Journal of Hydrogen Energy*, vol. 45, no. 39, pp. 20240–20249, 2020.

[7] H. Wen, J. Guo, Y. F. Jin, Z. F. Zhao, and Z. J. Yu, "Research status and trend of CO generation mechanism and control technology in coal mines," *Safety in Coal Mines*, vol. 46, no. 6, pp. 175–177, 2015.

[8] J. C. Li, "Analysis and prevention of CO overrun in full-mechanized caving mining face," *Coal Mining Technology*, vol. 17, no. 5, pp. 91–94, 2012.

[9] Y. Xue, F. Gao, Y. N. Gao, X. Liang, Z. Z. Zhang, and Y. Xing, "Thermo-hydro-mechanical coupled mathematical model for controlling the pre-mining coal seam gas extraction with slotted boreholes," *International Journal of Mining Science and Technology*, vol. 27, no. 3, pp. 473–479, 2017.

[10] X. W. Zhai, L. J. Ma, and J. Deng, "Study and application of CO content prediction model to upper corner of coal mining face," *Coal Science and Technology*, vol. 39, no. 11, pp. 59–62, 2011.

[11] H. L. Jia, M. G. Yu, and Y. L. Xu, "Analysis on the genetic type and mechanism identification of carbon monoxide in the coal-mine," *Journal of China Coal Society*, vol. 38, no. 10, pp. 1812–1818, 2013.

[12] B. Yu, C. Y. Liu, J. X. Yang, and J. R. Liu, "Mechanism of strong pressure reveal under the influence of mining dual system of coal pillar in Datong mining area," *Journal of China Coal Society*, vol. 39, no. 1, pp. 40–46, 2014.

[13] Y. Chen, H. W. Zhang, Z. H. Zhu, B. Yu, and L. J. Huo, "Research on the law overburden movement and failure under the influence of double period coal seam mining," *The Chinese Journal of Geological Hazard and Control*, vol. 25, no. 3, pp. 67–73, 2014.

[14] G. S. Tang, Z. H. Zhu, Y. L. Han, and Z. Li, "Relationship between overburden strata movement and strata behavior during dual system seam mining based on microseismic monitoring technology," *Journal of China Coal Society*, vol. 42, no. 1, pp. 212–218, 2017.

[15] X. B. Meng, "Safety and high efficient mining technology of ultra thick seam with double system interaction in Datong mining area," *Coal Science and Technology*, vol. 45, no. 8, pp. 114–120, 2017.

[16] X. Zhang, C. B. Deng, and X. F. Wang, "Study on dynamic deformation of overlying strata and pressure behavior law for extraction of multiple coal seams," *Coal Science and Technology*, vol. 45, no. 9, pp. 103–108, 2017.

[17] B. Yu, B. W. Xia, and P. Yu, "Effect of hard roof breaking on gas emission in fully-mechanized sublevel caving mining of extremely thick coal seam," *Journal of China Coal Society*, vol. 43, no. 8, pp. 2243–2249, 2018.

[18] Y. Xue, P. G. Ranjith, F. Dang et al., "Analysis of deformation, permeability and energy evolution characteristics of coal mass around borehole after excavation," *Natural Resources Research*, vol. 29, no. 5, pp. 3159–3177, 2020.

[19] Z. Z. Cao, P. Xu, Z. H. Li, M. X. Zhang, Y. Zhao, and W. L. Shen, "Joint bearing mechanism of coal pillar and backfilling body in roadway backfilling mining technology," *CMC-Computers Materials & Continua*, vol. 54, no. 2, pp. 137–159, 2018.

[20] W. L. Shen, J. B. Bai, W. F. Li, and X. Y. Wang, "Prediction of relative displacement for entry roof with weak plane under the effect of mining abutment stress," *Tunnelling and Underground Space Technology*, vol. 71, pp. 309–317, 2018.

[21] Y. Xue, J. Liu, F. Dang, X. Liang, S. Wang, and Z. Ma, "Influence of CH_4 adsorption diffusion and CH_4-water two-phase flow on sealing efficiency of caprock in underground energy storage," *Sustainable Energy Technologies and Assessments*, vol. 42, article 100874, 2020.

[22] B. H. Yao, Z. W. Chen, J. P. Wei, T. H. Bai, and S. M. Liu, "Predicting erosion-induced water inrush of karst collapse pillars using inverse velocity theory," *Geofluids*, vol. 2018, Article ID 2090584, 18 pages, 2018.

[23] Y. Xue, J. Liu, P. G. Ranjith, X. Liang, and S. Wang, "Investigation of the influence of gas fracturing on fracturing characteristics of coal mass and gas extraction efficiency based on a multi-physical field model," *Journal of Petroleum Science and Engineering*, vol. 206, article 109018, 2021.

[24] Z. Z. Cao, F. Du, Z. H. Li, Q. T. Wang, P. Xu, and H. X. Lin, "Research on instability mechanism and type of ore pillar based on the fold catastrophe theory," *CMES-Computer Modeling in Engineering & Science*, vol. 113, no. 3, pp. 287–306, 2017.

[25] L. Zhu, F. Dang, Y. Xue, K. Jiao, and W. Ding, "Multivariate analysis of effects of microencapsulated phase change materials on mechanical behaviors in light-weight aggregate concrete," *Journal of Building Engineering*, vol. 42, article 102783, 2021.

Hindawi
Geofluids
Volume 2021, Article ID 7089832, 10 pages
https://doi.org/10.1155/2021/7089832

Research Article

Flow Mechanism and Strength Characteristics of Textile Reinforced Concrete Mixed with Colloidal Nano-SiO_2

Ping Xu[1], **Rui Shi**[1], **Chao Wang**[2], **Yuhao Cui**[1], and **Minxia Zhang**[1]

[1] *School of Civil Engineering, Henan Polytechnic University, Jiaozuo, 454000 Henan, China*
[2] *China Construction Second Engineering Bureau Ltd., East China Company, Shanghai 200120, China*

Correspondence should be addressed to Chao Wang; ecc_cwang@163.com

Received 19 April 2021; Accepted 31 July 2021; Published 11 August 2021

Academic Editor: Yi Xue

In order to develop textile reinforced concrete (TRC) with good flowability and strength, colloidal nano-SiO_2 (CNS) is adopted to improve the performance of TRC. The flowability, compressive strength, flexural strength, and four-point bending tests of TRC matrix with CNS are carried out, and the changes of internal micromorphological characteristics of TRC matrix are analyzed by combining with scanning electron microscopy. The results show that the CNS has an inhibitory effect on the flowability of TRC matrix, and the greater the amount of admixture is, the smaller the slump expansion of TRC matrix is. The compressive strength and flexural strength of TRC matrix show a trend of increasing and then decreasing as the amount of CNS increases, and the compressive strength reaches the maximum at each age (7 d, 14 d, 28 d) when CNS and silica fume replace 5% cement by 1 : 4 equal mass. The flexural strength reaches the maximum at each age (7 d, 14 d, 28 d) when 5% cement is replaced by CNS and silica fume with 3 : 7 equal mass. The flexural strength increases with the increase of CNS admixture. It is found by electron microscope scanning that the incorporation of CNS consumes more $Ca(OH)_2$, refines the $Ca(OH)_2$ crystal size, and generates more C-S-H gels. These C-S-H gels are distributed in a net-like pattern inside the concrete, filling the internal pores, effectively densifying the interfacial transition zone between the cementitious material and the aggregates, and optimizing the internal structure.

1. Introduction

Textile reinforced concrete (TRC) has the superior characteristics of crack resistance, impact resistance, and durability properties, which has been widely applied in lightweight thin-walled structures, such as large span arches, shells, and domes [1–3]. TRC matrix has a better flowability because of the coarse aggregates completely replaced by the fine aggregates with different gradations, but the strength, stiffness, and elastic modulus of TRC matrix are adversely affected [4, 5]. Therefore, developing a fine-grained matrix concrete with good strength and flowability is the first step is to achieve the excellent performance of TRC. In recent years, nanotechnology has made effective progress in improving the mechanical and work-ability properties of cement composites [6].

More studies have shown that incorporation of CNS results in significant increase in compressive and flexural strength of concrete [7, 8]. Hani [9] compared the change in compressive strength of self-compacting concrete at different water-cement ratios after incorporation of appropriate amount of nano-SiO_2 and found higher compressive strength at larger water-cement ratio. Adak et al. [10] studied the effect of nano-SiO_2 on the strength and durability of fly ash based geopolymer mortar and found that the compressive and flexural strength of the oligomeric mortar with 6% nano-SiO_2 added was significantly improved after 28 days. Gülşan [11] found that the combined use of silica nanoparticles and steel fibers greatly increased the compressive strength and flexural properties of the material. Madadi [12] also found that the effect of silica nanoparticles on improving the bond strength of reinforced concrete was greater compared to that of fibers. In addition, incorporation of silica nanoparticles improved the durability of concrete [13]. A study by Li [14] showed that the combined addition of silica fume and nano-SiO_2 further improved the corrosion resistance of sulfate and chloride ions. Nano-SiO_2 also improved the high temperature resistance of concrete. Wang [15] studied the mechanical properties and microstructure at 25°C, 200°C, 400°C, and 600°C by static load test, scanning electron microscopy, and X-ray diffraction and found that the addition of nano-SiO_2 improved the high temperature performance of concrete at different temperatures. There are two reasons why the mechanical properties of concrete are enhanced by the addition of nano-SiO_2, either because the addition of silica nanoparticles improves the early hydration reaction of concrete [16–18] or because the nanoparticles act as fillers to fill the interfacial transition zone between aggregates and improve the denseness of concrete [19–21]. In summary, it can be tentatively judged that it is a viable option to introduce nano-SiO_2 into the preparation of TRC for improving the mechanical properties of TRC [22, 23]. Therefore, it is the focus of this study to investigate the mechanism of the effect of nano-SiO_2 on the mechanical properties of TRC matrix.

However, a number of studies have shown that the incorporation of nano-SiO_2 affects the flowability of concrete. Yu [24] investigated the effect of nano-SiO_2 on the hydration and microdevelopment of ultra-high performance concrete and found that the viscosity of ultra-high performance concrete increased with the addition of nano-SiO_2. This resulted in more air retention in the mixture and increased porosity of the concrete. Mosavinezha [25] found that the addition of water reducer and air inducing agent (AEA) at 2% and 0.2% by weight of cement, respectively, improved the poor matrix fluidity caused by the addition of nano-SiO_2. Puetens [26] investigated the effect of nano-SiO_2 and carbon nanotubes on self-compacting concrete and found that nano-SiO_2 inhibited concrete segregation, increased water demand, and reduced flowability, but the addition of fly ash reduced the loss of flowability properties. Therefore, it is important to study the mechanism of the effect of nano-SiO_2 on the fluidity of TRC matrix and analyze its microscopic mechanism in order to make the aggregates of TRC can have good workability in the preparation process.

In this paper, a high-performance TRC matrix is formulated by using CNS instead of silica fume to compare the difference in performance between the CNS and silica fume-doped TRC matrix. The changes in the microstructure of the TRC matrix are analyzed to compare the differences between them in improving the interfacial properties and to reveal the mechanism of the effect of CNS on the performance of fine-grained concrete. These experiments in this paper are designed to further investigate the effect of nano-SiO_2 on the flowability and strength of TRC matrix.

2. Test Materials and Test Design

2.1. Materials

2.1.1. Cementitious materials. The cementitious material consists of cement, fly ash, and silica fume. The P. O 42.5 cement has a specific surface area of 362 m^2/kg and apparent density of 3.11 g/m^3. The specific surface area of silica fume (SF) is 30000 m^2/kg and apparent density of 2.23 g/m^3. The cementitious material chemical composition is shown in Table 1.

TABLE 1: Chemical compositions of cementitious materials (w_t/%).

Materials	SiO_2	CaO	Al_2O_3	Fe_2O_3	MgO	Loss
Cement	22.85	60.16	6.18	3.85	2.15	4.81
Fly ash	49.91	3.72	37.69	4.40	0.55	3.73
Silica fume	93.52	0.32	0.31	0.73	0.12	3.81

2.1.2. Colloidal Nano-SiO_2 (CNS). The nano-SiO_2 is made of colloidal nano-SiO_2 (CNS) with an average particle size of 13 nm, a solid content of 30%, and a sample purity of more than 99%. The physical properties are shown in Table 2.

2.1.3. Sand. Two types of river sand with particle sizes of 0 ~ 0.6 mm and 0.6 ~1.2 mm are used for the experiments, to ensure good working performance of fine-grained concrete.

2.1.4. Water reducer. Polycarboxylic acid high efficiency water reducer with water reduction rate > 30% is used to preparate the TRC matrix.

2.2. Mix Properties. In this test, silica fume is mixed with CNS for the TRC matrix with a water-cement ratio of 0.38, a cement-sand ratio of 0.7.20% cement is replaced by equal mass of fly ash in the cementitious material, and 5% cement is replaced by equal mass of silica fume and CNS in different proportions. The amount of CNS is 0.5%, 1%, 1.5%, and 2%, respectively, according to the solid content of nano-SiO_2 as a percentage of the mass of cementitious material. The amount of water reducer is 0.7% of the total mass of cementitious material. The mix properties of TRC matrix are shown in Table 3.

2.3. Test Method

2.3.1. Specimen Preparation. The TRC matrix is mixed by a forced mixer. Firstly, sands of two different grain sizes are mixed for 2 minutes; then, cement, fly ash, and silica fume are added to the mixer for 5 minutes dry to mix the sand with the cementitious material. Then, the water reducer is added to the mixer with 1/4 of water and mixed at slow speed for 2 minutes, pouring the CNS and the remaining water into the mixture, mixing quickly for 1 minute, and finally loading to the standard triplex test mold with the specification of 40 mm × 40 mm × 160 mm for molding. When the CNS is mixed with more, it is properly vibrated according to the test condition. The molded specimens are placed in the standard curing room for 24 h and then demolded. The demolded specimens are placed in the standard curing room (temperature (20 ± 2°C), relative humidity 95% or more) and cured to different ages and then tested for compressive and flexural strength.

2.3.2. Slump Expansion. In this paper, the slump expansion test is used to evaluate the fluidity of TRC matrix after CNS modification according to GB/T 2419-2005 [27]. For the slump expansion test, a slump cylinder with an upper opening diameter of 100 mm, a lower opening diameter of 200 mm, and a height of 300 mm is used. Firstly, the aggregate mix was poured into the slump cylinder, and each time

Table 2: Physical properties of CNS.

Product model	Appearance	SiO_2 content	pH	Density	Viscosity	Particle size
GS-30	Lightly milky	30.5%	9.6	1.204 g/cm^3	6.2 cP	13 nm

Table 3: Mix properties of TRC matrix (kg/m^3).

Number	Cement	Fly ash	Silica fume	CNS	Sand (mm) 0 ~ 0.6	Sand (mm) 0.6 ~1.2	Water	Water reducer	Flowability (cm)
A	472	168	35	—	325	650			82
S1	472	168	31.6	11.3	325	650			76
S2	472	168	28.2	22.5	325	650	256.5	6.1	69
S3	472	168	25	33.8	325	650			38
S4	472	168	21.5	45	325	650			33

Note: No. A is the reference group; S1 to S4 are the CNS modified groups.

the amount poured was 1/3 of the volume of the slump cylinder. Then, the slump cylinder was lifted vertically and smoothly so that the concrete could flow freely, when the concrete is no longer flowing, measure the diameter of the two extensions in the mutual vertical direction and as shown in Figure 1. In order to meet the self-compaction requirement of the TRC matrix, the flow expansion is not less than 550 mm.

Figure 1: Test of slump flow.

2.3.3. Compressive Strength and Flexural Strength. The test is carried out according to GB/T 17671-1999 to study the effect of different dosings of CNS on the compressive strength and flexural strength of fine-grained concrete [28]. The flexural strength is tested by using 40 mm × 40 mm × 160 mm prismatic specimens, three specimens are formed for each ratio, and the loading speed is constant at 50 N/s. After the flexural strength test, the fractured specimens are taken for the compressive strength test, and the loading speed is 2.4 kN/s for each group of three specimens.

2.3.4. Four-Point Bending Test. The flexural strength of the TRC is tested by the four-point bending test, which consists of a woven fiber mesh and a matrix doped with nano-SiO_2, with the dimensions of 280 mm × 50 mm × 12 mm. The mold is demolded after 24 h of curing at room temperature, then standard curing is carried out, and the formed sheet is loaded by the four-point bending test. The schematic diagram of the formed sheet and the four-point bending test are shown in Figure 2.

2.3.5. Microscopic Tests. After the specimen is maintained to 60 days for compressive testing, a small number of fragments are removed as samples for testing. The small pieces are impregnated in anhydrous ethanol to terminate hydration before the sample test and dried in a vacuum drying oven at 60°C for half a day, and after drying, the sample surface is gold plated with 20 nm for conductivity by vacuum sputtering [29]. The test acceleration voltage is 10-15 kV, and the acceleration current is adjusted according to the image quality.

3. Discussion and Analysis of Test Results

3.1. Effect of CNS on the Flowability of TRC Matrix. The variation of slump expansion of fine-grained concrete at 0, 0.5%, 1.0%, 1.5%, and 2% of CNS admixture is shown in Figure 3. The slump expansion of TRC matrix decreases in different magnitudes with the increase of CNS admixture. The slump expansion of TRC matrix decreases by 59.8% compared with the TRC matrix without CNS, when the amount of CNS is 2%. When the amount of CNS is increased from 0.5% to 1.5%, the slump expansion of fine-grained concrete is reduced by 25.6%, 32.9%, and 53.7% relative to that of unadulterated CNS. The incorporation of water reducer thins the thickness of the surface water and improves the fluidity by repulsion between cement particles, but the amount of filled water does not change. The average particle size of silica particles in CNS is 13 nm, which fills the cement particle gap and improves the compactness, reducing the amount of filling water on the one hand, but increasing the specific surface area on the other hand. Therefore, in the case of the constant water-cement ratio, the effect of CNS on the slump flow of fine-grained concrete depends on the contrast between its filling effect and surface water absorption effect.

The addition of CNS affects the fluidity of concrete for two main reasons. On the one hand, because CNS has a large specific surface area, with the increase of CNS admixture, the

(a) Preparation of specimens (b) Four-point bending test

Figure 2: Textile reinforced concrete and four-point bending test.

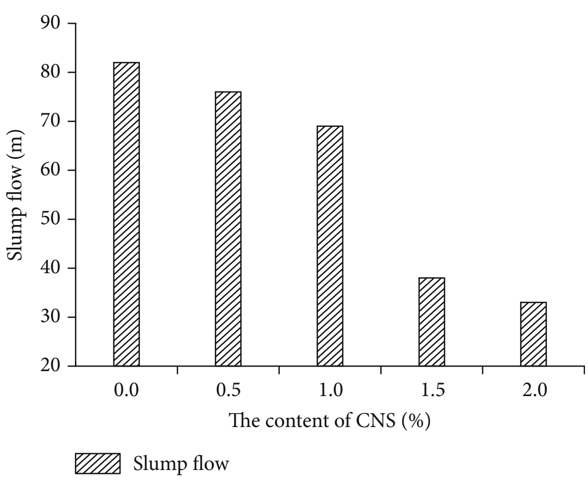

Figure 3: Slump flow expansion of TRC matrix.

required surface water increases rapidly, which increases the water requirement of concrete. On the other hand, CNS further refines the fineness of the cementitious material, which has strong water absorption and is easy to produce flocculation during the mixing process, wrapping the surrounding water in it. Under the combined effect of the above factors, the free water around the cement particles is reduced, thus decreasing the fluidity of the TRC matrix. The slump expansion of fine-grained concrete decreases slowly, when the amount of CNS is between 0 and 1%; when the amount of CNS is greater than 1%, the slump expansion of fine-grained concrete is less than 550 mm and no longer meets the liquidity requirements.

3.2. Effect of CNS on the Compressive Strength of TRC Matrix. The changes of postfolding compressive strength of fine-grained concrete at different ages (7 d, 14 d, 28 d) with the increase of CNS admixture are shown in Figure 4. The postfolding compressive strength of fine-grained concrete at each age increases from 0 to 1.5%. Compared with the compressive strength of the reference group (mixed with 5% silica fume), the compressive strength of each modified group increases by 17.4%, 23.9%, and 8.8% at the age of 7 days, shown in Figure 4(a). The compressive strength of each modified group increases by 16.6%, 28.9%, and 16.6% at the age of 14 days, shown in Figure 4(b). The compressive strength of each modified group increases by 4.6%, 14.9%, and 1.8% at the age of 28 days, shown in Figure 4(c). The compressive strength of each modified group at the age of 60 days increases by 9.4%, 19.9%, and 12.7%, respectively, shown in Figure 4. The compressive strength of fine-grained concrete at each age shows a decreasing trend as the amount of CNS admixture continues to increase to 2%. When the appropriate amount of CNS is incorporated into the fine-grained concrete (less than 1.5%), due to the extremely small particle size of CNS (average particle size of 13 nm), it increases the matrix compactness by refining the internal pores of fine-grained concrete and finally improves the compressive strength of the specimens.

On the one hand, the incorporation of CNS forms monomers of silicon (e.g., $-OSi(OH)_3$, $-OSi(OH)_2$) in the fine-grained concrete, and these monomers combine with $Ca(OH)_2$ generated by the reaction of cement to form C-S-H gels filled into the microscopic pores of fine-grained concrete, thus defensing the microstructure of the matrix and improving the compressive strength of the specimens. On the other hand, the test uses a large proportion of SiO_2 and Al_2O_3 in the fly ash, the fly ash activity is low, and the ratio of $n(SiO_2)/n(Al_2O_3)$ in the slurry has a greater degree of influence on its compressive strength. With the increase of CNS admixture, the concentration of silicon monomer in the matrix gradually increases, promoting the secondary hydration reaction of fly ash and the formation of three-dimensional mesh structure of silica-aluminate gel. When the amount of CNS is greater than the optimal value of 1%, the system of excessive SiO_2 is easy to deposit on the surface of the cement particles, combined with H_2O reaction, reducing the water required for cement hydration, unfavorable to the polymerization reaction, and reducing the compressive strength of fine-grained concrete gradually.

3.3. Effect of CNS on the Flexural Strength of TRC Matrix. The variation law of flexural strength of fine-grained concrete at different ages (7 d, 14 d, 28 d) with the increase of CNS admixture is shown in Figure 5. The postfolding compressive strength of fine-grained concrete at all ages increases in different magnitudes, when the amount of CNS is increased

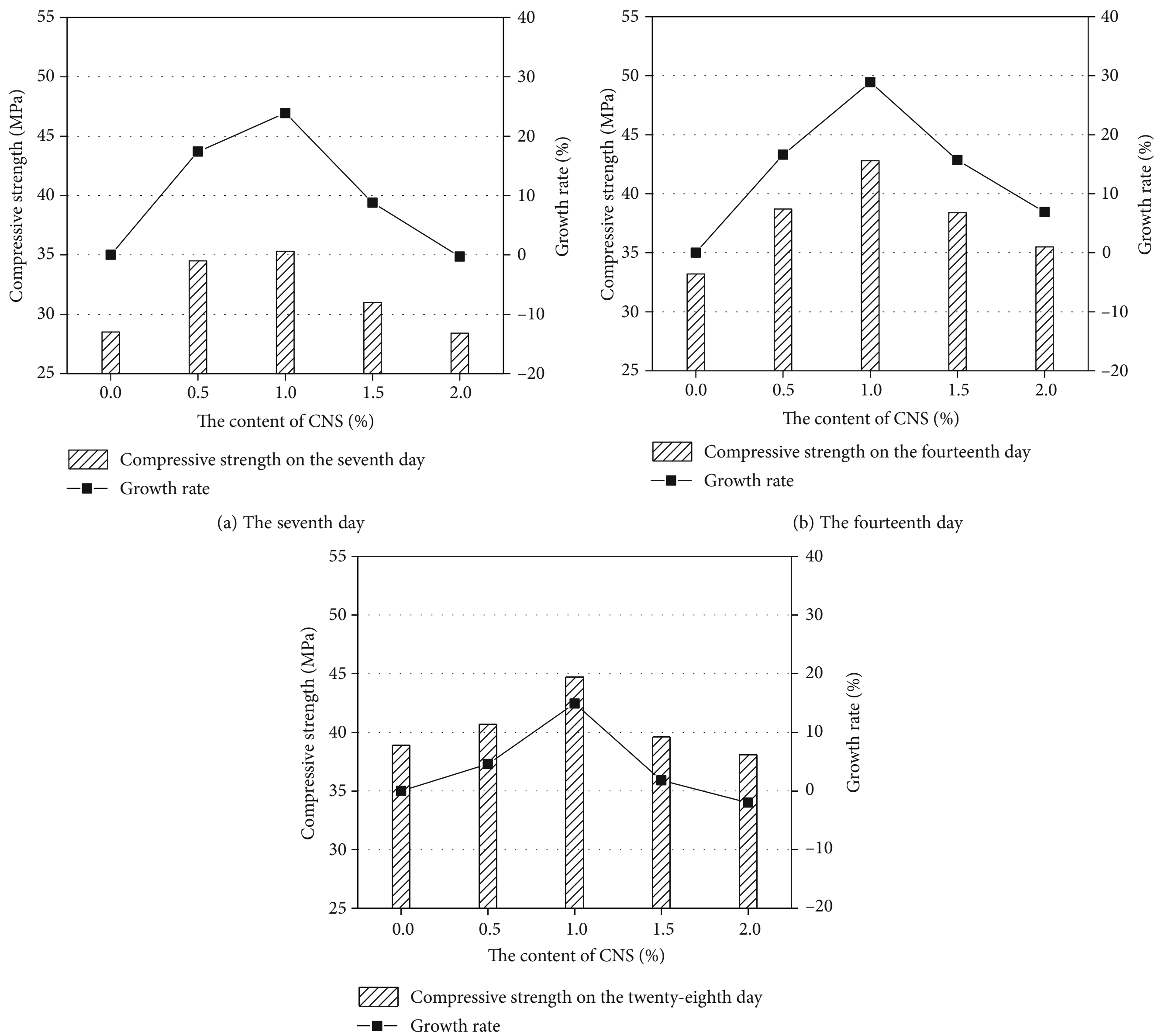

(a) The seventh day

(b) The fourteenth day

(c) The twenty-eighth day

Figure 4: Effect of CNS dosing on compressive strength at different ages.

from 0 to 2%. Compared with the base group (with 5% silica fume), the flexural strength of each modified group increases by 0%, 25%, 44.4%, and 14.4% at 7 days of age, shown in Figure 5(a)and 5.9%, 17.6%, 23.5%, and 19.6% at 14 days of age, shown in Figure 5(b). The flexural strength of each modified group increases by 9.5%, 12.7%, 23.8%, and 19.6% at 28 days of age, respectively, shown in Figure 5(c). With the continuous increase of CNS admixture, the growth of flexural strength of fine-grained concrete at each age shows a trend of first increase and then decrease.

When the admixture amount is 1.5%, the flexural strength at all ages reaches the maximum. After adding CNS, the cement particle gaps are filled by nano-SiO_2, which reacts with $Ca(OH)_2$, and the hydration product of cement. Hydrated calcium silicate gel is distributed between cement particles in a net shape and connected cement particles together. In the process of concrete tension, it weakens the pore stress concentration and increases the tensile stress of the matrix. Since the denser the internal structure of concrete is, the higher the energy required to be absorbed during crack expansion is, and the increase of flexural strength is facilitated.

3.4. Effect of CNS on the Bending Capacity of TRC. The bending cracking stress and ultimate stress of TRC with different doping of CNS are shown in Figure 6, and the bending cracking stress and bending ultimate stress of the specimens are significantly increased with the increase of CNS doping. The flexural cracking stresses of TRC with 0.5, 1, 1.5, and 2 CNS doping increase by 2.3%, 8.6%, 34.1%, and 95.5%, respectively, and the flexural ultimate stresses increase by 49.4%, 56.8%, 51.4%, and 72.7%, respectively, compared with

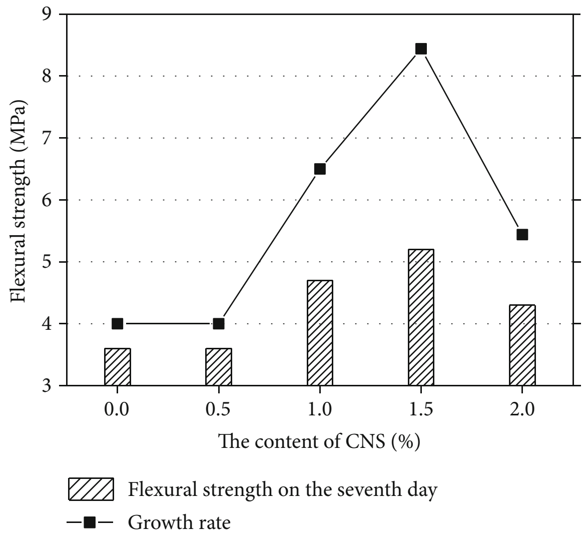

(a) The seventh day

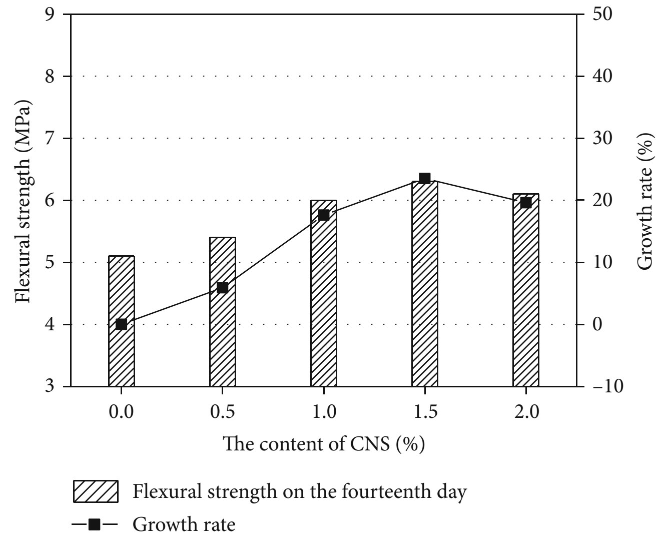

(b) The fourteenth day

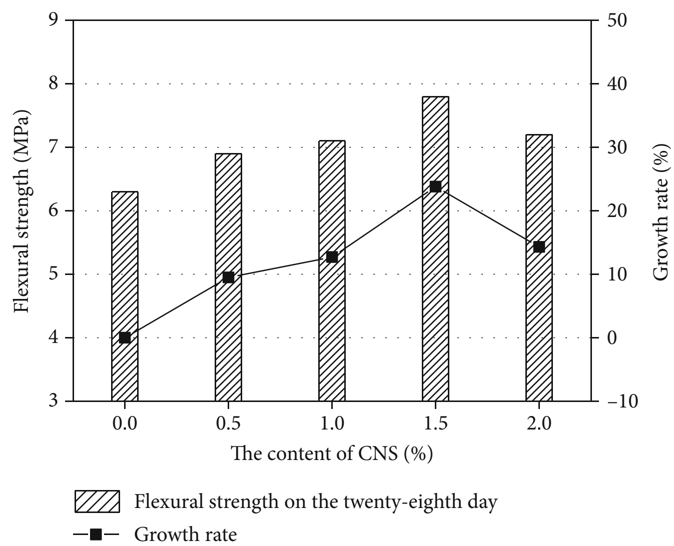

(c) The twenty-eighth day

Figure 5: Effect of CNS doping on flexural strength at different ages.

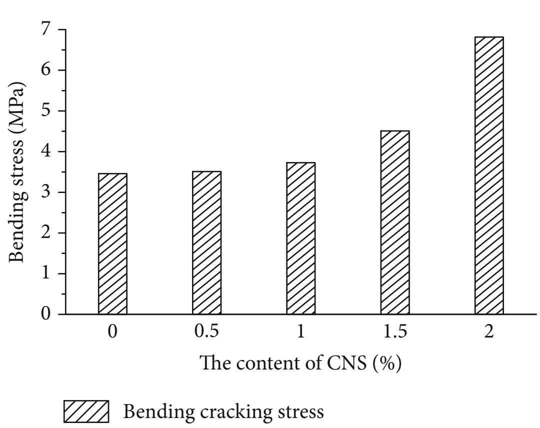

(a) The bending cracking stress

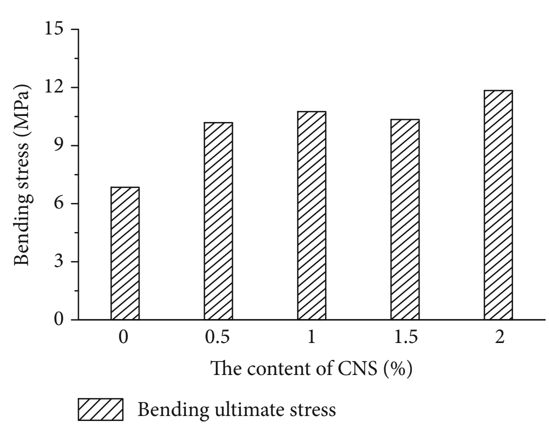

(b) The bending ultimate stress

Figure 6: Bending cracking stress and ultimate stress of TRC with different doping of CNS.

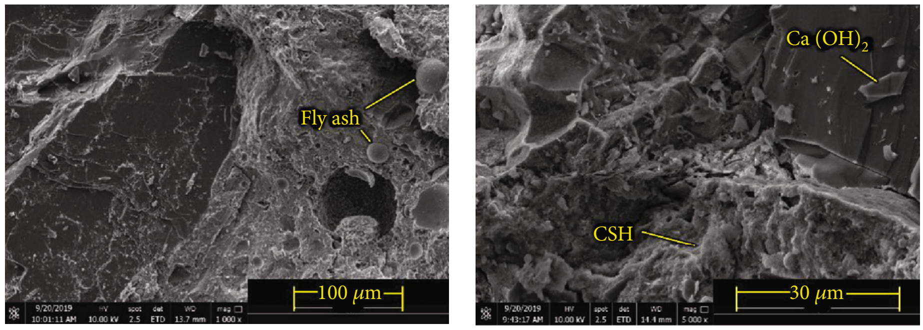

(a) Fly ash (b) Hydration products

Figure 7: Microscopy images of fine grained concrete.

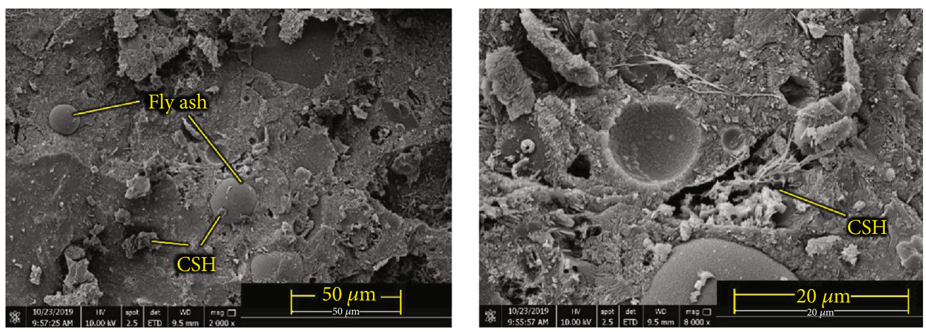

(a) Hydration products on the surface of fly ash (b) Flocculent C-S-H gel

Figure 8: Microscopy images of designed fine grained concrete with 0.5% CNS.

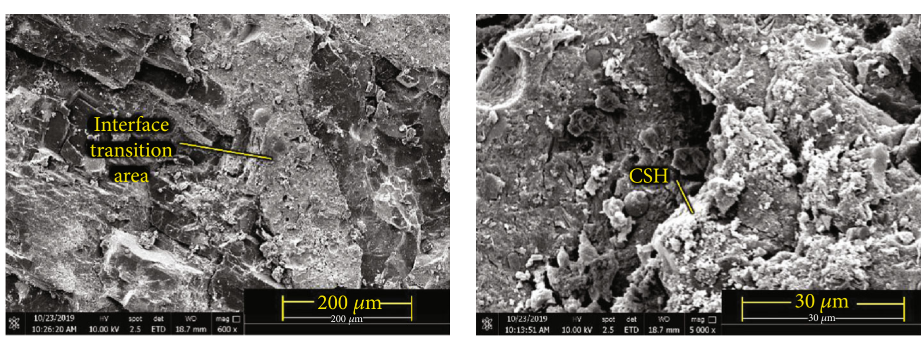

(a) The interface transition area (b) Hydration products

Figure 9: Microscopy images of designed fine grained concrete with 1% CNS.

those of TRC without CNS doping. When basalt fiber fabric is laid out, the load-bearing capacity of TRC sheet is higher than that of the sheet specimens without CNS, and the load-bearing capacity of the sheet increases with the increase of CNS doping in the dosing range of this test. Therefore, the bending test data of each group of specimens show that the higher the doping of CNS is, the more beneficial for improving the flexural load bearing capacity of TRC in the doping range of this test is.

The main reason for the lower strength of the TRC without CNS is that the strength of the fine-grained concrete is lower, the fluidity is poorer, and less fine-grained concrete is invaded inside the fiber bundles. Only the outer fiber roving is bonded to the matrix, and the inner and outer fiber filaments are not synergistically stressed during the stressing process of the thin plate. Therefore, the inner fiber yarn is pulled out sequentially, and bond slip damage occurs, which leads to a decrease in specimen load. However, for the specimens with CNS, the presence of CNS makes the hydration reaction of the TRC matrix more adequate and the bonding with the fibers more tight; therefore, the bending cracking stress of TRC is enhanced by the external nano-SiO_2 doping.

3.5. Microscopic Morphology Analysis. Scanning electron microscopy analysis results demonstrating the internal microstructural morphology of mixed-doped fine-grained concrete and CNS after 28 days of curing are shown in Figures 7–9. A common feature is demonstrated in all of these micromorphological feature maps. When CNS is employed together with silica fume, the interface between the aggregate particles and the hardened cement matrix is effectively densified, resulting in a denser bond between the aggregate and cement interface and an increase in the hardness of the interface transition zone. In addition to the change in interface transition, other structures in the matrix become dense.

The microscopic morphology of the benchmark group is shown in Figure 7. When it is magnified to 1000 times, the natural fine sand particles are tightly bound to the cement paste interface; in addition, the fly ash are not involved in hydration, silica fume particles form solid glass spheres, and hollow spherical shells exist. The surface of the spheres is smooth, and no hydration products are generated, indicating that the hydration reaction of fly ash and silica fume is incomplete, which plays the role of filler. When is magnified to 5000 times, the honeycomb pores between the interface of the aggregate and the cement paste are obvious. The partially intact $Ca(OH)_2$ crystals are attached to the surface of the aggregate and are arranged in a directional distribution, tending to form a directional layer, which is conducive to the emergence of pores and microcracks.

The changes in the microstructure of the fine-grained concrete with the addition of 0.5% CNS are shown in Figure 8, comparing the benchmark group specimens. At a magnification of ×2000, the hydration products are shown on the surface of the fly ash. The synthesized C-S-H gel is mainly presented as flocs or flakes, wrapped around the fly ash in a laminar distribution, and a small amount of layered $Ca(OH)_2$ crystals is observed as the reaction residue of the synthesized C-S-H gel. When it is magnified to ×8000, the fibrous filamentous hydration products form a continuous whole, filling the microscopic cracks within the concrete. The hydration product crystals grow in empty spaces (e.g., larger capillaries) or in entrapped pores, refining the pores and densifying the concrete structure.

The change in the interfacial transition zone between the fine-grained concrete cement matrix and the aggregate particles is shown in Figure 9, when 1.0% CNS is added. The void space between the cement paste and the aggregate particles is completely filled with hydration products, and it is difficult to observe $Ca(OH)_2$ crystals in the interfacial transition zone. On the one hand, the CNS volcanic ash effect consumes a large number of calcium hydroxide crystals, generating more C-S-H gels, reducing the voids, and compacting the interfacial transition zone and cement paste structure; on the other hand, in the hardening stage of the matrix of cementitious materials containing CNS and silica ash, there is a lack or almost no water-filled space around the concrete, and the aggregate is surrounded by a dense and hard matrix with a dense and homogeneous structure.

In summary, the enhancement of the TRC matrix by CNS incorporation is mainly reflected in the strengthening of the interfacial transition zone. One is that the micronized silica fume plays a filling role on the interfacial transition zone, and more importantly, the SiO_2 in CNS reacts with the $Ca(OH)_2$ to generate a C-S-H gel that is more dense than $Ca(OH)_2$, which reduces the voids in the interfacial transition zone.

4. Conclusion

(1) As the water-to-cement ratio is constant, the effect of CNS on the fluidity of the TRC matrix depends on its filling effect and the surface water absorption effect. As the CNS content increases, the slump expansion of fine-grained concrete decreases slowly, when the CNS content is 0%~1%. Besides, the decreased amplitude becomes larger, and the fluidity is poor, when the content is more than 1%

(2) On the one hand, silicon monolayers are formed in fine-grained concrete after adding CNS. These monolayers form Ca $(OH)_2$ that is formed by cement hydration reaction C-S-H, and the gel is filled into the microscopic pores of fine-grained concrete. On the other hand, fly ash secondary hydration is promoted to improve the compressive strength of fine-grained concrete. With the increase of CNS content, the compressive strength of different ages increases first and then decreases. When the CNS content is 1, the compressive strength of each age is the largest

(3) The filling effect of CNS makes the hydrated calcium silicate gel distribute between cement particles in a network. During the tensile process of concrete, the pore stress concentration is weakened, and the tensile stress of the matrix is increased. Thus, the flexural strength of fine-grained concrete is improved. With the increase of CNS content, the flexural strengths in different ages increase first and then decrease. When the CNS is 1.5, the flexural strength of each age is the largest

(4) A large amount of $Ca(OH)_2$ crystals with directional distribution in the interface transition region are consumed by the use of CNS, which reduce the internal pores, and dense the internal structure, and effectively improve the interfacial properties between aggregate particles and hardened cement matrix, thereby enhancing the strength of fine-grained concrete

Data Availability

The data used to support the findings of this study are included within the article.

Conflicts of Interest

The authors declare that they have no conflicts of interest.

Acknowledgments

The Youth Key Teacher Project of Henan Provincial Colleges and Universities (2017GGJS054), Financial Supports from the Key Science and Technology Program of Henan Province, China (No. 202102310253), Joint Funds of the National Natural Science Foundation of China (No. U1904188), the Doctor Foundation of Henan Polytechnic University (No. B2016-67), and the Science and Technology Project of Henan

Provincial Department of Transportation, China (No. 2019J-2-13) are gratefully appreciated.

References

[1] J. Hegger and S. Voss, "Investigations on the bearing behaviour and application potential of textile reinforced concrete," *Engineering Structures*, vol. 30, no. 7, pp. 2050–2056, 2008.

[2] V. Mechtcherine, "Novel cement-based composites for the strengthening and repair of concrete structures," *Construction and Building Materials*, vol. 41, pp. 365–373, 2013.

[3] R. Contamine, A. S. Larbi, and P. Hamelin, "Contribution to direct tensile testing of textile reinforced concrete (TRC) composites," *Materials Science & Engineering A*, vol. 528, no. 29-30, pp. 8589–8598, 2011.

[4] N. Shafiq, R. Kumar, M. Zahid, and R. Tufail, "Effects of modified metakaolin using nano-silica on the mechanical properties and durability of concrete," *Materials*, vol. 12, no. 14, p. 2291, 2019.

[5] Y. Xue, F. Gao, Y. N. Gao, X. Liang, Z. Z. Zhang, and Y. Xing, "Thermo-hydro-mechanical coupled mathematical model for controlling the pre- mining coal seam gas extraction with slotted boreholes," *International Journal of Mining Science and Technology*, vol. 27, no. 3, pp. 473–479, 2017.

[6] T. Suwan, P. Jitsangiam, and P. Chindaprasirt, "Influence of nano-silica dosage on properties of cement paste incorporating with high calcium fly ash," *Key Engineering Materials*, vol. 4874, pp. 9–13, 2020.

[7] Z. Z. Cao, Y. L. Ren, Q. T. Wang, B. H. Yao, and X. C. Zhang, "Evolution mechanism of water-conducting channel of collapse column in karst mining area of Southwest China," *Geofluids*, vol. 2021, Article ID 6630462, 8 pages, 2021.

[8] Y. Xue, P. G. Ranjith, F. Dang et al., "Analysis of deformation, permeability and energy evolution characteristics of coal mass around borehole after excavation," *Natural Resources Research*, vol. 29, no. 5, pp. 3159–3177, 2020.

[9] N. Hani, O. Nawawy, K. S. Ragab, and M. Kohail, "The effect of different water/binder ratio and nano-silica dosage on the fresh and hardened properties of self-compacting concrete," *Construction and Building Materials*, vol. 165, no. 20, pp. 504–513, 2018.

[10] D. Adak, M. Sarkar, and S. Mandal, "Effect of nano-silica on strength and durability of fly ash based geopolymer mortar," *Construction and Building Materials*, vol. 70, no. 20, pp. 453–459, 2014.

[11] M. E. Gülşan, R. Alzeebaree, A. A. Rasheed, A. Niş, and A. E. Kurtoğlu, "Development of fly ash/slag based self-compacting geopolymer concrete using nano-silica and steel fiber," *Construction and Building Materials*, vol. 211, pp. 271–283, 2019.

[12] A. Madadi, H. Eskandari-Naddaf, and M. N. Nejad, "Evaluation of bond strength of reinforcement in concrete containing fibers, micro-silica and nano-silica," *Journal of Stress Analysis*, vol. 3, no. 1, pp. 11–19, 2018.

[13] T. A. Tawfik, M. A. El-Yamani, and S. A. El-Aleem, "Effect of nano-silica and nano-waste material on durability and corrosion rate of steel reinforcement embedded in high-performance concrete," *Asian Journal of Civil Engineering*, vol. 20, no. 1, pp. 135–147, 2019.

[14] L. G. Li, J. Y. Zheng, and P. L. Ng, "Cementing efficiencies and synergistic roles of silica fume and nano-silica in sulphate and chloride resistance of concrete," *Construction and Building Materials*, vol. 223, pp. 965–975, 2019.

[15] Y. G. Wang, S. P. Li, H. Peter, and Y. H. Fan, "Mechanical properties and microstructure of basalt fibre and nano-silica reinforced recycled concrete after exposure to elevated temperatures," *Construction and Building Materials*, vol. 247, 2020.

[16] C. Gunasekara, M. Sandanayake, Z. Zhou, D. W. Law, and S. Setunge, "Effect of nano-silica addition into high volume fly ash-hydrated lime blended concrete," *Construction and Building Materials*, vol. 253, p. 119205, 2020.

[17] J. Wang, Y. Cheng, L. Yuan et al., "Effect of nano-silica on chemical and volume shrinkage of cement-based composites," *Construction and Building Materials*, vol. 247, p. 118529, 2020.

[18] Y. Xue, J. Liu, F. Dang, X. Liang, S. Wang, and Z. Ma, "Influence of CH_4 adsorption diffusion and CH_4-water two-phase flow on sealing efficiency of caprock in underground energy storage," *Sustainable Energy Technologies and Assessments*, vol. 42, article 100874, 2020.

[19] N. Zabihi and M. Hulusi Ozkul, "The fresh properties of nano silica incorporating polymer-modified cement pastes," *Construction and Building Materials*, vol. 168, no. 7, pp. 570–579, 2018.

[20] W. L. Shen, J. B. Bai, W. F. Li, and X. Y. Wang, "Prediction of relative displacement for entry roof with weak plane under the effect of mining abutment stress," *Tunnelling and Underground Space Technology*, vol. 71, pp. 309–317, 2018.

[21] Y. Yue, Y. Zhou, F. Xing, G. Gong, B. Hu, and M. Guo, "An industrial applicable method to improve the properties of recycled aggregate concrete by incorporating nano-silica and micro- $CaCO_3$," *Journal of Cleaner Production*, vol. 259, article 120920, 2020.

[22] J. Yu, M. Zhang, G. Li, J. Meng, and C. Leung, "Using nano-silica to improve mechanical and fracture properties of fiber- reinforced high-volume fly ash cement mortar," *Construction and Building Materials*, vol. 239, article 117853, 2020.

[23] Y. Xue, T. Teng, F. Dang, Z. Ma, S. Wang, and H. Xue, "Productivity analysis of fractured wells in reservoir of hydrogen and carbon based on dual-porosity medium model," *International Journal of Hydrogen Energy*, vol. 45, no. 39, pp. 20240–20249, 2020.

[24] R. Yu, P. Spiesz, and H. J. H. Brouwers, "Effect of nano-silica on the hydration and microstructure development of Ultra-High Performance Concrete (UHPC) with a low binder amount," *Construction and Building Materials*, vol. 65, no. 9, pp. 140–150, 2014.

[25] S. H. G. Mosavinezhad and G. F. Pasikhani, "Fresh performance and corrosion resistance of self-compacting concrete containing nano-silica," *Journal of Research in Science and Engineering*, vol. 1, no. 11, 2019.

[26] J. Puentes, G. Barluenga, and I. Palomar, "Effects of nano-components on early age cracking of self-compacting concretes," *Construction & Building Materials*, vol. 73, no. 6, pp. 89–96, 2014.

[27] Y. Xue, J. Liu, P. G. Ranjith, X. Liang, and S. Wang, "Investigation of the influence of gas fracturing on fracturing characteristics of coal mass and gas extraction efficiency based on a multi-physical field model," *Journal of Petroleum Science and Engineering*, vol. 206, article 109018, 2021.

[28] Z. Z. Cao, P. Xu, Z. H. Li, M. X. Zhang, Y. Zhao, and W. L. Shen, "Joint bearing mechanism of coal pillar and backfilling body in roadway backfilling mining technology," *CMC-Computers Materials & Continua*, vol. 54, no. 2, pp. 137–159, 2018.

[29] L. Zhu, F. Dang, Y. Xue, K. Jiao, and W. Ding, "Multivariate analysis of effects of microencapsulated phase change materials on mechanical behaviors in light-weight aggregate concrete," *Journal of Building Engineering*, vol. 42, article 102783, 2021.

Hindawi
Geofluids
Volume 2021, Article ID 8073602, 9 pages
https://doi.org/10.1155/2021/8073602

Research Article

Catastrophe Mechanism of Stress-Fissure Coupling Field in Mining Close Distance Seams in Southwest China

Suo Jie,[1] Li Zhen-hua ,[2,3] Huang Cun-han,[2,3] Cao Zheng-zheng,[2,3] Xu You-lin,[4] and Chen Zu-guo[5]

[1]School of Geoscience and Technology, Southwest Petroleum University, Chengdu, 610500 Sichuan, China
[2]School of Energy Science and Engineering, Henan Polytechnic University, Jiaozuo, 454000 Henan, China
[3]Collaborative Innovation Center of Coal Work Safety and Clean High Efficiency Utilization, Jiaozuo, 454000 Henan, China
[4]Institute of Mining Engineering, Guizhou Institute of Technology, Guiyang, 550003 Guizhou, China
[5]Xintian Coal Mine, Yonggui Energy Development Co., Ltd., Qianxi, 551500 Guizhou, China

Correspondence should be addressed to Li Zhen-hua; jzlizhenh@163.com

Received 23 April 2021; Revised 22 May 2021; Accepted 19 July 2021; Published 2 August 2021

Academic Editor: Kai Yao

For the sake of studying the catastrophe mechanism of stress-fissure coupling field in mining close distance seams in southwest China, a test working face in Guizhou province in southwest China is adopted and researched by the methods of numerical calculation and similar experiment. When the working face advances to 180 m in 4# coal seam in a similar experiment, the overlying rock breaks to the central base plate of Yulongshan limestone, and the conductive fractures run through the Changxing limestone karst cave and Yulongshan limestone karst cave. When the 1402 working face advances to 350 m, the top of vertical karst caves in the middle of the model produces extrusion damage, forming a penetrating water inrush passage. When the 1402 working face advances to 480 m, the top slab of the working face comes under periodic weighting with the short step. Besides, the mining of 9# coal seam starts after 4# coal seam in mining close distance seams. When the working face in 9# coal seam advances to 340 m in numerical simulation, the maximum opening of the overburden fractures is 51.16 mm. The fractures in the roof are mainly caused by the periodic breaking and falling of the basic roof, connected with the floor fractures of 4# coal seam. When the working face in 9# coal seam advances to 500 m, the maximum opening of the overburden fracture is 93.09 mm. Specifically, as the working face advances, the opening of fracture in the roof after collapse of the basic roof periodically is mainly greater than 5 mm, and the compaction closure is mainly 1 mm-5 mm. The fractures in the gob floor are mainly 0.1 mm-1 mm, and the fracture opening of the collapsed rock mass in the gob is mainly 1 mm-5 mm and greater than 5 mm. The karst caves in the overburden reduce the periodic weighting step of working face and play a guiding role in the direction of fracture development and water inflow passage formation. The karst caves are connected to surface waterfall holes and trap pits, and atmospheric precipitation recharges the water in the caves. The research results can be treated as an important basis for the prevention and treatment for water inrush disaster in mining close distance seams in the karst area of southwest China.

1. Introduction

China is one of the countries with the most extensive karst distribution and the close distance seams in the world [1]. Meanwhile, China has the largest coal mining production in the world [2]. Therefore, there are many coal mines in the karst area in China [3]. However, the ecological environment of the karst mining area is fragile [4]. The underground mining of coal seam causes rock strata movement and induces the development of mining-induced fractures of karst caves in the overburden, which has a great impact on the ecological balance in the karst area [5, 6]. Specifically, the water inrush disaster is easily induced in the downward mining in close distance seams in the karst mining area. For example, the water inrush disasters in downward mining caused by karst caves occurred in the Xintian coal mine in

Guizhou province, which greatly affected the safety mining production [7, 8]. Therefore, it is of great significance to research the evolution mechanism of water inrush passage in the overburden induced by karst caves in downward mining, in order to guarantee the safe mining in the karst mine area.

The scholars at home and aboard have carried out lots of research on the evolution mechanism of water inrush passage in the overburden induced by mining. Liu et al. [9] researched the mechanism of the karst water burst and its prevention countermeasures in Yuanliangshan tunnel systematically, which shows that the karst water burst in tunnels is a gradually developed process, influenced by water pressure, different filling materials, and the plastic zones around the tunnel. Zhao et al. [10] established a nonlinear model of coupled seepage-pipe flows to study the change of flow state of water inrush of confined karst cave, with the introduction of the equivalent hydraulic conductivity of pipe flow for the water inrush of confined karst cave. Jiao et al. [11] investigated the mechanism of delayed groundwater inrush from a covered karst cave in coal seam floor through the analysis of the formation of karst cave with special environment and physical process, in order to prevent the delayed groundwater inrush occurring from a covered karst cave in coal seam floor in north China coalfield. Zhao et al. [12] established the linkage analysis between fluid-solid coupling and strength reduction method of water bursting from concealed confined karst cave before roadway, on the basis of fluid-solid coupling theory of water bursting from confined karst cave and strength reduction method of rock pillar to prevent water inrush. Zhu et al. [13] established four kinds of a generalized model of the overlying rock cave collapse, respectively, under the action of mining; meanwhile, it was mainly analyzed on the basis of the conceptual model of the causes for the collapse caused by the mining. Pan et al. [14] applied a self-developed new type of model test system to the solid-fluid coupling model tests on lagging water-inrush of karst cave and revealed the variation of the multifield information such as displacement, stress, and seepage pressure effectively. Wang et al. [15] established a frustum model for the instability of tunnel face considering the influences of the location and size of the cavern on the stability of the intermediate rock wall, in order to study the bearing capacity and failure mode of the intermediate rock wall in the presence of orthogonal high-pressure caverns in front of horseshoe tunnels. Zhu et al. [16] built the model of mining under karst caves and analyzed the stratum movement law and the failure characteristics of karst caves, in order to study the development law of mining-induced fracture and its influences on fracture development of karst caves when mining in karst area.

The above research results are focus on the evolution mechanism of water inrush passage in the overburden induced by mining, which provide the significant reference for safe and high-efficiency mining [17–20]. In consideration of the wide spread of close distance seams and karst zone in a mining area in China, the disastrous mechanism of stress-fissure coupling field and prevention for water inrush in close distance seams have not been revealed recently. Therefore, it is obvious that the catastrophe mechanism of stress-fissure coupling field in mining close distance seams in southwest China has not been researched systematically and deeply [21, 22]. Based on the mining and geological condition of 1402 working face in Xintian coal mine in Guizhou province, the catastrophe mechanism of stress-fissure coupling field in mining close distance seams in southwest China is studied, by the physical similarity experiment and numerical calculation simulation. The research results can be treated as an important basis for the prevention and treatment for water inrush disaster in mining close distance seams in the karst area of southwest China.

2. Physical Similarity Experiment for Water Inrush Passage Evolution

2.1. Physical Similarity Model. The 1402 working face in the Xintian coal mine has a strike length of 147 m and a dip length of 1148 m. The single strike longwall mining method is adopted for coal mining. The main coal seams are 4# coal seam and 9# coal seam. The mining heights of two coal seams are 4 m and 3 m, and the mining depths are 262 m and 294 m, respectively. According to the geological and mining conditions of the 1402 working face in the Xintian coal mine, there are five large karst caves arranged in the overburden rock in Figure 1, marked as 1# cave, 2# cave, 3# cave, 4# cave, and 5# cave. Specifically, 1# cave and 2# cave are on the left side in physical similarity experiment, and 1# cave is above 2# cave; and 5# cave are in the right side in physical similarity experiment, and there are 3# cave and 4# cave in the middle position from left to right in physical similarity experiment. Meanwhile, the shape characteristics of 1# cave and 2# cave are horizontal caves from top to bottom, and 3# cave is a combination of the longitudinal cave and inclined cave, 4# cave is a vertical cave, and 5# cave is a combination of the horizontal cave, vertical cave, and inclined cave. The spatial position of 1# cave and 2# cave are distributed vertically; besides, 1# cave, 3# cave, 4# cave, and 5# cave are distributed horizontally.

In order to study the spatial and temporal evolution of the mining-induced fracture of Changxing formation chert and the Yulong section chert during the mining of 4# coal seam, physical similarity experimental research for water inrush passage evolution is carried out. The basic physical and mechanical parameters of each rock formation are shown in Table 1, based on the comprehensive histogram of the working face and relevant experiments. The physical similarity model is left with 60 m protective coal pillars on the left and right boundaries. The mining direction is from left to right, with 2 hours interval between each mining.

2.2. Experiment Results. When the 1402 working face advances to 180 m, the overlying rock breaks to the central base plate of Yulongshan limestone, the conductive fractures run through the Changxing limestone karst cave and Yulongshan limestone karst cave, and the delaminations occur between the central and lower Yulongshan limestone. Large damage occurs to the near-horizontal bead-like karst

Figure 1: Physical similarity model.

Table 1: Physical and mechanical properties of rock mass.

No.	Lithology	Height (m)	Buried depth (m)	Density (kg/m^3)	Volume modulus (GPa)	Shearing modulus (GPa)	Internal friction angle (°)	Internal cohesion (MPa)	Tensile strength (MPa)
1	Limestone	180	183	2800	3.06	2.39	42	6.53	5.70
2	Marl	15	198	2750	2.27	1.56	38	4.43	3.53
3	Mudstone	12	210	2670	1.48	0.65	28	2.14	1.38
4	Limestone	30	240	2800	3.06	2.39	42	6.53	5.70
5	Siltstone	10	250	2840	1.94	0.90	33	2.65	2.10
6	Muddy siltstone	3	253	2770	2.50	1.16	35	3.15	2.31
7	Siltstone	5	258	2840	1.94	0.90	33	2.65	2.10
8	4# coal	4	262	1500	1.18	0.55	34	1.56	1.12
9	Muddy siltstone	6	268	2770	2.50	1.16	35	3.15	2.31
10	Mudstone	4	272	2670	1.48	0.65	28	2.14	1.38
11	Siltstone	3	275	2800	2.78	1.28	37	3.64	2.25
12	Siltstone	6	281	2840	1.94	0.90	33	2.65	2.10
13	Fine-grained sandstone	4	285	2800	2.78	1.28	37	3.64	2.25
14	Siltstone	6	291	2840	1.94	0.90	33	2.65	2.10
15	9# coal	3	294	1500	1.18	0.55	34	1.56	1.12
16	Siltstone	3	297	2840	1.94	0.90	33	2.65	2.10

cave located in the lower part. Large damage occurs in the near-horizontal bead-like karst cave located in the lower part. The right-hand boundary of the karst cave is subjected to tensile stress and the rupture surface develops upwards along the right-hand boundary of karst caves, with a small amount of rock at the top of the lateral karst cave collapsing into the karst cave. The central and upper parts of the Yulongshan section are disturbed and remain in a stable structure, as shown in Figure 2.

When the 1402 working face advances to 290 m, the overburden fractures continue to develop upwards, reaching the top of Yulongshan limestone and forming two fracture faces. Due to the guiding effect of karst caves on the expansion of the fractures, the through-fracture surface on the side of the opening cut passes through the beaded karst caves in the middle of Yulongshan limestone. There is a vertical karst cave on the upper left side of 1402 working face, which is skewed to the left side of the model by a certain angle, and runs through the upper, middle, and lower parts of the limestone in the Yulongshan section. The gushing fractures enter at the bottom of the karst cave and penetrate at the top, creating a rupture surface, as shown in Figure 3.

When the 1402 working face advances to 350 m, the top of vertical karst caves in the middle of the model produces extrusion damage. The limestone on the top of the cave collapses, and the bottom is subjected to tensile stress to produce open fractures, forming a penetrating water inrush passage. Due to the continuous compaction of broken rocks in the mined-out area, the broken rock layer further revolves and descends, and the conduction fractures behind the mined-out area are gradually closed by squeezing, as shown in Figure 4.

Figure 2: Water inrush passage in the overburden (mining distance is 180 m).

Figure 3: Water inrush passage in the overburden (mining distance is 290 m).

Figure 4: Water inrush passage in the overburden (mining distance is 350 m).

The periodic weighting is the roof pressure phenomena caused by the periodical collapse of the basic roof in the fractured zone. When the 1402 working face advances to 480 m, the top slab of the working face comes under periodic weighting with the short step. The large stress concentration causes a shear break downwards at the boundary of the central part of the cavern. The cavern in the middle of Changxing limestone has a guiding effect on the development of the fractures so that the fractures pass through the rounded cavern of the Changxing limestone up to the top of the working face. When the trapezoidal fractured rock comes into contact with the mined-out area, the overburden stresses are further transferred to the mined-out area, and eventually, the overburden as a whole forms a stable structure, as shown in Figure 5.

It is obvious that karst caves play a guiding role in the direction of fracture development and water inflow passage formation. The water inflow passage develops from bottom to top, and when it develops to a certain height, it expands towards the karst caves and, finally, leads to the karst caves. When the fractures are sufficiently developed, the conductive fractures tend to be formed between two caves.

Figure 5: Water inrush passage in the overburden (mining distance is 480 m).

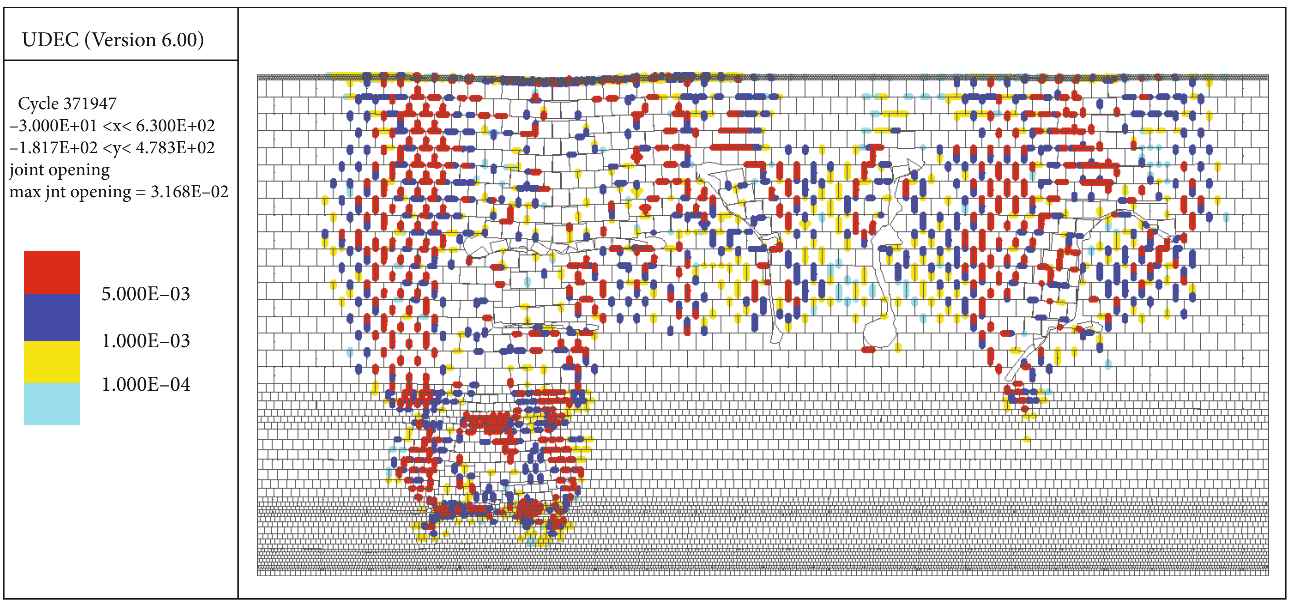

Figure 6: Mining-induced fracture field (mining distance is 180 m in 4# coal seam).

3. Numerical Calculation Simulation for Water Inrush Passage Evolution

The evolution of the mining-induced fracture field of the cavernous overburden at the 1402 working face is researched by numerical calculation simulation in this section, and the scheme is designed by downward mining, namely, the 4# coal seam in mined firstly, followed by mining the 9# coal seam. The numerical simulation model is established in UDEC numerical software, on the basis of the mining geological conditions of 1402 working face, with five karst caves in the overburden. The Mohr-Coulomb model is chosen as the constitutive model, and the Coulomb slip model of surface contact is chosen as the joint constitutive model. The length and the height of the numerical model are 600 m and 297 m, respectively. The mining heights of 4# coal seam and 9# coal seam are 4 m and 3 m, and the mining depths are 262 m and 294 m, respectively. The left and right boundary in the numerical simulation model is the fixed horizontal velocity boundary condition, and the bottom boundary in the numerical simulation model is the fixed vertical velocity boundary condition. The advance length in 4# coal is 400 m, and each step is 20 m; besides, the advance length of 9# coal seam is 400 m, and each step is 20 m. The evolution law of the fracture field during each mining process is analyzed.

3.1. Mining-Induced Fracture Field in 4# Coal Seam. When the working face in 4# coal seam advances to 180 m, the mining-induced fracture field in the overburden is shown in Figure 6. The maximum opening degree of the fracture is 31.68 mm. The fractures in the overlying roof of the working face are mainly concentrated at the front and rear ends of the stope, and the fracture opening is mainly greater than 5 mm. The fractures in the stope floor are mainly 0.1 mm-1 mm. After the collapsed rock mass in the gob is compacted, the fracture opening is mainly greater than 1 mm.

Specifically, the fracture opening greater than 5 mm is mainly used to analyze the penetration characteristics of water inrush passage between overlying karst caves. The 1# cave and 2# cave have a thorough connection. The

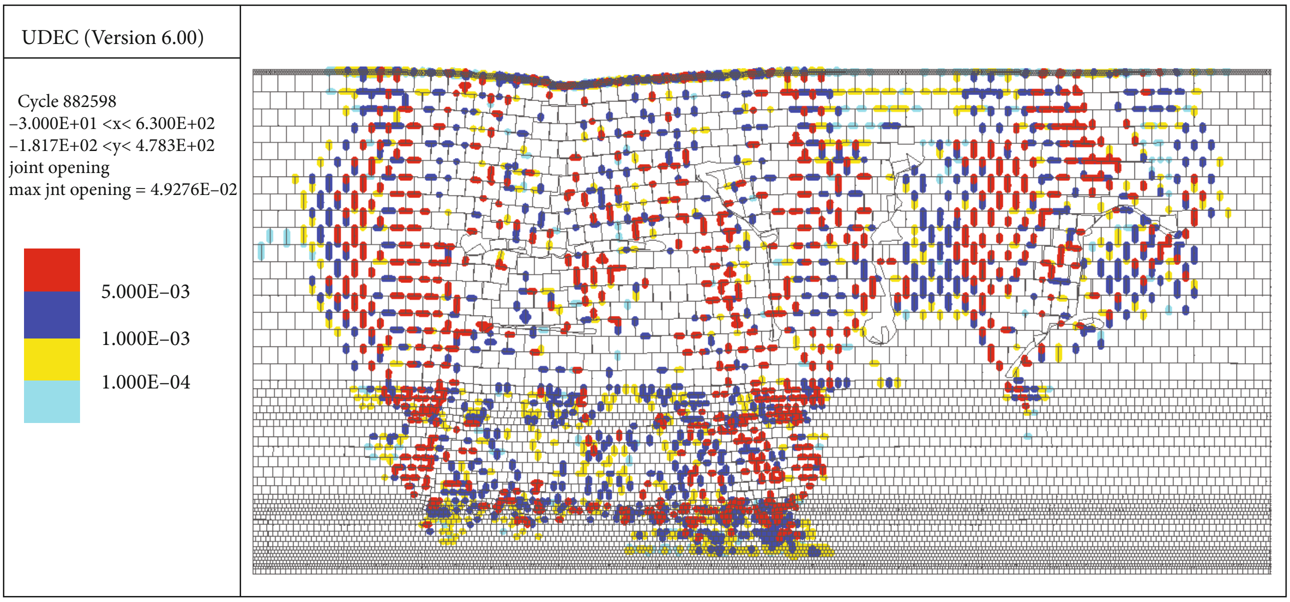

Figure 7: Mining-induced fracture field (mining distance is 320 m in 4# coal seam).

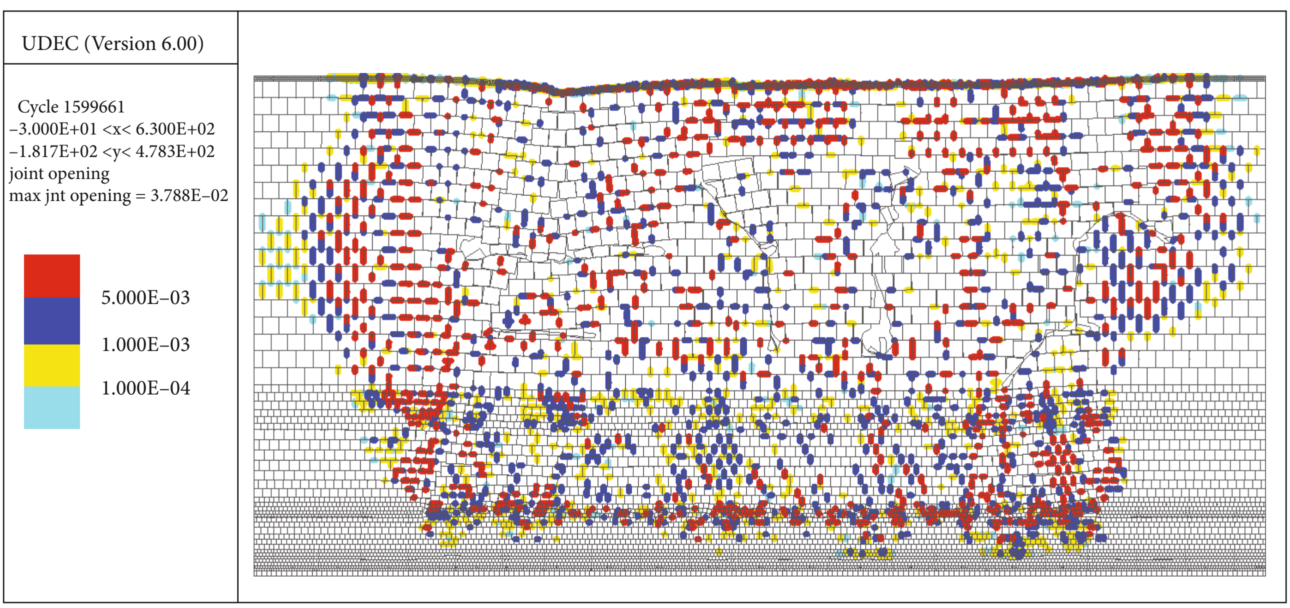

Figure 8: Mining-induced fracture field (mining distance is 500 m in 4# coal seam).

overburden fractures in 1# cave develop up to the surface, and the overburden fractures in 2# cave connect downward to the working face, forming a water inrush passage from the surface to the working face through 1# cave and 2# cave. Meanwhile, the opening degree of secondary development fractures in 3# cave is mainly 1 mm-5 mm, and the opening degree of secondary development fractures in 4# cave is mainly 0.1 mm-1 mm, and the overlying rock fractures of 5# cave basically have no secondary development. Therefore, when the working face in 4# coal seam advances from 100 m to 180 m, the water in the aquifer flows into the working face through the vertical water inrush passage.

When the working face in 4# coal seam advances to 320 m, the mining-induced fracture field is shown in Figure 7. The maximum opening of the overburden fracture is 49.27 mm. The fractures in the roof are mainly concentrated at the front and rear ends of the stope, and the opening degree is mainly greater than 5 mm. The fractures in the bottom of the working face are mainly 1 mm-5 mm, and the bottom of the gob is mainly 0.1 mm-1 mm. After the collapsed rock mass in the mined-out area is compacted, the fracture opening is mainly greater than 1 mm. As the working face advances, the mining-induced fractures in the roof form after the basic roof collapsed periodically, decrease from greater than 5 mm to 1 mm-5 mm, and finally compacted to 0.1 mm-1 mm.

Specifically, the fractures in 3# cave develop upward to the surface and connect downward to the working face,

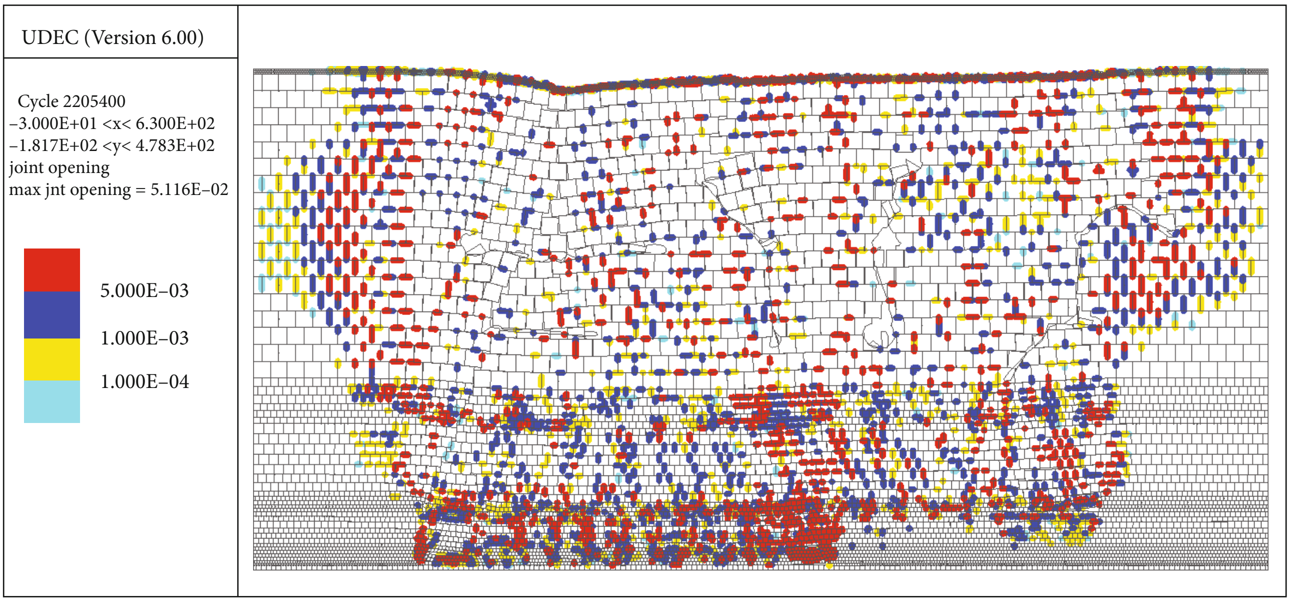

Figure 9: Mining-induced fracture field (mining distance is 340 m in 9# coal seam).

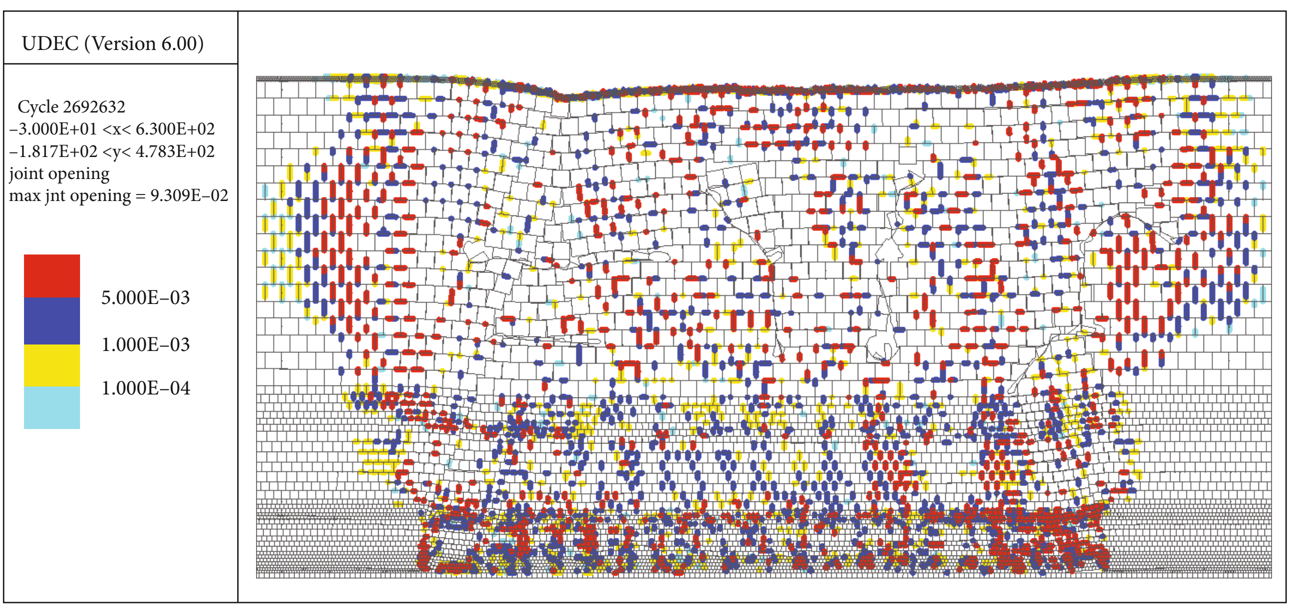

Figure 10: Mining-induced fracture field (mining distance is 500 m in 9# coal seam).

forming a water inrush passage connecting the 3# cave to the surface and the working face. Meanwhile, 1# cave, 3# cave, and 4# cave are connected through the secondary developed fractures in the overburden. The opening degree of the secondary developed fractures of 4# cave has increased from 0.1 mm-1 mm to 1 mm-5 mm and greater than 5 mm.

When the working face in 4# coal seam advances to 500 m, the mining-induced fracture field is shown in Figure 8. The maximum opening of the overburden fracture is 37.88 mm. The fractures in the overlying roof are mainly concentrated at the front and rear ends of the stope, especially at the working face, and the fracture opening is mainly greater than 5 mm. The fractures on the bottom of the working face are mainly 1 mm-5 mm, while the fractures on the bottom of the working face are mainly 0.1 mm-1 mm after the compaction of the collapsed rock. The fractures on the collapsed rock are mainly 1 mm-5 mm and greater than 5 mm. As the working face advances, the opening of the fractures in the roof after the collapse of the basic roof is mainly greater than 5 mm, and the compaction closure is 1 mm-5 mm.

Specifically, the overburden fractures in 4# cave and 5# cave develop up to the surface and connect downward to the working face, forming a water inrush passage connecting 4# cave and 5# cave to the surface and working face, respectively. Meanwhile, 4# cave and 5# cave are connected by secondary developed fractures, and the opening of the overburden fracture at the upper right of 5# cave has increased from 1 mm-5 mm to greater than 5 mm. When the 4# coal seam is mined, the overlying karst caves are formed with transverse intersecting fractures. The secondary developed fractures of the karst caves develop upward to the surface and connect downward to the stope, forming the good water inrush passages in the overburden.

3.2. Mining-Induced Fracture Field in 9# Coal Seam. The mining of 9# coal seam starts after 4# coal seam in downward mining. When the working face in 9# coal seam advances to 340 m, the mining-induced fracture field is shown in Figure 9. The maximum opening of the overburden fractures is 51.16 mm. The fractures in the roof are mainly caused by the periodic breaking and falling of the basic roof, connected with the floor fractures of 4# coal seam. The opening of the fractures is more than 5 mm, forming the water inrush passage from the gob in 4# coal seam to the working face in 9# coal seam.

Specifically, as the working face advances, the opening of fracture in the roof after collapse of the basic roof periodically is mainly greater than 5 mm, and the compaction closure is mainly 1 mm-5 mm. The fractures in the gob floor are mainly 0.1 mm-1 mm, and the fracture opening of the collapsed rock mass in the gob is mainly 1 mm-5 mm and greater than 5 mm.

When the working face in 9# coal seam advances to 500 m, the mining-induced fracture field is shown in Figure 10. The maximum opening of the overburden fracture is 93.09 mm. The fractures in the roof are mainly caused by the periodic breaking and falling of the basic roof, connected with the floor fractures in 4# coal seam. The opening of the fractures is greater than 5 mm, forming the water inrush passage from the gob in 4# coal seam to the working face in 9# coal seam.

Specifically, with the advance of working face, the opening of mining-induced fracture in the roof is greater than 5 mm, and the compaction closure is 1 mm-5 mm. The opening of fractures on the main floor is 0.1 mm-1 mm, while those of collapsed rock mass in the gob are 1 mm-5 mm and greater than 5 mm. The working face in 9# coal seam has little effect on the evolution of water inrush passage induced by karst caves in the overburden.

4. Conclusions

(1) The cavities in the overburden reduce the periodic weighting step of the working face. On the one hand, the caves accelerate the breakage of the overburden; on the other hand, the caves intensify the development of the overburden fractures and form ultrahigh water inrush passage in the overburden. The karst caves in the overburden hydraulic fracture zone are strongly affected by mining, and the fracture opening at the cave is larger than that of the intact rock layer

(2) Karst caves in the overburden play a guiding role in the direction of fracture development and water inflow passage formation. The water inflow passage develops from bottom to top, and when it develops to a certain height, it expands towards the karst caves and, finally, leads to the karst caves. When the fractures are sufficiently developed, the conductive fractures tend to be formed between two caves. The secondary developed fractures of karst caves develop upward to the surface and connect downward to the stope

(3) The water inrush passage is formed with the Yulongshan limestone caves by the influence of the working face. The caves are connected to surface waterfall holes and trap pits, and atmospheric precipitation recharges the water in the caves. The overlying rock is subjected to periodic breakage. The cavern is connected to the lower overburden hydraulic fractures and forms a hydraulic passage with the surrounding trap pillars, eventually forming a water inrush passage between the working face and the karst caves

Data Availability

The data used to support the findings of this study are included within the article.

Conflicts of Interest

The authors declare that they have no conflicts of interest.

Acknowledgments

This work was supported by the National Natural Science Foundation of China (51774110, 41972175, 52004082), the Strategic Consulting Research Project of Henan Institute for China Engineering Science and Technology Development Strategy (2021HENZT03), the Natural Science Foundation of Henan Province (202300410170), and the Fundamental Research Funds for the Universities of Henan Province (NSFRF200302).

References

[1] S. C. Li, K. Wang, L. P. Li, Z. Q. Zhou, S. S. Shi, and S. Liu, “Mechanical mechanism and development trend of water-inrush disasters in karst tunnels,” *Chinese Journal of Theoretical and Applied Mechanics*, vol. 49, no. 1, pp. 22–30, 2017.

[2] L. Y. Yu, L. J. Han, J. L. Ran, S. Q. Yang, and C. M. Zheng, “Comprehensive geological prediction of filling cavity and treatment of mud inrush for yangling tunnel,” *Journal of Basic Science and Engineering*, vol. 24, no. 6, pp. 1256–1267, 2016.

[3] M. Q. Zhang, Q. Y. Zeng, and B. Yang, “Water release mechanism of caverns of karst tunnels and case studies,” *Chinese Journal of Geotechnical Engineering*, vol. 32, no. 10, pp. 1543–1550, 2010.

[4] Y. Xue, J. Liu, P. G. Ranjith, X. Liang, and S. Wang, “Investigation of the influence of gas fracturing on fracturing characteristics of coal mass and gas extraction efficiency based on a multi-physical field model,” *Journal of Petroleum Science and Engineering*, vol. 206, article 109018, 2021.

[5] Z. Z. Cao, P. Xu, Z. H. Li, M. X. Zhang, Y. Zhao, and W. L. Shen, “Joint bearing mechanism of coal pillar and backfilling body in roadway backfilling mining technology,” *CMC-Computers Materials & Continua*, vol. 54, no. 2, pp. 137–159, 2018.

[6] H. X. Lin, F. Yang, Z. Z. Cao, Y. Wang, and X. J. Jiao, "Disastrous mechanism of water discharge in abandoned gob above the stope in mining extra-thick coal seam," *Geofluids*, vol. 2021, 2021.

[7] Y. Xue, J. Liu, F. Dang, X. Liang, S. Wang, and Z. Ma, "Influence of CH4 adsorption diffusion and CH4-water two-phase flow on sealing efficiency of caprock in underground energy storage," *Sustainable Energy Technologies and Assessments*, vol. 42, article 100874, 2020.

[8] B. H. Yao, Z. W. Chen, J. P. Wei, T. H. Bai, and S. M. Liu, "Predicting erosion-induced water inrush of karst collapse pillars using inverse velocity theory," *Geofluids*, vol. 2018, 2018.

[9] Z. W. Liu, M. C. He, and S. R. Wang, "Study on karst waterburst mechanism and prevention countermeasures in yuanliangshan tunnel," *Rock and Soil Mechanics*, vol. 27, no. 2, pp. 228–232, 2006.

[10] Y. L. Zhao, S. G. Zhang, W. Wan, W. J. Wang, L. Cai, and Q. Y. Peng, "Solid-fluid coupling-strength reduction method for karst cave water inrush before roadway based on flow state conversion theory," *Chinese Journal of Rock Mechanics and Engineering*, vol. 33, no. 9, pp. 1852–1862, 2014.

[11] Y. Jiao and H. B. Bai, "Mechanism of delayed groundwater inrush from covered karst cave in coal seam floor," *Journal of China Coal Society*, vol. 38, no. s2, pp. 377–382, 2013.

[12] Y. L. Zhao, P. Cao, W. Wan, W. J. Wang, S. G. Zhang, and S. H. Zou, "Fluid-solid coupling analysis of water bursting catastrophe from concealed confined karst cave before roadway," *Journal of Central South University (Science and Technology)*, vol. 45, no. 5, pp. 1598–1604, 2014.

[13] C. Q. Zhu, Y. J. Huang, Z. Zhou, and Z. Q. Zhang, "The karst cave detection and its collapse generalized model under the effects of mining in huping coal mine," *Journal of Hunan University of Science & Technology (Natural Science Edition)*, vol. 33, no. 4, pp. 7–13, 2018.

[14] D. D. Pan, S. C. Li, Z. H. Xu et al., "Model tests and numerical analysis for water inrush caused by karst caves filled with confined water in tunnels," *Chinese Journal of Geotechnical Engineering*, vol. 40, no. 5, pp. 828–836, 2018.

[15] Z. J. Wang, J. Y. Gao, P. Zhang, X. Guan, and X. F. Ji, "Stability analysis of tunnel face in high-pressure karst tunnels based on catastrophe theory," *Chinese Journal of Geotechnical Engineering*, vol. 41, no. 1, pp. 95–103, 2019.

[16] C. Q. Zhu, D. G. Cui, Z. Zhou, Q. F. Li, and Y. J. Huang, "Similar simulation of mining-induced fissure development law and cave destruction character when mining in karst area," *Chinese Journal of Underground Space and Engineering*, vol. 15, no. 1, pp. 93–100, 2019.

[17] Y. Xue, P. G. Ranjith, F. Dang et al., "Analysis of deformation, permeability and energy evolution characteristics of coal mass around borehole after excavation," *Natural Resources Research*, vol. 29, no. 5, pp. 3159–3177, 2020.

[18] Z. Z. Cao, F. Du, Z. H. Li, Q. T. Wang, P. Xu, and H. X. Lin, "Research on instability mechanism and type of ore pillar based on the fold catastrophe theory," *CMES-Computer Modeling in Engineering & Science*, vol. 113, no. 3, pp. 287–306, 2017.

[19] W. L. Shen, J. B. Bai, W. F. Li, and X. Y. Wang, "Prediction of relative displacement for entry roof with weak plane under the effect of mining abutment stress," *Tunnelling and Underground Space Technology*, vol. 71, pp. 309–317, 2018.

[20] Y. Xue, F. Gao, Y. N. Gao, X. Liang, Z. Z. Zhang, and Y. Xing, "Thermo-hydro-mechanical coupled mathematical model for controlling the pre-mining coal seam gas extraction with slotted boreholes," *International Journal of Mining Science and Technology*, vol. 27, no. 3, pp. 473–479, 2017.

[21] Y. Xue, T. Teng, F. Dang, Z. Ma, S. Wang, and H. Xue, "Productivity analysis of fractured wells in reservoir of hydrogen and carbon based on dual-porosity medium model," *International Journal of Hydrogen Energy*, vol. 45, no. 39, pp. 20240–20249, 2020.

[22] Z. Z. Cao, Y. L. Ren, Q. T. Wang, B. H. Yao, and X. C. Zhang, "Evolution mechanism of water-conducting channel of collapse column in karst mining area of Southwest China," *Geofluids*, vol. 2021, 2021.

Hindawi
Geofluids
Volume 2021, Article ID 5541512, 11 pages
https://doi.org/10.1155/2021/5541512

Research Article

Study on Micro Displacement Mechanism of Hydraulic Fracturing by Oil Displacement Agent at High Pressure

Fengjiao Wang[1,2] **Xu Wang,**[1] **Yikun Liu**[1] **Qingjun Deng,**[3] **Jianan Hu,**[4] **and Yingbo Lv**[4]

[1]*Laboratory of Enhanced Oil Recovery of Education Ministry, Northeast Petroleum University, Daqing, 163318 Heilongjiang, China*
[2]*Daqing Oilfield Co. Ltd., Postdoctoral Res Ctr, Daqing Heilongjiang 163453, China*
[3]*No. 1 Oil Production Plant CNPC (China), Daqing, Heilongjiang 163318, China*
[4]*Fuyu Oil Production Plant, Jilin Oilfield, Songyuan, Jilin 138000, China*

Correspondence should be addressed to Yikun Liu; liuyikun@nepu.edu.cn

Received 26 February 2021; Revised 27 May 2021; Accepted 5 July 2021; Published 23 July 2021

Academic Editor: Chuangzhou Wu

The type-III oil formations in Daqing Oilfield are the representatives of medium-low permeability reservoirs in ultrahigh water cut oilfields of China, which is characterized by bad connectivity of pores and throats, dispersed residual oil distribution, and difficult to displace effectively. In order to produce the residual oil, we propose a new EOR (enhanced oil recovery) method which is hydraulic fracturing by an oil displacement agent at high pressure. In this paper, firstly, we have performed three sets of displacement experiments under different conditions to provide the basis for the analysis of changes in core pore structure and wettability. Next, overburden pressure porosity and permeability tests were used to analyze the effect of the injection of an oil displacement agent at high pressure on core physical properties. Correspondingly, the constant speed mercury injection tests were used to determine the radius distribution of pore throat and change of seepage resistance under different displacement conditions. Moreover, the scanning electron microscopy (SEM) tests of cores were carried out to observe and analyze changes in pore-throat size and connectivity, mineral particle accumulation, and cementation before and after hydraulic fracturing by an oil displacement agent at high pressure. Finally, core wettability tests were conducted to discuss and analyze the rule of core wettability change in hydraulic fracturing by an oil displacement agent at high pressure, and its mechanism of wettability changes. Research shows that increasing the formation energy is the most important mechanism of EOR by a fracturing-seepage-displacement method. Additionally, the type of an oil displacement agent has less effect. After an oil displacement agent at high pressure is injected to fracture the formation, it not only provides efficient flow channel and larger sweep volume for an oil displacement agent. Under the flushing action of high-pressure injection fluid, the original way of line or point contact between mineral particles gradually changes to free particles. Therefore, the pore throat size increases, some larger pores are formed, and the overall flow resistance decreases. After the injection of fluid at high pressure, the energy in formation has increased and the core wettability changes from oil-wet to weakly water-wet. This is not only because the residual oil on the pore surface is flushed by high pressure; in addition, the adsorption of an oil displacement agent on the rock surface reduces the liquid-solid interface energy and changes the wettability, thus improving the oil displacement efficiency.

1. Introduction

Nowadays, about 70% of Chinese oil production is still exploited from the old oilfields. For a period of time in the future, the old oilfields will still be the main Chinese oil supply [1–5]. Take Daqing Oilfield of China as an example, at present, water driving is still the main way of oil development. The general water cut is about 92.7%, but the recovery rate is only about 35%: thus, there is great potential for further EOR in this area [6–9]. Additionally, the remaining oil mainly exists in medium-low permeability reservoirs. While these reservoirs are always bad in physical properties and the distribution of remaining oil is relatively dispersed, it is difficult to inject the oil displacement agent and, definitely, the remaining oil is difficult to be produced [10, 11]. Therefore, there is an urgent need for a reasonable oil formation improvement method that can effectively produce the oil and release the dispersed remaining oil.

The development experience of large oilfields in the United States and Russia shows that oil production is a process of gradual improvement, which is mainly reflected in the increasingly reservoir hierarchy division and the increasing density of well pattern [12–14]. With the continuous hierarchy division of reservoir and interwell infill in multilayer sandstone reservoir, the injection-production pressure system is constantly improved and strengthened. In the process of oil production, from primary oil recovery, secondary oil recovery to tertiary oil recovery, reservoir energy supplement has always been one of the most important methods to EOR [15–18]. Elastic energy recovery, dissolved gas driving, gas driving, steam huff and puff, and so on, the mechanism of EOR is essential to maintain or increase the formation energy. After all, enough pressure is the fundamental driving force of crude oil development; enough pressure difference ensures the successful exploitation of crude oil sustainable development.

Hydraulic fracturing, as a direct and effective stimulation measure, has been widely used in oilfields all over the world. With the exploration, development, and utilization of shales and other unconventional reservoirs, hydraulic fracturing has become a necessary means to result in complex fracture systems instead of simple planar fractures and provide flow channel for oil and gas [19–21]. For a long time, the fracturing fluid with high viscosity and low filtration has been widely used in the fracturing operation domestically and overseas [22–24]. These fracturing fluids generally have the advantages of high viscosity and low fluid loss. The commonly used fracturing fluids are represented by guanidine or modified guanidine. Vegetable gum water-based fracturing fluid is one of the most commonly used fracturing fluids, which is used earlier. Its high viscosity and low fluid loss can satisfy the needs of fracturing and carrying sand [25–27]. In order to further improve the fracturing performance effect, various fracturing fluid systems have been developed successively, such as crosslinked polymer gel fracturing fluid system [28], foam fracturing fluid system [29], VES fracturing fluid system [30, 31], cellulose fracturing fluid system, and so on [32]. These developments have improved the temperature resistance, shear resistance, sand carrying capacity, and wall building performance of the fracturing fluid system.

Since the first hydraulic fracturing well was constructed in 1947, hydraulic fracturing has always been used to establish a high-speed flow channel to increase oil and gas production and injection [33, 34]. At the later stage of oilfield development, it is difficult to effectively use the dispersed remaining oil in medium-low permeability reservoirs. In view of the above problems, our research team proposed a new EOR method: hydraulic fracturing by an oil displacement agent with high pressure. In this method, the oil displacement agent with low initial viscosity is used as fracturing fluid, and the oil displacement agent is carried to the target reservoir by the way of hydraulic fracturing. The oil displacement agent is rapidly pushed to the enrichment position of remaining oil through fractures, so as to achieve the higher efficiency of oil displacement. The process of hydraulic fracturing is transformed into the process of fracturing-seepage-oil displacement along the direction of perpendicular to the fracture. In this way, the displacement agent can quickly enter the pores; thus, the contact time and distance between the oil displacement agent and the formation can be shortened effectively. So it can solve the problems of higher fracturing fluid loss and lower utilization efficiency of the oil displacement agent in the traditional injection process. As we all know, the oil recovery depends on effective swept volume and oil displacement efficiency. Only when the swept volume reaches a certain extent, the oil displacement efficiency can be improved; only by effectively improving the liquid absorption capacity of medium-low permeability layers or small-medium pores in the reservoir can the swept volume be expanded and the oil recovery be greatly enhanced [35–37]. This new EOR method of fracturing-seepage-oil displacement combines the advantages of increased formation pressure, expanded swept volume, and enhanced oil displacement efficiency.

In this paper, aiming at the hydraulic fracturing by an oil displacement agent with high pressure we proposed, a series of studies on micro displacement mechanism has been carried out. The natural core parameters, including permeability, porosity, pore throat structure, and wettability, were tested by overburden porosity and permeability instrument, constant speed mercury injection instrument, scanning electron microscope (SEM), contact angle instrument, and oil displacement device. We have designed a series of experiments to compare and analyze the effects on micropore structure of cores under different conditions, including oil displacement at conventional speed, oil displacement by water at high pressure, and oil displacement by oil agent displacement at high pressure. On this basis, we clarified the micro oil displacement mechanism of hydraulic fracturing by an oil displacement agent at high pressure.

2. Materials and Methods

2.1. Experimental Materials. In this EOR method, as the oil displacement agent was injected under the condition of high pressure and would fracture the reservoir, it could also be regarded as the fracturing fluid. The oil displacement agent was the surfactant (petroleum sulfonate), which was provided by the Daqing Oilfield Downhole Operation Branch Company. The fracturing fluid used in the comparison experiment was water. The water in the experiments was prepared in the on-site construction of the Downhole Operation Branch Company. The oil in the experiments was simulated oil, which was a mixture of degassed and dehydrated crude oil and light hydrocarbon oil in Daqing Oilfield. The viscosity of the simulated oil was 8.86 mPa·s at 45°C. The cores in the experiments were natural cores, which were taken from the type-III formations of No.1 oil production plant in Daqing Oilfield. The diameter of natural core was 2.5 cm, and the permeability was in the range of $100 \times 10^{-3}\,\mu m^2$ to $200 \times 10^{-3}\,\mu m^2$.

2.2. Instrument and Facilities. In this study, we carried out three sets of displacement experiments under different conditions to provide the basis for the analysis of changes in core pore structure and wettability at first. Based on them, overburden pressure porosity and permeability tests, core pore radius distribution test, microstructure change test, and wettability change test were performed. The main device used in the experiments included an overlaying pressure pore-permeability instrument, constant speed mercury injection instrument, scanning electron microscope (SEM), and contact angle tester. The microscopic pore structure parameters of the core were measured by a constant speed mercury injection instrument. A Fei Tecnai G2 F20 scanning electron microscope (SEM) from Gatan Company, USA, was used to test the micromorphology of natural cores. The equipment used in oil displacement experiments mainly includes an advection pump, pressure gauge, and oil displacement agent container. Except for the advection pump, the other facilities were placed in an oven with a constant temperature of 45°C. The displacement pressure was provided by the advection pump, and the fluid in the intermediate container was injected into the cores. In order to compare the effects of conventional displacement and fracturing-seepage-displacement methods at high pressure on the microscopic pore throat structure and wettability changes of cores, we had designed three sets of experiments, including the following: (a) oil displacement at conventional speed, the injection rate was 0.1 mL/min and the injection volume was 30 PV (pore volume); (b) hydraulic fracturing by water flooding at high pressure, the injection pressure was 20 MPa and the injection volume was 30 PV; (c) hydraulic fracturing by oil displacement agent flooding at high pressure, the injection pressure was 20 MPa and the injection volume was 30 PV. Combined with the SEM test, the influence of different displacement conditions on the microstructure changes of cores was analyzed through the core samples after displacement obtained in this experiment. The schematic diagram of the experimental set-up is shown in Figure 1.

2.3. Experimental Methods. In this study, there were four experiments that were conducted to reveal the micro displacement mechanism of hydraulic fracturing by an oil displacement agent at high pressure to EOR. The detailed experimental methods and procedures of each experiment are as follows.

2.3.1. Methods for Measurement of Core Porosity and Permeability. The same natural core was cut into four segments of equal in length, and permeability and porosity tests were carried out under four different conditions. The experiment was performed with an overburden pressure pore-permeability instrument as shown in Figure 2. (1) A natural core with a diameter of about 2.5 cm was selected, and it should be dried; (2) the selected natural cores were cut into four parts with the same in length, and the target cores were loaded into the core gripper of the overburden pressure pore-permeability instrument; after setting the confining pressure parameters, the cores were loaded to measure the porosity; (3) the ratio of gas flow rate to core volume of the gas tank under constant pressure was calculated by computer, and the porosity could be obtained; (4) after the porosity measurement was over, the system began to enter the stage of the permeability measurement. The computer calculated the core permeability by calculating the pressure drop rate under the gas tank and other flow conditions.

2.3.2. Conventional Mercury Injection Measurement of Core Parameters. The microscopic pore structure parameters of the core were measured by a constant speed mercury injection instrument as shown in Figure 3. (1) A natural core with a diameter of about 2.5 cm was selected, and it should be washed with toluene oil and then dried; (2) measurement of the physical properties of the target core, including permeability measured with gas, volume, mass, and density; (3) the target core was loaded into the constant speed mercury injection instrument, and mercury was injected under the set pressure. After the pressure stabilized, the pressure and mercury injection volume were recorded to improve the injection pressure, and the above experimental process was repeated. (4) The injection pressure was equal to the capillary pressure corresponding to the pore radius where mercury could be injected, and the capillary radius corresponding to the capillary pressure was equal to the pore throat radius of the core. By continuously increasing the injection pressure, the capillary pressure curve could be obtained, and the distribution probability of different pore radius could be calculated by combining the volume of mercury injected.

2.3.3. Method for Measurement of Core Microscopic Morphology. The core morphology was observed by a scanning electron microscope shown in Figure 4. (1) Core sample production: use a burette to absorb a small amount of core debris, evenly coated in clean and fixed sample box, serial reserve; (2) freezing and drying samples: the prepared samples were quickly transferred to the E7400cryotrans refrigerating platform, then slowly poured into liquid nitrogen for freezing and vacuuming, and then rapidly heated up. The water in the sample froze and sublimated to get dry samples; (3) gold spraying: the sample was placed in a certain vacuum high voltage electric field, the high voltage electric field ionizes the air, and then the sample surface was coated with a layer of conductive metal film; (4) electron microscope scanning: the samples were placed under the scanning electron microscope and observed in the sample room. Pictures were selected to observe the microscopic morphology of each sample, and the characteristics of different systems were evaluated and analyzed.

2.3.4. Core Wettability Analysis. The wettability experiment mainly used contact angle measuring instrument SDC-200S as shown in Figure 5. Wettability is the interaction between oil and water and reservoir rock under reservoir conditions, which determines the microscopic and original distribution state of reservoir fluid in rock channels and plays a determination role in the recovery of crude oil in oil production. (1) The columnar natural core was selected, and the core was ground until the surface was smooth. The titration volume of the microsyringe needle was set as 3.00 μL, the sample table was used to collect distilled water, and the camera was used to record this process; (2) after setting the baseline

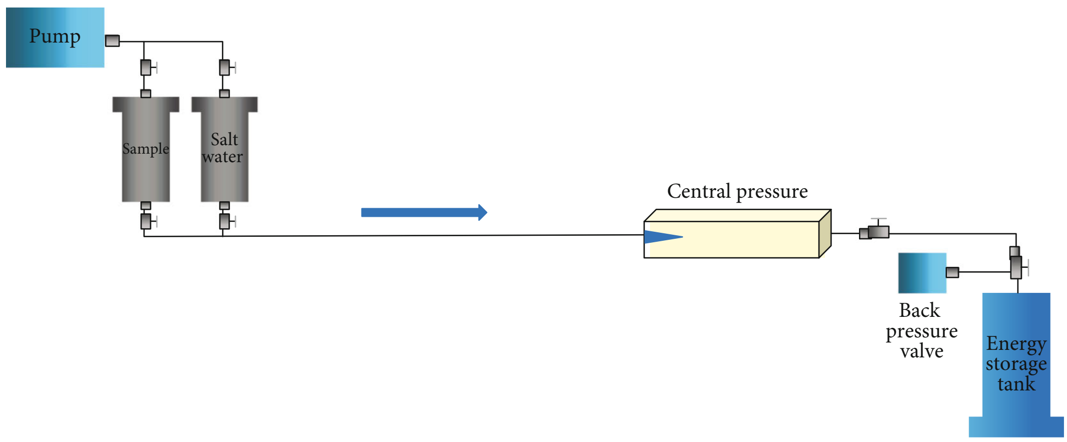

Figure 1: Schematic diagram of the experimental set-up.

Figure 2: Overburden pressure porosity instrument.

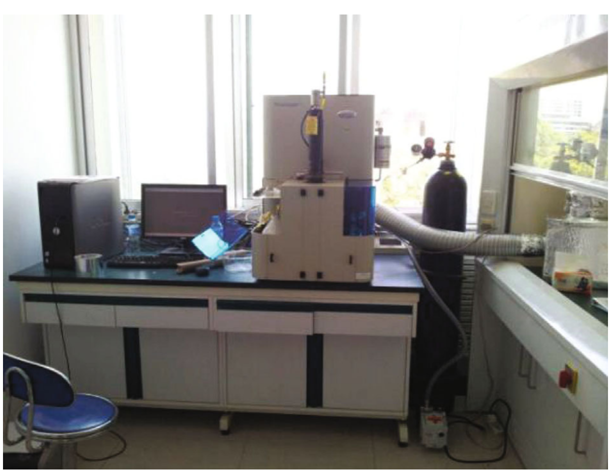

Figure 3: Constant speed mercury injection instrument.

position and the fitting function, the droplet contour could appear on the droplet image and the droplet connection could be obtained tentacles; (3) the systematic error of the effective result should be less than 5%. In order to minimize the error, three different measuring points were randomly selected on the same core, and the average value of the effective result was taken as the core contact angle; (4) the core was taken out after soaking in distilled water for a period of time, and the change of foundation angle after soaking was measured after drying. (5) The system error of the contact angle measuring instrument was less than 5%; (6) measurement of wettability after conventional water flooding: the wettability of the core after displacement was measured, i.e., steps (1)-(5) were repeated. (7) Measurement of core wettability after fracturing by water flooding formed at high pressure: steps (1)-(5) were repeated. (8) Measurement of core wettability after fracturing by surfactant flooding formed at high pressure: steps (1)-(5) were repeated.

The self-priming method was used to measure the core wettability index as shown in

$$I_w = \frac{w_a}{w_a + w_w}, \tag{1}$$

$$I_o = \frac{w_o}{w_o + w_b}, \tag{2}$$

$$I_{w-o} = I_w - I_o, \tag{3}$$

where I_w denotes the wettability index of oil phase; I_o denotes the wettability index of water phase; I_{w-o} denotes the Amott-Harvey index; w_a denotes the amount of crude oil discharged by spontaneous absorption; w_w denotes the amount crude oil discharged by water driving; w_o denotes the amount of water discharged by spontaneous oil absorption; w_b denotes the amount of water discharged by oil flooding.

The wettability grading standards are shown in Table 1.

3. Results and Discussions

3.1. Test Results of Porosity and Permeability Changes in Natural Cores. The natural cores 17-1 and 21-2 of the type-III formations of the No.1 oil production plant in Daqing Oilfield were selected and quartered. They tested the porosity and permeability of the cores in its original state, conventional water injection displacement, hydraulic fracturing by water flooding at high pressure, and hydraulic fracturing by oil displacement agent flooding at high pressure. The core parameter test results are shown in Table 2.

Figure 4: FEI Tecnai G2 20 scanning electron microscope.

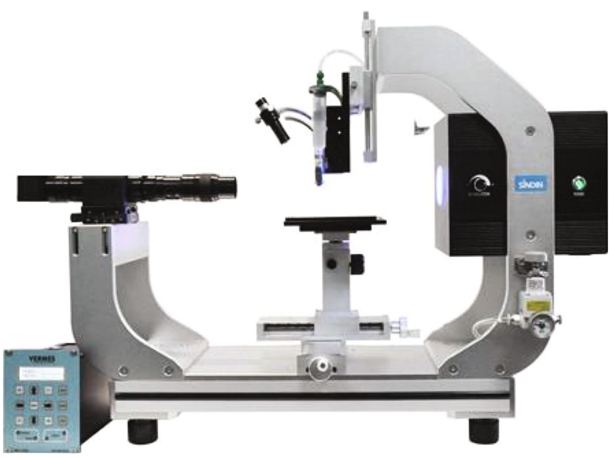

Figure 5: SDC-200S contact angle tester.

The measurement results of porosity and permeability under different displacement conditions of natural cores 17-1 and 21-2 are as shown in Figures 6 and 7, respectively. Obviously, for the cores in the original state and after water flooding under conventional injection rate, the porosity and permeability changed little. However, for the cores under hydraulic fracturing by water or an oil displacement agent at high pressure, the porosity and permeability were significantly increased. In particular, the permeability of core 17-1 and core 21-2 was increased by about $50 \times 10^{-3}\,\mu\text{m}^2$ after displacement at high pressure. It showed that high injection pressure greatly improved the percolation capacity of the reservoirs. It is worth noting that the change of core porosity and permeability parameters was mainly related to the increase of reservoir energy and high-pressure flushing, but less affected by the injected fluid. Namely, whether the injection fluid was water or oil displacement agent, the effect was not obvious.

3.2. Test Results of Core Pore Structure by SEM. The pore structure tests of natural cores were performed by SEM under four states, including original state, conventional water injection displacement (injection rate: 0.1 mL/min, 30 PV), hydraulic fracturing by water flooding at high pressure (injection pressure: 20 MPa, 30 PV), and hydraulic fracturing by an oil displacement agent at high pressure (injection pressure: 20 MPa, 30 PV). The experimental results of core 17-1 are shown in Figure 8.

Figure 8(a) shows the original state of the type-III core before fracturing. The pores were filled with kaolinite, and the clay on the surface of the particles was not obvious. Additionally, the development phenomenon of intergranular pores was not obvious and the mineral particles contacted with each other in the form of points or lines. After conventional injection water displacement as shown in Figure 8(b), the occurrence state and pore form of the mineral had no obvious change. The main components of the core were complete, and no feldspar was damaged or corroded. However, when the core was displaced by high-pressure injection fluid as shown in Figures 8(c) and 8(d), the supporting mode of the skeleton particles had changed. The cementing materials at the cementation between particles were migrated to other parts under the high-pressure injection fluid washing. The original contact relationship between the particles gradually changed to the contact mode with free particles, and the number of connected pores and throat increased. The experimental results showed that in the process of fracturing and oil displacement, the fracturing fluid stored energy at the fracture after hydraulic fracturing, and the fracturing fluid formed a large energy field at the fracture and percolated into the matrix. In the process of fracturing-seepage-displacement, the permeability and porosity of natural core increased. The change of core basic parameters was mainly related to energy enhancement.

3.3. Test Results of Conventional Mercury Injection. In order to study the change of pore structure of matrix cores under different displacement methods, a conventional mercury injection instrument was used to measure the natural cores of type-III formations of Daqing Oilfield. The mercury injection test results of the core under the original state are shown in Figure 9. The test results of hydraulic fracturing by oil displacement agent (surfactant) flooding at high pressure are shown in Figure 10. Table 3 shows the measurement results of core pore result parameters under different displacement conditions.

The results showed that the maximum pore radius and average pore radius of the cores became larger, and the pore distribution range became smaller, and the pore distribution tended to be more stable as the fracturing fluid flowed into the matrix under the action of increasing energy of the fracturing fluid. After injecting the oil displacement agent at high pressure, the greater the contribution rate of pore and throat to permeability in the range of 6.3 μm to 10 μm, the higher the distribution frequency of pore throat radius in this range. At present, the main outlet channel radius and effective seepage channel radius were usually used to describe the contribution of pore throat radius to permeability. The outlet channel radius referred to the distribution range of pore throat radius corresponding to the peak value of permeability contribution distribution curve. Before oil displacement agent flooding at high pressure, the distribution frequency

Table 1: The wettability grading standards.

Wettability index	Wettability grade				
	Oil-wet	Weak oil-wet	Neutral	Weak water-wet	Water-wet
The wettability index of oil phase	1~0.8	0.7~0.6	Approximate	0.3~0.4	0~0.2
The wettability index of water phase	0~0.2	0.3~0.4		0.7~0.6	1~0.8
$I = I_w - I_o$	[-1,-0.1]		(-0.1,0.1)	(0.1,1]	

Table 2: Results of porosity and permeability measurements in natural cores.

Core number	The experimental scheme	Porosity measured with gas (%)	Overburden pressure porosity (%)	Effective permeability ($\times 10^{-3}\ \mu m^2$)
17-1	Original state (predisplacement)	23.8	22.4	86.0
	Water driving under conventional injection rate	24.0	22.7	93.2
	Hydraulic fracturing by water at high pressure	25.5	24.5	134.6
	Hydraulic fracturing by oil displacement agent at high pressure	25.0	24.2	127.4
21-2	Original state (predisplacement)	24.6	23.8	113.6
	Water driving under conventional injection rate	25.0	24.1	120.2
	Hydraulic fracturing by water at high pressure	28.2	26.3	166.3
	Hydraulic fracturing by oil displacement agent at high pressure	29.4	26.5	175.5

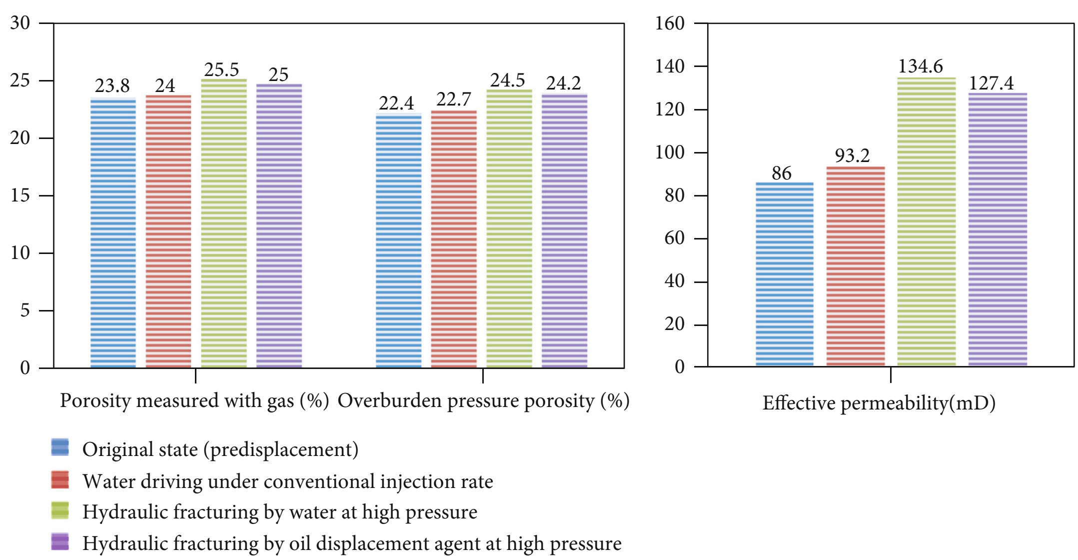

Figure 6: Results of porosity and permeability measurements of core 17-1.

peak of pore throat radius appeared in the range of 4 μm to 6.3 μm; after oil displacement agent flooding at high pressure, the distribution frequency peak of pore throat radius appeared in the range of 6.3 μm to 10 μm. This showed that high-pressure displacement made the core pore size generally increase, the fluid flow resistance in the core became smaller, and the seepage capacity was improved.

3.4. Test and Analysis Results of Core Wettability Test. In order to study the influence of the high-pressure oil displacement agent on the wettability of matrix core, contact angle tests under different displacement conditions were carried out. Contact angle test results of core 17-1 are shown in Figure 11. According to Equations (1)–(3), we calculated the wetting index under four experimental conditions of core 17-1 and core 21-2, as shown in Figure 12.

The natural cores of the type-III formation in the No.1 oil production plant of Daqing Oilfield were of weak oil-wet type as shown in Figure 11(a), and the wettability of the cores was still of oil-wet type after water flooding under conventional

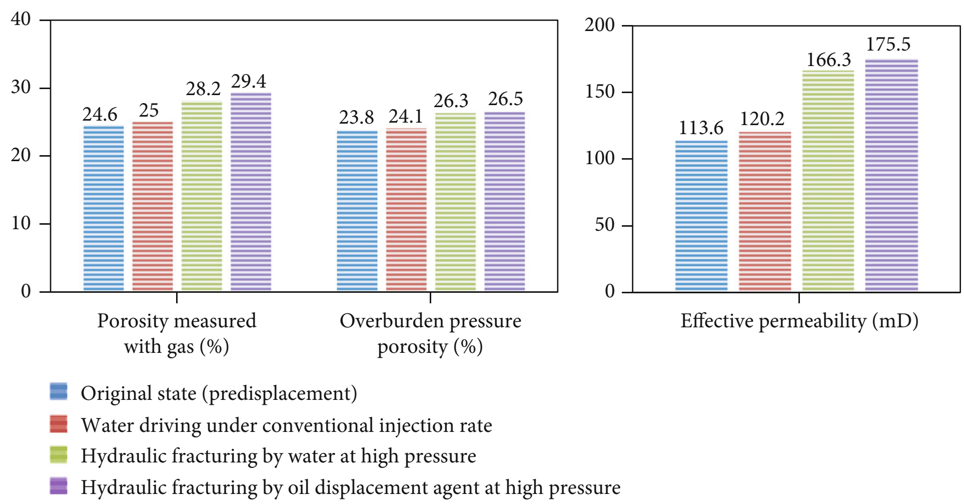

Figure 7: Results of porosity and permeability measurements of core 21-2.

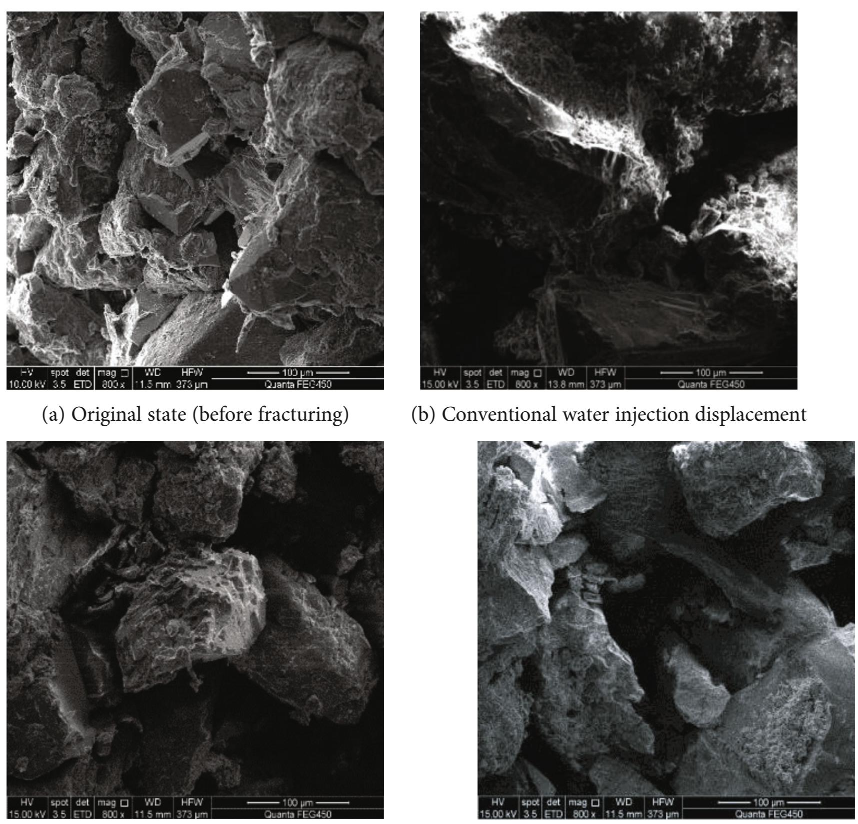

(a) Original state (before fracturing)

(b) Conventional water injection displacement

(c) Fracturing by water at high pressure

(d) Fracturing by an oil displacement agent at high pressure

Figure 8: Changes of core pore structure in different states of core 17-1.

injection rate as shown in Figure 11(b). After injecting water into the core at high pressure, the wetting angle decreased obviously, and the wettability of pore wall changed from oil-wet to weak water-wet as shown in Figure 11(c). In addition, when the injected fluid at high pressure was replaced by an oil displacement agent (surfactant in this paper), the wetting angle of the core wall decreased further as shown in Figure 11(d). It was the combined effect of high-pressure injection of an oil displacement agent and the surfactant on reducing interfacial tension. From the change of wettability index of core 17-1 and core 21-2, the average value also changed from negative to positive after high-pressure injection.

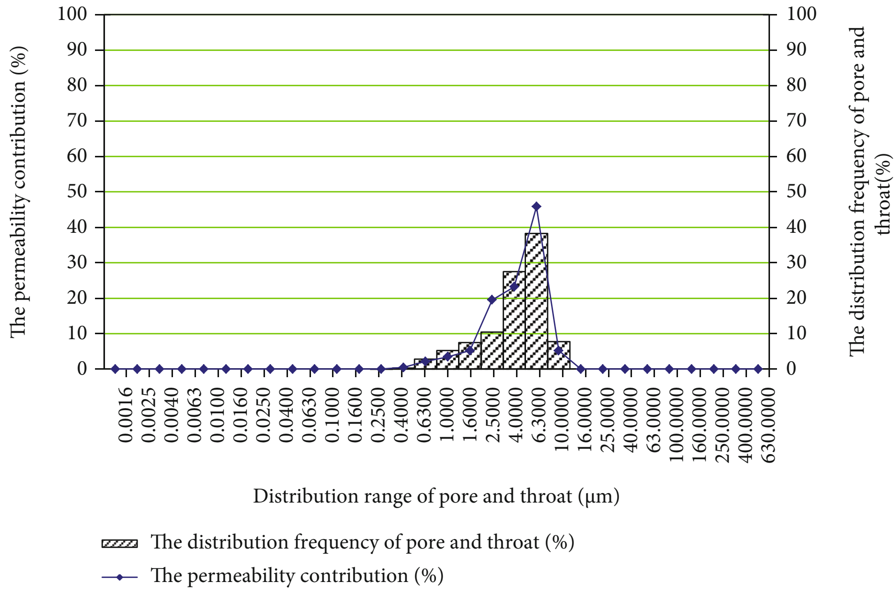

Figure 9: Core pore radius distribution results under the original state of core 21-2.

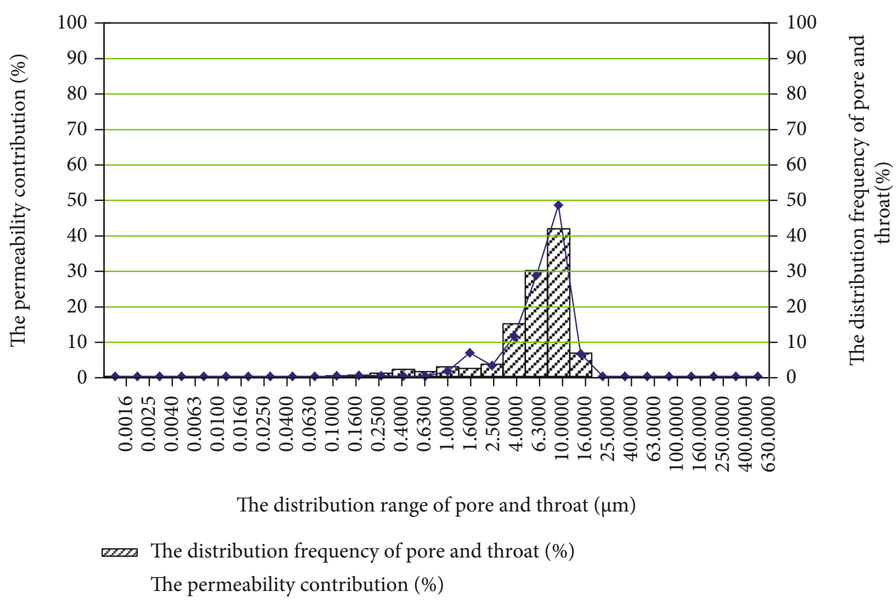

Figure 10: Core pore radius distribution results under the state of hydraulic fracturing by an oil displacement agent (surfactant) with high flow rate displacement of core 21-2.

Table 3: The measurement results of core pore parameters under different displacement methods.

Experimental scheme	Maximum pore radius (μm)	Average pore radius (μm)
Core original parameters (before displacement)	13.82	4.736
Core original parameters (after fracturing and driving by surfactant) (20 MPa)	21.23	7.401

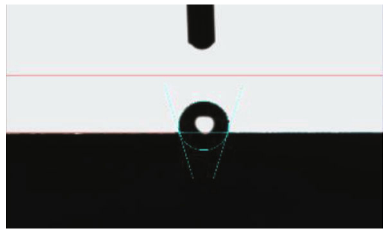

(a) Contact angle = 102.6°

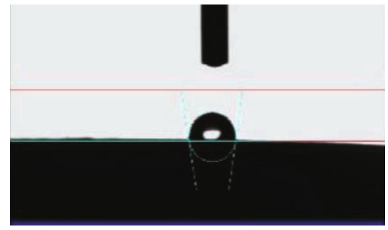

(b) Contact angle = 98.7°

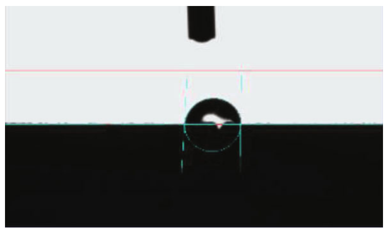

(c) Contact angle = 87.5°

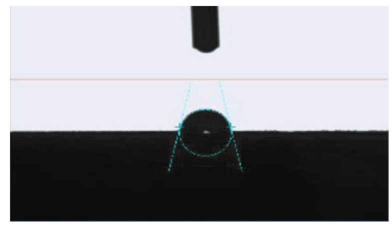

(d) Contact angle = 80.6°

Figure 11: The measurement of contact angle test of core 17-1.

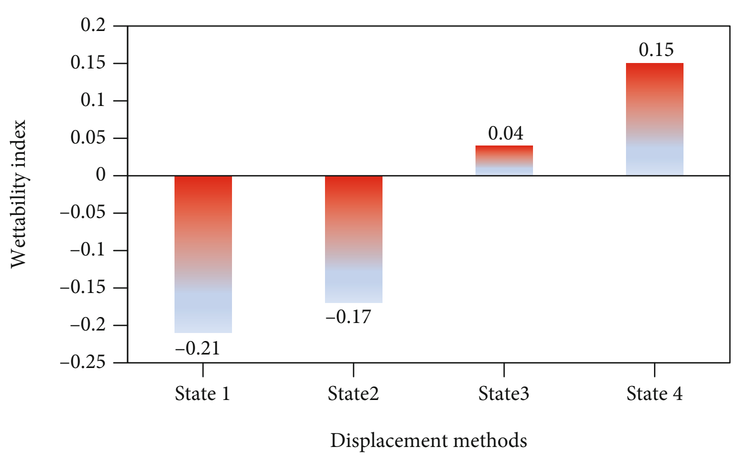

Figure 12: Average wetting index of core 17-1 and core 21-2 under four states (state 1 denotes the original state; state 2 denotes the state of water driving under conventional injection rate; state 3 denotes the state of fracturing by water at high pressure; state 4 denotes the state of fracturing by an oil displacement agent at high pressure).

On the one hand, injection fluid at high pressure effectively increased the formation energy, and the residual oil on the pore wall was stripped due to high-speed injection which was the main EOR mechanism of this method; on the other hand, the adsorption area of surfactant molecules on the pore surface was increasing, and the adsorption was dominated by monolayer, which reduced the liquid-solid interface energy and caused the wetting inversion of pore surface, thus improving the oil displacement efficiency. Besides, the type of injection fluid had little effect on it.

In a word, from the perspective of EOR, it may be the best choice to improve sweep volume and oil displacement efficiency at the same time. However, from the point of view of practical application in oilfields, the proposed approach is water injection at high pressure in general. The hydraulic fracturing method is used to bring the displacement fluid to the formation and provide energy to it.

4. Conclusions

(1) The most important mechanism of EOR by the fracturing-seepage-displacement method is to increase the formation energy by high-pressure injection of an oil displacement agent. Injection fluid displacement at high pressure can significantly increase the core permeability and porosity. It is worth mentioning that the type of injection fluid has little effect

(2) In the process of fracturing and oil displacement, the injection fluid forms a large energy field around the

fracture and then, it will penetrate into the matrix at high-pressure injection of an oil displacement agent. The original way of line or point contact between mineral particles gradually changes to free particles. Therefore, the pore throat size increases, some larger pores are formed, and the overall flow resistance decreases

(3) After injection of an oil displacement agent at high pressure, the phenomenon of wetting inversion occurs at the pore wall, which changes from oil-wet to weakly water-wet. The main reason is the high-pressure scouring of injected fluid, which leads to the stripping of residual oil on the pore wall. Besides, if the injected fluid is surfactant, it will also play a role in reducing the interfacial tension. In this way, the displacement efficiency has been improved

Data Availability

The data used to support the findings of this study are included within the article.

Conflicts of Interest

The authors declare that they have no conflicts of interest regarding the publication of this paper.

Acknowledgments

This research was supported by the National Natural Science Foundation of China (Youth Project) (Grant No. 51804076), China Postdoctoral Science Foundation Postdoctoral (No. 2021M690528), Projects in Heilongjiang Province (Grant No. LBH-Z20035), Youth Science Foundation of Northeast Petroleum University (Grant No. 2019NL-02), and Research Initiation Foundation of Northeast Petroleum University (Grant No. 2019KQ15).

References

[1] Q. L. Du, "Variation law and microscopic mechanism of permeability in sandstone reservoir during long-term water flooding development," *Acta Petrolei Sinica*, vol. 37, no. 9, pp. 115–1164, 2016.

[2] S. Yuan and Q. Wang, "New progress and prospect of oilfields development technologies in China," *Petroleum Exploration and Development*, vol. 45, no. 4, pp. 698–711, 2018.

[3] L. Sun, X. Wu, W. Zhou, X. Li, and P. Han, "Technologies of enhancing oil recovery by chemical flooding in Daqing oilfield, NE China," *Petroleum Exploration and Development*, vol. 45, no. 4, pp. 673–684, 2018.

[4] D. Jia, H. Liu, J. Zhang et al., "Data-driven optimization for fine water injection in a mature oil field," *Petroleum Exploration and Development*, vol. 47, no. 3, pp. 674–682, 2020.

[5] C. Jiaqing, W. Qiangqiang, X. Jianhong et al., "Development status and prospect of water pre-separation technology for produced liquid in high water-cut oil well," *Acta Petrolei Sinica*, vol. 41, no. 11, pp. 1434–1444, 2020.

[6] X. Gao, S. O. Xinmin, M. Xinli et al., "Quantitative characterization of the hidden remaining oil controlled by reservoir architecture at extra high water cut stage," *Acta Petrolei Sinica*, vol. 37, no. z2, pp. 99–111, 2016.

[7] J. Wang, C. Shi, S. Ji, G. Li, and Y. Chen, "New water drive characteristic curves at ultra-high water cut stage," *Petroleum Exploration and Development*, vol. 44, no. 6, pp. 1010–1015, 2017.

[8] X. Wang, H. Dang, and T. Gao, "Method of moderate water injection and its application in ultra-low permeability oil reservoirs of Yanchang oilfield, NW China," *Petroleum Exploration and Development*, vol. 45, no. 6, pp. 1094–1102, 2018.

[9] Q. N. Yu, Y. K. Liu, S. Liang, S. Tan, Z. Sun, and Y. Yu, "Mechanism experiment of enhanced oil recovery by surfactant flooding: a case study of Daqing placanticline oilfield," *Petroleum Exploration and Development*, vol. 46, no. 6, pp. 1138–1147, 2019.

[10] M. Zhou, J. Bu, J. Wang, X. Guo, J. Huang, and M. Huang, "Study on three phase foam for enhanced oil recovery in extra-low permeability reservoirs," *Oil & Gas Science and Technology*, vol. 73, no. 8, p. 55, 2018.

[11] Y. Long, R. Wang, B. Zhu et al., "Enhanced oil recovery by a suspension of core-shell polymeric nanoparticles in heterogeneous low-permeability oil reservoirs," *Nanomaterials*, vol. 9, no. 4, p. 600, 2019.

[12] Y. S. Gurav, A. Y. Dandekar, S. L. Patil, and S. D. Patwardhan, "Application of design of experiments for well pattern optimization in Umiat oil field: a natural petroleum reserve of Alaska case study," in *SPE/IATMI Asia Pacific Oil & Gas Conference and Exhibition*, Bali, Indonesia, 2019.

[13] D. A. Novikov, S. A. Pavlova, D. Yu Kuznetsov, S. V. Ryzhkova, and A. A. Chernikov, "Contemporary development state of reservoir Yu1, the Verkh-Tarskoe oilfield (south of Western Siberia)," *Journal of Physics: Conference Series*, vol. 1451, no. 1, article 012008, 2020.

[14] J. Bingyu, "Progress and prospects of enhanced oil recovery technologies at home and abroad," *Oil & Gas Geology*, vol. 33, no. 1, pp. 111–117, 2012.

[15] J. Lu, P. J. Liyanage, S. Solairaj et al., "New surfactant developments for chemical enhanced oil recovery," *Journal of Petroleum Science & Engineering*, vol. 120, pp. 94–101, 2014.

[16] E. Georges Lwisa and A. R. Abdulkhalek, "Enhanced oil recovery by nitrogen and carbon dioxide injection followed by low salinity water flooding for tight carbonate reservoir: experimental approach," *IOP Conference Series: Materials Science and Engineering*, vol. 323, p. 012009, 2018.

[17] Q. You, Q. Wen, J. Fang, M. Guo, Q. Zhang, and C. Dai, "Experimental study on lateral flooding for enhanced oil recovery in bottom- water reservoir with high water cut," *Journal of Petroleum Science and Engineering*, vol. 174, pp. 747–756, 2019.

[18] O. Massarweh and A. S. Abushaikha, "The use of surfactants in enhanced oil recovery: a review of recent advances," *Energy Reports*, vol. 6, pp. 3150–3178, 2020.

[19] F. Zhang, B. Damjanac, and S. Maxwell, "Investigating hydraulic fracturing complexity in naturally fractured rock masses using fully coupled multiscale numerical modeling," *Rock Mechanics and Rock Engineering*, vol. 52, no. 12, pp. 5137–5160, 2019.

[20] F. Zhang, E. Dontsov, and M. Mack, "Fully coupled simulation of a hydraulic fracture interacting with natural fractures with a hybrid discrete-continuum method," *International Journal*

Numerical and Analytical Methods in Geomechanics, vol. 41, no. 13, pp. 1430–1452, 2017.

[21] F. Zhang, X. Wang, M. Tang et al., "Numerical investigation on hydraulic fracturing of extreme limited entry perforating in plug-and-perforation completion of shale oil reservoir in Changqing oilfield, China," *Rock Mechanics and Rock Engineering*, vol. 54, no. 6, pp. 2925–2941, 2021.

[22] T. Guo, S. Zhang, Z. Qu, T. Zhou, Y. Xiao, and J. Gao, "Experimental study of hydraulic fracturing for shale by stimulated reservoir volume," *Fuel*, vol. 128, pp. 373–380, 2014.

[23] R. Barati and J.-T. Liang, "A review of fracturing fluid systems used for hydraulic fracturing of oil and gas wells," *Journal of Applied Polymer Science*, vol. 131, no. 16, pp. 318–323, 2014.

[24] Y. Guo, B. Fang, Y. Luo, X. Qiu, B. Guan, and K. Li, "Research progress of high temperature fracturing fluid," *Oilfield Chemistry*, vol. 35, no. 3, pp. 545–549, 2018.

[25] H. Liu and D. Xiao, "A novel low-damage vegetable gum-based fracturing fluid and its application in low-permeability reservoirs," *Acta Petrolei Sinica*, vol. 33, no. 3, pp. 343–350, 2008.

[26] M. Alohaly, A. BinGhanim, R. Rahal, and S. Rahim, "Seawater fracturing fluid development challenges: a comparison between seawater-based and freshwater-based fracturing fluids using two types of guar gum polymers," in *Spe Kingdom of Saudi Arabia Technical Symposium & Exhibition*, Dammam, Saudi Arabia, 2016.

[27] C. Wang, Z. Zhang, J. du, X. Li, M. Zhao, and Z. Zhang, "Titanium-based nanoscale cross-linker for guar gum fracturing fluid: effects on rheological behaviour and proppant-carrying ability," *Micro & Nano Letters*, vol. 14, no. 10, pp. 1096–1101, 2019.

[28] M. Zhao, Y. Li, Z. Xu et al., "Dynamic cross-linking mechanism of acid gel fracturing fluid," *Colloids and Surfaces A Physicochemical and Engineering Aspects*, vol. 607, p. 125471, 2020.

[29] K. Zhang, Z. Zhao, M. Tang et al., "A new type of experimentally proposed in situ heat/gas clean foam fracturing fluid system," *Journal of Petroleum Exploration and Production Technology*, vol. 10, no. 8, pp. 3419–3436, 2020.

[30] Y. Chen, T. Pope, and J. Lee, "Novel CO_2-emulsified viscoelastic surfactant fracturing fluid system," in *SPE European Formation Damage Conference*, Sheveningen, The Netherlands, 2005.

[31] W. Kang, S. J. Mushi, H. Yang, P. Wang, and X. Hou, "Development of smart viscoelastic surfactants and its applications in fracturing fluid: a review," *Journal of Petroleum Science and Engineering*, vol. 190, article 107107, 2020.

[32] Z. Gao, C. Dai, X. Sun, Y. Huang, M. Gao, and M. Zhao, "Investigation of cellulose nanofiber enhanced viscoelastic fracturing fluid system: increasing viscoelasticity and reducing filtration," *Colloids and Surfaces A: Physicochemical and Engineering Aspects*, vol. 582, pp. 123938–123938, 2019.

[33] J. D. Bredehoeft, R. G. Wolff, W. S. Keys, and E. Shuter, "Hydraulic fracturing to determine the regional in situ stress field, Piceance Basin, Colorado," *Geological Society of America Bulletin*, vol. 87, no. 2, p. 250, 1976.

[34] T. W. Teklu, X. Li, Z. Zhou, N. Alharthy, L. Wang, and H. Abass, "Low-salinity water and surfactants for hydraulic fracturing and EOR of shales," *Journal of Petroleum Science & Engineering*, vol. 162, pp. 367–377, 2018.

[35] S. Pingping, Y. Shiyi, D. Baorong, S. Jie, and S. Kuiyou, "Influence factors of oil displacement efficiency and sweep effeiciency in chemical flooding," *Petroleum Exploration and Development*, vol. 31, no. 1, pp. 1–4, 2004.

[36] J. Geng, H. Fan, Y. Zhao, and W. Kang, "A correlation between interfacial tension, emulsifying ability and oil displacement efficiency of ASP system for Daqing crude oil," *Petroleum Science & Technology*, vol. 36, no. 24, pp. 2151–2156, 2018.

[37] Z. Liu, Y. Li, R. Leng, Z. Liu, X. Chen, and H. Hejazi, "Effects of pore structure on surfactant/polymer flooding-based enhanced oil recovery in conglomerate reservoirs," *Petroleum Exploration and Development*, vol. 47, no. 1, pp. 134–145, 2020.

Hindawi
Geofluids
Volume 2021, Article ID 5558678, 14 pages
https://doi.org/10.1155/2021/5558678

Research Article

Case Studies of Comprehensive Gas Control Method during Fully Mechanized Caving of Low-Permeability Ultrathick Coal Seams

Bangyou Jiang,[1] **Shitan Gu**,[1] **Wenshuai Li**,[2] **Guangchao Zhang**,[1] **and Jihua Zhang**[3]

[1]*State Key Laboratory of Mining Disaster Prevention and Control Co-Founded by Shandong Province and the Ministry of Science and Technology, Shandong University of Science and Technology, Qingdao 266590, China*
[2]*Shandong Provincial Key Laboratory of Civil Engineering Disaster Prevention and Mitigation, Shandong University of Science and Technology, Qingdao 266590, China*
[3]*Faculty of Architecture and Civil Engineering, Huaiyin Institute of Technology, Huai'an, Jiangsu 223001, China*

Correspondence should be addressed to Shitan Gu; chinasdgst@163.com and Wenshuai Li; lwsnote@163.com

Received 17 February 2021; Accepted 10 July 2021; Published 22 July 2021

Academic Editor: Yi Xue

Slicing fully mechanized caving mining is a standard high-efficiency mining method for ultrathick coal seams. However, the effectiveness of gas control has accentuated the difficulty in fully mechanized top coal caving of low-permeability ultrathick coal seams. This study focused on mining the No. 9-15 coal in Liuhuanggou Coal Mine, Xinjiang Province, China. To this aim, the results of theoretical analyses and field tests were combined to explore a comprehensive gas control method for fully mechanized caving of low-permeability ultrathick coal seams. The No. (9-15)06 panel was a top-slicing panel of the No. 9-15 coal with a mining height of 9 m. Gas analysis results revealed that gas emissions in the No. (9-15)06 panel are mainly sourced from the coal wall, caving top coal, goaf, and neighboring coal seams. Based on gas source separation, a comprehensive gas control method was proposed. The proposed method was based on the combination of gas predrainage alongside the coal seam, high-position drilling on the top, preburial of pipes in the goaf, and pressure-balancing ventilation. The permeability and gas predrainage were enhanced by hydraulic fracturing in low-permeability coal seams. According to the characterizations of coal seam and crustal stress distribution, the arrangement of the boreholes and backward-segmented fracturing technology were designed. From the field results, the coal seam presented a remarkable prefracturing under hydraulic fracturing. Besides, the mean gas predrainage from the boreholes was enhanced by four times compared to the prehydraulic fracturing state. Finally, using the proposed comprehensive control method based on the gas sources, field tests were performed in the No. (9-15)06 panel. The measured results demonstrated that gas concentration in the return airflow is fluctuated within a range of 0.05% to 0.35%. The proposed gas control method can provide an insightful reference for other similar projects.

1. Introduction

Slicing fully mechanized mining is a high-efficiency mining method for ultrathick seams in China. However, most of China's coal fields include high gas and low permeability [1, 2]. Ultrathick seams with low permeability are commonly deficient in gas predrainage. When using the fully mechanized mining method, a significant amount of gas is emitted from coal seams. The high concentration and accumulation of gas in fractures can easily trigger a formidable accident such as a gas explosion in the overlying strata of the goaf and threaten production safety in the mines [3, 4]. Numerous attempts have been made to develop useful gas drainage and discharge methods and achieve adequate gas control by the fully mechanized mining of low-permeability ultrathick coal seams.

Fan and Wang focused on fully mechanized mining of ultrathick mines in Tashan Mine and proposed the gas in the goaf can be controlled by combining vertical surface drilling and high-position gas drainage roadways [5]. However, for the mines with great burial depth, the cost of gas drainage by drilling a significant number of vertical holes is high. According to the characteristics of longwall coal mining in Australia, Guo et al. projected a gas drainage and discharge method for the goaf using horizontal drilling [6]. They exhibited a good drilling operation in the construction of the roof fracturing zone. Furthermore, Zhang et al. examined the development rules for the roof fracturing zone when using high-dipping longwall coal caving and the related effect on gas drainage [7]. They designed an optimal construction layer during high-position drilling for gas drainage and discharged from the No. 704 panel of Baojishan Mine [7]. Moreover, Liu addressed gas accumulation at the upper corner of the goaf in a fully mechanized panel for tilted ultrathick coal seams [8]. This technique was successfully applied in Wudong Mine [8] by preburying gas drainage and discharge pipes in the goaf.

In previous studies, a straight-line construction was performed for gas drainage in surface and underground drilling operations. Recently, new means of gas drainage are provided by directional drilling in coal mines. In this regard, boreholes can be drilled in coal seams along with a preset direction [9]. Taking Daning Mine, Shanzi, China, as an example, Lu et al. carried out the directional drilling in coal seams for gas predrainage and achieved favorable results [10]. Li et al. proposed a new inverse π-type drilling mode for gas drainage and discharge and realized the gas comprehensively controlled through passing the caving zone, fracture zone, and coal seams in the working face [11]. In contrast to traditional drilling, the directional drilling of the coal seam exhibits a series of advantages, including strong adaptability, high drilling proportion, and good efficiency of gas drainage. Although these advantages are appropriate to gas control in directional drilling of coal seams, they should be pretty permeable.

For low-permeability coal seams, drilling alongside the coal seam has a poor gas drainage performance; therefore, some fracturing techniques are necessary for prefracturing in coal seams and enhancing their permeability. Deep-hole loosening blasting is a common prefracturing technique in coal seams [12, 13]. However, this technique has certain shortcomings. The dynamic shock wave produced in the deep-hole blasting can easily damage the surrounding rocks in the tunnel and lead to more difficulty controlling the rock deformation. Also, unreasonable deep-hole blasting schemes trigger numerous accidents such as gas explosions and coal and gas outbursts. Many scholars performed numerous studies and explored some methods such as hydraulic fracturing for enhancing the permeability in coal seams [14–16]. Hydraulic fracturing refers to drilling boreholes in the coal seams, followed by generating fractures through high-pressure water as a medium. In these enclosed boreholes, hydraulic pressure is utilized to overcome the tensile strength of surrounding rocks [17]. After hydraulic fracturing, the initial fractures are formed in the coal, and numerous secondary fractures are produced [17]. Gas transport channels can be increased while promoting the desorption of adsorbed gas, thereby leading an increase in coal permeability and range [18, 19]. In recent years, some scholars developed directional hydraulic fracturing and pulsed hydraulic fracturing techniques [20, 21].

Moreover, the effective gas control has always remained a technical difficulty in the fully mechanized mining of low-permeability ultrathick coal seams. As described earlier, some scholars have proposed numerous gas control methods and attained favorable results. In the fully mechanized mining of low-permeability ultrathick coal seams, gas has various sources and is significantly challenging to control. Currently, one method addressing the control of multi-source gas in the working face is lacking. This study focused on mining the No. 9-15 coal in Liuhuanggou Coal Mine, Xinjiang Province, China, and innovatively proposed a comprehensive gas control method. It is based on the gas emission analysis in which gas predrainage alongside the coal seam, high-position drilling on the top, preburial of pipes in the goaf, and pressure-balancing ventilation are combined. Considering the poor gas predrainage effect for low-permeability coal seams, the permeability and gas predrainage are enhanced by hydraulic fracturing. In this regard, a scheme of hydraulic fracturing is designed, and the performance of the prefracturing and permeability enhancement in the coal seams is verified through field measurements. Lastly, the proposed source-separation comprehensive gas control method's effectiveness and reliability are validated using long-term field tests. The proposed gas control concept and methods can provide a valuable reference for other similar projects.

2. Case Study

2.1. Mining and Geological Conditions. As shown in Figure 1, the No. 9-15 coal seam, with a mean thickness of 32.94 m and a mean inclination angle of 24°, is the primary mineable coal seams in Liuhuanggou Coal Mine. The coal seam has excellent hardness and undeveloped fractures. Also, the measured gas content and gas pressure in the No. 9-15 coal seam were 3.85 m^3/t and 0.5 MPa, respectively. Besides, the permeability coefficient ranged from 0.011814 to 0.061668 m^2/MPa^2 d, and the attenuation coefficient of gas flow was 1.03-1.28 d^{-1} in the borehole, suggesting a low-permeability coal seam.

No. 7 and No. 4-5 coal seams were also located above the No. 9-15 coal seam with mean thicknesses of 2.31 m and 7.18 m, respectively. Specifically, the No. 7 coal seam was unrecoverable. The gas content in No. 7 and No. 4-5 coal seams was 4.14 m^3/t and 3.5 m^3/t, respectively. The distance between No. 4-5 and No. 7 coal seams was 1.85 m, while the distance between No. 7 and No. 9-15 coal seams was 20.95 m. As illustrated in Figure 2, the roof strata of the No. 9-15 coal seam are mainly composed of siltstones and mudstones.

As an operating background in this study, the No. (9-15)06 panel was selected, 60 m away from the No (9-15)04 goaf. North of the (9-15)06 panel is the area of unmined coal. The No. (4-5)04 goaf is located on the inclined top of the north part, and the No. (4-5)02 goaf is right above the No. (9-15)06 panel. The tailgate in the No. (9-15)06 panel is inside staggered the tailgate in the No. (4-5)02 panel with a distance of 23 m, while the headgate in the No. (9-15)06 panel is inside staggered the headgate in the No. (4-5)02 panel with a distance of 11 m. A slicing mining method was used for the No. 9-15 coal seam. In the No. (9-15)06 panel, a fully mechanized longwall caving method was used to

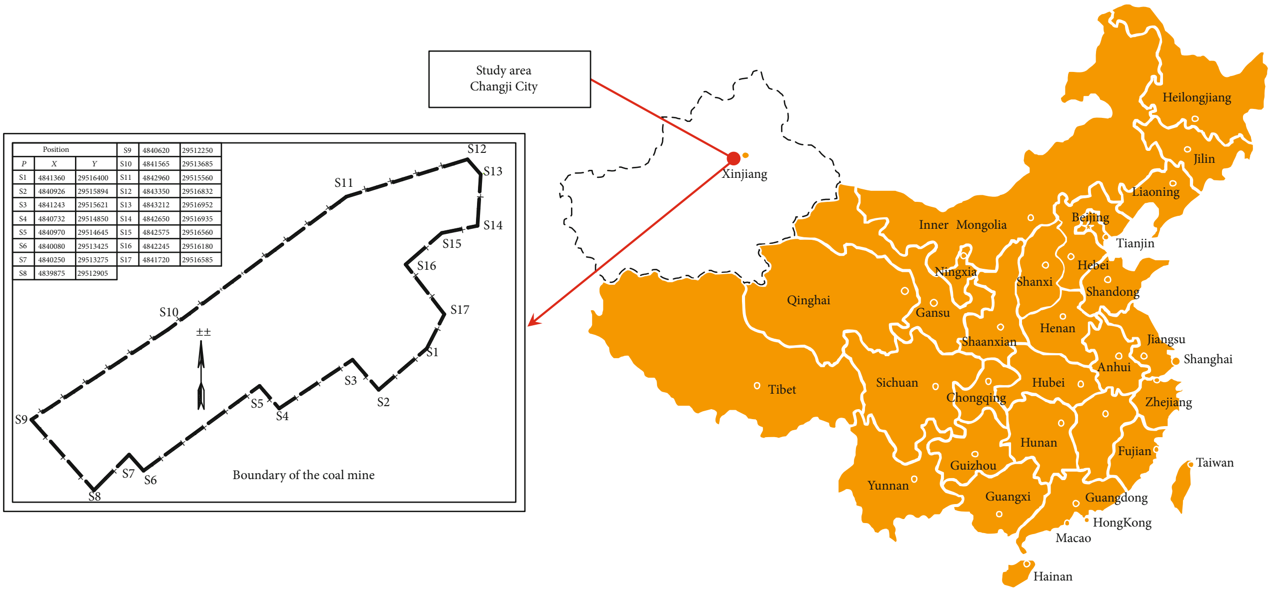

Figure 1: Locational map of Liuhuanggou Coal Mine, China.

top-slicing the No. 9-15 coal, with a mining height of 9 m and a mechanized mining height of 3 m. The strike length and inclined length of the working face were 1045 m and 100 m, respectively.

2.2. Coal Seam Mechanical Parameters. To measure the related mechanical parameters of the No. 9-15 coal seam, the No. 9-15 coal samples were collected from the tailgate. Because of the significant sample thickness, coal samples were sliced into three layers: the upper, middle, and lower slices. Coal samples were processed into standard cylindrical specimens with different sizes (e.g., Φ50mm × 100 mm and Φ50mm × 25 mm). Then, an MTS815 electrohydraulic servo rock tester was used to perform uniaxial compressive, triaxial compressive, and Brazilian disk splitting tests. The due parameters were then acquired on the standard samples, including uniaxial compressive strength (σ_c), tensile strength (σ_t), elasticity modulus (E), Poisson's ratio (υ), cohesive force (C), and internal friction angle (φ). Each test was repeated five times, and then the results were averaged. Table 1 lists the mechanical parameters of the No. 9-15 coal seam. The mean uniaxial compressive strength of the No. 9-15 coal was 35.35 MPa, suggesting excellent coal seam hardness. Owing to poor permeability, gas predrainage performance on the coal seam was far from ideal. During mining in the No. (9-15)06 panel, gas control was crucial.

2.3. In Situ Measurement of Crustal Stress. To gain an in-depth knowledge of the crustal stress distribution in the Liuhuanggou Mine, in situ measurements were performed. The accuracy of in situ measurement was related to selected methods and sensors. As the stress relief method, a CSIRO hollow inclusion stress gauge was used to possess numerous advantages, including the accuracy, reasonable distribution of numerous strain gauges, and a wide application range. The measuring points should be selected far from the areas with complex geological structures and significant mining effects on this subject. Figure 3 shows five measuring points of crustal stress selected in this study. Also, in situ stress measurement points of crustal stress and borehole layout parameters are listed in Table 2. Drilling depth ranges from 10 m to 12.8 m with dominant lithology between fine sandstone and siltstone. Besides, Figure 4 displays the in situ crustal stress measurement results in Liuhuanggou Mine, in which σ_H, σ_h, and σ_V denote the maximum horizontal stress, the minimum horizontal stress, and the principal vertical stress, respectively. The dominant azimuth angle and direction of σ_H and σ_h were 230° and 140°, respectively. Figure 4 shows the crustal stress direction at each measuring point.

Moreover, Figure 5 illustrates the stress field in Liuhuanggou Mine that $\sigma_V > \sigma_H > \sigma_h$. As shown in Figure 5, vertical stress dominates the crustal stress field, and various principal stresses increase with increasing burial depth. As a result, vertical stress was slightly smaller than the weight of the overlying strata per unit area. Based on the method of least squares regression (R^2), the following equations were written between various main principal stresses and burial depth (h).

$$\begin{cases} h = 16.7\sigma_V + 244, R^2 = 0.60 \\ h = 13.0\sigma_V + 302, R^2 = 0.50 \\ h = 18.3\sigma_V + 304, R^2 = 0.74. \end{cases} \quad (1)$$

2.4. Analysis of Gas Sources in the No. (9-15)06 Panel. Many scholars believe that gas emission sources in the working face mining are coal walls, fallen coal, goaf, and neighboring coal seams [22]. Four main gas emission sources were identified in the No. (9-15)06 working face by analyzing the arrangement and surrounding mining conditions.

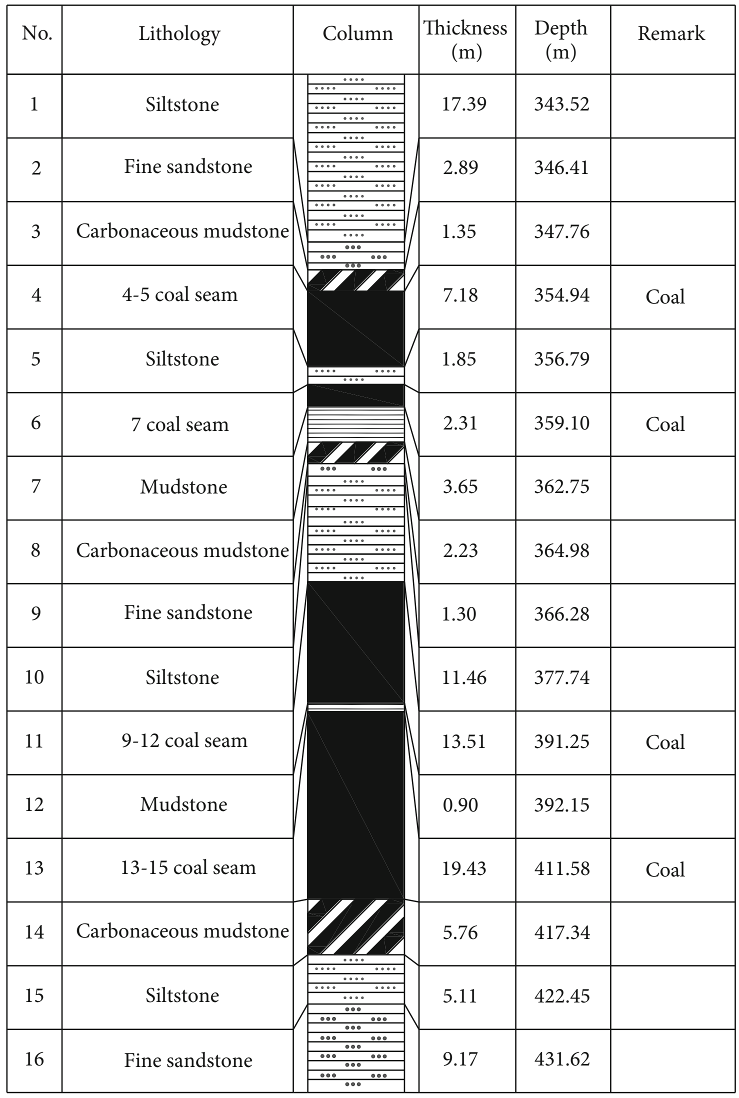

Figure 2: Stratigraphy column of test site from Liuhuanggou Coal Mine, China.

Table 1: Mechanical properties of the No. 9-15 coal.

Lithology	σ_c (MPa)	σ_t (MPa)	E (GPa)	υ	C (MPa)	φ (°)
9-15 coal upper	39.06	1.96	3.84	0.26	3.8	40
9-15 coal middle	35.44	2.04	3.79	0.21	4.4	41
9-15 coal lower	31.56	1.91	2.32	0.23	3.9	42
Average	35.35	1.97	3.29	0.23	4.03	41

2.4.1. Gas Emission Quantity from Coal Walls (Q_1). When the working face was to be moved forward, fresh coal walls were exposed to the air. Then, the pressure balance was broken after reliving the rock pressure. Due to a gas pressure gradient in the coal, gas was emitted through coal fractures towards the working face.

2.4.2. Gas Emission Quantity from Top Coal Caving (Q_2). Before caving the top coal in the working face, the top coal was first fully broken under supporting pressure. The original gas pressure balance in the coal seam was then broken during the crushing of the top coal. Hence, the adsorbed gas in the coal seam was converted into a stable state of free gas and then emitted into the working face during top coal caving.

2.4.3. Gas Emission Quantity from the Goaf (Q_3). Using the fully mechanized caving method, the recovery ratio in the No. (9-15)06 panel was about 85%, and a significant amount of coal would be left in the goaf. Therefore, gas from the unmined coal was the main source of the emitted gas in the goaf. Also, the top layer mining in the No. 9-15 coal seam affected the bottom coal seam mining by generating numerous fractures and emitting a significant amount of gas.

2.4.4. Gas Emission Quantity from the Neighboring Coal Seams (Q_4). As shown in Figure 2, the No. 7 and No. 4-5 coal seams locate right above the No. 9-15 coal with a distance of 20.95 m and 22.8 m, respectively, and include a high content of gas. After mining the No. (9-15)06 panel, the No. 7 and No. 4-5 coal seams were located in the roof caving zone, in

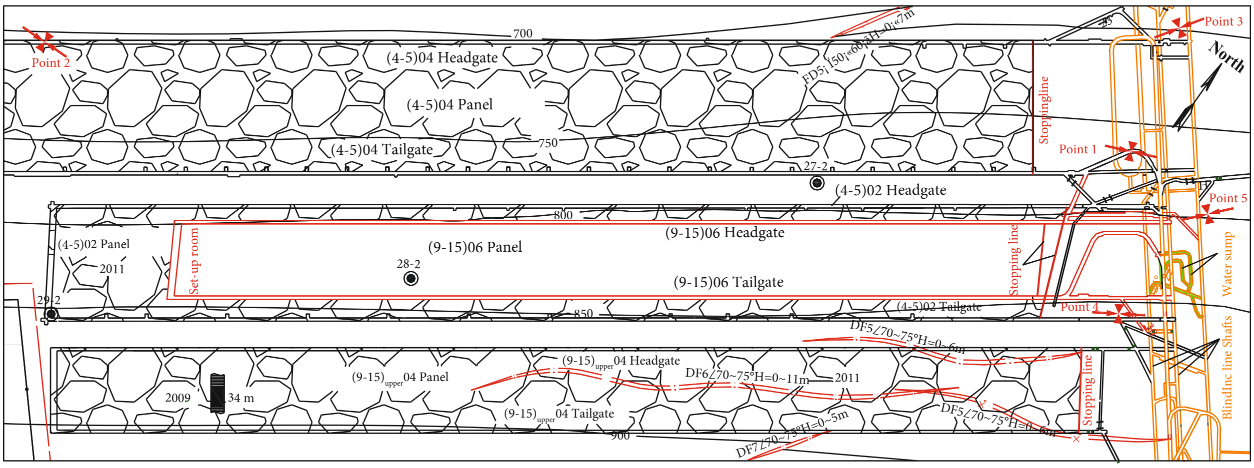

FIGURE 3: Layout of the No. (9-15)06 panel from Liuhuanggou Coal Mine, China.

TABLE 2: In situ stress measurement points and borehole layout parameters.

No.	Drilling depth (m)	Azimuth (°)	Elevation angle (°)	Depth (m)	Lithology
I	12.8	331	5	346	Fine sandstone
II	12.0	325	10	482	Fine sandstone
III	10.0	328	5	448	Fine sandstone
IV	10.5	320	41	360	Siltstone
V	10.6	50	41	405	Siltstone

which a connection was made between the No. (9-15)06 panel and the No. (4-5)02 goaf. Besides, the gas emitted from the No. 7 and No. 4-5 coal seams was accumulated in the overlying strata of the goaf in the No. (9-15)06 panel.

To conclude, the total gas emission (Q) from the No. (9-15)06 panel equals the sum of the gas emission from the above sources, i.e., $Q = Q_1 + Q_2 + Q_3 + Q_4$. Q_1 and Q_2 can be lowered by gas predrainage alongside the coal seams [23]. The gas from latter two sources accumulated in fractures in the overlying goaf strata. As a result of this accumulation, the friction in fractures of overlying strata quickly triggers a gas explosion in the goaf and threatens the production safety in the working face. Therefore, effective measures are required for drainage or dilution for the gas accumulated on the top of the goaf (i.e., $Q_3 + Q_4$).

3. Increasing the Permeability of Coal Seam by Hydraulic Fracturing

From the No. 9-15 coal seam, the performance of gas predrainage was weak due to high strength and poor permeability. Therefore, prefracturing was first performed on the coal seam to enhance the permeability by hydraulic fracturing and improve the coal seam's gas predrainage effect.

3.1. Crack Initiation Pressure. Crack initiation pressure refers to the maximum water pressure during hydraulic fracturing. Numerous factors affect the initiation pressure, including burial depth of the coal seam, crustal stress, coal mechanical properties, and original cracks. According to the hydraulic fracturing theory [14, 24–26], tensile cracks dominate the hydraulic fracturing process. Under the action of water pressure in the boreholes and the crustal stress field, when the tensile stress on the tip of the cracks exceeds the tensile strength σ_t, cracks develop gradually. The initiation pressure P_{k1} can be estimated (Equation (2)) by ignoring the water seepage effect from the boreholes on the surrounding media [26]:

$$P_{k1} \geq 3\sigma_3 - \sigma_1 + \sigma_t, \tag{2}$$

where σ_1 and σ_3 denote the maximum and minimum principal stresses, respectively, and σ_t denotes the coal tensile strength.

Besides, gas pressure significantly affects crack initiation and propagation under hydraulic fracturing [27]. Based on statistics from a large number of coal mines in China, Li et al. carried out a regression analysis and determined the following relationship between crack initiation pressure P_{k2}, burial depth of the coal seam H, and gas pressure P_0 [19]:

$$P_{k2} = 0.023H + 1.293P_0 + 2.04. \tag{3}$$

According to the minimum pressure principle, the minimum value between P_{k1} and P_{k2} was selected as the initiation pressure of the coal seam (P_k):

$$P_k = \min \{P_{k1}, P_{k2}\}. \tag{4}$$

In this study, the mean burial depth of the working face was approximately 420 m, the mean unit weight of the overlying strata was 23 kN/m^3, and the gas pressure of the coal seam was 0.5 MPa. Also, the maximum and minimum principal stresses in the study area were 10.54 MPa and 6.34 MPa, respectively. From Table 1, the

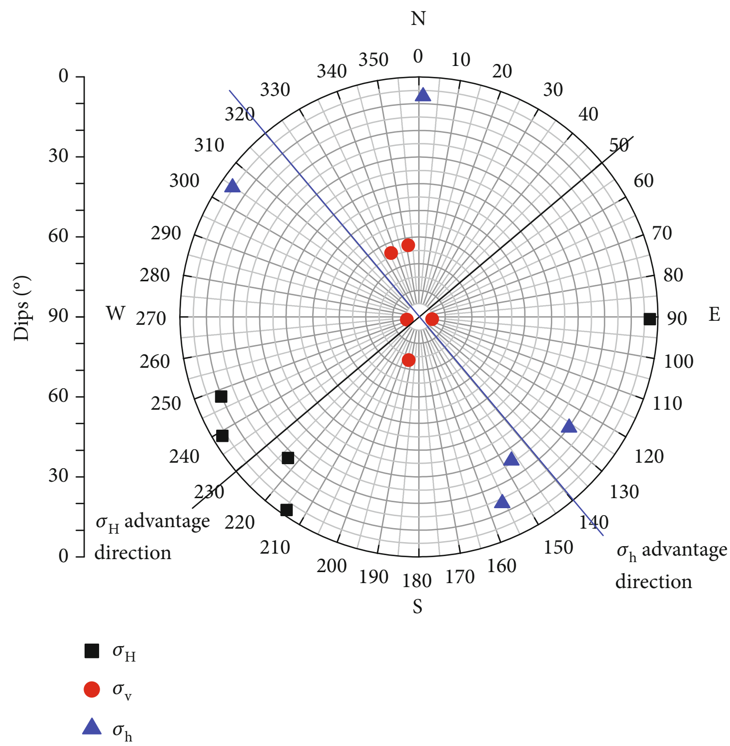

FIGURE 4: In situ stress directions of Liuhuanggou Coal Mine.

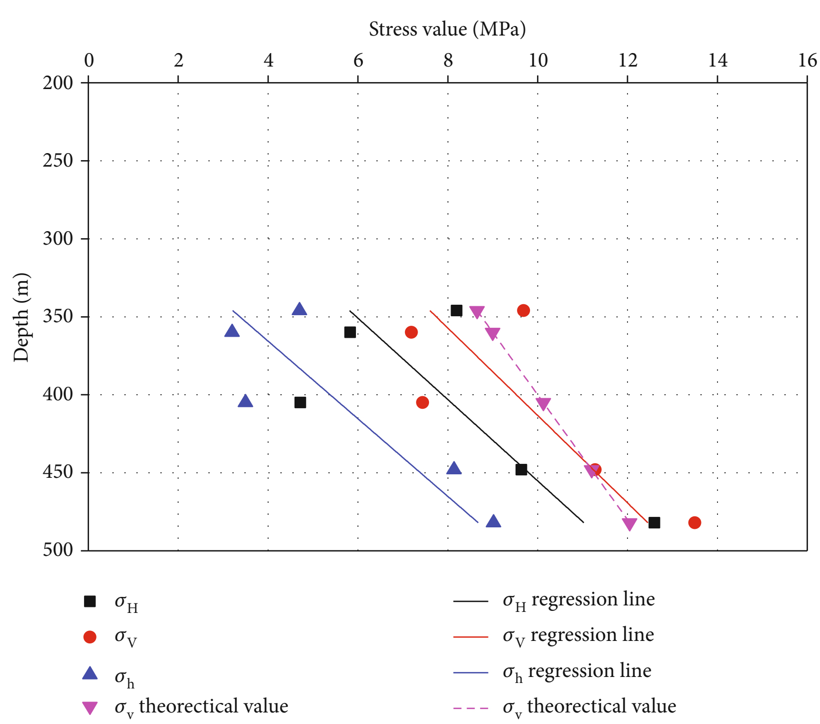

FIGURE 5: In situ stress magnitude (MPa) vs. depth (m) of Liuhuanggou Coal Mine.

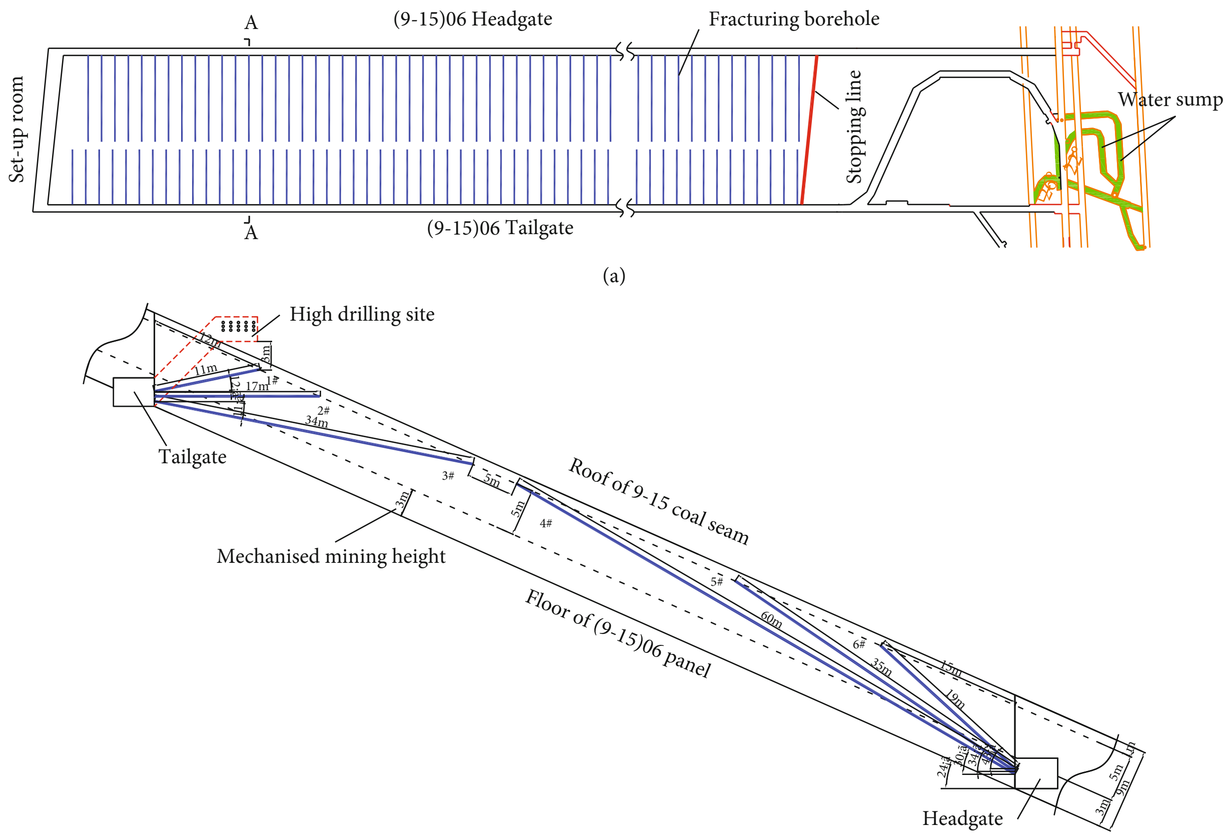

Figure 6: Layout of hydraulic fracturing borehole. (a) Plane of hydraulic fracturing borehole. (b) Profile of hydraulic fracturing borehole.

average tensile strength of the No. 9-15 coal was 1.97 MPa. P_{k1} and P_{k2} equal 10.45 MPa and 10.74 MPa, respectively. Therefore, P_k is10.45 MPa.

3.2. *Enhancing Coal Seam Permeability by Hydraulic Fracturing*

3.2.1. Arrangement of Hydraulic Fracturing Boreholes. The spatial positions of the hydraulic fracturing and high-position gas drainage in boreholes on the roof of the working face were analyzed to avoid damages to gas drainage boreholes. This analysis was based on geological and engineering conditions of the No. (9-15)06 panel and coal seam characteristics. Figure 6 shows an arrangement of the hydraulic fracturing in boreholes. A set of boreholes with a diameter of 75 mm were arranged on the inner sides of the tailgate and headgate. The first group of boreholes was arranged 15 m from the set-up room of the No. (9-15)06 panel, and the interval between every two groups of boreholes is 8 m. Table 3 lists the detailed parameters of boreholes.

3.2.2. Main Equipment. Many field equipment sets are used for hydraulic fracturing, including a high-pressure water injection pump, water tank, flow controller, pressure gauge, and high-pressure water pipe. The maximum pressure of the water injection pump was 35 MPa, and the water flow velocity was 200 L/min.

Table 3: Detailed borehole parameters.

Location	Number	Dip angle, °	Diameter, mm	Length, m	Height of the orifice from the floor of roadway, m
	1	12	75	11	1.5
Tailgate	2	0	75	17	1.0
	3	-11	75	34	0.5
	4	30	75	60	1.5
Headgate	5	34	75	35	1.8
	6	43	75	19	2.1

3.2.3. Sealing of Boreholes. Borehole sealing is a critical make-or-break step that determines the effectiveness of hydraulic fracturing. At present, cement and other particular hole packers were used for sealing [19]. The latter was used in the present field test. Under high-pressure water, the rubber gasket was compressed, then expanded radially in the hole packer, and reached the inner wall of the hole to achieve a seal. The use of this method provided a high sealing efficiency with a simple operating process in boreholes. However, this process sets high requirements on the boreholes, such as the high construction quality and the smooth borehole wall.

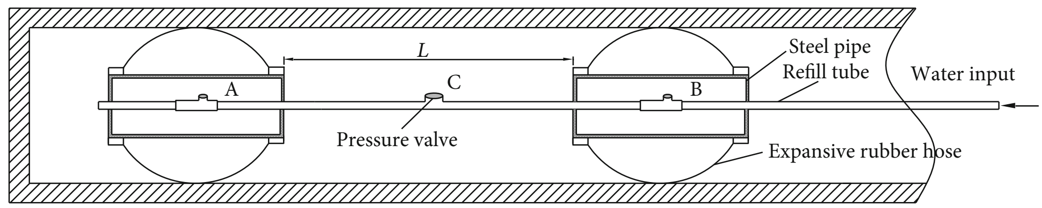

Figure 7: A schematic diagram of sectional sealing in low-permeability coal seams.

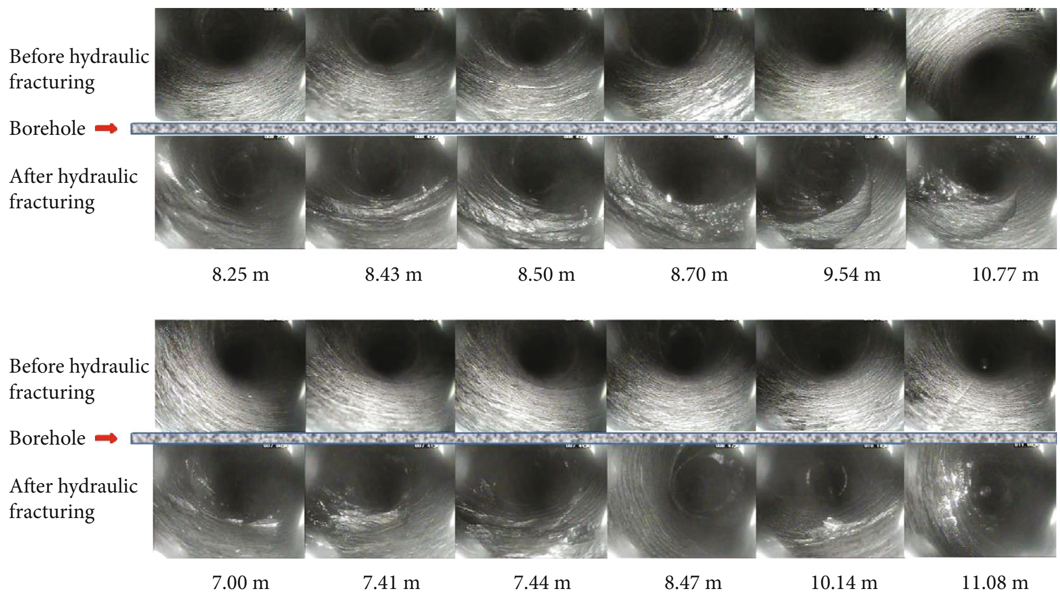

Figure 8: Fracture distribution contrast of part boreholes before and after hydraulic fracturing.

3.2.4. Fracturing Technology. Spatial propagation of hydraulic fractures directly affects the permeability enhancement of coal seams. The hydraulic fractures are always propagated parallel to the maximum principal stress and perpendicular to the minimum principal stress [17, 28–30].

According to in situ measurement results, the vertical stress was dominated the crustal stress in Liuhuanggou Mine. The dominant angle of the minimum horizontal stress was 140°. The angle between the dominant direction of the minimum horizontal stress and the gate axis of the panel was about 84°. Hydraulic fractures are most likely to propagate radially from the borehole; therefore, a backward-segmented fracturing technology was adopted to enhance hydraulic fracturing performance. Figure 7 illustrates the present borehole sealing method. Two-hole packers were connected in series, and the spacing distance between them (denoted as L) was the sectional fracturing length. In this study, L equals 8-10 m. As shown in Figure 7, the initiation pressure of valve in hole packer A equals in hole sealer B, and both are smaller than the initiation pressure of valve C. Thus, the fracturing and sealing of local borehole can be achieved.

3.3. Verification of Permeability Enhancement of the Coal Seam via Hydraulic Fracturing. To evaluate the enhancement of permeability in the coal seam by the hydraulic fracturing, the following two methods were used for the accuracy: borescope examination and borehole gas emission quantity measurement.

3.3.1. Borescope Examination. A stratum detector was employed for examining fracturing results in the borehole before and after the hydraulic fracturing. This study emphasizes both crack initiation and propagation behaviors in the borehole. Figure 8 shows the distribution of cracks in the borehole before and after the hydraulic fracturing. The inner wall of the initial borehole was complete in shape, while few original cracks were found in the borehole. After the hydraulic fracturing, cracks were propagated radially or in a spiral pattern from the borehole wall. This result correlates with the distribution of crustal stress in the test region, which was consistent with the predicted results as described above. In conclusion, the coal seam showed satisfactory prefracturing performance.

3.3.2. Measurement of Gas Emission Quantity from the Borehole. Before and after the hydraulic fracturing, gas predrainage flows were monitored using an orifice plate flow meter [31]. The gas flow in the borehole can be calculated as Equations (5) and (6):

$$Q_m = kb\sqrt{\Delta h}\delta_p\delta_T, \tag{5}$$

$$Q_c = Q_m X, \tag{6}$$

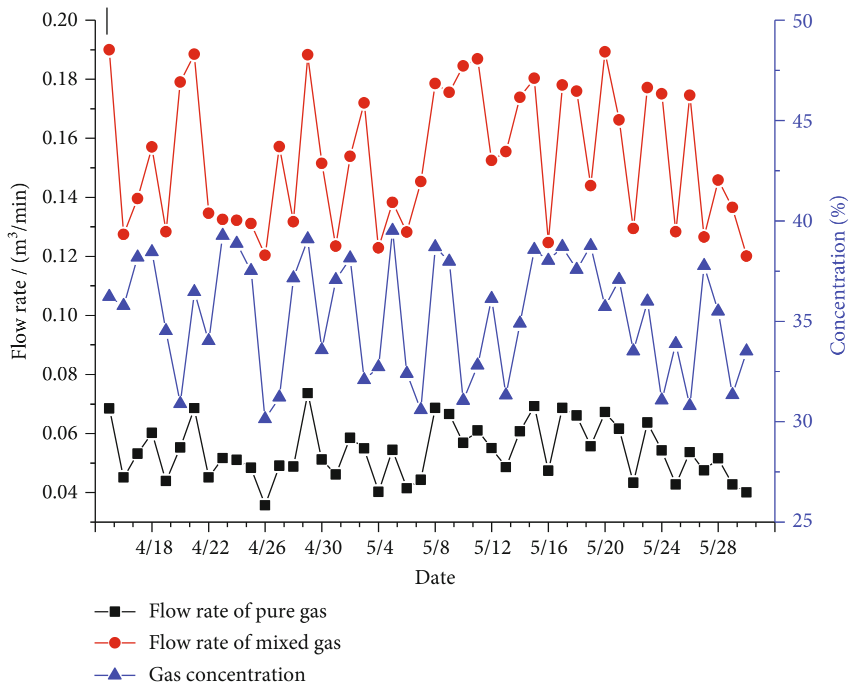

(a)

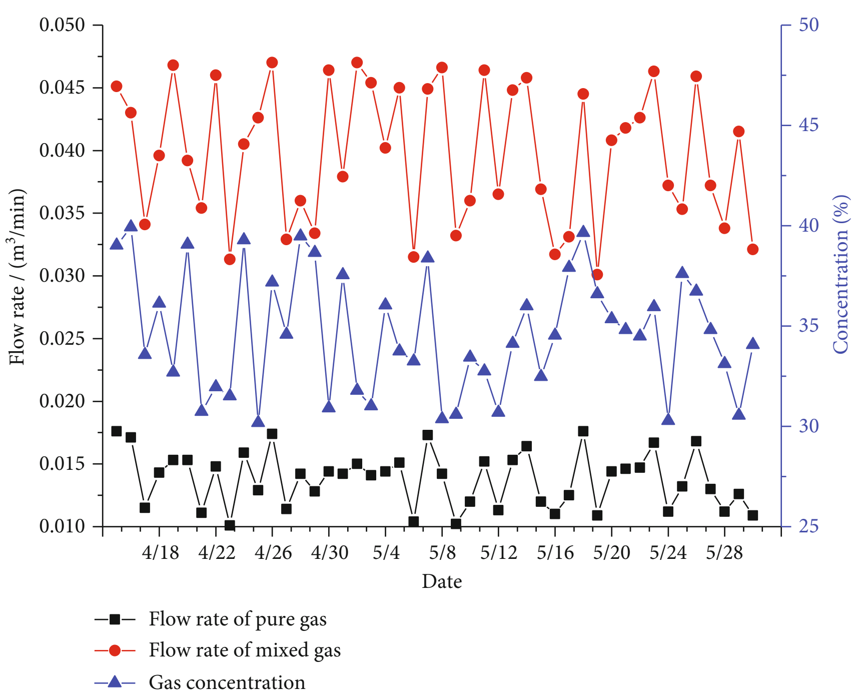

(b)

FIGURE 9: Variation of predrainage gas volume of single-hole with time. (a) Borehole after hydraulic fracturing. (b) Original borehole.

where Q_m and Q_c denote the flow of drained gas mixture and pure gas, respectively, in m^3/min. X denotes gas concentration (%) in the gas mixture, and k is the actual characteristic coefficient of orifice flow. b is the correction coefficient of gas concentration ($b = \sqrt{1/(1 - 0.00446X)}$), and Δh is the difference between the measured pressure (mmH_2O) of the front and rear ends in the hole plate. δ_p denotes the correction coefficient of gas pressure ($\delta_p = \sqrt{P_T/760}$). 760 is the standard atmospheric pressure. P_T denotes the measured absolute pressure (mmHg) at the windward end of the hole plate. δ_T denotes the correction coefficient of temperature ($\delta_T = \sqrt{293/(273 + t)}$). 293 is

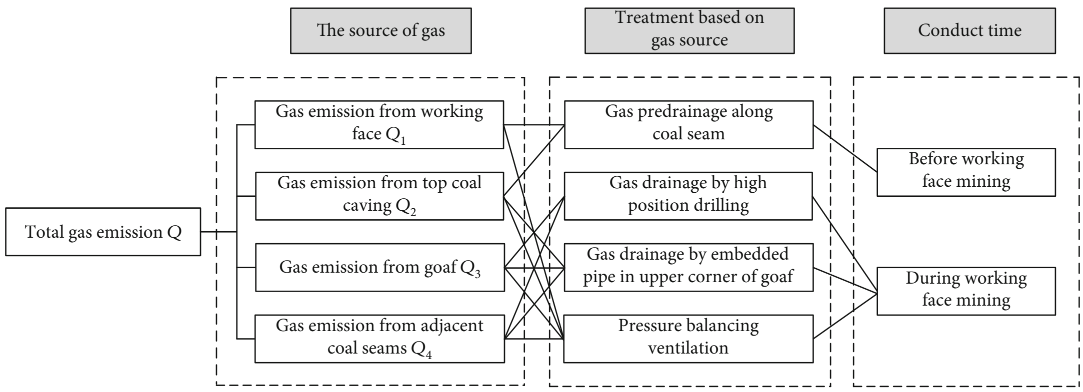

Figure 10: Comprehensive control method based on gas sources.

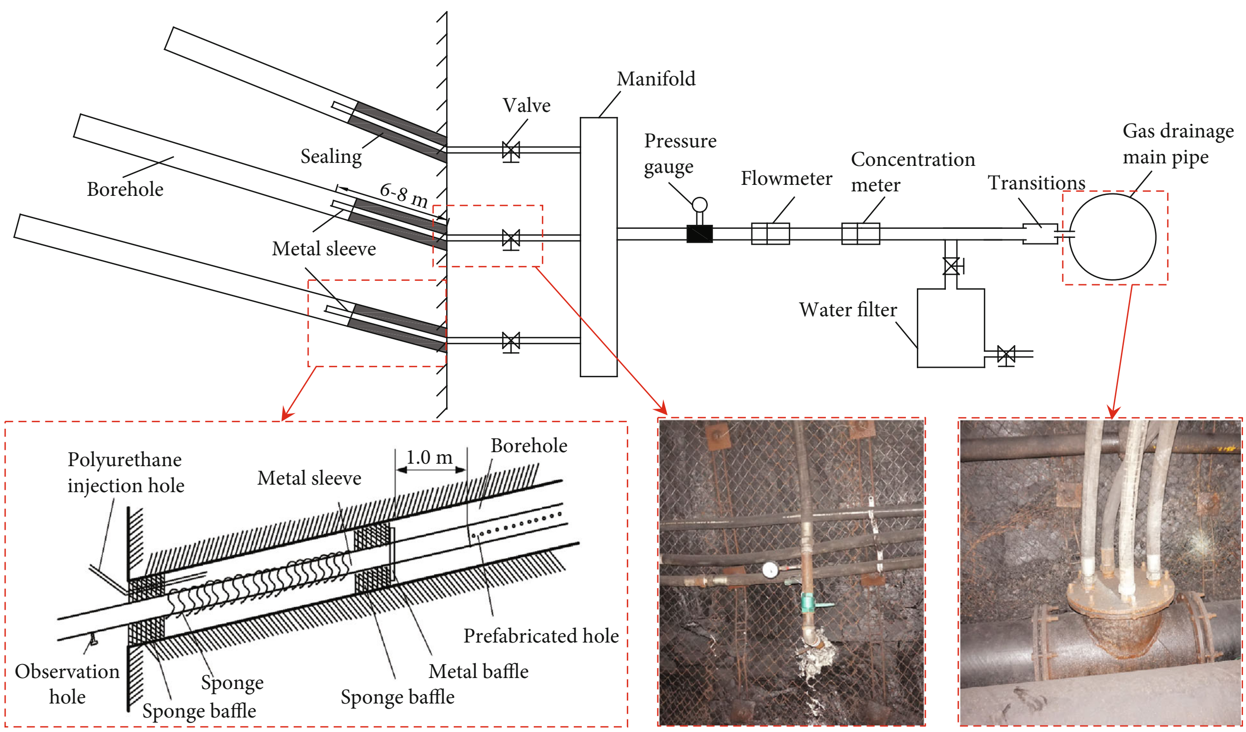

Figure 11: Scheme of gas predrainage in the low-permeability coal seam.

the standard absolute temperature (°C). Also, t denotes the temperature (°C) at the measuring point in the gas pipe.

Furthermore, the U-shaped differential pressure gauge readings were obtained and substituted into Equations (5) and (6) to calculate the exhausted gas mixture and pure gas. Figure 9 presents a plot of the results from the various rules of gas predrainage quality in the borehole before and after the hydraulic fracturing. After implementing hydraulic fracturing, the mean gas predrainage quantity from the borehole was enhanced by nearly four times the original value. Besides, in low-permeability hard coals, fractures were propagated around the borehole after the hydraulic fracturing. Therefore, the permeability of the surrounding coal seams was increased, and the performance of gas predrainage was remarkably improved.

4. Comprehensive Gas Control Based on Sources

A comprehensive gas control method was proposed by analyzing four main gas emission sources in the No. (9-15)06 panel (Figure 10). Before mining in the panel, the quantity of Q_1 and Q_2 was lowered by performing gas predrainage in the coal seam. During the working face mining, the gas was accumulated in the caving zone. In doing so, the fracture zone ($Q_3 + Q_4$) was discharged through high-position boreholes on the roof. Meanwhile, drainage pipes were buried along with the tailgate in the panel to address the gas accumulation in the upper corner. Also, pressure-balancing ventilation was implemented during the working face mining. To prevent the air leakage and gas emission in the goaf, the

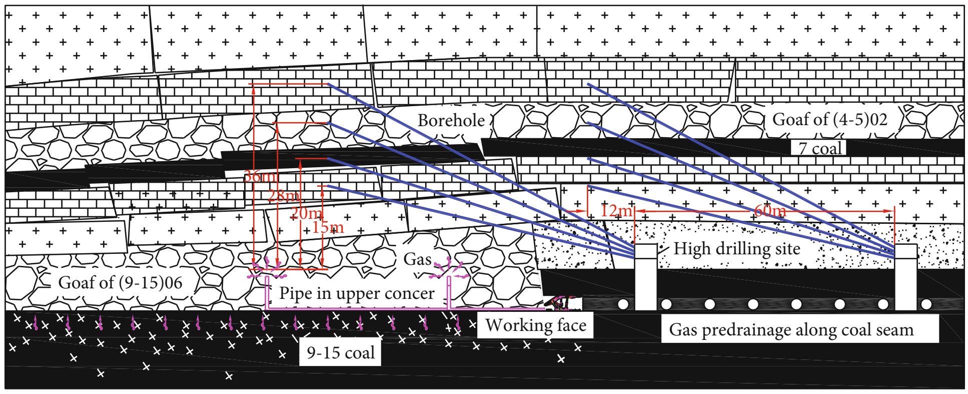

(a)

(b)

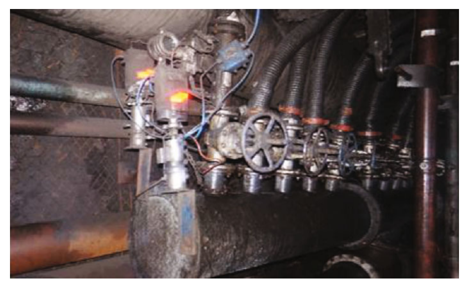

(c)

Figure 12: Gas drainage in roof caving and fissure zones of the No. (9-15)06 panel. (a) Overburden structure of (9-15)06 panel and roof high-level gas drainage boreholes. (b) Boreholes in high drilling site. (c) Metering installation of gas drainage.

difference between the measured pressures of two gate roads was reduced by adjusting the ventilation parameters.

4.1. Gas Predrainage in the Coal Seam. Hydraulic fractured boreholes were also used as gas predrainage holes before the working face mining for the gas predrainage in the coal seam (Figure 11). Accordingly, two purposes were obtained by predrainage holes: the enhancement of gas predrainage and reduction of construction volume.

The system of gas predrainage in the coal seam mainly consists of drainage pipe, filter pipe, collecting pipe, and hole-sealing materials (Figure 11). The auxiliary devices include the flow meter, the concentration meter, and the pressure gauges. Also, metal sleeves with a diameter of 40 mm and a wall thickness of 3 mm were put in each fractured borehole, and small-diameter holes were arranged at one of the sleeves' ends. Two sections of the sleeves were arranged around each borehole, and each section was 3-4 m in length. After installation of the sleeves, boreholes were sealed using polyurethane (PU). It is important to note that hole-sealing depth should not exceed the burial depth of the gas drainage pipe in the borehole. Lastly, the sleeves were connected with the gas drainage header pipes, providing a negative pressure of 25 kPa.

4.2. Drainage of Gas from the Caving Zone via High-Position Boreholes. Gas emitted from pressure relief in the coal seam floor was an essential gas source in the mining panel. After the working face mining, the overlying strata underwent fracturing and formed the bent subsidence zone, the fracture zone, and the caving zone [32–35]. Meanwhile, many layered and vertical fractures were produced [36, 37], and gas was accumulated in these regions. The accumulation of emitted gas from No. 4-5 coal, No. 7 coal, and No. 9-15 coal increased the gas accidents. Therefore, based on gas predrainage in the coal seam before the mining, long-strike holes were drilled in the high-position drilling site on the roof. It was performed for discharging the gas accumulated in the caving and fracture zones during working face mining (Figure 12). The high-position drilling site was located in the tailgate of the No. (9-15)06 panel. Drilling sites were set at an interval of 60 m. In each drilling site, 16 long boreholes in 4 rows were arranged alongside the strike of the coal seam in a fan-shaped distribution.

4.3. Gas Drainage at the Upper Corner of the Panel. The gas produced in pressure relief from the floor can rush into the goaf and enter the upper corner, resulting in an abundance of gas in the corner. To avoid the above problem, gas drainage pipes were buried at the air return corner on the top of the goaf during working face mining (Figure 12).

4.4. Pressure-Balancing Ventilation for Reducing Air Leakage in the Goaf. The air supply is generally increased for diluting the gas concentration in the return airflow for the panels with

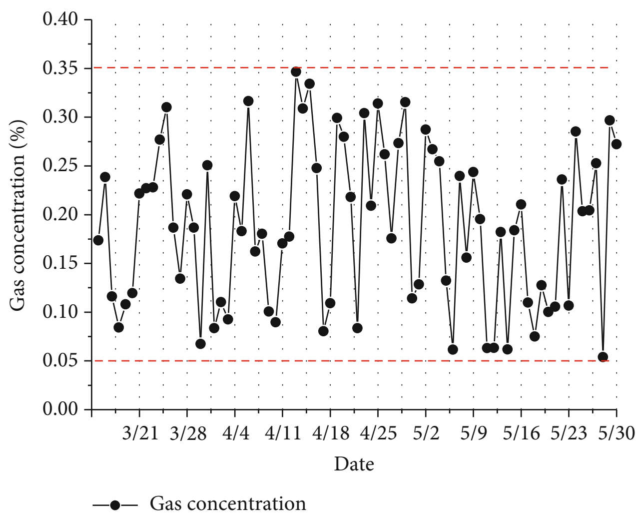

Figure 13: Variation law of gas concentration in return air flow of the No. (9-15)06.

U-shaped ventilation. It is an incorrect practice. Increasing the quantity of air supply in the panel blindly can increase the difference in the measured air pressure between the goaf and the panel and air leakage in the panel, leading to an increase in gas emission in the goaf and gas concentration in the panel return airflow [38]. On that basis, pressure-balancing ventilation was adopted to reduce the difference in the measured pressure between two sides in the air intake and return roadways. By the way, the distribution of the ventilation system's pressure was changed [39]. Accordingly, the air leakage can be lowered to inhibit gas emissions from the goaf's upper corner.

4.5. Gas Analysis. A long-term field test was performed in the No. (9-15)06 panel using the comprehensive control method based on the gas sources. Overall, gas was adequately controlled. Figure 13 displays the monitoring of gas concentration in the panel during the working face mining. The gas concentration in the return airflow fluctuated within a range of 0.05% to 0.35%. The maximum gas concentration was no greater than 0.35%, below the early warning value of 0.5%.

5. Conclusions

Gas control has always been a key problem during slice mining of ultrathick coal seams with a high content of gas. This study examined the No. (9-15)06 panel with a mean thickness of 32.94 m in Liuhuanggou Coal Mine. The No. 9-15 coal seam included low-permeability ultrathick coal seams with a high content of gas. The No. (9-15)06 panel was the top-slicing working face of the No. 9-15 coal, using a fully mechanized top coal caving with a mining height of 9 m. A significant content of gas was emitted from the panel in the working face mining.

Based on the arrangement in the No. (9-15)06 panel and the surrounding mining condition, gas in the panel had four emission sources: from the coal wall, gas top coal caving, the goaf, and the neighboring coal seams. In this study, a comprehensive control method based on gas sources was proposed for the panel. Before the working face mining, gas emissions from the coal walls and top coal caving were lowered via gas predrainage alongside the coal seam. After the working face mining, gas accumulated in the caving and fracturing zones was drained using long-strike boreholes in the high-position drilling site. Drainage pipes were buried in the upper corner of the goaf to avoid gas accumulation emitted from destressed floor coal seams. During the working face mining, pressure-balancing ventilation caused the reduction of air leakage in the goaf and gas emission from the goaf.

Due to the great hardness and poor permeability of the No. 9-15 coal seam, conventional gas predrainage methods were not properly performed on the coal seam. Using hydraulic fracturing caused the enhancement of the permeability in the coal seam. Also, the backward-segmented technology was designed for improving hydraulic fracturing performance. To validate the superiority of the proposed method, the prefracturing performance of the coal seam was evaluated using borescope examination and gas emission test. Field test results demonstrated that the fractures can be developed in the coal seam around the boreholes after hydraulic fracturing. Fractures were mainly initiated radially from the borehole wall and then propagated in a spiral pattern consistent with crustal stress measurements. After the hydraulic fracturing, the mean gas predrainage was enhanced by four times.

Finally, a long-term field test was performed in the No. 9-15 panel to validate the superiority of the proposed comprehensive control method based on the gas sources. Long-term monitoring results indicated that the gas concentration in the return airflow fluctuates within a range of 0.05%~0.35%. No warning of excessive gas appeared in the panel. An adequate gas control can effectively ensure mining safety in the panel.

Data Availability

The data used to support the findings of this study are available from the corresponding authors upon request.

Conflicts of Interest

The authors declare no conflicts of interest.

Acknowledgments

This research is supported by the Natural Science Foundation of China (52004144), Natural Science Foundation of Shandong Province, China (ZR2019BEE001, ZR2018MEE009), and Key Research and Development Projects of Shandong Province, China (2019GSF111038). The authors thank the anonymous referees for their careful reading of this paper and valuable suggestions.

References

[1] X. L. Yang, G. C. Wen, H. T. Sun et al., "Environmentally friendly techniques for high gas content thick coal seam stimulation—multi-discharge CO_2 fracturing system," *Journal of Natural Gas Science and Engineering*, vol. 61, pp. 71–82, 2019.

[2] T. Q. Xia, F. B. Zhou, J. S. Liu, and F. Gao, "Evaluation of the pre-drained coal seam gas quality," *Fuel*, vol. 130, pp. 296–305, 2014.

[3] F. X. Jiang, L. H. Kong, and C. G. Liu, "Gas emission laws of fully-mechanized sublevel caving mining in extra-thick coal seam," *Journal of China Coal Society*, vol. 36, no. 3, pp. 407–411, 2011.

[4] W. Wang, Y. P. Cheng, H. F. Wang et al., "Fracture failure analysis of hard-thick sandstone roof and its controlling effect on gas emission in underground ultra-thick coal extraction," *Engineering Failure Analysis*, vol. 54, pp. 150–162, 2015.

[5] Y. P. Fan and Y. B. Wang, "Study on measures to control methane in goaf in mechanized mining extremely thick face of Tashan coal mine," *China Safety Science Journal*, vol. 26, no. 12, pp. 116–121, 2016.

[6] H. Guo, C. Todhunter, Q. D. Qu, and Z. Y. Qin, "Longwall horizontal gas drainage through goaf pressure control," *International Journal of Coal Geology*, vol. 150-151, pp. 276–286, 2015.

[7] Y. Zhang, B. Zhang, L. Li, S. Q. Zhang, J. K. Liu, and J. J. Zhao, "Study on the effect of roof fracture development on gas drainage in steep full-mechanized caving mining," *Journal of Mining and Safety Engineering*, vol. 31, no. 5, pp. 809–813, 2014.

[8] Z. Q. Liu, "Gas drainage effect analysis of buried pipes in steeply inclined thick coal seam fully-mechanized caving face," *Coal Science and Technology*, vol. 45, no. S1, pp. 74–76, 2017.

[9] F. H. An, Z. F. Wang, H. M. Yang et al., "Application of directional boreholes for gas drainage of adjacent seams," *International Journal of Rock Mechanics and Mining Sciences*, vol. 90, pp. 35–42, 2016.

[10] S. Q. Lu, Y. P. Cheng, J. M. Ma, and Y. B. Zhang, "Application of in-seam directional drilling technology for gas drainage with benefits to gas outburst control and greenhouse gas reductions in Daning coal mine, China," *Natural Hazards*, vol. 73, no. 3, pp. 1419–1437, 2014.

[11] Y. K. Li, S. Y. Wu, B. S. Nie, and Y. K. Ma, "A new pattern of underground space-time tridimensional gas drainage: a case study in Yuwu coal mine, China," *Energy Science & Engineering*, vol. 7, no. 2, pp. 399–410, 2019.

[12] J. Liu, Z. G. Liu, K. Gao, and E. L. Jiang, "Application of deep borehole blasting to top-coal pre-weakening and gas extraction in fully mechanized caving," *Chinese Journal of Rock Mechanics and Engineering*, vol. 33, pp. 3361–3367, 2014.

[13] W. C. Zhu, C. H. Wei, S. Li, J. Wei, and M. S. Zhang, "Numerical modeling on destress blasting in coal seam for enhancing gas drainage," *International Journal of Rock Mechanics and Mining Sciences*, vol. 58, pp. 179–190, 2013.

[14] B. Bohloli and C. J. D. Pater, "Experimental study on hydraulic fracturing of soft rocks: influence of fluid rheology and confining stress," *Journal of Petroleum Science and Engineering*, vol. 53, no. 1-2, pp. 1–12, 2006.

[15] C. Z. Yan, H. Zhang, G. H. Sun, and X. R. Ge, "A 2d fdem-flow method for simulating hydraulic fracturing," *Chinese Journal of Rock Mechanics and Engineering*, vol. 1, pp. 67–75, 2015.

[16] D. Lockner and J. D. Byerlee, "Hydrofracture in Weber Sandstone at high confining pressure and differential stress," *Journal of Geophysical Research*, vol. 82, no. 14, pp. 2018–2026, 1977.

[17] J. Adachi, E. Siebrits, A. Peirce, and J. Desroches, "Computer simulation of hydraulic fractures," *International Journal of Rock Mechanics and Mining Sciences*, vol. 44, no. 5, pp. 739–757, 2007.

[18] C. Zhai, X. Z. Li, and Q. G. Li, "Research and application of coal seam pulse hydraulic fracturing technology," *Journal of China Coal Society*, vol. 36, no. 12, pp. 1996–2001, 2011.

[19] Q. Li, B. Lin, and C. Zhai, "A new technique for preventing and controlling coal and gas outburst hazard with pulse hydraulic fracturing: a case study in Yuwu coal mine, China," *Natural Hazards*, vol. 75, no. 3, pp. 2931–2946, 2015.

[20] C. Zhai, M. Li, C. Sun, J. G. Zhang, W. Yang, and Q. G. Li, "Guiding-controlling technology of coal seam hydraulic fracturing fractures extension," *International Journal of Mining Science & Technology*, vol. 22, no. 6, pp. 831–836, 2012.

[21] Q. Li, B. Lin, and C. Zhai, "The effect of pulse frequency on the fracture extension during hydraulic fracturing," *Journal of Natural Gas Science and Engineering*, vol. 21, pp. 296–303, 2014.

[22] W. Zhou, L. Yuan, G. L. Zhang et al., "A new method for determining the individual sources of goaf gas emissions: a case study in Sihe Coal Mine," *Journal of China Coal Society*, vol. 43, no. 4, pp. 1016–1023, 2018.

[23] Y. Xing and F. Zhang, "Optimizing borehole spacing for coal seam gas pre-drainage," *Journal of Geophysics and Engineering*, vol. 16, no. 2, pp. 399–410, 2019.

[24] M. K. Rahman and A. H. Joarder, "Investigating production-induced stress change at fracture tips: Implications for a novel hydraulic fracturing technique," *Journal of Petroleum Science and Engineering*, vol. 51, no. 3-4, pp. 185–196, 2006.

[25] B. X. Huang, X. L. Zhao, S. L. Chen, and J. W. Liu, "Theory and technology of controlling hard roof with hydraulic fracturing in underground mining," *Chinese Journal of Rock Mechanics and Engineering*, vol. 36, no. 12, pp. 2954–2970, 2017.

[26] M. K. Hubbert and D. G. Willis, "Mechanics of hydraulic fracturing," *Transactions of Society of petroleum engineers of AIME*, vol. 210, pp. 153–168, 1957.

[27] B. Q. Lin, J. Meng, J. Ning, M. B. Zhang, Q. G. Li, and Y. Liu, "Research on dynamic characteristics of hydraulic fracturing in coal body containing gas," *Journal of Mining and Safety Engineering*, vol. 29, no. 1, pp. 106–110, 2012.

[28] B. X. Huang, C. Y. Liu, J. H. Fu, and H. Guan, "Hydraulic fracturing after water pressure control blasting for increased fracturing," *International Journal of Rock Mechanics and Mining Sciences*, vol. 48, no. 6, pp. 976–983, 2011.

[29] G. Li, C. A. Tang, L. C. Li, and Z. Z. Liang, "Numerical simulation of 3D hydraulic fracturing process," *Chinese Journal of Geotechnical Engineering*, vol. 32, no. 12, pp. 1875–1881, 2010.

[30] Y. Xue, J. Liu, P. G. Ranjith, X. Liang, and S. Wang, "Investigation of the influence of gas fracturing on fracturing characteristics of coal mass and gas extraction efficiency based on a multi-physical field model," *Journal of Petroleum Science and Engineering, article*, vol. 206, p. 109018, 2021.

[31] Y. X. Cao, J. S. Zhang, L. Tian, H. Zhai, G. T. Fu, and J. H. Tang, "Research and application of CO^2 gas fracturing for gas control in low permeability coal seams," *Journal of China Coal Society*, vol. 42, no. 10, pp. 2631–2641, 2017.

[32] B. Y. Jiang, S. T. Gu, L. G. Wang, G. C. Zhang, and W. S. Li, "Strainburst process of marble in tunnel-excavation-induced stress path considering intermediate principal stress," *Journal of Central South University*, vol. 26, no. 4, pp. 984–999, 2019.

[33] N. Jiang, D. W. Yin, J. B. Ma, L. Han, H. Y. Pan, and Q. Yin, "Effects of water immersion on the long-term bearing characteristics of crushed gangue in goaf," *Geofluids*, vol. 2021, Article ID 6675984, 2021.

[34] J. Wang, J. G. Ning, J. Q. Jiang, and T. T. Bu, "Structural characteristics of strata overlying of a fully mechanized longwall face: a case study," *Journal of the South African Institute of Mining and Metallurgy*, vol. 118, pp. 1195–1204, 2018.

[35] X. S. Liu, Y. L. Tan, J. G. Ning, Y. W. Lu, and Q. H. Gu, "Mechanical properties and damage constitutive model of coal in coal-rock combined body," *International Journal of Rock Mechanics and Mining Sciences*, vol. 110, pp. 140–150, 2018.

[36] W. Y. Guo, Y. L. Tan, F. H. Yu et al., "Mechanical behavior of rock-coal-rock specimens with different coal thicknesses," *Geomechanics and Engineering*, vol. 15, no. 4, pp. 1017–1027, 2018.

[37] K. Fang, T. B. Zhao, Y. B. Zhang, Y. Qiu, and J. H. Zhou, "Rock cone penetration test under lateral confining pressure," *International Journal of Rock Mechanics and Mining Sciences*, vol. 119, pp. 149–155, 2019.

[38] B. Q. Lin, S. N. Zhou, and R. G. Zhang, "Methane controlling technique at the upper corner of the goaf in u- type ventilation face," *Journal of China Coal Society*, vol. 22, no. 5, pp. 63–67, 1997.

[39] G. Wang, R. Wang, M. M. Wu, L. Xin, X. H. Zhou, and C. W. Liu, "Prevention and control technology of harmful gas intrusion in close-up coal seam under fire area," *Journal of China Coal Society*, vol. 42, no. 7, pp. 1765–1775, 2017.

Hindawi
Geofluids
Volume 2021, Article ID 3277131, 12 pages
https://doi.org/10.1155/2021/3277131

Research Article

Numerical Analysis on the Storage of Nuclear Waste in Gas-Saturated Deep Coal Seam

Teng Teng,[1,2,3] Yuming Wang,[1] Xiaoyan Zhu,[1] Xiangyang Zhang,[2] Sihai Yi,[3,4] Guowei Fan,[1] and Bin Liu[2]

[1] *Beijing Key Laboratory for Precise Mining of Intergrown Energy and Resources, China University of Mining and Technology-Beijing, Beijing 100083, China*
[2] *Key Laboratory of Safety and High-Efficiency Coal Mining, Ministry of Education (Anhui University of Science and Technology), Huainan 232001, China*
[3] *State Key Laboratory of Water Resource Protection and Utilization in Coal Mining, Beijing 100011, China*
[4] *School of Safety Engineering, North China Institute of Science and Technology, Langfang 065201, China*

Correspondence should be addressed to Teng Teng; t.teng@cumtb.edu.cn and Xiangyang Zhang; xyzhang@aust.edu.cn

Received 23 April 2021; Accepted 23 June 2021; Published 12 July 2021

Academic Editor: Jia Liu

Nuclear power has contributed humanity a lot since its successful usage in electricity power generation. According to the global statistics, nuclear power accounts for 16% of the total electricity generation in 2020. However, the rapid development of nuclear power also brings up some problems, in which the storage of nuclear waste is the thorny one. This work carries out a series of modeling and simulation analysis on the geological storage of nuclear waste in a gas-saturated deep coal seam. As the first step, a coupled heat-solid-gas model with three constitutional fields of heat transfer, coal deformation, and gas seepage that based on three governing conservation equations is proposed. The approved mechanical model covers series of interactive influences among temperature change, dual permeability of coal, thermal stress, and gas sorption. As the second step, a finite element numerical model and numerical simulation are developed to analyze the storage of nuclear waste in a gas-saturated deep coal seam based on the partial differential equations (PDE) solver of COMSOL Multiphysics with MATLAB. The numerical simulation is implemented and solved then to draw the following conclusions as the nuclear waste chamber heats up the surrounding coal seam firstly in the initial storage stage of 400 years and then be heated by the far-field reservoir. The initial velocity of gas flow decreases gradually with the increment of distance from the storage chamber. Coal gas flows outward from the central storage chamber to the outer area in the first 100 years when the gas pressure in the region nearby the central storage chamber is higher than that in the far region and flows back then while the temperature in the outer region is higher. The modeling and simulation studies are expected to provide a deep understanding on the geological storage of nuclear waste.

1. Introduction

Nuclear power has provided a large amount of electric energy for human. It has the potential to be a major, global, scalable, and carbon-free energy source in the future. Nuclear power has serviced human beings as a continuous supply for the energy for more than sixty years since 1954, when a small Obninsk plant was founded in Russia. By the year 2019, more than four hundred and forty nuclear power plants in the world were producing about 10% of the electricity [1–3]. The three largest countries in the world for nuclear power generation are America, Japan, and France. America has more than 100 nuclear power units with a total capacity of 98.2 GW. In the year 2019, the generated nuclear power in America accounts for more than 30% of the total nuclear power in the world with the amount of 809 TWh [4]. Japan is developed in nuclear power that it is the second largest producer of nuclear power, where the nuclear power accounts for one-third of the country's total electricity generation [5]. In France, the nuclear power accounts for more than 70% of the country's electricity generation based on fifty-eight operational units with the installed capacity of 63.1

GW [6]. Although the nuclear power provides the energy to support the development of human, it also caused many thorny problems. Nuclear waste storage has always been a vexing and intractable problem. As we know, the nuclear waste is one kind of radioactive scrap that has a significant impact on human health if not disposed properly, and the average life of a nuclear reactor is just about a few decades. As a result, more and more nuclear waste is released every year. Researches have put forward various possible methods to store the waste nuclear after its reactor after considering different factors, such as the policies and techniques. Geological storage in deep georeservoir seems to be the most potential possibility for the disposal of nuclear waste that has caused high attention in the field. It means that the nuclear waste is to be transferred and stored promptly in a repository in the deep underground target formation once it is removed from the reactor.

Scholars at home and abroad have carried out a lot of researches on the underground storage of nuclear waste. The general design of the deep geological storage chamber requires a shielding tank that to cover the nuclear waste. The tank is then placed in a host rock formation. At present, different kinds of rock formations have been discussed for the feasibility of nuclear waste storage. In 2007, McKinley et al. [7] have published a good overview on the developing process about the choices for the stratigraphic formation. To summarize, the formations with rock types such as salt rock, clay stone, and granite are the possible targets to be host rocks for geological storage of nuclear waste. Based on a series of experiments, Jia et al. [8] analyzed the storage of nuclear waste in saturated hard clay; they also established an elastoplastic damage model for the deformation of the surrounding rock under a complex thermal-hydro-mechanical condition. Moog et al. [9] reported the ultralow seepage characteristics of granite and considered the storage of nuclear waste in a granite formation. Plúa et al. [10] introduced a large-scale modeling of the underground storage of high-level radioactive waste into Callovo-Oxfordian claystone and proposed a new method of numerical analysis. In their numerical work, the chamber of nuclear waste is considered to be stored in a deep formation of claystone, which has been selected as an industrial trial plot for geological disposal in France. Bentonite has favourable characteristics of plasticity, swelling capacity, colloid filtration, low hydraulic conductivity, high retardation of key radionuclides, and the stability in complex geological environments that it is treated as one kind of security component in the industrial storage engineering for different types of the nuclear waste [11]. Abdel-Karim et al. [12] collected the sand and sandstone samples from the Inshas rad-waste disposal site and examined the geochemical-physical properties in the Atomic Energy Agency. The results show that the samples has high contents of the interstitial Fe_2O_3 and Al_2O_3, which are important components to prevent the pollutant transport via adsorption. The Inshas rad-waste disposal site has a high possibility to meet the requirements of the nuclear waste storage as the presented high contents of the interstitial Fe_2O_3 and Al2O3 were important agents for preventing pollutants transport via adsorption. Based on the field data that were collected from a specific spot from the southeastern coast of Sweden and the experimental results that were obtained from the Aspo Hard Rock Laboratory on, Tiren et al. [13] adopt a three-dimensional (3D) visualization method to model a hypothetical site for the storage of a high-level nuclear waste (HLNW). In their model, the chamber is located in the granitoid formation of the trans-Scandinavian igneous belt with a depth of 500 meters. The research results show that the hypothetical conditions are of great feasibility for the storage of high-level nuclear waste. In 2010, Streimikiene and Mikalauskiene [14] analyzed and compared the challenges in the storages of geological carbon and nuclear waste in Lithuania. They also evaluated the cost for the development of the nuclear and carbon capture as well as the storage technologies. That is because Lithuania was faced with the final closure of the Ignalina nuclear power station and the storage of nuclear waste in that year. In China, researchers have conducted a lot of survey analysis from the surface and the subsurface aspects by the mapping and underground borehole exploration practices in the candidate sites. They have gotten comprehensive geological, hydrogeological, and geophysical data. The final result is that the Xinchang site in the Beishan region was selected as China's first underground research laboratory site [15]. Although scholars have considered couplings in the storage of nuclear waste in coal seam, few people take the characteristics of gas-saturated environment into consideration.

The geological storage of nuclear waste causes complex changes to the storage chamber and rocks. Their nature and performance are expected to change according to the internal and external conditions through the whole heating and cooling process of nuclear waste. As these processes donate potential influences on the engineering safety, it is necessary to identify and understand the environment changes in the surrounding rock profoundly in order to ensure the relevant safety requirements. Among the environment changes induced by nuclear waste storage, the thermo-hydro-mechanical-chemical (THMC) couplings are difficulties that urgently need to be resolved. Bernier et al. [16] points out that the complicated interactions among the thermofield, hydrofield, mechanical field, and chemical fields would affect the transport of radionuclide in the storage chamber and its surrounding environment. The ultimate degree of influence depends on the dynamic nature of the waste and the surroundings. By using the thermohydrological variables, Sasaki and Rutqvist [17] developed a methodology to approximately represent the stress in host rock and the changes of permeability that were induced by stress. A coupled thermo-hydro-mechanical simulation by using a TOUGH-FLAC simulator was established. Research results show that the developed methodology in the TH-coupled simulation matches the calculated data from the THM-coupled simulation over a simulated timeframe of over 10,000 years. To research the responses of the surrounding rocks under thermal loads under the background of deep geological radioactive waste storage, the French National Radioactive Waste Management Agency did a series of experiments including the in situ experiments at the Meuse/-Haute-Marne Underground Research Laboratory [18]. The thermomechanical behaviors of the steel sleeve, equipped with strain gauges, displacement sensors, and temperature sensors are well discussed. They also monitored the evolution of the annular space and studied the thermo-hydro-mechanical behavior of the near or far rock under different pore pressures and temperatures through the sensors that are installed in peripheral boreholes. Considering the change of extreme climate, Boulton et al. [19] simulated the thermo-hydro-mechanical impacts of extreme climate on the lithosphere, which might extend deep into the reservoir. The research results show that the glaciation has impacts on a depth scale. It required to be considered in a safety analysis for deep lithosphere storage of long-lived radionuclides in areas that have been prone to glaciation in the past. Holton et al. [20] described an efficient means to evaluate the maximum temperature constraint of the deformation that is to place a waste container. They find that sodium montmorillonite will undergo mineral alteration when the temperature increases significantly, which will reduce the expansion property of the material. At an approximate underground environment of nuclear waste storage in laboratory, Zhang [21] observed the thermo-hydro-mechanical behaviors of the indurated Opalinus clay rocks extensively. The results show that the maximum temperature for nuclear waste is over one hundred degrees centigrade. In large-scale deep geological disposal, the hydrogen embrittlement may occur in titanium vessels once oxygen is depleted. Therefore, Zhang et al. [22] predicted the potential danger of the high-level nuclear waste container caused by embrittlement; the hydrogen entry into titanium was studied at different temperatures in a simulated deep geological environment of Beishan, which was the preselected HLNW storage area in China. Ström et al. [23] presented an overview of the bedrock and surface modeling work that comprises a major part of the site characterization in Sweden, called site descriptions. The site-descriptive models involves a multidisciplinary interpretation of geology, rock mechanics, thermal properties, hydrogeology, hydrogeochemistry, transport properties, and ecosystems using input in the form of available data for the surface and from deep boreholes. Salama et al. [24] explored the anisotropic geologic repositories on the high-level nuclear waste disposal. Numerical results show that even a slight difference in anisotropy of thermal conductivity of host rock with direction could have interesting effects on temperature fields, and the temperature contours are aligned more towards the principal direction of anisotropy. Furthermore, it is found that the larger the peak temperature in the buffer zone, the smaller the anisotropy angle and vice versa. To better understand the processes of geological nuclear waste storage, Dupray et al. [25] proposed a case study for sensitivity analysis by using a thermo-hydro-mechanical finite element approach including a consistent thermoplastic constitutive model for unsaturated soils. The model features a coupled thermo-hydro-mechanical approach of the water retention curve. Various couplings were studied separately and in combination in order to determine the significance of each. The change of temperature caused by geological storage of nuclear waste has attracted the attention of most scholars; however, the study on the coupled interactive effects among temperature, surrounding rock/coal, and gas in the nuclear waste storage is still lacking.

To study the storage of nuclear waste in gas-saturated deep coal seam, this paper carried out a mechanical modeling and numerical simulation work. The theoretical heat-solid-gas coupling model has three components of heat transfer, gas seepage, and solid deformation that are governed by three conservation equations. Before the establishment of thermal energy conservation equation, the temperature decay evolution of nuclear waste was well discussed. For coal deformation, the mechanical equilibrium is obviously applicable with the considerations of thermal stress and gas pressure. The migration of gas in both coal matrix and fracture network satisfies the mass conservation equation, and gas flow obeys a Darcy's law. By using a PDE solver of COMSOL Multiphysics with MATLAB, the approved mechanical model is successfully implemented into a numerical model and solved as a numerical simulation in Section 3. Section 4 analyzes and quantifies the numerical results on the storage of nuclear waste in gas-saturated deep coal seam. The conclusions and understandings are drawn in the last Section 5, which are expected to provide a deep understanding on the geological storage of nuclear waste.

2. Modeling on the Storage of Nuclear Waste

There are three typical fields of the diffusion of thermal energy, deformation of coal seam, and the escaping of gas that interplays each other in the storage of nuclear waste in a gas-saturated coal seam. Before modeling, we assume that the surrounding coal is in close contact with the nuclear waste tanks. The governing equation for each physical field is established in this section as follows.

2.1. Evolution of Temperature with Time for the Nuclear Waste Tank. As the residual reaction of nuclear waste is exhausted, the temperature of the nuclear waste storage chamber decreases gradually [26]. In order to clarify the temperature attenuation evolution of nuclear waste itself, related data are collected and analyzed from the domestic and overseas research achievement, a simple and practical semiempirical curve for the evolution of temperature is obtained. Figure 1 shows the temperature attenuation curve of nuclear waste, in which the points represent the reported date by Zheng et al. [27]. From Figure 1, one can find that the temperature of nuclear waste decreases with the storage time from the initial temperature of 370 K to the final temperature of 298 K after about 4000 years. In the first 1500 years, the temperature of nuclear reactor decreases at an increasing rate, whereas the decreasing rate of temperature slows down gradually in the later 2500 years. Thus, the evolution of temperature with time for the nuclear reactor can be fitted by a logistic function as

$$T = 291.8 + \frac{75.2}{1 + (t/1638.2)^{3.52}}, \tag{1}$$

where T is the temperature of the nuclear reactor, K and t is the storage time in unit of year. As is seen in Figure 1, the

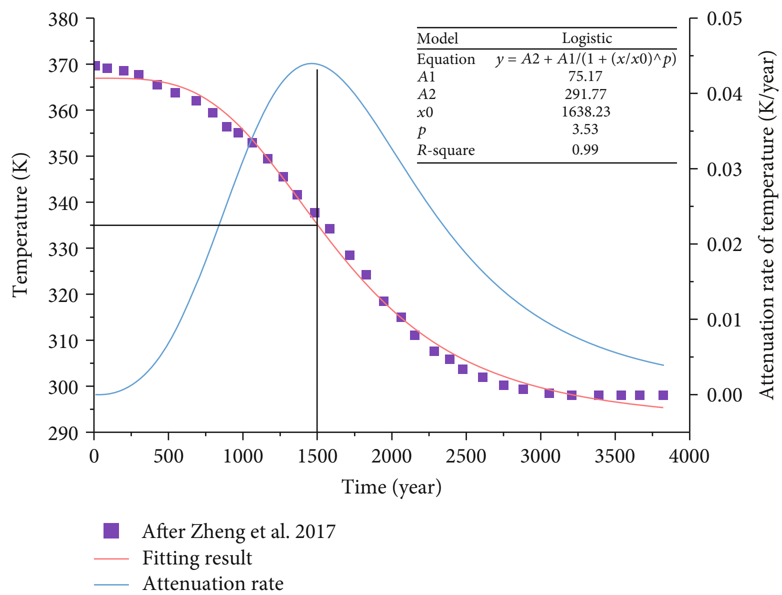

FIGURE 1: Temperature attenuation curve of nuclear reactor.

fitting result is well matched with the reported data from Zheng et al. [27].

2.2. Diffusion of Thermal Energy. The total heat flux in coal seam contains the heat conduction and convection that can be expressed as [28]

$$v_T = -K_T \nabla T + \rho_g \rho_c C_g v_g, \tag{2}$$

where v_T is the total heat flux velocity, (J/(m^2·s)); K_T is the effective coefficient for the thermal conductivity of gas-saturated coal, (J/(m·s·K)); ΔT is the increase of temperature, K; ρ_g and ρ_c represent the densities of gas and coal, respectively, kg/m^3; C_g is the specific heat constants of gas, kJ/(kg·K); and v_g is the vector of gas velocity, m/s.

According to Darcy's law, v_g can be expressed as [29, 30]

$$v_g = -\frac{k}{\mu} \nabla p_g, \tag{3}$$

where μ donates the dynamic viscosity of the gas, Pa·s; k is the permeability of the coal seam, m^2; and the pressure gradient ∇p_g, Pa/s, can be expressed as

$$\nabla p = \frac{\partial p_g}{\partial x} i + \frac{\partial p_g}{\partial y} j + \frac{\partial p_g}{\partial z} k. \tag{4}$$

The energy conservation in the coal seam obeys an energy conservation equation as [31]

$$\frac{\partial (C_q T)}{\partial t} + p_g \nabla \cdot v_g + \nabla \cdot v_T = Q_T, \tag{5}$$

where C_q donates the specific heat capacity of gas-saturated coal, kJ/(kg·K).

Substituting Equations (2)–(4) into Equation (5), one obtains the energy conservation equation as

$$C_q \frac{\partial T}{\partial t} + p_g \nabla \cdot \left(-\frac{k}{\mu} \nabla p_g \right) - K_T \nabla^2 T + \rho_c C_g \nabla \cdot \left[\rho_g - \frac{k}{\mu} \nabla p_g \right] = Q_T. \tag{6}$$

2.3. Deformation of Coal Seam. During the storage period of nuclear waste, the changes of temperature and gas pressure will trigger the gas desorption deformation and thermal expansion. According to Teng et al. [32], the deformation that was induced by gas desorption is related with the gas pressure and the change of temperature as

$$\varepsilon_s = \frac{\varepsilon_L p_g}{P_L + p_g} e^{-c_T \Delta T / \left(1 + c_p p_g\right)}, \tag{7}$$

where ε_s is the gas sorption-induced volumetric stain; ε_L is the deformation parameter; and P_L, c_T, and c_p are the coefficients for gas sorption. Thermal expansion ε_T is linearly dependent on the change of temperature as $\varepsilon_T = \alpha_T \Delta T$, where α_T is the coefficient of thermal expansion.

To establish the deformation model, the coal seam is assumed to deform as one kind of elastic material where the stress σ_{ij} and strain ε_{ij} has following relation [33]:

$$\sigma_{ij} = 2G\varepsilon_{ij} + \left(\frac{2G\nu}{1 - 2\nu} \varepsilon_{kk} + \alpha p_g - K \alpha_T T - K \varepsilon_s \right) \delta_{ij}, \tag{8}$$

where α is Biot's coefficients for coal; G and K are the shear and bulk modulus of coal, MPa, respectively; ν is Poisson's

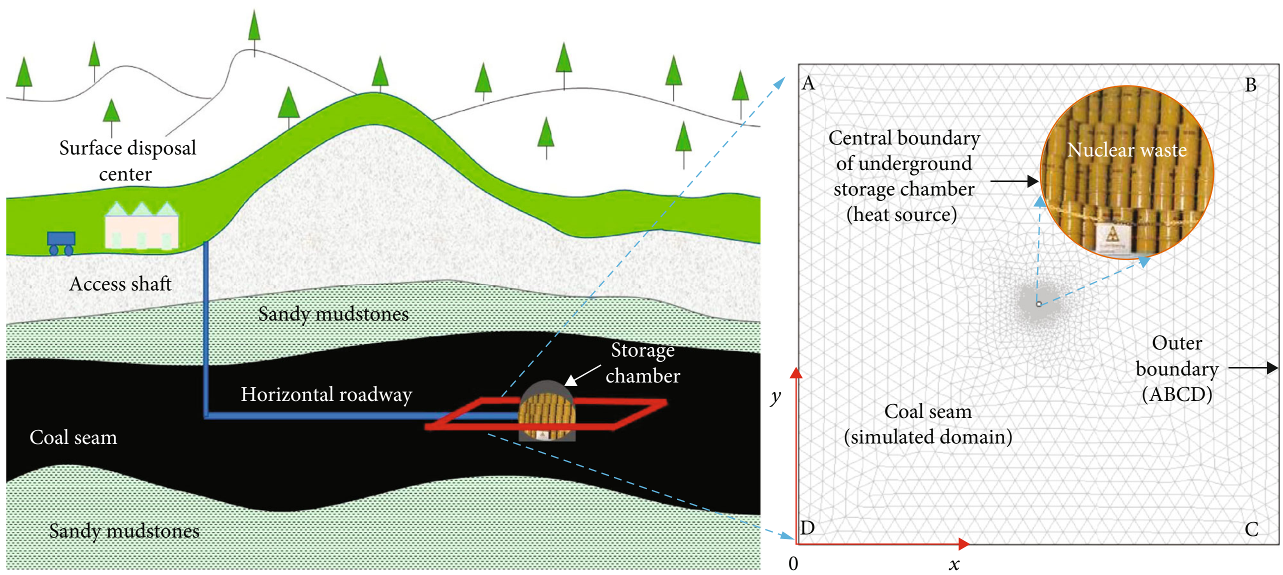

(a) Schematic diagram of nuclear waste storage in coal mine

(b) Numerical geometry: a top view section

FIGURE 2: Schematic diagram of the numerical model.

TABLE 1: Parameters for numerical simulation.

Parameter	Value used
Elasticity for coal (E, MPa)	2713
Poisson's ratio (ν)	0.339
Coal density (ρ_c, kg/m^3)	1.25×10^3
Coefficient for sorption deformation (ε_L, kg/m^3)	0.0156
Initial permeability of coal matrix (k_{m0}, mD)	0.002
Initial permeability of coal fracture system (k_{f0}, mD)	1
Initial porosity of coal matrix (ϕ_{m0})	0.05
Methane dynamic viscosity (μ, Pa·s)	1.84×10^{-5}
Langmuir volume constant (η_s, m^3/kg)	0.048
Langmuir pressure constant (P_L, MPa)	1.57
Pressure coefficient (c_p, MPa^{-1})	0.07
Temperature coefficient (c_T, K^{-1})	0.02
Pressure at standard condition (p_a, MPa)	0.103
Thermal expansion coefficient for solid coal matrix (α_T, K^{-1})	2.4×10^{-5}
Specific heat capacity of gas (C_g, kJ/(kg·K))	1.25
Specific heat capacity of coal (C_q, kJ/(kg·K))	1.62
Thermal conductivity of coal (K_T, J/(m·s·K))	0.2

ratio; and δ_{ij} donates the Kronecker delta which is defined as 1 if $i = j$ and 0 if $i \neq j$.

2.4. Gas Escaping in Coal Seam. The storage of nuclear waste leads to a redistribution of coalbed methane in coal and rock formations as it changes the temperature. Coal is often treated as a dual-porous medium that contains the coal matrix and the fracture network; the escaping of gas in both the matrix and fracture systems obeys the mass conservation equation in same type as [34]

$$\frac{\partial m_g}{\partial t} + \nabla \cdot \left(\rho_g v_g\right) = Q_g, \tag{9}$$

in which, Q_g is the gas source; the gas density ρ_g can be expressed by the gas pressure as

$$\rho_g = \frac{M_g}{RT} p_g, \tag{10}$$

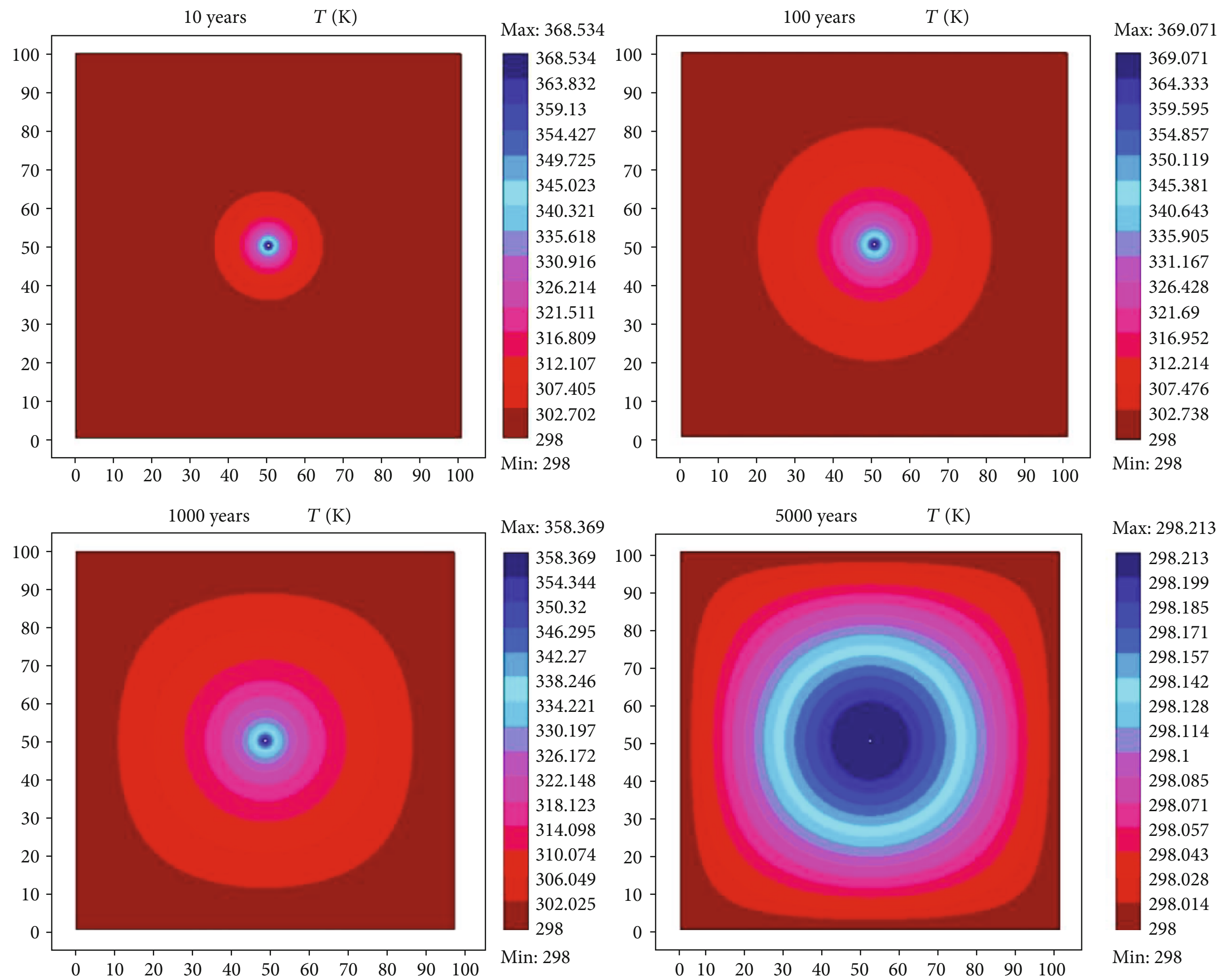

Figure 3: Spatial distribution of the reservoir temperature after 10, 100, 1000, and 5000 years.

where R and M_g are the universal gas constant and the molar mass of gas.

According to [35, 36], the transfer of gas in coal matrix and fracture network is proportional to the pressure gradient as

$$Q_g = \frac{M_g}{\tau RT}\left(p_{gm} - p_{gf}\right), \tag{11}$$

where τ is a coefficient for the desorption time and p_{gm} and p_{gf} represent the gas pressures in coal matrix and coal fracture network, MPa, respectively.

In coal matrix, gas is stored in both adsorption state and free state. The gas content m_{gf} can be expressed as

$$m_{gm} = \rho_g \phi_m + \frac{\eta_s p_g}{P_L + p_g} e^{-c_T \Delta T/\left(1+c_p p_g\right)}, \tag{12}$$

where η_s is the adsorption volume coefficient, kg/m^3. In the fracture network, gas is stored in free gas state, where the gas content m_{gf} is

$$m_{gf} = \rho_g \phi_f, \tag{13}$$

where ϕ_m and ϕ_f are the porosity of coal matrix and fracture network, respectively.

The permeability of coal matrix and fracture network can be expressed as [33, 35]

$$k_m = k_{m0}\left[\frac{1 + \alpha\left(\Delta\varepsilon_v + \Delta p_m/K_s - \Delta\varepsilon_s - \alpha_T \Delta T\right)}{\phi_{m0}}\right]^3, \tag{14}$$

$$k_f = k_{f0} e^{-3c_f \Delta\sigma_{ij}}, \tag{15}$$

where c_f is the compressibility for the fracture network.

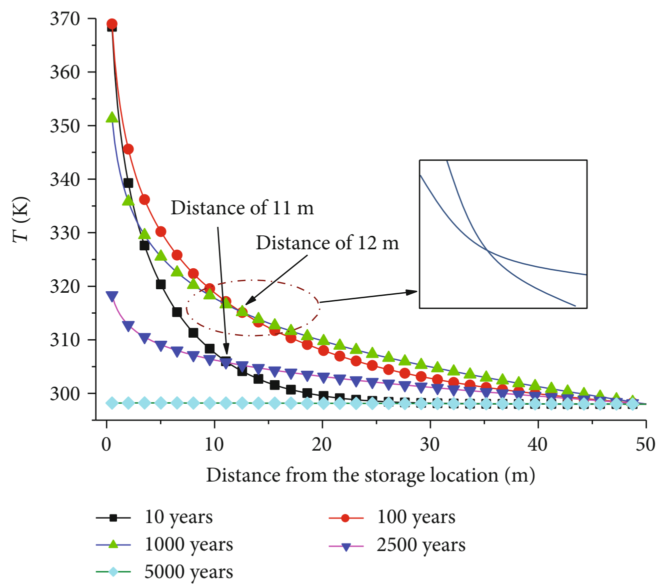

FIGURE 4: Evolution of reservoir temperature with the storage distance after different storage times.

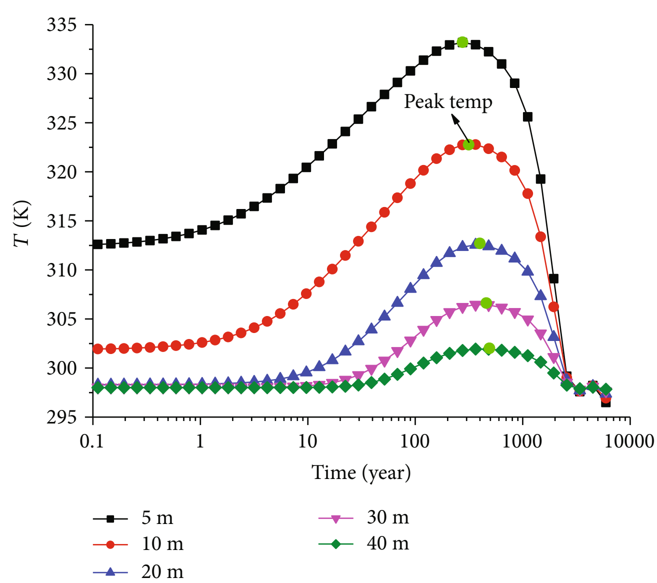

FIGURE 5: The evolution of reservoir temperature with time at different storage distances.

Equations (6), (8). and (9) make up a fully coupled heat-solid-gas coupling model for the storage of waste nuclear in deep coal seam. It is obviously difficult to solve an analytical solution for this proposed nonlinear partial differential model. However, the numerical solution can be well solved by a PDE solver, COMSOL Multiphysics with MATLAB in a powerful PDE-based multiphysics modeling environment.

3. Geological Environment and Model Establishment

The buried depth of target coal seam is 800 m, and there is a few of underground water above or below the formation. The roof and floor of the coal seam are sandy mudstone that has not been disturbed significantly from coal mining. The nuclear waste is supposed to be stored in the coal chambers that are remained in the previous coal mining practice. Figure 2(a) shows the schematic diagram of nuclear waste storage in deep coal seam. One can find a vertical shaft and a horizontal roadway for the access of storage chamber. The nuclear waste is processed at the ground surface disposal center and then transported to the storage chamber.

To simplify the calculation, a planar slice in Figure 2(b) can feasibly represent the basic computational area based on the plane strain hypothesis. The rectangular geometry of ABCD is selected for simulation with a circular storage chamber. The length of the rectangular model is 100 m, and the diameter of the central chamber is 8 m. In coal seam, the in situ gas pressure and temperature are 3.5 MPa and 298 K, respectively. The displacements for boundary AD

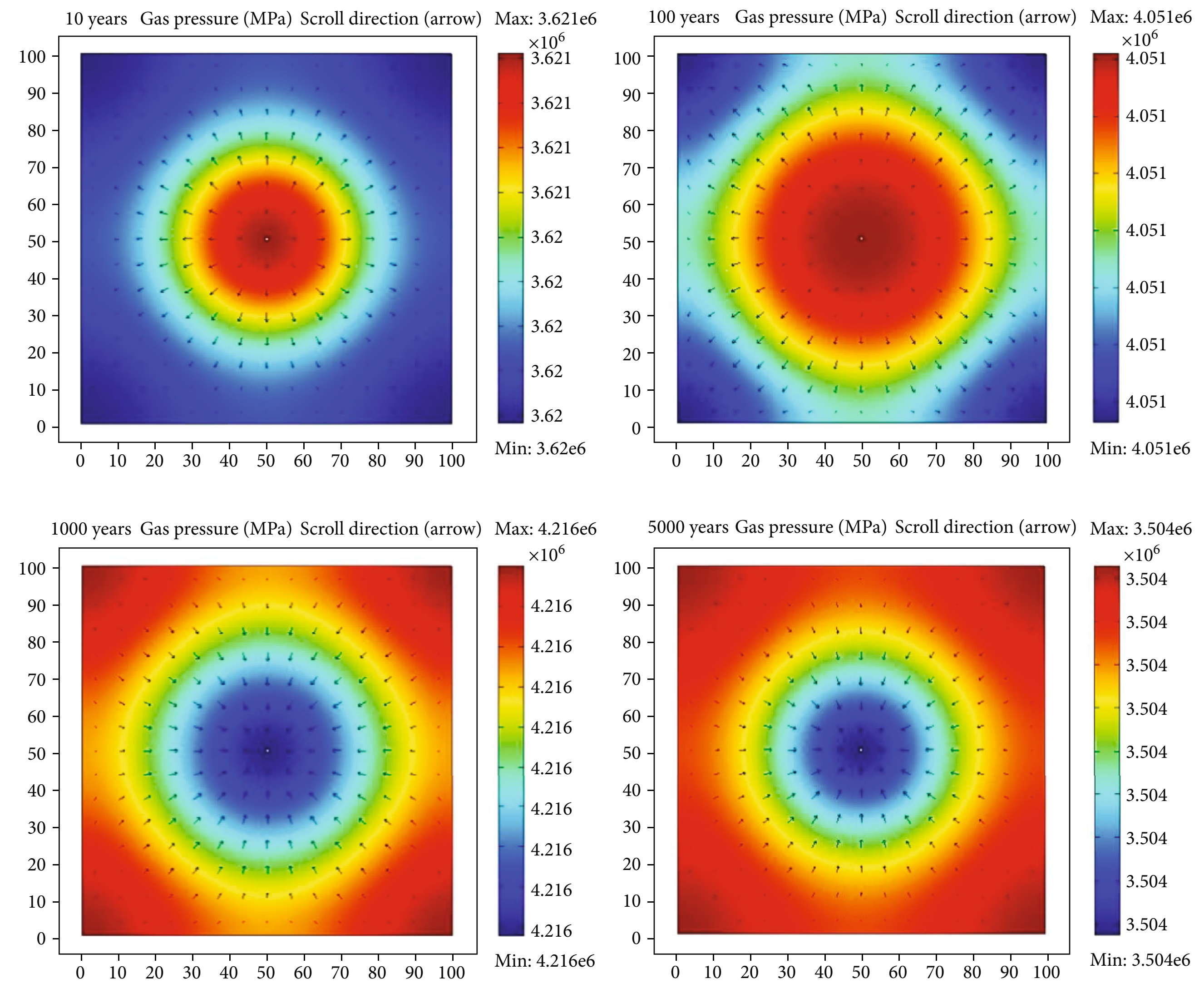

Figure 6: Distribution of gas pressure.

and BC are restrained in the x-direction while the displacements for boundary AB and DC are restrained in the y-direction. The central boundary is free for stress and constraint for displacement in the model. For the situation of coal seam gas, the boundary ABCD is treated as a symmetric boundary in both the matrix and fracture system where the gas flow and distribution have symmetry to these boundaries, and the central boundary is an airtight boundary with no flux. For the transfer of temperature, the boundary ABCD is given a constant temperature of 298 K while the central boundary has a time-dependent temperature that has been illustrated in Equation (1). Other simulation parameters are taken from literatures or determined from the conventional mechanical properties of coal and rock. Table 1 lists the main simulation parameters.

4. Analysis of Numerical Results

4.1. Spatial Evolution of Reservoir Temperature. Figure 3 shows the spatial distribution of the reservoir temperature after different storage time of 10, 100, 1000, and 5000 years. From Figure 3, one can find that the affected area of reservoir temperature gradually grows larger with the storage time of the nuclear waste. After the first 10 years of storage, the influence of nuclear waste on reservoir temperature mainly occurs within a range of about 15 m from the storage chamber, where the decreasing gradient of temperature with the increasing distance is very large. The storage of the nuclear waste has little impact in the more open range of area with the distance that is larger than 15 m. After the storage of 100 years, the increment of reservoir temperature is mainly concentrated within a distance of about 30 meters from the storage chamber, whereas the average temperature increment of the reservoir does not exceed 2°C at the further area. After the storage of 1000 years, the affecting distance of reservoir temperature by the central storage of nuclear waste reaches to 40 meters. By this time, the maximum value of reservoir temperature is significantly reduced to 358.4°C. This is because the temperature of nuclear waste decreases a lot after 1000 years. When the storage time reaches 5000 years, the

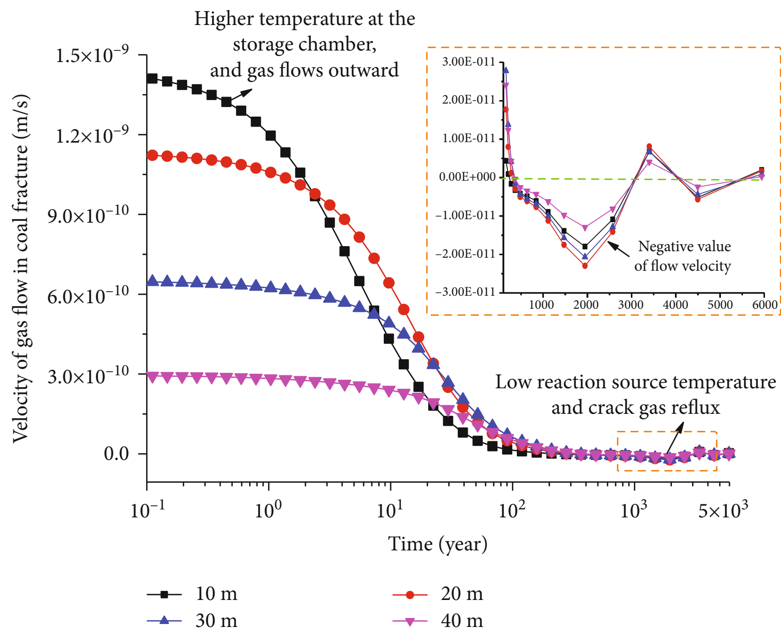

Figure 7: Velocity of gas flow in the fracture network.

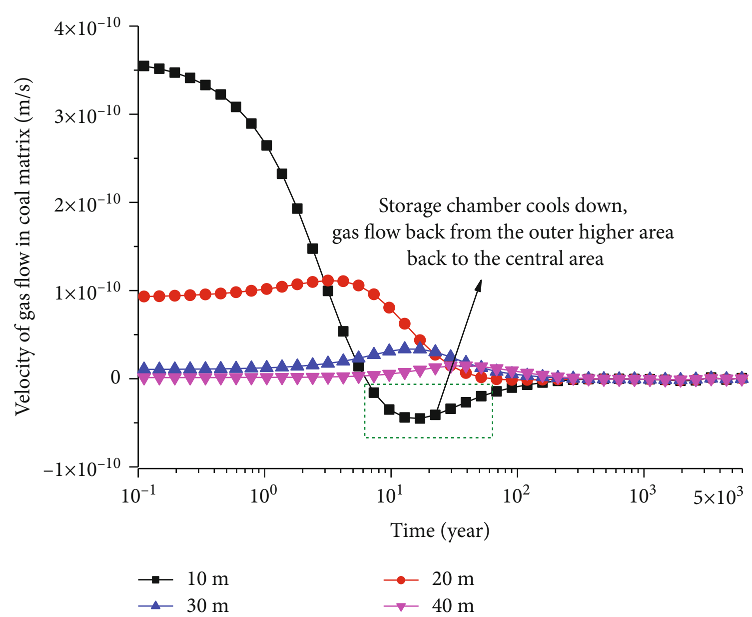

Figure 8: Velocity of gas flow in the coal matrix.

temperature of the whole coal seam drops to its initial temperature of 298 K after the depletion of the stored nuclear waste reaction.

Figure 4 is the quantitative evolution of reservoir temperature with the storage distance at different storage times. It shows that the nuclear waste source heats up the very adjacent surrounding coal reservoir firstly and then be heated by the far-field reservoir. As a result the evolution curves of reservoir temperature with the storage distance after different storage time get crossed, and the crossing points get close to the central chamber with storage time.

4.2. Evolution of Reservoir Temperature over Time. Figure 5 reflects the evolution of reservoir temperature over time at the storage distance of 5, 10, 20, 30, and 40 m from the nuclear waste chamber. It shows that the temperature rises firstly and then decreases over time. Due to the continuous decay of the nuclear waste reaction over time, the heat produced the nuclear itself decreases gradually; thus, the temperature of nuclear waste deceases over time. In the earlier stage of nuclear waste storage (about 200 to 400 years), the nuclear reaction heats up the surrounding coal seam, as a result the temperature rises gradually. When the nuclear reaction weakens, the temperature of the nuclear waste decreases, and the heat in heated seam conducts both toward to the central and the outer areas that resulting in a decrease of the temperature in coal seam. Taking the distance of 5 m as an example, one can find that the peak temperature is 333°C after a storage time of 200 years. The reservoir temperature rises with time before this time and decreases after then. Figure 5 also shows that the peak temperature value decreases with the distance from the central chamber, and the corresponding storage time for the peak temperature increases. For example, the peak temperature at the distance of 10, 20, 30, and 40 m are 322°C, 312°C, 306°C, and 301°C, at the corresponding storage year of 275, 352, 371, and 398, respectively.

4.3. Evolution of Gas Pressure in Coal Seam. Figure 6 represents to the distribution of gas pressure in coal seam after the storage time of 10, 100, 1000, and 5000 years. The change of temperature results in a series of coal-gas-temperature couplings, such as the enhancement of gas sorption, the expansion of coal matrix, and the increment of gas pressure. In Figure 6, it can be clearly seen that the gas pressure in the region nearby the central storage chamber is higher than that at the far region after 10 and 100 years, and coal seam gas flows outward from the central storage chamber to the outer area. At the storage time of 1000 and 5000 years, the temperature in the outer area is higher than the central area, where the gas flows back. This is the response of the change of reservoir temperature, as the gas pressure is sensitive to the changes of temperature.

4.4. Gas Flow in Coal Seam. Figures 7 and 8 show the velocity of gas flow at different distances in the coal matrix and the fracture network, respectively. From Figures 7 and 8, one can find that the initial velocity of gas flow decreases gradually with the increase of distance. For coal fracture network, the initial values are 1.42, 1.11, 0.65, and 0.3 nm/s at the position with distance of 10, 20, 30, and 40 m, respectively. For coal matrix, the corresponding initial values of flow velocity are 0.35, 0.1, 0, and 0 nm/s, respectively. Due to the high initial temperature of the nuclear waste and its fast cooling down, coal gas flows back. As a result, the velocity of gas flow decreases gradually or finally reverses to the opposite direction, especially at the region with short distance from the chamber. For example, gas flow is an obvious negative value at the distance of 10 m in coal matrix between the storage year that ranges from 6 to 110.

5. Conclusions

In this study, a coupled heat-solid-gas model with three constitutional fields of heat transfer, coal deformation, and gas seepage is developed for to analyze the geological storage of nuclear waste in a gas-saturated deep coal seam. The model covers a series of interactive influences among temperature change, dual permeability of coal, thermal stress, and gas sorption. It is then applied to a numerical simulation in the PDE solver of COMSOL Multiphysics with MATLAB. Hence, the following conclusions can be drawn from this study:

(1) In the initial storage stage of 400 years, the nuclear waste storage heats up the surrounding coal seam firstly and then be heated by the far-field reservoir. After the storage of 100 years, the increment of reservoir temperature is mainly concentrated within a distance of about 30 meters from the storage chamber, while the average temperature increase of the reservoir does not exceed 2°C at the further area. After 1000 years, the affecting distance of reservoir temperature by the central storage of nuclear waste affects reaches to 40 meters

(2) The initial velocity of gas flow decreases gradually with the increasing distance from the storage chamber. Gas pressure in the region nearby the central storage chamber is higher than that in the far region after 10 and 100 years, and coal seam gas flows outward from the central storage chamber to the outer area. After the storage time of 1000 and 5000 years, the temperature in the outer region is higher than the central region, and the gas flows back

The proposed heat-solid-gas model and simulation analysis are expected to improve the current understandings on the geological storage of nuclear waste.

Data Availability

Some calculation parameters are used in the numerical simulation in this work. All these parameters are derived from the historical documents and related experimental studies that are listed in Table 1.

Conflicts of Interest

I would like to make the following statement about the article's conflict of interest on behalf of all co-authors: (a) the article is organized under the joint efforts of all the authors, and the authors have agreed on the order in which the papers should be signed. (b) This article is the original work that has never been published in other places previously and will not be submitted for publication elsewhere during this period of submission. (c) The manuscript has been approved for submission by all the authors listed.

Acknowledgments

The paper is supported by the National Natural Science Foundation (52004285, U1910206), the Fundamental Research Funds for the Central Universities (2021YQNY06) from China University of Mining and Technology-Beijing, and the Open Fund of Key Laboratory of Safety and High-efficiency Coal Mining (JYBSYS2019101). This paper expresses deep gratitude to all the above supports.

References

[1] D. Themann and A. Brunnengräber, "Using socio-technical analogues as an additional experience horizon for nuclear waste management a comparison of wind farms, fracking,

carbon capture and storage (CCS) with a deep-geological nuclear waste disposal (DGD)," *Utilities Policy*, vol. 70, no. 6, p. 101181, 2021.

[2] F. G. F. Gibb, "High-temperature, very deep, geological disposal: a safer alternative for high-level radioactive waste?," *Waste Management*, vol. 19, no. 3, pp. 207–211, 1999.

[3] Z. Y. Ma, R. Pathegama Gamage, T. Rathnaweera, and L. Kong, "Review of application of molecular dynamic simulations in geological high- level radioactive waste disposal," *Applied Clay Science*, vol. 168, no. 2, pp. 436–449, 2019.

[4] L. Ortiz, G. Volckaert, and D. Mallants, "Gas generation and migration in Boom Clay, a potential host rock formation for nuclear waste storage," *Engineering Geology*, vol. 64, no. 2-3, pp. 287–296, 2002.

[5] F. Liang and X. G. Liu, "Analysis on the characteristics of geologic disposal waste arising from various partitioning and conditioning options," *Annals of Nuclear Energy*, vol. 85, no. 11, pp. 371–379, 2015.

[6] J. P. Busby, J. R. Lee, S. Kender, J. P. Williamson, and S. Norris, "Modelling the potential for permafrost development on a radioactive waste geological disposal facility in Great Britain," *Proceedings of the Geologists Association*, vol. 126, no. 6, pp. 664–674, 2015.

[7] I. G. McKinley, W. Russell Alexander, and P. C. Blaser, "Development of geological disposal concepts," *Radioactivity in the Environment*, vol. 9, no. 6, pp. 41–76, 2007.

[8] Y. Jia, G. Duveau, and J. F. Shao, "Thermo-hydromechanical modeling in saturated hard clay and application to nuclear waste storage," in *Soil and Rock Behavior and Modeling*, ASCE Library, 2006.

[9] H. C. Moog, F. Bok, C. M. Marquardt, and V. Brendler, "Disposal of nuclear waste in host rock formations featuring high-saline solutions - implementation of a thermodynamic reference database (THEREDA)," *Applied Geochemistry*, vol. 55, no. 4, pp. 72–84, 2015.

[10] C. Plúa, M. N. Vu, G. Armand et al., "A reliable numerical analysis for large-scale modelling of a high-level radioactive waste repository in the Callovo-Oxfordian claystone," *International Journal of Rock Mechanics and Mining Sciences*, vol. 140, no. 4, p. 104574, 2021.

[11] A. E. Milodowski, S. Norris, and W. R. Alexander, "Minimal alteration of montmorillonite following long-term interaction with natural alkaline groundwater: implications for geological disposal of radioactive waste," *Applied Geochemistry*, vol. 66, no. 5, pp. 184–197, 2016.

[12] A. M. Abdel-Karim, A. A. Zaki, W. Elwan, M. R. el-Naggar, and M. M. Gouda, "Geological and contaminant transport assessment of a low level radioactive waste disposal site," *Journal of Geochemical Exploration*, vol. 197, no. 2, pp. 174–183, 2019.

[13] S. A. Tirén, P. Askling, and S. Wänstedt, "Geologic site characterization for deep nuclear waste disposal in fractured rock based on 3D data visualization," *Engineering Geology*, vol. 52, no. 3-4, pp. 319–346, 1999.

[14] D. Streimikiene and A. Mikalauskiene, "Analysis of possible geological storage of CO_2 and nuclear waste in Lithuania," *Renewable & Sustainable Energy Reviews*, vol. 14, no. 6, pp. 1600–1607, 2010.

[15] J. Wang, L. Chen, R. Su, and X. Zhao, "The Beishan underground research laboratory for geological disposal of high-level radioactive waste in China: planning, site selection, site characterization and in situ tests," *Journal of Rock Mechanics and Geotechnical Engineering*, vol. 10, no. 3, pp. 411–435, 2018.

[16] F. Bernier, F. Lemy, P. de Cannière, and V. Detilleux, "Implications of safety requirements for the treatment of THMC processes in geological disposal systems for radioactive waste," *Journal of Rock Mechanics and Geotechnical Engineering*, vol. 9, no. 3, pp. 428–434, 2017.

[17] T. Sasaki and J. Rutqvist, "Estimation of stress and stress-induced permeability change in a geological nuclear waste repository in a thermo-hydrologically coupled simulation," *Computers and Geotechnics*, vol. 129, no. 1, p. 103866, 2021.

[18] F. Bumbieler, C. Plúa, S. Tourchi et al., "Feasibility of constructing a full-scale radioactive high-level waste disposal cell and characterization of its thermo-hydro-mechanical behavior," *International Journal of Rock Mechanics and Mining Sciences*, vol. 137, no. 1, p. 104555, 2021.

[19] G. Boulton, T. Chan, R. Christiansson et al., "Thermo-hydro-mechanical (T-H-M) impacts of glaciation and implications for deep geologic disposal of nuclear waste," *Elsevier Geo-Engineering Book Series*, vol. 2, no. 1, pp. 299–304, 2004.

[20] D. Holton, S. Myers, G. Carta, A. Hoch, M. Dickinson, and N. Carr, "Application of a novel approach to assess the thermal evolution processes associated with the disposal of high-heat-generating waste in a geological disposal facility," *Engineering Geology*, vol. 211, no. 8, pp. 102–119, 2016.

[21] C. L. Zhang, "Thermo-hydro-mechanical behavior of clay rock for deep geological disposal of high-level radioactive waste," *Journal of Rock Mechanics and Geotechnical Engineering*, vol. 10, no. 5, pp. 992–1008, 2018.

[22] Q. C. Zhang, Y. L. Huang, W. Sand, and X. Wang, "Effects of deep geological environments for nuclear waste disposal on the hydrogen entry into titanium," *International Journal of Hydrogen Energy*, vol. 44, no. 23, pp. 12200–12214, 2019.

[23] A. Ström, J. Andersson, K. Skagius, and A. Winberg, "Site descriptive modelling during characterization for a geological repository for nuclear waste in Sweden," *Applied Geochemistry*, vol. 23, no. 7, pp. 1747–1760, 2008.

[24] A. Salama, M. F. el Amin, and S. Y. Sun, "Numerical investigation of high level nuclear waste disposal in deep anisotropic geologic repositories," *Progress in Nuclear Energy*, vol. 85, no. 11, pp. 747–755, 2015.

[25] F. Dupray, C. Li, and L. Laloui, "THM coupling sensitivity analysis in geological nuclear waste storage," *Engineering Geology*, vol. 163, no. 8, pp. 113–121, 2013.

[26] R. Jonny, L. G. Zheng, and F. Chen, "Modeling of coupled thermo-hydro-mechanical processes with links to geochemistry associated with bentonite-backfilled repository tunnels in clay formations," *Rock Mechanics and Rock Engineering*, vol. 47, no. 1, pp. 167–186, 2014.

[27] L. G. Zheng, J. Rutqvist, H. Xu, and J. T. Birkholzer, "Coupled THMC models for bentonite in an argillite repository for nuclear waste: illitization and its effect on swelling stress under high temperature," *Engineering Geology*, vol. 230, no. 11, pp. 118–129, 2017.

[28] W. C. Zhu, C. H. Wei, J. Liu, H. Y. Qu, and D. Elsworth, "A model of coal-gas interaction under variable temperatures," *International Journal of Coal Geology*, vol. 86, no. 2-3, pp. 213–221, 2011.

[29] Y. Jin, X. Li, M. Y. Zhao, X. Liu, and H. Li, "A mathematical model of fluid flow in tight porous media based on fractal

assumptions," *International Journal of Heat and Mass Transfer*, vol. 108, no. 3, pp. 1078–1088, 2017.

[30] S. Harpalani and A. Schraufnagel, "Measurement of parameters impacting methane recovery from coal seams," *International Journal of Coal Geology*, vol. 8, no. 4, pp. 369–384, 1990.

[31] C. Wang, J. Feng, J. Liu, M. Wei, C. Wang, and B. Gong, "Direct observation of coal-gas interactions under thermal and mechanical loadings," *International Journal of Coal Geology*, vol. 131, no. 9, pp. 274–287, 2014.

[32] T. Teng, Y. X. Zhao, F. Gao, J. G. Wang, and W. Wang, "A fully coupled thermo-hydro-mechanical model for heat and gas transfer in thermal stimulation enhanced coal seam gas recovery," *International Journal of Heat and Mass Transfer*, vol. 125, no. 10, pp. 866–875, 2018.

[33] Z. W. Chen, J. S. Liu, D. Elsworth, L. D. Connell, and Z. Pan, "Impact of CO_2 injection and differential deformation on CO_2 injectivity under in-situ stress conditions," *International Journal of Coal Geology*, vol. 81, no. 2, pp. 97–108, 2010.

[34] Y. Xue, J. Liu, P. G. Ranjith, X. Liang, and S. Wang, "Investigation of the influence of gas fracturing on fracturing characteristics of coal mass and gas extraction efficiency based on a multi-physical field model," *Journal of Petroleum Science and Engineering*, vol. 206, no. 109018, pp. 1–19, 2021.

[35] T. Q. Xia, F. B. Zhou, J. S. Liu, J. Kang, and F. Gao, "A fully coupled hydro-thermo-mechanical model for the spontaneous combustion of underground coal seams," *Fuel*, vol. 125, no. 6, pp. 106–115, 2014.

[36] Y. Xue, T. Teng, F. Dang, Z. Ma, S. Wang, and H. Xue, "Productivity analysis of fractured wells in reservoir of hydrogen and carbon based on dual-porosity medium model," *International Journal of Hydrogen Energy*, vol. 45, no. 39, pp. 20240–20249, 2020.

Hindawi
Geofluids
Volume 2021, Article ID 5510535, 15 pages
https://doi.org/10.1155/2021/5510535

Research Article

Study on Water Characteristic Curve and Shear Characteristics of Typical Unsaturated Silty Clay in Shaoxing

Ruiqian Wu,[1] **Youzhi Tang**,[1] **Shaohe Li**,[2] **Wei Wang**,[1] **Ping Jiang**,[1] **and Guang Yang**[1]

[1]*School of Civil Engineering, Shaoxing University, Shaoxing 312000, China*
[2]*School of Civil Engineering, Zhejiang Institute of Industrial Technology, Shaoxing 312000, China*

Correspondence should be addressed to Wei Wang; wellswang@usx.edu.cn

Received 25 February 2021; Revised 6 May 2021; Accepted 16 June 2021; Published 9 July 2021

Academic Editor: Yi Xue

In order to probe into one simplified method to predict the shear strength of Shaoxing unsaturated silty clay, the test method combining unsaturated soil consolidation instrument and conventional direct shear instrument is used to study the shear strength, and the method is compared and verified with the results of equal suction direct shear test. The research results show that the soil water characteristic curve fitted by the measured data points and VG model has obvious stage characteristics in the range of 0~38 kPa, 38~910 kPa, and 910~10000 kPa. The shear strength of unsaturated soil measured by consolidation meter combined with conventional direct shear test is in good agreement with that measured by equal suction direct shear test in the range of 0~500 kPa. The results show that the shear strength, total cohesion, and effective internal friction angle of soil increase slightly with the increase of matric suction in the range of 0~38 kPa. When the matric suction increases from 38 kPa to 500 kPa, the shear strength and total cohesion force of the soil have similar stage characteristics with the SWCC, which first increases and then tends to be stable, while the effective internal friction angle changes slightly. Finally, taking the air-entry value as the demarcation point, an improved model of unsaturated shear strength is proposed by analyzing the error value. Compared with the measured value, the absolute value of relative error is basically kept in the range of 5%~10%, which is close to the measured value.

1. Introduction

Unsaturated soils widely exist in nature, and their engineering properties are quite different from saturated soils. The soils above the groundwater level are generally considered as unsaturated soils. With the change of seasons and rainfall, the unsaturated state is constantly changing. The failure of foundation and slope occurs easily, and it brings great threat to the safety of buildings and structures [1, 2]. Ciabatta et al. [3] have shown that a large amount of rainfall caused by changing global climate may cause more frequent slope failure. It has serious impact on the safety of human life and property. Rahardjo et al. [4] studied the residual soil slope, and they found that the high and steep residual soil slope could be safe in the dry period and only collapsed in the rainy season. The phenomena indicate that the stability of the slope is related to the additional shear strength of the unsaturated zone above the groundwater level. The infiltration of rainwater during rainfall affects the negative pressure of the pore water which decreases the additional shear strength of the unsaturated soils and leads to slope failure easily [1, 5–7].

In order to improve the properties of saturated and unsaturated soils, some scholars try to add inorganic cementitious materials such as cement into the soils [8, 9] or add cement, nano, fiber, and other mixed materials [10–12]. Obviously, in theory and in practice, it is very important to understand and investigate the characteristics especially the shear strength of unsaturated soils directly, which exist widely in nature. Mohr-Coulomb strength theory has been confirmed by a large number of tests and engineering practice. It can accurately determine the shear strength of saturated soil. However, at the beginning of the 20th century, the strength of unsaturated soil was similarly predicted by the Mohr-Coulomb shear strength formula for saturated soil.

Until later, with the development of the mechanics of unsaturated soil, many scholars have done a lot of research on the relationship between the shear strength of unsaturated soil and matric suction [13–18]. Idinger and Wu [19] showed that the matric suction reduced the shrinkage effect of granular soil and increased the total cohesion, while the effective angle of internal friction did not change too much; Rasool and Kuwano [20] studied the influence of matric suction on the shear strength of unsaturated silty soil, and they found the relationship between matric suction and shear strength was nonlinear; Pujiastuti et al. [21] pointed out that the total cohesion and effective angle of internal friction of unsaturated sand will increase with the increase of matric suction, but the shear strength increase a little. Khalili et al. [22] studied the mechanical behavior of unsaturated soils and found that the total cohesion increased linearly within the range of high matric suction. Çokça and Tilgen [23] studied the relationship between the shear strength of Ankara compacted clay and matric suction and found that the matric suction and shear strength were correlated positively. Inevitably, Mohr-Coulomb shear strength formula will lead to errors when it is used to predict the shear strength of unsaturated soils.

In geotechnical engineering practice, permeability coefficient, shear strength, and other relevant indexes describing the behavior of unsaturated soils can be obtained indirectly by using the soil-water characteristic curves [24–30]. According to the influence of matric suction on the cohesion and internal friction angle of unsaturated soil, many scholars used the Mohr-Coulomb strength failure criterion of saturated soil and the measured shear strength parameters of saturated soil and soil-water characteristic curve to predict the shear strength of unsaturated soil. For example, Vanapalli et al. [31] proposed a nonlinear shear strength calculation model related to soil-water characteristic curve of soil mass. Oberg and Sallfors [32] presented a formula for calculating the shear strength of unsaturated soils in combination with soil saturation and matric suction. Tang et al. [33] discussed the feasibility of using conventional direct shear instrument combined with the initial soil-water characteristic curve of 0 pressure to estimate the strength of unsaturated soil.

This paper conducted three experiments, respectively, for the unsaturated soil consolidation test, conventional direct shear test, and equal suction direct shear test. The unsaturated soil consolidation test can obtain soil-water characteristic curve, which describes the relationship between matric suction and water content of soils and reflects the water-holding capacity of soils under suction [33]. The conventional direct shear test is to obtain the shear strength of the soil with different water contents, which reflects the relationship between the different water content and the shear strength; the equal suction direct shear test can directly obtain the shear strength of the soil under different matric suction states. It is difficult to measure the required test analysis data in a short time because of the time-consuming of the constant suction direct shear test. However, the unsaturated soil consolidation test combined with conventional direct shear test can achieve the same test purpose as the direct shear test with equal suction, and the time consumption is relatively short. In this paper, the influence of matric suction on the shear strength of soil is analyzed by combining the unsaturated soil consolidation test with the conventional direct shear test and by comparing and checking the partial equal suction direct shear test. At the same time, based on the soil-water characteristic curve fitted by VG model, the shear strength prediction values of three typical models are calculated, and the model is improved through error analysis.

2. Test Materials and Preparation

2.1. Test Materials. The test soil sample is taken from the bottom of a cutting foundation pit in Keqiao District, Shaoxing, and the basic physical property indexes of the test materials are shown in Table 1. It can be seen from the table that the particle size of the soil sample is mainly between 0.005 mm and 0.075 mm, among which the average sand content is 21.43%, the average silt content is 64.52%, the clay content is 14.05%, and plastic index is 12.5, which is between 10 and 17. According to the code of *Engineering Classification Standard of Soil* (GB/T50145-2007) [34], it is judged to be low liquid limit silty clay.

2.2. Sample Preparation. In this experiment, remolded soil samples are dried, crushed, and sieved for 2 mm, and then, the natural stacking quartering method is used for diagonal sampling. Through theoretical calculation, the required distilled water is evenly sprayed on the surface of remolded soil sample and fully mixed, and then, the soil sample is prepared into a loose shape, sealed in a moisture retaining plastic bag, and placed in a moisture container for more than 48 h, so that the moisture in the soil can be fully transported and mixed evenly. According to the requirements for soil sample preparation in *Standards for Geotechnical Test Methods* [35], a disc-shaped sample with a diameter of 61.8 mm and a height of 20 mm is prepared by the layered compaction method with different dry density.

2.3. Test Scheme. The unsaturated soil consolidation instrument (SDSWCC) used in the test is made in Nanjing TKA company, and it is shown in Figure 1. According to the code of *Technical specifications for highway subgrade construction* [36], the compactness of urban secondary trunk roads is not less than 93%, and branch roads are not less than 90%. The water content is close to the optimal water content $\omega_{op} = 18.4\%$. Therefore, this test selects the lowest compaction degree (Dc = 0.90) of the silty clay of the cutting base. In various natural unsaturated soils, the matric suction range that affects the shear strength of the soil is usually 0~500 k Pa [17, 37–39]. Therefore, in this study, the matric suction range of the unsaturated soil consolidation test is taken as 0~500 kPa. The saturated sample is put into the unsaturated soil consolidation instrument, and apply the matric suction path of 1 kPa, 25 kPa, 50 kPa, 75 kPa, 100 kPa, 150 kPa, 200 kPa, 250 kPa, 300 kPa, 400 kPa, and 500 kPa to the sample in sequence to dehydration test. The stability standards of deformation and drainage during the test are as follows: the vertical deformation and displacement do not exceed 0.01 mm/2 h and 0.01 cm^3/2 h, respectively, and

Table 1: Basic physical properties of soil samples.

Liquid limit (ω_L)/%	Plastic limit (ω_P)/%	Plastic limit index (I_P)/%	Relative density (d_S)	Maximum dry density ($\rho_{d\ max}$)/g·cm^{-3}	Optimal water content (ω_{op})/%	Grain composition (mm) and its content (%)		
						Clay <0.005	Silt 0.005~0.075	The sand >0.075
30.3	17.8	12.5	2.72	1.68	18.4	14.05	64.52	21.43

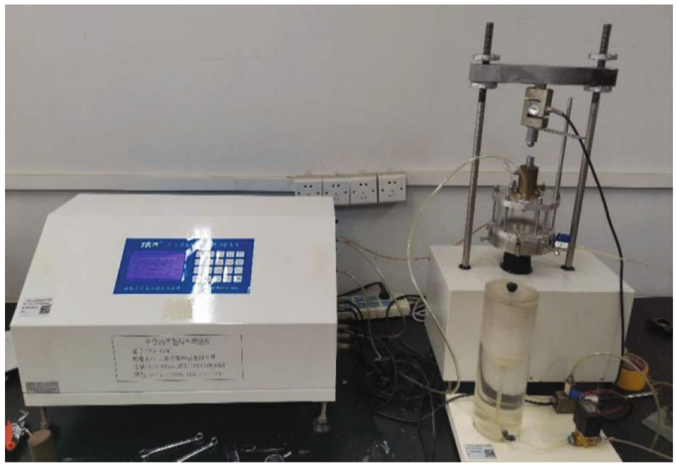

Figure 1: Unsaturated soil consolidation instrument.

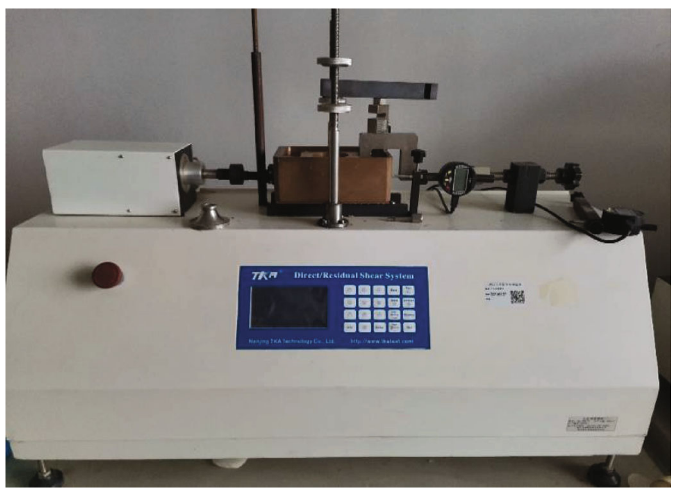

Figure 2: Fully automatic direct shear instrument.

the suction time of each stage is not less than 48 h. In order to reduce the error of displacement calculation, the pipeline at the bottom of the ceramic plate is bubble washed every 1 d during the test, so as to eliminate the influence of the air at the bottom of the ceramic plate.

This test is *t* unsaturated soil direct shear test with the same degree of compaction (Dc = 0.90, $\rho_d = 1.51\,\mathrm{g{\cdot}cm^{-3}}$) under different water content of the test instrument is made from Nanjing TKA production of fully automatic saturated soil direct shear instrument, as shown in Figure 2. Based on the soil-water characteristic curve obtained in the above test (Figure 2), samples are taken according to the volume water content corresponding to the matric suction of 25 kPa, 38 kPa, 50 kPa, 75 kPa, 100 kPa, 150 kPa, 200 kPa, 300 kPa, 400 kPa, and 500 kPa, and the volume water content corresponding to the suction path is 43.3%, 41.8%, 40.4%, 37.4%, 34.8%, 30.8%, 28.8%, 24.4%, 22.3%, and 20.9%, respectively. Three samples of each water content are prepared, and vertical stress of 50, 100, and 200 kPa is imposed for the direct shear test. The shear rate in the test is 0.0032 mm/min. The water content is measured by the drying method. To ensure the water content retaining constant, an impermeable plastic film is placed between the permeable stone and the soil sample during the test to reduce water loss.

The equal suction direct shear test equipment is from unsaturated soil direct shear instrument produced by Nanjing TKA LTD., as shown in Figure 3, which uses the axis translation technology to realize the direct shear test of matric suction control for samples with different saturations. In order to carry out comparative study, the samples are prepared with the optimal water content of 18.4% and compactness of 0.90 ($\rho_d = 1.51\,\mathrm{g{\cdot}cm^{-3}}$). The test consists of three stages, respectively, suction balance stage, equal suction consolidation stage, and equal suction shear stage. Combined with the regional characteristics of Shaoxing unsaturated silty clay, the matric suction is set at 0 kPa, 25 kPa, 50 kPa, 75 kPa,100 kPa, 150 kPa, 200 kPa, 300 kPa, 400 kPa, and 500 kPa, and the net vertical stress is 50 kPa, 100 kPa, and 200 kPa, respectively. In order to adapt to the characteristics of homogeneous and slow dissipation of pore pressure and pore water pressure in unsaturated soil during direct

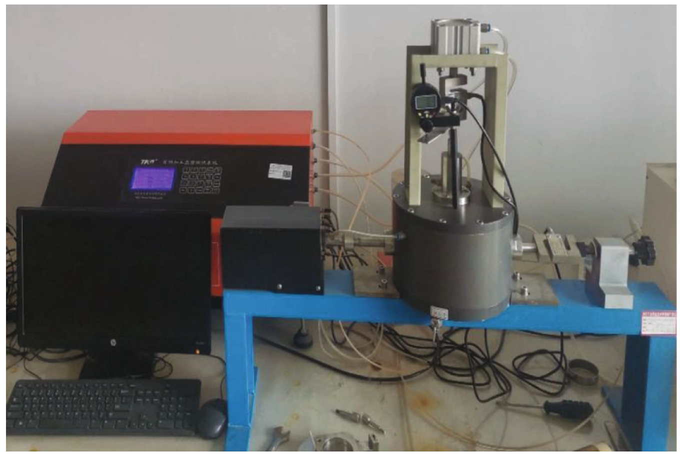

Figure 3: Unsaturated soil direct shear instrument.

Table 2: Corresponding values of matric suction and water content in unsaturated soil consolidation test.

Matric suction/(kPa)	1	25	50	75	100	150	200	300	400	500
Mass water content/(%)	29.7	28.8	27.8	24.9	22.1	20.5	19.0	16.8	15.0	13.4
Volume water content/(%)	44.9	43.5	42.0	37.6	33.4	31.0	28.7	25.4	22.7	20.2

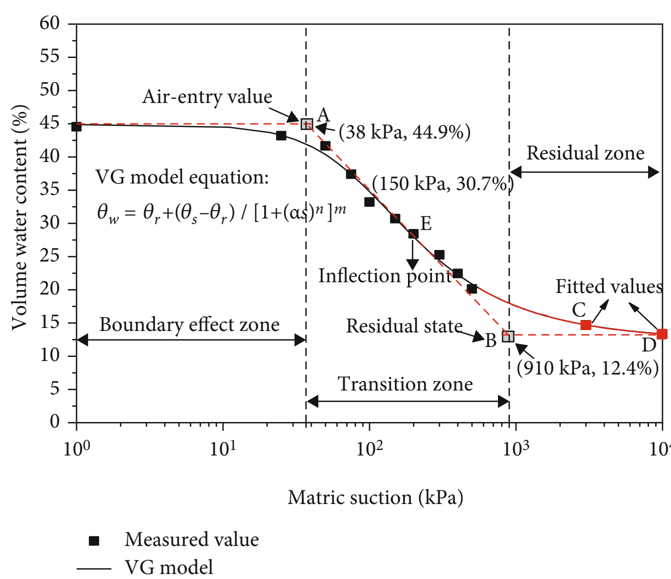

Figure 4: Fitting results of test data of soil-water characteristic curve.

shear test, the shear rate of the sample is 0.0032 mm/min and the horizontal displacement is 6 mm. After each sample is sheared, part of the soil is taken from the shear plane, and the water content after shearing is measured by drying method.

3. Test Results and Analysis

3.1. Unsaturated Soil Consolidation Test Results and Analysis. Under the action of different matric suction, the mass water content corresponding to the equilibrium and stable of the sample by the consolidation test of unsaturated soils is shown in Table 2. The measured mass water content is converted into the corresponding volume water content to establish the relationship between the volume water content and the matric suction, as shown in Figure 4. It can be seen that the volume water content shows a significant downward trend with the increase of matric suction. At the beginning, the volume water content drops slowly, then the curve steepens, and the rate of decline increases obviously. However, with the

Table 3: Basic parameters of VG model.

Model	Fitting parameters					Fitting correlation coefficient R^2
	α	n	m	θ_s/%	θ_r/%	
VG model	0.0122	1.733	0.423	44.9	12.4	0.9949

further increase of matric suction, the decreasing rate of moisture content in the sample volume gradually slows down.

Since most of the model equations describing the soil-water characteristic curve are based on experience and the shape of the curve, many scholars have proposed different model equations. The representative soil-water characteristic curve equations include Gardner equation [40], Brooks-Corey model [41], Van Genuchten model [29], and Fredlund and Xing model [30]. Among them, the parameters of the Van Genuchten model have a dear physical meaning, and its fitting effect is perfect, so it is widely used in practice. Therefore, the curve between matric suction and volume water content of unsaturated silty clay in this paper is fitted with the Van Genutchen model, and its expression is as follows:

$$\theta_w = \theta_r + \frac{(\theta_s - \theta_r)}{[1 + |as|^n]^m}, \tag{1}$$

where θ_w is the volumetric water content (%); θ_s is the saturated volumetric water content; θ_r is the residual volumetric water content; s is the matric suction (kPa); α is the parameter related to the inlet value (kPa^{-1}); n is parameters related to the degree of drainage; m is a parameter related to residual water content, where $m = 1 - 1/n$.

The logarithm of matric suction is made as abscissa, and volume water content is taken as ordinate, and VG model is used to fit the test data. The soil-water characteristic curve fitted by measured data points and VG model is shown in Figure 4. Among them, matric suction 0~500 kPa is the measured value fitting range, and 500~10000 kPa is the model prediction range. Basic parameters of the fitting are shown in Table 3. Among them, the parameters α, n, m, θ_s, and θ_r are obtained by inputting the VG model formula and the corresponding values of matric suction and water content measured in the experiment into Origin Software for fitting. As can be seen from Figure 4, the soil-water characteristic curve fitted by VG model shows an inverse "S" shape with obvious three stages. This result is similar to the law of dividing the soil-water characteristic curve dehydration process into three stages: boundary effect zone, transition zone, and unsaturated residual zone. The air-entry value of soil sample is 38 kPa, the residual volume water content is 12.4%, and the matric suction corresponding to the turning point of soil-water characteristic curve is 150 kPa. Within the value of 500 kPa matric suction, the soil-water characteristic curve fitted by the measured value shows obvious two-stage characteristics, which corresponding to the boundary area and transition area of the typical soil-water characteristic curve, respectively. In the boundary area ($s = 0 \sim 38$ kPa), the volume water content of soil did not decrease obviously with the increase of matric suction. This is because the initial water content of the sample is close to saturation, and the pore pressure is small which the gas in the soil can only be suspended in water in the form of closed bubbles and flow together with the water. At this time, the soil loses less water and is close to the saturated soil. When the matric suction increases to the air-entry value and reaches the transition zone ($38\,\text{kPa} \le s \le 910\,\text{kPa}$), the soil sample begins to lose water rapidly at a certain rate. This is due to the increase of pore pressure, and the water in the soil will be gradually discharged by gas and occupied a larger pore channel. With the further increase of pore pressure, more water will be discharged from the soil, and the soil water content will decrease rapidly. When the matric suction is in the unsaturated residual zone ($s \ge 910$ kPa), and the pore pressure continues to increase and the water in the soil is little or no longer discharged, it is considered that the soil has reached the residual water content.

Compared with the typical soil water characteristic curve, due to the limitation of the test instrument, the maximum air intake value of the clay plate is 500 kPa, and the data corresponding to the residual zone cannot be measured by the instrument, so the residual area of the sample can only be predicted by fitting. At present, many definitions of residual matric suction are based on experience. They do not have clear physical meaning and theoretical support. For example, Sillers and Fredlund and Sillers et al. [42, 43] think that the matric suction corresponding to the residual water content is 3000 kPa. They also think that the residual state is the state that pore water in soil changes from capillary action to adsorption force. This definition is quite popular at present. Based on the recommendations of Sillers and Fredlund and Sillers et al. [42, 43], this paper assumes that the residual matric suction is 3000 kPa for fitting, as shown in the curve of the end of measured value to point C in Figure 4. Obviously, the volume water content corresponding to the matric suction of 3000 kPa is not the residual volume water content. Through repeated fitting calculation, the residual matric suction is finally assumed to be 10000 kPa, as shown in the curve to point D in Figure 4, the fitting effect of this region is better, and the corresponding residual volume water content is 12.4%.

3.2. Direct Shear Test and Result Analysis

3.2.1. Relationship between Shear Strength and Matric Suction. Table 4 shows the corresponding shear strength values of the conventional direct shear test under different volume water contents and the equal suction direct shear test under different matric suction. Among them, the corresponding matric suction in the data column of the conventional direct shear test is obtained from the matric suction

Table 4: The corresponding shear strength values of the conventional direct shear test and the equal suction direct shear test.

	Conventional direct shear test			Equal suction direct shear test		
Volume water content/%	Matric suction/kPa	Vertical stress/kPa	Shear strength/kPa	Matric suction/kPa	Net vertical stress/kPa	Shear strength/kPa
		50	36.3		50	36.3
44.9	1	100	54.8	1	100	54.8
		200	91.8		200	91.8
		50	39.9		50	43.3
43.3	25	100	58.2	25	100	62.4
		200	94.8		200	100.6
		50	42.4		/	/
41.8	38	100	61.2	/	/	/
		200	98.5		/	/
		50	55.6		50	57.0
40.4	50	100	75.1	50	100	77.6
		200	114.1		200	118.8
		50	64.2		/	/
37.4	75	100	84.3	/	/	/
		200	124.5		/	/
		50	72.3		50	69.8
34.8	100	100	92.5	100	100	91.5
		200	132.9		200	134.7
		50	76.3		50	80.3
30.8	150	100	97.2	150	100	102.6
		200	139.4		200	147.4
		50	81.3		50	84.5
28.8	200	100	102.4	200	100	109.1
		200	144.7		200	154.2
		50	87.4		50	93.7
24.4	300	100	109.2	300	100	116.9
		200	152.7		200	163.3
		50	92.5		50	99.3
22.3	400	100	114.5	400	100	122.3
		200	158.6		200	168.3
		50	96.8		50	103.5
20.9	500	100	119.5	500	100	127.1
		200	164.8		200	174.1

corresponding to the volume water content in the soil-water characteristic curve.

The corresponding shear strengths of the conventional direct shear test and equal suction direct shear test under different matric suction are shown in the same figure, as shown in Figure 5. It can be seen from the figure that the shear strength of unsaturated silty clay samples changes with matric suction at different vertical normal stresses, and the change trend of boundary effect zone and transition zone is basically consistent with the soil water characteristic curve. In the boundary effect zone (0~38 kPa), a small matric suction can still slightly increase the shear strength of the soil, when the matric suction is less than the air-entry value comparing to the fully saturated state. The soil is in an unsaturated state, in the transition zone (38~500 kPa). The shear strength changes in two stages with the change of the matric suction. When the matric suction increases from 38 kPa to 200 kPa, the shear strength increases rapidly and the corresponding volume water content at this stage is 41.8%~28%, and the lower limit volume water content is close to that of plastic limit. The increase rate of shear strength gradually decreases after the matric suction exceeds 200 kPa. Combining with the soil-water characteristic curve, it can be found that the transition zone can also be divided into two stages,

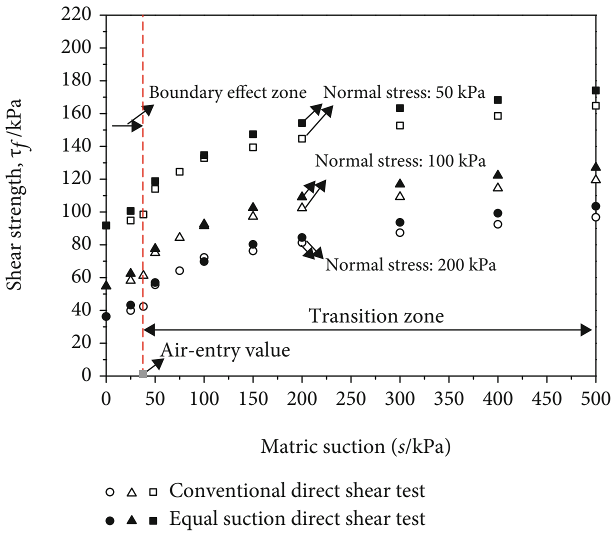

FIGURE 5: The relationship between shear strength and matric suction.

namely, the main transition zone and the secondary transition zone. Taking the matric suction as 200 kPa as the demarcation point, the shear strength in the main transition zone increases rapidly with the matric suction comparing with the secondary transition zone. This is similar to the results of Çokça and Tilgen [44], Bai and Liu [45], Pandya et al. [13], and Khalili et al. [22].

It can be found that the shear strength change trends measured by the two methods are relatively consistent comparing the two test results. When the matric suction is less than the air-entry value, the shear strength of the equal suction direct shear test is basically equal to that of the conventional direct shear test. When the matric suction is in the transition zone, the shear strength of equal suction direct shear test is generally higher than that of conventional direct shear test. Due to the limited range of the matric suction force applied by this test instrument, the results of the matric suction force exceeding 500 kPa cannot be compared.

3.2.2. Relationship between Shear Strength and Matric Suction. In order to avoid the limitation of Bishop equation, Sillers et al. [43] used two independent stress state variables to study the mechanical properties of unsaturated soils. Through a lot of laboratory tests and theoretical analysis, the theoretical formula of the shear strength of unsaturated soils with net normal stress and matric suction as two variables:

$$\tau_f = c' + (\sigma - u_a) \tan \varphi' + (u_a - u_w) \tan \varphi^b, \qquad (2)$$

where φ^b represents the rate at which the shear strength increases with the matric suction $(u_a - u_w)$, which is simply referred to as the internal friction angle of adsorption. If $c' + (u_a - u_w) \tan \varphi^b$ is replaced by c in the formula (1), the shear strength formula of unsaturated soil can be rewritten as formula (2):

$$\tau_f = c + (\sigma - u_a) \tan \varphi', \qquad (3)$$

where $c = c' + (u_a - u_w) \tan \varphi^b$, in which c is the intercept of total cohesion, which is referred to as total cohesion in this article. The total cohesive force c of unsaturated soil is composed of the cohesive force c' in the saturated state and the shear strength $(u_a - u_w) \tan \varphi^b$ caused by the matric suction in the unsaturated state.

Based on the above formula, the total cohesion and effective internal friction angle of soil samples at different volume water contents are obtained according to the results of conventional direct shear tests. By transforming the soil-water characteristic curve into the corresponding matric suction, the relationship between total cohesion and effective internal friction angle with matric suction can be obtained. The strength index of the equal suction direct shear test is obtained by applying the corresponding shear strength of different matric suction. Through calculation, the corresponding shear strength parameters of the conventional direct shear test and equal suction direct shear test under different volume water content and matrix suction are shown in Table 5. Among them, the corresponding matric suction in the data column of the conventional direct shear test is obtained from the matric suction corresponding to the volume water content in the soil-water characteristic curve.

Figures 6 and 7 show the relationship between the total cohesive and effective internal friction angle with the matric suction of equal suction direct shear test and conventional direct shear test. It can be seen from the figures that the total cohesion and effective internal friction angle have different rules of change with the matric suction. With the increase of matric suction, the total cohesion increases nonlinearly and tends to be stable gradually, and its characteristics are synchronous with the shear strength. The effective internal friction angle increases slightly with the increase of the matric suction, and the size is close to the internal friction angle when the soil is saturated, and its change characteristics are not synchronized with the shear strength. According to the geotechnical engineering investigation report of Shaoxing area, the typical silty clay in Shaoxing area is marine sedimentary soil, and the particles are in thin sheet shape. The particles are connected by edge to edge and edge to surface, and the arrangement is directional, with the characteristics of flocculent structure. It contains plant debris, a small amount of flaky particles filled in the coarse particles, clay minerals, silt particles, and humus which adsorb by each other. But microscopically, there is still a very small amount of gas present in the tiny corners of individual pores, the resulting very low suction force plays a role in connecting soil particles, and the lubrication of water between the soil particles is reduced. Therefore, compared with the fully saturated state, the total cohesion and effective internal friction angle of the soil are slightly increased. In the transition zone, the soil is in unsaturated state, the air entering the pores increases gradually, the moisture in the pores

Table 5: Shear strength parameters corresponding to conventional direct shear test and equal suction direct shear test.

Conventional direct shear test	Volume water content/%	44.9	43.3	41.8	40.4	37.4	34.8	30.8	28.8	24.4	22.3	20.9
	Matric suction/kPa	1	25	38	50	75	100	150	200	300	400	500
	Total cohesion/kPa	17.8	21.6	23.7	36.1	44.1	52.1	55.3	60.2	65.7	70.4	74.1
	Effective internal friction angle/°	20.3	20.1	20.5	21.3	21.9	22	22.8	22.9	23.5	23.8	24.4
Equal suction direct shear test	Matric suction/kPa	1	25	/	50	/	100	150	200	300	400	500
	Total cohesion/kPa	17.8	23.4	/	35.5	/	47.4	57.1	63.1	69.6	75.5	79.2
	Effective internal friction angle/°	20.3	20.9	/	22.4	/	23.4	24.1	24.3	24.9	24.7	25.2

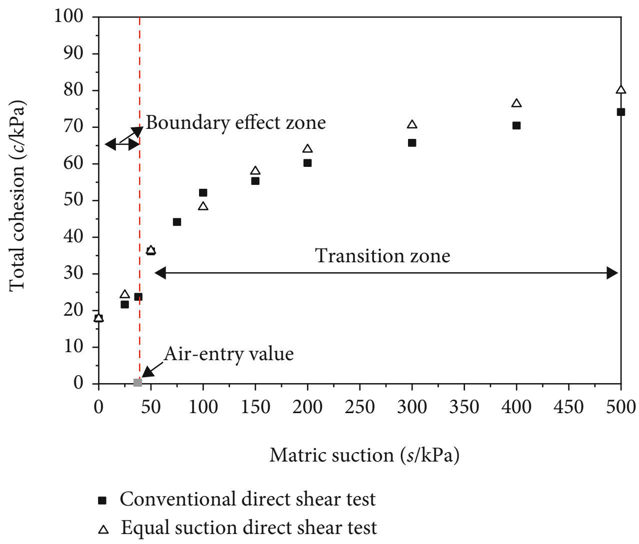

Figure 6: Relationship between total cohesion and the matric suction.

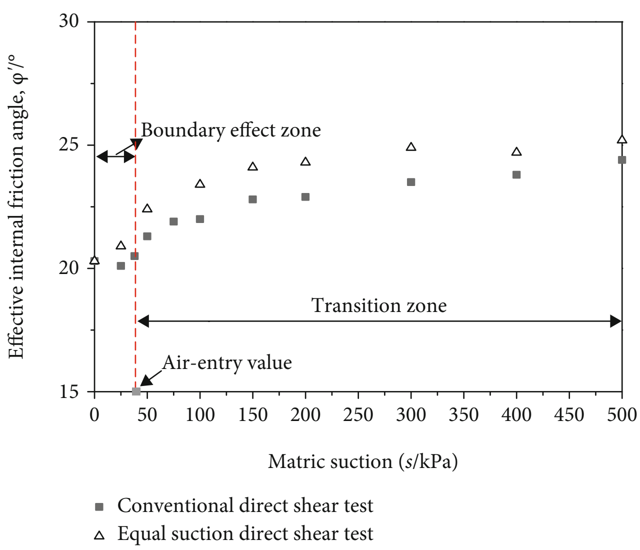

Figure 7: Relationship between the effective internal friction angle and the matric suction.

decreases correspondingly, the matric suction generated by the difference of pore pressure and water pressure increases, and with the change of air-water interface shrinkage membrane, the surface tension generated increases gradually with the increase of air in the pore, so the total cohesion of soil increases. At the same time, as the pore gas entering the soil increases, the moisture gradually decreases, and the lubrication between soil particles is reduced due to moisture, so the effective internal friction angle of the soil increases slightly. However, when the matric suction increased to a certain extent, the water content in the soil would not be discharged any more, and the water content in the soil would remain unchanged, eventually making the total cohesion in the soil gradually stabilized.

By comparing the data points obtained from the two tests, it can be found that in the boundary region ($s \le 38$ kPa), the total cohesion and effective internal friction angle under the equal suction direct shear test and the conventional direct shear test have little change, which is basically the same as that under the saturated state. In the transition zone ($38\,\text{kPa} \le S \le 500\,\text{kPa}$), when the matric suction force is lower than 100 kPa, the total cohesion measured by the equal suction direct shear test is smaller than the total cohesion measured by the conventional direct shear test, and when the suction direct shear test exceeds 100 kPa, the total cohesion is greater than that measured by the conventional direct shear test. However, the effective internal friction angle measured by the equal suction direct shear test is always greater than the effective internal friction angle measured by the conventional direct shear test.

From the above analysis, it can be concluded that with the increase of matric suction, the shear strength and total cohesion of the soil increase significantly, and the effective internal friction angle changes less. It can be considered that the contribution of matric suction to the shear strength is more reflected in the increase in total cohesion.

4. Prediction Model and Improved Model of Shear Strength Based on Soil-Water Characteristic Curve

According to the above analysis, as the matric suction increases, the effective internal friction angle of the soil changes only slightly, while the cohesive force changes significantly, so the change of the effective internal friction angle is ignored. In order to consider only the contribution of matric suction to shear strength, the effect of net vertical normal stress on shear strength should be excluded. Therefore, if the net vertical normal stress is 0, the increment of cohesion

Table 6: The shear strength contribution value and absolute relative error data table corresponding to different matric suction.

Matric suction/kPa	Measured value/kPa	Model 1/kPa	Model 2/kPa	Model 3/kPa	Improved model/kPa	Absolute relative error of model 1/%	Absolute relative error of model 2/%	Absolute relative error of model 3/%	Absolute relative error of improved model/%
1	0	0	0	0	0	0	0	0	0
25	3.8	11.6	8.4	4	4	67.2	54.8	5.3	5
38	5.9	14.1	12.2	5.9	5.9	58.2	51.6	0	0
50	18.3	15.9	15.3	7.5	17.9	13.1	16.4	59.0	2.2
75	26.3	19.1	20.5	10.4	25.2	27.4	22.1	60.5	4.2
100	34.3	21.7	24.4	12.9	30.1	36.7	28.9	62.4	12.2
150	37.5	26.1	30.6	17.1	36.3	30.4	18.4	54.4	3.2
200	42.4	29.7	34	20.7	40.1	30.0	19.8	51.2	3.1
300	47.9	35.5	39.4	27.1	44.9	25.9	17.7	43.4	6.3
400	52.6	40.5	43.2	33	48.3	23.0	17.9	37.3	8.2
500	56.3	44.8	46.3	38.6	51.0	20.4	17.8	31.4	9.4

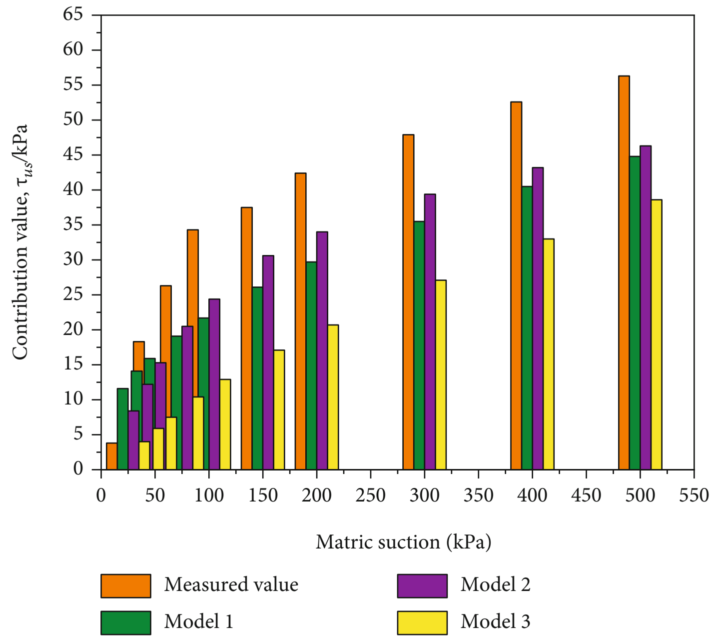

Figure 8: Comparison of calculated and measured values of the three models.

obtained from saturated state to unsaturated state is the contribution value of matric suction to shear strength. Based on the research of unsaturated soils, Khalili and Khabbaz [46], Vanapalli et al. [31], Lamborn [47], and others earlier proposed different prediction models for the shear strength of unsaturated soils, which have wide applicability. Without considering the influence of the net vertical normal stress and only considering the contribution of the matric suction to the shear strength, three models of the contribution of the shear strength can be obtained, namely, model 1, model 2, and model 3, as (4)~(6):

$$\tau_{us} = (u_a - u_w)^{0.45}(u_a - u_w)_b^{0.55} \tan \varphi', \tag{4}$$

$$\tau_{us} = (u_a - u_w)\left(\frac{\theta_w - \theta_r}{\theta_s - \theta_r}\right) \tan \varphi', \tag{5}$$

$$\tau_{us} = (u_a - u_w)\theta_w \tan \varphi', \tag{6}$$

where τ_{us} is the contribution value of the matric suction to the shear strength.

According to the results of the direct shear test, the measured shear strength contribution value can be obtained. The internal friction angle $\varphi' = 20.3°$ at saturated state of soil and the soil-water characteristic curve parameters $(u_a - u_w)_b = 38$ kPa, $\theta_s = 44.89\%$, and $\theta_r = 12.4\%$ fitted by VG model are substituted into equations (4)~(6) to calculate the contribution value of shear strength under model 1~model 3, as shown in Table 6. According to the results in Table 6, the calculated shear strength contribution values of the three models are compared with the measured values, as shown in Figure 8. It can be clearly seen from the bar graph that the shear strength contribution value calculated by model 1, model 2, and model 3 differs greatly from the measured value and is significantly lower than the measured value. The error analysis of the three models is performed, and the calculation results are shown in Table 6. The relationship between the absolute relative error of the three models and the change of the matric suction is represented by a bar graph, as shown in Figure 9. It can be seen from Figure 9 that the absolute value of the relative error calculated by the three models has a large dispersion. The absolute relative error calculated by model 1 and model 2 reached the maximum in the boundary area, 67.2% and 54.8%, respectively, while the absolute relative error calculated by model 3 is close to 0 in the boundary area, and the fitting effect is good. However, in the transition region, the absolute values of relative errors calculated by model 1 and model 2 are mostly in the range of 20%~35%, while those of model 3 are mostly in the range of 35%~60%. The average errors of the three models are 33.2%, 26.5%, and 40.5%. Due to the large error, the three calculation models cannot be directly used in the transition zone to calculate the contribution of the matric suction to the shear strength, and a new improved model needs to be established.

According to the literature [48], taking the matric suction value corresponding to the air-entry value and the residual volume water content as the dividing line, the soil can be divided into the boundary zone, the transition zone, and the unsaturated residual zone. According to the comparison of the absolute relative error calculated by the above model 1 to model 3, in the boundary zone, that is, the matric suction is less than the air-entry value, only the absolute relative error of model 3 is about 5%, which is in line with the actual allowable error range. Therefore, taking the air-entry value of the soil 38 kPa as the dividing line and based on the formula proposed by Lamborn [47], when the matric suction is less than the air intake value, the relationship between the matric suction and the shear strength contribution value is formula (6); when the matric suction is greater than 38 kPa, as the matric

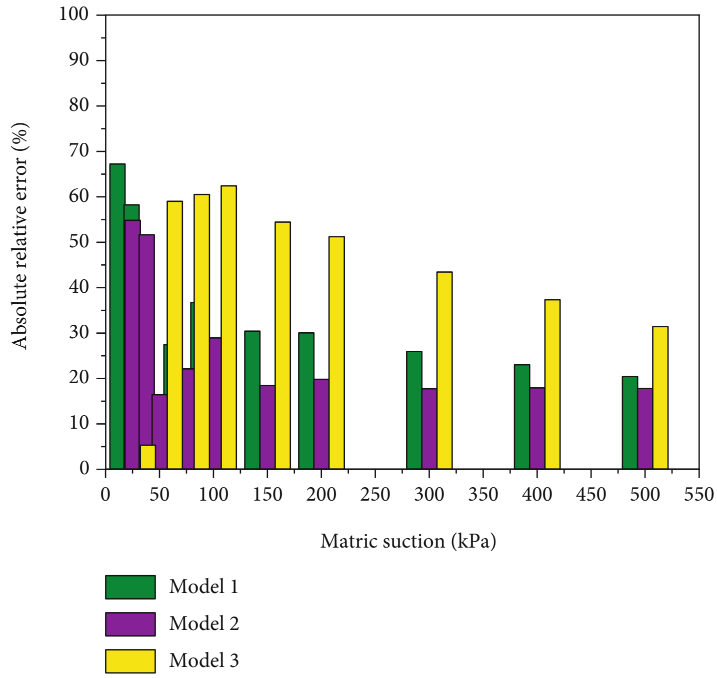

Figure 9: The variation of absolute relative error of the three models with matric suction.

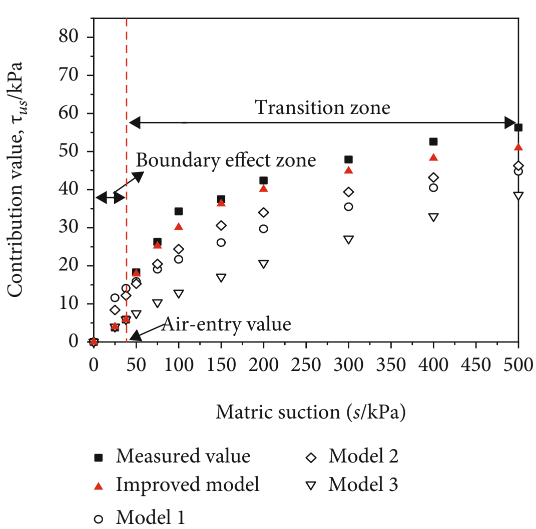

Figure 10: Comparison of the shear strength contribution values of the improved model and the three models with the measured values.

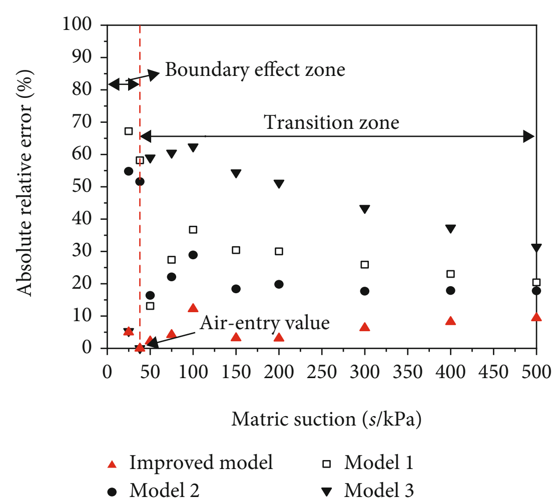

Figure 11: Comparison of absolute relative error between the improved model and the three models with the change of matric suction.

suction continues to increase, the contribution rate of the matric suction to the shear strength gradually decreases. Therefore, 38 kPa is used as the initial zero point, and the subsequent matric suction minus 38 kPa is used as the matric suction increase. According to the conversion relationship between matric suction and volume water content in reference [31], the expression of the contribution of matric suction to shear strength can be given as follows:

$$\tau_{us} = \frac{(u_a - u_w)\tan\varphi'}{\left[1 + \alpha\left((u_a - u_w) - (u_a - u_w)_b\right)^n\right]^m}. \quad (7)$$

Combining equations (6) and (7), the calculation model of the contribution value of matric suction to shear strength can be obtained as follows:

$$\tau_{us} = \begin{cases} (u_a - u_w)\theta_w \tan\varphi', (u_a - u_w) < (u_a - u_w)_b, \\ \dfrac{(u_a - u_w)\tan\varphi'}{\left[1 + \alpha\left((u_a - u_w) - (u_a - u_w)_b\right)^n\right]^m}, (u_a - u_w) \geq (u_a - u_w)_b. \end{cases} \quad (8)$$

According to the foregoing, substituting $\varphi' = 20.3°$, $(u_a - u_w)_b = 38$ kPa, $\alpha = 0.0.0122$, $n = 1.733$, and $m = 0.423$

into improved model (8), the shear strength under different matric suction can be obtained contribution value and compare with the measured value and predicted values of three models, as shown in Figure 10. The relationship between the absolute value of the relative error of model 1, model 2, model 3, and the improved model and matric suction is shown in Figure 11. It can be seen from the figure that, except for the absolute relative error between the actual measured value and the calculated value of the improved model, which exceeds 10%, the absolute relative error of the remaining measured value and the calculated value of the model is within 10%. The average absolute value of relative error of the improved model is 5.4% through calculation within the range of matric suction measured. Compared with the absolute value of relative error of model 1 to model 3, the mean value of absolute value of relative error obtained by the improved model decreases by 27.8%, 21.1%, and 35.1%, respectively, which shows the effectiveness of the improved model.

Therefore, the improved model formula for the shear strength of Shaoxing unsaturated silty clay is as follows:

$$\tau_f = \begin{cases} c' + (\sigma - u_a)\tan\varphi' + (u_a - u_w)\theta_w \tan\varphi', & (u_a - u_w) < (u_a - u_w)_b, \\ c' + (\sigma - u_a)\tan\varphi' + \dfrac{(u_a - u_w)\tan\varphi'}{\left[1 + \alpha\left((u_a - u_w) - (u_a - u_w)_b\right)^n\right]^m}, & (u_a - u_w) \geq (u_a - u_w)_b. \end{cases} \quad (9)$$

5. Conclusions

(1) The soil water characteristic curve fitted by VG model combined with the strength measured by conventional direct shear test is in good agreement with that measured by equal suction direct shear test of unsaturated soil. Within a certain range, the shear strength and total cohesive force of the soil increase nonlinearly with the increase of matric suction, which has similar phase characteristics of the soil-water characteristic curve, and the effective internal friction angle changes little

(2) By analyzing the physical meaning of the air-entry value and taking the air-entry value as the demarcation point, an improved model of the shear strength of unsaturated silty clay in this paper is proposed. The absolute value of the error between the shear strength contribution value calculated by the improved model and the measured value is basically within 10%. Compared with the average absolute relative error of model 1 to model 3, the absolute relative error of the improved model decreases by 27.8%, 21.1%, and 35.1%, respectively, which shows the effectiveness of the improve model

The research in this paper can simplify the testing method of unsaturated soil shear strength, save time, and provide new ideas for the popularization and application of unsaturated soil shear strength theory in engineering practice.

Data Availability

The data used to support the findings of this study are available from the corresponding author upon request.

Conflicts of Interest

The authors declare no conflicts of interest.

Acknowledgments

This research was funded by the Zhejiang Provincial Natural Science Foundation of China (Grant number Q20E080042) and the Scientific research project of Zhejiang education department (Grant number Y201839206).

References

[1] S. Jeong, K. Lee, J. Kim, and Y. Kim, “Analysis of rainfall-induced landslide on unsaturated soil slopes,” *Sustainability*, vol. 9, no. 7, pp. 1280–1299, 2017.

[2] J. Kim, S. Jeong, and R. A. Regueiro, “Instability of partially saturated soil slopes due to alteration of rainfall pattern,” *Engineering Geology*, vol. 147, pp. 28–36, 2012.

[3] L. Ciabatta, S. Camici, L. Brocca et al., “Assessing the impact of climate-change scenarios on landslide occurrence in Umbria Region,” *Journal of Hydrology*, vol. 541, no. A, pp. 285–295, 2016.

[4] H. Rahardjo, A. Satyanaga, E. C. Leong, and Y. S. Ng, “Effects of groundwater table position and soil properties on stability of slope during rainfall,” *Journal Geotechnical and Geoenvironmental*, vol. 136, no. 11, pp. 1555–1564, 2010.

[5] B. S. Par, H. Cho, and S. P. Youn, “Analysis and evaluation of stability for the reactivated landslide along deep-seated weakness zones,” *International Journal of Industrial Engineering: Theory, Applications, and Practice*, vol. 7, no. 3, p. 2016, 2016.

[6] H. Rahardjo, Y. Kim, N. Gofar, E. C. Leong, C. L. Wang, and J. L. H. Wong, “Field instrumentations and monitoring of GeoBarrier System for steep slope protection,” *Transportation Geotechnics*, vol. 16, pp. 29–42, 2018.

[7] H. Rahardjo, T. T. Lim, M. F. Chang, and D. G. Fredlund, “Shear strength characteristics of a residual soil in Singapore,” *Canadian Geotechnical Journal*, vol. 32, pp. 60–77, 1995.

[8] Y. Liu, F. H. Lee, S. T. Quek, E. J. Chen, and J. T. Yi, “Effect of spatial variation of strength and modulus on the lateral compression response of cement-admixed clay slab,” *Géotechnique*, vol. 65, no. 10, pp. 851–865, 2015.

[9] Y. Liu, L. Q. He, Y. J. Jiang, M. M. Sun, E. J. Chen, and F. H. Lee, “Effect of in-situ water content variation on the spatial

variation of strength of deep cement-mixed clay," *Géotechnique*, vol. 69, no. 5, pp. 391–405, 2019.

[10] N. Li, Y. Zhu, F. Zhang, S. M. Lim, W. Wu, and W. Wang, "Unconfined compressive properties of fiber-stabilized coastal cement clay subjected to freeze-thaw cycles," *International Journal of Engineering Science*, vol. 9, no. 143, pp. 356–363, 2021.

[11] W. Wang, J. Li, and J. Hu, "Unconfined mechanical properties of nanoclay cement compound modified calcareous sand of the South China Sea," *Advances in Civil Engineering*, vol. 2020, Article ID 6623710, 16 pages, 2020.

[12] W. Wang, Y. Li, and K. Yao, "Strength properties of nano-MgO and cement stabilized coastal silty clay subjected to sulfuric acid attack," *Marine Georesources & Geotechnology*, vol. 38, no. 10, pp. 1177–1186, 2020.

[13] S. Pandya, A. Sachan, S. Pandya, and A. Sachan, "Variation of collapse potential and stiffness degradation with matric suction of compacted unsaturated cohesive soil," *International Journal of Industrial Engineering: Theory, Applications, and Practice*, vol. 28, no. 7, pp. 1329–1337, 2017.

[14] Q. Zhai, H. Rahardjo, A. Satyanaga, and G. Dai, "Estimation of unsaturated shear strength from soil–water characteristic curve," *Acta Geotechnica*, vol. 3, no. 5, pp. 253–269, 2019.

[15] A. M. Elsharief and O. A. Abdulaziz, "Effects of matric suction on the shear strength of highly plastic compacted, Innovative Geotechnics for Africa-Bouassida," *Khemakhem & Haffoudhi (Eds.)*, vol. 63, no. 58, pp. 97–103, 2015.

[16] F. Champiré, A. Fabbri, J. C. Morel, H. Wong, and F. McGregor, "Impact of relative humidity on the mechanical behavior of compacted earth as a building material," *Construction and Building Materials*, vol. 1, no. 27, pp. 77-78, 2016.

[17] R. Schnellmann, H. Rahardjo, and H. R. Schneider, "Unsaturated shear strength of a silty sand," *Engineering Geology*, vol. 162, no. 23, pp. 88–96, 2013.

[18] S. Nam, M. Gutierrez, P. Diplas, and J. Petrie, "Determination of the shear strength of unsaturated soils using the multistage direct shear test," *Engineering Geology*, vol. 122, no. 3-4, pp. 272–280, 2011.

[19] G. Idinger and W. Wei, "Shear Strength of Granular Soil Under Saturated and Unsaturated Conditions," *Recent Advances in Geotechnical Research, Springer Series in Geomechanics and Geoengineering*, vol. 7, no. 7, pp. 79–89, 2019.

[20] A. M. Rasool and J. Kuwano, "Role of matric suction on shear strength of unsaturated compacted soil at low confining stress. Proceedings of GeoShanghai 2018 International Conference," *Multi-Physics Processes in Soil Mechanics and Advances in Geotechnical Testing*, vol. 13, no. 23, pp. 120–128, 2018.

[21] H. Pujiastuti, A. Rifa'i, A. D. Adi, and T. F. Fathani, "The effect of matric suction on the shear strength of unsaturated sandy clay," *International Journal of Geomate*, vol. 14, no. 42, pp. 112–119, 2018.

[22] N. Khalili, A. Russell, A. Khoshghalb, S. Frydman, and R. Baker, "Matrix Suction and Shear Strength of Unsaturated Clay," in *Unsaturated Soils: Research & Applications*, CRC Press, 2014.

[23] C. Erdal and P. Hüseyin Tilgen, "Shear strength-suction relationship of compacted Ankara clay," *Applied Clay Science*, vol. 49, pp. 400–404, 2010.

[24] J. Kim, W. Hwang, and Y. Kim, "Y. Kim (2018), "Effects of hysteresis on hydro-mechanical behavior of unsaturated soil"," *Engineering Geology*, vol. 245, pp. 1–9, 2018.

[25] A. Ahmed, M. Sahadat Hossain, M. S. Khan, K. Greenwood, and A. Shishani, "Moisture var-iation in expansive subgrade through field instrumentation and geophysical testing," *Engineering Geology*, vol. 1, pp. 45–58, 2018.

[26] Q. Zhai and H. Rahardjo, "H. Rahardjo (2015), "Estimation of permeability function from the soil–water characteristic curve"," *Engineering Geology*, vol. 199, pp. 148–156, 2015.

[27] S. W. Tyler and S. W. Wheatcraft, "Fractal process in soil water retention," *Water Resources Research*, vol. 26, no. 5, pp. 1047–1054, 1990.

[28] M. Feng and D. G. Fredlund, "Hysteretic influence associated with thermal conductivity sensor measurements," in *Proceedings from Theory to the Practice of Unsaturated Soil Mechanics in Association with the 52nd Canadian Geotechnical Conference and Unsaturated Soil Group*, pp. 651–657, Regina Sask, 1999.

[29] M. T. Van Genuchten, "A close-form equation for predicting the hydraulic conductivity of unsaturated soils," *Soil Science Society of America Journal*, vol. 44, no. 56, pp. 892–898, 1980.

[30] D. G. Fredlund and A. Xing, "Equations for the soil-water characteristic curve," *Canadian Geotechnical Journal*, vol. 31, no. 4, pp. 521–532, 1994.

[31] S. K. Vanapalli, D. G. Fredlund, D. E. Pufahl, and A. W. Clifton, "Model for the prediction of shear strength with respect of soil suction," *Canadian Geotechnical Journal*, vol. 33, no. 3, pp. 379–392, 1996.

[32] A. L. Oberg and G. Sallfors, "Determination of shear strength parameters of unsaturated silts and based on the water retention curve," *Geotechnical Testing Journal*, vol. 20, no. 1, pp. 40–48, 1997.

[33] C. Tang, R. Borden, and M. Gabr, "A simplified direct shear testing procedure to evaluate unsaturated shear strength," *Geotechnical Testing Journal*, vol. 41, no. 2, pp. 223–234, 2018.

[34] Ministry of Construction of the People's Republic of China, General Administration of quality supervision, inspection and Quarantine of the people's Republic of China, *Engineering Classification Standard of Soil GB/T50145-2007*, China Planning Press, Beijing, 2008.

[35] Ministry of Water Resources of the People's Republic of China, *Standards for Geotechnical Test Methods GB/T50123-2019[S]*, China Planning Press, Beijing, 2019.

[36] Ministry of Transport of the People's Republic of China, *Technical Code for Construction of Highway Subgrade JTG/T 3610-2019 [S]*, People's Communications Press, Beijing, 2019.

[37] E. J. Macari, R. Laureano, and J. Hoyos, "Mechanical behavior of an unsaturated soil under multi-axial stress states," *Geotechnical Testing Journal.*, vol. 24, no. 1, pp. 14–22, 2001.

[38] J. D. Mendes and G. Toll, "Influence of initial water content on the mechanical behavior of unsaturated sandy clay soil," *International Journal Of Geomechanics*, vol. 16, no. 6, pp. D4016005-1–D401600518, 2016.

[39] M. Rosone, C. A. Farulla, and A. Ferrari, "Shear strength of a compacted scaly clay in variable saturation conditions," *Acta Geotechnica*, vol. 11, no. 1, pp. 37–50, 2016.

[40] W. R. Gardner, "Some steady-state solutions of the moisture flow equations with application to evaporation from a water table," *Soil Science*, vol. 85, no. 4, pp. 228–232, 1958.

[41] H. Brooks and A. T. Corey, *Conference of Hydraulic Properties of Porous Media*, Colorado State University. Hydrol. Paper, 1964.

[42] W. S. Sillers and D. G. Fredlund, “Statistical assessment of soil-water characteristic curve models for geotechnical engineering,” *Canadian Geotechnical Journal*, vol. 38, no. 6, pp. 1297–1313, 2001.

[43] W. S. Sillers, D. G. Fredlund, and N. Zakerzadeh, *Mathematical Attributes of Some Soil-Water Characteristic Curve Models*, Springer, Netherlands, 2001.

[44] E. Çokça and H. Tilgen, “Shear strength-suction relationship of compacted Ankara clay,” *Applied Clay Science*, vol. 49, no. 4, pp. 400–404, 2010.

[45] F. Q. Bai and S. H. Liu, “Measurements of the shear strength of an expansive soil by combining a filter paper method and direct shear tests,” *Geotechnical Testing Journal*, vol. 35, no. 3, pp. 451–459, 2013.

[46] N. Khallili and M. H. Khabbaz, “A unique relationship for χ for the determination of the shear strength of unsaturated soils,” *Geotechnique*, vol. 48, no. 5, pp. 681–687, 1998.

[47] M. J. Lamborn, *A Micromechanical Approach to Modeling Partly Saturated Soils*, Texas A & M University, College Station, 1986.

[48] D. G. Fredlund and H. Rahardjo, *Soil Mechanics for Unsaturated Soils*, China Architecture and Building Press, Beijing, 1997.

Hindawi
Geofluids
Volume 2021, Article ID 5560762, 20 pages
https://doi.org/10.1155/2021/5560762

Research Article

Analysis of Seepage and Displacement Field Evolutionary Characteristics in Water Inrush Disaster Process of Karst Tunnel

Yongbiao Lai,[1] Shuo Li,[2] Jiaqi Guo ,[2,3] Zhengguo Zhu,[3] and Xin Huang[2]

[1]*China Construction Railway Investment Construction Group Ltd., Beijing 102601, China*
[2]*School of Civil Engineering, Henan Polytechnic University, Jiaozuo 454003, China*
[3]*State Key Laboratory of Mechanical Behaviour and System Safety Traffic Engineering Structures, Shijiazhuang Tiedao University, Shijiazhuang, 050043 Hebei, China*

Correspondence should be addressed to Jiaqi Guo; gjq519@163.com

Received 25 February 2021; Revised 4 May 2021; Accepted 15 June 2021; Published 9 July 2021

Academic Editor: Chuangzhou Wu

Water inrush of tunnel is one of the most common geological disasters in the karst strata in China. Aiming at the rock mass with a quasi-masonry structure in the water-resistant strata between karst cavity with high pressure water and tunnel and the shortcomings of theoretical analysis, traditional numerical simulation, and physics model test for describing and reflecting this special structure of rock mass, a Discrete Element Method considering the fluid-solid coupling effect and structural characteristics of rock mass is employed to study the disaster process of water inrush and the evolutionary characteristics of catastrophe information like seepage pressure and displacement under condition of different karst water pressure, tunnel depth, and lateral pressure coefficient. Research results show the following: (1) the seepage pressure and displacement increase with the increase of kart water pressure. The seepage pressure demonstrates a decreasing state from top to bottom in water-resistant strata, and the time of arrival to a stable value for the seepage pressure shows the time effect. (2) The larger the tunnel depth, the greater the coalescence and distribution scope of fracture and the more likely the water inrush to occur in a short time. The stability of water-resistant strata decreases on the whole with the growth of tunnel depth. (3) The increase of lateral pressure coefficient can restrain the fracture development and strengthen stability. The fracture state is significantly influenced by a lateral pressure coefficient. The results of numerical simulation are consistent with those obtained by a model test. Research and analysis based on energy are a promising train of thought for studying the disaster process of water inrush in a karst tunnel.

1. Introduction

Since the 21st century, with the rapid advancement of west development strategy of Chinese national economy, the focus of tunnel construction has gradually shifted to the Western Mountain and karst area. However, complex karst geological structures, especially various scale concealed karst cavities and underground rivers, make the construction of tunnel face the serious threat of water inrush in the abovementioned areas. The karst cavities with high water pressure and high concealment around a tunnel, inducing the suddenness and unpredictable water inrush disaster, are more dangerous than the karst structures exposed by tunnel excavation [1]. In the absence of presupport and prereinforcement, if the water-resistant strata between the tunnel and the concealed cavity with high water pressure cannot withstand the combined effect of karst water pressure and excavation disturbance, fractures will generate, propagate, and then coalesce with each other, eventually causing water inrush disaster and serious economic losses and casualties [2–7]. During the construction process, the Malujing Tunnel of the Yiwan Railway encountered a series of large-scale karst cavities, dissolved fissures, and sinkholes, and more than 10 large scale water and mud inrush disasters occurred successively. Among them, two weighty disasters occurred on January 21, 2006, and April 11, 2008, resulting in 15 deaths and a delay of more than two years [8]. Qiyueshan tunnel encountered a total of 187 large-scale karst pipelines, karst cavities, fault zones with high pressure water and other unfavourable geologies. As a result, 18 times of water inrush disasters occurred, and the cumulative value of water discharge reached to $6.3 \times 10^6\,m^3$, which led to a sharp increase in the cost of construction [9, 10]. The study on the disaster process of water inrush and evolutionary characteristics of accompanying catastrophe information is of great significance for control and preventing water inrushes in karst tunnel.

Lots of scholars have done many researches on disaster mechanism of water inrush and catastrophe information characteristics by theoretical analysis, numerical simulation, and physical model tests up to now. In terms of theoretical research, Xu et al. [11] proposed a semianalytical solution to determine the minimum safe thickness of water-resistant strata for resisting water inrush from filling-type karst cavities based on the principle of the slice method. Fu et al. [12] derived the computational formula of the minimum safety thickness for preventing the collapse of rock pillar when a tunnel is excavated above a karst cave. Guo et al. [13] used the Schwarz alternating method to identify the critical water-resistant thickness and analysed the influence of karst water pressure. Xin et al. [14] established an attribute recognition model for safe thickness assessment between a concealed karst cave and tunnel based on the attribute mathematic theory. Yang et al. [15] studied the minimum safe thickness of rock plug and obtained its analytical expression. In the field of numerical simulation, Qin et al. [16] analysed the distribution law of releasable elastic strain energy and failure zone under different widths of concealed karst cave by FLAC3D. Shan et al. [17] proposed a comprehensive numerical analysis method to determinate the safe thickness, and its rationality and effectiveness have been proved by field tests. Pan et al. [18] investigated the mechanism of lagging water inrush in tunnel construction due to the proximity of a karst cavern with confined water via numerical simulations. Li [19] analysed the catastrophic process of water inrush in the water-resistant strata induced by unloading damage under strong seepage by RFPA flow. With respect to physical model tests, Liang et al. [20] analysed the evolutionary laws of stress, displacement, and water pressure by a physical model test of water inrush in tunnel excavation. Yang et al. [21] studied the disaster process and failure model of water-resistant strata. Pan et al. [22] conducted a solid-fluid coupling model tests on lagging water inrush of karst tunnel and researched the evolutionary process of disaster information under different karst water pressures.

The previous researches and achievements as above for the stability and disaster process of the water-resistant strata promoted the advancement in this field and provided a solid foundation for further study in this paper. However, there are some shortcomings about theoretical analysis and physical model test. A theoretical analysis method can be only used to assess the overall instability of water-resistant strata in the end under some simplifications and assumptions. At the meantime, theoretical analysis is difficult to analyse and describe the disaster process of water inrush with highly nonlinear characteristics. As for physical model tests, there exist some disadvantages of expense, time, and acquisition of information. Numerical simulation is an effective and convenient tool for the simulation of disaster process of the water-resistant strata and water inrush with some unique advantages compared with theoretical analysis method and physical model testing method. The water-resistant strata are basically regarded as porous continuous medium in the aforementioned studies by the use of numerical simulation, which ignores the fracture condition in the water-resistant strata and misestimates the fluid-solid coupling effect. Therefore, for reflecting the real structure properties of water-resistant strata, it is very necessary to employ a numerical method that can consider the initial discontinuities (shown in Figure 1) and accurately describe the initiation and propagation of these discontinuities considering fluid-solid coupling (shown in Figure 1).

In the limestone strata, discontinuities such as beddings and cross joints intersect with each other and cut the rock mass into numerous relatively discrete blocks, called quasi-masonry structure seen in Figure 1. Figure 1 visually shows the disaster process of water inrush in the water-resistant strata with a quasi-masonry structure. The upper part of Figure 1 illustrates the structure of limestone in the karst area and the spatial relationship of cavity with high pressure water and tunnel. The lower half of Figure 1 is the sketch to intuitively indicate the disaster process of water inrush from karst cavity after tunnel excavation. As show in Figure 1, the disaster process of water inrush is the macroresult of the initiation, propagation, and coalescence of the initial discontinuities under tunnel excavation disturbance and karst water pressure. Therefore, the structure characteristics of the water-resistant strata and water-rock interaction in the rock mass with quasi-masonry structure play the important role in the disaster process of water inrush and evolutionary characteristics of catastrophe information like seepage pressure and displacement. The new method based on the DEM (UDEC) and fictitious joint technology is adopted to really simulate the disaster process of water-resistant strata under the combined effect of different karst water pressure, tunnel depth, and lateral pressure coefficient [23, 24]. The evolutionary characteristic of seepage pressure and displacement is analysed under different conditions, and the influential mechanism of karst water pressure, tunnel depth, and lateral pressure coefficient is revealed. The achievements are of great significance for early warning and prevention for water inrush of karst tunnel.

2. Numerical Modeling

2.1. Model Generation. Figure 2 shows the numerical model used in this simulation to analyse the catastrophic evolution process of water inrush from a water-filled karst cavity above the tunnel in the limestone strata with the quasi-masonry structure. For this model to ensure the simulation effect and computing efficiency, the range is $80\,m \times 71\,m$; the three-centred circular tunnel section with height of 9.5 m, span of 8.5 m, and buried depth of 500 m is adopted to simulate a more real tunnel cross section and tunnel depth. The concealed karst cavity above tunnel with water pressure (p) is generalized to an ellipse with a long axis of 20 m and a minor axis of 12 m, which can be identified and positioned by collaborative exploration method integrating geological identification, geophysical inversion, and drilling; and the

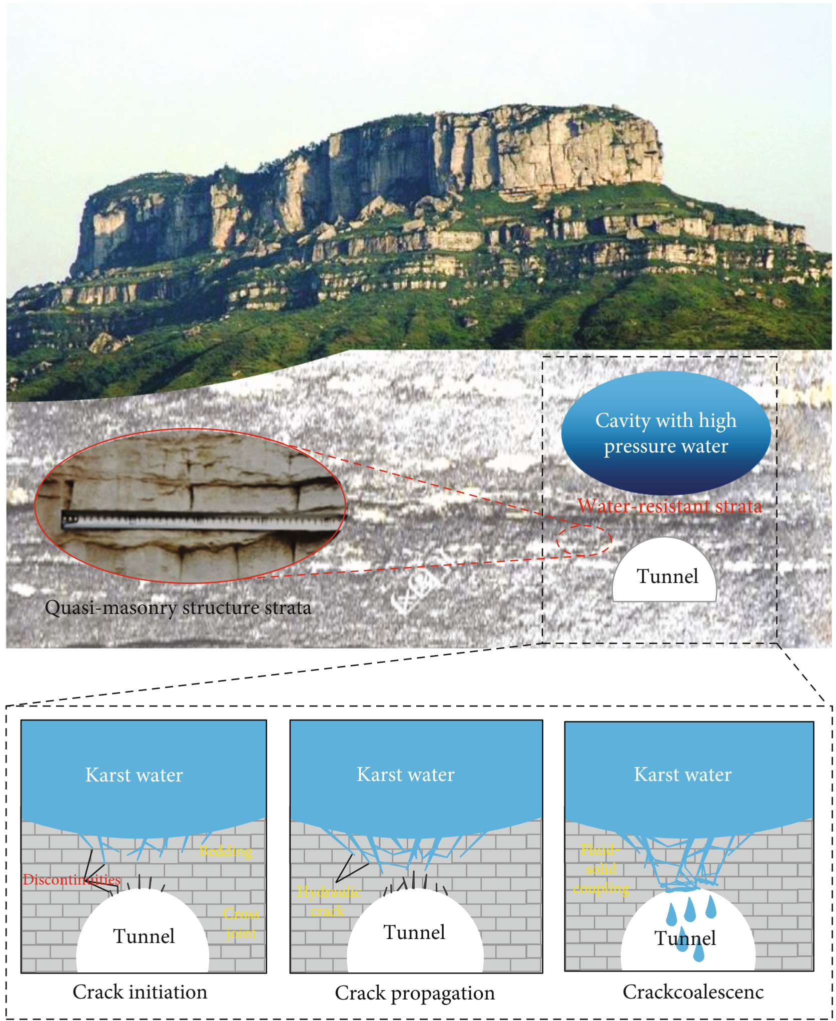

Figure 1: Sketch of quasi-masonry structure of water-resistant strata and water inrush process.

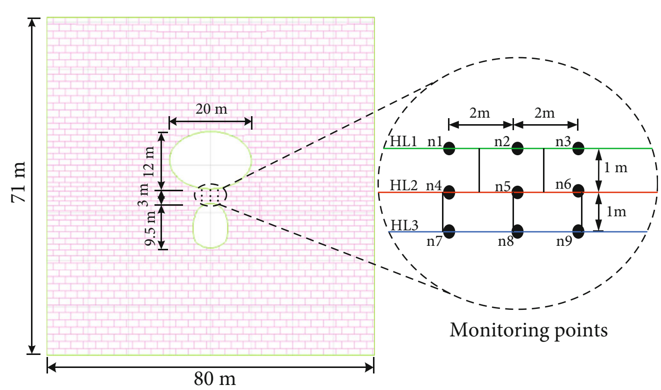

Figure 2: Simulation calculation model and measuring point arrangement.

water-resistant strata between cavity and tunnel are 3 m in thickness. Given the features of the quasi-masonry structure in karst strata, the blocks are divided into many small rectangles by the beddings and the crossed joints. A row of blocks bounded by upper and lower beddings is one limestone layer with the thickness of 1 m, and the number of the layer is 71. So, according to the range of model, tunnel dimension, and scale of karst cavity, the initial numerical model generates with the help of the command of *Generate*; and then, karst cavity generated in the model and the influence of karst cavity generation are reset. Finally, the full model is intersected by beddings and cross joints through *Jset* and *crack*, and the numerical model has been built as shown in Figure 2, as possibly similar to the actual structural features of the limestone strata. To acquire the disaster information like seepage pressure and displacement during the instability process of water-resistant strata, the typical 9 measuring points n1~3, n4~6, and n7~9 (shown in Figure 2) are, respectively, set up on horizontal lines HL1, HL2, and HL3 with a horizontal distance for 2 m and a vertical distance of 1 m between the adjacent points, which, respectively, are located on the three beddings and at the intersection point of the bedding and cross joint for easily and effectively reflecting the displacement and seepage information of the sharp change points in the disaster process.

2.2. Material Constitutive Models and Properties. The mechanical properties of model are defined by the use of the mechanical parameters of the blocks and those of the joints between blocks. In this numerical simulation, the material of rock block system is regarded as a large number of deformable microblocks (cons = 3, Mohr-Coulomb plasticity model adopted for the balance between computational accuracy and easy acquisition of mechanical parameters), bound together by contacts. The jcons = 5 (joint model residual), Coulomb slip with residual strength, is utilized to model the mechanical behaviour of discontinuities. In this model, an internal flag is set for each discontinuity segment when the shear strength of discontinuities is exceeded. If a discontinuity was fractured, the discontinuity friction angle and discontinuity cohesion are set to residual values. Therefore, the microparameters of the block and the discontinuity are required to input; they are shown in Table 1 based on the previous research of authors [25] and Table 2 [26], respectively.

2.3. Boundary Conditions. After finishing the cutting of all the block (beddings and joints) and the defining of the mechanical properties of model, the boundary and initial conditions were added on the numerical model, as shown in Figure 3. The concerned are defined as follows in Figure 3: $kq_0 + \gamma h$ is the stress value at bottom sides of the left and right boundaries of the numerical model; $q_0(\gamma H)$ is the overburden pressure of the model; k is the lateral pressure coefficient; γ is the bulk density of rock mass; h is the height of the model. According to the tunnel depth (H), the weight of the overlying rock mass was converted into a vertical uniform load (q_0) applied on the top boundary of the model. A stress boundary was also exerted on the left and right sides of the model with a lateral pressure coefficient (k). The bottom side was bounded by displacement boundary. The karst water pressure (p) in karst cavity is regarded as a constant and acted vertically on the boundary of the cavity. Numerical simulations for fully coupled fluid-solid interaction with saturated flow and initiation and propagation of hydraulic fracture are carried out in the following order: stress balance and state reset, tunnel excavation, acquiring the disaster information, and stop under the condition of combination.

2.4. Calculation Scheme. Karst water pressure, tunnel depth, and lateral pressure coefficient are three important influential factors that affect the stability condition and disaster process of the water-resistant strata. To figure out the disaster process of water inrush in karst tunnel and the evolutionary characteristics of catastrophe information like seepage pressure and displacement under condition of different karst water pressure, tunnel depth, and lateral pressure coefficient, a series of numerical simulations are conducted to the seepage pressure, displacement of the kinetics and dissipated energy of the water-resistant strata were simulated and analysed based on the above modeling method in the condition of different conditions. Table 3 shows the influential factors and their calculation scheme in this research. The cases 1~3, 4~6, and 7~9 are used to study the effect of water pressure (p), tunnel depth (H), and lateral pressure coefficient (k) on the disaster process and catastrophe information characteristics of the water-resistant strata, respectively. During the calculation, the fluid flow calculator is on for considering the solid-fluid coupling, and the mechanical time duration t for the increment of cycling lasts for 80 ms.

The seepage pressure characterizes the water pressure value, water pressure distribution, and crack propagation in the water-resistant strata, and vertical displacement to reflect the stability of the water-resistant strata of the n1~n9 of nine monitoring points on HL1, HL2, and HL3 is collected and recorded. Energy is the essential dynamics of crack propagation and rock mass failure under any circumstances. The failure process of rock is accompanied by energy accumulation, energy dissipation and energy release. In order to analyse the stability of the water-resistant strata from the energy point of view in stability analysis based on energy properties, the kinetic energy as one kind of the released energy and the dissipated energy of the model system are calculated and recorded by use of UDEC program in the disaster process of water inrush.

3. Influence of Karst Water Pressure (p)

3.1. Seepage Field Analysis of the Water-Resistant Strata under Different p. Table 4 demonstrates the evolutionary process of the seepage field in the water-resistant strata under the three cases of tunnel depth of 500 m, lateral pressure coefficient of 1.2, and different karst water pressure (case 1: $p = 1$ MPa, case 2: $p = 2$ MPa, and case 3: $p = 3$ MPa) at $t = 10$ ms, 40 ms, and 80 ms. Thus, this table is subdivided into 9 subfigures; every 3 subfigures in one column show the evolutionary process of seepage field in the water-resistant strata, which also illustrate the progressive failure process of the water-resistant strata. And every 3 subfigures in one row are a comparison of the 3 seepage fields under the different karst water pressure at the same mechanical duration time.

The columns in Table 4 show that the karst water in the cave splits the original closed bedding layers and cross joints and makes the water-resistant strata failure to form many cracks in the upper and middle part under the combined effect of tunnel excavation and karst water pressure at the beginning of the stress release of the surrounding rock mass ($t = 10$ ms). Then, with further stress release ($t = 40$ ms and $t = 80$ ms), the cracks furtherly propagate and the fracture range continuously extends in the water-resistant strata, and the failure degree of the water-resistant strata increases

Table 1: Block and joint mechanical parameters in numerical simulation.

Unit weight (γ)	Elastic bulk modulus (E)	Poisson's ratio (μ)	Internal angle of friction (φ)	Cohesion (c)
24 kN/m^3	18 GPa	0.2	35	10 MPa

Table 2: Joint mechanical parameters in numerical simulation.

Joint normal stiffness (jkn)	Joint shear stiffness (jks)	Joint cohesion (coh)	Joint friction angle (f)	Joint residual cohesion (resc)	Joint residual friction angle (resf)
222.2 Pa·m^{-1}	222.2 GPa·m^{-1}	0.15 MPa	25°	0 MPa	25°

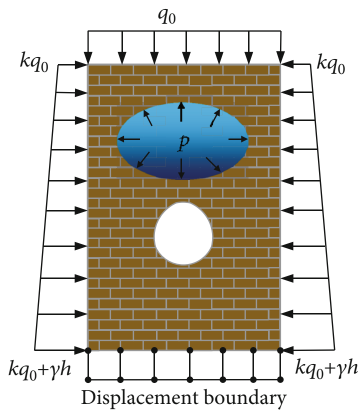

Figure 3: Boundary conditions of numerical simulation model.

with the increase of time in the meantime. At $t = 80$ ms, the water-resistant strata have the tendency of instability and the water inrush channel initially forms in the case of $p = 2$ MPa and $p = 3$ MPa. In this disaster process, the propagation feature of cracks and the distribution range of water pressure significantly show the time effect and the structure influence of the water-resistant strata.

With the increase of time, it is clear to find that the seepage scope in the water-resistant strata extends obviously and the fracture degree increases quickly with the increase of karst water pressure from the three columns in Table 4. For the first column ($p = 1$ MPa), relatively fewer cracks induced by karst water pressure and tunnel excavation are generated in the upper and middle parts of the water-resistant strata, and the cracks does not propagate the vault of the tunnel. Therefore, the macroscopic water inrush channel does not form, and the water-resistant strata are in the stable condition. The seepage pressure of each measuring points illustrates a decreasing state from HL1 to HL3, but the seepage pressure is the constant value because the cracks stop propagating and seepage pressure develops fully. For the middle column ($p = 2$ MPa), the larger fracture zone and seepage scope generate, and the fracture degree is more serious and the water inrush channel basically forms. For the third column ($p = 3$ MPa), these above characteristics are more prominent. Taking the seepage pressure of n7~n9 measuring points on HL3 as example, the seepage pressure of n7~n9 measuring points at $t = 80$ ms is still increasing while the water-resistant strata are in the fracture process by comparing with the first column ($p = 1$ MPa). These phenomena revel that the karst water pressure is the important reason of the water-resistant strata.

Figure 4 shows the trend of seepage pressure at the 9 measuring points. It is found that the seepage pressure of the 9 measuring points in the water-resistant strata increases with the increase of kart water pressure p from Figure 4. The time of arrival to a steady-state value for the seepage pressure at different measuring point varies obviously, and even the seepage pressure at some measuring points has been fluctuating in Figure 4. The reasons for the abovementioned phenomenon are as follows: (1) after tunnel excavation, under the action of excavation disturbance and karst water pressure, the karst water gradually infiltrates into the originally closed fissures, and the seepage pressure increases gradually. When the seepage pressure exceeds the critical pressure of fracture, the cracks begin to initiate and propagate. No matter whether the water-resistant strata are unstable or not finally (It is related to karst water pressure), under the action of three levels of karst water pressure in this paper, the cracks in the water-resistant strata can always extend to n1~n6 measuring points in the middle and upper parts of the water-resistant strata. Therefore, the seepage pressure at these measuring points can always reach a certain stable value before the formation of macrowater inrush channel in the water-resistant strata or when the fracture stops propagating, as shown in Figures 4(a) and 4(b). Because the location of n4~n6 is lower than that of n1~n3 in water-resistant strata, the propagation time for the cracks channelling the cave with high water pressure to reach n4~n6 is relatively long, and therefore, it takes a long time for the seepage pressure of n4~n6 to increase to a stable value. The stable values of seepage pressure at n1~n3 measuring points are close to the karst water pressure, but the stable value of seepage pressure at n4~n6 is relatively smaller, as shown in Figures 4(a) and 4(b); (2) when the karst water pressure is 1 MPa, the cracks in the water-resistant strata can only propagate to a certain position, and water inrush does not occur. Because the water-resistant strata are stable, the seepage pressure of n7~n9 measuring points set up at the bottom of the water-resistant strata reaches a smaller stable value than that of n1~n6 measuring points. When the karst water pressure is 2 MPa and 3 MPa, at $t = 80$ ms, the seepage pressure of n7~n9 is also increasing while the water-resistant strata are still fracturing, especially when $p = 3$ MPa, as shown in Figure 4(c).

Table 3: The calculation scheme for the three influential factors.

Study objectives	Case number	Karst water pressure (p)	Tunnel depth (H)	Lateral pressure coefficient (k)
Effect of karst water pressure (p)	1	1 MPa	500 m	1.2
	2	2 MPa	500 m	1.2
	3	3 MPa	500 m	1.2
Effect of tunnel depth (H)	4	2 MPa	300 m	1.2
	5	2 MPa	500 m	1.2
	6	2 MPa	800 m	1.2
Effect of lateral pressure coefficient (k)	7	2 MPa	500 m	0.8
	8	2 MPa	500 m	1.2
	9	2 MPa	500 m	1.6

Table 4: The seepage pressure distribution in the water-resistant strata under the three cases of $p = 1$, 2, and 3 MPa at $t = 10$, 40, and 80 ms.

t	$p = 1$ MPa	$p = 2$ MPa	$p = 3$ MPa
10 ms	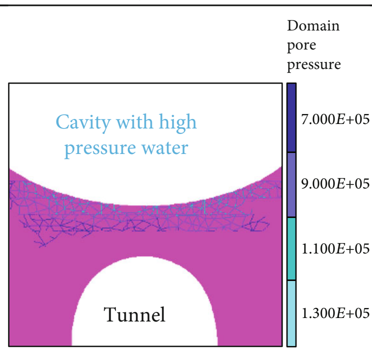	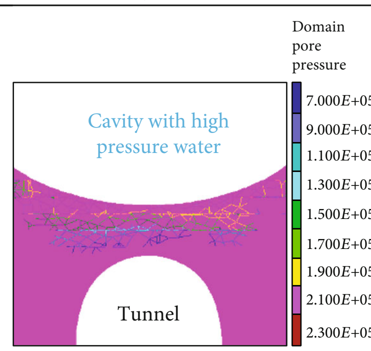	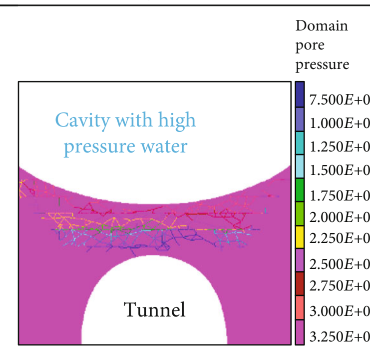
40 ms	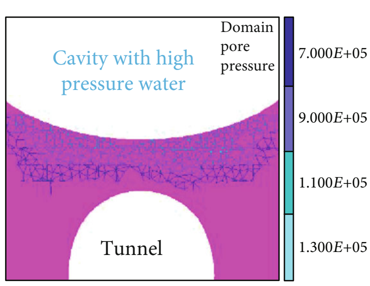	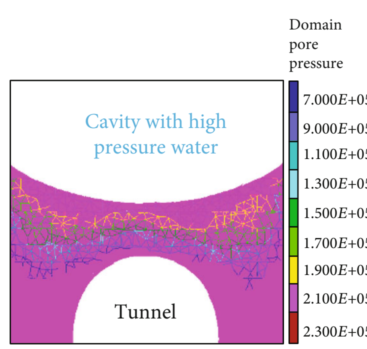	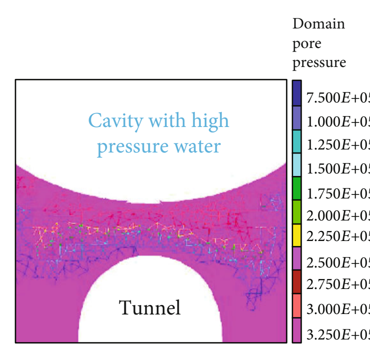
80 ms	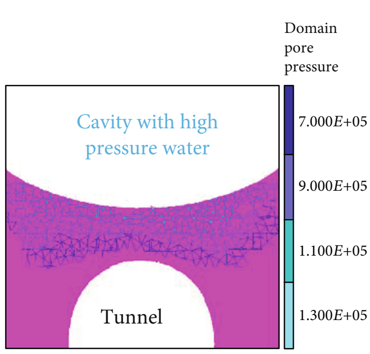	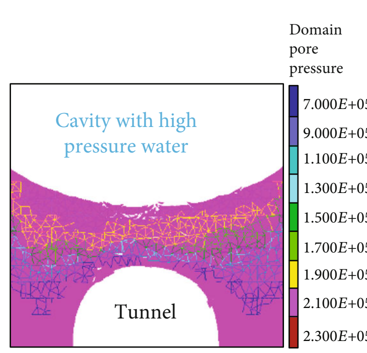	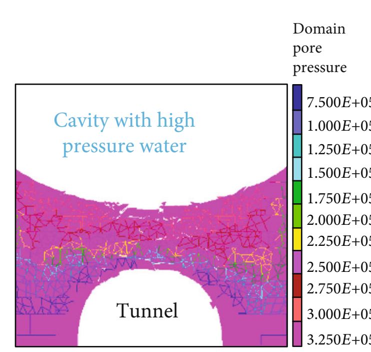

3.2. Displacement Field Analysis of the Water-Resistant Strata under Different p. Table 5 shows the displacement field under the three cases of $p = 1$, 2, and 3 MPa at $t = 10$, 40, and 80 ms. Taking the second column in Table 5 ($p = 2$ MPa) as an example, we analyse the displacement evolution characteristics of the water-resistant strata in the disaster process of water inrush. After the tunnel excavation, the water-resistant strata have displaced to some extent due to

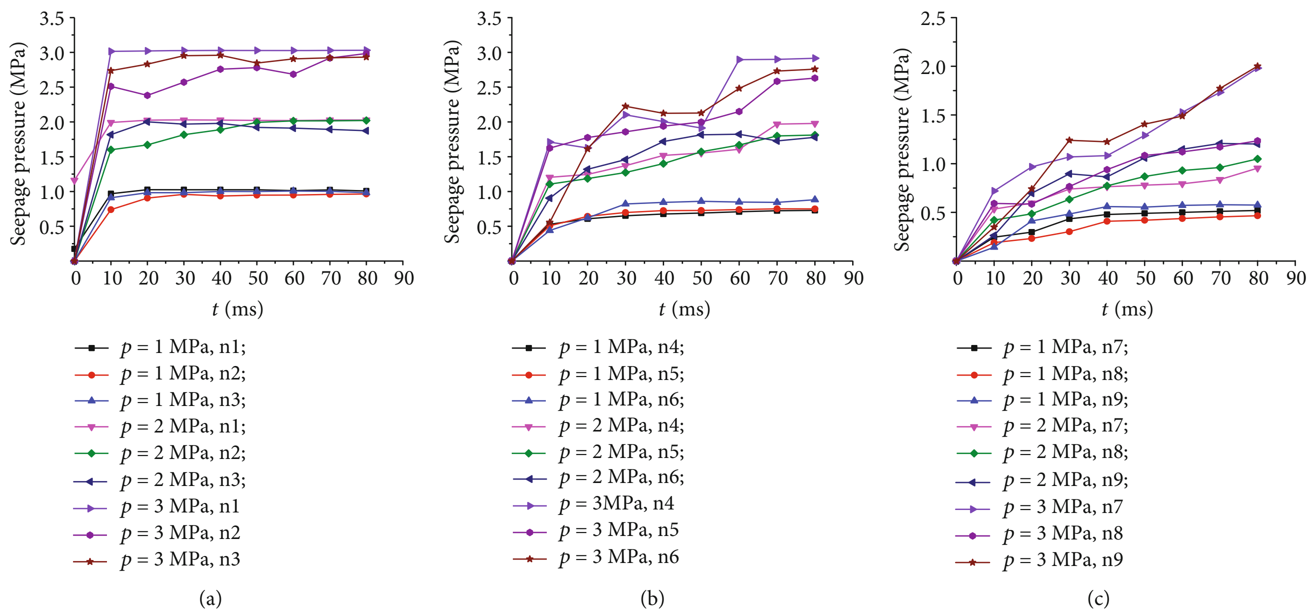

FIGURE 4: The trend of seepage pressure at the 9 measuring points in the conditions of $p = 1$, 2, and 3 MPa: (a) n1~n3 on HL1; (b) n4~n6 on HL2; (c) n7~n9 on HL3.

excavation effect in the early stage of stress release of the surrounding rock mass ($t = 10$ ms), with significant deformation towards the interior of tunnel and slight displacement near the karst cave. As the stress continues to be released ($t = 40$ ms), the seepage scope in the water-resistant strata is getting larger and larger, and the damage region extends rapidly. The seepage crack and seepage pressure in the water-resistant strata totally increase with various degrees, which causes the displacement of the water-resistant strata near tunnel vault continue to increase. And the fracture degree of the water-resistant strata furtherly increases, but overall, the water-resistant strata are still in a stable state. However, when $t = 80$ ms, the overall displacement of the water-resistant strata increases significantly, and meanwhile, the cracks propagate quickly and coalesce with each other making the water-resistant strata into fracture condition. The water-resistant strata become unstable due to severe fragmentation.

Although the disaster process of water-resistant strata is similar under the three cases of $p = 1$, 2, and 3 MPa, the influence difference of karst water pressure on the stability of water-resistant strata cannot be ignored. When $p = 1$ MPa, the vertical displacement of the water-resistant strata in the condition of stability is relatively small. But as p increases to 2 MPa and 3 MPa, the water-resistant strata have undergone the failure at $t = 80$ ms, and it can be clearly observed that the fracture degree and vertical displacement of the water-resistant strata at the top of the tunnel increase continuously with the increase of p. The number, width, and connectivity degree of the hydraulic fractures increase at the same time, and the speed of fracture and instability accelerates. The increase of the water pressure in the karst cave has a greater impact on the collapse of the water-resistant strata. The persistent fluid-solid coupling effect ultimately leads to the failure and overall instability of the water-resistant strata. From Table 5, we can also find that the fracture zone is growing greater and greater with the increase of p. The fracture zone between the cave and the tunnel has a downward displacement and is divided into many smaller fragments, which released the stress acting on the rock mass below the fracture zone, and hence, the rock mass shows a slightly upward displacement.

Figure 5 shows the variation process of vertical displacement at the 9 measuring points in the water-resistant strata with $p = 1$, 2, and 3 MPa. Comparing the vertical displacement of the same measuring points, it is obvious that the vertical displacement increases significantly with the increase of p, which illustrates that the karst water pressure has an obvious influence on the displacement of the water-resistant strata. In detail, when $p = 1$ MPa, the displacement increases almost linearly and steadily with increase of the time. But when p is 2 MPa or 3 MPa, the displacement of the same measuring point parabolically and quickly grows with the growth speed accelerating and the growth rate increasing. This is because the higher karst water pressure makes it easier to generate cracks in the water-resistant strata and furtherly forms the water inrush channel. Meantime, the higher karst water pressure can also exert a downward load on the water-resistant strata. Both of these factors contribute to the displacement of the water-resistant strata. The displacement of n2 on HL1 is greater than that of n1 or n3 under the effect of the same p. The same thing as above, the vertical displacement of n5 and n8 on HL2 and HL3 is larger that indicates the displacement of arch crown is greater than that of both sides of arch shoulders. In another words, the arch crown of tunnel is fractured severely compared with other locations.

4. Influence of Tunnel Depth (H)

4.1. Seepage Field Analysis of the Water-Resistant Strata under Different H. Table 6 shows the evolution processes of

Table 5: The vertical displacement contour under the three cases of $p = 1$, 2, and 3 MPa at $t = 10$, 40, and 80 ms.

<table>
<tr><th>t</th><th>p = 1 MPa</th><th>p = 2 MPa</th><th>p = 3 MPa</th></tr>
<tr><td>10 ms</td><td>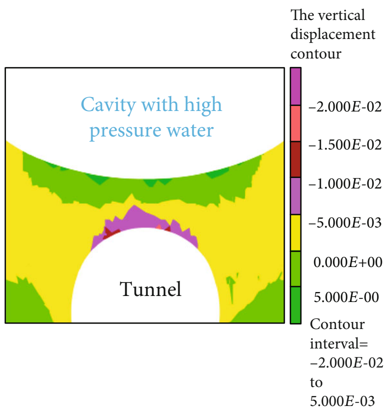</td><td>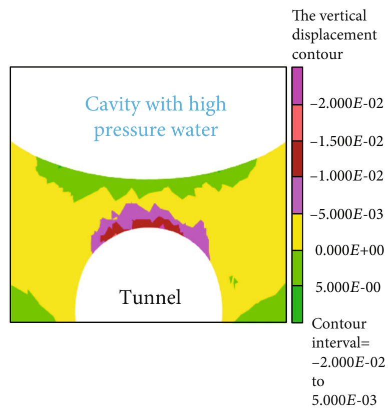</td><td>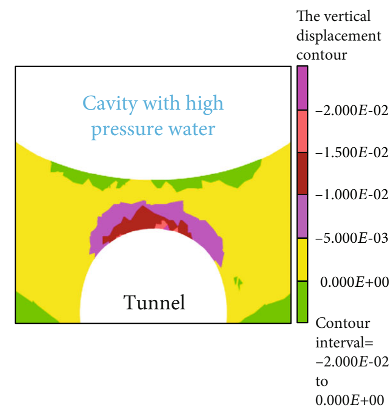</td></tr>
<tr><td>40 ms</td><td>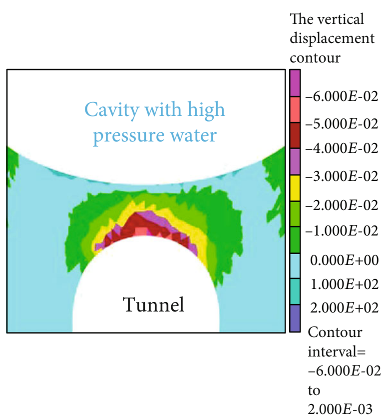</td><td>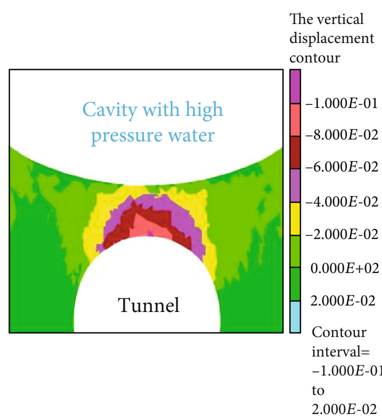</td><td>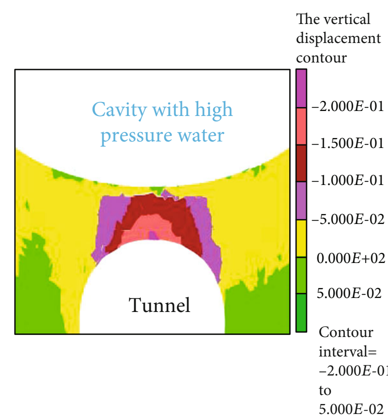</td></tr>
<tr><td>80 ms</td><td>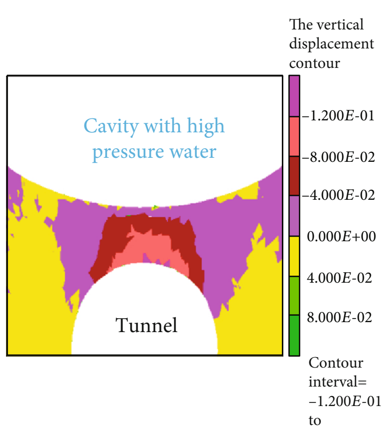</td><td>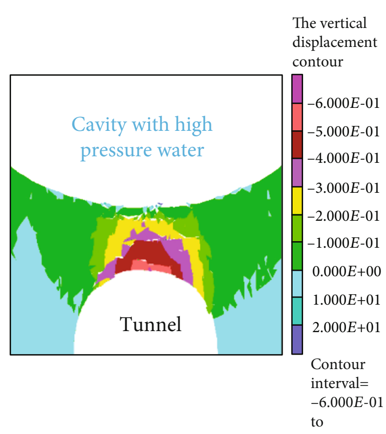</td><td>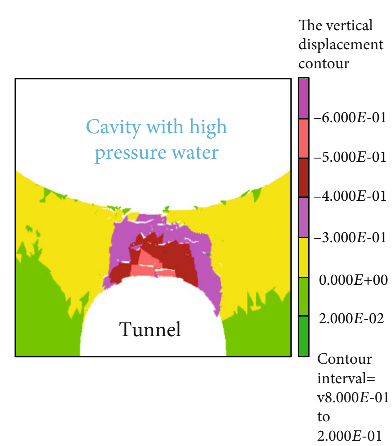</td></tr>
</table>

the seepage field in the water-resistant strata under the three cases of karst water pressure of 2 MPa, lateral pressure coefficient of 1.2, and tunnel depth (case 4: $H = 300$ m, case 5: $H = 500$ m, and case 6: $H = 800$ m) at $t = 10$ ms, 40 ms, and 80 ms. The column is the mechanical duration time, and the row is the different tunnel depth. Similar to the evolutionary process of seepage field in Section 3.1, for each tunnel depth, the karst water also infiltrates downward in the water-resistant strata to the vault, spandrel, and hance of the tunnel gradually. But the velocity of water seepage and crack propagation varies greatly with tunnel depth, and the formation time of water inrush channel is different in the condition of three kinds of tunnel depth. In the initial stage ($t = 10$ ms), the karst water ingresses into the water-resistant strata for a short distance, far from the tunnel vault for the situation of $H = 300$ m. But when H increases to 500 m or 800 m, the water is about to penetrate the water-resistant strata. Therefore, it can be concluded that the deeper the tunnel is buried, the more likely it is that water inrush happens in the initial stage. What is more, by comparing the distribution area of water with the same t, but varied H, it is clear that the distribution area of water and hydraulic fractures in the water-

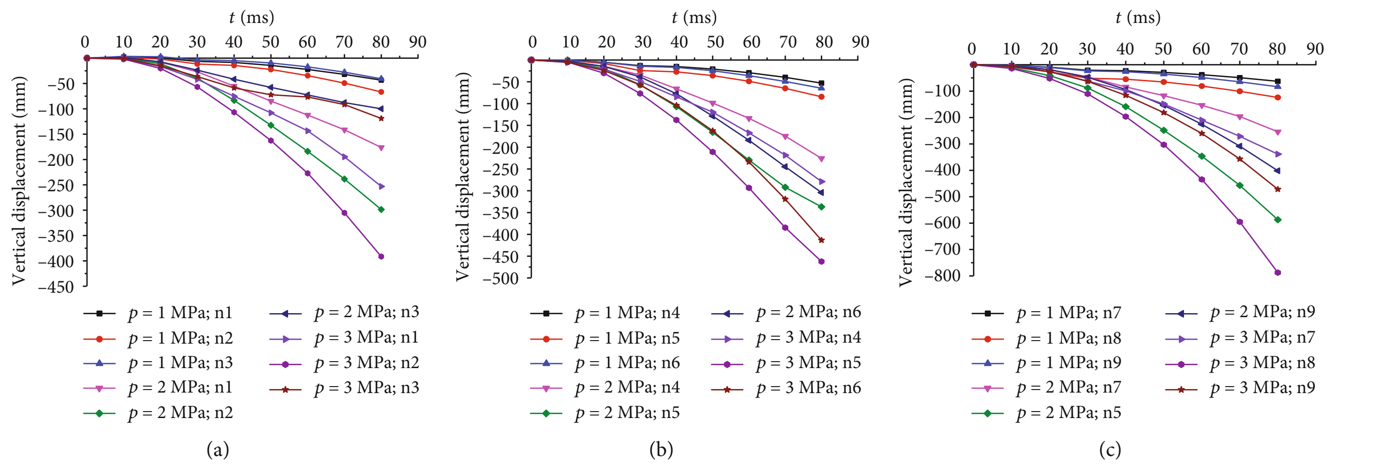

Figure 5: The trend of vertical displacement at the 9 measuring points in the conditions of $p = 1$, 2, and 3 MPa: (a) n1~n3 on HL1; (b) n4~n6 on HL2; (c) n7~n9 on HL3 with $p = 1$, 2 and 3 MPa.

resistant strata obviously increase with the increase of tunnel depth. At $t = 80$ ms, water inrush basically occurs under all three cases, but the fracture and water inrush scale in the condition of $H = 500$ m is larger than those in $H = 300$ m and reaches the maximum in $H = 800$ m, which reveals that the scale of fracture and water inrush increases with the growth of tunnel depth. This phenomenon shows that under the effect of water pressure and tunnel excavation disturbance, the larger the tunnel depth, the greater the scale and coalescence of fractures formed in the water-resistant strata, which can speed up the formation of channel and the occurrence of water inrush disaster.

Figure 6 shows diachronic evolution characteristics of the seepage pressure at the 9 measuring points in the condition of $H = 300$, 500, and 800 m under tunnel excavation disturbance and karst water pressure ($p = 2$ MPa). It is found that the seepage pressure of n1~n3 measuring points on HL1 quickly reaches a certain stable value close to karst water pressure in a short time from Figure 6(a), and the seepage pressure of n1~n3 is little different in the condition of $H =$ 300, 500, and 800 m finally. The growth of seepage pressure of n4~n9 measuring points is relatively slow by comparison with that of n1~n3 measuring points, and the deeper the tunnel depth, the greater the seepage pressure of measuring points on HL2 and HL3 in Figures 6(b) and 6(c). These indicate that as the tunnel depth increases, the number and connectivity of hydraulic fractures formed in the water-resistant strata become larger, and the smoother hydraulic fractures can be formed in the water-resistant strata in a relatively short time, resulting in water inrush disaster, which is in accordance with the above analysis.

4.2. Displacement Field Analysis of the Water-Resistant Strata under Different H. Table 7 shows the displacement contour under the three cases of $H = 300$, 500, and 800 m at $t = 10$, 40, and 80 ms. In Table 7, the evolutionary process of the water-resistant strata base on the displacement is similar to that demonstrated in Table 6, but it still varies considerably between each other due to the different tunnel depth. At the initial stage ($t = 10$ ms), the water-resistant strata have a small upward displacement in the upper part (near the cavity side) and a larger displacement on the lower part (near the tunnel side); the magnitude and distribution of these two kinds of displacement widen with increasing of tunnel depth. The reasons for these can be analysed as follows: the water-resistant strata can be simplified as a rock column under loads at the top, left, and right sides after tunnel excavation. The top side is subjected to 2 MPa of water pressure from the cavity, and the lower side is unstressed, while the left and right sides are subject to higher stress, approximately 8.6 MPa in $H = 300$ m, 14 MPa at 500 m, and 23 MPa at 800 m (these values are calculated by $\sigma = k\gamma H$, taking $H = 800$ m for example, $\sigma = k\gamma H = 1.2 \times 24 \times 800 = 23$ MPa). It can be seen that the left and right sides are subject to much greater compressive stress than the top and bottom sides. Due to the lower stress on the top and bottom sides in the unconstrained or weak constraint state, the beddings are prone to splitting failure taking into account that the direction of the beddings is parallel to the direction of stress acting on the left and right sides. According to the Poisson effect, a simplified rock column will deform laterally and some cracks, nearly paralleling to the upper and lower boundaries, generate in the water-resistant strata. Because of the loading difference on the top and bottom sides as mentioned earlier, the upward displacement on the upper side near the karst cavity is less than downward displacement on the lower side near the tunnel. Moreover, the greater the tunnel depth, then the greater the stress on the left and right sides of the water-resistant strata and, subsequently, the larger the lateral deformation, assuming lateral pressure coefficient was kept constant in the increase process of tunnel depth.

Therefore, in the initial stage ($t = 10$ ms) for Table 7, as the tunnel depth increases, the larger the area of upward displacement in the upper part of the water-resistant strata and the larger the area of downward displacement in the lower part, the larger the magnitude of the upward and downward displacements. However, because the downward displacement is always greater than the upward

Table 6: The seepage pressure distribution in the water-resistant strata under the three cases of $H = 300$, 500, and 800 m at $t = 10$, 40, and 80 ms.

t	$H = 300$ m	$H = 500$ m	$H = 800$ m
10 ms	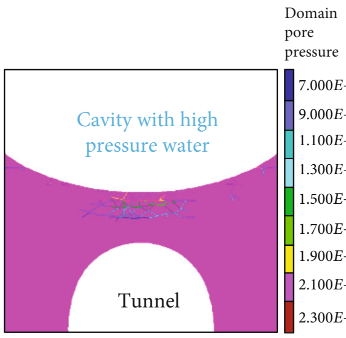	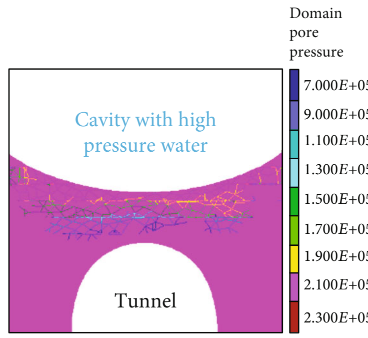	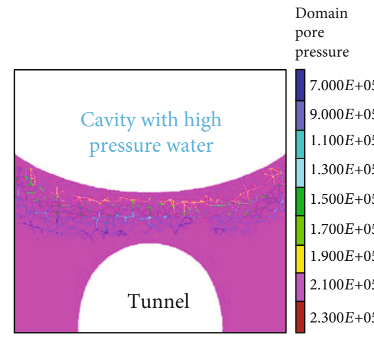
40 ms	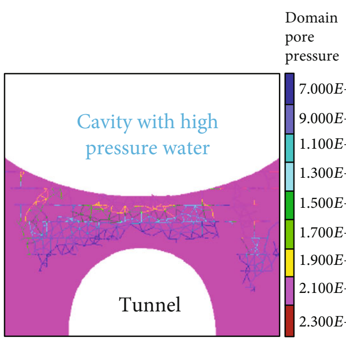	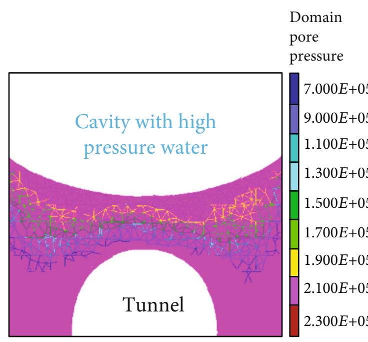	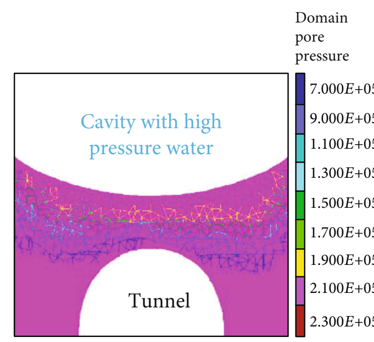
80 ms	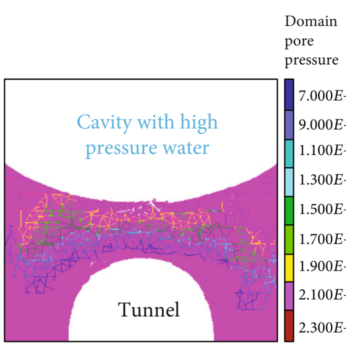	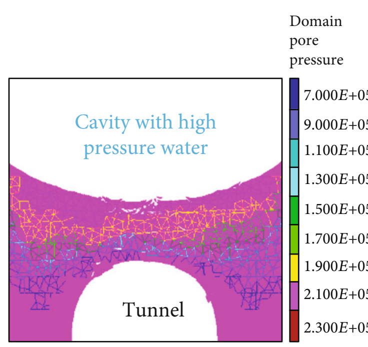	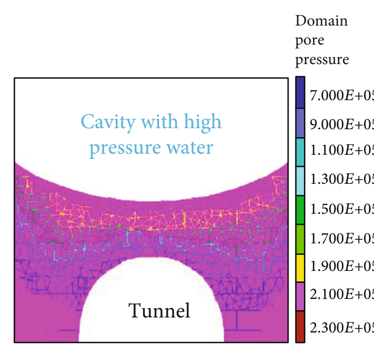

displacement, the area of downward displacement in the upper part of the water-resistant strata furtherly expands, resulting in the tendency of upward displacement in the upper part being weakened and offset and the deformation of water-resistant strata being mainly based on the upward displacement as shown in the second and third rows from Table 7. These analyses for the influence of tunnel depth on the displacement evolution characteristics in the water-resistant stability at the different times can be used to reveal the influence mechanism on the vertical displacement of karst water pressure in Table 5.

Figure 7 shows diachronic evolution characteristics of the vertical displacement at the 9 measuring points on HL1, HL2, and HL3 in the condition of $H = 300$, 500, and 800 m. For the varied properties of any measuring point in this figure, it is easy to find that the vertical displacement and its growth speed or growth rate have a small difference between the two cases of $H = 300$ m and $H = 500$ m, but far greater than those of $H = 800$ m. For the former two cases, the change trend of the vertical displacement at each point is relatively uniform, and the water-resistant strata shows a clear tendency of instability failure. But for the later, the vertical displacement of each measuring point is significantly reduced, which indicates that the larger horizontal tectonic stress is beneficial for the stability of water-resistant strata between karst cavity and tunnel. Besides, the vertical displacement of arch crown greater than that of both sides of arch shoulders is verified again.

5. Influence of Lateral Pressure Coefficient (k)

5.1. Seepage Field Analysis of the Water-Resistant Strata under Different k. Table 8 shows the evolutionary processes of the seepage field in the water-resistant strata under the three cases of karst water pressure of 2 MPa, tunnel depth of 500 m, and lateral pressure coefficient (case 7: $k = 0.8$, case 8: $k = 1.2$, and case 9: $k = 1.6$) at $t = 10$ ms, 40 ms, and 80 ms. The column is the mechanical duration time, and the row is

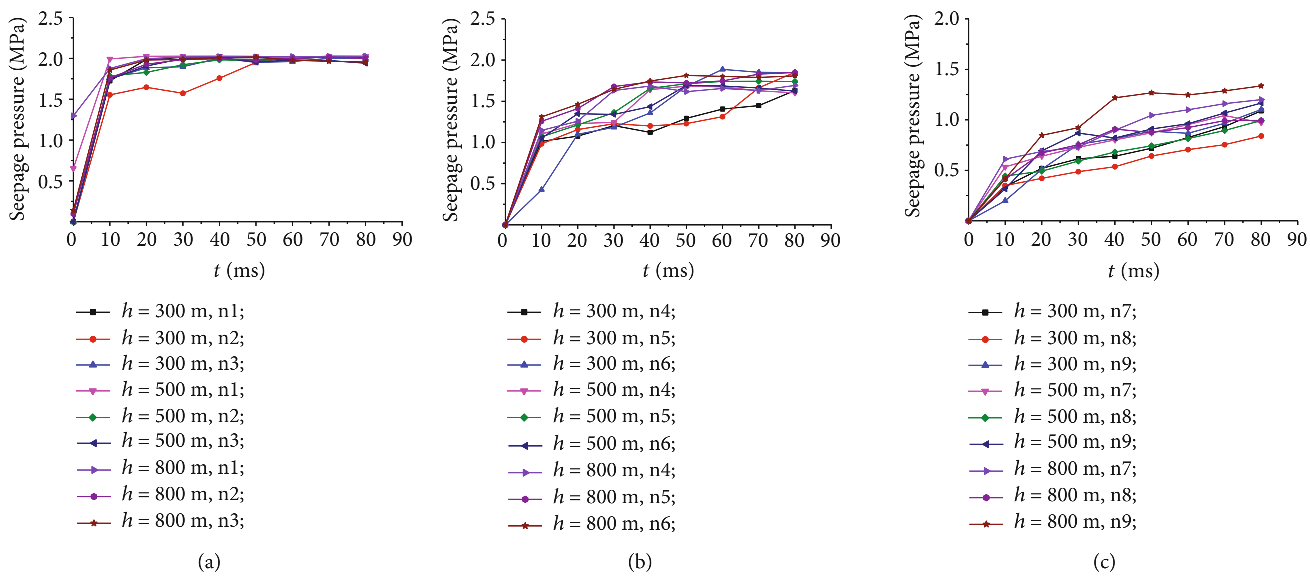

Figure 6: The trend of seepage pressure at the 9 measuring points in the conditions of $H = 300$, 500, and 800 m: (a) n1~n3 on HL1; (b) n4~n6 on HL2; (c) n7~n9 on HL3.

the different lateral pressure coefficient. The karst water also infiltrates downward from the upper part to the bottom part in the water-resistant strata. The lateral pressure coefficient has some influences on the seepage pressure and seepage distribution scope by comparison with the results of three cases. It is found that the fracture at $t = 80$ ms under the condition of $k = 0.8$ is more serious than that of another two cases of $k = 1.2$ and $k = 1.6$. It is indicated that the smaller the lateral pressure coefficient, the more serious the fracture of the water-resistant strata.

Figure 8 shows the trend of seepage pressure at the 9 measuring points under the three cases of $k = 0.8$, 1.2, and 1.6, respectively. No matter what the value of lateral pressure coefficient is, the cracks in the water-resistant strata always easily propagate to the n1~n3 measuring points in the upper part of the water-resistant strata, and the dissipated energy is less because the above measuring points are closer to the boundary of karst cavity. As a result, the seepage pressure of n1~n3 measuring points always reaches a stable value which is close to the karst water pressure in karst cavity, as shown in Figure 8(a). Because the n4~n6 measuring points have a relatively long distance with karst cavity, the process of cracks channelling the cavity with high water pressure to reach the n4~n6 measuring points on HL2 will dissipate more energy. Therefore, the seepage pressure of n4~n6 measuring points reaches a relatively stable low value, approximately 1.5 MPa~1.8 MPa as shown in Figure 8(b). At $t = 80$ ms, the water-resistant strata are still in the process of the seepage pressure accumulating-crack initiation and propagation, reaccumulating-crack initiation and propagation again under the three cases of $k = 0.8$, 1.2, and 1.6. As shown in Figure 8(c), the larger lateral pressure coefficient causes the increase of normal stress in crack in the water-resistant strata and then raises the critical water pressure as the threshold for hydraulic fracturing failure of cracks. Therefore, the fracture degree is higher and the fracture scope is larger under the low lateral pressure coefficient of $k = 0.8$, and the seepage pressure of the n7~n9 measuring points in the lower part of the water-resistant strata develops fully and is higher correspondingly under the circumstance of this lateral pressure coefficient.

5.2. Displacement Field Analysis of the Water-Resistant Strata under Different k. Table 9 shows the evolution processes of the displacement field in the water-resistant strata under the three cases of $k = 0.8$, 1.2, and 1.6 at $t = 10$ ms, 40 ms, and 80 ms. The disaster process of water-resistant strata based on displacement evolution is generally similar to Table 5 and Table 7. But the vertical displacement significantly differs from each other because of the different lateral pressure coefficient. In the different condition of $k = 0.8$, 1.2, and 1.6, the extension of the upward displacement area in the upper part of the water-resistant strata and the magnitude of the displacement increase with the increase of k. The underlying reason for this phenomenon is due to an increase of normal stress on the hydraulic cracks and its consequence of the critical water pressure for crack initiation arising from the horizontal load increase exerted on the left and right side of the water-resistant strata. It is very clear that the fracture zone and the vertical displacement decrease with the increase of k at $t = 40$ ms and 80 ms mainly due to the increase of horizontal load realized by the lateral pressure coefficient. The fracture state is different in the water-resistant strata under the different lateral pressure coefficient. When the lateral pressure coefficient is relatively large ($k = 1.2$ or 1.6), the development trend of fracture is restrained by a larger lateral pressure coefficient and the fracture state is in the underdeveloped condition. However, the water-resistant strata are in the fractured state due to propagation and coalesce of hydraulic cracks for the smaller lateral pressure

Table 7: The vertical displacement contour under the three cases of $H = 300$, 500, and 800 m at $t = 10$, 40, and 80 ms.

t	$h = 300$ m	$h = 500$ m	$h = 800$ m
10 ms	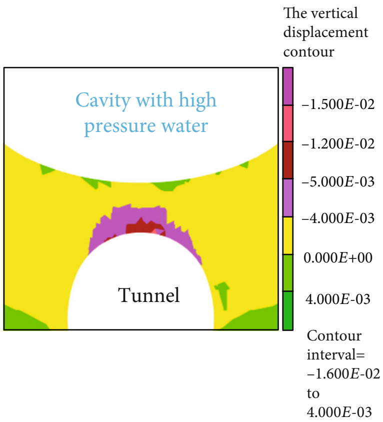	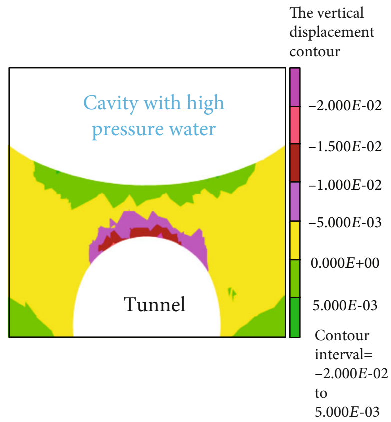	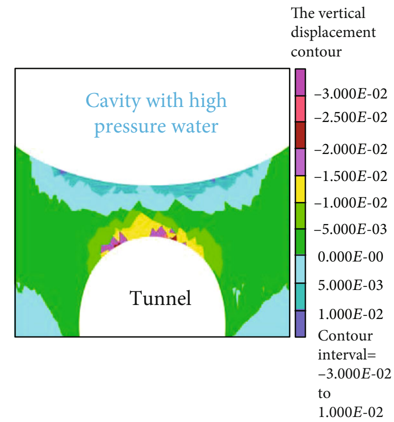
40 ms	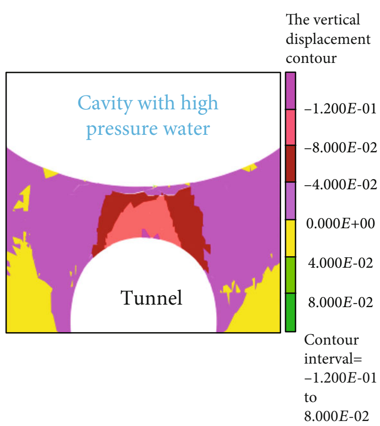	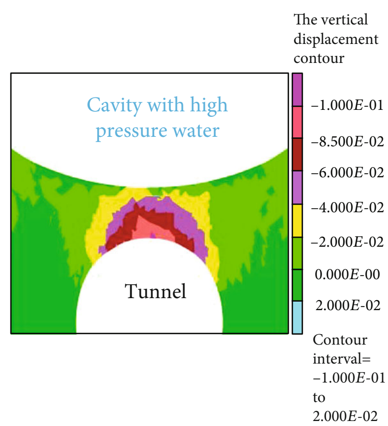	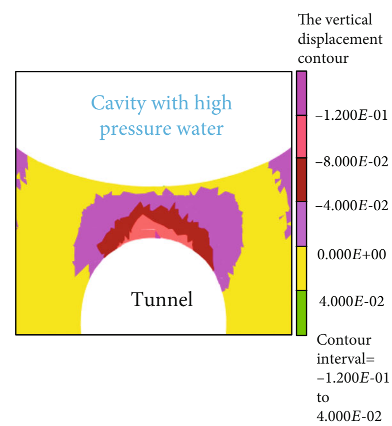
80 ms	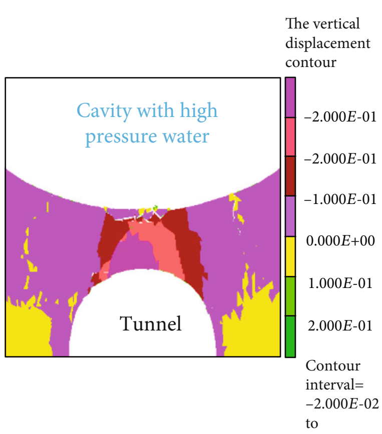	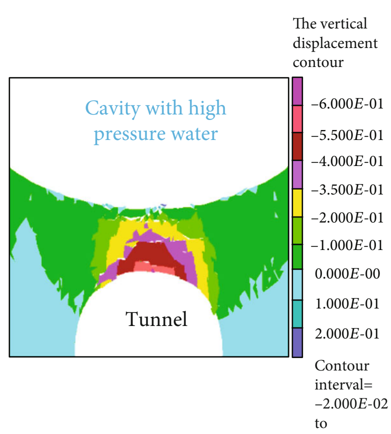	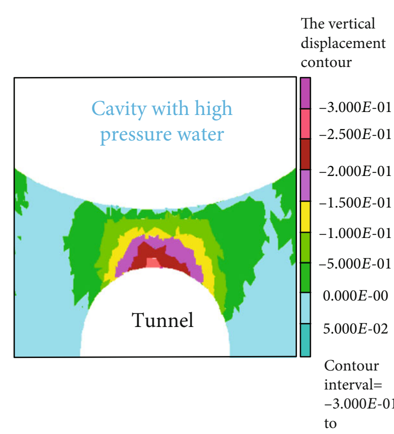

coefficient ($k = 0.8$), and the water inrush channel has fully formed at $t = 80$ ms. It is concluded that the increase of lateral pressure coefficient can restrain the fracture development of the water-resistant strata and strengthen its stability from Table 9 and its systemic analysis.

Figure 9 shows the trend of the vertical displacement development of the 9 measuring points under the three cases of $k = 0.8$, 1.2, and 1.6, respectively. Obviously, the vertical displacement of the same measuring points decreases significantly with the increase of k. Under the condition that the lateral pressure coefficient is same, the closer to the tunnel vault and the deformation of the water-resistant strata are greater. For $k = 1.2$ or 1.6, the vertical displacement of the water-resistant strata is obviously smaller, but for $k = 0.8$, the vertical displacement of the water-resistant strata increases rapidly and the final value of the vertical displacement at $t = 80$ ms is much larger than that for $k = 1.2$ or 1.6. The vertical displacement in the lower part of the water-

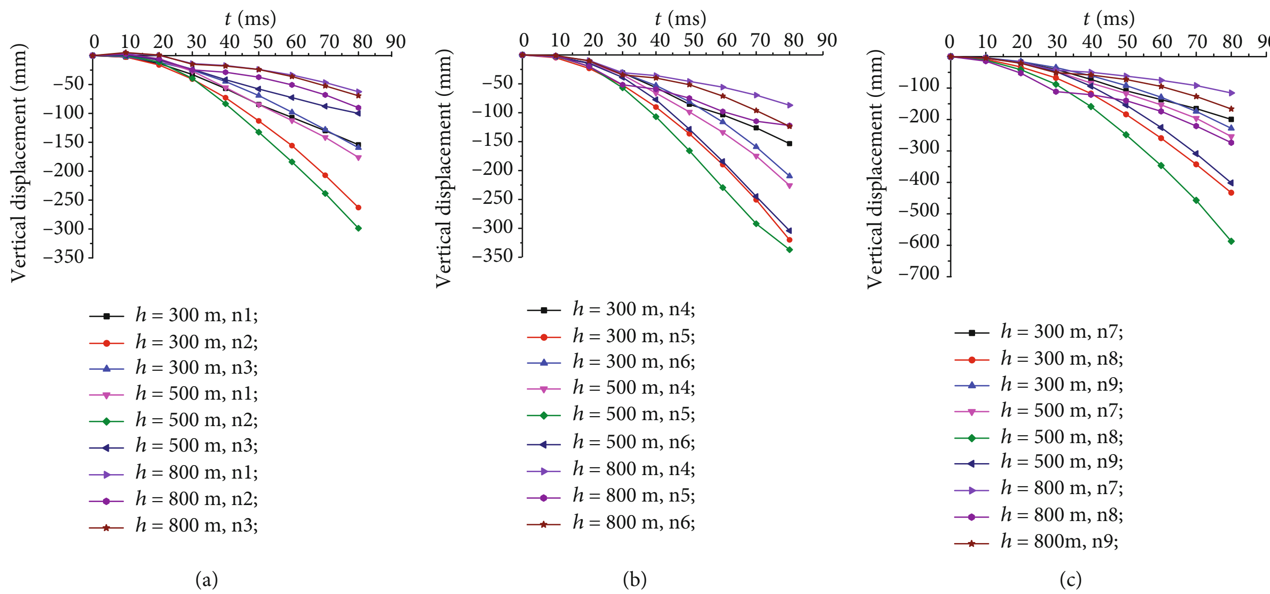

Figure 7: The vertical displacement at the 9 measuring points in the conditions of $H = 300$, 500, and 800 m: (a) n1~n3 on HL1; (b) n4~n6 on HL2; (c) n7~n9 on HL3.

resistant strata increases continuously with the decrease of k. It indicates that the smaller value of k is unfavourable to the stability of the water-resistant strata.

6. Discussion

6.1. Comparative Analysis with Results of Previous Model Test. The main methods to study water inrush of karst tunnel are theoretical analysis, model test, field test, and numerical simulation. In the theoretical analysis method, it is difficult to analyse and describe the water inrush disaster process with highly nonlinear problems in mathematics. A field test is not used to carry out batch tests with multiple factors and variable conditions as desired and seriously threatens the tester's safety. Therefore, theoretical analysis and field test are suitable to be used as the main research method for water inrush of karst tunnel. According to schedule, the model test and numerical simulation can be used as the effective ways to carry out water inrush research and really simulate the disaster process of the water-resistant strata considering the coupling of various influential factors. The model test has many disadvantages of great expense, time-consuming, and lacking of ability to obtain the information in full field and microdynamic process. Numerical simulation can solve the above problems, and it has the function of visualizing the dynamic disaster process of water inrush and can rupture the microinformation. Therefore, numerical simulation is a promising, effective, and convenient method for studying water inrush of karst tunnel, but the validity of the results using this method needs to be verified by a model test and other methods.

In the published literature about water inrush of karst tunnel, researches on the influence of tunnel depth and lateral pressure coefficient on the stability of water-resistant strata by means of model test have not yet been found. A few scholars have done some researches on the influence of karst water pressure on the water-resistant strata stability, which provides the possibility to compare the research results in this paper through numerical simulation with previous results utilizing model test. Yang et al. conducted some physics model tests to study the disaster process of water-resistant strata and analysed the evolutionary properties of seepage pressure in the water-resistant strata with the increase of karst water pressure [21]. Zhu used a self-developed testing system to study the influence of the karst water pressure on the deformation and deterioration of the water-resistant strata and found that the vertical displacement of the water-resistant strata gradually increased with the growth of karst water pressure [27]. The research results of this article are highly consistent with the abovementioned achievements obtained by the use of model tests, which proves the reliability of the numerical simulation method and the effectiveness of conclusions in this paper.

6.2. Comprehensive Effect of Three Kinds of Influential Factors. The instability and then water inrush of the water-resistant strata between tunnel and karst cavity with high pressure water are essentially a manifestation of local failure in surrounding rock mass of karst tunnel under the combined action of karst water pressure and disturbance of tunnel excavation. Karst water pressure is one kind of load directly acting on the water-resistant strata and causes fluid-solid coupling effect in the disaster process of the water-resistant strata. We can see that the seepage and failure scope extend obviously and the fracture degree increases quickly with the increase of karst water pressure from Table 4. Therefore, the water pressure of karst cavity is the effective factor affecting the stability analysis of water-resistant strata based on the research of this paper and many published papers by theoretical analysis, numerical simulation, model tests, and field tests [28].

Table 8: The seepage pressure distribution in the water-resistant strata under the three cases of $k = 0.8$, 1.2, and 1.6 at $t = 10$, 40, and 80 ms.

t	$k = 0.8$	$k = 1.2$	$k = 1.6$
10 ms	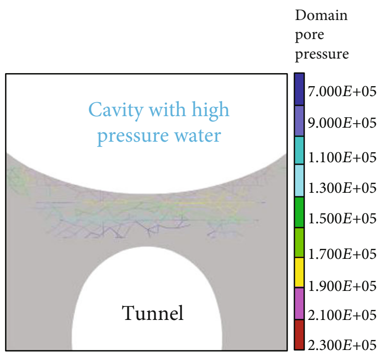	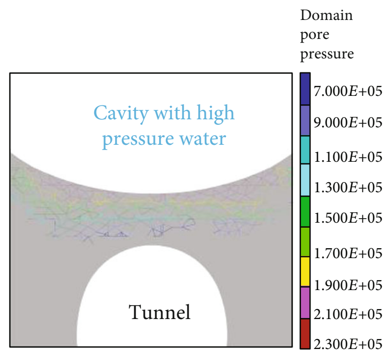	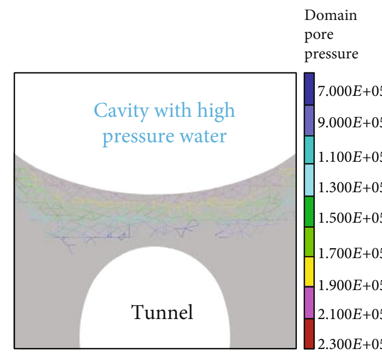
40 ms	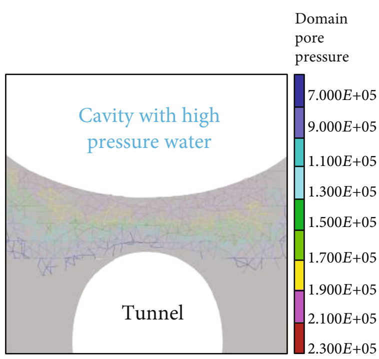	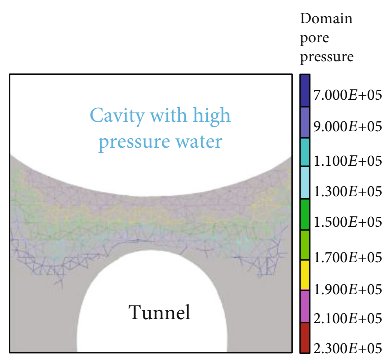	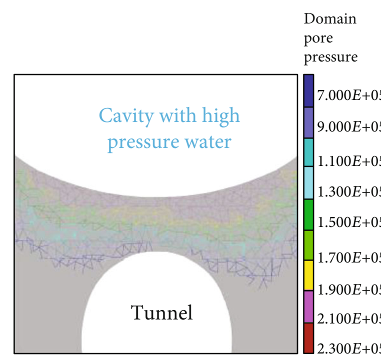
80 ms	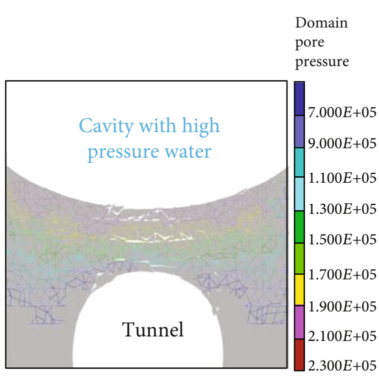	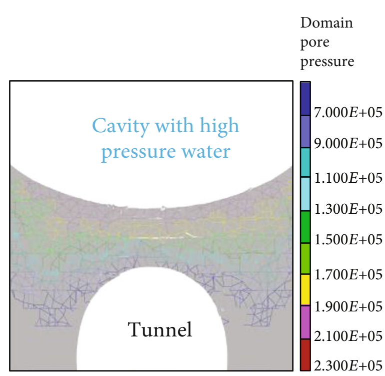	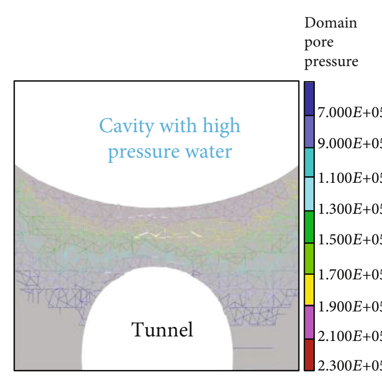

If tunnel is not constructed in strata, the water-resistant strata do not exist and the problems of the water-resistant strata stability will not exist. Tunnel excavation disturbance makes the water-resistant strata lose the lower support from the rock mass, and therefore, the water-resistant strata are in the unloading and stress adjustment condition and the critical water pressure of the water-resistant strata failure will decrease, eventually causing the water-resistant strata instability and water inrush. The degree of the unloading and stress adjustment is directly related to the geostress environment of the tunnel-karst system that is mainly determined by the tunnel depth and lateral pressure coefficient, and in consequence, tunnel depth and lateral pressure coefficient are the influential parameters for the water-resistant strata stability. Tables 6–9 and Figures 6–9 illustrate that the stability of water-resistant strata between karst cavity and tunnel decreases on the whole with the growth of tunnel depth, but with the decline of lateral pressure coefficient.

At present, there are few researches on the comprehensive effect of karst water pressure, tunnel depth, and lateral pressure coefficient on the stability of water-resistant strata. Zhang et al. established the theoretical relationship between stress intensity factor of crack tip in surrounding rock mass and tunnel depth under excavation unloading disturbance [29]. Guo and Qiao analysed the tendency of critical water pressure for the water-resistant strata failure with the normal stress on the crack in the water-resistant strata [30]. According to these above achievements, it is concluded that tunnel depth can strengthen the stress intensity factor, decreasing the water-resistant strata stability, and the lateral pressure coefficient is able to heighten the critical water pressure, for the stability. These conclusions are consistent with the

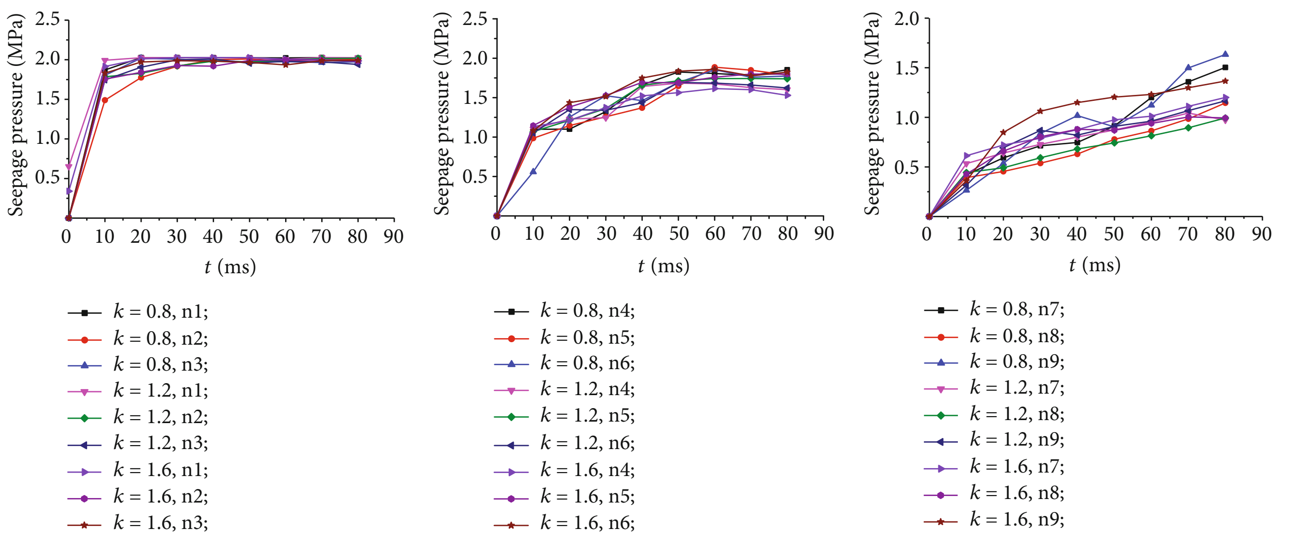

(a) (b) (c)

Figure 8: The trend of seepage pressure at the 9 measuring points in the conditions of $k = 0.8$, 1.2, and 1.6: (a) n1~n3 on HL1; (b) n4~n6 on HL2; (c) n7~n9 on HL3.

obtained results in Sections 4 and 5. These mean that tunnel depth amplifies the effect of karst water pressure p and the lateral pressure coefficient weakens the influence of p.

6.3. Stability Analysis Based on Energy Evolutionary Properties. As mentioned before, the water-resistant strata with quasi-masonry structure composed of discrete small rock blocks, bedding, and cross joints are heterogeneous, discontinuous, nonlinear, and highly discrete. Therefore, it is difficult to accurately and quantitatively describe the mechanical behaviour of all discrete blocks, joints, and cracks in the analysis of the instability process of water-resistant strata and evolution characteristics of water inrush under the condition that laboratory tests to investigate the behaviour of small-scale rock samples and structure planes are unlikely to accurately reflect the real state. However, this complicated phenomenon can be dealt with and grasped from the whole utilizing the theories of system science. As a whole, karst cavity, tunnel, and the water-resistant strata (surrounding rock mass) are regarded as an open system [19]. There exists always the energy exchange between this system and environment, and the process of water inrush in karst tunnel is seen as the energy release process of the above system. In this process, energy dissipation is caused by crack initiation-propagation-coalesce and plastic deformation in the water-resistant strata. The rock fragments separated from the water-resistant strata move at a certain speed, and these blocks release the system energy [31]. Therefore, the dissipated and kinetic energy can be used as an index to characterize the disaster condition of water-resistant strata [32].

Taking three cases under different karst water pressure of $p = 1$, 2, and 3 MPa in Section 3 as examples, the evolutionary characteristics of the dissipated and kinetic energy (U_d and U_k) in the disaster process of water inrush, calculated by the energy calculation module of UDEC program, is shown in Figures 10 and 11. In the period of 0~20 ms, the evolutionary processes of U_k and U_d are almost identical. During this period, a few cracks develop steadily and obvious displacement appears in the water-resistant strata. But after 20 ms, U_d gradually tends to one constant value and U_k fast reduces a lower value for $p = 1$ MPa, which indicates that the hydraulic cracks gradually stop propagating and the water-resistant strata are in the condition of stability for avoiding water inrush. These phenomena are well consistent with those revealed in Table 4 and Figure 4. But in the cases of $p = 2$ or 3 MPa, U_k and U_d increase rapidly with the increase of p , and their growth rates also increase. These indicate that the cracks continue to propagate and the propagation speed is accelerated. The number of hydraulic cracks continues to increase, and displacement continues to accelerate. Then, the water-resistant strata become unstable and water inrush occurs, although the U_d and U_k in conditions of $p = 2$ MPa and $p = 3$ MPa have the same evolutionary trend in Figures 10 and 11. But after 20 ms, by comparing the two cases of $p = 2$ MPa and $p = 3$ MPa, not only the kinetic energy and dissipated energy of the system are significantly different, but also the growth rate of U_d and U_k is also the same situation. It demonstrates that the greater the karst water pressure, the more likely to be failure and water inrush. These results are good agreement with the displacement and cracks in Tables 4 and 5.

6.4. Engineering Measures to Control and Prevent Water Inrush. The global karst distribution area is 22 million square kilometres, which accounts for 15% of the global land area. Among them, mainly concentrated distribution was in Yunnan-Guizhou Plateau and Hunan-Guangxi Hilly Basin in China; Massif Central, Ural Mountains in Russia; and Indiana State and Kentucky State in the Middle East of the United States. It is inevitable that the tunnel will expose karst structure or closely pass through the affected area when some

Table 9: The vertical displacement contour under the three cases of $k = 0.8$, 1.2, and 1.6 at $t = 10$, 40, and 80 ms.

t	$k = 0.8$	$k = 1.2$	$k = 1.6$
10 ms	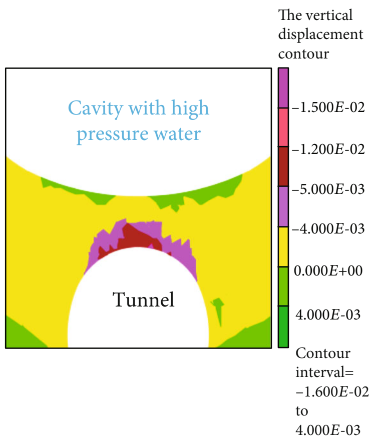	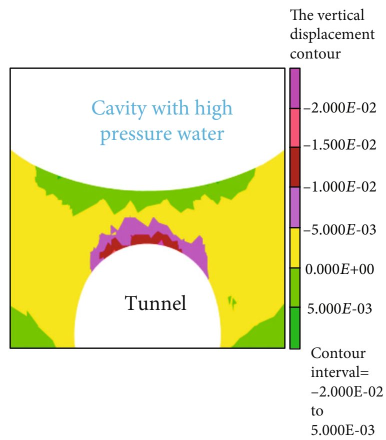	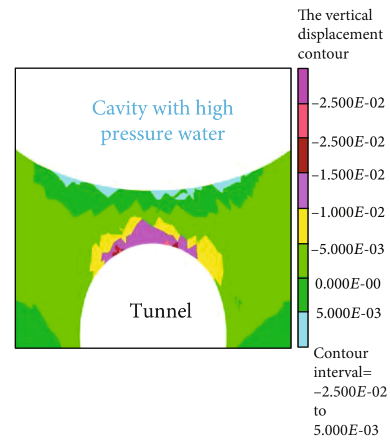
40 ms	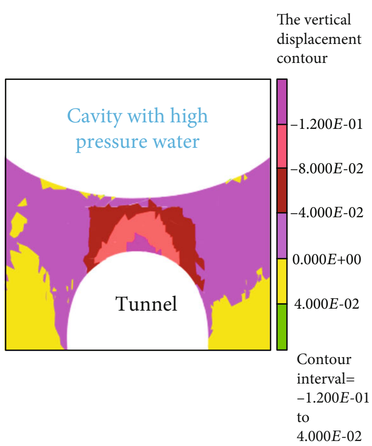	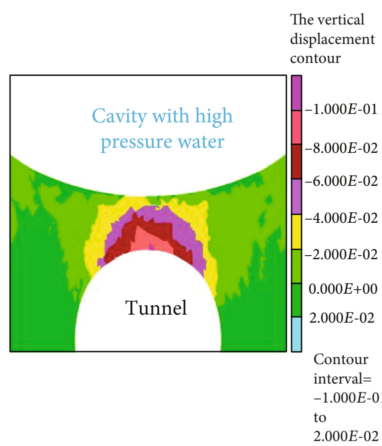	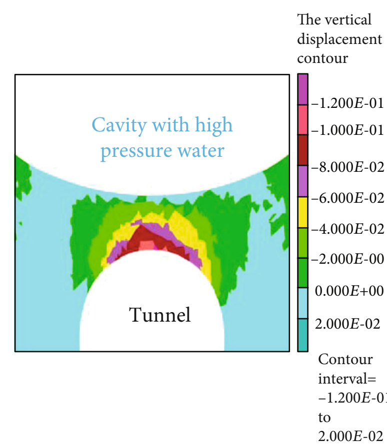
80 ms	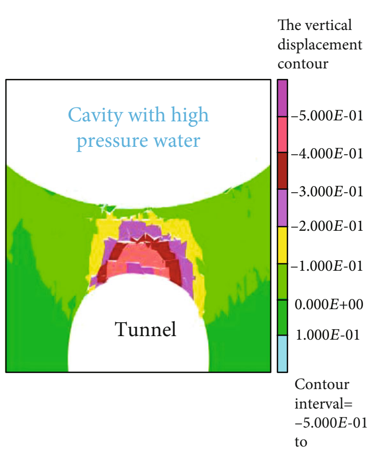	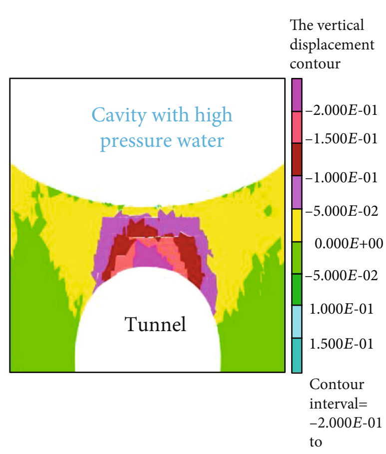	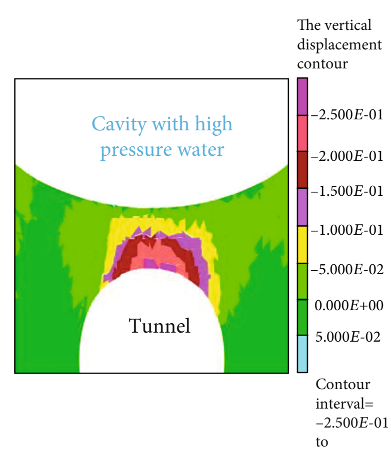

tunnels are planned to be constructed in the karst area. Water inrush disaster is often caused by the instability of water-resistant strata [33]. The results of this paper show that karst water pressure, tunnel depth, and lateral pressure coefficient have obvious effects on the water-resistant strata stability. Tunnel depth and lateral pressure coefficient are important consideration factors in tunnel design stage (route selection). But these are the immutable geological environment in the construction stage of tunnel. This part mainly discusses the control and prevention measures of water inrush disaster in karst tunnel from the perspective of influential law of karst water pressure. Figure 12 shows the variation characteristics of seepage pressure and vertical displacement of n2, n5, and n8 under three cases of $H = 500$ m, $k = 1.2$, and $p = 1$ MPa, 2 MPa, and 3 MPa at $t = 10$ ms, 40 ms, and 80 ms. According to Figure 12, the seepage pressure and vertical displacement of the three measuring points increase obviously with the increase of karst water pressure. Therefore, karst water

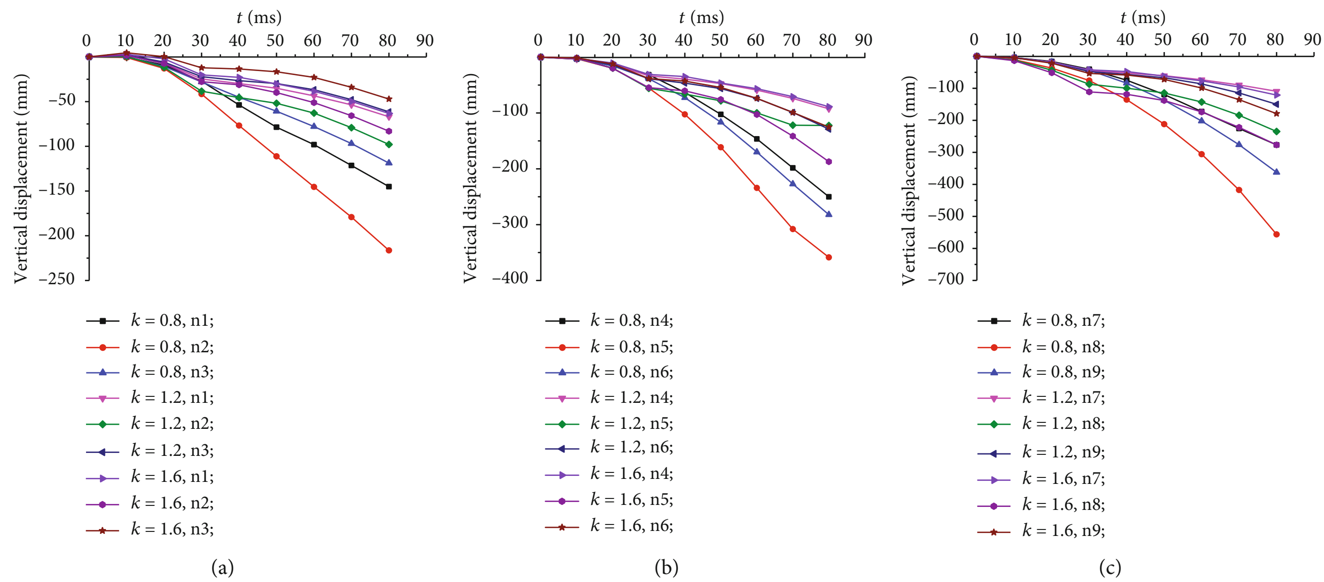

FIGURE 9: The vertical displacement at the 9 measuring points in the conditions of $k = 0.8$, 1.2, and 1.6: (a) n1~n3 on HL1; (b) n4~n6 on HL2; (c) n7~n9 on HL3.

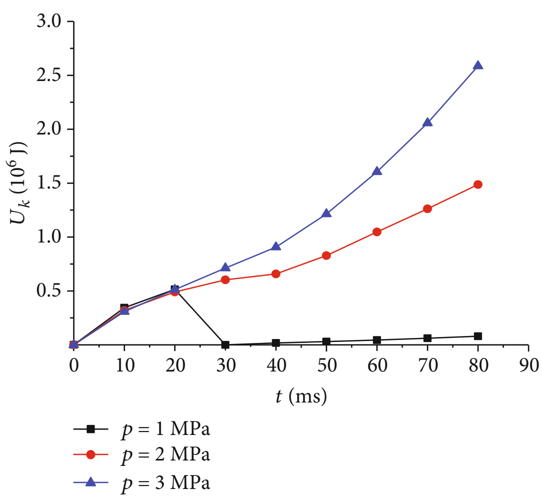

FIGURE 10: The evolution process of U_k of the system with $p = 1$, 2, and 3 MPa.

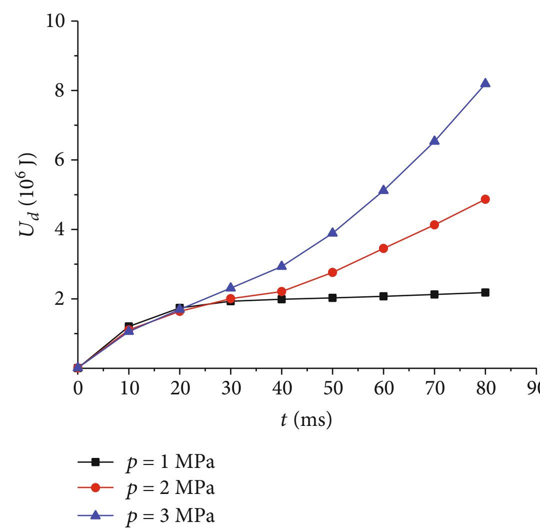

FIGURE 11: The evolution process of U_d of the system with $p = 1$, 2, and 3 MPa.

pressure in the cavity is an extremely important factor affecting the water-resistant strata stability, and additionally, the water-resistant performance and impermeability are also critical to control and prevent water inrush.

According to the above analysis, the pros and cons aspects of karst water pressure and water-resistant performance of the rock mass between cavity with high water pressure and tunnel, mainly considered during the process of the game process of the instability of water-resistant strata and water inrush, are the key to control and prevent water inrush disaster of karst tunnel. The water inrush disaster of karst tunnel is caused by reducing the critical water pressure of water-resistant strata failure due to tunnel excavation disturbance, and hence, reducing karst water pressure and increasing the critical water pressure of rock mass are the main measures to contain water inrush of karst tunnel. Some draining holes or tunnels are usually set up to release the stored energy in karst cavity and reduce karst water pressure in the engineering practice. Finally, the above method makes karst water pressure in karst tunnel smaller than the critical water pressure of water-resistant strata failure, and then the water inrush disaster in karst is avoided successfully. Another method of increasing the critical water pressure of the water-resistant strata is mainly achieved by improving the water-resistant performance of rock mass itself. In engineering practices, on the one hand, the partial excavation of small section and short progress is adopted to avoid excessive excavation disturbance and protect the water-resistant performance of the rock mass. On another hand, grouting and

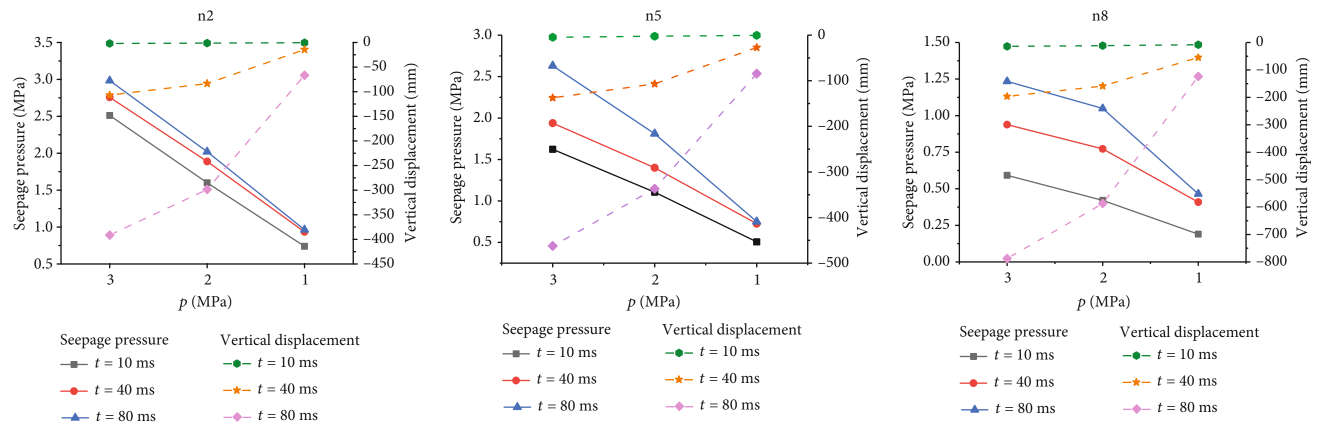

(a) n2 (b) n5 (c) n8

Figure 12: Relationship between seepage pressure and vertical displacement of three measuring points and karst water pressure at different time.

other prereinforcement method are implemented to reinforce the water-resistant strata and improve the water-resistant performance and impermeability [34–36].

7. Conclusions

Water inrush is one of the main geological disasters in the karst tunnel excavation. To investigate the evolutionary characteristics of seepage pressure and displacement in the disaster process of water inrush under different combined conditions of karst water pressure, tunnel depth, and lateral pressure coefficient, a series of numerical simulation analyses based on DEM were conducted utilizing the numerical models considering the quasi-masonry structure properties of water-resistant strata. Some conclusions can be drawn in the following:

(1) The seepage pressure of measuring points increases with the increase of kart water pressure. The seepage pressure illustrates a decreasing state from HL1 to HL3 and the time of arrival to a stable value for the seepage pressure at different measuring point varies obviously, and it shows the time effect. The displacement increases almost linearly with time under lower karst pressure, and the corresponding relationship curve demonstrates parabolical properties in condition of higher karst water pressure. The fracture area, fracture degree, and seepage pressure level increase quickly with the increase of karst water pressure

(2) The velocity of water seepage and crack propagation varies greatly with tunnel depth. The area and magnitude of displacement in the water-resistant strata increase with tunnel depth. The distribution area of water and hydraulic fractures obviously increase with the increase of tunnel depth. The larger the tunnel depth, the greater the scale and coalescence of fractures formed and the more likely the water inrush to occur in a short time. The stability of water-resistant strata decreases on the whole with the growth of tunnel depth

(3) No matter what the value of lateral pressure coefficient is, the seepage pressure of n1~n3 measuring points always reach a stable value which is close to the karst water pressure and those of n4~n9 reaches a relatively stable lower value. The vertical displacement decrease with the increase of lateral pressure coefficient. The larger lateral pressure coefficient raises the critical water pressure. The increase of lateral pressure coefficient can restrain the fracture development and strengthen stability. The fracture state is different under the different lateral pressure coefficients

(4) The research results of this article by numerical simulation are highly consistent with the achievements obtained utilizing model tests. Tunnel depth amplifies the effect of karst water pressure p, and lateral pressure coefficient weakens the influence of p. Stability analysis based on energy properties can be the important method to analyse and characterize the disaster process and condition of the water-resistant strata. In view of the important influence on the stability of water-resistant strata, the pros and cons aspects of karst water pressure and water-resistant performance are the key to control and prevent water inrush in karst tunnel

Data Availability

The raw/processed data required to reproduce these findings cannot be shared at this time as the data also form part of an ongoing study.

Conflicts of Interest

The authors declare that they have no conflicts of interest.

Acknowledgments

This study was financially supported by the National Natural Science Foundation of China (Grant No. 51778215), the National Key Basic Research and Development Plan (973 Plan) Project (Grant No. 2013CB036003), the China Postdoctoral Science Foundation Fund (Grant No. 2018M631114), and the Open Foundation of the State Key Laboratory (KF2020-07).

References

[1] Q. L. Cui, S. L. Shen, Y. S. Xu, H. N. Wu, and Z. Y. Yin, "Mitigation of geohazards during deep excavations in karst regions with caverns: a case study," *Engineering Geology*, vol. 11, pp. 194–204, 2015.

[2] Y. X. Lv, Y. J. Jiang, H. Wei, M. Cao, and Y. Mao, "A review of the effects of tunnel excavation on the hydrology, ecology, and environment in karst areas: current status, challenges, and perspectives," *Journal of Hydrology*, vol. 586, p. 124891, 2020.

[3] S. C. Li, Z. Q. Zhou, L. P. Li, Q. Q. Zhang, and S. S. Shi, "Risk assessment of water inrush in karst tunnels based on attribute synthetic evaluation system," *Tunnelling and Underground Space Technology incorporating Trenchless Technology Research*, vol. 38, pp. 50–58, 2013.

[4] P. Jeannin, A. Yves, and D. Malard, "Assessing karst-hydraulic hazards in tunneling—the Brunnmühle spring system—Bernese Jura, Switzerland," *Environmental Earth Sciences*, vol. 74, no. 12, pp. 7655–7670, 2015.

[5] Y. J. Zhao, F. G. Wang, C. S. Li, Y. Q. Cao, H. L. Tian, and L. Borrelli, "Study of the corrosion characteristics of tunnel fissures in a karst area in Southwest China," *Geofluids*, vol. 2018, 19 pages, 2018.

[6] Y. G. Xue, F. M. Kong, D. H. Qiu, M. X. Sun, and Y. Zhao, "The classifications of water and mud/rock inrush hazard: a review and update," *Bulletin of Engineering Geology and the Environment*, vol. 80, no. 3, pp. 1907–1925, 2021.

[7] X. X. Liu, S. L. Shen, Y. S. Xu, and Z. Y. Yin, "Analytical approach for time-dependent groundwater inflow into shield tunnel face in confined aquifer," *International Journal for Numerical and Analytical Methods in Geomechanics*, vol. 42, no. 4, pp. 655–673, 2018.

[8] M. Q. Zhang and S. W. Liu, "The analysis on the features of karst water burst in the Yuanliangshan tunnel," *Chinese Journal of Geotechnical Engineering*, vol. 27, no. 4, pp. 422–426, 2005.

[9] Y. Zhuo and G. Q. Sun, "Grouting construction technology of high pressure and rich water fault F11 in Qiyueshan tunnel," *Engineering Science*, vol. 11, no. 12, pp. 82–86, 2009.

[10] J. Q. Guo, G. Y. Wang, and L. W. Ren, "Geological features of karst and its development pattern of Yiwan railway," *The Chinese Journal of Geological Hazard and Control*, vol. 24, no. 2, pp. 72–78, 2013.

[11] Z. H. Xu, J. Wu, S. C. Li, B. Zhang, and X. Huang, "Semianalytical solution to determine minimum safety thickness of rock resisting water inrush from filling-type karst caves," *International Journal of Geomechanics*, vol. 18, no. 2, pp. 1–11, 2018.

[12] H. Fu, L. H. Zhao, T. H. Ling, and X. L. Yang, "Rock mass collapse mechanism of concealed karst cave beneath deep tunnel," *International Journal of Rock Mechanics and Mining Sciences*, vol. 91, pp. 133–138, 2017.

[13] J. Q. Guo, J. X. Chen, F. Chen, S. X. Huang, and H. Y. Wang, "Using the Schwarz alternating method to identify critical water-resistant thickness between tunnel and concealed cavity," *Advances in Civil Engineering*, vol. 2018, 15 pages, 2018.

[14] H. Xin, S. C. Li, Z. H. Xu, M. Guo, and X. S. Shi, "An attribute recognition model for safe thickness assessment between concealed karst cave and tunnel," *Journal of Central South University*, vol. 26, no. 4, pp. 955–969, 2019.

[15] Z. H. Yang, Y. X. Li, J. S. Xu, and H. B. Xiao, "Upper bound stability analysis for confining rocks considering the circular existence of filled karst cave around tunnels," *Journal of Hunan Univeristy (Natural Science)*, vol. 44, no. 5, pp. 122–131, 2017.

[16] L. Qin, L. Wei, J. X. Chen, Y. B. Luo, and P. Huang, "Stability analysis of water-resistant strata in karst tunnel based on releasable elastic strain energy," *Mathematical Problems in Engineering*, vol. 2017, 9 pages, 2017.

[17] R. L. Shan, X. N. Zhang, and M. Lu, "Numerical application of safe thickness between a tunnel and surrounding concealed caves," *Geotechnical and Geological Engineering*, vol. 36, no. 1, pp. 95–104, 2018.

[18] D. D. Pan, S. C. Li, Z. H. Xu, P. Lin, and X. Huang, "Experimental and numerical study of the water inrush mechanisms of underground tunnels due to the proximity of a water-filled karst cavern," *Bulletin of Engineering Geology and the Environment*, vol. 78, no. 8, pp. 6207–6219, 2019.

[19] L. P. Li, *Study on CatastroPhe Evolution Mechansim of Karst Water Inrush and Its Eengineering Application of High Risk Karst Tunnel*, [Ph.D. thesis], Shandong University, Jinan, 2009.

[20] D. X. Liang, Z. Q. Jiang, S. Y. Zhu, Q. Sun, and Z. W. Qian, "Experimental research on water inrush in tunnel construction," *Natural Hazards*, vol. 81, no. 1, pp. 467–480, 2016.

[21] W. M. Yang, Z. D. Fang, X. Yang, S. S. Shi, and J. Wang, "Experimental study of influence of karst aquifer on the law of water inrush in tunnels," *Water*, vol. 10, no. 9, pp. 1–24, 2018.

[22] D. D. Pan, S. C. Li, Z. H. Xu, L. P. Li, and W. Lu, "Model tests and numerical analysis for water inrush caused by karst caves filled with confined water in tunnels," *Chinese Journal of Geotechnical Engineering*, vol. 40, no. 5, pp. 828–836, 2018.

[23] F. Zhang, E. Dontsov, and M. Mack, "Fully coupled simulation of a hydraulic fracture interacting with natural fractures with a hybrid discrete-continuum method," *International Journal for Numerical and Analytical Methods in Geomechanics*, vol. 41, no. 13, pp. 1430–1452, 2017.

[24] F. S. Zhang, B. Damjanac, and S. Maxwell, "Investigating hydraulic fracturing complexity in naturally fractured rock masses using fully coupled multiscale numerical modeling," *Rock Mechanics and Rock Engineering*, vol. 52, no. 12, pp. 5137–5160, 2019.

[25] J. Q. Guo, *Study on Against-Inrush Thickness and Water Burst Mechanism of Karst Tunnel*, [Ph.D. thesis], Beijing Jiaotong University, Beijing, 2011.

[26] Z. Y. He, *Study on Progressive Failure and Safety Thickness of Water-Resistant Strata during Karst Tunnel Constructed by Drilling and Blasting Method*, M.S. Dissertation, Henna polytechnic university, Jiaozuo Henan, 2017.

[27] W. X. Zhu, *Study on Mechanism of Water Inrush in Muddy Limestone Karst Tunnel After Wetting and Drying Cycles*, [Ph.D. thesis]., China University of Mining and Technology, Beijing, 2018.

[28] Z. Huang, X. Z. Li, S. J. Li, K. Zhao, and R. Zhang, "Investigation of the hydraulic properties of deep fractured rocks around underground excavations using high-pressure injection tests," *Engineering Geology*, vol. 245, pp. 180–191, 2018.

[29] F. D. Zhang, B. J. Shen, and Y. H. Kang, "Water inrush failure mechanism of mining floor under unloading effect," *Rock and Soil Mechanics*, vol. 37, no. 2, pp. 431–438, 2016.

[30] J. Q. Guo and C. S. Qiao, "Study on water-inrush mechanism and safe thickness of rock wall of karst tunnel face," *Journal of the China Railway Society*, vol. 34, no. 3, pp. 105–111, 2012.

[31] J. Q. Jiang, "Research on mechanical behaviours and seismic stability of reinforced red-sandstone granular soil retaining wall," [Ph.D. thesis], Central South University, Changsha, 2010.

[32] Z. J. Zhang, J. B. Zhu, B. Wang, Z. J. Feng, and B. Lu, "The damage and shear dilation property evolution based on energy dissipation mechanism of gneissic granite," *Chinese Journal of Rock Mechanics and Engineering*, vol. 37, no. S1, pp. 3441–3448, 2018.

[33] S. S. Lin, S. L. Shen, A. Zhou, and Y. S. Xu, "Novel model for risk identification during karst excavation," *Reliability Engineering & System Safety*, vol. 209, pp. 107435–107448, 2021.

[34] N. Zhang, S. L. Shen, A. N. Zhou, and H. M. Lyu, "Challenges of earth-pressure-balance tunnelling in weathered granite with boulders," *Proceedings of the Institution of Civil Engineers-Geotechnical Engineering*, vol. 2020, pp. 1–37, 2020.

[35] E. Khalid, S. L. Shen, W. C. Cheng, and A. Arulrajah, "Cutter-disc consumption during earth pressure balance tunnelling in mixed strata," *Proceedings of the Institution of Civil Engineers-Geotechnical Engineering*, vol. 171, no. 4, pp. 363–376, 2018.

[36] K. Elbaz, S.-L. Shen, Y. Tan, and W.-C. Cheng, "Investigation into performance of deep excavation in sand covered karst: a case report," *Soils and Foundations, JGS*, vol. 58, no. 4, pp. 1042–1058, 2018.

Hindawi
Geofluids
Volume 2021, Article ID 6668644, 12 pages
https://doi.org/10.1155/2021/6668644

Research Article

Fracture Propagation and Hydraulic Properties of a Coal Floor Subjected to Thick-Seam Longwalling above a Highly Confined Aquifer

Shaodong Li,[1] **Gangwei Fan**,[1,2] **Dongsheng Zhang**,[3] **Shizhong Zhang**,[1] **Liang Chen**,[3] **Shang Ren**,[1] **and Yibo Fan**[1]

[1]*School of Mines, China University of Mining & Technology, No. 1 University Road, Xuzhou, Jiangsu 221116, China*
[2]*Key Laboratory of Deep Coal Resource Mining, China University of Mining & Technology, Ministry of Education, No. 1 University Road, Xuzhou, Jiangsu 221116, China*
[3]*State Key Laboratory of Coal Resources and Safe Mining, China University of Mining & Technology, No. 1 University Road, Xuzhou, Jiangsu 221116, China*

Correspondence should be addressed to Gangwei Fan; fangw@cumt.edu.cn

Received 7 December 2020; Accepted 13 June 2021; Published 3 July 2021

Academic Editor: Yong Liu

The high-pressure and water-rich confined aquifer occurring in the Ordovician limestone sequence poses great threats to the routine production of underground longwall mining. Considering the intense cooperation of mining disturbance and water pressure, water-conducting fractures within a coal seam floor can connect the lower aquifer and upper goaf, and this hydraulic behavior is considered the root of water inrush hazard and water loss or contamination. In this paper, the panel 4301 of the Longquan coal mine serves as the case where the panel works closely above the floor with high water pressure. By the combination of physical and numerical modelling approaches, the variation characteristics of fracture development and volumetric strain of floor rocks subjected to mining disturbance are analyzed. A numerical computation model is constructed based on the volumetric strain-permeability equation obtained by curve fitting, and on such basis, the impacts of different mining parameters on floor rock permeability are studied. The results show that the floor rocks experience fracture generation, extension, and convergence procedures as the workface advances along the longitudinal direction, and fractures appearing in front of the workface are more developed. In the whole process of coal seam extraction, the volumetric strain profile exhibits "Λ" shape and an inverted saddle shape before and after overburden strata collapse. By controlling a single variable, the paper reveals that panel height is of greater impact on floor permeability changes than panel length and panel width.

1. Introduction

Coal resource plays an important role in China's economic development, and the coal mines in North China contribute to 90% of the total output. The safety production of coal mines in such an extensive area attracts much attention [1, 2]. However, in the base floor of north coalfields, there exists the Ordovician karst aquifer, and because of its high pressure and water abundance, groundwater loss or contamination or even mine flooding catastrophe is likely to occur as long as mining-induced hydraulic channels bridge the immediate floor and the aquifer in Ordovician limestone. Long-term and large-scale coal resource exploitation triggers substantial fractures between the coal seam floor and confined aquifer. Such connective fractures can drastically affect groundwater equilibrium, and further, the loss of water resource would disturb the subsurface flow regime and give rise to irreversible ecological deterioration [3–5]. Currently, a great number of coal-producing enterprises are leaving traditional mode and transforming to green and water-conserved mining mode. In this context, the study on deformation, failure, and hydraulic property variation of a coal seam floor above a highly confined aquifer is of great significance for providing best water-conserved mining practice for North China.

In recent years, the failure mechanism of a longwall panel floor above a confined aquifer attracted great concerns [6–9]. For example, Liu et al. [10] conducted mathematical modelling to describe the failure of an inclined coal seam floor above confined water and calculated the failure depth after mining based on semi-infinite element theory. Lu and Wang [11] revealed that rock mass fracturing may experience three steps with the mined-out area enlarging, which included minor fracture initiation as the first step, fracture extension as the second, and fracture propagation through the whole rock mass as the third. By means of physical and numerical modelling methods, Hu et al. [12] studied the delay behavior of coal seam floor failure under the coupling effect of confined water and connective cracking regime. Liang et al. [13] analyzed coal seam floor failure under the impacts of mining-induced stress redistribution and uneven pressure caused by confined water; by establishing a two-dimensional hydraulic model and a key stratum stability model, the theoretical profile of failure and stable areas of an inclined floor was obtained. Such studies are mainly associated with the failure depth of a coal seam floor subjected to low water pressure or with the propagation profile of rock mass fractures. In fact, for the case where the longwall panel is just located closely above the highly confined aquifer in the paper, it is more challenging on account of larger water pressure, higher confined water-conducting zone, and greater risk of water inrush into the workface. So considering the safety of longwall panels exposed to such extreme circumstances, it is important to understand the mechanism of coal seam floor deformation and failure.

At present, many scholars have obtained various strain-permeability curves by means of experiments [14–18]. However, such studies were mainly based on small-scale rock samples, and for those cases where mining operations work above a highly confined aquifer, the whole panel floor shall be considered together. In this context, mining parameters are critical factors contributing to floor permeability enhancement. In fact, research achievements in this field are limited, and most of them are associated with the overburden rather than floor rocks [19–21]. For example, Khanal et al. [22] studied how different geometries of the longwall panel affect the permeability of overburden strata by means of numerical modelling and obtained the corresponding variation law of permeability. It is inappropriate to directly apply such laws like this kind to the coal seam floor. Therefore, the study of mining parameters affecting floor permeability in the case of a highly confined aquifer is necessary for the in situ preservation of deep-seated confined water.

From the perspective of water-conserved mining, the paper takes panel 4301 of the Longquan coal mine as the geological background. At first, panel floor fracturing and permeability variation with workface advancing are studied using physical modelling. A function between the volumetric strain and permeability of floor rocks is obtained by curve fitting, which is considered suitable to such geological conditions of the Longquan coal mine. Then, a numerical modelling approach is employed to evaluate the impact of panel height, panel width, and plane length on floor permeability. Such works can be taken as reference for profiling the permeability variation of a coal seam floor above a highly confined aquifer.

2. Geological Overview

There is no limestone outcrop in the Longquan coalfield. Due to the existence of thick overlying strata and no lateral recharge from atmospheric precipitation and surface runoffs, the water entering karst rock groups is derived from the infiltration of atmospheric precipitation through the northwestern, western, and southwestern carbonate outcrops, with some other derived from the leaking recharge across the major dislocation. As a result, the water flow path is of a significant distance extending from the south and northwest to southeast. At the same time, there is no natural discharge path in such an area, but only artificial water supply wells that can be considered discharge points. As a whole, Ordovician limestone water flowing from the west to east and reaching panel 4301 is the only exhalent region in the paper. The floor of the no. 4 coal seam in the Longquan coal mine bears Ordovician limestone water inrush coefficient of 0.036~0.097 MPa/m. The coalfield can be divided into 7 areas, as shown in Figure 1. According to the critical value of water inrush coefficient of 0.06 MPa/m, it can be seen from Figure 1(a) that there are water inrush risks in the northeast area and panel 4301 of the mine. Panel 4301 is 720 m in length and 250 m in width, using a top coal caving method to extract the coal seam with height 6.47 m. The elevation of the panel ranges from +525.2 m to +630.5 m. Affected by the confined limestone water in Taiyuan and Ordovician formations, the panel floor suffers high water pressure that is 4.97~6.29 MPa in the natural state. The lithological sequence of panel 4301 is exhibited in Figure 1(b).

3. Deformation and Failure Characteristics

3.1. Physical Modelling. In order to understand the stress condition and failure rule of the coal seam floor subjected to mining disturbance and high water pressure as well as the caving and movement behavior of overburden strata, the physical modelling method is employed here to emulate the phased excavation process. For constructing the physical model, various parameters of each stratigraphic unit are calculated via similarity theory. Then, a self-developed high-pressure water simulator is adopted.

According to the fundamental principles of similarity theory, the ratio of similitude is 100 : 1 in geometry, 10 : 1 in time, 1.7 : 1 in volume-weight, and 170 : 1 in both elastic modulus and strength. Such a physical model is mainly composed of sand, lime, gypsum, and pure water. The detailed contents and proportions of each ingredient are listed in Table 1.

Based on the experimental platform, a plane physical model with 2500 mm, 2200 mm, and 30 mm in length, height, and thickness, respectively, is established. This model emulates the 226 m thick lithological sequence, and the above

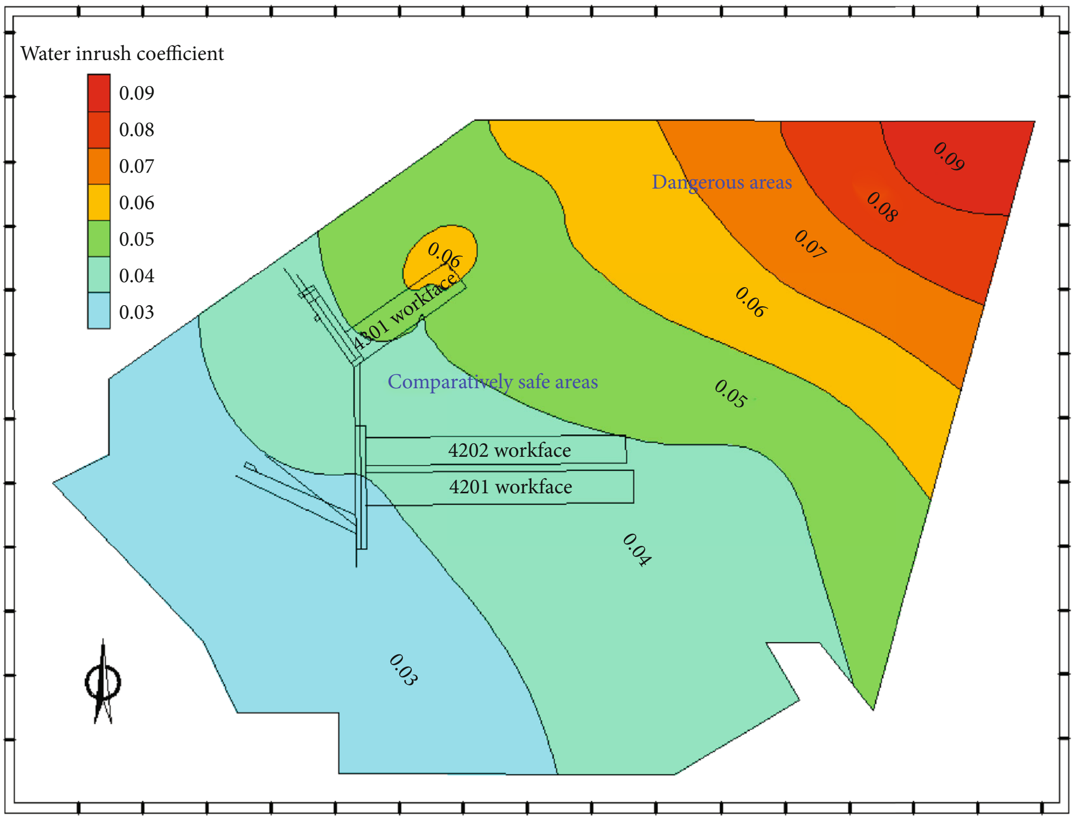

(a)

Columnar	NO.	Lithology	Thickness (m)	Hydrogeological feature	Interlayer spacing (m)	Geological time
		Loess and river stone	23.93	Loose aquifer		Quaternary
		Sandstone, sandy mudstone	423.64	Aquifuge		Permian
	K_5	Fine sandstone	2.5	Weak aquifer		
		Sandstone, sandy mudstone	52.12	Aquifuge	55.65	
	K_4	Siltstone	3.53	Weak aquifer		
	4#	Coal	6.25			Carboniferous
		Sandstone, sandy mudstone	23.18	Aquifuge	53.72; 120.54~156.19	
	K_3	Coarse sandstone	14.24	Weak aquifer		
	L_3	Limestone	1.23	Weak aquifer		
		Fine sandstone, coarse sandstone	15.07	Aquifuge		
	7#	Coal	1.0			
		Mudstone, medium sandstone	10.53	Aquifuge	24.91	
	L_2	Limestone	5.95	Weak aquifer		
		Mudstone	7.93	Aquifuge		
	L_1	Limestone	0.5	Weak aquifer		
	9#	Coal	13.71			
		Mudstone, sandstone	19.59	Aquifuge	27.20~62.85	
	K_1	Fine sandstone	4.06	Weak aquifer		
	C_2b	Limestone	2.44	Weak aquifer		Ordovician
		Mudstone, clay rock	1.11~36.76	Aquifuge		
	O_2f^2	Limestone	65.0~105.0	Weak-medium aquifer		
	O_2f^1	Gypsum unit	15.0~25.0	Aquiclude		
	O_2m	Limestone	150.0	Medium-strong aquifer		

(b)

Figure 1: Geological data of the Longquan coal mine: (a) contour map of Ordovician limestone water inrush coefficient of the no. 4 coal seam in the Longquan coal field; (b) lithological sequence of the 4301 panel.

Table 1: Parameters and material ratio of the physical model.

No.	Lithology	Thickness (m)	Strength (MPa) Uniaxial compression	Uniaxial tension	Simulated thickness (cm)	Quality (kg) Sand	Lime	Gypsum
1	Sandy mudstone	16	18.3	0.9	16	168	27.2	28.8
2	Siltstone	21	29.4	1.6	21	214.2	23.1	37.1
3	Mudstone	3	16.2	0.7	3	33.6	2.4	5.4
4	Sandy mudstone	9	18.3	0.9	9	94.5	15.3	16.2
5	Fine sandstone	3	37.6	2.1	3	34.5	4.5	4.5
6	Sandy mudstone	12	18.3	0.9	12	126	20.4	21.6
7	Mudstone	2	16.2	0.7	2	22.4	1.6	3.6
8	Sandy mudstone	16	18.3	0.9	16	168	27.2	28.8
9	Siltstone	3	29.4	1.6	3	30.6	3.3	5.3
10	Mudstone	4	16.2	0.7	4	44.8	3.2	7.2
11	Sandy mudstone	4	18.3	0.9	4	42	6.8	7.2
12	Carbonaceous mudstone	2	24.8	1.2	2	22.4	3.2	6.3
13	Aluminum-containing mudstone	5	26.9	1.4	5	54.5	3.2	6.2
14	Sandy mudstone	7	18.3	0.9	7	73.2	11.9	12.6
15	Siltstone	4	29.4	1.6	4	44.2	4.4	7.1
16	4# coal	6	10	0.6	6	61.8	10.8	11.3
17	Fine sandstone	6	37.6	2.1	6	69	9	9
18	Sandy mudstone	12	18.3	0.9	12	126	20.4	21.6
19	Fine sandstone	5	37.6	2.1	5	57.5	7.5	7.5
20	Coarse sandstone	14	47.8	3.5	14	144.6	30.8	31.2
21	L3 limestone	1	38.3	2.9	1	9.6	1.8	1.7
22	Fine sandstone	10	37.6	2.1	10	115	15	15
23	Siltstone	5	29.4	1.6	5	55.6	5.5	21.2
24	Medium sandstone	5	42.6	3.2	5	53.4	11	12.1
25	Mudstone	6	16.2	0.7	6	67.2	4.8	10.8
26	L2 limestone	6	38.3	2.9	6	57.6	10.8	10.5
27	Mudstone	8	16.2	0.7	8	89.6	6.4	14.4
28	L1 limestone	1	38.3	2.9	1	9.6	1.8	1.7
29	9# coal	14	10	0.6	14	144.2	25.2	26.4
30	Mudstone	7	16.2	0.7	7	78.4	5.6	12.6
31	Siltstone	9	29.4	1.6	9	93.4	9.9	21.2
32	Limestone	2	38.3	2.9	2	19.2	3.6	3.5
33	Fine sandstone	4	37.6	2.1	4	46	6	6
34	Limestone	3	38.3	2.9	3	28.8	5.4	5.3

375 m thick strata to the earth's surface are not modelled but simulated by 148 kN stress using a gravity loading device, as shown in Figure 2. Therefore, in accordance with the vertical geostress gradient, a simulated gravitational force being 148 kN is adopted. The actual workface advances at the speed of 6 m/d, and according to similarity theory regarding geometry and time, the extraction height in the physical model is 6 cm, and each excavation at the 6 cm spacing interval is executed per 2.4 h. On the other hand, a 30 cm long coal seam is reserved on both sides to eliminate negative consequences induced by boundary effects. The physical model configuration is shown in Figure 2. Also, a set of self-developed spring installations are arranged along the panel floor to emulate the high pressure supported by confined water. Each unit of the spring group comprises two iron plates connected through two springs, and both plates are 30 cm, 10 cm, and 1 cm in length, width, and thickness, respectively. According to Hooke's law and similarity theory, the stress onto the coal seam floor provided by the spring group shall reach 6 MPa prior to model construction.

3.2. Floor Fracture Development. The panel floor undergoes complicated loading and unloading processes due to mining operations. After accumulating and releasing energies, rock mass cracks and various fractures with different dimensions initiate. Such minor secondary fractures would extend and

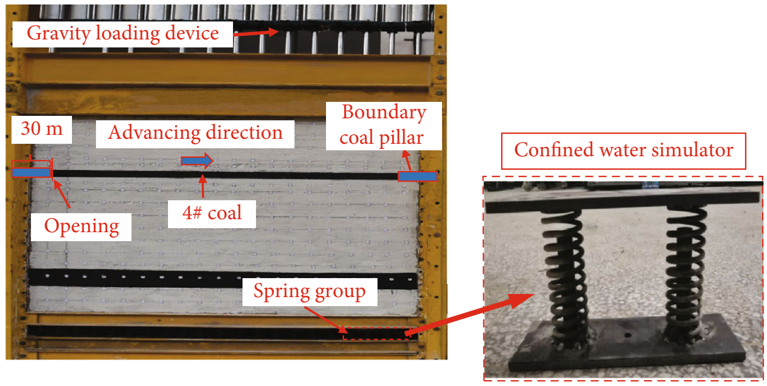

Figure 2: Configuration and components of the physical model.

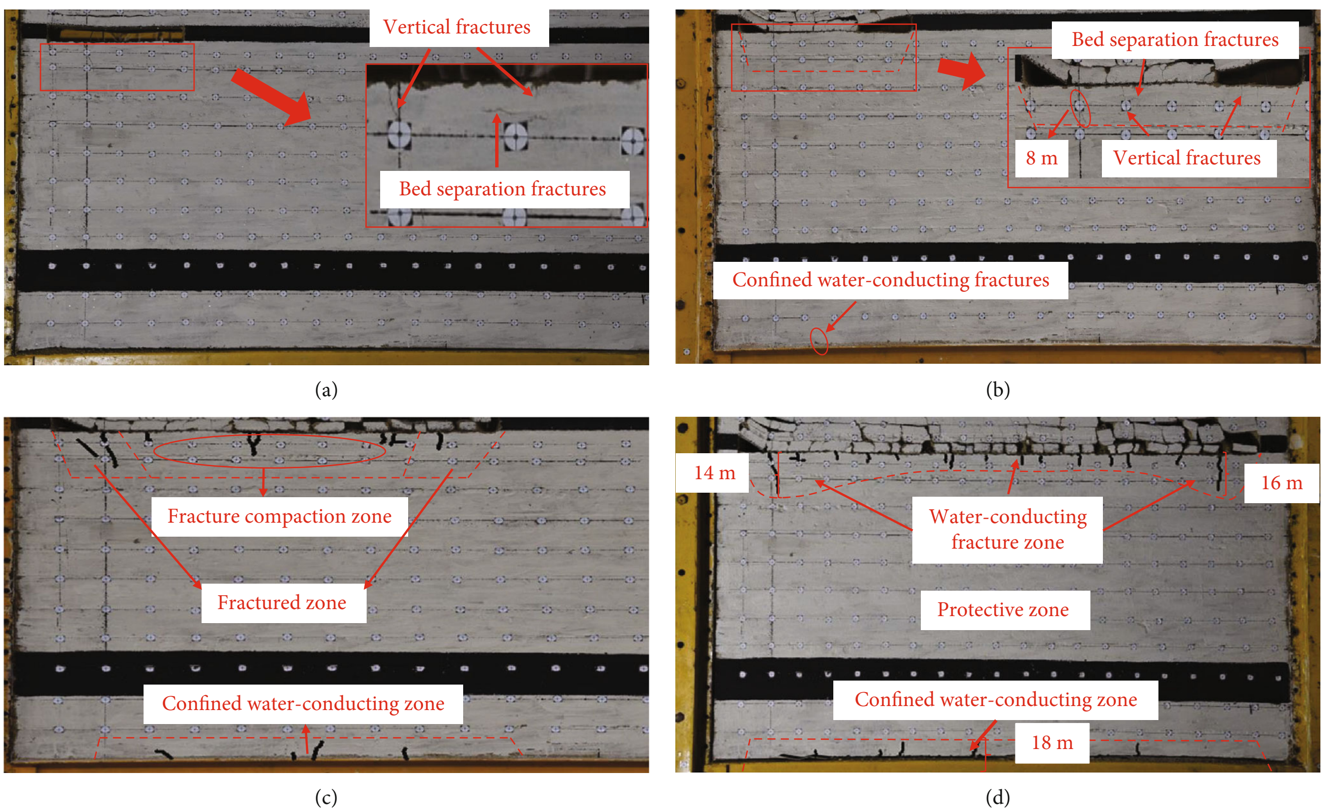

Figure 3: Floor fracturing profile with workface advancing: (a) workface advances 36 m; (b) workface advances 66 m; (c) workface advances 102 m; (d) workface advances 186 m.

expand when subjected to mining disturbance and then tend to converge after overburden collapses. It can be seen from Figure 3(a) that, as the workface advances 36 m, small-scale bedding plane separation comes into being, and in the meantime, such a separation extends 5 m along the longitudinal direction with vertical fractures thereof reaching 0.1 m in openness. In the middle of the mined-out area, there are two minor vertical fractures, while the immediate roof is still stable and floor fracture is developing with depth reaching 6 m. As the workface further progresses, roof failure occurs and the fractures forming in the floor area gradually shrink because of the gravity of collapsed overburden strata, as shown in Figure 3(b).

When the fractures at the middle of the void tend to converge, novel fractures initiate in front of the workface and vertical fractures nearby the setup room, go deep, and extend 8 m approximately. Above the confined water area, there are also a number of minor fractures propagating upward with the workface advancing. When the 102 m long coal seam is excavated, as shown in Figure 3(c), floor fracture achieves its maximum depth, 14.8 m, and some at the middle of the void are compacted. Figure 3(d) shows that the floor area

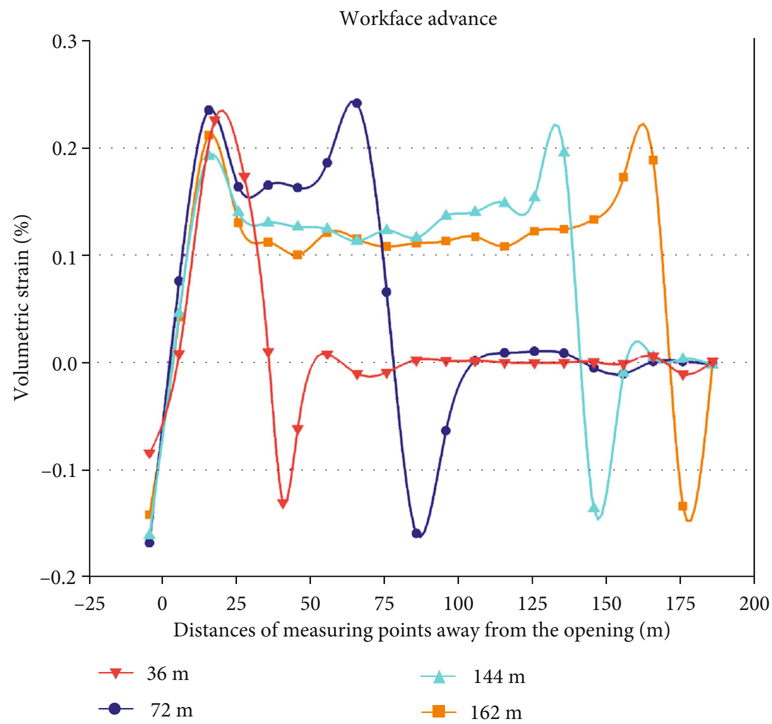

FIGURE 4: Volumetric strain curves of strata 5 m below the panel floor while mining progresses.

TABLE 2: Choice of volumetric strain-permeability curves.

Name of paper	Lithology	Geological time	Sampling location	Other characteristics
Fan et al. [19]	Sandstone	Quaternary	Yili, Xinjiang	Weakly cemented
Yu et al. [28]	Red sandstone	Quaternary	Ganzhou, Jiangxi	Ordinary
Xia et al. [29]	Sandstone	Carboniferous	Taiyuan, Shanxi	Ordinary

Notes: the floor of the studied coal seam is mainly composed of ordinary Carboniferous sandstone, and this coal mine is located in Taiyuan, Shanxi Province.

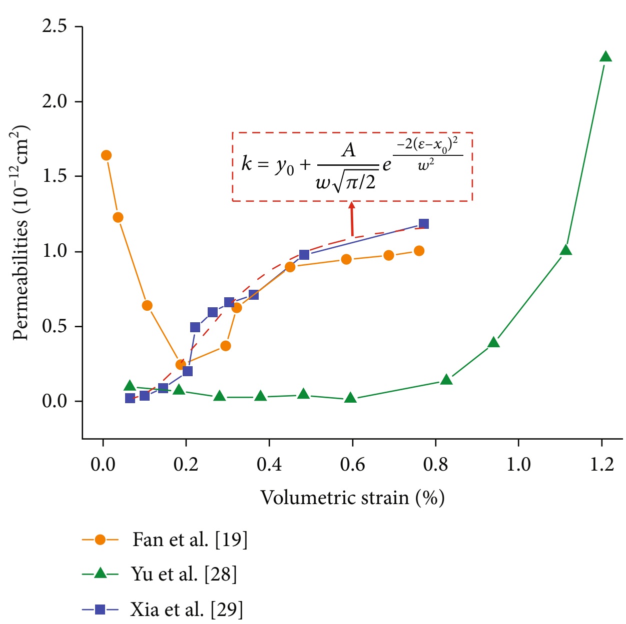

FIGURE 5: Curves of volumetric strain vs. permeability obtained by different scholars.

can be divided into three zones from the immediate floor down, including fractured zone, intact water-resisting zone, and confined water-conducting zone. In detail, the fractured zone is like an inverted saddle, reaching its maximum depth in the area below the lateral ribs. Mining-induced fractures in front of the workface are of the greatest developing degree and reach the greatest depth, 16 m in the vertical direction. In addition, the thickness of the confined water-conducting zone is about 18 m.

3.3. Floor Deformation. The study on bulking deformation can be achieved on the basis of surfaces rather than lines by virtue of an approach, namely, "four-point surrounded area." The bulking deformation ratio determined in this manner shall have more value in application [23]. So, according to the formula of "four-point surrounded area" approach, the volumetric strain of the floor is calculated regardless of the impacts of physical model thickness on volumetric strain in the simulated mining process.

$$\varepsilon = \frac{S' - S}{S}, \quad (1)$$

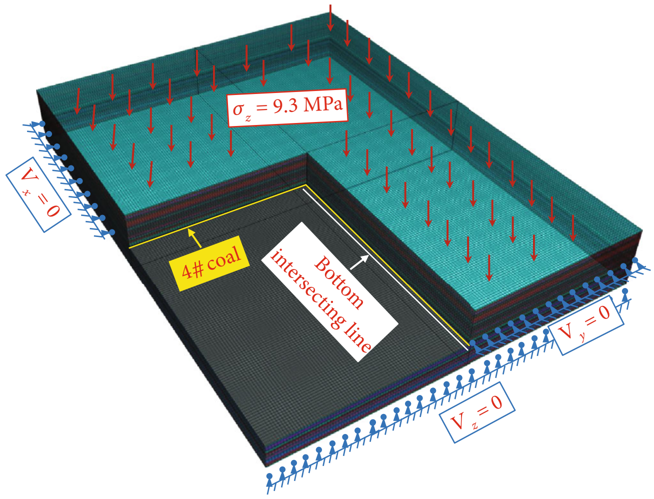

FIGURE 6: Configuration of the 3D numerical model.

where ε is the volumetric strain of rock mass; S the area of the coal seam floor before mining, a constant value; and S' is the area of the coal seam floor after mining.

As mining operation progresses, floor rocks in different depths see similar variation law in terms of the volumetric strain. Therefore, the layer that is 5 m below the 4# coal seam floor is selected and its volumetric strain is analyzed in detail. Relevant data are listed in Figure 4.

When the workface advances 36 m, the rock mass 10 m behind the opening is compressed because of abutment pressure effect and shows volumetric strain decline, -0.00085 in minimum. Similar impacts can also be demonstrated by floor rocks within 11 m range in front of the workface, where the frontal abutment pressure makes such rocks compressively deformed and volumetric strain reduced to -0.00131. At the present time, roof strata have not collapsed and floor strata below the mined-out area are being in a stress unloading state. Considering the tension effect, volumetric strain of the rock mass increases and peaks at 0.00226. It can be seen that the bulking deformation ratio profile of the panel floor is "Λ" shaped. Then, the maximum volumetric strain reaches 0.00241 and the minimum reaches -0.00168 as the workface advances 72 m, where floor rocks in the middle of the mined panel experience slight decrease in volumetric strain due to the gradual compaction of collapsed media. When the 144 m long coal seam is excavated, the maximum volumetric strain changes to 0.0192, with the minimum to -0.00149. The bulking deformation ratio profile shows that its peak value nearby the setup room is lower than that nearby the frontal rib, because the compaction degree of collapsed overburden is higher in the setup room area. Such recompaction of fallen rocks on the panel floor reaches equilibrium, and volumetric strain of floor rocks in the middle of the panel void becomes stable when the workface advances 162 m. Here, the maximum volumetric strain is still distributed in the panel void 7~9 m behind the frontal rib, with the value peaking at 0.00236. In contrast, volumetric strain of the coal seam floor 8~10 m in front of the workface reaches the lowest, -0.00134, and the bulking deformation profile extends like an inverted saddle.

4. Impacts of Mining Parameters on Floor Rock Permeability

Through the above analysis of floor deformation characteristics in a physically simulated coal mining process, the reason that deformation and failure trigger groundwater loss can be rooted from the changes in floor rock permeability. In fact, the more developed the fractures, the higher the volumetric strain and permeability. In order to investigate the impact degree of different mining parameters on floor rock permeability, three geometric factors regarding panel height, length, and width are selected in the context of the 4# coal seam of the Longquan coal mine. Such investigation results are of significant value in supporting theoretical references to the panel geometry setting under the condition of water-conserved mining.

4.1. Volumetric Strain-Permeability Curve Fitting. In order to characterize the change of permeability under hydraulic coupling, different scholars have established many theoretical models based on the assumption of small elastic deformation [24–27]. However, in order to study the permeability evolution of the mining floor, some scholars will use the volume strain permeability relationship to study [28, 29]. Fan et al. conducted an experimental study on the permeability of weakly cemented sandstone and obtained the relationship between volumetric strain and permeability of weakly cemented rocks [19]. Similarly, Yu et al. [30] studied the permeability property of rock samples along different stress paths and obtained a curve of sandstone. Other curves for Carboniferous rocks drilled from North China were also obtained by Xia et al. [31] by means of servo permeability tests. The lithological characteristics of different rock samples and their corresponding volumetric strain-permeability curves are shown in Table 2 and Figure 5, respectively.

As mentioned in Table 2, the floor of the 4# coal seam in the Longquan coal mine is mainly composed by sandstone and it can be seen that the sampling location and geological time of studied floor rocks in this paper have a good

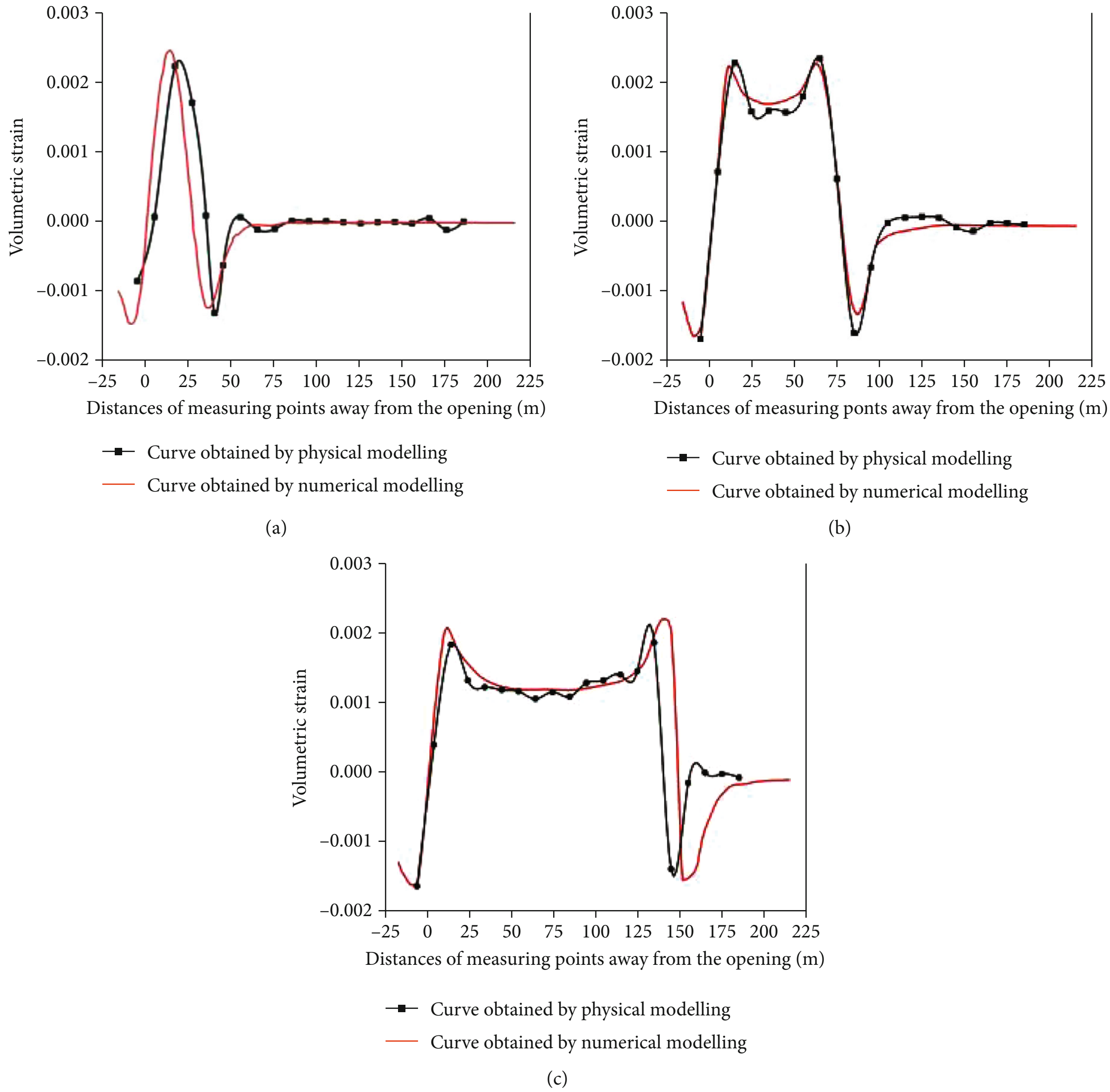

FIGURE 7: Comparison of volumetric strain obtained by physical modelling and numerical modelling in different advancing distances: (a) workface advances 36 m; (b) workface advances 72 m; (c) workface advances 144 m.

agreement with those in the paper [29]. Therefore, the curve of sandstone volumetric strain and permeability obtained by Xia et al. is fitted by virtue of Gaussian function, which gives the results as

$$k = y_0 + \frac{A}{w\sqrt{\pi/2}} e^{-2(\varepsilon - x_0)^2/w^2}, \tag{2}$$

where k is the permeability and ε is the volumetric strain, and for other constant parameters, there are $y_0 = 2.53944 \times 10^{-12}$, $A = -4.3916 \times 10^{-13}$, $w = 0.13984$, and $x_0 = -0.04739$.

4.2. Numerical Modelling. The 3D numerical model established via the FLAC3D software is shown in Figure 6 [32]. The model is 2000 m, 1500 m, and 252 m in length, width, and height, respectively. The top surface bears a vertical stress of 9.3 MPa, and the bottom bears a water pressure of 6 MPa. In addition, the displacement of the bottom and four laterals are fixed; this numerical model shares the same stratigraphic sequence with the above constructed physical

TABLE 3: Schemes of numerical simulation.

Scheme	Panel height (m)	Panel width (m)	Panel length (m)
1	4	250	800
2	6	250	800
3	8	250	800
4	4	500	800
5	4	750	800
6	4	250	1000
7	4	250	1200

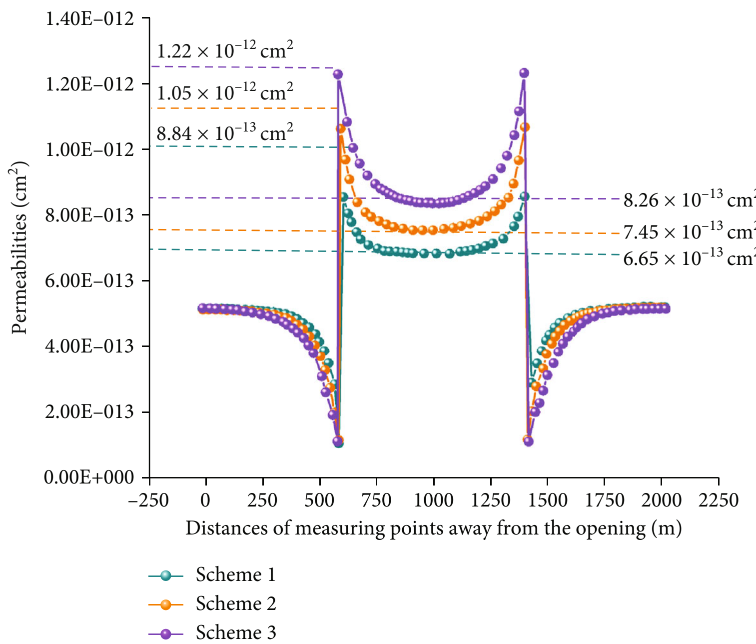

Figure 8: Curve of floor permeability in response to different panel heights.

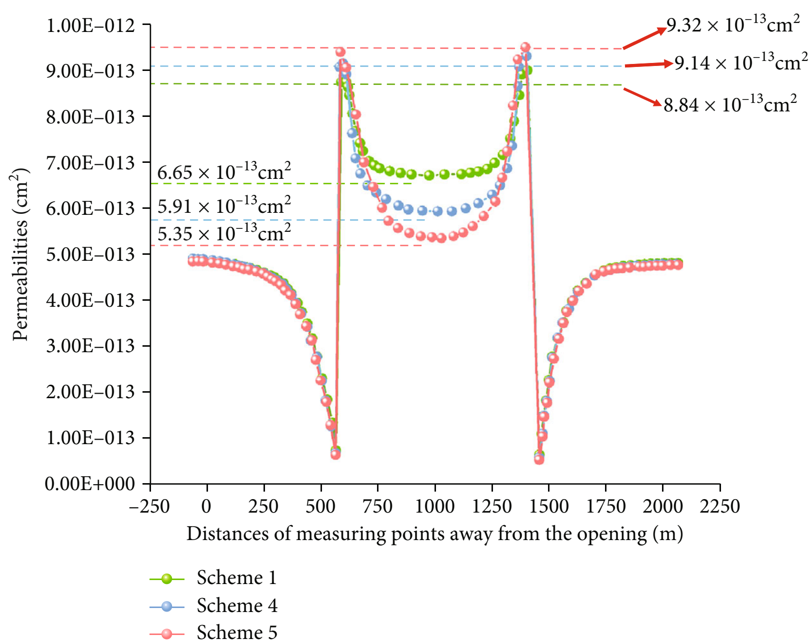

Figure 9: Curve of floor permeability in response to different panel widths.

model. A monitoring line is placed 5 m below the coal seam—rock floor interface to collect the volumetric strain variation of floor rocks. The purpose of this operation is to verify the appropriateness and rationality of the numerical model by a volumetric strain indicator. The curve describing the volumetric strain variation with coal seam excavation is shown in Figure 7.

The volumetric strain obtained by numerical modelling-based computation in three excavation periods is compared with that by physical modelling. The results show that the maximum volumetric strain reaches 0.00241 when the panel works 36 m, with the minimum reaching -0.00155. In the case of 72 m, the volumetric strain of the floor in the middle of the panel void decreases, while that in the rib area is the highest, reaching 0.00231, and that below both lateral coal bodies is the lowest, reaching -0.00164. As the workface advances 144 m, the maximum and minimum volumetric strains are 0.0229 and -0.00166, respectively. In general, the greatest difference ratio of the numerical model to the physical model only accounts for 6.6%, and both curves share a similar evolution trend, suggesting a good agreement between both models.

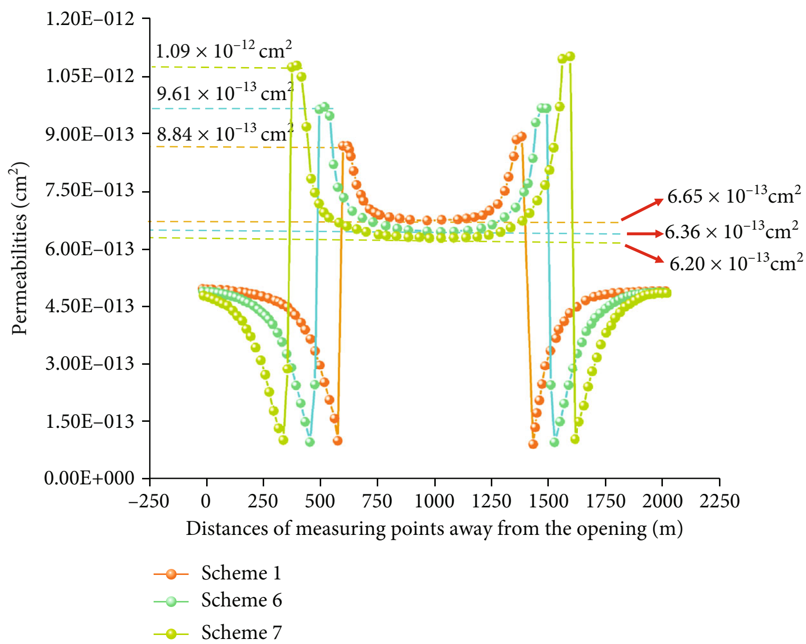

Figure 10: Curve of floor permeability in response to different panel lengths.

Formula (2) is input into the FLAC3D software to study the impacts of panel height, width, and length on floor permeability. According to the geological conditions of the 4# coal seam, panel height is considered 4 m, 6 m, and 8 m, respectively, with panel width 250 m, 500 m, and 750 m and panel length 800 m, 1000 m, and 1200 m. There are totally 7 simulation schemes in line with the approach, namely, single variable control. Such designed schemes can be compared with each other to analyze the impacts of different panel geometries on floor permeability. So a measuring line is arranged 5 m below the coal seam floor to obtain the permeability of the rock blocks with the centroid located along this line. The maximum value amongst calculated permeability is taken to participate in the subsequent comparison. Simulation schemes are listed in Table 3.

4.3. Simulation Result Analysis. Figure 8 shows that, when the two horizontal geometries (panel length and width) are considered fixed, the maximum permeability of floor rocks reaches 8.84×10^{-13} cm^2 in the case of 4 m panel height, while this value increases to 1.06×10^{-12} cm^2 in 6 m panel height and then to 1.22×10^{-12} cm^2 in 8 m panel height. It can be seen that there is a positive correlation between the maximum permeability of floor rocks and panel height. In fact, the minimum permeability also sees the same variation law due to the results that it reduces from 6.65×10^{-13} cm^2 to 7.45×10^{-13} cm^2 and to 8.26×10^{-13} cm^2 with panel height increasing from 4 m and 6 m to 8 m. It is speculated that for the same horizontal geometries, greater panel height gives rise to stronger depressurization effect on floor rocks. The compaction degree of collapsed overburden onto the panel floor becomes lower, and the permeability goes higher as a consequence.

The other scenario is shown in Figure 9, in which panel width changes along a gradient, but other geometries including panel height and length are fixed. The results show that the maximum permeability of floor rocks goes higher as panel width enlarges: 8.84×10^{-13} cm^2 in 250 m panel width, 9.14×10^{-13} cm^2 in 500 m panel width, and 9.32×10^{-13} cm^2 in 750 m panel width. However, its impact on permeability changes is weaker than the above analyzed factor, panel height. There is a totally different phenomenon in terms of the minimum permeability that decreases from 6.65×10^{-13} cm^2 in 250 m panel width to 5.91×10^{-13} cm^2 in 500 m panel width and then to 5.35×10^{-13} cm^2 in 750 m panel width. The reason behind it accords with the impact of panel length on floor permeability.

The last scenario is shown in Figure 10; when the two geometries regarding panel height and width are fixed, the maximum permeability of floor rocks reaches 8.84×10^{-13} cm^2 in the case of 800 m panel length. This value increases to 9.61×10^{-13} cm^2 in 1000 m panel length and then to 1.09×10^{-12} cm^2 in 1200 m panel length. In general, the impact of such a geometric factor is still weaker than that of panel height. The minimum permeability of the compressed area below the panel void demonstrates a different trend, with the value reducing from 6.20×10^{-13} cm^2 to 6.36×10^{-13} cm^2 and to 6.65×10^{-13} cm^2. The phenomenon that the minimum permeability of floor rocks decreases with the increase in panel length can be attributed to the wider scope for collapsed overburden, which makes the compaction onto the panel floor stronger, and the minimum value of floor permeability is resultantly lower.

In general, the three geometric factors including panel height, length, and width affect floor permeability to different extents. Comparison results show that the impact degree of panel height is the highest, followed by panel length and width.

5. Conclusion

Based on the case regarding panel 4301of the Longquan coal mine, the paper establishes a physical model for capturing panel floor failure characteristics. Floor fractures experience three stages including initiation, propagation, and convergence with the workface progressing. Two ribs witness the strongest fracturing behavior, where the fractures extend to the depth of 16 m. The fractures developing at the middle of goaf gradually converge due to caved rock reconsolidation. The fractured zone presents an inverted saddle shape in the floor area.

With coal seam excavation, the volumetric strain of floor rocks experiences a decrease-increase-decrease sequence. Before roof caving, the floor rocks below the middle of goaf have the maximum volumetric strain; after roof caving, two areas at an 8-10 m distance from two ribs exhibit the maximum volumetric strain. The volumetric strain profile changes from Λ shape to an inverted saddle shape.

Deformation and failure characteristics of floor rocks show that the more developed the floor fractures, the higher the floor permeability. The paper investigates the impact of panel height, panel length, and panel width on floor permeability by a fitted volumetric strain-permeability equation. The numerical modelling results indicate that the impact degree of panel height ranks first, followed by panel length and panel width.

Data Availability

The data of this manuscript is tested in the laboratory of State Key Laboratory of Coal Resources and Safe Mining, China University of Mining and Technology, which is available to authorized users.

Conflicts of Interest

The authors declare that they have no conflicts of interest.

Acknowledgments

The authors are grateful to the Longquan coal mine in Shanxi for the support. This work was financially supported by the National Natural Science Foundation (grant number 51774268), the Key Research and Development Project of Shanxi Province (grant number 20201101009), the Assistance Program for Future Outstanding Talents of China University of Mining and Technology (grant number 2020WLJCRCZL96), and the Postgraduate Research & Practice Innovation Program of Jiangsu Province.

References

[1] Q. Wu, B. X. Hu, L. Wan, and C. M. Zheng, “Coal mine water management: optimization models and field application in North China,” *Hydrological Sciences Journal*, vol. 55, no. 4, pp. 609–623, 2010.

[2] J. H. He, W. P. Li, and W. Qiao, “P-H-q evaluation system for risk assessment of water inrush in underground mining in North China coal field, based on rock-breaking theory and water-pressure transmission theory,” *Geomatics, Natural Hazards and Risk*, vol. 9, no. 1, pp. 524–543, 2018.

[3] M. R. Hasan, H. Rashid, and A. K. Paul, “Environmental impact of coal mining: a case study on Barapukuria coal mining industry, Dinajpur, Bangladesh,” *Journal of Environmental Science and Natural Resources*, vol. 6, no. 2, pp. 207–212, 2015.

[4] J. S. Caine, J. Evans, and C. B. Forster, “Fault zone architecture and permeability structure,” *Geology*, vol. 24, no. 11, pp. 1025–1028, 1996.

[5] D. L. Dong, W. J. Sun, and S. Xi, “Water-inrush assessment using a GIS-based Bayesian network for the 12-2 coal seam of the Kailuan Donghuantuo coal mine in China,” *Mine Water and the Environment*, vol. 31, no. 2, pp. 138–146, 2012.

[6] B. L. Zhang and Z. B. Meng, “Experimental study on floor failure of coal mining above confined water,” *Arabian Journal of Geosciences*, vol. 12, no. 4, p. 114, 2019.

[7] L. M. Yin, K. Ma, J. T. Chen, Y. C. Xue, Z. Q. Wang, and B. Q. Cui, “Mechanical model on water inrush assessment related to deep mining above multiple aquifers,” *Mine Water and the Environment*, vol. 38, no. 4, pp. 827–836, 2019.

[8] S. Aghababaei, G. Saeedi, and H. Jalalifar, “Risk analysis and prediction of floor failure mechanisms at longwall face in Parvadeh-I coal mine using rock engineering system (RES),” *Rock Mechanics and Rock Engineering*, vol. 49, no. 5, pp. 1889–1901, 2016.

[9] H. F. Lu, X. Y. Liang, N. Shan, and Y.-K. Zhang, “Study on the stability of the coal seam floor above a confined aquifer using the structural system reliability method,” *Geofluids*, vol. 2018, Article ID 9580271, 15 pages, 2018.

[10] W. T. Liu, D. R. Mu, X. X. Xie, L. Yang, and D. W. Wang, “Sensitivity analysis of the main factors controlling floor failure depth and a risk evaluation of floor water inrush for an inclined coal seam,” *Mine Water and the Environment*, vol. 37, no. 3, pp. 636–648, 2018.

[11] Y. L. Lu and L. G. Wang, “Numerical modeling of mining-induced fracturing and flow evolution in coal seam floor based on micro-crack growth,” *Journal of Mining & Safety Engineering*, vol. 32, pp. 889–897, 2015.

[12] Y. B. Hu, W. P. Li, Q. Q. Wang, S. L. Liu, and Z. K. Wang, “Evolution of floor water inrush from a structural fractured zone with confined water,” *Mine Water and the Environment*, vol. 38, no. 2, pp. 252–260, 2019.

[13] Z. Z. Liang, W. C. Song, and W. T. Liu, “Theoretical models for simulating the failure range and stability of inclined floor strata induced by mining and hydraulic pressure,” *International Journal of Rock Mechanics and Mining Sciences*, vol. 132, p. 104382, 2020.

[14] G. Fan, M. Chen, D. Zhang et al., “Experimental study on the permeability of weakly cemented rock under different stress states in triaxial compression tests,” *Geofluids*, vol. 2018, Article ID 9035654, 9 pages, 2018.

[15] J. Heiland, “Permeability of triaxially compressed sandstone: influence of deformation and strain-rate on permeability,” *Pure and Applied Geophysics*, vol. 160, no. 5-6, pp. 889–908, 2003.

[16] S. Harpalani and G. L. Chen, “Influence of gas production induced volumetric strain on permeability of coal,” *Geotechnical & Geological Engineering*, vol. 15, no. 4, pp. 303–325, 1997.

[17] S. A. Mathias, S. Nielsen, and R. L. Ward, “Storage coefficients and permeability functions for coal-bed methane production under uniaxial strain conditions,” *Transport in Porous Media*, vol. 130, no. 2, pp. 627–636, 2019.

[18] M. Hamoud, R. Chalaturnyk, and J. Leung, "Experimental studies of shear-induced changes in two-phase relative permeability," *Arabian Journal of Geosciences*, vol. 13, no. 14, p. 686, 2020.

[19] G. W. Fan, S. Z. Zhang, B. B. Cao, D. S. Zhang, and C. G. Zhang, "Impact of mine panel size on hydraulic permeability of weakly cemented strata," *Sustainability*, vol. 12, no. 6, p. 2396, 2020.

[20] T. R. C. Aston, R. N. Singh, and B. N. Whittaker, "The effect of test cavity geology on the in situ permeability of coal measures strata associated with longwall mining," *International Journal of Mine Water*, vol. 2, no. 4, pp. 19–34, 1983.

[21] D. P. Adhikary and H. Guo, "Modelling of longwall mining-induced strata permeability change," *Rock Mechanics and Rock Engineering*, vol. 48, no. 1, pp. 345–359, 2015.

[22] M. Khanal, H. Guo, and D. Adhikary, "3D numerical study of underground coal mining induced strata deformation and subsequent permeability change," *Geotechnical and Geological Engineering*, vol. 37, no. 1, pp. 235–249, 2019.

[23] A. P. He, H. Fu, Y. B. Lu, and B. J. Huo, "Analysis method on swelling deformation of protected seam in the process of protective coal seam exploitation," *Journal of Safety Science and Technology*, vol. 12, no. 8, pp. 60–67, 2016.

[24] Y. Xue, T. Teng, F. N. Dang, Z. Y. Ma, S. H. Wang, and H. B. Xue, "Productivity analysis of fractured wells in reservoir of hydrogen and carbon based on dual-porosity medium model," *International Journal of Hydrogen Energy*, vol. 45, no. 39, pp. 20240–20249, 2020.

[25] J. Liu, X. Liang, Y. Xue, K. Yao, and Y. Fu, "Numerical evaluation on multiphase flow and heat transfer during thermal stimulation enhanced shale gas recovery," *Applied Thermal Engineering*, vol. 178, article 115554, 2020.

[26] Z. L. Fan, G. W. Fan, D. S. Zhang et al., "Optimal injection timing and gas mixture proportion for enhancing coalbed methane recovery," *Energy*, vol. 222, article 119880, 2021.

[27] Z. L. Fan, D. S. Zhang, G. W. Fan et al., "Non-Darcy thermal-hydraulic-mechanical damage model for enhancing coalbed methane extraction," *Journal of Natural Gas Science and Engineering*, vol. 98, p. 104048, 2021.

[28] Z. J. Lu and S. Z. Li, "Experimental study on permeability and strain characteristics of coal containing gas," *Safety in Coal Mines*, vol. 51, no. 6, pp. 1–4, 2020.

[29] X. Chen, C. A. Tang, J. Yu, J. F. Zhou, and Y. Y. Cai, "Experimental investigation on deformation characteristics and permeability evolution of rock under confining pressure unloading conditions," *Journal of Central South University*, vol. 25, no. 8, pp. 1987–2001, 2018.

[30] J. Yu, S. J. Chen, X. Chen, Y. Z. Zhang, and Y. Y. Cai, "Experimental investigation on mechanical properties and permeability evolution of red sandstone after heat treatments," *Journal of Zhejiang University-SCIENCE A*, vol. 16, no. 9, pp. 749–759, 2015.

[31] X. H. Xia, W. F. Yang, D. W. Cui, L. T. Liu, J. J. Zhao, and P. P. Zhao, "Test study on penetrabillty of floor rock in stope," *Mining Safety & Environmental Protection*, vol. 33, no. 22, pp. 20–22, 2006.

[32] S. Z. Zhang, G. W. Fan, S. Y. Jiang, Z. L. Fan, S. D. Li, and H. N. Ni, "Dual-hazard control mechanism of burst-prone and spontaneous combustion coalface considering effect of retreat speed," *Energy Reports*, vol. 7, pp. 278–288, 2021.

Hindawi
Geofluids
Volume 2021, Article ID 5557125, 13 pages
https://doi.org/10.1155/2021/5557125

Research Article

The Evolutionary Characteristics of Reservoir Microstructure under Long-Term Waterflooding Development and Its Fractal Description

Fengjiao Wang,[1,2] Xu Wang,[1] Yikun Liu,[1] Qingjun Deng,[3] Jianjun Xu,[4] Yong Zhang,[5] and Huaiyuan Li[6]

[1]*Laboratory of Enhanced Oil Recovery of Education Ministry, Northeast Petroleum University, Daqing, 163318 Heilongjiang, China*
[2]*Daqing Oilfield Co. Ltd., Postdoctoral Res Ctr, Daqing, Heilongjiang 163453, China*
[3]*No. 1 Oil Production Plant CNPC (China), Daqing, Heilongjiang 163318, China*
[4]*Chongqing Branch of Daqing Oilfield Co. Ltd., Daqing 163001, China*
[5]*Yingtai Oil Production Plant of Jilin Oilfield, Songyuan, Jilin 138000, China*
[6]*Oil & Gas Engineering Institute of Jilin Oilfield Company, Jilin 138000, China*

Correspondence should be addressed to Yikun Liu; shenliujili@163.com

Received 26 February 2021; Revised 30 April 2021; Accepted 22 May 2021; Published 9 June 2021

Academic Editor: Guanglei Zhang

Generally, long-term waterflooding development often leads to the change of reservoir pore and clay mineral composition, which results in the change of permeability and wettability. In order to explore the relationship between core micropore structure and water cut, based on physical simulation experiments and fractal theory, we proposed a fractal evolutionary model to describe the evolution characteristics of microstructure of long-term water driving reservoirs. In this paper, core pore structure by SEM was first conducted to analyze the change of core pore structure before and after waterflooding under the conditions of magnification of 200 times, 800 times, and 2000 times, respectively. Then, conventional and constant rate mercury injection tests were combined to perform the comparative analysis of core structural parameters before and after waterflooding. Finally, a micropore-throat structure evolution model of core was established. Research shows that the connectivity of larger pores becomes better after long-term water driving, the degree of heterogeneity weakens, and the micro heterogeneity of small pores becomes stronger and stronger. The throat characteristics change in a complex manner, the radius tends to increase, and the sorting becomes better, while the connectivity of small throat changes complex. In general, the heterogeneity of throat increases with the time of water injection in reservoirs with low porosity and permeability. On the basis of fractal theory and variation characteristics of rock pore structure in water driving reservoirs, we have established a micropore-throat structure evolution model of core pore-throat characteristics. This fractal evolution model quantitatively characterized the complexity and evolution law of pore structure and clarified the relationship between fractal dimension of core pore structure and water cut under different stages of water driving.

1. Introduction

Daqing Oilfield is the largest continental multilayer sandstone reservoir in China. After more than 60 years of long-term water injection development, the comprehensive water cut is over 95%, and it has been fully entered and is a typical representative of ultrahigh water cut oilfield [1–3]. The long-term waterflooding development results in the change of reservoir pore and clay mineral composition, which leads to the change of permeability and wettability. The permeability of reservoirs with high permeability greater than 1300×10^{-3} μm^2 increases, while that of reservoirs with permeability lower than 300×10^{-3} μm^2 decreases, and the static heterogeneity of reservoirs intensifies [4]. With the further increase of water cut, especially in the extra high water cut period, the oil and water two-phase seepage capacity are increasing, and the water phase permeability is rising sharply, resulting in serious low efficiency and invalid circulation, greatly reducing the development efficiency, and causing great economic losses. In particular, long-term waterflooding leads to low resistance seepage channel at the bottom of high-permeability layer, which is usually called "dominant seepage channel" or "large channel." It makes the injected fluid channeling and greatly reduces the utilization rate of injected fluid, which is very unfavorable for reservoir development.

In Sazhong study area of Daqing Oilfield, there are fluvial-delta facies deposits under the condition of large shallow lake basin. There are 11 types of sand bodies, including flood plain facies, distributary plain facies, delta inner front facies, and delta outer front facies. The total thickness of the strata is about 500 m, and it is composed of 10 oil layer groups, 43 sandstone groups, 144 small layers, 158 subdivided sedimentary units, and hundreds of small sand beds and argillaceous rocks. The permeability difference of the single layer is as high as dozens to more than one hundred times, and the thickness of the single layer is from 0.2 m to 20 m, which superimposed each other vertically and distributed staggered on the horizontal surface. The sedimentary microfacies developed and formed a very complex reservoir system. The average viscosity of crude oil is 9.2 mPa·s. The permeability is in the range of $100 \times 10^{-3}\,\mu m^2$ to $2000 \times 10^{-3}\,\mu m^2$, and most of them are in the range of $500 \times 10^{-3}\,\mu m^2$ to $1500 \times 10^{-3}\,\mu m^2$. The development of oilfield in Sazhong study area was a gradual process. During the 60 years of development, the exploit objects changed from thick layers to thin layers, the strata combination gradually refined division, the injection-production well spacing changed from large to small, and the reserve utilization changed from good to bad. From the perspective of the whole Daqing Oilfield, the reservoir physical properties of Sazhong study area are very well, and the long-term injection fluid development leads to the development of dominant seepage channels. Therefore, in the ultrahigh water cut stage, the phenomenon of inefficient and ineffective circulation is extremely serious. In the final analysis, it is the change of microscopic pore-throat structure caused by long-term injection fluid erosion in these formations, which leads to the change of seepage law.

Reservoir pore structure heterogeneity is one of the key factors of oil remaining distribution and EOR (enhanced oil recovery), especially in the long-term waterflooding reservoir. The long-term waterflooding will lead to the change of reservoir microscopic pore structure. In this case, the quantitative study of the changing law of the reservoir microscopic heterogeneity is the most important to guide the adjustment of oilfield scheme, quantitative description of remaining oil, tertiary oil recovery, and EOR. A large number of scholars domestic and overseas have done a lot of related research on this issue and have obtained rich research results. The research methods mainly include the following: well logging data evaluation method [5], laboratory rock casting thin section [6], scanning electron microscope (SEM) [7], nuclear magnetic resonance (NMR) [8], and conventional high-pressure mercury injection [9], as well as two emerging technologies, namely, fractal theory and CT scanning method to construct network model, for qualitative, semiquantitative, and quantitative description of reservoir pore structure [10, 11]. Golsanami et al. [12] divided the target area under the T2 curve by NMR into eight porosity bins and estimated each bin's value from the seismic attributes using neural networks (NN). Their research work showed that by using the incremental porosity under the T2 curve, this curve could be synthesized using the seismic attributes. Thomeer and Libny et al. applied the conventional mercury injection experiment method to test capillary pressure curve, and they had obtained the pore-throat size, connectivity, and the parameters of the seepage ability [13, 14]. The constant speed mercury injection experiment method had been more and more applied to the study of pore structure, as it could overcome the disadvantages of conventional high-pressure mercury intrusion method with better quantitative characterization of reservoir microscopic pore structure [15]. Meanwhile, the geomechanical properties of the reservoir could not be neglected while studying the porosity-permeability changes. Golsanami et al. introduced a novel approach to obtain geomechanical parameters through investigating the relationship between geomechanical parameters and Archie's coefficients. The obtained results of this study provided new insights into the simultaneous evolution of the reservoir's mechanical and petrophysical characteristic [16]. Many domestic scholars have studied the variation law of reservoir physical property parameters after long-term waterflooding development, mainly through laboratory waterflooding experiments and coring tests. Guan et al. [17] applied laboratory experimental data such as oil well sealed coring and long core waterflooding experiment in the ultrahigh water cut period to study the variation law of physical property parameters and pore structure parameters. The study concluded that with the intensities of reservoir waterflooding, reservoir physical property parameters, pore structure parameters, and seepage characteristics all changed fundamentally. Wu et al. [18] study the sandstone reservoir physical characteristics and the changing law of the reservoir parameters, and research showed that due to long-term waterflooding, the permeability of sandstone reservoir and moisture content increased, the stratigraphic particles were rushed out, and clay mineral containing basin reduces clever grain of support way and the pore network connectivity, higher permeability, and reservoir wettability by oil into strong hydrophilic. Yin [19] studied through many years the testing data of inspection wells and laboratory core waterflooding experiment of distributary channel sand body of Daqing Oilfield waterflooding process reservoir parameter variation characteristics, and it showed that after long-term water erosion, sample average pore-throat radius and median pore-throat radius, pore throat in reservoir large number, and the permeability contribution rate increase. Li [20] believed that the dynamic geological process of reservoir development fluid was the main reason for the change of reservoir macro parameters. The connectivity of pore throat was improved, the separation of throat was better, the clay minerals were reduced, and the wettability of rock particles was transformed to hydrophilic.

Currently, the fractal geometry, which is an effective tool to characterize the pore structure of reservoirs [21–23], is widely utilized when conducting the research on pore and throat analysis. Katz and Thompson [24] first used fractal geometry theory to analyze pore structure in porous media and pointed out that both pore space and pore interface of porous media have fractal structure. It is demonstrated that the multiscale and statistically self-similar fractal behavior is always observed for the pore structure of porous media [25, 26]. Angulo et al., Perez and Chopra, Shen et al., Li, Li and Horne [27–31], and many other scholars domestic and overseas had put forward different mathematical models to calculate the fractal dimension of pore structure using mercury intrusion data combined with fractal theory and achieved many remarkable results. Li and Zhao [32] derived a mathematical model for determining oil production of spontaneous imbibition by the fractal theory for tight oil reservoir. And the fractal production mode showed a power law relationship between the oil production rate of spontaneous imbibition and time. Chen et al. [33] developed a theoretical model of liquid flow through porous media and numerically analyzed to investigate the role of pore structure on liquid flow behaviors in porous media. In the model, the Sierpinski fractal was utilized to construct the geometry structure of porous media. In the study of Chen et al. [34], they demonstrated that one special bridge function, which was a function of the apparent length and tortuosity fractal dimension, could characterize the relationship of pore structures between two dimensions (2-D) and three dimensions (3-D), and it could serve as a conversion bridge of the radius to determine the capillary pressure curve. In view of the evolution characteristics of micropore-throat structure of long-term waterflood reservoir, most scholars described it through laboratory experiments and field coring data, but few scholars proposed to apply fractal theory to it to realize the quantitative characteristics of its change law in theory.

In this paper, we studied and analyzed the influence and evolution mechanism of long-term waterflooding development on the microscopic pore structure of rocks. Firstly, the structural characteristics of cores before and after long-term waterflooding development were compared by scanning electron microscopy (SEM) under the conditions of magnification of 200 times, 800 times, and 2000 times, respectively. Then, combined with conventional and constant rate mercury injection tests, the effects of long-term water injection before and after on core pore radius distribution, throat radius distribution, permeability contribution rate, and other parameters were studied. And on that basis, based on the fractal theory and the evolution model of pore structure in different water cut stages during long-term water injection, a micropore-throat structure evolution model of core was established, and the mathematical relationship between water cut and fractal dimension of pore structure of core was obtained, which quantitatively characterized the complexity and evolution law of pore structure.

2. Materials and Methods

2.1. Experimental Materials. The experimental oil was simulated oil, which was a mixture of degassed and dehydrated crude oil and light hydrocarbon oil in Daqing Oilfield. The viscosity of the simulated oil was 8.86 mPa·s at 45°C. The experimental water was prepared from No. 1 oil production plant of Daqing Oilfield. The experimental cores were natural cores, which were taken from the type-I formation of No. 1 oil production plant in Daqing Oilfield. The diameter of natural core was 2.5 cm, and the permeability was in the range of $100 \times 10^{-3}\ \mu m^2$ to $2000 \times 10^{-3}\ \mu m^2$.

2.2. Instrument and Facilities. The main instrument used in the experiment include conventional mercury injection meter, conventional mercury injection meter, and constant speed mercury meter. The microscopic pore structure parameters of the core were measured by conventional mercury injection apparatus and constant speed mercury meter. Fei Tecnai G2 F20 scanning electron microscope (SEM) from Gatan Company, USA, was used to test the micromorphology of natural core before and after long-term water driving.

2.3. Experimental Methods. In this paper, we mainly did three aspects of the research work. Firstly, the core profiles before and after long-term waterflooding development were observed by SEM, and the changes of microscopic pores and throat characteristics were compared. Moreover, the evolution characteristics of core pore radius, throat radius, permeability contribution rate, and other parameters before and after long-term waterflooding development were compared and analyzed by conventional mercury injection test and constant rate mercury injection experiment. Finally, the fractal model of long-term water driving core under different water cut conditions was established based on fractal theory. The specific research methods are as follows.

2.3.1. Scanning Electron Microscopy Methods of Natural Cores. (1) Sample preparation: use a burette to absorb a small amount of core debris, evenly spread it in a clean and fixed sample box, and number it for standby; (2) freezing and drying the samples: transferring the prepared samples to E7400 cryotrans to freeze the table quickly, pouring liquid nitrogen for freezing and vacuumizing slowly, then raising the temperature quickly, and sublimating the water in the samples after freezing to obtain dry samples; (3) gold spraying: the sample was placed in a high-voltage electric field with a certain degree of vacuum, the high-voltage electric field ionized the air, and then, a conductive metal film was plated on the surface of the sample; (4) scanning electron microscope: the samples were placed under the scanning electron microscope and observed in the sample room. The pictures were selected to observe the micromorphology of each sample, and the changes of core microstructure before and after waterflooding were compared and analyzed

2.3.2. Method of Mercury Intrusion Test. (1) The natural cores with a diameter of about 2.5 cm were selected, and the natural cores must be dried after washing with toluene oil. (2) Determine the physical properties of the target cores, including gas permeability, volume, mass, and density. *For the conventional mercury injection test*: (3) put the target cores into the core chamber of mercury injection instrument, injected mercury under the set pressure, recorded the pressure value and mercury volume after the pressure was stable, increased the injection pressure, and repeated the record of the above experimental data. *For the constant speed mercury injection test*: (4) the target core was put into the core chamber of mercury instrument, and mercury was injected into the throat and pore of rock sample at a very low constant speed (0.00005 ml/min), so as to ensure that the mercury injection process was carried out under quasi-static state. It was assumed that the interfacial tension and contact angle remain unchanged during the mercury injection process, and the capillary system pressure increases gradually as mercury entered the throat. At the moment when mercury broke through the throat limit and enters the pore, the mercury pressure was released and the whole system pressure fell back. (5) It was considered that the injection pressure was equivalent to the capillary pressure corresponding to the pore space of mercury, and the capillary radius corresponding to the capillary pressure was equivalent to the pore-throat radius of the core. The capillary pressure curve could be obtained by continuously increasing the injection pressure. Combined with the volume of mercury, the distribution probability corresponding to different pore radius ranges could be calculated.

2.3.3. Fractal Evolution Model Establishment of Microscopic Pore-Throat Structure after Long-Term Waterflooding. The spatial distribution of pore and throat in porous media has statistical self-similarity [35–37]. The characteristic parameters of pore structure obtained by SEM test and mercury injection method cannot reflect the general law of pore spatial distribution and quantitatively characterize the self-similarity of pore structure. Based on mercury injection test data and fractal geometry theory, the theoretical model of evolution characteristics of microscopic pore throat in long-term water-driven cores was established, which was of significance for analyzing the change of core structure parameters under the action of water injection scour.

According to the fractal geometry theory, the number of pores with pore-throat radius greater than r of the reservoir $N(r)$ and r satisfies the following power ratio relation conditions in Equation (1) [38]:

$$N(r < L) = \int_{r}^{r_{\max}} f(r)dr = C_1 r^{-D_f}, \tag{1}$$

where $r_{\max}$ is the maximum pore-throat radius in the reservoir, μm; $f(r)$ is the probability density function; $N(r)$ is the number of pores of radius r; L is the object size; D_f is the fractal dimension of the microscopic pore structure, which is in the range of 2 to 3; C_1 is a constant.

Then, the micropore distribution of the reservoir has the fractal self-similar characteristics.

In this case, the fractal representation of pore-size distribution is as Equation (2) [39, 40]:

$$F = \left(\frac{r}{r_{\max}}\right)^{3-D_f}. \tag{2}$$

Correspondingly, the fractal representation of mercury injection capillary pressure curve is as Equation (3):

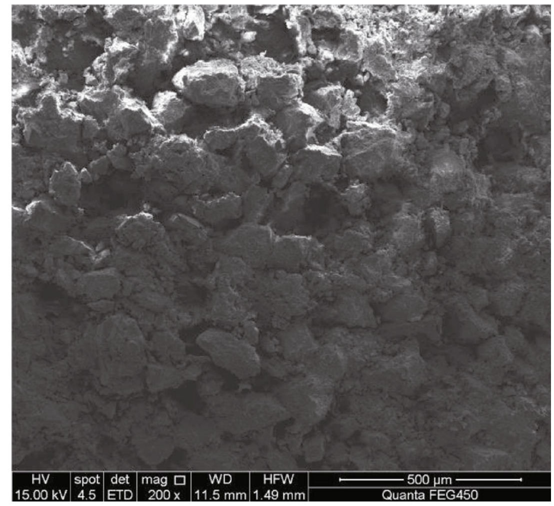

Figure 1: Enlarge image 200 times before water drive.

$$F = \left(\frac{p_c}{p_{\min}}\right)^{D_f-3}, \tag{3}$$

where F is the wetting phase saturation of mercury injection capillary pressure curve under reservoir conditions, fraction; $p_{\min}$ is the capillary pressure corresponding to the maximum pore-throat radius in the mercury injection capillary pressure curve under reservoir conditions, namely, the inlet capillary pressure, MPa; p_c is the capillary pressure, MPa.

Take the logarithm of both sides of Equation (3) and we can get Equation (4):

$$\lg F = \left(-D_f + 3\right) \lg p_{\min} + \left(D_f - 3\right) \lg p_c. \tag{4}$$

According to Equation (4), it can be clearly seen that in log-log coordinates, the wetting phase saturation S has a linear relationship with capillary pressure p_c. Therefore, the linear regression analysis of Equation (4) can be carried out by combining the test data obtained from conventional mercury injection and constant rate mercury injection, and the fractal dimension D_f can be obtained by the slope of the line. By the corresponding intercept, the capillary force $p_{\min}$ at the inlet and outlet can be obtained.

In order to truly reflect the distribution of pore structure of rock, the accuracy can be improved by using the method of piecewise fitting in the analysis of pore structure with great difference. In this paper, large pores and small pores are counted separately to calculate the fractal dimension of pore structure, respectively.

Then, the fractal models of pore distribution and capillary pressure curve are, respectively, as in Equation (5) and Equation (6).

For the larger pores,

$$F = \left(\frac{r_P}{r_{P,\max}}\right)^{3-D_P}, F = \left(\frac{p_{P,c}}{p_{P,\min}}\right)^{D_P-3}, \tag{5}$$

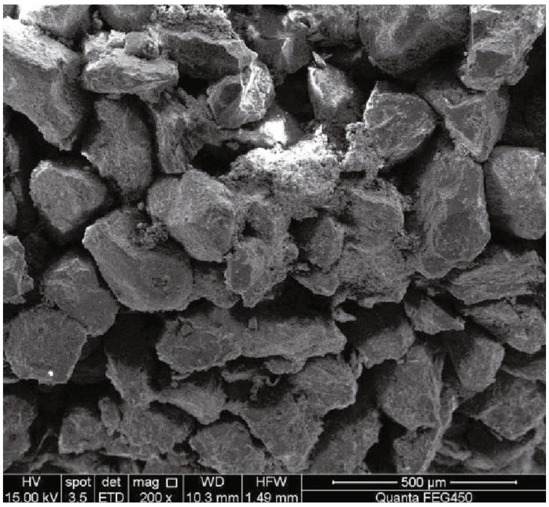

Figure 2: Enlarge image 200 times after water drive.

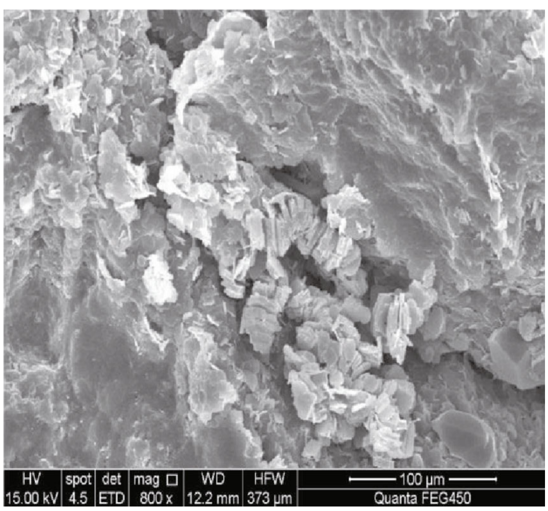

Figure 3: Enlarge image 800 times before water drive

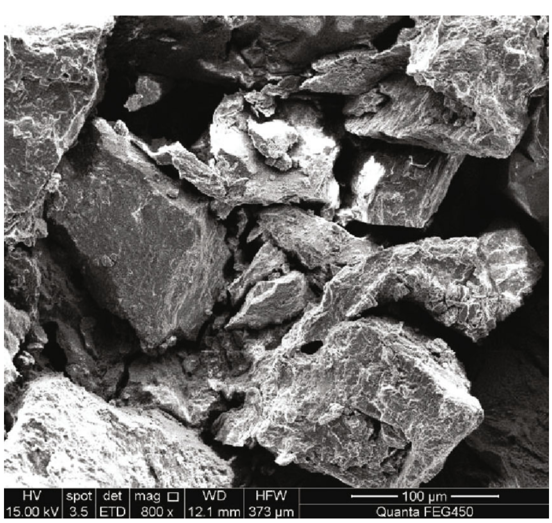

Figure 4: Enlarge image 800 times after water drive.

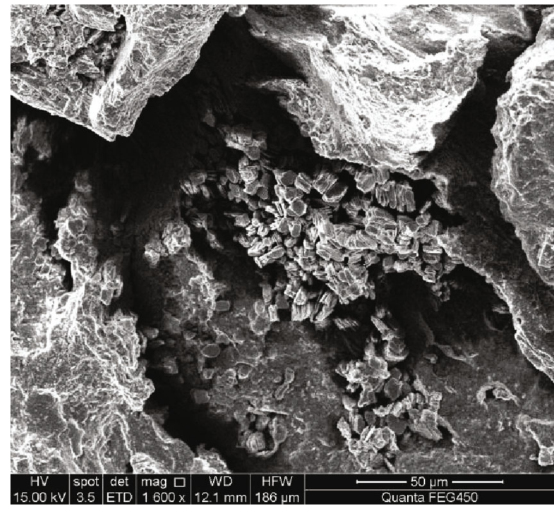

Figure 5: Enlarge images 2000 times before water drive.

and for the smaller pores,

$$F = \left(\frac{r_T}{r_{T,\max}}\right)^{3-D_T}, F = \left(\frac{p_{T,c}}{p_{T,\min}}\right)^{D_T-3}, \tag{6}$$

where D_P is the fractal dimension of larger pores; D_T is the fractal dimension of smaller pores; $r_{P,\max}$ is the largest pore of larger pores, μm; $r_{T,\max}$ is the smallest pore of smaller pores, μm; $p_{P,\min}$ is the minimum capillary pressure corresponding to the larger pores on the capillary pressure curve, MPa; $p_{T,\min}$ is the minimum capillary pressure corresponding to the smaller pores on the capillary pressure curve, MPa; r_P is the pore radius of larger pores, μm; r_T is the pore radius of smaller pores, μm; $p_{P,c}$ is the capillary pressure when the pore radius is r_P, MPa; $p_{T,c}$ is the capillary pressure when the pore radius is r_T, MPa.

3. Results and Discussions

3.1. Test Results of Core Pore Structure by SEM. In order to more clearly compare and analyze the changes of core pore structure before and after waterflooding, SEM scanning images were magnified by about 200 times, 800 times, and 1600 times, respectively, to conduct the related research work.

In Figures 1 and 2, the pore structures before and after waterflooding were imaged by scanning electron microscopy (SEM) at 200 times magnification. At low magnification, the clastic particles were well developed, and the clay mineral particles were closely arranged before waterflooding. The clastic rock particles were unevenly filled with argillaceous clay minerals, etc., with more content, more developed pores, and uneven distribution. After long-term waterflooding, core pores were more developed, intergranular pore connectivity was better, particle dissolution and quartz secondary enlargement were developed, and secondary intergranular pores were developed in pores.

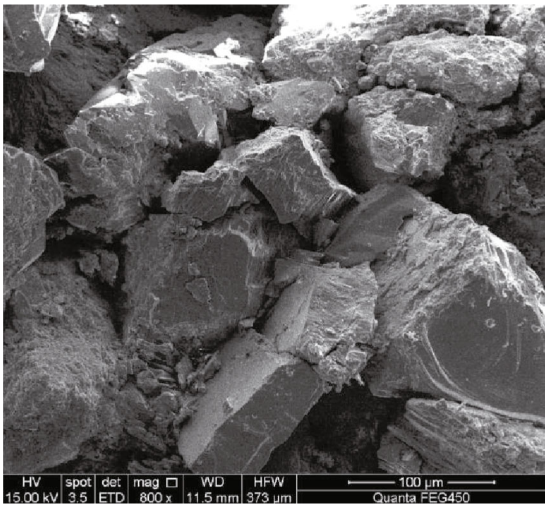

FIGURE 6: Enlarge images 2000 times after water drive.

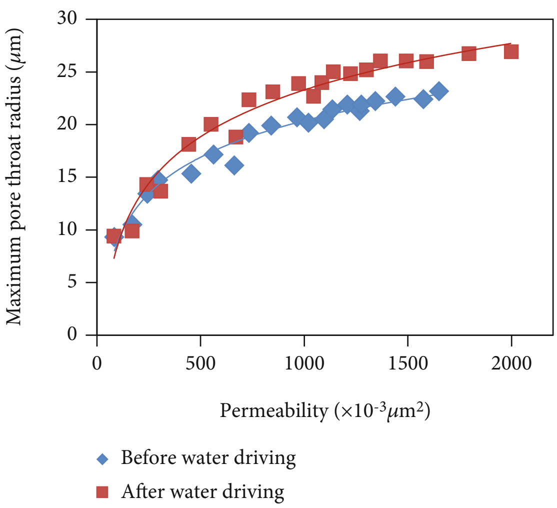

FIGURE 7: Relationship between the maximum pore-throat radius and permeability before and after water driving.

With the increase of magnification of core scanning electron microscope images, the mineral skeleton and filling components could be seen more obviously. Figures 3 and 4 showed the pore structure pictures of cores before and after waterflooding at a magnification of 800 times, respectively. Before waterflooding, it could be found that the clastic rocks were filled with leaf-like kaolinite and authigenic quartz, and the liritization was developed on the granules. The main component of the core was complete, and the phenomenon of feldspar damage and dissolution occurred locally. After waterflooding, it was obvious to observe the mineral skeleton left after the dissolution of minerals, and part of the clay minerals filled in the pores was washed away, and the average total amount of clay minerals decreased, which indicated that the overall pore structure inside the core had undergone a great change, from small pores to large and sublarge pores. The secondary development of quartz at the grain edge was increased, part of feldspar was broken, and the cements were

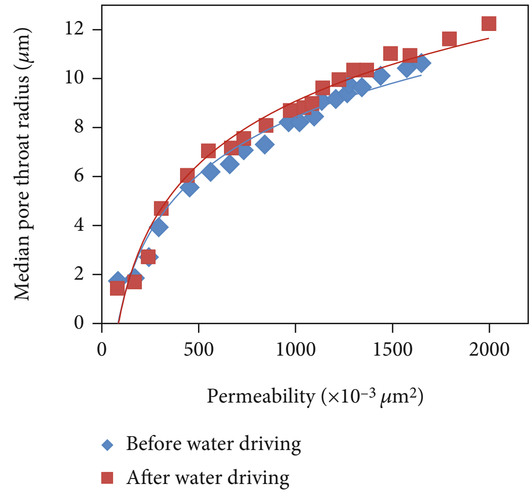

FIGURE 8: Relationship between the median pore-throat radius and permeability before and after water driving.

reduced. The local pores were also blocked due to clay mineral scouring and migration, making the pore roar smaller.

Figure 5 was the pore structure images of the core before waterflooding at a magnification of 2000 times. It could be observed that the pores were filled with kaolinite, with the presence of page-like, worm-like kaolinite and some chlorite. In addition, typical quartz could be seen, and the development of intergranular pores was not obvious. Figure 6 showed the pore structure images of the core after waterflooding at 2000 times magnification. Compared with that before waterflooding, it was observed that the dissolution of kaolinite in the pores was very obvious. The dissolved kaolinite fragments existed in the pores. There were few intact kaolinites in pieces. After alteration of feldspar, illite clay film was formed on the surface, and some quartz was secondary increased. Some secondary pores were formed, forming large pore channels, and the intergranular pores were enlarged.

In conclusion, before waterflooding, the reservoir pores were mainly intergranular pores with weak dissolution, smooth grain edges and developed mesopores, narrow distribution range, and single type. After long-term injection water erosion, reservoir properties changed. The dissolution and destruction of rock particles and the migration of original filling materials mainly expanded the intergranular pores and dissolution pores, and large intergranular pores, dissolution pores, and even macropores appeared, but there were also partly dissolved, broken content of settling down in the fine pore throat, made pore become smaller. Therefore, long-term water washing could increase the variation range of pore-throat distribution, with various types, macropore throat and micropore throat appeared and accompanied one after another, and the distribution of pores and throats were very different in vertical and transverse directions.

3.2. Results of Core Pore Structure by Mercury Injection Test before and after Waterflooding. In order to find out the influence of long-term waterflooding on the pore structure of cores in different permeability ranges, we selected 20 cores

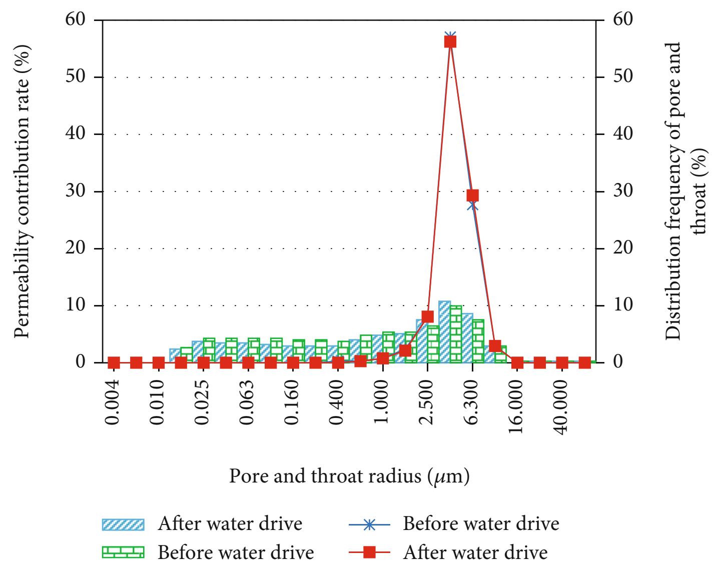

Figure 9: Pore-throat distribution frequency and permeability contribution before and after waterflooding ($k_A = 195 \times 10^{-3}\ \mu m^2$).

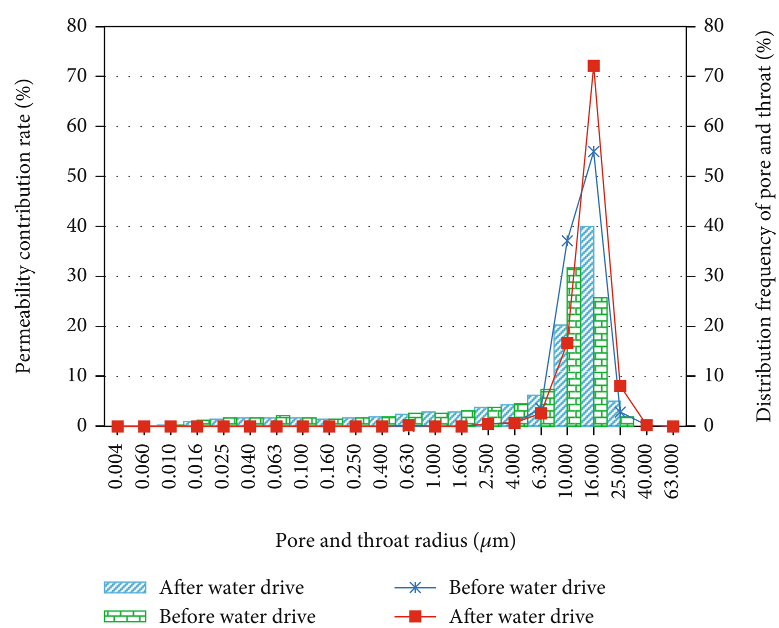

Figure 10: Pore-throat distribution frequency and permeability contribution before and after waterflooding ($k_A = 1610 \times 10^{-3}\ \mu m^2$).

from different types of reservoirs in the No. 1 oil production plant of Daqing Oilfield for this study. In addition, in order to ensure the accuracy of the experimental results, we performed long-term waterflooding on these core samples at standard displacement rates, and the injection volume was up to 1500 times the pore volume.

3.2.1. Changes of Permeability and Pore Radius before and after Waterflooding. Figure 7 showed the relationship between the maximum pore-throat radius and permeability of these core samples before and after waterflooding. Figure 8 shows the relationship between the median pore-throat radius and permeability before and after waterflooding of these core samples.

The results showed that the pore-throat size of the reservoir changed obviously after long-term waterflooding. On the whole, the median and maximum pore-throat radius increased. It could be seen from Figures 7 and 8 that after long-term waterflooding, the median pore-throat radius of rock sample increased by 1.62 μm and 0.97 μm on average, with an increase of 15.2%; the maximum pore-throat radius increased by 3.72 μm and 2.64 μm on average, with an increase of 12.9%. Moreover, there was a good correlation between the median radius of pore throat and core permeability before and after waterflooding. As is known to all, the median value of pore-throat radius is an important index to evaluate the quality of reservoir, which reflects the lowest value of pore radius accounting for more than 50% of the

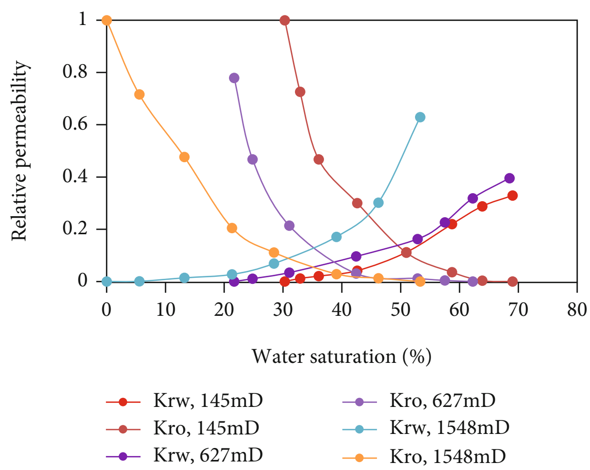

Figure 11: Imbibition and drainage relative permeability curves of type-I, type-II, and type-III.

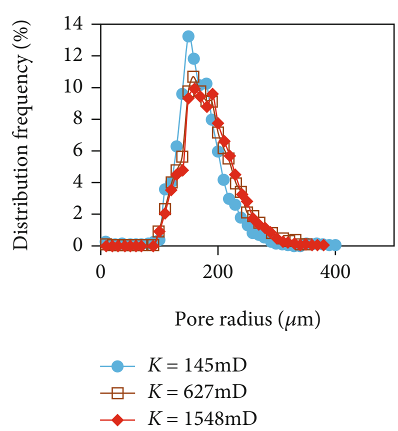

Figure 12: Pore radius before water driving.

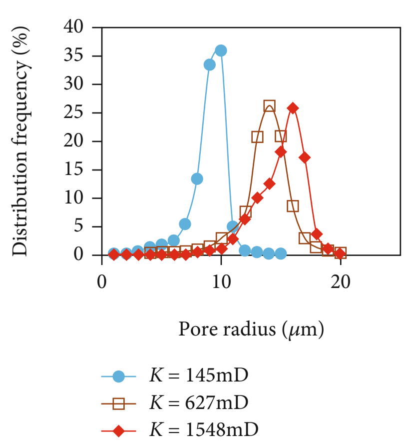

Figure 13: Throat radius before water driving.

pore volume of rock sample. That was to say, the increase of the median pore-throat radius indicated that the radius of large pore throat, which accounted for more than 50% of the pore volume of rock sample after waterflooding, was increasing. After long-term waterflooding, the pore-throat structure of sandstone changed, the pore-throat radius of reservoir increased, and the permeability was enhanced.

3.2.2. Pore-Throat Distribution and Permeability Contribution Rate before and after Waterflooding. In order to compare and analyze the variation of pore-throat distribution frequency and permeability contribution rate of rock samples with different permeability before and after waterflooding, the distribution variation of pore-throat distribution frequency and permeability contribution rate of rock samples with different permeability levels were compared and analyzed by using constant velocity mercury injection experimental parameters of rock samples. Figure 9 showed the distribution of pore-throat distribution frequency and permeability contribution rate before and after waterflooding, taking core A with lower permeability ($k = 195 \times 10^{-3}$ μm^2) as an example. Figure 10 showed the distribution of pore-throat distribution frequency and permeability contribution rate before and after waterflooding, taking core B with higher permeability ($k = 1610 \times 10^{-3}$ μm^2) as an example.

The results showed that on the whole, for high-permeability core samples, the increase of pore-throat distribution frequency and permeability contribution rate after waterflooding was greater; on the contrary, for low-permeability core samples, the change of pore-throat distribution frequency and permeability contribution rate before and after waterflooding was small or even slightly decreased. This was because the core with large permeability was denuded by fine particles after long-term waterflooding and forms more connected dominant seepage channels, which enhanced the flow ability of fluid and increases the apparent permeability. For the core with low permeability, the sorting of rock particles was poor, and the small particles stripped by long-term waterflooding had filled the larger holes to a certain extent, so it was possible to reduce the permeability.

3.2.3. Results of Constant Rate Mercury Injection Test. In Daqing Oilfield, three typical cores were taken from the type-I formation, the type-II formation, and the type-III formation, respectively, and the permeability was 145×10^{-3} μm^2, 627×10^{-3} μm^2, and 1548×10^{-3} μm^2, respectively. The influence of long-term waterflooding on their respective pore-throat structure was analyzed. The original imbibition and drainage curves were shown in Figure 11. The pore distribution before water driving was shown in Figure 12, and the throat radius distribution before water driving was shown in Figure 13. Under different permeability conditions, the pore radius distribution of rock sample had no obvious change, and the pore structure distribution tended to be normal distribution. Different from this, the throat radius distribution of samples was different with different permeability and presented certain regularity. For the samples with high permeability, the throat radius distribution was relatively wide; for the samples with low permeability, the throat radius distribution became narrow, and the peak value was concentrated in the small throat. The throat radius corresponding to the throat distribution peak value of three rock samples with different permeability is 10.3 μm, 14.7 μm, and 17 μm,

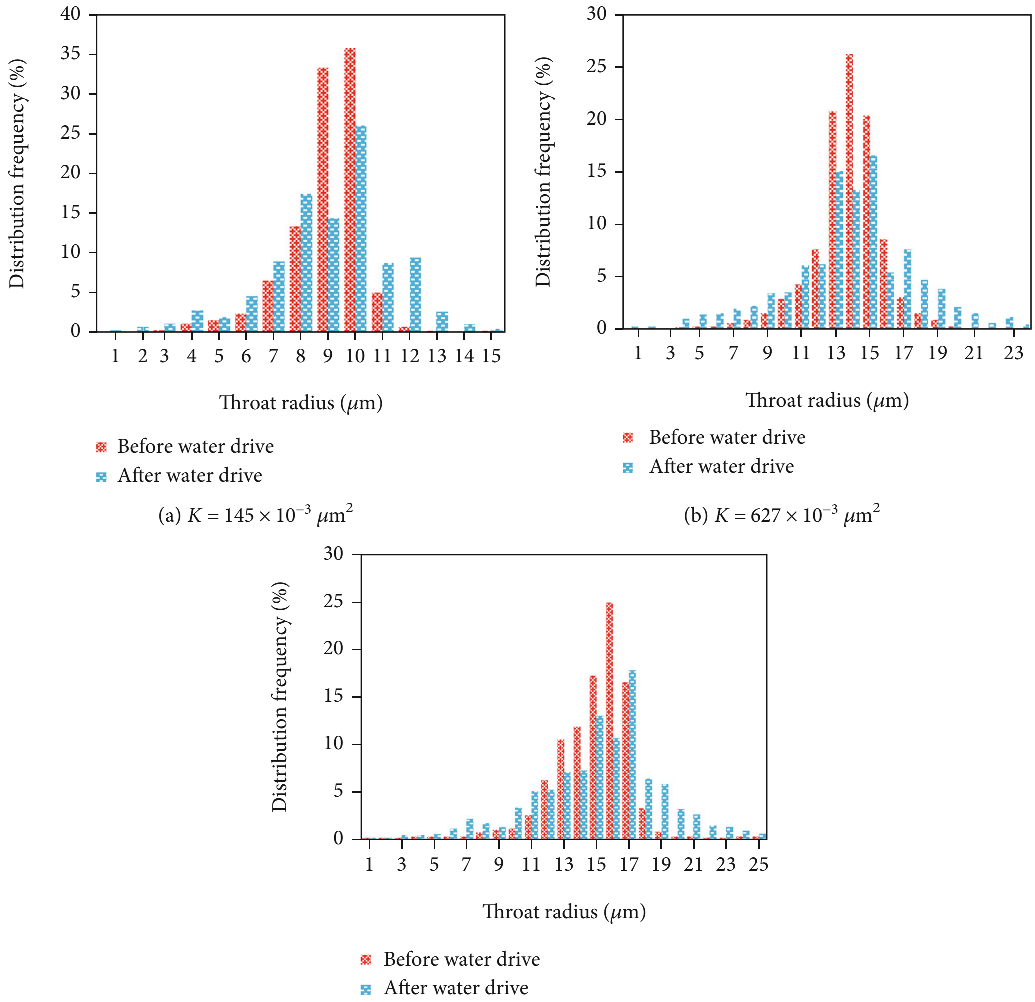

(a) $K = 145 \times 10^{-3}\ \mu m^2$

(b) $K = 627 \times 10^{-3}\ \mu m^2$

(c) $K = 1548 \times 10^{-3}\ \mu m^2$

Figure 14: Throat radius after water driving.

Table 1: The fractal dimension analysis results of different water cut stages of core B.

Scope	Water cut	Slope	Intercept	D	p_{min} (MPa)	R^2
Larger pores	0	0.5786	0.8422	2.437	0.036264	0.9919
	0.75	0.6258	0.9183	2.3892	0.035141	0.9966
	0.85	0.6597	0.9808	2.357	0.033487	0.9982
	0.95	0.7393	1.1480	2.206	0.030154	0.9955
Smaller pores	0	0.1990	0.5192	2.801	0.001712	0.9988
	0.75	0.1728	0.5545	2.827	0.000942	0.9972
	0.85	0.1534	0.5908	2.844	0.000742	0.9980
	0.95	0.1229	0.6202	2.878	0.000044	0.9968

respectively, and the throat radius increased with the increase of rock sample permeability. This shows that the throat characteristics, rather than the pore characteristics, control the seepage characteristics of rock samples. The throat radius distribution of the cores above after water driving was shown in Figure 14.

According to Figure 14, the contribution of throat with small radius to permeability decreased in lower permeability core and increased slightly near the peak value, but some throat was blocked. For the medium permeability core, the pore passage of some throat was unobstructed due to the clay falling off after waterflooding, which enhanced the fluid seepage ability. It was possible that some relatively large throat appears after long-term waterflooding. For high-permeability core, the main flow path changed before and after waterflooding. The throat with radius of 1-11 μm and

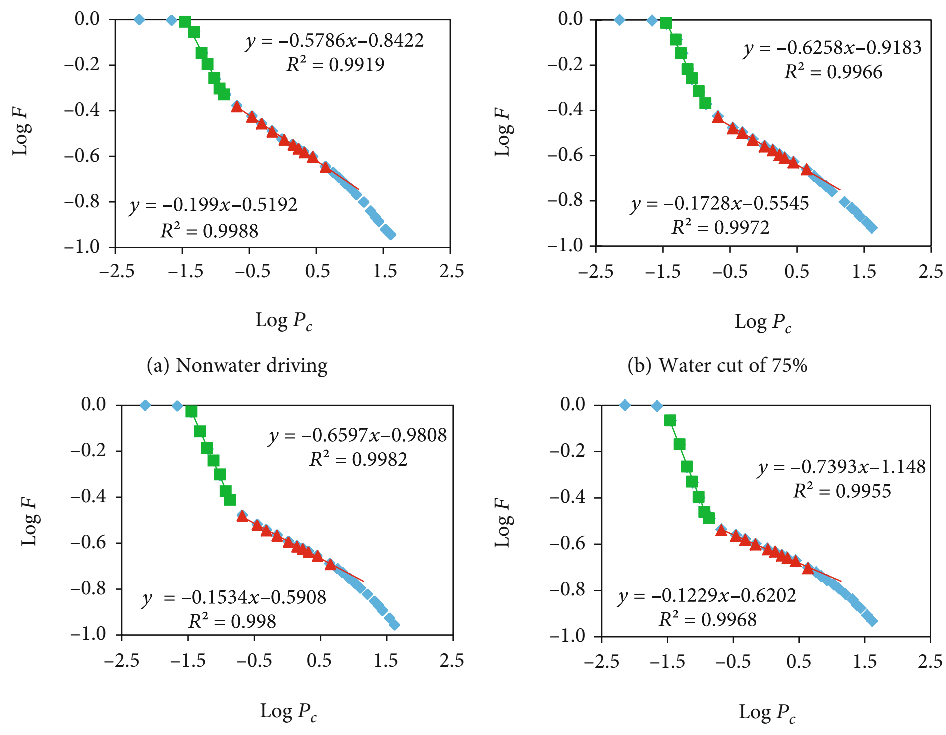

FIGURE 15: Double logarithm curves of core capillary pressure and water saturation.

17-20 μm increased the contribution to the flow after waterflooding, and there was a new throat with radius of 21-25 μm, which indicated that the pore channel of some throat was unobstructed due to the clay falling off after waterflooding, so that the flow capacity of fluid was enhanced. It was possible that some relatively large throat appeared after waterflooding. At the same time, part of the pore throat was blocked. This showed that high-permeability reservoir was very conducive to the development of dominant permeability channel.

3.3. Fractal Description of Core Pore Structure after Long-Term Waterflooding. In order to study the influence of long-term waterflooding on micropore structure, it is necessary to calculate the fractal dimension of core pore structure at different water cut stages and analyze the fractal characteristics. Core sample B had experienced a long-term waterflooding experiment, which was taken as an example to analyze the influence of long-term waterflooding on micropore structure. Based on the constant pressure mercury injection experimental data of core sample B (permeability $1548 \times 10^{-3}\ \mu m^2$) in four different water cut stages of initial nonwater driving, water driving at water cut of 75%, water driving at water cut of 85%, and water driving at water cut of 95%, the fractal dimension of core pore was analyzed by Equation (4). Under the double logarithm coordinate system, S_w and $p_{\min}$ should be in line with each other. The fractal dimension D could be obtained from the slope of the straight line, and the entrance capillary force $p_{\min}$ could be obtained from the intercept.

The fractal characteristics of core pore structure in four water cut stages of core sample B were analyzed by two-stage fitting method. The upper section reflected the pore structure characteristics of large pore throat and the lower section reflected the pore structure characteristics of small pore. The analysis results were shown in Figure 14. The fractal dimension analysis results of different water cut stages of core B were shown in Table 1.

According to Figure 15, the fractal dimension of macropore in different water cut stages was obviously smaller than that of small pore throat, which indicated that the pore structure of macropore throat was better than that of small pore throat; more importantly, after long-term waterflooding, the fractal dimension of macropore throat decreased with the increase of water cut, the macropore throat would become larger and larger, the inner wall would be smooth, and the homogeneity coefficient would increase; the fractal dimension of small pore throat would increase. The number increased with the increase of water content, reflecting the enhancement of micro heterogeneity driven by water. According to the analysis results of mercury injection data, with the increase of water cut after long-term waterflooding, the radius of pore throat increased, but the complexity of pore-throat structure increased. The macropore throat became larger and larger, and the micro heterogeneity of small pore throat became stronger and more complex. In this way, the injected water would preferentially enter into the macropore throat, which also created conditions for the formation to have a dominant channel. The change range of fractal dimension was small before the water content was

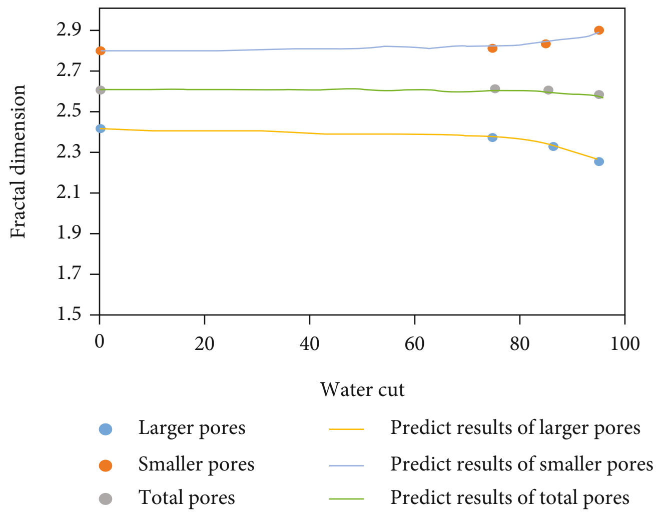

Figure 16: Comparison curves between actual data and prediction data of evolutionary model.

75%, but the change range of fractal dimension was large between 75% and 95%.

The fractal dimension of macropore throat and pinhole throat had the following relation with the fractal dimension of total pore throat as shown in Equation (7).

$$D_{\text{total}} = \frac{\left(D_{high} + D_{low}\right)}{2}, \tag{7}$$

where D_{total} denotes the fractal dimension of total pore throat, D_{high} denotes the fractal dimension of the larger pore throat, and D_{low} denotes the fractal dimension of the smaller pore throat.

The formation process of macropore can be seen as two processes: the increase of local reservoir permeability and the decrease of local reservoir permeability at the same time. However, the microscopic essence of macropore is reflected in the change of fractal dimension of pore structure. Moreover, the evolution law of fractal dimension of pore structure with the change of water cut in different reservoir rock properties is different. Therefore, the reservoir pore structure is established. The mathematical model of dynamic evolution mode of fractal dimension of structure can combine macro and micro to quantitatively solve the problem of mathematical description of the formation and evolution of macropores.

Under the condition of short-term waterflooding in Daqing Oilfield, the effect of injected water on reservoir erosion and immersion is not obvious, which shows that the fractal dimension of reservoir rock changes little in the initial stage, and it belongs to a gentle increasing stage. With the increase of injected water and waterflooding time, the long-term erosion and immersion of injected water has a great effect on pore structure. However, due to the limitation of rock cementation strength and clay content, the change of reservoir fractal dimension tends to be gentle from the end of ultrahigh water cut to 98% water cut. In general, the evolution of fractal dimension of pore structure in Daqing Oilfield is first gentle, then rising, and then gentle. According to the change of fractal dimension, the exponential evolution model can be used to characterize the evolution of fractal dimension in the middle and low water cut stage, but after the high water cut stage, the change model of fractal dimension can be established according to the half rising half ridge distribution function [41] as shown in Equation (8) and Equation (9).

For the reservoir dominated by larger pores and throats,

$$D = \begin{cases} D_{\max} e^{-C_1 f_w} & f_w \le 80\%, \\ D_{\max} - D_{\max}\lambda_{D\max}\left\{\frac{1}{2} - \frac{1}{2}\sin\left(\frac{\pi}{1-1/2}\left(f_w - \frac{1+1/2}{2}\right)\right)\right\} & 80\% < f_w \le 98\%, \end{cases} \tag{8}$$

and for the reservoir dominated by smaller pores and throats,

$$D = \begin{cases} D_{\min} e^{C_1 f_w} & f_w \le 80\%, \\ D_{\min} + D_{\min}\lambda_{D\min}\left\{1/2 + 1/2\sin\left(\frac{\pi}{1-1/2}\left(f_w - \frac{1\text{-}1/2}{2}\right)\right)\right\} & 80\% < f_w \le 98\%, \end{cases} \tag{9}$$

where $D_{\min}$ and $D_{\max}$ are both the fractal dimension at the water cut of 75%; C_1 is a fractal coefficient; $\lambda_{D\max}$ denotes a multiple decrease of fractal dimension, which is determined by rock properties; $\lambda_{D\min}$ denotes a multiple increase of fractal dimension, which is determined by rock properties; f_w denotes the water cut, fraction.

Based on the fractal evolution model of pore structure under different water cut conditions, the relationship between fractal dimension and water cut was calculated by using the data in Table 1, as shown in Figure 16. It can be seen that the fractal evolution mathematical model of pore throat is in good agreement with the actual test data. Therefore, it can quantitatively characterize the evolution of fractal dimension of reservoir micropore structure.

4. Conclusions

(1) Long-term waterflooding will lead to the dissolution of some minerals; part of the clay minerals filled in the pores will be washed away, the average total amount of clay minerals will be reduced, the overall pore structure of the core has changed greatly, and most of the pores will become larger. At the same time, due to the erosion and migration of clay minerals, local pores are also blocked, making a small part of pores smaller

(2) Long-term waterflooding and scouring will cause complex changes in the microscopic pore structure of the reservoir, and the overall pore characteristics will tend to become better. The connectivity of larger pores becomes better, and the degree of heterogeneity decreases. On the contrary, the microscopic heterogeneity of small pores becomes stronger and stronger. In general, the heterogeneity of the reservoir with low porosity and permeability increases with the passage of water injection time. These evolutionary characteristics will undoubtedly lead to the injected water preferring to enter the larger pores and throats, which will create conditions for the formation of dominant channels

(3) Based on the fractal theory and the evolution model of pore structure in different water cut stages during long-term water injection, a micropore-throat structure evolution model of core was established, and the mathematical relationship between water cut and fractal dimension of pore structure of core was obtained, which quantitatively characterized the complexity and evolution law of pore structure. The larger the fractal dimension was, the more serious the microscopic heterogeneity was

Data Availability

The data used to support the findings of this study are included within the article.

Conflicts of Interest

The authors declare that they have no conflicts of interest regarding the publication of this paper.

Acknowledgments

This research was supported by the National Natural Science Foundation of China (Youth Project) (Grant No. 51804076), Heilongjiang Provincial Natural Science Foundation (Youth Project) (Grant No. QC2018047), Youth Science Foundation of Northeast Petroleum University (Grant No. 2019NL-02), and Research Initiation Foundation of Northeast Petroleum University (Grant No. 2019KQ15).

References

[1] L. Zhu, Q. Du, X. Jiang et al., "Characteristics and strategies of three major contradiction for continental facies multi-layered sandstone reservoir at ultra-high water cut stage," *Acta Petrolei Sinica*, vol. 36, no. 2, pp. 210–216, 2015.

[2] Q. Du, "Variation law and microscopic mechanism of permeability in sandstone reservoir during long-term water flooding development," *Acta Petrolei Sinica*, vol. 37, no. 9, pp. 1159–1164, 2016.

[3] J. Q. Chen, Q. Q. Wang, J. H. Xiao et al., "Development status and prospect of water pre-separation technology for produced liquid in high water-cut oil well," *Acta Petrolei Sinica*, vol. 41, no. 11, pp. 1434–1444, 2020.

[4] Q. L. Du, B. Q. Song, and L. H. Zhu, "Challenges and countermeasures of the waterflooding development for Lasaxing Oilfields during extra-high watercut period," *Petroleum Geology & Development in Daqing*, vol. 38, no. 5, pp. 189–194, 2019.

[5] H. L. Bian, J. Guan, Z. Q. Mao, X. D. Ju, and G. Q. Han, "Pore structure effect on reservoir electrical properties and well logging evaluation," *Applied Geophysics*, vol. 11, no. 4, pp. 374–383, 2014.

[6] R. G. Loucks, "Revisiting the importance of secondary dissolution pores in tertiary sandstones along the Texas Gulf Coast," *Gulf Coast Association of Geological Societies Transactions*, vol. 55, pp. 447–455, 2005.

[7] Y. Li, J. Yang, Z. Pan, and W. Tong, "Nanoscale pore structure and mechanical property analysis of coal: an insight combining AFM and SEM images," *Fuel*, vol. 260, article 116352, 2020.

[8] J. Yan, X. He, S. Zhang et al., "Sensitive parameters of NMR T2 spectrum and their application to pore structure characterization and evaluation in logging profile: a case study from Chang 7 in the Yanchang Formation, Heshui area, Ordos Basin, NW China," *Marine and Petroleum Geology*, vol. 111, pp. 230–239, 2020.

[9] L. Hao-ran, H. Xu-ri, Y. cheng, and T. Zheng-wu, "Study of low-permeability sandstone by unidirectional mercury intrusion porosimetry," *Chemistry and Technology of Fuels and Oils*, vol. 54, no. 4, pp. 476–483, 2018.

[10] L. Zhang, J. Li, H. Tang, and J. Guo, "Fractal pore structure model and multilayer fractal adsorption in shale," *Fractals*, vol. 22, no. 3, article 1440010, 2014.

[11] Y. Yang and S. Liu, "Estimation and modeling of pressure-dependent gas diffusion coefficient for coal: a fractal theory-based approach," *Fuel*, vol. 253, pp. 588–606, 2019.

[12] N. Golsanami, X. Zhang, W. Yan et al., "NMR-based study of the pore types' contribution to the elastic response of the reservoir rock," *Energies*, vol. 14, no. 5, pp. 1513–1538, 2021.

[13] J. H. M. Thomeer, "Introduction of a pore geometrical factor defined by the capillary pressure curve," *Journal of Petroleum Technology*, vol. 12, no. 3, pp. 73–77, 1960.

[14] L. Leal, R. Barbato, A. Quaglia, J. C. Porras, and H. Lazarde, "Bimodal behavior of mercury-injection capillary pressure curve and its relationship to pore geometry, rock-quality and production performance in a laminated and heterogeneous reservoir," in *SPE Latin American and Caribbean Petroleum Engineering Conference*, Buenos Aires, Argentina, 2001.

[15] C. Zhang, Y. Cheng, and C. Zhang, "An improved method for predicting permeability by combining electrical measurements and mercury injection capillary pressure data," *Journal of Geophysics and Engineering*, vol. 14, no. 1, pp. 132–142, 2017.

[16] N. Golsanami, E. Bakhshi, W. Yan et al., "Relationships between the geomechanical parameters and Archie's coefficients of fractured carbonate reservoirs: a new insight," *Energy Sources, Part A: Recovery, Utilization, and Environmental Effects*, vol. 2, pp. 1–25, 2020.

[17] C. Guan, W. Hu, Y. Li, R. Ma, and Z. Ma, "Prediction of oil-water relative permeability with a fractal method in ultra-high water cut stage," *International Journal of Heat and Mass Transfer*, vol. 130, pp. 1045–1052, 2019.

[18] S. Y. Wu, "Variation rule of oil layer parameters washed by long-term injected water and its impact on development effect," *Petroleum Geology and Recovery Efficiency*, vol. 11, no. 2, pp. 9–11, 2004.

[19] S. F. Yin, "Variation characteristics of the reservoir parameters in the development course of the waterflooding for the distributary channel sandbodies," *Petroleum Geology & Oilfield Development in Daqing*, vol. 34, no. 4, pp. 69–72, 2015.

[20] Y. Li, "Variation rule of macro parameters and dynamic model of oil reservoirs in continental faulted basin," *Acta Petrolei Sinica*, vol. 26, no. 2, pp. 65–68, 2005.

[21] S. W. Tyler and S. W. Wheatcraft, "Fractal processes in soil water retention," *Water Resources Research*, vol. 26, no. 5, pp. 1047–1054, 1990.

[22] B. Yu and J. Li, "Some fractal characters of porous media," *Fractals*, vol. 9, no. 3, pp. 365–372, 2001.

[23] Z. Wu, C. Cui, Y. Ye, X. Cheng, and J. Trivedi, "A fractal model for quantitative evaluating the effects of spontaneous imbibition and displacement on the recovery of tight reservoirs," *Journal of Petroleum Science and Engineering*, vol. 198, article 108120, 2021.

[24] A. J. Katz and A. H. Thompson, "Fractal sandstone pores: implications for conductivity and pore formation," *Physical Review Letters*, vol. 54, no. 12, pp. 1325–1328, 1985.

[25] B. B. Mandelbrot, *The Fractal Geometry of Nature*, Freeman, New York, 1983.

[26] B. Yu, "Analysis of flow in fractal porous media," *Applied Mechanics Reviews*, vol. 61, no. 5, article 50801, 2008.

[27] R. F. Angulo, V. Alvarado, and H. Gonzalez, "Fractal dimensions from mercury intrusion capillary tests," in *SPE Latin America Petroleum Engineering Conference*, Caracas, Venezuela, 1992.

[28] G. Perez and A. K. Chopra, "Evaluation of fractal models to describe reservoir heterogeneity and performance," *SPE Formation Evaluation*, vol. 12, no. 1, pp. 65–72, 1997.

[29] P. P. Shen, M. X. Liu, and F. S. Jia, "Application of fractal techniques in reservoir development," in *SPE International Oil and Gas Conference and Exhibition in China*, Beijing, China, 1998.

[30] K. W. Li, "Characterization of rock heterogeneity using fractal geometry," in *SPE International Thermal Operations and Heavy Oil Symposium and Western Regional Meeting*, Bakersfield, California, 2004.

[31] K. Li and R. N. Horne, "Fractal modeling of capillary pressure curves for the geysers rocks," *Geothermics*, vol. 35, no. 2, pp. 198–207, 2006.

[32] K. Li and H. Zhao, "Fractal prediction model of spontaneous imbibition rate," *Transport in Porous Media*, vol. 91, no. 2, pp. 363–376, 2012.

[33] Y. Chen, C. Shen, P. Lu, and Y. Huang, "Role of pore structure on liquid flow behaviors in porous media characterized by fractal geometry," *Chemical Engineering and Processing: Process Intensification*, vol. 87, pp. 75–80, 2014.

[34] X. Chen, G. Yao, C. Luo et al., "Capillary pressure curve determination based on a 2-D cross-section analysis via fractal geometry: a bridge between 2-D and 3-D pore structure of porous media," *Journal of Geophysical Research: Solid Earth*, vol. 124, no. 3, pp. 2352–2367, 2019.

[35] E. P. Verrecchia, "On the relationship between the pore-throat morphology index ("a") and fractal dimension (D f) of pore networks in carbonate rocks; discussion," *Journal of Sedimentary Research*, vol. 65, no. 4a, pp. 701-702, 1995.

[36] L. Kouqi, O. Mehdi, and K. Lingyun, "Fractal and multifractal characteristics of pore throats in the Bakken Shale," *Transport in Porous Media*, vol. 126, pp. 579–598, 2019.

[37] Y. Jin, W. Z. Quan, J. H. Qin, X. H. Liu, J. L. Zheng, and H. B. Song, "Quantitative characterization of complex assembly in fractal pore-throat porous media," *Meitan Xuebao/Journal of the China Coal Society*, vol. 45, no. 5, pp. 1845–1854, 2020.

[38] W. Li, H. Zhao, S. Li, W. Sun, L. Wang, and B. Li, "A fractal model of effective stress of porous media and the analysis of influence factors," *Results in Physics*, vol. 8, pp. 920–925, 2018.

[39] W. Hua, *Nonlinear Percolation Mechanism and Dynamic Evaluation Model of Thief Zone at Ultra-High Water Cut Stage*, Northeast Petroleum University, 2017.

[40] B. Xiao, J. Fan, and F. Ding, "Prediction of relative permeability of unsaturated porous media based on fractal theory and Monte Carlo simulation," *Energy & Fuels*, vol. 26, no. 11, pp. 6971–6978, 2012.

[41] Z. H. Dai, Y. Liu, X. Q. Qiu, and J. S. Han, "Condition evaluation approach of protective devices based on fuzzy comprehensive evaluation with variable weight," *Electrical Measurement & Instrumentation*, vol. 58, no. 4, pp. 150–157, 2021.

Hindawi
Geofluids
Volume 2021, Article ID 5552791, 12 pages
https://doi.org/10.1155/2021/5552791

Research Article

Application of Modified Hoek–Brown Strength Criterion in Water-Rich Soft Rock Tunnel

Xianghui Deng, Yuncai Wang, Rui Wang, Daohong Xia, and Zhiqing Zhao

School of Civil and Architecture Engineering, Xi'an Technological University, Xi'an 710021, China

Correspondence should be addressed to Rui Wang; wangrui@xatu.edu.cn

Received 6 February 2021; Revised 11 April 2021; Accepted 29 May 2021; Published 7 June 2021

Academic Editor: Chuangzhou Wu

When a tunnel is excavated in the water-rich soft rock stratum, the strength of the soft rock is greatly reduced due to the seepage of groundwater. The condition may result in engineering accidents, such as large deformation, limit invasion, and even local collapse of the tunnel. Therefore, it is very important to research the stability of the surrounding rock in the water-rich soft rock tunnel. The water-rich disturbance factor considering the seepage influence of groundwater and blasting disturbance is proposed, and the generalized Hoek–Brown strength criterion is modified on the basis of the immersion softening test of soft rock. In accordance with the classical elastic–plastic mechanics theory, the stress, strain, and displacement calculation formulas of the tunnel surrounding rock are derived. The displacement of tunnel surrounding rock is analyzed using the derived formula and the modified Hoek–Brown strength criterion and then compared with the measured value. Results show that the displacement of surrounding rock, which is calculated by modified Hoek–Brown strength criterion considering water-rich disturbance factor and the displacement calculation formula, is close to the measured deformation of surrounding rock in water-rich soft rock tunnel, and the error is small. Therefore, the modified Hoek–Brown strength criterion can be applied to the water-rich soft rock tunnel, and the derived displacement calculation formula can accurately calculate the deformation of tunnel surrounding rock. It is of great significance to the study of surrounding rock stability of water-rich soft rock tunnel.

1. Introduction

With the rapid development of highway tunnels and railway tunnels in China, more and more tunnels need to be built in water-rich soft rock strata [1]. Water is an important factor affecting the deformation and failure mode of soft rock [2]. Usually, water negatively affects the mechanical properties, long-term strength, and stability of soft rock [3]. In most cases, due to the disturbance of tunnel excavation, the state of groundwater changes, thereby significantly changing the strength of the surrounding rock. It is an important reason for affecting the stability of surrounding rock in soft rock tunnel [4, 5]. Therefore, studying the influence of groundwater on the stability of surrounding rock in the water-rich soft rock stratum is important.

In the past 30 years, many scholars have found that groundwater has a great influence on the stability of surrounding rock after tunnel excavation. Some scholars have conducted a number of studies on the softening effect of water on the soft rock strength and deformation and have made considerable achievements. For example, Yang et al. [6] studied the microstructure and failure characteristics of argillaceous slate under different immersion time. They found that with the extension of immersion time, the internal pores of rock samples gradually increased, and the failure mode gradually developed from splitting failure to shear failure. Shakoor and Barefield [7] studied the change in sandstone strength under different water contents. They found that within the range of water content lower than 20%, the strength of surrounding rock decreased significantly with the increase in water content. However, when the water content was higher than 20%, the strength decreased insignificantly. Nara et al. [8] studied the microstructure of shale under different immersion time and found that the increase rate of internal cracks increased with the extension of immersion time. Azhar et al. [9] tested and analyzed the mechanical properties of clay-rich sandstone under different immersion time and found that the elastic modulus and compressive strength decreased with the increase of immersion time. Zhang et al. [10] studied the failure characteristics of soft rock under different immersion time and analyzed the failure mode of tunnel when water gushing occurred. Sun et al. [11] studied the softening characteristics and failure mode of rock under different immersion time and analyzed the failure mode of tunnel under different water contents. Bian et al. [12] considered the shale of Huangjialing tunnel as the research object, studied the changes in mineral composition and microstructure under different immersion time, analyzed the failure modes under different immersion time, and predicted the failure modes of the tunnel under different water contents.

The above research results only analyzed the softening properties and failure modes of soft rock after immersion, which can be used to study the mechanism of large deformation of water-rich soft rock tunnel and predict the failure mode of the tunnel. However, it cannot be used to analyze the stability of tunnels. In tunnel construction, the stability of surrounding rock is often judged by monitoring the deformation of surrounding rock. If the cumulative deformation of surrounding rock is small, the surrounding rock of tunnel is considered to be stable; on the contrary, if the cumulative deformation of surrounding rock is large, it is considered that the stability of surrounding rock is poor, and corresponding measures should be taken to strengthen support, such as temporary inverted arch, biological improvement grouting reinforcement [13, 14], and other measures to strengthen support. The deformation of surrounding rock during tunnel excavation should be calculated for the analysis of tunnel surrounding rock stability. In the calculation of surrounding rock displacement, selecting the appropriate calculation method and strength criterion can obtain more accurate calculation results. Considering the deformation capacity of surrounding rock, Thirukumaran et al. [15] proposed a stability analysis method of tunnel vault rock mass, which can be used to analyze the stability of the surrounding rock. But there is still a large gap between the calculation results of simplifying the vault rock block to a rectangular block and the actual deformation. To make up for the deficiency that the Mohr–Coulomb strength criterion can only describe the linear failure characteristics of rock, Hoek and Brown [16] proposed Hoek–Brown strength criterion, which can reflect the nonlinear failure characteristics, on the basis of Griffith's theoretical research results. Hoek et al. [17] improved the Hoek–Brown strength criterion and proposed the generalized Hoek–Brown strength criterion with wider applicability. Meanwhile, the blasting disturbance factor (D) and the geological strength index (GSI) were introduced to calculate the parameters. Sonmez and Ulusay [18] comprehensively considered the geological strength index and the disturbance effect in actual construction and corrected the blasting disturbance factor, which can calculate the displacement of tunnel surrounding rock more accurately. However, due to the cumbersome calculation process, it is less used at present. Chen et al. [19, 20] based on the damage law of rock and the reduction effect of cohesion and internal friction on the stability of rock proposed the damage evolution equation of fractured rock mass and established the damage constitutive equation of rock, which can be used for the stability analysis of fractured rock mass. Lee and Pietruszczak [21] proposed the method of numerical difference and considered the softening law of strength parameters, such as cohesion, internal friction angle, and dilatancy angle. They deduced the displacement analysis formula of tunnel surrounding rock by using the generalized Hoek–Brown strength criterion, which makes the calculation results more suitable for the actual tunnel deformation. Xia et al. [22] used the strength reduction method and catastrophe theory to study the stability of surrounding rock and applied the research theory to practical engineering, which achieved good results. Wu et al. [23] combined the Levenberg-Marquardt optimization technique with complex variable differential method and proposed a modified optimization technique for stress-seepage coupling problem, which can accurately and effectively estimate multiple rock mass parameters. Xue et al. [24] established a seepage model, which can simulate groundwater flow from aquifer to fault by coupling the Darcy flow model and the Fokheimer flow model and can be used to analyze the stability of tunnel when fractured rock mass gushes water.

The existing research results can accurately calculate the deformation of the tunnel surrounding rock in the natural state. However, the softening effect of groundwater on soft rock is not considered. There is still a large error in the calculation of the surrounding rock displacement in a water-rich soft rock tunnel. Thus, the stability of the surrounding rock of the water-rich soft rock tunnel cannot be accurately analyzed. Therefore, the variation law of physical and mechanical properties of soft rock is analyzed through the immersion softening test of soft rock. On this basis, the water-rich disturbance factor considering the influence of groundwater on the mechanical properties of soft rock is proposed. It is introduced into the generalized Hoek–Brown strength criterion for modification. The modified Hoek–Brown strength criterion can be applied to the displacement calculation and stability analysis of water-rich soft rock tunnel. The applicability of the modified Hoek–Brown strength criterion is verified by monitoring data in engineering practice.

2. Water Immersion Softening Test of Soft Rock Specimens

2.1. Preparation of Specimens. The rock samples are obtained from the face of the Xiejiapo tunnel, which is a water-rich soft rock tunnel, and the lithology is mainly carbonaceous phyllite. In accordance with the requirements of "Test method standard for engineering rock mass" (GB/T50266-2013) and on the basis of the actual test scheme and conditions, the rock specimens were made into cylindrical blocks with a diameter of 50 mm and height of 100 mm, as shown in Figure 1. The height-diameter ratio is not less than 2.0, the diameter error is less than 3 mm, and the nonparallelism of the end face is less than 0.05 mm. The end face of the rock sample is perpendicular to the axis, and the maximum deviation is less than 0.25 degrees, which is in line with the provisions of the International Society of Rock Mechanics (ISRM) for rock samples.

Figure 1: Prepared phyllite specimens.

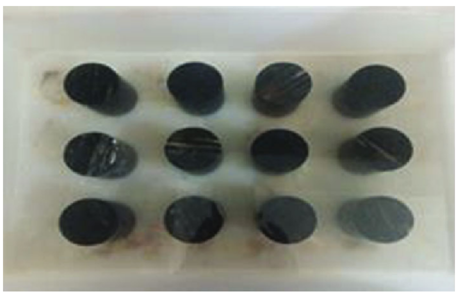

Figure 2: Phyllite specimen immersed in water.

The surface integrity of the initially processed rock samples was examined to prevent the large discreteness of the test data. The RSM-SY5(T) nonmetallic acoustic testing instrument was used to detect the wave velocity of the rock samples. The rock samples with no evident surface defects and similar wave velocity were selected for the test.

2.2. Test Scheme and Equipment. The prepared samples were divided into five groups with three blocks in each group. Five groups of test blocks were placed in a 50 cm × 45 cm × 30 cm tank, and water was added until the samples were completely submerged, as shown in Figure 2. Five groups of test blocks were immersed for 0, 30, 90, 180, and 270 days. The P-wave velocity test, porosity test, and uniaxial compression test of soft rock under different immersion time were carried out to study the softening characteristics of soft rock.

2.2.1. P-Wave Velocity Test. The P-wave velocity of the samples soaked for 0, 30, 90, 180, and 270 days was tested. The test equipment was RSM-SY5(T) acoustic wave tester, as shown in Figure 3. Three P-wave velocity tests were carried out on each sample, and the average value of the three tests was considered the P-wave velocity value of the sample.

2.2.2. Porosity Test. The porosity test was carried out when the samples were soaked for 0, 30, 90, 180, and 270 days. The test equipment was MesoMR23-060 H-I nuclear magnetic resonance instrument. Prior to the nuclear magnetic test, the specimen required vacuum saturation. The porosity of material was calculated accurately by analysing the relaxation behaviour of proton in rock under a magnetic field.

2.2.3. Uniaxial Compression Test. Uniaxial compression tests were carried out by YA-2000 digital pressure testing machine, as shown in Figure 4. Uniaxial compression tests were carried out on specimens immersed in water for 0, 30,

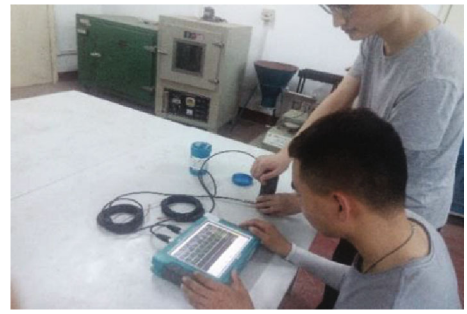

Figure 3: P-wave velocity test.

Figure 4: Uniaxial compression test.

90, 180, and 270 days. The load was applied at the loading rate of 0.5 kN per second and continuously collected until the test block was destroyed.

2.3. Mechanical Properties of Soft Rock under Different Immersion Time. The parameters of soft rock under different immersion time are obtained by analysing the test data, as shown in Table 1.

Generally, the lithology of surrounding rock in the same section is similar. Table 1 shows that the mechanical properties of the soft rock are the same under the same immersion time, therefore, it can be considered that the mechanical properties of the surrounding rock at the same section in water-rich soft rock tunnel are the same. Poisson's ratio of soft rock does not change significantly with the extension of immersion time. The change trend of elastic modulus and uniaxial compressive strength gradually reduced in the early stage and then stabilized. The experimental data were fitted by exponential function, power function, and logarithmic function, and the corresponding mathematical model was established. The functional relationship between immersion time and elastic modulus and compressive strength was obtained. The fitting formula and correlation coefficient are shown in Table 2.

Considering the correlation coefficient and relative error, the formula with the highest fitting degree was determined, as shown in Formula (1).

$$\begin{cases} E_t = 0.894 E_0 e^{-3\times10^{-3} t}, \\ \sigma_{ct} = 0.949 \sigma_0 e^{-1\times10^{-3} t}, \end{cases} \tag{1}$$

Table 1: Parameters of soft rock under different immersion time.

Test specimen number	Immersion time (t/d)	Compressive strength (σ_c/MPa)	Poisson ratio (μ)	Elastic modulus (E/GPa)	P-wave velocity (V/m·s^{-1})	Porosity (n/%)
1-1	0	23.58	0.337	33.214	2650	0.467
1-2	0	23.40	0.348	33.383	2647	0.446
1-3	0	22.96	0.333	32.656	2539	0.421
2-1	30	18.12	0.336	30.007	2638	0.572
2-2	30	18.45	0.332	30.131	2609	0.568
2-3	30	18.32	0.337	29.952	2629	0.583
3-1	90	14.35	0.337	26.935	2578	0.762
3-2	90	15.13	0.330	27.917	2541	0.695
3-3	90	14.96	0.329	27.272	2558	0.707
4-1	180	10.92	0.336	25.029	2501	1.098
4-2	180	11.38	0.327	24.960	2458	0.974
4-3	180	11.10	0.336	25.510	2418	1.063
5-1	270	9.96	0.328	24.929	2449	1.218
5-2	270	9.82	0.334	24.137	2439	1.196
5-3	270	10.58	0.336	25.017	2321	1.101

Table 2: Fitting formula and correlation coefficient comparison table.

Form of fitting function	Fitting formula	Correlation coefficient
Exponential function	$E_t = 0.894E_0e^{-3\times10^{-3}t}$	0.998
	$\sigma_{ct} = 0.949\sigma_0e^{-1\times10^{-3}t}$	0.985
	$V_t = 1.007V_0e^{-3\times10^{-4}t}$	0.995
	$(1-n_t) = (1-n_0)e^{-3\times10^{-5}t}$	0.971
Power function	$E_t = 0.864E_0t^{-0.094}$	0.859
	$\sigma_{ct} = 0.944\sigma_0t^{-0.035}$	0.822
	$V_t = 0.994V_0t^{-0.008}$	0.681
	$(1-n_t) = 1.455(1-n_0)t^{0.0624}$	0.764
Polynomial function	$E_t = 0.0001t^2 - 0.0555t + E_0$	0.977
	$\sigma_{ct} = 0.0002t^2 + 0.0721t + \sigma_0$	0.977
	$V_t = -0.00002t^2 - 0.8588t + V_0$	0.809
	$(1-n_t) = -0.000005t^2 + 0.004t + (1-n_0)$	0.967

where σ_{ct} is the uniaxial compressive strength of soft rock when the soaking time is t; σ_0 is the uniaxial compressive strength of the soft rock in the natural state,$\sigma_0 = 23.313$MPa; E_t is the elastic modulus of soft rock when the soaking time is t; E_0 is the elastic modulus of soft rock in the natural state, $E_0 = 33.084$GPa; t is immersion time.

The change in P-wave velocity and porosity can reflect the change in mechanical properties. Therefore, the P-wave velocity and rock porosity in Table 1 are analyzed. The table shows that with the extension of soaking time, the P-wave velocity of soft rock decreased gradually in the early stage and stabilized in the later stage. On the contrary, with the extension of soaking time, the porosity increased slowly in the early stage and then increased rapidly. The P-wave velocity and porosity of soft rock were fitted with the immersion time, and the formula with the highest fitting degree was selected, as shown in Formula (2), as follows:

$$\begin{cases} V_t = 1.007V_0e^{-3\times10^{-4}t}, \\ (1-n_t) = (1-n_0)e^{-3\times10^{-5}t}, \end{cases} \tag{2}$$

where V_t is the P-wave velocity of soft rock when the soaking time is t; V_0 is the P-wave velocity of soft rock in the natural state, $V_0 = 2612m\cdot s^{-1}$; n_t is the porosity of soft rock when the soaking time is t; n_0 is the porosity of soft rock in the natural state, $n_0 = 0.4445\%$.

3. Modified Hoek–Brown Strength Criterion

3.1. Generalized Hoek–Brown Strength Criterion. In 1980, based on the theoretical research results of Griffith, Hoek and Brown [16] proposed Hoek–Brown strength criterion through a large number of rock tests, which can reflect the nonlinear failure characteristics of rock mass and make up for the deficiency of linear Mohr–Coulomb strength criterion. Then, Hoek et al. [17] improved the Hoek–Brown strength criterion and proposed a generalized Hoek–Brown strength criterion with wider applicability, such as Formula (3), as follows:

$$\sigma_1 = \sigma_3 + \sigma_c \left[m_b \frac{\sigma_3}{\sigma_c} + s \right]^{\alpha}, \quad (3)$$

where σ_c is the compressive strength of rock; m_b, s, and α are the parameters related to rock lithology. Hoek introduced the geological strength index (GSI) for the calculation to determine the three parameters. Then, considering the influence of blasting and other construction measures on the stability of surrounding rock, the blasting disturbance factor (D) is introduced. The specific calculation formula is shown in Formula (4), as follows:

$$\begin{cases} m_b = m_i \exp\left(\dfrac{\mathrm{GSI} - 100}{28 - 14D}\right), \\ s = \exp\left(\dfrac{\mathrm{GSI} - 100}{9 - 3D}\right), \\ \alpha = 0.5 + \dfrac{1}{6}\left[\exp\left(-\dfrac{\mathrm{GSI}}{15}\right) - \exp\left(\dfrac{-20}{3}\right)\right], \end{cases} \quad (4)$$

where m_i is the m value of the rock block without joints and beddings; it can be obtained by referring to the relevant specifications through the lithology, hardness, and mineral composition of the rock; D is the blasting disturbance factor, which can be determined by the lithology and construction of surrounding rock; GSI is the geological strength index of rock.

3.2. Water-Rich Disturbance Factor. To apply the Hoek–Brown strength criterion to the water-rich soft rock tunnels, the softening effect of groundwater should be considered. To a certain extent, the change in the mechanical properties of soft rock after immersion can reflect the seepage influence of groundwater on the mechanical properties of surrounding rock in soft rock tunnel.

The elastic modulus of rock is an index used to describe the elastic deformation resistance of rock, so it can best reflect the change of mechanical properties of rock. According to the water immersion softening test of soft rock and the principle of damage mechanics, the change in elastic modulus under water-rich condition is used to characterise the influence of groundwater on soft rock, and the water-rich influence factor is proposed. The definition is shown in Formula (5), as follows:

$$D_\omega = 1 - \frac{E_\omega}{E_0}, \quad (5)$$

where D_ω is the water-rich influence factor, the value range is $0 \le D_\omega \le 1$; E_ω is the elastic modulus value after the influence of rich water that can be obtained by substituting the specific immersion time into E_t; E_0 is the elastic modulus under natural state.

The elastic modulus can be obtained by uniaxial compression test of rock and analysis of stress-strain curve. The porosity and P-wave velocity of rock can be obtained only by simple nondestructive test, and the test is relatively simple and fast. Therefore, the P-wave velocity and porosity are selected to calculate the damage variable of rock. According to the propagation theory of elastic wave in rock, the P-wave velocity of rock is related to elastic modulus, Poisson's ratio, and rock density, such as Formula (6), as follows:

$$V_P = \sqrt{\frac{E(1-\mu)}{\rho(1+\mu)(1-2\mu)}}, \quad (6)$$

where V_P is the P-wave velocity, which is different under different conditions. The P-wave velocity can be obtained by substituting different soaking time into Formula (2). E is the elastic modulus, which is different under different conditions. Elastic modulus can be obtained by substituting different soaking time into Formula (1). μ is the Poisson's ratio, and ρ is the density.

According to the results of the water immersion softening test, the Poisson's ratio of the soft rock has no evident change after soaking and can be ignored. Substitute the equality transformation of Formula (6) into Formula (5). At the same time, the relationship between the density and porosity of rock mass under unit mass is substituted into the water-rich influence factor, and the expression is shown in Formula (7), as follows:

$$D_\omega = 1 - \frac{1 - n_\omega}{1 - n_0} \frac{{V_\omega}^2}{{V_0}^2}, \quad (7)$$

where n_ω is the porosity of soft rock affected by water-rich conditions; n_0 is the porosity of soft rock before experiencing the influence of water-rich conditions; V_ω is the P-wave velocity affected by water-rich conditions; V_0 is the P-wave velocity of soft rock before experiencing the influence of water-rich conditions.

The relationship among P-wave velocity, porosity, and immersion time is substituted into the expression of the water-rich influence factor to accurately calculate the water-rich influence factor under different working conditions. The water-rich influence factor with timeliness is obtained, such as Formula (8), as follows:

$$D_{\omega t} = 1 - \frac{1 - n_t}{1 - n_0}\frac{V_t^{\,2}}{V_0^{\,2}} = 1 - 1.014e^{-6.3\times10^{-4}t}, \tag{8}$$

where $D_{\omega t}$ is a water-rich influence factor considering timeliness.

According to the results of the soft rock immersion softening test, after 180 days of soft rock immersion, the changes in various parameters are small and tend to be stable. It can be assumed that in the water-rich section of the soft rock tunnel, the t value greater than 180 can be selected to calculate the water-rich influence factor; in the natural state, $t = 0$ can be selected for calculation.

For water-rich soft rock tunnels, the effects of blasting disturbance and water-rich on tunnels should be considered simultaneously. In this regard, a water-rich disturbance factor considering blasting disturbance and groundwater effect is established. According to the principle of strain equivalence, the blasting disturbance factor is the first disturbance effect, and the water-rich disturbance factor is the second disturbance effect. Combined with the damage coupling principle in damage mechanics theory, the second disturbance effect can only affect other parts except for the first disturbance effect. Then, the expression of water-rich disturbance factor is defined in Formula (9), as follows:

$$D_m = D + D_\omega - DD_\omega, \tag{9}$$

where D_m is the water-rich disturbance factor considering the blasting disturbance factor and the water-rich influence factor; D is the blasting disturbance factor; D_ω is the water-rich influence factor.

By substituting Formula (8) into Formula (9), the expression of water-rich disturbance factor with timeliness can be obtained, as shown in Formula (10), as follows:

$$D_{mt} = 1 + 1.014D\,e^{-6.3\times10^{-4}t} - 1.014\,e^{-6.3\times10^{-4}t}, \tag{10}$$

where D_{mt} is a water-rich disturbance factor with timeliness. The blasting disturbance factor D value can be determined in accordance with the lithology and construction of the site. In the water-rich section of the soft rock tunnel, the t value greater than 180 can be selected to calculate the water-rich influence factor; in the natural state, $t = 0$ can be selected for calculation.

3.3. Modified Hoek–Brown Strength Criterion. From the parameter solution Formula (4), obtaining the three parameters m_b, s, and α in the modified Hoek–Brown strength criterion, the geological strength index value is required in addition to the value of water-rich disturbance factor. Hashemi et al. [25] proposed the method of estimating the GSI value by RMR value. Barton [26] proposed the relationship between RMR_{89} and rock mass quality index Q. Q was also related to the P-wave velocity of the rock mass. The specific relationship is shown in Formula (11), as follows:

$$\begin{cases} \mathrm{GSI} = \mathrm{RMR}_{89} - 5, \\ \mathrm{RMR}_{89} = 15\lg Q + 50, \\ Q = 10^{V_p/1000-3.5}, \end{cases} \tag{11}$$

where RMR_{89} is the geological classification parameter of the RMR geomechanical classification method, $\mathrm{RMR}_{89} > 23$; Q is the rock mass quality index, and V_P is the P-wave velocity.

After substituting Formula (2) into Formula (11), the geological strength index value of soft rock under water-rich conditions with timeliness can be obtained, as shown in Formula (12), as follows:

$$\mathrm{GSI}_t = 39.45e^{-3\times10^{-4}t} - .75, \tag{12}$$

where GSI_t is a geological strength index with timeliness.

By substituting time-dependent water-rich disturbance factor and time-dependent geological strength index into the parameter solving Formula (4), the parameters in the modified Hoek–Brown strength criterion can be obtained using Formula (13), as follows:

$$\begin{cases} m_b = m_i \exp\left(\dfrac{39.454e^{-3\times10^{-4}t} - 107.5}{14\left(1 + 1.014e^{-6.3\times10^{-4}t} - 1.014e^{-6.3\times10^{-4}t}D\right)}\right), \\ s = \exp\left(\dfrac{39.454e^{-3\times10^{-4}t} - 107.5}{3\left(2 + 1.014e^{-6.3\times10^{-4}t} - 1.014e^{-6.3\times10^{-4}t}D\right)}\right), \\ \alpha = 0.5 + \dfrac{1}{6}\left[\exp\left(-2.630e^{-3\times10^{-4}t} + 0.5\right) - \exp\left(\dfrac{-20}{3}\right)\right]. \end{cases} \tag{13}$$

Combined with the water-rich condition of the tunnel, the water-rich time t of the tunnel is reasonably selected and substituted into Formula (13). Each parameter value in the Hoek–Brown strength criterion under different water-rich conditions can be obtained and then used to calculate the displacement of the tunnel surrounding rock.

4. Deformation Analysis of Surrounding Rock

The problem of deep tunnel excavation can be simplified as the "thick wall cylinder" problem in elastic–plastic mechanics. The inner diameter of "cylinder" is the diameter of tunnel excavation, and the outer diameter can be ideally regarded as infinite. The deformation of the corresponding position of the tunnel surrounding rock can be obtained by calculating the displacement of the inner wall of the "thick wall cylinder."

4.1. Fundamental Assumptions. Prior to the elastic–plastic analysis of the deformation of tunnel surrounding rock, the rock mass is assumed to be continuous, homogeneous, and isotropic. The lithology of the surrounding rock in each part of the tunnel is consistent. At the same time, assuming the surrounding rock is an ideal linear elastic body, the plastic zone strain of the tunnel conforms to the Hoek–Brown strength criterion. The excavation mechanical model of the tunnel is shown in Figure 5.

As shown in Figure 5, the excavation radius of the tunnel is r_0; the radius of the plastic zone of the surrounding rock of the tunnel is R_0, and the elastic zone of the surrounding rock of the tunnel is infinite. P_0 is the initial stress of the surrounding rock during tunnel excavation, and P_i is the supporting resistance of the supporting structure.

4.2. Surrounding Rock Stress Analysis

4.2.1. Stress Analysis in Elastic Zone. The stress component of any point in the elastic zone of the surrounding rock is only related to the distance to the centre of the tunnel. It is independent of the position of the point. The stress of any point in the elastic zone of surrounding rock is only related to the radius and independent of the angle. The stress equilibrium equation and geometric equation at any point in the elastic zone of surrounding rock are shown in Formula (14), as follows:

$$\begin{cases} \dfrac{d\sigma_r}{dr} + \dfrac{\sigma_r - \sigma_\theta}{r} = 0, \\ \varepsilon_r = \dfrac{dx}{dr}, \\ \varepsilon_\theta = \dfrac{x}{r}, \end{cases} \tag{14}$$

where σ_r is the radial stress at any point in the elastic zone; σ_θ is the tangential stress at any point in the elastic zone; r is the distance from any point in the elastic zone to the centre of the tunnel; x is the radial displacement of any point in the elastic zone; ε_r is the radial strain at any point in the elastic zone; ε_θ is the tangential strain at any point in the elastic zone.

On the boundary of the elastic zone and plastic zone of the surrounding rock, the stress of the elastic zone is the same as that of the plastic zone. Therefore, the stress expression of any point in the elastic zone of the surrounding rock can be obtained, as shown in Formula (15), as follows:

$$\begin{cases} \sigma_r = P_0\left(1 - \dfrac{r_0^2}{r^2}\right) + \sigma_R \dfrac{r_0^2}{r^2}, \\ \sigma_\theta = P_0\left(1 + \dfrac{r_0^2}{r^2}\right) - \sigma_R \dfrac{r_0^2}{r^2}, \end{cases} \tag{15}$$

where P_0 is the initial ground stress; σ_R is the radial stress at the boundary of the elastic zone and plastic zone of the surrounding rock; r_0 is the excavation radius of the tunnel.

4.2.2. Stress Analysis in Plastic Zone. In polar coordinates, the expression of Hoek–Brown strength criterion is shown in Formula (16), as follows:

$$\sigma_\theta = \sigma_r + \sigma_c\left(m_b \frac{\sigma_r}{\sigma_c} + s\right)^\alpha. \tag{16}$$

Formula (16) is substituted into the first formula of Formula (14), and the formula is integrally calculated. Considering the boundary condition $r = r_0$, $\sigma_r = P_i$, the stress expression of the plastic zone can be obtained, as shown in Formula (17), as follows:

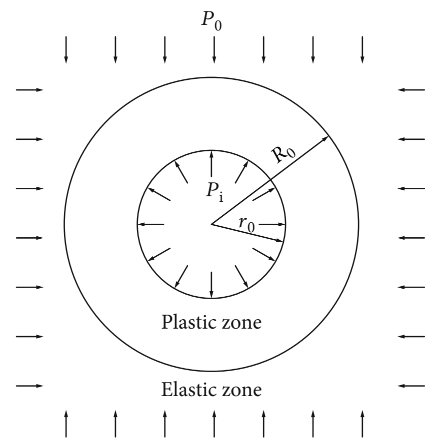

Figure 5: Mechanical model diagram of tunnel excavation.

$$\begin{cases} \sigma_r = \dfrac{\sigma_c}{m_b}\left[m_b(1-\alpha)\ln\left(\dfrac{r}{r_0}\right) + \left(m_b\dfrac{P_i}{\sigma_c} + s\right)^{1-\alpha}\right]^{1/1-\alpha} - \dfrac{\sigma_c}{m_b}s, \\ \sigma_\theta = \dfrac{\sigma_c}{m_b}\left[m_b(1-\alpha)\ln\left(\dfrac{r}{r_0}\right) + \left(m_b\dfrac{P_i}{\sigma_c} + s\right)^{1-\alpha}\right]^{1/1-\alpha} - \dfrac{\sigma_c}{m_b}s, \\ +\sigma_c\left[m_b(1-\alpha)\ln\left(\dfrac{r}{r_0}\right) + \left(m_b\dfrac{P_i}{\sigma_c} + s\right)^{1-\alpha}\right]^{\alpha/1-\alpha}, \end{cases} \tag{17}$$

where P_i is the supporting resistance of the supporting structure.

On the boundary of the elastic–plastic zone of the surrounding rock, where $r = R_0$, the stress in the elastic zone is the same as that in the plastic zone, where $\sigma_\theta^e = \sigma_\theta^p$, $\sigma_r^e = \sigma_r^p$. According to Formula (15), we can obtain the following:

$$\sigma_r^e + \sigma_\theta^e = 2P_0, \tag{18}$$

where σ_θ^e is the tangential stress in the elastic zone, σ_θ^p is the tangential stress in the plastic zone, σ_r^e is the radial stress in the elastic zone, $\sigma_r^p$is the radial stress in the elastic zone, and P_0 is the initial ground stress.

The radius of the plastic zone can be calculated by Formulas (17) and (18), as shown in Formula (19), as follows:

$$\begin{aligned} 2P_0 = {} & \frac{2\sigma_c}{m_b}\left[m_b(1-\alpha)\ln\left(\frac{r}{r_0}\right) + \left(m_b\frac{P_i}{\sigma_c} + s\right)^{1-\alpha}\right]^{1/1-\alpha} \\ & - \frac{2\sigma_c}{m_b}s + \sigma_c\left[m_b(1-\alpha)\ln\left(\frac{r}{r_0}\right) + \left(m_b\frac{P_i}{\sigma_c} + s\right)^{1-\alpha}\right]^{\alpha/1-\alpha}. \end{aligned} \tag{19}$$

Substituting the radius of the plastic zone into Formula (17), the radial stress of the elastic zone and plastic zone boundary of the surrounding rock can be calculated by

Formula (20), as follows:

$$\sigma_R = \frac{\sigma_c}{m_b}\left[m_b(1-\alpha)\ln\left(\frac{R_p}{r_0}\right) + \left(m_b\frac{P_i}{\sigma_c}+s\right)^{1-\alpha}\right]^{1/1-\alpha} - \frac{\sigma_c}{m_b}s. \quad (20)$$

4.3. Displacement Analysis of Surrounding Rock. The rock mass has an initial ground stress P_0. Tunnel excavation causes the redistribution of surrounding rock stress, resulting in the stress increment, and then the displacement of tunnel surrounding rock.

When the surrounding rock is in the elastic zone, Formula (15) can deduce the stress increment of the surrounding rock by using Formula (21), as follows:

$$\begin{cases} \Delta\sigma_r = P_0\left(1-\frac{R_p^2}{r^2}\right) + \sigma_R\frac{R_p^2}{r^2} - P_0 = -\frac{R_p^2}{r^2}(P_0-\sigma_R), \\ \Delta\sigma_\theta = P_0\left(1+\frac{R_p^2}{r^2}\right) - \sigma_R\frac{R_p^2}{r^2} - P_0 = \frac{R_p^2}{r^2}(P_0-\sigma_R). \end{cases} \quad (21)$$

According to the stress–strain equation of the surrounding rock under polar coordinates, the stress–strain equation of surrounding rock under stress increment can be obtained using Formula (22), as follows:

$$\varepsilon_\theta = \frac{1-\mu^2}{E}\left(\Delta\sigma_\theta - \frac{\mu}{1-\mu}\Delta\sigma_r\right), \quad (22)$$

where μ is Poisson's ratio; E is the elastic modulus, ε_θ is the strain increment, $\Delta\sigma_\theta$ is the increment of tangential stress, and $\Delta\sigma_r$ is the increment of radial stress.

Substituting stress increment in Formula (21) into constitutive Formula (22) and combining geometric equation (14), the displacement of the elastic zone can be calculated using Formula (23), as follows:

$$x = \frac{1+\mu}{E}\frac{R_p^2}{r}(\sigma_R - P_0), \quad (23)$$

when $r = R_0$, the displacement of the elastic zone and plastic zone boundary of the surrounding rock can be calculated using Formula (24), as follows:

$$x_p = \frac{(1+\mu)(\sigma_R - P_0)}{E}R_p, \quad (24)$$

where x_p is the displacement of the boundary between the elastic zone and plastic zone, R_0 is the radius of the plastic zone; P_0 is the initial ground stress; σ_R is the radial stress at the boundary of the elastic zone and plastic zone; μ is Poisson's ratio; E is elastic modulus.

The plastic deformation of the tunnel surrounding rock mainly considers the shape change. Assuming the tunnel surrounding rock is an incompressible material, the deformation is shown in Formula (25), as follows:

$$\varepsilon_v = \varepsilon_r + \varepsilon_\theta + \varepsilon_z = 0. \quad (25)$$

In Formula (25), ε_v is the volumetric strain, ε_r is the radial strain, ε_θ is the tangential strain, and ε_z is the axial strain.

In elastic–plastic mechanics, "thick-walled cylinder" is a plane strain problem, considering $\varepsilon_z = 0$. According to the continuity of tunnel surrounding rock deformation, the plastic zone displacement of the tunnel surrounding rock can be calculated using Formula (26), as follows:

$$x = \frac{1+\mu}{E}(\sigma_R - P_0)\frac{R_p^2}{r}. \quad (26)$$

In the plastic zone and the tunnel excavation boundary, where $r = r_0$, combined with Formula (23) and considering Formula (17), the surrounding displacement of the tunnel surrounding rock can be obtained using Formula (27), as follows:

$$x = \frac{1+\mu}{E}\frac{R_p^2}{r_0}\left\{\frac{\sigma_c}{m_b}\left[m_b(1-\alpha)\ln\left(\frac{R_p}{r_0}\right) + \left(m_b\frac{P_i}{\sigma_c}+s\right)^{1-\alpha}\right]^{1/1-\alpha} - \frac{\sigma_c}{m_b}s - P_0\right\}. \quad (27)$$

The displacement of the surrounding rock of the water-rich soft rock tunnel can be obtained through the displacement formula of the tunnel surrounding rock and the solution formula of each parameter.

5. Engineering Application

5.1. Engineering Situation. The newly-built Xiejiapo tunnel is a typical water-rich soft rock tunnel in Ankang–Langao Expressway, located in Hanbin District, Ankang City, Shaanxi Province. The tunnel is a separate one-way two-lane tunnel. The entrance pile number of the left line of the tunnel is ZK 15 + 200, and the exit pile number is ZK18 + 090, which is 2870 m long. The entrance pile number of the right line of the tunnel is K15 + 210, the exit pile number is K18 + 090, and the length is 2880 m. The maximum buried depth of the tunnel is approximately 234.0 m. The lithology of the entire strata in the tunnel site area is relatively complex, mainly phyllite of Meiziya Formation of Lower Silurian, which is grey and Brown. The surrounding rock of the tunnel is a thin sheet structure with silk lustre, and the strength is low in wet state. It is easily softened in water. The surrounding rock mass in the tunnel is broken, and the joint fissure is developed. It has poor ability to resist weathering, poor self-stability, and easy to collapse. The surrounding rock grade is V.

Groundwater is developed in the tunnel site area; it is mainly composed of pore fissure water of quaternary loose rock and basic fissure water. The surrounding rock is under water-rich conditions for a long time. The tunnel has a net width of 11.77 m and a net height of 8.80 m. The internal radius of the arch wall is 6.05 m, and the internal radius is

17.0 m in the inverted arch. The tunnel is in the Qinling fold tectonic belt, and the Dabashan fault zone passes through it. Tunnel construction is prone to collapse and water inrush events.

5.2. Theoretical Analysis of the Displacement of Surrounding Rock of Xiejiapo. The water-rich section ZK17 + 730 − ZK 17 + 760 and the natural state section ZK17 + 500 − ZK17 + 530 of Xiejiapo tunnel are selected as the research objects. In the water-rich section, the surrounding rock is always in the state of immersion, and it can be considered that the surrounding rock is in the state of immersion for 300 days. The surrounding rock is assumed to be immersed for 300 days, and in the natural state, the surrounding rock is assumed to be immersed for 0 days. The displacement of the surrounding rock is calculated considering the actual construction situation.

5.2.1. Determining the Parameters. The surrounding rock of the tunnel is mainly carbonaceous phyllite. According to the lithology of carbonaceous phyllite observed on site, $m_i = 7$. According to the blasting evaluation results of field tunnel engineering, the blasting disturbance factor $D = 0.45$. According to the tunnel equivalent radius value method, $r_0 = 9.60$. At the same time, different t values are substituted into Formula (13) to obtain the parameters of Hoek–Brown strength criterion, as shown in Tables 3 and 4.

5.2.2. Initial Ground Stress. The initial vertical ground stress of the tunnel only considers the self-weight of the surrounding rock in Formula (28), as follows:

$$P_0 = \gamma h. \tag{28}$$

In Formula (28), P_0 is the initial ground stress, γ is the bulk density, and h is the buried depth of the tunnel. The average buried depth of the water-rich section and natural state section of soft rock tunnel is 130 m. Thus, the initial stress of the tunnel can be calculated, $P_0 = 3.63\text{MPa}$.

5.2.3. Support Resistance. According to the provisions of "Specification for design of highway tunnels" (JTG 3370.1-2018), the formula for calculating the vertical surrounding rock pressure at the arch of deep-buried tunnels is shown in Formula (29), as follows:

$$q = 0.45 \times 2^{s-1} \times \gamma \times [1 + i(B - 5)], \tag{29}$$

where q is the surrounding rock pressure of the tunnel arch, and the unit is kN/m^2; s is the level of surrounding rock; B is the tunnel width, the unit is m; i is related to tunnel width B, $i = 0.1$. Support resistance of the initial support in vertical direction can be calculated, $P_i = 256.20\text{kPa}$.

5.2.4. Surrounding Rock Deformation. According to the vertical initial stress and vertical support resistance, the parameters in Tables 2 and 3 are substituted into the calculation formula of surrounding rock displacement (20), and the range of plastic zone of the surrounding rock can be calculated. Then, the parameters are substituted into Formula (27), and the vault subsidence of the tunnel surrounding rock can be calculated. The calculation results are shown in Table 5.

Table 3: Parameters of the generalized Hoek-Brown strength criterion.

t	D	GSI	m_b	s	α	σ_c
0	0.4500	31.815	0.30232	0.000135	0.51977	23.314
360	0.4500	31.815	0.30232	0.000135	0.51977	7.917

Table 4: Parameters of the modified Hoek-Brown strength criterion.

t	D_m	GSI_t	m_b	s	α	σ_c
0	0.4500	31.815	0.30223	0.000135	0.51977	23.314
360	0.5616	27.790	0.19400	0.000052	0.52592	7.917

Table 5: Calculation results of tunnel vault surrounding rock deformation.

Immersion time (d)	The displacement using generalized Hoek-Brown strength criterion (mm)	Displacement using Hoek-Brown strength criterion considering water-rich disturbance factor (mm)
0	43.51	43.51
360	44.33	54.53

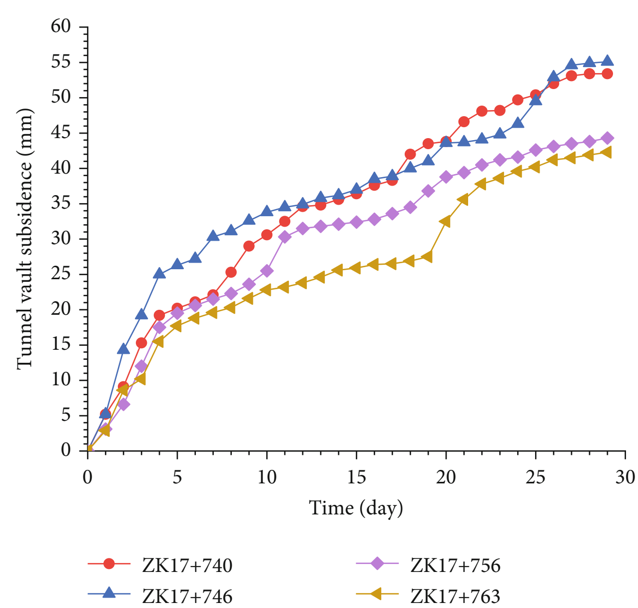

Figure 6: Temporal curve of vault subsidence monitoring section.

Table 4 shows that when the generalized Hoek–Brown strength criterion is used to calculate the vault settlement of the tunnel, the calculation results of the natural section and the water-rich section are similar. However, when the modified Hoek–Brown strength criterion is used, the vault settlement of the water-rich section is evidently larger than that of the natural section. When calculating the displacement

Table 6: Displacement of surrounding rock under different strength criterion.

Section number	Section	The deformation value of tunnel vault (mm)	The displacement using generalized Hoek-Brown strength criterion		Displacement using modified Hoek-Brown strength criterion	
			Theoretical value (mm)	Relative error (%)	Theoretical value (mm)	Relative error (%)
1	ZK17 + 740	53.6 mm	44.33 mm	-20.91%	54.53 mm	1.71%
2	ZK17 + 746	55.1 mm	44.33 mm	-24.30%	54.53 mm	-1.05%
3	ZK17 + 756	44.3 mm	43.51 mm	-1.81%	43.51 mm	-1.81%
4	ZK17 + 763	42.3 mm	43.51 mm	2.78%	43.51 mm	2.78%

of the tunnel vault in the natural state, the calculation results of the modified Hoek–Brown strength criterion are the same as those of the generalized Hoek–Brown strength criterion. This is mainly because the modified Hoek-Brown strength criterion in natural state can be transformed into generalized Hoek-Brown strength criterion, so the displacement calculation results are the same. When calculating the displacement of tunnel vault in the water-rich section, the modified Hoek-Brown strength criterion can comprehensively consider the softening effect of water on rock mass, so the calculated displacement value of the modified Hoek-Brown strength criterion is significantly larger than that of the generalized Hoek-Brown strength criterion.

5.3. Field Displacement of the Surrounding Rock of the Xiejiapo Tunnel. According to the requirements of the "Technical specification for monitoring and measuring highway tunnels" (DB13/T 2177-2015), combined with the construction of the Xiejiapo tunnel, ZK17 + 740 and ZK17 + 746 are selected in the water-rich section ZK17 + 730 – ZK17 + 760, and ZK17 + 515 and ZK17 + 521 are selected in the natural state section ZK17 + 500 – ZK17 530. The tunnel vault subsidence of the four sections is monitored and measured, and the monitoring measurement results are drawn into the vault subsidence temporal curve, as shown in Figure 6.

The figure shows that the vault subsidence values of the four sections are 53.6, 55.1, 44.3, and 42.3 mm. The deformation of surrounding rock in the natural section is obviously smaller than that in the water-rich section, and the stability time of surrounding rock in the natural section is obviously earlier than that in the water-rich section.

5.4. Comparative Analysis. The field monitoring measurement results are compared with the theoretical calculation results, and the error is shown in Table 6.

It can be seen from Table 6 that in the natural state, the displacement of surrounding rock calculated by the generalized Hoek-Brown strength criterion is close to the measured value, and the calculation error is small, so it has good applicability. As the generalized Hoek-Brown strength criterion fails to consider the softening effect of rock mass in the water-rich section of the tunnel, the calculation error of displacement is large when calculating the settlement of the vault. However, the modified Hoek-Brown strength criterion can better consider the disturbance of rich water on lithology and can accurately calculate the displacement of surrounding rock. Therefore, the displacement calculation is closer to the field test results, and the error is small. This shows that the modified Hoek-Brown strength criterion is more suitable for water-rich soft rock tunnel, and the analysis of surrounding rock stability in water-rich soft rock tunnel is more accurate.

6. Conclusions

Through the immersion softening test, the softening law of the mechanical properties of soft rock under the groundwater seepage influence is obtained, and on this basis, the water-rich influencing factor is established. Combined with the disturbance characteristics when the water-rich soft rock tunnel excavated, the water-rich disturbance factor is introduced to modify the generalized Hoek-Brown strength criterion. Using the "thick wall cylinder" problem in elastic-plastic mechanics theory, the calculation formula of tunnel surrounding rock displacement is obtained. By comparing the monitoring value and theoretical calculation value of surrounding rock displacement in practical engineering, the applicability of the modified Hoek-Brown strength criterion is verified. The main conclusions are as follows:

(1) Through the immersion softening test of soft rock, it was found that the Poisson's ratio of soft rock did not change significantly with the extension of immersion time. The uniaxial compressive strength, elastic modulus, and P-wave velocity of soft rock decreased rapidly at the beginning of immersion and then gradually stabilized. On the contrary, the porosity of soft rock changes little at the beginning of immersion and then increases rapidly. On this basis, the variation formula of physical and mechanical indexes of soft rock with immersion time is fitted

(2) According to the damage of elastic modulus of soft rock after immersion, the concept of water-rich influence factor is proposed. Combined with the disturbance characteristics of water-rich soft rock tunnel excavation, the water-rich disturbance factor considering both blasting disturbance and groundwater softening is established. Based on this, the generalized Hoek-Brown strength criterion is modified

(3) In the water-rich section of Xiejiapo tunnel, the relative error between the vault subsidence displacement obtained by the modified Hoek-Brown strength criterion and the field monitoring measurement is small, so the modified Hoek-Brown strength criterion can be applied to the displacement calculation and the stability analysis of water-rich soft rock tunnel

Data Availability

The raw/processed data required to reproduce these findings cannot be shared at this time as the data also form part of an ongoing study.

Conflicts of Interest

The authors declare that they have no conflicts of interest.

Acknowledgments

This research was financially supported by the National Natural Science Foundation of China (Grant No. 51408054 sponsored) and the Natural Science Foundation of Shaanxi Provincial Department of Science and Technology (2017JM5136).

References

[1] S. B. Tang, "The effects of water on the strength of black sandstone in a brittle regime," *Engineering Geology*, vol. 239, pp. 167–178, 2018.

[2] C. Yu, S. Tang, C. Tang et al., "The effect of water on the creep behavior of red sandstone," *Engineering Geology*, vol. 253, pp. 64–74, 2019.

[3] R. Wang, X. Deng, Y. Meng, D. Yuan, and D. Xia, "Case study of modified H-B strength criterion in discrimination of surrounding rock loose circle," *KSCE Journal of Civil Engineering*, vol. 23, no. 3, pp. 1395–1406, 2019.

[4] Z. A. Erguler and R. Ulusay, "Water-induced variations in mechanical properties of clay-bearing rocks," *International Journal of Rock Mechanics and Mining Sciences*, vol. 46, no. 2, pp. 355–370, 2009.

[5] M. Duda and J. Renner, "The weakening effect of water on the brittle failure strength of sandstone," *Geophysical Journal International*, vol. 192, no. 3, pp. 1091–1108, 2012.

[6] C. Yang, Y. Tang, W. Wang, and S. Wang, "Experimental study on the softening characteristics of argillaceous slate with water," *Civil Engineering Journal*, vol. 26, no. 4, pp. 544–554, 2017.

[7] A. Shakoor and E. H. Barefield, "Relationship between unconfined compressive strength and degree of saturation for selected sandstones," *Environmental and Engineering Geoscience*, vol. 15, no. 1, pp. 29–40, 2009.

[8] Y. Nara, R. Nakabayashi, and M. Maruyama, "Influences of electrolyte concentration on subcritical crack growth in sandstone in water," *Engineering Geology*, vol. 179, pp. 41–49, 2014.

[9] M. U. Azhar, H. Zhou, F. Yang et al., "Water-induced softening behavior of clay-rich sandstone in Lanzhou Water Supply Project, China," *Journal of Rock Mechanics and Geotechnical Engineering*, vol. 12, no. 3, pp. 557–570, 2020.

[10] G.-H. Zhang, Y.-Y. Jiao, H. Wang, Y. Cheng, and L.-B. Chen, "On the mechanism of inrush hazards when Denghuozhai Tunnel passing through granite contact zone," *Tunneling and Underground Space Technology*, vol. 68, pp. 174–186, 2017.

[11] X. Sun, G. Li, C. Zhao, Y. Liu, and C. Miao, "Investigation of deep mine shaft stability in alternating hard and soft rock strata using three-dimensional numerical modeling," *Processes*, vol. 7, 2019.

[12] K. Bian, J. Liu, Z. Liu et al., "Mechanisms of large deformation in soft rock tunnels: a case study of Huangjiazhai Tunnel," *Bulletin of Engineering Geology and the Environment*, vol. 78, 2019.

[13] C. Wu, J. Chu, S. Wu, and Y. Hong, "3D characterization of microbially induced carbonate precipitation in rock fracture and the resulted permeability reduction," *Engineering Geology*, vol. 249, pp. 23–30, 2019.

[14] C. Wu, J. Chu, S. Wu, L. Cheng, and L. von Paassen, "Microbially induced calcite precipitation along a circular flow channel under a constant flow condition," *Acta Geotechnica*, vol. 14, no. 3, pp. 673–683, 2019.

[15] S. Thirukumaran, B. Indraratna, E. T. Brown, and P. K. Kaiser, "Stability of a rock block in a tunnel roof under constant normal stiffness conditions," *Rock Mechanics and Rock Engineering*, vol. 49, no. 4, pp. 1587–1593, 2016.

[16] E. Hoek and E. T. Brown, "Empirical strength criterion for rock masses," *Journal of Geotechnical and Geoenvironmental Engineering*, vol. 106, no. 9, pp. 1013–1035, 1980.

[17] E. Hoek, C. T. Torres, and B. Corcum, "Hoek-Brown failure criterion Proceedings of the North American Rock Mechanics Society," *Toronto: Mining Innovation and Technology*, vol. 1, pp. 267–273, 2002.

[18] H. Sonmez and R. Ulusay, "Modifications to the geological strength index (GSI) and their applicability to stability of slopes," *International Journal of Rock Mechanics and Mining Sciences*, vol. 36, no. 6, pp. 743–760, 1999.

[19] Y. Chen, H. Lin, R. Cao, and C. Zhang, "Slope stability analysis considering different contributions of shear strength parameters," *International Journal of Geomechanics*, vol. 21, no. 3, p. 04020265, 2021.

[20] Y. Chen, H. Lin, Y. Wang, and Y. Zhao, "Damage statistical empirical model for fractured rock under freezing-thawing cycle and loading," *Geofluids*, vol. 2020, 12 pages, 2020.

[21] Y. K. Lee and S. Pietruszczak, "A new numerical procedure for elasto-plastic analysis of a circular opening excavated in a strain-softening rock mass," *Tunnelling and Underground Space Technology*, vol. 23, no. 5, pp. 588–599, 2008.

[22] C. Xia, C. Xu, and Z. Xu, "Study of the strength reduction DDA method and its application to mountain tunnel," *International Journal of Computational Methods*, vol. 9, no. 3, p. 1250041, 2012.

[23] C. Wu, Y. Hong, Q. Chen, and S. Karekal, "A modified optimization algorithm for back analysis of properties for coupled stress-seepage field problems," *Tunnelling and Underground Space Technology*, vol. 94, p. 103040, 2019.

[24] Y. Xue, Y. Liu, F. Dang et al., "Assessment of the nonlinear flow characteristic of water inrush based on the Brinkman and Forchheimer seepage model," *Water*, vol. 11, no. 4, p. 855, 2019.

[25] M. Hashemi, S. Moghaddas, and R. Ajalloeian, "Application of rock mass characterization for determining the mechanical

properties of rock mass: a comparative study," *Rock Mechanics and Rock Engineering*, vol. 43, no. 3, pp. 305–320, 2010.

[26] N. Barton, "Some new _Q_ -value correlations to assist in site characterisation and tunnel design," *International Journal of Rock Mechanics and Mining Sciences*, vol. 39, no. 2, pp. 185–216, 2002.

Hindawi
Geofluids
Volume 2021, Article ID 5599977, 13 pages
https://doi.org/10.1155/2021/5599977

Research Article

Study on Critical Hydraulic Gradient Theory of Flow Soil Failure in Cohesive Soil Foundation

Mei Zhou, Faning Dang, Yutao Li, Jiulong Ding, and Jun Gao

Institute of Geotechnical Engineering, Xi'an University of Technology, Xi'an, Shaanxi 710048, China

Correspondence should be addressed to Faning Dang; dangfn@163.com

Received 26 February 2021; Revised 21 April 2021; Accepted 20 May 2021; Published 2 June 2021

Academic Editor: Chuangzhou Wu

The current formula of critical hydraulic gradient is not adapted to solve critical hydraulic gradient of cohesive soil. Assume that the seepage failure mode of the cohesive soil foundation was cylindrical or inverted circular truncated cone, based on the calculation formula of the critical hydraulic gradient of *Terzaghi*, the analytical formula of the critical hydraulic gradient considering the influence of the shear strength of the soil was derived. Then, the seepage failure process of the clay layer was simulated numerically, and the effects of the clay layer thickness, failure radius, and shear strength indexes on the critical hydraulic slope were analyzed. The comparison results show that the numerical test results are in good agreement with the calculated results of the new formula. In addition, the critical hydraulic gradient of sandy loam and loess under different working conditions was studied severally by a self-made permeation failure instrument. The results show that the critical hydraulic gradient decreases with the increase of soil thickness and failure radius, and the maximum error between the test and the corresponding formula results is no more than 16%.

1. Introduction

Infiltration is one of the important factors of engineering accidents such as dams and foundation pits, which can drive people to deeply explore the characteristics of seepage failure for better prevention and control of the occurrence of engineering accidents [1, 2]. According to the investigation, it is found that a lot of researches on the critical conditions of soil seepage failure have been conducted and hence some useful conclusions have been obtained. For example, *Wu* et al. used biogrouting and other methods to analyze the permeability characteristics of soil and coal mass [3–6]. *Zhang* et al. developed a new fluid–solid coupled numerical approach by combining the dynamic fluid mesh (DFM) method with the DEM, which can be applied to analyze the seepage mechanism of soil; in addition, the stress-strain behavior for soil subjected to internal erosion was studied by three-dimensional DEM modeling [7–10]. The crack direction of the soil during the infiltration process is an important factor affecting the seepage failure. *Rabczuk* and Belytschko proposed a model that can be used to simulate soil crack propagation [11, 12]. A famous formula was proposed by *Terzaghi* for calculating the critical hydraulic gradient according to the balance principle of self-gravity, hydrostatic buoyancy, and seepage force of soil particles in water [13]. *Changxi* considered the influence of the shape resistance of soil particles [2] to the critical hydraulic gradient based on the former theory. *Israr* and Indraratna obtained a calculation method of hydraulic gradient considering the friction between particles in the soil by introducing a stress reduction coefficient [14, 15]. The soil effective stress and the stress reduction of fine particles were combined by *Wang* et al. who put forward a formula for calculating critical hydraulic gradient of fine particles in sandy soil [16]. *Jiang* equated the pores of clay into circular pipes with uniform distribution and subsequently analyzed the critical condition of seepage failure of clay from the perspective of pipe flow, and finally, the mathematical relationship between the pore diameter and the critical condition was established [17]. *Wu* and Gao established the calculation formula of critical hydraulic gradient in case where piping happened, based on the particle gradation curve and porosity of the soil [18]. The empirical formula of critical hydraulic gradient of piping, which was expressed via confining pressure [19, 20], was performed by *Luo* et al. The whole process from occurrence to failure of the soil flow was reproduced by *Tang* et al., using the similar model [21]. Based on seepage test, the low and high critical hydraulic gradients corresponding to the local flow and global loss of fine particles were defined by *Liang et al.* [22]. *Yang* et al. studied the influence of stress state on the critical hydraulic gradient and permeability coefficient of soil through indoor tests [23–25].

It is well known that critical hydraulic slope is an important basis to judge whether seepage failure will occur in soil. Therefore, it is an inevitable topic to study critical hydraulic slope. Although there are many theoretical formulas for the critical condition of seepage failure, however, there is no unified method so far to calculate the critical hydraulic gradient, when the flow soil failure phenomenon of the clay foundation occurs. In view of this situation, this paper considers the effect of clay shear strength; based on the existing theoretical results, the formula which can calculate the critical hydraulic gradient of cohesive soil foundation when the flow soil occurrence is derived, and its rationality is verified by a series of numerical experiments and laboratory tests.

2. Establish an Analytical Formula for Critical Hydraulic Gradient of Cohesive Soil Foundation

At present, the *Terzaghi* formula is often used to calculate the critical hydraulic slope for seepage failure of foundation, which is given by

$$i_{\mathrm{cr}} = \frac{\gamma'}{\gamma_w} = (1-n)(G_s-1), \tag{1}$$

where i_{cr} is the critical hydraulic gradient, G_s is the relative density of soil particles, and n is the porosity.

It is evident that Eq. (1) neglects the influence of friction resistance between soil particles when calculating the critical hydraulic gradient [26], while the critical hydraulic gradient of cohesive soil foundation is bound up with its shear strength, and therefore, this formula falls into a failure to solve the critical hydraulic gradient of cohesive soil foundation. As a result of this factor that we just have analyzed, the following study is going to take into account the effects of cohesive soil shear strength and to modify the formula of critical hydraulic gradient.

Assuming that there is a double-layer building foundation, the upper and lower layers are cohesive soil layer and sand gravel layer, respectively, in which there is weak area in the clay layer, as shown in Figure 1(a). Besides, the water head difference between the top and bottom of the clay layer is $\triangle h$, the seepage failure will occur in the weak area of the clay layer as soon as $\triangle h$ exceeds a certain critical value. This paper assumes that the failure mode of flow soil in cohesive soil foundation is (b) or (c) in Figure 1.

2.1. Cylinder Failure Mode. Take the cylinder with radius r and clay layer thickness h as the soil separation body to analyze its stress state, as shown in Figure 1(b). It is easy to see that the cylinder subjects to upward seepage force and downward effective gravity, and the separation body will trend to move upward when the former is greater than the latter. At the same time, there is a downward shear force on the boundary of the separation body. According to the equilibrium condition of the force, the following formula can be obtained.

$$J = G + \tau, \tag{2}$$

where J, G, and τ are the total seepage force, effective gravity of soil, and shear force between the separated body and the surrounding soil, respectively. J and G can be represented as follows:

$$J = j\bullet V = i\gamma_w\bullet\pi r^2 h, \tag{3}$$

$$G = \gamma\bullet\pi r^2 h. \tag{4}$$

Theoretically, when the shear force is equal to the shear strength of the soil multiplied by the area of the shear surface, the hydraulic gradient in Eq. (2) is the critical hydraulic gradient for seepage failure of the clay foundation, i.e., the shear force of soil in critical state is given by

$$\tau = (c + \sigma \tan\varphi)\bullet 2\pi r h. \tag{5}$$

Substituting Eqs. (3)-(5) into Eq. (2), the latter is written as

$$i_{\mathrm{cr}}\gamma_w\bullet\pi r^2 h = \gamma\bullet\pi r^2 h + (c + \sigma\tan\varphi)\bullet 2\pi r h. \tag{6}$$

Eq. (7) can be acquired by moving the term and simplifying of Eq. (6):

$$i_{\alpha} = \frac{\gamma}{\gamma_w} + \frac{2(c + \sigma\tan\varphi)}{\gamma_w\bullet r}, \tag{7}$$

where σ is the average normal stress on the failure surface, since the failure surface is vertical, and the average normal stress is theoretically equal to the average static earth pressure, which is expressed by Eq. (8).

$$\sigma = \frac{1}{2}\gamma' h K_0. \tag{8}$$

The critical hydraulic gradient calculation formula of the cohesive soil foundation when the failure mode is a cylinder can be obtained by substituting Eq. (8) into Eq. (7), which is written as

$$i_{\mathrm{cr}} = \frac{\gamma}{\gamma_w} + \frac{2\left(c + 1/2\gamma' h K_0 \tan\varphi\right)}{\gamma_w\bullet r}, \tag{9}$$

where γ_w is the weight of water, equaling to $9.8\,\mathrm{kN/m^3}$; γ' is the effective unit weight of soil, $\mathrm{kN/m^3}$; c is the cohesion,

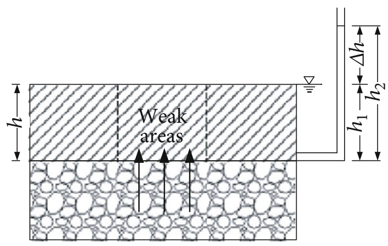

(a) Clay layer under the effect of water head difference

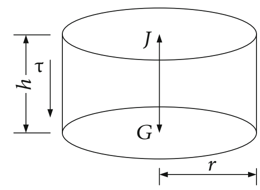

(b) Cylinder failure mode

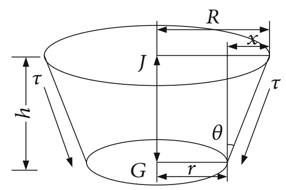

(c) Inverted frustum of a cone failure mode

Figure 1: Schematic diagram of seepage failure of clay layer.

kPa; φ is the internal friction angle, °; K_0 is the lateral pressure coefficient of soil, which is calculated by $K_0 = 1 - \sin\varphi$.

2.2. Inverted Frustum of a Cone Failure Mode. Supposing the radius of the upper and lower surfaces of the separation body of the inverted frustum of a cone is R and r, respectively, the thickness of the clay layer is h, and the angle between the generatrix and the axis is θ, as shown in Figure 1(c). According to the equilibrium conditions of gravity, seepage force, and vertical component of shear force on the boundary surface, the results are as follows:

$$J = G + \tau\cos\theta, \tag{10}$$

$$i_{cr}\gamma_w V = \gamma V + (c + \sigma\tan\varphi)A\cos\theta, \tag{11}$$

where V and A are the volume and side area of the inverted frustum of a cone, respectively.

It can be seen from Figure 1(c) that the radius difference between the upper and lower surfaces of the inverted frustum of a cone is $x(x = h\tan\theta)$, the relationship between the R and r is expressed as $R = r + h\tan\theta$, and the length of the busbar is $l\,(l = \sqrt{h^2 + (R-r)^2} = h\sqrt{1+\tan^2\theta})$.

The expressions of the side area and volume of the inverted frustum of a cone are as follows:

$$\begin{aligned} A &= \pi l(R + r) = \pi h\sqrt{1+\tan^2\theta}(r + h\tan\theta + r) \\ &= \pi h\sqrt{1+\tan^2\theta}(2r + h\tan\theta), \end{aligned} \tag{12}$$

$$V = \frac{\pi h}{3}\left(R^2 + r^2 + Rr\right) = \frac{\pi h}{3}\left[3r^2 + 3rh\tan\theta + h^2\tan^2\theta\right]. \tag{13}$$

Substituting Eq. (12) and Eq. (13) into Eq. (11) and then simplifying related items, Eq. (11) can be expressed as follows:

$$\begin{aligned} i_{cr} &= \frac{\gamma}{\gamma_w} + \frac{(c+\sigma\tan\varphi)}{\gamma_w} \bullet \frac{A\cos\theta}{V} = \frac{\gamma}{\gamma_w} + \frac{(c+\sigma\tan\varphi)}{\gamma_w} \\ &\quad \bullet \frac{\pi h\sqrt{1+\tan^2\theta}(2r + h\tan\theta)\cos\theta}{\pi h/3\left[3r^2 + 3rh\tan\theta + h^2\tan^2\theta\right]} \\ &= \frac{\gamma}{\gamma_w} + \frac{3(c+\sigma\tan\varphi)}{\gamma_w} \bullet \frac{(2r + h\tan\theta)}{\left[3r^2 + 3rh\tan\theta + h^2\tan^2\theta\right]}, \end{aligned} \tag{14}$$

where σ is the average normal stress on the failure surface and can be calculated by Eq. (15).

$$\sigma = \frac{1}{2}\gamma' h K_0\cos\theta. \tag{15}$$

When the failure mode is a cylinder, the calculation formula for the critical hydraulic gradient of the cohesive soil foundation will be obtained if we substitute Eq. (15) into Eq. (14), which is written as

$$\begin{aligned} i_{cr} &= \frac{\gamma}{\gamma_w} + \frac{3\left(c + 1/2\gamma' hK_0\cos\theta\tan\varphi\right)}{\gamma_w} \\ &\quad \bullet \frac{(2r + h\tan\theta)}{\left[3r^2 + 3rh\tan\theta + h^2\tan^2\theta\right]}. \end{aligned} \tag{16}$$

When $\theta = 0°$, Eq. (16) is simply reduced to Eq. (9), which indicates sufficiently that Eq. (16) is the most general expression of critical hydraulic gradient for seepage failure of cohesive soil foundation.

3. Analysis on Calculation Formula of Critical Hydraulic Gradient of Cohesive Soil Foundation

It is assumed that the form of flow soil failure in the cohesive soil foundation is an inverted frustum of a cone, and Eq. (16) is a function with five related variables, which is related to clay layer thickness, failure radius, two strength parameters, and stress diffusion angle. Given a basic working condition, that is, the clay layer thickness is 2 m, the failure radius of lower surface of soil layer is 2 m, the cohesion is 25 kPa, the internal friction angle and stress diffusion angle are both 20°, and then the influence of these five parameters on the critical hydraulic gradient of cohesive soil foundation is analyzed.

3.1. Influence of Clay Layer Thickness on Critical Hydraulic Gradient of Cohesive Soil Foundation. Taking the thickness of clay layer as a variable, the influence of clay layer thickness on the critical hydraulic gradient is analyzed by comparing the critical hydraulic gradient under two conditions of considering and ignoring the clay layer thickness. The results are shown in Figure 2.

It can be seen from Figure 2 that the critical hydraulic gradient would decrease in proportion to the clay layer thickness when considering the influence of clay layer thickness on the critical hydraulic gradient. The smaller the clay layer thickness is, the smaller the critical hydraulic slope difference between the two conditions is. For example, when the failure radius is 2 m, the maximum difference is 8.45% when the clay layer thickness is less than 2 m; when the clay layer thickness is less than 0.5 m, the maximum difference is only 2.59%; therefore, when the clay layer thickness is relatively thin relative to the range of soil layer, its influence on the critical hydraulic slope of cohesive soil can be ignored. It should be noted that the critical hydraulic gradient and the critical head difference are completely different concepts, and the critical head difference is positively correlated with the clay layer thickness.

3.2. Influence of Failure Radius on Critical Hydraulic Gradient of Cohesive Soil Foundation. The relation curve between the critical hydraulic gradient and the failure radius is shown in Figure 3, from which it can be seen that when the failure radius is small, the critical hydraulic slope decreases rapidly with the increase of the failure radius; with the increase of failure radius, the slope of $i_{cr} \sim r$ curve decreases, and the critical hydraulic gradient decreases with the increase of failure radius. Generally speaking, the critical hydraulic gradient decreases inversely with the increase of failure radius. In brief, the critical hydraulic gradient decreased as the failure radius increased; the reason is that the larger the failure radius (other conditions being equal), the smaller the constraint effect of cohesion at the boundary of clay layer weak zone on soil mass is, and the lower the head difference needed for soil seepage failure is, thus the smaller the critical hydraulic slope is. When the failure radius is greater than 3 m, several groups of $i_{cr} \sim r$ curves tend to coincide; when the failure radius is greater than 5 m, the critical hydraulic gradient of cohesive soil tends to a fixed value.

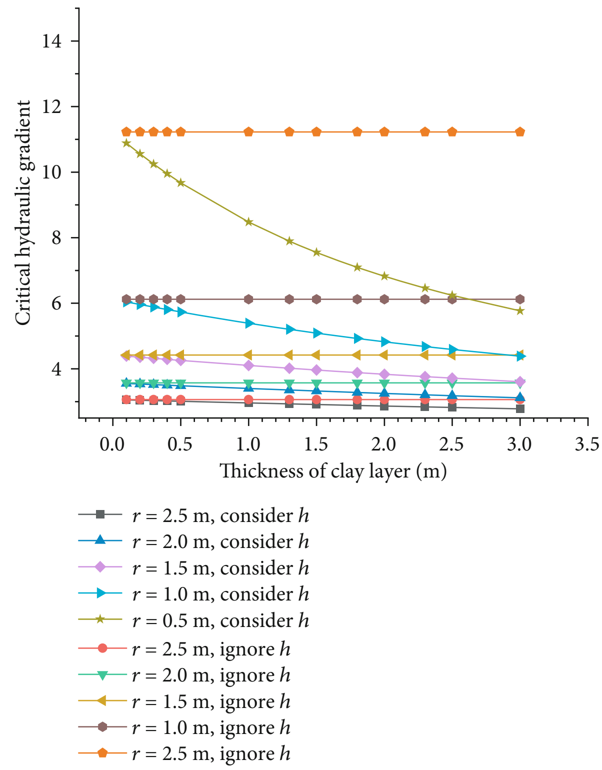

Figure 2: The curve between critical hydraulic gradient and thickness of clay layer.

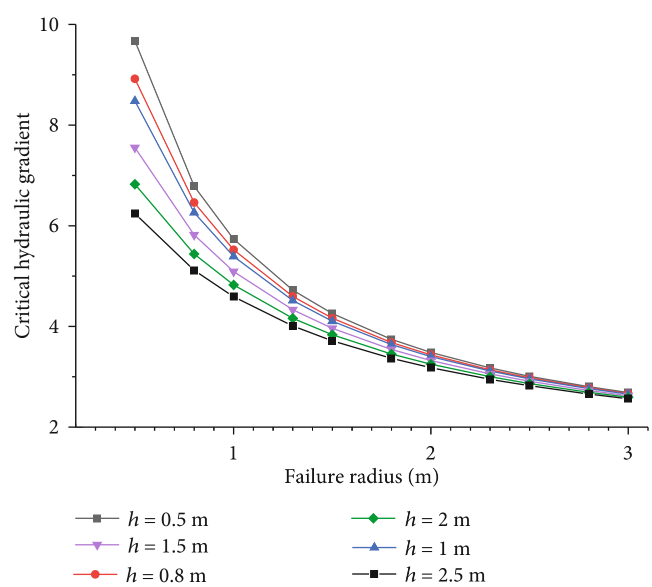

Figure 3: The curve between critical hydraulic gradient and failure radius.

To conclude, in the case that the radius of the failure opening is determined, Eq. (16) can be adopted to calculate the critical hydraulic gradient in the actual foundation pit or dam engineering; on the contrary, the hydraulic gradient corresponding to the failure radius of 5 m is taken as the critical hydraulic gradient.

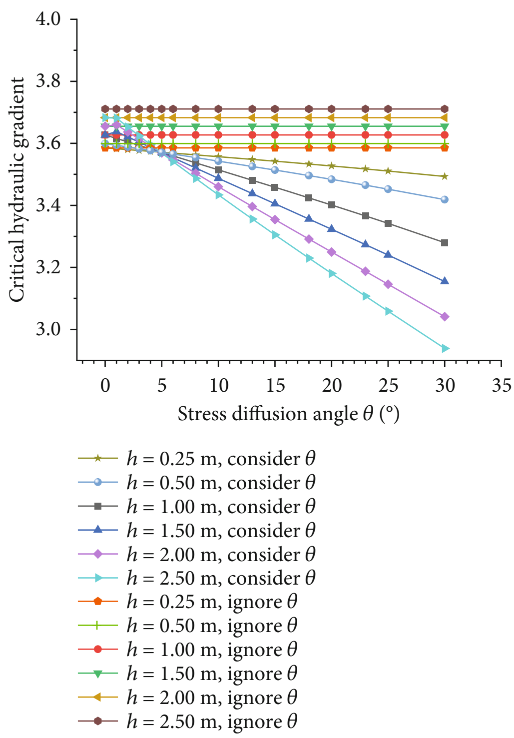

FIGURE 4: The curve between critical hydraulic gradient and angle of stress dispersion.

3.3. Influence of Stress Diffusion Angle on Critical Hydraulic Gradient of Cohesive Soil Foundation. It can be seen from Figure 4 that the stress diffusion angle has a certain influence on the critical hydraulic gradient; the critical hydraulic gradient decreases slightly with the increase of the stress diffusion angle. Moreover, the influence of the stress diffusion angle on the critical hydraulic slope is related to the clay layer thickness. The thicker the clay layer, the greater the influence of the stress diffusion angle on the critical hydraulic gradient; on the contrary, the smaller the influence is, the smaller the difference of the critical hydraulic gradient corresponding to considering and ignoring the stress diffusion angle. When $h = 0.25$ m and $\theta = 0 \sim 30^\circ$, the maximum difference is about 4.59%. Generally speaking, the clay layer thickness with flow soil failure is thin, and thus, the influence of stress diffusion angle on the critical hydraulic gradient can be ignored.

3.4. Influence of Internal Friction Angle on Critical Hydraulic Gradient of Cohesive Soil Foundation. The relation curve between the critical hydraulic gradient and the internal friction angle is shown in Figure 5, from which it can be seen that the internal friction angle has a certain influence on the critical hydraulic gradient, and the critical hydraulic gradient increases slightly with the increase of internal friction angle. Moreover, the influence of the internal friction angle on the critical hydraulic slope is related to the clay layer thickness; the thicker the clay layer, the greater the influence of the internal friction angle on the critical hydraulic gradient. When $h = 2.5$ m and $\varphi = 0^\circ \sim 30^\circ$, the maximum error is 5.16%; when $h = 0.5$ m and $\varphi = 0^\circ \sim 30^\circ$, the maximum error is 1.13%. In general, the influence of internal friction angle

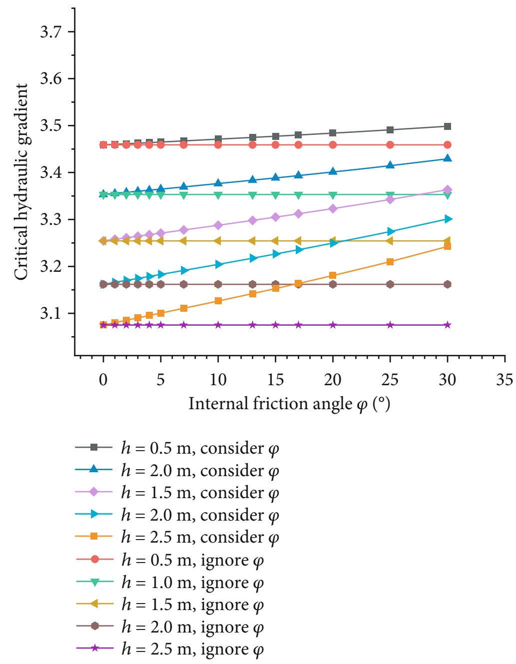

FIGURE 5: The curve between critical hydraulic gradient and internal friction angle.

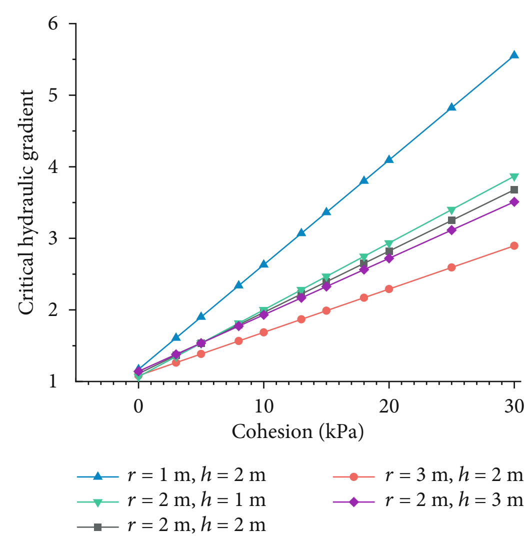

FIGURE 6: The curve between critical hydraulic gradient and cohesion.

on the critical hydraulic gradient of cohesive soil is so weak that it is negligible.

3.5. Influence of Cohesion on Critical Hydraulic Gradient of Cohesive Soil Foundation. The relation curves between the critical hydraulic gradient and cohesion under different working conditions are shown in Figure 6. By comparing the $i_{cr} \sim c$ relation curves under different working conditions, it can be found that the critical hydraulic gradient increased as the failure radius increased. The reason for this correlation is that the greater the cohesion of the soil (other conditions are the same), the stronger the constraint action of the soil

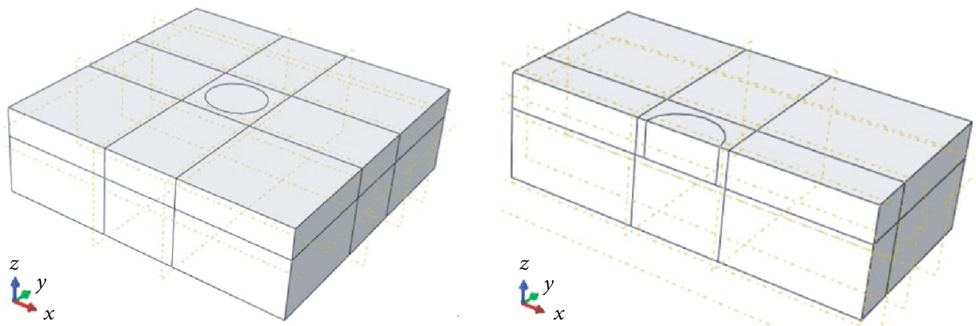

(a) Model diagram (b) z-x section at half-length along the y-axis of the model

Figure 7: Schematic diagram of finite element model.

is, and the greater the head difference is required for the clay layer to permeate, thus the greater the critical hydraulic slope is. Moreover, it is obvious that there is a great difference between the critical hydraulic slope under the conditions of considering cohesion and ignoring cohesion. For example, "$h = 2$ m,$r = 2$ m,$c = 5$ kPa," the critical hydraulic gradient considering cohesion is 1.54, and the critical hydraulic gradient ignoring cohesion is 1.11, and the difference between them is as high as 27.9%. This shows that if the critical hydraulic gradient formula of noncohesive soil is used to calculate the critical hydraulic gradient of cohesive soil foundation, it is necessary to consider the influence of cohesion on the critical hydraulic gradient; it is shown that there is a big error in calculating the critical hydraulic gradient of cohesive soil foundation by using the formula of critical hydraulic gradient of noncohesive soil, which further indicates that it is necessary to consider the influence of cohesion on the critical hydraulic gradient.

3.6. Further Discussion on the Formula of Critical Hydraulic Gradient of Cohesive Soil Foundation. The failure mode of the inverted frustum of a cone of the clay foundation is similar to the punching failure of the inverted foundation, and the value of θ can be determined by imitating the calculation method of the stress diffusion angle in the foundation treatment. When the buried depth of foundation (H) is equal to zero, the stress begins to diffuse from the bottom of the foundation; when the H is greater than zero, the stress begins to diffuse from the $H/3$ above the bottom of the foundation, and the variation range of the stress diffusion angle is approximately equal to the internal friction angle of the soil [27]. It can be considered as the foundation model which the buried depth is zero to exam, when the upward seepage force acts on the bottom of the weak zone of the clay layer, and the seepage force begins to spread upward from the bottom of the clay layer. The θ is stress diffusion angle which can be normally defined as clay's internal friction angle φ, viz., $\theta = \varphi$.

In general, the internal friction angle of saturated soft clay is pretty small [28], which usually can be ignored in engineering practices; in addition, the thickness of the viscous soil layer is generally less than 1 m, when there is an occurrence of flow soil failure, if $\varphi = 0 \sim 10°$, so $K_0 \cos\theta \tan\varphi = 0 \sim 0.14$, and the error between the calculation results of considering φ or not is no more than 5%, and hence, Eq. (16) can be simplified into the following equation.

Table 1: Model parameter table.

Material type	E MPa	k cm/s	e	ρ_{sat} g/cm^3
Clay layer	20	5e-8	0.75	2.0
Weak clay area	18	1e-7	0.85	1.95
Gravel layer	45	5e-3	0.55	2.05

$$i_{cr} = \frac{\gamma}{\gamma_w} + \frac{2c}{\gamma_w \bullet r}. \tag{17}$$

4. Numerical Test Verification on Rationality of Analytical Formula for Critical Hydraulic Gradient of Cohesive Soil Foundation

In this part, the seepage failure process of the viscous soil layer is simulated by finite element software, and the influences of the thickness of the clay layer, the radius of the weak zone of the clay layer, the cohesion, and the angle of internal friction on the critical hydraulic slope are analyzed. The results of the numerical simulation and Eq. (16) are compared to verify the rationality of the new formula in this paper.

The size of the numerical model is $20 \times 20 \times 6$ m, as shown in Figure 7(a), in which the upper and lower layers are clay layer (2 m) and sand and gravel layer (4 m), respectively. Moreover, a cylindrical weak area with radius of 2 m is set in the center of clay layer, and the model parameters are shown in Table 1. The elastic-plastic constitutive model and Mohr-Coulomb criterion are adopted in the calculation. The model has a total of 28288 nodes and 31467 elements, and the element type is C3D20RP. In addition, the lateral boundary of the model is constrained by normal direction, the top pore pressure is set to zero, and the bottom is fully constrained and applied.

According to the direct tensile test results of clay in reference [29], the peak tensile strain of clay with a moisture content of 14%~17% is about 0.15%~0.34%. Combined with the research results of relevant literature and a large number of

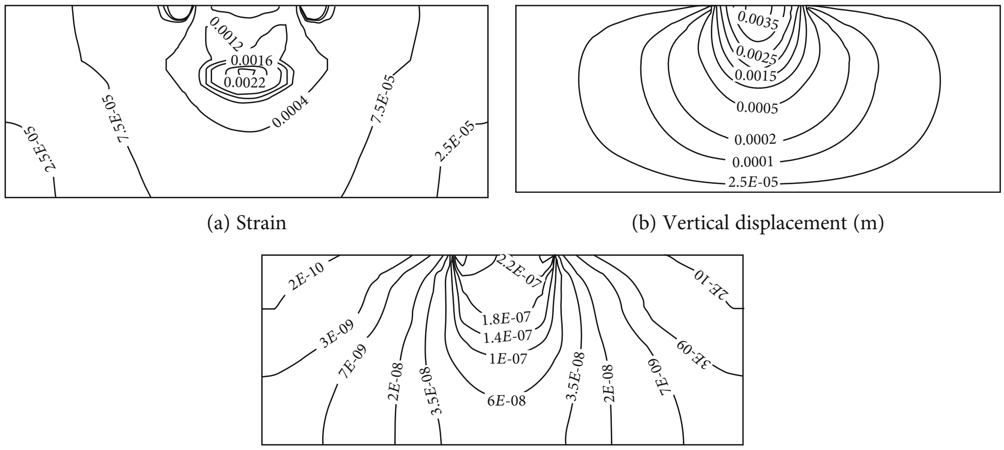

(a) Strain (b) Vertical displacement (m)

(c) Flow velocity (m/s)

FIGURE 8: Seepage failure contour cloud map.

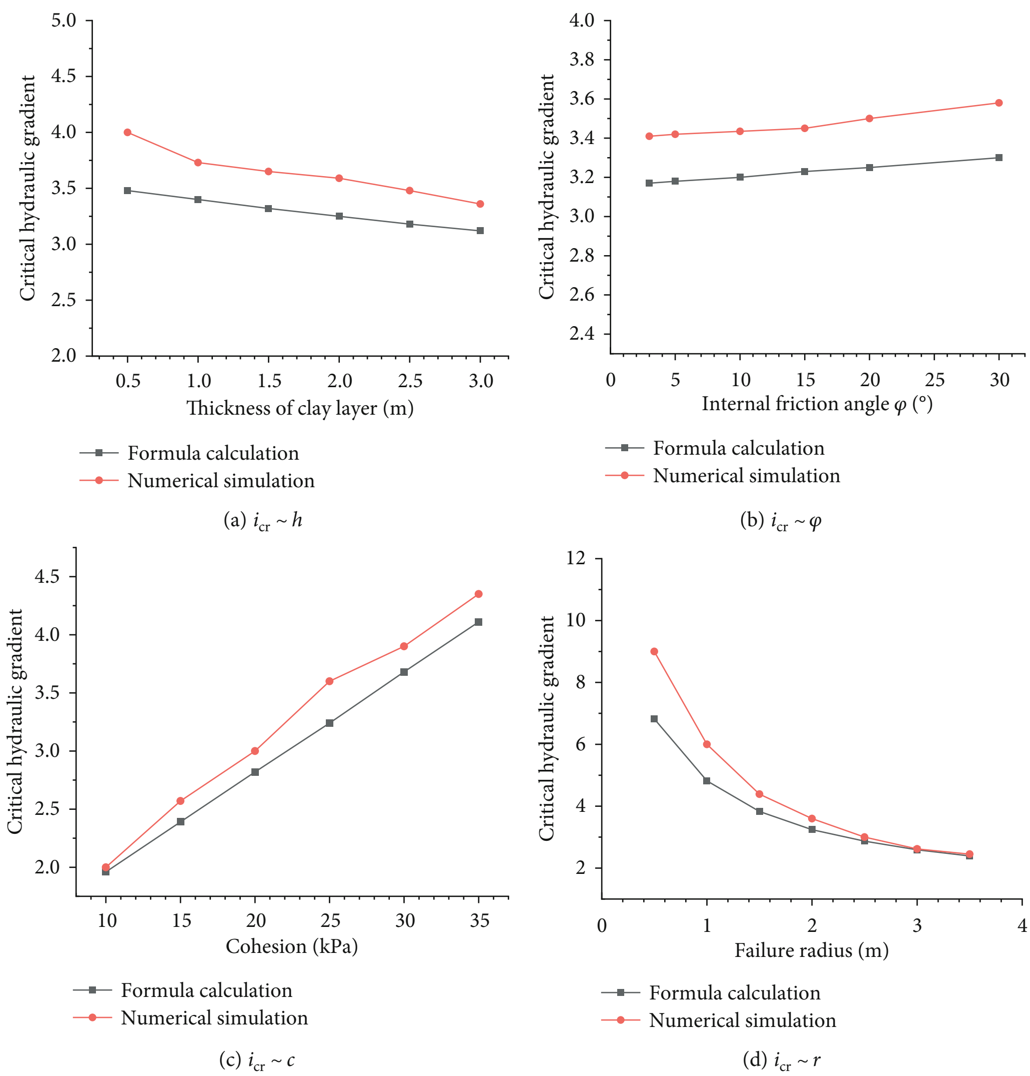

(a) $i_{cr} \sim h$ (b) $i_{cr} \sim \varphi$

(c) $i_{cr} \sim c$ (d) $i_{cr} \sim r$

FIGURE 9: Comparison between the formula solution and numerical simulation results.

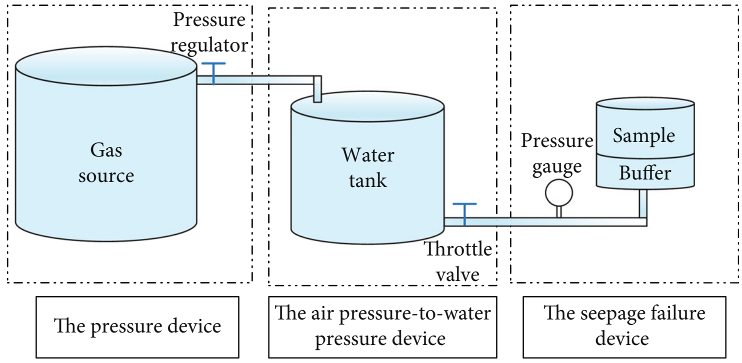

FIGURE 10: Schematic diagram of test facility.

numerical test results, this paper stipulates that the flow failure of clay layer occurs when the strain reaches 0.2~0.3%. Take the z - x section at 1/2 length along the y-axis direction of the model, as shown in Figure 7(b). When seepage failure occurs in basic working conditions, the contour cloud map of strain, vertical displacement, and flow velocity at this section are shown in Figure 8.

Figures 9(a)–9(d) show the relation curves of "critical hydraulic gradient-clay layer thickness," "critical hydraulic gradient-internal friction angle," "critical hydraulic gradient cohesion," and "critical hydraulic gradient-failure radius", respectively. The following conclusions can be drawn from the analysis of them: (a) The change law of the two curves of "critical hydraulic slope-clay layer thickness" obtained by the formula calculation and numerical simulation is basically consistent, and the rule is that the critical hydraulic slope decreases with the increase of clay layer thickness. The maximum difference between the numerical simulation results and the formula results is about 7%. (b) When the internal friction angle is used as a variable, the results of numerical simulation and formula calculation show that the critical hydraulic gradient is positively correlated with the internal friction angle, and the maximum difference between the two results is about 8%. In general, the internal friction angle has little effect on the critical hydraulic gradient of cohesive soil foundation. When the internal friction angle changes from 3° to 20°, the change rate of critical hydraulic gradient calculated by Eq. (16) is about 2.5%, and the change rate of numerical simulation results is about 3.6%; therefore, the influence of internal friction angle on critical hydraulic gradient can be ignored. (c) The "critical hydraulic gradient cohesion" curve obtained by numerical simulation is in good agreement with the corresponding calculation results of Eq. (16), which all show that the critical hydraulic gradient has a positive correlation with cohesion. The reason is that the greater the cohesion of soil is, the higher the shear strength of soil is, the greater the force between the soil particles that needs to be overcome to cause seepage failure, and the greater the critical hydraulic gradient of the cohesive soil is. (d) The law reflected by the two curves of "critical hydraulic gradient-failure radius" obtained by the formula calculation and numerical simulation is basically consistent. When the failure radius is less than the thickness of the clay layer, the critical hydraulic gradient increases rapidly with the decrease of the failure radius; on the contrary, when the failure radius is greater than the thickness of the clay layer, the critical hydraulic gradient decreases gradually with the increase of the failure radius.

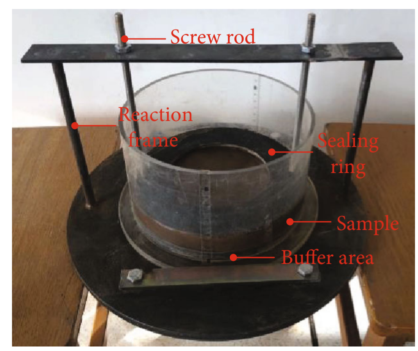

FIGURE 11: Seepage failure device.

In general, although there is a certain degree of error between the formula calculation results and the numerical experiment results, the results of the two are basically the same. The reason for the error may be that the failure shape of the weakened area of the clay layer is assumed to be a cylinder failure mode or an inverted frustum of a cone failure mode in the derivation of Eq. (16). However, the failure shape is not limited during the numerical experiment. Therefore, there is a certain error between the two calculation results.

After the above comparison, it can be considered that it is feasible to use Eq. (16) to calculate the critical hydraulic gradient of the cohesive soil foundation.

5. Experiment Verification

5.1. Experiment Equipment. The self-made test instrument is composed of the pressure device, air pressure-to-water pressure conversion device, and seepage failure device, as shown in Figure 10, whose main functions can not only control the thickness of the clay layer and the size of the seepage failure opening, but also make an application of controllable variable head pressure or constant head pressure to the cohesive soil samples.

The air pressure-to-water pressure conversion device with an air inlet at the top is connected with the gas source

Table 2: Main parameters of soil sample.

Soil type	Porosity (n)	Dry density (g/cm^3)	Water content (%)	Cu	Cohesion (kPa)	Internal friction angle
Sandy loam	0.8	1.50	14.5	2.70	5.25	15.84°
Loess	0.6	1.70	16	2.71	20.5	24.01°

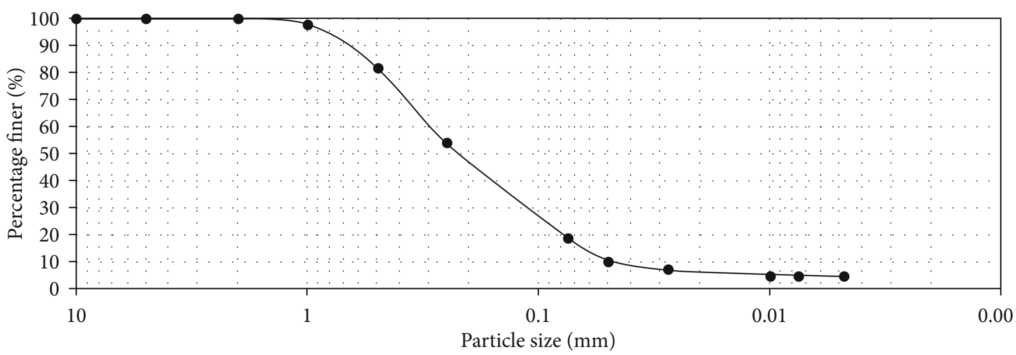

(a) Particle size distribution curve of sandy loam

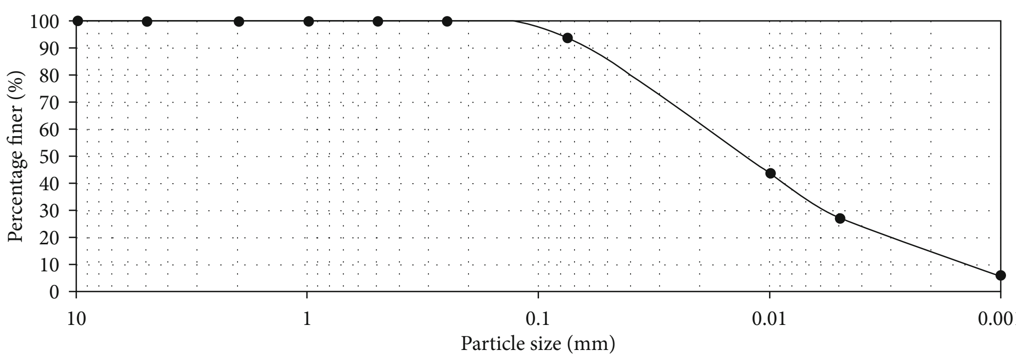

(b) Particle size distribution curve of loess

Figure 12: Particle size distribution curve of soil sample.

through the high-pressure pipe, so as to apply air pressure to the water tank. In addition, a water outlet at the device bottom is connected to the bottom of the seepage failure device through a high-pressure pipe, in order to apply water pressure to the bottom of the samples. Meanwhile, the flow velocity and water pressure measure are controlled by the throttle valve and pressure gauge, respectively.

The seepage failure device is set on the pedestal, shown in Figure 11. The test soil samples are fixed by the self-made reaction frame whose beam equips two screw rods, and the bottom of the screw rods can install the sealing ring with different inner diameters that can contact closely with the surface of the soil samples, which not only can change the exposed size of the soil samples but also prevent the concentrated leakage at the inside wall of the glass bucket. Moreover, it is necessary to note that pervious stone and filter paper must be placed at the bottom of the soil sample during the experiment so that the water pressure is applied evenly to the soil sample.

5.2. Experiment Plans. The previous research experiences show that apart from the physical properties of the soil, the thickness of the clay layer and the radius of the failure opening are great related to the critical hydraulic gradient of cohesive soil foundations. Therefore, this paper focuses on influences of clay layer thickness and failure radius on the critical hydraulic gradient. The soil samples are taken from the loess of Bin County and the sandy loam of The Yellow River beach of Yinchuan, both of which are remolded soil. The main parameters are shown in Table 2, and the particle size distribution is shown in Figure 12.

Table 3: Soil sample size table.

Sample No.	Radius (cm)	Height (cm)	Sample No.	Height (cm)	Radius (cm)
H1/S1	5	1	HR1/SR1	2	1
H2/S2	5	3	HR2/SR2	2	2
H3/S3	5	5	HR1/SR3	2	4
H4/S4	5	7.5	HR1/SR4	2	8
H5/S5	5	10	HR5/SR5	2	10

The loess soil samples with numbers as H1, H2, H3, H4, and H5 and the sandy loam soil samples with numbers as S1, S2, S3, S4, and S5 are, respectively, prepared for studying the influence of clay layer thickness on critical hydraulic gradient. Similarly, the loess soil samples with numbers as HR1,

(a) The first stage

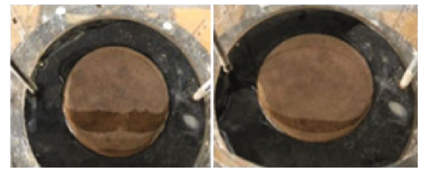

(b) The second stage

(c) The third stage

(d) The fourth stage

FIGURE 13: Diagram of seepage failure process of soil sample HR1/SR3.

HR2, HR3, HR4, and HR5 and the sandy loam soil samples with numbers as SR1, SR2, SR3, SR4, and SR5 are, respectively, prepared for studying the influence of failure radius on critical hydraulic gradient. The sample sizes are shown in Table 3.

5.3. Experiment Process. Before the test, keep the water pipe tightly connected to the gas source and water tank and not to the bottom of the seepage failure device temporarily, and the pipe mouth be open. Next, inject about 1200 mL water into the water tank and turn on the gas source, and the air pressure should be applied slowly to the tank by controlling the pressure regulating valve, and then, connect the pipe to the bottom of the seepage failure device when water overflows from the end of water pipe equipped with a pressure gauge. When the experiments are carrying out, the seepage failure process can be realized by step-by-step pressurization. The specific operation method is to apply a small water pressure to the soil sample at the beginning by adjusting the pressure regulating valve and observe the soil sample under the water pressure for 30 minutes continuously. If the seepage phenomenon changes continuously within 30 minutes, the observation time should be extended until the phenomenon becomes stable, and then, increase the water pressure (0.002 MPa) to observe the next stage. It should be noted that when the critical point of osmotic failure is nearly reached, the pressure is applied step by step at the order of 0.0005 MPa. The characteristics of losing a large amount of soil particles and of increasing seepage water volume per unit time significantly and of having an apparent soil bulge occurrence can act as a criterion for estimating the seepage failure or not of the soil samples. The water pressure value when the seepage failure happen is converted into the height of water head Δh, and the critical hydraulic gradient is $i_{cr} = \Delta h/L$, where L is the thickness of the soil samples.

5.4. Experimental Results. According to the experimental phenomena, the seepage failure of soil samples can be divided into the following four stages (see Figure 13): (a) There is a small amount of water slowly seeping out, no uplift occurrence at the top of the soil samples, and no seepage channel on the soil samples' side surface. (b) With the increase of water pressure, the top of soil samples slightly rises, and the amount of clear water seepage increases gradually. (c) Cracks first appear on the upper surface of the soil samples along the inner edge of the iron ring, and the uplift phenomenon on the upper surface of soil continues to intensify, and at the same time, a little bit of soil particle suspension begins to occur on the upper surface of the soil samples. (d) With the progress of the seepage failure tests, the surface cracks of the soil samples gradually expand, and in the center of the uplift part of soil samples, cracks can be found and therefore can infer that there is a seepage channel in the sample interior so that it leads to an abrupt emergence of a large amount of soil particle suspension, which means that the soil samples fall into seepage failure. The seepage failure process of soil sample is shown in Figure 13.

TABLE 4: Critical hydraulic gradient results of soil samples.

Sample codes	i_{cr}/formula solutions	i_{cr}/test results	Sample codes	i_{cr}/formula solutions	i_{cr}/test results
HR1	281.79	240	H1	81.1	80
HR2	170.35	150	H2	74.56	73.33
HR3	94.87	100	H3	68.81	64
HR4	65.87	60	H4	62.60	58.67
HR5	50.54	45	H5	57.31	54
SR1	77.87	70	S1	21.70	20
SR2	46.06	45	S2	20.32	18.33
SR3	25.55	22.5	S3	19.08	16
SR4	17.86	15	S4	17.69	15.33
SR5	13.84	12.5	S5	16.48	14

The test and formula calculation results of different soil samples are shown in Table 4; in addition, the relation curves of "critical hydraulic gradient-failure radius" and "critical hydraulic slope-sample height" are, respectively, shown in Figure 14.

5.4.1. Influence of Failure Radius on Critical Hydraulic Gradient. The results show that the critical hydraulic gradient of cohesive soil foundation decreases with the increase of failure radius. The reason is that the larger the failure

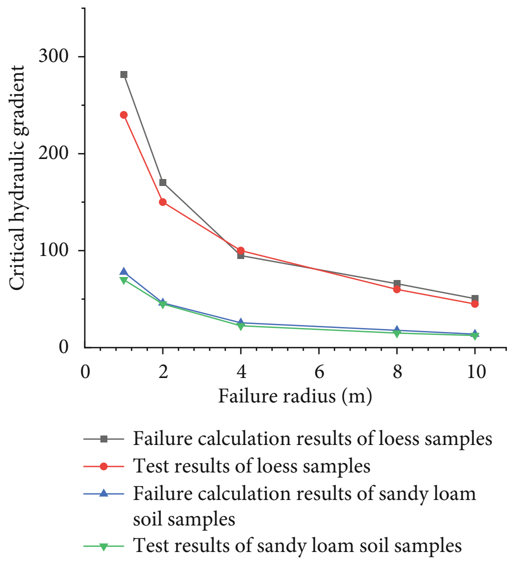

(a) The relation curve of "critical hydraulic gradient-failure radius"

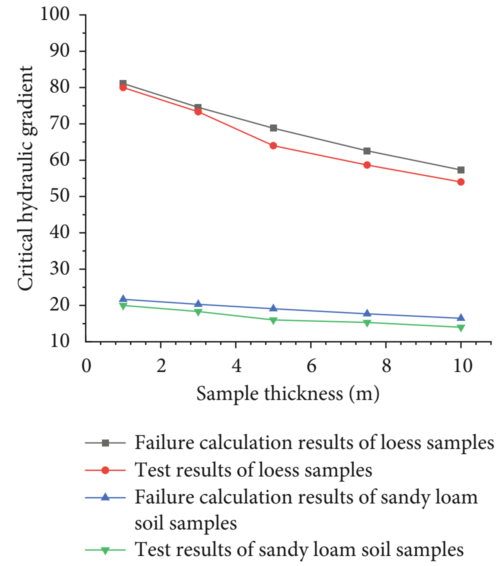

(b) The relation curve of "critical hydraulic gradient-sample thickness"

Figure 14: Comparison of formula solution and seepage test results.

Table 5: Results of experiments and calculation for critical hydraulic gradient.

Soil type	Dry density (g/cm^3)	Initial water content	Sample water content	Soil sample volume	i_{cr}/literature test	i_{cr}/formula calculation
Clay [31]	1.70	5.1%	20.1%	120 cm^3	110	119.96
Silty clay [32]	1.70	5.1%	20.1%	120 cm^3	70	77.67
Silty clay [32]	1.61	22.5%	20%	120 cm^3	45	49.17

radius is, the smaller the constraint of the soil cohesion on the surrounding soil will be; therefore, the smaller the upward seepage force needed for the seepage failure and the smaller the critical hydraulic gradient will be. It is easy to see from Figure 14(a) that if the failure radius is constant, the critical hydraulic gradient of loess is always greater than that of sandy loam. When the corresponding failure radius increases from 1 cm to 4 cm, for loess and sandy loam, the critical hydraulic gradient all drops greatly, decreasing by 62.3% and 17.4%, respectively. As the failure radius is larger than 4 cm, the decline trend of critical hydraulic gradient is relatively gentle. The reason may be that when the failure radius is equal to 4 cm in this tests, the seepage channel is easy to be formed inside the soil sample, which is conducive to the seepage failure of the soil sample. Moreover, the results of "critical hydraulic gradient-failure radius" obtained by seepage failure tests match highly to the corresponding calculation results of the new formula in this paper. The maximum difference value between the test results and the formula solutions is less than 16%, whether the soil samples are loess or sandy loam.

5.4.2. Influence of Soil Sample Thickness on Critical Hydraulic Gradient. In analyzing Figure 14(b), it can be seen that when the soil sample thickness is constant, the critical hydraulic gradient of loess is always greater than that of sandy loam soil. The overall trend is that the critical hydraulic gradient of cohesive soil foundation decreases slowly with the increase of soil sample thickness, and when the thickness of soil samples increases from 1 cm to 10 cm, the critical hydraulic gradient of loess soil and sandy loam soil decreases by 2.64% and 0.58%, respectively. It is worth noting here that the thicker the clay layer, the decrease of the critical hydraulic gradient rather than the decrease of the critical damage head.

When the soil samples are loess, the maximum difference value between the critical hydraulic determined by the tests and the calculation results of the formula is less than 10%. When the soil sample thickness is thin, the difference between the test results and the formula calculation results is greatly small, and the difference increases as the increase of soil sample thickness. The difference increases from 1.36% to about 7% when the soil sample thickness increases from 1 cm to 5 cm. For sandy loam soil, this maximum difference value is less than 15%, like the loess soil samples, in which the difference is smaller when the soil sample thickness is thinner. The reason for this may lie in the thicker the soil samples are, the more difficult to saturate; therefore, incomplete saturation phenomenon may exist, besides a small amount of soil is in aggregate form where distribute pores may also cause the internal stability of the entire soil to decrease, and the impermeability of fine particles cannot be better utilized [30].

5.5. Comparison of Formula Solution and Reference Test Results. In order to further verify the rationality of Eq. (16), the test data in references [31, 32] are taken as the original data, which are substituted into Eq. (16) for analysis and comparison. In reference [31], the internal friction angle of clay and silty clay is 20° and 23°, respectively, and the cohesion is 22.5 kPa and 15 kPa, respectively; in reference [32], the internal friction angle of silty clay is 22° and the cohesion is 9.5 kPa, and the results are shown in Table 5. It can be seen that the calculation results of the formula are close to the experimental results of references [31, 32].

6. Conclusion

Based on the calculation method of critical hydraulic gradient of *Terzaghi*, a formula for calculating the critical hydraulic gradient of soil foundation considering the influence of shear strength of soil is established in this paper, which is validated with both numerical simulations and experimental tests. The conclusions are as follows:

(1) According to the equilibrium relationship among the upward seepage force, the downward effective gravity and the shear force of the cohesive soil foundation, the calculation formula of the critical hydraulic gradient of the cohesive soil foundation is derived

(2) The results obtained by numerical simulation are in good agreement with the corresponding calculation results of the new formula. In addition, the maximum difference value between the critical hydraulic gradient calculated by the formula and the seepage failure test results is about 16%, which is sufficient to indicate that the formula is feasible

(3) The influence of the stress diffusion angle and the internal friction angle on the critical hydraulic gradient can be ignored when the internal friction angle does not exceed 10°

(4) The newly established formula can provide a theoretical basis for the mechanism analysis of dams, foundation pits, and other projects after destruction and contribute a reference basis to the design of dams and foundation pits, so as to reduce or avoid the occurrence of engineering safety accidents

Data Availability

Data supporting the results of this study can be obtained from the article.

Conflicts of Interest

The authors declare that they have no known competing financial interests or personal relationships that could have appeared to influence the work reported in this paper.

Acknowledgments

This paper was supported by the National Natural Science Foundation of China (Nos.: 51979225 and 51679199), the Ministry of Water Resources Public Welfare Industry Research Project (No.: 201501034-04), and the Shaanxi Key Laboratory of Science and Technology Innovation Project (No.: 2014SZS15-Z01).

References

[1] R. U. Naihua and N. Yunguang, *Embankment Dam· Incidents and Safety of Large Dams*, China Water Power Press, Beijing, 2001.

[2] M. A. O. Changxi, *Seepage Computation Analysis & Control*, Water Resources and Electric Power Press, Beijing, 2002.

[3] C. Wu, J. Chu, S. Wu, and Y. Hong, "Wu S.etal. 3D characterization of the microbially induced carbonate precipitation within rock fracture and the resulted permeability reduction," *Engineering Geology*, vol. 249, pp. 23–30, 2019.

[4] C. Wu, J. Chu, S. Wu, L. Cheng, and L. A. van Paassen, "Microbially induced calcite precipitation along a circular flow channel under a constant flow condition," *Acta Geotechnica*, vol. 14, no. 3, pp. 673–683, 2019.

[5] Y. Xue, J. Liu, F. Dang, X. Liang, S. Wang, and Z. Ma, "Influence of CH_4 adsorption diffusion and CH_4-water two-phase flow on sealing efficiency of caprock in underground energy storage," *Sustainable Energy Technologies and Assessments*, vol. 42, article 100874, 2020.

[6] Y. Xue, P. G. Ranjith, F. Dang et al., "Analysis of deformation, permeability and energy evolution characteristics of coal mass around borehole after excavation," *Natural Resources Research*, vol. 29, no. 5, pp. 3159–3177, 2020.

[7] F. Zhang, T. Wang, F. Liu, M. Peng, J. Furtney, and L. Zhang, "Modeling of fluid-particle interaction by coupling the discrete element method with a dynamic fluid mesh: implications to suffusion in gap-graded soils," *Computers and Geotechnics*, vol. 124, article 103617, 2020.

[8] F. Zhang, M. Li, M. Peng, C. Chen, and L. Zhang, "Three-dimensional DEM modeling of the stress-strain behavior for the gap-graded soils subjected to internal erosion," *Acta Geotechnica*, vol. 14, no. 2, pp. 487–503, 2019.

[9] M. An, F. Zhang, D. Elsworth, Z. Xu, Z. Chen, and L. Zhang, "Friction of Longmaxi shale gouges and implications for seismicity during hydraulic fracturing," *Journal of Geophysical Research-Solid Earth*, vol. 125, no. 8, article e2020JB019885, 2020.

[10] F. Zhang, B. Damjanac, and S. Maxwell, "B. Damjanac, S. Maxwell. Investigating hydraulic fracturing complexity in naturally fractured rock masses using fully coupled multiscale numerical modeling," *Rock Mechanics and Rock Engineering*, vol. 52, no. 12, pp. 5137–5160, 2019.

[11] T. Rabczuk and T. Belytschko, "Cracking particles: a simplified meshfree method for arbitrary evolving cracks," *International Journal for Numerical Methods in Engineering*, vol. 61, no. 13, pp. 2316–2343, 2004.

[12] H. Ren, X. Zhuang, and T. Rabczuk, "Dual-horizon peridynamics: a stable solution to varying horizons," *Computer Methods in Applied Mechanics and Engineering*, vol. 318, pp. 762–782, 2017.

[13] K. V. Terzaghi, "Der grundbruch an stauwerken und seine verhuetung," *Wasserkraft*, vol. 17, no. 24, pp. 445–449, 1922.

[14] J. Israr and B. Indraratna, “Study of critical hydraulic gradients for seepage-induced failures in granular soils,” *Journal of Geotechnical and Geoenvironmental Engineering*, vol. 145, no. 7, article 04019025, 2019.

[15] M. LI and R. J. Fannin, “A theoretical envelope for internal instability of cohesion less soil,” *Geotechnique*, vol. 62, no. 1, pp. 77–80, 2012.

[16] M. Wang, Y. Jiang, L. Yu, Y. Dong, and R. Duan, “Calculation method of starting critical hydraulic slope of fine particles in sandy soil,” *Rock and Soil Mechanics*, vol. 41, no. 8, pp. 2515–2524, 2010.

[17] F. Jiang, “Discussion on formula derivation and test of critical hydraulic condition of cohesive soil,” *Chinese Journal of Underground Space and Engineering*, vol. 13, no. 6, pp. 1472–1476, 2017.

[18] M. Wu and G. Gao, “Research on prediction method of critical gradient for piping of sand and gravel soils,” *Rock and Soil Mechanics*, vol. 40, no. 3, pp. 1–10, 2019.

[19] Y. Luo, B. Su, J. Sheng, and M. Zhan, “New understanding of piping mechanism,” *Journal of Geotechnical Engineering*, vol. 33, no. 12, pp. 1895–1902, 2011.

[20] Y. Luo, Q. Wu, M. Zhan, and J. Sheng, “Experimental study on critical piping gradient of suspended cutoff wall gravel foundation considering stress state,” *Rock and Soil Mechanics*, vol. 33, no. S1, pp. 73–78, 2012.

[21] Y. Tang, W. Shi, and X. Zhang, “The experiments study and theoretical analyses on piping and flow soil,” *Shanghai Land & Resources*, vol. 1, pp. 25–31, 2003.

[22] Y. Liang, T. C. J. Yeh, Y. Zha, J. Wang, M. Liu, and Y. Hao, “T C J YEH, Y Y ZHA..Onset of suffusion in gap-graded soils under upward seepage(article),” *Soils and Foundations*, vol. 57, no. 5, pp. 849–860, 2017.

[23] J. Yang, Y. Cai, and Y. Zhu, “Experimental study on contact soil flow considering stress condition,” *Yangtze River*, vol. 41, no. 7, pp. 79–81, 2010.

[24] F. Dang, H. Liu, X. Wang, H. Xue, and Z. Ma, “Emperimental of study on the relevance between stress state and seepage failure of Sandy-gravel soil,” *Chinese Journal of Rock Mechanics and Engineering*, vol. 34, no. 9, pp. 1909–1917, 2015.

[25] Z. Jiang, W. Wang, S. Feng, and H. Zhong, “Empirical formulas of permeability of clay based on effective pore ratio,” *Journal of Hydraulic Engineering*, vol. 44, no. 12, pp. 1498–1505, 2013.

[26] K. Zhang and S. Liu, *Soil Mechanics(The third edition)*, China Building Industry Press, Beijing, 2010.

[27] X. Dong, J. Ma, Z. Hu, J. Li, and L. Xu, “Study on foundation stress dispersion effect in saturated sand based on centrifugal model test,” *Railway Standard Design*, vol. 62, no. 1, pp. 84–88, 2018.

[28] Y. Mai, “Earth pressure of saturated soft clay,” *Port & Waterway Engineering*, vol. 320, no. 9, pp. 3–6, 2000.

[29] X. Zhang, Q. Zhang, and Q. Gao, “Development and application of geotechnical direct tension test devices,” *Chinese Journal of Geotechnical Engineering*, vol. 36, no. 7, pp. 1309–1315, 2014.

[30] M. Zhou, *Study on Critical Hydraulic Slope of Fluid Soil Failure on Cohesive Soil*, Xi 'an University of Technology, 2020.

[31] L. Jianguo, *Seepage Failure Test and Numerical Simulation of Cohesive Soil*, Hefei University of Technology, 2015.

[32] Q. He, *Exprimental Study on Seepage Failure and Long-Term Seepage Degradation of Clay*, Hefei University of Technology, 2017.

Hindawi
Geofluids
Volume 2021, Article ID 9957731, 9 pages
https://doi.org/10.1155/2021/9957731

Research Article

Human Activities Increase the Nitrogen in Surface Water on the Eastern Loess Plateau

Yuxian Hu,[1] **Ke Zhang**,[1] **Yuan Li**,[1] **Yanan Sun**,[2] **Hongyan Li**,[1] **and Gaiqiang Yang**[1]

[1]*School of Environment Science and Engineering, Taiyuan University of Science and Technology, Taiyuan, Shanxi 030024, China*
[2]*Ecology and Environment Bureau of Lvliang City, Lvliang, Shanxi 033000, China*

Correspondence should be addressed to Yuxian Hu; 7817231@qq.com and Yuan Li; liyuan_198711@sina.com

Received 25 March 2021; Revised 30 April 2021; Accepted 18 May 2021; Published 1 June 2021

Academic Editor: Yi Xue

Human activities have greatly accelerated the input of nitrogen into waters, resulting in water quality degradation. Facing the water crisis of nitrogen pollution, the state of surface water in arid areas needs close attention. Although numerous studies have indicated that waters' nitrogen is often impacted by land use covers, the correlation between the two remains obscure. This paper explored the spatial relationship between anthropogenic activity and waters' nitrogen on the eastern Loess Plateau, based on the Geographic Information System (GIS) spatial analysis using land use covers. There were 3 human land use types and 2 nitrogen indices used to assess the rivers' state at the watershed scale. The results showed that rivers' nitrogen was closely associated with human land use covers. Nitrogen pollution was most serious in urban areas. This study provided new evidence for the relationship between anthropogenic activities and river ecology. The findings may be helpful for policymakers to make strategic decisions of water resource management and land use planning in arid areas.

1. Introduction

Nitrogen (N) is one of the most important nutrients for ecosystem function and also a limiting factor for the productivity of many ecosystems in the world [1]. Nitrogen pollution can cause adverse ecological effects on the environment, including soil acidification, hypoxia, and subsequent fish death [2]. High concentration of nitrogen is the main factor leading to eutrophication of the water environment, resulting in the reduction of biodiversity and deterioration of water quality [3]. To make matters worse, some high levels of nitrogen forms in drinking water increase the risk of human disease [4]. How to make rational use of nitrogen and reduce the negative effects of nitrogen while meeting human needs has become a scientific challenge that human beings must solve in the 21st century [5].

About 99% of the global nitrogen is stable atmospheric nitrogen, which is not available to ecosystems unless it is converted into active nitrogen species, such as nitrate (NO_3^-), nitrite (NO_2^-), ammonia (NH_3), and ammonium (NH_4^+), and organic nitrogen [6]. Through nitrogen fixation, plants make inorganic nitrogen exist in soil in the form of NO_3^-, NO_2^-, and ammonia nitrogen (NH_3-N). Through rainfall erosion and surface runoff, inorganic nitrogen in soil migrates to water [7]. Biological nitrogen fixation can input $120\ \mathrm{Tg\,N\,yr^{-1}}$ nitrogen to the ecosystem [8]. Due to the nonuniformity of the spatial distribution of nitrogen flux, there are great differences in the nitrogen cycle in different regions of the world. Human beings enlarge the differences and make the process more complicated. Human activities have greatly accelerated the input of nitrogen into water, resulting in water quality degradation, including eutrophication, acidification, and nitrate pollution [9–15].

Anthropogenic nitrogen entering waters comes from industrial, municipal, residential, and agricultural sources [16]. Nitrogen deposition from fossil fuel combustion in the atmosphere is another important anthropogenic nitrogen source, which is discharged into surface water. Chemical inputs to water bodies are also classified by point sources (such as municipal wastewater treatment plants) and nonpoint sources (such as agricultural activities and atmospheric deposition). Annual nitrogen fixation from human sources

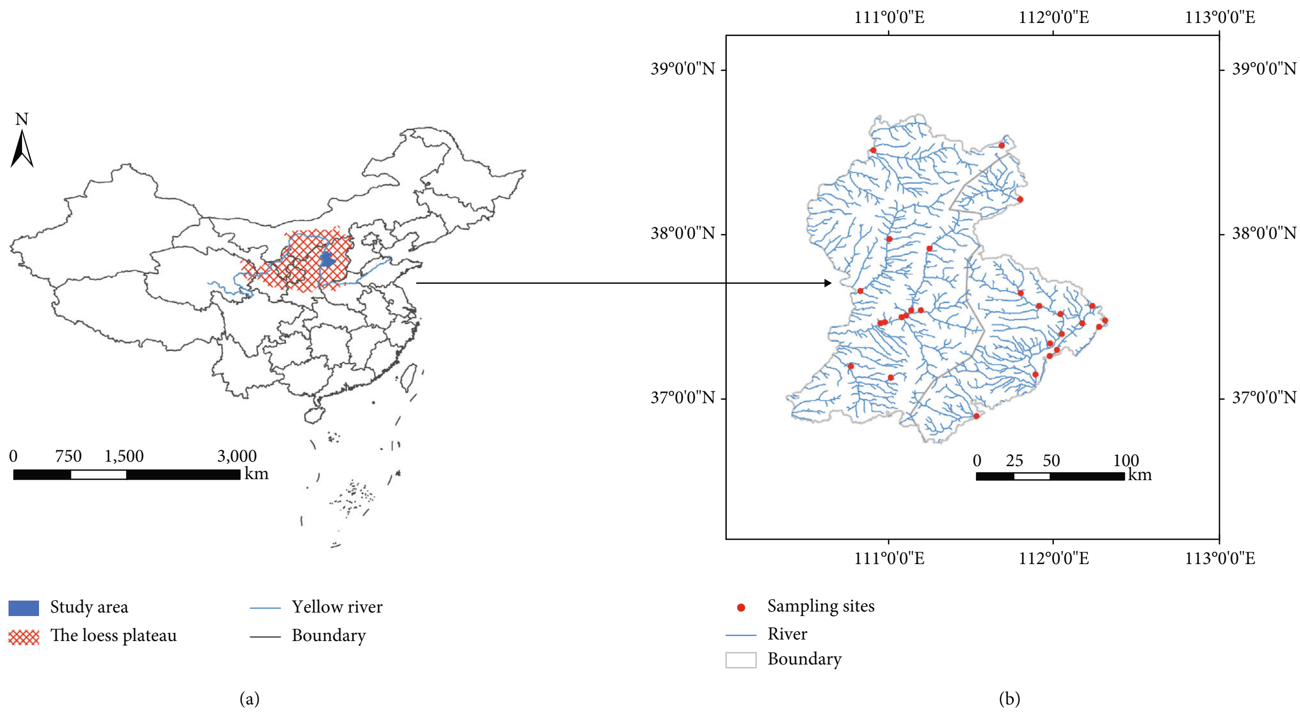

Figure 1: Location of the Loess Plateau, study area, and sampling sites.

has exceeded that from natural sources [17]. As time goes on, human activities increase the input of nitrogen into water. The nitrogen load of major rivers in the United States has increased [18]. It is expected that the nitrogen input into the water body will continue to increase all over the world. Kroeze and Seitzinger [19] predicted that by 2050, 90% of the dissolved inorganic nitrogen load in the world's rivers will be anthropogenic.

The water quality of several major rivers in northern China, Huaihe River, Yellow River, Haihe River, Liaohe River, and Heilongjiang River, cannot meet the Class III standard of China's surface water, plus China has large nitrogen fertilizer applications but lower nitrogen utilization efficiency, which greatly increases the nitrogen accumulation in waters [20]. Soil nitrogen may also increase because of the interference of human activities, such as the large amount of nitrogen fertilizer application in farmland and urban soil covered by impervious layers. Schlesinger [21] traced the final fate of 150 Tg nitrogen per year from human emissions. It was found that there was about 9 Tg N yr^{-1} nitrogen accumulating in the biosphere. Human activities have profoundly influenced the long-term dynamics of nitrogen concentrations in rivers, lakes, and aquifers worldwide. Under the disturbance of human activities, the reserves of terrestrial ecosystems may be increasing [22].

Land use/cover change (such as farmland expansion, afforestation, deforestation, urbanization, and industrialization) increases the vulnerability of the water ecosystem, which is an important way and response of human activities to the surface environment [23]. Nitrogen in industry, city, and people's life mainly comes from sewage. Agricultural nitrogen fertilizers include fertilizers, nitrogen-fixing crops, human and animal excreta, and soil erosion caused by land use changes such as deforestation and grassland reclamation. Construction sites also contribute to nitrogen input into the water body [24]. Nitrogen concentration in surface water is strongly affected by land use in settlement areas, especially by agriculture [25]. Zhao and Huang [26] found that nitrate concentration decreased with the increase of woodland proportion. Changing a paddy field to dry land or construction land will increase water yield while changing a water area to a paddy field or dry land will reduce water yield. The transfer of land use to the surface with a high evaporation rate will reduce runoff [27]. Agricultural coverage explained the 69% variability of mean nitrate concentrations in the Mediterranean river basin during the 25 years (1981–2005) [28]. In fact, land use is always associated with fertilization (cropland) and soil erosion (conversion of natural vegetation to arable land), which increases the concentration of nitrogen in the rivers discharging disturbed catchments.

Land use change plays an extremely important role in the fields of ecological environment, climate change, and food production. It plays a very important role in maintaining biodiversity and water environment systems. Land use/cover has become the main cause of global change [29]. However, few studies focused on the spatial relationship between land use and waters' nitrogen. In particular, the water ecosystem-based management in the arid areas lacked strong technical support. Here, we seek to develop a strategy to study the impact of human activities on surface water through a case study of a typical arid area in the Loess Plateau of northern China. Specifically, we analyzed the characteristics of different land use covers and waters' nitrogen by adopting remote sensing and field investigation. Our results contribute to a better understanding of the ecological effects that anthropogenic activities have on different landscape configurations

Table 1: Descriptive statistics of the nitrogen concentrations in Yellow River and Fen River Basins.

Basin	Nitrogen (mg/L)							
	NH_3-N				TN			
	Minimum	Maximum	Mean	SD	Minimum	Maximum	Mean	SD
Yellow River	0.11	13.20	1.82	2.55	2.09	22.30	10.42	4.83
Fen River	0.10	34.10	4.28	5.91	1.47	70.50	17.48	14.75

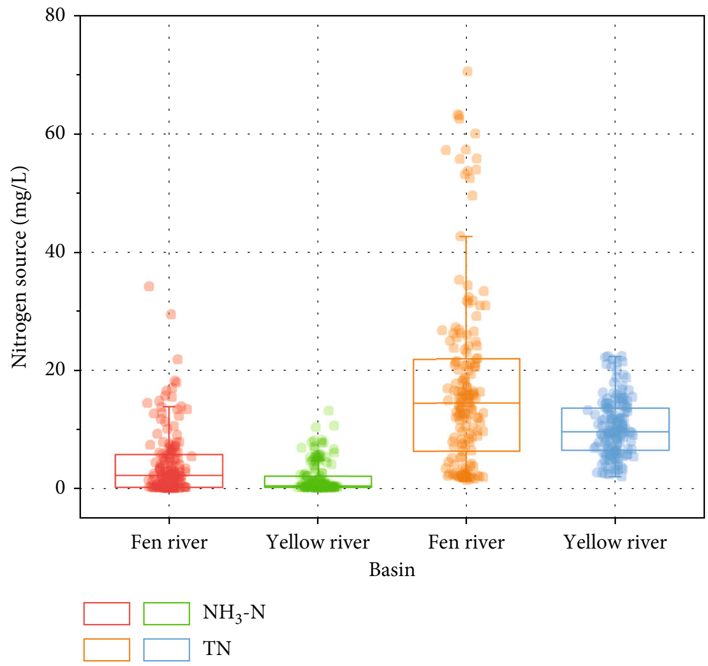

Figure 2: Box plots of NH_3-N and TN concentrations in Fen River and Yellow River Basins.

Table 2: Seasonal variations of the nitrogen concentrations in Yellow River and Fen River Basins.

Basin	Nitrogen (mg/L)							
	NH_3-N (dry season)				TN (dry season)			
	Minimum	Maximum	Mean	SD	Minimum	Maximum	Mean	SD
Yellow River	0.11	13.20	3.32	3.39	2.09	22.20	11.59	6.03
Fen River	0.12	34.10	7.35	8.11	1.47	63.10	21.25	18.20
Basin	NH_3-N (wet season)				TN (wet season)			
	Minimum	Maximum	Mean	SD	Minimum	Maximum	Mean	SD
Yellow River	0.22	5.71	1.21	1.74	2.75	20.60	9.52	3.81
Fen River	0.10	9.09	2.19	2.73	1.99	7.05	14.71	13.50

in the study area. This research will provide scientific guidance for water ecosystem management and regional sustainable development for maintaining ecological balance and regulating anthropogenic activities in arid areas.

2. Materials and Methods

2.1. Study Area. Loess covers about 10% of the earth's land surface and lies in semiarid zones [30]. The Loess Plateau of China is located in the middle reach of the Yellow River in northwestern China [31]. The Loess Plateau (Figure 1(a)) is the most concentrated and largest loess area on the earth. The Loess Plateau is more than 1000 kilometers long from east to west and 750 kilometers wide, with a total area of 6.4×10^5 km^2. It is located on the second step of China, with an altitude of 800–3000 meters.

Lvliang City (Figure 1(b)) is located in the west of Loess Plateau and the west of Shanxi Province. It is located between a latitude of 36°43′N and 38°43′N and a longitude of 110°22′E and 112°19′E. The city basically belongs to the temperate continental monsoon climate zone, cold in winter and hot in summer, with four distinct seasons. The total area of the

Table 3: The variations of the nitrogen concentrations in Yellow River and Fen River Basins during January to December in 2019.

Nitrogen (mg/L)	Month											
NH_3-N	1	2	3	4	5	6	7	8	9	10	11	12
Yellow River	4.26	3.66	2.64	1.75	2.11	1.50	1.58	0.53	0.54	0.72	0.92	2.05
Fen River	10.41	8.99	5.56	4.78	5.85	3.51	0.95	2.10	1.78	1.45	3.34	2.42
Eastern Loess Plateau	8.76	7.67	4.74	3.79	4.62	2.92	1.40	1.55	1.31	1.26	2.45	2.62
TN	1	2	3	4	5	6	7	8	9	10	11	12
Yellow River	12.30	12.54	9.07	12.68	10.67	10.56	10.66	7.35	9.72	9.82	10.09	10.01
Fen River	21.96	23.67	15.23	20.51	14.40	14.91	15.62	13.58	15.85	16.63	19.44	18.07
Eastern Loess Plateau	20.03	21.49	13.85	18.89	14.05	14.42	14.70	11.84	14.37	15.04	16.71	16.14

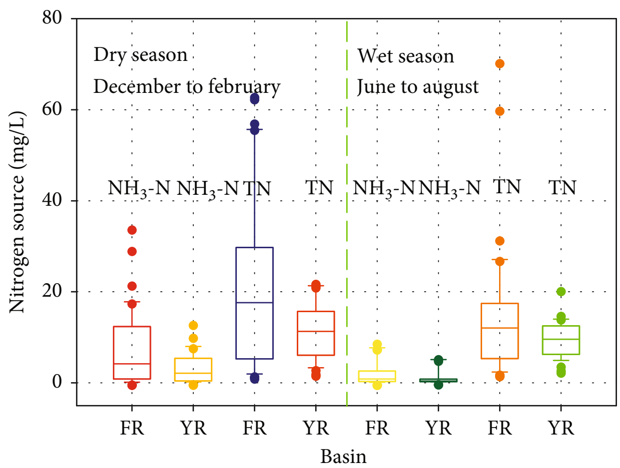

Figure 3: Temporal variations of NH_3-N and TN concentrations in dry and wet seasons.

city is 2.1×10^5 km^2, and the average annual precipitation is only 472 mm. Lvliang has wide loess coverage, broken terrain, steep slope, less flat land, rare vegetation, and serious soil erosion.

2.2. Sampling Strategy

2.2.1. Sample Collection. The surface water samples were collected from 28 rivers in the Loess Plateau. The sampling time was from January to December 2019 (the dry and wet seasons), and the sampling frequency was tested once a month, which was from Yellow River and Fen River Basins. The details of the sampling sites are shown in Figure 1(b). The water samples were stored in 5.0 L polypropylene (PP) bottles, which were prewashed with the water samples 3 times before collection. All the samples were stored at 4°C for no more than 7 days before the analysis.

2.2.2. Sample Determination. We determined TN and NH_3-N using the methods of potassium persulfate ultraviolet spectrophotometry and Nessler's reagent colorimetry with reference to GB3838-2002. The standard of TN and NH_3-N in this paper referred to the Class III standard value of surface water (1 mg L^{-1}).

2.3. Data Statistics and Analyses. We conducted box plots to compare the spatiotemporal variations of nitrogen concentrations based on SigmaPlot 14.0 (Systat Inc., US). Data on human land use was collected from the Resource Environment Data Cloud Platform (http://www.resdc.cn/) and was accurate to 1 km. Considering the heterogeneous distribution of sampling scatters, inverse distance weighting (IDW) interpolation was used to evaluate the spatiotemporal distribution and density of nitrogen [32]. We predicted the spatial distributions of eutrophication and water quality state using Kriging interpolation based on ArcGIS 10.2 (ESRI Inc., US).

3. Results and Discussions

3.1. Spatial Variations of Nitrogen Concentrations. The spatial variations of nitrogen concentrations are shown in Table 1. The range of NH_3-N is in 0.11–13.20 mg L^{-1} (mean 1.82 ± 2.55 mg L^{-1}) and 0.10–34.10 mg L^{-1} (mean 4.28 ± 5.91 mg L^{-1}) in Yellow River (YR) and Fen River (FR) Basins, respectively. The range of TN was in 2.09–22.30 mg L^{-1} (mean 10.42 ± 4.83 mg L^{-1}) and 1.47–70.50 mg L^{-1} (mean 17.48 ± 14.75 mg L^{-1}) in YR and FR, respectively. All the mean concentrations of NH_3-N and TN (>1.0 mg L^{-1}) exceeded the Class III standard of surface water (shorter form Class III). As shown in Figure 2, both NH_3-N and TN in FR were higher than those in YR. The nitrogen in FR had more volatility than that in YR to the spatial distribution.

Lvliang is a hilly and ravine area with a shortage of water resources and inconvenient transportation and is relatively closed to external communication. The population is mostly concentrated in the small river basin near the two sides of Lvliang Mountain. Lots of studies have proved that agriculture (fertilizer), population, and industry increased nitrogen input in the river basin [33]. In the Yellow River Basin, most areas are rural land, and the industries in the basin are not well developed. Therefore, industrial wastewater does not have a major impact on nitrogen transportation. The nitrogen load is sufficiently impacted by fertilizer use and population growth. In addition, the wastewater and soil erosion in the Loess Plateau intensified the input and transportation of nutrients (phosphorus) [34]. The Lvliang area is the most serious area of soil erosion in the Yellow River Basin. Considering the western part of the FR basin is high and the eastern part is low, the pollutants in the west basin are easily spread in FR. Excess nitrogen is enriched in surface water, which can negatively affect water quality and cause eutrophication.

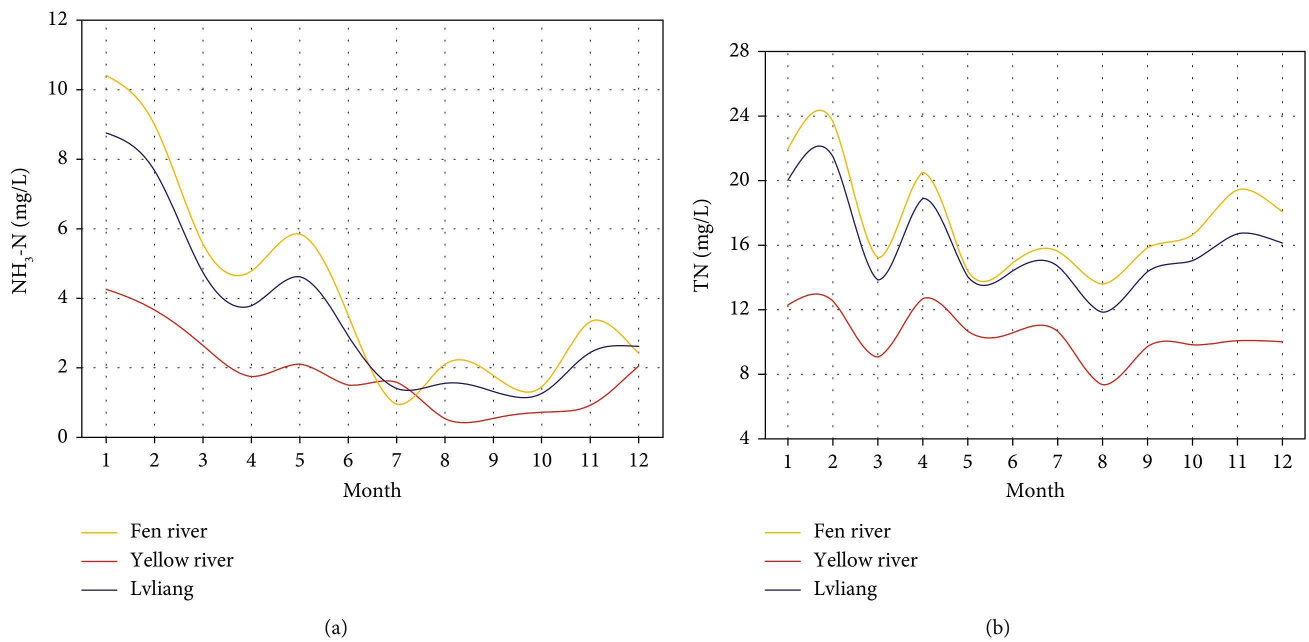

Figure 4: Comparison of NH_3-N and TN concentrations during January to December in 2019.

3.2. Temporal Variations of Nitrogen Concentrations. The Loess Plateau is a typical semiarid area with a wide range, which is short of water due to its low precipitation and high evaporation. The annual precipitation is 538.6 mm, and the annual evaporation is 1120 mm [35, 36]. The unreasonable and excessive development of water resources leads to the serious consequences of the reduction of groundwater storage. Some rivers even dried up in the dry season.

We calculated and compared the nitrogen concentrations in the wet/dry season and every month (Tables 2 and 3; Figures 3 and 4). The results showed that the NH_3-N in the dry season (YR: 3.32, FR: 7.35 mg L^{-1}) was higher than that in the wet season (July to September: YR: 1.21, FR: 2.19 mg L^{-1}). The NH_3-N in FR in dry and wet seasons had more volatility. The NH_3-N was highest in YR (4.26 mg L^{-1}) and FR (10.41 mg L^{-1}) in January. Rainfall is the major source of surface water supply in FR and YR. Precipitation has a certain dilution effect on the NH_3-N concentration in the rainy season. The dry season is the main period of farmers applying nitrogen and nitrogen-containing substances, and nutrients easily enter the surface water with rainfall and runoff [37]. These are the important reasons for the high nitrogen content in the dry season.

The above research results also showed TN (dry season: YR: 11.59, FR: 21.25 mg L^{-1}; wet season: YR: 9.52, FR: 14.71 mg L^{-1}). The TN was highest in YR (12.68 mg L^{-1}) and in FR in February (23.67 mg L^{-1}). TN is defined as the total amount of dissolved inorganic nitrogen and dissolved organic nitrogen in water. Figure 4 shows that the change of TN is mainly due to the change of NH_3-N, which means NO_3^--N is basically unchanged. The NO_3^--N is the main existing form of dissolved inorganic nitrogen in the Fen River [35]. NO_3^--N is the final product of oxidative decomposition of nitrogenous organic compounds, which indicates that the FR is polluted not only by agricultural pollution but also by industrial pollution. In the dry season, TN is 23.67 mg L^{-1} which means that the river in the FR region is extremely polluted.

3.3. Relationship between Nitrogen and Human Land Use. We predicted the spatial distribution of nitrogen in YR and FR, based on GIS interpolation (Figure 5). The results showed that the concentrations of NH_3-N were mostly <3.0 mg L^{-1} and 3.0–6.0 mg L^{-1} in YR and FR, respectively. The concentrations of TN were mostly 5.0–10.0 mg L^{-1} and 15.0–30.0 mg L^{-1} in YR and FR, respectively. The NH_3-N (12.0–13.4 mg L^{-1}) and TN (45.0–63.0 mg L^{-1}) were highest in the east of the study area. It should be noted that the NH_3-N and TN were much higher in FR than in YR. As shown in Table 4, the human land use in the Yellow River Basin (1.4%) was smaller than that in the Fen River Basin (8.12%). The land use types have an obvious impact on the nitrogen concentration distributions in FR. The sampling sites of the FR were mostly located near the Fen River Reservoir Two. There are some industrial facilities and human activities around this area. The sewage is discharged around the sampling sites. The results showed that high nitrogen contents should be related to anthropogenic sources, such as domestic sewage, animal manure and nitrogenous fertilizer, and industrial sewage. Xing and Liu [38] pointed that the TN in the Yellow River is mainly formed by soil organic nitrogen. Figure 5 shows that the highest TN region is at the southeast of Lvliang, the land use type of which is rural land. Another possible reason is that Lvliang's Fen River comes from the Taiyuan Basin, so the Taiyuan Basin might also be a source of nitrogen pollution in FR. Human beings affect surface water quality by interfering with land use and cover types [39]. The dynamic characteristics of water quality, nutrient density, and landscape will be affected [40]. The loss of nitrogen and sulfur in the landscape has a great

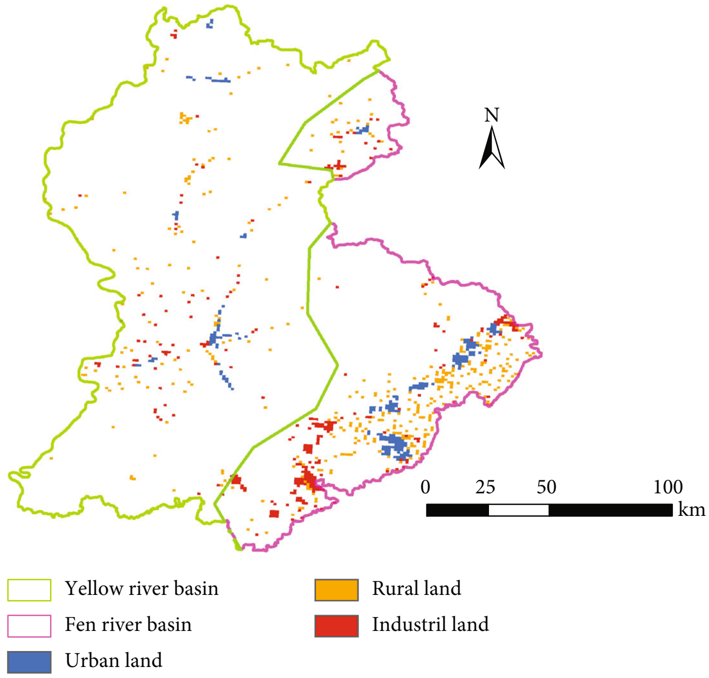

(a)

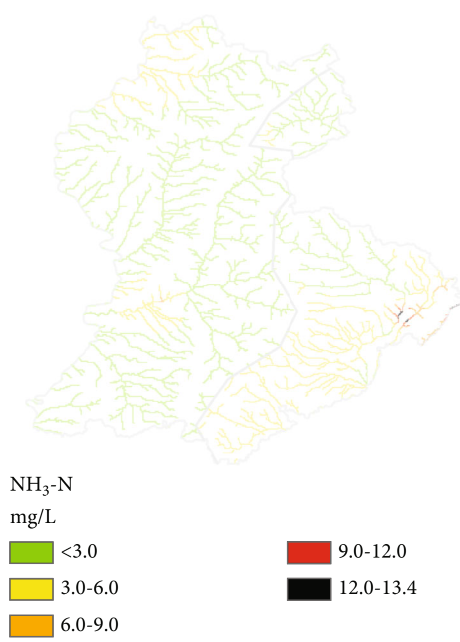

(b)

Figure 5: Continued.

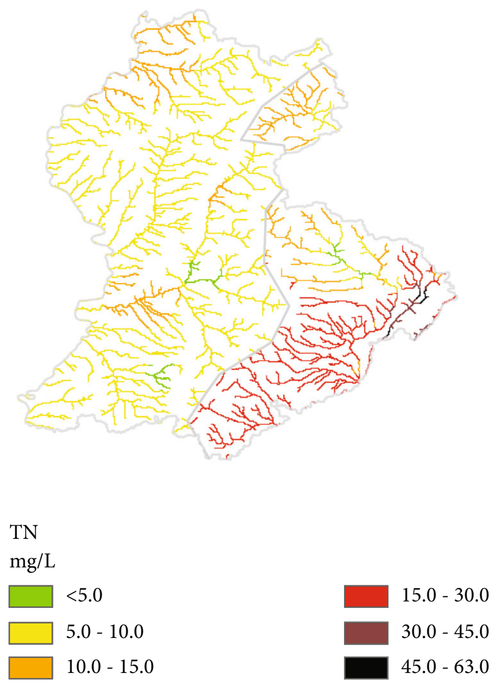

(c)

Figure 5: Spatial distribution of human land use (a), NH_3-N (b), and TN (c) in surface water on the eastern Loess Plateau.

Table 4: Comparison of the human land use in Yellow River and Fen River Basins.

Basin	Land use type (%)			
	Human land	Urban land	Rural land	Industrial land
Yellow River	1.40	0.39	0.65	0.36
Fen River	8.12	2.33	3.02	2.77

impact on the water quality of rivers, estuaries, and coastal waters.

Lvliang is located in the central of Shanxi Province, which has high GDP, population density, and concentrated industry. The large numbers of artificial land use in this area might be the cause of nitrogen pollution. In order to reduce the risk of water quality degradation, policymakers should carry out management and care assessment mechanisms at the source of rivers and pollution in accordance with the principle of Beneficiary Pays Principle and User Pays Principle. They should focus on the proportion of complete interference land use types by increasing the area of green land and natural water.

4. Conclusions

A GIS spatial analysis based on land use covers was used to understand the correlation between anthropogenic activity and rivers' nitrogen. The results showed that rivers' nitrogen was closely associated with human land use covers. Nitrogen pollution was most serious in urban areas. The method used in this study was effective and feasible for assessing the rivers' nitrogen under the background of different anthropogenic activities.

Our results suggest caution in developing cities and industries and stress the importance of sustainable intensification of land use. Overall, people have to a fair extent managed to protect water resource security and ecological sustainability. This research provided useful results concerning the relevant management decisions to reduce anthropogenic disturbance to the water resource management and land use planning in arid areas.

Data Availability

The data used to support the findings of this study are included within the article.

Conflicts of Interest

The authors declare that they have no known competing financial interests or personal relationships that could have appeared to influence the work reported in this paper.

Authors' Contributions

The contributions of the authors involved in this study are as follows: conceptualization: Yuxian Hu and Gaiqiang Yang; data curation: Yuxian Hu, Yanan Sun, and Hongyan Li; funding acquisition: Yuxian Hu, Gaiqiang Yang, and Hongyan Li; investigation: Yuxian Hu and Ke Zhang; supervision: Yuxian Hu and Ke Zhang; writing—original draft: Yuxian Hu; and writing—review and editing: Yuxian Hu and Yuan Li.

Acknowledgments

This work was partially supported by the Shanxi Natural Fund (No. 201901D111251), the Teaching reform and innovation project of colleges and universities of Shanxi (No. J2017081), the National Natural Science Foundation of China (No. 51709195), and the Shanxi Provincial Key Research and Development Project (International Cooperation) (No. 201803D421095).

References

[1] Q. Wang, D. Sun, W. Hao, Y. Li, X. Mei, and Y. Zhang, "Human activities and nitrogen in waters," *Acta Ecologica Sinica*, vol. 32, no. 4, pp. 174–179, 2012.

[2] I. Paredes, F. Ramírez, M. Forero, and A. Green, "Stable isotopes in helophytes reflect anthropogenic nitrogen pollution in entry streams at the Doñana World Heritage Site," *Ecological Indicators*, vol. 97, pp. 130–140, 2019.

[3] P. Shi, Y. Zhang, J. Song et al., "Response of nitrogen pollution in surface water to land use and social- economic factors in the Weihe River watershed, northwest China," *Sustainable Cities and Society*, vol. 50, p. 101658, 2019.

[4] F. Sajedi Hosseini, A. Malekian, B. Choubin et al., "A novel machine learning-based approach for the risk assessment of nitrate groundwater contamination," *Science of the Total Environment*, vol. 644, pp. 954–962, 2018.

[5] Y. Yu, Z. Jin, G. Chu, J. Zhang, and Y. Zhao, "Effects of valley reshaping and damming on surface and groundwater nitrate on the Chinese Loess Plateau," *Journal of Hydrology*, vol. 584, p. 124702, 2020.

[6] F. Mackenzie, L. Ver, C. Sabine, M. Lane, and A. Lerman, "C N P S global biogeochemical cycles and modeling of global change," in *Interactions of C N P and S Biogeochemical Cycles and Global Change*, vol. vol. 14 of NATO ASI series, pp. 1–61, Springer-Verlag, Berlin Heidelberg, 1993.

[7] S. G. Gardner, J. Levison, B. L. Parker, and R. C. Martin, "Groundwater nitrate in three distinct hydrogeologic and land-use settings in southwestern Ontario, Canada," *Hydrogeology Journal*, vol. 28, no. 5, pp. 1891–1908, 2020.

[8] J. Galloway, E. Cowling, S. Seitzinger, and R. Socolow, "Reactive nitrogen: too much of a good thing?," *Ambio*, vol. 31, no. 2, p. 60, 2002.

[9] Q. Guan, L. Feng, X. Hou, G. Schurgers, and J. Tang, "Eutrophication changes in fifty large lakes on the Yangtze Plain of China derived from MERIS and OLCI observations," *Remote Sensing of Environment*, vol. 246, article 111890, 2020.

[10] H. Kim, S. Yu, J. Oh et al., "Assessment of nitrogen application limits in agro-livestock farming areas using quantile regression between nitrogen loadings and groundwater nitrate levels," *Agriculture, Ecosystems & Environment*, vol. 286, p. 106660, 2019.

[11] P. Murdoch and J. Stoddard, "The role of nitrate in the acidification of streams in the Catskill Mountains of New York," *Water Resources Research*, vol. 28, no. 10, pp. 2707–2720, 1992.

[12] Y. Xue, J. Liu, F. Dang, X. Liang, S. Wang, and Z. Ma, "Influence of CH_4 adsorption diffusion and CH_4-water two-phase flow on sealing efficiency of caprock in underground energy storage," *Sustainable Energy Technologies and Assessments*, vol. 42, p. 100874, 2020.

[13] Y. Xue, F. Gao, and X. Liu, "Effect of damage evolution of coal on permeability variation and analysis of gas outburst hazard with coal mining," *Natural Hazards*, vol. 79, no. 2, pp. 999–1013, 2015.

[14] Y. Xue, P. G. Ranjith, F. Gao et al., "Mechanical behaviour and permeability evolution of gas-containing coal from unloading confining pressure tests," *Journal of Natural Gas Science and Engineering*, vol. 40, pp. 336–346, 2017.

[15] Y. Xue, P. G. Ranjith, F. Dang et al., "Analysis of deformation, permeability and energy evolution characteristics of coal mass around borehole after excavation," *Natural Resources Research*, vol. 29, no. 5, pp. 3159–3177, 2020.

[16] J. Allan and M. Castillo, *Stream Ecology: Structure and Function of Running Waters*, Springer, The Netherlands, second ed. edition, 2007.

[17] F. Chapin, M. Power, and J. Cole, "Coupled biogeochemical cycles and earth stewardship," *Frontiers in Ecology & the Environment*, vol. 9, no. 1, p. 3, 2011.

[18] D. Fowler, C. Steadman, D. Stevenson et al., "Effects of global change during the 21st century on the nitrogen cycle," *Atmosphere Chemistry Physics*, vol. 15, no. 24, pp. 13849–13893, 2015.

[19] C. Kroeze and S. Seitzinger, "Nitrogen inputs to rivers, estuaries and continental shelves and related nitrous oxide emissions in 1990 and 2050: a global model," *Nutrient Cycling in Agroecosystems*, vol. 52, no. 2/3, pp. 195–212, 1998.

[20] X. Chen, Z. Cui, M. Fan et al., "Producing more grain with lower environmental costs," *Nature*, vol. 514, no. 7523, pp. 486–489, 2014.

[21] W. H. Schlesinger, "On the fate of anthropogenic nitrogen," *Proceedings of the National Academy of Sciences of the United States of America*, vol. 106, no. 1, pp. 203–208, 2009.

[22] B. Gu, D. Liu, X. Wu, Y. Ge, Y. Min, and J. Chang, "Utilization of waste nitrogen for biofuel production in China," *Renewable & Sustainable Energy Reviews*, vol. 15, no. 9, pp. 4910–4916, 2011.

[23] H. Tu and H. Chen, "From deforestation to afforestation: effect of slopeland use policies on land use/cover change in Taiwan," *Land Use Policy*, vol. 99, article 105038, 2020.

[24] M. Martínková, C. Hesse, V. Krysanova, T. Vetter, and M. Hanel, "Potential impact of climate change on nitrate load from the Jizera catchment (Czech Republic)," *Physics & Chemistry of the Earth Parts*, vol. 36, no. 13, pp. 673–683, 2011.

[25] Y. Yan, L. Wang, J. Li et al., "Diatom response to climatic warming over the last 200 years: a record from Gonghai Lake, North China," *Palaeogeography Palaeoclimatology Palaeoecology*, vol. 495, pp. 48–59, 2018, (in Chinese).

[26] X. Zhao and M. Huang, "Spatial distribution of nitrogen of topsoil in the Wangdonggou Watershed of the Loess Plateau," *Research of Soil and Water Conservation*, vol. 26, pp. 62–67, 2019, (in Chinese).

[27] Y. Zheng, C. Duarte, J. Chen, D. Li, Z. Lou, and J. Wu, "Remote sensing mapping of macroalgal farms by modifying thresholds in the classification tree," *Geocarto International*, vol. 34, no. 10, pp. 1098–1108, 2019.

[28] L. Lassaletta, H. Garcia-Gomez, B. S. Gimeno, and J. Rovira, "Agriculture-induced increase in nitrate concentrations in stream waters of a large Mediterranean catchment over 25 years (1981-2005)," *Science of the Total Environment*, vol. 407, no. 23, pp. 6034–6043, 2009.

[29] F. Zhang, T. Tashpolat, H. Kung, and J. Ding, "The change of land use/cover and characteristics of landscape pattern in arid areas oasis: an application in Jinghe, Xinjiang," *Geo Spatial Information Science*, vol. 13, no. 3, pp. 174–185, 2010.

[30] J. Zhou, S. Li, X. Liang et al., "First report on the sources, vertical distribution and human health risks of legacy and novel per- and polyfluoroalkyl substances in groundwater from the Loess Plateau, China," *Journal of Hazardous Materials*, vol. 404, p. 124134, 2021.

[31] T. Huang, B. Ma, Z. Pang, Z. Li, Z. Li, and Y. Long, "How does precipitation recharge groundwater in loess aquifers? Evidence from multiple environmental tracers," *Journal of Hydrology*, vol. 583, p. 124532, 2020.

[32] Y. Li, Y. Bi, W. Mi, S. Xie, and J. Li, "Land-use change caused by anthropogenic activities increase fluoride and arsenic pollution in groundwater and human health risk," *Journal of Hazardous Materials*, vol. 406, article 124337, 2021.

[33] M. Gregory, M. David, and Z. Gertner, "Nitrate flux in the Mississippi River," *Nature*, vol. 414, no. 6860, pp. 166-167, 2001.

[34] Y. Tao, M. Wei, E. Ongley, L. Zicheng, and C. Jingsheng, "Long-term variations and causal factors in nitrogen and phosphorus transport in the Yellow River, China," *Estuarine, Coastal and Shelf Science*, vol. 86, no. 3, pp. 345–351, 2010.

[35] Z. Meng, Y. Yang, Z. Qin, and L. Huang, "Evaluating temporal and spatial variation in nitrogen sources along the lower reach of Fenhe River (Shanxi Province, China) using stable isotope and hydrochemical tracers," *Water*, vol. 10, no. 2, p. 231, 2018.

[36] Y. Yang and B. Fu, "Soil water migration in the unsaturated zone of semiarid region in China from isotope evidence," *Hydrology and Earth System Sciences*, vol. 21, pp. 1–24, 2017.

[37] W. Shao, J. Cai, J. Liu et al., "Impact of water scarcity on the Fenhe River Basin and mitigation strategies," *Water*, vol. 9, no. 1, p. 30, 2017.

[38] M. Xing and W. Liu, "Using dual isotopes to identify sources and transformations of nitrogen in water catchments with different land uses, Loess Plateau of China," *Environmental Science & Pollution Research*, vol. 23, no. 1, pp. 388–401, 2016.

[39] Y. Wang, "Urban land and sustainable resource use: unpacking the countervailing effects of urbanization on water use in China, 1990-2014," *Land Use Policy*, vol. 90, p. 104307, 2020.

[40] P. Shi, Y. Zhang, Z. Li, P. Li, and G. Xu, "Influence of land use and land cover patterns on seasonal water quality at multi-spatial scales," *Catena*, vol. 151, pp. 182–190, 2017.

Hindawi
Geofluids
Volume 2021, Article ID 6661107, 15 pages
https://doi.org/10.1155/2021/6661107

Review Article

Deterioration of Physical and Mechanical Properties of Rocks by Cyclic Drying and Wetting

Zhizhen Zhang[1,2] **Yixin Niu**[1] **Xiaoji Shang**[1] **Peng Ye,**[1] **Rui Zhou,**[2] **and Feng Gao**[1]

[1]*State Key Laboratory for Geomechanics and Deep Underground Engineering, School of Mechanics and Civil Engineering, China University of Mining and Technology, Xuzhou 221116, China*
[2]*State Key Laboratory of Coal Mine Safety Technology, China Coal Technology & Engineering Group Shenyang Research Institute, Shenfu Demonstration Zone, 113122, China*

Correspondence should be addressed to Zhizhen Zhang; zzzhang@cumt.edu.cn and Xiaoji Shang; shangxj2016@cumt.edu.cn

Received 25 February 2021; Accepted 3 May 2021; Published 28 May 2021

Academic Editor: Guanglei Zhang

Both surface and underground rocks in nature often undergo repeated drying and wetting. The dry-wet cycle is a weathering effect that includes physical and chemical processes, which has varying degrees of degradation effects on the physical and mechanical properties of rocks. This paper analyzes and discusses this kind of rock degradation based on the existing literature data. First, the deterioration degree of various physical and mechanical properties (including density, P-wave velocity, porosity, static and dynamic compressive/tensile strength, and fracture toughness) is summarized as the number of dry-wet cycles increases. Secondly, the possible degradation mechanism of the dry-wet cycle is explained in terms of clay mineral swelling, solute migration, and microcrack evolution. Then, the damage constitutive model of the rock after cyclic dry-wet treatment is introduced. Finally, the issues that need to be studied in the future are put forward.

1. Introduction

Rock is the most common geological material in projects such as oil and gas development, coal mining, and hydroelectric power generation. In engineering practice, rocks are commonly affected by dry and wet cycles, for example, the surrounding rock of reservoir bank slope engineering by the influence of daily and seasonal changes of water level (see Figure 1) [1–4]; the thin granite veneer cladding panels installed on the exterior of buildings subjected to environmental weathering [5]; tunnel excavation under the influence of groundwater level fluctuation [6]; the slope stability of open-pit coal mine affected by rainfall (see Figure 2) [7]; the tailings pond by the impact of abandoned tailings discharge and pumping [8]; the swelling rock of the base and slope of the water conveyance channel (see Figure 3) [9–11]; the coastal rock masses affected by tides [12–15]; the stone monuments, sculptures, and historical sites affected by acid rain erosion [16, 17]; the subgrade and surrounding rock of railway tunnel [18]; the retaining dam of an underground reservoir [19]. After the dry-wet cycle, the physical and mechanical properties of the rock will change to varying degrees, and the changes are very important to the design, construction, and operation of rock projects.

In recent years, with the continuous progress of research on water-rock interactions, the effects of dry-wet cycles on the degradation of rock properties have gradually attracted wide attention from scholars. The dry-wet cycle test was first used as an experimental method to study the durability of rocks after weathering, and it was often used as a comparison with freeze-thaw cycles and cold-heat cycles [18, 20–26]. Ito et al. [27] carried out the freeze-thaw cycle and dry-wet cycle test of rocks in cold regions and found that the influence of the dry-wet cycle on the rock sample is almost equal to or even more serious than the freeze-thaw cycle. The experiment of Loubser [28] found that water saturation does not seem to be the main factor affecting the degree of rock deterioration, and the influence of the number of wet and dry cycles is more significant. At present, most experiments have found that the rock samples deteriorate

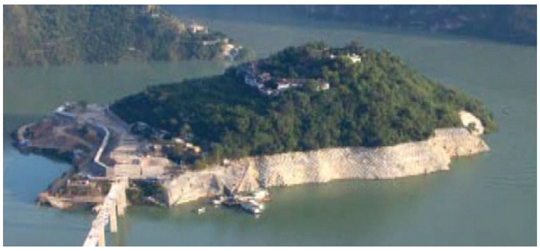

Figure 1: The famous scenic spot at the Three Gorges Reservoir, Baidicheng, whose reinforcement slope is designed to resist periodic reservoir fluctuations [1].

(a) Local landslide (b) Overall collapse

Figure 2: Landslides and collapses caused by rainfall [7].

Figure 3: The bedrock of Saranbe River, experiencing seasonal cycles of dry and wet [9].

significantly after the cyclic dry-wet treatment. However, there are still experiments found that the discrete difference of the dry-wet cycle test samples masks the degradation effect on the rock samples [20].

The dry-wet cycle itself is a weathering mechanism, and the properties of weathered substances are affected by the way of wetting [29]. In response to this problem, different scholars have adopted different cyclic dry-wet treatment methods (see Table 1). The cyclic dry-wet treatment methods are roughly divided into three types: the real wet-dry cycle of natural soaking and room temperature drying, the accelerated dry-wet cycle of vacuum pressure saturation and high temperature drying, and the mixed cycle treatment of the two (as seen in Figure 4). In the drying process, the rock deterioration is the greatest when the drying temperature is 60°C, that is, the porosity increases rapidly and the water absorption is the most [30].

Table 2 details the changes in the physical and mechanical properties of the rock samples with different lithologies in different tests after a certain number of dry and wet cycles. It was found that the physical and mechanical properties of the rock samples were degraded to varying degrees in most of the tests, but even the same type of rock differed significantly in different tests due to its different composition. In Chen et al.'s [6]test on altered granite, the reduction in internal friction angle reached an astonishing 93.76%, while Hale et al. [20] considered that the dry-wet cycle had no obvious deterioration effect on the rock sample when compared with the freeze-thaw cycle test. From Liu et al. [31] and Zhao et al.'s [32]separate experiments on sandstones with different clay content, it can be seen that the level of clay content is an important factor in the degree of rock degradation caused by the dry-wet cycle.

From the above, it is necessary to summarize the influence of dry and wet cycles on the physical and mechanical properties of rocks. In this article, we mainly reviewed the rock degradation after cyclic dry-wet treatment from three aspects, namely, quantitative characterization of degradation degree, degradation mechanism, and degradation constitutive model.

2. Rock Deterioration Degree after Dry-Wet Cycle

Due to the huge differences in the mineral composition of different types of rock samples, their physical and mechanical properties are very different, resulting in different sensitivity of rocks to water. Therefore, the effects of wet and dry cycles on rock degradation are different. This paper selected published test results from different researchers and normalizes them to make them comparable. The degradation degree of a certain physical and mechanical parameter is characterized by its relative change, that is, the ratio of the difference between the parameter value of the rock sample after the dry-wet cycle and the initial value to the initial value.

$$R_n = \frac{V_n - V_0}{V_0} \times 100\%, \quad (1)$$

where R_n is the degradation degree, V_n is the parameter value of the rock sample after the dry-wet cycle, and V_0 is the initial value.

2.1. Physical Properties. The physical properties of rock mainly include density, elastic wave velocity, porosity, water absorption, magnetic susceptibility, resistivity, thermal conductivity, radioactivity, and durability, which are the basis for the formation of various geophysical fields. The infiltration of water on the rock causes the salt inside the rock to dissolve, and the water reacts with the rock minerals chemically, which changes the internal composition and microstructure of the rock, which in turn leads to the deterioration of its physical properties. Take Zhou et al.'s test results as a representative [33], during the dry-wet cycle; this infiltration occurs repeatedly, and various physical properties of the rock change to varying degrees (as shown in Figure 5). It can be

Table 1: Different cyclic dry-wet treatment methods.

Rock type	Reference	Sample size	Wetting-drying cycle method	
			Wetting	Drying
Mudstone	Y. Zhao et al. [39]	Cylinder 25 ∗ 50 mm	Vacuum-saturated 24 h	Oven dried at 60°C for 24 h
Red-Bed sandstone	Z. Zhang et al. [36]	Cylinder 50 ∗ 100 mm	Vacuum-saturated 4 h and pure water saturated at room temperature for 44 h	Oven dried at 45°C for 20 h and drying in vacuum pump for 4 h
Sandstone	P. Yuan et al. [30]	Cylinder 50 ∗ 25 mm	Pure water saturated for 24 h	Oven dried at 60°C for 24 h
Chlorite	X. Yang et al. [7]	Cylinder 50 ∗ 100 mm	1/4 L, 1/2 L, 3/4 L of sample L each for 2 h and 1 L for 48 h	Room temperature dried for 7 d
Sandstone	K. Xie et al. [1]	Cylinder 50 ∗ 100 mm	Vacuum-saturated 4 h and pure water saturated for 44 h	Oven dried at 50°C for 24 h and room temperature vacuum-dried 4 h
Altered rock	Z. Qin et al. [8]	Cylinder 50 ∗ 100 mm	Water saturated for 24 h	Oven dried at 105°C for 12 h
Argillaceous limestone	B. Meng et al. [35]	Cylinder 50 ∗ 100 mm	Vacuum-saturated 3 d	Room temperature dried for 3 d
Red sandstone	G. Khanlari et al. [22]	Cylinder 50 ∗ 100 mm	Water saturated for 24 h	Oven dried at 110°C for 24 h

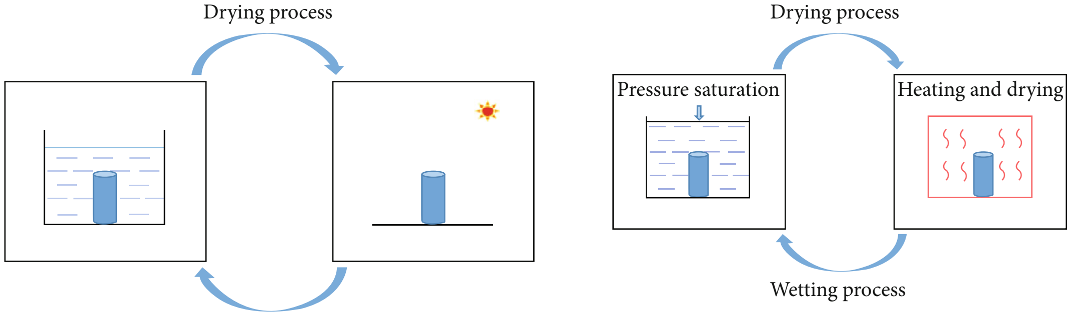

(a) The natural soaking and room temperature drying (b) The vacuum pressure saturation and high temperature drying

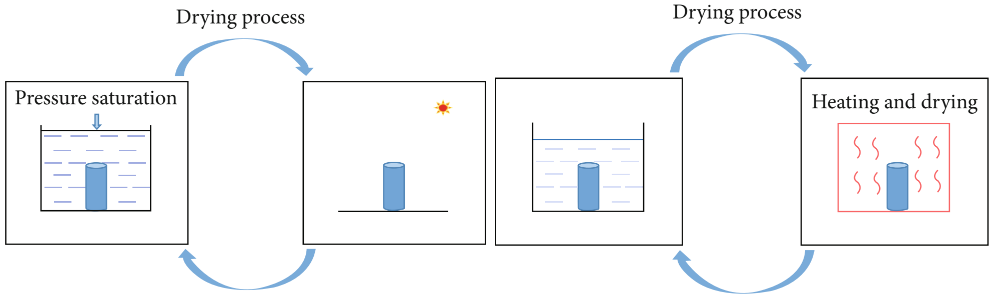

(c) The mixed treatment methods

Figure 4: Three types of cyclic dry and wet treatment methods.

seen that with the increase in the number of dry and wet cycles, the dry weight, P-wave velocity, and slake durability index of the rock sample gradually decrease, while the porosity and water absorption gradually increase. It is worth noting that the decrease in dry weight and slake durability index is relatively small. Since the ability of rock materials to hold water depends to a large extent on their porosity, the water absorption and porosity of the rock sample will change simultaneously, which has a good linear relationship [34]. From the perspective of the change trend, the deterioration rate is faster before the 20th-30th cycle and then tends to be stable. As the number of cycles increases, the damage effect caused by the water-rock interaction on the rock is reduced. The relationship between these physical parameters and the number of dry-wet cycles can usually be described by an exponential equation [34, 35].

Among the various physical properties of rocks, the P-wave velocity is affected by the characteristics of the internal pores and water content of the rock, and its monitoring methods are relatively simple and widely used. In addition, it is also related to mechanical parameters such as elastic modulus and strength, so it is a very important petrophysical

Table 2: Deterioration of different rocks after cyclic dry-wet treatment.

Rock type	Reference	Max n	Max variation: Physical properties		Max variation: Mechanical properties	
Sandstone	Z. Zhou et al. [33]	50	ρ	-5.69%	—	
			W_a	+16.91%		
			P	+12.48%		
			v_p	-24.64%		
			SDI	-3.07%		
Sandstone joint	J. Fang et al. [43]	20	S_p	-8.98%	JRC	-6.47%
			S_v	-8.62%	JCS	-44.21%
			S_z	-8.75%	φ	-8.93%
			S_{dr}	-4.96%		
Red-sandstone	B. Du et al. [37]	20	ρ	-3.62%	UCS	-18.28%
			v_p	-24.93%		
Shaly sandstone	X. Liu et al. [31]	20	—	—	UCS	-68.69%
					E	-70.02%
Low clay sandstone	Z. Zhao et al. [32]	15	—	—	TS	-5%
Mudstone	M. Hu et al. [90]	15	Weight loss	-60.7%	E	-14.17%
					K	-15%
					G	-15.22%
					φ	-19.31%
					c	-55.31%
Altered granite	X. Chen et al. [6]	60	P	+33.86%	UCS	-50.22%
					E	-63.84%
					φ	-93.76%
					c	-53.90%
Black ignimbrites	A. Özbek [21]	50	v_p	-8.33%	UCS	-16.08%
			ρ	-6.1%		
			P	+13.99%		
			W_a	+12.18%		

n is the number of dry-wet cycles, ρ is the density, W_a is the water content, P is the porosity, v_p is the P-wave velocity, S_p is the largest bulge on the joint surface, S_v is the largest valley on the joint surface, S_z is the largest drop on the joint surface, and S_{dr} is the expansion area ratio of the joint surface (indicating the complexity of the joint surface); JRC is the roughness coefficient of the joint, JCS is the compressive strength of the joint surface, SDI is the slake durability index, φ is the internal friction angle, c is the cohesive force, UCS is the uniaxial compressive strength, TS is the tensile strength, E is the elastic modulus, G is the shear modulus, and K is the bulk modulus.

parameter. In laboratory tests, P-wave velocity is often used in the selection of rock samples to reduce the dispersion of rock samples as much as possible [31]. A large number of test results show that with the increase of the number of dry-wet cycles, the P-wave velocity of rock samples decreases to varying degrees. Figure 6 shows the changes of P-wave velocity in different experiments based on previous literature, and Figure 7 shows the degradation degree of P-wave velocity. It can be seen that even if it is all sandstone, the P-wave velocity variation law is very different due to the different producing areas and the subtle differences in the test methods. The difference between different types of rocks is even greater. For example, for ignimbrite rocks with different colors [21], although the initial wave velocity is different, the degradation degree of the P-wave velocity is within 10% as the number of wet and dry cycles increases. However, for the sandstone samples in different tests, not only the initial wave velocity is greater than that of the ignimbrite rock, but the degradation degree can reach nearly 20% [34] or even more than 20% [36, 37] after a small number of wet and dry cycles. In addition, the water temperature will also accelerate the deterioration of the P-wave velocity [30]. To put it simply, the velocity of P-wave propagation in the air is much smaller than that in the solid, and it is equivalent to increasing the probability of P-wave propagation in the air due to the increasing rock porosity after dry-wet cycles, so the P-wave velocity is decreasing [38]. And if these pores are filled with water, the P-wave velocity in the water is much greater than that in the air, and the water completely replaces the air in the pores and microcracks in the saturated state, so the

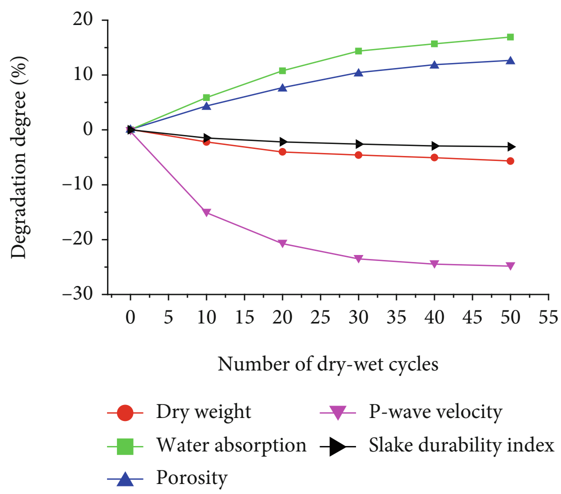

Figure 5: Degradation degree of physical properties of sandstone after dry-wet cycles [33].

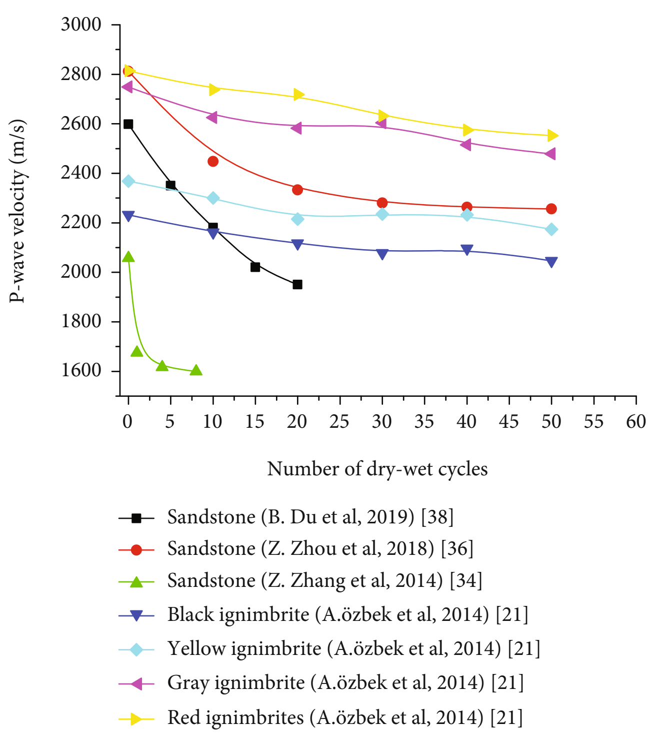

Figure 6: Variation of P-wave velocity after different dry-wet cycles.

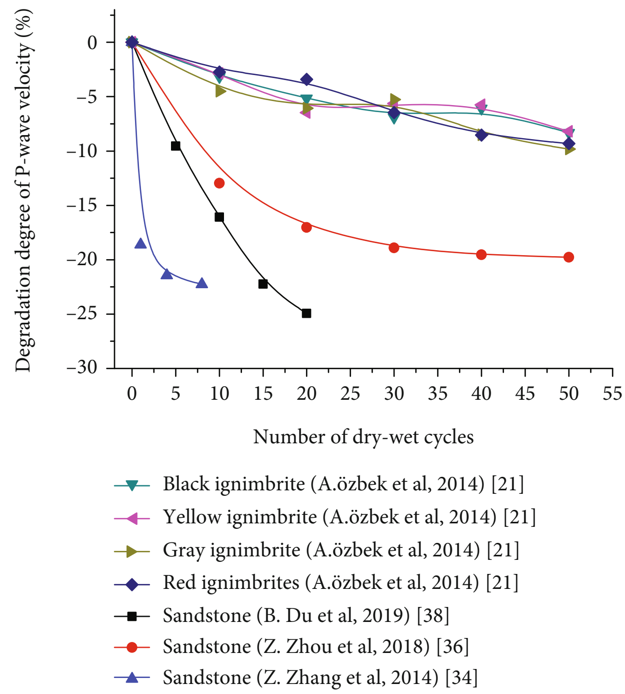

Figure 7: Degradation degree of P-wave velocity after different dry-wet cycles.

deterioration rate of the sample in the dry state is much greater than that in the saturated state [34, 38]. But in general, as the number of wet and dry cycles increases, the P-wave velocity across the sample would decrease under both dry and saturated conditions. This can be explained by increased porosity and density loss [38].

Rock porosity and pore size distribution are the macroscopic manifestations of the initiation, development, and expansion of internal microscopic cracks, which can be measured by nuclear magnetic resonance (NMR), mercury intrusion porosimetry (MIP), scanning electron microscopy (SEM) and other test methods. Figure 8 shows the porosity of the rock samples in different tests with the number of dry-wet cycles. It is found that the porosity of the rock shows a differential increase with the increase of the number of dry-wet cycles, which roughly obeys the linear relationship with different slopes [39]. Regardless of whether it is ignimbrite rock or sandstone, the porosity increases by about 20% after 50 dry-wet cycles, while it can exceed 40%, up to 44.4% for mudstone samples drilled from Simianshan [39]. The increase in porosity will cause the deterioration of the mechanical properties such as uniaxial compressive strength (UCS) and elastic modulus of the rock sample. The relationship between UCS and porosity can be quantitatively described by an exponential function [39]. The dry-wet cycle not only increases the porosity of the rock but also changes its pore structure, causing the pores to change from small pores (0.01~0.1 μm) to larger pores (0.1~1.0 μm) [35]. The pore size distribution is concentrated in two intervals and has an optimal value. As the number of cycles increased, the optimal pore size increases, and the corresponding component decreases. This variation may be related to the periodic water-rock interaction [39].

2.2. Mechanical Properties. The influence of dry-wet cycles on the physical properties of rocks eventually leads to the deterioration of mechanical properties, which is manifested in the static compressive and tensile strength, dynamic compressive and tensile strength, fracture toughness, elastic modulus, friction angle, cohesion, etc. decrease to varying degrees, which can usually be described by an exponential function [35].

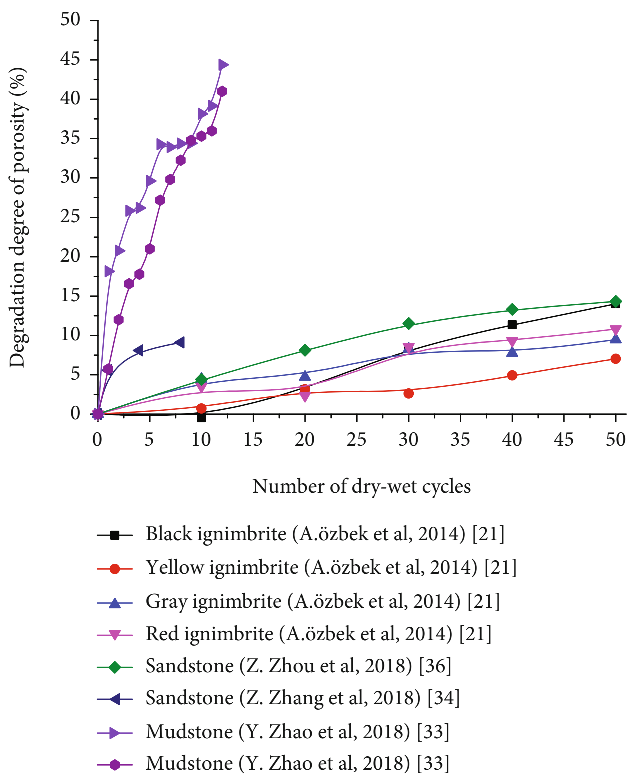

Figure 8: Degradation degree of porosity after different dry-wet cycles.

The strength properties of rocks would be significantly deteriorated after the cyclic dry-wet treatment. Khanlari et al. [22], Özbek [21], Zhao et al. [32], Huang et al. [40], and Chen et al. [41] performed static compression tests after dry and wet cycles on sandstone, melted limestone, mudstone, and coalstone, respectively. All of the results shown that with the increase of the number of dry and wet cycles, the uniaxial compressive strength and triaxial compressive strength of the rock sample decreased to varying degrees. There are relatively few studies on the static tensile strength of rocks after wet and dry cycles. Zhao et al. [32] conducted a Brazilian split test on a sandstone with low clay content and found that the deteriorating effect of dry and wet cycles on static tensile strength is not significant. In the rock dynamic compression test, Du et al. [37] found that the dynamic compressive strength of the sample is related to the number of wet and dry cycles and the loading rate. Taking the influence of the loading rate into account, he proposed a decay function to predict the long-term dynamic compressive strength of sandstone considering the number of wet and dry cycles. Zhou et al. [34] established an empirical equation based on experimental results, describing the influence of strain rate and the number of wet-dry cycles on the dynamic compressive strength of rock materials. Because the stress path involving surrounding rock in tunneling is an unloading process, that is, it can be regarded as a dynamic tensile process, Zhou et al. [33] and Li et al. [42] and others conducted related experiments and found that the cyclic dry-wet treatment increases the density, complexity, and connectivity of microcracks, which also significantly degrades the dynamic compressive strength of the rock. The shear strength of jointed rock mass would also deteriorate after drying and wet cycles, which is caused by the changes in the micromorphology and joint wall strength of the joint surface [43].

According to the total number of wet and dry cycles in the test and the interval between monitoring points, the number of dry and wet cycles below 20 is considered a short-term test, and more than 20 times is considered a long-term test. Figures 9 and 10 show the changes of the uniaxial compression strength degradation in different tests under short-term and long-term wet and dry cycles. In the long-term dry-wet cycle test, since the monitoring point interval is at least 10 dry-wet cycles, the nonlinear changes within the 10 dry-wet cycles are ignored, and there is no obvious regularity on the whole, and the uniaxial compressive strength is even enhanced to some extent. In the short-term test, the uniaxial compressive strength of the rock changes drastically when the number of dry-wet cycles is less than 5, and changes more steadily when it is greater than 5.

The dry-wet cycle also has a certain degradation effect on the fracture toughness of the rock. Hua et al. [44–46] pointed out that the tensile strength of sandstone and the fracture toughness of type I and type II cracks all decrease with the increase of the number of dry-wet cycles, and there is a good linear relationship between the fracture toughness of type I crack and tensile strength. Cyclic wet and dry treatments can also degrade cohesion and friction angle. Figure 11 shows that uniaxial tensile strength, elastic modulus, cohesion, and internal friction angle all decrease to varying degrees with the increase in the number of wet and dry cycles. However, some studies have shown that the influence of dry-wet cycles on sandstone cohesion is different from the influence on friction angle. The change in cohesion in the wet-dry cycle is similar to the change in the peak strength, while the friction angle seems to have nothing to do with the wet-dry cycles [36].

2.3. Chemical Corrosion. Water has dissolution, erosion, and softening effects on rocks [47–52]. However, in many cases, rocks are affected by the coupling of chemical corrosion and dry-wet cycles. Therefore, many scholars have also done related research about the deterioration of rocks under non-neutral dry-wet cycles. Smith [53] systematically studied the weathering of desert rocks due to temperature, moisture, and salt and chemical reactions. Yuan et al. [54, 55] studied the mechanical properties and ion change characteristics of sandstone under pH = 4, 7, and 9, respectively. Feng et al. [56] lists the chemical reaction equations of various materials in sandstone under acid-base and neutral conditions. Sun et al. [16] used MgSO4 solutions of different concentrations (4%, 6%, 8%) to saturate sandstone and found that compared with pure water wet and dry cycles, the threshold was reached at 30 times of dry and wet cycles, and the P-wave velocity began to rise in the reverse direction, and the tensile strength suddenly dropped sharply. It was found that the color brightness and thermal conductivity of the rock sample showed a good linear relationship with the tensile strength.

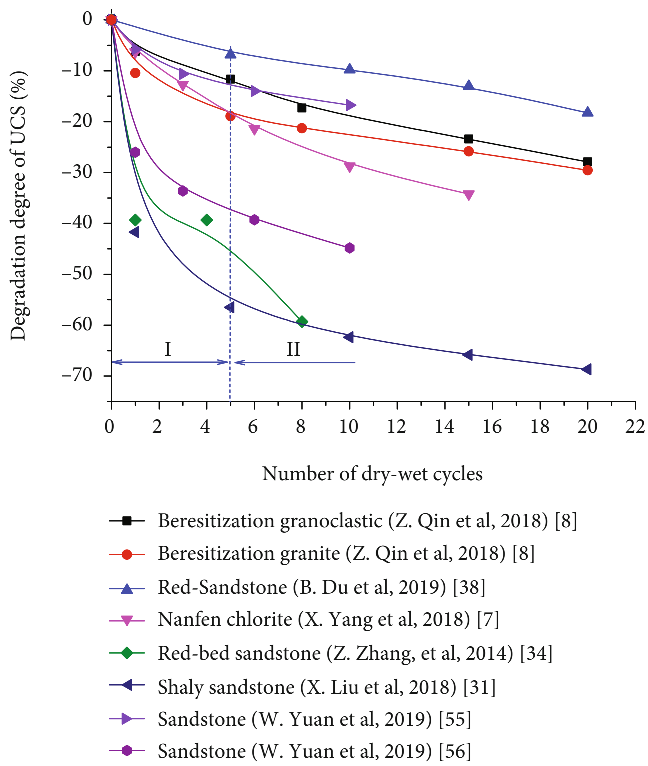

Figure 9: Degradation degree of UCS after short-term dry-wet cycles.

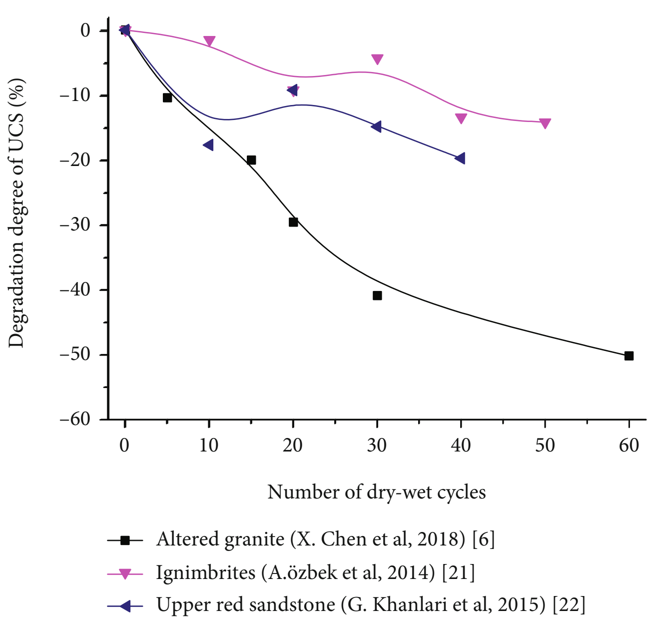

Figure 10: Degradation degree of UCS after long-term dry-wet cycles.

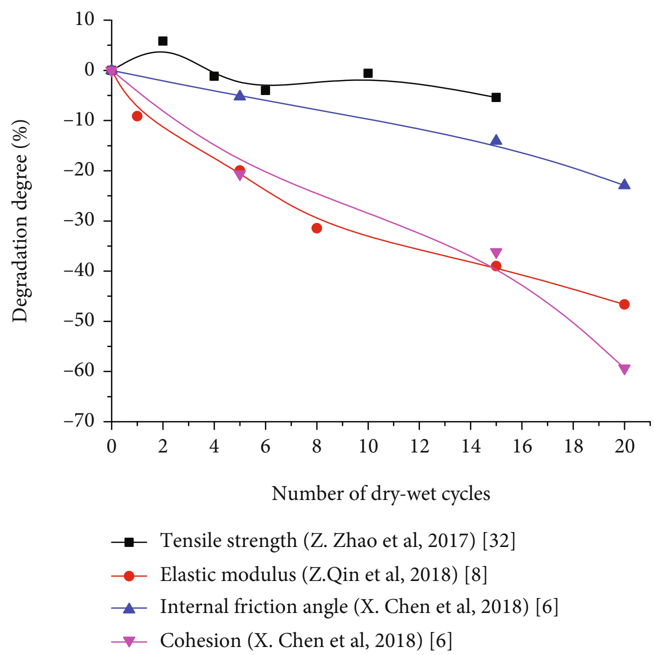

Figure 11: Degradation degree of several mechanical properties after different dry-wet cycles.

3. Rock Deterioration Mechanism after Dry-Wet Cycle

3.1. Soaking and Drying-Soaking Cycle. During the dry-wet cycle, there is a compound effect of soaking and drying-soaking alternately. It can also be considered as a fatigue damage process of water to rocks. Van Eeckhout [47] summarized five possible mechanisms for the impact of water soaking on the strength degradation of rocks, that is, reduction in fracture energy, reduction in capillary tension, increase in pore pressure, reduction in friction coefficient, and degradation due to chemical corrosion. In order to distinguish the effects of soaking and drying-soaking cycles, Zhao et al. [32] conducted a comparison test of pure soaking (16 days) and dry-wet cycles (soaking lasting 15 days) on low clay sandstone. The test results show that the rock strength decreased by 59% after 16 days of pure water immersion, while it decreased by only 5% after 15 wet and dry cycles. However, this test has a relatively big problem: the test state of the rock samples is different, that is, the pure water immersion test inevitably requires the rock sample to be tested in a saturated state, while the dry-wet cycle rock sample strength test is in a dry state. In terms of fracture behavior, the dynamic fracture initiation, propagation toughness, and crack propagation velocity of saturated specimen were apparently lower than that of dry ones at the same loading rate [57]. Although there is a strong correlation between the moisture content of rock samples and the deterioration of various physical properties [58–64], there is no obvious difference in the degradation of rocks with different moisture content after wet and dry cycles [65].

Whether the rock sample is in a saturated state or a dry state after the dry-wet cycle, its strength is very different.

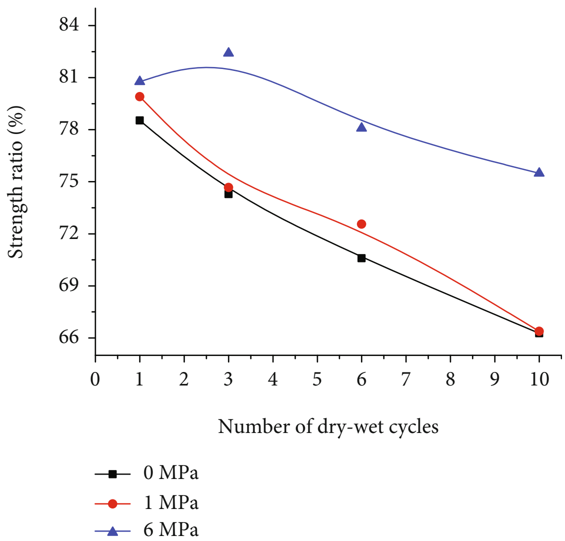

Figure 12: Strength ratio of saturated rock samples to dry rock samples after the same number of dry-wet cycles (after [54]).

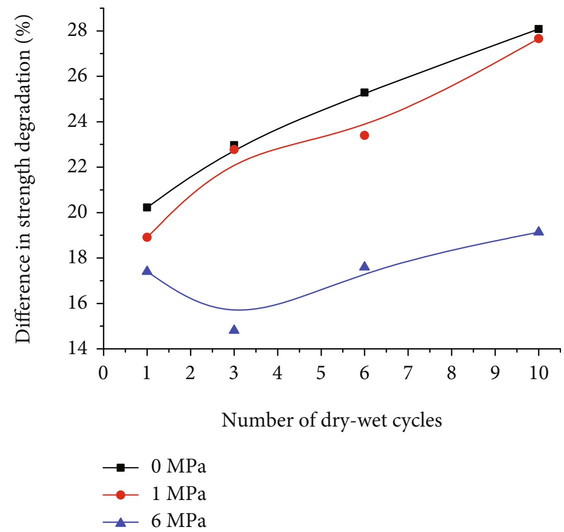

Figure 13: Difference in strength degradation between the saturated state and the dry state under different wet and dry cycles and confining pressure (after [54]).

Yuan et al. [54, 55] conducted strength tests on sandstones in different states. Figure 12 shows the strength ratio of saturated rock samples to dry rock samples after the same number of dry-wet cycles. It can be seen that as the number of dry-wet cycles increases, the saturation-dry strength ratio decreases significantly, which means that the difference between the strength of saturated rock samples and dry rock samples is getting larger and larger. This downward trend contains information about dry-wet cycle damage. Furthermore, the greater the confining pressure, the smaller the decrease, and the saturation-dry strength ratio under high confining pressure (6 MPa) is significantly greater than that under low confining pressure (0 MPa). Figure 13 shows the difference in strength degradation between the saturated state and the dry state under different wet and dry cycles and confining pressure. The strength degradation difference is defined as the ratio of the strength difference after n wet and dry cycles to the initial strength. It is found that the strength deterioration difference under low confining pressure gradually increases with the increase of the number of dry and wet cycles, while the trend is not obvious under high confining pressure. The enhancement effect of the confining pressure partially covers the deterioration caused by the dry and wet cycle.

3.2. Clay Content and Swelling Behavior. The swelling behavior of rock is often related to its clay composition. Clay minerals mainly include montmorillonite, illite, chlorite, kaolinite, and serpentine. These minerals would swell after absorbing water and eventually lead to rock damage and destruction [66–70]. The cyclic dry-wet treatment process would cause repeated expansion and contraction of clay components, and moisture fluctuation is the main reason [71–74]. The volume of expanded clay changes with the fluctuation of water, which causes the air pressure in the pores to rise sharply, and finally ruptures to form cracks. This irreversible phenomenon is called “air breakage” [75]. On the other hand, there would be obvious argillization phenomena after undergoing wetting-drying cycles, which weakens the cementation between mineral grains in the rock and smooths the shape of the grains themselves [36]. The increase in saturation will also increase the dissolution of clay minerals and the lubricity between mineral particles. Therefore, these effects significantly reduce the strength and deformation properties of the rock [35] and also reduce its brittleness, resulting in the failure mode of the specimen from extension failure to shear failure [36]. It should also be noted that the dissolution and precipitation of soluble substances are accompanied by substance migration. Beck et al. [76] observed the surface of limestone samples after 50 dry-wet cycles and found that the appearance of the limestone changed in color, becoming slightly brown, and a hard thin layer appeared in about 20% of the place, similar to the oxide layer on the metal, and the surface roughness of the rock sample decreased. The reason is that during the saturation process, the soluble matter dissolves, and during the subsequent drying process, the soluble matter migrates to the surface of the rock sample along with the water vapor, where it crystallizes out again. This phenomenon is macroscopically manifested as the reversibility of rock properties to a certain extent, that is, the strength recovery occurs in the dry state [77, 78] (as shown in Figures 12 and 13).

The internal microscopic damage caused by the dry-wet cycle would vary depending on the amount of clay content. Lin et al. [79] found that the fracture mechanism of all dry sandstones is mainly intracrystalline fracture, while saturated sandstones with high chlorite content mainly intracrystalline fracture and saturated sandstones with low chlorite content intercrystalline fracture. Wang et al. [80] observed that argillaceous rocks have a certain irreversible deformation regardless of whether they are wet or dry. The form is a typical 1 μm open-pore microcrack network: the former is located in the block and/or inclusion-matrix interface of the clay matrix; the latter mainly exists in the block of clay matrix. For rocks with low clay mineral content, the main degradation mechanism is to reduce the fracture energy and friction coefficient, while the possible softening, expansion, and dissolution behavior of clay minerals can only play a small role [32]. In short, the content of clay components is a key component factor that affects the effect of dry-wet cycles on rock degradation.

3.3. Microstructure Evolution. By means of scanning electron microscopy (SEM) observation, image analysis, and discrete element simulation, the microscopic morphology and structure of the rock surface, including the particles contact network, particles force chains distribution, microcrack diameter, length, and area, can be obtained. After cyclic drying and wetting treatment, the microstructure of rocks changes from a well-organized dense structure stage to a porous stage and then to a cracking stage [1, 6, 7, 30, 31, 34–37, 45, 80–82]. Microcracks in the rock grow and expand, and their density, length, complexity, and interconnectivity increase. At the same time, the size, shape, and distribution of pores also undergo significant changes, and the grains are also degraded. These changes are the main reason for the degradation of mechanical properties [33, 34]. The initiation and propagation of microcracks are mainly the result of cyclic loading and unloading of tensile stress caused by water absorption and desorption of rocks in the cyclic wetting and drying process [30].

Figure 14 shows the SEM images of the rock surfaces after different wet-dry cycles. When the rock sample does not absorb water, the microstructure of the particles shows a clear outline without obvious overlap. After the water-rock interaction, the microstructure of the rock sample surface is no longer compact and uniform, and the particle shape gradually changes from blocky and flat to flocculent and disordered [83]. When the number of wetting and drying cycles reaches more than 10 times, the microstructure of the rock changes greatly compared with the natural state [6, 82]. The original small pores gradually infiltrated and merged into large pores, and the phenomenon of stacking and overlapping and massive precipitation appeared, and the shape of the grains changed from a clear, neat, and dense edge to a mud layer. When the number of wetting and drying cycles reaches more than 30 times, the pores further expand and become larger, and obvious microcracks appear.

The dry-wet cycle has a great deteriorating effect on the dynamic energy absorption of the rock. Yuan et al. [84] found that the fracture surface energy of the sandstone sample decreases due to the stress transformation between sandstone mineral particles during the dry-wet cycle. Hu et al. [85] analyzed the degradation mechanism of the rock during the dry-wet cycle by considering the temperature-induced stress, load, and fluid effect, that is, temperature-induced stress and applied load cause tensile stress inside the rock sample and compressive stress on the surface; when the stress generated by the temperature and the overburden load is greater than the tensile strength of the rock sample, the internal cracks begin to expand, providing a channel for the action of water, and the contact area between water and rock is increasing; under the action of hydraulic fracturing and weakening, the fractures are connected and the width of the fractures increases, which eventually leads to failure.

In summary, the development process of rock microstructure after cyclic drying and wet treatment is roughly shown in Figure 15. Without wet and dry treatment, the mineral particles are tightly connected by cement, and the shape of the particles is clear and sharp. After 1 to 10 cycles of dry and wet treatment, the soluble matter dissolves and migrates, resulting in small erosion pores between the particles, but the morphology of the particles does not change much. After 10 to 30 wet and dry cycles, the pores gradually become larger, the dissolved substances fall off and settle on the edges of the pores, and the mineral particles become apparently smooth. After more than 30 wet and dry cycles, microcracks appear between the particles, the surface roundness of the mineral particles is larger, the cohesive force is greatly reduced, and secondary cracks also appear in the particles, which tend to be looser and disintegration breakage. It should be noted that the number of dry and wet cycles mentioned above is only an approximate number. For different rocks, these specific times are different, but the whole process of change is roughly the same.

4. Rock Deterioration Constitutive Model after Dry-Wet Cycle

Macroscopically, the mass loss of rock samples, P-wave velocity attenuation, relative changes in water content, elastic modulus, friction angle, and cohesion; microscopically, the CT number of CT scanning, and the characteristic parameters of microscopic cracks obtained by SEM image processing include quantity, size and surface area; in addition, statistical parameters, fractal dimensions, etc. can all be used as damage variables. The constitutive model of rock damage is difficult to be unified due to the complexity of damage variables [86–89]. Based on different damage variables, the constitutive equations describing the deterioration of rocks after drying and wet cycles are also different. Hu et al. [90] established the damage constitutive equation under the coupling action of the dry-wet cycle and the load based on the influence of temperature and the number of dry-wet cycles on the attenuation rate, combined with the damage evolution equation based on the energy principle. Du et al. [91] separated macroscopic damage variables and microscopic damage variables and constructed the constitutive equation of sandstone after impact load and dry-wet cycle coupling. Wang et al. [92] proposed an improved *D-C* equation to describe the initial compression stage and the residual stage after the peak during rock deformation. Wang et al. [93] proposed a damage nonlinear Burgers viscoelastic-plastic (DNBVP) model considering the effect of saturation-dehydration cycles by introducing a nonlinear viscoplastic body and a damage variable describing dry-wet cycles and then derived the three-dimensional creep equations of the new model and identified its creep parameters. Furthermore, Wang et al. [94] proposed four kinds of functions including an exponentially decreasing function, a linearly decreasing function, a linearly increasing function, and an exponentially increasing function to express the relationships between the shear modulus, viscoelastic

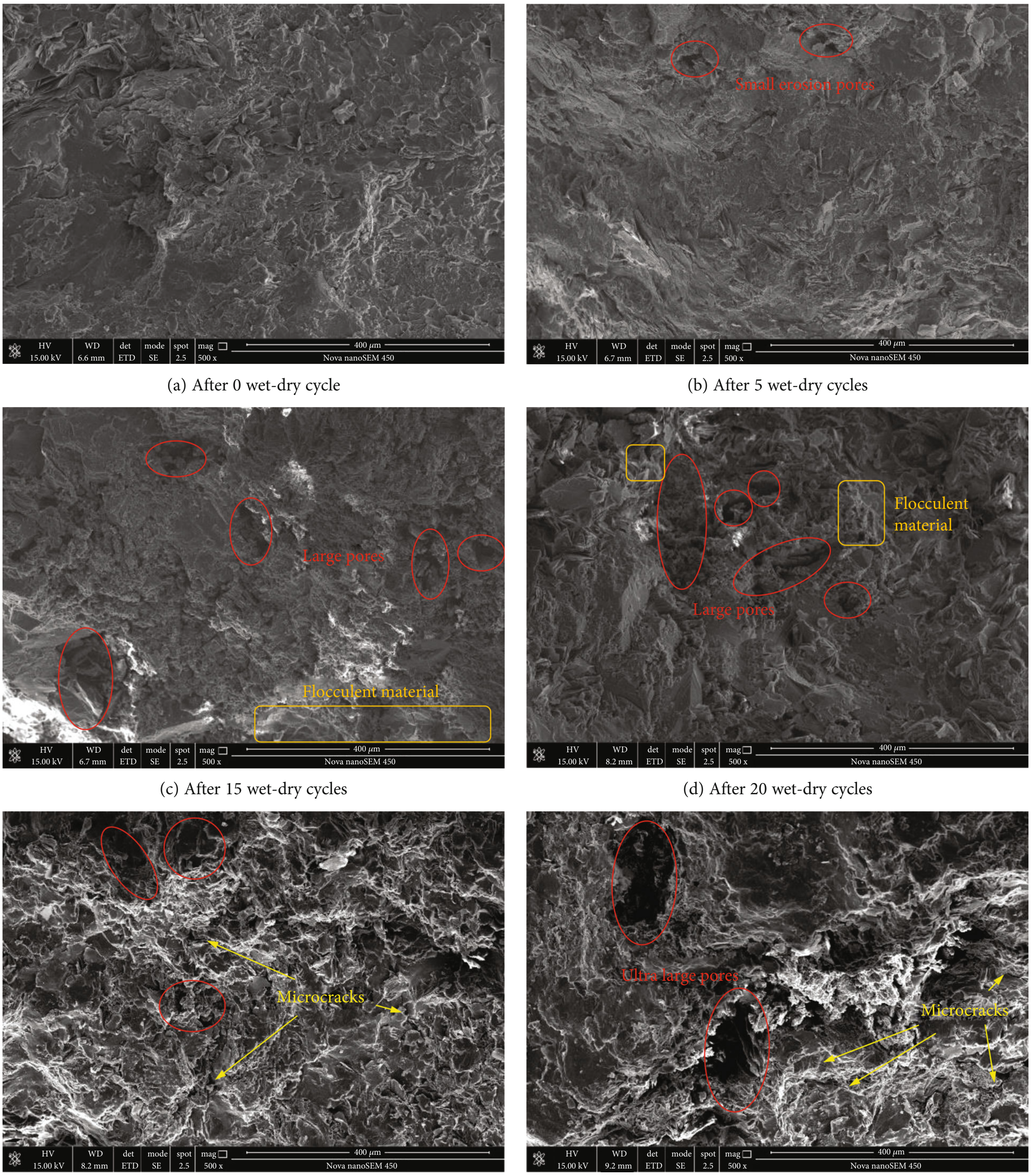

(a) After 0 wet-dry cycle

(b) After 5 wet-dry cycles

(c) After 15 wet-dry cycles

(d) After 20 wet-dry cycles

(e) After 30 wet-dry cycles

(f) After 60 wet-dry cycles

Figure 14: SEM images of rock surfaces after different wet-dry cycles (after [6]).

parameters of the Burgers model, and the deviatoric stress under different dry-wet cycles. Through comparative analysis, it is found that the theoretical curves generated using proposed four kinds of functions are in good agreement with the experimental data. Liu et al. [95] proposed a damage variable considering the combined influence of cyclic wetting-drying and loading and further established an improved damage model which considers the effect of cyclic wetting-drying on internal friction angle and the nonlinear deformation characteristics in the fissure closure stage with statistical damage mechanics. The determination method for the parameters in the proposed damage model was also introduced. He et al. [96] explored the deterioration features and acoustic wave parameters and resistivity (AWPR) of the sandstone in cyclic wetting and drying experiments and proposed a cumulative damage model in the light of the AWPR through the instantaneous damage analysis. Huang et al. [97] investigated the physical and mechanical properties under

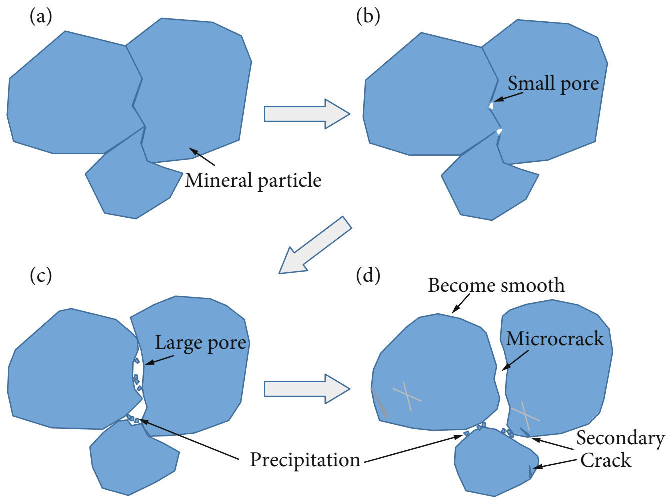

Figure 15: Diagrams of the microstructure development process after different wet-dry cycles. (a) 0 times; (b) 1-10 times; (c) 10-30 times; (d) >30 times.

acid dry-wet cycles and established a constitutive model of uniaxial compression based on Weibull damage variable, which has the best effect in acid solution with less cycle times or pH value of solution greater than 6. Zhang et al. [98] derived an evolution model of the disintegration breakage of red-bed soft rock using the Morgan-Mercer-Florin (MMF) model, measured the disintegration behaviours of red-bed soft rock by the disintegration ratio, and derived a new formula to calculate the disintegration ratio based on the concept of the traditional disintegration ratio using the established model. Xu et al. [99] established a traditional strength prediction model based on P-wave velocity combined with the damage theory and Lemaitre strain equivalence hypothesis and then proposed a modified model considering both the drying-wetting cycle number and confining pressures.

In shale gas development and other engineering practices, the study of rock mass diffusion and seepage equations is very important [100–102]. There are few studies on the influence of the dry-wet cycle on the law of water migration. Van der Hoven [103] conducted a detailed analysis of the unsaturated flow and solute transport of the high-porosity matrix rock during the dry-wet cycle, and the modeling results indicated that the advective flux of solutes from the fractures into the matrix during wetting was greater than from the matrix back into the fractures during drying, resulting in a net storage of solutes in the matrix, and the rock system behaved more like a fully saturated system where diffusion is the dominant transport process between fractures and matrix with the increase of number of dry-wet cycles.

5. Conclusions and Prospects

This article summarizes the geological and engineering scenarios of the dry-wet cycle and the research results of the rock degradation effect. Through the collection and normalization of the dry-wet cycle test data in the existing literature, the degradation degree and mechanism of the physical and mechanical properties of rocks are analyzed. The main conclusions are as follows.

(1) As the number of wet and dry cycles increases, the physical properties (including dry weight, P-wave velocity, porosity, water absorption, and durability index) and mechanical properties of rocks (including static compressive/tensile strength, elastic modulus, dynamic compressive/tensile strength, shear strength, fracture toughness, cohesion, and internal friction angle) would all experience different degrees of deterioration

(2) The possible mechanisms of the influence of dry-wet cycles on rock degradation include reduction of fracture energy, reduction of capillary tension, increase of pore pressure, reduction of friction coefficient, chemical corrosion, mineral dissolution, expansion and softening, and solute migration

(3) The content of clay components is a key factor that affects the effect of dry-wet cycles on rock degradation. The degradation mechanism of rocks with different clay content is also different

(4) The evolution of rock microstructures, especially microcracks, after dry-wet cycles is closely related to changes in the physical and mechanical properties

Based on these conclusions, we need to focus on the following aspects in the future. First, what is the actual dry and wet cycle process (frequency and mode) in nature? Second, what is the mineral composition and structure of the rock? What are the components of the solution? What kind of chemical, biological, physical, and mechanical interactions occur between the solution and the rock? Third, what kind of theoretical model is used or established to describe the dry-wet cycle process so as to predict the degradation behavior of the physical and mechanical properties of rocks?

Data Availability

The data used to support the findings of this study are available from the corresponding author upon request.

Conflicts of Interest

The authors declare that there is no conflict of interest regarding the publication of this paper.

Acknowledgments

The authors are supported by the National Natural Science Foundation of China (Grant nos. 42030810 and 51934007) and the Fundamental Research Funds for the Central Universities (Grant no. 2017QNA31).

References

[1] K. Xie, D. Jiang, Z. Sun, J. Chen, W. Zhang, and X. Jiang, "NMR, MRI and AE statistical study of damage due to a low number of wetting-drying cycles in sandstone from the three gorges reservoir area," *Rock Mechanics and Rock Engineering*, vol. 51, no. 11, pp. 3625–3634, 2018.

[2] X. Liu, Z. Wang, Y. Fu, W. Yuan, and L. Miao, "Macro/micro-testing and damage and degradation of sandstones under dry-wet cycles," *Advances in Materials Science and Engineering*, vol. 2016, Article ID 7013032, 2016.

[3] X. Min, G. M. Ren, and X. Lei, "Deformation and mechanism of landslide influenced by the effects of reservoir water and rainfall, Three Gorges, China," *Natural Hazards*, vol. 68, no. 2, pp. 467–482, 2013.

[4] T. Zhang, E. Yan, J. Cheng, and Y. Zheng, "Mechanism of reservoir water in the deformation of Hefeng landslide," *Journal of Earth Science*, vol. 21, no. 6, pp. 870–875, 2010.

[5] S. Noor-E-Khuda and F. Albermani, "Flexural strength of weathered granites under wetting-drying cycles: implications to steel structures," *Advanced Steel Construction*, vol. 15, no. 3, pp. 225–231, 2019.

[6] X. Chen, P. He, and Z. Qin, "Damage to the microstructure and strength of altered granite under wet-dry cycles," *Symmetry*, vol. 10, no. 12, p. 716, 2018.

[7] X. Yang, J. Wang, D. Hou, C. Zhu, and M. He, "Effect of dry-wet cycling on the mechanical properties of rocks: a laboratory-scale experimental study," *Processes*, vol. 6, no. 10, p. 199, 2018.

[8] Z. Qin, X. Chen, and H. Fu, "Damage features of altered rock subjected to drying-wetting cycles," *Advances in Civil Engineering*, vol. 2018, Article ID 5170832, 2018.

[9] T. Inoue, S. Yamaguchi, and J. M. Nelson, "The effect of wet-dry weathering on the rate of bedrock river channel erosion by saltating gravel," *Geomorphology*, vol. 285, pp. 152–161, 2017.

[10] C. Zhang, Z. Cai, Y. Huang, and H. Chen, "Laboratory and centrifuge model tests on influence of swelling rock with drying-wetting cycles on stability of canal slope," *Advances in Civil Engineering*, vol. 2018, Article ID 4785960, 2018.

[11] X. Gong, L. Xiao, Z. Zhao et al., "Spatial variation of polycyclic aromatic hydrocarbons (PAHs) in surface sediments from rivers in hilly regions of Southern China in the wet and dry seasons," *Ecotoxicology Environmental Safety*, vol. 156, pp. 322–329, 2018.

[12] A. S. Trenhaile, "Modelling tidal notch formation by wetting and drying and salt weathering," *Geomorphology*, vol. 224, pp. 139–151, 2014.

[13] A. Trenhaile, "Tidal wetting and drying on shore platforms: an experimental study of surface expansion and contraction," *Geomorphology*, vol. 76, no. 3-4, pp. 316–331, 2006.

[14] J. I. Kanyaya and A. S. Trenhaile, "Tidal wetting and drying on shore platforms: an experimental assessment," *Geomorphology*, vol. 70, no. 1-2, pp. 129–146, 2005.

[15] E. F. McBride and M. D. Picard, "Origin of honeycombs and related weathering forms in Oligocene Macigno Sandstone, Tuscan coast near Livorno, Italy," *Earth Surface Processes and Landforms*, vol. 29, no. 6, pp. 713–735, 2004.

[16] Q. Sun and Y. Zhang, "Combined effects of salt, cyclic wetting and drying cycles on the physical and mechanical properties of sandstone," *Engineering Geology*, vol. 248, pp. 70–79, 2019.

[17] M. Akin and A. Ozsan, "Evaluation of the long-term durability of yellow travertine using accelerated weathering tests," *Bulletin of Engineering Geology and the Environment*, vol. 70, no. 1, pp. 101–114, 2011.

[18] Z. Zeng and L. Kong, "Effect of wetting-drying-freezing-thawing cycles on the swelling behaviour of the Yanji mudstone," *Environmental Earth Sciences*, vol. 78, no. 15, p. 435, 2019.

[19] F. T. Wang, N. N. Liang, and G. Li, "Damage and failure evolution mechanism for coal pillar dams affected by water immersion in underground reservoirs," *Geofluids*, vol. 2019, 2019.

[20] P. A. Hale and A. Shakoor, "A laboratory investigation of the effects of cyclic heating and cooling, wetting and drying, and freezing and thawing on the compressive strength of selected sandstones," *Environmental & Engineering Geoscience*, vol. 9, no. 2, pp. 117–130, 2003.

[21] A. Ozbek, "Investigation of the effects of wetting-drying and freezing-thawing cycles on some physical and mechanical properties of selected ignimbrites," *Bulletin of Engineering Geology and the Environment*, vol. 73, no. 2, pp. 595–609, 2014.

[22] G. Khanlari and Y. Abdilor, "Influence of wet-dry, freeze-thaw, and heat-cool cycles on the physical and mechanical properties of Upper Red sandstones in central Iran," *Bulletin of Engineering Geology and the Environment*, vol. 74, no. 4, pp. 1287–1300, 2015.

[23] K. Cui, G. Wu, X. Wang, and W. Chen, "Behaviour of slate following freeze-thaw and dry-wet weathering processes," *Quarterly Journal of Engineering Geology and Hydrogeology*, vol. 50, no. 2, pp. 117–125, 2017.

[24] K. Hall, E. KOSTER, and H. FRENCH, "The interconnection of wetting and drying with freeze-thaw: some new data in periglacial processes and landforms," *Zeitschrift für Geomorphologie. Supplementband*, vol. 71, no. 1, pp. 1–11, 1988.

[25] A. Prick, "Dilatometrical behaviour of porous calcareous rock samples subjected to freeze-thaw cycles," *Catena*, vol. 25, no. 1-4, pp. 7–20, 1995.

[26] D. T. Nicholson and F. H. Nicholson, "Physical deterioration of sedimentary rocks subjected to experimental freeze–thaw weathering," *Earth Surface Processes and Landforms: The Journal of the British Geomorphological Research Group*, vol. 25, no. 12, pp. 1295–1307, 2000.

[27] Y. Ito, Y. Kusakabe, and S. Anan, "Experimental study on rock deterioration by repetition of freezing and thawing, and by repetition of dry and wet in cold region," in *Engineering Geology for Society and Territory*, vol. 5, pp. 1293–1297, Urban Geology, Sustainable Planning and Landscape Exploitation, 2015.

[28] M. J. Loubser, "Weathering of basalt and sandstone by wetting and drying: a process isolation study," *Geografiska Annaler Series a-Physical Geography*, vol. 95, no. 4, pp. 295–304, 2013.

[29] K. Hall and A. Hall, "Weathering by wetting and drying: some experimental results," *Earth Surface Processes and Landforms*, vol. 21, no. 4, pp. 365–376, 1996.

[30] P. Yuan, N.-N. Wei, Q.-Y. Ma, and J.-C. Chang, "Coupled effect of water temperature and cyclic wetting and drying on dynamic mechanical characteristics of sandstone," *Advances in Civil Engineering*, vol. 2019, Article ID 8167651, 2019.

[31] X. Liu, M. Jin, D. Li, and L. Zhang, "Strength deterioration of a Shaly sandstone under dry-wet cycles: a case study from the Three Gorges Reservoir in China," *Bulletin of Engineering Geology and the Environment*, vol. 77, no. 4, pp. 1607–1621, 2018.

[32] Z. Zhao, J. Yang, D. Zhang, and H. Peng, "Effects of wetting and cyclic wetting-drying on tensile strength of sandstone with a low clay mineral content," *Rock Mechanics and Rock Engineering*, vol. 50, no. 2, pp. 485–491, 2017.

[33] Z. Zhou, X. Cai, D. Ma, L. Chen, S. Wang, and L. Tan, "Dynamic tensile properties of sandstone subjected to wetting and drying cycles," *Construction and Building Materials*, vol. 182, pp. 215–232, 2018.

[34] Z. Zhou, X. Cai, L. Chen, W. Cao, Y. Zhao, and C. Xiong, "Influence of cyclic wetting and drying on physical and dynamic compressive properties of sandstone," *Engineering Geology*, vol. 220, pp. 1–12, 2017.

[35] B. Meng, H. Jing, W. Zhu, and H. Su, "Influences of saturation and wetting-drying cycle on mechanical performances of argillaceous limestones from Liupanshan tunnel, China," *Advances in Materials Science and Engineering*, vol. 2019, Article ID 9236172, 2019.

[36] Z. Zhang, Q. Jiang, C. Zhou, and X. Liu, "Strength and failure characteristics of Jurassic Red-Bed sandstone under cyclic wetting–drying conditions," *Geophysical Journal International*, vol. 198, no. 2, pp. 1034–1044, 2014.

[37] B. Du, H. Bai, and G. Wu, "Dynamic compression properties and deterioration of red-sandstone subject to cyclic wet-dry treatment," *Advances in Civil Engineering*, vol. 2019, Article ID 1487156, 2019.

[38] C. Liu, Y. Wu, X. F. Zhang et al., "Propagation of shock waves in dry and wet sandstone: experimental observations, theoretical analysis and meso-scale modeling," *Defence Technology*, vol. 14, no. 5, pp. 513–521, 2018.

[39] Y. Zhao, S. Ren, D. Jiang, R. Liu, J. Wu, and X. Jiang, "Influence of wetting-drying cycles on the pore structure and mechanical properties of mudstone from Simian Mountain," *Construction and Building Materials*, vol. 191, pp. 923–931, 2018.

[40] S. Huang, J. Wang, Z. Qiu, and K. Kang, "Effects of cyclic wetting-drying conditions on elastic modulus and compressive strength of sandstone and mudstone," *Processes*, vol. 6, no. 12, 2018.

[41] S. Chen, T. Jiang, H. Wang, F. Feng, D. Yin, and X. Li, "Influence of cyclic wetting-drying on the mechanical strength characteristics of coal samples: a laboratory-scale study," *Energy Science & Engineering*, vol. 7, no. 6, pp. 3020–3037, 2019.

[42] S. Li, C. Li, W. Yao, R. Zhang, and Z. Zhang, "Impact of wetting-drying cycles on dynamictensile strength of rock," *Thermal Science*, vol. 23, pp. 115–115, 2019.

[43] J. Fang, H. Deng, Y. Qi, Y. Xiao, H. Zhang, and J. Li, "Analysis of changes in the micromorphology of sandstone joint surface under dry-wet C strength and failure characteristics of Jurassic Red-Bed sandstone under cyclic wetting-drying conditions cycling," *Advances in Materials Science and Engineering*, vol. 2019, Article ID 8758203, 2019.

[44] W. Hua, S. Dong, Y. Li, and Q. Wang, "Effect of cyclic wetting and drying on the pure mode II fracture toughness of sandstone," *Engineering Fracture Mechanics*, vol. 153, pp. 143–150, 2016.

[45] W. Hua, S. Dong, F. Peng, K. Li, and Q. Wang, "Experimental investigation on the effect of wetting-drying cycles on mixed mode fracture toughness of sandstone," *International Journal of Rock Mechanics and Mining Sciences*, vol. 93, pp. 242–249, 2017.

[46] W. Hua, S. Dong, Y. Li, J. Xu, and Q. Wang, "The influence of cyclic wetting and drying on the fracture toughness of sandstone," *International Journal of Rock Mechanics and Mining Sciences*, vol. 78, pp. 331–335, 2015.

[47] E. M. Van Eeckhout, "The mechanisms of strength reduction due to moisture in coal mine shales," *International Journal of Rock Mechanics and Mining Sciences & Geomechanics Abstracts*, vol. 13, no. 2, pp. 61–67, 1976.

[48] A. Hawkins and B. McConnell, "Sensitivity of sandstone strength and deformability to changes in moisture content," *Quarterly Journal of Engineering Geology and Hydrogeology*, vol. 25, no. 2, pp. 115–130, 1992.

[49] E. Verstrynge, R. Adriaens, J. Elsen, and K. Van Balen, "Multi-scale analysis on the influence of moisture on the mechanical behavior of ferruginous sandstone," *Construction and Building Materials*, vol. 54, pp. 78–90, 2014.

[50] Z. Zhou, X. Cai, Y. Zhao, L. Chen, C. Xiong, and X.-b. Li, "Strength characteristics of dry and saturated rock at different strain rates," *Transactions of Nonferrous Metals Society of China*, vol. 26, no. 7, pp. 1919–1925, 2016.

[51] Z. Zhou, X. Cai, D. Ma, W. Cao, L. Chen, and J. Zhou, "Effects of water content on fracture and mechanical behavior of sandstone with a low clay mineral content," *Engineering Fracture Mechanics*, vol. 193, pp. 47–65, 2018.

[52] T. S. Rötting, L. Luquot, J. Carrera, and D. J. Casalinuovo, "Changes in porosity, permeability, water retention curve and reactive surface area during carbonate rock dissolution," *Chemical Geology*, vol. 403, pp. 86–98, 2015.

[53] B. Smith, "Weathering processes and forms," in *Geomorphology of Desert Environments*, pp. 69–100, Springer, 2009.

[54] W. Yuan, X. Liu, and Y. Fu, "Chemical thermodynamics and chemical kinetics analysis of sandstone dissolution under the action of dry-wet cycles in acid and alkaline environments," *Bulletin of Engineering Geology and the Environment*, vol. 78, no. 2, pp. 793–801, 2019.

[55] W. Yuan, X. Liu, and Y. Fu, "Study on deterioration of strength parameters of sandstone under the action of dry-wet cycles in acid and alkaline environment," *Arabian*

Journal for Science and Engineering, vol. 43, no. 1, pp. 335–348, 2018.

[56] X. Feng, W.-x. Ding, H. Yao, Q. Cui, and S. Chen, *Coupled Chemical-Stress Effect on Rock Fracturing Process*, Science Press, Beijing, 2010.

[57] Z. Zhou, X. Cai, D. Ma et al., “Water saturation effects on dynamic fracture behavior of sandstone,” *International Journal of Rock Mechanics and Mining Sciences*, vol. 114, pp. 46–61, 2019.

[58] N. Price, “The compressive strength of coal measure rocks,” *Colliery Engineering*, vol. 37, no. 437, pp. 283–292, 1960.

[59] N. J. Price, “The influence of geological factors on the strength of coal measure rocks,” *Geological Magazine*, vol. 100, no. 5, pp. 428–443, 1963.

[60] P. Colback and B. Wiid, “The influence of moisture content on the compressive strength of rocks,” *Geophysics*, 1965.

[61] J. Feda, “The influence of water content on the behaviour of subsoil, formed by highly weathered rocks,” in *1st ISRM Congress*, pp. 283–288, International Society for Rock Mechanics and Rock Engineering, 1966.

[62] M. Ruiz, “Some technological characteristics of twenty six Brazilian rock types,” in *Proc. 1st Cong. Int. Soc. Rock Mech*, pp. 115–119, 1966.

[63] L. Burshtein, “Effect of moisture on the strength and deformability of sandstone,” *Soviet Mining*, vol. 5, no. 5, pp. 573–576, 1969.

[64] B. Vásárhelyi, “Some observations regarding the strength and deformability of sandstones in dry and saturated conditions,” *Bulletin of Engineering Geology and the Environment*, vol. 62, no. 3, pp. 245–249, 2003.

[65] P. D. Sumner and M. J. Loubser, “Experimental sandstone weathering using different wetting and drying moisture amplitudes,” *Earth Surface Processes and Landforms*, vol. 33, no. 6, pp. 985–990, 2008.

[66] M. Gysel, “Design of tunnels in swelling rock,” *Rock Mechanics and Rock Engineering*, vol. 20, no. 4, pp. 219–242, 1987.

[67] H. Einstein, “Tunnelling in difficult ground—swelling behaviour and identification of swelling rocks,” *Rock Mechanics and Rock Engineering*, vol. 29, no. 3, pp. 113–124, 1996.

[68] M. Barla, *Tunnels in Swelling Ground–Simulation of 3D Stress Paths by Triaxial Laboratory Testing*, Unpublished Doctoral Dissertation, Politecnico di Torino, 1999.

[69] B. Hawlader, Y. Lee, and K. Lo, “Three-dimensional stress effects on time-dependent swelling behaviour of shaly rocks,” *Canadian Geotechnical Journal*, vol. 40, no. 3, pp. 501–511, 2003.

[70] B. Hawlader, K. Lo, and I. Moore, “Analysis of tunnels in shaly rock considering three-dimensional stress effects on swelling,” *Canadian Geotechnical Journal*, vol. 42, no. 1, pp. 1–12, 2005.

[71] S. Huang, R. Speck, and Z. Wang, “The temperature effect on swelling of shales under cyclic wetting and drying,” *in International journal of rock mechanics and mining sciences & geomechanics abstracts*, vol. 32, no. 3, pp. 227–236, 1995.

[72] O. J. Pejon and L. V. Zuquette, “Analysis of cyclic swelling of mudrocks,” *Engineering Geology*, vol. 67, no. 1-2, pp. 97–108, 2002.

[73] R. Doostmohammadi, M. Moosavi, T. Mutschler, and C. Osan, “Influence of cyclic wetting and drying on swelling behavior of mudstone in south west of Iran,” *Environmental Geology*, vol. 58, no. 5, pp. 999–1009, 2009.

[74] M. R. Vergara and T. Triantafyllidis, “Swelling behavior of volcanic rocks under cyclic wetting and drying,” *International Journal of Rock Mechanics and Mining Sciences*, vol. 80, pp. 231–240, 2015.

[75] R. Taylor and D. Spears, “The breakdown of British coal measure rocks,” *International Journal of Rock Mechanics and Mining Sciences & Geomechanics Abstracts*, vol. 7, no. 5, pp. 481–501, 1970.

[76] K. Beck and M. Al-Mukhtar, “Cyclic wetting-drying ageing test and patina formation on tuffeau limestone,” *Environmental Earth Sciences*, vol. 71, no. 5, pp. 2361–2372, 2014.

[77] Q. Pham, F. Vales, L. Malinsky, D. N. Minh, and H. Gharbi, “Effects of desaturation-resaturation on mudstone,” *Physics and Chemistry of the Earth, Parts A/B/C*, vol. 32, no. 8-14, pp. 646–655, 2007.

[78] D. Yang, M. Bornert, S. Chanchole, H. Gharbi, P. Valli, and B. Gatmiri, “Dependence of elastic properties of argillaceous rocks on moisture content investigated with optical full-field strain measurement techniques,” *International Journal of Rock Mechanics and Mining Sciences*, vol. 53, pp. 45–55, 2012.

[79] M. L. Lin, F. Jeng, L. Tsai, and T. Huang, “Wetting weakening of tertiary sandstones—microscopic mechanism,” *Environmental Geology*, vol. 48, no. 2, pp. 265–275, 2005.

[80] L. L. Wang, M. Bornert, E. Heripre, D. S. Yang, and S. Chanchole, “Irreversible deformation and damage in argillaceous rocks induced by wetting/drying,” *Journal of Applied Geophysics*, vol. 107, pp. 108–118, 2014.

[81] L. Zeng, J. Liu, Q. F. Gao, and H. Bian, “Evolution characteristics of the cracks in the completely disintegrated carbonaceous mudstone subjected to cyclic wetting and drying,” *Advances in Civil Engineering*, vol. 2019, Article ID 1279695, 2019.

[82] X. Yang, J. Wang, C. Zhu, M. He, and Y. Gao, “Effect of wetting and drying cycles on microstructure of rock based on SEM,” *Environmental Earth Sciences*, vol. 78, no. 6, 2019.

[83] F.-S. Jeng, M.-L. Lin, and T.-H. Huang, “Wetting deterioration of soft sandstone-microscopic insights,” in *ISRM International Symposium*, International Society for Rock Mechanics and Rock Engineering, 2000.

[84] P. Yuan and Q. Y. Ma, *Energy Analyses of Uniaxial Impact Compressive Tests for Coalmine Sandstone After Cyclic Wetting and Drying*, Rock Engineering and Rock Mechanics: Structures in and on Rock Masses, 2014.

[85] M. Hu, Y. Liu, J. Ren, R. Wu, and Y. Zhang, “Laboratory test on crack development in mudstone under the action of dry-wet cycles,” *Bulletin of Engineering Geology and the Environment*, vol. 78, no. 1, pp. 543–556, 2019.

[86] A. Minardi, A. Ferrari, R. Ewy, and L. Laloui, “Nonlinear elastic response of partially saturated gas shales in uniaxial compression,” *Rock Mechanics and Rock Engineering*, vol. 51, no. 7, pp. 1967–1978, 2018.

[87] Z. Wang, H. Shi, and J. Wang, “Mechanical behavior and damage constitutive model of granite under coupling of temperature and dynamic loading,” *Rock Mechanics and Rock Engineering*, vol. 51, no. 10, pp. 3045–3059, 2018.

[88] L. Liu, W. Xu, L. Zhao, Q. Zhu, and R. Wang, “An experimental and numerical investigation of the mechanical behavior of granite gneiss under compression,” *Rock Mechanics and Rock Engineering*, vol. 50, no. 2, pp. 499–506, 2017.

[89] L. Berto, A. Saetta, and D. Talledo, "Constitutive model of concrete damaged by freeze-thaw action for evaluation of structural performance of RC elements," *Construction and Building Materials*, vol. 98, pp. 559–569, 2015.

[90] M. Hu, Y. Liu, L. Song, and Y. Zhang, "Constitutive model and damage evolution of mudstone under the action of dry-wet cycles," *Advances in Civil Engineering*, vol. 2018, Article ID 9787429, 2018.

[91] B. Du and H. Bai, "A damage constitutive model of red sandstone under coupling of wet-dry cycles and impact load," *Shock and Vibration*, vol. 2019, Article ID 7692424, 2019.

[92] Z. Wang, X. Liu, X. Yang, and Y. Fu, "An improved Duncan-Chang constitutive model for sandstone subjected to drying-wetting cycles and secondary development of the model in FLAC(3D)," *Arabian Journal for Science and Engineering*, vol. 42, no. 3, pp. 1265–1282, 2017.

[93] X. Wang, B. Lian, and W. Feng, "A nonlinear creep damage model considering the effect of dry-wet cycles of rocks on reservoir bank slopes," *Water*, vol. 12, no. 9, 2020.

[94] X. Wang, B. Lian, J. Wang, W. Feng, and T. Gu, "Creep damage properties of sandstone under dry-wet cycles," *Journal of Mountain Science*, vol. 17, no. 12, pp. 3112–3122, 2020.

[95] X. Liu, Q. Liu, S. Huang, B. Liu, and J. Liu, "Effects of cyclic wetting-drying on the mechanical behavior and improved damage model for sandstone," *Marine Georesources & Geotechnology*, pp. 1–11, 2020.

[96] Y. He, K. Wang, Y. Ji, G. Wu, and M. Zhao, "Evaluation of cumulative damage of sandstone under cyclic wetting and drying through acoustic wave parameters and resistivity testing," *Journal of New Materials for Electrochemical Systems*, vol. 23, no. 4, pp. 256–261, 2020.

[97] X. Huang, J. Pang, G. Liu, and Y. Chen, "Experimental study on physicomechanical properties of deep sandstone by coupling of dry-wet cycles and acidic environment," *Advances in Civil Engineering*, vol. 2020, Article ID 2760952, 2020.

[98] Z. T. Zhang and W. H. Gao, "Effect of different test methods on the disintegration behaviour of soft rock and the evolution model of disintegration breakage under cyclic wetting and drying," *Engineering Geology*, vol. 279, p. 105888, 2020.

[99] Z. H. Xu, G. L. Feng, Q. C. Sun, G. D. Zhang, and Y. M. He, "A modified model for predicting the strength of drying-wetting cycled sandstone based on the P-wave velocity," *Sustainability*, vol. 12, no. 14, 2020.

[100] J. Deng, W. Zhu, and Q. Ma, "A new seepage model for shale gas reservoir and productivity analysis of fractured well," *Fuel*, vol. 124, pp. 232–240, 2014.

[101] C. Freeman, "A numerical study of microscale flow behavior in tight gas and shale gas," in *SPE Annual Technical Conference and Exhibition*Society of Petroleum Engineers.

[102] A. Beskok and G. E. Karniadakis, "Report: a model for flows in channels, pipes, and ducts at micro and nano scales," *Microscale Thermophysical Engineering*, vol. 3, no. 1, pp. 43–77, 1999.

[103] S. J. Van der Hoven, D. K. Solomon, and G. R. Moline, "Modeling unsaturated flow and transport in the saprolite of fractured sedimentary rocks: effects of periodic wetting and drying," *Water Resources Research*, vol. 39, no. 7, 2003.

Hindawi
Geofluids
Volume 2021, Article ID 5516997, 13 pages
https://doi.org/10.1155/2021/5516997

Research Article

Determination of Mining-Induced Changes in Hydrogeological Parameters of Overburden Aquifer in a Coalfield, Northwest China: Approaches Using the Water Level Response to Earth Tides

Qingyu Xu,[1,2] **Guangcai Wang**,[1,2] **Xiangyang Liang**,[3] **Shen Qu**,[1,2] **Zheming Shi**,[1,2] **and Xianbin Wang**[1,2]

[1]*State Key Laboratory of Biogeology and Environmental Geology & MOE Key Laboratory of Groundwater Circulation and Environment Evolution, China University of Geosciences, Beijing 100083, China*
[2]*School of Water Resources and Environment, China University of Geosciences, Beijing 100083, China*
[3]*Xi'an Research Institute of China Coal Technology & Engineering Group, Xi'an 710077, China*

Correspondence should be addressed to Guangcai Wang; wanggc@pku.edu.cn

Received 2 March 2021; Revised 26 April 2021; Accepted 15 May 2021; Published 24 May 2021

Academic Editor: Yi Xue

The determination of changes in hydrogeological properties (e.g., permeability and specific storage) of aquifers disturbed by mining activity is significant to groundwater resource and ecological environment protection in coal mine areas. However, such parameters are difficult to continuously measure in situ using conventional hydrogeological methods, and their temporal changes associated with coal mining are not well understood. The response of well water level to Earth tides provides a unique probe to determine the in situ hydrogeological parameters and their variations. In this study, the tidal responses of well water level were employed to characterize the changes in hydrogeological parameters of the overburden aquifer induced by longwall mining in a coalfield, northwest China. Based on the long-term hourly recorded water level data, two analytical models were used to determine the temporal changes of permeability and specific storage of the overburden aquifer. The results showed that the hydrogeological parameters changed with the longwall coal face advance. When the longwall coal face approached the wells, the aquifer permeability increased several to dozens of times, and the response distance ranged from 80 m to 300 m. The specific storage decreased before the coal face reached wells and recovered after the coal face passed. The results of this study indicate that the hydrogeological parameter changes induced by coal mining are related to the location of the well relative to the coal face and the stress distribution in the overburden aquifer. This study revealed the changes in permeability and specific storage associated with the mining disturbance which could have great significance for quantitative assessment of the impact of mining on overburden aquifer.

1. Introduction

Underground coal mining could change the structure and properties of the overburden aquifers due to surrounding rock stress changes and cause deformation which results in subsidence or settlement of the ground surface. The slight changes of stress and strain in the rock mass can be reflected in the change of pore pressure or well water level through seepage flow or the transfer of hydrostatic pressure [1]. Furthermore, high-intensity groundwater pumping and draining as well as strong mining vibration during the mining processes may cause the clogging or unclogging of fissures/-fractures in aquifers and the resultant hydrogeological property changes. Therefore, the hydrogeological parameters (e.g., permeability and specific storage) can be used as an indicator of the deformation of the aquifer associated with mining activities.

Groundwater flow in the overburden aquifer during longwall mining is governed by a complex interaction between roof caving and ground subsidence, pore pressure, and permeability changes and is influenced by in situ geological and hydrogeological conditions [2]. The parameter variations of the overlying aquifer during longwall mining have been studied by many researchers. During mining, the rock failure above a longwall coal face may increase the aquifer permeability [3, 4]. After mining, the permeability in the fractured zone may decrease due to stress reestablishment and fracture closure [5, 6]. The aquifer permeability and specific storage could be varied up to two or three orders of magnitude due to mining [7]. However, temporal changes in hydrogeological properties are still not well characterized and understood because it is difficult to evaluate the continuous variation of aquifer parameters due to the lack of corresponding methods. Generally, numerical modeling [4, 8, 9] and laboratory and in situ experiments [10–12] are utilized to evaluate the parameter variations of the overlying aquifer during mining. However, numerical modeling usually needs a lot of observation and experimental data and needs to simplify the boundary conditions and formation structures, which could cause uncertainty of the results. The laboratory and in situ experiments, such as the pumping test, are expensive, time-consuming, and not suitable for long-term continuous observation. As a result, we need an in situ, convenient, and inexpensive way to obtain continuous hydrogeological parameters during mining activity. The methods based on the tidal response of the well water level provide a plausible way to such requirements.

The theoretical development on the response of well-aquifer systems to Earth tidal loading has been well documented since the 1960s [13–16]. It has been known that the well water level in a well-confined aquifer can be a good measure of the crustal solid tide strain [17]. The water level in a well fluctuates in response to pressure head variations caused by the dilation of the aquifer under the Earth tidal loading [14]. Because time is needed for water to flow into or out of the well, there exists a phase shift between the tidal dilation of the aquifer and the water level response in the well. The amplitude and phase shift of the well water level to Earth tides are the functions of aquifer transmissivity, storage coefficient, and the period of the harmonic disturbance [18, 19]. Therefore, tidal response of well water level can be used to determine aquifer parameters such as permeability and specific storage. On the basis of the theory, two well-known classical models, the vertical flow model and horizontal flow model, were proposed [18, 19]. This method provides a way to determine the in situ hydrogeological parameters and has been used in some research fields such as aquifer deformations induced by earthquakes [20–23]. However, only a few studies have investigated the strain changes and fracture development under continuous mining disturbance using the tidal response of well water level, which may be different from the earthquake-induced changes that are mainly caused by transient stresses. The temporal changes of the hydrogeological parameters associated with coal mining are still not well understood.

To study the changes in hydrogeological parameters of aquifer disturbed by mining activity, we observed the tidal response of well water level in three wells in Ningtiaota Coalfield, northwest China. The spectral and tidal analyses were applied to identify and extract the tidal components in the well water level. The permeability and specific storage were estimated by two models (vertical flow model and horizontal flow model). The variation characteristics of permeability and specific storage associated with the process of coal face advancing were also investigated.

2. Study Area

The Ningtiaota Coalfield is located in the northern Shaanxi Province, northwest China (Figure 1). The regional stratum was generally characterized by a monoclinic layer that was gently inclined to the northwest, with a dip angle of about 1 degree. The stratum sequences from top to bottom are the Quaternary Holocene alluvium (Q_4^{al}) and eolian sand (Q_4^{eol}), the Upper Pleistocene Salawusu Group (Q_3s), the Middle Pleistocene Lishi Group (Q_2l), the Neogene Pliocene Baode Group (N_2b), the Middle Jurassic Zhiluo Group (J_2z), and the Yan'an Group (J_2y) (Table 1). So far, according to the geological investigation, mine construction, and production, no faults or folds were found in this area.

A coal seam is located at the top of the fourth section of the Yan'an Group, and the coal-bearing sequences extend approximately horizontally. The thickness of the overburden layers of the excavated coal seams varies from 2 m to 247 m. Aquifers were classified according to drill core logging and pumping tests. In the light of lithology, the top Quaternary strata Q_3s, Q_4^{eol}, and Q_4^{al} comprise fine-grained sand, sandy soil, and sandy clay, which are considered unconfined aquifers. The Lishi Group (Q_2l) and Baode Group (N_2b) are characterized as sandy clay and clay, which are considered an aquitard. The direct overburden aquifer of the coal-bearing sequence is the Jurassic Zhiluo Group (J_2z) fractured aquifer, with well-developed weathered medium-coarse-grained gravel-bearing sandstone. The source of water in the underground tunnel was found to be mainly from this aquifer during coal mining. Compared with the Yan'an Group (J_2y), a more intense weathering process has occurred in the Zhiluo Group (J_2z). Although similar in lithology, they are quite different in structures. We could also obtain the same aquifer classification from the pumping test. As shown in Table 1, the values of aquifer parameters of the Yan'an Group (J_2y) are much smaller than those of the Zhiluo Group (J_2z). Furthermore, there are weak hydraulic connections between Quaternary and Jurassic aquifers [24].

The S1229 coal face is about 4 km in length, 260 m in width, and with a mining height of around 5.7 m. The S1229 coal face is located in the middle of the coalfield, and several coal faces in the north had already been excavated. The S1229 coal face excavation started in September 2015 in a westward direction (Figure 2(a)) and ended in September 2017. During this period, the total water inflow in the underground tunnel is observed (Figure 2(b)).

3. Observations

Three wells (J7, J10, and J14) are used to monitor the water level from the start of mining of the S1229 coal face in September 2015 through September 2017. J7 is located directly above the S1229 coal face. J10 is about 122 meters away from the south side of the S1229 coal face. J14 is chosen as the comparable well because it is far away from the S1229 coal

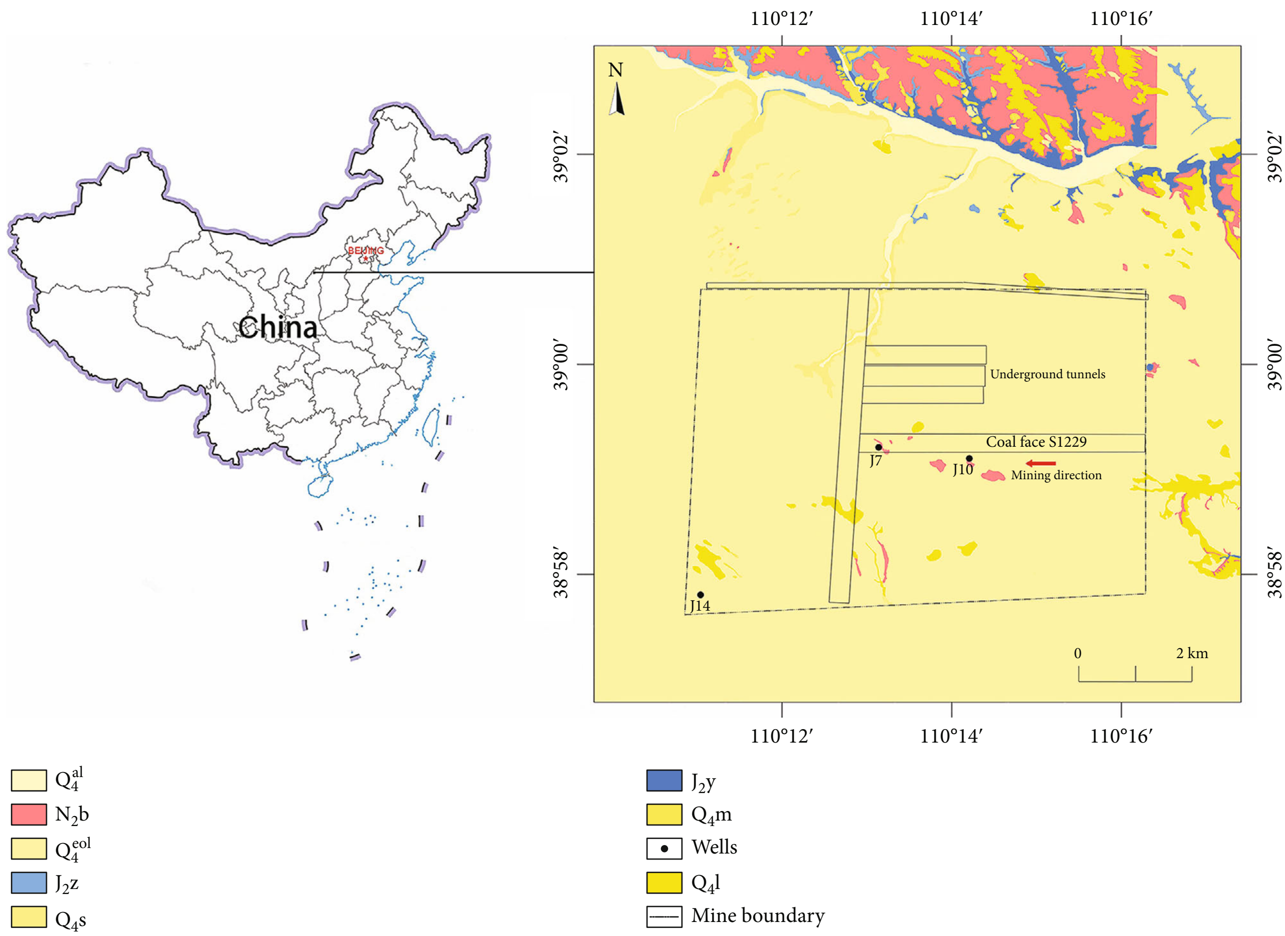

Figure 1: Geological map with location of longwall coal faces, boreholes of Ningtiaota Coalfield.

face and least affected by mining activity. Information on well structures is shown in Figure 3 and detailed in Table 2. All of the wells were instrumented with pressure sensors (levelogger) to measure the height of the water column above the sensors with the sampling frequency of one hour. The accuracy of the pressure sensors is ±0.05% of the full scale for sensors with a range of 100 ft and a resolution of 24 bits of the same scale. To evaluate the effects of the barometric pressure, a pressure transducer (barologger) was also set up in the air inside well J7. Besides, rainfall data are obtained from the weather station we installed in the mining district. Figure 4 shows the observations of the water level and barometric and precipitation data during S1229 coal face excavation. The sensor in J7 was taken out for about one week in April 2017, so there was no recorded water level data during this period. Otherwise, all the data is continuous.

As shown in Figure 4, the water level in J7 declined gradually since the start of mining. From the start of mining to June 2017, the water level in J7 declined 4 m gradually; by this time, the longwall excavation zone was about 300 m away from J7. In March 2017, the J7 water level appeared two abnormal fluctuations. The water level dropped rapidly from June 2017; the water level had dropped 42 m when mining reached the position beneath the J7 well in the middle of August. Because of the rapid decrease of the water level, the sensor was exposed to the air and failed to record data on August 16. Two days later, the water level rose steadily, and then, an instantaneous decrease was observed on August 25. Unfortunately, 15 days after the S1229 coal face passed the J7 well, the borehole was damaged and subsequent water level data was missing.

The water level variations are different in J10 compared with those of J7. One noticeable difference is that the water level in J10 started declining rapidly when the longwall excavation zone was approximately 200 m away in February 2017, and then, the water level kept falling until the S1229 coal face excavation ended.

The water levels in J7 and J10 varied greatly, while there is no distinct change in the water level in J14. Besides, there were no significant water level changes with the rainfall. Combining Figure 2 with Figure 4, it is obvious that the dramatic changes in the water level of J7 and J10 are related to the mining of the S1229 coal face.

4. Methods

The variation of aquifer parameters in coal mining areas mainly results from the disturbance of geological media caused by mining activities and mine drainage. This variation can be directly reflected in the water level. Based on the

Table 1: The stratum and aquifer parameters by pumping test of Ningtiaota Coalfield.

Stratum System	Series	Group	Lithology	Thickness	Hydraulic conductivity (m/d)	Specific capacity (L/s m)
Quaternary	Holocene (Q_4)	Aeolian sand (Q_4^{eol}) Alluvium (Q_4^{al})	Fine-grained sand	0-39.08 Ave 9.2 0-6.05	0.2701-6.42	0.055-0.244
	Upper Pleistocene (Q_3)	Salawusu (Q_3s)	Sandy soil, sandy clay	0-27.53 Ave 7.61	0.448-6.883	0.001376-0.5435
	Middle Pleistocene (Q_2)	Lishi (Q_2l)	Sandy soil, sandy clay	0-6.5		
Neogene	Pliocene (N_2)	Baode (N_2b)	Sandy clay, clay	0-103.37 Ave 60.8		
Jurassic	Middle Jurassic (J_2)	Zhiluo (J_2z)	Sandstone, mudstone	13.58-42.53	0.0179-2.277	0.0078~0.4461
		Yanan (J_2y)	Sandstone, mudstone, coal seam	170.52-240.9 Ave 208.97	0.000269-0.0003	0.0000652-0.00058

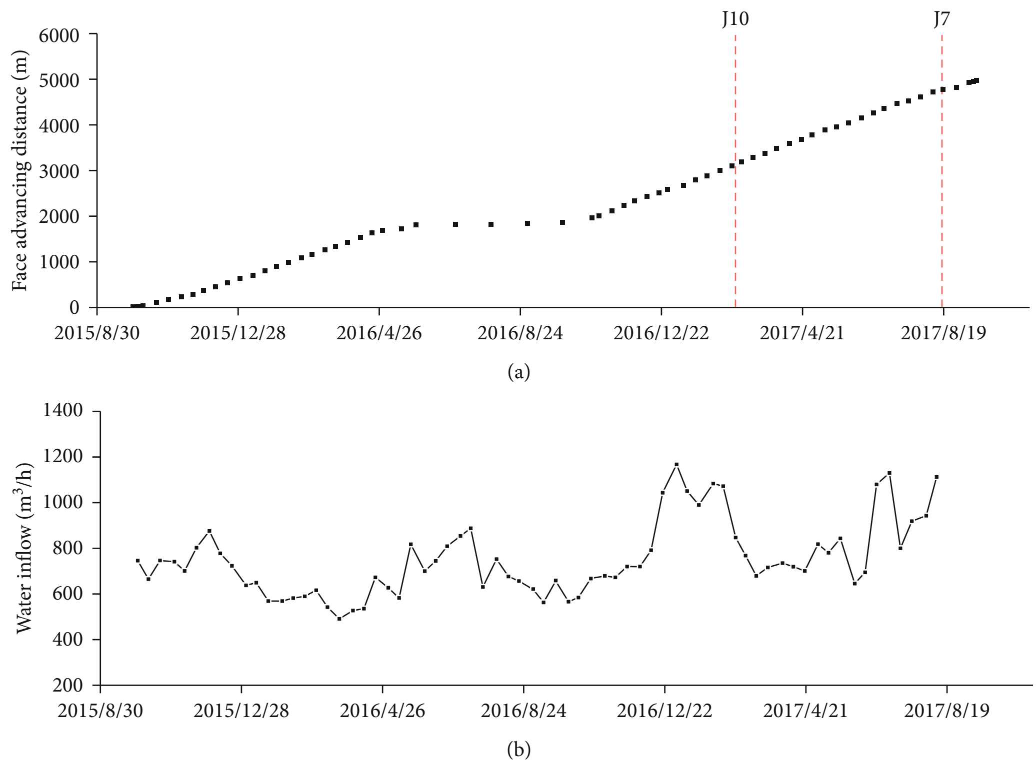

Figure 2: (a) S1229 panel advancing distance and (b) water inflow of entire coalfield. Red vertical dash lines show the times when the longwall excavation zone is closest to the J10 and J7 wells, respectively.

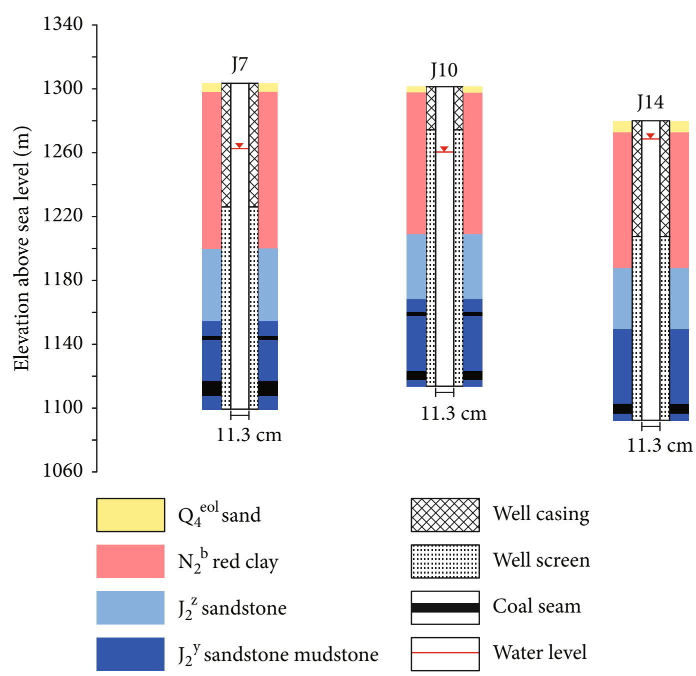

Figure 3: Well construction information.

continuous time series of water levels, we extract the solid tide component in the well water level by tidal analysis, and then, we utilize two analytical models to calculate the aquifer parameters.

4.1. Spectral and Tidal Analysis. First, we conducted a spectral analysis to identify the tidal components based on the water level data at three wells and local barometric pressure data, in which a band-pass filter of 0.8 to 2.2 cycles/day was

Table 2: Monitored wells in mining areas.

Well	Radius (cm)	Total depth (m)	Casing depth (m)	Coal seam depth (m)	Surface elevation (m)	Distance from startup (m)
J7	11.3	203.3	78.0	185.5	1310.2	4755
J10	11.3	171.1	30.0	141.0	1309.7	3162
J14	11.3	188.4	72.0	174.2	1283.5	8368

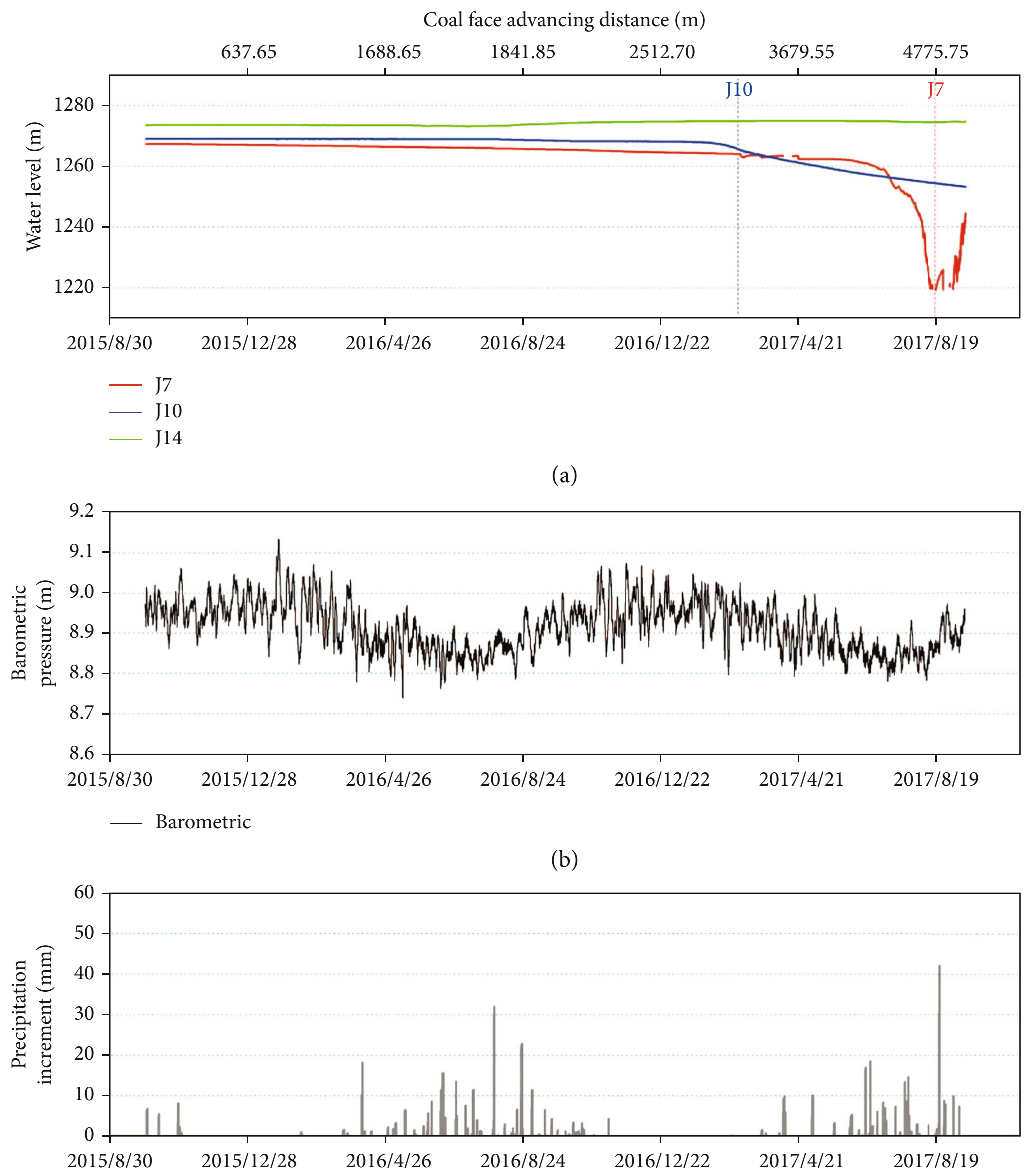

Figure 4: The observed hourly spaced record for (a) water levels, (b) barometric pressures, and (c) rainfall. The blue and red vertical dash lines show the times when the longwall excavation zone is closest to the J10 and J7 wells, respectively. The coal face advancing distance is the distance from the coal face startup.

used to eliminate the long-term trend of the water level data and the high-frequency noise. Although there may be dozens of tidal constituents that can be analyzed, the main lines of the spectrum of the tidal potential are due to the O1, K1, M2, S2, and N2 tides [18]. The N2 constituent was neglected due to its small amplitude. Therefore, we used four tidal constituents, O1, K1, M2, and S2, in the frequency domain analysis. Then, a program Baytap 08 is used to measure the phase and amplitude responses of water level for each tidal constituent and the corresponding errors. We also set local barometric pressure as an auxiliary series to eliminate the effect of barometric pressure on the water level. The study site is far from the ocean, so the ocean tide is ignored.

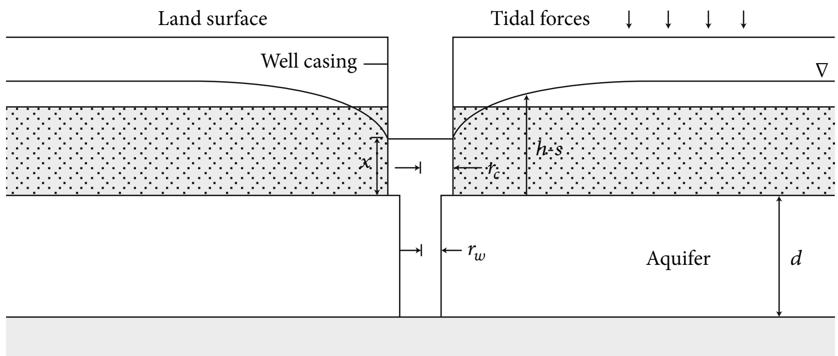

Figure 5: Illustration of an idealized well in a confined aquifer. Note: r_c is the inner radius of the casing. r_w is the screened portion of the well. s is the drawdown of the pressure head. d is the aquifer thickness.

4.2. Analytical Model. Figure 5 shows an idealized well in a confined aquifer. We assumed that the aquifer is two-dimensional isotropic, homogenous, and laterally extensive. The water level (x) in the well fluctuates in response to pressure head (h) variations caused by the dilation of the aquifer under the tidal forces. The amplitude and phase lag of well water level are the functions of the inner radius of the casing (r_c), radius of the screened portion of the well (r_w), aquifer transmissivity, and storage coefficient [18, 19]. Two analytical models determining the functional relationships, i.e., horizontal flow model and vertical flow model, were developed and have been widely used [18, 19]. We used a horizontal flow model, in which the flow to the well is radial, to determine the aquifer parameters [18]. However, the observed phase shift of J10 and J14 is positive, which may be caused by leakage to the water table [19] and cannot be described by a horizontal flow model. As a result, we need a vertical flow model applied to J10 and J14. Therefore, we use a horizontal flow model to calculate the hydrogeological parameters for the J7 well and use a vertical flow model to calculate the hydrogeological parameters for the other wells.

4.2.1. Horizontal Flow Model. As mentioned above, in a well-confined aquifer, both the phase lag and amplitude of well water level are the function of transmissivity and storage coefficient of aquifer [18]. Therefore, we can calculate the permeability and specific storage according to the phase shift and amplitude response. Analysis was based on the analytical solution proposed by Hsieh et al. [18]; the amplitude response A and phase shift η can be represented as

$$A = \left|\frac{x_0}{h_0}\right| = \left(E^2 + {}^2\right)^{-1/2}, \tag{1}$$

$$\eta = \arg\left(\frac{x_0}{h_0}\right) = -\tan^{-1}\left(\frac{F}{E}\right), \tag{2}$$

where

$$E \approx 1 - \frac{\omega {r_c}^2}{2T} \mathrm{Kei}(\alpha_w), \tag{3}$$

$$F \approx \frac{\omega {r_c}^2}{2T} \mathrm{Ker}\,(\alpha_w), \tag{4}$$

$$\alpha_w = \left(\frac{\omega S}{T}\right)^{1/2} r_w, \tag{5}$$

$$S = S_s d. \tag{6}$$

The amplitude response A is the ratio between the amplitude of water level oscillations and that of earth tidal dilation strain, and the phase shift η is the time lag of the water level oscillations relative to that of the imposed dilation strain. x_0 is the complex amplitude of water level fluctuation, and h_0 is the complex amplitude of pressure head fluctuation. T is the transmissivity (m^2/s), S_s is the specific storage (1/m), S is the storage coefficient, Ker (α_w) and Kei(α_w) are the real and imaginary parts of zero-order Kelvin function, r_w is the radius of the well (m), r_c is the inner radius of the casing (m), and ω is the frequency of the tide (rad/s).

4.2.2. Vertical Flow Model. When the water head gradient is vertical, the well water level tidal response can be simulated by periodic loading applied at the surface of a half-space and finite layer [19, 25]. The boundary condition at the water table is drained, and at the infinite depth, the boundary is undrained [26]. The pore pressure is related to the surface load, and its magnitude is the amplitude response A. Wang [25] presented an analytical solution to the water level tidal response under this condition. The amplitude response A is given by

$$A = \left|\frac{x_0}{h_0}\right| = \gamma\sigma_0 \left[1 - 2\exp\left(-\frac{z}{\delta}\right)\cos\frac{z}{\delta} + \exp\left(-\frac{2z}{\delta}\right)\right]^{1/2}, \tag{7}$$

where

$$\delta = \sqrt{\frac{2D}{\omega}}. \tag{8}$$

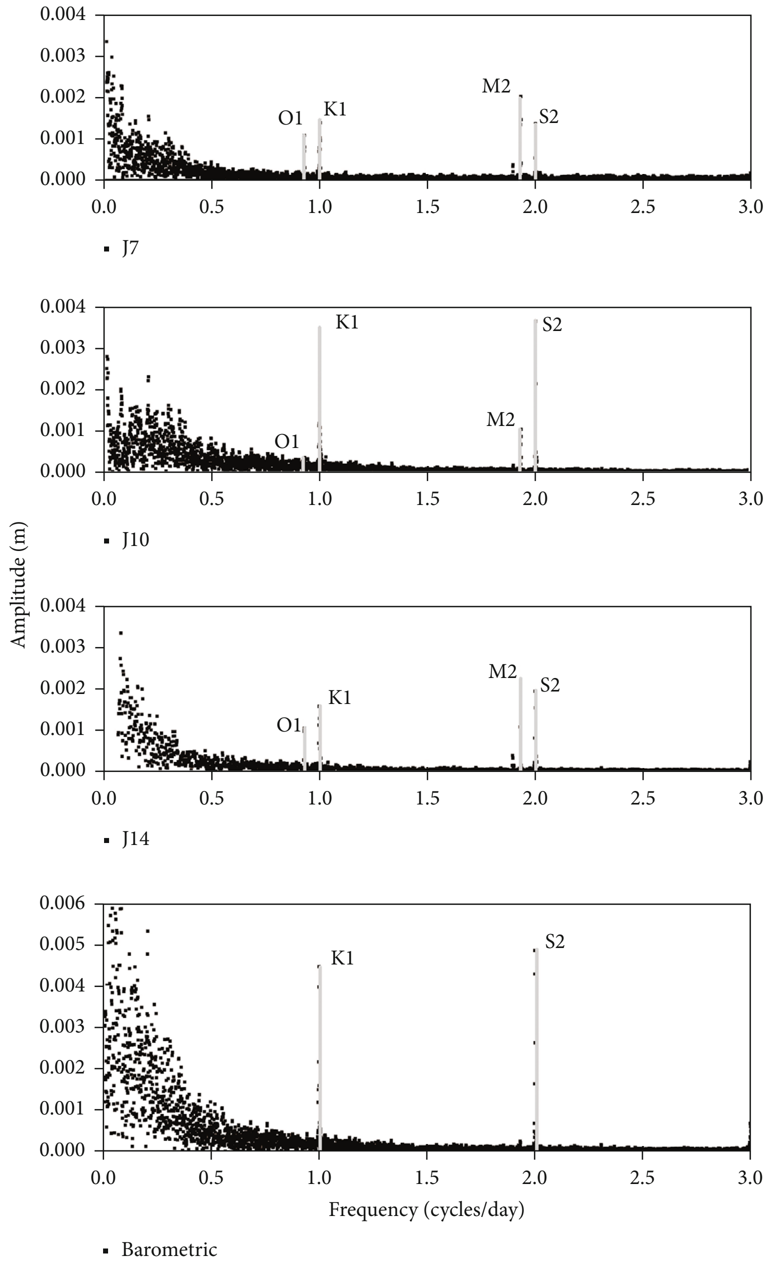

Figure 6: The amplitude spectrum of water level and barometric pressure data from September 2015 to September 2017. The vertical gray lines indicate the K1, O1, M2, and S2 tidal constituents.

The phase shift η is given by

$$\eta = \arg\left(\frac{x_0}{h_0}\right) = \tan^{-1}\left\{\frac{\exp\left(-z/\delta\right)\sin\left(z/\delta\right)}{1-\exp\left(-z/\delta\right)\cos\left(z/\delta\right)}\right\}, \quad (9)$$

where $\gamma\sigma_0$ is the amplitude of pore pressure, z is the depth from the water table, and D is the hydraulic diffusivity which equals the division of transmissivity T and storage coefficient S.

To get the values of T and S separately, we used a simplified method to determine the specific storage S_S [17]. The specific storage can be defined as

$$S_S = \rho g[(1-n)\alpha + n\beta], \quad (10)$$

and the relation of water level to tidal dilation strain can be shown as

$$x = \frac{\varepsilon_v}{\rho g[(1-n)\alpha + n\beta]}, \quad (11)$$

where ρ is the fluid density (kg/m^3), g is the acceleration of gravity (m/s^2), n is the porosity of the aquifer, α is the compressibility of the rock (MPa^{-1}), β is the compressibility of the fluid (MPa^{-1}), and ε_v is the aquifer dilation strain (volume strain). By combining equations (10) and (11), S_S can be shown as

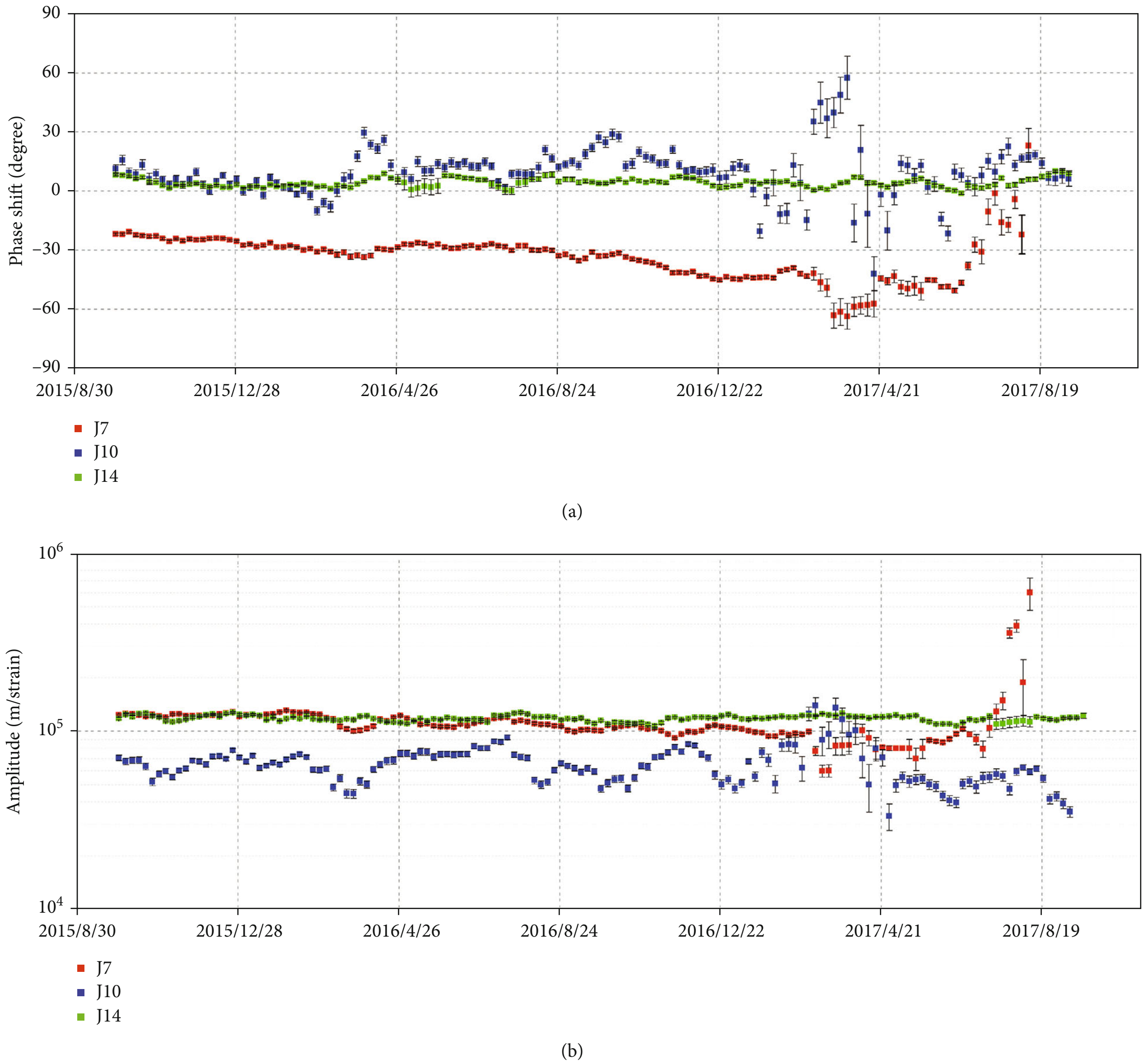

Figure 7: Phase shift (a) and amplitude response (b). The different colors show the results for different wells.

$$S_S = \frac{\varepsilon_v}{x}. \tag{12}$$

If the barometric pressure effects are removed from the tidal analysis, the aquifer dilation strain ε_v is equal to the tidal dilation strain ε. Thus, equation (12) can be rewritten as

$$S_S = \frac{\varepsilon}{x} = \frac{1}{A}. \tag{13}$$

Therefore, storage coefficient S can be obtained according to equations (6) and (13), and the corresponding transmissivity T can be calculated by

$$T = DS = DS_s d. \tag{14}$$

5. Results

5.1. Spectrum of Water Level. The results of the spectral analysis are shown in Figure 6. It can be seen that tidal constituents at O1, K1, S2, and M2 of all the wells are clear, which indicated a good response to tidal loading. The spectra of the barometric pressure, however, show only two clear constituents at K1 and S2, which means that the K1 and S2 constituents in water level are greatly affected by barometric pressure. Also, the O1 constituents in all wells are smaller than M2. Therefore, we focused on the tidal response at the frequency of M2, which has relatively large signal-to-noise ratios, and it is less affected by barometric loading.

5.2. Tidal Response and Hydrogeological Parameters. Figure 7 clearly shows that there are no obvious changes in phase and amplitude response of well water level at the J14 well;

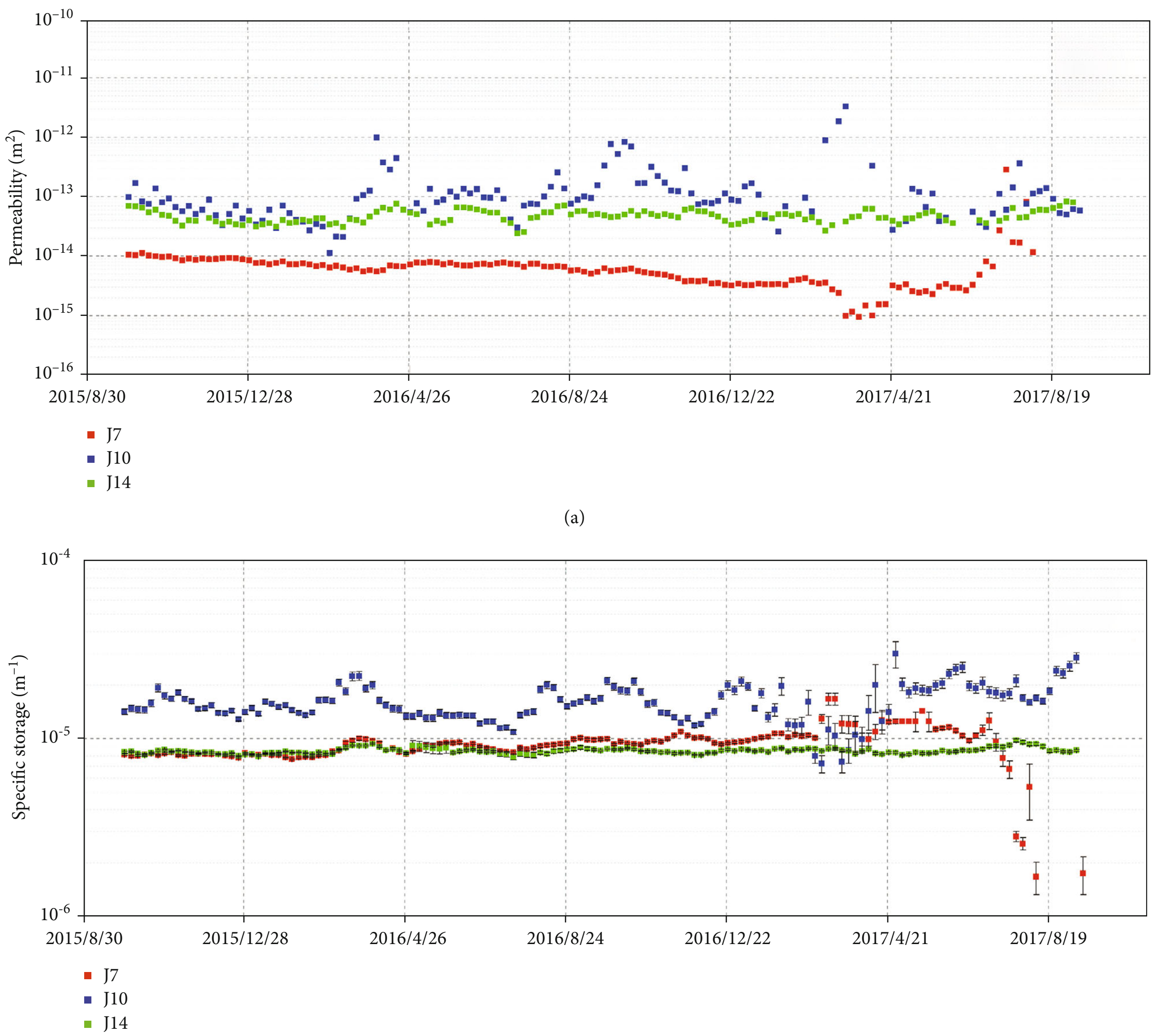

Figure 8: (a) Permeability and (b) specific storage. The different colors show the results for different wells.

however, the phase and amplitude response of J7 and J10 changed significantly when the longwall excavation zone approached each well. The phase shift of the J7 well decreased firstly and then increased during the mining. From the start of mining to June 2017, the phase shift of J7 declined gradually (25°). The phase shift of J7 started increasing as the coal face approached and eventually undermined the coal beneath the borehole, and the increment is 42°. The phase shift of J10 increased by 40° during the times when the longwall coal face approached the borehole and recovered about two months later. Furthermore, the phase shift of the J7 well dropped 14 degrees in March 2017 and recovered after a month. We infer that the sudden drop of phase shift might be related to the two unexpected water level drops in the J7 well as mentioned before. At that time, the work face is still about 1400 meters away from the J7 well. Though the amplitude changes are relatively insensitive compared with the phase shift changes [20], the amplitude response in J7 and J10 shows a relatively good agreement with phase shift changes (Figure 7(b)).

Based on the measured phase and amplitude response, we use two models to calculate the transmissivity (T) and storage coefficient (S); the relationship between transmissivity (T) and permeability (k) is

$$k = \frac{\mu}{\rho g d} T, \tag{15}$$

where k is the permeability (m^2), μ is the dynamic viscosity (Pa·s), ρ is the density (kg/m^3), g is the gravitational acceleration (m/s^2), and d is aquifer thickness (m). The storage coefficient (S) can be obtained by equation (6). The calculated permeability k and storage coefficient of the formation surrounding these three wells are shown in Figure 8. The permeability of the J7 and J10 wells exhibited a similar trend to that

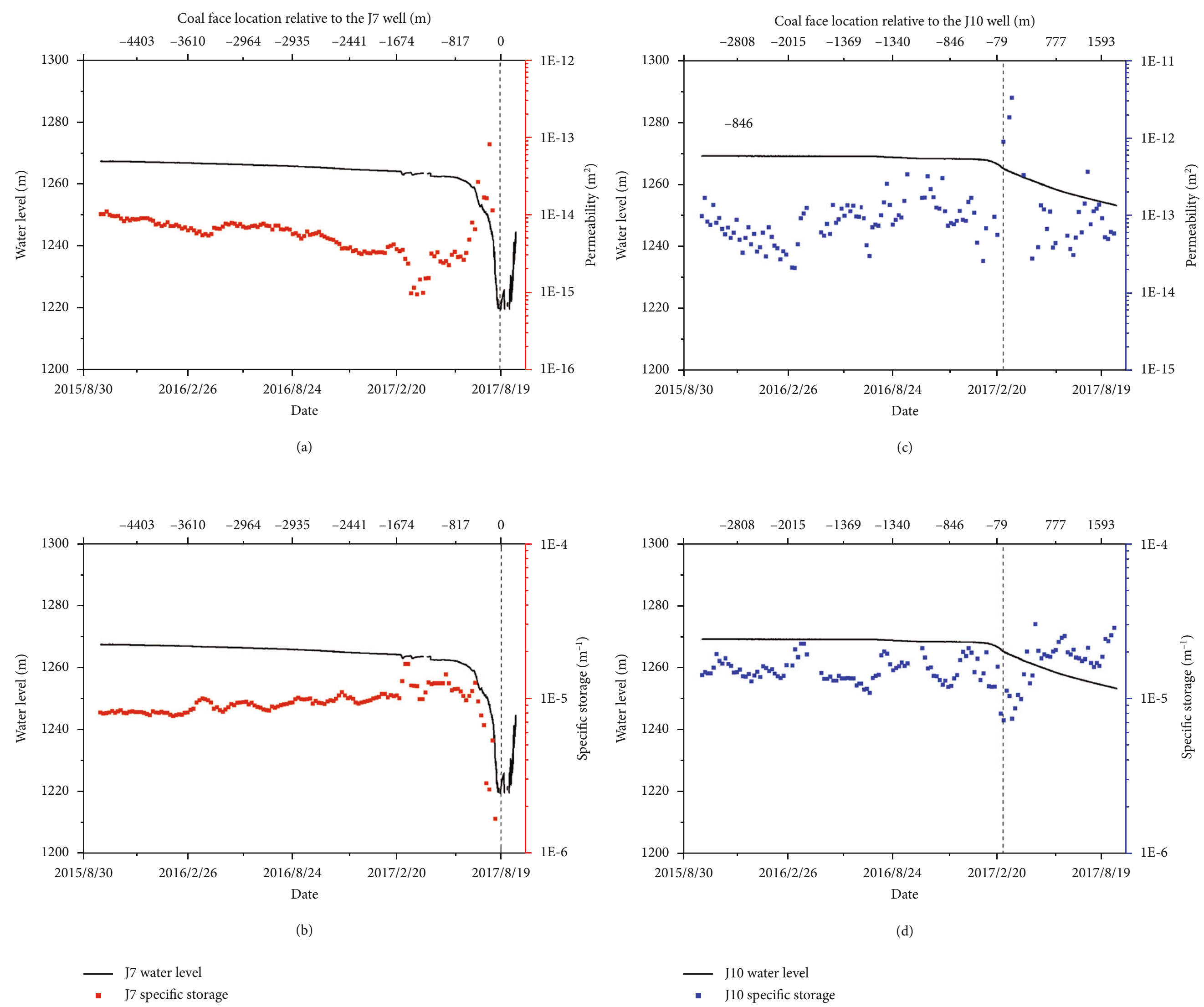

Figure 9: Variations of water level, permeability, and specific storage of J7 and J10 as a function of longwall coal face location relative to borehole location. Negative values represent a coal face location before it reaches the borehole location, where positive values represent the location of the coal face after undermining. The dash lines show the times when the longwall excavation zone is closest to the J10 and J7 wells, respectively.

of the phase shift. When the longwall excavation zone approached the wells, both the J7 and J10 permeability has increased by several to dozens of times.

6. Discussion

6.1. Aquifer Hydrogeological Parameter Changes during Mining. Figure 9 shows the variation in water level, permeability, and specific storage of J7 and J10 as a function of coal face location with respect to borehole location. The permeability of J7 and J10 declined gradually at first which was similar to the change in water level. In March 2017, the changes of permeability and specific storage of J7 are related to the two abnormal water level fluctuations as mentioned before. The earlier aquifer hydrogeological parameter changes may be related to slow depressurization and dewatering [27]. It is worth noting that during this period, the values of the parameters in J10 are relatively variable compared with that of J7. This might be due to the strong effect of the barometric pressure in the J10 well (Figure 6).

As the water levels change rapidly, the permeability and specific storage of J7 started to change drastically when the coal face was approximately 300 m away from the J7 well and eventually undermined the well. During this period, the value of permeability increased from $4.81 \times 10^{-15}\,\mathrm{m}^2$ to $1.15 \times 10^{-14}\,\mathrm{m}^2$ (Figure 9(a)), and the value of specific storage decreased from $1.04 \times 10^{-5}\,\mathrm{m}^{-1}$ to $5.32 \times 10^{-6}\,\mathrm{m}^{-1}$. The variation in the values of J10 was similar to J7. An obvious increase in permeability was observed to be from $5.57 \times 10^{-14}\,\mathrm{m}^2$ to $3.27 \times 10^{-12}\,\mathrm{m}^2$ when the coal face was about 80 m away from J10 (Figure 9(c)). When the coal face was about 300 m away from the J10 well, the specific storage of J10 started to decline until the coal face eventually undermined the well and subsequently recovered to its previous value.

These results may be explained by the fact that the permeability is controlled by mining-induced stress [8, 11]. The tensile stress in front of the work face possibly creates new fractures, which could increase the permeability of the aquifer around the wells. With the advance of the coal face, the tensile stress converts to compressive stress after the coal face undermined the well [28, 29]. In this case, the permeability of the aquifer around the wells will decrease due to formation compression and fracture closure.

The decrease of specific storage is due to the reduction of pore water pressure and porosity induced by drainage and aquifer compression. It is worth mentioning that the specific storage of J10 recovered to its previous level in the postclosure period. The increase of the specific storage of J10 after the coal face passed may be interpreted by aquifer rebound [30].

6.2. Water Level Changes Associated with Mining. From the start of mining, the water level of J7 and J10 is relatively stable or gradually decreased, which can be attributed to slow depressurization and dewatering of other mining faces elsewhere in the coalfield. Rapid declines in water levels occurred when the longwall excavation zone approached J7 and J10 wells, and the water level of J7 drops significantly faster than that of J10. The sharp water level drops in J7 and J10 are likely due to dewatering via the new fracture created by fracturing and dilation of joints [31].

Combined with the variation in water level and aquifer hydrogeological parameters, the aquifer deformation around J7 and J10 wells might be elastic during mining. For a deep confined aquifer, the hydraulic head recovery may not be related to recharge [32], and the recovery of the J7 water level might be related to the water released by partial closure of fractures during the formation compression [30, 32]. It is interesting to note that no recovery was observed in the water level in the J10 well while the hydrogeological parameters of J10 recovered to their previous level after the coal face passed as mentioned before. Therefore, it can be inferred that the continuous decline of the water level in the J10 well is probably due to the continuous leakage from the aquifer around the J10 well to other connected aquifers.

6.3. Uncertainty and Future Perspectives. There are some uncertainties of the estimated results. Due to the lack of field monitoring strain data, we can only determine aquifer parameters based on the theoretical solid tides, which may lead to error in the estimations. In the period of the drastic change of the well water level, the standard deviations of calculated phase and amplitude are relatively large, which leads to the corresponding uncertainty of estimated permeability and specific storage. Besides, we were unable to make a complete evaluation of the aquifer parameter changes of the J7 well due to the missing subsequent recovery water level data of the well. Nevertheless, this study showed the primary characteristics of the aquifer parameter changes under coal mining and demonstrated that the tidal effects of the well water level can be effectively used to investigate such changes. It is worth noting that mining-induced changes in hydrogeological parameters of overburden aquifer may be related to site-specific structures and operations of coal mines. It is expected that more research would be conducted in the future to improve the accuracy of parameter estimations and to further understand the changes in aquifer structure and properties and hydrological circle caused by mining.

7. Conclusion

In this paper, we use the method of the tidal response of well water level to explore the changes in hydrogeological parameters of the overburden aquifer in the mining area. Based on the long-term water level monitoring data, two analytical models were used to determine the temporal changes of hydrogeological parameters under mining disturbance. The main conclusions can be drawn as follows:

(1) The permeability of aquifer can increase by several to dozens of times when the longwall excavation zone approached the monitoring wells; the response distances of aquifer deformation to mining can be up to 300 m

(2) During mining, the drawdown of water level in wells is likely due to dewatering via the new fracture created by mining; the well water level and hydrogeological parameters may be recovered after the work face passed, possibly due to the rebound effects of aquifer

(3) The changes in well water level and hydrogeological parameters in different monitoring sites (wells) showed different characteristics, which may be related to the well and aquifer structures as well as the positions of the monitoring wells relative to the coal face

The results of this study could enhance our understanding of the hydrogeological parameter changes in the overburden aquifers and could have implications for groundwater protection and safety of mining in coal mine areas.

Data Availability

The data supporting the results of this article are included within the article and can be obtained from the corresponding author (wanggc@pku.edu.cn) upon request.

Conflicts of Interest

The authors declare no conflicts of interest.

Acknowledgments

This work is supported by the National Natural Science Foundation of China (41272269). We thank Dr. Liang Guo and Mr. Ziguan Wang for valuable discussions and assistance in field sampling.

References

[1] B. Zhu, Q. Wu, J. Yang, and T. Cui, "Study of pore pressure change during mining and its application on water inrush

prevention: a numerical simulation case in Zhaogezhuang coalmine, China," *Environmental Earth Sciences*, vol. 71, no. 5, pp. 2115–2132, 2014.

[2] D. P. Adhikary and H. Guo, "Modelling of longwall mining-induced strata permeability change," *Rock Mechanics and Rock Engineering*, vol. 48, no. 1, pp. 345–359, 2015.

[3] R. Fawcett, S. Hibberd, and R. Singh, "An appraisal of mathematical models to predict water inflows into underground coal workings," *International Journal of Mine Water*, vol. 3, no. 2, pp. 33–54, 1984.

[4] B. A. Poulsen, D. Adhikary, and H. Guo, "Simulating mining-induced strata permeability changes," *Engineering Geology*, vol. 237, pp. 208–216, 2018.

[5] J. Zhang and B. Shen, "Coal mining under aquifers in China: a case study," *International Journal of Rock Mechanics and Mining Sciences*, vol. 41, no. 4, pp. 629–639, 2004.

[6] K. Miyakawa, T. Nohara, T. Tokiwa, and M. Yamazaki, "Seven-year history of vertical hydraulic diffusivity related to excavation around an underground facility," *International Journal of Rock Mechanics and Mining Sciences*, vol. 70, pp. 332–342, 2014.

[7] S. J. Schatzel, C. Ö. Karacan, H. Dougherty, and G. V. R. Goodman, "An analysis of reservoir conditions and responses in longwall panel overburden during mining and its effect on gob gas well performance," *Engineering Geology*, vol. 127, pp. 65–74, 2012.

[8] J. Liu and D. Elsworth, "Three-dimensional effects of hydraulic conductivity enhancement and desaturation around mined panels," *International Journal of Rock Mechanics and Mining Sciences*, vol. 34, no. 8, pp. 1139–1152, 1997.

[9] W. X. Wang, W. H. Sui, B. Faybishenko, and W. T. Stringfellow, "Permeability variations within mining-induced fractured rock mass and its influence on groundwater inrush," *Environmental Earth Sciences*, vol. 75, no. 4, p. 326, 2016.

[10] C. Booth, "The effects of longwall coal mining on overlying aquifers," *Geological Society, London, Special Publications*, vol. 198, no. 1, pp. 17–45, 2002.

[11] C. Özgen Karacan and G. Goodman, "Hydraulic conductivity changes and influencing factors in longwall overburden determined by slug tests in gob gas ventholes," *International Journal of Rock Mechanics and Mining Sciences*, vol. 46, no. 7, pp. 1162–1174, 2009.

[12] Z. Huang, Z. Jiang, S. Zhu, X. Wu, L. Yang, and Y. Guan, "Influence of structure and water pressure on the hydraulic conductivity of the rock mass around underground excavations," *Engineering Geology*, vol. 202, pp. 74–84, 2016.

[13] H. H. Cooper, J. D. Bredehoeft, I. S. Papadopulos, and R. R. Bennett, "The response of well-aquifer systems to seismic waves," *Journal of Geophysical Research*, vol. 70, no. 16, pp. 3915–3926, 1965.

[14] J. D. Bredehoeft, "Response of well-aquifer systems to Earth tides," *Journal of Geophysical Research*, vol. 72, no. 12, pp. 3075–3087, 1967.

[15] R. I. Acworth and T. Brain, "Calculation of barometric efficiency in shallow piezometers using water levels, atmospheric and earth tide data," *Hydrogeology Journal*, vol. 16, no. 8, pp. 1469–1481, 2008.

[16] T. J. Burbey, "Fracture characterization using Earth tide analysis," *Journal of Hydrology*, vol. 380, no. 3-4, pp. 237–246, 2010.

[17] G. H. Rhoads and E. S. Robinson, "Determination of aquifer parameters from well tides," *Journal of Geophysical Research*, vol. 84, no. B11, p. 6071, 1979.

[18] P. A. Hsieh, J. D. Bredehoeft, and J. M. Farr, "Determination of aquifer transmissivity from Earth tide analysis," *Water Resources Research*, vol. 23, no. 10, pp. 1824–1832, 1987.

[19] E. Roeloffs, "Poroelastic techniques in the study of earthquake-related hydrologic phenomena," in *Advances in Geophysics Volume 37*, no. 37pp. 135–195, Elsevier, 1996.

[20] J. E. Elkhoury, E. E. Brodsky, and D. C. Agnew, "Seismic waves increase permeability," *Nature*, vol. 441, no. 7097, pp. 1135–1138, 2006.

[21] L. Xue, H. B. Li, E. E. Brodsky et al., "Continuous permeability measurements record healing inside the Wenchuan earthquake fault zone," *Science*, vol. 340, no. 6140, pp. 1555–1559, 2013.

[22] G. Lai, H. Ge, L. Xue, E. E. Brodsky, F. Huang, and W. Wang, "Tidal response variation and recovery following the Wenchuan earthquake from water level data of multiple wells in the nearfield," *Tectonophysics*, vol. 619-620, pp. 115–122, 2014.

[23] Z. Shi, G. Wang, C.-y. Wang, M. Manga, and C. Liu, "Comparison of hydrological responses to the Wenchuan and Lushan earthquakes," *Earth and Planetary Science Letters*, vol. 391, pp. 193–200, 2014.

[24] X. Huang, G. Wang, X. Liang, L. Cui, L. Ma, and Q. Xu, "Hydrochemical and stable isotope (δD and δ18O) characteristics of groundwater and hydrogeochemical processes in the Ningtiaota Coalfield, Northwest China," *Mine Water and the Environment*, vol. 37, no. 1, pp. 119–136, 2018.

[25] H. Wang, *Theory of Linear Poroelasticity*, Princeton Univ. Press, Princeton, NJ, 2000.

[26] L. Xue, E. E. Brodsky, J. Erskine, P. M. Fulton, and R. Carter, "A permeability and compliance contrast measured hydrogeologically on the San Andreas Fault," *Geochemistry, Geophysics, Geosystems*, vol. 17, no. 3, pp. 858–871, 2016.

[27] P. Hsieh, "Deformation-induced changes in hydraulic head during ground-water withdrawal," *Ground Water*, vol. 34, no. 6, pp. 1082–1089, 1996.

[28] S. G. Wang, D. Elsworth, and J. S. Liu, "Permeability evolution during progressive deformation of intact coal and implications for instability in underground coal seams," *International Journal of Rock Mechanics and Mining Sciences*, vol. 58, pp. 34–45, 2013.

[29] Y. Lu, L. Cheng, Z. Ge, B. Xia, Q. Li, and J. Chen, "Analysis on the initial cracking parameters of cross-measure hydraulic fracture in underground coal mines," *Energies*, vol. 8, no. 7, pp. 6977–6994, 2015.

[30] K. David, W. A. Timms, S. L. Barbour, and R. Mitra, "Tracking changes in the specific storage of overburden rock during longwall coal mining," *Journal of Hydrology*, vol. 553, pp. 304–320, 2017.

[31] C. J. Booth and E. D. Spande, "Potentiometric and aquifer property changes above subsiding longwall mine panels, Illinois Basin Coalfield," *Groundwater*, vol. 30, no. 3, pp. 362–368, 1992.

[32] C. J. Booth, "Confined-unconfined changes above longwall coal mining due to increases in fracture porosity," *Environmental and Engineering Geoscience*, vol. 13, no. 4, pp. 355–367, 2007.

Hindawi
Geofluids
Volume 2021, Article ID 5512729, 16 pages
https://doi.org/10.1155/2021/5512729

Research Article

Evaluation of the Water Yield of Coal Roof Aquifers Based on the FDAHP-Entropy Method: A Case Study in the Donghuantuo Coal Mine, China

Yaowen Zhang[1,2] **Lili Zhang**[2] **Haijun Li**[2] **and Baoming Chi**[2]

[1]*Key Laboratory of Earthquake Engineering and Engineering Vibration, Institute of Engineering Mechanics, China Earthquake Administration, Harbin, Heilongjiang 150080, China*
[2]*School of Ecology and Environment, Institute of Disaster Prevention, Sanhe, Hebei 065201, China*

Correspondence should be addressed to Lili Zhang; zhanglili@cidp.edu.cn

Received 26 February 2021; Revised 23 April 2021; Accepted 3 May 2021; Published 24 May 2021

Academic Editor: Guanglei Zhang

The water yield of coal seam roof aquifers is the key factor for evaluating and controlling water disasters in coal seam roofs. To evaluate the water yield of the sandstone aquifer in the roof of the Carboniferous-Permian Damiaozhuang Formation no. 8 coal seam in the Donghuantuo Mine, North China, seven main controlling factors affecting the water yield of sandstone aquifers are determined, including the permeability coefficient, consumption of drilling fluid, core recovery, aquifer thickness, brittle-plastic rock thickness ratio, fault scale index, and fault point density. Further, the fuzzy Delphi analytic hierarchy process (FDAHP) and entropy weight method (EWM) are used to calculate the subjective and objective weights of each main factor, respectively, and a combination weight model (CWM) is proposed based on the least square method to compose the comprehensive weights. Then, an improved water yield property index (IWYPI) model is established, and the water yield zoning map of sandstone aquifers is acquired. Engineering practice shows that the evaluation accuracy of the water yield property index (IWYPI) model based on the CWM is as high as 93.75%, which is 18.75% and 12.5% higher than that of the water yield property index (WYPI) model based on the FDAHP and EWM, respectively. The research results propose a novel method for evaluating the water yield of coal seam roof aquifers and can provide scientific guidance for the prevention and control of water disasters in the no. 8 coal seam roof of the Donghuantuo Coal Mine.

1. Introduction

As the largest coal mining country in the world, China also has some of the most serious mine water disasters [1–3]. Especially with the large-scale development of deep resources, the prevention and control of water disasters remains a top priority and is complicated by many problems and challenges. Control and utilization of China's groundwater resources remain a major research topic in coal mine safety production and scientific mining research [4–6]. From 2000 to 2011, there were 1089 coal mine water accidents in China with a total death toll of 4329 [7]. In particular, North China-type coalfields in China not only suffer from the problem of water inrushes from coal seam floors but also face the threat of water catastrophes from coal seam roofs [8]. The sufficient and necessary conditions for the occurrence of water disasters in coal seam roofs are that mining and caving touch water-filled aquifers, and the corresponding areas have high water yields, i.e., the aquifer provides the material for the water inrush from the coal seam roof, and the water yield of the aquifer directly determines the amount and duration of the water inrush [9]. Therefore, how to effectively evaluate the water yield of coal seam roof aquifers and how to delineate the zones of coal seam roofs with high water yields based on reality has important guiding significance and practical value for the prevention and control of coal mine roof water disasters.

Studying the water yield properties of aquifers is essential for preventing and controlling water disasters in coal seam roofs, and several assessment methods have been developed in recent decades. Geophysical prospecting and pumping test methods have been widely used and play an active role in the evaluation of aquifer water yields [10–17]. However, these two methods have problems, such as being the only method considered, a heavy workload, a high cost, and a limited control range, which limit their application [18]. Another important method is the analytic hierarchy process (AHP) water yield property index method [19], which uses geographic information systems (GIS) to fuse multisource geoscience information and to comprehensively reflect the results of water yield evaluations with various influencing factors and the differences and relationships among these factors. Compared with the geophysical prospecting method and the water pumping test method, the AHP has many potential advantages, but the weights of the factors influencing the water yield in this method are highly subjective as they are based on expert opinions; in addition, it is difficult to reach consistency in the judgement matrix in this method for more than four factors [20, 21]. Grey theory, BP neural networks, fuzzy clustering methods, and principal component analysis methods have been introduced for the evaluation of water yields, strengthening the evaluation of the water yield [22–25]. However, these methods have limitations in practical application, and they fail to address uncertain factors such as insufficient sample sizes, data information fusion, or subjective fuzzy evaluation in the evaluation process. For example, grey theory requires many water inrush examples and calculates the weight of each index according to the correlation coefficient between the index of each example and water inflow; however, when the amount of data is insufficient, the evaluation results are likely to deviate greatly [26]. The BP neural network model often results in overfitting, which usually leads to a local minimum and a slow convergence speed problem [27]. The fuzzy clustering method is theoretical and difficult to combine with actual mining areas [28]. However, principal component analysis effectively eliminates the influence of information superposition among evaluation indexes [29], but it compromises by making the evaluation index value fuzzy to reduce the dimensionality of the variables [30].

In summary, there are certain limitations to evaluate the water yield of an aquifer using any one method alone. Therefore, this paper proposes a water yield evaluation method based on the coupling of the fuzzy Delphi analytic hierarchy process (FDAHP) and entropy weight method (EWM) and applies it to evaluate the water yield of the sandstone aquifer in the roof of the Donghuantuo Coal Mine in a North China-type coalfield. The FDAHP and EWM are combined to determine the weight of each influencing factor. Considering the opinions of a group of decision-making experts, the problems of large errors from single-person evaluations and difficult consistency of the judgement matrix in the AHP are effectively avoided, and the characteristics of measured data are considered, thereby realizing the organic integration of subjective and objective weights and improving the accuracy and reliability of the evaluation results. Based on this, an improved water yield property index (IWYPI) model is established. The analysis results compared with engineering practice data are used to validate than the IWYPI model as an operational tool to evaluate the water yield of the no. 8 coal seam roof aquifer in the Donghuantuo Coal Mine. The obtained water yield zoning map of the sandstone aquifer provides a detailed scientific basis for ensuring safe coal mine production and roof water disaster prevention.

2. The Study Area

2.1. Physical Geography. The Donghuantuo Coal Mine is a typical North China Carboniferous-Permian coalfield with extremely complex hydrogeological conditions. During the construction period of the mine, the maximum water inflow reached 62.84 $m^3 \cdot min^{-1}$, and many water inrush accidents have occurred. At present, as the increase of the depth of coal mining, the threat of water hazards will continue to increase [31]. The Donghuantuo Mine is located in Tangshan City, Hebei Province (Figure 1). It is approximately 10 km east to Tangshan Station and 14 km south to Xugezhuang Station. The mine is within alluvial plain terrain; there are neither hills nor rivers in the mine area. The terrain is flat and high in the northeast and low in the southwest. The elevation of the terrain ranges from 2 to 23 m, and the topographic slope is 1.6. The climate of the mine area is continental: hot and rainy in summer and cold and windy in winter. The temperature ranges from 39.6 to -21°C with an average of 11.1°C. The average annual rainfall is 614.7 mm, and the average annual evaporation is 1321.1 mm. There is no surface water system in the mine area.

2.2. Geological Conditions. The Donghuantuo Coal Mine is in the northwestern Kaiping Coalfield. The strata of the Kaiping Coalfield are North China-type deposits. According to the strata exposed by boreholes, the study area contains Ordovician, Carboniferous, Permian and Quaternary strata. The coal-bearing strata in the mine are Carboniferous and Permian. The total thickness of the coal seams is 19.70 m, which includes the no. 8, no. 9, no. 11 and no. 12-1 main coal seams.

The mine is located on both sides of the Chezhoushan syncline, which is part of a coal-bearing structure in the western Kaiping Coalfield. Its main structural controls are those of the Neocathaysian system, and the structural lines are mostly NE-trending. The syncline is a large coal-bearing syncline with a long and narrow asymmetrical dip to the southwest. The strike of the syncline axis is approximately N60°E, and the synclinal axis slopes to the northwest.

Strata on both sides of the syncline vary greatly. The strata in the southeast wing are gentle with an inclination of approximately 20°, while the strata in the northwest wing are steep with an inclination of approximately 70°. The main structural form of the mine is the monoclinic structure in the southeastern wing of the Chezhoushan syncline. The fault structure is well developed in the mine, and the strike of the fault is mostly consistent with the direction of the syncline axis (Figure 2).

2.3. Hydrogeological Characteristics of the Mine. In this study, the main coal seam is the no. 8 coal seam, the direct water-filled aquifer is a Permian sandstone fractured aquifer, and the indirect water-filled aquifer is a Quaternary bottom gravel aquifer. There is a weak permeable aquifer between these two

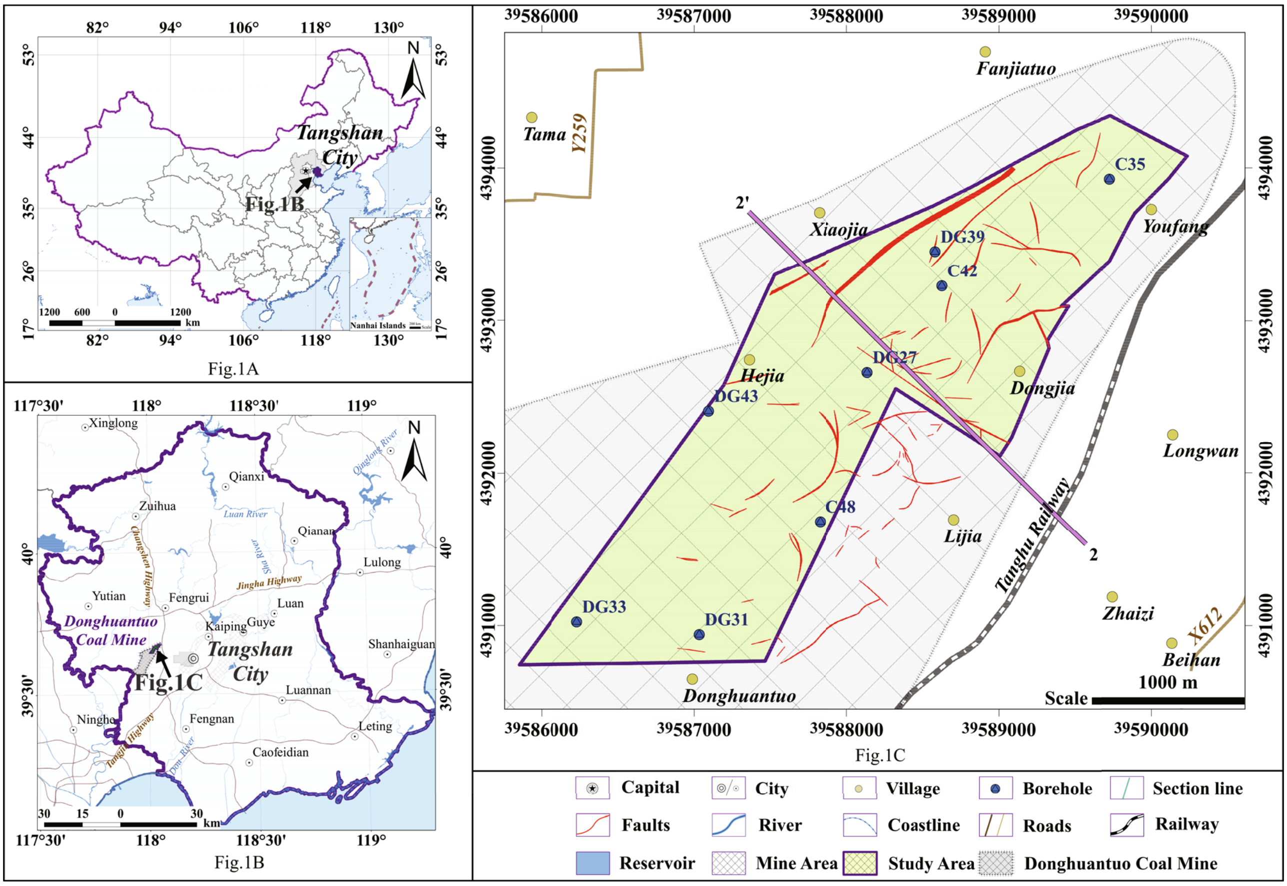

FIGURE 1: Map showing the location of the study area.

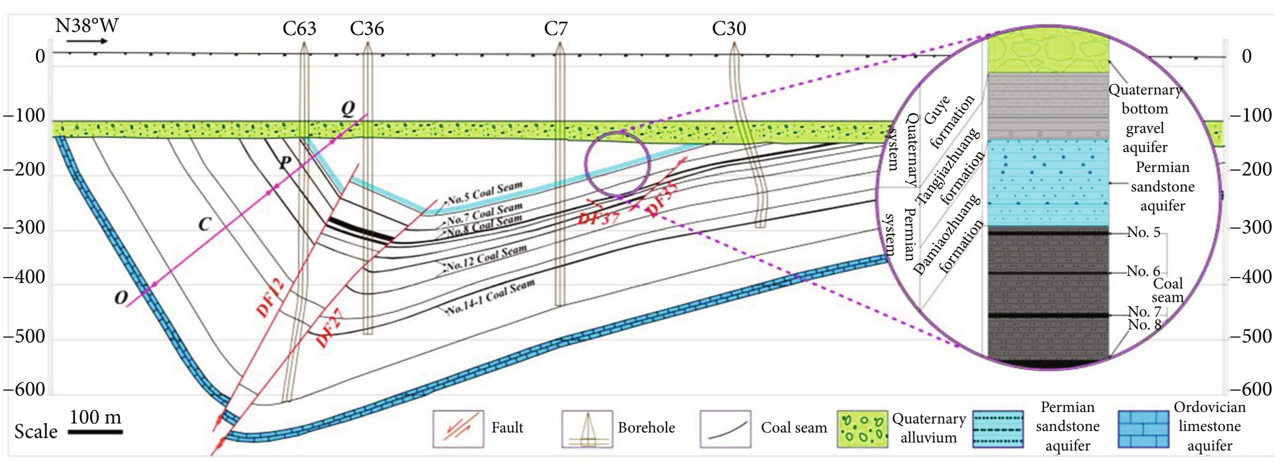

FIGURE 2: 2-2′ geological profile of the study area.

aquifers (Figure 2). The Permian sandstone fractured aquifer is the main threat to safely mining the no. 8 seam.

The Permian sandstone fractured aquifer is dominated by coarse sandstone and gravel-bearing giant sandstone with unequal grains and muddy siliceous cementation. This aquifer has extensive direct contact with the bottom gravel aquifer, and the gravel aquifer is the recharge source, so water is abundant and not easily drained. The specific capacity of boreholes is 0.016-1.806 $L{\cdot}s^{-1}{\cdot}m^{-1}$, and the permeability coefficient is 0.369-10.492 $m{\cdot}d^{-1}$.

The topographic difference between the outcrops in the two wings reveals that the northwest wing is a recharge area, and the southeast wing is an excretion area under natural conditions. The Permian sandstone fractured aquifer receives pore water from the bottom pebble beds of the Quaternary aquifer along the northwest wing. There has been a fundamental change in the groundwater movement arising from the operation of the mine, with the underground mining area becoming a drainage area and the outcrop zones near the mining area of the north and south flanks becoming a recharge area. At present, groundwater drainage is achieved by mine pumping.

3. Data

3.1. Major Controlling Factors of the Aquifer Water Yield. A thorough analysis of the hydrogeological data of the mining area was performed to generate a thematic database of multivariate geological information to comprehensively reflect the water yield of the water-filled aquifer. This analysis comprised seven factors: the permeability coefficient, consumption of flushing fluid, aquifer thickness, ratio of brittle-plastic rock thickness, core recovery rate, fault point density, and fault scale index (Figures 3 and 4).

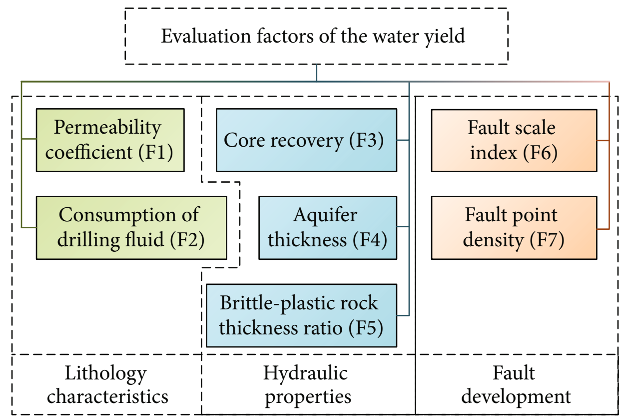

Figure 3: Major controlling factors of the water yield evaluation.

(1) The permeability coefficient is a constant representing the permeability of rock strata. Generally, the higher the permeability coefficient is, the more permeable the rock. The permeability of the Permian sandstone fractured aquifer in the study increased gradually from northeast to southwest in the range of 1.05-2.15 $m \cdot d^{-1}$

(2) The consumption of drilling fluid can reflect the permeability of the drilled rock. There is a certain degree of drilling fluid leakage when drilling through an aquifer. The larger the amount of leakage is, the better the development degree and connectivity of the voids in the strata. The flushing fluid consumption of the Permian sandstone fractured aquifer in the study area increased gradually from northeast to southwest within a range of 0.1-14.5 $m^3 \cdot h^{-1}$

(3) Aquifer thickness is the prerequisite for determining the water yield and the primary factor affecting the occurrence of groundwater. Generally, the thicker the aquifer is, the greater its water content. In the study area, the closer the Permian sandstone fractured aquifer was to the syncline axis, the thicker the aquifer was. The overall thickness increased gradually from northeast to southwest within a range of 140-230 m.

(4) The ratio of the brittle-to-plastic rock thickness can be used as an index to qualitatively judge the permeability of sandstone fractured aquifers. In the case of failure due to tectonic stress, the fracture characteristics reflected by lithologies with different mechanical properties are quite different. The stress release of brittle sandstone mainly occurs in the form of shear and tensile failures. Fractures and joints are relatively developed in the sandstone layer, which greatly enhances the permeability. Plastic clay rocks release their stress in the form of plastic deformation under a load action, which results in minimal changes to its permeability. Therefore, in general, the larger the ratio of brittle-to-plastic rock thickness is, the higher the permeability of the aquifer. The lithology of the Permian sandstone fractured aquifer in the study area is mainly medium and fine sandstone. Brittle rocks are much thicker than plastic rocks. Except in some individual sections, the ratio of the brittle-to-plastic rock thickness gradually decreased from northeast to southwest in the study area, ranging from 1.05-2.35.

(5) Core recovery refers to the ratio of the core length to the drilling depth, which is expressed as a percentage. Core recovery is a rock quality index used to express the integrity of a rock mass. The lower the core rate is, the more fragmented the rock and the better its connectivity. The core recovery rate of the Permian sandstone fractured aquifer in the study area gradually decreased from northeast to southwest, ranging from 0.87 to 0.99.

(6) The density of fault points refers to the number of intersections and endpoints of faults in a unit area. Intersections and endpoints of faults form in space and along planes and have certain rules for development. The higher the fault point density is, the more developed the rock mass fissures and the higher the water content and water conductivity. There are many faults in the study area that are widely distributed. The geological profile shows that most of the faults cut the Permian sandstone fissure aquifer. The high density of fault points in the middle and southern parts of the study area indicates that the water yield of the Permian sandstone fractured aquifer is obviously affected by faults.

(7) The fault size index is the sum of the product of the fault throw and strike lengths of all faults in the unit area, as shown by

$$F = \frac{\sum_{i=1}^{n} L_i H_i}{S}, \tag{1}$$

where F is the fault size index, H_i is the fault throw of the i^{th} fault (m), L_i is the strike length of the i^{th} fault

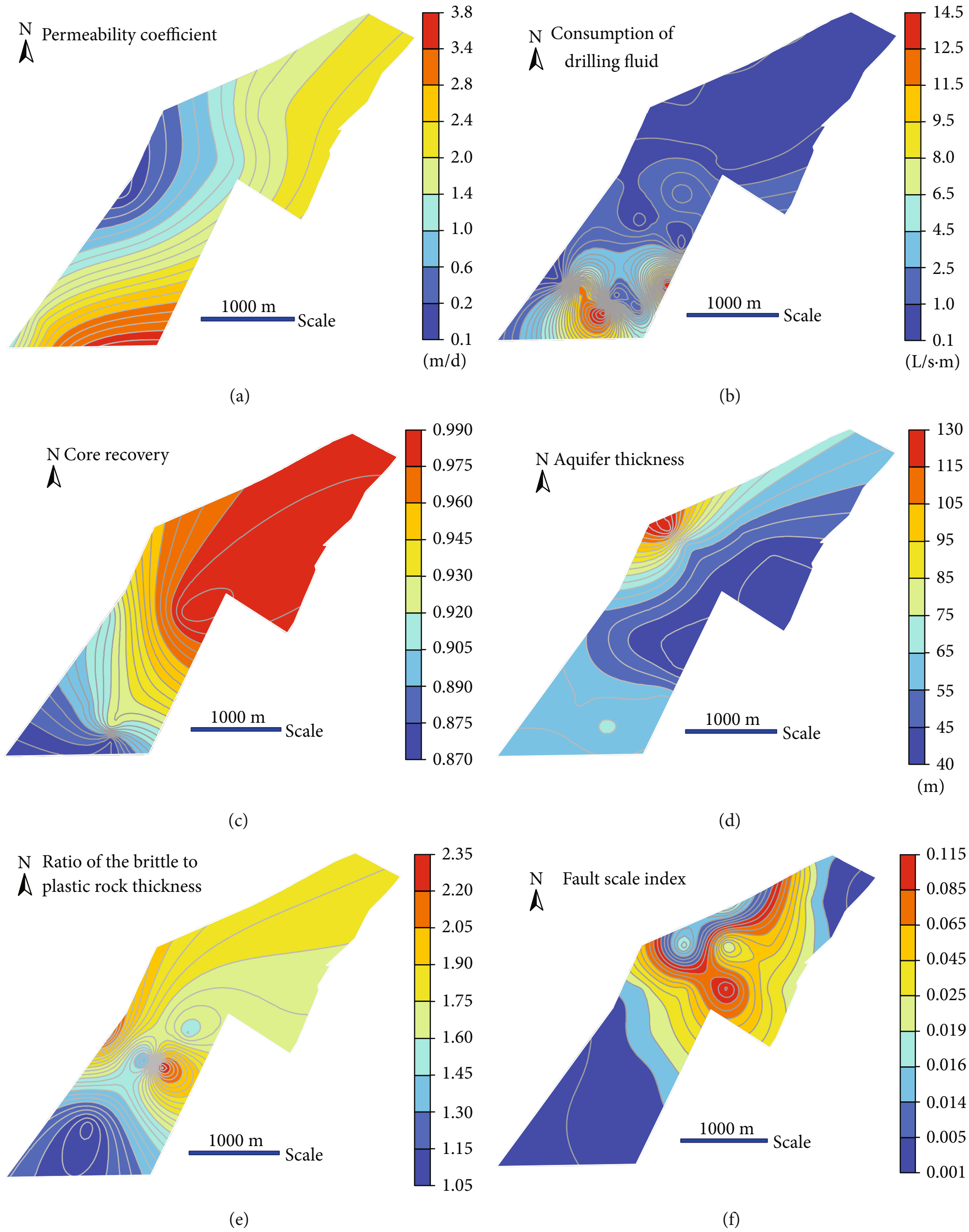

Figure 4: Continued.

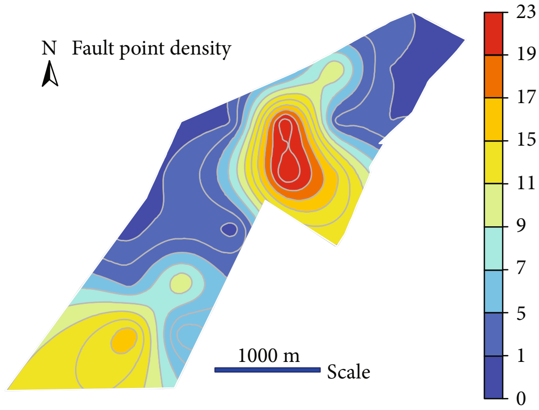

(g)

FIGURE 4: Thematic map of multiple geological factors for the water-filled aquifer in the no. 8 coal seam roof.

in the unit area (m), N is the number of faults within the unit area, and S is the unit area (m^2).

The fault size index comprehensively reflects the size and development of faults. The larger the fault size index is, the larger the groundwater recharge scope and occurrence space and the higher the water yield of the faults. The large-scale index of faults in the central and northern parts of the study area indicates that the area is disturbed by faults, and faults may serve as water-filling sources or conduits to increase the possibility of roof water inrushes.

3.2. Data Normalization. Taken individually, components of multivariate geological information provide only a limited reflection of the aquifer water yield, and data integration is necessary to comprehensively reflect the aquifer water yield. The physical quantities of aquifers represented by multivariate geological information are different. To achieve data integration, the limitations of different physical dimensions must first be eliminated. Normalization of data is a feasible way to achieve this, and Equations (2) and (3) were used to normalize the factors from the established multivariate geological information database, which were positively and negatively correlated with the water yield, respectively.

$$y_i = \frac{x_i - x_{\min}}{x_{\max} - x_{\min}}, \quad (2)$$

$$y_i{}' = \frac{x_{\max} - x_i}{x_{\max} - x_{\min}}. \quad (3)$$

y_i and $y_i{}'$ are the normalized value for positive and negative factor respectively, while $x_{\max}$ and $x_{\min}$ are the maximum and minimum of the original data, respectively. In this paper, the evaluation factors were normalized by Equation (2), with the exception of the core recovery factor, which was calculated by Equation (3).

4. Methods

4.1. Procedures. To acquire a relatively reasonable and accurate evaluation of the water yield of the coal roof aquifer, the comprehensive weight should be determined by considering the fuzziness of the comprehensive evaluation process, the decision-making experience of the expert group, and the differential information of the evaluation factor.

Based on the scientific quantification of multiple factors, the synthesized evaluation applies comprehensive coupling of the FDAHP and EWM, as shown in Figure 5.

4.2. Determination of the Factor Weights

4.2.1. Subjective Weights by the FDAHP. The FDAHP is a fuzzy group decision-making method that integrates fuzzy mathematics appraisal and the AHP and the Delphi group decision-making method [32, 33]. The relative importance matrix (Table 1) for all determined factors according to each expert's judgement value by the Saaty scale method is essential and the basis of generating a pairwise comparison matrix.

According to expert opinions, F1, F2,…, F7 are the evaluation factors, while a_{ij} is defined as the relative importance comparison judgement value for a pair of factors and is obtained by the F_i value divided by the F_j value. Therefore, ten 7×7 pairwise comparison judgement matrices for each expert were generated.

$$A = \begin{bmatrix} 1 & a_{12} & \cdots & a_{17} \\ \frac{1}{a_{12}} & 1 & \cdots & a_{27} \\ \vdots & \vdots & \ddots & \vdots \\ \frac{1}{a_{17}} & \frac{1}{a_{27}} & \cdots & 1 \end{bmatrix}. \quad (4)$$

Then, a group of fuzzy pairwise comparison matrices was established by making use of the triangular fuzzy number b_{ij}, which was calculated using Equation (5) and consisted of pessimistic, moderate, and optimistic comparison judgements of the evaluation factor according to the opinions of ten experts.

$$b_{ij} = \left(\alpha_{ij}, \beta_{ij}, \gamma_{ij}\right). \quad (5)$$

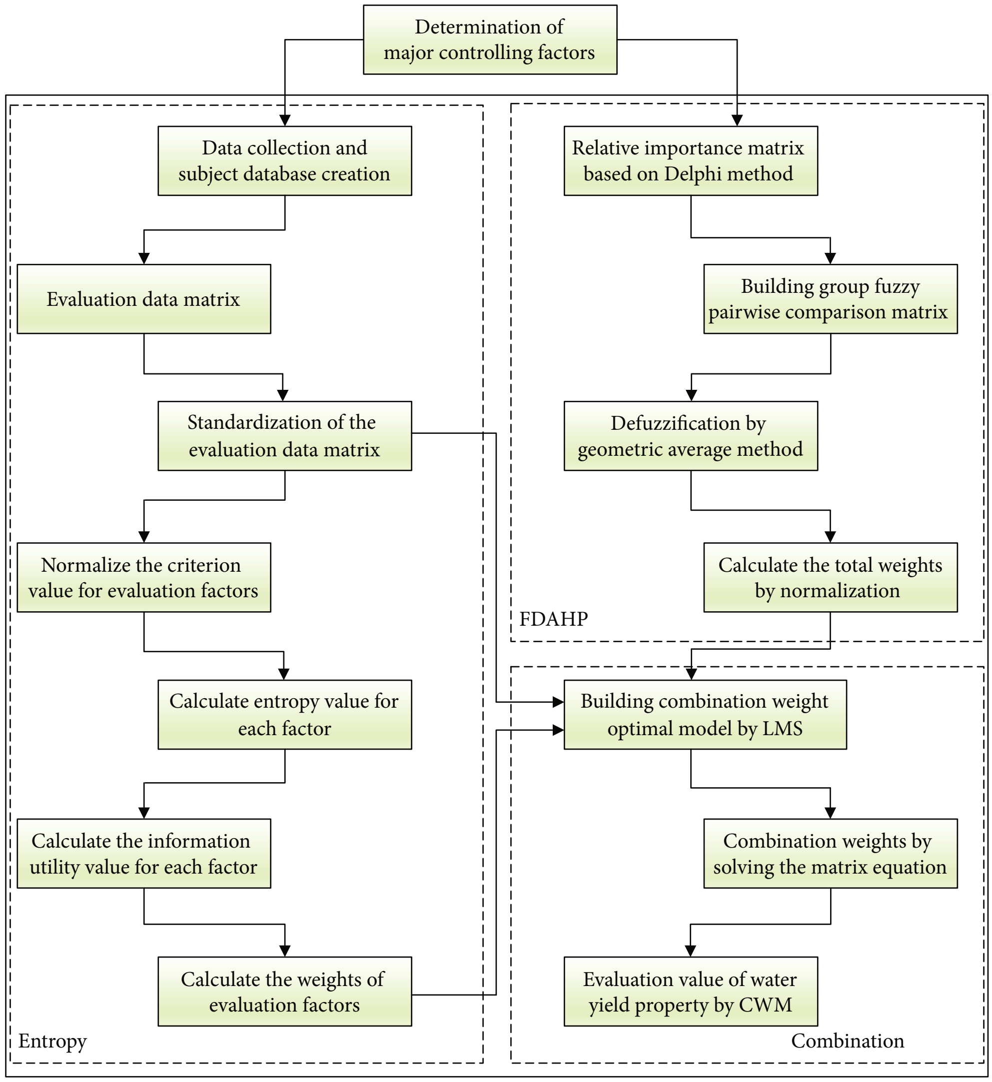

Figure 5: Flowchart of the methodology.

Table 1: Relative importance matrix of evaluation factors.

Factor	Expert 1 (E1)	Expert 2 (E2)	Expert 3 (E3)	Expert 4 (E4)	Expert 5 (E5)	Expert 6 (E6)	Expert 7 (E7)	Expert 8 (E8)	Expert 9 (E9)	Expert10 (E10)
Permeability coefficient (F1)	9	9	9	8	9	8	9	9	9	9
Consumption of drilling fluid (F2)	4	4	5	4	5	4	4	4	4	4
Core recovery (F3)	3	4	3	5	3	3	3	4	5	3
Aquifer thickness (F4)	8	8	7	8	7	9	7	8	7	7
Brittle-plastic rock thickness ratio (F4)	3	3	3	3	3	3	4	4	3	3
Fault scale index (F5)	4	4	4	4	5	4	4	3	4	5
Fault point density (F6)	3	2	3	2	2	3	3	2	2	3

$\alpha_{ij} \le \beta_{ij} \le \gamma_{ij}$, and they are obtained separately by Equations (6), (7), and (8). Furthermore, the established group fuzzy pairwise comparison matrix in this paper is shown in Table 2.

$$\alpha_{ij} = \min\left(b_{ijk}\right), \quad k = 1, 2, \cdots, p, \tag{6}$$

$$\beta_{ij} = \left(\prod_{k=1}^{m}\left(b_{ijk}\right)\right)^{1/m}, \quad k = 1, 2, \cdots, p, \tag{7}$$

$$\gamma_{ij} = \max\left(b_{ijk}\right), \quad k = 1, 2, \cdots, p. \tag{8}$$

Table 2: Group fuzzy pairwise comparison matrix.

	F1	F2	F3	F4	F5	F6	F7
F1	(1.00, 1.00, 1.00)	(1.80, 2.15, 2.25)	(1.80, 2.56, 3.00)	(1.13, 1.27, 1.50)	(2.25, 2.83, 3.00)	(1.80, 2.21, 3.00)	(3.00, 3.25, 4.50)
F2	(0.44, 0.46, 0.56)	(1.00, 1.00, 1.00)	(0.80, 1.19, 1.67)	(0.50, 0.59, 0.71)	(1.00, 1.32, 1.67)	(0.80, 1.03, 1.33)	(1.33, 1.51, 2.50)
F3	(0.33, 0.39, 0.56)	(0.60, 0.84, 1.25)	(1.00, 1.00, 1.00)	(0.38, 0.50, 0.83)	(0.75, 1.11, 1.67)	(0.60, 0.87, 1.33)	(1.00, 1.27, 2.50)
F4	(0.67, 0.78, 0.89)	(1.40, 1.69, 2.00)	(1.20, 2.01, 2.67)	(1.00, 1.00, 1.00)	(1.75, 2.26, 2.67)	(1.40, 1.77, 2.67)	(2.00, 2.59, 3.50)
F5	(0.33, 0.35, 0.44)	(0.60, 0.76, 1.00)	(0.60, 0.90, 1.33)	(0.38, 0.44, 0.57)	(1.00, 1.00, 1.00)	(0.60, 0.76, 1.00)	(1.00, 1.12, 1.50)
F6	(0.33, 0.45, 0.56)	(0.75, 0.97, 1.25)	(0.75, 1.15, 1.67)	(0.38, 0.57, 0.71)	(1.00, 1.32, 1.67)	(1.00, 1.00, 1.00)	(1.00, 1.47, 2.50)
F7	(0.22, 0.31, 0.33)	(0.40, 0.66, 0.75)	(0.40, 0.79, 1.00)	(0.29, 0.39, 0.50)	(0.67, 0.90, 1.00)	(0.40, 0.68, 1.00)	(1.00, 1.00, 1.00)

In the following defuzzification process, the geometric average method is applied to acquire the relative fuzzy weights for each factor. The group fuzzy weight vector and the fuzzy weights vector are determined by calculating Equations (9) and (10) successively.

$$r_i = (a_{i1} \otimes a_{i2} \otimes \cdots \otimes a_{in})^{1/n}, \tag{9}$$

$$w_i = r_i \otimes (r_1 \otimes r_2 \otimes \cdots \otimes r_n)^{-1}. \tag{10}$$

The two triangular fuzzy numbers $[a_1, a_2, a_3]$ and $[b_1, b_2, b_3]$ are calculated using

$$a \oplus b = [a_1 + b_1, a_2 + b_2, a_3 + b_3], \tag{11}$$

$$a \otimes b = [a_1 \times b_1, a_2 \times b_2, a_3 \times b_3], \tag{12}$$

$$a^{-1} = \left[a3^{-1}, a2^{-1}, a1^{-1}\right]. \tag{13}$$

Finally, the weights for each evaluation factor were obtained by the normalization of the fuzzy weight vector (w_i^L, w_i^M, w_i^N) by calculating Equation (14), and the results are shown in Table 3.

$$Ui = \frac{\left(w_i^L \times w_i^M \times w_i^N\right)^{1/3}}{\sum_{i=1}^{m} \left(w_i^L \times w_i^M \times w_i^N\right)^{1/3}}. \tag{14}$$

4.2.2. Objective Weights by the EWM. As a quantitative objective weighting method, the EWM can determine the factor weights according to the degree of variation in the major controlling factors by using information entropy to measure the uncertainty and heterogeneity of the factor value distribution.

For a certain factor value, the uneven distribution usually shows a significant difference in heterogeneity and manifests as a higher entropy but a lower entropy weight. Therefore, the existing objective criteria for weighting could avoid the influence of subjective factors as much as possible.

To obtain information entropy for each evaluation factor by the EWM [34], the standardized matrix Y_{ij} was established and expressed as Equation (15), which consisted of standardized data with 5787 evaluation units from united spatial thematic data of 7 evaluation factors calculated by Equations (2) and (3). Thus, $i = 1, 2, 3, \cdots, 5787$, and $j = 1, 2, 3, \cdots, 7$ in this paper.

Table 3: Calculated group fuzzy weights and total weights by the FDAHP.

Evaluation factors	Group fuzzy weights	Total weights
F1	(0.1796, 0.2663, 0.3866)	0.2647
F2	(0.0824, 0.1237, 0.1971)	0.1263
F3	(0.0644, 0.1041, 0.1934)	0.1092
F4	(0.1333, 0.2104, 0.3236)	0.2088
F5	(0.0624, 0.0930, 0.1486)	0.0953
F6	(0.0715, 0.1205, 0.1953)	0.1191
F7	(0.0449, 0.0820, 0.1216)	0.0766

$$Y = \left[Y_{ij}\right] = \begin{bmatrix} y_{11} & y_{12} & \cdots & y_{17} \\ y_{21} & y_{22} & \cdots & y_{27} \\ \vdots & \vdots & \ddots & \vdots \\ y_{57871} & y_{57872} & \cdots & y_{57877} \end{bmatrix}. \tag{15}$$

Then, Y_{ij} was normalized to calculate the projected outcome P_{ij} of the j^{th} factor by

$$P_{ij} = \frac{Y_{ij}}{\sum_{i=1}^{m} Y_{ij}}. \tag{16}$$

Then, the information entropy E_j could be defined as Equation (17), as shown in Table 4.

$$E_j = -(\ln m)^{-1} \sum_{i=1}^{m} P_{ij} \ln P_{ij}. \tag{17}$$

The diversification degree of information based on the j^{th} factor value d_j could be expressed as $d_j = 1 - E_j$, and the entropy weights of each factor were calculated by following Equation (18) and are shown in Table 4.

$$V_j = \frac{d_j}{\sum_{j=1}^{n} d_j}. \tag{18}$$

4.2.3. Total Weights by the CWM. Whereas the a priori weighting method FDAHP can provide subjective weights by considering the fuzziness of the evaluation process by group decision-making, and the EWM can determine the objective assessment with good stability upon attribute preference, the combination weight model (CWM) based on the optimization method is proposed in this paper. In situations that consider both the experience of a group of experts and the objective datum situation, the CWM can provide practical and reasonable weights.

The judgement basis of the CWM can be expressed as follows: the total deviation between the FDAHP calculations and the EWM result should be as small as possible. Therefore, the optimization model that applies the least square method to combine the subjective weight of a group of experts u_j with the objective entropy weight v_j is established as [35]

$$\min\ D(w)=\sum_{i=1}^{m}\sum_{j=1}^{n}\left\{\left[\left(u_j-w_j\right)Y_{ij}\right]^2+\left[\left(v_j-w_j\right)Y_{ij}\right]^2\right\}, \tag{19}$$

$$\text{s.t.}\quad \sum_{j=1}^{n} w_j=1, \tag{20}$$

$$w_j>0. \tag{21}$$

Furthermore, the CWM optimization model can be expressed as Equation (22) by the Lagrangian transformation.

$$\begin{bmatrix} A & e \\ e^T & 0 \end{bmatrix}\times\begin{bmatrix} w_j \\ \lambda \end{bmatrix}=\begin{bmatrix} B \\ 1 \end{bmatrix}. \tag{22}$$

The diagonal matrix A and the vector matrices e, W, and B are defined as Equations (23) to (26), respectively.

$$A=\operatorname{diag}\left[\sum_{i=1}^{m}Y_{i1}^2, \sum_{i=1}^{m}Y_{i2}^2,\cdots,\sum_{i=1}^{m}Y_{\text{in}}^2\right], \tag{23}$$

$$e=[1,1,\cdots,1]^T, \tag{24}$$

$$w_j=[w_1,w_2,\cdots,w_n]^T, \tag{25}$$

$$B=\left[\sum_{i=1}^{m}\frac{1}{2}(u_1+v_1)Y_{i1}^2, \sum_{i=1}^{m}\frac{1}{2}(u_2+v_2)Y_{i2}^2,\cdots,\sum_{i=1}^{m}\frac{1}{2}(u_n+v_n)Y_{\text{in}}^2\right]^T. \tag{26}$$

In this paper, the 7×7 matrix A was established by calculating the square sum of each factor, as shown by Equation (27), and the subjective weight u_j in Equation (26) was obtained from the FDAHP weighting process, while the objective weight v_j was acquired based on the measured information entropy of controlling factors by the EWM method.

$$A=\begin{bmatrix} 1661.2474 & 0 & 0 & 0 & 0 & 0 & 0 \\ 0 & 755.0315 & 0 & 0 & 0 & 0 & 0 \\ 0 & 0 & 1585.8033 & 0 & 0 & 0 & 0 \\ 0 & 0 & 0 & 547.9346 & 0 & 0 & 0 \\ 0 & 0 & 0 & 0 & 1310.3613 & 0 & 0 \\ 0 & 0 & 0 & 0 & 0 & 445.8467 & 0 \\ 0 & 0 & 0 & 0 & 0 & 0 & 1097.3887 \end{bmatrix}. \tag{27}$$

Finally, the CWM weights were acquired by calculating Equation (28), and the combination weight 5787 coupling of the subjective weight u_j and objective entropy weight v_j is shown in Table 5.

$$W_j=A^{-1}\times\left[B+\frac{1-e^TA^{-1}B}{e^TA^{-1}e}\times e\right]. \tag{28}$$

4.3. Evaluation of the IWYPI Model. The distribution of the aquifer water yield is controlled by a combination of factors; therefore, the comprehensive analysis of multisource information is considered to be the best method to evaluate the water yield of coal roof aquifers [36–38]. Based on the statistical values of 7 influencing factors of 36 boreholes in the northern no. 2 mining area and central mining area of the Donghuantuo Coal Mine, this paper first standardizes these factors and then applies the spatial information processing and analysis function of GIS to integrate the information of the 7 factors affecting the aquifer water yield.

On this basis, combined with the CWM composed of the FDAHP and EWM, an IWYPI model is established by adding linear weights to quantitatively describe the comprehensive influence of aquifer lithology, aquifer hydraulic properties, and fault characteristics of different weight combinations on the aquifer water yield. The calculation formula is shown by

$$\mathrm{WI}=\sum_{j=1}^{n}W_j * f_j(x,y). \tag{29}$$

Table 4: The entropy and entropy weights of evaluation factors.

Factor	F1	F2	F3	F4	F5	F6	F7
Entropy E	0.9841	0.9446	0.9715	0.9749	0.9788	0.9118	0.9752
Entropy weight V	0.0615	0.2137	0.1101	0.0967	0.0819	0.3405	0.0956

Table 5: The calculated weights of evaluation factors by the FDAHP, EWM, and CWM.

Factor	F1	F2	F3	F4	F5	F6	F7
FDAHP weight U	0.2647	0.1263	0.1092	0.2088	0.0953	0.1191	0.0766
Entropy weight V	0.0615	0.2137	0.1101	0.0967	0.0819	0.3405	0.0956
Combination weight W	0.1631	0.1701	0.1096	0.1527	0.0886	0.2298	0.0861

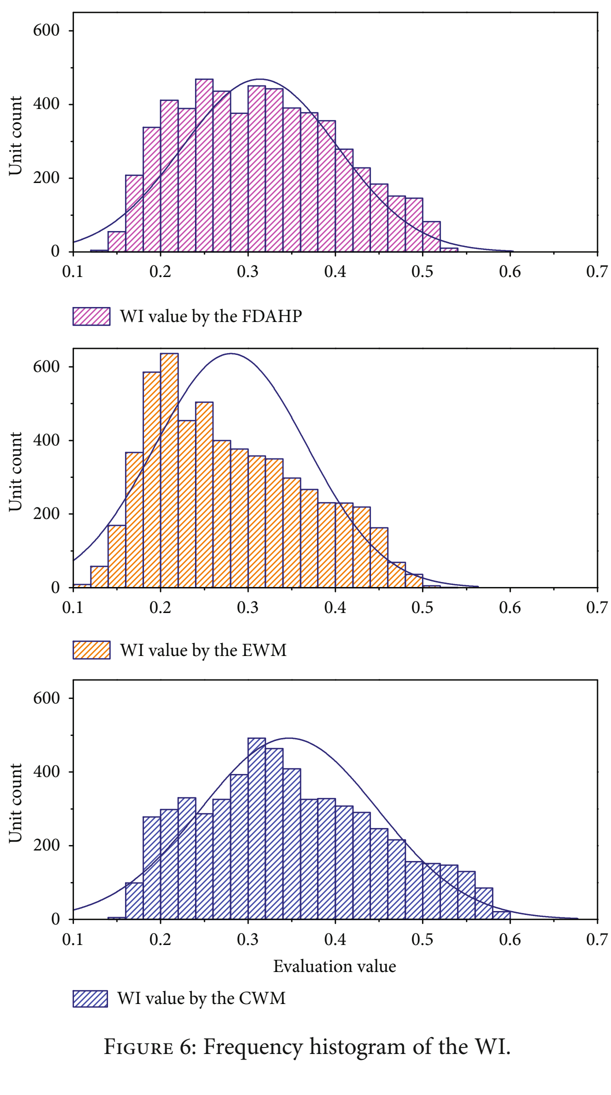

Figure 6: Frequency histogram of the WI.

where WI is the aquifer water yield property index; j is the factor number; n is the number of factors, which is 7 in this paper; W_j is the weight value of the j^{th} factor; $f_j(x, y)$ is the standard value of the j^{th} factor; and (x, y) are geographic coordinates.

The IWYPI model in this paper is established according to Equation (29) and shown as Equation (30). Correspondingly, the water yield property index (WYPI) model weighted by the FDAHP and EWM can also be calculated by Equation (29).

$$\begin{aligned} \mathrm{WI} = {} & 0.1631 * f_1(x, y) + 0.1701 * f_2(x, y) \\ & + 0.1096 * f_3(x, y) + 0.1527 * f_4(x, y) \\ & + 0.0086 * f_5(x, y) + 0.2298 * f_6(x, y) \\ & + 0.0861 * f_7(x, y). \end{aligned} \tag{30}$$

5. Results and Discussion

5.1. Results. According to the IWYPI and WYPI models, which have different weighting methods, the water yield zoning maps of the roof sandstone aquifer of the no. 8 coal seam are constructed by using GIS spatial superposition and reclassification functions, and a frequency histogram of WI values calculated by the three methods is acquired (Figure 6). As shown in Figures 7–9, there are differences in the evaluated WI values calculated from the different methods, with a larger value indicating a higher water yield. The WI values calculated by the FDAHP are 0.1549~0.5941, the WI values calculated by the EWM are 0.1131~0.5216, and the WI values calculated by the CWM are 0.1357~0.5271. Furthermore, the corresponding classification thresholds of WI values for four levels are determined by the natural break algorithm embedded in the GIS classification method. Therefore, the least square sum of the WI value and corresponding mean value are obtained by iterative grouping for determining thresholds. According to the classification threshold (Table 6), the water yield is divided into the following zones: poor, medium, rich, and richer; the distribution of partitions for each evaluation result is shown in Figures 7–9.

As shown in Figures 7–9, the overall trends of the results of the evaluation of the aquifer water yield by the three methods are consistent. The results are also cross-verified, which indicates that the water yield of the sandstone aquifer in the no. 8 coal seam roof in the Donghuantuo Mine ranges from poor to richer, among which the rich and richer zones are mainly distributed in the southern and middle regions, the medium zones are mainly distributed in the northern and middle regions, and the poor zones are mainly distributed in the northeast and central and western regions. As shown in Figures 4(a)–4(g), the difference in the water yield in the study area is mainly related to the aquifer permeability

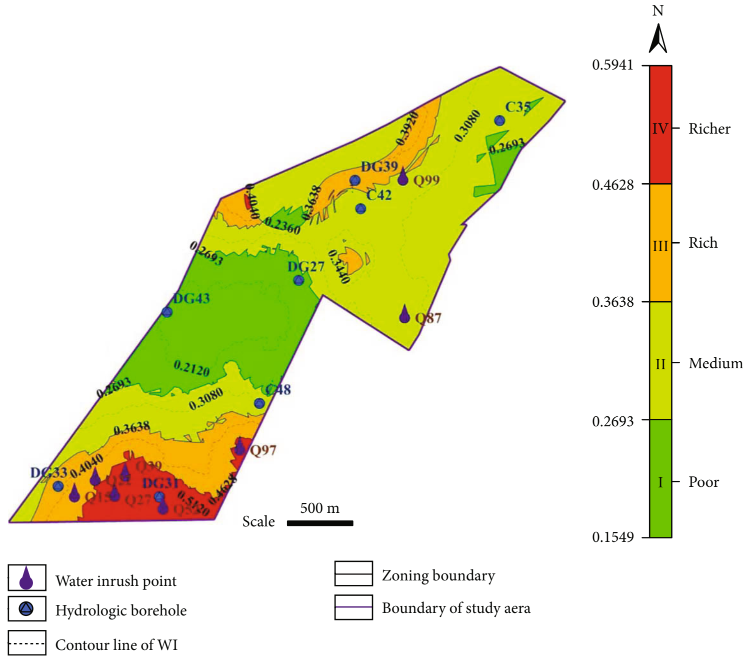

Figure 7: Water yield zoning map based on the WYPI model weighted by the FDAHP.

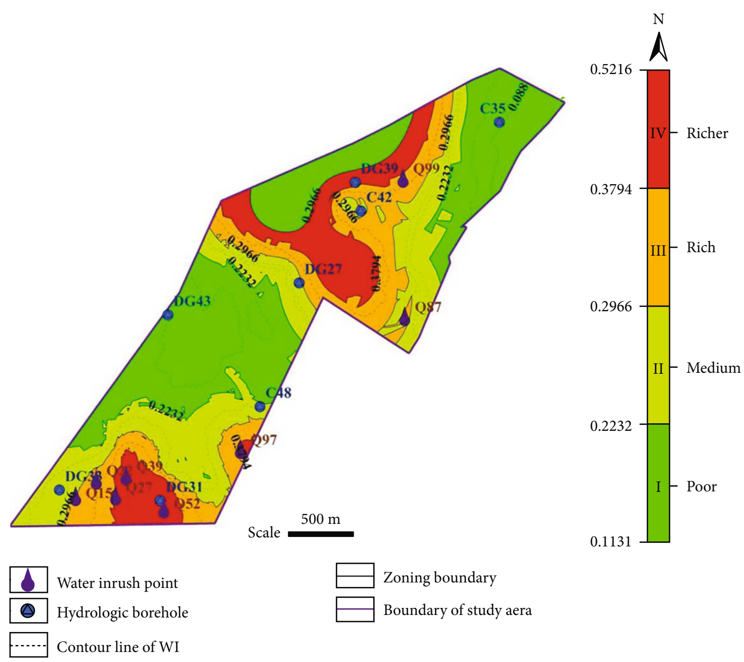

Figure 8: Water yield zoning map based on the WYPI model weighted by the EWM.

coefficient, thickness, and fault development, and the water yield in the zones with high values of these factors is relatively high. For example, the permeability coefficient and consumption of drilling fluid in the southern part of the study area are high, so the evaluation results of the three methods in the south indicate zones with rich-richer water yields. The fault scale index and fault point density in the middle of the study area are high, and the evaluation results of the middle of the study area by the three methods indicate medium-richer water yields. In contrast, except for the ratio of the brittle-to-plastic rock thickness, the water yield in areas with low index values is relatively poor, such as in the central and western regions of the study area, and the evaluation results of the three methods indicate zones with poor water yields.

5.2. Engineering Practice. According to the Regulations for Coal Water Prevention and Control in China [39], the theoretical evaluation of the aquifer water yield is based on a unit of water inflow (represented by q); however, the pumping test

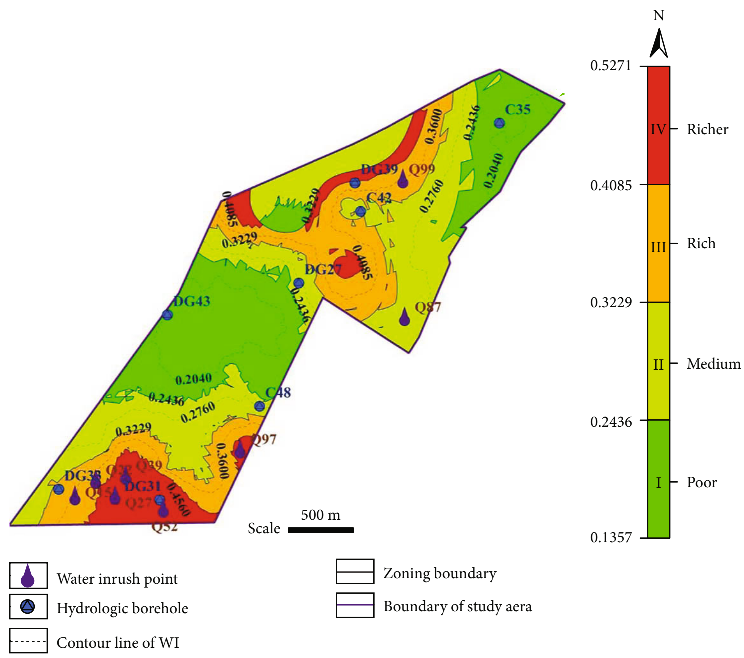

FIGURE 9: Water yield zoning map based on the IWYPI model weighted by the CWM.

TABLE 6: Classification thresholds of WI values by the FDAHP, EWM, and CWM.

Partition code	Water yield zone	WI value by the FDAHP	WI value by the EWM	WI value by the CWM
Zone I	Poor	0.1549-0.2693	0.1131-0.2232	0.1357-0.2436
Zone II	Medium	0.2694-0.3638	0.2233-0.2966	0.2437-0.3229
Zone III	Rich	0.3639-0.4628	0.2967-0.3794	0.3230-0.4085
Zone IV	Richer	Greater than 0.4628	Greater than 0.3794	Greater than 0.4085

TABLE 7: Specified and revised classification standard for the water yield.

	Specified level	Specified q ($L{\cdot}s^{-1}{\cdot}m^{-1}$)		Partition code	Revised level	Revised q ($L{\cdot}s^{-1}{\cdot}m^{-1}$)	Q ($m^3{\cdot}min^{-1}$)
Specified classification standard	Weak	$q \leq 0.1$	Revised classification standard	Zone I	Poor	$q \leq 0.1$	$Q < 0.2$
	Medium	$0.1 < q \leq 1.0$		Zone II	Medium	$0.1 < q \leq 1.0$	$0.2 \leq q < 1.0$
	Rich	$1.0 < q \leq 5.0$		Zone III	Rich	$1.0 < q \leq 1.5$	$1.0 \leq q < 2.0$
				Zone IV	Richer	$q > 1.5$	$q \geq 2.0$
	Extremely rich	$q > 5.0$		—	—	—	—

boreholes in the coalfield are generally limited in number and unevenly distributed. It is difficult to scientifically and reasonably divide the water yield of the aquifer by the q value. Therefore, the FDAHP, EWM, and CWM methods were used to establish a multisource geoscience information fusion WYPI model and an IWYPI model, which provide the more comprehensive scientific basis for the evaluation of the aquifer water yield.

Validation is the key to verifying results [40, 41]. The unit water inflow of the pumping test boreholes (represented by q) can directly indicate the water yield of aquifers. When data on the unit water inflow of the borehole are lacking, the inflow of the water inrush point (represented by Q) can also be used as the direct basis of the aquifer water yield. Therefore, the q and Q values are reliable bases to verify the evaluation results of different methods.

The q value can be divided into four grades (Table 7), poor, medium, rich, and extremely rich, according to the Regulations for Coal Water Prevention and Control in China. According to Table 7, the q values of 8 boreholes in the sandstone aquifer of the no. 8 coal roof in the study area are analysed. Among these q values, the boreholes with a medium water yield account for 50%, and the boreholes with both poor and rich water yields account for 25%; the maximum q value of the boreholes is $1.806\,L{\cdot}s^{-1}{\cdot}m^{-1}$, which is a rich water yield, and no boreholes with extremely rich water yields are found. To make the evaluation results of water yield zoning more convenient for conducting mine water

Table 8: Validation between the evaluation results and actual results.

Type and no. of verification case		Name	Measured q ($L{\cdot}s^{-1}{\cdot}m^{-1}$)	Measured Q ($m^3{\cdot}min^{-1}$)	Actual Judgment	WYPI result by the FDAHP		WYPI result by the EWM		IWYPI result by the CWM	
Hydrologic borehole	1	C35	0.086	—	I	II	Disagree	I	Agree	I	Agree
	2	DG39	0.110	—	II	III	Disagree	IV	Disagree	III	Disagree
	3	C42	0.143	—	II	II	Agree	II	Agree	II	Agree
	4	DG27	0.183	—	II	I	Disagree	II	Agree	II	Agree
	5	DG43	0.018	—	I	I	Agree	I	Agree	I	Agree
	6	C48	0.610	—	II	II	Agree	II	Agree	II	Agree
	7	DG33	1.222	—	III	III	Agree	II	Disagree	III	Agree
	8	DG31	1.806	—	IV	IV	Agree	IV	Agree	IV	Agree
Water inrush point	9	Q99	—	1.80	III	II	Disagree	III	Agree	III	Agree
	10	Q87	—	0.90	II	II	Agree	III	Disagree	II	Agree
	11	Q97	—	2.00	IV	IV	Agree	IV	Agree	IV	Agree
	12	Q15	—	1.02	III	III	Agree	III	Agree	III	Agree
	13	Q22	—	1.00	III	III	Agree	III	Agree	III	Agree
	14	Q39	—	4.57	IV	IV	Agree	IV	Agree	IV	Agree
	15	Q52	—	4.00	IV	IV	Agree	IV	Agree	IV	Agree
	16	Q27	—	3.19	IV	IV	Agree	IV	Agree	IV	Agree

prevention and control work in the Donghuantuo Coal Mine, the rich water yields can be further subdivided, that is, the rich water yield ($1{\sim}5\,L{\cdot}s^{-1}{\cdot}m^{-1}$) in the "Regulations" can be further divided into rich ($1{\sim}1.5\,L{\cdot}s^{-1}{\cdot}m^{-1}$) and richer ($1.5{\sim}2\,L{\cdot}s^{-1}{\cdot}m^{-1}$) water yields, as shown in Table 7. The revised classification standard of the water yield is suitable for the Donghuantuo Coal Mine. In the actual coal mining project of the Donghuantuo Coal Mine, the Q value is used to classify the water yield by taking the maximum inflow of each water inrush point in the Donghuantuo Mine in the last 10 years as the classification basis (Table 7).

Therefore, to verify the accuracy of the evaluation results of the FDAHP, EWM, and CWM, the evaluation results are compared with the actual engineering data, and a verification test is carried out. A total of 16 engineering test samples were collected, including 8 water inrush points and the q values of 8 boreholes in the Permian sandstone aquifer, and the evaluation results were tested. The evaluation results of these three methods and the actual results of 18 test samples are shown in Table 8. The results show that the coincidence degrees of the evaluation results of the FDAHP, EWM, and CWM with the actual results are 75%, 81.25%, and 93.75%, respectively; that is, the accuracy of the CWM is the highest.

6. Discussion

Through the verification of the evaluation results of the three methods, the evaluation ability of the CWM is the best, and its correctness percentage is as high as 93.75%, which is 18.75% and 12.5% higher than that of the FDAHP and EWM, respectively. The results of the FDAHP, EWM, and CWM are compared to determine the differences among the three evaluation methods. There are differences in the proportional area of each water yield grade evaluated by different methods (Figure 10).

According to the proportional area of each water yield grade from small to large, the water yields evaluated by the FDAHP and CWM are IV, III, I, and II, and the water yield grades evaluated by the EWM are IV, III, II, and I. This shows that the proportional area evaluated by the EWM for the poor water yield is relatively large, while for rich and richer water yields, which more easily cause water disasters in coal seam roofs, the proportional areas calculated by the FDAHP, EWM, and CWM are 24.19%, 33.95%, and 33.56%, respectively; this indicates that the proportional areas evaluated by the FDAHP for the rich and richer water yield areas are relatively small. Two main reasons account for these differences: (1) the FDAHP focuses on the influence of hydraulic properties of aquifers on the water yield and underestimates the influence of fault development characteristics on the water yield. For example, water inrush point Q99 is located in the fault development area and is affected by normal fault DF25 with a fault distance of 9 m. The aquifer fissure at this point is developed, with the water inflow reaching $1.8\,m^3{\cdot}min^{-1}$ and the aquifer having a rich water yield. However, the FDAHP classifies it as a medium water yield, which is inconsistent with the actual situation. (2) The EWM overemphasizes the difference in fault development characteristics in the study area but weakens the important influence of the aquifer permeability coefficient and thickness on the water yields. For example, the q value of the DG33 borehole is $1.22\,L{\cdot}s^{-1}{\cdot}m^{-1}$, and the sandstone aquifer where it is located is 60 m thick, with a permeability coefficient of $2.2\,m{\cdot}d^{-1}$, which is a rich water yield. It is unreasonable to characterize it as a medium water yield based on the EWM. Thus, the CWM takes into account both the recommendations of the experts and the internal relations among various

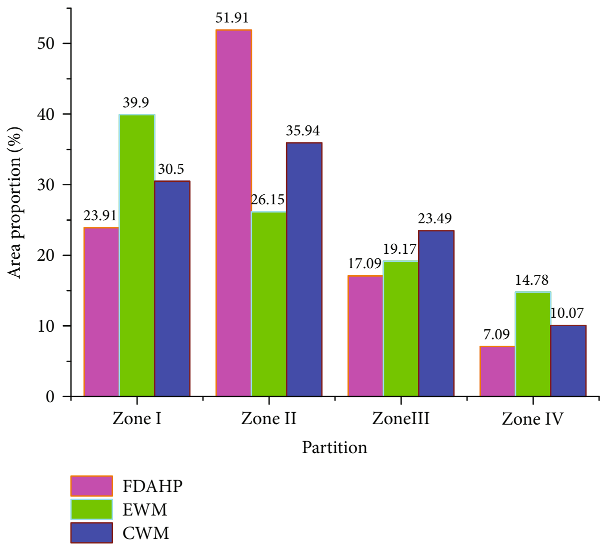

Figure 10: The proportional area of partition types for different results.

factors of the water yield; the CWM effectively reflects the joint control of the aquifer lithology, hydraulic characteristics, and fault factors on the water yield of the sandstone aquifer of the no. 8 coal seam roof in the study area, making the evaluation results more closely follow reality; moreover, the CWM can analyse the water yield characteristics of the coal seam roof more reasonably and accurately.

7. Conclusions

(1) Aquifers with rich and richer water yields provide the material source for water disasters in coal seam roofs, and they are also a prominent problem threatening the safe production of coal seams. It is necessary but challenging to evaluate the water yield of coal roof aquifers. The IWYPI model of coal roof aquifers is proposed and applied to evaluate the water yield of the sandstone aquifer in the no. 8 coal seam roof in the Donghuantuo Coal Mine. The factors that affect the water yield are the permeability coefficient, consumption of drilling fluid, core recovery, aquifer thickness, brittle-plastic rock thickness ratio, fault scale index, and fault point density. The IWYPI model established by the CWM takes into account the internal relations between the opinions of experts and various factors influencing the water yield; this model effectively reflects the common control of aquifer lithology, hydraulic characteristics, and fault factors on the aquifer water yield and overcomes the problem that there are generally limited amounts of water inflow data for boreholes in mines

(2) Engineering practice shows that the accuracy of the IWYPI model based on the CWM is as high as 93.75%, which is 18.75% and 12.5% higher than that of the WYPI model based on the FDAHP and EWM, respectively. The evaluation results show that the zones with rich and richer water yields are mainly distributed in the southern and middle regions, the zones with medium water yields are mainly distributed in the northern and middle regions, and the zones with poor water yields are mainly distributed in the northeast, central, and western regions. The IWYPI model provides favourable technical support for the prevention and control of water disasters in coal seam roofs and has important practical significance for ensuring safe coal mine production.

Data Availability

The data that support the findings of this study are available from the corresponding author upon reasonable request.

Conflicts of Interest

The authors declare no conflict of interest.

Acknowledgments

This study is financially supported by the National Natural Science Foundation of China (Granted No. 41702264), National Key Research and Development Program of China (2016YFC0402803-02), and China Three Gorges Group Co., Ltd. Project (0799217).

References

[1] S. N. Dong, L. W. Zheng, S. L. Tang, and P. Z. Shi, "A scientometric analysis of trends in coal mine water inrush prevention and control for the period 2000–2019," *Mine Water and the Environment*, vol. 39, no. 1, pp. 3–12, 2020.

[2] W. Qiang, L. Yuanzhang, and Y. Liu, "Using the vulnerable index method to assess the likelihood of a water inrush through the floor of a multi-seam coal mine in China," *Mine Water and the Environment*, vol. 30, no. 1, pp. 54–60, 2011.

[3] B. Li, X. Q. Wang, Z. J. Liu, and T. Li, "Study on multi-field catastrophe evolution laws of water inrush from concealed karst cave in roadway excavation: a case of Jiyuan coal mine," *Geomatics, Natural Hazards and Risk*, vol. 12, no. 1, pp. 222–243, 2021.

[4] H. F. Duan and L. J. Zhao, "New evaluation and prediction method to determine the risk of water inrush from mining coal seam floor," *Environmental Earth Sciences*, vol. 80, no. 1, 2021.

[5] Y. Zeng, Q. Wu, S. Liu, Y. Zhai, H. Lian, and W. Zhang, "Evaluation of a coal seam roof water inrush: case study in the Wangjialing coal mine, China," *Mine Water and the Environment*, vol. 37, pp. 174–184, 2018.

[6] S. Chen, D. Yin, F. Cao, Y. Liu, and K. Ren, "An overview of integrated surface subsidence-reducing technology in mining areas of China," *Natural Hazards*, vol. 81, no. 2, pp. 1129–1145, 2016.

[7] J. W. LaMoreaux, Q. Wu, and Z. Wanfang, "New development in theory and practice in mine water control in China," *Carbonates and Evaporites*, vol. 29, no. 2, pp. 141–145, 2014.

[8] H. Yin, Y. Shi, H. Niu et al., "A GIS-based model of potential groundwater yield zonation for a sandstone aquifer in the Juye Coalfield, Shangdong, China," *Journal of Hydrology*, vol. 557, pp. 434–447, 2018.

[9] Y. F. Zeng, Q. Wu, X. Du et al., “Further research on 'water-richness index method' for evaluation of aquifer water abundance,” *Journal of China Coal Society*, vol. 45, no. 7, pp. 2423–2431, 2020.

[10] S. P. Neuman, “On methods of determining specific yield,” *Ground Water*, vol. 25, no. 6, pp. 679–684, 1987.

[11] W. C. Walton and C. F. McLane, “Aspects of groundwater supply sustainable yield,” *Ground Water*, vol. 51, no. 2, pp. 158–160, 2013.

[12] H. Nampak, B. Pradhan, and M. A. Manap, “Application of GIS based data driven evidential belief function model to predict groundwater potential zonation,” *Journal of Hydrology*, vol. 513, pp. 283–300, 2014.

[13] P. Sander, M. M. Chesley, and T. B. Minor, “Groundwater assessment using remote sensing and GIS in a rural groundwater project in Ghana: lessons learned,” *Hydrogeology Journal*, vol. 4, no. 3, pp. 40–49, 1996.

[14] R. Dhakate, D. K. Chowdhary, V. V. S. Gurunadha Rao, R. K. Tiwary, and A. Sinha, “Geophysical and geomorphological approach for locating groundwater potential zones in Sukinda chromite mining area,” *Environmental Earth Sciences*, vol. 66, no. 8, pp. 2311–2325, 2012.

[15] Y. LI, J. YANG, Z. PAN, S. MENG, K. WANG, and X. NIU, “Unconventional natural gas accumulations in stacked deposits: a discussion of upper Paleozoic coal-bearing strata in the east margin of the Ordos basin, China,” *Acta Geologica Sinica - English Edition*, vol. 93, no. 1, pp. 111–129, 2019.

[16] Y. Li, D. Z. Tang, X. Hao, D. Elsworth, and Y. J. Meng, “Geological and hydrological controls on water coproduced with coalbed methane in Liulin, eastern Ordos basin, China,” *AAPG Bulletin*, vol. 99, no. 2, pp. 207–229, 2015.

[17] Y. Li, Y. B. Wang, J. Wang, and Z. J. Pan, “Variation in permeability during CO_2-CH_4 displacement in coal seams: part 1 - experimental insights,” *Fuel*, vol. 263, article 116666, 2020.

[18] M. Qiu, F. J. Huang, Y. Wang, and T. Guan, “Prediction model of water yield property based on GRA, FAHP and TOPSIS methods for Ordovician top aquifer in the Xinwen coalfield of China,” *Environmental Earth Sciences*, vol. 79, no. 10, 2020.

[19] Q. Wu, Z. L. Fan, S. Q. Liu, Y. W. Zhang, and W. J. Sun, “Water-richness evaluation method of water-filled aquifer based on the principle of information fusion with GIS: water-richness index method,” *Journal of China Coal Society*, vol. 36, no. 7, pp. 1124–1128, 2011.

[20] T. L. Saaty, *The Analytic Hierarchy Process: Planning, Priority Setting, Resource Allocation*, McGraw-Hill, New York, USA, 1980.

[21] L. Q. Shi, M. Qiu, Y. Wang, X. Qu, and T. Liu, “Evaluation of water inrush from underlying aquifers by using a modified water-inrush coefficient model and water-inrush index model: a case study in Feicheng coalfield, China,” *Hydrogeology Journal*, vol. 27, no. 6, pp. 2105–2119, 2019.

[22] Q. Wu, K. Xu, W. Zhang, and Z. Wei, “Roof aquifer water abundance evaluation: a case study in Taigemiao, China,” *Arabian Journal of Geosciences*, vol. 10, no. 11, 2017.

[23] H. J. Gong, S. L. Liu, and Y. F. Zeng, “Evaluation researchon water-richness of aquifer based on BP artificial neural network,” *Coal Technology*, vol. 37, no. 9, pp. 181-182, 2018.

[24] L. M. Fan, L. Q. Ma, Y. H. Yu, S. Wang, and Y. Xu, “Water-conserving mining influencing factors identification and weight determination in northwest China,” *International Journal of Coal Science and Technology*, vol. 6, no. 1, pp. 95–101, 2019.

[25] W. Zhai, W. Li, Y. Huang et al., “A case study of the water abundance evaluation of roof aquifer based on the development height of water-conducting fracture zone,” *Energies*, vol. 13, no. 16, p. 4095, 2020.

[26] L. L. Xiao, Q. Wu, C. Niu et al., “Application of a new evaluation method for floor water inrush risk from the Ordovician fissure confined aquifer in Xiayukou coal mine, Shanxi, China,” *Carbonates and Evaporites*, vol. 35, no. 3, 2020.

[27] Y. Li and M. Song, “Coal mine safety evaluation with V-fold cross-validation and BP neural network,” *Journal of Computers*, vol. 5, no. 9, 2010.

[28] Y. Wang, W. F. Yang, M. Li, and X. Liu, “Risk assessment of floor water inrush in coal mines based on secondary fuzzy comprehensive evaluation,” *International Journal of Rock Mechanics and Mining Sciences*, vol. 52, pp. 50–55, 2012.

[29] B. Li, Q. Wu, and Z. Liu, “Identification of mine water inrush source based on PCA-FDA: Xiandewang coal mine case,” *Geofluids*, vol. 2020, Article ID 2584094, 8 pages, 2020.

[30] W. T. Liu, Q. Li, J. Y. Zhao, and B. Fu, “Assessment of water inrush risk using the principal component logistic regression model in the Pandao coal mine, China,” *Arabian Journal of Geosciences*, vol. 11, no. 16, 2018.

[31] H. S. Tian, Y. Q. Hong, and Y. J. Ma, “Hydrogeology characteristics and measures of water prevention in Donghuantuo mine in Kailuan,” *Ground Water*, vol. 31, no. 3, pp. 110–113, 2009.

[32] Z. Yang, W. P. Li, J. H. He, and Y. Liu, “An assessment of water yield properties for weathered bedrock zone in Northern Shaanxi Jurassic coalfield: a case study in Jinjitan coal mine, Western China,” *Arabian Journal of Geosciences*, vol. 12, no. 23, 2019.

[33] M. Hayaty, M. R. Tavakoli Mohammadi, A. Rezaei, and M. R. Shayestehfar, “Risk assessment and ranking of metals using FDAHP and TOPSIS,” *Mine Water and the Environment*, vol. 33, no. 2, pp. 157–164, 2014.

[34] X. Li, “Topsis model with entropy weight for eco geological environmental carrying capacity assessment,” *Microprocessors and Microsystems*, vol. 82, article 103805, 2021.

[35] E. Hou, Z. Ji, X. Che et al., “Water abundance prediction method of weathered bedrock based on improved AHP and the entropy weight method,” *Journal of China Coal Society*, vol. 44, no. 10, pp. 3164–3173, 2019.

[36] I. Chenini, A. B. Mammou, and M. el May, “Groundwater recharge zone mapping using GIS–based multi-criteria analysis: a case study in Central Tunisia (Maknassy Basin),” *Water Resources Management*, vol. 24, no. 5, pp. 921–939, 2010.

[37] N. S. Magesh, N. Chandrasekar, and J. P. Soundranayagam, “Delineation of groundwater potential zones in Theni district, Tamil Nadu, using remote sensing, GIS and MIF techniques,” *Geoscience Frontiers*, vol. 3, no. 2, pp. 189–196, 2012.

[38] I. Park, Y. Kim, and S. Lee, “Groundwater productivity potential mapping using evidential belief function,” *Groundwater*, vol. 52, no. S1, pp. 201–207, 2014.

[39] State Administration of Work Safety, State Administration of Coal Mine Safety, *Regulations for Mine Water Prevention and Control*, China Coal Industry Publishing House, Beijing, China, 2009.

[40] K. A. N. Adiat, M. N. M. Nawawi, and K. Abdullah, "Assessing the accuracy of GIS-based elementary multi criteria decision analysis as a spatial prediction tool - a case of predicting potential zones of sustainable groundwater resources," *Journal of Hydrology*, vol. 440-441, pp. 75–89, 2012.

[41] W. J. Guo, J. H. Zhao, L. M. Yin, and D. Kong, "Simulating research on pressure distribution of floor pore water based on fluid-solid coupling," *Arabian Journal of Geosciences*, vol. 10, no. 1, 2017.

Hindawi
Geofluids
Volume 2021, Article ID 5533945, 12 pages
https://doi.org/10.1155/2021/5533945

Research Article

CO_2-Driven Hydraulic Fracturing Trajectories across a Preexisting Fracture

Qi Zhang,[1,2,3] Jiehao Wang ,[4] Yufeng Gao,[1,2] Shengfei Cao,[1,2] Jingli Xie,[1,2] Like Ma,[1,2] and Yuemiao Liu[1,2]

[1]*Beijing Research Institute of Uranium Geology (BRIUG), 10, Xiao-Guan-Dong-Li, P.O. Box 9818, Beijing 100029, China*
[2]*CNNC Key Laboratory on Geological Disposal of High-Level Radioactive Waste, 10, Xiao-Guan-Dong-Li, P.O. Box 9818, Beijing 100029, China*
[3]*State Key Laboratory for Geomechanics & Deep Underground Engineering, China University of Mining & Technology, Xuzhou, 221116 Jiangsu, China*
[4]*Department of Energy and Mineral Engineering, EMS Energy Institute and G3 Center, Pennsylvania State University, University Park PA 16802, USA*

Correspondence should be addressed to Jiehao Wang; jiehao.wang89@gmail.com

Received 29 January 2021; Revised 18 March 2021; Accepted 8 April 2021; Published 29 April 2021

Academic Editor: Guanglei Zhang

Defining the trajectory of hydraulic fractures crossing bedding planes and other fractures is a significant issue in determining the effectiveness of the stimulation. In this work, a damage evolution law is used to describe the initiation and propagation of the fracture. The model couples rock deformation and gas seepage using the finite element method and is validated against classical theoretical analysis. The simulation results define four basic intersection scenarios between the fluid-driven and preexisting fractures: (a) inserting—the hydraulic fracture inserts into a bedding plane and continues to propagate along it; (b) L-shaped crossing—the hydraulic fracture approaches the fracture/bedding plane then branches into the plane without crossing it; (c) T-shaped crossing—the hydraulic fracture approaches the fracture/bedding plane, branches into it, and crosses through it; (d) direct crossing—the hydraulic fracture crosses one or more bedding planes without branching into them. The intersection scenario changes from (a) → (b) → (c) → (d) in specimens with horizontal bedding planes when the stress ratio β ($\beta = \sigma_y/\sigma_x$) increases from 0.2 to 5. Similarly, the intersection type changes from (d) → (c) → (a) with an increase in the bedding plane angle α ($0^\circ \rightarrow 90^\circ$). Stiffness of the bedding planes also exerts a significant influence on the propagation of hydraulic fractures. As the stiffness ratio $\overline{E_1}/\overline{E_2}$ increases from 0.1 to 0.4 and 0.8, the seepage area decreases from 22.2% to 41.8%, and the intersection type changes from a T-shaped crossing to a direct crossing.

1. Introduction

The production of environmentally friendly unconventional gas has increased rapidly in recent years including shale gas, gas from tight sandstones, and coal bed methane [1–4], obviating the recovery of hydrocarbons from conventional reservoirs and coal [5, 6]. In the US, unconventional gas accounted for 46% of total production of natural gas in 2016 [7]. However, the permeability of these unconventional reservoirs is extremely low (less than 0.1 mD) [8, 9], necessitating massive hydraulic fracturing to improve production [10]. At present, water is the primary fracturing fluid due to its low cost and ready availability [11–15]. However, water-based fracturing may be constrained in water-deficient areas since fracturing treatments for a single reservoir may consume more than 227 m^3 [16]. In addition, the disposal of the large amount of flowback water that is precharged with dissolved pollutants may adversely affect potable aquifers, induce seismicity [17], and pose a potential risk to public health [18]. Recently, laboratory experiments indicate that gas may be a superior candidate to water for fracturing. These results show that the breakdown pressures of gas fracturing are lower than those for water fracturing [19, 20]. Compared to fractures induced by water, those induced by gas have rougher surfaces, more tortuous paths, and a larger potential to form a complex fracture network, in turn potentially resulting in higher surface flow-transfer surface areas and reduced conductive flow lengths [10, 19, 21]. Additionally, the adsorption capacity of CO_2 is 4-20 times of that of methane [22, 23], enabling the competitive replacement of methane by CO_2 and the cosequestration of CO_2.

Shale is a sedimentary rock containing bedding planes [24], which exert a significant influence on the propagation of hydraulic fractures. Indeed, the complex fracture network created by hydraulic fracturing may, in part, result from the intersection scenarios between hydraulic fractures and bedding planes [25–28]. Thus, it is of vital importance to understand the behavior of hydraulic fractures intersecting bedding planes during propagation.

A variety of studies focus on the behavior of hydraulic fractures intersecting preexisting bedding planes, including theoretical analyses, laboratory experiments, and numerical simulations. Multiple crossing criteria have been proposed using different methods, such as linear elastic fracture mechanics [29], theory of dislocations [30], and systematic analysis [31].

Laboratory hydraulic fracturing experiments conducted on rock containing bedding planes investigate the controls on intersection behavior from different perspectives. Hydraulic fracturing experiments in prefractured shale indicate that hydraulic fractures tend to cross a preexisting fracture only under high differential stresses and at high angles of approach [32]. Three forms of intersections were obtained in experiments when hydraulic fractures propagate in rock with cemented natural fractures [33], including (1) the hydraulic fracture bypassing the natural fracture, (2) the hydraulic fracture arresting into and diverting along the natural fracture, a (3) a combination of bypass and diversion. Also, the impact of permeability, fluid flow rate, friction coefficient, stress coefficient, and form of the bedding planes are shown to impact the nature of the intersection and potential crossing [34–36].

Numerical simulation is an effective way to study the intersection relation between hydraulic fractures and bedding planes. Such approaches have explored the physics of fracture-inhomogeneity interactions, indicating that hydraulic fracture branching and diversion are the result of inhomogeneity [37, 38]. Investigations of the interaction between hydraulic fractures and bedding planes have utilized discrete element methods (DEM) [39, 40], displacement discontinuity methods (DDM) [41], and extended finite element methods (XFEM) [42]. However, the finite element method (FEM) combining with damage theory is also an effective way to simulate the fracture initiation and propagation. The intersection mechanism between the fluid-driven fracture and bedding planes using FEM is rarely reported.

In this work, a coupled hydraulic-mechanical model is proposed where a damage evolution law is employed. It is then solved by FEM using COMSOL and MATLAB and utilized to simulate the fracturing processes. The intersection scenarios between hydraulic fractures and bedding planes under several conditions are numerically researched.

2. Governing Equations

We develop a damage-based hydraulic-mechanical model that follows the evolution of damage around a borehole with a propagating fluid-driven fracture. The model couples fluid and mechanical deformations to define the geometry of the resulting fluid-driven fracture.

2.1. Rock Deformation Equation. According to the elastic theory, the constitutive equation considering the influence of pore pressure can be written as

$$\sigma_{ij} = 2G\varepsilon_{ij} + 2G\frac{\nu}{1-2\nu}\varepsilon_v\delta_{ij} - \eta p\delta_{ij}, \tag{1}$$

where σ_{ij} is the stress tensor, G is the shear modulus of rock, ε_{ij} is the strain tensor, ν is Poisson's ratio of rock, $\varepsilon_v = \varepsilon_{11} + \varepsilon_{22} + \varepsilon_{33}$ is the volumetric strain, δ_{ij} is the Kronecker delta, η is the Biot coefficient, and p is the pore pressure.

Combining the modified constitutive equation, the geometric equation, and the equilibrium equation, the modified Navier-type equation can be written as

$$Gu_{i,jj} + \frac{G}{1-2\nu}u_{j,ji} - \eta p,_i + f_i = 0, \tag{2}$$

where u is the displacement vector and f_i is the component of the body force.

2.2. Gas Flow Equation. The governing equation for CO_2 flow based on mass balance can be defined as

$$\frac{\partial m}{\partial t} + \nabla \cdot \left(\rho_g q_g\right) = Q_m, \tag{3}$$

where m is the CO_2 mass per volume of rock, ρ_g is the CO_2 density, q_g is the seepage velocity of CO_2, Q_m is the source of CO_2, and t is the time variable.

According to Darcy's law, the seepage velocity of CO_2 can be defined as

$$q_g = -\frac{k}{\mu_g}\nabla p, \tag{4}$$

where k is the permeability of the shale rock and μ_g is the viscosity of CO_2.

The shale rock is assumed saturated with the injected CO_2; therefore, CO_2 mass per volume of rock can be written as $m = \rho_g\phi$ (ϕ is the porosity of the rock). And CO_2 will transfer from the gaseous to the supercritical state when the pressure reaches 7.43 MPa (the temperature is kept at 350 K). As shown in Figure 1, the density and viscosity of CO_2 change dramatically when the phase change occurs. Base on the above, the first item of equation (3) can be induced as [13]

$$\frac{\partial m}{\partial t} = \phi\frac{\partial \rho_g}{\partial t} + \rho_g\frac{\partial \phi}{\partial t} = \phi c\rho_g\frac{\partial p}{\partial t}, \tag{5}$$

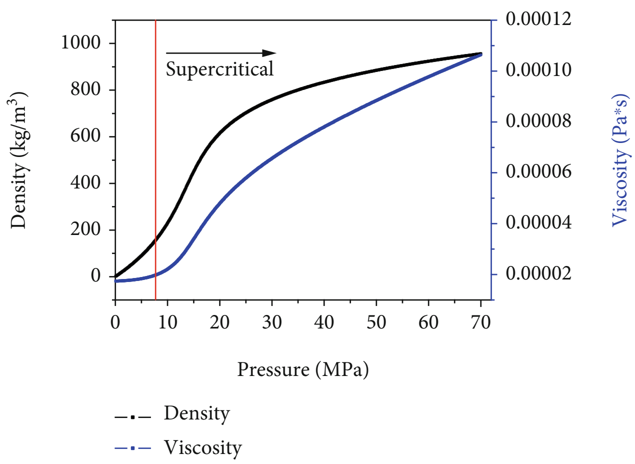

Figure 1: The evolution of density and viscosity of CO_2 versus pressure at 350 K.

where $c = (1/\rho_g)(\partial \rho_g/\partial p)$ is the compressibility coefficient of CO_2 which can be calculated from Figure 1.

Substituting equations (4) and (5) into equation (3), the CO_2 continuity equation is shown as

$$\phi c \rho_g \frac{\partial p}{\partial t} + \nabla \cdot \left(-\frac{k}{\mu_g} \rho_g \nabla p \right) = Q_m. \tag{6}$$

2.3. Damage Evolution Law. A damage evolution law based on representative elemental volume (REV) is used in this study to describe the initiation and propagation of hydraulic fracture in numerical samples with bedding planes. The evolution of stress-strain of REV under uniaxial tension or compression is shown in Figure 2. Shear or tension damage is initiated when the stress state of a REV meets the Mohr-Coulomb criterion or the maximum tensile stress criterion, as expressed by

$$H_1 = \sigma_1 - f_{t0} = 0, \tag{7}$$

$$H_2 = -\sigma_3 + \sigma_1 \frac{1 + \sin\varphi}{1 - \sin\varphi} - f_{c0} = 0, \tag{8}$$

where σ_1 and σ_3 are the first principal stress and third principal stress, respectively; f_{t0} and f_{c0} are the tensile strength and compressive strength of the REV, respectively; φ is the internal friction angle; and H_1 and H_2 are the threshold functions. Once a REV begins to get damage, the evolution of its stress-strain relation can be described by a nonlinear function as shown in Figure 2. A damage variable D is used to represent the damage level and is defined as [43]

$$D = \begin{cases} 0, & H_1 < 0, H_2 < 0, \\ 1 - \left| \dfrac{\varepsilon_t}{\varepsilon_1} \right|^2, & H_1 = 0, dH_1 > 0, \\ 1 - \left| \dfrac{\varepsilon_c}{\varepsilon_3} \right|^2, & H_2 = 0, dH_2 > 0, \end{cases} \tag{9}$$

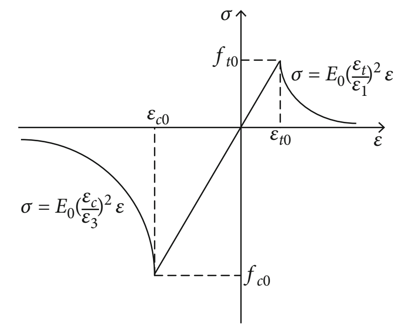

Figure 2: The damage constitutive criterion of REVs under uniaxial stress conditions.

where ε_1 and ε_3 are the first principal stain and the third principal strain, respectively, and ε_t and ε_c are the tensile strain and compressive strain, respectively.

For a damaged REV, the elastic modulus decreases but the permeability increases correspondingly as the damage variable increases. The evolution of elastic modulus and permeability with damage variable D can be defined as follows:

$$E = E_0 (1 - D), \tag{10}$$

$$k = k_0 \exp(\alpha_k D), \tag{11}$$

where E and E_0 are the elastic modulus and the initial elastic modulus of a REV, respectively; k_0 is the initial permeability of a REV; and α_k is the damage-permeability effect coefficient to define the influence of damage on permeability.

2.4. Rock Heterogeneity. Shale is a kind of sedimentary rock which is heterogeneous. Previous studies indicated that the heterogeneity of rock plays an important role on the propagation of microcracks [44]. And many studies have shown that Weibull distribution can well characterize the heterogeneity of rock [13, 45]. In this work, the Weibull distribution is introduced to describe the heterogeneity of shale rock. Mechanical parameters of REVs (strength and elastic modulus) are assumed to satisfy the Weibull distribution function, and the probability density function is written as

$$f(u) = \frac{\xi}{z_0} \left(\frac{z}{z_0} \right)^{\xi - 1} \exp\left[-\left(\frac{z}{z_0} \right)^{\xi} \right], \tag{12}$$

where z represents the mechanical parameter of REVs, z_0 is the average value of the mechanical parameter, and ξ is the heterogeneity coefficient.

3. Verification and Implementation of the Proposed Numerical Model

We use a finite element method to solve the proposed numerical model and obtain numerical results, and we compare the numerical results with two classical analytical results to verify the effect of the proposed model.

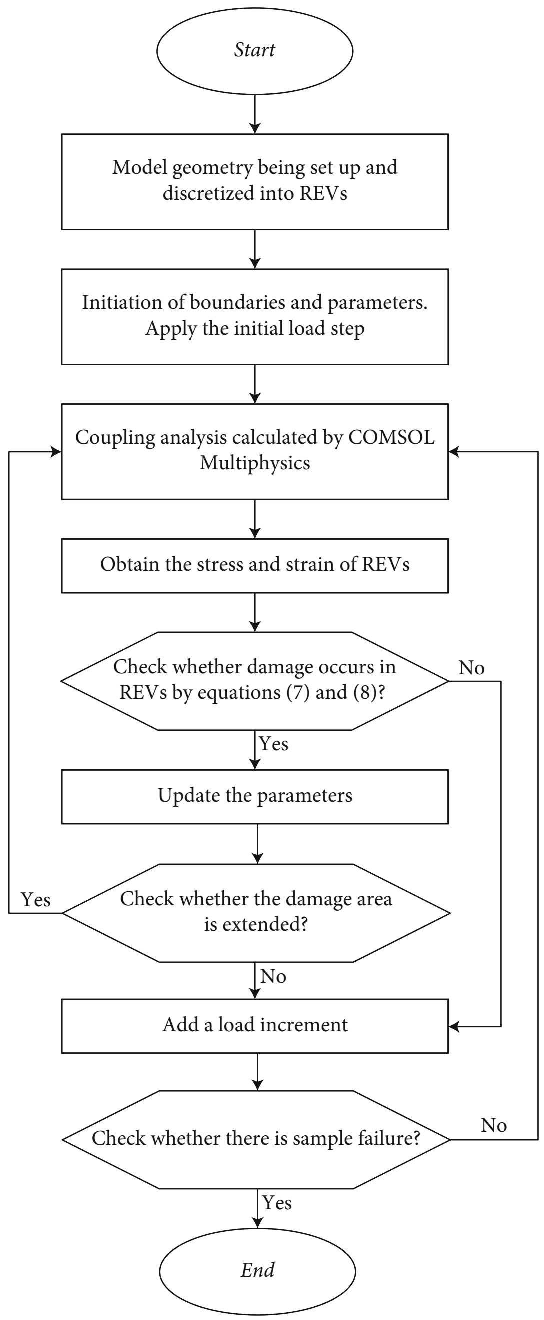

FIGURE 3: Primary solution procedures for the numerical model.

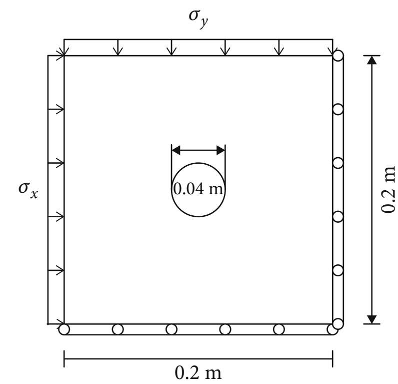

FIGURE 4: The numerical geometry for verification.

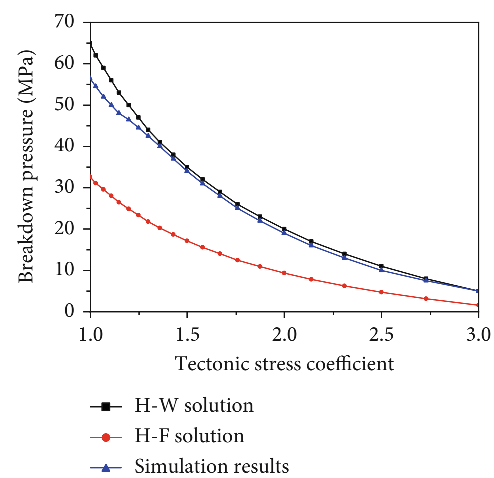

FIGURE 5: The breakdown pressures under different tectonic stress coefficients obtained by H-W solution, H-F solution, and numerical simulation.

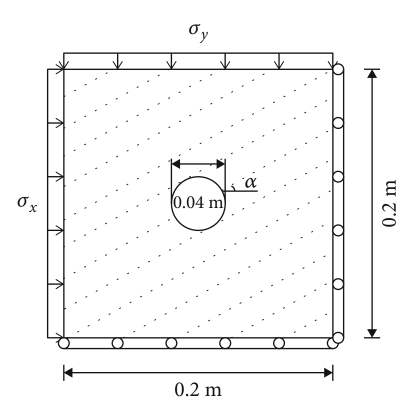

FIGURE 6: The numerical geometry for fracturing experiments.

3.1. Model Implementation. The numerical model is established in the previous section. Due to the complex coupled relationship between solid mechanics field and fluid seepage field, it is difficult to obtain an analytical solution. Therefore, the finite element method (FEM) is adopted to solve these coupled equations. The primary procedures are summarized as shown in Figure 3:

(a) After setting up the model geometry, the geometry is discretized into a series of REVs. Then, the initial mechanical parameters are defined at the REV scale and the boundary conditions are applied correspondingly

(b) Numerical calculation is conducted by COMSOL Multiphysics at the initial load step. After calculation, the stress and strain of REVs are obtained for the following analysis

Table 1: The parameters used in simulations.

Parameters	Rock matrix	Bedding plane
Average elastic modulus of REVs (GPa)	36	18
Poisson's ratio	0.225	0.25
Average tensile strength of REVs (MPa)	6.2	3.1
Average compressive strength of REVs (MPa)	62	31
Initiate porosity	0.01	0.015
Initiate permeability (m^2)	10^{-18}	$1.5 * 10^{-17}$
Internal friction angle (rad)	0.368	0.368
Initiate pore pressure (MPa)	1	1
Heterogeneity coefficient	6	6

(c) According to criterions (7) and (8), all REVs will be checked whether the damage occurs; this step is completed via MATLAB

(d) The damage variable of damaged REVs can be calculated according to equation (9), then the elastic modulus and permeability of the damaged REVs are updated with equations (10) and (11)

(e) Numerical simulation is conducted with the updated parameters, and the simulation results are compared with results of the former iteration step. If the damage area expands, steps (c)–(e) are repeated; otherwise, step (f) is applied

(f) The boundary conditions are updated in the next load increment

3.2. Model Verification. In this part, the proposed model for simulating the propagation of the hydraulic fracture is validated. There are two classical theoretical solutions for forecasting the breakdown pressure in terms of far-field stresses, tensile strength, and initial pore pressure. One is proposed by Hubbert and Willis [46] (the H-W solution) for impermeable rock whilst the other one is presented by Haimson and Fairhurst [47] (the H-F solution) for permeable rock. These two solutions can be expressed by

$$P_{\mathrm{HW}} = \sigma_t + 3\sigma_3 - \sigma_1 - p_0, \quad (13)$$

$$P_{\mathrm{HF}} = \frac{\sigma_t + 3\sigma_3 - \sigma_1 - p_0}{2 - \eta(1-2\nu)/(1-\nu)} - p_0, \quad (14)$$

where P_{HW} and P_{HF} are the breakdown pressures of the H-W solution and the H-F solution, respectively; σ_t is the tensile strength of the shale rock; and p_0 is the initial pore pressure of the shale rock.

In this part, the tensile strength of the shale rock is 6 MPa, the initial pore pressure of the rock is 1 MPa, the initial permeability of the rock is 10^{-18} m^2, the Biot coefficient is 0.1, and Poisson's ratio of the rock is 0.225. The model geometry for verification is shown in Figure 4. The vertical in situ stress σ_y is kept at 30 MPa, while the horizontal in situ stress varies from 10 MPa to 30 MPa. And a tectonic stress ratio β ($\beta = \sigma_y/\sigma_x$) is introduced. The breakdown pressures under different tectonic stress ratios obtained by the H-W solution, H-F solution, and numerical simulation are shown in Figure 5. The results showed that the simulation results are a little bit smaller than the H-W solutions but greater than the H-F solutions, since the permeability of shale rock in this part is close to the permeability adopted in the H-W solution. The similar results can be also found in simulations conducted by Lu et al. [48] and Zhang et al. [45]; this verifies the accuracy of the model coupling rock deformation and gas seepage and the numerical implementation, though no bedding planes are involved in this part.

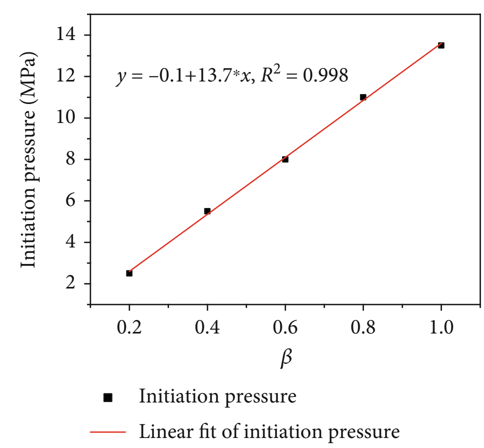

Figure 7: The fracture initiation pressure of specimen versus stress ratio β.

4. Numerical Settings

Shale rock naturally contains bedding planes with different directions owing to geological deposition and folding. These bedding planes in different directions play a significant role in the propagation of the hydraulic fracture. Thus, numerical samples with bedding planes in different directions are adopted in this work. As shown in Figure 6, the numerical sample is a 2D plane rectangle (0.2 m × 0.2 m) with a borehole (0.04 m in diameter) in its center. The dotted lines in the numerical sample represent bedding planes of which the thickness has a uniform value of 2 mm. Bedding planes are distributed uniformly in the numerical sample, and the distance between two adjacent bedding planes is 0.02 m. It

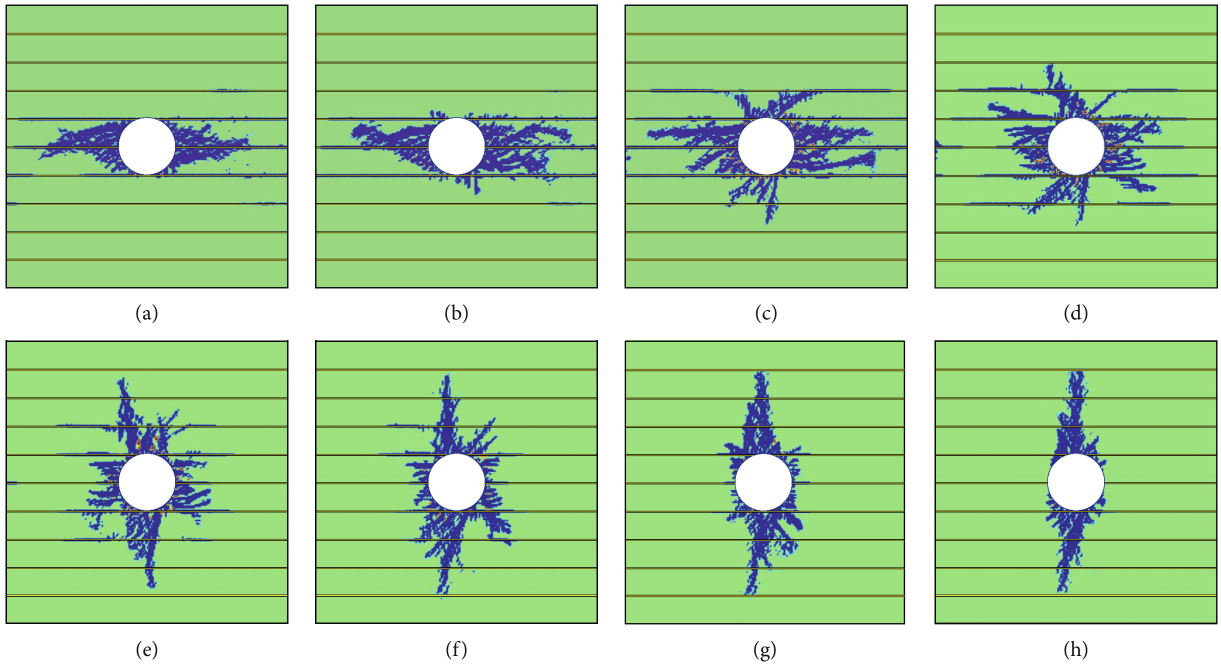

Figure 8: The distribution of hydraulic fractures in horizontal bedding plane samples under different stress ratios. (a) $\sigma_x = 5$ MPa, $\sigma_y = 1$ MPa ; (b) $\sigma_x = 5$ MPa, $\sigma_y = 2$ MPa; (c) $\sigma_x = 5$ MPa, $\sigma_y = 3$ MPa; (d) $\sigma_x = 5$ MPa, $\sigma_y = 4$ MPa; (e) $\sigma_x = 4$ MPa, $\sigma_y = 5$ MPa; (f) $\sigma_x = 3$ MPa, $\sigma_y = 5$ MPa; (g) $\sigma_x = 2$ MPa, $\sigma_y = 5$ MPa; (h) $\sigma_x = 1$ MPa, $\sigma_y = 5$ MPa. (The black lines represent bedding planes.)

should be noted that α is the angle between the bedding plane and the horizontal direction. As for boundary settings, loads applied on the left boundary and top boundary represent horizontal in situ stress and vertical in situ stress, respectively. And the right boundary and bottom boundary are set as rollers. All boundaries are set as no-flow boundaries except for the borehole, on which the fracturing fluid is injected with an injection rate of 0.0053 m^3/s. The parameters used in the simulations can be found in Table 1.

5. Results and Discussion

The physical processes for CO_2-driven hydraulic fracture trajectories across a bedding plane are simulated. Besides, the evolution of intersection scenarios between hydraulic fractures and bedding planes under several conditions (stress ratio, bedding plane angle, and bedding plane stiffness) is obtained and discussed.

5.1. Effect of Stress Ratio

5.1.1. Simulation Results. A series of numerical simulation tests were conducted to study the impact of stress ratio on the propagation of hydraulic fractures. Eight stress ratios were used in this study which are $\beta = \sigma_y/\sigma_x = 1$ MPa/5 MPa (0.2), 2 MPa/5 MPa (0.4), 3 MPa/5 MPa (0.6), 4 MPa/5 MPa (0.8), 5 MPa/4 MPa (1.25), 5 MPa/3 MPa (1.67), 5 MPa/2 MPa (2.5), and 5 MPa/1 MPa (5). Bedding planes were set as horizontal for all numerical samples in this part, and boundary settings and mechanical parameters can be found in Section 4.

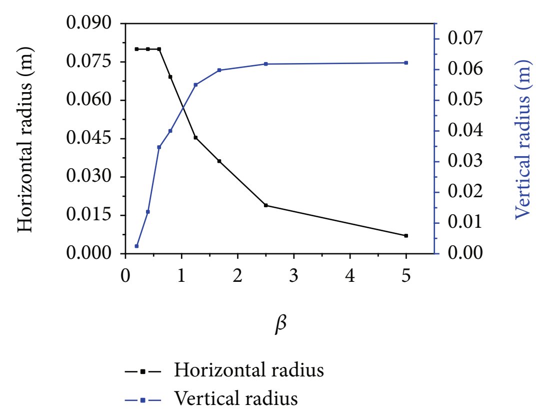

Figure 9: The horizontal radius and vertical radius of hydraulic fractures under different stress ratios.

In Figure 7, the fracture initiation pressure means the injection pressure at the borehole when damage first occurs in numerical samples. It should be noted that the horizontal in situ stress is kept at 5 MPa while the vertical in situ stress increases from 1 MPa to 5 MPa. It can be seen from the results that the fracture initiation pressure increases from 2.4 MPa to 13.5 MPa as the stress ratio increases from 0.2 to 1. And the relation between the fracture initiation pressure and the stress ratio can be fitted by a linear function.

Figure 8 shows the distribution of hydraulic fractures in samples with horizontal bedding planes under different stress ratios. As for stress ratio $\beta = 0.2$, the main hydraulic fracture propagates horizontally, that is, the direction of the maximum principal stress. Also, hydraulic fractures are observed

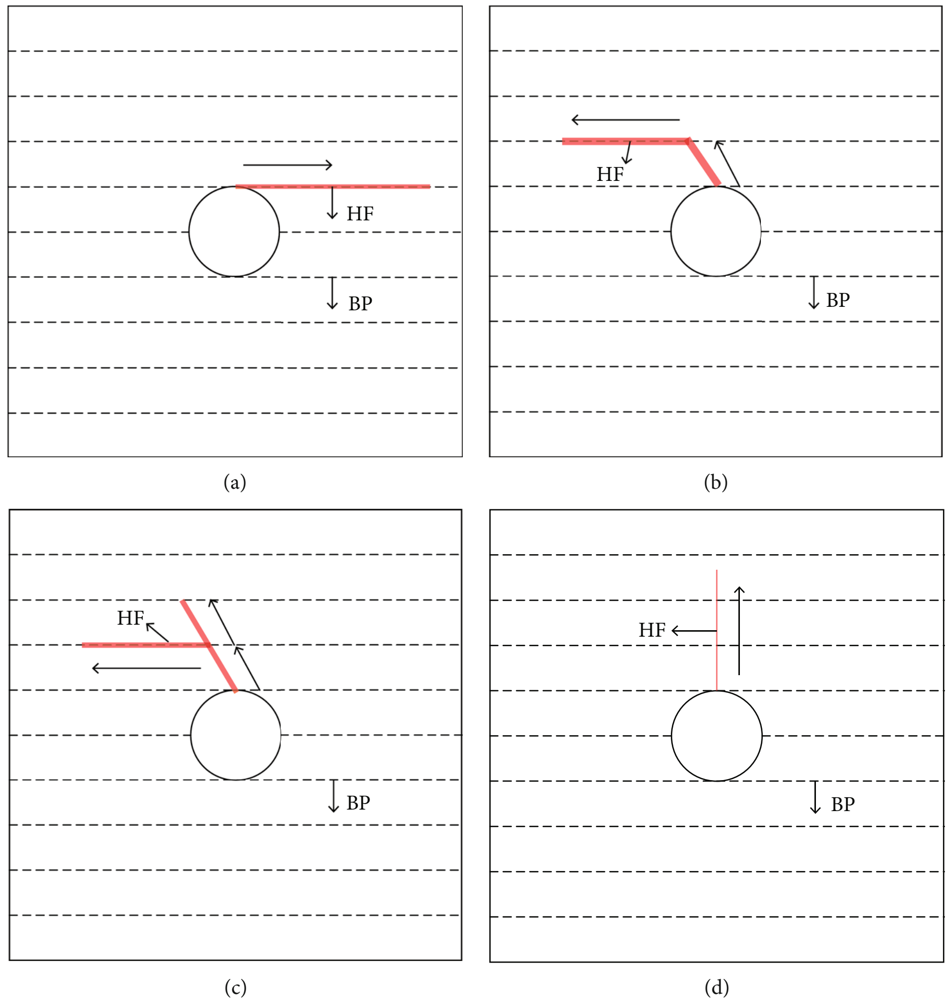

FIGURE 10: Four intersection scenarios between hydraulic fractures (HF) and bedding planes (BP): (a) inserting, (b) L-shape crossing, (c) T-shape crossing, and (d) direct crossing.

inserting into bedding planes because of their lower strength and elastic modulus compared with the rock matrix. No fracture propagates along the vertical direction. When the stress ratio $\beta = 0.6$, hydraulic fractures mainly propagate along the horizontal direction or insert into bedding planes. Some fractures are observed approaching the bedding plane and then branching into it or directly crossing through the bedding plane. As for $\beta = 0.8$, the propagation of hydraulic fractures in the horizontal direction is not as deep as the case of $\beta = 0.6$. Hydraulic fractures branching into and crossing through the bedding planes can be observed in the vertical direction. In the following cases, vertical stress remains at 5 MPa, while horizontal stress varies from 4 MPa to 1 MPa. For the stress ratio $\beta = 1.25$ and $\beta = 1.67$, the intersection scenarios of hydraulic fractures and bedding planes are similar with the case of $\beta = 0.8$, containing hydraulic fractures crossing through bedding planes, approaching bedding planes, and then branching into and crossing through bedding planes. However, the propagation of hydraulic fractures in the horizontal direction is gradually restricted. As for $\beta = 2.5$ and $\beta = 5$, a main vertical hydraulic fracture is formed along the direction of the maximum principal stress and almost no horizontal hydraulic fractures are observed in this condition. Based on the above results, it is indicated that the bedding plane and stress ratio have a significant influence on the distribution of hydraulic fractures. The horizontal radius and vertical radius of hydraulic fractures under different stress ratios is shown in Figure 9, which can reflect the fracturing area in a specific case. When the stress ratio β increases from 0.2 to 5, the horizontal radius decreases first dramatically and then slowly from 0.08 m to 0.007 m, whilst the vertical radius increases first sharply and then gradually from 0.00243 m to 0.0622 m.

5.1.2. Intersection Scenario between the Hydraulic Fracture and Bedding Plane. Understanding the complexity of the fracture network is of vital importance for hydraulic fracturing design. The fracture network near the gas reservoirs is formed through propagation and combination of basic intersection scenarios. Thus, the basic intersection types between the hydraulic fracture and bedding plane are summarized in this subsection.

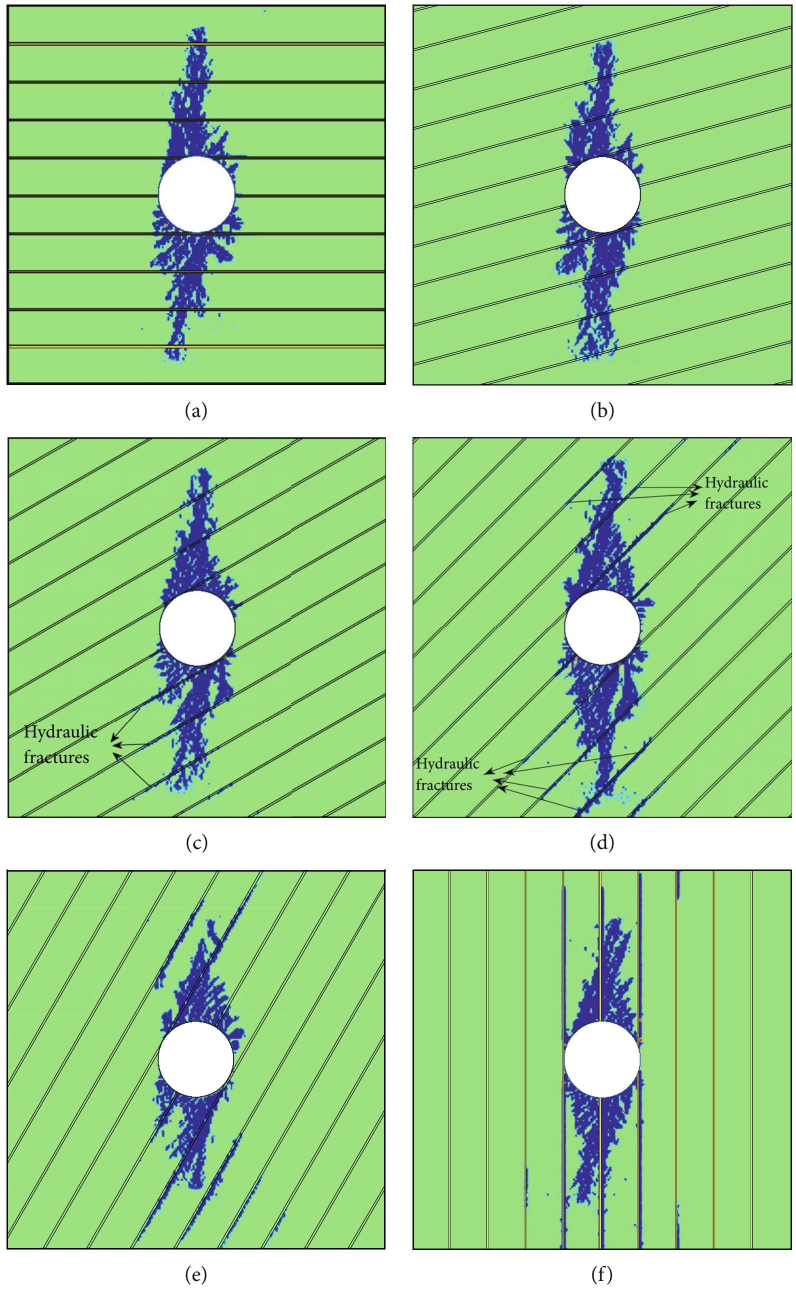

Figure 11: The distribution of hydraulic fractures in specimens with different bedding plane angles: (a) $\alpha = 0°$, (b) $\alpha = 15°$, (c) $\alpha = 30°$, (d) $\alpha = 45°$, (e) $\alpha = 60°$, and (f) $\alpha = 90°$.

Based on the simulation results above, four types of intersection scenarios between hydraulic fractures and bedding planes are shown in Figure 10. (a) Inserting: the hydraulic fracture inserts into a bedding plane and continues to propagate along it, i.e., the hydraulic fracture is arrested by the bedding plane. (b) L-shaped crossing: the hydraulic fracture approaches the fracture/bedding plane then branches into the plane without crossing it. (c) T-shaped crossing: the hydraulic fracture approaches the fracture/bedding plane, branches into it, and crosses through it. (d) Direct crossing: the hydraulic fracture crosses one or more bedding planes without branching into them. It indicates that the intersection types vary from (a) → (b) → (c) → (d) with the increase of stress ratio β in specimens with the horizontal bedding planes.

5.2. Effect of Bedding Plane Angle. Numerical simulations were performed to study the effect of the bedding plane angle on the propagation of hydraulic fractures. Six kinds of specimens with different bedding plane angles ($\alpha = 0°$, $\alpha = 15°$, $\alpha = 30°$, $\alpha = 45°$, $\alpha = 60°$, and $\alpha = 90°$) were used in this part. The horizontal in situ stress and vertical in

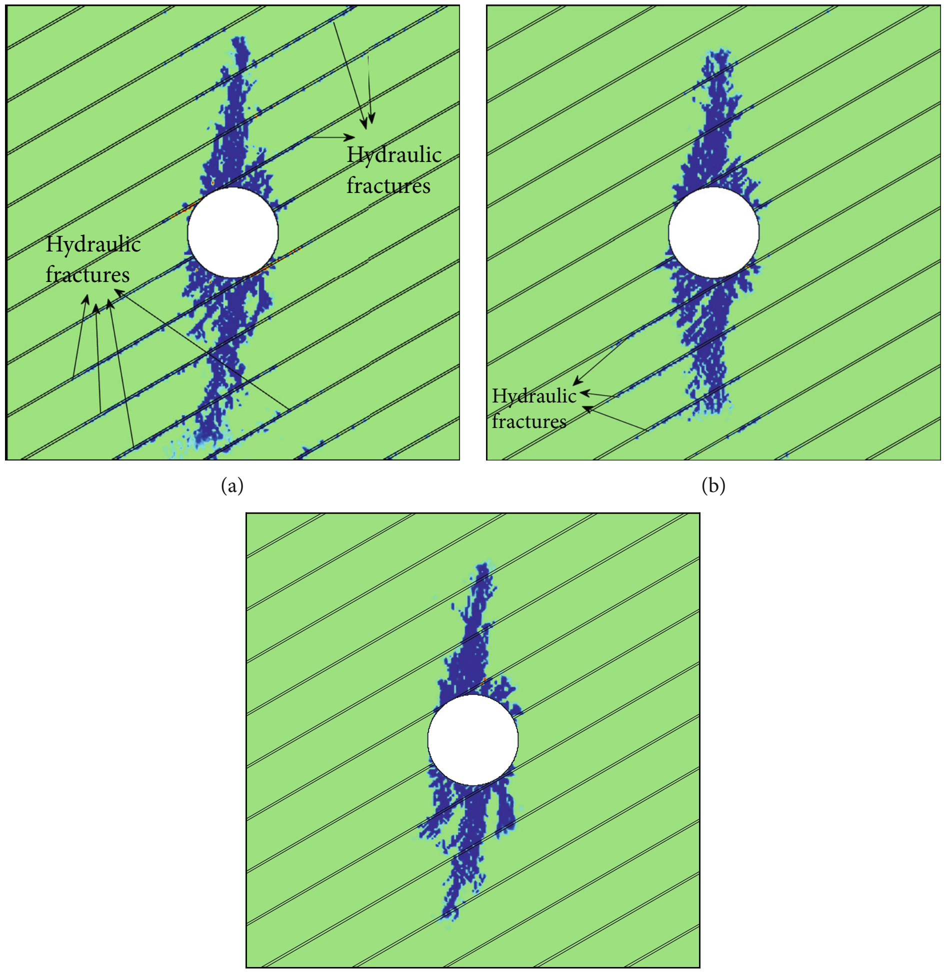

Figure 12: The distribution of hydraulic fractures in specimens with different levels of stiffness of bedding planes: (a) $\overline{E_1}/\overline{E_2} = 0.1$, (b) $\overline{E_1}/\overline{E_2} = 0.4$, and (c) $\overline{E_1}/\overline{E_2} = 0.8$.

situ stress were kept at 1 MPa and 5 MPa, respectively. And other boundary settings and mechanical parameters can be found in Section 4.

The distribution of hydraulic fractures in specimens with different bedding plane angles is shown in Figure 11. For the bedding plane angle $\alpha = 0^\circ$, a vertical main fracture is formed crossing through bedding planes since the vertical in situ stress is five times of the horizontal in situ stress. When $\alpha = 15^\circ$, the distribution of hydraulic fractures is similar with the former case ($\alpha = 0^\circ$). The results indicate that the bedding planes with angle $\alpha = 15^\circ$ do not have an obvious influence on the propagation of hydraulic fractures. With the bedding plane angle increasing to 30°, the intersection type between the hydraulic fracture and bedding plane changes from direct crossing to T-shaped crossing. It should be noted that only a small amount of hydraulic fractures branch into the bedding planes. As for the bedding angle $\alpha = 45^\circ$, the T-shaped crossing is the primary intersection scenario; more hydraulic fractures branch into the bedding planes compared with the case of $\alpha = 30^\circ$. With the bedding plane angle increasing to 60°, the results show that the intersection scenario changes from T-shaped crossing to inserting; no crossing scenario is observed in this condition. When the bedding plane angle $\alpha = 90^\circ$, hydraulic fractures propagate along the vertical direction or insert into bedding planes. The results indicate that the intersection type changes from (d) → (c) → (a) with the increase of the bedding plane angle α.

5.3. Effect of Bedding Plane Stiffness. Three numerical tests were performed to research the behavior of hydraulic fractures propagating in specimens with different levels of stiffness of bedding planes. The stiffness (elastic modulus $\overline{E_2}$) of the rock matrix was fixed whilst three different levels of stiffness of bedding planes (elastic modulus $\overline{E_1}$) were used in this part ($\overline{E_1}/\overline{E_2} = 1/10$, $\overline{E_1}/\overline{E_2} = 4/10$, and $\overline{E_1}/\overline{E_2} = 8/10$). The bedding plane angle α was 30° in the specimen, and the horizontal in situ stress and vertical in situ stress were 1 MPa and 5 MPa, respectively. Again, the boundary settings and the injection rate are the same as those defined in Section 4.

Figure 12 shows the distribution of hydraulic fractures in specimens with different levels of stiffness of bedding planes. For the case of $\overline{E_1}/\overline{E_2} = 1/10$, when the hydraulic fracture approaches the bedding plane, it is easy to branch into the

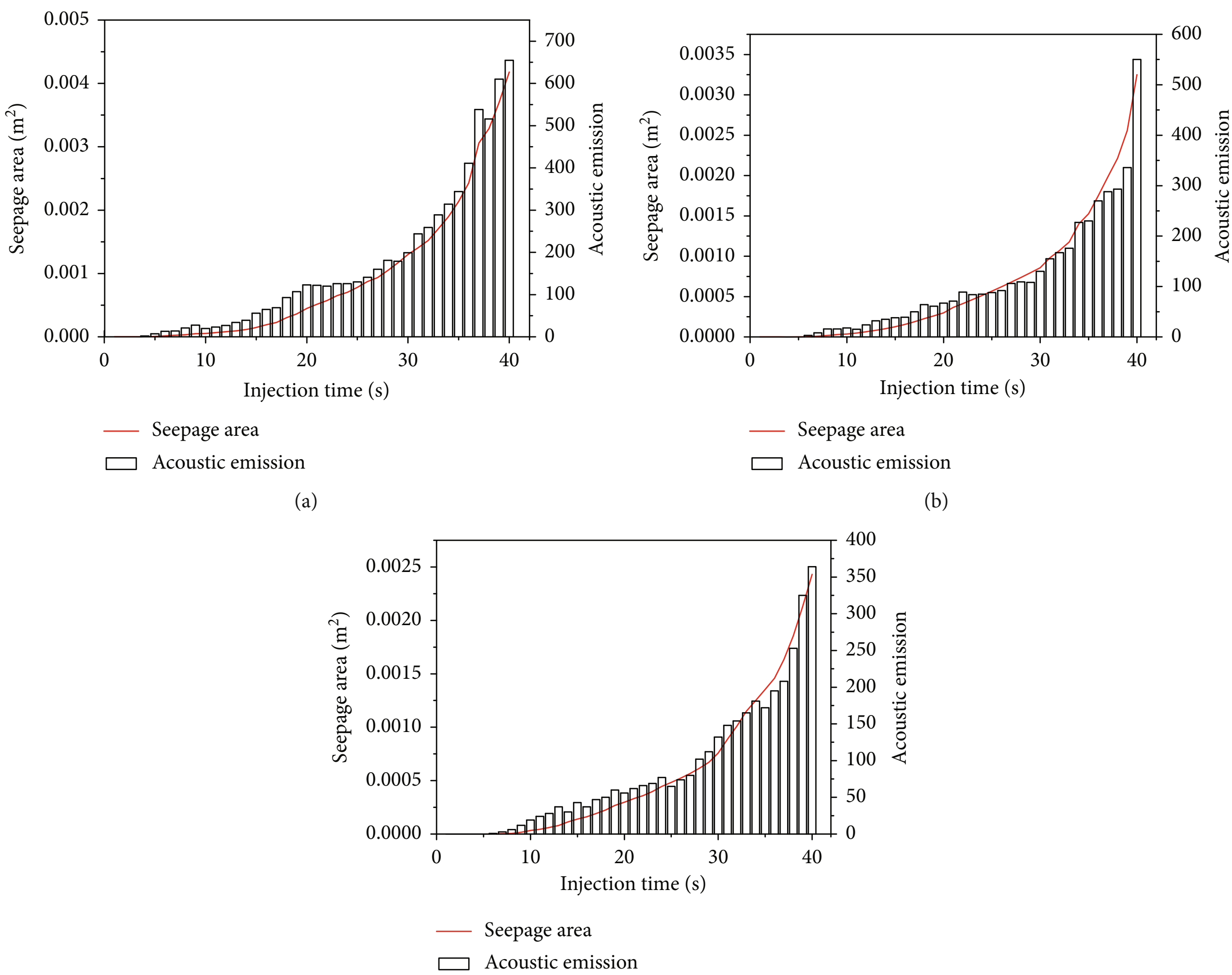

(a) (b) (c)

Figure 13: The development of seepage area and acoustic emission with different levels of stiffness of bedding planes: (a) $\overline{E_1}/\overline{E_2} = 0.1$, (b) $\overline{E_1}/\overline{E_2} = 0.4$, and (c) $\overline{E_1}/\overline{E_2} = 0.8$.

bedding plane since the stiffness of the bedding plane is much smaller than that of the rock matrix. T-shaped crossing is formed between hydraulic fractures and bedding planes. Comparing the case of $\overline{E_1}/\overline{E_2} = 4/10$ with the former one ($\overline{E_1}/\overline{E_2} = 1/10$), it can be found that the number of hydraulic fractures branching into bedding planes decreases. T-shaped crossing is also observed in this case. For the case of $\overline{E_1}/\overline{E_2} = 8/10$, a vertical main fracture is formed crossing bedding planes, and direct crossing is the intersection scenario between the hydraulic fracture and bedding plane. The results show that the intersection type changes from T-shaped crossing to direct crossing with the increase of the bedding plane stiffness. Besides, the bedding plane stiffness has an obvious impact on the development of the seepage area and acoustic emission (Figure 13). It should be noted that the acoustic emission is recorded from the number of damaged REVs per second. In all three cases, the seepage area increases slowly in the initiate stage (1 s–30 s) then increases rapidly. For the case of $\overline{E_1}/\overline{E_2} = 1/10$, the seepage area is $0.00418\,\mathrm{m}^2$ at time $t = 40$ s, and the highest acoustic emission is 655. When the stiffness ratio $\overline{E_1}/\overline{E_2}$ increases from 0.1 to 0.4 and 0.8, the seepage area decreases 22.2% and 41.8% to $0.00325\,\mathrm{m}^2$ and $0.00243\,\mathrm{m}^2$, respectively, whilst the highest acoustic emission decreases to 550 and 364, respectively. The results indicate that hydraulic fractures are formed more easily, and a relatively more complex intersection scenario is obtained with a lower stiffness of the bedding plane.

6. Conclusions

Understanding the mechanism of the intersection scenario between hydraulic fractures and bedding planes is of vital importance for creating a complex fracture network and improving the recovery of unconventional resources. In this work, a coupled hydraulic-mechanical model is developed where a damage evolution law is used to describe the initiation and propagation of hydraulic fractures. This model is then used to conduct a series of numerical simulations to investigate the propagation of hydraulic fractures in specimens with bedding planes. The following conclusions can be obtained:

(1) Stress ratio has a vital impact on the intersection scenario between a hydraulic fracture and a bedding plane. Four types of intersection scenarios are summarized based on the study: (a) inserting—the hydraulic fracture inserts into a bedding plane and continues to propagate along it; (b) L-shaped crossing—the hydraulic fracture approaches the fracture/-bedding plane then branches into the plane without crossing it; (c) T-shaped crossing—the hydraulic fracture approaches the fracture/bedding plane, branches into it, and crosses through it; (d) direct crossing—the hydraulic fracture crosses one or more bedding planes without branching into them. The simulation results indicate that intersection types vary from (a) → (b) → (c) → (d) in specimens with horizontal bedding planes when the stress ratio β increases from 0.2 to 5. Besides, the fracture initiation pressure increases from 2.4 MPa to 13.5 MPa while the stress ratio increases from 0.2 to 1

(2) The bedding plane angle can also greatly affect the propagation of hydraulic fractures. The results show that the intersection type changes from (d) → (c) → (a) with the increase of the bedding plane angle α ($0^\circ \rightarrow 90^\circ$)

(3) We also investigate the influence of bedding plane stiffness on the propagation of hydraulic fractures. The results indicate that the intersection type changes from the T-shaped crossing to the direct crossing with the increase of the bedding plane stiffness. When the stiffness ratio $\overline{E_1}/\overline{E_2}$ increases from 0.1 to 0.4 and 0.8, the seepage area decreases 22.2% and 41.8% and the highest acoustic emission decreases from 655 to 550 and 364, respectively

Data Availability

The numerical simulation data used to support the findings of this study are available from the corresponding author upon reasonable request.

Conflicts of Interest

The authors declare that they have no conflicts of interest.

Acknowledgments

This work was supported by the National Natural Science Foundation of China (51804339).

References

[1] J. Fan, P. Liu, J. Li, and D. Jiang, “A coupled methane/air flow model for coal gas drainage: model development and finite-difference solution,” *Process Safety and Environmental Protection*, vol. 141, pp. 288–304, 2020.

[2] P. Liu, J. Fan, D. Jiang, and J. Li, “Evaluation of underground coal gas drainage performance: mine site measurements and parametric sensitivity analysis,” *Process Safety and Environmental Protection*, vol. 148, pp. 711–723, 2021.

[3] C. McGlade, J. Speirs, and S. Sorrell, “Unconventional gas–a review of regional and global resource estimates,” *Energy*, vol. 55, pp. 571–584, 2013.

[4] Y. Xue, P. G. Ranjith, F. Dang et al., “Analysis of deformation, permeability and energy evolution characteristics of coal mass around borehole after excavation,” *Natural Resources Research*, vol. 29, no. 5, pp. 3159–3177, 2020.

[5] L. M. McKenzie, R. Z. Witter, L. S. Newman, and J. L. Adgate, “Human health risk assessment of air emissions from development of unconventional natural gas resources,” *Science of the Total Environment*, vol. 424, pp. 79–87, 2012.

[6] D. J. Rozell and S. J. Reaven, “Water pollution risk associated with natural gas extraction from the Marcellus shale,” *Risk Analysis*, vol. 32, no. 8, pp. 1382–1393, 2012.

[7] C. Zou, Z. Yang, D. He et al., “Theory, technology and prospects of conventional and unconventional natural gas,” *Petroleum Exploration and Development*, vol. 45, no. 4, pp. 604–618, 2018.

[8] J. Liu, X. Liang, Y. Xue, K. Yao, and Y. Fu, “Numerical evaluation on multiphase flow and heat transfer during thermal stimulation enhanced shale gas recovery,” *Applied Thermal Engineering*, vol. 178, p. 115554, 2020.

[9] C. W. Spencer, “Review of characteristics of low-permeability gas reservoirs in western United States,” *AAPG Bulletin*, vol. 73, no. 5, pp. 613–629, 1989.

[10] Y. Jia, Y. Lu, D. Elsworth, Y. Fang, and J. Tang, “Surface characteristics and permeability enhancement of shale fractures due to water and supercritical carbon dioxide fracturing,” *Journal of Petroleum Science and Engineering*, vol. 165, pp. 284–297, 2018.

[11] D. Ma, H. Duan, Q. Zhang et al., “A numerical gas fracturing model of coupled thermal, flowing and mechanical effects,” *Computers, Materials & Continua*, vol. 65, no. 3, pp. 2123–2141, 2020.

[12] J. Wang, D. Elsworth, and M. K. Denison, “Propagation, proppant transport and the evolution of transport properties of hydraulic fractures,” *Journal of Fluid Mechanics*, vol. 855, pp. 503–534, 2018.

[13] J. Wang, D. Elsworth, Y. Wu, J. Liu, W. Zhu, and Y. Liu, “The influence of fracturing fluids on fracturing processes: a comparison between water, oil and SC-CO2,” *Rock Mechanics and Rock Engineering*, vol. 51, no. 1, pp. 299–313, 2018.

[14] Q. Zhang, D. Ma, Y. Wu, and F. Meng, “Coupled thermal–gas–mechanical (TGM) model of tight sandstone gas wells,” *Journal of Geophysics and Engineering*, vol. 15, no. 4, pp. 1743–1752, 2018.

[15] Q. Zhang, D. Ma, J. Liu, J. Wang, X. Li, and Z. Zhou, “Numerical simulations of fracture propagation in jointed shale reservoirs under CO_2 fracturing,” *Geofluids*, vol. 2019, Article ID 2624716, 13 pages, 2019.

[16] C. T. Montgomery and M. B. Smith, “Hydraulic fracturing: history of an enduring technology,” *Journal of Petroleum Technology*, vol. 62, no. 12, pp. 26–40, 2010.

[17] D. Elsworth, C. J. Spiers, and A. R. Niemeijer, “Understanding induced seismicity,” *Science*, vol. 354, no. 6318, pp. 1380-1381, 2016.

[18] D. Rahm, “Regulating hydraulic fracturing in shale gas plays: the case of Texas,” *Energy Policy*, vol. 39, no. 5, pp. 2974–2981, 2011.

[19] Q. Gan, D. Elsworth, J. S. Alpern, C. Marone, and P. Connolly, "Breakdown pressures due to infiltration and exclusion in finite length boreholes," *Journal of Petroleum Science and Engineering*, vol. 127, pp. 329–337, 2015.

[20] J. Zhou, G. Liu, Y. Jiang et al., "Supercritical carbon dioxide fracturing in shale and the coupled effects on the permeability of fractured shale: an experimental study," *Journal of Natural Gas Science and Engineering*, vol. 36, pp. 369–377, 2016.

[21] P. Hou, F. Gao, Y. Ju, Y. Yang, Y. Gao, and J. Liu, "Effect of water and nitrogen fracturing fluids on initiation and extension of fracture in hydraulic fracturing of porous rock," *Journal of Natural Gas Science and Engineering*, vol. 45, pp. 38–52, 2017.

[22] S. Duan, M. Gu, X. Du, and X. Xian, "Adsorption equilibrium of CO_2 and CH_4 and their mixture on Sichuan basin shale," *Energy & Fuels*, vol. 30, no. 3, pp. 2248–2256, 2016.

[23] R. Ershadnia, C. D. Wallace, and M. R. Soltanian, "CO_2 geological sequestration in heterogeneous binary media: effects of geological and operational conditions," *Advances in Geo-Energy Research*, vol. 4, no. 4, pp. 392–405, 2020.

[24] I. C. Bourg, "Sealing shales versus brittle shales: a sharp threshold in the material properties and energy technology uses of fine-grained sedimentary rocks," *Environmental Science & Technology Letters*, vol. 2, no. 10, pp. 255–259, 2015.

[25] Y. Han, J. Hampton, G. Li, N. R. Warpinski, and M. J. Mayerhofer, "Investigation of hydromechanical mechanisms in microseismicity generation in natural fractures induced by hydraulic fracturing," *SPE Journal*, vol. 21, no. 1, pp. 208–220, 2016.

[26] R. Liu, Y. Jiang, N. Huang, and S. Sugimoto, "Hydraulic properties of 3D crossed rock fractures by considering anisotropic aperture distributions," *Advances in Geo-Energy Research*, vol. 2, no. 2, pp. 113–121, 2018.

[27] S. Maxwell, *Microseismic Imaging of Hydraulic Fracturing: Improved Engineering of Unconventional Shale Reservoirs*, Society of Exploration Geophysicists, 2014.

[28] J. Wang, D. Elsworth, and M. K. Denison, "Hydraulic fracturing with leakoff in a pressure-sensitive dual porosity medium," *International Journal of Rock Mechanics and Mining Sciences*, vol. 107, pp. 55–68, 2018.

[29] C. E. Renshaw and D. D. Pollard, "An experimentally verified criterion for propagation across unbounded frictional interfaces in brittle, linear elastic materials," *International Journal of Rock Mechanics and Mining Sciences & Geomechanics Abstracts*, vol. 32, no. 3, pp. 237–249, 1995.

[30] M. Thiercelin and E. Makkhyu, *Stress field in the vicinity of a natural fault activated by the propagation of an induced hydraulic fracture*, ARMA: American rock mechanics association, Vancouver, Canada, 2007.

[31] D. Chuprakov, O. Melchaeva, and R. Prioul, "Injection-sensitive mechanics of hydraulic fracture interaction with discontinuities," *Rock Mechanics and Rock Engineering*, vol. 47, no. 5, pp. 1625–1640, 2014.

[32] T. L. Blanton, "An experimental study of interaction between hydraulically induced and pre-existing fractures," in *SPE unconventional gas recovery symposium*, Society of Petroleum Engineers, 1982.

[33] J. E. Olson, B. Bahorich, and J. Holder, "Examining hydraulic fracture: natural fracture interaction in hydrostone block experiments," in *SPE hydraulic fracturing technology conference*, Society of Petroleum Engineers, 2012.

[34] S. C. Blair, R. K. Thorpe, and F. E. Heuze, "Laboratory observations of the effect of geological discontinuities on hydrofracture propagation," in *Proceeding of the 30th US Symposium on Rock Mechanics*, Morgantown, West Virginia, 1989.

[35] S. C. Blair, R. K. Thorpe, and F. E. Heuze, "Propagation of fluid-driven fractures in jointed rock. Part 2–physical tests on blocks with an interface or lens," *International Journal of Rock Mechanics and Mining Sciences & Geomechanics Abstracts.*, vol. 27, no. 4, pp. 255–268, 1990.

[36] T. Guo, S. Zhang, Z. Qu, T. Zhou, Y. Xiao, and J. Gao, "Experimental study of hydraulic fracturing for shale by stimulated reservoir volume," *Fuel*, vol. 128, pp. 373–380, 2014.

[37] F. E. Heuze, R. J. Shaffer, A. R. Ingraffea, and R. H. Nilson, "Propagation of fluid-driven fractures in jointed rock. Part 1–development and validation of methods of analysis," *International Journal of Rock Mechanics and Mining Sciences & Geomechanics Abstracts.*, vol. 27, no. 4, pp. 243–254, 1990.

[38] R. J. Shaffer, R. K. Thorpe, F. E. Heuze, and A. R. Ingraffea, "Numerical and physical studies of fluid-driven fracture propagation in jointed rock," in *the 25th US Symposium on Rock Mechanics (USRMS)*, American Rock Mechanics Association, 1984.

[39] Y. Wang, X. Li, R. Zhou, and C. Tang, "Numerical evaluation of the shear stimulation effect in naturally fractured formations," *Science China Earth Sciences*, vol. 59, no. 2, pp. 371–383, 2016.

[40] F. Zhang, E. Dontsov, and M. Mack, "Fully coupled simulation of a hydraulic fracture interacting with natural fractures with a hybrid discrete-continuum method," *International Journal for Numerical and Analytical Methods in Geomechanics*, vol. 41, no. 13, pp. 1430–1452, 2017.

[41] H. Gu, E. Siebrits, and A. Sabourov, "Hydraulic fracture modeling with bedding plane interfacial slip," in *SPE Eastern Regional/AAPG Eastern Section Joint Meeting*, Society of Petroleum Engineers, 2008.

[42] A. Dahi Taleghani and J. E. Olson, "How natural fractures could affect hydraulic-fracture geometry," *SPE Journal*, vol. 19, no. 1, pp. 161–171, 2013.

[43] W. C. Zhu and C. A. Tang, "Micromechanical model for simulating the fracture process of rock," *Rock Mechanics and Rock Engineering*, vol. 37, no. 1, pp. 25–56, 2004.

[44] Q. Zhang, D. Ma, J. Liu, K. Zhang, and Z. Fan, "Numerical studies on the failure process of heterogeneous rock material with preexisting fracture under uniaxial compression," *Advances in Civil Engineering*, vol. 2018, Article ID 9203549, 12 pages, 2018.

[45] X. Zhang, J. G. Wang, F. Gao, Y. Ju, and J. Liu, "Impact of water and nitrogen fracturing fluids on fracturing initiation pressure and flow pattern in anisotropic shale reservoirs," *Computers and Geotechnics*, vol. 81, pp. 59–76, 2017.

[46] M. Hubbert and D. Willis, "Mechanics of hydraulic fracturing," *Transactions of the AIME*, vol. 210, no. 1, pp. 153–168, 1957.

[47] B. Haimson and C. Fairhurst, "Initiation and extension of hydraulic fractures in rocks," *Society of Petroleum Engineers Journal*, vol. 7, no. 3, pp. 310–318, 1967.

[48] Y. L. Lu, D. Elsworth, and L. G. Wang, "Microcrack-based coupled damage and flow modeling of fracturing evolution in permeable brittle rocks," *Computers and Geotechnics*, vol. 49, pp. 226–244, 2013.

Hindawi
Geofluids
Volume 2021, Article ID 6631744, 16 pages
https://doi.org/10.1155/2021/6631744

Research Article

Particle Flow Simulation of Failure Characteristics of Deep Rock Influenced by Sample Height-to-Width Ratios and Initial Stress Level under True-Triaxial Unloading

Haoyu Rong,[1] **Guichen Li**,[1] **Jiahui Xu**,[1] **Ruiyang Bi**,[1] **Yuantian Sun**,[1] **Yaqiao Hu**,[2] **and Guoliang Bai**[3]

[1]*School of Mines, Key Laboratory of Deep Coal Resource Mining, Ministry of Education of China, China University of Mining and Technology, Xuzhou, Jiangsu 221116, China*
[2]*Tongling Nonferrous Metals Group Holdings Co., Ltd. Technology Center, Tongling, Anhui 244000, China*
[3]*Tangshan Branch, Ecological Environment Technology Co., Ltd., China Coal Technology and Engineering Group Corp., Tangshan 063012, China*

Correspondence should be addressed to Guichen Li; liguichen@126.com

Received 21 December 2020; Revised 12 February 2021; Accepted 31 March 2021; Published 21 April 2021

Academic Editor: Kai Yao

The micromechanism of the effects of different height/width ratios (H/W) and initial stress levels on unloading characteristics of deep rock was investigated based on PFC3D true-triaxial unloading simulation. The results show that the increase of H/W will increase the movement speed of rock particles and intensify the acoustic emission (AE) activity inside the rock. With the increase of H/W, the failure mode of rock changes from splitting failure to tensile-shear failure. With increasing initial stress level, the particle velocity and overall fragmentation degree of rock increase. However, the increase of lateral stress will limit the coalescence of microfractures and weaken AE activity in the rock. Under unloading condition, the bonds between particles generally crack along the unloading direction, and the tensile effect is more pronounced under the condition of low initial stress level and high H/W. Under unloading condition, the variable energy of rock increases with increasing H/W and initial stress level, and the kinetic energy of rock particles increases with increasing H/W. The increase of initial stress level will increase the kinetic energy of rock particles when H/W is high.

1. Introduction

The instability and failure of surrounding rock caused by excavation unloading effect is a huge problem faced by deep underground engineering. It is important to master the unloading characteristics of deep rock mass, which is necessary to improve the stability of surrounding rock and give full play to the optimal effect of support [1–5].

The mechanical properties of deep rock are affected by its stress environment. The deformation and failure characteristics of rock under different stress levels are different. Qiu et al. [6] investigated the unloading strength, deformation law, and expansion characteristics of marble under different unloading initial damage levels and unloading path and revealed the control effect of unloading initial damage degree and unloading path. Xu et al. [7] studied the influence of initial stress and unloading rate on the deformation and failure mechanism of Jinping marble under true-triaxial compression. Hou et al. [8] examined the effects of unloading rate on the deformation and failure of surrounding rock under different confining pressures. Zhang et al. and Yin et al. [9, 10] performed test and numerical simulation under different stress levels to investigate the deformation and failure characteristics of rock. Li et al. and Ma et al. [11, 12] carried out laboratory tests and obtained the failure mode and spalling strength of rock under different confining pressures.

The research shows that the deformation and failure characteristics of surrounding rock are not only affected by the change of stress level but also related to the specific size [13–15]. Some scholars have studied the mechanical

Table 1: Microparameters of the calibrated PFC3D model.

Microparameter	Description	Calibrated value
R_{min} (mm)	Minimum particle radius	1.5
$R_{max}R_{min}$	Particle radius ratio	1.66
E_c (GPa)	Effective modulus	15
k^*	Normal-to-shear stiffness ratio	1.5
μ	Particle friction coefficient	0.5
$\bar{E}_c$ (MPa)	Bond effective modulus	15
$\bar{k}^*$	Bond normal-to-shear stiffness ratio	1.5
$\bar{\sigma}_n$ (MPa)	Normal bond strength (mean ± SD)	30 ± 5
$\bar{\tau}_n$ (MPa)	Shear bond strength (mean ± SD)	60 ± 5
λ	Bond width multiplier	1

Table 2: Test and simulation results.

Method	Uniaxial compression strength (σ_c (MPa))	Young's modulus (E (GPa))	Poisson's ratio (ν)	Sample size ($R \times H$ (mm))
PFC simulation	154.03	22.46	0.16	25 × 100
Laboratory test	154.27	22.89	0.17	25 × 100

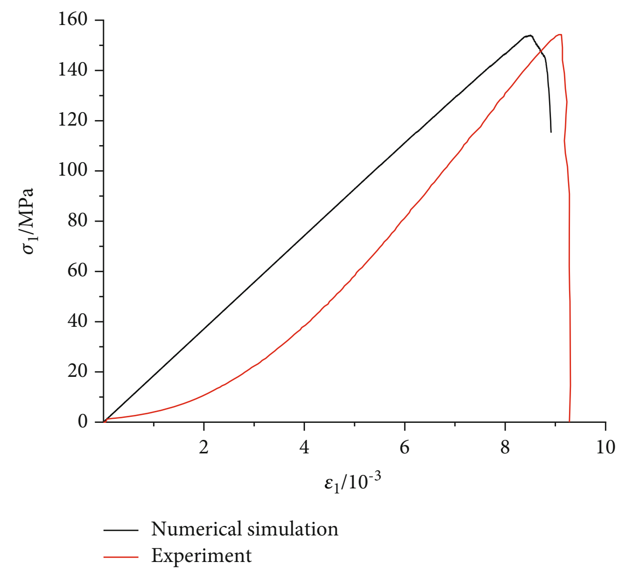

Figure 1: Stress-strain curves obtained from the laboratory test and PFC simulation.

Table 3: Initial stress level.

Stress level	σ_1 (MPa)	σ_2 (MPa)	σ_3 (MPa)
S1	40	10	5
S2	50	20	10
S3	60	40	20

properties of rocks with different sizes. Mogi and Bažant et al. [16, 17] found that with increasing length/diameter ratio, the rock strength will decrease significantly. Li et al. [18] observed that the macrofailure mode of rock is affected by the change of height/width ratios (H/W). Zhao et al. [19, 20] presented the results of an experimental study on strainburst behaviors of rock with different H/W under the condition of true-triaxial unloading. Li et al. and Chen et al. [21, 22] studied the effects of different H/W on the true-triaxial unloading characteristics of rock. However, these studies only focus on the macrolevel, and the failure mechanism of rock at the microlevel has not been studied. The mesomechanism of the influence of H/W and initial stress on the unloading characteristics of deep rocks is still unclear.

For the macrolevel study of mechanical properties of high-stress rock mass, predecessors have done a lot of basic work. At present, it is necessary to further explore the failure mechanism of deep rock under different conditions from the microlevel. The particle flow code (PFC) discrete element method can conveniently handle discontinuum problems and effectively simulate discontinuous phenomena such as the cracking and separation of a medium, offering an important means for studying the failure mechanism of rock-like media [23–25]. Wu et al. [26] conducted PFC simulation of unloading rockburst test and obtained the microfracture phenomenon and process of rock sample under different stress states. Huang et al. [27] analyzed the strength failure behavior and crack evolution mechanism of granite containing noncoplanar holes based on PFC simulation and laboratory tests. Bahaaddini et al. [28] used PFC to numerically investigate the influence of the geometrical parameters of jointed rock masses on the mechanical properties of the joints. Mohammad et al. [29] established a new rock strength criterion based on true-triaxial tests and PFC simulation. Valdez et al. [30] used PFC to study the influence of fracture roughness and microfractures on the mechanical responses of rock joints. The above studies show that the PFC can be used to investigate rock deformation and failure characteristics from the microlevel and that the simulation results are basically consistent with the actual results.

To further explain the mechanical behavior of deep rock, unloading tests were carried out in the present study through PFC3D true-triaxial simulation. The stress-strain relationship, failure modes, and crack evolution process of deep rock under different H/W and initial stress level were analyzed from macro- and microperspectives.

2. Numerical Simulation Scheme

2.1. Construction of a Numerical Model. PFC3D is used in the present study for true-triaxial numerical simulation. The parallel bond model (PBM), a commonly adopted contact model, is selected. In this model, the bond breakage leads to an immediate decrease in the macrostiffness [23, 31], and

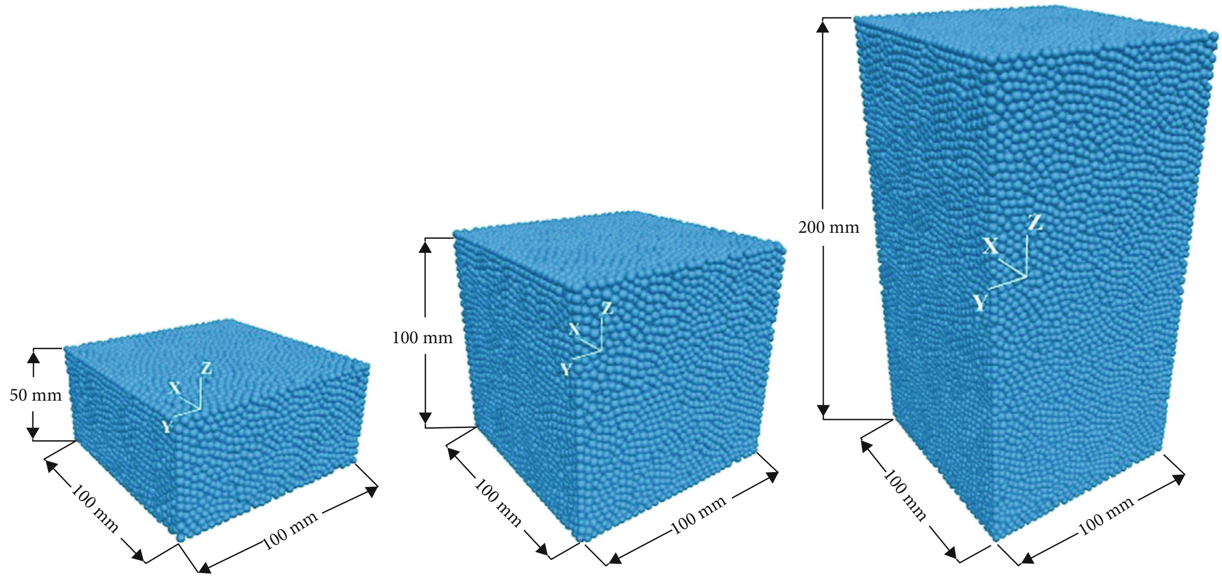

FIGURE 2: Numerical model.

hence, the characteristics of rock material failure can be reflected well.

Microparameters are used in PFC3D to characterize the mechanical properties of particles and bonds. Therefore, first, the calculated macroparameters of the sample must be compared with the laboratory test results, then the microparameters must be adjusted, and finally, a set of parameters that make the simulation results consistent with the test results must be determined and used for subsequent simulation calculations. The rock physical and mechanical parameters were obtained by uniaxial compression of granite standard samples. Rock samples tested were granite which is typically hard and brittle rock found in Anhui province. According to the relationship between the macro- and microparameters of the model [32–35], the trial-and-error method is used to calibrate microparameters, the experimental results are matched by continuously adjusting the microparameters, and the obtained microparameters are shown in Table 1.

Table 2 shows the laboratory test results and PFC simulation results. The comparison in Figure 1 reveals that the stress-strain characteristics of the discrete element model are basically consistent with the laboratory test results (note that the experimental curve exhibits a nonlinear increase due to the presence of microfractures in the granite specimens at the compaction stage, whereas the simulation curve shows a linear increase because of the relatively uniform contact between particles in the PFC3D model), indicating that the overall mechanical properties of the rock can be captured by using the PBM model and calibrated microparameters in the PFC.

2.2. Test Procedure. Due to the influence of excavation unloading effect, the surrounding rock is in the state of tangential stress concentration and radial stress reduction. Therefore, in order to study the unloading characteristics of deep rock under different stress levels and H/W (height/width ratio) and simulate the stress state of surrounding rock of deep tunnel, the specific steps are as follows: (1) the simulation adopts the force loading mode. Firstly, load σ_1, σ_2, and σ_3 to the set stress level, as shown in Table 3; (2) keep the other five stresses unchanged and remove the unloading surface stress and stabilize for 2000 steps; (3) keep the σ_2 and σ_3 unchanged and load σ_1 with 0.1 MPa/step until the specimen fails.

The H/W of the specimen is set in three groups, and the specific size is shown in Figure 2, in which the normal direction along the negative direction of the X-axis is the unloading surface.

3. Simulation Results

3.1. Stress-Strain Relationship. Figure 3 shows the relationship between the complete stress-strain curve and AE under different H/W and initial stress level. In the figure, the black curve corresponds to the axial stress, the red curve corresponds to the number of AE events, and the blue curve corresponds to the total number of microfractures (F_a). It can be seen from the figure that the stress-strain curve obtained by simulation experienced an elastic stage, a plastic stage, and a postpeak failure stage (due to the influence of the PFC loading mechanism, there is no compaction stage in the curves obtained from numerical simulation). It can be found that the nonlinear stage of the curve is short. After reaching the peak value, the fractures in the specimen rapidly expand and penetrate, and the stress-strain curve drops rapidly. The deformation and failure of the sample showed obvious brittleness.

Combined with Table 4, the results indicate that when H/W is constant, the peak stress and peak strain (the corresponding ε_1 at the peak stress) increase with increasing initial stress level. Under the three H/W conditions, the peak stress increases by 16% to 19%, and the peak strain increases by 12% to 14%. The results show that the strength of rock will

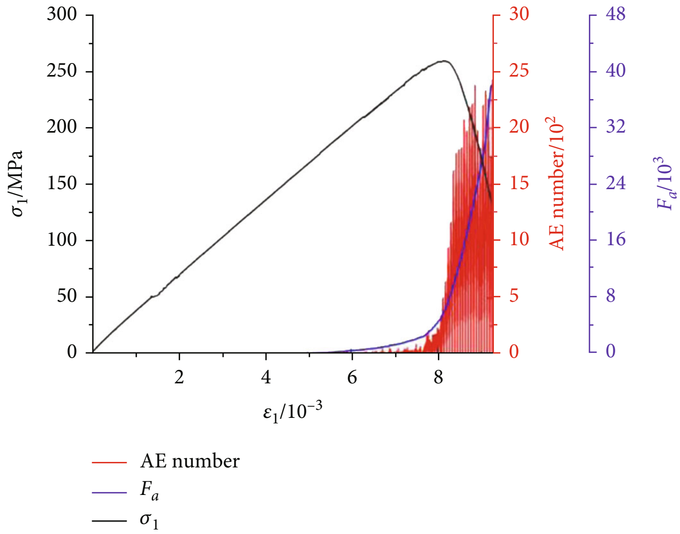

(a) $L/H = 0.5$, S1

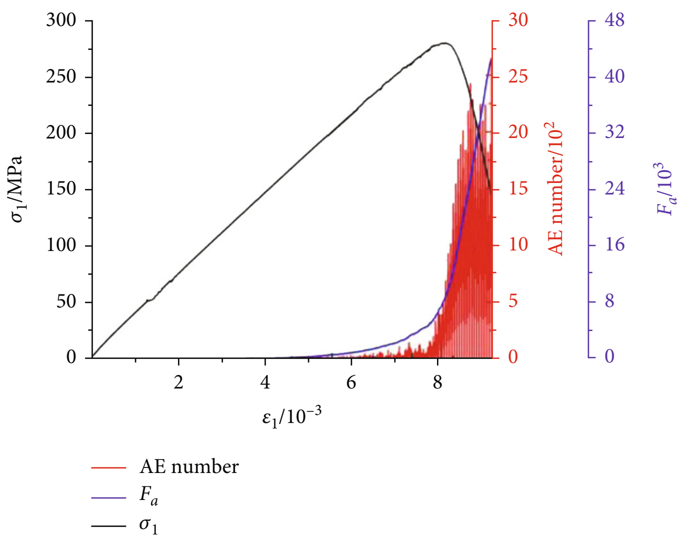

(b) $L/H = 0.5$, S2

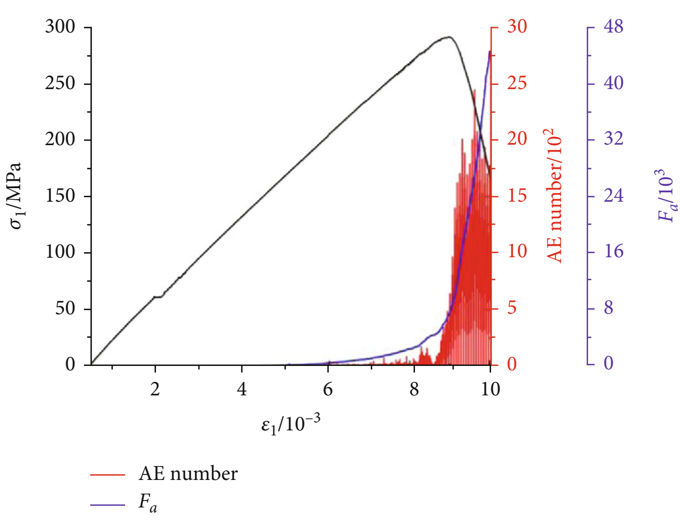

(c) $L/H = 0.5$, S3

Figure 3: Continued.

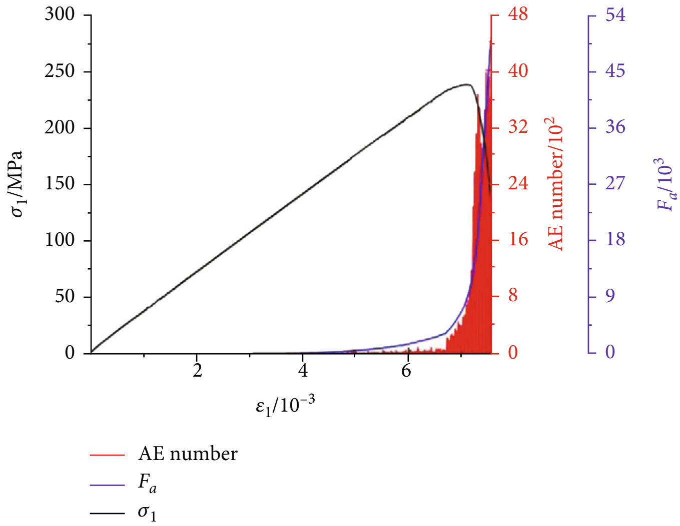

(d) $L/H = 1$, S1

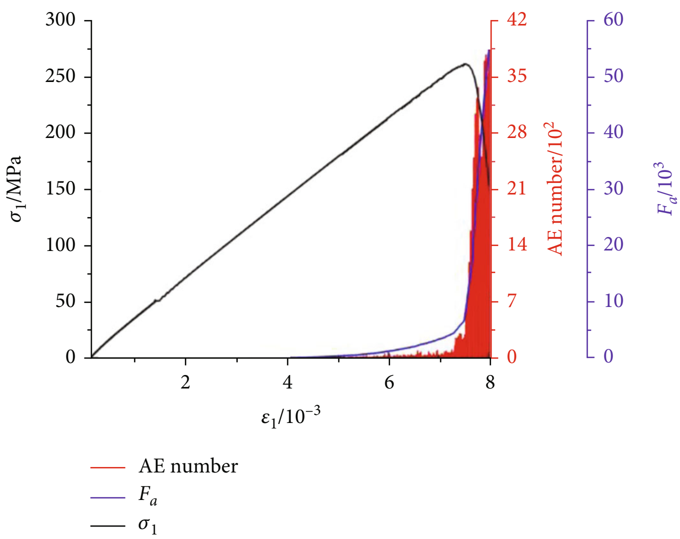

(e) $L/H = 1$, S2

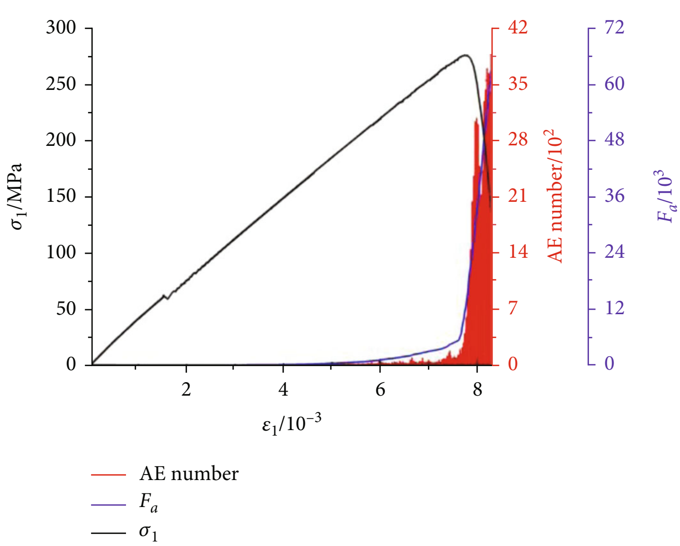

(f) $L/H = 1$, S3

Figure 3: Continued.

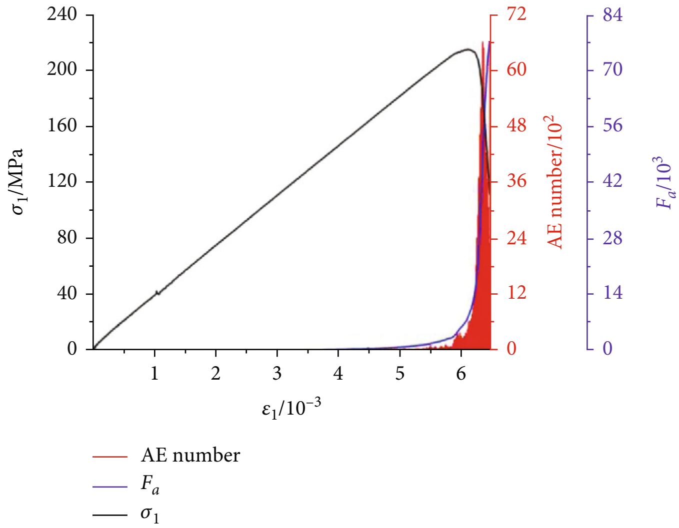

(g) $L/H = 2$, S1

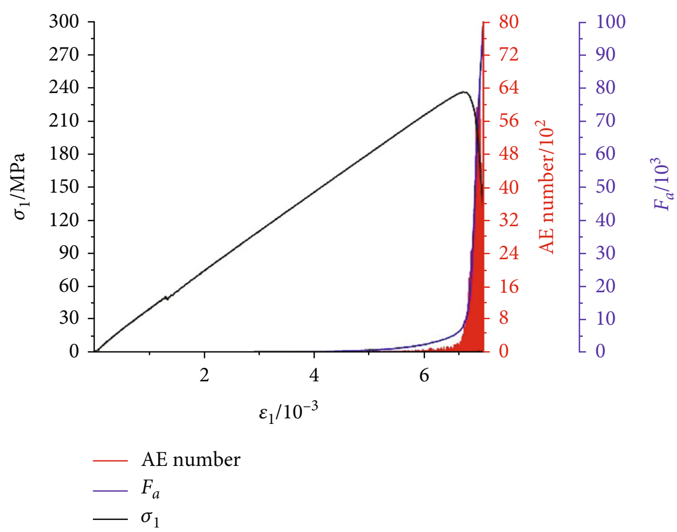

(h) $L/H = 2$, S2

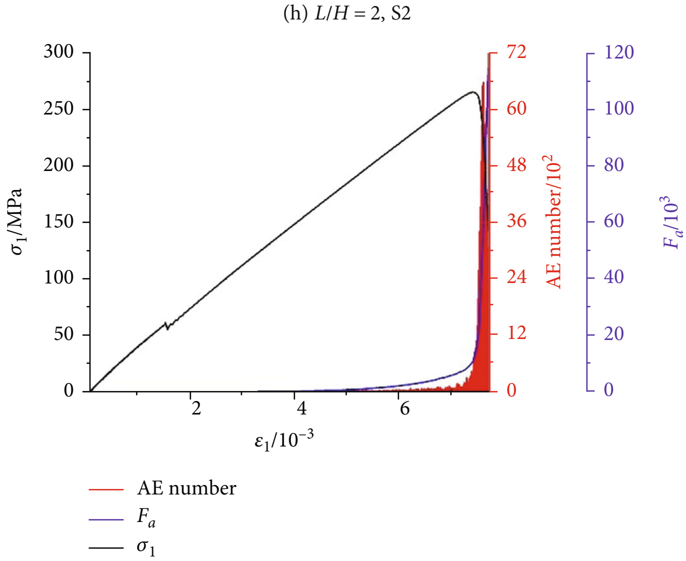

(i) $L/H = 2$, S3

Figure 3: Relationship between complete stress-strain curve and AE.

Table 4: Simulation results.

Stress level	Peak stress σ_1 (MPa)			Peak strain $\varepsilon_1/10^{-3}$		
	$L/H = 0.5$	$L/H = 1$	$L/H = 2$	$L/H = 0.5$	$L/H = 1$	$L/H = 2$
S1	251.71	237.42	212.09	8.01	7.11	6.11
S2	278.13	259.26	236.84	8.79	7.54	6.72
S3	290.79	272.21	251.38	8.97	7.74	6.97

Table 5: AE simulation results.

Stress level	Peak value of AE events			Total number of microfractures		
	$L/H = 0.5$	$L/H = 1$	$L/H = 2$	$L/H = 0.5$	$L/H = 1$	$L/H = 2$
1	2485	3971	6518	38227	50884	76435
2	2431	3743	6332	41963	55549	98766
3	2449	3648	6084	45991	61937	114869

be improved with increasing lateral stress, and the ductility of rock will be more obvious with increasing lateral stress, which shows the transformation trend from brittleness to ductility. Under the same initial stress level, the peak stress and peak strain decrease with increasing H/W. The peak stress and peak strain decrease by 14% to 16% and 22% to 24%, respectively. This shows that the strength of rock will be reduced with increasing H/W, and the brittleness of rock will be more pronounced with increasing H/W.

3.2. Acoustic Emission (AE) Simulation Results. Through the monitoring of information such as time, space, and the fracture intensity generated by AE signals during the rock fracture process, the process of rock crack initiation, development, and coalescence can be derived. In the PFC program, particles are used to construct a computational model, where the bonds between particles are broken under external force and microfractures are generated. Therefore, the rupture initiation and evolution in the model can be simulated to effectively reproduce the AE mechanism of the rock [36–38]. PFC is used in this study to simulate the AE characteristics of the rock unloading failure under different H/W and different initial stress level. Figure 3 shows that before reaching the peak value, the number of microfractures in the sample and the number of AE events increase only slightly, but when the stress reaches the peak value, both start to increase rapidly, and the curve of total number of microfractures exhibits a steep rise. This phenomenon is consistent with the characteristics of brittle failure of granite under unloading conditions.

Combined with Table 5, it can be found that under the same stress level, the peak value of AE event number and the total number of microfractures increase with increasing H/W. Under the three stress levels, the peak AE event number increases by 1.48 to 1.62 times, the total number of microfractures increases by 64.4% to 90.9%, and the failure progress of the rock is the most severe under the condition of H/W = 2. Under the same H/W conditions, the total number of microfractures increases with increasing initial stress level, while the peak value of AE events decreases with increasing initial stress level. Under the three H/W conditions, the peak value of AE events decreases by 2.2% to 8.1%, which indicates that the AE activity is more severe in the progress of rock failure when the initial stress level is low, and the increase of lateral stress will limit the coalescence of microfractures.

3.3. Rock Failure Mode. Table 6 shows schematic diagrams of the typical macrofailure of specimens obtained by simulation under different conditions; the red and yellow parts represent the tensile and shear failure of bond between particles, respectively. It can be seen from the figure that under different conditions, the bonds in the specimen mainly fail under tension, and the splitting fracture and inclined shear fracture extending from unloading surface the interior of the rock can be observed; the failure mode is tensile-shear failure.

As shown in Table 6, under the same H/W condition, with the increase of initial stress level, the overall fragmentation degree of the specimen increases. The specimen macrofailure mode gradually changes from shear failure to tensile-shear failure, and the number of splitting fractures in the specimen increases significantly. Under the condition of H/W = 1, 2, it can be found that under the condition of initial stress level of S1, the interior of the specimen is penetrated by oblique shear fractures, and there are a few splitting fractures. When the initial stress levels are S2 and S3, the rock plate formed by splitting appears near the unloading surface of the specimen. Under the same initial stress level, the overall fragmentation degree of the specimen decreases with increasing H/W. The overall fragmentation of the specimen was relatively high under the condition of H/W = 0.5, and the splitting failure is the main failure mode when H/W is low.

4. Discussion

4.1. Analysis of Micromechanism of Rock Failure. Figure 4 shows the proportion of shear fractures in rock microfractures under different conditions. It can be found that the bond between rock particles mainly fail under tension. With increasing stress level, the proportion of microfractures formed by shear failure increases gradually, and the tension

TABLE 6: Macrofailure mode of specimen.

Failure mode

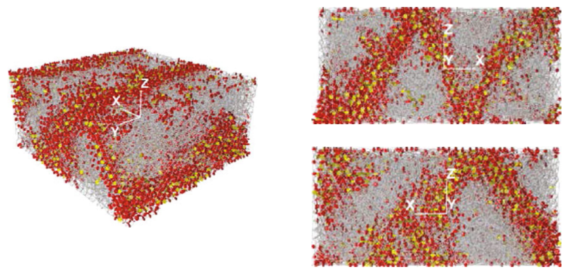

(a) S1

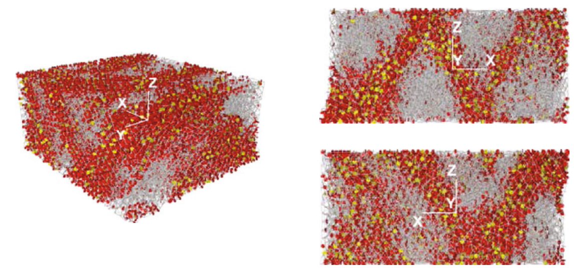

(b) S2

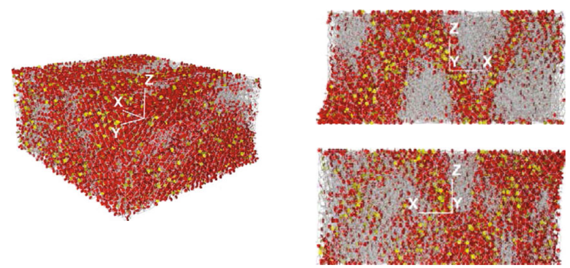

(c) S3

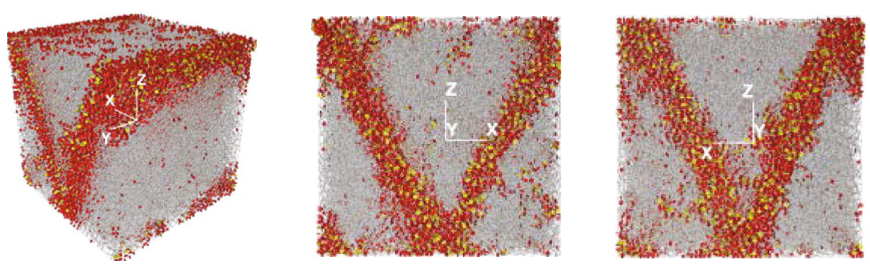

(a) S1

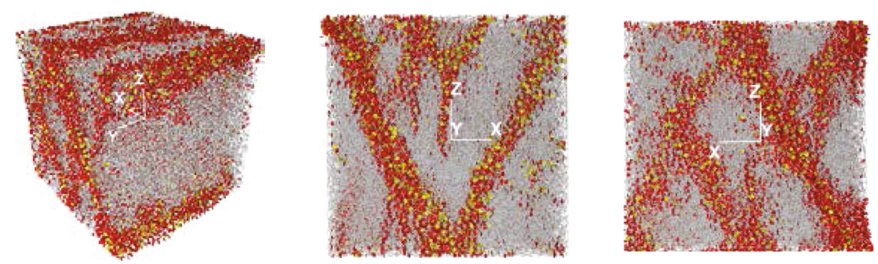

(b) S2

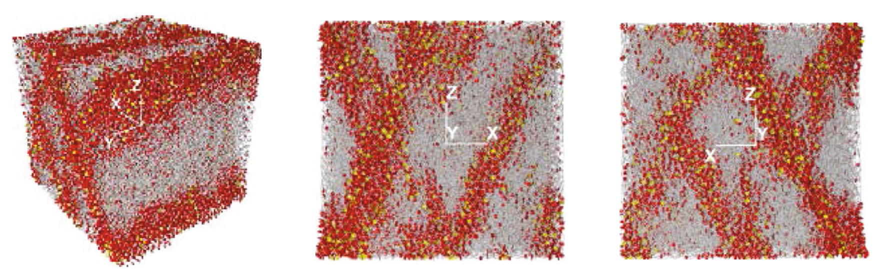

(c) S3

Table 6: Continued.

Failure mode

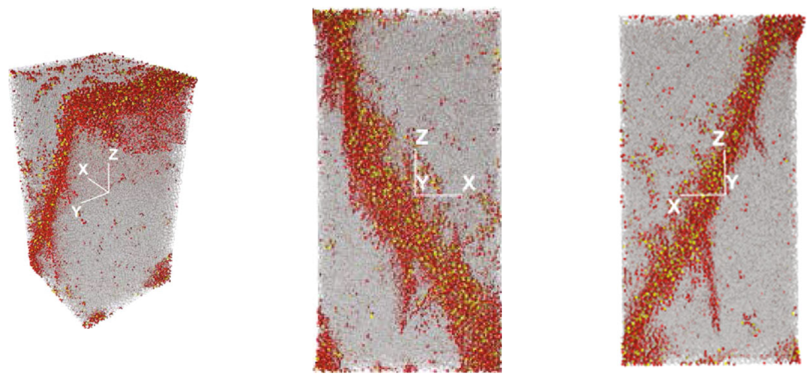

(a) S1

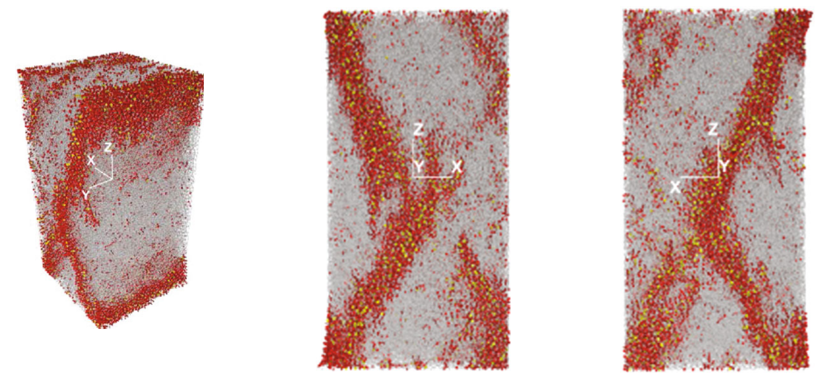

(b) S2

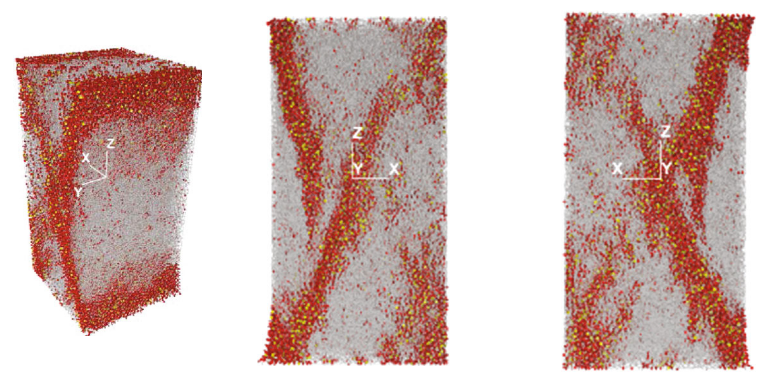

(c) S3

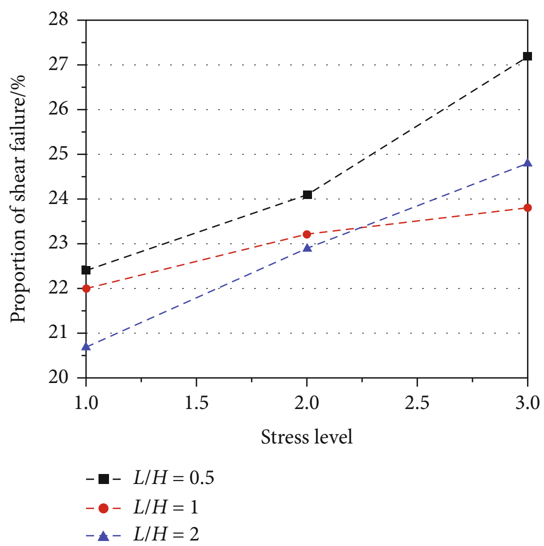

FIGURE 4: Proportion of shear fractures in rock microfractures.

effect between rock particles gradually weakens. When the stress level is S1 and S2, the proportion of shear fracture decreases with increasing H/W, while the proportion of shear fracture decreases first and then increases with increasing H/W at stress level of S3. It can be found that when H/W = 2 and the initial stress level is S1, the tension effect is more pronounced between particles.

To further explain the micromechanism of rock failure under different conditions, the particle motion of typical samples is analyzed. The velocity distribution in the specimen is shown in Table 7.

It can be seen from the table that particles in the rock mainly move along the unloading direction, and the closer the particles are to the unloading surface, the higher their velocities are. Combined with Table 4, it can be seen that the rock specimen first fails near the unloading surface and gradually expands to the interior. The fragmentation degree of the specimen near the unloading surface is relatively high; this is consistent with the true-triaxial unloading test, which shows that the deformation of the specimen exhibits strong expansion along the unloading direction. According to the velocity and movement direction of rock particles in the table, the formation of fractures in rock is mainly attributed to the following: (1) local particles move in the same direction but at different velocities. The particle velocity at the unloading surface is larger than that in the inner part of the specimen, the velocity of particles in front being higher than that of particles in the rear, which eventually form the splitting fractures; (2) local particles move relative to each other at a certain angle (<180°) and velocities are different, forming tensile-shear fractures, i.e., under the combined tensile-shear action.

It can be found that the velocity of rock particles increases with increasing H/W and initial stress level. According to Table 7, when the initial stress level is constant, under the condition of higher H/W, the velocity of rock particles is higher, the deformation and failure progress and AE activity of rock are more intense, but the overall fragmentation degree of rock is low. Under constant H/W, the increase of initial stress level will make the rock accumulate more energy and improve the velocity of particles in the rock, the fractures in the rock developed and propagated relatively fully, and the overall fragmentation degree of rock will be higher. But the increase of lateral stress will limit the coalescence and connection of microfractures in the rock and weaken AE activity in the process of rock failure.

As shown in Figure 5, taking the distribution of the angles of microfractures in rock under the condition of H/W = 1 and initial stress level of S3 as an example (Dip is the dip angle of the microfracture plane, and dip-direction is the angle between the inclination of the microfracture plane and the Y-axis), it can be found that dip of the microfracture plane is mostly concentrated at 90°, and dip-direction of the microfracture plane is mostly concentrated between -90° and 90°. Indicating that due to the unloading effect, the bonds in the rock under unloading conditions generally crack along the unloading direction. Combined with Table 7, it can be found that the specimen is under tension along the unloading direction, and the tensile force exerted on the bonds in the specimen exceeds its normal strength, leading to the tensile failure of the bonds.

4.2. Energy Evolution of Rock. Figures 6 and 7 show the strain energy and kinetic energy evolution curves under different conditions. From an energy perspective, rock failure is the result of the combined effect of the accumulation and transformation of energy, including internal strain energy and dissipative energy. Taking the patterns of strain energy and kinetic energy evolution as an example, it can be found that the strain energy in the rock increases continuously during the test process. When it is close to failure, the strain energy is rapidly released and converted into dissipative energy and kinetic energy acting on the development and expansion of fractures. The kinetic energy is basically zero in the prepeak stage (the kinetic energy increases slightly due to the unloading effect when unloading the unloading surface stress, then decreases rapidly and tends to zero), and the kinetic energy of particles increases rapidly when it is close to failure, which results in the rapid development and coalescence of microfractures in the rock and leads to the failure of the rock.

It can be found from Figures 6 and 7 that under constant H/W, the strain energy of the specimen increases with increasing initial stress level, which indicates that the increase of the lateral stress improves the strength of the rock and makes the rock accumulate more energy during the test. When H/W = 0.5, the kinetic energy changes little with increasing initial stress level but increases with increasing initial stress level under the conditions of H/W = 1 and 2, which indicates that the increase of the initial stress level has little effect on the evolution of kinetic energy of rock particles. Under constant initial stress level, the strain energy and kinetic energy of the specimen increase with increasing H/W, and the energy release is more rapid with increasing H/W, which indicates that the increase of H/W will make the rock accumulate more energy and accelerate the process

Table 7: The velocity distribution in the specimen.

	Velocity field		Failure mode	
S1, H/W = 0.5	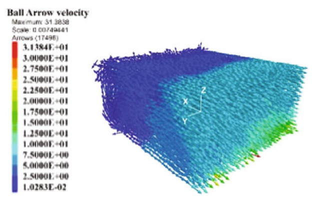	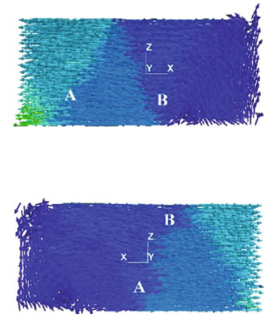	(A) Tension failure 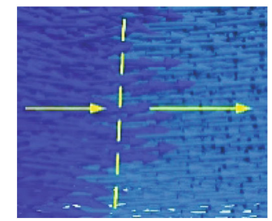	(B) Tension-shear failure 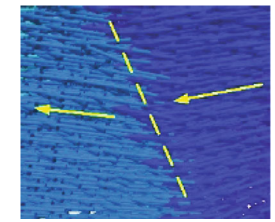
S3, H/W = 0.5	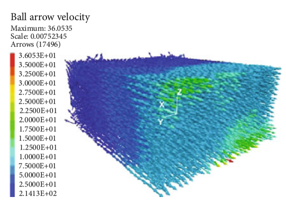	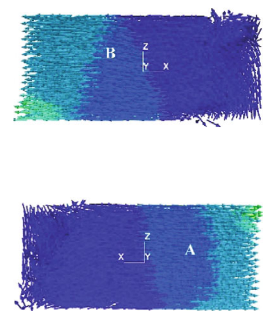	(A) Tension failure 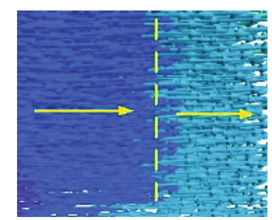	(B) Tension-shear failure 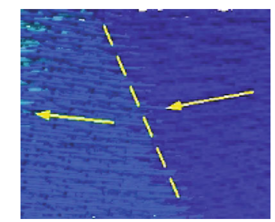
S3, H/W = 1	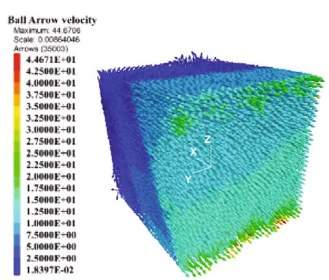	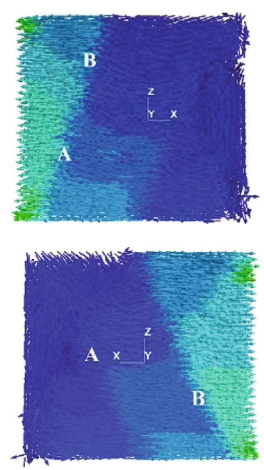	(A) Tension failure 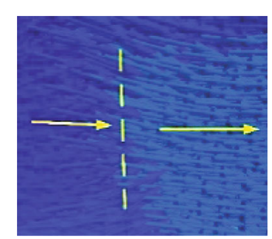	(B) Tension-shear failure 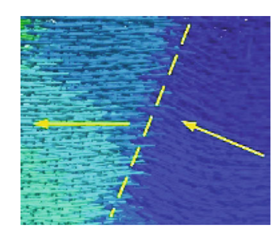

Table 7: Continued.

	Velocity field	Failure mode	
S3, H/W = 2	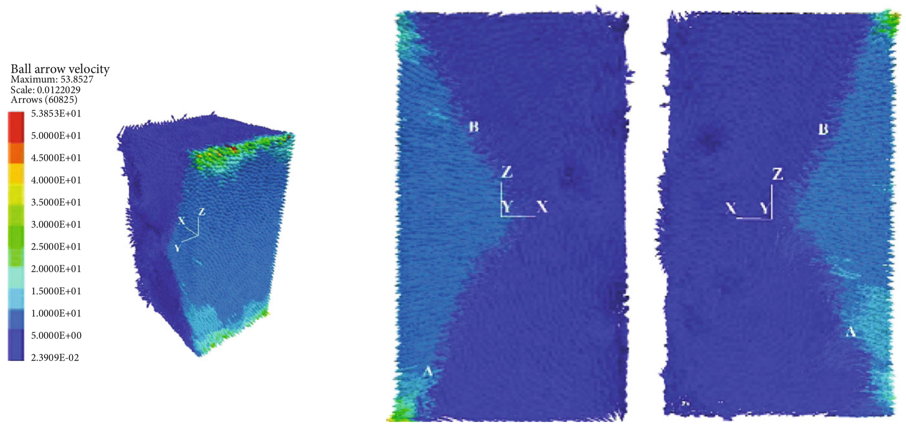	(A) Tension failure (B) Tension-shear failure	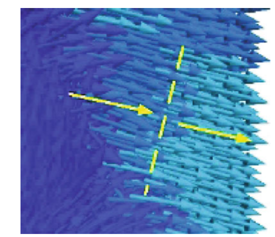 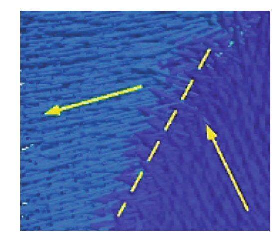

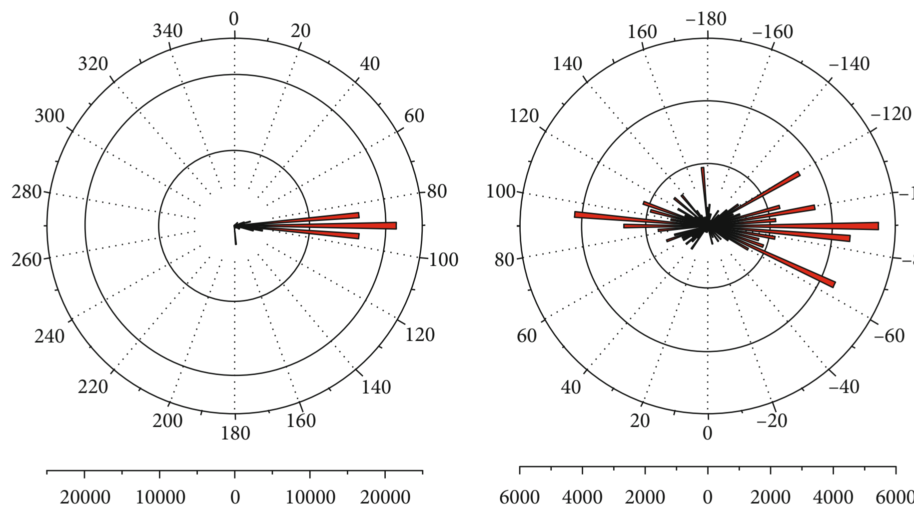

(a) Dip

(b) Dip-direction

Figure 5: Distribution of the angles of the microfractures.

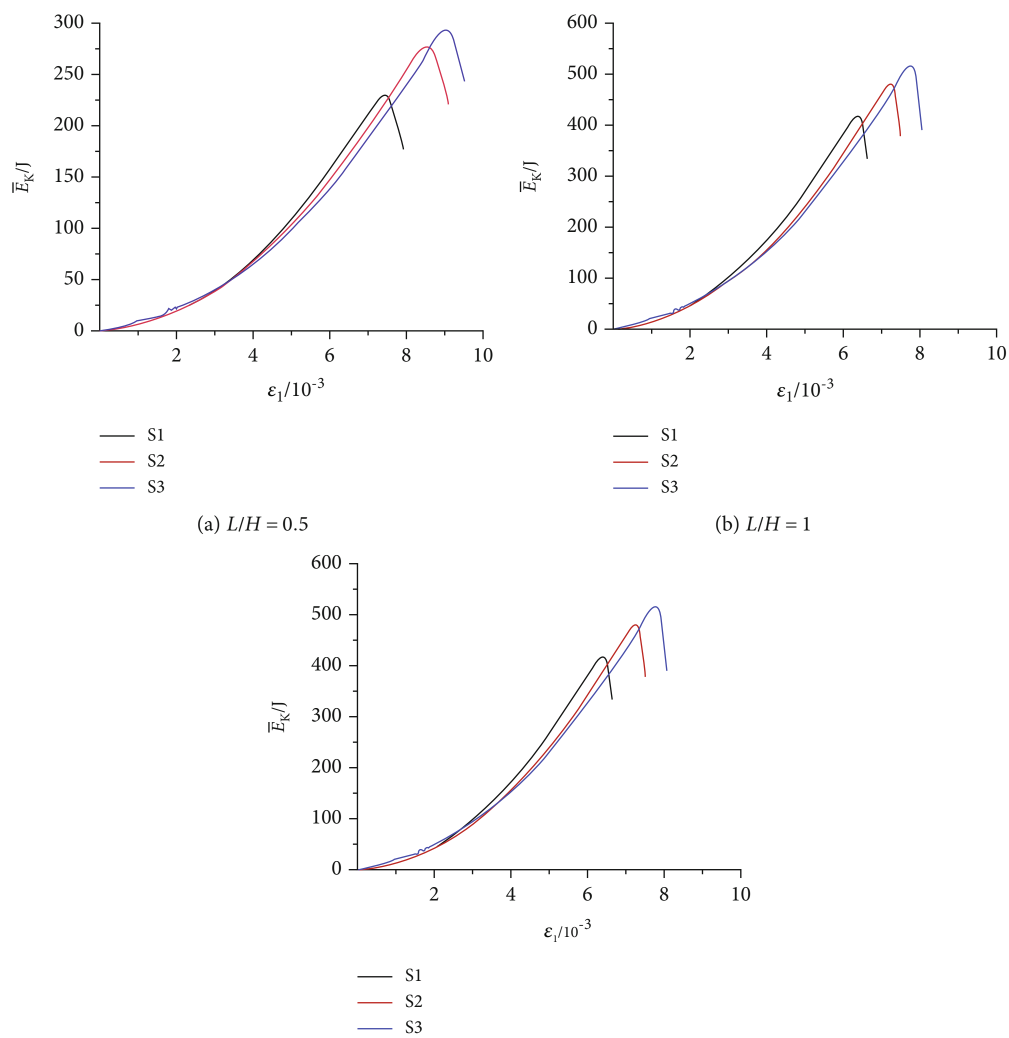

(a) $L/H = 0.5$

(b) $L/H = 1$

(c) $L/H = 2$

Figure 6: Curves of the strain energy evolution.

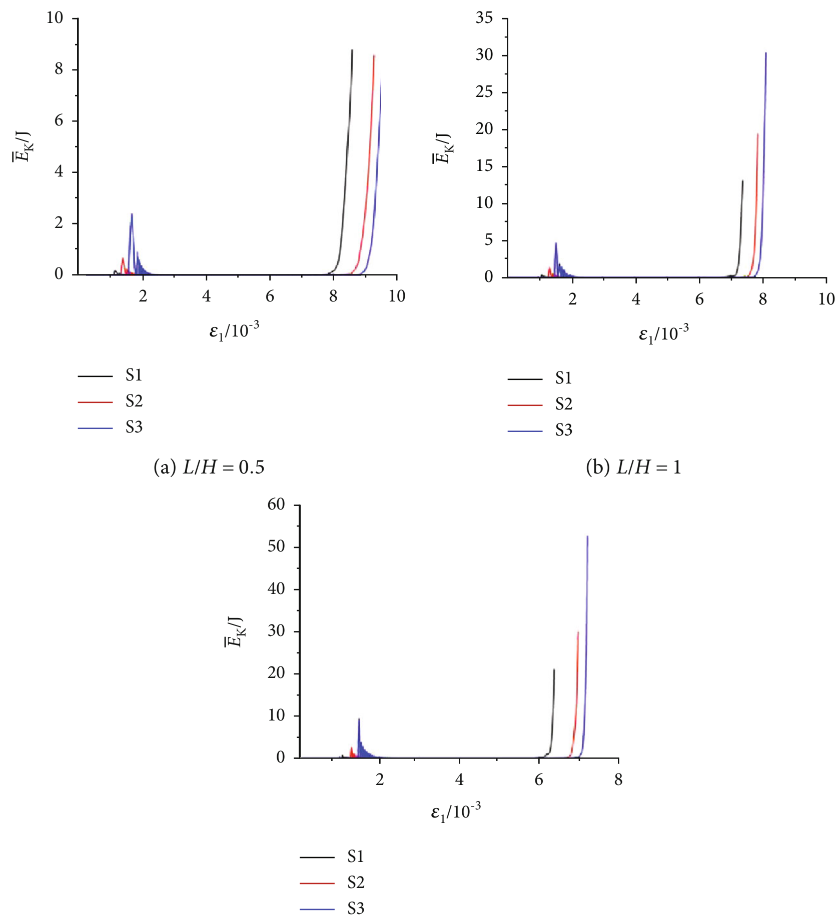

(a) $L/H = 0.5$

(b) $L/H = 1$

(c) $L/H = 2$

FIGURE 7: Curves of the kinetic energy evolution.

of energy transformation, which makes the rock more likely to be damaged.

5. Conclusion

The effects of different H/W and initial stress levels on unloading characteristics of deep rock were investigated based on PFC3D true-triaxial unloading simulation. The conclusions drawn are as follows:

(1) The increase of H/W will increase the velocity of rock particles. During the test process, the deformation and failure of rock and the activity of AE are more intense, and the failure of the rock showed obvious brittleness. When the H/W is low, the splitting failure is the main failure mode of rock, and with increasing H/W, the failure mode of rock gradually changes into tensile-shear failure

(2) With increasing initial stress level, the particle velocity and overall fragmentation degree of rock increase. However, the increase of lateral stress will limit the coalescence of microfractures and weaken AE activity in the rock

(3) Under unloading condition, the main failure mode of bond is tensile failure, and the bonds between particles generally crack along the unloading direction, and the tensile effect is more pronounced under the condition of low initial stress level and high H/W

(4) Under unloading condition, the variable energy of rock increases with increasing H/W and initial stress level, and the kinetic energy of rock particles increases with increasing H/W. When H/W is low, the change of initial stress level has little effect on kinetic energy, while the increase of initial stress level will increase the kinetic energy of rock particles when H/W is high

Data Availability

The data used to support the findings of this study are available from the corresponding author upon request.

Conflicts of Interest

The authors declare that they have no conflicts of interest.

Acknowledgments

The work presented in this paper was supported by the projects of "Supported by the Fundamental Research Funds for the Central Universities (2020ZDPY0221)" and "Tangshan Science and Technology Development Plan Funded Project (19150251E)."

References

[1] Q. L. Ha, "Loading and unloading rock masses mechanics," *Chinese Journal of Geotechnical Engineering*, vol. 20, no. 1, p. 114, 1998.

[2] J. L. Li, *Unloading Rock Mass Mechanics*, China Water Power Press, Beijing, China, 2003.

[3] M. C. He, H. P. Xie, and S. P. Peng, "Study on rock mechanics in deep mining engineering," *Chinese Journal of Rock Mechanics and Engineering*, vol. 24, no. 16, pp. 2804–2813, 2005.

[4] H. P. Xie, "Research framework and anticipated results of deep rock mechanics and mining theory," *Advanced Engineering Sciences*, vol. 49, no. 2, pp. 1–16, 2017.

[5] Y. T. Sun, G. C. Li, H. Basarir, A. Karrech, and M. R. Azadi, "Laboratory evaluation of shear strength properties for cement-based grouted coal mass," *Arabian Journal of Geosciences*, vol. 12, no. 22, p. 11, 2019.

[6] S. L. Qiu, X. T. Feng, C. Q. Zhang, and J. B. Yang, "Experimental research on mechanical properties of deep marble under different initial damage levels and unloading paths," *Chinese Journal of Rock Mechanics and Engineering*, vol. 31, no. 8, pp. 1686–1697, 2012.

[7] H. Xu, X.-T. Feng, C. Yang, X. Zhang, Y. Zhou, and Z. Wang, "Influence of initial stresses and unloading rates on the deformation and failure mechanism of Jinping marble under true triaxial compression," *International Journal of Rock Mechanics and Mining Sciences*, vol. 117, pp. 90–104, 2019.

[8] G. Y. Hou, J. P. Liang, T. Hu et al., "Unloading rate effects on the deformation and damage of the surrounding rock under different confining pressure," *Chinese Journal of Rock Mechanics and Engineering*, vol. 38, no. 3, pp. 433–444, 2019.

[9] Y. Zhang, T. Zhao, Y. Yin, Y. Tan, and Y. Qiu, "Numerical research on energy evolution in granite under different confining pressures using Otsu's digital image processing and PFC2D," *Symmetry-Basel*, vol. 11, no. 2, p. 131, 2019.

[10] P.-F. Yin, S.-Q. Yang, W.-L. Tian, and J.-L. Cheng, "Discrete element simulation on failure mechanical behavior of transversely isotropic rocks under different confining pressures," *Arabian Journal of Geosciences*, vol. 12, no. 19, 2019.

[11] X. Li, M. Tao, C. Wu, K. Du, and Q. Wu, "Spalling strength of rock under different static pre-confining pressures," *International Journal of Impact Engineering*, vol. 99, pp. 69–74, 2017.

[12] T. Ma, D. Ma, and Y. Yang, "Fractal characteristics of coal and sandstone failure under different unloading confining pressure tests," *Advances in Materials Science and Engineering*, vol. 2020, Article ID 2185492, 11 pages, 2020.

[13] X. B. Li, J. R. Yao, and K. Du, "Prelimenary study for induced fracture and non-explosive continuous mining in high-geostress hard rock mine—a case study of Kaiyang phosphate mine," *Chinese Journal of Rock Mechanics and Engineering*, vol. 6, pp. 1101–1111, 2013.

[14] J. A. Hudson, S. L. Crouch, and C. Fairhurst, "Soft, stiff and servo-controlled testing machines: a review with reference to rock failure," *Engineering Geology*, vol. 6, no. 3, pp. 155–189, 1972.

[15] H. P. Xie, R. D. Peng, Y. Ju, and H. W. Zhou, "On energy analysis of rock failure," *Chinese Journal of Rock Mechanics and Engineering*, vol. 24, no. 15, pp. 2603–2608, 2005.

[16] K. Mogi, "Some precise measurements of fracture strength of rocks under uniform compressive stress," *Rock Mechanics and Engineering Geology*, vol. 4, pp. 41–55, 1966.

[17] Z. P. Bažant and Y. Xiang, "Size effect in compression fracture: splitting crack band propagation," *Journal of Engineering Mechanics*, vol. 123, no. 2, pp. 162–172, 1997.

[18] D. Li, C. C. Li, and X. Li, "Influence of sample height-to-width ratios on failure mode for rectangular prism samples of hard rock loaded in uniaxial compression," *Rock Mechanics and Rock Engineering*, vol. 44, no. 3, pp. 253–267, 2011.

[19] X. G. Zhao and M. Cai, "Influence of specimen height-to-width ratio on the strainburst characteristics of Tianhu granite under true-triaxial unloading conditions," *Canadian Geotechnical Journal*, vol. 52, no. 7, pp. 890–902, 2015.

[20] F. Zhao and M. C. He, "Size effects on granite behavior under unloading rockburst test," *Bulletin of Engineering Geology and the Environment*, vol. 76, no. 3, pp. 1183–1197, 2017.

[21] X. Li, F. Feng, D. Li, K. Du, P. G. Ranjith, and J. Rostami, "Failure characteristics of granite influenced by sample height-to-width ratios and intermediate principal stress under true-triaxial unloading conditions," *Rock Mechanics and Rock Engineering*, vol. 51, no. 5, pp. 1321–1345, 2018.

[22] Z. Chen, L. Huang, X. Li, L. Weng, and S. Wang, "Influences of the height to diameter ratio on the failure characteristics of marble under unloading conditions," *International Journal of Geomechanics*, vol. 20, no. 9, 2020.

[23] Itasca, *PFC3D (Particle Flow Code in Three Dimensions) version 5.0*, Itasca Consulting Group, Minneapolis, USA, 2016.

[24] X. Ding, L. Zhang, H. Zhu, and Q. Zhang, "Effect of model scale and particle size distribution on PFC3D simulation results," *Rock Mechanics and Rock Engineering*, vol. 47, no. 6, pp. 2139–2156, 2014.

[25] J. W. Park and J. J. Song, "Numerical simulation of a direct shear test on a rock joint using a bonded- particle model," *International Journal of Rock Mechanics and Mining Sciences*, vol. 46, no. 8, pp. 1315–1328, 2009.

[26] S. C. Wu, Y. Zhou, and B. Gao, "Study of unloading tests of rock burst and PFC^{3D} numerical simulation," *Chinese Journal of Rock Mechanics and Engineering*, vol. 29, Supplement 2, pp. 4082–4088, 2010.

[27] Y. H. Huang, S. Q. Yang, P. G. Ranjith, and J. Zhao, "Strength failure behavior and crack evolution mechanism of granite containing pre-existing non-coplanar holes: experimental study and particle flow modeling," *Computers and Geotechnics*, vol. 88, pp. 182–198, 2017.

[28] M. Bahaaddini, G. Sharrock, and B. K. Hebblewhite, "Numerical investigation of the effect of joint geometrical parameters on the mechanical properties of a non-persistent jointed rock mass under uniaxial compression," *Computers and Geotechnics*, vol. 49, pp. 206–225, 2013.

[29] M. H. Mehranpour, P. H. S. W. Kulatilake, M. Xingen, and M. He, "Development of new three-dimensional rock mass strength criteria," *Rock Mechanics and Rock Engineering*, vol. 51, no. 11, pp. 3537–3561, 2018.

[30] A. V. Valdez, S. Morel, A. Marache, M. Hinojosa, and J. Riss, "Influence of fracture roughness and micro-fracturing on the

mechanical response of rock joints: a discrete element approach," *International Journal of Fracture*, vol. 213, no. 2, pp. 87–105, 2018.

[31] S. X. Deng, Y. L. Zheng, L. P. Feng, P. Y. Zhu, and Y. Ni, "Application of design of experiments in microscopic parameter calibration for hard rocks of PFC^{3D} model," *Chinese Journal of Geotechnical Engineering*, vol. 41, no. 4, pp. 655–664, 2018.

[32] T. Koyama and L. Jing, "Effects of model scale and particle size on micro-mechanical properties and failure processes of rocks–a particle mechanics approach," *Engineering Analysis with Boundary Elements*, vol. 31, no. 5, pp. 458–472, 2007.

[33] B. Yang, Y. Jiao, and S. Lei, "A study on the effects of microparameters on macroproperties for specimens created by bonded particles," *Engineering Computations*, vol. 23, no. 6, pp. 607–631, 2006.

[34] J. Yoon, "Application of experimental design and optimization to PFC model calibration in uniaxial compression simulation," *International Journal of Rock Mechanics and Mining Sciences*, vol. 44, no. 6, pp. 871–889, 2007.

[35] H. Rong, G. Li, D. Liang, C. Sun, S. Zhang, and Y. Sun, "Numerical investigation on the evolution of mechanical properties of rock affected by micro-parameters," *Applied Sciences-Basel*, vol. 10, no. 14, p. 4957, 2020.

[36] J. F. Hazzard and R. P. Young, "Simulating acoustic emissions in bonded-particle models of rock," *International Journal of Rock Mechanics and Mining Sciences*, vol. 37, no. 5, pp. 867–872, 2000.

[37] X.-p. Zhang, Q. Zhang, and S. Wu, "Acoustic emission characteristics of the rock-like material containing a single flaw under different compressive loading rates," *Computers and Geotechnics*, vol. 83, pp. 83–97, 2017.

[38] Y. Zhou, S. C. Wu, X. L. Xu, W. Sun, and X. P. Zhang, "Particle flow analysis of acoustic emission characteristics during rock failure process," *Chinese Journal of Rock Mechanics and Engineering*, vol. 32, no. 5, pp. 951–959, 2013.

Hindawi
Geofluids
Volume 2021, Article ID 9932932, 19 pages
https://doi.org/10.1155/2021/9932932

Research Article

Instability Mechanism of Extraction Structure in Whole Life Cycle in Block Caving Mine

Zhi-Yuan Xia,[1,2,3] **Zhuo-Ying Tan**,[1,2,3] **and Lei Zhang**[4]

[1]*School of Civil & Resource Engineering, University of Science and Technology Beijing, Beijing 100083, China*
[2]*State Key Laboratory of High-Efficient Mining and Safety of Metal Mine, Ministry of Education, University of Science and Technology Beijing, Beijing 100083, China*
[3]*Beijing Key Laboratory of Urban Underground Space Engineering, University of Science and Technology Beijing, Beijing 100083, China*
[4]*China Xinxing Mining and Chemical Co., Ltd., Beijing 100083, China*

Correspondence should be addressed to Zhi-Yuan Xia; zhiyuanxia1991@126.com

Received 4 March 2021; Revised 19 March 2021; Accepted 27 March 2021; Published 15 April 2021

Academic Editor: Yi Xue

In the whole life cycle of the extraction structure in block caving mine from the beginning of roadways excavation to the end of ore drawing, there are many factors affecting the stability of the extraction structure. The investigation in the mine site shows that the extraction structure often presents the law of repeated instability. In order to reveal the mechanism of repeated instability of the extraction structure, the whole life cycle of extraction structure can be divided into three stages, namely, the formation stage of extraction structure, the undercutting stage without initial caving, and the ore caving and drawing stage. The three-dimensional finite difference software $FLAC^{3D}$ was used to establish the numerical model of the extraction structure in the whole life cycle in the block caving method. The process of ore caving and ore drawing was replaced by manual excavation of the caving area above the undercut space and applying stress on the major apex. The stress and displacement evolution laws of the extraction structure in three stages of the whole life cycle were studied and compared with the instability characteristics of the extraction structure on mine site. The whole life cycle instability mechanism of the extraction structure in Tongkuangyu mine is revealed; the research results show that the extraction structure near the advancing undercut front is prone to producing compressive stress concentration under the action of the surrounding rock stress arch in the stope; if the rock mass shear failure condition is reached, the instability of the extraction structure occurs. The extraction structure near the advancing undercut front is gradually transferred to the area under the undercut space with undercut increase, and the tensile stress concentration gradually appears in the sidewall of ore loading roadway and the tip of major apex; if the tensile strength of the rock mass in the extraction structure is exceeded, the instability occurs again. It is helpful to reduce the probability of the instability of the extraction structure to promote the overburden ore caving as soon as possible after the undercutting begins.

1. Introduction

With the increasingly fierce market competition in recent years, the use of efficient mining methods and large-scale automatic equipment has become a trend in mining industry. Block caving is a low-cost, high efficiency, and large-scale mining method; block caving mining is the preferred method for mining deep mineral resources because of its small amount of rock drilling and large production capacity [1–3]. The extraction structure of the block caving method is the general term of a series of roadways and chambers used for ore drawing between the undercut level and the production level [4, 5]. The extraction structure undertakes the task of ore drawing. Once the extraction structure is damaged, the caved ores cannot be transported from the production level. Therefore, the stability of the extraction structure is very important, which is one of the key factors for the successful application of the block caving method. Due to the long service life of the extraction structure in the block caving mine and many factors affecting the

(a) (b)

Figure 1: Instability of extraction structure in Tongkuangyu mine: (a) collapse of the ore loading roadway and (b) bending of steel arch frame in ore drawing roadway.

stability, the maintenance of the extraction structure is difficult and the risk of instability is high.

Many experts have studied the instability reasons of the extraction structure during the process of block caving mining. Trueman et al. [6–8] studied the effect of undercut mode, horizontal stress, and other factors on the extraction structure of block caving method by using theoretical analysis, numerical simulation, and other methods, and related control measures was proposed. Rojas et al. [9, 10] monitored the stress and microseismic events of the production roadways to explore reasons of the instability of the extraction structure during the ore caving stage. Pierce et al. [11–13] studied the force of ore bulk on the extraction structure in the ore drawing stage, and the research results showed that unbalanced ore drawing was not conducive to the stability of the extraction structure, and the maximum vertical stress of the ore drawing roadway can reach 12 times of the vertical stress at the bottom of the ore bulk. Castro et al. [14, 15] used laboratory physical experiment to explore the vertical stress of extraction structure during the ore drawing stage, and the research conclusions presented that the vertical stress was mainly influenced by the area of ore drawing area and the distance between the monitoring point and the ore drawing advancing front.

In the whole life cycle of the extraction structure of the block caving mine from the beginning of roadways excavation to the end of ore drawing, there are many factors affecting its stability. Under the condition of large horizontal in situ stress, it is found that the extraction structure often presents the law of repeated instability. Previous studies have not really revealed the repeated instability mechanism of the extraction structure in the whole life cycle in the block caving method. Xia et al. [16–18] revealed the reasons for the repeated instability mechanism of the extraction structure during the process of undercutting but did not take into account the influence of the ore caving stage. In order to reveal the mechanism of repeated instability of the extraction structure, the whole life cycle of the extraction structure can be divided into three stages, namely, the formation stage of extraction structure, the undercutting stage without initial caving, and the ore caving and drawing stage. Based on the engineering background of Tongkuangyu mine, a typical block caving mine in China, the evolution characteristics of stress and displacement of the extraction structure in the whole life cycle of block caving were simulated by using three-dimensional finite difference software FLAC^{3D}, and the simulation results were compared with the instability characteristics of the extraction structure in mine site. The instability mechanism of the extraction structure in the whole life cycle is revealed, which is of great significance to ensure the safety of block cave mining.

2. Instability Characteristics of Extraction Structure in Tongkuangyu Mine

The instability characteristics of the extraction structure are mainly manifested on the damage of the production roadway, the collapse of the major apex, the deformation of the undercut roadway, and the dislocation of the ventilation shaft; it is shown in Figure 1.

Based on the site investigation and analysis of the damage area of production level in Tongkuangyu mine, the spatial and temporal evolution process of the instability area of the extraction structure over the years was reviewed, and the following instability laws can be found:

(1) A large proportion of the instability area of the extraction structure occurs in the range of 20-30 m near the advancing undercut front, which shows the ground pressure failure of the ore drawing and ore loading roadways

(2) With the advancement of undercutting, some instability areas of the extraction structure appear repeated instability after repair, and there is also a certain proportion of instability under the undercut space, which shows the repeated failure of ore drawing and ore loading roadways

(3) With the increase of the undercut area, the damage area of the production level gradually increases, and the ground pressure behavior becomes more intense

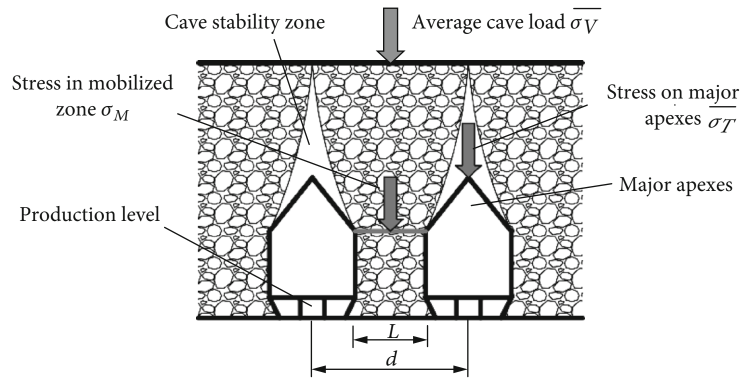

Figure 2: Schematic diagram of extraction structure under ore bulk force [11].

3. Establish of Extraction Structure Numerical Model in Whole Life Cycle

3.1. Numerical Model Establish Method. The three-dimensional finite difference software FLAC^{3D} was used to establish the numerical model. FLAC^{3D} software is suitable for simulating the stress and deformation of continuous medium, and thus, it has advantages in studying the stress of the extraction structure formation stage and the undercutting stage when the overburden ore does not form caving. However, FLAC^{3D} is not suitable for the simulation study of overburden rock caving and ore bulk drawing. Particle flow code (PFC) and 3 dimension distinct element code (3DEC) have great advantages in simulating ore bulk flow and ore caving, but it is inefficient in the calculation of a large-scale mining model. It is necessary to design the modeling method reasonably to study the stress of the extraction structure in the ore caving stage by FLAC^{3D}.

In view of the undercutting stage when the overburden ore did not form the initial caving, three undercut units were preset. The stress state of the extraction structure after excavation of each undercut unit was monitored, respectively. It could be used to study the stress evolution of the extraction structure with the increase of the undercut area.

The study of stress evolution law of the extraction structure during the caving stage did not involve the display of caving process, and only studied the stress state of the extraction structure before and after ore caving in the process of undercutting. Therefore, in the process of modeling, the command flow could be used to manually excavate the preset three domed caving areas step by step. The scope of the caving area was determined according to the following principles, the approximate range was firstly determined according to the plastic zone of overburden strata simulated by each step of undercutting, and then, the optimization was carried out according to the observed caving range in the upper panel roadway of the mine. After the area of undercut unit reaches the area of initial caving, the first domed caving area was excavated manually with command flow. With the advancement of undercutting, the other two caving areas were excavated manually in turn. Thus, the dynamic process of collapse could be transformed into a static process, and the stress evolution law of the extraction structure in the process of caving stage could be monitored and studied.

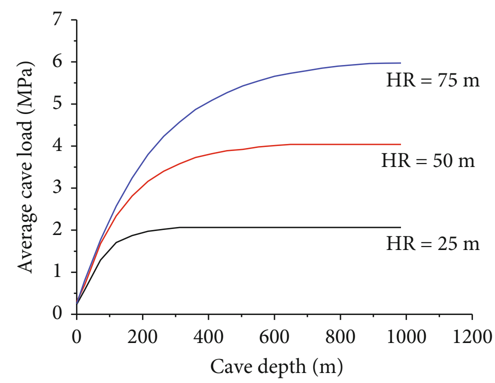

Figure 3: Function diagram of average stress at the bottom of ore bulk [11].

The model of the ore drawing stage after overburden ore caving was established by drawing on the conclusion of force analysis of ore bulk on the extraction structure studied by Pierce [9]. The stress of ore bulk acting on the extraction structure is mainly transferred through the major apexes. In the process of ore drawing, the flow of internal ore produces the equilibrium stress arch. Due to the influence of the equilibrium arch of the ore bulk, the vertical stress on the top of the major apexes is different from that on the bottom of the ore bulk, and it is shown in Figure 2. From formula (1), the stress acting on the top of the major apexes is 1.6 times as large as the average vertical stress at the bottom of the ore bulk in the stope.

$$\frac{\bar{\sigma}_T}{\sigma_V} = \frac{d}{d-l}, \tag{1}$$

where d is the distance between the adjacent ore loading roadway, and it is 30 m in Tongkuangyu mine and l is the length of drawbell, and it is 11 m in Tongkuangyu mine. The buried depth of undercut level in the main sublevel in the 530 panel in Tongkuangyu mine is 536 m. The average vertical stress at the bottom of ore bulk in stope is about 1.5 MPa by interpolation according to the functional relationship in Figure 3. Thus, the vertical stress acting on the top of the major apex is 2.4 MPa. A uniform stress of 2.4 MPa can be applied at the tip of the major apexes below

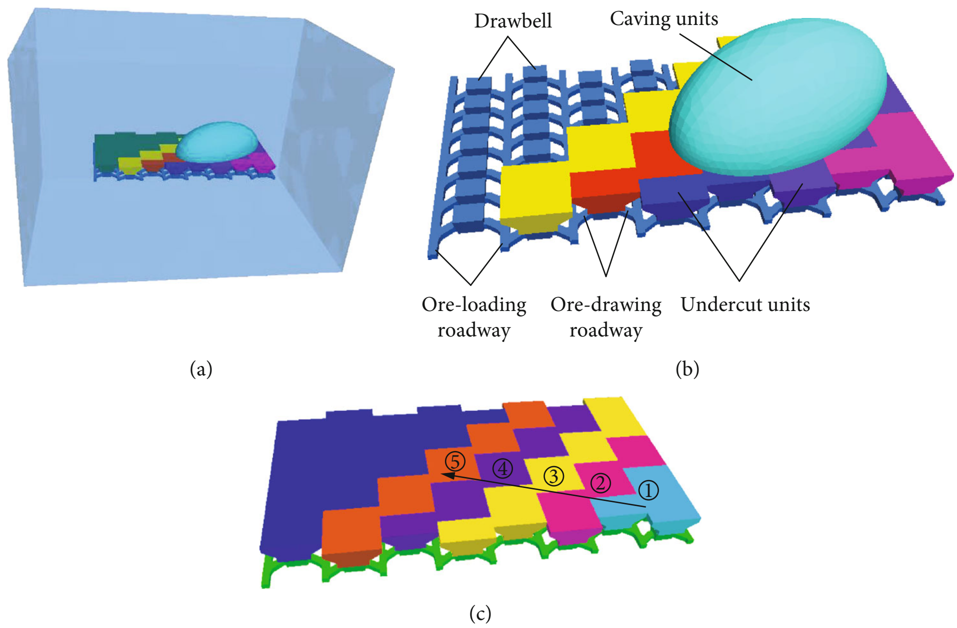

FIGURE 4: Numerical model: (a) overall structure of the model, (b) internal structure of the model, and (c) excavation sequence of the undercut unit.

TABLE 1: Rock mass mechanical parameters in the numerical model.

Items	Elasticity modulus, E (GPa)	Bulk density, ρ (kg/m^3)	Cohesive strength, C (MPa)	Shear modulus, G (GPa)	Internal friction angle, φ (°)	Tensile strength, σ_t (MPa)	Poisson ratio, μ
Value	5.99	2740	6.6	2.45	42.58	6.62	0.22

the caving space to replace the ore bulk in the ore drawing process above the extraction structure. Therefore, the dynamic simulation of the discontinuous medium was transformed into the static simulation of the continuous medium, and the stress evolution process of extraction structure in the ore drawing stage can be studied.

To sum up, through a reasonable conception of the modeling method and numerical simulation based on three-dimensional finite difference software FLAC^{3D}, the stress evolution process in the whole life cycle of the extraction structure could be effectively studied, and then, the instability mechanism of extraction structure could be explored.

3.2. Model Structure Parameters. The overall structure of the model is shown in Figure 4(a), and the internal structure of the model is shown in Figure 4(b). The range of the model is taken from the local range of the main sublevel in the 530 panel of the No.4 orebody in Tongkuangyu mine. The model has 410 m strike length, 291 m vertical strike length, and 310 m height, and 1942313 units in total. According to the needs of the research content, a total of 9 ore loading roadways, 60 ore drawing roadways, and 60 drawbells are arranged at the production level, and the burial depth of production level is 545 m. The top open face of the drawbell is 13 m × 10 m (length × width), the bottom open face is 11 m × 6.4 m (length × width), and the height is 10 m. The net cross-section of ore drawing roadways and ore loading roadways is 3.8 m × 3.2 m (width × height). The distance between the production level and the undercut level is 10 m; the distance between the adjacent ore loading roadway is 30 m; the ore drawing roadways are arranged in the branch herring bone type with the distance of 15 m. The undercut level is arranged above the extraction structure, and five undercut units are arranged from right to left. The undercut height is 12 m, and the undercut units are arranged in the diagonal direction step by step, which makes the simulation more in line with the actual situation of undercutting in Tongkuangyu mine. Three caving units are arranged above the undercut level; it is shown in Figure 4(b).

3.3. Strength Criteria and Boundary Conditions. The Mohr-Coulomb criterion was used in this calculation. Many parameters in the Hoek-Brown criterion could calculate rock mass failure with fissures [19–21]. In order to effectively describe the influence of fissures on the strength of rock mass in the numerical model, the equivalent calculation of some parameters was needed between the Hoek-Brown criterion and Mohr-Coulomb criterion. The rock mass mechanical parameters in the numerical model are shown in Table 1.

The vertical stress in the numerical model changes linearly with the depth. According to the buried depth of the ore body and the average rock mass density, the vertical stress was applied on the top plane of the model. The measured in situ stress was applied inside the model, the horizontal movement is limited on the side of the model, and the vertical movement is limited on the bottom plane of the model.

The in situ stresses applied inside the model are as follows:

$$\sigma_x = 22.8954 - 0.0399Z, \tag{2}$$

$$\sigma_y = 11.6484 - 0.0204Z, \tag{3}$$

$$\sigma_z = 14.6600 - 0.0269Z. \tag{4}$$

3.4. Numerical Simulation Steps of Extraction Structure in Whole Life Cycle. The simulation process of the numerical model was carried out according to the actual undercutting mode of Tongkuangyu mine. The extraction structure was formed firstly, and then, the undercutting level was excavated; the specific steps were as follows:

(1) The three-dimensional model was established, and the initial stress and boundary conditions were applied to form the initial equilibrium. At this time, the rock mass was in the in situ stress state

(2) The extraction structure was formed by excavating ore loading roadways, ore drawing roadways, and drawbells

(3) The undercut level was divided into five units along the diagonal direction and was pushed in ladder type, as shown in Figure 4(c); each color represented one undercut unit. Two undercut units were excavated step by step to form major apexes firstly; the initial caving was not formed in this stage. The stress and displacement state of major apexes and production roadways were monitored and analyzed

(4) With the excavation of the remaining three undercut units step by step, three ore caving areas were excavated in turn, which represented the continuous caving of overburden ore. At the same time, the vertical downward uniform stress was applied on the major apexes formed under the caving area, which represented the stress exerted on the extraction structure by the ore bulk. The stress and displacement state of major apexes and production roadways were monitored and analyzed

4. Mechanical Effect of Extraction Structure in Whole Life Cycle

4.1. Stress Evolution Characteristics of Extraction Structure in Whole Life Cycle

4.1.1. Evolution Characteristics of Maximum Principal Stress of Extraction Structure. The evolution characteristic contour of the maximum principal stress in the *XOY* cutting plane of the production level in each stage is shown in Figure 5, and the evolution characteristic contour of the maximum principal stress of in the *XOZ* cutting plane of the extraction structure are shown in Figure 6. In all contours, the negative value represents the compressive stress, and the positive value represents the tensile stress. The red area in the contour is the high stress concentration area of the maximum principal stress, and its value negative, so it exists in the form of compressive stress.

The extraction structure is formed after excavating ore loading roadways, ore drawing roadways, and drawbells. It can be seen from Figures 5(a) and 6(a) that the compressive stress is concentrated on the two sidewalls of the ore loading roadways and ore drawing roadways in a small range, the maximum value is 40.5 MPa, and the stress concentration factor is 1.8. Most range of the whole extraction structure is not in the stress concentration area, so the overall stability of the extraction structure is not affected when the excavation is completed.

It can be seen from Figures 5(b)–5(d), with the advancement of undercutting, the compressive stress concentration on the production level under the undercut space is gradually released. The maximum principal stress is positive, so it turns into the state of tensile stress. There is only a small range of compressive stress concentration at the production level under the undercut boundary on the right side. The compressive stress concentration gradually shifts to near the advancing undercut front, and the area of compressive stress concentration gradually expands. The stress concentration on the first ore loading roadways and ore drawing roadways in front of the advancing undercut front increases obviously after undercutting. After excavation of the third undercut unit, the maximum compressive stress of the production level near the advancing undercut front reaches 46.2 MPa, which is 12.7 percent higher than that of the extraction structure initially formed, and the compressive stress concentration factor reaches 2. As shown in Figures 6(b)–6(d), after the formation of the major apex, it is in the area where the compressive stress decreases.

With the continuous increase of the undercut area, the overburden ore collapses after reaching the hydraulic radius. As shown in Figures 5(d) and 5(e), the concentration degree of compressive stress of production level near the advancing undercut front slightly decreases after the overburden ore caving. As shown in Figures 5(e)–5(g), with the continuous caving of overburden ore, the compressive stress of production level near the advancing undercut front continues to increase. The maximum compressive stress of the ore drawing level in front of the advancing line reaches 53.2 MPa after excavation of the fifth undercut unit and third caving unit, which is 29.5 percent higher than that of the extraction structure initially formed, and the compressive stress concentration factor reaches 2.3.

4.1.2. Evolution Characteristics of Minimum Principal Stress of Extraction Structure. The evolution characteristics contour of the minimum principal stress in the XOY cutting plane of the production level in each stage are shown in Figure 7, and the evolution characteristic contour of the minimum principal stress in the *XOZ* cutting plane of the extraction structure are shown in Figure 8. The red area in the contour is the high stress concentration area of the minimum principal stress, which is positive, so it exists in the form of tensile stress.

The extraction structure is formed after excavating ore loading roadways, ore drawing roadways, and drawbells. It can be seen from Figures 7(a) and 8(a) that the tensile stress

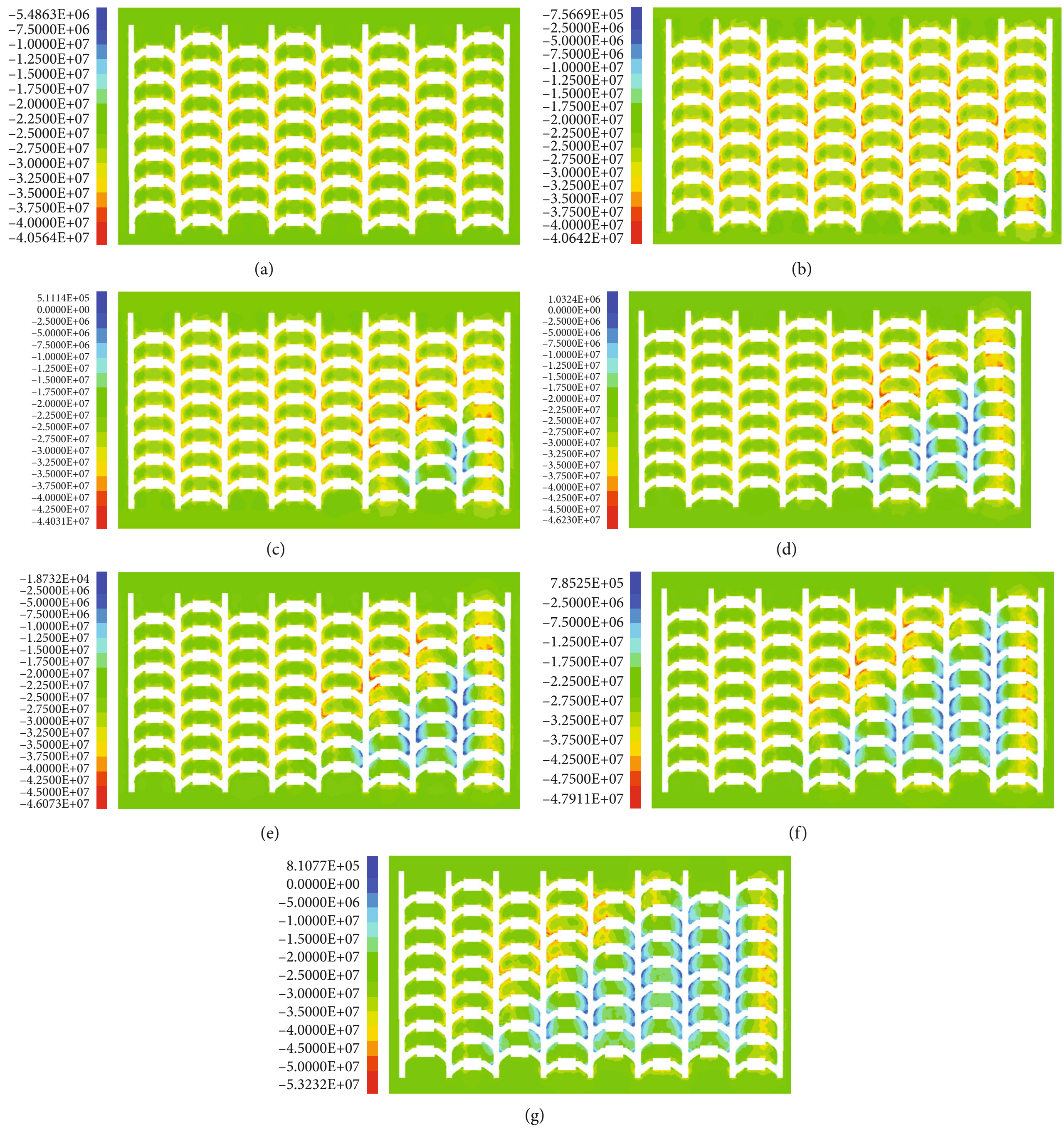

Figure 5: Evolution characteristic contour of the maximum principal stress in the *XOY* cutting plane of the production level: (a) after the formation of the extraction structure, (b) after excavation of the first undercut unit, (c) after excavation of the second undercut unit, (d) after excavation of the third undercut unit, (e) after initial caving, (f) after excavation of the fourth undercut unit and second caving unit, and (g) after excavation of the fifth undercut unit and third caving unit.

is concentrated on the intersections of the ore loading roadways and ore drawing roadways in a small range; the minimum value is 2.5 MPa. Most range of the whole extraction structure is not in the stress concentration area, so the overall stability of the extraction structure is not affected when the excavation is completed. By comparing Figure 5(a) with Figure 7(a), it is found that tensile stress concentration rather than compressive stress concentration is easy to occur at the intersections of ore loading roadways and ore drawing roadways after the extraction structure formation.

It can be seen from Figures 7(c) and 8(d) that, with the advancement of undercutting, the tensile stress concentration on the production level under the undercut space is gradually obvious, and the disturbance is gradually increased. At the initial stage of the formation of the extraction structure, tensile stress concentration was on the intersections.

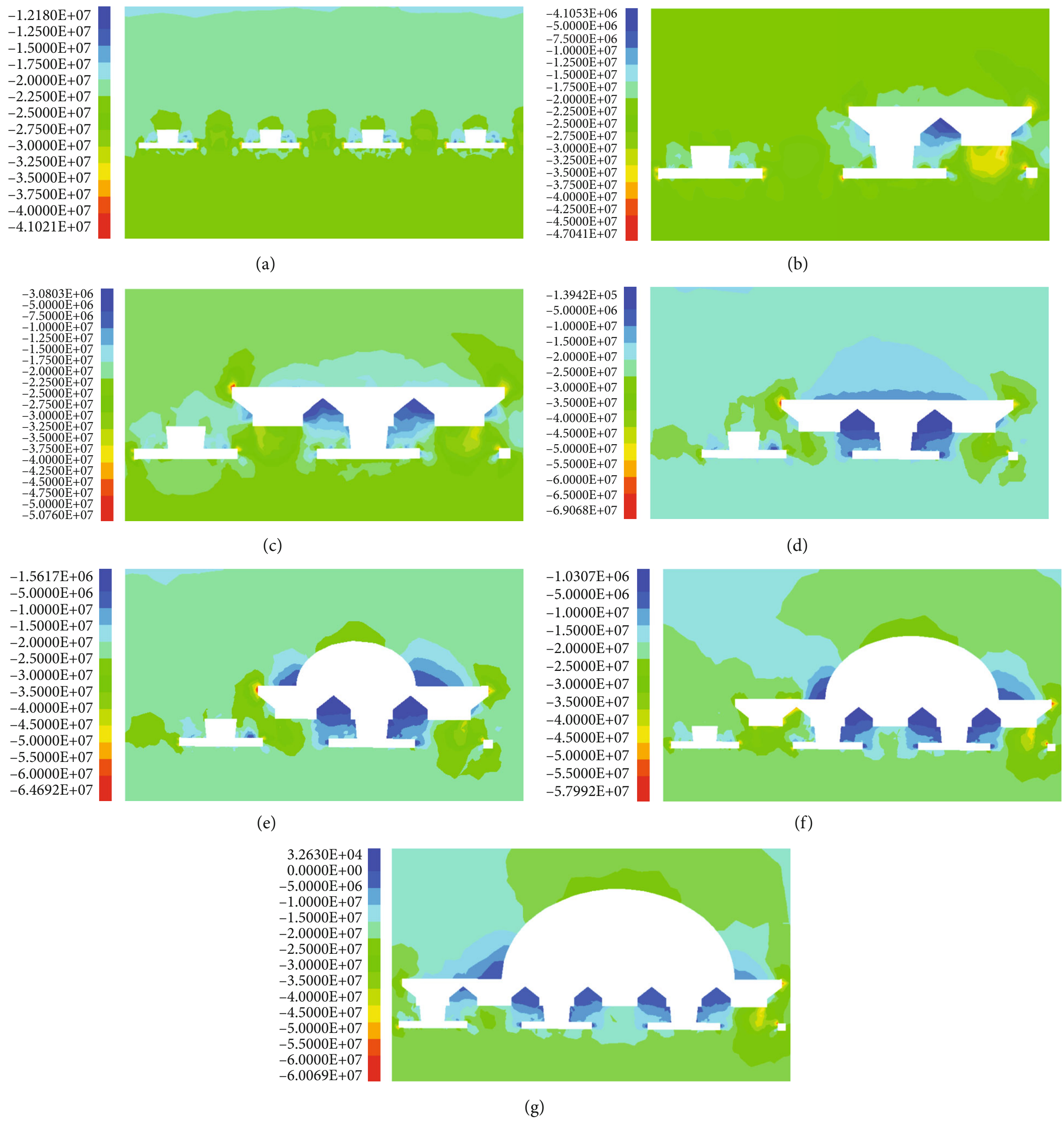

FIGURE 6: Evolution characteristic contour of the maximum principal stress in the XOZ cutting plane of the extraction structure: (a) after the formation of the extraction structure, (b) after excavation of the first undercut unit, (c) after excavation of the second undercut unit, (d) after excavation of the third undercut unit, (e) after initial caving, (f) after excavation of the fourth undercut unit and second caving unit, and (g) after excavation of the fifth undercut unit and third caving unit.

After excavation of the third undercut unit, both sidewalls of the ore loading roadways and ore drawing roadways under the undercut space are affected by high tensile stress. The maximum tensile stress is 5.8 MPa, which is 1.3 times as large as the extraction structure initially formed. It can be seen from Figures 8(b)–8(d) that the tensile stress is concentrated on the tip of the pillar after the major apex formation; after three steps of undercutting, the maximum tensile stress on the tip of major apex increases from 2 MPa to 4 MPa.

With the continuous increase of the undercut area, the overburden ore caves and the ore bulk fall on the extraction structure under the undercut space. At this time, the orderly ore drawing is carried out. It can be seen from Figures 7(d)–7(e) and 8(d)–8(e) that, after the ore body bulk falls down and starts to extract ores, the maximum tensile stress concentrated on the two sidewalls of ore loading roadways and ore drawing roadways under the undercut space decreases from 5.8 MPa to 3.8 MPa, and the maximum tensile stress

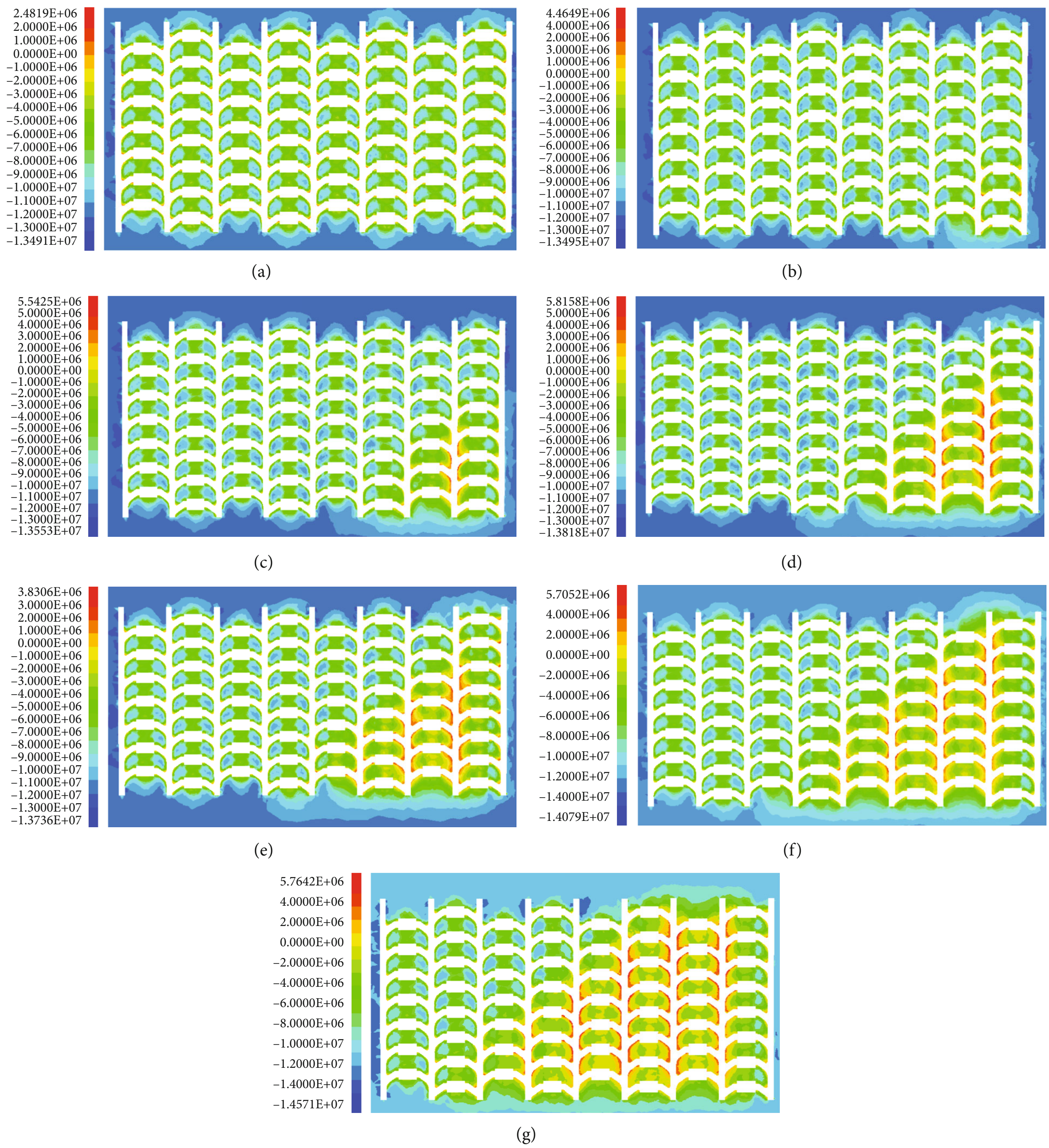

Figure 7: Evolution characteristic contour of the minimum principal stress in the *XOY* cutting plane of the production level: (a) after the formation of the extraction structure, (b) after excavation of the first undercut unit, (c) after excavation of the second undercut unit, (d) after excavation of the third undercut unit, (e) after initial caving, (f) after excavation of the fourth undercut unit and second caving unit, and (g) after excavation of the fifth undercut unit and third caving unit.

concentrated on the major apex decreases from 4 MPa to 2.5 MPa. The range of tensile stress concentration on the extraction structure is also slightly reduced, so the ore bulk on the extraction structure can effectively reduce the tensile stress concentration of the extraction structure under the undercut space. It can be seen from Figures 7(e)–7(g), with the advance of undercutting, the continuous caving of the overburden ore, and the orderly ore drawing, the tensile stress concentrated on the two sidewalls of ore loading roadways and ore drawing roadways under the undercut space gradually increases; after excavation of the fifth undercut unit and third caving unit, the maximum tensile stress increases to 5.7 MPa. It can be seen from Figures 8(e)–8(g) that, with the continuous process of undercutting and caving, the ore bulk accumulated on the extraction structure increases gradually, the ore drawing point also increases gradually, and the range of tensile stress concentration on the extraction structure decreases gradually, but the tensile stress concentrated

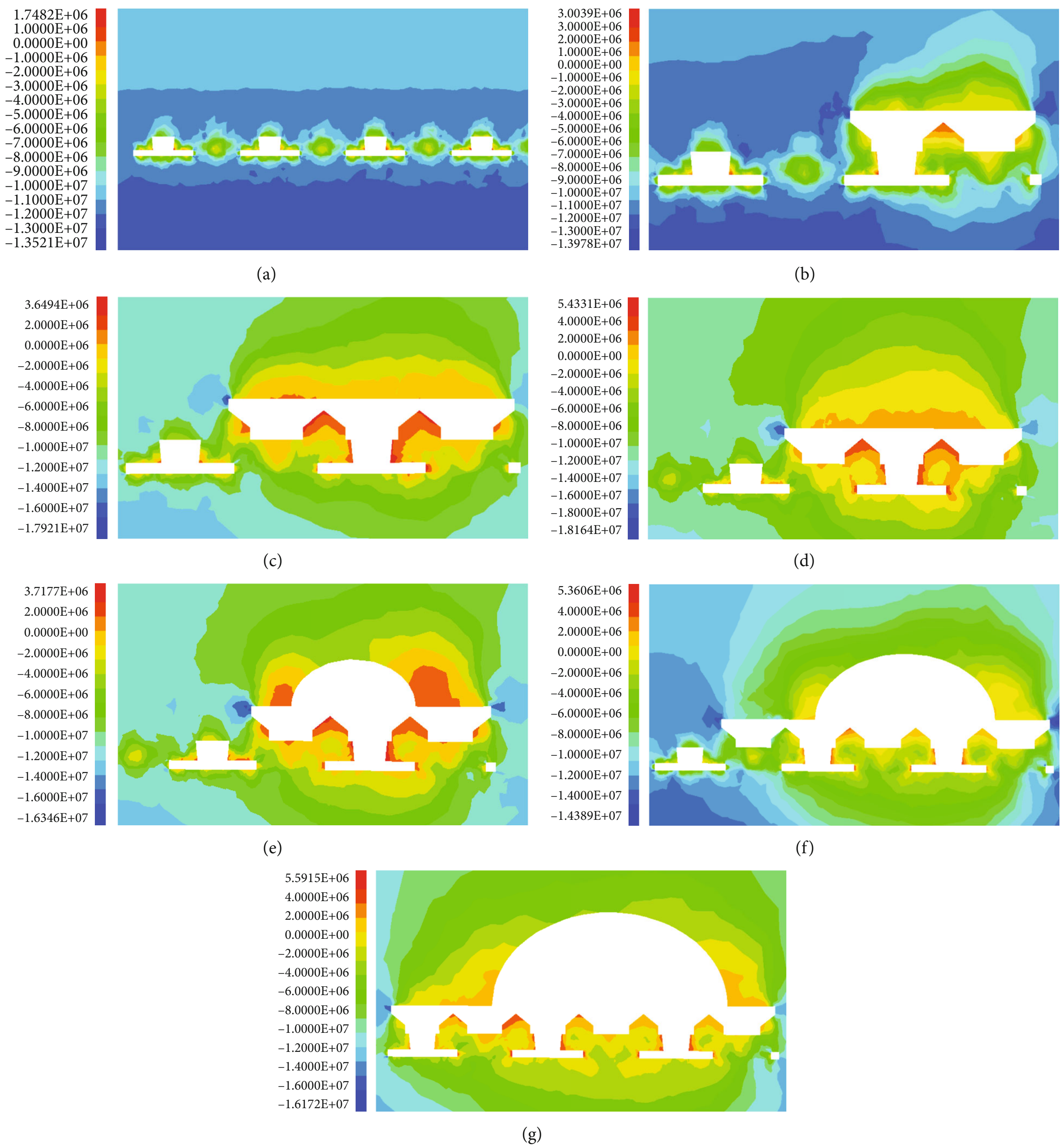

Figure 8: Evolution characteristic contour of the minimum principal stress in the *XOZ* cutting plane of the extraction structure: (a) after the formation of the extraction structure, (b) after excavation of the first undercut unit, (c) after excavation of the second undercut unit, (d) after excavation of the third undercut unit, (e) after initial caving, (f) after excavation of the fourth undercut unit and second caving unit, and (g) after excavation of the fifth undercut unit and third caving unit.

on the tip of major apex continues to increase. After excavation of the fifth undercut unit and third caving unit, the maximum tensile stress concentrated on the tip of major apex reaches 4 MPa.

It can be seen from the comparison of Figures 5 and 7, with the advancement of undercutting, the production level near the advancing undercut front gradually shifts to the location under the undercut space, and the high compressive stress concentrated on the two sidewalls of ore loading roadways and ore drawing roadways gradually turns to high tensile stress concentration.

4.2. Displacement Evolution Characteristics of Extraction Structure in Whole Life Cycle

4.2.1. Evolution Characteristics of Horizontal Displacement of Extraction Structure. The evolution characteristic contour of the horizontal displacement in the *XOY* cutting plane of the

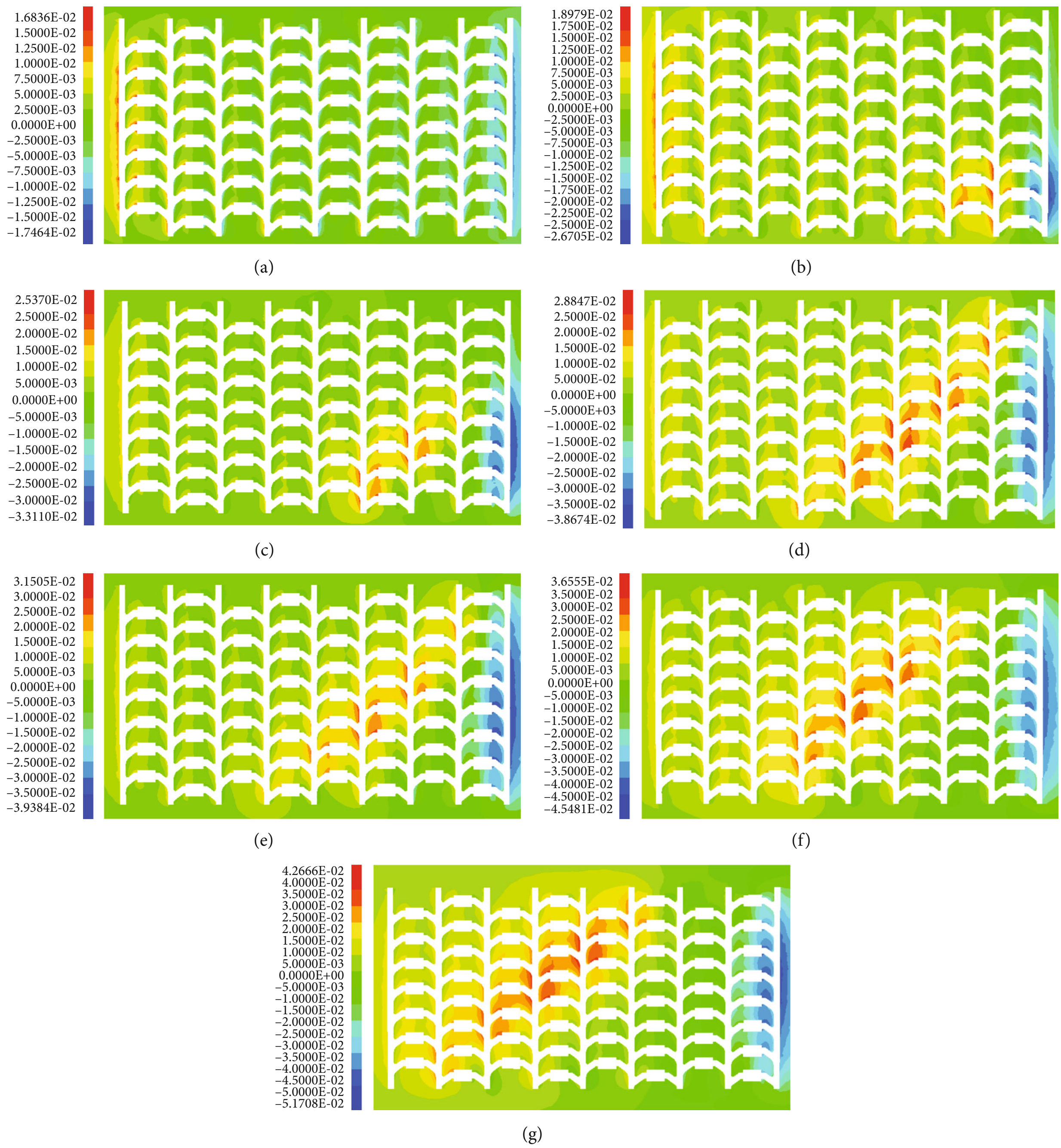

Figure 9: Evolution characteristic contour of the horizontal displacement in the *XOY* cutting plane of the production level: (a) after the formation of the extraction structure, (b) after excavation of the first undercut unit, (c) after excavation of the second undercut unit, (d) after excavation of the third undercut unit, (e) after initial caving, (f) after excavation of the fourth undercut unit and second caving unit, and (g) after excavation of the fifth undercut unit and third caving unit.

production level in each stage are shown in Figure 9, and the evolution characteristic contour of the horizontal displacement of the *XOZ* cutting plane of the extraction structure are shown in Figure 10. The red area in the contour is the area with larger displacement along the positive directions of x -axis, and the blue area in the contour is the area with larger displacement along negative directions of the x-axis.

The extraction structure is formed after excavating ore loading roadways, ore drawing roadways, and drawbells. It can be seen from Figure 9(a) that the sidewalls of ore loading roadways located on the boundary of production level are deformed, the sidewalls wall of ore loading roadways located on the left boundary is deformed to the right, and the sidewalls of ore loading roadways located on the right boundary is deformed to the left; the maximum value is only 16.8 mm. It can be seen from Figure 10(a) that the two sidewalls of drawbells move closer; the maximum horizontal displacement value is 18.3 mm. In general, the displacement of the roadway is not large after the initial formation of the extraction structure, which cannot affect the mining production.

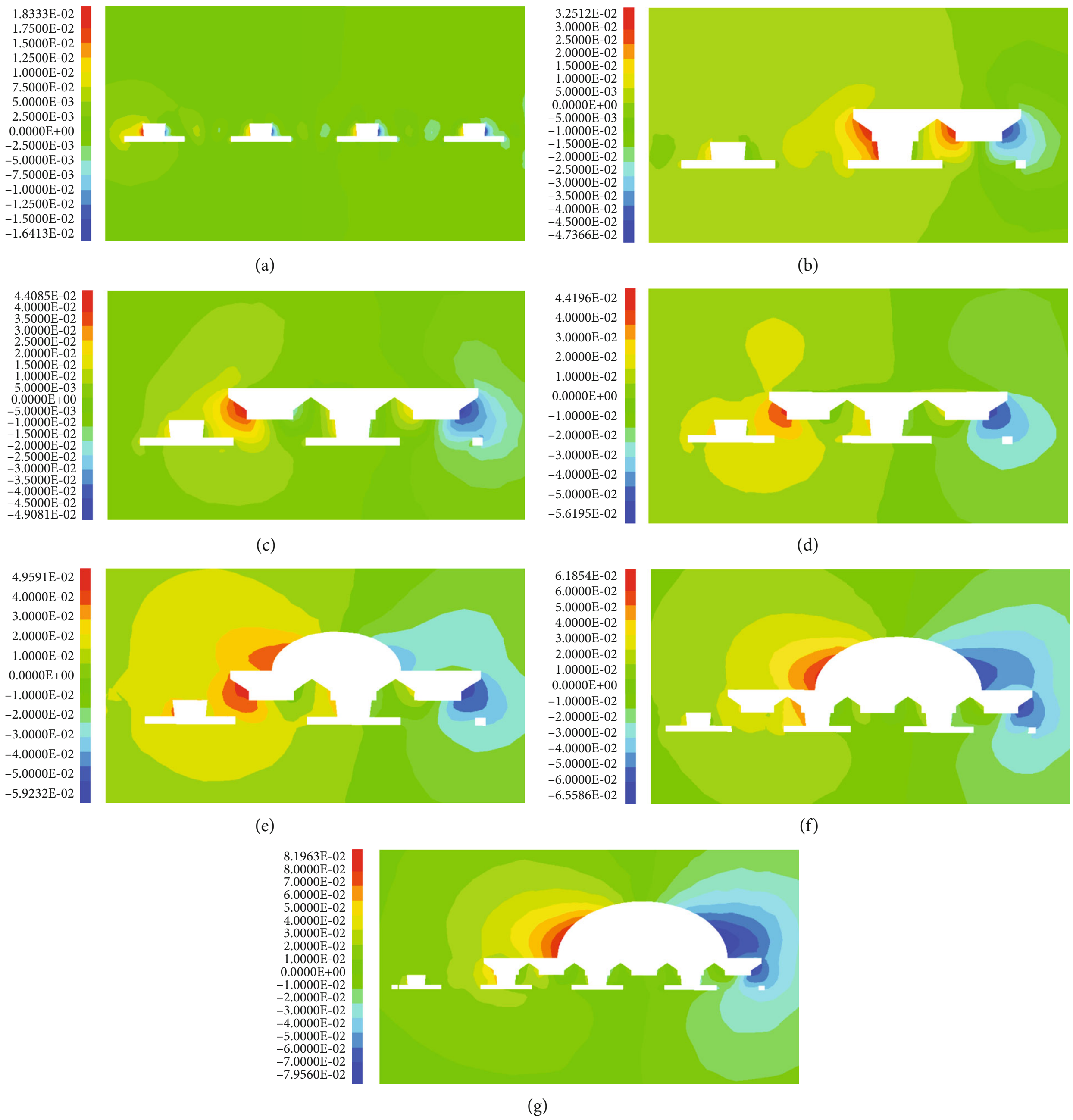

Figure 10: Evolution characteristic contour of the horizontal displacement in the *XOZ* cutting plane of the extraction structure: (a) after the formation of the extraction structure, (b) after excavation of the first undercut unit, (c) after excavation of the second undercut unit, (d) after excavation of the third undercut unit, (e) after initial caving, (f) after excavation of the fourth undercut unit and second caving unit, and (g) after excavation of the fifth undercut unit and third caving unit.

It can be seen from Figures 9(b)–9(d) that, with the advancement of undercutting, the sidewalls of ore loading roadways near the advancing undercut front are deformed to the right, and the displacement of the left sidewall is larger than that of the right sidewall; moreover, the displacement increases with the increase of the undercut area. After three steps of undercutting, the displacement value increases from 18.9 mm to 28.8 mm. It can be seen from Figures 10(b)–10(d) that the left sidewalls of the first drawbells near the undercut front are deformed to the right; after three steps of undercutting, the displacement increases from 18.3 mm to 30.2 mm. The displacement of major apexes near the undercut front is deformed to the right; after three steps of undercutting, the displacement increases from 18.3 mm to 30.2 mm.

It can be seen from Figures 9(e)–9(g) and 10(e)–10(g) that, after the overburden ore caving, with the continuous increase of the undercut area, the deformation of ore loading roadways, major apexes, and drawbells at the undercutting boundary increases continuously. After excavation of the fifth undercut unit and third caving unit, the maximum displacement of the sidewalls of ore loading roadways near the advancing undercut front increases to 42.6 mm, and the

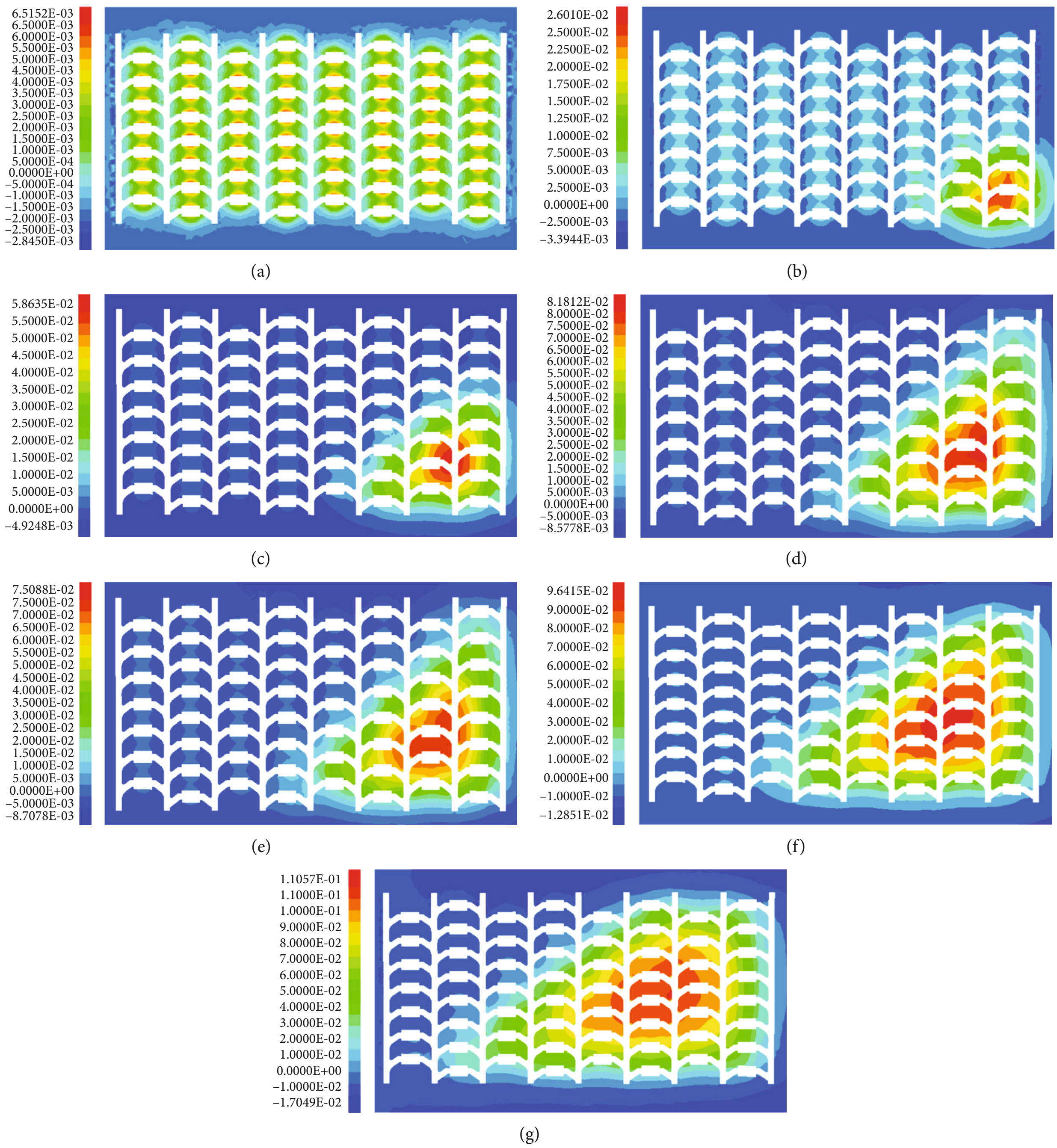

Figure 11: Evolution characteristic contour of the vertical displacement in the *XOY* cutting plane of the production level: (a) after the formation of the extraction structure, (b) after excavation of the first undercut unit, (c) after excavation of the second undercut unit, (d) after excavation of the third undercut unit, (e) after initial caving, (f) after excavation of the fourth undercut unit and second caving unit, and (g) after excavation of the fifth undercut unit and third caving unit.

maximum horizontal displacement of the sidewalls of ore loading roadways, major apexes, and drawbells near the advancing undercut front increases to 42.6 mm, 53.4 mm, and 53 mm, respectively.

4.2.2. Evolution Characteristics of Vertical Displacement of Extraction Structure. The evolution characteristic contour of the vertical displacement in the *XOY* cutting plane of the production level in each stage are shown in Figure 11, and the evolution characteristic contour of the vertical displacement in the *XOZ* cutting plane of the extraction structure are shown in Figure 12. The red area in the contour is the area with larger displacement along the positive directions of z-axis, and the blue area in the contour is the area with larger displacement along the negative directions of z-axis.

The extraction structure is formed after excavating ore loading roadways, ore drawing roadways, and drawbells. It can be seen from Figures 11(a) and 12(a) that the roof of the drawbells subsides, and the subsidence value is 18.3 mm. Slight floor heave occurs in the floor of ore loading roadways and

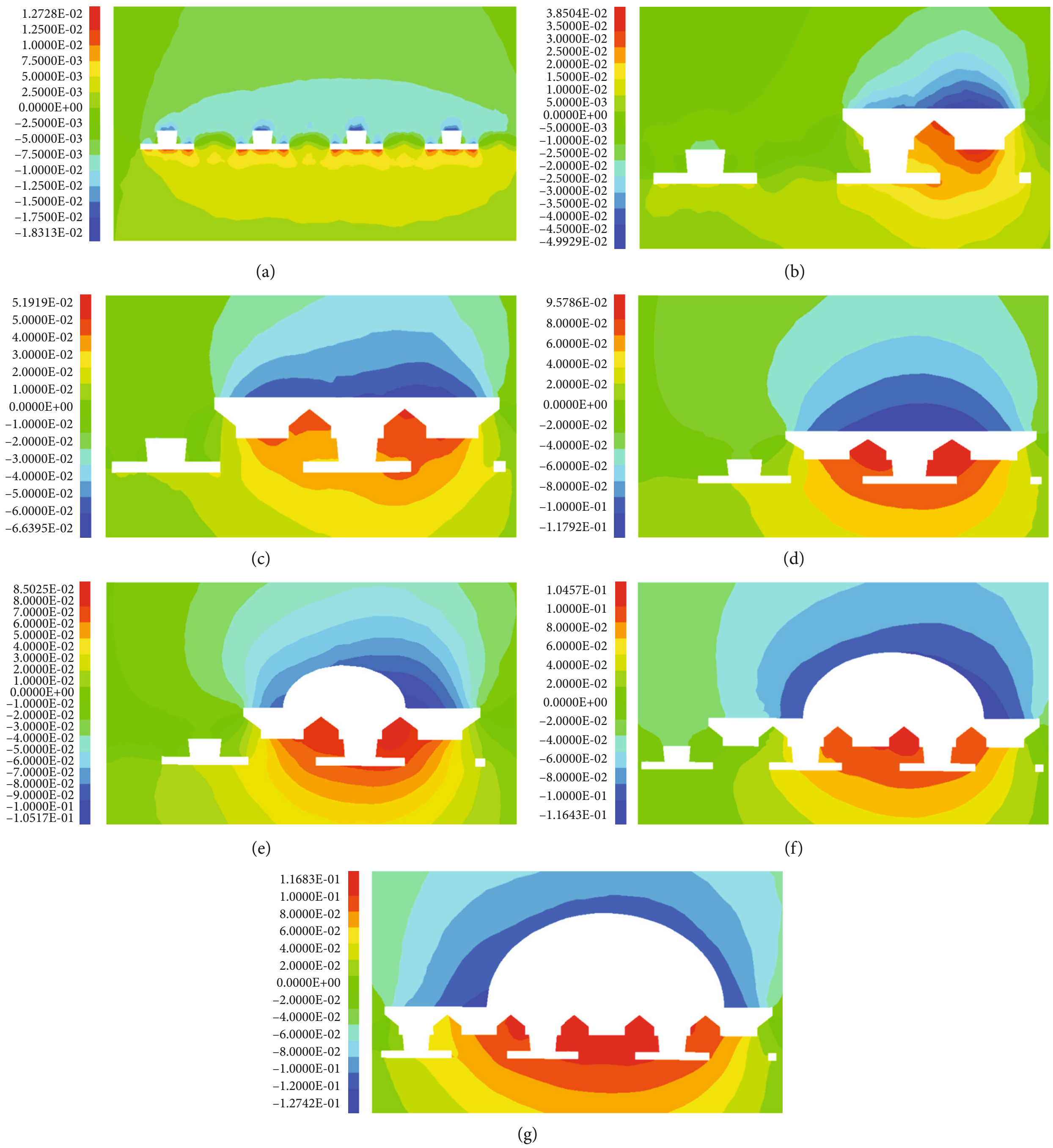

Figure 12: Evolution characteristic contour of the vertical displacement in the *XOZ* cutting plane of the extraction structure: (a) after the formation of the extraction structure, (b) after excavation of the first undercut unit, (c) after excavation of the second undercut unit, (d) after excavation of the third undercut unit, (e) after initial caving, (f) after excavation of the fourth undercut unit and second caving unit, and (g) after excavation of the fifth undercut unit and third caving unit.

drawbells, and the floor heave value is 12.7 mm. The vertical displacement of other parts of the extraction structure is small, which does not affect the mining activities at all.

It can be seen from Figures 11(b)–11(d) and 12(b)–12(d) that, with the advancement of undercutting, the vertical displacement of the extraction structure under the undercut space increases with the increase of the undercutting area; after three steps of undercutting, the maximum vertical displacement of the floor of ore loading roadways, major apexes, and the floor of drawbells under the undercut space increases from 27.3 mm, 30.8 mm, and 21.4 mm to 77.4 mm, 95.7 mm, and 77.9 mm, respectively.

It can be seen from Figures 11(d)–11(e) and 12(d)–12(e) that, after the overburden ore caving, the upward displacement of the extraction structure under the undercut space decreases slightly. However, it can be seen from Figures 11(e)–11(g) and 12(e)–12(g) that, with the continuous increase of the undercut area, the upward displacement of the extraction

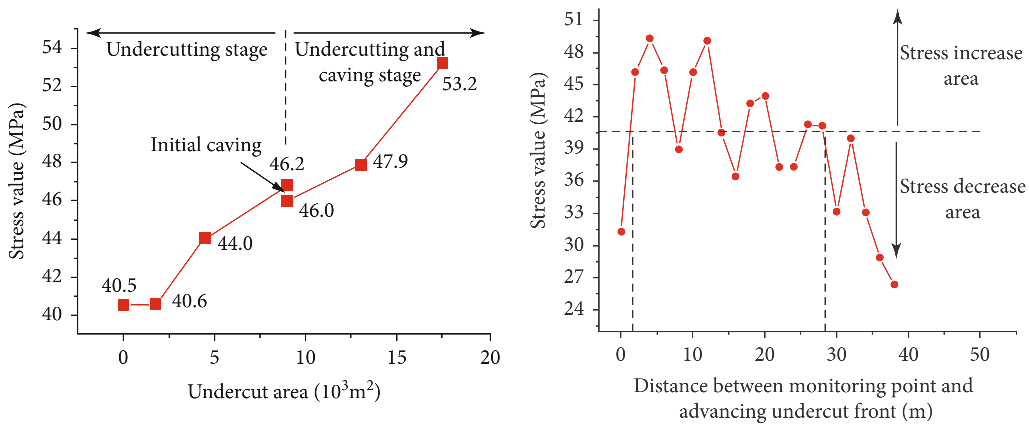

(a) (b)

FIGURE 13: Variation law of compressive stress of the extraction structure near the advancing undercut: (a) variation law of maximum compressive stress with undercut area increasing and (b) spatial distribution of compressive stress near the advancing undercut.

structure under the undercut space increases continuously, the value of ore-loading roadways floor, major apexes, and drawbells floor under the undercut space increases to 102 mm, 98.5 mm, and117mm, respectively.

It can be seen from the comparison of Figures 9 and 12, with the advancing of undercutting, the horizontal displacement of the extraction structure near the advancing undercut front becomes larger, while the vertical displacement of the extraction structure under the undercut space becomes larger.

5. Instability Mechanism of Extraction Structure in Whole Life Cycle

5.1. Instability Mechanism of Extraction Structure near the Advancing Undercut Front. In order to study the instability mechanism of the extraction structure near the advancing undercut front, it is necessary to deeply analyze the stress and displacement variation laws of the extraction structure in the stage of undercutting and ore caving. According to the analysis of stress evolution characteristics of the extraction structure, the extraction structure is mainly affected by the compressive stress near the advancing undercut front. Therefore, the stress monitoring points were set at the production level near the advancing undercut front. The variation law of the maximum compressive stress with the undercut area is shown in Figure 13(a). Undercut area 0 in the figure represents the stress state of the extraction structure before undercutting.

According to the analysis in Figure 13(a), it can be found that before the initial caving of the overburden ore, with the continuous increase of the undercut area, the concentration degree of compressive stress in the production level near the advancing undercut front becomes more and more obvious. The main reason is that the stress arch is formed around the undercut space after undercutting. With the continuous increase of the undercut area, the span of the stress arch increases, and the weight of the overburden ore gradually increases; the degree of stress concentration in the range of stress arch becomes more and more high. It can be shown that the compressive stress of the extraction structure increases near the advancing undercut front. According to the Mohr-Coulomb criterion, if the shear failure condition of the rock mass with the extraction structure is reached, the ground pressure failure occurs. When the undercutting reaches the hydraulic radius of caving, the overburden ore produces initial caving, and the weight of overburden ore can be reduced. Therefore, the compressive stress in the range of the stress arch is reduced, which shows that the compressive stress of the extraction structure decreases slightly near the advancing undercut front. Thus, effective measures should be taken in time to induce the overburden ore caving after the undercutting, which can help to reduce the compressive stress concentration on the extraction structure near the advancing undercut front. After that, with the continuous undercutting, the stope span continued to increase; the weight of overburden ore borne by the stress arch increases continuously in general, although the process is accompanied by the collapse of ore. Therefore, the stress of the extraction structure near the advancing undercut front, and if the support is weak in production level, the ground pressure behavior become more and more intense. It can be shown as the ground pressure failure of ore loading roadways and ore drawing roadways.

In order to study the influence range of the stress arch near the advancing undercut front in the continuous caving stage, the stress monitoring points are arranged at the first ore loading roadway in front of the undercut front in the fifth undercut step. The spatial distribution of the compressive stress on the two sidewalls of the ore loading roadway near the advancing undercut front is shown in Figure 13(b). The highest compressive stress value of 40.6 MPa after the formation of the extraction structure is taken as the baseline, and the stress of monitoring points higher than the baseline stress value are located in the stress increasing area, while the stress of monitoring points lower than the baseline stress value are located in the stress decreasing area. It can be seen from the analysis in Figure 13(b) that the position 2 m~28 m in front of the advancing undercut front is in the affected range of the stress arch and in the stress increasing area. Therefore,

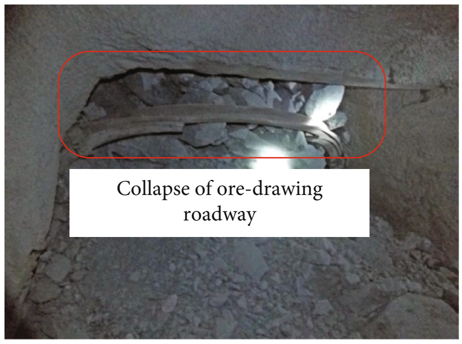

(a)

(b)

FIGURE 14: Instability characteristics of the extraction structure near the advancing undercut: (a) collapse of ore drawing roadway and (b) seriously deformed sidewall.

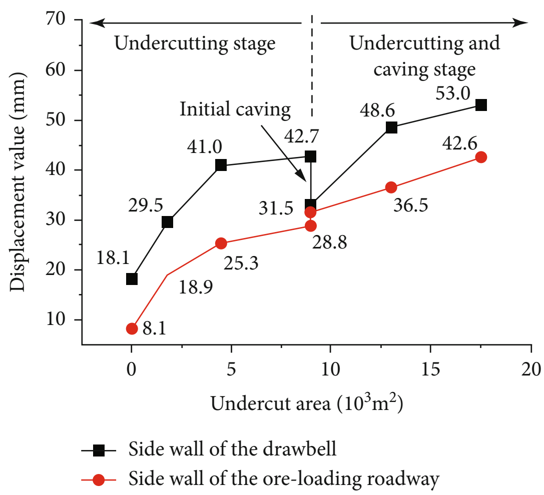

FIGURE 15: Variation law of maximum horizontal displacement with undercut area increasing.

during the process of undercutting, if the support of the extraction structure in front of advancing undercut front is weak or meets the extraction structure with low rock strength, the instability of extraction structure occurs. Therefore, the instability of the extraction structure can be found as early as 28 m in front of the advancing undercut front. The collapse of an ore drawing roadway is shown in Figure 14(a), and the seriously deformed sidewall of ore drawing through a vein is serious, as shown in Figure 14(b). The instability characteristics, occurrence time, and law of the extraction structure in front of the advancing undercut front are consistent with the numerical simulation results.

In order to study the deformation law of the extraction structure in front of the advancing undercut front, the displacement monitoring points are arranged at the production level. It is found that the horizontal displacement of the extraction structure in front of the advancing line is more obvious than the vertical displacement. The x-direction horizontal displacement analysis of the left sidewall of the ore drawing roadway and drawbell is shown in Figure 15.

It can be seen from Figure 15 that, with the increase of the undercut area, the displacement of the extraction structure in front of the advancing undercut front continues to increase and the deformation only decreases slightly after the initial caving. It shows that the collapse of the overburden ore as soon as possible is helpful to reduce the horizontal deformation of the extraction structure in front of the advancing undercut front. According to the field investigation, the sidewall deformation of the ore drawing in front of the advancing undercut front is serious, and it moves closer to the undercut space. As shown in Figure 14(b), the sidewall failure phenomenon is consistent with the numerical analysis results.

5.2. Instability Mechanism of Extraction Structure under Undercut Space. In order to study the instability mechanism of the extraction structure mechanism of the extraction structure under undercut space, it is necessary to deeply analyze the stress and displacement variation laws of the extraction structure in the stage of undercutting and ore caving. According to the analysis of stress evolution characteristics of the extraction structure, the extraction structure is mainly affected by the tensile stress under undercut space. Therefore, the stress monitoring points were set at the sidewalls of the ore loading roadway and the tip of major apex under undercut space. The variation law of the maximum tensile stress with the undercut area is shown in Figure 16(a). Undercut area 0 in the figure represents the stress state of the extraction structure before undercutting; no major apexes are formed at this time, so the tensile stress value of the major apex is missing.

It can be seen from the analysis in Figure 16(a) that, before the formation of the initial caving of the overburden ore, with the continuous increase of the undercut area, the tensile stress concentration degree of the sidewall of ore loading roadway and tip of the major apex under the undercut space becomes more and more obvious. It is mainly because of the combined action of high horizontal tectonic stress and vertical stress after undercutting that the extraction structure produces vertical upward bending deformation. In order to resist the bending deformation, the extraction structure produces higher tensile stress. After the initial caving of the overburden ore, the ore bulk falls on the extraction structure and begins to extract ores orderly. At this time, the tensile stress concentration on the sidewall of the ore loading roadway and tip of the major apex under the undercut space is

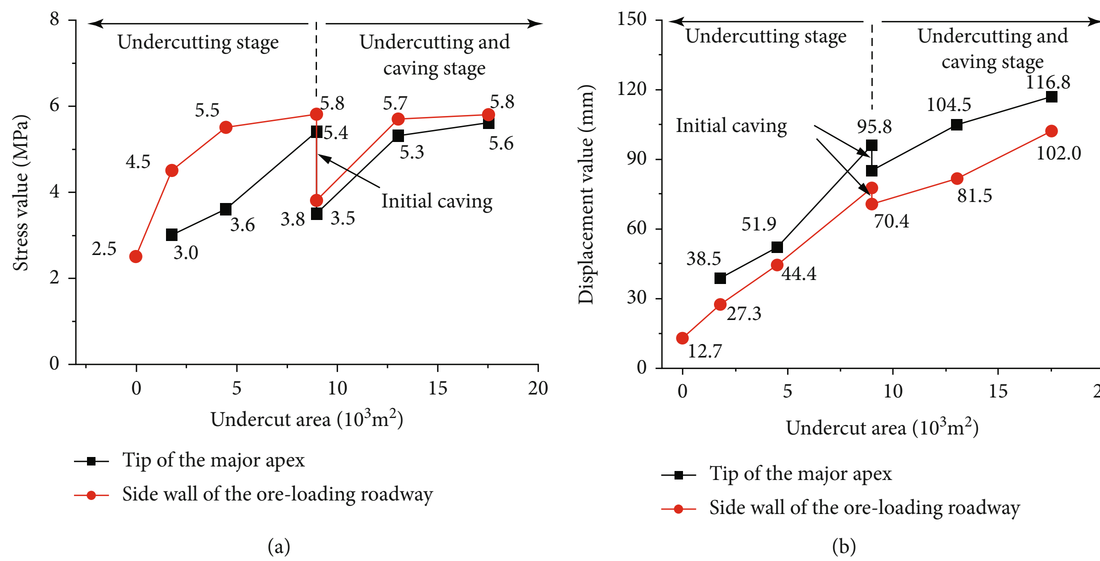

Figure 16: Stress and displacement evolution laws of extraction structure under undercut space: (a) variation law of maximum tensile stress with undercut area increasing and (b) variation law of maximum vertical displacement with undercut area increasing.

released to a certain extent. Measures should be taken to promote the collapse of the overburden ore in time after undercutting, which can effectively reduce the tensile stress concentration on the extraction structure under the undercut space. However, with the continuous increase of the undercut area and overburden ore caving, the stope space becomes larger and larger, and the bending deformation of the extraction structure becomes larger and larger, so the tensile stress concentration on the extraction structure continues to increase. At this time, if the stress exceeds the tensile strength of the rock mass of the extraction structure, the instability of the extraction structure occurs. The tensile stress on both sidewalls of the ore loading roadway under the undercut space is always higher than that on the tip of major apex, which indicates that the ore loading roadway is easier to be damaged than the major apex, and the support should be strengthened.

In order to study the deformation law of the extraction structure under the undercut space, the displacement monitoring points are arranged at the production level. It is found that the vertical displacement of the extraction structure under the undercut space is more obvious than the horizontal displacement. The upward displacement analysis of the floor of the ore drawing roadway and major apex is shown in Figure 16(b). With the increase of the undercut area, the vertical displacement of the extraction structure under the undercut space continues to increase, which shows that upward displacement of the ore drawing roadway floor and major apex increases. The deformation only decreases slightly after the initial caving, which indicates that the caving of the ore bulk and orderly ore drawing in the stope can help to reduce the vertical deformation of the extraction structure. Compared with Figures 16(a) and 16(b), it can be found that the tensile stress concentration on the extraction structure increases with the increase of the upward deflection of the extraction structure under the undercut space. It can be concluded that the tensile stress of the extraction structure under the undercut space is due to the resistance to the bending deformation of the extraction structure towards the undercut space. The upward deflection of the substructure is weakened after the initial caving, so the tensile stress concentration on the extraction structure is weakened, which helps to maintain the stability of the extraction structure. The rib spalling in the ore loading roadway is shown in Figure 17(a), and the floor heave in the ore loading roadway is shown in Figure 17(b); the results of the numerical analysis are consistent with the ground pressure failure phenomenon of field investigation.

5.3. Repeated Instability Mechanism of Extraction Structure in the Whole Life Cycle. In order to explore the mechanism of repeated instability of extraction structure in the whole life cycle, the stress variation law of the same position of the extraction structure with the undercut step is analyzed, as shown in Figure 18. Step 0 in Figure 18 is the state of the extraction structure when the undercutting is not carried out. After the first and second steps of undercutting, the monitoring point is located in the extraction structure in front of the advancing undercut front. After the third step of undercutting, the monitoring point is located in the extraction structure under the undercut space.

It can be seen from the analysis in Figure 18 that the maximum principal stress of the extraction structure in front of the advancing undercut front increases rapidly from 38.8 MPa to 43.3 MPa when the advancing undercut front is close to the monitoring point, and the sign is negative, so the extraction structure in front of the advancing undercut front is in the concentration area of compressive stress at this time. After the third step of undercutting, the extraction structure of the monitoring point is under the undercut space. At this time, the compressive stress gradually decreases to 5.2 MPa, while the minimum principal stress becomes positive and increases to 3.3 MPa, and the monitoring point of the extraction structure is in the tensile stress concentration area at this time. It

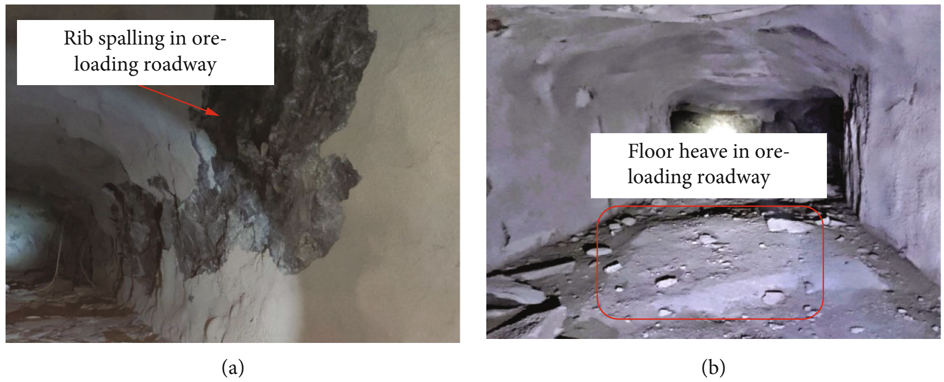

FIGURE 17: Instability characteristics of extraction structure under undercut space: (a) rib spalling in the ore loading roadway, (b) floor heave in the ore loading roadway (Figure 17 is reproduced from [19]).

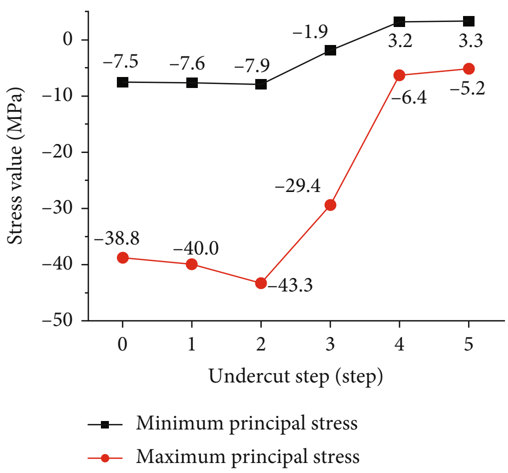

FIGURE 18: Stress variation law of extraction structure at the same position.

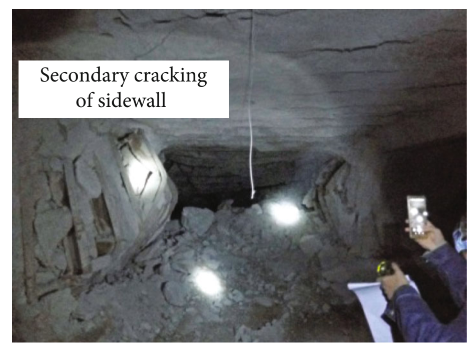

FIGURE 19: Secondary ground pressure damage of ore-loading roadway after supporting.

can be seen that the extraction structure in front of the advancing undercut front mainly presents compressive stress concentration, and the extraction structure under the undercut space mainly presents tensile stress concentration. With the gradual advancement of the undercutting, the extraction structure presents compressive stress concentration firstly and then tensile stress concentration at the same position. It is possible that the extraction structure can be damaged twice. As shown in Figure 19, the ore loading roadway is damaged again after the support.

In conclusion, the instability mechanism of the extraction structure in the whole life cycle in the block caving mine is summarized as follows: During the process of block caving mining under high level tectonic stress, with the advancement of undercutting, the stress of extraction structure presents the stress variation law that compressive stress concentration is prior to the tensile stress concentration. The schematic diagram of the instability mechanism of the extraction structure is shown in Figure 20. The stress arch is formed around the undercut space after undercutting; the spatial form presents as an egg-shaped thick wall structure with the long axis in the direction of the undercut advance and the short axis along the direction of the undercut front, and the stope is surrounded by an egg-shaped thick wall structure. The extraction structure in front of the advancing undercut front is under the influence of the compressive stress increasing area, and the extraction structure under the undercut space is in the compressive stress unloading area and the tension stress increasing area. With the continuous increase of undercutting area and stope span, the weight of overburden ore borne by stress arch above undercut space is increasing, and the compressive stress of the extraction structure in front of the advancing undercut front increases continuously. According to the Mohr-Coulomb criterion, when the stress reaches the shear failure condition of the rock mass of the extraction structure, the ground pressure damage occurs, and the instability of the extraction structure can be caused with the increase of the damage range. As the undercutting continues, the extraction structure located on compression stress concentration area is gradually transferred to the position under the undercut space. Affected by the higher horizontal tectonic stress and vertical stress, the excavation space is squeezed, and the extraction structure produces upward bending deformation. In order to resist the bending deformation, the extraction structure gradually changes to the tension state. With the increasing of the undercut space, the concentration degree of tensile stress becomes higher and higher. When the tensile stress of the extraction structure exceeds the tensile strength of the rock mass, the ground pressure damage occurs again. Therefore,

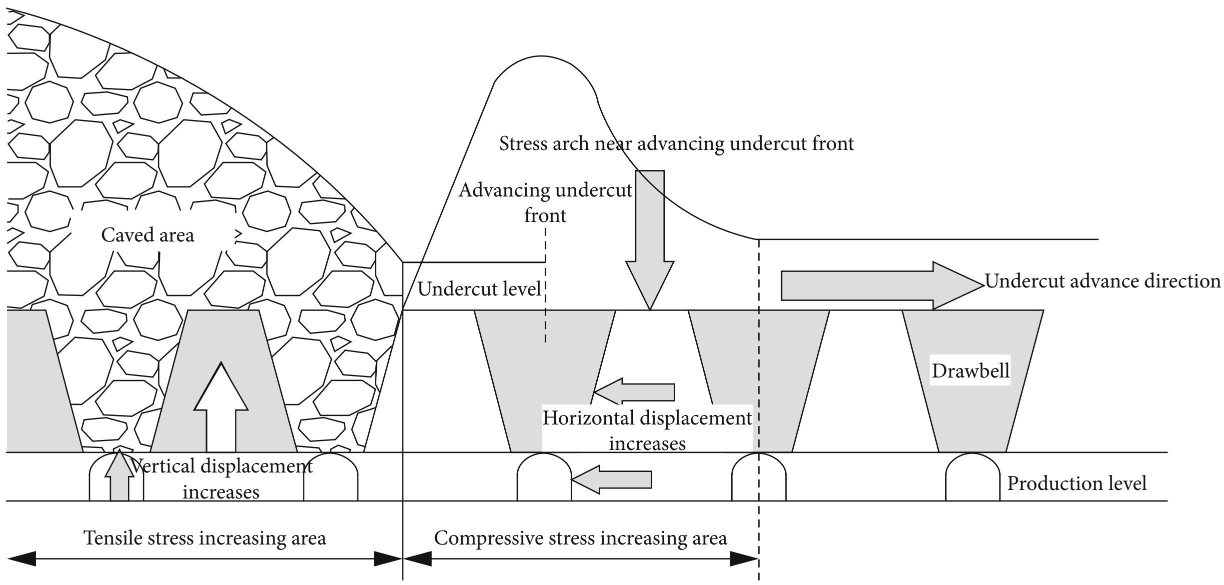

Figure 20: Schematic diagram of instability mechanism of extraction structure.

during the process of mine production, repeated instability of extraction structure may occur. With the increase of undercut area, the stress value increases gradually, and the ground pressure behavior becomes intense. At the same time, in the early stage of undercutting, to induce the overburden ore caving timely, orderly ore drawing can reduce the compressive stress concentration on the extraction structure in front of the advancing undercut front and the tensile stress concentration on the extraction structure under the undercut space. A combined support form of bolt mesh cable shotcreting and floor concrete reverse arch should be established before the high stress formation in front of advancing undercut front, which could effectively control the loose deformation of the surrounding rock of the ore drawing roadway, and increase the stability of the extraction structure.

6. Conclusions

The three-dimensional numerical model of the extraction structure in the whole life cycle in the block caving method was established; the stress and displacement evolution laws obtained are consistent with the instability characteristics of the extraction structure in mine site. The following conclusions can be drawn:

(1) The extraction structure near the advancing undercut front is prone to produce compressive stress concentration under the action of the surrounding rock stress arch in the stope; if the rock mass shear failure condition is reached, the instability of the extraction structure occurs

(2) The extraction structure near the advancing undercut front is gradually transferred to the area under the undercut space with undercut increase, and the tensile stress concentration gradually appears in the sidewall of ore-loading roadway and the tip of major apex; if the tensile strength of rock mass in extraction structure is exceeded, the instability occurs again

(3) To induce the overburden ore caving as soon as possible can reduce the compressive stress concentration on the extraction structure in front of the advancing undercut front and the tensile stress concentration on the extraction structure under the undercut space, which is helpful to reduce the probability of the instability of the extraction structure

Data Availability

The data used to support the findings of this study are available from the corresponding author upon request.

Conflicts of Interest

The authors declare that they have no conflicts of interest.

Acknowledgments

This research was supported by the National Natural Science Foundation of China (Grant No. 51574015).

References

[1] K.-S. Woo, E. Eberhardt, D. Elmo, and D. Stead, "Empirical investigation and characterization of surface subsidence related to block cave mining," *International Journal of Rock Mechanics and Mining Sciences*, vol. 61, pp. 31–42, 2013.

[2] J. P. Hurtado, N. Díaz, E. I. Acuña, and J. Fernández, "Shock losses characterization of ventilation circuits for block caving production levels," *Tunnelling and Underground Space Technology*, vol. 41, pp. 88–94, 2014.

[3] R. Trueman, R. L. Castro, and A. Halim, "Study of multiple draw-zone interaction in block caving mines by means of a

large 3D physical model," *International Journal of Rock Mechanics and Mining Sciences*, vol. 45, no. 7, pp. 1044–1051, 2008.

[4] V. Sánchez, R. L. Castro, and S. Palma, "Gravity flow characterization of fine granular material for block caving," *International Journal of Rock Mechanics and Mining Sciences*, vol. 114, pp. 24–32, 2019.

[5] R. Rafiee, M. Ataei, R. KhalooKakaie, S. E. Jalali, F. Sereshki, and M. Noroozi, "Numerical modeling of influence parameters in cavabililty of rock mass in block caving mines," *International Journal of Rock Mechanics and Mining Sciences*, vol. 105, pp. 22–27, 2018.

[6] R. Trueman, M. Pierce, and R. Wattimena, "Quantifying stresses and support requirements in the undercut and production level drifts of block and panel caving mines," *International Journal of Rock Mechanics and Mining Sciences.*, vol. 39, no. 5, pp. 617–632, 2002.

[7] R. J. Butcher, "Design rules for avoiding draw horizon damage in deep level block caves," *Journal of the Southern African Institute of Mining and Metallurgy*, vol. 99, no. 2, pp. 151–155, 1999.

[8] P. J. Bartlett, *Planning, Implementation, Operation and Monitoring of a Cave Mining Method with Coarse Fragmentation with Reference to Cave Mining at Premier*, University of Pretoria, 1998.

[9] E. Rojas, R. Molina, A. Bonani, and H. Constanzo, "The preundercut caving method at the El Teniente mine, Codelco Chile," in *Massmin 2000 Proceedings*, vol. 29, pp. 261–266, Brisbane, Australia, 2000.

[10] G. V. Fernandes, K. Bosman, D. Angus, W. de Beer, and T. Urbancic, "Mapping cave front growth utilising the collective behaviour of seismicity and velocity fields," in *Caving 2018, Fourth International Symposium on Block and Sublevel Caving*, pp. 577–588, Vancouver, Canada, October, 2018.

[11] M. Pierce, "Forecasting vulnerability of deep extraction level excavations to draw-induced cave loads," *Journal of Rock Mechanics and Geotechnical Engineering*, vol. 11, no. 3, pp. 527–534, 2019.

[12] H. Sahupala, C. Brannon, S. Annavarapu, and K. Osborne, "Recovery of extraction pillars in the deep ore zone (DOZ) block cave, PT freeport Indonesia," in *Massmin 2008, 5th International Conference & Exhibition on Mass Mining*, pp. 191–202, Lulea, Sweden, 2008.

[13] M. Orellana, C. Cifuentes, and J. Díaz, "Caving experiences in Esmeralda sector, El Teniente mine," in *3rd International Symposium on Block and Sublevel Caving*, pp. 78–90, Santiago, Chile, June 2014.

[14] R. Castro, R. Gómez, M. Pierce, and J. Canales, "Experimental quantification of vertical stresses during gravity flow in block caving," *International Journal of Rock Mechanics and Mining Sciences*, vol. 127, p. 104237, 2020.

[15] R. Castro, *Study of the Mechanisms of Gravity Flow for Block Caving*, The University of Queensland, 2006.

[16] Z. Xia, Z. Tan, and Y. Miao, "Damage evolution mechanism of extraction structure during mining gently dipped orebody by block caving method," *Geotechnical and Geological Engineering*, vol. 38, no. 4, pp. 3891–3902, 2020.

[17] Z. Xia, Z. Tan, Q. Pei, and J. Wang, "Ground pressure damage evolution mechanism of extraction level excavations induced by poor undercutting in block caving method," *Geotechnical and Geological Engineering*, vol. 37, no. 5, pp. 4461–4472, 2019.

[18] Z. Xia and Z. Tan, "Study on instability mechanism of extraction structure under undercut space based on thin plate theory in block caving method," *Shock and Vibration*, vol. 2021, no. 2, Article ID 5548213, p. 11, 2021.

[19] Y. Zhang, Y. Jiang, D. Asahina, and C. Wang, "Experimental and numerical investigation on shear failure behavior of rock-like samples containing multiple non-persistent joints," *Rock Mechanics and Rock Engineering*, vol. 53, no. 10, pp. 4717–4744, 2020.

[20] C. Wu, J. Chu, S. Wu, and Y. Hong, "3D characterization of microbially induced carbonate precipitation in rock fracture and the resulted permeability reduction," *Engineering Geology*, vol. 249, pp. 23–30, 2019.

[21] C. Wu, J. Chu, S. Wu, L. Cheng, and L. A. van Paassen, "Microbially induced calcite precipitation along a circular flow channel under a constant flow condition," *Acta Geotechnica*, vol. 14, no. 3, pp. 673–683, 2019.

Hindawi
Geofluids
Volume 2021, Article ID 6671829, 10 pages
https://doi.org/10.1155/2021/6671829

Research Article

A Complex Network Approach for Quantitative Characterization and Robustness Analysis of Sandstone Pore Network Structure

Yuhao Hu,[1,2] Guannan Liu ,[1,2,3] Feng Gao,[2,3] Fengtian Yue,[2,3] and Tao Gao[2,3]

[1]*Jiangsu Key Laboratory of Coal-Based Greenhouse Gas Control and Utilization, Mechanics and Civil Engineering Institute, China University of Mining and Technology, Xuzhou, Jiangsu 221116, China*
[2]*State Key Laboratory for Geomechanics and Deep Underground Engineering, China University of Mining and Technology, Xuzhou, Jiangsu 221116, China*
[3]*Laboratory of Mine Cooling and Coal-Heat Integrated Exploitation, China University of Mining and Technology, Xuzhou, Jiangsu 221116, China*

Correspondence should be addressed to Guannan Liu; guannanliu@cumt.edu.cn

Received 6 December 2020; Revised 16 March 2021; Accepted 29 March 2021; Published 7 April 2021

Academic Editor: Guanglei Zhang

The rational characterization and quantitative analysis of the complex internal pore structure of rock is the foundation to solve many underground engineering problems. In this paper, CT imaging technology is used to directly characterize the three-dimensional pore network topology of sandstone with different porosity. Then, in view of the problem, which is difficult to quantify the detailed topological structure of the sandstone pore networks in the previous study, the new complex network theory is used to characterize the pore structure. PageRank algorithm is based on the number of connections between targets as a measure index to rank the targets, so the network degree distribution, average path length, clustering coefficient, and robustness based on PageRank algorithm and permeability-related topological parameters are studied. The research shows that the degree distribution of sandstone pore network satisfies power law distribution, and it can be characterized by scale-free network model. The permeability of rock is inversely proportional to the average path length of sandstone network. The sandstone pore network has strong robustness to random disturbance, while a small number of pores with special topological properties play a key role in the macroscopic permeability of sandstone. This study attempts to provide a new perspective of quantifying the microstructure of the pore network of sandstone and revealing the microscopic structure mechanism of macroscopic permeability of pore rocks.

1. Introduction

Reservoir rocks contain huge numbers of pores with different sizes and complex shapes, and most part of the pores are connected with each other under the natural or artificial intervention, which is the main space for the migration of underground oil and gas. The connectivity of rock pore network directly affects the fluid flow behavior in geotechnical engineering [1–3]. However, the pore network of rock is highly complex. Accurately revealing the connectivity of micro and nanoscale and quantitatively analyzing the internal relationship between their microstructure and macroscopical permeability are the key problems to enhance the oil and gas recovery [4–7]. In order to study the microseepage mechanism of porous rock, scholars put forward the research methods based on continuum mechanics and pore network structure, respectively.

Based on the research method of continuum mechanics, Zhang et al. [8] coupled the gas flow control equation, coal deformation equation, and porosity model and established the permeability evolution model of multiporosity coal seam. Mitra et al. [9] studied the permeability variation of coal samples under the competitive mechanism of effective stress and adsorption expansion deformation. Pan et al. [10] studied the influence mechanism of effective stress on the permeability of coal samples, and the results show that the permeability of coal samples changed exponentially with gas pressure. Peng et al. [11] pointed out that under the same boundary conditions, there are significant differences in permeability of coal samples of different scales, and the sensitivity of permeability to confining pressure is also different. Pan [12] measured the permeability of coal samples in parallel, oblique, and vertical bedding directions. Lin and Zhou [13] found that the permeability of coal samples with parallel bedding is most closely related to the confining pressure effect and then studied the variation law of coal seam permeability with stress evolution under the action of in situ stress. Cao et al. [14] found by measuring the permeability of outburst raw coal that the permeability of coal seam first decreased and then increased with the gas pressure. Gao et al. [15] used the hybrid network theory to analyze the network parameters, modularization, and pore aggregation degree of sandstone with different porosity. This method can quantitatively analyze the structural parameters that cannot be quantified by traditional connectivity analysis and fractal dimension analysis. Ye et al. [16] established a dual pore network model of rock and analyzed the variation trend of permeability of coating model with microscopic parameters such as porosity distribution, average path length, and throat length distribution. Gong et al. [17] proposed a fractal reconstruction model of rock pore structure based on improved simulated annealing algorithm. The influences of pore radius and average pore shape factor on the pore structure characteristics of sandstone were analyzed from eight pore structure parameters, including pore number per unit volume, porosity, average pore size, pore volume, minimum maximum pore radius, and minimum average pore radius.

In order to analyze the influence mechanism of micropore structure on the permeability of porous rocks, Darabi et al. [18] studied the gas seepage process in dense porous media. Assuming that the porous media is composed of nano to millimeter pores, considering the influence of capillary roughness, the apparent permeability model was obtained. Singh et al. [19] obtained a new apparent permeability model by using analytical method without considering slippage effect. There are no empirical parameters in the model, which are only related to pore size, pore shape, temperature, gas properties, and average reservoir pressure. Yu et al. [20] proposed the fractal analysis model of porous media permeability and proposed the analytical expressions of fractal dimension, porosity, and microstructure of single-phase and multiphase porous media for the first time. Miao et al. [21, 22] extended the theory of fractal porous media to fracture network and constructed the fractal model of fracture network area density, which relates the structural parameters of fracture network, such as fracture size, fractal dimension, and porosity. Liu et al. [23] discussed the influence of size effect on permeability by combining seepage mechanics research method and Monte Carlo method to characterize fracture distribution mechanism. Li et al. [24, 25] developed a fully coupled multidomain multiphysics model to simulate the interactions between the fractured, nonfractured, and hydraulic fracture domains, taking into account the differences in properties and interactions between the fractured, nonfractured, and hydraulic fracture domains. Liu et al. [26–28] characterized pores and fractures by fractal dimension of pore, fractal dimension of curved capillary, and fractal dimension of fracture length. Coupled the fractal theory of porous media with the multifield model of coal seam, they established a multifield coupling mechanical model considering the influence of fissure and pore structure. Li et al. [29] used Frenkel-Halsey-Hill method to obtain the fractal dimension of pores used to characterize the pores and obtained the structural parameters used to characterize the natural organic matter such as aliphatic chain length, aromatic carbon condensation degree, and hydrocarbon generation potential by peak fitting of infrared spectra. Considering the geometric parameters of porous media, including porosity, liquid saturation, fractal dimension of granular matrix and liquid phase, and fractal dimension of bending of liquid phase, Qin et al. [30] proposed a theoretical model of effective thermal conductivity of porous media with rough surface. Li et al. [31] discussed the influence of pore characteristic parameters such as fractal dimension of curvature, fractal dimension of pore, and minimum to maximum capillary diameter ratio on relative permeability. A detailed comparison is made between the continuous method and the pore material prevention method as shown in Table 1.

Table 1: Comparison of continuous method and pore network method.

Characterization methods	Continuum methods	Pore network methods
Same parameters	Porosity	Porosity
Different parameters	/	Number of pores Average pore diameter Number of throat Coordination number Clustering coefficient

Firstly, based on continuum mechanics, the influence of micropore structure is generally not considered. Secondly, traditional reservoir structure analysis methods, such as Euler number and fractal dimension, are difficult to characterize the detailed topological properties of the pore network characteristics comprehensively and quantitatively. In order to solve the problem of scientific and quantitative characterization of microconnectivity characteristics of porous rock pores from the perspective of complex network theory, the topological structure and robustness characteristics of sandstone pore network were studied after obtaining CT images of sandstone with different porosity.

2. Extraction of Core Pore Network

Based on X-ray micron CT, four groups of two-dimensional tomography images of sandstone with different porosity are obtained, as shown in Figure 1. The experimental data comes from Professor Blunt's team of Imperial University of Technology. The data is public. The rock and equipment used in the experiment and the acquisition method of experimental data can be found on the official website of the team. See Acknowledgments for the website. The image shown in

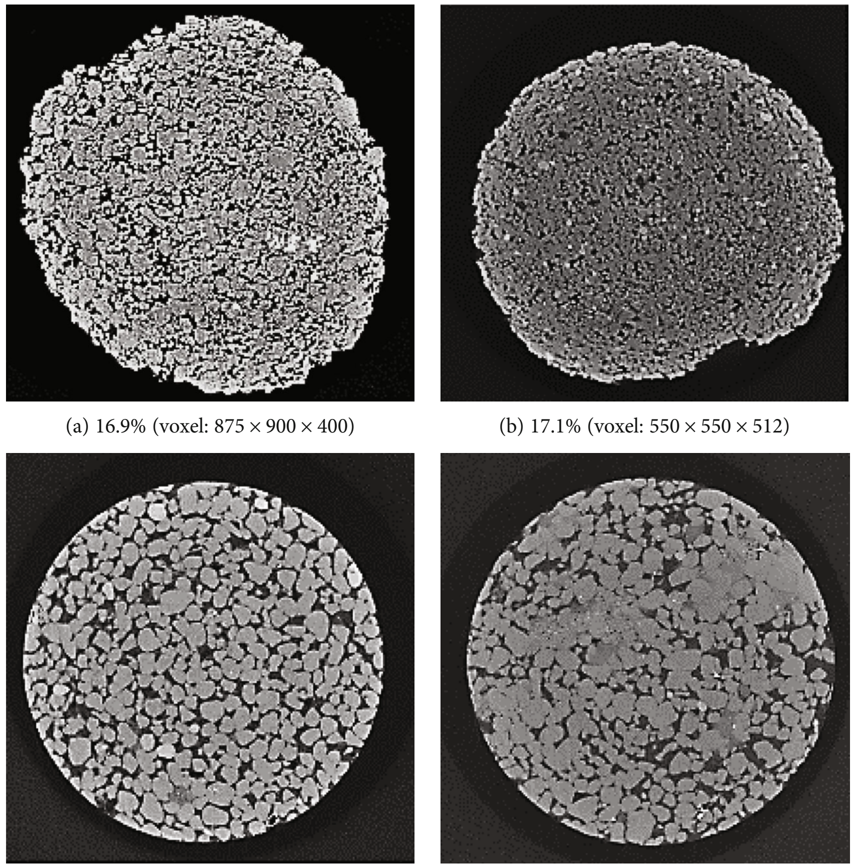

(a) 16.9% (voxel: 875 × 900 × 400) (b) 17.1% (voxel: 550 × 550 × 512)

(c) 24.6% (voxel: 950 × 950 × 300) (d) 34.0% (voxel: 950 × 950 × 350)

Figure 1: X-ray tomography images of sandstone with different porosity.

Figure 1 is one of the slices of each sample. The gray level of each pixel in a two-dimensional image indicates the point density value. Considering that the area outside the rock sample is assigned black, it is eliminated for the analysis process, and the rectangular area is selected as the research object in the sample.

3. Topological Structure Analysis of Pore Network Model

In the research process of pore network structure, we use the network analysis software GEPHI, which has the function of searching and eliminating dead pores. Generally, pores with a diameter of less than 10 nm are micropores, pores with a diameter of 10 nm-100 nm are small pores, macropores with a diameter of 1000 nm-100000 nm, and cracks with a diameter of over 100000 nm [32]. The basic parameters of sandstone samples with different porosity are shown in Table 1. From Table 2, it can be seen that when the porosity is small, such as 16.9% and 17.1%, the number and of nodes in the pore network model are large. When the porosity is large, such as 24.6% and 34%, the number of nodes in the pore network model is small, and it is less than 1/4 of that of the rock sample of which porosity is 16.9%. The main reason is that the smaller the porosity is, the smaller the particle size of the sandstone is, the smaller the volume of pore and pore throat is, so that the number of nodes in the network is more. The results show that the porosity is inversely proportional to the size of the pore network (the number of nodes).

Euler number and fractal dimension are usually used in the analysis of pore structure, and the topological structure of the pore network is difficult to be quantitatively analyzed. In this paper, the complex network theory analysis method is introduced into the pore network structure analysis, and the parameters such as the degree distribution, the clustering coefficient, and the average path length are calculated, respectively. The number of pore throat attached to a certain pore is defined as degree, which is usually expressed by k. In order to analyze the degree distribution of sandstone pore network, we counted the proportion of pores with different degrees to the total number of nodes expressed with $P(k)$, as shown in Figure 2. From Figure 2, it is known that the degree distribution curves of sandstone samples with different porosity have obvious long-tail characteristics. Different from the normal distribution, where most of the data are concentrated near the median, the distribution of sandstone pore network is more consistent with the scale-free network model which obeys the power law distribution.

The degree distribution is mainly used to measure the connected characteristics of the single pore in the sandstone pore network. In order to further explore the degree of aggregation between pores, the clustering coefficient is calculated.

Table 2: Structural parameters of sandstone pore network.

Porosity φ	Node number N	Edge number M	Permeability K (mD)	Resolution R (μm)
16.9%	8301	14381	224	9.1
17.1%	8345	12360	259	9.0
24.6%	1945	4697	3898	5.0
34.0%	1266	3833	13169	4.9

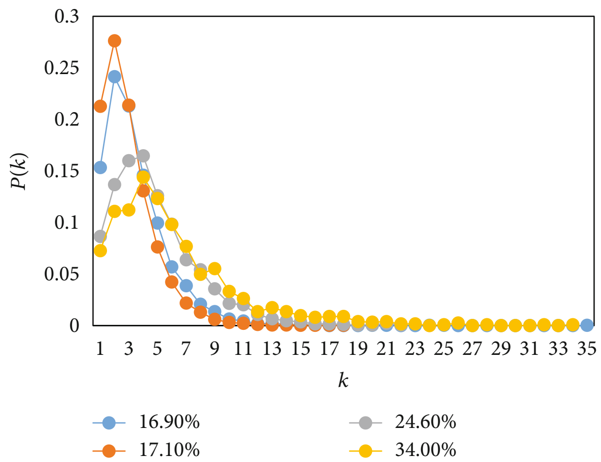

Figure 2: Degree distribution of sandstone pore networks.

Assumed that pore i in a pore network has k_i pores connected to it. The k_i pores are called the neighbor pores of pore i. There is a maximum of $k_i(k_i - 1)/2$ throats among the neighbor pores of pore i. The ratio between the number of the actual throat number N_i among pore i's neighbor pores and the number of the most probable throat number $k_i(k_i - 1)/2$ is defined as the clustering coefficient of pore i, which is expressed as C_i.

$$C_i = \frac{2N_i}{k_i(k_i - 1)}. \tag{1}$$

The value of C_i changes between 0 and 1 in the network. The larger the C_i is, the more the throats among pore i and its neighbor pores are. The distribution of the pore network clustering coefficient of sandstone with different porosity is shown in Figure 3. The horizontal axis is the number of the pore node. As shown in Figure 3, the clustering coefficients of most of the pores are less than 0.6. Only a small number of pores are closely connected to the pores of the surrounding pores. These small amounts of pores may play an important role in the permeability of sandstone.

In order to measure the transmission efficiency of the network, the complex network theory gives a metric parameter "the average path length." The average path length L of the sandstone network is the average number of throats between each pair of pores in the network.

$$L = \frac{2}{N(N-1)} \sum_{i=1}^{N-1} \sum_{j=i+1}^{N} d_{ij}. \tag{2}$$

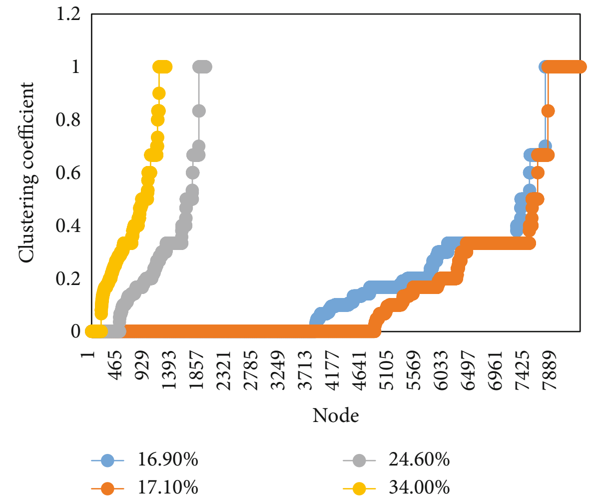

Figure 3: Distribution of clustering coefficient of sandstone pore network.

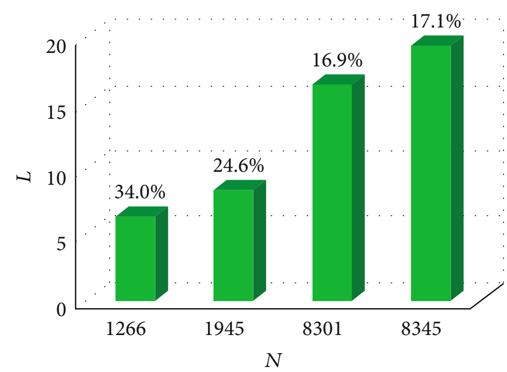

Figure 4: Distribution of average path length of sandstone pore network.

where N is the number of pores in the network. d_{ij} is the minimum number of throats between any two nodes of the network i and j.

The average path length distribution of pore network in sandstone samples with different porosity is shown in Figure 4. From Figure 4, it is known that the average path length of the sandstone pore network is proportional to the number of pores, and it is inversely proportional to the porosity. And the greater the porosity, the larger the permeability of sandstone and the smaller the average path length would be.

4. Analysis of the Robustness of Pore Network

Usually, we do not consider the importance of a single pore in the whole percolation network when analyzing the pore structure. In order to investigate whether a single or a small number of pores will lead to significant changes in the transmission efficiency of the whole seepage network, that is, whether the permeability of the rock network depends on a small number of important pores, we

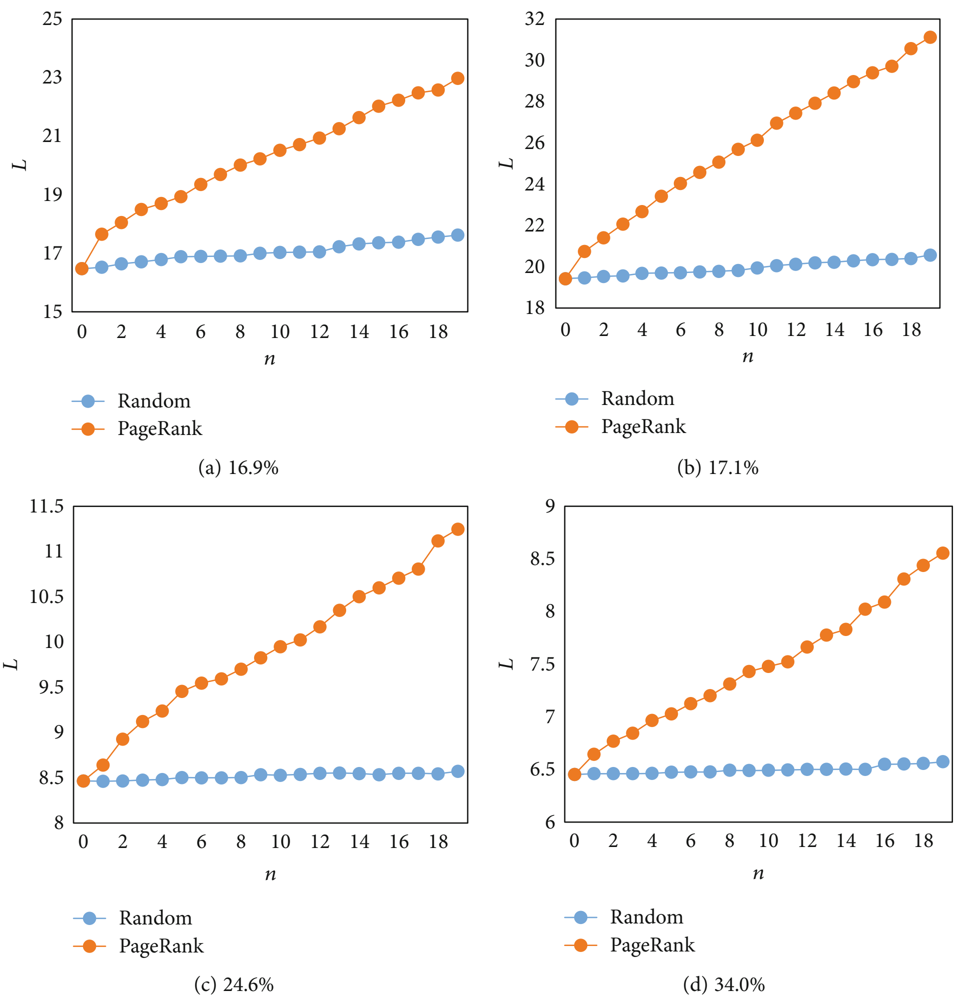

FIGURE 5: The robustness curve of sandstone with different porosity.

have studied the robustness of the sandstone pore network.

In the network science, the average path length is the key parameter to measure the transmission efficiency of the network. The smaller the average path length is, the higher the network transmission efficiency is. We eliminate the pore nodes in the pore network based on two methods and then discuss the evolution process of network transmission efficiency. Method 1: random elimination; method 2: elimination based on PageRank algorithm.

As the sorting algorithm in the complex network theory, the PageRank algorithm is based on the network topology as the importance of the network node importance. The basic idea of the PageRank algorithm is that the pore network is regarded as graph $G = (V, E)$, where V is the number of notes and E is the number of edges. Give each node an initial PageRank value. Suppose there is an edge (v_i, v_j) between node v_i and node v_j, then node v_i throws a ticket to the node v_j. Using $C'(i)$ to represent the number of edges connected with node i, then node v_i contributes a PageRank value of $P'(i)/C'(i)$ to the node v_j. The algorithm process is as follows.

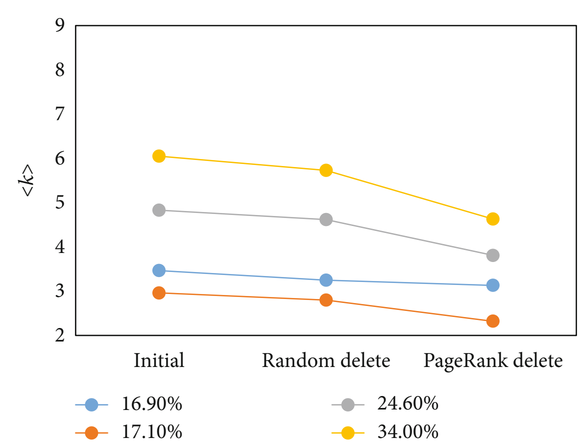

FIGURE 6: Average degree change curve under different elimination schemes.

First, define the initial PageRank value for each node v_i:

$$P'_0(i) = \frac{1}{(n+1)}, 0 < i \leq n. \tag{3}$$

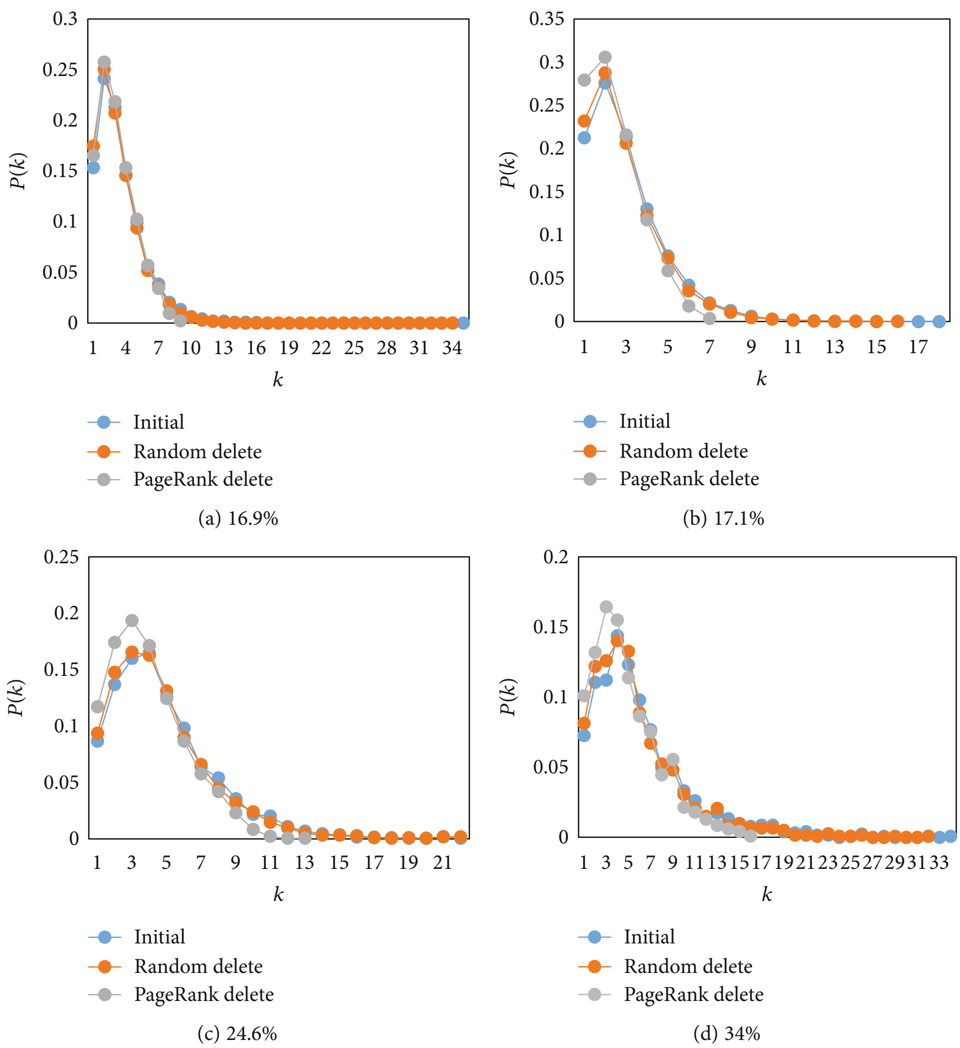

Figure 7: Pore network degree distribution of sandstone under different deletion schemes.

After the s times of iteration, the PageRank value of each node is as follows:

$$P'_s(i) = (1-d) + d \times \sum_{(V_j, V_i)\in E} \frac{P'_{s-1}(j)}{C'(j)}, 0 < i \le n, \qquad (4)$$

where d is a damping factor ($0 < d < 1$), which represents the probability of connecting a node. In this iterative way, multiple rounds are iterated until the PageRank value converges or when the sum of the PageRank value changes of all nodes is less than the custom threshold. Then, the pores are sorted according to the PageRank values.

The evolution process of the average path length is calculated as shown in Figure 5 according to two schemes, which are random deletion and PageRank-sorted deletion from the most important node. The horizontal coordinate axis is the number of deleting nodes, and the total amount of removing pores is 5% of the total number of pores. It can be seen from Figure 5 that when the pores in the sandstone pore network are randomly deleted, the average path length of the sandstone pore network increases only slightly. When the PageRank algorithm was used to rank the importance of pores and remove important nodes, the average path length increased significantly. It can be concluded that in the sandstone pore network, a small number of important nodes selected by the PageRank algorithm play a crucial role in the permeability of the whole macroscopic network. In the process of underground oil and gas exploitation, under the action of ground stress, adsorption, and desorption, if these key pores are plugged, it may cause significant change in the whole network permeability [19–22].

The variation curve of the average degree of pore network of sandstone under the two node elimination schemes is shown in Figure 6. As shown in Figure 6, compared with random deleting nodes, the decrease of pore average degree in the node deletion scheme based on PageRank algorithm is more obvious. That is, the overall connectivity of the sandstone pore network has been obviously weakened. In order to analyze the specific evolution process of the network degree distribution, we calculated the contrast curves before and after the deletion of the pores, as shown in Figure 7.

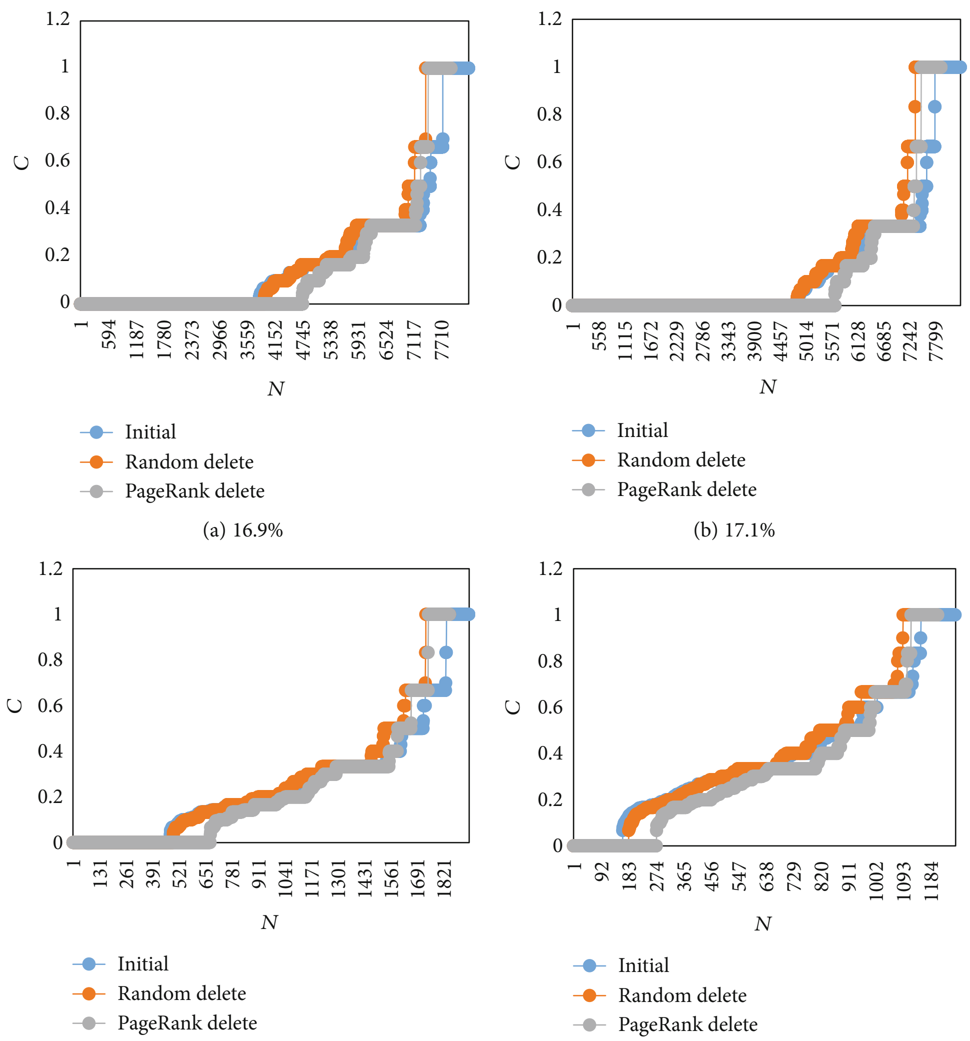

(a) 16.9%

(b) 17.1%

(c) 24.6%

(d) 34.0%

Figure 8: Clustering coefficients of sandstone pore network under different elimination schemes.

From Figure 7, it is known that random deleting nodes have little influence on the overall pore network degree distribution, and the curves before and after deletion are basically coincided. And before and after the node deletion based on the PageRank algorithm, the data of the back section of the curve are significantly reduced. The main reason is that the PageRank algorithm sorted the more important nodes, whose degree is larger, that is, the connectivity is stronger. Therefore, most of the nodes which have been deleted by the second scheme are the nodes with the large degree. This is also the reason for the obvious decrease in the average degree of the deletion method based on PageRank scheme in Figure 6.

The clustering coefficient is the coefficient that indicates the degree of node aggregation. This property is the clustering characteristic of the network. According to Figure 8, the distribution of the clustering coefficient of sandstone pore network has little change under different deletion schemes. In order to analyze the overall aggregation degree of sandstone pore network, we calculated the average clustering coefficient of pore network of different porosity sandstone, as shown in Figure 9.

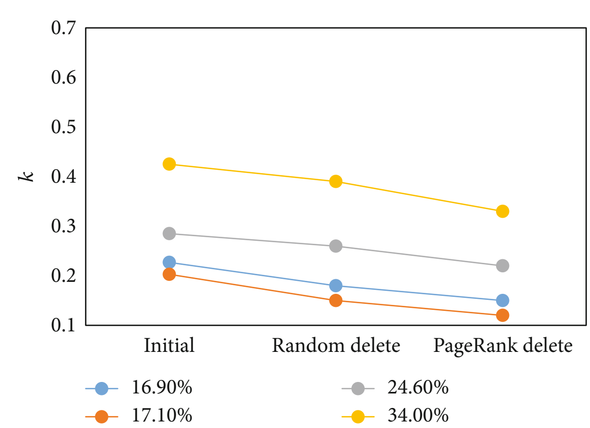

Figure 9: Comparison of the average clustering coefficient of sandstone pore network under different elimination schemes.

Compared with Figures 8 and 9, we can see that although the distribution of clustering coefficients changes slightly before and after the deletion, the average clustering coefficient

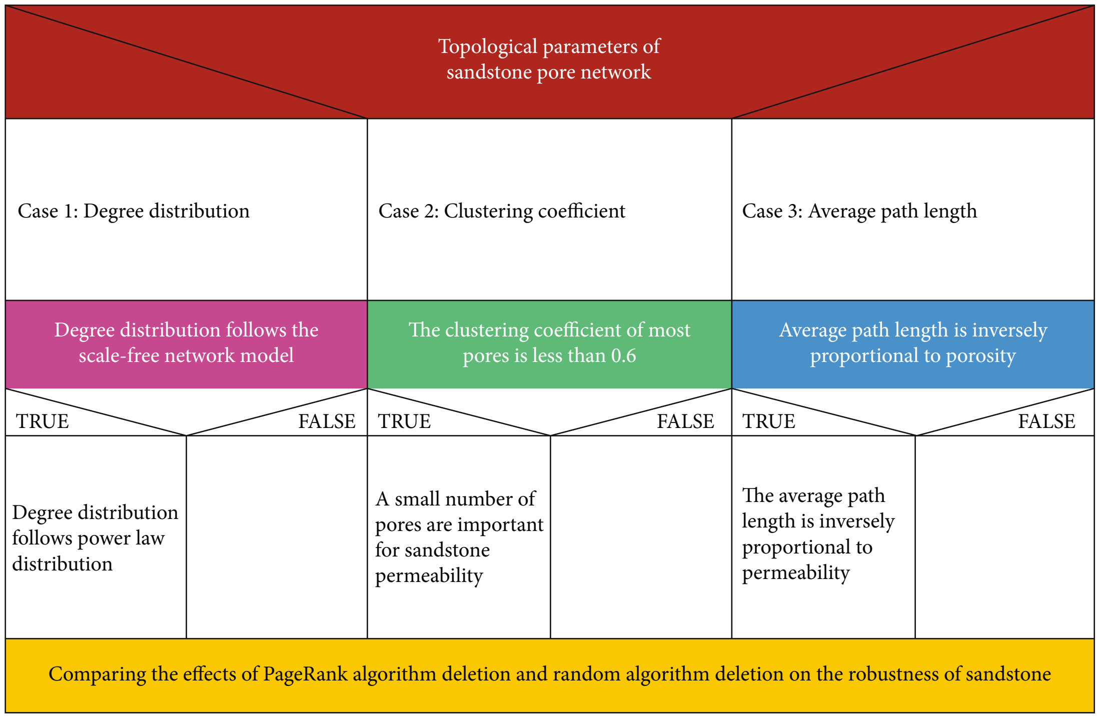

FIGURE 10: N-S diagram of the overall process of pore network analysis.

of the network has been significantly reduced. Especially the deletion method based on the PageRank algorithm, the clustering coefficients of the four porosity sandstone networks have decreased by about 0.1. The main reason is that the PageRank algorithm elimination scheme deletes a large number of nodes with large degree. That is, a large number of edges (throats) have been deleted, which leads to a significant reduction in the overall connectivity of the network. The pore network analysis process is shown in Figure 10.

5. Conclusions and Discussion

In this work, the complex network theory is used to study the characteristics of rock network. The degree distribution, clustering coefficient distribution, and average path length of the three-dimensional pore network are discussed, and the robustness of the network is also analyzed. The conclusions are as follows:

(1) Compared with the random model, the porosity distribution is more consistent with the scale-free network model of power-law distribution, that is, the porosity network of sandstone has no obvious characteristic value

(2) The average path length of sandstone pore network is directly related to the network size. The larger the aperture volume, the smaller the number of network nodes and the smaller the average path length. PageRank is a function defined in the pore network structure. It gives a positive real number for each pore, which indicates the importance of the pore and forms a vector as a whole. The higher the PageRank value is, the more important the pore is. Compared with the random model scheme, the average path length of the PageRank deletion scheme is much more significant than that of the random model scheme when the same few nodes are deleted by the PageRank algorithm, which may have a greater impact on the permeability of the whole sandstone pore network [20, 21]

(3) The pore network of sandstone is robust to random deletion. However, a few special nodes selected by the PageRank algorithm are deleted, which greatly reduces the transmission performance of the network. By comparing the stochastic model with the PageRank algorithm model, it is shown that the special pore structure plays a key role in the connectivity of the whole network. Based on the influence of the robustness of sandstone pore network on permeability, it can be used to select the position with strong robustness as the production well location in engineering, so as to ensure the stability of permeability and gas production.

Data Availability

Data used to support the results from the experimental results can be obtained at the university of British imperial, and access to sites is as follows: https://www.imperial.ac.uk/earth-science/research/research-groups/perm/research/pore-scale-modelling/micro-ct-images-and-networks/.

Conflicts of Interest

The authors declare that they have no conflicts of interest.

Acknowledgments

This research was funded by the open fund of Jiangsu Key Laboratory of Coal-based Greenhouse Gas Control and Utilization (Grant No. 2017B06). The data and methods for this study are from the website of Imperial College London, UK, which is linked below: https://www.imperialL.ac.uk/earth-science/research/research-groups/perm/research/pore-scale-modelling/micro-ct-images-and-networks/.

References

[1] J. Zeng, J. Liu, W. Li, Y. K. Leong, D. Elsworth, and J. Guo, "Evolution of shale permeability under the influence of gas diffusion from the fracture wall into the matrix," *Energy & Fuels*, vol. 34, no. 4, pp. 4393–4406, 2020.

[2] J. Zeng, X. Wang, J. Guo, F. Zeng, and F. Zeng, "Modeling of heterogeneous reservoirs with damaged hydraulic fractures," *Journal of Hydrology*, vol. 574, pp. 774–793, 2019.

[3] Y. Xue, T. Teng, F. Dang, Z. Ma, S. Wang, and H. Xue, "Productivity analysis of fractured wells in reservoir of hydrogen and carbon based on dual-porosity medium model," *International Journal of Hydrogen Energy*, vol. 45, no. 39, pp. 20240–20249, 2020.

[4] J. Liu, X. Liang, Y. Xue, K. Yao, and Y. Fu, "Numerical evaluation on multiphase flow and heat transfer during thermal stimulation enhanced shale gas recovery," *Applied Thermal Engineering*, vol. 178, p. 115554, 2020.

[5] H. Wang, R. Shi, D. Deng, Y. Jiang, G. Wang, and W. Gong, "Characteristic of stress evolution on fault surface and coal bursts mechanism during the extraction of longwall face in Yima mining area, China," *Journal of Structural Geology.*, vol. 136, p. 104071, 2020.

[6] H. Wang, S. Xue, R. Shi, Y. Jiang, W. Gong, and L. Mao, "Investigation of fault displacement evolution during extraction in longwall panel in an underground coal mine," *Rock Mechanics and Rock Engineering*, vol. 53, no. 4, pp. 1809–1826, 2020.

[7] C. Wang, J. Zhang, Y. Zang et al., "Time-dependent coal permeability: impact of gas transport from coal cleats to matrices," *Journal of Natural Gas Science and Engineering*, vol. 88, p. 103806, 2021.

[8] S. Zhang, J. Liu, M. Wei, and D. Elsworth, "Coal permeability maps under the influence of multiple coupled processes," *International Journal of Coal Geology*, vol. 187, pp. 71–82, 2018.

[9] A. Mitra, S. Harpalani, and S. Liu, "Laboratory measurement and modeling of coal permeability with continued methane production: part 1–laboratory results," *Fuel*, vol. 94, pp. 110–116, 2012.

[10] Z. Pan, L. D. Connell, and M. Camilleri, "Laboratory characterisation of coal reservoir permeability for primary and enhanced coalbed methane recovery," *International Journal of Coal Geology*, vol. 82, no. 3-4, pp. 252–261, 2010.

[11] Y. Peng, Q. Qi, Z. Deng, and H. Li, "Experimental study on permeability sensitivity of coal sample to confining pressure considering scale effect," *Journal of China Coal Society*, vol. 33, no. 5, pp. 509–513, 2008.

[12] R. Pan, *Permeability Evolution Characteristics of Loaded Coal Body and Its Application in Relief Gas Drainage*, China University of Mining and Technology, 2014.

[13] B. Lin and S. Zhou, "Experimental study on gas permeability of coal sample," *Journal of China Institute of Mining and Technology*, vol. 1, pp. 24–31, 1987.

[14] S. Cao, P. Guo, Y. Li et al., "Effect of gas pressure on permeability characteristics of raw coal," *Journal of China Coal Society*, vol. 35, no. 4, pp. 595–599, 2010.

[15] F. Gao, Y. Hu, G. Liu, and Y. Yang, "Experiment study on topological characteristics of sandstone coating by micro CT," *Coatings*, vol. 10, no. 12, p. 1143, 2020.

[16] D. Ye, G. Liu, F. Gao, X. Zhu, and Y. Hu, "A study on the structure of rock engineering coatings based on complex network theory," *Coatings*, vol. 10, no. 12, p. 1152, 2020.

[17] L. Gong, L. Nie, and Y. Xu, "Geometrical and topological analysis of pore space in sandstones based on X-ray computed tomography," *Energies*, vol. 13, no. 15, p. 3774, 2020.

[18] H. Darabi, A. Ettehad, F. Javadpour, and K. Sepehrnoori, "Gas flow in ultra-tight shale strata," *World Journal of Engineering*, vol. 6, no. 3, pp. 7–15, 2009.

[19] H. Singh, F. Javadpour, A. Ettehadtavakkol, and H. Darabi, "Nonempirical apparent permeability of shale," *SPE Reservoir Evaluation & Engineering*, vol. 17, no. 3, pp. 414–424, 2014.

[20] B. Yu and P. Cheng, "A fractal permeability model for bi-dispersed porous media," *International Journal of Heat and Mass Transfer*, vol. 45, no. 14, pp. 2983–2993, 2002.

[21] T. Miao, B. Yu, Y. Duan, and Q. Fang, "A fractal analysis of permeability for fractured rocks," *International Journal of Heat and Mass Transfer*, vol. 81, pp. 75–80, 2015.

[22] T. Miao, S. Yang, Z. Long, and B. Yu, "Fractal analysis of permeability of dual-porosity media embedded with random fractures," *International Journal of Heat and Mass Transfer*, vol. 88, pp. 814–821, 2015.

[23] R. Liu, Y. Jiang, B. Li, S. Wang, and S. Xun, "Numerical calculation of directivity of equivalent permeability coefficient of rock fracture network," *Rock and Soil Mechanics*, vol. 35, no. 8, pp. 2394–2400, 2014.

[24] W. Li, Z. J. Liu, J. Zeng et al., "A fully coupled multidomain and multiphysics model for evaluation of shale gas extraction," *Fuel*, vol. 278, article 118214, 2020.

[25] W. Li, Z. J. Liu, and Y. Leong, "A fully coupled multidomain and multiphysics model for shale gas production," in *Presented at the 5th ISRM Young Scholars' Symposium on Rock Mechanics and International Symposium on Rock Engineering for Innovative Future, 1-4 December*, Okinawa, Japan, 2019https://www.onepetro.org/conference-paper/ISRM-YSRM-2019-063.

[26] G. Liu, B. Yu, D. Ye, F. Gao, and J. Liu, "Study on evolution of fractal dimension for fractured coal seam under multi field coupling," *Fractals*, vol. 28, no. 4, article 2050072, 2020.

[27] G. Liu, J. Liu, L. Liu, D. Ye, and F. Gao, "A fractal approach to fully-couple coal deformation and gas flow," *Fuel*, vol. 240, pp. 219–236, 2019.

[28] G. Liu, D. Ye, F. Gao, and J. Liu, "A dual fractal poroelastic model for characterizing fluid flow in fractured coal masses," *Geofluids*, vol. 2020, Article ID 2787903, 13 pages, 2020.

[29] K. Li, S. Kong, P. Xia, and X. Wang, "Microstructural characterisation of organic matter pores in coal-measure shale,"

Advances in Geo-Energy Research, vol. 4, no. 4, pp. 372–391, 2020.

[30] X. Qin, Y. Zhou, and A. P. Sasmito, "An effective thermal conductivity model for fractal porous media with rough surfaces," *Advances in Geo-Energy Research*, vol. 3, no. 2, pp. 149–155, 2019.

[31] Z. Li, Y. Duan, Q. Fang, and M. Wei, "A study of relative permeability for transient two-phase flow in a low permeability fractal porous medium," *Advances in Geo-Energy Research*, vol. 2, no. 4, pp. 369–379, 2018.

[32] Q. Yu, *Mine Gas Prevention*, China University of Mining and Technology Press, 1992.

Hindawi
Geofluids
Volume 2021, Article ID 5545067, 16 pages
https://doi.org/10.1155/2021/5545067

Research Article

Speculum Observation and Trajectory Measurement in Gas Extraction Drilling: A Case Study of Changling Coal Mine

Enbiao Zhao,[1] Kangnan Li ,[1] Xin Yang ,[2] and Nan Deng[3]

[1]*Beijing Key Laboratory for Precise Mining of Intergrown Energy and Resources, China University of Mining & Technology (Beijing), Beijing 100083, China*
[2]*School of Civil and Resources Engineering, University of Science and Technology Beijing, Beijing 100083, China*
[3]*China Coal Research Institute, Beijing 100013, China*

Correspondence should be addressed to Kangnan Li; knli541@126.com and Xin Yang; xinyangbk89@163.com

Received 22 February 2021; Revised 14 March 2021; Accepted 24 March 2021; Published 1 April 2021

Academic Editor: Yi Xue

Coal will still be China's basic energy for quite a long time. With the increase of mining depth, gas content and pressure also increase. The problems of gas emission and overrun affect the safety and efficient production of coal resource to a certain extent. In this work, the field test of gas drainage borehole peeping and trajectory measurement in coal seam of Changling coal mine are carried out. These coal seams include C_5^b coal seam, upper adjacent C_5^a coal seam, C_6^a coal seams, C_6^c in lower adjacent strata, and C_5^b coal seam in high-level borehole. The view of gas drainage borehole peeping and trajectory measurement in the working seam, upper adjacent layer, lower adjacent layer, and high position are obtained. It is found that the hole collapses at the position of about 20 m in both adjacent strata and high-level boreholes, and there are a lot of cracks in the high-level boreholes before 12 m. The deviation distance of high-level borehole is large, and the actual vertical deviation of upper adjacent layer is small. Finally, the strategies to prevent the deviation of drilling construction are put forward. It includes four aspects: ensuring the reliability of drilling equipment, reasonably controlling the drilling length, standardizing the drilling, and reasonably selecting the drilling process parameters.

1. Introduction

For quite a long time in the future, coal is still China's main energy and important chemical raw materials, supporting the rapid and stable development of China's national economy [1–5]. More than 90% of China's coal mines are mainly underground mining. The complex coal seam occurrence conditions bring serious threat to coal mine safety production, even inducing personal injury [6–10]. In recent years, relying on scientific and technological progress, coal mine safety production situation continues to improve. Coal mining enterprises have higher requirements for gas drainage technology and pay more attention to the related problems of drainage drilling.

The curvature of drilling trajectory in extraction will lead to the blank area in the coal seam extraction, which greatly affects the gas drainage effect and may lead to coal-gas outburst, gas explosion, and other gas accidents. The main reasons are geological factors and technological factors [11–14]. The main geological factors are the anisotropy of rocks and the interbedding of soft and hard rocks. Coal rock with bedding, schistosity, and other structural characteristics has obvious anisotropy in drillability, which easily leads to borehole bending. In addition, the technical reasons such as uneven drilling foundation, too long drill pipe, incorrect vertical axis installation, and the technological reasons such as too much bit pressure, too high drilling speed, and too much flushing fluid will lead to the bending of the drilling hole. These will lead to the deviation of the final hole position from the target location. Borehole peeper can be used to detect coal seam structure, geological structure, roadway roof separation, borehole quality, and roadway grouting effect. Especially in the study of fracture zone development law, it can be displayed intuitively and clearly through the display, and it can also measure the trajectory of gas drainage borehole [15–17].

Scholars in various countries have done a lot of research on the principle and prevention of gas drainage borehole bending. Polak et al. [18, 19] established a new theoretical model of drill pipe and hole wall contact. Through the field test, it is found that the model can better estimate and predict the contact force and corresponding deformation of drill pipe, which provides a basis for controlling the drilling direction of drill pipe. Lueke et al. [20, 21] analyzed in detail the influence of geological conditions, drill pipe pressure, bit structure, borehole diameter, drilling depth, and other factors on borehole deviation during drilling. Based on the field test, it is proposed that the deviation prevention device can be installed at the appropriate position to reduce the deviation of the borehole. Based on the angular displacement sensor and communication module, Manacorda et al. [22] proposed and designed a bit radar equipment for directional drilling. The device can transmit the actual position of the bit in real time, which provides a reference for effectively controlling the drilling direction. Matheus et al. [23, 24] analyzed the shortcomings of existing drilling trajectory control and presented an adjustment method combining drill pipe control and prediction. It focuses on the application value of new rotary steering system (RSS) in drilling, providing a new method to control the movement of drill pipe in real time during drilling. Li [25] used wireless digital compass inclinometer to measure the coordinates of the drilled hole in Chambishi mine, Zambia. He calculated and compared the actual coordinates with the design coordinates to get the final offset. Liang et al. [26] analyzed the causes of borehole deviation from three aspects of geological factors, technological factors, and operation technical factors, summarizing the regularity of borehole deviation and the measures to prevent borehole deviation. Zhu et al. [27] invented a compound drilling device for deviation prevention and straight drilling while drilling, which can effectively improve the drilling speed and the ability of deviation prevention and correction in vertical wells and monitor the deviation change in real time with high stability and low cost. Ding et al. [28] analyzed the problems and error sources in the past drilling construction and gave a method for calculating the trajectory of borehole. Wang et al. [29, 30] proposed and designed angle compensation correction method and designed the evaluation index of borehole correction effect in view of serious deviation of pressure relief gas drainage borehole trajectory in 2603 working face of Liyazhuang coal mine. Zhao et al. [31] analyzed the geological, technical, and technological factors the causing borehole bending in drilling engineering construction. They put forward the preventive measures of correctly installing construction equipment and adopting reasonable drilling tool structure. Zhao [32] presents that the main factors of borehole bending can be attributed to three aspects: formation structure, drilling pressure, and equipment installation. He put forward corresponding preventive measures according to different reasons.

In order to investigate the development and trajectory of gas drainage borehole fracture zone in coal mine, the Changling coal mine is taken as a case. By peeping at the high-level boreholes of C_5^b coal seam, upper adjacent layer C_5^a coal seam, lower adjacent layer C_6^a and C_6^c coal seam, and C_5^b coal seam high-level drilling in Changling coal mine, the development law of borehole fracture zone was investigated, and the trajectory of construction holes of 1250 and 4000 drilling rigs was measured to determine the trajectory of gas drainage holes and explore the deviation law of drilling trajectory.

2. General Situation of Mine and Layout of Boreholes

2.1. General Situation of Mine. Changling coal mine is located in the southeast of Zhaotong City, Yunnan Province. The designed production capacity of the mine is 0.6 million t/a. Mining depth is from +1800 m to +1400 m elevation. The mining area is 11.399 km^2. The mine is divided into two levels of mining. The first level elevation is +1560 m, and the second level elevation is +1520 m. The mine is divided into five mining areas, and the mining sequence is 101 mining area, 102 mining area, 201 mining area, 202 mining area, and 203 mining area. Plan of excavation engineering in mining area is shown in Figure 1. There are only three minable coal seams in the mine, namely, C_5^b, C_6^a, and C_6^c. The dip angle of coal seam is 2 degrees to 10 degrees, and most of them are below 8 degrees with small coal seam spacing. The coal seam characteristics are shown in Table 1.

2.2. Drilling Layout. The design technical parameters of C_5^b coal seam gas drainage borehole are shown in Table 2. The layout of coal seam boreholes is shown in Figure 2.

There are six construction boreholes in the C_5^b coal seam. Two short boreholes in the working seam, numbered C_5^b-C_{1-1} and C_5^b-C_{1-2}, are used for the drilling peeping and trajectory measurement. Two long boreholes in the working seam (constructed by 4000 drilling rig), numbered C_5^b-C_{2-1} and C_5^b-C_{2-2}, are used for the drilling peeping and trajectory measurement. Two high-level boreholes, numbered C_5^b-A_{3-1} and C_5^b-B_{2-1}, are used for borehole peeping and trajectory measurement. Two construction boreholes in the C_5^a coal seam, numbered C_5^a-C_{2-1} and C_5^a-C_{2-2}, are used for the borehole trajectory measurement. Two construction boreholes in the C_6^a coal seam, numbered C_6^a-C_{2-1} and C_6^a-C_{2-2}, are used for the borehole trajectory measurement. Two construction boreholes in the C_6^c coal seam, numbered C_6^c-C_{2-1} and C_6^c-C_{2-2}, are used for the borehole trajectory measurement.

3. Overview of Test Equipment

3.1. Drilling Equipment

3.1.1. ZY-1250 Full Hydraulic Drilling Rig for Coal Mine. ZY-1250 full hydraulic drilling rig for coal mine is composed of seven parts: pump station, operating platform, power head, frame, column, and drilling tool. It is mainly suitable for drilling gas drainage holes, drainage holes, coal seam water injection holes, grouting fire prevention holes, geological exploration holes, and various engineering holes in coal mines. It is suitable for all kinds of coal seams and strata with rock firmness coefficient f less than or equal to 8. The cross-

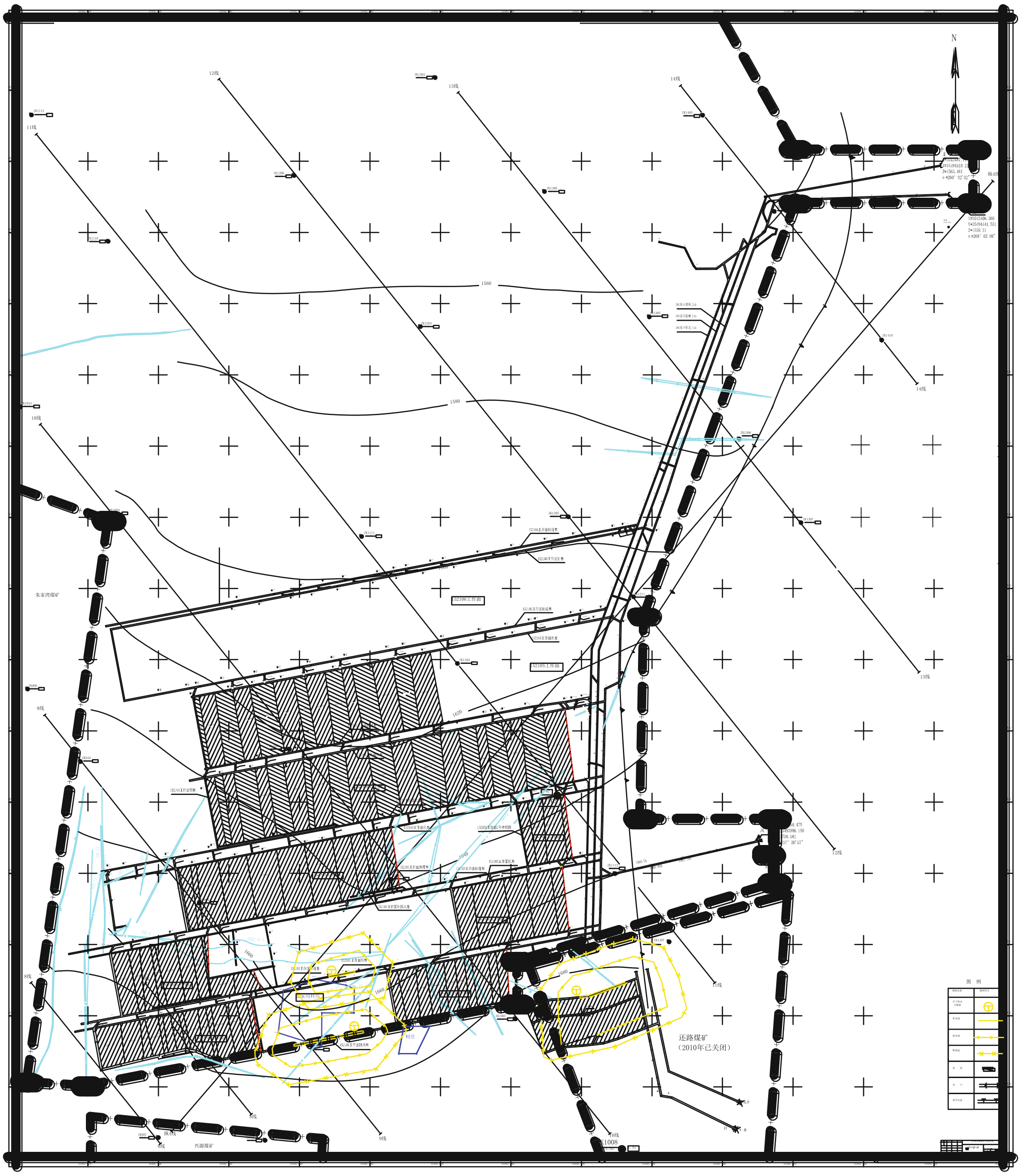

Figure 1: Excavation plan of 101 mining area of Changling coal mine.

sectional area of roadway for drilling rig is more than or equal to 6.5 m^2.

3.1.2. LD4000ZYWL00II (SZ2) Crawler Full Hydraulic Drilling Rig for Coal Mine. LD4000ZYWL00II (SZ2) crawler full hydraulic drilling rig for coal mine is mainly composed of bottom car, support rotation, work surface, frame, operation platform, pump station, gripper, guide sleeve, pipeline system, drilling tool, rear water braid, and other components. It is mainly used for drilling gas drainage hole, grouting fire prevention hole, coal seam water injection hole, outburst prevention and pressure relief hole, geological exploration hole, and other engineering holes. It is suitable for all kinds of coal seams and strata with rock firmness coefficient f less than or equal to 10. The drill can walk independently and turn in place. The cross-sectional area of roadway for drilling rig is more than 9 m^2. Or the width is more than 3 m, and the height is more than 3 m. The pump station converts the electric energy into hydraulic energy, and the pressure oil from the oil pump drives the motor and the propulsion cylinder to complete various actions of the drilling rig. The hydraulic system adopts the linkage oil circuit. Through the setting of each function selection valve, by operating the rotation and advance/retreat handle, it can realize the positive/negative

Table 1: Coal seam characteristics.

Coal seam	Coal seam thickness			Layers of gangue $\frac{\text{Maximum} - \text{Minimum}}{\text{Average}}$	Thickness of gangue (m) $\frac{\text{Maximum} - \text{Minimum}}{\text{Average}}$	Apparent density (t/m^3)	Recoverable range and reserve ratio
	Minimum	Maximum	Average				
C_1	0.8	1.05	0.89	-1 – 3/2	-0.03 – 0.14/0.08	1.70	Sporadic recoverable with 2% reserves
C_5^a	0.8	1.42	1.09	-0 – 3/1	-0 – 0.29/0.03	1.60	The recoverable area is 23%, and the reserves account for 5.3%
C_5^b	0.86	5.51	2.75	$-\frac{0-18}{3.3}$	$-\frac{0-6.9}{0.16}$		The whole area is recoverable, accounting for 69.7% of the total reserves
C_6^a	0.8	2.48	1.28	$-\frac{0-9}{2}$	$-\frac{0-0.56}{0.14}$	1.65	Recoverable area 50%, reserves 13%
C_6^c	0.8	1.56	0.97	-0 – 5/0.7	-0 – 0.45/0.05	1.65	Recoverable area 52%, reserves 10%

Table 2: Basic parameters of coal seam gas drainage borehole.

Number	Coal seam	Place	Dip angle (°)	Azimuth (°)	Drilling depth (m)	Aperture (mm)	Drilling type
C_5^b-C_{1-1}	C_5^b	152106 track lane, which is 1000 m and 1030 m away from the gateway	-3	350	70	75	Down bedding
C_5^b-C_{1-2}			-3	350	70	75	
C_5^b-C_{2-1}		152106 track lane, which is 500 m and 530 m away from the gateway	-3	350	100	94	
C_5^b-C_{2-2}			-3	350	100	94	
C_5^b-A_{3-1}	C_5^b	152105 track lane, which is 300 m away from the gateway	+14	230	80	75	High-level drilling
C_5^b-B_{2-1}		152105 track lane, which is 200 m away from the gateway	+14	285	80	75	
C_5^a-C_{2-1}	C_5^a	152106 track lane, which is 500 m and 530 m away from the gateway	+3	350	70	75	Up crossing
C_5^a-C_{2-2}			+3	350	70	75	
C_6^a-C_{2-1}	C_6^a	152106 track lane, which is 500 m and 530 m away from the gateway	-10	350	70	75	Down crossing
C_6^a-C_{2-2}			-10	350	70	75	
C_6^c-C_{2-1}	C_6^c	152106 track lane, which is 500 m and 530 m away from the gateway	-15	350	70	75	Down crossing
C_6^c-C_{2-2}			-15	350	70	75	

rotation, forward/backward of the power head, the loosening/clamping of the chuck and gripper, and the corresponding linkage functions.

3.2. Drilling Peeping and Trajectory Measurement System. The ZKXG30 mine drilling imaging track detection device is a high-tech equipment for comprehensive detection of drilling. The product integrates the functions of drilling photography, peeping (video), imaging, and track measurement and completes the workload of the previous four tests in one test. Meanwhile, it can obtain drilling dynamic video, local high-definition photos, full drill hole wall expanded plan, and drilling space track, which is efficient and fast. The instrument includes low-power embedded dual core processor, high-definition high-speed digital camera, and military grade high-precision space angle measuring device, which is supplemented by advanced control algorithm and image processing algorithm and other software systems to realize all functions synchronously. The product design fully considers the actual working environment of the coal mine and strives for simple operation, stable system performance, simple, and reliable. The system structure of the ZKXG30 mining borehole imaging track detection device (track) is shown in Figure 3.

4. Test Principle and Steps

4.1. Introduction of the Device Structure. The ZKXG30 mine drilling imaging track detection device (track) is mainly composed of host, probe, and sounder. The host is mainly composed of internal system, external interface, and battery pack. The external interface includes probe port, sounder port, operation control knob interface, and charger interface. The internal system mainly includes ARM dual core processor and data storage unit. The internal system is connected with external components through external interfaces. Under

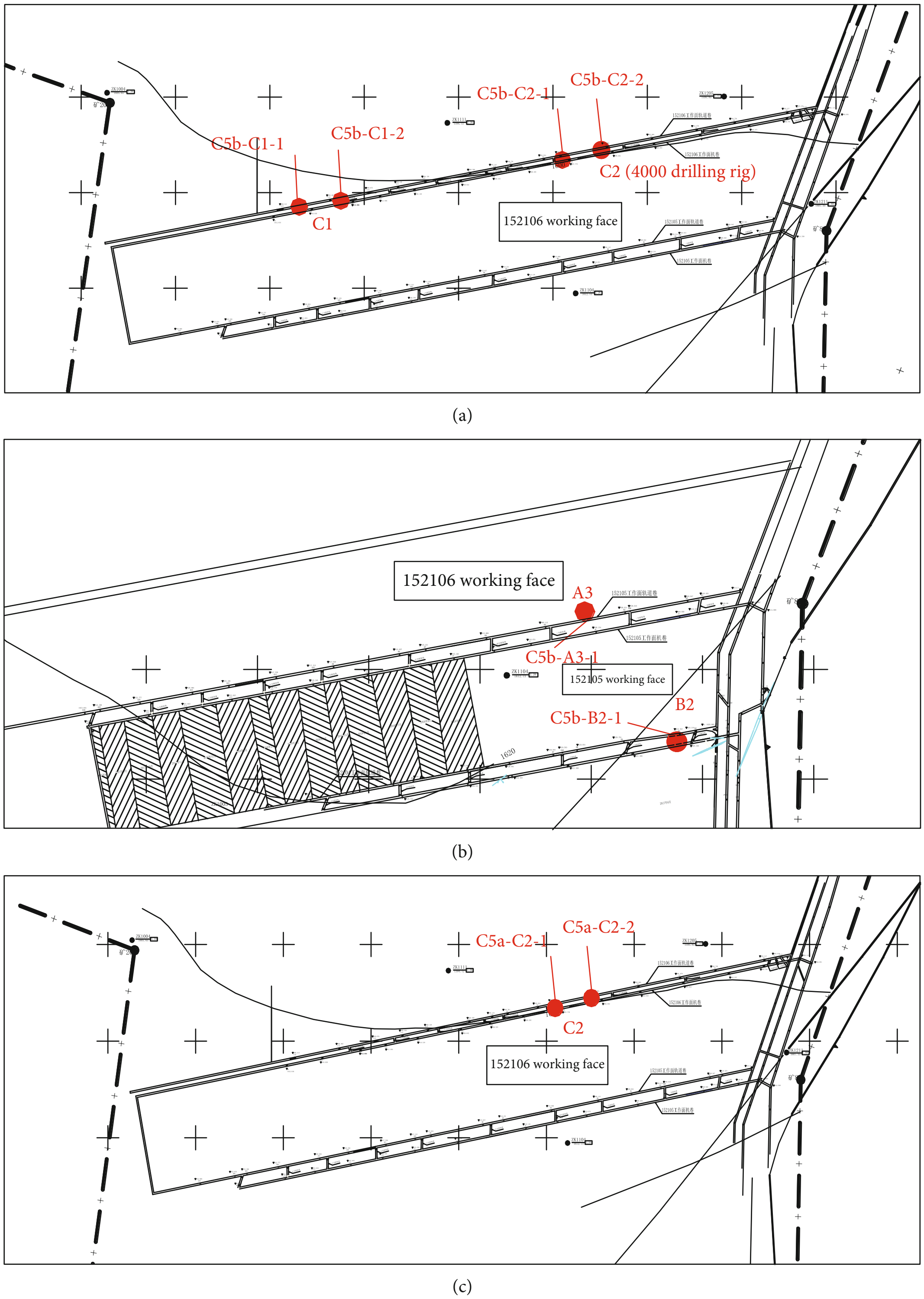

Figure 2: Continued.

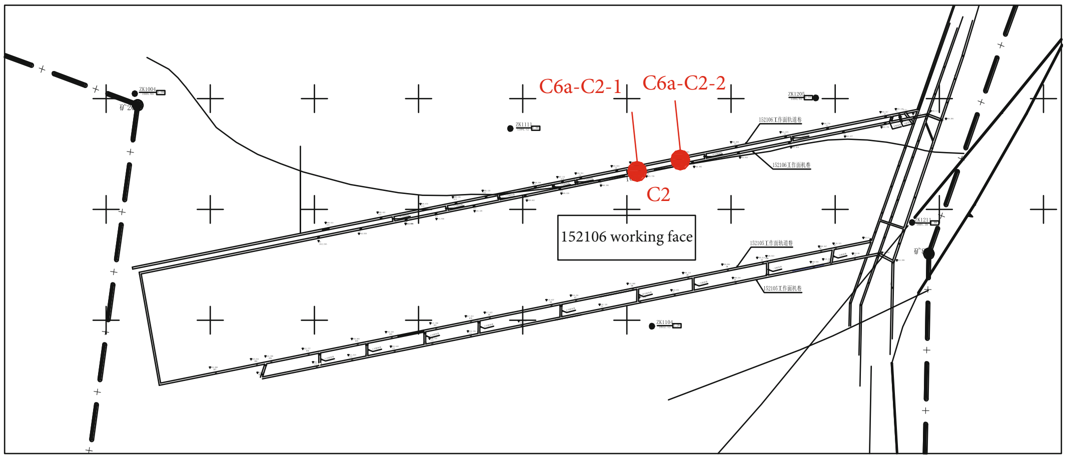

(d)

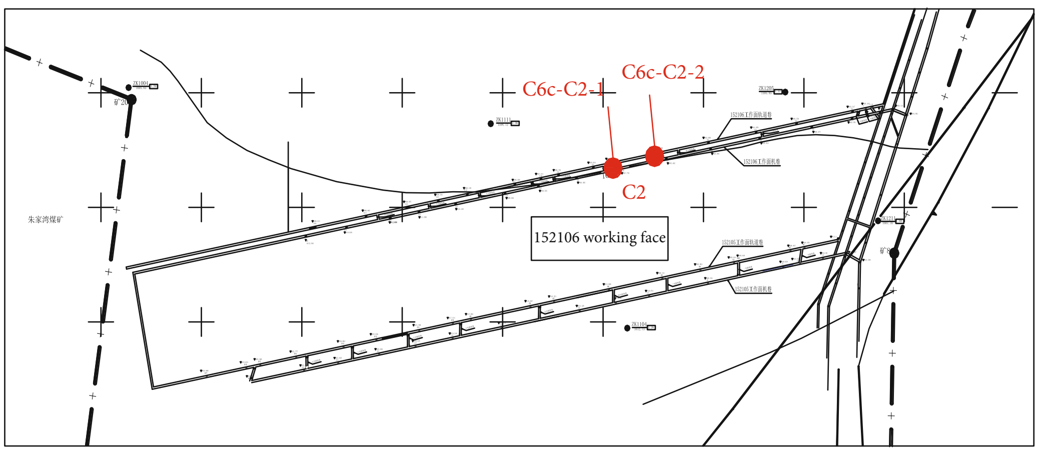

(e)

Figure 2: (a) Layout of boreholes for peeping and trajectory measurement in $C_5{}^b$ coal seam. (b) Layout of high-level boreholes peeping and trajectory measurement in $C_5{}^b$ coal seam. (c) Layout of trajectory survey boreholes in $C_5{}^a$ coal seam. (d) Layout of trajectory survey boreholes in $C_6{}^a$ coal seam. (e) Layout of trajectory survey boreholes in $C_6{}^c$ coal seam.

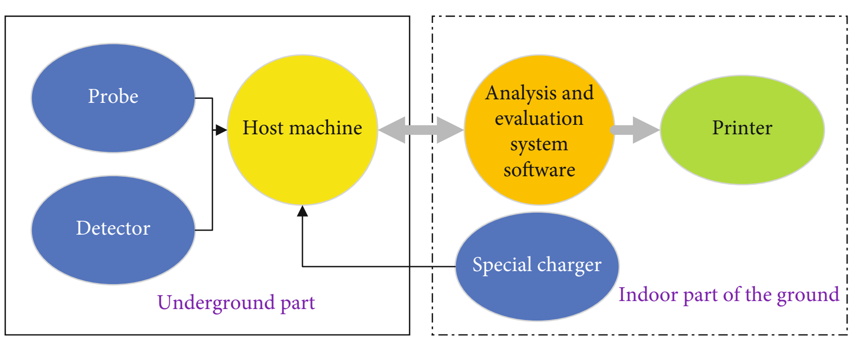

Figure 3: ZKXG30 mining borehole imaging track detection device (track) system structure diagram.

the control of the software system, the functions of track acquisition, display, storage, and data transmission are realized. The principle block diagram of the instrument is shown in Figure 4.

4.2. Test Principle. The ZKXG30 mining borehole imaging track detection device mainly includes ZKXG30-Z mining borehole imaging track detection device host, ZKXG30-T/T(a)/T(b) mining borehole imaging track detection device probe, ZKXG30-S mining borehole imaging track detection device depth encoder, and other main components, as well as video transmission cable, signal cable, push rod, and other accessories. The sounder is used to record the depth of the probe in the borehole. ZKXG30-T(b) mine drilling imaging

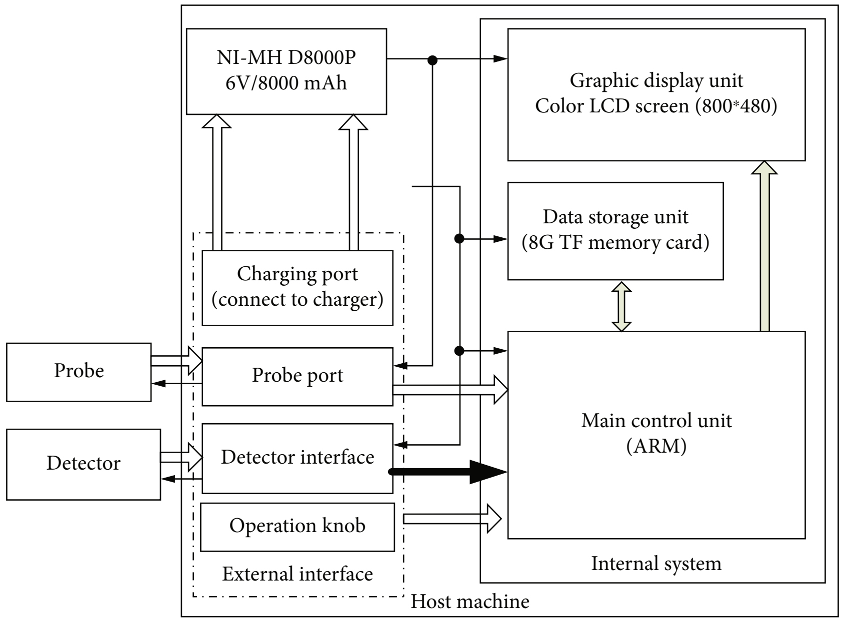

Figure 4: Block diagram of host structure.

trajectory detection device has a built-in LED white light emitting diode (with brightness adjustment circuit), and a camera, which is used to capture the hole wall image, and a built-in high-performance three-dimensional electronic compass, which is used to measure the drilling azimuth and inclination of the probe position. The ZKXG30-T(a) mine drilling imaging trajectory detection device has built-in high-performance three-dimensional electronic compass, which is used to measure the drilling azimuth and inclination of the probe position. The video signal, control signal, and compass digital signal in the probe are transmitted to the host through the mine intrinsically safe communication cable. The host receives the probe signal and the depth pulse signal of the sounder, calculates the depth position of the probe, and processes the video signal such as image recording, matching, and splicing. Video recording can be full hole or partial. Video and image matching and splicing are carried out simultaneously. As the probe continues to move into the hole, the whole hole wall is automatically matched and spliced into a complete plane expansion. While processing the image, the host computer can display the real-time monitoring image and the stitched unfolded image and can switch the display of borehole trajectory projection. The saved data can be played back and browsed. After connecting with PC, the instrument can be used as a U disk, which is convenient to copy and paste files.

4.3. Test Steps

4.3.1. Drilling Preparation. The diameter of the drilling probe shall not be less than 30 mm, and the depth shall be within 100 m, so as to ensure that the drilling has a certain elevation angle. Therefore, the water can flow out freely and keep as straight as possible to avoid step holes. After drilling, it needs to be placed for 10 minutes. After the fog in the hole disappears, it can be detected to ensure that the probe window will not condense water vapor.

4.3.2. Technical Staffing. At least 3 field operators are required for drilling exploration in deep roadway, excluding drilling personnel. One probe operator is responsible for using the push rod to push the probe slowly and smoothly into the drilling hole. Another cable operator is responsible for passing the cable through the depth decoder at a constant speed, and the last one host operator is responsible for controlling the host.

4.3.3. Device Connection. Connecting probe: both ends of the cable are fixed with 7-core waterproof plug. The plug is connected with the probe, and the plug cap is tightly fixed with the probe

Detector installation: the tripod is stably placed under the air port, and the probe cable is installed on the pulley

Connecting to the host: the other end of the 7-core video cable is connected to the host signal interface, and the 4-core cable connects the detector interface with the host deep interface

4.3.4. Equipment Operation. The equipment operation includes (1) power on self-test; (2) adjust the screen brightness; (3) drilling imaging detection device connection probe debugging: (a) turning on the host and entering the imaging detection mode, (b) setting the parameters, (c) menu selection, (d) adjusting the inner diameter and pulse distance, and (e) image acquisition; and (4) drilling track detection device connection probe debugging: (a) turning on the host and enter the track detection mode, (b) parameter setting, and (c) image acquisition, as shown in Figure 5.

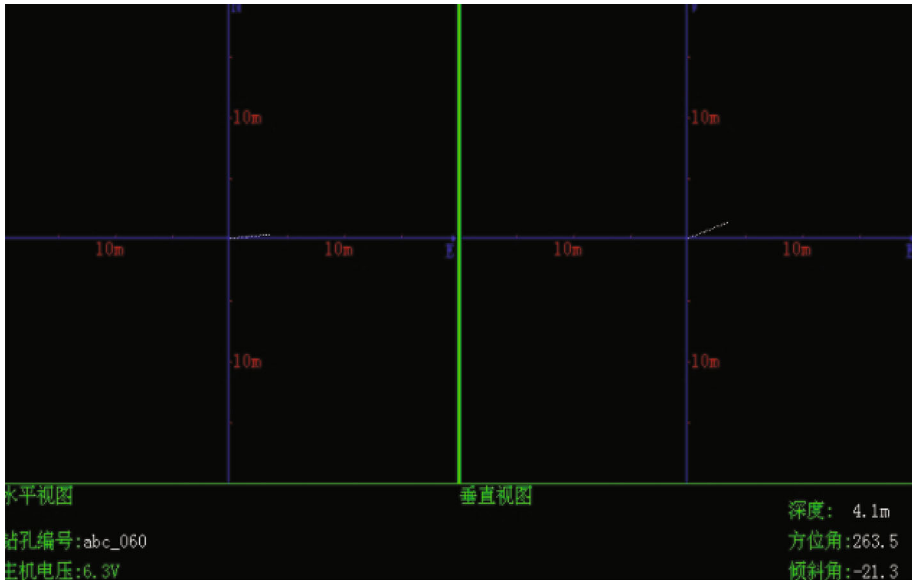

Figure 5: Image acquisition interface.

5. Test Results and Countermeasures

5.1. Drilling Peep Results. The peep results of this coal seam, upper adjacent layer, lower adjacent layer, and high-level gas drainage boreholes are shown in Figures 6–10.

Through peeping at the coal seam, upper adjacent layer, lower adjacent layer, and high-level gas drainage boreholes, the results show that the integrity of the boreholes in the coal seam is well. There is no obvious macrocracks, but there is water accumulation. Although the water in the borehole is ventilated and drained after the completion of drilling construction, there is still a certain length of water immersion in the depth of the down bedding drilling, which will directly affect the gas drainage effect. Due to the influence of drilling opening at 0-1 m of the hole opening in the lower adjacent layer, the hole collapse is very serious. The integrity of the borehole at 1-6 m is good, but the surrounding fissures are obviously developed. The borehole at 8-10 m begins to collapse obviously, and the borehole at 10 m completely collapses. The overall quality of the borehole is very poor. Compared with the lower adjacent layer, the integrity of the upper adjacent layer is better. However, there are obvious through type axial fractures. The borehole is completely collapsed at about 18 m.

There are a lot of cracks in the high-level borehole before 12 m. When selecting the high-level borehole for gas drainage, attention should be paid to the sealing distance of the borehole greater than 12 m. Otherwise, the gas concentration will decrease, and the gas drainage efficiency will be affected. The hole collapse occurred at the position of about 20 m in both adjacent strata and high-level boreholes, and the high-level boreholes collapsed seriously, which basically blocked the boreholes. In the follow-up gas drainage process, it will affect the drainage flow in varying degrees, resulting in the decline of drainage efficiency.

5.2. Prevention Measures of Hole Collapse. In view of the above experimental results, the prevention of hole collapse can be carried out from the following aspects. In the specific construction, according to the drilling speed, drilling pressure, rock powder, backwater, and lithology changes, the accurate judgment is made. Usually, clean water can be used as the flushing fluid. If the condition is not allowed and only circulating water can be selected, the bottom of cage should be kept in a clean state to avoid contamination by debris and rock powder, which will lead to the drill bit buried and paste, and eventually collapse. The drilling speed and feed pressure of the drilling rig should also be well controlled. If the rock stratum is relatively soft, the speed and pressure should be appropriately reduced according to the actual situation, and the footage height should also be appropriate. In case of hole collapse, the lithology and specific location of the starting section should be judged quickly and accurately, and the effective measures should be taken in time.

The operator should have practical experience and skilled technology, and be able to find the hole collapse in time, and adjust the drilling feed pressure and speed according to the coal and rock conditions. If the coal and rock are relatively soft, the drilling pressure and drilling speed should be appropriately reduced, the lifting frequency of drill pipe should be increased, and the coal and rock powder in the hole should be discharged in time, so as to reduce or avoid the drilling accidents.

According to the hardness of the rock in the hole, the bit type is selected to improve the drilling efficiency. When the rock is soft and the water invasion time is long, the hole collapse is easy to occur. The work should not be stopped during the shift handover, so as to facilitate the rapid construction and reduce the probability of hole collapse.

In the process of drilling, if the rock is soft, the drilling speed should be slowed down at this time, and the hole

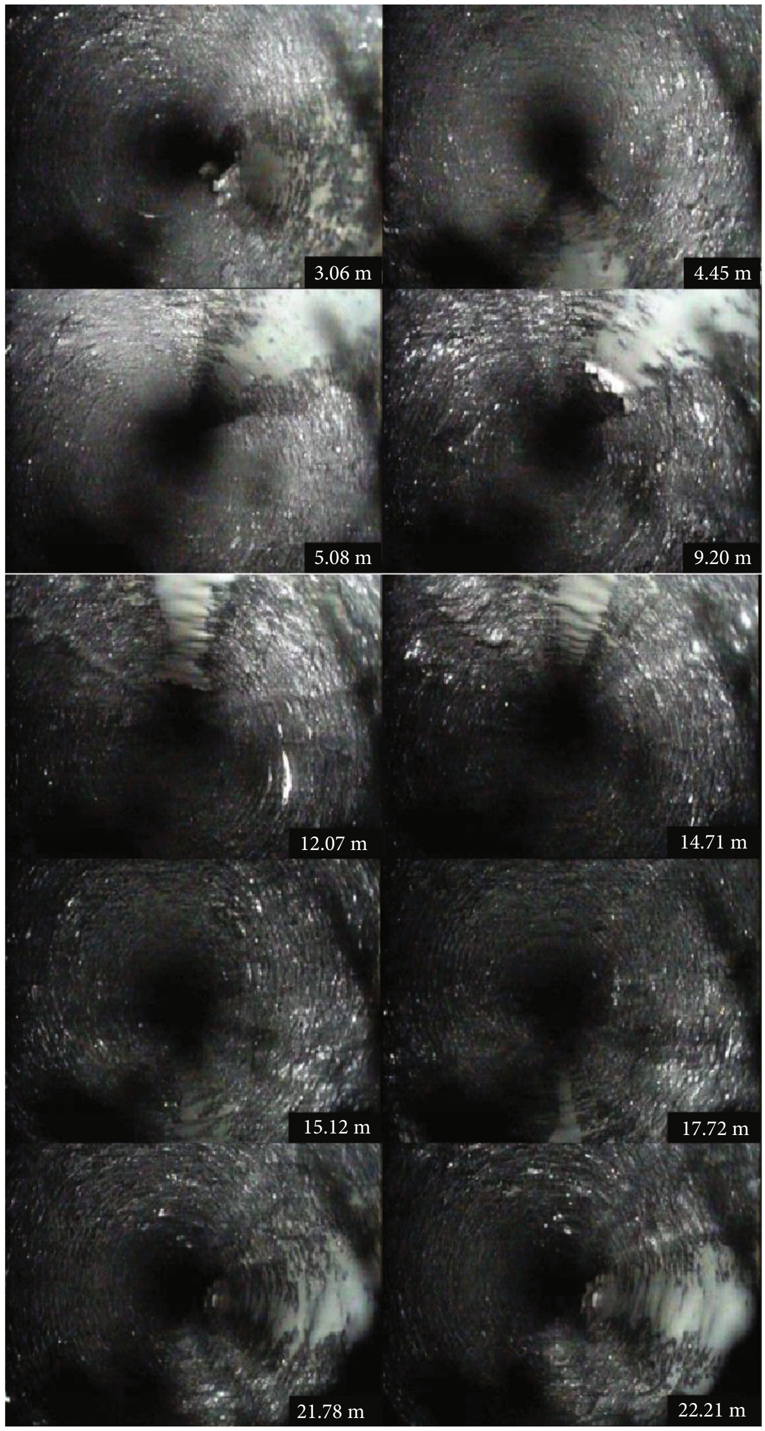

FIGURE 6: View of gas drainage borehole in C_5^b coal seam.

should be swept repeatedly after passing through the soft rock to avoid sticking. If the rotary resistance is large and the pump is choked, the feed pressure should be stopped to ensure the water circulation. Then, the drilling tool is moved up and down, continuing to work after removing obstacles. When there is abnormal phenomenon, it is forbidden to lift the drilling tool by force.

When drilling stops, the drilling tool is lifted to a height of 3 m to 5 m from the bottom of the hole. When there is clear water in the hole, it can be stopped, so as to avoid the phenomenon of buried drilling. When drilling again, the drilling slag in the hole should be washed clean, and the process speed of drilling to the bottom of the hole should be slowed down. It can work normally after reaching the bottom of the hole.

5.3. Trajectory Measurement Results. The three-dimensional schematic diagram of peeping results of borehole

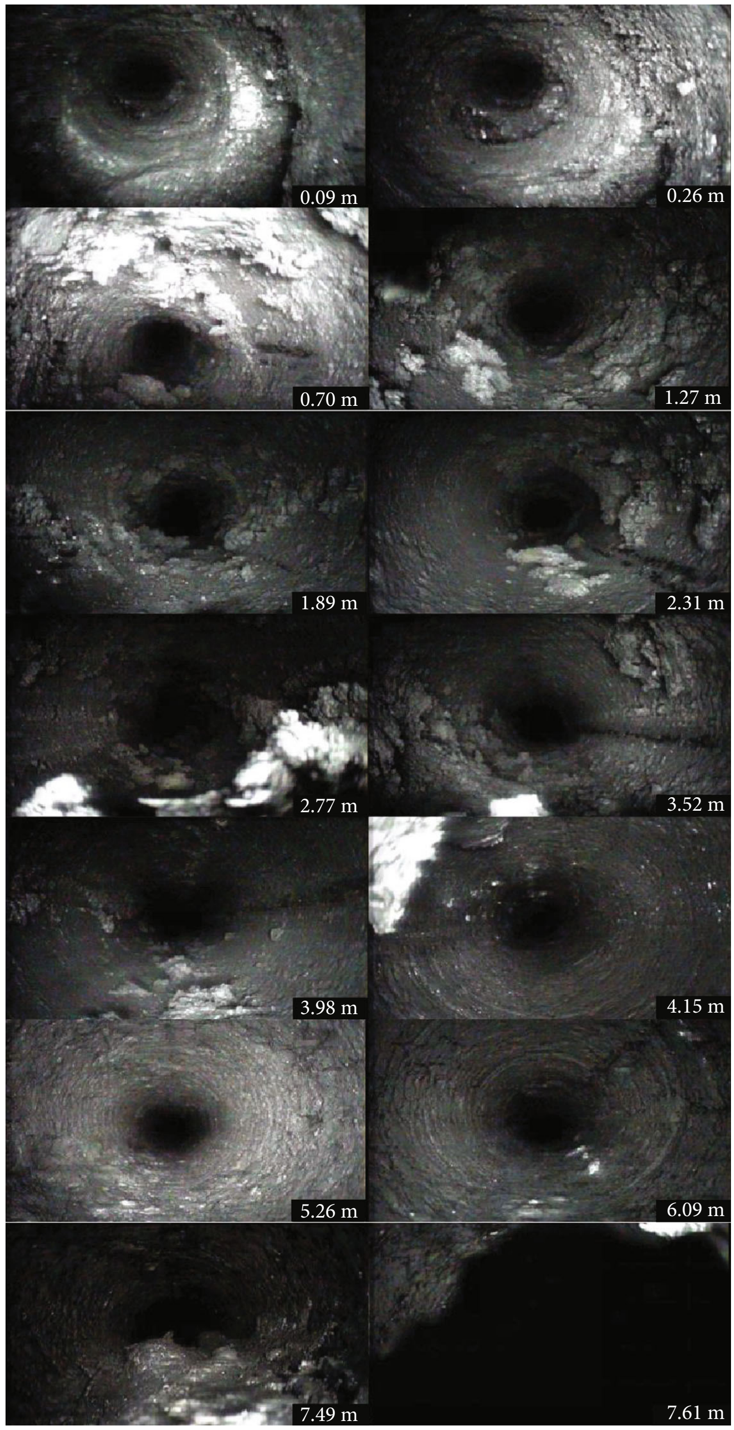

Figure 7: View of gas drainage boreholes in lower adjacent layer C_6^a coal seam.

trajectory measurement is shown in Figure 11, and the horizontal projection, East-West projection, and North-South projection are shown in Figures 12–14.

The trajectory measurement of gas drainage boreholes in C_5^a, C_5^b, C_6^a, and C_6^c coal seams was carried out on site, including 6 boreholes in C_5^b coal seam and 2 boreholes in each adjacent coal seam. The trajectory measurement results and trajectory deviation of gas drainage boreholes in working seam, upper adjacent layer, lower adjacent layer, and high position are shown in Table 3. The average values of deviation of borehole inclination, azimuth deviation of borehole, and vertical height deviation are listed in the table. In the data, a positive sign indicates upward deviation, and a negative sign indicates downward deviation. The actual measurement results show that the dip angles of the boreholes in the coal seam, the high-level boreholes, and the upper adjacent layers all deviate downward, while the dip angles of the boreholes

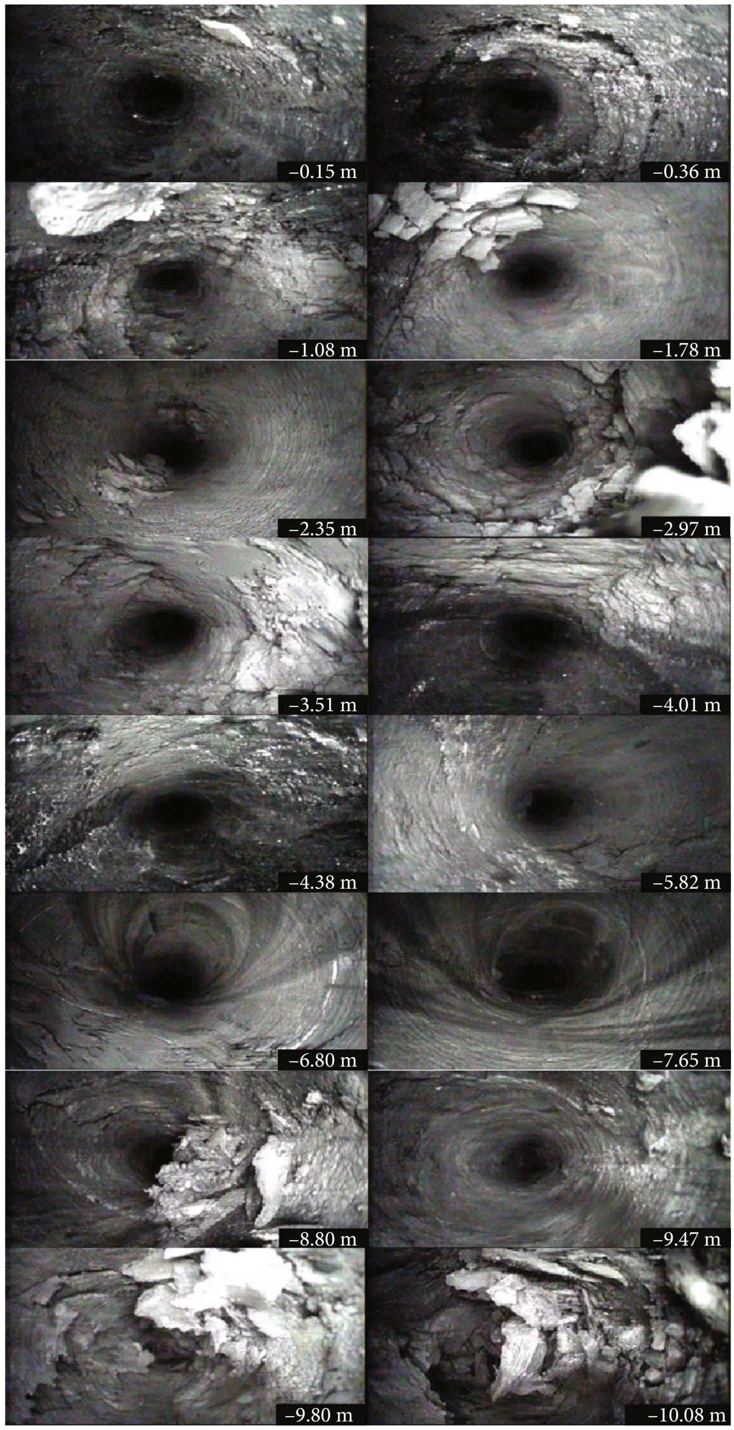

FIGURE 8: View of gas drainage boreholes in lower adjacent layer C_6^c coal seam.

in the lower adjacent layers deviate upward. The azimuth deviation of high position borehole is the largest and that of upper adjacent layer borehole is the smallest. The deviation distance of high-level borehole is the largest, and the average vertical height of downward deviation is 5.8 m. The actual vertical height deviation of upper adjacent layer is the smallest, and the average vertical height of downward deviation is 0.8 m.

5.4. Prevention Measures of Deviation in Drilling Construction. In view of the above experimental results, we think that the prevention of drilling construction deviation can be carried out from the following aspects.

(1) *Ensure Reliable Drilling Equipment*. Good equipment is the premise of accurate drilling construction. Reasonable drilling rig and BHA (bottom hole

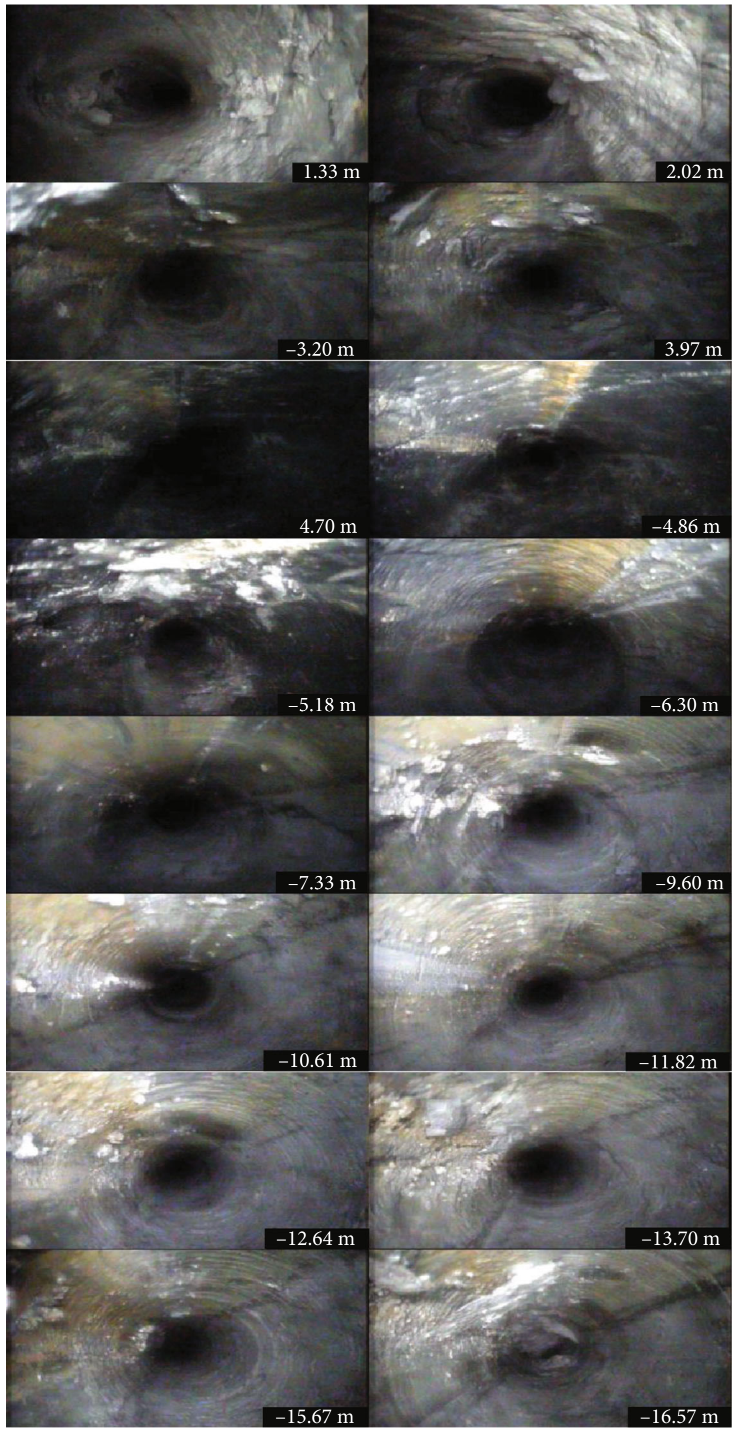

FIGURE 9: View of C_5^a gas drainage borehole in upper adjacent layer.

assembly) should be selected according to the geological conditions, and the drilling rig and BHA should be maintained regularly to ensure the stable and reliable state of drilling equipment. Drilling deviation correction technology should be actively applied to reduce the bending degree of drilling as much as possible

(2) *Reasonable Control of Drilling Length*. "Borehole deviation" increases with the increase of borehole depth, and long borehole is easy to form gas drainage goaf at the bottom of borehole. Therefore, from the perspective of controlling borehole deviation, the design and construction length of borehole should be reduced as far as possible on the

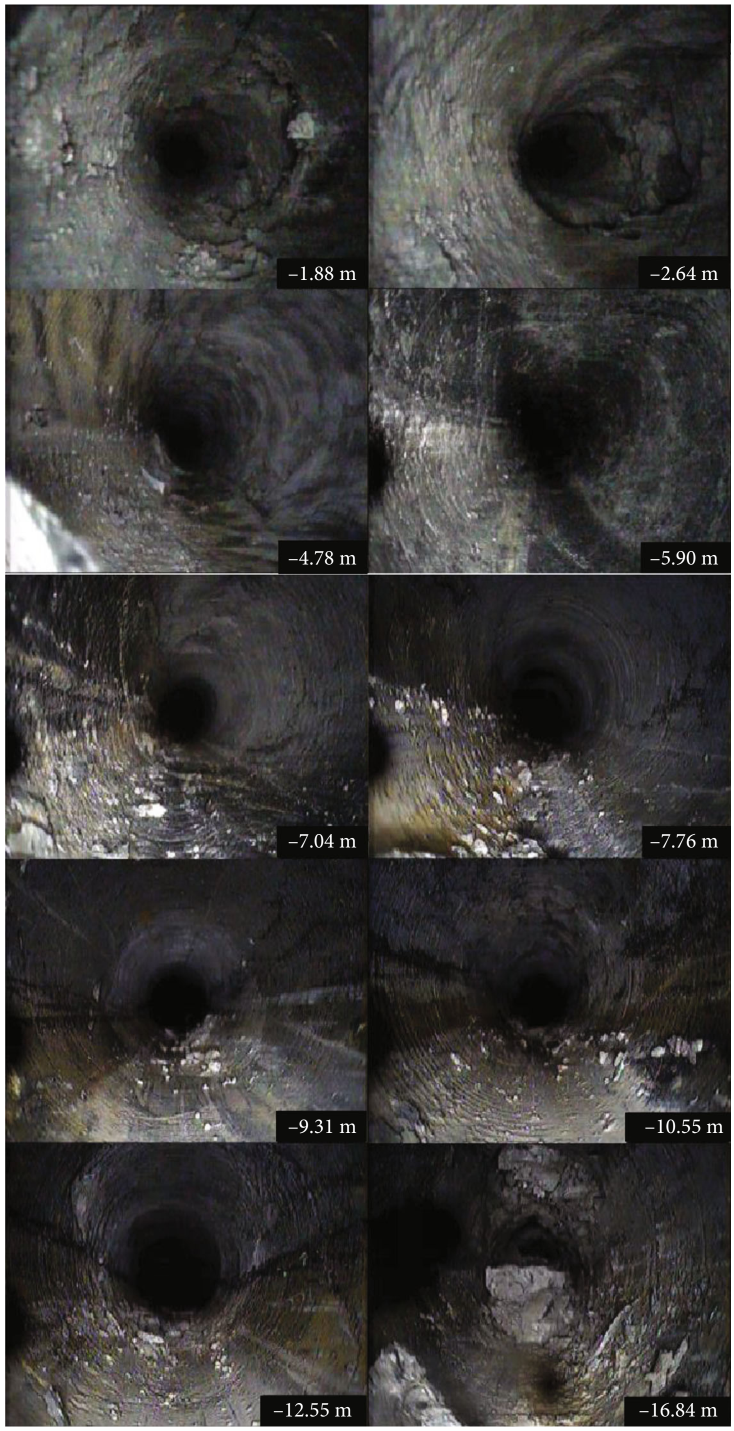

Figure 10: View of high-level borehole in C_5^b coal seam.

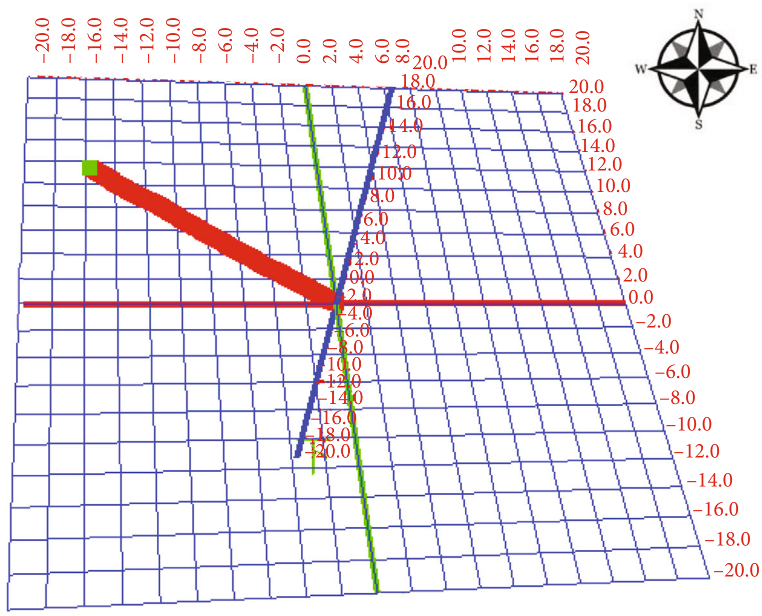

Figure 11: Main control page of borehole track of gas drainage.

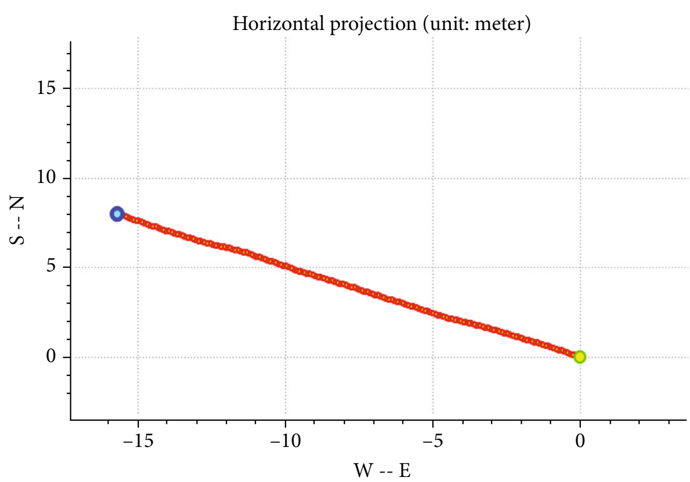

Figure 12: Horizontal projection of gas drainage borehole.

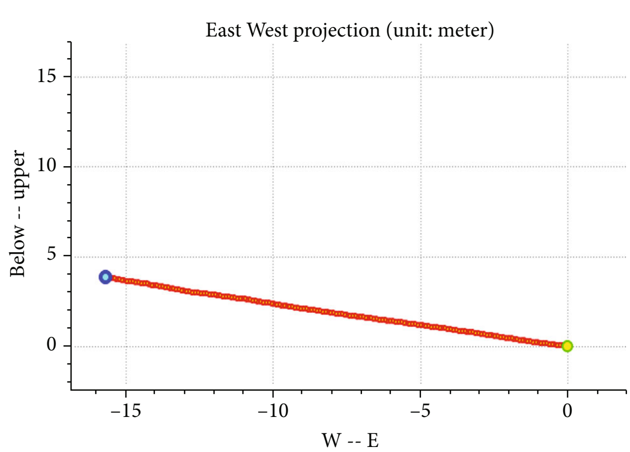

Figure 13: East-West projection of gas drainage borehole.

premise of ensuring full coverage of borehole control area

(3) *Scientific and Standardized Drilling*. The deviation of drilling angle is one of the main reasons for the deviation of drilling. We should change the traditional opening method of manual measurement such as compass and slope gauge and try to use advanced equipment and technology to locate the hole

(4) *Reasonable Selection of Drilling Parameters*. According to the different geological conditions, mechanical properties of coal and rock mass, and drilling construction process parameters, the drilling construction process parameters such as feed force, rotation speed, and flushing fluid flow are reasonably selected to reduce the drilling deviation

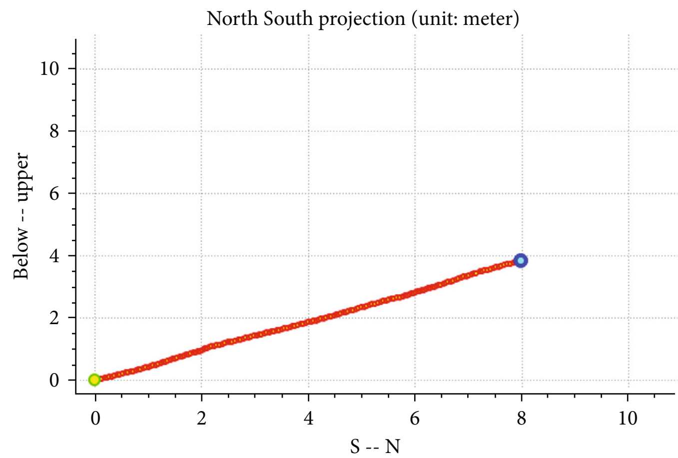

Figure 14: North-South projection of gas drainage borehole.

Table 3: Gas drainage borehole trajectory measurement results (average value).

Borehole type	Deviation of borehole inclination (°)	Azimuth deviation of borehole (°)	Vertical height deviation (m)
This coal seam drilling	-2.4	+1.8	-3.3
High-level drilling	-4.2	+2.2	-5.8
Upper adjacent layer drilling	-0.6	-0.6	-0.8
Lower adjacent layer drilling	+1.8	+1.3	+2.5

6. Conclusions

In this work, the field test of gas drainage borehole peeping and trajectory measurement in coal seam of Changling coal mine are carried out. The conclusions are as follows.

(1) By peeping at the boreholes of C_5^b coal seam, upper adjacent layer C_5^a coal seam, lower adjacent layer C_6^a and C_6^c coal seam, and C_5^b coal seam high-level drilling in Changling coal mine, it can be concluded that the integrity of boreholes in this coal seam is good. There is no obvious macrocracks, but there is water accumulation. The phenomenon of hole collapse occurs at the position of about 20 m in both adjacent strata and high-level boreholes, which will directly affect the gas drainage effect. There are a lot of cracks in the high-level boreholes before 12 m. When high-level boreholes are selected for gas drainage, the sealing distance should be greater than 12 m

(2) The dip angles of the boreholes in the coal seam, the high-level boreholes, and the upper adjacent layers all deviate downward, while the dip angles of the boreholes in the lower adjacent layers deviate upward. The deviation distance of the high-level boreholes is the largest. The average vertical height of the downward deviation is 5.8 m. The actual vertical height deviation of the upper adjacent layers is the smallest, and the average vertical height of the downward deviation is 0.8 m

(3) Through the experiment, we put forward four strategies to prevent the deviation of drilling construction: ensuring the reliability of drilling equipment, reasonably controlling the drilling length, standardizing the drilling, and reasonably selecting the drilling process parameters

Data Availability

The data used to support the findings of this study are available from the corresponding author upon request.

Conflicts of Interest

The authors certify that they have no conflicts of interest.

Acknowledgments

This research was funded by the National Natural Science Foundation of China (51874314, 52004291, 51974161).

References

[1] D. Jia, Y. Qiu, C. Li, and Y. Cai, "Propagation of pressure drop in coalbed methane reservoir during drainage stage," *Advances in Geo-Energy Research*, vol. 3, no. 4, pp. 387–395, 2019.

[2] K. Wang and F. Du, "Coal-gas compound dynamic disasters in China: a review," *Process Safety and Environmental Protection*, vol. 133, pp. 1–17, 2020.

[3] H. Wang, B. Tan, Z. Shao, Y. Guo, Z. Zhang, and C. Xu, "Influence of different content of FeS_2 on spontaneous combustion characteristics of coal," *Fuel*, vol. 288, p. 119582, 2021.

[4] S. Liu, X. Li, D. Wang, and D. Zhang, "Experimental study on temperature response of different ranks of coal to liquid

nitrogen soaking," *Natural Resources Research*, vol. 30, no. 2, pp. 1467–1480, 2021.

[5] W. Liang, Y. Zhao, J. Liu, D. Elsworth, Z. Feng, and J. Cai, "Advances in in-situ modified mining by fluidization and in unconventional geomechanics," *Advances in Geo-Energy Research*, vol. 5, no. 1, pp. 1–4, 2021.

[6] F. Du, K. Wang, X. Zhang, C. Xin, L. Shu, and G. Wang, "Experimental study of coal-gas outburst: insights from coal-rock structure, gas pressure and adsorptivity," *Natural Resources Research*, vol. 29, no. 4, pp. 2481–2493, 2020.

[7] F. Du and K. Wang, "Unstable failure of gas-bearing coal-rock combination bodies: insights from physical experiments and numerical simulations," *Process Safety and Environmental Protection*, vol. 129, pp. 264–279, 2019.

[8] C. Xin, F. Du, K. Wang, C. Xu, S. Huang, and J. Shen, "Damage evolution analysis and gas-solid coupling model for coal containing gas," *Geomechanics and Geophysics for Geo-Energy and Geo-Resources*, vol. 7, no. 1, 2021.

[9] J. Liu, X. Liang, Y. Xue, K. Yao, and Y. Fu, "Numerical evaluation on multiphase flow and heat transfer during thermal stimulation enhanced shale gas recovery," *Applied Thermal Engineering*, vol. 178, p. 115554, 2020.

[10] H. Wang, X. Fang, F. Du et al., "Three-dimensional distribution and oxidation degree analysis of coal gangue dump fire area: a case study," *Science of the Total Environment*, vol. 772, 2021.

[11] Y. Cai, F. Xi, and H. Cheng, "Causes and prevention measures of borehole bending," *Shangpin yu zhiliang*, vol. 7, pp. 85-86, 2011.

[12] C. Dong, "Directional drilling technology and development tendency in underground mine," *Coal Science and Technology*, vol. 43, no. 5, pp. 106–110, 2015.

[13] W. Wang, "Harm and preventive measures of borehole bending in coalfield geological drilling," *Heilongjiang Science*, vol. 5, no. 5, p. 170, 2014.

[14] L. Du, "Analysis on the causes of borehole bending and its preventive and corrective measures," *Public Communication of Science & Technology*, vol. 5, no. 7, pp. 182–189, 2013.

[15] Y. Chen and T. Yan, "Computer system of the function of tracking well trajectory and predicting hitting the target of drill holes," *Earth Science-Journal of China University of Geosciences*, vol. 22, no. 4, pp. 432–435, 1997.

[16] X. Li, Z. Cao, and Y. Xu, "Characteristics and trends of coal mine safety development," *Energy Sources, Part A: Recovery, Utilization, and Environmental Effects*, pp. 1–19, 2020.

[17] K. Wang and F. Du, "Experimental investigation on mechanical behavior and permeability evolution in coal-rock combined body under unloading conditions," *Arabian Journal of Geosciences*, vol. 12, no. 14, 2019.

[18] M. A. Polak and A. Lasheen, "Mechanical modelling for pipes in horizontal directional drilling," *Tunnelling and Underground Space Technology*, vol. 16, no. 1, pp. 47–55, 2001.

[19] E. Cheng and M. A. Polak, "Theoretical model for calculating pulling loads for pipes in horizontal directional drilling," *Tunnelling and Underground Space Technology*, vol. 22, no. 5-6, pp. 633–643, 2007.

[20] J. S. Lueke and S. T. Ariaratnam, "Surface heave mechanisms in horizontal directional drilling," *Journal of Construction Engineering and Management*, vol. 131, no. 5, pp. 540–547, 2005.

[21] J. S. Lueke, "Surface heave associated with horizontal directional drilling construction techniques," University of Alberta, Alberta, Canada, 2005.

[22] G. Manacorda, M. Miniati, A. Simi et al., "A bore-head GPR for horizontal directional drilling (HDD) equipment," in *Proceedings of the 15th International Conference on Ground Penetrating Radar*, pp. 745–750, Brussels, Belgium, 2014.

[23] J. Matheus, M. Ignova, and P. Hornblower, "A hybrid approach to closed-loop directional drilling control using rotary steerable systems," *IFAC Proceedings Volumes*, vol. 45, no. 8, pp. 84–89, 2012.

[24] C. Figueredo, "Enhanced RSS technology pushes drilling envelope," *Journal of Petroleum Technology*, vol. 66, no. 3, pp. 32–35, 2014.

[25] J. Li, "Analysis on the causes of borehole deviation," *Science and technology of West China*, vol. 12, no. 2, pp. 9–11, 2013.

[26] W. T. Liang, W. P. Zou, K. Han, and Z. J. Gu, "Analysis of reasons for declination of drillhole," *Mining Engineering*, vol. 7, no. 2, pp. 65–67, 2009.

[27] B. Zhu, Z. Du, and Z. Dang, "Compound drilling device for deviation prevention and straight drilling while drilling: China," 2011, 201874461.

[28] Z. Ding and K. Zhou, "The analysis of gas drainage drilling skew law in a coal mine," *Coal Mine Modernization*, vol. 6, pp. 89–91, 2014.

[29] H. Wang, S. Li, H. Shuang, Z. Du, L. You, and L. Liu, "Pressure-relief gas drainage technique by high level borehole in lateral high drainage roadway," *Journal of Central South University (Science and Technology)*, vol. 47, no. 4, pp. 1319–1326, 2016.

[30] H. Wang, Z. Du, Q. Fan, H. Shuang, J. Xie, and L. You, "Inclination measuring and deviation correction technology of pressure released gas drainage borehole in external dislocated high level gateway," *Coal Science and Technology*, vol. 43, no. 8, pp. 77–81, 2015.

[31] T. Zhao, "Causation of borehole deviation and measures to prevent and rectify," *Coal geology of China*, vol. 21, no. S1, pp. 62-63, 2009.

[32] Z. Zhao, G. Liu, Z. Duan, and Y. Zhao, "Causes and preventive measures of borehole inclination," *Ground Water*, vol. 6, pp. 96–98, 2007.

Hindawi
Geofluids
Volume 2021, Article ID 5520548, 15 pages
https://doi.org/10.1155/2021/5520548

Research Article

The Prediction Model of Super Large Subsidence in High Water Table Coal Mining Areas Covered with Thick Unconsolidated Layer

Yueguan Yan,[1] Weitao Yan ,[2] Jibo Liu,[3] and Junting Guo[4]

[1]The College of Geoscience and Surveying Engineering, China University of Mining and Technology, Beijing 100083, China
[2]School of Surveying and Land Information Engineering, Henan Polytechnic University, Jiaozuo, Henan 454003, China
[3]College of Mining Engineering, Guizhou University of Engineering Science, Guizhou 551700, China
[4]State Key Laboratory of Groundwater Protection and Utilization by Coal Mining, Beijing 102009, China

Correspondence should be addressed to Weitao Yan; yanweitao@hpu.edu.cn

Received 15 January 2021; Revised 25 January 2021; Accepted 30 January 2021; Published 30 March 2021

Academic Editor: Yi Xue

In mining engineering, after the extraction of underground resources, the maximum surface subsidence is usually less than the mining thickness of coal seam. However, under the condition of thick loose layer, some special phenomena appear in surface subsidence, for example, the maximum surface subsidence value is greater than the mining thickness of coal seam. This special phenomenon cannot be predicted by traditional subsidence prediction methods. To solve this problem, by using the numerical simulation software Fast Lagrangian analysis of continua (Flac), we study the changing rules of subsidence with different strata lithology and unconsolidated layer thickness and reveal the formation mechanism of this law. The results show that the effect of the thick unconsolidated layer on the hard rock is greater than that of the soft rock. When the rock is soft, the unconsolidated layer moves as a whole following the bedrock during the whole mining process. The surface subsidence decreases approximately linearly with the thickness ratio increase of the unconsolidated layer to bedrock. However, when the rock is hard or medium hard, there are supporting structures formed inside the rock stratum, which has supporting effect on the overlying strata. The surface subsidence undergoes three proportional sections, first increases, then decreases, and finally increases with the thickness ratio increase of the unconsolidated layer to bedrock. Combined with these laws, based on the theory that the rock strata space can be completely compressed gradually, we derive the calculation method of surface subsidence under the condition of thick unconsolidated layer and apply it to practice. The results show that the prediction results are consistent with the actual situation and meet the engineering requirements. The research results can provide a reference for the subsidence prediction of similar conditions.

1. Introduction

The exploitation of underground coal resources has accelerated the economic development, but at the same time, it has also brought about great economic [1–3], environmental, and ecological damage problems [4–10], such as water accumulation on the subsidence area, cracks on the surface, settlement of residential land, and house damage, etc. For a long time, scholars have been studying and analyzing the mining subsidence under general conditions from the aspects of subsidence law [11–14], subsidence mechanism [15, 16], subsidence prediction [17–19], subsidence control method [20, 21] and obtained many research results, which have been applied in the field.

For describing the law of surface subsidence, the indexes of subsidence, slope, curvature, horizontal displacement, and horizontal strain are commonly used at present. Generally speaking, when mining horizontal or gently inclined seams, slope is the first derivative of subsidence, curvature is the second derivative of subsidence, horizontal displacement is proportional to subsidence, and horizontal strain is the first derivative of horizontal displacement [22]. It can be seen that subsidence is the main evaluation index. To express the degree of subsidence, the concept of subsidence factor is often used, especially in mining subsidence prediction. Subsidence factor is an important parameter, which indicates the ratio between the maximum subsidence value of the surface and the vertical thickness of the coal seam when the gob has reached the critical size.

$$q = \frac{W_O}{M \cos \alpha}, \quad (1)$$

where q is the subsidence factor, W_O is the surface maximum subsidence value, M is the mining thickness of coal seam, and α is the dip angle of coal seam.

Generally, the empirical value of subsidence factor can be determined according to the lithology of overlying strata, as shown in Table 1.

From the table, we can see that the subsidence coefficient is generally less than 1.0. That is, the surface subsidence value is less than the thickness of underground mining coal. However, through the analysis of a large number of measured data, it is found that under the condition of thick loose layer, there is a peculiar phenomenon: the surface maximum subsidence value is greater than the mining thickness of coal seam. In eastern and central China, there are many mine areas covered with the thick unconsolidated layer and the water table is high. Large-scale surface subsidence usually leads to the large area of surface water accumulation (Figure 1), which easily submerges the farmland and farmhouses, seriously damaging the local ecosystem.

Based on the measured data, the surface subsidence rule under the thick unconsolidated layer was studied. A variety of phenomena show that the surface subsidence rules with the thick unconsolidated layer have its particularity and the subsidence has been beyond the scope of traditional concepts. The maximum subsidence value of the surface is greater than the mining thickness of coal seam, the range of surface subsidence is wider, the horizontal movement value of some measuring points at the boundary is greater than the subsidence value, the active period is intense and concentrated, and the surface subsidence is stable for a long time (He et al., 1994). The research results under general conditions are not suitable for mining in thick unconsolidated layer.

This paper chose the Huainan mine area as the research object. Based on the numerical simulation method, with different lithology and different thickness ratio of unconsolidated layer and bedrock, the subsidence changing rules of different layers are studied. A revised formula for calculating subsidence is put forward accordingly. The research results have important theoretical and practical significance for enriching the theory of surface subsidence, protecting the surface buildings and ecological environment, reducing mining damage, improving the economic benefits of coal production enterprises, avoiding industrial and agricultural disputes, and realizing the sustainable development of coal industry.

Table 1: Empirical value of surface subsidence factor.

Lithology	Hard	Medium hard	Soft
Subsidence factor	0.40-0.65	0.65-0.85	0.80-1.00

2. Experimental Region and Research Method

2.1. Experimental Region. The experimental region is located in Huaihe alluvial plain (Figure 2(a)). The mining area is flat. There are no faults in this area, and the geological structure is simple. The groundwater depth in this area is about 1 m, which is typical in high water table coal mining areas. Coal seam 8 is a stable mineable coal seam with a thickness of 1.19-5.87 m and an average thickness of 3.25 m. The roof is dominated by sandstone, while the floor is mudstone and sandy mudstone. Through the analysis of rock characteristics and physical mechanics properties, the comprehensive lithology of overlying strata is medium hard.

The panel 11118 is arranged in coal seam 8. The length along the inclination and strike direction of panel 11118 is 162 m and 620 m, respectively (Figure 2(b)). The average mining thickness is 5.0 m, and the average mining depth is 550 m. The unconsolidated layer thickness is about 300 m, and the bedrock thickness is about 250 m. The mining method adopts comprehensive mechanized coal mining with full height at one time, and the roof was managed by full caving method. The mining-induced damage to the ground structures is shown in Figure 3.

2.2. Research Method. Taking into account the geological and mining material of panel 11118, a two-dimension numerical model was built by using software Flac. The mining subsidence model has dimensions of length = 2000 m and height = 600 m. The model strata are simplified, and there are six layers from bottom to top. The lowest strata are floor mudstone with the thickness of 45 m. Overlying the strata is coal seam, and the thickness is 5 m. The immediate roof is sandstone with 10 m thickness. Above the immediate roof are siltstone and fine sandstone, and the thickness is 90 m and 150 m, respectively. The top is unconsolidated layer with the thickness of 300 m. The comprehensive lithology of overlying strata is medium hard. Coal seam dip angle is 0°. The value of panel length is 800 m. This model assumes that the rock failure obeys Mohr-Coulomb strength criterion. The numerical simulation design is showed in Figure 4. In this paper, H_s is the thickness of the unconsolidated layer, H_j is the thickness of bedrock, and H is the mining depth.

For comparison and analysis, the other two models were built based on the prototype of medium-hard rock numerical model. The models only change the physical mechanics parameters, and the strata geometry size and name remain the same as the prototype. According to the knowledge of rock mechanics, the harder the lithology is, the greater the density, elasticity module, Poisson ratio, tensile strength, internal frictional angle, and cohesive force are. Therefore, taking medium hard as the prototype, the parameters of soft rock stratum are 0.9 times of medium hard, while those of hard rock stratum

Figure 1: Surface water accumulation.

are 1.1 times. The soft, medium-hard, and hard models with different physical mechanics parameters are shown in Table 2.

3. Experimental Results and Analysis

3.1. Subsidence Changing Rules of Different Lithology and Strata under Thick Unconsolidated Layer. The model was mined 5 m height at one time, and the excavation dimension was 800 m. The maximum subsidence value and subsidence factor of different layers with soft, medium-hard, and hard rock could be obtained from immediate roof to surface with 50 m interval value. Subsidence curves of immediate roof, unconsolidated layer and bedrock interface (hereinafter referred to as interface in this paper), and surface with different lithology are shown in Figure 5.

Changing curves are shown in Figure 6 of subsidence factor of different layers in the soft, medium-hard, and hard lithology strata and unconsolidated layer.

Figure 6 indicates that no matter the rock lithology whether soft or hard, the subsidence factor decreases linearly with the increase of vertical distance from the layer to goaf.

If the overlying strata are hard lithology, in the process of the rock damage and subsidence, the fracture zones not only produce the vertical cracks of rock but also produced a large number of bed separation cracks along the strata level. These fissures and fractures form a large amount of compressible space in bedrock. Under the action of thick unconsolidated layer, these compressible spaces are recompressed, and the compression is large. This causes the subsidence factor in bedrock to decrease rapidly with the increase of vertical distance from the layer to goaf.

If the bedrock is soft lithology, overburden is not easy in order to produce the bed separation cracks in the process of the rock subsidence and less compressible space formed. Under the action of the thick unconsolidated layer, the compressible spaces are recompressed, but the compression is smaller than the hard rock. Therefore, the subsidence factor in soft bedrock decreases slower than that in hard rock with the increase of vertical distance from the layer to goaf.

Therefore, there is more compressible space in hard rock than in soft rock, and the subsidence factor of hard rock is less than that of the soft rock under the same condition. When the lithology is medium hard, the change of subsidence factor falls in between.

However, the unconsolidated layer variation has nothing to do with the strata lithology and the changing trend of unconsolidated layer is the same. All of them move as a whole. The subsidence factor of unconsolidated layer inside changes little and decreases linearly with the increase of vertical distance from bedrock to surface. The change range of unconsolidated layer is close to the soft rock. Therefore, it is stated that the unconsolidated layer has a certain expansion, which can play a supporting role to the surface.

3.2. Subsidence Changing Rules of Surface and Interface with Different Unconsolidated Layer Thickness. To study the effect of different unconsolidated layer thickness on the subsidence factor, keeping the rock size, thickness of coal seam, mining dimension, nature of unconsolidated layer, and the rock lithology conditions unchanged, the thickness of unconsolidated of 100 m, 200 m, 400 m, 500 m, and 600 m was simulated.

Starting from the direct roof of coal seam to the surface, taking 50 m as interval, the variation curves of subsidence factors of soft, medium-hard, and hard rock strata and different thickness of loose strata are drawn. As shown in Figure 7, the direct roof is 0 m from the vertical distance of goaf, and the interface of loose strata and bedrock is 250 m from the vertical distance of goaf. The maximum vertical distance in abscissa means the position of the surface.

From the analysis of Figure 7, it can be seen that the subsidence factors of all layers in rock mass and loose stratum decrease with the increase of vertical distance from the layer to goaf, and the variation range is different. With the increase of the thickness of unconsolidated layer, the variation range of subsidence factor with different lithological strata is different. When the bedrock is weak, the subsidence factor of the interface between the unconsolidated layer and the bedrock changes slightly. When the thickness of the unconsolidated layer increases from 200 m to 600 m, the subsidence factor is about 0.90-0.92. Nevertheless, when the bedrock is hard, the subsidence factor of the interface changes greatly when the thickness of the unconsolidated layer increases from 100 m to 600 m, from 0.38 to 0.82. Such a wide range of changes indicates that the increase of the unconsolidated layer thickness increases the load on the underlying bedrock

(a)

Figure 2: Continued.

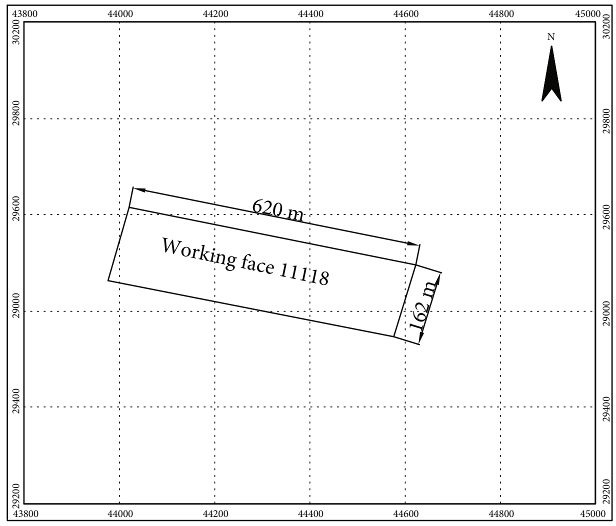

(b)

Figure 2: Study site. (a) Location of Huainan coal mine in China, the original image is quoted from national platform for common geospatial information services; (b) roadway layout of 11118 working face.

(a) Surface water ponding

(b) Surface crack

(c) Damage to the house

Figure 3: Problem map induced by mining subsidence.

and greatly increases the space compression of the bedrock.

4. Discussion

4.1. Subsidence Mechanism Analysis. For further analysis, the maximum subsidence values and subsidence factors of surface and interface are calculated based on different lithology and thickness ratios of unconsolidated layer to bedrock. The variation curves are drawn in Figure 8.

Combines with Figure 8, we can reveal the subsidence mechanism from two dimensions of lithology and thickness ratio of unconsolidated layer to bedrock.

(1) When the bedrock lithology is weak, the subsidence factor of the interface is larger, and the change range is smaller than others (Figure 9). This indicates that after the soft rock is affected by mining, there is almost no supporting structure and compressible space formed in the bedrock. The main performance

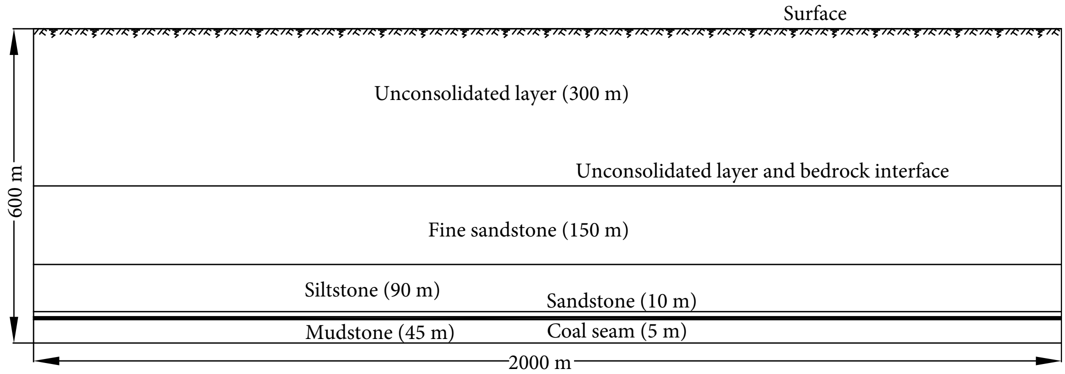

FIGURE 4: Numerical simulation design.

of overlying strata is overall subsidence. The increase of unconsolidated layer thickness is equivalent to the increase of mining depth, which leads to the surface subsidence factor approximately linearly reduced with the increase of thickness ratio

(2) When the bedrock lithology is hard or medium hard, there is more supporting structure and compressible space formed within the strata. The increase of unconsolidated layer thickness is equivalent to the increase of load on bedrock, which leads to the compressible space in the bedrock gradually reduced. Moreover, the larger the unconsolidated layer thickness is, the greater the reduction degree of compressible space within the bedrock is. Through the experiment, it is found that the subsidence factor of the interface increases linearly with the increase of the thickness ratio. However, the surface subsidence factor has certain fluctuation, which can be roughly divided into three proportional sections

   (a) Proportional section one: when the thickness of the unconsolidated layer is less than 1.2 times that of the bedrock (Figure 10(a)). With the increase of the unconsolidated layer thickness, the load on the bedrock increases gradually, and the compressible space with poor structure inside the stratum is compressed. At this time, the subsidence factors of the surface and the interface have the same trend, both of which increase. However, the total supporting force of supporting structure in bedrock is greater than the pressure of overlying loose layer and its own gravity

   (b) Proportional section two: when the unconsolidated layer thickness is between 1.2 and 2.0 times that of the bedrock (Figure 10(b)). With the increase of the unconsolidated layer thickness, the load on the bedrock increases gradually with the increase of the unconsolidated layer thickness. However, due to the existence of strong braced structure, the increase of subsidence factor at the interface is smaller than that at proportional section one. At the same time, the increase of unconsolidated layer thickness is equivalent to the increase of mining depth, resulting in the decrease of surface subsidence factor. That is, the subsidence factor of interface and surface has opposite development trend at this proportional section

   (c) Proportional section three: when the unconsolidated layer thickness is larger than 2.0 times that of the bedrock (Figure 10(c)). With the increase of unconsolidated layer thickness, the load on the bedrock becomes larger, and the strong braced structure inside the stratum is collapsed. At this time, the surface subsidence factor increases again, and the change trend of the interface subsidence factor is the same again

4.2. Inversion Method of Subsidence Factor under the Condition of Thick Unconsolidated Layer. We use the probability integral method to predict overburden and surface subsidence. The probability integral method is an influence function method, which is based on the extraction of the infinitesimal elements of an area. The surface subsidence induced by the extraction of a unit coal seam is as follows:

$$W_e(x) = \frac{1}{r} e^{-\pi\left(x^2/r^2\right)}. \tag{2}$$

If we integrate the whole space, the calculation formula for any surface point subsidence is as follows:

$$W(x, y) = \frac{Mq \cos \alpha}{r^2} \int_0^{D_3} \int_0^{D_1} e^{-\pi\left(\left((x-s)^2+(y-t)^2\right)/r^2\right)} dtds, \tag{3}$$

where $W(x, y)$ is the surface subsidence value of point (x, y), $M$is the mining height, q is the subsidence factor, α is the inclination angle of coal seam, r is the major influence radius, and D_3 and D_1 are the length and width of the panel, respectively.

The predicted results mainly include subsidence (w), inclination (i), curvature (k), horizontal displacement (u),

Table 2: Physical mechanics parameters of numerical simulation.

Lithology	Strata name	Thickness (m)	Density (kg/m^3)	Block dimension a (m)	Block dimension b (m)	Elastic modules (GPa)	Poisson ratio	Tensile strength (MPa)	Internal frictional angle (°)	Cohesive force (MPa)
Soft	Unconsolidated layer	300	1800	30	15	0.18	0.30	0.002	15	0.01
	Fine sandstone	150	2396	20	10	5.72	0.24	3.1	27	8.75
	Siltstone	90	2364	20	10	5.35	0.23	8.2	31	9.57
	Sandstone	10	2394	10	5	5.75	0.24	4.2	18	6.81
	Coal seam	5	1260	5	2.5	4.32	0.22	2.2	16	1.70
	Mudstone	45	2277	30	15	5.27	0.23	3.4	32	10.24
Medium hard	Unconsolidated layer	300	1800	30	15	0.18	0.30	0.002	15	0.01
	Fine sandstone	150	2662	20	10	6.36	0.27	3.4	30	9.72
	Siltstone	90	2627	20	10	5.94	0.25	9.1	34	10.63
	Sandstone	10	2660	10	5	6.39	0.27	4.7	20	7.57
	Coal seam	5	1400	5	2.5	4.80	0.24	2.4	18	1.89
	Mudstone	45	2530	30	15	5.85	0.25	3.8	35	11.38
Hard	Unconsolidated layer	300	1800	30	15	0.18	0.30	0.002	15	0.01
	Fine sandstone	150	2928	20	10	7.00	0.30	3.7	33	10.69
	Siltstone	90	2890	20	10	6.53	0.28	10.0	37	11.69
	Sandstone	10	2926	10	5	7.03	0.30	5.2	22	8.33
	Coal seam	5	1540	5	2.5	5.28	0.26	2.6	20	2.08
	Mudstone	45	2783	30	15	6.44	0.28	4.2	39	12.52

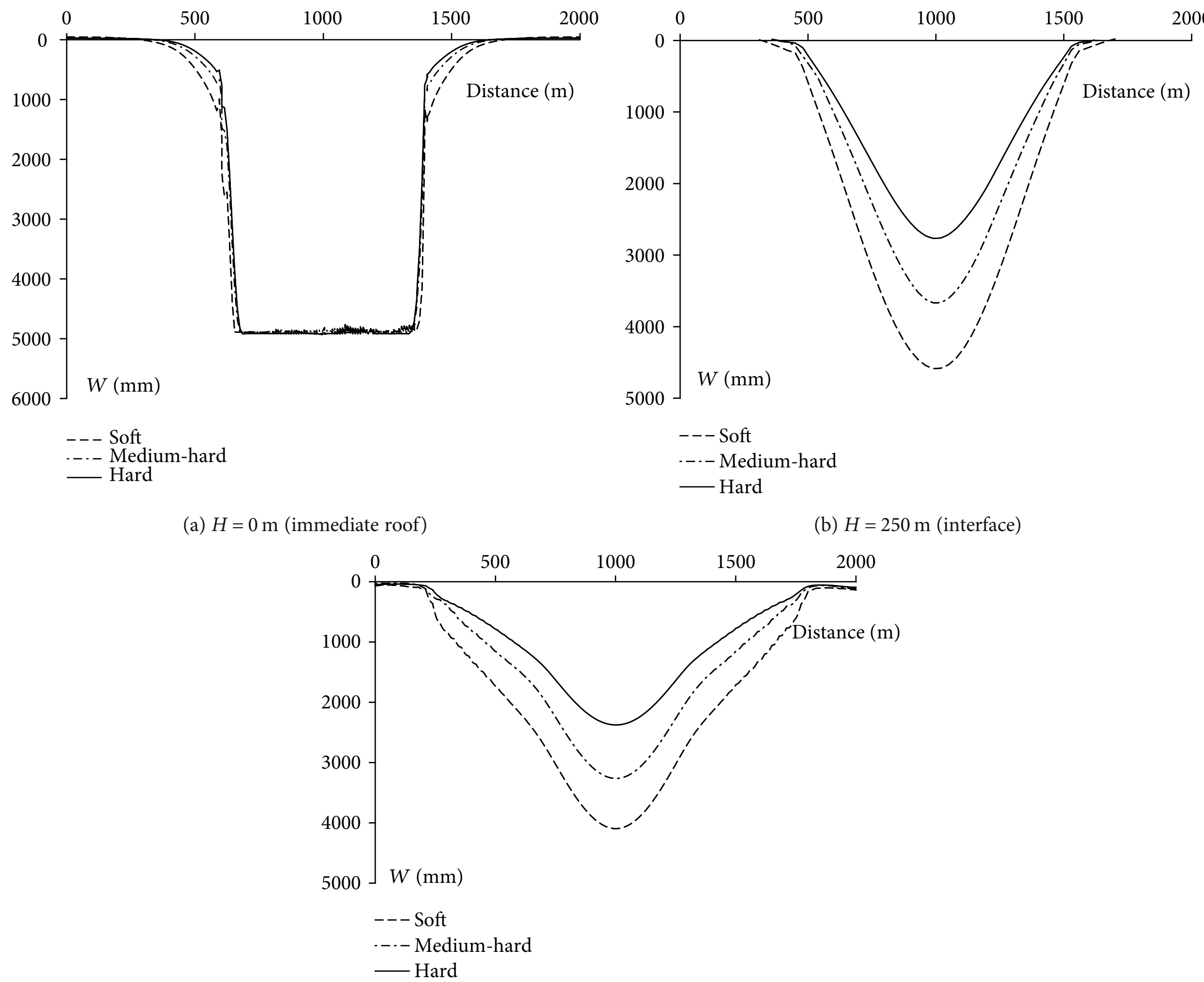

(a) $H = 0$ m (immediate roof)

(b) $H = 250$ m (interface)

(c) $H = 550$ m (surface)

Figure 5: Subsidence curves of different layers with different lithology.

and horizontal deformation (ε). Among them, inclination, curvature, horizontal displacement, and horizontal deformation can be derived from subsidence. Therefore, subsidence is the most important.

$$\begin{aligned} i_{12} &= \frac{w_1 - w_2}{l_{12}}, \\ k &= \frac{i_{12} - i_{23}}{0.5(l_{12} + l_{23})}, \\ u &= bri, \\ \varepsilon &= brk. \end{aligned} \tag{4}$$

Subsidence is mainly determined by the parameter of subsidence factor. Therefore, this paper mainly studies the calculation method of subsidence factor under the condition of thick loose layer. In general, the law of overburden subsidence and surface subsidence is mainly determined by bedrock, and the subsidence factor can be selected according to the traditional experience (Table 1). However, under the condition of thick unconsolidated layer, the subsidence law is determined by both bedrock and unconsolidated layer; the surface shows specificity. Therefore, we need to consider the comprehensive influence of rock and soil on the subsidence to study the subsidence factor. Thus, we take the continuous corrective effect of the unconsolidated layer on the subsidence into consideration and deduced the calculation formula of the subsidence factor under the condition of thick unconsolidated layer.

Given the subsidence correction factor is k_s (Figure 11), which is induced by the multifactor comprehensive influence of unconsolidated layer, for an area element Δs at the maximum subsidence position of the interface, after subsidence, the bedrock provides the compressible space $mq_j\Delta s$ for the unconsolidated layer. Assume that the compressible space is compressed n times, and it is completely compacted.

After the compressible space is compressed for the first time, the new subsidence space $mq_s{}'\Delta s$ appears on the ground surface, as follows:

$$m \times q_j \times \Delta s = k_s \times m \times q_S' \times \Delta s, \tag{5}$$

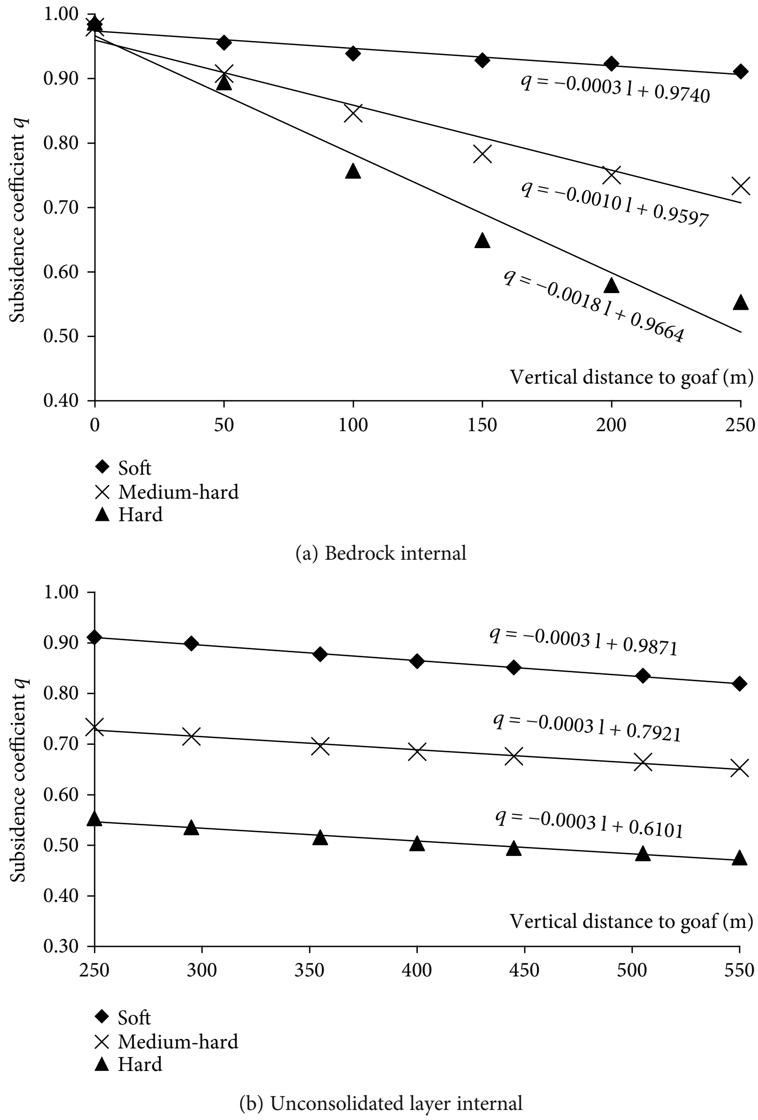

Figure 6: Changing curves of subsidence factor in soft, medium-hard, and hard lithology strata.

namely,

$$m \times q_j = k_s \times m \times q_s'. \tag{6}$$

After the compressible space is second compressed, the subsidence space $mq_s''\Delta s$ appears on the ground surface, as follows:

$$m \times q_s' = k_s \times m \times q_s''. \tag{7}$$

Similarly, after the compressible space is compressed n times, the subsidence space $mq_s\Delta s$ appears on the ground surface, as follows:

$$m \times q_s^{n-1} = k_s \times m \times q_s. \tag{8}$$

Combined with the formula above,

$$m \times q_j = k_s{}^n \times m \times q_s, \tag{9}$$

namely,

$$q_s = \frac{q_j}{k_s^n}, \tag{10}$$

where m is the mining thickness (m), H_s is the unconsolidated layer thickness (m), and n is the compress time.

Now calculate n. The subsidence correction factor of unconsolidated layer is k_s and i is the compress time.

$$h_i = \frac{mq_j \cos\alpha}{k_s{}^i}. \tag{11}$$

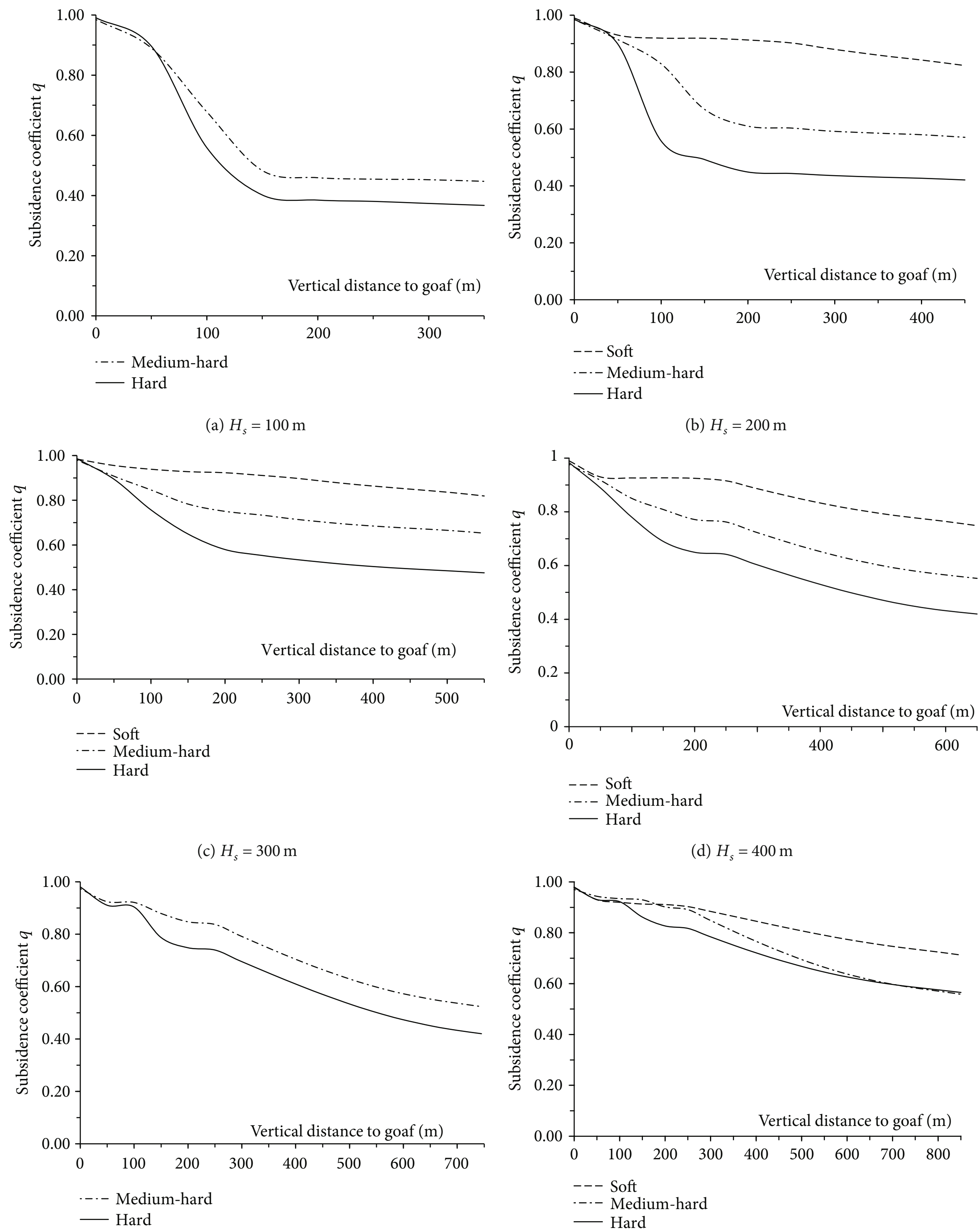

(a) $H_s = 100\,\mathrm{m}$ (b) $H_s = 200\,\mathrm{m}$ (c) $H_s = 300\,\mathrm{m}$ (d) $H_s = 400\,\mathrm{m}$ (e) $H_s = 500\,\mathrm{m}$ (f) $H_s = 600\,\mathrm{m}$

Figure 7: Subsidence factor changing curves of soft, medium, and hard lithology strata and different thickness of unconsolidated layers.

After the compressible space is compressed n times,

$$h = h_1 + h_2 + \cdots + h_n, \tag{12}$$

namely,

$$h = \frac{mq_j \cos\alpha}{k_s - 1}\left(1 - \frac{1}{k_s^{\,n}}\right). \tag{13}$$

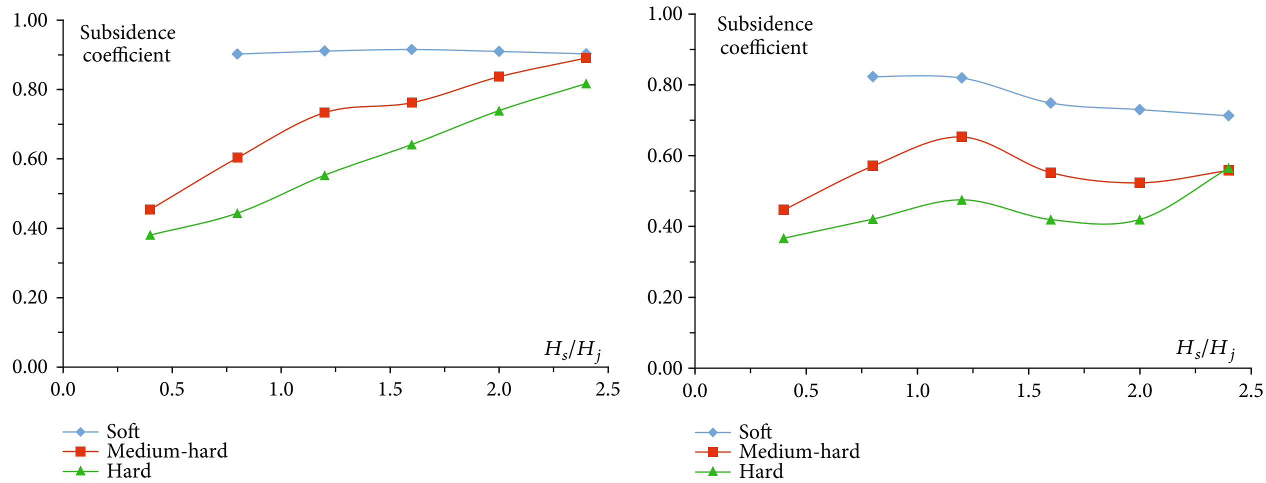

(a) Interface (b) Surface

Figure 8: Surface and interface subsidence factor change curves with different thickness ratio of different lithology bedrock and unconsolidated layer.

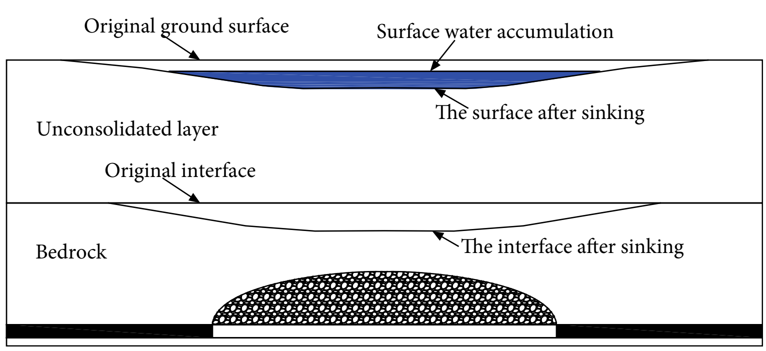

Figure 9: Schematic diagram of overburden subsidence of soft rock.

Let h be equal to H_s. So

$$H_s = \frac{mq_j \cos\alpha}{k_s - 1}\left(1 - \frac{1}{k_s{}^n}\right). \tag{14}$$

Therefore, the relationship of subsidence correction factor k_s and compress times n is

$$n = \frac{\ln\left[1 - \left(H_s/mq_j \cos\alpha\right)(k_s - 1)\right]}{\ln(1/k_s)}, \tag{15}$$

where α is the dip angle of coal seam.

To simplify the calculation, n can be obtained by the following formula:

$$n = \frac{H_s}{mq_j \cos\alpha}. \tag{16}$$

Therefore, the surface subsidence factor q_s is

$$q_s = \frac{q_j}{k_s^n}. \tag{17}$$

4.3. Determination of Subsidence Factor. The surface subsidence is the appearance of the mining influence on the surface under the joint action of bedrock and loose layer. The mining influence first propagates in the bedrock, then transfers to the loose layer through the interface, and finally to the surface. To accurately invert the surface subsidence factor, it is necessary to study the propagation law of mining influence within the bedrock, determining the subsidence factor at the interface and then to study the propagation law of the mining influence within the unconsolidated layer, determining the surface subsidence factor.

4.3.1. For Interface. According to the above analysis, when the bedrock is medium-hard or hard lithology and the thickness ratio of unconsolidated layer to bedrock is larger than 2.0, the supporting structure in the rock mass is gradually collapsed, which leads to the increase of interface subsidence factor. This phenomenon can be regarded as lithologic softness. Therefore, when predicting any point subsidence in the interior space of bedrock under thick unconsolidated layer, especially in medium-hard and hard lithology, the interface subsidence factor cannot be calculated according to the conventional experience. Referring to the regulation,

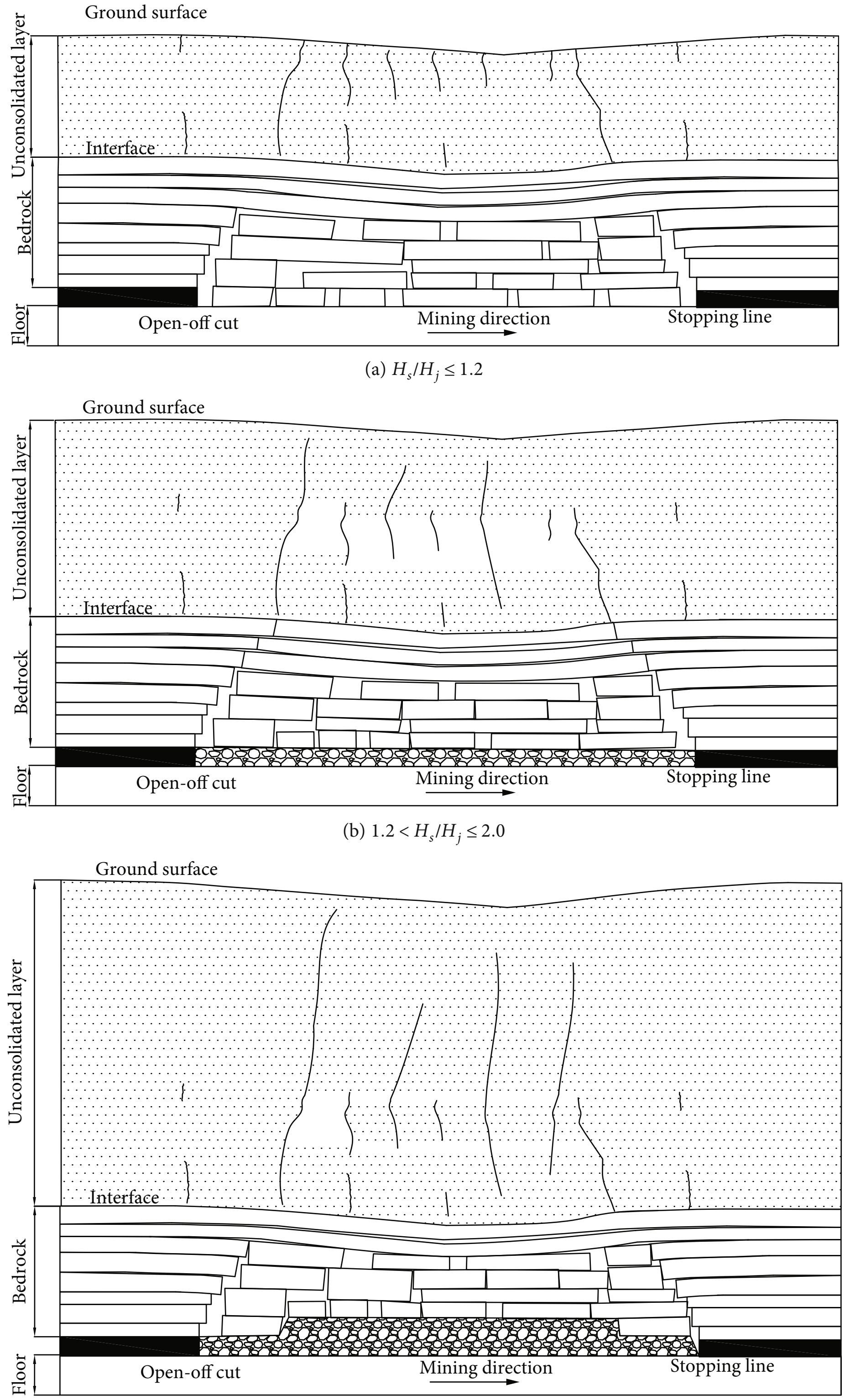

(a) $H_s/H_j \leq 1.2$

(b) $1.2 < H_s/H_j \leq 2.0$

(c) $H_s/H_j > 2.0$

FIGURE 10: Schematic diagram of overburden subsidence of hard or medium-hard rock.

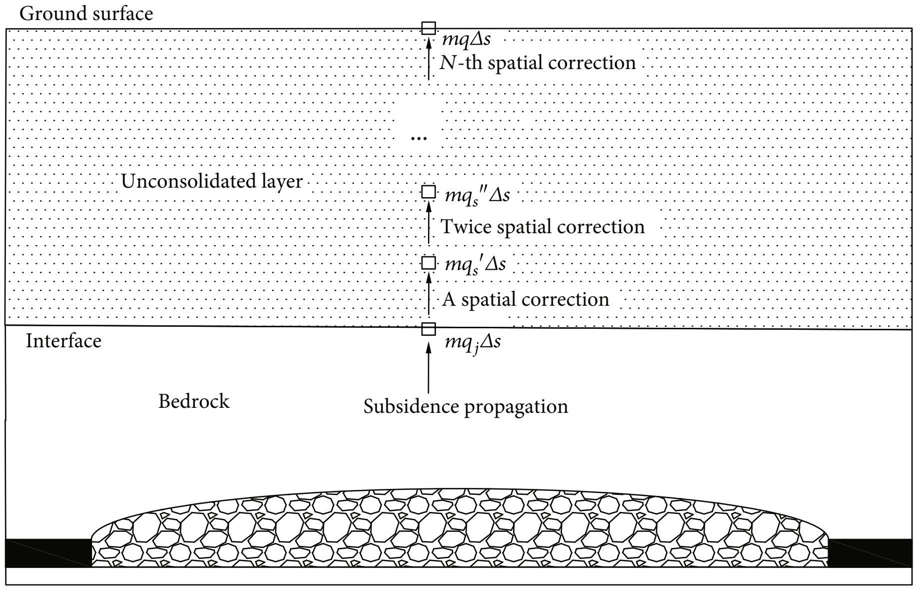

Figure 11: Correction process of subsidence factor.

the interface subsidence factor q_j can be obtained from Figure 11 as follows:

$$q_j = \begin{cases} 0.80 \sim 1.00 & \text{soft lithology} \\ 0.65 \sim 0.85 & \text{medium-hard lithology } H_s \le 1.2H_j, \\ 0.40 \sim 0.65 & \text{hard lithology} \end{cases} \tag{18}$$

$$q_j = \begin{cases} 0.75 \sim 1.00 & \text{soft lithology} \\ 0.65 \sim 0.75 & \text{medium-hard, hardlithology} \end{cases} \quad 1.2H_j < H_s \le 2.0H_j, \tag{19}$$

$$q_j = 0.80\text{-}1.00 \text{ soft, medium-hard, hard lithology } H_s > 2.0H_j. \tag{20}$$

4.3.2. For Surface. According to formula (17), to calculate the surface subsidence factor, we need to know the value of q_j, k_s, and n. Use formulas (18)–(20) to determine q_j and formula (16) to calculate n. Generally speaking, k_s is variety in different mine areas and does not suffer the effect of dip angle of coal seam and the rock lithology. For convenience in use, the theory lookup table calculated from formula (17) is shown in Table 3.

From Table 3, we can get the relevant data and calculate the surface subsidence factor.

4.4. Application Scope. The application of this method is limited. When the movement of the strata above the gob is only affected by self-weight and overburden pressure, the larger the thickness ratio, the higher the accuracy of parameter inversion. However, when a place has a wide range of geological structures (e.g., faults and folds) or geological events (e.g., earthquakes), the subsidence boundary shape model is unsuitable.

Table 3: Lookup table of theoretical value of k_s and q_s/q_j.

n q_s/q_j k_s	50	100	150	200	250	300	350	400	450	500
0.995	1.28	1.65	2.12	2.73	3.50	4.50	5.78	7.43	9.54	12.26
0.996	1.22	1.49	1.82	2.23	2.72	3.33	4.07	4.97	6.07	7.42
0.997	1.16	1.35	1.57	1.82	2.12	2.46	2.86	3.33	3.87	4.49
0.998	1.11	1.22	1.35	1.49	1.65	1.82	2.02	2.23	2.46	2.72
0.999	1.05	1.11	1.16	1.22	1.28	1.35	1.42	1.49	1.57	1.65
1.000	1.00	1.00	1.00	1.00	1.00	1.00	1.00	1.00	1.00	1.00
1.001	0.95	0.90	0.86	0.82	0.78	0.74	0.70	0.67	0.64	0.61
1.002	0.90	0.82	0.74	0.67	0.61	0.55	0.50	0.45	0.41	0.37
1.003	0.86	0.74	0.64	0.55	0.47	0.41	0.35	0.30	0.26	0.22
1.004	0.82	0.67	0.55	0.45	0.37	0.30	0.25	0.20	0.17	0.14
1.005	0.78	0.61	0.47	0.37	0.29	0.22	0.17	0.14	0.11	0.08
1.006	0.74	0.55	0.41	0.30	0.22	0.17	0.12	0.09	0.07	0.05
1.007	0.71	0.50	0.35	0.25	0.17	0.12	0.09	0.06	0.04	0.03
1.008	0.67	0.45	0.30	0.20	0.14	0.09	0.06	0.04	0.03	0.02
1.009	0.64	0.41	0.26	0.17	0.11	0.07	0.04	0.03	0.02	0.01
1.010	0.61	0.37	0.22	0.14	0.08	0.05	0.03	0.02	0.01	0.01

5. Case Study

The rock lithology of Bai Shan colliery in Huai Bei mine area is medium hard. The thickness of unconsolidated layer and the bedrock is 145 m and 64 m, respectively. The coal seam thickness is 2.1 m, and the dip angel of coal seam is 10°. The strike length of the workface is 500 m, and the tendency length is 175 m. The measured surface subsidence factor is 1.25.

Table 4: The calculated value of $1/k_s^{82}$ and q_s/q_j.

k_s	$1/k_s^{82}$	q_s/q_j $n = 50$	$n = 82$	$n = 100$
0.995	1.5084	1.28	1.5168	1.65
0.996	1.3891	1.22	1.4528	1.49
0.997	1.2794	1.16	1.4016	1.35
0.998	1.1784	1.11	1.3504	1.22
0.999	1.0855	1.05	1.3184	1.11
1.000	1.0855	1.00	1.28	1.00
1.001	0.9213	0.95	1.248	0.90
1.002	0.8489	0.90	1.2288	0.82
1.003	0.7822	0.86	1.2032	0.74
1.004	0.7208	0.82	1.184	0.67
1.005	0.6643	0.78	1.1712	0.61
1.006	0.6123	0.74	1.1584	0.55
1.007	0.5644	0.71	1.1456	0.50
1.008	0.5203	0.67	1.1392	0.45
1.009	0.4796	0.64	1.1328	0.41
1.010	0.4422	0.61	1.1264	0.37

Based on the geological and mining condition, $H_s/H_j = 2.3$ and $H_s > 2.0H_j$. According to formula (20), the interface subsidence factor is as follows:

$$q_j = 0.85. \tag{21}$$

Compress times n:

$$n = \frac{H_s}{mq_j \cos \alpha} = \frac{145}{2.1 * 0.85 * \cos 10^\circ} = 82, \tag{22}$$

$$\frac{q_s}{q_j} = \frac{1}{k_s^{82}}. \tag{23}$$

Combined with Table 4, the value of q_s/q_j can be obtained by linear interpolation when $n = 82$. In addition, the value of $1/k_s^{82}$ is calculated by k_s. The values of both are shown in Table 4. According to formula (20), the two should be equal. By searching Table 4, we can see that when $k_s = 1$, the two are basically equal. Therefore, the unconsolidated layer subsidence correction factor k_s of Bai Shan colliery can be obtained, $k_s = 0.995$. q_s is greater than q_j. It is stated that the surface subsidence aggravates because of the aquifer water loss and soil secondary consolidation.

Correspondingly, the value of q_s/q_j is 1.5168. Then, the calculated surface subsidence coefficient is

$$q_{sc} = 1.5168 * q_j = 1.5168 * 0.85 = 1.29. \tag{24}$$

To evaluate the prediction precision, the relative error is used. The relative error is

$$f = \frac{|q_{sa} - q_{sc}|}{q_{sa}}, \tag{25}$$

where f is the relative error, q_{sa} is the actual surface subsidence factor, and q_{sc} is the calculated surface subsidence factor.

Bring in the value and calculate the relative error.

$$f = \frac{|q_{sa} - q_{sc}|}{q_{sa}} = \frac{|1.25 - 1.29|}{1.25} = 5\%. \tag{26}$$

The results show that the relative error is less than 10%, which can meet the engineering requirements and can better predict the subsidence of overburden rock.

6. Conclusions

(1) This paper presents an inversion method of subsidence based on geological conditions. By using this method, the case that the surface subsidence is greater than the mining thickness can be inverted, which is not available in other methods

(2) Numerical simulation is used to reveal the variation law of surface mining-induced subsidence under different lithology and thickness ratio. For soft rock, the surface subsidence decreases approximately linearly with the thickness ratio increase of the unconsolidated layer to bedrock. However, for hard or medium-hard rock, the surface subsidence undergoes three proportional sections, first increases, then decreases, and finally increases with the thickness ratio increase of the unconsolidated layer to bedrock

(3) Based on the theory that the rock strata space can be completely compressed gradually, from the perspective of lithology, we have revealed the mechanism of the above laws

(4) The case study of this inversion method has been carried out. The results show that the inversion effect is good, and the relative error is only 5%

Data Availability

The data used to support the findings of this study are available from the corresponding author upon request.

Conflicts of Interest

The authors declare that there is no conflict of interest regarding the publication of this paper.

Acknowledgments

This research work has been supported by the National Natural Science Foundation of China (50974122 and U1810203), the Specialized Research Fund for the Doctoral Program of Higher Education of China (20110023110014), the Key Scientific Research Projects of Higher Education Institutions in Henan Province (20A440005), the Youth Backbone Teacher Support Program of Henan Polytechnic University (2019XQG-07), the Fundamental Research Funds for the Universities of Henan Province (NSFRF200314), the Henan Scientific and Technological Project (212102310012), the Science and Technology Cooperative Planning of Guizhou Province (LH [2017]097), and the High-Level Talents Fund of Guizhou University of Engineering Science (G2015005). All those financial supports are gratefully acknowledged.

References

[1] S. Sinha, R. N. Bhattacharya, and R. Banerjee, "Surface iron ore mining in eastern India and local level sustainability," *Resources Policy*, vol. 32, no. 1-2, pp. 57–68, 2007.

[2] P. R. Helm, C. T. Davie, and S. Glendinning, "Numerical modelling of shallow abandoned mine working subsidence affecting transport infrastructure," *Engineering Geology*, vol. 154, pp. 6–19, 2013.

[3] P. Hadi, Y. B. Alireza, and N. Mehdi, "Impact of ground surface subsidence due to underground mining on surface infrastructure: the case of the Anomaly No. 12 Sechahun, Iran," *Environmental Earth Sciences*, vol. 78, p. 409, 2019.

[4] Z. Liu, B. Cui, Y. Liang, H. Guo, and Y. Li, "Study on foundation deformation of buildings in mining subsidence area and surface subsidence prediction," *Geotechnical and Geological Engineering*, vol. 37, no. 3, pp. 1755–1764, 2019.

[5] J. Zhang and L. Chong, "The discussion of the surface and building deformation in the coal mining subsidence area," *Shanxi Architecture*, vol. 38, no. 9, pp. 83-84, 2012.

[6] X. M. Cui, Y. G. Gao, and D. B. Yuan, "Sudden surface collapse disasters caused by shallow partial mining in Datong coalfield, China," *Natural Hazards*, vol. 74, no. 2, pp. 911–929, 2014.

[7] F. G. Bell, T. R. Stacey, and D. D. Genske, "Mining subsidence and its effect on the environment: some differing examples," *Environmental Geology*, vol. 40, no. 1-2, pp. 135–152, 2000.

[8] S. Saha, S. K. Pattanayak, E. O. Sills, and A. K. Singha, "Undermining health: environmental justice and mining in India," *Health & Place*, vol. 17, no. 1, pp. 140–148, 2011.

[9] L. M. Fan, X. D. Ma, and R. J. Ji, "The progress of research engineering practice of water-preserved coal mining in western eco-environment frangible area," *Journal of China Coal Society*, vol. 40, no. 8, pp. 1711–1717, 2015.

[10] Z. Jinhai, J. Ning, Y. Liming, and B. Liyang, "The effects of mining subsidence and drainage improvements on a waterlogged area," *Bulletin of Engineering Geology and the Environment*, vol. 78, no. 5, pp. 3815–3831, 2019.

[11] J. J. Chen, Y. F. Zou, and W. B. Guo, "Study on the relationship between subsidence factor and mining degree under a thick alluvium stratum," *Journal of Mining and Safety Engineering*, vol. 29, no. 2, pp. 250–254, 2012.

[12] J. Ju and J. Xu, "Surface stepped subsidence related to top-coal caving longwall mining of extremely thick coal seam under shallow cover," *International Journal of Rock Mechanics and Mining Sciences*, vol. 78, pp. 27–35, 2015.

[13] J. Liu, X. Liang, Y. Xue, K. Yao, and Y. Fu, "Numerical evaluation on multiphase flow and heat transfer during thermal stimulation enhanced shale gas recovery," *Applied Thermal Engineering*, vol. 178, article 115554, 2020.

[14] Q. Qu, J. Xu, R. Wu, W. Qin, and G. Hu, "Three-zone characterisation of coupled strata and gas behaviour in multi-seam mining," *International Journal of Rock Mechanics and Mining Sciences*, vol. 78, pp. 91–98, 2015.

[15] L. Chen, X. Feng, W. Xie, and D. Xu, "Prediction of water-inrush risk areas in process of mining under the unconsolidated and confined aquifer: a case study from the Qidong coal mine in China," *Environmental Earth Sciences*, vol. 78, no. 8, p. 706, 2016.

[16] W. Yan, H. Dai, and J. Chen, "Surface crack and sand inrush disaster induced by high-strength mining: example from the Shendong coal field, China," *Geosciences Journal*, vol. 22, no. 2, pp. 347–357, 2018.

[17] C. Q. Ma, H. Z. Li, and P. P. Zhang, "Subsidence prediction method of solid backfilling mining with different filling ratios under thick unconsolidated layers," *Arabian Journal of Geosciences*, vol. 10, no. 78, pp. 1–12, 2017.

[18] G. Ren, G. Li, and M. Kulessa, "Application of a generalised influence function method for subsidence prediction in multi-seam longwall extraction," *Geotechnical and Geological Engineering*, vol. 32, no. 4, pp. 1123–1131, 2014.

[19] W. T. Yan, J. J. Chen, and Y. G. Yan, "A new model for predicting surface mining subsidence: the improved lognormal function model," *Geosciences Journal*, vol. 23, no. 1, pp. 165–174, 2019.

[20] W. Liu, J. Xu, W. Zhu, and S. Wang, "A novel short-wall caving zone backfilling technique for controlling mining subsidence," *Energy Science & Engineering*, vol. 7, no. 5, pp. 1–14, 2019.

[21] D. Y. Xuan and J. L. Xu, "Grout injection into bed separation to control surface subsidence during longwall mining under villages: case study of Liudian coal mine, China," *Natural Hazards*, vol. 73, no. 2, pp. 883–906, 2014.

[22] J. Z. Wang, Y. S. Li, X. Zhou, L. Wu, and S. Wei, "Ground movement caused by mining under thick alluvium," *Journal of China Coal Society*, vol. 22, no. 1, pp. 18–21, 1997.

Hindawi
Geofluids
Volume 2021, Article ID 5570846, 11 pages
https://doi.org/10.1155/2021/5570846

Research Article

Tunnel Behaviour Caused by Basement Excavation in Clay

Huasheng Sun, Jihua Zhang, Guodong Zhao, and Hao Wang

Huaiyin Institute of Technology, 89 North Beijing Road, Huai'an 223001, China

Correspondence should be addressed to Jihua Zhang; zhangjh84@hyit.edu.cn

Received 18 January 2021; Revised 21 February 2021; Accepted 11 March 2021; Published 30 March 2021

Academic Editor: Yi Xue

Many researchers have investigated the effect of basement excavation on tunnel deformation. However, the influence of consolidation on the interaction of basement-tunnel-soil is rarely considered or systematically studied in clay. In this study, three-dimensional coupled-consolidation finite element analyses were conducted to investigate the effect of consolidation on the tunnel response to excavation. An advanced nonlinear constitutive model was adopted, and numerical parametric investigations were conducted to study the effect of the excavation depth, tunnel stiffness, soil permeability coefficient, and consolidation time on the tunnel response. The results revealed that the basement excavation led to stress release, which caused tunnel heave. Owing to the dissipation of excess negative pore water pressure, the tunnel heave further increased to become approximately twice as large compared with that observed when the foundation pit excavation had just been completed. As the consolidation time increased, the longitudinal tunnel heave and tunnel diameter change caused by the foundation pit excavation gradually increased, but the growth rate was slower down. When the consolidation time changed from 50 days to 150 days, the maximum tunnel heave at the crown and the maximum tunnel diameter change increased by 1.18 and 1.48 times, respectively. The soil's permeability coefficient did not have a significant effect on the tunnel heave at the crown nor on the tunnel diameter change. The results obtained by this study are expected to be useful as an engineering reference for the analysis of soil structure problems in clay.

1. Introduction

With the further progress of urbanization, the foundation pit engineering appears constantly, most of which are located in structures and densely populated areas. In current foundation pit engineering design, not only the effect of adjacent structures on the foundation pit but also the effect of foundation pit excavation on adjacent structures should be considered. The former is mainly to ensure that reasonable measures are taken to ensure the safety of foundation pit excavation and foundation construction, while the latter is to consider the excessive deformation of adjacent buildings caused by the excessive deformation of foundation pit, thus affecting the safety of structures. If appropriate measures are not taken, the adjacent structures will be damaged, causing serious economic losses and huge social impact. As a major engineering problem in urban underground space construction, it is essential to predict and evaluate the interaction between foundation pit excavation and adjacent structures.

The deformation of adjacent tunnels as a result of basement excavation is such a typical problem in this kind of major engineering problems. To investigate the effect of tunnels due to a nearby basement excavation, numerous studies have been conducted using field tests [1–5], centrifuge model tests [6–10], and analytical and numerical methods [11–27].

Burford [1] reported that the excavation of the large basement of the Shell Centre in London Clay resulted in an upward displacement between 20 mm and 30 mm for the underlying Bakerloo line tunnel. After 27 years, the maximum uplift measured under the basement of the southbound Bakerloo tunnel was 50 mm, while that of the northbound tunnel was 41 mm. It is shown that the release of overburden pressure will lead to long-term uplift of a tunnel in London clay. Shi et al. [10] carried out three-dimensional centrifuge tests to investigate tunnel responses due to overlying basement excavation in lightly (overconsolidation ratio (OCR) = 1.7) and heavily overconsolidated (OCR = 6.0) kaolin clays. It is found that special attention should be paid to long-term rather than short-term tunnel responses.

However, most previous studies investigating the tunnel deformation caused by basement excavation mainly focused on the short-term tunnel response [2, 4–6, 8, 9, 11, 14–27]. The field monitoring of a tunnel affected by foundation pit excavation in clay revealed that the long-term heave of the tunnel in clay is very large, and the time required to reach the steady state is very long [1]. Thus, it seems that the subway tunnel response on clay ground is highly dependent on time. Therefore, in the analysis of the existing tunnel response in clay, it is important to consider the short-term response systematically from the foundation pit excavation construction period and the long-term response after the construction is completed.

Prediction of tunnel response induced by excavation is becoming one of the major tasks for geotechnical engineers. The use of the numerical method to analyse the interaction between excavation and the existing tunnel is frequent [11, 13–20, 22, 23, 28, 29]. It is well known that a soil model in the numerical method should capture the state-, strain-, and path-dependent soil stiffness even at small strains and path- and state-dependent soil strength. In addition, the consolidation characteristics should be considered in clay. In order to investigate the influence of a basement excavation on the tunnel behaviour in dry sand precisely, Ng et al. [8] carried out two centrifuge model tests to investigate this issue. Several numerical analyses based on these centrifuge model tests were conducted by adopting the hypoplasticity model for sand, and it was found that the hypoplasticity model can more effectively capture the soil behaviour compared with the previously reported centrifuge model test [9, 16, 18, 19]. Mašín and Herle [30] developed a basic hypoplastic model to predict the clay behaviour at medium to large strain levels. To account for strain-dependent and path-dependent soil stiffness at small strains, Mašín [31] improved the basic hypoplastic model by incorporating the concept of the intergranular strain [32]. The improved model was used by Najser et al. [33] and the computed ground deformations agree with the measured results. However, numerical simulation considering the state-, strain-, and path-dependent soil stiffness even at small strains, the path- and state-dependent soil strength, and the consolidation characteristics of soil has not been reported in literatures to investigate the interaction of foundation pit excavation and existing tunnel.

Considering the abovementioned issues, the aim of this paper was to investigate the tunnel behaviour and elucidate the internal law and mechanism of tunnel deformation resulting from basement excavation in clay. To this end, three-dimensional coupled-consolidation numerical analyses using the clay hypoplasticity model were carried out to simulate the long-term response of a tunnel subjected to basement excavation in clay. Numerical parametric investigations were also conducted to study the influence of the basement excavation depth, soil and tunnel property, and the consolidation effect on the tunnel response.

2. Material and Methods

The software ABAQUS (Version 6.17; ABAQUS, Inc.) was adopted to conduct numerical analyses, wherein the hypoplastic model of clay with user-defined subroutine was established by Mašín [34, 35].

2.1. Finite Element Model. The finite element mesh shown in Figure 1 was constructed on the basis of the model test reported by Ng et al. [8]. In this model, the finite element mesh dimension was 18 m in length, 18 m in width, and 9 m in depth in the prototype. The tunnel diameter was 6 m in the prototype. The other dimensions of basement excavation and retaining wall were the same as that in the model test. It should be noted that the centrifuge model tests were conducted in sand but the finite element was carried out in clay. For the boundary condition, roller supports were adopted at the vertical surfaces and pin supports were adopted at the bottom of the model. Soil-water coupling analysis theory was adopted. The groundwater level was set on the model top, and the bottom of the model was set as an undrained boundary. To simulate the recharge of external groundwater during the foundation pit excavation, the pore pressure at the side boundaries of the model was set as hydrostatic pressure and remained unchanged throughout the analysis process. The top surface of the model was set as a free drainage boundary. The element types of the soil, retaining wall, and tunnel were C3D8P, C3D8, and S4, respectively. Interface elements were used at the soil-tunnel and at the soil-retaining wall interfaces. The setting method can be referred to document reported by Ng et al. [16].

2.2. Constitutive Model and Related Parameters. It is essential to adopt a constitutive model which can simulate the soil behaviour varying with strain from small to large levels. A clay hypoplastic model proposed by Mašín [31] was used to predict the behaviour of the clay. The original model requires five parameters: φ_c', N, λ^*, κ^*, and r to predict the behaviour of clay from medium to large strain levels. The other five parameters, namely, R, m_T, m_R, β_r, and χ are required to predict the soil response in the small-strain range. The physical meaning of these parameters was shown in Table 1. Mašín [36] reported the calibration of the parameters for London Clay in the hypoplastic clay model. Table 1 summarizes the parameters for London Clay used in this study. The tunnel and retaining wall were simulated as a linear elastic material. Both their Young's modulus and Poisson's ratio are 70 GPa and 0.2, respectively.

2.3. Numerical Simulation Process. The finite element simulation process before soil consolidation is essentially the same as the centrifugal model test process. The tunnel and retaining structure were simulated using the "wished in place" method, which assumes that the tunnel and retaining structure already exist before the foundation pit excavation. Gravity was applied in the way of the physical force, and the analysis is based on the excess pore pressure. The simulation process is summarized as follows:

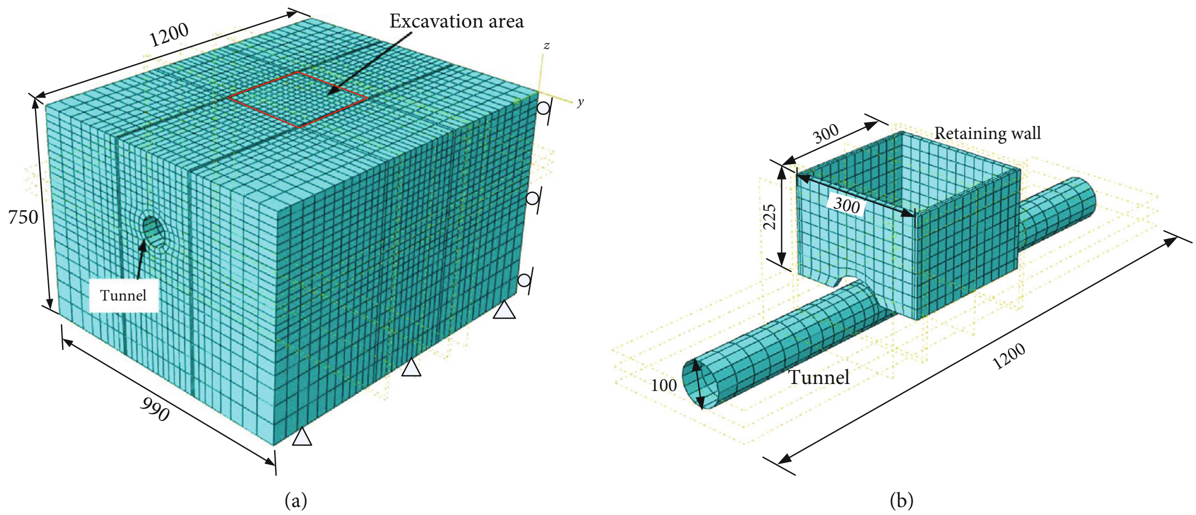

FIGURE 1: (a) Finite element model and (b) retaining wall and tunnel (all dimensions in model scale, unit: mm).

TABLE 1: Parameters of London Clay in the clay hypoplastic model [36].

Parameters	Physical meaning	Values
N	Control the position of the isotropic normal compression line	1.375
λ^*	Control the slope of the isotropic normal compression line	0.11
κ^*	Control the slope of the isotropic unloading line	0.016
φ_c'	The critical state friction angle	22.6°
r	Control the shear stiffness	0.4
m_{R}	Parameter controlling the initial (very-small-strain) shear Modulus upon 180°strain path reversal and in the initial loading	1×10^{-4}
m_{T}	Parameter controlling the initial shear modulus upon 90° Strain path reversal	4.5
R	The size of the elastic range (in the strain space)	4.5
β_r	Control the rate of degradation of the stiffness with strain	0.2
χ	Control the rate of degradation of the stiffness with strain	6

(1) The initial stress field of the soil is established under the 1 g condition. The initial stress in the tunnel and retaining structure is the same as that of the surrounding soil

(2) Gradually increase the acceleration of gravity until 60 g

(3) Simulate the excavation process using the birth-death element method and complete the excavation in three steps of 3 m each

(4) After the basement excavation is completed, the consolidation time of 50, 100, 150, and 200 days is set to investigate the effect of the surrounding soil's consolidation on the tunnel deformation

3. Interpretation of Calculated Results

3.1. Tunnel Heave along the Tunnel Axis. Figure 2 shows the calculated tunnel heave resulting from the basement excavation and subsequent consolidation for 100 days. With the increase of foundation pit excavation depth, the tunnel heave increases gradually. After the foundation pit excavation, the calculated tunnel heave was 0.020%H_{e} under the basement centre, wherein, H_{e} is the basement depth. After consolidation for 100 days, the calculated maximum value of the tunnel heave was 0.041%H_{e}. The measured maximum tunnel heave given by Ng et al. [8] is 0.023%H_{e}, 0.051%H_{e}, and 0.074%H_{e} for each excavation depth 3 m, 6 m, and 9 m, respectively. This is because different soil media are used in each case although using the same size of the model equipment. By comparing the tunnel heave calculated for different stages in clay, it is found that the maximum tunnel heave as a result of stress relief after immediately excavation was approximately half of the magnitude after consolidation for 100 days. Thus, it is concluded that the consolidation effect on the tunnel heave is significant. Moreover, the effect of consolidation on the tunnel heave is approximately the same as when the basement construction has just been completed, which is analogous to the case reported by Burford [1] and

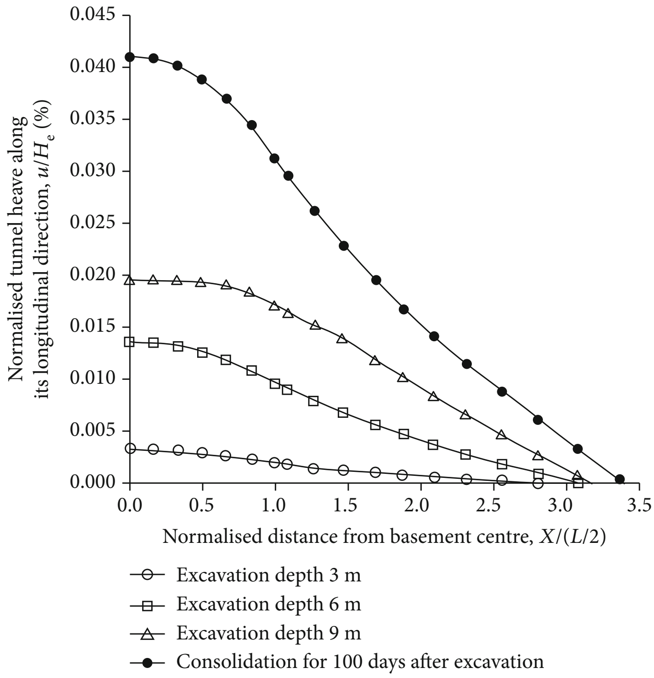

FIGURE 2: Normalised tunnel displacement along tunnel axis.

Shi et al. [10]. This enlightens us that, in engineering practice, it is necessary to pay close attention to the long-term influence of foundation pit excavation on tunnel displacement in clay. Once the foundation pit is exposed for a long time or the superstructure construction is too long, corresponding measures should be taken to control the tunnel displacement to prevent the tunnel lining from being damaged due to excessive deformation.

3.2. Vertical Stress Change in Soil at Tunnel Crown. To deeply understand the mechanism of the consolidation effect's influence on the tunnel's longitudinal deformation, the results for the vertical stress change at the longitudinal tunnel crown are shown in Figure 3. As can be seen, when the foundation pit excavation was completed, the vertical stress of the soil at the tunnel crown decreased owing to the stress release, and the maximum variation was approximately −8 kPa. The vertical stress variation in the excavated area of the foundation pit was approximately nonlinear. Because of the stress concentration, the soil stress at the bottom of the retaining structure rapidly increased, the maximum value was approximately 22 kPa, and the stress variation exceeded the maximum allowable stress change value specified by the BD [37] (±20 kPa). The soil stress change after the retaining structure sharply decreased and was within 20 kPa. Because of the excavation unloading, a large amount of soil stress was released and the tunnel moved upward, while the soil behind the retaining structure moved into the pit, and the soil behind the wall settled. The friction force generated by the relative movement of the soil and the retaining structure prevented the upward movement of the tunnel behind the wall, which resulted in tunnel uplift. After 100 days of excavation, the effective stress at the top of the tunnel and directly below the centre of the foundation pit increased by 11 kPa relative to the initial value. According to the principle of effective stress, with the dissipation of excess pore water pressure, the effective stress in the soil at the tunnel crown gradually increased. This is consistent with existing observation data for foundation pit excavation in clay [38, 39].

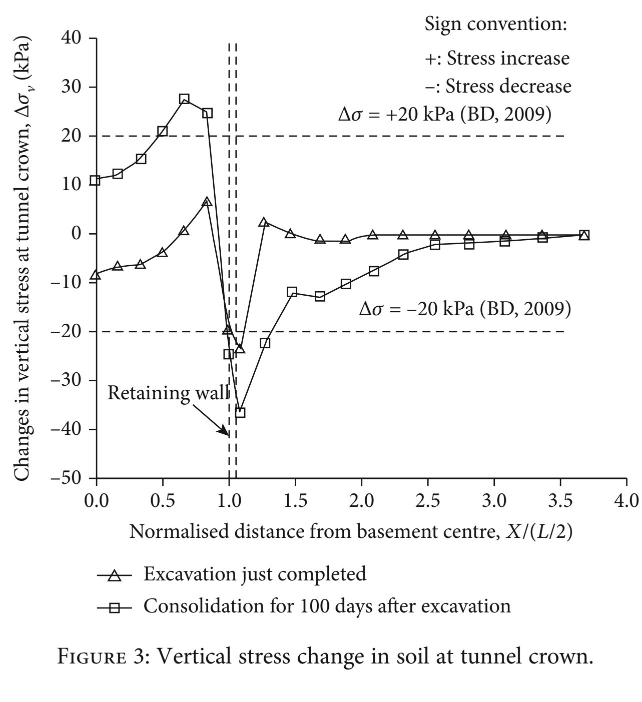

FIGURE 3: Vertical stress change in soil at tunnel crown.

3.3. Tunnel Deformation in the Transverse Direction. Figure 4 shows the variation of the tunnel diameter change with the

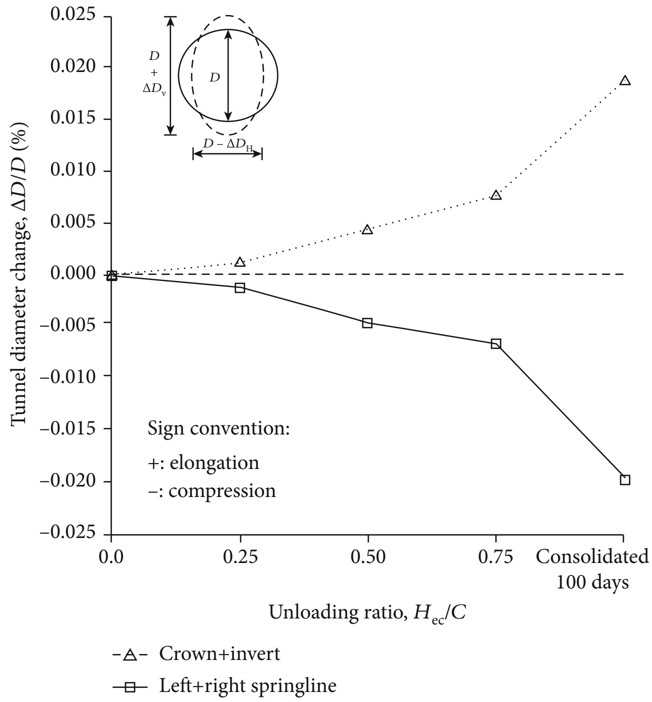

Figure 4: Tunnel diameter change in transverse direction in clay.

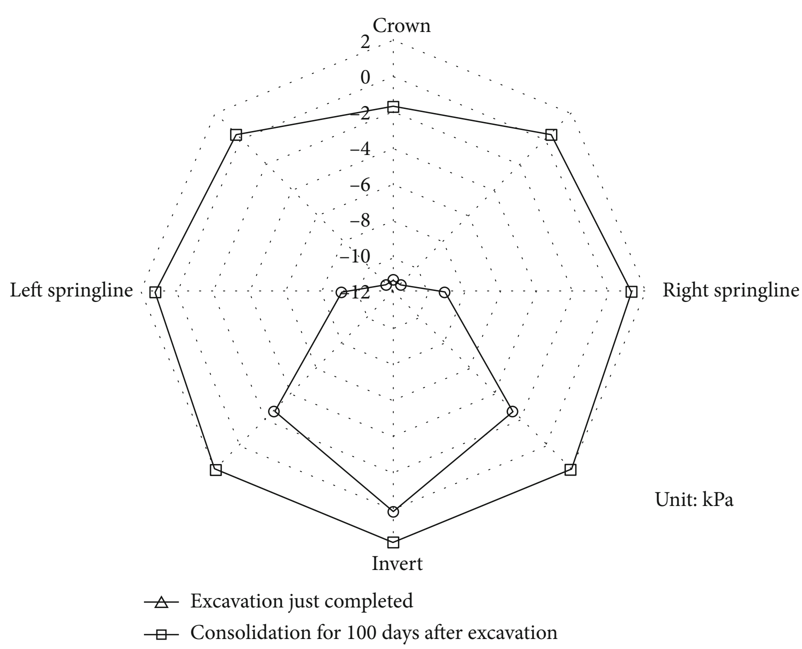

Figure 5: Earth pressure change around tunnel lining in clay.

excavation unloading ratio and consolidation time. The unloading ratio is defined as the ratio of the excavation depth of the foundation pit to the cover-depth of the tunnel. The positive value of the ordinate indicates the stretching of the tunnel diameter, while the negative value indicates the compression of the tunnel diameter. As can be seen in the figure, the excavation unloading of the foundation pit directly above the tunnel led to the vertical extension and horizontal compression of the tunnel. As the unloading ratio increased, the vertical diameter of the tunnel gradually elongated and the horizontal diameter gradually compressed. When the basement excavation was completed, the vertical elongation (ΔD_V) of the tunnel was 0.008%D and horizontal compression (ΔD_H) of the tunnel was 0.007%D (D is the tunnel diameter). After 100 days of consolidation following the excavation, the vertical elongation (ΔD_V) and horizontal

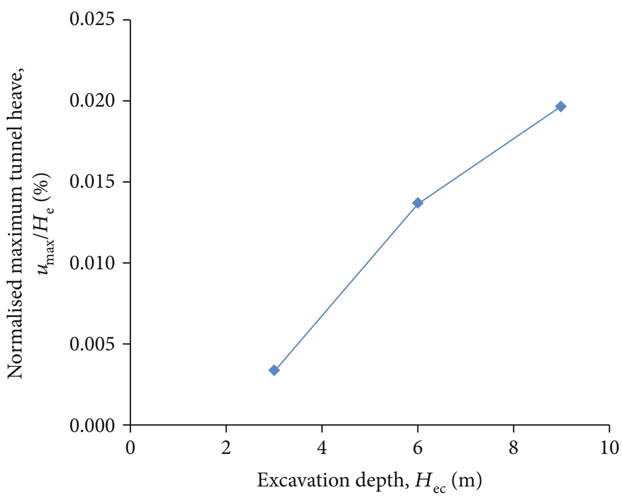

FIGURE 6: Tunnel heave as a result of different basement excavation depth in clay.

compression (ΔD_H) of the tunnel were 0.019%D and 0.020%D, respectively, both of which are approximately twice as large as that observed when the foundation pit was completed. According to the BTS [40], the allowable maximum value of tunnel deformation ($(\Delta D_V + \Delta D_H)/2$) is 2%. Therefore, the tunnel deformation is within the allowable range.

3.4. Earth Pressure Change around Tunnel Lining. Figure 5 shows the change of earth pressure in tunnel's cross-section after the foundation pit excavation. The tunnel's cross-section was located directly below the basement's excavation centre. Because of the symmetry, the earth pressure around the tunnel was symmetrically distributed. The stress release above the arch line of the tunnel was greater than that of the soil below the arch line. The vertical stress release of the soil around the tunnel was greater than that in the horizontal direction. Therefore, the tunnel diameter was vertically stretched and horizontally compressed, as shown in Figure 4. Additionally, as shown in Figure 5, the earth pressure above the tunnel springlines changed more than that below the springlines, which resulted in overall tunnel uplift. After 100 days of consolidation following the foundation pit excavation, as a result of the dissipation of excess negative pore water pressure, the earth pressure acting on the tunnel crown increased while the change at the invert was small, which resulted in the further increase of tunnel lining deformation, as shown in Figure 4.

4. Parametric Investigation

4.1. Effect of Basement Excavation Depth. Figure 6 shows the effect of the basement excavation depth on the maximum tunnel displacement at the crown in clay. The basement had variable depth of 3 m, 6 m, and 9 m. The computed maximum tunnel displacement was 0.003%H_e, 0.013%H_e, and 0.020%H_e, respectively. It is found that the maximum tunnel displacement in the longitudinal direction increased gradually as the basement depth increased; however, the growth rate slowed down.

4.2. Effect of Tunnel Lining Stiffness. Figure 7 shows the effect of the tunnel lining stiffness on the distribution of tunnel heave along tunnel axis and the maximum tunnel heave in clay. Considering that the tunnel material is unchanged, for convenience, the bending rigidity of the tunnel ($E_t I_t$) is replaced by the elastic modulus of the tunnel (E_t). As can be seen, the tunnel distribution shape was basically the same for different tunnel lining stiffness. The tunnel stiffness did not affect the main influence area caused by basement excavation. The maximum tunnel displacement decreased linearly with the logarithm of the tunnel lining stiffness.

4.3. Effect of Soil Permeability Coefficient. The effect of the soil permeability coefficient on the tunnel longitudinal heave is shown in Figure 8. Let the soil permeability coefficient in the foundation model be $K_0 = 3.6 \times 10^{-6}$ m/s and compare the other two different working conditions, that is, $K_1 = 3.6 \times 10^{-5}$ m/s and $K_2 = 3.6 \times 10^{-4}$ m/s. As illustrated in Figure 8, the longitudinal uplift of the tunnel increased with the permeability coefficient. When the permeability coefficient of the basic model increased by 10 times and 100 times, the longitudinal uplift of the tunnel increased by 15% and 17%, respectively. As can be seen, the soil permeability coefficient only has a small effect on the tunnel uplift deformation. When the permeability coefficient of the soil increased more than 10 times, the maximum tunnel heave underwent a minor change.

4.4. Effect of Soil Consolidation Time. Figure 9 illustrates the variation of the tunnel longitudinal heave with the consolidation time. After the foundation pit excavation was completed, the soil consolidation time was set to 50, 100, 150, and 200 days, respectively. Compared with the completion of the foundation pit excavation, the maximum uplift of the tunnel crown increased by 0.90, 1.10, 1.15, and 1.18 times, respectively. As can be seen, the consolidation effect had a significant effect on the tunnel heave. As the consolidation time increased, the maximum uplift at the crown of the tunnel gradually increased, but the growth rate slowed down. Compared with 150 days of consolidation, the maximum tunnel uplift only changed by 2.6% for 200 days of consolidation. As can be seen, the consolidation can be considered to have completed 150 days after the foundation pit excavation.

Figure 10 illustrates the variation of tunnel diameter change in the cross-section with the consolidation time. With the increase of the unloading ratio, the vertical diameter of the tunnel gradually elongated and the horizontal diameter gradually compressed. After the foundation pit excavation was completed, the soil consolidation time was set to 50, 100, and 150 days. Compared with the completion of the basement excavation, the maximum elongation of the tunnel cross-section lining increased by 1.10, 1.44, and 1.48 times, respectively. As can be seen, the consolidation effect had a significant effect on the deformation of the tunnel lining in the transverse direction. As the consolidation time increased,

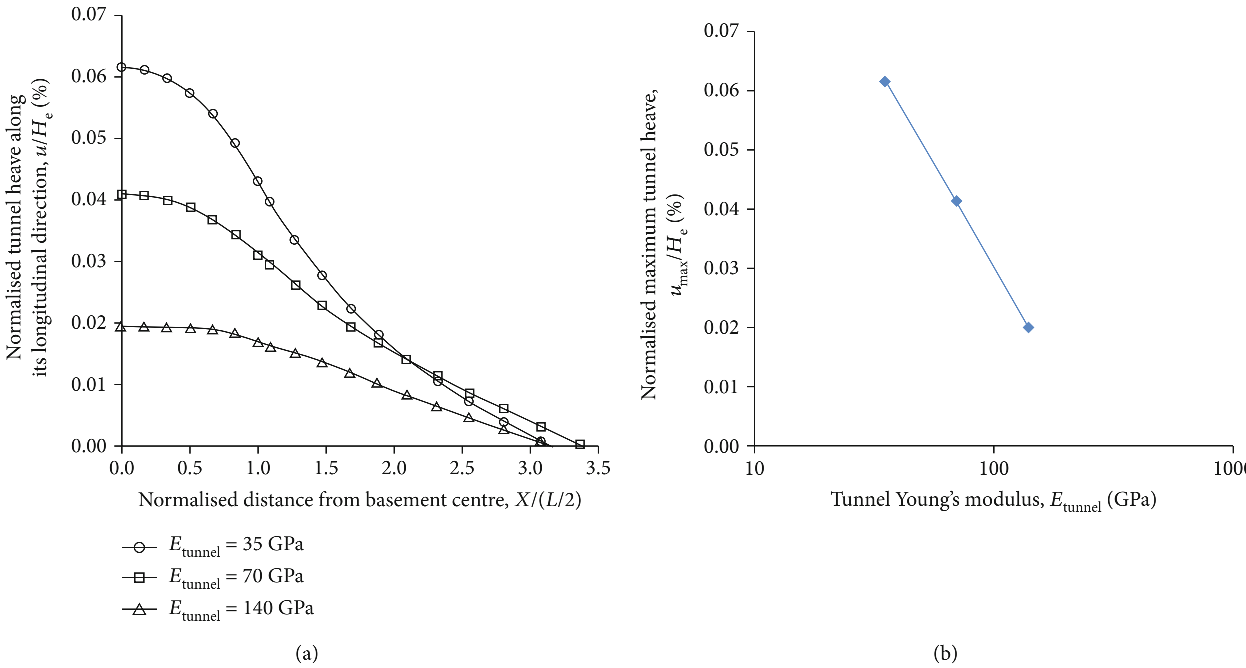

FIGURE 7: Influence of tunnel Young's modulus on (a) tunnel heave along its axis and (b) maximum tunnel displacement in clay.

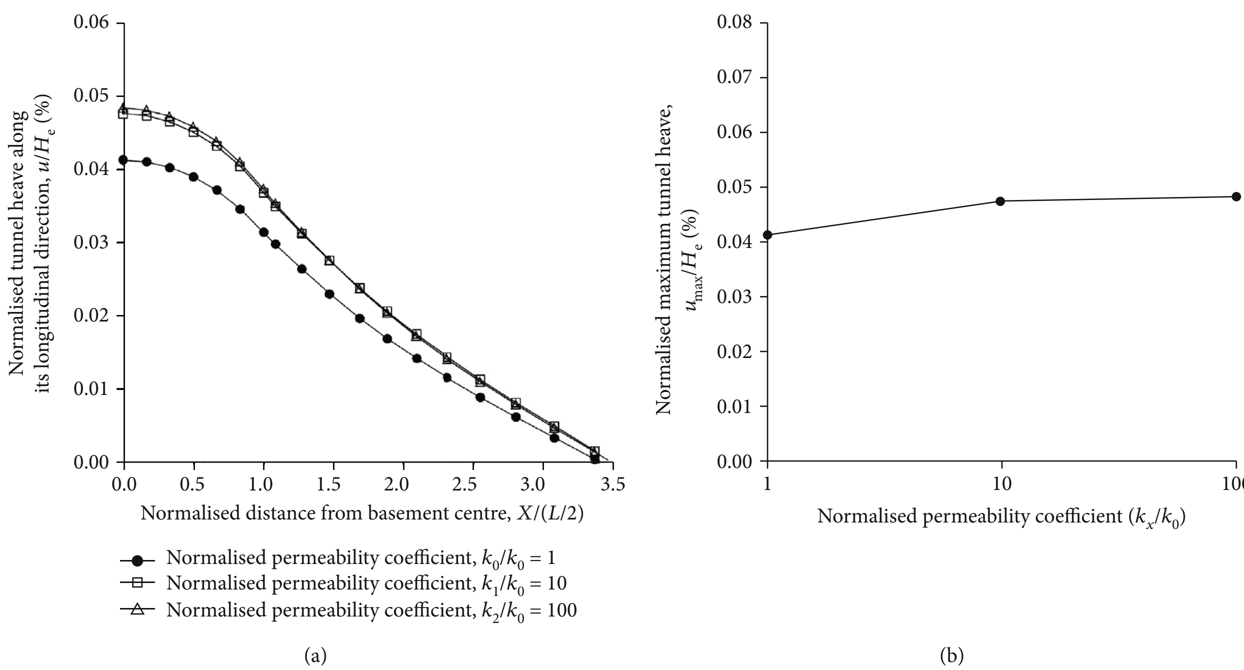

FIGURE 8: Effect of soil permeability on (a) tunnel heave along its axis and (b) maximum tunnel heave in clay.

the tunnel diameter change gradually increased, but the growth rate slowed down and finally tended toward stability.

Figure 11 shows the variation of the vertical stress change in soil at the tunnel crown with the consolidation time. As can be seen, when the foundation pit excavation was completed, the vertical stress of the soil at tunnel crown decreased owing to stress release, and the maximum variation was approximately -8 kPa. After the completion of the foundation pit excavation, as the consolidation time increased, the effective vertical stress gradually increased, which led to the gradual increase of the tunnel longitudinal uplift, as shown in Figure 9. Additionally, it can be seen that, when the consolidation time was greater than 100 days, the vertical stress changed only slightly, which led to the good stability of the tunnel's longitudinal uplift, as shown in Figure 9.

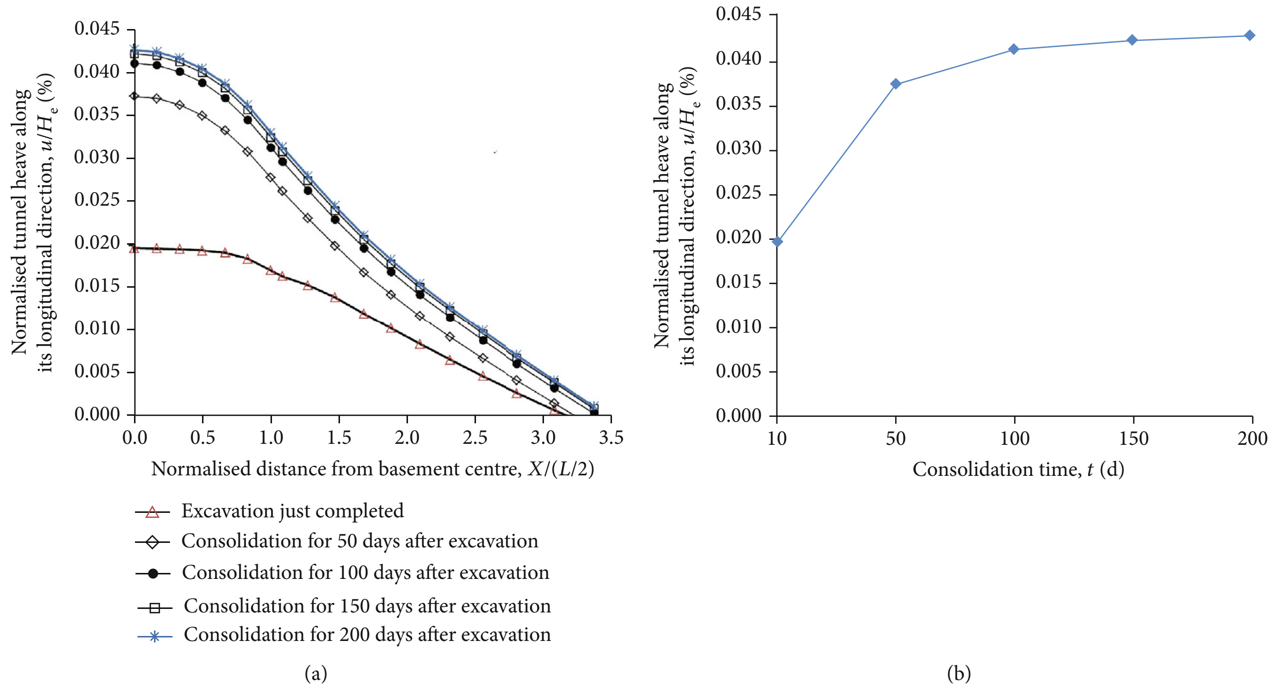

Figure 9: Effect of consolidation time on (a) tunnel heave in longitudinal direction and (b) maximum tunnel heave in clay.

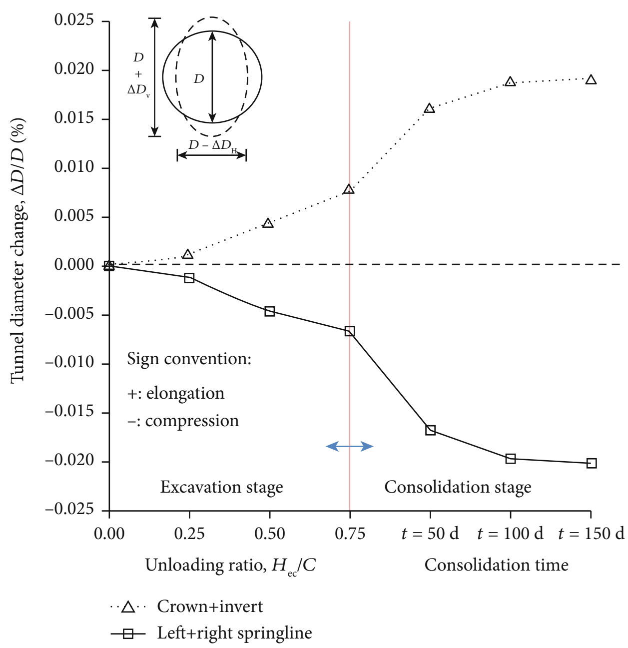

Figure 10: Effect of consolidation time on tunnel diameter change in clay.

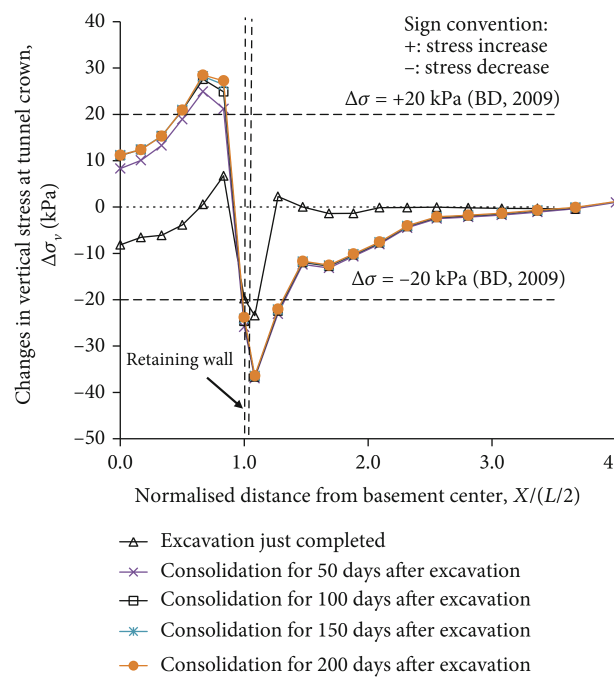

Figure 11: Soil vertical stress change at tunnel crown for different consolidation times.

Figure 12 shows the relationship between the variation of the earth pressure acting at the tunnel lining and the consolidation time. After the foundation pit excavation was completed, as the consolidation time gradually increased, the pore water pressure of the soil around the tunnel gradually dissipated, and the earth pressure acting on the tunnel lining gradually increased, which led to the further increase of the tunnel lining deformation, as shown in Figure 10. When the consolidation time was more than 100 days, the earth pressure acting on the tunnel cross-section did not change much, which led to the good stability of the tunnel cross-section lining deformation, as shown in Figure 10.

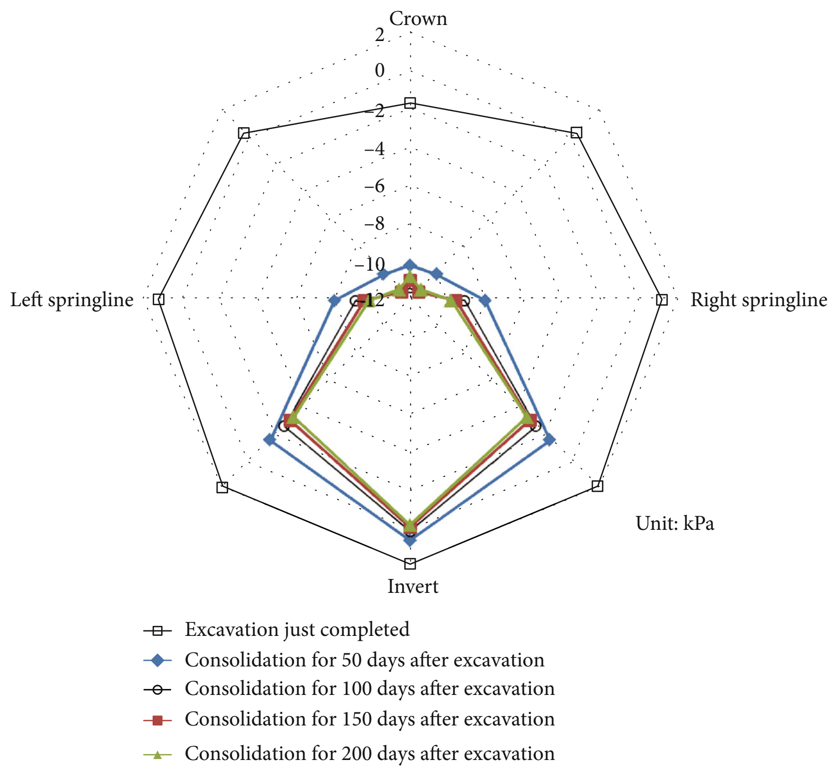

FIGURE 12: Soil pressure change around tunnel lining for different consolidation times.

5. Conclusions

Based on the centrifugal model test, this paper investigated the effect of basement excavation on long-term tunnel deformation using the clay hypoplasticity model, which considers the small-strain, stress-path dependence, and soil consolidation characteristics. The influence law and mechanism of the consolidation effect on the long-term deformation caused by excavation were investigated. Numerical parametric investigations were also carried out to study the tunnel response. The main conclusions drawn from this study are summarized as follows:

(a) The unloading of the basement excavation resulted in stress release, which caused tunnel heave. The tunnel heave further increased by approximately two times compared with that observed when the foundation pit excavation had just been completed. The foundation pit excavation directly above the tunnel resulted in the vertical extension and horizontal compression of the tunnel. As the unloading ratio increased, the vertical diameter of the tunnel gradually elongated and the horizontal diameter gradually compressed. Owing to the effect of further consolidation, the tunnel diameter change continuously increased by approximately two times compared with that at the end of the foundation pit excavation. Thus, it is concluded that the consolidation effect has a significant effect on the longitudinal and transverse deformation of the tunnel

(b) Owing to the excavation and subsequent consolidation process, the maximum tunnel heave increased with the basement depth, but the growth rate slowed down. Additionally, the maximum tunnel heave decreased linearly with the logarithm of the tunnel lining stiffness. As the consolidation time increased, the longitudinal uplift and tunnel diameter change gradually increased, but the growth rate was slow. When the consolidation time changed from 50 to 150 days, the maximum tunnel heave at the crown and the maximum tunnel diameter change increased by 1.18 and 1.48 times, respectively

(c) As the soil permeability coefficient gradually increased, the tunnel longitudinal uplift and tunnel diameter change gradually increased. When the permeability coefficient of the soil increased by 10 times and 100 times, the maximum uplift of the tunnel increased by 15% and 17%, and the tunnel diameter change increased by 2% and 11%. Thus, the soil's permeability coefficient did not have a significant effect on the tunnel heave at the crown nor on the tunnel diameter change

Data Availability

The computed data used to support the findings of this study are included within the article.

Conflicts of Interest

The authors declare that they have no conflicts of interest.

Acknowledgments

This study was sponsored by the National Natural Science Foundation of China (Grant number 51708245 and Grant number 51904112), the Natural Science Foundation of Jiangsu Province (Grant number BK20160426), and the Natural Science Foundation for Colleges and Universities in Jiangsu Province (19KJA430017). We thank Liwen Bianji, Edanz Editing China (http://www.liwenbianji.cn/ac), for editing the English text of a draft of this manuscript.

References

[1] D. Burford, "Heave of tunnels beneath the Shell Centre. London, 1959–1986," *Géotechnique*, vol. 38, no. 1, pp. 135–137, 1988.

[2] C. T. Chang, C. W. Sun, S. Duann, and R. N. Hwang, "Response of a Taipei Rapid Transit System (TRTS) tunnel to adjacent excavation," *Tunnelling and Underground Space Technology*, vol. 16, no. 3, pp. 151–158, 2001.

[3] B. Liu, D. W. Zhang, C. Yang, and Q. B. Zhang, "Long-term performance of metro tunnels induced by adjacent large deep excavation and protective measures in Nanjing silty clay," *Tunnelling and Underground Space Technology*, vol. 95, article 103147, 2020.

[4] K. Lo and J. Ramsay, "The effect of construction on existing subway tunnels–a case study from Toronto," *Tunnelling and Underground Space Technology*, vol. 6, no. 3, pp. 287–297, 1991.

[5] B. Simpson and P. J. Vardanega, "Results of monitoring at the British Library excavation," *Proceedings of the Institution of Civil Engineers-Geotechnical Engineering*, vol. 167, no. 2, pp. 99–116, 2014.

[6] H. Huang, X. Huang, and D. Zhang, "Centrifuge modelling of deep excavation over existing tunnels," *Proceedings of the Institution of Civil Engineers - Geotechnical Engineering*, vol. 167, no. 1, pp. 3–18, 2014.

[7] F. Y. Meng, R. P. Chen, S. L. Liu, and H. N. Wu, "Centrifuge modeling of ground and tunnel responses to nearby excavation in soft clay," *Journal of Geotechnical and Geoenvironmental Engineering*, vol. 147, no. 3, article 04020178, 2021.

[8] C. W. W. Ng, J. W. Shi, and Y. Hong, "Three-dimensional centrifuge modelling of basement excavation effects on an existing tunnel in dry sand," *Canadian Geotechnical Journal*, vol. 50, no. 8, pp. 874–888, 2013.

[9] C. W. W. Ng, J. W. Shi, D. Mašín, H. S. Sun, and G. H. Lei, "Influence of sand density and retaining wall stiffness on three-dimensional responses of tunnel to basement excavation," *Canadian Geotechnical Journal*, vol. 52, no. 11, pp. 1811–1829, 2015.

[10] J. W. Shi, C. Ding, C. W. W. Ng, H. Lu, and L. Chen, "Effects of overconsolidation ratio on tunnel responses due to overlying basement excavation in clay," *Tunnelling and Underground Space Technology*, vol. 97, article 103247, 2020.

[11] M. Doležalová, "Tunnel complex unloaded by a deep excavation," *Computers and Geotechnics*, vol. 28, no. 6-7, pp. 469–493, 2001.

[12] Z. F. Hu, Z. Q. Yue, J. Zhou, and L. G. Tham, "Design and construction of a deep excavation in soft soils adjacent to the shanghai metro tunnels," *Canadian Geotechnical Journal*, vol. 40, no. 5, pp. 933–948, 2003.

[13] X. Huang, H. F. Schweiger, and H. W. Huang, "Influence of deep excavations on nearby existing tunnels," *International Journal of Geomechanics*, vol. 13, no. 2, pp. 170–180, 2013.

[14] R. Liang, W. Wu, F. Yu, G. Jiang, and J. Liu, "Simplified method for evaluating shield tunnel deformation due to adjacent excavation," *Tunnelling and Underground Space Technology*, vol. 71, pp. 94–105, 2018.

[15] H. L. Liu, P. Li, and J. Y. Liu, "Numerical investigation of underlying tunnel heave during a new tunnel construction," *Tunnelling and Underground Space Technology*, vol. 26, no. 2, pp. 276–283, 2011.

[16] C. W. W. Ng, H. S. Sun, G. H. Lei, J. W. Shi, and D. Mašín, "Ability of three different soil constitutive models to predict a tunnel's response to basement excavation," *Canadian Geotechnical Journal*, vol. 52, no. 11, pp. 1685–1698, 2015.

[17] J. S. Sharma, A. M. Hefny, J. Zhao, and C. W. Chan, "Effect of large excavation on deformation of adjacent MRT tunnels," *Tunnelling and Underground Space Technology*, vol. 16, no. 2, pp. 93–98, 2001.

[18] J. W. Shi, C. W. W. Ng, and Y. H. Chen, "Three-dimensional numerical parametric study of the influence of basement excavation on existing tunnel," *Computers and Geotechnics*, vol. 63, pp. 146–158, 2015.

[19] J. W. Shi, Z. Z. Fu, and W. L. Guo, "Investigation of geometric effects on three-dimensional tunnel deformation mechanisms due to basement excavation," *Computers and Geotechnics*, vol. 106, pp. 108–116, 2019.

[20] H. S. Sun, Y. D. Chen, J. H. Zhang, and T. S. Kuang, "Analytical investigation of tunnel deformation caused by circular foundation pit excavation," *Computers and Geotechnics*, vol. 106, pp. 193–198, 2019.

[21] H. S. Sun and W. B. Sun, "Effect of soil reinforcement on tunnel deformation as a result of stress relief," *Applied Sciences*, vol. 9, no. 7, p. 1420, 2019.

[22] H. S. Sun, L. W. Wang, S. W. Chen, H. W. Deng, and J. H. Zhang, "A precise prediction of tunnel deformation caused by circular foundation pit excavation," *Applied Sciences*, vol. 9, no. 11, p. 2275, 2019.

[23] H. S. Sun, L. W. Wang, Y. D. Chen, Y. Dong, J. H. Zhang, and W. B. Sun, "Nonlinear analysis of tunnel deformation and mechanisms of stress transfer caused by basement excavation," *Soil Mechanics and Foundation Engineering*, vol. 55, no. 5, pp. 298–304, 2018.

[24] J. F. Zhang, J. J. Chen, J. H. Wang, and Y. F. Zhu, "Prediction of tunnel displacement induced by adjacent excavation in soft soil," *Tunnelling and Underground Space Technology*, vol. 36, pp. 24–33, 2013.

[25] Z. Zhang, M. Huang, and W. Wang, "Evaluation of deformation response for adjacent tunnels due to soil unloading in excavation engineering," *Tunnelling and Underground Space Technology*, vol. 38, pp. 244–253, 2013.

[26] Z. Zhang, M. Zhang, and Q. Zhao, "A simplified analysis for deformation behavior of buried pipelines considering disturbance effects of underground excavation in soft clays," *Arabian Journal of Geosciences*, vol. 8, no. 10, pp. 7771–7785, 2015.

[27] G. Zheng and S. W. Wei, "Numerical analyses of influence of overlying pit excavation on existing tunnels," *Journal of*

Central South University of Technology, vol. 15, Supplementary 2, pp. 69–75, 2008.

[28] Y. Xue, P. G. Ranjith, F. Dang et al., "Analysis of deformation, permeability and energy evolution characteristics of coal mass around borehole after excavation," *Natural Resources Research*, vol. 29, no. 5, pp. 3159–3177, 2020.

[29] Y. Xue, T. Teng, F. Dang, Z. Ma, S. Wang, and H. Xue, "Productivity analysis of fractured wells in reservoir of hydrogen and carbon based on dual-porosity medium model," *International Journal of Hydrogen Energy*, vol. 45, no. 39, pp. 20240–20249, 2020.

[30] D. Mašín and I. Herle, "State boundary surface of a hypoplastic model for clays," *Computers and Geotechnics*, vol. 32, no. 6, pp. 400–410, 2005.

[31] D. Mašín, "A hypoplastic constitutive model for clays," *International Journal for Numerical and Analytical Methods in Geomechanics*, vol. 29, no. 4, pp. 311–336, 2005.

[32] A. Niemunis and I. Herle, "Hypoplastic model for cohesionless soils with elastic strain range," *Mechanics of Cohesive-frictional Materials*, vol. 2, no. 4, pp. 279–299, 1997.

[33] J. Najser, D. Mašin, and J. Boháč, "Numerical modelling of lumpy clay landfill," *International Journal for Numerical and Analytical Methods in Geomechanics*, vol. 36, no. 1, pp. 17–35, 2012.

[34] D. Mašín, "A hypoplastic constitutive model for clays with meta-stable structure," *Canadian Geotechnical Journal*, vol. 44, no. 3, pp. 363–375, 2007.

[35] ABAQUS, Inc, *ABAQUS User's and Theory Manuals; Version 6.17*, ABAQUS, Inc., Providence Rhode Island, RI, USA, 2017.

[36] D. Mašín, *Development and applications of hypoplastic constitutive models [Ph.D. thesis]*, Charles University in Prague, Zech Republic, 2009.

[37] BD, *Practice Note for Authorized Persons APP-24. Technical Notes for Guidance in Assessing the Effects of Civil Engineering Construction/Building Development on Railway Structures and Operations*, Building Department of the Government of HKSAR (BD), Hongkong, China, 2009.

[38] G. W. Clough and M. W. Reed, "Measured behavior of braced wall in very soft clay," *Journal of Geotechnical Engineering*, vol. 110, no. 1, pp. 1–19, 1984.

[39] R. J. Finno, D. K. Atmatzidis, and S. B. Perkins, "Observed performance of a deep excavation in clay," *Journal of Geotechnical Engineering*, vol. 115, no. 8, pp. 1045–1064, 1989.

[40] BTS, *Specification for Tunnelling*, Thomas Telford, London, UK, British Tunnelling Society (BTS), 2000.

Hindawi
Geofluids
Volume 2021, Article ID 6671982, 13 pages
https://doi.org/10.1155/2021/6671982

Research Article

Unsteady Approximate Model of Grouting in Fractured Channels Based on Bingham Fluid

Bo Ren, Lianguo Wang, Hao Fan, Ke Ding, Kai Wang, and Chongyang Jiang

State Key Laboratory for Geomechanics and Deep Underground Engineering, China University of Mining and Technology, Xuzhou, Jiangsu 221116, China

Correspondence should be addressed to Lianguo Wang; cumt_lgwang@163.com

Received 1 December 2020; Revised 17 January 2021; Accepted 16 March 2021; Published 28 March 2021

Academic Editor: Jia Liu

It is of great significance for the improvement of grouting technology and engineering practice to master the flow law of grout between parallel plates. However, the traditional calculation model ignores the influence of the inertia term and only considers the stable flow of slurry, so there is a big error in some cases. It is difficult to solve the motion equation of a Bingham fluid considering the inertial force term directly. Combined with the relationship between the steady-state flow equation of a Bingham fluid and a Newtonian fluid, the approximate unsteady-state flow equation of a Bingham fluid suitable for describing slurry flow is constructed. In addition, according to the unsteady flow equation, the relationship between the time and distance of slurry flow in parallel plate fractures can be obtained, and the simplified conditions of the Bingham fluid unsteady flow model are given. Finally, the accuracy of the flow equations and the simplified conditions are verified by experiments and numerical calculations.

1. Introduction

Grouting technology is widely used in many fields such as mining, tunneling, landfilling of municipal solid waste, storage of nuclear waste, and development and utilization of underground space. In coal mining, a soft rock roadway is often strengthened by grouting to prevent roadway damage or large deformation during roadway excavation [1–4]. Bad geological bodies such as lava and faults will have many adverse effects on the construction during the tunneling process. Grouting into the faults can increase the integrity of the rock mass and ensure safe and efficient construction [5–7]. Landfill of municipal solid waste [8, 9] requires grouting and antiseepage treatment in the buried pits that have been dug in advance to avoid water and soil pollution caused by toxic gas and liquid penetration. In the same way, nuclear waste storage [10, 11] also needs to consider the environmental impact of radioactive materials and consider strengthening the surrounding areas of the rock to avoid irreparable damage. In the long run, the scope of human activities is becoming wider and wider, and the use of underground space is gradually being put on the agenda. The use of underground space will certainly use grouting technology. So far, the method of grouting is more environmentally friendly, economical, and effective than other methods.

However, in a grouting project, the important construction parameters such as slurry water-cement ratio, grouting pressure, and time are often judged by experience. Studying the flow of slurry in the fractured rock mass can guide on-site grouting and can aid in properly designing the grouting parameters [12]. A grouting project is of great significance. Therefore, it is becoming more and more important to study the characteristics of the slurry itself and the flow of the slurry in the rock mass [13].

Fracture is the medium into which the slurry flows in a rock mass, and the simplest type is the smooth parallel plate fracture. By studying the parallel plate fracture, the flow law of the slurry in the rock mass can be well grasped, so some scholars have studied this problem and have obtained a series of results. Among them, the cubic law [14–16] has been widely used because of its accuracy and simplicity. Through theoretical derivation, it is found that the cubic law can be obtained from the Navier-Stokes (N-S) equation [17, 18]. To be precise, the cubic law is the theoretical solution of an incompressible Newtonian fluid doing steady laminar flow in smooth parallel fractures. However, grouting materials are mostly non-Newtonian fluids. Therefore, more flow equations have been proposed. Wereley and Pang [19] proposed a flow equation for the steady laminar flow of an incompressible Bingham fluid in smooth parallel fractures. Yan and Koplik [20] derived the flow equation of the steady laminar flow of an incompressible power law fluid in a smooth parallel fracture. Zou et al. [21] also obtained the flow equation of a Herschel-Bulkley (H-B) fluid which is more general.

The above models all have the same disadvantage, that is, they ignore the effect of inertial terms. In some cases, there is a large calculation error. In addition, at present, many grouting materials have a very short solidification time, ranging from a few seconds to a few tens of seconds, and the viscosity changes significantly with time, so it is necessary to take the inertial term into account in the equation derivation. There is a "flow core" when a Bingham fluid flows. Therefore, the unsteady flow equation of a Bingham fluid needs to be divided into two sections. The equation is complicated and difficult to solve. In this paper, the unsteady-state flow model between parallel plates of a Newtonian fluid considering inertial force is first derived. Combined with the relationship between the steady-state solution of a Bingham fluid and a Newtonian fluid, the approximate unsteady-state flow equation of a Bingham fluid suitable for describing slurry flow is constructed and the approximate solution is verified by numerical calculation. Then, based on the unsteady-state flow model, the calculation method of the flow distance of slurry in the fractures of smooth parallel plates is obtained, and the simplified condition of a Bingham fluid unsteady-state flow model is given. Finally, different models are used to calculate the mud diffusion distance under different conditions, and the correctness of the simplified conditions is also proven.

2. Theoretical Model

2.1. Steady-State Flow Model of Slurry in Fracture. Firstly, the steady-state flow equation is derived based on 2D N-S equations, and the coordinate system is shown in Figure 1. The derivation process is based on the following assumptions:

(1) The flow state of slurry is laminar flow

(2) The slurry is incompressible

(3) The grouting process has reached a stable state

(4) The property of slurry does not change during grouting

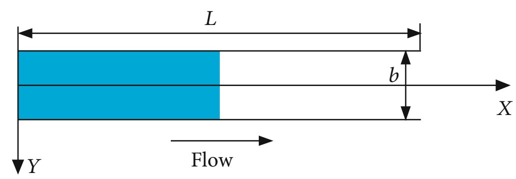

FIGURE 1: Diagram of a parallel plate fracture channel.

The differential equation of viscous fluid motion is expressed by stress:

$$\begin{cases} \dfrac{\partial u}{\partial t} + \dfrac{u\partial u}{\partial x} + \dfrac{v\partial u}{\partial y} = f_x + \dfrac{1}{\rho}\left(\dfrac{\partial p_{xx}}{\partial x} + \dfrac{\partial \tau_{xy}}{\partial y}\right), \\ \dfrac{\partial v}{\partial t} + \dfrac{u\partial v}{\partial x} + \dfrac{v\partial v}{\partial y} = f_y + \dfrac{1}{\rho}\left(\dfrac{\partial p_{yy}}{\partial y} + \dfrac{\partial \tau_{yx}}{\partial x}\right). \end{cases} \quad (1)$$

The constitutive equation of a Newtonian fluid is shown as follows:

$$\begin{pmatrix} p_{xx} & \tau_{xy} \\ \tau_{yx} & p_{yy} \end{pmatrix} = \mu \begin{pmatrix} 2\dfrac{\partial u}{\partial x} & \dfrac{\partial u}{\partial y} + \dfrac{\partial v}{\partial x} \\ \dfrac{\partial v}{\partial x} + \dfrac{\partial u}{\partial y} & 2\dfrac{\partial v}{\partial y} \end{pmatrix} - \begin{pmatrix} p & 0 \\ 0 & p \end{pmatrix}. \quad (2)$$

The continuity equation for incompressible fluids is shown as follows:

$$\frac{\partial u}{\partial x} + \frac{\partial v}{\partial y} = 0. \quad (3)$$

Bring equation (2) and equation (3) into equation (1) to obtain the N-S equation [22], and we have

$$\begin{cases} \dfrac{\partial u}{\partial t} + \dfrac{u\partial u}{\partial x} + \dfrac{v\partial u}{\partial y} = f_x - \dfrac{1}{\rho}\dfrac{\partial p}{\partial x} + \dfrac{\mu}{\rho}\left(\dfrac{\partial^2 u}{\partial x^2} + \dfrac{\partial^2 u}{\partial y^2}\right), \\ \dfrac{\partial v}{\partial t} + \dfrac{u\partial v}{\partial x} + \dfrac{v\partial v}{\partial y} = f_y + \dfrac{1}{\rho}\dfrac{\partial p}{\partial y} + \dfrac{\mu}{\rho}\left(\dfrac{\partial^2 v}{\partial x^2} + \dfrac{\partial^2 v}{\partial y^2}\right). \end{cases} \quad (4)$$

According to the four hypotheses mentioned above, we can get

$$\begin{aligned} v &= 0, \\ \frac{\partial v}{\partial x} &= \frac{\partial v}{\partial y} = 0, \\ \frac{\partial u}{\partial x} &= 0. \end{aligned} \quad (5)$$

Therefore, the two-dimensional problem is simplified into a one-dimensional problem. The definite condition that makes it easy to get the problem is shown as follows:

$$\begin{gathered}\mu\frac{\partial^2 u}{\partial y^2}+\frac{\Delta P}{L}=0,\\ \left.\frac{\partial u}{\partial y}\right|_{y=0}=0,\\ u|_{y=\pm(b/2)}=0.\end{gathered}\tag{6}$$

The velocity distribution equation can be solved as follows:

$$u=\frac{b^2}{8\mu}\frac{\Delta P}{L}\left[1-\left(\frac{2y}{b}\right)^2\right].\tag{7}$$

Integral along the Y direction to obtain the average velocity equation, we have

$$\bar{u}=\frac{1}{b}\int_{-(b/2)}^{(b/2)}udy=-\frac{b^2}{12\mu}\frac{\Delta P}{L}.\tag{8}$$

Similarly, equations of the average velocity of a non-Newtonian fluid can be obtained. The average velocity equation of the steady flow of a Bingham fluid is shown as follows:

$$\bar{u}=\frac{2}{b}\int_{y_0}^{(b/2)}udy+b_0u|_{y=y_0}=-\frac{b^2}{12\mu}\frac{\Delta P}{L}\left(1-\frac{b_0}{b}\right)^2\left(1+\frac{1}{2}\frac{b_0}{b}\right),\tag{9}$$

where $b_0=-(2\tau_0 L/\Delta p)$, which is the width of the "flow core," like Figure 2.

Similarly, for a power law fluid, when we calculate the steady-state flow equation of a power law fluid, we only need to replace the constitutive equation of the fluid [4, 20, 23]:

$$\begin{gathered}\tau=K\dot{\gamma}^n,\\ \dot{\gamma}=\frac{1}{2}\sqrt{4\left(\frac{\partial u}{\partial x}\right)^2+2\left(\frac{\partial u}{\partial y}+\frac{\partial v}{\partial x}\right)^2+4\left(\frac{\partial v}{\partial y}\right)^2}.\end{gathered}\tag{10}$$

And then we can get,

$$\begin{gathered}K\frac{\partial}{\partial y}\left(\frac{\partial u}{\partial y}\right)^n+\frac{\Delta P}{L}=0,\\ \left.\frac{\partial u}{\partial y}\right|_{y=0}=0,\\ u|_{y=\pm(b/2)}=0.\end{gathered}\tag{11}$$

It is not difficult to acquire the steady-state average velocity equation of a power law fluid:

$$\bar{u}=-\frac{n}{4n+2}\left(\frac{\Delta P}{2KL}\right)^{(1/n)}b^{(n+1/n)}.\tag{12}$$

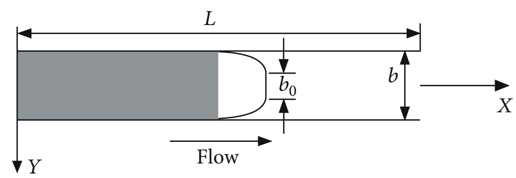

Figure 2: Velocity distribution of a Bingham fluid in a parallel plate fracture channel.

It is not easy to directly calculate the flow equation of an H-B fluid by the N-S equation. Therefore, based on the relationship between this model and the constitutive equation of the model mentioned above, the flow equation of an H-B fluid is obtained by analogy. The average velocity equation obtained is consistent with the research results of other scholars [21, 24].

$$\bar{u}=-\frac{n}{4n+2}\left(\frac{\Delta P}{2KL}\right)^{(1/n)}b^{(n+1/n)}\left(1-\frac{b_0}{b}\right)^{(n+1/n)}\left(1+\frac{n}{n+1}\frac{b_0}{b}\right).\tag{13}$$

2.2. Unsteady Flow Model of Slurry in Fracture. The above formula is based on the assumption of stable flow. Next, we only keep assumptions (1), (2), and (4) to further derive the unsteady flow equation. The influence of inertia force must be taken into account in the establishment of unsteady-state equations. The first is the unsteady flow solution based on a Newtonian fluid:

$$\begin{gathered}\frac{\partial u}{\partial t}-\frac{\mu}{\rho}\frac{\partial^2 u}{\partial y^2}=\frac{\Delta P}{\rho L},\\ u(0,y)=u_0(y),\\ \frac{\partial u}{\partial y}(t,0)=0,\\ u\left(t,-\frac{b}{2}\right)=u\left(t,\frac{b}{2}\right)=0.\end{gathered}\tag{14}$$

Solving equation (14) is a pure mathematical process. First of all, it needs to be divided into two subproblems, and then the solutions of the two subproblems are superposed to get the original solution.

Subproblem 1.

$$\begin{gathered}\frac{\partial u}{\partial t}-\frac{\mu}{\rho}\frac{\partial^2 u}{\partial y^2}=0,\\ u(0,y)=u_0(y),\\ \frac{\partial u}{\partial y}(t,0)=0,\\ u\left(t,-\frac{b}{2}\right)=u\left(t,\frac{b}{2}\right)=0.\end{gathered}\tag{15}$$

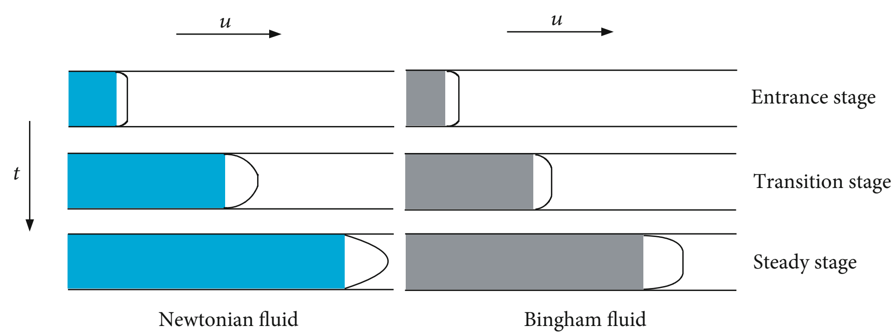

FIGURE 3: Distribution diagram of velocity in the entrance stage, the transition stage, and the steady stage when a Newtonian fluid and a Bingham fluid flow in fractures.

Subproblem 2.

$$\begin{gathered}\frac{\partial u}{\partial t}-\frac{\mu}{\rho}\frac{\partial^2 u}{\partial y^2}=\frac{\Delta P}{\rho L},\\ u(0,y)=0,\\ \frac{\partial u}{\partial y}(t,0)=0,\\ u\left(t,-\frac{b}{2}\right)=u\left(t,\frac{b}{2}\right)=0.\end{gathered}\tag{16}$$

The solution of Subproblem 1 is as follows:

$$u_1(y,t)=\sum_{k=1}^{\infty}a_k e^{-(k\pi/b)^2(\mu/\rho)t}\sin\left(\frac{k\pi}{b}y+\frac{k\pi}{2}\right),\quad (k=1,2,\cdots),\tag{17}$$

where $a_k=(2/b)\int_{-(b/2)}^{(b/2)}u_0(y)\sin((k\pi/b)y+(k\pi/2))dx$.

The solution of Subproblem 2 is as follows:

$$u_2(y,t)=\frac{b^2\Delta P}{12\mu L}\sum_{k=1}^{\infty}f_Y(y)f_T(t),\quad (k=1,2,\cdots).\tag{18}$$

$$\begin{gathered}f_Y(y)=24\left(\frac{1}{k\pi}\right)^3\left[(-1)^{k+1}+1\right]\sin\left(\frac{k\pi}{b}y+\frac{k\pi}{2}\right),\\ f_T(t)=1-e^{-(k\pi/b)^2(\mu/\rho)t}.\end{gathered}\tag{19}$$

When the initial velocity $u_0(y)=0$ in Subproblem 1, the solution of Subproblem 1 is always equal to 0. Therefore, the solution of the original problem is equal to the solution of Subproblem 2.

$$u_{new}(y,t)=u_2(y,t).\tag{20}$$

According to equation (18), the unsteady solution of a Newtonian fluid flowing in parallel plates can be divided into three terms: the first term is the average velocity term representing the magnitude of the velocity, the second term is the velocity distribution term related to the coordinates, and the third is the time-dependent attenuation term.

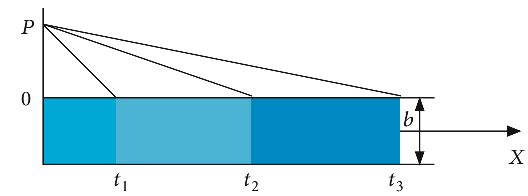

FIGURE 4: Pressure distribution diagram during grouting in a dry fracture.

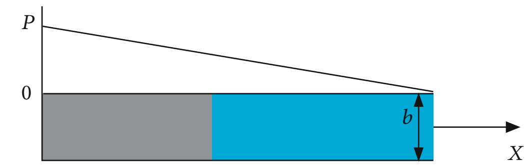

FIGURE 5: Schematic diagram of pressure distribution when grouting in water-saturated fractures.

TABLE 1: Fracture parameters and slurry parameters used in calculation.

Injection pressure (kPa)	Length (m)	Aperture (m)	Density (kg/m^3)	Plastic viscosity (Pa · s)	Yield stress (Pa)
10	0.1	0.001	1540	0.014	0.94

It is assumed that the time for a Newtonian fluid and a Bingham fluid to reach steady flow from 0 is the same. The unsteady flow equation of a Bingham fluid can be obtained by combining the relationship between the steady flow velocity equation of a Bingham fluid [25] and the steady solution of a Newtonian runny nose (equation (7)).

$$u_{bin}(y,t)=u_{new}(y,t)\cdot f_{trans1}(y),\tag{21}$$

$$\begin{gathered}f_{trans1}(y)=\frac{1-(2y/b)^2-2(b_0/b)(1-(2|y|/b))}{1-(2y/b)^2},\\ \left(\frac{b_0}{2}<|y|<\frac{b}{2}\right).\end{gathered}\tag{22}$$

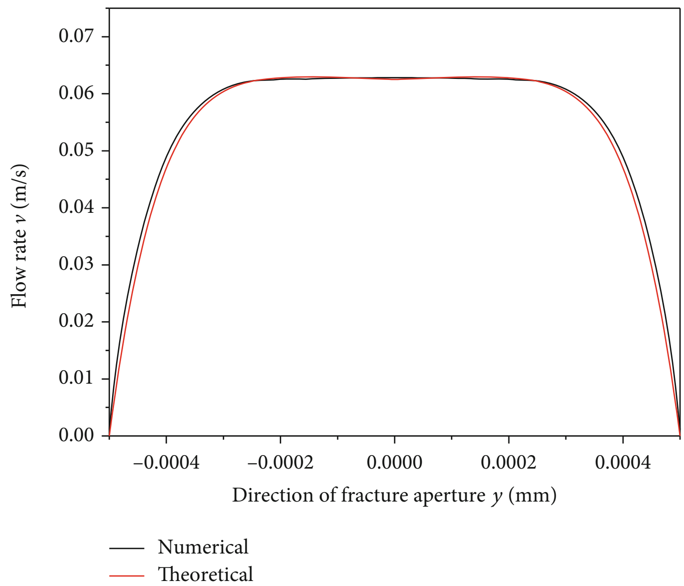

(a) $t = 0.001$ s

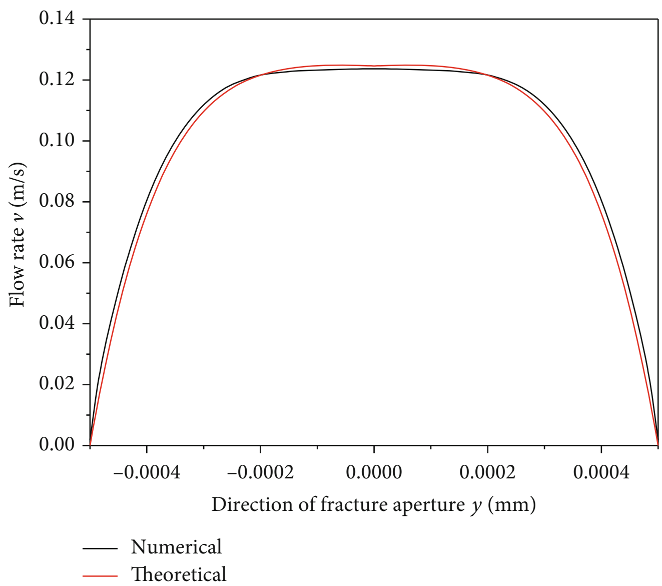

(b) $t = 0.002$ s

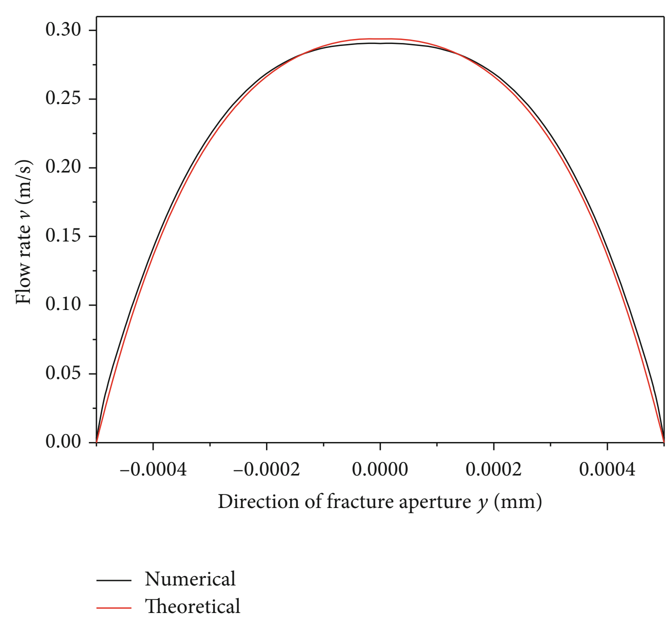

(c) $t = 0.005$ s

Figure 6: Continued.

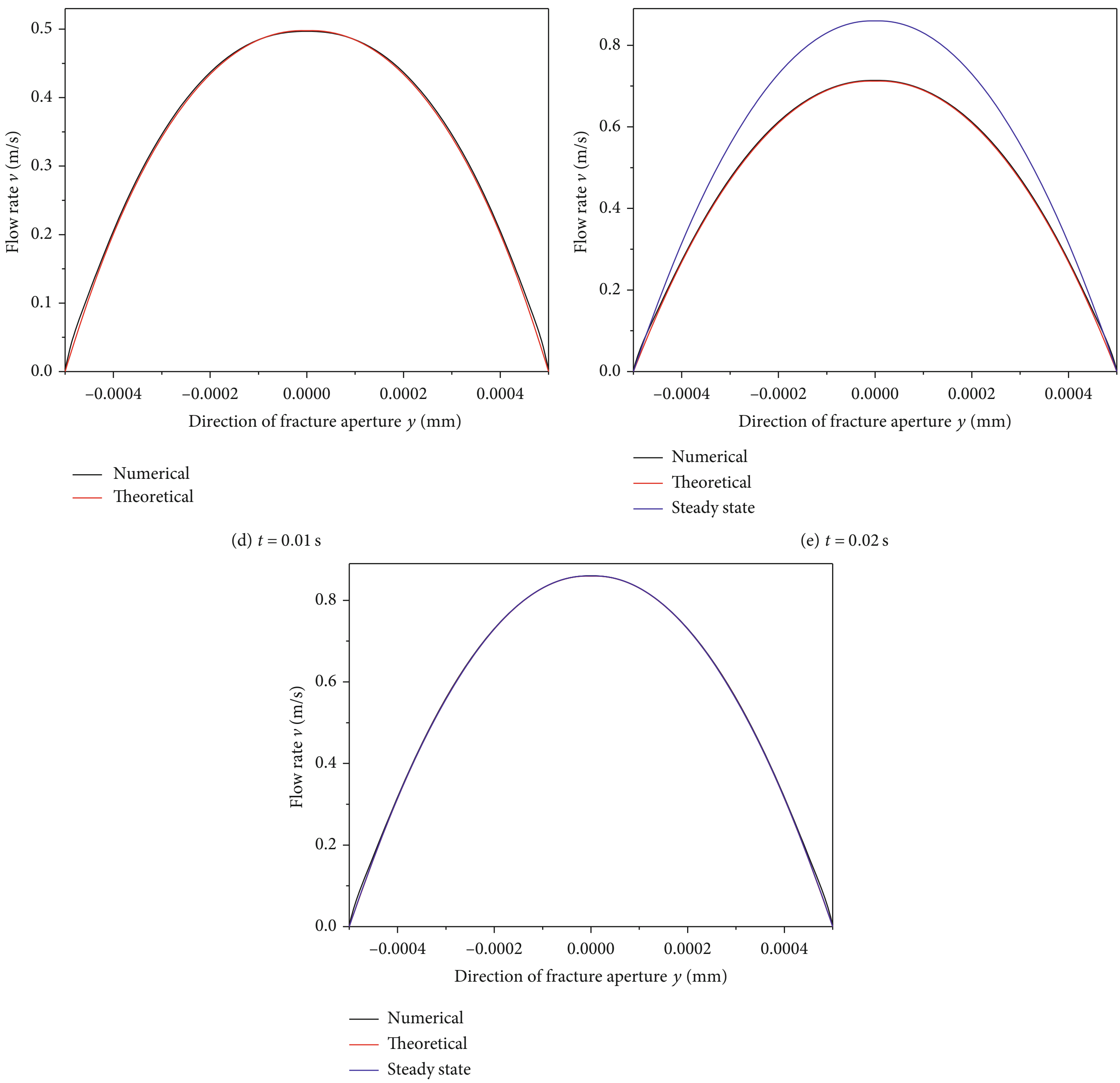

(d) $t = 0.01$ s

(e) $t = 0.02$ s

(f) $t = 0.1$ s

Figure 6: Relationship between velocity distribution curve and time when slurry flows in fractures.

Through the unsteady solution of a Newtonian fluid and a Bingham fluid, we can get the fluid flow process in a parallel plate, which will go through the entrance stage, transition stage, and stable stage. The entrance stage is located at the entrance of the parallel plate, which is generally very short in length. In this stage, the boundary effect has not affected the whole flow layer, even for a Newtonian fluid; its velocity distribution will show a similar shape of "flow core." In the transition stage, the boundary effect has affected the whole flow layer, but the influence of inertial force has not disappeared, and the velocity distribution is still changing. When it comes to the stable stage, the influence of the inertial term has disappeared, and the fluid enters a stable flow state (see Figure 3).

3. Model Application and Simplification

3.1. Model Application. The derivation of the unsteady flow solution of a Bingham fluid is not only to understand the flow pattern of the slurry in the fissure, but more importantly to obtain the parameters or methods that are of great significance to grouting engineering.

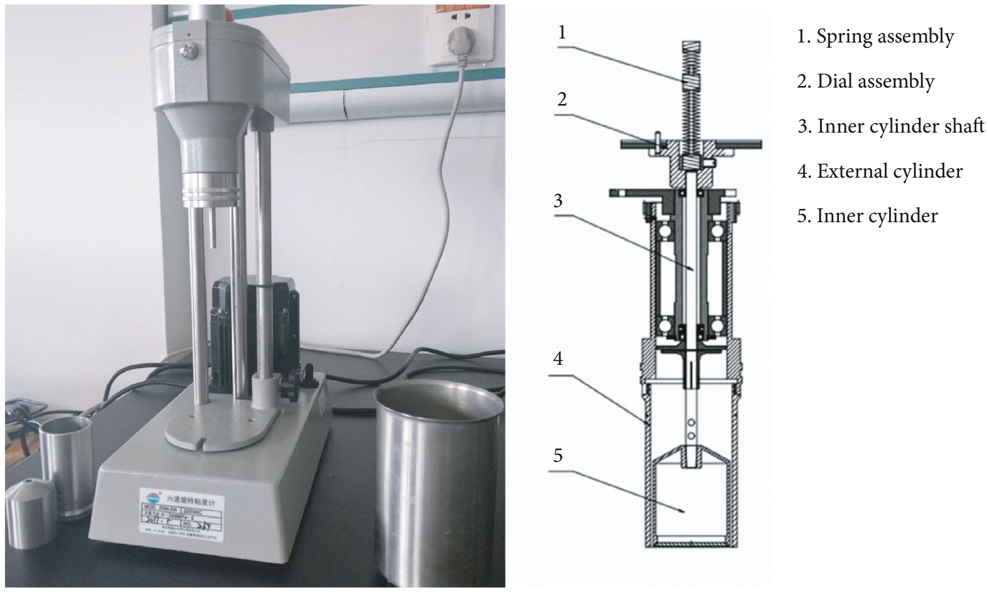

Figure 7: ZNN-D6 viscometer physical figure and schematic diagram of key parts.

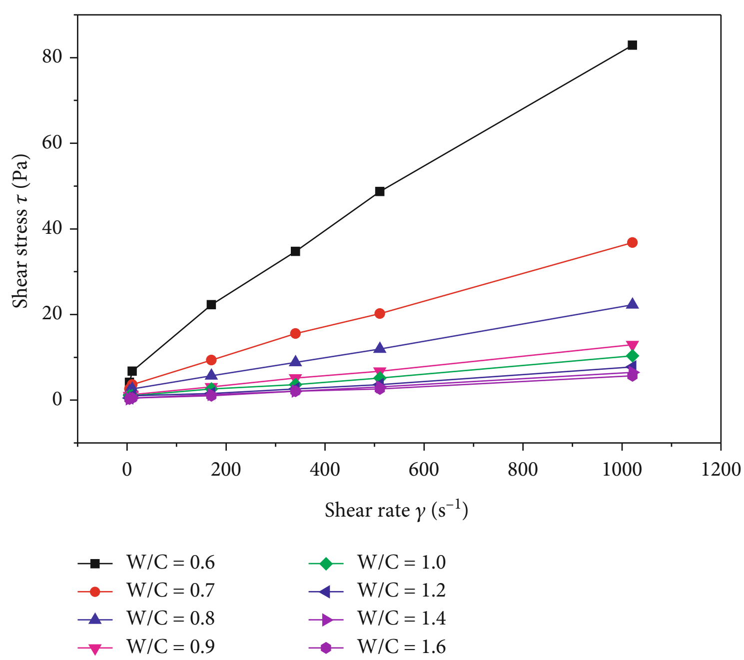

Figure 8: Rheological curves of ordinary Portland cement slurry with different water-cement ratios.

According to $b_0 = -(2\tau_0 L/\Delta p)$, when $b_0 = b$, the slurry will stop flowing. At this time, the critical pressure gradient is the starting pressure gradient of the slurry, and the critical length is the farthest distance that the slurry can reach in the fracture.

$$\left(\frac{\Delta p}{L}\right)_{cr} = -\frac{2\tau_0}{b}, \tag{23}$$

$$L_{\max} = -\frac{\Delta p b}{2\tau_0}. \tag{24}$$

In addition, through further processing of the unsteady-state equation, the corresponding relationship between grouting time and slurry flow distance can be obtained. Also based on Newtonian fluids, equation (18) is integrated to obtain the average velocity:

$$\bar{u}_{\text{new}} = \frac{1}{b}\int_{-(b/2)}^{(b/2)} u(y,t)dy = \frac{2b^2\Delta P}{\mu l}\sum_{k=1}^{\infty}\left(\frac{1}{k\pi}\right)^4\left[(-1)^{k+1}+1\right]^2 f_T(t). \tag{25}$$

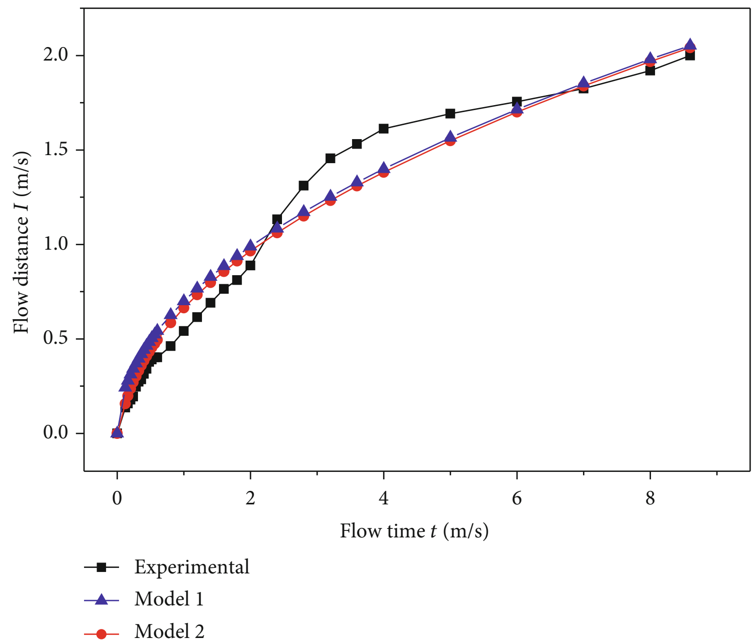

Figure 9: The relationship between flow time and flow distance when water flows in a fracture. Model 1 is the result of the iterative calculation of equation (8), and model 2 is the result of direct calculation using equation (26).

Since $\bar{u} = (dI/dt)$ [13], replace the left side of equation (25), which can be obtained after an integral operation:

$$I_{\text{new}}^2 = \frac{4b^2 \Delta P}{\mu} \sum_{k=1}^{\infty} \left(\frac{1}{k\pi}\right)^4 \left[(-1)^{k+1} + 1\right]^2 F_T(t), \tag{26}$$

$$F_T(t) = t + \left(\frac{b}{k\pi}\right)^2 \frac{\rho}{\mu} e^{-(k\pi/b)^2 (\mu/\rho) t} - \left(\frac{b}{k\pi}\right)^2 \frac{\rho}{\mu}. \tag{27}$$

According to the previous assumption, the average velocity of a Bingham fluid in the fracture is as follows:

$$\begin{aligned} \bar{u}_{\text{bin}} &= f_{\text{trans2}} \bar{u}_{\text{new}}, \\ f_{\text{trans2}} &= \left(1 - \frac{b_0}{b}\right)^2 \left(1 + \frac{1}{2}\frac{b_0}{b}\right). \end{aligned} \tag{28}$$

The relationship between time and distance of a Bingham flow in fractures is as follows:

$$I_{\text{bin}}{}^2 = f_{\text{trans2}} \frac{4b^2 \Delta P}{\mu} \sum_{k=1}^{\infty} \left(\frac{1}{k\pi}\right)^4 \left[(-1)^{k+1} + 1\right]^2 F_T(t). \tag{29}$$

In the differential calculation, approximate processing is also adopted. When integrating the flow distance I, ignoring b_0 will also change with I. Therefore, in the actual calculation, it is necessary to correct the value of b_0 by using an iterative method.

Although the relationship between the slurry flow time and the distance in the fracture has been obtained, it is necessary to distinguish fractures before calculation. Here, fractures are divided into dry fracture and water-saturated fracture according to whether there is water in the fracture before grouting. Different types of fractures use slightly different equations to predict slurry diffusion.

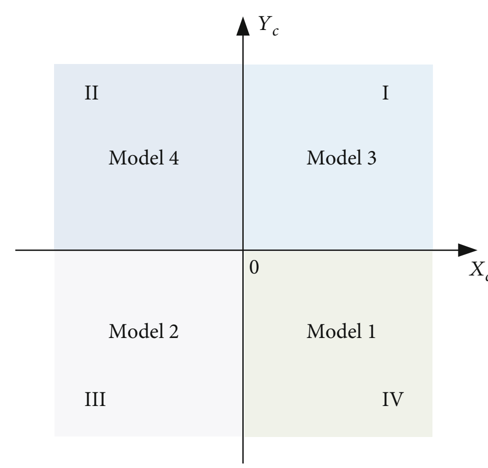

Figure 10: Schematic diagram of discrimination space.

First of all, for the dry fracture, it is considered that there is only air inside the fracture before grouting, and the air has high permeability and compressibility, so the influence of air on the slurry flow is not considered here, that is, the gas-liquid two-phase flow is not considered. The traditional method is to use the steady-state flow equation of slurry for iterative calculation, but at the initial stage of slurry diffusion, the diffusion distance tends to zero, that is, the pressure gradient tends to infinity (see Figure 4), and the calculated velocity is also very large, so it is difficult to choose the appropriate initial iteration value. One method is to use reverse iteration

Table 2: Calculation results of four models for slurry flow distance under different conditions.

Aperture, b (mm)	Pressure, P (MPa)	Time, t (s)	Diffusion distance, I (m) Model 1	Model 2	Model 3	Model 4
0.1	0.1	0.01	0.0094	0.0093	0.0093	0.0093
0.1	0.1	1	0.0937	0.0937	0.0908	0.0908
0.1	0.1	100	0.9366	0.9366	0.6990	0.6990
0.1	1	0.01	0.0296	0.0295	0.0296	0.0295
0.1	1	1	0.2962	0.2962	0.2933	0.2933
0.1	1	100	2.9617	2.9617	2.6899	2.6899
0.1	10	0.01	0.0937	0.0933	0.0936	0.0932
0.1	10	1	0.9366	0.9365	0.9337	0.9337
0.1	10	100	9.3659	9.3658	9.0836	9.0835
1	0.1	0.01	0.0937	0.0606	0.0934	0.0605
1	0.1	1	0.9366	0.9326	0.9084	0.9046
1	0.1	100	9.3659	9.3655	6.990	6.9898
1	1	0.01	0.2962	0.1916	0.2959	0.1914
1	1	1	2.9617	2.9492	2.9332	2.9209
1	1	100	29.6174	29.6162	26.8995	26.8984
1	10	0.01	0.9366	0.6058	0.9363	0.6057
1	10	1	9.3659	9.3263	9.3372	9.2979
1	10	100	93.6586	93.6546	90.8355	90.8318
10	0.1	0.01	0.9366	0.0774	0.9337	0.0774
10	0.1	1	9.3659	6.0578	9.0836	5.9391
10	0.1	100	93.6586	93.2633	69.9001	69.6849
10	1	0.01	2.9617	0.2447	2.9589	0.2447
10	1	1	29.6174	19.1566	29.3320	19.0370
10	1	100	296.1744	294.9246	268.9949	267.9673
10	10	0.01	9.3659	0.7739	9.3630	0.7739
10	10	1	93.6586	60.5785	93.3722	60.4586
10	10	100	936.5858	932.6333	908.3553	904.6386

[26]. Take cubic law as an example, the iteration formula is as follows:

$$I_n = I_{n+1} - \bar{u}_{n+1}(t_{n+1} - t_n),$$
$$\bar{u}_{n+1} = \frac{\Delta P b^2}{12\mu I_{n+1}}. \tag{30}$$

When the fracture water is saturated, it is assumed that both the slurry and the water are incompressible. Since the pressure ladder will not decrease with the increase of the diffusion distance (see Figure 5), the diffusion distance of the slurry can be directly calculated as follows:

$$I_{\text{bin}} = \int_0^t \bar{u}_{\text{bin}}(\tau)d\tau = f_{\text{trans2}} \frac{2b^2 \Delta P}{\mu L} \sum_{k=1}^{\infty} \left(\frac{1}{k\pi}\right)^4 \left[(-1)^{k+1} + 1\right]^2 F_T(t). \tag{31}$$

3.2. Simplified Conditions. It can be seen from equation (19) that the attenuation coefficient in the time-dependent attenuation term is inversely proportional to the square of fracture opening, inversely proportional to the density of slurry, and directly proportional to the viscosity of slurry. The development trend of grouting materials is that the viscosity of slurry is decreasing and the density is increasing, which leads to an increase in the time it takes for the slurry to reach steady flow. Especially for the fractures with a large opening, the influence of inertia force cannot be ignored, and the grouting time and flow distance calculated by the steady-state formula are no longer applicable. According to the formula calculation, for the centimeter fracture, it takes nearly 60 s for the slurry to reach the stable state. In the process of coal mining, the grouting time often used for roadway reinforcement is about 200-300 s, which also shows that the influence of inertia force cannot be ignored.

When using the Bingham fluid unsteady flow equation to calculate the flow distance of slurry in the fracture, the relative error is ensured to be less than 5%, and the following simplified condition is obtained:

$$\frac{\mu t}{\rho b^2} \geq 0.3035. \tag{32}$$

Table 3: Applicability of the first three models.

Aperture, b (mm)	Pressure, P (MPa)	Time, t (s)	Relative error Model 1	Model 2	Model 3
0.1	0.1	0.01	√	√	√
0.1	0.1	1	√	√	√
0.1	0.1	100	×	×	√
0.1	1	0.01	√	√	√
0.1	1	1	√	√	√
0.1	1	100	×	×	√
0.1	10	0.01	√	√	√
0.1	10	1	√	√	√
0.1	10	100	√	√	√
1	0.1	0.01	×	√	×
1	0.1	1	√	√	√
1	0.1	100	×	×	√
1	1	0.01	×	√	×
1	1	1	√	√	√
1	1	100	×	×	√
1	10	0.01	×	√	×
1	10	1	√	√	√
1	10	100	√	√	√
10	0.1	0.01	×	√	×
10	0.1	1	×	√	×
10	0.1	100	×	×	√
10	1	0.01	×	√	×
10	1	1	×	√	×
10	1	100	×	×	√
10	10	0.01	×	√	×
10	10	1	×	√	×
10	10	100	√	√	√

Note: if the relative error is less than 5%, it is √, otherwise it is ×.

The time-dependent terms of the non-steady-state model quickly decay to 0, and they can be replaced by those of the steady-state model:

$$\tau_0\sqrt{\frac{t}{-3\mu\Delta P}} \leq 0.062. \tag{33}$$

The size of the "flow core" is negligible with respect to the fracture opening, so the Newtonian fluid model can be used instead of the Bingham fluid model.

4. Results and Verification

4.1. Numerical Simulation of Bingham Fluid Flow in Fracture. The numerical calculation results are compared with the calculation results of equation (21). The fracture and slurry parameters selected here [27] are shown in Table 1.

According to the calculation results (see Figure 6), firstly, the approximate solution of the unsteady flow of a Bingham fluid between parallel plates obtained in this paper is highly consistent with the numerical results. Secondly, it also shows that the three stages of velocity distribution mentioned above do exist. It needs to be explained that in the stable stage, the velocity distribution does not observe "flow core," because the size of "flow core" ($b_0 = 1.88e-5$ m) is too small relative to the fracture opening.

4.2. Related Tests

4.2.1. Rheological Property Test of Cement Slurry. In order to study the flow law of a slurry, the first step is to study the flow characteristics of the slurry itself, that is, the rheology of the slurry [28–30]. The commonly used rheological models of slurry include the Newtonian fluid model, the Bingham fluid model, the power law fluid model, and the H-B fluid model. In this paper, a ZNN-D6 rotational viscometer (see Figure 7) is used to test the rheological property of ordinary Portland cement (OPC) slurry, and the rheological curves of the OPC slurry under different water-cement ratios are obtained (see Figure 8). When the water-cement ratio (W/C) of the cement slurry is more than 0.7 but less than 1.0, the rheological curve is basically straight and the intercept between the curve and coordinate Y axis is obviously not zero, that is to say, there is yield stress. Therefore, we think that the water-cement slurry is more suitable for the Bingham fluid model than the OPC slurry with W/C of 0.7~1.0, which is also consistent with the research of other scholars [31]. In the subsequent calculation of the slurry flow distance under different conditions, the slurry parameters of W/C = 0.8 in this experiment are selected.

4.2.2. Experiment of Unsteady Fracture Flow of Water. In the derivation of the relationship between the diffusion distance and time of slurry, the differential relationship of $\bar{u} = dI/dt$ is adopted, so in order to verify equation (26), the experiment of water flowing in the parallel plate fracture is designed. After processing the experimental data, the results obtained and the theoretical calculation results are drawn in Figure 9, which prove the correctness of the differential relationship. At the same time, the correctness of equation (29) can also be guaranteed.

4.3. Application of Simplified Conditions. Based on formulas (23) and (24), we design two discriminant conditions X_c and Y_c:

$$\begin{aligned} X_c &= \frac{\mu t}{\rho b^2} - 0.3035, \\ Y_c &= \tau_0\sqrt{\frac{t}{-3\mu\Delta P}} - 0.062. \end{aligned} \tag{34}$$

According to the discriminant conditions, the discriminant space corresponding to the model can be divided into four quadrants (see Figure 10). According to the previous analysis, the entire space can be calculated using model 4, but when the discriminant conditions (X_c, Y_c) fall in quadrant II, only model 4 can be

Table 4: Discriminant coordinates obtained under different conditions and their quadrants in the discriminant plane.

Aperture, b (mm)	Pressure, P (MPa)	Time, t (s)	Discriminant coordinates	Quadrant
0.1	0.1	0.01	(11.5715, -0.0591)	IV
0.1	0.1	1	(1187.2, -0.0331)	IV
0.1	0.1	100	(118750, 0.2267)	I
0.1	1	0.01	(11.5715, -0.0611)	IV
0.1	1	1	(1187.2, -0.0529)	IV
0.1	1	100	(118750, 0.0293)	I
0.1	10	0.01	(11.5715, -0.0617)	IV
0.1	10	1	(1187.2, -0.0591)	IV
0.1	10	100	(118750, -0.0331)	IV
1	0.1	0.01	(-0.1847, -0.0591)	III
1	0.1	1	(11.5715, -0.0331)	IV
1	0.1	100	(1187.2, 0.2267)	I
1	1	0.01	(-0.1847, -0.0611)	III
1	1	1	(11.5715, -0.0529)	IV
1	1	100	(1187.2, 0.0293)	I
1	10	0.01	(-0.1847, -0.0617)	III
1	10	1	(11.5715, -0.0591)	IV
1	10	100	(1187.2, -0.0331)	IV
10	0.1	0.01	(-0.3023, -0.0591)	III
10	0.1	1	(-0.18475, -0.0331)	III
10	0.1	100	(11.5715, 0.2267)	I
10	1	0.01	(-0.3023, -0.0611)	III
10	1	1	(-0.18475, -0.0529)	III
10	1	100	(11.5715, 0.0293)	I
10	10	0.01	(-0.3023, -0.0617)	III
10	10	1	(-0.18475, -0.0591)	III
10	10	100	(11.5715, -0.0331)	IV

used for calculation (to ensure that the model error is within 5%); when the discriminant conditions (X_c, Y_c) fall into quadrant IV, all four models can guarantee relatively high accuracy; when the discriminant conditions (X_c, Y_c) fall in quadrant II, model 2 can be used for approximate calculation; finally, when the judgment condition (X_c, Y_c) is in quadrant I, model 3 can be used for approximate calculation.

In order to further verify the feasibility of the criteria, using the experimentally obtained cement slurry with W/C = 0.8, plastic viscosity is 0.019, yield stress is 2.18, and density is 1600. The slurry flow distance under different conditions is calculated. Among them, model 1 represents the steady-state Newtonian fluid (equation (8)), model 2 represents the unsteady-state Newtonian fluid (equation (26)), model 3 refers to the steady-state Bingham fluid (equation (9)), and model 4 represents the unsteady-state Bingham fluid (equation (29). The calculation results are shown in Table 2.

Taking model 4 as the standard, first judge its applicability based on the relative errors of the other three models (see Table 3), and then calculate the discriminant coordinates under different conditions to get Table 4 through the comparison table. The results in Tables 3 and 4 verify the accuracy of the discrimination method.

5. Conclusion

The unsteady flow equation of a Newtonian fluid in a parallel plate fracture is derived in detail based on the N-S equation. Combining the steady-state flow equations of a Newtonian fluid and a Bingham fluid, the unsteady-state flow equation of a Bingham fluid which is more suitable for describing slurry flow is constructed. The application conditions of the new model are analyzed. We can get the following conclusions:

(1) We have deduced the relationship between the flow time and flow distance of a Bingham fluid in the parallel plate fractures, and proved the accuracy of the derivation process through experiments

(2) The unsteady flow equation of a Bingham fluid makes up for the traditional model's inability to consider the influence of inertial forces on the calculation results, and the slurry flow velocity distribution is divided into the inlet section, the transition section, and the stable section through calculation

(3) We have provided the judgment condition that the unsteady flow equation of a Bingham fluid simplifies the traditional model. After bringing in the calculation criterion of specific construction parameters, we choose whether to use the traditional model and which model to use

The flow equations of power law fluids and H-B fluids can be calculated with reference to the proposed ideas, which can be used for the flow calculation of a high water-cement ratio slurry. In future research, the effect of fracture roughness and tortuosity on slurry flow should also be studied. At the same time, changes in the rheology of the cement slurry over time should be considered.

Abbreviations

u, v: Flow velocity of fluid in x and y directions
p, τ: Area force acting on fluid microelements
f_x, f_y: Volume force acting on fluid microelements
μ: Newtonian fluid viscosity, corresponding to the plastic viscosity of a Bingham fluid
ρ: Fluid density
L: Length of the fracture
b: Aperture of the fracture
b_0: The width of the "flow core"
ΔP: Pressure difference across the fracture
K: Consistency coefficient of a power law fluid and a Herschel-Bulkley fluid
$\dot{\gamma}$: Shear rate
n: The rheological index of a power law fluid and a Herschel-Bulkley fluid
I: The flow distance of the fluid in the fracture at a certain moment (the length from the end of the fluid to the inlet).

Data Availability

The raw/processed data required to reproduce these findings cannot be shared at this time as the data also forms part of an ongoing study.

Conflicts of Interest

The authors declare that they have no conflicts of interest.

References

[1] L. Sun, H. Wu, B. Yang, and Q. Li, "Support failure of a high-stress soft-rock roadway in deep coal mine and the equalized yielding support technology: a case study," *International Journal of Coal Science & Technology*, vol. 2, no. 4, pp. 279–286, 2015.

[2] H. Wang, C. Jiang, P. Zheng, W. Zhao, and N. Li, "A combined supporting system based on filled-wall method for semi coal-rock roadways with large deformations," *Tunnelling and Underground Space Technology*, vol. 99, article 103382, 2020.

[3] Y. Wang, B. Liu, and Y. Qi, "A risk evaluation method with an improved scale for tunnel engineering," *Arabian Journal for Science and Engineering*, vol. 43, no. 4, pp. 2053–2067, 2018.

[4] Y. Wang, C. Shu, L. M. Yang, and H. Z. Yuan, "A decoupling multiple-relaxation-time lattice Boltzmann flux solver for non-Newtonian power-law fluid flows," *Journal of Non-Newtonian Fluid Mechanics*, vol. 235, pp. 20–28, 2016.

[5] Z. P. Li, S. C. Li, Q. S. Zhang et al., "Study on parameters of grouting reinforced circle for water-rich and soft fault fracture zone in tunnel," *Applied Mechanics and Materials*, vol. 470, pp. 925–929, 2013.

[6] J. Yang, C. Zhang, J. Fu, S. Wang, X. Ou, and Y. Xie, "Pre-grouting reinforcement of underwater karst area for shield tunneling passing through Xiangjiang River in Changsha, China," *Tunnelling and Underground Space Technology*, vol. 100, article 103380, 2020.

[7] M. Zhu, X. Gong, X. Gao, S. Liu, and J. Yan, "Remediation of damaged shield tunnel using grouting technique: serviceability improvements and prevention of potential risks," *Journal of Performance of Constructed Facilities*, vol. 33, no. 6, p. 04019062, 2019.

[8] G. Dai, Y. Sheng, S. Li, and Y. Zhang, "Experimental study on mechanical properties of anti-seepage slurry in landfill," *Modern Physics Letters B*, vol. 32, no. 34n36, p. 1840065, 2019.

[9] K. N. Zhang, Y. G. Chen, F. Y. Deng, and Q. Y. Tian, "Retention of clay-solidified grouting curtain to Cd 2+, Pb 2+ and Hg 2+ in landfill of municipal solid waste," *Journal of Central South University of Technology*, vol. 11, no. 4, pp. 419–422, 2004.

[10] N. C. Collier, K. P. Travis, F. G. Gibb, and N. B. Milestone, "Characteristics of cementitious paste for use in deep borehole disposal of spent fuel and high level wasteforms," *MRS Proceedings*, vol. 1744, pp. 205–210, 2015.

[11] H. Eichhorn, "Industrial complex for solid radwaste management (ICSRM) at Chernobyl nuclear power plant functionality of the facilities. Factors of success," *Atw. Internationale Zeitschrift fuer Kernenergie*, vol. 57, no. 2, pp. 105–107, 2011.

[12] M. Axelsson and G. Gustafson, "A robust method to determine the shear strength of cement-based injection grouts in the field," *Tunnelling and Underground Space Technology*, vol. 21, no. 5, pp. 499–503, 2006.

[13] H. M. Kim, J. W. Lee, M. Yazdani, E. Tohidi, H. R. Nejati, and E. S. Park, "Coupled viscous fluid flow and joint deformation analysis for grout injection in a rock joint," *Rock Mechanics and Rock Engineering*, vol. 51, no. 2, pp. 627–638, 2018.

[14] S. Denetto and A. M. Kamp, "Cubic law evaluation using well test analysis for fractured reservoir characterization," in *SPE Annual Technical Conference and Exhibition*, Society of Petroleum Engineers, 2016.

[15] J. Funehag and Å. Fransson, "Sealing narrow fractures with a Newtonian fluid: model prediction for grouting verified by field study," *Tunnelling and Underground Space Technology*, vol. 21, no. 5, pp. 492–498, 2006.

[16] P. A. Witherspoon, J. S. Wang, K. Iwai, and J. E. Gale, "Validity of cubic law for fluid flow in a deformable rock fracture," *Water Resources Research*, vol. 16, no. 6, pp. 1016–1024, 1980.

[17] N. Weng, Q. Wang, J. Li, J. Lyu, H. Zhang, and W. Yao, "Liquid penetration in metal wire mesh between parallel plates under normal gravity and microgravity conditions," *Applied Thermal Engineering*, vol. 167, p. 114722, 2020.

[18] R. W. Zimmerman and I. W. Yeo, "Fluid flow in rock fractures: from the Navier-Stokes equations to the cubic law," *Geophysical Monograph-American Geophysical Union*, vol. 122, pp. 213–224, 2000.

[19] N. M. Wereley and L. Pang, "Nondimensional analysis of semi-active electrorheological and magnetorheological dampers using approximate parallel plate models," *Smart Materials and Structures*, vol. 7, no. 5, pp. 732–743, 1998.

[20] Y. Yan and J. Koplik, "Flow of power-law fluids in self-affine fracture channels," *Physical Review E*, vol. 77, no. 3, article 036315, 2008.

[21] L. Zou, U. Hakansson, and V. Cvetkovic, "Yield-power-law fluid propagation in water-saturated fracture networks with application to rock grouting," *Tunnelling and Underground Space Technology*, vol. 95, p. 103170, 2020.

[22] A. G. Petrov and I. S. Kharlamova, "The solutions of Navier-Stokes equations in squeezing flow between parallel plates," *European Journal of Mechanics - B/Fluids*, vol. 48, pp. 40–48, 2014.

[23] A. R. De Castro and M. Agnaou, "Numerical investigation of the apparent viscosity dependence on Darcy velocity during

the flow of shear-thinning fluids in porous media," *Transport in Porous Media*, vol. 129, no. 1, pp. 93–120, 2019.

[24] S. G. Cherny and V. N. Lapin, "3D model of hydraulic fracture with Herschel-Bulkley compressible fluid pumping," *Procedia Structural Integrity*, vol. 2, pp. 2479–2486, 2016.

[25] L. Zou, U. Hakansson, and V. Cvetkovic, "Cement grout propagation in two-dimensional fracture networks: impact of structure and hydraulic variability," *International Journal of Rock Mechanics and Mining Sciences*, vol. 115, pp. 1–10, 2019.

[26] F. Xiao, Z. Zhao, and H. Chen, "A simplified model for predicting grout flow in fracture channels," *Tunnelling and Underground Space Technology*, vol. 70, pp. 11–18, 2017.

[27] M. Eriksson, M. Friedrich, and C. Vorschulze, "Variations in the rheology and penetrability of cement-based grouts—an experimental study," *Cement and Concrete Research*, vol. 34, no. 7, pp. 1111–1119, 2004.

[28] M. Axelsson, G. Gustafson, and Å. Fransson, "Stop mechanism for cementitious grouts at different water-to-cement ratios," *Tunnelling and Underground Space Technology*, vol. 24, no. 4, pp. 390–397, 2009.

[29] W. Qing, Z. Qing, S. Tang et al., "The rheological test and application research of glass fiber cement slurry based on plugging mechanism of dynamic water grouting," *Construction and Building Materials*, vol. 189, pp. 119–130, 2018.

[30] O. Turan, N. Chakraborty, and R. J. Poole, "Laminar Rayleigh-Benard convection of yield stress fluids in a square enclosure," *Journal of Non-Newtonian Fluid Mechanics*, vol. 171-172, pp. 83–96, 2012.

[31] Q. Liu, G. Lei, X. Peng, C. Lu, and L. Wei, "Rheological characteristics of cement grout and its effect on mechanical properties of a rock fracture," *Rock Mechanics and Rock Engineering*, vol. 51, no. 2, pp. 613–625, 2018.

Hindawi
Geofluids
Volume 2021, Article ID 5535321, 11 pages
https://doi.org/10.1155/2021/5535321

Research Article

Mechanism and Characteristics of $CH_4/CO_2/H_2O$ Adsorption in Lignite Molecules

Zhihui Wen,[1,2,3] **Yunpeng Yang**,[1,2] **Qi Wang**,[1,2] **and Banghua Yao**[1,2,3]

[1]*School of Safety Science and Engineering, Henan Polytechnic University, Jiaozuo 454000, China*
[2]*State Key Laboratory Cultivation Base for Gas Geology and Gas Control (Henan Polytechnic University), Jiaozuo 454000, China*
[3]*State Collaborative Innovation Center of Coal Work Safety and Clean-Efficiency Utilization, Jiaozuo 454000, China*

Correspondence should be addressed to Zhihui Wen; wenzhihui@hpu.edu.cn

Received 21 January 2021; Revised 19 February 2021; Accepted 9 March 2021; Published 20 March 2021

Academic Editor: Yi Xue

Adsorption characteristics of coalbed methane (CBM) are significant to investigate the absorption of coal, shale, and porous media. In particular, adsorption characteristics of CH_4, CO_2, and H_2O play an important role in predicting CBM output and geologic sequestration potentials of CO_2 in research fields of CO_2-enhanced CBM recovery (CO_2-ECBM) and sequestration of CO_2. In this work, adsorption characteristics of CH_4, CO_2, and H_2O in lignite molecules were simulated through the grand canonical Monte Carlo (GCMC) method and molecular dynamics (MD) method. Research results demonstrated that given the same temperature and pressure, the ultimate adsorption capacity of lignite per unit to H_2O is the highest, followed by those of CO_2 and CH_4 successively. All isothermal adsorption curves conform to the "I-type" characteristics. In the saturated molecular configuration, gas molecules show different distribution patterns at two sides of the lignite molecule chain. Lignite has typical physical adsorption to CH_4 and CO_2, with adsorption energy provided by nonbonding energy. However, lignite has both physical adsorption and chemical adsorption to H_2O, with adsorption energy provided by both nonbonding energy and hydrogen bond energy. High temperature is against adsorption of CH_4, CO_2, and H_2O. Temperature might inhibit adsorption of gas molecules. Research conclusions lay foundations for the exploitation and development of CBM and relevant studies on sequestration of CO_2.

1. Introduction

Recently, the energy problem has become an important global research field. With the increasing exhaustion of fossil fuels, it is crucial to find new energies [1, 2]. Coalbed methane (CBM), a high-efficiency, environmental-friendly, and rich energy source, has been highly concerned by scholars and experts [3–7]. It is the best substitute for fossil fuels at present. CBM is mainly composed of CH_4, CO_2, H_2O, O_2, and some other trace gases, and 80%-90% of CBM are adsorbed on the surface of the coal matrix [8, 9]. According to estimations, the global CBM resources are higher than 200,000 billion m^3. China also possesses abundant CBM reserves, and it is the third-largest CBM reserve in the world. There are about 35,000 billion m^3 of CBM resources in more than 2,000 m of buried depth, including about 12,000 m^3 of explored reserves and 23,000 m^3 of future reserves. There is a great development potential of CBM resources in China [10, 11]. Meanwhile, exploiting CBM before coal mining can avoid the occurrence of outburst of gas and gas explosion effectively. Injecting CO_2 to enhance coalbed methane (CO_2-ECBM) has been widely concerned by many scholars because it can not only displace the methane in coal but also reduce the greenhouse gas effect by geological storage [12, 13]. Many studies have demonstrated that the total pore volume of coals is mainly determined by micropores (<2 nm) and mesopores (2-50 nm) [14–16]. Therefore, elaborating the microscale adsorption characteristics and mechanism of coals is critical to adopt effective CO_2-ECBM measures and gas disaster control technologies. Therefore, it is very necessary to carry out molecular simulation on adsorption of CH_4, CO_2, and H_2O in coal matrix molecules.

With the development of scientific technology, the molecular adsorption mechanism between adsorbent and adsorbate can be discussed through computer molecular simulation. Microscopic technology is very suitable to study adsorption behavior of nanometer and submicron pores of coals [17]. Matranga et al. [18] simulated the adsorption behavior of CH_4, CO_2, and N_2 on activated carbons by the grand canonical Monte Carlo (GCMC) method, finding that the adsorption capacity and adsorption heats of CO_2 are higher than those of CH_4 and N_2. Narkiewicz and Mathews [19] introduced an adsorption position corresponding to the CO_2 adsorption of low-volatile soft coals and methane molecular capacity and model through molecular simulation. Zhang et al. [20] discussed adsorption effects of benzene ring and side chains of coal surface molecules to CH_4, CO_2, N_2, and O_2 through molecular simulation. Xiang et al. [21] concluded adsorption capacities of CH_4, CO_2, and H_2O, molecular configuration, and effects of oxygen-containing functional groups on adsorption performance of Yanzhou coal through GCMC and MD methods. Mosher et al. [14] carried out a molecular simulation to explore competitive adsorption behaviors of CH_4 and CO_2 in micropores and middle pore structures of coals. Dang et al. [22] and Song et al. [23] studied adsorption behaviors of CH_4, CO_2, and H_2O in low-rank coals by using density functional theory (DFT) and MD, finding that high temperature is against adsorption of CH_4, CO_2, and H_2O in coal matrix and oxygen-functional groups and nitrogen-containing functional groups of coal can influence adsorption greatly. Xu et al. [24] studied molecular behaviors that CO_2 promotes CH_4 desorption in coals. You et al. [25] simulated the interaction between subbituminous coals and water through MD simulation and found that water molecules are easy to be adsorbed by carboxyls. Li et al. [26] calculated and discussed adsorption capacities of CH_4, CO_2, and N_2 in coal silt models, finding a relationship in adsorption capacities of three gases with the increase of silt width: $H_2O > CH_4 > N_2$. Gao et al. [27] simulated adsorption characteristics of lignite through GCMC and MD methods. Results showed that the adsorption isotherm of single gas conformed to the Langmuir equation and the CO_2 enjoys obvious advantages in the competitive adsorption of multiple gases. Hu et al. [28] and You et al. [29] studied self-diffusion and mutual diffusion of CH_4, CO_2, and multicomponent gases through the MD method.

Although many works have been reported, only few concentrate on adsorption characteristics of CH_4, CO_2, and H_2O in lignite. Besides, lignite reserves account for 47% of total coal reserves, indicating that lignite has great potentials in CBM development and sequestration of CO_2. In this study, adsorption characteristics of CH_4, CO_2, and H_2O in lignite which possesses a great reserve were discussed with the classical GCMC and MD method. Moreover, the stable configuration of lignite molecules was discussed, and the saturated adsorption capacity and saturated molecular configuration of lignite molecules were simulated. The variation law of adsorption energy of different adsorbates in lignite molecules was analyzed, and the microscopic mechanism of CH_4, CO_2, and H_2O adsorption in lignite molecules was elaborated. Research conclusions provide theoretical supports to study adsorption performances of different adsorbates in lignite molecules.

2. Methodology

2.1. Brown Coal Structure Construction. Coal is a type of porous heterogeneous solids with complicated physical and chemical structures. The basic structural unit of coals includes a regular part and irregular part. The regular part is composed of benzene rings, heterocyclic rings, alicyclic rings, and hydroaromatic rings, and it forms the core part of the structural unit of coals. The irregular part is composed of functional groups which are connected to the regular part and side chains of alkyls. Among studies of the molecular structure of coals, more than 130 molecular structures have been proposed yet [30]. Among them, the Given model [31], Wiser model [32], and Solomon model [33] are representative ones. In particular, the Wiser model is regarded as a relatively comprehensive and reasonable model to describe lignite with a low degree of metamorphism, and this model can reflect the modern concept of the molecular structure of coals. The Wiser model can explain surface chemical and other reactive properties of lignite. Therefore, it is widely applied in simulation studies related to lignite molecules [17, 26, 33]. The Wiser model ($C_{184}H_{155}N_3O_{20}S_3$) has basic features of lignite, including a single aromatic ring which is linked and cross-linked through the aliphatic side chain. It is applicable to the molecular simulation study of gas adsorption of lignite. The plane molecular structure of the Wiser model is shown in Figure 1.

In this work, Materials Studio (MS) was used to carry out the simulation calculation. In the MS, 3D lignite molecular structural units were constructed according to the molecular formula ($C_{184}H_{155}N_3O_{20}S_3$), and they were defined as a molecular fragment. The initial 3D space structure of lignite molecules was gained by adding hydrogen until saturation. In the Condensed-phase Optimized Molecular Potentials for Atomistic Simulation Studies (COMPASS), the smart technique was chosen to optimize the initial 3D spatial structure of lignite molecules. The number of iteration steps, convergent standard accuracy, and energy deviation were set as 100,000, fine, and 0.0001 kcal/mol, respectively. The acting energies of Coulomb electrostatic force and Van der Waals (VDW) force were set at the atomic state, and charges carried on the lignite molecular structure were distributed automatically by a force field. Potential energy surfaces were searched through annealing added with energy disturbance to recognize the point with the lowest energy in the system. The frame with the lowest energy was chosen as the stable structure of the molecular structural model of lignite. The optimized 3D structure of lignite molecules is shown in Figure 2.

In order to verify the accuracy of the constructed molecular model of lignite, unit cells were added through setting of density to the stable molecular model of lignite in Figure 2 by using the Amorphous Cell module. The constructed unit cells were processed by MD optimization and annealing, thus getting stable configuration and energy distribution of unit cells under different densities. The molecular structure at the lowest system energy is the most stable. At this moment, the density corresponding to the system energy is the optimal density after adding periodic boundary conditions. The

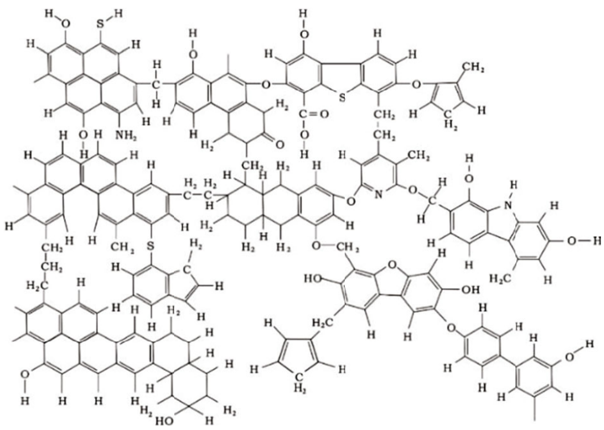

Figure 1: Molecular plane structure of the Wiser model [28].

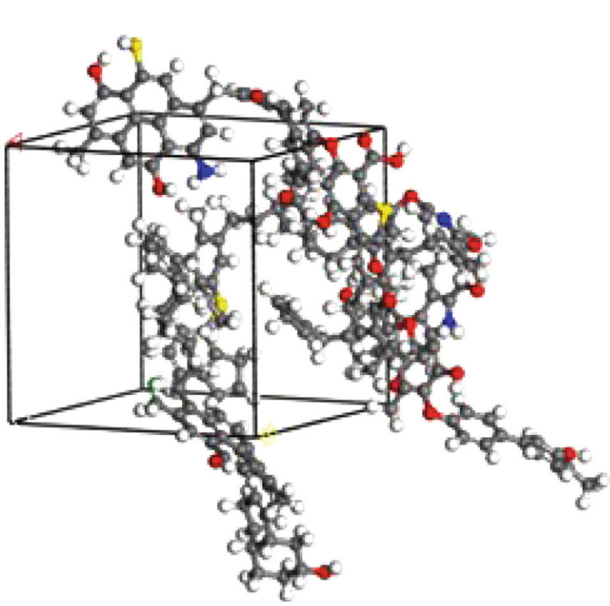

Figure 2: Stable molecular model of lignite. Color scheme: C: black; H: gray; O: red; N: blue; S: yellow.

variation laws of unit cell system energy of lignite with density are shown in Figure 3.

It can be seen from Figure 3(b) that with the increase in system density, system energy of lignite molecules presents a "V-shaped" variation after unit cells are added in. The system energy of unit cells of lignite fluctuates when the molecular density is between 1.20 g/cm^3 and 1.26 g/cm^3 (Figure 3(a)). When the molecular system density of lignite is 1.23 g/cm^3, the system energy of unit cells reaches the minimum. Besides, the system energy of unit cells shows an upward trend with the increase and decrease of system density. In other words, the system energy of unit cells of lignite reaches the lowest when the system density is 1.23 g/cm^3. Under this circumstance, the molecular structure of lignite is the most stable and the molecular configuration of lignite is the optimal one when periodic boundary conditions are added in. This conforms to the mean lignite density (1.21 g/cm^3) which is calculated in References [34, 35]. Therefore, the constructed model can be used to investigate the adsorption characteristics in lignite molecules. At this moment, the unit cell size of lignite molecules is 1.5745695 nm × 1.5745695 nm × 1.5745695 nm.

2.2. Force Field. In molecular simulation calculations, various types of force fields are used, including (a) the classic fields, such as the MM force field, AMBER force field, CHARMM force field, and CVFF force field, and (b) the second generation fields, such as the COMPASS force field. The existing force field has been highly applicable to description of macromolecular substances and biomacromolecules [26, 36–38]. The molecular force field is formed by a set of potential functions and dynamic constant. The total molecular energy is the sum of kinetic energies and potential energies. Potential energy of molecules can be expressed in a simple geometric coordinate function.

The force field used in this study is a second-generation field. The force field is designed to accurately calculate various properties, structures, spectra, thermodynamic properties, and other expected parameters of a molecule. Thus, in addition to incorporating an enormous amount of experimental data, the derivation of the force-field constant refers to the exact quantum calculation results. Due to the use of varying parameters, second-generation force fields can be divided into various types: CFF91, CFF95, PCFF, and MMFF93.

An appropriate force field should be able to reproduce experimental results quantitatively. We have used different force fields, such as polymer-consistent force field (PCFF), Dreiding, condensed phase optimized molecular potential for atomistic simulation studies (COMPASS), and universal force field, to calculate the density of the lignite molecule model. The results indicated that the density computed through Dreading force field was the closest to the experimental values. The PCFF force field selected for this study was derived from the CFF91 force field, which is suitable for the study of polymers and organic matter. In addition to the parameters of the force field of CFF91, PCFF contains the force-field parameters of inert gas atoms, such as He, Kr, and metal atoms. These parameters could be used to reckon the molecular system containing these atoms.

The total energy of a molecule was considered to be the sum of the kinetic and potential energies. The bonding energy includes energy of slip keys (E_b), bending energy of bond angle (E_θ), torsion energy of the bond dihedron (E_φ), bending energy of bond angle surface (E_χ), and crossing energy (E_{cross}). The nonbonding energy covers Coulomb electrostatic force (E_c) and VDW force (E_v). The total energy of the molecular simulation system (E_{total}) can be expressed as

$$\mathrm{E_{total}} = \mathrm{E_b} + \mathrm{E}_\theta + \mathrm{E}_\varphi + \mathrm{E}_\chi + \mathrm{E_{cross}} + \mathrm{E_v} + \mathrm{E_c}. \quad (1)$$

E_b of atoms can be expressed as

$$\mathrm{E_b} = \sum_b \left[K_2(b-b_0)^2 + K_3(b-b_0)^3 + K_4(b-b_0)^4\right], \quad (2)$$

where K_2, K_3, and K_4 are the elastic constant of chemical bonds, respectively. b and b_0 are the chemical bond length

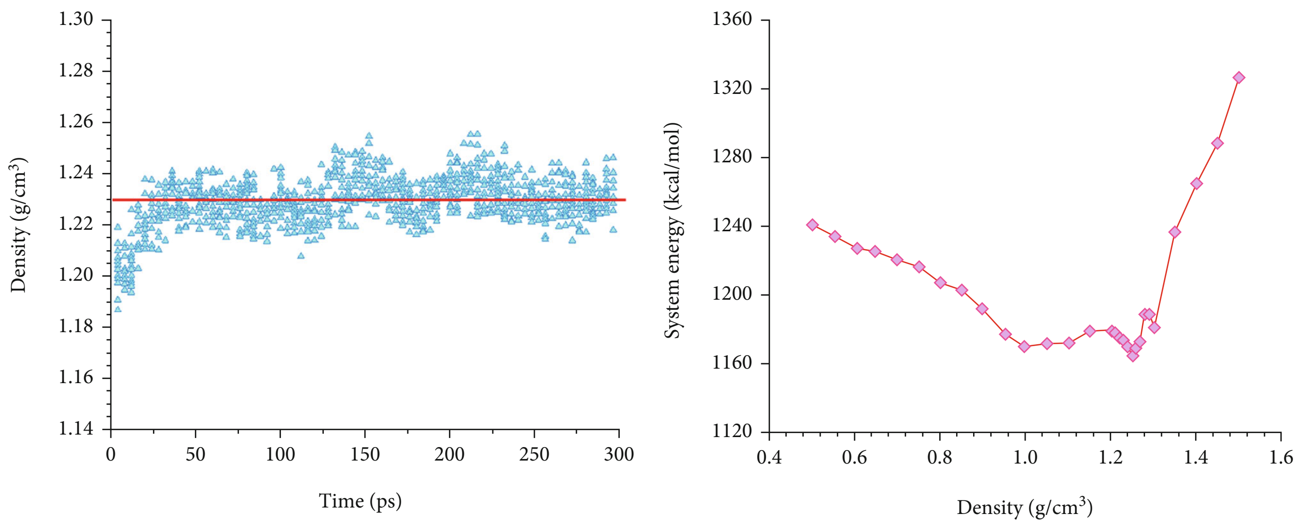

(a) Density change during annealing kinetics

(b) System energy change with density

FIGURE 3: Variation of energy with density in unit cell system of lignite.

and bond length at the equilibrium state, respectively. With the decrease of the elastic constant, the vibrational frequency and vibration amplitude slow down and decrease, respectively. E_θ can be expressed as

$$\mathrm{E}_\theta = \sum_\theta \left[H_2(\theta-\theta_0)^2 + H_3(\theta-\theta_0)^3 + H_4(\theta-\theta_0)^4\right], \quad (3)$$

where θ and θ_0 are the bond angle and bond angle at the equilibrium state, respectively. H_2, H_3, and H_4 are the bending elastic constants of the bond angle, respectively. E_φ can be expressed as

$$\mathrm{E}_\varphi = \sum_\varphi \left\{V_1\left[1-\cos\left(\varphi-\varphi_1^0\right)\right] + V_2\left[1-\cos\left(2\varphi-\varphi_2^0\right)\right] + V_3\left[1-\cos\left(3\varphi-\varphi_3^0\right)\right]\right\}, \quad (4)$$

where V_2, V_3, and V_4 are the torsion elastic constant of the dihedral angle. φ refers to four adjacent dihedral angles which are not formed by atoms on the same plane. φ_0 can be used to reflect the dihedral angle in the initial stage. E_χ can be expressed as

$$\mathrm{E}_\chi = \sum_\chi K_\chi \chi^2, \quad (5)$$

where K_χ is the bending elastic constant of the bond angle out of the plane. χ denotes the bending angle out of the plane. E_{cross} of bonds, bond angles, and dihedral angles can be expressed as

$$\begin{aligned}\mathrm{E}_{\mathrm{cross}} = &\sum_b \sum_{b'} F_{bb'}(b-b_0)\left(b'-b_0'\right) + \sum_\theta \sum_{\theta'} F_{\theta\theta'}(\theta-\theta_0) \\ &\cdot \left(\theta'-\theta_0'\right) + \sum_b \sum_\theta F_{b\theta}(b-b_0)(\theta-\theta_0) \\ &+ \sum_{\mathrm{b}} \sum_\varphi (\mathrm{b}-\mathrm{b}_0)[V_1\cos\varphi + V_2\cos 2\varphi + V_3\cos 3\varphi] \\ &+ \sum_{\mathrm{b}'} \sum_\varphi \left(\mathrm{b}'-\mathrm{b}_0'\right)[V_1\cos\varphi + V_2\cos 2\varphi + V_3\cos 3\varphi] \\ &+ \sum_\theta \sum_\varphi (\theta-\theta_0)[V_1\cos\varphi + V_2\cos 2\varphi + V_3\cos 3\varphi] \\ &+ \sum_\varphi \sum_\theta \sum_{\theta'} K_{\theta\varphi\varphi'}\cos\varphi(\theta-\theta_0)\left(\theta'-\theta_0'\right),\end{aligned} \quad (6)$$

where $F_{bb'}$ is an extended coupling elastic constant, $F_{\theta\theta'}$ denotes the bending coupling elastic constant, $F_{b\theta}$ refers to the coupling elastic constant of extended bending, and $\mathrm{K}_{\theta\varphi\varphi'}$ refers to the coupling elastic constant of torsional bending. E_c can be expressed as

$$\mathrm{E}_c = \sum_{\mathrm{i,j}} \frac{q_i q_j}{r_{ij}}, \quad (7)$$

where $\mathrm{q_i}$ and $\mathrm{q_j}$ are the quantity of electric charge of atoms. $\mathrm{r_{ij}}$ refers to the distance between two atoms. The nonbonded VDW forces (E_v) can be expressed as

$$\mathrm{E}_v = 4\varepsilon_{ij}\left[\left(\frac{\sigma_{ij}}{r_{ij}}\right)^{12} - \left(\frac{\sigma_{ij}}{r_{ij}}\right)^6\right], \quad (8)$$

where $\varepsilon_{\mathrm{ij}}$ is the effective dielectric constant between two atoms and σ_{ij} is the potential parameter which changes according to the atom type.

2.3. Implementation of Simulation

2.3.1. Optimization of Adsorbate. Molecular structures of adsorbates CH_4, CO_2, and H_2O are plotted by Skirt in MS, and a 3D atom document of gas molecules is constructed. The plotted molecular structures of adsorbates were cleaned, followed by optimization of molecular mechanical structures and annealing processing under the Focite module. In this process, parameters were set consistent with those in Section 2 for molecular optimization of coals.

2.3.2. Simulation Scheme and Parameter Setting. This study is a GCMC simulation based on the Sorption module in MS software. During simulation, the number of gas molecules is added to the coal surface one by one. The coal surface will release heats after adsorption with gas molecules, leading to the energy of the system declining gradually. The system energy reaches the minimum at saturated adsorption of gas molecules in coal structures. Under this circumstance, the number of gas molecules adsorbed on the coal surface is the maximum adsorption capacity of the coal surface to the gas molecule.

During GCMC simulation of adsorption behaviors based on the Sorption module, the task term chose "adsorption isotherm," and the interaction force between lignite molecules and gas molecules chose "Ewald" and "atom-based." The electrostatic force was calculated by Ewald, and the VDW force was calculated by the atom-based method. The interaction between lignite molecules and gas molecules was described by the Lennard-Jones (LJ) 12-6 electric potentials [39]. Meanwhile, classical Metropolis rules were used to accept or reject production, disappear, translation, and rotation of gas micromolecules to assure that the system is at the lowest energy state [40]. The temperature in simulation was cycled five times automatically. Step length was adjusted and calculated automatically. The whole simulation involved 2×10^7 Monte Carlo steps. The first 10^7 steps were set to reach the adsorption equilibrium of the system, while the rest 10^7 steps were for sampling and statistics of relevant thermodynamic parameters.

This work is to construct an optimized stable configuration of lignite for adsorbent, and the adsorbates are CH_4, CO_2, and H_2O molecules. The simulation adopted 0.00 MPa~10.00 MPa pressure and periodic boundary conditions. Two situations were involved in the simulation:

(1) The adsorption characteristics of CH_4, CO_2, and H_2O in lignite molecules under the temperature of 303.15 K were simulated. The saturated adsorption configuration was analyzed, and the evolution laws of energies in the adsorption process were discussed

(2) Effects of simulation temperatures (283.15 K, 303.15 K, and 323.15 K) on CH_4, CO_2, and H_2O in lignite were analyzed

The adsorption capacity gained in the simulation refers to the number of gas molecules adsorbed in a single unit cell. Its unit is moleculars/u.c., but the unit of adsorption capacity in a conventional experiment is cm^3/g. These adsorption capacities in different units can be converted according to the following formula:

$$1 \text{ moleculars/u.c.} = 1/N \times 10^3 \div M = 1/N \div M \times V_{mol}, \quad (9)$$

where N is the Avogadro's constant which values 6.02×10^{23}. M refers to the mass of a single unit cell, and it is 4.08017×10^{-21} g. V_{mol} refers to the molar volume of gas under standard conditions, and it is 22.4×10^3 cm^3/mol.

3. Results and Discussion

3.1. Adsorption Isotherms and Adsorption Capacity. The adsorption performance of coal is usually expressed by the adsorption isotherm of coal. The adsorption isotherm refers to the curve of the change of coal's adsorption gas volume with gas pressure at a certain fixed temperature. A large number of research results at home and abroad show that when coal adsorbs gas, the adsorption isotherm conforms to the Langmuir adsorption equation expressed as

$$V = \frac{abp}{1 + bp}, \quad (10)$$

where V is adsorption capacity (cm^3/g), a is Langmuir adsorption constant (cm^3/g), b is Langmuir adsorption constant (1/MPa), and p is gas pressure (MPa).

Firstly, GCMC molecular simulation on adsorption isotherm of single pure CH_4, CO_2, or H_2O was carried out under 303.15 K and 0.00 MPa~10.00 MPa. Results are shown in Figure 4.

Evident differences in adsorption capacities of CH_4, CO_2, and H_2O in lignite are observed in Figure 4. In particular, with the increase in adsorption pressure, the adsorption capacity soars up in the low-pressure stage. However, such growth rate declines significantly when the adsorption pressure reaches a fixed value. This indicates that the pressure can promote adsorption behavior. In view of the upward trend of adsorption capacity of lignite per unit mass, the H_2O adsorption in lignite is significantly faster than those of CO_2 and CH_4 in the low-pressure stage. The CO_2 adsorption in lignite is the second fast, and the CH_4 adsorption is the slowest. In the high-pressure stage, the adsorption rates of CH_4, CO_2, and H_2O in lignite tend to be stable. The simulation results could describe adsorption characteristics of CH_4, CO_2, and H_2O on the lignite surface well by using the Langmuir equation. The gained isothermal curves show good "I-type" characteristics [41], which conform to previous research results [21, 22, 42]. It can be seen from Figure 4 that given the same temperature and pressure, the ultimate adsorption capacities of CH_4, CO_2, and H_2O in lignite per unit mass observe the laws of $H_2O > CO_2 > CH_4$. This was consistent with previous research results based on simulation [16, 17, 21, 26].

3.2. Adsorption Saturation Configuration. The saturated molecular configuration of lignite molecules cannot be displayed clearly due to the influences of a single unit cell. The molecular configuration of the unit cell was extended for

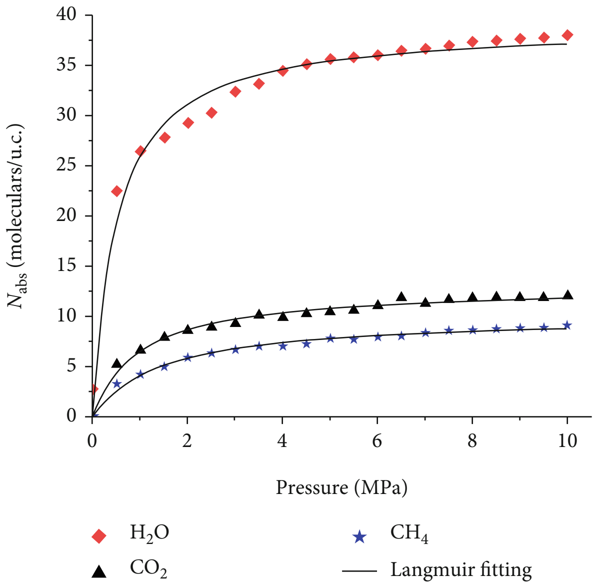

FIGURE 4: Adsorption isotherms of lignite on CH_4, CO_2, and H_2O.

one time along the direction *AB* through the task term "supercell" in the Build module of MS software. The molecular configuration of CH_4, CO_2, and H_2O in lignite molecular cells was observed from a different perspective.

The saturated molecular configurations of CH_4, CO_2, and H_2O adsorption in lignite molecules are shown in Figure 5. Distributions of the adsorbed CH_4, CO_2, and H_2O molecules in lignite molecules can be seen clearly, and all adsorbate molecules distribute at two sides of the lignite molecular chain. Specifically, CH_4 molecules are in clustering distribution and present the conformation of pairwise crossing ethane. CO_2 molecules are in parallel or crossing and even vertical arrangement. For the H_2O molecules, the hydrogen atoms point to the coal molecules or oxygen atoms in surrounding H_2O molecules as a response to the hydrogen bond energy.

Under the same condition, the adsorbed quantities of CH_4, CO_2, and H_2O in the saturated configuration of lignite vary. The adsorbed quantity of H_2O is far higher than those of CH_4 and CO_2, and the adsorbed quantity of CO_2 is higher than that of CH_4, indicating that CO_2 adsorption is more advantageous than CH_4 adsorption in lignite. With respect to the adsorbed quantity of CH_4, CO_2, and H_2O, there is a law of $H_2O > CO_2 > CH_4$, which conforms to the variation law of isothermal adsorption curves gained from simulation.

For coal molecules with fixed pore diameter distributions, the MD diameters of adsorbates (0.38 nm, 0.33 nm, and 0.265 nm for CH_4, CO_2, and H_2O molecules) determine their adsorption behaviors in coals. Only when coals with pore diameter larger than the diameter of adsorbates can the adsorbates be absorbed effectively [26]. When lignite adsorbs CH_4, CO_2, and H_2O, it is found that molecular diameter is inversely proportional to adsorption capacity. This proves that the adsorption capacity of H_2O in lignite is higher than those of CH_4 and CO_2. In fact, the interaction between lignite molecules and H_2O molecules is stronger in the adsorption process, which is mainly caused by different interaction energies during gas molecular adsorption in lignite.

3.3. Adsorption Energy. During the simulation process, the energy of the unit cell system after every adding of adsorbate molecules can be recorded. This energy is the difference between energy of the adsorption composite structure and energies of adsorbents and adsorbates. The adsorption energy can be calculated according to

$$\Delta E_{\mathrm{ads}} = E_{\mathrm{adsorbent/adsorbate}} - E_{\mathrm{adsorbent}} - E_{\mathrm{adsorbate}}, \tag{11}$$

where ΔE_{ads} is the adsorption energy of adsorbates after the occurrence of adsorption; $E_{\mathrm{adsorbent/adsorbate}}$ is the total energy of the whole adsorption system after the occurrence of adsorption behaviors; $E_{\mathrm{adsorbent}}$ is the energy of adsorbent before adsorption, that is, energy of lignite cell model; and $E_{\mathrm{adsorbate}}$ is the energy of adsorbates before adsorption, which refers to energies of CH_4, CO_2, and H_2O molecular models.

Heats are released during gas molecule adsorption, thus resulting in the decreasing energy of the whole system. With the increase in the number of adsorbate molecules, the total system energy after adsorption presents a downward trend until reaching the minimum. Subsequently, no adsorption occurs by adding adsorbate molecules. Instead, there are molecular repulsions and the total system energy increases gradually. The number of adsorbate molecules when the total system energy is the lowest refers to the saturated adsorption capacity of the adsorbate.

3.3.1. Energy Change of Adsorbed CH_4 Gas Molecules. It can be seen from Figure 6 that E_c and E_v play positive roles in the adsorption process of CH_4 before saturated adsorption in lignite molecular cells. However, E_c makes a tiny contribution, and E_v takes the dominant role in the adsorption of CH_4. The total system energy reaches the lowest, and the system achieves the saturation state after the unit cell adsorbs 7 CH_4 molecules. Subsequently, the adsorption system begins to repel CH_4 molecules after adding gas molecules.

3.3.2. Energy Change of Adsorbed CO_2 Gas Molecules. It can be seen from Figure 7 that E_c, E_v, and $E_{\text{b-H}}$ play positive roles in the adsorption process of CO_2 before saturated adsorption in lignite molecular cells. However, $E_{\text{b-H}}$ makes a tiny contribution, while E_c and E_v take the dominant role in the adsorption of CO_2. The total system energy reaches the lowest and the system achieves the saturation state after the unit cell adsorbs 9 CO_2 molecules. Subsequently, the adsorption system begins to repel CO_2 molecules after adding gas molecules.

3.3.3. Energy Change of Adsorbed H_2O Gas Molecules. It can be seen from Figure 8 that the changes of system energy during H_2O adsorption in lignite molecular cells are more complicated. E_c is the primary contributor to system energy, followed by $E_{\text{b-H}}$. The contribution of E_v is basically zero before the adsorbed quantity of H_2O molecules is lower than 12. After the adsorbed quantity of H_2O is higher than 12, E_v becomes negative energy against adsorption of H_2O molecules. Such repulsion effect increases with the increase of adsorbed quantity of H_2O molecules until reaching saturated

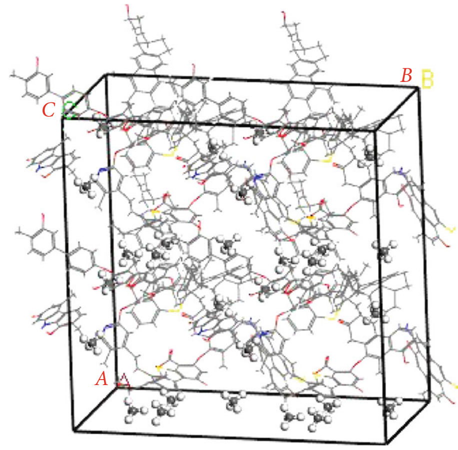

(a) Saturated adsorption configuration of CH_4

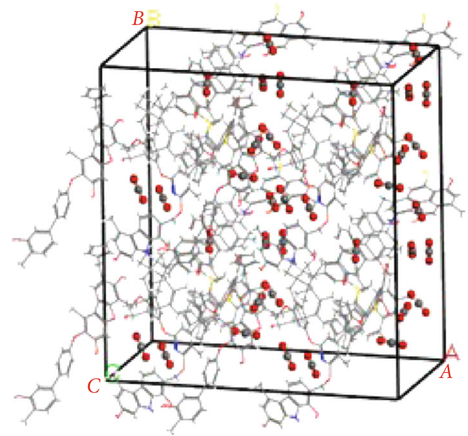

(b) Saturated adsorption configuration of CO_2

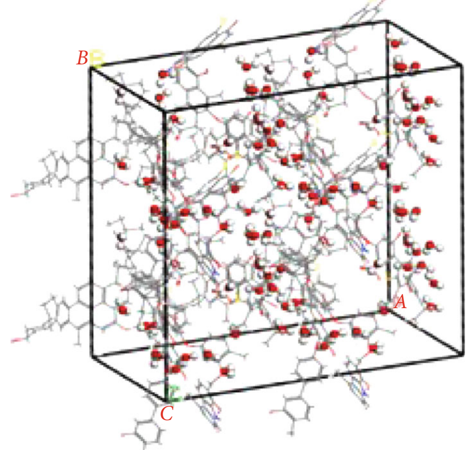

(c) Saturated adsorption configuration of H_2O

FIGURE 5: Saturated adsorption configuration of CH_4, CO_2, and H_2O adsorbed on lignite. Color scheme: C: black; H: gray; O: red; N: blue; S: yellow.

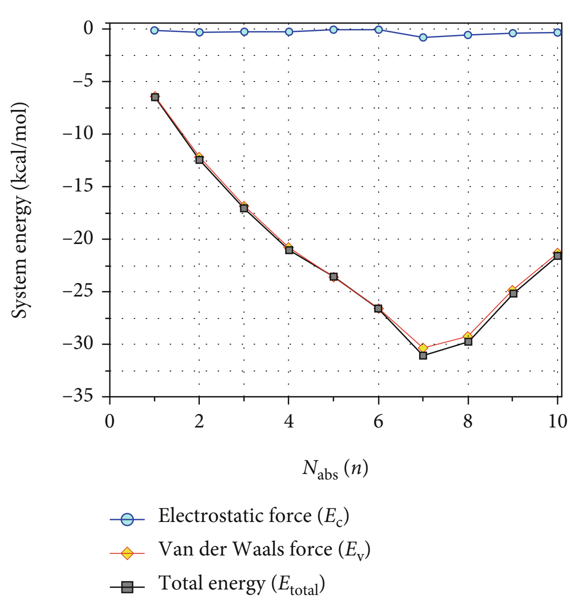

FIGURE 6: Energy changes during unit cell adsorption of different amounts of CH_4 molecules.

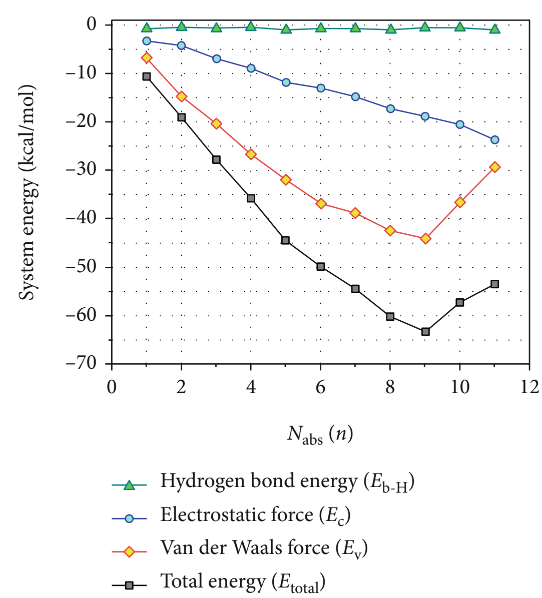

FIGURE 7: Energy changes during unit cell adsorption of different amounts of CO_2 molecules.

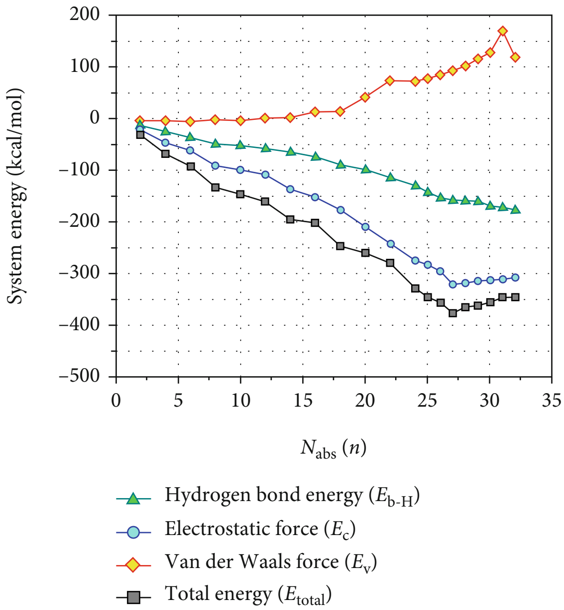

FIGURE 8: Energy changes during unit cell adsorption of different amounts of H_2O molecules.

adsorption. Although E_v hinders adsorption, the growth amplitude of the sum of E_c and E_{b-H} which are positive to the adsorption is higher than the growth amplitude of E_v, thus keeping the adsorption. The total system energy reaches the lowest, and the system achieves the saturation state after the unit cell adsorbs 27 H_2O molecules. Subsequently, the adsorption system begins to repel H_2O molecules after adding gas molecules. During the repulsive interaction stage, E_c and $E_{b\text{-}H}$ are major repulsive energies, while E_v turns to be the energy that consumes repulsion effect.

According to system energy changes during CH_4, CO_2, and H_2O adsorption in lignite molecules, it can be seen that

(1) system energies after CH_4, CO_2, and H_2O adsorption in lignite molecules drop significantly. With respect to the reduction amplitudes, there is a law of $H_2O > CO_2 > CH_4$, indicating that H_2O adsorption capacity in coals is the highest, followed by adsorption capacities of CO_2 and CH_4 [14, 17, 21, 23, 26]

(2) single ignite molecular cells reach the saturated adsorption state and the system energy is the lowest after adsorbing 7 CH_4 molecules, 9 CO_2 molecules, or 27 H_2O molecules. With continuous adding of adsorbate molecules, the adsorption system begins to repel gas molecules and the total system energy increases gradually [21]

(3) in the process of CH_4, CO_2, and H_2O adsorption in lignite molecules, adsorption of CH_4 and CO_2 is typical physical adsorptions. The adsorption energy of CH_4 is provided by E_v in the nonbonding energy, while the adsorption energy of CO_2 is provided by E_c and E_v in the nonbonding energy together. Adsorption of H_2O involves both chemical and physical adsorptions, and the adsorption energy of H_2O is attributed to both nonbonding energy and $E_{b\text{-}H}$. This conforms to previous research conclusions [23, 43–45]

3.4. Effects of Temperature on Adsorption Behaviors. Isothermal curves of CH_4, CO_2, and H_2O adsorptions in lignite under 0.00~10.00 MPa and at different temperatures (283.15 K, 303.15 K, and 323.15 K) are shown in Figure 9.

Based on single-gas adsorption in lignite molecules, it can be seen clearly that temperature can inhibit adsorption. This can be explained as follows. CH_4, CO_2, and H_2O adsorptions in coals which are porous media belong to physical adsorption, and thermal movement of gas molecules is intensified with the increase of system temperature, thus increasing kinetic energy of adsorbate molecules. Under this circumstance, the probability for gas molecules to get rid of binding of adsorption energy increases. In particular, the probability of VDW force which promotes desorption increases, and the difficulties of capturing adsorbed gas molecules on the coal surface are increased, thus reducing adsorbing capacity [44, 46, 47]. Meanwhile, the gas molecular adsorption on the coal surface is a heat-releasing process, and temperature rise is against the heat releasing, which is the reason for decreasing adsorption capacity of lignite [48, 49].

4. Conclusions

In this work, adsorption characteristics of CH_4, CO_2, and H_2O molecules in lignite are discussed through a simulation. The selection optimization and simulation methods of the lignite molecular models are elaborated thoroughly. Moreover, adsorption capacities of CH_4, CO_2, and H_2O in lignite molecules, saturated molecular configuration, evolutions of adsorption energies, and influences of temperature on adsorption behavior are analyzed. Some major conclusions could be drawn:

(1) The classical Wiser model can reflect the basic features of low-metamorphism lignite comprehensively. After molecular dynamics optimization and annealing process, the lignite molecular structure becomes more compacted and has stronger stereo perception. Based on a density energy simulation, the constructed lignite molecular model is proved applicable to simulation of adsorption characteristics

(2) Adsorption capacities of CH_4, CO_2, and H_2O in lignite are significantly different. Given the same temperature and pressure, H_2O shows the highest ultimate adsorption capacity of these three gases in unit mass of lignite, followed by CO_2 and CH_4 successively. The isothermal curves present well "I-type" characteristics

(3) A single lignite molecular cell reaches saturated adsorption upon 7 CH_4 molecules, 9 CO_2 molecules, or 27 H_2O molecules. The molecular configurations of lignite molecules to CH_4, CO_2, and H_2O gases are extracted, finding that all gas molecules distribute

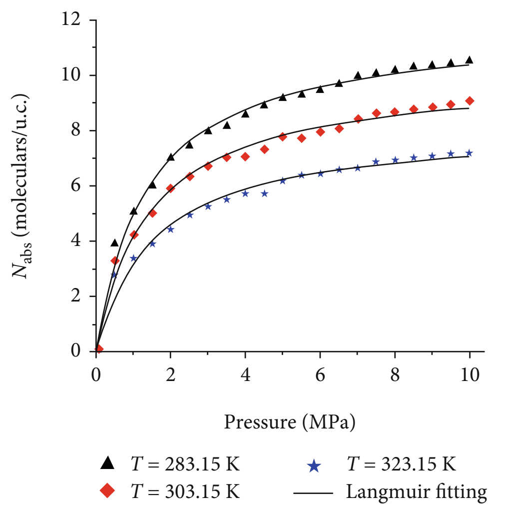

(a) The lignite adsorption isotherms of CH_4 at different temperatures

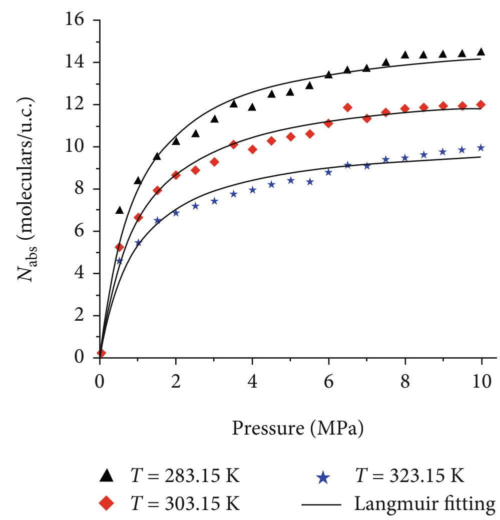

(b) The lignite adsorption isotherms of CO_2 at different temperatures

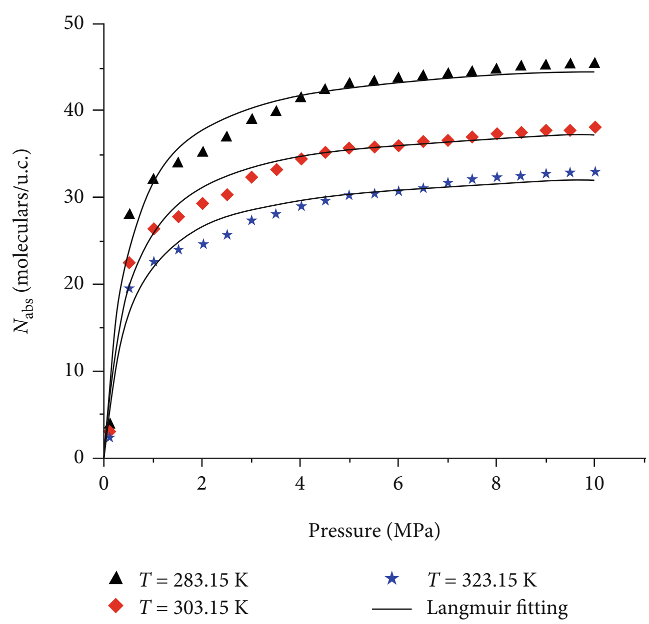

(c) The lignite adsorption isotherms of H_2O at different temperatures

Figure 9: The lignite adsorption isotherms of CH_4, CO_2, and H_2O at different temperatures.

at two sides of the lignite molecular chain. Specifically, CH_4 molecules are in clustering distributions and form a pairwise crossing ethane conformation. CO_2 molecules are in parallel or crossing and even vertical arrangement. H_2O molecules point to the coal molecules or oxygen atoms in surrounding H_2O molecules as a response to the hydrogen bond energies

(4) The CH_4 and CO_2 adsorptions in lignite are typical physical adsorption, and adsorption energies are provided by nonbonding energies. However, H_2O adsorption involves both physical and chemical adsorptions, with adsorption energies provided by both nonbonding energy and hydrogen bond energy

(5) Temperature can inhibit adsorption of lignite since CH_4 CO_2 and H_2O adsorptions in lignite are physical adsorptions. With the increase of temperature, thermal movement of gas molecules is intensified. As a result, kinetic energy of adsorbate molecules increases, and the difficulties of adsorbed gas molecules are increased. Temperature rise is not in favor of the adsorption-induced heat releasing

Data Availability

The data used to support the findings of this study are included within the article.

Conflicts of Interest

The authors declare that they have no conflicts of interest.

Acknowledgments

This work was supported by the National Natural Science Foundation of China (Grant No.: 51974109), the Program for Leading Talents in Scientific and Technological Innovation of Henan Province (Grant No.: 204200510032), the Scientific and Technological Projects of Henan Province (Grant No.: 202102310220), the Plan of Key Scientific Research Project of Colleges and Universities in Henan Province (Grant No.: 20A620001), the Natural Science Foundation of Henan Province of China (Grant No.: 202300410182), and the Henan Polytechnic University Doctoral Fund (Grant No.: B2019-55).

References

[1] J. X. Yang, Y. Q. He, and X. Y. Zhang, "Energy development trend and the coal enterprises'countermeasures in China under the background of low-carbon economy," *China Mining Magazine*, vol. 19, no. 8, pp. 58–61, 2010.

[2] L. L. Si, H. T. Zhang, J. P. Wei, B. Li, and H. K. Han, "Modeling and experiment for effective diffusion coefficient of gas in water- saturated coal," *Fuel*, vol. 284, p. 118887, 2021.

[3] C. Mcglade, J. Speirs, and S. Sorrell, "Unconventional gas – a review of regional and global resource estimates," *Energy*, vol. 55, pp. 571–584, 2013.

[4] A. Stephen, A. Adebusuyi, and A. Baldygin, "Bioconversion of coal: new insights from a core flooding study," *RSC Advances*, vol. 4, no. 43, pp. 22779–22791, 2014.

[5] T. A. Moore, "Coalbed methane: a review," *International Journal of Coal Geology*, vol. 101, pp. 36–81, 2012.

[6] Y. Xue, T. Teng, F. Dang, Z. Ma, S. Wang, and H. Xue, "Productivity analysis of fractured wells in reservoir of hydrogen and carbon based on dual-porosity medium model," *International Journal of Hydrogen Energy*, vol. 45, no. 39, pp. 20240–20249, 2020.

[7] J. Liu, X. Liang, Y. Xue, K. Yao, and Y. Fu, "Numerical evaluation on multiphase flow and heat transfer during thermal stimulation enhanced shale gas recovery," *Applied Thermal Engineering*, vol. 178, p. 115554, 2020.

[8] X. Liu, D. Song, X. He, Z. Wang, M. Zeng, and L. Wang, "Quantitative analysis of coal nanopore characteristics using atomic force microscopy," *Powder Technology*, vol. 346, pp. 332–340, 2019.

[9] X. Liu, Z. Wang, D. Song, X. He, and T. Yang, "Variations in surface fractal characteristics of coal subjected to liquidCO2-phase change fracturing," *International Journal of Energy Research*, vol. 44, no. 11, pp. 8740–8753, 2020.

[10] X. Wang and B. Lin, "How to reduce $_{CO\ 2}$ emissions in China's iron and steel industry," *Renewable and Sustainable Energy Reviews*, vol. 57, pp. 1496–1505, 2016.

[11] X. F. Xian, "The present situation of coal-bed methane mining and utilization in our country and looking forward to its industrialization," *Journal of Chongqing University*, vol. 15, no. 1, pp. 1–5, 2000.

[12] Y. K. Ma, B. S. Nie, X. Q. He, X. C. Li, J. Q. Meng, and D. Z. Song, "Mechanism investigation on coal and gas outburst: an overview," *International Journal of Minerals, Metallurgy and Materials*, vol. 27, no. 7, pp. 872–887, 2020.

[13] Z. Liao, X. Liu, D. Song et al., "Micro-structural damage to coal induced by liquid CO_2 phase change fracturing," *Natural Resources Research*, vol. 30, no. 1, pp. 1613–1627, 2021.

[14] K. Mosher, J. J. He, Y. Y. Liu, E. Rupp, and J. Wilcox, "Molecular simulation of methane adsorption in micro- and mesoporous carbons with applications to coal and gas shale systems," *International Journal of Coal Geology*, vol. 109, pp. 36–44, 2013.

[15] V. Prabu and N. Mallick, "Coalbed methane with CO_2 sequestration: an emerging clean coal technology in India," *Renewable & Sustainable Energy Reviews*, vol. 50, pp. 229–244, 2015.

[16] M. S. A. Perera, "Influences of CO2injection into deep coal seams: a review," *Energy & Fuels*, vol. 31, no. 10, pp. 10324–10334, 2017.

[17] W. N. Zhou, H. B. Wang, Z. Zhang, H. X. Chen, and X. L. Liu, "Molecular simulation of CO_2/CH_4/H_2O competitive adsorption and diffusion in brown coal," *RSC Advances*, vol. 9, no. 6, pp. 3004–3011, 2019.

[18] K. R. Matranga, A. L. Myers, and E. D. Glandt, "Storage of natural gas by adsorption on activated carbon," *Chemical Engineering Science*, vol. 47, no. 7, pp. 1569–1579, 1992.

[19] M. R. Narkiewicz and J. P. Mathews, "Visual representation of carbon dioxide adsorption in a low-volatile bituminous coal molecular model," *Energy & Fuels*, vol. 23, no. 10, pp. 5236–5246, 2009.

[20] S. J. Zhang, C. W. Li, and C. Ding, "Molecular fragment model of coal surface and molecular mechanics simulation of gas adsorption," *Mining Research and Development*, vol. 30, no. 1, pp. 88–91, 2010.

[21] J. H. Xiang, F. G. Zeng, H. Z. Liang, B. Li, and X. X. Song, "Molecular simulation of the CH_4/CO_2/H_2O adsorption onto the molecular structure of coal," *Scientia Sinica(Terrae)*, vol. 44, no. 7, pp. 1418–1428, 2014.

[22] Y. Dang, L. M. Zhao, X. Q. Lu, J. Xu, and P. P. Sang, "Molecular simulation of CO_2/CH_4 adsorption in brown coal: effect of oxygen-, nitrogen-, and sulfur-containing functional groups," *Applied Surface Science*, vol. 423, pp. 33–42, 2017.

[23] Y. Song, J. Bo, and L. Wu, "Molecular simulation of CH_4/CO_2/H_2O competitive adsorption on low rank coal vitrinite," *Physical Chemistry Chemical Physics*, vol. 19, no. 27, pp. 17773–17788, 2017.

[24] H. Xu, W. Chu, and X. Huang, "CO_2 adsorption-assisted CH_4 desorption on carbon models of coal surface: a DFT study," *Applied Surface Science*, vol. 375, pp. 196–206, 2016.

[25] X. F. You, M. He, W. Zhang, H. B. Wei, Q. Q. He, and L. Li, "Molecular dynamics simulations and contact angle of surfactant at the coal–water interface," *Molecular Simulation*, vol. 44, no. 9, pp. 722–727, 2018.

[26] S. G. Li, Y. Bai, H. F. Lin, C. M. Shu, M. Yan, and L. W. Bin, "Molecular simulation of adsorption of gas in coal slit model under the action of liquid nitrogen," *Fuel*, vol. 255, p. 115775, 2019.

[27] D. M. Gao, H. Lin, J. R. Wang, and D. Zheng, "Molecular simulation of gas adsorption characteristics and diffusion in micropores of lignite," *Fuel*, vol. 269, p. 117443, 2020.

[28] H. X. Hu, L. Du, Y. F. Xing, and X. C. Li, "Detailed study on self- and multicomponent diffusion of CO_2 、CH_4, gas mixture in coal by molecular simulation," *Fuel*, vol. 187, pp. 220–228, 2017.

[29] J. You, L. Tian, C. Zhang, H. X. Yao, W. Dou, and B. Fan, "Adsorption behavior of carbon dioxide and methane in bituminous coal: a molecular simulation study," *Chinese Journal of Chemical Engineering*, vol. 24, no. 9, pp. 1275–1282, 2016.

[30] J. P. Mathews and A. L. Chaffee, "The molecular representations of coal – a review," *Fuel*, vol. 96, pp. 1–14, 2012.

[31] P. H. Given, "The distribution of hydroxyl in coal and its relation to coal structure," *Fuel*, vol. 39, pp. 147–158, 1960.

[32] J. H. Shinn, "Towards an understanding of the coal structure," *Fuel Processing Technology*, vol. 63, no. 8, pp. 483–497, 1984.

[33] Y. Zhang, L. X. Zhou, and J. Zhang, "Simplified Solomon pyrolysis model and simulation of no formation in swirling coal combustion," *Journal of Chemical Industry and Engineering (China)*, vol. 54, no. 9, pp. 1274–1278, 2003.

[34] M. L. Connolly, "Solvent-accessible surfaces of proteins and nucleic acids," *Science*, vol. 221, no. 4612, pp. 709–713, 1983.

[35] B. Q. Dai, A. Hoadley, and L. Zhang, "Characteristics of high temperature C-CO_2 gasification reactivity of Victorian brown coal char and its blends with high ash fusion temperature bituminous coal," *Fuel*, vol. 202, pp. 352–365, 2017.

[36] X. J. Li, L. Y. Cai, and H. Xu, "Feasibility study on coal seam gas flow based on molecular dynamics simulation," *Safety in Coal Mines*, vol. 39, no. 7, pp. 84–87, 2008.

[37] Z. S. Li, Y. J. Zhao, X. N. Jia, and L. R. Zhang, "Development of molecular dynamics computer simulation," *Mechanical Management and Development*, vol. 23, no. 2, pp. 174–176, 2008.

[38] Y. H. Wen, R. Z. Zhu, F. X. Zhou, and C. Y. Wang, *Main Techniques of Molecular Dynamics Simulation*, vol. 1, pp. 65–73, 2003.

[39] Z. Y. Gao, S. K. Lv, J. D. Li, P. F. Yang, and C. M. Chen, "Micro-mechanism of water molecule adsorption on lignite surfaces," *Journal of Chinese Society of Power Engineering*, vol. 36, no. 4, pp. 258–264, 2016.

[40] N. Metropolis, A. W. Rosenbluth, M. N. Rosenbluth, A. H. Teller, and E. Teller, "Equation of state calculations by fast computing machines," *Journal of Chemical Physics*, vol. 21, no. 6, pp. 1087–1092, 1953.

[41] H. Chen, J. M. Li, and B. Sun, "Application of characteristics of the coal isothermal adsorption curve in coalbed methane research," *Journal of Chongqing University of Science and Technology*, vol. 13, no. 2, pp. 24–26, 2011.

[42] J. F. Zhang, M. B. Clennell, K. Y. Liu, D. N. Dewhurst, M. Pervukhina, and N. Sherwood, "Molecular dynamics study of CO_2 sorption and transport properties in coal," *Fuel*, vol. 177, pp. 53–62, 2016.

[43] G. C. Chen and X. F. Xian, "Ab intio study on the interaction between CH_4 and the coal surface," *Journal of Chongqing University*, vol. 23, no. 3, pp. 77–79, 2000.

[44] Y. J. Cui, L. W. Zhong, and Q. Zhang, "The quantum chemical study on different rank coals surface interacting with methane," *Journal of China Coal Society*, vol. 32, no. 3, pp. 292–295, 2007.

[45] A. A. Sizova, V. V. Sizov, and E. N. Brodskaya, "Molecular mechanisms of the effect of water on CO_2/CH_4 mixture adsorption in slitlike carbon pores," *Colloid Journal*, vol. 80, no. 4, pp. 439–446, 2018.

[46] T. J. Zhang, H. J. Xu, and S. G. Li, "The effect of temperature on the adsorbing capability of coal," *Journal of China Coal Society*, vol. 34, no. 6, pp. 802–805, 2009.

[47] L. Si, J. Wei, Y. Xi et al., "The influence of long-time water intrusion on the mineral and pore structure of coal," *Fuel*, vol. 290, article 119848, 2021.

[48] L. W. Zhong, Y. Z. Zheng, and Z. R. Yuan, "The adsorption capability of coal under integrated influence of temperature and pressure and predicted of content quantity of coal bed gas," *Journal of China Coal Society*, vol. 27, no. 6, pp. 581–585, 2002.

[49] H. G. Sui and J. Yao, "Effect of surface chemistry for CH_4/CO_2 adsorption in kerogen: a molecular simulation study," *Journal of Natural Gas Science and Engineering*, vol. 31, pp. 738–746, 2016.

Hindawi
Geofluids
Volume 2021, Article ID 5570884, 10 pages
https://doi.org/10.1155/2021/5570884

Research Article

Study on the Development Height of Overburden Water-Flowing Fracture Zone of the Working Face

Ke Ding[1] **Lianguo Wang**[1] **Wenmiao Wang**[2] **Kai Wang,**[1] **Bo Ren**[1] **and Chongyang Jiang**[1]

[1]*State Key Laboratory for Geomechanics and Deep Underground Engineering, China University of Mining and Technology, Xuzhou, Jiangsu 221116, China*
[2]*School of Mines, China University of Mining and Technology, Xuzhou, Jiangsu 221116, China*

Correspondence should be addressed to Lianguo Wang; cumt_lgwang@163.com

Received 9 February 2021; Revised 9 February 2021; Accepted 4 March 2021; Published 18 March 2021

Academic Editor: Yi Xue

Mining-induced fractures in underground coal mining face affect the stability of overburdens and provide preferential channels for water and material transfer in the underground environment. Therefore, to study the development of water-flowing fracture zones in overburdens of working face and goaf is of great significance for roof control, gas drainage, water resistance, disaster reduction, and efficient mining from the mining. In this study, a new method for predicting the development of overburden water-flowing fracture zone height (DHOWFFZ) was proposed based on the characteristics of overburden rock in No. 3 coal seam of Xin'an Coal Mine. First, the stope of No. 3 coal seam exhibits a rock stratum structure of mudstone and sandstone overlapping. Considering this characteristic, the overburden strata of No. 3 coal seam are divided into several "mudstone-sandstone" rock stratum groups. Furthermore, the ultimate tensile deformation of soft rock is greater than that of hard rock. It is proposed to judge the development degree of penetrating fracture in each rock stratum by adopting the elongation rate of mudstone intermediate layer. Meanwhile, the DHOWFFZ of "mudstone sandstone" composite rock stratum structure in the 3402 working face of No. 3 coal seam is calculated to be smaller than 43.1 m according to the actual situation. Finally, the DHOWFFZ in the 3402 working face was measured in the field, which verifies the rationality of the new DHOWFFZ prediction method. The research results provide new ideas for the prediction of DHOWFFZ and are helpful for future research in related fields.

1. Introduction

The repaid development of China's economic situation is pushing large-scale coal mining area growth and development. However, the large-scale mining of coal resources has caused great damage to the surrounding environment and communities and brought irreparable losses to people's production and life [1–3]. These problems are all related to the deformation and damage of the overburdens caused by the mining of coal resources. Therefore, how to effectively predict the deformation and cracking of the overburdens of the mining coal seams has a very important practical significance for the protection of the overlying aquifers and surface water resources and the prediction of mine water damage accidents [4–6].

The overburden water-flowing fracture zone is not only an important indicator reflecting the damage of overburdens but also a crucial channel for water flowing into the goaf and causing various mine disasters. Therefore, the development height of overburden water-flowing fracture zone (DHOWFFZ) is an important technical parameter for safe mining under a mine water body. Its height is an intuitive description of the shape of the water-flowing fracture zone. At present, field observation is the most accurate method to determine the DHOWFFZ, and the commonly used observation methods include underground double-end water plugging observation method, surface drilling flushing fluid consumption observation method, high-density resistivity method, and television imaging method [7–9]. However, the traditional empirical formula method is generally adopted in the prediction of DHOWFFZ currently in China because the complex field observation operation may affect the efficient production in coal mines. The traditional empirical formula method is $H = (1 \sim 3)(m - S_A)/(K_A - 1)m$, where H is DHOWFFZ; m is the coal seam thickness; S_A is the settlement value of the rock beam at the gangue is generally selected according to the empirical value; and K_A is the coefficient of broken expansion of the fallen rock strata at the gangue of the rock beam [10, 11]. In recent years, extensive in-depth researches have been conducted on the prediction of DHOWFFZ, showing promising results. The empirical formula for DHOWFFZ prediction in China is developed based on the summary of vast data obtained during coal mining. Since only the mining thickness of coal seam is considered in the formula, the calculated results are quite different from the actual measured results in practical application, indicating certain limitations [12]. When investigating DHOWFFZ, scholars at home and abroad have recognized the deficiency of the empirical formula method and have proposed various new theories and methods to accurately estimate the value of DHOWFFZ research. Abbas et al. [13] proposed a new parameter influencing the DHOWFFZ, namely, the lithology proportion factor of hard rock, which avoided the statistical determination of uniaxial compressive strength involved in the classification of various roof types in the currently used standards; Hu et al. [14] put forward a new DHOWFFZ prediction method based on the position of key overburdens strata. Chai et al. [15] established a GA-SVR mining DHOWFFZ prediction model and verified by practice that the accuracy of the model could meet the actual requirements. Adhikary and Guo [16] revealed a theoretical DHOWFFZ calculation method for fully mechanized mining by constructing three models, i.e., (i) a complete mechanical model of rock stratum suspension, (ii) a model of rock stratum overhanging, and (iii) breaking and a mechanic model of broken rock block. Huang et al. [17] proposed a new DHOWFFZ prediction method of calculating overlying bedrock composite structure and rock stratum tensile deformation. In general, current researches on the DHOWFFZ are still in the stage of exploration and experience accumulation.

The roof of coal seam in Xin'an Coal Mine is composed of mudstone and sandstone. Each rock stratum possesses a "mudstone-sandstone" composite structure comprising a lower layer of hard sandstone and an upper layer of soft mudstone. In this study, based on the characteristics of mudstone and sandstone crosscombination in the roof of No. 3 coal seam in Xin'an Coal Mine. A new method for calculating the DHOWFFZ is proposed in light of the calculation method of horizontal tensile deformation of soft rock stratum. The method works by calculating the elongation rates of mudstone intermediate layers in rock stratum groups and analyzing the law of fracture development in rock strata. The new DHOWFFZ prediction method is suitable for "mudstone-sandstone" composite rock stratum structure.

2. Analysis of the Influence of "Mudstone-Sandstone" Composite Rock Stratum Structure on the Development of Water-Flowing Fracture Zone

2.1. Engineering Geology. Xin'an Coal Mine is located in Liuzhuang Town, Weishan County, Shandong Province, China. The surface above the mine is Weishan Lake which covers an area of about 1266 km^2. Coal-bearing strata of the mine belong to Shanxi Formation and Taiyuan Formation, and No. 3 coal seam with an average thickness of 8.7 m is the main mining coal seam. No. 3 coal seam is affected by two layers of aquifers in the mine: (1) the first is a sandstone karst fracture aquifer located 55-89 m above No. 3 coal seam. With a thickness of 12.6-21.1 m and a unit water inflow of 0.02483-0.79245 L/s·m, the aquifer belongs to a weak to medium water-rich aquifer. (2) The second is roof and floor sandstone aquifers in No. 3 coal seam. The roof and floor sandstones, both mainly composed of fine sandstone, are 8.0-45.4 m and 4.1-10.6 m in thickness, respectively. With a unit water inflow of 0.0369-0.16434 L/s·m, the aquifers belong to weak water-rich fractured confined aquifers. To avoid the effect of water-flowing fracture zone on the water body, the development rule of water-flowing fracture zone is analyzed by taking the 3402 working face of Xin'an Coal Mine as an example. The position of 3402 working face is displayed in Figure 1.

The ground elevation and elevation of the 3402 working face are +31.56~+32.52 m and -525.6~-604.2 m, respectively. The mining coal seam is No. 3 coal seam whose average thickness and average dip angle are 8.7 m is 9°, respectively. The overburden roof, which belongs to medium hard rock strata in terms of overall structure, is mainly composed of mudstone and sandstone. The specific rock structure within 70 m of overburdens above the working face is exhibited in Figure 2.

As can be seen from Figure 2, there are 9 layers of weak mudstones and sandy mudstones and 7 layers of hard fine sandstones and siltstones within 70 m of overburdens above the working face. The overburdens are characterized by obvious stratification. From No. 3 sandy mudstone upward, each layer of mudstone is separated by a layer of sandstone, and the overburdens exhibit a rock stratum structure of mudstone and sandstone overlapping. Moreover, each layer of mudstone shares a similar thickness with the adjacent layer of sandstone above.

The roof rock was collected from the 3402 working face of No. 3 coal seam in Xin'an Coal Mine and processed into cylindrical samples with a diameter of 50 mm and heights of 100 mm and 25 mm and cubic samples with a side length of 100 mm. Then, sample density was obtained using MH-300Z mineral rock densitometer. Further, classical mechanical testing was performed to obtain their uniaxial compression strength, tensile strength, and shear resistance, as shown in Figures 3–5. The corresponding data acquired were analyzed to obtain the mechanical parameters of each rock layer.

The test results of mechanical parameters of rock layers within 70 m above the roof of No. 3 coal seam in Xin'an Coal Mine are listed in Table 1. It can be known by testing the basic mechanical parameters that the mechanical properties of sandstone layers in the roof differ slightly, and those of

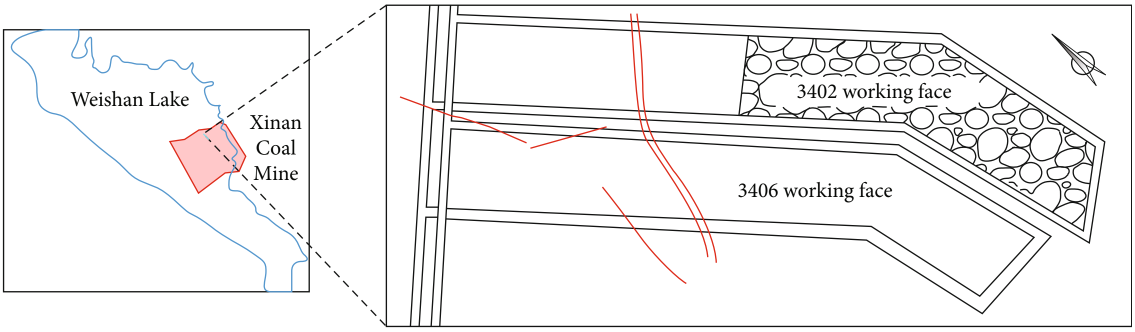

Figure 1: Position map of 3402 working face.

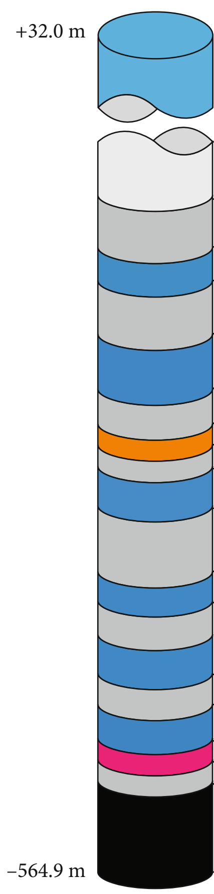

Order	Lithology	Thickness (m)	Distance to coal seam roof (m)	Rock association
18	Conglomerate	17.3	67.7	
17	Mudstone	4.3	50.4	Rock formation 7
16	Fine sandstone	3.0	46.1	
15	Mudstone	4.8	43.1	Rock formation 6
14	Fine sandstone	4.6	38.3	
13	Mudstone	2.4	33.7	Rock formation 5
12	Siltstone	1.5	31.3	
11	Mudstone	1.4	29.8	Rock formation 4
10	Fine sandstone	3.8	28.4	
9	Mudstone	6.7	24.6	Rock formation 3
8	Fine sandstone	2.5	17.9	
7	Mudstone	3.3	15.4	Rock formation 2
6	Fine sandstone	4.0	12.1	
5	Mudstone	2.4	8.1	Rock formation 1
4	Fine sandstone	3.0	5.7	
3	Sandy mudstone	1.3	2.7	
2	Mudstone	1.4	1.4	
1	No.3 coal	8.7	0	

Figure 2: Overburden stratum structure.

mudstone layers in the roof are also similar. Besides, the strength of sandstone is greater than that of mudstone.

2.2. Analysis of "Mudstone-Sandstone" Composite Rock Stratum Structure. Numerous previous studies have revealed that after the coal seam is mined, the overburdens bend and subside in the form of stratum groups. In each stratum group, a layer of hard rock at the bottom drives the upper layers of softer rock to move synchronously and coordinately. The movement and combination of rock strata are determined by the strength factors (including lithology, thickness, elastic modulus) of each rock stratum. The upper rock stratum with low strength factors will move simultaneously with the lower rock stratum with high strength factors, and the ultimate elongation rate of upper rock stratum with low strength factors is higher than that of lower rock stratum with high strength factors [18].

The fully mechanized caving coal mining technology is adopted in the working face of No. 3 coal seam in Xin'an Coal Mine. As the working face advances, the relatively weak mudstone 1.4 m above No. 3 coal seam and sandy mudstone 1.3 m above No. 3 coal seam will collapse together with the remaining coal in the process of coal caving. As illustrated in Figure 1, from No. 4 rock stratum upwards, the roof of No. 3 coal seam exhibits a rock stratum structure of mudstone and sandstone overlapping, and each layer of

Figure 3: Uniaxial compression test.

Figure 4: Brazilian splitting test.

Figure 5: Shear resistance experiment.

mudstone shares a similar thickness with the adjacent layer of sandstone above. According to this characteristic, the roof overburden strata of No. 3 coal seam are divided into 7 rock stratum groups, each comprising a sandstone layer and a mudstone layer. Since the strength of sandstone is greater than that of mudstone and the thicknesses of mudstone and sandstone are similar in each group, it can be inferred that the fracture development of each rock stratum group is controlled by the movement of sandstone in the lower part, and the mudstone and sandstone move synchronously and coordinately. In addition, since the ultimate elongation deformation of soft rock is greater than that of hard rock [19], it is assumed that when the mudstone fails to form a fracture as it undergoes tensile deformation, the water-flowing fracture zone develops at most to the rock stratum group where the mudstone is located. Therefore, the maximum DHOWFFZ can be determined by analyzing and judging whether mudstone tensile deformation in each rock stratum group can lead to the formation of enough penetrating fractures which enable water to flow smoothly.

2.3. Analysis of Rock Stratum Deformation Criterion for the DHOWFFZ. According to the above analysis, with the overburden strata divided into groups, the judgment of DHOWFFZ can be transformed into the analysis of tensile deformation of the 7 layers of mudstone. Since the mudstone above the working face is soft rock, compared with the original horizontal state, the mudstone in the deformed state will be elongated as it bends and subsides, as shown in Figure 6. The tensile deformation value of the soft layer is a comprehensive parameter reflecting the development of fractures in rock strata. The fracture development degree and hydraulic conductivity of soft rocks share a direct causal relationship with the tensile deformation of rock [20]. Hence, the elongation rate of mudstone intermediate layer can be regarded as a criterion to analyze the fracture development degree and hydraulic conductivity of "mudstone-sandstone" composite rock stratum structure.

The deformation curve of mudstone is divided into three sections, namely, the approximately horizontal section in the middle and the elongated curve sections on both sides. The deformation increased by the subsidence and elongation of rock intermediate layer is mainly concentrated in the curve sections of the subsided basin. Therefore, the deformation rate ε of rock intermediate layer can be expressed as

$$\varepsilon = \frac{(l_1 - l_0)}{l_0}, \tag{1}$$

where l_0 is the length of rock intermediate layer before bending and deformation and l_1 is the arc length of the curve sections of rock intermediate layer after bending and deformation.

By means of fitting the two arcs, two parameters required for the calculation of layer elongation rate ε are obtained:

$$l_0 = h_j(\cot \delta_0 + \cot \varphi_0), \tag{2}$$

$$l_1 = \left(w_j^2 + l_0^2\right) \text{artsin}\left[2w_j l_0 / \left(w_j^2 + l_0^2\right)\right] \pi / (180 \times 2w_j),. \tag{3}$$

where h_j is the height of the jth rock intermediate layer (m); $h_j = \sum_{i=1}^{j-1} h_i + h_0/2$ in which $\sum_{i=1}^{j-1} h_i$ is the total thickness of

Table 1: Test results of physical and mechanical parameters.

Sample No.	Rock name	Uniaxial compressive strength (MPa)	Average (MPa)	Tensile strength (MPa)	Average (MPa)	Elastic modulus(GPa)	Average (GPa)	Bulk density (g/cm^3)	Average (g/cm^3)
1	No. 4 fine sandstone	69.91		9.47		6.65		2.56	
2	No. 6 fine sandstone	65.33		8.55		8.60		2.58	
3	No. 8 fine sandstone	69.07		9.21		8.01		2.55	
4	No. 10 fine sandstone	71.26	69.78	9.55	9.25	7.88	8.29	2.56	2.54
5	No. 12 siltstone	73.63		9.90		10.07		2.43	
6	No. 14 fine sandstone	70.08		9.33		8.24		2.56	
7	No. 16 fine sandstone	68.52		8.74		8.59		2.54	
8	No. 3 sandy mudstone	28.57		2.11		2.96		2.43	
9	No. 5 mudstone	21.43		1.80		2.73		2.35	
10	No. 7 mudstone	24.18		1.91		2.74		2.41	
11	No. 9 mudstone	21.66		2.36		3.52		2.39	
12	No. 11 mudstone	30.40	25.61	1.42	1.76	2.99	2.96	2.39	2.39
13	No. 13 mudstone	27.43		1.17		2.73		2.35	
14	No. 15 mudstone	25.63		1.55		3.11		2.40	
15	No. 17 mudstone	25.61		1.76		2.89		2.37	
16	No. 18 conglomerate	55.70	55.70	6.63	6.63	6.80	6.80	2.63	2.63

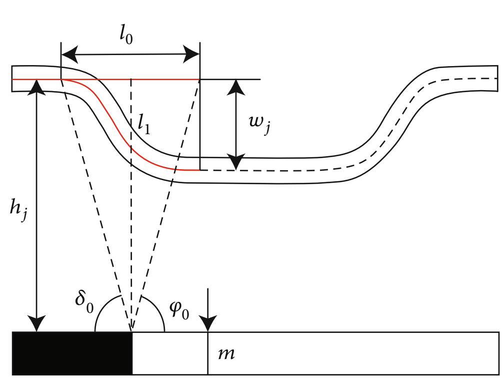

Figure 6: Sketch map of tensile deformation of rock stratum.

lower layers (m); h_0 is the thickness of the rock layer, m; δ_0 is the mining boundary angle of the coal seam; φ_0 is the angle of full mining; and w_j is the maximum subsidence of the rock stratum group where the jth layer of mudstone is located (m).

According to the research [21], the size of free movement space of rock stratum is a key factor that determines the bending and subsidence of rock stratum and the full development of penetrating fractures. And the free space formed after mining of coal seams will be filled by fractured and expanded overburden rock. By taking into account the bulking coefficient of each rock layer, the maximum subsidence w_j of a certain mudstone intermediate layer in the "mudstone-sandstone" composite rock stratum structure can be calculated according to Equation (4):

$$w_j = m - \sum_{i=1}^{j-1} h_i(k_i - 1), \tag{4}$$

where m is the mining thickness of coal seam (m) and k_i is the residual bulking coefficient of sandstone in the ith group below.

Table 2: Calculation parameters of layer elongation rate.

Rock layer	Height of rock intermediate layer (m)	Cot δ_0	Cot φ_0	Mining thickness (m)	Bulking coefficient of rock layer	Maximum subsidence of rock layer (m)	Layer elongation rate ε
No. 5 mudstone	8.64	0.577	0.577	8.70	1.14	5.92	22.07%
No. 7 mudstone	15.49	0.577	0.577	8.70	1.13	5.16	5.54%
No. 9 mudstone	22.99	0.577	0.577	8.70	1.12	4.60	2.15%
No. 11 mudstone	30.84	0.577	0.577	8.70	1.11	3.64	0.70%
No. 13 mudstone	34.24	0.577	0.577	8.70	1.11	3.33	0.53%
No. 15 mudstone	42.44	0.577	0.577	8.70	1.11	2.56	0.12%
No. 17 mudstone	49.99	0.577	0.577	8.70	1.10	2.18	0.09%

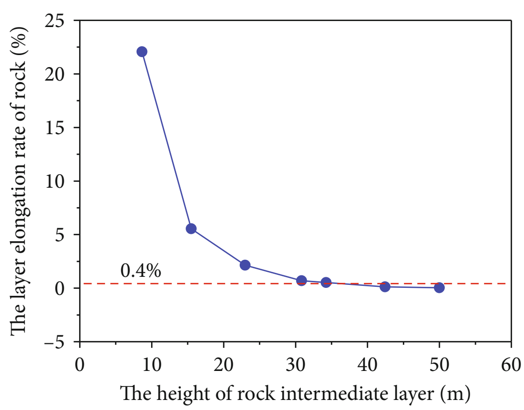

Figure 7: Relationship curve between the layer elongation rate of rock and the height of rock intermediate layer.

The elongation rate of a certain mudstone intermediate layer above the coal seam roof can be obtained by combining Equations (1)–(4). It can be seen that the elongation rate ε of a rock layer is mainly affected by factors such as the height of the rock stratum group, the thickness of the stratum, the bulking coefficient of sandstone in the rock stratum group, the boundary angle, and the angle of full mining.

The bulking coefficient of caved immediate roof in the goaf can be measured in the field, but that of upper rock strata can hardly be accurately measured in the field. The value of bulking coefficient, however, directly influences the subsidence space of different rock strata. According to the researches [22, 23], the smaller the size of fragmented rock block is, the greater the bulking coefficient is. Besides, in the vertical direction, with the increase of distance from the goaf, the size of fragmented rock block increases rapidly, and the residual bulking coefficient of it gradually decreases as a logarithmic function. The relationship between the average bulking coefficient k and the distance from the mining coal seam hi (i.e., the total thickness of lower rock strata) can be expressed by the function $k = \mathrm{kz} - 0.017\ln \mathrm{hi}$ (hi < 100) where kz is the bulking coefficient of the immediate roof below [24–26]. $\cot \delta_0 = \cot \varphi_0 = 0.577$ in accordance with Regulations on Coal Pillar Retention and Coal Mining under Buildings, Water Bodies, Railways and Main Shafts [5]. The data of working face suggest that the recovery rate of the 3402 working face is 80%. Given the recovery rate, the actual mining height of coal in the working face is about 6.96 m, and the rest of coal and roof strata are broken together and left in the goaf. Therefore, kz takes the value of the bulking coefficient of coal, namely, 1.17, according to the field test. Combined with Figure 2, the values of calculation parameters of the elongation rate of mudstone intermediate layer are given in Table 2.

For full comparison and explanation, the elongation rates of mudstone intermediate layers in these rock stratum groups were collated, based on which the fitting curve between the layer elongation rate of rock and the height of rock intermediate layer was plotted, as disclosed in Figure 7.

As can be observed from Figure 7, the relationship between the layer elongation rate of rock and the height of rock intermediate layer is a negative exponential function. The closer the rock layer is to the working face, the higher its layer elongation rate is, indicating that the more seriously it bends and subsides. As the height of rock layer increases, the layer elongation rate decreases as a negative exponential function. For soft rocks such as mudstone and sandy mudstone, the critical elongation rate of the rock layer is over 0.4%. That is, when the elongation rate of the rock layer is lower than 0.4%, the upward development of the water-flowing fracture zone can be restrained. Thus, the elongation rate drops from 0.53% to 0.12% from No. 13 mudstone to No. 15 mudstone, which is a turning point for the layer elongation rate. After passing this turning point, the elongation rates of mudstone layers are all lower than 0.4%. This demonstrates that no penetrating fractures are generated in No. 15 mudstone which basically stays out of the range of the

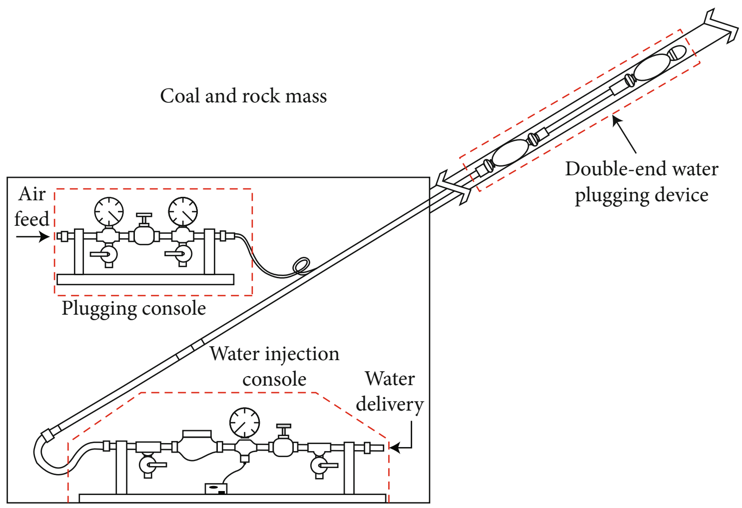

Figure 8: Working principle of observation instrument.

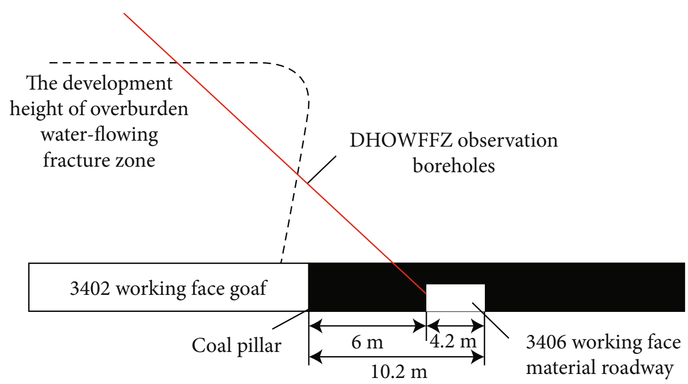

Figure 9: Schematic diagram of measurement borehole arrangement.

water-flowing fracture zone. It can be concluded that the DHOWFFZ does not exceed the height of the 6th rock stratum group, namely, 43.1 m.

3. Field Measurement of DHOWFFZ

The field measurement was conducted by the method of underground double-end water plugging observation with the aid of a DHOWFFZ observation instrument. The working principle and structure of the observation instrument are shown in Figure 8. Observation points were arranged in the adjacent 3406 working face material roadway, and DHOWFFZ observation boreholes were constructed to the roof above the goaf of the 3402 working face. The coal pillar in the section is 6 m wide. The length of each constructed observation borehole should exceed the expected DHOWFFZ a little. During the observation, the method of plugging and water injection observation in sections (each observation section: 1-2 m long) was adopted to observe the DHOWFFZ from the bottom of the borehole to the top of it. In the observation process, the water leakage amount will differ greatly when the probe reaches different areas inside and outside the fracture zone. Therefore, the fracture development degree and water conductivity of rock layer can be judged by the changes in water leakage amounts in the rock layer sections. In this way, the DHOWFFZ can be determined accurately. The schematic diagram of DHOWFFZ observation borehole arrangement is presented in Figure 9.

The results of DHOWFFZ observation are shown in Figure 10. The elevation angle of borehole is 40-45°. It is calculated that before the borehole depth reaches 9 m, the borehole is located in the rock mass above the protective coal pillar of the working face. In this section, the rock stratum is less affected by mining, so no observation was conducted here [27]. When the water leakage amount becomes large (generally about 20-30 L/min), the borehole has penetrated into the fracture zone. With the increase of borehole depth, the water leakage amount drops rapidly to about 5-10 L/min which means that the rock layer in this section no longer conducts water. The results of water injection observation reveals that the water leakage amount of borehole 1 changes greatly at the borehole depth of 50.8 m and the vertical depth of 38.9 m (an obvious turning point). It can thus be judged that the DHOWFFZ measured through borehole 1 is about 38.9 m. Similarly, the DHOWFFZs measured through boreholes 2, 3, 4, 5, 6, and 7 are given in Table 3.

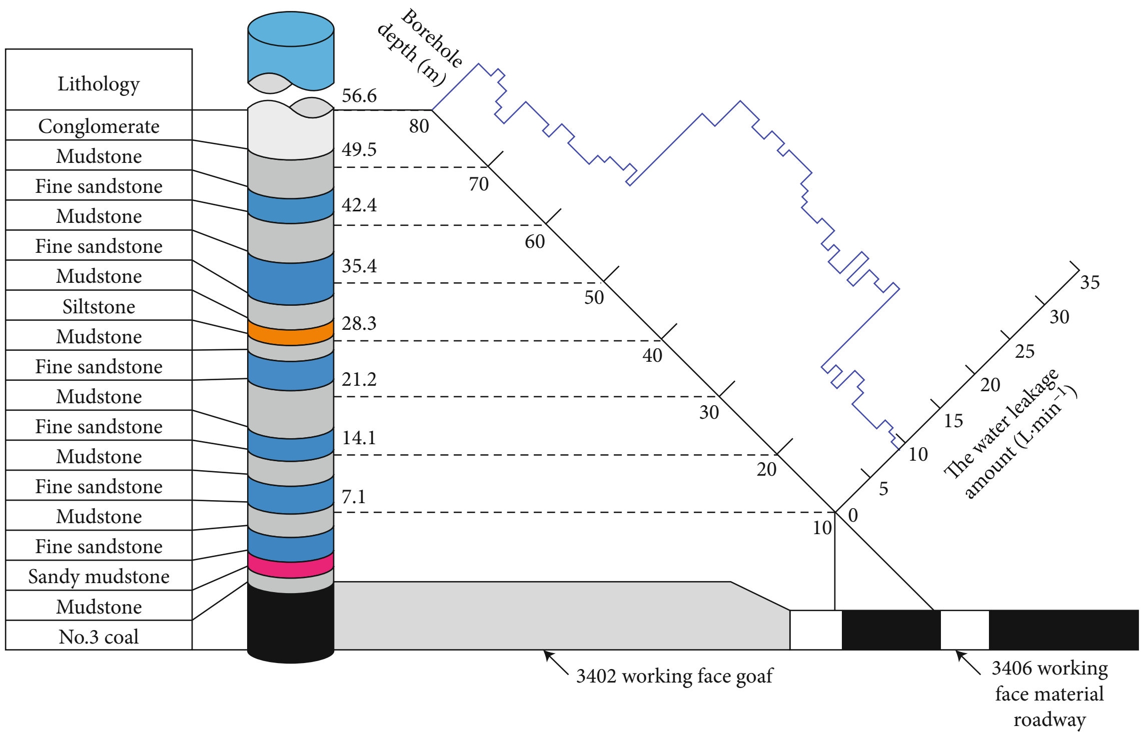

Figure 10: Water leakage amount of borehole 1.

Table 3: Measuring results of water-flowing fracture zone.

Observation borehole	Elevation angle (°)	Length (m)	Height of water-flowing fracture zone (m)
Borehole 1	45	80	38.9
Borehole 2	40	85	35.9
Borehole 3	43	80	39.6
Borehole 4	45	80	38.2
Borehole 5	40	85	36.4
Borehole 6	45	80	41.3
Borehole 7	42	85	39.7

Here is a comparison between the theoretical analysis and the field measurement. The theoretical analysis shows that the DHOWFFZ is smaller than 43.1 m; the water-flowing fracture zone finally develops into the rock layer below No. 14 fine sandstone; and No. 14 fine sandstone is classified into the range of the bending subsidence zone. The field measurement suggests that the DHOWFFZs all lie in the range of 35.9-41.3 m which is in line with the theoretical calculation results and does not exceed the height from the goaf to No. 15 mudstone (43.1 m). This demonstrates that although No. 15 mudstone undergoes a certain bending and subsidence, its tensile fracture only develops in the middle and lower parts of the rock stratum, and its subsidence is not enough to cause the development of a penetrating fracture which covers the whole thickness of the rock. Thereby, it can be inferred that the final DHOWFFZ will not exceed the height of No. 15 mudstone. In the field application, considering a certain safety factor, the maximum value (41.3 m) measured on site is taken as the DHOWFFZ. The field measurement results verify the rationality of the DHOWFFZ prediction method of "mudstone-sandstone" composite rock stratum structure based on the soft rock elongation rate. This indicates that for the "mudstone-sandstone" composite rock stratum structure, it is reasonable to judge the development degree of penetrating fracture in the rock stratum by adopting the elongation rate of the mudstone intermediate layer. By virtue of this method, the range of DHOWFFZ can be obtained.

4. Conclusions

(1) By combining the actual geological characteristics of Xin'an Coal Mine with the results of laboratory mechanical tests, the rock stratum structure characteristics in the stope of Xin'an Coal Mine are obtained as follows: The overburden roof exhibits a rock stratum structure of mudstone and sandstone overlapping, and each layer of mudstone shares a similar thickness with the adjacent layer of sandstone above. However, their mechanical properties differ significantly. A layer of hard rock at the bottom drives the upper layers of softer rock to move synchronously and coordinately. Therefore, the overburden rock strata are divided into several "mudstone-sandstone" rock stratum groups, each comprising one lower sandstone layer with high strength factors and one upper mudstone layer with low strength factors. The overburdens of the working face are gradually developed upward in the form of the abovementioned "mudstone-sandstone" rock stratum groups.

(2) In light of the literature, the ultimate tensile deformation of soft rock is greater than that of hard rock. Therefore, only when the soft mudstone in a rock stratum group bends and deforms and undergoes the formation of a penetrating fracture can the rock stratum group be completely classified as a part of the water-flowing fracture zone. It is proposed to judge the development degree of penetrating fracture in each rock stratum by adopting the elongation rate of mudstone intermediate layer, and the range of DHOWFFZ is judged according to the changes in the elongation rate of the mudstone layer in each rock stratum group. Through calculation, the DHOWFFZ of "mudstone-sandstone" composite rock stratum structure in the 3402 working face is smaller than 43.1 m.

(3) The DHOWFFZ in the 3402 working face was measured in the field, and the measured results are all smaller than the theoretically predicted values. The field measurement verifies the rationality of the DHOWFFZ prediction method of "mudstone-sandstone" composite rock stratum structure based on the soft rock elongation rate. Furthermore, it is determined that the water-flowing fracture zone will not affect the overburden aquifer above No. 3 coal seam of Xin'an Coal Mine, and the mining of No. 3 coal seam is safe and feasible.

Data Availability

The data used to support the findings of this study are included within the article.

Conflicts of Interest

The authors declare that they have no conflicts of interest.

Acknowledgments

This study was supported by the National Key Research and Development Program of China (No. 2017YFC0603004) and the support is gratefully acknowledged.

References

[1] W. B. Guo, Y. F. Zou, and Q. L. Hou, "Fractured zone height of longwall mining and its effects on the overburden aquifers," *International Journal of Mining Science and Technology*, vol. 22, no. 5, pp. 603–606, 2012.

[2] D. P. Adhikary and H. Guo, "Modelling of longwall mining-induced strata permeability change," *Rock Mechanics and Rock Engineering*, vol. 48, no. 1, pp. 345–359, 2015.

[3] Z. Zhao, W. Sun, S. J. Chen, D. W. Yin, H. Liu, and B. S. Chen, "Determination of critical criterion of tensile-shear failure in Brazilian disc based on theoretical analysis and meso-macro numerical simulation," *Computers and Geotechnics*, vol. 134, article id 104096, p. 62, 2021.

[4] Y. L. Tan, Q. Ma, Z. H. Zhao et al., "Cooperative bearing behaviors of roadside support and surrounding rocks along gob-side," *Geomechanics and Engineering*, vol. 18, no. 4, pp. 439–448, 2019.

[5] State Bureau of Coal Industry, *Specification for Coal Pillar Retention and Coal Mining in Buildings, Water Bodies, Railways and Main Wells and Alley*, Coal Industry Press, Beijing, 2017.

[6] Y. Tai, H. C. Xia, and T. J. Kuang, "Failure characteristics and control technology for large-section chamber in compound coal seams-a case study in Tashan Coal Mine," *Energy Science and Engineering*, vol. 8, no. 4, pp. 1353–1369, 2020.

[7] W. Y. Guo, Y. Qiu, T. B. Zhao, Y. L. Tan, S. Lan, and W. G. Chen, "Influence of the variable stoping speed on the occurrence mechanism of rock burst," *Geomatics, Natural Hazards and Risk*, vol. 10, no. 1, pp. 2094–2105, 2019.

[8] S. C. Hu, Y. L. Tan, H. Zhou et al., "Anisotropic modeling of layered rocks incorporating planes of weakness and volumetric stress," *Energy Science and Engineering*, vol. 8, no. 3, pp. 789–803, 2020.

[9] B. Ghabraie, G. Ren, X. Zhang, and J. Smith, "Physical modelling of subsidence from sequential extraction of partially overlapping longwall panels and study of substrata movement characteristics," *International Journal of Coal Geology*, vol. 140, pp. 71–83, 2015.

[10] Y. Zhang, S. H. Tu, Q. H. Bai, and J. J. Li, "Overburden fracture evolution laws and water-controlling technologies in mining very thick coal seam under water-rich roof," *International Journal of Mining Science and Technology*, vol. 23, no. 5, pp. 693–700, 2013.

[11] W. Y. Guo, Q. H. Gu, T. L. Tan, and S. C. Hu, "Case studies of rock bursts in tectonic areas with facies change," *Energies*, vol. 12, no. 7, p. 1330, 2019.

[12] C. Liu, J. H. Xue, G. F. Yu, and X. Y. Cheng, "Fractal characterization for the mining crack evolution process of overlying strata based on microseismic monitoring technology," *International Journal of Mining Science and Technology*, vol. 26, no. 2, pp. 295–299, 2016.

[13] A. Majdi, F. P. Hassani, and M. Y. Nasiri, "Prediction of the height of destressed zone above the mined panel roof in longwall coal mining," *International Journal of Coal Geology*, vol. 98, no. 1, pp. 62–72, 2012.

[14] G.-L. Hu, W.-B. Zhu, and X.-Z. Wang, "New method to predict the height of fractured water-conducting zone by location of key strata," *Journal of China Coal Society*, vol. 37, no. 5, pp. 762–769, 2012.

[15] H. B. Chai, J. P. Zhang, and C. H. Yan, "Prediction of water-flowing height in fractured zone of overburdens strata based on GA-SVR," *Journal of Mining & Safety Engineering*, vol. 35, no. 2, pp. 359–365, 2018, (In Chinese).

[16] V. Palchik, "Bulking factors and extents of caved zones in weathered overburden of shallow abandoned underground workings," *International Journal of Rock Mechanics and Mining Sciences*, vol. 79, pp. 227–240, 2015.

[17] W. P. Huang, Y. F. Gao, B. Wang, and J. R. Liu, "Evolution rule and development height of permeable fractured zone under combined-strata structure," *Journal of Mining & Safety Engineering*, vol. 34, no. 2, pp. 330–335, 2017, (In Chinese).

[18] G. W. Cheng, C. X. Chen, T. H. Ma, H. Y. Liu, and C. N. Tang, "A case study on the strata movement mechanism and surface deformation regulation in Chengchao underground iron mine," *Rock Mechanics and Rock Engineering*, vol. 50, no. 4, pp. 1011–1032, 2017.

[19] B. Ghabraie, G. Ren, J. Smith, and L. Holden, "Application of 3D laser scanner, optical transducers and digital image processing techniques in physical modelling of mining-related strata movement," *International Journal of Rock Mechanics and Mining Sciences*, vol. 80, pp. 219–230, 2015.

[20] W. Y. Guo, F. H. Yu, Y. L. Tan, and T. B. Zhao, "Experimental study on the failure mechanism of layer-crack structure," *Energy Science & Engineering*, vol. 7, no. 6, pp. 2351–2372, 2019.

[21] H. Hu, X. Lian, and Y. Li, "Physical experiments on the deformation of strata with different properties induced by underground mining," *Journal of Engineering Science and Technology Review*, vol. 9, no. 1, pp. 74–80, 2016.

[22] E. Fathi Salmi, M. Nazem, and M. Karakus, "Numerical analysis of a large landslide induced by coal mining subsidence," *Engineering Geology*, vol. 217, pp. 141–152, 2017.

[23] B. Ghabraie, K. Ghabraie, G. Ren, and J. Smith, "Numerical modelling of multistage caving processes: insights from multi-seam longwall mining-induced subsidence," *International Journal for Numerical and Analytical Methods in Geomechanics*, vol. 41, no. 7, pp. 959–975, 2017.

[24] Y. Xue, T. Teng, F. Dang, Z. Ma, S. Wang, and H. Xue, "Productivity analysis of fractured wells in reservoir of hydrogen and carbon based on dual-porosity medium model," *International Journal of Hydrogen Energy*, vol. 45, no. 39, pp. 20240–20249, 2020.

[25] M. An, F. Zhang, D. Elsworth, Z. Xu, Z. Chen, and L. Zhang, "Friction of Longmaxi shale gouges and implications for seismicity during hydraulic fracturing," *Journal of Geophysical Research: Solid Earth*, vol. 125, no. 8, article e2020JB019885, 2020.

[26] F. Zhang, B. Damjanac, and S. Maxwell, "Investigating hydraulic fracturing complexity in naturally fractured rock masses using fully coupled multiscale numerical modeling," *Rock Mechanics and Rock Engineering*, vol. 52, no. 12, pp. 5137–5160, 2019.

[27] Z. Meng, X. Shi, and G. Li, "Deformation, failure and permeability of coal-bearing strata during longwall mining," *Engineering Geology*, vol. 208, pp. 69–80, 2016.

Hindawi
Geofluids
Volume 2021, Article ID 5564786, 12 pages
https://doi.org/10.1155/2021/5564786

Research Article

Grouting Fractured Coal Permeability Evolution Based on Industrial CT Scanning

Li Tao,[1,2,3] Yao Banghua ,[3,4] Liu Yong ,[3,4] and Wang Dengke[3,4]

[1]*School of Emergency Management and Safety Engineering, China University of Mining & Technology-Beijing, Beijing 100083, China*
[2]*School of Electrical Engineering & Automation, Henan Polytechnic University, Jiaozuo 454000, China*
[3]*State Collaborative Innovation Center of Coal Work Safety and Clean-Efficiency Utilization, Jiaozuo 454000, China*
[4]*School of Safety Science and Engineering, Henan Polytechnic University, Jiaozuo 454000, China*

Correspondence should be addressed to Yao Banghua; yaobanghua@126.com

Received 11 January 2021; Revised 17 February 2021; Accepted 5 March 2021; Published 17 March 2021

Academic Editor: Yi Xue

Gas extraction from coal seams in China faces various middle-term and long-term problems, such as the poor sealing quality and low extraction rate. The mean gas extraction concentration is only 30%. Studying the flowing laws of the grout and fracture plugging mechanism is of important significance to improve the sealing quality and increase the gas extraction efficiency. For this reason, a new coal-based grouting material was prepared in this study, and its parameters such as viscosity were tested. Moreover, a grouting theoretical model with considerations of the flowing of the grout and coal fracture plugging by migration and deposition of slurry particles was constructed. The crack distribution before and after the grouting of fractured coal samples was scanned with an industrial CT, and the fracture distribution of coal samples was reconstructed using an independently compiled MATLAB program. Meanwhile, the variations of the coal permeability before and after the grouting were tested. On this basis, this study built a numerical calculation model of the grouting in fractured coal samples to simulate the leakage stoppage and permeability reduction mechanism of the coal-based sealing material grouting. Results demonstrate that (1) according to the experimental test results, the new coal-based grouting materials achieve a good fracture plugging effect, and the fractures in coal samples after the grouting are filled densely by the grouting particles. (2) According to the simulation results, the permeability of grouting coal samples declines quickly and then tends to be stable. The overall permeability of coal samples and the fracture permeability are decreased by 93.5% and more than 99.9% in average, respectively. (3) Influences of the grouting pressure on the permeability variation of coal samples were investigated through a numerical simulation. It was found that a reasonable grouting pressure for coal samples is about 0.3 MPa. (4) The numerical simulation reproduces the whole process of the grout flowing and the fracture filling. The variation laws of the diffusion and the permeability of the grout which are calculated through a numerical simulation agree well with the experimental results, which verifies the reasonability of the model. Research conclusions can provide important significance in theory and practice to disclose the leakage stoppage and the permeability reduction mechanism of the borehole grouting during the gas extraction and strengthen the sealing effects of extraction boreholes.

1. Introduction

With the vertical extension of coal mining in China, disasters like coal and gas outburst are intensifying increasingly. Gas extraction is an important technical mean to develop and use gas resources and prevent gas disaster accidents in coal mines [1, 2]. Nevertheless, gas extraction from coal seams generally has low extraction efficiency in China, and the mean gas extraction concentration is only 30% [3]. This is because due to the general poor sealing quality, a lot of air in the roadway enters into the borehole along the surrounding rock fractures under the effect of negative extraction pressure, thus causing air leakage (Figure 1). At present, the grouting sealing technique like "two-plugging and one-grouting" is a common sealing technique in gas extraction [1]. The principle of "two-plugging and one-grouting" is to

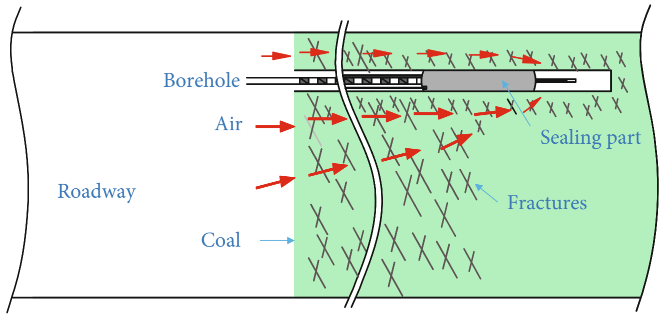

Figure 1: Air leakage in boreholes for gas extraction.

inject some condensable grout into the fractures or pores of coal mass to improve the physical and mechanical properties of coal masses and thereby increase their antipermeability and stability [4–6]. Therefore, exploring the flowing and diffusion laws of grout and fracture sealing mechanism of coal masses has important engineering significance to guide the sealing effect of boreholes and increase the gas extraction efficiency.

With respect to existing studies on the flowing and diffusion laws of grout, scholars have developed a grouting theory of rock masses with boreholes, a grouting theory of fractured rock masses, a splitting grouting theory, a compaction grouting theory, and a dynamic grouting theory [7–11]. With respect to the grouting theory of fractured rock masses, Baker deduced a flow equation of Newtonian fluid in fractures under the assumption that the fractures are parallel smooth fractures with equal widths [12, 13]. Mu et al. [14] established a grout diffusion model in a single random fracture. Xiao et al. [15] calculated the relation curve between the extension distance of grout in fractures of a panel and the grouting time. Based on the flowing theory of viscous fluid, Xiaolong et al. [16] built a radial diffusion model of grout in single-plane fracture under anhydrous conditions. Gustafson et al. [8] assumed that the grouting pressure is a constant value and studied the flowing law of grout in a single-plane fracture based on the Bingham body constitutive model. Draganović et al. [17] developed a short-slot model between two assembled discs with constrictions to investigate the filtration and penetration length of cement-based grout. Yang et al. [18] carried out a numerical simulation study on the diffusion process of cement-based grout with a single rough crack through a finite element method. Saeidi et al. [19] studied the influences of crack characteristics on grout flowing and penetration length in fractured rock masses through a numerical simulation based on discrete element software (Udec). Wenjun [20] built a diffusion and flow model of the route in fractured rock masses with consideration of the variations of the viscosity of the grout with time. With consideration of time-varying characteristics of the viscosity of grout, Qingsong et al. [21] constructed a theoretical model of grout diffusion in horizontal fractures under a constant grouting speed.

The sealing effect of grout in fractured rock masses is mainly reflected by the changes of fracture and permeability. With respect to studies on the permeability of grouting rock masses, Renshu et al. [22] analyzed the fracture variations of mudstone samples before and after grouting through CT scanning under laboratory conditions and evaluated the fracture sealing effect by a method based on fractal dimension. Yue [23] tested the permeability of coal samples after grouting and carried out an intuitive analysis of the influences of grouting viscosity on the sealing effect of coal mass. Ning et al. [24] carried out a numerical simulation study of the variation laws of permeability of rock masses after grouting. Based on an independently developed large triaxial seepage-grouting multifunctional platform, Qi et al. [25] investigated the evolutionary characteristics of the permeability of rock masses before and after grouting through an experiment. Rentai et al. [26] gained the relationship between the fracture of rock masses and osmotic coefficient through a drilling analysis, analyzed the flowing law of grout during the grouting process through the flow dimension theory, and evaluated the sealing effect of rock grouting. Guangxuan et al. [27] developed an experimental system of 3-dimensional penetrating grouting model and implemented a grouting test on sandstone samples, getting time-varying laws of porosity, permeability, and grouting pressure of samples. Sun et al. [28] proposed a coupling HM model based on the coupling effect between grout and rock mass and discussed the grouting process through a numerical simulation. Moreover, they analyzed the influences of geostress on anisotropic permeability characteristics of grouting rock masses. Xu et al. [29] discussed the leakage stoppage and permeability reduction of grouting in deep-fractured rock masses through an independently developed physical simulation platform of grouting.

In the above studies, the mathematical model of describing the diffusion and flow laws of grout is mature. Associated studies have made beneficial discussions on the flowing and diffusion laws and sealing effect of grout. However, most of the existing studies assume coal and rock masses as an ideal isotropic body [30–33] or set the fracture distribution based on a random function [34]. Uncertainty of the initial fracture distribution influences the reliability of the calculation results directly, thus making existing studies difficult to describe the motion law and diffusion scope of grout accurately. Moreover, the associated studies hardly have considered the physical essence of fracture and permeability changes of coal and rock masses caused by sedimentation of grout particles, and they cannot predict the leakage stoppage and permeability

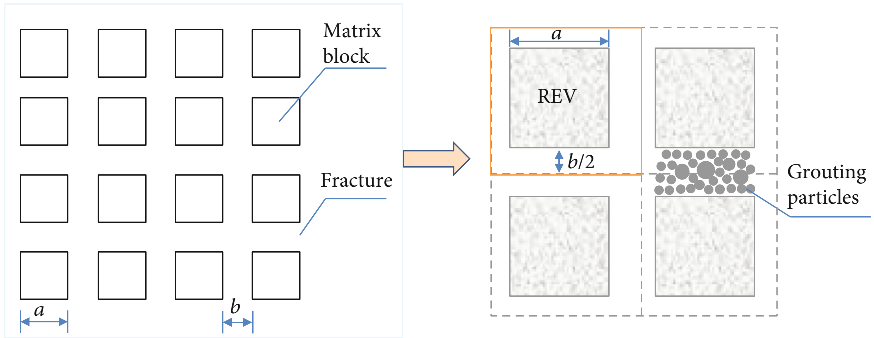

Figure 2: Sketch of the physical model for broken coal with grouting.

reduction characteristics of grout in coal samples reliably. Furthermore, it lacks of a systematic study on flowing characteristics and performance in leakage stoppage and permeability reduction of the new coal-based grouting material. Based on the distribution law of fracture field in coals which was gained from practical CT scanning, this study reflected the fracture evolution seepage law of grout in coal masses scientifically with considerations to the fracture evolution, leakage stoppage, and permeability reduction mechanism of grouting caused by diffusion deposition of grouting particles. Research conclusions lay the foundation for the optimization of grouting-based sealing of boreholes during gas extraction. This study has important theoretical and practical significance.

2. Theoretical Grouting-Based Sealing Model of Surrounding Rock Fractures

Through grouting of fractured coal and rock masses, the grout is driven by the grouting pressure and flows along fractures in coal masses. Grouting particles deposit in block the fractures, thus influencing the permeability of coal mass. To establish an evolutionary model of the permeability of fractured coal masses after grouting, some basic hypotheses were set up:

(1) Grouting particles are incompressible, and the injection concentration remains constant

(2) Effects of stress changes on the fractures of coal mass are ignored in the grouting process

(3) The deposition process of grouting particles is irreversible. In other words, the separation process of deposited grouting particles is ignored.

2.1. Definition. Based on the aforementioned assumptions, a representative element for a typical coal microstructure is shown in Figure 2. The length L (m) and volume V (m3) of the element are expressed as

$$L = a + b, \tag{1}$$

$$V = (a + b)^3, \tag{2}$$

where a (m) is the length of the matrix and b (m) is the aperture of the fracture.

The total voidage φ (%) of an element is written as

$$\varphi = \frac{(a+b)^3 - a^3}{(a+b)^3} \cong \frac{3b}{a}. \tag{3}$$

It should be noted that $b \ll a$.

2.2. Mass Conservation Equations for Particles. To study the sediment characteristics of the grouting particles, the dynamic mass conservation equations for the particles were calculated based on a three-dimensional representative element, as illustrated in Figure 3.

Grouting particles have migration and sediment processes inside a representative element. For the migration process, the average seepage velocity of an element can be defined as $\vec{q}_i$ (m/s). In the direction of x_i ($i = 1,2,3$), the mass increase of particles flowing into the element in a unit time can be calculated as

$$-\frac{\partial (C\rho_s q_i)}{\partial x_i} V \tag{4}$$

where C (%) is the particle concentration (i.e., particle saturation) and ρs (kg/m3) denotes the density of grouting particles.

Figure 3 Illustration of a three-dimensional characteristic element. M_i is the mass change of solids due to convection, defined as $M_i = C\rho_s q_i$.

In the direction of x_i, the mass flowing into the element due to the sediment should be expressed as

$$-\frac{\partial M_i}{\partial x_i} V (i = 1, 2, 3). \tag{5}$$

For the element, the total mass flowing can be expressed as the summation of the three directions:

$$-\sum_{i=1}^{3} \left(\frac{\partial M_i}{\partial x_i} V \right). \tag{6}$$

For the sediment process, the total mass flowing into the element can be expressed as

$$-\frac{\partial \varphi}{\partial t} \rho_s V \tag{7}$$

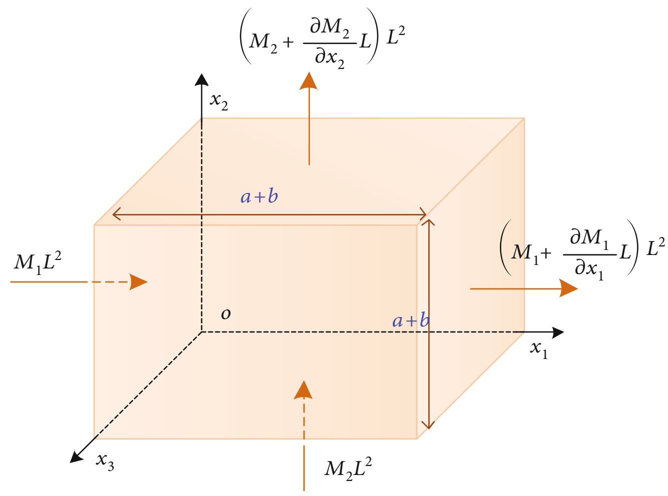

Figure 3: Sketch of a representative element for broken coal.

According to the mass conservation law for the unit element, giving the mass conservation equation for particles as

$$\frac{\partial}{\partial t}(C\varphi\rho_s)V=-\sum_{i=1}^{3}\left(\frac{\partial M_i}{\partial x_i}V\right)-\frac{\partial\varphi}{\partial t}\rho_s V, \tag{8}$$

Equation (8) can be simplified as

$$\frac{\partial}{\partial t}(C\varphi)+\nabla\cdot\left(C\vec{q}\right)=-\frac{\partial\varphi}{\partial t}. \tag{9}$$

2.3. Water Mass Conservation Equations. In a similar way as Equation (9), the mass conservation equation for water flow can be derived as

$$\frac{\partial[\varphi(1-C)]}{\partial t}+\nabla\cdot\left[(1-C)\vec{q}\right]=0. \tag{10}$$

2.4. Evolution of the Fracture Aperture and Permeability. According to that study [35, 36], the evolution of fracture aperture was affected by the particles concentration as well as the seepage velocity. The following equations have been developed to determine the evolution of the fracture aperture:

$$\frac{\partial\varphi}{\partial t}=C\cdot K_{dep}, \tag{11}$$

$$K_{dep}=\frac{3(1-\varphi)u}{2D_c}\eta. \tag{12}$$

The relationship between element permeability and fracture aperture can be expressed as

$$k=\frac{b^3}{12a}, \tag{13}$$

$$\frac{k}{k_0}=\left(\frac{b}{b_0}\right)^3. \tag{14}$$

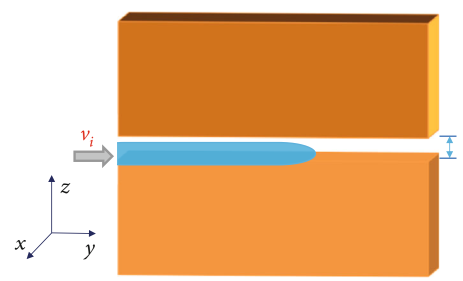

Figure 4: Sketch of grouting flow in coal fracture.

2.5. Grout Flow. The schematic diagram of the flow of grouting slurry in the coal cracks is shown in Figure 4. According to the related study [37], the velocity equation describing the flow of grout can be obtained:

$$q_i=-\frac{k}{\eta}\nabla p_i\left(1-\frac{\lambda}{|\nabla p_i|}\right), \tag{15}$$

where

$$\lambda=\frac{4\tau_s}{b}. \tag{16}$$

τ_s is the yield stress of the grouting slurry, which can be obtained by the test.

Equations (9)–(16) compose the coupled processes of coal fracture grouting under sediment effects. The above governing equations will be implemented into COMSOL Multiphysics next to understand the grouting mechanism in coal fractures.

3. Grouting Test of Fractured Coal Samples

3.1. Preparation of Grout and Viscosity Test. It can be seen from Figure 5 that a new grouting material was prepared by water, curing agent, expansive agent, and coal powder with grain size lower than 100 meshes. Grout samples with different water-solid ratios were prepared, and variations of their

FIGURE 5: Raw materials of grouting.

TABLE 1: Proportioning scheme of water-solid ratio.

Water-solid ratio	Mass of coal powder (g)	Curing agent (g)	Expansive agent (g)	Water (g)
0.5	500	2	400	451
0.8	500	2	400	721.6
0.9	500	2	400	811.8
1	500	2	400	902
1.5	500	2	400	1353
2	500	2	400	1804

viscosities were tested by experiments. The proportioning schemes of water-solid ratio are shown in Table 1.

We test the viscosity of grout samples by using a Brinell viscosity rotation tester, and the time-varying test results and fitting curves of viscosity of grout samples with different water-solid ratios are shown in Figure 6. Clearly, the initial apparent viscosity is negatively correlated with water-solid ratio. This is because the internal frictional resistance of the grout decreases with the increase of free water content in the grout. Moreover, the apparent viscosity of grout samples with different water-solid ratios presents an upward trend as time goes on, because the grout samples condense gradually and the internal frictional resistance increases accordingly.

3.2. Experimental System and Steps. Grouting and experimental systems of fractured coal samples are shown in Figure 7. It is mainly composed of three experimental systems, namely, permeability test system, CT scanning system, and grouting test system. The permeability test system is to measure the permeability of coal samples before grouting. The CT scanning system is to acquire the initial fracture distribution in coal samples through CT scanning and then carry out a grouting test of coal samples: (1) coal samples were wrapped with silicon seals and then loaded into a closed cavity. The lower valve was kept open. (2) The upper valve was connected to the grouting pipeline, and it was kept open. (3) The prepared grouting materials were added by a manual pressure pump and then the grouting test began. (4) In the grouting test, the grouting pressure was maintained at 0.2 MPa, and the upper valve was closed at 30 min. The grouting pipeline and manual pressure pump were cleaned. (5) The closed cavity was open, and coal samples were taken out. The grouting air chamber was cleaned for later use. After finishing the grouting process, the permeability test and CT scanning test of coal samples were performed again.

3.3. Experimental Results and Analysis. CT scanning results of coal sample 1# before and after grouting are shown in Figure 8. It can be seen from Figure 8(a) that the main fractures extend gradually from the upper to bottom of the coal samples, and the fractures are relatively wide. In this process, fractures incline toward one side, and two fractures which could extend to other sides could be seen at the upper end and at 1/3 of the coal samples. The width of these two fractures was relatively low. The main fracture developed two branches after reaching the middle position of the coal samples. One branch stops extension after reaching one side surface, and the other branch was twisted after reaching the side surface and then extended to the lower position of coal samples. This branch was relatively narrow, and it only could be seen from images. In Figure 9(b), the main fracture of coal samples was filled completely by the grouting material. In branch fractures, grouting materials cannot run through the whole fracture channel due to the small width, big sinuosity, and poor connectivity. There are few grouting particles in branches.

CT scanning results of coal sample 2# before and after grouting are shown in Figure 9. It can be seen from Figure 9(a) that there is a big fracture on the upper position of the coal sample. It extends from top to bottom, then inclines toward the side surface after reaching 1/3 of the upper position of the coal sample, and finally disappears. No other evident fracture structure is found in the coal samples. However, white minerals form a dense distribution at 1/3 of the lower position of the coal sample. Figure 9(b) shows that the fracture shows good connectivity, and it is filled completely by the grout, forming good cementation between the grouting materials and the fracture wall.

With reference to the permeability test of coal samples [38–43], the permeability of coal samples before and after grouting was tested through a triaxial gas seepage experimental system of coal and rock masses. Test conditions and results are listed in Table 2. Clearly, permeability of coal samples after grouting declines significantly compared to the initial value. The permeability of coal samples 1# and 2# is decreased by 93.0% and 95.5%, respectively.

4. Numerical Modeling of Grouting in Fractured Coal Masses

4.1. Construction of a Numerical Model. In the above experiments, coal samples before grouting were scanned using an industrial CT, through which the internal fracture distribution of coal mass was gained. It can be seen from

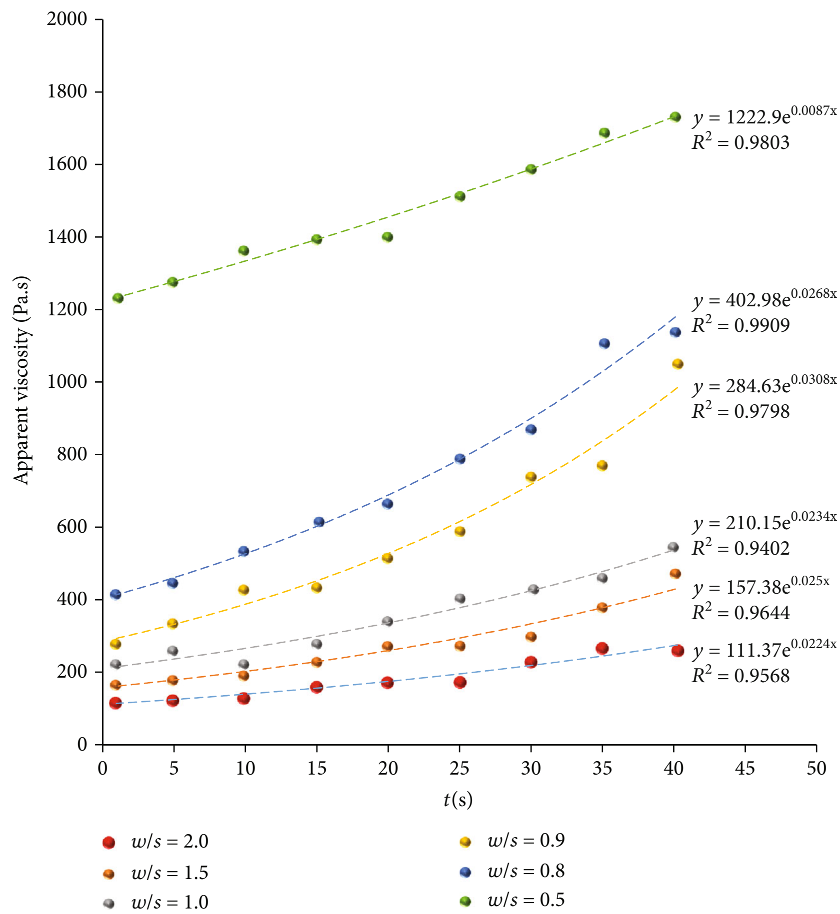

Figure 6: Time-varying curves of viscosity of grout samples with different water-solid ratios.

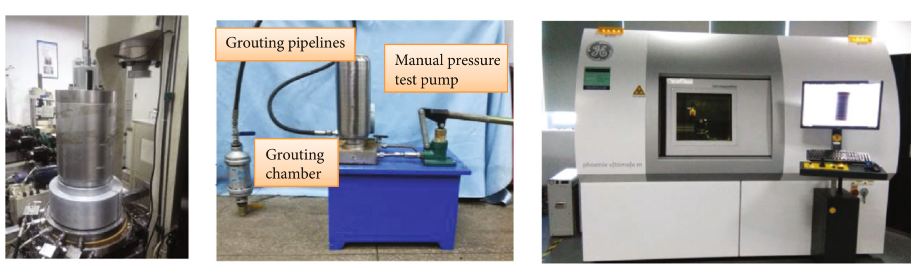

Figure 7: Experimental systems.

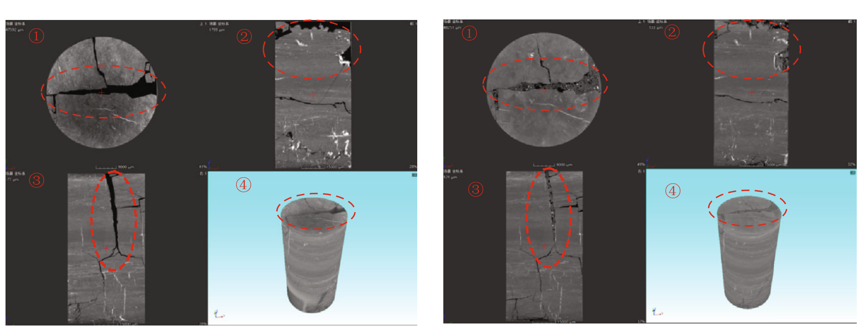

(a) (b)

Figure 8: CT scanning results of coal sample 1#: (a) before grouting, (b) after grouting.

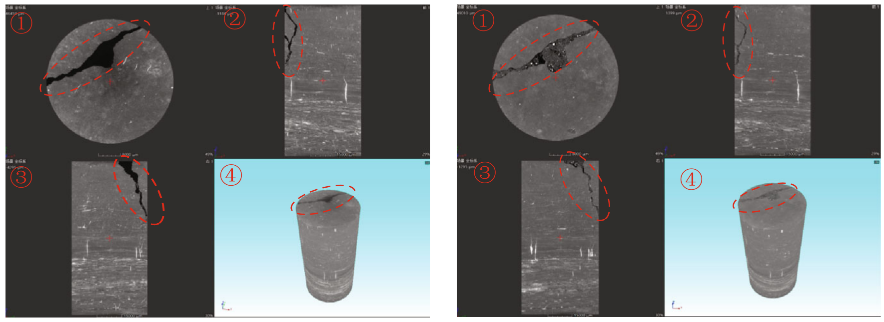

(a) (b)

Figure 9: CT scanning results of coal sample 2#: (a) before grouting, (b) after grouting.

Table 2: Variations of permeability of coal samples before and after grouting.

No.	Initial permeability (k_0/mD)	Permeability after grouting (k_1/mD)	Reduction $(k_0 - k_1)/k_0$
1	37.0 mD	2.6 mD	93.0%
2	6.7 mD	0.3 mD	95.5%

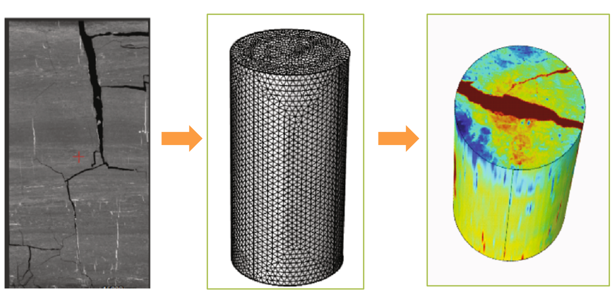

(a) (b) (c)

Figure 10: Numerical calculation model of grouting in fractured coal samples. (a) CT scanning fracture. (b) Model meshing. (c) Numeralization fracture distribution.

Figure 10(a) that the diameter and height of coal samples were set 50 mm and 100 mm, respectively. A numerical calculation model which was consistent with the dimension of coal samples was built (Figure 10(b)), in which the mesh generation is tetrahedral mesh, and the number is about 80000. Boundary conditions for numerical simulation were set according to the experimental conditions. Specially, the grouting pressures on the upper surface and lower surface of coal samples were set as 0.2 MPa and 0, respectively. There were no permeable boundaries surrounding the coal samples. Initial condition is as follows: the initial grout concentration of the model was 0, and CT scanning slices of coal samples were processed by the independently compiled MATLAB program. The generated documents were input into a finite element numerical simulation software COMSOL, getting the initial fracture distribution diagram of coal samples. In Figure 10(c), the initial permeability distribution of coal samples was gained by combining the permeability test results of coal samples based on the above results. Main parameters of numerical simulation are listed in Table 3.

4.2. Numerical Simulation Results and Analysis

4.2.1. Grouting Pressure. The cloud maps of the variation of grouting pressure in coal samples 1# and 2# with time are shown in Figures 11 and 12, respectively. As the grouting process continues, the grouting pressure of coal samples diffuses gradually from top to bottom. Pressure distribution runs through the coal samples at 200 s, indicating that the grout flows from the lower end to the upper end of the coal samples. Pressure in fractures tends to be stable after 2000 s. It also can be seen that the grouting pressure in coal sample 1# diffuses relatively slowly, and the pressure in the end fracture has not reached the maximum at 200 s. By combining with CT scanning maps, this is the consequence of wide fractures and good permeability on the upper surface of coal samples, but narrow fractures and poor permeability on the lower surface of coal samples. Grouting pressure diffuses quickly in coal sample 2# due to the short fracture, and the pressure was stable at 100 s.

4.2.2. Permeability of Coal Samples. The cloud maps of permeability variations of coal samples 1# and 2# with time are shown in Figures 13 and 14. Clearly, the permeability at the fracture of coal samples is far higher than that in the nonfractured zones in the beginning of grouting. As grouting continues, the fractures are filled by the grout, and the permeability declines continuously. Permeability at the fracture of coal masses is similar to that in the nonfractured zones after 2000 s. Besides, the fracture on the upper end of coal samples is blocked firstly in the grouting process, and the permeability declines quickly. As the grout diffuses downward continuously, the permeability at the lower position of coal samples decreases gradually. Finally, the fractures that run through the coal samples are filled by grout. Specifically, the permeability in the upper section of the fracture of coal sample 1# decreases quickly, while the permeability at the lower branch of the fracture decreases slowly. This is attributed to the small width of the branch and the slow flowing of the grout. Similar phenomenon of permeability variation is observed for the coal sample 2#. The slow reduction of permeability in the lower section of the fracture is attributed to

Table 3: Main parameters for simulation.

Grout density $kg\,m^{-3}$	Grouting pressure MPa	Water-solid ratio	Viscosity Pa s	Sedimentation coefficient h^{-1}	a m	Yield stress MPa
1340	0.2	1.5	$\eta = 154.55e^{0.0254t}$	80	0.1	55.6

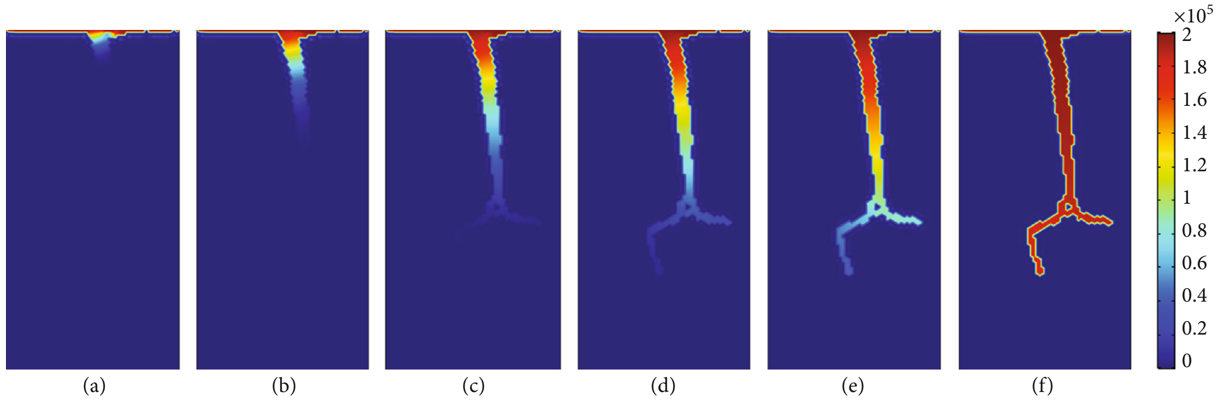

Figure 11: Cloud map of the variation of grouting pressure distribution with time (coal sample 1#). (a) $t = 1$ s. (b) 10 s. (c) 50 s. (d) 100 s. (e) 200 s. (f) 2000 s.

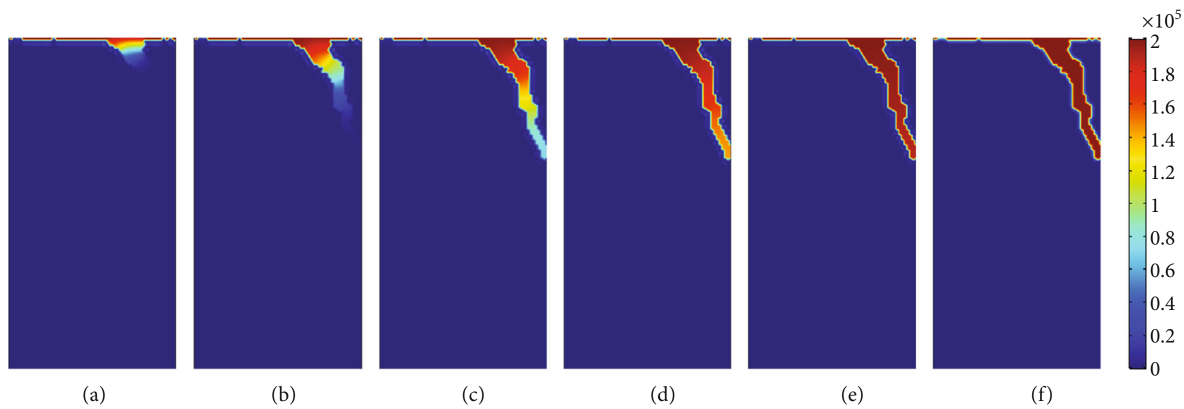

Figure 12: Cloud map of the variation of grouting pressure distribution with time (coal sample 2#). (a) $t = 1$ s. (b) 10 s. (c) 50 s. (d) 100 s. (e) 200 s. (f) 2000 s.

the small width in the middle position, which influences the flow velocity of the grout in the lower section of the fracture.

The variation curves of permeability of grouting coal samples with time, which are gained from the numerical simulation, are shown in Figure 15. The numerical simulation results of permeability of coal samples before and after grouting are listed in Table 4. Clearly, the overall permeability of coal samples decreases gradually, and the mean reduction amplitude is 93.5%. Specifically, the initial permeability of coal sample 1# is 36.9 mD, and it decreases gradually with the increase of grouting time. The overall permeability decreases by 92.2% to 2.86 mD at 2000 s. The initial permeability of coal sample 2# is 6.6 mD, and it decreases gradually as the grouting continues. The overall permeability of coal sample 2# is decreased by 94.8% to 0.34 mD at 2000 s. According to the comparison of experimental results, the numerical simulation results conform to the experimental results, which verify the accuracy of the theoretical model.

The variation curves of the overall fracture permeability of coal samples with grouting time which are gained from numerical simulation are shown in Figure 16. Clearly, the variation trend of fracture permeability is consistent with the overall permeability of coal samples. Differently, the initial fracture permeability is higher and the reduction amplitude is larger. The fracture permeability of coal samples can be decreased by at least 99.9%.

4.3. Effects of Grouting Pressure on Permeability Reduction of Coal Samples. Grouting pressure can influence the grouting effect significantly in the grouting process. In this section, the variation law of permeability of coal samples with time under different grouting pressures was discussed by taking

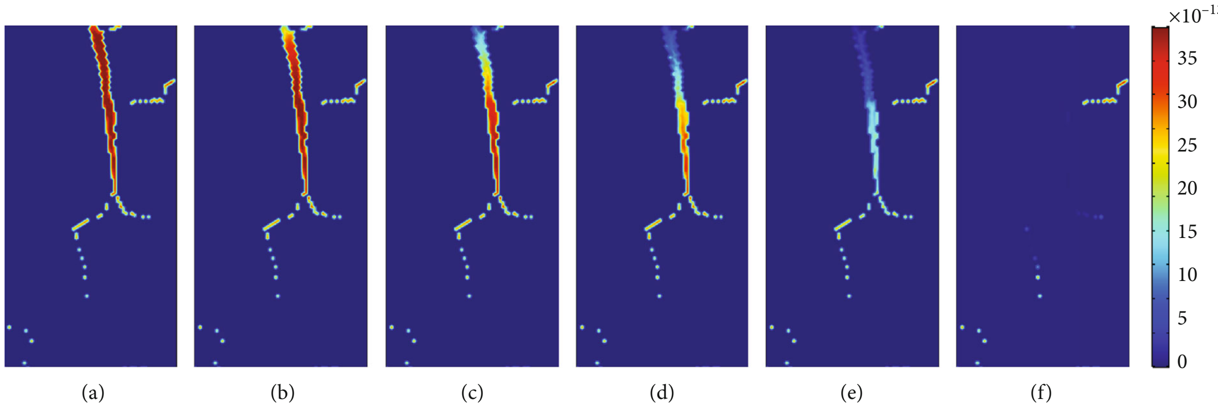

Figure 13: Cloud map of variation of permeability distribution with time (coal sample 1#). (a) $t = 1$ s. (b) 10 s. (c) 50 s. (d) 100 s. (e) 200 s. (f) 2000 s.

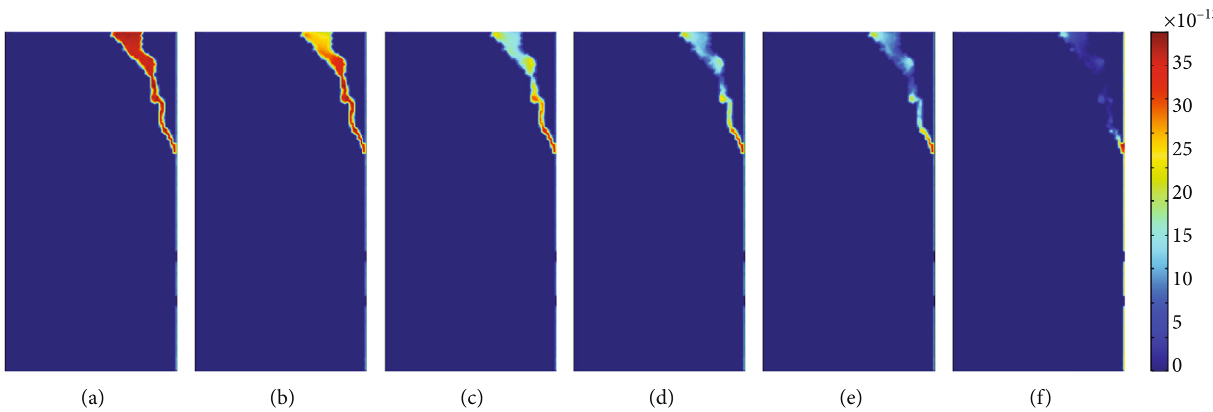

Figure 14: Cloud map of variation of permeability distribution with time (coal sample 2#). (a) $t = 1$ s. (b) 10 s. (c) 50 s. (d) 100 s. (e) 200 s. (f) 2000 s.

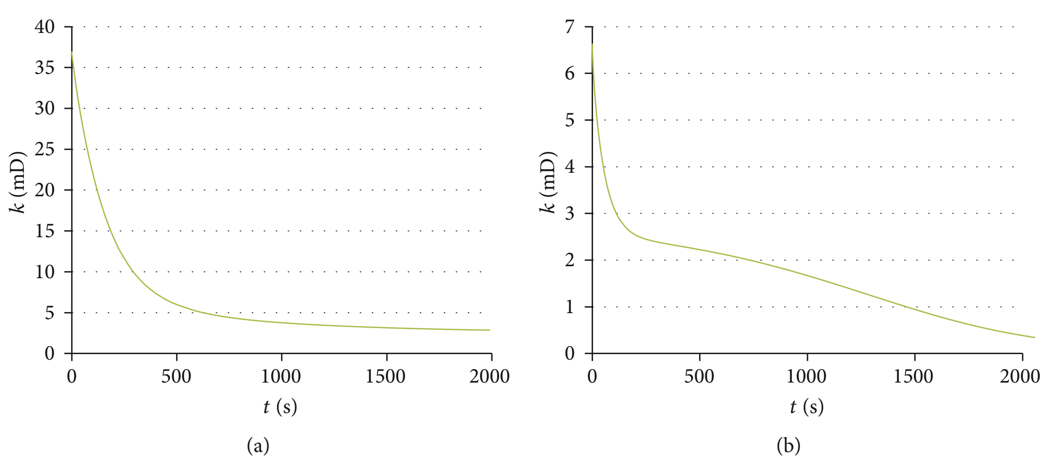

Figure 15: Variation curves of overall permeability of coal samples with time. (a) Coal sample 1#. (b) Coal sample 2#.

coal sample 1#, for example. The results can provide theoretical supports to select the reasonable grouting pressure in the grouting engineering. The variation curve of permeability of coal sample 1# with time under different grouting pressures is shown in Figure 17. Clearly, permeability of coal sample 1# decreases by 89.6% from 37 mD to 3.83 mD when the grouting pressure is 0.1 MPa. When the grouting pressure is 0.2 MPa, the permeability decreases by 92.2% from 37 mD to 2.86 mD. When the grouting pressure is 0.3 MPa, the permeability decreases by 92.5% from 37 mD to 2.78 mD.

Table 4: Numerical simulation on permeability variations of coal samples before and after grouting.

No.	Initial permeability kn_0/mD	Permeability after groutin kn_1/mD	Reduction amplitude $(kn_0 - kn_1)/kn_0$	Error between numerical simulation and experiment %
1	36.9	2.86	92.2%	0.86%
2	6.6	0.34	94.8%	0.73%

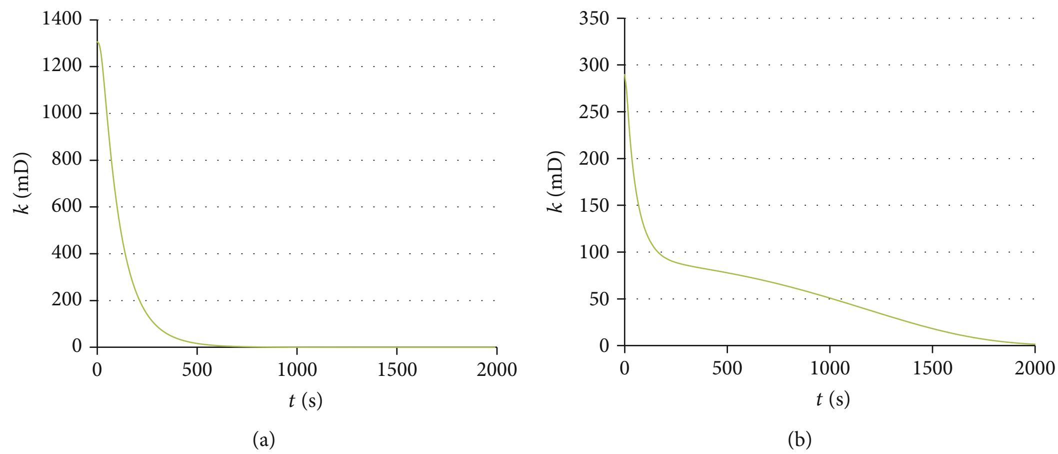

Figure 16: Variation curves of fracture permeability of coal samples with time. (a) Coal sample 1#. (b) Coal sample 2#.

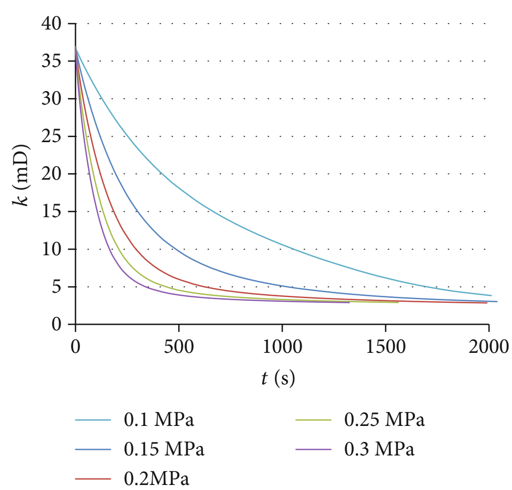

Figure 17: Variation curves of permeability of coal samples under different grouting pressures.

Obviously, the variation velocity of permeability of coal samples increases significantly with the grouting pressure when it is lower than 0.25 MPa. However, the variation curves of permeability of coal samples are almost consistent when the grouting pressure exceeds 0.25 MPa. In a word, the optimal grouting pressure of coal samples under this condition is about 0.25 MPa.

5. Discussions

Disclosing leakage stoppage and permeability reduction mechanism of grouting in fractured coal masses has important theoretical significance to strengthen the borehole sealing effect during gas extraction. Since existing theoretical studies hardly consider the variation of fracture and permeability of coal and rock masses caused by the deposition of grouting particles and it is difficult to describe the research status of motion law of grout accurately due to the uncertain initial fracture distribution in the numerical simulation study, authors prepared a new coal-based grouting material and tested the parameters of this grouting material (e.g., viscosity). Moreover, a theoretical grouting model of coal fracture filling with consideration of the flowing of grout and deposition of grouting particles was built up. A "visual" analysis of fracture structures in coal masses was realized by industrial CT scanning. The leakage stopping and permeability reduction mechanism of coal mass is investigated by using a numerical simulation software COMSOL. Research conclusions provide references to the quantitative analysis of the motion law of grouting particles and strengthening the borehole sealing effect for gas extraction. However, grout deposition and fracture filling involve relatively complicated physical and chemical processes. For instance, the chemical properties of grouting materials may change with time and the deposited particles can be changed into suspending particles again. In this study, the deposition process was simplified, and key attentions were paid to the physical outcomes of fracture filling by deposited grouting particles. Secondly, CT scanning and observation analysis of the whole grouting process are impossible due to limitations of experimental conditions. This study only carried out CT scanning and permeability test of coal samples at the initial state and after the grouting, but the "visual" experiment over the whole grouting process still needs improvement and updating of experimental means. In addition, this study is still under laboratory conditions and scale. The diffusion law and blocking mechanism of grout under engineering sale and complicated conditions are still needed.

6. Conclusions

In this study, a new coal-based grouting material is prepared, and its parameters such as viscosity are tested. A theoretical grouting model of the coal fracture filling with consideration of the flowing of the grout and the deposition of grouting particles is constructed. The leakage stoppage and the permeability reduction mechanism of the coal mass is investigated by using a numerical simulation software COMSOL. Some major conclusions can be drawn:

(1) Fractured coal masses are viewed as a fractured medium. With consideration of the deposition of grouting particles, the mass conservation equation of grouting particles, grout flow equation, and fracture evolutionary equation are deduced. Besides, a grout mass variable seepage model of the leakage stoppage and permeability reduction of fractured coal masses is constructed. This lays a theoretical base to disclose the leakage stoppage and permeability reduction mechanism of the grouting in fractured coal masses

(2) The permeability of fractured coal samples before and after the grouting is tested by an experiment. It was found that the proposed coal-based grouting materials can fill in coal fractures completely, thus significantly decreasing the permeability after the grouting. This proves that the coal-based grouting materials can block fractures significantly

(3) The model is reconstructed based on the real-time industrial CT scan of fractures, and CT scanning images after the reconstruction are input into the numerical simulation software COSMOL by using the independently compiled MATLAB. The whole process of the grout flowing and the fracture filling is simulated, getting the variation laws of the permeability of coal samples. Moreover, the reasonable grouting pressure of coal samples is analyzed. Numerical simulation results conform well with the CT scanning distribution of coal-based grouting materials and the permeability variation in coal samples. This further verifies the reliability of the proposed theoretical model.

Data Availability

The data used to support the findings of this study are included within the article.

Conflicts of Interest

The authors declare that they have no conflicts of interest.

Acknowledgments

This project is supported by the Natural Science Foundation of Henan (No. 202300410182), the National Natural Science Foundation of China (No. 51904095, U1704129, 51774110, and 51774118), the Scientific and Technological Projects of Henan Province (No. 202102310220), and the Plan of Key Scientific Research Projects of Colleges and Universities in Henan Province (No. 20A620001).

References

[1] C. Ö. Karacan, M. Cotè, S. Phipps, and F. A. Ruiz, "Coal mine methane: A review of capture and utilization practices with benefits to mining safety and to greenhouse gas reduction," *International Journal of Coal Geology*, vol. 86, no. 2-3, pp. 121–156, 2011.

[2] B. Yu, C. Su, and D. Wang, "Study of the features of outburst caused by rock cross-cut coal uncovering and the law of gas dilatation energy release," *International Journal of Mining Science and Technology*, vol. 25, no. 3, pp. 453–458, 2015.

[3] L. Wang and Y. P. Cheng, "Drainage and utilization of Chinese coal mine methane with a coal-methane co- exploitation model: analysis and projections," *Resources Policy*, vol. 37, no. 3, pp. 315–321, 2012.

[4] J. He and K. Dong, "Research on rational sealing depth of gas drainage borehole in large section roadway," *China Coal*, vol. 40, no. 2, pp. 101–104, 2014.

[5] Z. Ge, Y. Lu, J. Tang, B. Xia, and X. Mei, "Optimization and application of sealing material and sealing length for hydraulic fracturing borehole in underground coal mines," *Arabian Journal of Geosciences*, vol. 8, no. 6, article 1488, pp. 3477–3490, 2015.

[6] S. Li, Q. Zhang, Q. Zhang, and R. Liu, "Protection against water or mud inrush in tunnels by grouting: a review," *Journal of Rock Mechanics and Geotechnical Engineering*, vol. 8, no. 5, pp. 753–766, 2016.

[7] J. Y. Rafi and H. Stille, "Basic mechanism of elastic jacking and impact of fracture aperture change on grout spread, transmissivity and penetrability," *Tunnelling and Underground Space Technology*, vol. 49, pp. 174–187, 2015.

[8] G. Gustafson, J. Claesson, and Å. Fransson, "Steering parameters for rock grouting," *Journal of Applied Mathematics*, vol. 2013, Article ID 269594, 9 pages, 2013.

[9] Z. Zhou, X. Du, Z. Chen, and Y. Zhao, "Grouting diffusion of chemical fluid flow in soil with fractal characteristics," *Journal of Central South University*, vol. 24, no. 5, pp. 1190–1196, 2017.

[10] Y. E. Fei, C. Zhi, and G. O. U. Chang-fei, "Back-filled grouting compaction model of shield tunnel based on spherical cavity expansion," *Journal of Traffic and Transportation Engineering*, vol. 14, no. 1, pp. 35–42, 2014.

[11] X. F. Liu, J. G. Wang, K. Huang, and F. Li, "Experimental study on dynamic water grouting of modified water-soluble polyurethane," *KSCE Journal of Civil Engineering*, vol. 23, no. 9, pp. 3897–3906, 2019.

[12] W. H. Baker, "Planning and performing structural chemical grouting," *American Society of Civil Engineers*, vol. 1, 2010.

[13] C. Baker-Muler, *Comments on paper rock stabilization in rock mechanics*, Springer-Verlag, New York, 1974.

[14] W. Q. Mu, L. C. Li, T. H. Yang, G. Yu, and Y. Han, "Numerical investigation on a grouting mechanism with slurry-rock

coupling and shear displacement in a single rough fracture," *Bulletin of Engineering Geology and the Environment*, vol. 78, no. 8, pp. 6159–6177, 2019.

[15] F. Xiao, Z. Y. Zhao, and H. M. Chen, "A simplified model for predicting grout flow in fracture channels," *Tunnelling and Underground Space Technology*, vol. 70, pp. 11–18, 2017.

[16] X. L. Li, D. Jin, F. M. Wang, Y. H. Zhong, and B. Zhang, "Diffusion model of an ideal expansible grout in single fracture," *Chinese Journal of Rock Mechanics and Engineering*, vol. 37, no. 5, pp. 1207–1217, 2018.

[17] A. Draganović and H. Stille, "Filtration and penetrability of cement-based grout: study performed with a short slot," *Tunnelling and Underground Space Technology*, vol. 26, no. 4, pp. 548–559, 2011.

[18] Y. Ping and S. Xueqing, "Single fracture grouting numerical simulation based on fracture roughness in hydrodynamic environment," *Electronic Journal of Geotechnical Engineering*, vol. 20, pp. 59–67, 2015.

[19] O. Saeidi, H. Stille, and S. R. Torabi, "Numerical and analytical analyses of the effects of different joint and grout properties on the rock mass groutability," *Tunnelling and Underground Space Technology*, vol. 38, no. 38, pp. 11–25, 2013.

[20] W. Ruan, "Spreading model of grouting in rock mass fissures based on time-dependent behavior of viscosity of cement-based grouts," *Chinese Journal of Rock Mechanics and Engineering*, vol. 24, no. 15, pp. 2709–2714, 2005.

[21] Q. Zhang, L. Zhang, X. Zhang, R. T. Liu, M. T. Zhu, and D. Z. Zheng, "Grouting diffusion in a horizontal crack considering temporal and spatial variation ofviscosity," *Chinese Journal of Rock Mechanics and Engineering*, vol. 34, no. 6, pp. 1198–1210, 2015.

[22] R. S. Yang, H. J. Xue, D. M. Guo et al., "Laboratory grouting experiment based CT analysis of grouted soft rocks in deep mines," *Journal of China Coal Society*, vol. 41, no. 2, pp. 345–351, 2016.

[23] Y. Yu, *Experimental study on mechanical properties and permeability of coal with grouting reinforcement*, Harbin:Heilongjiang University of Science and Technology, 2015.

[24] L. Ning, Z. Ping, and Y. Jianwen, "Numerical modeling of grouting in geoengineering," *Chinese Journal of Rock Mechanics and Engineering*, vol. 21, no. 3, pp. 326–330, 2002.

[25] Q. Li, W. Z. Chen, J. Q. Yuan, Y. X. Wang, and H. Wan, "Evaluation of grouting reinforcement effect for karst filling medium based on seepage-erosion theory," *Chinese Journal of Rock Mechanics and Engineering*, vol. 39, no. 3, pp. 1–9, 2020.

[26] L. I. U. Rentai, Z. Zhuo, L. I. Shucai, and Z. Qingsong, "Pre-excavation grouting to prevent water inflow of jointed rock in underground construction," *Journal of Southwest Jiaotong University*, vol. 54, no. 1, pp. 48–54, 2019.

[27] G. X. Zhu, Q. S. Zhang, X. Feng et al., "Study on the filtration mechanism in permeation grouting using the particle deposition probability model," *Advanced Engineering Sciences*, vol. 52, no. 5, pp. 125–135, 2020.

[28] L. Sun, G. Grasselli, Q. Liu, and X. Tang, "Coupled hydro-mechanical analysis for grout penetration in fractured rocks using the finite-discrete element method," *International Journal of Rock Mechanics and Mining Sciences*, vol. 124, article 104138, 2019.

[29] Z. Xu, X. Zhou, G. Gao, X. Feng, and C. Liu, "Full-scale physical modelling of fissure grouting in deep underground rocks," *Tunnelling and Underground Space Technology*, vol. 89, pp. 249–261, 2019.

[30] S. Berrone, C. Canuto, S. Pieraccini, and S. Scialò, "Uncertainty quantification in discrete fracture network models: stochastic fracture transmissivity," *Computers & Mathematics with Applications*, vol. 70, no. 4, pp. 603–623, 2015.

[31] X. Han, J. Chen, Q. Wang, Y. Li, W. Zhang, and T. Yu, "A 3D fracture network model for the undisturbed rock mass at the Songta Dam Site based on small samples," *Rock Mechanics & Rock Engineering*, vol. 49, no. 2, pp. 611–619, 2016.

[32] M. Li, S. Han, S. Zhou, and Y. Zhang, "An improved computing method for 3D mechanical connectivity rates based on a polyhedral simulation model of discrete fracture network in rock masses," *Rock Mechanics & Rock Engineering*, vol. 51, no. 6, article 1423, pp. 1789–1800, 2018.

[33] C. Yan and H. Zheng, "Three-dimensional hydromechanical model of hydraulic fracturing with arbitrarily discrete fracture networks using finite-discrete element method," *International Journal of Geomechanics*, vol. 17, no. 6, article 04016133, 2017.

[34] S. Deng, X. Wang, J. Yu, Y. Zhang, Z. Liu, and Y. Zhu, "Simulation of grouting process in rock masses under a dam foundation characterized by a 3D fracture network," *Rock Mechanics & Rock Engineering*, vol. 51, no. 6, article 1436, pp. 1801–1822, 2018.

[35] Q. Liu, X. Cui, and C. Zhang, "Permeability reduction model of particles deposit in porous medium considering changeable porosity," *Chinese Journal of Rock Mechanics and Engineering*, vol. 35, pp. 3308–3314, 2016.

[36] L. Huawei, *The study on the penetration property of red mud filtrate and transport process of contaminant*, BEIJING JIAOTONG UNIVERSITY, BeiJing, 2015.

[37] F. Ye, X. Han, and N. Qin, "Displacement infiltration diffusion model of binghamian grouts as backfill grouting of shield tunne," *Journal of Tongji University. Natural Science*, vol. 47, no. 12, pp. 1720–1726, 2019.

[38] W. Jianping, D. Wang, and W. Le, "Comparison of permeability between two kinds of loaded coal containing gas samples," *Journal of China Coal Society*, vol. 38, no. S1, pp. 93–99, 2013.

[39] D. Ma, H. Duan, X. Cai, and Z. Li, "A global optimization-based method for the prediction of water inrush hazard from mining floor," *Water*, vol. 10, no. 11, pp. 1–18, 2018.

[40] D. Ma, J. Wang, and Z. Li, "Effect of particle erosion on mining-induced water inrush hazard of karst collapse pillar," *Environmental Science and Pollution Research International*, vol. 26, no. 19, pp. 19719–19728, 2019.

[41] W. Jianping, W. Le, and W. Dengke, "Experimental study of moisture content influences on permeability of coal containing gas," *Journal of China Coal Society*, vol. 39, no. 1, pp. 97–103, 2014.

[42] Y. Xue, P. G. Ranjith, F. Dang et al., "Analysis of deformation, permeability and energy evolution characteristics of coal mass around borehole after excavation," *Natural Resources Research*, vol. 29, no. 5, pp. 3159–3177, 2020.

[43] J. Liu, X. Liang, Y. Xue, K. Yao, and Y. Fu, "Numerical evaluation on multiphase flow and heat transfer during thermal stimulation enhanced shale gas recovery," *Applied Thermal Engineering*, vol. 178, article 115554, 2020.

Hindawi
Geofluids
Volume 2021, Article ID 6616315, 16 pages
https://doi.org/10.1155/2021/6616315

Research Article

Constraints of Pore-Bulk Strain Ratio and Interference Time on the Evolution of Coal Permeability during CO_2 Injection

Guannan Liu,[1,2,3] **Jishan Liu**,[4] **and Feng Gao**[1,2]

[1]*State Key Laboratory for Geomechanics and Deep Underground Engineering, China University of Mining and Technology, Xuzhou, Jiangsu 221116, China*
[2]*Laboratory of Mine Cooling and Coal-heat Integrated Exploitation, China University of Mining and Technology, Xuzhou 221116, China*
[3]*Beijing Key Laboratory for Precise Mining of Intergrown Energy and Resources, China University of Mining and Technology, Beijing 100083, China*
[4]*School of Engineering, The University of Western Australia, WA 6009, Australia*

Correspondence should be addressed to Guannan Liu; guannanliu@cumt.edu.cn

Received 6 December 2020; Revised 20 February 2021; Accepted 5 March 2021; Published 16 March 2021

Academic Editor: Guanglei Zhang

CO_2 injection into coal seam triggers a series of processes that are coupled all together through a permeability model. Previous studies have shown that current permeability models cannot explain experimental data as reported in the literature. This knowledge gap defines the goal of this study. We hypothesize that this failure originates from the assumption that the pore strain is the same as the bulk strain in order to satisfy the Betti-Maxwell reciprocal theorem. This assumption is valid only for the initial state without gas sorption and deformation and for the ultimate state with uniform gas sorption and uniform deformation within the REV (representative elementary volume). In this study, we introduce the pore-bulk strain ratio and interference time to characterize the process of gas sorption and its associated nonuniform deformation from the initial state to the ultimate state. This leads to a new nonequilibrium permeability model. We use the model to fully couple the coal deformation and gas flow. This new coupled model captures the impact of coal local transient behaviors on gas flow. Results of this study clearly show that coal permeability is constrained by the magnitudes of initial and ultimate pore-bulk strain ratios and interference time, that current permeability data in the literature are within these bounds, and that the evolutions of coal permeability all experience similar stages from the initial value to the ultimate one.

1. Introduction

CO_2 is the main contributor to the greenhouse effect. CO_2 sequestration in deep nonexploitable coal seams can simultaneously reduce CO_2 emissions and enhance coalbed methane recovery (CO_2-ECBM), which has great potential for development [1–4]. The study of coal permeability evolution is the main problem to enhance gas recovery of reservoir [5–7]. When the gas pressure drops to the desorption point, the adsorbed gas enters into pores, the matrix shrinks, and the pores' volume increases [8–10]. In the process of gas injection, solid-gas coupling leads to significant differences in permeability, and its evolution process is highly complex.

In the past few decades, several coupling models have been proposed to interpret the permeability change during CO_2 injection. Based on the Langmuir model, a finite element model was proposed to investigate the coupling of sorption-induced deformation and coal seam gas flow process [11]. A multiphase flow model for the gas injection process considering the coupling of matrix deformation and heat conduction process was proposed [12]. Then, the single-porosity elastic model to study the evolution process of porosity and permeability of CO_2 gas injection under in situ stress, taking into account the deformation and flow process of micropore and fracture, was revised [13, 14]. A dual porosity model considering the statistical properties of geological parameters, which can introduce relatively large errors, was proposed [15]. The effects of directional compaction, single fracture, and anisotropic expansion on coalbed methane reservoirs through a dual porosity model were discussed [16]. Based on the multiple porosity model, the relationship between matrix strain and macro permeability of coal by introducing the strain splitting function was studied [17]. Two nonequilibrium models with two different nonlinear adsorption isotherms, i.e. nonlinear Freundlich and Langmuir adsorption isotherms, were developed [18]. The change of fracture porosity and permeability caused by coal matrix shrinkage into the dual pore model to study the quasisteady flow in unconventional reservoirs was introduced [19, 20]. Although these models have been used to interpret and match some experimental data, the interaction between coal matrix and fracture induced by the adsorption-induced strain has not been understood well.

Previous model conclusions [15, 21] are inconsistent with experimental data of huge changes in coal permeability caused by coal swelling. The experimental data are sensitive to the change of stress and pore pressure, especially for low permeability coal seams. Using transient pulse attenuation technology, it is found that the compressibility of face cleats is considerably sensitive to the sorption-induced swelling/shrinkage and offers significant effects on the coal permeability [22]. The adsorption and desorption energy of CO2 gas significantly affects the volume change of microscopic and macroscopic pores in coal, resulting in the expansion/contraction and permeability fluctuation of coal [23].Previous models usually only studied the ultimate equilibrium permeability, but neglected its evolution process. Studies [14, 22, 23] show that for low permeability coal seams, it often takes a long time for permeability to evolve to the final equilibrium state during gas injection. To solve this problem, a series of research was conducted [24–26] to study the change process of the intermediate nonequilibrium state in the process of coalbed methane exploitation. In recent years, a new functional relationship between coal permeability and fracture aperture was defined [27], and the evolution process of coal permeability from the initial equilibrium state to final equilibrium state was analyzed. However, the study on the division of fracture and matrix-induced strain by adsorption usually adopts the method of single or discrete fracture explicitly embedded into the models.

In this study, the explicit approach as adopted in previous studies is transformed into a continuous approach. The explicit method uses geometric methods to characterize the fracture pore structure, such as digital core method and fracture discrete network method. However, due to its high computational requirements, the analysis of large-scale multifield coupling problems is still limited [5, 6]. In the process of gas adsorption, coal will undergo uneven deformation, which will lead to the change of throat and channel length in the internal pores; so, the pore-bulk strain ratio is introduced to characterize this change process. Under the coupling effect of stress, the change of pore pressure in coal will lead to the change of permeability. The pore volume strain ratio and interference time proposed in this work can quantitatively characterize the gas adsorption process and the accompanying nonuniform evolution process from the initial state to the final state. Thus, a new multifield coupling model of nonequilibrium permeability including fracture pore dual scale is established. Compared with the previous models, this new coupling model captures the influence of local transient behavior of coal on gas flow from the perspective of interference time. The results of this study are reported in the following sections.

2. Governing Equations

Coal seam is a typical dual porosity medium under the action of in situ stress [28–31]. The deformation caused by the adsorption process is one of the main inducements of coal seam permeability. Firstly, considering the pore adsorption strain ratio, a dual porosity model is established and coupled to the solid deformation equation under the influence of effective stress. The following assumptions are made for coal deformation and gas seepage process:

(1) The deformation process of coal meets linear elasticity

(2) The effect of anisotropy is not considered

(3) Gas viscosity coefficient is a constant

(4) Gas in the pores is saturated

2.1. Permeability Model. The ratio of pore strain and bulk strain induced by adsorption can be expressed as [32]:

$$\varepsilon_{sp} = \psi(\varepsilon_{sb}), \tag{1}$$

where ε_{sp} is the pore strain induced by sorption, ε_{sb} is the bulk strain of coal induced by sorption, and ψ is the function of ε_{sb}. According to Taylor expansion, Eq.(1) can be expressed as

$$\varepsilon_{sp} = \gamma\varepsilon_{sb}, \tag{2}$$

where $\gamma = \partial\psi/\partial\varepsilon_{sb}|_{\varepsilon_{sb}=0}$. Experimental results [15] show that the sorption-induced strain of pore is larger than that of bulk, and the two strains can be regarded as equal only when they are in the equilibrium state.

At the beginning of gas injection, the pressure in fracture is greater than that in matrix. So, gas permeates into the matrix, and the amount of adsorbed gas in the matrix increases. Then, the volume expands, and the fracture volume decreases as shown in Figure 1. We can draw the conclusion that the sign of the fracture strain is opposite to that of the matrix strain. In addition, coal porosity is usually very small ($0.001 < \phi < 0.03$); so, the sorption-induced strain of matrix is approximately equal to that of bulk. Then, the sigh of the sorption-induced fracture strain is opposite to that of bulk, i.e., at the initial state $\gamma_0 < 0$. The initial value of γ can be expressed as [33]:

$$\gamma_0 = \frac{C_f E}{3(\nu - 1)}, \tag{3}$$

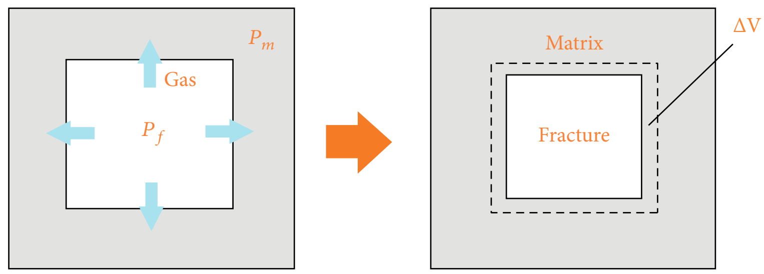

FIGURE 1: Block volume evolution induced by gas transfer between fracture and matrix.

where C_f is the coal compressibility, E is the Young's modulus of coal, and ν is the Poisson ratio of coal.

The characteristic interference time τ_1 is determined by the onset of pressure interference between two hydro fractures spaced $2d$ (as shown in Figure 2) apart and defined by [34]:

$$\tau_1 = \frac{d^2}{\lambda_i}. \tag{4}$$

λ_i is the hydraulic diffusivity of gas under the initial reservoir pressure and temperature (p_i, T), which can be measured by experiment. Pore structure, temperature, pressure, and gas composition have an important influence on the hydraulic diffusion coefficient, but here we ignore the change of temperature and pressure, assuming that the gas is an ideal gas, and considering the homogeneous reservoir; so, the hydraulic diffusion coefficient λ_i is considered to be a constant.

When coal reaches the final equilibrium state, the strain ratio $\gamma = 1$, which means pore strain induced by sorption, is equal to the bulk strain. In combination with equation (3), we assume that the adsorption strain ratio changes linearly from the initial state to the final equilibrium state. As shown in Figure 3, γ can be expressed as

$$\gamma = \begin{cases} \dfrac{1-\gamma_0}{\tau_1} \cdot \tau + \gamma_0, 0 \le \tau < \tau_1 \\ 1, \tau_1 \le \tau \end{cases}. \tag{5}$$

The change rate of pore volume can be expressed as [11, 35]:

$$\frac{\Delta V}{V} = -\frac{1}{K}(\bar{\sigma} - \alpha p) + \varepsilon_s, \tag{6}$$

$$\frac{\Delta V_p}{V_p} = -\frac{1}{K_p}(\bar{\sigma} - \alpha p) + \gamma \varepsilon_s, \tag{7}$$

where $V = V_p + V_s$, V is total volume of porous coal, V_p is the pore volume of porous coal, and V_s is solid volume of porous coal. $\bar{\sigma}$ is the mean compressive stress, α is the Biot coefficient, p is the gas pressure. ε_s is the gas

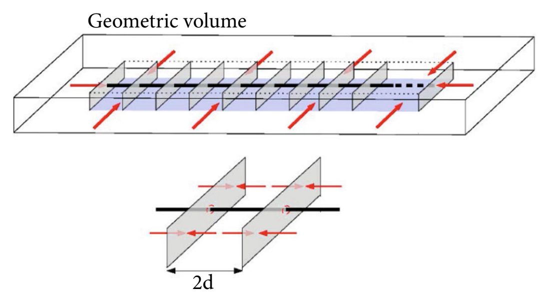

FIGURE 2: Schematic diagram of the artificial fracturing structure.

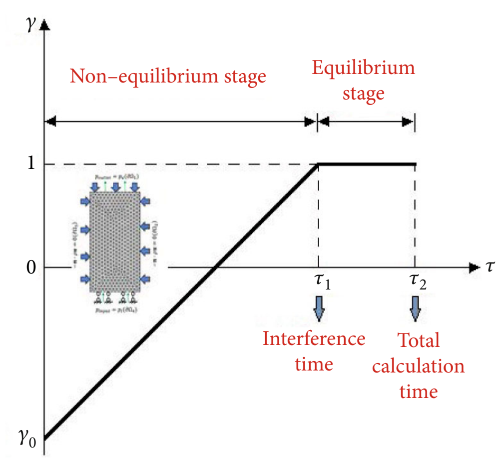

FIGURE 3: Schematic diagram of the change of adsorption strain ratio γ.

sorption-induced strain, K is the bulk modulus of coal, and K_p is the bulk modulus of pores.

$$K_p = \frac{\phi}{\alpha} K, \tag{8}$$

$$\frac{\Delta V}{V} = \frac{\Delta V_s}{V_s} + \frac{\Delta \phi}{1-\phi}, \tag{9}$$

$$\frac{\Delta V_p}{V_p} = \frac{\Delta V_s}{V_s} + \frac{\Delta \phi}{\phi(1-\phi)}, \tag{10}$$

where ϕ is the porosity of coal. Combined Eq.(6)–(10), we obtain

$$\begin{aligned}\Delta\phi &= \phi(\bar{\sigma}-\alpha p)\left[-\frac{1}{K_p}+\frac{1}{K}\right]+\phi(\gamma-1)\varepsilon_s \\ &= \frac{\phi-\alpha}{K}(\bar{\sigma}-\alpha p)+\phi(\gamma-1)\varepsilon_s.\end{aligned} \tag{11}$$

Substitute $\varepsilon_v=-(1/K)(\bar{\sigma}-\alpha p)+\varepsilon_s$ into Eq.(11), we obtain

$$\Delta\phi=(\alpha-\phi)\left(\varepsilon_v-\varepsilon_s+\frac{p}{K_s}\right)+\phi(\gamma-1)\varepsilon_s, \tag{12}$$

where K_s is the bulk modulus of coal grains. Then,

$$\begin{aligned}\phi-\phi_0 &= (\alpha-\phi)(S-S_0)+\phi(\gamma-1)(\varepsilon_s-\varepsilon_{s0}) \\ &= (\alpha-\phi)(S-S_0)+\phi(\gamma-1)\left(\varepsilon_s-\varepsilon_L\frac{p_0}{P_L+p_0}\right),\end{aligned} \tag{13}$$

where $S=\varepsilon_v+(p/K_s)-\varepsilon_s$, $S_0=(p_0/K_s)-\varepsilon_L p_0/(p_0+p_L)$, p_0 is the initial gas pressure, ε_{s0} is initial gas sorption-induced strain, p_L is the Langmuir pressure coefficient, and ε_L is the Langmuir volumetric strain constant; so, we obtain

$$\phi=\frac{\phi_0+\alpha(S-S_0)}{1+(S-S_0)-(\gamma-1)(\varepsilon_s-\varepsilon_L(p_0/P_L+p_0))}. \tag{14}$$

Find the partial derivatives of the equations on both sides of Eq. (11):

$$\frac{\partial\phi}{\partial t}=\frac{\alpha-2\phi+\phi\gamma}{1+2S-\gamma S-S_0}\frac{\partial S}{\partial t}. \tag{15}$$

The governing equations of gas flow can be expressed as

$$\left[\phi+\frac{\rho_c p_a V_L P_L}{(p+P_L)^2}\right]\frac{\partial p}{\partial t}+p\frac{\partial\phi}{\partial t}-\nabla\cdot\left(\frac{k}{\mu}p\nabla p\right)=Q_s, \tag{16}$$

where V_L is the Langmuir volume coefficient, k is the permeability, μ is the gas viscosity, and Q_s is source term of gas flow, $Q_s=\omega(p_f-p_m)$. Experiments [11, 12] show that the relationship between porosity and permeability of coal can be expressed as

$$\frac{k}{k_0}=\left(\frac{\phi}{\phi_0}\right)^3. \tag{17}$$

Combined Eq. (16) with Eq.(17), we can obtain the permeability of the pore system and fracture system:

$$k_m=k_{m0}\left[\frac{\phi_{m0}+\alpha(S_m-S_{m0})}{1+(S_m-S_{m0})-(\gamma-1)(\varepsilon_{ms}-\varepsilon_L(p_{m0}/P_L+p_{m0}))}\cdot\frac{1}{\phi_{m0}}\right]^3,$$

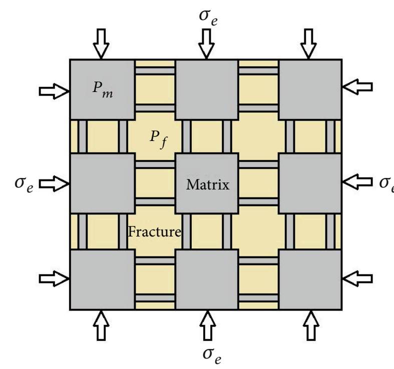

Figure 4: Dual porosity coal structure.

$$k_f=k_{f0}\left[\frac{\phi_{f0}+\alpha(S_f-S_{f0})}{1+(S_f-S_{f0})-(\gamma-1)\left(\varepsilon_{fs}-\varepsilon_L\left(p_{f0}/P_L+p_{f0}\right)\right)}\cdot\frac{1}{\phi_{f0}}\right]^3, \tag{18}$$

where subscript m denotes matrix and f denotes fractures.

2.2. Governing Equation of Coal Deformation. The structure of the dual porosity model is shown in Figure 4. The equilibrium equation of matrix and fracture can be expressed as

$$\sigma_{ij}+f_i=0, \tag{19}$$

where σ_{ij} is the component of stress tensor, and f_i is the component of body force. The relationship between coal deformation and stress induced by adsorption can be expressed as [36]

$$\varepsilon_{ij}=\frac{1}{2G}\sigma_{ij}-\left(\frac{1}{6G}-\frac{1}{9k}\right)\sigma_{kk}\delta_{ij}+\frac{\alpha}{3K}p\delta_{ij}+\frac{\varepsilon_s}{3}\delta_{ij}, \tag{20}$$

where G is the elastic shear modulus, $\sigma_{kk}=\sigma_{11}+\sigma_{22}+\sigma_{33}$, and δ_{ij} is the Kronecker delta. According to the Langmuir equation, the sorption-induced strain can be expressed as

$$\varepsilon_s=\varepsilon_L\frac{p}{P_L+p}. \tag{21}$$

Combined Eq. (19) with Eq. (20), the governing equation of coal deformation can be expressed as [37, 38]

$$Gu_{i,kk}+\frac{G}{1-2\mu}u_{k,ki}-\alpha p_i-K\varepsilon_{s,i}+f_i=0. \tag{22}$$

2.3. Governing Equation of Gas Flow. According to the state of occurrence, gas in the coal reservoir can be divided into two parts: the adsorption phase and the free phase. The total mass can be described by the following equations:

$$m_m=\rho_{gm}\phi_m+\rho_{ga}\rho_c\frac{V_L p_m}{p_m+P_L}, \tag{23}$$

$$m_f = \rho_{gf}\phi_f + \rho_{ga}\rho_c \frac{V_L p_f}{p_f + P_L}, \tag{24}$$

where m_m and m_f, respectively, denote the mass of gas in matrix and fracture. ρ_{gm} and ρ_{gf}, respectively, denote the gas density in matrix and fracture. ρ_{ga} denotes the gas density in standard condition. ρ_c denotes coal density. Based on the conservation law of mass, the governing equation of gas mass can be expressed as

$$\frac{\partial m}{\partial t} + \nabla \cdot \left(\rho_g q_g\right) = Q_s, \tag{25}$$

where t is the time. ρ_g is the gas density, and q_g is Darcy's flow velocity. Neglecting the effect of gravity, Darcy's flow can be expressed as

$$\dot{q}_g = -\frac{k}{\mu}\nabla p, \tag{26}$$

where $\dot{q}_g$ represents the derivation of q_g. Substituting Eqs.(23), (24), and (26) into Eq.(25), the mass conservation equation of the gas can be expressed as [11, 39, 40]

$$\left[\phi_m + \frac{\rho_c p_a V_L P_L}{(p_m + P_L)^2}\right]\frac{\partial p_m}{\partial t} + p_m \frac{\partial \phi_m}{\partial t} - \nabla \cdot \left(\frac{k_m}{\mu} p_m \nabla p_m\right) = Q_s,$$
$$\left[\phi_f + \frac{\rho_c p_a V_L P_L}{\left(p_f + P_L\right)^2}\right]\frac{\partial p_f}{\partial t} + p_f \frac{\partial \phi_f}{\partial t} - \nabla \cdot \left(\frac{k_f}{\mu} p_f \nabla p_f\right) = -Q_s, \tag{27}$$

where p_a is the atmospheric pressure, $p_a = 101.325 kPa$.

2.4. Coupled Governing Equation. The dual porosity model proposed in this paper considers the pore strain induced by adsorption as a linear relationship with the bulk strain. The coal deformation governing equation is rewritten as

$$G u_{i,kk} + \frac{G}{1-2\mu} u_{k,ki} - \alpha p_i - \frac{K\varepsilon_L P_L}{(p + P_L)^2} p_i + f_i = 0. \tag{28}$$

There is no deformation in the coal at initial pressure, and the porosity evolution equation in the gas injection process is

$$\frac{\partial \phi}{\partial t} = \frac{\alpha - \phi}{1 + S}\left[\frac{\partial \varepsilon_v}{\partial t} + \frac{1}{K_s}\frac{\partial p}{\partial t} - \frac{\varepsilon_L P_L}{(p + P_L)^2}\frac{\partial p}{\partial t}\right], \tag{29}$$

where $\varepsilon_v = \varepsilon_{11} + \varepsilon_{22} + \varepsilon_{33}$ is the volume strain of coal. Substituting Eq. (8) for Eq. (5), we obtain the coal bed gas flow equation of the pore system and fracture system:

Table 1: Property parameters of simulation model against experimental data.

Parameter	Value
Young's modulus of coal, E(MPa)	3600
Possion's ratio of coal, ν	0.35
Density of coal, ρ_c(kg/m^3)	1.25×10^3
Density of methane, ρ_g(kg/m^3)	1.784
Methane dynamic viscosity, μ(Pa · s)	1.493×10^{-5}
Langmuir pressure constant, P_L(MPa)	1.43
Langmuir volumetric strain constant, ε_L	0.004
Hydraulic diffusivity of gas, λ_i(m^2/s)	1.42×10^{-7}
Distance between two hydro fractures spaced, $2d$(m)	8
Cleat compressibility, C_f(MPa^{-1})	3.2×10^{-7}

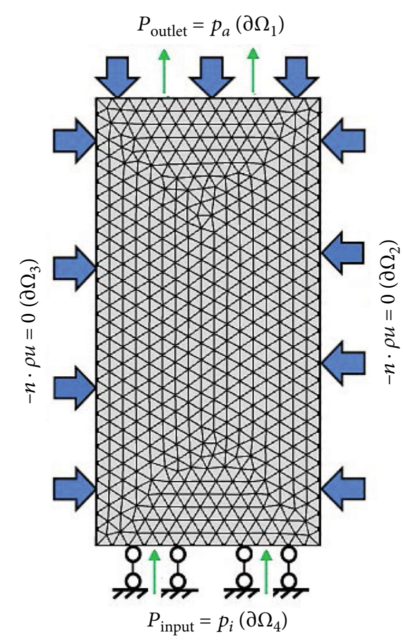

Figure 5: Simulation model for the case of CO_2 injection.

$$\left[\phi_m + \frac{\rho_{mc} p_a V_L P_L}{(p_m + P_L)^2} + \frac{(\alpha - \phi_m)p_m}{(1 + S_m)K_s} - \frac{(\alpha - \phi_m)\varepsilon_L P_L p_m}{(1 + S_m)(p_m + P_L)^2}\right]\frac{\partial p_m}{\partial t}$$
$$-\nabla \cdot \left(\frac{k_m}{\mu} p_m \nabla p_m\right) = Q_s - \frac{(\alpha - \phi_m)_L p_m}{(1 + S_m)}\frac{\partial \varepsilon_v}{\partial t},$$

$$\left[\phi_f + \frac{\rho_{fc} p_a V_L P_L}{\left(p_f + P_L\right)^2} + \frac{\left(\alpha - \phi_f\right)p_f}{(1 + S_f)K_s} - \frac{\left(\alpha - \phi_f\right)\varepsilon_L P_L p_f}{(1 + S_f)\left(p_f + P_L\right)^2}\right]\frac{\partial p_f}{\partial t}$$
$$-\nabla \cdot \left(\frac{k_f}{\mu} p_f \nabla p_f\right) = -Q_s - \frac{\left(\alpha - \phi_f\right)_L p_f}{(1 + S_f)}\frac{\partial \varepsilon_v}{\partial t}. \tag{30}$$

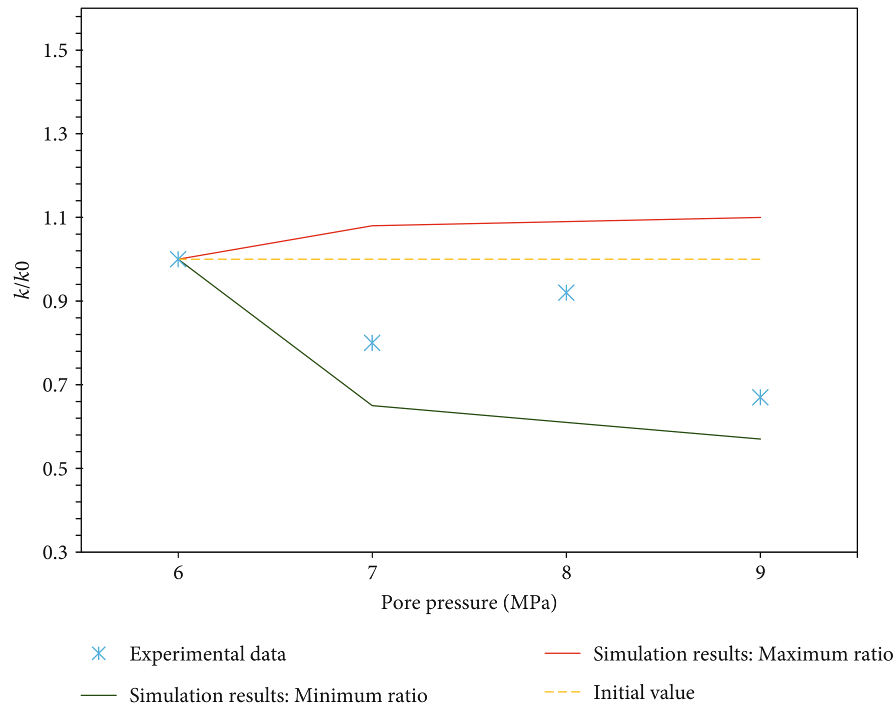

Figure 6: Comparison between experimental data and simulation results for the case of confining pressure $p = 24$ MPa.

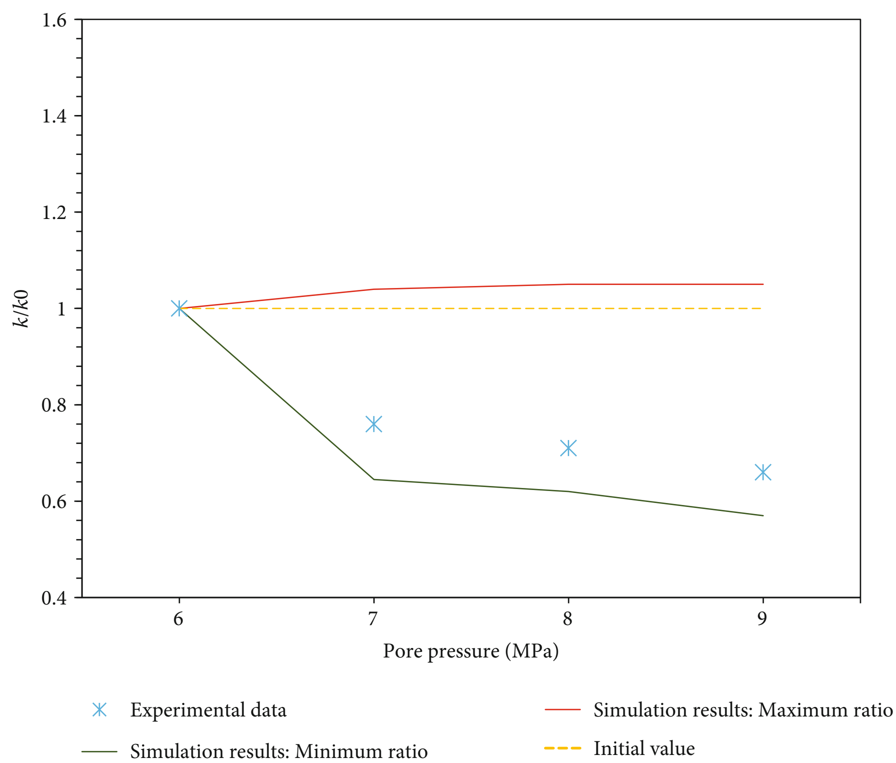

Figure 7: Comparison between experimental data and simulation results for the case of confining pressure $p = 20$ MPa.

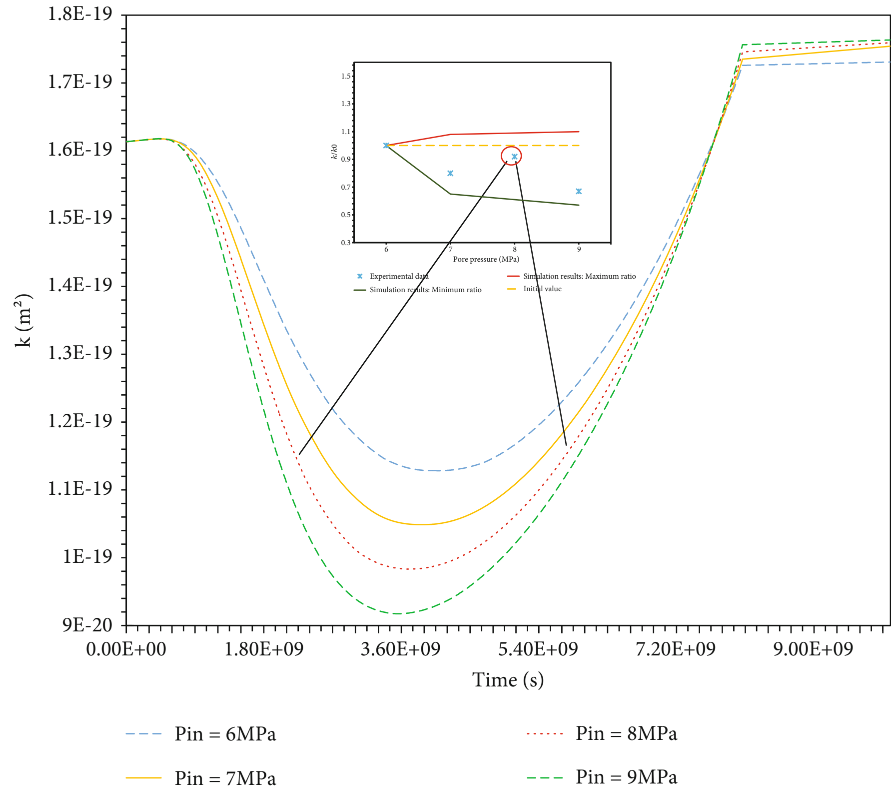

Figure 8: Evolution of permeability with different injection pressures for the case of confining pressure $p = 24$ MPa.

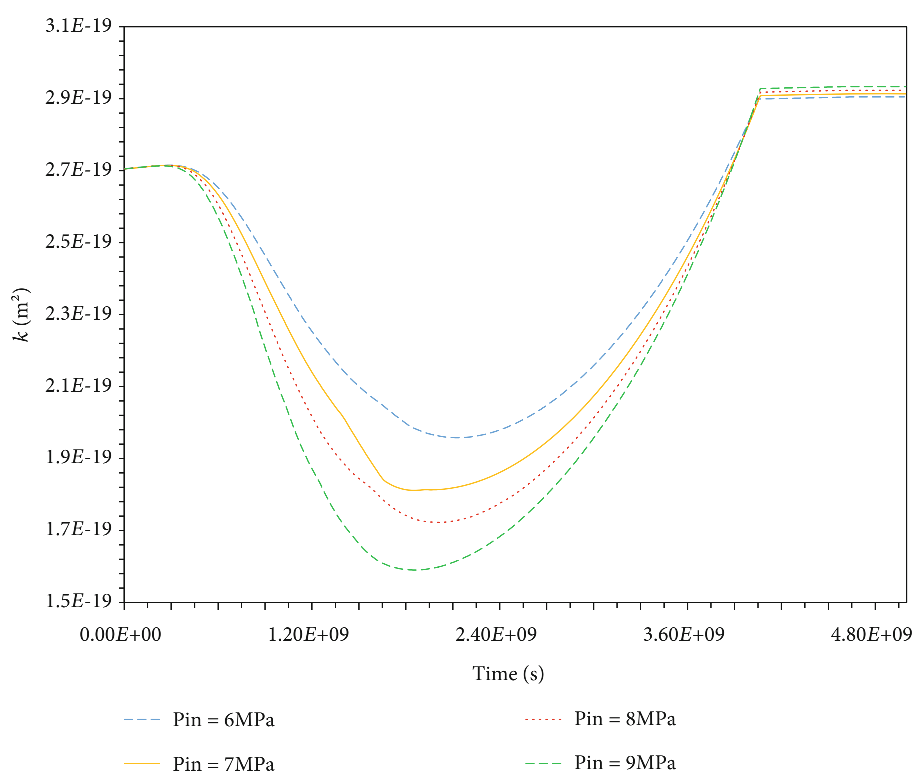

Figure 9: Evolution of permeability with different injection pressures for the case of confining pressure $p = 20$ MPa.

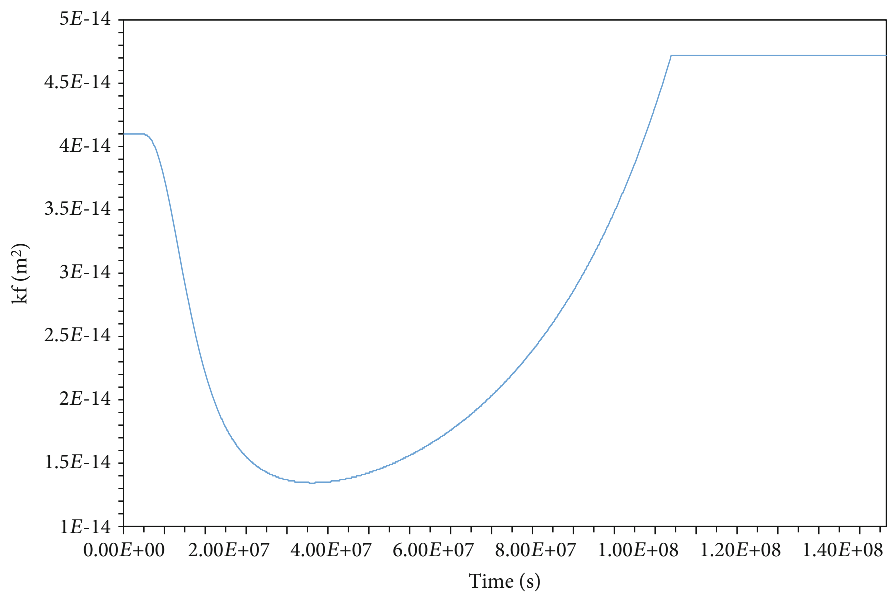

Figure 10: Permeability evolution process of fracture system of model I.

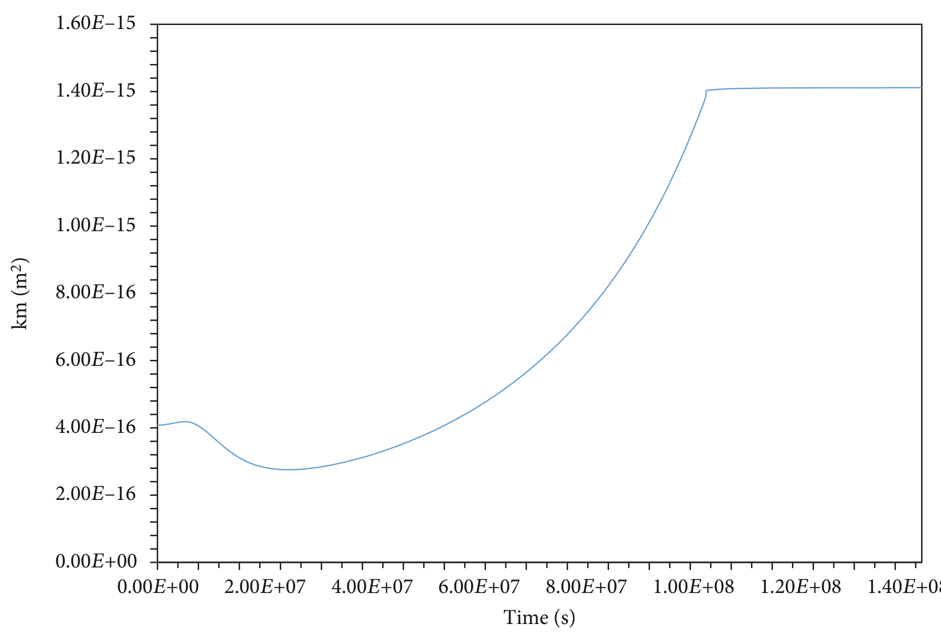

Figure 11: Permeability evolution process of pore system of model I.

3. Model Verifications against Experimental Data

The process of gas seepage in dual porosity media is highly nonlinear both in time and space. The governing equations of gas seepage in dual porosity media are partial differential equations, which are difficult to obtain analytical solutions. In this paper, the multiphysical coupling software COMSOL is used for numerical solution. In order to verify the correctness of the model, we compare the simulation results with the experimental data [41].The material property parameters used in the calculation model are shown in Table 1.

The simulation model is a square domain with the size of 0.076 m × 0.038 m. CO_2 is injected at the bottom of the model, and the outlet is the upper boundary. The gas injection pressure varies from 6 MPa to 9 MPa. The bottom boundary is hinge constraint, and the upper, left, and right boundaries are uniformly distributed, as shown in Figure 5. The numerical results are compared with two sets of laboratory data (confining pressure 24 MPa and 20 MPa, respectively), as shown in Figures 6 and 7. The two experimental cases are simulated as follows: the permeability evolution process of each experiment from the initial equilibrium state to the final equilibrium state is calculated (Figures 8 and 9). The red lines in Figures 6 and

8 represent the upper limit of permeability simulation results under different injection pressures, and the green lines represent the lower limit of permeability simulation results. It is found that the experimental results may not reach the equilibrium state of permeability evolution.

According to Figures 6 and 7, the coupling model proposed in this paper is in good agreement with the experimental data. According to Figures 8 and 9, the evolution of permeability in CO_2 gas injection can be divided into four stages: (1) when CO_2 is injected into coal, the pore space becomes larger, and the permeability increases with the increase of fracture pressure. (2) The gas pressure in fracture is larger than that in matrix. The gas begins to diffuse from fracture to matrix. The volume of the matrix expands, the volume of the fracture shrinks, and the permeability of coal decreases. (3) With the gradual diffusion of gas into the matrix, only local expansion deformation has an impact on the permeability of coal, and the permeability increases gradually, and (4) the pressure of the matrix and pore is in equilibrium with each other, the coal mass is uniformly expanded, and the coupling process is stable.

From Figures 6 and 7, it can be seen that coal permeability is affected by the injection pressure. Figures 8 and 9 correspond to the evolution of permeability with time under different injection pressures of Figures 6 and 7, respectively. Each point of the measured data in Figures 6 and 7 corresponds to the specific location of the corresponding curve in Figures 8 and 9. Because the curve is not monotonous, the measured data mostly correspond to the two points of the curve, as shown in Figure 8. When the gas injection reaches the final stable state, the permeability value is the upper limit of the permeability curve. Figures 6 and 7 show that the measured permeability values lie between the upper and lower limits, indicating that the measured permeability values may not reach the final equilibrium state, which may due to the low porosity of coal samples. The permeability evolution process of the fracture and pore system of model I is not a monotone line, which can be seen in Figures 10 and 11.

4. Numerical Experiments

4.1. Permeability Tests under the Condition of Constant Confining Stress. The boundary conditions of the numerical model are shown in Figure 5. The gas parameters of dual porosity coal are shown in the following table, which comes from previous experiments (Robertson E.P. and Christiansen R.L., 2005). The size of the calculation model is $0.1\,\text{m} \times 0.05\,\text{m}$. The lower boundary is fixed hinge constraint, and the upper, left, and right boundaries are subjected to uniform pressure 7 MPa. There is no mass transfer on the left boundary and the right boundary. CO_2 is injected from the bottom of the model and outflows from the upper boundary. The inlet pressure is 4.8 MPa, and outlet pressure is atmospheric pressure. The parameters of coal and gas for simulation are shown in Table 2.

The permeability evolution process of the coal fracture system and pore system is shown in Figures 5 and 6. According to Figures 5 and 6, during the process of gas injection, the permeability change rule of the pore system and fracture system is similar, which includes four stages: increasing, decreasing, then gradually restoring, and finally balancing. The permeability of the pore system is changing more obviously. The reason is that the porosity of pore system is small, and the small change of pore volume will have a more obvious impact on its permeability.

Table 2: Property parameters of coal and gas.

Parameter	Value
Young's modulus of coal, E(MPa)	5100
Possion's ratio of coal, ν	0.39
Density of coal, $\rho_c(\text{kg/m}^3)$	1.25×10^3
Density of methane, $\rho_g(\text{kg/m}^3)$	1.784
Methane dynamic viscosity, $\mu(\text{Pa} \cdot \text{s})$	1.493×10^{-5}
Langmuir pressure constant, P_L(MPa)	2.75
Langmuir volumetric strain constant, ε_L	0.01
Hydraulic diffusivity of gas, $\lambda_i(\text{m}^2/\text{s})$	1.1×10^{-7}
Distance between two hydro fractures spaced, $2d$(m)	7
Cleat compressibility, $C_f(\text{MPa}^{-1})$	1.04×10^{-7}

Table 3: Simulation strategies.

Case 1	Impact of adsorptive strain ratios on the resulting response $\gamma = -100, -150, -200$
Case 2	Impact of interference time on the resulting response $\tau = 7 \times 10^7, 9 \times 10^7, 1.1 \times 10^8\text{s}$
Case 3	Impact of gas injection pressure on the resulting response $P_{in} = 4.1, 4.8, \text{and } 5.5\,\text{MPa}$

In this paper, a dual porosity model considering the adsorption strain ratio is proposed. The effects of three main factors on permeability evolution during gas injection are analyzed, including

(1) Adsorption strain ratio

(2) Interference time

(3) Gas injection pressure

The simulation parameters of different cases are shown in Table 3. The evolution of permeability with different adsorptive strain ratios during gas injection is shown in Figures 12–14. According to Figures 12–14 below, although the adsorption strain ratio does not affect the permeability after the final equilibrium state of gas injection, the lower limit of permeability decreases obviously when the absolute value of the adsorption strain ratio increases.

The comparison of the evolution process of permeability with the interference time is shown in Figure 13. According to Figure 13, we obtain that the difference of permeability is mainly the lower limit of the permeability evolution process

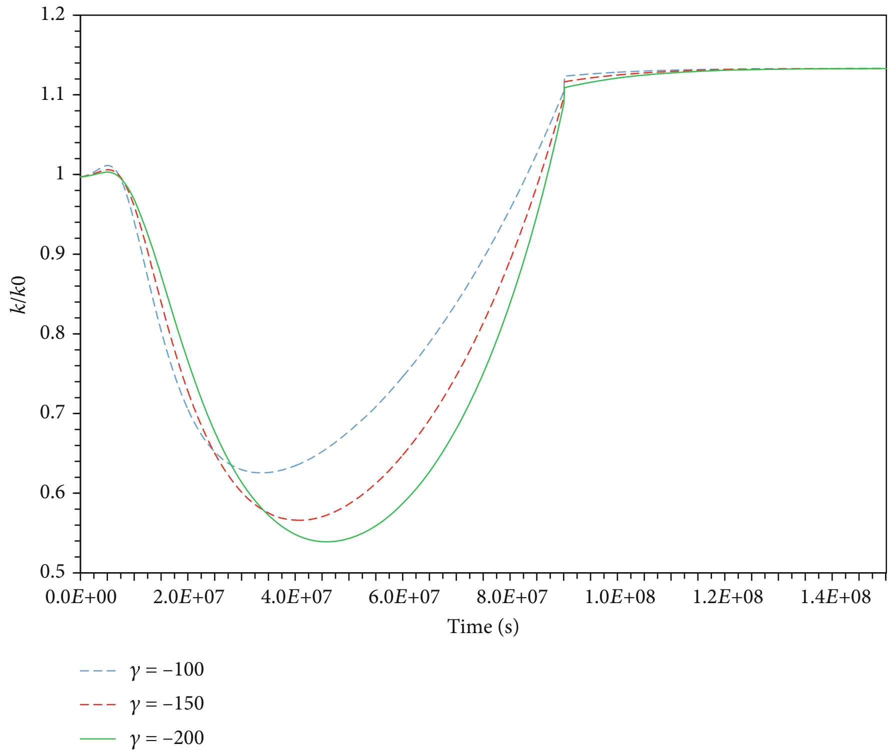

FIGURE 12: Evolution of permeability with different γ of model I.

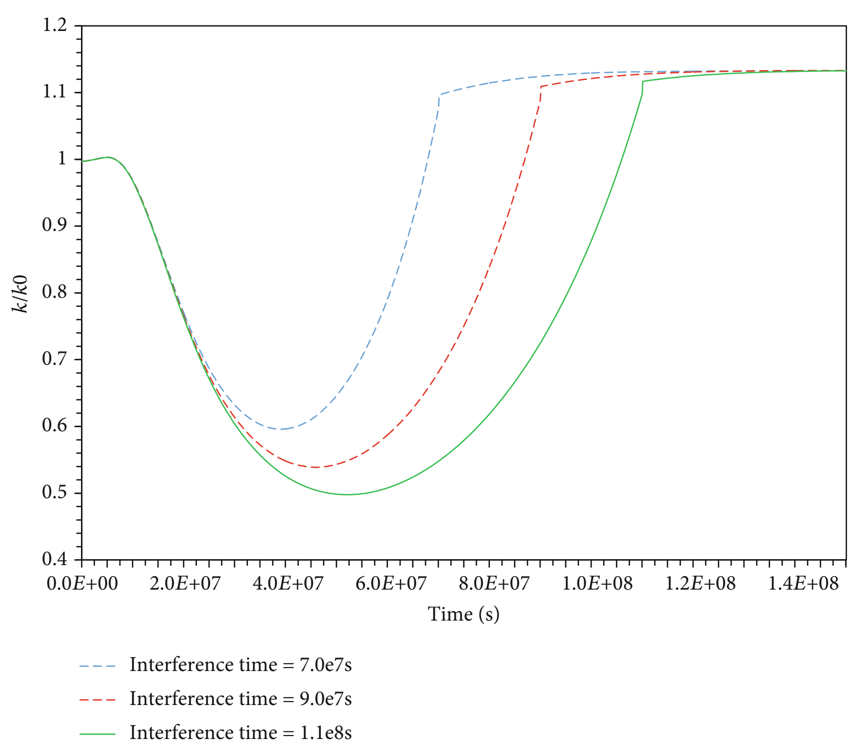

FIGURE 13: Evolution of permeability with different interference times of model I.

when the coal interference time is different. And the lower limit of permeability is inversely proportional to the stable time required for gas diffusion in the coal.

When the confining pressure is maintained at 7 MPa, the evolution of coal permeability with gas injection pressure is shown in Figure 14. It can be seen from Figure 14

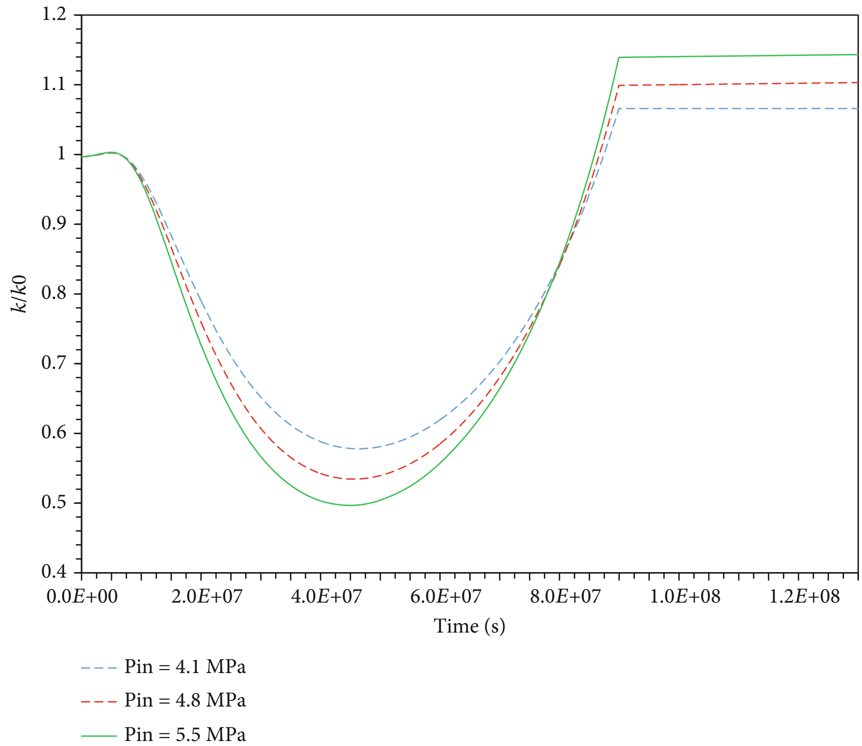

FIGURE 14: Evolution of permeability with different injection pressures of model I.

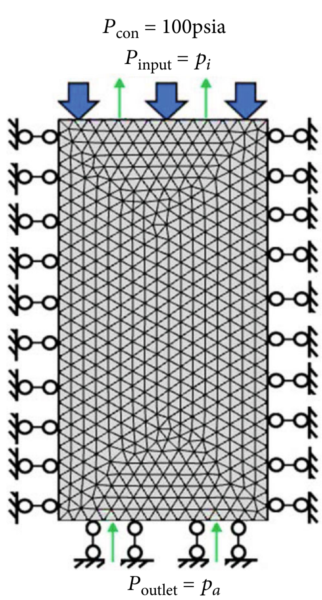

FIGURE 15: Simulation model II for the case of gas injection.

that with the increase of the injection pressure, the lower limit of permeability value gradually decreases, and the upper limit gradually increases in the process of coal permeability evolution. The upper limit is at the final equilibrium state of the curve.

TABLE 4: Property parameters of coal and gas.

Parameter	Value
Young's modulus of coal, E(MPa)	4900
Possion's ratio of coal, ν	0.39
Density of coal, ρ_c (kg/m^3)	1.25×10^3
Density of methane, ρ_g (kg/m^3)	1.784
Methane dynamic viscosity, μ(Pa · s)	1.493×10^{-5}
Langmuir pressure constant, P_L(MPa)	2.69
Langmuir volumetric strain constant, ε_L	0.008
Hydraulic diffusivity of gas, λ_i (m^2/s)	9.35×10^{-11}
Cleat compressibility, C_f (MPa^{-1})	7.5×10^{-8}

4.2. Permeability Tests under the Condition of Three Roller Constrains. The boundary condition of model II is shown in Figure 15. The property parameters are shown in Table 4. Evolution of the coal fracture and pore permeability under the condition of three roller constrains is shown in Figures 16 and 17.

According to Figures 16 and 17, it can be seen that the fracture system and pore system of coal of model II in the process of gas injection also include four stages: first rising, decreasing, restoring, and finally balancing. The change of permeability of pore system is more obvious.

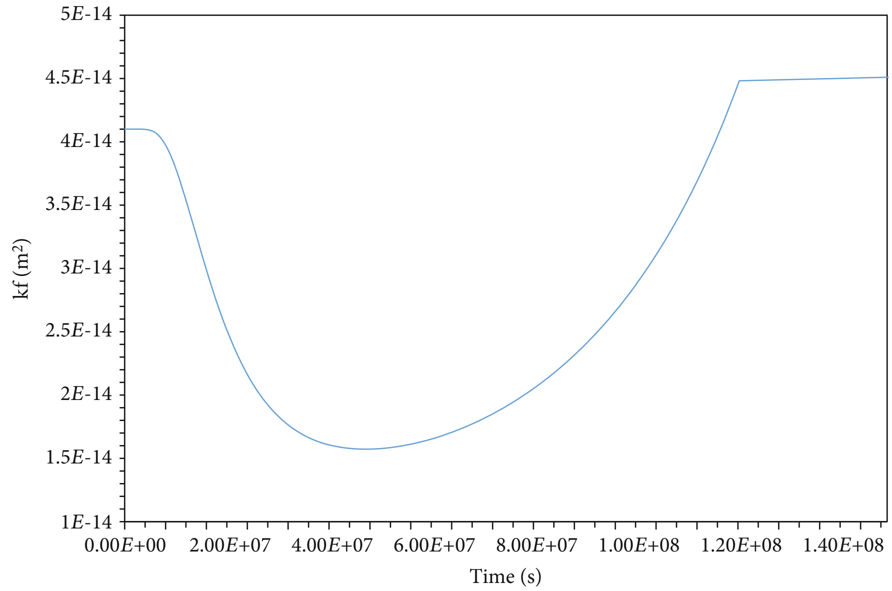

Figure 16: Permeability evolution process of the fracture system of model II.

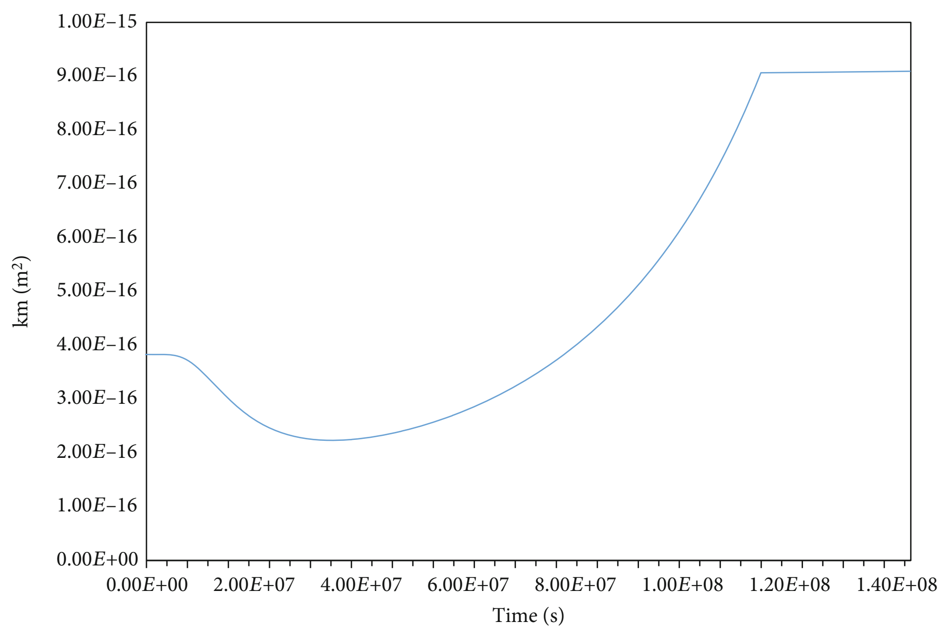

Figure 17: Permeability evolution process of the pore system of model II.

The simulation parameters of different cases are shown in Table 5.

The influence of coal adsorption strain ratio γ on the permeability evolution process in the CO_2 injection process of model II is shown in Figure 18. According to Figure 18, the permeability after final equilibrium is the same under different adsorption strain ratios. The lower limit of permeability is proportional to γ.

The evolution process of the permeability of model II varies with the interference time is shown in Figure 19. It can be seen from Figure 19 that with the increase of coal

Table 5: Simulation strategies.

Case 1	Impact of adsorptive strain ratios on the resulting response $\gamma = -100, -150, -200$
Case 2	Impact of interference time on the resulting response $\tau = 7.6 \times 10^7, 9.6 \times 10^7, 1.16 \times 10^8$s
Case 3	Impact of gas injection pressure on the resulting response $P_{in} = 4.1, 4.8,$ and 5.5 MPa

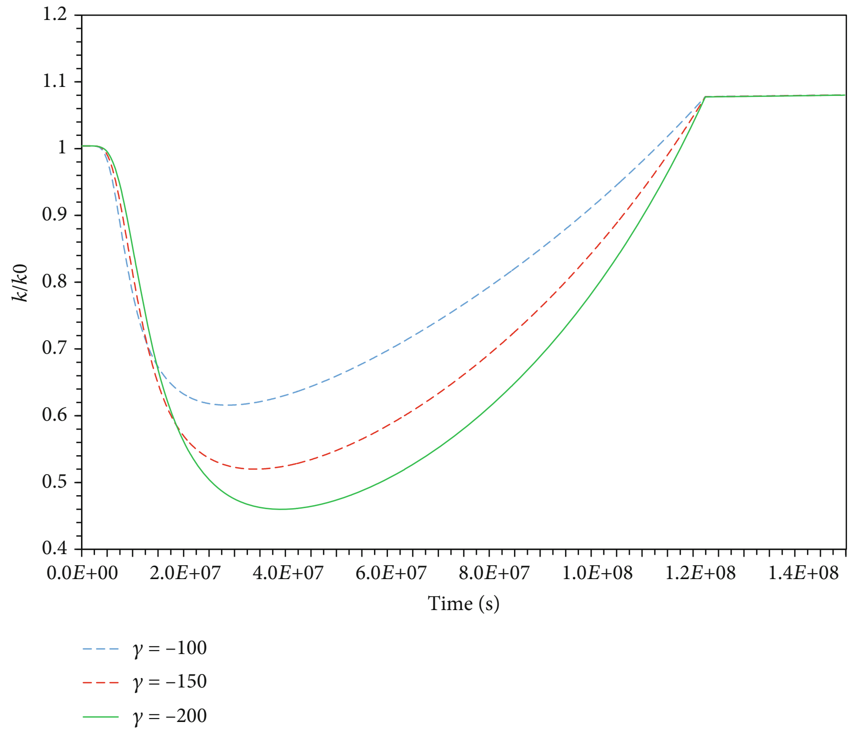

Figure 18: Evolution of permeability with different γ of model II.

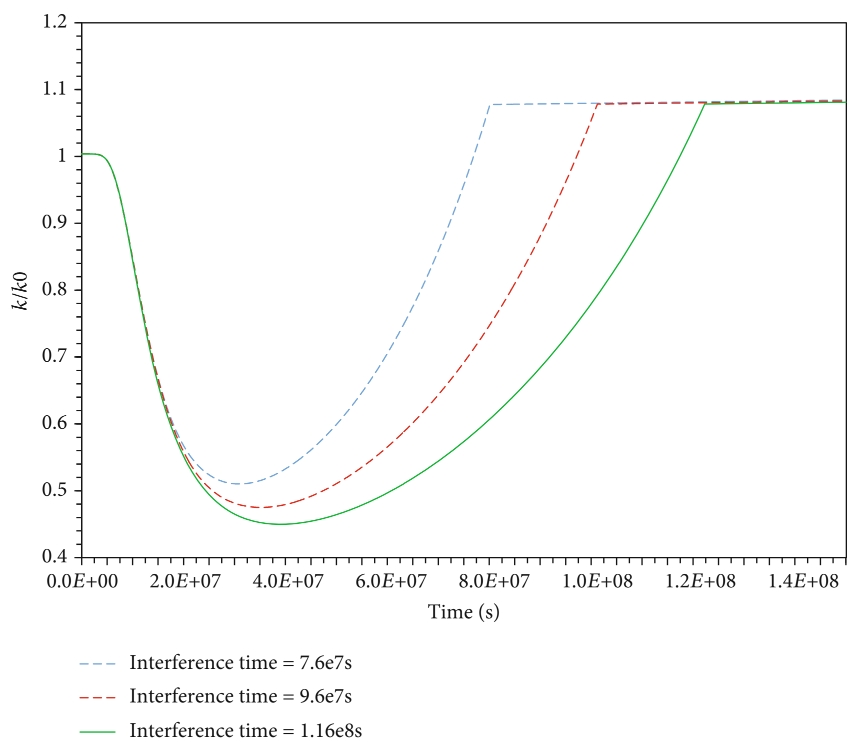

Figure 19: Evolution of permeability with different interference times of model II.

interference time, the lower limit of the permeability curve gradually decreases; that is, the change of coal porosity is more obvious. However, due to the constant gas injection pressure, when the coupling process of coal deformation and gas permeability is eventually balanced, the permeability of coal with different interference times is unchanged.

The evolution process of permeability under different gas injection pressures is shown in Figure 20. It can be seen from

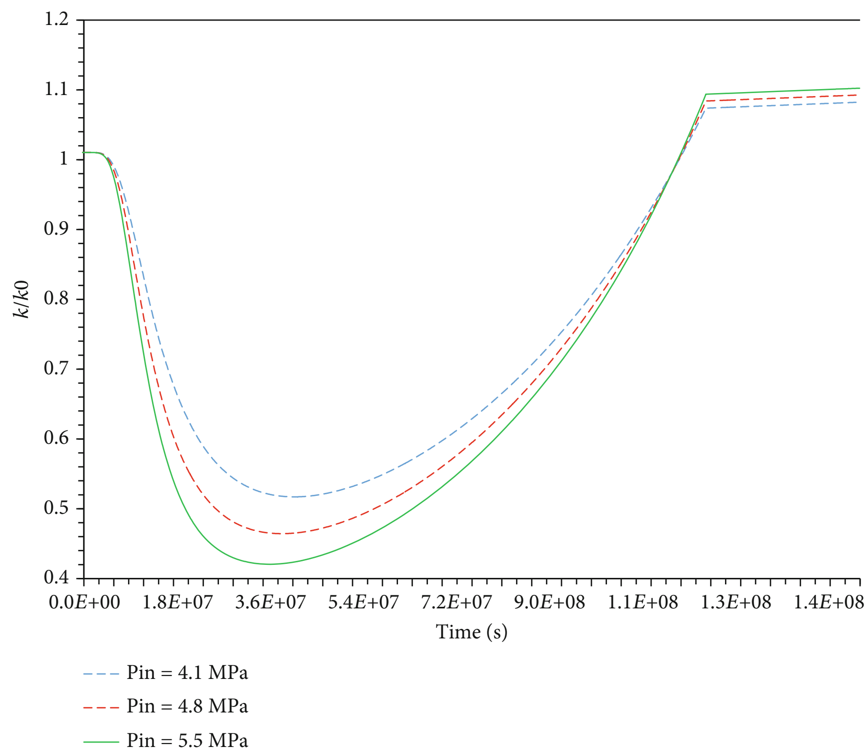

Figure 20: Evolution of permeability with different injection pressures of model II.

Figure 20 that the upper limit of permeability is at the final equilibrium state, which is proportional to the injection pressure, while the lower limit of permeability value is inversely proportional to the injection pressure. The permeability under different injection pressures after equilibrium has little difference. The main reason is that the free expansion deformation is limited by the roller constraints; so, the model cannot expand freely.

5. Conclusions

A nonequilibrium coal permeability model is developed to quantify the impact of local transient behaviors on gas flow triggered by gas injection. Based on the results of this study, the following conclusions can be drawn:

(1) The permeability of coal is restricted by the initial and ultimate pore-body strain ratio and the disturbance time. The equilibrium permeability is determined by the initial and the limit pore volume strain ratio, and the evolution time from the initial to the limit equilibrium permeability is determined by the interference time

(2) It is assumed in the literature that the current permeability data are measured under equilibrium conditions, but are distributed within the permeability range described by the equilibrium value. This suggests that the equilibrium hypothesis of those experiments may not be valid

(3) The coal permeability from the initial value to the final value all experienced a similar evolution stage. The injection pressure leads to an initial increase, and the fracture diffuses to the periphery, leading to a gradual decrease. The diffusion region expands from the fracture to the whole matrix region, leading to recovery, and finally reaches the equilibrium permeability

Data Availability

The data used to support the findings of this study are included within the article.

Conflicts of Interest

The author(s) declare(s) that they have no conflicts of interest.

Acknowledgments

This work was supported by the Fundamental Research Funds for the Central Universities (Grant No. 2020ZDPYMS02).

References

[1] J. D. N. Pone, M. Hile, P. M. Halleck, and J. P. Mathews, "Three-dimensional carbon dioxide-induced strain distribution within a confined bituminous coal," *International Journal of Coal Geology*, vol. 77, no. 1-2, pp. 103–108, 2009.

[2] P. Au, J. Liu, and Y. Leong, "Yield stress and microstructure of washed oxide suspensions at the isoelectric point: experimental and model fractal structure," *Rheologica Acta*, vol. 55, no. 10, pp. 847–856, 2016.

[3] C. Wang, J. Liu, J. Feng, M. Wei, C. Wang, and Y. Jiang, "Effects of gas diffusion from fractures to coal matrix on the evolution of coal strains: Experimental observations," *International Journal of Coal Geology*, vol. 162, pp. 74–84, 2016.

[4] S. Mazumder and K. H. Wolf, "Differential swelling and permeability change of coal in response to CO2 injection for ECBM," *International Journal of Coal Geology*, vol. 74, pp. 123–138, 2007.

[5] K. Li, S. Kong, P. Xia, and X. Wang, "Microstructural characterisation of organic matter pores in coal-measure shale," *Advances in Geo-Energy Research*, vol. 4, no. 4, pp. 372–391, 2020.

[6] R. Liu, B. Li, and Y. Jiang, "A fractal model based on a new governing equation of fluid flow in fractures for characterizing hydraulic properties of rock fracture networks," *Computers and Geotechnics*, vol. 75, pp. 57–68, 2016.

[7] X. Qin, Y. Zhou, and A. P. Sasmito, "An effective thermal conductivity model for fractal porous media with rough surfaces," *Advances in Geo-Energy Research*, vol. 3, no. 2, pp. 149–155, 2019.

[8] G. Liu, B. Yu, D. Ye, F. Gao, and J. Liu, "Study on evolution of fractal dimension for fractured coal seam under MULTI-FIELD coupling," *Fractals*, vol. 28, no. 4, article 2050072, 2020.

[9] G. Liu, B. Yu, F. Gao, D. Ye, and F. Yue, "Analysis of permeability evolution characteristics based on dual fractal coupling model for coal seam," *Fractals*, vol. 28, no. 7, article 2050133, 2020.

[10] G. Liu, J. Liu, L. Liu, D. Ye, and F. Gao, "A fractal approach to fully-couple coal deformation and gas flow," *Fuel*, vol. 240, pp. 219–236, 2019.

[11] H. B. Zhang, J. Liu, and D. Elsworth, "How sorption-induced matrix deformation affects gas flow in coal seams: a new FE model," *International Journal of Rock Mechanics and Mining Sciences*, vol. 45, no. 8, pp. 1226–1236, 2008.

[12] J. Rutqvist and C. Tsang, "A study of caprock hydromechanical changes associated with CO_2-injection into a brine formation," *Environmental Geology*, vol. 42, no. 2-3, pp. 296–305, 2002.

[13] Y. Wu, J. Liu, D. Elsworth, Z. Chen, L. Connell, and Z. Pan, "Dual poroelastic response of a coal seam to CO_2 injection," *International Journal of Greenhouse Gas Control*, vol. 4, no. 4, pp. 668–678, 2010.

[14] W. Li, J. Liu, J. Zeng, Y. Leong, and D. Elsworth, "A fully coupled multidomain and multiphysics model for shale gas production," in *5th ISRM Young Scholars' Symposium on Rock Mechanics and International Symposium on Rock Engineering for Innovative Future*, Okinawa, Japan, 2019.

[15] M. Lu and L. D. Connell, "A statistical representation of the matrix–fracture transfer function for porous media," *Transport in Porous Media*, vol. 86, no. 3, pp. 777–803, 2011.

[16] J. G. Wang, J. Liu, and A. Kabir, "Combined effects of directional compaction, non-Darcy flow and anisotropic swelling on coal seam gas extraction," *International Journal of Coal Geology*, vol. 109-110, pp. 1–14, 2013.

[17] Y. Peng, J. Liu, M. Wei, Z. Pan, and L. D. Connell, "Why coal permeability changes under free swellings: new insights," *International Journal of Coal Geology*, vol. 133, pp. 35–46, 2014.

[18] N. Joshi, C. S. P. Ojha, P. K. Sharma, and C. A. Madramootoo, "Application of nonequilibrium fracture matrix model in simulating reactive contaminant transport through fractured porous media," *Water Resources Research*, vol. 51, no. 1, pp. 390–408, 2015.

[19] R. Upadhyay and S. Laik, "A computational approach to determine average reservoir pressure in a coalbed methane (CBM) well flowing under dominant matrix shrinkage effect," *Transport in Porous Media*, vol. 116, no. 3, pp. 1167–1188, 2017.

[20] J. Li, W. Yu, D. Guerra, and K. Wu, "Modeling wettability alteration effect on well performance in Permian basin with complex fracture networks," *Fuel*, vol. 224, pp. 740–751, 2018.

[21] Y. Xue, T. Teng, F. Dang, Z. Ma, S. Wang, and H. Xue, "Productivity analysis of fractured wells in reservoir of hydrogen and carbon based on dual-porosity medium model," *International Journal of Hydrogen Energy*, vol. 45, no. 39, pp. 20240–20249, 2020.

[22] J. Zeng, J. Liu, W. Li, Y. K. Leong, D. Elsworth, and J. Guo, "Evolution of shale permeability under the influence of gas diffusion from the fracture wall into the matrix," *Energy & Fuels*, vol. 34, no. 4, pp. 4393–4406, 2020.

[23] G. Liu, D. Ye, F. Gao, and J. Liu, "A Dual Fractal Poroelastic Model for Characterizing Fluid Flow in Fractured Coal Masses," *Geofluids*, vol. 2020, Article ID 2787903, 13 pages, 2020.

[24] J. Zeng, X. Wang, J. Guo, F. Zeng, and F. Zeng, "Modeling of heterogeneous reservoirs with damaged hydraulic fractures," *Journal of Hydrology*, vol. 574, pp. 774–793, 2019.

[25] W. Li, J. Liu, J. Zeng et al., "A fully coupled multidomain and multiphysics model for evaluation of shale gas extraction," *Fuel*, vol. 278, article 118214, 2020.

[26] Y. Peng, J. Liu, Z. Pan, L. D. Connell, Z. Chen, and H. Qu, "Impact of coal matrix strains on the evolution of permeability," *Fuel*, vol. 189, pp. 270–283, 2017.

[27] X. X. Liu, J. C. Sheng, J. S. Liu, and Y. Hu, "Evolution of coal permeability during gas injection—from initial to ultimate equilibrium," *Energies*, vol. 11, no. 10, p. 2800, 2018.

[28] J. Liu, X. Liang, Y. Xue, K. Yao, and Y. Fu, "Numerical evaluation on multiphase flow and heat transfer during thermal stimulation enhanced shale gas recovery," *Applied Thermal Engineering*, vol. 178, article 115554, 2020.

[29] J. Zeng, X. Wang, J. Guo, F. Zeng, and Q. Zhang, "Composite linear flow model for multi-fractured horizontal wells in tight sand reservoirs with the threshold pressure gradient," *Journal of Petroleum Science and Engineering*, vol. 165, pp. 890–912, 2018.

[30] H. Wang, R. Shi, D. Deng, Y. Jiang, G. Wang, and W. Gong, "Characteristic of stress evolution on fault surface and coal bursts mechanism during the extraction of longwall face in Yima mining area, China," *Journal of Structural Geology*, vol. 136, article 104071, 2020.

[31] H. Wang, S. Xue, R. Shi, Y. Jiang, W. Gong, and L. Mao, "Investigation of fault displacement evolution during extraction in longwall panel in an underground coal mine," *Rock Mechanics and Rock Engineering*, vol. 53, no. 4, pp. 1809–1826, 2020.

[32] M. Lu and D. L. Connell, "Swell of coal matrix induced by gas sorption and its partition to pore volume and bulk strains - a critical parameter for coal permeability," in *44th US rock*

mechanics symposium and 5th U.S.-Canada rock mechanics symposium, pp. 27–30, Salt Lake City, UT, 2010.

[33] L. Connell, Z. Pan, M. Lu, D. D. Heryanto, and M. Camilleri, "Coal permeability and its behaviour with gas desorption, pressure and stress," in *SPE Asia Pacific Oil & Gas Conference and Exhibition*, pp. 18–20, Brisbane, Queensland, Australia, 2010.

[34] W. T. Patzek, D. B. Silin, S. M. Benson, and G. I. Barenblatt, "On vertical diffusion of gases in a horizontal reservoir," *Transport in Porous Media*, vol. 51, no. 2, article 5088959, pp. 141–156, 2003.

[35] J. Liu, J. Wang, Z. Chen, S. Wang, D. Elsworth, and Y. Jiang, "Impact of transition from local swelling to macro swelling on the evolution of coal permeability," *International Journal of Coal Geology*, vol. 88, no. 1, pp. 31–40, 2011.

[36] F. Zhou, T. Xia, X. Wang, Y. Zhang, Y. Sun, and J. Liu, "Recent developments in coal mine methane extraction and utilization in China: a review," *Journal of Natural Gas Science and Engineering*, vol. 31, pp. 437–458, 2016.

[37] M. Wei, J. Liu, X. Feng, C. Wang, and F. Zhou, "Evolution of shale apparent permeability from stress-controlled to displacement-controlled conditions," *Journal of Natural Gas Science and Engineering*, vol. 34, pp. 1453–1460, 2016.

[38] P. Cao, J. Liu, and Y. Leong, "Combined impact of flow regimes and effective stress on the evolution of shale apparent permeability," *Journal of Unconventional Oil and Gas Resources*, vol. 14, pp. 32–43, 2016.

[39] Z. X. Liu, Z. C. Feng, Q. M. Zhang, D. Zhao, and H. Guo, "Heat and deformation effects of coal during adsorption and desorption of carbon dioxide," *Journal of Natural Gas Science and Engineering*, vol. 25, pp. 242–252, 2015.

[40] X. Cui and R. M. Bustin, "Volumetric strain associated with methane desorption and its impact on coalbed gas production from deep coal seams," *AAPG Bulletin*, vol. 89, no. 9, pp. 1181–1202, 2005.

[41] M. S. A. Perera, P. G. Ranjith, and S. K. Choi, "Coal cleat permeability for gas movement under triaxial, non-zero lateral strain condition: a theoretical and experimental study," *Fuel*, vol. 109, pp. 389–399, 2013.

Hindawi
Geofluids
Volume 2021, Article ID 5578636, 18 pages
https://doi.org/10.1155/2021/5578636

Research Article

Characteristics of Stress, Crack Evolution, and Energy Conversion of Gas-Containing Coal under Different Gas Pressures

Zhizhen Zhang[1,2] **Yixin Niu,**[1] **Xiaoji Shang**[1] **Xingguang Liu,**[3,4] **and Feng Gao**[1]

[1]*State Key Laboratory for Geomechanics and Deep Underground Engineering, School of Mechanics and Civil Engineering, China University of Mining and Technology, Xuzhou 221116, China*
[2]*State Key Laboratory of Coal Mine Safety Technology, China Coal Technology & Engineering Group Shenyang Research Institute, Shenfu Demonstration Zone 113122, China*
[3]*College of Mining and Safety Engineering, Shandong University of Science and Technology, Qingdao 266590, China*
[4]*Mine Disaster Prevention and Control-Ministry of State Key Laboratory Breeding Base, Shandong University of Science and Technology, Qingdao 266590, China*

Correspondence should be addressed to Zhizhen Zhang; zzzhang@cumt.edu.cn and Xiaoji Shang; shangxj2016@cumt.edu.cn

Received 5 February 2021; Revised 23 February 2021; Accepted 26 February 2021; Published 15 March 2021

Academic Editor: Guanglei Zhang

In order to study the meso-mechanism of deformation, crack evolution, and energy conversion of gas-containing coal under loads, considering the gas pressure and adsorption expansion, the gas-solid coupling calculation program of MatDEM software was developed, and the triaxial compression process of gas-containing coal under different gas pressures was numerically simulated. The results show that the strength and stiffness of gas-containing coal decrease with the increase of gas pressure. During the loading process, the permeability of the coal sample decreases first and then increases, while the initial permeability, minimum permeability, and maximum permeability all decrease with the increase of gas pressure. There are far more shear cracks in coal samples than tension cracks, and the number of cracks increases simultaneously with the peak stress drop. With the increase of gas pressure, the macroscopic cracks in coal samples gradually change from large-angle shear cracks to multiple intersecting small-angle ones, and the coal sample gradually changes from brittle failure to ductile. There is an initial accumulation of elastic energy inside the gas-bearing coal, and the dissipated damping heat presents a stage change. As the loading stress level increases, the gas pressure gradually produces a degrading effect. The rockburst tendency of gas-bearing coal changes from weak to none with the increase of gas pressure, which is related to the evolution of the accumulated elastic energy and dissipated damping energy in the coal.

1. Introduction

China is the largest coal producer and consumer in the world, and coal accounts for nearly 70% of the country's total energy consumption. More than 50% of the mined coal seams in the country are high gas coal seams. Gas disasters are the mine disasters with the largest coal mine casualties and losses in China. Gas is the main cause of gas disasters such as coal and gas outbursts and gas explosions [1–3]. Gas-containing coal is a typical heterogeneous multiphase medium composed of coal solid particles, free gas, and adsorbed gas. The mechanical and nonmechanical effects of free gas and adsorbed gas make the mechanical properties and permeability characteristics of gas-containing coals very different from those of ordinary coals [4, 5]. Therefore, studying the stress, deformation, crack evolution, and energy conversion of gas-containing coal with gas-solid coupling under gas pressures is very important for the understanding and prevention of gas disasters.

The influence of gas-solid coupling on the deformation and failure process of gas-containing coal can be divided into two aspects.

(1) The effect of coal structure on gas flow in the mechanical process is as follows: the pore structure and volume of coal change under loads, which will

cause internal gas pressure fluctuations and gas permeability changes. He [6] found that the gas escape pressure decreases intermittently during the compression process and reaches the maximum at the peak stress. The permeability test found that the gas permeability gradually decreases during the initial compaction and elastic stage and starts to increase at the failure stage when a large number of cracks are generated and connected [7, 8]. Wei found [9] that the effective gas permeability of the raw coal sample decreases nonlinearly under the condition of constant effective stress with increasing water content

(2) The influence of gas pressure on coal structure is as follows: gas seepage causes pore pressure disturbance, and the pore pressure acts on the pore structure to cause crack propagation and structural instability. Many different tests have shown that the strength of gas-containing coal samples decreases to varying degrees with the increase of gas pressure [7–9]. Liang and Wang [10] conducted triaxial compression tests on gas-containing coal and found that the brittleness of coal increases significantly with increasing gas pressure. The mechanical action of pore gas and the nonmechanical action of adsorbed gas simultaneously affect the deformation and strength characteristics of coal. For methane-based gas, the adsorption of methane on the pore structure surface will cause the adsorption structure surface to expand, resulting in adsorption expansion stress, which has a greater impact on the overall structure [11–16]

Numerical simulation is an effective method for studying the mechanical behavior of gas-containing coal under load. Most of the domestic and foreign solutions for gas-solid coupling numerical simulation of gas-containing gas are studied by the method of continuum mechanics [17–20]. Zhao and Kaunda [17] performed numerical simulations on gas-containing coal pillars under different gas pressures based on FLAC3D software and analyzed the strength of impact tendency under different sizes. Yang [18] proposed an improved anisotropic permeability model based on the theory of linear elastic pore mechanics, assuming that coal is a transversely isotropic fractured medium. Similarly, Tao et al. [19] analyzed the change of permeability according to the Klinkenberg effect of gas adsorption, which is in good agreement with the experiments. However, for coal and rock, which are essentially discontinuous materials, the discrete element method may be more suitable and accurate, and it is more convenient to know the mechanical response on the mesoscale. In this paper, considering the gas pressure and adsorption expansion, we developed a simulation method for the gas-solid coupling of porous media on the MatDEM software platform (http://matdem.com), and based on this, we studied the mechanical characteristics of gas-containing coal during triaxial compression including grain stress, pore pressure, macroscopic deformation and failure, crack evolution, and energy conversion.

2. Numerical Test Platform and Assumption

2.1. Numerical Test Platform. Gas-containing coal is a discontinuous structure composed of mineral particles and gas, and the particle flow software can be used to simulate this discontinuous feature. By setting the properties of the basic particles, the meso-material structure of the coal can be reflected essentially, and the overall mechanical properties of the coal can be obtained.

The MatDEM software platform uses the particle discrete element method and is developed by Liu Chun and his team at Nanjing University in China. MatDEM software has the function of self-training materials. It only needs to input 6 macromechanical parameters to automatically obtain the material's micromechanical parameters. Compared with general commercial discrete element software, such as PFC, which directly sets the bond strength between particles, it greatly saves the time to adjust model parameters. Using innovative GPU matrix calculation method and 3D contact algorithm, MatDEM realizes 15 million 3D element motion calculations per second (where in 2D is 40 million elements), and the number and calculation speed of calculation element are more than 30 times that of some commercial software (3 million 3D elements, and 10 million 2D elements). It has been successfully applied in slope instability [21], hob breaking rock [22, 23], rock compaction failure [24], etc. The advantage of MatDEM in modelling the gas-solid coupling problems is that the number of simulation units is more, the calculation is faster, and it can reach the level of one million units in the 2D case, providing calculation support for future engineering-scale simulations. Therefore, we choose this software platform to study the gas-solid coupling of gas-containing coal in this paper.

2.2. Assumption. The gas-solid coupling effect of coal is a very complex issue. Considering the two most important mechanical effects of gas on the pore structure during the gas-solid coupling process, that is, the mechanical effect of pore pressure on the structure and the adsorption and expansion of the pore structure surface. The basic assumptions are as follows:

(1) Ignore the gas exchange process in the adsorption and desorption process, and only consider the gas permeation behavior caused by the pore pressure difference

(2) The temperature and viscosity of the gas migration process remain unchanged, that is, isothermal adsorption and percolation

(3) The gas permeability of adjacent pores follows the cubic law

(4) The simulation test conditions are quasistatic

In fact, gas exchange mainly affects the mechanical properties of coal through the process of adsorption and desorption, and the structural expansion and contraction caused by this process have been realized by changing the particle diameter in real-time in the simulation. However, considering gas

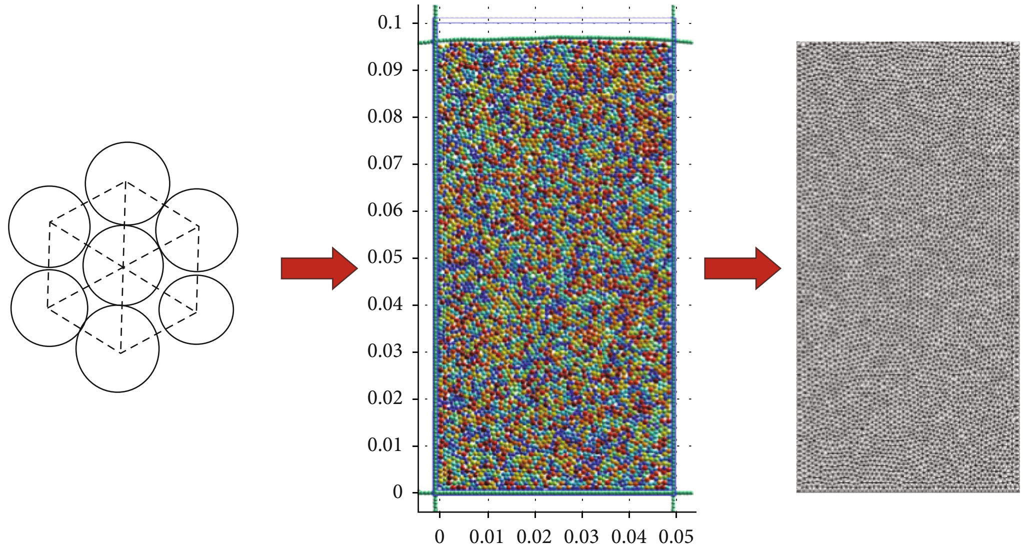

Figure 1: Numerical model of gas-containing coal sample and triangulation network.

Table 1: Microscopic parameters for numerical simulation.

Average normal stiffness/MPa	20.0460
Average tangential stiffness/MPa	7.1590
Average breaking force/N	11.8780
Average shear resistance/N	37.6636

exchange in the process of gas percolation requires a more complicated dual-medium permeation model. The gas adsorption will cause the supersaturated gas inside the pores to be absorbed, and the gas desorption will fill the expansion space caused by the destruction of the pore structure, both of which will reduce the gas pressure difference between adjacent pores and inhibit gas penetration and diffusion.

3. Gas-Solid Coupling Process

3.1. Pore Structure and Initial Aperture of Pore Throat. The numerical model of gas-containing coal consists of round particles and interparticle pores. Through the Delaunay triangulation method, the particles are divided into triangular networks, and the gas storage area of the pores is composed of blank areas formed naturally after the accumulation of round particles. Therefore, the area of each pore area (two-dimensional) can be calculated from the coordinates and radius of the particles. The seepage channel is considered as the gap between the particles, and the length of the channel is simply the average of the diameters of the two particles. The seepage direction is perpendicular to the connecting direction of the two particles. The model and the triangular network are shown in Figure 1. The average radius of coal samples is 0.3 mm, with a total of 14,726 particles. 27945 pores are formed by the triangular splitting. After the model is stacked, the length and width are 97 mm and 51 mm, respectively. According to the laboratory test [8], the macroscopic elastic modulus, compressive strength, Poisson's ratio, density, and internal friction coefficient are 9.53 GPa, 63.9 MPa, 0.15, 1650 kg·m^{-3}, and 0.35 in order. The microscopic parameters of the model are calculated by the macro-micro conversion formula [25], which is listed in equations (1)–(6), as shown in Table 1.

$$K_n = \frac{\sqrt{2}Ed}{4(1-2\nu)}, \tag{1}$$

$$K_s = \frac{\sqrt{2}(1-5\nu)Ed}{4(1+\nu)(1-2\nu)}, \tag{2}$$

$$X_b = \frac{3K_n + K_s}{6\sqrt{2}K_n(K_n + K_s)} \cdot T_u \cdot d^2, \tag{3}$$

$$F_{S_0} = \frac{1-\sqrt{2}\mu_p}{6} \cdot C_u \cdot d^2, \tag{4}$$

$$\mu_p = \frac{2\sqrt{2}+\sqrt{2}I}{2+2I}, \tag{5}$$

$$I = \left[\left(1+\mu_i^2\right)^{1/2} + \mu_i\right]^2, \tag{6}$$

where K_n is the interelement normal stiffness, K_s is the shear stiffness, X_b is the breaking displacement, F_{S_0} is the shear resistance, μ_p is the coefficient of friction, E is the Young's modulus, ν is the Poisson's ratio, T_u is the tensile strength, C_u is the compressive strength, and μ_i is the coefficient of intrinsic friction.

At the contact point between particles, it is assumed that there is an initial aperture a_0. The initial aperture setting allows fluid flow in the fluid channel formed by the two particles even when they are tightly compacted, thereby simulating the initial matrix permeability of the material. The aperture of the channel depends on the contact force between

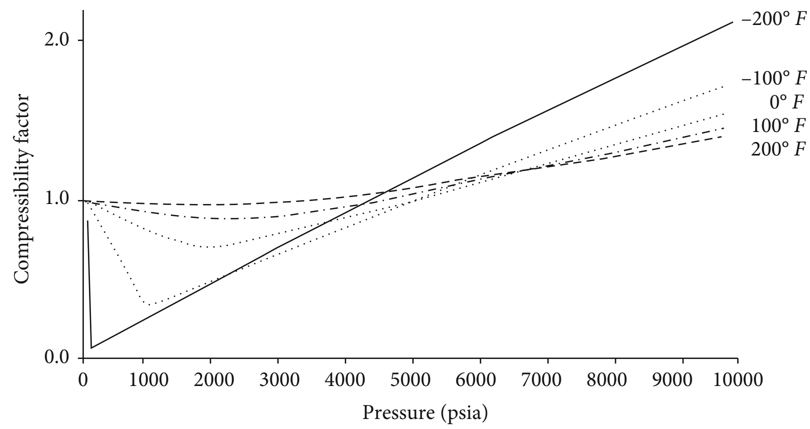

Figure 2: Change curve of gas compressibility factor [27].

the particles. When the normal contact force between the particles is the compression force, the pore aperture is

$$a = \frac{a_0 F_0}{F + F_0}, \tag{7}$$

where F is the compression force between two particles, and F_0 is the compression force when the pore aperture is reduced to half of the initial size.

When two cemented particles are stretched, or the cementation is broken to form a connected domain, the pore aperture is:

$$a = a_0 + \alpha(d - R_1 - R_2), \tag{8}$$

where d is the distance between two particles, R_1 and R_2 are the radii of the two particles, respectively, and α is a dimensionless coefficient. The value of α is 1.

3.2. Gas Pressure Calculation. There is free gas in coal pores, which is a state of free motion and has the characteristics of conventional gas, so the gas state equation is generally used to describe its physical characteristics. However, when the ideal gas state equation is applied to CH4 and other gases, there will be deviations. It is generally described by Van der Waal's equation [26]. In practical applications, the gas compression factor Z is often introduced, namely,

$$p = \frac{nZRT}{V}, \tag{9}$$

where p is the gas pressure, Pa; V is the gas volume, m^3; n is the total amount of gas, mol; T is the gas temperature, K; R is the ideal gas constant, about 8.31441 J/(mol·k); Z is the compressibility factor, its value changes with temperature and pressure, as shown in Figure 2 [27].

3.3. The Mechanical Effect of Gas Pressure on Pore Structure. As mentioned above, the mechanical effect of gas pressure on coal is mainly manifested and that pore pressure promotes pore deformation and destruction and volume expansion of coal particles due to gas adsorption. The former is achieved by applying body force in the direction of the particle line to the particles forming the pores, and the latter is achieved by changing the diameter. Aiming at the adsorption expansion of coal, Wu [28] obtained the expansion linear strain formula of the coal sample under constraints based on the pore structure model, surface physical chemistry, and elastic mechanics theory, which is

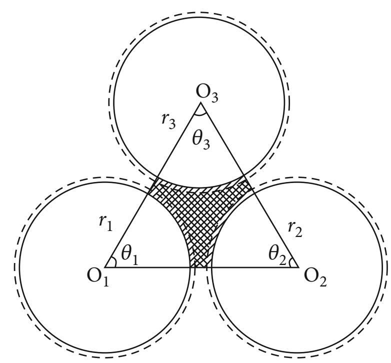

Figure 3: Schematic diagram of adsorption expansion.

$$\varepsilon_s = \frac{2a_m \rho RT(1 - 2\nu) \ln(1 + b_m p)}{EV_m}, \tag{10}$$

where a_m is the limit adsorption capacity under the reference pressure, about 19.95 m^3/t; b_m is the adsorption equilibrium constant of coal, about 1.081 MPa^{-1}; ρ is the apparent density of coal, t/m^3; V_m is the molar volume, $V_m = 22.4 \times 10^{-3}$ m^3/mol.

The arc of the particle as the adsorption surface is shown in Figure 3, due to the adsorption expansion, the overall diameter of the particle increases and the pore volume decreases. Therefore, the change in particle diameter due to pressure change is

$$\mathrm{dr} = \frac{r_i \theta_i}{2\pi} \varepsilon_s = \frac{r_i \theta_i a_m \rho RT(1 - 2\nu) \ln(1 + b_m p)}{\pi EV_m}, \tag{11}$$

where r_i and θ_i are the particle radius and the central angles of the arc of the pore, respectively.

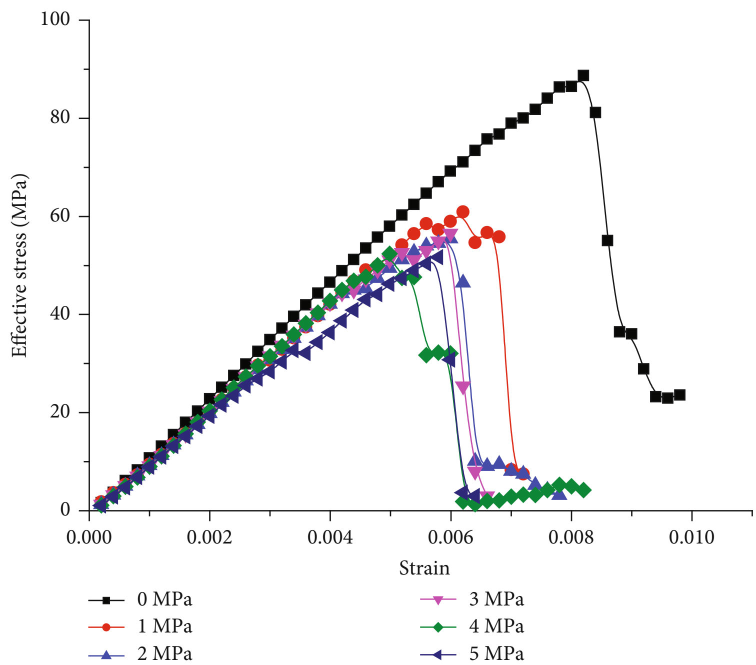

Figure 4: Effective stress-strain curves under different gas pressure with confining pressure of 10 MPa.

4. Numerical Simulation Results and Analysis

The numerical model of gas-containing coal is shown in Figure 1, and the conventional triaxial compression numerical simulation is performed. The confining pressure is 10 MPa, and the gas pressure is 0 MPa, 1 MPa, 2 MPa, 3 MPa, 4 MPa, and 5 MPa, respectively. The stress and strain, the number of tensile cracks and shear cracks, elastic energy, and damping heat dissipation are simultaneously monitored, and the deformation and failure mechanism of gas-containing coal during the loading process is analyzed from both macroscopic and microscopic aspects.

4.1. Stress-Strain Curves. The stress-strain curve reflects the deformation and strength characteristics of the gas-containing coal during the whole process of deformation and failure. Figure 4 shows the effective stress-strain curves of the gas-containing coal samples under different gas pressures at a confining pressure of 10 MPa. When the gas pressure is 0 MPa, the effective stress is the axial stress. When the gas pressure is not 0, the effective stress is equal to the measured stress minus the initial pore stress after adsorption expansion equilibrium. The gas-containing coal sample went through five deformation stages from the initial hydrostatic pressure state to failure: compaction stage, elastic deformation stage, crack propagation stage, postpeak failure stage, and residual stage. (1) Compaction stage: this stage cannot be represented in a typical discrete element simulation, but it exists in laboratory experiments. The pores in the coal sample are compacted, and some cracks are closed, resulting in a nonlinear deformation of the coal sample at the initial stage of loading. However, during the triaxial compression test, the confining pressure caused some of the primary defects in the coal sample to be compacted and closed before the axial compression load, resulting in the compaction stage of the stress-strain curve of the coal sample being less obvious. The higher the gas pressure, the smaller the effective confining pressure of the coal sample, the more primary defects in the coal sample at the initial stage of axial compression, and the more obvious the compaction stage of the stress-strain curve of the gas-containing coal sample. (2) Elastic deformation stage: the stress-strain relationship conforms to Hooke's law. In this stage, the original defects of the coal sample are compacted, new cracks are not produced in large numbers, and the deformation of the coal sample is mainly reversible elastic deformation. (3) Crack propagation stage: the stress-strain curve of gas-containing coal presents obvious nonlinearity, the slope of the curve gradually decreases, and the stiffness of the coal sample decreases significantly. At this stage, a large number of microcracks in the coal sample are dense and confluent, forming larger macrocracks. (4) Postpeak failure stage: due to the stress drop of the coal sample, the deviator stress-axial strain curve of the gas-containing coal is curved downward and shows a nonlinear change. The slope of the curve is negative. At this stage, the microcracks in the coal sample merge and form the connected macroscopic crack surface, the effective bearing area of the coal sample gradually decreases with the crack propagation, and the bearing capacity of the coal sample decreases accordingly. (5) Residual stage: after the stress drops to a certain level, it remains basically unchanged, while the strain continues to increase. This is because under the action of confining pressure, the friction between the crack surfaces provides a stable residual bearing capacity for the coal sample, but the shear slip of the crack surface causes the coal sample to continue to deform.

The peak strength quantitatively characterizes the maximum bearing capacity of gas-containing coal. Figure 5 shows the variation of the peak strength of the coal sample with the

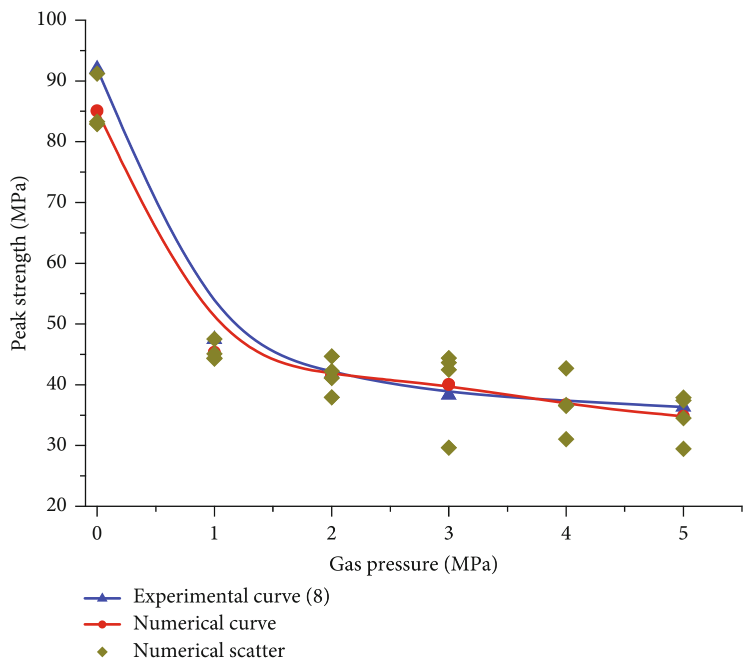

FIGURE 5: Variation of peak strength of coal sample with gas pressure.

gas pressure. It can be seen that as the gas pressure increases, the peak strength of the coal sample gradually decreases, roughly index relationship. Both pore gas pressure and adsorbed gas have a weakening effect on the carrying capacity of coal samples. The pore gas pressure acting on the inside of the coal sample particles weakens the confining pressure to close the coal sample cracks, promotes the crack propagation, and reduces the ability to resist damage. The adsorbed gas on the surface of coal particles weakens the cohesive force of the internal structure of the coal sample, making it easier to generate internal cracks in the coal sample. However, since the change of the adsorbed gas under unit gas pressure decreases with the increase of gas pressure, the change of peak strength of coal sample under unit gas pressure also decreases with the increase of gas pressure, so the attenuation range of peak strength of coal sample gradually decreases with the increasing gas pressure. Since the particles in the discrete element method are randomly generated by a random function, the models obtained under different random parameters are completely different in detail. Figure 5 shows the average results of multiple models, which are in good agreement with the experimental results [8].

The elastic modulus quantitatively characterizes the deformation properties of gas-containing coal. Figure 6 shows the normalized elastic modulus of a coal sample as a function of gas pressure. It can be seen that as the gas pressure increases, the elastic modulus decays exponentially. When the gas pressure is small, the elastic modulus has a larger change range, and when the gas pressure is higher than 2 MPa, the change range is reduced. This is because the adsorbed gas on the surface of coal particles weakens the bonding force between coal particles and reduces their ability to resist deformation. The experimental studies of many scholars have shown that the higher the gas pressure, the

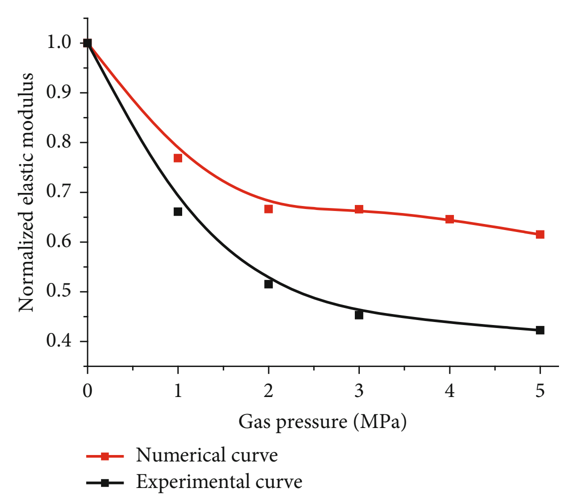

FIGURE 6: Variation of normalized elastic modulus of coal sample with gas pressure.

smaller the change in the amount of adsorbed gas caused by the change in unit gas pressure. Therefore, as the gas pressure increases, the change in elastic modulus caused by the change in unit gas pressure becomes smaller. In the numerical simulation, the spring stiffness between discrete particles does not change, so the elastic modulus is basically unchanged in the elastic phase. The decrease in elastic modulus is mainly caused by the stress drop associated with local structural instability, so the numerical simulation value is higher than the experimental value.

4.2. Permeability. Figure 7 shows the change of permeability during loading under different gas pressures. It can be seen

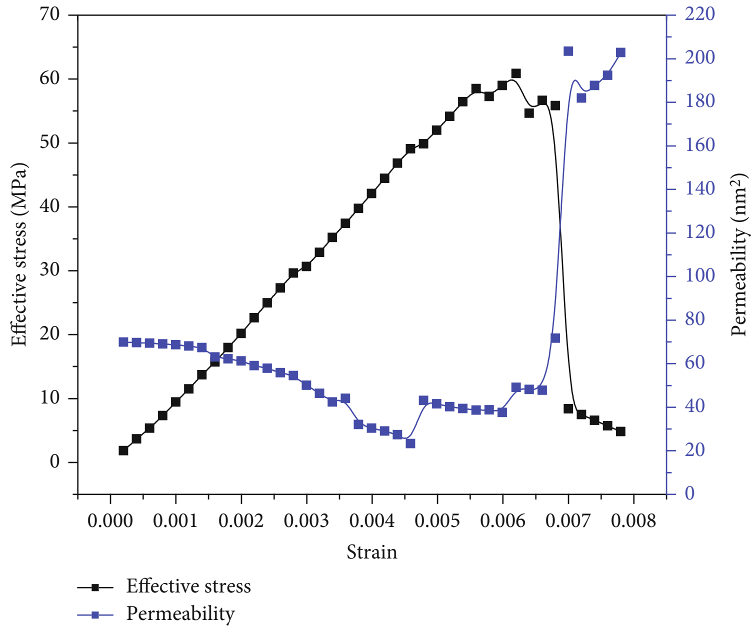

(a) 1 MPa

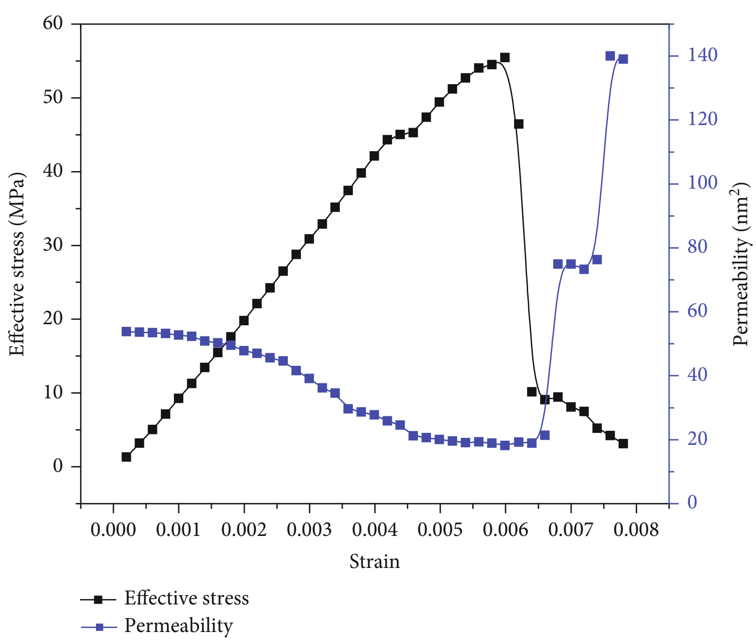

(b) 2 MPa

Figure 7: Continued.

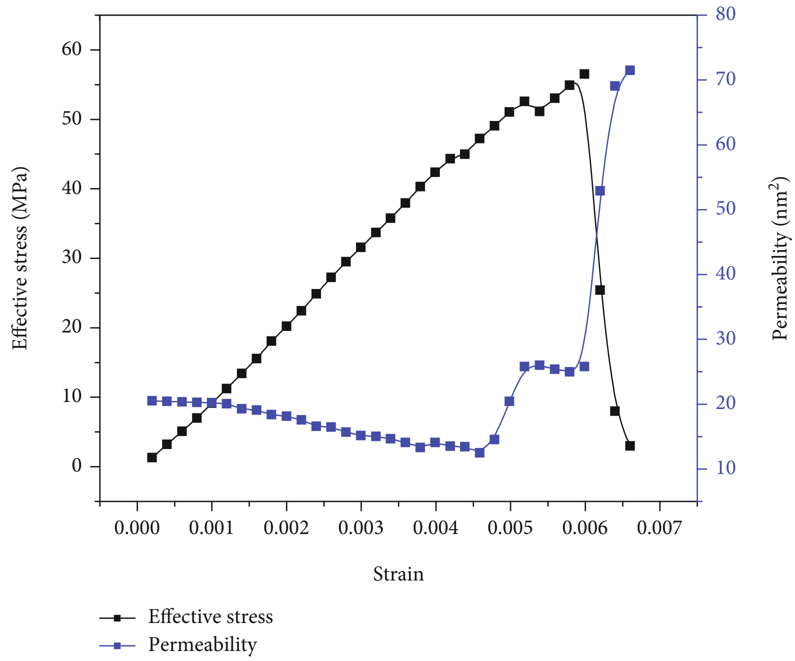

(c) 3 MPa

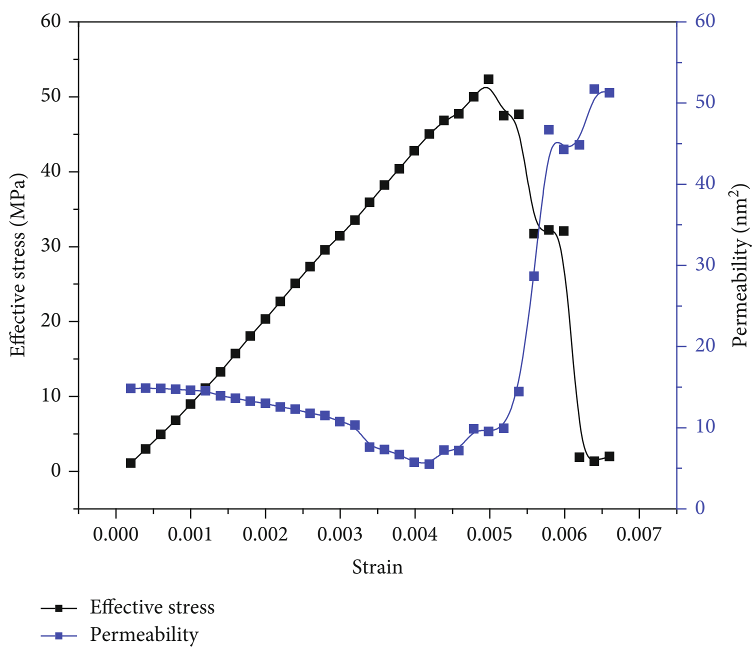

(d) 4 MPa

Figure 7: Continued.

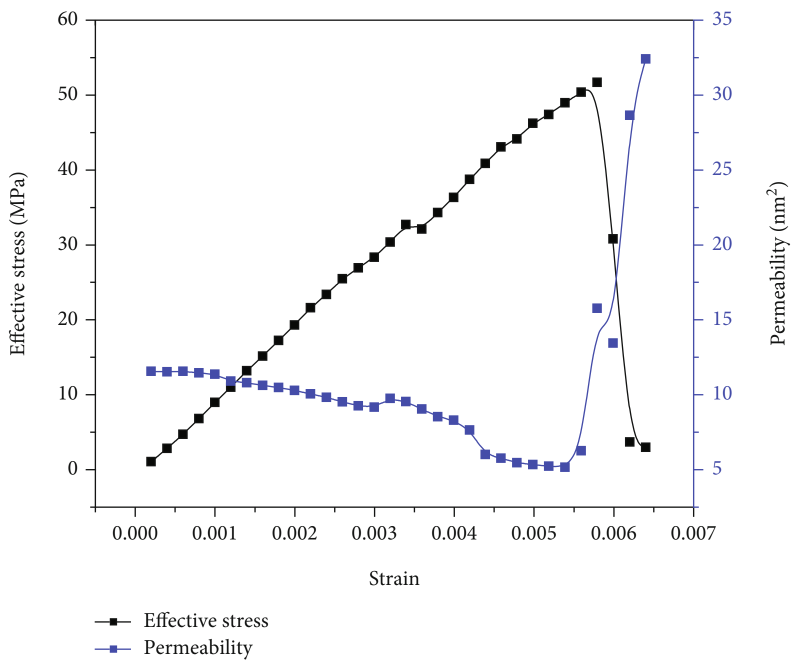

(e) 5 MPa

Figure 7: Changes of stress and permeability with strain under different gas pressure.

that the permeability of gas-containing coal decreases first and then increases during the deformation and failure process. During the compaction and elastic deformation stages of coal sample deformation, the primary cracks and pores of the coal sample are gradually closed, and the newly generated cracks do not form effective macroscopic cracks that penetrate the entire model, and matrix infiltration dominates. As the axial load increases, the effective stress and axial strain of the coal sample gradually increase. The initiation and propagation of cracks in the coal sample provide a new channel for gas flow. The change trend of coal sample permeability gradually changes from decreasing to increasing. The effective deviator stress corresponding to the starting point of coal sample permeability increase is generally about 90% of the peak deviator stress, and the axial strain is about 85% of the peak axial strain. During the crack propagation stage of the coal sample, with the increase of the deviator stress and axial strain of the coal sample, the propagation and convergence of the cracks gradually increase the permeability of the coal sample. Because no macroscopic cracks are formed in the coal sample at this stage, the permeability increases slowly, and the permeability of the coal sample at the peak point of deviator stress is lower than the initial permeability, that is, the permeability at the zero point. In the postpeak failure stage, the formation of macroscopic cracks in the coal sample prompts the coal sample's permeability to increase rapidly and quickly exceeds the initial permeability. In the residual stage, the shear slip and propagation of the cracks in the coal sample continue to increase the permeability with the increase of axial strain. However, since no new macroscopic cracks are formed, the rate of increase in permeability is lower than the postpeak failure stage. It can be seen that the evolution of permeability in the process of deformation and failure of gas-containing coal has obvious stage characteristics and correspond to the five stages of deformation and failure. The evolution characteristics of permeability in each stage are closely related to the law of crack change. The crack propagation in a coal sample not only determines the macroscopic stress-strain characteristics but also determines its permeability evolution characteristics.

In addition, the initial permeability, minimum permeability, and maximum permeability of coal samples all decrease with the increase of gas pressure, and the greater the gas pressure, the smaller the permeability attenuation caused by the increase of unit gas pressure. This is because the volume expansion of solid particles caused by gas adsorption occupies the space of cracks and pores under stress constraints, the gas flow channel is blocked, and the permeability is also reduced. The volume expansion of coal solid particles is directly proportional to the adsorbed gas content, and the higher the gas pressure, the smaller the change in the adsorbed gas volume caused by the change in unit gas pressure. Therefore, the higher the gas pressure, the smaller the increase in volume expansion of solid particles caused by the change of unit gas pressure, and the corresponding permeability attenuation amplitude also decreases.

4.3. Particle Stress and Pore Pressure. The temporal and spatial distribution and evolution of the particle stress and pore stress in the coal sample can be calculated, which is not available in laboratory tests. To save space, a sample with a gas pressure of 5 MPa is shown here. Figure 8 shows the axial particle stress distribution of gas-containing coal samples under different stress levels. Before the peak stress, as the load increases, the high-stress area of the internal particles is transferred downward from the top of the model and is

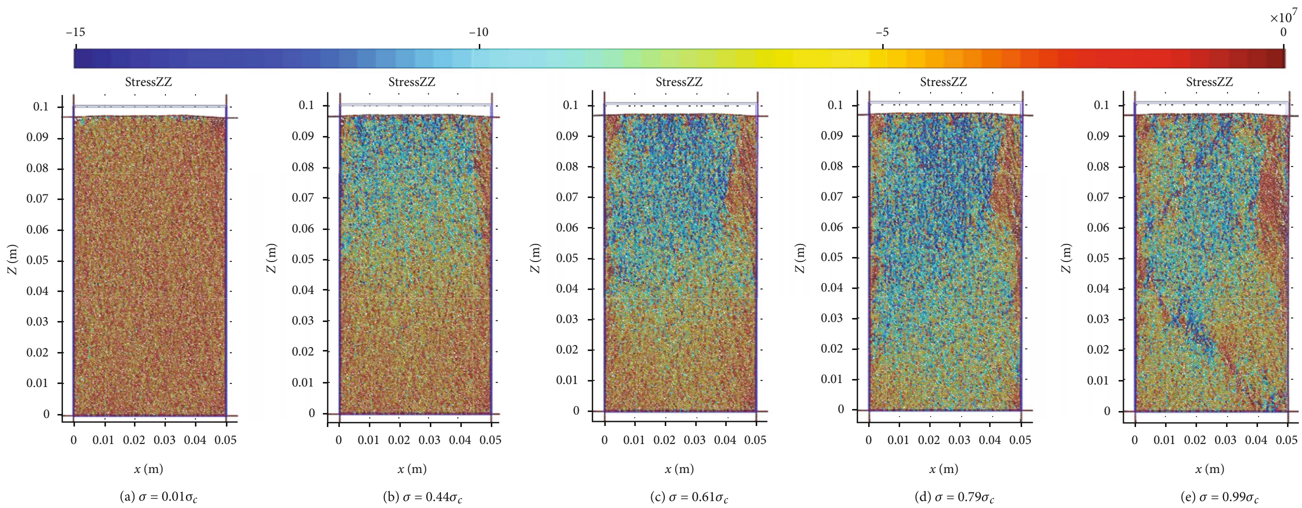

Figure 8: Axial stress distribution of particles under different stress levels in gas-containing coal.

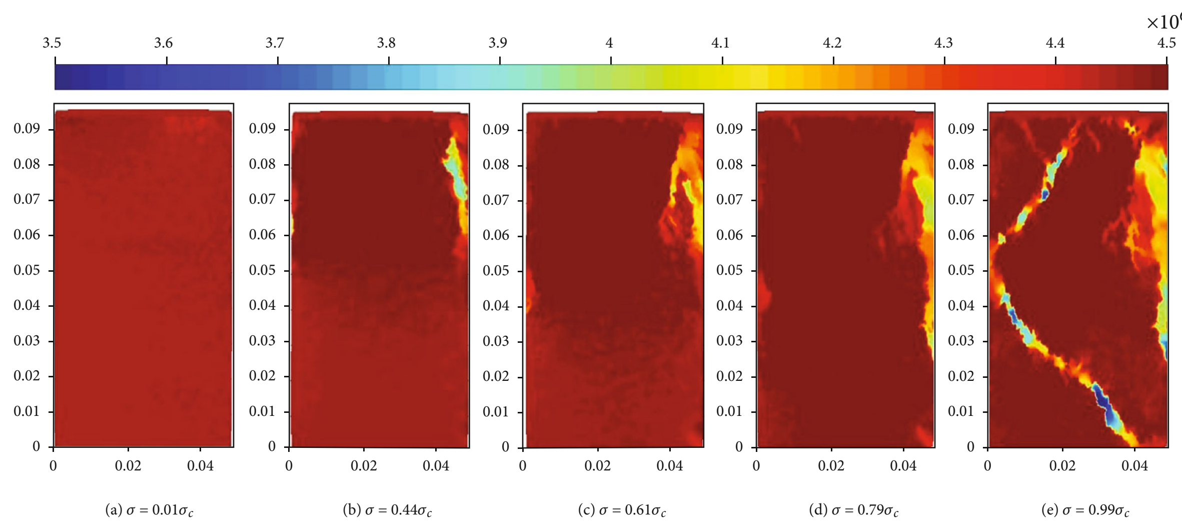

Figure 9: Pore pressure distribution under different stress levels in gas-containing coal.

accompanied by local failure of the upper right part. After the peak stress, macroscopic connected cracks are generated, and high-stress particles are concentrated in the unstabilized overall structure. The particles near the crack also concentrated a large supporting stress, maintaining the stability of the current load state.

Figure 9 shows the pore pressure distribution of gas-containing coal under different stress levels. Since the gas pressure at the upper end is kept constant during the loading process, the internal gas mass is conserved, and the pores between the particles become larger during the deformation and failure process, and the gas pressure calculated by equation (9) will decrease. The particle adsorption pressure is the average value of the surrounding pore pressure, which will also reduce the particle diameter and the expansion stress, resulting in a greater degradation effect.

4.4. Cracks. Figure 10 shows the distribution and evolution of cracks in coal samples under different gas pressures. From a macropoint of view, the failure of coal samples under different gas pressures is mainly caused by two macroscopic cracks intersecting on the left side of the model. With the increase of gas pressure, the crack intersection point moves to the middle part of the sample, and the macrocracks in the upper half of the crack bifurcate, and the structural damage becomes more serious. The reason may be that the loading mode is the displacement control of the upper pressure plate, the stress is transmitted from top to bottom, and the upper end is damaged first. Although the number of balances is sufficient to simulate the quasistatic process, in order to dissipate the internal energy of the model as soon as possible, the empirical damping [25] used makes the compaction and mechanical effects of the upper part more significant. Therefore, the higher the gas pressure, the earlier the main cracks that cause instability in the upper part initiate and expand. It can also be seen that with the increase of gas pressure, the macroscopic cracks in the coal sample change from large-angle shear cracks to multiple intersecting small-angle

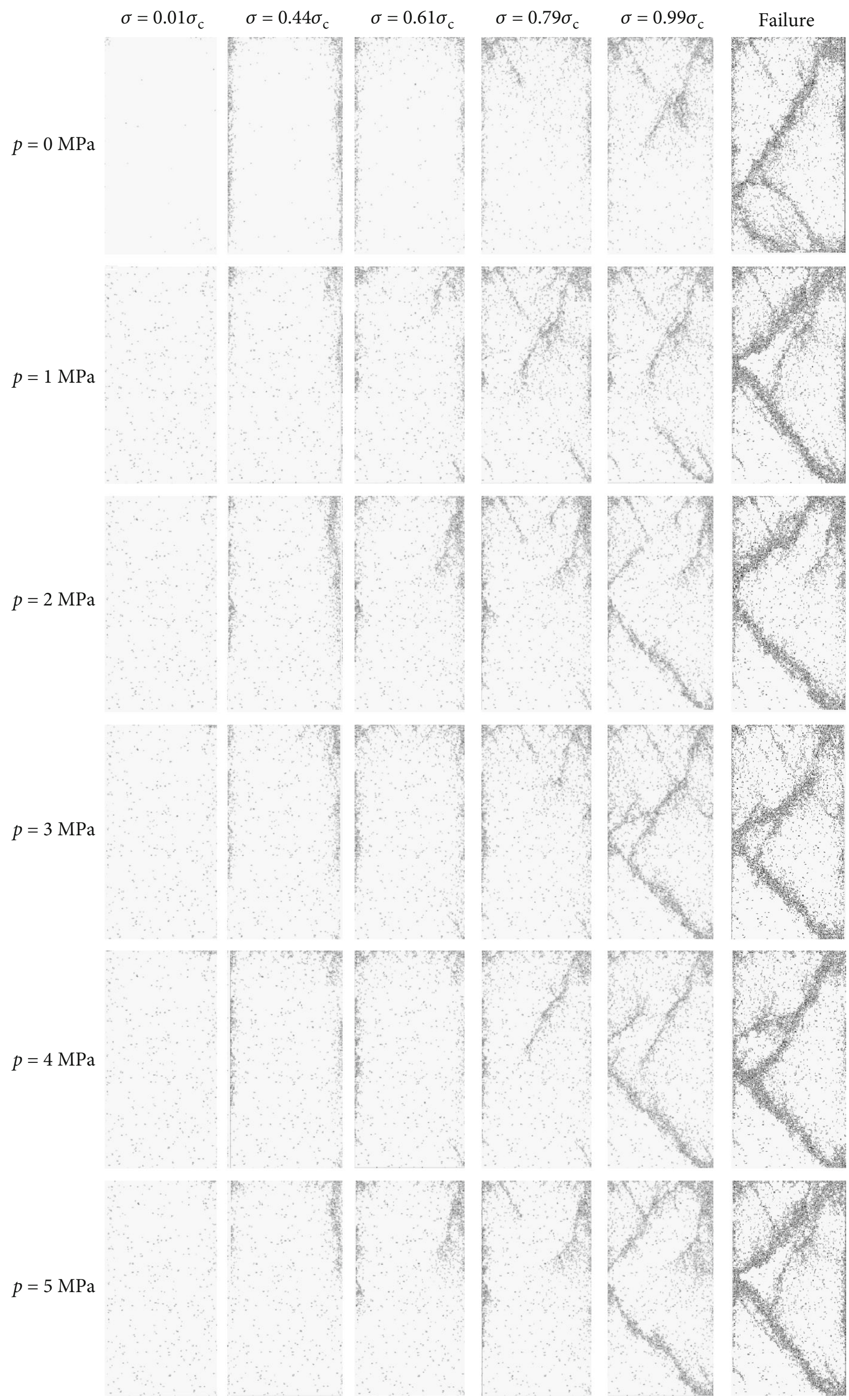

Figure 10: Distribution and evolution of cracks in gas-containing coal under different gas pressures.

shear cracks, and the failure mode gradually changes from brittle shear to ductile shear. This may be because the adsorbed gas in the coal sample reduces the cohesive force between coal particles, softens the coal sample to a certain extent, and weakens the brittleness of the coal sample.

It can also be seen from Figure 10 that under the same stress level, the higher the gas pressure, the more the number of cracks. We counted the number of cracks in the coal sample during the entire loading process. Taking into account the different mechanisms of crack generation, the numbers of tensile cracks, shear cracks, and total cracks were counted, as shown in Figure 11. It can be seen that the change of the number of cracks in the deformation and failure process of coal samples under different gas pressures has a similar law,

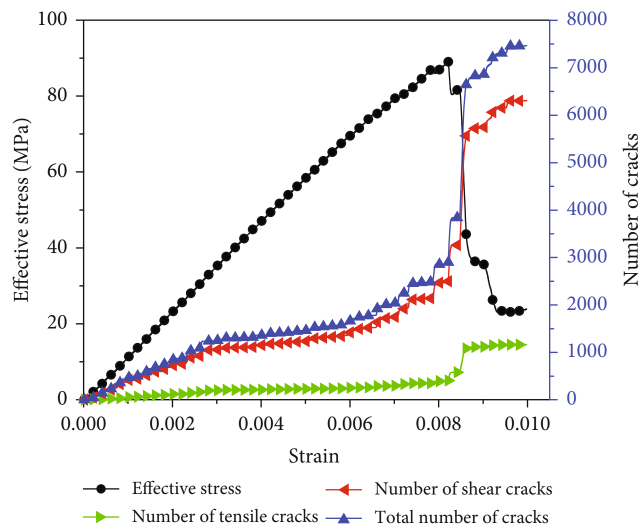

(a) 0 MPa

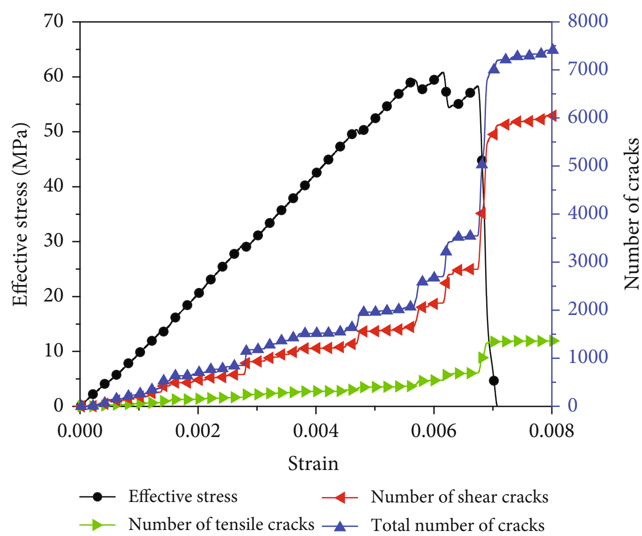

(b) 1 MPa

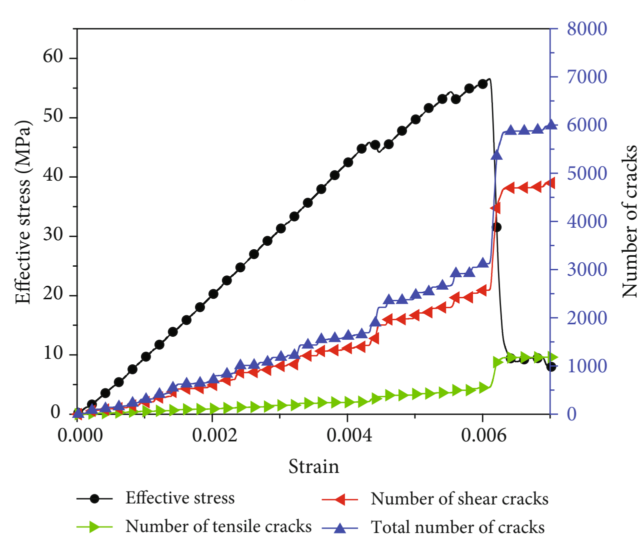

(c) 2 MPa

Figure 11: Continued.

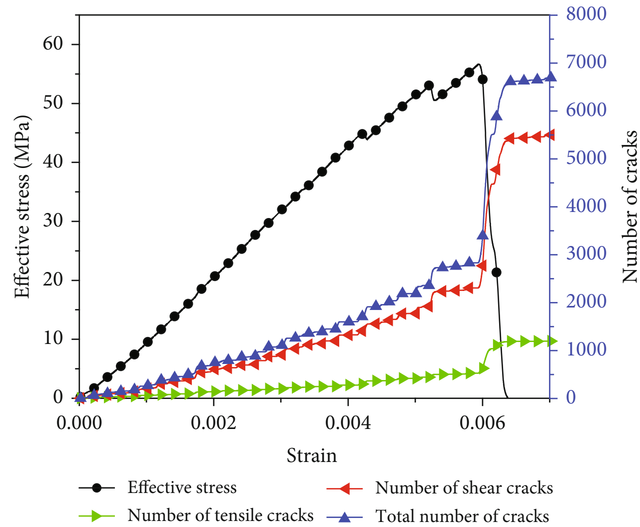

(d) 3 MPa

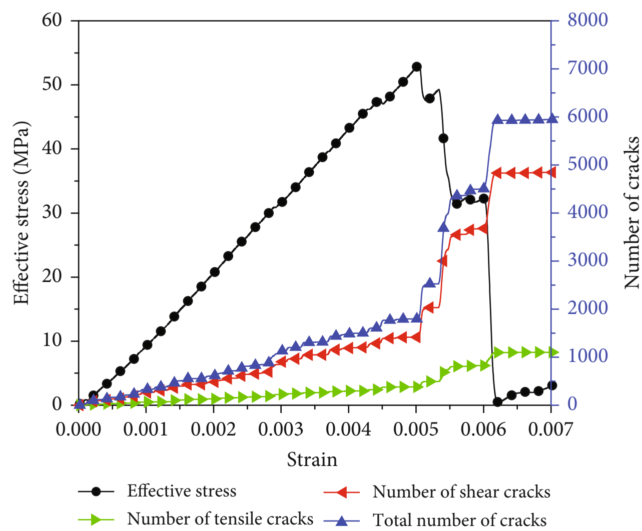

(e) 4 MPa

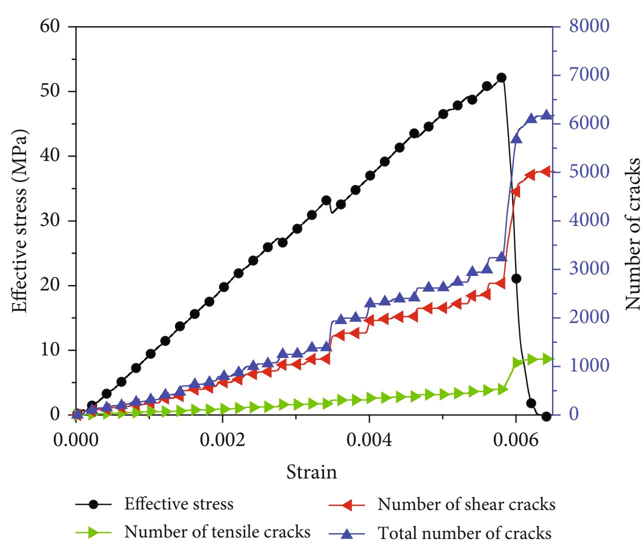

(f) 5 MPa

Figure 11: Changes of the number of cracks in gas-containing coal during deformation and failure.

which can be roughly divided into the following four stages: slow growth stage, rapid growth stage, violent growth stage, and steady stage. (1) Slow growth stage: this stage corresponds to the compaction stage and the elastic deformation stage of the coal sample. As the load increases, microcracks in the coal sample initiate and slowly expand, the total number of cracks rises slowly, and appears to be disorderly and random in space (see Figure 10), and most of them are shear cracks, while tension cracks are almost absent. (2) Rapid growth stage: this stage corresponds to the crack growth stage. The microcracks in the coal sample are gradually dense and merge to form larger cracks. As the axial strain increases, the total number of cracks rises rapidly. Shear cracks account for the majority, but tensile cracks increase significantly. The predominant gathering area of cracks gradually formed in space (see Figure 10). (3) Violent growth stage: corresponds to the postpeak failure stage from the peak point. The cracks propagate rapidly and converge to form a connected main crack, and a large amount of energy is released instantly, causing violent cracking activities. Near the peak point, the crack number curve rises approximately vertically. (4) Steady stage: corresponding to the residual stage of the coal sample deformation. At this stage, the cracks in the coal sample slip and propagate, and almost no new cracks are formed.

Gas affects the crack evolution properties of coal samples. With the increase of gas pressure, the slow growth stage of cracks is shorter, and the increase in the number of cracks in the violent growth stage is smaller. It can also be seen from Figure 10 that the coal sample under the gas pressure of 0 MPa has very few cracks before 60% of the peak stress, while the coal sample under the gas pressure of 5 MPa has a considerable number of microcracks in the initial stage of loading. This is because the gas has a weakening effect on the coal sample, so that the coal sample starts to initiate and propagate cracks at a lower stress level. When the gas pressure is 0 MPa, the increase in the number of cracks in the violent growth stage accounts for more than 70% of the final total number of cracks, while it is only about 50% when the gas pressure is 5 MPa. This indicates that with the increase of gas pressure, the severity of the damage of gas-containing coal samples gradually weakened, and the brittle failure gradually changed to ductile failure.

4.5. Energy. The energy in the discrete element model mainly includes mechanical energy and thermal energy. Mechanical energy includes kinetic energy, gravitational potential energy, and elastic potential energy, which transform into each other in various forms and are transformed into heat energy under the action of friction, fracture, and damping. The total heat in the model is the sum of damping heat, fracture heat, and friction heat.

The cementation between particles can be regarded as a set of orthogonal springs, which are normal spring and tangential spring, corresponding to normal stiffness and tangential stiffness. Through the tangential stiffness, normal stiffness, fracture displacement, and other parameters between particles, energy changes such as elastic energy, dissipation damping heat, and fracture heat can be calculated. The elastic energy of the system is the elastic energy stored by all springs. The kinetic energy of the system is the sum of the kinetic energy of all particles. For a tangential spring, the maximum static friction force limits its deformation, and the friction heat is calculated by the static friction force and the relative shear displacement of the particles. The fracture heat is the heat directly converted by the elastic potential energy of the spring between particles, assuming that the spring stops vibrating immediately after breaking. The damping heat is equal to the product of the damping force on the particle and the moving distance, which is the heat generated by damping which weakens the elastic wave and dissipates the kinetic energy in the particle system [29].

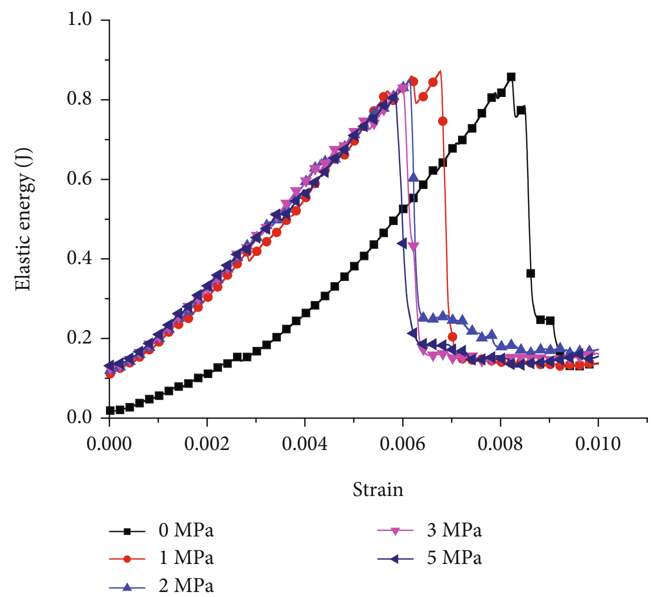

Figure 12: Changes of the elastic energy during deformation and failure under different gas pressures.

Figure 12 shows the changes in the elastic energy of gas-containing coal during deformation and failure under different gas pressures. The pore structure expands in volume after adsorbing gas, resulting in expansion stress. The internal particles are squeezed and stretched due to the cementation, resulting in initial elastic deformation and accumulating initial elastic energy. The maximum accumulated elastic energy at the peak stress decreases with the increase of gas pressure. When the sample is unstable, the elastic energy is released largely, and the residual elastic energy is basically unchanged under the action of confining pressure after the peak point.

Figure 13 shows the change of the dissipated damping heat during deformation and failure under different gas pressures. Dissipated damping heat, as the cumulative sum of dissipated energy, has four distinct stages in the process of deformation and failure. First, when the strain is less than 0.003, the dissipated damping heat is basically the same under different gas pressures, and it grows approximately linearly, that is, the overall energy dissipation of the system is mainly stress wave dissipation. In stage II, the greater the gas pressure, the more damping heat is dissipated, indicating

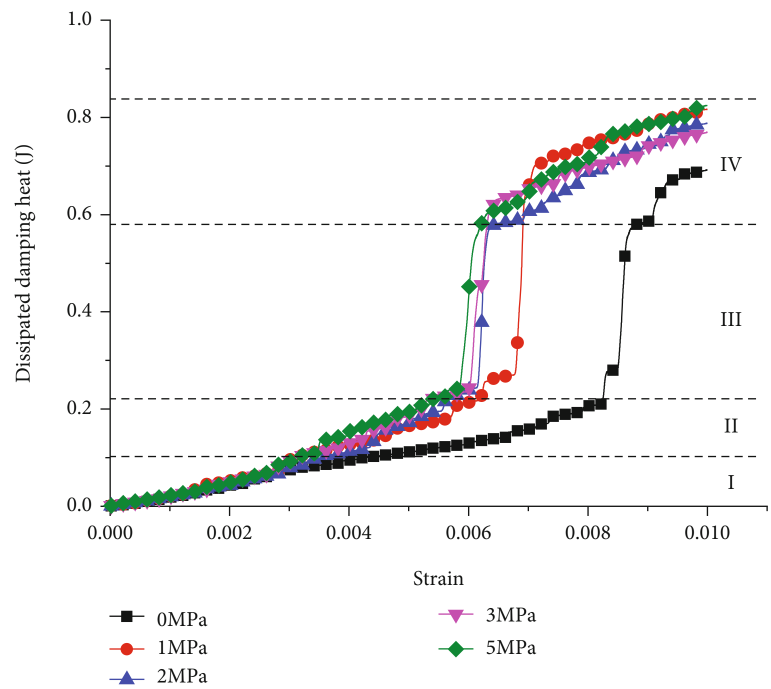

Figure 13: Changes of dissipated damping heat in the process of deformation and failure under different gas pressures.

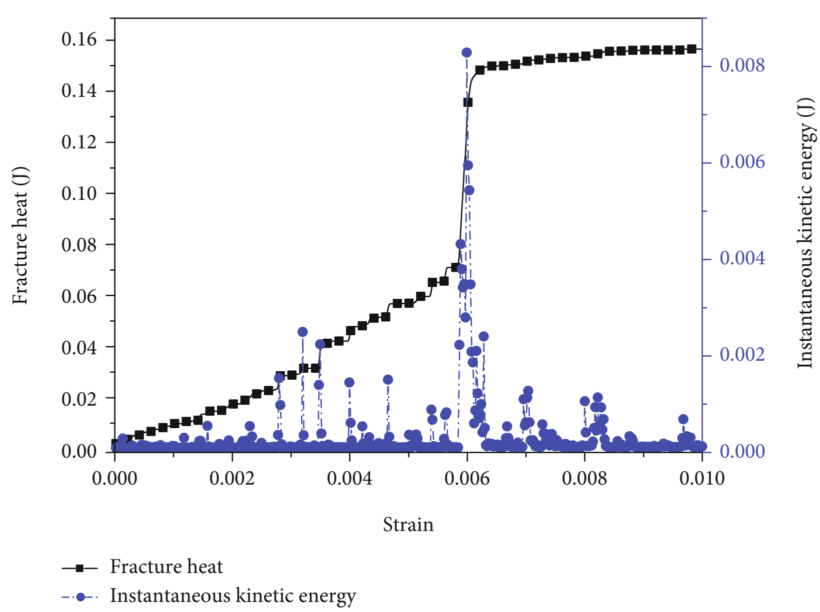

Figure 14: Change of fracture heat and instantaneous kinetic energy of gas-containing coal.

that a certain amount of instantaneous kinetic energy generated inside the bond is dissipated after the bond fractures, and the gas pressure gradually produces a degrading effect, as shown in Figure 14. Stage III is the stage of macroscopic instability and destruction, a large number of bonds are broken, and the dissipation energy rises sharply; stage IV is the residual stage after the peak, and the energy dissipation gradually tends to be stable.

4.6. Rockburst Tendency. According to the National Standard of the People's Republic of China "Method for Measuring the Classification Index of Rockburst Tendency of Coal GB/T 25217.2-2010," the impact energy index of coal can be used as the evaluation standard. The impact energy index K_E is obtained from the whole stress-strain curve of the rock and is defined as the ratio of the area under the stress-strain curve before and after the peak point, that is, the ratio of the energy stored by the rock before the peak strength to the energy required for failure after the peak.

$$K_E = \frac{A_e}{A_x}, \tag{12}$$

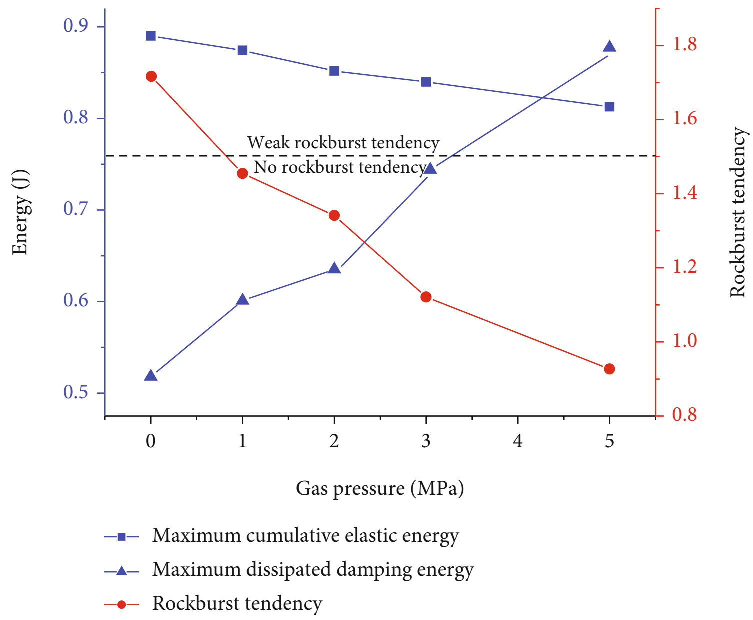

Figure 15: Changes of the rockburst tendency and energy of coal samples with different gas pressures.

where A_e is the energy stored by the rock before the peak strength, and A_x is the energy required for failure after the peak point. When K_E is between 1.5 and 2, the coal sample has a weak rockburst tendency, and when it is less than 1.5, there is no rockburst tendency.

Figure 15 shows the rockburst tendency and energy accumulation and release of coal samples under different gas pressures. It can be found that the cumulative elastic energy before the peak point decreases approximately linearly with the increase of gas pressure, while the dissipated damping energy increases in the failure stage after the peak point relatively large, which causes the overall rockburst tendency of coal to change from weak to none. Liu et al. [4] conducted uniaxial compression tests on gas-containing coal under different gas pressures and evaluated their rockburst tendency according to 4 different indexes, including dynamic failure time, elastic energy index, impact energy index, and uniaxial compressive strength. All test results have reached the same conclusion. Xue et al. [30, 31] studied the influence of gas pressure on coal and rock bursting tendency based on the energy method and found that the impact energy index, effective impact energy index, and residual energy index all decrease with the increase of gas pressure. The change of rockburst tendency can also be confirmed by the abovementioned crack evolution law. In the coal seam which has typical dynamic hazards, there is a critical value of gas pressure. When the gas pressure is higher than the critical value, gas outburst is the main disaster. When the gas pressure is lower than the critical value, the rockburst is the main disaster [30].

5. Conclusions

Through the fluid-solid coupling simulation of gas-containing coal, considering gas pressure and adsorption expansion, from the perspectives of macromechanical behavior, permeability, microcrack evolution, energy accumulation and release, the deformation, and failure mechanism of gas-containing coal under different gas pressures is analyzed. The main conclusions are as follows.

(1) In the discrete element method, the adsorption and expansion of gas-containing coal can be effectively simulated by increasing the particle diameter. Based on the MatDEM software, a gas-solid coupling simulation method for porous media has been developed

(2) The compressive strength and elastic modulus of gas-containing coal decrease with the increase of gas pressure. The pore gas pressure acting on the inside of the coal sample particles weakens the confining pressure to close the coal sample cracks, promotes the crack propagation, and reduces the ability to resist damage. The adsorbed gas on the surface of coal particles weakens the bonding force between coal particles and reduces their ability to resist deformation

(3) During the process of deformation and failure of gas-containing coal, the permeability of coal samples first decreases and then increases. The initial permeability, minimum permeability, and maximum permeability of coal samples all decrease with the increase of gas pressure, and the greater the gas pressure, the smaller the decrease in permeability caused by the increase in unit gas pressure

(4) With the increase of gas pressure, the macroscopic cracks in the coal sample gradually changed from large-angle shear cracks to multiple intersecting small-angle shear cracks. The number of cracks at the same stress level increases, and the increase in the number of cracks during the violent growth stage becomes small. The coal sample gradually changed from brittle failure to ductile failure

(5) The cumulative elastic energy before the peak strength decreases approximately linearly with the increase of gas pressure, while the increase of dissipated damping energy is relatively large, and the overall rockburst tendency of coal samples changes from weak to no

Data Availability

The data used to support the findings of this study are available from the corresponding author upon request.

Conflicts of Interest

The authors declare that there is no conflict of interest regarding the publication of this paper.

Acknowledgments

The authors are supported by the National Natural Science Foundation of China (Grant Nos. 51934007 and 42030810), and the Fundamental Research Funds for the Central Universities (Grant No. 2017QNA31).

References

[1] V. Hudecek, “Analysis of safety precautions for coal and gas outburst-hazardous strata,” *Journal of Mining Science*, vol. 44, no. 5, pp. 464–472, 2008.

[2] J. Shepherd, L. K. Rixon, and L. Griffiths, “Outbursts and geological structures in coal mines: a review,” *International Journal of Rock Mechanics and Mining Science & Geomechanics Abstracts*, vol. 18, no. 4, pp. 267–283, 1981.

[3] Y. K. Ma, B. S. Nie, X. Q. He, X. C. Li, J. Q. Meng, and D. Z. Song, “Mechanism investigation on coal and gas outburst: an overview,” *International Journal of Minerals Metallurgy and Materials*, vol. 27, no. 7, pp. 872–887, 2020.

[4] X. Liu, X. Wang, E. Wang et al., “Effects of gas pressure on bursting liability of coal under uniaxial conditions,” *Journal of Natural Gas Science and Engineering*, vol. 39, pp. 90–100, 2017.

[5] T. B. Zhao, Y. C. Yin, Y. L. Tan, P. Wei, and J. C. Ju, “Bursting liability of coal research of heterogeneous coal based on particle flow microscopic test,” *Meitan Xuebao/Journal of the China Coal Society*, vol. 39, no. 2, pp. 280–285(6), 2014.

[6] M. He, C. Wang, D. Li, J. Liu, and X. Zhang, “Desorption characteristics of adsorbed gas in coal samples under coupling temperature and uniaxial compression,” *Yanshilixue Yu Gongcheng Xuebao/Chinese Journal of Rock Mechanics and Engineering*, vol. 29, no. 5, pp. 865–872, 2010.

[7] R. S. Lv, B. Li, Z. Song, and G. Liu, “Experimental investigation on permeability and mechanical deformation of coal containing gas under load,” *Advances in Civil Engineering*, vol. 2018, Article ID 7341523, 10 pages, 2018.

[8] X. G. Liu, *Study on the Deformation and Failure Characteristics and the Permeation Behavior of Gas-Saturated Coal*, China University of Mining and Technology, Jiangsu, 2013.

[9] C. F. Wei, “Research on fluid-solid coupling model of loaded coal containing gas and its application, [Ph.D. thesis],” Henan Polytechnic University, Henan, 2014.

[10] B. Liang and Y. J. Wang, “The experimental research on the effect of gas on mechanical properties and mechanical response of coal,” *Chinese Journal of Geotechnical Engineering*, vol. 17, no. 5, pp. 12–18, 1995.

[11] J. Cao, L. Dai, H. Sun et al., “Experimental study of the impact of gas adsorption on coal and gas outburst dynamic effects,” *Process Safety and Environmental Protection*, vol. 128, pp. 158–166, 2019.

[12] D. M. Gao, J. R. Wang, L. Hong, and D. Zheng, “The characteristics of gas adsorption in micropores and its influence on coal and gas outburst,” *Fresenius Environmental Bulletin*, vol. 28, no. 12, pp. 9443–9451, 2019.

[13] L. Hong, D. M. Gao, J. R. Wang, and D. Zheng, “A distinguishing method of coal and gas outburst based on the adsorption capacity in pores,” *Energy Sources, Part A: Recovery, Utilization, and Environmental Effects*, vol. 42, no. 11, pp. 1402–1411, 2020.

[14] Y. Liu, Y. M. Zhu, S. M. Liu, W. Li, and X. Tang, “Temperature effect on gas adsorption capacity in different sized pores of coal: experiment and numerical modeling,” *Journal of Petroleum Science and Engineering*, vol. 165, pp. 821–830, 2018.

[15] F. K. Wang, Y. P. Liang, X. L. Li, L. Li, J. Li, and Y. Chen, “Orthogonal experimental study on multifactor conditions for gas desorption in coal,” *Advances in Civil Engineering*, vol. 2019, Article ID 3028721, 12 pages, 2019.

[16] Z. H. Shen, L. Zhou, H. L. Li, Z. H. Lu, and J. C. Cai, “Experimental and numerical study on the anisotropic and nonlinear gas flow behavior of a single coal fracture under loading,” *Energy & Fuels*, vol. 34, no. 4, pp. 4230–4242, 2020.

[17] H. C. Zhao and R. B. Kaunda, “Numerical assessment of the influences of gas pressure on coal burst liability,” *Energies*, vol. 11, no. 2, p. 260, 2018.

[18] D. S. Yang, X. Y. Qi, W. Z. Chen, S. G. Wang, and F. Dai, “Numerical investigation on the coupled gas-solid behavior of coal using an improved anisotropic permeability model,” *Journal of Natural Gas Science and Engineering*, vol. 34, pp. 226–235, 2016.

[19] Y. Q. Tao, D. Liu, J. Xu, S. J. Peng, and W. Nie, “Investigation of the Klinkenberg effect on gas flow in coal matrices: a numerical study,” *Journal of Natural Gas Science and Engineering*, vol. 30, pp. 237–247, 2016.

[20] M. Y. Tang, P. X. Zheng, C. S. Zheng, Z. X. Hu, J. H. Wang, and G. L. Dai, “Numerical analysis and prediction of coal mine methane drainage based on gas–solid coupling model,” *Tehnicki Vjesnik-Technical Gazette*, vol. 26, no. 3, pp. 752–761, 2019.

[21] C. G. Zhu, C. Liu, Q. Xu, W. Hu, and X. Y. Zhang, “Discrete element numerical simulation research on friction heat in sliding zone of the landslide,” *Journal of Engineering Geology*, vol. 27, no. 3, pp. 651–658, 2019.

[22] L. W. Liang, C. Liu, Y. Qin, C. G. Zhu, and S. Deng, “Discrete element modeling and numerical simulation of rock breaking by hob based on MatDEM,” *Hazard Control in Tunnelling and Underground Engineering*, vol. 1, no. 3, pp. 116–122, 2019.

[23] Y. D. Xue, J. Zhou, F. Zhao, and X. Li, “Rock breaking mechanism of TBM cutter based on MatDEM,” *Rock and Soil Mechanics*, vol. 41, no. S1, pp. 337–346, 2020.

[24] C. Liu, Y. Qin, Q. Tang, and T. C. Le, “Numerical simulation of compacted failure in porous sandstone based on discrete element method,” *Journal of Guilin University of Technology*, vol. 37, no. 3, pp. 536–540, 2017.

[25] C. Liu, D. D. Pollard, and B. Shi, “Analytical solutions and numerical tests of elastic and failure behaviors of close-packed lattice for brittle rocks and crystals,” *Journal of Geophysical Research Solid Earth*, vol. 118, no. 1, pp. 71–82, 2013.

[26] R. D. Zucker and O. Biblarz, *Fundamentals of Gas Dynamics*, John Wiley & Sons, New Jersey, 2nd edition, 2002.

[27] B. L. Evans, “Compressibility of natural gas,” *Journal of Canadian Petroleum Technology*, vol. 14, no. 2, pp. 157–162, 1952.

[28] S. Y. Wu, W. Zhao, and Y. Y. Guo, “Parametric correlation between expansion deformation of coal mass and adsorption thermodynamics,” *Journal of Northeastern University (Natural Science)*, vol. 26, no. 7, pp. 683–686, 2005.

[29] C. Liu, Q. Xu, B. Shi, S. Deng, and H. H. Zhu, “Mechanical properties and energy conversion of 3D close-packed lattice model for brittle rocks,” *Computers & Geosciences*, vol. 103, pp. 12–20, 2017.

[30] Y. Xue, F. Gao, T. Teng, and Y. Xing, “Effect of gas pressure on rock burst proneness indexes and energy dissipation of coal samples,” *Geotechnical and Geological Engineering*, vol. 34, no. 6, pp. 1737–1748, 2016.

[31] Y. Xue, F. Dang, Z. Cao et al., “Deformation, permeability and acoustic emission characteristics of coal masses under mining-induced stress paths,” *Energies*, vol. 11, no. 9, p. 2233, 2018.

Hindawi
Geofluids
Volume 2021, Article ID 6649824, 14 pages
https://doi.org/10.1155/2021/6649824

Research Article

Experimental Study on Influence of Chemical Corrosion on Mechanical Property of Fissured Granite

Fan Zhang,[1] Tao He,[1] JunjieKang,[1] and Dawei Hu[2]

[1]*School of Civil Engineering, Architecture and Environment, Hubei University of Technology, Wuhan 430068, China*
[2]*State Key Laboratory of Geomechanics and Geotechnical Engineering, Institute of Rock and Soil Mechanics, Chinese Academy of Sciences, Wuhan 430071, China*

Correspondence should be addressed to Dawei Hu; dwhu@whrsm.ac.cn

Received 21 November 2020; Revised 7 February 2021; Accepted 25 February 2021; Published 12 March 2021

Academic Editor: Kai Yao

The effect of chemical corrosion and natural joints on the damage characteristics and strength of rock masses is highly important for the construction of rock engineering and energy extraction. Therefore, the intact granite is processed into prefabricated fissured granite specimens with a fissure angle of 0°, 30°, and 45°. Chemical corrosion tests are then performed on the prefabricated fissured granites. The pH of the solution gradually becomes neutral; the mass loss of the granite specimens and the mineral compositions of the fissure surface are measured and analyzed. The scanning electron microscopy (SEM) and uniaxial compression tests are performed on the granite specimens after chemical corrosion. After chemical corrosion, the surface of the fissure becomes loose. The various mineral components of the specimens have been changed to different degrees or converted into other mineral components. The peak strength and elastic modulus of the prefabricated fissured granites with the three fissure angles present a clear decrease, as the time of chemical corrosion increases. The stress intensity factors at the fissured tip are also analyzed. The stress intensity factors of the specimens with a fissure angle of 0°, 30°, and 45° decrease from 0.017, 0.35, and 0.84 to 0.013, 0.30, and 0.74 $\mathrm{MPa{\cdot}m^{1/2}}$, respectively, as the time of the chemical corrosion increases. And the chemical corrosion has the largest effect on the intensity factors of the specimens with a fissure angle of 45° among the three angles. These experimental results could improve the understanding of the long-term stability of underground engineering in the multifield coupling environment.

1. Introduction

Due to the function of crustal movement and weathering, a large number of fissures with different sizes are induced inside rocks. In the underground of rock engineering such as underground energy storage, oil extraction, gas extraction, and geothermal extraction, the initiation, propagation, and penetration of these fissures are closely related to the instability and destruction of rock engineering.

The natural fissures of rocks are the decisive factor for the stability of underground rock engineering. A large number of experimental studies have focused on the physicomechanical properties of fissured granite, such as ultrasound characteristic strength, elastic modulus, and fracture behaviors [1–4]. In addition to the traditional analysis of mechanical parameters of fissured granites, some scholars confirm that the fracture criterion is related to the properties of the rock, prefabricated cracks, and types of loading [5]. Simultaneously, secondary cracks and wing cracks are observed [6, 7] during the uniaxial and biaxial compression tests by using rock-like models with prefabricated fissures. In the tip of crack, the tensile crack and petal crack [8] are observed by an experimental study on marbles with a 3-D surface flaw. In order to supplement previous research results, crack propagation [9, 10] and coalescence [11, 12] with prefabricated fissures have been extensively studied by experimental and simulation research. For example, Wu et al. [13] distinguished coalescence modes of three rock bridges: stretch-stretch, shear-shear, and stretch-shear mode by the DIC and CT methods. The simulation of granites with prefabricated joints by PFC shows that granites usually generate tensile fracture with low confining pressure, tensile-shear mixed fracture with medium confining pressure, and shear fracture with high confining pressure [14]. The simulated crack growth, coalescence, and type are highly consistent with the experimental results by using the method of finite element with unstructured mesh of tetrahedral element [15]. Simultaneously, there is also research on the mechanical properties and expansion modes of granite with two kinds of joints. Rezania et al. [16] conducted the numerical simulation and experimental research on granite with two side cracks and an opening with a tunnel; the results showed that the fissured angle has a great influence on the mechanical properties, stress distribution, and crack propagation of granite. Yang et al. [17] summarized the propagation and aggregation mode of cracks in the stage of loading through the experimental and simulation study on granite with two holes and a fissure.

In addition, in the underground engineering constructions such as coal mining, the geological repository of radioactive wastes and tunnels, surrounding rocks, will be inevitably immersed in the environment of saturated water because of the groundwater. The aggressive ions in the water will affect the mechanical properties of surrounding rocks and the stability of the tunnel, which weakens the mechanical property of the rocks [18]. Therefore, it is of great importance to study the mechanical properties of rocks under the action of chemical corrosion.

In recent years, many scholars have carried out a series of studies on the physical and mechanical properties of various rock materials after corrosion by water and chemical solutions. Corrosive solutions, such as NaCl and NaOH, obviously have a great influence on the rate of crack growth of quartz [19]. Dunning et al. [20] analyzed the role of the chemical environment in frictional deformation, including stress corrosion cracking and grinding. The failure mechanism of rock mass after chemical corrosion has become a hot topic. For example, Karfakis and Akram [21] carried out the strain energy index and fracture toughness tests on three kinds of rocks under five environments and researched the mechanism of modification of rock characteristics under the chemical corrosion. Sausse et al. [22] conducted the research on the fissured permeability of granites under the action of water and rock and discussed the evolution law of permeability of granites. Min et al. [23] proposed a model about the mechanical and transport characteristics of fissured rock. Croizé et al. [24] conducted the uniaxial compression test on crushed calcite to investigate the physical properties of rocks and their evolution during fault zone processes. Yu et al. [25] proposed the damage variables to be used to describe the corrosion damage. The development of computer technology has also accelerated the progress of scientific research on rock mechanics [26, 27]. For example, the parallel bond stress corrosion model [28] is obtained by adding the damage rate law, which can well simulate the chemical corrosion reaction of rock under the action of aqueous solution. And this model can also be used to predict the macrogradation of mechanical properties caused by chemical corrosion and simulate the evolution process of microdamage [29]. Mohtarami et al. [30] developed an extended finite element code that could reproduce the singularity in anisotropic and uneven environments after chemical corrosion.

However, the previous research results mostly focus on the mechanical and physical properties of intact rock masses after chemical corrosion. Considering the complexity of the underground environment and natural joints, the rock mass is inevitably affected by the chemical-stress coupling. Therefore, it is essential to carry out research on the mechanical characteristics of fissured granites with various angles after chemical corrosion. This paper carries out research on the physical and mechanical properties of fissured granite after chemical corrosion (0, 30, 60, and 90 days) and analyzes the variations of mineral composition and microstructure of fissured granites after chemical corrosion. Simultaneously, the stress intensity factors of the fissured tip after chemical corrosion are calculated and analyze the change mechanism of the stress intensity factors at the fissured tip. The results can provide a theoretical basis for the stability analysis of underground engineering.

2. Test Preparation

2.1. Specimen Preparation. The rock specimens in the experiment are sampled from Yueyang, Hunan province, China, with a dense structure and good macroscopic homogeneity. And the natural density is 2.6 g/cm^3. The average mass fractions of the main mineral components are quartz (30%), sodium feldspar (19.67%), and potassium feldspar (24.49%), and the specimen also contains a small amount of biotite (11.71%), chlorite (7.18%), and illite (6.95%). The granite specimens are processed into cylindrical standard specimens of $\varphi 50 \times 100$ mm. The processed accuracy of the specimens (including the parallelism, straightness, and perpendicularity of the granites) is controlled by the suggested methods of the International Society of Rock Mechanics and Rock Engineering (IRSM). Therefore, the surface of the specimens is smooth and without obvious defects. The Mohs hardness of granites is about 7 [31], which is a species of hard granite. Since the cutting thickness of fissured specimens is large, prefabricated fissures adopt the water-jet cutting technique to process the specimens [32]. The length of the prefabricated fissure is 20 mm, the width is 1 mm, and the maximum depth of cutting is 50 mm. The prefabricated fissures, respectively, have inclinations with $\alpha = 0^\circ$, 30°, and 45° (Figure 1).

2.2. Specimen Processing. Groundwater contains amounts of various ions such as Na^+, Ca^{2+}, SO_4^{2-}, Mg^{2+}, Cl^-, and HCO_3^-. When granites are immersed in the environment of ionic solution, multiple mineral ingredients will react with chemical solution such as decomposition reaction, oxidation-reduction reaction, and single displacement reaction. And the chemical reactions deteriorate the mechanical property of granites. However, the contents of Na^+ and Cl^- in the ionic solution are more [33]. Therefore, the granite specimens are immersed in a glass vessel, which contains an oversaturated NaCl solution with the concentration of 5.4 mol/L and pH = 2. The vessel is sealed with Vaseline to prevent evaporation of water. The test, respectively, selects 30, 60, and 90 days as immersed time. To ensure the accuracy of the experimental results, the temperature of a test is a constant temperature (22°C). During the immersion of the specimens, this paper measured the change of the pH value of the solution and the

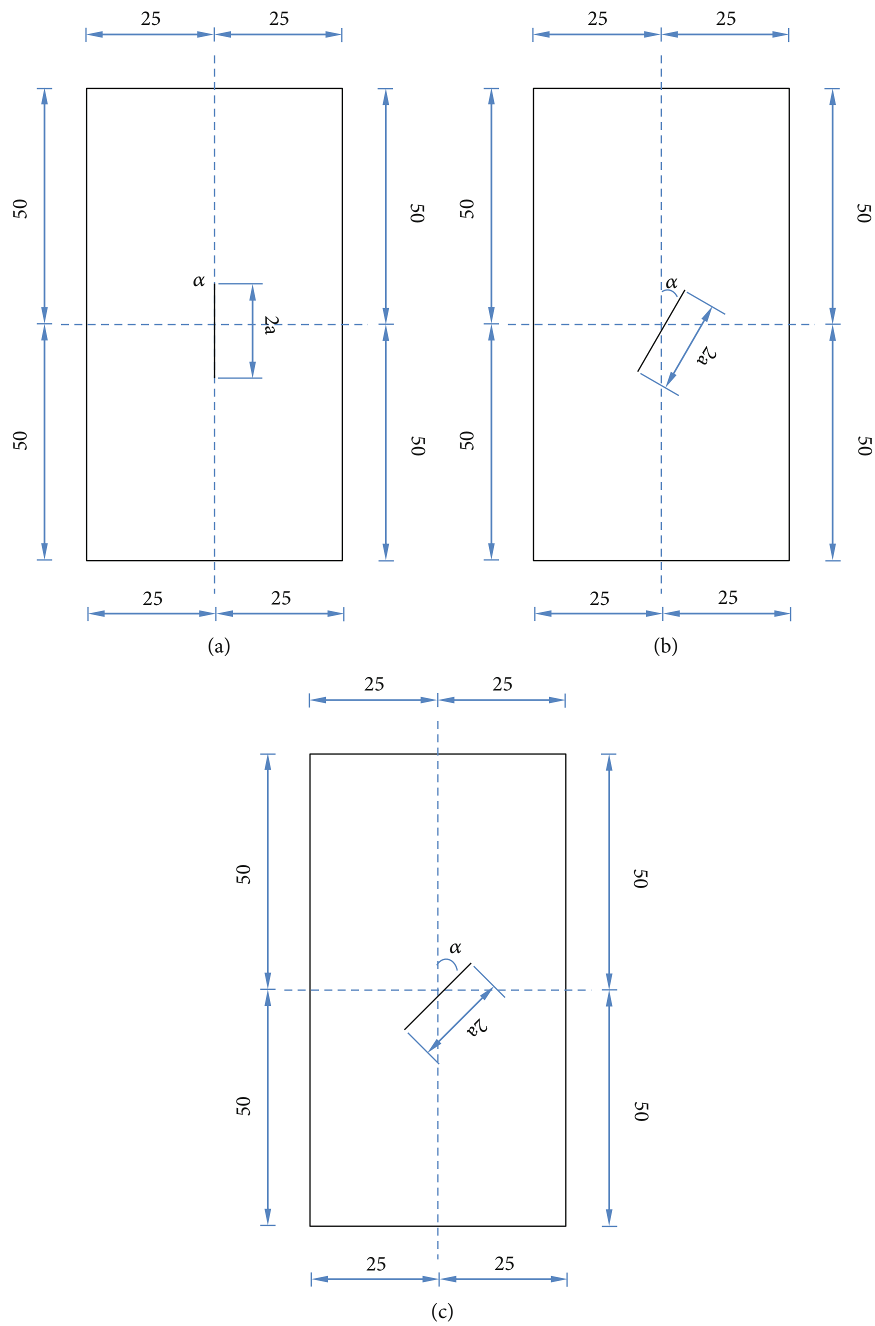

Figure 1: Prefabricated fissured specimen with different inclinations: (a) specimen with $\alpha = 0^\circ$, (b) specimen with $\alpha = 30^\circ$, and (c) specimen with $\alpha = 45^\circ$, 2a = 20 mm.

quality of the specimens. To ensure the accuracy of the specimens on quality measurement and reduce random errors, after the specimens are taken out, they are dried at 105°C in an electric drying oven with constant temperature and the specimens are completely dried for 24 hours. Then, the quality of specimens is measured.

2.3. Test Equipment and Test Process. The uniaxial compression test is completed using a Thermo-Hydro-Mechanical-Chemical (THMC) coupling test system in this paper [34], which includes a triaxial pressure chamber, an antiforce framework with high strength, an electrohydraulic servo pump with high pressure, a microcomputer system, a strain monitoring with acquisition system, and accessory in Figure 2.

The test process of this article is as follows. The fissured specimens with $\alpha = 0^\circ$, 30°, and 45° after chemical corrosion for 0, 30, 60, and 90 days are pasted axial strain gauges and radial strain gauges on both sides of the plane corresponding of cylindrical shaft of specimens. Then, specimens after treatment are put into the triaxial stress chamber, which connects with strain monitoring with the acquisition system. The test

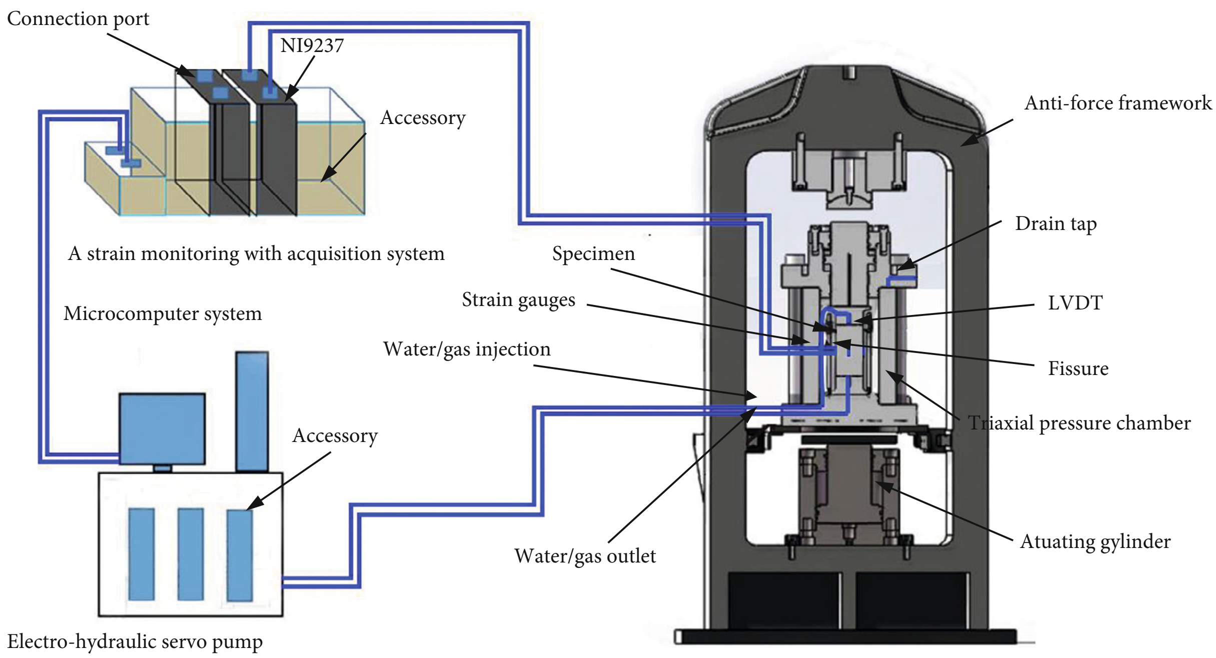

Figure 2: THMC coupling test system (after [34]).

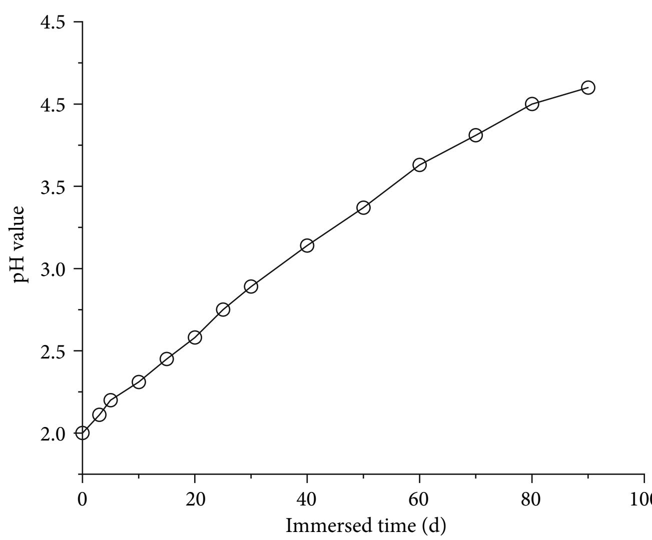

Figure 3: Variation curve of the pH value with the change of immersed time.

is a uniaxial compression test, the axial force loading is applied under the control mode of axial displacement, and the loading rate is 0.01 mm/min.

3. Experimental Results

3.1. Chemical Corrosion for Prefabricated Fissured Granite. After the chemical corrosion, the pH value of the solution gradually increases with the increase of the immersed time, and the increasing rate in the stage of initial immersion is large and then gradually flattens out (Figure 3). Figure 4 shows the mass loss of the specimens, which undergoes a rapid decrease to a gradual balance. Because the active mineral content of the initial granite surface is relatively high, H^+ ions are quickly consumed in the chemical solution; as the reaction progresses, the granite surface active minerals decrease, resulting in a decrease in the chemical dissolution rate. Simultaneously, the decrease of H^+ also leads to an increase in the pH value of the solution, and the pH value tends to stabilize with the progress of the reaction [35].

In order to analyze the degree of mass loss of prefabricated fissured granites with different inclinations, a mass loss rate K_t was defined in Equation (1), M_t is the mass of specimens after chemical corrosion, and M_0 is the initial mass of specimens without chemical corrosion [36].

$$K_t = \frac{(M_t - M_0)}{M_0} \times 100\%. \quad (1)$$

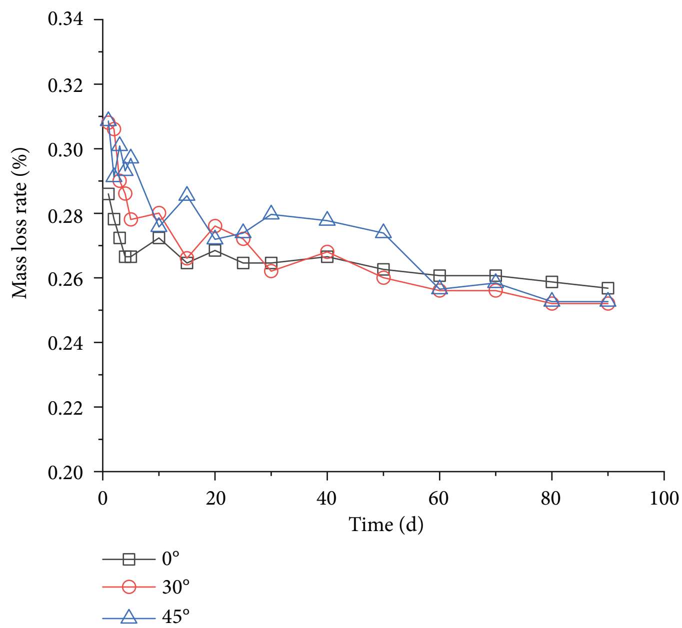

Figure 4: Variation curves of mass of specimens under the action of chemical solution.

Table 1: Contents of the main minerals of granites during the immersed process.

Immersed time (d)	The contents of main mineral components (%)					
	Quartz	Sodium feldspar	Mica	Chlorite	Potassium feldspar	Illite
0	30.00	19.67	11.71	7.18	24.49	6.95
30	26.19	29.53	15.23	10.04	12.91	6.11
60	34.52	27.75	11.70	6.08	14.46	5.50
90	37.20	24.51	6.61	10.13	9.07	12.49

To more intuitively analyze the influence of chemical corrosion on the composition of fissured granite, the X-ray diffraction test is proceeded on the surface of granites after chemical corrosion for 0, 30, 60, and 90 days, and the results of the content of main minerals are shown in Table 1 and Figure 5. The contents of mica and potassium feldspar show a downward trend during the immersion process, and the decreasing rates of mass percentage are, respectively, 43.55% and 62.96% after chemical corrosion for 90 days. This phenomenon is attributed to the reaction of mica and potassium feldspar in an acidic environment (Equations (2) and (3)) [36, 37]. However, the content of quartz and sodium feldspar slightly ascends with the increase of the immersed time, and the content of chlorite appears to fluctuate. Firstly, the hydrolysis rate of quartz is slower than other types of minerals, and quartz has a lower sensitivity to acidic solutions. Moreover, mica and potassium feldspar will also generate a certain amount of colloidal quartz during the chemical reaction. Secondly, potassium feldspar will produce K^+ in the process of hydrolysis, and the increase of the concentration of K^+ is likely to lead to the formation of sodium feldspar [38]. The mass percentage of illite does not significantly change after chemical corrosion for 60 days but significantly increases after chemical corrosion for 90 days, because illite is a kind of potassium-rich mineral, and potassium feldspar can form illite in an acidic environment. Furthermore, after potassium feldspar is corroded in an acidic solution for 90 days, a large amount of K^+ appear in the corrosive solution, which reacts with sodium feldspar to form illite (Equations (4) and (5)) [39]. In short, after the chemical composition of granites reacts with the acid solution, the chemical composition of granites has changed, leading to the change of the mechanical and physical properties of granites.

The reaction of mica with the acidic solution is written as follows:

$$KAl_3Si_3O_{10}(OH)_2 + 10H^+ = 3Al^{3+} + 3SiO_2 + 6H_2O + K^+ \tag{2}$$

The reaction of potassium feldspar with the chemical solution is written as follows:

$$KAlSi_3O_8 + 4H^+ = Al^{3+} + 3SiO_2 + 2H_2O + K^+ \tag{3}$$

The reaction of formation of illite is written as follows:

$$\begin{aligned} 3NaAlSi_3O_8 + K^+ + 2H^+ + H_2O = KAl_3Si_3O_{10}(OH)_2 + 3Na^+ \\ + 6SiO_2 + H_2O \end{aligned} \tag{4}$$

$$3KAlSi_3O_8 + 2H^+ + H_2O = KAl_3Si_3O_{10}(OH)_2 + 2K^+ + 6SiO_2 + H_2O \tag{5}$$

The Scanning Electron Microscope (SEM) tests are performed to observe the microstructure variations of the fissure surface of the granite specimens after chemical corrosion for 0, 30, 60, and 90 days, and the results are shown in Figure 6.

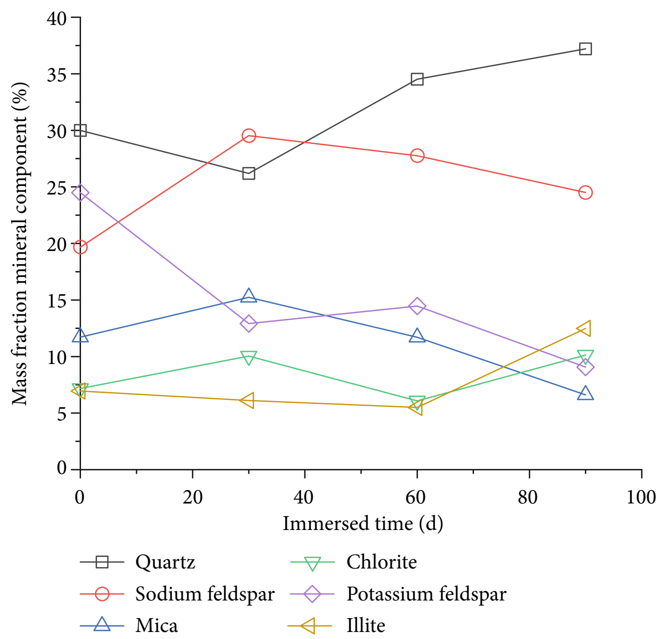

FIGURE 5: Variation curves of the main mineral content during the immersion process.

The fissure surfaces of the granite specimens are damaged to varying degrees after chemical corrosion.

At the initial stage, the surface texture is dense and the cemented surface is complete without chemical corrosion and only a small quantity of fine mineral particles could be observed. The size of crystal particles is clearly distinct (Figure 6(a)). After chemical corrosion for 30 days, local degradation of cemented surface of the specimens can be observed. The microstructure appears loose; fine particles and crystals increase. A lot of small cracks begin to appear, and the edges and corners begin to become smooth (Figure 6(b)). After chemical immersion for 60 and 90 days, the cemented surface is completely destroyed. The surface texture of the fissure becomes loose, and small cracks begin to connect so that the internal edges and corners gradually disappear. A large number of small particles and crystals appear. The structure of honeycomb appears, and secondary pores significantly increase (Figures 6(c) and 7(d)) [36].

3.2. Mechanical Properties of Fissured Granite after Chemical Corrosion

3.2.1. Stress-Strain Curves. To study the effect of chemical corrosion on the mechanical property of fissured granites with different inclinations, three kinds of fissured granite specimens with $\alpha = 0°$, $30°$, and $45°$ are, respectively, immersed in the oversaturated NaCl solution of pH = 2 for 0, 30, 60, and 90 days. The uniaxial compression tests are performed on the granite specimens with $\alpha = 0°$, $30°$, and $45°$ after chemical corrosion for 0, 30, 60, and 90 days, and the environment temperature of the test is 22°C.

Figure 7 shows stress-strain curves for granites with $\alpha = 0°$, $30°$, and $45°$ without chemical corrosion under the uniaxial compression test. The compaction stage of fissured specimens with $\alpha = 45°$ has a shorter time by comparing with the specimens with $\alpha = 0°$ and the specimens with $\alpha = 30°$, once the microcracks are compacted, which soon enter the elastic deformation stage. Moreover, the specimen with $\alpha = 0°$ shows ductile failure when it fails. However, when the loading pressure is close to the peak strength of the specimens with $\alpha = 30°$ and $\alpha = 45°$, the principal stress drops instantly, which shows a kind of brittle failure.

Due to space constraints, the paper only gives the stress-strain curves of the specimens with $\alpha = 0°$ after chemical corrosion in Figure 8. According to the stress-strain curves of fissured granite after chemical corrosion, the duration of the initial compaction stage is relatively long for specimens without chemical corrosion. The stress-strain curves of specimens without chemical corrosion in the compaction stage have an obvious concave downward trend. However, the compaction stage of specimens after chemical corrosion is relatively short. Particularly, the specimens are immersed for 90 days. The result shows that the chemical corrosion will shorten the compaction stage of fissured granite and accelerates the destruction speed of the specimens, resulting in a decrease in the peak value of the specimens. The specimens without chemical corrosion basically maintain a linear change before reaching the peak value, and the elastic stage is longer than the specimens after chemical corrosion, and there is no obvious yield point. However, the elastic stage of the specimens becomes shorter after chemical corrosion. The specimens after chemical corrosion for 90 days have the shortest elastic stage. It is indicated that chemical corrosion has damaged the internal structure of the granite, causing the granite to quickly enter the destruction stage. When the stress-strain curve reaches the peak strength, it can be seen that the specimens after chemical corrosion are instantaneously broken, the peak value has a significant drop, and strain even rebounds (specimens after chemical corrosion for 90 days), which presents a brittle failure. However, the

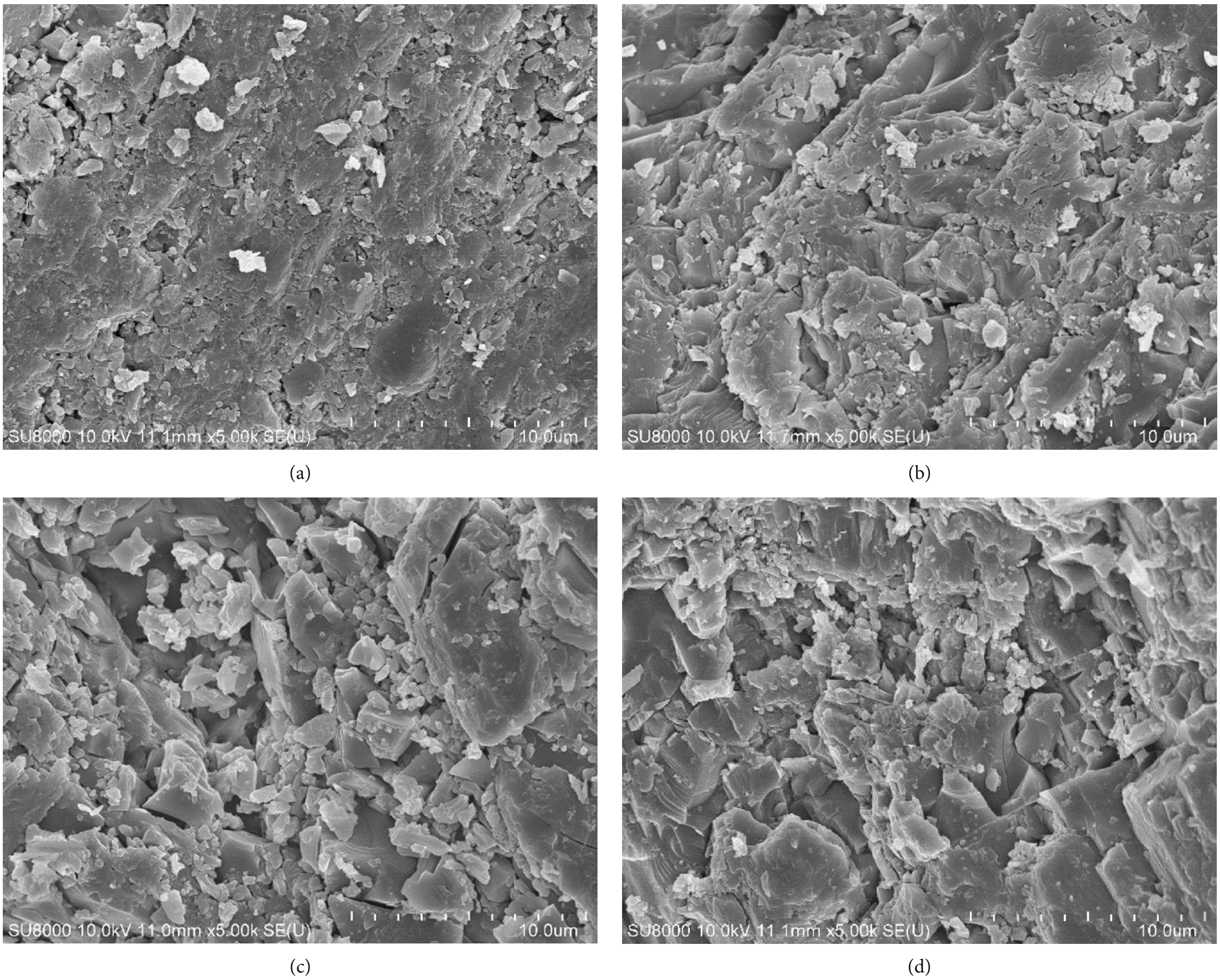

Figure 6: SEM images of fissure surface of granite: (a) without immersion, (b) 30 days, (c) 60 days, and (d) 90 days.

specimens without chemical corrosion show a ductile failure, and there is no instant drop of principal stress.

It can be seen in Figure 9 that the expansion path of the granite specimens is relatively bent. And a few of paths even deviate from the failure path. It is due to the heterogeneity of composition of granite. The strength of each composition is naturally different, and then, the resistance of fissured propagation of granites is also different.

3.2.2. Peak Strength and Elastic Modulus. To further study the effect of chemical corrosion on the mechanical properties of fissured granites, this paper selects the maximum value of the stress as the peak strength and approximately 40% to 60% of the linear part in the elastic stage of the stress-strain curve to calculate slope as the elastic modulus [34] by using the following formula:

$$E = \frac{\sigma_{a60} - \sigma_{a40}}{\varepsilon_{a60} - \varepsilon_{a40}}, \tag{6}$$

where σ_{a40} and σ_{a60} are 40% and 60% of the peak strength, respectively. ε_{a40} and ε_{a60} are 40% and 60% of the axial strain in each stress-strain curve, respectively.

Figure 10 shows the variation curve of the elastic modulus of fissured granite with $\alpha = 0^\circ$, 30°, and 45°. Figure 11 shows the effect of prefabricated fissures on the peak strength of granite. The mechanical parameters are calculated, and the results are shown in Table 2. It is not difficult to find that the prefabricated fissures have a significant influence on the mechanical parameters of granite from the experimental results. As the fissured angles increase, the elastic modulus and peak strength both show a tendency to attenuate.

Based on the test results of stress-strain curves after chemical corrosion in Figure 8, it is indicated that the longer time granites are immersed in the chemical solution, the bigger chemical damage is acted on the granites. Therefore, chemical damage has a significant influence on the mechanical parameters of granite. The following part of this article explores the influence of chemical corrosion on the

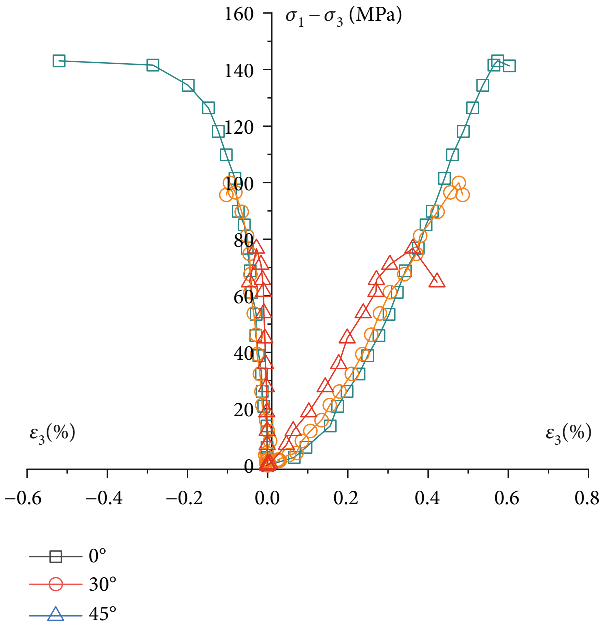

FIGURE 7: Stress-strain curves of fissured granites with $\alpha = 0^\circ$, 30°, and 45° under the uniaxial compression test without chemical corrosion.

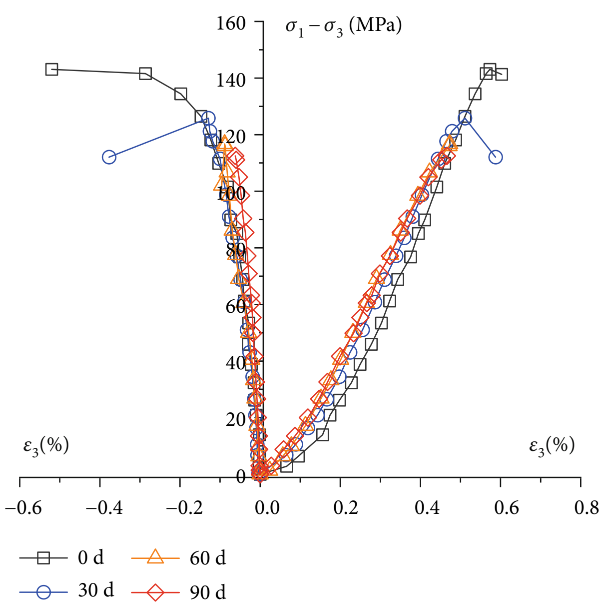

FIGURE 8: Stress-strain curves of fissured granites of uniaxial compression test under the action of chemical corrosion ($\alpha = 0^\circ$ specimen after chemical corrosion for 30, 60, and 90 days).

mechanical properties of fissured granites through the relevant mechanical parameters of granites.

Figure 12 shows the variation curves of elastic modulus of fissured granites with $\alpha = 0^\circ$, 30°, and 45° after chemical corrosion for 30, 60, and 90 days. Figure 13 shows the variation curves of peak strength of fissured granites with $\alpha = 0^\circ$, 30°, and 45° after chemical corrosion for 30, 60, and 90 days. It can be seen from Figures 12 and 13 that the mechanical parameters of prefabricated fissured granites with $\alpha = 0^\circ$, 30°, and 45° have changed to a certain extent after chemical corrosion for 30, 60, and 90 days. According to the above method of calculating the peak strength and elastic modulus, the mechanical parameters of the fissured granites after chemical corrosion for 30, 60, and 90 days are calculated. The results of peak strength and elastic modulus of fissured granite with $\alpha = 0^\circ$, 30°, and 45° after chemical corrosion for 30, 60, and 90 days are recorded in Table 3.

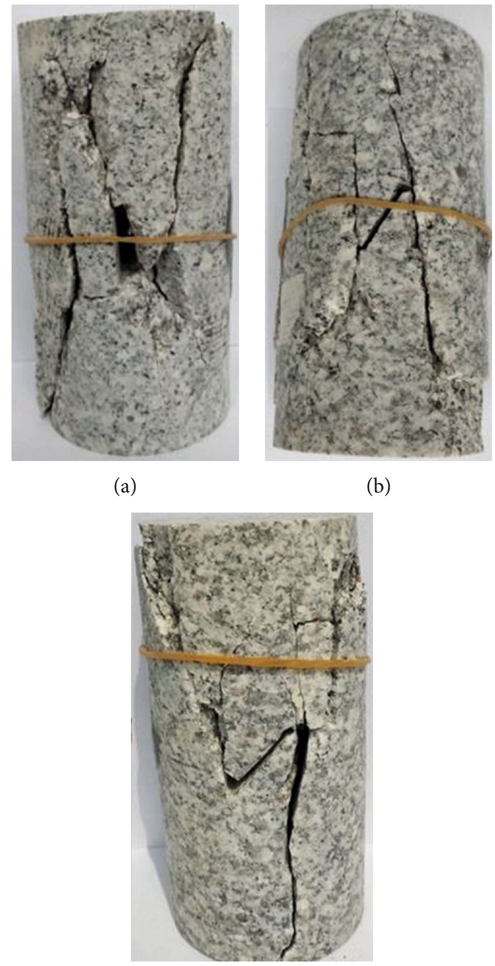
(a) (b)

(c)

FIGURE 9: Crack initiation of prefabricated fissured granite with different inclination under the uniaxial compression test: (a) specimen with $\alpha = 0^\circ$, (b) specimen with $\alpha = 30^\circ$, and (c) specimen with $\alpha = 45^\circ$.

As shown in Figure 13, after chemical corrosion for 30, 60, and 90 days, the peak strength of prefabricated fissured granite with different inclination shows a decreasing trend on the whole. Through the experimental values of the peak strength in Table 3, it can be seen that the peak strength of specimens with $\alpha = 0^\circ$ decreases from 140.88 to 112.50 MPa, and the degradation amplitude of the peak strength of the specimens with $\alpha = 0^\circ$ is 10.60%, 17.17%, and 20.14%, respectively. The peak strength of specimens with $\alpha = 30^\circ$ decreases from 100.73 to 85.34 MPa, and the degradation amplitude of the specimens with $\alpha = 30^\circ$ is 9.22%, 10.20%, and 15.28%, respectively. The peak strength of specimens with $\alpha = 45^\circ$

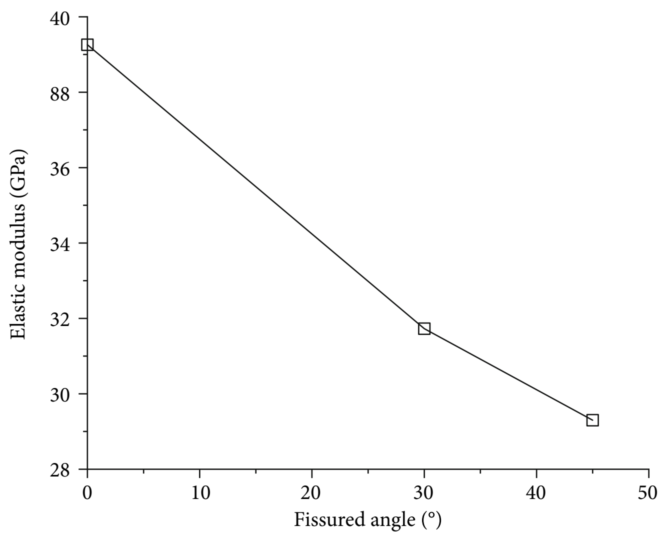

Figure 10: Variation of elastic modulus of fissured granites with $\alpha = 0°$, $30°$, and $45°$.

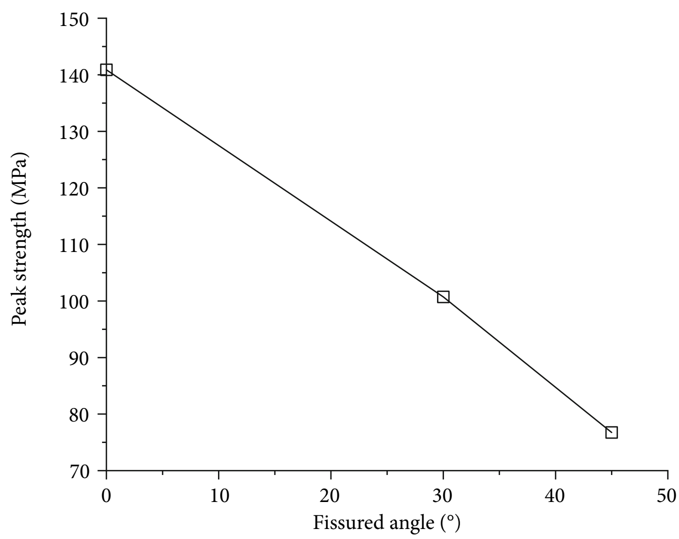

Figure 11: Variation of peak strength of fissured granites with $\alpha = 0°$, $30°$, and $45°$.

Table 2: Results of fissured granites with different inclination under uniaxial compressive test.

Fissured angle (°)	Peak strength (MPa)	Elastic modulus (GPa)
0	140.88	39.26
30	100.73	31.73
45	76.75	29.33

decreases from 75.75 to 67.19 MPa, and the degradation amplitude of the specimens with $\alpha = 45°$ is -0.12%, 7.92%, and 12.46%, respectively.

It can be seen from Figure 12 that the elastic modulus of granites with different inclinations show a gradually decreasing tendency with the increase of immersed time of chemical solution. Combined with the value of elastic modulus in Table 3, the average values of elastic modulus of specimens with $\alpha = 0°$ descend from 39.26 to 33.17 GPa after the chemical corrosion for 90 days. And after chemical corrosion for 30, 60, and 90 days, the degradation amplitude of the elastic modulus of the specimens with $\alpha = 0°$ is 2.06%, 5.99%, and 15.51%, respectively. Granites with other fissured angles have similar results. For example, descending from 31.73 to 26.96 GPa, the degradation amplitude is -1.70%, 10.53%, and 15.03%, respectively (specimens with $\alpha = 30°$). Descending from 29.33 to 21.91 GPa, the degradation amplitude is, respectively, -3.10%, 10.47%, and 25.30% (specimens with $\alpha = 45°$). Through the above analysis, it can be seen that the mechanical parameters of specimens with $\alpha = 30°$ and $\alpha = 45°$ slightly increase after chemical corrosion for 30 days. Because granite has the heterogeneity of material itself and the fissure has an error in size, the change of microstructure and the degree of corrosion softening are slightly different under the action of the chemical solution, leading to different mechanical characteristics of

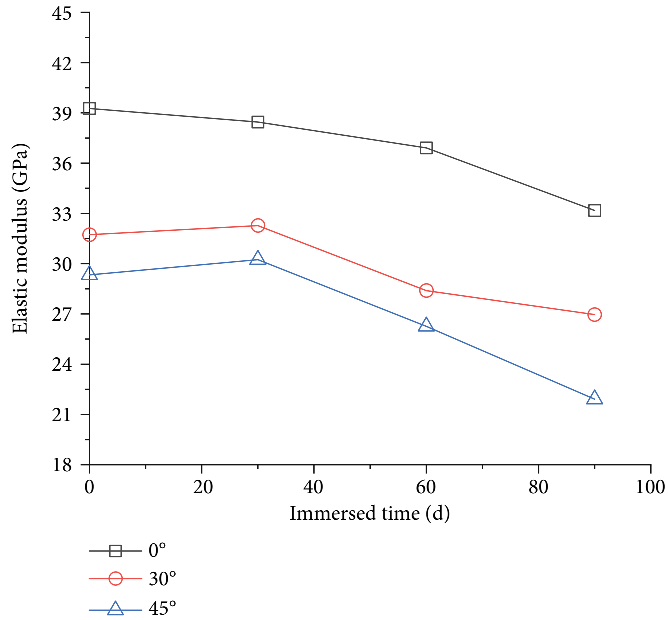

FIGURE 12: Variation of elastic modulus of fissured granite with $\alpha = 0^{\circ}$, 30°, and 45° after chemical corrosion for 30, 60, and 90 days.

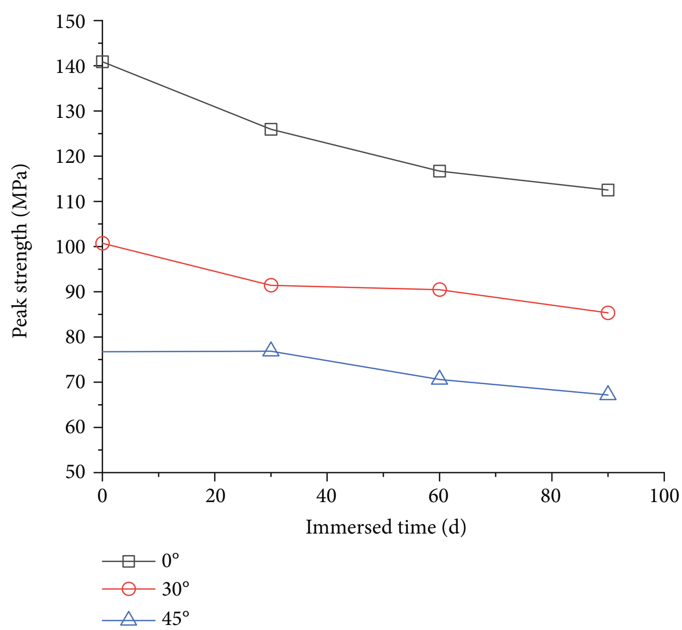

FIGURE 13: Variation of peak strength of fissured granite with $\alpha = 0^{\circ}$, 30°, and 45° after chemical corrosion for 30, 60, and 90 days.

TABLE 3: The results of the uniaxial compression test of fissured granites under the action of chemical solution.

Immersed time (d)	0°		30°		45°	
	Peak strength (MPa)	Elastic modulus (GPa)	Peak strength (MPa)	Elastic modulus (GPa)	Peak strength (MPa)	Elastic modulus (GPa)
0	140.88	39.26	100.73	31.73	76.75	29.33
30	125.94	38.45	91.44	32.27	76.84	30.24
60	116.69	36.91	90.46	28.39	70.61	26.26
90	112.50	33.17	85.34	26.96	67.19	21.91

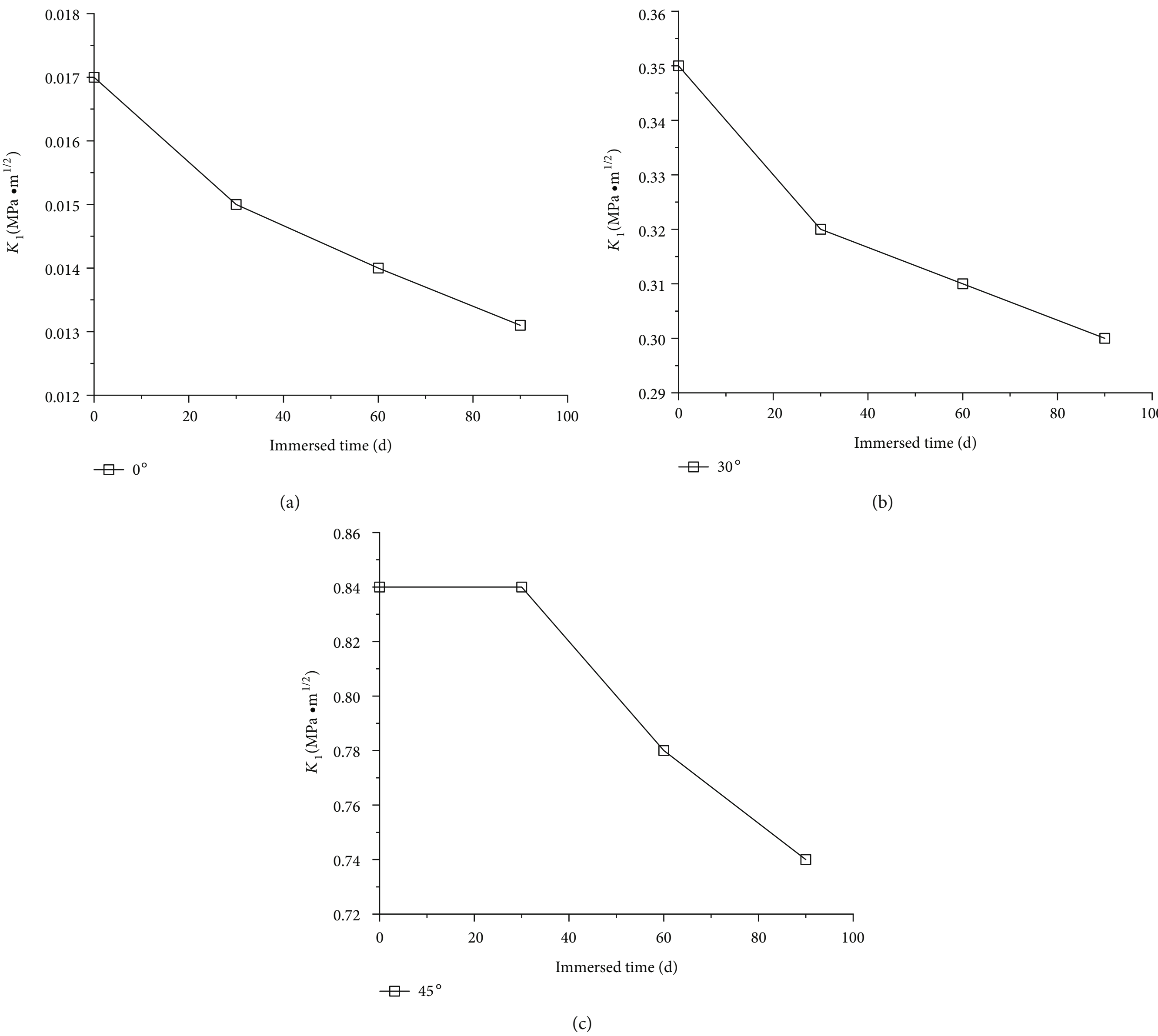

Figure 14: Variation of K_1 under the action of chemical solution.

some specimens and occurrence of discreteness phenomenon [40, 41].

4. Discussion

4.1. Evolutions of Stress Intensity Factors under the Action of Chemical Solution. In order to better understand the evolution of the stress field at the tip of the fissure after chemical corrosion, stress intensity factors are analyzed to investigate the effect of chemical solution on the fracture characteristics of fissured granite.

From previous research results, we can know that the process of failure of rock masses containing joints, I-type tensile failure, and II-type shear failure both exist, but II-type shear failure is difficult to observe [42]. More importantly, there is no clear boundary between the two destruction modes. Brace and Bombolakis [43] carried out tests on a glass model with prefabricated fissure and propose the slip-tension fracture model to study mechanical characteristics of brittle materials under the action of compression, which believes that I-type tensile failure is dominated in the mechanism of slip fracture. Therefore, the model of sliding fracture can better simulate the two types of shear-tension mixed failures in the process of compressive failure of granites. In the present work, an improved slipping crack model [44] is adopted, and the formula for stress intensity factors is written as

$$\frac{K_1}{\sigma_1\sqrt{\pi a}} = \frac{-\mu[(1+\lambda)-(1-\lambda)\cos\gamma]\sin\gamma}{\pi\sqrt{L^*+L}} + \frac{(1-\lambda)\sin 2\gamma\sin\gamma}{\pi\sqrt{L+L^*}} - \lambda\sqrt{L}, \quad (7)$$

where K_1 is the I-type strength stress factors, μ is the friction coefficient of the fissured surface, γ is the angle of crack initiation, $L^* = 8/(3\pi^2)$, $L = l/a$, l is the length of fissure after chemical corrosion, and λ is the ratio of the confining pressure to the axial pressure. Considering the uniaxial compression testis applied in this work, a simplified formula of stress intensity factors is rewritten as

$$\frac{K_1}{\sigma_1\sqrt{\pi a}} = \frac{-\mu[1-\cos\gamma]\sin\gamma}{\pi\sqrt{L+L^*}} + \frac{\sin 2\gamma \sin\gamma}{\pi\sqrt{L+L^*}}. \quad (8)$$

After the chemical corrosion, the extent of fissure growth is not obvious in the macroscopic view; therefore, the length of fissure is considered to be a constant during the chemical corrosion. According to Equation (8), the I-type stress intensity factors of specimens with $\alpha = 0^\circ$, 30°, and 45° after chemical corrosion for 30, 60, and 90 days are calculated and the results are shown in Figure 14.

It can be seen from Figure 14 that the stress intensity factors of the specimens with $\alpha = 0^\circ$, 30°, and 45° generally show the downward trend, as the immersed time of the chemical solution increases. And under the same chemical corrosion time, the changes in intensity factors of the specimens with $\alpha = 45^\circ$ are the largest among the three angles.

4.2. Analysis of Mechanism of Stress Intensity Factors. The plastic zone of the fissured tip has a decisive effect in the fracture toughness of granite during the process of destruction of granite. When the chemical solution erodes the granite specimens, the chemical solution molecule is driven to the fissure of granites under the action of concentration gradient of chemical solution. The active ions of solution react with the mineral molecules such as adsorption reaction and hydration reaction. The chemical bond connecting with grains in the fissured tip appears fracture under the action of H^+ [45]. The process of water-rock reaction deteriorates the seepage channels of the fissured surface and the mechanical property of the fissured surface. The active ions in the chemical solution cause the mineral particles to migrate and dissolve, and form caves and microfissures inside the fissures, leading to an increase of porosity of the fissured surface, weaken the seepage performance and pore pressure of the fissured surface, and increase secondary pore [36]. Under the long-term chemical corrosion of the fissure tip of granite, microcracks both appear at the top and bottom of the fissures (see Figure 6), leading to a decrease of mechanical properties of the plastic zone at the fissured tip and increase of fissured length and a large quantity of stress concentration in the plastic zone [46]. Therefore, as the chemical corrosion time increases, the stress intensity factors at the fissure gradually decrease.

From a previous study, it can be known that as the fissured angle increases, the crack initiation stress becomes smaller, leading to initiate easily in the fissured tip. Simultaneously, a large number of cracks initiate, leading to stress concentration at the crack tip [47]. It is seen that there is no obvious stress concentration of specimens with $\alpha = 0^\circ$ during the loading process (Figure 9(a)). The failure mode of the specimens with $\alpha = 0^\circ$ is a simple compression failure and does not depend on the influence of the fissure. Consequently, the tension crack propagates along the direction of paralleling to prefabricated fissured surface. Nevertheless, the fissured granite of other angles reaches the crack initiation stress, and wing cracks and antiwing cracks gather and appear at the fissured tip, leading to stress concentration that occurs at the fissured tip (Figures 9(b) and 9(c)). As the loading progresses, the cracks penetrate and lead to the destruction of the specimens [48]. The stress intensity factors are a parameter that reflects the concentration of the stress field at the fissured tip. Therefore, from the above analysis, the specimen with $\alpha = 0^\circ$ is a simple compression failure. There is almost no stress concentration at the prefabricated fissured tip. Therefore, the stress intensity factors of the specimens with $\alpha = 0^\circ$ are the smallest or even close to 0, while the specimens with $\alpha = 30^\circ$ and $\alpha = 45^\circ$ have a large quantity of stress concentration at the fissured tip, and the chemical corrosion has the largest effect on the intensity factors of the specimens with $\alpha = 45^\circ$ among the three angles.

5. Conclusions

In this paper, granites are processed into three kinds of standard cylindrical fissured specimens with different inclinations. First, a chemical corrosion test is performed, and then, the specimens before and after immersion are proceeded to the uniaxial compression test. Based on the physical and mechanical experiment data of granite, this paper analyzes the damage effect of fissures on the mechanical properties of granite and chemical solutions on the physical and mechanical property of fissured granite. It is found that, during the immersed process, the pH value of the solution gradually becomes neutral and maintains at 4.1, and the mass loss gradually increases, and the pH value and rate of mass loss greatly change in the early immersed stage; the main mineral content of the fissured surface significantly changes. After the chemical corrosion, the surface of the fissure becomes loose and secondary micropore increases. As the time of chemical corrosion increases, the peak strength of fissured granite with $\alpha = 0^\circ$, 30°, and 45° has decreased in varying degrees (from 140.88, 100.73, and 76.75 to 112.50, 85.34, and 67.19 MPa, respectively). Simultaneously, the modulus of fissured granites with $\alpha = 0^\circ$, 30°, and 45° also shows similar variation trends (from 39.26, 31.73, and 29.33 to 33.17, 26.96, and 21.91 GPa, respectively). Furthermore, the chemical corrosion shortens the compaction stage of the fissured granite, reduces the elastic stage of the fissured granite, and accelerates the failure of fissured granite. The stress intensity factors of the specimens with $\alpha = 0^\circ$, 30°, and 45° decrease from 0.017, 0.35, and 0.84 to 0.013, 0.30, and 0.74 MPa·m$^{1/2}$, respectively, as the time of the chemical corrosion increases, and the chemical corrosion has the largest effect on the intensity factors of the specimens with $\alpha = 45^\circ$ among the three kinds of specimens.

Data Availability

All the data used to support the findings of this study are included within the article.

Conflicts of Interest

The authors have declared that we have no financial and personal relationships with other people or organizations that can inappropriately influence our work.

Acknowledgments

This work was jointly supported by the National Key Research and Development Program of China (Nos. 2018YFC0809600 and 2018YFC0809601), the Natural Science Foundation of China (grant numbers 51979100 and 51779252), and the Major Technological Innovation Projects of Hubei (No. 2017AAA128).

References

[1] Y. Ichikawa, K. Kawamura, K. Uesugi, Y. S. Seo, and N. Fujii, "Micro- and macrobehavior of granitic rock: observations and viscoelastic homogenization analysis," *Computer methods in applied mechanics and engineering*, vol. 191, no. 1-2, pp. 47–72, 2001.

[2] M. Prudencio and M. van Sint Jan, "Strength and failure modes of rock mass models with non-persistent joints," *International Journal of Rock Mechanics and Mining Sciences*, vol. 44, no. 6, pp. 890–902, 2007.

[3] S. Q. Yang, X. R. Liu, and H. W. Jing, "Experimental investigation on fracture coalescence behavior of red sandstone containing two unparallel fissures under uniaxial compression," *International Journal of Rock Mechanics and Mining Sciences*, vol. 63, pp. 82–92, 2013.

[4] S. Q. Yang, Y. H. Huang, and P. G. Ranjith, "Failure mechanical and acoustic behavior of brine saturated-sandstone containing two pre-existing flaws under different confining pressures," *Engineering Fracture Mechanics*, vol. 193, pp. 108–121, 2018.

[5] L. N. Germanovich, R. L. Salganik, A. V. Dyskin, and K. K. Lee, "Mechanisms of brittle fracture of rock with pre-existing cracks in compression," *Pure and Applied Geophysics*, vol. 143, no. 1-3, pp. 117–149, 1994.

[6] A. Bobet, "The initiation of secondary cracks in compression," *Engineering Fracture Mechanics*, vol. 66, no. 2, pp. 187–219, 2000.

[7] W. Han, Y. Jiang, H. Luan, Y. du, Y. Zhu, and J. Liu, "Numerical investigation on the shear behavior of rock-like materials containing fissure-holes with FEM-CZM method," *Computers and Geotechnics*, vol. 125, article 103670, 2020.

[8] R. H. C. Wong, C. M. Law, K. T. Chau, and W. S. Zhu, "Crack propagation from 3-D surface fractures in PMMA and marble specimens under uniaxial compression," *International Journal of Rock Mechanics and Mining Sciences*, vol. 41, no. 3, pp. 37–42, 2004.

[9] H. Lee and S. Jeon, "An experimental and numerical study of fracture coalescence in pre-cracked specimens under uniaxial compression," *International Journal of Solids and Structures*, vol. 48, no. 6, pp. 979–999, 2011.

[10] B. Vásárhelyi and A. Bobet, "Modeling of crack initiation, propagation and coalescence in uniaxial compression," *Rock Mechanics and Rock Engineering*, vol. 33, no. 2, pp. 119–139, 2000.

[11] R. H. C. Wong, K. T. Chau, C. A. Tang, and P. Lin, "Analysis of crack coalescence in rock-like materials containing three flaws– part I: experimental approach," *International Journal of Rock Mechanics and Mining Sciences*, vol. 38, no. 7, pp. 909–924, 2001.

[12] P. Yin, R. H. C. Wong, and K. T. Chau, "Coalescence of two parallel pre-existing surface cracks in granite," *International Journal of Rock Mechanics and Mining Sciences*, vol. 68, pp. 66–84, 2014.

[13] T. H. Wu, Y. T. Gao, Y. Zhou, and J. Li, "Experimental and numerical study on the interaction between holes and fissures in rock-like materials under uniaxial compression," *Theoretical and Applied Fracture Mechanics*, vol. 106, article 102488, 2020.

[14] W. Yao, Y. Cai, J. Yu, J. Zhou, S. Liu, and B. Tu, "Experimental and numerical study on mechanical and cracking behaviors of flawed granite under triaxial compression," *Measurement*, vol. 145, pp. 573–582, 2019.

[15] S. Mondal, L. Olsen-Kettle, and L. Gross, "Simulating damage evolution and fracture propagation in sandstone containing a preexisting 3-d surface flaw under uniaxial compression," *International Journal for Numerical and Analytical Methods in Geomechanics*, vol. 43, no. 7, pp. 1448–1466, 2019.

[16] M. Rezania, M. Panahandeh, S. M. J. Razavi, and F. Berto, "Experimental study of the simultaneous effect of nano-silica and nano-carbon black on permeability and mechanical properties of the concrete," *Theoretical and Applied Fracture Mechanics*, vol. 104, article 102391, 2019.

[17] S. Q. Yang, T. Xu, L. He, H. W. Jing, S. Wen, and Q. L. Yu, "Numerical study on failure behavior of brittle rock specimen containing pre- existing combined flaws under different confining pressure," *Archives of Civil and Mechanical Engineering*, vol. 15, no. 4, pp. 1085–1097, 2015.

[18] S. Xie and J. Shao, "Elastoplastic deformation of a porous rock and water interaction," *International Journal of Plasticity*, vol. 22, no. 12, pp. 2195–2225, 2006.

[19] B. K. Atkinson and P. G. Meredith, "Stress corrosion cracking of quartz: a note on the influence of chemical environment," *Tectonophysics*, vol. 77, no. 1-2, pp. T1–T11, 1981.

[20] J. Dunning, B. Douglas, M. Miller, and S. McDonald, "The role of the chemical environment in frictional deformation: stress corrosion cracking and comminution," *Pure and Applied Geophysics*, vol. 143, no. 1-3, pp. 151–178, 1994.

[21] M. G. Karfakis and M. Akram, "Effects of chemical solutions on rock fracturing," *International journal of rock mechanics and mining sciences & geomechanics abstracts*, vol. 30, no. 7, pp. 1253–1259, 1993.

[22] J. Sausse, E. Jacquot, B. Fritz, J. Leroy, and M. Lespinasse, "Evolution of crack permeability during fluid-rock interaction. Example of the Brezouard granite (Vosges, France)," *Tectonophysics*, vol. 336, no. 1-4, pp. 199–214, 2001.

[23] K. B. Min, J. Rutqvist, and D. Elsworth, "Chemically and mechanically mediated influences on the transport and mechanical characteristics of rock fractures," *International Journal of Rock Mechanics and Mining Sciences*, vol. 46, no. 1, pp. 80–89, 2009.

[24] D. Croizé, K. Bjørlykke, J. Jahren, and F. Renard, "Experimental mechanical and chemical compaction of carbonate sand," *Journal of Geophysical Research: Solid Earth*, vol. 115, no. B11, 2010.

[25] L. Yu, Z. Zhang, J. Wu, R. Liu, H. Qin, and P. Fan, "Experimental study on the dynamic fracture mechanical properties of

limestone after chemical corrosion," *Theoretical and Applied Fracture Mechanics*, vol. 108, article 102620, 2020.

[26] A. Ghazvinian, V. Sarfarazi, W. Schubert, and M. Blumel, "A study of the failure mechanism of planar non-persistent open joints using PFC2D," *Rock Mechanics and Rock Engineering*, vol. 45, no. 5, pp. 677–693, 2012.

[27] S. Portier and F. D. Vuataz, "Developpement des capacites de modelisation des interactions acides-roche et des dissolutions de mineraux au cours des tests de stimulation acide de type RMA realises sur le site SGS de Soultz-sous-Forets (France)," *Comptes Rendus Geoscience*, vol. 342, no. 7-8, pp. 668–675, 2010.

[28] D. O. Potyondy, "Simulating stress corrosion with a bonded-particle model for rock," *International Journal of Rock Mechanics and Mining Sciences*, vol. 44, no. 5, pp. 677–691, 2007.

[29] S. G. Li, R. K. Huo, B. Wang et al., "Experimental study on physicomechanical properties of sandstone under acidic environment," *Advances in Civil Engineering*, vol. 2018, Article ID 5784831, 15 pages, 2018.

[30] E. Mohtarami, A. Baghbanan, M. Eftekhari, and H. Hashemolhosseini, "Investigating of chemical effects on rock fracturing using extended finite element method," *Theoretical and Applied Fracture Mechanics*, vol. 89, pp. 110–126, 2017.

[31] S. H. Hoseinie, M. Ataei, and R. Mikaiel, "Comparison of some rock hardness scales applied in drillability studies," *Arabian Journal for Science and Engineering*, vol. 37, no. 5, pp. 1451–1458, 2012.

[32] G. Aydin, I. Karakurt, and K. Aydiner, "An investigation on surface roughness of granite machined by abrasive waterjet," *Bulletin of materials science*, vol. 34, no. 4, pp. 985–992, 2011.

[33] V. Sunitha, B. M. Reddy, J. A. Khan, and M. R. Reddy, "Groundwater geochemistry in the southeastern part of Anantapur District, Andhra Pradesh, with special reference to fluoride distribution and its impact on health," *Journal of Environmental Science & Engineering*, vol. 56, no. 2, pp. 153–160, 2014.

[34] F. Zhang, J. Zhao, D. Hu, F. Skoczylas, and J. Shao, "Laboratory investigation on physical and mechanical properties of granite after heating and water-cooling treatment," *Rock Mechanics and Rock Engineering*, vol. 51, no. 3, article 1350, pp. 677–694, 2018.

[35] H. Li, I. I. Eshiet, Y. Sheng, Z. Zhong, X. Liu, and D. Yang, "A parallel-bonded chemical corrosion model for discrete element modelling of chemically corroded limestone," *Engineering Fracture Mechanics*, vol. 202, pp. 297–310, 2018.

[36] S. Miao, M. Cai, Q. Guo, P. Wang, and M. Liang, "Damage effects and mechanisms in granite treated with acidic chemical solutions," *International Journal of Rock Mechanics and Mining Sciences*, vol. 88, pp. 77–86, 2016.

[37] F. Zhang, J. Zhao, D. Hu, Q. Sheng, and J. Shao, "Creep strain and permeability evolution in cracked granite subjected to triaxial stress and reactive flow," *Geofluids*, vol. 2018, Article ID 4653937, 10 pages, 2018.

[38] R. H. Lander and L. M. Bonnell, "A model for fibrous illite nucleation and growth in sandstones," *AAPG bulletin*, vol. 94, no. 8, pp. 1161–1187, 2010.

[39] R. H. Worden and S. Morad, "Clay minerals in sandstones: controls on formation, distribution and evolution," *International Association of Sedimentologists. Special Publication*, vol. 34, pp. 3–42, 1999.

[40] Y. Ju, K. Luxbacher, X. Li et al., "Micro-structural evolution and their effects on physical properties in different types of tectonically deformed coals," *International Journal of Coal Science & Technology*, vol. 1, no. 3, pp. 364–375, 2014.

[41] S. J. Miao, X. P. Lai, X. G. Zhao, and F. H. Ren, "Simulation experiment of AE-based localization damage and deformation characteristic on covering rock in mined-out area," *International Journal of Minerals, Metallurgy and Materials*, vol. 16, no. 3, pp. 255–260, 2009.

[42] A. Bobet and H. H. Einstein, "Fracture coalescence in rock-type materials under uniaxial and biaxial compression," *International Journal of Rock Mechanics and Mining Sciences*, vol. 35, no. 7, pp. 863–888, 1998.

[43] W. F. Brace and E. G. Bombolakis, "A note on brittle crack growth in compression," *Journal of Geophysical Research*, vol. 68, no. 12, pp. 3709–3713, 1963.

[44] J. M. Kemeny, "A model for non-linear rock deformation under compression due to sub-critical crack growth," *International journal of rock mechanics and mining sciences & geomechanics abstracts*, vol. 28, no. 6, pp. 459–467, 1991.

[45] A. E. Blum and A. C. Lasaga, "The role of surface speciation in the dissolution of albite," *Geochimica et Cosmochimica Acta*, vol. 55, no. 8, pp. 2193–2201, 1991.

[46] Y. Cai, J. Yu, G. F. Fu, and H. Li, "Experimental investigation on the relevance of mechanical properties and porosity of sandstone after hydrochemical erosion," *Journal of Mountain Science*, vol. 13, no. 11, pp. 2053–2068, 2016.

[47] S. Q. Yang, "Crack coalescence behavior of brittle sandstone samples containing two coplanar fissures in the process of deformation failure," *Engineering Fracture Mechanics*, vol. 78, no. 17, pp. 3059–3081, 2011.

[48] C. H. Park and A. Bobet, "Crack initiation, propagation and coalescence from frictional flaws in uniaxial compression," *Engineering Fracture Mechanics*, vol. 77, no. 14, pp. 2727–2748, 2010.

Hindawi
Geofluids
Volume 2021, Article ID 6655823, 13 pages
https://doi.org/10.1155/2021/6655823

Research Article

An Influence Study of Face Length Effect on Floor Stability under Water-Rock Coupling Action

Baojie Fu [1,2] and Bo Wang [3,4]

[1] *School of Mining and Safety Engineering, Anhui University of Science and Technology, Road Taifeng No. 168, Huainan, Anhui 232001, China*
[2] *Key Laboratory of Coal Mine Safety and Efficiently Caving of Ministry of Education, Anhui University of Science and Technology, Huainan, Anhui 232001, China*
[3] *CCTEG Chongqing Research Institute, Chongqing 400037, China*
[4] *School of Mechanics and Civil Engineering, China University of Mining and Technology, Xuzhou, Jiangsu 221116, China*

Correspondence should be addressed to Baojie Fu; bjfu@aust.edu.cn

Received 25 November 2020; Revised 21 January 2021; Accepted 22 February 2021; Published 10 March 2021

Academic Editor: Chuangzhou Wu

The Taiyuan Formation limestone aquifer and Ordovician limestone aquifer are widely distributed in the coal seam floor of coal measures in North China; the water hazard safety problem of the stope floor under the influence of mining is very prominent. The risk of the water inrush from the coal seam floor is closely related to the degree of full exploitation, so it is necessary to study the stability of the stope floor under aquifer conditions, especially the influence of the working face length effect on floor stability. Through numerical simulation of water-rock coupling action, the mine pressure behaviors of the water-resisting floor under different face lengths were analyzed based on the measured formation permeability coefficient. The Fish program was used to adjust rocks entering the plastic failure state into a strain softening model to investigate the influence of the face length effect, the damage degree of the water-resisting floor, and the morphology and deformation bearing capacity of the failure zone. The results show the following: (1) the face length effect is one of the main influence factors of the failure mode and failure degree of surrounding rocks in the stope; (2) as the face length increases, the obvious pressure relief zone of surrounding rocks presents a staged change, and the obvious pressure relief zone at the seam roof and floor is in an obvious "reverse saddle shape"; (3) the closer to the seam floor, the more remarkable the rock softening characteristic because of the compaction action of gangues caving from the roof; and (4) the rock mass close to the seam floor undergoes local tensile failure, and the water-resisting floor near the coal wall at two sides mainly bears compaction-shear action, leading to compression-shear failure of the rock mass at the floor and formation of water-conducting fractures. The study results can provide a reference for taking precautionary measures of safety mining above a confined aquifer.

1. Introduction

The Taiyuan Formation limestone aquifer and Ordovician limestone aquifer are widely distributed in the coal seam floor of coal measures in North China. However, due to the relatively poor mechanical strength of the aquifer medium, and the large scale of the underground mining stope space, the water hazard safety problem of the stope floor under the influence of mining is very prominent. The risk of the water inrush from the coal seam floor is closely related to the degree of full exploitation. Mining activities destroy the balance of the original ground stress. Then, the surrounding rock stress in the stope will then undergo redistribution, leading to interactions between permeability characteristics of the rock mass medium and stress state, thereby forming water-rock coupling action [1]. The surrounding rocks in the stope will experience deformation and failure under the action of a new stress field. The rock masses will suffer from fracturing expansion, shear deformation, and displacement because of fracturing, extruding, and softening and corroding actions of confined water. Consequently, the porosity and connectivity of structural planes in the rock mass will be enhanced to strengthen the permeability of rock masses and groundwater inrush pathways can be easily formed [2].

Various factors influence the floor stability in a stope. Many Chinese and foreign scholars have conducted investigation work on influence factors such as floor lithology, water-resisting floor thickness, water pressure, face length, structure, and coal seam occurrence state, analyzing the load-carrying characteristics and deformation failure laws of the stope floor with one factor of combining multiple factors and obtaining important research results [3–8]. Wang et al. [9] used the discrete element fluid-structure interaction (FSI) simulation method to perform simulation analysis of the evolution laws of floor stress and seepage during the coal mining process above a confined aquifer. Zheng et al. [10] established a jointed rock mass seepage-damage coupling model and applied it to the prediction of water inrush disasters in mines. The studies carried out by other scholars [11–16] have deepened the understanding of the breeding and evolution process of the water inrush from the seam floor and provided a certain scientific basis for the prevention and treatment engineering practice of the water inrush from the seam floor. Most existing research is conducted on the theoretical basis of the traditional elastic-plastic mechanics or phenomenological damage mechanics, resulting in imperfect simulation of rock mesostructural damage and permeability evolution arising out of this. Thus, in-depth studies need to be implemented on damage, rupture, permeability change, and formation of the water inrush pathway of rock masses at the seam floor under different mining conditions.

The increasing working face length will undoubtedly enlarge the scope of mining influence and intensity of mine pressure behaviors, deepen the damage scope of the floor, and effectively reduce the thickness of water-resisting strata. Therefore, the working face length is one of the key factors influencing the failure depth of the stope floor. However, when geological conditions are unchanged, the mine pressure behaviors under different face lengths and the influence mechanism on the floor stability remain to be further discussed. Thus, a strain softening model was introduced into the floor failure zone based on hydrogeological conditions in Group A coal mining of the Panxie Coal Mine of the Huainan Mining Group to investigate the influence mechanism of face length effect on floor stability.

2. Stress-Bearing Zoning and Failure Mechanism of the Floor

The coal seam and surrounding rock are in a stress balance state under the primary rock stress state, while the excavation of the coal seam or rock strata will damage the stress balance state and cause the redistribution of surrounding rock stress, finally leading to deformation and failure [17]. Affected by the forward supporting pressure, the coal seam and floor within a certain distance from the front of the working face are located in a pressurization zone, so the seam floor at this location is compressed. This zone is called the compression zone (Zone B in Figure 1). As the working face continues to advance, the area from the working face to the rear goaf is in a pressure relief zone. The floor rocks of this part are converted from a compression state into an expansion state. The floor heave will be generated on the working face, and cracks of rock bedding stratification will appear. This zone is called the expansion and pressure relief zone (Zone D in Figure 1). Between Zones B and D, the rock strata within this scope are gradually transited from a compression state into a pressure relief state. The deformation state is also transited from compression into expansion. This area is called a transition zone (Zone C in Figure 1). After the working face is advanced again, the rock masses caving in the goaf are compacted by the overlying strata, and this part of the floor is located within the new pressurization zone again due to the overburden pressure. Then, it is converted from an expansion state into a compaction state again (Zone E in Figure 1).

Each point at the floor rock strata will undergo the process of "compaction-stress relief-recompression" with the advancement of the working face [18]. The crack ratio in the floor rock strata is changed due to the action of these stresses. Three crack types, namely, vertical tension, bedding, and shear, arise. Accordingly, this part of floor strata loses its water-resisting ability, and the floor failure depth refers to the depth of rock strata, causing the failure of the seam floor with a certain depth and water-conducting ability due to the combined action of factors such as mine pressure during the mining process of the working face.

3. Permeability Test of Floor Strata

3.1. Site Conditions. The A1 and A3 seams are mainly mined in Group A of the Panxie Mining Area of the Huainan Mining Group, and the average dip angle is 10°; the coal thickness at the A1 seam is within 1.56~7.77 m (average value: 2.8 m); the coal thickness at the A3 seam is 2.09–9.17 m (average value: 5.8 m). The spacing between the two coal seams is 1~5 m, and they are combined into one seam at the local part. Strong Taiyuan Formation limestone and Ordovician limestone aquifers occur at the seam floor, where the Taiyuan Formation limestone aquifer C_3^3 at 28.1 m away from the A3 seam floor is a strong aquifer, resulting in potential water-induced damage to coal mining of Group A. The thickness and water pressure of the C_3^3 aquifer are 7.8 m and 4.5 MPa, respectively. The positional relationship of the working face and lithological histogram is shown in Figure 2.

3.2. Permeability Test. The test rock specimens, namely, sandstone, mudstone, sandy mudstone, and limestone at the floor of Coal Group A1, were collected from the field. Each rock was processed into five blocks, and standard specimen dimensions were obtained: height $H = 100$ mm and sectional diameter $d = 50$ mm. The instantaneous permeability test of the rock specimens was conducted on an MTS816 electrohydraulic servo rock mechanics experimental system. The test principles are shown in Figures 3 and 4.

The volumes of both pressure stabilizers in the pore pressure system are B; their pressures are p_1 and p_2, respectively;

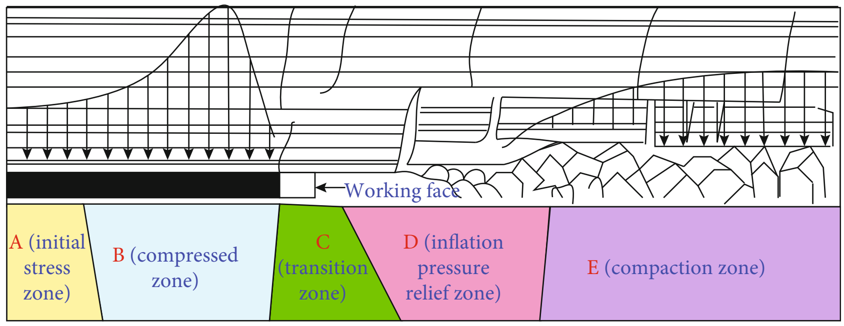

Figure 1: Simulated diagram of the coal seam floor failure.

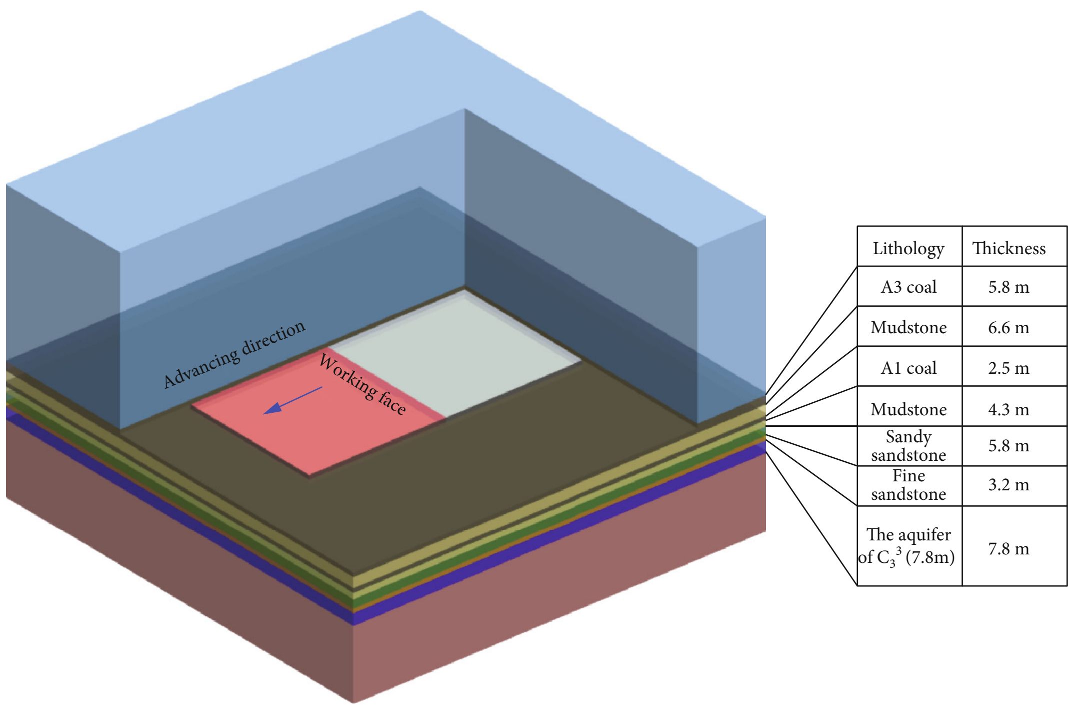

Figure 2: Working face arrangement and lithologic column.

and the height and cross-sectional area of each rock specimen are H and A, respectively. As the pressures at two ends of each rock specimen are different at the initial time ($p_{10} > p_{20}$), the pressure gradient $\xi_0 = (p_{20} - p_{10})/H$ exists, and the liquid in water tank 1 enters water tank 2 through the rock specimen. Then, the pressure in water tank 1 is continuously lowered while that in water tank 2 is continuously elevated until the pressures in the two water tanks become equal and reach an equilibrium state. The mass flow of liquid entering the rock specimen from water tank 1 is set as q. If the pore water of the rock specimen is saturated, then the mass flow of liquid flowing into water tank 2 from the rock specimen is also q, and the seepage velocity in the rock specimen is $V = q/\rho A$. According to the fluid compressibility, the following can be obtained:

$$\frac{1}{c_f} = \rho \frac{dp_1}{d\rho}. \tag{1}$$

The relational expressions $d\rho = -q dt/B$ and $q = \rho A V$ indicate that

$$\frac{dp_1}{dt} = -\frac{AV}{c_f B}. \tag{2}$$

Similarly,

$$\frac{dp_2}{dt} = -\frac{AV}{c_f B}. \tag{3}$$

The following can be obtained through (2) and (3):

$$\frac{d(p_2 - p_1)}{dt} = 2\frac{AV}{c_f B}, \tag{4}$$

$$V = \frac{c_f B H}{2A} \frac{d\xi}{dt}, \tag{5}$$

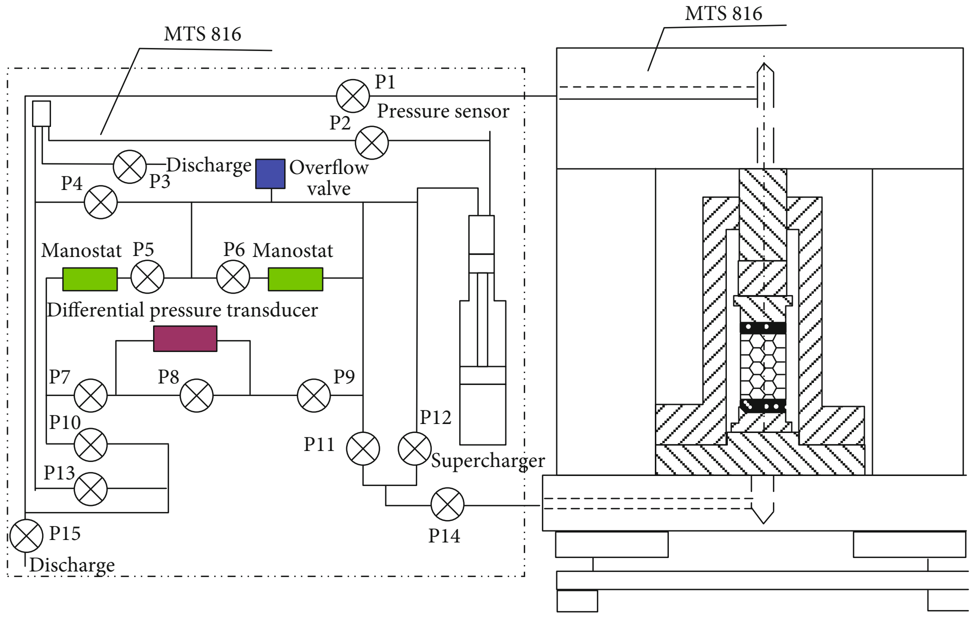

Figure 3: MTS816 rock mechanics permeability experimental system.

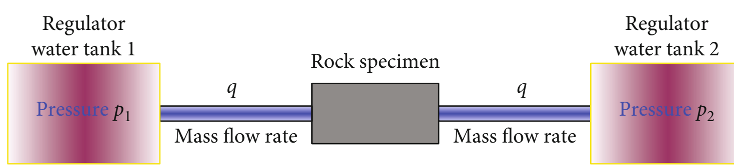

Figure 4: Mechanical model of the transient permeation experimental system.

where ξ is the pressure gradient of the rock specimen, namely, $\xi = (p_2 - p_1)/H$.

For Darcy's flow, the relationship between the seepage velocity and the pressure gradient follows Darcy's law, that is,

$$\xi = -\frac{\mu}{k_D} V, \tag{6}$$

where μ is the dynamic viscosity of seeping liquid and k_D is the permeability of Darcy's flow in the rock specimen.

Equation (5) is substituted into Equation (6) to obtain

$$\frac{d\xi}{dt} = -2\frac{Ak_D}{c_f BH\mu}\xi. \tag{7}$$

The sampling time interval and the total number of sampling times were set as τ and n, respectively, in the test. The pore pressure gradient is ξ_f at the sampling ending time $t_f = n\tau$. We use the integral of Equation (7) to obtain

$$\ln \frac{\xi_0}{\xi_f} = 2\frac{Ak_D t_f}{c_f BH\mu}. \tag{8}$$

In Equation (8), pressure gradients ξ and ξ_0 are negative, ξ_0/ξ is positive, so $\ln(\xi_0/\xi)$ is significant. The permeability and permeability coefficient of the rock specimen can be obtained through Equation (8):

$$k_D = \frac{c_f BH\mu}{2t_f A} \ln \frac{\xi_0}{\xi_f} = \frac{c_f BH\mu}{2t_f A} \ln \frac{p_{10} - p_{20}}{p_{1f} - p_{2f}}, \tag{9}$$

$$K = \frac{k_D \gamma}{\mu}, \tag{10}$$

where γ is the specific gravity of the liquid.

Equations (9) and (10) are formulas used to calculate the permeability K_D and permeability coefficient K in the stress-strain whole-process instantaneous permeability test of the rock specimens, which was performed on an MTS816 rock mechanics experimental system.

To guarantee the sealing property of the rock specimen, the stains on cylindrical surfaces of the rock specimen, pressure head, and porous disc were wiped away first. Then, these cylindrical surfaces were intertwined with a layer of plastic insulating tapes in a spiral form from bottom to top. A segment of the thermal-shrinking plastic jacket was cut off to cover rock specimens, porous discs, and upper and lower pressure heads. The plastic jacket was uniformly baked using an electric blower so that the plastic jacket fitted in well with the insulating tape. Information like experimental parameters, components, and number of rock specimens was recorded on the insulating tape. Finally, insulating tapes were

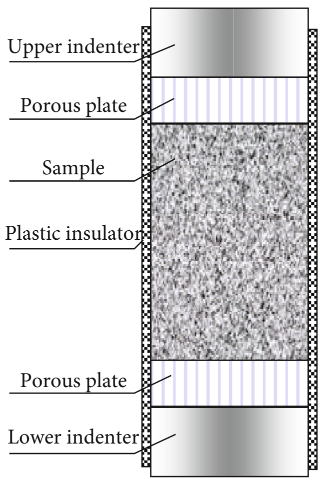

FIGURE 5: Sealing of rock sample.

used to twine the upper and lower parts of the plastic jacket. Rock specimens, pressure heads, and porous discs were encapsulated together using the plastic insulating tape and thermal-shrinking plastic jacket. Sealing of the rock sample is shown in Figure 5.

3.3. Analysis of Test Results. In the test, the confining pressure p_c was set as 4 MPa. The seeping liquid was water, where its mass density ρ, dynamic viscosity μ, and compression coefficient c_f were $1{,}000\,\mathrm{kg/m^3}$, $1.01 \times 10^{-3}\,\mathrm{Pa \cdot s}$, and $0.472 \times 10^{-9}\,\mathrm{Pa^{-1}}$, respectively. The volume of pressure stabilizer B was $0.32 \times 10^{-3}\,\mathrm{m^3}$. According to the time series of the pore pressure difference acquired in the test, the permeability coefficient K of Darcy's flow is calculated according to Equation (10).

3.3.1. Whole Stress-Strain Permeability Characteristics of Sandstone. Figure 6 provides the strain ε-dependent change laws of the sandstone permeability coefficient K. The data analysis indicates the following. (1) In the elastic deformation phase, a small number of microcracks in the sandstone specimen start presenting tensile deformation as the strain increases. Moreover, the porosity is elevated, the permeability coefficient K is gradually enlarged, but the increased rate of K is low in this phase. (2) After the strain satisfies $\varepsilon > 0.0106$, the permeability coefficient K abruptly increases and reaches the maximum value: $K_{max} = 278.02 \times 10^{-11}\,\mathrm{m \cdot s^{-1}}$. The increased amplitude reaches 4~20 times that in the elastic deformation phase. In reality, the cracks in the specimen are expanded, fused together, and run through each other. An evident damaged macrostructural plane is already formed. When the strain satisfies $\varepsilon > 0.0118$, the permeability coefficient K declines rapidly, and the decreased amplitude is approximately 50%. (3) Under $\varepsilon > 0.0133$, the permeability coefficient K is decreased slowly and stabilized at $K_{max} = 124.83 \times 10^{-11}\,\mathrm{m \cdot s^{-1}}$, approximately. In this phase, some large cracks and the space of the damaged structural plane are filled by small crushed particles as the failure degree is aggravated. Consequently, the porosity and the permeability

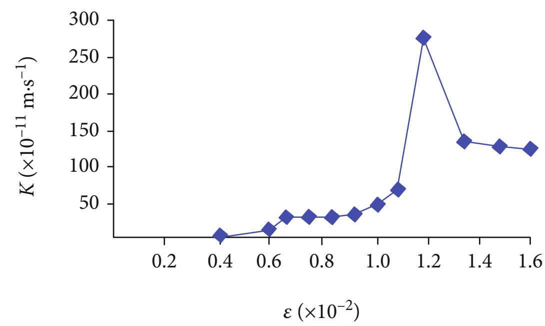

FIGURE 6: Variation curve of the permeability coefficient K with strain ε.

coefficient K decline. The confining pressure p_c also exerts a limiting effect on crack expansion.

3.3.2. Mudstone Whole Stress-Strain Permeability Characteristics. Figure 7 shows the change laws of the mudstone permeability coefficient K with strain ε. The data analysis indicates the following. (1) Relative to sandstone and limestone, the permeability coefficient K of mudstone is small, meaning that mudstone has better water-resisting performance than sandstone and limestone. (2) Similar to sandstone and limestone, the permeability coefficient K of the mudstone specimen increases slowly in the elastic deformation phase with the increase of strain. It increases rapidly when approaching the peak deformation point and tends to be a steady value in the residual deformation phase. (3) During the entire stress-strain permeability test process, the change amplitude of the permeability coefficient K of the mudstone specimen is not large, only being $K = 0.24 \times 10^{-13}\,\mathrm{m \cdot s^{-1}} \sim 68.79 \times 10^{-13}\,\mathrm{m \cdot s^{-1}}$. The permeability coefficient K in the residual deformation phase is stabilized at approximately $31.28 \times 10^{-13}\,\mathrm{m \cdot s^{-1}}$. (4) The strain of the mudstone specimen is larger than those of sandstone and limestone when the maximum permeability coefficient K_{max} is reached. K_{max} is reduced by three orders of magnitude than those of sandstone and limestone.

3.3.3. Whole Stress-Strain Permeability Characteristics of Sandy Mudstone. The change laws of the permeability coefficient K of sandy mudstone with strain ε are presented in Figure 8. The curve analysis shows the following. (1) For the sandy mudstone specimen, the change law of its permeability coefficient K is similar to that of mudstone on the whole as the strain ε increases. (2) The permeability coefficient K of the sandy mudstone specimen is slightly larger. During the entire stress-strain permeability test, the change amplitude of its permeability coefficient K is not large, only being $K = 2.84 \times 10^{-12}\,\mathrm{m \cdot s^{-1}} \sim 61.37 \times 10^{-12}\,\mathrm{m \cdot s^{-1}}$. (3) The strain ε of the sandy mudstone specimen is approximate to that of mudstone when the maximum permeability coefficient K_{max} is reached, indicating approximate plasticity of sandy mudstone and mudstone.

3.3.4. Limestone Whole Stress-Strain Permeability Characteristics. Figure 9 shows the change laws of the

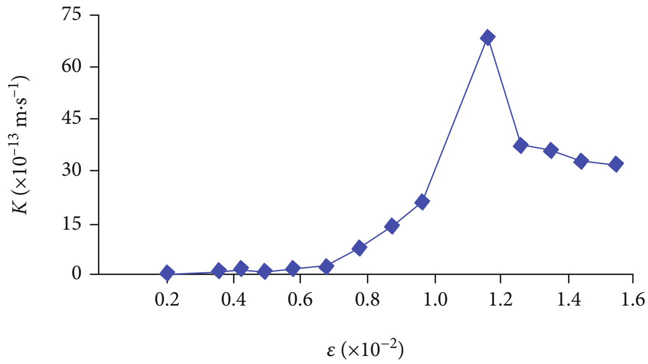

FIGURE 7: Variation curve of the permeability coefficient K with strain ε.

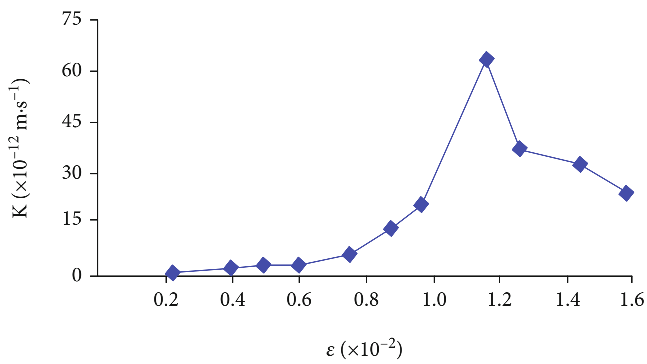

FIGURE 8: Variation curve of the permeability coefficient K with strain ε.

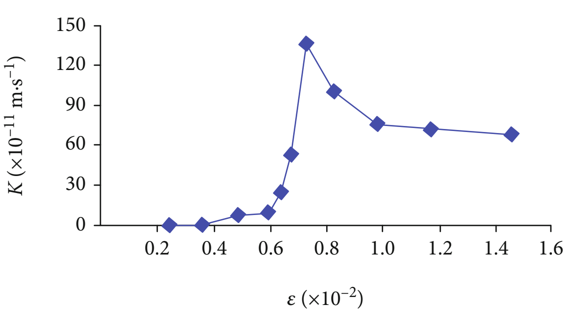

FIGURE 9: Variation curve of the permeability coefficient K with strain ε.

permeability coefficient K of limestone with strain ε. The curve analysis indicates the following. (1) The permeability coefficient K of the limestone specimen is reduced by 50% in comparison with that of sandstone, manifesting better compactness of limestone than sandstone. (2) The permeability coefficient K of the limestone specimen is slightly increased in the elastic deformation phase as the strain ε increases, indicating few effective pores in the rock specimen. Only a small number of microfractures are under tensile deformation. (3) When the strain satisfies $\varepsilon > 0.0063$, the permeability coefficient K is increased rapidly and reaches the maximum value $K_{max} = 134.82 \times 10^{-11} \mathrm{m \cdot s^{-1}}$. At this time, macrocracks exist in the rock specimen. (4) Similar to sandstone, the permeability coefficient K of the limestone specimen is in a rapid decline process under the condition of $\varepsilon > 0.0084$, but it is finally stabilized at approximately $K_{max} = 66.89 \times 10^{-11} \mathrm{m \cdot s^{-1}}$.

4. Numerical Analysis of Face Length Effect under Water-Rock Coupling Action

4.1. Mechanical Model of the Floor Failure Zone. During the FLAC3D numerical calculation process, the stress-strain curve is linear before the element reaches a yield point, and only elastic strain ε^{e} is generated in this phase, namely,

$$\varepsilon = \varepsilon^{e}, \tag{11}$$

where ε is the total element strain.

After the element yields, the total strain consists of elastic strain ε^{e} and plastic strain ε^{p}, namely,

$$\varepsilon = \varepsilon^{e} + \varepsilon^{p}. \tag{12}$$

The subsequent yield surface of the rock is related not only to the instantaneous stress state but also to the plastic deformation history. If the rock is regarded as the isotropic material and equivalent plastic shear strain ε^{ps} as the parameter recording the plastic loading history of rock material, then the postpeak subsequent yield surface [19] can be expressed as

$$\phi(\sigma_1, \sigma_2, \sigma_3, \varepsilon^{ps}) = 0, \tag{13}$$

Table 1: Physicomechanical parameters of rock layers.

Lithology	Density (kg/m^3)	Elastic modulus (GPa)	Poisson's ratio	Cohesion (MPa)	Friction angle (°)	Tensile strength (MPa)
Sandy mudstone	2,467	1.6	0.36	1.8	30	0.8
Siltstone	2,531	3.2	0.32	2.3	31	1.0
Grit	2,602	8.3	0.21	5.3	35	2.1
Coal	1,320	1.0	0.39	1.2	26	0.4
Mudstone	2,368	1.3	0.35	1.6	31	0.7
Fine sandstone	2,545	7.2	0.24	4.2	32	2.2
Limestone	2,680	6.4	0.26	4.4	33	2.1

where σ_1, σ_2, and σ_3 are the principal stresses in three directions.

When the rock is under a peak state, it satisfies the Mohr–Coulomb criterion. When it is under the postpeak state, the characteristic parameters (namely, cohesion and internal friction angle) used to describe this state will be changed. Therefore, two parameters, which can reflect the postpeak strain softening characteristics, that is, generalized cohesion $\bar{c}$ and generalized internal friction angle $\bar{\varphi}$, are introduced to describe the stress level on the Mohr–Coulomb yield surface. The subsequent yield criterion can be expressed by Equation (14), as follows:

$$f = \sigma_1 - \sigma_3 \frac{1+\sin\bar{\varphi}(\Delta\varepsilon^{\mathrm{ps}})}{1-\sin\bar{\varphi}(\Delta\varepsilon^{\mathrm{ps}})} + 2\bar{c}(\Delta\varepsilon^{\mathrm{ps}})\sqrt{\frac{1+\sin\bar{\varphi}(\Delta\varepsilon^{\mathrm{ps}})}{1-\sin\bar{\varphi}(\Delta\varepsilon^{\mathrm{ps}})}}, \tag{14}$$

$$\Delta\varepsilon^{\mathrm{ps}} = \left\{\frac{1}{2}\left(\Delta\varepsilon_1^{\mathrm{ps}} - \Delta\varepsilon_m^{\mathrm{ps}}\right)^2 + \frac{1}{2}\left(\Delta\varepsilon_m^{\mathrm{ps}}\right)^2 + \frac{1}{2}\left(\Delta\varepsilon_3^{\mathrm{ps}} - \Delta\varepsilon_m^{\mathrm{ps}}\right)^2\right\}^{1/2}, \tag{15}$$

where $\Delta\varepsilon_m^{\mathrm{ps}}$ is the main increment of plastic shear strain, $\Delta\varepsilon_m^{\mathrm{ps}} = (1/3)(\Delta\varepsilon_1^{\mathrm{ps}} + \Delta\varepsilon_3^{\mathrm{ps}})$, $m = 1, 2, 3$.

4.2. Water-Rock Coupling Model. When the FSI mechanism of the rock mass is simulated using FLAC3D, the rock mass is regarded as a porous medium, and the fluid flow in the porous medium conforms to Darcy's law and satisfies the Biot FSI equation as follows:

$$\begin{cases} G\,.\cdot^2 u_j - (\lambda + G)\dfrac{\partial\varepsilon_{\mathrm{v}}}{\partial x_j} - \dfrac{\partial p}{\partial x_j} + f_{xj} = 0, \\ K\,.\cdot^2 p = \dfrac{1}{S}\dfrac{\partial p}{\partial t} - \dfrac{\partial\varepsilon_{\mathrm{v}}}{\partial t}, \end{cases} \tag{16}$$

where λ and G are the lame constants; p is the pore water pressure; ε_{v} is the volume strain; x_j, u_j, and f_{xj}, $-j$ are the directional coordinates, displacement, and body force, respectively; $.\cdot$ is the Laplace operator; and S is the elastic storativity.

Equation (16) is an expression based on the Biot classical percolation theory, where $\partial p/\partial x_j$ reflects the influence of the seepage field on a solid skeleton, and its essence is that the pore pressure generated in the fluid flow influences the effective stress of a solid skeleton, influencing its deformation. $\partial\varepsilon_{\mathrm{v}}/\partial t$ expresses the influence of volume deformation of a solid skeleton on the seepage field. The classical Biot equation can characterize the interaction between pore pressure dissipation and deformation of the medium skeleton very well.

4.3. Establishment and Analysis of a Numerical Model. The A1 and A3 seams are mainly mined in Group A of the Panxie Mining Area of the Huainan Mining Group, and the average dip angle is 10°; the coal thickness at the A1 seam is 2.8 m; the coal thickness at the A3 seam is 5.8 m. The spacing between the two coal seams is 1~5 m; Strong Taiyuan Formation limestone and Ordovician limestone aquifers occur at the seam floor, where the Taiyuan Formation limestone aquifer $C_3^{\ 3}$ at 28.1 m away from the A3 seam floor is a strong aquifer, resulting in potential water-induced damage to coal mining of Group A. The thickness and water pressure of the $C_3^{\ 3}$ aquifer are 7.8 m and 4.5 MPa, respectively. The dimensions of the established model were 300 m (length) × 300 m (width) × 212 m (height). The model was divided into 210,112 elements. The Mohr–Coulomb yield criterion was used, and the attribute of strain softening was judged and assigned via Fish language after the floor rock reached yield failure. The model boundary conditions were as follows. Front, rear, left, and right boundaries were fixed in directions x and y, and the bottom was a full-constrained boundary, and the top boundary was set as stress constraint (the top boundary stress is 12 MPa, the buried depth is 520 m, and the average rock weight is 2500 kg/m^3). The boundary condition of seepage was as follows. A boundary with fixed water pressure was used at the bottom to simulate confined water of the limestone aquifer, and the others were water-resisting boundaries. The goaf was a water drainage boundary after mining of the working face. No water was present in the goaf. The fixed water pressure was 0 at the boundary, and physical and mechanical parameters of rock strata are seen in Table 1. The stress, displacement, and plastic zone distribution laws of the water-resisting floor during the A3 coal mining under face lengths of 120, 160, and 200 m were analyzed. The interface is set in the roof and floor of the coal seam to avoid model zone embedding; the mining simulation of the working face adopts the method of gradual excavation to simulate the mining process of the working face, and the excavation step is taken as the periodic mining press step.

4.4. Simulation Result

4.4.1. Maximum Principal Stress. After the coal mining, the rocks within a certain scope of the roof and floor will undergo

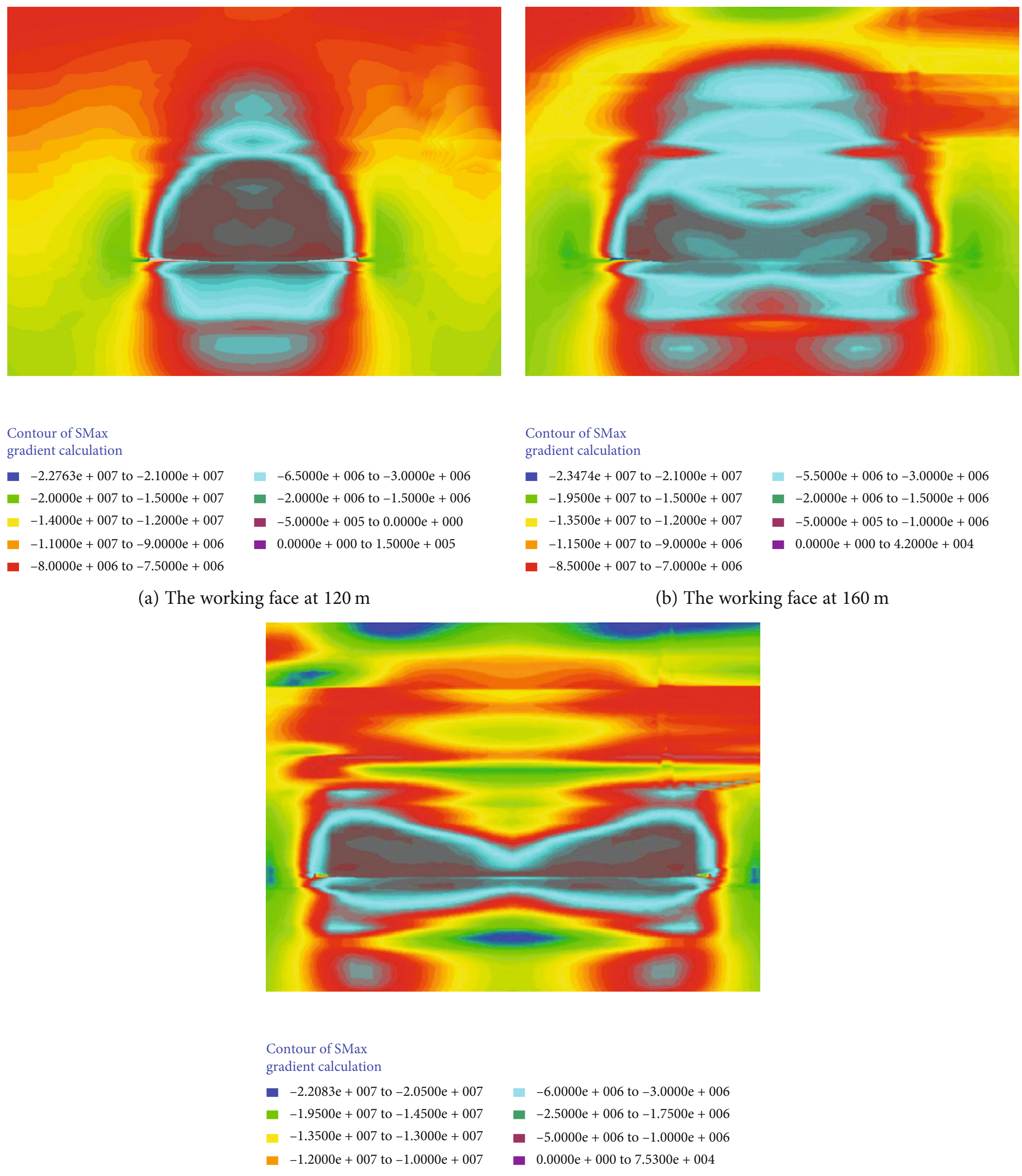

(a) The working face at 120 m

(b) The working face at 160 m

(c) The working face at 200 m

Figure 10: Stress distribution of rock.

pressure relief to different degrees. As the mining size is enlarged, the scope of influence of coal mining on surrounding rocks in the stope will also be enlarged, and the pressure relief degree and morphology of the pressure relief zone will present staged features.

As shown in Figure 10(a), the stope roof presents a "semicircular arch" pressure relief zone under a face length of 120 m, and the maximum principal stress in the zone is –2.0~0.12 MPa, where the roof strata near two ends of the stope are tensioned while other scopes are compressed. The pressure relief zone at the stope floor is divided into upper and lower parts by using the aquifer as the boundary, where the upper pressure relief zone is in a "basin shape." In particular, an obvious pressure relief zone appears within the 6–7 m scope near the stope floor. The maximum principal stress value is −2.0~0 MPa. This obvious pressure relief zone is under an obvious "reverse saddle shape."

Figure 10(b) shows that the pressure relief zone at the stope roof is "saddle-shaped" under a face length of 160 m and an advancement distance of 160 m. Under compaction of gangues caving from the coal seam roof, the pressure in a large scope at the middle of the stope is increased to

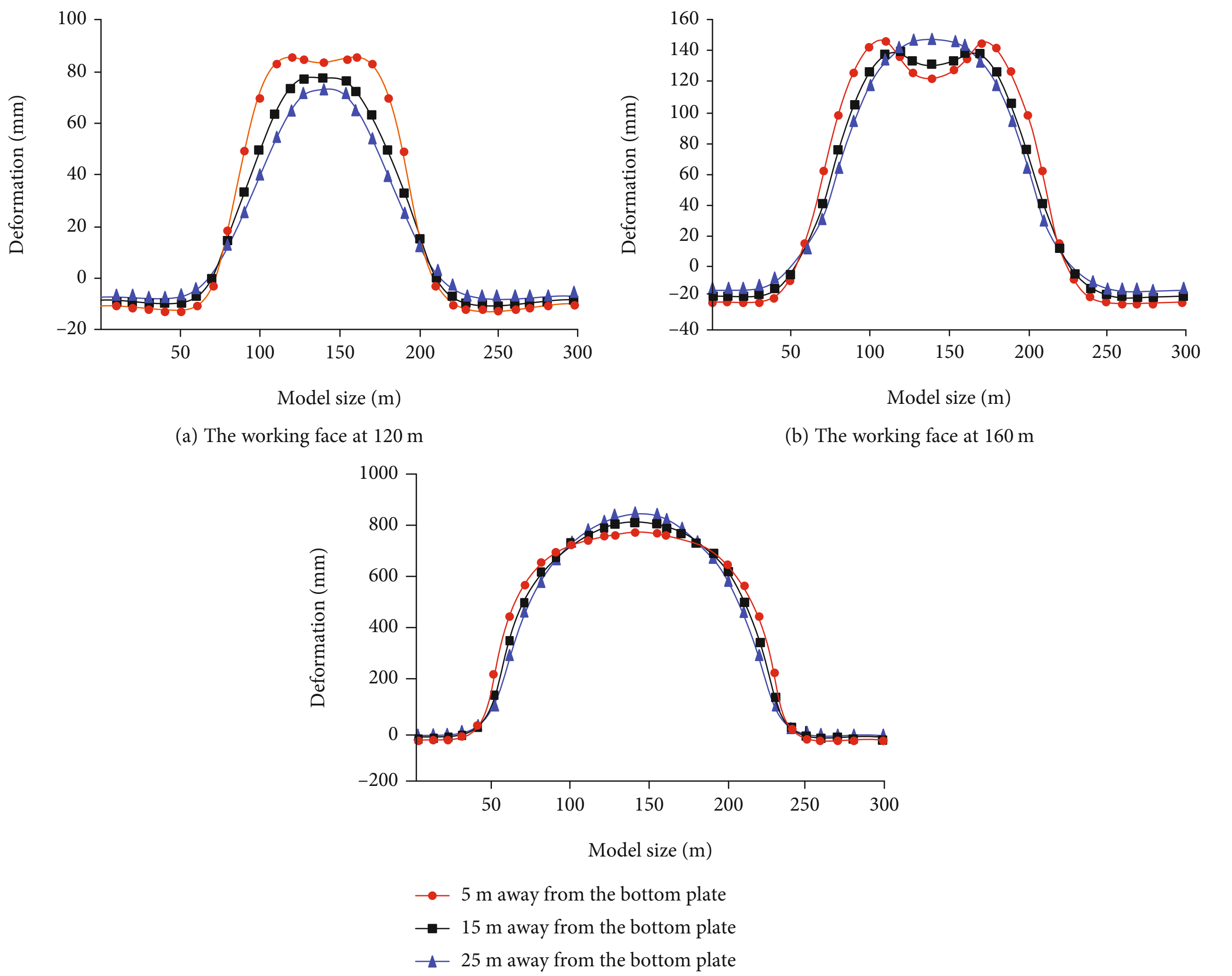

(a) The working face at 120 m

(b) The working face at 160 m

(c) The working face at 200 m

FIGURE 11: Floor movement and deformation curve.

−3.0~1.0 MPa, and obvious pressure relief takes place at the position 11.0–14.0 m away from the roof at two ends of the stope. The pressure value is within −1.0~0.04 MPa.

Corresponding to the stope roof, the pressure relief zone at the seam floor is in a "reverse saddle shape," where the stress close to the middle position of the stope is higher than those at two sides.

The situation under a face length of 200 m is shown in Figure 10(c). Under the actions of water pressure and mining stress, the relative movement deformation of rock strata at the roof and floor is enlarged, and a compaction zone is formed within a certain scope in the middle of the working face. Two stress arches are formed in the large pressure relief zone of the roof and floor of the stope, and the arch angles are located in the compaction zone between the floor and the goaf, presenting an even more obvious "saddle shape." The stress inside the obvious pressure relief zone at the floor ranges from −1.0 MPa to 0.07 MPa, being within the 14.0~18.0 m scope of the floor.

4.4.2. Floor Deformation. The influence scope of coal mining on the floor is enlarged with the increase of the face length, so the movement deformations at different rock strata in the floor are enlarged. Due to the water-rock coupling action, the displacement laws of upper and lower rock strata in the aquifer of the seam floor will be analyzed in the simulation, as shown in Figure 11.

After coal mining, the entity coal side is compressed, the deformation is turned into a negative value, the floor rock strata in the stope undergo pressure relief, and the floor heaves are formed, so the deformation value becomes positive. As the face length increases, the heave deformation is gradually enlarged. For example, at 5.0 m from the floor, the maximum heave deformations under face lengths of 120, 160, and 200 m are 83, 148, and 786 mm, respectively.

Based on the rock strain softening characteristics in the floor failure zone, the closer to the seam floor, the more obvious the rock softening characteristics due to the compaction of gangues caving from the roof. Under a face length of 120 m, as shown in Figure 11(a), the deformation curve at 5.0 m from the floor is slowed down somehow within a certain scope in the middle of the stope. The heave deformation is higher than the 15.0 m displacement curve of the floor by 13 mm, indicating that the failure depth is over 5.0 m. The failure depth at the

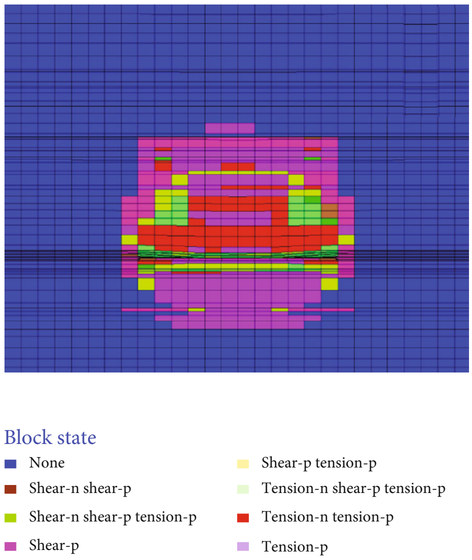

(a) The working face at 120 m

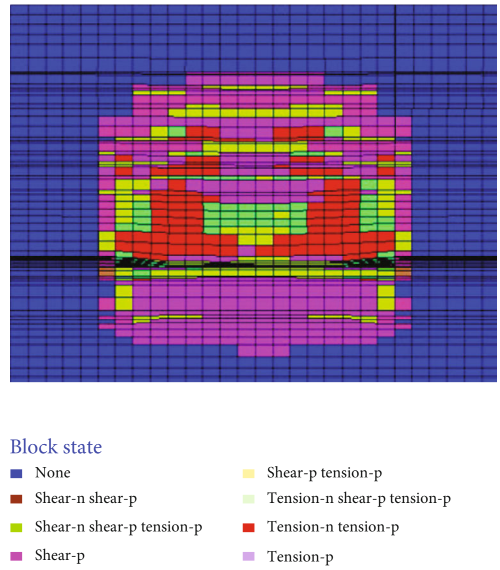

(b) The working face at 160 m

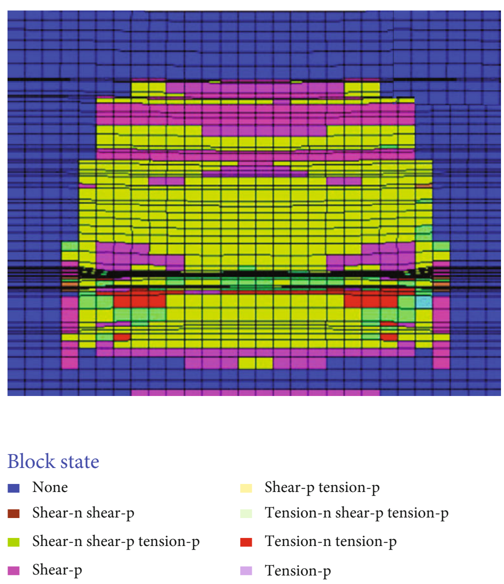

(c) The working face at 200 m

Figure 12: Plastic zone distribution.

floor is approximately 15.0 m under a face length of 160 m, as shown in Figure 11(b). At the time, the deformation curves at 5.0 and 15.0 m from the floor are slowed down within a certain scope at the middle of the stope, which are lower than the corresponding positions of the 25.0 m displacement curve by 21 and 12 mm, respectively. Therefore, the obvious failure depth of the floor is 15.0~25.0 m under a face length of 200 m, as shown in Figure 11(c).

Under the water-rock coupling action, the influence degree borne by the rock strata below the aquifer is relatively low, and the displacement quantity is within 20~–20 mm. Under a face length of 120 m, the deformation in the corresponding floor zone in the stope is turned positive. However, when the face length is 160–200 m, the deformation in the middle of this zone becomes negative while those at the two sides are positive. The deformation curve is under the wavy line shape.

The displacement and deformation curves of different strata of the roof under different face lengths indicate that the 30.0~45.0 m scope at two sides of the stope is a roof and floor unobvious contact zone. Other scopes constitute the zone of significant roof/floor interaction.

4.4.3. Distribution of the Plastic Zone. Following the coal mining, the load-bearing state of the water-resisting floor is turned from compression into tension. As the advancement distance of the working face is continuously increased, the tensile action borne by the rock mass close to the seam floor within a certain scope at the rear of the stope becomes

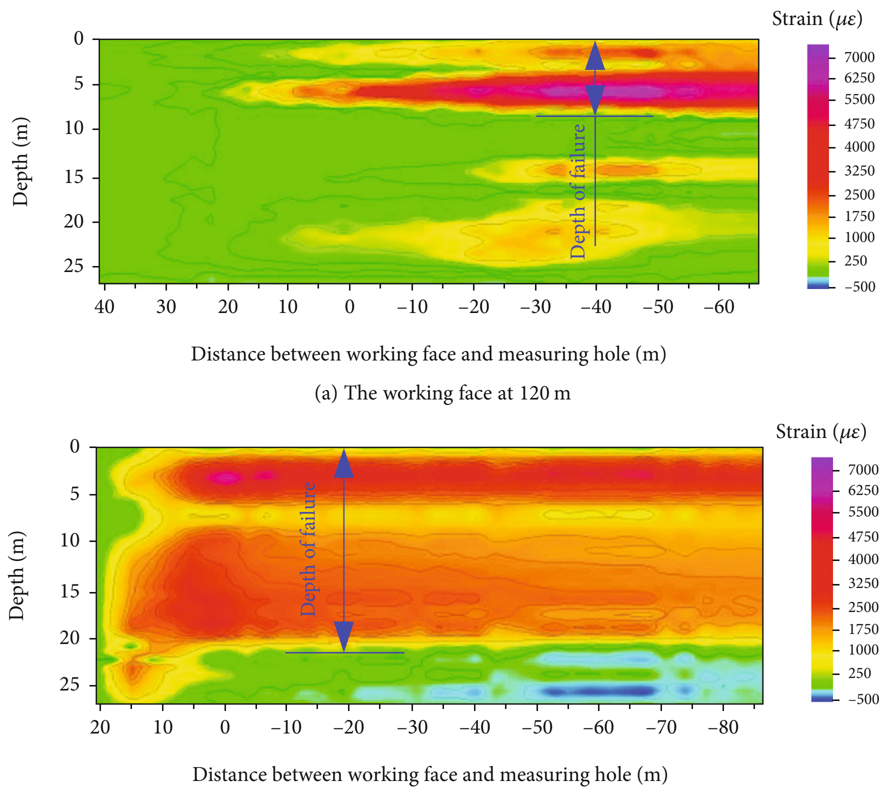

(a) The working face at 120 m

(b) The working face at 200 m

Figure 13: Depth of floor failure by the electrical method test.

increasingly obvious. Local tensile failure will occur when the tensile stress exceeds the tensile strength of the rock mass. The water-resisting layer of the seam floor near the coal wall at two sides of the stope mainly bears compression-shear action. The compressive stress is also elevated as the advancement distance increases. As a result, the compression-shear action strength is continuously reinforced, and the rock mass at the floor will undergo compression-shear failure when the strength of the rock mass is exceeded.

FLAC3D judges whether the element enters plastic deformation via the Mohr–Coulomb criterion, but the plastic failure of rock strata does not indicate the formation of water-conducting fractures. The strain softening characteristic was assigned to the plastic deformation element. Whether the element had water-conducting ability after secondary failure was judged through Equation (4). The simulation analysis manifests that under a face length of 120 m, water-conducting zones are formed at the 5.6 m tensile failure depth at the middle of the floor and 8.8 m compression-shear failure depth at two ends, as shown in Figure 12(a). When the face length is 160 m, the tensile failure depth at the middle of the stope does not obviously change. The compression-shear failure depth at two ends is elevated to 16.2 m, and the communication trend with the floor aquifer becomes evident, as shown in Figure 12(b). With the increase in the face length, the influence scope borne by the floor from coal mining is enlarged. Under the face length of 200 m, the tensile failure zone at the middle of the stope is extended downward, reaching 13.2 m, and the compression-shear depth at two ends becomes 22.3 m, as shown in Figure 12(c).

5. Engineering Verification

The 11123 working face of Panji Coal Mine 2 is the working face of the Group A coal mine in the Panxie Mining Area. Here, the ground elevation is +19.5~+22.5 m and the elevation of the working face is −429.9~−497.5 m. The average thickness of the A3 coal seam is 5.5 m with a dip angle of 10°. It is classified as a stable coal seam. Influenced by the sliding and fault between coal seams within the scope of the working face, the face length 500 m forward from the cutting hole is 120 m, and the rear face length is increased to 200 m. To analyze the scope of the floor failure depth under different face lengths, the optical fiber and electrical integrated test system was laid by drilling holes on the floor to conduct continuous monitoring. The physical properties and strain change characteristics of the floor during the rock stratum mining process were acquired, followed by the analysis of failure depth. As shown in Figure 13, the floor failure depth is approximately 8.2 m under the face length of 120 m and approximately 21.6 m under the face length of 200 m. The measurement result accords with the numerical analysis result.

6. Conclusion

(1) By analyzing the permeability characteristics of limestone, mudstone, sandy mudstone, and sandstone in

a coal mine, the numerical calculation model of floor stability under a confined aquifer is established. The strain softening characteristics are judged by using the Fish function, and then the mechanical behavior, bearing capacity, and deformation of floor rock are described, and the floor failure degree under different working face lengths is obtained; compared with the measured data, the feasibility of this method is verified

(2) The face length effect is one of the main influence factors of the failure mode and failure degree of surrounding rocks in the stope. As the face length increases, the obvious pressure relief zone of surrounding rocks presents a staged change. When the size of the working face is short, the stope roof presents a "semicircular arch" pressure relief zone, and the obvious pressure relief zone within a certain scope at the stope floor is in an unobvious "reverse saddle shape." When the size of the working face is long, the obvious pressure relief zone at the seam roof and floor is in an obvious "reverse saddle shape" due to the compaction action of gangues caving from the seam roof

(3) Based on the strain softening characteristic of rocks in the roof failure zone, the closer to the seam floor, the more remarkable the rock softening characteristic because of the compaction action of gangues caving from the roof. The floor deformation characteristic corresponds to the stress distribution in the floor pressure relief zone. The 30–45 m scope at two sides of the stope is a roof/floor unobvious contact zone, and other scopes constitute a zone with significant roof/floor interaction

(4) After the coal is mined, the rock mass close to the seam floor undergoes local tensile failure, and the water-resisting floor near the coal wall at two sides mainly bears compaction-shear action. The influence scope of mining is enlarged with the increase of the face length, leading to compression-shear failure of the rock mass at the floor and formation of water-conducting fractures

Data Availability

The others can access the data supporting the conclusions of the study from this research article. The nature of the data is the laboratory experimental data, the field observation data, and the theoretical calculation data. The laboratory experimental data used to support the findings of this study are included within the article; mainly, the mechanical parameters used to support the findings of this study are available from the corresponding author upon request.

Conflicts of Interest

The authors declare that they have no conflicts of interest.

Acknowledgments

The work presented in this paper is financially supported by the National Natural Science Foundation of China (No. 51674007) and the Natural Science Foundation of Chongqing (cstc2020jcyj-msxmX1052). The authors gratefully acknowledge the assistance of the Huainan Mining Group at the Anhui University of Science and Technology for providing access to the mine, data, and physical resources necessary to complete this work.

References

[1] L. Xiaoli, "Study on the theory and application of multi-scale behavior of water-rock coupling," Tsinghua University, Beijing, 2008.

[2] F. Meimei and M. Xianbiao, "Experimental research on fracture evolution law of water-resisting strata in coal seam floor above aquifer," *Chinese Journal of Rock Mechanics and Engineering*, vol. 28, no. 2, pp. 336–341, 2009.

[3] T. Min, "Study on the growth height of separation fracture of mining rock in Panxie area," *Journal of China Coal Society*, vol. 29, no. 6, pp. 641–645, 2004.

[4] L. Dejun, "The stress distribution of the goaf and its relationship of water inrush," *Safety in Coal Mines*, vol. 7, pp. 35–39, 1988.

[5] G. Yingbin, L. Haimei, and L. Junchen, "Research of No.9coal seam floor's fracture regularity in Xiandewang Coal Mine," *Journal of China Coal Society*, vol. 28, no. 2, pp. 121–125, 2003.

[6] S. Longqing and H. Jin, "Floor water inrush mechanism and prediction," China University of Mining and Technology Press, Beijing, 2004.

[7] H. Weiyue and Y. Shangxian, "Dynamic mechanism of water inrush from floor of mining face," *Chinese Journal of Rock Mechanics and Engineering*, vol. 29, no. 1, pp. 3344–3348, 2010.

[8] Z. Yujun, L. Shucai, Q. Sifeng, and L. Liping, "A catastrophe model for floor water-resisting key stratum instability induced by dynamic disturbance," *Rock and Soil Mechanics*, vol. 31, no. 8, pp. 2361–2366, 2010.

[9] W. Jinan, W. Xianhao, and C. Shaojie, "Fracture and seepage characteristics in the floor strata when mining above a confined aquifer," *Journal of China University of Mining & Technology*, vol. 41, no. 4, pp. 536–542, 2012.

[10] Z. Shaohe, Z. Weishen, and W. Shufa, "Study on the coupling problem between flow and solid of mine in confined aquifer," *Chinese Journal of Rock Mechanics and Engineering*, vol. 19, no. 4, pp. 421–424, 2000.

[11] C. Jisheng, "Numerical simulation study on water inrush mechanism of working face under high confined water," Shandong University of Science and Technology, Qingdao, 2006.

[12] H. Yaoqing, Y. Guochao, and S. Xiuwe, "Study on physical and numerical simulation of water inrush prediction theory for coal mining above confined aquifer," *Chinese Journal of Rock Mechanics and Engineering*, vol. 27, no. 1, pp. 9–15, 2008.

[13] Y. Xiaoge, "Study on broken depth of damage floor," Shandong University of Science and Technology, Qingdao, 2011.

[14] Y. Qingdao, "The possibility of detecting water in the Ordovician carbonate with objective seismic exploration," *Journal of China Coal Society*, vol. 27, no. 1, pp. 36–40, 2002.

[15] J. Fuxing, L. Weijian, Y. Genxi, and L. Wei, "Coupling study of microseismic monitoring and numerical simulation for tectonic activation," *Chinese Journal of Rock Mechanics and Engineering*, vol. 29, no. A2, pp. 3590–3597, 2010.

[16] J. Fuxing, Y. Genxi, W. Cunwen, Z. Dangyu, and G. Yongqiang, "Application of high-precision microseismic monitoring technique to water inrush monitoring in coal mine," *Chinese Journal of Rock Mechanics and Engineering*, vol. 27, no. 9, pp. 1932–1938, 2008.

[17] L. Shucai, "Mechanism of water inrush from coal seam floor and continuous survey of fractured zones in coal seam floor," China University of Mining Technolony, Xuzhou, 2008.

[18] P. L. Gong, Y. Q. Hu, Y. S. Zhao, and D. Yang, "Three-dimension simulation study on law of deformation and breakage of coal floor on mining above aquifer," *Chinese Journal of Rock Mechanics and Engineering*, vol. 24, no. 23, pp. 4396–4402, 2005.

[19] J. W. Zhou, W. Y. Xu, M. W. Li, X. Q. Zhou, and C. Shi, "Application of rock strain softening model to numerical analysis of deep tunnel," *Chinese Journal of Rock Mechanics and Engineering*, vol. 28, no. 6, pp. 1116–1127, 2009.

Hindawi
Geofluids
Volume 2021, Article ID 6664925, 9 pages
https://doi.org/10.1155/2021/6664925

Research Article

Changing Characteristics of Sandstone Pore Size under Cyclic Loading

Jiaguang Kan,[1] Guichen Li,[1] Nong Zhang ,[1,2] Peng Wang ,[1] Changliang Han,[1] and Shun Wang[1]

[1]*Key Laboratory of Deep Coal Resource Mining of the Ministry of Education, School of Mines, China University of Mining and Technology, Xuzhou 221116, China*
[2]*Open Laboratory for Large-Scale Scientific Instruments, Jiangsu Normal University, Xuzhou, 221116 Jiangsu, China*

Correspondence should be addressed to Nong Zhang; zhangnong@cumt.edu.cn and Peng Wang; wangpeng19@cumt.edu.cn

Received 16 December 2020; Revised 22 January 2021; Accepted 7 February 2021; Published 5 March 2021

Academic Editor: Yi Xue

The size and distribution of pores in rocks are closely related to their physical and mechanical properties. It is important to study the structure and distribution of pore size inside the rock to assess the risk of damage to a given rock volume. These characteristics were studied under different pressures, pore diameters, and pore throat size distribution laws using a UTM5540 electronic universal testing machine, magnetic resonance imaging scanning, and low field nuclear magnetic resonance spectroscopy with cyclic loading on yellow sandstone. We found the following. (1) Under 0–10 MPa load, the peaks of the sandstone T_2 spectrum move left as load increases, and the porosity of the sandstone decreases. The peak area of the middle relaxation spectrum increases as pressure increases from 10 to 20 MPa, and a peak for the long relaxation time spectrum appears. (2) Under 0–10 MPa load, the spectral peak associated with a large pore moves left and decreases in area as pressure increases. Under 10–20 MPa load, the large-pore spectral peak moves right and increases in area as pressure increases. (3) Under the applied 0–10 MPa load, the porosity of water-saturated sandstone gradually decreases, and the sandstone NMR images darken with increasing load. The porosity of saturated sandstone gradually increases under 10–20 MPa pressure, and its NMR image brightens. (4) The number of small pore throats increases with increasing load, but the number of large- and medium-sized pore throats decreases. From 0 to 15 MPa, crack (>1 micron) abundance decreases, and fractures are generated by compaction under a 20 MPa load. The pore interconnectivity is enhanced, as are the number and size of pores in the sandstone. With continuing increasing pressure, the numbers of pores and penetration of cracks increase, which damages the sandstone.

1. Introduction

The characteristics of pores in sandstone are closely related to the rock's physical and mechanical properties [1–6]. The pores' size, structure, and distribution not only determine the mechanical properties of the rock but are also the key factors affecting the permeability of the rock [7–12]. Therefore, to ensure the stability of rock formations in coal mining, it is important to study how the internal pore size and pore state in sandstone change under stress and to study the resulting damage to the body of rock.

Previous studies have used various methods to explore the relationship between the internal microstructural changes of sandstone and externally imposed stress. Common methods include numerical simulation, computerized tomography (CT) scans, acoustic emission tests, electron microscopy, and mercury intrusion. For example, Wu [13–15] studied the pore throat size and proportion of sandstone through mercury intrusion experiments. Ren and Yang [16–18] combined triaxial loading and CT scanning experiments through CT image analysis of the sandstone failure process under triaxial or uniaxial loading to reveal microscopic damage and the crack propagation law of the sandstone failure process. However, these experimental methods have the disadvantages of large errors, damage to the sample, and invisible static processes.

Low-field nuclear magnetic resonance (NMR) technology has the advantages of being nondestructive, using smaller sample volume, having a rapid detection speed, and having dynamic visibility, and it has therefore been widely used to measure porosity, permeability, pore size distribution, and displacement among other physical properties of the medium being studied [19–24]. Zhang [25, 26] combined nuclear magnetic resonance and triaxial compression methodologies to study the crack propagation law of granite under different confining pressures and measured the stress-change curve and T_2 spectrum of granite under different confining pressure conditions. With increasing axial load, the T_2 spectrum peak, spectrum area, and porosity of granite gradually increased, and the degree of damage inside the rock continued to increase. Porosity increased exponentially with increasing axial load, which resulted in damage to the rock as cracks penetrated and increased in number. Zhou [27] studied the mechanism of damage to rock under triaxial compression using NMR technology to determine the functional relationship between porosity and damage and conducted "stress-strain," porosity, and relaxation time (T_2) measurements. Quantitative analysis of the damage spectrum and triaxial compression established a tensor relationship as the rock is damaged. Hu [28, 29] studied the meso-scale damage evolution characteristics of the internal pore structure of unloaded rock masses using NMR and triaxial unloading experiments on marble. They found that with increasing unloading confining pressure ratio, the elastic deformation of the rock gradually transformed into plastic deformation, the size of the small pores in the rock sample increased, and the size and number of the large pores increased. The porosity of the rock sample increased with increasing unloading confining pressure ratio, and the growth rate progressively increased.

In summary, there are insufficient studies on the structure and distribution of pores in sandstone under the influence of cyclic mining stress. Using low-field nuclear magnetic resonance spectroscopy, this study evaluates the evolution in pore size in fine yellow sandstone under cyclic loading and obtains the T_2 spectrum and characteristics of changes in pore throats in fine yellow sandstone under cyclic loading. It provides a reference for future research on the damage and destruction of sandstone and on the stability of the surrounding rocks of mining roadways.

2. Materials and Methods

2.1. Experimental Sample. The selected samples are cylindrical fine yellow sandstone with a size of 25 mm × 60 mm. The measured uniaxial compressive strength of the sandstone is 26 MPa, and the maximum deformation is 0.9 mm. The stress and deformation curve of sandstone are shown in Figure 1.

2.2. Experimental Equipment. The equipment used in this experiment includes a low-temperature and high-pressure nuclear magnetic resonance spectrometer (Suzhou Newmai Analytical Instruments Co., Ltd.) and a UTM5540 electronic universal testing machine (Figure 2). Nuclear magnetic resonance is used to measure the T_2 spectrum, porosity, pore size, and pore throat distribution of the sample and to conduct NMR imaging of water-saturated sandstone under cyclic loading. Magnetic field strength was 0.3 ± 0.05 T, magnet frequency was 10.64–14.90 MHz, pulse control accuracy was 0.1 Hz, and pulse accuracy was 100 ns.

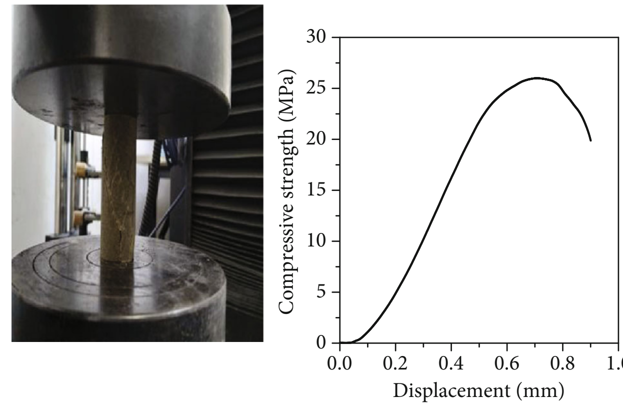

Figure 1: Sandstone stress-strain curve.

ZYB-2 vacuum pressure saturation device is used as supporting equipment, sample chamber size: Φ 150 × 300 mm, withstand voltage: 50 MPa, power supply voltage: AC220 V/50 Hz, vacuum pumping rate: 4 L/s, and manual pump: 210 ml/50 MPa. The core is vacuumized with vacuum device and then soaked with liquid of certain specification under vacuum condition to make the core absorb the liquid fully. In order to speed up the absorption rate, a certain external pressure is applied to the core and liquid during the soaking process, and the external pressure can be determined according to the porosity and tightness of the core.

The electronic universal testing machine is used to apply different uniaxial compression forces to sandstone; the maximum test force is 50 kN, the test force measurement range is 2%–100% FS, the test force measurement range is within ±1%, the displacement resolution is 0.001 mm, and the displacement display value has relative error of ±0.5% and relative speed error ± <1% of the set value.

2.3. Experimental Procedures. The UTM5540 electronic universal testing machine was used to apply cyclic loads to sandstone samples, and then, water-saturated sandstone was scanned using NMR to obtain T_2 spectra and porosity, pore size, and pore throat distribution measurements. NMR images were obtained under different loads. The complete methodology is as follows.

(1) The sandstone sample is placed in the core chamber of the vacuum pressure saturation device, and after vacuum treatment, the valve of the core chamber is opened to allow water to enter the core chamber such that the experimental sample reaches a state of complete water saturation

(2) When the temperature of the permanent magnet is 32 ± 0.01°C, a coil suitable for the size of the experimental sample is installed, and a standard oil sample is used to calibrate the central frequency of the NMR instrument. By adjusting the appropriate parameters,

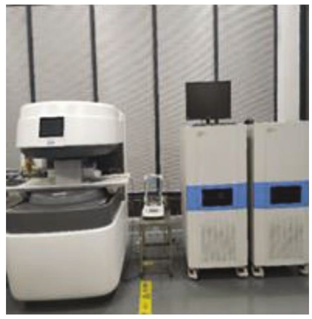

(a)

(b)

Figure 2: Main experimental equipment: (a) low-temperature and high-pressure nuclear magnetic resonance spectrometer; (b) UTM5540 electronic universal testing machine.

the signal volume curve after the hard pulse CPMG (Carr-Purcell-Meiboom-Gill) sequence scans the standard oil sample decreases smoothly

(3) The standard oil sample is removed and added to the test sample, then scanned with the adjusted CPMG sequence to obtain the T_2 spectrum of the experimental sample, followed by determination of the T_2 spectrum of each sample in turn. The T_2 spectrum is then inverted with an analytical tester to obtain the porosity and pore size distribution map of each sample

(4) The UTM5540 electronic universal testing machine was used to sequentially apply pressures of 5, 10, 15, and 20 MPa to the sandstone. After the load reached the selected pressure value, it was maintained for 30 minutes

(5) The loaded sandstone sample is scanned again with the adjusted CPMG sequence to obtain its T_2 spectrum, porosity, and pore size distribution

3. Results and Discussion

3.1. Characteristics of the Sandstone T_2 Spectrum under Cyclic Loading. Through the above experimental process, the T_2 spectrum of sandstone under different loads is shown in Figure 3.

The relaxation time of hydrogen atoms in the pore water is an indicator of the sample's environment. The longer the relaxation time, the weaker the binding of the water molecules and the larger the pore size. We divide relaxation time into short (0.01–10 ms), medium (10–100 ms), and long (100–1000 ms) durations.

The peak distribution of sandstone T_2 spectrum under different loads is shown in Table 1. The relaxation time of sandstone in the untreated state is indicated by four spectral peaks. The short relaxation time is mainly concentrated in 0.5-4 ms. After pressure of 5 MPa is applied, short relaxation peak of 0.07~0.16 ms disappears, and the termination time of the medium and long relaxations decreases. Both sets of peaks move to the left, and the maximum relaxation time shortens. Applying a pressure of 10 MPa, the spectral peaks for a relaxation time of 0.1 ms disappear, which leaves three spectral peaks indicating relaxation time. The maximum relaxation time also decreases to 100 ms, the peak associated with long relaxation time eventually disappears, the sandstone continues to be compacted, and the size of the pores further decreases. When a pressure of 15 MPa is applied, a short relaxation time peak of 0.01–0.1 ms appears, and five relaxation time peaks are observed. The newly added short relaxation time peaks indicate the presence of tiny pores caused by small displacements and dislocations of the cemented particles inside the sandstone under the new pressure. The maximum relaxation time of the newly appearing long relaxation time peak is 174 ms, and a larger pore diameter is produced. After applying a pressure of 20 MPa, the spectral peaks for short relaxation times of 0.01 ms to 0.1 ms disappeared, and the relaxation time peaks all moved to the right relative to their position under 15 MPa, which indicates that the new micropores continued to expand after further compression. Under 20 MPa pressure, the penetration degree of the pore diameter increases, and more large pores are produced. As pressure increased, the formation of macroscopic cracks continued until the sandstone was destroyed.

3.2. Evolution of Pore Characteristics of Saturated Sandstone under Cyclic Loading. According to the NMR measurement results, the pore size distribution of the sandstone as obtained by inversion is shown in Figure 4.

According to their results, Yao [30] classified pore sizes in rock by radius (r) into small pores ($r < 0.1\,\mu$m), mesopores ($0.1\,\mu\text{m} < r < 1\,\mu$m), and large pores ($r > 1\,\mu$m). According to the analysis shown in Figure 4, in the original state of the sandstone, the micropores yielded two spectral peaks, and there were no pores in the size range of 0 to 0.01 μm. The large pores and mesopores all had one spectral peak distribution, but the large pores yielded smaller peak areas and were few in number. When a pressure of 5 MPa was applied, tiny pores measuring 0.001–0.01 μm appeared, and the height and area of the peak associated with these pores in the original state decreased. The two spectral peaks resulting from the large and medium pores became connected under a pressure of 5 MPa. The peak associated with large pores moved to the left while the area of the peak decreased, which indicates that the sample was compacted under the new applied pressure.

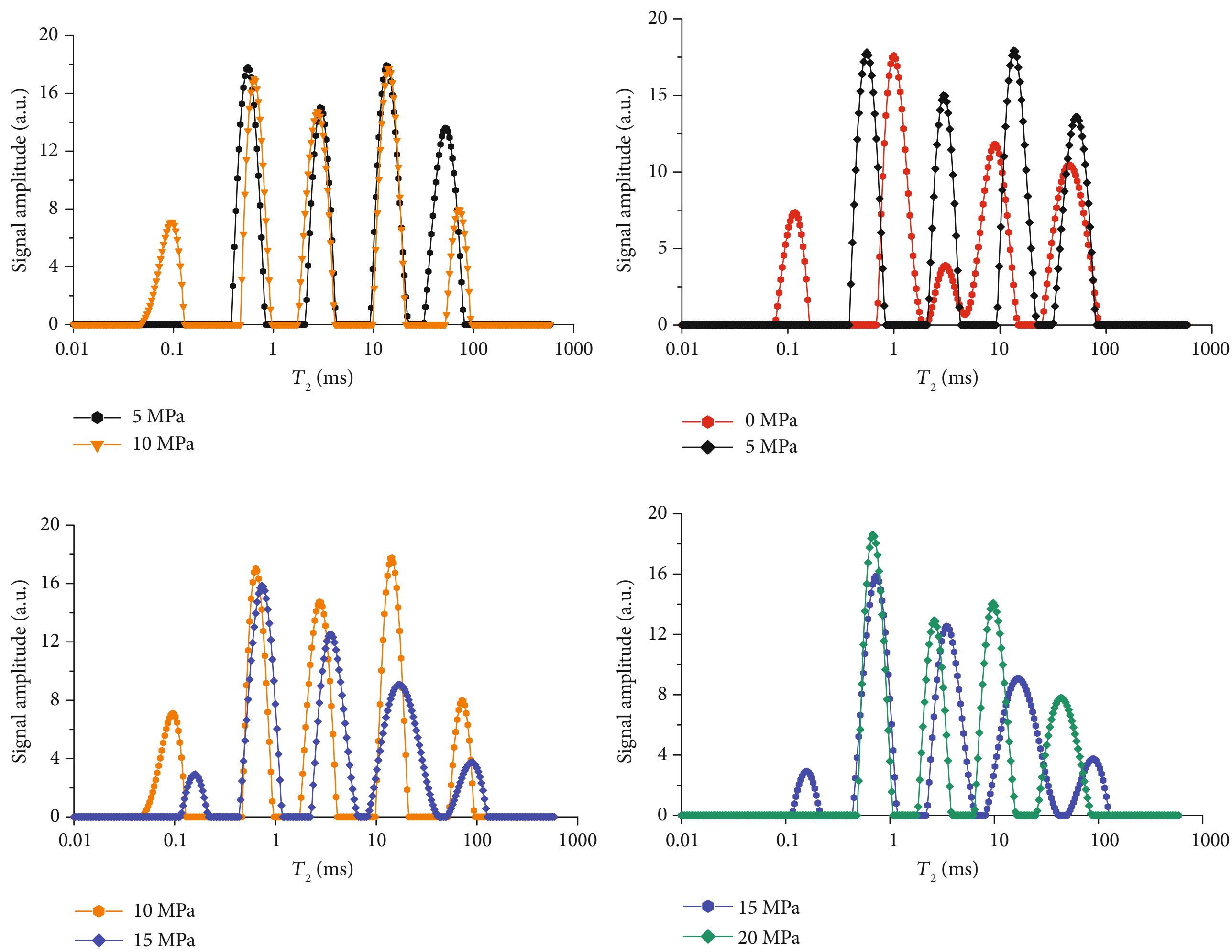

Figure 3: Peak distribution of sandstone T_2 spectrum under different loads.

Table 1: Peak distribution of sandstone T_2 spectrum under different loads.

Load	Spectral peak starting and ending time/ms (area)				
0 MPa	0.07~0.16 (107.7)	0.68~1.93 (280.7)	1.99~14.89 (269.3)		24.18~87.07 (232.4)
5 MPa	0.21~0.44 (143.4)	1.50~2.14 (300.5)	8.27~17.11 (259.2)		39.26~86.5 (88.7)
10 MPa	0.05~0.13 (109.1)	0.47~0.97 (220.4)	1.74~2.73 (229.9)	9.83~21.05 (245.6)	58.80~96.6 (87.7)
15 MPa	0.11~0.22 (34.1)	0.44~1.12 (275.5)	2.21~6.72 (225.1)	7.99~42.08 (238.6)	48.33~127.43 (60.0)
20 MPa	0.48~1.07 (266.3)	1.80~3.99 (173.5)	6.27~16.52 (224.4)		25.03~87.07 (172.1)

When a pressure of 10 MPa was applied, the newly generated micropore spectrum peak generated under 5 MPa disappeared, and the micropore spectrum peak continued to move to the left, which indicates that the sandstone was further compacted, while the large-pore and mesopore spectrum peak area was generally unchanged and moved slightly to the left. When 15 MPa pressure was applied, a peak appeared at 0.001 μm, the micropore spectrum peak moved to the right and increased in area, and the 1–10 μm macropore spectrum peak appeared. This indicates that small pores begin to be generated inside the sandstone under 15 MPa pressure and that the sizes of large pores and mesopores increase under pressure. When a pressure of 20 MPa was applied, the peak at 0.001 μm disappeared, and the diameter of the small pores of about 0.001 μm size expanded. Although the peak associated with large pore size moved to the left, the peak area was greatly increased. This indicates that pore size inside the sandstone continued to expand. As the pressure was increased to the uniaxial compressive strength, the internal pore of the sandstone expanded and penetrated to form macroscopic cracks until the sandstone was destroyed.

3.3. Sandstone Porosity and NMR Imaging under Cyclic Loading. The unpressurized saturated rock sample was

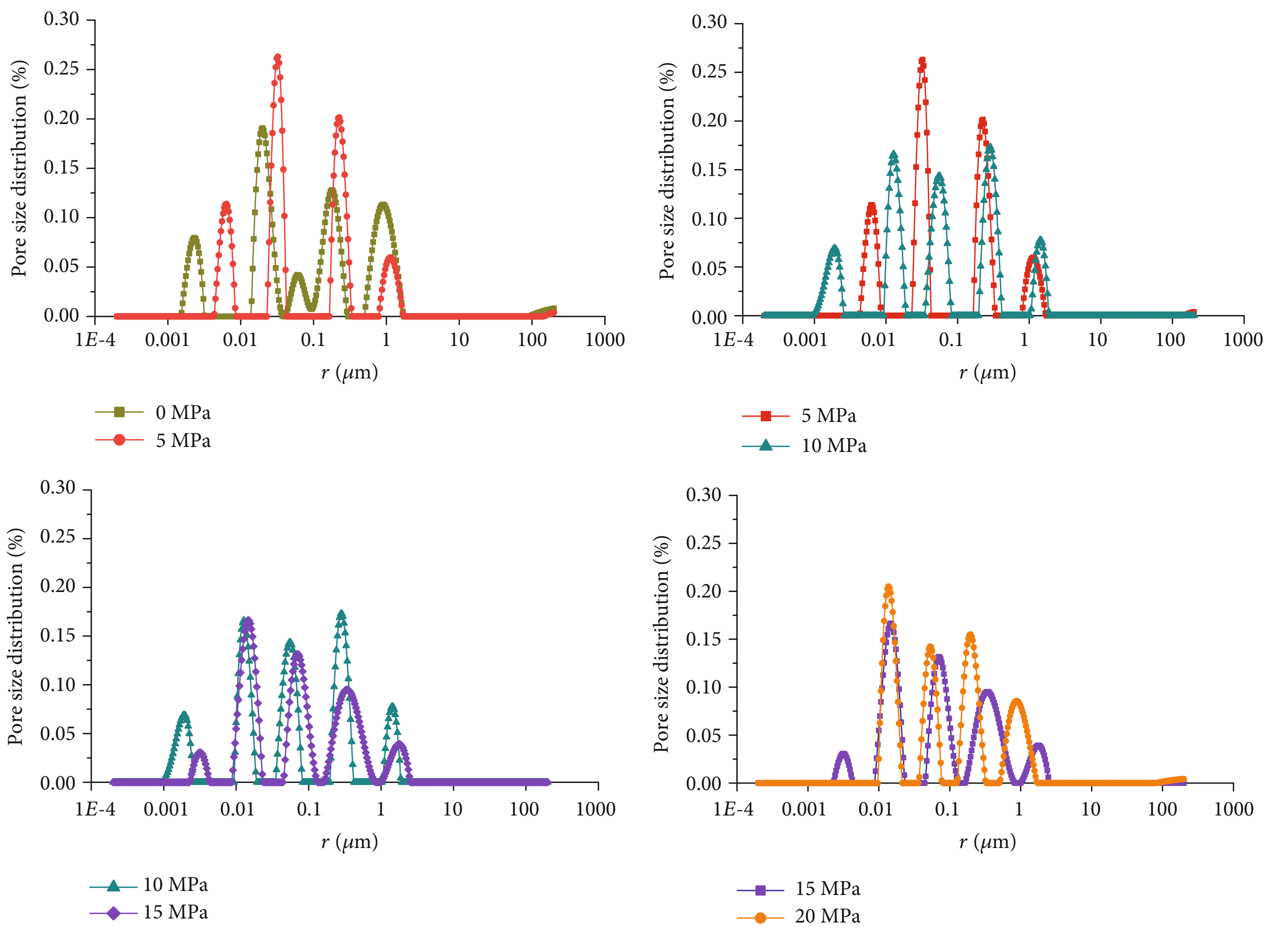

FIGURE 4: Pore size distribution of sandstone under different loads.

scanned by NMR, and then, different uniaxial compressive stresses were applied to the sandstone and maintained for 30 minutes. After unloading, the sample was scanned with NMR. The porosity of the sandstone under different loading conditions is shown in Figure 5.

According to the analysis in Figure 5, the porosity of all sandstones decreased under 5 MPa pressure, which indicates that the voids inside the sandstone were compacted and closed under that pressure. The porosity of sandstone decreased significantly because there were more large pores inside the sandstone, and the decreasing pore size under compression led to a larger decrease in porosity. When the pressure reached 10 MPa, the porosity decreased slowly, the internal fractures of the sandstone continued to be compacted and closed, and the porosity decreased. When pressure increased to 15 MPa, the porosity of the sandstone slowly increased, which indicates that the pores and pore throats inside the sandstone began to expand and that the speed of expansion was greater than the speed of compaction and closure. Cracks began to develop, and porosity increased. Under 20 MPa pressure, the porosity of the sandstone continued to increase, and the rate of increase was faster than that at 15 MPa, which indicates that the small pores in the sandstone continued to develop, and the existing pores began to penetrate the cracks and expand, and porosity increased.

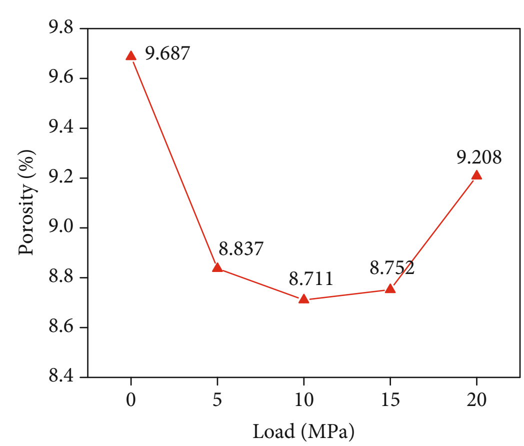

FIGURE 5: The porosity of sandstone varies with different load states.

Low-temperature and high-pressure nuclear magnetic resonance spectroscopy was used to perform NMR imaging of sandstone under cyclic loading at various pressure states Niu-Spin Echo (soft pulse imaging) was selected for the imaging sequence, and the sandstone magnetic resonance imaging results are shown in Figure 6.

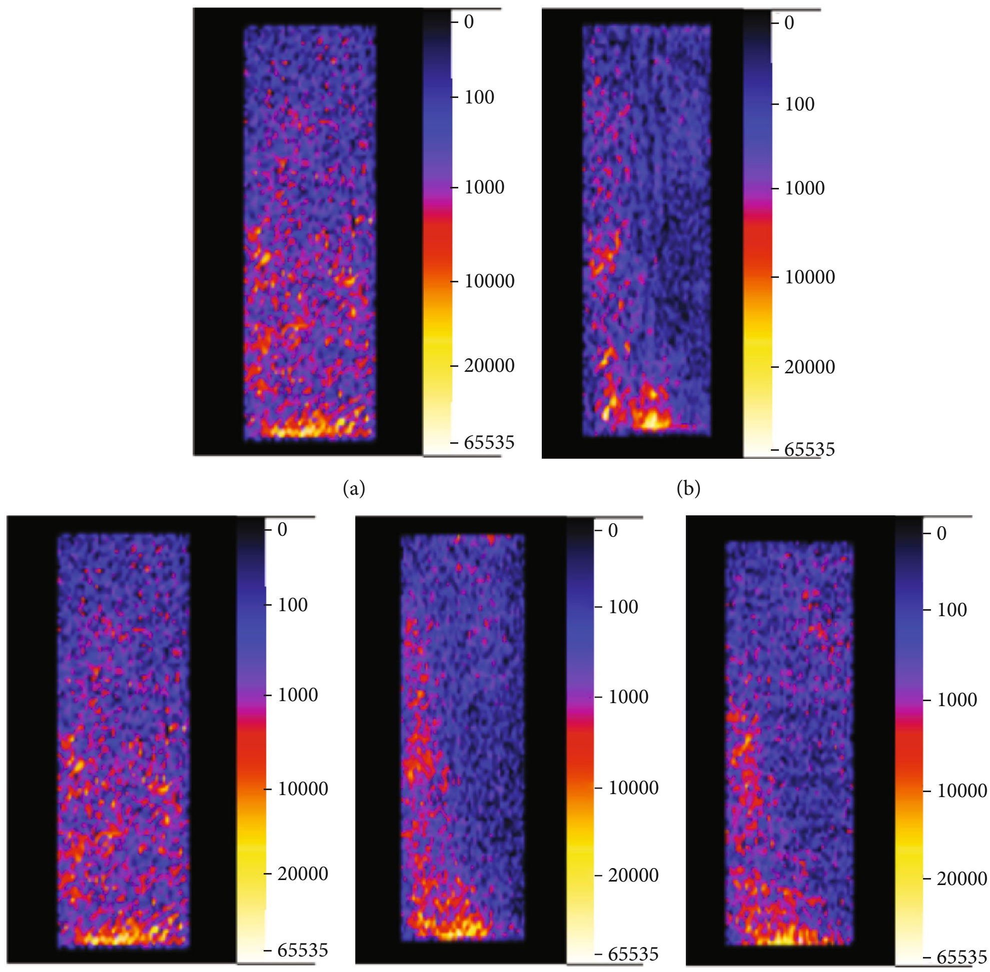

Figure 6: NMR images of sandstone under different loads.

Table 2: Sandstone pore throat distribution under different load.

Proportion/% Load	Pore throat size/μm 0 ~ 0.1	0.1 ~0.16	0.16~0.25	0.25~ 0.4	0.4 ~ 0.63	0.63~ 1	1 ~ 1.6	1.6 ~ 2.5	2.5 ~ 4
0 MPa	4.742	0.870	1.305	0.343	0.804	2.289	1.008	0.019	0
5 MPa	4.710	0	0.777	1.980	0.061	0.966	0.987	0	0
10 MPa	5.459	0	0.503	1.876	0.018	0.623	0.678	0.177	0
15 MPa	5.405	0.211	0.382	1.241	0.793	0.092	0.241	0.392	0
20 MPa	4.843	0.415	1.673	0.384	0.143	0.986	0.893	0.008	0

According to the NMR image analysis of sandstone:

(1) When no load was applied (0 MPa), the pores inside the sandstone were mainly distributed in the middle and lower parts. The upper part was darker, the particles were cemented well, and the diameter of the pores was small. At the edge of the lower part, the color was bright and evenly distributed, the diameter of the pores was larger, and the pores were unevenly distributed in the sandstone

(2) After a load of 5 MPa, the left half and bottom of the sandstone image became brighter, and pores were mainly distributed in this region. The right half was darker than when no load was applied. Compared with the image when no load was applied, the number of blocks with uniform brightness had decreased, which indicates that some of the cracks inside the sandstone were compressed and closed under a load of 5 MPa and that the sandstone was initiating compaction

Table 3: Ratio of pore throat of different types of sandstone under different loads.

Proportion/% Load	Pore throat size/μm Tiny pore throat (0 ~0.25 μm)	Large and medium-sized pore throat (0.25~ 1 μm)	Crack (>1 μm)
0 MPa	6.917	3.436	1.027
5 MPa	5.487	3.007	0.987
10 MPa	5.962	2.571	0.855
15 MPa	6.001	2.126	0.633
20 MPa	6.931	1.513	0.902

(3) After a load of 10 MPa, the bright area at the bottom of the sandstone was less bright than that after 5 MPa, the area of uniform brightness was smaller, and the color of the upper left section was darker. The right half was darker than it was at 5 MPa, and the darker region was larger. The pores were mainly distributed in the lower left and bottom of the sample. Under 10 MPa, the voids inside the sandstone were compressed, closed, and further compacted. Under a load of 15 MPa, the upper right part of the sandstone image became brighter than it was at 10 MPa; the center-right, lower left, and bottom sections became brighter, and the total area of the brighter area increased. This indicates that under a load of 15 MPa, new pores began to form inside the sandstone

(4) After a load of 20 MPa, the image tone of the left half of the sandstone was almost the same as that after 15 MPa, and the area of uniform brightness did not significantly change in size. The upper right section of the sandstone was brighter than it was under 15 MPa. Sections with brighter colors began to merge, which indicates that larger cracks began to penetrate the sandstone under this pressure. Furthermore, the rate of new pore generation increased, and the porosity of the sandstone increased

3.4. Characteristics of Sandstone Pore Throats under Cyclic Loading. According to the NMR measurement results, the pore throat distribution of sandstone is determined and presented in Table 2. According to the size of pore throats, pore throats can be divided into small pore throats (0–0.25 μm), medium to large pore throats (0.25–1 μm), and cracks (>1 μm). According to this classification, the proportions of different types of pore throat in sandstone under cyclic loading can be established, as presented in Table 3.

As indicated in Table 3, the number of micropore throats increased with increasing pressure. Under the pressure of 0-10 MPa, the size of large and medium-sized pore throat decreases, and new micropore throat is formed, which leads to the increase of the number of micropore throat. The increase in the number of micropore throats under pressure of 10–20 MPa indicated newly generated micropore throats in the sandstone. Under this pressure, the internal pore of the sandstone begins to penetrate to form the micropore throats. At 0–5 MPa, the number of large and medium pore throats decreases as a result of compaction. Under pressure of 5–20 MPa, there was minimal change, and the number of pore throats only decreases at a pressure of 15 MPa. It may be that the sample was further compacted under this pressure, which led to a decrease in the number of pore throats. When pressure was increased to 20 MPa, the number of large, medium, and small pore throats all increases, which indicates that the degree of pore penetration inside the sandstone had increased.

Cracks (>1 μm) were gradually compacted and closed under a pressure of 0–15 MPa. Under 20 MPa pressure, the number of cracks increased sharply, the degree of penetration of the sandstone pores increased, and the number and size of pore throats increased. As pressure was further increased, the number of pore throats increased, and the cracks expanded until the sandstone was destroyed.

4. Conclusions

(1) Under increasing load from 0 to 10 MPa, the relaxation peak of the sandstone T_2 spectrum moves to the left, and the porosity of sandstone decreases. Under a load of 10–20 MPa, the area of the medium relaxation time spectrum peak increases with pressure, and a long relaxation time spectrum peak appears. At 0–10 MPa, the large-pore spectrum peak moves to the left with increasing load, and the area under the spectrum peaks decreases, as does the porosity of the sandstone. The spectrum peaks of large and medium pores under pressures of 10–20 MPa move to the right with increasing area as load increases

(2) Under increasing load from 0 to 10 MPa, water absorption and porosity of the saturated sandstone gradually decrease, and the sandstone NMR image becomes darker. Under a load of 10–20 MPa, water absorption and porosity of saturated sandstone gradually increase with increasing pressure, and its NMR image tone becomes brighter

(3) With increasing load, the number of tiny pore throats increases, and the number of large and medium pore throats decreases. Under pressures of 0–15 MPa, the number of cracks (>1 μm) decreases, and these are gradually closed by compaction. Under a load of

20 MPa, the number of cracks increases, and the degree of penetration of sandstone pores increases. The number and size of pore throats increase with pressure, until cracks expand to the point where the sandstone is destroyed

Data Availability

The data used to support the findings of this study are included within the article.

Conflicts of Interest

The authors declare that there is no conflict of interest regarding the publication of this paper.

Acknowledgments

The paper is financially supported by the National Natural Science Foundation of China (52074263, 52034007) and the Fundamental Research Funds for the Central Universities (2014QNA47).

References

[1] X. C. Shi, “*Study on deformation and failure of overlying strata and evaluation of its permeability in coal mining*,” China university of mining and technology (Beijing), Beijing, China, 2016.

[2] J. Y. Zhang, “Opens pure and crystal-clear.Development of rock mesoscopic damage visualization system and study on evolution law of pore and fracture structure,” Taiyuan university of technology, Taiyuan, China, 2019.

[3] J. H. Cui and Q. F. Liang, “Experimental and simulation analysis of the influence of pore size on rock mechanical properties,” *Journal of Shaoxing College of Arts and Sciences (Natural Science)*, vol. 39, no. 3, pp. 38–45, 2019.

[4] X. Hao, W. Du, Y. Zhao et al., “Dynamic tensile behaviour and crack propagation of coal under coupled static- dynamic loading,” *International Journal of Mining Science and Technology*, vol. 30, no. 5, pp. 659–668, 2020.

[5] L. N. Y. Wong and H. H. Einstein, “Systematic evaluation of cracking behavior in specimens containing single flaws under uniaxial compression,” *International Journal of Rock Mechanics and Mining Sciences*, vol. 46, no. 2, pp. 239–249, 2009.

[6] J. Y. Teng, J. X. Tang, Y. N. Zhang, J. C. Duan, and J. B. Wang, “Damage and destruction process and characteristics of uniaxial compression substratum water-bearing shale,” *Rock and Soil Mechanics*, vol. 38, no. 6, pp. 1629–1638, 2017.

[7] Z. Xie, N. Zhang, J. Wang, Z. Xiang, and C. Zhang, “Study on magnetic resonance characteristics of coal sample under progressive loads,” *Applied Sciences*, vol. 10, no. 18, p. 6526, 2020.

[8] Z. X. Liu, W. Wang, J. A. Luo, and G. H. Miu, “Research on energy evolution analysis method in uniaxial rock compression test,” *Journal of China Coal Society*, vol. 45, no. 9, pp. 3131–3139, 2020.

[9] Y. C. Zhou, *Research on Energy Evolution Analysis Method in Uniaxial Rock Compression Test*, Shandong agricultural university, Taian, China, 2019.

[10] D. Liang, N. Zhang, L. Xie, G. Zhao, and D. Qian, “Damage and fractal evolution trends of sandstones under constant-amplitude and tiered cyclic loading and unloading based on acoustic emission,” *International Journal of Distributed Sensor Networks*, vol. 15, no. 7, 2019.

[11] C. Zhang, S. H. Tu, Y. X. Zhao, W. Wang, and X. He, “Numerical simulation study of three-axis fluid-solid coupling discrete element based on seepage experiment,” *Journal of Mining Sciences*, vol. 4, no. 1, pp. 23–33, 2019.

[12] K. L. Zhan, J. H. Xue, and Z. X. Liu, “Evolution law of energy under cyclic loading and unloading of rock,” *Coal Mine Safety*, vol. 50, no. 3, pp. 49–52, 2019.

[13] C. Wu, S. Q. Wang, Y. Cai et al., “The sandstone pore throat division of Zhiluo Formation in Binchang mining area based on mercury injection method,” *Coal Mine Safety*, vol. 50, no. 3, pp. 31–34, 2019.

[14] C. R. Clarkson, N. Solano, R. M. Bustin et al., “Pore structure characterization of North American shale gas reservoirs using USANS/SANS, gas adsorption, and mercury intrusion,” *Fuel*, vol. 103, pp. 606–616, 2013.

[15] Y. J. Hou, Y. H. Liu, P. Hu, and Z. Wang, “Nonlinear dynamics of Kuroshio intrusion in the Luzon Strait,” *Science China (Earth Sciences)*, vol. 60, no. 4, pp. 761–769, 2017.

[16] J. X. Ren, X. R. Ge, Y. B. Pu, W. Ma, and Y. L. Zhu, “CT real-time analysis of the evolution characteristics of uniaxial microscopic damage in rock,” *Journal of Civil Engineering*, vol. 3, no. 6, pp. 99–104, 2000.

[17] G. S. Yang, D. Y. Xie, C. Q. Zhang, and Y. B. Pu, “CT identification of rock damage characteristics,” *Journal of Rock Mechanics and Engineering*, vol. 1, pp. 48–54, 1996.

[18] J. X. Ren, X. R. Ge, and Y. B. Pu, *Dynamic Analysis of CT Mesoscopic Damage Evolution Mechanism in the Whole Process of Rock Failure*, no. 2, 2000Xi'an road traffic university, 2000.

[19] H. Q. Wang, C. D. Fu, L. J. Jing, and Y. Z. Jiang, “Application of nuclear magnetic resonance imaging technology in rock physics experiments,” *Logging Technology*, vol. 2, pp. 95–97, 2005.

[20] J. C. Sun, J. P. Chen, Z. M. Yang, X. W. Liu, and Y. J. Liu, “Experimental study on nuclear magnetic resonance response characteristics of shale core,” *Science and Technology Journal*, vol. 30, no. 14, pp. 25–30, 2012.

[21] K. E. Washburn, E. Anderssen, S. J. Vogt et al., “Simultaneous Gaussian and exponential inversion for improved analysis of shales by NMR relaxometry,” *Journal of Magnetic Resonance*, vol. 250, pp. 7–16, 2015.

[22] K. E. Washburn and J. E. Birdwell, “Multivariate analysis of ATR-FTIR spectra for assessment of oil shale organic geochemical properties,” *Organic Geochemistry*, vol. 63, pp. 1–7, 2013.

[23] C. Shen, C. X. Ouyang, D. Ruan, and Q. Wu, “Fractal characteristics of pore structure of tight sandstone reservoir – a case study of Fuyang reservoir in Xinli oilfield,” *Chinese Science and Technology Papers*, vol. 14, no. 12, pp. 1334–1340, 2019.

[24] Q. Zhang, Y. H. Dong, and S. Q. Tong, “NMR experimental study on water absorption process and characteristics of sandstone,” *Journal of the University of Chinese Academy of Sciences*, vol. 34, no. 5, pp. 610–617, 2017.

[25] L. Zhang, F. H. Ren, M. Han, Z. Yang, Y. C. Sun, and K. Liu, “Study on fracture development and damage rule of granite

before peak of triaxial compression based on nuclear magnetic resonance technology," *Coal Mine Safety*, vol. 49, no. 9, pp. 87–90, 2008.

[26] X. B. Li, L. Wong, X. F. Xie, and Q. H. Wu, "Experimental study on nuclear magnetic resonance characteristics of damage evolution of hard rock containing holes under dynamic and static loading," *Journal of Rock Mechanics and Engineering*, vol. 10, pp. 1985–1993, 2015.

[27] K. P. Zhou, Z. X. Hu, F. Gao, M. Q. Wang, and Z. Yang, "Research on triaxial compression damage law of marble based on nuclear magnetic resonance technology," *Geotechnical Mechanics*, vol. 35, no. 11, pp. 3117–3122, 2014.

[28] Z. X. Hu, K. P. Zhou, J. L. Li, F. Gao, and M. Q. Wang, "Nuclear magnetic resonance (NMR) testing of microdamage evolution of unloaded rock mass," *Journal of University of Science and Technology Beijing*, vol. 16, no. 12, pp. 1567–1574, 2014.

[29] D. T. Nicholson and F. H. Nicholson, "Physical deterioration of sedimentary rocks subjected to experimental freeze–thaw weathering," *Earth Surface Processes and Landforms*, vol. 25, no. 12, pp. 1295–1307, 2000.

[30] Y. Yao, D. Liu, J. Liu, and S. Xie, "Assessing the water migration and permeability of large intact bituminous and anthracite coals using NMR relaxation spectrometry," *Transport in Porous Media*, vol. 107, no. 2, pp. 527–542, 2015.

Hindawi
Geofluids
Volume 2021, Article ID 6633517, 10 pages
https://doi.org/10.1155/2021/6633517

Research Article

Disastrous Mechanism of Water Discharge in Abandoned Gob above the Stope in Mining Extra-Thick Coal Seam

Haixiao Lin,[1] **Feng Yang**,[1] **Zhengzheng Cao**,[1] **Yue Wang**,[1] **and Xiaojian Jiao**[1,2]

[1]*School of Civil Engineering, Henan Polytechnic University, Jiaozuo, 454000 Henan, China*
[2]*Henan Polytechnic Industrial Technology Research Institute Co. Ltd., Jiaozuo, 454000 Henan, China*

Correspondence should be addressed to Zhengzheng Cao; caozz@hpu.edu.cn

Received 9 January 2021; Revised 7 February 2021; Accepted 20 February 2021; Published 4 March 2021

Academic Editor: Guanglei Zhang

The Datong mining area is a typical double system coal seam mining area in China, where the Jurassic and Carboniferous coal seams are mined simultaneously. The upper Jurassic coal seam has been largely mined, leaving a large amount of gob area. Besides, a large amount of harmful water is accumulated. With the exploitation of the 3-5# extra-thick coal seam in the Carboniferous system, the scope of overburden damage is greatly increasing, and the mining fracture field is further developed. Once the mining-induced fractures connect with the overlying gob, it is easy to induce the water discharge disaster. With the mining geological conditions of the 8202 working face in the Tongxin coal mine as references, the disastrous mechanism of water discharge in the abandoned gob above the stope in the mining extra-thick coal seam is researched by numerical simulation with the UDEC numerical software, and the research results are obtained. The water in the overlying gob percolates through the mining-induced fractures in the higher key layer forming a "shower" seepage pattern. The water in the above gob converges in the key fracture channel, flowing into the working face. The seepage in the fractures in the high key stratum experiences the process of increase, decrease, and stabilization, related with the stretching and extrusion deformation between the high key stratum blocks. Compared with other fractures, the flow rates in the No.2 and No.4 fractures in the far field key lay are larger, because the fractures are in the tension state, forming the "saddle-shaped" flow pattern. The influencing distance of mining-induced seepage is about 80 m in front of the working face. The research results provide a guided reference for the prediction and prevention of water discharge disaster in an abandoned gob above the stope in a mining extra-thick coal seam.

1. Introduction

The Datong coal mining area is a typical dual system of coal seam in China, where the Jurassic and Carboniferous coal seams are mined simultaneously [1, 2]. At present, the Jurassic coal mining is almost finished, and the Carboniferous 3-5# extra-thick coal seam is the key mining zone in the Tongxin mine [3, 4]. The harmful water in the gob comes from rainfall, rivers, and the overlying aquifer. The mining thickness of the 3-5# extra-thick coal seam is 14-20 m, which increases the overburden breakage height and fracture development height [5, 6]. When the fracture filed in the overburden communicates with the mining gob in the upper Jurassic coal seam, the accumulated water in the gob is released to the working face in the Carboniferous 3-5# extra-thick coal seam, through a mining-induced fracture channel, leading to the water drainage disaster [7–9]. Therefore, it is of great significance to accurately grasp the disastrous mechanism of water discharge in the abandoned gob above the stope in mining the extra-thick coal seam, which provides references for the prevention and control of water drainage disaster.

The significant researches on the disastrous mechanism of water discharge in abandoned gob have been carried out by scholars at home and aboard. Meng [10] determined the cracking connection in the overburden strata above the double system seam mining, with the double system seam mining in the Datong mining area as an engineering background. Du et al. [11] developed the porous medium two-phase water-sand flow testing system and researched the influence of sand, the particle sizes of broken rock mass, and the porosity of porous medium on water-sand inrush disaster. Yang et al. [12] built a three field coupled nonlinear flow model based on the essentially flow translation, from laminar flow in the aquifer to turbulence flow in the tunnel, in the process of collapsing pillar water inrush. Ju et al. [13] summarized the research progress on the evolution law of mining-induced water conducted zone in overburden, and the water-preserved mining countermeasures or solutions, according to the theories and practices in water-preserved coal mining under water in China. Hou et al. [14] analyzed the water inrush law with the influencing factors by building an experimental platform and performing a water inrush experiment and established the prediction method for water inrush from ground cracks. Zhang [15] expounded the idea, technical principle, and key technology of water-controlled coal mining technology in detail and solved the problems of large coal resource losses caused by different types of waterproof coal pillar technology in coal mining under a traditional water body. Yang et al. [16] built the overlying rock combination bearing structure model and studied the occurrence mechanism of bedrock fissure conduction working face and water-containing loose layer caused by the cutting-top compression frame of the working face. Zhang et al. [17] analyzed the limit equilibrium conditions of water and sand burst in fractures through the mechanics model of sand body inrush in fractures and carried out the simulation experiments of water and sand burst in fractures under different initial water pressures.

It is obvious that research results of water inrush disaster in the coal mine have been achieved systematically [18–20]. However, the researches on the disastrous mechanism of water discharge in an abandoned gob above the stope in a mining extra-thick coal seam (coal seam thickness is larger than 8 m) have been rarely performed. Besides, the mining fracture in the 8202 working face in the Datong mining area is different from the conventional mining situation, since the mining thickness of the 3-5# extra-thick coal seam is 14-20 m [21, 22]. Based on the mining geological conditions at the 8202 working face in the Tongxin mine of the Datong mining area, the disastrous mechanism of water discharge in an abandoned gob above the stope in a mining extra-thick coal seam is studied in this article, by means of numerical simulation with the UDEC numerical calculation software. This study provides a theoretical basis for the prediction and prevention of the water discharge disaster in an abandoned gob above the stope in a mining extra-thick coal seam.

2. Numerical Calculation Model of Water Discharge Disaster

UDEC (Universal Distinct Element Code) is the numerical calculation program based on the theory of the discrete element method [23, 24]. According to the mining geological conditions in the 8202 working face of the Tongxin coal mine, the mining height of the upper Jurassic 14# coal is 4 m, while that of the lower Carboniferous 3-5# coal seam is 15 m; besides, the average distance between the two coal seams is 160 m, and the buried depth of 3-5# coal seam is 480 m. The key point in the numerical calculation is to study the relationship between the fracture of the key layer and the evolution law of the seepage field with the mining of the 3-5# coal seam. The numerical calculation model has the length of 500 m, the height of 194 m, and the mining depth of 488 m. The numerical model is shown in Figure 1.

The boundary condition of both sides is the velocity boundary condition, the horizontal direction is fixed, and the bottom boundary of the model is fixed in the vertical direction. Besides, the vertical stress on the upper boundary is 8.6 MPa, which is the converted by the overburden on the upper part of the model. Both the sides and bottom of the model are set as the impermeable boundary, that is, there is no water supply, but seepage pressure exchange can be carried out at this boundary. The top of the model has a free boundary that can be supplied from the top according to changes in water pressure. When the 14# coal seam is being mined, the hydraulic boundary is applied in the way of fixed water pressure. After the mining of the 3-5# coal seam, the water pressure in the gob is set as zero. When the harmful water enters the space, the pressure is set as zero. Besides, the physical parameters of the rock mass are shown in Table 1, and the percolation mechanical parameters of joints are shown in Table 2. The data for the numerical calculation in Tables 1 and 2 are obtained by the rock mechanics experiments.

Therefore, the numerical calculation scheme is determined. In the numerical calculation, the 14# coal seam is firstly mined, and the mining width is 300 m, with 100 m pillars on both sides left to eliminate the boundary effect. The mining width of the 3-5# coal seam is 300 m, with 15 m each step, when the mining of the 14# coal seam is finished, and the development law of the overburden fracture and seepage field is analyzed.

3. Spatial and Temporal Evolution Law of Water Discharge Disaster

After the 14# coal seam is mined, the water pressure distribution of the overburden in initial equilibrium is shown in Figure 2, when the water pressure in the gob is 0.1 MPa before the mining of the 14# coal seam. It is indicated that the pore pressure of the surrounding rock in the middle of the mining gob is bigger, and that in both ends is smaller. The key layer refers to the strata which control the whole or partial overburden movement from the overburden to the surface [25].

When the 8202 working face in the 3-5# coal seam advances to 30 m, the initial caving of the direct roof occurs, and the transverse cracks on the top rapidly develop to the bottom of key layer 1. The pore pressure in the top of key layer 3 (far field key layer) is the maximum value 0.3183 MPa. The maximum pore pressure of the roof in the unexploited area in the 3-5# coal seam is 0.2929 MPa, as shown in Figure 3. From the perspective of flow velocity distribution, the water flow in the floor at both ends is the largest, with a maximum of 0.78 m^3/s, since both ends of the gob of the 14# coal mine have the maximum fracture depth and fracture opening degree. It is located within 1 m below the floor at both ends, and the flow outside 1 m below the floor drops to $1.4 \times 10^{-6}\ m^3/s$ rapidly, with a great change in

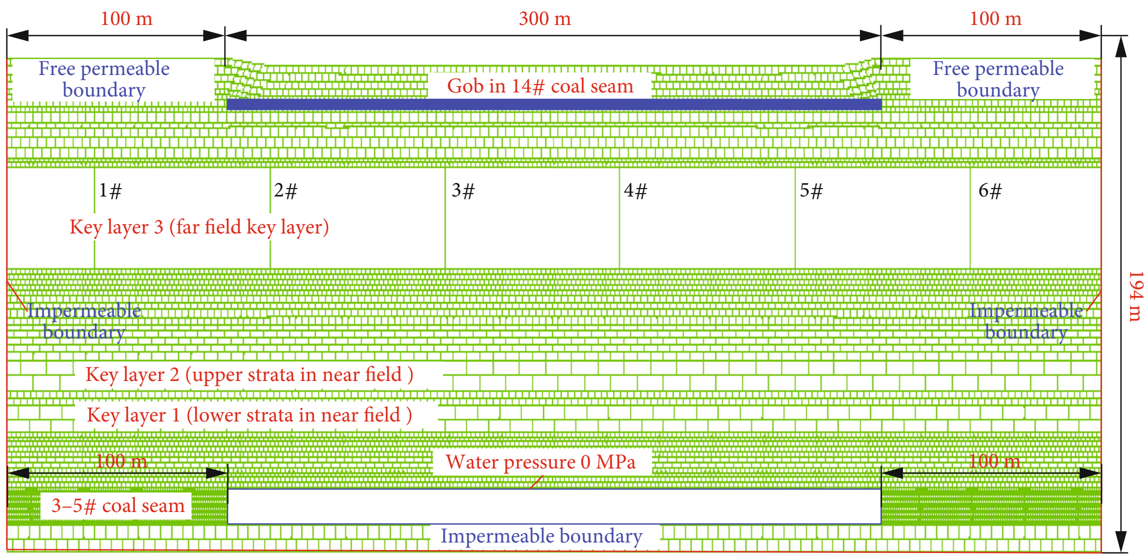

Figure 1: The numerical calculation model.

Table 1: The physical parameters of rock mass.

Rock strata	K (GPa)	G (GPa)	d (N·m^{-3})	f (°)	C (MPa)	t (MPa)
Coal seam	3.89	1.59	1426	42	2.01	1.6
Sandy mudstone	30.35	14.74	2693	35	12.5	4.4
Siltstone	18.50	16.02	2604	34	4.8	4.89
Fine sandstone	19.79	19.86	2700	34	4.8	6.4
Medium sandstone	23.24	15.93	2654	35	12.5	5.72
Coarse sandstone	10.85	7.5	2540	35	12.5	2.56

Table 2: The percolation mechanical parameters of joints.

Rock strata	f (°)	jperm (Pa^{-1}·s^{-1})	azero (m)	ares (m)
Coal seam	30	83	0.0001	0.00001
Sandy mudstone	32	100	0.0001	0.00001
Siltstone	30	128	0.0002	0.00003
Fine sandstone	30	143	0.0003	0.00004
Medium sandstone	33	178	0.0002	0.00003
Coarse sandstone	32	246	0.0004	0.00006

magnitude. At the same time, it is also noted that prefabricated primary joints in the key layer 3 (far key layer) also have the seepage phenomenon, but the flow rate is 2.472×10^{-8} m^3/s, with the extremely low seepage flow. In addition, the maximum flow rate in the roof of the 3-5# coal seam is 5.553×10^{-8} m^3/s, and it is located at 7 m in the direct roof, which is derived from the extremely low seepage generated through the primary fracture, as shown in Figure 4. According to the flow velocity vector distribution in the initial caving of the direct roof, the flow not only percolates downward along the longitudinal fracture but also percolates along the transverse fracture, and the flow confluence or separation occurs at a node, as shown in Figure 5.

When the 8202 working face in the 3-5# coal seam advances to 90 m, the initial caving of key layer 1 occurs. Because the key layer 1 is 22 m away from the top plate of the 3-5# coal seam, the rock layer cannot form a stable structure, so it collapses into the gob with revolving instability and becomes part of the caving zone. The distance between the key layer 1 and the key layer 2 is only 6 m. The overburden movement deformation caused by the fracture of the key layer 1 has a significant impact on the key layer 2 and its upper layers, resulting in obvious longitudinal and transverse fractures in the key layer 2. At the same time, due to the breakage of key layer 1, the maximum pore pressure in the mining area increases to 0.3909 MPa, as shown in Figure 6. The flow distribution in the initial caving of key layer 1 is obtained. The fractures in the overburden above the key layer 1 develop further, and water in the gob penetrates downward through primary fractures in key layer 3 (far field key layer) at a small flow rate and enters the key seepage channel of the working face. The flow rate in the key layer 3 (far field key layer) increases to 5.374×10^{-8} m^3/s, and the maximum flow rate in the working face reaches 5.374×10^{-8} m^3/s, which increases by nearly 10 times, as shown in Figure 7. According to the flow velocity vector distribution in the initial caving of key layer 1, as shown in Figure 8, the water in the far field key layer in the primary joint seepage phenomenon begins to appear, along with the increase of the fracture opening in key layer 3. Besides, the phenomenon of the water seepage in the lower rock layer is more obvious in the primary joint with a large opening, and the water seepage is concentrated in the gob.

When the 8202 working face in the 3-5# coal seam advances to 120 m, the initial caving of key layer 2 occurs. Because the key layer 2 is 37 m away from the top plate of the 3-5# coal seam, the rock layer cannot form a stable

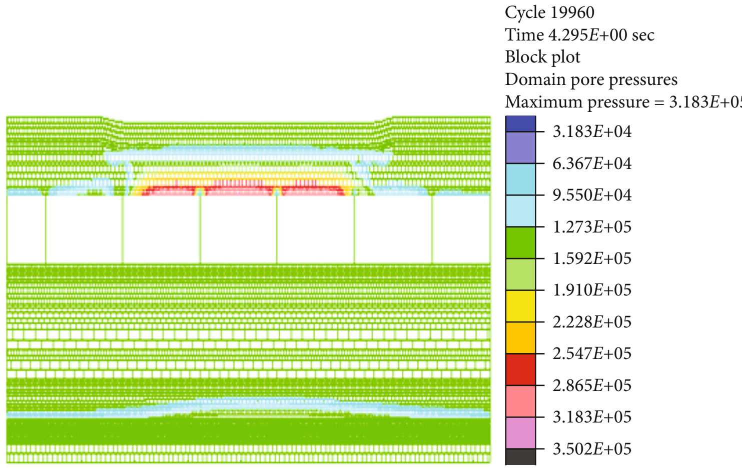

Figure 2: The water pressure distribution in initial equilibrium.

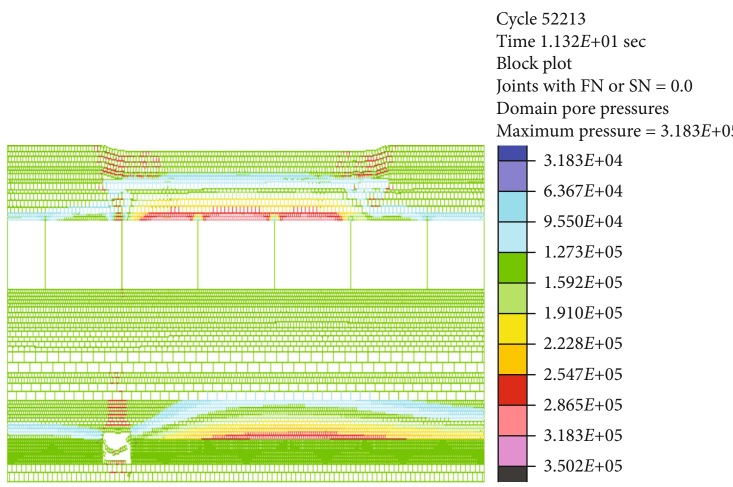

Figure 3: The pore pressure distribution in initial caving of direct roof.

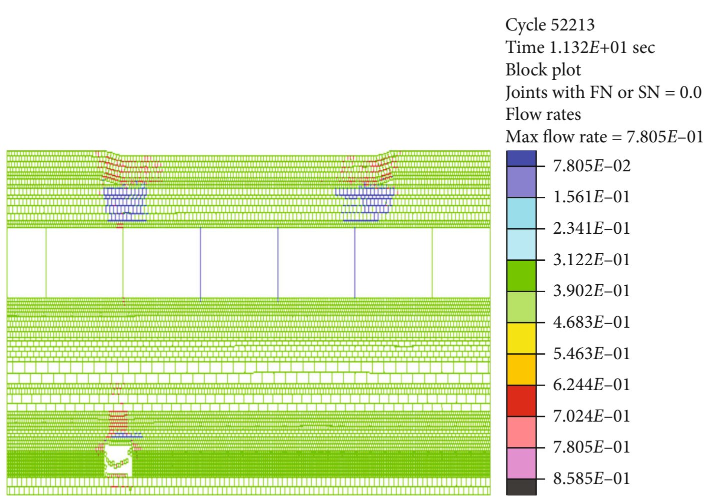

Figure 4: The flow distribution in initial caving of direct roof.

structure, so it caves into the gob and becomes part of the caving zone. After the breakage of key layer 2, tensile fractures appear in the lower part of key layer 3 (far field key layer) above the central position of the gob and in the upper part of key layer 3 far from the mining center. Meanwhile, the maximum pore pressure at the top of key layer 3 decreases to

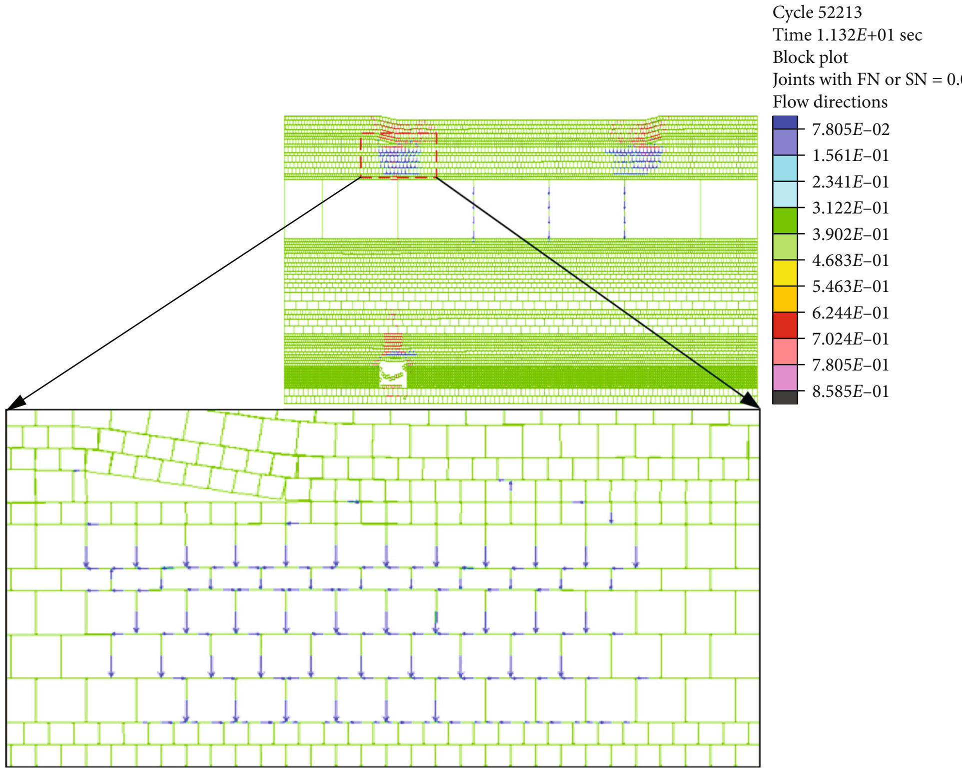

Figure 5: The flow velocity vector distribution in initial caving of direct roof.

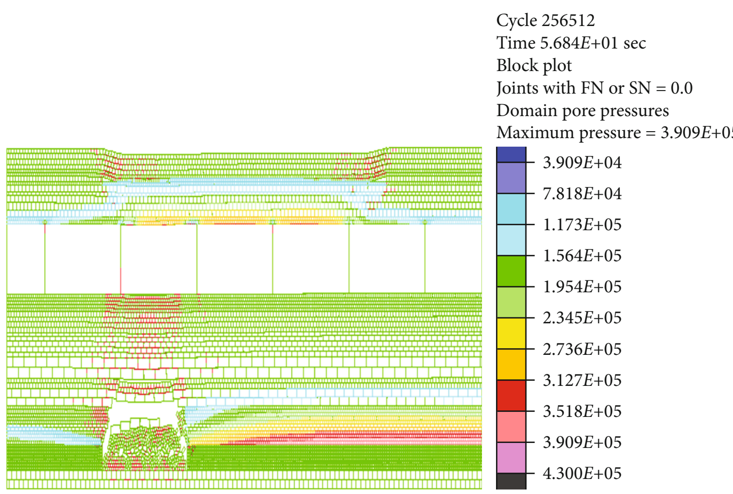

Figure 6: The pore pressure distribution in initial caving of key layer 1.

0.3174 MPa, while the pore pressure in the unexploited area of the coal seam increases to 0.4283 MPa, as shown in Figure 9. The flow distribution in the initial caving of key layer 2 is obtained in Figure 10; the water seepage flow of the No.1 fracture in the far field key layer reaches $7.736 \times 10^{-8}\ m^3/s$, the No.2 fracture seepage flow is $6.623 \times 10^{-8}\ m^3/s$, the No.3 fracture seepage flow is $7.071 \times 10^{-8}\ m^3/s$, the No.4 fracture seepage flow is $8.394 \times 10^{-8}\ m^3/s$, and the No.5 fracture seepage flow is $2.089 \times 10^{-8}\ m^3/s$. The seepage flows in the No.1 and No.4 fractures are greater than those in the No.2 and No.3 fractures, affected by mining in advance. At this time, the maximum flow rate in the 8202 working face reaches $1.224 \times 10^{-3}\ m^3/s$. The flow velocity vector distribution in the initial caving of key layer 2 is obtained in Figure 11. The water flowing velocity increases in the far field key layer, along with the increase of the fracture opening, and the water seepage flows as a “shower” form. The “shower” seepage pattern is the blue line under the far field key layer in Figure 10. Besides, there are water flows along both the longitudinal fractures and the horizontal fractures, and the overall flow direction eventually permeates to the key fracture channel of the gob in the 8202 working face.

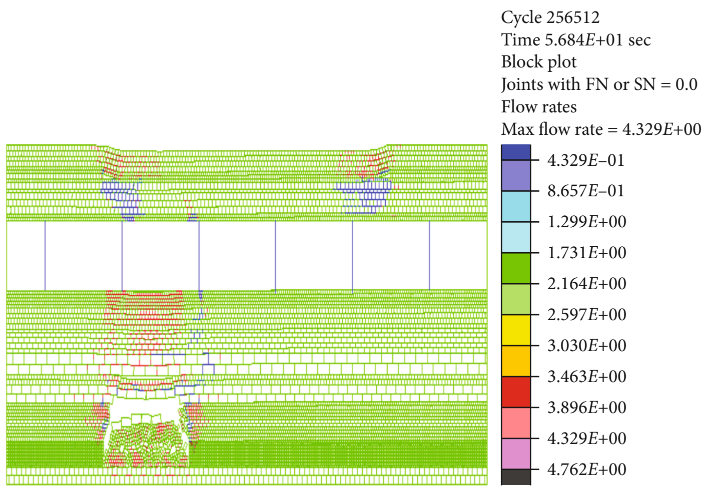

Figure 7: The flow distribution in initial caving of key layer 1.

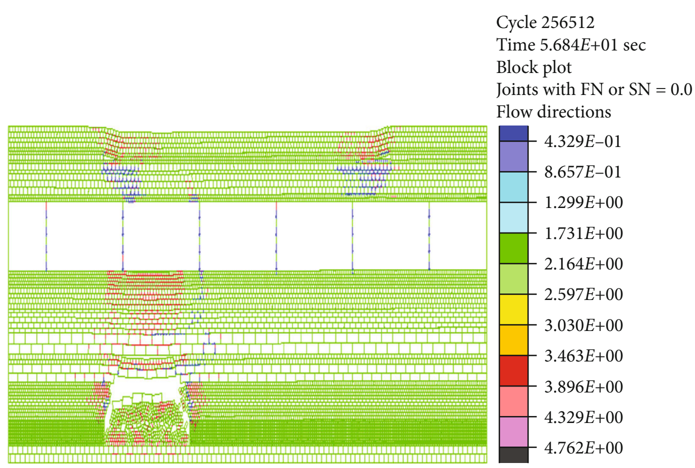

Figure 8: The flow velocity vector distribution in initial caving of key layer 1.

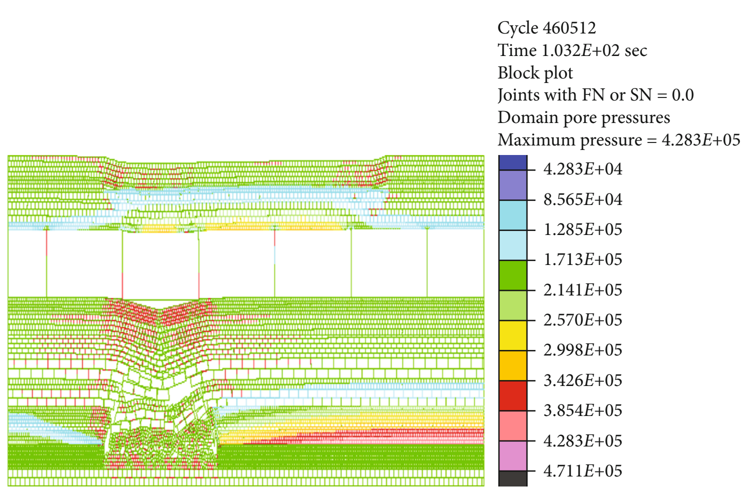

Figure 9: The pore pressure distribution in initial caving of key layer 2.

When the 8202 working face in the 3-5# coal seam advances to 180 m, the initial caving of key layer 3 (far field key layer) occurs, and the key layer 3 forms a stable structure of the voussoir beam. After the breakage of the rock strata, the middle part of the upper rock stratum is in the state of compression, and the fractures appear in the state of inter-layer dislocation. The two clamped ends of the voussoir beam in key layer 3 are tensile fractures, which are the key channel

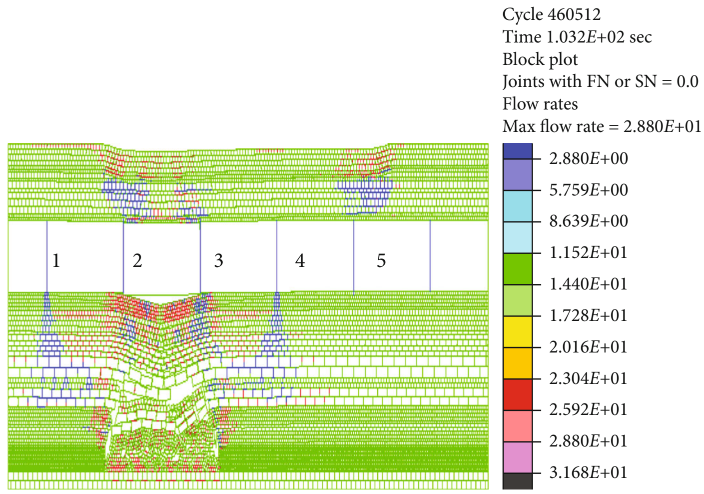

Figure 10: The flow distribution in initial caving of key layer 2.

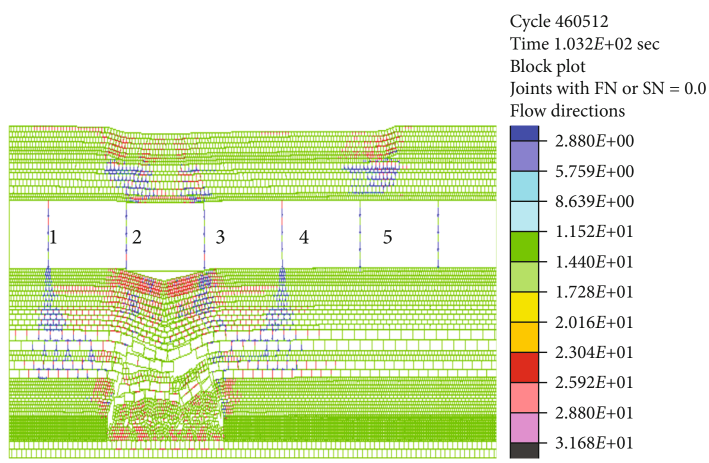

Figure 11: The flow velocity vector distribution in initial caving of key layer 2.

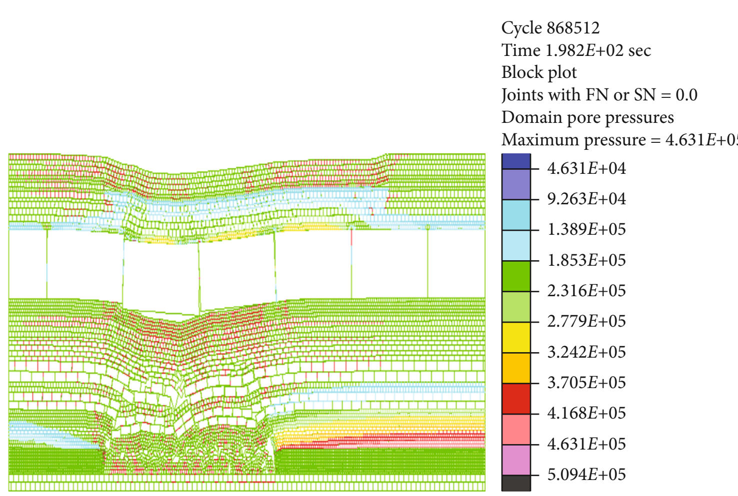

Figure 12: The pore pressure distribution in initial caving of key layer 3.

for water flowing into the working face. Besides, the largest pore pressure at the top of key layer 3 slightly reduced to 0.3159 MPa, while the pore pressure in the unexploited area of the coal seam increases to 0.4631 MPa, as shown in Figure 12. The flow distribution in the initial caving of key layer 3 is shown in Figure 13. The water seepage flow of the

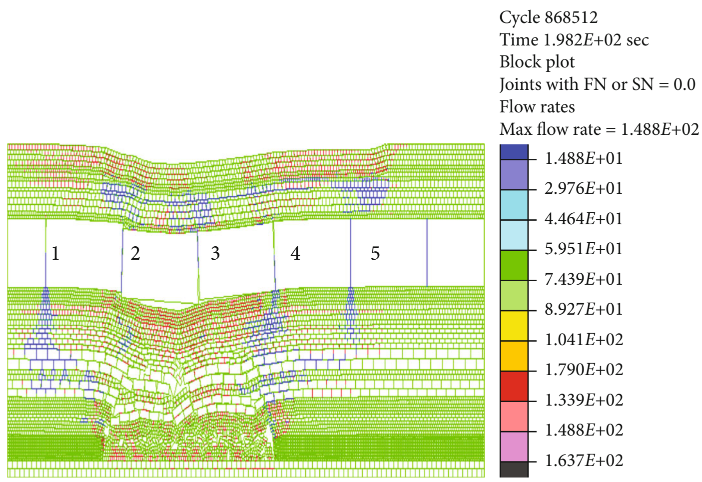

Figure 13: The flow distribution in initial caving of key layer 3.

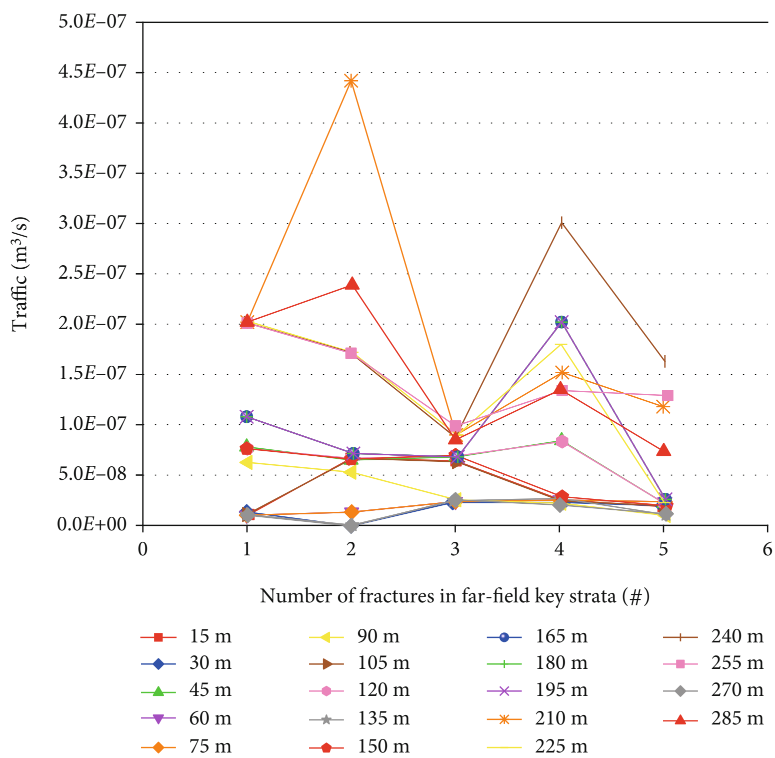

Figure 14: The fracture flow distribution curve in key layer 3 (far field key layer).

No.1 fracture in the far field key layer reaches 1.064×10^{-7} m^3/s, the No.2 fracture seepage flow reaches 9.598×10^{-8} m^3/s, the No.3 fracture seepage flow reaches 6.967×10^{-8} m^3/s, the No.4 fracture seepage flow reaches 1.608×10^{-7} m^3/s, and the No.5 fracture seepage flow reaches 8.368×10^{-8} m^3/s. Meanwhile, the maximum flow in the 8202 working face reaches 2.342×10^{-3} m^3/s.

It is obvious that the development of mining-induced fractures experiences several states of "small-expansion-peak-closure-stable," with the advance of the 8202 working face. The No.1 fracture is located outside of the stope, so the fracture development is in the open state in the whole process. The No.2 fracture is located at 20 m inside the cut hole, and its seepage velocity is the maximum, which forms the permanent fracture passage. Besides, the influence distance of mining-induced seepage is about 80 m in front of the working face, and the range of the seepage stability zone is about 165 m-265 m behind the gob.

The fracture flow distribution curve in key layer 3 is obtained in Figure 14. The No.3 fracture is located in the center position of key layer 3, and the upper part is in the state of compression, which is difficult for the seepage of water in the above gob; therefore, the flow rate in the No.3 fracture is smaller. Compared with other fractures, the flow rates in the No.2 and No.4 fractures are larger, because the fractures are in the tension state, forming the "saddle-shaped" flow pattern.

4. Conclusions

(1) When the 8202 working face in the 3-5# coal seam advances to 90 m, the initial caving of key layer 1 occurs, and the rock layer cannot form a stable structure, collapsing into the gob. The water in the overlying gob percolates through the fractures in the higher key layer forming a "shower" seepage pattern. The water in the above gob converges in the key fracture channel and then flows into the working face

(2) When the 8202 working face in the 3-5# coal seam advances to 120 m, the initial caving of key layer 2 occurs, and the rock layer cannot form a stable structure. The fracture seepage in the high key stratum experiences the process of increase, decrease, and stabilization, which is related with the stretching and extrusion deformation between the high key stratum blocks in the process of working face propulsion

(3) When the 8202 working face in the 3-5# coal seam advances to 180 m, the initial caving of key layer 3 occurs, and the key layer 3 forms a stable structure of the voussoir beam. The influence distance of the mining-induced seepage is about 80 m in front of the working face, and the range of the seepage stability zone is about 165 m-265 m behind the gob. Compared with other fractures, the flow rates in the No.2 and No.4 fractures are larger, forming the "saddle-shaped" flow pattern

Data Availability

The data used to support the findings of this study are included within the article.

Conflicts of Interest

The authors declare that they have no conflicts of interest.

Acknowledgments

This work was supported by the National Natural Science Foundation of China (52004082), the Natural Science Foundation of Henan Province (202300410170), the Foundation for Higher Education Key Research Project by Henan Province (18A440012), the Ph.D. Programs Foundation of Henan Polytechnic University (B2021-57), the Fundamental Research Funds for the University of Henan Province (NSFRF200302), the Postdoctoral Research Projects of Henan Province, the Scientific and Technological Development Project for Coal Mine Safety Production by Henan Province (HN19-59), the Virtual Simulation Experiment Teaching Project of Henan Province, and the Research and Practice Project of Educational and Teaching Reformation of Henan Polytechnic University (2019JG074).

References

[1] S. X. Yin, Y. Wang, H. C. Yin et al., "Mechanism and full-time-space prevention and control technology of water inrush from Ordovician and thin limestone in deep mines," *Journal of China Coal Society*, vol. 45, no. 5, pp. 1855–1864, 2020.

[2] D. Ma, H. Y. Duan, W. T. Liu, X. T. Ma, and M. Tao, "Water–sediment two-phase flow inrush hazard in rock fractures of overburden strata during coal mining," *Mine Water and the Environment*, vol. 39, no. 2, pp. 308–319, 2020.

[3] Y. Xue, P. G. Ranjith, F. N. Dang et al., "Analysis of deformation, permeability and energy evolution characteristics of coal mass around borehole after excavation," *Natural Resources Research*, vol. 29, no. 5, pp. 3159–3177, 2020.

[4] J. Liu, X. Liang, Y. Xue, K. Yao, and Y. Fu, "Numerical evaluation on multiphase flow and heat transfer during thermal stimulation enhanced shale gas recovery," *Applied Thermal Engineering*, vol. 178, p. 115554, 2020.

[5] B. H. Yao, J. P. Wei, D. K. Wang, Y. G. Wang, and H. T. Zhang, "A numerically simulated model on the water-inrush risk under the geo-condition of thin rock-mass with thick-loose bed in Sima coal mine," *Journal of Safety and Environment*, vol. 14, no. 4, pp. 137–141, 2014.

[6] D. Ma, H. Y. Duan, X. B. Li, Z. H. Li, Z. L. Zhou, and T. B. Li, "Effects of seepage-induced erosion on nonlinear hydraulic properties of broken red sandstones," *Tunnelling and Underground Space Technology*, vol. 91, p. 102993, 2019.

[7] W. L. Shen, J. B. Bai, W. F. Li, and X. Y. Wang, "Prediction of relative displacement for entry roof with weak plane under the effect of mining abutment stress," *Tunnelling and Underground Space Technology*, vol. 71, pp. 309–317, 2018.

[8] Y. Xue, F. Gao, T. Teng, and Y. Xing, "Effect of gas pressure on rock burst proneness indexes and energy dissipation of coal samples," *Geotechnical and Geological Engineering*, vol. 34, no. 6, pp. 1737–1748, 2016.

[9] J. T. Chen, L. M. Yi, W. B. Sun, C. Lu, S. C. Zhang, and X. Z. Sun, "Development and application of new deep solid-fluid coupling similar materials," *Chinese Journal of Rock Mechanics and Engineering*, vol. 34, pp. 3956–3964, 2015.

[10] X. B. Meng, "Safety and high efficient mining technology of ultra thick seam with double system interaction in Datong mining area," *Coal Science and Technology*, vol. 45, no. 8, pp. 114–120, 2017.

[11] F. Du, Z. H. Li, G. H. Jiang, and Z. Q. Chen, "Types and mechanism of water-sand inrush disaster in west coal mine," *Journal of China Coal Society*, vol. 42, no. 7, pp. 1846–1853, 2017.

[12] T. H. Yang, W. H. Shi, H. L. Liu, B. Yang, X. Yang, and Z. B. Liu, "A non-linear flow model based on flow translation and its application in the mechanism analysis of water inrush through collapse pillar," *Journal of China Coal Society*, vol. 42, no. 2, pp. 315–321, 2017.

[13] J. F. Ju, J. L. Xu, Q. S. Li, W. B. Zhu, and X. Z. Wang, "Progress of water-preserved coal mining under water in China," *Coal Science and Technology*, vol. 46, no. 1, pp. 12–19, 2018.

[14] E. K. Hou, X. Y. Che, T. W. Long, Z. N. Ye, and Q. Wen, "Prediction method of water inrush from ground cracks in shallow buried seams," *Journal of China Coal Society*, vol. 45, no. 12, pp. 4154–4162, 2020.

[15] Y. J. Zhang, "Principle and key technologies of controlled water mining and practice of fully-mechanized mining under soft sandstone aquifer," *Journal of China Coal Society*, vol. 45, no. 10, pp. 3380–3388, 2020.

[16] J. Z. Yang, B. Zhang, X. Y. Fu, Z. Q. Wu, and W. B. Ji, "Formation mechanism of water and sand inrush channel in shallow buried bedrock face," *Journal of China Coal Society*, vol. 45, no. 12, pp. 4144–4153, 2020.

[17] S. C. Zhang, Y. Y. Li, J. P. Li, W. H. Yang, G. L. Wang, and Z. J. Wen, "Experimental studies on variation characteristics of physical parameters during water and sand burst through mining fractures," *Journal of China Coal Society*, vol. 45, no. 10, pp. 3548–3555, 2020.

[18] Y. Xue, T. Teng, F. N. Dang, Z. Ma, S. Wang, and H. Xue, "Productivity analysis of fractured wells in reservoir of hydrogen and carbon based on dual-porosity medium model," *International Journal of Hydrogen Energy*, vol. 45, no. 39, pp. 20240–20249, 2020.

[19] Z. Z. Cao, P. Xu, Z. H. Li, M. X. Zhang, Y. Zhao, and W. L. Shen, "Joint bearing mechanism of coal pillar and backfilling body in roadway backfilling mining technology," *CMC-Computers Materials & Continua*, vol. 54, no. 2, pp. 137–159, 2018.

[20] J. L. Xu, X. Z. Wang, W. T. Liu, and Z. G. Wang, "Effects of primary key stratum location on the height of water flowing fracture zone," *Chinese Journal of Rock Mechanics and Engineering*, vol. 28, pp. 380–385, 2009.

[21] Y. Xue, F. Gao, Y. N. Gao, X. Liang, Z. Z. Zhang, and Y. Xing, "Thermo-hydro-mechanical coupled mathematical model for controlling the pre- mining coal seam gas extraction with slotted boreholes," *International Journal of Mining Science and Technology*, vol. 27, no. 3, pp. 473–479, 2017.

[22] M. Faraji, A. Rezagholilou, M. Ghanavati, A. Kadkhodaie, and D. A. Wood, "Breakouts derived from image logs aid the estimation of maximum horizontal stress: a case study from Perth Basin, Western Australia," *Advances in Geo-Energy Research*, vol. 5, no. 1, pp. 8–24, 2021.

[23] Z. Z. Cao, F. Du, Z. H. Li, Q. T. Wang, P. Xu, and H. X. Lin, "Research on instability mechanism and type of ore pillar based on the fold catastrophe theory," *CMES-Computer Modeling in Engineering & Science*, vol. 113, no. 3, pp. 287–306, 2017.

[24] Z. H. Li, C. Z. ZhaiI, and L. F. Li, "Experimental study on water inrush mechanism due to floor faults activation in mining above confined aquifer," *Journal of Central South University (Science and Technology)*, vol. 46, no. 5, pp. 1806–1811, 2015.

[25] M. R. Mohammadi, H. Bahmaninia, S. Ansari et al., "Evaluation of asphaltene adsorption on minerals of dolomite and sandstone formations in two and three-phase systems," *Advances in Geo-Energy Research*, vol. 5, no. 1, pp. 39–52, 2021.

Hindawi
Geofluids
Volume 2021, Article ID 6616331, 21 pages
https://doi.org/10.1155/2021/6616331

Research Article

Measurement and Investigation on 1-D Consolidation Permeability of Saturated Clay considering Consolidation Stress Ratio and Stress History

Le Zhang[1], **Faning Dang**[1,2,3], **Jun Gao**[1], **and Jiulong Ding**[1]

[1]*School of Civil Engineering and Architecture, Xi'an University of Technology, Xi'an 710048, China*
[2]*State Key Laboratory of Eco-Hydraulics in Northwest Arid Region, Xi'an University of Technology, Xi'an 710048, China*
[3]*Shaanxi Key Laboratory of Loess Mechanics and Engineering, Xi'an University of Technology, Xi'an 710048, China*

Correspondence should be addressed to Faning Dang; dangfn@163.com

Received 17 December 2020; Revised 19 January 2021; Accepted 4 February 2021; Published 2 March 2021

Academic Editor: Chuangzhou Wu

To study the influence of consolidation stress ratio and stress history on 1-D consolidation permeability of saturated clay, one-dimensional consolidation permeability tests were carried out with GDS triaxial device. The results indicated that the permeability coefficient and void ratio of normally and overconsolidated saturated clay decreased with the increase of consolidation stress ratio under different consolidation stress ratios but the same stress history. And the amount of final sample's compression increased with the increase of the consolidation stress ratio. Under the condition of the same consolidation stress ratio but different stress history, the amount of final compression of the overconsolidated saturated clay was smaller than that of the normally consolidated saturated clay. Besides, the stress difference σ_{dv} between consolidation pressure σ and gravity stress σ_{cz} was fitted to the amount of the final sample's compression, and a good linear relationship between the stress difference σ_{dv} and the amount of the final sample's compression under each consolidation pressure was obtained. The results showed that it is necessary to consider the influence of consolidation stress ratio and stress history simultaneously on 1-D consolidation permeability of saturated clay. Meanwhile, it can accurately predict the amount of the final sample's compression after knowing the gravity stress. Moreover, a model prediction analysis was conducted on the saturated clay and recommended to use the modified Kozeny-Carman's equation to predict the permeability coefficient of Luochuan saturated clay during one-dimensional consolidation.

1. Introduction

Saturated clay (especially soft soil) has a considerable areal distribution range in China's coastal and inland areas. Due to the fact that soft clay foundation has the characteristics of high compressibility and low permeability, the duration of consolidation deformation tends to be longer. Therefore, the prediction of foundation settlement and settlement rate has become a major problem in engineering design [1]. In recent years, some new foundation improvement methods have been proposed, such as biogrouting and drainage powder sprayed piles [2, 3]. And the relationship between the foundation settlement and the time is always based on the one-dimensional Terzaghi's consolidation theory. The theory assumed that the permeability coefficient k, initial void ratio e, and compressibility coefficient a are all constant during the consolidation process, and the permeability of water in the soil obeys Darcy's law. However, some simplified assumptions are often not met in actual projects and can be extremely complicated. Davis and Raymond [4] obtained the analytical solution of the one-dimensional nonlinear consolidation equation. And Xie et al. [5] proposed an analytical solution for one-dimensional nonlinear consolidation of double-layered soils based on Davis. A method for simulating nonlinear characteristics of soil during compression by the hyperbolic curve was developed according to the compression behavior of soil [6]. Dumais and Konrad [7] established a one-dimensional model for the consolidation of thawed soil by using the relationship among effective stress, void ratio, and permeability coefficient. Yin and Feng [8, 9] stated that the variable compressibility must be considered in settlement calculation of soft soil stratum and proposed a new simplified method to calculate the settlement of a thick soil layer by considering the nonlinear compressibility. Besides, a one-dimensional nonlinear consolidation theory considering the thermal effect was established, which showed that the pore water dissipation rate or consolidation rate considering the secondary consolidation and temperature was higher than that when only considering secondary consolidation [10]. Some researchers have also conducted one-dimensional consolidation nonlinear studies on layered foundations. Xia et al. [11] assumed that the change in compressibility and permeability of the soil during the consolidation process was proportional, and the analytical solution of one-dimensional nonlinear consolidation for layered saturated soft soil was derived based on e-log σ' and e-log k_v relations. An analytical solution for one-dimension consolidation of a clay layer with variable compressibility and permeability under a ramp loading was derived based on the assumption that the initial effective stress of the clay layer remains constant with depth [12]. To consider the limitation of Terzaghi's theory, Lekha et al. [13] presented a generalized theory for the vertical consolidation of a compressible medium with finite thickness, and an analytical closed-form solution was obtained for vertical consolidation considering the variation in the compressibility and permeability. Moreover, Abbasi et al. [14] derived a one-dimensional nonlinear partial differential equation for the prediction of consolidation characteristics of soft clays considering variable values for C_v and took into consideration the changes in C_v during consolidation.

However, the aforementioned one-dimensional nonlinear consolidation models were based on the assumption of Darcy's flow. The characteristics of the non-Darcy's flow of water in the soil during one-dimensional consolidation have long been recognized. Mishra and Patra [15], Liu et al. [16], and Zhao and Gong [17] have studied the consolidation characteristic of saturated clay by considering the non-Darcy's flow. Li et al. [18] proposed a nonlinear model of consolidation by considering the non-Darcy's flow and stress history and found that the consolidation rate of overconsolidated soil with the non-Darcy's flow was slower than that with Darcy's flow. Moreover, Terzaghi's one-dimensional consolidation equation was modified and generalized based on the non-Darcy's flow in the soil [19]. However, the consolidation theory which can consider both geometrical nonlinearity and non-Darcy's flow is rarely reported. Li et al. [20] proposed a model for soft clay, which can allow for these two factors simultaneously, and the results showed that the difference between the consolidation rates caused by the non-Darcy's and Darcy's flows is significant. Besides, some researchers have also considered the effect of stress history on the one-dimensional consolidation [21–24] and have proposed one-dimensional nonlinear consolidation equations considering stress history.

Besides, the Terzaghi's one-dimensional consolidation theory assumed that the external load is applied instantaneously and remains unchanged during the consolidation process. However, the load acting on the foundation generally increases gradually with the construction process, and it is impossible to have "instantaneous" loading as assumed by Terzaghi. Schiffman [25] gave a theoretical solution to this situation. Next, Olson [26] proposed the mathematical solution of the average degree of consolidation in the first-order linear loading process. In recent years, some researchers have also conducted one-dimensional consolidation analysis under ramp loading mode according to different working conditions. Liu and Ma [27] studied the one-dimensional consolidation of soft ground with impeded boundaries under a depth-dependent ramp load. Similarly, Sun et al. [28] also introduced the exponentially time-growing drainage boundary and investigated the one-dimensional consolidation problem of soil under a ramp load. This one-dimensional consolidation theory can be utilized to describe the asymmetric drainage characteristics of the top and bottom drainage surfaces of the actual soil layer. However, the present solution is just for homogeneous soil. Tian et al. [29] obtained an analytical solution of excess pore-water pressure under a multistage load and the continuous drainage boundary. A different conclusion from Terzaghi's one-dimensional consolidation theory was obtained; that is, the degree of consolidation is also related to the applied time-dependent load. In the same year, a new simplified method was developed to calculate the settlement of multilayer soft soils exhibiting creep subjected to the multistage loading under a one-dimensional straining condition [30]. The advantage of this new simplified method is that the soft soils at both the normally consolidated state and overconsolidated state are considered in this approach by the "equivalent time" concept.

For further studying the nature of saturated clay permeability and consolidation, many researchers conducted laboratory tests on saturated clay. Experiments on the change characteristics of soil permeability coefficient under different head pressures were carried out and obtained that the permeability coefficient of soft soil decreased with the decreased of void ratio [31]. The consolidation and permeability combined tests of Xiaoshan soft clay were carried out by Qi [32] and showed that the compressibility and permeability of overconsolidated soils vary nonlinearly with the consolidation pressure during consolidation. Besides, Wen [33] had studied the one-dimensional consolidation theory of double-layered soil considering effects of stress history and revealed that the settlement was smaller and the rate of consolidation was greater than that of the one without considering the effects of the stress history. Moreover, the initial static stress state of the natural foundation soil; i.e., consolidation stress σ_1 and σ_3 or consolidation stress ratio K_c, where $K_c = \sigma_1/\sigma_3$, is also different. The effect of consolidation stress ratio on the pore pressure characteristics of saturated undisturbed loess under different stress paths was studied and showed that the effect of stress path on pore pressure characteristics during equal pressure consolidation was significantly different from that during K_0 consolidation [34].

Through reviewing the relevant studies, it was found that the influence of the initial stress state (consolidation stress ratio K_c) and stress history of natural foundation soil on the one-dimensional consolidation and permeability characteristics of saturated clay was rarely considered and only involved the properties of normally consolidated soil or overconsolidated soil on the one hand. In this study, the GDS-advanced consolidation device was utilized to conduct a series of one-dimensional consolidation-permeability combined tests under ramp loading on the loess silty clay in Luochuan, Shaanxi. Then, the effects of consolidation stress ratio and stress history on one-dimensional consolidation permeability of saturated clay were explored based on test results. Finally, a model prediction analysis was performed which is aimed at selecting a model suitable for predicting the permeability coefficient of Luochuan saturated clay.

2. Test and Method

2.1. Sample Preparation and Method. The clay soil samples used in this study were loess-like silty clay taken from Luochuan, Shaanxi. The sampling depth is 7-8 m, and the main physical properties of the silty clay are illustrated in Table 1.

Due to the heterogeneity of undisturbed clay samples, the samples used in this study were all saturated homogeneous remolded soil samples, and the preparation processes were as follows:

(1) Firstly, the soil was air-dried, ground, and sieved through a 2 mm sieve. Then, the air-dried moisture content was measured after fully mixing. The soil was prepared to a moisture content (11.6%) that can be used for sample preparation. Finally, the prepared soil was placed in a plastic bag and sealed for 24 hours to allow moisture equalization

(2) The moisture content of the prepared soil sample was measured, and the mass of soil required for sample preparation was calculated. In this study, the pressure sampling method was used for sample preparation, and the samples with 3.91 cm in diameter and 8 cm in height were used. The sample was divided evenly into five layers during sample preparation. For making better contact between the sample layers, the contact surface should be shaved before each compaction. According to the e-log p curve, the preconsolidation pressure of Luochuan silty clay was 115 kPa, and the soil was considered to be in a normally consolidated state. Therefore, the remolded soil samples were consolidated under a pressure of 115 kPa. After the consolidation was completed, the soil samples were considered to be in a normally consolidated state

(3) To reflect the influence of consolidation stress ratio on one-dimensional consolidation permeability of saturated clay, a consolidation test was conducted under the condition of $K_c = 1.5$ firstly, and it was obtained that the amount of soil compression reached 10 mm when the consolidation stress was 600 kPa. According to the Chinese standard for the geotechnical testing method (GB/T 50123; National Standards of People's Republic of China 2019), the sample was considered to be damaged when the strain reaches 15%. Therefore, the consolidation stress ratio was taken as 1, 1.3, and 1.5, respectively

2.2. Experimental Device. A GDS triaxial device imported from the UK was used for the one-dimensional consolidation and permeability tests, as shown in Figure 1. The test device can not only perform traditional consolidation tests but also perform permeability tests under the condition of the constant consolidation pressure, which can directly measure the permeability coefficient under various consolidation stress levels. For conducting the consolidation permeability test for saturated remolded soil samples, a set of saturated soil base and dual-channel sample cap was redesigned and processed to achieve the connection of back pressure controller with sample's base and cap, which ensured that the water drained from the upper and lower ends of the sample was drained into the back pressure controller. Hence, the sample's volume change can be accurately measured. The schematic diagram of the GDS device was shown in Figure 2.

2.3. Test Procedure. For studying the one-dimensional consolidation permeability characteristics of saturated clays considering the initial consolidation state and consolidation stress ratio, one-dimensional consolidation permeability tests were performed. The specific test steps were as follows:

(1) Before loading the sample into the pressure chamber, the base and sample cap were vented to reduce the volume of gas entering the sample as much as possible when the sample was saturated with back pressure

(2) After completion of the sample preparation, the soil sample was saturated by the vacuum saturation method firstly and then by the back pressure. When the pore pressure coefficient B was close or equal to 1, the sample was considered to be fully saturated

(3) Then, the sample was consolidated by applying consolidation stress with a constant duration of 24 h at each stress level. When the pore pressure dissipated completely, the axial deformation was basically unchanged, and the volume change became stable; the consolidation was considered complete. The specific test scheme is shown in Table 2, and the schematic diagram of multistage ramp loading is shown in Figure 3. In Figure 3, t_{j1}-t_{j4} represented the time required to reach each level of load, and t_{j1}-$t_{j4} = 30$ mins. t_1-t_4 represented the total duration of consolidation at each stage, and $t_1 = t_2 = \cdots = t_4 = 24$ h

(4) Subsequently, the permeability test was performed by the water head difference formed by the back pressure and the bottom pressure. To ensure that the effective stress acting on the soil sample remains unchanged in the process of the permeability test, the following equation must be satisfied between the pressure

$$p_1 - p_2 \geq p_2 - p_3, \tag{1}$$

where p_1 is confining pressure, p_2 is back pressure, and p_3 is bottom pressure. The bottom pressure is always 0 kPa in this

Table 1: Physical properties of intact Q_3 loess.

Specific gravity G_s	Water content w (%)	Dry density ρ_d (g/cm^3)	Liquid limit w_L (%)	Plastic limit w_P (%)	Particle size fraction (%) >0.075 mm	0.075~0.005 mm	<0.005 mm	Soil classification
2.7	13.3	1.34	28.4	19.2	4	73	23	Silty clay

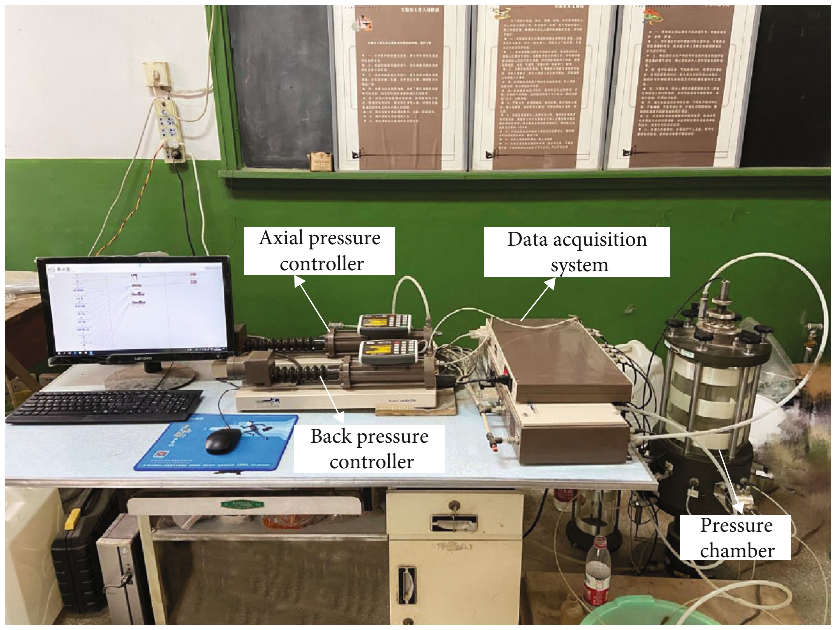

Figure 1: GDS triaxial device.

study, and the duration of permeability induced from water head difference is 70 min. The test plan is listed in Table 3.

To study the influence of stress history on the one-dimensional consolidation permeability of saturated clay, the consolidation stress with the same increment was applied. In this study, the double-drainage condition was adopted, and the one-dimensional consolidation diagram of the saturated clay layer is shown in Figure 4.

3. Result and Discussion

3.1. Effect of Consolidation Stress Ratio on One-Dimensional Consolidation Permeability of Normally Consolidated Saturated Clay

3.1.1. Permeability Test Results and Analysis. When the consolidation stress ratio $K_c = 1$, 1.3, and 1.5, the relationship curves of permeability coefficient k and void ratio e with consolidation stress σ in one-dimensional consolidation permeability of normally consolidated soil are shown in Figures 5 and 6, respectively.

It can be seen from Figure 5 that the initial permeability coefficients at three consolidation stress ratios were the same before applying consolidation stress. The permeability coefficient k decreased with the increase of consolidation stress, which was independent from the consolidation stress ratio. And the permeability coefficient decreased as the consolidation stress ratio increased under the same consolidation stress. On the whole, the permeability coefficient showed a nonlinear decreasing trend with the increase of consolidation stress. As the consolidation stress continued to increase, the rate at which the permeability coefficient k decreased as the consolidation stress increased gradually slows down.

The consolidation stress ratio K_c had a certain effect on the permeability coefficient k. As the consolidation stress increased, the smaller the consolidation stress, the greater the effect of the consolidation stress ratio on the permeability coefficient. Besides, the permeability coefficient is an important parameter for the consolidation analysis of saturated clay. Therefore, it is necessary to study the consolidation stress ratio on one-dimensional consolidation permeability of saturated clay.

In the one-dimensional consolidation process of saturated clay, the determination of the void ratio e, compression coefficient a_v, and compression modulus E_s is the same as the traditional consolidation test method.

The void ratio e_i of the sample after consolidation stability under various consolidation pressures can be obtained from

$$e_i = e_0 - (1 + e_0) \cdot \frac{\sum \Delta h_i}{h_0}, \tag{2}$$

where e_0 and h_0 are the void ratio and initial height of the sample after back pressure saturation, e_i is the void ratio of the sample after consolidation stability, and $\sum \Delta h_i$ is the cumulative compression of the sample at the level of

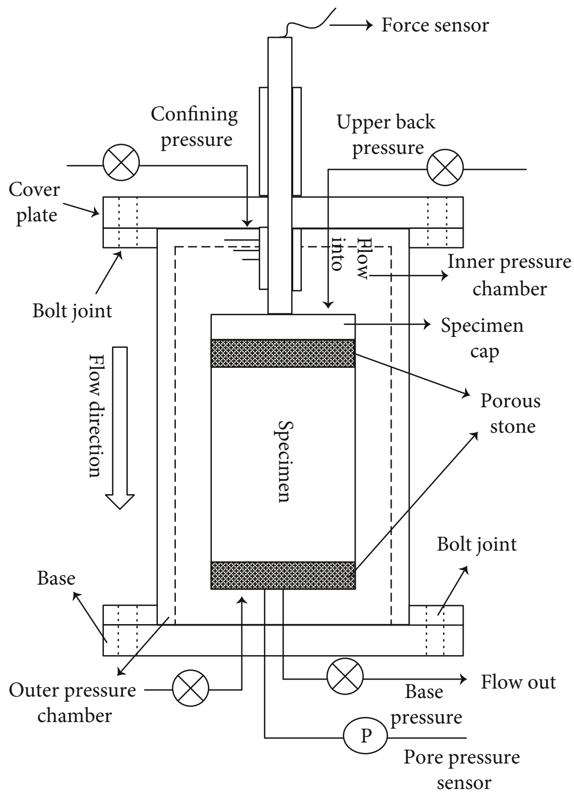

Figure 2: Schematic diagram of pressure application for consolidation and permeability tests.

Table 2: Scheme and procedure of staged consolidation test.

Consolidation state	Loading step
Normally consolidated	115→140→165→190→215 kPa
Overconsolidated	115→25→50→75→100 kPa

consolidation stress σ_i. Then, the height of the sample after compression is expressed by

$$h = h_0 - \sum \Delta h_i. \quad (3)$$

The compression coefficient a_v in a certain stress range can be yield by

$$a_v = \frac{e_i - e_{i+1}}{\sigma_{i+1} - \sigma_i}, \quad (4)$$

where e_i and e_{i+1} are the void ratios corresponding to σ_i and σ_{i+1}, respectively, σ_i and σ_{i+1} are the consolidation stress values of a certain level and the next level, respectively.

The compression modulus E_s in a certain stress range can be obtained by

$$E_s = \frac{1 + e_0}{a_v}. \quad (5)$$

According to Equations (2), (3), (4), and (5), the deformation parameters of the sample during the consolidation process are illustrated in Table 4. The definition of each parameter in Table 4 was the same as above. For example, the amount of compression, void ratio, compressibility, and compression modulus of the corresponding sample under the consolidation stress of 165 kPa were the calculated results of various parameters within the range of consolidation stress of 140-165 kPa.

In this study, the void ratio after back pressure saturation was taken as the initial void ratio e_0 of the sample. It can be seen from Figure 6 that the corresponding initial void ratio e_0 when $K_c = 1$, 1.3, and 1.5 was 1.015. It also can be seen from Equation (2) that the void ratio e during the consolidation stage is related to the initial void ratio e_0, initial height h_0 , and the cumulative compression of the sample $\sum \Delta h_i$ under certain consolidation stress.

From Figure 6, the void ratio decreased with the increase of consolidation stress. When $\sigma = 215$ kPa, the corresponding void ratios of $K_c = 1.0$, 1.3, and 1.5 were 0.904, 0.876, and 0.834, respectively. After obtaining the amount of sample's compression, the variation curve of void ratio and time can be drawn, which is shown in Figure 7.

Both Figures 5 and 6 show the nonlinear characteristics of the soil sample during the consolidation process. As increased with the consolidation stress, the pore volume of the soil decreased continuously due to the drainage of pore water, which resulted in the permeability coefficient of the soil was continuously decreasing. The reduction of the void ratio was also related to the consolidation stress ratio K_c to a certain extent. When $K_c = 1$, 1.3, and 1.5, the corresponding reductions for the void ratio were 10.97%, 13.70%, and 17.79%, which illustrated the importance of considering the consolidation stress ratio on one-dimensional consolidation permeability of saturated clay in this study.

It can be seen from Figure 7 that the void ratio e showed a stepwise downward trend with time. The void ratio of the sample hardly changes during the permeability stage, and the change of the sample's void ratio mainly occurred during the consolidation stage.

3.1.2. Consolidation Test Results and Analysis. The consolidation coefficient is an important parameter in both geotechnical and geoenvironmental engineering [35]. According to the Terzaghi's one-dimensional consolidation theory, the consolidation coefficient of the sample can be obtained according to

$$C_v = \frac{k(1 + e_1)}{a_v \cdot \gamma_w}, \quad (6)$$

where C_v represents the consolidation coefficient of the soil (cm^2/s); k is the permeability coefficient (cm/s); e_1 is the initial void ratio; a_v is the compression coefficient in a certain consolidation stress range (MPa^{-1}); and γ_w is the unit weight of water (chosen as 10 kN/m^3). In this study, the initial void ratio and the initial height were determined by assuming that the completed state of the previous level of stress consolidation is the initial state of this level.

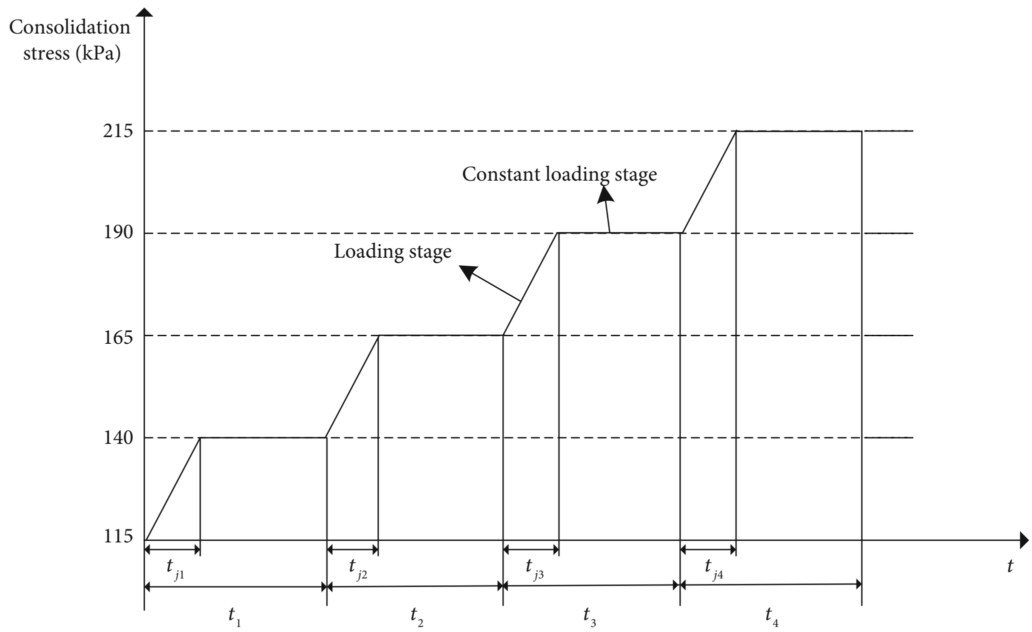

Figure 3: Schematic diagram of multistage ramp loading.

Table 3: Permeability test scheme.

Consolidation state	Consolidation stress (kPa)	Water head difference (kPa)
Overconsolidated	25	5, 10
	50	10, 20
	75	10, 20
	100	20, 40
Normally consolidated	140	20, 40, 60
	165	20, 40, 60, 80
	190	20, 40, 60, 80
	215	20, 40, 60, 80, 100

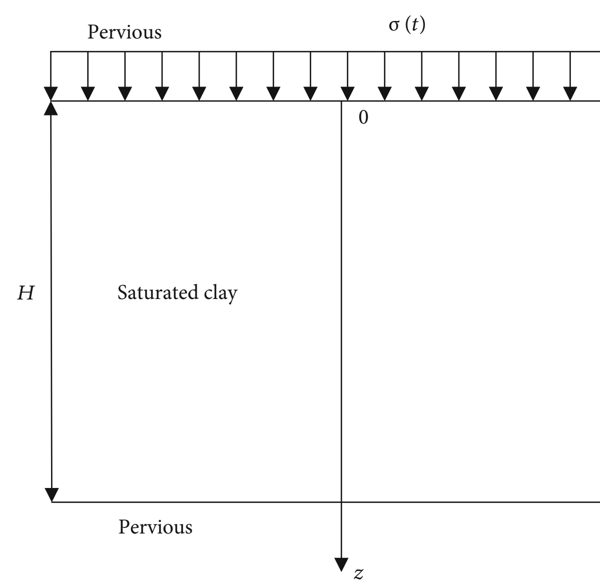

Figure 4: One-dimensional consolidation sketch.

According to Equation (6), the consolidation coefficients of the sample with $K_c = 1$, 1.3, and 1.5 are shown in Table 5. Following Table 5, the C_v-σ relationship curve was plotted with the consolidation stress σ as the abscissa and the consolidation coefficient C_v as the ordinate, which is shown in Figure 8.

It can be seen from Figure 8 that when $K_c = 1$, 1.3, and 1.5, the consolidation coefficient C_v showed a trend of increasing first and then decreasing with the increase of consolidation stress. Some researchers have also studied the changing law of consolidation coefficient with consolidation stress and time during the process of consolidation [14, 36]. It was found that with the increase of consolidation stress, the change of consolidation coefficient was not only monotonously increasing or decreasing. Li et al. [36] established the consolidation coefficient expression related to pore development and revealed that the development of the sample pore greatly affected the changing law of the consolidation coefficient. In the consolidation process, the consolidation coefficient of the soil was a variable, which was related to the effective stress acting on the soil sample. The consolidation coefficient was an increasing function relative to the void ratio under a relatively lower effective stress level. With the soil sample being further compressed, the void ratio continued to decrease, which resulted in a decrease in the consolidation coefficient. As shown in Figure 8, the consolidation stress ratio had an obvious influence on the consolidation coefficient, but it did not affect the distribution shape of the consolidation coefficient. The larger the consolidation stress ratio, the smaller the consolidation coefficient.

The relationship curve between the amounts of sample's compression and time is shown in Figure 9.

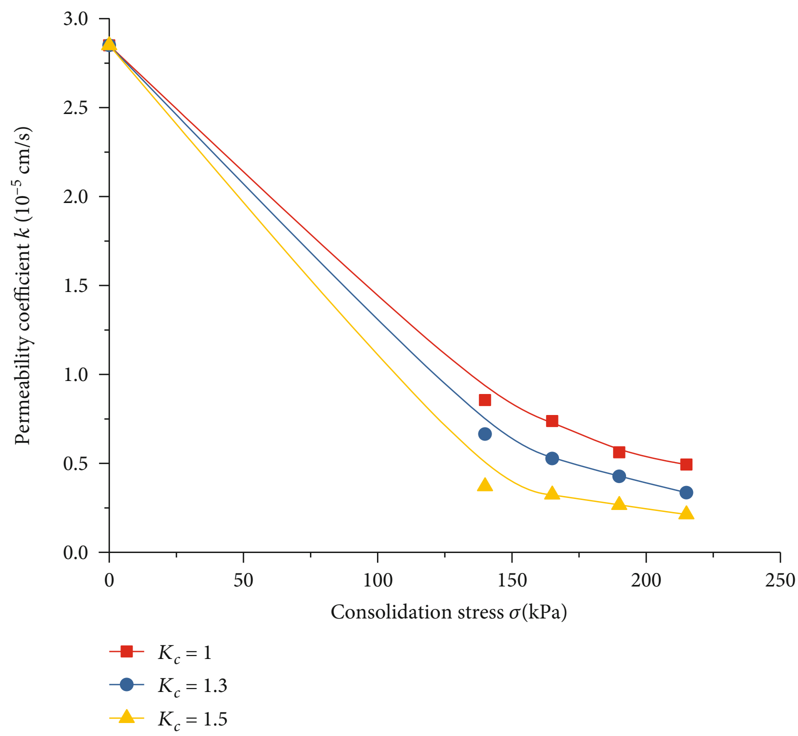

Figure 5: The curve of permeability coefficient of normally consolidation clay with consolidation pressure at different consolidation stress ratios.

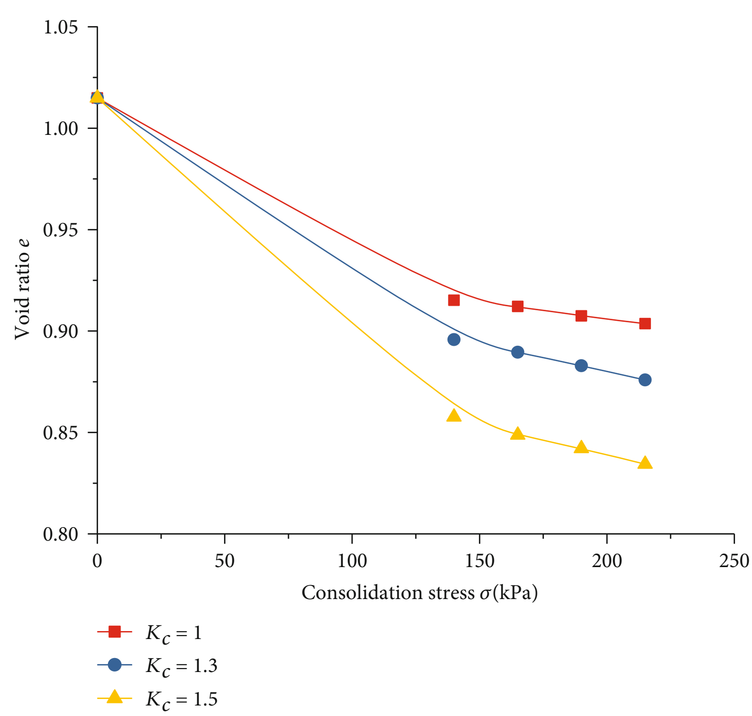

Figure 6: The curve of void ratio of normally consolidation clay with consolidation pressure at different consolidation stress ratios.

Table 4: Calculation results of mechanical parameters of normally consolidation clay during consolidation.

Consolidation stress ratio K_c	Consolidation stress (kPa)	Sample's compression (mm)	Sample's height after compression (mm)	Void ratio e	Compression coefficient (MPa^{-1})	Compression modulus E_s
1	140	3.96	76.03	0.915	0.71	2.83
	165	4.08	75.91	0.912	0.12	16.46
	190	4.27	75.72	0.907	0.19	10.72
	215	4.43	75.56	0.904	0.17	12.16
1.3	140	4.73	75.26	0.896	0.85	2.37
	165	4.98	75.01	0.890	0.25	8.13
	190	5.24	74.75	0.883	0.27	7.57
	215	5.52	74.47	0.876	0.28	7.20
1.5	140	6.24	73.75	0.858	1.12	1.79
	165	6.60	73.39	0.849	0.36	5.63
	190	6.86	73.13	0.842	0.27	7.57
	215	7.17	72.82	0.834	0.31	6.59

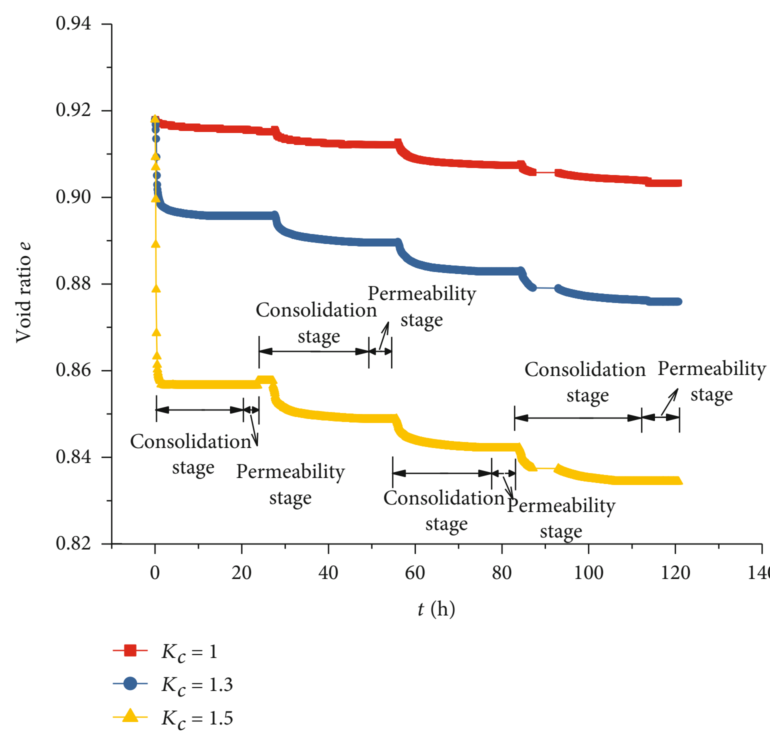

Figure 7: The curve of void ratio of normally consolidation clay with time.

It can be seen from Figure 9 that the amount of sample's compression increased stepwise with time under three consolidation stress ratios. The amount of sample's compression at the permeability stage was almost 0 mm, and the sample's compression mainly occurred at the consolidation stage. It can also be seen from the figure that the amount of sample's final compression corresponding to $K_c = 1$, 1.3, and 1.5 were 4.43, 5.52, and 7.17 mm, respectively. Therefore, considering the initial stress state of the soil in the one-dimensional consolidation of saturated clay plays a good role in accurately predicting the final settlement of the soil in the future.

Figure 10 displays the variation curve of the permeability coefficient of normally saturated clay with the void ratio in the logarithm coordinate. Taking the slope of the linear fitting line as permeability index C_k and C_k corresponding to $K_c = 1$, 1.3, and 1.5 was expressed by C_{k1}, $C_{k1.3}$, and $C_{k1.5}$, respectively. Then, $C_{k1} = 0.047$, $C_{k1.3} = 0.067$, and $C_{k1.5} = 0.093$.

It can be seen from Figure 10 that the permeability coefficient k of the sample decreased as the void ratio decreased. When the consolidation stress $\sigma = 215$ kPa, the corresponding permeability coefficients of $K_c = 1$, 1.3, and 1.5 were as follows: 0.493×10^{-5} cm/s, 0.335×10^{-5} cm/s, and 0.213×10

Table 5: Calculated value of consolidation coefficient.

Consolidation stress ratio K_c	Consolidation stress (kPa)	Consolidation coefficient (10^{-5} cm^2/s)
1	140	0.230
	165	1.152
	190	0.571
	215	0.567
1.3	140	0.148
	165	0.401
	190	0.302
	215	0.225
1.5	140	0.061
	165	0.167
	190	0.184
	215	0.128

$^{-5}$ cm/s, which was about the initial permeability coefficient 0.173, 0.118, and 0.075 times. The greater the K_c, the greater the amplitude of variation.

Figure 11 represents the relation curve of the void ratio of normally consolidated saturated clay with the consolidation stress. The compression index corresponding to $K_c = 1$, 1.3, and 1.5 was represented by C_{c1}, $C_{c1.3}$, and $C_{c1.5}$. Therefore, C_{c1}, $C_{c1.3}$, and $C_{c1.5}$ were equal to 0.063, 0.106, and 0.123, respectively, where the compression index was a maximum when $K_c = 1.5$.

It can be seen from the e-log σ curve in Figure 11 that the void ratio decreased as the consolidation pressure increased, and the greater the consolidation stress ratio K_c, the smaller the void ratio e. The test results showed the nonlinearity of the one-dimensional consolidation of the soil sample.

3.1.3. Analysis of Compression Curve. For a homogeneous soil layer with a natural gravity of γ, at any depth z under the natural ground, the vertical self-weight stress σ_{cz} of the soil is equal to the gravity of the soil column per unit area. That is,

$$\sigma_{cz} = \sum_{i=1}^{n} \gamma_i h_i, \tag{7}$$

where σ_{cz} is the vertical effective self-weight stress of the soil at any depth z under the natural ground (kPa); n is the total number of soil layers within the depth z; h_i is the thickness of the ith soil layer (m); γ_i is the natural unit weight of the ith soil layer; and the effective unit weight is taken for the soil layer below the groundwater level (kN/m^3).

The sampling depth is 7-8 m, and its self-weight stress σ_{cz} is in the range of 106.4 ~ 121.6kN. The preconsolidation pressure is 115 kPa, and the soil is considered to be in the normally consolidated state. Therefore, it was determined that the self-weight stress of the sample used in the study was 115 kPa. Then, the difference σ_{dv} between the consolidation pressure σ applied in the test and the self-weight stress σ_{cz} of the soil layer was expressed by

$$\sigma_{\mathrm{dv}} = \sigma - \sigma_{\mathrm{cz}}. \tag{8}$$

The calculated values of the difference between the consolidation pressure and the self-weight stress of the soil layer when the consolidation stress ratio $K_c = 1$ are listed in Table 6. The fitted relation curve between the amount of sample's final compression s_f and σ_{dv} is shown in Figure 12.

It can be seen from Figure 12 that the stress difference σ_{dv} had a good linear relationship with the amount of sample's final compression at each consolidation pressure. After knowing the self-weight stress of the soil, the amount of final compression of the sample can be predicted more accurately, which had an important application value to the engineering.

3.2. Effect of Consolidation Stress Ratio on One-Dimensional Consolidation Permeability of Overconsolidated Saturated Clay. As mentioned above, the preconsolidation pressure of Luochuan loess-like silty clay σ_c was 115 kPa. Therefore, the consolidation stress applied to the soil sample was 25, 50, 75, and 100 kPa, and the corresponding overconsolidation ratios (OCR) are 4.6, 2.3 1.5, and 1.2, respectively.

3.2.1. Permeability Test Results and Analysis. Table 7 shows the measured values of the permeability coefficient at various consolidation pressures for overconsolidated soil.

According to Table 7 and Equation (2), the relationship curves of permeability coefficient, void ratio, and consolidation stress at different consolidation stress ratios K_c were drawn, which are shown in Figures 13 and 14.

As can be seen from Figures 13 and 14, for overconsolidated soils, both the permeability coefficient and the void ratio decreased with increasing consolidation pressure at different consolidation stress ratios, and the larger K_c, the smaller e and k. Taking the consolidation stress ratio $K_c = 1.0$ as an example, the permeability coefficients when the consolidation stress was 50, 75, and 100 kPa were reduced by 24.20%, 26.66%, and 43.48%, respectively, compared with that at 25 kPa. Besides, the permeability coefficient and void ratio of overconsolidated soil decreased with the increase of the consolidation stress ratio at the same consolidation pressure. This phenomenon was the same as that of normally consolidated soil; that is, the permeability coefficient was related to the sample's void ratio, and the larger the consolidation stress ratio, the smaller the sample's void ratio.

3.2.2. Consolidation Test Results and Analysis. According to Equations (2), (3), (4), and (5), the deformation parameters of consolidation and the amount of compression of overconsolidated soils were calculated, as shown in Table 8.

According to Table 8, the relationships between the sample's void ratio and compression over time during the consolidation and compression process are shown in Figures 15 and 16.

It can be seen from Figure 15 that the amount of sample's compression increased with time during the one-dimensional consolidation of the overconsolidated soil. And the sample's compression mainly occurred during the consolidation stage.

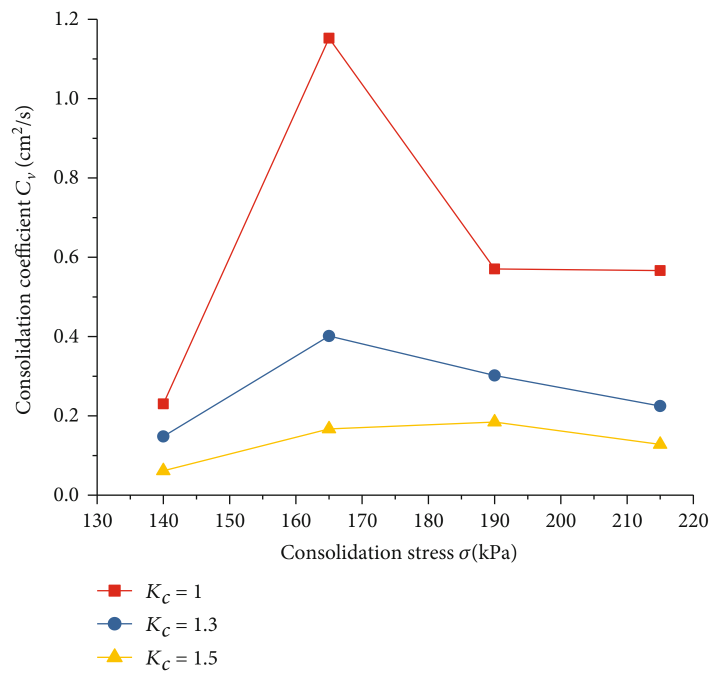

Figure 8: The curve of consolidation coefficients of normally consolidation clay with consolidation pressure at different consolidation stress ratios.

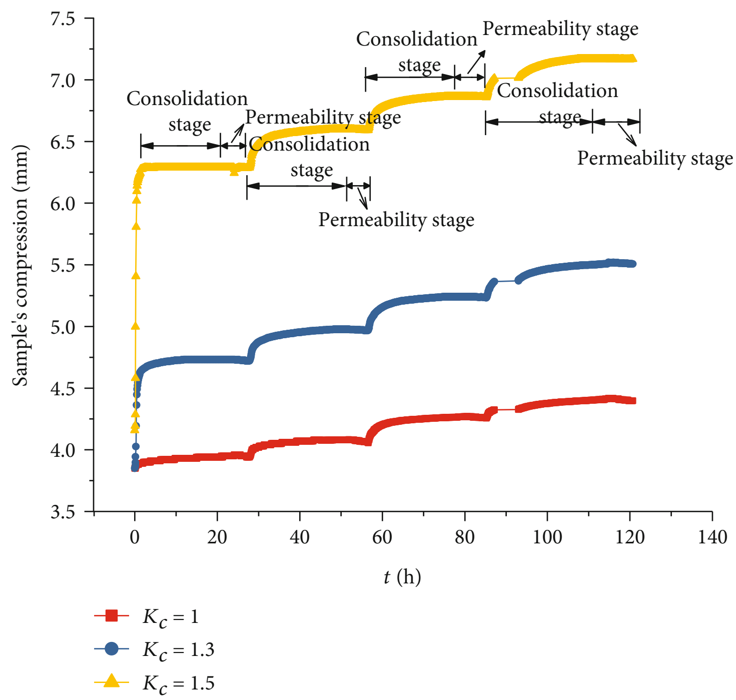

Figure 9: The curve of normally consolidation clay compression with time at different consolidation stress ratios.

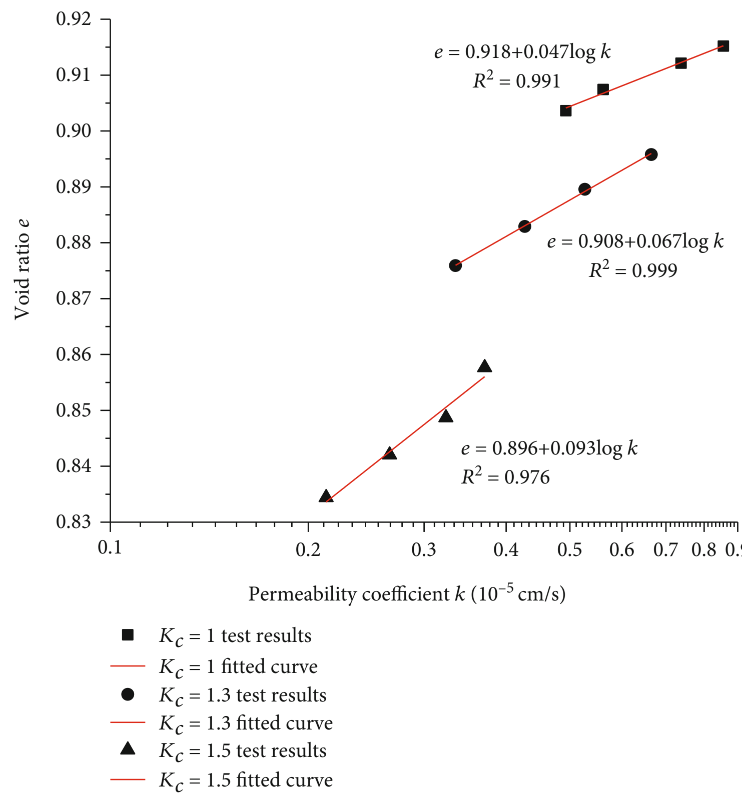

Figure 10: e-log k curve.

Taking the consolidation stress ratio $K_c = 1$ as an example, when the consolidation stress was 25, 50, 75, and 100 kPa, the corresponding amount of sample's compression was 3.23, 3.31, 3.41, and 3.53 mm, respectively. However, the amount of sample's compression during the permeability stage under the corresponding consolidation stress hardly changed. The amount of final sample's compression varied with different consolidation stress ratios. When $K_c = 1$, 1.3, and 1.5, the amount of final sample's compression was 3.53, 3.92, and 4.57 mm, respectively, which revealed that the greater the consolidation stress ratio, the greater the final sample's compression.

Accordingly, from Figure 16, it can be seen that the void ratio of the sample gradually decreased with time, and the variation of the void ratio mainly occurred in the consolidation stage, while hardly changing in the permeability stage. Different consolidation stress ratios resulted in a different final void ratio of the sample. That is, when $K_c = 1$, 1.3, and 1.5, the corresponding void ratio was 0.926, 0.916, and 0.900, respectively. In other words, the greater the consolidation stress ratio, the smaller the final void ratio of the sample. The final void ratio was reduced by 8.76%, 9.73%, and 11.35% compared with the initial void ratio.

3.2.3. Compression Curve Analysis. According to Equations (7) and (8), the difference between the consolidation pressure of saturated clay and the self-weight stress of the soil layer can be obtained. Only the calculated values when $K_c = 1$ are listed in Table 9.

The relationship curve between the stress difference σ_{dv} and the amount of final sample's compression s_f was linearly fitted, as shown in Figure 17.

It can be seen from Figure 17 that there was a good linear relationship between the stress difference of overconsolidated soil and the amount of final sample's compression under each consolidation pressure, and the amount of final compression of overconsolidated soil can be accurately predicted after knowing the self-weight stress of soil.

3.3. Effect of Stress History on One-Dimensional Consolidation and Permeability of Saturated Clay. The compressibility and permeability of soil play an important role in consolidation, which are closely related to stress history [33]. The research results showed that the settlement of the foundation was smaller and the consolidation development was faster when the stress history effect was considered. Besides, the settlement development rate increased with the increase of preconsolidation pressure.

According to the obtained test results, a series of consolidation and settlement curves of normally and overconsolidated soil under the condition of a certain consolidation stress ratio K_c (and $K_c = 1$) was acquired.

Figure 18 is the variation curve of the amount of sample's compression with the time of normally and overconsolidated saturated clay during the consolidation process when the consolidation stress ratio $K_c = 1$. It can be seen from the figure that the amount of compression of

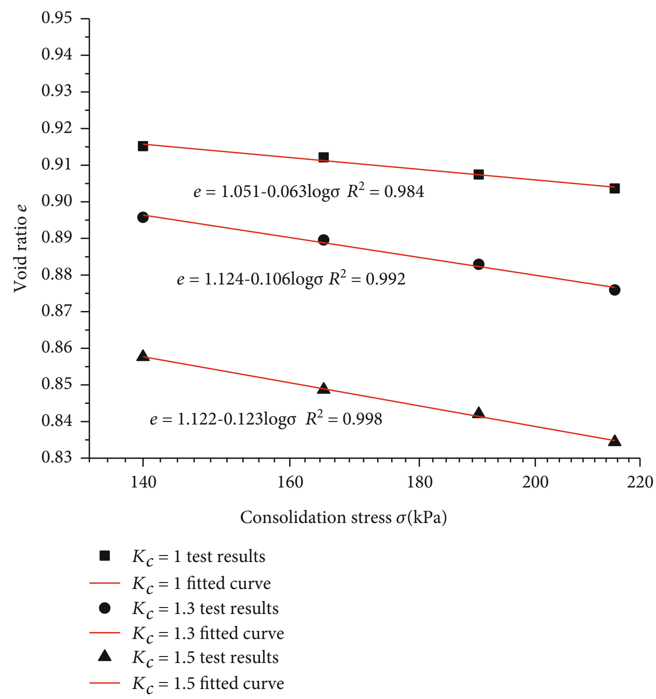

Figure 11: e-log σ curve.

Table 6: Stress calculations of normally consolidation clay.

Stress state	σ (kPa)	σ_{cz} (kPa)	σ_{dv} (kPa)
Normally consolidated	140	115	25
	165		50
	190		75
	215		100

overconsolidated soil was less than that of normally consolidated soil during the same consolidation time. Hu [37] used the semianalytical method to study the one-dimensional linear and nonlinear consolidation behavior of single-layer overconsolidated saturated soil foundation. The results revealed that the settlement of the foundation was smaller and the consolidation developed faster when the influence of stress history was considered, which was consistent with the conclusion of this study. That is, the amount of final compression of the overconsolidated soil under the 5th continuous load was 3.53 mm, while the normally consolidated soil was 4.43 mm.

Figures 19 and 20 are the variation curve of the void ratio e and the permeability coefficient k with the consolidation pressure during the process of one-dimensional consolidation permeability of normally and overconsolidated saturated clay.

It can be seen from Figure 19 that the void ratio of normally and overconsolidated clays decreased monotonously with the increase of consolidation stress during the process of one-dimensional consolidation permeability. Accordingly, the permeability coefficient decreased nonlinearly with the increase of consolidation stress. The compressibility and permeability of soil in the overconsolidation stage were much less than that in the normally consolidation stage.

As can be seen from Figures 18, 19, and 20, considering the stress history was of great significance for one-dimensional consolidation of saturated clay when the consolidation stress ratio K_c was constant. However, stress history did not affect the relationship between the permeability coefficient and void ratio.

4. Model Prediction of Saturated Clay Permeability Coefficient

All fields of geotechnical engineering are closely related to the permeability of rock and soil [38, 39]. In engineering practice, it is particularly important to accurately and quickly predict the permeability coefficient of saturated clay. The previous section proposed that stress history did not affect the relationship between permeability coefficient and void ratio; thus, only the permeability coefficient of normally consolidated saturated clay was predicted in this section. The study selected the prediction equations of permeability coefficient considering the initial consolidation state proposed by Gao et al. [40], Stokes flow permeability coefficient equation, and consolidation degree permeability equation to predict the permeability coefficient of saturated clay in Luochuan, Shaanxi.

(1) When expressed by the permeability coefficient prediction equations proposed by Gao et al. [40], there were

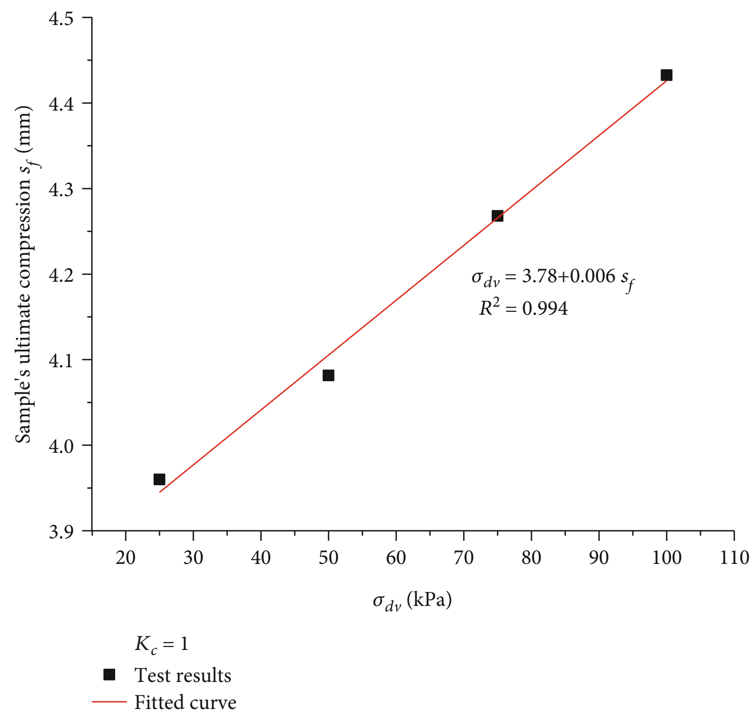

Figure 12: The relation curve between soil ultimate compression and stress difference.

$$k = k_0 \frac{1+e_0}{e_0^2} \frac{\left(e_0 - C_c \lg\left(\left(\sigma_0 + \Delta\sigma\right)/\sigma_0\right)\right)^2}{1 + e_0 - C_c \lg\left(\left(\sigma_0 + \Delta\sigma\right)/\sigma_0\right)}, \tag{9}$$

$$k = k_0 \frac{1+e_0}{e_0^3} \frac{\left(e_0 - C_c \lg\left(\left(\sigma_0 + \Delta\sigma\right)/\sigma_0\right)\right)^3}{1 + e_0 - C_c \lg\left(\left(\sigma_0 + \Delta\sigma\right)/\sigma_0\right)}. \tag{10}$$

Equations (9) and (10) were the permeability coefficient prediction equations for normally consolidated soil based on the Darcy's permeability coefficient equation and the Kozeny-Carman's permeability coefficient equation, respectively, where k_0 and e_0 are the initial permeability coefficient and void ratio of the soil, respectively

(2) When expressed by the Stokes flow permeability coefficient equation, there was

$$k = \frac{\gamma_{wz} R^2 e}{8\eta(1+e)}, \tag{11}$$

where R is the radius of the capillary (cm); η is the dynamic viscosity coefficient of free water (g·s·cm^{-2}); γ_{wz} is the weight of free water (kN/m^3); and e is the void ratio of soil. According to the method used by Gao et al. [40], during the soil compression process, the basic physical parameters such as the dynamic viscosity coefficient of water, and the weight of free water are constant; only the permeability coefficient and void ratio are changing. Therefore, these constant physical parameters can be expressed by the initial permeability coefficient k_0 and the initial porosity ratio e_0. Equation (11) yields

Table 7: Permeability coefficient at various consolidation pressures.

Consolidation stress ratio K_c	Consolidation stress (kPa)	Average permeability coefficient k (10^{-5} cm/s)
1	25	1.504
	50	1.140
	75	1.103
	100	0.850
1.3	25	0.802
	50	0.650
	75	0.615
	100	0.513
1.5	25	0.776
	50	0.604
	75	0.563
	100	0.476

$$\frac{\gamma_{wz} R^2}{8\eta} = k_0 \frac{1+e_0}{e_0}. \tag{12}$$

Substituting Equation (12) into Equation (11), the permeability coefficient of soil was obtained as Equation (13).

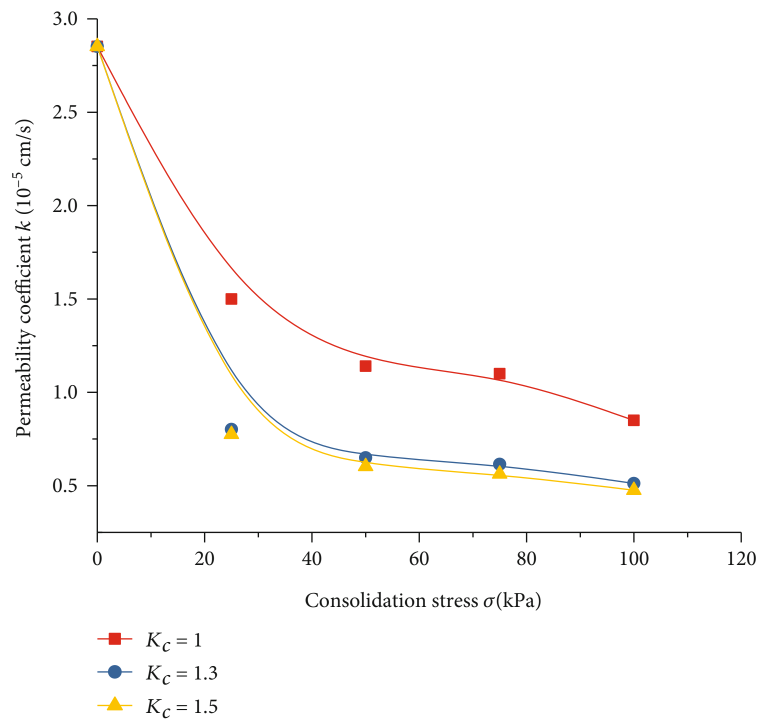

Figure 13: The curve of permeability coefficient of overconsolidation clay with consolidation pressure at different consolidation stress ratios.

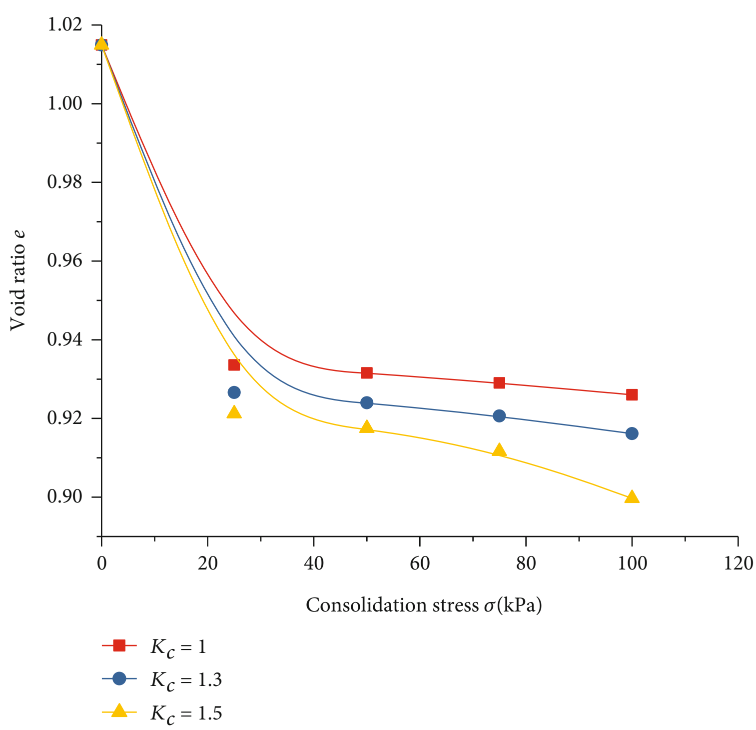

Figure 14: The curve of the void ratio of overconsolidation clay with consolidation pressure at different consolidation stress ratios.

Table 8: Calculation results of deformation parameters of overconsolidation clay during consolidation.

Consolidation stress ratio K_c	Consolidation stress (kPa)	Sample's compression (mm)	Sample's height after compression (mm)	Void ratio e	Compression coefficient (MPa^{-1})	Compression modulus (MPa)
1	25	3.23	76.76	0.934	3.25	0.62
	50	3.31	76.68	0.932	0.08	25.00
	75	3.41	76.58	0.929	0.10	20.00
	100	3.53	76.46	0.926	0.12	16.66
1.3	25	3.51	76.48	0.927	3.53	0.57
	50	3.61	76.38	0.924	0.10	19.38
	75	3.74	76.25	0.921	0.13	15.04
	100	3.92	76.07	0.916	0.18	11.20
1.5	25	3.72	76.27	0.921	3.75	0.54
	50	3.87	76.12	0.918	0.15	13.62
	75	4.10	75.89	0.912	0.23	8.61
	100	4.57	75.42	0.900	0.48	4.22

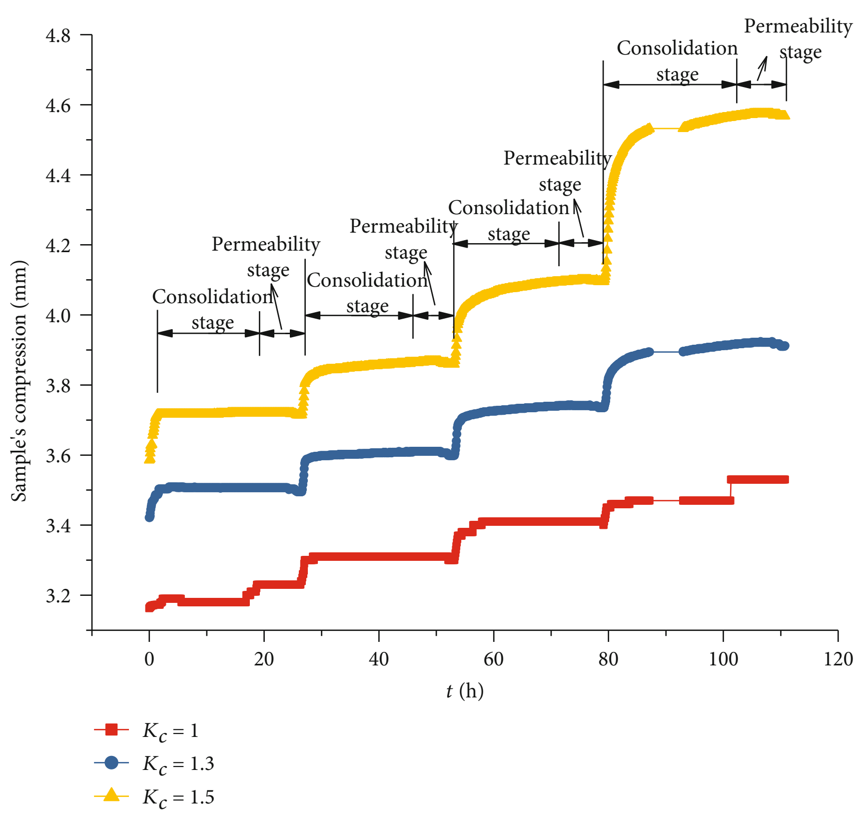

Figure 15: The curve of overconsolidation clay compression with time at different consolidation stress ratios.

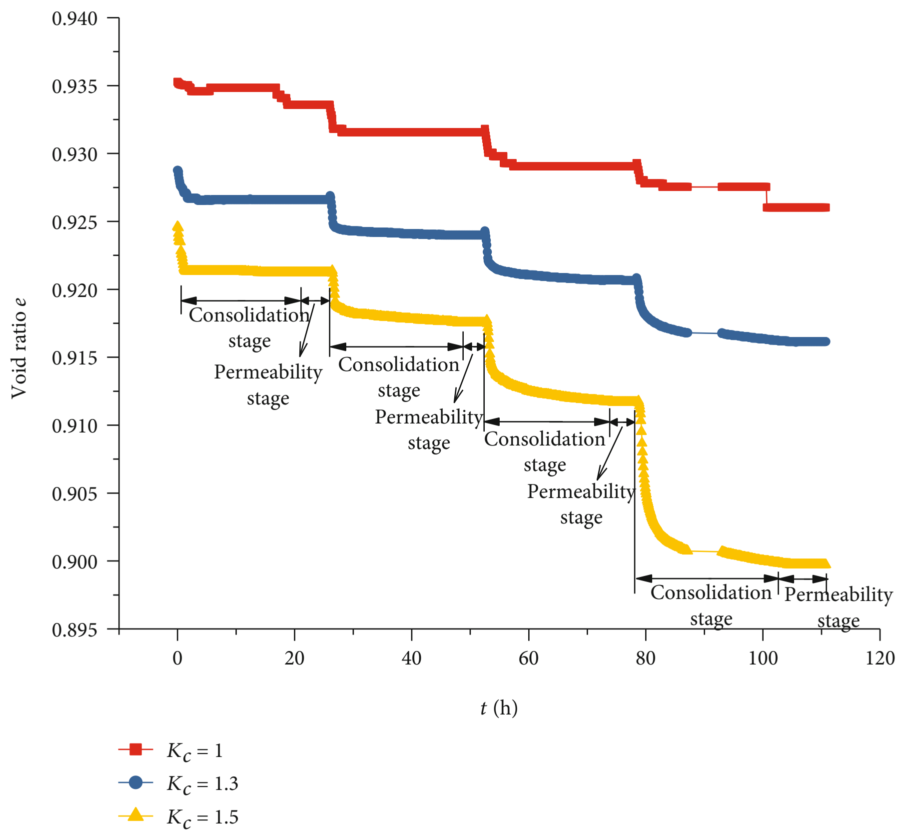

FIGURE 16: The curve of overconsolidation void ratio with time at different consolidation stress ratios.

TABLE 9: Stress calculations of overconsolidation clay.

Stress state	σ (kPa)	σ_{cz} (kPa)	σ_{dv} (kPa)
Overconsolidation	25	115	-90
	50		-65
	75		-40
	100		-15

$$k = k_0 \frac{1+e_0}{e_0} \frac{e}{1+e}. \tag{13}$$

For normally consolidated soil, it is assumed that the self-weight stress acting on the midpoint of the soil layer is σ_0, the corresponding initial void ratio is e_0, and the additional stress is $\Delta\sigma$; then actual stress is $(e_0 + \Delta\sigma)$, and the corresponding void ratio is

$$e = e_0 - C_c \lg \frac{\sigma_0 + \Delta\sigma}{\sigma_0}. \tag{14}$$

Submitting Equation (14) into Equation (13), the permeability coefficient equation for one-dimensional consolidation of normally consolidated soil was obtained as

$$k = k_0 \frac{1+e_0}{e_0} \frac{e_0 - C_c \lg\left((\sigma_0+\Delta\sigma)/\sigma_0\right)}{1+e_0 - C_c \lg\left((\sigma_0+\Delta\sigma)/\sigma_0\right)} \tag{15}$$

(3) When expressed by the consolidation degree permeability equation, there was

$$k = C_v \gamma_{wz} \frac{a_v}{1+e}, \tag{16}$$

where C_v is the consolidation coefficient (cm^2/s); γ_{wz} is the weight of free water (kN/m^3); and a_v is the compression coefficient (MPa^{-1})

In the same way as the Stokes equation, the equation of the permeability coefficient of normally consolidated soil under one-dimensional consolidation can be obtained as

$$k = k_0 \frac{1+e_0}{1+e_0 - C_c \lg\left((\sigma_0+\Delta\sigma)/\sigma_0\right)}. \tag{17}$$

According to the measured results of one-dimensional consolidation permeability tests and Equations (9), (10), (15), and (17), the comparison between the predicted value and the measured value of the permeability coefficient of normally consolidated saturated clay can be obtained as shown in Figure 21.

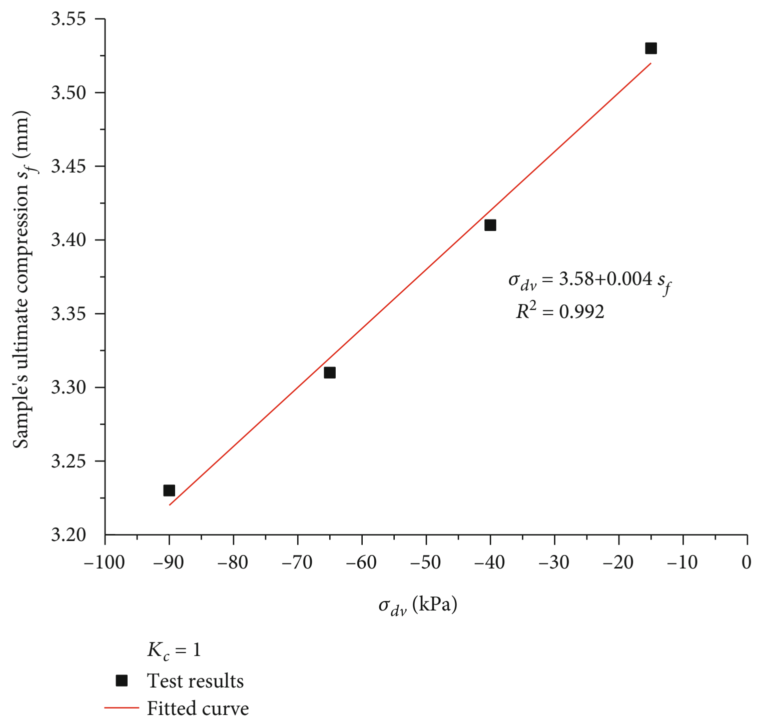

FIGURE 17: The relation curve between overconsolidation clay ultimate compression and stress difference.

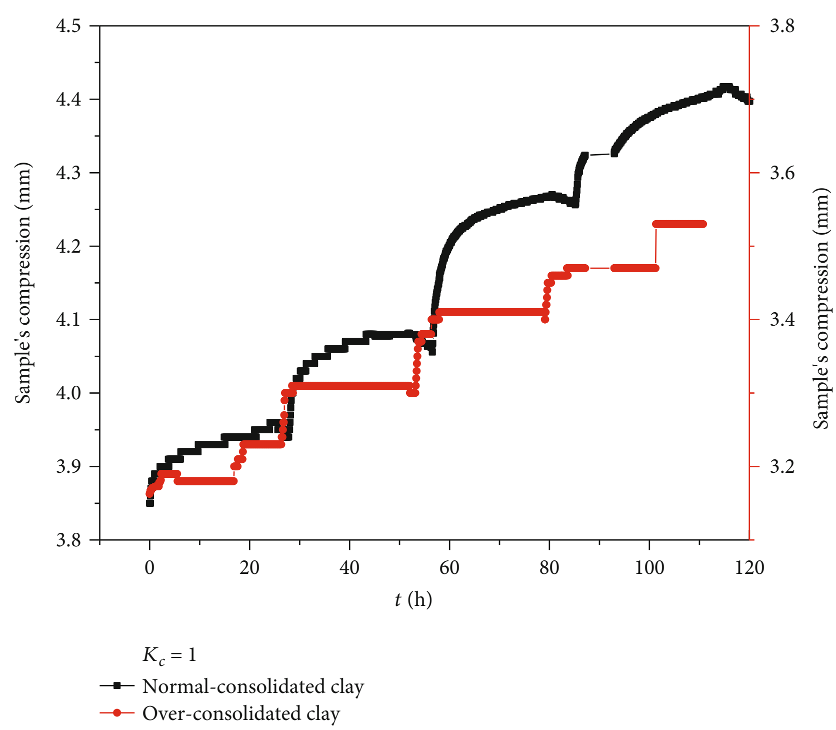

FIGURE 18: The curve of compression with time considering the influence of stress history.

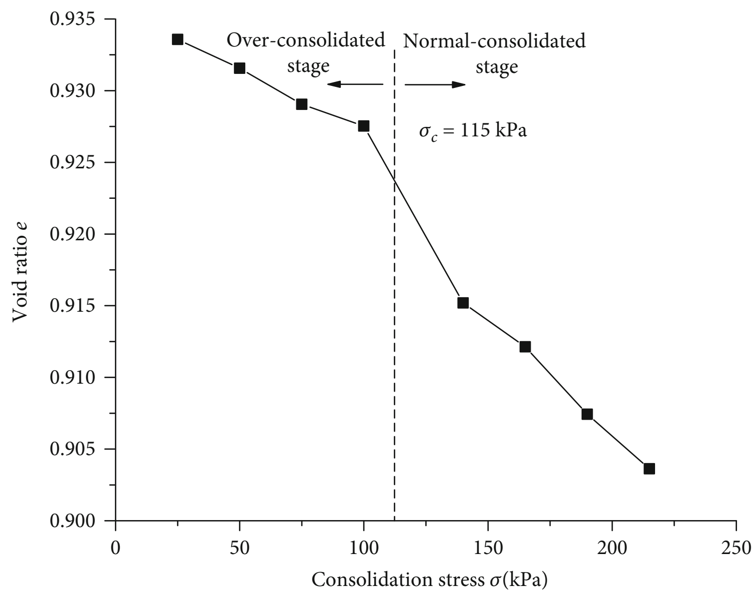

Figure 19: Variation curve of the void ratio with consolidation pressure during one-dimensional consolidation of normally and overconsolidation saturated clays.

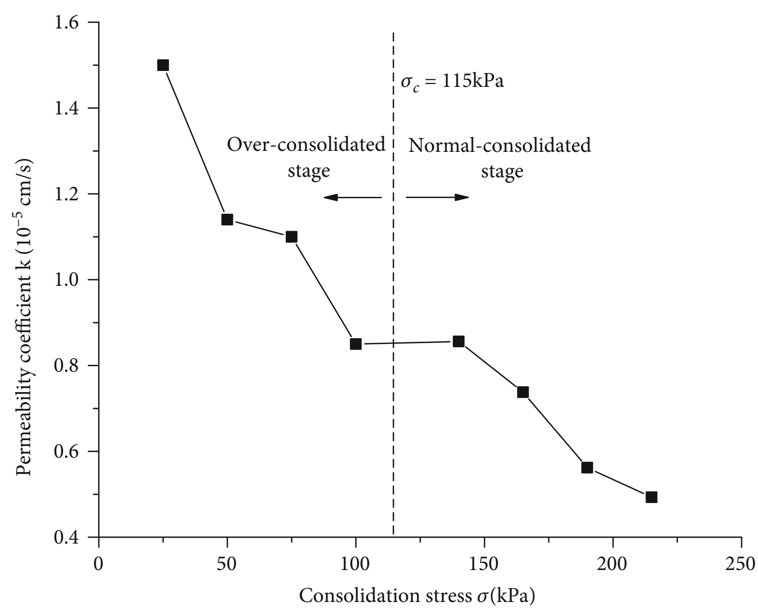

Figure 20: Variation curve of permeability coefficient with consolidation pressure during one-dimensional consolidation of normally and overconsolidation saturated clays.

It was found in Figure 21 that the predicted values of the permeability coefficient and the measured value were consistent with the change of the consolidation stress. The measured value of permeability coefficient was in the order of 10^{-5}~10^{-6}, while the permeability coefficient calculated by Stokes equation and consolidation degree equation was in the order of 10^{-5}, which was quite different from the measured value. The calculated values of the modified Darcy's permeability coefficient equation and modified Kozeny-Carman's permeability coefficient equation proposed by Gao et al. [40] were close to the measured values. Besides, it can be seen from the figure that the permeability coefficient calculated by the modified Kozeny-Carman's permeability coefficient equation is almost coincided with the measured value. Therefore, it was more appropriate to use the modified Kozeny-Carman's permeability coefficient equation to predict the saturated clay permeability coefficient in Luochuan.

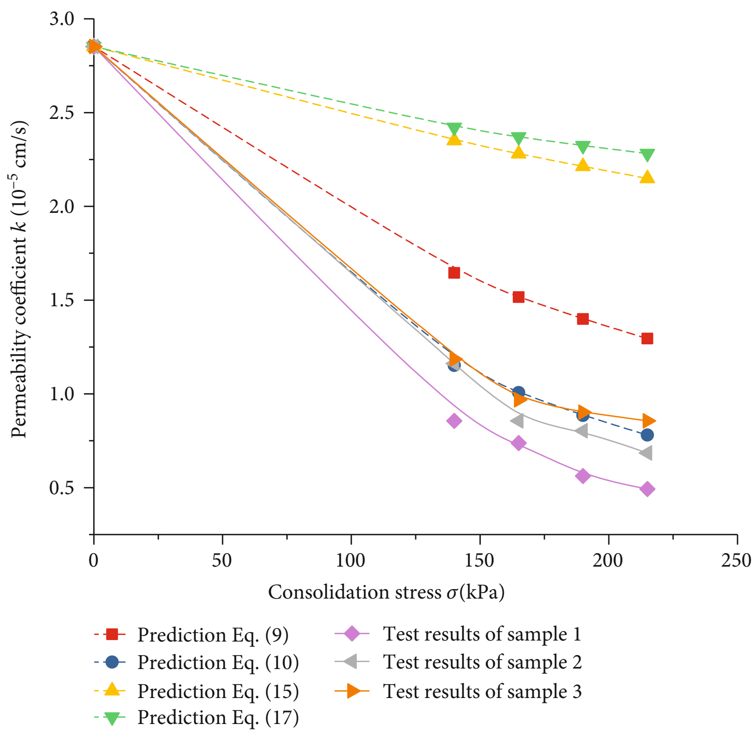

Figure 21: The comparison of the measured and predicted values of one-dimensional consolidation permeability coefficient of normally consolidated soil.

5. Conclusion

In this study, a series of one-dimensional consolidation permeability tests under different consolidation stress ratio K_c and different stress history were carried out. Moreover, a model for predicting the permeability coefficient of the saturated clay in Luochuan, Shaanxi, was recommended by comparing several models. The following conclusions can be drawn:

(1) The permeability coefficient and void ratio of normally and overconsolidation saturated clay decreased with the increase of K_c, and the amount of sample's compression increased with the increase of K_c. When $K_c = 1$, 1.3, and 1.5, the corresponding amounts of sample's final compression of normally consolidated soil were 4.43, 5.52, and 7.17 mm, and those of overconsolidated soil were 3.53, 3.92, and 4.57 mm

(2) Fitting the difference σ_{dv} between the consolidation pressure σ and the soil self-weight stress σ_{cz} with the amount of final sample's compression s_f, it was concluded that the stress difference σ_{dv} between the consolidation pressure and the self-weight stress of the soil layer and the amount of final compression under each consolidation pressure had a good linear relationship. After knowing the self-weight stress of the soil, the amount of final sample's compression can be predicted more accurately, which had an important application value for the engineering

(3) The compressibility and permeability of the soil in the overconsolidation stage are much smaller than that in the normally consolidation state under the same consolidation stress ratio but different consolidation states. Meanwhile, the amount of compression of overconsolidated saturated clay was less than that of normally consolidated saturated clay during the same consolidation time; that is, the amount of final sample's compression of overconsolidated soil was 3.53 mm, while that of normally consolidated soil was 4.43 mm under the condition of $K_c = 1$

(4) The permeability coefficient of Luochuan saturated clay in Shaanxi was predicted using the modified Darcy's permeability coefficient equation, the modified Kozeny-Carman's permeability coefficient equation, the Stokes flow permeability coefficient equation, and the consolidation degree permeability equation. The results showed that the calculated permeability coefficient of the modified Kozeny-Carman's permeability coefficient equation was in good agreement with the measured value. Therefore, it was recommended to use the modified Kozeny-Carman's equation to predict the permeability coefficient of Luochuan saturated clay during one-dimensional consolidation

Data Availability

The data used to support the findings of this study are available from the corresponding author upon request.

Conflicts of Interest

The authors declare that they have no known competing financial interests or personal relationships that could have appeared to influence the work reported in this paper.

Authors' Contributions

Le Zhang is responsible for the investigation, testing, conceptualization, software, and writing of the original draft. Faning Dang is involved in the conceptualization and methodology. Jun Gao is also involved in the methodology and analyzed the data. Jiulong Ding performed the tests.

Acknowledgments

This study is sponsored by the National Natural Science Foundation of China (Nos. 51979225 and 51679199), the Special Funds for Public Industry Research Projects of the Ministry of Water Resources (No. 201501034-04), the Key Laboratory for Science and Technology Coordination & Innovation Projects of Shaanxi Province (No. 2014SZS15-Z01), and the Natural Science Foundation of Shaanxi Province (No. 2020JQ-584). The authors gratefully acknowledge the financial and technical support from these sources.

References

[1] L. Y. Sun, *One-Dimensional Consolidation Experiment and Theory of Saturated Clay Based on Non-Darcy Flow*, Dissertation, Zhengzhou University, 2011.

[2] C. Wu, J. Chu, S. Wu, L. Cheng, and L. A. van Paassen, "Microbially induced calcite precipitation along a circular flow channel under a constant flow condition," *Acta Geotechnica*, vol. 14, no. 3, pp. 673–683, 2018.

[3] C. Wu, J. Chu, S. Wu, and Y. Hong, "3D characterization of microbially induced carbonate precipitation in rock fracture and the resulted permeability reduction," *Engineering Geology*, vol. 249, pp. 23–30, 2018.

[4] E. H. Davis and G. P. Raymond, "A non-linear theory of consolidation," *Geotechnique*, vol. 15, no. 2, pp. 161–173, 1965.

[5] K. H. Xie, X. Y. Xie, and W. Jiang, "A study on one-dimensional nonlinear consolidation of double-layered soil," *Computers and Geotechnics*, vol. 29, no. 2, pp. 151–168, 2002.

[6] J. Y. Shi, L. A. Yang, W. B. Zhao, and Y. X. Liu, "Research of one-dimensional consolidation theory considering nonlinear characteristics of soil," *Journal of Hohai University*, vol. 29, no. 1, pp. 1–5, 2001.

[7] S. Dumais and J. M. Konrad, "One-dimensional large-strain thaw consolidation using nonlinear effective stress – void ratio – hydraulic conductivity relationships," *Canadian Geotechnical Journal*, vol. 55, no. 3, pp. 414–426, 2018.

[8] J. H. Yin and W. Q. Feng, "A new simplified method and its verification for calculation of consolidation settlement of a clayey soil with creep," *Canadian Geotechnical Journal*, vol. 54, no. 3, pp. 333–347, 2017.

[9] W. Q. Feng and J. H. Yin, "Development and verification of a new simplified method for calculating settlement of a thick soil layer with nonlinear compressibility and creep," *International Journal of Geomechanics*, vol. 20, no. 3, article 04019184, 2020.

[10] Q. Liu, Y. B. Deng, and T. Y. Wang, "One-dimensional nonlinear consolidation theory for soft ground considering secondary consolidation and the thermal effect," *Computers and Geotechnics*, vol. 104, pp. 22–28, 2018.

[11] C. Q. Xia, A. F. Hu, J. Cui, W. X. Lv, and K. H. Xie, "Analytical solutions for one-dimensional nonlinear consolidation of saturated soft layered soils," *Rock and Soil Mechanics*, vol. 39, no. 8, pp. 2858–2864, 2018.

[12] C. X. Li, J. S. Huang, L. Z. Wu, L. Z. Lu, J. F. Lu, and C. Q. Xia, "Approximate analytical solutions for one-dimensional consolidation of a clay layer with variable compressibility and permeability under a ramp loading," *International Journal of Geomechanics*, vol. 18, no. 11, article 06018032, 2018.

[13] K. R. Lekha, N. R. Krishnaswamy, and P. Basak, "Consolidation of clays for variable permeability and compressibility," *Journal of Geotechnical and Geoenviromental Engineering*, vol. 129, no. 11, pp. 1001–1009, 2003.

[14] N. Abbasi, H. Rahimi, A. A. Javadi, and A. Fakher, "Finite difference approach for consolidation with variable compressibility and permeability," *Computers and Geotechnics*, vol. 34, no. 1, pp. 41–52, 2007.

[15] A. Mishra and N. R. Patra, "Long-term response of consolidating soft clays around a pile considering non-Darcian flow," *International Journal of Geomechanics*, vol. 19, no. 6, article 04019040, 2019.

[16] Z. Y. Liu, Y. Y. Xia, M. S. Shi, J. C. Zhang, and X. M. Zhu, "Numerical simulation and experiment study on the characteristics of non-Darcian flow and rheological consolidation of saturated clay," *Water*, vol. 11, no. 7, article 1385, 2019.

[17] X. D. Zhao and W. H. Gong, "Numerical solution of nonlinear large strain consolidation based on non-Darcian flow," *Mathematical Problems in Engineering*, vol. 2019, Article ID 745068, 14 pages, 2019.

[18] C. X. Li, C. Xu, and K. H. Xie, "Nonlinear consolidation of clayed soil considering non-Darcy flow and stress history," *Rock and Soil Mechanics*, vol. 38, no. 1, pp. 91–100, 2017.

[19] Y. Z. Jiu, Z. Y. Liu, J. C. Yue, and L. Y. Sun, "One-dimensional consolidation with a consideration of non-Darcy flow and self-gravity stress," *Journal of Tongji University (Natural Science)*, vol. 40, no. 4, pp. 541–548, 2012.

[20] C. X. Li, C. J. Wang, M. M. Lu, J. F. Lu, and K. H. Xie, "One-dimensional large-strain consolidation of soft clay with non-Darcian flow and nonlinear compression and permeability of soil," *Journal of Central South University*, vol. 24, no. 4, pp. 967–976, 2017.

[21] S. Sica, L. Pagano, and A. Modaressi, "Influence of past loading history on the seismic response of earth dams," *Computers and Geotechnics*, vol. 35, no. 1, pp. 61–85, 2008.

[22] X. B. Li, K. H. Xie, and F. Q. Chen, "One dimensional consolidation and permeability tests considering stress history and rheological characteristic of soft soils," *Journal of Hydraulic Engineering*, vol. 44, no. 1, pp. 18–25, 2013.

[23] K. H. Xie, J. B. Wen, H. W. Ying, and A. F. Hu, "One-dimensional consolidation theory of double-layered soil considering effects of stress history," *Journal of Zhejiang University (Engineering Science)*, vol. 41, no. 7, pp. 1126–1131, 2007.

[24] W. Q. Lv, Z. L. Dong, P. S. Chen, and H. H. Mo, "Research on relationship between permeability coefficient and consolidation stress of normal consolidation clay," *Rock and Soil Mechanics*, vol. 30, no. 3, pp. 769–773, 2009.

[25] R. L. Schiffman, “Consolidation of soil under time-dependent loading and varying permeability,” *Proceedings of the Highway Research Board*, vol. 37, pp. 584–617, 1958.

[26] R. E. Olson, “Consolidation under time-dependent loading,” *Journal of the Geotechnical Engineering Division*, vol. 103, no. 1, pp. 55–60, 1977.

[27] J. C. Liu and Q. Ma, *One-Dimensional Consolidation of Soft Ground with Impeded Boundaries under Depth-Dependent Ramp Load*, First International Symposium on Pavement and Geotechnical Engineering for Transportation Infrastructure, 2013.

[28] M. Sun, M. F. Zong, S. J. Ma, W. B. Wu, and R. Z. Liang, “Analytical solution for one-dimensional consolidation of soil with exponentially time-growing drainage boundary under a ramp load,” *Mathematical Problems in Engineering*, vol. 2018, Article ID 9385615, 10 pages, 2018.

[29] Y. Tian, W. Wu, G. Jiang et al., “One-dimensional consolidation of soil under multistage load based on continuous drainage boundary,” *International Journal for Numerical and Analytical Methods in Geomechanics*, vol. 44, no. 8, pp. 1170–1183, 2020.

[30] W. Q. Feng, J. H. Yin, W. B. Chen, D. Y. Tan, and P. C. Wu, “A new simplified method for calculating consolidation settlement of multi-layer soft soils with creep under multi-stage ramp loading,” *Engineering Geology*, vol. 264, article 105322, 2020.

[31] S. F. Zou, J. Z. Li, Z. J. Wang, L. Lan, W. J. Wang, and X. Y. Xie, “Seepage test and empirical models for soils based on GDS apparatus,” *Journal of Zhejiang University (Engineering Science)*, vol. 51, no. 5, pp. 856–862, 2017.

[32] T. Qi, *Theoretical and Experimental Studies on One-dimensional Nonlinear Consolidation of Soft Soil*, Dissertation, Zhejiang University, 2008.

[33] J. B. Wen, *Study on One-dimensional Consolidation Theory of Layered Soils Considering the Effect of Stress History*, Dissertation, Zhejiang University, 2007.

[34] C. L. Chen, C. M. Cao, F. Chu, and J. T. Wang, “Effects of consolidation stress ratio on pore water pressure characteristics of saturated intact loess under different stress paths,” *Journal of Xi’an University of Technology*, vol. 25, no. 3, pp. 328–332, 2009.

[35] G. J. Cai, S. Y. Liu, and A. J. Puppala, “Predictions of coefficient of consolidation from CPTU dissipation tests in Quaternary clays,” *Bulletin of Engineering Geology and the Environment*, vol. 77, no. 2, pp. 337–350, 2012.

[36] B. Li, Y. G. Fang, and Z. F. Ou, “Asymptotic solution for the one-dimensional nonlinear consolidation equation including the pore evolution effect,” *International Journal of Geomechanics*, vol. 18, no. 10, article 04018125, 2018.

[37] H. Y. Hu, *Study on One-dimensional Consolidation Theory of Saturated Soil Considering the Effect of Stress History*, Dissertation, Zhejiang University, 2004.

[38] Y. Xue, T. Teng, F. Dang, Z. Ma, S. Wang, and H. Xue, “Productivity analysis of fractured wells in reservoir of hydrogen and carbon based on dual-porosity medium model,” *International Journal of Hydrogen Energy*, vol. 45, no. 39, pp. 20240–20249, 2019.

[39] J. Liu, X. Liang, Y. Xue, K. Yao, and Y. Fu, “Numerical evaluation on multiphase flow and heat transfer during thermal stimulation enhanced shale gas recovery,” *Applied Thermal Engineering*, vol. 178, 2020.

[40] J. Gao, F. N. Dang, J. L. Ding, C. Yang, and L. Zhang, “Research on soft soil consolidation calculation method considering the impacts of initial consolidation state,” *Chinese Journal of Rock Mechanics and Engineering*, vol. 38, no. Supp 1, pp. 3189–3196, 2019.

Hindawi
Geofluids
Volume 2021, Article ID 6693888, 15 pages
https://doi.org/10.1155/2021/6693888

Research Article

Theoretical Analysis on Stress and Deformation of Overburden Key Stratum in Solid Filling Coal Mining Based on the Multilayer Winkler Foundation Beam Model

Chao Ma[1], **Xiaoqian Guo**[2], **Lianying Zhang**[1], **Aihong Lu**[2], **Xianbiao Mao**[2], **and Bing Li**[1]

[1] *Xuzhou University of Technology, Xuzhou 221008, China*
[2] *School of Mechanics and Civil Engineering, China University of Mining and Technology, Xuzhou 221008, China*

Correspondence should be addressed to Aihong Lu; xzlah@126.com

Received 20 December 2020; Revised 17 January 2021; Accepted 31 January 2021; Published 27 February 2021

Academic Editor: Jia Liu

Solid backfill coal mining (SBCM) is a green mining technology which can effectively alleviate the environmental problems induced by traditional coal mining techniques, such as surface subsidence, water resources loss, coal gangue occupation, and pollution. In this study, a multilayer Winkler foundation beam model for the overburden key strata is proposed, and the model with two key strata is solved. The subsidence, rotating angle, inner force, and stress of the overburden key strata are systematically analyzed under various backfill elastic modulus, mining height, and soft layer thickness. The results show that the subsidence of the key strata exhibit "basin"-shape curves, and the backfill elastic modulus, mining height, and the thickness of the soft strata have significant influences on the subsidence of the key strata. The shear stress, horizontal stress, and vertical stress of key stratum can be effectively reduced by increasing the backfill elastic modulus. The increase of mining height has little influence on the stress of key stratum that close to the coal seam (key stratum #1), but has a significant effect on the stress of key stratum that above the soft layers (key stratum #2). On the contrary, the effect of increasing soft layer thickness on the stress of key stratum is opposite to that of increasing mining height. In addition, the shear failure of key stratum #1 at mining boundary and the tensile failures on both sides of mining boundary should be preferentially considered in SBCM engineering design. Due to the low shear stress level of key stratum #2, the tensile failure on both sides of the mining boundary should be mainly considered.

1. Introduction

Solid backfill coal mining (SBCM) is a coal mining technology in which underground coal resources are replaced by backfill [1, 2]. The backfill normally consists of industrial wastes, such as coal gangue and fly ash [3–5]. In this respect, SBCM can effectively alleviate the environmental problems caused by gangue discharge in coal mining, including occupying the ground and spontaneous combustion [6–9]. Besides, SBCM can improve the mining rate efficiently, especially for mining the coal resources under the surface water bodies, buildings, and railways (roads) [1]. In addition, compared with the traditional underground coal mining technology, the backfill can support the overburden strata in SBCM, which can effectively reduce a series of problems caused by overburden strata deformation and failure, such as surface subsidence [10, 11] and water resources loss [12–16]. Therefore, it is of great significance to study the deformation and stress distribution of overburden strata for SBCM engineering.

The research on SBCM mainly focuses on the backfill material and the overburden control. At present, the mechanical properties, components, and particle sizes of backfill materials have relatively systematic research results [17–21]. However, to the best of our knowledge, there are few theoretical and numerical modeling studies on the overburden strata control.

For the numerical simulation studies, Zha et al. studied the characteristics of overburden deformation and movement by the numerical simulation [22]; Huang et al. analyzed the effect of compaction rates of backfill on controlling movement of overburden and surface subsidence by UDEC [23]; Li et al. proposed a backfill material model that considers the coefficient of horizontal pressure and numerically simulated the overburden movement deformation characteristics by Flac^{3D} [24]. However, the above works only focus on the characteristics of overburden movement and deformation without considering the stress distribution and failure of the overburden key strata. Zhang et al. proposed a negative exponential function model of backfill materials and simulated the deformation and stress distribution of overburden of SBCM by the software of Abaqus [25]. However, this work did not pay attention to the stress distribution of overburden key strata.

For the theory studies, Miao et al. proposed an equivalent mining height theory, which assumes that the actual mining height of SBCM can be equivalent to the deformation of backfill [2]. Based on this theory, the Winkler foundation beam model of the upper roof was established, and the analytical solution of the subsidence and internal force of the old roof were obtained. Similar to the work of Miao et al., Chen et al. proposed a beam model for elastic foundation of roof and systematically analyzed the influences of mining depth and backfill foundation coefficient on roof subsidence [26]. In addition, Li et al. simplified the basic roof into a thin plate, proposed a thin plate model for the overburden key strata of SBCM, and systematically analyzed the influence of compaction rate of backfill on deformation of overburden key strata [27]. The above theoretical models only consider the key stratum close to the coal seam, and the load on the key stratum is simplified to uniformly distribute; however, in practical SBCM engineering, there are usually several key strata, and their deformations are not necessarily uniform subsidence, resulting in complicated load distribution on the key stratum. Consequently, the previous theory models cannot capture the stress and deformation of the key strata appropriately. In addition, the previous studies mainly focus on the deformation of overburden, but it is necessary to grasp the fracture cases of the key stratum such as the key stratum for water retention in overburden. Therefore, the stress distribution of key stratum, in overburden, should also be systematically studied.

In this study, a multilayer beam model of SBCM based on Winkler foundation theory is established, and the case with 2 key strata is solved. The subsidence, internal forces, stresses distribution, and failure characteristics of key strata are systematically analyzed under various elastic modulus of backfill, mining heights, and thicknesses of soft layers.

2. Mechanical Mole of Overburden Strata in SBCM

In longwall mining, the overburden strata movement and deformation along tilt direction of the working face are the same, except both ends of working face. Therefore, the overburden strata mechanical model in the central stope can be simplified to a plane strain problem, shown as Figure 1. Using the filled mining technology to replace the coal resources with filled materials which has adequate filling rate and compaction, the movement of overburden only induces slight bending deformation. Consequently, the overburden under solid filling mining only has continuous deformation, rather than discontinuous deformations such as the fracture of rock stratum and the development of fracture zone above the stope. That is, the theory of continuum mechanics can be employed to study the overburden deformation and land subsidence induced by solid filling mining.

To study the deformation characteristics of the overburden in longwall mining, the overburden structure can be simplified to a laminated beam on elastic foundation, shown in Figure 2(a). Moreover, based on the symmetry, only half of the model is considered, shown in Figure 2(b). The boundary condition of the model is that the horizontal displacement of left side is fixed, and both the horizontal and vertical displacement of the infinity at right side are fixed. For the case that the depth of coal seam is relatively shallow, it is more probably to have only one key stratum in the overburden. Because of this, the simplified single-layer beam on elastic foundation model, which is easily to be solved through the basic beam theory, could be used to study the overburden deformation. However, the above single beam model is inapplicable for the cases that the overburden has more than one key stratum. Therefore, a new elastic foundation beam model including more than one beams should be developed. Based on the key stratum theory, the overburden can be classified as key stratum and soft layer. In the model shown in Figure 2, the soft layer can be simplified to elastic foundation because of the small deformation in SBCM. Consequently, the model in Figure 2 can be further simplified to a multilayer Winkler foundation beam model, shown in Figure 3. In this model, all of the overburden key strata are simplified to beams, and the backfill, coal, and soft layer are simplified to elastic foundation. K_1-K_n denote the elastic foundation coefficients of soft layer 1 to n, K_{11} and K_{12} represent the elastic foundation coefficients of backfill and coal, respectively.

3. Model Solution

3.1. Double-Layer Winkler Foundation Beam Model. Based on the model in Figure 3, a double-layer Winkler foundation beam model is established, shown in Figure 4. In this model, the two key strata are simplified to beams, while the backfill, coal, and soft layer are simplified to elastic foundation. K_{11}, K_{12}, and K_2 are the elastic foundation coefficients of backfill, coal, and soft layer, respectively. q is the weight of the rock and topsoil layers. In the actual geological conditions, the soft layer normally consists of several soft strata, resulting in that K_2 is an equivalent parameter, which could be calculated as follows:

$$k_2 = \frac{\sum_1^i k_i h_i}{\sum_1^i h_i}, \tag{1}$$

where k_i and h_i are the foundation coefficient and thickness of layer i in the soft layers, respectively.

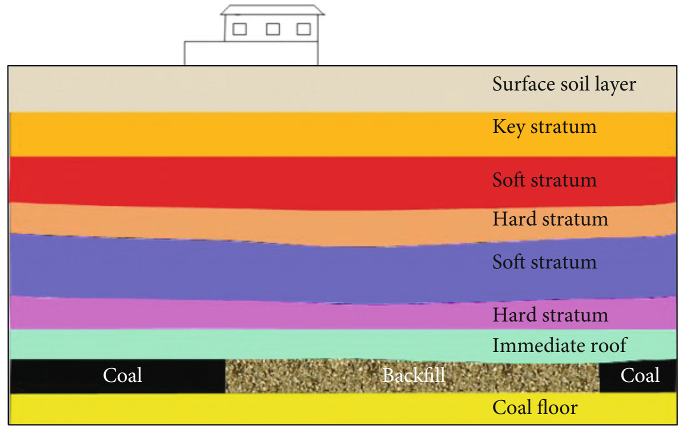

FIGURE 1: Schematic diagram of overburden rock deformation behavior of solid filling mining.

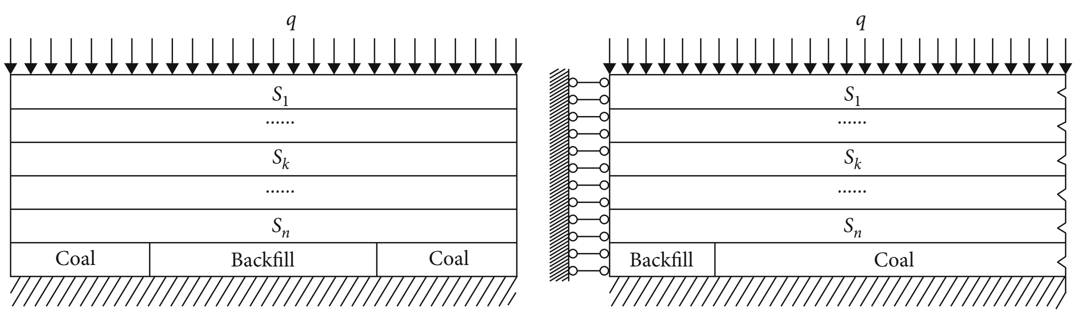

(a) (b)

FIGURE 2: Continuous beam model of solid close pack mining.

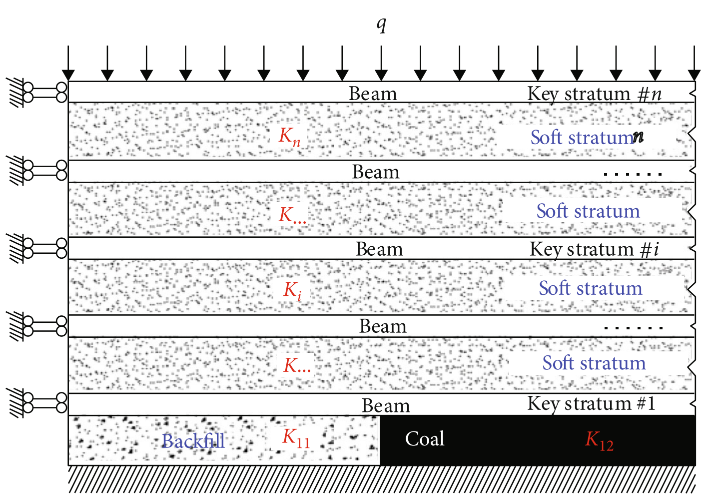

FIGURE 3: Multilayer Winkler foundation beam model of overburden in filled mining.

According to the multilayer beam model on Winkler foundation, the foundation coefficient K has a significant influence on overburden deformation, so it is necessary to solve the Winkler elastic foundation coefficient. According to the Winkler hypothesis, the elastic foundation coefficient of rock stratum can be calculated as follows:

$$k = \frac{E}{h}, \tag{2}$$

where E is the elastic modulus of the rock strata.

In Winkler foundation beam theory, the deflection at any point on the foundation surface is proportional to the pressure on the unit area of the point.

$$P(x) = k \cdot \omega(x), \tag{3}$$

where $P(x)$ is the support force of the foundation to the beam and $w(x)$ is the deflection equation of the beam. The relation between $w(x)$, load, and $P(x)$ is

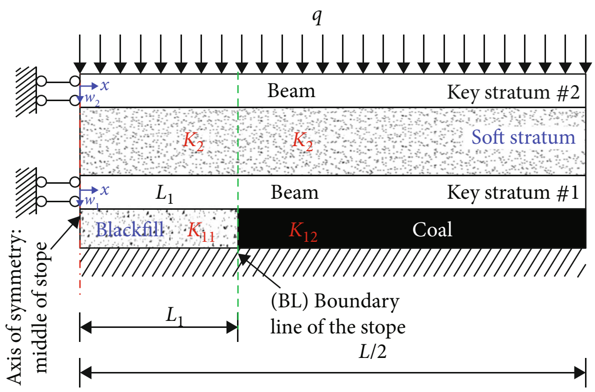

FIGURE 4: Double-layer Winkler foundation beam model.

$$EI\frac{d^4\omega}{dx^4} = q(x) - p(x). \tag{4}$$

Here, $q(x)$ and EI are the load concentration and flexural rigidity of the beam, respectively. According to Eq. (4), the governing equation of the double-layer Winkler foundation beam model can be obtained as follows:

$$\left\{E_1I_1\frac{d^4\omega_{11}}{dx^4} + k_{11}\cdot\omega_{11} = k_2(\omega_{21}-\omega_{11}) + q_1 + q_{\text{soft}} \quad 0 \le x < L_1, \right. \tag{5}$$

$$\left\{E_2I_2\frac{d^4\omega_{21}}{dx^4} + k_2\cdot(\omega_{21}-\omega_{11}) = q + q_2 \quad 0 \le x < L_1, \right. \tag{6}$$

$$\left\{E_1I_1\frac{d^4\omega_{12}}{dx^4} + k_{12}\cdot\omega_{12} = k_2(\omega_{22}-\omega_{12}) + q_1 + q_{\text{soft}} \quad L_1 \le x \le \frac{L}{2}, \right. \tag{7}$$

$$\left\{E_2I_2\frac{d^4\omega_{22}}{dx^4} + k_2\cdot(\omega_{22}-\omega_{12}) = q + q_2 \quad L_1 \le x \le \frac{L}{2}, \right. \tag{8}$$

where $\omega_{ij}(x)$ is the deflection equation of key stratum i, subscript $j = 1$ represents the part of the key stratum above the stope, and $j = 2$ represents the part of the key stratum above the unmined coal seam. q_1, q_2, and q_{soft} are the weight of key stratum #1, key stratum #2, and soft layer, respectively, which determined by equations$q_1 = \rho_1 gh_1$, $q_2 = \rho_2 gh_2$, and $q_{\text{soft}} = \rho_{\text{soft}} gh_{\text{soft}}$, in which ρ and h are the densities and thicknesses of the rock strata. By adding Eqs. (5) and (6), it can be obtained that

$$E_1I_1\frac{d^4\omega_{11}}{dx^4} + E_2I_2\frac{d^4\omega_{21}}{dx^4} + k_{11}\cdot\omega_{11} = q_{pl}, \tag{9}$$

where $q_{pl} = q + q_1 + q_2 + q_{\text{soft}}$. The fourth derivative of both sides of Eq. (5) with respect to x can be obtained as follows:

$$E_2I_2\frac{d^4\omega_{21}}{dx^4} = \frac{E_1I_1E_2I_2}{k_2}\frac{d^8\omega_{11}}{dx^8} + \frac{k_{11}+k_2}{k_2}\cdot E_2I_2\cdot\frac{d^4\omega_{11}}{dx^4}. \tag{10}$$

Substitute Eq. (10) into Eq. (9).

$$\begin{cases} A\dfrac{d^8\omega_{11}}{dx^8} + B\dfrac{d^4\omega_{11}}{dx^4} + k_{11}\cdot\omega_{11} = q_{pl}, \\ A = \dfrac{E_1I_1E_2I_2}{k_2}, \\ B = \left(\dfrac{k_{11}+k_2}{k_2}\cdot E_2I_2 + E_1I_1\right). \end{cases} \tag{11}$$

The above equation is an 8-order linear inhomogeneous differential equation with constant coefficients, of which the solution is the general solution of secondary differential equation plus a particular solution of the inhomogeneous equation. For the secondary differential equation of Eq. (11), its characteristic equation is as follows:

$$A\cdot r^8 + B\cdot r^4 + k_{11} = 0. \tag{12}$$

The above equation can be converted to

$$\begin{cases} \left(r^4 + \dfrac{B}{2A}\right)^2 = M, \\ M = \dfrac{B^2}{4A^2} - \dfrac{k_{11}}{A}. \end{cases} \tag{13}$$

Substituting A and B in Eq. (11) into Eq. (13), it is easy to get $M > 0$; then,

$$r^4 = \pm\sqrt{M} - \frac{B}{2A}, \tag{14}$$

It is obvious that $\sqrt{M} - B/2A < 0$, the solution of the characteristic (Eq. (13)) can be obtained as follows:

$$\begin{cases} r_1 = \dfrac{\sqrt{2}}{2}\left(\dfrac{B}{2A}-\sqrt{M}\right)^{1/4} + \dfrac{\sqrt{2}}{2}\left(\dfrac{B}{2A}-\sqrt{M}\right)^{1/4}\cdot i, \\ r_2 = -\dfrac{\sqrt{2}}{2}\left(\dfrac{B}{2A}-\sqrt{M}\right)^{1/4} - \dfrac{\sqrt{2}}{2}\left(\dfrac{B}{2A}-\sqrt{M}\right)^{1/4}\cdot i, \\ r_3 = -\dfrac{\sqrt{2}}{2}\left(\dfrac{B}{2A}-\sqrt{M}\right)^{1/4} + \dfrac{\sqrt{2}}{2}\left(\dfrac{B}{2A}-\sqrt{M}\right)^{1/4}\cdot i, \\ r_4 = \dfrac{\sqrt{2}}{2}\left(\dfrac{B}{2A}-\sqrt{M}\right)^{1/4} - \dfrac{\sqrt{2}}{2}\left(\dfrac{B}{2A}-\sqrt{M}\right)^{1/4}\cdot i, \\ r_5 = \dfrac{\sqrt{2}}{2}\left(\dfrac{B}{2A}+\sqrt{M}\right)^{1/4} + \dfrac{\sqrt{2}}{2}\left(\dfrac{B}{2A}+\sqrt{M}\right)^{1/4}\cdot i, \\ r_6 = -\dfrac{\sqrt{2}}{2}\left(\dfrac{B}{2A}+\sqrt{M}\right)^{1/4} - \dfrac{\sqrt{2}}{2}\left(\dfrac{B}{2A}+\sqrt{M}\right)^{1/4}\cdot i, \\ r_7 = -\dfrac{\sqrt{2}}{2}\left(\dfrac{B}{2A}+\sqrt{M}\right)^{1/4} + \dfrac{\sqrt{2}}{2}\left(\dfrac{B}{2A}+\sqrt{M}\right)^{1/4}\cdot i, \\ r_8 = \dfrac{\sqrt{2}}{2}\left(\dfrac{B}{2A}+\sqrt{M}\right)^{1/4} - \dfrac{\sqrt{2}}{2}\left(\dfrac{B}{2A}+\sqrt{M}\right)^{1/4}\cdot i. \end{cases} \tag{15}$$

The real and imaginary part of Eq. (15) are denoted as real_i and imag_i, respectively, and combining with the Euler formula, the solution of Eq. (11) is as follows:

$$\omega_{11}(x) = \sum_{i=0}^{3}\Big(C_{2i+1}e^{\mathrm{real}_{2i+1}x}\cos\left(\mathrm{imag}_{2i+1}\cdot x\right) + C_{2i+2}e^{\mathrm{real}_{2i+2}x}\sin\left(-\mathrm{imag}_{2i+2}\cdot x\right)\Big) + \frac{q_{pl}}{k_{11}}, \tag{16}$$

where q_{pl}/k_{11} is a particular solution of Eq. (11). Based on the relation between ω_{11} and ω_{21} in Eq. (5), ω_{21} can be expressed as follows:

$$\omega_{21} = \frac{E_1 I_1}{k_2}\frac{d^4\omega_{11}}{dx^4} + \frac{k_{11}+k_2}{k_2}\omega_{11} - \frac{q_1 + q_{\mathrm{soft}}}{k_2}. \tag{17}$$

Equation (16) and Eq. (17) are the deflection equations of the part of key strata #1 and #2 above the goaf. In the same way, ω_{12} and ω_{22} can also be obtained.

$$\omega_{12}(x) = \sum_{i=4}^{7}\Big(C_{2i+1}e^{\mathrm{real}_{2i+1}x}\cos\left(\mathrm{imag}_{2i+1}\cdot x\right) + C_{2i+2}e^{\mathrm{real}_{2i+2}x}\sin\left(-\mathrm{imag}_{2i+2}\cdot x\right)\Big) + \frac{q_{pl}}{k_{12}}, \tag{18}$$

$$\omega_{22} = \frac{E_1 I_1}{k_2}\frac{d^4\omega_{12}}{dx^4} + \frac{k_{12}+k_2}{k_2}\omega_{12} - \frac{q_1 + q_{\mathrm{soft}}}{k_2}. \tag{19}$$

Equations (16)–(19) are the analytical solutions of the double-layer Winkler foundation beam model for solid backfill coal mining, but there are still 16 integral constants to be determined. Firstly, according to the boundary condition, the key strata at the infinitely far from stope are not affected by mining, and its bending moment and rotating angle are zero.

$$\begin{cases} M_{12}(x) \to 0, \\ \theta_{12}(x) \to 0, \\ M_{22}(x) \to 0, \\ \theta_{22}(x) \to 0, \\ x \to \infty. \end{cases} \tag{20}$$

Combined with Eqs. (15), (18), and (19), it can be easily obtained that $C_9 = C_{12} = C_{13} = C_{16} = 0$. In addition, the rotating angle and shearing force are 0 when $x = 0$, and the deflection, rotating angle, bending moment, and shearing force are continuous when $x = L_1$; then,

$$\begin{cases} Q_{11}(0) = 0, \\ \theta_{11}(0) = 0, \\ Q_{21}(0) = 0, \\ \theta_{21}(0) = 0, \\ x = 0, \end{cases}
\quad
\begin{cases} \omega_{11}(L_1) = \omega_{12}(L_1), \\ \theta_{11}(L_1) = \theta_{12}(L_1), \\ M_{11}(L_1) = M_{12}(L_1), \\ Q_{11}(L_1) = Q_{12}(L_1), \\ x = L_1, \end{cases}
\quad
\begin{cases} \omega_{21}(L_1) = \omega_{22}(L_1), \\ \theta_{21}(L_1) = \theta_{22}(L_1), \\ M_{21}(L_1) = M_{22}(L_1), \\ Q_{21}(L_1) = Q_{22}(L_1), \\ x = L_1, \end{cases} \tag{21}$$

where θ, M, and Q are the rotating angle, bending moment, and shearing force of the key strata, respectively, and the relations of them with deflection are as follows:

$$\begin{cases} \theta(x) = \dfrac{d\omega(x)}{dx}, \\ M(x) = -EI\dfrac{d^2\omega(x)}{dx^2}, \\ Q(x) = -EI\dfrac{d^3\omega(x)}{dx^3}. \end{cases} \tag{22}$$

Based on the above equations, Eq. (21) can be used to obtain the linear system of equations with respect to the remaining 12 integral constants. Furthermore, the expressions for $\omega_1(x)$ and $\omega_2(x)$ can be obtained. The details of expressions are not listed here since they are too long.

3.2. n-Layer Winkler Foundation Beam Model. For the multi-layer Winkler foundation beam model that with n key strata in SBCM, the governing equation can be easily obtained according to Eqs. (5)–(8).

$$\begin{cases} E_1 I_1\dfrac{d^4\omega_{11}}{dx^4} + k_{11}\cdot\omega_{11} = k_2(\omega_{21} - \omega_{11}) + q_1 + q_{\mathrm{soft1}} & 0 \le x < L_1, \\ E_2 I_2\dfrac{d^4\omega_{21}}{dx^4} + k_2\cdot(\omega_{21} - \omega_{11}) = k_3\cdot(\omega_{31} - \omega_{21}) + q_2 + q_{\mathrm{soft2}} & 0 \le x < L_1, \\ \cdots\cdots & \\ E_i I_i\dfrac{d^4\omega_{i1}}{dx^4} + k_i\cdot\left(\omega_{i1} - \omega_{(i-1)1}\right) = k_{(i+1)}\cdot\left(\omega_{(i+1)1} - \omega_{i1}\right) + q_i + q_{\mathrm{soft}i} & 0 \le x < L_1, \\ \cdots\cdots & \\ E_n I_n\dfrac{d^4\omega_{n1}}{dx^4} + k_n\cdot\left(\omega_{n1} - \omega_{(n-1)1}\right) = q + q_n & 0 \le x < L_1, \end{cases}$$

Table 1: The calculation parameters.

q/MPa	h_1/m	h_2/m	ρ_1/Kg/m^3	ρ_2/Kg/m^3	ρ_{soft}/Kg/m^3	E_1/GPa	E_2/GPa	E_{coal}/GPa	E_{soft}/GPa	L/m	L_1/m
1.0	10	20	2500	2500	2000	6.0	6.0	1.0	2.0	800	200

Table 2: The calculation schemes.

Scheme #1			Scheme #2			Scheme #3		
E_{fill}/MPa	h/m	h_s/m	E_{fill}/MPa	h/m	h_s/m	E_{fill}/MPa	h/m	h_s/m
80				3.0				20
100				3.5				40
120	3.0	50	100	4.0	50	100	3.0	60
140				4.5				80
160				5.0				100

$$\begin{cases} E_1 I_1 \dfrac{d^4\omega_{12}}{dx^4} + k_{12}\cdot\omega_{12} = k_2(\omega_{22}-\omega_{12}) + q_1 + q_{soft1} & L_1 \le x < \dfrac{L}{2}, \\ E_2 I_2 \dfrac{d^4\omega_{22}}{dx^4} + k_2\cdot(\omega_{22}-\omega_{12}) = k_3\cdot(\omega_{32}-\omega_{22}) + q_2 + q_{soft2} & L_1 \le x < \dfrac{L}{2}, \\ \cdots\cdots \\ E_i I_i \dfrac{d^4\omega_{i2}}{dx^4} + k_i\cdot\left(\omega_{i2}-\omega_{(i-1)2}\right) = k_{(i+1)}\cdot\left(\omega_{(i+1)2}-\omega_{i2}\right) + q_i + q_{softi} & L_1 \le x < \dfrac{L}{2}, \\ \cdots\cdots \\ E_n I_n \dfrac{d^4\omega_{n2}}{dx^4} + k_n\cdot\left(\omega_{n2}-\omega_{(n-1)2}\right) = q + q_n & L_1 \le x < \dfrac{L}{2}. \end{cases} \tag{23}$$

By solving the double-layer Winkler foundation beam model, it is concluded that the key process is to get the solution of 8-order differential equation. For a three-layer beam, the order of the differential equation will increase to 12. The increase in number of layers will increase the order of the equations, resulting that is difficult to get the analytical expression of the key strata deformation of overburden. In order to solve the above equations, the corresponding program should be compiled with the help of mathematical calculation software and the numerical method should be applied.

4. Result and Discussion

According to the solution of the double-layer Winkler foundation beam model, the deformation, stress and inner force of the key strata are systematically analyzed under various elastic modulus E_{fill}, mining height h, soft layer thickness h_s, the calculation parameters, and schemes are shown in Tables 1 and 2. Based on the mechanical properties of backfill [3, 6, 20], the E_{fill} is determined as 80-160 MPa.

4.1. Deformation of the Key Strata. Figures 5 and 6 show the curves of key strata subsidence w and rotating angle θ with the distance to the middle of the stope (x) under various elastic modulus of backfill, mining heights, and thicknesses of soft layers. It can be seen that the subsidence curves of overburden key strata under all cases exhibit the "basin" shaped, which remains almost unchanged in a large range in the middle of stope, but decreases sharply near the BL (boundary line of the stope, Figure 4). This characteristic reflects that its rotating angle firstly rises and then falls with the increase of distance x from the middle of stope.

With the increase of the elastic modulus of backfill, the peak value of subsidence of key stratum #1 decreases significantly. The range of subsidence curve "basin" gradually increases, while the horizontal scope of rotating angle that dramatically rises decreases, indicating that the role of filling material on supporting key stratum #1 is gradual significant. However, with the increase of the elastic modulus of the backfill, the increase of the "basin" range of the key stratum #2 is not significant, and its rotation-angle starts to increase at $x = 110$ m under all of the E_{fill}. It is indicated that the elastic modulus of the backfill only has a great influence on the bending deformation of the key stratum #2, while slight influence on the location of bending.

With an increase in mining height, the subsidence of the key strata increase gradually. While the "basin" area decreases gradually, and the range of rotating angle increases gradually, which indicates that the greater the mining height is, the more significant the bending deformation of the overburden key stratum is. With the increase of the thickness of the soft layers, both the subsidence and "basin" range of key stratum #1 gradually rise, and the range of the rotating angle also increases. However, the above characteristic of key stratum #2 is opposite to that of key stratum #1. In addition, by comparing the subsidence curves of key strata #1 and #2, it can be seen that the subsidence of the two strata is almost the same in a larger range in the middle of the stope, indicating that the subsidence in this range is caused by the compressive deformation of backfill and the vertical downward movement only occurs in the 2 key strata and the soft layers.

4.2. Internal Force of Overburden Key Strata. Figure 7 shows the bending moment curves of key strata with the distance to the middle of the stope under various elastic modulus of backfill, mining height, and thickness of soft layers, where points A and B represent the location of which bending moment is 0 in key strata #1 and #2, respectively. As can be seen that the bending moment curve shapes of the two key strata are analogical, the bending moment is almost 0 in the location of the key strata that far from the BL while the

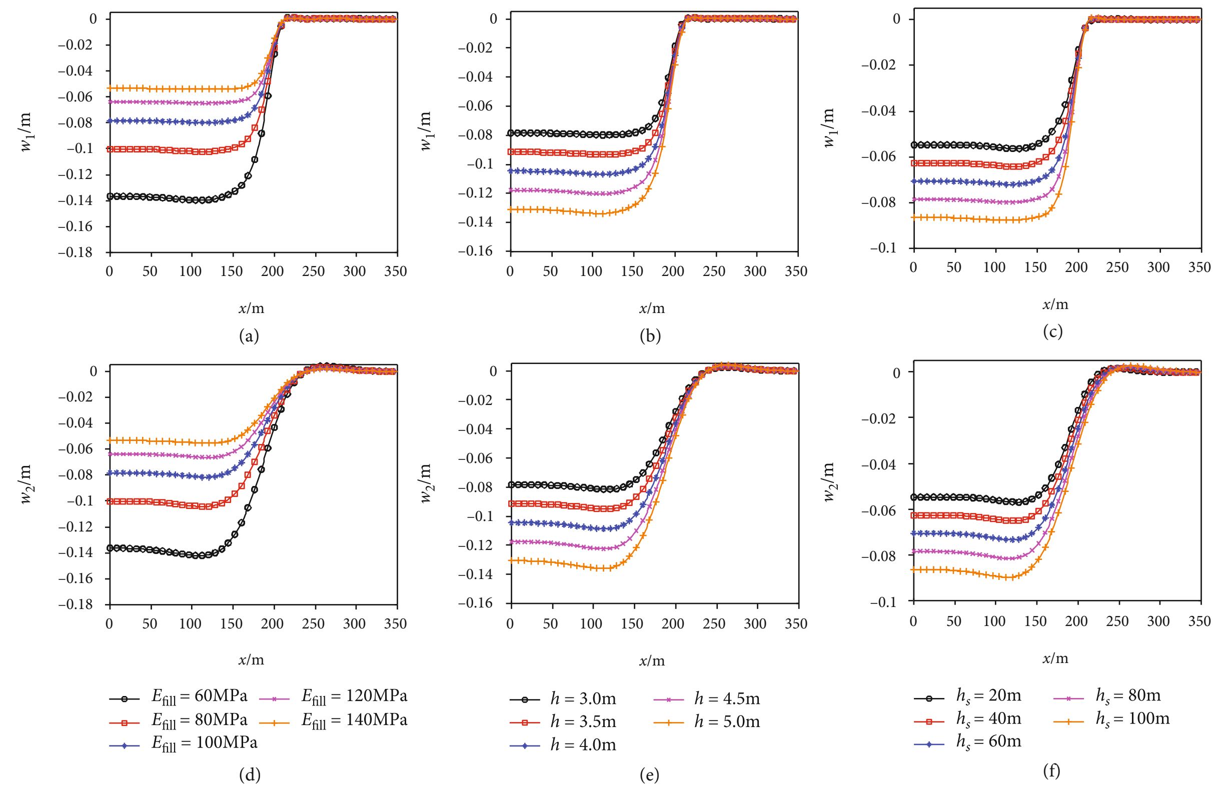

Figure 5: The curves of key strata subsidence with the distance to the middle of the stope under various (a, d) elastic modulus of backfill, (b, e) mining height, and (c, f) thickness of soft layers.

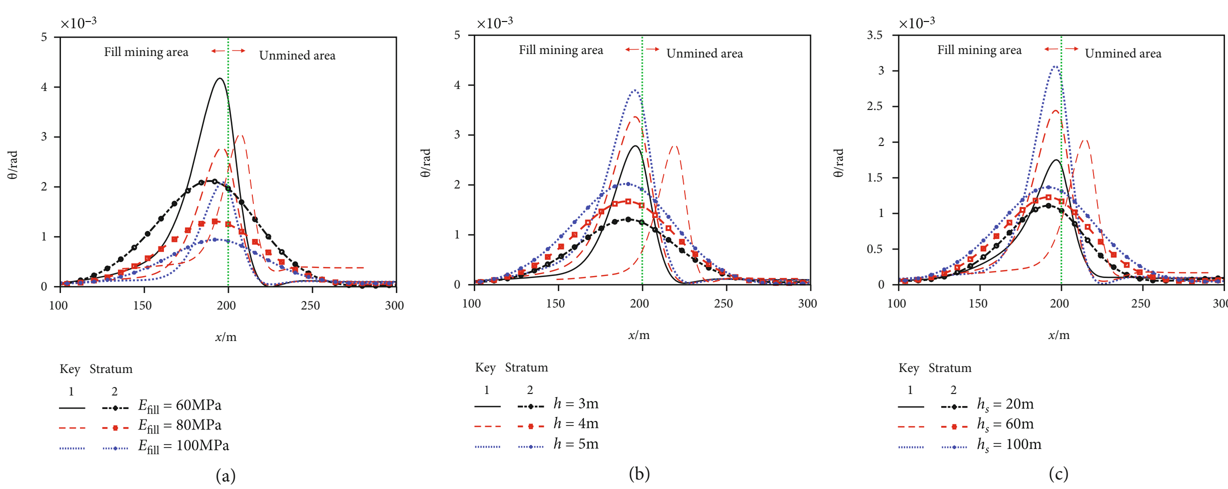

Figure 6: The curves of key strata rotating angle with the distance to the middle of the stope under various (a) elastic modulus of backfill, (b) mining height, and (c) thickness of soft layers.

bending moment increases or decreases sharply at both sides of BL. Bending moments of the key strata at left of point A (or B) is negative, indicating that the horizontal deformation is extension in the upper part and compression in lower part, while the right of point A (or B) is opposite. Moreover, the maximum of negative bending moment is located at the left of BL, while the peak of positive bending moment is located on the right. Furthermore, with the increase of E_{fill} and the decrease of h and h_s, the peak of bending moment decreases. The E_{fill} and h_s have a significant effect on the bending moment, which is relatively slightly influenced by h.

Figure 8 shows the shear force curves of key strata with the distance to the middle of the stope under various elastic modulus of backfill, mining height, and thickness of soft layers. It can be seen that the shear force distributions of the two key strata are obvious different. For the key stratum #1, the shear force peak locates at BL, where the shear force has a sudden change, caused by the concentration force at

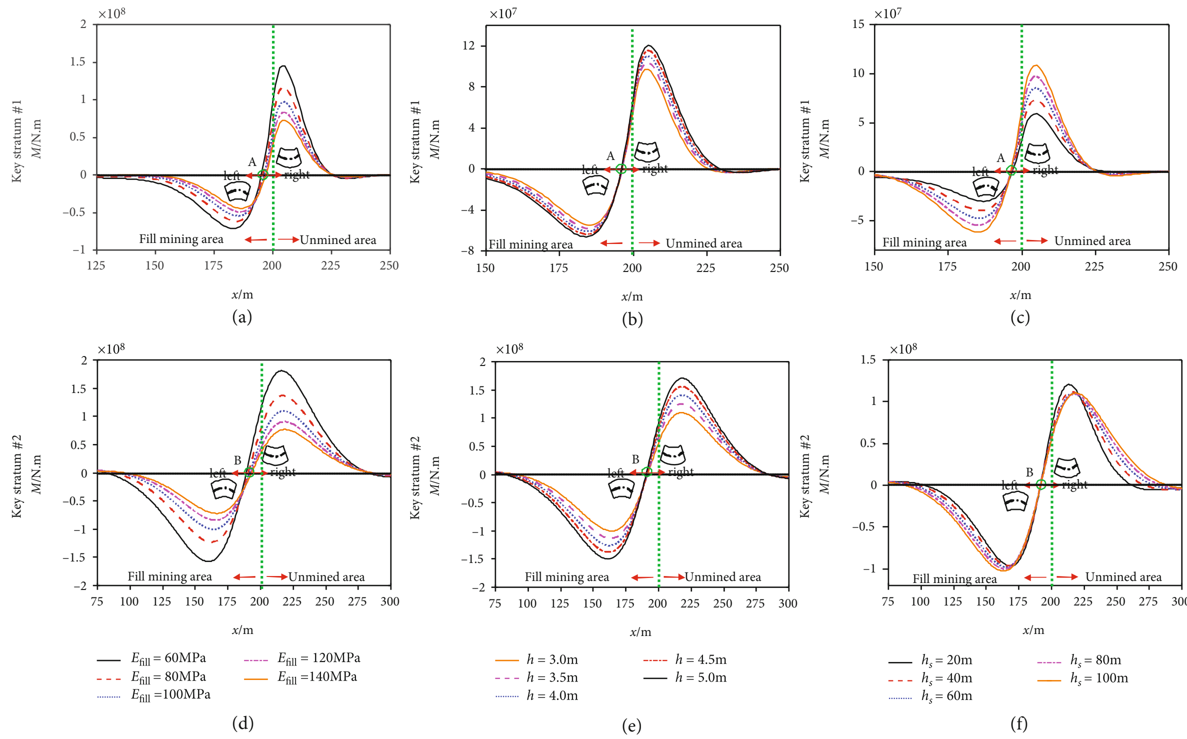

FIGURE 7: The bending moment curves of key strata with the distance to the middle of the stope under various (a, d) elastic modulus of backfill, (b, e) mining height, and (c, f) thickness of soft layers.

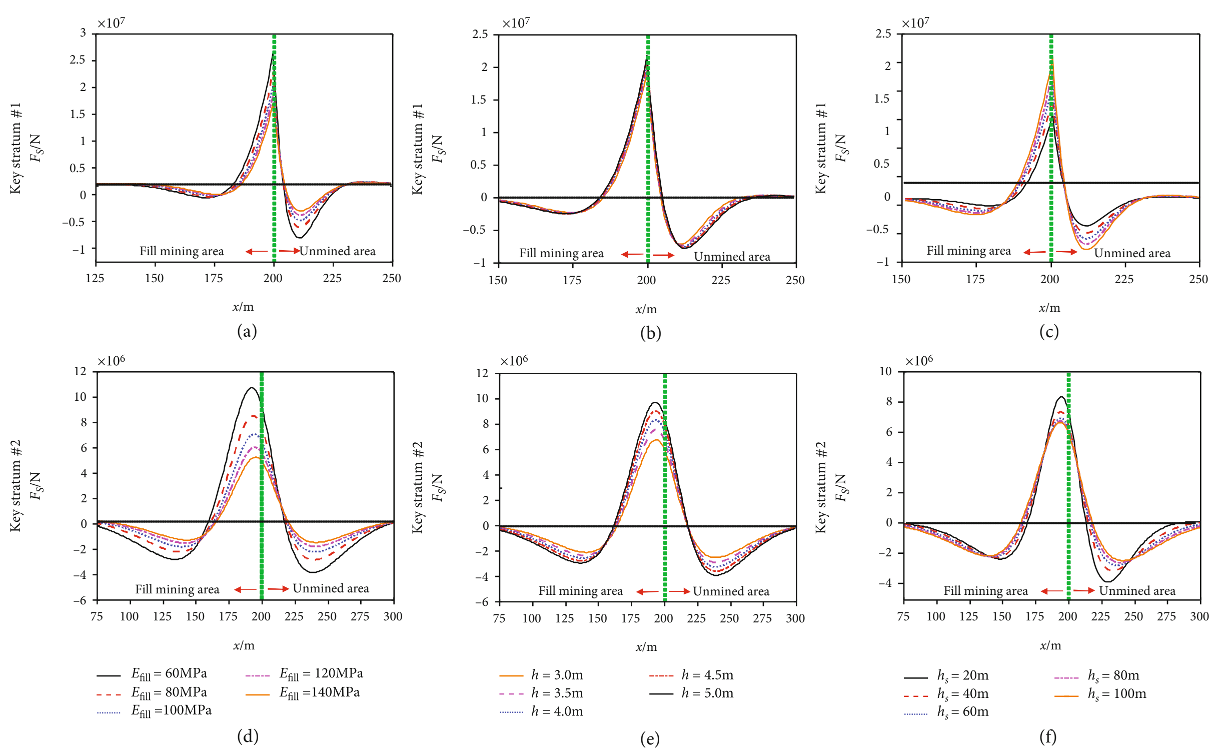

FIGURE 8: The shear force curves of key strata with the distance to the middle of the stope under various (a, d) elastic modulus of backfill, (b, e) mining height, and (c, f) thickness of soft layers.

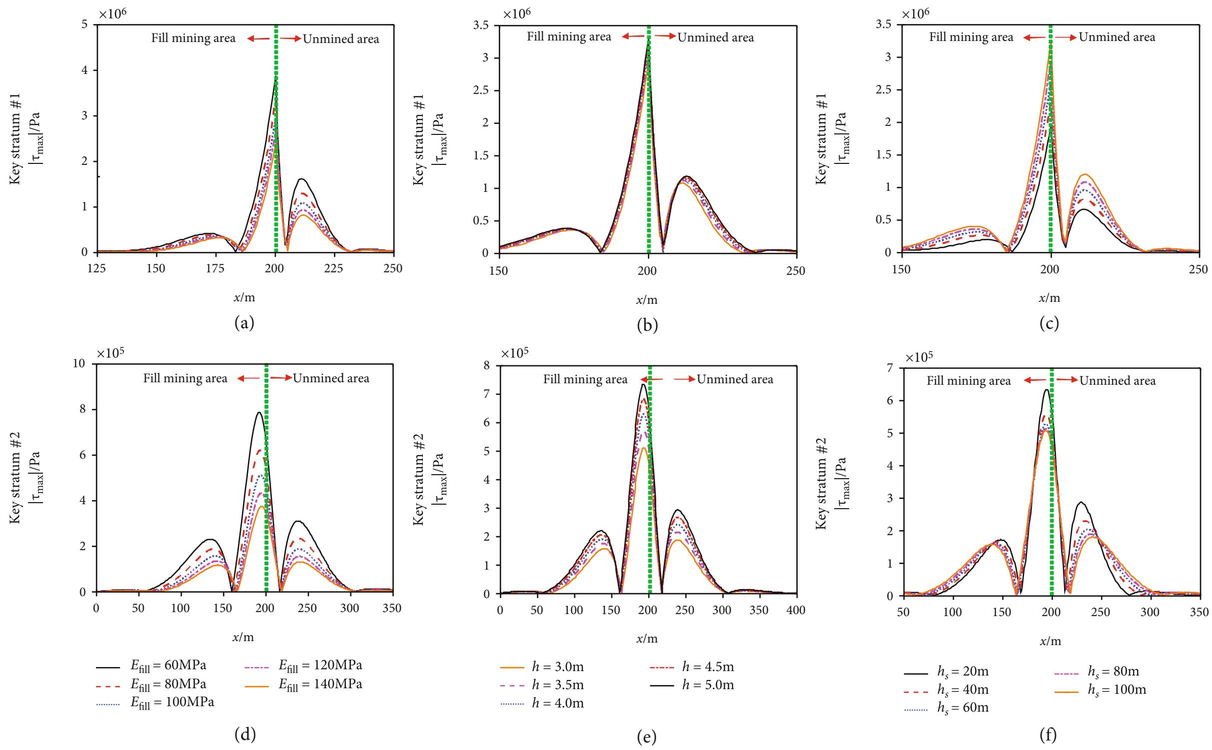

FIGURE 9: The shear stress distribution of key strata with the distance to the middle of the stope under various (a, d) elastic modulus of backfill, (b, e) mining height, and (c, f) thickness of soft layers.

the location of $x = 200$ due to greater stiffness difference between backfill and coal. For the key stratum #2, the shear force peak is located to the left of BL, which is significantly lower than that of key stratum #1. Moreover, with the increase of the elastic modulus of the backfill, the shear force peak of the two key strata decreases. When E_{fill} increases from 60 MPa to 140 MPa, the shear force peak of the key stratum #1 decreases by 38.5% and #2 decreases by 52.4%. Therefore, it is effective to prevent the shear fracture of the key strata by increasing the elastic modulus of the backfill. In addition, with the increase of the thickness of the soft layer, the shear force of key stratum #2 decreases gradually, but the shear peak of key stratum #1 increases significantly. Consequently, it should be fully considered in engineering design that the thickness of the soft layer is significant on the shear failure of key stratum #1. Besides, mining height has little influence on the shear force of key stratum #1, and the shear peak of key stratum #2 changes moderately.

4.3. Stress of Overburden Key Strata. For rectangular beam, bending moment and maximum normal stress, shear force, and maximum shear stress have the following relations:

$$\begin{cases} \sigma_{max} = \dfrac{M}{W}, \\ \tau_{max} = \dfrac{3F_s}{2A}, \end{cases} \tag{24}$$

where W and A are the section modulus in bending and section area, respectively. According to the above equations, it is easy to obtain the absolute value of maximum horizontal stress and shear stress distribution of the two key strata, shown in Figures 9 and 10. It can be seen that distributions of the horizontal stress in the two key strata are similar, and the maximum values are located on the right of BL. Therefore, in the engineering design of solid backfill mining, the key strata tensile fracture at right of BL should be preferentially considered, because of the lower tensile strength of the rock material. For the maximum shear stress, the position of key stratum #1 is located on BL, while the position of key stratum #2 is located on the left of BL. Consequently, the shear strength of these two positions should attract more attentions in the design of solid backfill mining. In addition, with the increase of the elastic modulus of the backfill, the maximum horizontal stress and shear stress of the two key strata decrease significantly, indicating that improving the compaction of the backfill can effectively prevent the fracture of the key strata. However, with the increase of mining height, the maximum horizontal stress and shear stress of key stratum #1 change slightly, but the ones of key strata #2 increase significantly, and this characteristic denotes that special attention should be paid to the fracture of key stratum #2 in large mining height backfill engineering. Besides, with the increase of the thickness of the soft layer, the peak value of the horizontal stress and the shear stress of the key stratum #1 increase significantly, while the peak value of key stratum #2 slightly decreases. Therefore, it should attract more attentions to the fracture of the key stratum #1 with larger thickness of the soft layer in the engineering geological condition.

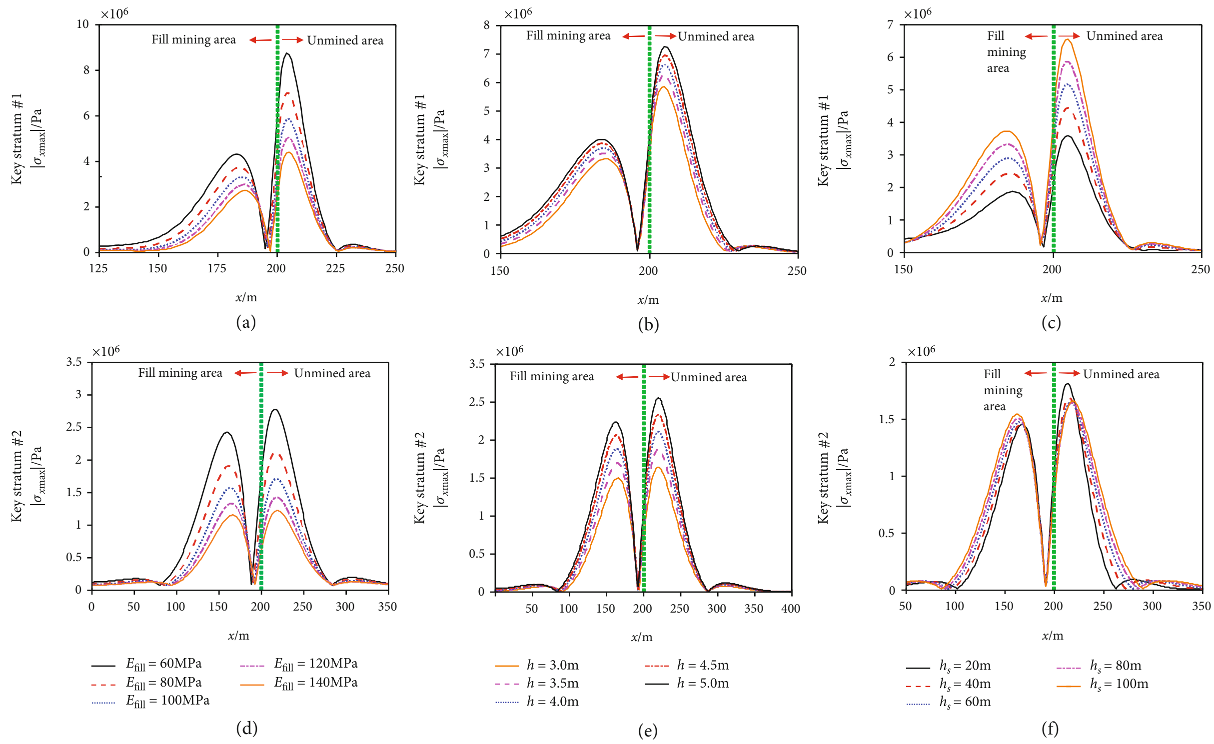

Figure 10: The horizontal stress distribution of key strata with the distance to the middle of the stope under various (a, d) elastic modulus of backfill, (b, e) mining height, and (c, f) thickness of soft layers.

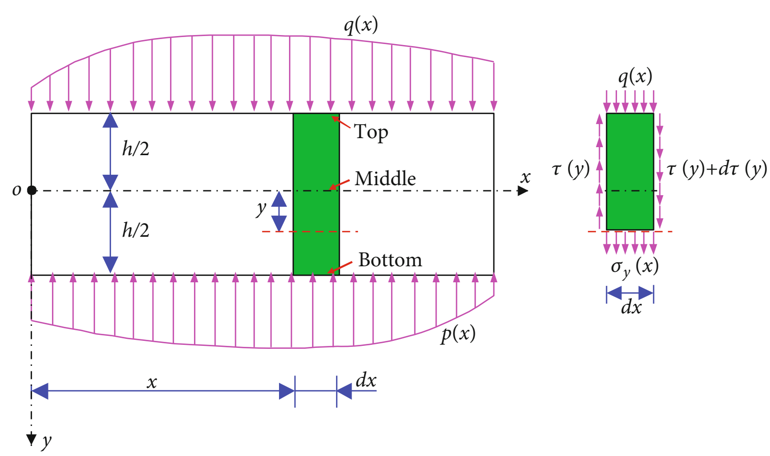

Figure 11: Force analysis diagram of beam microelement.

The vertical stress distribution is also an important aspect to analyze the damage of underground coal mining. For the Winkler foundation beam, the upper surface is subjected to vertical downward distributed load, while the lower surface is subjected to vertical upward distributed load due to the support of the foundation. Therefore, the foundation beam is generally under compressive stress in the vertical direction. In order to analyze the vertical stress distribution characteristics of the beam, a microelement dx in the beam is taken into account. The microelement is cut by a cross section that is perpendicular to y direction, and the part of the microelement above the cross section is taken as a research object, of which the force analysis diagram is shown in Figure 11. According to the equilibrium conditions, the following equation can be obtained.

$$b \cdot q(x)dx + b\sigma_y dx + \int_{-h/2}^{y} b \cdot [\tau(y) + d\tau(y)]dy = \int_{-h/2}^{y} b \cdot \tau(y)dy. \tag{25}$$

Based on the distribution characteristics of shear stress in the beam section in bending, it can be obtained that

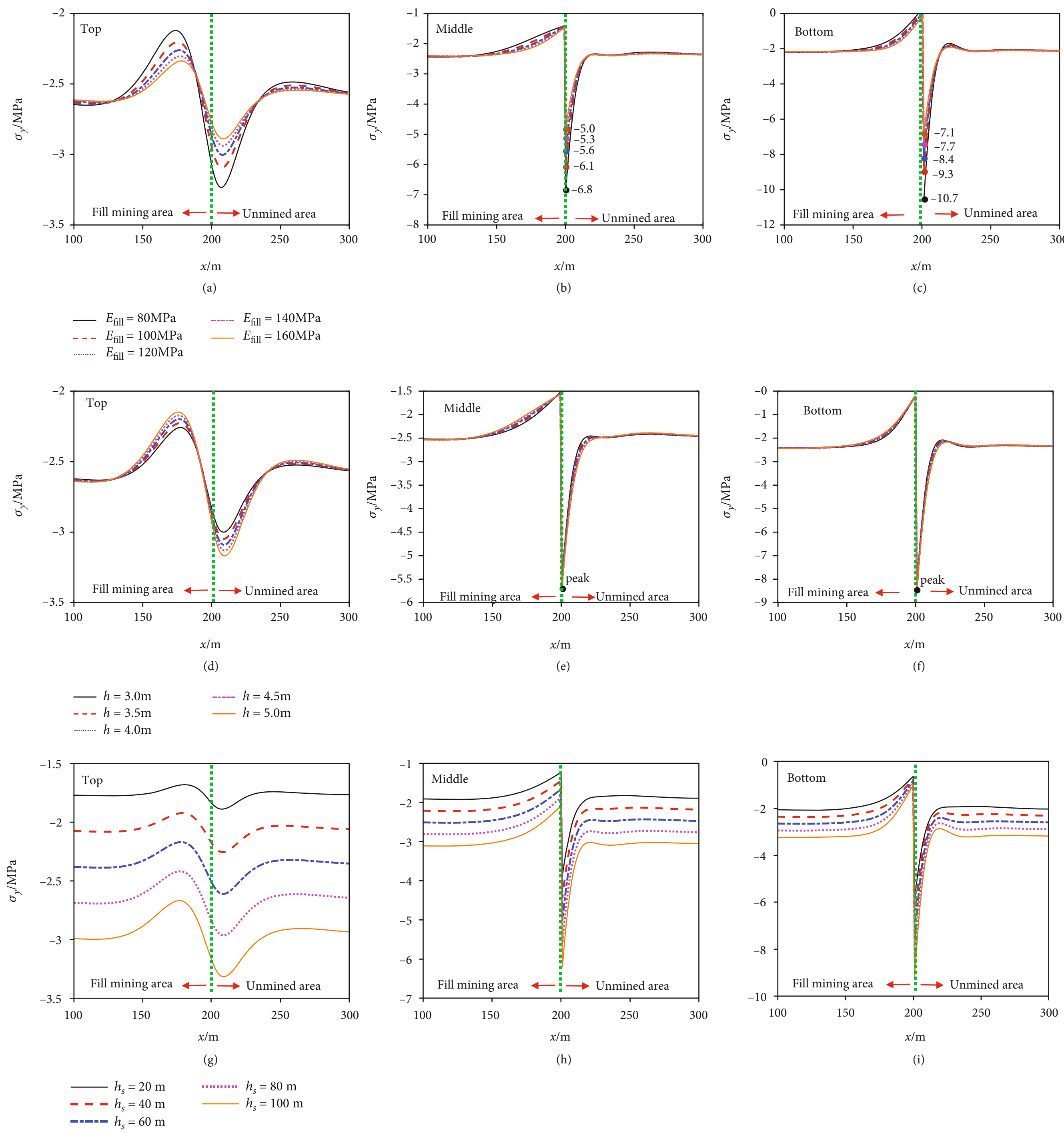

FIGURE 12: Vertical stress distribution of the key stratum #1 at top, middle, and bottom under various (a–c) E_{fill}, (d–f) h, and (g–i) h_s.

$$\begin{cases} \int_{-h/2}^{y} d\tau(y)dy = \int_{-h/2}^{y} \frac{dF_s}{2I_z}\left(\frac{h^2}{4} - y^2\right)dy = D \cdot dF_s, \\ D = \frac{1}{2I_z}\left(-\frac{1}{3}y^3 + \frac{1}{4}h^2 y + \frac{1}{12}h^3\right). \end{cases} \tag{26}$$

Combining Eqs. (25) and (26), the vertical stress can be expressed as follows:

$$\sigma_y = -D\frac{dFs}{dx} - q(x). \tag{27}$$

According to Eqs. (5), (7), and (22), the vertical stress can be expressed with$p(x)$, $q(x)$, and y.

$$\sigma_y = -D[p(x) - q(x)] - q(x). \tag{28}$$

Equation (28) is the vertical stress expression of beam on Winkler foundation. Based on the Eq. (30), the vertical

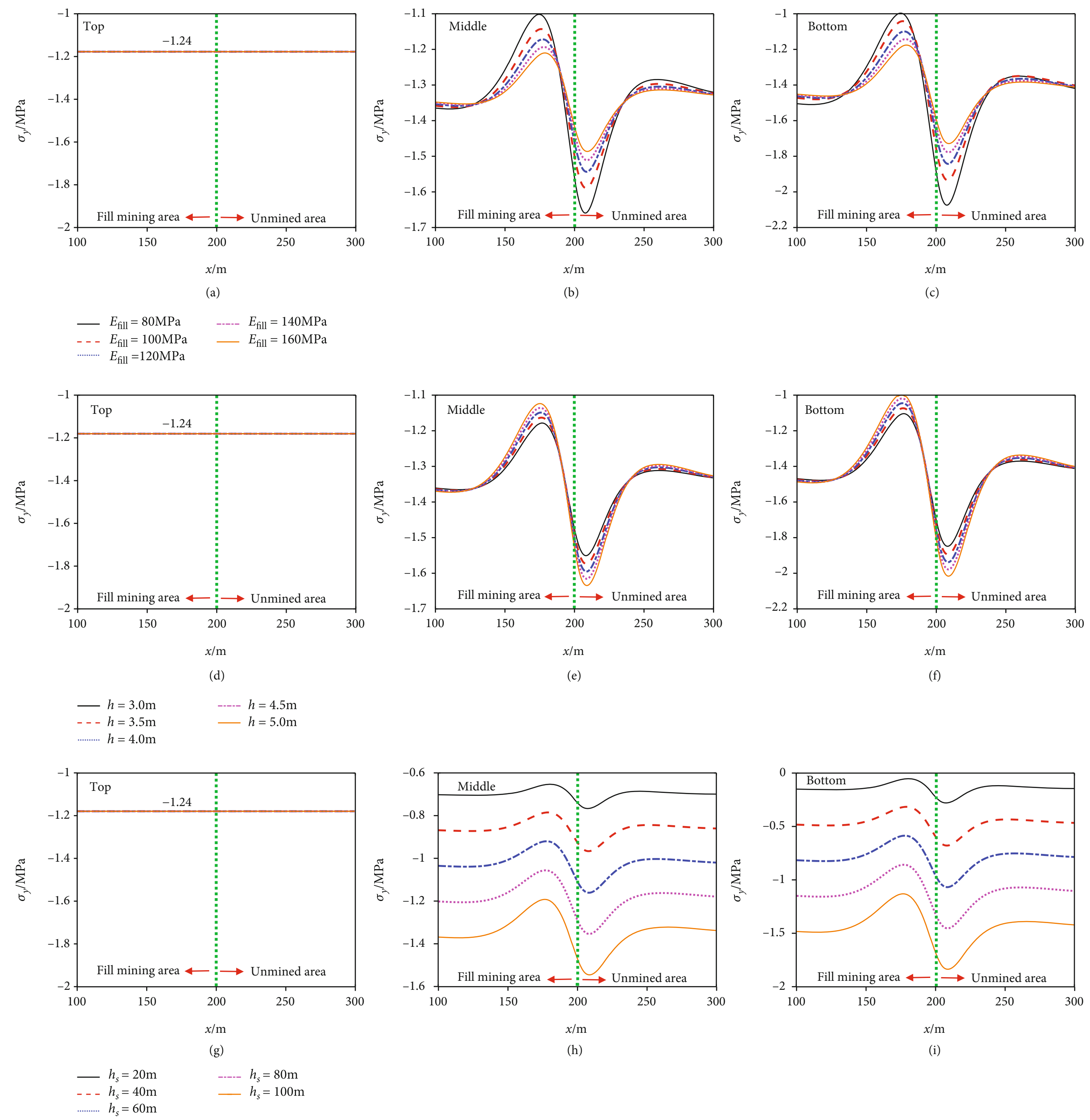

FIGURE 13: Vertical stress distribution of the key stratum #2 at top, middle, and bottom under various (a–c) E_{fill}, (d–f) h, and (g–i) h_s.

stresses of key strata #1 and #2 under various E_{fill}, h, and h_s can be easily obtained, of which the distribution is shown in Figures 12 and 13.

For key stratum #1, it can be seen that the maximum and minimum values of vertical stresses are located on both sides of BL, and the vertical stress of key stratum #1 changes sharply at this location because of the sudden change in shear force. For key stratum #2, differing from key stratum #1, there is no mutation value. The maximum vertical stress is located on the right of BL. In addition, the vertical stress peak of key stratum #1 is significantly greater than that of key stratum #2. With the increase of the elastic modulus of the backfill, the vertical stress peaks, located on the bottom, of the two key strata decrease significantly. With the increase in mining height, the peak of vertical stress in key stratum #1 almost unchanged, while the one of key stratum #2 gradually increases. With the increase of thickness of soft layer, the vertical stress of both key strata increases. Within the scope of the model, the increase in the load on the top of key strata #1 results in increasing the support force from soft layer to key stratum #2.

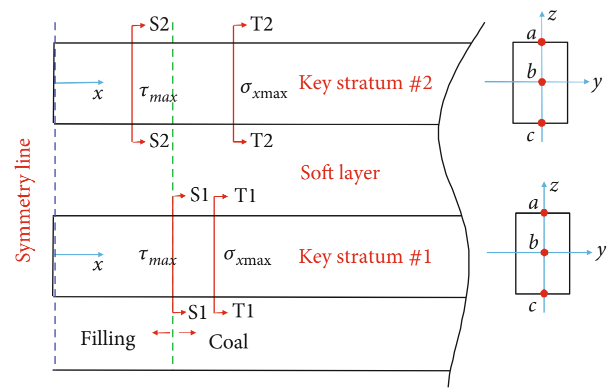

Figure 14: The section positions of the maximum tensile stress and shear stress.

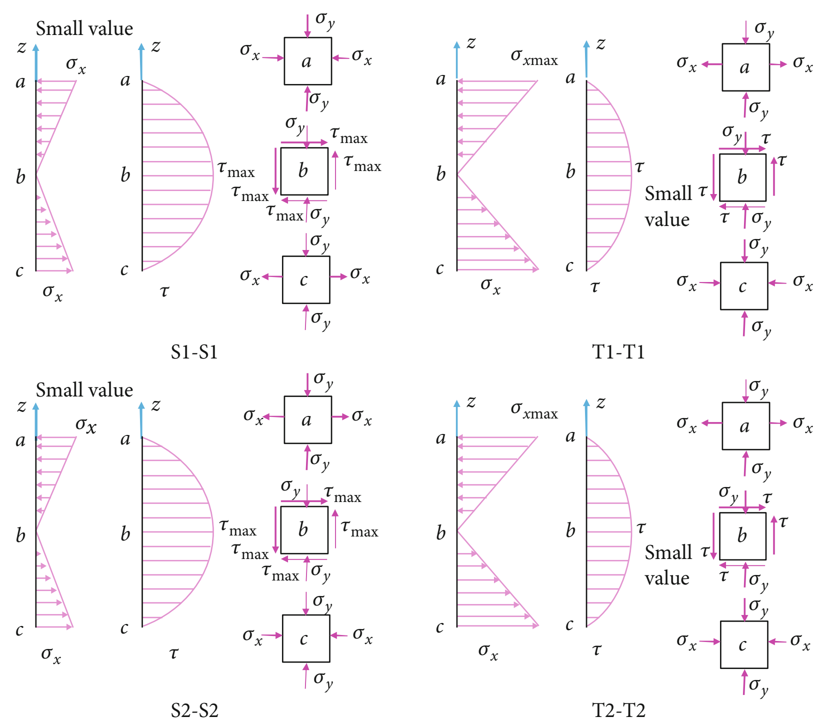

Figure 15: The horizontal stress, shear stress characteristics, and stress states of each section.

5. Strength Analysis of Overburden Key Strata

Generally, rock material is typical brittle material, of which failure forms include tensile failure and shear failure. Tensile failure is generally determined by the maximum tensile stress criterion, while shear failure is determined by the More-Coulomb model. According to the horizontal stress and shear stress distribution of the key strata, their maximum values are distributed in different locations. Besides, stresses of different locations on the same cross section are also different on the basis of the stress distribution of rectangular section beam under transverse bending. Consequently, it is necessary to study the stress state in different locations of the cross section which has the maximum tensile stress and shear stress for further analyzing the strength of the key strata. Figure 14 shows the section positions of the maximum tensile stress and shear stress of the two key strata. Where points a, b, and c represent the top, middle, and bottom of the beam at the same section, respectively. According to the stress distribution characteristics of the key strata, the horizontal stress, shear stress characteristics, and stress states of each section are shown in Figure 15. It can be seen that the most dangerous point in the S1-S1 section of the key stratum #1 is point b, because the horizontal tensile stress is low at point c of S1-S1 section. The horizontal stress of point b in section S1-S1 is 0, which is mainly affected by shear stress and vertical stress. According to the More-Coulomb criterion, the $\tau_{\max}$ should meet the following requirements:

$$\tau_{\max} \leq \frac{c}{n} = [c], \tag{29}$$

where c is the cohesive force of the key stratum material, n is the safety factor, and $[c]$ is the allowable cohesive force. In addition, the dangerous location of section T1-T1 is at the point c, and its strength should meet the maximum tensile stress criterion.

$$\sigma_{\max} \le \frac{\sigma_t}{n} = [\sigma_t], \tag{30}$$

where σ_t is the tensile strength of the key stratum material and $[\sigma_t]$ is the allowable tensile stress. For key stratum #2, its strength condition is the same with that of key stratum #1 according to its stress distribution and state.

To summarize, the strength condition of key strata in solid backfill mining is as follows:

$$\begin{cases} \tau_{\max} \le \dfrac{c}{n} = [c], \\ \sigma_{\max} \le \dfrac{\sigma_t}{n} = [\sigma_t]. \end{cases} \tag{31}$$

6. Conclusion

(1) A multilayer Winkler foundation beam model of the overburden strata in SBCM is established, and its analytical solution is obtained. According to the theoretical analysis results, the subsidence of key strata in overburden shows a "basin"-shape curve, and all of the backfill elastic modulus, mining height, and soft layer thickness have significant influences on the subsidence of key strata

(2) The maximum shear stress of the key stratum close to the coal seam is located on BL, while the one of the key stratum above the soft strata is located on the cross section that horizontal position of which is on the right of BL. The maximum horizontal stresses of both key strata are located to the cross section that horizontal position of which is on the right of BL

(3) The shear stress, horizontal stress, and vertical stress of both the two key strata can be effectively reduced by increasing the elastic modulus of backfill. The increase of mining height has negligible influence on the shear and vertical stresses of key stratum #1, but has a significant influence on the all of the stresses of key stratum #2. The increase of the soft layer thickness has remarkable influence on the horizontal and shear stress of key stratum #1, but has slight influence on the stress of key stratum #2

(4) In the engineering design of SBCM, the shear failure of key stratum #1 at BL and the tensile failures on both sides of BL should be preferentially considered. Due to the low shear stress level of key stratum #2, the tensile failure on both sides of BL should be mainly considered

Data Availability

The data used to support the findings of this study are included within the article.

Conflicts of Interest

The authors declare that they have no conflicts of interest.

Acknowledgments

Ma Chao acknowledges the Key Research and Development Program of Xuzhou (No. KC20176) and Natural Science Foundation of the Jiangsu Higher Education Institutions of China (19KJB430037). Zhang Lianying was supported by the National Natural Sciences Foundation of China (No. 51974296 and No. 52074240), the Outstanding Innovation Team of Jiangsu Province (Safety of Engineering Structure under Complex Environmental), "333" Project of Jiangsu Province, the Key Research and Development Program of Xuzhou (No. KC18090), and the Innovation Capacity Building Program of Xuzhou (No. KC18241).

References

[1] J. Q. Zhang, Y. J. Zhou, and Y. L. Huang, "Integrated technology of fully mechanized solid backfill mining," *Coal Science and Technology*, vol. 40, no. 11, pp. 10–13, 2012.

[2] X. X. Miao, Y. L. Huang, F. Ju, X. B. Mao, G. L. Guo, and J. X. Zhang, "Strata movement theory of dense backfill mining," *Journal of China University of Mining & Technology*, vol. 41, no. 6, pp. 863–867, 2012.

[3] M. Li, J. Zhang, W. Song, and D. M. Germain, "Recycling of crushed waste rock as backfilling material in coal mine: effects of particle size on compaction behaviours," *Environmental Science and Pollution Research*, vol. 26, no. 9, pp. 8789–8797, 2019.

[4] D. Ma, J. Zhang, H. Duan et al., "Reutilization of gangue wastes in underground backfilling mining: overburden aquifer protection," *Chemosphere*, vol. 264, no. 1, article 128400, 2021.

[5] J. Zhang, F. Jiang, J. Yang, W. Bai, and L. Zhang, "Rockburst mechanism in soft coal seam within deep coal mines," *International Journal of Mining Science and Technology*, vol. 27, no. 3, pp. 551–556, 2017.

[6] M. Li, J. Zhang, A. Li, and N. Zhou, "Reutilisation of coal gangue and fly ash as underground backfill materials for surface subsidence control," *Journal of Cleaner Production*, vol. 254, article 120113, 2020.

[7] N. Zhou, J. Zhang, S. Ouyang, X. Deng, C. Dong, and E. du, "Feasibility study and performance optimization of sand-based cemented paste backfill materials," *Journal of Cleaner Production*, vol. 259, article 120798, 2020.

[8] Z. Chuncai, L. Guijian, W. Dun, F. Ting, W. Ruwei, and F. Xiang, "Mobility behavior and environmental implications of trace elements associated with coal gangue: a case study at the Huainan Coalfield in China," *Chemosphere*, vol. 95, pp. 193–199, 2014.

[9] D. Ma, H. Duan, Q. Zhang et al., "A numerical gas fracturing model of coupled thermal, flowing and mechanical effects," *Computers, Materials & Continua*, vol. 65, no. 3, pp. 2123–2141, 2020.

[10] D. Turer, H. A. Nefeslioglu, K. Zorlu, and C. Gokceoglu, "Assessment of geoenvironmental problems of the Zonguldak province (NW Turkey)," *Environmental Geology*, vol. 55, no. 5, pp. 1001–1014, 2008.

[11] Y. Li, S. S. Peng, and J. Zhang, "Impact of longwall mining on groundwater above the longwall panel in shallow coal seams," *Journal of Rock Mechanics and Geotechnical Engineering*, vol. 7, no. 3, pp. 298–305, 2015.

[12] A. Karaman, P. Carpenter, and C. Booth, "Type-curve analysis of water-level changes induced by a longwall mine," *Environmental Geology*, vol. 40, no. 7, pp. 897–901, 2001.

[13] Y. Yu and L. Ma, "Application of roadway backfill mining in water-conservation coal mining: a case study in northern Shaanxi, China," *Sustainability*, vol. 11, no. 13, article 3719, 2019.

[14] J. Zhang, D. Li, and Y. Wang, "Predicting tunnel squeezing using a hybrid classifier ensemble with incomplete data," *Bulletin of Engineering Geology and the Environment*, vol. 79, no. 6, pp. 3245–3256, 2020.

[15] D. Ma, H. Duan, W. Liu, X. Ma, and M. Tao, "Water-sediment two-phase flow inrush hazard in rock fractures of overburden strata during coal mining," *Mine Water and the Environment*, vol. 39, no. 2, pp. 308–319, 2020.

[16] D. Ma, H. Duan, X. Li, Z. Li, Z. Zhou, and T. Li, "Effects of seepage-induced erosion on nonlinear hydraulic properties of broken red sandstones," *Tunnelling and Underground Space Technology*, vol. 91, article 102993, 2019.

[17] M. Li, J. Zhang, Z. Wu, and K. Sun, "Calculation and monitoring analysis of stress distribution in a coal mine gob filled with waste rock backfill materials," *Arabian Journal of Geosciences*, vol. 12, no. 14, p. 418, 2019.

[18] M. Li, G. Meng, J. Zhang, P. Huang, and D. M. Germain, "Sensitivity analysis of key factors influencing compression-induced deformation of waste rocks for backfilling to reduce environmental pollution," *Environmental Science and Pollution Research*, vol. 27, no. 14, pp. 16707–16717, 2020.

[19] M. Li, J. Zhang, G. Meng, Y. Gao, and A. Li, "Testing and modelling creep compression of waste rocks for backfill with different lithologies," *International Journal of Rock Mechanics and Mining Sciences*, vol. 125, article 104170, 2020.

[20] Y. L. Huang, J. M. Li, D. Ma, H. D. Gao, Y. Guo, and S. Ouyang, "Triaxial compression behaviour of gangue solid wastes under effects of particle size and confining pressure," *Science of The Total Environment*, vol. 693, article 133607, 2019.

[21] B. Li, H. Yan, J. Zhang, and N. Zhou, "Compaction property prediction of mixed gangue backfill materials using hybrid intelligence models: a new approach," *Construction and Building Materials*, vol. 247, article 118633, 2020.

[22] J. F. Zha, G. L. Guo, Y. X. Liu, and B. Wu, "The nonlinear features of waste deformation and its impaction on strata movement," *Journal of China Coal Society*, vol. 34, no. 8, pp. 1071–1075, 2009.

[23] Y. L. Huang, J. X. Zhang, Q. Zhang, S. J. Nie, and B. F. An, "Strata movement control due to bulk factor of backfilling body in fully mechanized backfilling mining face," *Journal of Mining and Safety Engineering*, vol. 29, no. 2, pp. 162–167, 2012.

[24] M. Li, J. X. Zhang, X. X. Miao, and Y. L. Huang, "Strata movement under compaction of solid back fill body," *Journal of China University of Mining and Technology*, vol. 43, no. 6, pp. 969–973+980, 2014.

[25] Q. Zhang, J. X. Zhang, Y. Chen, J. D. Ntigurirwa, and K. Q. Xia, "Moving set-up room theory of weakening the mining pressure caused by the backfilling body in solid backfilling mining," *Energy Science and Engineering*, vol. 8, no. 1, 2020.

[26] "An elastic base beam model of overlying strata movement during caol mining with gangue back-filling," *Journal of China University of Mining & Technology*, vol. 41, no. 1, pp. 14–19, 2012.

[27] "Strata movement under compaction of solid backfill body," *Journal of China University of Mining & Technology*, vol. 43, no. 6, pp. 969–980, 2014.

Hindawi
Geofluids
Volume 2021, Article ID 6630462, 8 pages
https://doi.org/10.1155/2021/6630462

Research Article

Evolution Mechanism of Water-Conducting Channel of Collapse Column in Karst Mining Area of Southwest China

Zhengzheng Cao, Yulou Ren, Qinting Wang, Banghua Yao, and Xinchao Zhang

International Joint Research Laboratory of Henan Province for Underground Space Development and Disaster Prevention, School of Civil Engineering, Henan Polytechnic University, Jiaozuo, 454000 Henan, China

Correspondence should be addressed to Qinting Wang; hpu_wangqt@126.com

Received 3 January 2021; Revised 29 January 2021; Accepted 16 February 2021; Published 26 February 2021

Academic Editor: Guanglei Zhang

There are many karst collapse columns in coal seam roof in the southern coal field in China, which are different from those in coal seam floor in the northern coal field, due to the stratum characteristics. The karst collapse column in coal seam roof tends to reactivate and conduct water and induce the serious water inrush disaster, when the karst collapse column communicates with the overlying aquifer. In order to reveal the evolution mechanism of water-conducting channel of collapse column in karst mining area of southwest China, the aquifers and water inflow rule in 1908 working face in Qianjin coal mine are analyzed. Besides, the particle size distribution and mineral component of collapse column are researched by the X-ray diffraction test and the screening method, which are the basis for researching the water inrush mechanism in karst collapse column. On this basis, the water inrush of roof collapse column under the influence of mining is researched by establishing the numerical calculation model with the UDEC numerical software. The results show that the water flowing into the 1908 working face comes from the Changxing formation aquifer and Yulongshan formation aquifer above the coal seam, and the proportion of coarse particles and fine particles in collapse column is 89.86% and 10.14%, respectively. With the advance of working face, the water-conducting channel connected the working face with the aquifer, or the surface is formed by collapse pits, karst caves, and collapse column. The research results can be treated as an important basis for the water-preserved mining in southern coal field in China.

1. Introduction

Water inrush disaster is one of the major safety accidents in coal mine. According to statistics, the direct economic loss caused by water inrush disaster ranks first among all kinds of coal mine accidents [1]. More precisely, the water inrush of collapse column has the characteristics of concealment, abruptness, large water inrush value, and high harm, which is the hotspot and difficulty in the disaster-causing mechanism of water inrush in coal mine [2]. The geological structure of collapse column exists between the coal resource of Longtan formation and the aquifer of overlying Changxing formation, due to the overlap between late Permian coalfield and karst area in south China, especially with Guizhou province as the center, which is different from those in coal seam floor in the northern coal field [3]. The karst collapse column in coal seam roof tends to reactivate and conduct water in the mining process of working face and induce the serious water inrush disaster, when the karst collapse column communicates with the overlying aquifer, which poses a serious threat to safety production in coal mines [4]. For example, the water inrush disasters of roof collapse column occurred in working face in Qianjin coal mine and Xintian coal mine in Guizhou province, which greatly affected the safety mining [5, 6]. Therefore, it is of great significance to research the water-conducting channel of collapse column in karst mining areas, in order to ensure the safe mining of working face in southwest China.

The scholars at home and aboard have carried out lots of research on the water-conducting channel of collapse column. Wang et al. [7] conducted variable mass seepage experiments for broken mudstone considering particle migration, by using a modified variable mass seepage experiment system on broken rock and study the water inrush mechanism of karst collapse column in different depths with coupled underground water pressure and compaction degree. Du et al. [8] studied the influence mechanisms of porosity of porous medium, the particle sizes of broken rock mass, and sand on water-sand inrush disaster, by using the self-developed porous medium two-phase water-sand flow testing system. Wu et al. [9] designed an experimental system for testing the seepage property of broken rock under the condition of mass loss and studied the effect of dissolution on the seepage property of broken rock. Based on the imagination between column pipeline of water inrush and thick wall canister, Yin et al. [10] generalized the former as column pipelines of uniform patterns and simulated with mechanical models of thick wall canisters. Song et al. [11] derived the criteria equation of elliptical cross section of thick cylinder collapse columns mechanical model in water inrush mode and predicted water inrush by karst collapse columns, by using complex function, elastic-plastic mechanics, and related theories. Li et al. [12] carried out the physical simulation experiment about mining effect on the activated collapse column, by the self-designed similar simulation experiment system, and observed the change laws of seepage field around collapse column and apparent resistivity. Yang et al. [13] researched the water inrush due to karst collapse columns, which is considered to be a coupled processes that can be characterized with Darcy equation in confined aquifer, Brinkman equation in fractured zone, and Navier-Stokes's equation in tunnel. Zhu et al. [14] established the formulation of a damage-based hydromechanical model based on elastic damage theory, by understanding the mechanism of water inrushes controlled by geologic structures is of vital importance for adopting effective measures to prevent their occurrence. Yao et al. [15] presented a mechanical model for water outburst of karst collapse pillar involving the processes of solid deformation, water flow, particles erosion, and migration and obtained the variation of porosity, seepage velocity, water pressure, and particle concentration as well as water inflow volume as the time.

The above research results are focus on the water inrush mechanism of collapse column in north China, where the water resource is the Ordovician limestone aquifer in floor of coal seam [16, 17]. However, the water resource of collapse column in southwest China is the Yulongshan and Changxing limestone aquifer in roof of coal seam, which is different from the water inrush of collapse column in north China [18]. Besides, the particle size distribution and mineral component of collapse column are not researched intensively, which are the basis for the water inrush mechanism of karst collapse column [19]. The water-preserved mining in karst area in southwest China has not researched. Therefore, the evolution mechanism of water-conducting channel of collapse column in karst mining area of southwest China is researched systematically, on the basis of the 1908 working face in Qianjin coal mine in Guizhou province. The research results can be treated as an important basis for the prevention and treatment of water inrush disaster in southern coal field in China.

2. Overview of Trial Working Face

2.1. Mining Geological Condition. Karst landforms are well developed in Qianjin coal mine, which is located at Meidongchang village, Jinpo township, Qianxi county, Bijie city, Guizhou province, such as peak cluster, depression, dissolving bucket, and karst cave [20, 21]. The 9# coal seam is the mining coal seam, and the thickness is basically stable, with an average thickness of 1.8 m and an average buried depth of 245 m. The trial engineering background is based on the 1908 working face in Qianjin coal mine. The strike length of 1908 working face is 403 m, and the cutting hole length is 104 m, and the dip angle of coal seam is $8\sim14^{\circ}$, and the average dip angle is 10°. Because the dip angle of coal seam is gentle, the longwall mining method is employed to mining the coal seam, and the caving method is employed to manage the roof. Atmospheric precipitation is mostly concentrated in underground caves and underground rivers, while surface water resources are scarce [22, 23]. A collapse column exists at a distance of 235 m from the working face to the cutting hole. The length of long axis of the collapse column is 32 m, and the length of the short axis is 18 m.

2.2. Hydrological Geological Condition. There are two limestone aquifers exist above the 1908 working face, which are Changxing formation aquifer near the coal seam and Yulongshan formation aquifer far from the coal seam. The Yulongshan formation aquifer is exposed in the central and southern areas in the mine field, and the average limestone thickness is 130 m. Geomorphology is diversity, such as peak cluster, depression, dissolve gully, stone bud, and dry karst cave. Besides, the depression is accompanied by falling-water holes, dissolving bucket, and vertical wells. Due to the strong development of surface karst fissure and underground karst pipeline, it is easy to collect a large amount of surface precipitation, which turns into karst fissure water and interlayer karst pipeline water. The Changxing formation aquifer is exposed in the north of the mine field, and the average thickness of limestone is 7 m. The limestone in outcrop area is strongly weathered, and the karst fissure is developed, which contains abundant karst fissure water. The gushing water at the 1908 working face comes from the Changxing formation aquifer and Yulongshan formation aquifer, conducted by the activated karst collapse column. According to the monitoring situation in 1908 working face in Qianjin coal, a large amount of water flow occurs in the working face, when the working face is 2 m away from the collapse column. Besides, the gushing water is affected by atmospheric precipitation. The water inflow in working face lags behind the atmospheric precipitation, and the water inflow begins to increase sharply in the rain after about two days.

3. Particle Distribution and Mineral Component of Collapse Column

The collapse column is the geological structure composed of fillings such as fine argillaceous and crushed rocks. The particle distribution and mineral component of collapse column are the basis for researching the water inrush mechanism of karst collapse column. The X-ray diffraction testing (XRD) and the screening method are carried out in this article, and the effect of particle distribution and mineral component on the seepage characteristic of collapse column is obtained.

3.1. Particle Distribution of Collapse Column. The dried particles of collapse column are screened by standard screens of different pore sizes and divided into different groups according to the particle size of standard screen diameters; then, the percentages of particle groups in the total amount are weighed and calculated. Specifically, a representative sample of dried collapse column weighed 500 g is poured into the standard screens. Then, vibrating the representative sample by the standard screens of different pore sizes, which is shown in Figure 1. Finally, the weight of particle remaining on each screen is weighed, and the particle size distribution of collapse column is obtained.

The particle size distribution of the collapse column is obtained through the standard screening test. These particles that cannot pass the minimum coarse screen (2 mm) are regarded as coarse particles (greater than 2 mm), while those that pass the minimum coarse screen are regarded as fine particles (less than 2 mm). The test result indicates that the proportion of coarse particles and fine particles is 89.86% and 10.14%, respectively. Besides, the particle size of 20-40 mm occupies the largest proportion (31.91%), followed by the particle size of 10-20 mm (21.08%). The mass loss of fine particles in collapse column in seepage accelerates the evolution and formation of water-conducting channel in karst mining area.

3.2. Mineral Component of Collapse Column. XRD (X-ray diffraction) is a diffraction pattern which is obtained by diffraction of X-rays in crystals [24, 25]. The mineral component of collapse column is measured by the X-ray diffraction test (XRD), which is shown in Figure 2. The XRD test result indicates that the content of illite is 68%, and the content of quartz is 17%, and the content of pyrite is 11%, and the total content of sphalerite, calcite, zincite, and anatase is 4%. The collapse column contains a large proportion of viscous minerals, such as illite, which are easy to transport along with water migration, causing the porosity expansion of collapse column, thereby triggering water inrush disaster of karst collapse column.

4. Numerical Simulation of Water Inrush of Roof Collapse Column

4.1. Numerical Calculation Model. UDEC (Universal Distinct Element Code) is the numerical calculation program based on the theory of discrete element method. The numerical calculation model is established, with reference to mining geological conditions of 1908 working face, which is shown in Figure 3. The length and the height of numerical model are 600 m and 245 m, respectively. Besides, the height of the collapse column is 186 m, and the upper boundary and lower boundary of the collapse column is 10 m and 30 m, respectively. There are two sinkholes in the surface and eight karst caves in limestone strata. The mining height and the mining depth of the coal seam are 2 m and 240 m, respectively.

The left and right boundary of the numerical calculation model is the velocity boundary condition, which are fixed horizontally, and the bottom boundary of the numerical calculation model is fixed vertically. Besides, the left boundary, right boundary, and bottom boundary of the numerical calculation model are set as impermeable boundary, while the top of the numerical calculation model is set as free permeable boundary. The water pressure of the aquifer in overlying limestone strata is 0.25 MPa. The mining step by step is adopted, and the mining length is 400 m. The material constitutive model is More-Coulomb model, and the joint constitutive model is coulomb slip model of surface contact. Besides, the physical parameters of rock mass are shown in Table 1, and the percolation mechanical parameters of joints are shown in Table 2.

Figure 1: Vibration classification screen.

4.2. Result Analysis. When the 1908 working face is mining to 140 m, the first weighting on the working face occurs. The distribution characteristics of mining-induced fracture field in overburden are shown in Figure 4, and the maximum opening of the fracture in overburden is 23.41 mm. The fractures in the roof of the working face are concentrated at the front and rear ends of the stope, and the fracture opening is greater than 5 mm. The fracture opening in floor is distributed at 0.1 mm-1 mm, and the fracture opening of the compacted rock mass in gob is distributed at 1 mm-5 mm. The first weighting on the working face has little effect on the collapse column. The first weighting in working face is the initial breakage of the basic roof, and the periodic weighting in working face is the periodic breakage of the basic roof.

When the 1908 working face is mining to 280 m, the distribution characteristics of mining-induced fracture field in overburden is shown in Figure 5, and the maximum opening of the fracture in overburden is 31.46 mm. The fractures in the roof of the working face are caused by periodic weighting in overburden, which are concentrated at the front and rear ends of the stope, and the fracture opening is greater than 5 mm. The fracture opening in floor is distributed at 0.1 mm-1 mm, and the fracture opening of the compacted rock mass in gob is distributed at 1 mm-5 mm.

The analysis of permeability characteristics of water-conducting channel in overburden is based on the fractures with the opening greater than 5 mm, since fractures with an opening greater than 5 mm belong to good water-conducting channels. From the transverse perspective, the fracture opening of collapse pits and karst caves above gob increases from 0.1 mm-1 mm to 1 mm-5 mm and greater

(a) The collected sample (b) The dried sample (c) The test sample

Figure 2: Mineral component of collapse column.

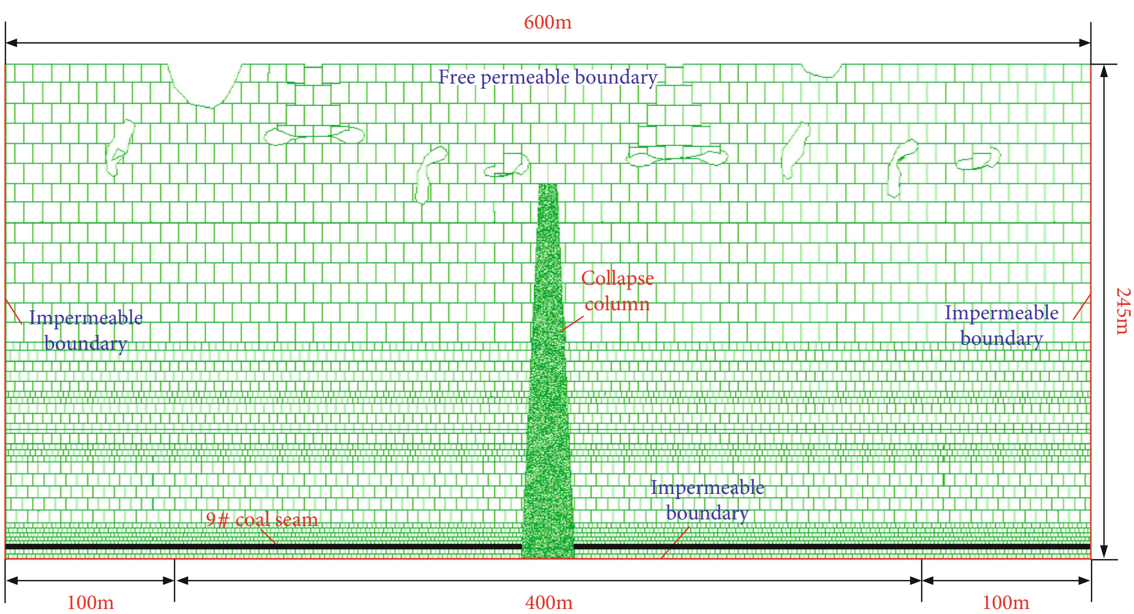

Figure 3: Numerical calculation model.

than 5 mm, and the collapse column is connected with the collapse pit and karst cave through the mining-inducing fractures in the surrounding rock. From the vertical perspective, the collapse column is effected by the mining of working face, and the fracture opening of collapse column close to the working face increases from less than 0.1 mm and 0.1 mm-1 mm to 1 mm-5 mm and greater than 5 mm. Therefore, the water-conducting channel connected the surface with the working surface is formed by collapse pits, karst caves, and collapse column. The velocity diagram of water flow in the water-conducting channel can be obtained, as shown in Figure 6.

When the 1908 working face is mining to 300 m, the working face is in the center of collapse column. The distribution characteristics of mining-induced fracture field in overburden are shown in Figure 7, and the maximum opening of the fracture in overburden is 23.64 mm. The fractures in the roof of the working face are concentrated at the front and rear ends of the stope, and the fracture opening increases from less than 0.1 mm and 0.1 mm-1 mm to greater than 5 mm. The fracture opening in floor of working face is distributed at 1 mm-5 mm, and the fracture opening in floor of gob is distributed at 0.1 mm-1 mm. The fracture opening of the compacted rock mass in gob is distributed at 1 mm-

Table 1: The physical parameters of rock mass.

Rock strata	h/m	K/GPa	G/GPa	d/N·m-3	f/°	C/MPa	t/MPa
Limestone	138	26.6	21.9	2800	42	6.53	5.7
Kern stone	4	21.3	16.7	2650	38	4.23	3.23
Limestone	20	26.6	21.9	2800	42	6.53	5.7
Siltstone	6	18.5	16.2	2800	37	3.64	2.25
Silty mudstone	13	19.4	9.5	2840	33	2.65	2.1
Fine sandstone	7	20.7	17.8	2800	37	3.64	2.25
Silty mudstone	9	19.4	9.5	2840	33	2.65	2.1
Fine sandstone	30	7	20.7	17.8	2800	37	3.64
Silty mudstone	5	19.4	9.5	2840	33	2.65	2.1
Fine sandstone	6	20.7	17.8	2800	37	3.64	2.25
Coal seam	2	3.89	1.59	1600	40	1.50	1.2
Argillaceous siltstone	5	21.0	12.6	2770	35	3.15	2.31
Collapse column	186	1.30	0.50	1300	35	0.5	0.5

Table 2: The percolation mechanical parameters of joints.

Rock strata	h/m	jkn/GPa	jks/GPa	jfric/°	jperm/Pa-1.s-1	ares/m	azero/m
Limestone	138	8.06	6.39	10	246	0.003	0.02
Kern stone	4	7.46	6.18	11	198	0.003	0.02
Limestone	20	8.06	6.39	10	246	0.003	0.02
Siltstone	6	4.58	2.73	8	128	0.003	0.02
Silty mudstone	13	8.06	6.39	11	100	0.003	0.02
Fine sandstone	7	4.58	2.73	10	143	0.003	0.02
Silty mudstone	9	8.06	6.39	11	100	0.003	0.02
Fine sandstone	30	4.58	2.73	10	143	0.003	0.02
Silty mudstone	5	8.06	6.39	11	100	0.003	0.02
Fine sandstone	6	4.58	2.73	10	143	0.003	0.02
Coal seam	2	4.09	2.50	10	85	0.0003	0.003
Argillaceous siltstone	5	4.58	2.73	15	95	0.003	0.02
Collapse column	186	3.46	2.20	14	330	0.010	0.08

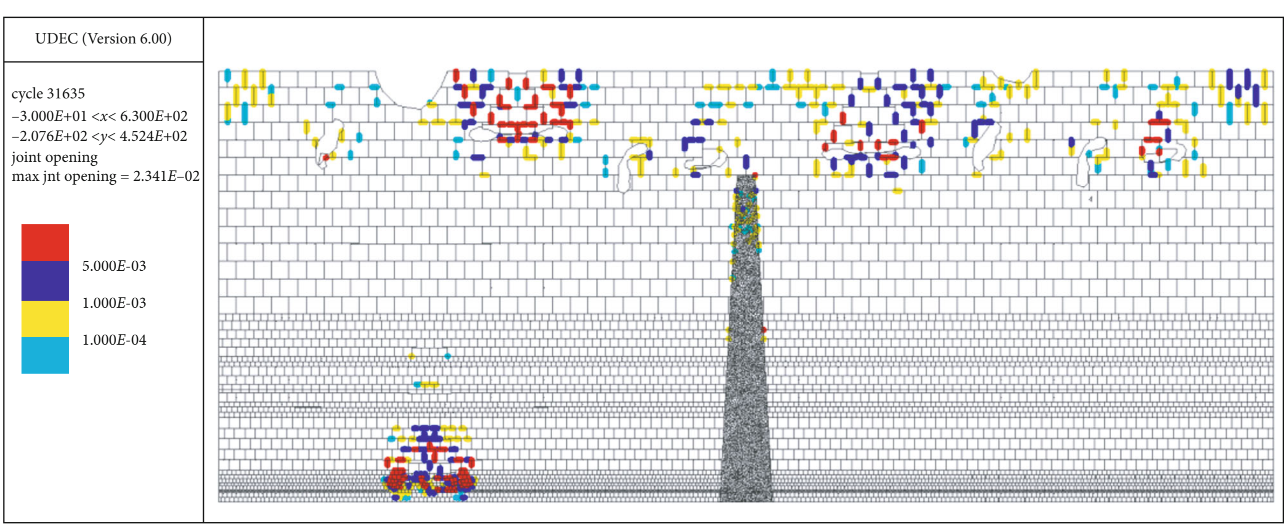

Figure 4: The mining-induced fracture field (the mining distance is 140 m).

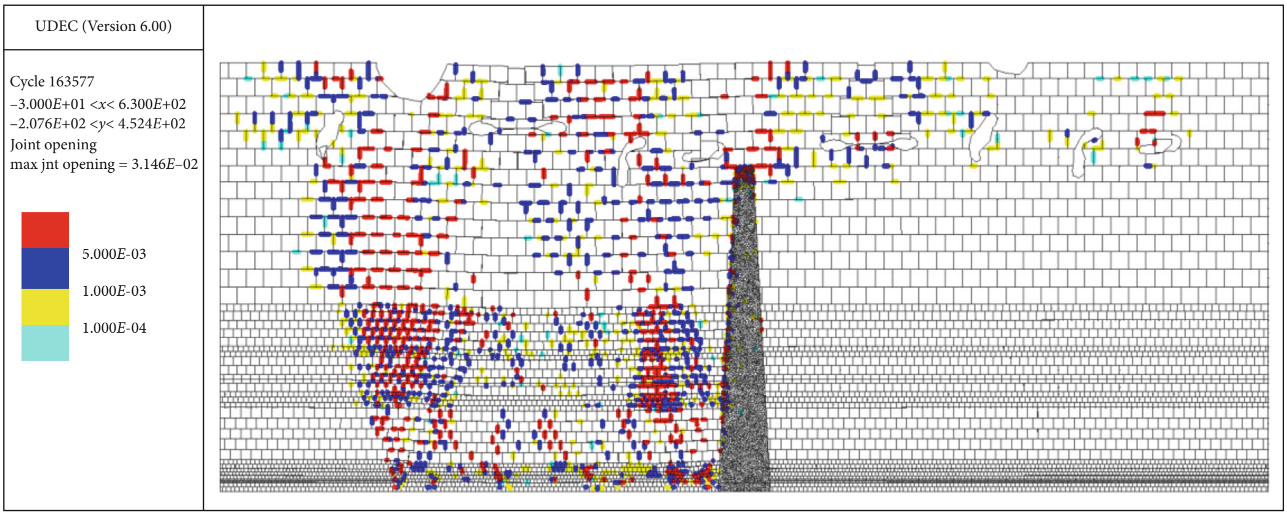

Figure 5: The mining-induced fracture field (the mining distance is 280 m).

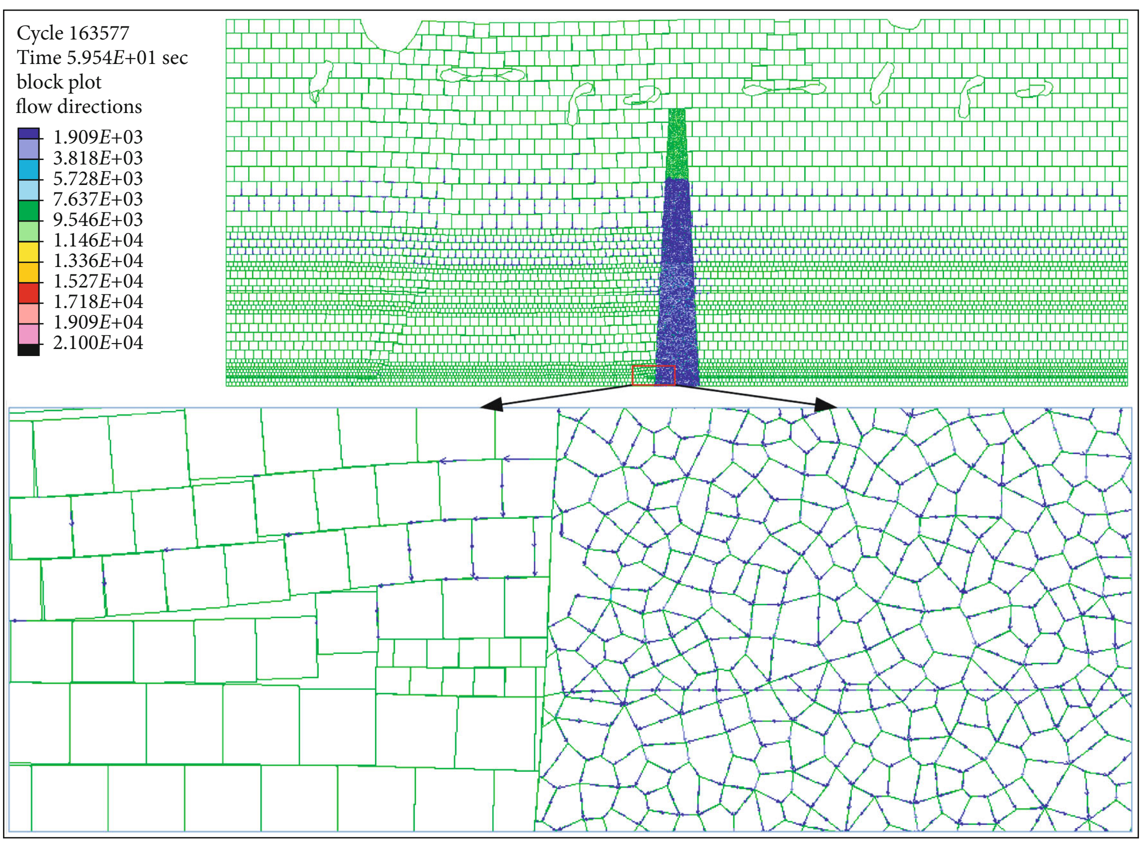

Figure 6: The velocity diagram of water flow (the mining distance is 280 m).

5 mm and greater than 5 mm. With the advance of the working face, the fracture opening of the basic roof formed by the periodic weighting decreases from greater than 5 mm to 1 mm-5 mm, due to the compaction effect.

When the 1908 working face is mining to 320 m, the collapse column lies behind the working face. The distribution characteristics of mining-induced fracture field in overburden are shown in Figure 8, and the maximum opening of the fracture in overburden is 29.46 mm. The fractures in the roof of the working face are concentrated at the front and rear ends of the stope, developed mostly in the area of collapse column.

The fracture opening at the lower end of collapse column is greater than 5 mm, and the fractures of karst cave on the upper right of collapse column develop to the surface, connected with the upper end of collapse column. The fracture opening in floor of working face is distributed at 1 mm-

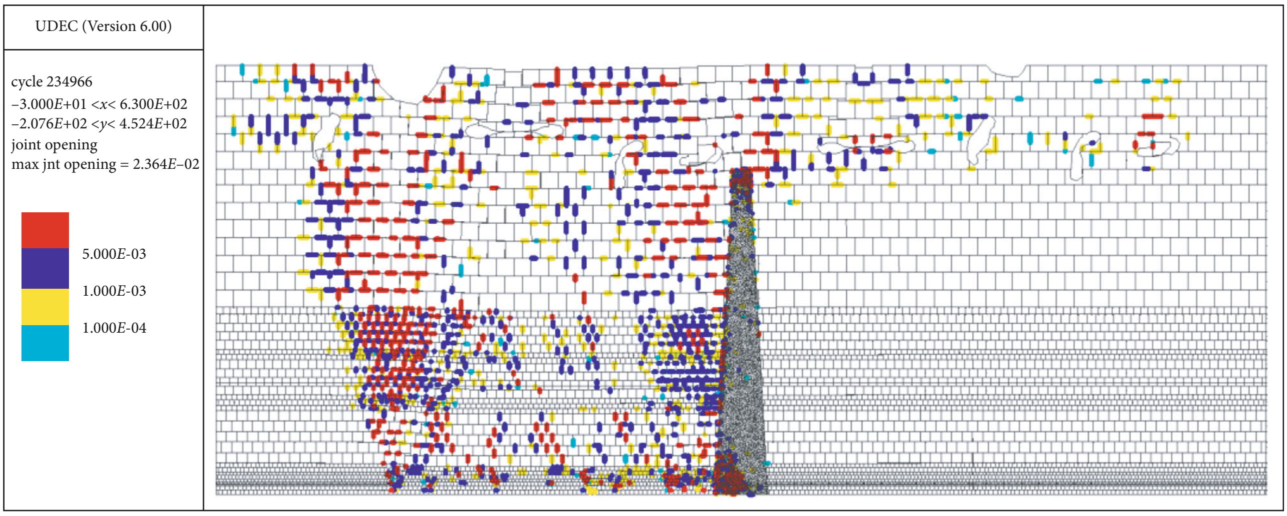

Figure 7: The mining-induced fracture field (the mining distance is 300 m).

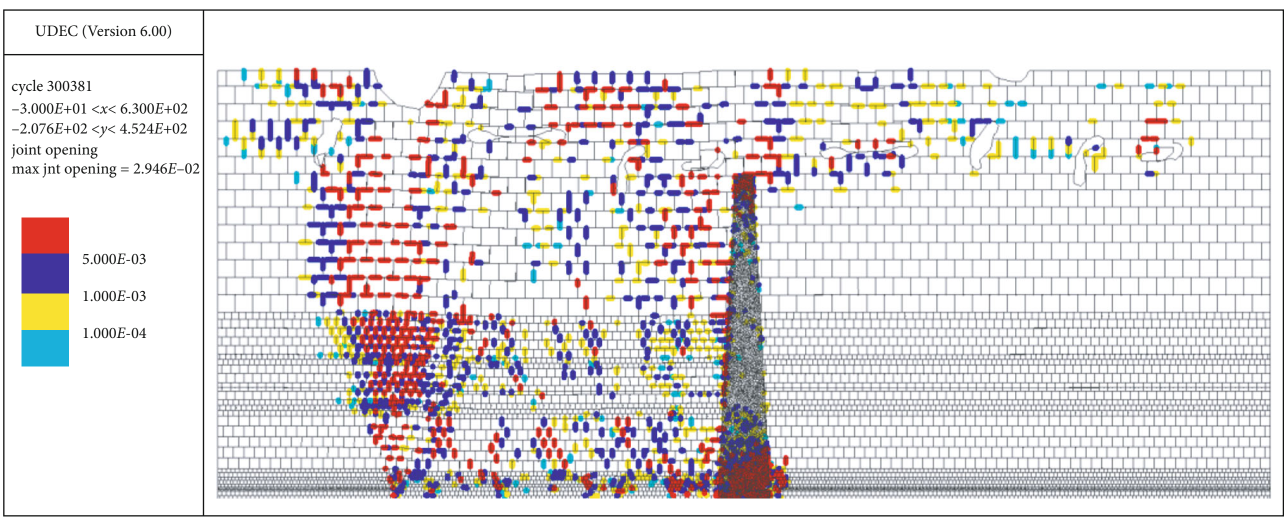

Figure 8: The mining-induced fracture field (the mining distance is 320 m).

5 mm, and the fracture opening in floor of gob is distributed at 0.1 mm-1 mm. The fracture opening of the compacted rock mass in gob is distributed at 1 mm-5 mm and greater than 5 mm. With the advance of the working face, the fracture opening of the basic roof formed by the periodic weighting decreases from greater than 5 mm to 1 mm-5 mm.

5. Conclusions

(1) The water flowing into the 1908 working face comes from the Changxing formation aquifer and Yulongshan formation aquifer above the coal seam, conducted by the activated karst collapse column. Besides, the water inrush quantity is affected by atmospheric precipitation, and the water inflow in working face lags behind the atmospheric precipitation; more precisely, the water inflow begins to increase sharply in the rain after about two days

(2) The proportion of coarse particles and fine particles in collapse column is 89.86% and 10.14%, respectively. Besides, the particle size of 20-40 mm occupies the largest proportion (31.91%), followed by the particle size of 10-20 mm (21.08%). Besides, the collapse column contains a large proportion of viscous minerals, such as illite, which are easy to transport along with water migration, triggering water inrush disaster of karst collapse column

(3) When the working face is in the center of collapse column, the maximum opening of the fracture is 23.64 mm. Besides, the collapse column is effected by the mining of working face, and the collapse column is connected with the collapse pit and karst cave through the mining-inducing fractures. Therefore, the water-conducting channel in overburden is formed, containing collapse pits in surface, karst caves, collapse column, and working face

Data Availability

The data used to support the findings of this study are included within the article.

Conflicts of Interest

The authors declare that they have no conflicts of interest.

Acknowledgments

This work was supported by the National Natural Science Foundation of China (52004082), the Natural Science Foundation of Henan Province (202300410170, 202300410182), the Fundamental Research Funds for the Universities of Henan Province (NSFRF200302, NSFRF180330), the Postdoctoral Research Projects of Henan Province, and the Scientific and Technological Development Project for Coal Mine Safety Production by Henan Province (HN19-59).

References

[1] S. X. Yin, H. Q. Lian, D. M. Liu, and H. C. Yin, “70 years of investigation on karst collapse column in North China coalfield: cause of origin, mechanism and prevention,” *Coal Science and Technology*, vol. 47, no. 11, pp. 1–29, 2019.

[2] D. Ma, H. Y. Duan, W. T. Liu, X. T. Ma, and M. Tao, “Water–sediment two-phase flow inrush hazard in rock fractures of overburden strata during coal mining,” *Mine Water and the Environment*, vol. 39, no. 2, pp. 308–319, 2020.

[3] H. L. Kong and L. Z. Wang, “Seepage problems on fractured rock accompanying with mass loss during excavation in coal mines with karst collapse columns,” *Arabian Journal of Geosciences*, vol. 11, no. 19, p. 585, 2018.

[4] Y. Xue, T. Teng, F. N. Dang, Z. Ma, S. Wang, and H. Xue, “Productivity analysis of fractured wells in reservoir of hydrogen and carbon based on dual-porosity medium model,” *International Journal of Hydrogen Energy*, vol. 45, no. 39, pp. 20240–20249, 2020.

[5] J. Liu, X. Liang, Y. Xue, K. Yao, and Y. Fu, “Numerical evaluation on multiphase flow and heat transfer during thermal stimulation enhanced shale gas recovery,” *Applied Thermal Engineering*, vol. 178, p. 115554, 2020.

[6] H. B. Bai, D. Ma, and Z. Q. Chen, “Mechanical behavior of groundwater seepage in karst collapse pillars,” *Engineering Geology*, vol. 164, pp. 101–106, 2013.

[7] L. Z. Wang, Z. Q. Chen, H. L. Kong, and X. Y. Ni, “An experimental study of the influence of seepage pressure and initial porosity on variable mass seepage for broken mudstone,” *Journal of Mining & Safety Engineering*, vol. 31, no. 3, pp. 462–468, 2014.

[8] F. Du, Z. H. Li, G. H. Jiang, and Z. Q. Chen, “Types and mechanism of water-sand inrush disaster in west coal mine,” *Journal of China Coal Society*, vol. 42, no. 7, pp. 1846–1853, 2017.

[9] J. Y. Wu, M. M. Feng, Z. Q. Chen, B. Y. Yu, and G. S. Han, “Dissolution effects on the seepage property of broken mudstone,” *Journal of Harbin Institute of Technology*, vol. 51, no. 2, pp. 117–125, 2019.

[10] S. X. Yin, S. X. Wang, and Q. Wu, “Water inrush patterns and theoretic criteria of karstic collapse columns,” *Chinese Journal of Rock Mechanics and Engineering*, vol. 23, no. 6, pp. 964–968, 2004.

[11] Y. Q. Song, X. Y. Wang, P. Cheng, C. J. Peng, and S. Xu, “The mechanical criterion and numerical simulation of thick-walled elliptical cylinder collapse column model under water inrush,” *Journal of China Coal Society*, vol. 36, no. 3, pp. 452–455, 2011.

[12] Z. H. Li, H. Xie, J. B. Li, and Z. H. He, “Experimental study of mining effect on collapse column activated water conducting mechanism,” *Journal of Central South University (Science and Technology)*, vol. 45, no. 12, pp. 4377–4383, 2014.

[13] T. H. Yang, J. S. Liu, and W. C. Zhu, “A coupled flow-stress-damage model for groundwater outbursts from an underlying aquifer into mining excavations,” *International Journal of Rock Mechanics and Mining Sciences*, vol. 44, no. 1, pp. 87–97, 2007.

[14] W. C. Zhu and C. H. Wei, “Numerical simulation on mining-induced water inrushes related to geologic structures using a damage-based hydromechanical model,” *Environmental Earth Sciences*, vol. 62, no. 1, pp. 43–54, 2011.

[15] B. H. Yao, Z. W. Chen, J. P. Wei, T. H. Bai, and S. M. Liu, “Predicting erosion-induced water inrush of karst collapse pillars using inverse velocity theory,” *Geofluids*, vol. 2018, Article ID 2090584, 18 pages, 2018.

[16] Y. Xue, P. G. Ranjith, F. N. Dang et al., “Analysis of deformation, permeability and energy evolution characteristics of coal mass around borehole after excavation,” *Natural Resources Research*, vol. 29, no. 5, pp. 3159–3177, 2020.

[17] Z. Z. Cao, P. Xu, Z. H. Li, M. X. Zhang, Y. Zhao, and W. L. Shen, “Joint bearing mechanism of coal pillar and backfilling body in roadway backfilling mining technology,” *CMC-Computers Materials & Continua*, vol. 54, no. 2, pp. 137–159, 2018.

[18] W. L. Shen, J. B. Bai, W. F. Li, and X. Y. Wang, “Prediction of relative displacement for entry roof with weak plane under the effect of mining abutment stress,” *Tunnelling and Underground Space Technology*, vol. 71, pp. 309–317, 2018.

[19] G. L. Liu, S. X. Yin, and Y. B. Wang, “Model of water inrush for thick wall cylinder at side face of paleo - sinkholes in North - China - type coalfields,” *Journal of Engineering Geology*, vol. 15, no. 2, pp. 284–287, 2007.

[20] D. Ma, H. Y. Duan, Q. Zhang et al., “A numerical gas fracturing model of coupled thermal, flowing and mechanical effects,” *Computers, Materials & Continua*, vol. 65, no. 3, pp. 2123–2141, 2020.

[21] Y. Xue, F. Gao, Y. N. Gao, X. Liang, Z. Z. Zhang, and Y. Xing, “Thermo-hydro-mechanical coupled mathematical model for controlling the pre- mining coal seam gas extraction with slotted boreholes,” *International Journal of Mining Science and Technology*, vol. 27, no. 3, pp. 473–479, 2017.

[22] Z. Z. Cao, F. Du, Z. H. Li, Q. T. Wang, P. Xu, and H. X. Lin, “Research on instability mechanism and type of ore pillar based on the fold catastrophe theory,” *CMES-Computer Modeling in Engineering & Science*, vol. 113, no. 3, pp. 287–306, 2017.

[23] W. Liang, Y. Zhao, J. Liu, D. Elsworth, Z. Feng, and J. Cai, “Advances in in-situ modified mining by fluidization and in unconventional geomechanics,” *Advances in Geo-Energy Research*, vol. 5, no. 1, pp. 1–4, 2021.

[24] B. Y. Zhang and Z. B. Lin, “Seepage property of crushed mudstone rock in collapse column,” *Advances in Civil Engineering*, vol. 2020, 2020.

[25] C. Gu, R. Qiu, S. Liu, Z. You, and R. Qin, “Shear thickening effects of drag-reducing nanofluids for low permeability reservoir,” *Advances in Geo-Energy Research*, vol. 4, no. 3, pp. 317–325, 2020.

Hindawi
Geofluids
Volume 2021, Article ID 6678608, 9 pages
https://doi.org/10.1155/2021/6678608

Research Article

Experimental Accuracy and Stability of Gas Outburst Experimental System

Yanbao Liu,[1,2] Haitao Sun ,[1,2] Bo Wang ,[1,2,3] Linchao Dai ,[1,2] and Jie Cao[1,2]

[1]*State Key Laboratory of the Gas Disaster Detecting, Preventing and Emergency Controlling, Chongqing 400037, China*
[2]*China Coal Technology and Engineering Group Chongqing Research Institute, Chongqing 400037, China*
[3]*School of Mechanics and Civil Engineering, China University of Mining and Technology, Xuzhou, Jiangsu 221116, China*

Correspondence should be addressed to Haitao Sun; dreamsht@163.com and Bo Wang; 21305@163.com

Received 20 November 2020; Revised 10 January 2021; Accepted 4 February 2021; Published 25 February 2021

Academic Editor: Yi Xue

Gas outburst is an important issue in deep coal mining. At present, the gas-rock coupling change mechanism and intensity prediction of gas outburst are not clear. The research of gas outburst simulation experiment is particularly important. The State Key Laboratory of Gas Disaster Monitoring and Emergency Technology of China independently developed a large-scale coal and gas outburst physical simulation test system. However, the influence of the design parameters of the testing machine on the stability and accuracy of the simulation experiment is unclear. The article analyzes the energy conversion in the process of gas outburst through experimental simulation phenomena and results. The experimental simulation results show that the energy released by the CO_2 gas in similar materials is the most important energy source. The cracks of similar materials increase the nominal volume of similar materials, and the deformation energy stored in similar materials slightly increases. The experimental simulation results are consistent with the actual situation on site. Combined with CAE simulation analysis, the displacement and pressure of the indenter of the experimental machine remained basically unchanged during the experiment, and the system did not produce resonance. Comprehensive analysis shows that the design of the test machine meets the simulation requirements.

1. Introduction

China's coal production and consumption have long ranked first in the world [1]. Coal and gas outburst accidents are one of the most serious disasters that plague the safe production of underground coal mines [2, 3]. Outburst accidents of large scales accounted for 32% of gas outburst accidents, and fatalities caused by such accidents accounted for 33.3% of all types of mine fatalities [4]. At the same time, China's shallow coal resources are gradually depleted, and the mining of deep coal resources is increasingly becoming a demand for the coal industry [5]. However, the coupling of coal and rock gas dynamic disasters in deep environments such as high ground stress, high gas pressure, and high ground temperature is more complicated [5–7]. Large-scale physical simulation analysis of this scientific problem is currently the most applicable research method [1, 8].

Coal and gas outburst is a mine dynamic disaster caused by a combination of factors such as crustal stress, gas pressure, and coal physical properties [9, 10]. Once coal and gas outburst occurs, a large amount of coal is thrown into the roadway space [11]. Once a large amount of gushing gas encounters a fire source, a gas explosion will occur, which destroys the mine production system and endangers the lives of workers. The mechanism and prediction of coal and gas outburst have always been a worldwide problem that the field of coal mine safety tries to solve [6, 7].

The understanding of the mechanism of gas outburst is still at the stage of hypothesis and is not unified, but the research on the physical model of gas outburst is similar [12–19]. The preparation stage for gas outburst is the energy accumulation stage. The magnitude of this energy varies with the elasticity of coal [9], and the release method of elastic potential varies with the mechanical properties of coal [2, 12]. The occurrence and development stages of the outburst are mainly completed by the action of gas in the coal [2]. When the coal is suddenly broken, the gas quickly changes from the adsorbed state to the free [2, 12]. At the same time,

Specifications	Parameter
Model size	$1.5 \times 0.8 \times 0.8 m^3$
Maximum gas pressure	6MPa
Bursting disc size	Φ0.3m
Maximum vertical force	3000t
Maximum horizontal force	2000t
Loading time	>30d
Tunnel geometry	Section $0.3 \times 0.3 m^2$, Total length 50m

FIGURE 1: Coal and gas outburst simulation experiment system.

the gas expansion further breaks the coal and throws it into the roadway [20], and the expansion work is proportional to the rate of gas release [2]. Due to the complexity of the coal and gas outburst mechanism, the use of large-scale coal and gas outburst testing equipment to explore the excitation conditions of coal and gas outburst in complex environments is the current development trend [5, 8, 11].

Focusing on the characteristics of deep coal mining, China Coal Science and Industry Group Chongqing Research Institute Co., Ltd. has researched and developed a deep mine coal and rock gas dynamic disaster simulation experiment system. The maximum vertical loading capacity of the experimental system is 25 MPa, the maximum horizontal loading capacity is 16 MPa, the system stiffness is 3×10^{10} N/m, the maximum gas pressure is 6 MPa, and the minimum ground temperature reaches 60°C [21].

The coal and gas outburst simulation experiment system is composed of six parts: mechanical loading system, sealing and outburst generation system, inflation system, simulated roadway system, monitoring system, and dust removal system, as shown in Figure 1. The experimental system can simulate all the processes (incubation, occurrence, evolution, and termination) of coal and gas outburst. In addition to studying the cause mechanism and dynamic evolution characteristics of coal and gas outburst disasters, it can also study the migration of coal and gas outburst two-phase flow in roadways and the separation and accumulation of coal dust. This experimental system provides support for research on mine coal and gas outburst disaster-prevention-control.

During the test, a large amount of elastic energy is stored in the testing machine. When the rock sample is damaged, the elastic energy stored in the testing machine is suddenly released, which causes the sample to be further severely damaged. In order to avoid such damage, the stiffness of the testing machine must be improved to meet the needs of the experiment. In addition, the gas outburst simulation experiment system is a limited space, while the deep gas outburst is in a nearly infinite space. The above problems will affect the stability and error of the gas outburst simulation experiment system.

The article uses this experimental system to simulate a coal and rock gas outburst accident on the 11-2 seam 1331 (1) conveyor tunnel driving face of Huainan Dingji Coal Mine on April 19, 2009. Analyze the energy change in the process of gas outburst through the phenomenon of experimental results, and then determine whether the design of the testing machine meets the requirements of the simulation test.

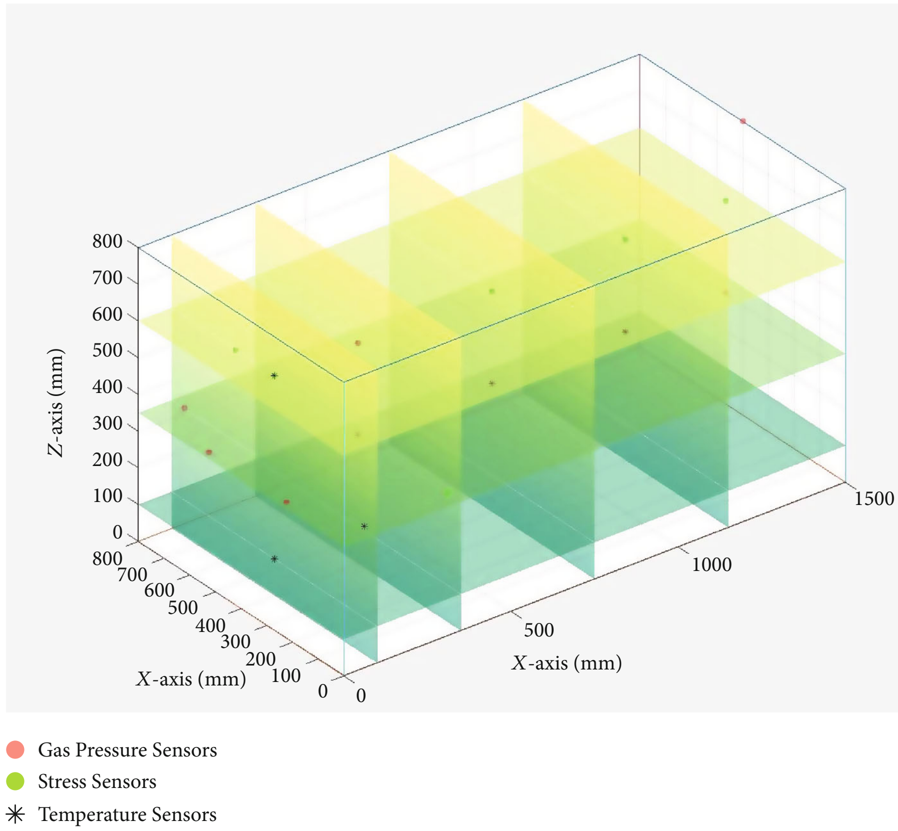

Figure 2: Position of the sensor in similar materials.

2. Simulation Experiment

The simulation experiment used CO_2 as the experimental gas, and the rock block in the experiment (the size is 1.5 m × 0.8 m × 0.8 m) is a self-made similar material. Pulverized coal is the main component of similar materials (mass ratio is 78.16%). In addition, the mass ratios of cement, sand, water, and activated carbon are 7%, 5.5%, 8.5%, and 0.84%, respectively. Similar materials are made by layering (4 layers). The precompression pressure is 25 MPa. The holding time for forming similar materials is 30 minutes, and the curing time for similar materials is 30 days. The mechanical properties of similar materials belong to soft rock. The uniaxial compressive strength of similar materials is 1.88 MPa, the elastic modulus is 178.62 MPa, the porosity is 2.99%, and the density is 1590 kg/m^3. The adsorption constants [2, 20] a and b of similar materials are 33.98 and 1.63, respectively. The similarity ratio of the material is 1 : 1.

While making the similar model, the sensors are arranged inside the similar model. A total of 31 sensors are arranged in the similar model, including 12 gas pressure sensors, 13 in situ stress sensors, and 6 temperature sensors, as shown in Figure 2.

After preparing similar rocks, it is charged with 0.2 MPa of CO_2 to displace the air in the similar model. After CO_2 displaces the air for a period of time, an initial lateral stress of 3.0 MPa and an axial stress of 16.0 MPa are applied to similar models. Continuing, we also injected CO_2 gas into the balance chamber of the explosive device and similar materials. We keep the pressure difference between the two sides of the bursting disc less than its bursting pressure 0.4 MPa and make similar materials basically reach the adsorption equilibrium. Fill the balance gas chamber of the device with overpressure gas greater than 0.4 MPa to induce protrusions. The computer records the data during the experiment in real time. The high-speed acquisition is started when the CO_2 gas outburst occurred. After the outburst of CO_2 gas, the distribution of pulverized coal in the roadway and the shape characteristics of the outburst holes are collected. The schematic diagram of the experimental process is shown in Figure 3.

3. Experimental Results

Before analyzing the experimental results, we obtained the stiffness of the testing machine through CAE simulation [22, 23]. It is found that the displacement in a certain direction has a linear relationship with the applied stress, as shown in Figure 4. The calculated longitudinal stiffness and transverse stiffness of the experimental machine are 1.5×10^{10} N/m and 4×10^{10} N/m, respectively. There is a mutual influence between the horizontal indenter displacement and the longitudinal indenter displacement of the experimental machine. When the longitudinal indenter is loaded, the displacement ratio of the horizontal indenter is -0.218; when the horizontal indenter is loaded, the displacement ratio of the longitudinal indenter is -0.243.

According to the similar proportion, the simulated outburst coal quantity is 39.74 t, and the actual outburst coal

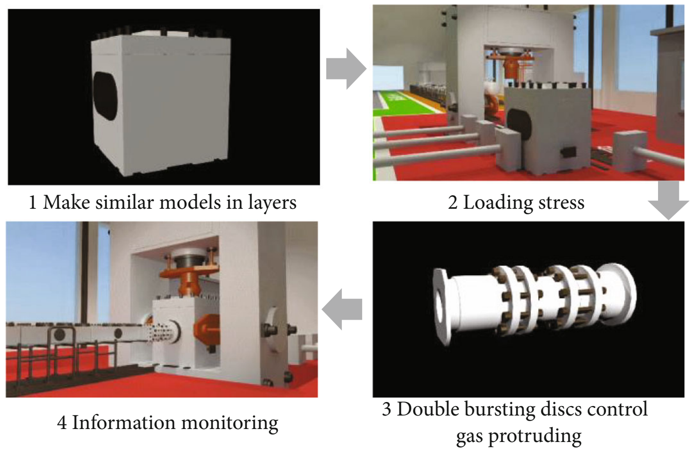

Figure 3: The schematic diagram of the experimental process.

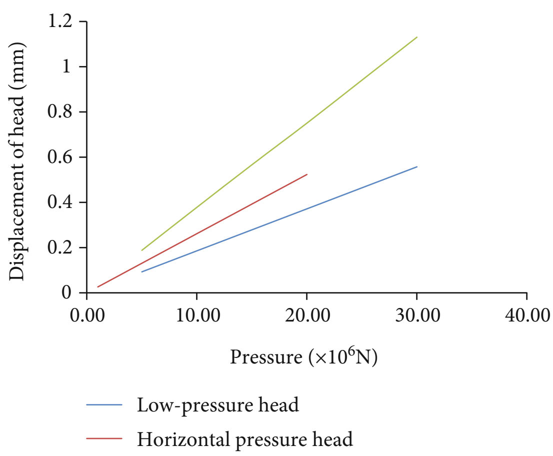

Figure 4: Indenter displacement curve of testing machine.

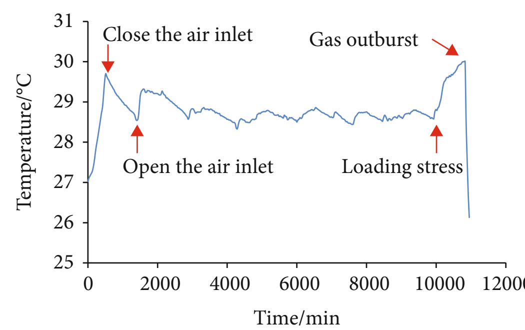

Figure 5: The gas temperature changes in similar materials during the experiment.

quantity in the field is 35 t. Considering the laboratory error and the statistical error of the field data, the experimental data are consistent with the actual situation in the field.

The energy storage in the experimental system before the gas outburst is calculated. The calculation results show that the deformation energy [24] of the experimental machine is 1.1×10^4 J, and the deformation energy stored in similar materials is 5.7×10^5 J. The volume of free CO_2 gas in similar materials is 0.028704 m^3, and the free gas storage energy is 1.17×10^4 J. The mass of CO_2 gas adsorbed in similar materials is 43.8 kg, which is greater than the mass of free CO_2 gas. The energy storage of adsorbed CO_2 gas will be much greater than that of free gas [9].

The gas outburst experiment is actually the conversion of energy [11]. There are mainly four energy conversion channels: changes in temperature of similar materials, energy is converted into kinetic energy of coal and air, energy is used for the rupture of similar materials, and energy is used for system dissipation. Damped vibration is the main channel for energy dissipation [11–13].

During the process of coal and gas outburst, the temperature of similar materials will change due to energy conversion and gas desorption. As shown in Figure 5, the temperature changes during the experiment. To prevent the temperature sensor from being damaged during the experiment, the thermocouple was placed in a cavity of similar material. The actual temperature measured by the thermocouple sensor is the temperature of CO_2 gas in similar materials. Therefore, the temperature of CO_2 gas is obviously affected by pressure, which is reflected in the process of CO_2 gas pressurization and saturation. The temperature dropped by 3 degrees after the gas outburst occurred, which was caused by the expansion of CO_2 gas. In this process, the energy released by the temperature decrease is about 403 J.

The shape of the hole after the CO_2 gas outburst is irregular semiellipsoid. The depth of the hole is about 15 cm, and the maximum width of the hole is 30 cm. The upper part of the coal wall in the hole showed obvious layered fracture. At the same time, most of the ejected coal is in the form of flakes, and the stacking height of the coal flakes accounts for more than 2/3 of the hole diameter.

During the outburst process, the broken similar materials are thrown into the tunnel and deposited under the action of gas, which reflects the strength of the outburst. In this similar simulation experiment, a total of 18.09 kg of similar materials were thrown out, and the farthest distance from the hole was 3.3 m. After the experiment, the cuttings in the roadway were divided into 5 areas for sampling, weighing, and screening. The results are shown in Figures 6 and 7. As shown in Figure 6, the quality of thrown cuttings is decreasing along

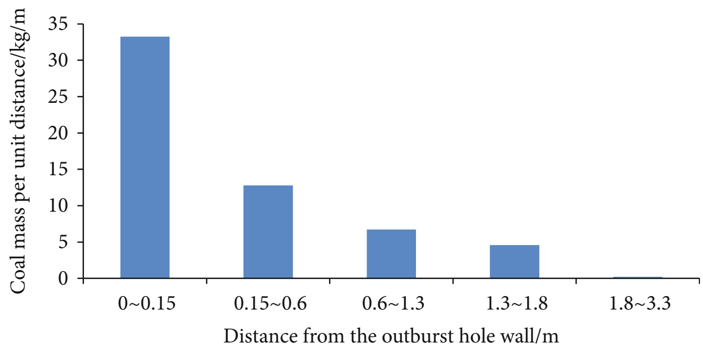

Figure 6: Mass distribution of thrown cuttings.

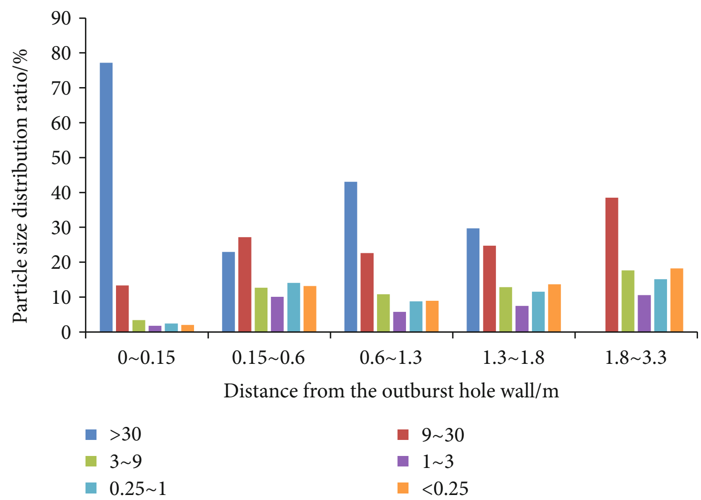

Figure 7: The particle size distribution diagram of thrown cuttings in different areas.

the roadway. Within 0.6 m from the hole, the mass of thrown cuttings accounts for 59.4%. Figure 7 shows the particle size distribution of cuttings thrown in different areas. Figure 7 shows that more than 80% of the cuttings in the hole (0~0.15 m) are larger than 9 mm. The particle size distribution of cuttings in other regions is the same, and the proportion of cuttings' particle size in each region shows a trend of first decreasing and then increasing as the particle size decreases. In each region, the cuttings with a particle size greater than 9 mm or less than 1 mm accounted for the majority, while the medium-sized cuttings accounted for a relatively small proportion. The energy used to throw out cuttings by calculation is about 550 J.

In the simulated gas outburst experiment, the gas pressure in similar rock blocks is shown in Figure 8. The similar material near the hole loses support due to sudden exposure, and the accumulated elastic energy and gas compression energy are quickly released. This causes similar materials to be broken and thrown out to form the initial protruding holes. After the outburst, similar rock blocks ruptured, forming integrated staggered fissures. The closer to the hole, the greater the crack density is. The gas pressure near the hole quickly decays to 0.0 MPa, as shown in Figure 8(a). The gas pressure in similar materials farther from the hole gradually decreases, as shown in Figure 8(b). There is still some gas in similar materials after the gas outburst. The energy stored in similar materials is not completely released [10]. After the initial pores are formed by the gas outburst, the test conditions have higher stress and lower porosity, and the crack density far away from the hole is small and gas permeability is weak. The newly desorbed CO_2 gas failed to accumulate enough energy to further break and throw similar materials, so the protrusion was terminated. Therefore, the duration of the outburst under the stress is shorter.

After the outburst occurs, the adsorbed CO_2 in similar materials is quickly desorbed and gushes out into the roadway space, causing the CO_2 concentration near the holes in the roadway to increase rapidly, reaching 15.4% in a very short time. With the end of the outburst, the CO_2 gas concentration gradually decreases. There is still a relatively stable source of CO_2 gas behind the protruding hole in a short time, so the concentration in the tunnel gradually reaches a stable value of 3.15%. By observing the gas pressure in similar rock blocks, it is concluded that after 2000 seconds, the mass of compressed free gas in similar materials accounts for 60% of the mass before the experiment. At the end of the experiment, the gas pressure in similar materials was generally around 0.2 MPa, and the CO_2 gas in similar materials was being stably released. Therefore, it is calculated that the

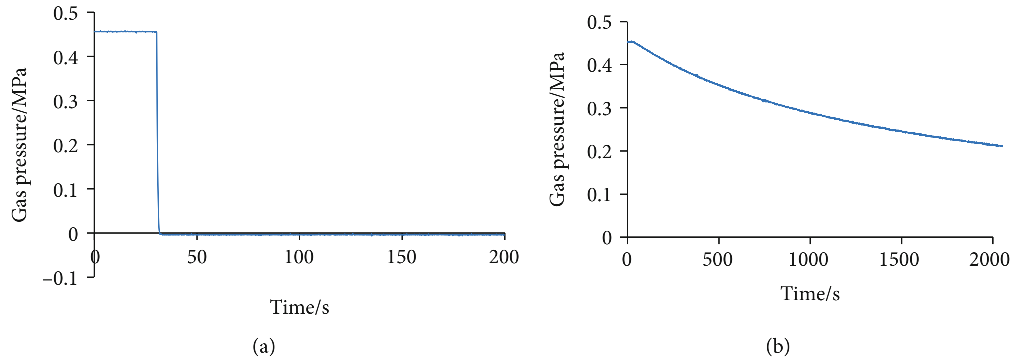

Figure 8: Gas pressure change curve.

energy released by CO_2 gas in similar materials is greater than 3500 J.

The uniaxial compression curve of a similar material sample is shown in Figure 9. A rough calculation shows that the energy density absorbed per unit volume of the standard sample is 22200 J/m^3 when it is broken. The damaged sample had multiple main fracture and was divided into several large pieces, but did not collapse. The elastic energy absorbed by the specimen under uniaxial compression is used for specimen failure and cracking. We believe that the energy density required for similar materials to form the cracks shown in Figure 9 is 22200 J/m^3. In the entire similar material, the broken bodies are concentrated in the hole, and the crack density in the similar material gradually decreases with the increase of the distance of the hole. According to the density of cracks in similar materials after the experiment, it can be estimated that the energy used for the destruction and cracking of similar materials during the experiment is about 2220 J.

The released energy comes from the decrease of temperature and the release of CO_2 gas compression energy in similar materials. The compression energy released by the CO_2 gas in similar materials is the most important energy source.

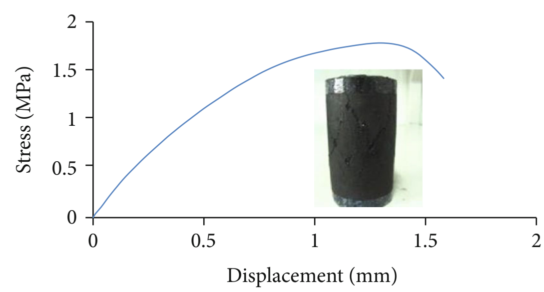

Figure 9: Uniaxial compression curve of similar materials.

4. Analysis of Testing Machine Parameters

Compared with the infinite space of on-site working conditions, the biggest difference is that the experimental system is a limited space. The parameters of the testing machine will determine the stability and accuracy of the simulation experiment system. This will be analyzed below.

First, analyze the influence of the stored deformation energy of the testing machine on the accuracy of the simulation experiment. The similar material after the CO_2 outburst still has the pressure-bearing capacity, and the stress of the internal observation point before and after the gas outburst is shown in Figure 10. It can be concluded from the figure that the stress near the hole of the similar material has decreased, while the stress far away from the hole has increased.

During the experiment, the displacement of the indenter of the testing machine was almost 0.0, and the stress increase of the indenter of the testing machine was about 0.1 MPa. This phenomenon is consistent with the observation of on-site working conditions. During the gas outburst experiment, the hydraulic cylinder of the testing machine was in a locked state. Therefore, the testing machine can be regarded as a compression spring with one end fixed and one end acting on similar materials. The increase in stress indicates that the spring is further compressed, and the mechanical energy stored by the testing machine increases. Experimental phenomena show that similar materials have new cracks, and these cracks increase the nominal volume of similar materials. The process of gas outburst is the process of expansion of similar materials. In addition, these cracks reduce the elastic modulus of similar materials. Through the above calculation and analysis, it can be judged that the deformation energy stored in similar materials has slightly increased. The energy increase of the testing machine and similar materials does not exceed 1000 J.

In the field conditions, the change of stress and strain at infinity is almost zero. During this experiment, the displacement of the indenter of the testing machine is very small, and the change in stress is very small. The stiffness of the testing machine meets the needs of gas outburst simulation experiments. The size of similar materials can be further increased to increase the accuracy of the simulation experiment.

Second, we analyze the impact of the vibration characteristics of the testing machine on the accuracy and stability of the simulation experiment [25]. According to the above analysis, the energy released during the experiment is greater than the energy absorbed by the system, and the excess energy is dissipated by the experimental system. Damping vibration of the experimental system is the main way of energy dissipation [26, 27]. According to the geometric structure of the experimental system, it is divided into experimental machines and similar materials. Gas outburst will cause

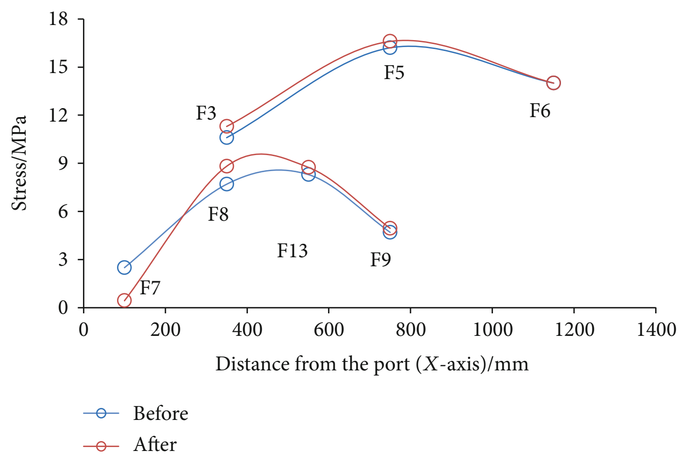

Figure 10: Stress of observation points in similar materials before and after gas outburst.

coupling vibration between the testing machine and similar materials. The vibration excitation of the testing machine comes from similar materials; the vibration excitation of similar materials comes from the vibration of the testing machine and the instantaneous release of energy when the gas burst occurred.

Data show that the natural vibration frequency of relatively complete rock is above 1000 Hz [28]. The test results show that the natural frequency of similar materials is 2170 Hz. Similar materials are similar to rocks, and the propagation speed of stress waves is between 3.2 and 7.0 km/s [29]. Therefore, in the experimental simulation process, the deformation of similar materials can be considered to be instantaneous. The damping ratio of similar materials is between 0.06 and 0.11 [30], while the damping ratio of broken rock is higher [31]. The process of stress wave propagation in similar materials is a process of energy dissipation. The higher the rock vibration frequency is, the faster the energy decay is. The frequency range of seismic waves excited by artificial earthquakes is generally between 2 and 50 Hz [32]. We can judge that the vibration excitation frequency of similar materials to the testing machine is in the range of 2-50 Hz.

We use the ANSYS WORKBENCH finite element software to analyze the natural frequency of the testing machine. The natural frequency and the vibration mode of testing machine are obtained by calculation. The natural frequencies of the first six orders of vibration are 22.47 Hz, 29.89 Hz, 43.01 Hz, 93.09 Hz, 99.971 Hz, and 128.35 Hz. The vibration excitation frequency of similar materials is low, so the high-order frequency vibration of the experimental machine does not need to be considered. The frequency of the fourth-order mode is 93.09 Hz, and this mode is the main vibration mode excited by similar materials. The excitation frequency received by the testing machine is lower than 93.09 Hz. The difference between the natural frequency of the testing machine and the excitation frequency is more conducive to energy dissipation. The analysis can show that the experimental system does not produce obvious resonance phenomenon during the experiment, which has little influence on the experimental results.

In site conditions, most of the energy is transmitted to the distant place in the form of seismic waves, and the energy is gradually dissipated in the process of transmission. In the experimental simulation, part of the vibration wave is reflected from the interface, and part of the vibration wave is absorbed by the testing machine. The greater the energy absorbed by the testing machine, the greater the simulation accuracy of the testing machine. Adding a damping structure to the testing machine enables the testing machine to absorb and dissipate more energy. The experimental simulation system in this article adds multiple high damping devices to absorb energy. In summary, the parameters of the testing machine have minimal impact on the accuracy of the simulation experiment.

5. Conclusions

In this paper, the simulation experiment of coal and gas outburst is carried out by using the simulation experiment system of deep-well coal and rock gas dynamic disaster. The energy conversion in the process of gas outburst is analyzed through experimental phenomena and results. Then, according to the experimental phenomenon and CAE simulation, the influence of the parameters of the testing machine on the stability and accuracy of the gas outburst simulation experiment is judged. The main conclusions obtained are as follows:

(1) Gas outburst is actually the transformation of energy. The released energy comes from the decrease of temperature and the release of CO_2 gas compression energy in similar materials. The compression energy released by the CO_2 gas in similar materials is the most important energy source

(2) Simulation experiments show that cracks increase the nominal volume of similar materials. These breaks reduce the elastic modulus of similar materials and slightly increase the deformation energy stored in similar materials

(3) The parameters of the testing machine satisfy the needs of the experiment. The displacement and pressure of the indenter remained basically unchanged during the experiment. The vibration excitation frequency transmitted to the testing machine is 2-50 Hz, and the natural frequency of the testing machine is 93.09 Hz. The system will not produce resonance to meet the needs of experimental stability. It is recommended to add a damping structure to the testing machine so that the testing machine can dissipate more energy

Data Availability

The data used to support the findings of this study are available from the corresponding author upon request.

Conflicts of Interest

The authors declare that they have no conflicts of interest.

Acknowledgments

This study was supported by the National Natural Science Foundation of China (51974358, 51874348, and 51774319), Science and Technology Innovation and Entrepreneurship Fund of China Coal Technology Engineering Group (2019-TD-QN037 and 2019-TD-QN040), Natural Science Foundation of Chongqing (cstc2020jcyj-msxmX1052 and cstc2019jcyj-msxmX0531), and Chongqing Science Fund for Distinguished Young Scholars (cstc2019jcyjjqX0019).

References

[1] C. Zhang, J. Xu, G. Yin, S. Peng, Q. Li, and Y. Chen, "A novel large-scale multifunctional apparatus to study the disaster dynamics and gas flow mechanism in coal mines," *Rock Mechanics and Rock Engineering*, vol. 52, no. 8, pp. 2889–2898, 2019.

[2] K. Jin, Y. Cheng, T. Ren et al., "Experimental investigation on the formation and transport mechanism of outburst coal-gas flow: implications for the role of gas desorption in the development stage of outburst," *International Journal of Coal Geology*, vol. 194, pp. 45–58, 2018.

[3] W. Yin, G. Fu, C. Yang, Z. Jiang, K. Zhu, and Y. Gao, "Fatal gas explosion accidents on Chinese coal mines and the characteristics of unsafe behaviors: 2000-2014," *Safety Science*, vol. 92, pp. 173–179, 2017.

[4] R. Liu, W. Cheng, Y. Yu, and Q. Xu, "Human factors analysis of major coal mine accidents in China based on the HFACS-CM model and AHP method," *International Journal of Industrial Ergonomics*, vol. 68, pp. 270–279, 2018.

[5] L. Yuan, "Control of coal and gas outbursts in Huainan mines in China: a review," *Journal of Rock Mechanics and Geotechnical Engineering*, vol. 8, no. 4, pp. 559–567, 2016.

[6] H. Sun, J. Cao, M. Li et al., "Experimental research on the impactive dynamic effect of gas-pulverized coal of coal and gas outburst," *Energies*, vol. 11, no. 4, p. 797, 2018.

[7] J. Cao, L. Dai, H. Sun et al., "Experimental study of the impact of gas adsorption on coal and gas outburst dynamic effects," *Process Safety and Environmental Protection*, vol. 128, pp. 158–166, 2019.

[8] Y. Lu, H. Wang, B. Xia, X. Li, Z. Ge, and J. R. Tang, "Development of a multi-functional physical model testing system for deep coal petrography engineering," *Rock Mechanics and Rock Engineering*, vol. 50, no. 2, pp. 269–283, 2017.

[9] J. Sobczyk, "A comparison of the influence of adsorbed gases on gas stresses leading to coal and gas outburst," *Fuel*, vol. 115, pp. 288–294, 2014.

[10] A.-D. Alexeev, V.-N. Revva, N.-A. Alyshev, and D. M. Zhitlyonok, "True triaxial loading apparatus and its application to coal outburst prediction," *International Journal of Coal Geology*, vol. 58, no. 4, pp. 245–250, 2004.

[11] B. Nie, Y. Ma, S. Hu, and J. Meng, "Laboratory study phenomenon of coal and gas outburst based on a mid-scale simulation system," *Scientific Reports*, vol. 9, no. 1, article 15005, 2019.

[12] H. Liu, B. Lin, J. Mou, and W. Yang, "Mechanical evolution mechanism of coal and gas outburst," *Rock Mechanics and Rock Engineering*, vol. 52, no. 5, pp. 1591–1597, 2019.

[13] S. Zhi and E. Derek, "The role of gas desorption on gas outbursts in underground mining of coal," *Geomechanics and Geophysics for Geo-Energy and Geo-Resources*, vol. 2, no. 3, pp. 151–171, 2016.

[14] T. Xu, C.-A. Tang, T.-H. Yang, W. C. Zhu, and J. Liu, "Numerical investigation of coal and gas outbursts in underground collieries," *International Journal of Rock Mechanics and Mining Sciences*, vol. 43, no. 6, pp. 905–919, 2006.

[15] H. Li, Z. Feng, D. Zhao, and D. Duan, "Simulation experiment and acoustic emission study on coal and gas outburst," *Rock Mechanics and Rock Engineering*, vol. 50, no. 8, pp. 2193–2205, 2017.

[16] J. Hongwei, H. Qianting, and L. Yanbao, "Failure mechanism of coal and gas outburst initiation," *Procedia Engineering*, vol. 26, pp. 1352–1360, 2011.

[17] G. Yin, C. Jiang, J. G. Wang, J. Xu, D. Zhang, and G. Huang, "A new experimental apparatus for coal and gas outburst simulation," *Rock Mechanics and Rock Engineering*, vol. 49, no. 5, pp. 2005–2013, 2016.

[18] Q. Tu, Y. Cheng, P. Guo, J. Jiang, L. Wang, and R. Zhang, "Experimental study of coal and gas outbursts related to gas-enriched areas," *Rock Mechanics and Rock Engineering*, vol. 49, no. 9, pp. 3769–3781, 2016.

[19] G. Wang, W. Cheng, Z. Qingtao, and L. Sun, "Design of simulation experiment and its application system of outburst in uncovering coal seam in cross-cut," *Rock and Soil Mechanics*, vol. 34, no. 4, pp. 1202–1210, 2013.

[20] A. Zhou, K. Wang, L. Wang, F. du, and Z. Li, "Numerical simulation for propagation characteristics of shock wave and gas flow induced by outburst intensity," *International Journal of Mining Science and Technology*, vol. 25, no. 1, pp. 107–112, 2015.

[21] J. Cao, H. Sun, B. Wang et al., "A novel large-scale three-dimensional apparatus to study mechanisms of coal and gas outburst," *International Journal of Rock Mechanics and Mining Sciences*, vol. 118, pp. 52–62, 2019.

[22] M.-W. Fu, M.-S. Yong, and T. Muramatsu, "Die fatigue life design and assessment via CAE simulation," *The International Journal of Advanced Manufacturing Technology*, vol. 35, no. 9-10, pp. 843–851, 2008.

[23] D. Krzikalla, A. Slíva, J. Měsíček, and J. Petrů, "On modelling of simulation model for racing car frame torsional stiffness

analysis," *Alexandria Engineering Journal*, vol. 59, no. 6, pp. 5123–5133, 2020.

[24] S. Zhang, W. Liu, and H. Lv, "Creep energy damage model of rock graded loading," *Results in Physics*, vol. 12, pp. 1119–1125, 2019.

[25] L. Dong, J. Wang, X. Li, and K. Peng, "Dynamic stability analysis of rockmass: a review," *Advances in Civil Engineering*, vol. 2018, Article ID 4270187, 22 pages, 2018.

[26] I. López, J.-M. Busturia, and H. Nijmeijer, "Energy dissipation of a friction damper," *Journal of Sound and Vibration*, vol. 278, no. 3, pp. 539–561, 2004.

[27] G. Bianchi, S. Cagna, N. Cau, and F. Paolucci, "Analysis of vibration damping in machine tools," *Procedia CIRP*, vol. 21, pp. 367–372, 2014.

[28] S. Li, S. Tian, W. Li, T. Yan, and F. Bi, "Research on the resonance characteristics of rock under harmonic excitation," *Shock and Vibration*, vol. 2019, 11 pages, 2019.

[29] J. Zhou, W. Lu, P. Yan, M. Chen, and G. Wang, "Frequency-dependent attenuation of blasting vibration waves," *Rock Mechanics and Rock Engineering*, vol. 49, no. 10, pp. 4061–4072, 2016.

[30] Z. Song and C. Su, "Computation of Rayleigh damping coefficients for the seismic analysis of a hydro-powerhouse," *Shock and Vibration*, vol. 2017, Article ID 2046345, 11 pages, 2017.

[31] Y. Takahashi, T. Sasaoka, W. Sugeng et al., "Study on prediction of ground vibration in consideration of damping effect by fragment in the rock mass," *Journal of Geoscience and Environment Protection*, vol. 6, no. 6, pp. 1–11, 2018.

[32] H. Yuan, X. Liu, Y. Liu, H. Bian, W. Chen, and Y. Wang, "Analysis of acoustic wave frequency spectrum characters of rock mass under blasting damage based on the HHT method," *Advances in Civil Engineering*, vol. 2018, Article ID 9207476, 8 pages, 2018.

Hindawi
Geofluids
Volume 2021, Article ID 6655443, 14 pages
https://doi.org/10.1155/2021/6655443

Research Article

Critical Conditions and Energy Transfer Characteristics of the Failure Process of Coal-Rock Combination Systems in Deep Mines

Haitao Sun,[1,2] Linchao Dai ,[1,2] Yanbao Liu,[1,2] and Hongwei Jin[3]

[1]*State Key Laboratory of the Gas Disaster Detecting, Preventing and Emergency Controlling, Chongqing 400037, China*
[2]*China Coal Technology and Engineering Group Chongqing Research Institute, Chongqing 400037, China*
[3]*School of Safety Engineering, Xi'an University of Science and Technology, Xi'an, Shanxi 710054, China*

Correspondence should be addressed to Linchao Dai; dailinchao@126.com

Received 7 December 2020; Revised 21 December 2020; Accepted 4 February 2021; Published 25 February 2021

Academic Editor: Timothy S. Collett

With the steady increase in the size, intensification, and modernization of coal production enterprises, the deep coal resources in large coal bases are gradually entering the mining stage. When the coal mining reaches the deep zone, the interactions between various underground dynamic hazards begin to occur. These interactions are affected by the engineering geological environment and can lead to the occurrence of severe compound hazards. When coal and gas outbursts occur and destabilize the mining area, the high geostress causes the multiphysical coupling effect of the laminated overburden system to become more pronounced. Therefore, we analyzed the development path of a coal-rock system under instability conditions from the perspective of coal–rock coupling, constructed a model of the coal-rock combination system's structure, and proposed three directions (i.e., strain softening, limit equilibrium, and dynamic instability) for the development of coal-rock system instability. Then, we established a model for the critical conditions of the system's failure process and elucidated that the release of the rock's elastic energy promoted the instability of the coal. Furthermore, we verified the established critical conditions through laboratory tests on a coal-rock combination structure and obtained the patterns of the rock energy transferring into the coal seam during the instability failure process of the coal–rock combination structure. When the coal–rock combination structure failed, the rock strain reached its maximum value and the strain rebound phenomenon occurred. The stored elastic strain energy released by the rock into the combination system accounted for 26% to 53% of the accumulated energy in the rock itself, and the released elastic energy and the new surface area of the crushed coal sample followed a logarithmic relationship. The findings of this study provide theoretical support for the identification and quantitative analysis of instability due to the dynamic hazards of coal-rock gas in deep mines.

1. Introduction

As the depth of coal mining increases, deep mining presents a complex mechanical environment that has been described as "three highs and one disturbance," i.e., high geostress, high geotemperature, high osmotic pressure, and strong mining disturbance, making the rock's mechanical behavior and the hazard characteristics in the deep zone significantly different from those in the shallow zone [1–5]. When coal mining reaches the deep zone, interactions begin to occur between the various underground dynamic hazards in the coal mine, resulting in compound hazards such as the rockburst-outburst compound dynamic hazard of coal–rock [6, 7], which is caused by the combined actions of multiple factors such as high stress, high gas pressure, and a hard roof under deep conditions and poses a serious problem in deep coal mining projects. Coal–rock dynamic hazards in deep mines are affected by the special engineering geological environment, which involves complex mechanisms of hazard formation, occurrence, and development. Numerous basic studies have been carried out on this topic. Several studies used the dynamic failure characteristics of rock specimens determined using a flexible testing machine to describe rockburst and to formulate the stiffness theory of rockburst [8, 9]. Based on the energy criterion of rockburst and coal and gas outbursts, other studies established a unified instability theory of rockburst and coal and gas outbursts and discussed the mechanism of the induction and transformation of dynamic hazards [10–16]. Compound dynamic hazards have been reclassified [17, 18]. Numerous studies have been conducted on the rockburst tendency, damage precursor information, acoustic emission characteristics, and electromagnetic radiation signals of coal–rock combinations, and the deformation characteristics and strength criteria of different coal–rock combinations have been discussed [19–28].

The deep high-stress environment significantly increases the risk of rockbursts in coal seams, roofs, and their combination structures. The elastic energy stored in coal–rock structures with a rockburst tendency is an important energy source for the occurrence of compound dynamic hazards. This elastic energy is used in the process of coal and rock dynamic hazards. The patterns of the accumulation, transformation, and dissipation of the elastic energy in the process of coal–rock dynamic hazard formation directly determine the probability and intensity of the hazards [29]. The experimental study of coal–rock combinations from an energy perspective helps to fundamentally investigate the failure mechanism of coal–rock combinations. When the coal–rock combination specimen yields, the proportion of the dissipated energy increases while that of the elastic energy decreases [30, 31]. Chen et al. [32] conducted uniaxial loading tests on coal–rock combinations with different proportions and found that the energy of the coal–rock sample is mainly distributed in the weak coal–rock seam, and regardless of the specific type of the coal–rock combination, the portion of energy in the coal is greater than 50%. Song et al. [33] carried out the conventional uniaxial and uniaxial cyclic loading tests on three types of samples (i.e., coal, rock, and coal-rock combinations) to reveal the failure modes and energy evolution law of underground coal during the mining process and found that the elastic energy stored in coal-rock combinations played a dominant role in the distribution of all input energy, accounting for more than 80% of it. And with the increase in cycle index, both the elastic energy stored in the sample and the dissipated energy increased in a quadratic function, and the failure process became more intense.

During the occurrence of coal–rock dynamic hazards in deep mines, the instability failure of coal–rock combinations is clearly influenced by the lithological characteristics of the coal seam and the roof, and the corresponding failure process is caused by the comprehensive effect of the roof–coal seam--floor system. Therefore, we simplified the coal–rock system to a rock+coal combination sample structure. Different types of coal–rock combination sample structures were constructed, and laboratory tests were carried out to investigate the patterns of accumulation, transformation, and dissipation and the quantitative characteristics of the energy in the rock sample and coal sample during the deformation and failure process of the coal–rock combination samples with different characteristics (i.e., combination types and lithologies). The mechanical criterion and energy failure characteristics of the compound failure of the bursting coal–rock combination sample structure were obtained to guide the prediction and the prevention and control of rockburst–outburst compound dynamic hazards in deep mines.

2. Analysis of Coal-Rock Combination System in Deep Mines

The roof–coal seam system in deep mines reaches the ultimate mechanical equilibrium state and fails under external loads and changes in the internal physical and mechanical properties. When the elastic strain energy accumulated by the system exceeds the energy consumed by the system at failure, intense rockburst occurs as the crushed coal–rock bodies are subjected to excess energy, resulting in coal–rock dynamic hazards. Because the elastic modulus of rock is much larger than that of coal, the strain of the rock part of the sample is much smaller than that of the coal part during the compression process. This leads to the failure of the system, which is manifested by the failure and fragmentation of the coal [34, 35]. During this process, from the system being compressed to the coal reaching its mechanical equilibrium state, which leads to the ultimate failure of the sample, both the coal and rock deform, and energy is accumulated continuously in the system. When the energy accumulated in the system reaches the limit the system can bear, the coal–rock combination structure undergoes instability failure, which causes the energy to be released rapidly, resulting in the deformation failure of the coal at the bottom. In the above process, the upper rock deforms under compression, and energy is continuously accumulated in the rock. Part of the accumulated energy acts on the rock itself, compacting the primary pores and fractures, while the other part of the energy is stored in the form of elastic energy. When the combination structure undergoes instability failure, the coal fails, the strength of the system decreases sharply, and the rock is unloaded. This passive unloading causes the strain rebound phenomenon in the rock; that is, the strain of the rock decreases. The elastic strain energy stored in the rock itself is released instantaneously, and part of the released elastic energy acts on the coal, exacerbating the failure of the coal and increasing the crushing degree of the coal. When the coal undergoes instability failure, it bears not only the effect of the accumulated energy of the system under the external load but also the effect of the elastic strain energy released by the rock. In different combination structures, the rock has different effects on the elastic strain energy of the coal and on the degree of aggravation of the coal failure.

Taking the coal–rock combination sample with an upper rock and lower coal structure as the research object, the roof–coal seam structure in a deep mine was simulated, and the model of the interaction between the coal seam and the rock layer in a deep mine was simplified using the similar model method, as shown in Figure 1. It is of great significance to analyze the failure characteristics and mechanical properties of different combination samples under uniaxial conditions, to investigate the quantitative patterns of energy conversion during the instability failure of combination samples, and to elucidate the mechanisms of compound dynamic hazards under deep mine conditions from an energy perspective.

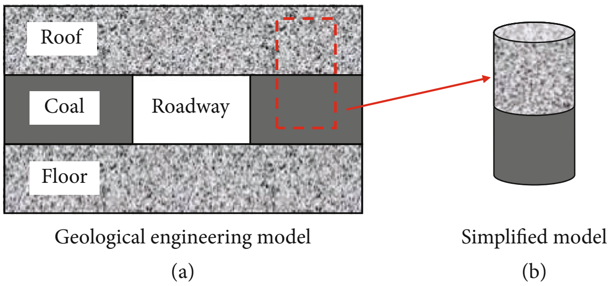

Figure 1: The structural mechanics model of coal-rock combination: (a) geological engineering model; (b) simplified model.

3. Critical Conditions for Instability Failure of Coal-Rock Combination System

In a coal–rock combination structure, the coal and rock have different physical and mechanical properties. The coal, the large number of microfractures and pores inside the coal, and the coal–rock interface jointly constitute the soft part of the combination structure, and the rock constitutes the hard part [36]. The coal–rock combination sample structure exhibits nonlinear mechanical properties, and the critical conditions for its instability failure and the criterion of the failure state are related to the physical and mechanical properties of the coal and the rock.

3.1. Criterion of the Failure State. To objectively describe the stress–strain relationship of the coal–rock combination structure under vertical mining stress during the advancement of the driving face, a simplified uniaxial loading model of the coal–rock combination structure was established, as shown in Figure 2.

Assuming that a and b are the rock block and coal block, respectively, each of which has an elasticity–strain softening constitutive relationship, the constitutive equation for the coal–rock combination material is shown in Figure 3 and the following equation:

$$\sigma = \begin{cases} E\varepsilon, & -\infty<\varepsilon \le \varepsilon_{\mathrm{c}}, \\ \sigma_{\mathrm{c}} - E_{\mathrm{t}}(\varepsilon - \varepsilon_{\mathrm{c}}), & \varepsilon_{\mathrm{c}} < \varepsilon \le \varepsilon_{\mathrm{r}}, \\ \sigma_{\mathrm{r}}, & \varepsilon_{\mathrm{r}} < \varepsilon \le +\infty, \end{cases} \quad (1)$$

where E is the elastic modulus of the material and E_{t} is the slope of the descending section of the curve, which is taken as a positive value. σ_{c} is the uniaxial compressive strength of the material; and ε_{c} is the compressive strain of the material when it reaches the uniaxial compressive strength, $\varepsilon_{\mathrm{c}} = \sigma_{\mathrm{c}}/E$. σ_{r} and ε_{r} are the strength and strain, respectively, of the material when it essentially loses its load-bearing capacity, that is, the starting point of the zero residual strength stage.

Suppose that the displacement at the top of a (i.e., the overall displacement of the combination sample) is u. The peak strains of a and b are ε_{ca} and ε_{cb}, respectively. Before b reaches the peak strength, both a and b are in the linear elastic stage, that is, in the first part of the constitutive equation.

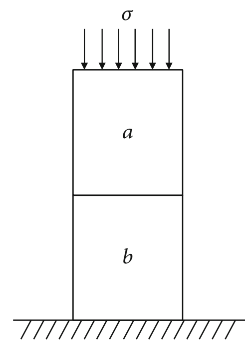

Figure 2: Coal-rock combination uniaxial loading model.

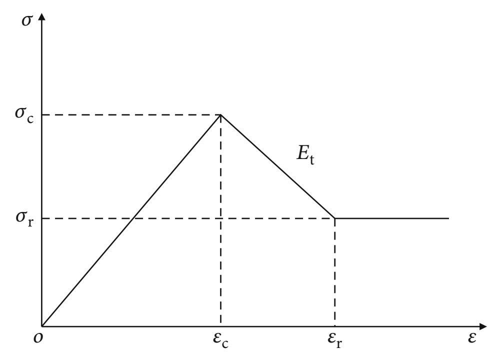

Figure 3: The elasticity-strain softening constitutive relationship.

The following relationship can be obtained by assuming that the stresses on a and b are equal during the compression:

$$\begin{cases} E_a\varepsilon_a S_a = E_b\varepsilon_b S_b, \\ \varepsilon_a l_a + \varepsilon_b l_b = u, \end{cases} \quad (2)$$

where E_a and E_b are the elastic moduli of the rock and coal, respectively; ε_a and ε_b are the strains of the rock and coal, respectively; S_a and S_b are the cross-sectional areas of the two blocks, respectively; and l_a and l_b are the heights of the corresponding rock block a and coal block b, respectively.

According to Equation (2), the stress–displacement relationship of the coal–rock combination structure in the linear elastic stage is

$$\sigma = E_a\varepsilon_a = \frac{E_a E_b S_b}{E_a S_a l_b + E_b S_b l_a} u, \quad (3)$$

where σ is the stress of the combination structure in the elastic stage. In this stage, the overall strain of the combination structure increases as the external load increases, and the system is in a stable state.

When the axial load gradually increases to a certain value, in the loading model, b reaches its peak strength first, and the failure of the combination sample occurs in the coal block. At this time, the constitutive relationship of b in the combination structure is expressed by the second part of the equation, that is, the slope section in Figure 3. a still satisfies the characteristics of the elastic stage, and the corresponding relationship is as follows:

$$\begin{cases} E_a \varepsilon_a S_a = [\sigma_{cb} - E_{tb}(\varepsilon_b - \varepsilon_{cb})] S_b \\ \varepsilon_a l_a + \varepsilon_b l_b = u \end{cases}. \quad (4)$$

Substitution of $\varepsilon_{cb} = \sigma_{cb}/E_b$ into Equation (4) gives

$$\varepsilon_a = \frac{E_b S_b \sigma_{cb} l_b + E_{tb} S_b \sigma_{cb} l_b - E_b S_b E_{tb} u}{(E_a S_a l_b - E_{tb} S_b l_a) E_b}. \quad (5)$$

Finally, the stress of the coal–rock combination structure is

$$\sigma = E_a \varepsilon_a = \frac{E_a}{E_b} \left(\frac{(E_b S_b \sigma_{cb}/l_a) + (E_{tb} S_b \sigma_{cb}/l_a)}{(E_a S_a/l_a) - (E_{tb} S_b/l_b)} - \frac{E_b E_{tb} S_b/l_a l_b}{(E_a S_a/l_a) - (E_{tb} S_b/l_b)} u \right). \quad (6)$$

When the external load causes b in the combination structure to fail completely, the combination structure completely loses its bearing capacity. b is in the third part of the constitutive equation, while a is still in the elastic stage, and the following relationship applies:

$$\sigma = \sigma_{rb}, \quad (7)$$

where σ_{rb} is the strength of coal block b when it loses its bearing capacity.

The failure state of the combination structure under uniaxial conditions can be divided into three stages, namely, the elastic (nonfailure) stage, the failure stage, and the postfailure stage, based on the constitutive equation of the coal–rock combination structure constructed under uniaxial conditions. Taking b with its relatively low strength in the structure as the research object and using the relative relationship between the ratio of the strain ε of b in the uniaxial compression process to the strain ε_c when it achieves its uniaxial compressive strength and the strain ε_r when it just completely loses its load-bearing capacity, the characteristics of each stage are as follows:

(1) When $\varepsilon \le \varepsilon_c$, the combination structure is in the elastic stage, and neither the coal nor the rock fails. As the external load increases, the strain of the coal and rock increases

(2) When $\varepsilon_c < \varepsilon \le \varepsilon_r$, the combination structure is in the failure stage. ε_c is the starting point of the instability failure of the combination structure, and it corresponds to the maximum stress point of the combination structure. After this point, the coal block fails and the stress decreases as the strain increases, exhibiting a sharp drop in the bearing capacity of the combination structure

(3) When $\varepsilon_r < \varepsilon$, the combination structure has completely lost its bearing capacity

3.2. Analysis of the Critical Conditions of Failure. According to Equations (3), (6), and (7), the expression or the stress on the coal–rock combination structure is

$$\sigma = \begin{cases} \dfrac{E_a E_b S_b}{E_a S_a l_b + E_b S_b l_a} u, & -\infty < \varepsilon_b \le \varepsilon_{cb}, \\ \dfrac{E_a}{E_b} \left(\dfrac{(E_b S_b \sigma_{cb}/l_a) + (E_{tb} S_b \sigma_{cb}/l_a)}{(E_a S_a/l_a) - (E_{tb} S_b/l_b)} - \dfrac{E_b E_{tb} S_b/l_a l_b}{(E_a S_a/l_a) - (E_{tb} S_b/l_b)} u \right), & \varepsilon_{cb} < \varepsilon_b \le \varepsilon_{rb}, \\ \sigma_{rb}, & \varepsilon_{rb} < \varepsilon_b \le +\infty. \end{cases} \quad (8)$$

Based on Equation (8), when the strain of b is within a certain range, the conditions of the instability failure of the overall combination sample structure can be obtained, as shown in Figure 4.

(1) For the first equation (section OA in Figure 4), every part of the combination structure is in the elastic stage. As the load on the combination structure increases, the displacements of the coal and rock increase, but the system remains in a stable state. The peak stress of this section is the peak stress σ_{cb} of b, which has a relatively low strength

(2) For the second equation, if $(E_a S_a/l_a) - (E_{tb} S_b/l_b) > 0$, the coefficient u is negative, and the combination structure is characterized by strain softening (section AB in Figure 4). In this stage, external work must be done to the system to increase the degree of damage to the system. However, if the external energy is input at a very low rate, even if the system can withstand less and less stress, the combination structure will not suddenly lose its bearing capacity, and thus, the system remains in a stable state

If $(E_a S_a/l_a) - (E_{tb} S_b/l_b) < 0$, the coefficient u is positive, and the equilibrium path of the system corresponds to section AD in Figure 4. The external load on the system decreases continuously, and the displacement at the top of the system increases (with downward displacement, i.e., the top surface of the system moving upward, which is negative); that is, the rebound phenomenon occurs. This means that while the system gradually loses its bearing capacity, it performs external work, and the elastic strain energy accumulated in the combination structure is released. The

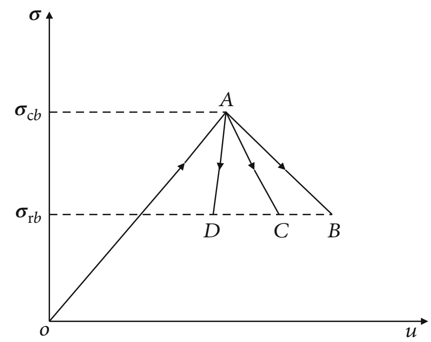

FIGURE 4: Balance path of coal-rock combination under uniaxial compression.

equilibrium path of section AD is from A to D; that is, the system performs external work and loses its bearing capacity. When the external constraints on the system are sufficiently small and thus, the system is unable to effectively perform external work, in addition to acting on the coal, the internal elastic strain energy may also be directly transformed into the kinetic energy of the rock block. Thus, the system will rapidly lose its stability and exhibit a dynamic effect.

If $(E_a S_a / l_a) - (E_{tb} S_b / l_b) = 0$, the coefficient u is negative infinity, and the equilibrium path of the system corresponds to section AC in Figure 4. In this case, the system is in a critical state. This means that as long as work is done externally by or to the system, it immediately loses all bearing capacity; that is, the combination structure is in a state of limit equilibrium.

(3) For the third equation, the equilibrium path of the system corresponds to the back section of point B in Figure 4. b in the combination structure has already undergone instability failure, and the strength of the sample is reduced. The external load is the residual strength of b.

According to the above analysis, $E_a S_a / l_a$ is the stiffness of a in the combination structure and characterizes the ability of a to resist elastic deformation when it is stressed during the elastic stage; and $E_{tb} S_b / l_b$ is the stiffness of b after failure and characterizes the ability of b to maintain its bearing capacity when displacement occurs during the strain-softening stage. The correspondence between $(E_a S_a / l_a) - (E_{tb} S_b / l_b)$ and 0 can be used as the critical condition for the combination structure in different failure states, and the critical point of instability failure of the combination structure can be determined accordingly. When its value is zero, the system is in a state of limit equilibrium. When its value is greater than zero, the damage degree of the combination structure increases if it is subjected to a large external load. When its value is less than zero, the damage to the combination structure is attributed to the combined actions of the external load and the rock block rebound energy, which may cause rapid instability failure.

3.3. Coal–Rock Elastic Modulus Correction Parameters. Due to the large number of pores and fractures in the coal, rock, and combination samples, they are strongly heterogeneous and anisotropic. Therefore, the elastic moduli of the rock samples and coal samples obtained in the experiment are not unique values but are dynamic variables related to the loading process. Considering the weakening effect of the coal–rock interface and the microfractures and pores inside the rock and coal on the elastic modulus and taking into account the influence of data discreteness due to the low number of experiments, the elastic modulus parameters of the coal and rock should be corrected in the data analysis.

In the coal–rock combination sample structure system, the rock is regarded as the hard part and is equivalent to a hard spring, while the coal is treated as the soft part and is equivalent to a soft spring, both of which satisfy Hooke's law, i.e., the two-part Hooke's model (TPHM) [37–41]. The structure of the coal–rock combination sample is a TPHM, in which the nonlinear behavior of the combination sample during the loading process is discussed. Using the basic assumptions, the coal and rock in the coal–rock combination sample are regarded as a soft body and a hard body, respectively. The force deformation process is shown in Figure 5. In Figure 5, F is the external force; H_R and H_C are the heights of the rock and coal, respectively, in the coal–rock combination before loading; D_R and D_C are the diameters of the rock and coal, respectively, in the coal–rock combination before loading; h_R and h_C are the heights of the rock and coal, respectively, in the coal–rock combination after loading; and d_R and d_C are the diameters of the rock and coal, respectively, in the coal–rock combination after loading. When only uniaxial compression and axial strain are considered, the change in the diameter of the combination sample before and after loading can be ignored, i.e., $D_{R=} d_R$ and $D_{C=} d_C$. Δ is the displacement of the coal–rock combination specimen before and after loading.

Under external force F, the coal–rock combination will undergo elastic deformation. According to Hooke's law,

$$d\sigma_R = m_R E_R d\varepsilon_R, \tag{9}$$

$$d\sigma_C = m_C E_C d\varepsilon_C, \tag{10}$$

where σ_R and σ_C are the stresses applied to the upper rock sample and the coal sample, respectively; E_R and E_C are the elastic moduli of the rock sample and coal sample, respectively; $\varepsilon_R$and ε_C are the axial strains of the rock sample and the coal sample, respectively; and m_R and m_C are the correction coefficients for the elastic moduli of the rock sample and the coal sample, respectively.

In the TPHM, the rock represented by a hard spring and the coal represented by a soft spring deform under the same force F. There are a large number of fractures in the coal, a considerable number of which are consistent with the direction of the principal stress and will develop and propagate as the principal stress increases, thereby leading to the failure of the coal and resulting in nonlinear elastic deformation or inelastic deformation.

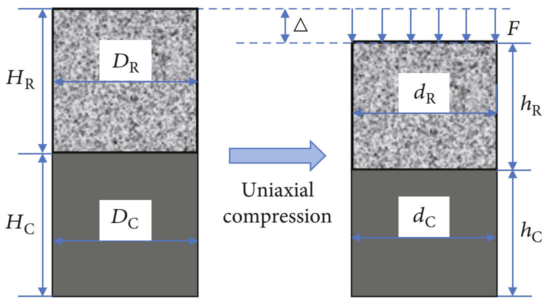

FIGURE 5: Schematic diagram of the deformation of the coal–rock combination under an external force.

The respective strains of the rock and coal in the combination sample are

$$d\varepsilon_R = -\frac{dh_R}{H_R}, \tag{11}$$

$$d\varepsilon_C = -\frac{dh_C}{H_C}. \tag{12}$$

Equations (9)–(12) were solved simultaneously to obtain the respective stresses of the rock and coal in the coal–rock combination as follows:

$$\begin{cases} \sigma_R = -\dfrac{m_R E_R}{H_R} h_R + C_1, \\ \sigma_C = -\dfrac{m_C E_C}{H_C} h_R + C_2, \end{cases} \tag{13}$$

where C_1 and C_2 are integration constants.

When the external force F is zero, under the initial conditions, $h_R = H_R$ and $h_c = H_c$, based on which $C_1 = m_R E_R$ and $C_2 = m_C E_C$. Substitution into Equation (13) leads to the correction parameters of the displacements, strains, and elastic moduli of the rock and coal in the combination sample structure as follows:

$$\begin{cases} \Delta R = h_R - H_R = -H_R \dfrac{\sigma_R}{m_R E_R}, \\ \Delta C = h_C - H_C = -H_C \dfrac{\sigma_C}{m_C E_C}. \end{cases} \tag{14}$$

$$\begin{cases} \varepsilon_R = \dfrac{\Delta R}{H_R} = \dfrac{h_R - H_R}{H_R} = -\dfrac{\sigma_R}{m_R E_R}, \\ \varepsilon_C = \dfrac{\Delta C}{H_C} = \dfrac{h_C - H_C}{H_C} = -\dfrac{\sigma_C}{m_C E_C}, \end{cases} \tag{15}$$

$$\begin{cases} m_R = -\dfrac{\sigma_R}{\varepsilon_R E_R}, \\ m_C = -\dfrac{\sigma_C}{\varepsilon_C E_C}. \end{cases} \tag{16}$$

4. Mechanical Experiment and Analysis of the Instability of the Coal-Rock Combination System

4.1. Experimental Design. The coal samples and rock samples required for the experiment were both collected from the Pingdingshan No. 5 Coal Mine. The coal-bearing strata in this mine are 556 to 1090 m thick, with an average of 796 m. There are 21 to 56 coal-bearing seams, including 8 minable and partially minable seams. Among them, the roof of the Geng 20 coal seam is dominated by sandstone and sandy mudstone, and its floor lithology is mostly sandstone and limestone. To meet the experimental needs, rock specimens with three different lithologies (i.e., coarse sandstone, fine sandstone, and siltstone) and raw coal specimens were prepared. According to their lithologies and coal–rock height ratios, two groups of different combination samples were prepared. Group A contained combination samples with different lithologies and with coal and rock heights of 50 mm each, as shown in Figure 6(a). Group B contained samples formed by bonding the siltstone specimens to the raw coal specimens. The ratios of the heights of the rock and coal in the specimens were 1 : 1, 1.5 : 1, and 2 : 1, and the total height of each sample was 100 mm, as shown in Figure 6(b).

The experiments were divided into 2 sets, as shown in Table 1. In set A, uniaxial compression tests were carried out on combination samples with three different lithologies, and the experiments were repeated three times for each type of combination sample. The experiments were numbered A11 through A33, for a total of 9 experiments. In set B, uniaxial compression tests were conducted on combination samples with three different height ratios, and the experiments were repeated three times for each height ratio. The experiments were numbered B11 through B33, for to a total of 9 experiments.

4.2. Experimental Results. A TAW-2000 microcomputer-controlled rock triaxial testing machine was used to carry out the uniaxial compression tests on the coal–rock combination samples, and a DH3818Y static strain tester was used to monitor the strain of the samples. The test equipment is shown in Figure 7. Figure 8 shows the stress-strain curve of the coarse sandstone-coal combination sample (A11). Figures 9(a)–9(c) show the failure modes of the coal–rock combination sample structures with different lithologies. Figures 10(a)–10(c) show the failure modes of the coal–rock combination sample structures with different height ratios.

As can be seen from Figure 9, when the coarse sandstone–raw coal combination samples underwent instability failure, a few cracks appeared in the rock part at the interface, and the coal basically maintained its integrity. The failure was concentrated in the pieces of lump coal, which still retained a certain amount of integrity. The fine sandstone–raw coal combination samples and the siltstone–raw coal combination samples were damaged severely. The coal was cut through, the damaged coal was in the form of small blocks and particles, and there were no notable cracks in the rock parts. Figure 10 shows that the structure of the combination samples with a rock–coal height ratio of 2 : 1 suffered the

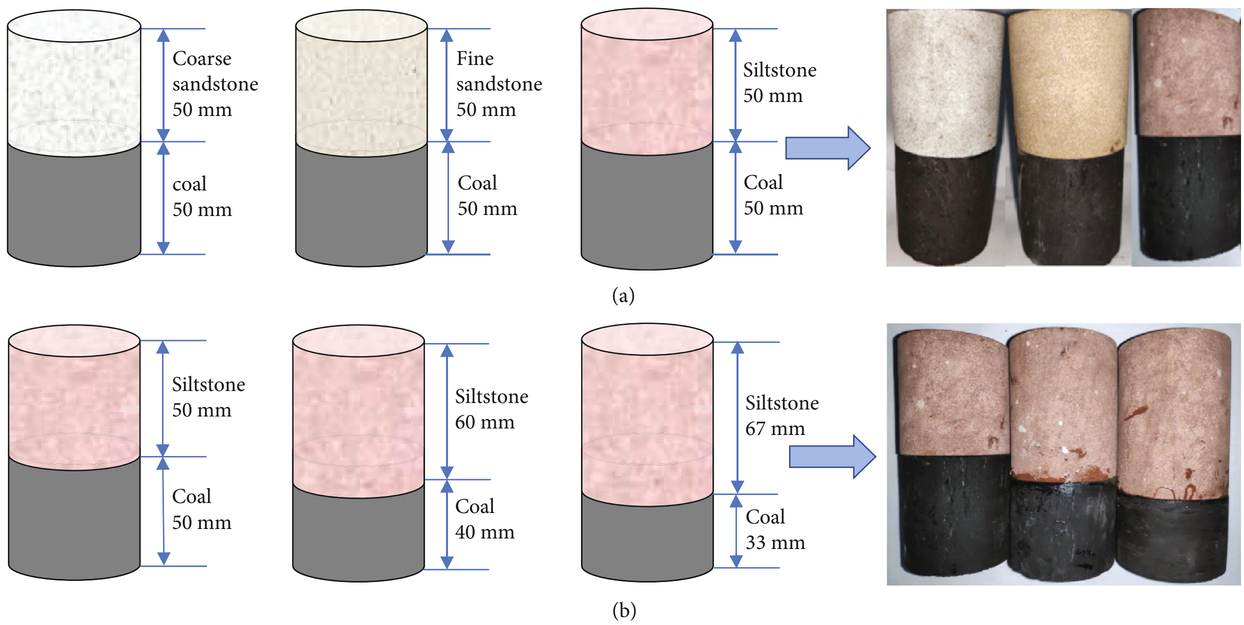

Figure 6: Schematic diagram of the deformation of the coal–rock combination under an external force: (a) combination samples with different lithologies; (b) combination samples with different height ratios.

Table 1: Experimental design.

Set A: samples with different lithologies				Set B: samples with different height ratios			
Coarse sandstone-coal	A11	A12	A13	Siltstone-coal height ratio 1 : 1	B11	B12	B13
Fine sandstone-coal	A21	A22	A23	Siltstone-coal height ratio 1.5 : 1	B21	B22	B23
Siltstone-coal	A31	A32	A33	Siltstone-coal height ratio 2 : 1	B31	B32	B33

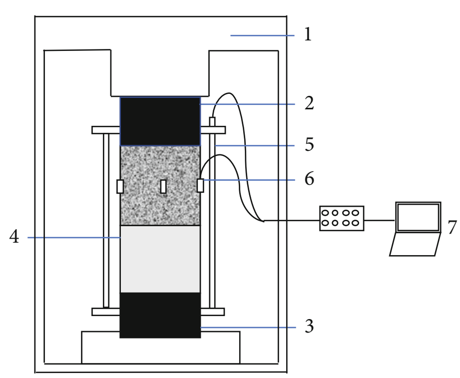

Figure 7: The test equipment. 1 the TAW-2000 testing machine, 2 upper indenter, 3 lower indenter, 4 coal-rock combination sample, 5 extensometer, 6 strain gauges, and 7 the DH3818Y static strain tester.

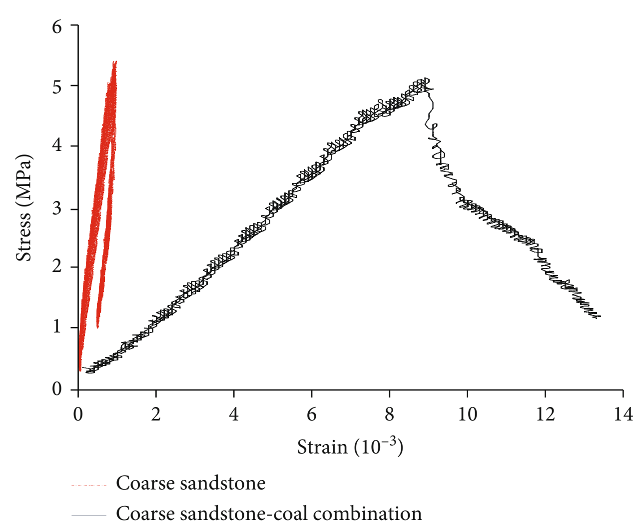

Figure 8: The stress-strain curve of the coarse sandstone-coal combination sample (A11).

most severe damage. The combination structure was completely destroyed, and the coal in the structure was shattered into powder. The damage to the structure of the combination samples with a rock–coal height ratio of 1.5 : 1 manifested as a large number of longitudinal cracks on the surface of the coal, resulting in the coal being cut through. Due to its internal failure, it no longer had a bearing capacity, and obvious dilatancy phenomenon occurred in the coal part under compression. The damage to the combination sample structures with a rock-coal height ratio of 1 : 1 was mainly manifested as a few pieces of coal falling off of the structure.

(a) (b) (c)

FIGURE 9: The failure modes of the coal–rock combination sample structures with different lithologies: (a) coarse sandstone-coal; (b) fine sandstone-coal; (c) siltstone-coal.

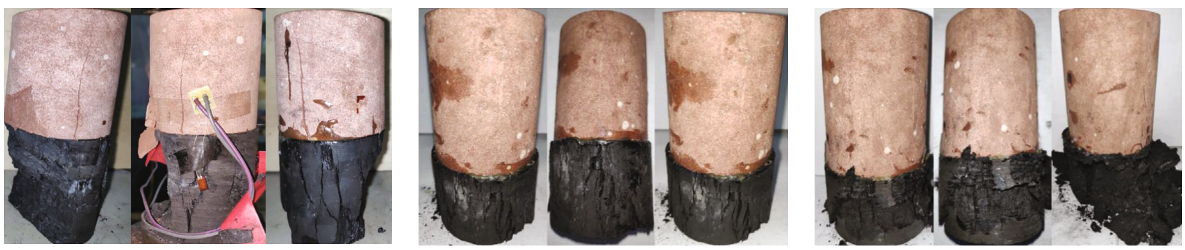

(a) (b) (c)

FIGURE 10: The failure modes of the coal–rock combination sample structures with different height ratios: (a) siltstone-coal height ratio 1 : 1; (b) siltstone-coal height ratio 1.5 : 1; (c) siltstone-coal height ratio 2 : 1.

TABLE 2: The critical equilibrium values for the failure of the two types of coal–rock combination sample structures with different lithologies and different height ratios.

Set A	$m_R E_a S_a / l_a$	$m_c E_b S_b / l_b$	Difference	Set B	$m_R E_a S_a / l_a$	$m_c E_b S_b / l_b$	Difference
A11	153.490	156.324	-2.834	B11	200.054	200.525	-0.471
A12	153.581	156.110	-2.529	B12	209.201	209. 669	-0.468
A13	157.802	159.573	-1.771	B13	206.072	206.508	-0.436
A21	180.778	181.845	-1.067	B21	244.145	244.436	-0.291
A22	175.587	176.664	-1.077	B22	241.743	241.945	-0.202
A23	178.998	180.079	-1.081	B23	245.242	245.455	-0.213
A31	197.935	198.566	-0.631	B31	301.323	301.446	-0.123
A32	195.588	196.289	-0.701	B32	305.901	306.083	-0.182
A33	196.145	196.799	-0.654	B33	304.851	304.983	-0.132

The coal could still maintain the combination structure to a certain extent after the failure of the coal, and the coal still had some bearing capacity.

The difference in the structural failure modes of the two different types of combination samples is mainly reflected in the failure of the coal. For the combination sample structures of different lithologies, a higher rock strength corresponded to a larger elastic modulus, so more elastic strain energy could be accumulated during its compression deformation. The elastic strain energy accumulated in the rock was released into the coal at the moment when the sample underwent instability failure, resulting in the differences in the failure modes of the coal. For the combination sample structures with different height ratios, a higher rock content corresponded to a higher sample strength, so more elastic strain energy accumulated during the rock compression process. When the combination sample failed, the deformation of the coal part was more violently and significant.

4.3. Critical Condition Verification Analysis. By substituting the experimental stress and strain data for the coal–rock combination structures used in the uniaxial compression tests into Equation (16), the correction parameters m_C and m_R for the elastic moduli of the coal and rock, respectively, were obtained. Then, these were substituted into Equation (8) to obtain the overall displacement–load function relationship of the corrected combination sample structures composed of rock block a and coal block b and the critical conditions for the failure of the corrected combination samples, as shown in Equation (17).

$$\sigma = \begin{cases} \dfrac{m_R E_a m_c E_b S_b}{m_R E_a S_a l_b + m_c E_b S_b l_a} u, & -\infty < \varepsilon_b \leq \varepsilon_{cb}, \\ \dfrac{m_R E_a}{m_c E_b} \left(\dfrac{(m_c E_b S_b \sigma_{cb}/l_a) + (m_c E_b S_b \sigma_{cb}/l_a)}{(m_R E_a S_a/l_a) - (m_c E_b S_b/l_b)} - \dfrac{m_c{}^2 E_b{}^2 S_b/l_a l_b}{(m_R E_a S_a/l_a) - (m_c E_b S_b/l_b)} u \right), & \varepsilon_{cb} < \varepsilon_b \leq \varepsilon_{rb}, \\ \sigma_{rb}, & \varepsilon_{rb} < \varepsilon_b \leq +\infty. \end{cases} \tag{17}$$

$m_R E_a S_a/l_a - m_b E_b S_b/l_b = 0$ indicates that the combination sample structure is in a critical state of limit equilibrium, and the combination structure will fail immediately when the external load increases. $m_R E_a S_a/l_a - m_b E_b S_b/l_b < 0$ indicates that the combination sample structure is in the failure state, and the coal part of the structure is subjected to the combined actions of the external work and rebound energy of the rock in the system. In the case of $m_R E_a S_a/l_a - m_b E_b S_b/l_b > 0$, if external work is done to the system, the degree of damage done to the combination sample structure will increase, and the system will still have a certain bearing capacity.

Taking the peak failure point of the combination sample as the research object, the coal in the sample at this moment reaches its peak strength and $\varepsilon_b \geq \varepsilon_{cb}$, but the rock part is still in the elastic stage. The structural failure characteristics of the combination sample expressed by Equation (17) are satisfied. Therefore, the critical equilibrium values for the failure of the two types of coal–rock combination sample structures with different lithologies and different height ratios can be calculated, as shown in Table 2.

As can be seen from Table 2, the critical equilibrium values of the different combination samples are all negative, and they approach 0 as the rock strength and the proportion of rock in the combination samples increase, indicating that the combination samples failed under the combined actions of the external work and the rebound energy of the rock. When the load on the system reached the maximum that the coal could withstand, the strain of the coal increased, exceeded its uniaxial compressive strength, and reached the peak strain, at which time the combination structure underwent instability failure. At this moment, the rock was still in its elastic stage; and the strain increased with increasing stress, reaching its maximum value at the peak point of the system's strain. After that, the strain of the rock decreased, exhibiting a trend opposite to that of the coal. The strain characteristics that the coal and rock exhibited at the system's strain peak point and in the moments thereafter indicate that the rock exerts rebound energy on the coal, which is consistent with the mechanical phenomenon represented by the calculated critical equilibrium value being less than 0.

5. Energy Transfer Characteristics during the Instability of the Coal-Rock System

5.1. Elastic Energy Test and Energy Transfer Analysis of the Coal–Rock Combination. The energy evolution of the loaded coal–rock system can be divided into three main processes: energy input, energy accumulation, and energy dissipation. In the loading process, without considering the damping dissipation and heat exchange, the energy input is mainly derived from the work done by the experimental machine on the combination sample. Part of the input energy is accumulated in the combination sample in the form of reversible elastic energy, and the other part is dissipated in the form of plastic deformation energy and damage energy, which is irreversible. When the accumulated elastic strain energy in the combination sample reaches a certain extent, the coal, which has a much smaller elastic modulus than the rock, undergoes instability failure due as it reaches the limit of its bearing capacity. Then, the rock part of the combination sample exhibits the passive unloading phenomenon, the stress and strain of the rock decrease, and the rock releases the stored elastic strain energy into the system. This part of the energy acts on the coal, aggravating the damage to the coal and increasing the degree of crushing. The coal part undergoes instability failure under the joint actions of the energy accumulated in the coal itself and the elastic strain energy transferred to the coal during the passive unloading of the rock part.

Based on the stress–strain curves of the rock part and the overall combination sample of the coal–rock combination sample structure under uniaxial compression until its failure (Figure 11), the following energy values are obtained: the energy accumulated before the peak of the corresponding combination sample (E_1), the energy consumed by the failure of the combination sample (E_2), the elastic energy accumulated by the rock part during uniaxial compression (U), and the elastic strain energy transferred to the coal during the passive unloading of the rock part (U_1), as shown in the following equation:

$$\begin{cases} E_1 = V_{\text{combination}} \displaystyle\int_{\text{OBI}} \sigma \mathrm{d}\varepsilon = S_{\text{OBI}} V_{\text{combination}}, \\ E_2 = V_{\text{combination}} \displaystyle\int_{\text{BIKE}} \sigma \mathrm{d}\varepsilon = S_{\text{BIKE}} V_{\text{combination}}, \\ U = V_{\text{rock}} \displaystyle\int_{\text{OAH}} \sigma \mathrm{d}\varepsilon = S_{\text{OAH}} V_{\text{rock}}, \\ U_1 = V_{\text{rock}} \displaystyle\int_{\text{NAD}} \sigma \mathrm{d}\varepsilon = S_{\text{NAD}} V_{\text{rock}}, \end{cases} \tag{18}$$

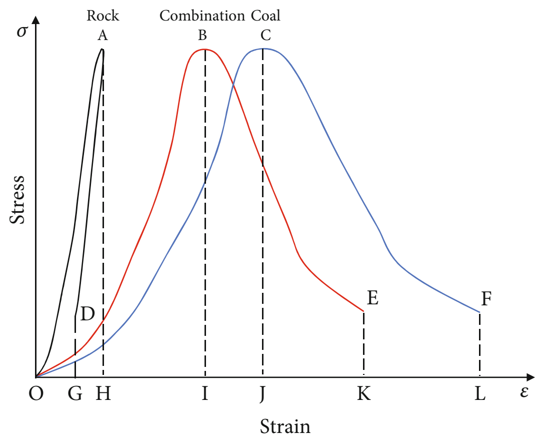

(a) The stress–strain curves of the overall combination

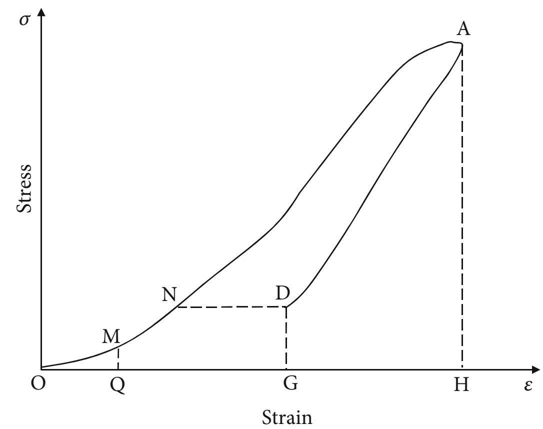

(b) The stress–strain curves of the rock part

FIGURE 11: The stress–strain curves of the rock part and the overall combination sample of the coal–rock combination sample structure under uniaxial compression until its failure.

TABLE 3: The calculation results of each research index.

No.	U_1 (J)	U (J)	E_1 (J)	U_1/U	Average U_1/U	$U_1/(E_1 - U + U_1)$	Average $U_1/(E_1 - U + U_1)$
A11	0.30537	1.16180	8.53295	26.28%		3.98%	
A12	0.28221	1.09508	7.72440	25.77%	26%	4.08%	4.0%
A13	0.27632	1.08330	7.70085	25.51%		4.01%	
A21	0.32342	1.15003	8.64285	28.12%		4.14%	
A22	0.32146	1.21675	8.63108	26.42%	28%	4.16%	4.1%
A23	0.34893	1.17358	9.44748	29.73%		4.05%	
A31	0.52988	1.31488	11.51988	40.30%		4.94%	
A32	0.54558	1.37375	12.17143	39.71%	40%	4.81%	4.9%
A33	0.50240	1.25993	11.00178	39.88%		4.90%	
B11	0.54558	1.31488	12.06545	41.49%		4.83%	
B12	0.53380	1.33843	11.85350	39.88%	41%	4.83%	4.8%
B13	0.54165	1.29918	12.20675	41.69%		4.73%	
B21	0.79599	1.77567	10.86754	44.83%		8.05%	
B22	0.81483	1.73799	10.99314	46.88%	46%	8.09%	8.1%
B23	0.79128	1.74742	10.74508	45.28%		8.08%	
B31	1.10429	2.09867	9.65715	52.62%		12.75%	
B32	1.182794	2.15624	10.18043186	54.85%	53%	12.85%	12.4%
B33	1.03625	2.04634	9.89786	50.64%		11.66%	

where S is the corresponding area under the stress-strain curve and V is the volume of the corresponding structure.

To describe the energy characteristics and transfer patterns, including their relationships with the failure state and failure severity, of the different combination samples during failure, the following indicators are proposed:

(1) U_1 intuitively reflects the influence of the elastic strain energy of the rock on the instability failure of the coal

(2) U_1/U reflects the difference in the ability of the rock parts of the different combination samples to release elastic strain energy

(3) $U_1/(E_1 - U + U_1)$ reflects the proportion of the energy contributed by the elastic strain energy released by the rock during the failure of the coal–rock combination

The indicators were calculated based on Figure 10 and Equation (18), and the specific results are shown in Table 3. The following can be seen from Table 3:

(1) During the failure process of the coal–rock combination, the greater the stored elastic strain energy released into the system by the rock (U_1), the higher the crushing degree of the coal after the failure of the combination structure. For the coal–rock combination samples of different lithologies, the greater the

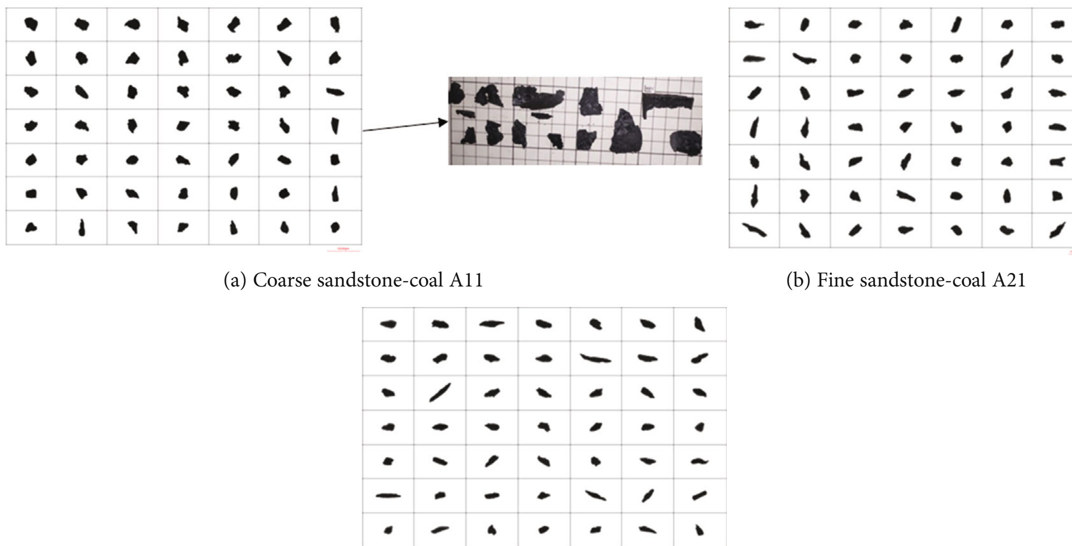

(a) Coarse sandstone-coal A11

(b) Fine sandstone-coal A21

(c) Siltstone-coal A31

Figure 12: The particle size statistics of the crushed coal samples after the failure of the different lithology combination structures.

strength of the roof rock, the greater the stored elastic strain energy released into the system by the rock. For the coal–rock combination samples with different height ratios, the smaller the coal–rock height ratio, the greater the stored elastic strain energy released into the system by the rock

(2) For the different combination specimens, the stored elastic strain energy released into the system by the rock accounts for a large proportion of the energy accumulated in the rock = $(U1/U)$, reaching 26% to 53%, whereas this part of the energy contributes a relatively small amount to the energy during the failure of the coal–rock combination $(U_1/(E_1 - U + U_1))$, only accounting for approximately 4% to 12.4%. During the failure process of the coal–rock combination, as the strength of the roof rock increased, U_1/U increased, whereas the change in $U_1/(E_1 - U + U_1)$ was not significant. As the coal–rock height ratio decreased, U_1/U increased, and $U_1/(E_1 - U + U_1)$ increased significantly. This indicates that, relative to the strength of the roof rock of the coal–rock combination, the coal–rock height ratio of the coal–rock combination plays a greater role in the failure of the coal–rock combination.

5.2. Test of the Crushing Degree of the Coal Sample. The compression failure of the combination samples under uniaxial conditions was a process involving energy accumulation, transfer, and release. To analyze the patterns of energy transfer and release during this process, it is necessary to study the crushing degree of the coal after failure. In essence, the crushing of the combination sample is a process in which, under the combined actions of the energy accumulated in the sample and the elastic strain energy released by the upper rock part, the coal is crushed into smaller pieces, creating new surfaces that separate the pieces from the original body. Therefore, there is an inevitable relationship between the sum of the elastic strain energy released by the rock and the energy accumulated in the coal (i.e., the crushing energy) and the new surface [42]. By analyzing the particle distribution of the crushed coal samples after the failure of the different combination samples and the crushing degree of the different combination samples, the newly added surface areas of the different combination samples were calculated and the relationship between the newly added surface area and the crushing energy was obtained. The particle size statistics of the crushed coal samples after the failure of the different combination structures were determined, and the typical results are shown in Figure 12. From the particle size and microscopic morphology, it can be seen that most of the broken coal-like particles are close to spherical or ellipsoidal, with only a few irregular shapes.

According to the new surface theory [43, 44], the coal crushing energy was all used to create new surfaces, the area of which was generated by the crushed coal:

$$S_{\text{New}} = \frac{6m}{\rho d_Z}, \tag{19}$$

where S_{New} is the newly added surface area of the crushed coal, m is the mass of the coal, ρ is the density of the coal, and d_Z is the converted diameter of the coal.

The newly added surface area of the different combination samples was calculated by Equation (19), as shown in Table 4.

As can be seen from Table 4, for the different coal–rock combination samples tested in the experiments, the mass of the crushed coal sample was relatively small, accounting for less than 5% of the total coal in the combination sample. The newly added surface areas of the different combination samples, which were provided by the crushed coal, reflect the crushing conditions of the samples. The larger the newly

Table 4: The newly added surface area of the different combination samples.

No.	Coal weight (g)	Crushed coal weight (g)	Crushed coal weight/coal weight (%)	Converted diameter (mm)	Newly added surface area (mm^2)
A11	127.0	6.3	4.96	1.6976	346813.148
A12	127.1	5.3	4.16	1.5867	371053.129
A13	127.8	6.1	4.77	1.5487	380157.551
A21	126.4	5.2	4.11	1.0826	543829.669
A22	126.4	4.8	3.79	1.1287	521617.790
A23	126.3	4.7	3.72	0.9828	599053.724
A31	126.2	4.6	3.64	0.8277	711308.445
A32	126.7	4.3	3.39	0.8177	720007.338
A33	126.3	4.1	3.24	0.7719	762728.333
B11	127.3	5.1	4.00	0.7828	752107.818
B12	127.4	4.9	3.84	0.7961	739542.771
B13	127.2	5.0	3.93	0.7840	750956.633
B21	101.6	4.8	4.72	0.6019	782522.014
B22	99.2	4.6	4.63	0.5979	787757.150
B23	100.3	4.7	4.68	0.5778	815160.955
B31	82.8	4.1	4.95	0.4423	878532.670
B32	80.1	3.8	4.74	0.4379	887360.128
B33	79.9	3.4	4.25	0.4308	901984.680

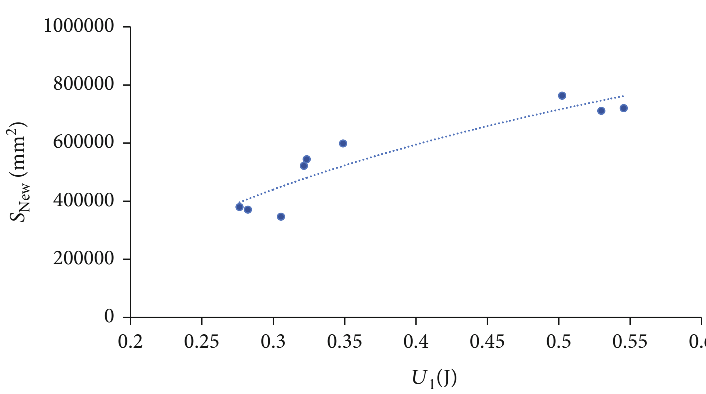

Figure 13: The relationship between S_{New} and U_1 of the different lithology combination structures.

added surface area, the higher the crushing degree of the coal, that is, the more severe the degree of instability failure.

To further illustrate the aggravating effect of the rock elastic energy on the failure of the coal, the newly added surface area was selected as the research object, and for the coal–rock combinations with different roof lithologies, the relationship between the newly added surface area and the stored elastic strain energy released into the system by the rock (U_1) was analyzed. The energy characteristics of the combination samples during instability failure under uniaxial conditions were analyzed from the perspective of coal crushing, as shown in Figure 13.

Figure 13 shows that as the rock strength of the coal–rock combination increased, the U_1 increased, which increased the crushing degree of the sample, leading to an increase in S_{New} of the crushed coal. Furthermore, there is a logarithmic relationship between the two, and the fitting relationship is $S_{New} = 537808 \ln (U_1) + 1087600$.

6. Conclusions

(1) Based on the analysis of the mechanical behaviors of the combination structures under uniaxial conditions, the relationship between the value of the critical equilibrium conditions of the sample ($m_R E_a S_a / l_a - m_c E_b S_b / l_b$) and the theoretical peak failure point value 0 is proposed and verified using experimental data. If the value is less than 0, the sample has undergone instability failure. If the value is greater than 0, the sample has not reached the limit state. If the value is 0, the sample is in a state of limit

equilibrium, and an increase in the external load will cause the sample to undergo instability failure

(2) The combination samples underwent instability failure under the combined actions of the external load and the rock's elastic energy. The stored elastic strain energy that was released into the combination sample system by the rock (U_1) accounts for approximately 26% to 53% of the energy accumulated by the rock, and the proportion of energy contributed to the failure of the coal–rock combination ($U_1/(E_1 - U + U_1)$) is approximately 4% to 12.4%. The values of these two energies are greater for the combination samples with different height ratios than for the combination samples with different lithologies

(3) The crushing degree of the coal characterizes the severity of the instability failure of the combination sample. The failure severity of the combination sample and the crushing degree of the coal are related to the ability of the rock in the sample to release the stored elastic strain energy into the combination sample system (U_1). The larger the U_1 value, the larger the increased surface area generated by the coal after the failure of the combination sample, and the more severely the coal is crushed, which leads to a higher degree of sample failure. Moreover, the stored elastic strain energy that is released into the combination sample system by the rock is logarithmically related to the increase in surface area

Data Availability

The data used to support the findings of this study are included within the article.

Disclosure

Meanwhile, the founding sponsors had no role in the design of the study; in the collection, analyses, or interpretation of data; in the writing of the manuscript; and in the decision to publish the results.

Conflicts of Interest

The authors declare no conflict of interest.

Authors' Contributions

The manuscript is approved by all authors for publication. All the authors listed have approved the manuscript that is enclosed.

Acknowledgments

This work is financially supported by the National Natural Science Foundation of China (51874348, 51974358, 51774319, 51574280), Chongqing Science Fund for Distinguished Young Scholars (cstc2019jcyjjqX0019), Science and Technology Innovation and Entrepreneurship Fund of China Coal Technology Engineering Group (2019-TD-QN040), Chongqing Science and Technology Innovation Leading Talent Support Program (CSTCCXLJRC201911), and National Key Research and Development Program (2016YFC0801402) which are gratefully acknowledged.

References

[1] M. C. He, H. P. Xie, S. P. Peng, and Y. D. Jiang, "Study on rock mechanics in deep mining engineering," *Chinses Journal of Rock Mechanical and Engineering*, vol. 24, no. 16, pp. 2803–2813, 2005.

[2] H. W. Zhou, H. P. Xie, and J. P. Zuo, "Developments in researches on mechanical behaviors of rocks under the condition of high ground pressure in the depths," *Advances in Mechanics*, vol. 35, no. 1, pp. 91–97, 2005.

[3] L. C. Dai, Y. B. Liu, J. Cao et al., "A Study on the energy condition and quantitative analysis of the occurrence of a coal and gas outburst," *Shock and Vibration*, vol. 2019, Article ID 8651353, 13 pages, 2019.

[4] J. G. Li, Q. T. Hu, M. G. Yu, X. L. Li, J. Hu, and H. M. Yang, "Acoustic emission monitoring technology for coal and gas outburst," *Energy Science & Engineering*, vol. 7, no. 2, pp. 443–456, 2019.

[5] G. C. Wen, H. T. Sun, J. Cao, Y. B. Liu, L. C. Dai, and B. Wang, "Simulation experiment system of coal and gas dynamic disaster in deep mine and its application in accident analysis," *Journal of China Coal Society*, vol. 45, no. 1, pp. 223–231, 2020.

[6] B. B. Gao, "Research status and prospect of compound dynamic disaster of deep mining in coal mine," *Safety in Coal Mines*, vol. 44, no. 11, pp. 175–178, 2013.

[7] F. Du, K. Wang, Y. Y. Guo, G. D. Wang, L. Wang, and Y. H. Wang, "The mechanism of rockburst-outburst coupling disaster considering the coal-rock combination: an experiment study," *Geomechanics and Engineering*, vol. 22, no. 3, pp. 255–264, 2020.

[8] N. G. W. Cook, "A note on rock burst considered as a problem of stability," *Journal of the Southern African Institute of Mining and Metallurgy*, vol. 65, pp. 437–446, 1965.

[9] И. М. Петухов, "Theory and practice of preventing rock burst," *Safety in Coal Mines*, vol. 5, pp. 39-40, 1988.

[10] Z. F. Zhu, "Research report of the laboratory of rock burst in Fushun Longfeng mine-study on using coal (rock) stiffness to establish impact index," *Journal of Fuxin Mining Institute*, vol. S1, pp. 43–56, 1985.

[11] M. T. Zhang, Z. H. Xu, Y. S. Pan, and Y. S. Zhao, "A united instability theory on coal(rock) burst and outburst," *Journal of China Coal Society*, vol. 16, no. 4, pp. 48–53, 1991.

[12] Y. S. Pan, "Integrated study on compound dynamic disaster of coal-gas outburst and rockburst," *Journal of China Coal Society*, vol. 41, no. 1, pp. 105–112, 2016.

[13] Z. Wang, G. Z. Yin, Q. T. Hu, and H. W. Jin, "Inducing and transforming conditions from rockburst to coal-gas outburst in a high gassy coal seam," *Journal of Mining and Safety Engineering*, vol. 27, no. 4, pp. 572–575,580, 2010.

[14] T. Li, M. F. Cai, J. A. Wang, D. C. Li, and J. Liu, "Discussion on relativity between rockburst and gas in deep exploitation," *Journal of China Coal Society*, vol. 30, no. 5, pp. 20–25, 2005.

[15] S. Y. Li, X. S. He, K. Pan et al., "Relationship between mining seismicity and gas outburst in coal mine-some scientific

questions of mining safety," *Physics*, vol. 36, no. 2, pp. 136–145, 2007.

[16] Y. Liu, C. P. Lu, B. Liu, Z. Y. Xiao, and H. Zhang, "Slip and instability mechanisms of coal-rock parting-coal structure (CRCS) under coupled dynamic and static loading," *Energy Science & Engineering*, vol. 7, no. 6, pp. 2703–2719, 2019.

[17] Q. T. Hu, S. N. Zhou, and X. Q. Zhou, "Mechanical mechanism of coal and gas outburst process," *Journal of China Coal Society*, vol. 33, no. 12, pp. 1368–1372, 2008.

[18] G. Z. Yin, X. Li, J. Lu, and M. H. Li, "Disaster causing mechanism of compound dynamic disaster in deep mining under static and dynamic load conditions," *Journal of China Coal Society*, vol. 42, no. 9, pp. 2316–2326, 2017.

[19] L. M. Dou, C. P. Lu, Z. L. Mou, Y. H. Qin, and J. M. Yao, "Intensity weakening theory for rockburst and its application," *Journal of China Coal Society*, vol. 30, no. 6, pp. 690–694, 2005.

[20] Y. X. Zhao, Y. D. Jiang, J. Zhu, and G. Z. Sun, "Experimental study on precursory information of deformations of coal-rock composite samples before failure," *Chinese Journal of Rock Mechanics and Engineering*, vol. 27, no. 2, pp. 339–346, 2008.

[21] J. P. Zou, Z. F. Wang, H. W. Zhou, J. L. Pei, and J. F. Liu, "Failure behavior of a rock-coal-rock combined body with a weak coal interlayer," *International Journal of Mining Science and Technology*, vol. 23, no. 6, pp. 907–912, 2013.

[22] J. P. Zou, Y. Chen, J. W. Zhang, J. T. Wang, Y. J. Sun, and G. H. Jiang, "Failure behavior and strength characteristics of coal-rock combined body under different confining pressures," *Journal of China Coal Society*, vol. 41, no. 11, pp. 2706–2713, 2016.

[23] J. P. Zou, Y. Chen, Y. J. Sun, G. H. Jiang, and J. T. Wang, "Investigation on whole failure nonlinear model for deep coal-rock combined bodies," *Journal of Mining Science and Technology*, vol. 2, no. 1, pp. 17–24, 2017.

[24] C. P. Lu, L. M. Dou, and X. R. Wu, "Experimental research on rules of rockburst tendency evolution and acoustic-electromagnetic effects of compound coal-rock samples," *Chinese Journal of Rock Mechanics and Engineering*, vol. 26, no. 12, pp. 2549–2555, 2007.

[25] J. X. Liu, C. A. Tang, W. C. Zhu, and T. H. Yang, "Rock-coal model for studying the rockburst," *Chinese Journal of Geotechnical Engineering*, vol. 26, no. 2, pp. 276–280, 2004.

[26] Z. J. Wen, X. Wang, L. J. Chen, G. Lin, and H. L. Zhang, "Size effect on acoustic emission characteristics of coal-rock damage evolution," *Advances in Materials Science and Engineering*, vol. 2017, Article ID 3472485, 8 pages, 2017.

[27] F. Du, K. Wang, G. D. Wang, Y. F. Jiang, C. P. Xin, and X. Zhang, "Investigation of the acoustic emission characteristics during deformation and failure of gas-bearing coal-rock combined bodies," *Journal of Loss Prevention in the Process Industries*, vol. 55, pp. 253–266, 2018.

[28] K. Yang, W. J. Liu, L. T. Dou, X. L. Chi, Z. Wei, and Q. Fu, "Experimental investigation into interface effect and progressive instability of coal-rock combined specimen," *Journal of China Coal Society*, vol. 45, no. 5, pp. 1691–1700, 2020.

[29] Q. X. Qi, Y. S. Pan, H. T. Li et al., "Theoretical basis and key technology of prevention and control of coal-rock dynamic disasters in deep coal mining," *Journal of China Coal Society*, vol. 45, no. 5, pp. 1567–1584, 2020.

[30] Y. Chen, J. P. Zuo, X. Wei, H. Q. Song, and Y. J. Sun, "Energy nonlinear evolution characteristics of the failure behavior of coal-rock combined body," *Chinese Journal of Underground Space and Engineering*, vol. 13, no. 1, pp. 124–132, 2017.

[31] L. Yang, F. Q. Gao, X. Q. Wang, and J. Z. Li, "Energy evolution law and failure mechanism of coal-rock combined specimen," *Journal of China Coal Society*, vol. 44, no. 12, pp. 3894–3902, 2019.

[32] G. B. Chen, Z. H. Qin, G. H. Zhang, T. Li, and J. K. Li, "Law of energy distribution before failure of a loaded coal-rock combined body," *Rock and Soil Mechanics*, vol. 41, no. 6, pp. 1–13, 2020.

[33] S. L. Song, X. S. Liu, Y. L. Tan, D. Y. Fan, Q. Ma, and H. L. Wang, "Study on failure modes and energy evolution of coal-rock combination under cyclic loading," *Shock and Vibration*, vol. 2020, Article ID 5731721, 16 pages, 2020.

[34] L. Biolzi, J. F. Labuz, and G. Muciaccia, "A problem of scaling in fracture of damaged rock," *International Journal of Rock Mechanics and Mining Sciences*, vol. 48, no. 3, pp. 451–457, 2011.

[35] A. Fakhimi and B. Hemami, "Axial splitting of rocks under uniaxial compression," *International Journal of Rock Mechanics and Mining Sciences*, vol. 79, no. 10, pp. 124–134, 2015.

[36] B. Mishra and D. Nie, "Experimental investigation of the effect of change in control modes on the post-failure behavior of coal and coal measures rock," *International Journal of Rock Mechanics and Mining Sciences*, vol. 60, pp. 363–369, 2013.

[37] Z. H. Chen, C. A. Tang, and R. Q. Huang, "A double rock sample model for rockbursts," *International Journal of Rock Mechanics and Mining Sciences*, vol. 34, no. 6, pp. 991–1000, 1997.

[38] H. Liu, J. Rutqvist, and J. G. Berryman, "On the relationship between stress and elastic strain for porous and fractured rock," *International Journal of Rock Mechanics and Mining Sciences*, vol. 46, no. 2, pp. 289–296, 2009.

[39] L. C. Li, H. H. Liu, and Y. Zhao, "Investigation on nonlinear elastic behavior of rocks based on a two-part Hooke's model," *Chinese Journal of Rock Mechanics and Engineering*, vol. 31, no. 10, pp. 2119–2126, 2012.

[40] Y. Xue, T. Teng, F. N. Dang, Z. Y. Ma, S. H. Wang, and H. B. Xue, "Productivity analysis of fractured wells in reservoir of hydrogen and carbon based on dual-porosity medium model," *International Journal of Hydrogem Energy*, vol. 45, no. 39, pp. 20240–20249, 2019.

[41] J. Liu, X. Liang, Y. Xue, K. Yao, and Y. Fu, "Numerical evaluation on multiphase flow and heat transfer during thermal stimulation enhanced shale gas recovery," *Applied Thermal Engineering*, vol. 178, article 115554, 2020.

[42] M. Li, J. X. Zhang, N. Zhou, and Y. L. Huang, "Effect of particle size on the energy evolution of crushed waste rock in coal mines," *Rock Mechanics and Rock Engineering*, vol. 50, no. 5, pp. 1347–1354, 2017.

[43] C. Y. Guo, X. F. Xian, X. H. Wu, W. J. Yao, and C. Y. Zhang, "The relationship among rock crushing energy, the Protodyakonov coefficient and rock strength," *Journal of Chongqing Jianzhu University*, vol. 30, no. 6, pp. 28–31, 2008.

[44] P. Coezkowski, J. Macoekewsli, and S. Bak, "Analysis of energy consumption of crushing processes – comparison of one-stage and two-stage processes," *Studia Geotechnica et Mechanica*, vol. 39, no. 2, pp. 17–24, 2017.

Hindawi
Geofluids
Volume 2021, Article ID 6657662, 13 pages
https://doi.org/10.1155/2021/6657662

Research Article

Permeability of Sand-Based Cemented Backfill under Different Stress Conditions: Effects of Confining and Axial Pressures

Cunli Zhu,[1,2] **Jixiong Zhang**,[1,2] **Nan Zhou**,[1,2] **Meng Li**,[1,2] **and Yaben Guo**[1,2]

[1]*School of Mines, China University of Mining and Technology, Xuzhou, 221116 Jiangsu, China*
[2]*State Key Laboratory of Coal Resources and Safe Mining, Xuzhou, 221116 Jiangsu, China*

Correspondence should be addressed to Nan Zhou; tb18020034b1@cumt.edu.cn

Received 13 December 2020; Revised 22 January 2021; Accepted 5 February 2021; Published 20 February 2021

Academic Editor: Guanglei Zhang

Sand-based cemented backfill (SBCB) mining technology is instrumental in utilizing coal resources buried under the water bodies. SBCB is exposed to the long-term action of mining-induced stresses in the goaf and groundwater permeating via microcracks along the rock strata. Studying the permeability evolution of SBCB under varying stress states is crucial for protecting coal and water resources below the aquifer. This study is focused on the influence law of different stress states on the SBCB permeability exposed to groundwater, which was tested under different axial and confining pressures using a laboratory seepage meter, particle size analyzer, scanning electron microscope (SEM), and X-ray diffractometer (XRD). Best-fitting quadratic polynomials linking the SBCB permeability with confining and axial pressures, respectively, were obtained via statistical processing of test results. The permeability gradually dropped within the elastic range as the confining and axial pressures increased. Moreover, an increase in the confining pressure caused a more dramatic reduction in the SBCB permeability than the axial pressure. Finally, the SBCB seepage mechanism under different stress states was revealed based on the particle size analysis, XRD patterns, and SEM microstructure. These findings are considered instrumental in substantiating safe mining of coal resources below the water bodies and above the confined groundwater.

1. Introduction

Most developed countries have limited oil and gas resources, which are imported or gradually replaced by green energy sources. China follows this trend and takes advantage of its abundant coal resources, in which share in the national primary energy consumption in 2020 exceeded 60% and is expected to remain high in the foreseeable future. In China, the occurrence conditions of coal resources are complex and highly variable. Most coal resources are located below the water bodies and above the confined groundwater [1–3]. Coal resources threatened by water account for over 27% of the total proven coal reserves. Waterproof coal pillars of large scale need to be left to mine these coal resources using the conventional methods [4, 5]. This implies considerable losses of the coal resources and, more importantly, the hidden danger of water burst of coal and rock masses and damage to the aquifer [6–8]. Figure 1(a) shows a transient fracture belt formed due to the rock strata's damage under the conventional mining conditions, resulting in the aquifer's damage.

Given this, some scholars have proposed backfilling and replacement to liberate the coal resources below the water bodies and above the confined groundwater [9–11]. Backfilling materials with high compaction and low permeability are usually needed to ensure the reliability of backfill mining. The sand-based cemented backfill (SBCB) method is a mining technology with small ecological and environmental damage [12–14]. SBCB has high compactness and good control against overlying strata deformation. This method has been extensively applied to the "three-under" coal resources in recent years [15–17]. Figure 1(b) shows the mine water's occurrence state via the SBCB method. The SBCB is made of fly ash, aeolian sand, and cement. Fly ash, as the product

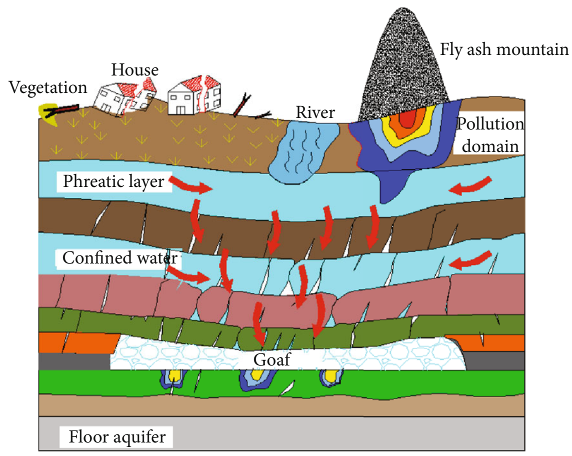

(a) Conventional mining method

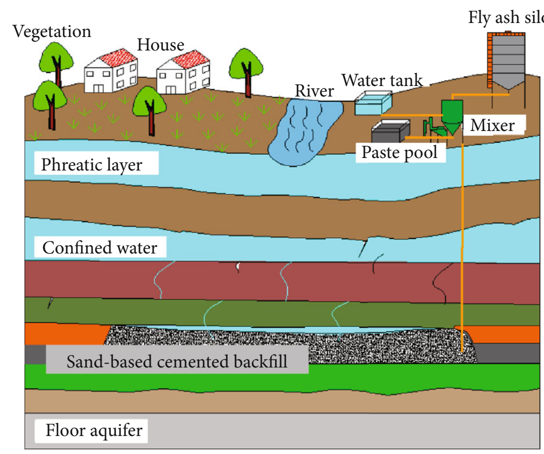

(b) Mining method with sand-based cemented backfill

Figure 1: Occurrence state of mine water under different mining methods.

of coal burning, may accumulate in large quantities on the ground surface. Making backfill aggregates with fly ash helps prevent its rainfall erosion, which otherwise carries many noxious elements underground, polluting the soil and groundwater resources [18–20]. Thus, the SBCB turns wastes into resources. Solid wastes, namely, fly ash and aeolian sand, are used for backfilling the goaf to liberate the coal resources, thereby increasing the economic benefit of the coal mine and protecting the environment [21, 22]. However, the aquifer's water may penetrate the roof strata and permeate, via the cracks, into the SBCB in the goaf. As a result, the SBCB is exposed to water [23]. As time progresses and the working face advances, water in the backfilled space invades the backfilling materials, deteriorating their strength. This phenomenon will affect the SBCB stability and control the aquifer and overlying strata deformation [24, 25]. In engineering practice, there is no assurance of whether the SBCB is eroded by groundwater and how the backfill changes permeability under different stress states.

Many studies have been conducted worldwide regarding SBCB permeability. Thus, Liu et al. [26] performed indoor triaxial seepage tests and analyzed the cracked backfill's permeability and strength features. They obtained the failure mode of the cracked sandstone backfill. Mamaghanian et al. [27] carried out a permeability study of a composite material similar to cemented backfill. They elaborated four different permeability models describing the observed patterns, which clarified the studied composite material's permeation performance under different pressures. Hou et al. [28] introduced a damage model and determined the damage evolution features of the prefabricated cracked backfill under the seepage-stress coupling effect. The above studies represent some of the preliminary explorations of the permeability of cemented backfills. However, most of them were concerned with the mechanical performance and model evaluations of the cemented backfill or provided the comparative analysis of permeability variation after modifying the cemented backfill. Very few of them examined evolutionary laws of the SBCB permeability.

Others have investigated the stress state effect on the permeability of concrete and rock strata. Santos and Barros [29] proposed a method for calculating the pressure imposed by the cemented backfill on the retaining wall under a high water level. They concluded that the ground pressure on the retaining wall was caused by water seepage in part of the soil bodies. Hou et al. [30] analyzed the seepage-stress coupling effect on the mechanical behavior, damage evolution law, and the microscopic structural response of cracked cemented gangue-fly ash backfill (CGFB). Barros and Santos [31] provided a numerical simulation of water permeation of soil bodies based on the boundary element method. They calculated the internal friction angle of soil and the inclined angle of the wall surface and plotted the variation diagram of ground pressure coefficient with seepage. Zhang et al. [32] analyzed the influence of confining pressure on permeability characteristics of granite and cracked slate. They clarified the effect of crack morphology on the permeation mechanism of different rock types. Zhou et al. [33] built a theoretical model quantifying the effects of crack-pore permeability coupling and hydromechanical coupling on soft rocks' damage behavior. The above studies of the stress state effect on permeability characteristics were mostly focused on the fractured confining rocks. However, few of them investigated SBCBs exposed to groundwater for a long period under different stress states.

This study is aimed at clarifying the stress state effect (which occurs at different burial depths) on the permeability of SBCB, which is mainly composed of aeolian sand, fly ash, cement, and water. Aeolian sand is used as aggregate, and fly ash and cement are used as binding materials. During hydration reaction, the smaller fly ash and cement particles fill the pores between the aeolian particles, enhancing the overall compaction and antiseepage performance of the SBCB. However, there are scarce data on the permeability variation pattern under different stress states for the SBCB long-term exposure to a moist goaf, which is depicted in Figure 1(b).


(a) Aeolian sand


(b) Fly ash


(c) Portland cement

Figure 2: Raw materials.

The current study explored the influence of axial pressure and confining pressure on the permeation performance of the SBCB exposed to the long-term action of groundwater. A seepage meter was used to measure the SBCB permeability under the above conditions, while the backfill microstructure was examined via an FEI Quanta 250 scanning electron microscope (SEM) and X-ray diffractometer (XRD). The performed single-factor analysis and the 2-factor 3-level orthogonal experiment revealed the influence of single factors and the combined effect of multiple factors on the SBCB permeation mechanism. The research findings are considered instrumental in substantiating the protection measures for mining under water bodies and ensuring green, safe mining of coal resources under the same type's geological conditions.

2. Materials and Methods

2.1. Test Materials. The raw materials used in the experiments were aeolian sand, fly ash, cement, and water. Aeolian sand and fly ash were collected from the superficial deposits in Yulin City, solid wastes generated by the Yulin Power Station (Shaanxi Province of China). The ordinary Portland cement was acquired from the Jinniu Coal Mine in Yulin City. Photos of raw materials for the experiment are presented in Figure 2, while their particle size distribution and XDR patterns are depicted in Figures 3 and 4, respectively.

2.1.1. Aeolian Sand. Aeolian sand usually serves as an aggregate of the cemented paste. Its particle size distribution and mineral composition play a decisive role in the SBCB's permeability. Figures 3(a) and 4(a) show the particle size distribution and the major mineral components of aeolian sand, respectively. As shown in Figure 3(a), the particle size of aeolian sand ranged between 168 and 571 μm, with an average value of 346.49 μm. The particle size of aeolian sand was small and evenly distributed. When used as an aggregate, the aeolian sand was conducive to enhancing the SBCB's compaction. According to the XRD patterns of the aeolian sand in Figure 4(a), the aeolian sand contained a large amount of quartz, feldspar, and calcite. Quartz existing in large quantities enhanced the SBCB's stability, improving the backfill's compressive resistance and optimizing its bearing capacity.

2.1.2. Fly Ash. Fly ash is usually applied as the binding material in the sand-based cemented paste. Figure 3(b) shows the particle size distribution of fly ash, ranging between 19 and 126 μm, with an average value of 64.683 μm. Therefore, the fly ash is conducive to the SBCB delivery. As indicated by the XRD patterns in Figure 4(b), fly ash contained many quartz and mullite but little muscovite. Chemically stable quartz improved the stability of the SBCB exposed to groundwater.

2.1.3. Cement. Ordinary Portland cement, which is generally a binding material, undergoes hydration reaction in the cemented paste. It is an important raw material for improving the strength and stability of the SBCB. Figure 3(c) shows the particle size distribution of cement, ranging between 6.9 and 99.3 μm, with an average value of 44.846 μm. Smaller particles usually have a more extensive contact area in the SBCB, thereby ensuring a complete hydration reaction. Figure 4(c) shows the XRD pattern of cement, which was rich in calcium silicate ($3CaO{\bullet}SiO_2$) and calcium carbonate and where dicalcium silicate was most abundant. Hydration of these minerals would significantly improve the SBCB strength.

2.2. Test Method

2.2.1. Seepage System. A seepage system of the cemented backfill was designed and constructed by the authors to analyze the stress state effect on the SBCB's permeability. This system consisted of the axial loading subsystem, seepage meter, confining pressure loading subsystem, hydraulic loading subsystem, and data monitoring subsystem. Figure 5 presents a schematic of the seepage system.

(1) Axial Loading System. A WAW-1000D series servohydraulic testing machine incorporated into the axial loading system was used to generate different stresses in the SBCB

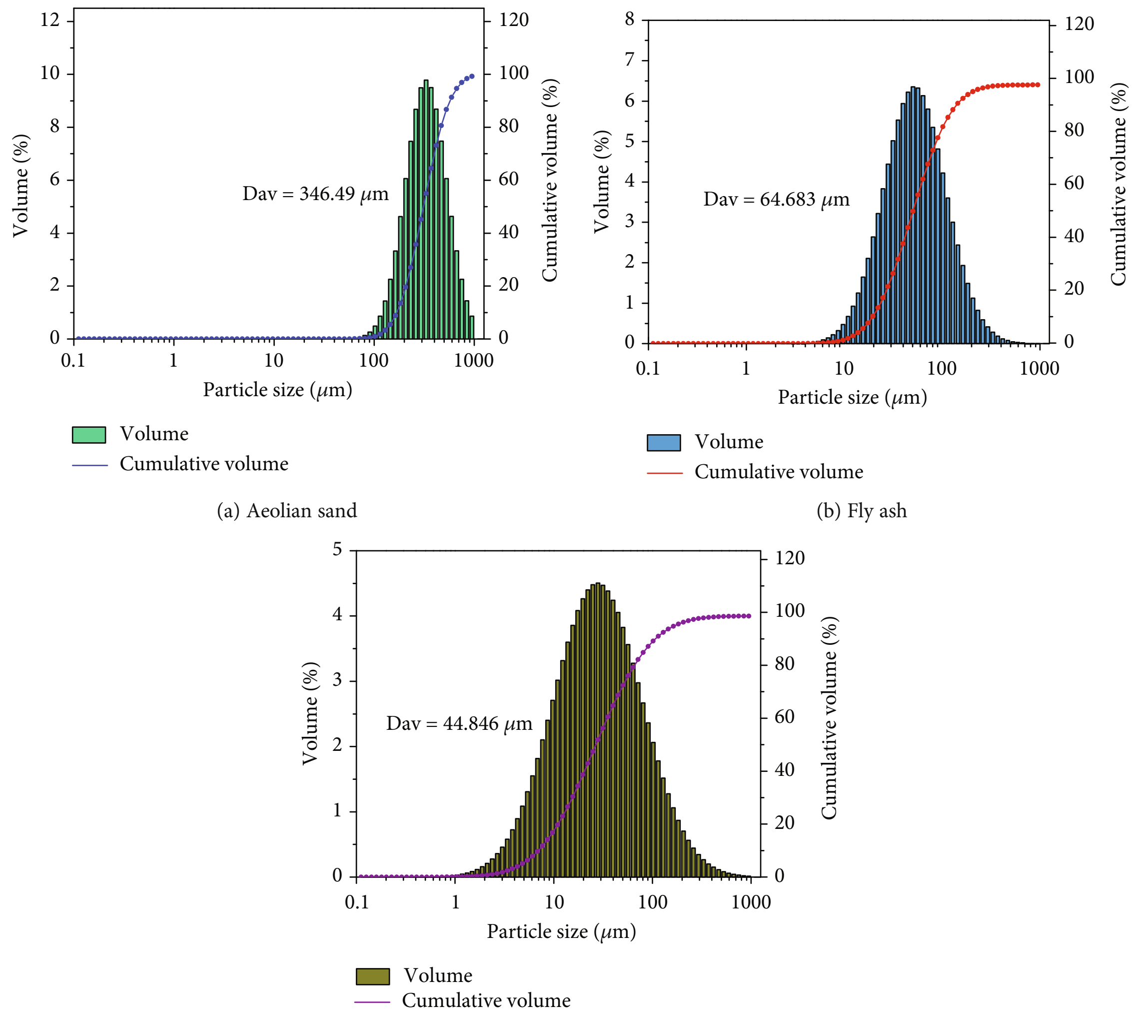

(a) Aeolian sand

(b) Fly ash

(c) Portland cement

FIGURE 3: Particle size distributions.

specimens. The maximum stroke of the servohydraulic testing machine was 250 mm, the loading rate was 0.2 mm/min, the display precision grade was 0.5, and the measuring range was 0~1000 kN.

(2) Hydraulic Loading System. The hydraulic loading system applied a seepage pressure to the SBCB. An ultra-high-pressure hydraulic pump was used to apply hydraulic loading. The hydraulic loading system consisted of a water tank, an energy accumulator, a wobble pump for pressure testing, a stop valve, a pressure gauge, and a pressure transmitter.

(3) Confining Pressure Loading System. The confining pressure loading system applied a constant confining pressure on the SBCB. This system ensured the water seepage into SBCB specimens and guaranteed the test reliability. A YE2-100L2-4 three-phase asynchronous motor drove the confining pressure loading system. The hydraulic oil was pumped into the seepage meter to apply a constant confining pressure to the specimens. The power was 3 kW, the frequency was 50 Hz, and the rotational speed was 1420 r/min, which satisfied the test requirements.

(4) Seepage Meter. The seepage meter was the core part of the entire experiment. The seepage meter was composed of the base, tank body, cap, upper press head, lower press head, and porous plate. The entire seepage process of the backfill specimens mainly proceeded in the seepage meter. Figure 6 shows photos of the seepage meter and its components.

(5) Data Collection and Monitoring System. During the seepage system's experimental process, the data were collected and recorded by combining the pressure transmitter with the paperless recorder. The paperless recorder monitored water pressure variations in the water tank over time. The permeability k_D of the backfill specimens was calculated as follows:

$$k_D = \frac{c_f B H \mu}{2 t_f A} \ln \frac{J_0}{J} = \frac{c_f B H \mu}{2 t_f A} \ln \left(\frac{p_{10} - p_{20}}{p_{1f} - p_{2f}} \right), \qquad (1)$$

where P_{10} and P_{20} are the initial pressures; P_{1f} and P_{2f} are pressures at time t; J is the pressure gradient at time t; c_f is the compressibility factor of the liquid; B is the water tank

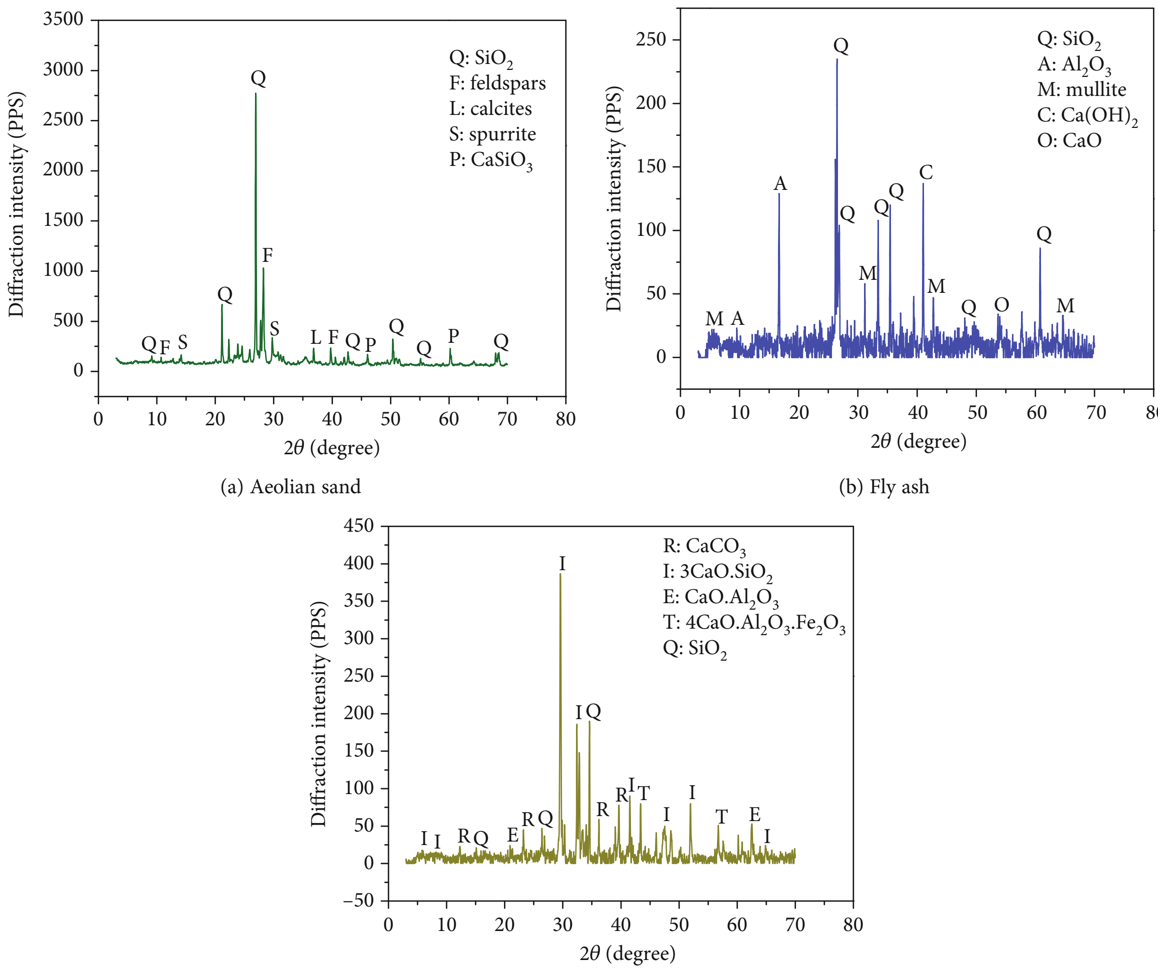

(a) Aeolian sand

(b) Fly ash

(c) Portland cement

FIGURE 4: XRD patterns of raw materials.

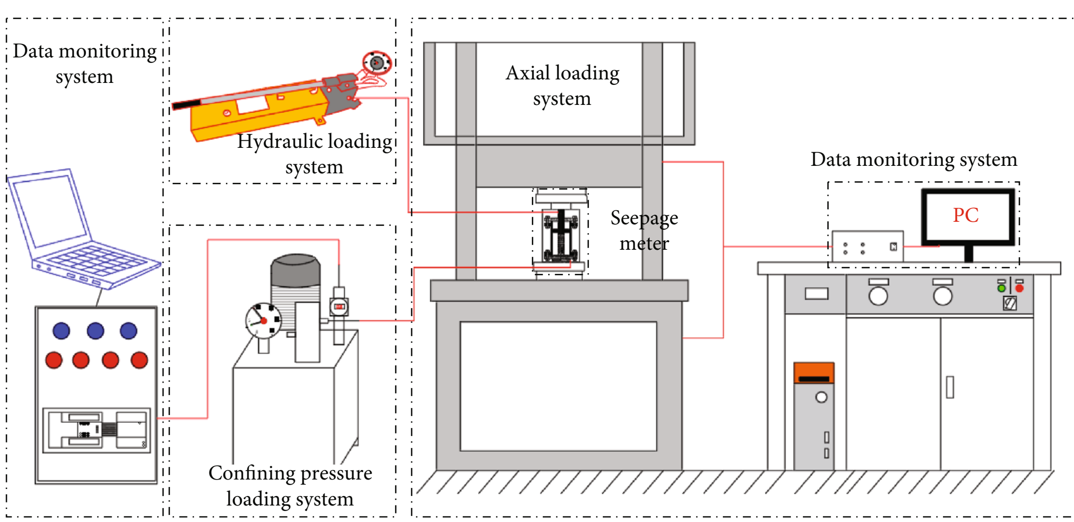

FIGURE 5: Schematic of the seepage system.

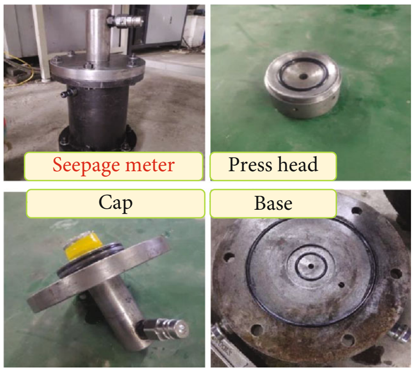

Figure 6: Photos of the seepage meter and its components.

volume; H is the specimen's height; μ is the dynamic viscosity of the seeping liquid; t is the time needed for the experiment; and A is the specimen cross-sectional area.

2.2.2. Microstructural Analysis. An FEI Quanta 250 SEM introduced by the Advanced Analysis and Computation Center of the China University of Mining and Technology was used for the microstructural analysis, as shown in Figure 7(a) An X-ray diffractometer was used to analyze the mineral composition of the raw materials. As shown in Figure 7(b), the X-ray diffractometer was composed of a sealed-tube X-ray source and an X-ray high-voltage generator for precise measuring of specimens' mineral composition.

2.2.3. Test Procedures. The test procedures included the following: determination of physical and chemical properties of raw materials, determination of the mix ratio of each component of the SBCB, preparation and pretreatment of specimens, and the seepage test of pretreated specimens using a WAW-1000D series servohydraulic testing machine. The effect of different stress states on the SBCB's permeability was analyzed based on the experimental results. The SBCB microstructure was observed via the SEM. The experimental workflow is depicted in Figure 8.

As seen in Figure 8, the particle size, chemical composition, and microstructure of the raw materials were first analyzed using the particle size analyzer, XRD, and SEM, respectively. After testing, the cemented paste was prepared by mixing fly ash, aeolian sand, cement, and water at a certain mix ratio according to the GB/T50080-2016 standard for the test method on the performance of ordinary fresh concrete. The paste was poured into a mold with a diameter of 50 mm and a height of 100 mm. The mold was gently shaken for 10-15 s to remove air bubbles from the paste. The paste was left to stand for 8 h and then removed from the mold. The specimen was then cured in a curing box for 28 d under a humidity of 95% and a temperature of $20 \pm 2^{\circ}$C.

According to the GB50218-94 standard for the test method of engineering rock masses, the cured specimens were prepared into standard specimens. A seepage experiment of SBCB was performed under different stress states according to the GB/T23561.12-2010 method for determining physicomechanical properties. After the seepage experiment, the specimens were dried for 12 h in a drying oven at 40°C to prepare them for microstructural analysis. The dried specimens were cut into a length of 10 mm, a width of 10 mm, and a height of 5 mm. Specimens were gold-sprayed to improve the electrical conductivity and hence facilitate the SEM observation. Finally, the effect of different stress states on the SBCB permeability under different stress states was analyzed based on the experimental results.

2.3. Experimental Scheme

2.3.1. Specimen Pretreatment. The specimens were cured for 28 d and then taken out. Each specimen was truncated to a height of 100 mm with a cutting machine. Next, the specimen's two end surfaces were ground flat with a polishing machine to ensure a flatness below 0.5 mm. The parallelism between the two end surfaces was below 0.02 mm. The specimens' machining precision was measured and satisfied the GB 50218-1994 standard for engineering classification of rock masses. The machined specimens were then soaked into the water to saturate them before the seepage test.

2.3.2. Variation Laws of SBCB Permeability under Different Confining Pressures. The aeolian sand mass was a fixed value, and the doping amount of other ingredients was expressed as their mass ratio to that of the aeolian sand. The raw materials' mix ratios for the SBCB preparation were as follows: the fly ash with a mass fraction of 78% accounted for 70%, and the cement for 15%. Secondly, after the dry material was evenly stirred, water was added slowly until its amount required by the mixing ratio was reached. The standard specimens of SBCB were prepared under this mixed ratio [32]. The axial pressure was fixed at 2.5 MPa, and different levels of confining pressure were set up at 1, 2, 3, and 4 MPa [34]. The S1, S5, S6, and S7 tests described in Table 1 were carried out. The variation rules of SBCB permeability under different confining pressures and constant axial pressures were identified.

2.3.3. Variation Rules of Permeability of SBCB under Different Axial Pressures. For standard specimens, the confining pressure was fixed at 3 MPa, while different axial pressures were set up at 2.5, 3.5, 4.5, and 5.5 MPa [34]. Tests S1, S2, S3, and S4 described in Table 1 were carried out. The variation rules of SBCB permeability under different axial pressures and constant confining pressures.

The 2-factor 3-level orthogonal experiment was designed, as shown in Table 1, to study the effect of different axial and confining pressures on the SBCB's permeability.

3. Experimental Results

3.1. Influence Rules of Confining Pressure on the SBCB Permeability. The constant axial pressure of 2.5 MPa was applied, while varying the confining pressures (1, 2, 3, and 4 MPa) to study the influence of a single factor on the SBCB permeability. Each group contained three specimens, and the average permeability value was taken of the three specimens. Table 2 shows the results of the permeability tests.

Figure 9(a) shows the best-fitting curve of the SBCB permeability under four different confining pressures. The

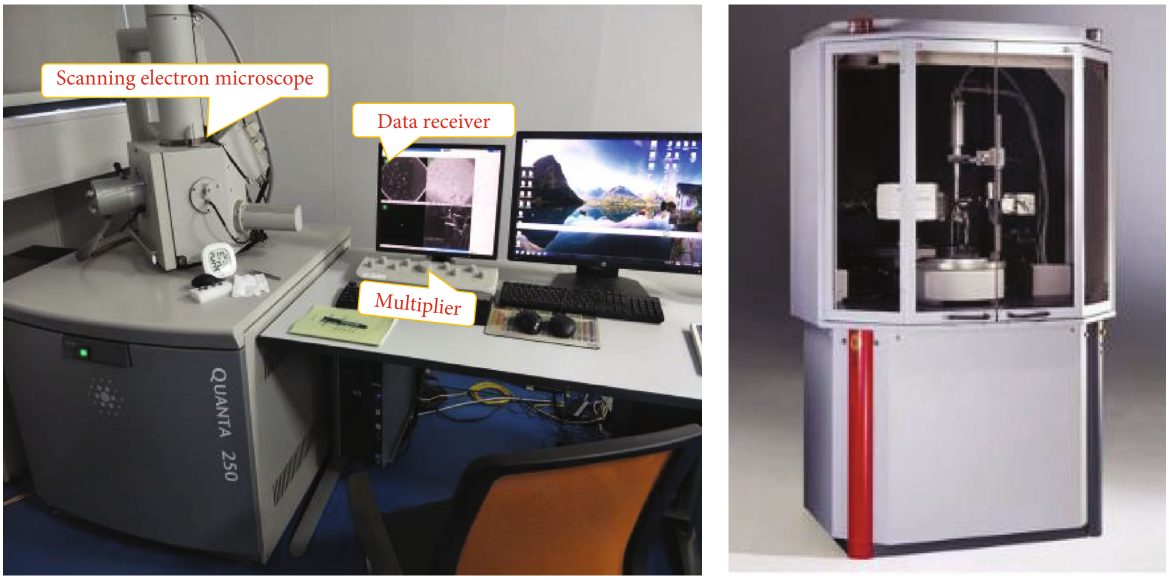

(a) Scanning electron microscope (SEM)

(b) X ray diffractometer (XRD)

Figure 7: Equipment used for microstructural analysis.

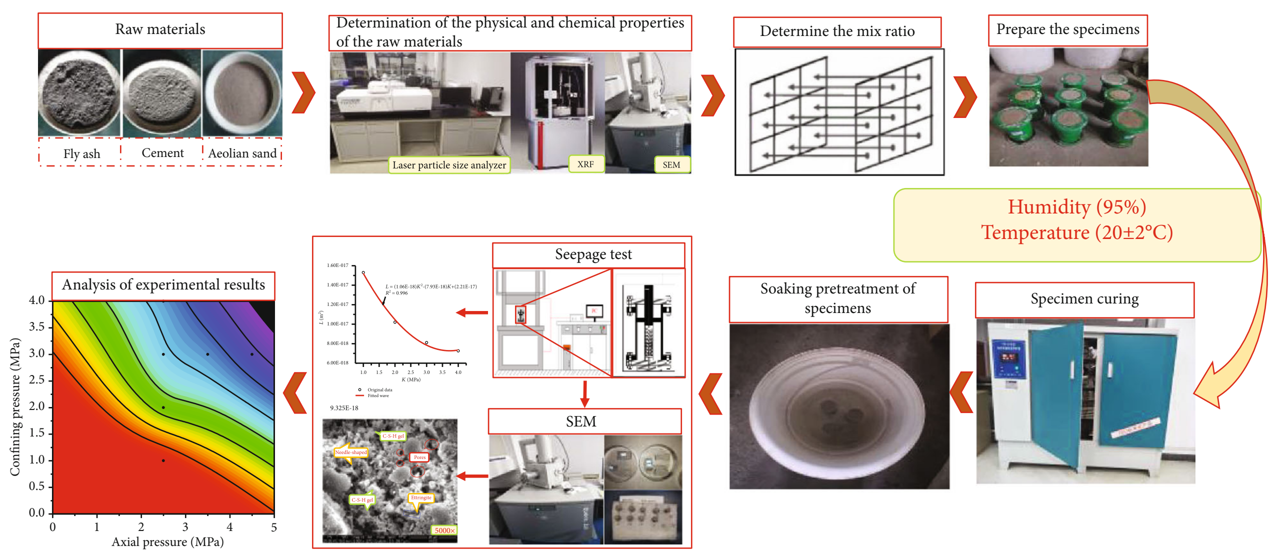

Figure 8: Experimental workflow.

Table 1: Orthogonal experiment design for the SBCB permeability under different stress states.

Experiment No.	Axial pressure (MPa)	Confining pressure (MPa)
S1	2.5	3.0
S2	3.5	3.0
S3	4.5	3.0
S4	5.5	3.0
S5	2.5	1.0
S6	2.5	2.0
S7	2.5	4.0

permeability was related to the confining pressure via a quadratic polynomial, in which equation and correlation coefficient $R^2 = 0.996$ are presented in Figure 9(a). As the confining pressure increased, the permeability decreased at a progressively slowing rate. As the confining pressure grew from 1 to 4 MPa, the permeability dropped from 1.53×10^{-17} to $7.26 \times 10^{-18}\,m^2$, i.e., by 52.5%. This was due to initially small confining pressure in the backfill, which still had pores to form seepage channels, leading to a higher permeability. But as the confining pressure increased, the pores inside the backfill were closed under compaction. The seepage channels were closed as well. Therefore, the permeability gradually decreased at a progressively slowing rate.

Table 2: Results of SBCB permeability tests under different confining pressures.

Axial pressure (MPa)	Confining pressure (MPa)	Permeability K_1 (m^2)	Permeability K_2 (m^2)	Permeability K_3 (m^2)	Average permeability $\bar{K}$
2.5	1.0	1.47×10^{-17}	1.65×10^{-17}	1.22×10^{-17}	1.53×10^{-17}
2.5	2.0	8.90×10^{-18}	1.29×10^{-17}	9.90×10^{-18}	1.02×10^{-17}
2.5	3.0	8.57×10^{-18}	5.27×10^{-18}	1.05×10^{-17}	8.11×10^{-18}
2.5	4.0	7.12×10^{-18}	6.92×10^{-18}	7.75×10^{-18}	7.26×10^{-18}

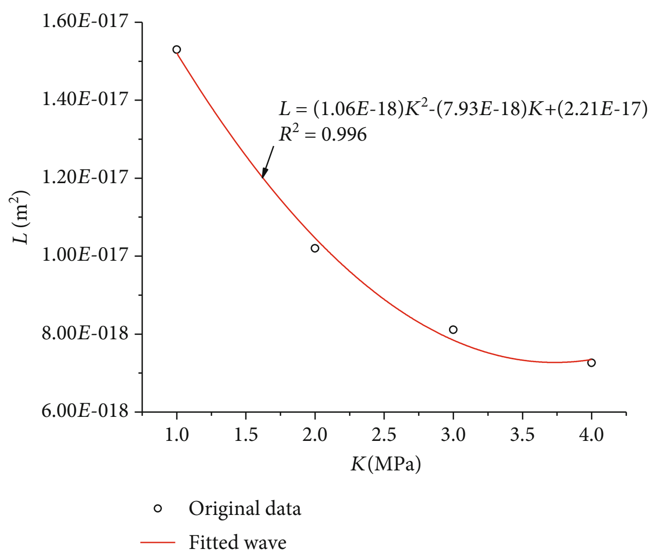

(a) Confining pressure

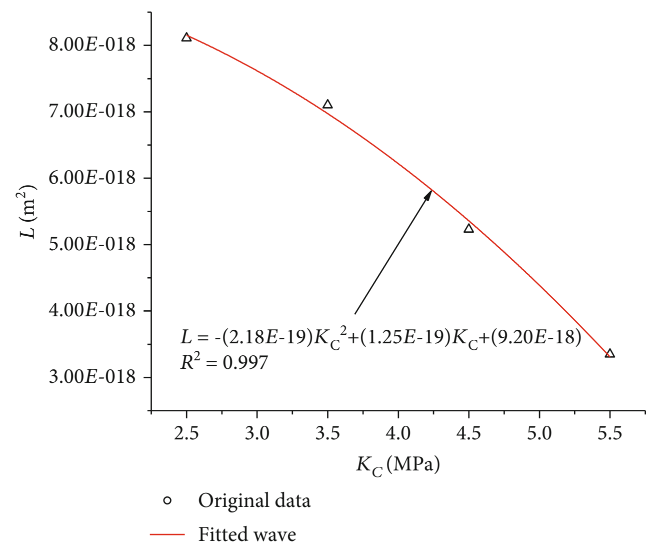

(b) Axial pressure

Figure 9: Permeability of SBCB under different stress states.

Table 3: Results of permeability testing of the SBCB under different axial pressures.

Axial pressure (MPa)	Confining pressure (MPa)	Permeability K_1 (m^2)	Permeability K_2 (m^2)	Permeability K_3 (m^2)	Average permeability $\bar{K}$
2.5	3.0	8.57×10^{-18}	5.27×10^{-18}	1.05×10^{-17}	8.11×10^{-18}
3.5	3.0	7.69×10^{-18}	6.67×10^{-18}	6.94×10^{-18}	7.10×10^{-18}
4.5	3.0	3.94×10^{-18}	7.52×10^{-18}	4.23×10^{-18}	5.23×10^{-18}
5.5	3.0	2.88×10^{-18}	2.84×10^{-18}	4.32×10^{-18}	3.35×10^{-18}

3.2. Influence Rules of Axial Pressure on the SBCB Permeability. The axial pressure effect on the permeability of the backfill was experimentally determined. During the experiment, a constant confining pressure of 3 MPa was applied, while the axial pressure was variable (2.5, 3.5, 4.5, and 5.5 MPa). Table 3 shows the SBCB permeability under different axial pressures. Figure 9(b) presents the best-fitting curve of SBCB permeability under different axial pressures. The permeability was related to the axial pressure via a quadratic polynomial, in which equation and correlation coefficient $R^2 = 0.997$ are given in Figure 9(b). As the axial pressure increased, the reduction amplitude of the permeability gradually grew. As the axial pressure increased from 2.5 to 5.5 MPa, the permeability dropped from 8.11×10^{-18} to 3.35×10^{-18} m^2, i.e., by 58.7%. This was because as the axial pressure increased, the pores inside the backfill were closed under compaction, resulting in a gradual decrease in permeability. Besides, the axial pressure direction was perpendicular to the seepage direction. As the axial pressure increased, the backfill specimens were compressed along the axial direction, thereby blocking the passage of water flow and accelerating the permeability reduction.

Under the action of confining pressure, the backfill was subjected to a transverse extruding force. The fractures' resulting compaction was slightly smaller than that exerted by the axial pressure on the backfill. Moreover, the confining pressure direction was parallel with the seepage direction, while the axial pressure direction was perpendicular to the

Table 4: Results of the orthogonal experiments on permeability.

Experiment No.	Axial pressure (MPa)	Confining pressure (MPa)	Permeability (m^2)
S1	2.5	3.0	8.11×10^{-18}
S2	3.5	3.0	7.10×10^{-18}
S3	4.5	3.0	5.23×10^{-18}
S4	5.5	3.0	3.35×10^{-18}
S5	2.5	1.0	1.53×10^{-17}
S6	2.5	2.0	1.02×10^{-17}
S7	2.5	4.0	7.26×10^{-18}

seepage direction. Thus, under different confining pressures, the fitted curve slope at the later stage was lower than the fitted curve's corresponding slope under different axial pressures.

3.3. Analysis of the Combined Effect of Multiple Factors. As shown by the above single-factor influence analysis, permeability's influencing factors mainly included confining pressure and axial pressure. In the goaf, the SBCB underwent a three-dimensional stress state. The permeability was influenced by both the confining pressure and axial pressure. An orthogonal experiment design was adopted to analyze multiple factors' combined effect on permeability to intuitively and accurately predict permeability's influence rules. The confining and axial pressures were taken as two influencing factors, each being allocated four levels. The orthogonal experiment design details and experimental results are listed in Table 4.

The range reflects the influence degree of different levels of various factors on the indicator of concern. The results of the orthogonal experiment in Table 4 were analyzed under each level of different factors. The results of range analysis of permeability under the combined action of different factors are summarized in Table 5.

It can be seen from Table 5 that the range of confining pressure was larger than that of the axial pressure. Different factors had a varying influence on the permeability of SBCB exposed to groundwater in the goaf. The confining pressure influenced the permeability of the backfill more significantly. The slope of the fitted curve of permeability in Figure 9(a) was considerably smaller than that of Figure 9(b). That is to say, the fitted curves of permeability under different stress states corresponded to the range analysis.

3.4. Influence Rules of Confining Pressure/Axial Pressure. The effect of different stress states (i.e., confining and axial pressures) on the backfill's permeability was analyzed in detail. The nephograms of permeability under different confining pressures/axial pressures were plotted based on the range analysis following the orthogonal experiment, as shown in Figure 10.

As indicated by the permeability isolines in Figure 10(a), the permeability was related to the confining/axial pressure in a roughly parabolic manner. The parabola's peak occurred under greater confining pressure, indicating that the confining pressure significantly influenced the backfill's permeability. According to Figure 10(b), with the confining pressure fixed at 0.5 MPa, the backfill's permeability varied less significantly as the axial pressure increased. When the confining pressure was increased to 2 MPa and then to 3 MPa, the permeability decreased considerably with the increasing axial pressure. This was because the backfill was subjected to larger axial and confining pressures simultaneously; both stresses acted on the backfill's contact surface within the range of elastic deformation. As a result, the backfill was densely compacted inside, leading to a more significant reduction in its permeability.

Table 5: Permeability range analysis.

Level	Axial pressure ($\times 10^{-18}$ Pa)	Confining pressure ($\times 10^{-18}$ Pa)
Level 1	10.2	15.3
Level 2	7.10	10.2
Level 3	5.23	5.95
Level 4	3.35	7.26
Range	6.85	9.35

4. Discussion

4.1. Analysis of the Seepage Mechanism of the SBCB under Different Confining Pressures. The influence of stress states on the SBCB permeability on the microscopic level was analyzed by preparing the SEM specimens after the seepage experiment under different stress states. The specimens' images under different stress states were magnified by the same factor, and their microstructure was observed via SEM.

Figure 11 shows the SEM patterns of the SBCB under different confining pressures. The particle size of the aeolian sand was the largest and varied between 168 and 571 μm. By contrast, fly ash and cement's particle sizes were smaller, with average values of 64.683 and 44.846 μm, respectively. Therefore, the fly ash and cement particles effectively filled the pores between the aeolian sand particles as aggregates. This structure offered greater compactness and smaller permeability of the backfill.

In Figure 11, the backfill specimens were all magnified by a factor of 5000 consistently. Under the confining pressure of 1 MPa (Figure 11(a)), many needle-/rod-like crystals appeared in the backfill. According to the XRD patterns, the needle-like crystals represented ettringite, which was relatively stable and contributed to the backfill's overall stability. After the hydration reaction, the fly ash was dispersed to form a gel, aggregated with the ettringite gel. The overall structure was loose, with many pores. Therefore, when confining pressure was 1 MPa at the early stage, the backfill's permeability was higher.

As the confining pressure increased to 3 and 4 MPa, as shown in Figures 11(c) and 11(d), a large amount of flocculated hydration product C-S-H was formed within the backfill. As the confining pressure continued to increase, the flocculated hydration product C-S-H overlapped in the middle of the backfill, increasing its compactness. Meanwhile, the

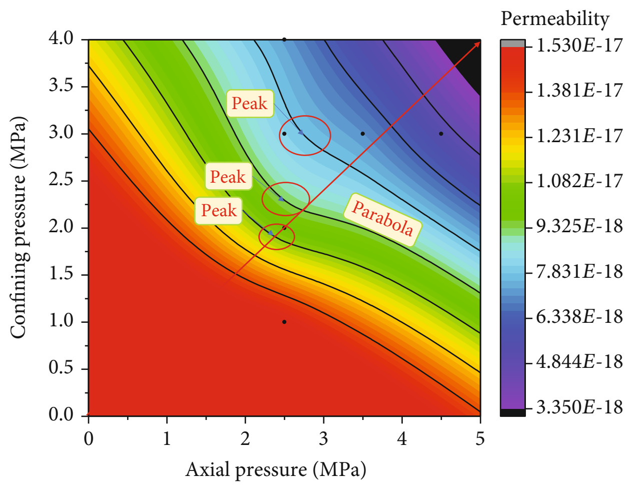

(a) Peak value of the parabola

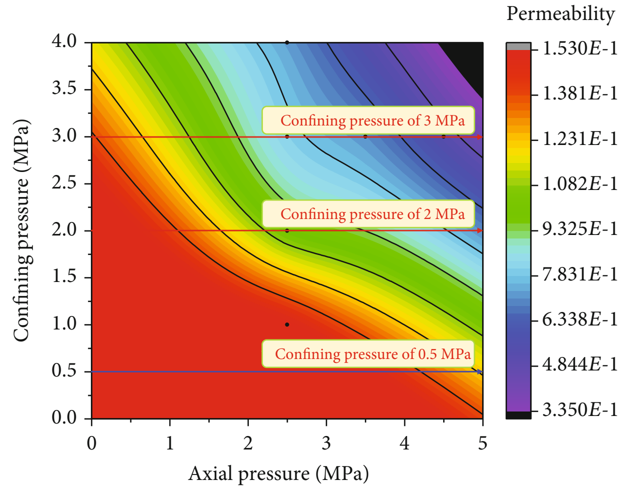

(b) Influence gradient

Figure 10: Influence of confining pressure/axial pressure on the SBCB permeability.

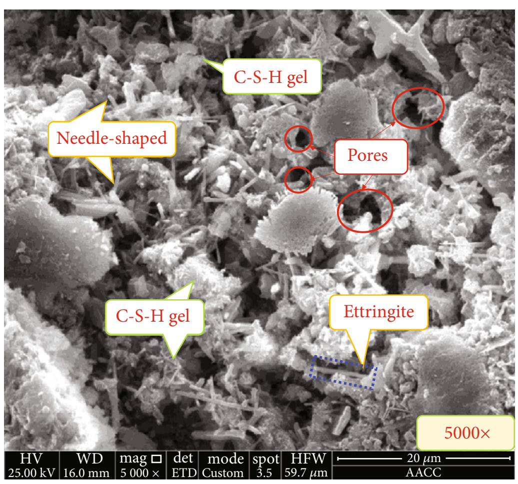

(a) 1 MPa

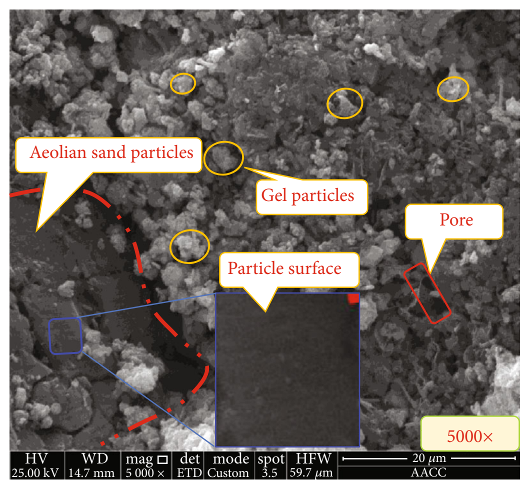

(b) 2 MPa

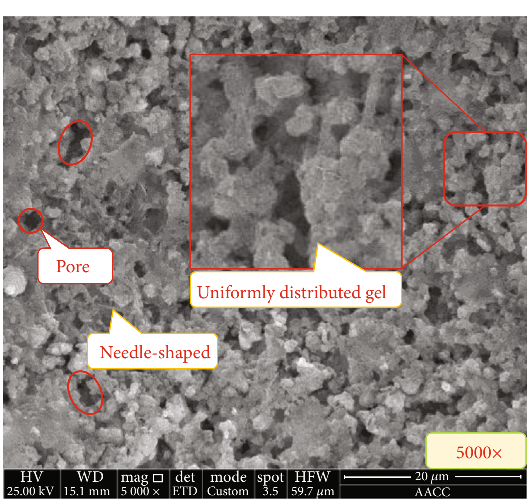

(c) 3 MPa

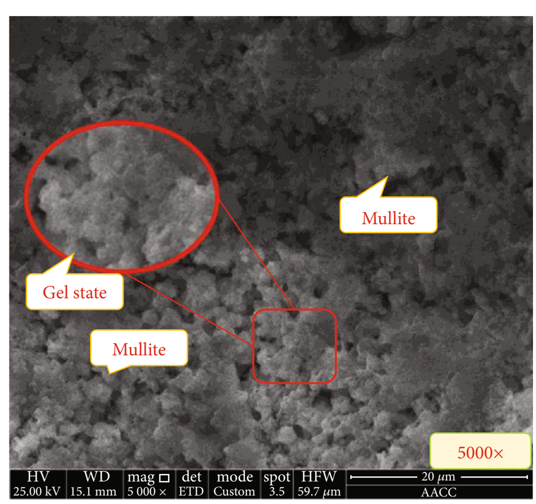

(d) 4 MPa

Figure 11: SEM patterns of SBCB under different confining pressures.

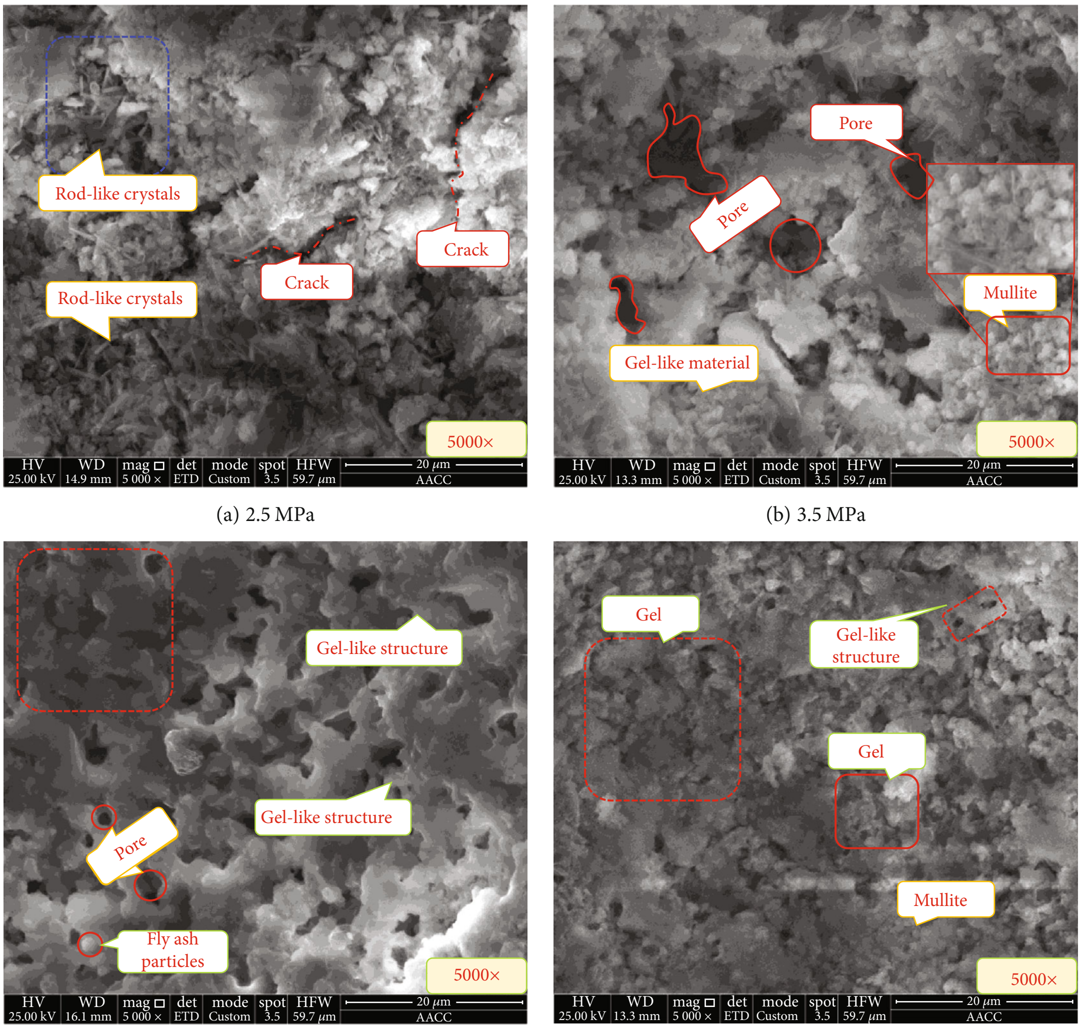

(a) 2.5 MPa

(b) 3.5 MPa

(c) 4.5 MPa

(d) 5.5 MPa

Figure 12: SEM patterns of the SBCB under different axial pressures.

number of needle-like crystals was considerably reduced. Therefore, the confining pressure had a more significant influence on the backfill's permeability.

4.2. Analysis of the Seepage Mechanism of the SBCB under Different Axial Pressures. The influence rules of axial pressure on the backfill's permeability were studied by comparing data for different confining pressures. Figure 12 shows the seepage mechanism of the SBCB under different axial pressures. The direction of axial pressure was parallel with the backfill's seepage direction, which was different from the case of the confining pressure. The direction of the axial pressure was perpendicular to the seepage direction of the backfill. This major distinction had a direct bearing on the seepage rules.

According to Figure 12, at the axial pressure of 2.5 MPa, more cracks appeared in the backfill, which was the major distinction from the confining pressure action. Moreover, a small amount of rod-like crystals, which were hydration products, appeared on the backfill particles' surface. The appearance of more cracks was mainly due to the loose structure within the backfill, which further led to a higher permeability at the early stage. As the axial pressure, which was perpendicular to the seepage direction, increased, the flocculated gel, as the fly ash's hydration product, was compressed vertically. The gel filled the pores between the backfill particles, reducing the porosity. Moreover, according to the XRD patterns shown in Figure 4, the aeolian sand contained many stable mineral components, such as quartz. Within the backfill, due to cement hydration and hardening at the early stage, fly ash was not involved in the hydration reaction and served as the filler between the cement particles, thus increasing the backfill's compactness.

Taken together, after the SBCB took shape, $Ca(OH)_2$ precipitated from cement due to hydration and was absorbed by the surfaces of fly ash particles. Meantime, the pozzolanic reaction proceeded as follows:

$$\begin{gathered} x\mathrm{Ca(OH)_2} + \mathrm{SiO_2} + n\mathrm{H_2O} \longrightarrow x\mathrm{CaO}\cdot\mathrm{SiO_2}\cdot(n+x)\mathrm{H_2O} \\ y\mathrm{Ca(OH)_2} + \mathrm{Al_2O_3} + n\mathrm{H_2O} \longrightarrow yx\mathrm{CaO}\cdot\mathrm{Al_2O_3}\cdot(n+y)\mathrm{H_2O} \end{gathered} \tag{2}$$

Fly ash and aeolian sand particles, acting as carriers, formed a flocculated gel by hydration reaction on the aeolian sand's particle surface. The flocculated gel tightly enveloped the aeolian sand particles to form a whole bulk, reducing the SBCB permeability.

5. Conclusions

A seepage system simulating the seepage mechanism of the SBCB was designed and tested. SBCB specimens were prepared with a fixed mix ratio. The backfill specimens' permeability and microstructure were studied under different stress states using a WAW-1000D series servohydraulic testing machine and SEM, respectively. The results obtained made it possible to draw the following conclusions:

(1) A particle size analyzer was employed to plot the normal distribution of the raw materials' particle size. The particle size of the aeolian sand ranged between 168 and 571 μm, with an average of 346.49 μm; that of the fly ash ranged from 19 to 126 μm, with an average of 64.683 μm; and that of the cement was between 6.9 and 99.3 μm, with an average of 44.846 μm. The XRD analysis revealed each raw material's mineral composition as the basis for subsequent macroscopic and microscopic studies of the backfill

(2) Permeability of the backfill specimens was studied under different confining pressures. The permeability was related to the confining pressure by a quadratic polynomial dependence. As the confining pressure increased, the permeability of the backfill gradually decreased. The confining pressure had a more significant influence on the permeability than the axial pressure. As the confining pressure increased from 1 to 4 MPa, the permeability dropped from 1.53×10^{-17} to 7.26×10^{-18} m^2, i.e., by 52.5%

(3) Permeability of backfill specimens was studied under different axial pressures. The permeability was related to the axial pressure by a quadratic polynomial dependence. As the axial pressure increased, the permeability decreased, at a progressively increasing rate. As the axial pressure increased from 2.5 to 5.5 MPa, the permeability decreased from 8.11×10^{-18} to 7.26×10^{-18} m^2, i.e., by 58.7%. The range of permeability under different confining and axial pressures was also analyzed. It was found that the confining pressure had a greater impact on the permeability of the backfill than the axial pressure

(4) The SBCB seepage mechanism under different stress states was investigated by SEM analysis. At small stresses, the backfill had a relatively loose structure and hence a higher permeability. As the stress increased, the flocculated gel C-S-H generated by the fly ash hydration at the later stage filled the pores between the aeolian sand particles, thus enhancing the backfill's compactness. The results of particle size analysis and XRD patterns confirmed that the confining pressure had a greater impact on the SBCB's permeability than the axial one

Data Availability

The latest data used to support the findings of this study are included within the article.

Conflicts of Interest

The authors declare that they have no conflicts of interest.

Acknowledgments

This study was financially supported by the National Key R&D Program of China (grant number 2018YFC0604706), the National Natural Science Foundation of China (grant number 51874287), and the Independent Research Project of State Key Laboratory of Coal Resources and Safe Mining, CUMT (grant number SKLCRSM19X006).

References

[1] D. Y. Zhang, W. H. Sui, and J. W. Liu, "Overburden failure associated with mining coal seams in close proximity in ascending and descending sequences under a large water body," *Mine Water and the Environment*, vol. 37, no. 2, pp. 322–335, 2018.

[2] D. B. Wang, X. B. Bian, H. Qin, D. L. Sun, and B. Yu, "Experimental investigation of mechanical properties and failure behavior of fluid-saturated hot dry rocks," *Natural Resources Research*, vol. 30, no. 1, pp. 289–305, 2021.

[3] L. L. Xiao, Q. Wu, C. Niu et al., "Application of a new evaluation method for floor water inrush risk from the Ordovician fissure confined aquifer in Xiayukou coal mine, Shanxi, China," *Carbonate Evaporite*, vol. 35, no. 3, article 97, 2020.

[4] M. L. Hu, W. L. Zhao, Z. Lu, J. X. Ren, and Y. P. Miao, "Research on the reasonable width of the waterproof coal pillar during the mining of a shallow coal seam located close to a reservoir," *Advances in Civil Engineering*, vol. 2019, Article ID 3532784, 14 pages, 2019.

[5] D. Ma, J. J. Wang, and Z. H. Li, "Effect of particle erosion on mining-induced water inrush hazard of karst collapse pillar," *Environemental Science and Pollution Research*, vol. 26, no. 19, pp. 19719–19728, 2019.

[6] L. Q. Ma, X. Du, F. Wang, and J. M. Liang, "Water-preserved mining technology for shallow buried coal seam in ecologically-vulnerable coal field: a case study in the Shendong coal field of China," *Disaster Advances*, vol. 6, pp. 268–278, 2013.

[7] Y. Suo, Z. Chen, S. S. Rahman, and H. Song, "Experimental and numerical investigation of the effect of bedding layer orientation on fracture toughness of shale rocks," *Rock Mechanics and Rock Engineering*, vol. 53, no. 8, pp. 3625–3635, 2020.

[8] D. B. Wang, Y. C. Dong, D. L. Sun, and B. Yu, "A three-dimensional numerical study of hydraulic fracturing with degradable diverting materials via CZM-based FEM," *Engineering Fracture Mechanics*, vol. 237, article 107251, 2020.

[9] W. B. Sun, Y. Wang, H. F. Qiu, and Z. W. Ding, "Numerical simulation study of strip filling for water-preserved coal

mining," *Environemental Science and Pollution Research*, vol. 27, no. 12, pp. 12899–12907, 2019.

[10] Q. Sun, J. X. Zhang, N. Zhou, and W. Y. Qi, "Roadway backfill coal mining to preserve surface water in Western China," *Mine Water and the Environment*, vol. 37, no. 2, pp. 366–375, 2018.

[11] X. J. Deng, J. X. Zhang, N. Zhou, B. de Wit, and C. T. Wang, "Upward slicing longwall-roadway cemented backfilling technology for mining an extra-thick coal seam located under aquifers: a case study," *Environment and Earth Science*, vol. 76, no. 23, p. 789, 2017.

[12] N. Zhou, J. X. Zhang, S. Y. Ouyang, X. J. Deng, C. W. Dong, and E. B. Du, "Feasibility study and performance optimization of sand-based cemented paste backfill materials," *Journal of Cleaner Production*, vol. 259, p. 120798, 2020.

[13] X. P. Shao, L. Wang, X. Li et al., "Study on rheological and mechanical properties of aeolian sand-fly ash-based filling slurry," *Energies*, vol. 13, no. 5, p. 1266, 2020.

[14] J. Li, S. Q. Zhang, Q. Wang et al., "Feasibility of using fly ash–slag-based binder for mine backfilling and its associated leaching risks," *Journal of Hazardous Materials*, vol. 400, p. 123191, 2020.

[15] J. P. Qiu, Y. L. Zhao, J. Xing, and X. G. Sun, "Fly ash/blast furnace slag-based geopolymer as a potential binder for mine backfilling: effect of binder type and activator concentration," *Advances in Materials Science and Engineering*, vol. 2019, Article ID 2028109, 12 pages, 2019.

[16] X. J. Deng, Z. X. Yuan, L. X. Lan, B. de Wit, and J. W. Zhang, "Roof movement and failure behavior when mining extra-thick coal seams using upward slicing longwall-roadway cemented backfill technology," *Advances in Materials Science and Engineering*, vol. 2020, Article ID 5828514, 15 pages, 2020.

[17] H. F. Liu, J. X. Zhang, B. Y. Li et al., "Environmental behavior of construction and demolition waste as recycled aggregates for backfilling in mines: leaching toxicity and surface subsidence studies," *Journal of Hazardous Materials*, vol. 389, p. 121870, 2020.

[18] Q. Sun, J. X. Zhang, W. Y. Qi, and M. Li, "Backfill mining alternatives and strategies for mitigating shallow coal mining hazards in the Western mining area of China," *Quarterly Journal of Engineering Geology and Hydrogeology*, vol. 53, no. 2, pp. 217–226, 2020.

[19] W. Y. Qi, Y. L. Huang, H. He, J. X. Zhang, J. M. Li, and M. Qiao, "Potential pollution of groundwater by dissolution and release of contaminants due to using gangue for backfilling," *Mine Water and the Environment*, vol. 38, no. 2, pp. 281–293, 2019.

[20] H. F. Liu, J. X. Zhang, W. Q. Zhang, F. Gao, H. Yan, and T. L. An, "Experimental investigation of perceptual characteristics of functional cemented backfilling materials in coal mines," *Minerals*, vol. 9, no. 1, p. 55, 2019.

[21] W. Y. Qi, J. X. Zhang, and Q. Zhang, "Compression of aggregates of acid-leached coal gangues: implications for coal mine backfill," *Advances in Materials Science and Engineering*, vol. 2018, Article ID 7056430, 13 pages, 2018.

[22] R. L. Zhang, L. N. Ma, P. Liu et al., "Influence mechanisms under different immersion methods and different strengths of concrete in corrosive environments, and verification via long-term field test," *Structural Concrete*, vol. 21, no. 5, pp. 1853–1864, 2020.

[23] Q. Sun, J. X. Zhang, and N. Zhou, "Early-age strength of aeolian sand-based cemented backfilling materials: experimental results," *Arabian Journal For Science And Engineering*, vol. 43, no. 4, pp. 1697–1708, 2018.

[24] C. Zhu, X. D. Xu, W. R. Liu et al., "Softening damage analysis of gypsum rock with water immersion time based on laboratory experiment," *IEEE Access*, vol. 9, pp. 125575–125585, 2019.

[25] D. Ma, J. X. Zhang, H. Y. Duan et al., "Reutilization of gangue wastes in underground backfilling mining: overburden aquifer protection," *Chemosphere*, vol. 264, article 128400, 2020.

[26] X. Y. Liu, Z. D. Zhu, and A. H. Liu, "Permeability characteristic and failure behavior of filled cracked rock in the triaxial seepage experiment," *Advances in Civil Engineering*, vol. 2019, Article ID 3591629, 12 pages, 2019.

[27] J. Mamaghanian, B. V. S. Viswanadham, and H. R. Razeghi, "Centrifuge model studies on geocomposite reinforced soil walls subjected to seepage," *Geosynthetics International*, vol. 26, no. 4, pp. 371–387, 2019.

[28] J. F. Hou, Z. P. Guo, W. Z. Liu, H. Z. Yang, and W. W. Xie, "Study on damage model and damage evolution characteristics of backfill with prefabricated fracture under seepage-stress coupling," *Advances in Materials Science and Engineering*, vol. 2020, Article ID 3642356, 2020.

[29] P. J. Santos and P. L. A. Barros, "Active earth pressure due to soil mass partially subjected to water seepage," *Canadian Geotechnical Journal*, vol. 52, no. 11, pp. 1886–1891, 2015.

[30] J. F. Hou, Z. P. Guo, W. Z. Liu, and Y. X. Zhang, "Mechanical properties and meso-structure response of cemented gangue-fly ash backfill with cracks under seepage- stress coupling," *Construction and Building Materials*, vol. 250, p. 118863, 2020.

[31] P. L. A. Barros and P. J. Santos, "Coefficients of active earth pressure with seepage effect," *Canadian Geotechnical Journal*, vol. 49, no. 6, pp. 651–658, 2012.

[32] X. B. Zhang, H. H. Chen, C. Yao et al., "Seepage characteristics of triaxial compression-induced fractured rocks under varying confining pressures," *International Journal of Geomechanics*, vol. 20, no. 9, article 04020160, 2020.

[33] C. Y. Zhou, L. Yu, F. F. You, Z. Liu, Y. H. Liang, and L. H. Zhang, "Coupled seepage and stress model and experiment verification for creep behavior of soft rock," *International Journal of Geomechanics*, vol. 20, no. 9, article 04020146, 2020.

[34] N. Zhou, H. B. Ma, S. Y. Ouyang, D. Germain, and T. Hou, "Influential factors in transportation and mechanical properties of aeolian sand-based cemented filling material," *Minerals*, vol. 9, no. 2, p. 116, 2019.

Hindawi
Geofluids
Volume 2021, Article ID 6672020, 10 pages
https://doi.org/10.1155/2021/6672020

Research Article

Key Strata Inducing Dynamic Disasters Based on Energy Condition: Criterion and Application

Chao Xu,[1,2,3] Gang Yang,[1] Haoshi Sun,[1] Liangliang Qin,[1] Kai Wang,[1,2] Bo Ren,[1,4] and Zhijie Wen[2,3]

[1]*School of Emergency Management and Safety Engineering, China University of Mining and Technology (Beijing), Beijing, China*
[2]*Beijing Key Laboratory for Precise Mining of Intergrown Energy and Resources, China University of Mining and Technology (Beijing), Beijing, China*
[3]*Key Laboratory of Mining Disaster Prevention and Control, Shandong University of Science and Technology, Qingdao, China*
[4]*National Engineering Research Center for Coal Mine Gas Control, Huainan, China*

Correspondence should be addressed to Zhijie Wen; 201527@cumtb.edu.cn

Received 15 December 2020; Revised 11 January 2021; Accepted 6 February 2021; Published 20 February 2021

Academic Editor: Chuangzhou Wu

The thick and hard rock strata (THRS) exist widely in coal measure strata, which control the movements of overlying rock strata in stopes. When THRS break, great energy is released, which could aggravate the risks of coal and gas outburst, rock burst, and other dynamic disasters. Therefore, the foundation and key of preventing dynamic disasters are to distinguish the THRS that could induce coal-rock dynamic disasters and to analyze the laws of rock stratum breaking and energy releasing. The paper proposed the theoretical calculation methods of the energy accumulation and attenuation of rock breaking which is greatly affected by the hanging length of rock strata and the spreading distance. One or more roof strata that play a leading role in inducing dynamic disasters of the underlying coal mass are defined as the key disaster-inducing strata (KDIS). The disaster-inducing coefficient (DIC) is defined and used as the criterion of KDIS. The greater the source energy, the shorter the spreading distance, and the smaller the attenuation coefficient are, the easier the roof strata are to become KDIS. The disaster-inducing ability of the main THRS was analyzed, and the igneous sill was judged as KDIS, taking the Yangliu Coal Mine as project background. The breaking laws of the igneous sill were obtained by the methods of UDEC numerical simulation and microseismic monitoring, which verified the criterion of KDIS.

1. Introduction

With the huge demand of economic development for energy and the gradual exhaustion of shallow coal resources, the depth of coal mining is increasing by 10-25 m per year in China [1, 2]. The deep mining conditions are more complex with complicated geological structure, higher in situ stress, higher gas pressure, and lower permeability and strength of coal [3]. Therefore, the typical dynamic disasters such as rock burst and coal and gas outburst in deep mines are more and more frequent and serious, compared with those in shallow mines [4–8]. Thick and hard rock strata (THRS) exist widely in coal measure strata, which control the movements of overlying rock strata in stopes because of the great thickness, hardness, and integrity. In case of THRS failure and instability, huge elastic energy is released and transmitted to the stopes, which aggravates the risk of coal and rock dynamic disasters (Figure 1) [9, 10].

In recent years, a series of coal and rock dynamic disasters occurred in the environment of THRS and caused huge casualties and property losses. For example, a rock burst accident that killed six miners was triggered by the fracturing of a 550 m-thick conglomerate rock stratum in the Qianqiu coal mine on March 27, 2014 [11]. One person died in a coal and gas outburst accident under a 120 m-thick igneous rock stratum in the Haizi coal mine on April 25, 2009 [12]. A water-gas ejection accident occurred with about 7800 m^3 of water and 166400 m^3 of gas which were ejected from the

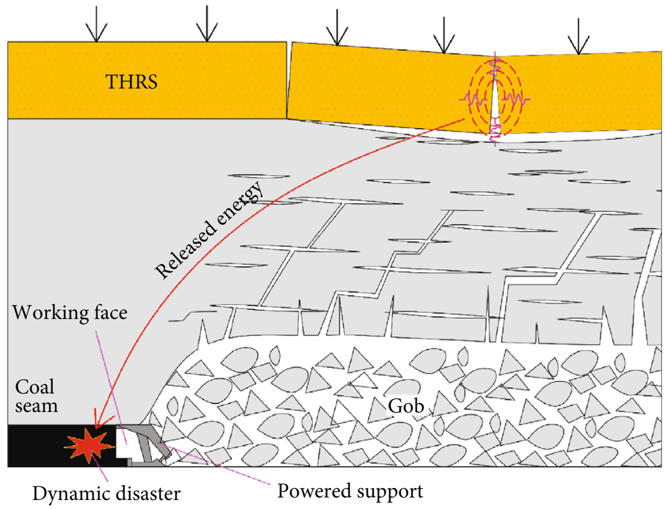

Figure 1: Schematic diagram of dynamic disasters induced by key strata.

bed-splitting space under the 43.6 m-thick igneous rock stratum in the Yangliu coal mine on July 17, 2011 [13]. These examples highlight the need to investigate the effects of the THRS failure on the coal-rock dynamic disasters.

The strata are composed of coal and rock layers with uneven thickness and different strength. An increasing number of studies have focused on the recognizing and failure behaviors of THRS [14]. The key strata [15], which are usually thick-hard strata, play an important role in overlying movement and may influence the mining-induced strata behaviors in the working face using top-coal caving method [16]. Based on the key strata theory, an overburden caving model is proposed to predict the multilayered hard strata behavior [17]. The concept of key strata in immediate roof (KSIR) was put forward, and the dynamic effect and control mechanism of KSIR were studied [18]. Three kinds of structural model, which are affected by the relative position of key strata in the overburden, are found and defined [19]. A roof structural model for large mining-height stopes was established based on their overlying rock structure [20]. In situ measurements via vertical boreholes were performed to determine the key strata, and an innovative solution to fracture high-level hard strata by ground hydraulic fracturing was proposed [21, 22]. A physical modeling system was established to explore the fracture mechanism of the hard roof, and the characteristics of acoustic emission signals during the process of hard roof failure were also studied [23]. The key strata breakage could bring great effects on the stress redistribution and energy storage of mining coal seams. The cause and mechanism of localized stress concentration and rock failure behavior in rock interlayer after protective seam exploitation were explored by numerical simulation, mechanical model, and field investigation [24]. The microseismic effects of hard and thick igneous strata separation and fracturing and the corresponding evaluation index of fracturing intensity were analyzed [9]. For controlling the behavior of the high-located main key stratum (HMKS), a new technique is proposed to add grout between the separated beds during mining [25]. However, there are less literatures on how to distinguish the key strata inducing coal-rock dynamic disasters.

In this paper, the laws of energy accumulation, spreading, and attenuation for the THRS instability was studied theoretically, the sensitivity of those influencing factors was analyzed, and then the concept and criterion of key disaster-inducing strata (KDIS) were put forward. Afterwards, the KDIS in Yangliu Coal Mine, Huaibei Coalfield, China, was distinguished, in which results were verified by the numerical simulations and microseismic monitoring.

2. Energy Spreading Laws of THRS Instability

The elastic energy accumulated in THRS will be released rapidly and then spread and attenuated in the surrounding rock mass when THRS breaks. The residual energy could have a certain degree of impact action on the underlying coal under the state of ultimate stress, easily causing the irreversible damage and even the dynamic disasters.

2.1. Theoretical Analysis for Energy Spreading Laws. According to the stress state of roof strata, the total of the accumulated energy E_0 is composed of the bending elastic energy, the volumetric strain energy, and the kinetic energy generated by rock strata movement [26], which is expressed by

$$E_0 = \frac{q^2 a_0^5}{576EI} + \frac{(1-2\mu)(1+2k)^2 q^2}{6E} + \frac{1}{2} m \left(\frac{\mathrm{d}u}{\mathrm{d}t}\right)^2, \quad (1)$$

where q is the overburden load, Pa; a_0 is hanging length of roof strata, m; E is the elasticity modulus, Pa; μ is Poisson's ratio; k is the ratio of horizontal stress to vertical stress; m is the mass of broken roof strata, kg; u is the displacement of roof strata movement, m; and I is the inertia moment of roof strata, m^4. For rectangular cross-section, $I = bh^3/12$, in which b and h are the width and height of the rectangle, respectively.

It is known that the total of the accumulated energy before the failure of THRS is positively correlated with the hanging length, overburden load, and kinematic velocity of THRS. The larger the hanging length, overburden load, and kinematic velocity, the greater the accumulated energy.

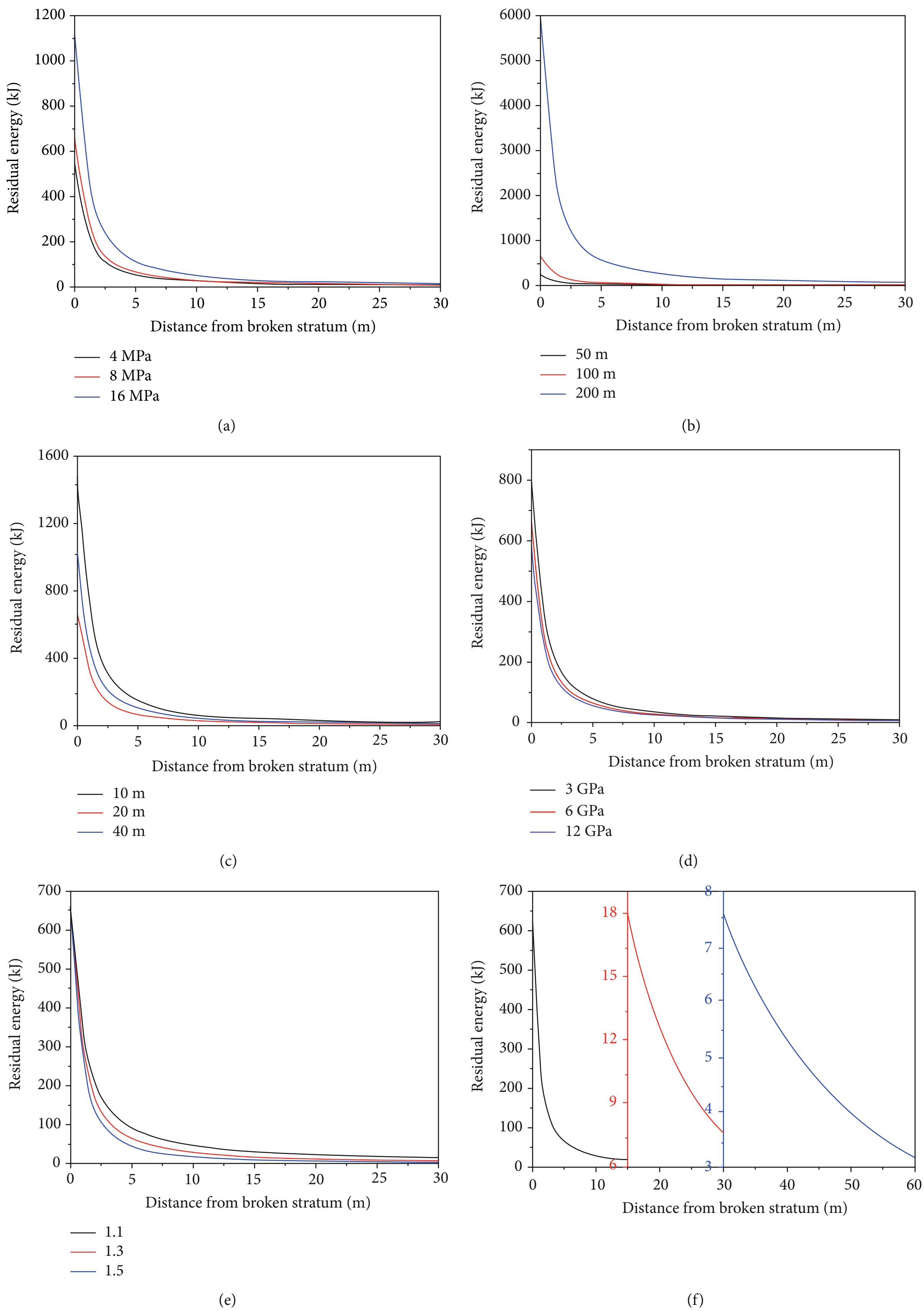

FIGURE 2: Sensitivity of influencing factors for energy spreading and attenuation. (a) Overburden load. (b) Hanging length of roof strata. (c) Thickness of roof strata. (d) Elasticity modulus of roof strata. (e) Mass of roof strata. (f) Energy attenuation coefficient.

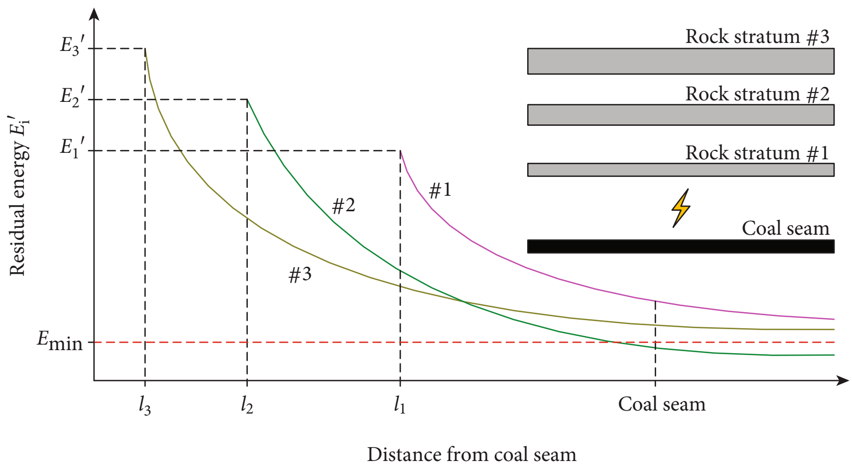

Figure 3: Energy attenuation laws for roof rock breakage against distance.

The energy will be released rapidly and then spread and attenuated in the surrounding rock mass when THRS breaks. However, only about 1%~10% of the energy is spread in the form of seismic waves while most of the energy is converted to heat during collisions of THRS with other rocks [27]. The energy of seismic waves decreases gradually in the form of power with the increase of spreading distance due to the heterogeneity and damping effect of rock strata. From the perspective of safety protection, it could be assumed that 10% of the energy is converted into seismic waves, and then the residual energy after attenuation E_0' is

$$E_0' = 0.1 E_0 l^{-\lambda}, \tag{2}$$

where l is the spreading distance, m, and λ is the energy attenuation coefficient that is related to the properties of the medium.

The residual energy decreases with the increasing of the energy spreading distance and attenuation coefficient. Assuming that the seismic waves are spread in m strata with the thickness of $h_1, h_2, h_3, \ldots, h_m$, in turn, the residual energy E_m' would be

$$E_m' = 0.1 E_0 \prod_1^m h_i^{-\lambda_i}. \tag{3}$$

It indicates that the THRS with the hanging length a_0 accumulates the energy E_0; when THRS breaks, the energy is spread in m strata with the thickness of $h_1, h_2, h_3, \ldots, h_m$ in turn and attenuated to E_m'.

2.2. Sensitivity of Influencing Factors for Energy Spreading. The energy accumulation and spread laws are related to many influencing factors, such as the overburden load, the hanging length, thickness, elasticity modulus and mass of roof strata, energy spreading distance, and attenuation coefficient based on the above formula. The sensitivity of influencing factors was obtained when they were assigned the different values (1 time, 2 times, and 4 times), assuming that the seismic waves were spread in the isotropous rock strata (Figure 2). When the load is increased by 2 times and 4 times, the initial seismic wave energy increases by 1.22 times and 2.08 times, respectively; however, when the hanging length is increased by 2 times and 4 times, the initial seismic wave energy increases by 2.55 times and 23.04 times, respectively. When the thickness and elasticity modulus of rock strata increase, the initial seismic wave energy decreases gradually, which is contrary to the common understanding. It is because that only the single influence of rock thickness or elasticity modulus on initial seismic wave energy is considered. In fact, the rock strata are more difficult to be broken and form larger hanging length when the thickness and elasticity modulus of rock strata increase and so the greater seismic wave energy will be released when the rock strata are broken [28]. The attenuation velocity of seismic wave energy increases with the increase of energy attenuation coefficient. If the energy attenuation coefficients are set as 1.1, 1.3, and 1.5, the seismic wave energy will be attenuated to 1/14, 1/22.6, and 1/36.5 of the initial values, respectively, when the seismic waves are spread 10 m. The seismic wave energy is attenuated in the form of powers with the increasing of spreading distance. The seismic wave energy will be attenuated to 1/33.8, 1/86.8, and 1/209.4 of the initial values, respectively, when the spreading distances increase by 2 times and 4 times from 15 m. The comprehensive analysis shows that the spread of seismic wave energy is greatly affected by the hanging length of rock strata and the spreading distance.

3. Concept and Criterion of KDIS

3.1. Concept of KDIS. Although most of the released energy has been dissipated, the residual energy may still induce dynamic disasters when the seismic waves were spread to the mining coal seam. Therefore, one or more roof strata that play a leading role in inducing dynamic disasters of the underlying coal mass are defined as the key disaster-inducing strata (KDIS). The residual energy not only depends on the size and mechanical properties of rock strata but also relates to the energy spreading distance and attenuation coefficient. The greater the source energy, the shorter

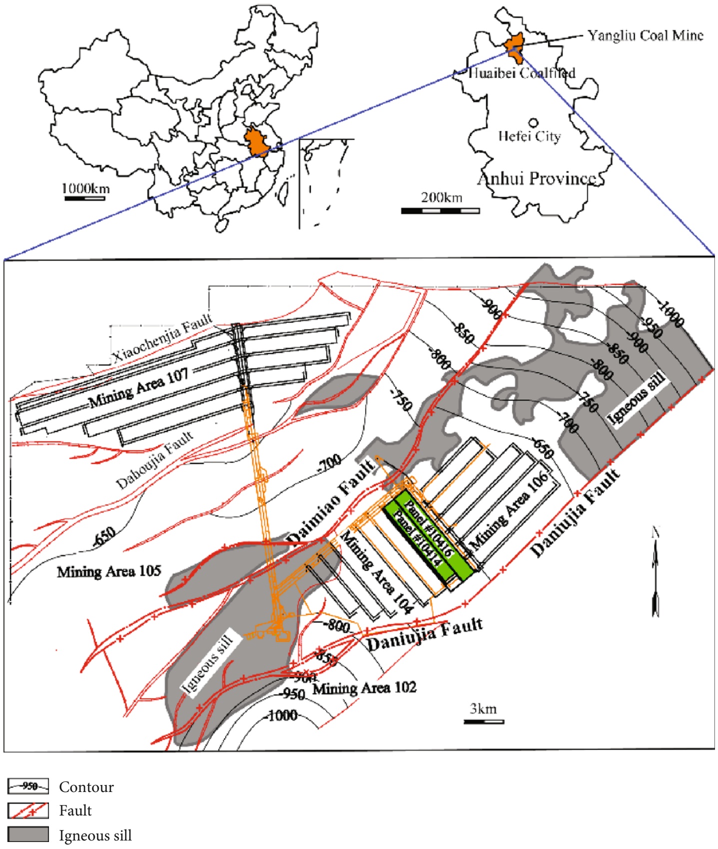

(a)

Rock thickness (m)	Depth (m)	Columnar	Lithology
43.60	485.07		Diorite
2.81	487.88		
1.16	489.04		Coal seam #7$_1$
7.62	496.66		Siltstone
1.60	499.38		Coal seam #7$_2$
1.89	501.27		
0.82	502.09		Coal seam #8$_1$
3.07	505.15		
9.26	514.41		Sandstone
2.23	516.64		Coal seam #8$_2$
2.25	518.89		
6.30	525.19		Siltstone
28.57	553.76		
11.45	565.21		Siltstone
5.24	570.45		
4.85	575.30		Siltstone
11.60	586.90		
3.54	590.44		Coal seam #10

(b)

Figure 4: Project background of Yangliu Coal Mine.

the spreading distance, and the smaller the attenuation coefficient are, the stronger the disaster-inducing ability of the roof strata is, and the easier the roof strata are to become KDIS. However, the key stratum of ground control mainly depends on the size and mechanical properties of the rock stratum itself [15]. Thus, the key stratum of ground control is not exactly equal to KDIS.

Figure 3 provides a better understanding of KDIS. When the rock stratum #1 that is close to the mining coal seam is broken, the residual energy may be larger than the minimum energy inducing dynamic disasters although the released energy is less. When the thicker rock stratum #2 is broken, more seismic wave energy is released but cannot induce dynamic disasters due to the relatively large distance from the mining coal seam. But for the thick rock stratum #3 which is the key stratum of ground control, great seismic wave energy is released when broken, and the residual energy is so large that could induce dynamic disasters although it is far from the mining coal seam. Therefore, the rock strata #1 and #3 are the KDIS, and the key stratum of ground control may be the KDIS under certain conditions.

3.2. Criterion of KDIS. During the process of dynamic disaster occurring, the crushing work is needed for crack propagation, debris stripping, and new surface forming of coal mass; the kinetic energy is needed for throwing the broken coal into the excavation space; the friction dissipation energy is also needed for overcoming the inner friction during the broken coal peeling and throwing. Thus, the total energy consumption is composed of the crushing work, the kinetic energy, and the friction dissipation energy. If the accumulated energy of mining coal mass is larger than the total energy consumption, the dynamic disasters will occur.

They are assumed that there are n overlying rock strata with the distances $l_1, l_2, l_3, \ldots, l_n$ from the mining coal seam, respectively, and that the seismic wave energy $E_1, E_2, E_3, \ldots, E_n$ will be released and attenuated with the average attenuation coefficient λ_0 when they are broken. The residual energy $E_1', E_2', E_3', \ldots, E_n'$ when spreading to the mining coal seam is, respectively

$$\begin{cases} E_1' = E_1 l_1^{-\lambda_0} \\ E_2' = E_2 l_2^{-\lambda_0} \\ E_3' = E_3 l_3^{-\lambda_0} \\ \cdots \\ E_n' = E_n l_n^{-\lambda_0}. \end{cases} \tag{4}$$

The ratio of the residual energy E_i' and the minimum energy inducing dynamic disasters $E_{\min}$ is defined as the disaster-inducing coefficient (DIC) ξ, that is $\xi = E_i'/E_{\min}$. Based on DIC, THRS are divided into three types: KDIS, the weak

Table 1: Criterion results of KDIS in Yangliu Coal Mine.

No.	#1	#2	#3	#4
Lithology	Sandstone	Siltstone	Sandstone	Igneous rock
Thickness (m)	4.8	11.5	9.3	43.6
Distance from coal seam #10 (m)	12	21	72	102
Extreme hanging length (m)	16.7	20.0	18.7	184.6
Released energy (MJ)	0.31	0.63	0.48	41.10
Residual energy spreading to coal seam #10 (kJ)	1.55	1.62	0.28	15.98
DIC	0.155	0.162	0.028	1.598
Criterion result	WDIS	WDIS	NDIS	KDIS

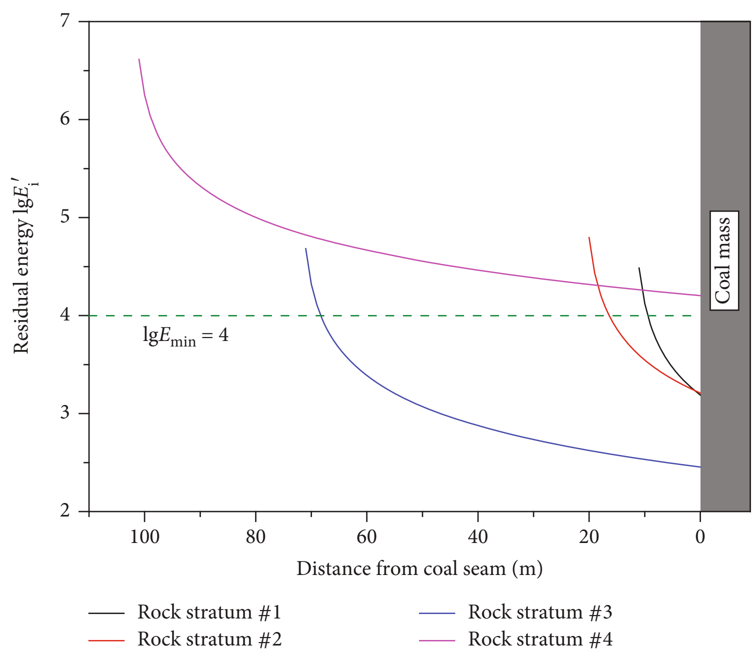

Figure 5: Energy attenuation laws of rock strata in Yangliu Coal Mine.

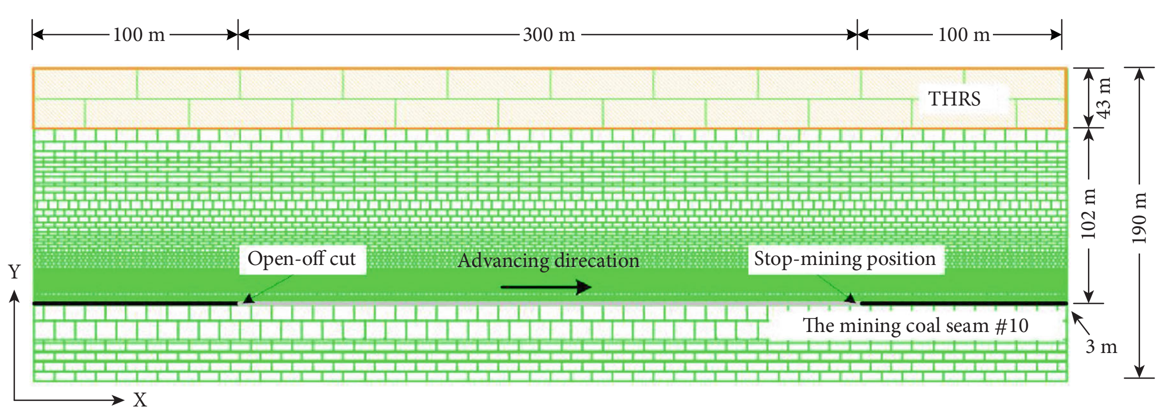

Figure 6: UDEC numerical model.

disaster-inducing stratum (WDIS), and the non-disaster-inducing stratum (NDIS). If $\xi \geq 1$, the broken rock strata could induce dynamic disasters, which are distinguished to be KDIS; if $0.1 \leq \xi < 1$, the broken rock strata may induce dynamic disasters considering in situ stress, mechanical properties of coal, and other factors, which are distinguished to be WDIS; if $\xi < 0.1$, the broken rock strata could not induce dynamic disasters, which are distinguished to be NDIS.

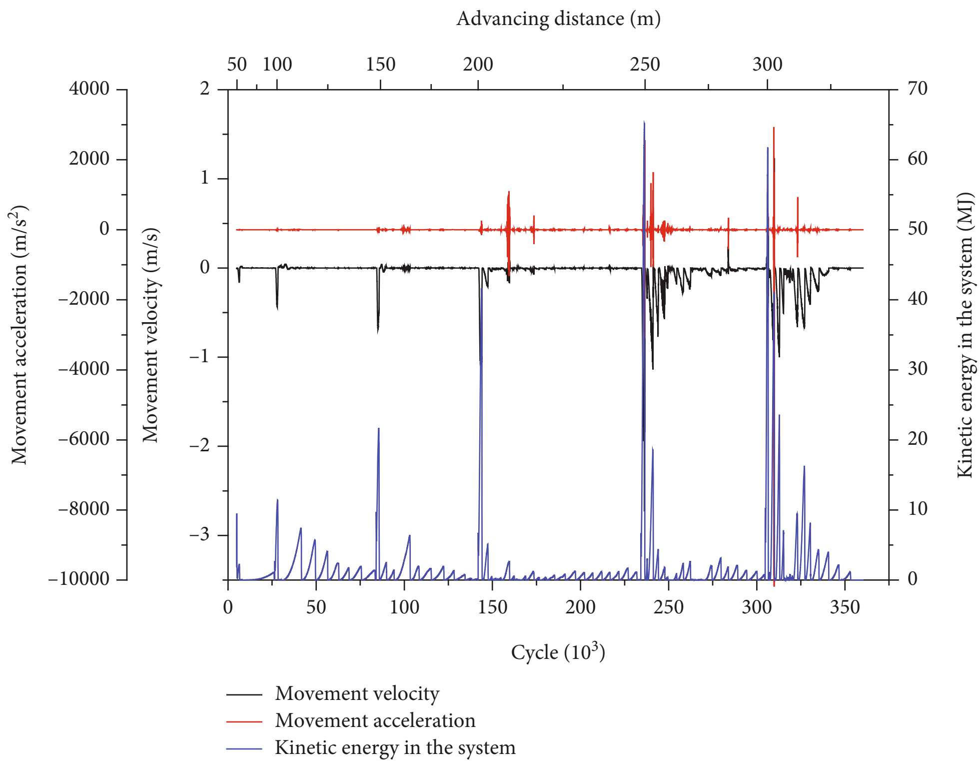

Figure 7: Movement laws of igneous sill.

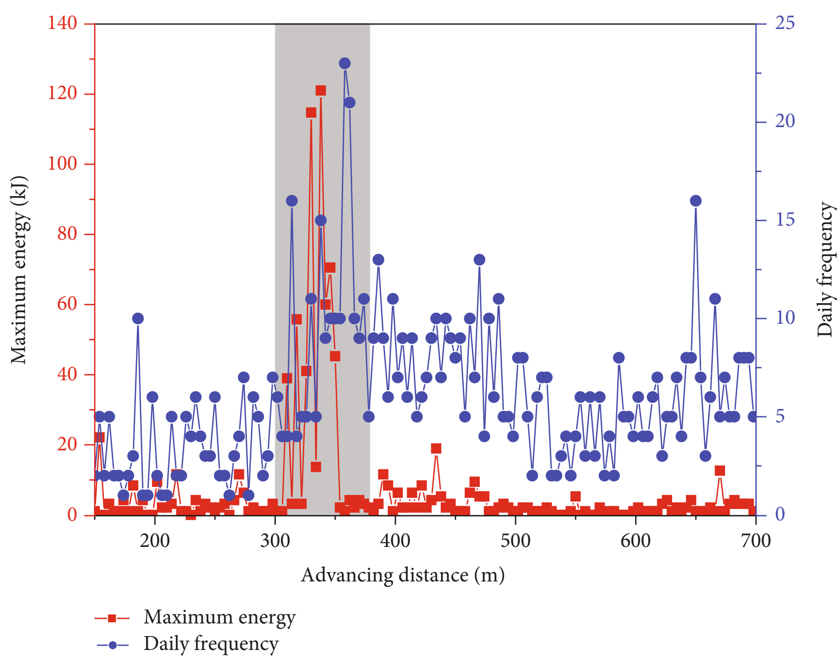

Figure 8: Daily frequency and maximum energy of the panel #10416.

4. Engineering Application

4.1. Project Background. Yangliu Coal Mine, the coal and gas outburst mine, is located in the north Anhui province, China. The coal seam #10 with the average thickness of 3.19 m is the main mining seam adopting the comprehensive mechanized mining method. The magmatic activities in Yangyan Coal Mine were quite intense, and almost all coal seams were affected by magmatic intrusion. The igneous sill, 43.6 m thick averagely and 102 m above the coal seam #10, is the key stratum of ground control (Figure 4). The panel #10414 and the adjacent panel #10416 of the coal seam #10 were mined in turn. According to the statistics, multiple dynamic disasters were induced by the movement and failure of the igneous sill during the two panels mining. The large amount of water and gas were ejected from the surface well when the panel #10414 was advanced 527 m [13]; the abnormal pressure on working face occurred when the panel #10416 was advanced 320 m [28].

4.2. Criterion Results of KDIS. It can be preliminarily analyzed from the column chart of coal-bearing strata that the four thick rock strata, 12 m, 21 m, 72 m, and 102 m above the coal seam #10, respectively, may have the ability to induce dynamic disasters. The released energy of the four rock strata breaking and the residual energy spreading to the coal seam #10 were calculated based on the above formula (Table 1 and Figure 5). Researches show that the minimum energy inducing dynamic disasters $E_{\min}$ is 10^4 orders of magnitude [29]. Assuming that the minimum energy inducing dynamic disasters in the coal seam #10 of Yangliu Coal Mine is 10 kJ for security, the DIC of the four rock strata were 0.155, 0.162, 0.028, and 1.598, respectively. So the rock strata #1 and #2 were judged to be WDIS, the stratum #3 to be NDIS, and the stratum #4 to be KDIS. The breaking of the stratum #4 could induce the dynamic disasters in coal seam #10.

4.3. Result Validation. The methods of UDEC numerical simulation and microseismic monitoring were adopted for verifying the THRS failure and energy releasing laws.

4.3.1. UDEC Numerical Simulation. The numerical model is 190 m high from 50 m below the coal seam #10 to the top of the igneous sill. The model size is 500 ∗ 190 m while the panel size is 300 ∗ 3 m and the coal pillars with 100 m width were set at each end (Figure 6). The Mohr-Coulomb criterion was selected, and the mechanical parameters of the coal and rock masses and joint surface were set as shown in the reference [26]. The bottom, left, and right boundaries of the model were set to obey the zero-displacement constraint, and the top boundary was loaded at 10 MPa. The excavation of the panel took place in six steps, each of which was 50 m.

The movement velocity and acceleration of the igneous sill and the kinetic energy in the system were recorded by the orders *yvel*, *yacc*, and *energy*, respectively (Figure 7). The movement velocity and acceleration of the igneous sill at the central position (250, 155) increased gradually with the workface advancing. When the workface was advanced 250 m, the movement velocity increased to the maximum of -2.6 m/s, the acceleration increased to about 3000 m/s^2, and the kinetic energy extended to the maximum of 59.3 MJ, which were consistent with the previous calculated results. When the workface advanced 300 m, the maximum of the movement velocity was 1.2 m/s and the acceleration increased to -9600 m/s^2 while the kinetic energy decreased to the 56.2 MJ due to the collision and rebound between the igneous sill and the underlying rock strata. It was indicated that the igneous sill had been broken when the workface was advanced 250~300 m, and the released kinetic energy was much larger than that of the common rock strata. The igneous sill would force greater impact on the underlying

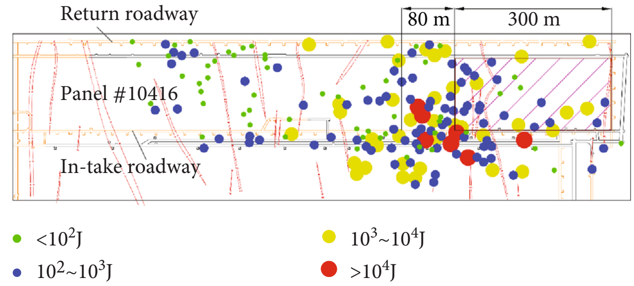

Figure 9: Microseismic event distribution.

coal seam and conformed to the characteristics of KDIS, which verified the above research results.

4.3.2. Microseismic Monitoring. The microseismic monitoring technology is a method to monitor the stability of engineering rock mass using the vibration waves emitted by the rock mass deformation and failure [30–32]. The SOS microseismic monitoring system was used to monitor the microseismic signals in real time in Yangliu Coal Mine. The daily frequency and maximum energy of seismic waves during the workface #10416 advancing are shown in Figure 8. When the workface #10416 was advanced 300~380 m, the igneous sill was broken with square form [28], and thus, the daily frequency and maximum energy of seismic waves increased obviously, the maximum of which were 121.1 kJ and 23 times, relatively, according with the characteristics of KDIS. The daily frequency and maximum energy returned to normal levels gradually with the workface #10416 advancing further. A large number of microseismic events with greater magnitude mainly occurred on the side of the intake roadway (Figure 9), which verified the laws of the igneous sill breaking and energy releasing.

5. Conclusions

In this paper, the laws of energy accumulation, spreading, and attenuation for the THRS instability were studied theoretically, the sensitivity of those influencing factors was analyzed, and then the concept and criterion of KDIS were put forward. Afterwards, the KDIS in Yangliu Coal Mine, Huaibei Coalfield, China, was distinguished, in which results were verified by the numerical simulations and microseismic monitoring. The main conclusions are as follows:

(1) The total of the accumulated energy is composed of the bending elastic energy, the volumetric strain energy, and the kinetic energy generated by rock strata movement, which is positively correlated with the hanging length, overburden load, and kinematic velocity. The energy of seismic waves decreases gradually in the form of power with the increase of spreading distance, the residual of which is negatively correlated with the energy spreading distance and attenuation coefficient. The spread of seismic wave energy is greatly affected by the hanging length of rock strata and the spreading distance, relatively

(2) One or more roof strata that play a leading role in inducing dynamic disasters of the underlying coal mass are defined as the KDIS. The greater the source energy, the shorter the spreading distance, and the smaller the attenuation coefficient are, the easier the roof strata are to become KDIS. The key stratum of ground control is not exactly equal to KDIS but may be the KDIS under certain conditions. The DIC is defined and used as the criterion of KDIS, based on which the THRS are divided into three types of KDIS, WDIS, and NDIS

(3) The disaster-inducing ability of the main THRS was analyzed and the igneous sill was judged as KDIS when the overlying coal seam #10 was mined, taking the Yangliu Coal Mine as project background. By the methods of UDEC numerical simulation and microseismic monitoring, it was revealed that the igneous sill was broken and greater energy than that of common rock strata was released resulting to the occurrence of abnormal pressure when the workface of the coal seam #10 was advanced 250~300 m, which verified the criterion of KDIS.

Data Availability

The data used to support the findings of this study are included within the article.

Conflicts of Interest

The authors declare that they have no conflicts of interest.

Acknowledgments

The work was supported by the National Natural Science Foundation of China (grant numbers 51974321, 51874314, and 51774292), Open Fund of Key Laboratory of Mining Disaster Prevention and Control (Grant No. MDPC202018), and Yueqi Young Scholar Project, China University of Mining & Technology (Beijing).

References

[1] S. Kong, Y. Cheng, T. Ren, and H. Liu, "A sequential approach to control gas for the extraction of multi-gassy coal seams from traditional gas well drainage to mining-induced stress relief," *Applied Energy*, vol. 131, pp. 67–78, 2014.

[2] C. Xu, Q. Fu, K. Wang, C. Guo, and X. Li, "Effects of the deviatoric stress ratio on the coal failure and permeability during deep mining," *Geotechnical and Geological Engineering*, vol. 38, no. 6, pp. 6093–6105, 2020.

[3] Y. Xue, T. Teng, F. Dang, Z. Ma, S. Wang, and H. Xue, "Productivity analysis of fractured wells in reservoir of hydrogen and carbon based on dual-porosity medium model," *International Journal of Hydrogen Energy*, vol. 45, no. 39, pp. 20240–20249, 2020.

[4] L. Dou, T. Chen, S. Gong, H. He, and S. Zhang, "Rockburst hazard determination by using computed tomography technology in deep workface," *Safety Science*, vol. 50, no. 4, pp. 736–740, 2012.

[5] H. Guo, L. Yuan, B. Shen, Q. Qu, and J. Xue, "Mining-induced strata stress changes, fractures and gas flow dynamics in multi-seam Longwall mining," *International Journal of Rock Mechanics and Mining Sciences*, vol. 54, pp. 129–139, 2012.

[6] P. Konicek, K. Soucek, L. Stas, and R. Singh, "Long-hole destress blasting for rockburst control during deep underground coal mining," *International Journal of Rock Mechanics and Mining Sciences*, vol. 61, pp. 141–153, 2013.

[7] C. Xu, G. Yang, K. Wang, and Q. Fu, "Uneven stress and permeability variation of mining-disturbed coal seam for targeted CBM drainage: a case study in Baode coal mine, Eastern Ordos Basin, China," *Fuel*, vol. 289, 2021.

[8] C. Zhang, L. Zhang, M. Li, and C. Wang, "A gas seepage modeling study for mitigating gas accumulation risk in upper protective coal seam mining process," *Geofluids*, vol. 2018, Article ID 8127207, 11 pages, 2018.

[9] C.-P. Lu, Y. Liu, H.-Y. Wang, and P.-F. Liu, "Microseismic signals of double-layer hard and thick igneous strata separation and fracturing," *International Journal of Coal Geology*, vol. 160–161, pp. 28–41, 2016.

[10] L. Dou, K. Yang, W. Liu, X. Chi, and Z. Wen, "Mining-induced stress-fissure field evolution and the disaster-causing mechanism in the high gas working face of the deep hard strata," *Geofluids*, vol. 2020, Article ID 8849666, 14 pages, 2020.

[11] G.-f. Wang, S.-y. Gong, Z.-l. Li, L.-m. Dou, W. Cai, and Y. Mao, "Evolution of stress concentration and energy release before rock bursts: two case studies from Xingan Coal Mine, Hegang, China," *Rock Mechanics & Rock Engineering*, vol. 49, no. 8, pp. 3393–3401, 2016.

[12] L. Wang, Y.-p. Cheng, C. Xu, F.-h. An, K. Jin, and X.-l. Zhang, "The controlling effect of thick-hard igneous rock on pressure relief gas drainage and dynamic disasters in outburst coal seams," *Natural Hazards*, vol. 66, no. 2, pp. 1221–1241, 2013.

[13] C. Xu, Y. Cheng, T. Ren, L. Wang, S. Kong, and S. Lu, "Gas ejection accident analysis in bed splitting under igneous sills and the associated control technologies: a case study in the Yangliu Mine, Huaibei Coalfield, China," *Natural Hazards*, vol. 71, no. 1, pp. 109–134, 2014.

[14] C. Wu, J. Chu, S. Wu, and Y. Hong, "3D characterization of microbially induced carbonate precipitation in rock fracture and the resulted permeability reduction," *Engineering Geology*, vol. 249, pp. 23–30, 2019.

[15] M. Qian, X. Miao, and X. Jialin, "Theorical study of key stratum in ground control," *Journal of China Coal Society*, vol. 21, no. 3, pp. 225–230, 1996.

[16] B. Yu, "Behaviors of overlying strata in extra-thick coal seams using top-coal caving method," *Journal of Rock Mechanics and Geotechnical Engineering*, vol. 8, no. 2, pp. 238–247, 2016.

[17] Z. Zhu, Y. Wu, J. Han, and Y. Chen, "Overburden failure and ground pressure behaviour of Longwall top coal caving in hard multi-layered roof," *Archives of Mining Sciences*, vol. 64, no. 3, pp. 575–590, 2019.

[18] Y. Yong, T. Shihao, Z. Xiaogang, and L. Bo, "Dynamic effect and control of key strata break of immediate roof in fully mechanized mining with large mining height," *Shock and Vibration*, vol. 2015, Article ID 657818, 11 pages, 2015.

[19] J. Ju and J. Xu, "Structural characteristics of key strata and strata behaviour of a fully mechanized Longwall face with 7.0 m height chocks," *International Journal of Rock Mechanics and Mining Sciences*, vol. 58, pp. 46–54, 2013.

[20] Z. Wen, E. Xing, S. Shi, and Y. Jiang, "Overlying strata structural modeling and support applicability analysis for large mining-height stopes," *Journal of Loss Prevention in the Process Industries*, vol. 57, pp. 94–100, 2019.

[21] B. Yu, R. Gao, T. Kuang, B. Huo, and X. Meng, "Engineering study on fracturing high-level hard rock strata by ground hydraulic action," *Tunnelling and Underground Space Technology*, vol. 86, pp. 156–164, 2019.

[22] B. Yu, J. Zhao, T. Kuang, and X. Meng, "In situ investigations into overburden failures of a super-thick coal seam for Longwall top coal caving," *International Journal of Rock Mechanics and Mining Sciences*, vol. 78, pp. 155–162, 2015.

[23] N. Li, E. Wang, M. Ge, and J. Liu, "The fracture mechanism and acoustic emission analysis of hard roof: a physical modeling study," *Arabian Journal of Geosciences*, vol. 8, no. 4, pp. 1895–1902, 2015.

[24] M. Zhang, H. Shimada, T. Sasaoka, K. Matsui, and L. Dou, "Evolution and effect of the stress concentration and rock failure in the deep multi-seam coal mining," *Environmental Earth Sciences*, vol. 72, no. 3, pp. 629–643, 2014.

[25] X.-y. Wang, W.-d. Wu, and B.-w. Wu, "Grouting of bed separation spaces to control sliding of the high-located main key stratum during Longwall mining," *Quarterly Journal of Engineering Geology and Hydrogeology*, vol. 53, no. 4, pp. 569–578, 2020.

[26] C. Xu, Q. Fu, X. Cui, K. Wang, Y. Zhao, and Y. Cai, "Apparent-depth effects of the dynamic failure of thick hard rock strata on the underlying coal mass during underground mining," *Rock Mechanics and Rock Engineering*, vol. 52, no. 5, pp. 1565–1576, 2019.

[27] J. Jiang, P. Zhang, L. Nie, H. Li, L. Xu, and W. Wang, "Fracturing and dynamic response of high and thick strata of hard rocks," *Chinese Journal of Rock Mechanics and Engineering*, vol. 33, no. 7, pp. 1366–1372, 2014.

[28] C. Xu, L. Yuan, Y. Cheng, K. Wang, A. Zhou, and L. Shu, "Square-form structure failure model of mining-affected hard rock strata: theoretical derivation, application and verification," *Environmental Earth Sciences*, vol. 75, no. 16, p. 1180, 2016.

[29] Z. Mu, "Study of burst-energy principle of rock burst induced by roof stratum and its application," *Journal of China University of Mining & Technology*, vol. 37, no. 6, pp. 149-150, 2008.

[30] H. He, L. Dou, A. Cao, and J. Fan, "Mechanisms of mining seismicity under large scale exploitation with multikey strata," *Shock and Vibration*, vol. 2015, Article ID 313069, 9 pages, 2015.

[31] J. He, L. Dou, S. Gong, J. Li, and Z. Ma, "Rock burst assessment and prediction by dynamic and static stress analysis based on micro-seismic monitoring," *International Journal of Rock Mechanics and Mining Sciences*, vol. 93, pp. 46–53, 2017.

[32] G. Cheng, L. Li, W. Zhu et al., "Microseismic investigation of mining-induced brittle fault activation in a Chinese coal mine," *International Journal of Rock Mechanics and Mining Sciences*, vol. 123, article 104096, 2019.

Hindawi
Geofluids
Volume 2021, Article ID 6696757, 12 pages
https://doi.org/10.1155/2021/6696757

Research Article

A New Unified Solution for Deep Tunnels in Water-Rich Areas considering Pore Water Pressure

Hao Fan, Lianguo Wang, Shuai Wang, and Chongyang Jiang

State Key Laboratory for Geomechanics and Deep Underground Engineering, China University of Mining and Technology, Xuzhou 221116, China

Correspondence should be addressed to Lianguo Wang; cumt_lgwang@163.com

Received 26 December 2020; Revised 24 January 2021; Accepted 28 January 2021; Published 20 February 2021

Academic Editor: Yi Xue

Pore water pressure has an important influence on the stresses and deformation of the surrounding rock of deep tunnels in water-rich areas. In this study, a mechanical model for deep tunnels subjected to a nonuniform stress field in water-rich areas is developed. Considering the pore water pressure, a new unified solution for the stresses, postpeak zone radii, and surface displacement is derived based on a strain-softening model and the Mogi-Coulomb criterion. Through a case study, the effects of pore water pressure, intermediate principal stress, and residual cohesion on the stress distribution, postpeak zone radii, and surface displacement are also discussed. Results show that the tangential stresses are always larger than the radial stress. The radial stress presents a gradually increasing trend, while the tangential stress presents a trend of first increasing and then decreasing, and the maximum tangential stress appears at the interface between the elastic and plastic zones. As the pore water pressure increases, the postpeak zone radii and surface displacement increase. Because of the neglect of the intermediate principal stress in the Mohr-Coulomb criterion, the postpeak zone radii, surface displacement, and maximum tangential stress solved by the Mohr-Coulomb criterion are all larger than those solved by the Mogi-Coulomb criterion. Tunnels surrounded by rock masses with a higher residual cohesion experience lower postpeak zone radii and surface displacement. Data presented in this study provide an important theoretical basis for supporting the tunnels in water-rich areas.

1. Introduction

Tunnels are one of the most basic facilities in water conservancy engineering, civil engineering, and mining engineering [1–3]. The stress distribution of the rock mass changes with the excavation of the tunnel, and the surrounding rock of the tunnel will be deformed if the redistributed stress exceeds the peak strength of the rock mass. Therefore, accurate calculation for the stress of the surrounding rock plays an important role in stability evaluation and support design of the tunnel [4–6].

In the past decades, a series of unified solutions based on different strength criteria have been proposed. Some common strength criteria, such as the Mohr-Coulomb criterion [7–10] and the Hoek-Brown criterion [11–14], were widely used to calculate the stress in the tunnel surrounding rock. However, the intermediate principal stress is not considered in these criteria, which caused an inaccurate result. In fact, the surrounding rock of the tunnel is always in a true triaxial stress environment [15, 16], and the intermediate principal stress has a nonnegligible influence on the strength of the rock mass. Therefore, it is of great significance that the intermediate principal stress be taken into consideration in the unified solution for deep tunnels.

Because of the underground faults, folds, and other special structures, the ratio of the vertical stress to horizontal stress is usually not equal to one. In this case, Galin [17] first analyzed the tunnel in a nonuniform stress field and deduced the radius of the plastic zone. However, Galin's solution only applies to frictionless rock mass. Detournay [18–20] extended Galin's result to other materials and obtained the boundary of the elastic and plastic zones. Tokar [21], Leitman and Villaggio [22], and Ochensberger et al. [23] also presented a series of analytical solutions for a circular wellbore in some certain cases based on Galin's solution.

It is known that the flowing water always exists in the underground rock mass, which has a certain impact on the stress distribution and deformation of the surrounding rock of the tunnel. Therefore, the influence of the pore water pressure should be considered in the elastic-plastic analysis for deep tunnels in water-rich areas [24–26]. In the present study, a mechanical model for deep tunnels subjected to a nonuniform stress field in water-rich areas is first established. Considering the pore water pressure, a new unified solution for the stresses, postpeak zone radii, and surface displacement is derived based on strain-softening model and Mogi-Coulomb criterion. Through a case study, the sensitivity of pore water pressure, intermediate principal stress, and residual cohesion on the stress distribution, postpeak zone radii, and surface displacement is analyzed.

2. Definition of the Problem

2.1. Mechanical Model of a Circular Tunnel. A circular tunnel of radius R_0 was excavated in an infinite rock mass (Figure 1). The vertical and horizontal stresses are σ_0 and $\lambda\sigma_0$, respectively, where λ is the lateral stress coefficient. A support pressure (P_i) is uniformly distributed along the excavation surface. The surrounding rock of the tunnel is subdivided into an elastic zone ("e"), plastic zone ("p"), and damage zone ("d"). The radii of the elastic, plastic, and damage zones are denoted by R_e, R_p, and R_d, respectively.

We assume that there is a pore water pressure (P_0) outside the elastic zone of the tunnel. Based on Darcy's law, the continuous differential equation of seepage is

$$\frac{\mathrm{d}^2 P_w}{\mathrm{d}r^2} + \frac{1}{r}\frac{\mathrm{d}P_w}{\mathrm{d}r} = 0, \tag{1}$$

where P_w is the pore water pressure at any point of the tunnel surrounding rocks.

Combined with the boundary condition of $P_w = 0$ at $r = R_0$ and $P_w = P_0$ at $r = R_e$, the pore water pressure can be derived by solving Equation (1):

$$P_w = P_0 \frac{\ln (R_0/r)}{\ln (R_0/R_e)}. \tag{2}$$

2.2. Strain-Softening Model. As shown in Figure 2, the experimental stress-strain curve of the rock mass can be simplified into a three-section line. The three straight lines correspond to the elastic zone, plastic zone, and damage zone, respectively.

3. Analytical Solution

3.1. Basic Equations. The Mogi-Coulomb criterion can be expressed as [27–29]

$$\sigma_{\theta i} = M\sigma_{ri} + N_i, \tag{3}$$

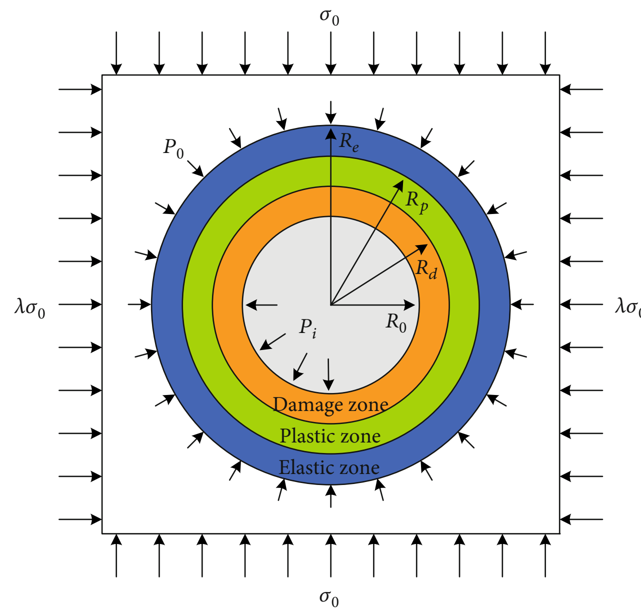

Figure 1: Mechanical model of tunnels subjected to a nonuniform stress field in water-rich area.

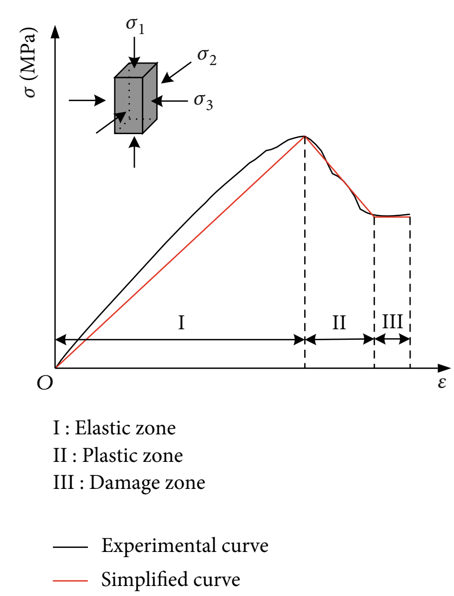

Figure 2: Total stress-strain curve of rock mass.

where $\sigma_{\theta i}$ and σ_{ri} are the tangential and radial stresses in the "i" region, respectively; $M = (\sqrt{3} + 2\sin\varphi)/(\sqrt{3} - 2\sin\varphi)$; φ is the internal friction angle; $N_i = 4c_i \cos\varphi/(\sqrt{3} - 2\sin\varphi)$; and c_i represents the cohesion in different zones. The symbol "i" can be replaced by "e," "p," and "d."

Taking the pore water pressure into consideration, the equilibrium differential equation in the "i" zone can be given as

$$\frac{\mathrm{d}\sigma_{ri}}{\mathrm{d}r} + \frac{\sigma_{ri} - \sigma_{\theta i}}{r} + \eta\frac{\mathrm{d}P_w}{\mathrm{d}r} = 0, \tag{4}$$

where η is the pore water pressure coefficient.

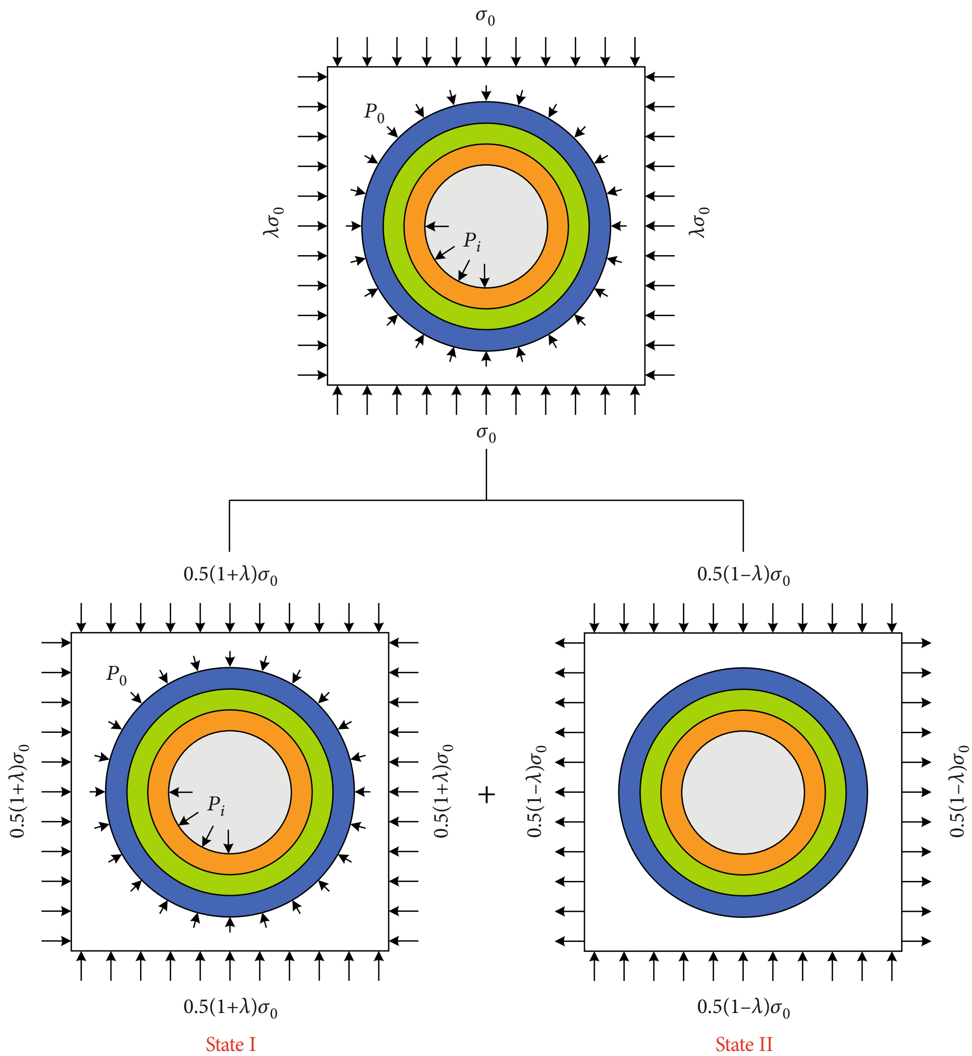

FIGURE 3: Mechanical model of surrounding rock in water-rich coal tunnel.

The geometric equation can be written as

$$\begin{cases} \varepsilon_{ri} = \dfrac{du_i}{dr}, \\ \varepsilon_{\theta i} = \dfrac{u_i}{r}, \end{cases} \tag{5}$$

where ε_{ri} and $\varepsilon_{\theta i}$ are the radial and tangential strains in the "i" zone, respectively, and u_i represents the displacement in the "i" zone.

The constitutive equations can be denoted as

$$\begin{cases} \varepsilon_r = \dfrac{1-\mu^2}{E}\left(\sigma_r - \dfrac{\mu}{1-\mu}\sigma_\theta\right), \\ \varepsilon_\theta = \dfrac{1-\mu^2}{E}\left(\sigma_\theta - \dfrac{\mu}{1-\mu}\sigma_r\right), \end{cases} \tag{6}$$

where μ and E are Poisson's ratio and Young's modulus of the rock mass, respectively.

In addition, the volume of the rock mass is always changing in the postpeak failure zone; the plastic-strain relationships can be developed based on the nonassociated flow rule as follows:

$$\varepsilon_{ri} + \beta_i \varepsilon_{\theta i} = 0, \tag{7}$$

where $\beta_i = (1 + \sin\psi_i)/(1 - \sin\psi_i)$; ψ_i is the dilation angle in the "i" zone.

3.2. Elastic Zone. The stress state of the circular tunnel in a nonuniform stress field can be decomposed into two parts (see Figure 3). In state I, the tunnel is subjected to a uniform pressure $(0.5(1+\lambda)\sigma_0)$, pore water pressure (P_w), and support pressure (P_i); the differential equation can be obtained by substituting Equations (2), (5), and (6) into Equation (3):

$$\frac{d^2 u_{e1}}{dr^2} + \frac{1}{r}\frac{du_{e1}}{dr} - \frac{u_{e1}}{r^2} = \frac{F\nu}{rE}, \tag{8}$$

where $F = \eta P_0/\ln(R_0/R_e)$ and $\nu = (1+\mu)(1-2\mu)/(1-\mu)$.

Solving Equation (8), the displacement and strains in state I can be easily obtained as

$$\begin{cases} u_{e1} = C_1 r + \dfrac{C_2}{r} + \dfrac{Fvr\ln r}{2E}, \\ \varepsilon_{re1} = C_1 - \dfrac{C_2}{r^2} + \dfrac{Fv}{2E}(\ln r + 1), \\ \varepsilon_{\theta e1} = C_1 + \dfrac{C_2}{r^2} + \dfrac{Fv\ln r}{2E}, \end{cases} \tag{9}$$

where C_1 and C_2 are integral constants.

The radial and tangential stresses can be derived by integrating Equations (6) and (9):

$$\begin{cases} \sigma_{re1} = \dfrac{EC_1}{(1+\mu)(1-2\mu)} - \dfrac{EC_2}{(1+\mu)r^2} + \dfrac{\eta F\ln r}{2(1-\mu)} + \dfrac{\eta F}{2}, \\ \sigma_{\theta e1} = \dfrac{EC_1}{(1+\mu)(1-2\mu)} + \dfrac{EC_2}{(1+\mu)r^2} + \dfrac{\eta F\ln r}{2(1-\mu)} + \dfrac{\mu\eta F}{2(1-\mu)}. \end{cases} \tag{10}$$

Considering the boundary condition $\sigma_r = 0.5(1+\lambda)\sigma_0 + P_0$ at $r = R_0$ and $\sigma_r = \sigma_r^{e-p}$ at $r = R_p$, the integral constants can be solved as follows:

$$\begin{aligned} C_1 = {} & \frac{v(1-\mu)}{E}\left[\frac{1}{2}(1+\lambda)\sigma_0 + P_0\right] \\ & + \frac{{R_p}^2}{{R_e}^2 - {R_p}^2}\frac{v(1-\mu)}{E}\left[\frac{1}{2}(1+\lambda)\sigma_0 + P_0 - \sigma_r^{e-p}\right] \\ & + \frac{\eta Fv}{2E}\frac{{R_p}^2}{{R_e}^2 - {R_p}^2}\ln\frac{R_p}{R_e} - \frac{\eta Fv(1-\mu)}{2E} - \frac{\eta Fv}{2E}\ln R_e, \\ C_2 = {} & \frac{1+\mu}{E}\frac{{R_e}^2{R_p}^2}{{R_e}^2 - {R_p}^2}\left[\frac{1}{2}(1+\lambda)\sigma_0 + P_0 - \sigma_r^{e-p}\right] \\ & + \frac{\eta F(1+\mu)}{2E(1-\mu)}\frac{{R_e}^2{R_p}^2}{{R_e}^2 - {R_p}^2}\ln\frac{R_p}{R_e}. \end{aligned} \tag{11}$$

The stresses in state I can be determined by substituting Equation (11) into Equation (10):

$$\begin{cases} \sigma_{re1} = \dfrac{1}{2}(1+\lambda)\sigma_0 + P_0 + \dfrac{\eta F}{2(1-\mu)}\ln\dfrac{r}{R_e} + \dfrac{{R_p}^2}{{R_p}^2 - {R_e}^2}\left(\dfrac{{R_e}^2}{r^2} - 1\right), \\ \left[\dfrac{1}{2}(1+\lambda)\sigma_0 + P_0 - \sigma_r^{e-p} + \dfrac{\eta F}{2(1-\mu)}\ln\dfrac{R_p}{R_e}\right], \\ \sigma_{\theta e1} = \dfrac{1}{2}(1+\lambda)\sigma_0 + P_0 + \dfrac{\eta F}{2}\dfrac{\ln(r/R_e) + 2\mu - 1}{1-\mu} - \dfrac{{R_p}^2}{{R_p}^2 - {R_e}^2}\left(\dfrac{{R_e}^2}{r^2} + 1\right), \\ \left[\dfrac{1}{2}(1+\lambda)\sigma_0 + P_0 - \sigma_r^{e-p} + \dfrac{\eta F}{2(1-\mu)}\ln\dfrac{R_p}{R_e}\right]. \end{cases} \tag{12}$$

In state II, the surrounding rock is subjected to a horizontal tension $(0.5(1-\lambda)\sigma_0)$ and a vertical pressure $(0.5(1-\lambda)\sigma_0)$. At $r = R_s$, the boundary condition can be written as follows:

$$\begin{cases} \sigma_x = -0.5(1-\lambda)\sigma_0, \\ \sigma_y = 0.5(1-\lambda)\sigma_0, \\ \tau_{r\theta} = 0. \end{cases} \tag{13}$$

Though coordinate transformation, Equation (13) can be re written as follows:

$$\begin{cases} \sigma_r = -0.5(1-\lambda)\sigma_0\cos 2\theta \\ \tau_{r\theta} = 0.5(1-\lambda)\sigma_0\sin 2\theta \end{cases} \tag{14}$$

At $r = R_0, \sigma_x = \tau_{r\theta} = 0$. Therefore, using semi-inverse method, the stresses in state II can be deduced as follows:

$$\begin{cases} \sigma_{re2} = -\dfrac{1}{2}(1-\lambda)\sigma_0\left(1 - 4\dfrac{{R_p}^2}{r^2} + 3\dfrac{{R_p}^4}{r^4}\right)\cos 2\theta, \\ \sigma_{\theta e2} = \dfrac{1}{2}(1-\lambda)\sigma_0\left(1 + 3\dfrac{{R_p}^4}{R^4}\right)\cos 2\theta. \end{cases} \tag{15}$$

Therefore, the stresses in the elastic zone considering pore water pressure can be obtained by superimposing Equations (12) and (15):

$$\begin{aligned} \sigma_{re} = {} & \frac{1}{2}(1+\lambda)\sigma_0 + P_0 + \frac{\eta F}{2(1-\mu)}\ln\frac{r}{R_e} + \frac{{R_p}^2}{{R_p}^2 - {R_e}^2}\left(\frac{{R_e}^2}{r^2} - 1\right) \\ & \cdot\left[\frac{1}{2}(1+\lambda)\sigma_0 + P_0 - \sigma_r^{e-p} + \frac{\eta F}{2(1-\mu)}\ln\frac{R_p}{R_e}\right] \\ & - \frac{1}{2}(1-\lambda)\sigma_0\left(1 - 4\frac{R_p^2}{r^2} + 3\frac{R_p^4}{r^4}\right)\cos 2\theta, \\ \sigma_{\theta e} = {} & \frac{1}{2}(1+\lambda)\sigma_0 + P_0 + \frac{\eta F}{2}\frac{\ln(r/R_e) + 2\mu - 1}{1-\mu} - \frac{{R_p}^2}{{R_p}^2 - {R_e}^2}\left(\frac{{R_e}^2}{r^2} + 1\right) \\ & \cdot\left[\frac{1}{2}(1+\lambda)\sigma_0 + P_0 - \sigma_r^{e-p} + \frac{\eta F}{2(1-\mu)}\ln\frac{R_p}{R_e}\right] \\ & + \frac{1}{2}(1-\lambda)\sigma_0\left(1 + 3\frac{R_p^4}{r^4}\right)\cos 2\theta. \end{aligned} \tag{16}$$

At the interface between the elastic and plastic zones, the radial and tangential stresses should satisfy Equation (3). Thus, σ_r^{e-p} can be derived by substituting Equation (16) into Equation (3):

$$\sigma_r^{e-p} = \frac{\left\{-2R_e^2[(1/2)(1+\lambda)\sigma_0 + P_0] + \eta F/2(1-\mu)\left[\left(R_p^2 - R_e^2\right)\left(\ln\left(R_p/R_e\right) + 2\mu - 1\right) - \left(R_p^2 + R_e^2\right)\ln\left(R_p/R_e\right)\right] + 2(1-\lambda)\sigma_0\cos 2\theta\left(R_p^2 - R_e^2\right) - N_e\left(R_p^2 - R_e^2\right)\right\}}{\left[M\left(R_p^2 - R_e^2\right) - R_p^2 - R_e^2\right]}. \tag{17}$$

The radial and tangential strains in the elastic zone can be derived by substituting Equation (14) into Equation (6):

$$\begin{cases} \varepsilon_{re} = C_1 - \dfrac{C_2}{r^2} + \dfrac{\eta F v}{2E}(\ln r + 1) - \dfrac{1+\mu}{2E}(1-\lambda)\sigma_0\left[1 - 4(1-\mu)\dfrac{R_p^2}{r^2} + 3\dfrac{R_p^4}{r^4}\right]\cos 2\theta, \\ \varepsilon_{\theta e} = C_1 + \dfrac{C_2}{r^2} + \dfrac{\eta F v \ln r}{2E} + \dfrac{1+\mu}{2E}(1-\lambda)\sigma_0\left(1 - 4\mu\dfrac{R_p^2}{r^2} + 3\dfrac{R_p^4}{r^4}\right)\cos 2\theta. \end{cases} \tag{18}$$

Using Equation (5), the displacement in the elastic zone can be easily obtained as

$$u_e = C_1 r + \frac{C_2}{r} + \frac{\eta F v r \ln r}{2E} + \frac{1+\mu}{2E}(1-\lambda)\sigma_0 \cdot \left(r - 4\mu\frac{R_p^2}{r} + 3\frac{R_p^4}{r^3}\right)\cos 2\theta. \tag{19}$$

3.3. Plastic Zone. In the plastic zone, the total strain of the surrounding rock consists of two parts: the plastic and the elastic part. Thus, the following equation can be easily given as

$$\begin{cases} \varepsilon_r = \varepsilon_{rp} + \varepsilon_r^{e-p}, \\ \varepsilon_\theta = \varepsilon_{\theta p} + \varepsilon_\theta^{e-p}. \end{cases} \tag{20}$$

The displacement differential equation in the plastic zone can be obtained by integrating Equations (5), (7), and (20):

$$\frac{\mathrm{d}u_p}{\mathrm{d}r} + \beta_p\frac{u_p}{r} = \varepsilon_r^{e-p} + \beta_p\varepsilon_\theta^{e-p}. \tag{21}$$

With the boundary condition of $u_p = u^{e-p}$ at $r = R_p$, the displacement in the plastic zone can be deduced by solving Equation (21):

$$u_p = \left[\frac{u^{e-p} - \varepsilon_r^{e-p}R_p}{\beta_p + 1}\right]\left(\frac{R_p}{r}\right)^{\beta_p} + \frac{\left(\varepsilon_r^{e-p} + \beta_p\varepsilon_\theta^{e-p}\right)r}{\beta_p + 1}. \tag{22}$$

Using Equation (5), the strains in the plastic zone can be obtained as

$$\begin{cases} \varepsilon_{rp} = \dfrac{\beta_p\left(\varepsilon_r^{e-p} - \varepsilon_\theta^{e-p}\right)}{\beta_p + 1}\left(\dfrac{R_p}{r}\right)^{\beta_p+1} + \dfrac{\varepsilon_r^{e-p} + \beta_p\varepsilon_\theta^{e-p}}{\beta_p + 1}, \\ \varepsilon_{\theta p} = \dfrac{\varepsilon_\theta^{e-p} - \varepsilon_r^{e-p}}{\beta_p + 1}\left(\dfrac{R_p}{r}\right)^{\beta_p+1} + \dfrac{\varepsilon_r^{e-p} + \beta_p\varepsilon_\theta^{e-p}}{\beta_p + 1}. \end{cases} \tag{23}$$

Previous studies indicated that the internal friction angle of the rock does not change significantly in the post-peak phase, and the rock strength is only related to cohesion. Assuming that the cohesion in the plastic zone decreases linearly (see Figure 4), the cohesion at any point in the plastic zone can be expressed as

$$\begin{aligned} c_p &= c_0 - \alpha\left(\varepsilon_{\theta p} - \varepsilon_\theta^{e-p}\right) \\ &= c_0 - \alpha\left[\frac{\varepsilon_\theta^{e-p} - \varepsilon_r^{e-p}}{\beta_p + 1}\left(\frac{R_p}{r}\right)^{\beta_p+1} + \frac{\varepsilon_r^{e-p} + \beta_p\varepsilon_\theta^{e-p}}{\beta_p + 1} - \varepsilon_\theta^{e-p}\right] \\ &= c_0 - \frac{\alpha\left(\varepsilon_\theta^{e-p} - \varepsilon_r^{e-p}\right)}{\beta_p + 1}\left[\left(\frac{R_p}{r}\right)^{\beta_p+1} - 1\right], \end{aligned} \tag{24}$$

where c_0 is the initial cohesion and α is the softening coefficient of the cohesion.

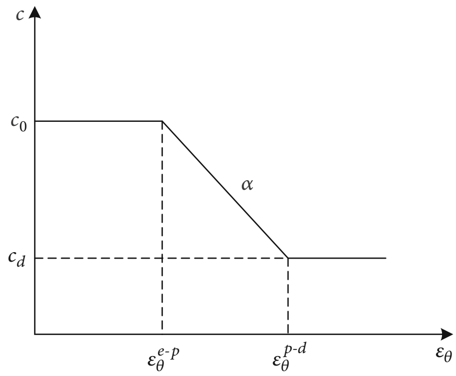

Figure 4: Softening model of the cohesion.

The equilibrium differential equation in the plastic zone can be rewritten by substituting Equations (2), (3), and (24) into Equation (4).

$$\frac{d\sigma_r}{dr} + \frac{(1-M)\sigma_r}{r} - \frac{4\cos\varphi}{\left(\sqrt{3}-2\sin\varphi\right)} \cdot \frac{\left\{c_0 - \alpha(\varepsilon_\theta^{e-p} - \varepsilon_r^{e-p})/\left(\beta_p+1\right)\left[\left(R_p/r\right)^{\beta_p+1} - 1\right]\right\}}{r} - \frac{\eta F}{r} = 0 \tag{25}$$

Combining the boundary condition of $\sigma_r = \sigma_r^{e-p}$ at $r = R_p$, the radial stress in the plastic zone can be obtained by solving Equation (25) as

$$\begin{aligned}\sigma_{rp} = {} & \left(\sigma_r^{e-p} - \frac{N_e + \eta F}{1-M}\right)\left(\frac{R_p}{r}\right)^{1-M} \\ & + \frac{4\cos\varphi/\left(\sqrt{3}-2\sin\varphi\right)\alpha(\varepsilon_\theta^{e-p} - \varepsilon_r^{e-p})}{\left(\beta_p+1\right)\left(\beta_p+M\right)} \cdot \left[\left(\frac{R_p}{r}\right)^{1+\beta_p} - \left(\frac{R_p}{r}\right)^{1-M}\right] \\ & + \frac{4\cos\varphi/\left(\sqrt{3}-2\sin\varphi\right)\alpha(\varepsilon_\theta^{e-p} - \varepsilon_r^{e-p})}{\left(\beta_p+1\right)(1-M)} \cdot \left[1 - \left(\frac{R_p}{r}\right)^{1-M}\right] + \frac{N_e + \eta F}{1-M}.\end{aligned} \tag{26}$$

3.4. Damage Zone. In the damage zone, the total strains of the surrounding rock are also composed of two parts as:

$$\begin{cases}\varepsilon_r = \varepsilon_{rd} + \varepsilon_r^{p-d} \\ \varepsilon_\theta = \varepsilon_{\theta d} + \varepsilon_\theta^{p-d}\end{cases} \tag{27}$$

where ε_r^{p-d} and ε_θ^{p-d} are the radial and tangential strains at the interface between the plastic and damage zones, respectively.

The displacement differential equation in the plastic zone can be obtained by integrating Equations (5), (7), and (27):

$$\frac{du_d}{dr} + \beta_d \frac{u_d}{r} = \varepsilon_r^{p-d} + \beta_d \varepsilon_\theta^{p-d}. \tag{28}$$

Considering the boundary condition of $u_d = u^{p-d}$ at $r = R_d$, the displacement in the plastic zone can be deduced by solving Equation (28):

$$u_d = \left[\frac{u^{p-d} - \varepsilon_r^{p-d} R_d}{\beta_d + 1}\right]\left(\frac{R_d}{r}\right)^{\beta_d} + \frac{\left(\varepsilon_r^{p-d} + \beta_d \varepsilon_\theta^{p-d}\right) r}{\beta_d + 1}. \tag{29}$$

Using Equation (5), the strains in the damage zone can be achieved as follows:

$$\begin{cases}\varepsilon_{rd} = \dfrac{\beta_d\left(\varepsilon_r^{p-d} - \varepsilon_\theta^{p-d}\right)}{\beta_p + 1}\left(\dfrac{R_d}{r}\right)^{\beta_p+1} + \dfrac{\varepsilon_r^{p-d} + \beta_d \varepsilon_\theta^{p-d}}{\beta_d + 1}, \\ \varepsilon_{\theta d} = \dfrac{\varepsilon_\theta^{p-d} - \varepsilon_r^{p-d}}{\beta_d + 1}\left(\dfrac{R_d}{r}\right)^{\beta_d+1} + \dfrac{\varepsilon_r^{p-d} + \beta_d \varepsilon_\theta^{p-d}}{\beta_d + 1}.\end{cases} \tag{30}$$

The equilibrium differential equation in the damage zone can be rewritten by substituting Equations (2) and (3) into Equation (4) as

$$\frac{d\sigma_r}{dr} + \frac{(1-M)\sigma_r - N_d}{r} - \frac{\eta F}{r} = 0. \tag{31}$$

Combining the boundary condition of $\sigma_r = P_i$ at $r = R_0$, the radial stress in the plastic zone can be obtained by solving Equation (31) as

$$\begin{cases}\sigma_{rd} = \left(p_i - \dfrac{N_d + \eta F}{1-M}\right)\left(\dfrac{R_0}{r}\right)^{1-M} + \dfrac{N_d + \eta F}{1-M}, \\ \sigma_{\theta d} = M\left(p_i - \dfrac{N_d + \eta F}{1-M}\right)\left(\dfrac{R_0}{r}\right)^{1-M} + \dfrac{M N_d + \eta F}{1-M}.\end{cases} \tag{32}$$

3.5. Radius of Postpeak Failure Zone. Because of the continuity of radial stress in the surrounding rock of the tunnel, the relationship between R_p and R_d can be established by combining with (26) and (32).

$$\left(\sigma_r^{e-p} - \frac{N_e + \eta F}{1-M}\right)\left(\frac{R_p}{R_d}\right)^{1-M} + \frac{N_e + \eta F}{1-M} + \frac{4\cos\varphi/\left(\sqrt{3} - 2\sin\varphi\right)\alpha(\varepsilon_\theta^{e-p} - \varepsilon_r^{e-p})}{\left(\beta_p + 1\right)\left(\beta_p + M\right)} \cdot \left[\left(\frac{R_p}{R_d}\right)^{1-\beta_p} - \left(\frac{R_p}{R_d}\right)^{1-M}\right] + \frac{4\cos\varphi/\left(\sqrt{3} - 2\sin\varphi\right)\alpha(\varepsilon_\theta^{e-p} - \varepsilon_r^{e-p})}{\left(\beta_p + 1\right)(1-M)}\left[1 - \left(\frac{R_p}{R_d}\right)^{1-M}\right] = \left(p_i - \frac{N_d + \eta F}{1-M}\right)\left(\frac{R_0}{R_d}\right)^{1-M} + \frac{N_d + \eta F}{1-M}. \tag{33}$$

According to Equation (24), the cohesion at $r = R_d$ can be expressed as follows:

$$c_d = c_0 - \frac{\alpha(\varepsilon_\theta^{e-p} - \varepsilon_r^{e-p})}{\beta_p + 1}\left[\left(\frac{R_p}{R_d}\right)^{\beta_p + 1} - 1\right]. \tag{34}$$

Subsequently, the radii R_p and R_d can be derived by integrating (33) and (34).

4. Case Study

The stress distribution and deformation of the tunnel surrounding rock are of great importance for the stability evaluation and support design of the tunnel. In order to study the influence of pore water pressure, intermediate principal stress, and residual cohesion on the stresses and displacement of the tunnel, the mechanical and geometrical parameters of the rock mass are shown in Table 1.

Table 1: Geometrical and mechanical parameters.

Parameters	Values
Radius of the tunnel, R_0 (m)	3
Initial stress, σ_0 (MPa)	16.2
Support pressure, P_i (MPa)	0
Lateral stress coefficient	1.5
Pore water pressure, P_0 (MPa)	5
Pore water pressure coefficient, η	1
R_e/R_0	12
Poisson's ratio, μ	0.25
Young's modulus, E (MPa)	2400
Initial cohesion, c_0 (MPa)	3.5
Residual cohesion, c_d (MPa)	1.5
Dilation angle, ψ_i (°)	10

4.1. Effect of Pore Water Pressure

4.1.1. Postpeak Zone Radii and Surface Displacement. Figure 5 shows the postpeak zone radii and surface displacement around the tunnel under different pore water pressure. The radii of plastic and damage zones and surface displacement all increase with the increase of pore water pressure. For example, as P_0 increases from 3 MPa to 6 MPa, the R_p, R_d, and u_0 values at the tunnel side increase by 0.85 m, 0.83 m, and 36.44 mm, with an increment of 20.48%, 22.61%, and 67.31%, respectively, and the R_p, R_d, and u_0 values at the tunnel crown increase by 0.77 m and 0.75 m, and 72.06 mm, with an increment of 13.62%, 14.24%, and 43.43%, respectively. Therefore, the pore water pressure exerts a crucial influence on the radii of plastic and damage zones and surface displacement.

4.1.2. Stress Distribution in Tunnel Surrounding Rock. Taking the tunnel crown as an example, the stress distribution based on different pore water pressure is shown in Figure 6. It can be seen that the tangential stresses are always larger than the radial stress. The radial stress presents a gradually increasing trend, while the tangential stress presents a trend of first increasing and then decreasing, and the maximum tangential stress appears at the interface between the elastic and plastic zones. As the pore water pressure increases, the maximum tangential stress increases and is farther away from the center of the tunnel.

4.2. Effect of Intermediate Principal Stress

4.2.1. Postpeak Zone Radii and Surface Displacement. In order to research the influence of intermediate principal stress on the tunnel deformation, the current analytical results are compared with the data obtained based on the Mohr-Coulomb criterion. As shown in Figure 7, because of the neglect of the intermediate principal stress in the Mohr-Coulomb criterion, the R_p, R_d, and u_0 values solved by the Mohr-Coulomb criterion are all larger than those solved by the Mogi-Coulomb criterion. For example, the R_p, R_d, and u_0 values at the tunnel side from the Mogi-Coulomb criterion are 4.73 m, 4.22 m, and 76.71 mm, respectively; however, the results from the Mohr-Coulomb criterion are 6.83 m, 5.95 m, and 130.69 mm, with an increment of 44.40%, 40.99%, and 70.37%, respectively.

4.2.2. Stress Distribution in Tunnel Surrounding Rock. The stress distribution at the tunnel crown based on two different criteria is shown in Figure 8. It can be seen that the intermediate principal stress has a significant effect on the stress distribution in the three zones. When the intermediate principal stress is ignored, the stress concentration and maximum tangential stress are larger, and the boundary between the plastic and elastic zones is closer to the tunnel center.

4.3. Effect of Residual Cohesion

4.3.1. Postpeak Zone Radii and Surface Displacement. Figure 9 shows the postpeak zone radii and surface displacement around the tunnel under different types of residual

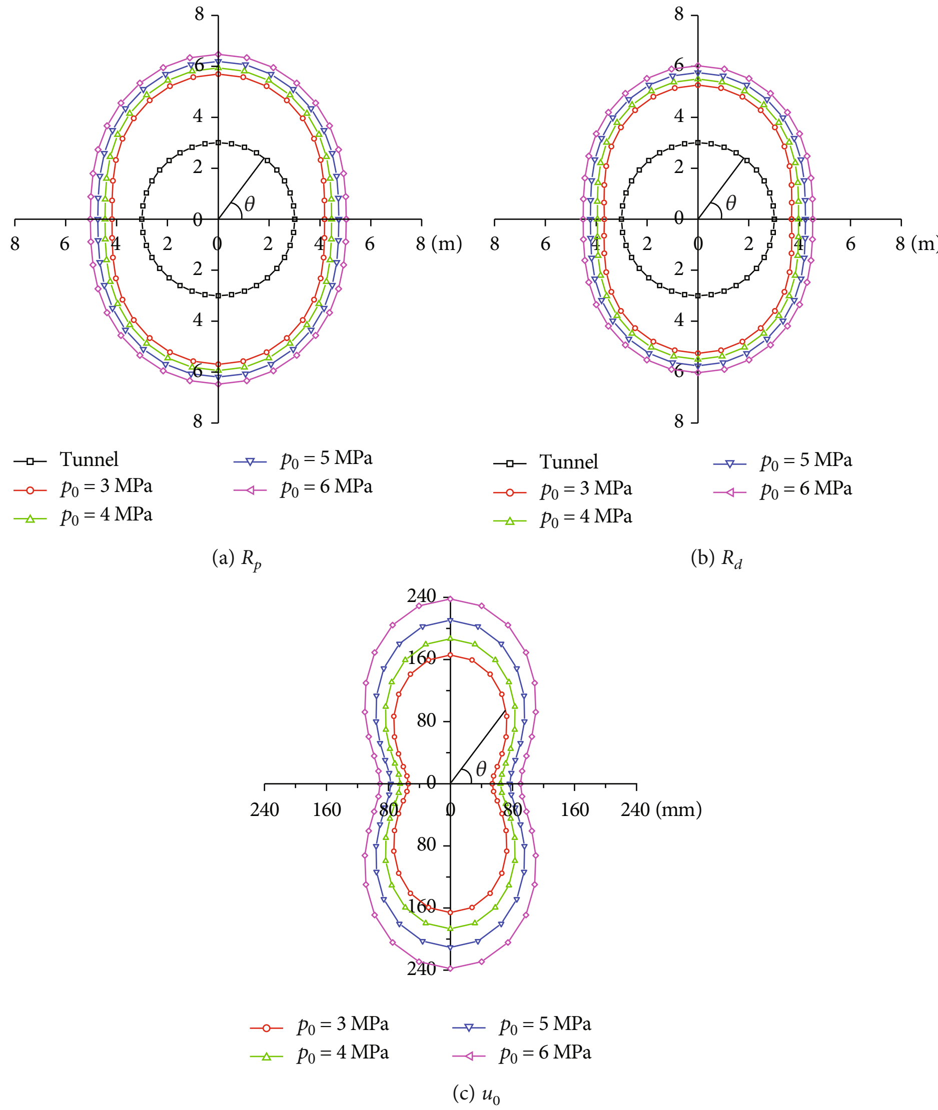

Figure 5: Postpeak zone radii and surface displacement around the tunnel under different pore water pressures.

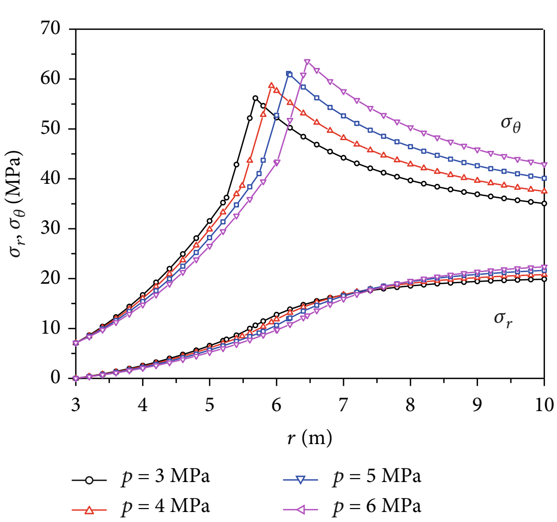

Figure 6: Comparison of stress distribution at the tunnel crown based on different pore water pressures.

cohesion. The radii of plastic and damage zones and surface displacement all decrease with the increase of residual cohesion. For example, as c_d increases from 1.5 MPa to 2.5 MPa, the R_p, R_d, and u_0 values at the tunnel side decrease by 1.34 m, 0.86 m, and 37.39 mm, with a reduction of 24.45%, 18.07%, and 37.59%, respectively, and the R_p, R_d, and u_0 values at the tunnel crown increase by 2.41 m and 1.94 m, and 164.56 mm, with a reduction of 32.01%, 28.24%, and 52.63%, respectively. Therefore, some measures, such as grouting, can be used to increase the residual cohesion of the rock mass and reduce the deformation of the tunnel.

4.3.2. Stress Distribution in Tunnel Surrounding Rock. The stress distribution based on different types of residual cohesion is shown in Figure 10. It can be seen that the radial stress is always in the increasing trend and the tangential stress is always larger than the radial stress, which are similar to those laws in Figures 6 and 9. As the residual cohesion increases,

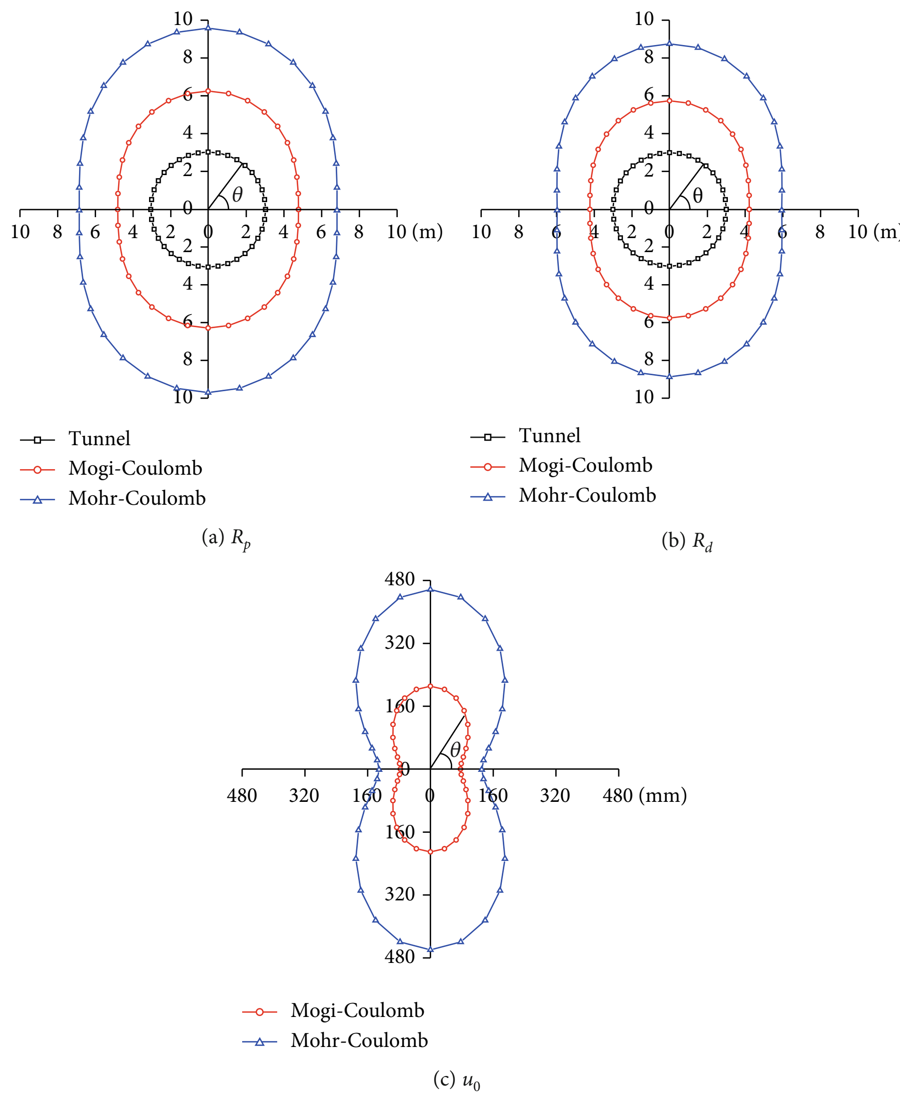

FIGURE 7: Postpeak zone radii and surface displacement around the tunnel under different strength criteria.

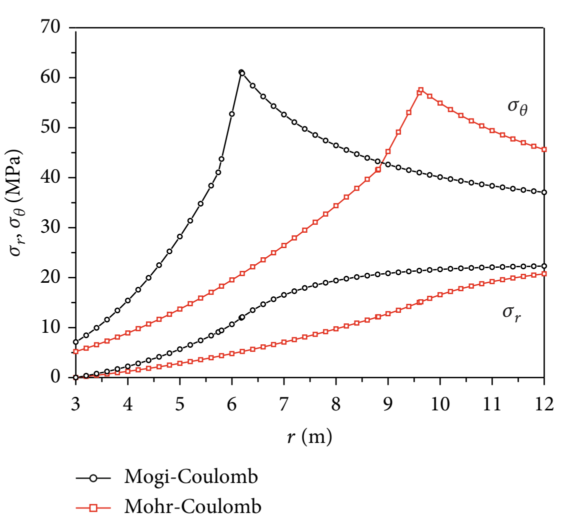

FIGURE 8: Comparison of stress distribution at the tunnel crown based on different strength criteria.

the maximum tangential stress increases slightly, but the boundary between the plastic and elastic zones moves farther away from the center of the tunnel.

5. Conclusions

Considering the pore water pressure, the stress distribution and postpeak zone radii in the surrounding rock of a deep tunnel in water-rich areas are deduced based on a strain-softening model and the Mogi-Coulomb criterion. The influence of pore water pressure, intermediate principal stress, and residual cohesion on the stress distribution and postpeak zone radii is also discussed. The conclusions can be summarized as follows:

(1) As for the stress distribution in the surrounding rock of a tunnel, the tangential stresses are always larger than the radial stress. The radial stress presents a gradually increasing trend, while the tangential stress

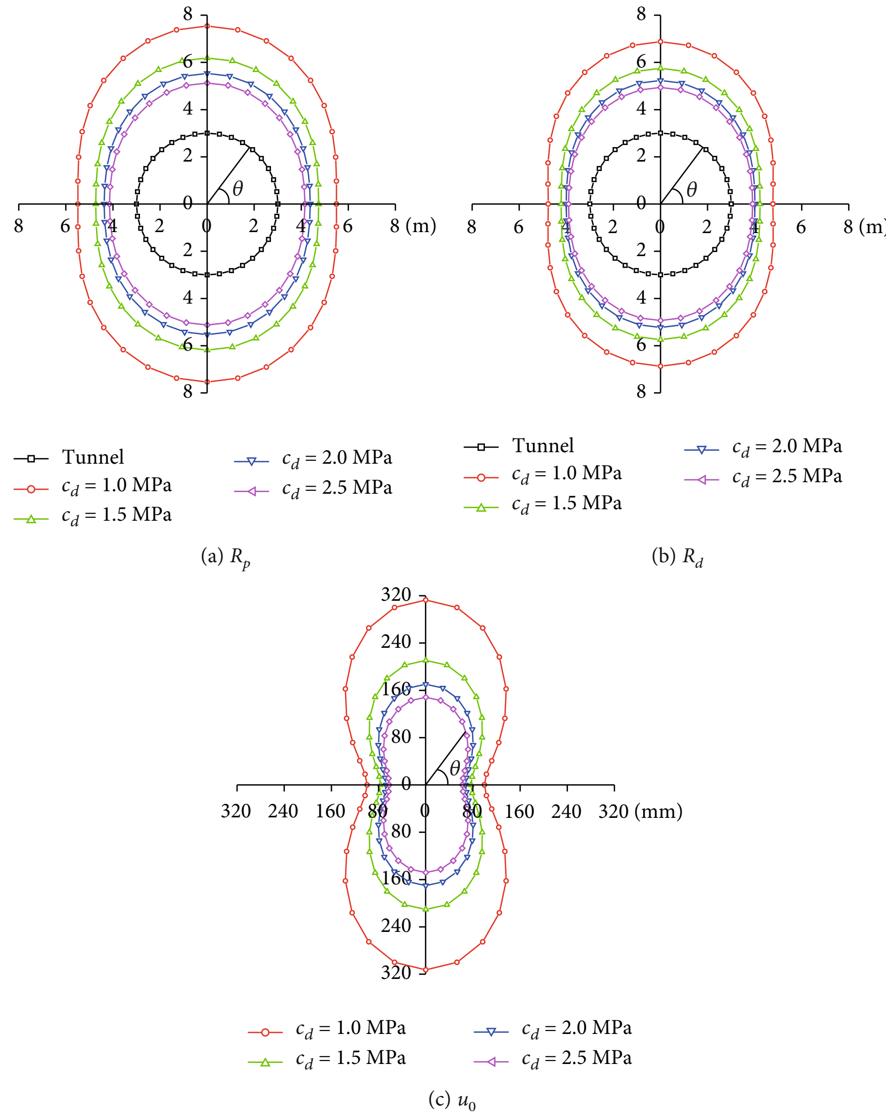

FIGURE 9: Postpeak zone radii and surface displacement around the tunnel under different types of residual cohesion.

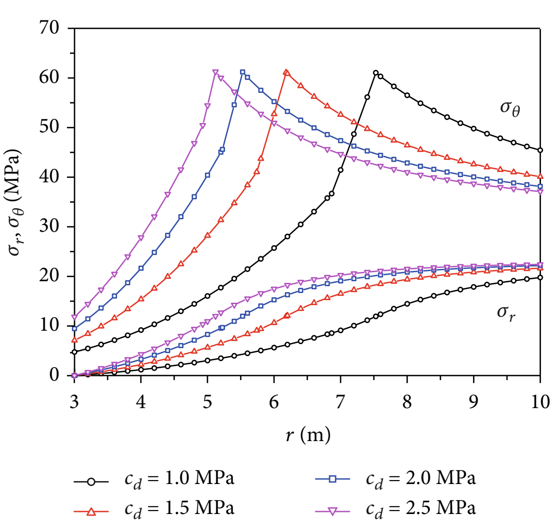

FIGURE 10: Comparison of stress distribution at the tunnel crown based on different types of residual cohesion.

presents a trend of first increasing and then decreasing, and the maximum tangential stress appears at the interface between the elastic and plastic zones

(2) The postpeak zone radii and surface displacement increase with the increasing pore water pressure and decreasing residual cohesion. The greater the pore water pressure, the farther the maximum tangential stress is from the center of the tunnel. Residual strength has little effect on the maximum tangential stress

(3) Because of the neglect of intermediate principal stress in the Mohr-Coulomb criterion, the postpeak zone radii, surface displacement, and maximum tangential stress solved by the Mohr-Coulomb criterion are all larger than those solved by the Mogi-Coulomb criterion. Therefore, opportune consideration of the intermediate principal stress can lead to a more reasonable tunnel support design

Data Availability

All data generated or analyzed during this study are included in this published article.

Conflicts of Interest

The authors declare that they have no conflicts of interest.

Authors' Contributions

The manuscript is approved by all authors for publication.

Acknowledgments

Financial support from the National Key Research and Development Program of China (No. 2017YFC0603004) and the China Postdoctoral Science Foundation funded project (No. 2020M671649) is gratefully acknowledged.

References

[1] B. Jiang, L. Wang, Y. Lu, S. Gu, and X. Sun, "Failure mechanism analysis and support design for deep composite soft rock roadway: a case study of the Yangcheng Coal Mine in China," *Shock and Vibration*, vol. 2015, Article ID 452479, 14 pages, 2015.

[2] Q. Guo, J. Pan, X. Wu, X. Xi, and M. Cai, "A new unified solution for circular tunnels based on generalized SMP criterion considering the strain softening and dilatancy," *Advances in Civil Engineering*, vol. 2019, Article ID 1684707, 10 pages, 2019.

[3] H. Fan, L. Wang, and W. Liu, "An analytical solution for stresses and deformations of tunnels in a non-uniform stress field based on strain-softening model and Mogi-Coulomb criterion," *Latin American Journal of Solids and Structures*, vol. 17, no. 1, pp. 1–16, 2020.

[4] Y. Xue, P. G. Ranjith, F. Dang et al., "Analysis of deformation, permeability and energy evolution characteristics of coal mass around borehole after excavation," *Natural Resources Research*, vol. 29, no. 5, pp. 3159–3177, 2020.

[5] Q. Zhang, B. S. Jiang, X. S. Wu, H. Q. Zhang, and L. J. Han, "Elasto-plastic coupling analysis of circular openings in elasto-brittle-plastic rock mass," *Theoretical and Applied Fracture Mechanics*, vol. 60, no. 1, pp. 60–67, 2012.

[6] B. Jiang, Q. Zhang, Y. He, and L. Han, "Elastioplastic analysis of cracked surrounding rocks in deep circular openings," *Chinese Journal of Rock Mechanics and Engineering*, vol. 26, pp. 982–986, 2007.

[7] K. Park and Y. Kim, "Analytical solution for a circular opening in an elastic-brittle-plastic rock," *International Journal of Rock Mechanics and Mining Sciences*, vol. 43, no. 4, pp. 616–622, 2006.

[8] Y. K. Lee and S. Pietruszczak, "A new numerical procedure for elasto-plastic analysis of a circular opening excavated in a strain-softening rock mass," *Tunnelling and Underground Space Technology*, vol. 23, no. 5, pp. 588–599, 2008.

[9] L. R. Alejano, A. Rodriguez-Dono, E. Alonso, and G. Fdez-Manín, "Ground reaction curves for tunnels excavated in different quality rock masses showing several types of post-failure behaviour," *Tunnelling and Underground Space Technology*, vol. 24, no. 6, pp. 689–705, 2009.

[10] R. Z. Mohammad and F. Ahmad, "Elastic-brittle-plastic analysis of circular deep underwater cavities in a Mohr-Coulomb rock mass considering seepage forces," *International Journal of Geomechanics*, vol. 15, pp. 1–10, 2015.

[11] S. K. Sharan, "Elastic-brittle-plastic analysis of circular openings in Hoek-Brown media," *International Journal of Rock Mechanics and Mining Science*, vol. 40, no. 6, pp. 817–824, 2003.

[12] S. K. Sharan, "Exact and approximate solutions for displacements around circular openings in elastic-brittle-plastic Hoek-Brown rock," *International Journal of Rock Mechanics and Mining Sciences*, vol. 42, no. 4, pp. 542–549, 2005.

[13] L. R. Alejano, E. Alonso, A. Rodríguez-Dono, and G. Fernández-Manín, "Application of the convergence-confinement method to tunnels in rock masses exhibiting Hoek-Brown strain-softening behaviour," *International Journal of Rock Mechanics and Mining Sciences*, vol. 47, no. 1, pp. 150–160, 2010.

[14] R. Chen and F. Tonon, "Closed-form solutions for a circular tunnel in elastic-brittle-plastic ground with the original and generalized Hoek–Brown failure criteria," *Rock Mechanics and Rock Engineering*, vol. 44, no. 2, pp. 169–178, 2011.

[15] Z. Li, L. Wang, Y. Lu, W. Li, K. Wang, and H. Fan, "Experimental investigation on true triaxial deformation and progressive damage behaviour of sandstone," *Scientific Reports*, vol. 9, no. 1, pp. 3386–3404, 2019.

[16] Y. Xue, T. Teng, F. Dang, Z. Ma, S. Wang, and H. Xue, "Productivity analysis of fractured wells in reservoir of hydrogen and carbon based on dual-porosity medium model," *International Journal of Hydrogen Energy*, vol. 45, no. 39, pp. 20240–20249, 2020.

[17] L. A. Galin, "Plane elastic-plastic problem: plastic regions around circular holes in plates and beams," *Prikladnaia Matematika i Mechanika*, vol. 10, pp. 365–386, 1946.

[18] E. Detournay, "An approximate statical solution of the elastoplastic interface for the problem of Galin with a cohesive-frictional material," *International Journal of Solids and Structures*, vol. 22, no. 12, pp. 1435–1454, 1986.

[19] E. Detournay and C. Fairhurst, "Two-dimensional elastoplastic analysis of a long, cylindrical cavity under non-hydrostatic loading," *International Journal of Rock Mechanics and Mining Science and Geomechanics Abstracts*, vol. 24, no. 4, pp. 197–211, 1987.

[20] E. Detournay and C. S. John, "Design charts for a deep circular tunnel under non-uniform loading," *Rock Mechanics and Rock Engineering*, vol. 21, no. 2, pp. 119–137, 1988.

[21] G. Tokar, "Generalization of Galin's problem to frictional materials and discontinuous stress fields," *International Journal of Solids and Structures*, vol. 26, no. 2, pp. 129–147, 1990.

[22] M. J. Leitman and P. Villaggio, "Plastic zone around circular holes," *Journal of Engineering Mechanics*, vol. 135, no. 12, pp. 1467–1471, 2009.

[23] W. Ochensberger, C. C. Celigoj, and M. H. Ulz, "Amendment to the Galin plane elastoplastic solution," *Journal of Engineering Mechanics*, vol. 139, no. 11, pp. 1658–1662, 2013.

[24] X. Li, S. Du, and B. Chen, "Unified analytical solution for deep circular tunnel with consideration of seepage pressure, grouting and lining," *Journal of Central South University*, vol. 24, no. 6, pp. 1483–1493, 2017.

[25] J. Pan, Q. Guo, F. Ren, and M. Cai, "Comparative analysis of different strength criteria for deep-buried rock roadway under

seepage," *Journal of China Coal Society*, vol. 44, no. 11, pp. 3369–3378, 2019.

[26] Y. J. Shin, B. M. Kim, J. H. Shin, and I. M. Lee, "The ground reaction curve of underwater tunnels considering seepage forces," *Tunnelling and Underground Space Technology*, vol. 25, no. 4, pp. 315–324, 2010.

[27] K. Mogi, "Effect of the intermediate principal stress on rock failure," *Journal of Geophysical Research*, vol. 72, no. 20, pp. 5117–5131, 1967.

[28] K. Mogi, "Fracture and flow of rocks under high triaxial compression," *Journal of Geophysical Research*, vol. 76, no. 5, pp. 1255–1269, 1971.

[29] B. C. Haimson and C. Chang, "A new true triaxial cell for testing mechanical properties of rock, and its use to determine rock strength and deformability of Westerly granite," *International Journal of Rock Mechanics and Mining Sciences*, vol. 37, no. 1-2, pp. 285–296, 2000.

Hindawi
Geofluids
Volume 2021, Article ID 6689966, 16 pages
https://doi.org/10.1155/2021/6689966

Research Article

Deformation Behavior of Mining beneath Flat and Sloping Terrains in Mountainous Areas

Zhao Jianjun,[1] **Wan Xun**,[1] **Shi Yanbing**,[1] **Wei Jiangbo**,[2] **and Min Lee Lee**[3]

[1]State Key Laboratory of Geohazard Prevention and Geoenvironment Protection, Chengdu University of Technology, 610059 Chengdu, China
[2]Shaanxi Provincial Key Laboratory of Geological Support for Coal Green Exploitation, Xi'an University of Science and Technology, 710054 Shaanxi, China
[3]Faculty of Science and Engineering, University of Nottingham Malaysia, 43500 Selangor, Malaysia

Correspondence should be addressed to Zhao Jianjun; j.j.zhao@qq.com

Received 27 November 2020; Revised 9 January 2021; Accepted 27 January 2021; Published 19 February 2021

Academic Editor: Yi Xue

Slope structures and surface terrains are two significant factors affecting the deformation behavior of mining slopes in mountainous areas. This research is aimed at investigating the deformation characteristics of a mining slope wielding Particle Flow Code (PFC), with 9 different mining configurations (i.e., horizontal distance from extracted panel center to slope shoulder, $D = -200$ m, −150 m, −100 m, −50 m, 0 m, 50 m, 100 m, 150 m, and 200 m). A representative slope in Faer Town, Liupanshui City, Guizhou Province, China, was selected, which was characterized by soft and hard interbedded rock strata. The results indicated that the overlying rock mass tended to move towards the sloping surface with mining beneath sloping terrain, which brought an asymmetrical subsidence funnel, and formed a wider relative disturbance range on the slope surface. With the vertical subsidence increasing additionally, the stability of the overall slope deteriorated. A safe mining range should be proposed based on evaluating the time-dependent deformation behavior at the slope shoulder and the overall slope stability.

1. Introduction

Longwall mining is one of the most generally adopted underground mining methods, particularly in mining areas with relatively uniform and thick coal beds [1]. Surface subsidence is the leading form of mining-induced geological hazards which has caused various adverse effects to the environment [2, 3].

Analyzing the mechanism of ground movement and estimating their magnitudes and geometries have long been the main concerns in risk management of mining operations. A reliable prediction of ground subsidence caused by the mining operations remains a great challenge [4]. An extracted panel formed, the deformation of the overlying rock mass depends on many factors, i.e., bedding structure, thickness, strength, discontinuous geometric, mechanical characteristics of the panel, thickness of the mined coal seam, and width and length of the extracted panel [5–8]. In addition to the properties of the coal seams and the overlying rock masses, in situ stress conditions, groundwater conditions, terrain gradient, mining method, process of extraction, and distribution of pillars may all add complexity to the ground subsidence estimation [4, 9, 10]. The ground deformation induced by the mining operation is thus a multifactor coupling problem in temporal and spatial scales.

The prediction of ground subsidence can be performed by various methods, such as numerical simulation, physical modelling, influence function method, empirical approach, and analytical technique [10–14]. In addition, with the advancement in geographic information system (GIS) and remote sensing (RS) technologies, the spatial database can be constructed to analyze the shape and magnitude of the subsidence [15, 16]. The capability of GPS network application in measuring ground horizontal displacement has made great contributions to monitoring and early warning systems for mining-induced geological hazards [17]. Application of geophysical methods enables geologists to develop a comprehensive understanding of fracture evolution in

Table 1: Distributions of mining-induced geological hazards in Liupanshui City on different strata (data compiled by end of 2016).

Types of geological hazards	Main distribution strata											Total
	C_2hn	C_3mp	P_2l	P_2m+q	P_3l	$P_3\beta$	T_1f	T_1y	T_1yn	T_2g	E	
Landslide	1	1	4	0	86	2	73	1	3	1	0	181
Collapse	0	0	0	2	9	1	19	2	6	0	1	39
Surface subsidence	0	0	2	1	69	2	37	4	8	0	0	122
Ground fissure	0	0	0	1	3	0	4	3	1	0	0	12
Debris flow	0	0	0	0	2	0	0	0	0	0	0	2
Total	1	1	6	4	169	8	133	10	18	1	1	356

the overburden rock masses induced by shallow mining activities [18, 19].

Many researchers performed numerical and physical modelling to estimate the subsidence of complex ground profiles. The physical modelling normally has difficulties dealing with an in situ stress state of rock mass (i.e., effect of gravitational force), which can be only simulated by geotechnical centrifuge [20, 21]. Performing a large geotechnical centrifuge test, however, can be extremely costly. The numerical simulation has been widely used to analyze mining slopes with complex geometries and simulate discontinuous and nonlinear mechanical behavior of rock masses [4, 9, 22–27]. The Discrete Element Method (DEM) is an efficient tool for analyzing instability of jointed rock slope, as proven by numerous successful cases [28–30].

There were in total 356 incidents of geological hazards (refer to Table 1) reported in the mountainous area in Liupanshui City, Guizhou Province, southwest of China. By the end of 2016, most of the hazards occurred on the P_3l and T_1f strata. A typical mining slope named Jianshanying slope in Faer Town, Liupanshui City, was selected. Wielding Particle Flow Code (PFC) to analyze deformation behavior with underground mining operations.

2. Mechanisms of Mining-Induced Slope Instability

Numerous previous studies reported that slopes subjected to underground mining are prone to caving and landslides [31–34]. There were 2 main models of mining-induced slope failures: (1) progressive rock falls and caving failures, which cause nearly vertical cliffs [25, 35], and (2) rock masses extruded from the slope toe causing holistic instability [36]. With underground extraction performed beyond the slope shoulder, most instabilities are initiated [37, 38].

According to Salmi et al. [4], the surface topography has a considerable impact on the mechanisms of mining-induced slope instability. Mining in hilly and mountainous terrains usually increases the risk of slope failure. In addition, mining beneath sloping terrains imposes an additional threat on ground subsidence, which usually occurs near a valley [35]. The coal seam extracted beneath flat terrains, the rock masses above the extracted panel were fragmented and caved into the panel immediately, and the fragmented rocks tend to fill the void forming a goaf. As a result of ascending step-loading imposed by the upper caving block, the stiffness of rock mass increases gradually [39]. The overburden strata remain intact and bend towards the extracted panel [40]. Owing to the expansibility of rock, the rock masses falling into the panel are subjected to lateral forces from the virgin strata, which rise gradually with the increase of depth and reach the maximum value at the coal pillar [41]. The boundary conditions on both sides of the extracted panel are identical, and hence, the magnitude and direction of lateral forces are completely symmetrical. Under the circumstances, there are different horizontal deformations in the rock masses, and it causes a symmetrical subsidence funnel on the surface [42]. In an extraction performed near or beneath a cliff, the lateral forces induced above the goaf (directed from the plateau towards the valley) are not counterbalanced by an identical force in the opposite direction. The rock mass near the valley has a greater horizontal displacement, and hence, an asymmetric subsidence funnel occurs on the slope surface.

The magnitude and shape of the surface subsidence, which is induced by mining operations under the condition of flat terrains, have been studied extensively. The localized deformation and overall instability constitute much more uncertainties attributed to the complex combination of terrains and structures in the sloping terrains. Studies on ground subsidence induced by mining activities in sloping terrains are still very limited. Several previous case studies of large-scale slope failures induced by mining include the Zhangjiawan collapse and Madaling landslide in Guizhou, China [36], and one of the largest contemporary landslides and mass movements reported at Nattai North, Australia [43], have drawn the global attention on the mass movement caused by mining activities and provoke the present study to be carried out.

This research is rooted in the exploration of mining-induced subsidence rules in P_3l and T_1f with Liupanshui City, Guizhou Province, China, as the typical. To be detailed, this research innovatively proposed 9 mining configurations for expounding the deformation behavior of mining beneath flat and sloping terrains by wielding Particle Flow Code, which is applied to the soft and hard interbedded and jointed slopes in the mountainous area. Furthermore, the time-dependent deformation was measured at the slope shoulder, as the transition part of the flat and sloping terrains, to propose a safe mining range, which was meaningful in the risk management of mining operations.

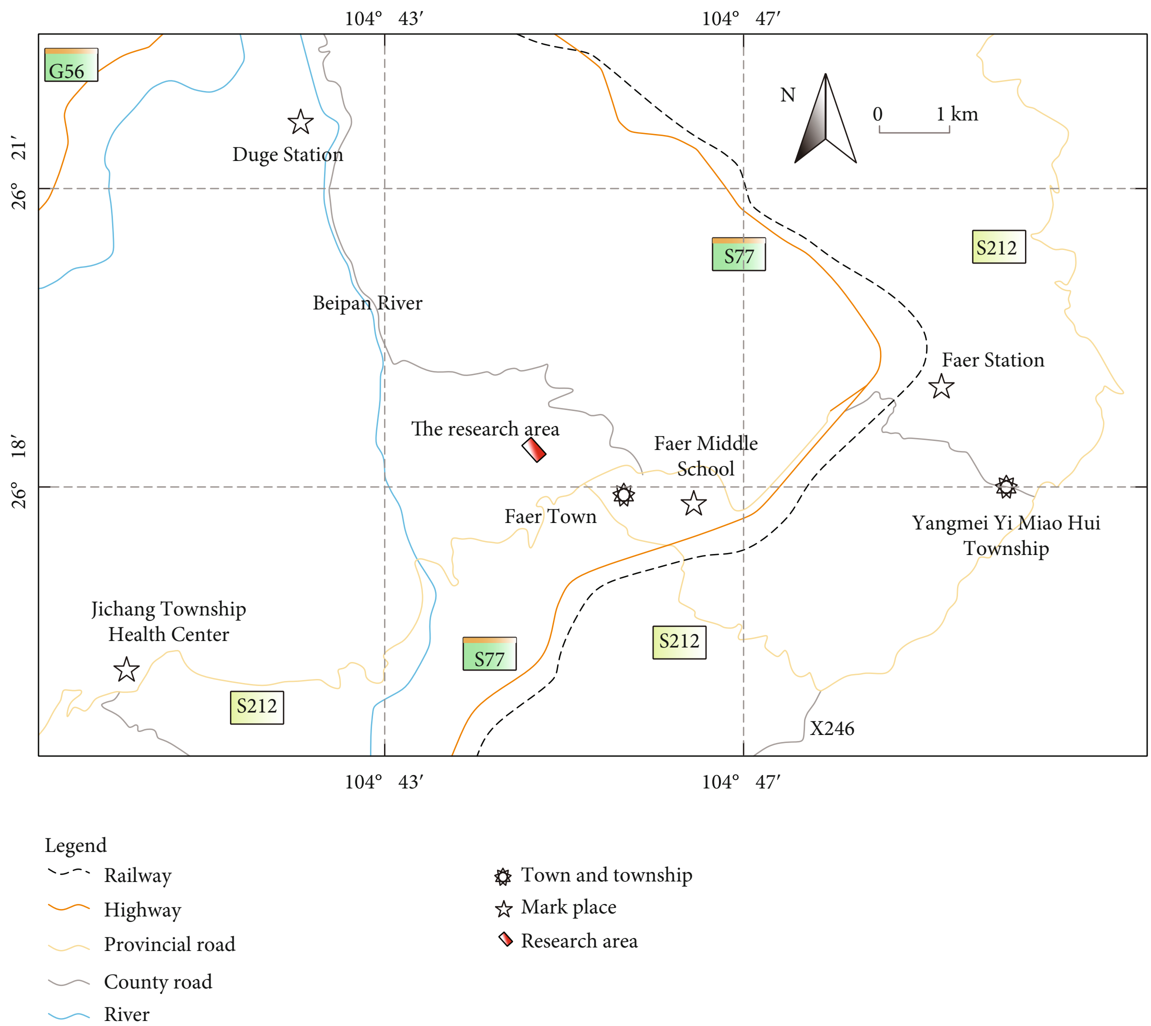

Figure 1: Location of study area.

3. Case Study

3.1. Model Development. Liupanshui City in Guizhou Province, China, is known for its proven coal resources and reserves. The city which is known as the "Southwest Coal Sea" has developed multistage coal seams on the P_3l stratum. In 2015, there were more than 800 mines in the city, while more than 400 landslide and ground subsidence incidents have been reported, which were mainly caused by improperly planned mining activities. In the present study, a mining slope named Jianshanying slope in Faer Town, Liupanshui City, was selected as the case study. The specific geographical coordinates of the study area are E104°44′11″ and N26°18′ 20″ (Figures 1 and 2).

In the western part of the Guizhou plateau, a low mountainous terrain was formed because of the tectonic erosion. Typically, both steep and gentle structures were formed in the mining slope. Most of the coal-bearing strata are located in the flat terrains, while the interbedded sandstone and mudstone are mainly located in the sloping terrains. The surface terrain of the Jianshanying slope was reasonably generalized to simplify the subsequent numerical modelling processes. Three sets of dominant joints were considered in each strata, and one set has the same tendency as the strata. The general stratifications of the slope are presented in Figure 3. Coal and mudstone formed the relatively weak strata in the slope, however, the effect of the stratified structure was not considered in them.

Mining slopes are typically prone to time-dependent failures in the form of ground subsidence and slope sliding [44]. After going through a long process of mining, 6 coal layers had been mined out beneath the Jianshanying mining slope forming a total of 13 mining panels. These mining activities had caused severe impact on the stability of the slope. To simplify the analysis, the present study only focused on the impact of mining with the first coal layer on the slope instability. Nine mining configurations with different horizontal distances (D) from the extracted panel center to slope shoulder (where the flat terrain intersected with the sloping terrain) were set, namely, $D = -200$ m, -150 m, -100 m, -50 m, 0 m, 50 m, 100 m, 150 m, and 200 m (see Figure 4 and Table 2). The width of each extracted panel along the strata dip direction was within the range of 150~250 m, while the thickness of the coal seam was ranging from 2 to 4 m in

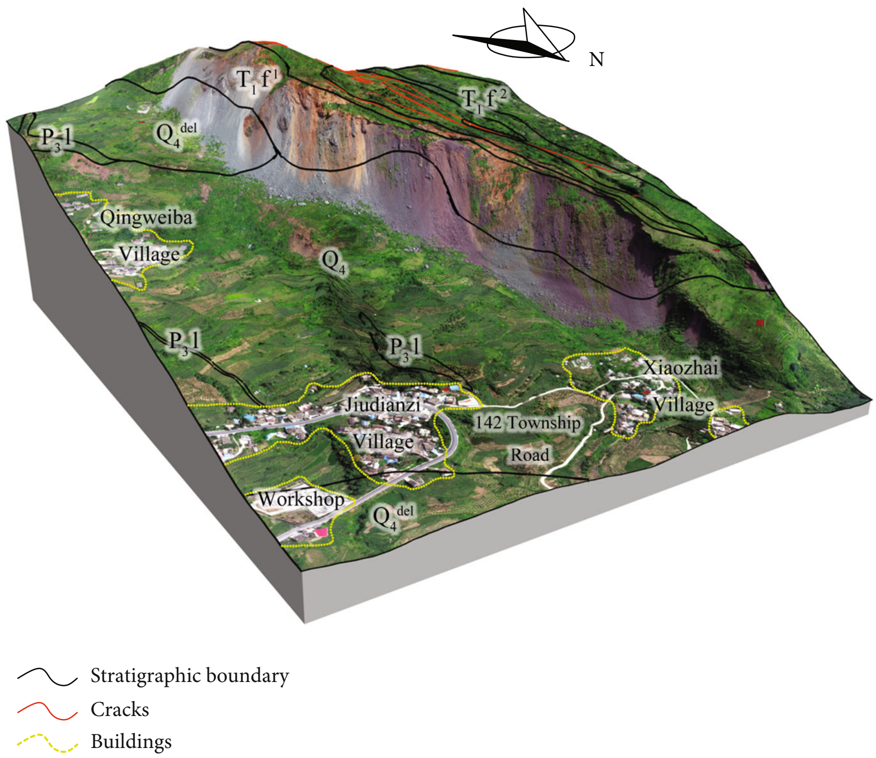

Figure 2: 3D terrains of Jianshanying mining slope.

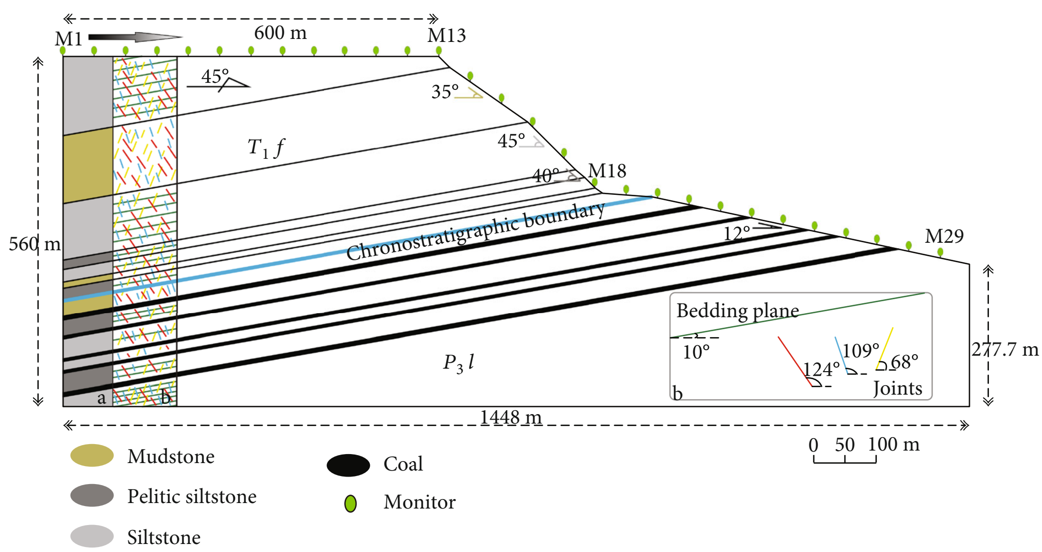

Figure 3: Generalized profile of mining slope model ("T_1f" is Feixianguan group and "P_3l" is Longtan group).

statistics. The width of the extracted panel and the thickness of the mined-out coal seam were fixed at 200 m and 6 m in practice. The above configurations were set to systematically study the influences of extracted panel depth, horizontal distance between the center of extracted panel and slope shoulder, and surface terrain condition on the instability of the mining slope. The extracted panel was located beneath a flat terrain with $D \leq -100$ m, while the extracted panel was beneath a sloping terrain with $D \geq 100$ m (Figure 4). A total of 29 monitoring points with a horizontal interval of 50 m were set in the numerical model, for revealing the deformation characteristics of the slope surface with various configurations.

3.2. Particle Flow Code. Rock masses are discontinuous medium, and hence, the use of the DEM is justifiable [4]. PFC (Particle Flow Code), a popular program based on the DEM, is widely used to simulate the macroscopic characteristics of rock-soil masses. The soil/rock aggregates are modelled as either rigid disks (2D) or spheres (3D), and they are

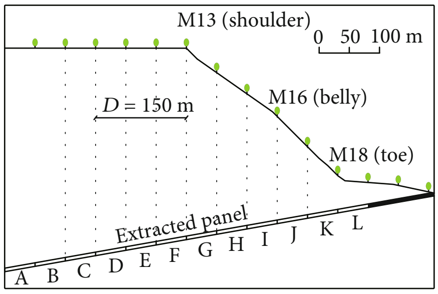

Figure 4: Mining configurations considered for numerical simulation.

connected by specific contact models as an equivalent model of rock-soil mass [45]. The PFC adopts the time step iterative calculation method (Figure 5). Newton's second law and the law of force and displacement are repeatedly applied in the calculation for updating the motion state of units in real-time, and the contact force and torque between the updated units are further determined by the force-displacement relationship [46].

The law of force-displacement reflects the contact relationship between particles, also the relationship between the contact force and relative motion. In the PFC model, the contact force ball-ball and ball-wall can be divided into normal force and transverse force (Equation (1)). The particles move and rotate under the action of unbalanced forces and unbalanced torques (Equations (2) and (3)). The motion equation of PFC is solved using the centered finite difference method in relation to time step (Δt). The translational and rotational acceleration ($\ddot{x}_i^{(t)}$ and $\dot{\omega}_i^{(t)}$) of particles at any time can be obtained from Equations (4) and (5). The translational velocity ($\dot{x}_i^{(t)}$), angular velocity ($\omega_i^{(t)}$), and displacement ($x_i^{(t)}$) of particle motion can be obtained from equation transformation (Equations (6), (7), and (8)). The definitions of the model parameters are summarized in Table 3:

$$\overrightarrow{F_i} = \overrightarrow{F_i^n} + \overrightarrow{F_i^s}, \tag{1}$$

$$\overrightarrow{F_i} = m\left(\overrightarrow{\ddot{x}_i} - \overrightarrow{g_i}\right), \tag{2}$$

$$\overrightarrow{M_i} = \overrightarrow{\dot{H}_i}, \tag{3}$$

$$\ddot{x}_i^{(t)} = \frac{1}{\Delta t}\left(\dot{x}_i^{(t+\Delta t/2)} - \dot{x}_i^{(t-\Delta t/2)}\right), \tag{4}$$

$$\dot{\omega}_i^{(t)} = \frac{1}{\Delta t}\left(\omega_i^{(t+\Delta t/2)} - \omega_i^{(t-\Delta t/2)}\right), \tag{5}$$

$$\dot{x}_i^{(t+\Delta t/2)} = \dot{x}_i^{(t-\Delta t/2)} + \left(\frac{F_i^{(t)}}{m} + g_i\right)\Delta t, \tag{6}$$

$$\omega_i^{(t+\Delta t/2)} = \omega_i^{(t-\Delta t/2)}\Big) + \left(\frac{M_i^{(t)}}{I}\right)\Delta t, \tag{7}$$

$$x_i^{(t+\Delta t)} = x_i^{(t)} + x_i^{(t+\Delta t/2)}\Delta t. \tag{8}$$

3.3. Rock Mass Parameters. In particle flow simulation, the macroscopic mechanical behaviors of the rock and soil masses are governed by the microscopic mechanical properties of particles, nevertheless, there is a highly nonlinear relationship between them. Typically, the transformations of the macroscopic and microscopic parameters are carried out by means of biaxial compression tests [47]. The most common set of siltstone and pelitic siltstone was selected for parameter calibration to avoid the discreteness of rock samples. The stress-strain curve obtained from the PFC simulation under the condition of no confining pressure was reasonably consistent with that of the laboratory (Figure 6). Both siltstone and pelitic siltstone showed significant brittle failure characteristics. The initial balance was carried out after gravity loading in the process of engineering scale simulation, and the increment of displacement and velocity during the process was cleared, and hence, the consistency of the stress-strain curve in the compaction stage was superfluous. The elastic modulus (E) and unconfined compressive strength (UCS) of siltstone and pelitic siltstone obtained from the laboratory and PFC are shown in Table 4; moreover, the fitting degree of their magnitude values is a measure index of calibration. Both mudstone and coal retrieved in the field had great discreteness with mechanical properties, which obstructed calibration by the PFC test. This research attempted to bring empirical values to the parameters of coal and mudstone, and the full mining model simulation was used in comparison with the actual situation. The parameter inversion method was used to adjust the rock block parameters as empirical.

The mechanical parameters of rock masses are generally smaller than those of intact rock with laboratory scale because of the size effect and discontinuity of rock masses [48]. Practically, the effects of bedding plane and dominant joints are often considered in simulation, and the equivalent jointed rock masses technology is applied. The smooth-joint model was chosen over the flat-joint model, which is poor in simulating the plane dilation mechanics, to reflect the constitutive relation. Furthermore, the smooth-joint model enabled the joint properties to a limited range on both sides of them, and a random joint model was formed to verify and correspond to the characteristics of the slope on-site. For this purpose, based on the laboratory mechanical experimental results, numerical simulation calibration testing, and the equivalent rock masses technique, the full mining model (the six-coal-seam mining model) simulation was used in comparison with the actual situation, which ensured that the simulation outputs were reasonably consistent with the actual field deformation (i.e., occurrence of deposition at the slope toe, presence of tensile cracks in the middle of the slope, and subsidence at the edge of slope), which was acquired through the UAV survey (Figure 7). In this paper, parameters related to rock and soil masses materials were obtained and adjusted by parameter inversion. The calibrated microscopic mechanical parameters of the rock masses, which were adopted for the PFC simulation of the Jianshanying mining slope, are summarized in Table 5.

Table 2: Details of mining configurations.

D (m)	-200	-150	-100	-50	0	50	100	150	200
Extracted panels	$A+B+C+D$	$B+C+D+E$	$C+D+E+F$	$D+E+F+G$	$E+F+G+H$	$F+G+H+I$	$G+H+I+J$	$H+I+J+K$	$I+J+K+L$
Panel depth (m)	345.5	336.6	328	319.2	310.1	261.5	217.1	170.9	112.1

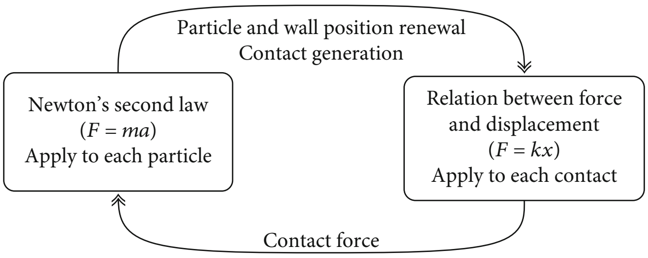

Figure 5: Workflow of PFC analysis.

Table 3: Definitions of symbols.

Symbol	Definition	Symbol	Definition
F_i	Contact force	$\dot{x}_i$	Translational velocity
F_i^n	Normal contact force	x_i	Displacement
F_i^s	Shear contact force	$\dot{\omega}_i$	Slew acceleration
g_i	Gravitational acceleration	ω_i	Angular velocity
M_i	Unbalance moment	I	Inertia moment
$\ddot{H}_i$	Angular momentum	Δt	Time step
$\ddot{x}_i$	Translational acceleration	m	Particle quality

4. Results of Numerical Analysis

4.1. Evaluation of Crack Propagation. In the panel extracted, tensile cracks initiated to propagate in the overburden materials. The cracks mainly aggregated at the boundary of the extracted panel and extended up to the surface [49]. Obviously, tensile cracks were observed beneath the slope shoulder with $D=-100$ m. The panel was extracted directly below the slope shoulder ($D=0$ m); the tensile cracks had developed in front of the slope shoulder and extended to the sloping terrain (Figure 8(e)). These results implied that there was an "aggregation" on the extension of tensile cracks beneath the slope shoulder.

According to Salmi et al. [50], neglecting the effect of stratum bedding in simulating mining-induced subsidence in flat terrains would yield a wider but shallower subsidence trough as compared with the field conditions. Therefore, the strata bedding surface and joints should be carefully modelled to improve the simulation outputs (Figure 3).

The sum of upside and downside crack angles ($\gamma+\beta$) was wielded to characterize the relative disturbance range of overburden rock masses. The term "relative" was used to indicate that the thickness of rock strata, which is above the extracted panel, was not taken into consideration. A low value of "$\gamma+\beta$ " indicated a large relative disturbance range, and vice versa (refer to Figure 9). The extracted panel is partially or completely located beneath the sloping terrains; the relative disturbance ranges for the cases were greater than those beneath the flat terrains. With the upside crack angle decreasing, the subsidence trough of the latter was wider than that of the former (see in Figure 8). Moreover, the propagations of tensile cracks at the extracted panel boundary were almost parallel with all mining configurations. The crushing of the coal pillar resulted in an increment in the distance between the position of boundary tensile cracks and the center of the extracted panel and hence altered the crack angle (Figure 10). The center of the extracted panel positioned in front of the slope shoulder; the otherness between upside and downside crack angles increased. The upside crack angle reached the minimum value of 64°, and the summation angle of "$\gamma+\beta$" reached the minimum value of 151° with $D=0$ m; moreover, the rock masses above the extracted panel were disturbed to the greatest.

4.2. Evaluation of Horizontal Displacement. Coal mining causes significant vertical deformations. For materials which are characterized by low compactness and high expansibility in the subsidence area, the lateral compression of the strata surrounding the extracted panel would increase and cause an expansion to the sloping terrains. Subsidence immediately causes lateral deformation with the constraining forces of surrounding rock mass. A lower confining pressure makes the effect of lateral deformation more prominent [41]. Therefore, symmetrical and high constraining forces make the lateral deformation inappreciable [51]. In sloping terrains, the overburden rock masses produce relatively low lateral constraining forces, which are insufficient to offset the dilatational forces of rock masses caving into the panel. As a result, the disturbed rock mass would displace towards the sloping terrains (Figure 10). The extraction panels are located at different positions; Figure 11 shows the lateral deformations of rock masses. The lateral deformation of overburden rock mass above the extracted panel was not symmetrical, with flat-sloping terrains as simulated. The lateral deformation beneath the flat terrain side was lower than that of the sloping side. The extraction panel was located close to the sloping terrain; the lateral deformation was intensified and caused an outcrop towards the sloping surface.

Bedding planes provided a suitable path for lateral movement of strata in both flat and sloping terrains. A bedding plane, with a low bonding strength, provided less resistance in the direction of the overburden material movement and hence caused the sliding between the layers. The "zigzag" horizontal displacement change zone can be seen in Figures 11 and 12.

Interestingly, lateral deformations towards the slope inner part were observed in the mudstone layer with $D<100$, with

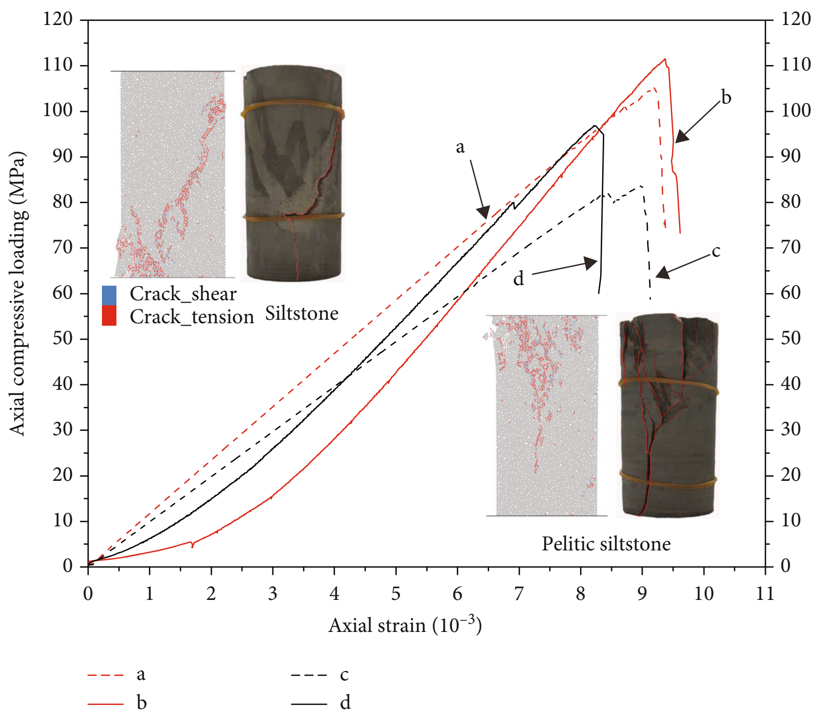

FIGURE 6: Stress-strain curves obtained from uniaxial compression tests (red lines: (a, b) represent siltstone; black lines: (c, d) represent pelitic siltstone. Solid lines are results obtained from laboratory tests, while dashed lines are results obtained from PFC calibration test).

TABLE 4: Uniaxial compression test results.

Parameter	Siltstone		Pelitic siltstone	
	Laboratory test	PFC test	Laboratory test	PFC test
E (GPa)	15.75	11.44	13.6	9.35
UCS (MPa)	111.49	105.26	96.87	83.76

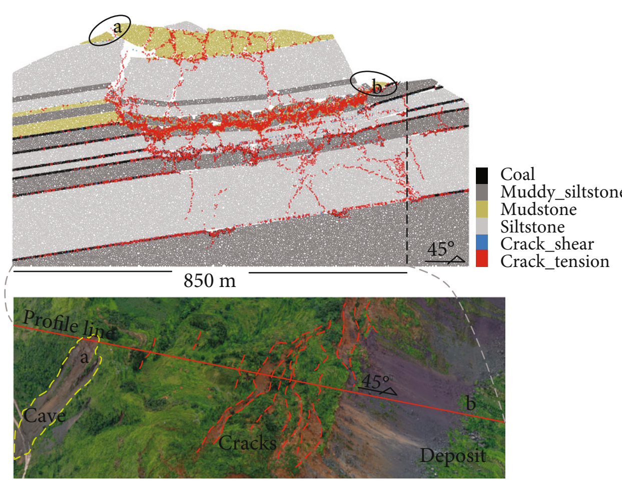

FIGURE 7: Comparisons of a typical PFC simulated deformation and the actual field observation.

the maximum value reaching 0.98 m (Figure 12(b)). However, there was no similar phenomenon in the mudstone directly above the extracted panel (Figure 11). With the in situ stress releasing, the materials at the slope shoulder poorly cemented were further loosed. Holding a more complete and dense layered structure, the siltstone and pelitic siltstone were subjected to stick-slip resistances along the bedding plane in the lateral motion. Conversely, the resultant force, including the gravitational force, redistributed stress, and the cementing force between the materials, leading to the deformation of mudstone.

A potential through slip plane appeared on the slope with $D = -100$ m (Figure 11(c)), which was initiated from the inner boundary of the extracted panel, extended upward to the goaf and the thin mudstone layer, and subsequently spread from the outer boundary of the extracted panel to the toe of the slope, causing the overall instability of slope. A horizontal displacement was observed of 0.4 m at the toe.

4.3. Evaluation of Surface Subsidence. The maximum surface subsidence is consistently located above the inner part of the extracted panel under various mining configurations in the countertilt slope. Furthermore, the sloping surface with thinner overburden materials has a larger maximum subsidence area, as indicated by the cases of $D \geq 0$ m (Figure 13(a)). These results proved that the slope has reached the "sufficient mining conditions" with $D \geq 0$ m. For obtaining the increment in surface subsidence beneath the sloping terrains, the maximum subsidence (W_0) of flat terrains was brought to the present research, which was referred to Equation (9) proposed by Zou [52] under the "sufficient mining conditions":

$$W_0 = qm \cos \alpha, \tag{9}$$

Table 5: Microstrength parameters used for PFC simulations.

Parameter	Definition	Siltstone	Pelitic siltstone	Mudstone	Coal
R_{min}	Minimum particle radius (m)	1.6	1.6	1.2	0.8
R_{max}/R_{min}	Particle radius ratio, uniform distribution	1.25	1.25	1.33	1.5
ρ	Particle density (kg/m^3)	2850	2650	3050	1850
E_c	Interparticle contact modulus (GPa)	7	6	2	2
K	Normal-to-shear stiffness ratio	1.8	2	2.2	2.4
μ	Microfriction coefficient	0.3	0.38	0.75	0.58
E_c'	Bond effective modulus (GPa)	7	6	2	2
K'	Bond normal-to-shear stiffness ratio	1.8	2	2.2	2.4
σ_c	Parallel bond normal strength (MPa)	35	30	10	9
τ_c	Parallel bond shear strength (MPa)	35	30	10	9
K_j	Joint stiffness ratio	1			
μ_j	Joint microfriction coefficient	0.35			

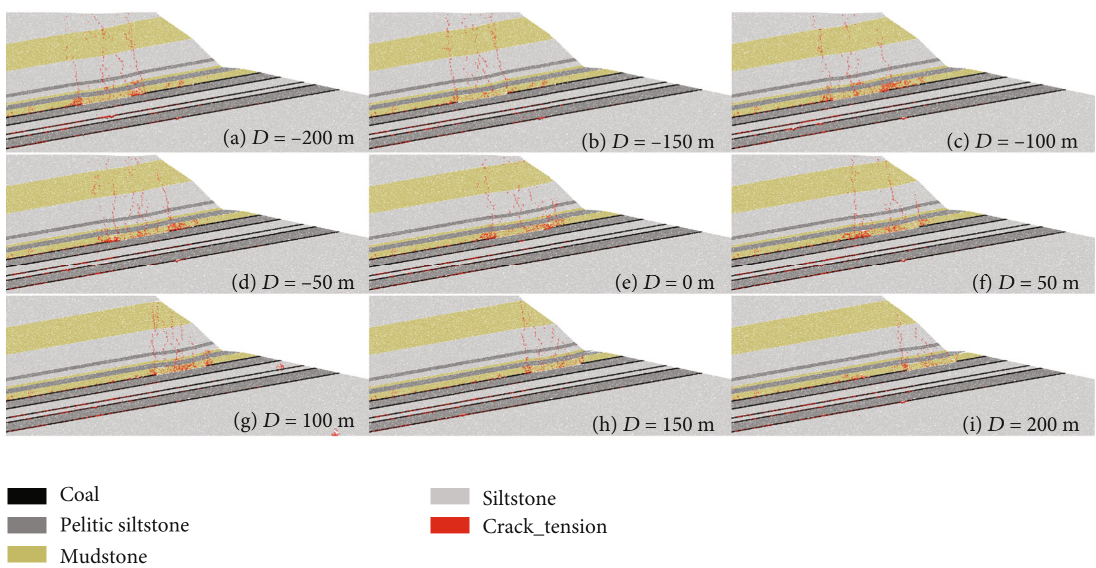

Figure 8: Crack propagations after coal seam extractions with different mining configurations.

where q is the subsidence coefficient under the "sufficient mining conditions," m is the thickness of the mining coal seam, and α is the dip angle of the coal seam.

Wielding the lithology comprehensive evaluation index (p) to characterize the degree of influence of lithology on surface subsidence [52]:

$$p = \frac{\sum_1^n h_i Q_i}{\sum_1^n h_i}, \tag{10}$$

where h_i is the thickness of overburden rock strata and Q_i is the lithologic classification index of overburden rock mass. The value of Q_i ranges from 0 to 1 for the first mining slope according to the hardness of the lithology. The Q_i values for the coal seam, mudstone, pelitic siltstone, and siltstone in this research were set at 0.9, 0.8, 0.4, and 0.05, respectively.

Based on the comprehensive evaluation index of lithology (p), the subsidence coefficient (q) of flat terrains under the "sufficient mining conditions" can be acquired by the following:

$$q = 0.45 + 0.5p. \tag{11}$$

From the above computations, W_0 for the 5 mining configurations with $D \geq 0$ m were 3.761 m ($D = 0$ m), 3.702 m ($D = 50$ m), 3.436 m ($D = 100$ m), 3.126 m ($D = 150$ m), and 3.294 m ($D = 200$ m). Accordingly, the increment in subsidence of sloping terrains as compared with the flat terrains was 2.761 m, 2.822 m, 3.101 m, 2.836 m, and 2.424 m, respectively.

Khanal et al. [53] suggested that the ratio of subsidence to thickness of overburden rock mass (S/T) could be positively correlated with the width to depth ratio of the mine (W/D_1). In this research, the thickness (T) and width (W) were fixed at 6 m and 200 m, respectively. The findings from the mining

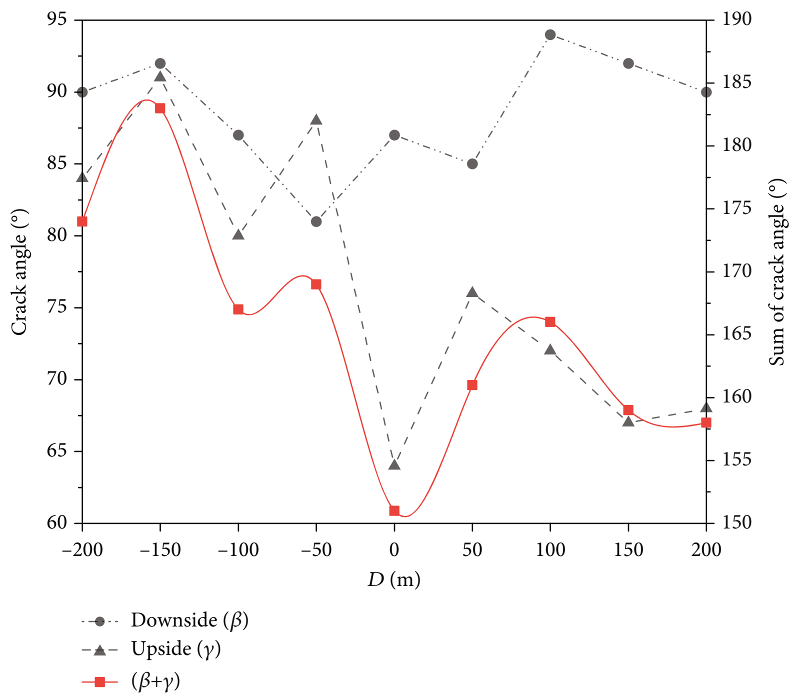

FIGURE 9: Changes in crack angle for different mining configurations.

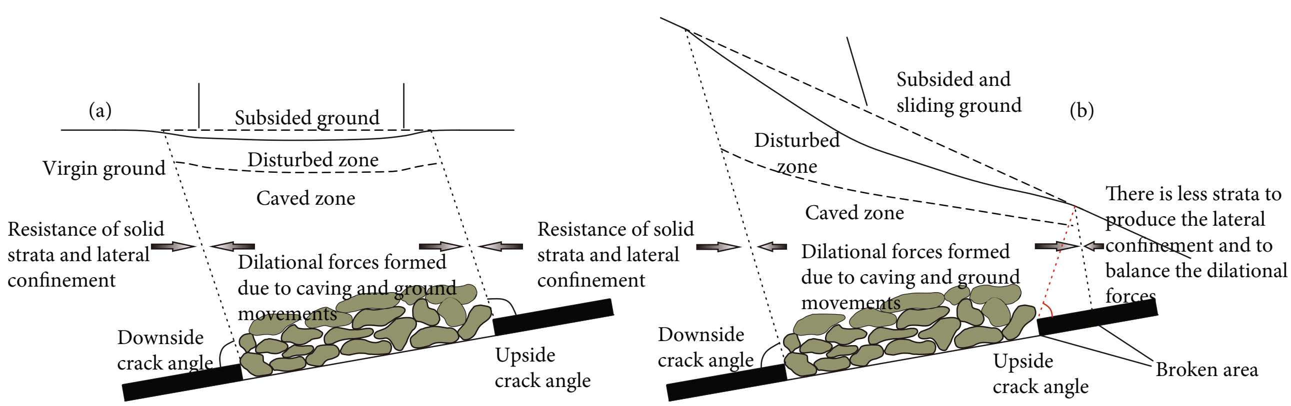

FIGURE 10: Mechanical mechanisms of mining-induced subsidence in (a) flat terrains and (b) sloping terrains (adapted from [41]).

configurations of $D < 100$ m showed consistency with that of Khanal et al. [53], but an opposite trend was observed with $D > 100$ m (Figure 13).

4.4. Evolution of Deformation at Slope Shoulder. The deformation behavior of the slope shoulder, a transition from flat terrains to sloping terrains, has been focused on in this research. The monitoring data of M13 was selected to characterize the deformation of rock mass at the slope shoulder. Figures 14–17 present the vertical and horizontal deformation characteristics of the rock mass over time under short-term and long-term conditions, respectively. The following findings are reported from the analyses:

(a) Short term

(i) Initiating the horizontal displacement and subsidence concurrently at the time step of 3000 with various mining configurations, which indicated that both the horizontal displacement and subsidence occurred right after the formation of the extracted panel

(ii) The extracted panel is located below the slope shoulder ($-100\text{ m} \leq D \leq 100\text{ m}$); the subsidence rate and value at the slope shoulder were higher than that in flat terrains

(b) Long term

(i) The rock mass at the slope shoulder showed prominent horizontal displacement (1.23 m) and subsidence (6.52 m) with $D = 0$ m and 50 m

(ii) The time required to stabilize the deformation at the slope shoulder was longer in flat terrain mining

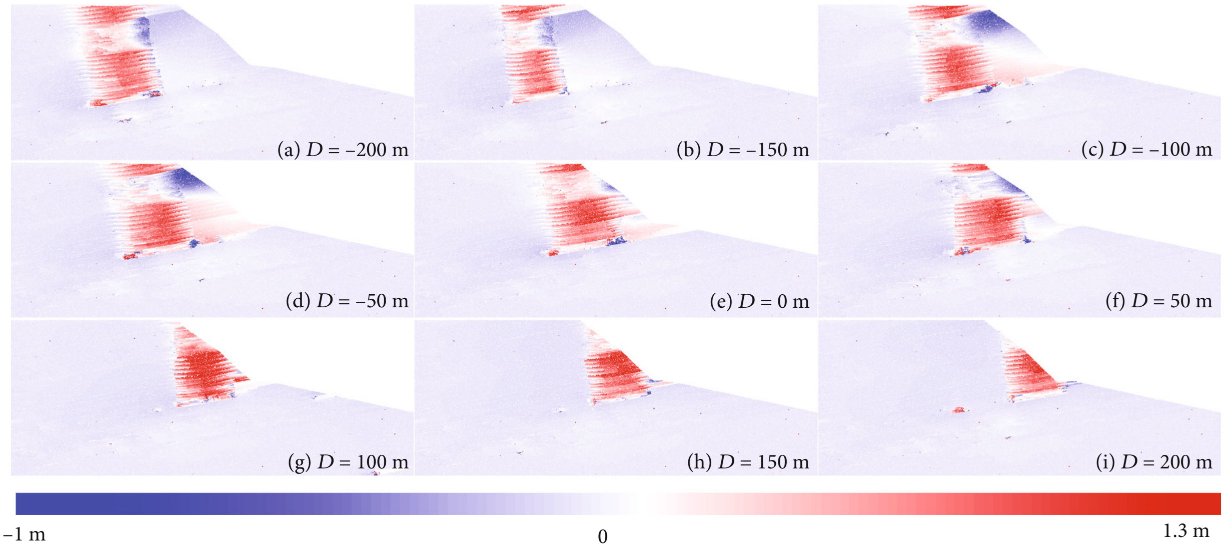

Figure 11: Contours of horizontal displacements after coal seam extractions with different mining configurations.

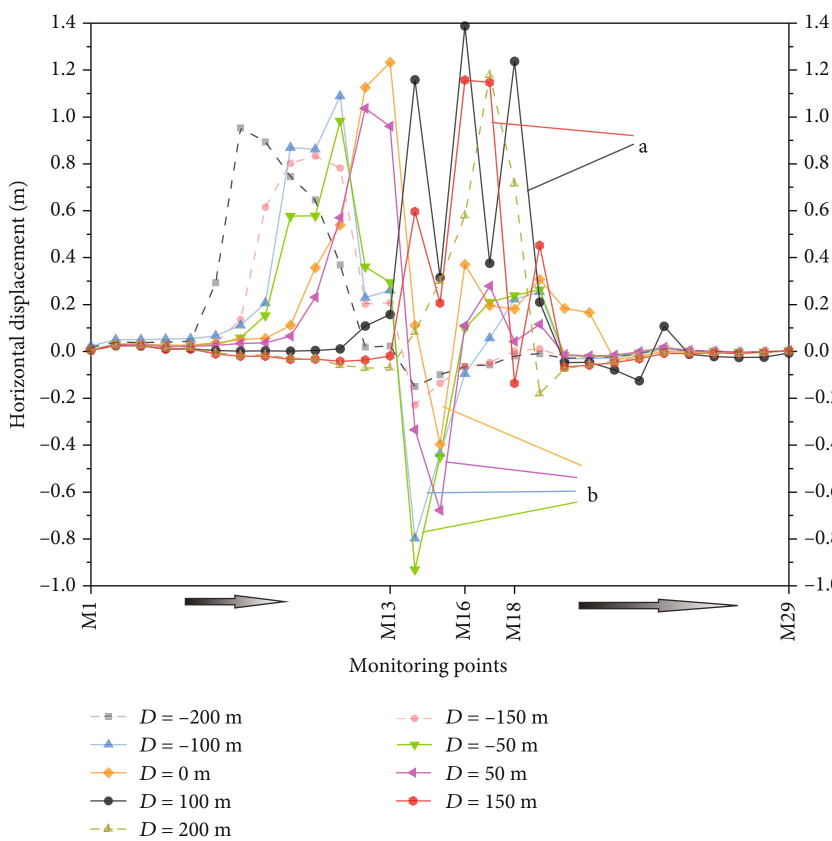

Figure 12: Horizontal displacement at the ground surface for different mining configurations.

(iii) The rock mass at the slope shoulder initially displaced horizontally towards the inner part and, subsequently, displaced outwards to the slope facing with $D < 0$ m. The horizontal displacement behavior depended on the location of the inner boundary of the extracted panel with $D \geq 0$ m. The rock mass at the slope shoulder displaced horizontally towards the direction of the slope facing with $D = 0$, 50, and 100 m. Observing a lower or negligible value with $D \geq 100$ m, which was identical to the cases of $D < 0$ m in the pattern of rock mass displacement

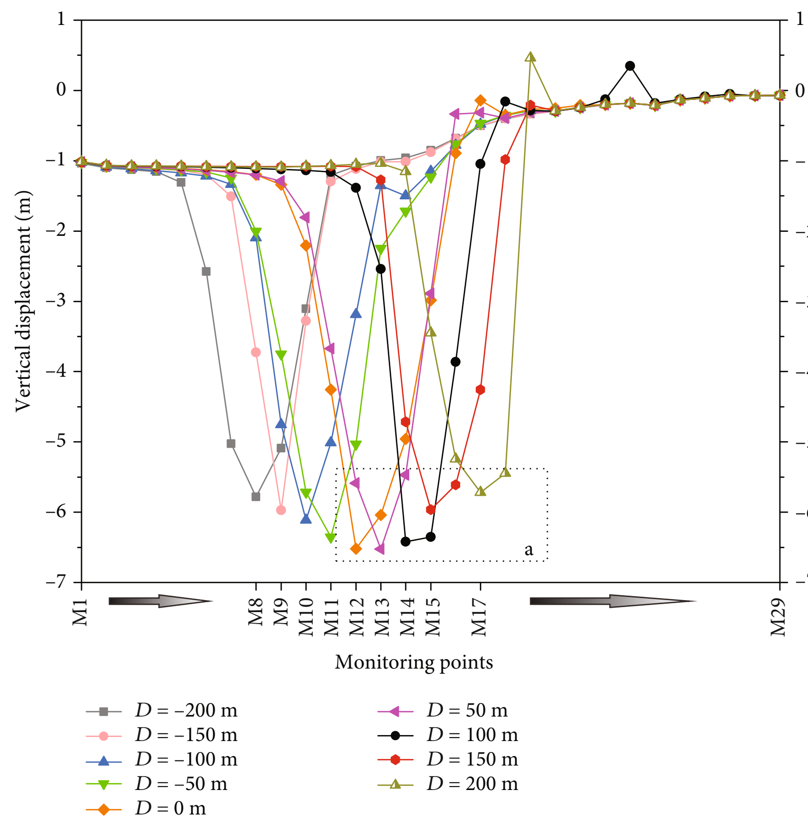

Figure 13: Vertical displacement at the ground surface for different mining configurations.

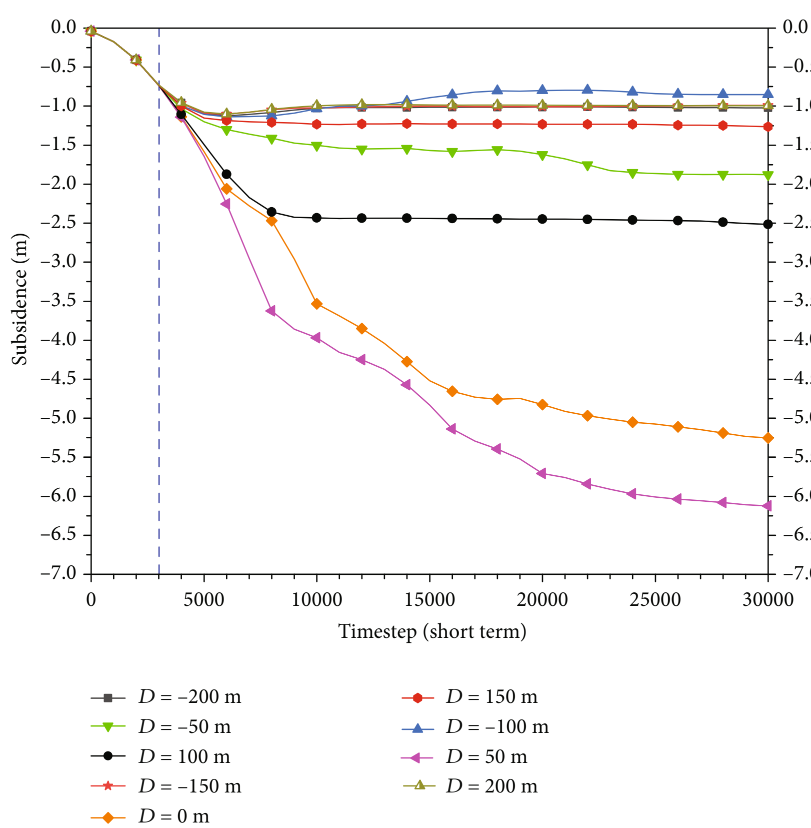

Figure 14: Variations in vertical displacement over time at slope shoulder for different mining configurations (short-term condition).

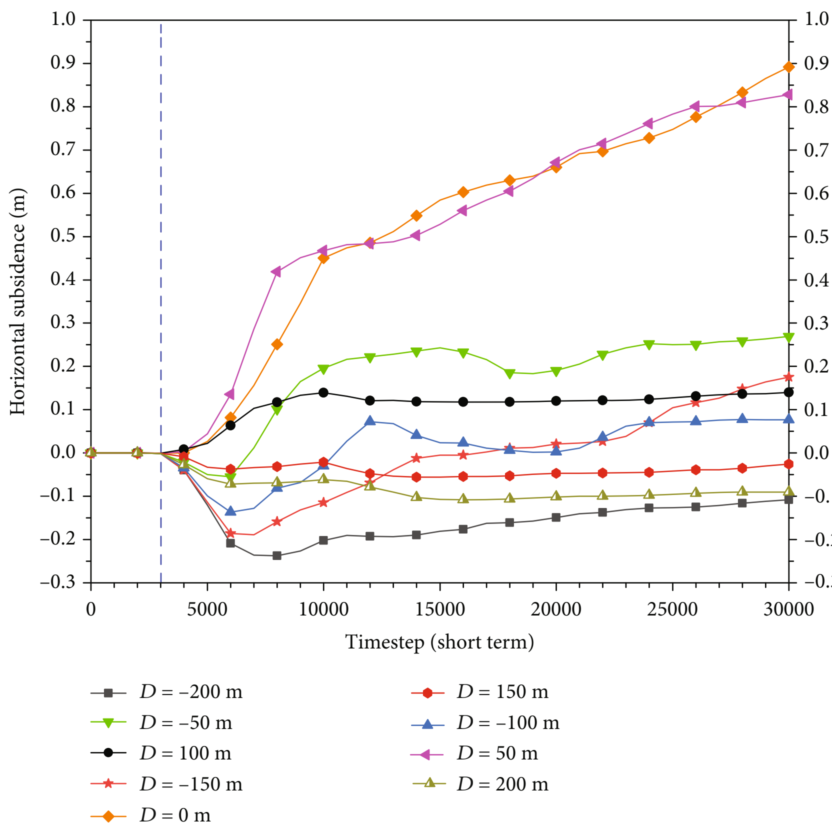

FIGURE 15: Variations in horizontal displacement over time at slope shoulder for different mining configurations (short-term condition).

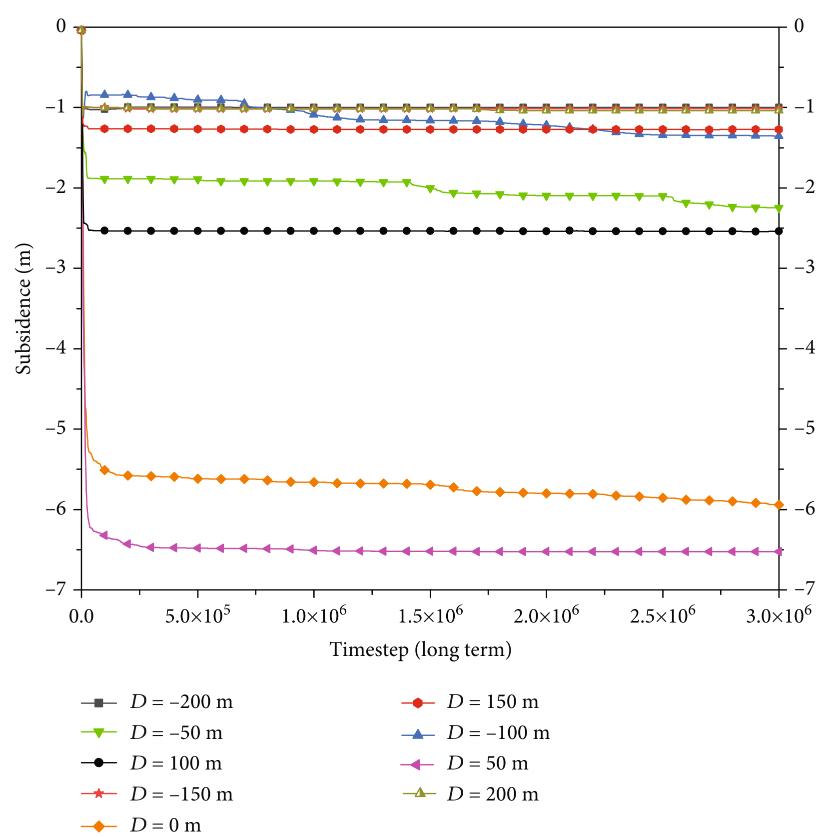

FIGURE 16: Variations in vertical displacement over time at slope shoulder for different mining configurations (long-term condition).

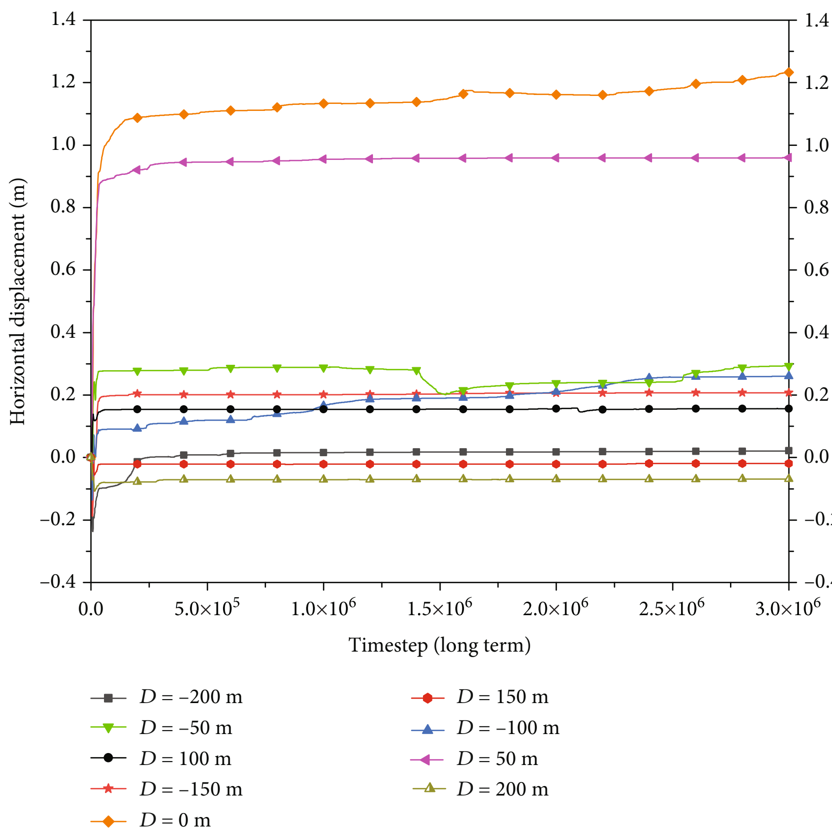

Figure 17: Variations in horizontal displacement over time at slope shoulder for different mining configurations (long-term condition).

5. Discussion

This research investigated the mechanical mechanisms of mining activities in flat and sloping terrains, with the considerations of deformation of overburden rock masses and propagation of tensile cracks. A model was established based on the typical mining-induced slope structure of a case study in southwest China. To the authors' knowledge, this is the first research reported on the use of PFC for analyzing the mining slope deformation behavior, with the extracted panel located beneath various complex terrains (i.e., flat terrain, slope shoulder, and sloping terrain). The time-dependent deformation characteristics of the rock mass at the slope shoulder were studied in detail. The sum of upside and downside crack angles was proposed to characterize the relative disturbance range of overburden rock mass, and reasonable and safe configurations of single-layered mining operations in mountainous areas were put forward.

It should be noted that the findings from the present research were handicapped by several limitations, such as the width of the extracted panel along the inclined strata was remained constant at 200 m, and the interval of two adjacent extracted panels in all mining configurations was kept at 50 m. In addition, the microstrength parameters of coal and pelitic siltstone were not derived from the uniaxial compression simulation by the PFC. Owing to these limitations, the functional relationship between surface subsidence and geological and geotechnical factors cannot be fully revealed in this research. These issues can be solved if the following future improvements are taken: (i) setting the extracted panel width as an independent variable and shortening the interval, (ii) increasing the number of samples for coal and pelitic siltstone and acquiring the mechanical parameters by wielding the support vector machine (SVM) coupled with the microstrength parameters by PFC, and (iii) setting the number of configurations of mining in sloping terrains to be 5 to 10 times of independent variables, for finding the regression relationship between the maximum subsidence and geological and geotechnical factors.

6. Conclusion

The present research investigated the deformation behavior of slopes under different mining configurations (i.e., horizontal distance from extracted panel center to slope shoulder, $D = -200$ m, -150 m, -100 m, -50 m, 0 m, 50 m, 100 m, 150 m, and 200 m) by wielding PFC. The Jianshanying mining slope, which was generalized based on the actual field investigation and laboratory experiment data, in Faer Town, Shuicheng county, Guizhou Province, was selected. Based on the laboratory mechanical experimental results, numerical simulation calibration testing, and the equivalent rock mass technique, the full mining model (the six-coal-seam mining model) simulation was used in comparison with the actual situation, which ensured the rationality of microstrength parameters of rock masses and joints. The following conclusions can be drawn for the study of deformation behavior of mining slopes in mountainous areas with gentle anti-incline overburden rock strata:

(i) Mining in mountainous areas usually meets with the risk of slope instability. The overlying rock masses tended to move towards the sloping surface with mining beneath sloping terrain, which brought an asymmetrical subsidence funnel, and formed a wider relative disturbance range on the slope surface. In particular, the rock masses above the extracted panel were disturbed to the greatest with $D = 0$ m

(ii) The constraining forces of overburden rock masses towards the valley decrease; mining beneath sloping terrains usually acquire larger subsidence (up to 3 m) and additional horizontal displacement (up to 1.4 m) than flat terrains. The "zigzag" horizontal displacement change zone formed with the control of bedding planes

(iii) It is important to remain the center position of the extracted panel behind the slope shoulder, beyond which the deformation rate and ultimate value of the rock mass at the slope shoulder would increase drastically. In addition, the boundary of the extracted panel should also be avoided to cross over the slope shoulder (i.e., $D \le -100$ m) to prevent an overall slope instability

Data Availability

The simulation codes and slope information used to support the findings of this study are available from the corresponding author upon request.

Conflicts of Interest

The authors declared that they have no conflicts of interest to this work. The authors declare that they do not have any commercial or associative interest that represents a conflict of interest in connection with the work submitted.

Acknowledgments

The authors would like to acknowledge the financial support from the State Key Laboratory of Geohazard Prevention and Geoenvironment Protection (Chengdu University of Technology) (Grant No. SKLGP2017Z016), the National Natural Science Foundation of China (Grant No. 41877273), the Innovative Research Groups of the National Natural Science Foundation of China (Grant No. 41521002), the Guizhou Provincial Geological Environment Monitoring Institute, and the Faer Coal Mine. These supports are gratefully acknowledged.

References

[1] A. Majdi, F. P. Hassani, and M. Y. Nasiri, "Prediction of the height of destressed zone above the mined panel roof in longwall coal mining," *International Journal of Coal Geology*, vol. 98, pp. 62–72, 2012.

[2] L. J. Donnelly, H. De La Cruz, I. Asmar, O. Zapata, and J. D. Perez, "The monitoring and prediction of mining subsidence in the Amaga, Angelopolis, Venecia and Bolombolo regions, Antioquia, Colombia," *Engineering Geology*, vol. 59, no. 1-2, pp. 103–114, 2001.

[3] M. Marschalko, I. Yilmaz, M. Bednárik, and K. Kubečka, "Influence of underground mining activities on the slope deformation genesis: Doubrava Vrchovec, Doubrava Ujala and Staric case studies from Czech Republic," *Engineering Geology*, vol. 147-148, pp. 37–51, 2012.

[4] E. F. Salmi, M. Nazem, and M. Karakus, "The effect of rock mass gradual deterioration on the mechanism of post-mining subsidence over shallow abandoned coal mines," *International Journal of Rock Mechanics and Mining Sciences*, vol. 91, pp. 59–71, 2017.

[5] H. G. Denkhaus, "Critical review of strata movement theories and their application to practical problems," *Journal of the Southern African Institute of Mining and Metallurgy*, vol. 64, no. 8, pp. 310–332, 1964.

[6] J. R. Dinsdale, "Ground pressure and pressure profiles around mining excavation," *Colliery Engineering*, vol. 12, pp. 406–409, 1935.

[7] M. R. Islam, D. Hayashi, and A. B. M. Kamruzzaman, "Finite element modeling of stress distributions and problems for multi-slice longwall mining in Bangladesh, with special reference to the Barapukuria coal mine," *International Journal of Coal Geology*, vol. 78, no. 2, pp. 91–109, 2009.

[8] M. M. Singh and F. S. Kendorski, "Strata disturbance prediction for mining beneath surface water and waste impoundments," in *Proceedings of the 1st Conference on Ground Control in Mining*, pp. 76–89, Morgantown, WV, USA, 1981.

[9] D. P. Sainsbury, B. L. Sainsbury, M. P. Board, and D. M. Loring, "Numerical back-analysis of structurally controlled cave initiation and propagation at the Henderson mine," in *45th US Rock Mechanics/Geomechanics Symposium*, p. 321, American Rock Mechanics Association, San Francisco, California, 2011.

[10] T. Unlu, H. Akcin, and O. Yilmaz, "An integrated approach for the prediction of subsidence for coal mining basins," *Engineering Geology*, vol. 166, pp. 186–203, 2013.

[11] B. Ghabraie, G. Ren, X. Zhang, and J. Smith, "Physical modelling of subsidence from sequential extraction of partially overlapping longwall panels and study of substrata movement characteristics," *International Journal of Coal Geology*, vol. 140, pp. 71–83, 2015.

[12] M. Karmis, A. Jarosz, P. Schilizzi, and Z. Agioutantis, "Surface deformation characteristics above undermined areas: experience from the eastern United States," *Civil Engineering Transactions*, vol. 29, no. 2, pp. 106–114, 1987.

[13] A. T. McCay, M. Valyrakis, and P. L. Younger, "A meta-analysis of coal mining induced subsidence data and implications for their use in the carbon industry," *International Journal of Coal Geology*, vol. 192, pp. 91–101, 2018.

[14] D. Zhang, G. Fan, L. Ma, and X. Wang, "Aquifer protection during longwall mining of shallow coal seams: a case study

in the Shendong Coalfield of China," *International Journal of Coal Geology*, vol. 86, no. 2-3, pp. 190–196, 2011.

[15] O. Düzgün, C. Künzer, and C. Özgen Karacan, "Applications of remote sensing and GIS for monitoring of coal fires, mine subsidence, environmental impacts of coal-mine closure and reclamation," *International Journal of Coal Geology*, vol. 86, no. 1, pp. 1-2, 2011.

[16] H. J. Oh and S. Lee, "Integration of ground subsidence hazard maps of abandoned coal mines in Samcheok, Korea," *International Journal of Coal Geology*, vol. 86, no. 1, pp. 58–72, 2011.

[17] E. Can, S. Kuşcu, and C. Mekik, "Determination of underground mining induced displacements using GPS observations in Zonguldak-Kozlu Hard Coal Basin," *International Journal of Coal Geology*, vol. 89, pp. 62–69, 2012.

[18] P. Hatherly, "Overview on the application of geophysics in coal mining," *International Journal of Coal Geology*, vol. 114, pp. 74–84, 2013.

[19] W.-d. Wu, J.-b. Bai, X.-y. Wang, Z.-j. Zhu, and S. Yan, "Field investigation of fractures evolution in overlying strata caused by extraction of the Jurassic and carboniferous coal seams and its application: case study," *International Journal of Coal Geology*, vol. 208, pp. 12–23, 2019.

[20] S. Zhang, X. Pei, S. Wang, R. Huang, X. Zhang, and Z. Chang, "Centrifuge model testing of a loess landslide induced by rising groundwater in Northwest China," *Engineering Geology*, vol. 259, article 105170, 2019.

[21] Y. G. Zhou, D. Meng, Q. Ma, B. Huang, D. S. Ling, and Y. M. Chen, "Centrifuge modeling of dynamic response of high fill slope by using generalized scaling law," *Engineering Geology*, vol. 260, p. 105213, 2019.

[22] Q. Bai, S. Tu, F. Wang, and C. Zhang, "Field and numerical investigations of gateroad system failure induced by hard roofs in a longwall top coal caving face," *International Journal of Coal Geology*, vol. 173, pp. 176–199, 2017.

[23] M. A. Coulthard and A. J. Dutton, "Numerical modelling of subsidence induced by underground coal mining," in *The 29th US Symposium on Rock Mechanics (USRMS)*, pp. 529–536, American Rock Mechanics Association, Minneapolis, Minnesota, 1988.

[24] M. Karmis, Z. Yu, and A. Jarosz, "Design considerations for subsidence control," *International Journal of Mining and Geological Engineering*, vol. 8, no. 4, pp. 357–368, 1990.

[25] L. J. Wardle and K. E. McNabb, "Three-dimensional numerical modelling of effects of subsidence on escarpments," in *Proceedings of the 11th International Congress On ground control in mining*, pp. 506–510, Wollongong, Australia, 1992.

[26] L. J. Wardle, "The use of numerical modeling for underground coal mine design," in *Analysis and Design Methods*, pp. 733–748, Pergamon, Oxford, UK, 1993.

[27] C. Zhang, R. Mitra, and B. Hebblewhite, "UDEC modeling of valley closure and upsidence," in *Continuum and Distinct Element Numerical Modeling in Geomechanics*, pp. 1–8, Itasca International Inc. Minneapolis, 2013.

[28] R. Bhasin and A. M. Kaynia, "Static and dynamic simulation of a 700-m high rock slope in western Norway," *Engineering Geology*, vol. 71, no. 3-4, pp. 213–226, 2004.

[29] E. F. Salmi and S. Hosseinzadeh, "Slope stability assessment using both empirical and numerical methods: a case study," *Bulletin of Engineering Geology and the Environment*, vol. 74, no. 1, pp. 13–25, 2015.

[30] M. Sharifzadeh, M. Sharifi, and S. M. Delbari, "Back analysis of an excavated slope failure in highly fractured rock mass: the case study of Kargar slope failure (Iran)," *Environment and Earth Science*, vol. 60, no. 1, pp. 183–192, 2010.

[31] P. J. N. Pells, "A note on escarpment instability associated with mining subsidence," in *Second Triennial Conference on Buildings and Structures Subject to Mine Subsidence*, pp. 66–73, Maitland, NSW, USA, 1991.

[32] P. J. N. Pells, J. C. Braybrooke, J. Mong, and G. P. Kotze, "Cliff line collapse associated with mining activities," in *Soil Slope Instability and Stabilisation*, pp. 359–385, Balkema, Rotterdam, Netherlands, 1987.

[33] A. Waddington and D. Kay, "The impacts of mine subsidence on creeks, river valleys and gorges due to underground coal mining operations," in *Proceedings of the 2003 Coal Operators Conference*, pp. 101–116, University of Wollongong & the Australasian Institute of Mining and Metallurgy Wollongong, Australasian, 2003.

[34] H. Zahiri, D. R. Palamara, P. Flentje, G. M. Brassington, and E. Baafi, "A GIS-based weights-of-evidence model for mapping cliff instabilities associated with mine subsidence," *Environmental Geology*, vol. 51, no. 3, pp. 377–386, 2006.

[35] M. Marschalko, I. Yilmaz, V. Křístková, M. Fuka, M. Bednarik, and K. Kubečka, "Determination of actual limit angles to the surface and their comparison with the empirical values in the upper Silesian Basin (Czech Republic)," *Engineering Geology*, vol. 124, pp. 130–138, 2012.

[36] J. J. Zhao, J. G. Xiao, M. L. Lee, and Y. T. Ma, "Discrete element modeling of a mining-induced rock slide," *SpringerPlus*, vol. 5, no. 1, p. 1633, 2016.

[37] D. B. Jones, H. J. Siddle, D. J. Reddish, and B. N. Whittaker, "Landslides and undermining: slope stability interaction with mining subsidence behaviour," in *7th ISRM Congress*, pp. 893–898, International Society for Rock Mechanics and Rock Engineering, Aachen, Germany, 1991.

[38] D. Page, *Mine Subsidence Devastates Sugarloaf: Video, Photos*, The NewcastleHerald, 2013.

[39] J. M. Galvin, *Ground Engineering-Principles and Practices for Underground Coal Mining*, Springer, 2016.

[40] J. E. Turney, A. Amundson, C. Greenman, B. K. Stover, and A. Bucknam, *Subsidence above Inactive Coal Mines: Information for the Homeowner*, Colorado Geological Survey, 1985.

[41] D. R. Kay, J. P. Barbato, and K. W. Mills, "Review of mechanisms resulting in observed upsidence and closure movements," in *Mine Subsidence 2007: Proceedings of the Seventh Triennial Conference on Mine Subsidence: A Community Issue-Mine Subsidence Technological Society*, pp. 197–205, University of Wollongong, Wollongong, 2007.

[42] D. R. Kay and J. P. Carter, *Effects of Subsidence on Steep Topography and Cliff Lines*, University of Sydney, Department of Architectural Science, 1992.

[43] D. M. Cunningham, "A rockfall avalanche in a sandstone landscape, Nattai North, NSW," *Australian Geographer*, vol. 19, pp. 221–229, 1988.

[44] I. Yilmaz and M. Marschalko, "A leaning historical monument formed by underground mining effect: an example from Czech Republic," *Engineering Geology*, vol. 133-134, pp. 43–48, 2012.

[45] J. Wei, Z. Zhao, C. Xu, and Q. Wen, "Numerical investigation of landslide kinetics for the recent Mabian landslide (Sichuan, China)," *Landslides*, vol. 16, no. 11, pp. 2287–2298, 2019.

[46] D. O. Potyondy and P. A. Cundall, “A bonded-particle model for rock,” *International Journal of Rock Mechanics and Mining Sciences*, vol. 41, no. 8, pp. 1329–1364, 2004.

[47] C. Shi, D. Li, K. Chen, and J. Zhou, “Failure mechanism and stability analysis of the Zhenggang landslide in Yunnan Province of China using 3D particle flow code simulation,” *Journal of Mountain Science*, vol. 13, pp. 891–905, 2016.

[48] E. T. Brown, “Estimating the mechanical properties of rock masses,” in *Proceedings of the 1st Southern Hemisphere International Rock Mechanics Symposium (SHIRMS), Australian Centre for Geomechanics*, pp. 3–21, Perth, Australia, 2008.

[49] G. Wang, M. Wu, R. Wang, H. Xu, and X. Song, “Height of the mining-induced fractured zone above a coal face,” *Engineering Geology*, vol. 216, pp. 140–152, 2017.

[50] E. F. Salmi, M. Nazem, and M. Karakus, “Numerical analysis of a large landslide induced by coal mining subsidence,” *Engineering Geology*, vol. 217, pp. 141–152, 2017.

[51] K. W. Mills, “Developments in understanding subsidence with improved monitoring,” in *Mine subsidence 2011: proceedings of the eighth triennial conference on Management of Subsidence. MineSubsidence Technological Society*, pp. 25–41, Sebel Kirkton Park, Hunter Valley, NSW, 2011.

[52] Y. F. Zou, “Research on calculation method of surface subsidence coefficient,” *Chinese Journal of Geotechnical Engineering*, vol. 3, pp. 112–115, 1997.

[53] M. Khanal, D. Adhikary, C. Jayasundara, and R. Balusu, “Numerical study of mine site specific multiseam mining and its impact on surface subsidence and chain pillar stress,” *Geotechnical and Geological Engineering*, vol. 34, no. 1, pp. 217–235, 2016.

Hindawi
Geofluids
Volume 2021, Article ID 5549168, 9 pages
https://doi.org/10.1155/2021/5549168

WILEY | Hindawi

Research Article

Numerical Simulation of Gas Ventilation Mode in Highway Gas Tunnel

Jihua Zhang ,[1] Yun Dong ,[1] Yadong Chen ,[1] Huasheng Sun ,[1] Jingke Wu ,[1] Weili Liu ,[2] Jiarui Chen ,[1] and Shiqiang Pan [3]

[1]*Faculty of Architecture and Civil Engineering, Huaiyin Institute of Technology, Huai'an, Jiangsu 223001, China*
[2]*School of Life Science and Food Technology, Huaiyin Institute of Technology, Huai'an, Jiangsu 223001, China*
[3]*Hunan Communications Research Institute Co., Ltd., Changsha, Hunan 410015, China*

Correspondence should be addressed to Jihua Zhang; zhangjh84@hyit.edu.cn

Received 8 January 2021; Revised 2 February 2021; Accepted 8 February 2021; Published 17 February 2021

Academic Editor: Yi Xue

When the mountain tunnel projects passing through the complex formation with coal, it happened along with disaster accidents such as gas outburst, gas combustion, and gas explosion. These disasters should seriously threaten the safety and life of the construction personnel and affect the normal operation of the tunnel construction. Ventilation is the most effective means to control gas, fire, dust, heat, and other disasters. To study the effects of different ventilation modes in highway gas tunnels, Fluent software was used to simulate forced ventilation, exhaust ventilation, and mixed ventilation in a high gas tunnel of a highway in Hunan. The distribution law of the airflow velocity and gas concentration of these three ventilation modes were obtained to determine the optimal ventilation system. It was shown that vortex zones of different ranges formed in the tunnel for all three ventilation modes, and the gas concentration was higher in the vortex zone than in other regions. Mixed ventilation of them is superior to the other two modes, showing the best ventilation effect with regard to airflow velocity and gas concentration.

1. Introduction

Currently, highway tunnel construction has expanded throughout China. Particularly with urban construction development, numerous traffic tunnels have arisen in the mountainous and hilly areas of China [1–3]. When these tunnel projects developing in depth, they often encounter the situation of crossing coal seam, which brings great security risks to tunnel construction. The tunnel is closed in the construction process, and the dust from driving and the blasting process and hazardous gases such as gas from the broken surrounding rock are likely to accumulate in the tunnel, which seriously threatens the safety of the workers [4–8]. Hence, adequate ventilation needs to be implemented in the tunnel [9–13] to dilute poisonous and hazardous gases in a timely manner and prevent the accumulation of explosive gases within the tunnel. Gas is a major risk source of tunnel construction safety. Because of the long ventilation distance and a large volume of gas emissions in a tunnel, ventilation via pipes is usually used to mitigate gas accumulation [14–17]. The study of the effects of different ventilation methods by pipes is critical for a reasonable selection of ventilation measures, improved ventilation efficiency, and a safe construction environment.

The tunnel studied here is in Jishou city, Hunan province, China. A coal seam was exposed during the excavation process, consisting of pork liver coal and asphaltic coal. These coals are tectonic coals, with high hardness and contain a large amount of gas with contents reaching 6.92 m^3/t. Furthermore, the methane concentration can reach 53.50% while the maximum absolute gas emission rate exceeds 75 m^3/min. After the exposure of the coal seam, the absolute gas emission rate exceeded 0.5 m^3/min for several consecutive days. According to "Technical Code for Railway Tunnel with Gas" and "Guidelines for Design of Highway Tunnel," together with the determination principle of the highest level in the tunnel gas work area, this tunnel was classified as a high gas tunnel. To guarantee the construction safety of this

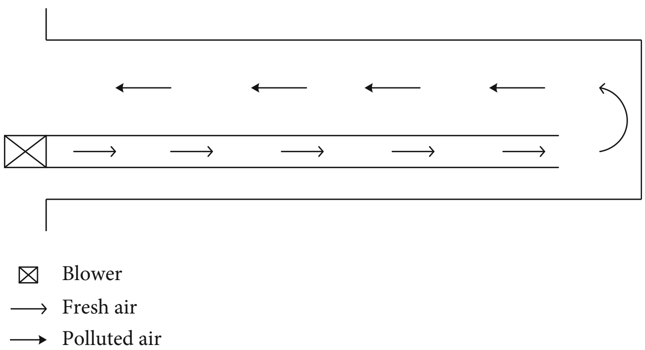

(a) Forced ventilation

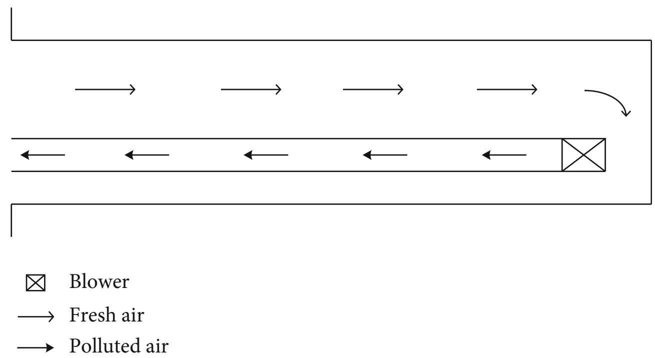

(b) Exhaust ventilation

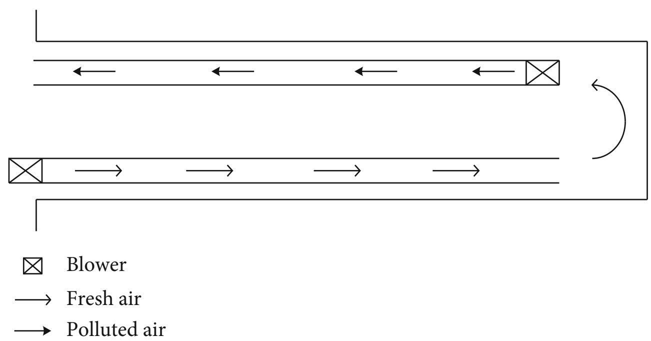

(c) Mixed ventilation

Figure 1: Schematic diagram of the ventilation model.

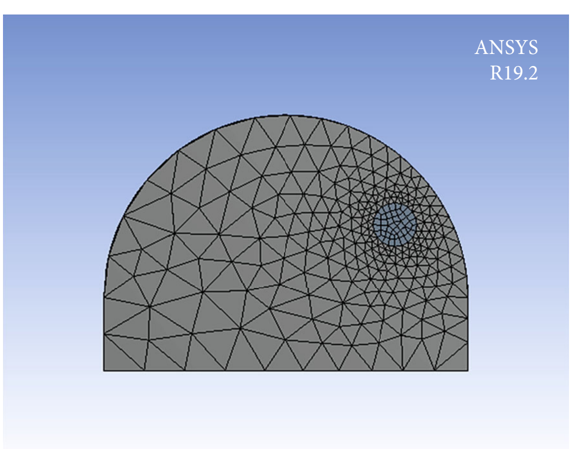

(a) Forced ventilation and exhaust ventilation

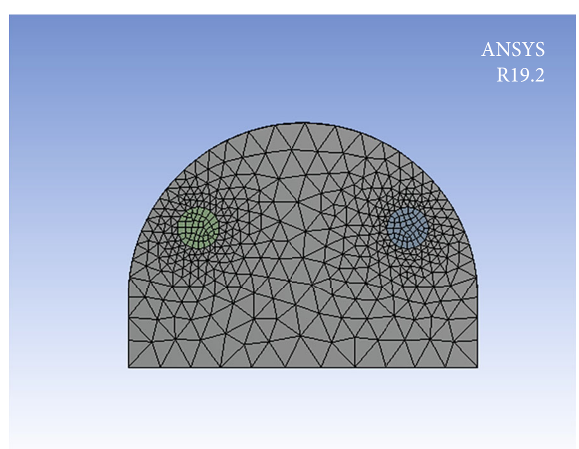

(b) Mixed ventilation

Figure 2: Schematic diagram of model meshing.

tunnel, effective measures of outburst prevention is necessary for penetration through the coal seam to suppress the gas concentration and gas pressure. This requires a scientific and rational configuration of the ventilation mode. Thus, in this paper, the hydrodynamics software Fluent was employed to simulate three different ventilation measures, forced ventilation, exhaust ventilation, and mixed ventilation, and the status of the transportation of fresh air and gas in different ventilation flow fields was obtained. Therefore, the efficiency of tunnel ventilation was able to be enhanced, and the safety of the workers was guaranteed using the results of this research.

2. Ventilation Modes of Air Pipe of Tunnel

In the driving construction of tunneling, ventilation by pipes can be divided into three types based upon the layout type of pipe and blower: forced ventilation, exhaust ventilation, and mixed ventilation [18–21]. When using forced ventilation, pipes deliver fresh air to the tunnel working face to suppress

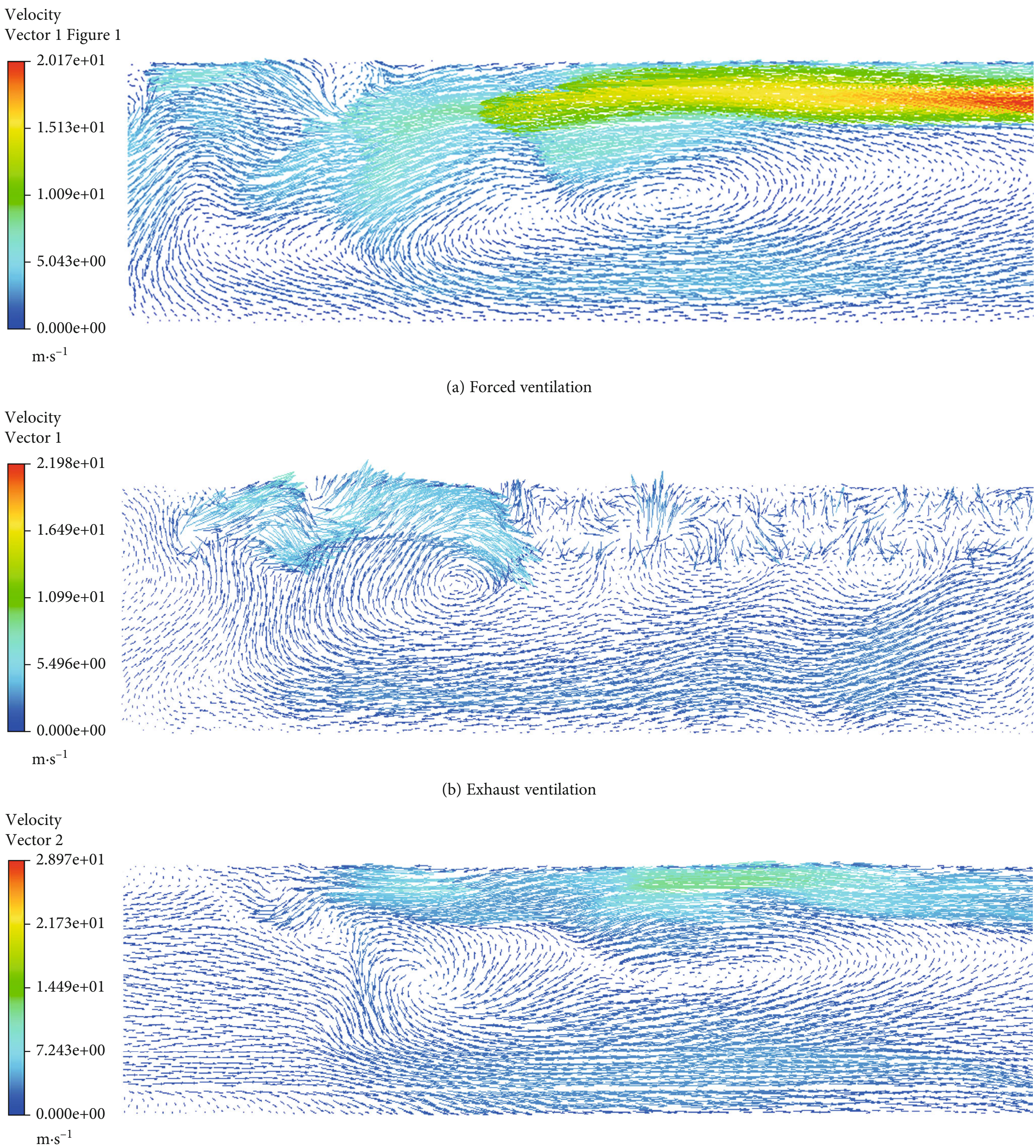

(a) Forced ventilation

(b) Exhaust ventilation

(c) Mixed ventilation

Figure 3: Wind flow velocity vector inside the tunnel.

the concentration of poisonous and hazardous gas in the air and discharge the polluted air through the tunnel portal. It has a short ventilation duration, an extensive effective range, and a favorable ventilation effect. Exhaust ventilation exhausts poisonous and hazardous gas at the tunnel's working face through negative-pressure pipes, provides fast ventilation, and is suitable for driving ventilation across a long tunnel. As a standard ventilation mode in tunnel construction, mixed ventilation uses a forced blower to dilute poisonous and hazardous gases at the working face and an exhaust blower to exhaust the polluted air through a ventilation pipe, which has the advantages of both the forced and exhaust ventilation modes so that the maximum ventilation efficiency can be

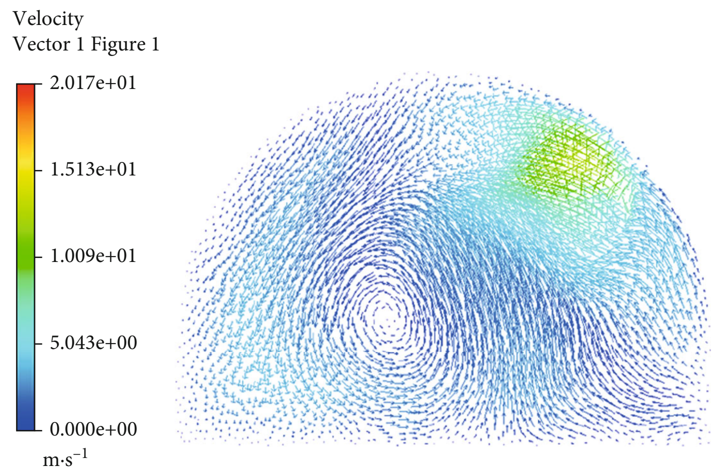

(a) Forced ventilation

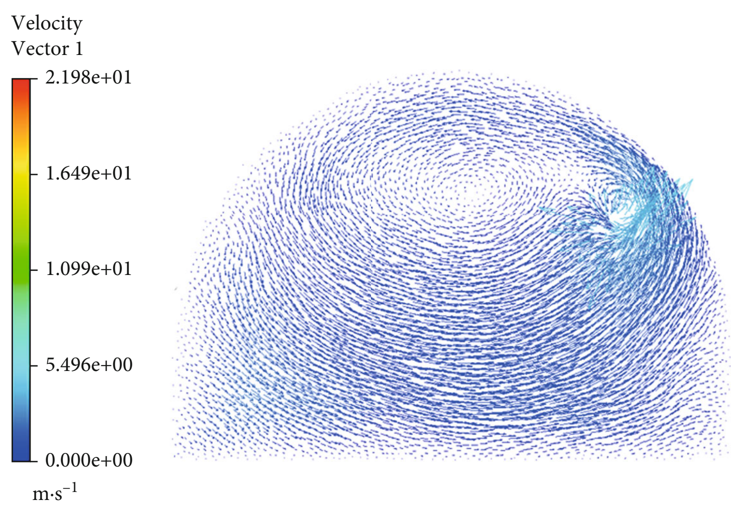

(b) Exhaust ventilation

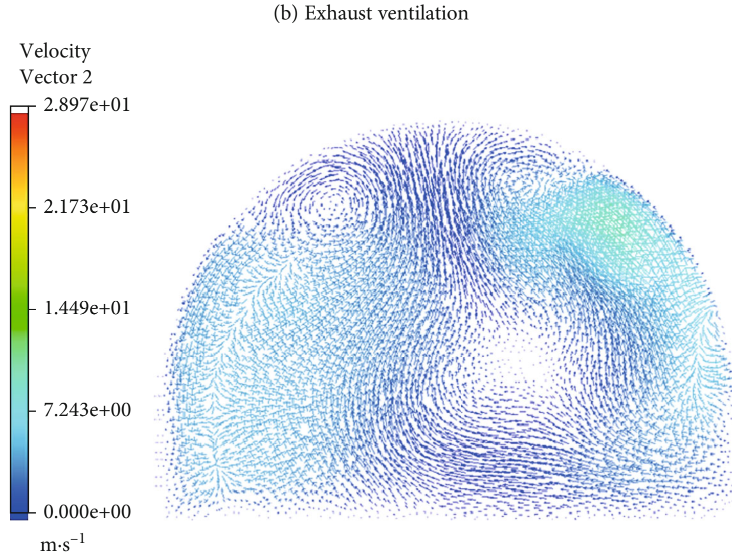

(c) Mixed ventilation

Figure 4: Tunnel section wind speed vector.

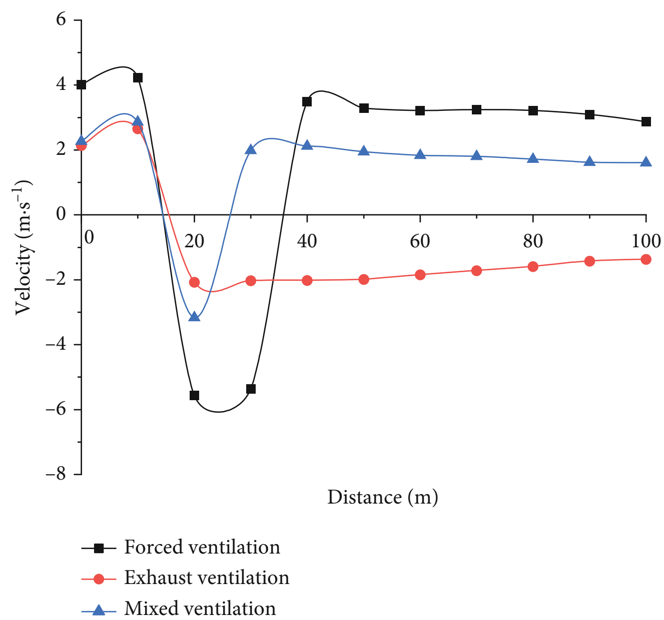

FIGURE 5: Curve of wind speed variation in the tunnel.

obtained, and it is especially suitable for ventilation of a long-distance tunnel.

3. Numerical Calculation Model

3.1. Calculation Model of Tunnel. The three-dimensional models of the three pipe ventilation modes of tunnel were established using Fluent software. The basic geometric dimensions of the tunnel were as follows: length was 100 m, cross-section was 10 m × 7 m straight wall circular arch (width × height), the diameter of the ventilation pipe was 1.2 m, and distance of pipe from the ground was 4 m. The tunnel ventilation model is simplified and shown in the schematic in Figure 1.

The mesh subdivision for the model was implemented by the preprocessor within Fluent software, and the generated mesh is shown in Figure 2.

3.2. Mathematical Model of Tunnel. When studying the airflow in the tunnel, the airflow was simplified as channel flow, and the airflow was modeled as nearly turbulent [22–26]. By referring to the tunnel ventilation condition, the $k-\varepsilon$ turbulence model was adopted in the calculation model [27–29], and thus, the $k-\varepsilon$ turbulence model was selected as the calculation model for gas diffusion [30–32]. The model solves the turbulent viscosity coefficient μ_i by establishing the equations of k and ε.

(1) Turbulent fluctuation kinetic energy equation (k equation)

$$\frac{\partial(\rho k v_i)}{\partial x_i} = \frac{\partial((\mu + (\mu_i/\sigma_k))(\partial k/\partial x_i))}{\partial x_i} + G_k - \rho\varepsilon, \quad (1)$$

where ρ is the fluid density, kg·m^{-3}; k is the turbulent kinetic energy, m^2·s^{-2}; v_i is the velocity component, m·s^{-1}; μ is the laminar viscosity coefficient, Pa·s; μ_i is the turbulent viscosity coefficient, Pa·s; σ_k is an empirical constant; G_k is the change rate of turbulent fluctuating kinetic energy caused by the change of average velocity gradient, which can be given by equation (2); ε is the turbulent kinetic energy dissipation rate, m^2·s^{-3}.

$$G_k = \mu_i \left(\frac{\partial v_i}{\partial x_j} + \frac{\partial v_j}{\partial x_i} \right) \frac{\partial v_i}{\partial x_j} \ (i,\ j = 1,\ 2,\ 3) \quad (2)$$

(2) Turbulent fluctuation kinetic energy dissipation equation (ε equation)

$$\frac{\partial(\rho\varepsilon v_i)}{\partial x_i} = \frac{\partial((\mu + (\mu_i/\sigma_\varepsilon))(\partial\varepsilon/\partial x_i))}{\partial x_i} + C_1 \frac{\varepsilon}{k} G_k - C_2 \rho \frac{\varepsilon^2}{k}, \quad (3)$$

where σ_k, C_1, and C_2 are empirical constants

3.3. Calculation of Boundary Conditions. The boundary conditions were determined as follows:

(1) The ventilation pipe in the tunnel was set as the inlet boundary, which used the velocity-inlet with the ventilation velocity of 20 m/s

(2) The exhaust opening of the blower was set as the inlet boundary with the type of mass-flow inlet and $Q = 2.7$ m^3/s

(3) The walls of the tunnel and ventilation pipe were subject to a fixed wall boundary with nonslip conditions

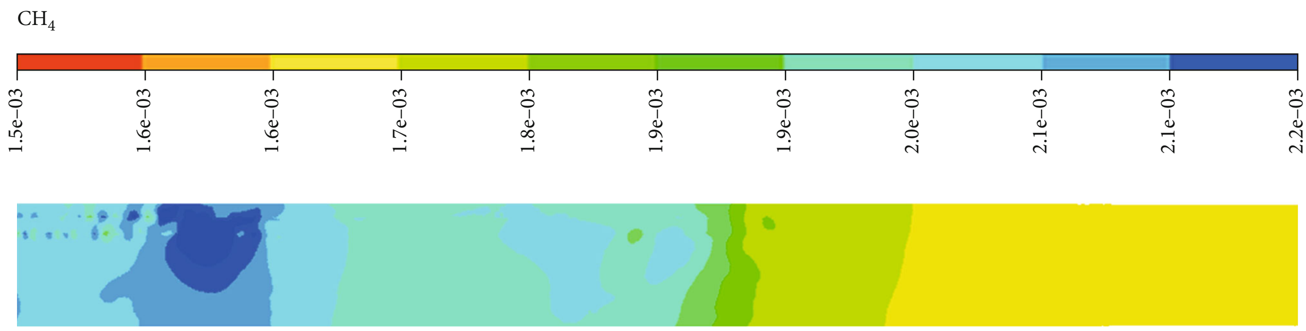

(a) Forced ventilation

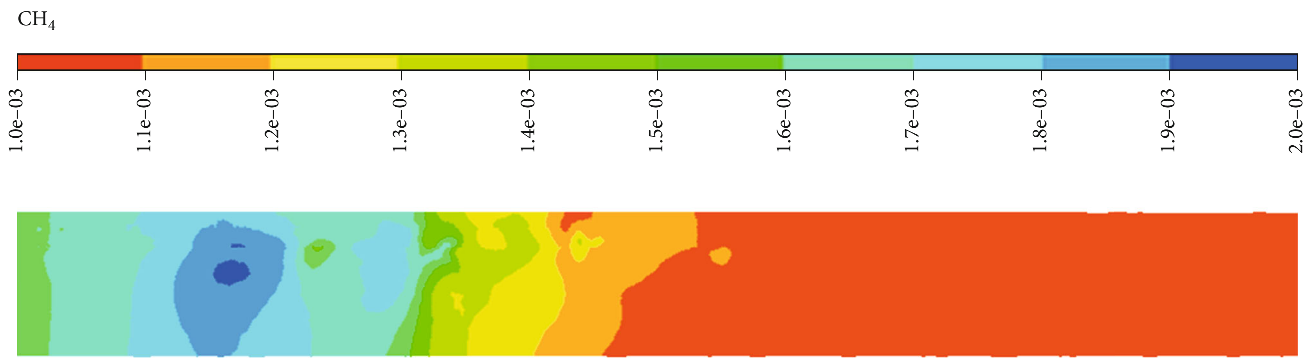

(b) Exhaust ventilation

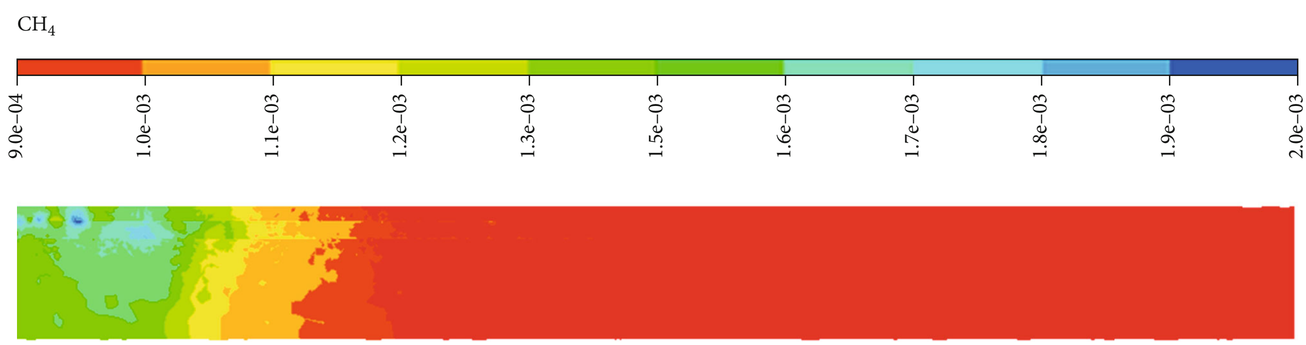

(c) Mixed ventilation

Figure 6: Distribution of gas concentration in the tunnel.

(4) Gas was emitted from the tunnel face with an emission rate of $0.5\,m^3/min$

4. Calculation Results and Analysis

4.1. Distribution of Airflow Velocity Field in the Tunnel. The tunnel face is the most likely location where gas is emitted and accumulated, and the ventilation effect of this location directly affects the ventilation status of the entire tunnel. Therefore, the local airflow field of the tunnel face is the focus of this numerical simulation study. To visually observe the distribution of the local airflow field in the tunnel, for the three ventilation modes, the velocity contours on the plane of the ventilation pipe center (plane $y = 4\,m$) and the cross-section of the tunnel which was 5 m away from the tunnel face (plane $z = 5\,m$) is analyzed as in Figures 3 and 4.

It can be observed in Figure 3 that in the forced ventilation, fresh air is delivered by the blower and the ventilation pipe to the tunnel face and lashes against the tunnel face; after mixing with the gas emitted through the tunnel face, the flow direction is altered due to rebounding on wall and backflow occurs towards the direction of the tunnel opening; a part of the airflow changes its direction under the effect of ventilation pipe opening jet flow and forms a vortex, and polluted air quickly accumulates in the vortex zone, which is the main factor influencing the exhaust of the polluted air. In exhaust ventilation, a suction region is formed around the blower, which sucks the gas emitted through the tunnel face and the air in the tunnel into the ventilation pipe for exhaustion from the tunnel. In the mixed ventilation mode, the airflow is delivered from the forced air pipe and mixed with gas, and then, the rotation of velocity occurs on the tunnel face so that most of the mixed gas is sucked into the ventilation pipe by the suction region formed by the blower before finally being exhausted out of the tunnel. It can be seen from the airflow velocity vectors on the tunnel cross-section

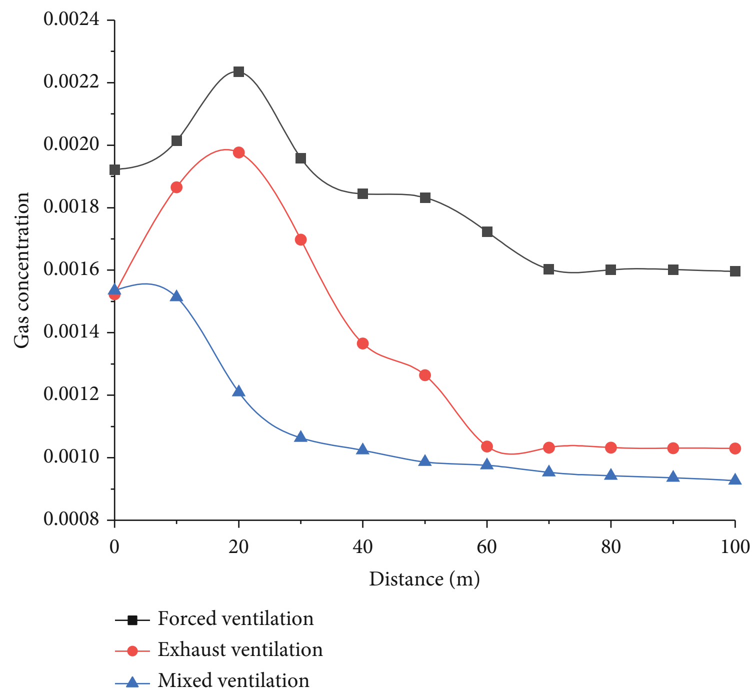

FIGURE 7: Variation curve of gas concentration in a tunnel under three ventilation modes.

in Figure 4 that for all three ventilation modes, the airflow velocity is always greater at the ventilation pipe and continuously dissipates out of the boundaries, and vortex zones of different sizes are produced for each three modes. Among them, the range of the vortex zone produced by mixed ventilation is relatively small. Overall, comparing the three ventilation modes: forced ventilation creates the most significant airflow velocity at the tunnel face. However, it is very likely to cause an extensive range of vortex zones in the ventilation pipe zone, resulting in gas accumulation; the airflow velocity of the exhaust ventilation is relatively small, which is against the gas exhaust and the inflow of fresh air; the airflow velocity is relatively large while the exhaust pipe exists in mixed ventilation, which enables the vectored flow of polluted air to the exhaust pipe, reducing the range of vortex zone and enhancing the ventilation efficiency.

To better understand the variation law of airflow velocity in a tunnel under the three ventilation modes, monitoring points for analyzing the airflow velocity variations were configured every 10 m along the tunnel centerline. The obtained airflow velocity variation curves are shown in Figure 5.

It can be observed in Figure 5 that for forced ventilation, the axial velocity of airflow 0~10 m from the tunnel face was around 4.1 m/s. The direction of the axial velocity of the airflow was altered at 15~35 m, resulting in airflow of -5.4 m/s. This indicates that a vortex zone formed in this region, in which airflow was subjected to rotational motion. Subsequently, the velocity direction was altered again, and finally, the polluted air was exhausted out of the tunnel at a constant velocity of 3.2 m/s. For exhaust ventilation, the axial velocity was 2.3 m/s in front of the tunnel face. The velocity decreased to -1.7 m/s at 15~30 m, and fresh air finally flowed into the tunnel at a velocity of -2.8 m/s. For mixed ventilation, the variation law of airflow velocity in the tunnel was similar to forced ventilation. From 0~10 m, the velocity was constant at 2.5 m/s and changed to -2.9 m/s at 15~25 m. The direction was then altered again. Finally, the air was exhausted out of the tunnel at a velocity of 1.8 m/s. It can be found by the velocity variations of the three ventilation modes that in the range of 15~30 m in front of the tunnel face, the airflow was inclined to form a vortex zone, which was likely to cause gas accumulation in the ventilation process. The range of the vortex zone can be derived by the range of the airflow velocity direction variation. Therefore, the range of the vortex zone was the largest in forced ventilation, followed by that in exhaust ventilation, and that in mixed ventilation was the smallest. This indicates that mixed ventilation showed the best ventilation efficiency.

4.2. Distribution Law of Gas Concentration in Tunnel. The study of the gas distribution law on the tunnel face is critical for the safe construction of a tunnel. Hence, the tunnel ($y = 0$ cross-section) center plane was selected to study the gas concentration distribution in a tunnel for the three ventilation modes. The obtained gas concentration distributions are shown in Figure 6.

Gas concentration monitoring points were located every 10 m along the tunnel's centerline, and the variation curves of gas concentration in the tunnel with distance were obtained for the three ventilation modes, as presented in Figure 7.

As shown in Figure 6, the gas concentration distributions tended to gradually decline along the direction from the opening of the ventilation pipe to the tunnel opening for all three ventilation modes. In the region where the ventilation pipe is located, a vortex formed due to the jet flow of the ventilation pipe acting on the recirculated flow further caused an increase in local gas concentration. The gas concentration was distinctly higher in the vortex zone than in other regions. High gas concentration areas were concentrated in the vortex zone and the region of the ventilation pipe. It can be seen in Figure 7 that for both the forced ventilation and exhaust ventilation, the gas concentration values in the tunnel first increased, then decreased, and finally stabilized. The gas concentration maximums were mainly identified in the vortex zones 15~20 m in front of the tunnel face, which were 0.22% and 0.18%, respectively. In the range of 20~60 m from the working face, the gas concentration value fell to 0.16% and 0.11% and finally stabilized. However, for mixed ventilation, the gas concentration was high next to the tunnel face, and with an increase in distance, it gradually declined until it stabilized. At the region 0~5 m in front of the tunnel face, the gas concentration reached its maximum at 0.15%. In the range of 5~30 m, the concentration sharply dropped to 0.11% and then tended to stabilize. Among the three ventilation modes, mixed ventilation resulted in the lowest values for both the concentration of gas accumulation in the tunnel and the mean concentration of gas. Therefore, the ventilation efficiency of mixed ventilation was greater than that of the other two.

5. Conclusions

In this paper, the ventilation processes of three ventilation modes in a gas tunnel were simulated by Fluent software. Through the simulation, the three ventilation modes were studied in terms of the airflow's transportation law inside the tunnel, the distribution law of airflow velocity, and the distribution law of gas concentration in the tunnel. The following conclusions were addressed.

Vortex zones of different ranges were formed in the ventilation pipe region in the tunnel for all three ventilation modes. The existence of a vortex zone caused an accumulation of gas and affected the efficiency of ventilation. Thereinto, forced ventilation showed the most significant airflow velocity. However, the range of the vortex zone was also the greatest. The airflow velocity caused by the mixed ventilation mode was relatively great without any large-range vortex zones forming, which is beneficial for improving tunnel ventilation efficiency.

Between the recirculation zone and the vortex zone, the gas concentration distributions in the tunnel were obviously different between the three ventilation methods. The gas concentration was clearly higher in the vortex zone than in other areas. In terms of the concentration of gas accumulation region in the tunnel and the mean concentration of gas, mixed ventilation resulted in lower values than the other two and showed the greatest efficiency of ventilation.

Data Availability

The data used to support the findings of this study are available from the corresponding author upon request.

Conflicts of Interest

The authors declare that there are no conflicts of interest regarding the publication of this paper.

Acknowledgments

This work was supported by the National Natural Science Foundation of China (Nos. 51904112, 51904113, 51804129, 51808246, and 51708245), the Scientific and Technological Guidance Project of Jiangsu Construction System (Nos. 2018ZD268 and 2017ZD246), the Natural Science Foundation for Colleges and Universities in Jiangsu Province (No. 17KJB620002), and the Natural Science Foundation of Jiangsu Province (No. BK20170457), 2019 Huaishang Talent Plan Program (Project Principals Jiarui Chen).

References

[1] Y. Zhao and P. F. Li, "A statistical analysis of China's traffic tunnel development data," *Engineering*, vol. 4, no. 1, pp. 3–5, 2018.

[2] K. R. Hong and H. H. Feng, "Development trends and views of highway tunnels in China over the past decade," *China Journal of Highway and Transport*, vol. 33, no. 12, pp. 62–76, 2020.

[3] K. R. Hong, "Development and thinking of tunnels and underground engineering in China in recent 2 years (from 2017 to 2018)," *Tunnel Construction*, vol. 39, no. 5, pp. 710–723, 2019.

[4] Q. Z. Sun and B. J. Fan, "Stress analysis and movement study on construction tunnel dust," *Coal Technology*, vol. 35, no. 5, pp. 176–178, 2016.

[5] K. Wang and F. Du, "Coal-gas compound dynamic disasters in China: a review," *Process Safety and Environmental Protection*, vol. 133, pp. 1–17, 2020.

[6] P. Peng, Y. Fang, Y. C. Zhou, and X. G. Chen, "Effect analysis and parameter optimization of forced ventilation during tunneling," *Railway Standard Design*, vol. 58, no. 7, pp. 102–106, 2014.

[7] Y. Xue, P. G. Ranjith, F. Dang et al., "Analysis of deformation, permeability and energy evolution characteristics of coal mass around borehole after excavation," *Natural Resources Research*, vol. 29, no. 5, pp. 3159–3177, 2020.

[8] R. H. Lin, G. Q. Li, N. L. Hu, J. Gong, and H. Yang, "Parameters optimization of combined ventilation in an excavation roadway of high-altitude mine," *China Mining Magazine*, vol. 26, no. 4, pp. 121–125, 2017.

[9] P. Wu, Z. B. Feng, S. J. Hu, and J. Cao, "Fast and accurate prediction of airflow and drag force for duct ventilation using wall-modeled large-eddy simulation," *Building and Environment*, vol. 141, no. 8, pp. 226–235, 2018.

[10] W. B. Ye, "Design method and modeling verification for the uniform air flow distribution in the duct ventilation," *Applied Thermal Engineering*, vol. 110, pp. 573–583, 2017.

[11] Y. D. Huang, X. L. Gong, Y. J. Peng, and C. N. Kim, "Effects of the solid curtains on natural ventilation performance in a subway tunnel," *Tunnelling and Underground Space Technology*, vol. 38, no. 9, pp. 526–533, 2013.

[12] E. Mostafa, I. B. Lee, S. H. Song et al., "Computational fluid dynamics simulation of air temperature distribution inside broiler building fitted with duct ventilation system," *Biosystems Engineering*, vol. 112, no. 4, pp. 293–303, 2012.

[13] Y. D. Huang, W. Gao, and C. N. Kim, “A numerical study of the train-induced unsteady airflow in a subway tunnel with natural ventilation ducts using the dynamic layering method,” *Biosystems Engineering*, vol. 22, no. 2, pp. 164–172, 2010.

[14] G. M. Xie, “Research on ventilation technology of high gas tunnel,” *Highway Engineering*, vol. 43, no. 3, pp. 263–267, 2018.

[15] X. Zhao, S. Q. Li, and F. Huang, “Advanced detection of coal seam and methane detection in highway gas tunnel,” *Highway Engineering*, vol. 44, no. 4, pp. 163–168,173, 2019.

[16] R. X. Li, H. W. Chen, S. Y. Zhou, and X. P. Liu, “Analysis on the genesis of gas in the tunnel with oil and gas and its safety management,” *Modern Tunnelling Technology*, vol. 56, no. 6, pp. 36–40,46, 2019.

[17] Z. Y. Zhou, P. Hu, Z. C. Han, and J. H. Chen, “Effect of heading face ventilation arrangement on regulation of dust distribution,” *Journal of Central South University(Science and Technology)*, vol. 49, no. 9, pp. 2264–2271, 2018.

[18] P. P. Cheng, H. N. Wang, L. Mi, Q. C. Liang, and J. Gao, “3D simulation on transporting of particle dust in horizontal duct,” *Chinese Journal of Environmental Engineering*, vol. 11, no. 10, pp. 5457–5464, 2017.

[19] P. Ntzeremes and K. Kirytopoulos, “Evaluating the role of risk assessment for road tunnel fire safety: a comparative review within the EU,” *Journal of Traffic and Transportation Engineering(English Edition)*, vol. 6, no. 3, pp. 282–296, 2019.

[20] R. Hansen, “Fire behaviour of multiple fires in a mine drift with longitudinal ventilation,” *International Journal of Mining Science and Technology*, vol. 29, no. 2, pp. 245–254, 2019.

[21] A. T. Zhou, K. Wang, L. G. Wu, and Y. W. Xiao, “Influence of gas ventilation pressure on the stability of airways airflow,” *International Journal of Mining Science and Technology*, vol. 28, no. 2, pp. 297–301, 2018.

[22] X. B. Kang, S. Luo, Q. S. Li, M. Xu, and Q. Li, “Developing a risk assessment system for gas tunnel disasters in China,” *Journal of Mountain Science*, vol. 14, no. 9, pp. 1751–1762, 2017.

[23] H. Rickard, “Fire behavior of mining vehicles in underground hard rock mines,” *International Journal of Mining Science and Technology*, vol. 27, no. 4, pp. 627–634, 2017.

[24] J. Li, T. Yu, X. Liang, P. Zhang, C. Chen, and J. Zhang, “Insights on the gas permeability change in porous shale,” *Advances in Geo-energy Research*, vol. 1, no. 2, pp. 69–73, 2017.

[25] Y. Zhao, S. Chen, X. Tan, and M. Hui, “New technologies for high-risk tunnel construction in Guiyang-Guangzhou high-speed railway,” *Journal of Modern Transportation*, vol. 21, no. 4, pp. 258–265, 2013.

[26] A. Bond, S. Benbow, J. Wilson et al., “Reactive and non-reactive transport modelling in partially water saturated argillaceous porous media around the ventilation experiment, Mont Terri,” *Journal of Rock Mechanics and Geotechnical Engineering*, vol. 5, no. 1, pp. 44–57, 2013.

[27] J. C. Fang, C. D. Zhang, Z. Z. Gou, and B. He, “Analysis of three dimensional dynamic numerical simulation of the construction ventilation of long tunnel,” *Highway Engineering*, vol. 42, no. 1, pp. 139–142,155, 2017.

[28] Y. Xue, F. Gao, Y. Gao, X. Liang, Z. Zhang, and Y. Xing, “Thermo-hydro-mechanical coupled mathematical model for controlling the pre- mining coal seam gas extraction with slotted boreholes,” *International Journal of Mining Science and Technology*, vol. 27, no. 3, pp. 473–479, 2017.

[29] C. P. Xin, F. Du, K. Wang, C. Xu, S. G. Huang, and J. T. Shen, “Damage evolution analysis and gas–solid coupling model for coal containing gas,” *Geomechanics and Geophysics for Geo-energy and Geo-resources*, vol. 7, no. 7, pp. 1–15, 2021.

[30] C. F. Wu, B. Jin, Z. Y. Chen, and Y. Liu, “Numerical simulation on combined ventilation in excavation roadway,” *Nonferrous Metals(Mine Section)*, vol. 67, no. 1, pp. 69–73,82, 2015.

[31] W. Shen, X. Li, A. Cihan, X. Lu, and X. Liu, “Experimental and numerical simulation of water adsorption and diffusion in shale gas reservoir rocks,” *Advances in Geo-energy Research*, vol. 3, no. 2, pp. 165–174, 2019.

[32] T. T. Long, K. P. Zhou, Q. F. Chen, and J. L. Li, “A simulated study on the ventilation effect of the heading face based on PMV index,” *Journal of Safety and Environment*, vol. 8, no. 3, pp. 122–125, 2008.

Hindawi
Geofluids
Volume 2021, Article ID 6639602, 9 pages
https://doi.org/10.1155/2021/6639602

Research Article

Triaxial Mechanical Properties and Micromechanism of Calcareous Sand Modified by Nanoclay and Cement

Wei Wang,[1] Jian Li,[1] and Jun Hu[2]

[1]School of Civil Engineering, Shaoxing University, Shaoxing, China 312000
[2]College of Civil Engineering and Architecture, Hainan University, Haikou, China 570228

Correspondence should be addressed to Jun Hu; hj7140477@hainanu.edu.cn

Received 29 December 2020; Revised 7 January 2021; Accepted 29 January 2021; Published 8 February 2021

Academic Editor: Yi Xue

Calcareous sand is developed by the fracture of marine biological skeleton under the impact of seawater. Calcareous sand is not transported in the process of deposition. Therefore, calcareous sand retains the characteristics of marine biological skeleton, low strength, and porous. In order to study the effect of nanoclay and cement on the modification of calcareous sand, a series of tests were carried out on the modified cement calcareous sand (CCS) with different content of nanoclay. In this study, the triaxial mechanical properties and failure modes of nanoclay and cement composite modified calcareous sand (NCCS) were studied through the triaxial UU test. Then, SEM tests were carried out on CCS and NCCS samples, and the micromechanism of nanoclay and cement composite modified Nanhai calcareous sand was analyzed. The results showed that (1) the shear properties of CCS could be improved by adding nanoclay. The optimum admixture ratio of nanoclay was 8%, and its peak stress was 23%-39% higher than that of CCS. (2) The peak stress and strain of NCCS showed a linear correlation. (3) Compared with CCS, the internal friction angle and cohesion of NCCS were increased by 5.2% and 52%, respectively. (4) Nanoclay could improve the compactness and structure of cement calcareous sand, and the macroscopic performance is the improvement of peak stress and cohesion.

1. Introduction

Calcareous sand is the accumulation of pieces of carbonate materials, which are usually developed from shell fragments and skeletal debris of marine organism [1, 2]. Due to the fact that calcareous sand did not undergo long-distance transportation in the process of deposition [3], there are many small pores in calcareous sand particles with irregular shapes and large edges. In the 1960s and 1970s, the engineering properties of calcareous sand have received global focus at both the academic and the practical levels [4, 5]. After that, the basic engineering properties of calcareous sand have been paid more attention to studies [6]. The compressive properties of calcareous sand are similar to nanoclay, which is significantly affected by the particle breakage [7]. In terms of shear performance, the shear strength and plastic deformation of calcareous sand are larger than conventional terrigenous sand [8]. In addition, calcareous sand displays a larger internal friction angle than terrigenous sand [9, 10]. The shear performance of calcareous sand is mainly affected by its grain failure and dilatancy [11, 12]. The above studies have shown that the physical properties of calcareous sand are different from conventional terrigenous sand; it retains the characteristics of marine biological skeleton, low strength easy fragmentation, and high compressibility.

In practical engineering, a question arises herein as to whether some materials can be adopted to effectively reinforce the calcareous sand in order to make it meet the requirements of bearing capacity. At present, the improvement measures of calcareous sand mainly include cement reinforcement, polymer reinforcement, and MICP microbial induction reinforcement. Cement, as a common gelling agent, exhibits a good effect in strengthening soft soil [13–15]. Therefore, some scholars began to study the reinforcement effect of cement on calcareous sand. The cyclic triaxial test was carried out on cement calcareous sand by Sharma and Fahey [16], and they found that cement can improve the shear strength of calcareous sand. Ismail et al. [17]

Table 1: Basic physical indexes of calcareous sand in a certain area of Sansha City.

Sand depth/m	Gravity/kN·m^{-3}	Cohesion/kPa	Internal friction angle/°	Compression modulus/MPa	Osmotic coefficient/cm·s^{-1}	Bearing capacity/kPa
25~30	18	5	30	10	8.0×10^{-2}	200

Table 2: Basic physical and mechanical indexes of cement.

Fineness/%	Initial setting time/min	Final setting time/min	Loss on ignition/%	Compressive strength/MPa		Flexural strength/MPa	
				3 d	28 d	3 d	28 d
3.4	210	295	1.4	26.9	48.1	4.9	9.0

Table 3: Technical indexes of nanoclay.

Components	Appearance	Montmorillonite content/%	Apparent density (g/cm^3)	Radius-thickness ratio	Layer thickness/nm	Moisture content/%
Montmorillonite derivatives	Light pink powder	96-98	0.45	200	≤25	≤3

studied the influence of different cementitious materials on calcareous soil shear performance via triaxial test, and the result showed that compared with calcite powder and gypsum powder, the cementation degree of silicate cement to calciferous sand was better. Wang et al. [18] studied the effect of cement content on the shear performance of calcareous sand through the triaxial test, and the result showed that the addition of cement could improve the shear strength of calcareous sand. The modification effect is optimal when the content of cement is 15%, and compared with ordinary calcareous sand, the strength is 1.7 times.

As the most promising material in the 21st century, nanomaterials have been widely used in various fields due to its excellent properties [19–22]. Gao and coworkers [23, 24] explored the influence of nano-MgO on the mechanical performance of soft clay via an unconfined compression test, and the research indicated that the engineering properties of soft clay could be improved by adding an appropriate amount of nano-MgO. Wang et al. [25] found that nano-MgO can modify the shear performance of cement silty clay through the direct shear test, and the optimal blending ratio is 5‰. As a common nanomaterial, nanoclay is also widely used in improving the performance of cement-based materials. An unconfined compression test for exploring the effect of nanoclay on the compressive properties of cement iron tailings is reported by Li et al. [26], and the result showed that the compressive property of cement iron tailing sand can be improved by adding 5%–10% nanoclay instead of cement. Zaid et al. [27] conducted the unconfined compression test on solidified soft soil with nanoclay and nano-CuO, respectively, and the result showed that the effect of nanoclay-cured soft soil was significantly better than that of nano-CuO. Li et al. [28] explored the effect of nanoclay on the shear performance of soft clay through the direct shear test, and the result showed that the addition of nanomontmorillonite can increase the shear strength and internal friction angle of the clay. Wang et al. [29] research showed that nanoclay could effectively improve the compressive properties of cement calcareous sand. Overall, nanoclay can improve the mechanical performance of soft soil and cement-based materials.

Table 4: Experimental design scheme.

Sample no.	Cement content/%	Nanoclay content/%	Water content/%	Curing age/d
CCS	10	0	30	7
NCCS-4	10	4	30	7
NCCS-6	10	6	30	7
NCCS-8	10	8	30	7
NCCS-10	10	10	30	7

In spite of a lot of reports have explored the mechanical performance of nanoclay solidified soft soil and cement-based materials, there are still few researches on mechanical performance of calciferous sand modified by nanomaterial and cement composite. Therefore, with the aim of addressing the above concerns, a systematic laboratory program was carried out to explore the effect of nanoclay content and confining pressure on the shear performance of CCS. And the SEM was used to analyze the micromechanism of NCCS. We hoped that the outcomes of this study will not only provide convincing evidence on the role of nanoclay in a mixture, but can also serve as a useful reference for engineering applications of NCCS in offshore engineering and for relevant theoretical developments.

2. Materials and Sample Preparation

2.1. Materials. In this test, the loose and unconsolidated calcareous sand was taken from an area of Yongxing Island,

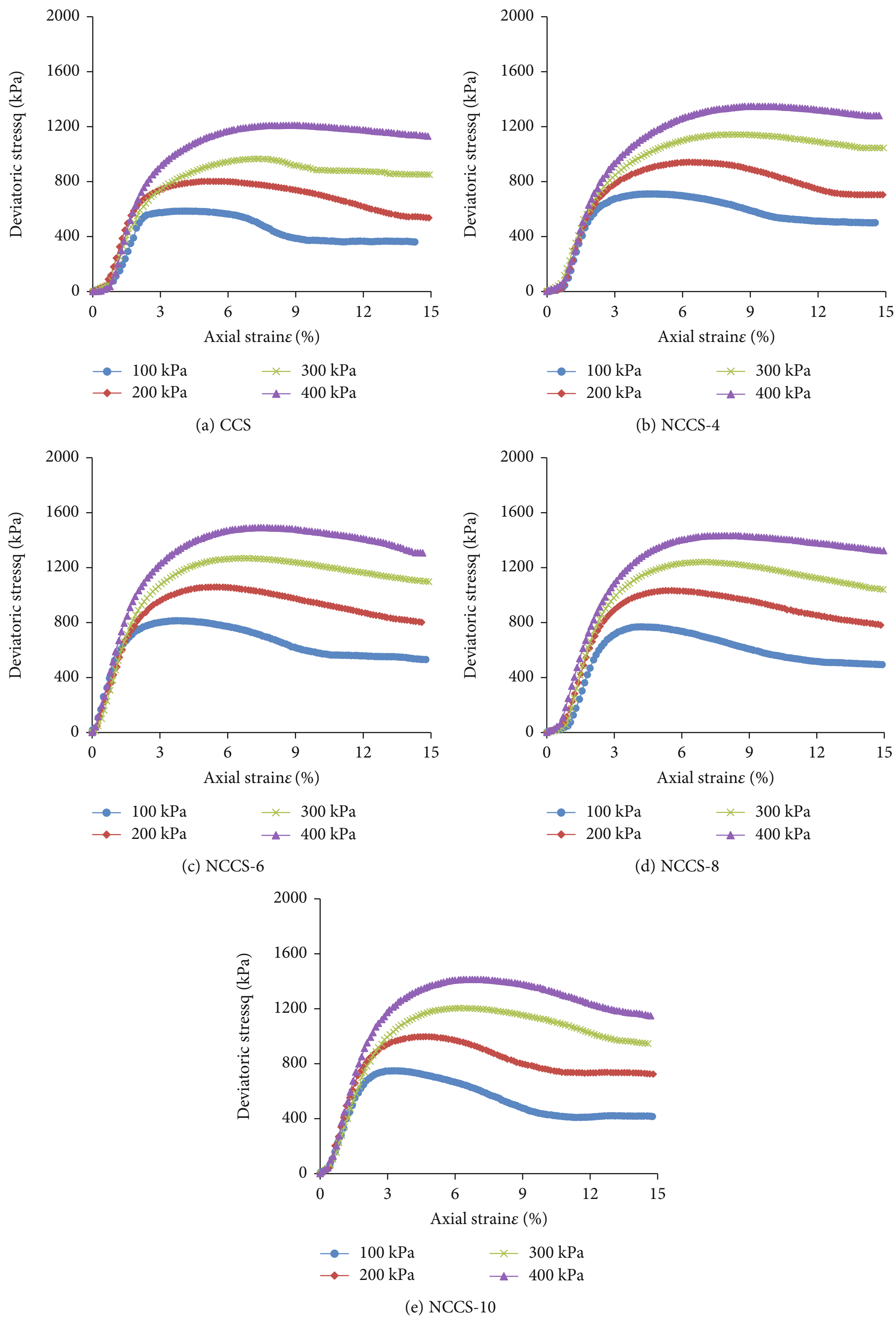

Figure 1: Stress-strain curves of CCS and NCCS.

Sansha City, Hainan Province. It generally showed white; meanwhile, red particles are present in calciferous sand due to the presence of coral debris. To remove any possible influence of particle size and grading, sieved calcareous sand (0.25-1 mm) was adopted as the base sand; all particle size is less than 2 mm. Basic mechanical indexes of calcareous sand are shown in Table 1. The cement used in the test was Lanting PO 32.5 ordinary silicate cement produced by Shaoxing Zhaoshan Building Materials Co., Ltd.; the basic physical mechanical indexes are shown in Table 2. Nanoclay is a faint yellow powder, produced by Hubei gold fine montmorillonite technology Co., Ltd, and its main technical indicators are shown in Table 3.

2.2. Experimental

2.2.1. Instrument. TKA-TTS-3S was used for the triaxial shear test, which was produced by Nanjing Texao Technology Co., Ltd. In this study, the unconsolidated and undrained (UU) test was performed on calcareous sand to investigate the effects of different confining pressure, such as 100, 200, 300, and 400 kPa, on NCCS shear performance. According to GBT 50123-2019 Geotechnical Test Standard [30], the shear rate of the specimen is set at 0.6 mm/min, and the test is stopped when the axial strain reaches 15%.

2.2.2. Experimental Scheme. Considering the effect of nanoclay content on the shear performance of CCS, cement content at 10% and water content at 30% were controlled in the test to explore the effects of different nanoclay content and confining pressure on triaxial shear properties of CCS. The experimental design is shown in Table 4.

2.3. Sample Preparation and Curing. According to the "GBT 50123-2019 Geotechnical Test Standard," the triaxial specimens in this test were all cylinders with diameter $D = 39.1$ mm and height $H = 80$ mm. Before the test, the dried calcareous sand was sieved through a 2 mm sieve to remove impurities such as small and medium shells and coral debris. The calcareous sand sample was compacted in 4 layers, 41 g of the calcareous sand mixed sand sample was weighed at each time. After each layer of compaction was completed, the surface of the calcareous sand sample needed to be roughened to ensure the internal integrity of the sample. Then the as-acquired sample was placed into a three-valve saturation device, and filter stones were placed at both ends of the sample; the filter paper was required to be placed between the filter stones and the sample to prevent calcareous sand particles from adhering to the filter stones. Due to the loose and non-caking characteristics of calcareous sand, the specimens needed to be maintained with a matrix for 4 days and then removed the matrix. Finally, the as-obtained sample was put into a curing room for curing.

3. Triaxial UU Test

3.1. Stress-Strain Curves. The effect of nanoclay content on the shear performance of CCS was explored in this test. Four confining pressures of 100, 200, 300, and 400 kPa were all test for four NCCS samples (0, 4%, 6%, 8%, and 10%). The stress-strain curves of NCCS with different nanoclay content were shown in Figure 1.

In Figure 1, the stress-strain curves of CCS and NCCS showed softening curves. The deviatoric stress showed a slight decrease after peak stress occurred in the CCS samples. When the confining pressure was from 400 kPa to 100 kPa, the softening trend of the stress-strain curves of CCS gradually increased. With the increase of nanoclay content, the softening trend of stress-strain curves of NCCS was gradually obvious.

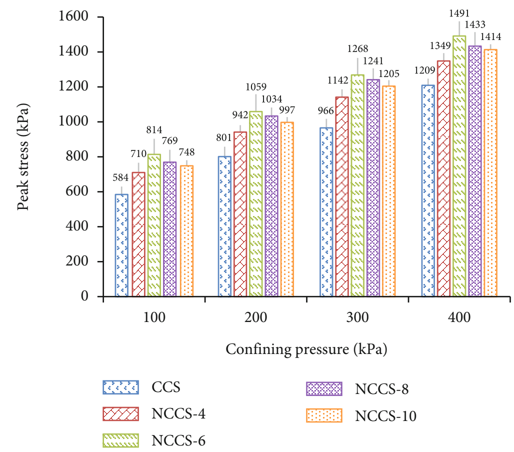

Figure 2: Relation of nanoclay content and peak stress of NCCS.

Table 5: Peak strain of CCS and NCCS (%).

Nanoclay content/%	Confining pressure/kPa			
	100	200	300	400
0	3.67	4.82	7.27	7.82
4	4.45	6.29	7.71	9.03
6	3.78	5.52	6.84	7.48
8	4.20	5.55	7.01	8.01
10	3.31	4.70	6.12	6.65

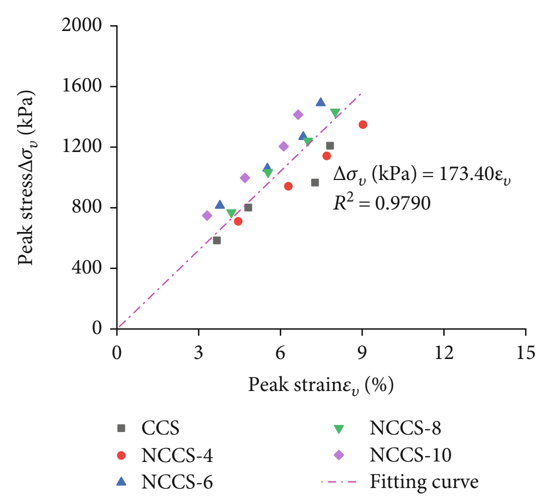

Figure 3: Relation of peak stress and peak strain of NCCS.

3.2. Effects of Nanoclay Content on Peak Stress of NCCS. Peak stress was the maximum deviatoric stress in the deviatoric stress-strain curve. Figure 2 showed the relation of nanoclay content and peak stress of NCCS.

As shown in Figure 2, the addition of nanoclay could improve the peak stress of CCS. When the confining pressure

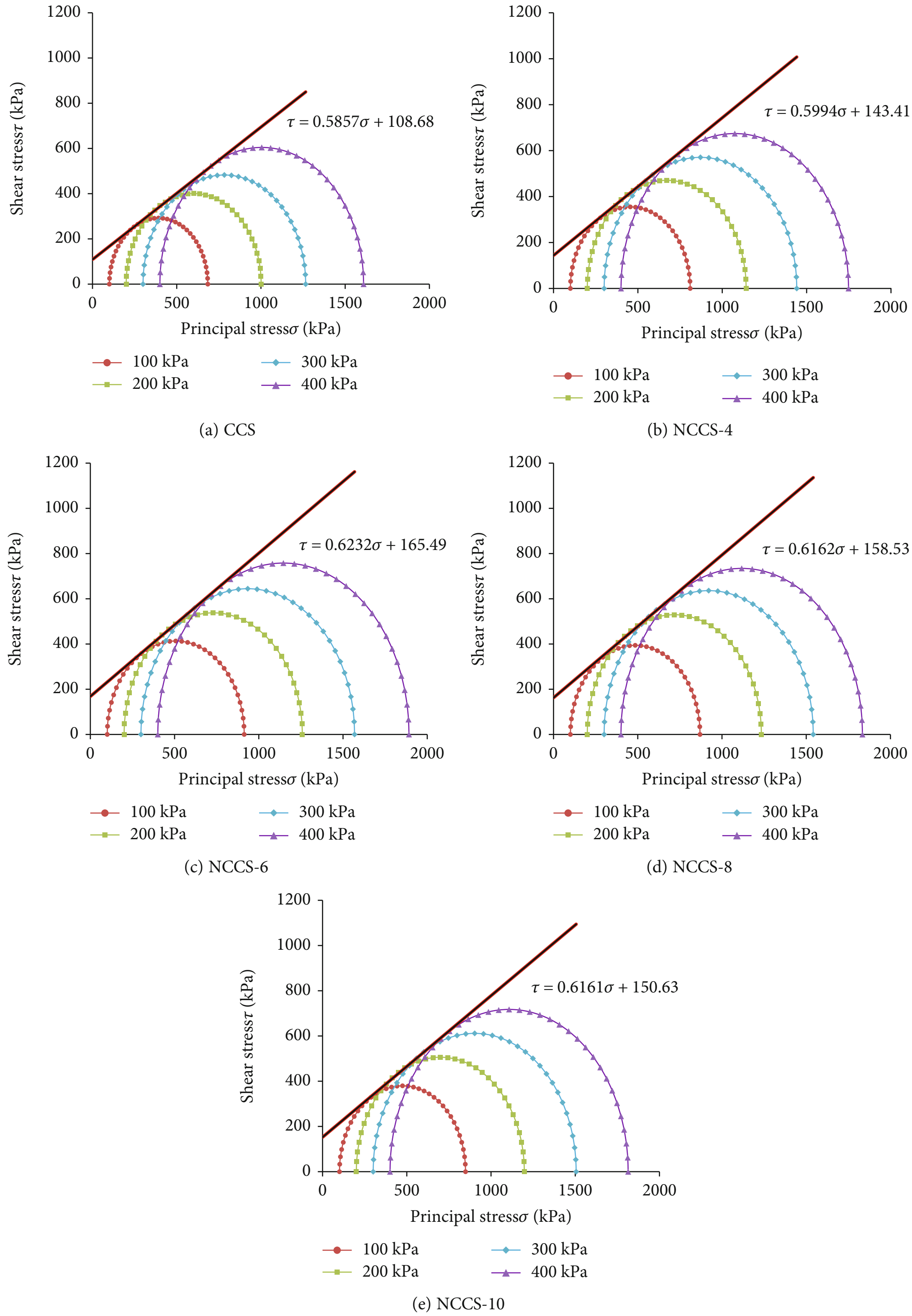

FIGURE 4: Strength envelopes of CCS and NCCS.

was within the range of 100 kPa to 400 kPa, the corresponding peak stress of CCS was 584 kPa, 801 kPa, 966 kPa, and 1209 kPa, respectively. Compared with CCS, the peak stress of NCCS-4, NCCS-6, NCCS-8, and NCCS-10 was increased by 12%–22%, 23%–39%, 19%–32%, and 17%–28%, respectively. Under the same confining pressure, the above data also indicated that with the increase of nanoclay content, the peak stress of NCCS increased first and then decreased.

In summary, the optimized nanoclay content of NCCS was 6%, and its peak stress was 23%–39% higher than CCS.

3.3. Peak Strain of NCCS. Table 5 lists peak strains CCS and NCCS.

As shown in Table 1, the peak strain of NCCS exhibited smaller under the smaller confining pressure. When the confining pressure increased, the peak strain of NCCS increased, indicating that NCCS had good ductility under the constraint of higher confining pressure. The peak strain and peak stress of NCCS with different content of nanoclay were compared. As shown in Figure 3, the peak stress and peak strain of NCCS were basically linear.

3.4. Shear Strength Index of NCCS. To further study the modification effect of nanoclay on CCS shear strength, the strength envelops of CCS and NCCS were drawn according to the Mohr-Coulomb theory, and the shear strength c and φ were obtained. The ultimate stress circle of CCS and NCCS under different confining pressure was shown in Figure 4.

As shown in Figure 4, when CCS and NCCS samples were in failure models, with the increase of the effective confining pressure, the diameter of the stress circle would gradually increase and the strength envelop presented a diagonal line, which was similar to the conclusion of cement soil research [31]. Du et al. [32] pointed out that in the triaxial UU test, the low saturation state of the sample would make the strength and confining pressure linearly increase. The reason mainly had the following two aspects; on the one hand, the initial water content of the CCS and NCCS samples was lower than the saturated water content. On the other hand, the hydration reaction of cement consumed water in the CCS and NCCS samples during curing. These two reasons caused both the CCS and NCCS samples to be in a low saturation state. Therefore, the existence of initial confining pressure would cause isotropic compression and the decrease of void ratio of the CCS and NCCS samples. With the increase of the confirmation pressure, the strength of the sample increased and the increment of pore pressure decreased [33]. In the process of shear failure, the effective stress of CCS and NCCS samples increased step by step as the confining pressure increased from 100 kPa to 400 kPa. It was further clarified that the diameter of the stress circle of CCS and NCCS will also increase. Therefore, different from the conventional soft soil triaxial UU test, the strength envelope of CCS and NCCS showed an obvious diagonal line, that is to say, the value of internal friction angle would be much greater than 0. This result indicated that the mechanical performance can be effectively improved by the addition of cement and nanoclay to calcareous sand.

Figure 5 showed the relation of nanoclay content and internal friction angle of NCCS. As exhibited in Figure 5, the internal friction angle of CCS was 30.36°, which was 0.36° higher than that of calcareous sand, indicating that the incorporation of cement has little effect on calcareous sand internal friction angle. The internal friction angle of NCCS-4, NCCS-6, NCCS-8, and NCCS-10 was 30.94, 31.93, 31.64, and 31.63, respectively, which was 1.9%, 5.2%, 4.2%, and 4.2% higher than CCS, indicating that nanoclay can rapidly increase the internal friction angle of NCCS when the content of nanoclay was small. When there was more nanoclay content, the increase of internal friction angle of NCCS tends to be gentle, even decreased. Therefore, for NCCS, with the increase of nanoclay content, the internal friction angle of NCCS generally increased first and then decreased; when the nanoclay content was 6%, the internal friction angle of NCCS reached maximum value, it increased by 5.2% compared with that of CCS.

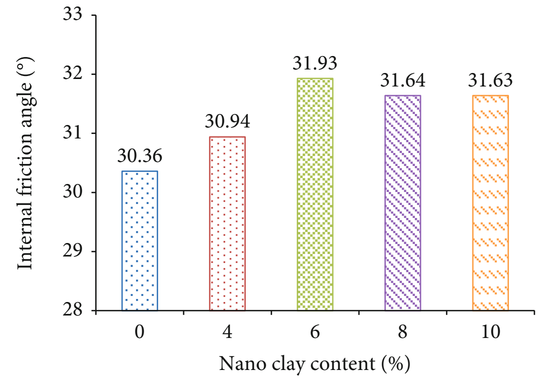

Figure 5: Relation of nanoclay content and internal friction angle of NCCS.

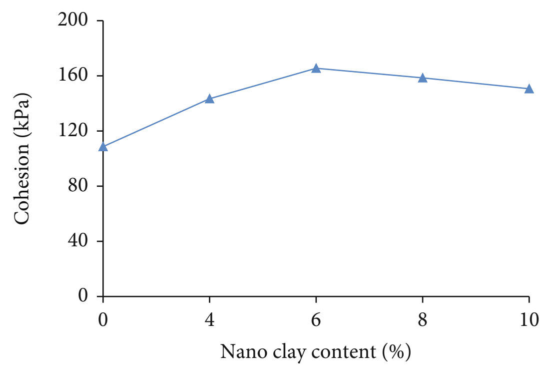

Figure 6: Relationship between nanoclay content and NCCS's cohesion.

Figure 6 showed the relation of nanoclay content and NCCS cohesion. According to Figure 6, the cohesion of CCS was 108.68 kPa, indicating that the incorporation of cement can significantly improve the cohesion of calcareous sand. The cohesion of CCS was further improved by the modification of nanoclay. The cohesion values for NCCS-4, NCCS-6, NCCS-8, and NCCS-10 were 143.41, 165.49, 158.53, and 150.63 kPa, respectively, 32%, 52%, 46%, and 39% higher than the cohesion of CCS values, respectively. Therefore, the incorporation of nanoclay could improve the cohesion of CCS. With the increase of nanoclay content, the cohesion of NCCS increased firstly and then decreased. When nanoclay content was 6%, cohesion of NCCS was the best value, which was 52% higher than CCS.

In summary, the modification of nanoclay could improve the shear properties of CCS. When nanoclay content was 6%, the internal friction angle and cohesion of NCCS reached the

(a) CCS

(b) NCCS

Figure 7: Failure characteristics of specimens.

maximum. In this case, cohesion of NCCS was 52% higher than CCS, while the internal friction angle was 5.2% higher than CCS. Therefore, the shear performance of NCCS was mainly achieved by enhancing the cohesion of CCS. The modification of nanoclay could improve the bite force between the particles in calcareous sand, while it was little effect on the internal friction of NCCS. The reason that nanoclay could improve the shear strength index of CCS can be attributed to: calcareous sand was loose sand particles with low cohesion, but the cementitious material produced by the hydration reaction of cement could increase the cohesive force between sand particles. The nanoclay particles were small and highly active, which could not only absorb water and expand to fill the pores but also promote the hydration reaction of cement and increase the production of cementitious substances. These two aspects could improve the bite force between sand particles, so as to improve the shear strength index of CCS.

3.5. Failure Characteristics. In order to deeply study the effect of nanoclay incorporation on the failure mode of CCS, the failure modes of CCS and NCCS samples were analyzed when the confining pressure was 300 kPa, as shown in Figure 7.

As depicted in Figure 7, CCS was drum-like failure in the middle without obvious cracks, while NCCS was inclined fracture failure. This may be due to the large number of pores in CCS, which had high compressibility under the constraint of certain confining pressure. After modified by nanoclay, the pores in NCCS were decreased and its compressibility was decreased, so that NCCS presented oblique inclined fracture failure.

4. Micromechanism

In order to investigate the micromechanism of shear performances of calcareous sand modified by nanoclay and cement, cement calcareous sand (CCS) and nanoclay-cement calcareous sand (NCCS) were characterized by scanning electron microscope. The microscopic features of CCS and NCCS were shown in Figures 7 and 8, respectively.

As depicted in Figure 8, the fibrous and flocculent water-insoluble gelling substances (C-S-H) were distributed in the spindle-shaped pores on the surface of calcareous sand, which indicated that the generation of hydration products can bond calcareous sand particles better. Meanwhile, the small particles of calcareous sand broken during the test also filled the pores of the larger particles of calcareous sand. As shown in Figure 9, there were many fine nanoclay particles and few plate-like massive substances in the microstructure of NCCS. The distribution of fine particles was irregular on the structural plane. And in addition, fibrous hydration products were generated between the particles of calcareous sand. Compared with CCS, the pores in the microstructure of NCCS were significantly reduced, and a relatively complete bulk structure appeared, indicating that the modification of nanoclay can improve the compactness of CCS. At macro level, the shear strength of NCCS increased.

There were two reasons why nanoclay modification can change the shear performance of CCS. On the one hand, the particle size of nanoclay was small, while the surface of calciferous sand had lots of spindle-shaped pores, thus, nanoclay could improve the shear strength of CCS by filling the pores on the surface of calciferous sand. On the other hand, nanoclay possesses a nucleation effect. Nanoclay could

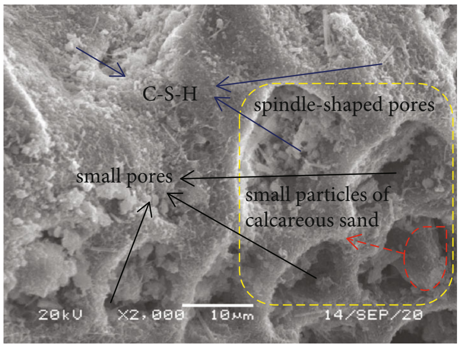

Figure 8: Microscopic features of CCS.

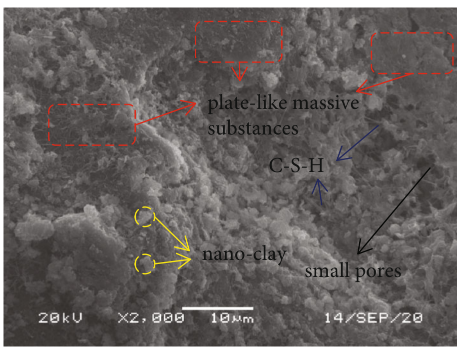

Figure 9: Microscopic features of NCCS.

adsorb free Ca ions in NCCS samples and promote the hydration reaction of cement in NCCS. To summarize, the modification of nanoclay could improve the compressibility and structure of NCCS, which further improves the shear strength of CCS.

5. Conclusions

The triaxial mechanical properties and micromechanism of CCS and NCCS with water content of 30% and cement content of 10% were investigated via triaxial UU shear tests. The following conclusions can be drawn:

(1) The stress-strain curves of both CCS and NCCS were softening curves

(2) The modification of nanoclay can improve the shear properties of the CCS. The optimum content of nanoclay is 6%, and its peak stress was 23% ~39% higher than CCS. Meanwhile, the cohesion of NCCS increased by 52% compared with CCS, and the internal friction angle increased by 5.2%

(3) NCCS exhibited good ductility under high confining pressure, and the peak deviatoric stress of NCCS with different content of nanoclay had a linear correlation with peak strain

(4) CCS was drum-like failure in the middle without obvious cracks, while NCCS was inclined fracture failure

(5) Due to the filling effect and nucleation effect, the modification of nanoclay could improve the compactness and structure of CCS, and the macroscopic performance was the improvement of peak stress and cohesion

Data Availability

All the data used to support the findings of this study are included within the article.

Conflicts of Interest

The authors declare no conflicts of interest.

Acknowledgments

This study was supported by the National Natural Science Foundation of China (51968019 and 41772311), the High level Talent Project of Hainan Basic and Applied Basic Research Plan (2019RC148 and 2019RC351), and the Hainan Natural Science Foundation (518QN307 and 519QN333).

References

[1] K. Qian, X. Z. Wang, J. W. Chen, and P. J. Liu, "Experimental study on permeability of calcareous sand for islands in the South China Sea," *Rock and Soil Mechanics*, vol. 38, no. 6, pp. 1557–1564, 2017.

[2] J. R. Zhang, C. Hua, M. X. Luo, and B. W. Zhang, "Particle breakage characteristics of calcareous sand under triaxial drained shear," *Chinese Journal of Geotechnical Engineering*, vol. 42, no. 9, pp. 1593–1602, 2020.

[3] M. Salem, H. Elmamlouk, and S. Agaiby, "Static and cyclic behavior of North Coast calcareous sand in Egypt," *Soil Dynamics & Earthquake Engineering*, vol. 55, pp. 83–91, 2013.

[4] H. Salehzadeh, D. C. Procter, and C. M. Merrifield, "Medium dense non-cemented carbonate sand under reversed cyclic loading," *International Journal of Civil Engineering*, vol. 4, no. 1, pp. 54–63, 2006.

[5] J. F. Nauroy and T. P. Le, "Driven pile and drilled and grouted piles in calcareous sands," in *The 17st Annual Offshore Technology Conference*, pp. 83–91, Houston, USA, 1985.

[6] H. Shahnazari, Y. Jafarian, M. A. Tutunchian, and R. Rezvani, "Undrained cyclic and monotonic behavior of Hormuz calcareous sand using hollow cylinder simple shear tests," *International Journal of Civil Engineering*, vol. 14, no. 4, pp. 209–219, 2016.

[7] M. R. Coop, "The mechanics of uncemented carbonate sands," *Geotechnique*, vol. 40, no. 4, pp. 607–626, 1990.

[8] J. Yang, J. H. Fan, and X. D. Li, "Shear test of calcareous sand and terrigenous sea sand," *China Water Transport*, vol. 18, no. 5, pp. 230-231, 2018.

[9] R. Rasouli, M. H. Rad, and H. Salehzadeh, "A comparison between the undrained shear behavior of carbonate and quartz sands," *International Journal of Civil Engineering*, vol. 12, no. 4, pp. 338–350, 2014.

[10] J. H. Wu, H. Lin, X. Y. Zhou, Y. C. Deng, and S. Yang, "Determination and variation of shear strength of unsaturated soil under action of water repellent agent," *Transactions of the*

Chinese Society of Agricultural Engineering, vol. 35, no. 6, pp. 123–129, 2019.

[11] J. M. Zhang, G. S. Jiang, and R. Wang, "Effect of particle breakage and dilatancy on shear strength of calcareous sand," *Rock and Soil Mechanics*, vol. 30, no. 7, pp. 2043–2048, 2009.

[12] Y. Dehnavi, H. Shahnazari, H. Salehzadeh, and R. Rezvani, "Compressibility and undrained behavior of Hormuz calcareous sand," *Electronic Journal of Geotechnical Engineering*, vol. 15, pp. 1684–1702, 2010.

[13] Y. Liu, F. H. Lee, S. T. Quek, E. J. Chen, and J. T. Yi, "Effect of spatial variation of strength and modulus on the lateral compression response of cement-admixed clay slab," *Geotechnique*, vol. 65, no. 10, pp. 851–865, 2015.

[14] Y. Liu, L. Q. He, Y. J. Jiang, M. M. Sun, E. J. Chen, and F.-H. Lee, "Effect of in situ water content variation on the spatial variation of strength of deep cement-mixed clay," *Geotechnique*, vol. 69, no. 5, pp. 391–405, 2019.

[15] Y. T. Pan, Y. Liu, A. Tyagi, F. H. Lee, and D. Q. Li, "Model-independent strength-reduction factor for effect of spatial variability on tunnel with improved soil surrounds," *Geotechnique*, 2021.

[16] S. S. Sharma and M. Fahey, "Evaluation of cyclic shear strength of two cemented calcareous soils," *Journal of Geotechnical and Geoenvironmental Engineering*, vol. 129, no. 7, pp. 609–618, 2003.

[17] M. A. Ismail, H. A. Joer, W. H. Sim, and M. F. Randolph, "Effect of cement type on shear behavior of cemented calcareous soil," *Journal of Geotechnical and Geoenvironmental Engineering*, vol. 128, no. 6, pp. 520–529, 2002.

[18] L. Wang, X. B. Lu, S. Y. Wang, J. Zhao, and A. L. Wang, "Experimental study on cementation of calcareous sand and its influence on mechanical properties," *Journal of Experimental Mechanics*, vol. 24, no. 2, pp. 133–143, 2009.

[19] P. Hosseini, A. Afshar, B. Vafaei, A. Booshehrian, and A. Esrafili, "Effects of nano-clay particles on the short-term properties of self-compacting concrete," *European Journal of Environmental and Civil Engineering*, vol. 21, no. 2, pp. 127–147, 2016.

[20] K. Yao, D. L. An, W. Wang, N. Li, C. Zhang, and A. Z. Zhou, "Effect of nano-mgo on mechanical performance of cement stabilized silty clay," *Marine Georesources and Geotechnology*, vol. 20, no. 2, pp. 250–255, 2020.

[21] D. Wang, L. N. Zhang, P. K. Hou, and X. Chen, "Research progress on application of nano-SiO2 in cement based materials," *Bulletin of the Chinese Ceramic Society*, vol. 39, no. 4, pp. 1003–1015, 2020.

[22] D. T. Niu, J. Q. He, Q. Fu, D. Li, and B. B. Guo, "Effect of carbon nanotubes on microstructure and durability of cement based materials," *Bulletin of the Chinese Ceramic Society*, vol. 48, no. 5, pp. 705–717, 2020.

[23] L. Gao, Z. Ren, and X. Yu, "Experimental study of nanometer magnesium oxide-modified clay," *Soil Mechanics and Foundation Engineering*, vol. 52, no. 4, pp. 218–224, 2015.

[24] L. Gao, K. Y. Ren, Z. Ren, and X. J. Yu, "Study on the shear property of nano-MgO-modified soil," *Marine Georesources & Geotechnology*, vol. 36, no. 4, pp. 465–470, 2018.

[25] W. Wang, Y. Li, K. Yao, A. Z. Zhou, and C. Zhang, "Strength properties of nano-MgO and cement stabilized coastal silty clay subjected to sulfuric acid attack," *Marine Georesources and Geotechnology*, vol. 3, 2019.

[26] N. Li, S. W. Lv, W. Wang, J. Guo, P. Jiang, and Y. Liu, "Experimental investigations on the mechanical behavior of iron tailings powder with compound admixture of cement and nano-clay," *Construction and Building Materials*, vol. 254, article 119259, 2020.

[27] H. M. Zaid, R. T. Mohd, and T. J. Ibtehaj, "Stabilization of soft soil using nanomaterials," *Research Journal of Applied Sciences*, vol. 8, no. 4, pp. 503–509, 2014.

[28] C. Li, J. L. Wu, and L. Chen, "Experimental study on influence of nano montmorillonite on properties of soft clay," *Journal of Wuhan Polytechnic University*, vol. 33, no. 2, pp. 72–76, 2014.

[29] W. Wang, J. Li, and J. Hu, "Unconfined mechanical properties of nanoclay cement compound modified calcareous sand of the South China Sea," *Advances in Civil Engineering*, vol. 2020, Article ID 6623710, 16 pages, 2020.

[30] GB/T 50123-2019, *Standard for Soil Test Method*, China Planning Press, 2019.

[31] F. Chen and W. B. Jian, "Triaxial test of basalt fiber cement soil," *Journal of Lanzhou University (Natural Sciences)*, vol. 52, no. 6, pp. 741–745, 2016.

[32] J. Du, G. Zheng, B. Liu, N. J. Jiang, and J. Hu, *Triaxial Behavior of Cement-Stabilized Organic Matter–Disseminated Sand*, Acta Geotechnica, 2020.

[33] J. Wang, G. Y. Ding, L. Y. Pan, Y. Q. Cai, and Y. F. Gao, "Study on mechanical properties and constitutive model of cement soil in static triaxial test," *Rock and Soil Mechanics*, vol. 31, no. 5, pp. 67–72, 2010.

Hindawi
Geofluids
Volume 2021, Article ID 6696882, 12 pages
https://doi.org/10.1155/2021/6696882

Research Article

Study on Seepage Simulation of High Pressure Grouting in Microfractured Rock Mass

Kai Wang, Lianguo Wang, Bo Ren, and Hao Fan

State Key Laboratory for Geomechanics and Deep Underground Engineering, China University of Mining and Technology, Xuzhou 221116, China

Correspondence should be addressed to Lianguo Wang; cumt_lgwang@163.com

Received 11 November 2020; Revised 22 December 2020; Accepted 9 January 2021; Published 3 February 2021

Academic Editor: Jia Liu

In coal mines, under high in situ stress and strong mining activity, roadway surrounding rock commonly contains large amounts of larger fractures and microfractures. Along with the large deformation and continuous rheology of the soft rock roadway, the fractures in the surrounding rock are likely to be compressed and closed, forming undeveloped microfractures, which hinder conventional grouting support methods. Based on the fluid-solid coupling between slurry seepage and microfracture deformation, a theoretical model of microfracture grouting seepage is established. A program for the analysis and calculation of microfracture grouting is developed to quantitatively describe the variation in slurry seepage distance and fracture opening. Numerical experiments are carried out to study the grouting seepage of microfractures under different grouting pressures and fracture opening conditions, and the variation rules for the spatial distribution of fracture opening and slurry seepage distance during grouting pressure are obtained. Fluid-solid coupling has a significant influence on grout seepage characteristics. The grouting pressure and the fracture opening changes are nonlinearly attenuated along the grout seepage direction.

1. Introduction

With continuously decreasing shallow coal resources, deep well coal mining is the future of coal mine development [1, 2]. Different from shallow coal mines, deep coal mines exist in high in situ stress environments with strong mining action, and deep coal mine roadways are particularly difficult [3–5]. As a common engineering support technology, grouting support can significantly reinforcement and prevent seepage in the surrounding rock [6–10]. Slurry is injected into the fractures in the surrounding rock by grouting pressure, filling the fractures, and cementing the rock mass together to improve rock mass bearing capacity. Grouting support plays a vital role in the surrounding rock reinforcement [11].

Under high in situ stress and strong mining stress, surrounding rock masses commonly contain large amounts of fractures, including large- and medium-sized fractures as well as microfractures (fracture opening $d \leq 0.1$ mm) [12–14]. With large deformation and continuous rheology of the surrounding rock, fractures in the rock mass are prone to squeezing and closing. A large number of underdeveloped and closed low-permeability microfractures exist in the surrounding rock [15–17]. Owing to the small fracture opening, cement particles cannot enter the microfractures, resulting in poor grouting and support effects as well as failure to achieve the expected reinforcement [18]. Subsequently, the roadway surrounding rock mass is seriously weakened, greatly reducing the overall stability of the surrounding rock [19–21].

Conventional grouting support is primarily carried out via lower grouting pressure. Based on infiltration theory, the grout spreads in the fractures or pores without destroying the structure of the rock mass [22]. However, due to the low permeability of microfractured rock masses, the injectability is poor. By increasing the grouting pressure, high pressure grouting technology can artificially reopen the originally closed fractures, improving the low-permeability of microfractured rock masses and achieving the desired support.

The grouting process is a process in which grout seepage and rock deformation are coupled together. Especially when the fracture opening is small, the fluid-solid coupling within the grouting process will be more significant [23, 24]. The

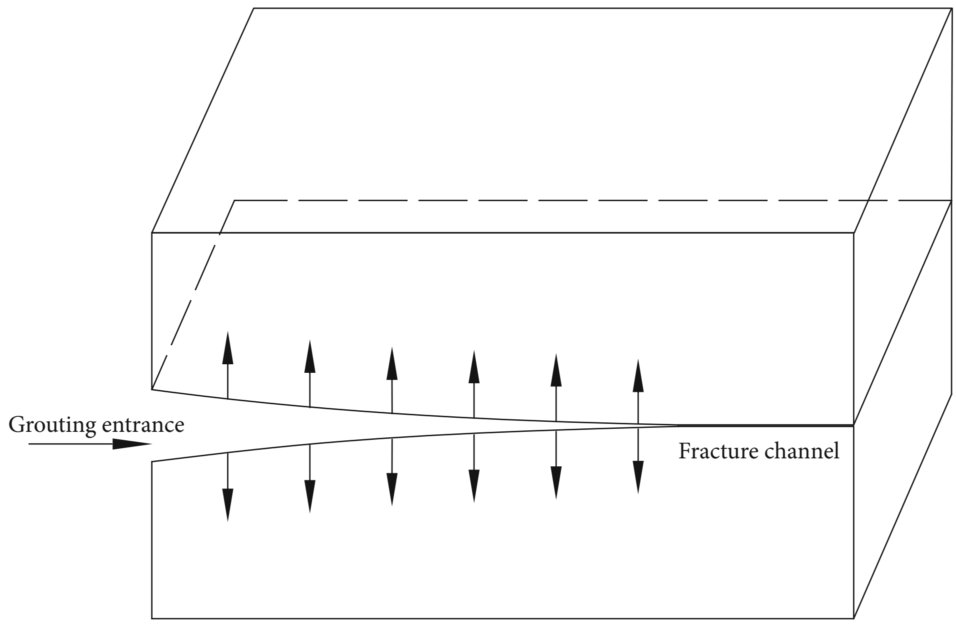

Figure 1: Schematic diagram of the slurry seepage process through a microfracture.

cement slurry enters the fracture due to grouting pressure, and the grouting pressure causes fracture to deform, changing the fracture opening and leading to variations in seepage characteristics [25, 26]. Most of the existing grouting seepage simulations are aimed at the characteristics of the law of the slurry seepage movement and do not take into account the combined effect of the slurry seepage and rock mass deformation during the slurry seepage process [27]. Especially under high pressure grouting conditions, microfractures will deform under the action of grouting pressure, which will cause changes in the seepage characteristics of the slurry [28–31]. Existing grouting seepage simulations lack descriptions of fracture deformation and slurry seepage characteristics under high pressure grouting conditions and are not suitable for the simulation of microfractured high pressure grouting slurry seepage characteristics [32–34]. Therefore, studying the seepage characteristics of high pressure grouting on microfractures considering fluid-solid coupling is of great significance to the study of grouting in microfractured rock masses [35].

In order to study the seepage characteristics of high pressure grouting on microfractures, a theoretical high pressure grouting model is established. In addition, a quantitative description of slurry seepage and fracture deformation during high pressure grouting for microfractures under the action of fluid-solid coupling is realized by employing the step-wise algorithm.

2. Methods

2.1. Mathematical Model Establishment. During grouting, the slurry and fractures are coupled, and slurry seepage and fracture deformation affect each other. The amount of grouting pressure determines the change in the fracture opening, and the change in fracture opening also determines the resistance of the slurry seepage [36–39]. During slurry seepage, the grouting pressure and fracture opening at each position are attenuated to varying degrees, which affect the slurry seepage process [40].

The seepage process in microfractures under high pressure grouting is as follows: the cement slurry enters the microfracture under the action of grouting pressure, and the grout flows into the fracture and exerts force on the fracture surfaces on both sides [14, 41]. Microfractures are opened due to the grouting pressure, allowing more cement slurry to enter the fracture channels. Assuming that there is a critical pressure, when the force overcomes the critical pressure for fracture deformation, the fracture opens and deforms perpendicular to the fracture surface, and the opening amount of the fracture is positively related to grouting pressure. During cement slurry flow, the slurry is subject to its own viscosity and resistance caused by the fracture surface, such that the grouting pressure and the amount of fracture opening will be attenuated along the seepage direction during slurry seepage. The schematic diagram of the seepage process of slurry flow through a microfracture is shown in Figure 1.

2.2. Basic Assumptions. In this contribution, we make the following assumptions:

(i) The fractures are flat, the fracture openings are uniformly distributed, and gravity does not affect grouting seepage

(ii) The rock mass on both sides of the fracture is isotropic and homogeneous, the upper and lower surfaces of the fracture meet the nonslip boundary condition, and the slurry flow velocity on the surface of the fracture is zero

(iii) The influence of the flow of cement slurry in the direction perpendicular to the fracture surface on the spatial distribution of grouting pressure in the slurry seepage direction is ignored

(iv) Only elastic deformation occurs in the rock mass on both sides of the fracture

(v) Cement slurry seepage only occurs within the fracture, and the reduction of the slurry caused by the rock mass penetrating both sides of the fracture is ignored

2.3. Slurry Seepage Control Equation. The constitutive model for a Bingham fluid is shown in formula (1):

$$\tau = \tau_0 + \mu \frac{dv}{dr}. \quad (1)$$

In the formula, τ is the shear stress, Pa·s, τ_0 is the initial yield stress, Pa·s, μ is the plastic viscosity Pa·s, v is the flow velocity, m/s, and r is the microbody half height, m.

We establish a rectangular coordinate system, in which the x direction is the direction of the fracture centerline, and the y direction is perpendicular to the fracture direction. The seepage model is shown in Figure 2. According to the force analysis of the microelement body, the shear stress distribution along the x direction can be obtained as

$$\tau = -r \frac{dp}{dx}. \quad (2)$$

The nucleus area of a Bingham fluid in the fracture centerline is

$$r_0 = -\tau_0 \left(\frac{dx}{dp}\right). \quad (3)$$

The range of the nuclear-retaining area needs to satisfy $r0 \le b/2$. Substituting it into formula (3), the starting pressure gradient of the slurry movement can be obtained:

$$\frac{dp}{dx} = \frac{2\tau_0}{b}. \quad (4)$$

Combining equations (1) and (2) gives the differential equation for the slurry velocity in the y direction:

$$\frac{dv}{dr} = \frac{r}{\mu}\frac{dp}{dx} + \frac{\tau_0}{\mu}. \quad (5)$$

When substituting the boundary condition $r = \pm b$, $v = 0$, considering $|r| \le r0$, $v = v(r = r_0)$, the velocity of the slurry distribution along the fracture width is obtained:

$$v = \begin{cases} -\dfrac{\mathrm{b}^2 - 4\mathrm{r}^2}{8\mu}\dfrac{\mathrm{dp}}{\mathrm{dx}} - \dfrac{\tau_0}{\mu}\left(\dfrac{\mathrm{b}}{2} - |\mathrm{r}|\right) & \left(r_0 \le |r| \le \dfrac{\mathrm{b}}{2}\right) \\ -\dfrac{\mathrm{b}^2 - 4\mathrm{r}^2}{8\mu}\dfrac{\mathrm{dp}}{\mathrm{dx}} - \dfrac{\tau_0}{\mu}\left(\dfrac{\mathrm{b}}{2} - \mathrm{r}_0\right) & |\mathrm{r}| \le r_0 \end{cases}. \quad (6)$$

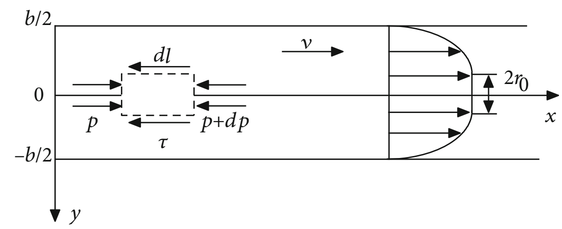

Figure 2: Bingham fluid seepage model.

Integrating the slurry flow velocity in the y direction and taking the average slurry velocity gives

$$\begin{aligned} \bar{v} &= \frac{b^2}{12\mu}\left[-\frac{dp}{dx} - 3\frac{\tau_0}{b} + \frac{4{\tau_0}^3}{b^3(dp/dx)^2}\right] \\ &= \frac{-\mathrm{b}^2}{12\mu}\frac{dp}{dx}\left(1 + 3\frac{\tau_0}{b}\frac{dx}{dp} - \frac{4{\tau_0}^3}{b^3(dp/dx)^3}\right). \end{aligned} \quad (7)$$

Substituting into equation (3) and ignoring the influence of higher order terms on the slurry, the average slurry flow velocity is

$$\bar{v} = \frac{-b^2}{12\mu}\frac{dp}{dx}\left(1 + 3\frac{r_0}{b} - \frac{4{\tau_0}^3}{b^3}\right). \quad (8)$$

In formula (8), we make

$$A = 1 + 3\frac{r_0}{b} - \frac{4{\tau_0}^3}{b^3}. \quad (9)$$

Then, obtain the slurry flow control equation:

$$\frac{dp}{dx} = \frac{-12\mu\bar{v}}{Ab^2}. \quad (10)$$

2.4. Fracture Deformation Control Equation. For microfractured rock masses, fracture surfaces are held in contact due to the in situ stress, which causes the force between the fracture surfaces to affect the fracture deformation [21]. During grouting, the cement slurry flows in the fractures and produces stress opposite to the in situ stress on the fracture surfaces. Assuming that there is a critical grouting pressure, when the grouting pressure is less than the critical pressure, the fracture opening does not change. When the grouting pressure is greater than the critical pressure, the grouting pressure causes the fracture to open, and the fracture opening degree increases with increasing grouting pressure. In this contribution, a constant pressure grouting method is adopted, meaning that the grouting pressure at the grouting port remains constant. During slurry seepage, the grouting pressure gradually decreases with increasing seepage distance. When the grouting pressure is less than the critical pressure, the fracture opening remains unchanged. When the grouting pressure is greater than the critical pressure, the fracture opening near the grouting port changes. As the seepage distance of the slurry increases, grouting pressure decreases. When grouting pressure decreases to the critical

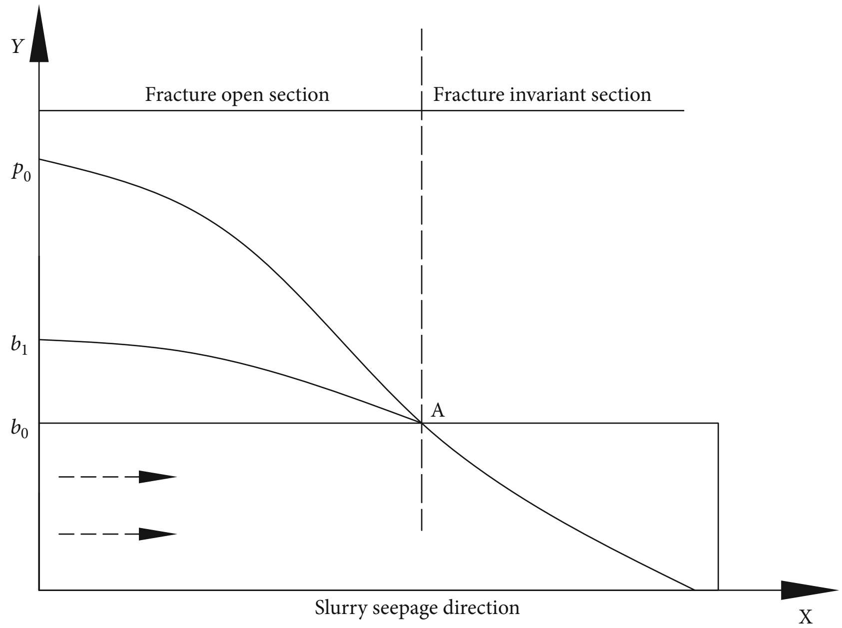

FIGURE 3: Curve of fracture opening and grouting pressure.

pressure, the fracture stops opening and stays the same. The curve of the fracture opening degree and grouting pressure is shown in Figure 3.

The governing equation of fracture opening during grouting can be obtained as [21]

$$b = \begin{cases} b_0 & (p < p_1) \\ b_0 + k_n(p - p_1) & (p > p_1) \end{cases}. \quad (11)$$

In the formula, b is the fracture opening, m, b_0 is the initial fracture opening, m, p is the grouting pressure, MPa, p_1 is the critical grouting pressure, MPa, k_n is the normal elastic coefficient, $k_n = D/E$, D is the grouting influence range, m, and E is the rock mass elastic modulus, Pa.

2.5. Step-Wise Algorithm for Microfracture High Pressure Grouting Seepage Process. Based on the step-wise algorithm, a microfracture high pressure grouting process analysis and calculation program is developed using the MATLAB software platform. The slurry seepage area is discrete using the same time interval Δt, and the slurry seepage area is divided into n finite elements. Combined with the fracture opening control equation, the recursive method is used to determine the time-step iterative solution according to the law of conservation of energy, which describes the grout seepage distance and fracture opening changes throughout the grouting process. The schematic diagram of the step-wise algorithm is shown in Figure 4.

The iterative calculation process for grout seepage and fracture deformation is as follows: for m iterations, the fracture opening b_i^m of each element node and the slurry seepage distance L_i^m of each element are obtained, and the grouting pressure p_j^m at each element node is determined using the recursion method. The obtained grouting pressure p_j^m is then used to recalculate the new fracture opening b_i^{m+1} and slurry seepage distance L_i^{m+1}, as well as judge whether the slurry seepage distance L_i^{m+1} at this time meets the convergence condition. If the convergence requirement is met, the current time step ends, and the next time step is calculated. If the convergence requirement is not met, the iteration continues until the convergence requirement is met.

The relative error between any two iteration results is

$$\varepsilon = \left| \frac{\sum_{i=1}^{n} L_i^m - \sum_{i=1}^{n} L_i^{m-1}}{\sum_{i=1}^{n} L_i^m} \right|. \quad (12)$$

$\sum_{i=1}^{n} L_i^m$ is the slurry seepage distance calculated after the nth iteration. When the error is less than 0.1%, the convergence condition is satisfied. When the convergence conditions are met, the seepage distance of each unit, the grouting pressure of each unit node, and the fracture opening are output.

The step-wise algorithm calculation flow chart written by MATLAB is shown in Figure 5.

3. Results and Discussion

3.1. Seepage Characteristic Analysis. The grouting cement is composed of a 1000 mesh ultrafine cement slurry, the water-cement ratio is 1.2, and the slurry flow pattern is that of a Bingham fluid, the measured slurry viscosity $\mu = 0.02$ Pa.s, the slurry yield stress $\tau_0 = 3.3$ Pa, and the original fracture opening $b = 100\,\mu$m. When the grouting pressure is 3 MPa, grouting time is 100 s, and the fracture opening is 100 μm (Figures 6 and 7). The spatial distribution curves of the grouting pressure and the fracture opening are obtained, respectively, with or without considering fluid-solid coupling.

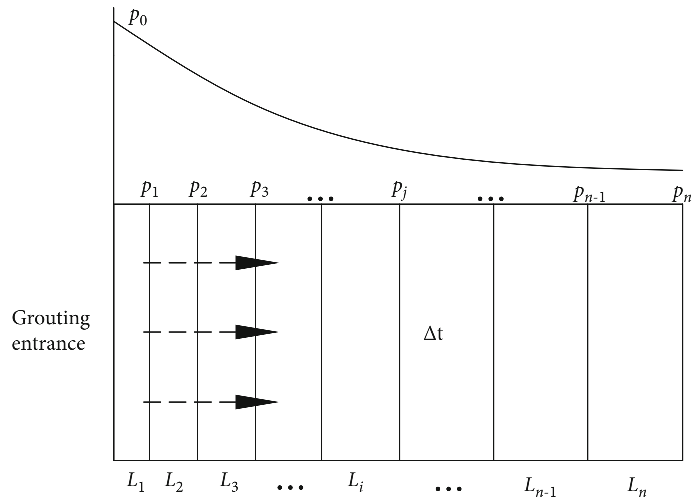

Figure 4: Schematic diagram of the step-wise algorithm. L_i represents the grout seepage distance of each grouting time unit ($i = 1 \sim n$), and p_j represents the grouting pressure of the node after each grouting time unit ($j = 1 \sim n$).

When fluid-solid coupling is not considered, the grouting pressure decays linearly from the entrance along the slurry seepage direction, the fracture opening remains unchanged at 100 μm, and the slurry seepage distance is 5 m. When fluid-solid coupling is considered, the grouting pressure and fracture opening both decrease nonlinearly from the entrance in the slurry seepage direction. The maximum fracture opening at the grouting entrance is 180 μm, 1.8 times the original fracture opening, and the slurry seepage distance is 6.4 m. 4.78 m away from the grouting entrance, the grouting pressure decays to the critical pressure. At this time, the fracture opening is reduced to the original fracture opening of 100 μm, and the fracture opening remains unchanged with increasing distance from the entrance. When grouting pressure is reduced to the critical grouting pressure, the grouting pressure changes from the original nonlinear decrease to a linear decrease. After grouting pressure is reduced to the extent that the fracture opening cannot be changed, the fracture opening remains the original value. When fluid-solid coupling is considered under the same grouting conditions, the grout seepage distance is larger than that without considering the fluid-solid coupling..

In order to examine the variation in fracture opening with grouting time at different positions (1 m, 2 m, 3 m, 4 m, and 5 m) from the grouting entrance, the variation curve of fracture opening vs. grouting time was obtained. The slurry pressure change curves are shown in Figures 8 and 9, respectively.

When the grouting time is 10 s, the fracture opening at 1 m away from the grouting inlet increases to 130 μm, while the fracture opening at 2 m, 3 m, 4 m, and 5 m away from the grouting entrance remained at 100 μm, without any change in fracture opening (Figure 8). When the grouting time is 20 s, the fracture opening at 1 m and 2 m away from the grouting entrance increases to 150 μm and 108 μm mm, respectively. The fracture opening at 3 m, 4 m, and 5 m away from the grouting entrance remained at 100 μm without any change in fracture opening. With increasing grouting time, the fracture opening at 1 m away from the grouting entrance increases from 130 μm at 10 s to 150 μm, an increase of 20 μm. When the grouting time is 40 s, the fracture openings at 1 m, 2 m, and 3 m away from the grouting entrance increases to 160 μm, 134 μm, and 101 μm, respectively. The fracture opening at 4 m and 5 m away from the grouting entrance remained at 100 μm, without any change in fracture opening. When the grouting time is 80 s, the fracture openings at 1 m, 2 m, 3 m, and 4 m away from the grouting entrance increases to 167 μm, 150 μm, 131 μm, and 108 μm, respectively. The fracture opening at 5 m away from the grouting entrance remained at 100 μm without any change in fracture opening. When the grouting time is 120 s, the fracture openings at 1 m, 2 m, 3 m, 4 m, and 5 m away from the grouting entrance increases to 170 μm, 157 μm, 142 μm, 125 μm, and 106 μm, respectively. The fracture opening at different positions gradually increases with increasing grouting time. The farther from the grouting entrance is, the later the change in fracture opening is, and the smaller the change in the fracture opening is. With continuously increasing grouting time, the coupling effect between fracture opening and slurry pressure continues, and the fracture opening continues to change; however, the influence degree gradually decreases.

When the grouting time is 10 s, the grouting pressure at 1 m and 2 m away from the grouting entrance is 1.84 MPa and 0.04 MPa, respectively (Figure 9). When the grouting time increases to 40 s, the grouting pressure at 1 m, 2 m, 3 m, and 4 m away from the grouting entrance is 2.47 MPa, 1.84 MPa, 1.02 MPa, and 0.04 MPa, respectively. When the grouting time increases to 80 s, the grouting pressure at 1 m, 2 m, 3 m, 4 m, and 5 m away from the grouting inlet is 2.64 MPa, 2.22 MPa, 1.75 MPa, 1.19 MPa, and 0.49 MPa, respectively. With continuously increasing grouting time, the grouting pressure gradually decreases compared to the initial grouting stage, and with increasing grouting time, the scope of influence will increase, and the degree of influence will relatively decrease.

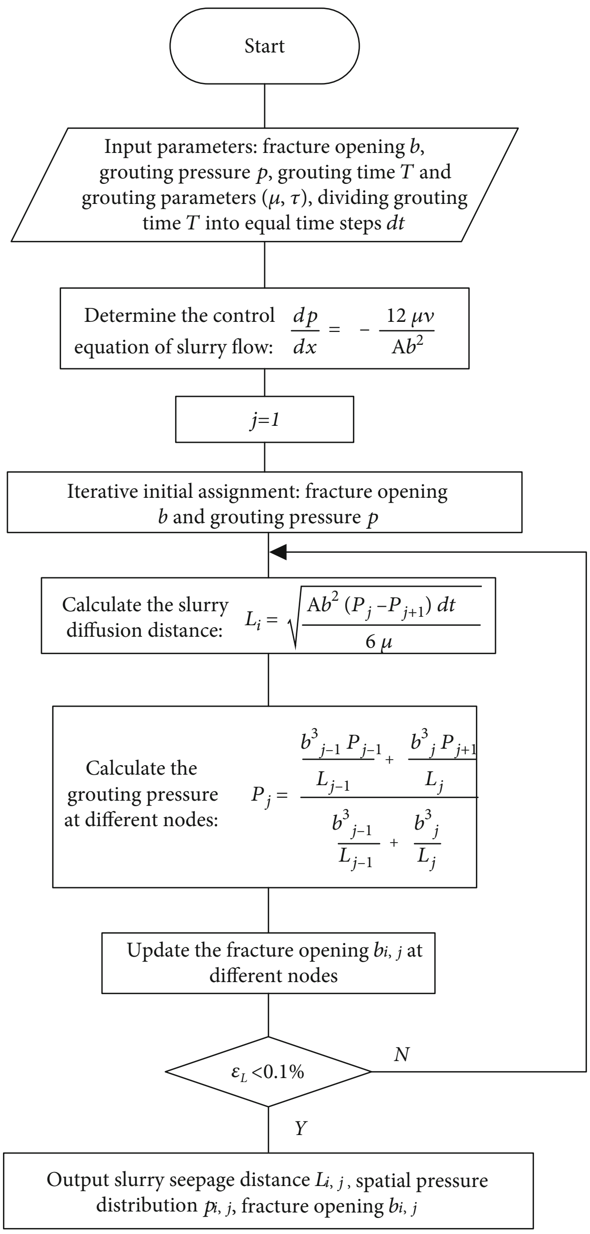

Figure 5: Flow chart of the step-wise algorithm.

3.2. Influence of Fracture Opening. When the grouting pressure is 3 MPa, and grouting time is 100 s, the relationship between slurry seepage distance and grouting time under varying fracture opening conditions (20 μm, 50 μm, 100 μm, 200 μm, and 300 μm) was calculated, and the influence of fracture opening on slurry seepage characteristics was analyzed (Figures 10 and 11).

Without considering fluid-solid coupling, when the fracture opening is 20 μm, the slurry seepage distance increases from 0.31 m at a grouting time of 10 s to 0.89 m at a grouting time of 80 s, an increase of 0.58 m (Figures 10 and 11). When the fracture opening is 100 μm, the slurry seepage distance increases from 1.58 m at a grouting time of 10 s to 4.47 m at a grouting time of 80 s. When the fracture opening is 300 μm, the slurry seepage distance increases from 4.74 m at 10 s to 13.41 m at 80 s. Considering the effect of fluid-solid coupling, when the fracture opening is 20 μm, the slurry seepage distance increases from 0.78 m at 10 s to 2.2 m at 80 s. When the fracture opening is 100 μm, the slurry seepage distance increases from 2.02 m at 10 s to 5.72 m at 80 s. When the fracture opening is 300 μm, the slurry seepage distance increases from 5.17 m at 10 s to 14.62 m at 80 s. Fracture opening has a significant influence on the slurry seepage distance. With increasing grouting time, the slurry seepage distance also increases. With increasing fracture opening at the same grouting time, the slurry seepage distance also increases. In the early stage of grouting seepage, the slurry seepage rate is relatively fast. As grouting continues, the slurry seepage rate gradually decreases. The larger the fracture opening is, the larger the grouting seepage rate will be. As fracture opening gradually decreases, the seepage rate of the grout will decrease accordingly.

In order to examine the influence of fracture opening on the spatial distribution characteristics of grouting pressure for a grouting pressure of 3 MPa and grouting time of 100 s, the conditions of different fracture openings (20 μm, 50 μm, 100 μm, 200 μm, and 300 μm) in the grouting simulation are analyzed. The spatial distribution curve of grouting pressure is shown in Figure 12.

For a fracture opening of 20 μm, the grouting pressure decays rapidly in the slurry seepage direction and decreases to 0 at 2.64 m from the grouting entrance (Figure 12). When the fracture opening is small, the slurry seepage resistance is very large, which rapidly reduces the grouting pressure inside the fracture and affects the slurry seepage. When the fracture opening is 50 μm, the grouting pressure decreases rapidly in the slurry seepage direction and decreases to 0 at 3.92 m from the grouting entrance; however, the reduced rate is smaller than that when the fracture opening is 20 μm. With increasing fracture opening, when the fracture opening is 300 μm, the grouting pressure decreases to 0 at 16.4 m from the grouting entrance. Results show that the smaller the fracture opening, the greater the decay grouting pressure rate and the shorter the seepage distance. With increasing fracture opening, grouting pressure decay rate decreases, and the slurry seepage distance increases.

3.3. Influence of Grouting Pressure. In order to examine the influence of grouting pressure on the grout seepage distance, calculate whether the grout diffusion distance with fluid-solid coupling under different grouting pressures (1 MPa, 2 MPa, 3 MPa, 5 MPa, and 8 MPa) and choose the fracture opening, the relationship between grouting pressure, and grout seepage distance of the grout when the grouting time is 100 μm and grouting time of 100 s is analyzed. The simulation results are shown in Figure 13.

Under a grouting pressure of 1 MPa, the slurry seepage distance is 2.38 m when fluid-solid coupling is not considered, and the slurry seepage distance is 2.88 m when fluid-solid coupling is considered. When considering fluid-solid coupling, the slurry seepage distance is slightly larger than that without considering fluid-solid coupling; however, there is little difference between them. When grouting pressure increases to 3 MPa, the slurry seepage distance is 5 m without

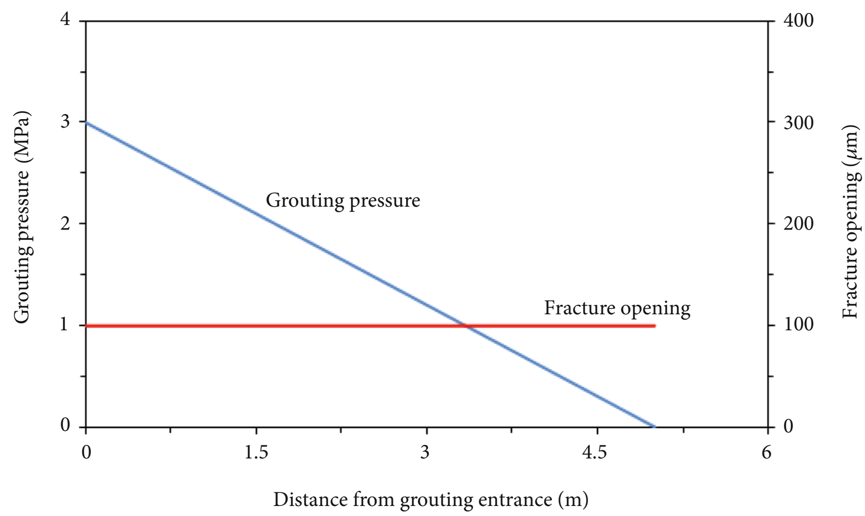

Figure 6: The curve of grouting pressure and fracture opening with no fluid-solid coupling.

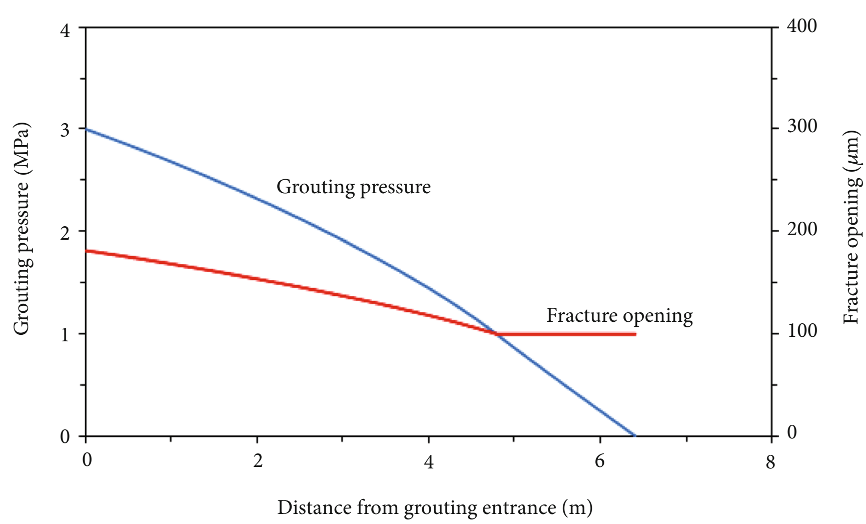

Figure 7: The curve of grouting pressure and fracture opening with fluid-solid coupling.

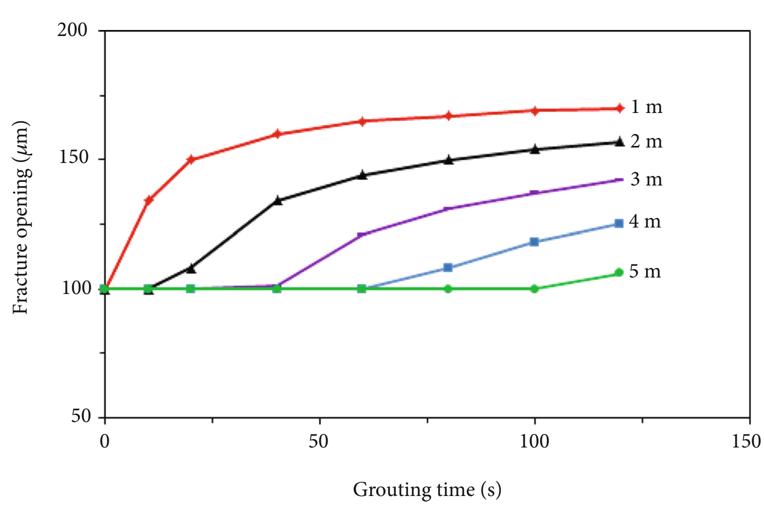

Figure 8: Curves of fracture opening vs. grouting time.

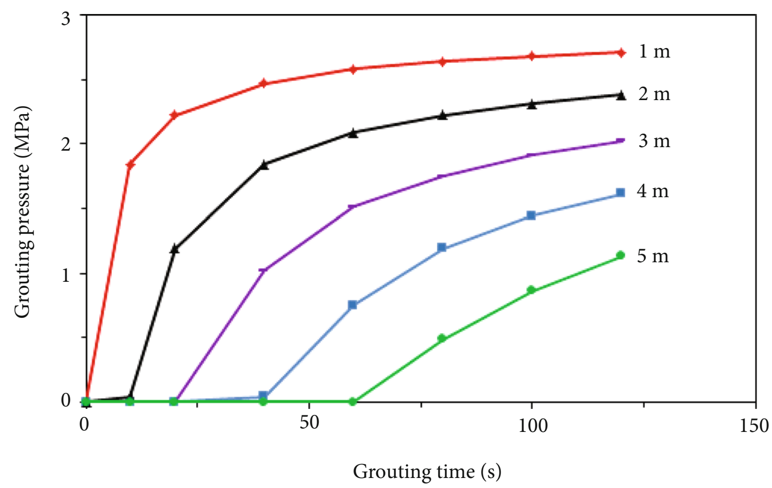

Figure 9: Curves of grouting pressure vs. grouting time.

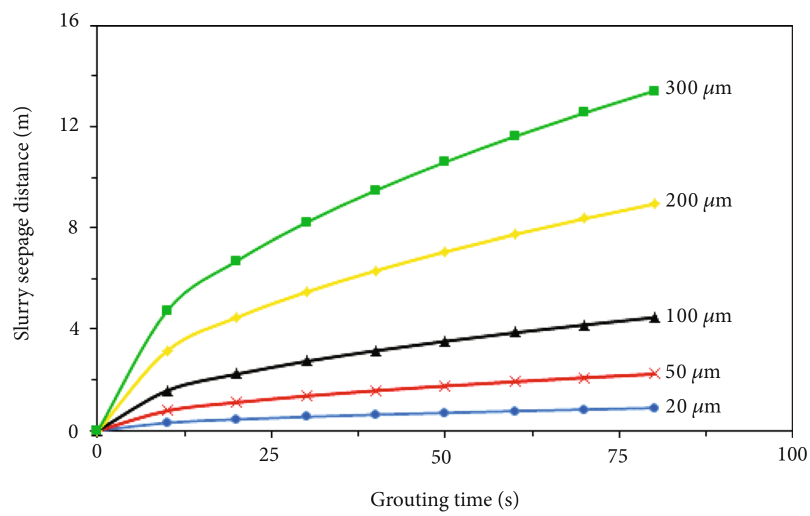

Figure 10: Slurry seepage distance for different fracture openings with no fluid-solid coupling.

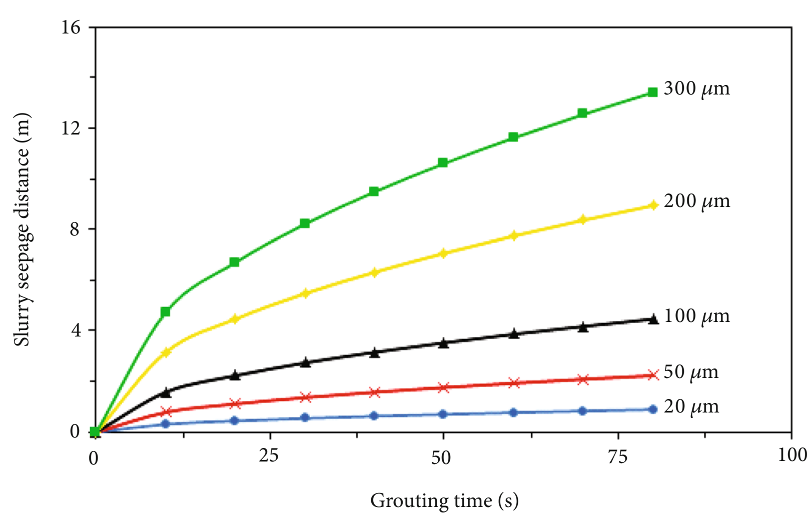

Figure 11: Slurry seepage distance for different fracture openings with fluid-solid coupling.

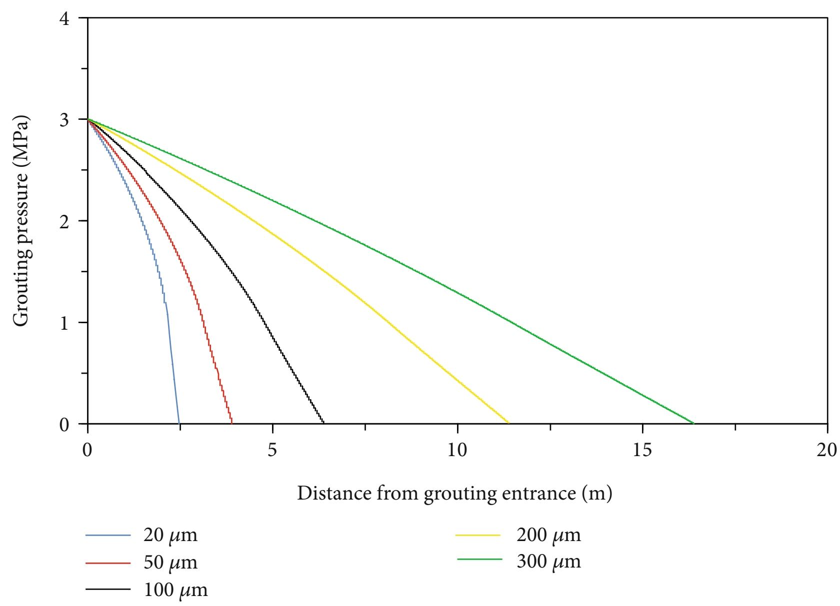

Figure 12: Curve of grouting pressure vs. distance for different fracture openings.

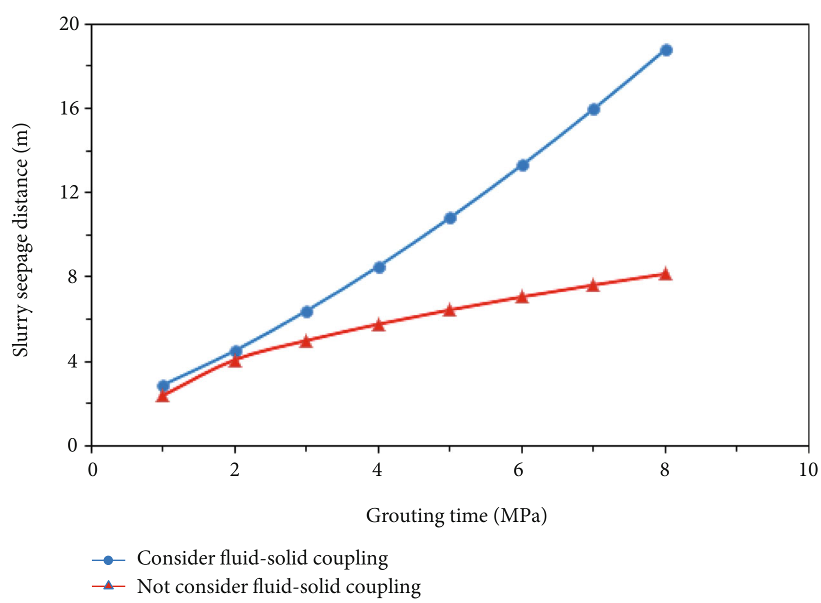

Figure 13: Slurry seepage distance under different grouting pressures.

considering fluid-solid coupling, and the slurry seepage distance increases by 2.62 m. Considering fluid-solid coupling, the slurry seepage distance is 6.41 m, and the slurry seepage distance increases by 3.53 m. When grouting pressure increases to 8 MPa, the slurry seepage distance is 8.16 m without considering fluid-solid coupling and 18.81 m when considering fluid-solid coupling. With increasing grouting pressure, the slurry seepage distance only increases from 2.38 m to 8.16 m without considering fluid-solid coupling; while when considering fluid-solid coupling, the slurry seepage distance increases from 2.88 m at the beginning to 18.8 m. When fluid-solid coupling is not considered, the resistance to slurry seepage is greater due to the constant fracture opening, and the slurry seepage distance is much smaller than that under fluid-solid coupling. When considering fluid-solid coupling, with increasing grouting pressure, the fracture opening also increases, the resistance of slurry seepage decreases, and the slurry seepage distance increases.

In order to study the influence of grouting pressure on fracture opening, the law between fracture opening change and grouting pressure under different grouting pressures (1 MPa, 2 MPa, 3 MPa, 5 MPa, and 8 MPa) was calculated, and various grouting pressures were obtained. The grouting pressure change curve and the fracture opening change curve

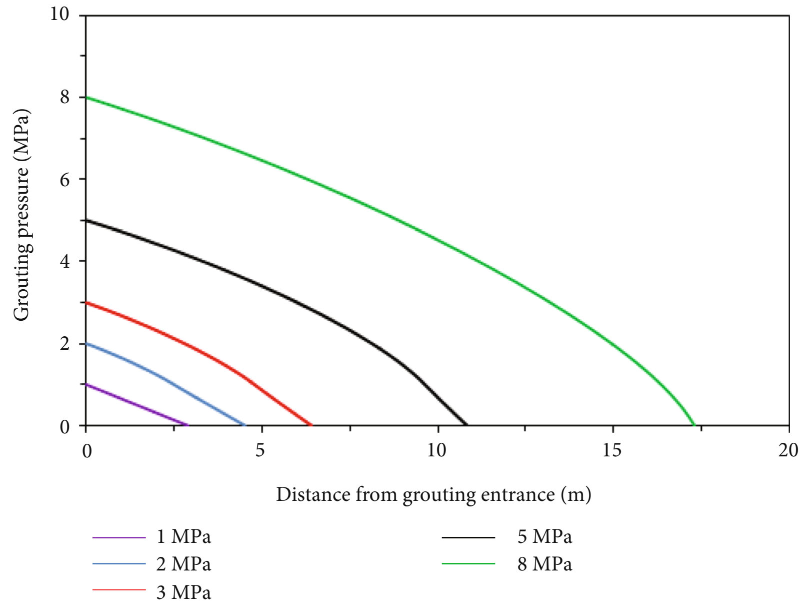

Figure 14: Curve of grouting pressure vs. distance for different grouting pressures.

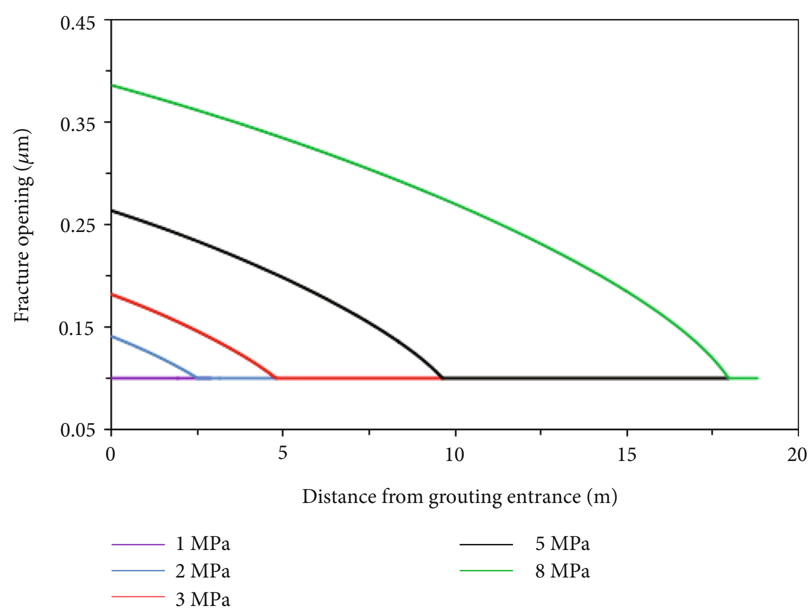

Figure 15: Curve of fracture opening vs. distance for different grouting pressures.

at different positions from the grouting inlet under pressure are shown in Figures 14 and 15, respectively.

As shown in Figures 14 and 15, when the grouting pressure is 1 MPa, grouting pressure decreases linearly along the slurry seepage direction and decreases to 0 at 2.86 m from the grouting entrance. The fracture opening remains unchanged at 100 μm. The grouting pressure is less than the critical pressure; therefore, the fracture opening does not change. When the grouting pressure increases to 2 MPa, the grouting pressure shows nonlinear attenuation along the slurry seepage direction, and when the grouting pressure is less than the critical pressure, the grouting pressure curve shows linear attenuation until it decreases to 0 at 4.51 m from the grouting entrance. The fracture opening at the fracture entrance is the most affected. The original fracture opening increases from 100 μm to 180 μm and shows nonlinear attenuation along the slurry seepage direction. With decreasing grouting pressure to the critical pressure, the fracture opening remains unchanged. When grouting pressure increases to 5 MPa, the grouting pressure also shows nonlinear attenuation along the grouting seepage direction. When the grouting pressure in the fracture channel attenuates to less than the critical pressure, the grouting pressure curve shows linear attenuation, until it decreases to 0 at 18.8 m from the grouting entrance. The fracture opening value at the entrance of the grouting increases to 380 μm, and it also decays nonlinearly along the grout seepage direction until the fracture opening remains unchanged. At the same position from the grouting entrance, as grouting pressure increases, the increase in the fracture opening also increases. The increase in fracture opening at the entrance of grouting is the largest, and it gradually decreases along the slurry seepage direction.

Overall, the change in grouting pressure and fracture opening shows a nonlinear attenuation trend during fracture seepage. As grouting pressure decreases nonlinearly along the slurry seepage direction, the fracture opening also decreases nonlinearly. When grouting pressure decreases to the critical pressure, the fracture opening decreases to the original fracture opening and remains unchanged until the slurry stops flowing. With increasing grouting pressure, the increase in fracture opening also increases, from 80 μm when the grouting pressure is 2 MPa to 280 μm when the grouting pressure is 8 MPa. Correspondingly, the affected fracture opening range also increases, from 2.5 m at 2 MPa to 17.96 m at 8 MPa, which is significantly affected by the grouting pressure.

4. Conclusions

(i) A step-wise algorithm in MATLAB was used to conduct numerical experiment on grouting slurry seepage in microfractures. The slurry seepage area is divided into multiple finite elements at the same time interval. According to the law of conservation of energy and the recursion method, a time-step iterative solution is used to quantitatively describe the change in grout seepage distance and fracture opening during grouting

(ii) Fluid-solid coupling has a significant influence on slurry seepage characteristics. At the same grouting time, the slurry seepage distance increases with increasing fracture opening. In the early stage of grout seepage, the slurry seepage rate is faster. With increasing grouting time, the slurry seepage rate gradually decreases, and the greater the fracture opening, the greater the slurry seepage rate

(iii) The grouting pressure and fracture opening are largest at the grouting entrance. Along the slurry seepage direction, the change in grouting pressure and fracture opening shows nonlinear attenuation trend. When grouting pressure decreases to the critical pressure, the fracture opening is linearly attenuated, and the fracture opening remains unchanged until the slurry stops flowing

Data Availability

The data used to support the findings of this study are included within the article.

Conflicts of Interest

The authors declare that they have no conflicts of interest regarding the publication of this paper.

Acknowledgments

We thank all project partners for many fruitful discussions. This paper was funded by the National Key Research and Development Program of China (2017YFC0603004) and the China Postdoctoral Science Foundation Funded Project (2020M671649).

References

[1] X. Chen, L. Li, L. Wang, and L. Qi, "The current situation and prevention and control countermeasures for typical dynamic disasters in kilometer-deep mines in China," *Safety Science*, vol. 115, pp. 229–236, 2019.

[2] W. Qiao, W. Li, and X. Zhang, "Characteristic of water chemistry and hydrodynamics of deep karst and its influence on deep coal mining," *Arabian Journal of Geosciences*, vol. 7, no. 4, pp. 1261–1275, 2014.

[3] Y. Sun, G. Li, J. Zhang, and J. Xu, "Failure mechanisms of rheological coal roadway," *Sustainability*, vol. 12, no. 7, p. 2885, 2020.

[4] Z. Xiao, J. Liu, S. Gu et al., "A control method of rock burst for dynamic roadway floor in deep mining mine," *Shock and Vibration*, vol. 2019, 16 pages, 2019.

[5] Y. Xue, Z. Cao, F. Du, and L. Zhu, "The influence of the backfilling roadway driving sequence on the rockburst risk of a coal pillar based on an energy density criterion," *Sustainability*, vol. 10, no. 8, p. 2609, 2018.

[6] M. Heidari and F. Tonon, "Ground reaction curve for tunnels with jet grouting umbrellas considering jet grouting hardening," *International Journal of Rock Mechanics and Mining Sciences*, vol. 76, pp. 200–208, 2015.

[7] R. Pan, Q. Wang, B. Jiang et al., "Failure of bolt support and experimental study on the parameters of bolt- grouting for supporting the roadways in deep coal seam," *Engineering Failure Analysis*, vol. 80, pp. 218–233, 2017.

[8] X. Sun, L. Wang, Y. Lu, B. Jiang, Z. Li, and J. Zhang, "A yielding bolt-grouting support design for a soft-rock roadway under high stress: a case study of the Yuandian No. 2 coal mine in China," *Journal of the Southern African Institute of Mining and Metallurgy*, vol. 118, no. 1, pp. 71–82, 2018.

[9] K. Wang, L. Wang, B. Ren, and H. Fan, "Understanding the effect of cementitious grouting pressure on micro-fracture permeability for rock reinforcement underground: a lab study," *Energies*, vol. 13, no. 16, p. 4225, 2020.

[10] Q. Wang, Q. Qin, B. Jiang, H. C. Yu, R. Pan, and S. C. Li, "Study and engineering application on the bolt-grouting reinforcement effect in underground engineering with fractured surrounding rock," *Tunnelling and Underground Space Technology*, vol. 84, pp. 237–247, 2019.

[11] X. Ni, C. Xu, and W. Li, "Numerical simulation of grouting in micro-fractured rock mass of metro tunnel considering effect of fluid-solid coupling," *Tunnel Construction*, vol. 38, no. 10, p. 1667, 2018.

[12] F.-j. Dong, Y. Cao, D.-z. Ren, and W. Sun, "Micro-fracture development impact factors analysis and its effects on well production of Hua-qing area Ordos Basin in China," *International Journal of Oil Gas and Coal Technology*, vol. 21, no. 1, pp. 39–56, 2019.

[13] M. Ezati, M. Azizzadeh, M. A. Riahi, V. Fattahpour, and J. Honarmand, "Characterization of micro-fractures in

carbonate Sarvak reservoir, using petrophysical and geological data, SW Iran," *Journal of Petroleum Science and Engineering*, vol. 170, pp. 675–695, 2018.

[14] H. Sun, L. Duan, L. Liu et al., "The influence of micro-fractures on the flow in tight oil reservoirs based on pore-network models," *Energies*, vol. 12, no. 21, p. 4104, 2019.

[15] P. Wang, Z. Wang, L. Shen, and L. Xin, "Lattice Boltzmann simulation of fluid flow characteristics in a rock micro-fracture based on the pseudo-potential model," *Energies*, vol. 11, no. 10, p. 2576, 2018.

[16] P. Zhu, C. Lin, H. Ren, Z. Zhao, and H. Zhang, "Micro-fracture characteristics of tight sandstone reservoirs and its evaluation by capillary pressure curves: a case study of Permian sandstones in Ordos Basin, China," *Journal of Natural Gas Science and Engineering*, vol. 27, pp. 90–97, 2015.

[17] Y. Xue, Y. Liu, F. Dang et al., "Assessment of the nonlinear flow characteristic of water inrush based on the Brinkman and Forchheimer seepage model," *Water*, vol. 11, no. 4, p. 855, 2019.

[18] Y. Li, C. Wu, and B.-A. Jang, "Effect of bedding plane on the permeability evolution of typical sedimentary rocks under triaxial compression," *Rock Mechanics and Rock Engineering*, vol. 53, no. 11, pp. 5283–5291, 2020.

[19] L. Wang, M. Li, and X. Wang, "Study of mechanisms and technology for bolting and grouting in special soft rock roadways under high stress," *Chinese Journal of Rock Mechanics and Engineering*, vol. 24, no. 16, pp. 2889–2893, 2005.

[20] J. Yang, Y. Cheng, and W. Chen, "Experimental study on diffusion law of post-grouting slurry in sandy soil," *Advances in Civil Engineering*, vol. 2019, 11 pages, 2019.

[21] L. Zhang, Q. Zhang, R. Liu, and S. Li, "Grouting mechanism in fractured rock considering slurry-rock stress coupling effects," *Chinese Journal of Geotechnical Engineering*, vol. 40, no. 11, pp. 2003–2011, 2018.

[22] H. Jiang, R. Zhong, and Z. Peng, "Study on preparation of chemical grouting and its hydraulic properties and application for water seepage safety," *Journal of Coastal Research*, vol. 94, no. sp1, p. 291, 2019.

[23] P. Li, Q. Zhang, X. Zhang, S. Li, X. Li, and J. Zuo, "Grouting diffusion characteristics in faults considering the interaction of multiple grouting," *International Journal of Geomechanics*, vol. 17, no. 5, article 04016117, 2017.

[24] B. T. Sun, X. Z. Ling, C. Ling, and G. R. Zhu, "Numerical simulation for diffusion and pressure distribution of permeation grouting," *Journal of Hydraulic Engineering*, vol. 38, no. 11, pp. 1402–1407, 2007.

[25] X. X. Zhang, J. G. Wang, F. Gao, and X. L. Wang, "Numerical study of fracture network evolution during nitrogen fracturing processes in shale reservoirs," *Energies*, vol. 11, no. 10, 2018.

[26] X. Zhang, J. G. Wang, X. Wang, and F. Gao, "Numerical simulations on the front motion of water permeation into anisotropic porous media," *Geofluids*, vol. 2019, 13 pages, 2019.

[27] Y. Wang, B. Liu, and Y. Qi, "A risk evaluation method with an improved scale for tunnel engineering," *Arabian Journal for Science and Engineering*, vol. 43, no. 4, pp. 2053–2067, 2018.

[28] M. Axelsson and G. Gustafson, "The PenetraCone, a new robust field measurement device for determining the penetrability of cementitious grouts," *Tunnelling and Underground Space Technology*, vol. 25, no. 1, pp. 1–8, 2010.

[29] A. Draganović and H. Stille, "Filtration and penetrability of cement-based grout: study performed with a short slot," *Tunnelling and Underground Space Technology*, vol. 26, no. 4, pp. 548–559, 2011.

[30] S. Mohajerani, A. Baghbanan, G. Wang, and S. F. Forouhandeh, "An efficient algorithm for simulating grout propagation in 2D discrete fracture networks," *International Journal of Rock Mechanics and Mining Sciences*, vol. 98, pp. 67–77, 2017.

[31] Z. Saada, J. Canou, L. Dormieux, and J. C. Dupla, "Evaluation of elementary filtration properties of a cement grout injected in a sand," *Canadian Geotechnical Journal*, vol. 43, no. 12, pp. 1273–1289, 2006.

[32] X. Chen, L.-s. Xu, and M. Xu, "Adaptive control system for grouting pressure stability based on fuzzy algorithm," *Journal of Intelligent & Fuzzy Systems*, vol. 31, no. 4, pp. 2231–2239, 2016.

[33] H. Stromsvik, J. C. Morud, and E. Grov, "Development of an algorithm to detect hydraulic jacking in high pressure rock mass grouting and introduction of the PF index," *Tunnelling and Underground Space Technology*, vol. 81, pp. 16–25, 2018.

[34] Y. Xue, T. Teng, F. Dang, Z. Ma, S. Wang, and H. Xue, "Productivity analysis of fractured wells in reservoir of hydrogen and carbon based on dual-porosity medium model," *International Journal of Hydrogen Energy*, vol. 45, no. 39, pp. 20240–20249, 2020.

[35] J. Liu, X. Liang, Y. Xue, K. Yao, and Y. Fu, "Numerical evaluation on multiphase flow and heat transfer during thermal stimulation enhanced shale gas recovery," *Applied Thermal Engineering*, vol. 178, p. 115554, 2020.

[36] G. Dai, Z. Zhang, G. Shi, S. Li, W. Shi, and X. Li, "Study on anti-seepage slurry of landfill site modified by sodium carboxymethyl cellulose," *International Journal of Modern Physics B*, vol. 33, no. 31, p. 1950377, 2019.

[37] G. Dai, J. Zhu, and G. Shi, "Analysis on the basic properties of PBFC anti-seepage slurry in landfill," *Applied Ecology and Environmental Research*, vol. 16, no. 6, pp. 7657–7667, 2018.

[38] W. Zhang, H. Zhou, and W. Guo, "Experimental study on seepage characteristics of fractured rock mass and its electrical response," *Journal of Hydrologic Engineering*, vol. 24, no. 7, article 04019017, 2019.

[39] S. Zhou, X. Zhang, D. Wu, and H. Di, "Mathematical modeling of slurry infiltration and particle dispersion in saturated sand," *Transport in Porous Media*, vol. 124, no. 1, pp. 91–116, 2018.

[40] J. Liu, K. Yao, Y. Xue, X. Zhang, Z. Chong, and X. Liang, "Study on fracture behavior of bedded shale in three-point-bending test based on hybrid phase-field modelling," *Theoretical and Applied Fracture Mechanics*, vol. 104, article 102382, 2019.

[41] H. Xie, Y. Ju, S. Ren, F. Gao, J. Liu, and Y. Zhu, "Theoretical and technological exploration of deep in situ fluidized coal mining," *Frontiers in Energy*, vol. 13, no. 4, pp. 603–611, 2019.

Hindawi
Geofluids
Volume 2021, Article ID 6637098, 11 pages
https://doi.org/10.1155/2021/6637098

Research Article

Slope Stability Analysis under Complex Stress State with Saturated and Unsaturated Seepage Flow

Zongyuan Ma, Caihui Zhu, Xiaoliang Yao, and Faning Dang

State Key Laboratory of Eco-Hydraulics in Northwest Arid Region, Xi'an University of Technology, 5 South Jinhua Road, Xi'an, Shaanxi 710048, China

Correspondence should be addressed to Caihui Zhu; zhucaihui@xaut.edu.cn

Received 3 November 2020; Revised 30 November 2020; Accepted 6 December 2020; Published 11 January 2021

Academic Editor: Guanglei Zhang

Seepage flow is one of the primary factors that trigger slopes and landslides' failure. In this study, the slope stability under saturated or unsaturated conditions is analyzed. The influence of a complex stress state on the slope stability with the saturated or unsaturated seepage flow is proposed in this paper. Firstly, an elastoplastic constituted model for the soil under a complex stress state is established and as a user subroutine of the finite element method code of FLAC. Secondly, the 2D and 3D problems of slope stability influenced by the saturated or unsaturated seepage flow are analyzed via the finite difference method with the influence of the complex stress state. Finally, the influence of the intermediate principal stress and the saturated or unsaturated seepage flow on the slope stability is analyzed in this study.

1. Introduction

Soil is a typical polyporous and multiphase material on our planet. Therefore, soils usually contain soil particles, pore water, and pore air. The soil can be divided into dry, saturated, and unsaturated states via the pore filling composition. The seepage flow of pore fluid will influence the stability of the soil significantly. Soil slope stability is one of the key and classical problems in soil mechanics. The variation of the water content in soil (due to underground water, seepage flow, or rainfall) is a vital influence factor for soil slope safety and stability. In recent years, soil slope stability, i.e., hill slope, embankment, and cutting high slope, is influenced by the water content variation due to climatic and anthropogenic factors [1–3]. Many true triaxial tests have verified that the intermediate principal stress has specific influences on mechanical behavior and strength characteristics of soil, and this problem was summarized by Ma et al. [4–6].

The factor of safety (FOS) is an essential parameter to determine the slope or landslide stability, and several methods have been suggested for FOS calculation, including analytical and numerical methods. The limit equilibrium method (LEM) is a general analytical method for slope stability analysis and FOS calculation, e.g., the circular slip surface method or the general methods of slices [7–11]. The limit analysis method is a semianalytic method for the problem of slope stability analysis. The stability of three-dimensional undrained slopes was analyzed by Li et al. using the numerical limit analysis method [12]. The FOS of a slope also can be calculated via the numerical method with the strength reduction method (SRM), e.g., finite element method (FEM) or finite difference method (FDM). SRM is a method that the original shear strength parameters (e.g., cohesion c and friction angle φ) of soil mass are divided by the strength reduction factor (SRF) to bring the slope to the point of failure. The shear strength parameters of the soil mass are decreased gradually by SRF until the slope becomes unstable, and the value of SRF when the failure is initiated is equal to FOS for the slope [13–16]. The numerical method has several advantages over the analytical method (e.g., LEM) for slope stability analysis, e.g., finding the critical failure surface automatically. The relationship between the LEM and SRM in slope stability analysis was discussed by Griffiths and Lane [17]. A model test for soil slope failure due to the seepage flow is proposed by Jia et al. [3]. The soil slope failure caused by rainfall and infiltration is analyzed by Chen et al. [1].

In this paper, an explicit finite difference elastoplastic model is developed based on the twin shear strength theory (TSST). TSST is proposed by Yu [18, 19] that takes the effect of intermediate principal stress on the failure of materials into account. The model is written in C++ and compiled as a dynamic link library file that can be loaded into an explicit finite difference code FLAC. According to the model test and field investigation, the stability analyses of an embankment slope and a high loess slope are performed with FLAC, where the complex stress state, groundwater level variation, and seepage flow are taken into account. The problems of fractured wells in a reservoir of hydrogen and carbon based on a dual-porosity medium model were discussed by Xue et al. and Liu et al., respectively [20, 21].

2. Theory and Method

2.1. Twin Shear Strength Theory. The principal stress form of TSST can be written as [18, 19]

$$\begin{cases} f = \sigma_1 - \dfrac{\alpha}{1+b}(b\sigma_2 + \sigma_3) - \sigma_t, & \text{when } \sigma_2 \le \dfrac{\sigma_1 + \alpha\sigma_3}{1+\alpha}, \\ f' = \dfrac{1}{1+b}(\sigma_1 + b\sigma_2) - \alpha\sigma_3 - \sigma_t, & \text{when } \sigma_2 \ge \dfrac{\sigma_1 + \alpha\sigma_3}{1+\alpha}, \end{cases} \tag{1}$$

where α is the ratio of tensile and compression yield strength, σ_t is the tensile yield strength, and b is the coefficient which reflects the influence of intermediate principal stress. The three principal stresses are denoted as $\sigma_1 \ge \sigma_2 \ge \sigma_3$, and the direction of principal stress is positive in tension and negative in compression. TSST can be written as the form of the strength parameters c and φ, which are widely used in geotechnical engineering; it follows that

$$\begin{cases} f = \dfrac{\cos\varphi}{(1+\sin\varphi)(1+b)}(b\sigma_2 + \sigma_3) - \sigma_1 + \dfrac{2C\cdot\cos\varphi}{1+\sin\varphi}, & \text{when } \sigma_2 \le \dfrac{1+\sin\varphi}{2}\sigma_1 + \dfrac{1-\sin\varphi}{2}\sigma_3, \\ f' = \dfrac{\cos\varphi}{1+\sin\varphi}\cdot\sigma_3 - \dfrac{1}{1+b}(\sigma_1 + b\sigma_2) + \dfrac{2C\cdot\cos\varphi}{1+\sin\varphi}, & \text{when } \sigma_2 \ge \dfrac{1+\sin\varphi}{2}\sigma_1 + \dfrac{1-\sin\varphi}{2}\sigma_3. \end{cases} \tag{2}$$

2.2. Explicit Finite Difference Form. From the incremental elastoplastic theory, the total strain can be written as

$$\Delta\varepsilon_i = \Delta\varepsilon_i^e + \Delta\varepsilon_i^p. \tag{3}$$

The elastic portion follows increment generalized Hooke's law:

$$\begin{cases} \Delta\sigma_1 = \alpha_1\Delta\varepsilon_1^e + \alpha_2(\Delta\varepsilon_2^e + \Delta\varepsilon_3^e), \\ \Delta\sigma_2 = \alpha_1\Delta\varepsilon_2^e + \alpha_2(\Delta\varepsilon_1^e + \Delta\varepsilon_3^e), \\ \Delta\sigma_3 = \alpha_1\Delta\varepsilon_3^e + \alpha_2(\Delta\varepsilon_1^e + \Delta\varepsilon_2^e), \end{cases} \tag{4}$$

where $\alpha_1 = K + 4G/3$, $\alpha_2 = K - 2G/3$, K is bulk modulus, and G is shear modulus. The tensor form of Eq. (4) is given:

$$\Delta\sigma_i = S_i(\Delta\varepsilon_1^e, \Delta\varepsilon_2^e, \Delta\varepsilon_3^e) = S_i(\Delta\varepsilon_n^e), \quad i = 1, 2, 3. \tag{5}$$

From the plastic flow rule, the plastic incremental deformation part can be determined:

$$\Delta\varepsilon_i^p = \lambda\frac{\partial g}{\partial\sigma_i}, \tag{6}$$

where g is plastic potential and λ is the plastic multiplier.

In order to deduce the expression of λ, the critical state between elastic and plastic is assumed: an increment stress $\Delta\sigma_n = (\sigma_1, \sigma_2, \sigma_3)$ loaded to a structure when $f(\sigma_n) = 0$, and the state of the structure has no change ($f(\sigma_n + \Delta\sigma_n) = 0$).

From Eq. (5), the component of increment stress $\Delta\sigma_n$ can be written as

$$\Delta\sigma_i = S_i(\Delta\varepsilon_n - \Delta\varepsilon_n^p). \tag{7}$$

Substituting Eq. (6) into Eq. (7) and simplifying

$$\Delta\sigma_i = S_i\left(\Delta\varepsilon_n - \lambda\frac{\partial g}{\partial\sigma_n}\right) = S_i(\Delta\varepsilon_n) - \lambda\cdot S_i\left(\frac{\partial g}{\partial\sigma_n}\right), \tag{8}$$

where $\lambda\cdot S_i(\partial g/\partial\sigma_n)$ is the corresponding stress of plastic strain. $f(\sigma_n + \Delta\sigma_n)$ can also be written as

$$f(\sigma_n + \Delta\sigma_n) = f(\sigma_n) + f^*(\sigma_n), \tag{9}$$

where $f(\sigma_n) = 0, f^*(\sigma_n) = f(\Delta\sigma_n) - f(0)$, and then, $f(\sigma_n + \Delta\sigma_n)$ follows:

$$f(\sigma_n + \Delta\sigma_n) = f^*(\Delta\sigma_n). \tag{10}$$

Substituting Eq. (8) into Eq. (10) and then $f(\sigma_n + \Delta\sigma_n)$ can be deduced:

$$f(\sigma_n + \Delta\sigma_n) = f^*(S_n(\Delta\varepsilon_n)) - \lambda\cdot f^*\left(S_n\left(\frac{\partial g}{\partial\sigma_n}\right)\right) = 0. \tag{11}$$

In order to process the material nonlinearity, the stress σ_i^N and σ_i^I is defined as follows [22]:

$$\sigma_i^N = \sigma_i + \Delta\sigma_i = \sigma_i + S_i(\Delta\varepsilon_n) - S_i(\Delta\varepsilon_n^p), \tag{12}$$

$$\sigma_i^I = \sigma_i + S_i(\Delta\varepsilon_n), \tag{13}$$

where $\Delta\varepsilon_n$ is the total strain of the elastic stage, σ_i^I is a stress tensor in the elastic stage, and σ_i^N is a stress tensor in the plastic stage. $f(\sigma_n^I)$ can be written as

$$f(\sigma_n^I) = f(\sigma_n + S_n(\Delta\varepsilon_n)) = f^*(S_n(\Delta\varepsilon_n)). \tag{14}$$

Substituting Eq. (14) into Eq. (11) and then λ can be deduced:

$$\lambda = \frac{f(\sigma_n^I)}{f^*(S_n(\partial g/\partial\sigma_n))}. \tag{15}$$

From Eqs. (6), (12), and (13), the expression σ_i^N can be deduced:

$$\sigma_i^N = \sigma_i^I - \lambda \cdot S_i\left(\frac{\partial g}{\partial\sigma_n}\right). \tag{16}$$

Eq. (2) can also be written as

$$\begin{cases} f = \dfrac{1}{(1+b)N_\varphi}(b\sigma_2 + \sigma_3) - \sigma_1 + \dfrac{2c}{\sqrt{N_\varphi}}, & \text{when } \sigma_2 \le \dfrac{1+\sin\varphi}{2}\sigma_1 + \dfrac{1-\sin\varphi}{2}\sigma_3, \\ f' = \dfrac{\sigma_3}{N_\varphi} - \dfrac{1}{1+b}(\sigma_1 + b\sigma_2) + \dfrac{2c}{\sqrt{N_\varphi}}, & \text{when } \sigma_2 \ge \dfrac{1+\sin\varphi}{2}\sigma_1 + \dfrac{1-\sin\varphi}{2}\sigma_3, \end{cases} \tag{17}$$

where $N_\varphi = (1+\sin\varphi)/(1-\sin\varphi)$. The nonassociated flow is employed, the dilation angle ψ substitutes the internal friction angle in Eq. (17) and as the equation of the plastic potential, where $N_\psi = (1+\sin\psi)/(1-\sin\psi)$, and the item of $\lambda \cdot S_i(\partial g/\partial\sigma_n)$ can be determined:

$$\begin{cases} S_1\left(\lambda\dfrac{\partial g}{\partial\sigma_1}, \lambda\dfrac{\partial g}{\partial\sigma_2}, \lambda\dfrac{\partial g}{\partial\sigma_3}\right) = \lambda\left(\dfrac{\alpha_2}{N_\psi} - \alpha_1\right), \\ S_2\left(\lambda\dfrac{\partial g}{\partial\sigma_1}, \lambda\dfrac{\partial g}{\partial\sigma_2}, \lambda\dfrac{\partial g}{\partial\sigma_3}\right) = \lambda\left\{\dfrac{b\cdot\alpha_1}{(1+b)N_\psi} + \alpha_2\left[\dfrac{1}{(1+b)N_\psi} - 1\right]\right\}, \\ S_3\left(\lambda\dfrac{\partial g}{\partial\sigma_1}, \lambda\dfrac{\partial g}{\partial\sigma_2}, \lambda\dfrac{\partial g}{\partial\sigma_3}\right) = \lambda\left\{\dfrac{\alpha_1}{(1+b)N_\psi} + \alpha_2\left[\dfrac{b}{(1+b)N_\psi} - 1\right]\right\}0, \\ \text{when } \sigma_2 \le \dfrac{1+\sin\phi}{2}\sigma_1 + \dfrac{1-\sin\phi}{2}\sigma_3, \end{cases}$$

$$\begin{cases} S_1\left(\lambda\dfrac{\partial g}{\partial\sigma_1}, \lambda\dfrac{\partial g}{\partial\sigma_2}, \lambda\dfrac{\partial g}{\partial\sigma_3}\right) = \lambda\left[\alpha_2\left(\dfrac{1}{N_\psi} - \dfrac{b}{1+b}\right) - \dfrac{\alpha_1}{1+b}\right], \\ S_2\left(\lambda\dfrac{\partial g}{\partial\sigma_1}, \lambda\dfrac{\partial g}{\partial\sigma_2}, \lambda\dfrac{\partial g}{\partial\sigma_3}\right) = \lambda\left[\alpha_2\left(\dfrac{1}{N_\psi} - \dfrac{1}{1+b}\right) - \dfrac{\alpha_1\cdot b}{1+b}\right], \\ S_3\left(\lambda\dfrac{\partial g}{\partial\sigma_1}, \lambda\dfrac{\partial g}{\partial\sigma_2}, \lambda\dfrac{\partial g}{\partial\sigma_3}\right) = \lambda\left(\alpha_1\dfrac{1}{N_\psi} - \alpha_2\right), \\ \text{when } \sigma_2 \ge \dfrac{1+\sin\phi}{2}\sigma_1 + \dfrac{1-\sin\phi}{2}\sigma_3. \end{cases} \tag{18}$$

Substituting Eq. (18) into Eq. (16), the component of σ_i^N yields

$$\begin{cases} \sigma_1^N = \sigma_1^I - \lambda\left(\alpha_2\dfrac{1}{N_\psi} - \alpha_1\right), \\ \sigma_2^N = \sigma_2^I - \lambda\left\{\alpha_1\dfrac{b}{(1+b)N_\psi} + \alpha_2\left[\dfrac{1}{(1+b)N_\psi} - 1\right]\right\}, \\ \sigma_3^N = \sigma_3^I - \lambda\left\{\alpha_1\dfrac{1}{(1+b)N_\psi} + \alpha_2\left[\dfrac{b}{(1+b)N_\psi} - 1\right]\right\}, \\ \text{when } \sigma_2 \le \dfrac{1+\sin\phi}{2}\sigma_1 + \dfrac{1-\sin\phi}{2}\sigma_3, \end{cases}$$

$$\begin{cases} \sigma_1^N = \sigma_1^I - \lambda\left[\alpha_2\left(\dfrac{1}{N_\psi} - \dfrac{b}{1+b}\right) - \dfrac{\alpha_1}{1+b}\right], \\ \sigma_2^N = \sigma_2^I - \lambda\left[\alpha_2\left(\dfrac{1}{N_\psi} - \dfrac{1}{1+b}\right) - \dfrac{\alpha_1\cdot b}{1+b}\right], \\ \sigma_3^N = \sigma_{31}^I - \lambda\left(\alpha_1\dfrac{1}{N_\psi} - \alpha_2\right), \\ \text{when } \sigma_2 \ge \dfrac{1+\sin\phi}{2}\sigma_1 + \dfrac{1-\sin\phi}{2}\sigma_3, \end{cases} \tag{19}$$

where the expression of λ is as follows:

$$\begin{aligned} \lambda &= \frac{f(\sigma_1^I, \sigma_2^I, \sigma_3^I)}{f(S_1(\partial g/\partial\sigma_1, \partial g/\partial\sigma_2, \partial g/\partial\sigma_3), S_2(\partial g/\partial\sigma_1, \partial g/\partial\sigma_2, \partial g/\partial\sigma_3), S_3(\partial g/\partial\sigma_1, \partial g/\partial\sigma_2, \partial g/\partial\sigma_3)) - f(0)}, \quad \text{when } \sigma_2 \le \frac{1+\sin\varphi}{2}\sigma_1 + \frac{1-\sin\varphi}{2}\sigma_3, \\ \lambda &= \frac{f'(\sigma_1^I, \sigma_2^I, \sigma_3^I)}{f'(f(S_1(\partial g/\partial\sigma_1, \partial g/\partial\sigma_2, \partial g/\partial\sigma_3), S_2(\partial g/\partial\sigma_1, \partial g/\partial\sigma_2, \partial g/\partial\sigma_3), S_3(\partial g/\partial\sigma_1, \partial g/\partial\sigma_2, \partial g/\partial\sigma_3))) - f'(0)}, \quad \text{when } \sigma_2 \ge \frac{1+\sin\varphi}{2}\sigma_1 + \frac{1-\sin\varphi}{2}\sigma_3. \end{aligned} \tag{20}$$

Table 1: Analysis and calculation parameters of slope stability under seepage flow condition.

Saturated seepage flow		Unsaturated seepage flow			
Permeability k (m/d)	Porosity n (%)	Residual volume water content θ_r	Saturated volume water content θ_s	α	m
0.6	50	0.0812 sorption	0.4155 sorption	0.0573 sorption	4.0974 sorption
		0.1028 desorption	0.4465 desorption	0.0325 desorption	7.4845 desorption

Eqs. (18) and (19) are the formats of Lagrangian explicit finite difference for the twin shear elastoplastic model. The model is written in the language of C++ and compiled as a file of dynamic link library that can be loaded in FLAC code [22]. Ma et al. propose a numerical study of gravel soil ground's dynamic compaction using the explicit discrete element method [23].

2.3. Slope Stability due to Saturated Seepage Flow. Due to groundwater level variations, the FOS of the slope is calculated according to the saturated seepage flow theory without the influence of unsaturation on slope stability during seepage flow. FOS values for a 2D slope (with the plane strain condition) are calculated by SRM using TSST. The FOS of the soil slope is calculated via SRM, i.e., the same factor SRF is applied to both of the shear strength parameters (c and φ). The reduced strength parameters (c_f and φ_f) are given by

$$c_f = \frac{c}{\mathrm{SRF}},\qquad \varphi_f = \arctan\left(\frac{\tan\varphi}{\mathrm{SRF}}\right), \tag{21}$$

where c and φ are the original cohesion and internal friction angle of the slope soil, c_f and φ_f are the cohesion and internal friction angle of soil after the reduction, and SRF (strength reduction factor) is the intensity reduction coefficient. The strength parameter of slope soil is divided by a reduction factor SRF step by step until the slope failure, and then, the value of SRF equals FOS of the slope. The values of SRF at the critical failure state of the slope are taken as FOS of the slope [17].

Analysis and calculation parameters for slope stability with seepage flow are shown in Table 1. Figure 1 shows the relationship between FOS and groundwater level calculated by saturated seepage. It can be seen from Figure 1 that under saturated seepage, the slope safety coefficient calculated according to Mohr-Coulomb theory is lower than 1.0 when the groundwater level is raised. The values of FOS are greater than 1.0 when the effect of intermediate principal stress is considered. The model test results in the literature [3] showed that the slope did not fail in the water injection stage (the groundwater level is raised), so the calculation results without taking the effect of intermediate principal stress into account do not agree with the actual situation. Figure 2 shows the maximum shear strain contours of the slope calculated according to TSST ($b = 1.0$) when the slope water level drops to $L/H = 1.0$ under saturated seepage condition. Figure 2 shows that the nonassociated flow ($\psi = 0$) calculation results show that there are multiple sliding surfaces of the slope. However, the results obtained by associated flow ($\psi = \varphi$) show only one sliding surface.

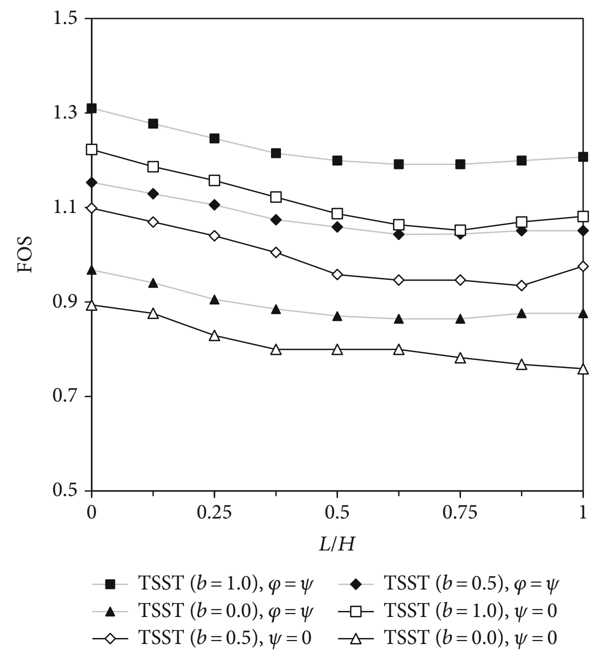

Figure 1: Relation between slope FOS and water level L/H during the falling of water level.

2.4. Slope Stability due to Unsaturated Seepage Flow. The effect stress σ^b can be formulated as follows using Bishop's unsaturated effect stress theory (compression is negative) [24]:

$$\sigma^b = \sigma - (S_w P_w + S_a P_a), \tag{22}$$

where σ is the total stress, S_w is the saturation of water, $S_a = 1 - S_w$ is the air saturation, and P_w and P_a are the water pressure and air pressure. TSST can establish the formula of unsaturated shearing strength, and TSST can be written by the twin shear stress (τ_{12} and τ_{23}) and normal stress (σ_{12} and σ_{23}) as follows [18, 19]:

$$\begin{cases} \tau_{13} + b\tau_{12} = C - \beta\left(\sigma_{13}^b + b\sigma_{12}^b\right), & \text{when } \tau_{12} + \beta\sigma_{12}^b \geq \tau_{23} + \beta\sigma_{23}^b, \\ \tau_{13} + b\tau_{23} = C - \beta\left(\sigma_{13}^b + b\sigma_{23}^b\right), & \text{when } \tau_{12} + \beta\sigma_{12}^b \leq \tau_{23} + \beta\sigma_{23}^b, \end{cases} \tag{23}$$

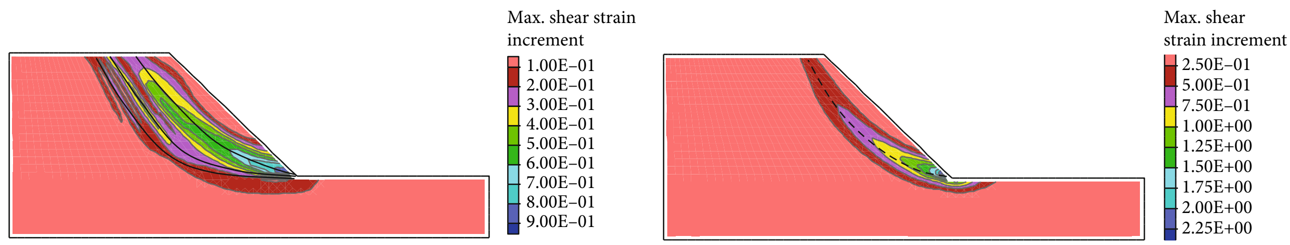

(a) Nonassociated flow $\psi = 0$ (b) Associated flow $\psi = \varphi$

FIGURE 2: Maximum shear strain counters obtained by TSST $b = 1.0$ when the water level drops to $L/H = 1.0$.

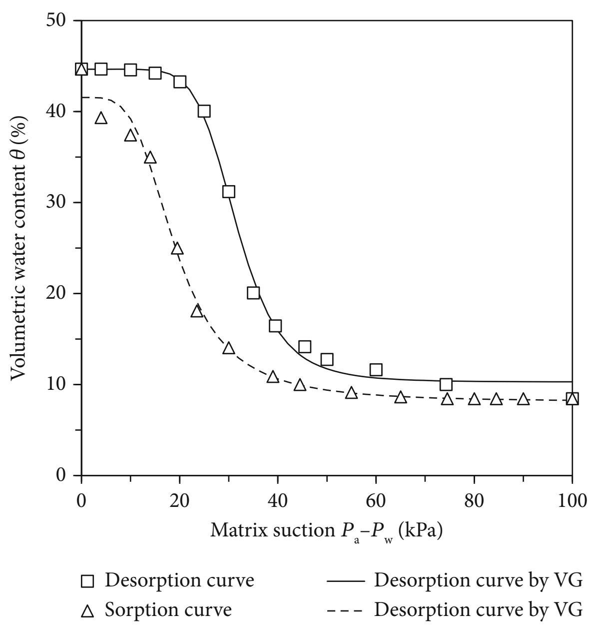

FIGURE 3: Soil-water characteristic curves.

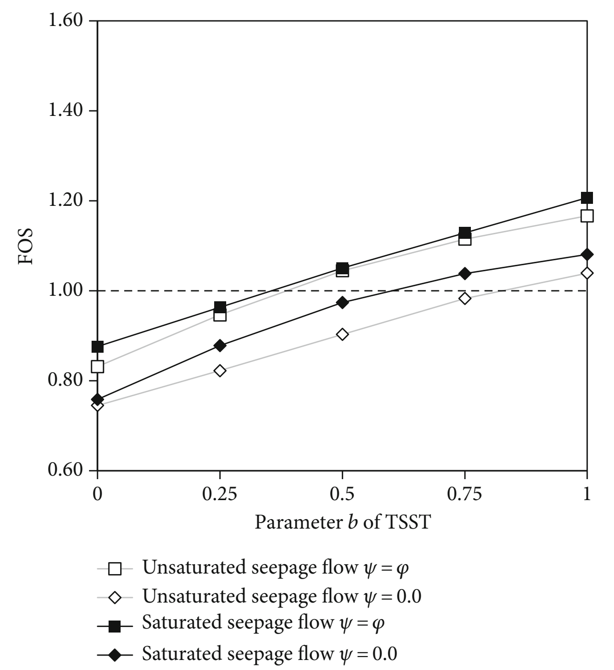

FIGURE 4: Relation between FOS and parameter b when the underground water level rises to the slope crest.

where β and C is the strength parameters and can be determined by cohesion c and friction angle φ ($\beta = \sin\varphi$, $C = 2c \cos\varphi$); TSST also can be formulated by c and φ as follows:

$$\begin{cases} \tau_{13} + b\tau_{12} = 2c\cos\varphi - \left(\sigma_{13}^{b} + b\sigma_{12}^{b}\right)\sin\varphi, & \text{when } \tau_{12} + \sigma_{12}^{b}\sin\varphi \geq \tau_{23} + \sigma_{23}^{b}\sin\varphi, \\ \tau_{13} + b\tau_{23} = 2c\cos\varphi - \left(\sigma_{13}^{b} + b\sigma_{23}^{b}\right)\sin\varphi, & \text{when } \tau_{12} + \sigma_{12}^{b}\sin\varphi \leq \tau_{23} + \sigma_{23}^{b}\sin\varphi, \end{cases} \tag{24}$$

where the normal stress σ_{12} and σ_{23} under the unsaturated condition is as follows:

$$\begin{cases} \sigma_{13}^{b} = \sigma_{13} - (S_w P_w + S_a P_a) = (\sigma_{13} - P_a) - S_w (P_a + P_w), \\ \sigma_{12}^{b} = \sigma_{12} - (S_w P_w + S_a P_a) = (\sigma_{12} - P_a) - S_w (P_a + P_w), \\ \sigma_{23}^{b} = \sigma_{23} - (S_w P_w + S_a P_a) = (\sigma_{23} - P_a) - S_w (P_a + P_w). \end{cases} \tag{25}$$

The shear strength formula of unsaturated soil can be established via substituting Eq. (25) into Eq. (24), and the shear strength formula of unsaturated soil can be obtained as follows:

$$\begin{cases} \tau_{13} + b\tau_{12} = 2c\cos\varphi - [(\sigma_{13} - P_a) + b(\sigma_{12} - P_a)]\sin\varphi + (1+b)[S_w(P_a - P_w)]\sin\varphi, & \text{when } \tau_{12} + (\sigma_{12} - P_a)\sin\varphi \geq \tau_{23} + (\sigma_{23} - P_a)\sin\varphi, \\ \tau_{13} + b\tau_{23} = 2c\cos\varphi - [(\sigma_{13} - P_a) + b(\sigma_{23} - P_a)]\sin\varphi + (1+b)[S_w(P_a - P_w)]\sin\varphi, & \text{when } \tau_{12} + (\sigma_{12} - P_a)\sin\varphi \leq \tau_{23} + (\sigma_{23} - P_a)\sin\varphi. \end{cases} \tag{26}$$

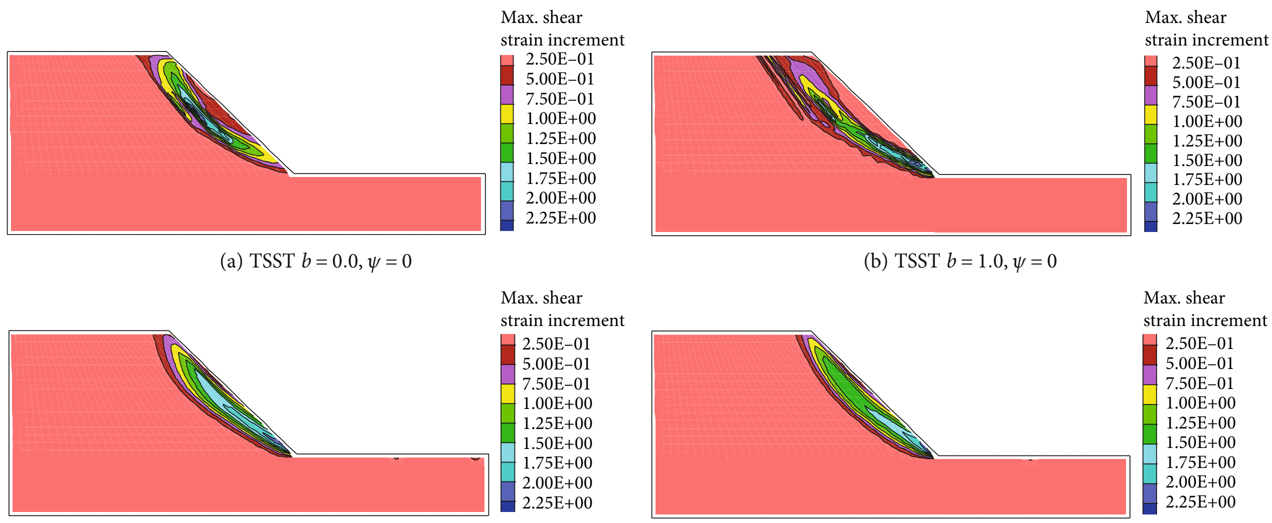

(a) TSST $b = 0.0$, $\psi = 0$

(b) TSST $b = 1.0$, $\psi = 0$

(c) TSST $b = 0.0$, $\psi = \varphi$

(d) TSST $b = 1.0$, $\psi = \varphi$

Figure 5: Maximum shear strain contours of slope (unsaturated seepage) when the water level drops to $L/H = 1.0$.

The principal shear stress (τ_{13}, τ_{12}, and τ_{23}) and normal stress (σ_{13}, σ_{12}, and σ_{23}) can be expressed as follows:

$$\begin{cases} \tau_{13} = \dfrac{\sigma_1 - \sigma_3}{2}, \\ \tau_{12} = \dfrac{\sigma_1 - \sigma_2}{2}, \\ \tau_{23} = \dfrac{\sigma_2 - \sigma_3}{2}, \\ \sigma_{13} = \dfrac{\sigma_1 + \sigma_3}{2}, \\ \sigma_{12} = \dfrac{\sigma_1 + \sigma_2}{2}, \\ \sigma_{23} = \dfrac{\sigma_2 + \sigma_3}{2}. \end{cases} \tag{27}$$

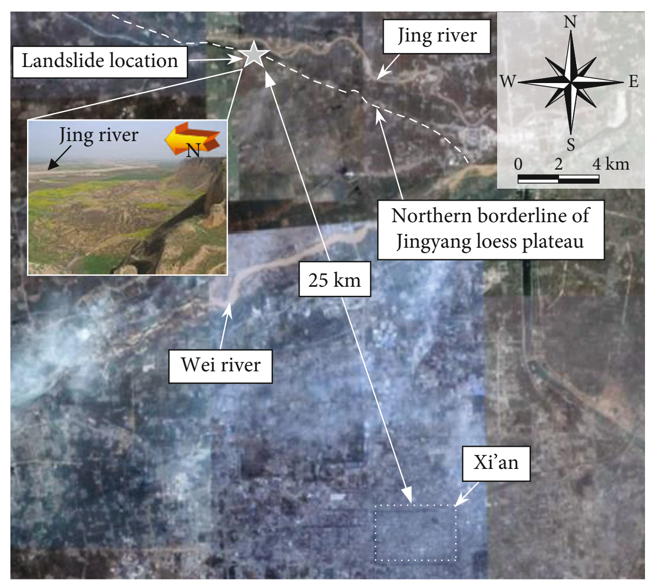

Figure 6: Location of the high loess slope and terrain of Jingyang loess plateau.

The shear strength formula of unsaturated soil also can be formulated via substituting Eq. (27) into Eq. (26):

$$\begin{aligned} &(1+b)\sigma_1 - b\sigma_2 - \sigma_3 = 4c\cos\varphi - [(1+b)\sigma_1 + b\sigma_2 + \sigma_3 - 2(1+b)P_a]\sin\varphi + 2(1+b)[S_w(P_a - P_w)]\sin\varphi, \quad \text{when } \sigma_1 - \sigma_2 + (\sigma_1 + \sigma_2 - 2P_a)\sin\varphi \ge \sigma_2 - \sigma_3 + (\sigma_2 + \sigma_3 - 2P_a)\sin\varphi, \\ &\sigma_1 + b\sigma_2 - (1+b)\sigma_3 = 4c\cos\varphi - [\sigma_1 + b\sigma_2 + (1+b)\sigma_3 - 2(1+b)P_a]\sin\varphi + 2(1+b)[S_w(P_a - P_w)]\sin\varphi, \quad \text{when } \sigma_1 - \sigma_2 + (\sigma_1 + \sigma_2 - 2P_a)\sin\varphi \le \sigma_2 - \sigma_3 + (\sigma_2 + \sigma_3 - 2P_a)\sin\varphi. \end{aligned} \tag{28}$$

The variation of suction $P_a - P_w$ of the unsaturated soil can be described by the empirical formula recommended by van Genuchten [25–27]:

$$\theta_w = \theta_r + \frac{\theta_s - \theta_r}{\{1 + [\alpha(P_a - P_w)]^m\}^{1-1/m}}, \tag{29}$$

where θ_w is the volume water content of the soil, R is the residual volume water content of the soil, and m is the measured parameters. The relationship between saturation S_w and volume water content θ_w is $\theta_w = S_w n$, where n is soil's porosity. The shear strength formula of unsaturated soil based on TSST and the empirical formula of SWCC van

Genuchten were used to analyze the stability analysis of unsaturated seepage slope in the slope model test in literature [3]. The lsqcurvefit function in Matlab's software is used to fit the data of the soil-water characteristic curve (SWCC) tested by literature [3] and the empirical formula proposed by van Genuchten. Figure 3 is the fitting result of SWCC data of the slope model test soil and the empirical formula of van Genuchten. It can be seen that the hygroscopic and dehumidification curves of slope soil have an obvious hysteretic relationship. The matric suction of the soil's unsaturated state in the calculation process is controlled by the empirical formula of van Genuchten, in which the stage of water level rise and fall is calculated by the fitting results of the empirical formula of van Genuchten in SWCC in Figure 3. According to the strength formula of unsaturated soil with TSST derived in the previous part, the slope's safety factor is calculated by the strength reduction method. The numerical calculation model and boundary conditions are consistent with the saturated seepage calculation. Figure 4 shows the slope to water injection after reaching the top, saturated and unsaturated seepage flow theory to calculate the safety factor of slope, and the relationship between the theory of parameter b; it can be seen that the value of FOS yielded by Mohr-Coulomb theory is less than 1.0 both under saturated and unsaturated conditions and does not agree with the results of the slope model test in literature [3]. The value of FOS yielded by TSST ($b = 1.0$) is greater than 1.0. Therefore, the intermediate principal stress influence should be considered in slope stability analysis due to the seepage flow. Figure 5 shows the maximum shear strain contours of slope under the unsaturated seepage when the water level dropped to $L/H = 1.0$ yield by Mohr-Coulomb and TSST. The calculation result yield by TSST ($b = 1.0$) in the associated flow ($\psi = 0$) shows that the multiple sliding surfaces have occurred. However, the calculation result yield by Mohr-Coulomb theory or associated flow ($\psi = \varphi$) shows that the slope only has one sliding surface.

2.5. Three-Dimensional Analysis of High Slope Stability due to Saturated Seepage Flow. The high loess slope is situated along the northern boundary of a loess plateau close to Jingyang, Shaanxi province, China. The distance from the high loess slope to the downtown of Xi'an is about 25 km. The Jing river flows beside the northern boundary of the loess plateau (see Figure 6). Due to the Jing river's erosion, many high loess slopes came into being along the northern loess plateau boundary. The northern loess plateau boundary is about 30 km long, the elevation of 30-90 m above the Jing river, and the slope angle is about 45-80°.

The landslide mass' length and width are about 400 and 410 m, respectively, and the slope angle is about 45-55°. Seven cross-sections are measured for the landslide mass in a longitudinal direction (see Figure 7). The continuous line represents the edge of the slope crest before the landslide event, and the dashed line represents the current edge of the slope crest, as shown in Figure 7. The cross-section sketch is drawn according to the topography data, as shown in Figure 8. The groundwater of the loess plateau is stored in a phreatic aquifer. In 1976, the groundwater level was kept equal to the Jing

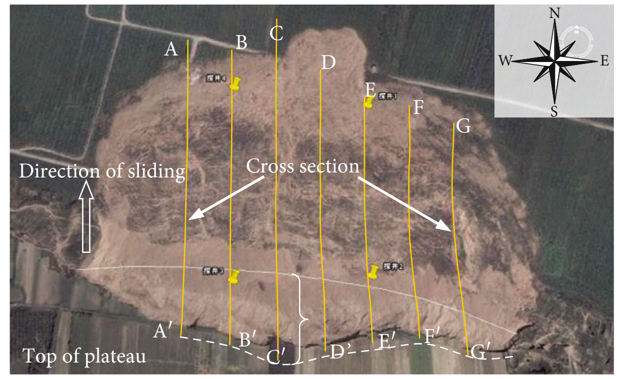

Figure 7: General view of landslide and cross-sections.

river (elevation is 380 m). However, large-scale irrigation and raining above the loess plateau induced a significant rise in the groundwater level. In 1992, the groundwater level's depth under the loess plateau was 37 m (elevation is 425 m). Since 1976, the landslides in this area have occurred over 40 times, which enormously influenced the local area.

A series of laboratory tests, including the particle-size analysis test and consolidated-undrained triaxial tests, were conducted. The particle-size analysis test shows that the percent of particles with diameters greater than 0.075 mm is 27.8%. The percent of particles with diameters less than 0.005 mm is greater than 10%. The plasticity index I_p ranges from 3.0 to 10.0. Therefore, the soil can be classified as clayey silt. The cohesion and internal friction angle of soil samples obtained from the consolidated-undrained triaxial test under different confining pressures are 3.56 kPa and 17.9°, respectively. Table 2 shows the physical properties of the soil samples from the high loess slope.

2.5.1. Influence of Intermediate Principal Stress and Groundwater Level. The previous terrain of the high loess slope before the landslide is created based on terrain from field investigation, and the three-dimensional model of high loess slope before the landslide event is established. The cross-sections of A-A′ and G-G′ are selected as the boundaries of two sides of the slope model, and the dimension and meshing of the model are shown in Figure 9. The dashed line represents the groundwater level, and h is the depth of groundwater under the loess plateau. Node O of the slope top on the cross-section of D-D′ is selected. The displacement of node O in the direction of the x-axis is recorded during the calculation process to analyze the slope stability. The calculation parameters are as follows: Young's modulus $E = 5.0$ MPa, Poisson's ratio $\nu = 0.33$, and dilation angle $\psi = 10°$. The calculations are performed under the groundwater level in 1976 ($h = 80$ m) and 1992 ($h = 37$ m) to compare the slope stability under different groundwater levels, respectively. The relationship between the displacement at node O in the x-direction and the unbalanced force rate with the different magnitude of b is shown in Figure 10. The unbalanced force rate can be defined as the maximum unbalanced force magnitude for all nodes divided by the average applied force magnitude for all the nodes. The equilibrium in the calculation is

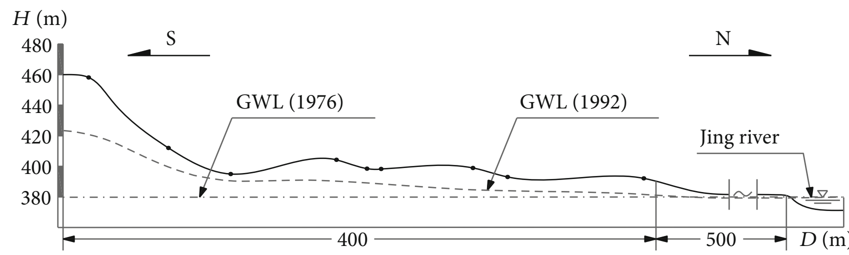

Figure 8: Sketch of the cross-section of D-D′.

Table 2: Physical properties of soil for high loess slope.

Density ρ (kg/m^3)	Specific gravity d_s	Water content w_n (%)	Void ratio e	Plasticity index I_p
1540	2.72	17.8	1.08	8.6

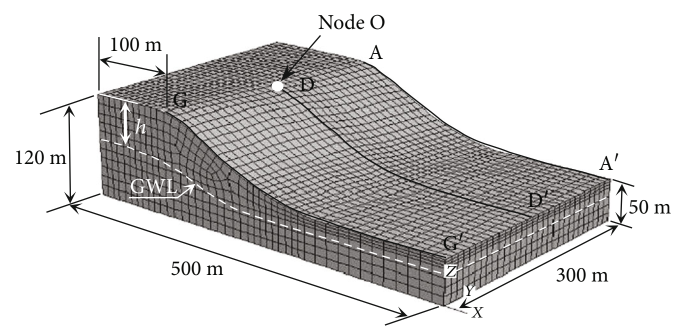

Figure 9: Meshing model of slope before landslide event.

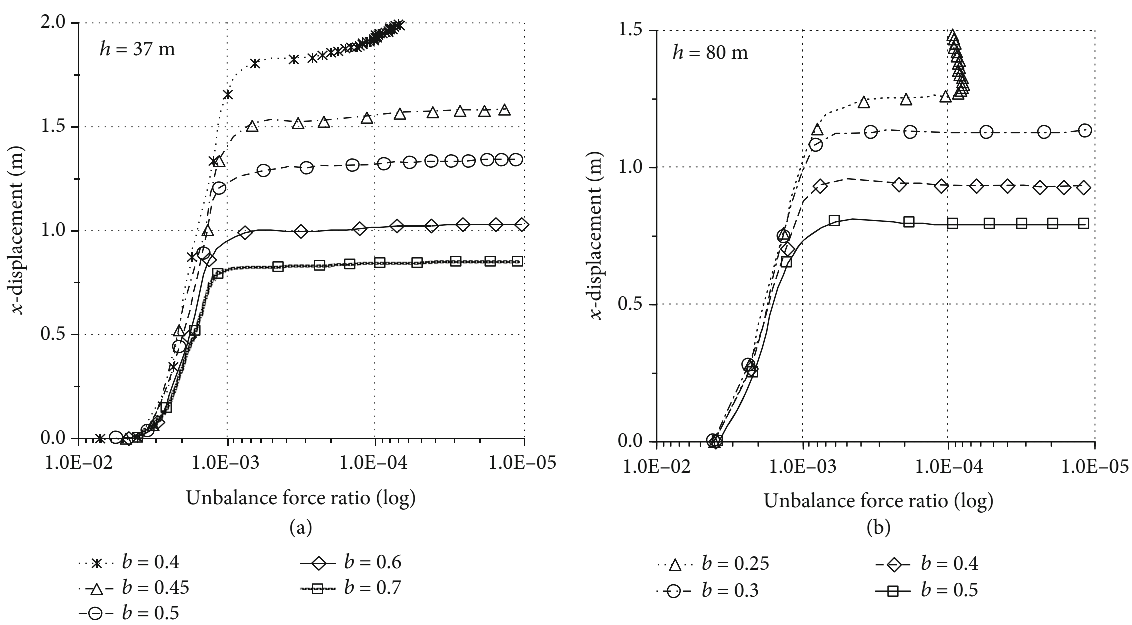

Figure 10: Relationship between x-displacement of node O and unbalanced force rate with different b.

closely related to the unbalanced force rate. By default, the ratio limit for convergence is 1.0×10^{-5}.

Figure 10 indicated that the slope changes towards instability with the decrease of the parameter b, and the slope failure occurs when the magnitude of b falls below a specific value. Because the high loess slope was stable before 1976, the stability analysis taking the intermediate principal stress' influence into account can reflect the actual situation more accurately. The factor of safety for the high loess slope is calculated via the strength reduction method. The strength

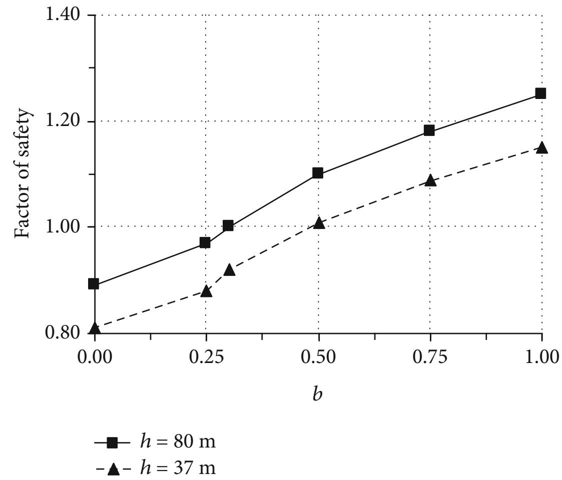

Figure 11: Relationship between FOS and b under the groundwater levels in 1976 and 1992.

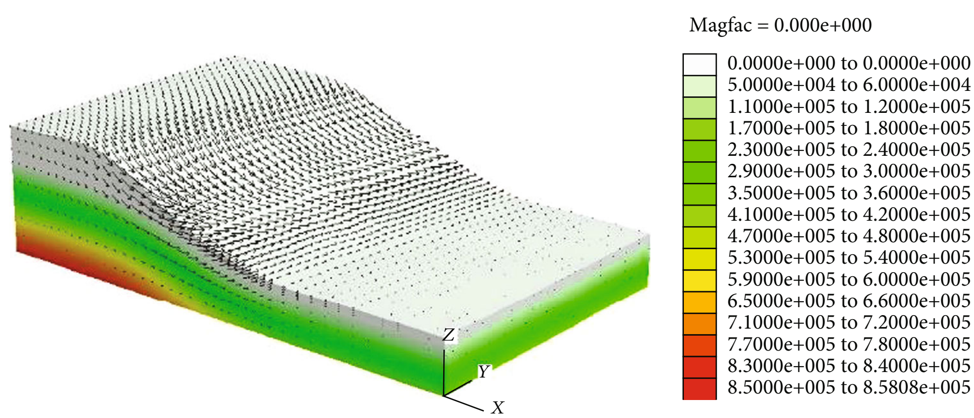

Figure 12: Pore-water pressure and displacement vector of slope in $h = 37$ m and $b = 0.5$.

parameters of soil mass are decreased gradually by a factor until the slope becomes unstable. The factor when the failure is initiated is the factor of safety for the slope. The relationship between FOS values and the magnitude of b under the groundwater level in 1976 and 1992 is shown in Figure 11. The same results can be observed from Figure 11, the values of FOS decreased with the decreasing value of the parameter b, and the values of FOS also decrease with the rising level of the groundwater. The magnitudes of b under the groundwater levels in 1976 and 1992 are equal to 0.3 and 0.5, respectively, when FOS values equal to 1.0. Figure 12 shows the pore-water pressure and displacement vector of slope in $h = 37$ m and $b = 0.5$. As shown in Figure 12, the high loess slope becomes unstable when $h = 37$ m and $b = 0.5$.

The stability analysis of the high loess slope during the rise in the groundwater level caused by raining and irrigation is performed with different depths ($h = 35$-50 m) of the groundwater level. Figure 13 shows the relationship between the displacement of node O in the x-direction and unbalanced force rate under different depths of the groundwater level when $b = 0.5$. The results suggest that the displacement of node O in the x-direction increases significantly as the groundwater rises gradually. The slope failure occurred until the depth of the groundwater level is close to 35 m.

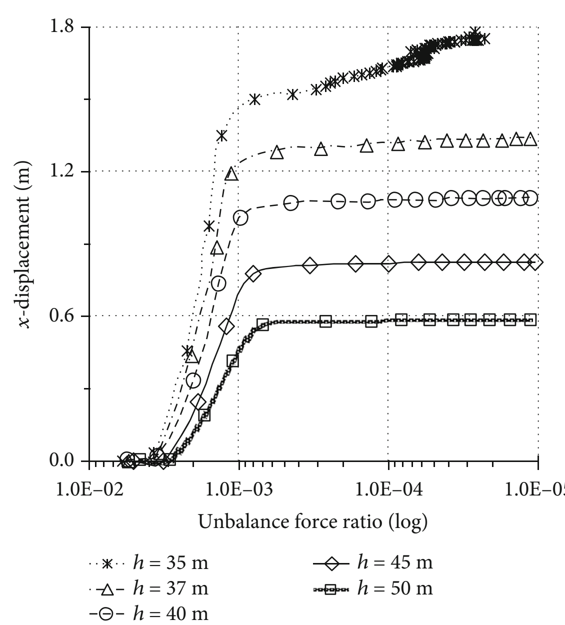

Figure 13: Relationship between displacement of node O in x -direction and unbalanced force rate ($b = 0.5$).

2.5.2. Influence of Seepage Flow. According to statistics, landslides of the loess area induced by the distinct change of the groundwater level occurred frequently during the shot-time raining in the rainy season. The rainfall in the district of Xi'an fluctuates seasonally, and the most rainfall is yielded during the months of July to September, and the time of raining is very short. The mean monthly rainfall of July to September is about 12.5-16.4% of the mean annual rainfall. For example, the total rainfall of 2003 is 898.7 mm, and the total rainfall of July in 2003 is close to 140 mm, which is about 15% of the total rainfall in 2003. The high loess slope on the southern bank of the Jing river slided in July of 2003. Thus, it is necessary to analyze the influence of the distinct rise of the groundwater level and seepage flow which are caused by raining and irrigation on the stability of the high loess slope.

Parameters of soil are the same as the calculation of no seepage flow, and the soil permeability is 0.1 m/d. The calculations of seepage flow and stress field are parallel performed, and the stress field of the slope is calculated by the mechanical strains caused by pore-water pressure changes. Based on the calculation results of groundwater depth $h = 80$ m, the calculation of seepage flow is performed with four scenarios: the rise of groundwater level $\Delta h = 30$ m, 35 m, 40 m, and 45 m under the loess plateau.

Comparing with the numerical results of no seepage, the results of seepage flow calculation show that the displacement of node O in the x-direction increases significantly when the unbalanced force rate is close to the target of convergence and the slope failure occurs suddenly when Δh reaches a certain value. However, the results of no seepage calculation show that the slope reaches a static state when the unbalanced force rate decreased. On the other hand, the x-displacement at node O from the seepage calculation is less than the result of no seepage calculation. This phenomenon suggests that the deformation of the loess slope is too limited to absorb the overload of seepage flow completely; thus, the sudden failure of the loess slope may occur more easily during the process of seepage flow.

3. Conclusion

The form of the explicit finite difference of the twin shear elastoplastic model is established and used to analyze the slope stability with saturated and unsaturated seepage flow. The following conclusions can be stated.

(1) The intermediate principal stress effect of soil strength greatly influences FOS of saturated and unsaturated slopes under the seepage flow condition. The results of slope stability analysis under saturated and unsaturated seepage flow indicate that the slope FOS calculated by Mohr-Coulomb strength theory is less than 1.0, which is not consistent with the results of the slope model test

(2) The saturated and unsaturated seepage calculation results show that the slope will have multiple sliding surfaces when the associated flow is used ($\psi = 0$). The comparison of slope stability analysis results under saturated and unsaturated seepage conditions shows that the shear dilatancy (flow rule) of the unsaturated soil has little influence on the slope stability, and it is mainly related to the unsaturated seepage mechanical behavior of the soil. In the case of saturated seepage, the soil's dilatancy (flow rule) significantly influences the slope stability under the condition of seepage, so the soil's dilatancy should be considered in the slope stability analysis under the condition of saturation

(3) The loess area's arid climate often causes a significant rise in the groundwater level due to the large-scale irrigation and seasonal rainfall. According to the numerical results, it is necessary to reduce the reclamation and irrigation of farmland along the loess plateau's boundary. The stability of the high loess slope can be enhanced

Data Availability

The FEM calculation and the graph data used to support the findings of this study are available from the corresponding author upon request.

Conflicts of Interest

The authors declare that they have no conflicts of interest.

Acknowledgments

This research described in this paper was funded by the National Natural Science Foundation of China (No. 51979225, 51308456).

References

[1] R. H. Chen, H. P. Chen, K. S. Chen, and H. B. Zhung, "Simulation of a slope failure induced by rainfall infiltration," *Environmental Geology*, vol. 58, no. 5, pp. 943–952, 2009.

[2] W. X. Jian, Z. J. Wang, and K. Yin, "Mechanism of the Anlesi landslide in the Three Gorges Reservoir, China," *Engineering Geology*, vol. 108, no. 1-2, pp. 86–95, 2009.

[3] G. W. Jia, T. L. T. Zhan, Y. M. Chen, and D. G. Fredlund, "Performance of a large-scale slope model subjected to rising and lowering water levels," *Engineering Geology*, vol. 106, no. 1-2, pp. 92–103, 2009.

[4] Z. Y. Ma, H. J. Liao, and F. N. Dang, "Influence of intermediate principal stress on the bearing capacity of strip and circular footings," *Journal of Engineering Mechanics*, vol. 140, no. 7, article 04014041, 2014.

[5] H. Matsuoka and T. Nakai, "Stress-deformation and strength characteristics of soil under three different principal stresses," *Proceedings of the Japan Society of Civil Engineers*, vol. 1974, no. 232, pp. 59–70, 1974.

[6] P. V. Lade and J. M. Duncan, "Cubical triaxial tests on cohesionless soil," *Journal of the Soil Mechanics and Foundations Division ASCE*, vol. 99, SM10, pp. 793–812, 1973.

[7] E. Spencer, "A method of analysis of the stability of embankments assuming parallel inter-slice forces," *Géotechnique*, vol. 17, no. 1, pp. 11–26, 1967.

[8] A. W. Bishop, "The use of the slip circle in the stability analysis of slopes," *Géotechnique*, vol. 5, no. 1, pp. 7–17, 1955.

[9] A. W. Bishop and N. Morgenstern, "Stability coefficients for earth slopes," *Géotechnique*, vol. 10, no. 4, pp. 164–169, 1960.

[10] N. R. Morgenstern and V. E. Price, "The analysis of the stability of general slip surfaces," *Géotechnique*, vol. 15, no. 1, pp. 79–93, 1965.

[11] S. K. Sarma, "Stability analysis of embankment and slopes," *Journal of Geotechnical Engineering Division ASCE*, vol. 105, no. 12, pp. 1511–1524, 1979.

[12] A. J. Li, R. S. Merifield, and A. V. Lyamin, "Limit analysis solutions for three dimensional undrained slopes," *Computers and Geotechnics*, vol. 36, no. 8, pp. 1330–1351, 2009.

[13] O. C. Zienkiewicz, C. Humpheson, and R. W. Lewis, "Associated and nonassociated visco-plasticity and plasticity in soil mechanics," *Géotechnique*, vol. 25, no. 4, pp. 671–689, 1975.

[14] J. M. Duncan, "State of the art: limit equilibrium and finite-element analysis of slopes," *Journal of Geotechnical Engineering Division ASCE*, vol. 122, no. 7, pp. 577–596, 1996.

[15] C. C. Swan and Y. K. Seo, "Limit state analysis of earthen slopes using dual continuum/FEM approaches," *International Journal for Numerical and Analytical Methods in Geomechanics*, vol. 23, no. 12, pp. 1359–1371, 1999.

[16] E. M. Dawson, W. H. Roth, and A. Drescher, "Slope stability analysis by strength reduction," *Géotechnique*, vol. 49, no. 6, pp. 835–840, 1999.

[17] D. V. Griffiths and P. A. Lane, "Slope stability analysis by finite elements," *Geotechnique*, vol. 49, no. 3, pp. 387–403, 1999.

[18] M.-H. Yu, *Unified Strength Theory and its Applications*, Springer, Berlin, 2004.

[19] M. Yu, *Generalized Plasticity*, Springer, Berlin, 2005.

[20] Y. Xue, T. Teng, F. N. Dang, Z. Y. Ma, S. Wang, and H. Xue, "Productivity analysis of fractured wells in reservoir of hydrogen and carbon based on dual-porosity medium model," *International Journal of Hydrogen Energy*, vol. 45, no. 39, pp. 20240–20249, 2020.

[21] J. Liu, X. Liang, Y. Xue, K. Yao, and Y. Fu, "Numerical evaluation on multiphase flow and heat transfer during thermal stimulation enhanced shale gas recovery," *Applied Thermal Engineering*, vol. 178, article 115554, 2020.

[22] Itasca Consulting Group, *Inc. Fast Lagrangian Analysis of Continua in 3 Dimensions, Version 2.0, User's Manual*, Itasca Consulting Group, Inc, USA, 1997.

[23] Z. Y. Ma, F. N. Dang, and H. J. Liao, "Numerical study of the dynamic compaction of gravel soil ground using the discrete element method," *Granular Matter*, vol. 16, no. 6, pp. 881–889, 2014.

[24] A. W. Bishop and G. E. Blight, "Some aspects of effective stress in saturated and partly saturated soils," *Géotechnique*, vol. 13, no. 3, pp. 177–197, 1963.

[25] M. T. van Genuchten, "A closed-form equation for predicting the hydraulic conductivity of unsaturated soils," *Soil Science Society of America Journal*, vol. 44, no. 5, pp. 892–898, 1980.

[26] D. G. Fredlund and H. Rahardjo, *Soil mechanics for unsaturated soils*, Wiley, New York, 1993.

[27] A. Rahimi, H. Rahardjo, and E. C. Leong, "Effect of hydraulic properties of soil on rainfall-induced slope failure," *Engineering Geology*, vol. 106, pp. 135–143, 2010.